

Springer

Handbook *of*

Metrology
and Testing

Czichos

Saito

Smith

Editors

**Springer Handbook
of Metrology and Testing**

Springer Handbook provides a concise compilation of approved key information on methods of research, general principles, and functional relationships in physics and engineering. The world's leading experts in the fields of physics and engineering will be assigned by one or several renowned editors to write the chapters comprising each volume. The content is selected by these experts from Springer sources (books, journals, online content) and other systematic and approved recent publications of physical and technical information.

The volumes will be designed to be useful as readable desk reference book to give a fast and comprehensive overview and easy retrieval of essential reliable key information, including tables, graphs, and bibliographies. References to extensive sources are provided.

Springer Handbook of Metrology and Testing

Horst Czichos, Tetsuya Saito, Leslie Smith (Eds.)

2nd edition
1017 Figures and 177 Tables



Springer

Editors

Horst Czichos
University of Applied Sciences Berlin
Germany

Tetsuya Saito
National Institute for Materials Science (NIMS)
Tsukuba, Ibaraki
Japan

Leslie Smith
National Institute of Standards and Technology (NIST)
Gaithersburg, MD
USA

ISBN: 978-3-642-16640-2 e-ISBN: 978-3-642-16641-9
DOI 10.1007/978-3-642-16641-9
Springer Heidelberg Dordrecht London New York

Library of Congress Control Number: 2011930319

© Springer-Verlag Berlin Heidelberg 2011

This work is subject to copyright. All rights are reserved, whether the whole or part of the material is concerned, specifically the rights of translation, reprinting, reuse of illustrations, recitation, broadcasting, reproduction on microfilm or in any other way, and storage in data banks. Duplication of this publication or parts thereof is permitted only under the provisions of the German Copyright Law of September 9, 1965, in its current version, and permission for use must always be obtained from Springer. Violations are liable to prosecution under the German Copyright Law.

The use of general descriptive names, registered names, trademarks, etc. in this publication does not imply, even in the absence of a specific statement, that such names are exempt from the relevant protective laws and regulations and therefore free for general use.

Production and typesetting: le-tex publishing services GmbH, Leipzig
Senior Manager Springer Handbook: Dr. W. Skolaut, Heidelberg
Typography and layout: schreiberVIS, Seeheim
Illustrations: le-tex publishing services GmbH, Leipzig & Hippmann GbR, Schwarzenbruck
Cover design: eStudio Calamar Steinen, Barcelona
Cover production: WMXDesign GmbH, Heidelberg
Printing and binding: Stürtz GmbH, Würzburg

Printed on acid free paper

Springer is part of Springer Science+Business Media (www.springer.com)

61/3180/YL 5 4 3 2 1 0

Preface to the 2nd Edition

The ability to measure and to compare measurements between laboratories is one of the cornerstones of the scientific method. Globalization of research, development and manufacture has produced greatly increased attention to international standards of measurement. It is no longer sufficient to achieve internal consistency in measurements within a local laboratory or manufacturing facility; measurements must now be able to be reproduced accurately anywhere in the world.

These demands are especially intense in materials science and technology, where many characterization methods are needed during the various stages of materials and product cycles. In order for new materials to be used and incorporated into practical technology, their most important characteristics must be known well enough to justify large research and development costs. The useful properties of materials are generally responses to external fields or loads under specific conditions. The stimulus field and environmental conditions must be completely specified in order to develop a reproducible response, and to obtain reliable characteristics and data. Standard test and calibration methods describe these conditions and the Springer Handbook of Materials Measurement Methods was developed to assist scientists and engineers in both industry and academe in this task.

In this second edition of the handbook, we have responded to reader's requests for a more complete treatment of the internationally recognized formal metrology system. The book title has been changed to reflect this emphasis and the handbook organized in five parts: (A) Fundamentals of Metrology and Testing, (B) Chemical and Microstructural Analysis, (C) Materials Properties Measurement, (D) Materials Perfor-

mance Testing, (E) Modeling and Simulation Methods. The initial chapters are new and present, inter alia:

- Methodologies of measurement and testing, conformity assessment and accreditation
- Metrology principles and organization
- Quality in measurement and testing, including measurement uncertainty and accuracy.

All the remaining chapters have been brought up to date by the same distinguished international expert that produced the first edition.

The editors wish again to acknowledge the critical support and constant encouragement of the Publisher. In particular, Dr. Hubertus von Riedesel encouraged us greatly with the original concept and Dr. Werner Skolaut has done the technical editing to the highest standards of professional excellence. Finally, throughout the entire development of the handbook we were greatly aided by the able administrative support of Ms Daniela Tied.

May 2011
 Horst Czichos
 Tetsuya Saito
 Leslie Smith

Berlin
 Tsukuba
 Washington



Horst Czichos



Tetsuya Saito



Leslie Smith

Preface to the 1st Edition

The ability to compare measurements between laboratories is one of the cornerstones of the scientific method. All scientists and engineers are trained to make accurate measurements and a comprehensive volume that provides detailed advice and leading references on measurements to scientific and engineering professionals and students is always a worthwhile addition to the literature. The principal motivation for this Springer Handbook of Materials Measurement Methods, however, stems from the increasing demands of technology for measurement results that can be used reliably anywhere in the world. These demands are especially intense in materials science and technology, where many characterization methods are needed, from scientific *composition–structure–property* relations to technological *performance–quality–reliability* assessment data, during the various stages of materials and product cycles.

In order for new materials to be used and incorporated into practical technology, their most important characteristics must be known well enough to justify large research and development costs. Furthermore, the research may be performed in one country while the engineering design is done in another and the prototype manufacture in yet another region of the world. This great emphasis on international comparison means that increasing attention must be paid to internationally recognized standards and calibration methods that go beyond careful, internally consistent, methods. This handbook was developed to assist scientists and engineers in both industry and academe in this task.

The useful properties of materials are generally responses to external fields under specific conditions.

The stimulus field and environmental conditions must be completely specified in order to develop a reproducible response. Standard test methods describe these conditions and the Chapters and an Appendix in this book contain references to the relevant international standards.

We sought out experts from all over the world that have been involved with concerns such as these. We were extremely fortunate to find a distinguished set of authors who met the challenge: to write brief chapters that nonetheless contain specific useful recommendations and resources for further information. This is the hallmark of a successful handbook. While the diverse nature of the topics covered has led to different styles of presentation, there is a commonality of purpose evident in the chapters that come from the authors' understanding of the issues facing researchers today.

This handbook would not have been possible without the visionary support of Dr. Hubertus von Riedesel, who embraced the concept and encouraged us to pursue it. We must also acknowledge the constant support of Dr. Werner Skolaut, whose technical editing has met every expectation of professional excellence. Finally, throughout the entire development of the handbook we were greatly aided by the able administrative support of Ms. Daniela Bleienberger.

March 2006
Horst Czichos
Tetsuya Saito
Leslie Smith

Berlin
Tsukuba
Washington

List of Authors

Shuji Aihara

Nippon Steel Corporation
Steel Research Laboratories
20-1, Shintomi Futtsu
293-8511 Chiba, Japan
e-mail: s-aihara@re.nsc.co.jp

Tsutomu Araki

Osaka University
Graduate School of Engineering Science
Machikaneyama, Toyonaka
560-8531 Osaka, Japan
e-mail: araki@me.es.osaka-u.ac.jp

Masaaki Ashida

Osaka University
Graduate School of Engineering Science
1-3 Machikaneyama-cho, Toyonaka
560-8531 Osaka, Japan
e-mail: ashida@mp.es.osaka-u.ac.jp

Peter D. Askew

IMSL, Industrial Microbiological Services Limited
Pale Lane
Hartley Wintney, Hants RG27 8DH, UK
e-mail: peter.askew@imsl-uk.com

Heinz-Gunter Bach

Heinrich-Hertz-Institut
Components/Integration Technology,
Heinrich-Hertz-Institute
Einsteinufer 37
10587 Berlin, Germany
e-mail: Heinz-Gunter.Bach@hhi.fraunhofer.de

Gun-Woong Bahng

Korea Research Institute of Standards and Science
Division of Chemical and Materials Metrology
Doryong-dong 1, POBox 102, Yuseoung
Daejeon, 305-600, South Korea
e-mail: gwbahng@kriss.re.kr

Claude Bathias

Conservatoire National des Arts et Métiers,
Laboratoire ITMA
Institute of Technology and Advanced Materials
2 rue Conté
75003 Paris, France
e-mail: bathias@cnam.fr

Günther Bayreuther

University of Regensburg
Physics Department
Universitätsstr. 31
93040 Regensburg, Germany
e-mail:
guenther.bayreuther@physik.uni-regensburg.de

Bernd Bertsche

University of Stuttgart
Institute of Machine Components
Pfaffenwaldring 9
70569 Stuttgart, Germany
e-mail: bernd.bertsche@ima.uni-stuttgart.de

Brian Brookman

LGC Standards Proficiency Testing
Europa Business Park, Barcroft Street
Bury, Lancashire, BL9 5BT, UK
e-mail: brian.brookman@lgcstandards.com

Wolfgang Buck

Physikalisch-Technische Bundesanstalt
Abbestrasse 2-12
10587 Berlin, Germany
e-mail: wolfgang.buck@ptb.de

Richard R. Cavanagh

National Institute of Standards
and Technology (NIST)
Surface and Microanalysis Science Division,
Chemical Science and Technology Laboratory (CSTL)
100 Bureau Drive, MS 8371
Gaithersburg, MD 20899, USA
e-mail: richard.cavanagh@nist.gov

Leonardo De Chiffre

Technical University of Denmark
Department of Mechanical Engineering
Produktionstorvet, Building 425
2800 Kgs. Lyngby, Denmark
e-mail: *ldch@mek.dtu.dk*

Steven J. Choquette

National Institute of Standards and Technology
Biochemical Science Division
100 Bureau Dr., MS 8312
Gaithersburg, MD 20899-8312, USA
e-mail: *steven.choquette@nist.gov*

Horst Czichos

University of Applied Sciences Berlin
BHT Berlin, Luxemburger Strasse 10
13353 Berlin, Germany
e-mail: *horst.czichos@t-online.de*

Werner Daum

Federal Institute for Materials Research
and Testing (BAM)
Division VIII.1 Measurement and Testing
Technology; Sensors
Unter den Eichen 87
12205 Berlin, Germany
e-mail: *werner.daum@bam.de*

Paul DeRose

National Institute of Standards and Technology
Biochemical Science Division
100 Bureau Drive, MS 8312
Gaithersburg, MD 20899-8312, USA
e-mail: *paul.derose@nist.gov*

Stephen L.R. Ellison

LGC Ltd.
Bioinformatics and Statistics
Queens Road, Teddington
Middlesex, TW11 0LY, UK
e-mail: *s.ellison@lgc.co.uk*

Anton Erhard

Federal Institute for Materials Research
and Testing (BAM)
Department Containment Systems for Dangerous
Goods
Unter den Eichen 87
12205 Berlin, Germany
e-mail: *anton.erhard@bam.de*

Uwe Ewert

Federal Institute for Materials Research
and Testing (BAM)
Division VIII.3 Radiology
Unter den Eichen 87
12205 Berlin, Germany
e-mail: *uwe.ewert@bam.de*

Richard J. Fields

National Institute of Standards and Technology
Materials Science and Engineering Laboratory
100 Bureau Drive
Gaithersburg, MD 20899, USA
e-mail: *richard.fields@nist.gov*

David Flaschenträger

Fraunhofer Institute for Structural Durability and
System Reliability (LBF)
Bartningstrasse 47
64289 Darmstadt, Germany
e-mail: *David.flaschentraeger@lbf.fraunhofer.de*

Benny D. Freeman

The University of Texas at Austin, Center for Energy
and Environmental Resources
Department of Chemical Engineering
10100 Burnet Road, Building 133, R-7100
Austin, TX 78758, USA
e-mail: *freeman@che.utexas.edu*

Holger Frenz

University of Applied Sciences Gelsenkirchen
Business Engineering
August-Schmidt-Ring 10
45665 Recklinghausen, Germany
e-mail: *frenz@fh-gelsenkirchen.de*

Jochen Gäng

JHP – consulting association for product reliability
Nobelstraße 15
70569 Stuttgart, Germany
e-mail: gaeng@jhp-beratung.de

Anja Geburtig

BAM Federal Institute for Materials Research and Testing
Division III.1, Dangerous Goods Packaging
Unter den Eichen 44-46
12203 Berlin, Germany
e-mail: anja.geburtig@bam.de

Mark Gee

National Physical Laboratory
Division of Engineering and Processing Control
Hampton Road
Teddington, TW11 0LW, UK
e-mail: mark.gee@npl.co.uk

Jürgen Goebbels

Federal Institute for Materials Research and Testing (BAM)
Radiology (VIII.3)
Unter den Eichen 87
12205 Berlin, Germany
e-mail: juergen.goebbels@bam.de

Manfred Golze

BAM Federal Institute for Materials Research and Testing
S.1 Quality in Testing
Unter den Eichen 87
12205 Berlin, Germany
e-mail: manfred.golze@bam.de

Anna A. Gorbushina

Federal Institute for Materials Research and Testing (BAM)
Department Materials and Environment
Unter den Eichen 87
12205 Berlin, Germany
e-mail: anna.gorbushina@bam.de

Robert R. Greenberg

National Institute of Standards and Technology
Analytical Chemistry Division
100 Bureau Drive, MS 8395
Gaithersburg, MD 20899-8395, USA
e-mail: robert.greenberg@nist.gov

Manfred Grinda

Landreiterweg 22
12353 Berlin, Germany
e-mail: manfred.grinda@t-online.de

Roland Grössinger

Technical University Vienna
Institut für Festkörperphysik
Wiedner Hauptstr. 8-10
Vienna, Austria
e-mail: rgroess@ifp.tuwien.ac.at

Yukito Hagihara

Sophia University
Faculty of Science and Technology, Department of Engineering and Applied Science
7-1 Kioi-cho, Chiyoda-ku
102-8554 Tokyo, Japan
e-mail: hagihara@me.sophia.ac.jp

Junhee Hahn

Korea Research Institute of Standards and Science (KRISS)
Division of Industrial Metrology
1 Doryong-dong, Yuseong-gu
Daejeon, 305-340, South Korea
e-mail: juny@kriss.re.kr

Holger Hanselka

Fraunhofer-Institute for Structural Durability and System Reliability (LBF)
Bartningstrasse 47
64289 Darmstadt, Germany
e-mail: holger.hanselka@lbf.fraunhofer.de

Werner Hässelbarth

Charlottenstr. 17A
12247 Berlin, Germany
e-mail: werner.haesselbarth@t-online.de

Martina Hedrich

BAM Federal Institute for Materials Research and Testing
S.1 Quality in Testing
Unter den Eichen 87
12205 Berlin, Germany
e-mail: martina.hedrich@bam.de

Manfred P. Hentschel

Federal Institute for Materials Research and Testing (BAM)
VIII.3, Nondestructive Testing
12200 Berlin, Germany
e-mail: manfred.hentschel@bam.de

Horst Hertel

Federal Institute for Materials Research and Testing (BAM)
Division IV.1
Unter den Eichen 87
12205 Berlin, Germany
e-mail: horst.hertel@bam.de

Daniel Hofmann

University of Stuttgart
Institute of Machine Components
Pfaffenwaldring 9
70569 Stuttgart, Germany
e-mail: daniel.hofmann@ima.uni-stuttgart.de

Xiao Hu

National Institute for Materials Science
World Premier International Center for Materials Nanoarchitectonics
Namiki 1-1
305-0044 Tsukuba, Japan
e-mail: hu.xiao@nims.go.jp

Ian Hutchings

University of Cambridge, Institute for Manufacturing
Department of Engineering
17 Charles Babbage Road
Cambridge, CB3 0FS, UK
e-mail: imh2@cam.ac.uk

Shoji Imatani

Kyoto University
Department of Energy Conversion Science
Yoshida-honmachi, Sakyo-ku
606-8501 Kyoto, Japan
e-mail: imatani@energy.kyoto-u.ac.jp

Hanspeter Ischi

The Swiss Accreditation Service (SAS)
Lindenweg 50
3003 Berne, Switzerland
e-mail: hanspeter.ischi@sas.ch

Bernd Isecke

Federal Institute for Materials Research and Testing (BAM)
Department Materials Protection and Surface Technologies
Unter den Eichen 87
12203 Berlin, Germany
e-mail: bernd.isecke@bam.de

Tadashi Itoh

Osaka University
Institute for NanoScience Design
1-3, Machikaneyama-cho, Toyonaka
560-8531 Osaka, Japan
e-mail: itoh@insd.osaka-u.ac.jp

Tetsuo Iwata

The University of Tokushima
Department of Mechanical Engineering
2-1, Minami-Jyosanjima
770-8506 Tokushima, Japan
e-mail: iwata@me.tokushima-u.ac.jp

Gerd-Rüdiger Jaenisch

Federal Institute for Materials Research and Testing (BAM)
Non-destructive Testing
Unter den Eichen 87
12205 Berlin, Germany
e-mail: gerd-ruediger.jaenisch@bam.de

Oliver Jann

Federal Institute for Materials Research
and Testing (BAM)
Environmental Material and Product Properties
Unter den Eichen 87
12205 Berlin, Germany
e-mail: oliver.jann@bam.de

Enrico Janssen

Fraunhofer Institute for Structural Durability and
System Reliability (LBF)
Bartningstrasse 47
64289 Darmstadt, Germany
e-mail: enrico.janssen@lbf.fraunhofer.de

Masanori Kohno

National Institute for Materials Science
Computational Materials Science Center
1-2-1 Sengen
305-0047 Tsukuba, Japan
e-mail: kohno.masanori@nims.go.jp

Toshiyuki Koyama

Nagoya Institute of Technology
Department of Materials Science and Engineering
Gokiso-cho, Showa-ku
466-8555 Nagoya, Japan
e-mail: koyama.toshiyuki@nitech.ac.jp

Gary W. Kramer

National Institute of Standards and Technology
Biospectroscopy Group, Biochemical Science
Division
100 Bureau Drive
Gaithersburg, MD 20899-8312, USA
e-mail: gary.kramer@nist.gov

Wolfgang E. Krumbein

Biogema
Material Ecology
Drakestrasse 68
12205 Berlin-Lichterfelde, Germany
e-mail: wek@biogema.de

George Lamaze

National Institute of Standards and Technology
Analytical Chemistry Division
100 Bureau Dr. Stop 8395
Gaithersburg, MD 20899, USA
e-mail: george.lamaze@nist.gov

Haiqing Lin

Membrane Technology and Research, Inc.
1306 Willow Road, Suite 103
Menlo Park, CA 94025, USA
e-mail: Haiqing.lin@mtrinc.com

Richard Lindstrom

National Institute of Standards and Technology
Analytical Chemistry Division
100 Bureau Drive
Gaithersburg, MD 20899-8392, USA
e-mail: richard.lindstrom@nist.gov

Samuel Low

National Institute of Standards and Technology
Metallurgy Division, Materials Science
and Engineering Laboratory
100 Bureau Drive, Mail Stop 8553
Gaithersburg, MD 20899, USA
e-mail: samuel.low@nist.gov

Koji Maeda

The University of Tokyo
Department of Applied Physics
Hongo, Bunkyo-ku
113-8656 Tokyo, Japan
e-mail: maeda@exp.t.u-tokyo.ac.jp

Ralf Matschat

Püttbergeweg 23
12589 Berlin, Germany
e-mail: ralf.matschat43@web.de

Willie E. May

National Institute of Standards
and Technology (NIST)
Chemical Science and Technology Laboratory (CSTL)
100 Bureau Drive, MS 8300
Gaithersburg, MD 20899, USA
e-mail: willie.may@nist.gov

Takashi Miyata

Nagoya University
Department of Materials Science and Engineering
464-8603 Nagoya, Japan
e-mail: miyata@numse.nagoya-u.ac.jp

Hiroshi Mizubayashi

University of Tsukuba
Institute of Materials Science
305-8573 Tsukuba, Japan
e-mail: mizuh@ims.tsukuba.ac.jp

Bernd R. Müller

BAM Federal Institute for Materials Research and Testing
Unter den Eichen 87
12205 Berlin, Germany
e-mail: bernd.mueller@bam.de

Rolf-Joachim Müller

Gesellschaft für Biotechnologische Forschung mbH
TU-BCE
Mascheroder Weg 1
Braunschweig, 38124, Germany
e-mail: rmu@gbf.de

Kiyofumi Muro

Chiba University
Faculty of Science, Department of Physics
1-33 Yayoi-cho, Inage-ku
283-8522 Chiba, Japan
e-mail: muro@physics.s.chiba-u.ac.jp

Yoshihiko Nonomura

National Institute for Materials Science
Computational Materials Science Center
Sengen 1-2-1, Tsukuba
305-0047 Ibaraki, Japan
e-mail: nonomura.yoshihiko@nims.go.jp

Jürgen Nuffer

Fraunhofer Institute for Structural Durability and System Reliability (LBF)
Bartningstrasse 47
64289 Darmstadt, Germany
e-mail: juergen.nuffer@lbf.fraunhofer.de

Jan Obrzut

National Institute of Standards and Technology
Polymers Division
100 Bureau Dr.
Gaithersburg, MD 20899-8541, USA
e-mail: jan.obrzut@nist.gov

Hiroshi Ohtani

Kyushu Institute of Technology
Department of Materials Science and Engineering
Sensui-cho 1-1, Tobata-ku
804-8550 Kitakyushu, Japan
e-mail: ohtani@matsc.kyutech.ac.jp

Kurt Osterloh

Federal Institute for Materials Research and Testing (BAM)
Division VIII.3
Unter den Eichen 97
12205 Berlin, Germany
e-mail: kurt.osterloh@bam.de

Michael Pantke

Federal Institute for Materials Research and Testing (BAM)
Division IV.1, Materials and Environment
12205 Berlin, Germany
e-mail: michael.pantke@bam.de

Karen W. Phinney

National Institute of Standards and Technology
Analytical Chemistry Division
100 Bureau Drive, Stop 8392
Gaithersburg, MD 20899-8392, USA
e-mail: karen.phinney@nist.gov

Rüdiger (Rudy) Plarre

Federal Institute for Materials Research and Testing (BAM)
Environmental Compatibility of Materials
Unter den Eichen 87
12205 Berlin, Germany
e-mail: ruediger.plarre@bam.de

Kenneth W. Pratt

National Institute of Standards and Technology
Analytical Chemistry Division
100 Bureau Dr., Stop 8391
Gaithersburg, MD 20899-8391, USA
e-mail: kenneth.pratt@nist.gov

Michael H. Ramsey

University of Sussex
School of Life Sciences
Brighton, BN1 9QG, UK
e-mail: m.h.ramsey@sussex.ac.uk

Peter Reich

Treppendorfer Weg 33
12527 Berlin, Germany
e-mail: peterreichberlin@email.de

Gunnar Ross

Magnet-Physik Dr. Steingroever GmbH
Emil-Hoffmann-Str. 3
50996 Köln, Germany
e-mail: ross@magnet-physik.de

Steffen Rudtsch

Physikalisch-Technische Bundesanstalt (PTB)
Abbestr. 2–12
10587 Berlin, Germany
e-mail: steffen.rudtsch@ptb.de

Lane Sander

National Institute of Standards and Technology
Chemical Science and Technology Laboratory,
Analytical Chemistry Division
100 Bureau Drive, MS 8392
Gaithersburg, MD 20899–8392, USA
e-mail: lane.sander@nist.gov

Erich Santner

Bürvigstraße 43
53177 Bonn, Germany
e-mail: esantner@arcor.de

Michele Schantz

National Institute of Standards and Technology
Analytical Chemistry Division
100 Bureau Drive, Stop 8392
Gaithersburg, MD 20899, USA
e-mail: michele.schantz@nist.gov

Anita Schmidt

Federal Institute for Materials Research and
Testing (BAM)
Unter den Eichen 44–46
12203 Berlin, Germany
e-mail: anita.schmidt@bam.de

Guenter Schmitt

Iserlohn University of Applied Sciences
Laboratory for Corrosion Protection
Frauenstuhlweg 31
8644 Iserlohn, Germany
e-mail: schmitt.g@fh-swf.de

Bernd Schumacher

Physikalisch-Technische Bundesanstalt
Department 2.1 DC and Low Frequency
Bundesallee 100
38116 Braunschweig, Germany
e-mail: bernd.schumacher@ptb.de

Michael Schütze

Karl-Winnacker-Institut
DECHEMA e.V.
Theodor-Heuss-Allee 25
Frankfurt am Main, 60486, Germany
e-mail: schuetze@dechema.de

Karin Schwibbert

Federal Institute for Materials Research
and Testing (BAM)
Division IV.1 Materials and Environment
12205 Berlin, Germany
e-mail: karin.schwibbert@bam.de

John H. J. Scott

National Institute of Standards and Technology
Surface and Microanalysis Science Division
100 Bureau Drive
Gaithersburg, MD 20899–8392, USA
e-mail: johnhenry.scott@nist.gov

Martin Seah

National Physical Laboratory
Analytical Science Division
Hampton Road, Middlesex
Teddington, TW11 0LW, UK
e-mail: martin.seah@npl.co.uk

Steffen Seitz

Physikalisch-Technische Bundesanstalt (PTB)
Dept. 3.13 Metrology in Chemistry
Bundesallee 100
38116 Braunschweig, Germany
e-mail: steffen.seitz@ptb.de

Masato Shimono

National Institute for Materials Science
Computational Materials Science Center
1–2–1 Sengen
305–0047 Tsukuba, Japan
e-mail: shimono.masato@nims.go.jp

John R. Sieber

National Institute of Standards and Technology
Chemical Science and Technology Laboratory
100 Bureau Drive, Stop 8391
Gaithersburg, MD 20899, USA
e-mail: john.sieber@nist.gov

Franz-Georg Simon

Federal Institute for Materials Research
and Testing (BAM)
Waste Treatment and Remedial Engineering
Unter den Eichen 87
12205 Berlin, Germany
e-mail: franz-georg.simon@bam.de

John Small

National Institute of Standards and Technology
Surface and Microanalysis Science Division
100 Bureau Drive, MS 8370
Gaithersburg, MD 20899, USA
e-mail: john.small@nist.gov

Melody V. Smith

National Institute of Standards and Technology
Biospectroscopy Group
100 Bureau Drive
Gaithersburg, MD 20899-8312, USA
e-mail: melody.smith@nist.gov

Petra Spitzer

Physikalisch-Technische Bundesanstalt (PTB)
Dept. 3.13 Metrology in Chemistry
Bundesallee 100
38116 Braunschweig, Germany
e-mail: petra.spitzer@ptb.de

Thomas Steiger

Federal Institute for Materials Research and
Testing (BAM)
Department of Analytical Chemistry; Reference
Materials
Richard-Willstätter-Straße 11
12489 Berlin, Germany
e-mail: thomas.steiger@bam.de

Ina Stephan

Federal Institute for Materials Research
and Testing (BAM)
Division IV.1 Biology in Materials Protection
and Environmental Issues
Unter den Eichen 87
12205 Berlin, Germany
e-mail: ina.stephan@bam.de

Stephan J. Stranick

National Institute of Standards and Technology
Department of Commerce, Surface
and Microanalysis Science Division
100 Bureau Dr.
Gaithersburg, MD 20899-8372, USA
e-mail: stranick@nist.gov

Hans-Henning Strehblow

Heinrich-Heine-Universität
Institute of Physical Chemistry
Universitätsstr. 1
40225 Düsseldorf, Germany
e-mail: henning@uni-duesseldorf.de

Tetsuya Tagawa

Nagoya University
Department of Materials Science and Engineering
464-8603 Nagoya, Japan
e-mail: tagawa@numse.nagoya-u.ac.jp

Akira Tezuka

National Institute of Advanced Industrial Science
and Technology
AIST Tsukuba Central 2
305-8568 Tsukuba, Japan
e-mail: tezuka.akira@aist.go.jp

Yo Tomota

Ibaraki University
Department of Materials Science,
Faculty of Engineering
4-12-1 Nakanarusawa-cho
316-8511 Hitachi, Japan
e-mail: tomota@mx.ibaraki.ac.jp

John Travis

National Institute of Standards and Technology
Analytical Chemistry Division (Retired)
100 Bureau Drive, MS 8312
Gaithersburg, MD 20899-8312, USA
e-mail: john.travis@nist.gov

Peter Trubiroha

Schlettstadter Str. 116
14169 Berlin, Germany
e-mail: peter.trubiroha@t-online.de

Gregory C. Turk

National Institute of Standards and Technology
Analytical Chemistry Division
100 Bureau Drive, Stop 8391
Gaithersburg, MD 20899, USA
e-mail: turk@nist.gov

Thomas Vetter

National Institute of Standards
and Technology (NIST)
Analytical Chemistry Division
100 Bureau Dr. Stop 8391
Gaithersburg, MD 20899-8391, USA
e-mail: thomas.vetter@nist.gov

Volker Wachtendorf

BAM Federal Institute for Materials Research and
Testing (BAM)
Division VI.3, Durability of Polymers
Unter den Eichen 87
12205 Berlin, Germany
e-mail: volker.wachtendorf@bam.de

Andrew Wallard

Pavillon de Breteuil
Bureau International des Poids et Mesures
92312 Sèvres, France
e-mail: fjoly@bipm.org

Joachim Wecker

Siemens AG
Corporate Technology, CT T DE
91050 Erlangen, Germany
e-mail: joachim.wecker@siemens.com

Wolfhard Wegscheider

Montanuniversität Leoben
General and Analytical Chemistry
Franz-Josef-Strasse 18
8700 Leoben, Austria
e-mail: wegschei@unileoben.ac.at

Alois Wehrstedt

DIN Deutsches Institut für Normung
Normenausschuss Materialprüfung (NMP)
Burggrafenstraße 6
10787 Berlin, Germany
e-mail: aloes.wehrstedt@din.de

Michael Welch

National Institute of Standards and Technology
100 Bureau Drive, Stop 8392
Gaithersburg, MD 20899, USA
e-mail: michael.welch@nist.gov

Ulf Wickström

SP Swedish National Testing and Research Institute
Department of Fire Technology
501 15 Borås, Sweden
e-mail: ulf.wickstrom@sp.se

Sheldon M. Wiederhorn

National Institute of Standards and Technology
Materials Science and Engineering Laboratory
100 Bureau Drive
Gaithersburg, MD 20899-8500, USA
e-mail: sheldon.wiederhorn@nist.gov

Scott Wight

National Institute of Standards and Technology
Surface and Microanalysis Science Division
100 Bureau Drive, Stop 8371
Gaithersburg, MD 20899-8371, USA
e-mail: scott.wight@nist.gov

Michael Winchester

National Institute of Standards and Technology
Analytical Chemistry Division
100 Bureau Drive, Building 227, Mailstop 8391
Gaithersburg, MD 20899, USA
e-mail: mrw@nist.gov

Noboru Yamada

Matsushita Electric Industrial Co., Ltd.
Optical Media Group, Storage Media Systems
Development Center
3-1-1 Yagumo-Nakamachi
570-8501 Moriguchi, Japan
e-mail: yamada.noboru@jp.panasonic.com

Rolf Zeisler

National Institute of Standards and Technology
Analytical Chemistry Division
100 Bureau Drive, MS 8395
Gaithersburg, MD 20899-8395, USA
e-mail: rolf.zeisler@nist.gov

Uwe Zscherpel

Federal Institute for Materials Research
and Testing (BAM)
Division "NDT – Radiological Methods"
Unter den Eichen 87
12205 Berlin, Germany
e-mail: uwez@bam.de

Adolf Zschunke

Rapsweg 115
04207 Leipzig, Germany
e-mail: zschunke35@aol.com

Contents

List of Abbreviations	XXV
------------------------------------	-----

Part A Fundamentals of Metrology and Testing

1 Introduction to Metrology and Testing	
<i>Horst Czichos</i>	3
1.1 Methodologies of Measurement and Testing	3
1.2 Overview of Metrology	9
1.3 Fundamentals of Materials Characterization	13
References	22
2 Metrology Principles and Organization	
<i>Andrew Wallard</i>	23
2.1 The Roots and Evolution of Metrology	23
2.2 BIPM: The Birth of the Metre Convention	25
2.3 BIPM: The First 75 Years	26
2.4 Quantum Standards: A Metrological Revolution	28
2.5 Regional Metrology Organizations	29
2.6 Metrological Traceability	29
2.7 Mutual Recognition of NMI Standards: The CIPM MRA	30
2.8 Metrology in the 21st Century	32
2.9 The SI System and New Science	34
References	37
3 Quality in Measurement and Testing	
<i>Michael H. Ramsey, Stephen L.R. Ellison, Horst Czichos, Werner Hässelbarth, Hanspeter Ischi, Wolfhard Wegscheider, Brian Brookman, Adolf Zschunke, Holger Frenz, Manfred Golze, Martina Hedrich, Anita Schmidt, Thomas Steiger</i>	39
3.1 Sampling	40
3.2 Traceability of Measurements	45
3.3 Statistical Evaluation of Results	50
3.4 Uncertainty and Accuracy of Measurement and Testing	68
3.5 Validation	78
3.6 Interlaboratory Comparisons and Proficiency Testing	87
3.7 Reference Materials	97
3.8 Reference Procedures	116
3.9 Laboratory Accreditation and Peer Assessment	126
3.10 International Standards and Global Trade	130
3.11 Human Aspects in a Laboratory	134
3.12 Further Reading: Books and Guides	138
References	138

Part B Chemical and Microstructural Analysis

4 Analytical Chemistry

<i>Willie E. May, Richard R. Cavanagh, Gregory C. Turk, Michael Winchester, John Travis, Melody V. Smith, Paul DeRose, Steven J. Choquette, Gary W. Kramer, John R. Sieber, Robert R. Greenberg, Richard Lindstrom, George Lamaze, Rolf Zeisler, Michele Schantz, Lane Sander, Karen W. Phinney, Michael Welch, Thomas Vetter, Kenneth W. Pratt, John H. J. Scott, John Small, Scott Wight, Stephan J. Stranick, Ralf Matschat, Peter Reich</i>		145
4.1	Bulk Chemical Characterization	145
4.2	Microanalytical Chemical Characterization	179
4.3	Inorganic Analytical Chemistry: Short Surveys of Analytical Bulk Methods	189
4.4	Compound and Molecular Specific Analysis: Short Surveys of Analytical Methods	195
4.5	National Primary Standards – An Example to Establish Metrological Traceability in Elemental Analysis	198
	References	199

5 Nanoscopic Architecture and Microstructure

<i>Koji Maeda, Hiroshi Mizubayashi</i>		205
5.1	Fundamentals.....	211
5.2	Crystalline and Amorphous Structure Analysis	232
5.3	Lattice Defects and Impurities Analysis	239
5.4	Molecular Architecture Analysis	258
5.5	Texture, Phase Distributions, and Finite Structures Analysis.....	269
	References	277

6 Surface and Interface Characterization

<i>Martin Seah, Leonardo De Chiffre</i>		281
6.1	Surface Chemical Analysis	282
6.2	Surface Topography Analysis	308
	References	326

Part C Materials Properties Measurement

7 Mechanical Properties

<i>Sheldon M. Wiederhorn, Richard J. Fields, Samuel Low, Gun-Woong Bahng, Alois Wehrstedt, Junhee Hahn, Yo Tomota, Takashi Miyata, Haiqing Lin, Benny D. Freeman, Shuji Aihara, Yukito Hagihara, Tetsuya Tagawa</i>		339
7.1	Elasticity	340
7.2	Plasticity	355

7.3	Hardness	366
7.4	Strength	388
7.5	Fracture Mechanics.....	408
7.6	Permeation and Diffusion	426
	References	442
8	Thermal Properties	
	<i>Wolfgang Buck, Steffen Rudtsch</i>	453
8.1	Thermal Conductivity and Specific Heat Capacity	454
8.2	Enthalpy of Phase Transition, Adsorption and Mixing.....	462
8.3	Thermal Expansion and Thermomechanical Analysis	469
8.4	Thermogravimetry	471
8.5	Temperature Sensors	471
	References	482
9	Electrical Properties	
	<i>Bernd Schumacher, Heinz-Gunter Bach, Petra Spitzer, Jan Obrzut, Steffen Seitz</i>	485
9.1	Electrical Materials	486
9.2	Electrical Conductivity of Metallic Materials.....	493
9.3	Electrolytic Conductivity.....	498
9.4	Semiconductors.....	507
9.5	Measurement of Dielectric Materials Properties.....	526
	References	537
10	Magnetic Properties	
	<i>Joachim Wecker, Günther Bayreuther, Gunnar Ross, Roland Grössinger</i>	541
10.1	Magnetic Materials	542
10.2	Soft and Hard Magnetic Materials: (Standard) Measurement Techniques for Properties Related to the $B(H)$ Loop	546
10.3	Magnetic Characterization in a Pulsed Field Magnetometer (PFM)	567
10.4	Properties of Magnetic Thin Films.....	579
	References	585
11	Optical Properties	
	<i>Tadashi Itoh, Tsutomu Araki, Masaaki Ashida, Tetsuo Iwata, Kiyofumi Muro, Noboru Yamada</i>	587
11.1	Fundamentals of Optical Spectroscopy.....	588
11.2	Microspectroscopy	605
11.3	Magneto-optical Measurement.....	609
11.4	Nonlinear Optics and Ultrashort Pulsed Laser Application	614
11.5	Fiber Optics	626
11.6	Evaluation Technologies for Optical Disk Memory Materials.....	641
11.7	Optical Sensing	649
	References	656

Part D Materials Performance Testing

12 Corrosion

<i>Bernd Isecke, Michael Schütze, Hans-Henning Strehblow</i>	667
12.1 Background	668
12.2 Conventional Electrochemical Test Methods	671
12.3 Novel Electrochemical Test Methods	695
12.4 Exposure and On-Site Testing	699
12.5 Corrosion Without Mechanical Loading	699
12.6 Corrosion with Mechanical Loading	705
12.7 Hydrogen-Induced Stress Corrosion Cracking	714
12.8 High-Temperature Corrosion	718
12.9 Inhibitor Testing and Monitoring of Efficiency	732
References	738

13 Friction and Wear

<i>Ian Hutchings, Mark Gee, Erich Santner</i>	743
13.1 Definitions and Units	743
13.2 Selection of Friction and Wear Tests	747
13.3 Tribological Test Methods	751
13.4 Friction Measurement	754
13.5 Quantitative Assessment of Wear	759
13.6 Characterization of Surfaces and Debris	764
References	767

14 Biogenic Impact on Materials

<i>Ina Stephan, Peter D. Askew, Anna A. Gorbushina, Manfred Grinda, Horst Hertel, Wolfgang E. Krumbein, Rolf-Joachim Müller, Michael Pantke, Rüdiger (Rudy) Plarre, Guenter Schmitt, Karin Schwibbert</i>	769
14.1 Modes of Materials – Organisms Interactions	770
14.2 Biological Testing of Wood	774
14.3 Testing of Organic Materials	789
14.4 Biological Testing of Inorganic Materials	811
14.5 Coatings and Coating Materials	826
14.6 Reference Organisms	833
References	838

15 Material–Environment Interactions

<i>Franz-Georg Simon, Oliver Jann, Ulf Wickström, Anja Geburtig, Peter Trubiroha, Volker Wachtendorf</i>	845
15.1 Materials and the Environment	845
15.2 Emissions from Materials	860
15.3 Fire Physics and Chemistry	869
References	883

16 Performance Control: Nondestructive Testing and Reliability Evaluation
Uwe Ewert, Gerd-Rüdiger Jaenisch, Kurt Osterloh, Uwe Zscherpel, Claude Bathias, Manfred P. Hentschel, Anton Erhard, Jürgen Goebbels, Holger Hanselka, Bernd R. Müller, Jürgen Nuffer, Werner Daum, David Flaschenträger, Enrico Janssen, Bernd Bertsche, Daniel Hofmann, Jochen Gäng..... 887

16.1 Nondestructive Evaluation 888

16.2 Industrial Radiology 900

16.3 Computerized Tomography – Application to Organic Materials 915

16.4 Computerized Tomography – Application to Inorganic Materials 921

16.5 Computed Tomography – Application to Composites and Microstructures 927

16.6 Structural Health Monitoring – Embedded Sensors 932

16.7 Characterization of Reliability 949

16.A Appendix 967

References 968

Part E Modeling and Simulation Methods

17 Molecular Dynamics
Masato Shimono..... 975

17.1 Basic Idea of Molecular Dynamics 975

17.2 Diffusionless Transformation 988

17.3 Rapid Solidification 995

17.4 Diffusion 1006

17.5 Summary 1010

References 1010

18 Continuum Constitutive Modeling
Shoji Imatani 1013

18.1 Phenomenological Viscoplasticity 1013

18.2 Material Anisotropy 1018

18.3 Metallothermomechanical Coupling 1023

18.4 Crystal Plasticity 1026

References 1030

19 Finite Element and Finite Difference Methods
Akira Tezuka..... 1033

19.1 Discretized Numerical Schemes for FEM and FDM 1035

19.2 Basic Derivations in FEM and FDM 1037

19.3 The Equivalence of FEM and FDM Methods 1041

19.4 From Mechanics to Mathematics:
 Equilibrium Equations and Partial Differential Equations 1042

19.5 From Mathematics to Mechanics:
 Characteristic of Partial Differential Equations 1047

19.6	Time Integration for Unsteady Problems	1049
19.7	Multidimensional Case	1051
19.8	Treatment of the Nonlinear Case	1055
19.9	Advanced Topics in FEM and FDM	1055
19.10	Free Codes	1059
	References	1059
20	The CALPHAD Method	
	<i>Hiroshi Ohtani</i>	1061
20.1	Outline of the CALPHAD Method	1062
20.2	Incorporation of the First-principles Calculations into the CALPHAD Approach	1066
20.3	Prediction of Thermodynamic Properties of Compound Phases with First-principles Calculations	1079
	References	1090
21	Phase Field Approach	
	<i>Toshiyuki Koyama</i>	1091
21.1	Basic Concept of the Phase-Field Method	1092
21.2	Total Free Energy of Microstructure	1093
21.3	Solidification	1102
21.4	Diffusion-Controlled Phase Transformation	1105
21.5	Structural Phase Transformation	1108
21.6	Microstructure Evolution	1110
	References	1114
22	Monte Carlo Simulation	
	<i>Xiao Hu, Yoshihiko Nonomura, Masanori Kohno</i>	1117
22.1	Fundamentals of the Monte Carlo Method	1117
22.2	Improved Algorithms	1121
22.3	Quantum Monte Carlo Method	1126
22.4	Bicritical Phenomena in O(5) Model	1133
22.5	Superconductivity Vortex State	1137
22.6	Effects of Randomness in Vortex States	1143
22.7	Quantum Critical Phenomena	1146
	References	1149
	Acknowledgements	1159
	About the Authors	1161
	Detailed Contents	1185
	Subject Index	1203

List of Abbreviations

μ TA	microthermal analysis	BBG	Bragg–Bose glass
A		bcc	body-centered-cubic
AA	arithmetic average	BCR	Bureau Communautaire de Référence
AAS	atomic absorption spectrometry	BCS	Bardeen–Cooper–Schrieffer
AB	accreditation body	bct	body-centered tetragonal
AC	alternating current	BE	Bauschinger effect
ACF	autocorrelation function	BEI	back-scattered electron imaging
ACVF	autocovariance function	BEM	boundary element method
ADC	analog-to-digital converter	BER	bit error rate
ADR	automated defect recognition	BESSY	Berlin Electron Storage Ring Company for Synchrotron Radiation
AED	atomic emission detector	BF	bright field
AEM	analytical electron microscopy	BG	Bose glass
AES	Auger electron spectroscopy	BIPM	Bureau International des Poids et Mesures
AF	antiferromagnetism	BIPM	International Bureau of Weights and Measures
AFGM	alternating field gradient magnetometer	BLRF	bispectral luminescence radiance factor
AFM	atomic force microscope	BOFDA	Brillouin optical-fiber frequency-domain analysis
AFNOR	Association Francaise de Normalisation	BOTDA	Brillouin optical-fiber time-domain analysis
AFRAC	African Accreditation Cooperation	BRENDA	bacterial restriction endonuclease nucleic acid digest analysis
AGM	alternating gradient magnetometer	BSI	British Standards Institute
ALT	accelerated lifetime testing	Bi-CGSTAB	biconjugate gradient stabilized
AMR	anisotropic magneto-resistance	C	
AMRSF	average matrix relative sensitivity factor	CAB	conformity assessment body
ANOVA	analysis of variance	CAD	computer-aided design
AOAC	Association of Official Analytical Chemists	CALPHAD	calculation of phase diagrams
APCI	atmospheric pressure chemical ionization	CANMET	Canadian Centre for Mineral and Energy Technology
APD	avalanche photodiodes	CARS	coherent anti-Stokes Raman spectroscopy
APEC	Asia-Pacific Economic Cooperation	CASCO	ISO Committee on Conformity Assessment
APLAC	Asian Pacific Accreditation Cooperation	CBED	convergent beam electron diffraction
APMP	Asian–Pacific Metrology Program	CC	consultative committee
ARDRA	amplified ribosomal DNA restriction analysis	CC	correlation coefficient
ARPES	angle-resolved photoemission spectroscopy	CCAUV	Consultative Committee for Acoustics, Ultrasound, and Vibration
AS	activation spectrum	CCD	charge-coupled device
ASE	amplified spontaneous emission	CCEM	Consultative Committee for Electricity and Magnetism
ASEAN	Association of South-East-Asian Nations	CCL	Consultative Committee for Length
ASTM	American Society for Testing and Materials	CCM	Consultative Committee for Mass and Related Quantities
ATP	adenosine triphosphate	CCPR	Consultative Committee for Photometry and Radiometry
ATR	attenuated total reflection		
B			
BAAS	British Association for the Advancement of Science		
BAM	Federal Institute for Materials Research and Testing, Germany		

CCQM	Comité Consultative pour la Quantité de Matière	CNRS	Centre National de la Recherche Scientifique
CCQM	Consultative Committee for Quantity of Matter Metrology in Chemistry	COMAR	Code d'Indexation des Matériaux de Référence
CCRI	Consultative Committee for Ionizing Radiation	COSY	correlated spectroscopy
CCT	Consultative Committee for Thermometry	CPAA	charged particle activation analysis
CCT	center-cracked tension	CPP	current-perpendicular-to-plane
cct	crevice corrosion temperature	cpt	critical pitting temperature
CCTF	Consultative Committee for Time and Frequency	CR	computed radiography
CCU	Consultative Committee for Units	CRM	certified reference material
CD	circular dichroism	CT	compact tension
CE	Communauté Européenne	CT	compact test
CE	Conformité Européenne	CT	computed tomography
CE	capillary electrophoresis	CTD	charge transfer device
CE	counter electrode	CTE	coefficient of thermal expansion
CEM	cluster expansion method	CTOD	crack-tip opening displacement
CEN	European Committee for Standardization	CTS	collaborative trial in sampling
CEN	European Standard Organization	CVD	chemical vapor deposition
CENELEC	European Electrotechnical Standardization Commission	CVM	cluster variation method
CERT	constant extension rate test	CW	continuous wave
CFD	computational fluid dynamics	CZE	capillary zone electrophoresis
CFL	Courant–Friedrichs–Lewy		
CFRP	carbon-fiber-reinforced polymer	D	
CG	coarse grained	DA	differential amplifier
CG	conjugate gradient	DA	drop amplifier
CGE	capillary gel electrophoresis	DAD	diode-array detector
CGHE	carrier gas hot extraction	DBTT	ductile-to-brittle transition temperature
CGPM	General Conference on Weights and Measures	DC	direct current
CI	carbonyl index	DCM	double crystal monochromator
CIEF	capillary isoelectric focusing	DDA	digital detector array
CIP	constrained interpolated profile	DEM	discrete element method
CIP	current-in-plane	DF	dark field
CIPM	Comité Internationale des Poids et Mesures	DFG	difference frequency generation
CIPM	International Committee of Weights and Measures	DFT	discrete Fourier transform
CITAC	Cooperation for International Traceability in Analytical Chemistry	DI	designated institute
CITP	capillary isotachopheresis	DIN	Deutsches Institut für Normung
CL	cathodoluminescence	DIR	digital industrial radiology
CLA	center line average	DLTS	deep-level transient spectroscopy
CM	ceramic matrix	DMM	double multilayer monochromator
CMA	cylindrical mirror analyzer	DMRG	density-matrix renormalization group
CMC	calibration and measurement capability	DMS	diluted magnetic semiconductor
CMC	ceramic matrix composite	DNA	deoxyribonucleic acid
CMM	coordinate-measuring machine	DNPH	2,4-dinitrophenylhydrazine
CMN	cerium magnesium nitrate	DOC	dissolved organic carbon
CMOS	complementary metal-oxide-semiconductor	DOS	density of states
CNR	contrast-to-noise ratio	DRP	dense random packing
		DS	digital storage
		DSC	differential scanning calorimeter
		DT	tomography density
		DTA	differential thermal analysis
		DTU	Danmarks Tekniske Universitet
		DWDD	domain-wall displacement detection
		DWDM	dense wavelength-division multiplexed

J			
JCGM	Joint Committee for Guides in Metrology	MECC	micellar electrokinetic capillary chromatography
JCTLM	Joint Committee for Traceability in Laboratory Medicine	MEIS	medium-energy ion scattering
JIS	Japanese Institute of Standards	MEM	maximum entropy method
		MEMS	microelectromechanical system
		MFC	mass-flow controller
		MFD	mode field diameter
		MFM	magnetoforce micrometer
		MIBK	methylisobutylketone
		MIC	microbially induced corrosion
		MID	measuring instruments directive
		MIS	metal-insulator-semiconductor
		MISFET	metal-insulator-semiconductor FET
		MITI	Ministry of International Trade and Industry
			meter, kilogram, and second
		MKS	meter, kilogram, second, and ampere
		MKSA	
		MLA	multilateral agreement
		MLE	maximum-likelihood estimation
		MLLSQ	multiple linear least squares
		MM	metal matrix
		MMC	metal matrix composite
		MMF	minimum mass fraction
		MO	magneto-optical
		MOE	modulus of elasticity
		MOKE	magneto-optic Kerr effect
		MOL	magneto-optical layer
		MON	monochromator
		MOS	metal-oxide-semiconductor
		MPA	Materialprüfungsamt
		MRA	multiregional agreement
		MRA	mutual recognition arrangement
		MRAM	magnetic random-access memory
		MRI	magnetic resonance imaging
		MRR	median rank regression
		MS	magnetic stirring
		MS	mass spectrometry
		MST	microsystems technology
		MSW	municipal solid waste
		MTJ	magnetic tunnel junction
		MUT	material under test
		MUVU	mobile UV unit
		MXCD	magnetic x-ray circular dichroism
		MoU	memorandum of understanding
K			
KC	key comparison		
KCDB	key comparison database		
KKS	Kim–Kim–Suzuki		
KLM	Kerr-lens mode-locking		
KT	Kosterlitz–Thouless		
L			
LBB	Ladyzhenskaya–Babuska–Brezzi		
LBZ	local brittle zone		
LC	liquid chromatography		
LC	liquid crystal		
LCF	low cycle fatigue		
LD	Lawrence–Doniach		
LD	laser device		
LD	laser diode		
LDOS	local density of states		
LDV	laser Doppler velocimeter		
LED	light-emitting diode		
LEFM	linear-elastic fracture mechanics		
LGC	Laboratory of the Government Chemist		
LIF	laser-induced fluorescence		
LJ	Lennard–Jones		
LNE	Laboratoire nationale de métrologie et d'essais		
LOC	limit of decision		
LOD	limit of detection		
LOD	limit of determination		
LOQ	limit of quantification		
LSCM	laser scanning confocal microscope		
LSDA	local spin density approximation		
LST	linear system theory		
LTS	low-temperature superconductor		
LVDT	linear variable differential transformer		
LVM	local vibrational mode		
M			
MAD	median absolute deviation		
MC	Monte Carlo		
MCA	multichannel analyzer		
MCD	magnetic circular dichroism		
MCDA	magnetic circular dichroic absorption		
MCP	microchannel plate		
MCPE	magnetic circular-polarized emission		
MD	molecular dynamics		
MDM	minimum detectable mass		
N			
NA	numerical aperture		
NAA	neutron activation analysis		
NAB	national accreditation body		
NACE	National Association of Corrosion Engineers		
NAFTA	North America Free Trade Association		
NBS	National Bureau of Standards		
ND	neutron diffraction		
NDE	nondestructive evaluation		

NDP	neutron depth profiling	PC	personal computer
NDT	nondestructive testing	PC	photoconductive detector
NEP	noise-equivalent power	PC	polycarbonate
NEXAFS	near-edge x-ray absorption fine structure	PCB	polychlorinated biphenyl
NFPA	National Fire Protection Association	PCF	photonic crystal fiber
NHE	normal hydrogen electrode	PCI	phase contrast imaging
NIR	near infrared	PCR	polymerase chain reaction
NIST	National Institute of Standards and Technology	PDMS	poly(dimethylsiloxane)
NMI	National Metrology Institute	PE	polyethylene
NMR	nuclear magnetic resonance	PE-HD	high-density polyethylene
NMi	Netherlands Measurement Institute	PE-LD	low-density polyethylene
NOE	nuclear Overhauser effect	PEELS	parallel electron energy loss spectroscopy
NPL	National Physical Laboratory	PEM	photoelectromagnetic
NPT	number pressure temperature	PERSF	pure element relative sensitivity factor
NR	natural rubber	PET	polyethylene terephthalate
NR	neutron reflectance	PFM	pulse field magnetometer
NRA	nuclear reaction analysis	PGAA	prompt gamma activation analysis
NRC-CRM	National Research Center for Certified Reference Materials	PHB	poly(β -hydroxy butyrate)
NRW	Nordrhein-Westfalen	PI	pitting index
NTC	negative temperature coefficient	PID	photoionization detector
		PIRG	path-integral renormalization group
		PIXE	particle-induced x-ray emission
		PL	photoluminescence
O		PLE	PL excitation
		PLZT	lanthanide-modified piezoceramic
OA	operational amplifier	PM	polymer matrix
OCT	optical coherence tomography	PMMA	poly(methyl methacrylate)
ODD	object-to-detector distance	PMT	photomultiplier tube
ODF	orientation distribution function	POD	probability of detection
ODMR	optically detected magnetic resonance	POF	polymer optical fiber
ODS	octadecylsilane	POL	polychromator
OES	optical emission spectroscopy/spectrometry	POM	particulate organic matter
OIML	International Organization of Legal Metrology	POS	proof-of-screen
OKE	optical Kerr effect	PSD	power-spectral density
OM	optical microscopy	PSDF	power spectral density function
OMH	Orzajos Meresugyi Hivatal	PSI	phase-shift interferometry
OPA	optical parametric amplifier	PSL	photostimulated luminescence
OPG	optical parametric generation	PT	phototube
OPO	optical parametric oscillator	PTB	Physikalisch-Technische Bundesanstalt
OR	optical rectification	PTC	positive temperature coefficient
ORD	optical rotary dispersion	PTFE	polytetrafluoroethylene
OSA	optical spectrum analyzer	PTMSP	poly(1-trimethylsilyl-1-propyne)
OSU	Ohio State University	PU	polyurethane
OTDR	optical time-domain reflectometry	PUF	polyurethane foam
		PV	photovoltaic
P		PVA	polyvinyl acetate
		PVC	polyvinyl chloride
PA	polyamide	PVD	physical vapor deposition
PAA	photon activation analysis	PVDF	polyvinylidene fluoride
PAC	Pacific Accreditation Cooperation	PWM	pulse-width modulation
PAC	perturbed angular correlation	PZT	lead zirconate titanate
PAH	polycyclic aromatic hydrocarbon		
PAS	positron annihilation spectroscopy	Q	
PBG	photonic band gap	QA	quality assurance
		QC	quality control

QE quantum effect
 QMR quasiminimal residual
 QMS quality management system
 QNMR quantitative proton nuclear magnetic resonance

R

RAPD random amplified polymorphic DNA
 RBS Rutherford backscattering
 RC resistor–capacitor
 RD rolling direction
 RDE rotating disc electrode
 RE reference electrode
 RF radiofrequency
 RFLP restriction fragment length polymorphism
 RG renormalization group
 RH relative humidity
 RI refractive index
 RM reference material
 RMO regional metrology organization
 RMR RM report
 RMS root mean square
 RNA nuclear reaction analysis
 RNAA radiochemical NAA
 RPLC reversed-phase liquid chromatography
 RRDE rotating ring-disc electrode
 rRNA ribosomal RNA
 RSF relative sensitivity factor

S

S/N signal-to-noise ratio
 SABS South African Bureau of Standards
 SAD selected area diffraction
 SADC MET Southern African Development Community Cooperation in Measurement Traceability
 SAMR small-angle magnetization-rotation
 SAQCS sampling and analytical quality control scheme
 SAXS small-angle x-ray scattering
 SBI single burning item
 SBR styrene butyl rubber
 SBS sick-building syndrome
 SC superconductivity
 SCA surface chemical analysis
 SCC stress corrosion cracking
 SCE saturated calomel electrode
 SCLM scanning confocal laser microscopy
 SD strength difference
 SDD silicon drift detector
 SE secondary electron
 SEC specific energy consumption
 SECM scanning electrochemical microscope
 SEI secondary electron imaging

SEM scanning electron microscopy
 SEN single-edge notched
 SENB4 four-point single-edge notch bend
 SER specific emission rate
 SFG sum frequency generation
 SFM scanning force microscopy
 SHE standard hydrogen electrode
 SHG second-harmonic generation
 SHM structural health monitoring
 SI International System of Units
 SI Système International d'Unités
 SIM Sistema Interamericano de Metrología
 SIMS secondary ion mass spectrometry
 SMSC study semiconductor
 SMU Slovenski Metrologicky Ustav
 SNOM scanning near-field optical microscopy
 SNR signal-to-noise ratio
 SOD source-to-object distance
 SOLAS safety of life at sea
 SOLZ second-order Laue zone
 SOP standard operating procedure
 SOR successive overrelaxation
 SP Swedish National Testing and Research Institute
 SPD singular point detection
 SPF superplastic forming
 SPH smooth particle hydrodynamics
 SPI selective polarization inversion
 SPM scanning probe microscopy
 SPM self-phase modulation
 SPOM surface potential microscope
 SPRT standard platinum resistance thermometer
 SPT sampling proficiency test
 SQUID superconducting quantum interference device
 SRE stray radiant energy
 SRET scanning reference electrode technique
 SRM standard reference material
 SRS stimulated Raman scattering
 SS spectral sensitivity
 SSE stochastic series expansion
 SST single-sheet tester
 SST system suitability test
 STEM scanning transmission electron microscopy
 STL stereolithographic data format
 STM scanning tunneling microscopy
 STP steady-state permeation
 STS scanning tunneling spectroscopy
 SUPG streamline-upwind Petrov–Galerkin
 SVET scanning vibrating electrode technique
 SVOC semi-volatile organic compound
 SW Swendsen–Wang
 SWLI scanning white-light interferometry
 SZ stretched zone
 SZW stretched zone width

T		V	
TAC	time-to-amplitude converter	VAMAS	Versailles Project on Advanced Materials and Standards
TBCCO	tellurium-barium-calcium-copper-oxide	VCSEL	vertical-cavity surface-emitting laser
TBT	technical barriers to trade	VDEh	Verein Deutscher Eisenhttenleute
TCD	thermal conductivity detector	VG	vortex glass
TCSPC	time-correlated single-photon counting	VIM	international vocabulary of basic and general terms in metrology
TDI	time-delayed integration	VIM	international vocabulary of metrology
TDS	thermal desorption mass spectrometry	VL	vortex liquid
TDS	total dissolved solid	VOC	volatile organic carbon
TEM	transmission electron microscopy	VOST	volatile organic sampling train
TFT	thin-film transistor	VSM	vibrating-sample magnetometer
TG	thermogravimetry	VVOC	very volatile organic compound
TGA-IR	thermal gravimetric analysis-infrared		
TGFSR	twisted GFSR	W	
THG	third-harmonic generation	WDM	wavelength division multiplexing
TIMS	thermal ionization mass spectrometry	WDS	wavelength-dispersive spectrometry
TIRFM	total internal reflection fluorescence microscopy	WE	working electrode
TLA	thin-layer activation	WFI	water for injection
TMA	thermomechanical analysis	WGMM	Working Group on Materials Metrology
TMR	tunnel magneto-resistance	WHO	World Health Organization
TMS	tetramethylsilane	WLI	white-light interferometry
TOF	time of flight	WTO	World Trade Organization
TPA	two-photon absorption	WZW	Wess–Zumino–Witten
TR	technical report	X	
TRIP	transformation induced plasticity	XAS	x-ray absorption spectroscopy
TS	tensile strength	XCT	x-ray computed tomography
TTT	time–temperature-transformation	XEDS	energy-dispersive x-ray spectrometry
TU	Technical University	XFL	photoemitted Fermi level
TVOC	total volatile organic compound	XMA	x-ray micro analyzer
TW	thermostat water	XMCD	x-ray magnetic circular dichroism
TWA	technical work area	XPS	x-ray photoelectron spectroscopy
TWIP	twinning induced plasticity	XPS	x-ray photoemission spectroscopy
TXIB	2,2,4-trimethyl-1,3-pentanediol diisobutyrate	XRD	x-ray diffraction
TXRF	total reflection x-ray fluorescence spectrometry	XRF	x-ray fluorescence
		XRT	x-ray topography
U		Y	
UBA	Bundesumweltamt	YAG	yttrium aluminum garnet
UHV	ultra-high vacuum	YIG	yttrium-iron garnet
UIC	Union Internationale des Chemins de Fer	YS	yield strength
ULSI	ultralarge-scale integration	Z	
USAXS	ultrasmall-angle scattering	ZOLZ	zero-order Laue zone
USP	United States Pharmacopeia	ZRA	zero-resistance ammetry
UT	ultrasonic technique		
UTS	ultimate tensile strength		
UV	ultraviolet		
UVSG	UV Spectrometry Group		
UXO	unexploded ordnance		

Part A Fundamentals

Part A Fundamentals of Metrology and Testing

1 Introduction to Metrology and Testing

Horst Czichos, Berlin, Germany

2 Metrology Principles and Organization

Andrew Wallard, Sèvres, France

3 Quality in Measurement and Testing

Michael H. Ramsey, Brighton, UK

Stephen L.R. Ellison, Middlesex, UK

Horst Czichos, Berlin, Germany

Werner Hässelbarth, Berlin, Germany

Hanspeter Ischi, Berne, Switzerland

Wolfhard Wegscheider, Leoben, Austria

Brian Brookman, Bury, Lancashire, UK

Adolf Zschunke, Leipzig, Germany

Holger Frenz, Recklinghausen, Germany

Manfred Golze, Berlin, Germany

Martina Hedrich, Berlin, Germany

Anita Schmidt, Berlin, Germany

Thomas Steiger, Berlin, Germany

1. Introduction to Metrology and Testing

This chapter reviews the methodologies of measurement and testing. It gives an overview of metrology and presents the fundamentals of materials characterization as a basis for

1. Chemical and microstructural analysis
2. Materials properties measurement
3. Materials performance testing

which are treated in parts B, C, and D of the handbook.

1.1 Methodologies of Measurement and Testing	3
1.1.1 Measurement	3
1.1.2 Testing.....	5

1.1.3 Conformity Assessment and Accreditation.....	7
1.2 Overview of Metrology	9
1.2.1 The Meter Convention	9
1.2.2 Categories of Metrology.....	9
1.2.3 Metrological Units	11
1.2.4 Measurement Standards	12
1.3 Fundamentals of Materials Characterization	13
1.3.1 Nature of Materials.....	13
1.3.2 Types of Materials	15
1.3.3 Scale of Materials	16
1.3.4 Properties of Materials.....	17
1.3.5 Performance of Materials	19
1.3.6 Metrology of Materials	20
References	22

In science and engineering, objects of interest have to be characterized by measurement and testing. Measurement is the process of experimentally obtaining quantity values that can reasonably be attributed to a property of

a body or substance. Metrology is the science of measurement. Testing is the technical procedure consisting of the determination of characteristics of a given object or process, in accordance with a specified method [1.1].

1.1 Methodologies of Measurement and Testing

The methodologies of measurement and testing to determine characteristics of a given object are illustrated in a unified general scheme in Fig. 1.1, which is discussed in the next sections.

1.1.1 Measurement

Measurement begins with the definition of the measurand, the quantity intended to be measured. The specification of a measurand requires knowledge of the kind of quantity and a description of the object carrying the quantity. When the measurand is defined, it must be related to a measurement standard, the realization of the definition of the quantity to be measured. The measurement procedure is a detailed description

of a measurement according to a measurement principle and to a given measurement method. It is based on a measurement model, including any calculation to obtain a measurement result. The basic features of a measurement procedure are the following [1.1].

- Measurement principle: the phenomenon serving as a basis of a measurement
- Measurement method: a generic description of a logical organization of operations used in a measurement
- Measuring system: a set of one or more measuring instruments and often other devices, including any reagent and supply, assembled and adapted to give information used to generate measured quan-

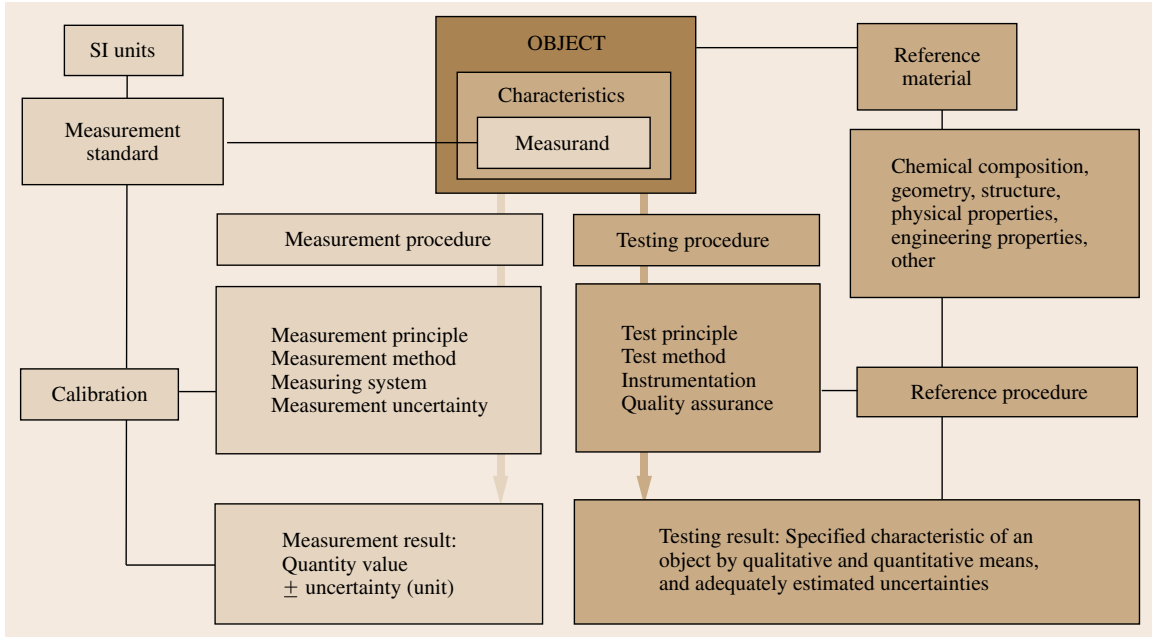


Fig. 1.1 The methodologies of measurement (light brown) and testing (dark brown) – a general scheme

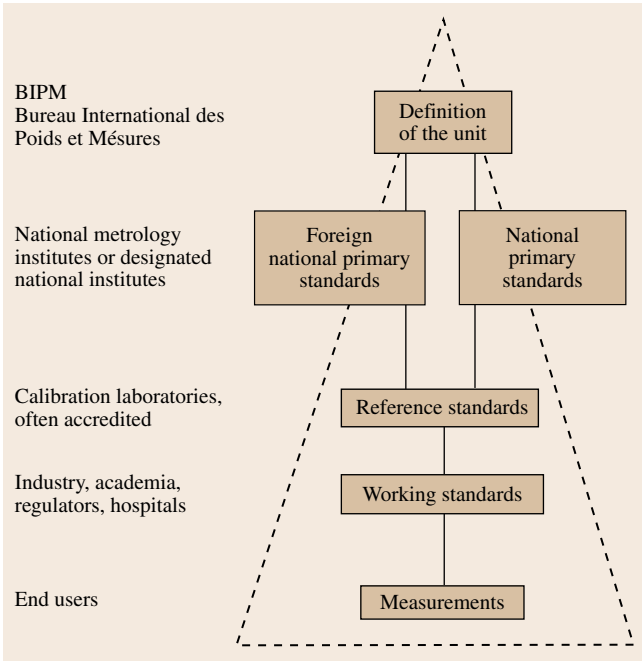


Fig. 1.2 The traceability chain for measurements

- Measurement uncertainty: a nonnegative parameter characterizing the dispersion of the quantity values being attributed to a measurand

The result of a measurement has to be expressed as a quantity value together with its uncertainty, including the unit of the measurand.

Traceability and Calibration

The measured quantity value must be related to a reference through a documented unbroken *traceability chain*. The *traceability of measurement* is described in detail in Sect. 3.2. Figure 1.2 illustrates this concept schematically.

The traceability chain ensures that a measurement result or the value of a standard is related to references at the higher levels, ending at the primary standard, based on the International System of Units (*le Système International d’Unités, SI*) (Sect. 1.2.3). An end user may obtain traceability to the highest international level either directly from a national metrology institute or from a secondary calibration laboratory, usually an accredited laboratory. As a result of various mutual recognition arrangements, internationally recognized traceability may be obtained from laboratories outside the user’s own country. Metrological timelines in traceability, defined as changes, however slight, in

tity values within specified intervals for quantities of specified kinds

all instruments and standards over time, are discussed in [1.2].

A basic tool in ensuring the traceability of a measurement is either the calibration of a measuring instrument or system, or through the use of a reference material. Calibration determines the performance characteristics of an instrument or system before its use, while reference material calibrates the instrument or system at time of use. Calibration is usually achieved by means of a direct comparison against measurement standards or certified reference materials and is documented by a calibration certificate for the instrument.

The expression “traceability to the SI” means traceability of a measured quantity value to a unit of the International System of Units. This means metrological traceability to a *dematerialized reference*, because the SI units are conceptually based on *natural constants*, e.g., the speed of light for the unit of length. So, as already mentioned and shown in Fig. 1.1, the characterization of the measurand must be realized by a *measurement standard* (Sect. 1.2.4). If a measured quantity value is an attribute of a *materialized object* (e.g., a chemical substance, a material specimen or a manufactured product), also an object-related traceability (speciation) to a *materialized reference* (Fig. 1.1) is needed to characterize the object that bears the metrologically defined and measured quantity value.

Uncertainty of Measurements

Measurement uncertainty comprises, in general, many components and can be determined in different ways [1.3]. *The Statistical Evaluation of Results* is explained in detail in Sect. 3.3, and the *Accuracy and Uncertainty of Measurement* is comprehensively described in Sect. 3.4. A basic method to determine uncertainty of measurements is the *Guide to the expression of uncertainty in measurement (GUM)* [1.4], which is shared jointly by the Joint Committee for Guides in Metrology (JCGM) member organizations (BIPM, IEC, IFCC, ILAC, ISO, IUPAC, IUPAP and OIML). The concept of the GUM can be briefly outlined as follows [1.5].

The GUM Uncertainty Philosophy.

- A measurement quantity X , whose value is not known exactly, is considered as a stochastic variable with a probability function.
- The result x of measurement is an estimate of the expectation value $E(X)$.

- The standard uncertainty $u(x)$ is equal to the square root of an estimate of the variance $V(X)$.
- *Type A uncertainty evaluation.* Expectation and variance are estimated by statistical processing of repeated measurements.
- *Type B uncertainty evaluation.* Expectation and variance are estimated by other methods than those used for type A evaluations. The most commonly used method is to assume a probability distribution, e.g., a rectangular distribution, based on experience or other information.

The GUM Method Based on the GUM Philosophy.

- Identify all important components of measurement uncertainty. There are many sources that can contribute to measurement uncertainty. Apply a model of the actual measurement process to identify the sources. Use measurement quantities in a mathematical model.
- Calculate the standard uncertainty of each component of measurement uncertainty. Each component of measurement uncertainty is expressed in terms of the standard uncertainty determined from either a type A or type B evaluation.
- Calculate the combined uncertainty u (the *uncertainty budget*). The combined uncertainty is calculated by combining the individual uncertainty components according to the law of propagation of uncertainty. In practice
 - for a sum or a difference of components, the combined uncertainty is calculated as the square root of the sum of the squared standard uncertainties of the components;
 - for a product or a quotient of components, the same *sum/difference* rule applies as for the relative standard uncertainties of the components.
- Calculate the expanded uncertainty U by multiplying the combined uncertainty with the coverage factor k .
- State the measurement result in the form $X = x \pm U$.

The methods to determine uncertainties are presented in detail in Sect. 3.4.

1.1.2 Testing

The aim of testing is to determine characteristics (attributes) of a given object and express them by qualitative and quantitative means, including adequately

estimated uncertainties, as outlined in the right-hand side of Fig. 1.1. For the testing methodology, metrology delivers the basis for the comparability of test results, e.g., by defining the units of measurement and the associated uncertainty of the measurement results. Essential tools supporting testing include reference materials, certified reference materials, and reference procedures.

- Reference material (RM) [1.6]: a material, sufficiently homogeneous and stable with regards to specified properties, which has been established to be fit for its intended use in measurement or in examination of nominal properties
- Certified reference material (CRM): a reference material, accompanied by documentation issued by an authoritative body and providing one or more specified property values with associated uncertainties and traceabilities, using a valid procedure
- Reference procedures [1.5]: procedures of testing, measurement or analysis, thoroughly characterized and proven to be under control, intended for
 - quality assessment of other procedures for comparable tasks, or
 - characterization of reference materials including reference objects, or
 - determination of reference values.

The uncertainty of the results of a reference procedure must be adequately estimated and appropriate for the intended use. Recommendations/guides for the de-

termination of uncertainties in different areas of testing include

- Guide for the estimation of measurement uncertainty in testing [1.7]
- Guide to the evaluation of measurement uncertainty for quantitative tests results [1.8]
- Guide for chemistry [1.9]
- Measurement uncertainty in environmental laboratories [1.10]
- Uncertainties in calibration and testing [1.11].

The methodology of testing combined with measurement is exemplified in Fig. 1.3 for the determination of mechanical characteristics of a technical object.

Generally speaking, the mechanical properties of materials characterize the response of a material sample to loading. The mechanical loading action on materials in engineering applications can basically be categorized as tension, compression, bending, shear or torsion, which may be static or dynamic. In addition, thermomechanical loading effects can occur. The testing of mechanical properties consists of measuring the mechanical loading stress (force/cross-sectional area = F/A) and the corresponding materials response (strain, elongation) and expressing this as a *stress–strain curve*. Its regimes and data points characterize the mechanical behavior of materials.

Consider for example *elasticity*, which is an important characteristic of all components of engineered structures. The elastic modulus (E) describes the rela-

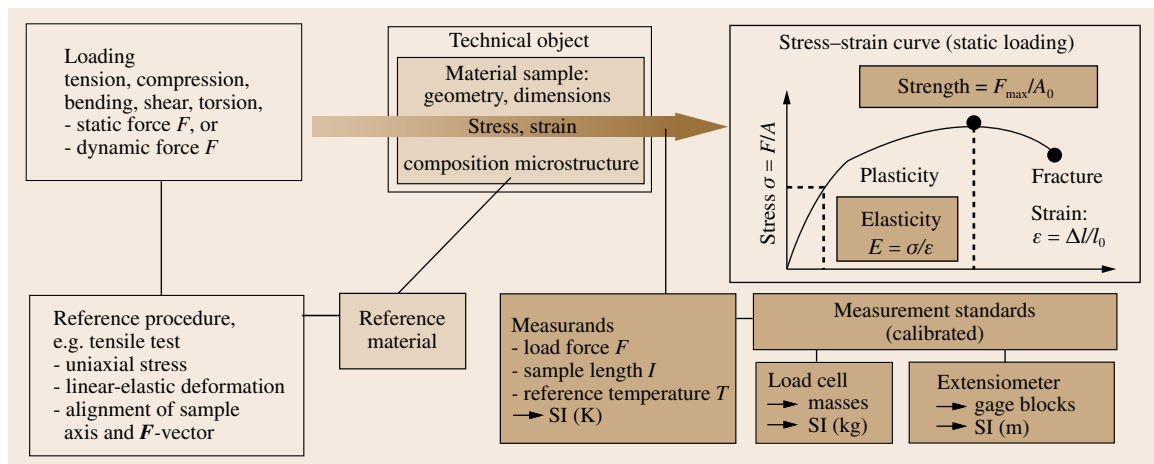


Fig. 1.3 The combination of measurement and testing to determine mechanical characteristics of the technical object

tion between a stress (σ) imposed on a material and the strain (ϵ) response of the material, or vice versa. The stimulus takes the form of an applied load, and the measured effect is the resultant displacement. The traceability of the stress is established through the use of a calibrated load cell and by measuring the specimen cross-sectional area with a calibrated micrometer, whereas the traceability of the strain is established by measuring the change in length of the originally measured gage length, usually with a calibrated strain gage. This, however, is not sufficient to ensure repeatable results unless a testing reference procedure, e.g., a standardized tensile test, is used on identically prepared specimens, backed up by a reference material.

Figure 1.3 illustrates the metrological and technological aspects.

- Metrologically, the measurands of the strength value are the force (F), area (A), and the length measurement (l) of the technical object, all at a reference temperature (T).
- Technologically and concerning testing, the mechanical characteristics expressed in a stress–strain curve depend on at least the following groups of influencing parameters, to be backed up by appropriate references.
 - The chemical and physical nature of the object: chemical composition, microstructure, and *structure–property relations* such as crystallographic shape-memory effects [1.12]; for example, strength values of metals are significantly influenced by alloying elements, grain size (fine/coarse), work-hardening treatment, etc.
 - The mechanical loading action and dependence on deformation amplitude: tension, compression, bending, shear, and torsion; for example, tensile strength is different from shear strength for a given material.
 - The time dependence of the loading mode forces (static, dynamic, impact, stochastic) and deviations from simple linear-elastic deformation (anelastic, viscoelastic or micro-viscoplastic deformation). Generally, the dynamic strength of a material is different from its static strength.

The combined measurement and testing methodologies, their operating parameters, and the traceability requirements are illustrated in a highly simplified scheme by the *confidence ring* [1.13] shown in Fig. 1.4.

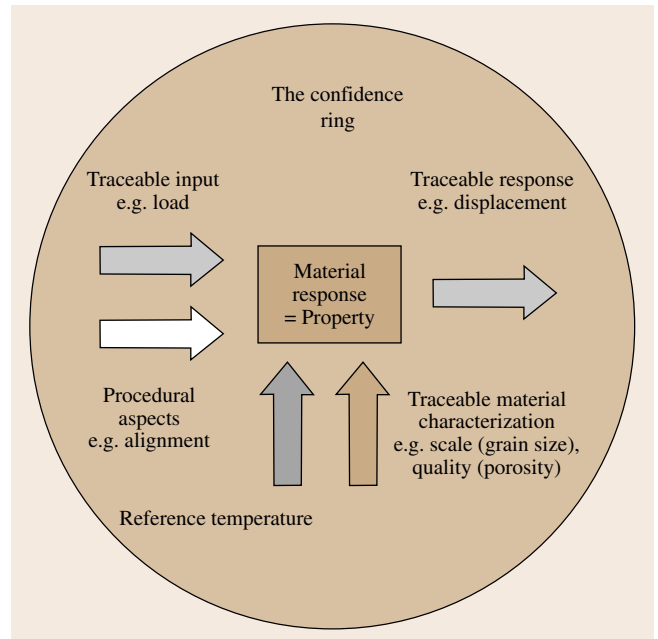


Fig. 1.4 Confidence ring for material property combined measurement and testing – note that separate traceability requirements apply to applied stimulus (load), response (displacement), and material characterization (grain size, porosity)

The confidence ring illustrates that, in measurement and testing, it is generally essential to establish reliable traceability for the applied stimulus and the resulting measured effect as well as for the measurements of any other quantities that may influence the final result. The final result may also be affected by the measurement procedure, by temperature, and by the state of the sample. It is important to understand that variation in measured results will often reflect material inhomogeneity as well as uncertainties associated with the test method or operator variability. All uncertainties should be taken into account in an *uncertainty budget*.

1.1.3 Conformity Assessment and Accreditation

In today's global market and world trade there is an increased need for *conformity assessment* to ensure that products and equipment meet specifications. The basis for conformity assessment are measurements together with methods of calibration, testing, inspection, and certification. The goal of conformity assessment

Table 1.1 Standards of conformity assessment tools

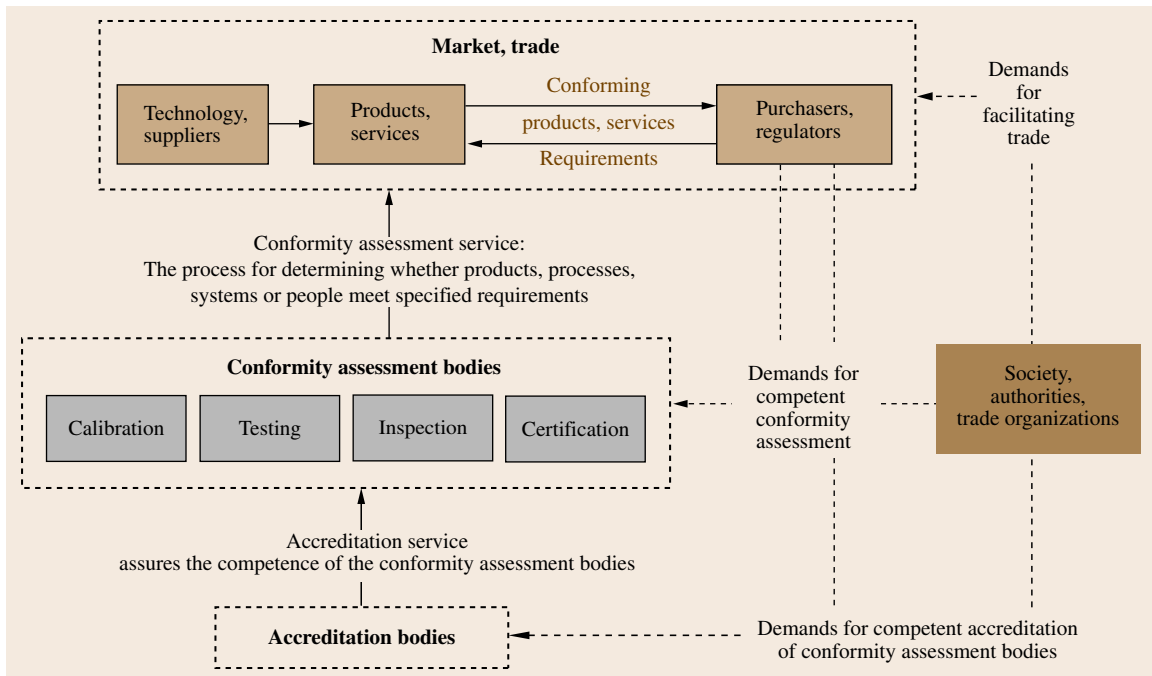
Tools for conformity assessment	First party Supplier, user	Second party Customers, trade associations, regulators	Third party Bodies independent from 1st and 2nd parties	ISO standards
Supplier's declaration	×			ISO/IEC 17050
Calibration, testing	×	×	×	ISO/IEC 17025
Inspection	×	×	×	ISO/IEC 17020
Certification			×	ISO 17021 ISO Guide 65

is to provide the user, purchaser or regulator with the necessary confidence that a product, service, process, system or person meets relevant requirements. The international standards relevant for conformity assessment services are provided by the ISO Committee on Conformity Assessment (CASCO). The conformity assessment tools are listed in Table 1.1, where their use by first parties (suppliers), second parties (customers, regulators, trade organizations), and third parties (bodies independent from both suppliers and customers) is indicated.

Along with the growing use of these conformity assessment tools there is the request for assurance of the competence of the conformity assessment bodies

(CABs). An increasingly applied and recognized tool for this assurance is *accreditation of CABs*.

The world's principal international forum for the development of laboratory accreditation practices and procedures is the International Laboratory Accreditation Cooperation (ILAC, <http://www.ilac.org/>). It promotes laboratory accreditation as a trade facilitation tool together with the recognition of competent calibration and testing facilities around the globe. ILAC started as a conference in 1977 and became a formal cooperation in 1996. In 2000, 36 ILAC members signed the ILAC Mutual Recognition Arrangement (MRA), and by 2008 the number of members of the ILAC MRA had risen to 60. Through the evaluation

**Fig. 1.5** Interrelations between market, trade, conformity assessment, and accreditation

of the participating accreditation bodies, the international acceptance of test data and the elimination of technical barriers to trade are enhanced as recommended and in support of the World Trade Organization

(WTO) Technical Barriers to Trade agreement. An overview of the interrelations between market, trade, conformity assessment, and accreditation is shown in Fig. 1.5.

1.2 Overview of Metrology

Having considered the methodologies of measurement and testing, a short general overview of metrology is given, based on *Metrology – in short* [1.5], a brochure published by EURAMET to establish a common metrological frame of reference.

1.2.1 The Meter Convention

In the middle of the 19th century the need for a world-wide decimal metric system became very apparent, particularly during the first universal industrial exhibitions. In 1875, a diplomatic conference on the meter took place in Paris, at which 17 governments signed the diplomatic treaty *the Meter Convention*. The signatories

decided to create and finance a permanent scientific institute: the *Bureau International des Poids et Mesures* (BIPM). The Meter Convention, slightly modified in 1921, remains the basis of all international agreement on units of measurement. Figure 1.6 provides a brief overview of the Meter Convention Organization (details are described in Chap. 2).

1.2.2 Categories of Metrology

Metrology covers three main areas of activities [1.5].

1. The definition of internationally accepted units of measurement

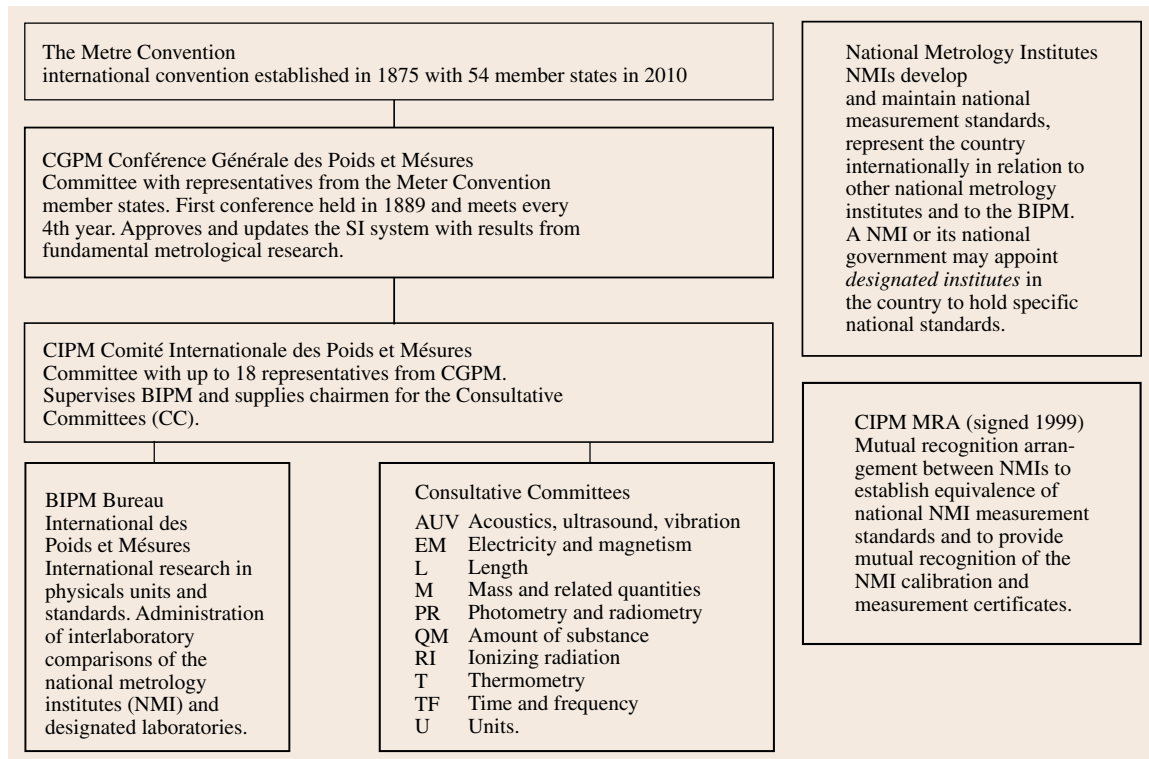


Fig. 1.6 The organizations and their relationships associated with the Meter Convention

2. The realization of units of measurement by scientific methods
3. The establishment of traceability chains by determining and documenting the value and accuracy of a measurement and disseminating that knowledge

Metrology is separated into three categories with different levels of complexity and accuracy (for details, see Chaps. 2 and 3).

Scientific Metrology

Scientific metrology deals with the organization and development of measurement standards and their maintenance. Fundamental metrology has no international definition, but it generally signifies the highest level of accuracy within a given field. Fundamental metrology may therefore be described as the top-level branch of scientific metrology.

Scientific metrology is categorized by BIPM into nine technical subject fields with different branches. The metrological calibration and measurement capabilities (CMCs) of the national metrology institutes (NIMs) and the designated institutes (DIs) are compiled together with *key comparisons* in the BIPM key comparison database (KCDB, <http://kcdb.bipm.org/>). All CMCs have undergone a process of peer evaluation by NMI experts under the supervision of the regional metrology organizations (RMOs). Table 1.2 shows the scientific metrology fields and their branches together with the number of registered calibration and measurement capabilities (CMCs) of the NMIs in 2010.

Industrial Metrology

Industrial metrology has to ensure the adequate functioning of measurement instruments used in industrial production and in testing processes. Systematic measurement with known degrees of uncertainty is one of the foundations of industrial quality control. Generally speaking, in most modern industries the costs bound up in taking measurements constitute 10–15% of production costs.

However, good measurements can significantly increase the value, effectiveness, and quality of a product. Thus, metrological activities, including calibration, testing, and measurements, are valuable inputs to ensure the quality of most industrial processes and quality of life related activities and processes. This includes the need to demonstrate traceability to international standards, which is becoming just as important as the measurement itself. Recognition of metrological competence at each level of the traceability chain can be established through mutual recognition agreements or arrangements, as well as through accreditation and peer review.

Legal Metrology

Legal metrology originated from the need to ensure fair trade, specifically in the area of weights and measures. The main objective of legal metrology is to assure citizens of correct measurement results when used in official and commercial transactions. Legally controlled instruments should guarantee correct measurement results throughout the whole period of use under working conditions, within given permissible errors.

Table 1.2 Metrology areas and their branches, together with the numbers of metrological calibration and measurement capabilities (CMCs) of the national metrology institutes and designated institutes in the BIPM KCDB as of 2010

Metrology area	Branch	CMCs
Acoustics, ultrasound, vibrations	Sound in air; sound in water; vibration	955
Electricity and magnetism	DC voltage, current, and resistance; impedance up to the megahertz range; AC voltage, current, and power; high voltage and current; other DC and low-frequency measurements; electric and magnetic fields; radiofrequency measurements	6586
Length	Laser; dimensional metrology	1164
Mass and related quantities	Mass; density; pressure; force; torque, viscosity, hardness and gravity; fluid flow	2609
Photometry and radiometry	Photometry; properties of detectors and sources; spectral properties; color; fiber optics	1044
Amount of substance	List of 16 amount-of-substance categories	4558
Ionizing radiation	Dosimetry; radioactivity; neutron measurements	3983
Thermometry	Temperature; humidity; thermophysical quantities	1393
Time and frequency	Time scale difference; frequency; time interval	586

For example, in Europe, the marketing and usage of the following measuring instruments are regulated by the European Union (EU) measuring instruments directive (MID 2004/22/EC)

1. Water meters
2. Gas meters
3. Electrical energy meters and measurement transformers
4. Heat meters
5. Measuring systems for liquids other than water
6. Weighing instruments
7. Taximeters
8. Material measures
9. Dimensional measuring systems
10. Exhaust gas analyzers

Member states of the European Union have the option to decide which of the instrument types they wish to regulate.

The International Organization of Legal Metrology (OIML) is an intergovernmental treaty organization established in 1955 on the basis of a convention, which was modified in 1968. In the year 2010, OIML was composed of 57 member countries and an additional 58 (corresponding) member countries that joined the OIML (<http://www.oiml.org/>) as observers. The purpose of OIML is to promote global harmonization of legal metrology procedures. The OIML has developed a worldwide technical structure that provides its members with metrological guidelines for the elaboration of national and regional requirements concerning the

manufacture and use of measuring instruments for legal metrology applications.

1.2.3 Metrological Units

The idea behind the metric system – a system of units based on the meter and the kilogram – arose during the French Revolution when two platinum artefact reference standards for the meter and the kilogram were constructed and deposited in the French National Archives in Paris in 1799 – later to be known as the Meter of the Archives and the Kilogram of the Archives. The French Academy of Science was commissioned by the National Assembly to design a new system of units for use throughout the world, and in 1946 the MKSA system (meter, kilogram, second, ampere) was accepted by the Meter Convention countries. The MKSA was extended in 1954 to include the kelvin and candela. The system then assumed the name the International System of Units (*Le Système International d'Unités*, SI). The SI system was established in 1960 by the 11th General Conference on Weights and Measures (CGPM): *The International System of Units (SI) is the coherent system of units adopted and recommended by the CGPM.*

At the 14th CGPM in 1971 the SI was again extended by the addition of the mole as base unit for amount of substance. The SI system is now comprised of seven base units, which together with derived units make up a coherent system of units [1.5], as shown in Table 1.3.

Table 1.3 The SI base units

Quantity	Base unit	Symbol	Definition
Length	Meter	m	The meter is the length of the path traveled by light in a vacuum during a time interval of $1/299\,792\,458$ of a second
Mass	Kilogram	kg	The kilogram is equal to the mass of the international prototype of the kilogram
Time	Second	s	The second is the duration of 9 192 631 770 periods of the radiation corresponding to the transition between the two hyperfine levels of the ground state of the cesium-133 atom
Electric current	Ampere	A	The ampere is that constant current which, if maintained in two straight parallel conductors of infinite length, of negligible circular cross-section, and placed one meter apart in vacuum, would produce between these conductors a force equal to 2×10^{-7} newtons per meter of length
Temperature	Kelvin	K	The kelvin is the fraction $1/273.16$ of the thermodynamic temperature of the triple point of water
Amount of substance	Mole	mol	The mole is the amount of substance of a system that contains as many elementary entities as there are atoms in 0.012 kg of carbon-12. When the mole is used, the elementary entities must be specified and may be atoms, molecules, ions, electrons, other particles, or specified groups of such particles
Luminous intensity	Candela	cd	The candela is the luminous intensity in a given direction of a source that emits monochromatic radiation of frequency 540×10^{12} Hz and has a radiant intensity in that direction of $1/683$ W per steradian

Table 1.4 Examples of SI derived units expressed in SI base units

Derived quantity	SI derived unit special name	Symbol	In SI units	In SI base units
Force	Newton	N		m kg s^{-2}
Pressure, stress	Pascal	Pa	N/m^2	$\text{m}^{-1} \text{kg s}^{-2}$
Energy, work, quantity of heat	Joule	J	N m	$\text{m}^2 \text{kg s}^{-2}$
Power	Watt	W	J/s	$\text{m}^2 \text{kg s}^{-3}$
Electric charge	Coulomb	C		s A
Electromotive force	Volt	V		$\text{m}^2 \text{kg s}^{-3} \text{A}^{-1}$
Electric capacitance	Farad	F	C/V	$\text{m}^{-2} \text{kg}^{-1} \text{s}^4 \text{A}^2$
Electric resistance	Ohm	Ω	V/A	$\text{m}^2 \text{kg s}^{-3} \text{A}^{-2}$
Electric conductance	Siemens	S	A/V	$\text{m}^{-2} \text{kg}^{-1} \text{s}^3 \text{A}^2$

SI derived units are derived from the SI base units in accordance with the physical connection between the quantities. Some derived units, with examples from mechanical engineering and electrical engineering, are compiled in Table 1.4.

1.2.4 Measurement Standards

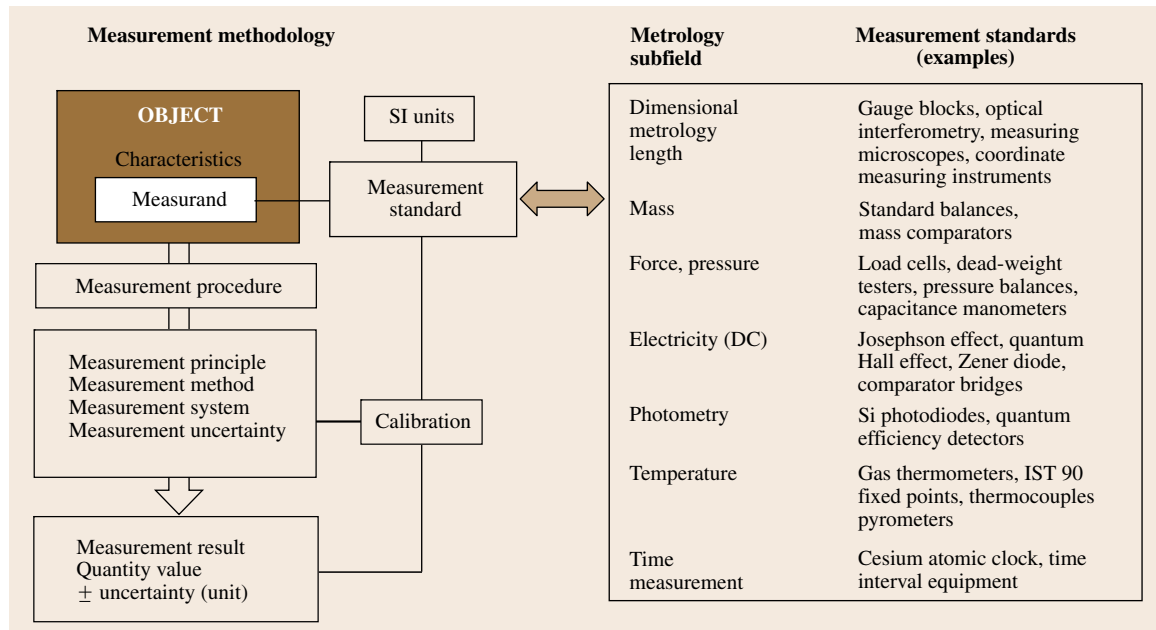
In the introductory explanation of the methodology of measurement, two essential aspects were pointed out.

1. Measurement begins with the definition of the measurand.

2. When the measurand is defined, it must be related to a measurement standard.

A measurement standard, or etalon, is the realization of the definition of a given quantity, with stated quantity value and associated measurement uncertainty, used as a reference. The realization may be provided by a material measure, measuring instrument, reference material or measuring system.

Typical measurement standards for subfields of metrology are shown in Fig. 1.7 in connection with the scheme of the measurement methodology (left-hand side of Fig. 1.1). Consider, for example, dimensional metrology. The meter is defined as the length of the path

**Fig. 1.7** Measurement standards as an integral part of the measurement methodology

traveled by light in vacuum during a time interval of $1/299\,792\,458$ of a second. The meter is realized at the primary level (SI units) in terms of the wavelength from an iodine-stabilized helium-neon laser. On sublevels, material measures such as gage blocks are used, and traceability is ensured by using optical interferometry to determine the length of the gage blocks with reference to the above-mentioned laser light wavelength.

A national measurement standard is recognized by a national authority to serve in a state or economy as the basis for assigning quantity values to other measurement standards for the kind of quantity concerned. An international measurement standard is recognized by signatories to an international agreement and intended to serve worldwide, e.g., the international prototype of the kilogram.

1.3 Fundamentals of Materials Characterization

Materials characterization methods have a wide scope and impact for science, technology, economy, and society, as materials comprise all natural and synthetic substances and constitute the physical matter of engineered and manufactured products.

For materials there is a comprehensive spectrum of *materials measurands*. This is due to the broad variety of metallic, inorganic, organic, and composite materials, their different chemical and physical nature, and the manifold attributes which are related to materials with respect to composition, microstructure, scale, synthesis, physical and electrical properties, and applications. Some of these attributes can be expressed in a metrological sense as numbers, such as density; some are Boolean, such as the ability to be recycled or not; some, such as resistance to corrosion, may be expressed as a ranking (poor, adequate, good, for instance); and some can only be captured in text and images [1.14]. As background for materials characterization methods, which are treated in parts B, C, D of the handbook, namely

- Chemical and microstructural analysis
- Materials properties measurement
- Materials performance testing

the essential features of materials are outlined in the next sections [1.15].

1.3.1 Nature of Materials

Materials can be natural (biological) in origin or synthetically processed and manufactured. According to their chemical nature, they are broadly grouped traditionally into inorganic and organic materials.

The physical structure of materials can be crystalline or amorphous, as well as mixtures of both structures. Composites are combinations of materials assembled together to obtain properties superior to those of their single constituents. Composites (C) are

classified according to the nature of their matrix: metal (MM), ceramic (CM) or polymer (PM) matrix composites, often designated as MMCs, CMCs, and PMCs, respectively. Figure 1.8 illustrates, with characteristic examples, the spectrum of materials between the categories natural, synthetic, inorganic, and organic.

From the view of *materials science*, the fundamental features of a solid material are as listed below.

- Material's atomic nature: the atomic elements of the Periodic Table which constitute the chemical composition of a material
- Material's atomic bonding: the type of cohesive electronic interactions between the atoms (or molecules) in a material, empirically categorized into the following basic classes.
 - Ionic bonds form between chemical elements with very different electron negativity (tendency

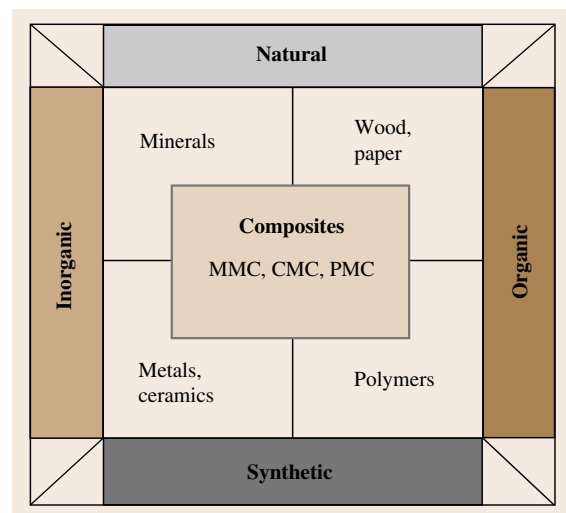


Fig. 1.8 Classification of materials

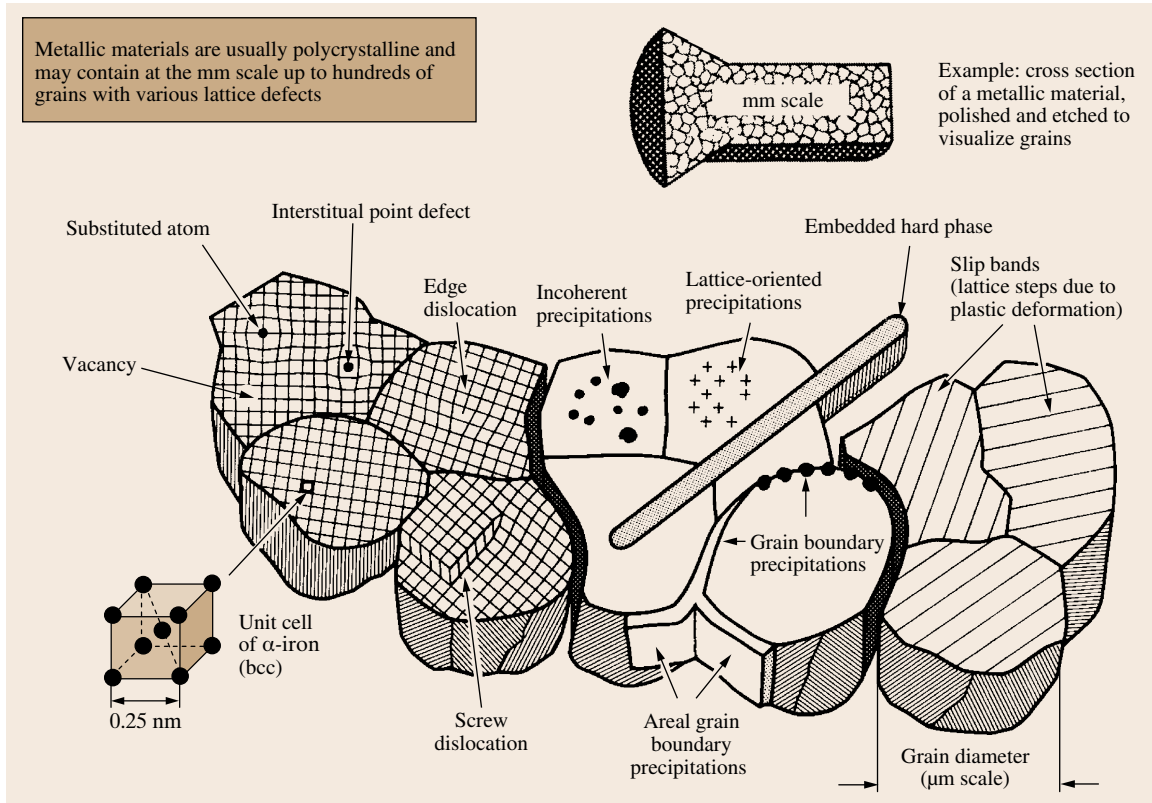


Fig. 1.9 Schematic overview on the microstructural features of metallic materials and alloys

to gain electrons), resulting in electron transfer and the formation of anions and cations. Bonding occurs through electrostatic forces between the ions.

- Covalent bonds form between elements that have similar electron negativities; the electrons are localized and shared equally between the atoms, leading to spatially directed angular bonds.
- Metallic bonds occur between elements with low electron negativities, so that the electrons are only loosely attracted to the ionic nuclei. A metal is thought of as a set of positively charged ions embedded in a sea of electrons.
- van der Waals bonds are due to the different internal electronic polarities between adjacent atoms or molecules, leading to weak (secondary) electrostatic dipole bonding forces.
- Material's spatial atomic structure: the amorphous or crystalline arrangement of atoms (or molecules) resulting from *long-range* or *short-range* bonding forces. In crystalline structures, it is characterized by unit cells which are the fundamental building blocks or modules, repeated many times in space within a crystal.
- Grains: crystallites made up of identical unit cells repeated in space, separated by grain boundaries.
- Phases: homogeneous aggregations of matter with respect to chemical composition and uniform crystal structure; grains composed of the same unit cells are the same phase.
- Lattice defects: deviations from ideal crystal structure.
 - Point defects or missing atoms: vacancies, interstitial or substituted atoms
 - Line defects or rows of missing atoms: dislocations
 - Area defects: grain boundaries, phase boundaries, and twins
 - Volume defects: cavities, precipitates.
- Microstructure: The microscopic collection of grains, phases, and lattice defects.

In addition to bulk materials characteristics, surface and interface phenomena also have to be considered.

In Fig. 1.9 an overview of the microstructural features of metallic materials is depicted schematically. Methods and techniques for the characterization of nanoscopic architecture and microstructure are presented in Chap. 5.

1.3.2 Types of Materials

It has been estimated that there are between 40 000 and 80 000 materials which are used or can be used in today's technology [1.14]. Figure 1.10 lists the main conventional *families* of materials together with examples of *classes*, *members*, and *attributes*. For the examples of attributes, necessary characterization methods are listed.

Metallic Materials and Alloys

In metals, the grains are the building blocks and are held together by the *electron gas*. The free valence electrons of the electron gas account for the high electrical and thermal conductivity, as well as for the optical gloss of metals. Metallic bonding, seen as the interaction between the total atomic nuclei and the electron gas, is not significantly influenced by displacement of atoms, which is the reason for the good ductility and formability of metals. Metals and metallic alloys are the most important group of the so-called *structural materials* whose special features for engineering applications are their mechanical properties, e.g., strength and toughness.

Semiconductors

Semiconductors have an intermediate position between metals and inorganic nonmetallic materials. Their most important representatives are the elements silicon and germanium, possessing covalent bonding and diamond structure; they are also similar in structure to III–V compounds such as gallium arsenide (GaAs). Being electric nonconductors at absolute zero temperature, semiconductors can be made conductive through thermal energy input or atomic doping, which leads to the creation of free electrons contributing to electrical conductivity. Semiconductors are important *functional materials* for electronic components and applications.

Inorganic Nonmetallic Materials or Ceramics

Atoms of these materials are held together by covalent and ionic bonding. As covalent and ionic bonding energies are much higher than those of metallic bonds, inorganic nonmetallic materials, such as ceramics, have high hardness and high melting temperatures. These materials are basically brittle and not ductile: In contrast to the metallic bond model, displacement of atomic dimensions theoretically breaks localized covalent bonds or transforms anion–cation attractions into anion–anion or cation–cation repulsions. Because of the lack of free valence electrons, inorganic nonmetallic materials are poor conductors of electricity and heat; this qualifies them as good insulators in engineering applications.

Organic Materials or Polymers and Blends

Organic materials, whose technologically most important representatives are the polymers, consist of macro-

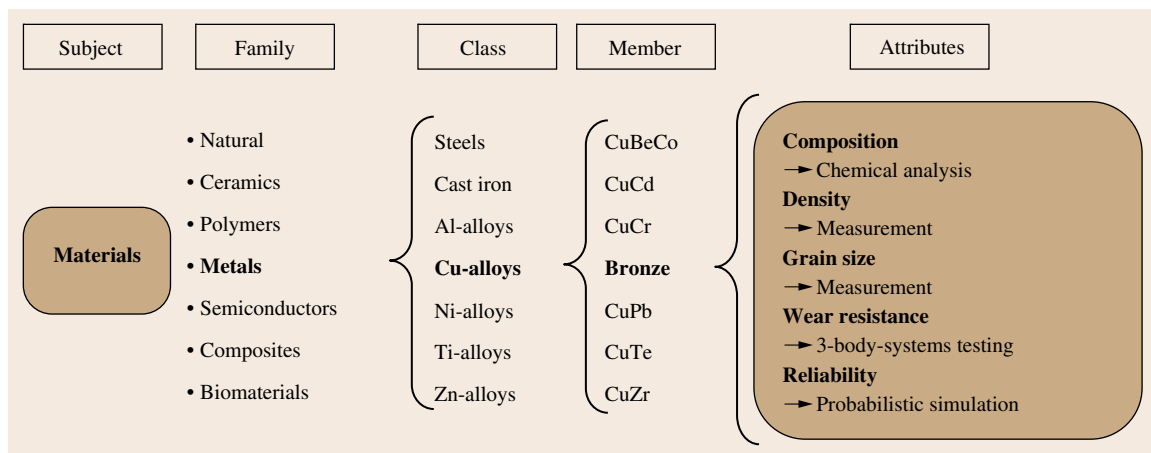


Fig. 1.10 Hierarchy of materials, and examples of attributes and necessary characterization methods

molecules containing carbon (C) covalently bonded with itself and with elements of low atomic number (e.g., H, N, O, S). Intimate mechanical mixtures of several polymers are called blends. In thermoplastic materials, the molecular chains have long linear structures and are held together by (weak) intermolecular (van der Waals) bonds, leading to low melting temperatures. In thermosetting materials, the chains are connected in a network structure and therefore do not melt. Amorphous polymer structures (e.g., polystyrene) are transparent, whereas crystalline polymers are translucent to opaque. The low density of polymers gives them a good strength-to-weight ratio and makes them competitive with metals in structural engineering applications.

Composites

Generally speaking, composites are hybrid creations made of two or more materials that maintain their identities when combined. The materials are chosen so that the properties of one constituent enhance the deficient properties of the other. Usually, a given property of a composite lies between the values for each constituent, but not always. Sometimes, the property of a composite is clearly superior to those of either of the constituents. The potential for such a synergy is one reason for the interest in composites for high-performance applications. However, because manufacturing of composites involves many steps and is labor intensive, composites may be too expensive to compete with metals and polymers, even if their properties are superior. In high-technology applications of advanced composites, it should also be borne in mind that they are usually difficult to recycle.

Natural Materials

Natural materials used in engineering applications are classified into natural materials of mineral origin, e.g., marble, granite, sandstone, mica, sapphire, ruby, or diamond, and those of organic origin, e.g., timber, India rubber, or natural fibres such as cotton and wool. The properties of natural materials of mineral origin, for example, high hardness and good chemical durability, are determined by strong covalent and ionic bonds between their atomic or molecular constituents and stable crystal structures. Natural materials of organic origin often possess complex structures with directionally dependent properties. Advantageous aspects of natural materials are ease of recycling and sustainability.

Biomaterials

Biomaterials can be broadly defined as the class of materials suitable for biomedical applications. They may be synthetically derived from nonbiological or even inorganic materials, or they may originate in living tissues. Products that incorporate biomaterials are extremely varied and include artificial organs; biochemical sensors; disposable materials and commodities; drug-delivery systems; dental, plastic surgery, ear, and ophthalmological devices; orthopedic replacements; wound management aids; and packaging materials for biomedical and hygienic uses. When applying biomaterials, understanding of the interactions between synthetic substrates and biological tissues is of crucial importance to meet clinical requirements.

1.3.3 Scale of Materials

The geometric length scale of materials covers more than 12 orders of magnitude. The scale ranges from

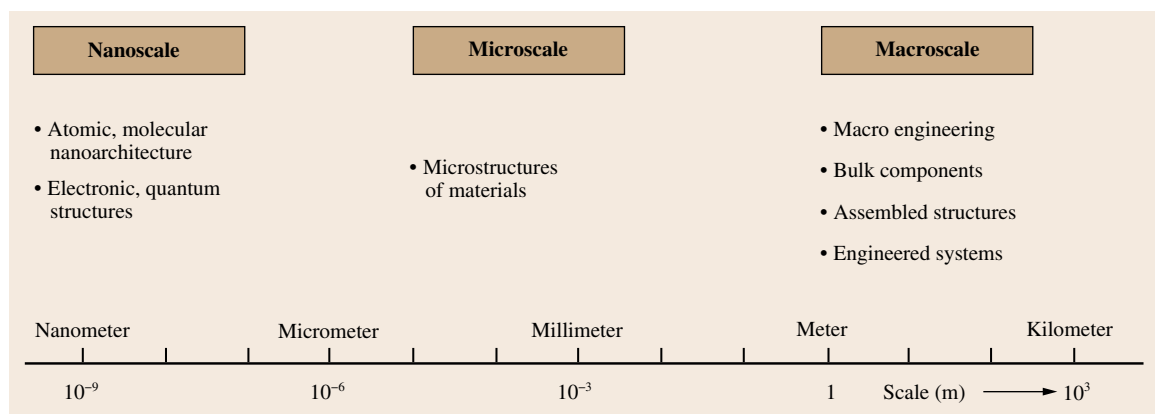


Fig. 1.11 Scale of material dimensions to be recognized in materials metrology and testing

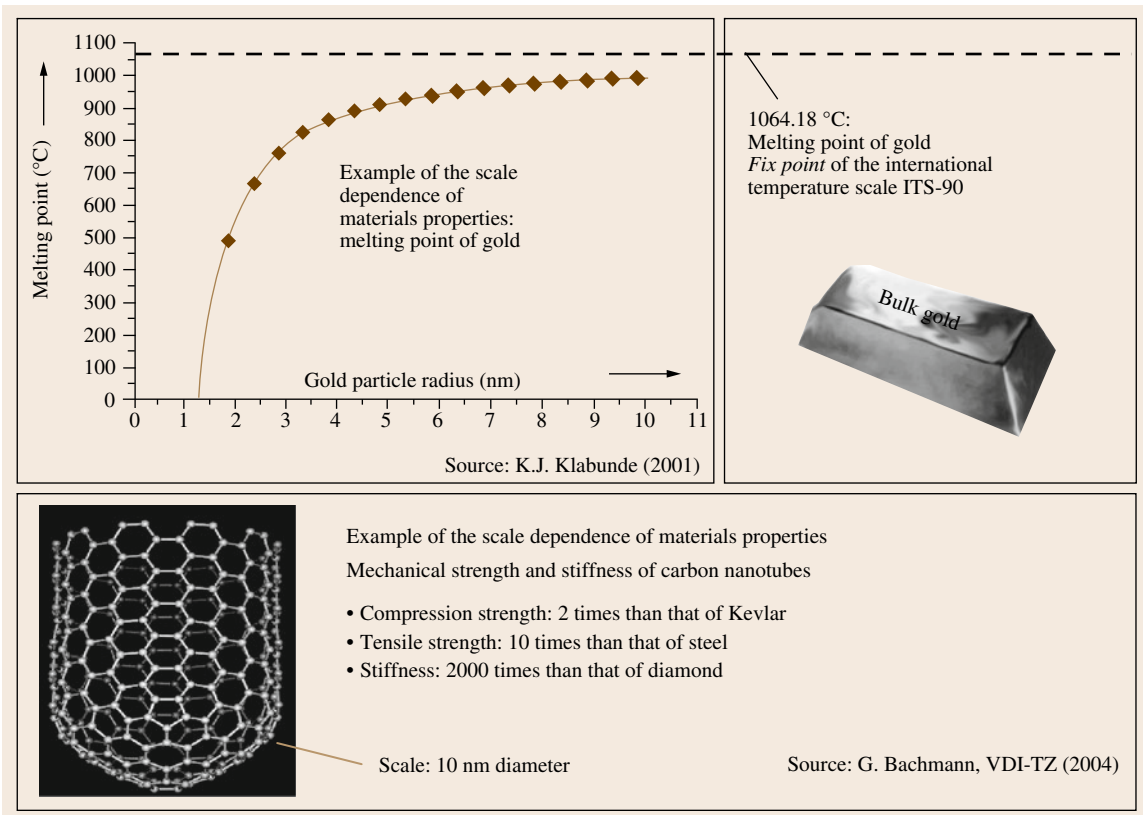


Fig. 1.12 Examples of the influence of scale effects on thermal and mechanical materials properties

the nanoscopic materials architecture to kilometer-long structures of bridges for public transport, pipelines, and oil drilling platforms for supplying energy to society. Figure 1.11 illustrates the dimensional scales relevant for today's materials science and technology.

Material specimens of different geometric dimensions have different bulk-to-surface ratios and may also have different bulk and surface microstructures. This can significantly influence the properties of materials, as exemplified in Fig. 1.12 for thermal and mechanical properties. Thus, scale effects have to be meticulously considered in materials metrology and testing.

1.3.4 Properties of Materials

Materials and their characteristics result from the processing of matter. Their properties are the response to extrinsic loading in their application. For every application, materials have to be engineered by processing, manufacturing, machining, forming or nanotechnology assembly to create structural, func-

tional or smart materials for the various engineering tasks (Fig. 1.13).

The properties of materials, which are of fundamental importance for their engineering applications, can be categorized into three basic groups.

1. Structural materials have specific mechanical or thermal properties for mechanical or thermal tasks in engineering structures.
2. Functional materials have specific electromagnetic or optical properties for electrical, magnetic or optical tasks in engineering functions.
3. Smart materials are engineered materials with intrinsic or embedded sensor and actuator functions, which are able to accommodate materials in response to external loading, with the aim of optimizing material behavior according to given requirements for materials performance.

Numerical values for the various materials properties can vary over several orders of magnitude for the different material types. An overview of the broad

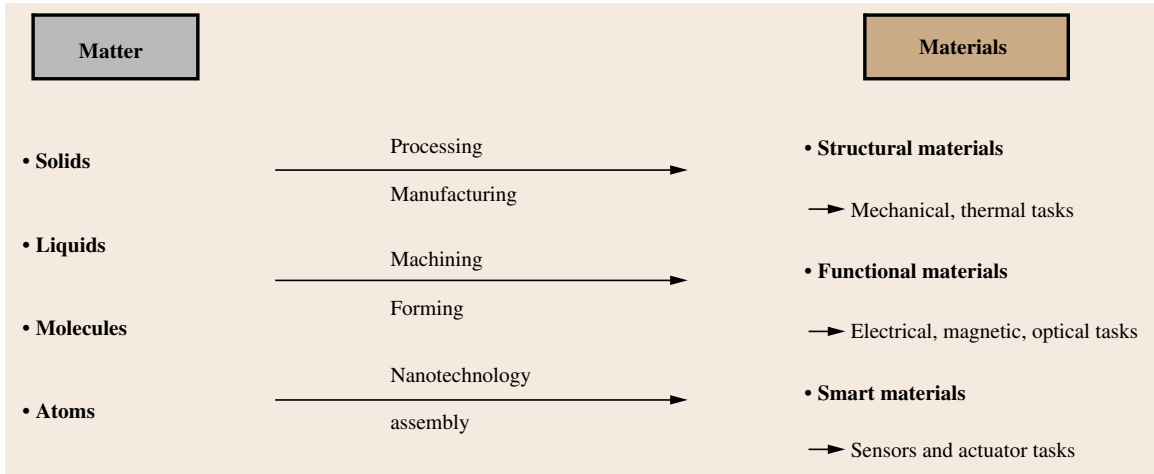


Fig. 1.13 Materials and their characteristics result from the processing of matter

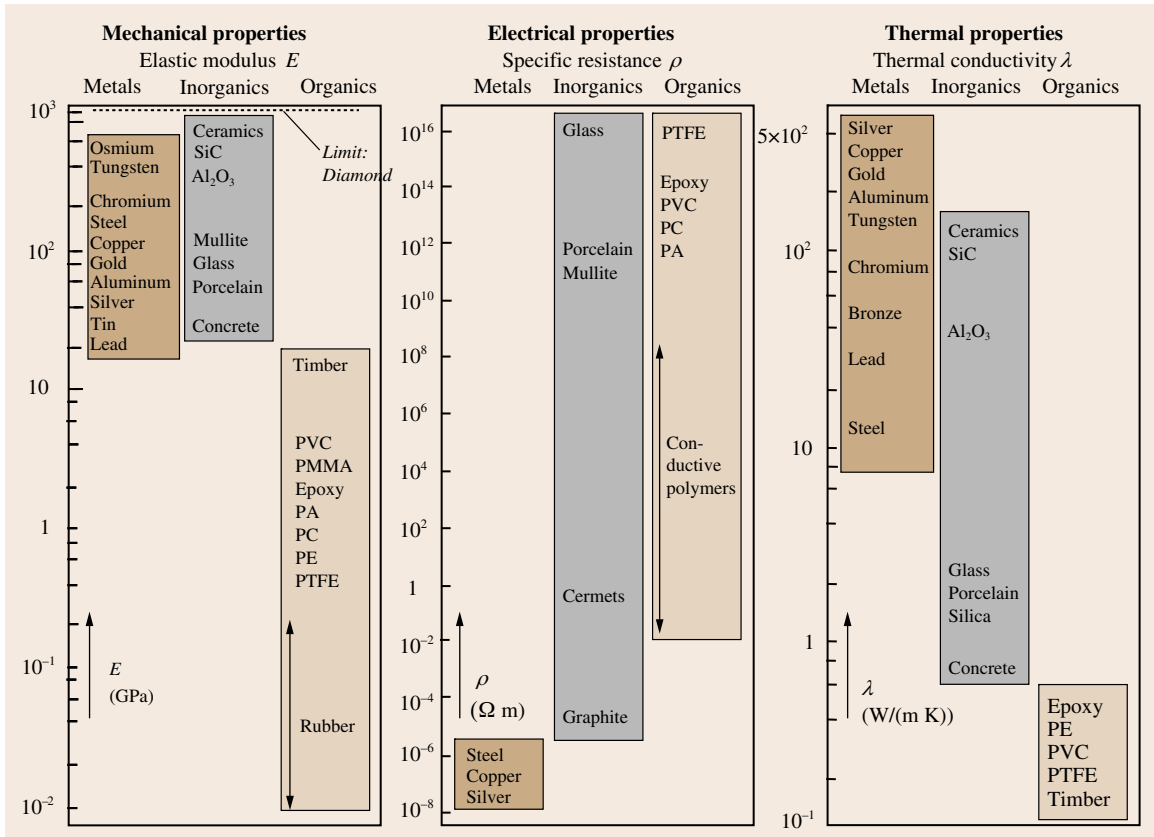


Fig. 1.14 Overview of mechanical, electrical, and thermal materials properties for the basic types of materials (metal, inorganic, or organic)

numerical spectra of some mechanical, electrical, and thermal properties of metals, inorganics, and organics is shown in Fig. 1.14 [1.16].

It must be emphasized that the numerical ranking of materials in Fig. 1.14 is based on *rough, average values* only. Precise data of materials properties require the specification of various influencing factors described above and symbolically expressed as

$$\begin{aligned} &\text{Materials properties data} \\ &= f(\text{composition–microstructure–scale,} \\ &\quad \text{external loading, } \dots) . \end{aligned}$$

1.3.5 Performance of Materials

For the application of materials as constituents of engineered products, performance characteristics such as quality, reliability, and safety are of special importance. This adds performance control and material failure analysis to the tasks of application-oriented materials measurement, testing, and assessment. Because all materials interact with their environment, materials–environment interactions and detrimental influences on

the integrity of materials must also be considered. An overview of the manifold aspects to be recognized in the characterization of materials performance is provided in Fig. 1.15.

The so-called materials cycle depicted schematically in Fig. 1.15 applies to all manmade technical products in all branches of technology and economy. The materials cycle illustrates that materials (accompanied by the necessary flow of energy and information) move in *cycles* through the technoeconomic system: from raw materials to engineering materials and technical products, and finally, after the termination of their task and performance, to deposition or recycling.

The operating conditions and influencing factors for the performance of a material in a given application stem from its structural tasks and functional loads, as shown in the right part of Fig. 1.15. In each application, materials have to fulfil technical functions as constituents of engineered products or parts of technical systems. They have to bear mechanical stresses and are in contact with other solid bodies, aggressive gases, liquids or biological species. In their functional tasks, materials always interact with their environment,

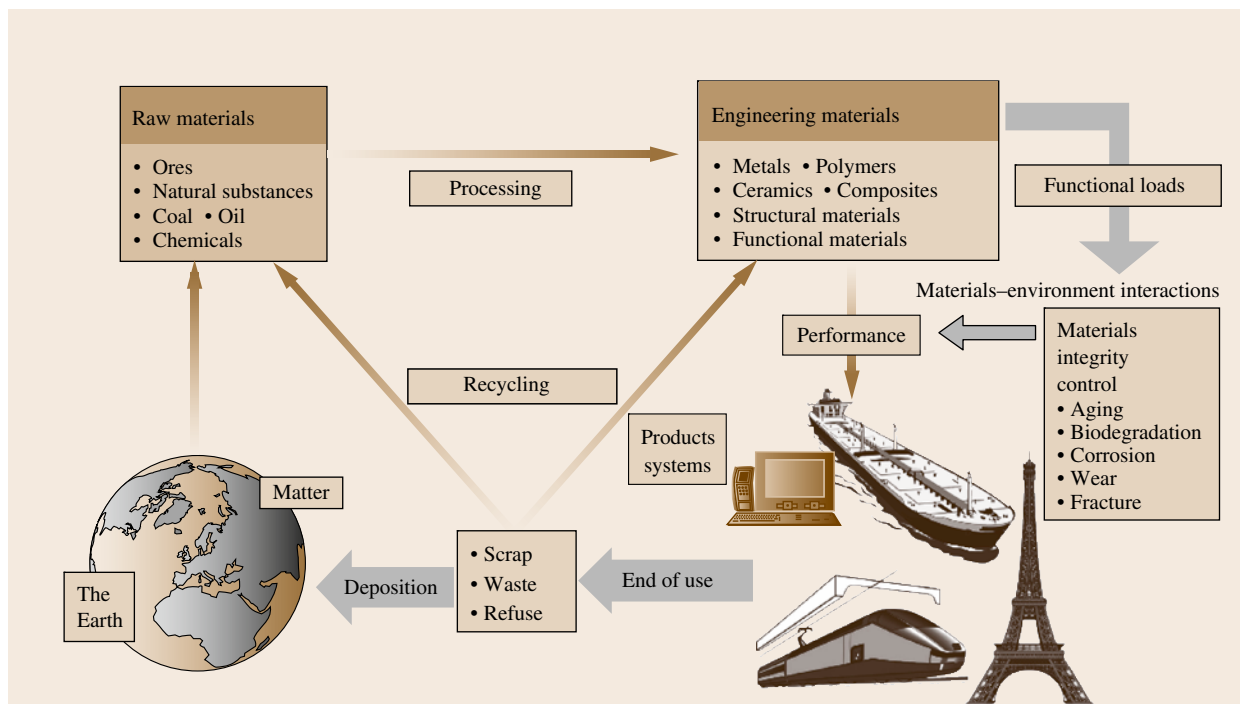


Fig. 1.15 The materials cycle of all products and technical systems

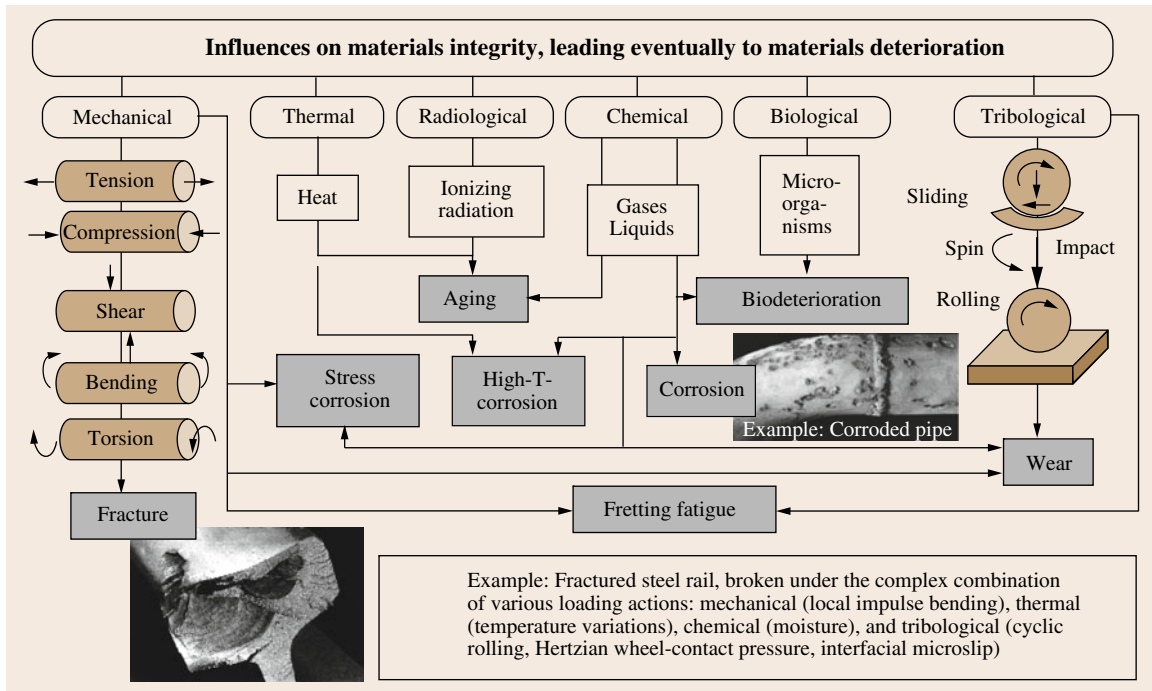


Fig. 1.16 Fundamentals of materials performance characterization: influencing phenomena

so these aspects also have to be recognized to characterize materials performance.

For the proper performance of engineered materials, materials deterioration processes and potential failures, such as materials aging, biodegradation, corrosion, wear, and fracture, must be controlled. Figure 1.16 shows an overview of influences on materials integrity and possible failure modes.

Figure 1.16 illustrates in a generalized, simplified manner that the influences on the integrity of materials, which are essential for their performance, can be categorized in mechanical, thermal, radiological, chemical, biological, and tribological terms. The basic materials deterioration mechanisms, as listed in Fig. 1.15, are aging, biodegradation, corrosion, wear, and fracture.

The deterioration and failure modes illustrated in Fig. 1.16 are of different relevance for the two elementary classes of materials, namely organic materials and inorganic materials (Fig. 1.8). Whereas aging and biodegradation are main deterioration mechanisms for organic materials such as polymers, the various types of corrosion are prevailing failure modes of metallic materials. Wear and fracture are relevant as materials deterioration and failure mechanisms for all types of materials.

1.3.6 Metrology of Materials

The topics of measurement and testing applied to materials (in short *metrology of materials*) concern the accurate and fit-for-purpose determination of the behavior of a material throughout its lifecycle.

Recognizing the need for a sound technical basis for drafting codes of practice and specifications for advanced materials, the governments of countries of the Economic Summit (G7) and the European Commission signed a Memorandum of Understanding in 1982 to establish the Versailles Project on Advanced Materials and Standards (VAMAS, <http://www.vamas.org/>). This project supports international trade by enabling scientific collaboration as a precursor to the drafting of standards. Following a suggestion of VAMAS, the Comité International des Poids et Mesures (CIPM, Fig. 1.6) established an ad hoc Working Group on the Metrology Applicable to the Measurement of Material Properties. The findings and conclusions of the Working Group on Materials Metrology were published in a special issue of *Metrologia* [1.17]. One important finding is the *confidence ring for traceability in materials metrology* (Fig. 1.4).

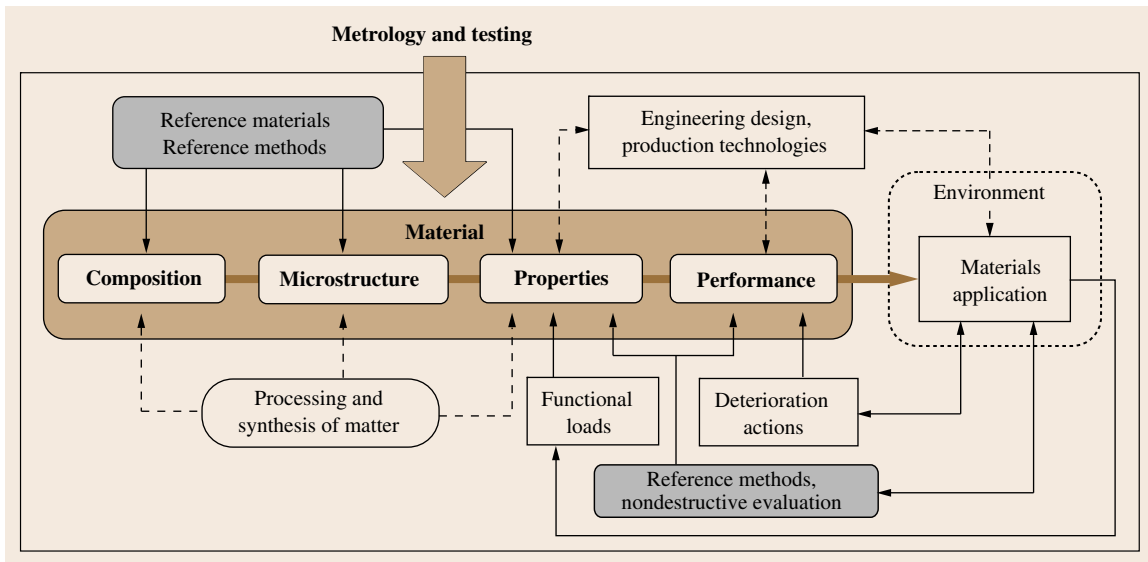


Fig. 1.17 Characteristics of materials to be recognized in metrology and testing

Materials in engineering design have to meet one or more structural, functional (e.g., electrical, optical, magnetic) or decorative purposes. This encompasses materials such as metals, ceramics, and polymers, resulting from the processing and synthesis of matter, based on chemistry, solid-state physics, and surface physics. Whenever a material is being created, developed or produced, the properties or phenomena that the material exhibits are of central concern. Experience shows that the properties and performance associated with a material are intimately related to its composition and structure at all scale levels, and influenced also by the engineering component design and production technologies. The final material, as a constituent of an engineered component, must perform a given task and must do so in an economical and societally acceptable manner. All these aspects are compiled in Fig. 1.17 [1.15].

The basic groups of materials characteristics essentially relevant for materials metrology and testing, as shown in the central part of Fig. 1.17, can be categorized as follows.

- *Intrinsic characteristics* are the material's composition and material's microstructure, described in Sect. 1.3.1. The intrinsic (inherent) materials characteristics result from the processing and syn-

thesis of matter. Metrology and testing to determine these characteristics have to be backed up by suitable reference materials and reference methods, if available.

- *Extrinsic characteristics* are the material's properties and material's performance, outlined in Sects. 1.3.4 and 1.3.5. They are *procedural characteristics* and describe the response of materials and engineered components to functional loads and environmental deterioration of the material's integrity. Metrology and testing to determine these characteristics have to be backed up by suitable reference methods and nondestructive evaluation (NDE).

It follows that, in engineering applications of materials, methods and techniques are needed to characterize intrinsic and extrinsic material attributes, and to consider also structure–property relations. The methods and techniques to characterize composition and microstructure are treated in part B of the handbook. The methods and techniques to characterize properties and performance are treated in parts C and D. The final part E of the handbook presents important modeling and simulation methods that underline measurement procedures that rely on mathematical models to interpret complex experiments or to estimate properties that cannot be measured directly.

References

- 1.1 BIPM: *International Vocabulary of Metrology*, 3rd edn. (BIPM, Paris 2008), available from <http://www.bipm.org/en/publications/guides/>
- 1.2 C. Ehrlich, S. Rasberry: Metrological timelines in traceability, *J. Res. Natl. Inst. Stand. Technol.* **103**, 93–106 (1998)
- 1.3 EUROLAB: Measurement uncertainty revisited: Alternative approaches to uncertainty evaluation, EUROLAB Tech. Rep. No. 1/2007 (EUROLAB, Paris 2007), <http://www.eurolab.org/>
- 1.4 ISO: *Guide to the Expression of Uncertainty in Measurement (GUM-1989)* (International Organization for Standardization, Geneva 1995)
- 1.5 P. Howarth, F. Redgrave: *Metrology – In Short*, 3rd edn. (Euramet, Braunschweig 2008)
- 1.6 ISO Guide 30: *Terms and Definitions of Reference Materials* (International Organization for Standardization, Geneva 1992)
- 1.7 T. Adam: *Guide for the Estimation of Measurement Uncertainty in Testing* (American Association for Laboratory Accreditation (A2LA), Frederick 2002)
- 1.8 EUROLAB: Guide to the evaluation of measurement uncertainty for quantitative tests results, EUROLAB Tech. Rep. No. 1/2006 (EUROLAB, Paris 2006), <http://www.eurolab.org/>
- 1.9 EURACHEM/CITAC Guide: *Quantifying Uncertainty in Analytical Measurement*, 2nd edn. (EURACHEM/CITAC, Lisbon 2000)
- 1.10 B. Magnusson, T. Naykki, H. Hovind, M. Krysell: *Handbook for Calculation of Measurement Uncertainty*, NORDTEST Rep. TR 537 (Nordtest, Espoo 2003)
- 1.11 R. Cook: *Assessment of Uncertainties of Measurement for Calibration and Testing Laboratories* (National Association of Testing Authorities Australia, Rhodes 2002)
- 1.12 J. Ma, I. Karaman: Expanding the repertoire of shape memory alloys, *Science* **327**, 1468–1469 (2010)
- 1.13 S. Bennett, G. Sims: Evolving needs for metrology in material property measurements – The conclusions of the CIPM Working Group on Materials Metrology, *Metrologia* **47**, 1–17 (2010)
- 1.14 M.F. Ashby, Y.J.M. Brechet, D. Cebon, L. Salvo: Selection strategies for materials and processes, *Mater. Des.* **25**, 51–67 (2004)
- 1.15 H. Czichos: Metrology and testing in materials science and engineering, *Measure* **4**, 46–77 (2009)
- 1.16 H. Czichos, B. Skrotzki, F.-G. Simon: Materials. In: *HÜTTE – Das Ingenieurwissen*, 33rd edn., ed. by H. Czichos, M. Hennecke (Springer, Berlin, Heidelberg 2008)
- 1.17 S. Bennett, J. Valdés (Eds.): Materials metrology, Foreword, *Metrologia* **47**(2) (2010)

2. Metrology Principles and Organization

This chapter describes the basic elements of metrology, the system that allows measurements made in different laboratories to be confidently compared. As the aim of this chapter is to give an overview of the whole field, the development of metrology from its roots to the birth of the Metre Convention and metrology in the 21st century is given.

2.1	The Roots and Evolution of Metrology	23	2.5	Regional Metrology Organizations	29
2.2	BIPM: The Birth of the Metre Convention	25	2.6	Metrological Traceability	29
2.3	BIPM: The First 75 Years	26	2.7	Mutual Recognition of NMI Standards: The CIPM MRA	30
2.4	Quantum Standards: A Metrological Revolution	28	2.7.1	The Essential Points of the MRA.....	30
			2.7.2	The Key Comparison Database (KCDB).....	31
			2.7.3	Take Up of the CIPM MRA	31
			2.8	Metrology in the 21st Century	32
			2.8.1	Industrial Challenges	32
			2.8.2	Chemistry, Pharmacy, and Medicine	33
			2.8.3	Environment, Public Services, and Infrastructures.....	34
			2.9	The SI System and New Science	34
			References	37	

2.1 The Roots and Evolution of Metrology

From the earliest times it has been important to compare things through measurements. This had much to do with fair exchange, barter, or trade between communities, and simple weights such as the stone or measures such as the cubit were common. At this level, parts of the body such as hands and arms were adequate for most needs. Initially, wooden length bars were easy to compare and weights could be weighed against each other. Various forms of balance were commonplace in early history and in religion. Egyptian tomb paintings show the Egyptian god Anubis weighing the soul of the dead against an ostrich feather – the sign of purity (Fig. 2.1). Noah's Ark was, so the Book of Genesis reports, 300 cubits long by 50 cubits wide and 30 cubits high. No one really knows why it was important to record such details, but the Bible, as just one example, is littered with metrological references, and the symbolism of metrology was part of early culture and art.

A steady progression from basic artifacts to naturally occurring reference standards has been part of the entire history of metrology. Metrologists are familiar with the use of the carob seed in early Mediterranean

civilizations as a natural reference for length and for weight and hence volume. The Greeks were early traders who paid attention to metrology, and they were known to keep copies of the weights and measures of the countries with which they traded.



Fig. 2.1 Anubis



Fig. 2.2 Winchester yard



Fig. 2.3 Imperial length standards, Trafalgar Square, London

The Magna Carta of England set out a framework for a citizen's rights and established *one measure throughout the land*. Kings and queens took interest in national weights and measures; Fig. 2.2 shows the Winchester yard, the bronze rod that was the British standard from 1497 to the end of the 16th century. The queen's mark we see here is that of Elizabeth the First (1558–1603). In those days, the acre was widely used as a measurement, derived from the area that a team of oxen could plow in a day. Plowing an acre meant that you had to walk 66 furlongs, a linear dimension measured in rods.

The problem with many length measurements was that the standard was made of the commonly available metals brass or bronze, which have a fairly large coefficient of expansion. Iron or steel measures were not developed for a couple of centuries. Brass and bronze therefore dominated the length reference business until the early 19th century, by which time metallurgy had developed enough – though it was still something of a black art – for new, lower-expansion metals to be used and reference temperatures quoted. The UK imperial

references were introduced in 1854 and reproduced in Trafalgar Square in the center of London (Fig. 2.3), and the British Empire's domination of international commerce saw the British measurement system adopted in many of its colonies.

In the mid 18th century, Britain and France compared their national measurement standards and realized that they differed by a few percent for the same unit. Although the British system was reasonably consistent throughout the country, the French found that differences of up to 50% were common in length measurement within France. The ensuing technical debate was the start of what we now accept as the metric system. France led the way, and even in the middle of the French Revolution the Academy of Science was asked to *deduce an invariable standard for all the measures and all the weights*. The important word was *invariable*. There were two options available for the standard of length: the second's pendulum and the length of the Earth's meridian. The obvious weakness of the pendulum approach was that its period depended on the local acceleration due to gravity. The academy therefore chose to measure a portion of the Earth's circumference and relate it to the official French meter. Delambre and Méchain, who were entrusted with a survey of the meridian between Dunkirk and Barcelona, created the famous *Mètre des Archives*, a platinum end standard.

The international nature of measurement was driven, just like that of the Greek traders of nearly 2000 years before, by the need for interoperability in trade and advances in engineering measurement. The displays of brilliant engineering at the Great Exhibitions in London and Paris in the 19th century largely rested on the ability to measure well. The British Victorian engineer Joseph Whitworth coined the famous phrase *you can only make as well as you can measure* and pioneered accurate screw threads. He immediately saw the potential of end standard gages rather than line standards where the reference length was defined by a scratch on the surface of a bar. The difficulty, he realized, with line standards was that optical microscopes were not then good enough to compare measurements of line standards well enough for the best precision engineering. Whitworth was determined to make the world's best measuring machine. He constructed the quite remarkable *millionth machine* based on the principle that touch was better than sight for precision measurement. It appears that the machine had a *feel* of about 1/10 of a thousandth of an inch. Another interesting metrological trend at the 1851 Great Exhibition was military: the word *calibrate* comes from the need to control the caliber of guns.

At the turn of the 19th century, many of the industrialized countries had set up national metrology institutes, generally based on the model established in Germany with the Physikalisch Technische Reichsanstalt, which was founded in 1887. The economic benefits of such a national institute were immediately recognized, and as a result, scientific and industrial organizations in a number of industrialized countries began pressing their governments to make similar investments. In the UK, the British Association for the Advancement of Science reported that, without a national laboratory to act as a focus for metrology, the country's industrial competitiveness would be weakened. The cause was taken up more widely, and the UK set up the National Physical Laboratory (NPL) in 1900. The USA created the National Bureau of Standards in 1901 as a result of similar industrial pressure. The major national metrology institutes (NMIs), however, had a dual role. In general, they were the main focus for national research programs on applied physics and engineering. Their scientific role in the development of units – what became the International System of Units, the SI – began to challenge the role of the universities in the measurement of fundamental constants. This was especially true after the development of quantum physics in the 1920s and 1930s. Most early NMIs therefore began with two major elements to their mission

- a requirement to satisfy industrial needs for accurate measurements, through standardization and verification of instruments; and
- determination of physical constants so as to improve and develop the SI system.

The new industries which emerged after the First World War made huge demands on metrology and, together with mass production and the beginnings of multinational production sites, raised new challenges which brought NMIs into direct contact with companies, so causing a close link to develop between them. At that time, and even up to the mid 1960s, nearly all calibrations and measurements that were necessary for industrial use were made in the NMIs, and in the gage rooms of the major companies, as were most measurements in engineering metrology. The industries of the 1920s, however, developed a need for electrical and optical measurements, so NMIs expanded their coverage and their technical abilities.

The story since then is one of steady technical expansion until after the Second World War. In the 1950s, though, there was renewed interest in a broader applied focus for many NMIs so as to develop civilian applications for much of the declassified military technology. The squeeze on public budgets in the 1970s and 1980s saw a return to core metrology, and many other institutions, public and private, took on the responsibility for developing many of the technologies, which had been initially fostered at NMIs. The NMIs adjusted to their new roles. Many restructured and found new, often improved, ways of serving industrial needs. This recreation of the NMI role was also shared by most governments, which increasingly saw them as tools of industrial policy with a mission to stimulate industrial competitiveness and, at the end of the 20th century, to reduce technical barriers to world trade.

2.2 BIPM: The Birth of the Metre Convention

A brief overview of the Metre Convention has already been given in Sect. 1.2.1. In the following, the historical development will be described.

During the 1851 Great Exhibition and the 1860 meeting of the British Association for the Advancement of Science (BAAS), a number of scientists and engineers met to develop the case for a single system of units based on the metric system. This built on the early initiative of Gauss to use the 1799 meter and kilogram in the Archives de la République, Paris and the second, as defined in astronomy, to create a coherent set of units for the physical sciences. In 1874, the three-dimensional CGS system, based on the centimeter, gram, and second, was launched by the BAAS.

However, the size of the electrical units in the CGS system were not particularly convenient and, in the 1880s, the BAAS and the International Electrotechnical Commission (IEC) approved a set of practical electrical units based on the ohm, the ampere, and the volt. Parallel to this attention to the units, a number of governments set up what was then called the Committee for Weights and Money, which in turn led to the 1870 meeting of the Commission Internationale du Mètre. Twenty-six countries accepted the invitation of the French Government to attend; however, only 16 were able to come as the Franco-Prussian war intervened, so the full committee did not meet until 1872. The result was the Metre Convention and the creation of the Bureau International



Fig. 2.4 Bureau International des Poids et Mesures, Sèvres

des Poids et Mesures (BIPM, International Bureau of Weights and Measures), in the old Pavillon de Breteuil at Sèvres (Fig. 2.4), as a permanent scientific agency supported by the signatories to the convention. As this required the support of governments at the highest level, the Metre Convention was not finally signed until 20 May 1875.

The BIPM's role was to *establish new metric standards, conserve the international prototypes* (then the meter and the kilogram) and *to carry out the comparisons necessary to assure the uniformity of measures throughout the world*. As an intergovernmental, diplomatic treaty organization, the BIPM was placed under the authority of the General Conference on Weights and Measures (CGPM). A committee of 18 scientific experts, the International Committee for Weights and Measures (CIPM), now supervises the running of the BIPM. The aim of the CGPM and the CIPM was, and still is, to assure the *international unification and development of the metric system*. The CGPM now meets every 4 years to review progress, receive reports from the CIPM on the running of the BIPM, and establish the operating budget of the BIPM, whereas the CIPM meets annually to supervise the BIPM's work.

When it was set up, the staff of the BIPM consisted of a director, two assistants, and the necessary number of employees. In essence, then, a handful of

people began to prepare and disseminate copies of the international prototypes of the meter and the kilogram to member states. About 30 copies of the meter and 40 copies of the prototype kilogram were distributed to member states by ballot. Once this was done, some thought that the job of the BIPM would simply be that of periodically checking (in the jargon, verifying) the national copies of these standards. This was a short-lived vision, as the early investigations immediately showed the importance of reliably measuring a range of quantities that influenced the performance of the international prototypes and their copies. As a result, a number of studies and projects were launched which dealt with the measurement of temperature, density, pressure, and a number of related quantities. The BIPM immediately became a research body, although this was not recognized formally until 1921.

Returning to the development of the SI, one of the early decisions of the CIPM was to modify the CGS system to base measurements on the meter, kilogram, and second – the MKS system. In 1901, Giorgi showed that it was possible to combine the MKS system with the practical electrical units to form a coherent four-dimensional system by adding an electrical unit and rewriting some of the equations of electromagnetism in the so-called rationalized form. In 1946, the CIPM approved a system based on the meter, kilogram, second, and ampere – the MKSA system. Recognizing the ampere as a base unit of the metric system in 1948, and adding, in 1954, units for thermodynamic temperature (the kelvin and luminous intensity (the candela), the 11th CGPM in 1960 coined the name *Système internationale d'Unités*, the SI. At the 14th CGPM in 1971, the present-day SI system was completed by adding the mole as the base unit for the amount of substance, bringing the total number of base units to seven. Using these base units, a hierarchy of derived units and quantities of the SI have been developed for most, if not all, measurements needed in today's society. A substantial treatment of the SI is to be found in the 8th edition of the SI brochure published by the BIPM [2.1].

2.3 BIPM: The First 75 Years

After its intervention in the initial development of the SI, the BIPM continued to develop fundamental metrological techniques in mass and length measurement but soon had to react to the metrological implications of

major developments in atomic physics and interferometry. In the early 1920s, Albert Michelson came to work at the BIPM and built an eponymous interferometer to measure the meter in terms of light from

the cadmium red line – an instrument which, although modified, did sterling service until the 1980s. In temperature measurement, the old hydrogen thermometer scale was replaced with a thermodynamic-based scale and a number of fixed points. After great debate, electrical standards were added to the work of the BIPM in the 1920s with the first international comparisons of resistance and voltage. In 1929, an electrical laboratory was added, and photometry arrived in 1939.

In these early days, it was clear that the BIPM needed to find a way of consulting and collaborating with the experts in the world's NMIs. The solution adopted is one which still exists and flourishes today. The best way of working was in face-to-face meetings, so the concept of a consultative committee to the CIPM was born. Members of the committee were drawn from experts active in the world's NMIs and met to deal with matters concerning the definitions of units and the techniques of comparison and calibration. The consultative committees are usually chaired by a member of the CIPM. Much information was shared, although for obvious logistical reasons, the meetings were not too frequent. Over the years, the need for new consultative committees grew in reaction to the expansion of metrology, and now 10 consultative committees exist, with over 25 working groups.

The CIPM is rightly cautious about establishing a new committee, but proposals for new ones are considered from time to time, usually after an initial survey through a working group. In the last 10 years, joint committees have been created to tackle issues such as the

international approach to the estimation of measurement uncertainties or to the establishment of a common vocabulary for metrology. Most of these joint committees bring the BIPM together with international or intergovernmental bodies such as the International Organization for Standardization (ISO), the International Laboratory Accreditation Cooperation (ILAC), and the IEC. As the work of the Metre Convention moves into areas other than its traditional activities in physics and engineering, joint committees are an excellent way of bringing the BIPM together with other bodies that bring specialist expertise – an example being the joint committee for laboratory medicine, established recently with the International Federation of Clinical Chemists and the ILAC.

The introduction of ionizing radiation standards to the work of the BIPM came when Marie Curie deposited her first radium standard at the BIPM in 1913. As a result of pressure, largely from the USSR delegation to the CGPM, the CIPM took the decision to deal with metrology in ionizing radiation.

In the mid 1960s, and at the time of the expansion into ionizing radiation, programs on laser length measurement were also started. These contributed greatly to the redefinition of the meter in 1983. The BIPM also acted as the world reference center for laser wavelength or frequency comparisons in much the same way as it did for physical artifact-based standards. In the meantime, however, the meter bar had already been replaced, in 1960, by an interferometric-based definition using optical radiation from a krypton lamp.

Table 2.1 List of consultative committees with dates of formation

Names of consultative committees and the date of their formation

(Names of consultative committees have changed as they have gained new responsibilities; the current name is cited)

Consultative Committee for Electricity and Magnetism, CCEM (1997, but created in 1927)
Consultative Committee for Photometry and Radiometry, CCPR (1971 but created in 1933)
Consultative Committee for Thermometry, CCT (1937)
Consultative Committee for Length, CCL (1997 but created in 1952)
Consultative Committee for Time and Frequency, CCTF (1997, but created 1956)
Consultative Committee for Ionizing Radiation, CCRI (1997, but created in 1958)
Consultative Committee for Units, CCU (1964, but replacing a similar commission created in 1954)
Consultative Committee for Mass and Related Quantities, CCM (1980)
Consultative Committee for Amount of Substance and Metrology in Chemistry, CCQM (1993)
Consultative Committee for Acoustics, Ultrasound, and Vibration, CCAUV (1999)

2.4 Quantum Standards: A Metrological Revolution

Technology did not stand still, and in reaction to the developments and metrological applications of superconductivity, important projects on the Josephson, quantum Hall, and capacitance standards were launched in the late 1980s and 1990s. The BIPM played a key role in establishing worldwide confidence in the performance of these new devices through an intense program of comparisons which revealed many of the systematic sources of error and found solutions to them. The emergence of these and other quantum-based standards, however, was an important and highly significant development. In retrospect, these were one of the drivers for change in the way in which world metrology organizes itself and had implications nationally as well as internationally.

The major technical change was, in essence, a belief that standards based on quantum phenomena were the same the world over. Their introduction sometimes made it unnecessary for a single, or a small number of, reference standards to be held at the BIPM or in a few of the well-established and experienced NMIs. Quantum-based standards were, in reality, available to all and, with care, could be operated outside the NMIs at very high levels of accuracy.

There were two consequences. Firstly, that the newer NMIs that wanted to invest in quantum-based standards needed to work with experienced metrologists in existing NMIs in order to develop their skills as rapidly as possible. Many of the older NMIs, therefore, became adept at training and providing the necessary experience for newer metrologists. The second consequence was an increased pressure for comparisons of standards, as the ever-conservative metrology community sought to develop confidence in new NMIs as well as in the quantum-based standards. These included frequency-stabilized lasers, superconducting voltage and resistance standards, cryogenic radiometers (for measurements related to the candela), atomic clocks (for the second), and a range of secondary standards.

Apart from its responsibility to maintain the international prototype kilogram (Fig. 2.5), which remains the last artifact-based unit of the SI, the BIPM was therefore no longer always the sole repository of an international primary reference standard. However there were, and still are, a number of unique reference facilities at the BIPM for secondary standards and quantities of the SI. Staff numbers had also leveled off at about 70.

If it was going to maintain its original mission of a scientifically based organization with responsibility

for coordinating world metrology, the BIPM recognized that it needed to discharge particular aspects of its treaty obligation in a different way. It also saw the increased value of developing the links needed to establish collaboration at the international and intergovernmental level. In addition, the staff had the responsibility to provide the secretariat to the 10 consultative committees of the CIPM as well as an increasing number of working groups. The last 10 years of the 20th century, therefore, saw the start of a significant change in the BIPM's way of working. During this period, it was also faced with the need to develop a world metrology infrastructure in new areas such as the environment, chemistry, medicine, and food. The shift away from physics and engineering was possible, fortunately, as a result of the changing way in which the SI units could be realized, particularly through the quantum-based standards. Other pressures for an increase in the BIPM's coordination role resulted from the increasingly intensive program of comparisons brought about by the launch of the CIPM's mutual recognition arrangement in the 1990s.

The most recent consequence of these trends was that the CIPM decided that the photometry and radiometry section would close due to the need to operate within internationally agreed budgets, ending nearly

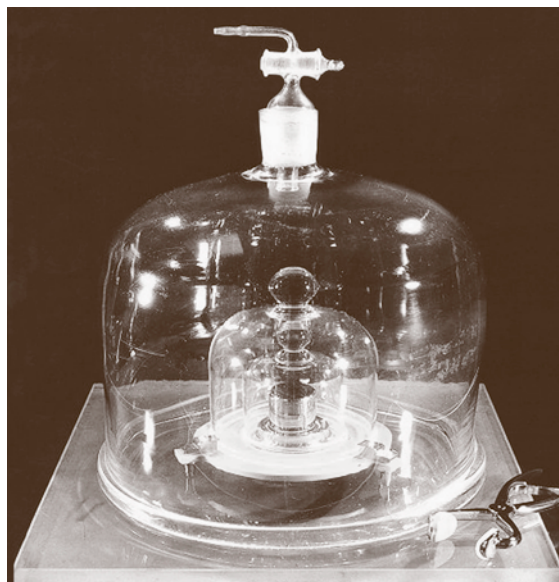


Fig. 2.5 International prototype kilogram (courtesy of BIPM)

70 years of scientific activity at the BIPM. Additional savings would also be made by restricting the work of the laser and length group to a less ambitious program.

A small, 130-year-old institution was therefore in the process of reinventing itself to take on and develop a changed but nevertheless unique niche role. This was still based on technical capabilities and laboratory work but was one which had to meet the changing, and expanding, requirements of its member states in a different

way. Much more also needed to be done as the benefits of precise, traceable measurement became seen as important in a number of the new disciplines for metrology. This change of emphasis was endorsed at the 2003 General Conference on Weights and Measures as a new 4 year work program (2005–2008) was agreed, as well as the first real-terms budget increase since the increase agreed in the mid 1960s which then financed the expansion into ionizing radiation.

2.5 Regional Metrology Organizations

The growth of the number of NMIs and the emergence of world economic groupings such as the Asia–Pacific Economic Cooperation and the European Union mean that regional metrological groupings have become a useful way of addressing specific regional needs and can act as a mutual help or support network. The first such group was probably in Europe, where an organization now named EURAMET emerged from a loose collaboration of NMIs based on the Western European Metrology Club. There are now five regional metrology organizations (RMOs): the Asian–Pacific Metrology Program (APMP) with perhaps the largest geographical coverage from India in the west to New Zealand in the east and extending into Asia, the Euro–Asian Cooperation in Metrology amongst the Central European Countries (COOMET), the European Association of National Metrology Institutes (EURAMET), the Southern African Development Community Cooperation in Measurement Traceability (SADC MET), and Sistema Interamericano de Metrología (SIM, Inter-American

Metrology System) which covers Southern, Central, and North America). The RMOs play a vital role in encouraging coherence within their region and between regions; without their help, the Metre Convention would be far more difficult to administer and its outreach to nonmembers – who may, however, be members of an RMO – would be more difficult.

Traditionally, NMIs have served their own national customers. It is only within the last 10 years that regional metrology organizations have started to become more than informal associations of national laboratories and have begun to develop strategies for mutual dependence and resource sharing, driven by concerns about budgets and the high cost of capital facilities. The sharing of resources is still, however, a relatively small proportion of all collaborations between NMIs, most of which are still at the research level. It is, of course, no coincidence that RMOs are based on economic or trading blocs and that these groupings are increasingly concerned with free trade within and between them.

2.6 Metrological Traceability

Traceability of measurement has been a core concern of the Metre Convention from its inception, as has been emphasized already in Sect. 2.1. Initially, a measurement is always made in relation to a more accurate reference, and these references are themselves calibrated or measured against an even more accurate reference standard. The chain follows the same pattern until one reaches the national standards. (For technical details see Chap. 3.)

The NMIs' job was to make sure that the national standards were traceable to the SI and were accurate enough to meet national needs. As NMIs themselves stopped doing all but the highest accuracy measurements and as accredited laboratories, usually

in the commercial sector, took on the more routine tasks, the concept of a national hierarchy of traceable measurements became commonplace, frequently called a national measurement system. In general, the technical capabilities of the intermediate laboratories are assured by their accreditation to the international documentary standards ISO/IEC 17025 by a national accreditation body, usually a member of the International Laboratory Accreditation Cooperation (ILAC) (Sect. 1.1.3). At the top of the traceability system, measurements were relatively few in number and had the lowest uncertainty. Progressing down the traceability chain introduced a greater level of uncertainty of measurement, and generally speaking, a larger number

of measurements are involved. Traceability itself also needed to be defined. The *international vocabulary of metrology (VIM)* defines traceability as [2.2]:

The property of a measurement result relating the result to a stated metrological reference through an unbroken chain of calibrations or comparisons each contributing to the stated uncertainty.

The important emphasis is on uncertainty of measurement (for a detailed treatment of measurement uncertainty, the reader is referred to the *Guide to the expression of uncertainty in measurement (GUM)* [2.3]) and the need for the continuous unbroken chain of measurement. Comparisons of standards or references are a common way of demonstrating confidence in the measurement processes and in the reference standards held either in the **NMIs** or in accredited laboratories. The national accreditation body usually takes care of these comparisons at working levels, sometimes called interlaboratory comparisons (**ILCs**) or proficiency testing (Sect. 3.6).

At the **NMI** level, the framework of the **BIPM** and the **CIPM**'s consultative committees (**CCs**) took care of the highest level comparisons. However, the increased relevance of traceable measurement to trade,

and the need for demonstrable equivalence of the national standards held at **NMIs**, and to which national measurements were traceable, took a major turn in the mid 1990s. This event was stimulated by the need, from the accreditation community as much as from regulators and trade bodies, to know just how well the **NMI** standards agreed with each other. Unlike much of the work of the consultative committees, this involved **NMIs** of all states of maturity working at all levels of accuracy. The task of comparing each and every standard was too great and too complex for the **CC** network, so a novel approach needed to be adopted. In addition, it became increasingly clear that the important concept was one of measurements traceable to the **SI** through the standards realized and maintained at **NMIs**, rather than to the **NMI**-based standards themselves. Not to develop and work with this concept would run the risk of creating technical barriers to trade (**TBTs**) if measurements in a certain country were legally required to be traceable to the **NMI** standards or if measurements made elsewhere were not recognized. The World Trade Organization was turning its attention towards the need for technical measurements to be accepted worldwide and was setting challenging targets for the reduction of **TBTs**. The metrology community needed to react.

2.7 Mutual Recognition of NMI Standards: The CIPM MRA

The result was the creation, by the **CIPM**, of a mutual recognition arrangement (**MRA**) for the recognition and acceptance of **NMI** calibration and test certificates. The **CIPM MRA** is one of the key events of the last few years, and one which may be as significant as the Metre Convention itself. The **CIPM MRA** has a direct impact on the reduction of technical barriers to trade and to the globalization of world business. The **CIPM MRA** was launched at a meeting of **NMIs** from member states of the Metre Convention held in Paris on 14 October 1999, at which the directors of the national metrology institutes of 38 member states of the convention and representatives of two international organizations became the first signatories.

2.7.1 The Essential Points of the MRA

The objectives of the **CIPM MRA** are

- to establish the degree of equivalence of national measurement standards maintained by **NMIs**,

- to provide for the mutual recognition of calibration and measurement certificates issued by **NMIs**, and
- thereby to provide governments and other parties with a secure technical foundation for wider agreements related to international trade, commerce, and regulatory affairs.

The procedure through which an **NMI**, or any other recognized signatory, joins the **MRA** is based on the need to demonstrate their technical competence, and to convince other signatories of their performance claims. In essence, these performance claims are the uncertainties associated with the routine calibration services which are offered to customers and which are traceable to the **SI**. Initial claims, called calibration and measurement capabilities (**CMCs**), are first made by the laboratory concerned. They are then first reviewed by technical experts from the local regional metrology organization and, subsequently, by other **RMOs**. The technical evidence for the **CMC** claims is generally based on the institute's performance in a number of comparisons

carried out and managed by the relevant CIPM consultative committees (CCs) or by the RMO. This apparently complex arrangement is needed because it would be technically, financially or organizationally impossible for each participant to compare its own SI standards with all others. The CIPM places particular importance on two types of comparisons

- international comparisons of measurements, known as CIPM key comparisons and organized by the CCs, which generally involve only those laboratories which perform at the highest level. The subject of a key comparison is chosen carefully by the CC to be representative of the ability of the laboratory to make a range of related measurements;
- key or supplementary international comparisons of measurements, usually organized by the RMOs and which include some of the laboratories which took part in the CIPM comparisons as well as other laboratories from the RMO. RMO key comparisons are in the same technical area as the CIPM comparison, whereas supplementary comparisons are usually carried out to meet a special regional need.

Using this arrangement, we can establish links between all participants to provide the technical basis for the comparability of the SI standards at each NMI. Reports of all the comparisons are published in the key comparison database maintained by the BIPM on its website (www.bipm.org).

These comparisons differ from those traditionally carried out by the CCs, which were largely for scientific reasons and which established the dependence of the SI realizations on the effects which contributed to the uncertainty of the realization. In CIPM and RMO key or supplementary comparisons, however, each participant carries out the measurements without knowing the results of others until the comparison has been completed. They provide, therefore, an independent assessment of performance. The CIPM, however, took the view that comparisons are made at a specific moment in time and so required participating NMIs to install a quality system which could help demonstrate confidence in the continued competence of participants in between comparisons. All participants have chosen to use the ISO/IEC 17025 standard and have the option of a third-party accreditation by an ILAC member or a self-declaration together with appropriate peer reviews.

The outcome of this process is that it gives NMIs the confidence to recognize the results of key and supplementary comparisons as stated in the database and

therefore to accept the calibration and measurement capabilities of other participating NMIs.

When drawing up its MRA, the CIPM was acutely aware that its very existence, and the mutual acceptance of test and calibration certificates between its members, might be seen as a technical barrier to trade in itself. The concept of associate members of the CGPM was therefore developed. An associate has, in general, the right to take part in the CIPM MRA but not to benefit from the full range of BIPM services and activities, which are restricted to convention members. Associate status is increasingly popular with developing countries, as it helps them gain recognition worldwide but does not commit them to the additional expense of convention membership, which may be less appropriate for them at their stage of development.

2.7.2 The Key Comparison Database (KCDB)

The key comparison database, referred to in the MRA and introduced in Sect. 1.2.2 (Table 1.2), is available on the BIPM website (www.bipm.org). The content of the database is evolving rapidly. Appendix A lists signatories, and appendix B contains details of the set of key comparisons together with the results from those that have been completed. The database will also contain a list of those old comparisons selected by the consultative committees that are to be used on a provisional basis. Appendix C contains the calibration and measurement capabilities of the NMIs that have already been declared and reviewed within their own regional metrology organization (RMO) as well as those other RMOs that support the MRA.

2.7.3 Take Up of the CIPM MRA

The KCDB data is, at the moment, largely of interest to metrologists. However, a number of NMIs are keen to see it taken up more widely, and there are several examples of references to the CIPM MRA in regulation. This campaign is at an early stage; an EU–USA trade agreement cites the CIPM MRA as providing an appropriate technical basis for acceptance of measurements and tests, and the USA's National Institute of Standards and Technology (NIST) has opened up a discussion with the Federal Aviation Authority (FAA) and other regulators as to the way in which they can use KCDB data to help the FAA accept the results of tests and certificates which have been issued outside the USA.

There is a range of additional benefits and consequences of the CIPM MRA. Firstly, anyone can use

the **KCDB** to look for themselves at the validated technical capability of any **NMI**. As a result, they can, with full confidence, choose to use its calibration services rather than those of their national laboratory and have the results of these services accepted worldwide. They can also use the **MRA** database to search for **NMIs** that can satisfy their needs if they are not available nationally. This easy access and the widespread and cheap availability of information may well drive a globalization of the calibration service market and will enable users to choose the supplier that best meets their needs. As the **MRA** is implemented, it will be a real test of market economics. Secondly, there is the issue of rapid turnarounds. Companies that have to send their standards away for calibration do not

have them available for in-house use. This can lead to costly duplication if continuity of an internal service is essential, or to a tendency to increase the calibration interval if calibrations are expensive. **NMIs** therefore have to concentrate increasingly on reducing turnaround times, or providing better customer information through calibration management systems. Some calibrations will always require reasonable periods of time away from the workplace because of the need for stability or because **NMIs** can only (through their own resource limitations) provide the service at certain times. This market sensitivity is now fast becoming built into service delivery and is, in some cases, more important to a customer than the actual price of a calibration.

2.8 Metrology in the 21st Century

In concluding this review of the work of the Metre Convention, it seems appropriate to take a glance at what the future may have in store for world metrology and, in particular, at the new industries and technologies which require new measurements.

2.8.1 Industrial Challenges

The success of the Metre Convention and, in particular, the recognized technical and economic benefits of the **CIPM MRA** – one estimate by the consulting company **KPMP** puts its potential impact on the reduction of **TBTs** at some €4 billion (see the **BIPM** website) – have attracted the interest and attention of new communities of users.

New Technologies

A challenge which tackles the needs of new industries and exploits new technologies is to enhance our ability to measure the large, the small, the fast, and the slow. Microelectronics, telecommunications, and the study and characterization of surfaces and thin films will benefit. Many of these trends are regularly analyzed by **NMIs** as they formulate their technical programs, and a summary can be found in the recent report to the 22nd **CGPM** by its secretary Dr. Robert Kaarls, entitled *Evolving Needs for Metrology in Trade, Industry, and Society and the Role of the BIPM*. The report can be found on the **BIPM** website (<http://www.bipm.org/>).

Materials Characterization

Of particular relevance to the general topic of this handbook, there has been an interest in a worldwide framework for traceable measurement of material characteristics. The potential need is for validated, accepted reference data to characterize materials with respect to their properties (see Part C) and their performance (see Part D). To a rather limited extent, some properties are already covered in a metrological sense (hardness, some thermophysical or optical properties, for example), but the vast bulk of materials characteristics, which are not intrinsic properties but system-dependent attributes (Sect. 1.3.6), remain outside the work of the convention. Therefore, relatively few **NMIs** have been active in materials metrology, but a group is meeting to decide whether to make proposals for a new sphere of Metre Convention activity. A report recommending action was presented to the **CIPM** in 2004 and will be followed up in a number of actions launched by the committee (Sect. 1.3.6).

Product Appearance

Another challenge is the focus by manufacturers on the design or appearance of a product, which differentiates it in the eyes of the consumer from those of their competitors. These rather subjective attributes of a product are starting to demand an objective basis for comparison. Appearance measurement of quantities such as gloss, or the need to measure the best conditions in which to display products under different lighting or pre-

sensation media (such as a TV tube, flat-panel display, or a printed photograph), or the response for different types of sounds combine hard physical or chemical measurements with the subjective and varying responses of, say, the human eye or ear. However, these are precisely the quantities that a consumer uses to judge textiles, combinations of colored products, or the relative sound reproduction of music systems. They are therefore also the selling points of the marketer and innovator. How can the consumer choose and differentiate? How can they compare different claims? Semisubjective measurements such as these are moving away from the carefully controlled conditions of the laboratory into the high street and are presenting exciting new challenges.

NMIs are already becoming familiar with the needs of their users for color or acoustical measurement services, which require a degree of modeling of the user response and differing reactions depending on environmental conditions such as ambient lighting or noise background. The fascination of this area is that it combines objective metrology with physiological measurements and the inherent variability of the human eye or ear, or the ways in which our brains process optical or auditory stimuli.

Real-Time In-Process Measurements

The industries of today and tomorrow are starting to erode one of the century-old metrology practices within which the user must bring their own instruments and standards to the NMI for calibration. Some of this relates to the optimization of industrial processes, where far more accurate, real-time, in-process measurements are made. The economics of huge production processes demand just-in-time manufacture, active data management, and sophisticated process modeling. By reliably identifying where subelements of a process are behaving poorly, plant engineers can take rapid remedial action and so identify trouble spots quickly. However, actual real-time systems measurements are difficult, and it is only recently that some NMIs have begun to address the concept of an industrial measurement system. New business areas such as this will require NMIs to work differently, if for no other reason than because their customers work differently and they need to meet the customers' requirements. Remote telemetry, data fusion, and new sensor techniques are becoming linked with process modeling, numerical algorithms, and approximations so that accurate measurement can be put, precisely, at the point of measurement. These users are already adopting the systems approach, and some NMIs are starting to respond to this challenge.

Quantum-Based Standards

There is a trend towards quantum-based standards in industry, as already highlighted in this chapter. This is a result of the work of innovative instrument companies which now produce, for example, stabilized lasers, Josephson-junction voltage standards, and atomic clocks for the mass market. The availability of such highly accurate standards in industry is itself testimony to companies' relentless quest for improved product performance and quality. However, without care and experience, it is all too easy to get the wrong answer. Users are advised to undertake comparisons and to cooperate closely with their NMIs to make sure that these instruments are operated with all the proper checks and with attention to best practice so that they may, reliably, bring increased accuracy closer to the end user [2.4]. Industry presses NMIs – rightly so – for better performance, and in some areas of real practical need, NMI measurement capabilities are still rather close to what industry requires. It is, perhaps, in these highly competitive and market-driven areas that the key comparisons and statements of equivalence that are part of the CIPM MRA will prove their worth. Companies specify the performance of their products carefully in these highly competitive markets, and any significant differences in the way in which NMIs realize the SI units and quantities will have a direct bearing on competitiveness, market share, and profitability.

2.8.2 Chemistry, Pharmacy, and Medicine

Chemistry, biosciences, and pharmaceuticals are, for many of us, the new metrology. We are used to the practices of physical and engineering metrology, and so the new technologies are challenging our understanding of familiar concepts such as traceability, uncertainty, and primary standards. Much depends here on the interaction between a particular chemical or species and the solution or matrix in which it is to be found, as well as the processes or methods used to make the measurement. The concept of reference materials (RMs) (Chap. 3) is well developed in the chemical field, and the Consultative Committee for Quantity of Matter Metrology in Chemistry (CCQM) has embarked on a series of RM and other comparisons to assess the state of the art in chemical and biological measurements.

Through the CIPM MRA, the international metrology community has started to address the needs and concerns of regulators and legislators. This has already brought the Metre Convention into the areas of laboratory medicine and food [genetically modified organisms

(GMOs), pesticides, and trace elements]. The BIPM is only beginning to tackle and respond to the world of medicine and pharmacy and has created a partnership with the International Federation of Clinical Chemistry (IFCC) and ILAC to address these needs in a Joint Committee for Traceability in Laboratory Medicine (JCTLM). This is directed initially at a database of reference materials which meet certain common criteria of performance. Recognition of the data in the JCTLM database will, in particular, help demonstrate compliance of the products of the in vitro diagnostic industry with the requirements of a recent directive [2.5] of the European Union. The BIPM has signed a memorandum of understanding with the World Health Organization to help pursue these matters at an international level.

2.8.3 Environment, Public Services, and Infrastructures

In the area of the environment, our current knowledge of the complex interactions of weather, sea currents, and the various layers of our atmosphere is still not capable of a full explanation of environmental issues. The metrologist is, however, beginning to make a recognized contribution by insisting that slow or small changes, particularly in large quantities, should be measured traceably and against the unchanging reference stan-

dards offered through the units and quantities of the SI system. Similar inroads are being made into the space community where, for example, international and national space agencies are starting to appreciate that solar radiance measurements can be unreliable unless related to absolute measurements. We await the satellite launch of a cryogenic radiometer, which would do much to validate and monitor long-term trends in solar physics. The relevance of these activities is far from esoteric. Governments spend huge sums of money in their efforts to tackle environmental issues, and it is only by putting measurements on a sound basis that we can begin to make sure that these investments are justified and are making a real difference in the long term.

Traceable measurements are beginning to be needed as governments introduce competition into the supply of public services and infrastructures. Where utilities, such as electricity or gas, are offered by several different companies, the precise moment at which a consumer changes supplier can have large financial consequences. Traceable timing services are now used regularly in these industries as well as in stock exchanges and the growing world of e-commerce. Global trading is underpinned by globally accepted metrology, often without users appreciating the sophistication, reliability, and acceptability of the systems in which they place such implicit trust.

2.9 The SI System and New Science

Science never stands still, and there are a number of trends already evident which may have a direct bearing on the definitions of the SI itself. Much of this is linked with progress in measuring the fundamental constants, their coherence with each other and the SI, and the continued belief that they are time and space invariant. Figure 2.6 shows the current relationships of the basic SI units defined in Sect. 1.2.3 (Table 1.3).

This figure presents some of the links between the base units of the SI (shown in circles) and the fundamental physical and atomic constants (shown in boxes). It is intended to show that the base units of the SI are linked to measurable quantities through the unchanging and universal constants of physics.

The base units of the International System of Units defined in Table 1.3 are

A = ampere
K = Kelvin

s = second
m = meter
kg = kilogram
cd = candela
mol = mole

The surrounding boxes, lines, and uncertainties represent measurable quantities.

The numbers marked next to the base units are estimates of the standard uncertainties of their best practical realizations.

The fundamental and atomic constants shown are

R_K = von Klitzing constant
K_J = Josephson constant
R_{K-90} and K_{J-90} : the conventional values of these constants, introduced on 1 January 1990
N_A = Avogadro constant
F = Faraday constant

G = Newtonian constant of gravitation
m_{12C} = mass of ^{12}C
m_e = electron mass
R_∞ = Rydberg constant
h = Planck constant
c = speed of light
μ_0 = magnetic constant
α = fine-structure constant
R = molar gas constant
k_B = Boltzmann constant
e = elementary charge

The numbers next to the fundamental and atomic constants represent the relative standard uncertainties of our knowledge of these constants (from the 2002 CODATA adjustment).

The grey boxes reflect the unknown long-term stability of the kilogram artifact and its consequent effects on the practical realization of the definitions of the ampere, mole, and candela.

Based on the fundamental SI units, derived physical quantities have been defined which can be expressed in

terms of the fundamental SI units, for example, the unit of force = mass \times acceleration is newton = mkg/s^2 , and the unit of work = force \times distance is joule = $\text{m}^2\text{kg/s}^2$. A compilation of the units which are used today in science and technology is given in the *Springer Handbook of Condensed Matter and Materials Data* [2.6].

There is considerable discussion at the moment [2.7] on the issue of redefinitions of a number of these base units. The driver is a wish to replace the kilogram artifact-based definition by one which assigns a fixed value to a fundamental constant, thereby following the precedent of the redefinition of the meter in 1983 which set the speed of light at 299 792 458 m/s. There are two possible approaches – the so-called watt balance experiment, which essentially is a measure of the Planck constant, and secondly a measurement of the Avogadro number, which can be linked to the Planck constant. For a detailed review of the two approaches and the scientific background see [2.8]. The two approaches, however, produce discrepant results, and there is insufficient convergence at the moment to enable a redefinition with uncertainty of a few parts in 10^8 . This uncertainty has been specified by the Consultative Committee for Mass

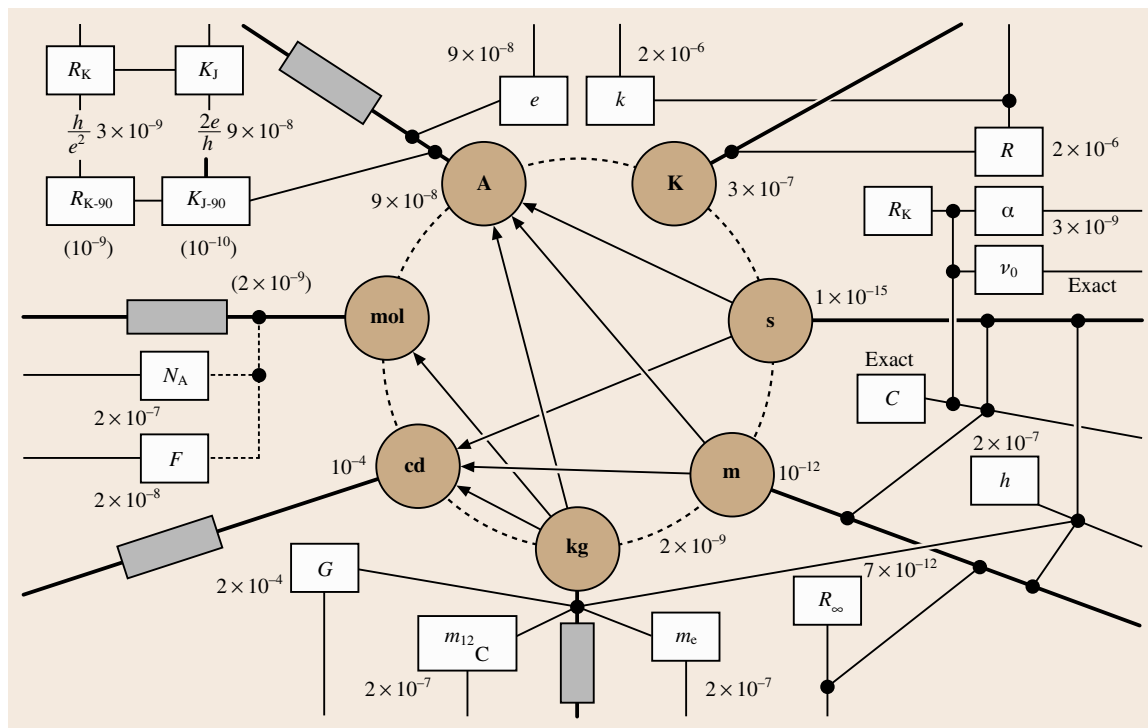


Fig. 2.6 Uncertainties of the fundamental constants (CODATA 2002, realization of the SI base units, present best estimates)

so as to provide for continuity of the uncertainty required and for minimum disturbance to the downstream world of practical mass measurements. If the Planck constant can be fixed, then it turns out that the electrical units can be related directly to the **SI** rather than based on the conventional values ascribed to the Josephson and von Klitzing constants by the **CIPM** in 1988 and universally referred to as R_{K-90} and J_{K-90} at the time of their implementation in 1990. A number of experiments are also underway to make improved measurements of the Boltzmann constant [2.9], which would be used to redefine the Kelvin, and finally a fixed value of the Planck constant with its connection to the Avogadro number would permit a redefinition of the mole.

This is, at the time of writing, a rapidly moving field, and any summary of the experimental situation would be rapidly overtaken by events. The reader is referred to the **BIPM** website (www.bipm.org), through which access to the deliberations of the relevant committees are available. However, the basic policy is now rather clear, and current thinking is that, within a few years and when the discrepancies are resolved, the General Conference on Weights and Measures will be asked to decide that four base units be redefined using

- a definition of the kilogram based on the Planck constant h ,
- a definition of the ampere based on a fixed value of the elementary charge e ,

- a definition of the Kelvin based on the value of the Boltzmann constant k_B , and
- a definition of the mole based on a fixed value of the Avogadro constant N_A .

The values ascribed to the fundamental constants would be those set by the CODATA group [2.10].

As a result, the *new SI* would be as shown diagrammatically in Fig. 2.7.

However, definitions are just what the word says – definitions – and there is a parallel effort to produce the *recipies* (called *mises en pratique*, following the precedent set at the time of redefining the meter) which enable their practical realizations worldwide.

When will all this take place? History will be the judge, but given current progress, the *new SI* could be in place by 2015. However, that will not be all.

New femtosecond laser techniques and the high performance of ion- or atom-trap standards may soon enable us to define the second in terms of optical transitions, rather than the current microwave-based one.

These are exciting times for metrologists. Trends in measurement are taking us into new regimes, and chemistry is introducing us to the world of reference materials and processes and to application areas which would have amazed our predecessors. What is, however, at face value surprising is the ability of a 130-year-old organization to respond flexibly and confidently to these

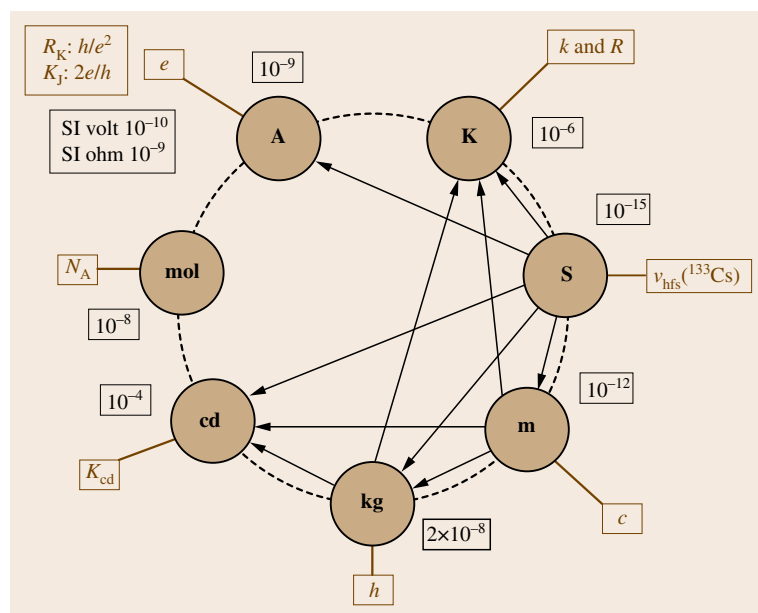


Fig. 2.7 Relations between the base units and fundamental constants together with the uncertainty associated with each link

changes. It is a tribute to our forefathers that the basis they set up for meter bars and platinum kilograms still applies to GMOs and measurement of cholesterol

in blood. Metrology is, truly, one of the oldest sciences and is one which continues to meet the changing needs of a changing world.

References

- 2.1 Bureau international des poids et mesures (BIPM): *The international system of units (SI)*, 7th edn. (BIPM, Sèvres 1998), see http://www.bipm.org/en/si/si_brochure
- 2.2 International Organization for Standardization (ISO): *International vocabulary of basic and general terms in metrology* (BIPM/IEC/IFCC/ISO/IUPAC/IUPAP/OIML, Genf 1993)
- 2.3 International Organization for Standardization (ISO): *Guide to the expression of uncertainty in measurement* (ISO, Genf 1993)
- 2.4 A.J. Wallard, T.J. Quinn: Intrinsic standards – Are they really what they claim?, *Cal Lab Mag.* **6**(6) (1999)
- 2.5 Directive 98/79/EC: See <http://www.bipm.org/en/committees/jc/jctlm>
- 2.6 W. Martienssen, H. Warlimont (Eds.): *Springer Handbook of Condensed Matter and Materials Data* (Springer, Berlin, Heidelberg 2005)
- 2.7 I.M. Mills, P.J. Mohr, T.J. Quinn, B.N. Taylor, E.R. Williams: Redefinition of the kilogram: A decision whose time has come, *Metrologia* **42**(2), 71–80 (2005)
- 2.8 http://www.sim-metrologia.org.br/docs/revista_SIM_2006.pdf
- 2.9 <http://www.bipm.org/wg/AllowedDocuments.jsp?wg=TG-SI>
- 2.10 <http://www.codata.org/index.html>

Quality in Me

3. Quality in Measurement and Testing

Technology and today's global economy depend on reliable measurements and tests that are accepted internationally. As has been explained in Chap. 1, metrology can be considered in categories with different levels of complexity and accuracy.

- Scientific metrology deals with the organization and development of measurement standards and with their maintenance.
- Industrial metrology has to ensure the adequate functioning of measurement instruments used in industry as well as in production and testing processes.
- Legal metrology is concerned with measurements that influence the transparency of economic transactions, health, and safety.

All scientific, industrial, and legal metrological tasks need appropriate *quality* methodologies, which are compiled in this chapter.

3.1	Sampling	40	3.4	Uncertainty and Accuracy of Measurement and Testing	68
	3.1.1 Quality of Sampling	40	3.4.1	General Principles	68
	3.1.2 Judging Whether Strategies of Measurement and Sampling Are Appropriate	42	3.4.2	Practical Example: Accuracy Classes of Measuring Instruments	69
	3.1.3 Options for the Design of Sampling	43	3.4.3	Multiple Measurement Uncertainty Components	71
3.2	Traceability of Measurements	45	3.4.4	Typical Measurement Uncertainty Sources	72
	3.2.1 Introduction	45	3.4.5	Random and Systematic Effects.....	73
	3.2.2 Terminology	46	3.4.6	Parameters Relating to Measurement Uncertainty: Accuracy, Trueness, and Precision ..	73
	3.2.3 Traceability of Measurement Results to SI Units.....	46	3.4.7	Uncertainty Evaluation: Interlaboratory and Intralaboratory Approaches	75
	3.2.4 Calibration of Measuring and Testing Devices	48	3.5	Validation	78
	3.2.5 The Increasing Importance of Metrological Traceability.....	49	3.5.1	Definition and Purpose of Validation	78
3.3	Statistical Evaluation of Results	50	3.5.2	Validation, Uncertainty of Measurement, Traceability, and Comparability.....	79
	3.3.1 Fundamental Concepts	50	3.5.3	Practice of Validation.....	81
	3.3.2 Calculations and Software	53	3.6	Interlaboratory Comparisons and Proficiency Testing	87
	3.3.3 Statistical Methods	54	3.6.1	The Benefit of Participation in PTs ..	88
	3.3.4 Statistics for Quality Control.....	66	3.6.2	Selection of Providers and Sources of Information	88
			3.6.3	Evaluation of the Results	92
			3.6.4	Influence of Test Methods Used.....	93
			3.6.5	Setting Criteria	94
			3.6.6	Trends	94
			3.6.7	What Can Cause Unsatisfactory Performance in a PT or ILC?.....	95
			3.6.8	Investigation of Unsatisfactory Performance	95
			3.6.9	Corrective Actions.....	96
			3.6.10	Conclusions	97
			3.7	Reference Materials	97
			3.7.1	Introduction and Definitions	97
			3.7.2	Classification	98
			3.7.3	Sources of Information	99
			3.7.4	Production and Distribution	100
			3.7.5	Selection and Use.....	101

3.7.6	Activities of International Organizations	104	3.9	Laboratory Accreditation and Peer Assessment	126
3.7.7	The Development of RM Activities and Application Examples	105	3.9.1	Accreditation of Conformity Assessment Bodies ...	126
3.7.8	Reference Materials for Mechanical Testing, General Aspects.....	107	3.9.2	Measurement Competence: Assessment and Confirmation	127
3.7.9	Reference Materials for Hardness Testing.....	109	3.9.3	Peer Assessment Schemes	130
3.7.10	Reference Materials for Impact Testing	110	3.9.4	Certification or Registration of Laboratories	130
3.7.11	Reference Materials for Tensile Testing	114	3.10	International Standards and Global Trade	130
3.8	Reference Procedures	116	3.10.1	International Standards and International Trade: The Example of Europe	131
3.8.1	Framework: Traceability and Reference Values ..	116	3.10.2	Conformity Assessment	132
3.8.2	Terminology: Concepts and Definitions	118	3.11	Human Aspects in a Laboratory	134
3.8.3	Requirements: Measurement Uncertainty, Traceability, and Acceptance	119	3.11.1	Processes to Enhance Competence – Understanding Processes.....	134
3.8.4	Applications for Reference and Routine Laboratories.....	121	3.11.2	The Principle of Controlled Input and Output.....	135
3.8.5	Presentation: Template for Reference Procedures.	123	3.11.3	The Five Major Elements for Consideration in a Laboratory ...	136
3.8.6	International Networks: CIPM and VAMAS	123	3.11.4	Internal Audits.....	136
3.8.7	Related Terms and Definitions	126	3.11.5	Conflicts.....	137
			3.11.6	Conclusions	137
			3.12	Further Reading: Books and Guides	138
			References		138

3.1 Sampling

Sampling is arguably the most important part of the measurement process. It is usually the case that it is impossible to measure the required quantity, such as concentration, in an entire batch of material. The taking of a sample is therefore the essential first step of nearly all measurements. However, it is commonly agreed that the quality of a measurement can be no better than the quality of the sampling upon which it is based. It follows that the highest level of care and attention paid to the instrumental measurements is ineffectual, if the original sample is of poor quality.

3.1.1 Quality of Sampling

The *traditional approach* to ensuring the quality of sampling is procedural rather than empirical. It relies initially on the selection of a correct sampling protocol for the particular material to be sampled under a particular circumstance. For example the material may be

copper metal, and the circumstance could be manufacturers' quality control prior to sale. In general, such a protocol may be specified by a regulatory body, or recommended in an international standard or by a trade organization. The second step is to train the personnel who are to take the samples (i.e., the samplers) in the correct application of the protocol. No sampling protocol can be completely unambiguous in its wording, so uniformity of interpretation relies on the samplers being educated, not just in how to interpret the words, but also in an appreciation of the rationale behind the protocol and how it can be adapted to the changing circumstances that will arise in the real world, without invalidating the protocol. This step is clearly related to the management of sampling by organizations, which is often separated from the management of the instrumental measurements, even though they are both inextricably linked to the overall quality of the measurement. The fundamental basis of the traditional approach

to assuring sampling quality is to assume that the correct application of a correct sampling protocol will give a representative sample, by definition.

An *alternative approach* to assuring sampling quality is to estimate the quality of sampling empirically. This is analogous to the approach that is routinely taken to instrumental measurement, where as well as specifying a protocol, there is an initial validation and ongoing quality control to monitor the quality of the measurements actually achieved. The key parameter of quality for instrumental measurements is now widely recognized to be the uncertainty of each measurement. This concept will be discussed in detail later (Sect. 3.4), but informally this uncertainty of measurement can be defined as the range within which the true value lies, for the quantity subject to measurement, with a stated level of probability. If the quantity subject to measurement (the measurand) is defined in terms of the batch of material (the sampling target), rather than merely in the sample delivered to the laboratory, then measurement uncertainty includes that arising from primary sampling. Given that sampling is the first step in the measurement process, then the uncertainty of the measurement will also arise in this first step, as well as in all of the other steps, such as the sampling preparation and the instrumental determination.

The key measure of sampling quality is therefore this sampling uncertainty, which includes contributions not just from the random errors often associated with sampling variance [3.1] but also from any systematic errors that have been introduced by sampling bias. Rather than assuming the bias is zero when the protocol is correct, it is more prudent to aim to include any bias in the estimate of sampling uncertainty. Such bias may often be unsuspected, and arise from a marginally incorrect application of a nominally correct protocol. This is equivalent to abandoning the assumption that samples are representative, but replacing it with a measurement result that has an associated estimate of uncertainty which includes errors arising from the sampling process.

Selection of the most appropriate sampling protocol is still a crucial issue in this alternative approach. It is possible, however, to select and monitor the appropriateness of a sampling protocol, by knowing the uncertainty of measurement that it generates. A judgement can then be made on the fitness for purpose (FFP) of the measurements, and hence the various components of the measurement process including the sampling, by comparing the uncertainty against the target value indicated by the FFP criterion. Two such FFP criteria are discussed below.

Two approaches have been proposed for the estimation of uncertainty from sampling [3.2]. The first or *bottom-up* approach requires the identification of all of the individual components of the uncertainty, the separate estimation of the contribution that each component makes, and then summation across all of the components [3.3]. Initial feasibility studies suggest that the use of sampling theory to predict all of the components will be impractical for all but a few sampling systems, where the material is particulate in nature and the system conforms to a model in which the particle size/shape and analyte concentration are simple, constant, and homogeneously distributed. One recent application successfully mixes theoretical and empirical estimation techniques [3.4]. The second, more practical and pragmatic approach is entirely empirical, and has been called *top-down* estimation of uncertainty [3.5].

Four methods have been described for the empirical estimation of uncertainty of measurement, including that from primary sampling [3.6]. These methods can be applied to any sampling protocol for the sampling of any medium for any quantity, if the general principles are followed. The simplest of these methods (#1) is called the *duplicate method*. At its simplest, a small proportion of the measurements are made in duplicate. This is not just a duplicate analysis (i. e., determination of the quantity), made on one sample, but made on a fresh primary sample, from the same sampling target as the original sample, using a fresh interpretation of the same sampling protocol (Fig. 3.1a). The ambiguities in the protocol, and the heterogeneity of the material, are therefore reflected in the difference between the duplicate measurements (and samples). Only 10% ($n \geq 8$) of the samples need to be duplicated to give a sufficiently reliable estimate of the overall uncertainty [3.7]. If the separate sources of the uncertainty need to be quantified, then extra duplication can be inserted into the experimental design, either in the determination of quantity (Fig. 3.1b) or in other steps, such as the physical preparation of the sample (Fig. 3.1d). This duplication can either be on just one sample duplicate (in an *unbalanced* design, Fig. 3.1b), or on both of the samples duplicated (in a *balanced* design, Fig. 3.1c).

The uncertainty of the measurement, and its components if required, can be estimated using the statistical technique called analysis of variance (ANOVA). The frequency distribution of measurements, such as analyte concentration, often deviate from the normal distribution that is assumed by classical ANOVA. Because of this, special procedures are required to accommodate outlying values, such as robust ANOVA [3.8]. This method

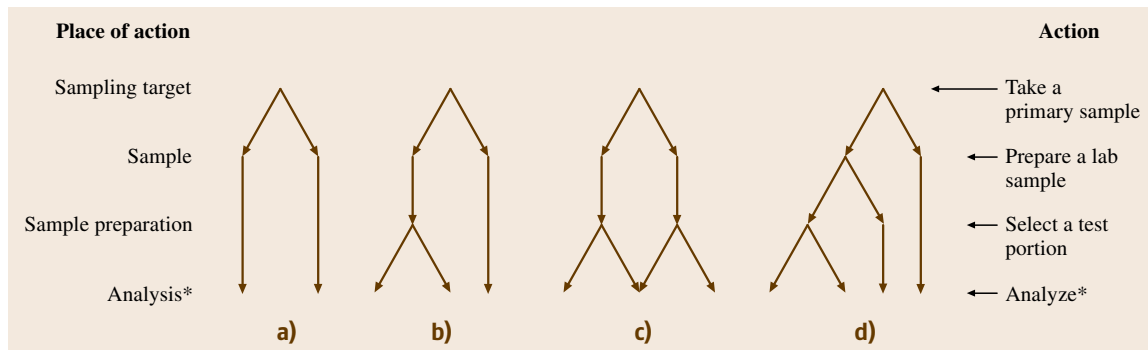


Fig. 3.1a–d Experimental designs for the estimation of measurement uncertainty by the duplicate method. The simplest and cheapest option (a) has single analyses on duplicate samples taken on around 10% ($n \geq 8$) of the sampling targets, and only provides an estimate of the random component of the overall measurement uncertainty. If the contribution from the analytical determination is required separately from that from the sampling, duplication of analysis is required on either one (b) or both (c) of the sample duplicates. If the contribution from the physical sample preparation is required to be separated from the sampling, as well as from that from the analysis, then duplicate preparations also have to be made (d). (*Analysis and Analyze can more generally be described as the determination of the measurand)

has successfully been applied to the estimation of uncertainty for measurements on soils, groundwater, animal feed, and food materials [3.2]. Its weakness is that it ignores the contribution of systematic errors (from sampling or analytical determination) to the measurement uncertainty. Estimates of analytical bias, made with certified reference materials, can be added to estimates from this method. Systematic errors caused by a particular sampling protocol can be detected by use of a different method (#2) in which different sampling protocols are applied by a single sampler. Systematic errors caused by the sampler can also be incorporated into the estimate of measurement uncertainty by the use of a more elaborate method (#3) in which several samplers apply the same protocol. This is equivalent to holding a *collaborative trial in sampling (CTS)*. The most reliable estimate of measurement uncertainty caused by sampling uses the most expensive method (#4), in which several samplers each apply whichever protocol they consider most appropriate for the stated objective. This incorporates possible systematic errors from the samplers and the measurement protocols, together with all of the random errors. It is in effect a sampling proficiency test (SPT), if the number of samplers is at least eight [3.6].

Evidence from applications of these four empirical methods suggests that small-scale heterogeneity is often the main factor limiting the uncertainty. In this case, methods that concentrate on repeatability, even with just one sampler and one protocol as in the duplicate method (#1), are good enough to give an acceptable approximation of the sampling uncertainty. Proficiency

test measurements have also been used in *top-down* estimation of uncertainty of analytical measurements [3.9]. They do have the added advantage that the participants are scored for the proximity of their measurement value to the true value of the quantity subject to measurement. This true value can be estimated either by consensus of the measured values, or by artificial spiking with a known quantity of analyte [3.10]. The score from such SPTs could also be used for both ongoing assessment and accreditation of samplers [3.11]. These are all new approaches that can be applied to improving the quality of sampling that is actually achieved.

3.1.2 Judging Whether Strategies of Measurement and Sampling Are Appropriate

Once methods are in place for the estimation of uncertainty, the selection and implementation of a correct protocol become less crucial. Nevertheless an appropriate protocol is essential to achieve fitness for purpose. The FFP criterion may however vary, depending on the circumstances. There are cases for example where a relative expanded uncertainty of 80% of the measured value can be shown to be fit for certain purposes. One example is using in situ measurements of lead concentration to identify any area requiring remediation in a contaminated land investigation. The contrast between the concentration in the contaminated and in the uncontaminated areas can be several orders of magnitude, and so uncertainty within one order (i.e., 80%) does not

result in errors in classification of the land. A similar situation applies when using laser-ablation inductively coupled plasma for the determination of silver to differentiate between particles of anode copper from widely different sources. The Ag concentration can differ by several orders of magnitude, so again a large measurement uncertainty (e.g., 70%) can be acceptable. One mathematical way of expressing this FFP criterion is that the measurement uncertainty should not contribute more than 20% to the total variance over samples from a set of similar targets [3.8]. A second FFP criterion also includes financial considerations, and aims to set an optimal level of uncertainty that minimizes financial loss. This loss arises not just from the cost of the sampling and the determination, but also from the financial losses that may arise from incorrect decisions caused by the uncertainty [3.12]. The approach has been successfully applied to the sampling of both contaminated soil [3.13] and food materials [3.14].

3.1.3 Options for the Design of Sampling

There are three basic approaches to the design/selection of a sampling protocol for any quantity (measurand) in any material. The first option is to select a previously specified protocol. These exist for most of the material/quantity combinations considered in Chap. 4 of this handbook. This approach is favored by regulators, who expect that the specification and application of a standard protocol will automatically deliver comparability of results between samplers. It is also used as a defense in legal cases to support the contention that measurements will be reliable if a standard protocol has been applied. The rationale of a standard protocol is to specify the procedure to the point where the sampler needs to make no subjective judgements. In this case the sampler would appear not to require any grasp of the rationale behind the design of the protocol, but merely the ability to implement the instructions given. However, experimental video monitoring of samplers implementing specified protocols suggests that individual samplers often do extemporize, especially when events occur that were unforeseen or unconsidered by the writers of the protocols. This would suggest that samplers therefore need to appreciate the rationale behind the design, in order to make appropriate decisions on implementing the protocol. This relates to the general requirement for improved training and motivation of samplers discussed below.

The second option is to use a theoretical model to design the required sampling protocol. Sampling

theory has produced a series of increasingly complex theoretical models, recently reviewed [3.15], that are usually aimed at predicting the sampling mass required to produce a given level of variance in the required measurement result. All such models depend on several assumptions about the system that is being modeled. The model of Gy [3.1], for example, assumes that the material is particulate, that the particles in the batch can be classified according to volume and type of material, and that the analyte concentration in a contaminated particle and its density do not vary between particles. It was also assumed that the volume of each particle in the batch is given by a constant factor multiplied by the cube of the particle diameter. The models also all require large amounts of information about the system, such as particle diameters, shape factors, size range, liberation, and composition. The cost of obtaining all of this information can be very high, but the model also assumes that these parameters will not vary in space or time. These assumptions may not be justified for many systems in which the material to be sampled is highly complex, heterogeneous, and variable. This limits the real applicability of this approach for many materials. These models do have a more generally useful role, however, in facilitating the prediction of how uncertainty from sampling can be changed, if required, as discussed below.

The third option for designing a sampling protocol is to adapt an existing method in the light of site-specific information, and monitor its effectiveness empirically. There are several factors that require consideration in this adaptation.

Clearly identifying the *objective of the sampling* is the key factor that helps in the design of the most appropriate sampling protocol. For example, it may be that the acceptance of a material is based upon the best estimate of the *mean* concentration of some analyte in a batch. Alternatively, it may be the *maximum* concentration, within some specified mass, that is the basis for acceptance or rejection. Protocols that aim at low uncertainty in estimation of the mean value are often inappropriate for reliable detection of the maximum value.

A *desk-based review* of all of the relevant information about the sampling target, and findings from similar targets, can make the protocol design much more cost effective. For example, the history of a contaminated land site can suggest the most likely contaminants and their probable spatial distribution within the site. This information can justify using *judgemental sampling* in which the highest sampling density is concentrated in

the area of highest predicted probability. This approach does however, have the weakness that it may be self-fulfilling, by missing contamination in areas that were unsuspected.

The actual *mode of sampling* varies greatly therefore, depending not just on the physical nature of the materials, but also on the expected heterogeneity in both the spatial and temporal dimension. Some protocols are designed to be random (or nonjudgemental) in their selection of samples, which in theory creates the least bias in the characterization of the measurand. There are various different options for the design of random sampling, such as stratified random sampling, where the target is subdivided into regular units before the exact location of the sampling is determined using randomly selected coordinates. In a situation where judgemental sampling is employed, as described above, the objective is not to get a representative picture of the sampling target. Another example would be in an investigation of the cause of defects in a metallurgical process, where it may be better to select items within a batch by their aberrant visual appearance, or contaminant concentration, rather than at random.

There may also be a question of the most appropriate *medium to sample*. The answer may seem obvious, but consider the objective of detecting which of several freight containers holds nuts that are contaminated with mycotoxins. Rather than sampling the nuts themselves, it may be much more cost effective to sample the atmosphere in each container for the spores released by the fungi that make the mycotoxin. Similarly in contaminated land investigation, if the objective is to assess potential exposure of humans to cadmium at an allotment site, it may be most effective to sample the vegetables that take up the cadmium rather than the soil.

The *specification of the sampling target* needs to be clear. Is it a whole batch, or a whole site of soil, or just the top 1 m of the soil? This relates to the objective of the sampling, but also to the site-specific information (e.g., there is bedrock at 0.5 m) and logistical constraints.

The next key question to address is the *number of samples* required (n). This may be specified in an accepted sampling protocol, but should really depend on the objective of the investigation. Cost-benefit analysis can be applied to this question, especially if the objective is the mean concentration at a specified confidence interval. In that case, and assuming a normal distribution of the variable, the Student t -distribution can be used to calculate the required value of n . A closely related question is whether *composite samples* should be

taken, and if so, what is the required number of increments (i). This approach can be used to reduce the uncertainty of measurement caused by the sampling. According to the theory of Gy, taking an i -fold composite sample should reduce the main source of the uncertainty by \sqrt{i} , compared with the uncertainty for a single sample with the same mass as one of the increments. Not only do the increments increase the sample mass, but they also improve the sample's ability to represent the sampling target. If, however, the objective is to identify maximum rather than mean values, then a different approach is needed for calculating the number of samples required. This has been addressed for contaminated land by calculating the probability of hitting an idealized hot-spot [3.16].

The *quantity of sample* to be taken (e.g., mass or volume) is another closely related consideration in the design of a specified protocol. The mass may be specified by existing practise and regulation, or calculated from sampling theory such as that of Gy. Although the calculation of the mass from first principles is problematic for many types of sample, as already discussed, the theory is useful in calculating the factor by which to change the sample mass to achieve a specified target for uncertainty. If the mass of the sample is increased by some factor, then the sampling variance should reduce by the same factor, as discussed above for increments. The mass required for measurement is often smaller than that required to give an acceptable degree of representativeness (and uncertainty). In this case, a larger sample must be taken initially and then reduced in mass, without introducing bias. This *comminution of samples*, or reduction in grain size by grinding, is a common method for reducing the uncertainty introduced by this subsampling procedure. This can, however, have unwanted side-effects in changing the measurand. One example is the loss of certain analytes during the grinding, either by volatilization (e.g., mercury) or by decomposition (e.g., most organic compounds).

The *size of the particles* in the original sampling target that should constitute the sample needs consideration. Traditional wisdom may suggest that a representative sample of the whole sampling target is required. However, sampling all particle sizes in the same proportions that they occur in the sampling target may not be possible. This could be due to limitations in the sampling equipment, which may exclude the largest particles (e.g., pebbles in soil samples). A representative sample may not even be desirable, as in the case where only the small particles in soil ($< 100 \mu\text{m}$) form the main route of human exposure to lead by hand-to-

mouth activity. The objectives of the investigation may require therefore that a specific size fraction be selected.

Contamination of samples is probable during many of these techniques of sampling processing. It is often easily done, irreversible in its effect, and hard to detect. It may arise from other materials at the sampling site (e.g., topsoil contaminating subsoil) or from processing equipment (e.g., cadmium plating) or from the remains of previous samples left in the equipment. The traditional approach is to minimize the risk of contamination occurring by careful drafting of the protocol, but a more rigorous approach is to include additional procedures that can detect any contamination that has occurred (e.g., using a **SPT**).

Once a sample has been taken, the protocol needs to describe how to *preserve the sample*, without changing the quantity subject to measurement. For some measurands the quantity begins to change almost immediately after sampling (e.g., the redox potential of groundwater), and in situ measurement is the most reliable way of avoiding the change. For other measurands specific actions are required to prevent change. For example, acidification of water, after filtration, can prevent adsorption of many analyte ions onto the surfaces of a sample container.

The final, and perhaps most important factor to consider in designing a sampling protocol is the logistical

organization of the samples within the investigation. Attention to detail in the unique numbering and clear description of samples can avoid ambiguity and irreversible errors. This improves the quality of the investigation by reducing the risk of gross errors. Moreover, it is often essential for legal traceability to establish an unbroken chain of custody for every sample. This forms part of the broader quality assurance of the sampling procedure.

There is no such thing as either a perfect sample or a perfect measurement. It is better, therefore, to estimate the uncertainty of measurements from all sources, including the primary sampling. The uncertainty should not just be estimated in an initial method validation, but also monitored routinely for every batch using a sampling and analytical quality control scheme (**SAQCS**). This allows the investigator to judge whether each batch of measurements are **FFP**, rather than to assume that they are because some standard procedure was nominally adhered to. It also enables the investigator to propagate the uncertainty value through all subsequent calculations to allow the uncertainty on the interpretation of the measurements to be expressed. This approach allows for the imperfections in the measurement methods and the humans who implement them, and also for the heterogeneity of the real world.

3.2 Traceability of Measurements

3.2.1 Introduction

Clients of laboratories will expect that results are correct and comparable. It is further anticipated that complete results and values produced include an estimated uncertainty. A comparison between different results or between results achieved and given specifications can only be done correctly if the measurement uncertainty of the results is taken into account.

To achieve comparable results, the traceability of the measurement results to **SI** units through an unbroken chain of comparisons, all having stated uncertainties, is fundamental (Sect. 2.6 *Traceability of Measurements*). Among others, due to the strong request from the International Laboratory Accreditation Cooperation (**ILAC**) several years ago, the International Committee for Weights and Measures (**CIPM**), which is the governing board of the International Bureau of Weights and Measures (**BIPM**), has realized under the scope

of the Metre Convention the **CIPM** mutual recognition arrangement (**MRA**) on the mutual recognition of national measurement standards and of calibration and measurement certificates issued by the national metrology institutes, under the scope of the Metre Convention. Details of this **MRA** can be found in Chap. 2 *Metrology Principles and Organization* Sect. 2.7 or at <http://www1.bipm.org/en/convention/mra/>.

The range of national measurement standards and best measurement capabilities needed to support the calibration and testing infrastructure in an economy or region can normally be derived from the websites of the respective national metrology institute or from the website of the **BIPM**. Traceability to these national measurement standards through an unbroken chain of comparisons is an important means to achieve accuracy and comparability of measurement results.

Access to suitable national measurement standards may be more complicated in those economies where

the national measurement institute does not yet provide national measurement standards recognized under the **BIPM MRA**. It is further to be noted that an unbroken chain of comparisons to national standards in various fields such as the chemical and biological sciences is much more complex and often not available, as appropriate standards are lacking. The establishment of standards in these fields is still the subject of intense scientific and technical activities, and reference procedures and (certified) reference materials needed must still be defined. As of today, in these fields there are few reference materials that can be traced back to **SI** units available on the market. This means that other tools should also be applied to assure at least comparability of measurement results, such as, e.g., participation in suitable proficiency testing programs or the use of reference materials provided by reliable and competent reference material producers.

3.2.2 Terminology

According to the *International Vocabulary of Metrology – Basic and General Concepts and Associated Terms (VIM 2008)* [3.17], the following definitions apply.

Primary Measurement Standard

Measurement standard established using a primary reference measurement procedure, or created as an artifact, chosen by convention.

International Measurement Standard

Measurement standard recognized by signatories to an international agreement and intended to serve worldwide.

National Measurement Standard, National Standard

Measurement standard recognized by national authority to serve in a state or economy as the basis for assigning quantity values to other measurement standards for the kind of quantity concerned.

Reference Measurement Standard, Reference Standard

Measurement standard designated for the calibration of other measurement standards for quantities of a given kind in a given organization or at a given location.

Working Standard

Measurement standard that is used routinely to calibrate or verify measuring instruments or measuring systems.

Note that a working standard is usually calibrated against a reference standard. Working standards may also at the same time be reference standards. This is particularly the case for working standards directly calibrated against the standards of a national standards laboratory.

3.2.3 Traceability of Measurement Results to SI Units

The formal definition of traceability is given in Chap. 2, Sect. 2.6 as: the property of a measurement result relating the result to a stated metrological reference through an unbroken chain of calibrations or comparisons, each contributing to the stated uncertainty. This chain is also called the traceability chain. It must, as defined, end at the respective primary standard.

The uncertainty of measurement for each step in the traceability chain must be calculated or estimated according to agreed methods and must be stated so that an overall uncertainty for the whole chain may be calculated or estimated. The calculation of uncertainty is officially given in the *Guide to the Expression of Uncertainty in Measurement (GUM)* [3.18]. The **ILAC** and regional organizations of accreditation bodies (see under peer and third-party assessment) provide application documents derived from the **GUM**, providing instructive examples. These documents are available on their websites.

Competent testing laboratories, e.g., those accredited by accreditation bodies that are members of the **ILAC MRA**, can demonstrate that calibration of equipment that makes a significant contribution to the uncertainty and hence the measurement results generated by that equipment are traceable to the international system of units (**SI** units) wherever this is technically possible.

In cases where traceability to the **SI** units is not (yet) possible, laboratories use other means to assure at least comparability of their results. Such means are, e.g., the use of certified reference materials, provided by a reliable and competent producer, or they assure at least comparability by participating in interlaboratory comparisons provided by a competent and reliable provider. See also Sects. 3.6 and 3.7 on *Interlaboratory Comparisons and Proficiency Testing* and *Reference Materials*, respectively.

The Traceability Chain

National Metrology Institutes. In most cases the national metrology institutes maintain the *national standards* that are the sources of traceability for the quantity

of interest. The national metrology institutes ensure the comparability of these standards through an international system of key comparisons, as explained in detail in Chap. 2, Sect. 2.7.

If a national metrology institute has an infrastructure to realize a given primary standard itself, this national standard is identical to or directly traceable to that *primary standard*. If the institute does not have such an infrastructure, it will ensure that its national standard is traceable to a primary standard maintained in another country's institute. Under <http://kcdb.bipm.org/AppendixC/default.asp>, the calibration and measurement capabilities (CMCs) declared by national metrology institutes are shown.

Calibration Laboratories. For *calibration laboratories* accredited according to the ISO/International Electrotechnical Commission (IEC) standard ISO/IEC 17025, accreditation is granted for specified calibrations with a defined calibration capability that can (but not necessarily must) be achieved with a specified measuring instrument, reference or working standard.

The *calibration capability* is defined as the smallest uncertainty of measurement that a laboratory can achieve within its scope of accreditation, when performing more or less routine calibrations of nearly ideal measurement standards intended to realize, conserve or reproduce a unit of that quantity or one or more of its values, or when performing more or less routine calibrations of nearly ideal measuring instruments designed for the measurement of that quantity.

Most of the accredited laboratories provide calibrations for customers (e.g., for organizations that do not have their own calibration facilities with a suitable measurement capability or for testing laboratories) on request. If the service of such an accredited calibration laboratory is taken into account, it must be assured that its scope of accreditation fits the needs of the customer. Accreditation bodies are obliged to provide a list of accredited laboratories with a detailed technical description of their scope of accreditation. <http://www.ilac.org/> provides a list of the accreditation bodies which are members of the ILAC MRA.

If a customer is using a nonaccredited calibration laboratory or if the scope of accreditation of a particular calibration laboratory does not fully cover a specific calibration required, the customer of that laboratory must ensure that

- the tractability chain as described above is maintained correctly,

- there is a concept to estimate the overall measurement uncertainty in place and applied correctly,
- the staff is thoroughly trained to perform the activities within their responsibilities,
- clear and valid procedures are available to perform the required calibrations,
- a system to deal with errors is applied, and the calibration operations include statistical process control such as, e.g., the use of control charts.

In-House Calibration Laboratories (Factory Calibration Laboratories). Frequently, calibration services are provided by in-house calibration laboratories which regularly calibrate the measuring and test equipment used in a company, e.g., in a production facility, against its reference standards that are traceable to an accredited calibration laboratory or a national metrology institute.

An in-house calibration system normally assures that all measuring and test equipment used within a company is calibrated regularly against working standards, calibrated by an accredited calibration laboratory. In-house calibrations must fit into the internal applications in such a way that the results obtained with the measuring and test equipment are accurate and reliable. This means that for in-house calibration the following elements should be considered as well.

- The uncertainty contribution of the in-house calibration should be known and taken into account if statements of compliance, e.g., internal criteria for measuring instruments, are made.
- The staff should be trained to perform the calibrations required correctly.
- Clear and valid procedures should be available also for in-house calibrations.
- A system to deal with errors should be applied (e.g., in the frame of an overall quality management system), and the calibration operations should include a statistical process control (e.g., the use of control charts).

To assure correct operation of the measuring and test equipment, a concept for the maintenance of that equipment should be in place. Aspects to be considered when establishing calibration intervals are given in Sect. 3.5.

The Hierarchy of Standards. The hierarchy of standards and a resulting metrological organizational structure for tracing measurement and test results within a company to national standards are shown in Fig. 3.2.

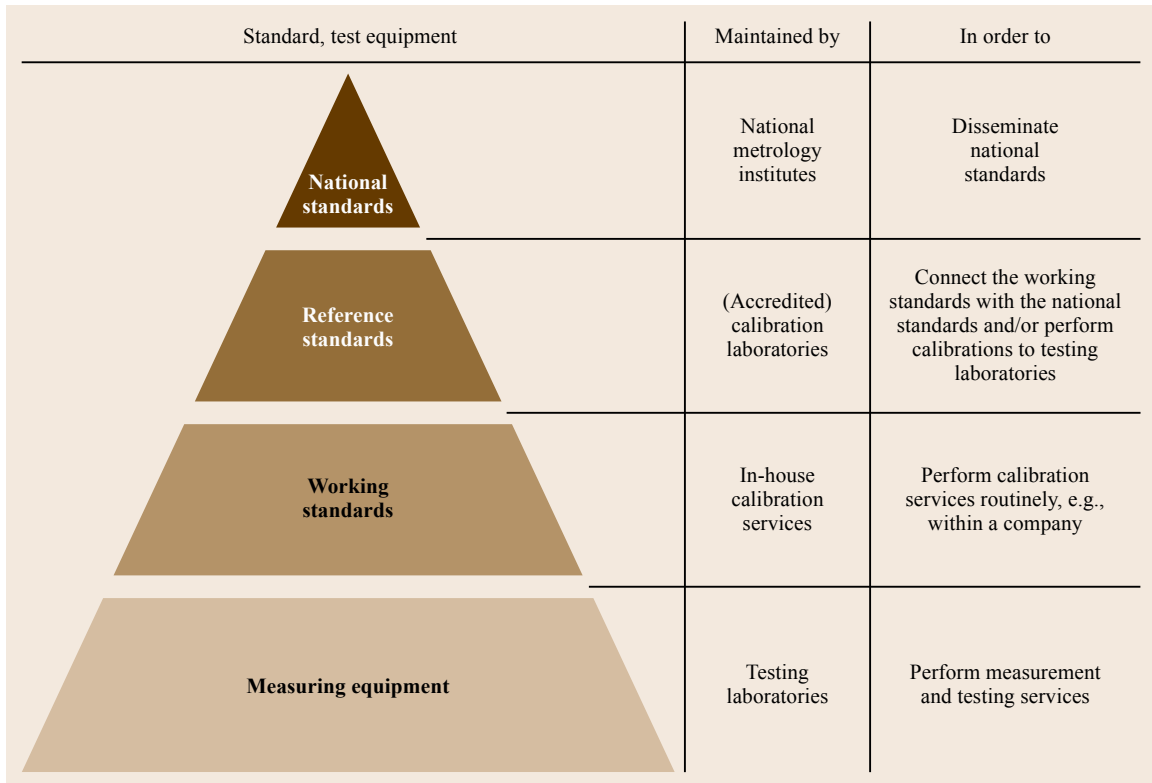


Fig. 3.2 The calibration hierarchy

Equipment used by testing and calibration laboratories that has a significant effect on the reliability and uncertainty of measurement should be calibrated using standards connected to the national standards with a known uncertainty.

Alternative Solutions

Accreditation bodies which are members of the [ILAC MRA](#) require accredited laboratories to ensure traceability of their calibration and test results. Accredited laboratories also know the contribution of the uncertainty derived through the traceability chain to their calibration and test results.

Where such traceability is not (yet) possible, laboratories should at least assure comparability of their results by alternative methods. This can be done either through the use of appropriate reference materials ([RM](#)) or by participating regularly in appropriate proficiency tests ([PT](#)) or interlaboratory comparisons. *Appropriate* means that the [RM](#) producers or the [PT](#) providers are competent or at least recognized in the respective sector.

3.2.4 Calibration of Measuring and Testing Devices

The [VIM 2008](#) gives the following definition for calibration:

Definition

Operation that, under specified conditions, in a first step, establishes a relation between the quantity values with measurement uncertainties provided by measurement standards and corresponding indications with associated measurement uncertainties and, in a second step, uses this information to establish a relation for obtaining a measurement result from an indication.

The operation of calibration and its two steps is described in [Sect. 3.4.2](#) with an example from dimensional metrology ([Fig. 3.10](#)).

It is common and important that testing laboratories regularly maintain and control their testing instruments, measuring systems, and reference and working standards. Laboratories working according to the [ISO/IEC 17025](#) standard as well as manufactur-

ers working according to, e.g., the ISO 9001 series of standards maintain and calibrate their measuring instruments, and reference and working standards regularly according to well-defined procedures.

Clause 5.5.2 of the ISO/IEC 17025 standard requires that:

Calibration programmes shall be established for key quantities or values of the instruments where these properties have a significant effect on the results.

Whenever practicable, all equipment under the control of the laboratory and requiring calibration shall be labeled, coded, or otherwise identified to indicate the status of calibration, including the data when last calibrated and the date or expiration criteria when recalibration is due. (Clause 5.5.8)

Clause 7.6 of ISO 9001:2000 requires that:

Where necessary to ensure valid results, measuring equipment shall be calibrated or verified at specified intervals, or prior to use, against measurement standards traceable to international or national measurement standards.

In the frame of the calibration programs of their measuring instruments, and reference and working standards, laboratories will have to define the time that should be permitted between successive calibrations (recalibrations) of the used measurement instruments, and reference or working standards in order to

- confirm that there has not been any deviation of the measuring instrument that could introduce doubt about the results delivered in the elapsed period,
- assure that the difference between a reference value and the value obtained using a measuring instrument is within acceptable limits, also taking into account the uncertainties of both values,
- assure that the uncertainty that can be achieved with the measuring instrument is within expected limits.

A large number of factors can influence the time interval to be defined between calibrations and should be taken into account by the laboratory. The most important factors are usually

- the information provided by the manufacturer,
- the frequency of use and the conditions under which the instrument is used,

- the risk of the measuring instrument drifting out of the accepted tolerance,
- consequences which may arise from inaccurate measurements (e.g., failure costs in the production line or aspects of legal liability),
- the cost of necessary corrective actions in case of drifting away from the accepted tolerances,
- environmental conditions such as, e.g., climatic conditions, vibration, ionizing radiation, etc.,
- trend data obtained, e.g., from previous calibration records or the use of control charts,
- recorded history of maintenance and servicing,
- uncertainty of measurement required or declared by the laboratory.

These examples show the importance of establishing a concept for the maintenance of the testing instruments and measuring systems. In the frame of such a concept the definition of the calibration intervals is one important aspect to consider. To optimize the calibration intervals, available statistical results, e.g., from the use of control charts, from participation in interlaboratory comparisons or from reviewing own records should be used.

3.2.5 The Increasing Importance of Metrological Traceability

An increasing awareness of the need for metrological underpinning of measurements can be noticed at least in the past years. Several factors may be the reason for this process, including

- the importance of quality management systems,
- requirements by governments or trading partners for producers to establish certified quality management systems and for calibration and testing activities to be accredited,
- aspects of legal reliability.

In a lot of areas it is highly important that measurement results, e.g., produced by testing laboratories, can be compared with other results produced by other parties at another time and quite often using different methods. This can only be achieved if measurements are based on equivalent physical realizations of units. Traceability of results and reference values to primary standards is a fundamental issue in competent laboratory operation today.

3.3 Statistical Evaluation of Results

Statistics are used for a variety of purposes in measurement science, including mathematical modeling and prediction for calibration and method development, method validation, uncertainty estimation, quality control and assurance, and summarizing and presenting results. This section provides an introduction to the main statistical techniques applied in measurement science. A knowledge of the basic descriptive statistics (mean, median, standard deviation, variance, quantiles) is assumed.

3.3.1 Fundamental Concepts

Measurement Theory and Statistics

The traditional application of statistics to quantitative measurement follows a set of basic assumptions related to ordinary statistics

1. That a given measurand has a value – the value of the measurand – which is unknown and (in general) unknowable by the measurement scientist. This is generally assumed (for univariate quantitative measurements) to be a single value for the purpose of statistical treatment. In statistical standards, this is the *true value*.
2. That each measurement provides an *estimate* of the value of the measurand, formed from an *observation* or set of observations.
3. That an observation is the sum of the measurand value and an *error*.

Assumption 3 can be expressed as one of the simplest statistical models

$$x_i = \mu + e_i,$$

in which x_i is the i -th observation, μ is the measurand value, and e_i is the error in the particular observation.

The error itself is usually considered to be a sum of several contributions from different sources or with different behavior. The most common partition of error is into two parts: one which is constant for the duration of a set of experiments (the *systematic error*) and another, the *random error*, which is assumed to arise by random selection from some distribution. Other partitioning is possible; for example, collaborative study uses a statistical model based on a systematic contribution (method bias), a term which is constant for a particular laboratory (the laboratory component of bias) but randomly distributed among laboratories, and a residual error for each observation. Linear calibration

assumes that observations are the sum of a term that varies linearly and systematically with measurand value and a random term; least-squares regression is one way of characterizing the behavior of the systematic part of this model.

The importance of this approach is that, while the value of the measurand may be unknown, studying the distribution of the observations allows inferences to be drawn about the probable value of the measurand. Statistical theory describes and interrelates the behaviors of different distributions, and this provides quantitative tools for describing the probability of particular observations given certain assumptions. Inferences can be drawn about the value of the measurand by asking what range of measurand values could reasonably lead to the observations found. This provides a range of values that can reasonably be attributed to the measurand. Informed readers will note that this is the phrase used in the definition of uncertainty of measurement, which is discussed further below.

This philosophy forms the basis of many of the routine statistical methods applied in measurement, is well established with strong theoretical foundations, and has stood the test of time well. This chapter will accordingly rely heavily on the relevant concepts. It is, however, important to be aware that it has limitations. The basic assumption of a point value for the measurand may be inappropriate for some situations. The approach does not deal well with the accumulation of information from a variety of different sources. Perhaps most importantly, real-world data rarely follow theoretical distributions very closely, and it can be misleading to take inference too far, and particularly to infer very small probabilities or very high levels of confidence. Furthermore, other theoretical viewpoints can be taken and can provide different insights into, for example, the development of confidence in a value as data from different experiments are accumulated, and the treatment of estimates based on judgement instead of experiment.

Distributions

Figure 3.3 shows a typical measurement data set from a method validation exercise. The tabulated data shows a range of values. Plotting the data in histogram form shows that observations tend to cluster near the center of the data set. The histogram is one possible graphical representation of the *distribution* of the data.

If the experiment is repeated, a visibly different data distribution is usually observed. However, as the

number of observations in an experiment increases, the distribution becomes more consistent from experiment to experiment, tending towards some underlying form. This underlying form is sometimes called the *parent* distribution. In Fig. 3.3, the smooth curve is a plot of a possible parent distribution, in this case, a *normal distribution* with a mean and standard deviation estimated from the data.

There are several important features of the parent distribution shown in Fig. 3.3. First, it can be represented by a mathematical equation – a distribution function – with a relatively small number of parameters. For the normal distribution, the parameters are the mean and population standard deviation. Knowing that the parent distribution is normal, it is possible to summarize a large number of observations simply by giving the mean and standard deviation. This allows large sets of observations to be summarized in terms of the distribution type and the relevant parameters. Second, the distribution can be used predictively to make statements about the likelihood of further observations; in Fig. 3.3, for example, the curve indicates that observations in the region of 2750–2760 mg kg⁻¹ will occur only rarely. The distribution is accordingly important in both describing data and in drawing inferences from the data.

Distributions of Measurement Data. Measurement data can often be expected to follow a normal distribution, and in considering statistical tests for ordinary

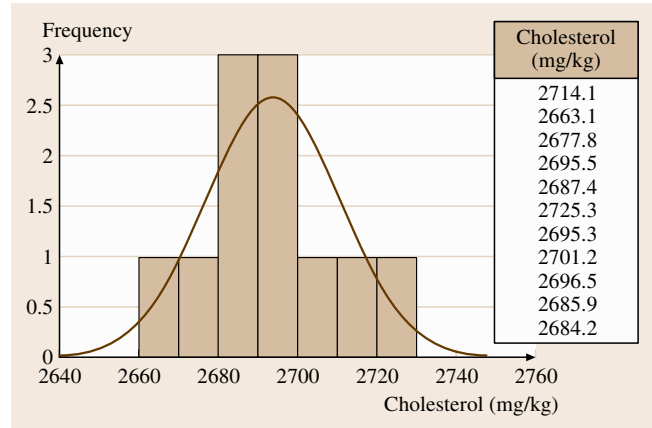


Fig. 3.3 Typical measurement data. Data from 11 replicate analyses of a certified reference material with a certified value of 2747±90 mg/kg cholesterol. The *curve* is a normal distribution with mean and standard deviation calculated from the data, with vertical scaling adjusted for comparability with the histogram

cases, this will be the assumed distribution. However, some other distributions are important in particular circumstances. Table 3.1 lists some common distributions, whose general shape is shown in Fig. 3.4. The most important features of each are

- The normal distribution is described by two independent parameters: the mean and standard deviation. The mean can take any value, and the standard

Table 3.1 Common distributions in measurement data

Distribution	Density function	Mean	Expected variance	Remarks
Normal	$\frac{1}{\sigma\sqrt{2\pi}} \exp\left(-\frac{(x-\mu)^2}{2\sigma^2}\right)$	μ	σ^2	Arises naturally from the summation of many small random errors from any distribution
Lognormal	$\frac{1}{\sigma\sqrt{2\pi}} \exp\left(-\frac{(\ln(x)-\mu)^2}{2\sigma^2}\right)$	$\exp\left(\mu + \frac{\sigma^2}{2}\right)$	$\exp(2\mu + \sigma^2) [\exp(\sigma^2) - 1]$	Arises naturally from the product of many terms with random errors. Approximates to normal for small standard deviation
Poisson	$\lambda^x \exp(-\lambda)/x!$	λ	λ	Distribution of events occurring in an interval; important for radiation counting. Approximates to normality for large λ
Binomial	$\binom{n}{x} p^x (1-p)^{(n-x)}$	np	$np(1-p)$	Distribution of x , the number of successes in n trials with probability of success p . Common in counting at low to moderate levels, such as microbial counts; also relevant in situations dominated by particulate sampling
Contaminated normal	Various			Contaminated normal is the most common assumption given the presence of a small proportion of aberrant results. The <i>correct</i> data follow a normal distribution; aberrant results follow a different, usually much broader, distribution

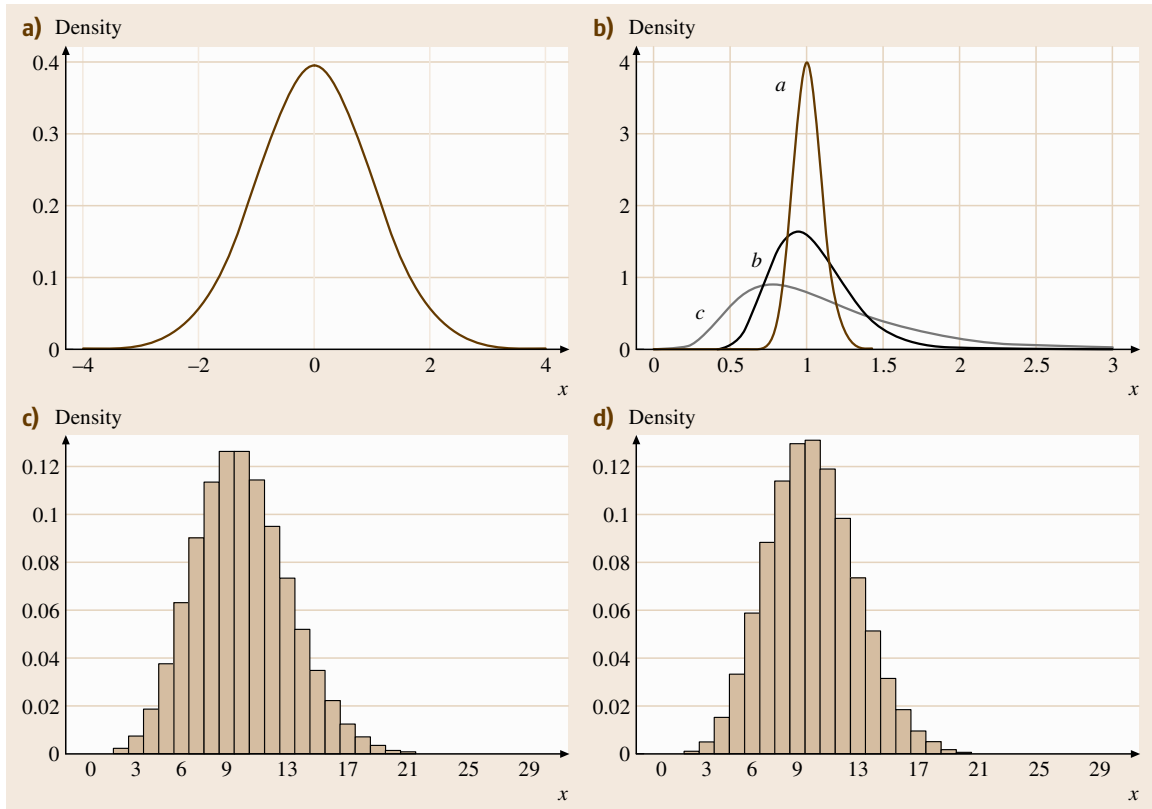


Fig. 3.4a-d Measurement data distributions. Figure 3.4 shows the *probability density function* for each distribution, not the probability; the area under each curve, or sum of discrete values, is equal to 1. Unlike probability, the probability density at a point x can be higher than 1. **(a)** The standard normal distribution (mean = 0, standard deviation = 1.0). **(b)** Lognormal distributions; mean on log scale = 0, standard deviation on log scale = a : 0.1, b : 0.25, c : 0.5. **(c)** Poisson distribution: $\lambda = 10$. **(d)** Binomial distribution: 100 trials, $p(\text{success}) = 0.1$. Note that this provides the same mean as **(c)**

deviation any nonnegative value. The distribution is symmetric about the mean, and although the density falls off sharply, it is actually infinite in extent. The normal distribution arises naturally from the additive combination of many effects, even, according to the central limit theorem, when those effects do not themselves arise from a normal distribution. (This has an important consequence for means; errors in the mean of even three or four observations can often be taken to be normally distributed even where the parent distribution is not.) Furthermore, since small effects generally behave approximately additively, a very wide range of measurement systems show approximately normally distributed error.

- The lognormal distribution is closely related to the normal distribution; the logarithms of values from

a lognormal distribution are normally distributed. It most commonly arises when errors combine multiplicatively, instead of additively. The lognormal distribution itself is generally asymmetric, with positive skew. However, as shown in the figure, the shape depends on the ratio of standard deviation to mean, and approaches that of a normal distribution as the standard deviation becomes small compared with the mean. The simplest method of handling lognormally distributed data is to take logarithms and treat the logged data as arising from a normal distribution. As the standard deviation becomes small relative to the mean, the lognormal distribution tends towards the normal distribution.

- The Poisson and binomial distributions describe counts, and accordingly are *discrete* distributions;

they have nonzero density only for integer values of the variable. The Poisson distribution is applicable to cases such as radiation counting; the binomial distribution is most appropriate for systems dominated by sampling, such as the number of defective parts in a batch, the number of microbes in a fixed volume or the number of contaminated particles in a sample from an inhomogeneous mixture. In the limit of large counts, the binomial distribution tends to the normal distribution; for small probability, it tends to the Poisson distribution. Similarly, the Poisson distribution tends towards normality for small probability and large counts. Thus, the Poisson distribution is often a convenient approximation to the binomial, and as counts increase, the normal distribution can be used to approximate either.

Distributions Derived from the Normal Distribution. Before leaving the topic of distributions, it is important to be aware that other distributions are important in analyzing measurement data with normally distributed error. The most important for this discussion are

- the t -distribution, which describes the distribution of the means of small samples taken from a normal distribution. The t -distribution is routinely used for checking a method for significant bias or for comparing observations with limits,
- the chi-squared distribution, which describes inter alia the distribution of estimates of variance. Specifically, the variable $(n-1)s^2/\sigma^2$ has a chi-squared distribution with $\nu = n-1$ degrees of freedom. The chi-squared distribution is asymmetric with mean ν and variance 2ν ,
- the F -distribution, which describes the distribution of ratios of variances. This is important in comparing the spread of two different data sets, and is extensively used in analysis of variance as well as being useful for comparing the precision of alternative methods of measurement.

Probability and Significance

Given a particular distribution, it is possible to make predictions of the probability that observations will fall within a particular range. For example, in a normal distribution, the fraction of observations falling, by chance, within two standard deviations of the mean value is very close to 95%. This equates to the probability of an observation occurring in that interval. Similarly, the probability of an observation falling more than 1.65 standard deviations above the mean value is close to 5%.

These proportions can be calculated directly from the area under the curves shown in Fig. 3.4, and are available in tabular form, from statistical software and from most ordinary spreadsheet software.

Knowledge of the probability of a particular observation allows some statement about the significance of an observation. Observations with high probability of chance occurrence are not regarded as particularly significant; conversely, observations with a low probability of occurring by chance are taken as significant. Notice that an observation can only be allocated a probability if there is some assumption or hypothesis about the true state of affairs. For example, if it is asserted that the concentration of a contaminant is below some regulatory limit, it is meaningful to consider how likely a particular observation would be *given this hypothesis*. In the absence of any hypothesis, no observation is more likely than any other. This process of forming a hypothesis and then assessing the probability of a particular observation *given the hypothesis* is the basis of significance testing, and will be discussed in detail below.

3.3.2 Calculations and Software

Statistical treatment of data generally involves calculations, and often repetitive calculation. Frequently, too, best practise involves methods that are simply not practical manually, or require numerical solutions. Suitable software is therefore essential. Purpose-designed software for statistics and experimental design is widely available, including some free and open-source packages whose reliability challenges the best commercial software. Some such packages are listed in Sect. 3.12 at the end of this chapter. Many of the tests and graphical methods described in this short introduction are also routinely available in general-purpose spreadsheet packages. Given the wide availability of software and the practical difficulties of implementing accurate numerical software, calculations will not generally be described in detail. Readers should consult existing texts or software for further details if required.

However, it remains important that the software used is reliable. This is particularly true of some of the most popular business spreadsheet packages, which have proven notoriously inaccurate or unstable on even moderately ill-conditioned data sets. Any mathematical software used in a measurement laboratory should therefore be checked using typical measurement data to ensure that the numerical accuracy is sufficient. It may additionally be useful to test software using more

extreme test sets; some such sets are freely available (Sect. 3.12).

3.3.3 Statistical Methods

Graphical Methods

Graphical methods refer to the range of graphs or plots that are used to present and assess data visually. Some have already been presented; the histogram in Fig. 3.3 is an example. Graphical methods are easy to implement with a variety of software and allow a measurement scientist to identify anomalies, such as outlying data points or groups, departures from assumed distributions or models, and unexpected trends, quickly and with minimal calculation. A complete discussion of graphical methods is beyond the scope of this chapter, but some of the most useful, with typical applications, are presented below. Their use is strongly recommended in routine data analysis.

Figure 3.5 illustrates some basic plots appropriate for reviewing simple one-dimensional data sets. Dot

plots and strip charts are useful for reviewing small data sets. Both give a good indication of possible outliers and unusual clustering. Overinterpretation should be avoided; it is useful to gain experience by reviewing plots from random normal samples, which will quickly indicate the typical extent of apparent anomalies in small samples. Strip charts are simpler to generate (plot the data as the x variable with a constant value of y), but overlap can obscure clustering for even modest sets. The stacked dot plot, if available, is applicable to larger sets. Histograms become more appropriate as the number of data points increases. Box plots, or box-and-whisker plots (named for the lines extending from the rectangular box) are useful for summarizing the general shape and extent of data, and are particularly useful for grouped data. For example, the range of data from replicate measurements on several different test items can be reviewed very easily using a box plot. Box plots can represent several descriptive statistics, including, for example, a mean and confidence interval. However, they are most commonly based on quartiles. Traditionally,

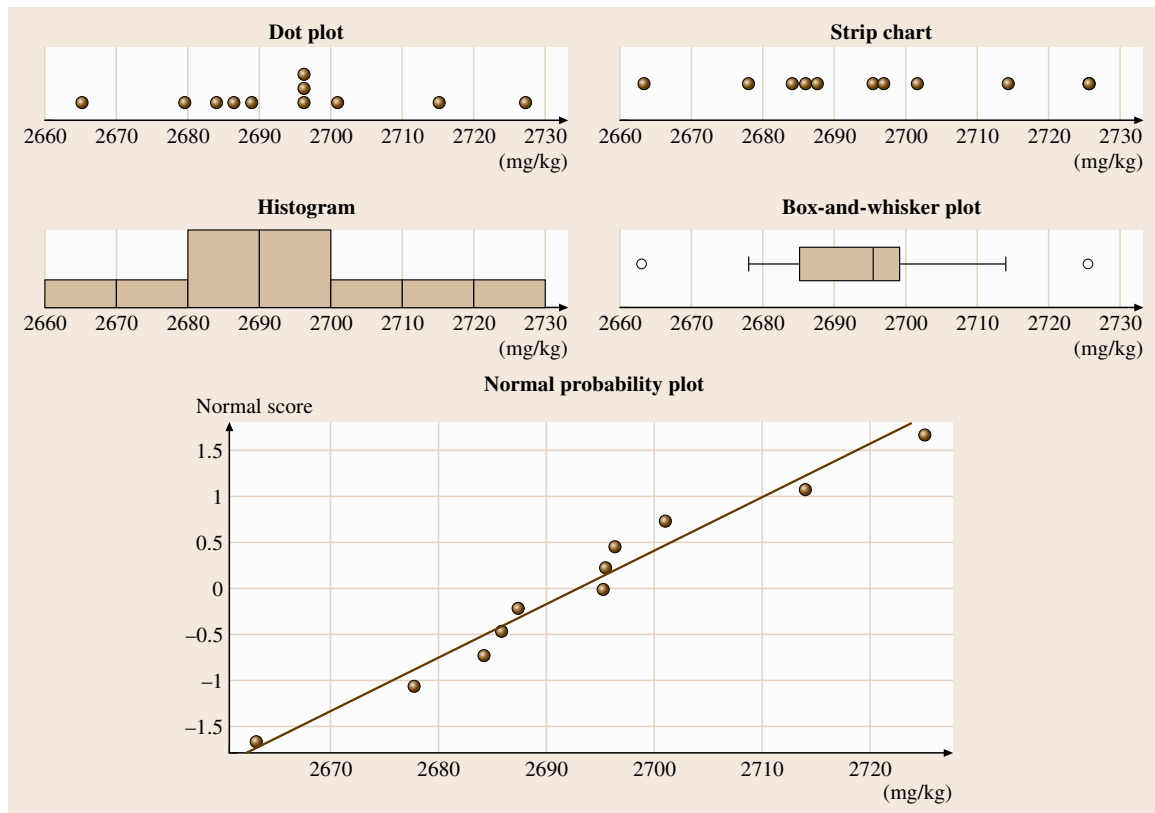


Fig. 3.5 Plots for simple data set review

the box extends from the first to the third quartile (that is, it contains the central 50% of the data points). The median is marked as a dividing line or other marker inside the box. The *whiskers* traditionally extend to the most distant data point within 1.5 times the interquartile range of the ends of the box. For a normal distribution, this would correspond to approximately the mean ± 2.7 standard deviations. Since this is just beyond the 99% confidence interval, more extreme points are likely to be outliers, and are therefore generally shown as individual points on the plot. Finally, a normal probability plot shows the distribution of the data plotted against the expected distribution assuming normality. In a normally distributed data set, points fall close to the diagonal line. Substantial deviations, particularly at either end of the plot, indicate nonnormality.

The most common graphical method for two-dimensional measurement data (such as measurand level/instrument response pairs) is a scatter plot, in which points are plotted on a two-dimensional space with dimensions corresponding to the dimensions of the data set. Scatter plots are most useful in reviewing data for linear regression, and the topic will accordingly be returned to below.

Planning of Experiments

Most measurements represent straightforward application of a measuring device or method to a test item. However, many experiments are intended to test for the presence or absence of some specific treatment effect – such as the effect of changing a measurement method or adjusting a manufacturing method. For example, one might wish to assess whether a reduction in preconditioning time had an effect on measurement results. In these cases, it is important that the experiment measures the intended effect, and not some external nuisance effect. For example, measurement systems often show significant changes from day to day or operator to operator. To continue the preconditioning example, if test items for short preconditioning were obtained by one operator and for long preconditioning by a different operator, operator effects might be misinterpreted as a significant conditioning effect. Ensuring that nuisance parameters do not interfere with the result of an experiment is one of the aims of good experimental design.

A second, but often equally important aim is to minimize the cost of an experiment. For example, a naïve experiment to investigate six possible effects might investigate each individually, using, say, three replicate measurements at each level for each effect: a total of

36 measurements. Careful experimental designs which vary all parameters simultaneously can, using the right statistical methods, reduce this to 16 or even 8 measurements and still achieve acceptable power.

Experimental design is a substantial topic, and a range of reference texts and software are available. Some of the basic principles of good design are, however, summarized below.

1. *Arrange experiments for cancellation*: the most precise and accurate measurements seek to cancel out sources of bias. For example, null-point methods, in which a reference and test item are compared directly by adjusting an instrument to give a zero reading, are very effective in removing bias due to residual current flow in an instrument. Simultaneous measurement of test item and calibrant reduces calibration differences; examples include the use of internal standards in chemical measurement, and the use of comparator instruments in gage block calibration. Difference and ratio experiments also tend to reduce the effects of bias; it is therefore often better to study differences or ratios of responses obtained under identical conditions than to compare absolute measurements.
2. *Control if you can; randomize if you cannot*: a good experimenter will identify the main sources of bias and control them. For example, if temperature is an issue, temperature should be controlled as far as possible. If direct control is impossible, the statistical analysis should include the nuisance parameter. *Blocking* – systematic allocation of test items to different strata – can also help reduce bias. For example, in a 2 day experiment, ensuring that every type of test item is measured an equal number of times on each day will allow statistical analysis to remove the between-day effect. Where an effect is known but cannot be controlled, and also to guard against unknown systematic effects, randomization should be used. For example, measurements should always be made in random order within blocks as far as possible (although the order should be recorded to allow trends to be identified), and test items should be assigned randomly to treatments.
3. *Plan for replication or obtaining independent uncertainty estimates*: without knowledge of the precision available, and more generally of the uncertainty, the experiment cannot be interpreted. Statistical tests all rely on comparison of an effect with some estimate of the uncertainty of the effect, usually based on observed precision. Thus, exper-

iments should always include some replication to allow precision to be estimated, or provide for additional information of the uncertainty.

4. *Design for statistical analysis: To consult a statistician after an experiment is finished is often merely to ask him to conduct a post-mortem examination. He can perhaps say what the experiment died of.* (R. A. Fisher, Presidential Address to the First Indian Statistical Congress, 1938). An experiment should always be planned with a specific method of statistical analysis in mind. Otherwise, despite the considerable range of tools available, there is too high a risk that no statistical analysis will be applicable. One particular issue in this context is that of *balance*. Many experiments test several parameters simultaneously. If more data are obtained on some combinations than others, it may be impossible to separate the different effects. This applies particularly to two-way or higher-order analysis of variance, in which interaction terms are not generally interpretable with unbalanced designs. Imbalance can be tolerated in some types of analysis, but not in all.

Significance Testing

General Principles. Because measurement results vary, there is always some doubt about whether an observed difference arises from chance variation or from an underlying, real difference. Significance testing allows the scientist to make reliable objective judgements on the basis of data gathered from experiments, while protecting against overinterpretation based on chance differences.

A significance test starts with some hypothesis about a true value or values, and then determines whether the observations – which may or may not appear to contradict the hypothesis – could reasonably arise by chance if the hypothesis were correct. Significance tests therefore involve the following general steps.

1. *State the question clearly, in terms of a null hypothesis and an alternate hypothesis:* in most significance testing, the null hypothesis is that there is no effect of interest. The alternate is always an alternative state of affairs such that the two hypotheses are mutually exclusive and that the combined probability of one or the other is equal to 1; that is, that no other situation is relevant. For example, a common null hypothesis about a difference between two values is: *there is no difference between the true val-*

ues ($\mu_1 = \mu_2$). The relevant alternate is that *there is a difference between the true values* ($\mu_1 \neq \mu_2$). The two are mutually exclusive (they cannot both be true simultaneously) and it is certain that one of them is true, so the combined probability is exactly 1.0. The importance of the hypotheses is that different initial hypotheses lead to different estimates of the probability of a contradictory observation. For example, if it is hypothesized that the (true) value of the measurand is exactly equal to some reference value, there is some probability (usually equal) of contradictory observations both above and below the reference value. If, on the other hand, it is hypothesized that the true value is less than or equal to the reference value, the situation changes. If the true value may be anywhere below or equal to the reference value, it is less likely that observations above the reference value will occur, because of the reduced chance of such observations from true values very far below the reference value. This change in probability of observations on one side or another must be reflected either in the choice of critical value, or in the method of calculation of the probability.

2. *Select an appropriate test:* different questions require different tests; so do different distribution assumptions. Table 3.2 provides a summary of the tests appropriate for a range of common situations. Each test dictates the method of calculating a value called the *test statistic* from the data.
3. *Calculate the test statistic:* in software, the test statistic is usually calculated automatically, based on the test chosen.
4. *Choose a significance level:* the significance level is the probability at which chance is deemed sufficiently unlikely to justify rejection of the null hypothesis. It is usually the measurement scientist's responsibility to choose the level of significance appropriately. For most common tests on measurement results, the significance level is set at 0.05,

Table 3.2 Common significance tests for normally distribution data. The following symbols are used: α is the desired significance level (usually 0.05); μ is the (true) value of the measurand; σ is the population standard deviation for the population described by μ (not that calculated from the data). \bar{x} is the observed mean; s is the standard deviation of the data used to calculate \bar{x} ; n is the number of data points. x_0 is the reference value; x_U, x_L are the upper and lower limits of a range. $\mu_1, \mu_2, \bar{x}_1, \bar{x}_2, s_1, s_2, n_1, n_2$ are the corresponding values for each of two sets of data to be compared ►

Test objective	Test name	Test statistic	Remarks
Tests on a single observed mean \bar{x} against a reference value or range			
Test for significant difference from the reference value x_0	Student <i>t</i> -test	$ x_0 - \bar{x} / (s / \sqrt{n})$	Hypothesis ($\mu = x_0$) against alternate ($x_0 \neq \mu$). Use a table of two-tailed critical values
Test for \bar{x} significantly exceeding an upper limit x_0	Student <i>t</i> -test	$(\bar{x} - x_0) / (s / \sqrt{n})$	Hypothesis ($\mu_1 = \mu_2$) against alternate ($\mu_1 > \mu_2$). Use a table of <i>one</i> -tailed critical values. Note that the sign of $x_0 - \bar{x}$ is retained
Test for \bar{x} falling significantly below a lower limit x_0	Student <i>t</i> -test	$(x_0 - \bar{x}) / (s / \sqrt{n})$	
Test for \bar{x} falling significantly outside a range $[x_L, x_U]$	Student <i>t</i> -test	$\max \left[\begin{array}{l} (x_L - \bar{x}) / (s / \sqrt{n}) \\ (\bar{x} - x_U) / (s / \sqrt{n}) \end{array} \right]$	Hypothesis: $x_L \leq \mu \leq x_U$ against the alternate $\mu < x_L, x_U < \mu$. Use a table of <i>one</i> -tailed critical values. This test assumes that the range is large compared with s , but $(x_U - x_L) > s$ gives adequate accuracy at the 5% significance level
Tests for significant difference between two means			
(a) With equal variance	Equal-variance <i>t</i> -test	$ \bar{x}_1 - \bar{x}_2 $	Hypothesis $\mu_1 = \mu_2$ against alternate ($\mu_1 \neq \mu_2$)
(b) With significantly different variance	Unequal-variance <i>t</i> -test		Use a table of two-tailed critical values. For equal variance, take degrees of freedom equal to $n_1 + n_2 - 2$. For unequal variance, take degrees of freedom equal to $\frac{(s_1^2/n_1 + s_2^2/n_2)^2}{[(n_1 - 1)/(s_1/n_1)^2 + (n_2 - 1)/(s_2/n_2)^2]}$
For testing the hypothesis $\mu_1 > \mu_2$ against the alternative $\mu_1 \leq \mu_2$, where μ_1 is the <i>expected</i> larger mean (not necessarily the larger observed mean), calculate the test statistic using $(\bar{x}_1 - \bar{x}_2)$ instead of $ \bar{x}_1 - \bar{x}_2 $ and use a one-tailed critical value			
Test n paired values for significant difference (constant variance)	Paired <i>t</i> -test	$ \bar{d} / (s_d / \sqrt{n})$, where $\bar{d} = \frac{1}{n} \sum_i x_{1,i} - x_{2,i}$ and $s_d = \frac{1}{n-1} \sum_i (x_{1,i} - x_{2,i})^2$	Hypothesis $\mu_d = 0$ against alternate $\mu_d \neq 0$. The sets must consist of pairs of measurements, such as measurements on the same test items by two different methods
Tests for standard deviations			
Test an observed standard deviation against a reference or required value σ_0	i) Chi-squared test	i) $(n-1)s^2/\sigma_0$	i) Compare $(n-1)s^2/\sigma_0$ with critical values for the chi-squared distribution with $n-1$ degrees of freedom
	ii) <i>F</i> -test	ii) s^2/σ_0	ii) Compare s^2/σ_0 with critical values for <i>F</i> for $(n-1)$ and infinite degrees of freedom For a test of $\sigma \leq \sigma_0$ against $\sigma > \sigma_0$, use the upper one-tailed critical value of chi-squared or <i>F</i> for probability α . To test $\sigma = \sigma_0$ against $\sigma \neq \sigma_0$, use two-tailed limits for chi-squared or compare $\max(s^2/\sigma_0, \sigma_0/s^2)$ against the upper one-tailed value for <i>F</i> for probability $\alpha/2$
Test for a significant difference between two observed standard deviations	<i>F</i> -test	s_{\max}^2/s_{\min}^2	Hypothesis: $\sigma_1 = \sigma_2$ against $\sigma_1 \neq \sigma_2$. s_{\max} is the larger observed standard deviation. Use the upper <i>one</i> -tailed critical value for <i>F</i> for a probability $\alpha/2$ using $n_1 - 1, n_2 - 1$ degrees of freedom
Test for one observed standard deviations s_1 significantly exceeding another (s_2)	<i>F</i> -test	s_1^2/s_2^2	Hypothesis: $\sigma_1 \leq \sigma_2$ against $\sigma_1 > \sigma_2$. Use the upper <i>one</i> -tailed critical value for <i>F</i> for a probability α using $n_1 - 1, n_2 - 1$ degrees of freedom
Test for homogeneity of variance among several groups of data	Levene's test	N/A	Levene's test is most simply estimated as a one-way analysis of variance performed on absolute values of group residuals, that is, $ x_{ij} - \hat{x}_j $, where \hat{x}_j is an estimate of the population mean of group j ; \hat{x}_j is usually the median, but the mean or another robust value can be used

or 5%. For stringent tests, 1% significance or less may be appropriate. The term *level of confidence* is an alternative expression of the same quantity; for example, the 5% level of significance is equal to the 95% level of confidence. Mathematically, the significance level is the probability of incorrectly rejecting the null hypothesis given a particular critical value for a test statistic (see below). Thus, one chooses the critical value to provide a suitable significance level.

5. *Calculate the degrees of freedom for the test:* the distribution of error often depends not only on the number of observations n , but on the number of degrees of freedom ν (Greek letter nu). ν is usually equal to the number of observations minus the number of parameters estimated from the data: $n - 1$ for a simple mean value, for example. For experiments involving many parameters or many distinct groups, the number of degrees of freedom may be very different from the number of observations. The number of degrees of freedom is usually calculated automatically in software.
6. *Obtain a critical value:* critical values are obtained from tables for the relevant distribution, or from software. Statistical software usually calculates the critical value automatically given the level of significance.
7. *Compare the test statistic with the critical value or examine the calculated probability (p -value).* Traditionally, the test is completed by comparing the calculated value of the test statistic with the critical value determined from tables or software. Usually (but not always) a calculated value higher than the critical value denotes significance at the chosen level of significance. In software, it is generally more convenient to examine the calculated probability of the observed test statistic, or p -value, which is usually part of the output. The p -value is always between 0 and 1; small values indicate a low probability of chance occurrence. Thus, if the p -value is below the chosen level of significance, the result of the test is significant and the null hypothesis is rejected.

Significance Tests for Specific Circumstances. Table 3.2 provides a summary of the most common significance tests used in measurement for normally distributed data. The calculations for the relevant test statistics are included, although most are calculated automatically by software.

Interpretation of Significance Test Results. While a significance test provides information on whether an observed difference could arise by chance, it is important to remember that statistical significance does not necessarily equate to practical importance. Given sufficient data, very small differences can be detected. It does not follow that such small differences are important. For example, given good precision, a measured mean 2% away from a reference value may be statistically significant. If the measurement requirement is to determine a value within 10%, however, the 2% bias has little practical importance.

The other chief limitation of significance testing is that a lack of statistical significance cannot prove the absence of an effect. It should be interpreted only as an indication that the experiment failed to provide sufficient evidence to conclude that there was an effect. At best, statistical insignificance shows only that the effect is not large compared with the experimental precision available. Where many experiments fail to find a significant effect, of course, it becomes increasingly safe to conclude that there is none.

Effect of Nonconstant Standard Deviation. Significance tests on means assume that the standard deviation is a good estimate of the population standard deviation and that it is constant with μ . This assumption breaks down, for example, if the standard deviation is approximately proportional to μ , a common observation in many fields of measurement (including analytical chemistry and radiological counting, although the latter would use intervals based on the Poisson distribution). In conducting a significance test in such circumstances, the test should be based on the best estimate of the standard deviation at the hypothesized value of μ , and not that at the value \bar{x} . To take a specific example, in calculating whether a measured value significantly exceeds a limit, the test should be based on the standard deviation at the limit, not at the observed value.

Fortunately, this is only a problem when the standard deviation depends very strongly on μ in the range of interest and where the standard deviation is large compared with the mean to be tested. For s/\bar{x} less than about 0.1, for example, it is rarely important.

Confidence Intervals

Statistical Basis of Confidence Intervals. A confidence interval is an interval within which a statistic (such as a mean or a single observation) would be expected to be observed with a specified probability.

Significance tests are closely related to the idea of confidence intervals. Consider a test for significant difference between an observed mean \bar{x} (taken from n values with standard deviation s) against a hypothesized measurand value μ . Using a t -test, the difference is considered significant at the level of confidence $1 - \alpha$ if

$$\frac{|\bar{x} - \mu|}{s/\sqrt{n}} > t_{\alpha, v, 2},$$

where $t_{\alpha, v, 2}$ is the two-tailed critical value of Student's t at a level of significance α . The condition for an *insignificant* difference is therefore

$$\frac{|\bar{x} - \mu|}{s/\sqrt{n}} \leq t_{\alpha, v, 2}.$$

Rearranging gives $|\bar{x} - \mu| \leq t_{\alpha, v, 2}s/\sqrt{n}$, or equivalently, $-t_{\alpha, v, 2}s/\sqrt{n} \leq \bar{x} - \mu \leq t_{\alpha, v, 2}s/\sqrt{n}$. Adding \bar{x} and adjusting signs and inequalities accordingly gives

$$\bar{x} - t_{\alpha, v, 2}s/\sqrt{n} \leq \mu \leq \bar{x} + t_{\alpha, v, 2}s/\sqrt{n}.$$

This interval is called the $1 - \alpha$ *confidence interval* for μ . Any value of μ within this interval would be considered consistent with \bar{x} under a t -test at significance level α .

Strictly, this confidence interval cannot be interpreted in terms of the probability that μ is within the interval $\bar{x} \pm t_{\alpha, v, 2}s/\sqrt{n}$. It is, rather, that, in a long succession of similar experiments, a proportion $100(1 - \alpha)\%$ of the calculated confidence intervals would be expected to contain the true mean μ . However, because the significance level α is chosen to ensure that this proportion is reasonably high, a confidence interval does give an indication of the range of values that can reasonably be attributed to the measurand, based on the statistical information available so far. (It will be seen later that other information may alter the range of values we may attribute to the measurand.)

For most practical purposes, the confidence interval is quoted at the 95% level of confidence. The value of t for 95% confidence is approximately 2.0 for large degrees of freedom; it is accordingly common to use the range $\bar{x} \pm 2s/\sqrt{n}$ as an approximate 95% confidence interval for the value of the measurand.

Note that, while the confidence interval is in this instance symmetrical about the measured mean value, this is by no means always the case. Confidence intervals based on Poisson distributions are markedly asymmetric, as are those for variances. Asymmetric confidence intervals can also be expected when the standard deviation varies strongly with μ , as noted above in relation to significance tests.

Before leaving the topic of confidence intervals, it is worth noting that the use of confidence intervals is not limited to mean values. Essentially any estimated parameter estimate has a confidence interval. It is often simpler to compare some hypothesized value of the parameter with the confidence interval than to carry out a significance test. For example, a simple test for significance of an intercept in linear regression (below) is to see whether the confidence interval for the intercept includes zero. If it does, the intercept is not statistically significant.

Analysis of Variance

Introduction to ANOVA. Analysis of variance (ANOVA) is a general tool for analyzing data grouped by some factor or factors of interest, such as laboratory, operator or temperature. ANOVA allows decisions on which factors are contributing significantly to the overall dispersion of the data. It can also provide a direct measure of the dispersion due to each factor.

Factors can be qualitative or quantitative. For example, replicate data from different laboratories are grouped by the qualitative factor *laboratory*. This single-factor data would require one-way analysis of variance. In an experiment to examine time and temperature effects on a reaction, the data are grouped by both time and temperature. Two factors require two-way analysis of variance. Each factor treated by ANOVA must take two or more values, or *levels*. A combination of factor levels is termed a *cell*, since it forms a cell in a table of data grouped by factor levels. Table 3.3 shows an example of data grouped by time and temperature. There are two factors (time and temperature), and each has three levels (distinct values). Each cell (that is, each time/temperature combination) holds two observations.

The calculations for ANOVA are best done using software. Software can automate the traditional manual calculation, or can use more general methods. For example, simple grouped data with equal numbers of replicates within each cell are relatively simple to ana-

Table 3.3 Example data for two-way ANOVA

Time (min)	Temperature (K)		
	298	315	330
10	6.4	11.9	13.5
10	8.4	4.8	16.7
12	7.8	10.6	17.6
12	10.1	11.9	14.8
9	1.5	8.1	13.2
9	3.9	7.6	15.6

lyze using summation and sums of squares. Where there are different numbers of replicates per cell (referred to as an unbalanced design), ANOVA is better carried out by linear modeling software. Indeed, this is often the default method in current statistical software packages. Fortunately, the output is generally similar whatever the process used. This section accordingly discusses the interpretation of output from ANOVA software, rather than the process itself.

One-Way ANOVA. One-way ANOVA operates on the assumption that there are two sources of variance in the data: an effect that causes the true mean values of groups to differ, and another that causes data within each group to disperse. In terms of a statistical model, the i -th observation in the j -th group, x_{ij} , is given by

$$x_{ij} = \mu + \delta_j + \varepsilon_{ij},$$

where δ and ε are usually assumed to be normally distributed with mean 0 and standard deviations σ_b and σ_w , respectively. The subscripts “b” and “w” refer to the between-group effect and the within-group effect, respectively. A typical ANOVA table for one-way ANOVA is shown in Table 3.4 (The data analyzed are shown, to three figures only, in Table 3.5). The important features are

- The row labels, *Between groups* and *Within groups*, refer to the estimated contributions from each of the two effects in the model. The *Total* row refers to the total dispersion of the data.
- The columns “SS” and “df” are the sum of squares (actually, the sum of squared deviations from the relevant mean value) and the degrees of freedom for each effect. Notice that the total sum of squares and degrees of freedom are equal to the sum of those in the rows above; this is a general feature of ANOVA, and in fact the between-group SS and df can be calculated from the other two rows.
- The “MS” column refers to a quantity called the mean square for each effect. Calculated by dividing the sum of squares by the degrees of freedom, it can be shown that each mean square is an estimated

variance. The between-group mean square (MS_b) estimates $n_w\sigma_b^2 + \sigma_w^2$ (where n_w is the number of values in each group); the within-group mean square (MS_w) estimates the within-group variance σ_w^2 .

It follows that, if the between-group contribution were zero, the two mean squares should be the same, while if there were a real between-group effect, the between-group mean square would be larger than the within-group mean square. This allows a test for significance, specifically, a one-sided F -test. The table accordingly gives the calculated value for $F (= MS_b/MS_w)$, the relevant critical value for F using the degrees of freedom shown, and the p -value, that is, the probability that $F \geq F_{\text{calc}}$ given the null hypothesis. In this table, the p -value is approximately 0.08, so in this instance, it is concluded that the difference is not statistically significant. By implication, the instruments under study show no significant differences.

Finally, one-way ANOVA is often used for interlaboratory data to calculate repeatability and reproducibility for a method or process. Under interlaboratory conditions, repeatability standard deviation s_r is simply $\sqrt{MS_w}$.

The reproducibility standard deviation s_R is given by

$$s_R = \sqrt{\frac{MS_b + (n_w - 1)MS_w}{n_w}}.$$

Two-Way ANOVA. Two-way ANOVA is interpreted in a broadly similar manner. Each effect is allocated a row in an ANOVA table, and each main effect (that is, the effect of each factor) can be tested against the within-group term (often called the residual, or error, term in higher-order ANOVA tables). There is, however, one additional feature found in higher-order ANOVA tables: the presence of one or more *interaction terms*.

By way of example, Table 3.6 shows the two-way ANOVA table for the data in Table 3.3. Notice the *Interaction* row (in some software, this would be labeled *Time:Temperature* to denote which interaction it referred to). The presence of this row is best understood

Table 3.4 One-way ANOVA. Analysis of variance table

Source of variation	SS	df	MS	F	P-value	F _{crit}
Between groups	8.85	3	2.95	3.19	0.084	4.07
Within groups	7.41	8	0.93			
Total	16.26	11				

Table 3.5 One-way ANOVA. Data analyzed

Instrument			
A	B	C	D
58.58	59.89	60.76	61.80
60.15	61.02	60.78	60.60
59.65	61.40	62.90	62.50

by reference to a new statistical model

$$x_{ijk} = \mu + A_j + B_k + AB_{jk} + \varepsilon_{ijk} .$$

Assume for the moment that the factor A relates to the columns in Table 3.3, and the factor B to the rows. This model says that each level j of factor A shifts all results in column j by an amount A_j , and each level k of factor B shifts all values in row k by an amount B_j . This alone would mean that the effect of factor A is independent of the level of factor B . Indeed it is perfectly possible to analyze the data using the statistical model $x_{ijk} = \mu + A_j + B_k + \varepsilon_{ijk}$ to determine these main effects – even without replication; this is the basis of so-called two-way ANOVA without replication. However, it is possible that the effects of A and B are not independent; perhaps the effect of factor A depends on the level of B . In a chemical reaction, this is not unusual; the effect of time on reaction yield is generally dependent on the temperature, and vice versa. The term AB_{jk} in the above model allows for this, by associating a possible additional effect with every combination of factor levels A and B . This is the interaction term, and is the term referred to by the *Interaction* row in Table 3.6. If it is significant with respect to the within-group, or error, term, this indicates that the effects of the two main factors are not independent.

In general, in an analysis of data on measurement systems, it is safe to assume that the levels of the factors A and B are chosen from a larger possible population. This situation is analyzed, in two-way ANOVA, as a *random-effects model*. Interpretation of the ANOVA table in this situation proceeds as follows.

Table 3.6 Two-way ANOVA table

Source of variation	SS	df	MS	F	P-value	F _{crit}
Time	44.6	2	22.3	4.4	0.047	4.26
Temperature	246.5	2	123.2	24.1	0.0002	4.26
Interaction	15.4	4	3.8	0.8	0.58	3.63
Within	46.0	9	5.1			
Total	352.5	17	154.5			

1. Compare the interaction term with the within-group term.
2. If the interaction term is *not* significant, the main effects can be compared directly with the within-group term, as usually calculated in most ANOVA tables. In this situation, greater power can be obtained by pooling the within-group and interaction term, by adding the sums of squares and the degrees of freedom values, and calculating a new mean square from the new combined sum of squares and degrees of freedom. In Table 3.6, for example, the new mean square would be 4.7, and (more importantly) the degrees of freedom for the pooled effect would be 13, instead of 9. The resulting p -values for the main effects drop to 0.029 and 3×10^{-5} as a result. With statistical software, it is simpler to repeat the analysis omitting the interaction term, which gives the same results.
3. If the interaction term *is* significant, it should be concluded that, even if the main effects are not statistically significant in isolation, their combined effect is statistically significant. Furthermore, the effects are not independent of one another. For example, high temperature and long times might increase yield more than simply raising the temperature or extending the time in isolation. Second, compare the main effects with the interaction term (using an F -test on the mean squares) to establish whether each main effect has a statistically significant additional influence – that is, in addition to its effect in combination – on the results.

The analysis proceeds differently where both factors are *fixed effects*, that is, not drawn from a larger population. In such cases, all effects are compared directly with the within-group term.

Higher-order ANOVA models can be constructed using statistical software. It is perfectly possible to analyze simultaneously for any number of effects and all their interactions, given sufficient replication. However,

in two-way and higher-order ANOVA, some cautionary notes are important.

Assumptions in ANOVA. ANOVA (as presented above) assumes normality, and also assumes that the within-group variances arise from the same population. Departures from normality are not generally critical; most of the mean squares are related to sums of squares of group means, and as noted above, means tend to be normally distributed even where the parent distribution is nonnormal. However, severe outliers can have serious effects; a single severe outlier can inflate the within-group mean square drastically and thereby obscure significant main effects. Outliers can also lead to spurious significance – particularly for interaction terms – by moving individual group means. Careful inspection to detect outliers is accordingly important. Graphical methods, such as box plots, are ideal for this purpose, though other methods are commonly applied (see *Outlier detection* below).

The assumption of equal variance (homoscedasticity) is often more important in ANOVA than that of normality. Count data, for example, manifest a variance related to the mean count. This can cause seriously misleading interpretation. The general approach in such cases is to transform the data to give constant variance (not necessarily normality) for the transformed data. For example, Poisson-distributed count data, for which the variance is expected to be equal to the mean value, should be transformed by taking the square root of each value before analysis; this provides data that satisfies the assumption of homoscedasticity to a reasonable approximation.

Effect of Unbalanced Design. Two-way ANOVA usually assumes that the design is balanced, that is, all cells are populated and all contain equal numbers of observations. If this is not the case, the order that terms appear in the model becomes important, and changing the order can affect the apparent significance. Furthermore, the mean squares no longer estimate isolated effects, and comparisons no longer test useful hypotheses.

Advanced statistical software can address this issue to an extent, using various modified sums of squares (usually referred to as type II, III etc.). In practise, even these are not always sufficient. A more general approach is to proceed by constructing a linear model containing all the effects, then comparing the residual mean square with that for models constructed by omitting each main effect (or interaction term) in turn. Significant differences in the residual mean square indicate a significant effect, independently of the order of specification.

Least-Squares Linear Regression

Principles of Least-Squares Regression. Linear regression estimates the coefficients α_i of a model of the general form

$$Y = \alpha_0 + \alpha_1 X_1 + \alpha_2 X_2 + \dots + \alpha_n X_n ,$$

where, most generally, each variable X is a *basis function*, that is, some function of a measured variable. Thus, the term covers both multiple regression, in which each X may be a different quantity, and polynomial regression, in which successive basis functions X are increasing powers of the independent variable (e.g., x , x^2 etc.). Other forms are, of course, possible. These all fall into the class of linear regression because they are linear in the coefficients α_i , not because they are linear in the variable X . However, the most common use of linear regression in measurement is to estimate the coefficients in the simple model

$$Y = \alpha_0 + \alpha_1 X ,$$

and this simple form – the form usually implied by the unqualified term *linear regression* – is the subject of this section.

The coefficients for the linear model above can be estimated using a surprisingly wide range of procedures, including robust procedures, which are resistant to the effects of outliers, and nonparametric methods, which make no distribution assumptions. In practise, by far the most common is simple least-squares linear regression, which provides the minimum-variance unbiased estimate of the coefficients when all errors are in the dependent variable Y and the error in Y is normally distributed. The statistical model for this situation is

$$y_i = \alpha_0 + \alpha_1 x_i + \varepsilon_i ,$$

where ε_i is the usual error term and α_i are the true values of the coefficients, with estimated values a_i . The coefficients are estimated by finding the values that minimize the sum of squares

$$\sum_i w_i [y_i - (a_0 + a_1 x_i)]^2 ,$$

where the w_i are weights chosen appropriately for the variance associated with each point y_i . Most simple regression software sets the weights equal to 1, implicitly assuming equal variance for all y_i . Another common procedure (rarely available in spreadsheet implementations) is to set $w_i = 1/s_i^2$, where s_i is the standard deviation at y_i ; this *inverse variance weighting* is the correct weighting where the standard deviation varies significantly across the y_i .

The calculations are well documented elsewhere and, as usual, will be assumed to be carried out by software. The remainder of this section accordingly discusses the planning and interpretation of linear regression in measurement applications.

Planning for Linear Regression. Most applications of linear regression for measurement relate to the construction of a calibration curve (actually a straight line). The instrument response for a number of reference values is obtained, and the calculated coefficients a_i used to estimate the measurand value from signal responses on test items. There are two stages to this process. At the validation stage, the linearity of the response is checked. This generally requires sufficient power to detect departures from linearity and to investigate the dependence of precision on response. For routine measurement, it is sufficient to reestablish the calibration line for current circumstances; this generally requires sufficient uncertainty and some protection against erroneous readings or reference material preparation.

In the first, validation, study, a minimum of five levels, approximately equally spaced across the range of interest, are recommended. Replication is vital if a dependence of precision on response is likely; at least three replicates are usually required. Higher numbers of both levels and replication provide more power.

At the routine calibration stage, if the linearity is very well known over the range of interest and the intercept demonstrably insignificant, single-point calibration is feasible; two-point calibration may also be feasible if the intercept is nonzero. However, since there is then no possibility of checking either the internal consistency of the fit, or the quality of the fit, suitable quality control checks are essential in such cases. To provide additional checks, it is often useful to run a minimum of four to five levels; this allows checks for outlying values and for unsuspected nonlinearity. Of course, for extended calibration ranges, with less well-known linearity, it will be valuable to add further points. In the following discussion, it will be assumed that at least five levels are included.

Interpreting Regression Statistics. The first, and perhaps most important, check on the data is to inspect the fitted line visually, and wherever possible to check a residual plot. For unweighted regression (i. e., where $w_i = 1.0$) the residual plot is simply a scatter plot of the values $y_i - (a_0 + a_1x_i)$ against x_i . Where weighted regression is used, it is more useful to plot the weighted residuals $w_i[y_i - (a_0 + a_1x_i)]$. Figure 3.6 shows an ex-

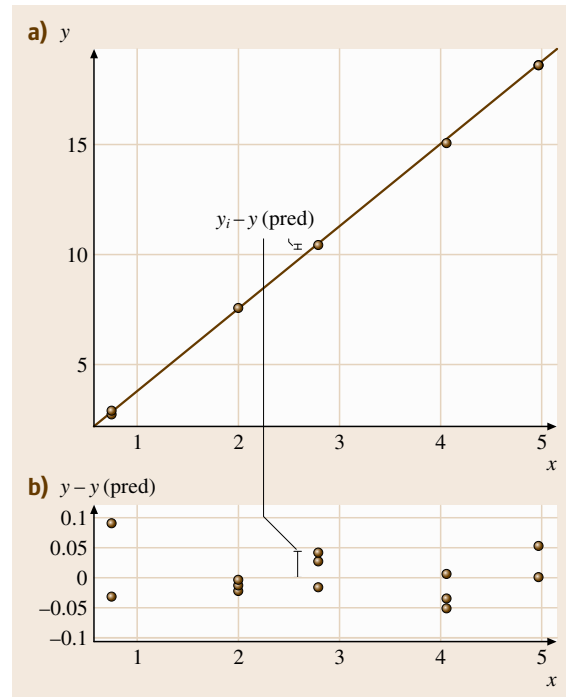


Fig. 3.6a,b Linear regression

ample, including the fitted line and data (Fig. 3.6a) and the residual plot (Fig. 3.6b). The residual plot clearly provides a much more detailed picture of the dispersion around the line. It should be inspected for evidence of curvature, outlying points, and unexpected changes in precision. In Fig. 3.6, for example, there is no evidence of curvature, though there might be a high outlying point at $x_i = 1$.

Regression statistics include the correlation coefficient r (or r^2) and a derived correlation coefficient r^2 (adjusted), plus the regression parameters a_i and (usually) their standard errors, confidence intervals, and a p -value for each based on a t -test for difference compared with the null hypothesis of zero for each.

The regression coefficient is always in the range -1 to 1 . Values nearer zero indicate a lack of linear relationship (not necessarily a lack of *any* relationship); values near 1 or -1 indicate a strong linear relationship. The regression coefficient will always be high when the data are clustered at the ends of the plot, which is why it is good practise to space points approximately evenly. Note that r and r^2 approach 1 as the number of degrees of freedom approaches zero, which can lead to overinterpretation. The adjusted r^2 value protects against this,

as it decreases as the number of degrees of freedom reduces.

The regression parameters and their standard errors should be examined. Usually, in calibration, the intercept a_0 is of interest; if it is insignificant (judged by a high p -value, or a confidence interval including zero) it may reasonably be omitted in routine calibration. The slope a_1 should always be highly significant in any practical calibration. If a p -value is given for the regression as a whole, this indicates, again, whether there is a significant linear relationship; this is usually well known in calibration, though it is important in exploratory analysis (for example, when investigating a possible effect on results).

Prediction from Linear Calibration. If the regression statistics and residual plot are satisfactory, the curve can be used for prediction. Usually, this involves estimating a value x_0 from an observation y_0 . This will, for many measurements, require some estimate of the uncertainty associated with prediction of a measurand value x from an observation y . Prediction uncertainties are, unfortunately, rarely available from regression software. The relevant expression is therefore given below.

$$s_{x_0} = \frac{s_{(y/x)}}{a_1} \left(w_0 + \frac{1}{n} + \frac{(y_0 - \bar{y}_w)^2}{a_1^2 \sum (w_i x_i^2 - n \bar{x}_w^2)} \right)^{1/2}$$

s_{x_0} is the *standard error of prediction* for a value x_0 predicted from an observation y_0 ; $s_{(y/x)}$ is the (weighted) residual standard deviation for the regression; \bar{y}_w and \bar{x}_w are the weighted means of the x and y data used in the calibration; n is the number of (x, y) pairs used; w_0 is a weighting factor for the observation y_0 ; if y_0 is a mean of n_0 observations, w_0 is $1/n_0$ if the calibration used unweighted regression, or is calculated as for the original data if weighting is used; s_{x_0} is the uncertainty arising from the calibration and precision of observation of y_0 in a predicted value x_0 .

Outlier Detection

Identifying Outliers. Measurement data frequently contain a proportion of extreme values arising from procedural errors or, sometimes, unusual test items. It is, however, often difficult to distinguish erroneous values from chance variations, which can also give rise to occasional extreme values. Outlier detection methods help to distinguish between chance occurrence as part of the normal population of data, and values that cannot reasonably arise from random variability.

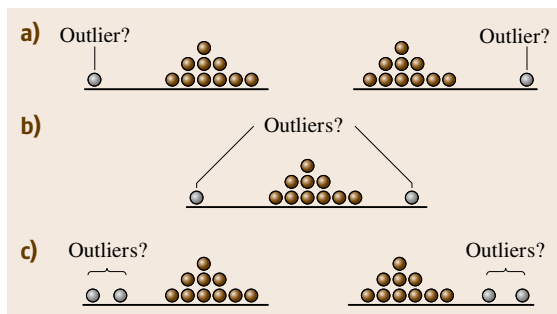


Fig. 3.7a–c Possible outliers in data sets

Graphical methods are effective in identifying possible outliers for follow-up. Dot plots make extreme values very obvious, though most sets have at least some apparent extreme values. Box-and-whisker plots provide an additional quantitative check; any single point beyond the whisker ends is unlikely to arise by chance in a small to medium data set. Graphical methods are usually adequate for the principal purpose of identifying data points which require closer inspection, to identify possible procedural errors. However, if critical decisions (including rejection – see below) are to be taken, or to protect against unwarranted follow-up work, graphical inspection should always be supported by statistical tests. A variety of tests are available; the most useful for measurement work are listed in Table 3.7. Grubb's tests are generally convenient (given the correct tables); they allow tests for single outliers in an otherwise normally distributed data set (Fig. 3.7a), and for simultaneous outlying pairs of extreme values (Fig. 3.7b, c), which would otherwise cause outlier tests to fail. Cochran's test is effective in identifying outlying variances, an important problem if data are to be subjected to analysis of variance or (sometimes) in quality control.

Successive application of outlier tests is permitted; it is not unusual to find that one exceptionally extreme value is accompanied by another, less extreme value. This simply involves testing the remainder of the data set after discovering an outlier.

Action on Detecting Outliers. A statistical outlier is only *unlikely* to arise by chance. In general, this is a signal to investigate and correct the cause of the problem. As a general rule, outliers should not be removed from the data set simply because of the result of a statistical test. However, many statistical procedures are seriously undermined by erroneous values, and long experience suggests that human error is the most common cause

Table 3.7 Tests for outliers in normally distributed data. The following assume an ordered set of data $x_1 \dots x_n$. Tables of critical values for the following can be found in ISO 5725:1995 part 2, among other sources. Symbols otherwise follow those in Table 3.2

Test objective	Test name	Test statistic	Remarks
Test for a single outlier in an otherwise normal distribution	i) Dixon's test	$n = 3 \dots 7 :$ $(x_n - x_{n-1}) / (x_n - x_1)$ $n = 8 \dots 10 :$ $(x_n - x_{n-1}) / (x_n - x_2)$ $n = 10 \dots 30 :$ $(x_n - x_{n-2}) / (x_n - x_3)$	The test statistics vary with the number of data points. Only the test statistic for a high outlier is shown; to calculate the test statistic for a low outlier, renumber the data in descending order. Critical values must be found from tables of Dixon's test statistic if not available in software
	ii) Grubb's test 1	$(x_n - \bar{x}) / s$ (high outlier) $(\bar{x} - x_1) / s$ (low outlier)	Grubb's test is simpler than Dixon's test if using software, although critical values must again be found from tables if not available in software
Test for two outliers on opposite sides of an otherwise normal distribution	Grubb's test 2	$1 - \left(\frac{(n-3)[s(x_3 \dots x_n)]^2}{(n-1)s^2} \right)$	$s(x_3 \dots x_n)$ is the standard deviation for the data excluding the two suspected outliers. The test can be performed on data in both ascending and descending order to detect paired outliers at each end. Critical values must use the appropriate tables
Test for two outliers on the same side of an otherwise normal distribution	Grubb's test 3	$(x_n - x_1) / s$	Use tables for Grubb's test 3
Test for a single high variance in l groups of data	Cochran's test	$C_{\bar{n}} = \frac{(s^2)_{\max}}{\sum_{i=1,l} s_i^2}$	$\bar{n} = \frac{1}{l} \sum_{i=1,l} n_i$

of extreme outliers. This experience has given rise to some general rules which are often used in processing, for example, interlaboratory data.

1. Test at the 95% and the 99% confidence level.
2. All outliers should be investigated and any errors corrected.
3. Outliers significant at the 99% level may be rejected unless there is a technical reason to retain them.
4. Outliers significant only at the 95% level should be rejected only if there is an additional, technical reason to do so.
5. Successive testing and rejection is permitted, but not to the extent of rejecting a large proportion of the data.

This procedure leads to results which are not unduly biased by rejection of chance extreme values, but are relatively insensitive to outliers at the frequency commonly encountered in measurement work. Note, however, that this objective can be attained without out-

lier testing by using robust statistics where appropriate; this is the subject of the next section.

Finally, it is important to remember that an outlier is only outlying in relation to some prior expectation. The tests in Table 3.7 assume underlying normality. If the data were Poisson distributed, for example, too many high values would be rejected as inconsistent with a normal distribution. It is generally unsafe to reject, or even test for, outliers unless the underlying distribution is known.

Robust Statistics

Introduction. Instead of rejecting outliers, robust statistics uses methods which are less strongly affected by extreme values. A simple example of a robust estimate of a population mean is the median, which is essentially unaffected by the exact value of extreme points. For example, the median of the data set (1, 2, 3, 4, 6) is identical to that of (1, 2, 3, 4, 60). The median, however, is substantially more variable than the mean when

the data are not outlier-contaminated. A variety of estimators have accordingly been developed that retain a useful degree of resistance to outliers without unduly affecting performance on normally distributed data. A short summary of the main estimators for means and standard deviations is given below. Robust methods also exist for analysis of variance, linear regression, and other modeling and estimation approaches.

Robust Estimators for Population Means. The median, as noted above, is a relatively robust estimator, widely available in software. It is very resistant to extreme values; up to half the data may go to infinity without affecting the median value. Another simple robust estimate is the so-called trimmed mean: the mean of the data set with two or more of the most extreme values removed. Both suffer from increases in variability for normally distributed data, the trimmed mean less so.

The mean suffers from outliers in part because it is a least-squares estimate, which effectively gives values a weight related to the square of their distance from the mean (that is, the *loss function* is quadratic). A general improvement can be obtained using methods which use a modified loss function. Huber (see Sect. 3.12 *Further Reading*) suggested a number of such estimators, which allocate a weight proportional to squared distance up to some multiple c of the estimated standard deviation \hat{s} for the set, and thereafter a weight proportional to distance. Such estimators are called M-estimators, as they follow from maximum-likelihood considerations. In Huber's proposal, the algorithm used is to replace each value x_i in a data set with z_i , where

$$z_i = \begin{cases} x_i & \text{if } \hat{X} - c \times \hat{s} < x_i < \hat{X} + c \times \hat{s} \\ \hat{X} \pm c \times \hat{s} & \text{otherwise} \end{cases},$$

and recalculate the mean \hat{X} , applying the process iteratively until the result converges. A suitable one-dimensional search algorithm may be faster. The estimated standard deviation is usually determined using a separate robust estimator, or (in Huber's proposal 2) iteratively, together with the mean. Another well-known approach is to use Tukey's biweight as the loss function; this also reduces the weight of extreme observations (to zero, for very extreme values).

Robust Estimators of Standard Deviation. Two common robust estimates of standard deviation are based on rank order statistics, such as the median. The first, the median absolute deviation (**MAD**), calculates the median of absolute deviations from the estimated mean

value \hat{x} , that is, median ($|x_i - \hat{x}|$). This value is not directly comparable to the standard deviation in the case of normally distributed data; to obtain an estimate of the standard deviation, a modification known as **MAD_e** should be used. This is calculated as **MAD**/0.6745. Another common estimate is based on the interquartile range (**IQR**) of a set of data; a normal distribution has standard deviation **IQR**/1.349. The **IQR** method is slightly more variable than the **MAD_e** method, but is usually easier to implement, as quartiles are frequently available in software. Huber's proposal 2 (above) generates a robust estimate of standard deviation as part of the procedure; this estimate is expected to be identical to the usual standard deviation for normally distributed data. **ISO 5725** provides an alternative iterative procedure for a robust standard deviation independently of the mean.

Using Robust Estimators. Robust estimators can be thought of as providing good estimates of the parameters for the good data in an outlier-contaminated set. They are appropriate when

- The data are expected to be normally distributed. Here, robust statistics give answers very close to ordinary statistics.
- The data are expected to be normally distributed, but contaminated with occasional spurious values, which are regarded as unrepresentative or erroneous. Here, robust estimators are less affected by occasional extreme values and their use is recommended. Examples include setting up quality control (**QC**) charts from real historical data with occasional errors, and interpreting interlaboratory study data with occasional problem observations.

Robust estimators are not recommended where

- The data are expected to follow nonnormal distributions, such as binomial, Poisson, chi-squared, etc. These generate extreme values with reasonable likelihood, and robust estimates based on assumptions of underlying normality are not appropriate.
- Statistics that represent the whole data distribution (including extreme values, outliers, and errors) are required.

3.3.4 Statistics for Quality Control

Principles

Quality control applies statistical concepts to monitor processes, including measurement processes, and

detect significant departures from normal operation. The general approach to statistical quality control for a measurement process is

1. regularly measure one or more typical test items (control materials),
2. establish the mean and standard deviation of the values obtained over time (ignoring any erroneous results),
3. use these parameters to set up warning and action criteria.

The criteria can include checks on stability of the mean value and, where measurements on the control material are replicated, on the precision of the process. It is also possible to seek evidence of emerging trends in the data, which might warn of impending or actual problems with the process.

The criteria can be in the form of, for example, permitted ranges for duplicate measurements, or a range within which the mean value for the control material must fall. Perhaps the most generally useful implementation, however, is in the form of a control chart. The following section therefore describes a simple control chart for monitoring measurement processes.

There is an extensive literature on statistical process control and control charting in particular, including a wide range of methods. Some useful references are included in Sect. 3.12 *Further Reading*.

Control Charting

A control chart is a graphical means of monitoring a measurement process, using observations plotted in a time-ordered sequence. Several varieties are in common use, including cusum charts (sensitive to sustained small bias) and range charts, which control precision. The type described here is based on a Shewhart mean chart. To construct the chart

- Obtain the mean \bar{x} and standard deviation s of at least 20 observations (averages if replication is used) on a control material. Robust estimates are recommended for this purpose, but at least ensure that no erroneous or aberrant results are included in this preliminary data.
- Draw a chart with date as the x -axis, and a y -axis covering the range approximately $\bar{x} \pm 4s$.
- Draw the mean as a horizontal line on the chart. Add two *warning limits* as horizontal lines at $\bar{x} \pm 2s$, and two further *action limits* at $\bar{x} \pm 3s$. These limits are approximate. Exact limits for specific probabil-

ities are provided in, for example, ISO 8258:1991 *Shewhart control charts*.

As further data points are accumulated, plot each new point on the chart. An example of such a chart is shown in Fig. 3.8.

Interpreting Control Chart Data

Two rules follow immediately from the action and warning limits marked on the chart.

- A point outside the action limits is very unlikely to arise by chance; the process should be regarded as out of control and the reason investigated and corrected.
- A point between the warning and action limits could happen occasionally by chance (about 4–5% of the time). Unless there is additional evidence of loss of control, no action follows. It may be prudent to remeasure the control material.

Other rules follow from unlikely sequences of observations. For example, two points outside the warning limits – whether on one side or alternate sides – is very unlikely and should be treated as actionable. A string of seven or more points above, or below, the mean – whether within the warning limits or not – is unlikely and may indicate developing bias (some recommendations consider ten such successive points as actionable). Sets of such rules are available in most textbooks on statistical process control.

Action on Control Chart Action Conditions

In general, actionable conditions indicate a need for corrective action. However, it is prudent to check that the control material measurement is valid before undertaking expensive investigations or halting a process. Taking a second control measurement is therefore advised, particularly for warning conditions. However, it is not sensible to continue taking control measurements until one falls back inside the limits. A single remeasurement is sufficient for confirmation of the out-of-control condition.

If the results of the second check do not confirm the first, it is sensible to ask how best to use the duplicate data in coming to a final decision. For example, should one act on the second observation? Or perhaps take the mean of the two results? Strictly, the correct answer requires consideration of the precision of the means of duplicate measurements taken over the appropriate time interval. If this is available, the appropriate limits can

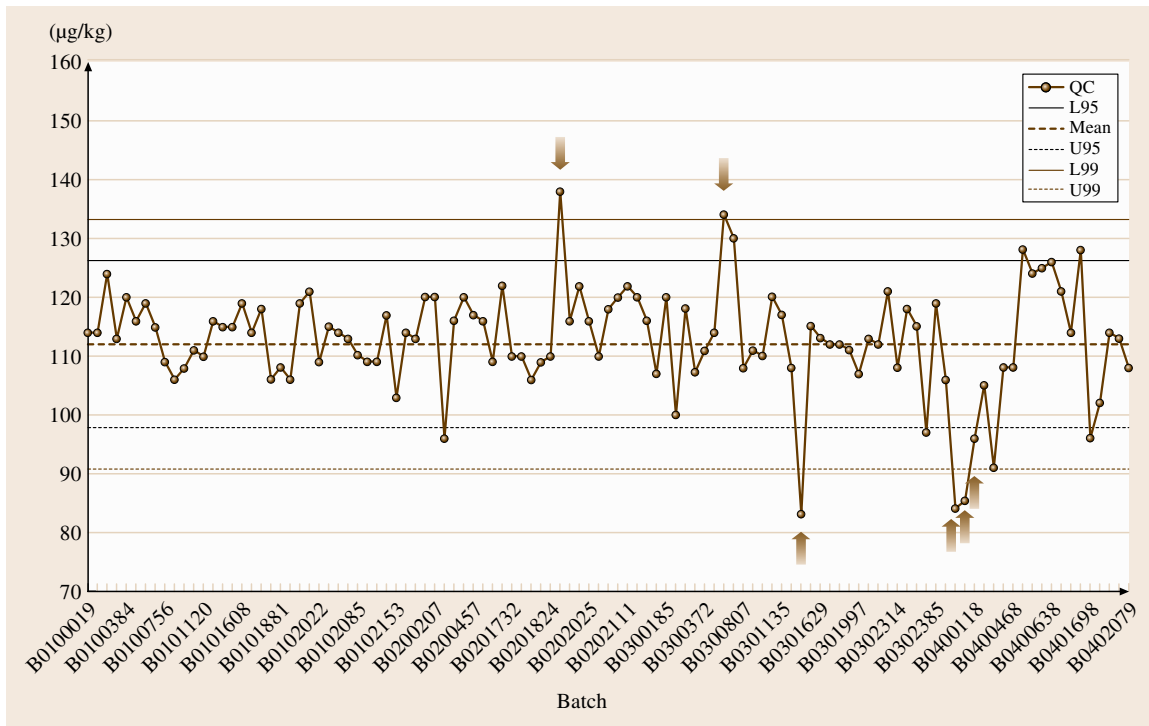


Fig. 3.8 QC chart example. The figure shows successive QC measurements on a reference material certified for lead content. There is evidence of loss of control at points marked by arrows

be calculated from the relevant standard deviation. If not, the following procedure is suggested: First, check whether the difference between the two observations is consistent with the usual operating precision (the results should be within approximately $2.8s$ of one another). If so, take the mean of the two, and compare this with new

limits calculated as $\bar{x} \pm 2s/\sqrt{2}$ and $\bar{x} \pm 3s/\sqrt{2}$ (this is conservative, in that it assumes complete independence of successive QC measurements; it errs on the side of action). If the two results do not agree within the expected precision, the cause requires investigation and correction in any case.

3.4 Uncertainty and Accuracy of Measurement and Testing

3.4.1 General Principles

In metrology and testing, the result of a measurement should always be expressed as the measured quantity value together with its uncertainty. The uncertainty of measurement is defined as a nonnegative parameter characterizing the dispersion of the quantity values being attributed to a measurand [3.17].

Measurement accuracy, which is the closeness of agreement between a measured quantity value and the true quantity value of a measurand, is a positive formulation for the fact that the measured value

is deviating from the true value, which is considered unique and, in practise, unknowable. The deviation between the measured value and the true value or a reference value is called the measurement error.

Since the 1990s there has been a conceptual change from the traditionally applied *error approach* to the *uncertainty approach*.

In the *error approach* it is the aim of a measurement to determine an *estimate of the true value* that is as close as possible to that single true value. In the *uncertainty approach* it is assumed that the information from

measurement only permits assignment of an *interval of reasonable values* to the measurand.

The master document, which is acknowledged to apply to all measurement and testing fields and to all types of uncertainties of quantitative results, is the *Guide to the Expression of Uncertainty in Measurement (GUM)* [3.19]. The Joint Committee for Guides in Metrology Working Group 1 (JCGM-WG1), author of the *GUM*, is producing a complementary series of documents to accompany the *GUM*.

The *GUM uncertainty philosophy* has already been introduced in Chap. 1, its essential points are

- A measurement quantity X , of which the true value is not known exactly, is considered as a stochastic variable with a probability function. Often it is assumed that this is a normal (*Gaussian*) distribution.
- The result x of a measurement is an estimate of the expectation value $E(X)$ for X .
- The standard uncertainty $u(x)$ of this measured value is equal to the square root of the variance $V(X)$.
- Expectation (quantity value) and variance (standard uncertainty) are estimated either
 - by statistical processing of repeated measurements (*type A uncertainty evaluation*) or
 - by other methods (*type B uncertainty evaluation*).
- The result of a measurement has to be expressed as a quantity value together with its uncertainty, including the unit of the measurand.

The methodology of measurement evaluation and determination of measurement uncertainty are compiled

in Fig. 3.9. The statistical evaluation of results has been described in detail in Sect. 3.3.

3.4.2 Practical Example: Accuracy Classes of Measuring Instruments

All measurements of quantity values for single measurands as well as for multiple measurands need to be performed with appropriate measuring instruments, devices for making measurements, alone or in conjunction with one or more supplementary devices.

The quality of measuring instruments is often defined through *limits of errors* as description of the *accuracy*.

Accuracy classes are defined [3.17] as classes of measuring instruments or measuring systems that meet stated metrological requirements that are intended to keep measurement errors or instrumental measurement uncertainties within specified limits under specified operating conditions. An accuracy class is usually denoted by a number or symbol adopted by convention. Analog measuring instruments are divided conventionally into accuracy classes of 0.05, 0.1, 0.2, 0.3, 0.5, 1, 1.5, 2, 2.5, 3, and 5. The accuracy classes p represent the maximum permissible relative measurement error in %. For example an accuracy class of 1.0 indicates that the limits of error – in both directions – should not exceed 1% of the full-scale deflection. In digital instruments, the limit of indication error is ± 1 of the least significant unit of the digital indication display.

In measuring instruments with an analog indication, the measured quantity is determined by the position

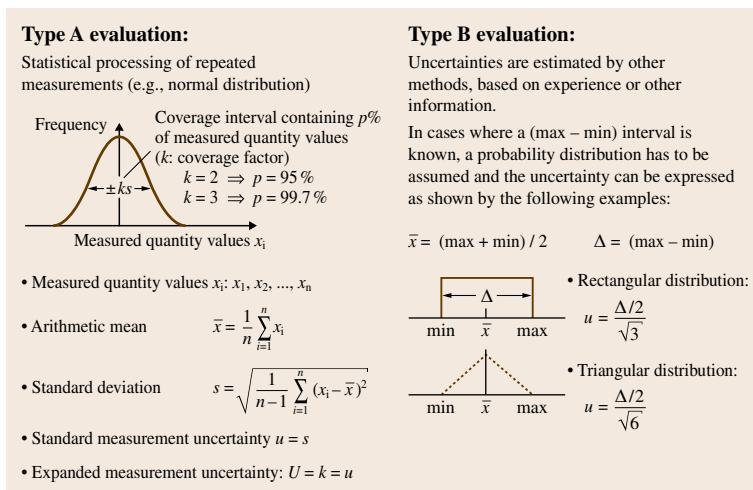
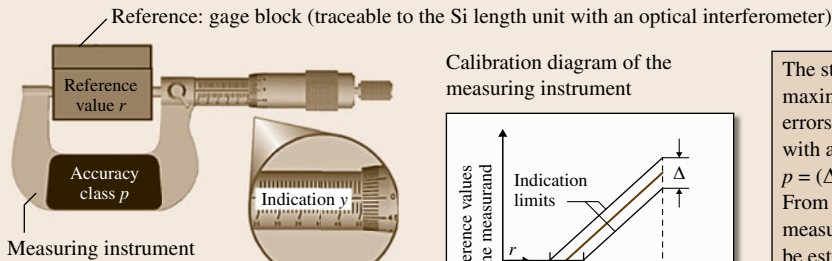


Fig. 3.9 Principles of measurement evaluation and determination of uncertainty of measurement for a single measurand x

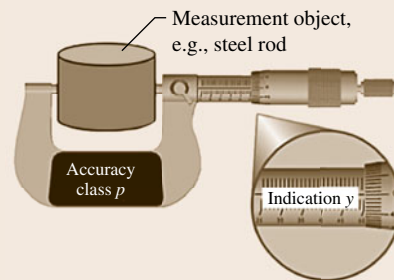
Measurement uncertainty of a single measurand with a single measuring instrument

Example from dimensional metrology

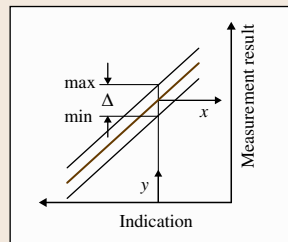
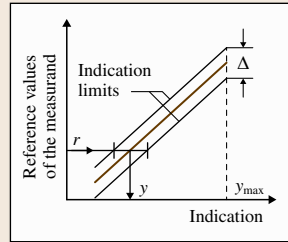
(1) Calibration of measuring instrument (measurand: length)



(2) Measurement



Calibration diagram of the measuring instrument



The strip Δ is the range of the maximum permissible measurement errors of a measuring instrument with an accuracy class $p = (\Delta / (2y_{\max})) \cdot 100$ [%]. From Δ or p , the instrument measurement uncertainty u_{instr} can be estimated in a type B evaluation. Assuming a rectangular distribution (Fig. 3.9) it follows that $u_{\text{instr}} = (\Delta/2)\sqrt{3}$, or $u_{\text{instr}} = ((p/100) \cdot y_{\max}) / \sqrt{3}$. The relative instrument measurement uncertainty [%] $\delta_{\text{instr}} = u_{\text{instr}} / u_{\text{max}}$ is given by $\delta_{\text{instr}} = p / \sqrt{3}$.

Measurement result:
Quantity value x
 \pm instrument measurement uncertainty u_{instr} .

Fig. 3.10 Method for obtaining a measurement result and estimating the instrument measurement uncertainty

of the indicator on the scale. The limits of errors (percentages) are usually given at the full-scale amplitude (maximum value of measurement range). From the accuracy class p , also the instrumental measurement uncertainty u_{instr} can be estimated. In Fig. 3.10, the method for obtaining a measurement result and measurement uncertainty for a single measurand with a single measuring instrument is shown.

As illustrated in Fig. 3.10, a measuring instrument gives as output an *indication*, which has to be related to the quantity value of the measurand through a calibration diagram. A calibration diagram represents the relation between indications of a measuring instrument and a set of reference values of the measurand. At the maximum indication value (maximum measurement range) y_{\max} the width Δ of the strip of the calibration diagram is the range of the maximum permissible measurement errors.

From the determination of Δ the accuracy class p in % follows as

$$p = \left(\frac{\Delta}{2y_{\max}} \right) \cdot 100 \text{ [%]}.$$

Note that, at indicator amplitudes lower than the maximum y_{\max} , the actual relative maximum permissible measurement errors p_{act} for the position y_{act} on the scale need to be determined as

$$p_{\text{act}} = p \cdot \left(\frac{y_{\max}}{y_{\text{act}}} \right).$$

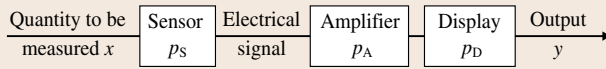
For the estimation of the standard measurement uncertainty it can be considered in an uncertainty estimation of type B that all values in the range between the limits of indications have the same probability – as long as no other information is available. This kind of distribution is called a rectangular distribution (Fig. 3.9). Therefore, the standard uncertainty is equal to

$$u_{\text{instr}} = \frac{(\Delta/2)}{\sqrt{3}} = \frac{((p/100) \cdot y_{\max})}{\sqrt{3}}.$$

Example 3.1: What is the measurement uncertainty of a measurement result obtained by a measurement with an analog voltmeter (accuracy class 2.0) with a maximum amplitude of 380 V, when the indicator is at 220 V?

Measurement uncertainty of a measurement system or measurement chain

Consider a measurement system, consisting in the simplest case of three components, namely a sensor (accuracy class p_S), an amplifier (accuracy class p_A) and a display (accuracy class p_D)



The measurement uncertainty of the system can be estimated by applying the law of the propagation of uncertainties (see Sect. 3.4.3)

$$u_{\text{System}}/|y| = \sqrt{(u_S^2/x_S^2 + u_A^2/x_A^2 + u_D^2/x_D^2)},$$

where $u_S/x_S + u_A/x_A, u_D/x_D$, are the relative instrument uncertainties of sensor, amplifier and display, which can be expressed by their accuracy classes as $p_S/\sqrt{3}, p_A/\sqrt{3}, p_D/\sqrt{3}$.

It follows that
$$u_{\text{System}}/|y| = \frac{\sqrt{(p_S^2 + p_A^2 + p_D^2)}}{\sqrt{3}}$$

For a measurement system of n components in line, the following formula characterizes the relative *uncertainty budget* of the measuring chain

$$\delta_{\text{chain}} = u_{\text{chain}}/|y| = \frac{\sqrt{(\sum p_i^2)}}{\sqrt{3}} \quad (i = 1 \dots n)$$

Consideration: actual relative maximum permissible measurement errors for 220 V and limits of error expressed in measurement units (V as scale divisions) are

$$p_{220,\text{rel}} = 2.0\% \cdot \frac{380 \text{ V}}{220 \text{ V}} = 3.5\% ;$$

$$p_{\text{abs}} = 380 \text{ V} \cdot \frac{2.0\%}{100\%} = 7.6 \text{ V} \quad (\text{limits of error})$$

$$u_{\text{instr,rel}} = \frac{p_{\text{rel}}}{\sqrt{3}} = \frac{3.5\%}{\sqrt{3}} = 2.0\% \quad \text{and}$$

$$u_{\text{instr,abs}} = \frac{p_{\text{abs}}}{\sqrt{3}} = \frac{7.6 \text{ V}}{\sqrt{3}} = 4.4 \text{ V} .$$

It is obvious that the relative standard uncertainties are smallest at y_{max} .

Since a rectangular distribution was assumed, it is not reasonable to apply the coverage factor k , because this approach assumes a Gaussian distribution. Instead, the standard uncertainty u_{instr} should be stated. It normally suffices to report the uncertainties to at most two significant digits – and also to provide information on how it was determined. Finally, the measurement uncertainty allows the experimenter to decide whether the used instrument is appropriate for his/the customer's needs.

Answer: The result of the example could be reported as 220 V \pm 4.4 V. The measurement uncertainty of the

Fig. 3.11 Method for estimating the measurement system uncertainty

instrument is reported as a standard uncertainty (coverage factor $k = 1$) and was obtained by type B evaluation only considering the instrument accuracy class.

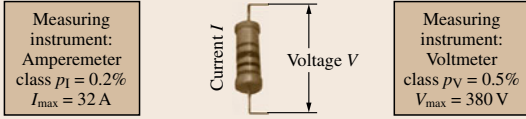
If instead of a single measuring instrument, a measuring system or a measuring chain is used, consisting in the simplest case of a sensor, an amplifier, and a display, the accuracy classes of the components of the measuring system can also be used to estimate the instrumental system uncertainty, as illustrated in Fig. 3.11.

3.4.3 Multiple Measurement Uncertainty Components

The method outlined in Figs. 3.9 and 3.10 considers only one single measurement quantity and only the sources covered by only one variable. However, very often uncertainty evaluations have to be related to functional combinations of measured quantities or uncertainty components $y = f(x_1, x_2, x_3, \dots, x_n)$. In these cases, for uncorrelated (i. e., independent) values, the single uncertainties are combined by applying the law of propagation of uncertainty to give the so-called combined measurement uncertainty

$$u_{\text{combined}}(y) = \sqrt{\sum \left(\frac{\partial f}{\partial x_i} \right)^2 u^2(x_i)} .$$

Example 1: Measurement of electrical resistance R



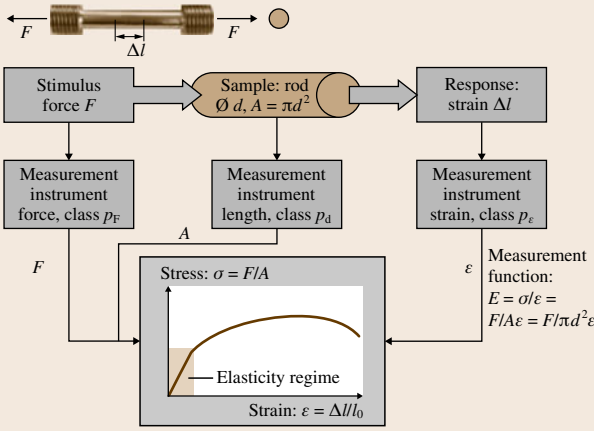
• Measurement function: $R = V/I$
 • Minimum combined measurement uncertainty (at the maximum of instrument range):

$$u_R/R_{\max} = \sqrt{(u_V^2/V^2 + u_I^2/I^2)} = \sqrt{((p_V \cdot V_{\max})^2/\sqrt{3}^2 \cdot V_{\max}^2 + (p_I \cdot I_{\max})^2/\sqrt{3}^2 \cdot I^2)}$$

$$u_R/R_{\max} = \sqrt{(p_V^2 + p_I^2)}/\sqrt{3}$$

$$u_R/R_{\max} = \sqrt{(0.5^2 + 0.2^2)}/\sqrt{3} = 0.31\%$$

Example 2: Measurement of elastic modulus E



• Minimum combined measurement uncertainty (at the maximum range of each instrument):

$$u_E/E_{\max} = \sqrt{(u_F^2/F_{\max}^2 + 4u_d^2/d_{\max}^2 + u_\epsilon^2/\epsilon_{\max}^2)}$$

$$u_E/E_{\max} = \sqrt{(p_F^2 + 4p_d^2 + p_\epsilon^2)}/\sqrt{3}$$

Fig. 3.12 Determination of the combined uncertainty of multiple measurands

From the statistical law of the propagation of uncertainties it follows that there are three basic relations, for which the resulting derivation becomes quite simple

1. for equations of the measurand involving only sums or differences

$$y = x_1 + x_2 + \dots + x_n \quad \text{it follows}$$

$$u_y = \sqrt{(u_1^2 + u_2^2 + \dots + u_n^2)}$$

2. for equations of the measurand involving only products or quotients

$$y = x_1 x_2 \dots x_n \quad \text{it follows}$$

$$\frac{u_y}{|y|} = \sqrt{\left(\frac{u_1^2}{x_1^2} + \frac{u_2^2}{x_2^2} + \dots + \frac{u_n^2}{x_n^2}\right)}$$

3. for equations of the measurand involving exponents

$$y = x_1^a x_2^b \dots x_n^z \quad \text{it follows}$$

$$\frac{u_y}{|y|} = \sqrt{\left(\frac{a^2 u_1^2}{x_1^2} + \frac{b^2 u_2^2}{x_2^2} + \dots + \frac{z^2 u_n^2}{x_n^2}\right)}$$

If the parameters are not independent from each other, the mutual dependence has to be taken into account by the covariances; see, e.g., GUM [3.19], but in practise they are often neglected for simplicity.

Also for multiple measurands or measurement instruments, it is possible to use the instrument accuracy class data and other information – if available – for the estimation of the demanded combined measurement uncertainty. The method for the determination of the combined uncertainty is shown in Fig. 3.12, exemplified with simple cases of two and three measurands.

However, for strict application of the measurement uncertainty approach, all uncertainty sources have to be identified and possible additional components not covered have to be considered. This is especially the case in the examples for such uncertainty sources that are not covered by p from the calibration experiment from which p is derived.

3.4.4 Typical Measurement Uncertainty Sources

While in the previous examples included in the accuracy class – which is obtained from calibration experiments – were considered, the GUM [3.19] requests to consider all components that contribute to the measurement uncertainty of a measured quantity. The various uncertainty sources and their contributions can be divided into four major groups, as has been proposed by the EUROLAB Guide to the Evaluation of Measurement Uncertainty for Quantitative Test Results [3.20]. Measurement uncertainty may depend on

1. the sampling process and sample preparation, e.g.,
 - the sample being not completely representative
 - inhomogeneity effects

- contamination of the sample
 - instability/degradation of the sample or other effects during sampling, transport, storage, etc.
 - the subsampling process for the measurement (e.g., weighing)
 - the sample preparation process for the measurement (dissolving, digestion)
2. the properties of the investigated object, e.g.,
 - instability of the investigated object
 - degradation/ageing
 - inhomogeneity
 - matrix effects and interactions
 - extreme values, e.g., small measured quantity/little concentration
 3. the applied measurement and test methods, e.g.,
 - the definition of the measurand (approximations, idealizations)
 - nonlinearities, extrapolation
 - different perception or visualization of measurands (different experimenters)
 - uncertainty of process parameters (e.g., environmental conditions)
 - neglected influence quantities (e.g., vibrations, electromagnetic fields)
 - environment (temperature, humidity, dust, etc.)
 - limits of detection, limited sensitivity
 - instrumental noise and drift
 - instrument limitations (resolution, dead time, etc.)
 - data evaluation, numerical accuracy, etc.
 4. the basis of the measurement, e.g.,
 - uncertainties of certified values
 - calibration values
 - drift or degradation of reference values/reference materials
 - uncertainties of interlaboratory comparisons
 - uncertainties from data used from the literature.

All possible sources for uncertainty contributions need to be considered, when the measurement uncertainty is estimated, even if they are not directly expressed in the measurement function. They are not necessarily independent from each other. They are partly of random and partly of systematic character.

3.4.5 Random and Systematic Effects

In the traditional error approach (Sect. 3.4.1) a clear distinction was made between so-called *random errors* and *systematic errors*. Although this distinction is not relevant within the uncertainty approach anymore, as it is

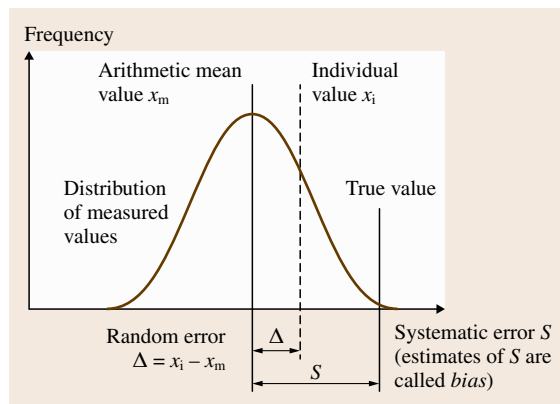


Fig. 3.13 Illustration of random and systematic errors of measured values

not unambiguous, the concept is nevertheless descriptive.

Random effects contribute to the variation of individual results in replicate measurements. Associated uncertainties can be evaluated using statistical methods, e.g., the experimental standard deviation of a mean value (type A evaluation).

Systematic errors result in the center of the distribution being shifted away from the true value even in the case of infinite repetitions (Fig. 3.13).

If systematic effects are known, they should be corrected for in the result, if possible. Remaining systematic effects must be estimated and included in the measurement uncertainty.

The consideration and inclusion of the various sources of measurement errors in the measurement result or the measurement uncertainty is illustrated in Fig. 3.14.

3.4.6 Parameters Relating to Measurement Uncertainty: Accuracy, Trueness, and Precision

The terms *accuracy*, *trueness*, and *precision*, defined in the ISO 3534 international standard characterize a measurement procedure and can be used with respect to the associated uncertainty.

Accuracy as an umbrella term characterizes the closeness of agreement between a measurement result and the true value of the measurand. If several measurement results are available for the same measurand from a series of measurements, accuracy can be split into trueness and precision. Trueness accounts for the closeness of agreement between the mean value and the true

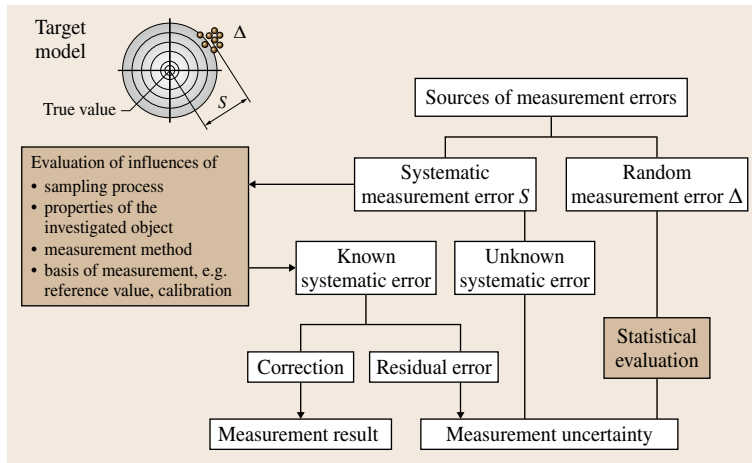


Fig. 3.14 Methodology of considering random and systematic errors in measurement

value. Precision describes the closeness of agreement of the individual values themselves.

The target model (Fig. 3.15) visualizes comprehensively the different possible combinations which result from true or wrong and precise or imprecise results.

Estimates of precision are commonly determined for repeated measurements and are valuable information with a view to the measurement uncertainty. They are strongly dependent on the conditions under which precision is investigated: repeatability conditions, reproducibility conditions, and intermediate conditions.

- Repeatability conditions mean that all parameters are kept as constant as possible, e.g.,
 - a) the same measurement procedure,
 - b) the same laboratory,
 - c) the same operator,
 - d) the same equipment,
 - e) repetition within short intervals of time.
- Reproducibility conditions imply those conditions for a specific measurement that may occur between different testing facilities, e.g.,
 - a) the same measurement procedure,
 - b) different laboratories,

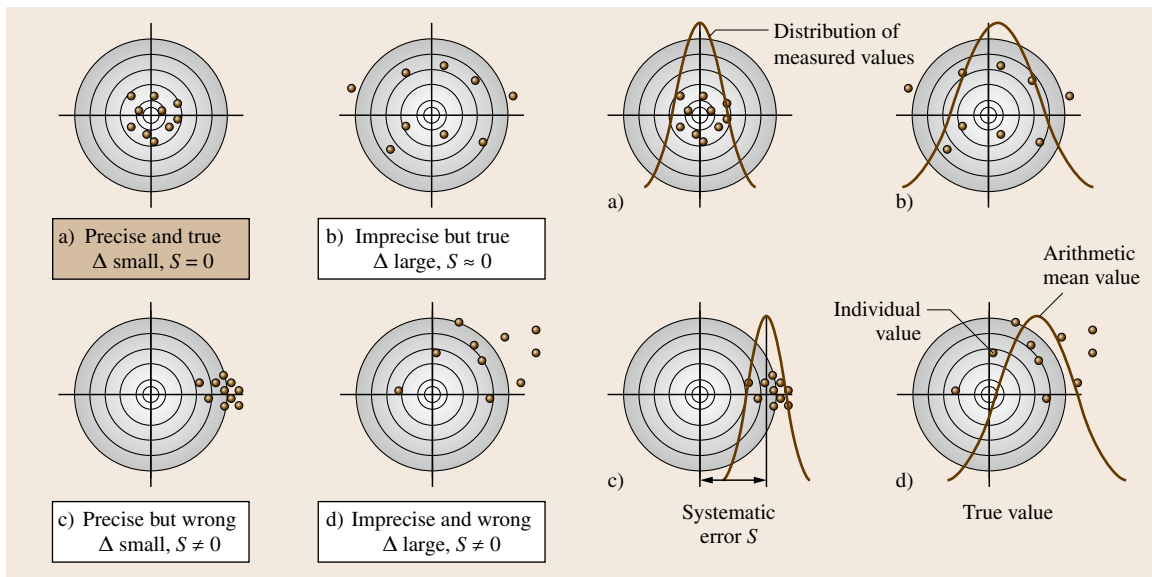


Fig. 3.15 Target model to illustrate trueness and precision. The center of the target symbolizes the (unknown) true value

- c) different operators,
- d) different equipment.
- Intermediate conditions have to be specified regarding which factors are varied and which are constant. For *within-laboratory reproducibility* the following conditions are used
 - a) the same measurement procedure,
 - b) the same laboratory,
 - c) different operators,
 - d) the same equipment (alternatively, different equipment),
 - e) repetition within long intervals of time.

3.4.7 Uncertainty Evaluation: Interlaboratory and Intralaboratory Approaches

For the evaluation of measurement uncertainties in practice, often many different approaches are possible. They all begin with the careful definition of the measurand and the identification of all possible components contributing to the measurement uncertainty. This is especially important for the sampling step, as primary sampling

effects are often much larger than the uncertainty associated with the measurement of the investigated object.

A convenient classification of uncertainty approaches is shown in Fig. 3.16. The classification is based on distinction between uncertainty evaluation carried out by the laboratory itself (called *intralaboratory approach*) and uncertainty evaluation based on collaborative studies in different laboratories (called *interlaboratory approach*). These approaches are compiled in the *EUROLAB Technical Report 1/2007 Measurement uncertainty revisited: Alternative approaches to uncertainty evaluation* [3.21].

In principle, four different approaches can be applied. The four approaches to uncertainty estimations outlined in Fig. 3.16 are briefly described in the following.

1) The Modeling Approach

This is the main approach to the evaluation of uncertainty and consists of various steps as described in Chap. 8 of the *GUM*.

For the modeling approach, a mathematical model must be set up, which is an equation defining the quan-

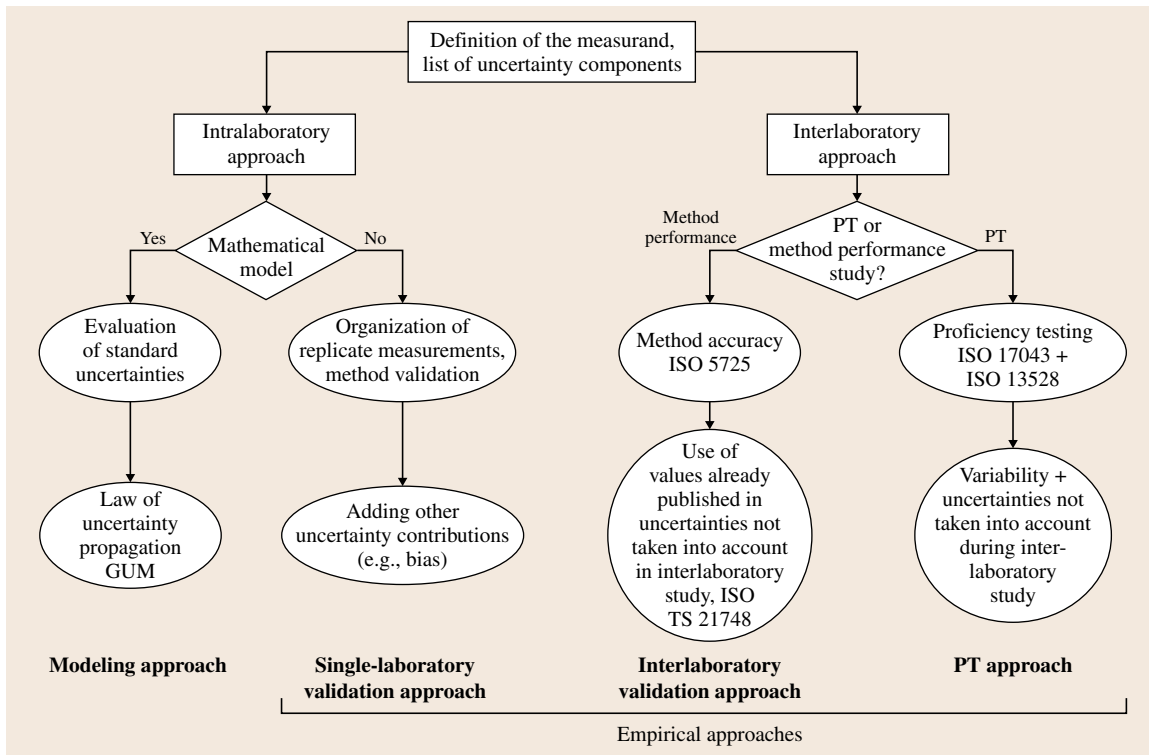


Fig. 3.16 A road map for uncertainty estimation approaches according to [3.21]

titative relationship between the quantity measured and all the quantities on which it depends, including all components that contribute to the measurement uncertainty.

Afterwards, the standard uncertainties of all the single uncertainty components are estimated. Standard deviations from repeated measurements are directly the standard uncertainties for the respective components (if normal distribution can be assumed). The combined uncertainty is then calculated by the application of the law of propagation of uncertainty, which depends on the partial derivatives for each input quantity. In strictly following the modeling approach, correlations also need to be incorporated.

Usually the expanded uncertainty U (providing an interval $y - U$ to $y + U$ for the measurand y) is calculated. For normal distribution, the coverage factor $k = 2$ is chosen typically. Finally, the measurement result together with its uncertainty should be reported according to the rules of the GUM [3.19]. These last two steps of course also apply to the other approaches (2–4).

Because full mathematical models are often not available or the modeling approach may be infeasible for economic or other reasons, the GUM [3.19] foresees that also alternative approaches may be used. The other approaches presented here are as valid as the modeling approach and sometimes even lead to more realistic evaluation of the uncertainty, because they are largely based on experimental data. These approaches are based on long experience and reflect common practise.

Even though the single-laboratory validation, inter-laboratory validation, and PT approaches also use statistical models as the basis for data analysis (which also be described as *mathematical models*) the term *mathematical model* is reserved for the modeling approach, and the term *statistical model* is used for the other approaches. The latter are also called *empirical approaches*.

2) The Single-Laboratory Validation Approach

If the full modeling approach is not feasible, in-house studies for method validation and verification may deliver important information on the major sources of variability. Estimates of bias, repeatability, and within-laboratory reproducibility can be obtained by organizing experimental work inside the laboratory. Quality control data (control charts) are valuable sources for precision data under within laboratory reproducibility conditions, which can be used to serve directly as standard uncertainties. Standard uncertainties of additional (missing) effects can be estimated and combined – see also under

point 5). If possible, during the repetition of the experiment, the influence quantities should be varied, and certified reference materials (CRMs) and/or comparison with definitive or reference methods should be used to evaluate the component of uncertainty related to the trueness.

3) The Interlaboratory Validation Approach

Precision data can also be obtained by utilizing method performance data and other published data (other than proficiency testing that the testing laboratory has taken part in itself, as this is considered in the PT approach). The reproducibility data can be used directly as standard uncertainty.

ISO 5725 *Accuracy (trueness and precision) of measurement methods and results* [3.22] provides the rules for assessment of repeatability (repeatability standard deviation s_r), reproducibility (reproducibility standard deviation s_R), and (sometimes) trueness of the method (measured as a bias with respect to a known reference value). Uncertainty estimation based on precision and trueness data in compliance with ISO 5725 [3.22] is extensively described in ISO/TS 21748 *Guidance for the use of repeatability, reproducibility and trueness estimates in measurement uncertainty estimation* [3.23].

4) The PT Approach: Use of Proficiency Testing (EQA) Data

Proficiency tests (external quality assessment, EQA) are intended to check periodically the overall performance of a laboratory. Therefore, the laboratory can compare the results from its participation in proficiency testing with its estimations of measurement uncertainty of the respective method and conditions.

Also, the results of a PT can be used to evaluate the measurement uncertainty. If the same method is used by all the participants in the PT scheme, the standard deviation is equivalent to an estimate of interlaboratory reproducibility, which can serve as standard uncertainty and, if required, be combined with additional uncertainty components to give the combined measurement uncertainty. If the laboratory has participated over several rounds, the deviations of its own results from the assigned value can be used to evaluate its own measurement uncertainty.

Combination of the Different Approaches to Uncertainty Evaluation

It is also possible – and often necessary – to combine the different approaches described above. For example, in the PT approach, sometimes missing components need

Table 3.8 Compilation of relevant documents on measurement uncertainty

Document	Reference	General	Modeling	Single laboratory	Inter-laboratory	PT
ISO (1993/1995), <i>Guide to the expression of uncertainty in measurement (GUM)</i>	[3.19]	×	×			
EURACHEM/CITAC (2000), <i>Quantifying uncertainty in analytical measurement</i> , 2nd edn.	[3.24]	×	×	×		
EUROLAB technical report no. 1/2002, <i>Measurement uncertainty in testing</i>	[3.25]	×				
EUROLAB technical report no. 1/2006, <i>Guide to the evaluation of measurement uncertainty for quantitative test results</i>	[3.20]	×	×	×		×
EUROLAB technical report no. 1/2007, <i>Measurement uncertainty revisited: Alternative approaches to uncertainty evaluation</i>	[3.21]	×	×	×	×	×
EA 4/16 (2004), <i>Guidelines on the expression of uncertainty in quantitative testing</i>	[3.26]	×	×	×	×	×
NORDTEST technical report 537 (2003), <i>Handbook for calculation of measurement uncertainty in environmental laboratories</i>	[3.27]			×	×	×
EA-4/02 (1999), <i>Expression of the uncertainty of measurement in calibration</i>	[3.28]		×			
ISO 5725 Accuracy (trueness and precision) of measurement methods and results (six parts)	[3.22]				×	
ISO 5725-3 Accuracy (trueness and precision) of measurement methods and results – Part 3: Intermediate measures of the precision of a standard measurement method	[3.22]			×		
ISO/TS 21748 <i>Guide to the use of repeatability, reproducibility, and trueness estimates in measurement uncertainty estimation</i>	[3.23]				×	
AFNOR FD X 07-021, <i>Fundamental standards – Metrology and statistical applications – Aid in the procedure for estimating and using uncertainty in measurements and test results</i>	[3.29]		×		×	
Supplement no. 1 to the GUM, <i>Propagation of distributions using a Monte Carlo method</i>	[3.30]		×			
ISO 13528 <i>Statistical methods for use in proficiency testing by interlaboratory comparison</i>	[3.31]					×
ISO/TS 21749 <i>Measurement uncertainty for metrological applications – Repeated measurements and nested experiments</i>	[3.32]			×		

to be added. This may be the case if the PT sample was a solution and the investigated object is a solid sample that needs to be dissolved first before undergoing the same measurement as the PT sample. Therefore, uncertainty components from the dissolving and possible dilution steps need to be added. These could be estimated by intralaboratory validation data or – especially for the dilution uncertainty – by repeated measurements from the resulting standard deviation.

Concerning the reliability of the methods described, it should be emphasized that there is no hierarchy; i. e., there are no general rules as to which method should be preferred. The laboratory should choose the most fit-for-purpose method of estimating uncertainty for its individual application. Also, the time and effort invested

in the uncertainty estimation should be appropriate for the purpose.

Finally there may be cases where none of the approaches described above is possible. For example for fire protection doors repeated measurements are not possible. Also, there may be no PT scheme available. For such cases, experience-based expert estimate (type B evaluation) may be the best option to estimate measurement uncertainty contributions.

A compilation of references (guidelines and standards) for the various approaches is given in Table 3.8 (adopted from the EUROLAB Technical Report 1/2007 [3.21]) together with the reference number and an indication (×) of which uncertainty evaluation approaches are addressed in the respective document.

3.5 Validation

The operation of a testing facility or a testing laboratory requires a variety of different prerequisites and supporting measures in order to produce trustworthy results of measurements. The most central of these operations is the actual execution of the test methods that yield these results. At all times it has therefore been vital to operate these test methods in a skillful and reproducible manner, which requires not only good education and training of the operator in all relevant aspects of performing a test method, but also experimental verification that the specific combination of operator, sample, equipment, and environment yields results of known and fit-for-purpose quality. For this experimental verification at the testing laboratory the term *validation* (also *validation of test methods*) was introduced some 20 years ago. Herein, test method and test procedure are used synonymously.

In the following it is intended to present purpose, rationale, planning, execution, and interpretation of validation exercises in testing. We will, however, not give the mathematical and statistical framework employed in validation, as this is dealt with in other chapters of the handbook.

3.5.1 Definition and Purpose of Validation

Definitions

Although in routine laboratory jargon a good many shades of meaning of *validation* are commonly associated with this word, the factual operation of a validation project encompasses the meaning better than words do. Nevertheless, a formal definition is offered in the standards, and the following is cited from EN-ISO 9000:2000 [3.33].

Validation. Confirmation, through the provision of objective evidence, that the requirements for a specific intended use or application have been fulfilled.

Objective Evidence. Data supporting the existence or verity of something.

Requirement. Need or expectation that is stated, generally implied or obligatory.

In ISO 17025 (*General Requirements for the Competence of Testing and Calibration Laboratories*), validation prominently features in Sect. 5.4 on technical requirements, and the definition is only slightly different: *Validation is the confirmation by examina-*

tion and the provision of objective evidence that the particular requirements for a specific intended use are fulfilled.

Although such definitions tend to be given in a language that makes it difficult to see their ramifications in practise, there are a couple of key features that warrant some discussion. Validation is (done for the purpose of) confirmation and bases this confirmation on objective evidence, generally data from measurements. It can be concluded that, in general, only carefully defined, planned, and executed measurements yield data that will permit a judgement on the fulfilment of requirements. The important point here is that the requirements have to be cast in such a way that permits the acquisition of objective evidence (data) for testing the question of whether these requirements are fulfilled.

Verification is frequently used in a manner indistinguishable from validation, so we also want to resort to the official definition in EN-ISO 9000:2000.

Verification. Confirmation, through the provision of objective evidence, that specified requirements have been fulfilled.

The parallels with validation are obvious, as verification is also confirmation, also based on objective evidence, and also tested against specified requirements, but apparently without a specific use in mind, which is part of the definition of validation. In practise, the difference lies in the fact that validation is cited in connection with test methods, while verification is used in connection with confirmation of data.

As the formal definitions are not operationally useful, it may be helpful to keep in mind the essentials offered from ISO 17025 that appear to be summarized in Chap. 5.4.5.3:

The range and accuracy of the values obtainable from validated methods (e.g. the uncertainty of the results, detection limit, selectivity of the method, linearity, limit of repeatability and/or reproducibility, robustness against external influences and/or cross-sensitivity against interference from the matrix of the sample/test object) as assessed for the intended use shall be relevant to the clients' needs.

This statement makes clear that there must be an assessment for the intended use, although the various figures of merit in parenthesis are inserted in a rather artificial manner into the sentence.

The view of Cooperation International Traceability in Analytical Chemistry (CITAC)/EURACHEM on validation is best summarized in Chap. 18 of the *Guide to Quality in Analytical Chemistry* [3.34], where the introductory sentence reads:

Checks need to be carried out to ensure that the performance characteristics of a method are understood and to demonstrate that the method is scientifically sound under the conditions in which it is to be applied. These checks are collectively known as validation. Validation of a method establishes, by systematic laboratory studies that the method is fit-for-purpose, i. e. its performance characteristics are capable of producing results in line with the needs of the analytical problem . . .

At this point we shall leave the normative references and try to develop a general-purpose approach to validation in the following.

Purpose

The major purpose in line with the formal definition is confirmation. Depending on the party concerned with the testing, the emphasis of such a confirmation may be slightly different.

The (future) operator of a test method has the need to acquire enough skill for performing the method and may also care to optimize the routine execution of this method. The laboratory manager needs to know the limits of operation of a test method, as well as the performance characteristics within these limits. The prospective customer, who will generally base decisions on the outcome of the testing operation, must know the limits and performance characteristics as well, in order to make an educated judgement on the reliability of the anticipated decisions. He/she must be the one to judge the fitness for purpose, and this can only be done on the basis of experimental trials and a critical appraisal of the data thereby generated.

In a regulated environment, such as the pharmaceutical or car industry, regulatory agencies are additional stakeholders. These frequently take the position that a very formalized approach to validation assures the required validity of the data produced. In these instances very frequently every experimental step to be taken is prescribed in detail and every figure to be reported is unequivocally defined, thereby assuring uniform execution of the validation procedures.

On a more general basis one can argue that validation primarily serves the following purposes.

1. Derivation of performance characteristics
2. Establishment of short- and long-term stability of the method of measurement, and setting of control limits
3. Fine-tuning of the standard operating procedure (SOP)
4. Exploitation of scope in terms of the nature and diversity of samples and the range of the values of the measurand
5. Identification of influence parameters
6. Proof of competence of the laboratory.

In simple words, validation for a laboratory/operator is about getting to know your procedure.

3.5.2 Validation, Uncertainty of Measurement, Traceability, and Comparability

Relation of Uncertainty, Traceability, and Comparability to Validation

Validation cannot be discussed without due reference to other important topics covered in this handbook. We therefore need to shed light on the terms uncertainty, traceability, and comparability, in order to demonstrate their relationship to method validation.

The existence of a recognized test method is the prerequisite for the mutual recognition of results. This recognition is based on reproducibility and traceability, whereby traceability to a stated and (internationally) accepted reference is an indispensable aid in producing reproducible results. This links a locally performed measurement to the world of internationally accepted standards (references, scales) in such a way that all measurements linked to the same standards give results that can be regarded as fractions and multiples of the same unit. For identical test items measured with the same test method this amounts to identical results within the limits of measurement uncertainty. Measurement uncertainty cannot be estimated without due consideration of the quality of all standards and references involved in the measurement, and this in turn necessitates the clear stating of all references, which has been defined as traceability earlier in this paragraph. In a way a tight connection of a result to a standard is realized by very well-defined fractions and multiples, all carrying small uncertainties. Well-defined fractions and multiples are thus tantamount to small measurement uncertainty.

Formal Connection of the Role of Validation and Uncertainty of Measurement

In a certain way, validation is linked to measurement uncertainty through optimization of the method of measurement: validation provides insight into the important influence quantities of a method, and these influence quantities are those that generally contribute most to measurement uncertainty. As a result of validation, the reduction of measurement uncertainty can be affected in one of two ways: (a) by tighter experimental control of the influence quantity, or (b) by suitable numerical correction of the (raw) result for the exerted

influence. By way of example, we consider the influence of temperature on a measurement. If this is significant, one may control the temperature by thermostating, or alternatively, one can establish the functional dependence of the measurement, note the temperature at the time of measurement, and correct the raw result using the correction function established earlier. Both these actions can be regarded as a refinement of the measurement procedure, constitute an improvement over the earlier version of the method (*optimization*), and necessitate changes in the written SOP.

A good measurement provides a close link of the result to the true value, albeit not perfectly so. Prior to validation, the result is

$$x_{ijk} = \mu + \varepsilon_{ijk} ,$$

x_{ijk} . . . result ; μ . . . true value ; ε_{ijk} . . . deviation .

The deviation is large and unknown in size and sign, and will give rise to a large uncertainty of measurement. A major achievement in a successful validation exercise is the identification of influence quantities and their action on the result. If, for instance, three (significant) influence quantities are identified, the result can be viewed as biased by these effects δ

$$x_{ijk} = \mu + \delta_i + \delta_j + \delta_k + \varepsilon_{ijk} ,$$

and in so doing the residual (and poorly understood) deviation ε_{ijk} is now greatly reduced as the effects of the identified quantities δ are quasi-extracted from the old ε_{ijk} . As the bias is now known in sign and size, δ s can be used for correcting the original x_{ijk} , which after validation can be viewed as the uncorrected raw result,

$$x_{ijk} - \delta_i - \delta_j - \delta_k = \mu + \varepsilon_{ijk} .$$

Alternatively – as is occasionally done in chemistry with recovery – the corrections can be ignored, and thus the raw results are left uncorrected.

Figure 3.17 highlights the central position of validation in the introduction of a new method of measurement in a testing laboratory.

From a blown-up view of the measurement problem (Fig. 3.18) one can see that, in reality, it can be broken down into three distinct steps: the measurement task as formulated by the customer, the formulation of the requirements in technical terms derived from the communicated measurement task, and the preliminary method devised from experience and/or literature that will serve as basis for the (first round of) validation.

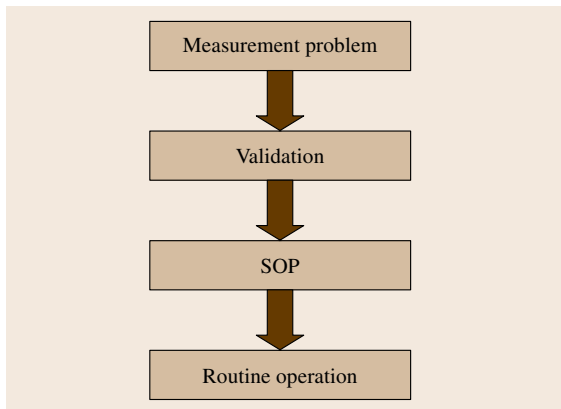


Fig. 3.17 Validation has a central place in the operation of a test method

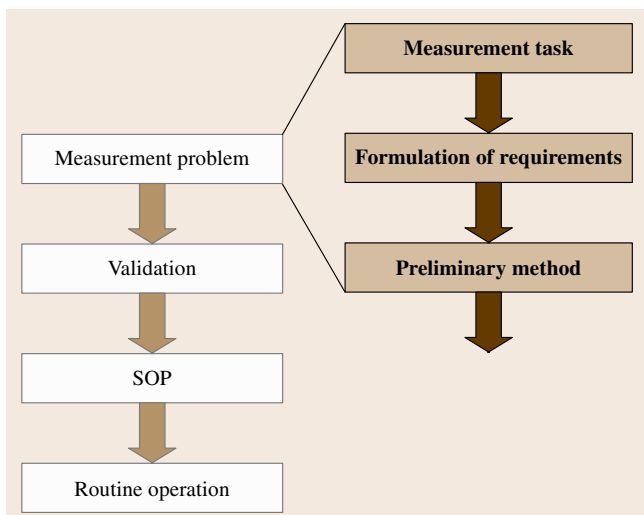


Fig. 3.18 Blown-up view of the measurement problem validation leads from the preliminary method to routine operation

3.5.3 Practice of Validation

Validation Plan

Prior to validation, a plan needs to establish which performance characteristics have to be established. This serves the purpose that in a clear succession of experiments test are applied that ultimately allow the assessment of the performance of the method with respect to the client's needs.

Therefore, a written plan must be laid out for the experiments performed in the course of validation, and the criteria to be met by the method in the course of validation must be established in this plan beforehand. It is then immediately obvious whether the method validated is suitable in the particular instance or not.

Validation is frequently planned by senior supervisory personnel or by staff specialized in validation with a good grasp of the client's needs. In regulated areas, such as pharmacy or food, fixed validation plans may be available as official documents and are not to be altered by laboratory personnel.

In any case it is advisable to have a separate standard operating procedure to cover the generic aspects of validation work.

Method Development and Purpose of Basic Validation

For a specified method as practised in a laboratory under routine conditions, method validation marks the end of preliminary method development. It serves the purpose of establishing the performance characteristics of a suitably adapted and/or optimized method, and also the purpose of laying down the limitation of reliable operation by either environmental or sample-related conditions. These limits are generally chosen such that the influence of changes in these conditions is still negligible relative to the required or expected measurement uncertainty. In chemical terms, this makes transparent which analytes (measurands) can be measured with a specific method in which (range of) matrices in the presence of which range of potential interferents.

If a method is developed for a very specific purpose, method validation serves to provide experimental evidence that the method is suitable for this purpose, i. e., for solving the specific measurement problem. In a sense, method validation is interlinked with method development, and care must be taken to draw a clear line experimentally between those steps. The validation plan forms the required delimitation.

Implicitly it is assumed that experiments for the establishment of performance characteristics are exe-

cuted with apparatus and equipment that operate within permissible specifications, work correctly, and are calibrated. Such studies must be carried out by competent staff with sufficient knowledge in the particular area in order to interpret the obtained results properly, and base the required decision regarding the suitability of the method on them.

In the literature there are frequent reports regarding results of interlaboratory comparison studies being used for the establishment of some method characteristics. There is, however, also found the situation in which a single laboratory requires a specific method for a very special purpose. The Association of Official Analytical Chemists (AOAC), which is a strong advocate of interlaboratory studies as a basis for method validation, established in 1993 the peer-verified method program [3.35], which serves to validate methods practised by one or a few laboratories only.

For an analytical result to be suitable for the anticipated purpose, it must be sufficiently reliable that every decision based on it will be trustworthy. This is the key issue regarding method validation performance and measurement uncertainty estimation.

Regardless of how good a method is and how skillfully it is applied, an analytical problem can only be solved by analyzing samples that are appropriate for this problem. This implies that sampling can never be disregarded.

Once a specific analytical question is defined by the client, it must be decided whether one of the established (and practised) methods meets the requirements. The method is therefore evaluated for its suitability. If necessary, a new method must be developed/adapted to the point that it is regarded as suitable. This process of evaluating performance (established by criteria such as selectivity, detection limits, decision limits, recovery, accuracy, and robustness) and the confirmation of the suitability of a method are the essence of method validation.

The questions considered during the development of an analytical procedure are multifaceted: Is a qualitative or a quantitative statement expected? What is the specific nature of the analyte (measurand)? What matrix is involved? What is the expected range of concentrations? How large a measurement uncertainty is tolerable? In practise, limitations of time and money may impose the most stringent requirements.

Confronted with altered or new analytical queries, the adaptation of analytical procedures for a new analyte, a new matrix, another concentration range or similar variations is frequently required. General analytical

trends may also require modifications or new developments of analytical procedures; a point in case are trends in miniaturization, as experienced in high-performance liquid chromatography (HPLC), flow photometry, capillary electrochromatography, hyphenation, etc.

Many analytical procedures are described in the scientific literature (books, journals, proceedings, etc.). These sources are frequently an appropriate basis for the development of new procedures. In many cases, there are also standards available with detailed documentation of the experimental procedure. If only general documentation is provided, it might be suitable as a starting point for the development of customized laboratory procedures.

Alternatively, the interchange of ideas with friendly laboratories can give impetus to the development of new or modified analytical procedures. Occasionally, a new combination of established analytical steps may lead to a new method.

There is also an increasing need for good cooperation between several disciplines, as it is hardly possible for a single person to independently develop complex methods in instrumental analysis. Also, the great flood of data from multichannel detection systems cannot be captured or evaluated by conventional procedures of data treatment, so additional interfaces are needed, particularly to information technology.

The basic validation exercise cannot cover the complete validation process, but is concerned mainly with those parts of validation that are indispensable in the course of development of an analytical procedure. Most importantly the scope of the method must be established, *inter alia* with respect to analytes, matrices, and concentration range within which measurements can be made in a meaningful way. In any case, the basic validation comprises the establishment of performance characteristics (also called figures of merit), with a clear emphasis on data supporting the estimation of measurement uncertainty.

Depth and Breadth of Validation

Regarding the depth and breadth of validation, ISO 17025 states that *validation shall be as extensive as is necessary to meet the needs in the given application or field of application*.

However, how does this translate into practical experimental requirements? As already stated earlier, it is clear that every analytical method must be available in the written form of an SOP. Until fitness for the intended use is proven through validation, all methods must be regarded as preliminary. It is not uncommon that the re-

sults of validation require revision of the SOP with regard to the matrix and the concentration range. This can be understood as laboratory procedures are based on a combination of SOP and validation as delimited by matrix, analyte, and this particular SOP. Here too, the close connection of SOP and validation is noteworthy.

Besides the type and number of different matrices and the concentration range for the application of the method, the extent of validation also depends markedly on the number of successive operations; for a multi-stage procedure, the extent and consequently the effort of validation will be much larger than for a single-stage procedure.

For the time sequence of basic validation there are also no fixed rules, but it seems appropriate to adopt some of the principles of method development for validation.

- Test of the entire working range, starting from one concentration
- Reverse inclusion of the separate stages into validation, starting with the study of the final determination
- Testing of all relevant matrices, starting with the testing of standards.

In all phases of validation, it must be ascertained that the method is performing satisfactorily, for instance, by running recovery checks alongside.

The final step must be the proof of trueness and reproducibility, e.g., on the basis of suitable reference materials.

Performance Characteristics

The importance of performance characteristics has been mentioned repeatedly in this text. These parameters generally serve to characterize analytical methods and – in the realm of analytical quality assurance – they serve to test whether a method is suitable to solve a particular analytical problem or not. Furthermore, they are the basis for the establishment of control limits and other critical values that provide evidence for the reliable performance of the method on an everyday basis.

The latter use of performance characteristics is a very significant one, and it is obvious that these performance characteristics are only applicable if established under routine conditions and in real matrices, and not under idealized and unrealistic conditions.

The actual selection of performance characteristics for validation depends on the particular situation and requirements. Table 3.9 gives an overview of the most relevant ones.

Table 3.9 Performance characteristics (after *Kromidas* [3.36])

Parameter	Comment
Trueness, accuracy of the mean, freedom from bias	The older English literature does not distinguish between accuracy and trueness
Precision	
– repeatability	
– reproducibility	ISO 5725 series: Accuracy, trueness, and precision
Linearity	
Selectivity	
Recovery	
Limit of detection (LOD)	
Limit of quantification (LOQ)	
Limit of determination (LOD)	
Limit of decision (LOC)	
Robustness, ruggedness	
Range	
Sensitivity	
Stability	
Accuracy	See <i>trueness</i>
Specificity	Often used synonymously with <i>selectivity</i>
Uncertainty of measurement	
expanded uncertainty	
Method capability	
Method stability/process stability	

Different emphasis is given to many of these parameters in the various standards. The most significant recent shift in importance is seen in ISO 17025, where the previously prominent figures of merit (*accuracy* and *precision*) are replaced by *uncertainty in measurement*.

The following performance characteristics are specifically emphasized in the CITAC/EURACHEM *Guide to Quality in Analytical Chemistry* of 2002.

- Selectivity and specificity (description of the measurand)
- Measurement range
- Calibration and traceability
- Bias/recovery
- Linearity
- Limit of detection/limit of quantitation
- Ruggedness
- Precision.

In ISO 17025 the performance characteristics are listed exemplarily:

e.g. the uncertainty of the results, detection limit, selectivity of the method, linearity, limit of repeatability and/or reproducibility, robustness against external influences and/or cross-sensitivity against interference from the matrix of the sample/test object.

From this wording it can be understood that the actual set of figures must be adapted to the specific problem. Selection criteria for the best set in a given situation will be discussed later.

Some of these performance characteristics are discussed in the following.

Some of these performance characteristics are discussed in the following.

Accuracy, Precision, and Trueness. There are different approaches for the proof of *accuracy* of results from a particular method. The most common one is by testing of an appropriate reference material, ideally a certified reference material, with certified values uncontested as known and true. A precondition, however, is obviously that such a material is available. It must also be noted that, when using this approach, most sampling and some of the sample preparation steps are not subjected to the test.

Numerically, the comparison of the results of a test method with a certified value is most frequently carried

out using a t -test, or alternatively the Doerffel test for significant deviations can be applied.

Trueness of results can also be backed up by applying a completely different measurement principle. This alternative method must be a well-established and recognized method. In this approach, only those steps that are truly independent of each other are subjected to a serious test for accuracy. For instance, if the same method of decomposition is applied in both procedures, this step cannot be taken as independent in the two procedures and therefore cannot be regarded as having been tested for accuracy by applying the alternative method of measurement.

In practise, the differences between the results from the two procedures are calculated, these differences are averaged, and their standard deviation is computed. Finally, a t -value from these results is obtained and compared with a critical t -value from the appropriate table. If the computed t -value is greater than the tabulated one, it can be assumed with a previously determined probability (e.g., 95%) that the difference between the two methods is indeed significant.

Another method to check the accuracy is the use of recovery studies (particularly useful for checking separation procedures), or balancing the analyte, applying mass balances or plausibility arguments.

In all of these considerations, there must always be due regard to the fact that trueness and precision are hardly independent from each other.

Precision can be regarded as a measure of dispersion between separate results of measurements. The standard deviation under repeatability, reproducibility or intermediate conditions, but also the relative standard deviation and variance, can be used as measures of precision. From the standard deviation, repeatability or reproducibility limits can be obtained according to [ISO 5725](#).

Which of these measures of precision is actually used is up to the analyst. It is, however, recommended to use the repeatability, reproducibility or intermediate standard deviation according to [ISO 5725](#).

The values of precision and trueness established in practise are always estimates that deviate in the operation of successive interlaboratory comparison studies or proficiency testing rounds.

Precision can therefore be regarded as a measure of dispersion (typical statistical measure: standard deviation) and trueness as a measure of location (typical statistical measure: arithmetic average), adding up to a combined measure of accuracy as a measure of disper-

sion and location: the deviation of a single value from the true one.

To avoid misunderstanding in the practical estimation of trueness and precision, the description of the experimental data underlying the computations must be done most carefully. For instance, it is of significant importance to know whether the data used are results of single determinations, or whether they were obtained from duplicate or triplicate measurements. Equally, the conditions under which these measurements were made must be meticulously documented, either as part of the [SOP](#) or independently. Important but neglected parameters might be the temperature constancy of the sample, constant time between single measurements, extraction of raw data, etc.

Calibration and Linearity. Valid calibration can be regarded as a fundamental prerequisite for a meaningful analytical measurement. Consequently, calibration frequently constitutes the first step in quality assurance. In short, the challenge is to find the dependence between signal and amount of substance (or concentration). Preconditions for reliable calibration are

- standards with (almost) negligible uncertainty (independent variable x),
- constant precision of the entire working range,
- useful model (linear or curved),
- random variation of deviations in signals,
- deviations distributed according to the normal distribution.

These criteria are ranked in order of decreasing importance. This means that all analytical work is meaningless unless there is a firm idea about the reliability of standards. Many methods of analysis have poorer precision at higher concentrations (larger absolute standard deviation) than at lower concentrations. In practise, this means that the working range must either be reduced or be subdivided into several sections, each with its own calibration function. Alternatively, the increase of standard deviation with increasing concentration can be established and used for calibration on the basis of weighted regression. In this case a confidence band cannot be given.

In all cases, it is advantageous to position the calibration function so that the majority of expected concentrations fall in the middle part of the curve.

The calibration function is therefore the mathematical model that best describes the connection between signal and concentration, and this function can be

straight or curved. The linearity of a measurement method determines the range of concentrations within which a straight line is the best description for the dependence of the signal on concentration.

A large deviation from linearity can be visually detected without problems. Alternatively, the dependence of signal on concentration is modeled by appropriate software in the way that best describes this dependence. A statistical *F*-test then shows deviations from linearity, or the correlation coefficients of the different models can be compared with each other; the closer the value is to 1, the better the fit of the model.

Recovery. Recovery is the ratio of a measured mean value under repeatability conditions to the true value of the analyte in the sample

$$R = \frac{\bar{x}}{x_t} 100,$$

where *R* is recovery (in %), \bar{x} is the mean value, and x_t is the true value.

Recovery data can be useful for the assessment of the entire method, but in a specific case it is applicable just for the experimental conditions, i.e., the matrix, etc. for which the mean value was determined.

If *R* is sufficiently well established, it can also be used for the correction of the results.

The following are the most important procedures for determining recoveries.

- **Certified reference materials:** the certified value is used as the true value in the formula above.
- **Spiking:** this procedure is widely practised either on a blank sample or on a sample containing the analyte.
- **Trueness:** if spiking is used at several concentration levels or if several reference materials are available over the concentration range of interest, *R* can be estimated from a regression line by testing the trueness of a plot of true (spiked) values versus measured values.
- **Mass balance:** tests are conducted on separate fractions of a sample. The sum of the results on each fraction constitute 100%. This tedious method is applied only in special cases.

Robustness. A method is robust (or rugged) if minor variations in the practise of the method do not lead to changes in the data quality. Robustness therefore is the degree of independence of the results from changes in the different influence factors. It is easily seen that

robustness is becoming a very major issue in routine operation of analytical methods.

For the determination of robustness, two different approaches are feasible.

Interlaboratory studies: The basic reasoning behind the usefulness of interlaboratory studies for robustness testing is the fact that the operation of a specific method in a sufficiently large number of laboratories (≥ 8) will always lead to random deviations in the experimental parameters.

Experimental design in a single laboratory: In a carefully designed study the relevant experimental parameters are varied within foreseen or potential tolerances and the effects of these perturbations on the results are recorded.

- Experimental parameters (also called factors) that are most likely to have an influence on the result are identified.
- For each experimental parameter the maximum deviation from the nominal value that might be seen in routine work is laid down.
- Experiments are run under these perturbed conditions.
- The results are evaluated to identify the truly influential experimental parameters.
- A strategy is devised to optimize the procedure with respect to the identified influences.

Relationship Between the Objective of a Method and the Depth of Validation

To present the basic considerations considered so far in a concrete form, it is useful to classify analytical methods according to their main purposes.

1. Methods for qualitative analysis
2. Methods for measuring main components, assaying
3. Methods for trace analysis
4. Methods for the establishment of physicochemical properties.

The requirements for validation that follow for the different classes of applications are given in Table 3.10.

These performance characteristics have already been described in an earlier part of the chapter and do not require further discussion. It should be stressed, however, that selectivity must be demonstrated in the course of validation by accurate and reliable measurements on real samples. A test of selectivity is at the same time a test of the influence of interference on the results.

Particular attention should also be drawn to the fact that the working range of a method of analysis is never

Table 3.10 Purpose of a method of measurement and the relevant performance characteristics in validation

	(a) Qualitative	(b) Main component/assay	(c) Trace analysis	(d) Phys.-chem. properties
Trueness		×	×	×
Precision		×	×	×
Linearity/working range		×	×	×
Selectivity	×	×	×	
Limit of detection	×		×	
Limit of determination			×	
Robustness	×	×	×	×

larger than that tested on real samples in the course of validation. Extrapolation to smaller or larger values cannot be tolerated.

In practise, this leads to a definition of the limit of determination by the sample with the smallest content for which data on trueness and precision are available. The lower limit of the working range therefore also defines the limit of determination; the upper limit of the working may sometimes be extended by suitable dilutions.

Frequency of Validation

The situation regarding the frequency of validation is comparable to the situation for the appropriate amount of validation; there are no firm and generally applicable rules, and only recommendations can be offered that help the person responsible for validation with a competent assessment of the particular situation. Some such recommendations can also be found in ISO 17025 Chap. 5.4.5. Besides those cases where a basic validation is in order, e.g., at the beginning of the lifecycle of a method, there is the recommendation to validate

standard methods used outside their intended scope, and amplifications and modifications of standard methods to confirm that the methods are fit for the intended use,

and

when some changes are made in the validated non-standard methods, the influence of such changes carried out should be documented and if appropriate a new validation should be carried out.

In routine work, regular checks are required to make sure that the fitness for the intended use is not compromised in any way. In practise this is best done by control charts.

It is fair to state that, in essence, the frequency and extent of revalidation depend on the problem and on the

magnitude of changes applied to previously validated methods. In a way it is therefore not time but a particular event that triggers the quest for revalidation. For a simple orientation and overview, some typical examples are addressed in Table 3.9.

If a new sample is analyzed, this might constitute the simplest event calling for validation measures. Depending on the method applied, this might be accomplished by adding an internal standard, by the method of standard additions, or by calling for duplicate measurements. If a new batch of samples is to be analyzed, it may be appropriate to take some additional actions, and it is easily seen that the laboratory supervisory personnel must incorporate flexibility in the choice of the appropriate revalidation action.

A special case is the training of new laboratory personnel, as the workload necessary may be significant, for instance, if difficult clean-up operations are involved. It may be advisable to have a backup operator trained in order to have a smooth transition from one operator to another without interruption of the laboratory workflow.

System Suitability Test

A system suitability test (SST) is an integral part of many analytical methods. The idea behind an SST is to view equipment, electronics, analytical operations, and samples as one system that can therefore be evaluated in total. The particular test parameters of an SST therefore critically depend on the type of method to be validated. In general, an SST must give confidence that the test system is operating without problems within specified tolerances. An SST is carried out with real samples, and it therefore cannot pinpoint problems with a particular subsystem.

Details can be found in pharmaceutical science literature, particularly in pharmacopeia. In the literature there are several examples for SST, e.g., for HPLC.

If an SST is applied regularly, it is generally laid down in a separate standard operating procedure.

Table 3.11 Event-driven actions in revalidation; adapted from [3.37]

Event	Action taken for revalidation
A new sample	Internal standard Standard additions Duplicate analysis
Several new samples (a new batch)	Blank(s) Recalibration Measurement of a standard reference material or a control check sample
New operator	Precision Calibration Linearity Limit of detection Limit of determination Control check sample(s)
New instrument	General performance check Precision Calibration Limit of detection Limit of determination Control check samples
New chemicals/standards	Identity check for critical parameters Laboratory standards
New matrix	Interlaboratory comparisons New certified reference material Alternative methods
Small changes in analytical methodology	Proof of identical performance over the concentration range and range of matrices (<i>method comparison</i>)

Report of Validation and Conclusions

Around the globe, millions of analytical measurements are performed daily in thousands of laboratories. The reasons for doing these measurements are extremely diverse, but all of them have in a common the characteristic that the cost of measurement is high, but the decisions made on the basis of the results of these measurements involve yet higher cost. In extreme cases, they can lead to fatal consequences; points in case are measurements in the food, toxicological, and forensic fields.

Results of analytical measurements are truly of foremost importance throughout life, demonstrating the underlying responsibility to ensure that they are correct. Validation is an appropriate means to demonstrate that the method applied is truly fit for purpose. For every method applied, a laboratory will have to rely

on validation for confidence in the operation of the method.

The elements of validation discussed in this chapter must ascertain that the laboratory produces, in every application of a method, data that are well defined with respect to trueness and precision. The basics of quality management aid in providing this confidence. Therefore, every laboratory should be prepared to demonstrate its competence on the basis of internal data not only for methods it has devised itself, but also for standard methods of analysis. Revalidation will eventually be required for all methods to keep this data up to date.

A laboratory accredited according to ISO 17025 must be able, at any time, to demonstrate the required performance by well-documented validation results.

3.6 Interlaboratory Comparisons and Proficiency Testing

Interlaboratory comparisons (ILCs) are a valuable quality assurance tool for measurement laboratories, since

they allow direct monitoring of the comparability of measurement and testing results. Proficiency tests (PTs)

are interlaboratory comparisons that are organized on a continuing or ongoing basis. **PTs** and **ILCs** are therefore important components in any laboratory quality system. This is increasingly recognized by national accreditation bodies (**NABs**) in all parts of the world, who are increasingly demanding that laboratories participate in **PTs** or **ILCs** where these are available and appropriate.

PTs and **ILCs** enable laboratories to benchmark the quality of their measurements. Firstly, in many **ILCs**, a laboratory's measurement results may be compared with reference, or true, values for one or more parameters being tested. Additionally, where applicable, the associated measurement uncertainties may also be compared. These reference values will be the best estimate of the true value, traceable to national or international standards or references. Reference values and uncertainties are determined by expert laboratories; these will often be national measurement institutes (**NMIs**).

However, not all **ILCs** and **PTs** will be used to determine reference values. In most of these cases, a laboratory will only be able to benchmark their results against other laboratories. In these situations, a consensus value for the true value will be provided by the organizer, which will be a statistical value based upon the results of the participating laboratories or a value derived from extended validation.

3.6.1 The Benefit of Participation in **PTs**

The primary benefit from participating in **PTs** and **ILCs** for a laboratory is the ability to learn from the experience. Organizers of **PTs** and **ILCs** usually see themselves in the role of teachers rather than policemen. **PTs** and **ILCs** are therefore viewed as educational tools, which can help the participating laboratories to learn from their participation, regardless of how successful the participation is.

There are many quality assurance tools available to laboratories, including

- appropriate training for staff,
- validation of methods for testing and calibration,
- use of certified reference materials and artifacts,
- implementation of a formal quality system and third-party accreditation,
- participation in appropriate **PTs** and **ILCs**.

It is usually recommended that all these tools be used by measurement laboratories. However, laboratories are now recognizing the particular importance of participation in **PTs** and **ILCs** as a quality tool. Of the tools

listed above, it is the only one that considers a laboratory's outputs, i. e., the results of its measurements. The other tools are input tools, concerned with quality assurance measures put in place to provide the infrastructure necessary for quality measurements.

As a consequence of this, appropriate use of participation in **PTs** and **ILCs** is of great value to laboratories in assessing the validity of the overall quality management system. Appropriate participation in **PTs** and **ILCs** can highlight how the quality management system is operating, where any problems may be found that have an effect on the measurement results expected. Regular participation can therefore form a continuous feedback mechanism, enabling the quality management system to be monitored and improved on an ongoing basis. In particular, following poor performance in a **PT** or **ILC**, laboratories should institute an investigation, which may result in corrective action being taken. This corrective action may involve changes to the quality management system and its documentation.

3.6.2 Selection of Providers and Sources of Information

There are literally thousands of **PTs** and **ILCs** offered during any year, across all measurement sectors, by reputable organizations across the world. Laboratories can gain information about available **PTs** and **ILCs** from a number of sources. These include

- the European Proficiency Testing Information System (**EPTIS**),
- national accreditation bodies (**NABs**),
- international accreditation bodies [e.g., the Asian Pacific Accreditation Cooperation (**APLAC**), **ILAC**, and the European Cooperation for Accreditation (**EA**)],
- peer laboratories.

National accreditation bodies (**NABs**) will hold, as part of their normal laboratory surveillance and assessment activities, a great deal of information about **PTs** and **ILCs** (or organizations that run **ILCs**). They will have noted, during laboratory surveillance visits, what these **PTs** and **ILCs** cover, how they operate, and how relevant they are to the laboratory's needs. **NABs** are therefore in a good position to provide information about available and appropriate **PTs** and **ILCs** and, in some cases, may advise on the suitability and quality of these. Some **NABs** also accredit **PT** providers, usually against **ISO** guide 43 part 1 (1997) and **ILAC** guide G13 (2000). These **NABs** will therefore have more detailed

information regarding accredited **PTs**, which they can pass on to laboratories.

International accreditation bodies such as **APLAC**, **ILAC** or **EA** will also have a significant body of information regarding international or regional **PTs** and **ILCs**. Additionally they may organize **PTs** and **ILCs** themselves, or associate themselves with specific **PTs** and **ILCs**, which they use for their own purposes, such as monitoring the efficacy of multilateral agreements (**MLAs**) or multiregional agreements. **APLAC**, for example, associates itself with a number of **ILCs**, which are usually organized by member accreditation bodies. **EA** may be involved with independent **PT** and **ILC** organizers, such as the Institute of Reference Materials and Measurements (**IRMM**) in Geel, Belgium, who organize the International Measurement Evaluation Programme (**IMEP**) series of **ILCs**.

The *European Proficiency Testing Information System* (**EPTIS**) is the leading international database of **PTs** and **ILCs**. **EPTIS** was originally set up with funding from the European Commission, and is now maintained by the German Federal Institute of Materials Testing (**BAM**) in Berlin. **EPTIS** contains over 800 **PTs** and **ILCs** across all measurement sectors excluding metrology. Although originally established as a database for the pre-May 2004 countries within the European Union, plus Norway and Switzerland, it has now been extended to include the new European Union (**EU**) countries, the USA, as well as other countries in South and Central America and Asia. **EPTIS** now enjoys the support of the International Laboratory Accreditation Conference (**ILAC**), and has the goal of extending its coverage to include potentially all providers of **PTs** and **ILCs** throughout the world. The database, however, is searchable by anyone, anywhere in the world. It is accessed online at www.eptis.bam.de. It can be searched for **PTs** by country, test sample type, measurement sector, or determinand. The details contained in **EPTIS** for each **PT** and **ILC** are comprehensive. These include

- organizer,
- frequency,
- scope,
- test samples,
- determinands,
- statistical protocol,
- quality system,
- accreditation status,
- fees payable.

Many of the entries also contain a link to the home page of the provider so that more in-depth information can be studied.

EPTIS also provides more general information on the subject of proficiency testing. Any laboratory wishing to find a suitable **PT** or **ILC** in which to participate is strongly advised to search **EPTIS** first. One warning must, however, be given. Although there is no cost to **PT** providers to have an entry on **EPTIS**, it is voluntary, and therefore there are a small number of **PTs** in the countries covered by **EPTIS** which are not listed.

Peer laboratories are a good source of information about available and appropriate **PTs** and **ILCs**. A laboratory working in the same field as your own may be a good source of information, particularly if they already participate in a **PT**, or have investigated participation in a **PT** or **ILC**. Although such laboratories may be commercial competitors, a **PT** or **ILC** that is appropriate for them is very likely to be appropriate for all similar laboratories in that measurement sector.

When a laboratory has obtained the information about available **ILCs** and **PTs**, there may be a need to make a decision.

- Is there more than one **ILC/PT** available? If so, which is the most appropriate for my laboratory?
- There is only one **ILC/PT** that covers my laboratory's needs. Is it appropriate for my laboratory to participate?

There are many issues that are appropriate to both the above questions. In order to make the correct decision, there are a number of aspects of the **ILCs/PTs** that must be understood. To select the most appropriate **ILC** or **PT**, or determine if an **ILC** or **PT** is appropriate for a specific laboratory, the following factors need to be considered.

- Test samples, materials or artifacts used.
- Measurands, and the magnitude of these measurands.
- What is the frequency of distribution for a **PT** scheme?
- Who are the participants?
- What quality system is followed by the organizer?
- In which country is the **ILC** or **PT** organized, and what language is used?
- What is the cost of participation?

We will consider these factors individually below.

Test Samples, Materials or Artifacts Used

The laboratory must satisfy itself that the test samples, materials or artifacts used in the **PT** or **ILC** are appropriate to their needs. The test materials should be of a type that the laboratory would normally or routinely test. They should be materials that are covered by the scope of the laboratory's test procedures. If the materials available in the **PT** or **ILC** are not fully appropriate – they may be quite similar but not ideal – the laboratory must make a judgement as to whether participation would have advantages. The laboratory could also contact the **PT** or **ILC** organizer to ask if the type of material appropriate to them could be included.

Measurands and the Levels of These Measurands

If the test materials in the **PT** or **ILC** are appropriate for the laboratory, then the question of the measured properties (measurands) needs to be taken into consideration. The measurands available should be the same as the laboratory would routinely measure. Of course, for those materials where many tests could be carried out, the **PT** or **ILC** may not routinely provide all of these. Again, the laboratory must make a judgement about whether the list of tests available is appropriate and fits sufficiently well with the laboratory's routine work to make participation worthwhile.

The origin of the samples is also important to many laboratories. The laboratory needs to know where and how they were prepared, or from which source they were obtained. For example, it is important to know whether they have been tested for homogeneity and/or stability. If so, where there is more than one measurand required for that material, the laboratory needs to know for which measurands. A good-quality **PT** or **ILC** will prepare sufficient units that surplus samples are available for participants later, particularly those who need them following poor performance.

What Is the Frequency of Distribution for a PT Scheme?

For **PT** schemes, rather than **ILCs**, the frequency of distributions, or rounds, is important. The frequency of **PTs** does vary from scheme to scheme and from sector to sector. Most **PTs** are distributed between two and six times a year, and a frequency of three or four rounds per year is quite common. The frequency is important for laboratories, in case of unsatisfactory performance in a **PT**, when the efficacy of corrective actions must be studied to ensure any problem has been properly corrected.

Who Are the Participants?

For any **PT** or **ILC**, it is important that a laboratory can compare its results with peer laboratories. Peer laboratories may not always be those who carry out similar tests.

Laboratories in different countries may have different routine test methods – these may be specified by regulation. In some cases, these test methods will be broadly equivalent technically, but in other cases their performance may be significantly different. In fact, in this case, this situation may not be recognized by laboratories or expert sectoral bodies. Comparison with results generated using such methods will be misleading.

Even within any individual country, there may be differences in the test methods used by laboratories. The **PT** or **ILC** organizer should be able to offer advice on which test methods may be used by participants, how these vary in performance, and what steps the organizer will follow to take these into account when evaluating the results.

The type of laboratories participating in a **PT** or **ILC** is also important. For a small nonaccredited laboratory, comparison with large, accredited laboratories or national measurement institutes (**NMIs**) may not be appropriate. The measurement capabilities of these different types of laboratories, and the magnitude of their estimated measurement uncertainties will probably be significantly different. The actual end use of results supplied by different types of laboratories to their customers will usually determine the level of accuracy and uncertainty to which these laboratories will work.

What Quality System Is Followed by the Organizer?

For laboratories who may rely significantly on participation in **PTs** or **ILCs**, or if they are accredited and are required to participate by their national accreditation body (**NAB**), as a major part of their quality system, it is important that the schemes they use are of appropriate quality. This gives laboratories a higher degree of confidence in the **PT** or **ILC**, and hence the actions they may need to take as a result of participating.

In recent years the concept of quality for **PTs** has gained more importance. **ISO/IEC** guide 43 parts 1 and 2 were reissued in 1997, and many **PT** and **ILC** organizers claim to follow this. In practise, this guide is very generic, but compliance with it does confer a higher level of quality. The development of the **ILAC** guide G13:2000 has, however, enabled many accreditation bodies throughout the world (including in countries

such as The Netherlands, Australia, the UK, Spain, Sweden, and Denmark) to offer accreditation of PT scheme providers as a service. Most accreditation bodies who offer this service accredit providers against a combination of ISO/IEC guide 43 and ILAC G13. Guide G13 is a considerably more detailed document and is generally used as an audit protocol. Not all NABs accredit PT and ILC organizers using these documents; some NABs in Europe prefer the approach of using ISO/IEC 17020, considering the PT or ILC organizers to be inspection bodies. In Europe, the policy of the EA is that it is not mandatory for NABs to provide this service, but that, if they do, they should accredit using a combination of ISO guide 43 part 1 (1997) and the ILAC guide G13:2000, which is also the preferred approach within APLAC.

Information on quality is listed on EPTIS, and now information on accreditation status is also included, at the request of ILAC.

Laboratories need to make a judgement on whether an accredited scheme is better than a nonaccredited scheme where a choice is available.

The quality of a PT or ILC is important, as the operation of such an intercomparison must fit well with the requirements of participating laboratories. All PTs and ILCs should have a detailed protocol, available to all existing and potential participating laboratories. The protocol clearly illustrates the modus operandi of the PT or ILC, including timescales, contacts, and the statistical protocol. The statistical protocol is the heart of any intercomparison, and should comprehensively show how data should be reported (e.g., number of replicates and reporting of measurement uncertainty), how the data is statistically evaluated, and how the results of the evaluation are reported to participating laboratories. Laboratories need to understand the principles of the statistical protocol of any PT or ILC in which they participate. This is necessary in order to understand how their results are evaluated, which criteria are used in this evaluation, and how these fit with the laboratory's own criteria for the quality and fitness for purpose of results. It is therefore important to find a PT or ILC that asks for data in an appropriate format for the laboratory and evaluates the data in a way that is broadly compatible with the laboratory's own procedures.

In Which Country Is the ILC or PT Organized, and What Language Is Used?

Where a laboratory has a specific need which cannot be met by a PT or ILC in their own country, or where a choice between PTs or ILCs exists where one or more

of these are organized in countries outside their own, the country of origin may be important.

The modus operandi of many PTs and ILCs may vary significantly between countries, particularly with regard to the statistical evaluation protocol followed. This may be important where a laboratory wants to take part in a PT or ILC that fits well with their own internal quality procedures.

More important for many laboratories is the language in which the PT or ILC documentation is written. A number of PTs or ILCs may be aimed mainly at laboratories in their own country and will use only their native language. Laboratories wishing to participate in such a PT or ILC will need to ensure that they have members of staff who can use this language effectively. Other PTs and ILCs are more international in nature, and may use more than one language. In particular, many of these will issue documents in English as a second language.

What Is the Cost of Participation?

If a laboratory has researched the available PTs and ILCs and has found more than one of these that could be appropriate, the final decision may often be made on the basis of cost.

Some laboratories see participation in PTs and ILCs as another cost that should be minimized. Some accredited laboratories see participation as an extra cost on top of what they already pay for accreditation.

Therefore, cost is an important factor for some laboratories. However, it should be noted that a less expensive scheme may not always provide the quality or service that is required for all the many benefits of participation in PTs and ILCs to be realized.

Some laboratories successfully negotiate with the organizers where cost is a real issue for them (e.g., very small laboratories, university laboratories, laboratories in developing economies, etc.). Laboratories should note that the cost of participation is not just the subscription that is paid to the organizer. The cost in time and materials of testing PT and ILC test materials or samples also needs to be taken into account.

What if There is no Appropriate PT or ILC for a Laboratory's Needs?

When the right PT or ILC does not exist, a laboratory can participate in one which is the best fit, or decide not to participate at all. In this case, reliance on other quality measures will be greater. A laboratory can approach a recognized organizer of PTs and ILCs to ask if an appropriate intercomparison can be organized. Also,

a laboratory may collaborate with a group of laboratories with similar needs (these groups will nearly always be quite small, otherwise a PT or ILC will probably already have been organized), to organize small inter-comparisons between themselves.

3.6.3 Evaluation of the Results

It is important for laboratories, when they have participated in any PT or ILC, to gain the maximum benefit from this. A major aspect of this is in the interpretation of the results from a PT or ILC, and how to use these results to improve the quality of measurements in the laboratory.

There are a number of performance evaluation procedures used in PT schemes. Two of the most widely used of these are outlined here.

1. Z-scores
2. E_n numbers.

Z-scores are commonly used in many PT schemes across the world, in many sectors. This performance evaluation technique is probably the most widely used on an international basis.

E_n numbers incorporate measurement uncertainty and are used in calibration studies and by many ILCs where the measurement uncertainty is an important aspect of the measurement process. E_n numbers are therefore used more commonly in physical measurement ILCs and PTs, where the measurement uncertainty concept is much better understood.

More examples of performance evaluation techniques can be found in the ISO standard for statistics used in proficiency testing, ISO 13528 (2005).

Z-Scores

Z-scores are calculated according to the following equation:

$$Z = (x_1 - X)/s ,$$

where x_1 is the individual result, X is the assigned or true value, and s is a measure of acceptability. For example, s can be a percentage of X : if X is 10.5, then if results should be within 20% of this to be awarded a satisfactory Z-score, the s will be 10% of 10.5, i. e., 1.05. It could also be a value considered by the organizer to be appropriate from previously generated precision data for the measurement. s may also be a statistically calculated value such as the standard deviation, or a robust measure of the standard deviation.

The assigned value can be either a *reference* value or a *consensus* value. Reference values are traceable and can be obtained, for example, from

- formulation (the test sample is prepared in a quantitative manner so that its properties and/or composition are known),
- reference measurement (the test sample has been characterized using a primary method, or traceable to a measurement of a certified reference material of a similar type).

Consensus values are obtained from the data submitted by participants in a PT or ILC.

Most schemes will classify Z-scores as

- satisfactory ($|Z| \leq 2$),
- questionable ($2 > |Z| > 3$),
- unsatisfactory ($|Z| \geq 3$).

These are broadly equivalent to internal quality control charts, which give warning limits (equivalent to a *questionable* result) and action limits (equivalent to an *unsatisfactory* result).

E_n Numbers

The equation for the calculation of E_n numbers is

$$E_n = \frac{x - X}{\sqrt{U_{\text{lab}}^2 + U_{\text{ref}}^2}} ,$$

where the assigned value X is determined in a reference laboratory, U_{ref} is the expanded uncertainty of X , and U_{lab} is the expanded uncertainty of a participant's result x .

E_n numbers are interpreted as follows.

- Satisfactory ($E_n \leq 1$)
- Unsatisfactory ($E_n > 1$).

Laboratories are encouraged to learn from their performance in PTs and ILCs. This includes both positive and negative aspects.

Action should be considered

- when an unsatisfactory performance evaluation has been obtained (this is mandatory for laboratories accredited to ISO/IEC 17025), or
- when two consecutive questionable results have been obtained for the same measurement, or
- when nine consecutive results with the same bias against the assigned value, for the same measurement, have been obtained. This would indicate that, although the measurements may have been very precise, there is a clear bias. Deviations from this

situation could easily take the measurements out of control.

The above guidelines should enable laboratories to use **PT** and **ILC** results as a way of monitoring measurement quality and deciding when action is necessary.

When interpreting performance in any **PT** or **ILC**, there are a number of factors that need to be considered to enable the performance to be placed into a wider context. These include

- the overall results in the intercomparison from all participating laboratories,
- the performance of different testing methods,
- any special characteristics or problems concerning the test sample(s) used in the intercomparison,
- bimodal distribution of results,
- other factors concerning the **PT** or **ILC** organization.

It is always advisable to look at any unsatisfactory performance in the context of all results for that measurement in the intercomparison. For example, if the majority of the results have been evaluated as satisfactory, but one single result has not, then this is very serious. However, if many participating laboratories have also been evaluated as unsatisfactory, then for each laboratory with an unsatisfactory performance, there is still a problem but it is less likely to be specific to each of those laboratories.

It is also a good idea to look at how many results have been submitted for a specific measurement. When there are only a few results, and the intercomparison has used a consensus value as the assigned value for the measurement, the confidence in this consensus value is greatly reduced. The organizer should provide some help in interpreting results in such a situation and, in particular, should indicate the minimum number of results needed.

3.6.4 Influence of Test Methods Used

In some cases, an unsatisfactory performance may be due, at least in part, to the test method used by the laboratory being inappropriate, or having lower performance characteristics than other methods used by other laboratories in the intercomparison.

If the **PT** or **ILC** organizer has evaluated performance using the characteristics of a standard method, which may have superior performance characteristics, then results obtained using test methods with inferior performance characteristics will be more likely to be evaluated as unsatisfactory. It is always suggested that

in such situations participating laboratories should compare their results against other laboratories using the same test method.

Some **PTs** and **ILC** will clearly differentiate between the various test methods used in the report, so the performance of each test method can be compared in order to see if there is a difference in precision of these test methods, and any bias between test methods can also be evaluated. The performance of all participating laboratories using the same test method can be studied, which should give laboratories information about both the absolute and relative performance of that test method in that intercomparison.

As has been previously stated, the test samples used in **PTs** and **ILCs** should be similar to those routinely measured by participating laboratories. A **PT** scheme may cover the range of materials appropriate to that scheme, so some may be unusual or extreme in their composition or nature for some of the participating laboratories. Such samples or materials should ideally be of a type seen from time to time by these laboratories. These laboratories should be able to make appropriate measurements on these test samples satisfactorily, if only to differentiate them from the test samples they would normally see. These unusual samples can, however, present measurement problems for laboratories when used in a **PT** or **ILC**, and results need to be interpreted accordingly.

In some cases, the value of the key measurands may be much higher or lower than what is considered to be a normal value. This can cause problems for laboratories, and results need to be interpreted appropriately, and lessons should be learned from this. If the values are in fact outside the scope of a laboratory's test methods, then any unsatisfactory performance may not be surprising, and investigation or corrective actions do not always need to be carried out.

One consequence of divergence of performance of different test methods, which may not necessarily be related to the test samples, is that a bimodal distribution of results is obtained. This is often caused by two test methods which should be, or are considered by experts in the appropriate technical sector to be, technically equivalent showing a significant bias. This could also arise from two different interpretations of a specific test method, or the way the results are calculated and/or reported. Problems that are typically encountered with reporting include the units or number of significant figures. When the assigned value for this measurement is a consensus value, this will have a more significant effect on result evaluation. Automatically, any smaller

group of laboratories will be evaluated as unsatisfactory, regardless. In extreme cases, the two distributions will contain the same number of results, and then the consensus value will lie between them, and probably most, if not all, results will be evaluated as unsatisfactory.

In these cases, the organizer of the PT or ILC should take action to ensure that the effect of this is removed or minimized, or no evaluation of performance is carried out in order that laboratories do not misinterpret the evaluations and carry out any unnecessary investigations or corrective actions.

Although organizers of PTs and ILCs should have a quality system in place, occasionally some problems will arise that affect the quality of the evaluation of performance that they carry out. These can include, for example,

- transcription errors during data entry,
- mistakes in the report,
- software problems,
- use of inappropriate criteria for evaluation of performance.

In these cases, the evaluation of the performance of participating laboratories may be wrong, and the evaluation must either be interpreted with caution or, in extreme situations, ignored. The organizer of the PT or ILC should take any necessary corrective action once the problem has been identified.

3.6.5 Setting Criteria

In setting the criteria for satisfactory performance in a PT or ILC, the organizer, with the help of any technical steering group, may need to make some compromises in order to set the most appropriate criteria that will be of value to all participating laboratories. These criteria should be acceptable and relevant to most laboratories, but for a small minority these may be inappropriate. From a survey carried out by the author in 1997, some laboratories stated that they chose to use their own criteria for performance evaluation, rather than those used by the PT or ILC organizer. For most of these laboratories, the criteria they chose were tighter than those used in the PT or ILC.

Laboratories are normally free to use their own criteria for assessing their PT results if those used by the scheme provider are not appropriate, since the PT provider can obviously not take any responsibility for participating laboratories' results. These criteria should be fit for purpose for the individual laboratory's situation, and should be applied consistently. Interpretation

of performance using these criteria should be carried out in the same manner as when using the criteria set by the PT or ILC organizer.

3.6.6 Trends

It is very useful to look at trends in performance in a PT that is carried out regularly. This is particularly useful when a laboratory participates at a relatively high frequency (e.g., once every 3 months).

Performance over time is the major example of this. The example in Fig. 3.19 shows how this may be illustrated graphically. This approach is recommended by experts rather than using statistical procedures, which may produce misleading information or hide specific problems.

The chart shows an example from a Laboratory of the Government Chemist (LGC) PT scheme of a graph showing performance over time. Z-scores for one measurement are plotted against the round number. In this case, the laboratory has reported results using three different test methods. This graph can be used to assess trends and to ascertain whether problems are individual in nature or have a more serious underlying cause.

Where more than one test method has been used, these can also be used to see if there is a problem with any individual method, or whether there is a calibration problem, which could be seen if more than one test method shows a similar trend.

In many PTs and ILCs there may be measurements that are requested to be measured using the same method, or are linked to each other technically in some way. Where all results for such linked measurements are unsatisfactory, the problem is likely to be generic,

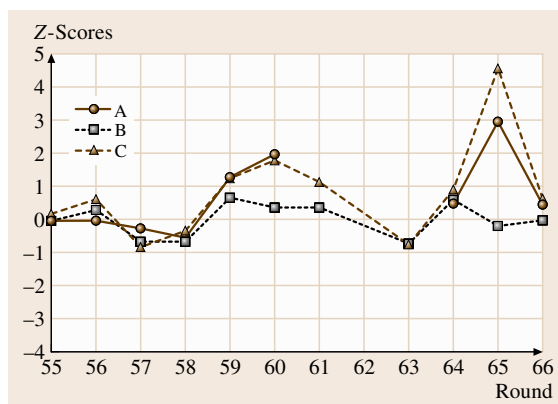


Fig. 3.19 Example graphical presentation of performance over time

and only one investigation and corrective action will be necessary.

Laboratory managers can gain information about the performance of individual staff on **PT** or **ILC** test samples. Information on each member of staff can be collated from **PT** and **ILC** reports and interpreted together with the information they should hold about which member of staff carried out the measurements.

Alternatively, where the test sample is of an appropriate nature, the laboratory manager can give the **PT/ILC** test sample(s) to more than one member of staff. Only one set of results needs to be reported to the organizer, but the results of appropriate members of staff can then be compared when the report is published.

Samples provided by the organizer should be tested in the same way as routine samples in order to get optimum feedback on performance. If this is not done, the educational benefit will be limited.

3.6.7 What Can Cause Unsatisfactory Performance in a **PT** or **ILC**?

There are many potential causes of unsatisfactory performance in any **PT** or **ILC**. These fall into two distinct categories.

- Analytical problems with the measurement itself
- Nonanalytical problems that usually occur after the measurement has been made.

Analytical errors include

- problems with calibration (e.g., the standard materials prepared to calibrate a measurement, or the accuracy/traceability of the calibration material),
- instrument problems (e.g., out of specification),
- test sample preparation procedures not being carried out properly,
- poor test method performance. This may be due to problems with the member of staff carrying out the measurement, or the appropriateness of the test method itself.

Nonanalytical errors include

- calculation errors,
- transcription errors,
- use of the wrong units or format for the reported result.

Any result giving rise to an unsatisfactory performance in a **PT** or **ILC** indicates that there is a problem in the laboratory, or a possible breakdown of the laboratory's quality system. It does not matter if the cause of

this unsatisfactory result was analytical or nonanalytical as the result has been reported. At this point, it must be remembered that the **PT** or **ILC** organizer is acting in the role of the laboratory's customer and is providing a service to examine the laboratory's quality system thoroughly by means of an intercomparison.

The author's own experience of the organization of **PTs** over 10 years has shown that 35–40% of unsatisfactory results are due to nonanalytical errors.

3.6.8 Investigation of Unsatisfactory Performance

Participation in appropriate **PTs** and **ILCs** is strongly recommended by most national accreditation bodies for accredited laboratories and those seeking accreditation. Some **NABs** will stipulate that participation is mandatory in certain circumstances. Additionally, some regulatory authorities and, increasingly, customers of laboratories, will also mandate participation in certain **PTs** and **ILCs** in order to assist in the monitoring of the quality of appropriate laboratories.

It is mandatory under accreditation to **ISO/IEC 17025** that an investigation be conducted for all instances of unsatisfactory performance in any **PT** or **ILC**, and to implement corrective actions where these are considered appropriate. All investigations into unsatisfactory performance in an intercomparison, and what, if any, corrective actions are implemented must be fully documented.

Some measurement scientists believe that unsatisfactory performance in any **PT** or **ILC** is in itself a noncompliance under **ISO/IEC 17025**. This is not true, although there are a few exceptions in regulatory **PTs** where participation is mandatory and specified performance requirements are stated. However, failure to investigate an unsatisfactory result is certainly serious noncompliance for laboratories accredited to **ISO/IEC 17025**.

It is generally recommended to follow the policy for the investigation of unsatisfactory performance in **PTs** and **ILCs** given by most national accreditation bodies, and the subsequent approach to taking corrective actions. All investigations should be documented, along with a record of any corrective actions considered necessary and the outcome of the corrective action(s).

There are a number steps that it is recommended should be taken when investigating unsatisfactory performance in any intercomparison. This should be done in a logical manner, working backwards.

Firstly, it should be checked that the **PT** or **ILC** organizer is not at fault. This should be done by ensuring that the report is accurate, that they have not entered any of the laboratory's data incorrectly, and that they have carried out all performance evaluations appropriately.

If the organizer has not made any errors, then the next check is to see that the result was properly reported. Was this done accurately, clearly, and in the correct units or format required by the **PT** or **ILC**?

If the result had been reported correctly and accurately, the next check is on any calculations that were carried out in producing the result.

If the calculations are correct, the next aspect to check is the status of the member of staff who carried out the measurement. In particular, was he or she appropriately trained and/or qualified for this work, and were the results produced checked by their supervisor or manager?

This should identify most sources of nonanalytical error. If no nonanalytical errors can be found, then analytical errors must be considered. When it appears that an unsatisfactory result has arisen due to analytical problems, there are a number of potential causes that should be investigated, where appropriate.

Poor calibration can lead to inaccurate results, so the validity of any calibration standards or materials must be checked to ensure that these are appropriate and within their period of use, and that the calibration values have been correctly recorded and used.

If the measurement has been made using an instrument – which covers many measurements – the status of that instrument should be checked (i. e., is it within its calibration period, and when was it last checked?). It is also recommended to check that the result was within the calibration range of the instrument.

Any **CRM**, **RM** or other **QC** material measured at the same time as the **PT** test sample should be checked with the result. If the result for such a material is acceptable, then a calibration or other generic measurement problem is unlikely to be the cause of the unsatisfactory performance.

Finally, the similarity of the test sample to routine test samples or, where appropriate, other samples tested in the same batch, should be noted.

This is not an exhaustive list, but covers the main causes.

When an investigation into unsatisfactory performance has indicated a potential cause, one or more corrective actions may need to be implemented. These include

- modifying a test method – which may then need revalidating,
- recalibration or servicing of an instrument,
- obtaining new calibration materials,
- changing the procedure for checking and reporting test results,
- considering whether any members of staff need further training, or retraining in particular test methods or techniques.

3.6.9 Corrective Actions

Corrective actions are not always necessary. Investigation of the situation may in fact conclude that

- no problem can be readily identified, and that the unsatisfactory result is just a single aberration – this needs monitoring, however, to ensure that this is not the beginning of a trend,
- there is a problem external to the laboratory – for example with the organize of the **PT** or **ILC**,
- the test sample from the **PT** or **ILC** is very unusual for the laboratory compared with the test samples they normally receive so that any corrective action will be of little or no value.

In some cases, it can prove very difficult for a laboratory to find the causes of unsatisfactory performance. Many **PT** and **ILC** organizers provide help to laboratories in such situations. It is always recommended to contact the organizer to ask for confidential help to solve such a problem. Many organizers have the expertise to give valuable advice, or can obtain the advice in strictest confidence from third parties.

Whatever is – or is not – done should be documented fully.

When corrective actions have been implemented, the laboratory needs to know that the actions have been successful. The corrective actions therefore need to be validated. The easiest way is to reanalyze the **PT** or **ILC** test sample. (If there is none remaining, some organizers will be able to provide another sample.) This will not, of course, be appropriate for checking nonanalytical errors. If the result from retesting agrees with the assigned value in the report, the corrective action can be considered to be successful. Alternatively (this is particularly true for more frequent **PTs**), it may be more appropriate to wait for the next round to be distributed and carry out the testing of the sample, so the efficacy of the corrective action can be assessed when the report is received. Doing both is the ideal situation, where appropriate, and

will give greater confidence that the corrective action has been effective.

In some cases, the nature of the problem is such that there must be significant doubt about the quality of results made for the test under investigation, and that this problem may have existed for some weeks or months. In fact, the problem will certainly have occurred since the last **PT** or **ILC** where satisfactory performance for the test had been obtained.

The investigation in such a situation therefore needs to be deeper in order to ascertain which results within this timeframe have a high degree of confidence, and which may be open to questions as to their validity.

There are other, secondary, benefits from participation in appropriate **PTs** or **ILCs**. These include

- help with method validation,
- demonstration of competence to internal and external customers, accreditation bodies, and regulatory bodies,
- evaluation of technical competence of staff, which can be used in conjunction with a staff training programme.

3.6.10 Conclusions

Participation in **PTs** and **ILCs** is a very good way for a laboratory to demonstrate its competence at carrying out measurements. This may be for internal use (giving good news and confidence to senior manage-

ment, for example) or giving positive feedback to the staff who carried out the measurements. Alternatively it may be used externally. Accreditation bodies, of course, will ask for evidence of competence from the results of **PTs** and **ILCs**. Regulatory authorities may ask for a level of **PT** or **ILC** performance from laboratories carrying out measurements in specific regulated areas. Customers of laboratories may require evidence of **PT** or **ILC** performance as part of their contractual arrangements. The laboratory can also be proactive in providing data to existing and potential customers to show their competence.

PT can also be used effectively in the laboratory as a tool for monitoring the performance of staff. This is particularly valuable for staff undergoing training, or who have been recently trained. The results obtained in an intercomparison can be used for this purpose, and appropriate feedback can be given. Where performance has been good, these results can be used as a specific example in a training record, and positive feedback should be given to the individual. Where performance has been less than satisfactory, it should be used constructively to help the individual improve, as part of any corrective action.

To conclude, **PTs** and **ILCs** are very important quality tools for laboratories. They can be used very effectively in contributing to the assessment of all aspects of a laboratory's quality system. The most valuable use of **PTs** and **ILC** participation is in the educational nature of proficiency testing.

3.7 Reference Materials

3.7.1 Introduction and Definitions

Role of Reference Materials in Quality

Assurance, Quality Control, and Measurement

Reference materials (**RMs**) are widely used for the calibration of measuring systems and the validation of measurement procedures, e.g., in chemical analysis or materials testing. They may be characterized for nominal properties (e.g., chemical structure, fiber type, microbiological species, etc.) and for quantitative values (e.g., hardness, chemical composition, etc.). Nominal property values are used for identification of testing objects, and assigned quality values can be used for calibration or measurement trueness control. The measurand needs to be clearly defined, and the quantity values need to be, where possible, traceable to the **SI** units of measurement, or to other internationally agreed

references such as the values carried by certified reference material [3.38].

The key characteristics of **RMs**, and therefore the characteristics whose quality needs to be assured, include the following: definition of the measurand, metrological traceability of the assigned property values, measurement uncertainty, stability, and homogeneity.

Users of reference materials require reliable information concerning the **RM** property values, preferably in the form of a certificate. The user and accreditation bodies will also require that the **RM** has been produced by a competent body [3.39, 40].

The producers of reference materials must be aware that the values they supply are invariably an indispensable link in the traceability chain. They must implement all procedures necessary to provide evidence internally and externally (e.g., by peer review, laboratory

intercomparison studies, etc.) that they have met the conditions required for obtaining traceable results at all times.

There are a number of authoritative and detailed texts on various aspects of reference materials, and these are listed in Sect. 7.3.4. Reference materials are an important tool in realizing a number of aspects of measurement quality and are used for method validation, calibration, estimation of measurement uncertainty, training, and for internal quality control (QC) and external quality assurance (QA) (proficiency testing) purposes.

Different types of reference materials are required for different functions. For example, a certified reference material would be desirable for method validation, but a working-level reference material would be adequate for QC [3.39].

Definition of RM and CRM [3.41]

Reference material (RM) is a material, sufficiently homogeneous and stable with reference to specified properties, which has been established to be fit for its intended use in measurement or in examination of nominal properties.

Certified reference material (CRM) is a reference material, accompanied by documentation issued by an authoritative body and providing one or more specified property values with associated uncertainties and traceabilities, using valid procedures.

Related Terms.

- *Quantity*: property of a phenomenon, body or substance, where the property has a magnitude that can be expressed as a number and a reference.
- *Quantity value*: number and reference together expressing the magnitude of a quantity.
- *Nominal property*: property of a phenomenon, body or substance, where the property has no magnitude.
- *Measurand*: quantity intended to be measured.
- *Metrological traceability*: property of a measurement result whereby the result can be related to a reference through a documented unbroken chain of calibrations, each contributing to the measurement uncertainty.
- *Measurement standard (etalon)*: realization of the definition of a given quantity, with stated quantity value and associated measurement uncertainty, used as a reference.
- *Reference material producer*: technically competent body (organization or firm, public or private) that is fully responsible for assigning the certified or prop-

erty values of the reference materials it produces and supplies which have been produced in accordance with ISO guides 31 and 35 [3.42].

- *European reference material (ERM)*: new standard in certified reference materials issued by three European reference materials producers (IRMM, BAM, LGC).
- *In-house reference material*: material whose composition has been established by the user laboratory by several means, by a reference method or in collaboration with other laboratories [3.43].
- *Primary method* [3.44]: method having the highest metrological qualities, whose operation can be completely described, and understood, and for which a complete uncertainty statement can be written in terms of SI units. A primary direct method measures the value of an unknown without reference to a standard of the same quantity. A primary ratio method measures the ratio of an unknown to a standard of the same quantity; its operation must be completely described by a measurement equation. The methods identified as having the potential to be primary methods are: isotope dilution mass spectrometry, gravimetry (covering gravimetric mixtures and gravimetric analysis), titrimetry, coulometry, determination of freezing point depression, differential scanning calorimetry, and nuclear magnetic resonance spectroscopy. Other methods such as chromatography, which has extensive applications in organic chemical analysis, have also been proposed.
- *Standard reference materials (SRMs)*: are certified reference materials issued by the National Institute of Standards and Technology (NIST) of the USA. SRM is a trademark.
- *Validation*: confirmation, through the provision of objective evidence, that the requirements for a specific intended use or application have been fulfilled [3.33].

3.7.2 Classification

Principles of Categorization

Physical, chemical character:

- Gases, liquids, solutions
- Metals, organics
- Inorganics

Preparation:

- Pure compounds, code of reference materials
- Natural or synthetic mixtures

- Artifacts and simulates
- Enriched and unenriched real-life samples

Function:

- Calibration of apparatus and measurement systems
- Assessment of analytical methods
- Testing of measurement devices
- Definition of measuring scales
- Interlaboratory comparisons
- Identification and qualitative analysis
- Education and training

Application field (this principle is mainly used in the catalogs of **RM** producers):

- Food and agriculture (meat, fish, vegetable, etc.)
- Environment (matter, soil, sediment, etc.)
- Biological and clinical (blood, urine, etc.)
- Metals (ferrous, nonferrous, etc.)
- Chemicals (gas, solvents, paints, etc.)
- Pure materials (chromatography, isotopes, etc.)
- Industrial raw materials and products (fuels, glass, cement, etc.)
- Materials for determination of physical properties (optical, electrical properties, etc.)

Metrological qualification **CMC**:

- Primary, secondary, and tertiary standards
- Reference, transfer, and working standards
- Amount of substance standards
- Chemical composition standards
- Gases, electrochemistry, inorganic chemistry, organic chemistry

Reliability:

1. Certified reference materials of independent institutions (**NIST**, **IRMM**, **BAM**, **LGC**)
2. **CRM** traceable to 1. of reliable producers (Merck, Fluka, Messer-Grießheim)
3. Reference materials derived from 1. or 2. (in-house **RM**, dilution, **RM** preparations)

3.7.3 Sources of Information

CRM Databases

Information about reference materials is available from a number of sources. The international database for certified reference materials Code d'Indexation des Matériaux de Référence (**COMAR**) contains information on about 10 500 **CMC** from about 250 producers in 25 countries. It can be accessed via the Internet [3.45]. Advisory services assist users identify the type of material

required for their task and identify a supplier. A number of suppliers provide a comprehensive range of materials including materials produced by other organizations and aim to provide a one-stop shop for users. An additional Internet database of natural matrix reference materials is published by the International Atomic Energy Agency (**IAEA**) [3.46].

Calibration and Measurement Capabilities (CMC) of the BIPM [3.47]

In 1999 the member states of the Metre Convention signed the mutual recognition arrangement (**MRA**) on measurement standards and on calibration and measurement certificates issued by national metrology institutes. Appendix C of the **CIPM MRA** is a growing collection of the calibration and measurements capabilities (**CMC**) of the national metrology institutes. The **CMC** database is available for everyone on the website of the Bureau International des Poids et Mesures (**BIPM**) and includes reference materials as well as reference methods.

The methods used are proved by key comparisons between the national metrology institutes. For chemical measurements the Comité Consultative pour la Quantité de Matière (**CCQM**) has been established. The **CMC** database provides a reliable service for customers all over the world to establish traceability.

Conferences and Exhibitions (Election)

PITTCON: annual; largest **RM** conference and exhibition in the USA
ANALYTICA: biannual; Munich
BERM: biannual; biological and environmental **RM**

Guides (Selection)

- **ISO** guide 30:1992/Amd 1:2008 – Terms and definitions used in connection with reference materials [3.38]
- **ISO** guide 31:2000 – Contents of certificates of reference materials [3.48]
- **ISO** guide 32:1997 – Calibration of chemical analysis and use of certified reference materials
- **ISO** guide 33:2000 – Uses of certified reference materials
- **ISO** guide 34:2009 – General requirements for the competence of reference material producers [3.42]
- **ISO** guide 35:2006 – Certification of reference materials – General and statistical principles
- **ISO/AWI** guide 79 – Reference materials for qualitative analysis – Testing of nominal properties

- ISO/CD guide 80 – Minimum requirements for in-house production of in-house-used reference materials for quality control
- ISO/NP guide 82 – Reference materials – Establishing and expressing metrological traceability of quantity values assigned to reference materials
- ISO/TR 10989:2009 – Reference materials – Guidance on, and keywords used for, RM categorization
- ISO/WD TR 11773 – Reference materials transportation
- ILAC-G9:2005 – Guidelines for the selection and use of reference materials
- ISO/REMCO (ISO-Committee on Reference Materials) document N 330 – List of producers of certified reference materials, information by task group 3 (*promotion*)
- 4E-RM guide (B. King) – Selection and use of reference materials [3.39]
- European Commission document BCR/48/93 (Dec. 1994) – Guidelines for the production and certification of Bureau Communautaire de Référence (BCR) reference materials
- ISO/REMCO – List of producers of certified reference materials
- RM report (RMR) (<http://www.rmreport.com/>)
- European Commission document BCR/48/93 (Dec. 1994) – Guidelines for the production and certification of BCR reference materials
- NIST publication 260-100 (1993) – Standard reference materials – handbook for SRM users
- IUPAC orange book – Recommended reference materials for the realization of physicochemical properties (ed. K.N. Marsh, Blackwell Scientific, 1987)
- World Health Organization (WHO) – Guidelines for the preparation and characterization and establishment of international and other standards and reference reagents for biological substances, technical report series no. 800 (1990)
- Subcontracting and selection of collaborators
- Sourcing of materials including synthesis
- Processing of materials including purification, grinding, particle size separation, etc.
- Packaging, storage, and design of dispatch processes
- Homogeneity and stability testing
- Development and validation of measurement methods, including consideration of the traceability and measurement uncertainty of measurement results
- Measurement of property values, including evaluation of measurement uncertainty
- Certification and sign-off of the RM
- Establishment of shelf-life
- Promotion, marketing, and sales of RM
- Postcertification stability monitoring
- Postcertification corrective action
- Other after-sales services
- QC and QA of quality systems and technical aspects of the work.

Certification Strategies [3.49]

Interlaboratory Cooperation Approach. The producer organizes interlaboratory comparisons of selected experienced laboratories, contributing independent measurements. Systematic uncertainties can be identified and minimized.

Elite Group Method Approach. Only a few qualified laboratories contribute to the certification by validated, independent measurement methods.

Primary Method Approach. Only primary methods (CIPM definition [3.44]) are used for certification. A blunder check is recommended.

Most BCR, BAM, and EURONORM reference materials are certified by the interlaboratory cooperation approach. NIST prefers, however, the latter methods.

Homogeneity and Stability [3.48]

The homogeneity of an RM has to be estimated and noted on the certificate. It describes the smallest amount (of a divisible material) or the smallest area (of a reference object) for which the certified values are accurate in the given uncertainty range.

The stability of a RM has to be stated in the certificate and has to be tested by control measurements (e.g., control charts). Time-dependent changes of the certified values within the uncertainty range are tolerated.

3.7.4 Production and Distribution

Requirements on RM Producers [3.42]

All or some of the following activities can be crucial in RM production, and their quality assessment can be crucial to the quality of the final RM.

- Assessment of needs and specification of requirements
- Financial planning and cost–benefit analysis

List of Suppliers (Examples)

Institutes. NIST (USA), LGC (UK), National Physical Laboratory (NPL, UK), Laboratoire d'Essais (LNE, France), BAM (Germany), PTB (Germany), NMJ (Japan), Netherlands Measurement Institute (NMI, The Netherlands), National Research Center for Certified Reference Materials (NRC-CRM, China), UNIM (Russia), Canadian Centre for Mineral and Energy Technology (CANMET, Canada), South African Bureau of Standards (SABS, South Africa), Orzajos Meresugyi Hivatal (OMH, Hungary), Slovenski Metrologicky Ustav (SMU, Slovak), Swedish National Testing and Research Institute (SP, Sweden), Główny Urząd Miar (GUM, Poland), IRMM (Europe).

Associations. Pharmacopeia, the European Network of Forensic Science (ENFS), Bureau Communautaire de Référence (BCR), European Committee for Iron and Steel Standardization (ECISS), Codex Alimentarius Committee (food standard program), Environmental Protection Agency (EPA, environment), UBA (Bundesumweltamt, environment), GDMB, Verein Deutscher Eisenhüttenleute (VDEh).

Companies (Branches). Sigma-Aldrich, LGC-Promotech, Merck, Fluka, Polymer Standard Service GmbH, Ehrenstorfer, Brammer Standard Company, Messer-Griesheim (gas), Linde (gas).

3.7.5 Selection and Use

Requirements on RM

Generally, the demand for reference materials exceeds supply in terms of the range of materials and availability. It is rare to have a choice of alternative RMs, and the user must choose the most suitable material available. It is important, therefore, that users and accreditation bodies understand any limitations of reference materials employed.

There are, however, several hundred organizations producing tens of thousands of reference materials worldwide. Producers include internationally renowned institutions such as NIST, collaborative government-sponsored programs such as the EU BCR program, semicommercial sectoral or trade associations such as the American Oil Chemicals Association, and an increasing number of commercial organizations. The distinction between government institutes and commercial businesses is disappearing with the privatization of a number of national laboratories.

Not all materials that are used as reference materials are described as such. Commercially available chemicals of varying purity, commercial matrix materials, and products from research programs are often used as standards or reference materials. In the absence of certification data provided by the supplier, it is the responsibility of the user to assess the information available and undertake further characterization as appropriate. Guidance on the preparation of reference materials is given in ISO guides 31, 34, and 35, and guides on the preparation of working-level reference materials are also available.

The suitability of a reference material depends on the details of the analytical specification. Matrix effects and other factors such as concentration range can be more important than the uncertainty of the certified value as detailed. The factors to consider include

- measurand, including analyte,
- measurement range (concentration),
- matrix match and potential interferences,
- sample size,
- homogeneity and stability,
- measurement uncertainty,
- value assignment procedures (measurement and statistical),
- the validity of the certification and uncertainty data,
- track record of both,
- availability of certificate.

The validity of the certification and uncertainty data, including conformance to key procedures of ISO guide 35.

Track record of both the producer and the material. For example, when an RM in use has been subjected to an interlaboratory comparison, cross-checked by the use of different methods, or there is experience of use in a number of laboratories over a period of years. Availability of a certificate and report conforming to ISO guide 31 is needed.

All or some of the requirements may be specified in the customer and analytical specification, but often it will be necessary for the analyst to use professional judgement. Finally, quality does not necessarily equate to small uncertainty, and fitness-for-purpose criteria need to be used [3.39].

Certificates and Supporting Reports. Ideally, a certificate complying with ISO guide 31 and a report covering the characterization, certification, and statistical analysis procedures, complying with ISO guide 35, will be

available. However, many **RM**, particularly older materials and materials not specifically produced as **RM**, may not fully comply with **ISO** guides 31 and 35. Alternative, equivalent information in whatever form available and that provides credible evidence of compliance can be considered acceptable. Examples include the following: technical reports, trade specifications, papers in journals or reports of scientific meetings, and correspondence with suppliers.

Assessment of the Suitability of Reference Materials. Laboratories must be able to explain and justify the basis of selection of all **RMs** and of course any decision not to use an **RM**. In the absence of specific information it is not possible to assess the quality of an **RM**. The rigor with which an assessment needs to be conducted depends on the criticality of the measurement, the level of the technical requirement, and the expected influence of the particular **RM** on the validity of the measurement. Only where the choice of **RM** can be expected to affect measurement results significantly is a formal suitability assessment required.

Requirements of ISO/IEC 17025 on Laboratories Measurement Traceability (§ 5.6 of ISO/IEC 17025) General (§ 5.6.1). (The symbol § refers to parts of **ISO 17025**.) All equipment used for tests and/or calibrations, including equipment for subsidiary measurements (e.g., for environmental conditions) having a significant effect on the accuracy or validity of the result of the test, calibration or sampling, shall be calibrated before being put into service. The laboratory shall have an established program and procedure for the calibration of its equipment.

Note that such a program should include a system for selecting, using, calibrating, checking, controlling, and maintaining measurement standards, reference materials used as measurement standards, and measuring and testing equipment used to perform tests and calibrations.

Specific Requirements (§ 5.6.2) Calibration (§ 5.6.2.1). § 5.6.2.1.1. For calibration laboratories, the program for calibration of equipment shall be designed and operated so as to ensure that calibrations and measurements made by the laboratory are traceable to the International System of Units [Système International d'Unités (**SI**)].

§ 5.6.2.1.2. There are certain calibrations that currently cannot be strictly made in **SI** units. In these cases calibration shall provide confidence in measurements by establishing traceability to appropriate measurement

standards such as: the use of certified reference materials provided by a competent supplier to give a reliable physical or chemical characterization of a material; the use of specified methods and/or consensus standards that are clearly described and agreed by all parties concerned. Participation in a suitable programme of interlaboratory comparisons is required where possible.

Testing (§ 5.6.2.2). § 5.6.2.2.1. For testing laboratories, the requirements given in § 5.6.2.1 apply for measuring and test equipment with measuring functions used, unless it has been established that the associated contribution from the calibration contributes little to the total uncertainty of the test result. When this situation arises, the laboratory shall ensure that the equipment used can provide the uncertainty of measurement needed. Note that the extent to which the requirements in § 5.6.2.1 should be followed depends on the relative contribution of the calibration uncertainty to the total uncertainty. If calibration is the dominant factor, the requirements should be strictly followed.

§ 5.6.2.2.2. Where traceability of measurements to **SI** units is not possible and/or not relevant, the same requirements for traceability to, for example, certified reference materials, agreed methods, and/or consensus standards, are required as for calibration laboratories (§ 5.6.2.1.2). (e.g., breath alcohol, pH value, ozone of air).

Reference Standards and Reference Materials (§ 5.6.3). Reference standards (§ 5.6.3.1). The laboratory shall have a programme and procedure for the calibration of its reference standards. Reference standards shall be calibrated by a body that can provide traceability as described in § 5.6.2.1. Such reference standards of measurement held by the laboratory shall be used for calibration only and for no other purpose, unless it can be shown that their performance as reference standards would not be invalidated. Reference standards shall be calibrated before and after any adjustment.

Reference materials (§ 5.6.3.2). Reference materials shall, where possible, be traceable to **SI** units of measurement, or to certified reference materials. Internal reference materials shall be checked as far as is technically and economically practicable.

Assuring the Quality of Test and Calibration Results (§ 5.9 of ISO/IEC 17025). The laboratory shall have quality control procedures for monitoring the validity of tests and calibrations undertaken. The resulting data shall be recorded in such a way that trends are de-

teable, and where practicable, statistical techniques shall be applied to the reviewing of the results. This monitoring shall be planned and reviewed and may include, but not be limited to, the following.

1. Regular use of certified reference materials and/or internal quality control using secondary reference materials
2. Participation in interlaboratory comparison or proficiency testing programmes
3. Replicate tests or calibrations using the same or different methods
4. Retesting or recalibration of retained items; correlation of results for different characteristics of an item.

Note that the selected methods should be appropriate for the type and volume of the work undertaken.

Application Modes

Method Validation and Measurement Uncertainty. Estimation of bias (the difference between the measured value and the true value) is one of the most difficult elements of method validation, but appropriate RMs can provide valuable information, within the limits of the uncertainty of the RM certified value(s) and the uncertainty of the method being validated. Although traceable certified values are highly desirable, the estimation of bias differences between two or more methods can be established by use of less rigorously certified RM. Clearly the RM must be within the scope of the method in terms of matrix type, analyte concentration, etc., and ideally a number of RM covering the full range of the method should be tested. Where minor modifications to a well-established method are being evaluated, less-rigorous bias studies can be employed.

Replicate measurements of the RM, covering the full range of variables permitted by the method being validated, can be used to estimate the uncertainty associated with any bias, which should normally be corrected for.

The uncertainty associated with an RM should be no greater than one-third of that of the sample measurement [3.38, 50].

Verification of the Correct Use of a Method. Successful application of a valid method depends on its correct use, with regard to both operator skill and the suitability of equipment, reagents, and standards. RM can be used for training, for checking infrequently used methods, and for trouble-shooting when unexpected results are obtained.

Calibration. Normally, a pure substance RM is used for calibration of the measurement stage of a method. Other components of the test method, such as sample digestion, separation, and derivatization, are, of course, not covered, and loss of analyte, contamination, and interferences and their associated uncertainties must be addressed as part of the validation of the method. The uncertainty associated with RM purity will contribute to the total uncertainty of the measurement. For example, an RM certified as 99.9% pure, with an expanded uncertainty $U(k=2)$ of 0.1%, will contribute an uncertainty component of 0.1% to the overall measurement uncertainty budget. In the case of trace analysis, this level of uncertainty will rarely be important, but for assay work, it can be expected to be significant.

Some other methods, such as x-ray-fluorescence (XRF) analysis, use matrix RM for calibration of the complete analytical process. In addition to a close matrix match, the analyte form must be the same in the samples and RM, and the analytical concentrations of the RM must span that of the samples.

ISO guide 32 provides additional useful information.

Quality Control and Quality Assurance (QC and QA). RM should be characterized with respect to homogeneity, stability, and the certified property value(s). For in-house QC, however, the latter requirement can be relaxed, but adequate homogeneity and stability are essential. Similar requirements apply to samples used to establish how well or badly measurements made in different laboratories agree. In the case of proficiency testing, homogeneity is essential and sample stability within the time scale of the exercise must be assessed and controlled. Although desirable, the cost of certifying the property values of proficiency testing samples often prohibits this being done, and consensus mean values are often used instead. As a consequence, there often remains some doubt concerning the reliability of assigned values used in proficiency testing schemes. This is because, although the consensus mean of a set of data has value, the majority is not necessarily correct and as a consequence the values carry some undisclosed element of uncertainty. The interpretation of proficiency testing data thus needs to be carried out with caution.

Errors and Problems of RM Use

Election of RM.

- Certificate not known
- Certificate not complete
- Required uncertainty unknown

- Contribution of calibration to total uncertainty of measurement unknown
- Wrong matrix simulation
- Precision of measurement higher than precision of certification of **RM**
- No need for a certified **RM**
- to propose, as far as necessary, action to be taken on reference materials required for **ISO** work,
- to deal with matters within the competence of the committee, in relation with other international organizations, and to advise the technical management board on action to be taken.

Handling of **RM**.

- Amount of **RM** too small
- Stability date exceeded
- Wrong preparation of in-house **RM**
- Wrong preparation of sample
- Matrix of sample and **RM** differ too much

Assessment of Values.

- Wrong correction of matrix effect
- Use of incorrect quantities (e.g., molality for unspecified analyte)
- Uncertainty budget wrong

3.7.6 Activities of International Organizations

Standardization Bodies

ISO. The International Organization for Standardization (**ISO**) is a worldwide federation of national standards bodies from some 130 countries. The scope of the **ISO** covers standardization in all fields except electrical and electronic standards, which are the responsibility of the **IEC** (see below).

IEC. The International Electrotechnical Commission (**IEC**), together with the **ISO**, forms a specialized system for worldwide standardization – the world’s largest nongovernmental system for voluntary industrial and technical collaboration at the international level.

ISO REMCO. **REMCO** is **ISO**’s committee on reference materials, responsible to the **ISO** technical management board [3.51]. The objectives of **REMCO** are

- to establish definitions, categories, levels, and classification of reference materials for use by **ISO**,
- to determine the structure of related forms of reference materials,
- to formulate criteria for choosing sources for mention in **ISO** documents (including legal aspects),
- to prepare guidelines for technical committees for making reference to reference materials in **ISO** documents,

ASTM. The American Society for Testing and Materials (**ASTM**) is the US standardization body with international activities. The committees of the **ASTM** are also involved in determining reference materials, providing cross-media standards, and working in other associated fields.

Accreditation Bodies

ILAC. International Laboratory Accreditation Cooperation (**ILAC**) and the International Accreditation Forum (**IAF**) are international associations of national and regional accreditation bodies. **ILAC** develops guides for production, selection, and use of reference materials.

EA. The European Cooperation for Accreditation (**EA**) is the regional organization for Europe. **EA** is directly contributing to the international advisory group on reference materials.

Metrology Organizations (Chap. 2)

BIPM. In 1875, a diplomatic conference on the metre took place in Paris, where 17 governments signed a treaty (the Metre Convention). The signatories decided to create and finance a scientific and permanent institute, the Bureau International des Poids et Mesures (**BIPM**).

CIPM. The Comité Internationale des Poids et Mesures (**CIPM**) supervises the **BIPM** and supplies chairmen for the consultative committees.

CCQM. The consultative committee for amount of substance (**CCQM**) is a subcommittee of the **CIPM**. It is responsible for international standards in chemical measurements, including reference materials.

OIML. The International Organization of Legal Metrology (**OIML**) was established in 1955 on the basis of a convention in order to promote global harmonization of legal metrology procedures. **OIML** collaborates with the Metre Convention and **BIPM** on international harmonization of legal metrology.

User Organizations (Users of RM)

EUROLAB. The European Federation of National Associations of Measurement, Testing, and Analytical Laboratories (**EUROLAB**) promotes cost-effective services, for which the accuracy and quality assurance requirements should be adjusted to actual needs. **EUROLAB** contributes to the international advisory group on reference materials.

EURACHEM. The European Federation of National Associations of Analytical Laboratories (**EURACHEM**) promotes quality assurance and traceability in chemical analysis. **EURACHEM** also contributes to the international advisory group on reference materials.

CITAC. The Cooperation for International Traceability in Analytical Chemistry (**CITAC**), a federation of international organizations, coordinates activities of international comparability of analytical results, including reference materials.

IAGRM. The International Advisory Group on Reference Materials (**IAGRM**) is the successor of the 4E/RM group (selection and use of reference materials). It coordinates activities of users, producers, and accreditation bodies in the field of reference materials. **IAGRM** published guides and policy papers. Presently, accreditation of reference materials producers according to **ISO** guide 34 is being discussed.

AOAC International. The Association of Official Analytical Chemists (**AOAC**) International also has a reference materials committee to develop **RM** for analytical chemistry.

IFCC. The International Federation of Clinical Chemistry and Laboratory Medicine (**IFCC**) develops concepts for reference procedures and reference materials for standardization and traceability in laboratory medicine.

Pharmacopeia. Pharmacopeias [European and US Pharmacopeia (**USP**)] provide analysts and researchers from the pharmaceutical industry and institutes with written standards and certified reference materials.

Codex Alimentarius Commission. This commission of the Food and Agriculture Organization (**FAO**) of the United Nations and the World Health Organization (**WHO**) deals with safety and quality in food analysis, including reference materials.

ENFSI. The Network of Forensic Science Institutes (**ENFSI**) recommends standards and reference materials for forensic analysis.

BCR. The Bureau Communautaire de Référence (**BCR**) of the European Commission has, since 1973, set up programs for the development of reference materials needed for European directives. The Institute of Reference Materials and Measurement (**IRMM**) in Geel is responsible for distribution.

3.7.7 The Development of RM Activities and Application Examples

Activities for the development of reference materials started as early as 1906 at the US National Bureau of Standards (**NBS**). In 1912, the first iron and steel reference materials were certified for carbon content in Germany by the Royal Prussian Materials Testing Institute **MPA**, predecessor of **BAM**, the Federal Institute for Materials Research and Testing.

As in other parts of the world, the production of **RM** in Europe was primarily organized nationally, but as early as 1958 three institutes and enterprises of France (F) and Germany (D) combined their efforts in issuing exclusively iron and steel **RM** under the common label **EURONORM**. In 1973, a supplier from the UK, and in 1998 a company from Sweden (S), joined this group (Fig. 3.20).

To overcome national differences, to avoid duplicate work, and to improve mutual acceptance, a new class of European reference materials (**ERM**) has been created. In October 2003, this initiative was launched by three major reference material producers in Europe: the Institute for Reference Materials and Measurements (**IRMM**), **BAM**, Germany, and the Laboratory of the Government Chemist (**LGC**), UK. **ERM** are certified reference materials that undergo uncompromising peer evaluation by the **ERM** Technical Board to ensure the highest quality and reliability according to the state of the art.

A similar initiative to commonly produce **CRM** in a harmonized way is currently taking place in the Asian Pacific region.

To illustrate reference materials and their impact for technology, industry, economy, and society some examples from sectors such as

1. currency,
2. industry,
3. food,
4. environment

are briefly presented.

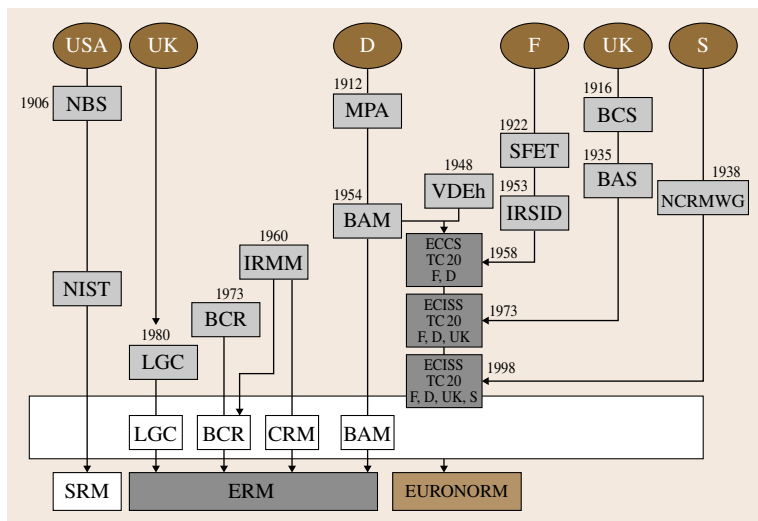


Fig. 3.20 Historical development of reference material activities in the USA and Western Europe (excerpt)

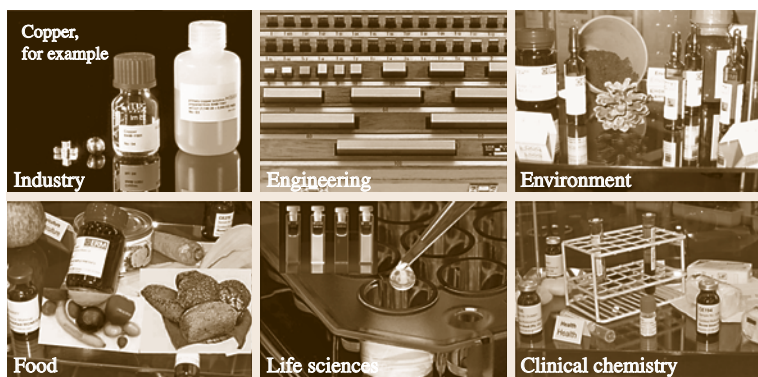


Fig. 3.21 Variety of reference materials highlighted by six fields of application

Currency

Since 2002, Europe has a new common currency: the Euro (€). To control and assure the alloy quality of the coins, several **ERM** have been issued (Fig. 3.22).

Industry

The automobile sector is an important industrial factor in all economies. There is a demand for automobiles to be exported also to countries with deviating standards for exhaust emission. Comparable, correct measurements are not only a national goal but a challenge with international implications. To support the detection of sulfur in gasoline, certified reference materials have been developed which cover the present legal limits in the European Union and in the USA (Fig. 3.23). These certified reference materials have two unique features:

They are the first **CRM** made from commercial gasoline, and they offer lower uncertainties than presently available materials.

In addition to **CRM**, also interlaboratory comparisons are needed to assess reliably the determination of harmful substances such as sulfur in diesel fuel (Fig. 3.24). While the International Measurement Evaluation Programme (**IMEP**) is open to any laboratory, in the key comparison studies of the Consultative Committee for the Amount of Substance (**CCQM-K**) only national metrology institutes are accepted as participants.

Food

Toxic components in food affect health and endanger quality of life. Foodstuffs and a large number of

other goods cross national borders. Legislation sets out limit values to protect consumers. RM such as ERM-BD475 *Ochratoxin A in roasted coffee* enable control (Fig. 3.25).

Environment

Harmful substances in industrial products may detrimentally influence technical functionality and may harm both man and the environment (Fig. 3.26). Consequently, CRM are needed to assess toxicity or show that industrial products are environmentally benign for the benefit of society and the economy.

3.7.8 Reference Materials for Mechanical Testing, General Aspects

In the area of mechanical testing, certified reference materials (CRM) are important tools to establish confidence and traceability of test results, as has been



Fig. 3.22 Certified reference materials representing Euro coin alloy

explained in Chap. 1 (Fig. 1.4). Usually, testing methods are defined in international ISO standards. In these standards, special focus is laid on direct calibration of all parts of the testing equipment as well as the related traceability of all measured values to national and/or international standards. Annual direct calibration is used to demonstrate this update of the measurement capabilities. Within the calibration interval only a few



- First CRMs from commercial gasoline
- Covering present legal limits in EU and USA
- Offer lower uncertainties (3.5–8.8%) than presently available materials

EF213
 Sample No: 0001
 Certified Reference Material
S in Petrol (low concentration)
 mass: 28.913 g
 Distributed by BAM, Unter den Eichen 87, 12205 Berlin, Germany
 Tel: +49 30 8184-0 Fax: +49 30 812023

Fig. 3.23 Certified reference material for sulfur content in gasoline

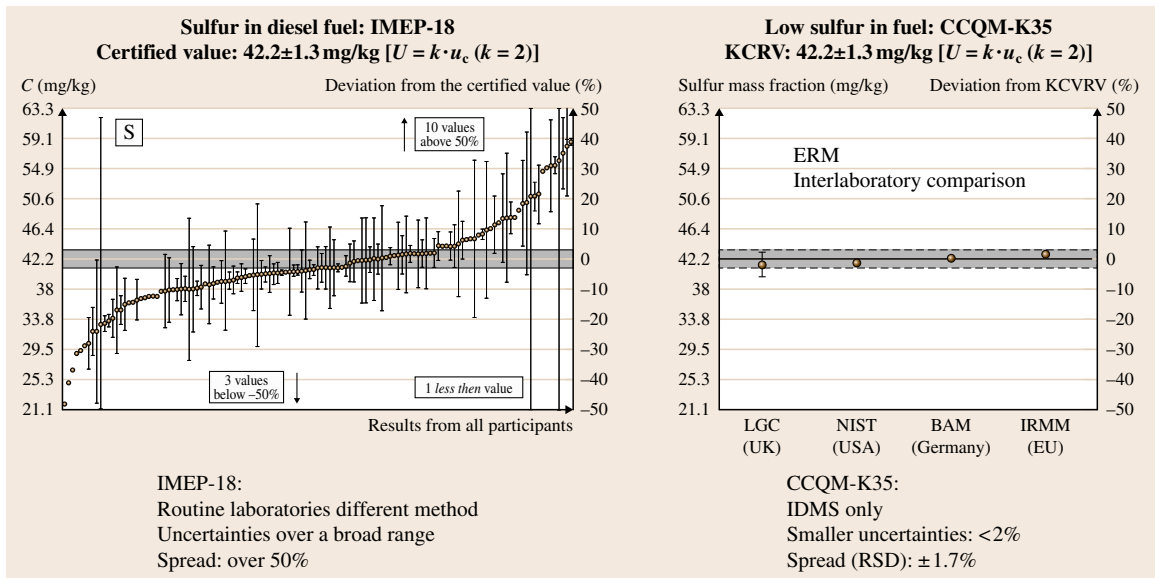


Fig. 3.24 International comparison results of sulfur measurements in fuel

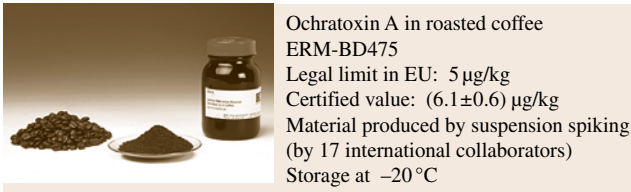


Fig. 3.25 Certified reference material meets legal limit: ochratoxin A in coffee

laboratories use the in-house specimen or rarely available certified reference material. Increasing demands from quality management systems and customers, and lower acceptable tolerances, will require effective use of CRM in the field of mechanical testing in the future as well. As a first result, new CRMs have been developed in the past few years, and their use is required or at least recommended in the updated ISO test standards.

The increasing demand for CRM in the field of mechanical testing is driven by growing requirements from quality management systems. The reliability of test results is no longer a question of yearly direct calibration and demonstrated traceability. Regulatory demands regarding product safety place higher requirements on the producer regarding the reliability of test results. The major question today is the documented, daily assurance that a test system is working properly in the defined range. Three main streams are driving the development of CRM in this field.

- Comparability of test results within company laboratories, producers, and customers must be reliably demonstrated. In this framework the validation of the capabilities of test methods is necessary.

- Customers and the market demand reduced product tolerances. This is only possible when the test method itself allows a judgement on the level of reduced values for trueness and precision.
- To establish measurement uncertainty budgets. Mathematical models are usually not practical in the field of mechanical testing because of the complexity of the parameters affecting the results.

Modern test systems, for example, for tensile testing of metals, are a combination of hardware, the measurement sensors themselves, additional measurement equipment, and computer hardware and software. Direct calibration reflects only one aspect of the overall functionality of the complete and complex test system. Additional measures and proofs are necessary to demonstrate that the system is working properly. The following independent aspects can be verified using CRM.

- The ability of the test system to produce true values. The calculated bias between the certified reference value and the mean value from a defined number of repeated tests using the CRM is calculated. The acceptable range for the bias is defined in the test standard itself (hardness test, Charpy impact test) or by the user (tensile test).
- The ability of the test system to produce precise results can be demonstrated. Usually the standard deviation of repeated tests using the CRM is calculated as a measure for the precision of the test system. Limitations of this value are defined in the test standard itself or by the user.
- The use of CRMs to establish the measurement uncertainty of a test system is an accepted procedure. The known uncertainty of the CRM in combination with the uncertainty calculated from the use

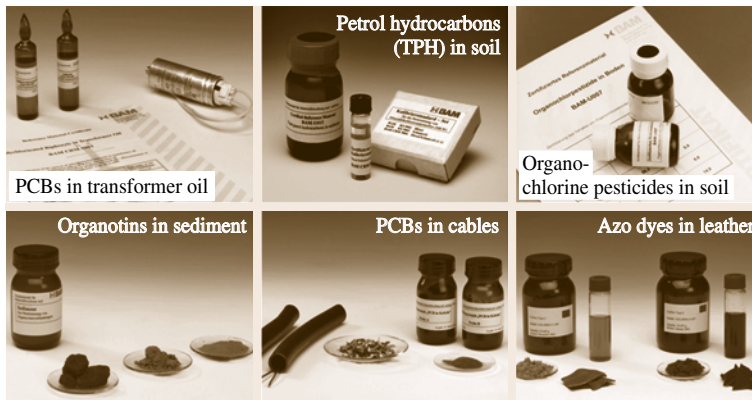


Fig. 3.26 Matrices of environmental or industrial origin certified for contents of organic toxins

of this CRM in the test systems is defined in the corresponding ISO test standard. With this uncertainty budget, smallest measurement tolerances can be established. The stability of an up-to-date test system must be documented. Quality control charts are rarely used in mechanical testing laboratories.

Accredited Producers of Reference Materials for Mechanical Testing

Certified Reference Material for Charpy Impact Test.

- EU Joint Research Centre Institute for Reference Materials and Measurements
Retieseweg 111
2440 Geel, Belgium

Certified Reference Material for Hardness Testing.

- MPA NRW Materialprüfungsamt Nordrhein-Westfalen
Marsbruchstraße 186
44287 Dortmund, Germany
- MPA-Hannover
Materialprüfanstalt für Werkstoffe und Produktionstechnik
An der Universität 2
30823 Garbsen, Germany

Certified Reference Material for Charpy Impact Test and Tensile Test.

- IfEP GmbH
Institut für Eignungsprüfung GmbH
Daimlerstraße 8
45770 Marl, Germany

3.7.9 Reference Materials for Hardness Testing

In hardness testing of metals (Sect. 7.3) indirect verification with certified hardness reference blocks is mandatory. The related standards ISO 6506 Brinell [3.52], ISO 6507 Vickers [3.53], and ISO 6508 Rockwell [3.54] define the relevant and acceptable criteria for a test system when using a CRM. After direct calibration, a final check of the whole system is done by using a material of defined hardness. The parameters assessed are the precision and repeatability of the measurements. In the related standards of the ISO 650X series individual requirements are defined for every test method. Prior to a test series, the certified reference block (Fig. 3.27) should be used to verify the trueness and precision of the measurement capability of the testing machine under the specified test conditions. If the

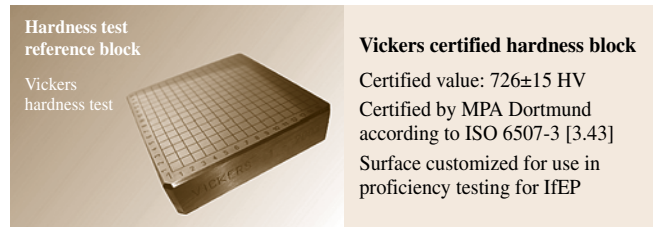


Fig. 3.27 Example of a hardness reference block

result shows an error or the repeatability exceeds the limits defined in the test standard, tests shall not be performed.

Example:

Vickers Hardness Test According to ISO 6507-1

The evaluation criteria are based on ISO 6507-2 [3.55], Table 4 (permissible repeatability of the testing machine r and r_{rel}) and Table 5 (error of the testing machine E_{rel}). The error of the testing machine E_{rel} is calculated according to (3.1)

$$E_{rel} = \frac{\bar{H} - H_C}{H_C} \cdot 100\% . \quad (3.1)$$

Examples of permissible error of the testing machine (3.2) stated in ISO 6507-2, Table 5 are

$$\begin{aligned} HV10 : -3\% \leq E_{rel} \leq 3\% \\ HV30 : -2\% \leq E_{rel} \leq 2\% . \end{aligned} \quad (3.2)$$

\bar{H} is the (arithmetic) mean value of the measurements on a given hardness block of certified reference value H_C .

For the determination of the repeatability (r and r_{rel}) both values of (3.3) must be calculated

$$\begin{aligned} r_{rel} &= \frac{d_{max} - d_{min}}{\bar{d}} \cdot 100\% , \\ r &= H_{max} - H_{min} . \end{aligned} \quad (3.3)$$

d_{max}/min are the maximum/minimum measured diagonal, and H_{max}/min are the maximum/minimum measured hardness in HV10/HV30.

According to ISO 6507-2, Table 4 the permissible repeatability is given by

$$r_{rel} < 2\% , \quad (3.4a)$$

$$r < 30HV10/HV30 . \quad (3.4b)$$

Both requirements must be fulfilled to guarantee an acceptable status of the testing machine prior to the test series.

Determination of Measurement Uncertainty. The results of testing the CRM are also used to establish the measurement uncertainty budget of the test procedure. The determination of the measurement uncertainty according to ISO 6507-1 is based on the UNCERT Code of Practice Nr. 14 [3.55] and GUM [3.18]. Additional to the CRM, this requires the measurement of hardness on a standard material. The results of these measurements are the mean values and the standard deviation. The expanded measurement uncertainty for the measurement done by one laboratory on the standard material is calculated according to (3.5) and (3.6).

$$U = 2\sqrt{u_E^2 + u_{CRM}^2 + u_{\bar{H}}^2 + u_{\bar{x}}^2 + u_{ms}^2}, \quad (3.5)$$

$$\tilde{U} = \frac{U}{\bar{X}_{CRM}} 100\% \quad (3.6)$$

with

U	Expanded measurement uncertainty
\tilde{U}	Relative expanded measurement uncertainty
u_E	Standard uncertainty according to the maximum permissible error
u_{CRM}	Standard measurement uncertainty of the certified reference block
$u_{\bar{H}}$	Standard measurement uncertainty of the laboratory testing machine measuring the hardness of the certified reference block
$u_{\bar{x}}$	Standard measurement uncertainty from testing the material
u_{ms}	Standard measurement uncertainty according to the resolution of the testing machine
\bar{X}_{CRM}	Certified reference value of the certified reference block.

The minimum level of relative expanded measurement uncertainty \tilde{U} is given by the combination of the fixed factors u_E , u_{CRM} , and u_{ms} .

This approach is used in the same manner for other hardness methods.

3.7.10 Reference Materials for Impact Testing

The Charpy impact test, also known as the Charpy V-notch test, is a standardized high-strain-rate test that determines the amount of energy absorbed by a material during fracture (Sect. 7.4.2). This absorbed energy is a measure of a given material's toughness and acts as a tool to study temperature-dependent brittle-ductile transition. It is widely applied in industry, since it is easy to prepare and conduct, and results can be obtained

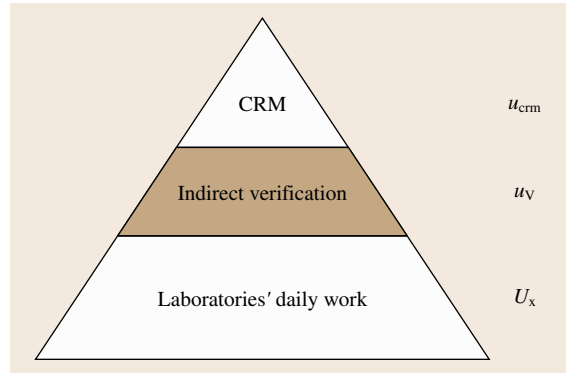


Fig. 3.28 Traceability chain of ISO 148

quickly and cheaply. However, a major disadvantage is that all results are only comparative. This may be commercially important when values obtained by these machines are so different that one set of results does not meet a defined specification while another, tested on a second machine, does not meet the requirements. To avoid disagreements, in the future, all machines have to be verified by testing certified reference test pieces. A testing machine is in compliance with the ISO 148-1:2008 international standard [3.56] when it has been verified using direct and indirect methods. Methods of verification (ISO 148-2:2008) [3.57] are

- The first method uses instruments for direct verification that are traceable to national standards. All specific parameters are calibrated individually. Direct methods are used yearly, when a machine is installed or repaired, or if the indirect method gives a nonconforming result.
- The second method is indirect verification, using certified reference test pieces to verify points on the measuring scale.

Additionally, the results of the indirect verification are used to establish the measurement uncertainty budget of the test system (Fig. 3.28).

Requirements for Reference Material and Reference Test Pieces. The preparation and characterization of Charpy test pieces for indirect verification of pendulum impact testing machines are defined in ISO 148-3:2008 [3.58].

The specimen shall be as homogeneous as possible. The ranges of absorbed energy that should be used in indirect verification are specified in ISO 148-3:2008 [3.58] and displayed in Table 3.12.

Table 3.12 Requirements for certified reference material in Charpy testing, according to ISO 148-3

Energy level	Range of absorbed energy
Low	< 30 J
Medium	≥ 30–110 J
High	≥ 110–200 J
Ultra high	≥ 200 J

Table 3.13 Permissible standard deviation in homogeneity testing

Energy KV_R	Standard deviation
< 40 J	≥ 2.0 J
≥ 40 J	≥ 5% of KV_R

One set of reference pieces (Fig. 3.29) contains five specimens. This set is accompanied by a certificate, which gives information on the production procedure, the certified reference value, and the uncertainty value.

Certified Energy of Charpy Reference Materials. Charpy RM specimens are produced in a batch of up to 2000 pieces. From this batch a representative number of samples are tested. The samples are destroyed to measure the absorbed energy. The average of all test results is defined as the certified value KV_R .

Qualification Procedure. The certified value can be determined using any method which is defined in ISO guides 34 and 35 [3.59].

Reference Machine. Sets of at least 25 test pieces are randomly selected from the batch. These sets are tested on one or more reference machines. The grand average of the results obtained from the individual machines is taken as the reference energy. The standard deviation in homogeneity testing is calculated according to ISO 148-3 [3.58] and must meet the requirements of Table 3.13, where KV_R is the certified KV value of the Charpy reference material.

Intercomparison Among Several Charpy Impact Machines. To reduce the effect of machines on the certified reference value, it is possible to perform tests on different impact testing machines; ISO guide 35 recommends at least six laboratories. The larger the number of testing machines used to assess the average of a batch of samples, the more likely it is that the average of the values obtained is true and unbiased. It is necessary that individual participating pendulums are high-quality

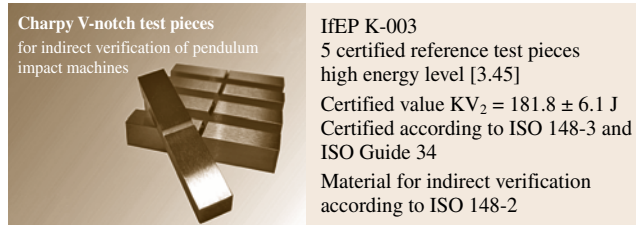


Fig. 3.29 Charpy reference test pieces according to ISO 148-3, for 2 mm striker (after [3.58])

instruments and that the laboratory meets minimum quality requirements, e.g., accreditation according to ISO/IEC 17025 [3.59].

Uncertainty of the Certified Energy Value of Charpy Reference Material. The uncertainty budget of the reference material is calculated using the basic model from ISO guide 35, which is in compliance with GUM. The uncertainty of the certified value of the Charpy reference material can be expressed as (3.7)

$$U_{RM} = \sqrt{u_{\text{char}}^2 + u_{\text{hom}}^2 + u_{\text{Its}}^2 + u_{\text{sts}}^2} \quad (3.7)$$

Here, u_{Its} means uncertainty due to long-term stability. Although steel properties are supposed to be stable, some producers limit their material to 5 years, within which u_{Its} is negligible.

u_{sts} means short-term stability. As stability is given for at least 5 years, this is negligible, too.

u_{hom} is given by (3.8)

$$u_{\text{hom}} = \frac{s_{RM}}{\sqrt{n_V}} \quad (3.8)$$

with

s_{RM} Standard deviation of the homogeneity study

n_V Number of specimens in one set of CRM (here five)

u_{char} is calculated according to (3.9), usually based on an interlaboratory comparison

$$u_{\text{char}} = \frac{s_p}{\sqrt{p}} \quad (3.9)$$

with

s_p Standard deviation of the interlaboratory comparison

p Number of participants

The better the within-instrument repeatability and between-instrument reproducibility, the smaller u_{char} will be.

The standard deviation of the interlaboratory comparison is calculated using (3.10)

$$s_p = \sqrt{\frac{1}{n-1} \sum_{i=1}^n (X_i - \bar{X})^2}, \quad (3.10)$$

with

- X_i Laboratories' mean value
- \bar{X} Grand mean
- n Number of participants

The coverage factor k is calculated using the Welch-Satterthwaite equation (3.11). The confidence level is usually set at 95%.

$$k = t_{95}(v_{\overline{KV}}) \quad \text{with} \quad v_{\overline{KV}} = \frac{u_{RM}^4}{u_{char}^4/v_{char} + u_{hom}^4/v_{hom}}. \quad (3.11)$$

Indirect Verification of the Impact Pendulum Method by Use of Reference Test Pieces

Indirect verification of an industrial machine is done using five specimens in random order and including all results in the average. The indirect verification shall be performed at least every 12 months. Substitution or replacement of individual test pieces by test pieces of another reference set is not permitted. These reference test pieces are used:

- For comparison between test results obtained with the machine and reference values obtained from the procedure described in ISO 148-3:2008 [3.58].
- To monitor the performance of a testing machine over a period of time, without reference to any other machine. This is done by laboratories to assure the internal quality of testing.

The indirect verification shall be performed at a minimum of two energy levels within the range of the testing machine. The absorbed energy level of the reference samples used shall be as close as possible to the lower and upper levels of the range of use in the laboratory. When more than two absorbed energy levels are used, other levels should be uniformly distributed between the lower and upper limits, subject to the availability of reference test pieces. The indirect verification shall be performed at the time of installation, or after moving the machine, or when parts have been replaced.

Evaluation of the Result. $KV_1, KV_2, \dots, KV_{n_V}$ are the absorbed energies at rupture of the n_V reference test pieces of a set, numbered in order of increasing value. The repeatability of the machine performance under the particular controlled conditions is characterized by (3.12)

$$b = KV_{n_V} - KV_1, \quad \text{i. e.} \quad KV_{\max} - KV_{\min}. \quad (3.12)$$

The maximum allowed repeatability values are given in Table 3.14.

Bias. The bias of the machine performance under the particular controlled conditions is characterized by (3.13)

$$B_V = \overline{KV}_V - KV_R, \quad (3.13)$$

with

$$\overline{KV}_V = \frac{\sum KV_i + \dots + KV_{n_V}}{n_V} \quad (3.14)$$

and $KV_R =$ certified reference value. The maximum allowed bias values are given in Table 3.14.

Measurement Uncertainty of the Results of Indirect Verification. The primary result of an indirect verification is the estimate of the instrument bias B_V (3.13). The standard uncertainty of the bias value $u(B_V)$ is equal to the combined standard uncertainties of the two terms in (3.15)

$$u(B_V) = \sqrt{\left(\frac{s_V}{\sqrt{n_V}}\right)^2 + u_{RM}^2}. \quad (3.15)$$

As a general rule, bias should be corrected for. However, due to wear of the anvil and hammer parts, it is difficult to obtain a perfectly stable bias value throughout the period between two indirect verifications. This is why the measured bias value is considered an uncertainty contribution, to be combined with its own uncertainty to obtain the uncertainty of the indirect verification result u_V (3.16)

$$u_V = \sqrt{u^2(B_V) + B_V^2}. \quad (3.16)$$

Table 3.14 Permissible limits in indirect verification according to ISO 148-2 [3.57]

Absorbed energy level	Repeatability b	Bias $ B_V $
< 40 J	≤ 6 J	≤ 4 J
≥ 40 J	$\leq 15\%$ of KV_R	$\leq 10\%$ of KV_R

To correct for the absorbed energy values measured with a pendulum impact testing machine, a term equal to $-B_V$ can be added. This requires that the bias value be firmly established and stable. Such a level of knowledge on the performance of a particular pendulum impact testing machine can only be achieved after a series of indirect verification and control chart tests, which should provide the required evidence regarding the stability of the instrument bias. Therefore, this practise is likely to be limited to the use of reference pendulum impact testing machines.

The coverage factor k is calculated using the Welch–Satterthwaite equation (3.17). The confidence level is usually set at 95%.

$$k = t_{95}(\nu_V) \quad \text{with} \quad \nu_V = \frac{u_V^4}{u^4(\overline{KV}_V)/\nu_B + u_{RM}^4/\nu_{RM} + B_V^4/\nu_B}. \quad (3.17)$$

The value of ν_B is $n_V - 1$; the value of ν_{RM} is taken from the reference material certificate. The number of verification test samples is most often five, and the heterogeneity of the samples is not insignificant. This is why the number of effective degrees of freedom is most often not large enough to use a coverage factor of k equal to 2.

Determination of the Uncertainty of a Related Test Result. This approach requires the results of the indirect verification process. This is the normative method of assessing the performance of the test machine with certified reference materials. The following principle factors contribute to the uncertainty of the test result.

- Instrument bias, identified by the indirect verification
- Homogeneity of the tested material
- Instrument repeatability
- Test temperature

Instrument Bias. Measured values are allowed to be corrected for if the bias is stable and well known. This is the case only when an acceptable number of repeated verifications have been performed. More often, a reliable bias is not known. In this case the bias is not corrected for, but it contributes to the uncertainty budget (3.16).

Homogeneity of the Test Material and Instrument Repeatability. The uncertainty of the test result $u(\bar{X})$ is

calculated using equation (3.18)

$$u(\bar{X}) = \frac{s_X}{\sqrt{n}}, \quad (3.18)$$

where s_X is the standard deviation of the values obtained on the n test samples.

In this factor the sample-to-sample heterogeneity of the material and the repeatability of the test method are cofounded. They cannot be identified individually. The value s_X is a conservative measure for the variation due to the material tested.

Temperature Bias. The effect of temperature bias on the measured absorbed energy is extremely material dependent. A general model cannot be formulated to solve the problem in terms of the uncertainty budget. It is recommended to report the test temperature and the related uncertainty in the test report. During the testing phase the temperature shall be kept as constant as possible.

Machine Resolution. Usually, the influence of the machine resolution r is negligible compared with the other factors. Only when the resolution is large and the measured values are low can the corresponding uncertainty be calculated using (3.19)

$$u(r) = \frac{r}{\sqrt{3}}, \quad (3.19)$$

where r is the machine resolution. The corresponding number of degrees of freedom is ∞ .

Combined and Expanded Uncertainty. To calculate the overall uncertainty the individual parts shall be combined according to (3.20)

$$u(\overline{KV}) = \sqrt{u^2(\bar{x}) + u_V^2 + u^2(r)}. \quad (3.20)$$

The number of tested samples in the Charpy impact test is usually low. In addition, the heterogeneity of the material leads to high values for $u(x)$. For this reason, the coverage factor shall not be selected as $k = 2$. To calculate the expanded uncertainty, the combined uncertainty is multiplied by a k -factor which depends on the degrees of freedom, calculated using (3.21)

$$k = t_{95}(\nu_V) \quad \text{with} \quad \nu_V = \frac{u^4 u(\overline{KV})}{u^4(\bar{X})/\nu_{\bar{X}} + u_V^4/\nu_V}. \quad (3.21)$$

With this number, the coverage factor k can be determined using tables published in GUM. Examples are shown in Table 3.15.

Table 3.15 Typical values of k with given ν

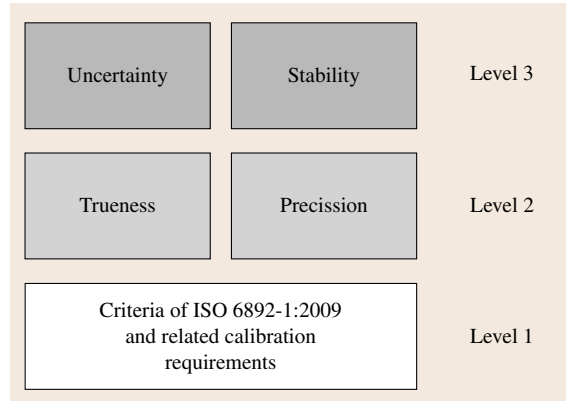
Degrees of freedom ν	Corresponding coverage factor k
8	2.31
9	2.26
10	2.23
11	2.20
12	2.18
13	2.16
14	2.14
15	2.13
16	2.12
17	2.11

3.7.11 Reference Materials for Tensile Testing

Tensile testing of metals according to ISO 6892-1:2009 [3.60] is one of most important methods to characterize materials and products. The methodology of tensile testing is described in Sect. 7.4.1 and illustrated in Fig. 3.30. The direct calibration of load and displacement is done on a regular base. However, the complexity of modern test systems requires additional measures to guarantee acceptable test results, including knowledge about measurement uncertainty. The international standard ISO 6892-1:2009 recommends use of reference materials to demonstrate the functionality of the whole test system. This is part of the concept to prove the capability of the whole measuring process and ensures the reliability of the tensile test system. In the majority of tensile tests, the proof strength $R_{p0.2}$, the ultimate strength R_m , and the elongation A are the resulting parameters.

Concept to Prove the Capability of a Tensile Test System

Level 1 – Requirements of the Test Standard. ISO 6892-1:2009 defines criteria regarding the basic status of acceptable test equipment. Specific requirements are formulated for the load and length measurements as well as for the elongation measuring device. All measurements must be in class 1, with maximum deviation of 1% (class 1) over the whole measurement range. The corresponding values are determined in the direct calibration process on a regular base, usually once a year. The weakness of the calibration process is that it is not possible to demonstrate the full functionality of the system. Many influencing factors such as the dimensions of the specimen used, the test speed, and the software settings are not evaluated in this process.

**Fig. 3.30** Schematic presentation of the IfEP accuracy concept

Level 2 – Trueness. The trueness of the measured values and the calculated results for strength and elongation can only be checked using reference material (Fig. 3.31). After the direct calibration, 25 specimens (round or flat) are tested under realistic laboratory conditions. The reference material used should have similar characteristics to material tested regularly.

The results are used to calculate the systematic deviation, the bias b for all characteristics (R_p , R_m , A , Z) as a measure of trueness using (3.22)

$$b = \bar{y} - \mu, \quad (3.22)$$

using \bar{y} , the mean value of 25 tests, and μ , the certified reference value.

According to ISO 5725-6 [3.61], Chap. 7.2.3.1.3 a judgement on the systematic deviation can be defined based on (3.23)

$$|b| < 2\sqrt{\sigma_R^2 - \sigma_r^2 \frac{(n-1)}{n}}, \quad (3.23)$$

using

- σ_R Reproducibility standard deviation
- σ_r Repeatability standard deviation
- n Number of repetitions

σ_R and σ_r are defined in the certification process. Table 3.16 shows an example of the allowed bias for 25 repetitions.

The use of 25 specimens allows reliable determination of the bias. This bias can be corrected for. If it is not corrected, it is included in the measurement uncertainty budget of the test system.

Table 3.16 Example for the allowed bias b , testing 25 certified specimens; calculation according to ISO 5725-6

Parameter	Maximum $ b $
$R_{p0,2}$	7.5 MPa
R_m	8.0 MPa
A	3.3%

Table 3.17 Example for maximum limits of repeatability standard deviation using 25 reference specimens, calculated according to ISO 5725-6

Parameter	S_{\max}
$R_{p0,2}$	4.2 MPa
R_m	2.6 MPa
A	0.8%

Precision. The precision of the test system can be evaluated using ISO 5725-6:2002, Chap. A7.2.3 *Measurement method for which reference material exists*. In this approach the standard deviation of laboratories' results for the tested reference material, S_r , is divided by the repeatability standard deviation, σ_r , of the certification process. The result is compared with the tabulated c^2 distribution according to (3.24)

$$\frac{S_r^2}{\sigma_r^2} < \frac{\chi_{(1-\alpha)}^2(\nu)}{\nu}, \quad (3.24)$$

using

S_r	Standard deviation when testing the CRM
σ_r	Repeatability standard deviation of the certification process
$\chi_{(1-\alpha)}^2(\nu)$	$(1 - \alpha)$ quartile of the χ^2 distribution
α	Significance level, here 0.01 or 1%
ν	$n - 1$ degrees of freedom

σ_r is defined in the certification process.

To define an acceptable maximum standard deviation for the test system (3.24) is transformed to define S_{\max} (3.25)

$$S_{\max} < \sqrt{\frac{\chi_{(1-\alpha)}^2(\nu)}{\nu} \sigma_r^2}. \quad (3.25)$$

For a significance level of 1% and 25 specimens tested, Table 3.17 shows example maximum standard deviations for various parameters of a tensile test system. The defined limits guarantee state-of-the-art test results.

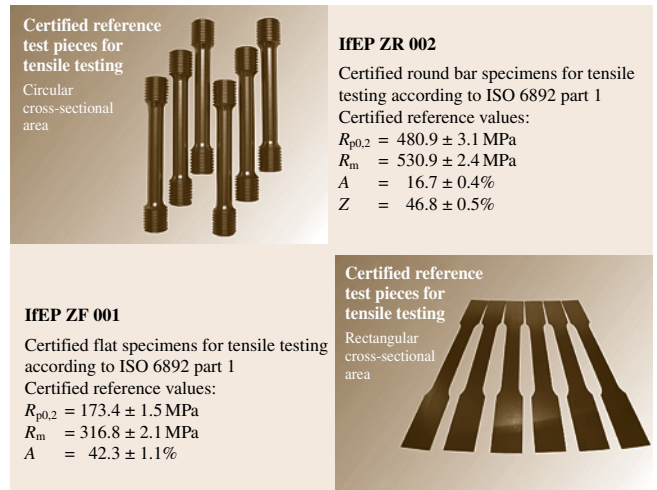


Fig. 3.31 Certified reference test pieces for the tensile test (after [3.58])

Level 3 – Measurement Uncertainty. The concepts of the guide to the expression of uncertainty in measurement, ISO/IEC guide 98-3:2008 [3.62], are used to establish the uncertainty budget.

The test standard ISO 6892-1:2009 recommends in appendix J.4 the use of a reference material to establish the uncertainty budget of the test system, to incorporate all elements of the test process itself. The concept to establish the uncertainty budget uses the approach defined in ISO 148-1:2009 for Charpy impact testing, which uses certified reference materials as well.

Uncertainty of the Systematic Deviation. The uncertainty budget is calculated using the uncertainty of the reference material itself combined with the standard deviation of the tested 25 reference specimens. The laboratory has to define their acceptable uncertainty level to judge the result for each individual parameter.

First, the uncertainty of the calculated bias from level 2 must be evaluated under the condition that the bias is within the defined limits of acceptable trueness (3.22). If this requirement is fulfilled, the uncertainty can be calculated using (3.26)

$$U_b = k \sqrt{\left(\frac{sv}{\sqrt{nv}}\right)^2 + u_{RM}^2}. \quad (3.26)$$

sv is the standard deviation of the results from the 25 (nv) reference specimens tested. The uncertainty of the

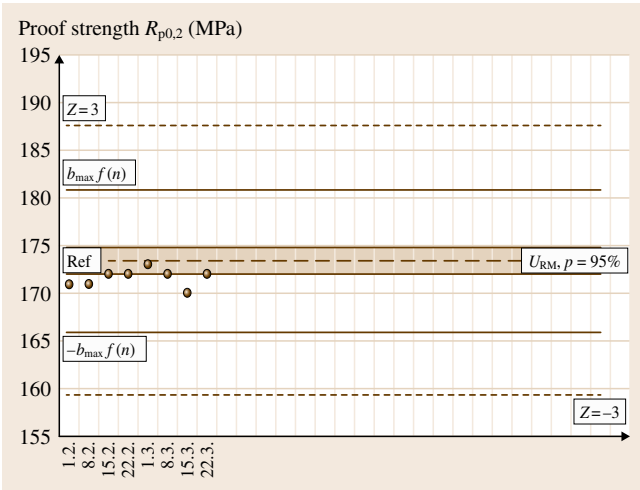


Fig. 3.32 Example quality control chart (proof strength, $R_{p0,2}$)

reference material is u_{RM} , defined in the certification process and stated in the certificate, divided by the coverage factor k_{RM} , also stated in the certificate.

Determination of the Coverage Factor k for 95% Confidence Level. The coverage factor k is calculated using (3.27)

$$k = t(v_{\text{eff}}), \tag{3.27}$$

where t is the value of the t -distribution for the effective number of degrees of freedom v_{eff} . The common confidence level is 95%.

The number of effective degrees of freedom v_{eff} is calculated using (3.28)

$$v_{\text{eff}} = \frac{u_b^4}{(s_V/\sqrt{n_V})^4/n_V - 1 + u_{RM}^4/v_{RM}}, \tag{3.28}$$

where v_{RM} is the number of degrees of freedom from the certification process, stated in the certificate of the reference material. The corresponding t -factor is tabulated in ISO/IEC guide 98-3:2008, Table G2.

3.8 Reference Procedures

3.8.1 Framework: Traceability and Reference Values

Establishing *traceability* of measurement results (Sect. 3.2) is a shared activity. A laboratory per-

Evaluation of the Influence of the Bias b on the Uncertainty Budget. Three different cases have to be analyzed.

- A laboratory is correcting their test results using the calculated bias b of level 2. This bias must be constantly checked afterwards using a quality control chart. In this case the bias is not an element of the uncertainty budget.
- A laboratory is not correcting their test results with their bias. The bias b is within the range of the established uncertainty budget. In this case the bias b is not included in the uncertainty budget.
- A laboratory is not correcting their test results with their bias. The bias b is outside of the range of the established uncertainty budget. In this case the bias must be included in the uncertainty budget using (3.29). This approach is similar to the procedure used in ISO 6507-1:2006.

$$U_{B_{\text{ukorr}}} = (U_{B_V} + |B|). \tag{3.29}$$

The uncertainty is considerably higher in this case, and it might be questionable whether this machine is working according to the state of the art.

Stability. The stability of the test system must be checked regularly. The established tool for this is a quality control chart in which the results of repeated tests are documented and evaluated. The basic condition is the use of the same reference material that was used to establish the trueness and precision of the test system. The number of repetitions (daily, weekly, monthly) depends on the level of confidence a laboratory wants to demonstrate. An example for a quality control chart is shown in Fig. 3.32. It must be noted that the limit values depend on the number of repeated tests in one run. The number of test specimens in one run (for example, 1 to 6) must be defined to establish statistically correct limits in the control chart. Basically, the maximum allowed bias b_{max} is calculated using (3.23). In case of only one specimen tested per run, the proof of trueness reduces to (3.30)

$$|b| < 2\sigma_R. \tag{3.30}$$

forming measurements of materials properties has to

- identify all the laboratory references that are relevant for a given result, e.g., *specify the working*

standard used for calibrating the measuring system,

- specify the relationship between the result and any laboratory reference used, e.g., *specify how the value of the working standard is used in a correction,*
- ensure that all those laboratory references are fit for purpose, e.g., *check the calibration status and the uncertainty of the working standard.*

As a complementary activity, the provider of a laboratory reference (e.g., *a calibration laboratory, performing calibration of working standards against reference standards*) has to

- ensure that the specification of the laboratory reference is valid, e.g., *operate a quality control program for the calibration of working standards,*
- establish traceability of the laboratory reference to a primary reference, e.g., *ensure traceability of the reference standard used for calibrating working standards against a primary standard.*

Laboratory references are by no means restricted to measurement standards used for calibration, reference materials used for bias investigation, and the like. Rather than relating measurement results to devices or materials, traceability relates measurement results to *reference values*, which may be associated with devices or materials but may also be of other origin. They include any data except for those generated in the measurement process and subsidiary measurements (e.g., for control of environmental conditions) which are utilized explicitly or implicitly in any stage of the measurement process, from preparation of measuring objects to data evaluation, and whose values are taken for granted.

Traceability relates measurement results to reference values.

Having raised the issue of a reference value, here are two current definitions.

- Definition 1: Quantity value used as a basis for comparison with values of quantities of the same kind. (VIM, 3rd edition, 2008 [3.63])
- Definition 2: Property value of a specified material or product that has been determined with an accuracy fit for use as a source of traceability for test results obtained on comparable materials or products. (Eurolab Position Paper, 2007 [3.64])

While originating from different fields – metrology and testing – these definitions are in fact very close, with

complete agreement concerning the basic requirement: the uncertainty of reference values must be known and fit for the intended use. Given this, the relevance of reference values with regard to the accuracy of specified measurements may be assessed as follows: a reference value is relevant to a measurement result, if the uncertainty associated with the reference value contributes significantly to the overall uncertainty of the measurement result.

Reference values need specified uncertainties.

Depending on the type of material and the property under consideration, there are three basic sources of reference values for materials properties: *reference data compilations, reference materials* (Sect. 3.7), and *reference procedures*.

- For
 - well-defined and commonly available materials (e.g., pure copper), and
 - well-investigated quantities (e.g., thermophysical)
 reference values may be taken from a recognized reference data compilation.
- For
 - certified reference materials (e.g., a copper alloy CRM CuZn37), and
 - certified properties (e.g., the mass fraction of nickel)
 reference values may be taken from the certificate of the reference material.
- For
 - real-life materials (e.g., a sample from a batch of raw copper), and
 - well-defined quantities (for the purpose at hand)
 reference values may be measured using a reference procedure, if available.

As a remark in passing, uncertainty statements in reference data compilations are generally poor. Strategies for improving this situation are

- *New measurements* – Example: in the framework of a Japanese national project [3.65], new measurements were made on thermophysical property data of key industrial materials to generate reference data with state-of-the-art uncertainty.
- *Reevaluation of original measurements* – Example: for an international standardization project [3.66], publications on measurements of virial coefficients of pure gases were reevaluated to estimate the un-

certainty of virial coefficient data used in a previous standard.

3.8.2 Terminology: Concepts and Definitions

Unlike for reference materials (Sect. 3.7), there are currently no internationally harmonized terminology, fundamental concepts, and basic requirements for reference measurements. Before reviewing current concepts and definitions for the notion of a reference procedure, there is an obvious question to address first: why use the term *procedure* instead of the more common term *method*?

Method versus procedure: According to current perception, a measurement method provides a generic description of measurements, specifying the kind of equipment to be used, the kind of measuring objects, and a sequence of operations, while a measurement procedure provides a detailed description of how to actually carry out measurements according to a given method using specified equipment on specified measuring objects.

Although this distinction is also made in the VIM [3.63], it is not yet part of standard terminology and is often disregarded even in current publications.

Method versus procedure: a subtle but important difference

In the scientific/technical literature, various different definitions of the term *reference procedure* are in use, falling into three main categories as follows.

1. Measurement procedure with established high quality of results, which can be used for the assessment of other measurement procedures; ... *results obtained using the procedure (proper implementation and validation assumed) serve as a benchmark for alternative procedures.*
2. Measurement procedures defining a quantity subject to measurement; ... *the property under consideration is in fact defined by the procedure.*
3. Measurement procedure prescribed by legal regulations for specific measurements; ... *to obtain valid results for regulatory purposes, the procedure must be used.*

In the last decade, approach (1) has clearly become the dominant concept, and in this section the term reference procedure is used in this sense. Below are three definitions with international scope [3.38, 67, 68]. Irrespective of their widely different origins – metrology, laboratory medicine, and reference materials – these definitions are very close and agree completely with respect to scope and requirements.

The term *reference procedure* has a wide range of connotations.

Obviously the term reference procedure applies equally to measurement, testing, and chemical analysis, i. e., all procedures for determining quantitative properties of materials, but the concept may also be extended to other fields.

Qualitative testing, i. e., determination of qualitative properties: qualitative properties are expressed by

Table 3.18 Definitions related to the concept of reference procedures

Reference procedure	Reference measurement procedure	Reference method
Procedure of testing, measurement or analysis, thoroughly characterized and proven to be under control, intended for quality assessment of other procedures for comparable tasks, or characterization of reference materials including reference objects, or determination of reference values. The uncertainty of the results of a reference procedure must be adequately estimated and appropriate for the intended use. (Euramet Guide [3.67])	Thoroughly investigated measurement procedure shown to have an uncertainty of measurement commensurate with the intended use, especially in assessing the trueness of other measurement procedures for the same quantity and in characterising reference materials. (ISO 15195 [3.68])	Thoroughly investigated method, clearly and exactly describing the necessary conditions and procedures, for the measurement of one or more property values that has been shown to have accuracy and precision commensurate with its intended use and that can therefore be used to assess the accuracy of other methods for the same measurement, particular in permitting the characterisation of a reference material. (ISO Guide 30 [3.38])

membership to one of several specified classes, and the uncertainty of a qualitative test result is an estimate of the probability that the result is incorrect.

Preparation of reference materials or reference objects: for example, the gravimetric preparation of mixtures of pure substances as reference materials of chemical composition, or the preparation of reference defects by spark erosion on metal specimens to be used as reference objects for nondestructive testing of pressure vessels.

Procedures for data evaluation: for example, uncertainty propagation, i. e., the calculation of combined standard uncertainty according to the GUM, is based on approximations that may not always be valid in practice. In case of doubt, Monte Carlo simulation may be used as a reference procedure to investigate whether uncertainty propagation is valid [3.69].

According to the definitions above, reference procedures for materials measurements can be used to

- validate (or calibrate) other measurement procedures that are used for a similar task and to determine their uncertainty,
- determine reference values for material properties that are embodied by a reference material or a reference object,
- determine reference data of materials properties for reference data compilations.

Another application of reference procedures could be measurements as the basis for important decisions, e.g., for authoritative evidence.

It should be noted that there are a number of alternative terms with a similar meaning. The term *primary method of measurement* has been developed for use in the Consultative Committee for Amount of Substance (CCQM), i. e., the international committee of the Metre Convention for metrology in chemistry. The term *definitive method* originates from the International Union of Pure and Applied Chemistry (IUPAC).

Primary Method of Measurement

A method having the highest metrological qualities, whose operation can be completely described and understood, and for which a complete uncertainty statement can be written down in terms of SI units (*Milton* and *Quinn* [3.44]).

Primary Reference Measurement Procedure

A reference measurement procedure used to obtain a measurement result without relation to a measurement standard for a quantity of the same kind [3.63]. From the

conceptional point of view, this is identical to the term primary method of measurement.

Definitive Method of Measurement

A method of exceptional scientific status that is sufficiently accurate to stand alone in the determination of a given property for the certification of a reference material. Such a method must have a firm theoretical foundation so that systematic error is negligible relative to the intended use. The property values must be measured directly in terms of the base units of measurement, or indirectly related through sound theoretical equations (adapted from IUPAC [3.70]).

3.8.3 Requirements: Measurement Uncertainty, Traceability, and Acceptance

The definition of a reference procedure presumes the existence of several procedures for a specified task. Given this, a reference procedure is qualified by the uncertainty of results that are proven to be fit for the purpose of providing reference values of the property under consideration.

Before addressing requirements for measurement quality, the basic condition that the procedure be one among several procedures for the same task requires a second thought. For measurement of *rationaly defined properties*, i. e., properties that are defined independently of the method of measurement, the concept is clear. There is a variety of measurement techniques available, and a reference procedure implements the best available technique, i. e., that with the capability of providing the most reliable results with the best available uncertainty.

Reference procedures for operationally defined properties?

However, the concept is also applicable to operationally defined properties, i. e., properties that are (to a significant degree) defined by a particular measurement method, often specified in a standard. In this case a reference procedure is a *reference implementation* of the defining measurement method, used to provide reference values for bench-marking *routine implementations*.

The scope of reference procedures implies a number of key requirements, concerning *measurement uncertainty*, *measurement traceability*, and *acceptance*, as follows. In addition to these, measurement quality con-

tol must be designed and executed at an appropriate level that is commensurate with provision of reliable reference values.

1. *The uncertainty of measurement results must be known.* The uncertainty of measurement is evaluated and specified in accordance with the GUM [3.71]. This entails that the uncertainty attributed to a measurement result accounts for all significant sources of uncertainty, and that every effort is taken to ensure that there is no significant residual bias that could compromise measurement results. The uncertainty of measurement may be evaluated using any of the following approaches or combinations thereof
 - Propagation of input uncertainties, based on a detailed mathematical model of the measurement process, as specified in the GUM [3.71];
 - Utilizing data from interlaboratory method-validation studies according to ISO 5725 [3.22];
 - Utilizing data from within-laboratory method-validation studies [3.26].
2. *The validity of the uncertainty claim must be demonstrated by interlaboratory comparisons.* Comparison with results obtained by other proficient laboratories, preferably using reference procedures based on independent measurement techniques, is generally accepted as the best way to challenge the uncertainty claimed for the results of a reference procedure. Agreement is taken to support the claim. Disagreement requires further action to identify the reason, e.g., underestimation of the uncertainty or significant bias not detected so far. As a recent example, the so-called key comparisons (KC) provide the basis for the acceptance of calibration and measurement capability (CMC) claims of national metrology institutes in the various peer reviews prior to publication (Sect. 3.8.6).
3. *The uncertainty of measurements results must be commensurate with their intended use as reference values.* The traditional policy concerning the use of reference values, e.g., in calibration, has been: the uncertainty of reference values (e.g., the uncertainty of a reference standard used to calibrate working standards) should be negligible compared with the target uncertainty of the result under consideration (e.g., the uncertainty of a working standard) and must not exceed one-third of that target uncertainty. The rationale for this requirement is unknown to the authors, but as a conjecture, the driver behind this requirement may have been the lack of techniques

for the statistical evaluation of data with specified uncertainty, e.g., least-squares regression with uncertainties in the independent variable. When using techniques designed for data without uncertainty on data with an associated uncertainty, one has to make sure that they still give valid results. To this end, the uncertainty associated with the data has to be negligible against the relevant statistical variability. Similarly the 1 : 3 rule mentioned above may be justified using the root-sum-of-squares addition of standard uncertainties

$$\sqrt{u^2 + \left(\frac{u}{3}\right)^2} = \sqrt{1.11u^2} = 1.05u \approx u .$$

Fitness for purpose concerning requirements on measurement uncertainty

Given appropriate techniques for uncertainty-based data evaluation, there is no need to require that the uncertainty of reference values be negligible. Instead, their contribution to the uncertainty of the final result may be determined, and limits on the uncertainty of reference values may be derived from target uncertainties.

4. *Measurement results must be traceable to recognized references.* Reference values constitute the endpoint of within-laboratory traceability chains. Unless a reference value happens to be a primary reference that is recognized by the relevant community, its traceability to an appropriate higher-level reference value has to be established. Reference measurements carried out by national metrology institutes according to measurement capabilities specified in the BIPM database (Sect. 3.8.6) are internationally recognized as providing traceability to SI units. Traceability of reference values embodied by certified reference materials (CRM) is currently under debate in various fora, concerning technical issues such as the traceability of consensus values from interlaboratory certification studies and quality management issues such as third-party assessments of CRM quality and accreditation of CRM producers. The BIPM database contains a number of entries for CRMs provided by national metrology institutes, which may therefore be utilized as internationally recognized sources of traceability.
5. *Reference procedures must be accepted as such by the relevant target groups.* Reference procedures have the potential to stand alone in the provision of reference values for the property in

question. Reference procedures are qualified as such in a validation study, where the performance of the procedure is investigated in appropriate detail, and the values of the relevant performance characteristics – in particular measurement uncertainty – are determined. However, as an equally important requirement, the relevant target groups have to be convinced of the merits of a candidate reference procedure before it can be used as such. These target groups will normally include customers of reference measurements, laboratories, research institutes, and technical associations in the respective field, but may also involve accreditation bodies and regulators. Results of appropriate interlaboratory comparisons will normally be the most convincing arguments in favor of a newly proposed reference procedure.

3.8.4 Applications for Reference and Routine Laboratories

Developing and maintaining a reference procedure often requires significant effort, money, and manpower, and the costs for operating a reference procedure are often significantly higher than for other procedures for the same task. Therefore, reference procedures are most often operated by reference laboratories (Sect. 3.8.7), e.g., for the provision of reference measurement services, the determination of reference data, and the characterization of reference materials or reference objects. However, it may also be profitable for laboratories engaged in routine measurement and testing to operate a reference procedure for dedicated tasks such as validation or calibration of routine procedures.

The key qualification of reference procedures is their potential to stand alone in the determination of reference values for the property in question. This is due to

- the high capability of the particular measurement technology, with respect to trueness (absence of bias), precision, robustness to interfering effects (measuring conditions and measuring objects), and
- the high level of performance evaluation, in particular concerning measurement uncertainty, and ongoing internal and external quality control for the reference procedure developed using this technology.

The main fields of application for reference procedures were already mentioned in the various definitions (Sect. 3.8.2).

Euramet Guide [3.67].

- Quality assessment of other procedures for comparable tasks
- Characterization of materials, including reference objects
- Determination of reference values

ISO 15195 [3.68].

- Assessing the trueness of other measurements procedures for the same quantity
- Characterizing reference materials

ISO Guide 30 [3.38].

- Assessing the accuracy of other methods for the same measurement
- Characterization of a reference material

VIM [3.63].

- Assessing the measurement trueness of measured quantity values obtained from other measurement procedures for quantities of the same kind
- Calibration
- Characterization of a reference material

Reference Data

Determination of reference data for materials property databases is a typical reference laboratory activity, requiring reference procedures with established uncertainty and traceability of measurement, and an appropriate level of measurement quality control.

Reference Measurements

An increasingly important application of reference procedures is the provision of reference values for proficiency testing of samples or specimens, as an activity for a single reference laboratory or a small group of reference laboratories. Utilizing traceable reference values with specified uncertainty as the target values in proficiency tests (PT) has the advantage of providing information to the participants about their level of measurement bias, while PTs using a consensus value of the participants' results only provide information about their comparability.

Reference values for proficiency testing: a key application field

The International Measurement Evaluation Programme (IMEP) of the IRMM, Geel [3.72] is a prominent example of a proficiency test utilizing reference values. Recently, provision of reference values for PT samples

or specimens has become a major activity for national metrology institutes for the dissemination of their measurement capabilities (Sect. 3.8.6).

Reference Materials

Reference materials are often characterized in interlaboratory studies that include a major number of expert laboratories utilizing a broad range of different measurement techniques. Alternative approaches include a small group of reference laboratories, or even a single reference laboratory, utilizing appropriate reference procedures as follows.

- Stand-alone determination of the property value under consideration in a single laboratory, utilizing an appropriate reference procedure, with check measurements using an independent method as a safeguard against blunders. In the chemistry field, this approach is often advocated by national metrology institutes, using primary methods of measurement such as isotope-dilution mass spectrometry.
- Collaborative determination, in a single laboratory using several independent reference procedures or several laboratories, using a reference procedure each. Given agreement within uncertainty limits, the results are combined into a mean value and an associated uncertainty.

Further information on strategies and procedures for characterization of reference materials is given in Sect. 3.7.

Validation of Routine Procedures

As another major field of application, reference procedures may be used to validate routine procedures for the same task. Similarly, routine procedures may be calibrated against reference procedures for the same task. To this end, measurements using the routine procedure and the reference procedure are carried out in parallel on appropriate samples or specimens, and the results are compared. The great benefit of this approach is that real-life samples may be used, thus avoiding the problem of mismatch between calibrants and measuring objects, which is often encountered using reference materials.

Validation and calibration of routine procedures: an alternative to the use of reference materials

When validating a routine procedure against a reference procedure, the task is to investigate whether the results

of the routine procedure (y) agree with those of the reference procedure (x). For this purpose, measurements using both procedures are carried out on a series of samples or specimens S_1, S_2, \dots, S_N with varying values of the property under consideration, yielding paired results $(y_1, x_1), (y_2, x_2), \dots, (y_N, x_N)$. These data are examined to see whether they are compatible with a straight line $y = x$. To this end, a straight line $y_i = ax_i + b$ is fitted to the calibration data (y_i, x_i) using, e.g., the method of least squares, and the joint confidence region for the slope a and the intercept b is determined. If this confidence region contains the point $(a = 1, b = 0)$, the test is positive, i.e., the results obtained using the routine procedure and the reference procedure are compatible with a straight line $y = x$. This means that the routine procedure is not significantly biased against the reference procedure, thus both procedures measure the same quantity, although most often with different uncertainties.

Calibration of Routine Procedures

Calibration of a routine procedure against a reference procedure makes use of the same experimental design, with a slightly different task: the measurement results are utilized to derive a correction for the results of the routine procedure, and to evaluate the uncertainty for the corrected results.

Often calibration is performed for a narrow measuring range, using a single sample or specimen S . With x_S denoting the result of the reference procedure and y_S that of the routine procedure, the difference $\Delta_S = y_S - x_S$ may be utilized to correct the results obtained using the routine procedure on similar samples or specimens according to $y_{\text{corr}} = y_{\text{meas}} - \Delta_S$. The uncertainty of the corrected result can be calculated by combining the precision of the routine procedure and the uncertainty associated with the correction. The latter uncertainty includes the measurement uncertainty of the reference procedure.

For extended measuring ranges, calibration often requires parallel measurement of several samples or specimens S_1, S_2, \dots, S_N . The results are used to derive a correction curve, e.g., by way of fitting a straight line $y_i = ax_i + b$ to the calibration data (y_i, x_i) and subsequent inversion according to $y_{\text{corr}} = (y_{\text{meas}} - b)/a$. The uncertainty of the corrected results may be calculated from the precision of the routine procedure and the uncertainty associated with the parameters of the calibration line. The latter uncertainty includes contributions from the measurement uncertainty of the reference procedure.

The approach outlined above is also applicable to another type of calibration, where, instead of a correction, the input/output behavior of a measuring system is determined. Here the task is to establish the relationship between the target quantity and the response (output) of the measuring system, e.g., temperature and current in case of a thermoelement. To this end, measurements using the procedure subject to calibration and the reference procedure are carried out in parallel on appropriate samples or specimens. A calibration curve is fitted to the calibration data, and this is used to convert measured responses into values of the target quantity. Again the advantage of using a reference procedure instead of reference materials or reference objects is that calibration can be carried out on real-life samples or specimens.

3.8.5 Presentation: Template for Reference Procedures

When dealing with a range of measurement or test procedures, it is useful to have the most important characteristics presented in a standard format. Most often these standards are sector specific, as e.g., ISO 78-2 [3.73], which specifies the presentation of procedures for chemical analysis. A generic template for the presentation of reference procedures was developed at the Federal Institute for Materials Research and Testing, Germany and is utilized in their catalog [3.74].

BAM catalog of reference procedures

According to this template, reference measurement procedures are presented as follows.

- *Title* – the title of the procedure.
- *Key words* – key words for the procedure.
- *Quantities and items measured* – the quantities measured, the kind of objects that can be investigated, and important measuring conditions.
- *Measuring range and uncertainty of measurement* – the range of values, i.e., the working range as a reference procedure, for each quantity measured, and an associated uncertainty range. Uncertainty of measurement is an expanded uncertainty according to the GUM [3.71] for an approximate confidence level of 0.95 (coverage factor $k = 2$), expressed as a relative uncertainty in % or as an absolute uncertainty in units of the quantity measured. For expressing an uncertainty range, different conventions may be used
 - referring to the lower and upper limit of the measuring range, respectively, or
 - specifying best-case and worst-case uncertainty.
- *Fields of application* – the kind of tasks for which the procedure is currently in use, or may be utilized as a reference: quality assessment of other procedures, characterization of reference materials and objects, determination of reference values, and other high-level tasks.
- *Methodology and instrumentation* – the method of measurement and essentials of the measuring system.
- *Qualification and quality assurance* – supporting evidence for the critical figures of merit, in particular measurement uncertainty (e.g., successful participation in interlaboratory comparisons), and efforts taken for measurement quality control.
- *Further information* – free-style presentation of additional information, in particular including pictures, diagrams, and references.

This template is also applicable to reference procedures for testing, even in cases of qualitative characteristics. Figure 3.33 shows an example taken from the BAM catalog [3.74].

3.8.6 International Networks: CIPM and VAMAS

One of the main services of national metrology institutes is to calibrate reference standards against national standards. Typically, these calibrations are performed by reference measurements, i.e., measurements using reference procedures of measurement.

On 14 October 1999 a multilateral agreement (the so-called CIPM MRA) was signed in Paris between 38 member states of the Metre Convention as well as two international organizations (the IAEA and IRMM). Currently the agreement has been signed by 48 member states, 32 associates of the General Conference on Weights and Measures (CGPM), and 3 international organizations (WMO, in addition to the above mentioned). This agreement had been drawn up by the International Committee of Weights and Measures (CIPM), its subject being the mutual recognition of national measurement standards and of the calibration and measurement certificates issued by national metrology institutes. The mutual recognition of national traceability systems aims to create a secure technical foundation for wider agreements in international trade, commerce, and regulatory affairs.

**X-ray Photoelectron Spectroscopy for Chemical Analysis of Surfaces (ESCA/XPS):
Precise Determination of Binding Energies on Nonconducting Samples**

Key words
Binding energy, ESCA, surface, chemical analysis, gold particle

Quantities and items tested
Binding energies of photoelectrons in nonconducting samples

Testing range	Uncertainty of results	
0 eV – 1040 eV	from 0,3 eV	to 1 eV

Fields of application
Quality assessment of other procedures for the determination of photoelectron binding energies of nonconducting samples. Determination of reference values of binding energies for users of the ESCA method in surface analysis laboratories.

Methodology and instrumentation
Determination of the static charge by using the Au 4f 7/2 photoemission signal of nm gold particles as a reference. With the help of the static charge value the ESCA spectrum is corrected. The identification of chemical species is now possible. The binding energy of the Au 4f 7/2 photoemission signal is given by ISO 15472. Traceability of ESCA measurements is possible by using this method.

Qualification and quality assurance
Traceability to SI units, Organization of interlaboratory tests. Participation in interlaboratory tests. The uncertainty of results was determined by a worldwide interlaboratory test launched under the auspices of the Versailles Project on Advanced Materials and Standards (VAMAS).

Contact:	Dr. Wolfgang Unger	Phone:	++49(0)30 8104 1823
E-mail:	wolfgang.unger@bam.de	Fax:	++49(0)30 8104 1827
Division VI.4: Surface Technologies		back to Catalogue of reference procedures	

Fig. 3.33 Example presentation of a reference procedure

This mutual recognition is far more than a formal act. The national measurement institutes concerned have to prove their competence and the reliability of their results in international intercomparisons – so-called key comparisons (KC) – and must operate an appropriate quality management system. For maximum transparency the results of these intercomparisons are published with free access on the Internet [3.75] by the International Office of Weights and Measures (BIPM) in Paris. In addition, the BIPM publishes another (freely accessible) Internet database [3.76] specifying the reference measurement services of the national metrology institutes – the so-called calibration and measurement capabilities (CMC).

BIPM databases for intercomparisons and reference measurements

These activities take place in close cooperation with the national metrology institutes and related designated institutes in the respective committees of the CIPM, the so-called consultative committees (CCs), one associated with each base quantity of the SI. Further information on the Metre Convention and the BIPM is given in Chap. 2.

Currently, the CMC database contains some 24 000 entries, specifying reference measurement procedures of the national metrology institutes and designated institutes for various metrology areas.

- *Acoustics, ultrasound, and vibration*
- *Electricity and magnetism*, including direct-current (DC) and alternating-current (AC) measurements, impedance, electric and magnetic fields, radio frequencies, and measurements on materials

- *Length*, including laser frequencies and dimensional metrology
- *Mass and related quantities*, including mass standards, force, pressure, density, hardness, torque, gravity, viscosity, and fluid flow
- *Photometry and radiometry*, including fiber optics and properties of detectors, sources, and materials
- *Amount of substance*, including high-purity chemicals, inorganic solutions, organic solutions, gases, water, metals and metal alloys, advanced materials, biological materials, food, fuels, sediments, soils, ores and particulates, other materials, pH, electrolytic conductivity, surfaces, films, and engineered nanomaterials
- *Ionizing radiation*, including dosimetry, radioactivity, and neutron measurements
- *Thermometry*, including temperature, humidity, and thermophysical quantities
- *Time and frequency*

In several of these CMC directories, entries for reference measurements of materials properties can be found. However, the reference procedures for materials measurements are a long way from covering the needs of materials metrology. Therefore, an initiative was recently taken by some of the leading national materials research institutes towards the International Committee of Weights and Measures, proposing to consider dedicated activities in the field of materials metrology.

A well-known international network for materials research and technology is the Versailles project on advanced materials and standards (VAMAS). VAMAS was founded in 1982, as a follow-up action from a G7 economic summit in Versailles, to provide a framework for international collaboration on prestandardization materials research, with scope to provide a technical basis for agreement on methodologies prior to the formal development of standards.

The Versailles project on advanced materials and standards

The main objective of VAMAS is to support trade in high-technology products through international collaborative projects aimed at providing the technical basis for drafting codes of practice and specifications for advanced materials. The scope of the collaboration embraces all agreed aspects of science and technology concerned with advanced materials including materials

technology, test methods, design methods, and materials databases that are required as a precursor to the drafting of standards.

Current member countries are Australia, Brazil, Canada, Taiwan, France, Germany, India, Italy, Japan, Mexico, South Africa, South Korea, UK, USA, and also the EC, but VAMAS is open to organizations from other countries to participate in research activities.

Technical work is done in various working groups, the so-called technical work areas (TWA), of which there are 16 currently

- Surface chemical analysis
- Polymer composites
- Superconducting materials
- Mechanical property measurement of thin films and coatings
- Performance-related properties of electroceramics
- Full-field optical stress and strain measurement
- Spectrometry of synthetic polymers
- Nanomechanics applied to scanning probe microscopy
- Tissue engineering
- Creep, crack, and fatigue growth in weldments
- Modulus measurements
- Polymer nanocomposites
- Nanoparticle populations
- Materials databases interoperability
- Organic electronics
- Quantitative microstructural analysis

Further information about VAMAS activities may be obtained from the VAMAS website [3.77].

Considering the need to involve the metrology community, VAMAS approached the CIPM. The CIPM established an ad hoc Working Group on Materials Metrology (WGMM) in 2005. The WGMM published its final report in 2008 [3.78], leading to the signature of a memorandum of understanding (MoU) between VAMAS and the BIPM. This MoU provides the framework for the activities on materials metrology of all CIPM Consultative Committees (CC), including the establishment of special working groups in selected CC, identification of key issues and priority areas, and the development of collaborative studies for the validation of reference test procedures and of CIPM appropriate pilot studies for addressing comparability. The current status of material metrology, including the activities of the CIPM and of VAMAS and covering a broad scope of application fields, is comprehensively outlined in a special edition of *Metrologia* [3.79].

3.8.7 Related Terms and Definitions

In Sect. 3.8.4 the term *reference laboratory* was introduced and utilized without any further explanation. Similarly to the term *reference procedure*, this term has recently been used on an increasing scale, but a widely accepted definition is not available yet. Table 3.19 gives two definitions, originating from rather different fields: testing and laboratory medicine [3.64, 68].

The concept of reference laboratories, as defined above, has a lot of similarity with that of calibration laboratories and may be seen as a generalization. Unfortunately, the authors are not aware of any officially designated reference laboratories in the field of materials measurements. Examples from other fields include

- EU community and national reference laboratories for regulatory residue analysis of veterinary drugs and for air pollution control,
- reference laboratories for clinical measurements.

The concept of reference laboratories could become a key issue in the future development of ISO/IEC 17025, but this will require comprehensive discussion in various fora. In the authors' opinion, the concept should designate functions rather than a formal status, with functions centered on the provision of reference values. This could include provision of

- reference measurements/tests, preferably using reference procedures,
- reference materials and reference objects,
- proficiency testing schemes.

Another basic term that is intimately related to many of the issues of this section is that of a *measurement standard*. Here are two definitions from the International Vocabulary of Basic and General Terms in Metrology (VIM).

Measurement Standard. Realization of the definition of a given quantity, with stated quantity value and associated measurement uncertainty, used as a reference (VIM, 2008 [3.63]).

Reference Measurement Standard. Measurement standard designated for the calibration of other measurement standards for quantities of the same kind in a given organization or at a given location (VIM, 2008 [3.63]).

The concept of a measurement standard embraces both reference materials and reference procedures (of measurement). Currently the notion of national measurement standards maintained and disseminated by national metrology institutes is moving away from tangible objects to measurement service delivery capabilities.

Table 3.19 Definitions of the term reference laboratory

Reference (testing) laboratory	Reference measurement laboratory
Testing laboratory which – in arrangement with a specified laboratory community or through appointment by a competent organisation provides reference values in a specified technical field, i. e. property values of materials or products to which test results can be related or traced back and whose quality is fit for this purpose. (Eurolab Position Paper, 2007 [3.64])	Laboratory that performs a reference measurement procedure and provides results with stated uncertainties. (ISO 15195 [3.68])

3.9 Laboratory Accreditation and Peer Assessment

3.9.1 Accreditation of Conformity Assessment Bodies

Accreditation is the formal recognition that laboratories and other conformity assessment bodies such as inspection bodies and bodies certifying products, quality management systems, environmental management

systems or personnel are competent to perform specified tasks such as tests or measurements.

Modern technologies in processing goods, just-in-time manufacturing of goods, subcontracting or outsourcing of activities to specialized organizations are demanding an established system to demonstrate competence and reliability of testing laboratories.

The word *accreditation* comes from the Latin *credere* (to believe, to be confident in) in which the word *dare*, meaning to give or to offer, is found. Accreditation therefore means *to give confidence*. People must be confident that accredited bodies provide their services with competence and reliability.

Accreditation should be understood as a system to maintain and continuously develop a laboratory's competence through competent assessments provided by accreditation bodies. It is designed to be a transparent process in which all the interested parties should have the possibility to become involved effectively. In this context, processes should also be understood as a host of small innovative steps with the goal of causing something new to arise. (For more about processes, see Sect. 3.9.)

Accreditation is defined in standards that are developed by ISO/CASCO. CASCO is the ISO committee on conformity assessment. ISO is the International Standards Organization, and CASCO is its conformity assessment cooperation. These standards specify the accreditation body's competence as well as the laboratory's competence. While accreditation bodies work according to the ISO/IEC 17011 standard, laboratories operate according to the ISO/IEC 17025 standard. In some special fields, such as in the field of the medical laboratories sector, specific standards have been developed as well. In other cases, sector-specific criteria are given in annexes to ISO/IEC 17025.

The goal of all of these standards is to ensure that the respective organizations are technically competent to perform well-defined services and that they have an adequate management system in place to ensure daily quality as defined by their clients.

Competence according to the spirit of all of these standards can be assured in the long term only when the accredited companies – and the accreditation bodies themselves – including all the persons involved, go through a permanent and conscious process.

It is obvious that conformity assessment bodies that continuously develop their competence in a systematic way have a large advantage in an increasingly competitive market. Accreditation recognizes the constant development of their competence and service quality. So far, accreditation should be seen as a structure to implement processes leading to competence, quality, and efficiency.

The task of an accreditation service is to assess whether a conformity assessment body (CAB) has the necessary technical competence, infrastructure, and organization to provide reliable services. The CAB's

procedures should be clearly structured and controlled in a defined way. CABs need specialized knowhow and to develop an adapted structure to allow systematic decisions and learning processes.

Having a look at how accreditation works makes the significance of this evident. Let us take cable transportation plants and operators as an example.

- Accredited calibration laboratories calibrate measuring equipment for material testing
- Accredited testing laboratories test mechanical, hydraulic, and electronic system components and assess their quality
- Accredited inspection bodies inspect the critical technical installations for final approval of cable transportations
- Accredited certification bodies for products certify security components of cable transportation. In delivering credible conformity certificates they recognize compliance of such components with security requirements
- Accredited certification bodies evaluate quality and environmental management systems of cable transportation manufacturers and operators
- Accredited certification bodies for personnel examine training and technical competence of specialists.

3.9.2 Measurement Competence: Assessment and Confirmation

Measurement and testing are important elements of conformity assessment, the formal recognition that a material or a product conforms with specified requirements. The institutions performing conformity assessment tasks are called conformity assessment bodies (CABs). CABs are organizations providing the following conformity assessment services: calibration, testing, inspection, management system certification, personnel certification, and product certification. Accreditation is a third-party attestation related to a conformity assessment body conveying formal demonstration of its competence to carry out specific conformity assessment tasks. An authoritative body that performs accreditation is called an accreditation body (AB, ISO/IEC 17011). The goals of accreditation are

- to assess and confirm the competence and service quality of conformity assessment bodies,
- to ensure worldwide acceptance of their reports and certificates through a highly reliable confidence-building process,

- to support the competitiveness of accredited bodies on the national and global market.

In the entire chain of production and services one must have confidence that accredited testing and conformity assessment bodies provide their services in a competent and reliable manner.

The following examples illustrate the tasks fulfilled by accredited bodies.

- Measuring instruments of manufacturers and service providers have to be calibrated in order to allow correct measurements. *Accredited calibration laboratories* execute this task with the required precision and traceability to the international system of units (ISO 31).
- In their daily life, consumers depend on reliable analyses and tests, e.g., in the fields of food products, electrotechnical appliances, and medical diagnostic analyses. *Accredited testing laboratories* carry out these analyses and tests in a reliable manner.
- Inspections have to be carried out in order to detect safety oversights in food products, medicine, and

technical installations at a given moment. *Accredited inspection bodies* fulfill these tasks reliably.

- Consumers and industry depend on the compliance of products with defined requirements. *Accredited certification bodies for products* attest to this conformity, after evaluation, in a credible way.
- *Accredited certification bodies for quality systems* deliver conformity certificates attesting to the conformity of quality systems to the standard requirements. This allows clients to be confident that these firms have structures and working procedures at their disposal that ensure a service that respects deadlines and corresponds to the agreed quality.
- *Accredited certification bodies for environmental management systems* attest through their conformity certificates that firms present the necessary conditions in order to continuously improve their environmental performance.
- A large number of firms depend on recognized specialists whose competence has to comply with defined criteria. Amongst these specialists we find welders, auditors, business consultants, and project managers. *Accredited certification bodies for personnel* attest to their technical competence so the economy can rely on these specialists.

In the light of the considerable costs of assessments and the long-term acceptance of accreditation as a tool to build confidence in reports and certificates, accreditation bodies are fully aware of the fact that the necessary added value can only be achieved if

- assessments are aimed at real objectives and values and not at formalism of standards,
- assessors are able to provide useful feedback to the ongoing processes in a competent and independent way.

Today, trade has become global, and export trade is vital to the development of any country's economy. The increasing development of globalization, the reduction of technical barriers to trade (TBTs), and the recognition of conformity certificates worldwide is leading to increasing competition not only between companies, but also between marketplaces and economic regions. Governments, industry, and the whole economy is challenged to face this situation. Specialist knowledge, use of modern technologies, and experience and competence in management and in the realization of modern scientific technical solutions are the way to face this development. Today, a competent and well-recognized infrastructure of conformity assessment bodies is a fun-

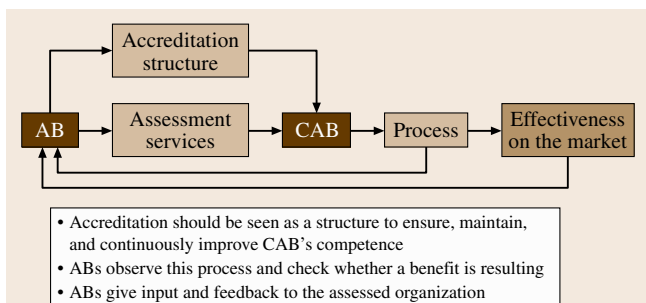


Fig. 3.34 Accreditation should be seen as a structure to implement processes leading to competence quality and efficiency

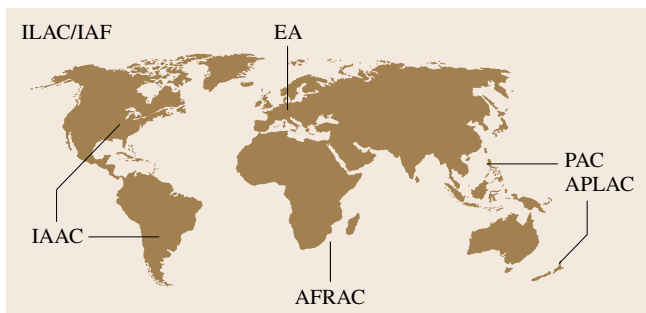


Fig. 3.35 Organizations of accreditation bodies in regions and worldwide

damental key factor for the economical success of a marketplace.

The technical barriers to trade (TBT) agreement encourages members of the World Trade Organization (WTO) to enter into mutual recognition agreements (MRAs) to enable assessments carried out in one country to be recognized in the other, based on reliable conformity assessments (TBT, Article 6):

Members shall ensure, whenever possible, that results of conformity assessment procedures in other Member's states are accepted, even when those procedures differ from their own, provided they are satisfied that those procedures offer an assurance of conformity with applicable technical regulations or standards equivalent to their own procedures. It is recognized that prior consultations may be necessary in order to arrive at a mutually satisfactory understanding.

The TBT agreements were one of the reasons for the establishment of accreditation bodies in the major trade groupings of the world (Fig. 3.33).

- ILAC:** International Laboratory Accreditation Cooperation (covers the field of laboratory accreditation and, together with the IAF, the field of accreditation of inspection bodies).
- IAF:** International Accreditation Forum (covers the field of the accreditation of certification bodies and, together with ILAC, the field of accreditation of inspection bodies).
- EA:** European Cooperation for Accreditation.
- IAAC:** Inter American Cooperation for Accreditation.
- PAC:** Pacific Accreditation Cooperation (active in the field of accreditation of certification bodies).
- APLAC:** Asian Pacific Accreditation Cooperation (active in the field of laboratory accreditation).
- AFRAC:** African Accreditation Cooperation.

These agreements help to eliminate major technical barriers to trade and, at the same time, reduce costs by removing the need for duplicate testing of products by both exporters and importers. Similar provisions, consistent with the TBT agreement, are being encouraged by regional trade groupings such as, e.g., the European Union (EU), the European Free Trade Association (EFTA), the Asia-Pacific Economic Cooperation (APEC) or the North America Free Trade Association (NAFTA) and the Association of South-East-Asian Nations (ASEAN) Free Trade Association (AFTA).

MRAs may be *bilateral* or *multilateral*. Over the past 20 years, a network of bilateral and multilateral MRAs have been established between laboratory accreditation bodies throughout the major trade regions.

An example illustrates this: within the framework of the *new and global approach concept* of the European Union, national standards are replaced by harmonized European directives, which define the fundamental requirements, especially with regard to the safety of a product. Products in compliance with these requirements are marked with the Communauté Européenne (CE) logo. They can be put into free circulation in the European Economic Area. In order to implement and maintain this concept globally, all states that participate need an infrastructure of competent and reliable calibration, testing, inspection, and certification bodies.

Multilateral Agreements. Agreements within accreditation bodies within regional trade groupings such as Europe (Fig. 3.36) ensure worldwide harmonization of accreditation. They create the basis for international recognition of testing reports and conformity certificates, especially on the technical level. Therefore, an important task of each country's accreditation bodies is to maintain the interests of the respective country in view of international organizations such as the European Cooperation for Accreditation (EA) in Europe, the International Laboratory Accreditation Cooperation (ILAC), and the International Accreditation Forum (IAF). Together with all their stakeholders, these organizations continuously establish recommendations and guidance for harmonization of accreditation criteria and evaluation testing procedures to ensure worldwide reli-

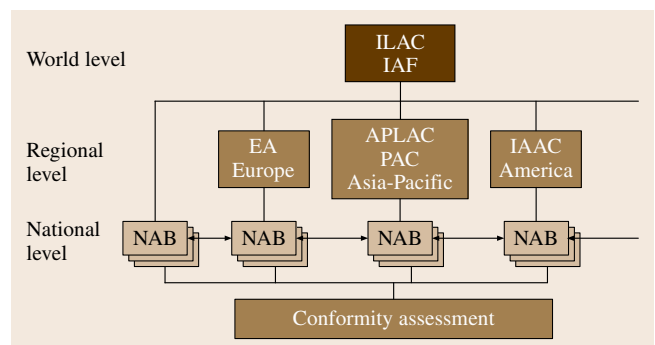


Fig. 3.36 The structure of the MLAs: The competence of the regional organizations is evaluated by ILAC and IAF, the regional organizations evaluate the national accreditation bodies, and these accredit the conformity assessment bodies

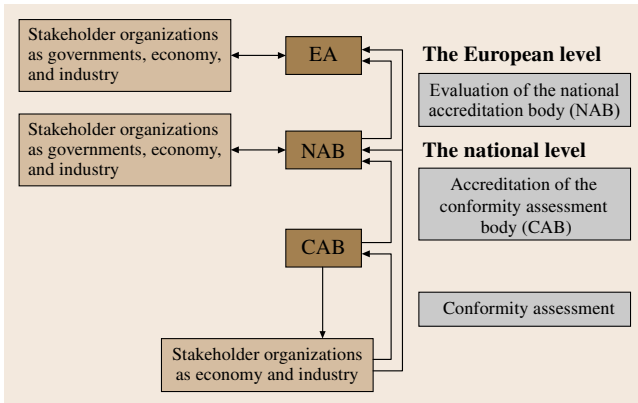


Fig. 3.37 Accreditation, an infrastructure offered to all interested parties

ability and recognition of testing reports and conformity certificates.

As a result, accreditation benefits from professional input and provides a structure to all the interested parties in order to

- establish confidence in testing reports and conformity certificates,
- develop competence in a continuous way,
- allow mutual recognition of testing reports and conformity certificates.

3.9.3 Peer Assessment Schemes

Peer assessment schemes follow basically the same goal as the accreditation process. Peer assessments schemes are private agreements with the aim of mutually assessing each other's competence. They are normally designed and performed by professional organizations in order to build confidence in their members' services.

3.10 International Standards and Global Trade

Standards are important tools for metrology and testing. A *standard* (French: *norme*, German: *Norm*) is defined as follows.

Standard: document, established by consensus and approved by a recognized body, that provides, for common and repeated use, rules, guidelines, or characteristics for activities and their result, aimed

By definition, such peer assessment schemes are second-party recognition schemes, while accreditation is clearly designed as a third-party recognition scheme. However they can provide a big help for its members.

3.9.4 Certification or Registration of Laboratories

The ISO 9001 standard is the well-known standard in the field of quality management systems (QMS) certification. This standard deals with quality management as generally applied to any types of companies. The ISO/IEC 17025 standard and laboratory accreditation are concerned with competence and quality and are specific for laboratories. An official communique (IAF/ILAC JWG/129) characterizes the differences between accreditation and certification as follows.

Certification

- means compliance with a standard or specification
- uses management system auditors who are certified by an independent body that meets internationally agreed criteria
- considers the total activities of an organization, and the scope of recognition is general.

Accreditation

- is the recognition of specific competence, and its scope is normally highly specific
- evaluates people skills and knowledge
- uses assessors who are recognized specialists in their fields
- evaluates the supporting management system for a specific activity
- involves practical tests as appropriate (proficiency testing and measurement audits).

at the achievement of the optimum degree of order in a given context (ISO guide 2).

The world principal forum for standardization is ISO, the International Organization for Standardization, an international-standard-setting body composed of representatives from various national standards organizations (<http://www.iso.org>). Founded in 1947 and with head-

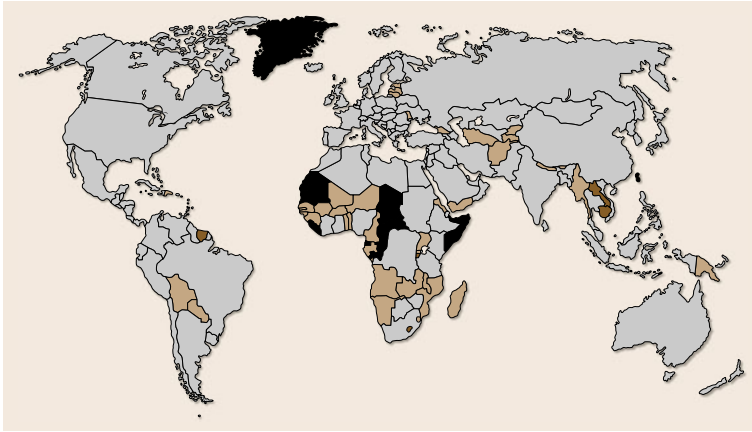


Fig. 3.38 A map of standards bodies who are ISO members (*grey*: members, *light brown*: correspondent members, *dark brown*: subscriber members, *black*: nonmembers)

quarters in Geneva, Switzerland, the organization publicizes worldwide proprietary industrial and commercial standards. While the ISO defines itself as a nongovernmental organization, it acts as a consortium with strong links to governments, setting standards that often become law, either through treaties or national standards. ISO has 163 national members, out of the 203 total countries in the world (Fig. 3.38).

International standards are standards developed by international standards organizations. They are available for consideration and use worldwide, and may be used either by direct application or by a process of modifying an international standard to suit local conditions. International standards are one way of overcoming technical barriers in international trade caused by differences among technical regulations and standards developed independently and separately

by each nation, national standards organization, or companies.

3.10.1 International Standards and International Trade: The Example of Europe

Consider, for example, the evolution of the European standardization system. A coherent collection of European standards has been developed by a large number of stakeholders, including industry, public authorities, research organizations, and special interest groups such as consumers, representing a wide range of sectors. Technical barriers to trade have thus been removed, ensuring the free movement of goods – an essential prerequisite for the economic functioning of the Common European Market (Fig. 3.39).

New approach for the European Economic Community (Legislation 1985) intending to ensure the four basic freedoms for movement of *goods, persons, services, capital*.

- Flexible regulatory framework providing access to the common market while protecting essential public requirements, e.g. safety, health, environment.
- *Essential requirements* defined in EU-Directives: from machinery to toys.
- The EU-Directives have to be transposed into national laws of the EU countries to become legally binding forces in the individual EU countries.
 - Note: the European Union in 2010 comprises 27 countries with 23 official languages for national laws and national legal regulations.
- Harmonized EN Standards define the technical details
 - Note: European EN Standards are valid in the whole EU, conflicting national standards have to be withdrawn.
- CE marking: the manufacturer declares that the product is safe and in conformity with the relevant EU-Directives.



Fig. 3.39 The role of harmonized standards for trade, the example of Europe

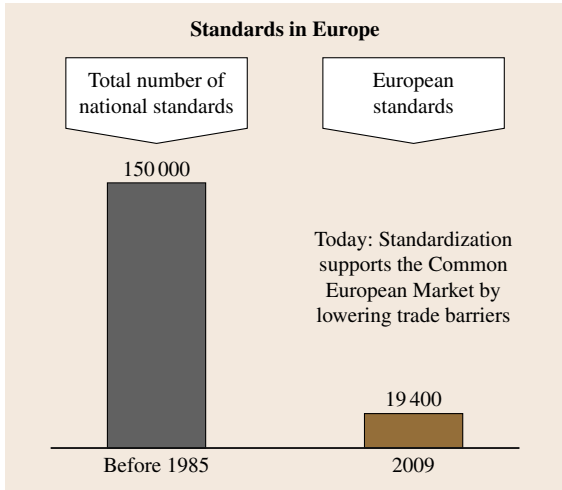


Fig. 3.40 Number of standards before and after formation of the European Union and the evolution of the Common European Market

There are now only three standardization organizations that coordinate, monitor, and support the relevant activities in Europe.

- **CENELEC** in the field of electrotechnical standardization (<http://www.cenelec.eu>)

- **ETSI** in the telecommunications sector (<http://www.etsi.eu>)
- **CEN** in all other fields of standardization (<http://www.cen.eu>).

The development of standardization in Europe is illustrated in Fig. 3.40. It shows that, before 1985, there were about 150 000 national standards in the European countries. Due to harmonization efforts of standards in the evolution process of the European Union (EU), there are now fewer than 20 000 harmonized standards in the EU. The business domains relating to the European standards in 2010, as compiled by the bureaus of the CEN/CENELEC Management Centre, are shown in Fig. 3.41.

As a prerequisite for global trade, international cooperation in standardization is necessary. The modalities of technical cooperation and exchange of information between the CEN and the ISO are laid down in the *Vienna Agreement*, while the *Dresden Agreement* regulates the cooperation between CENELEC and IEC (Fig. 3.42).

The purpose of these agreements is

- to make best use of available resources and thus avoid duplication of work, and
- to ensure that international and European standards are not only compatible, but identical.

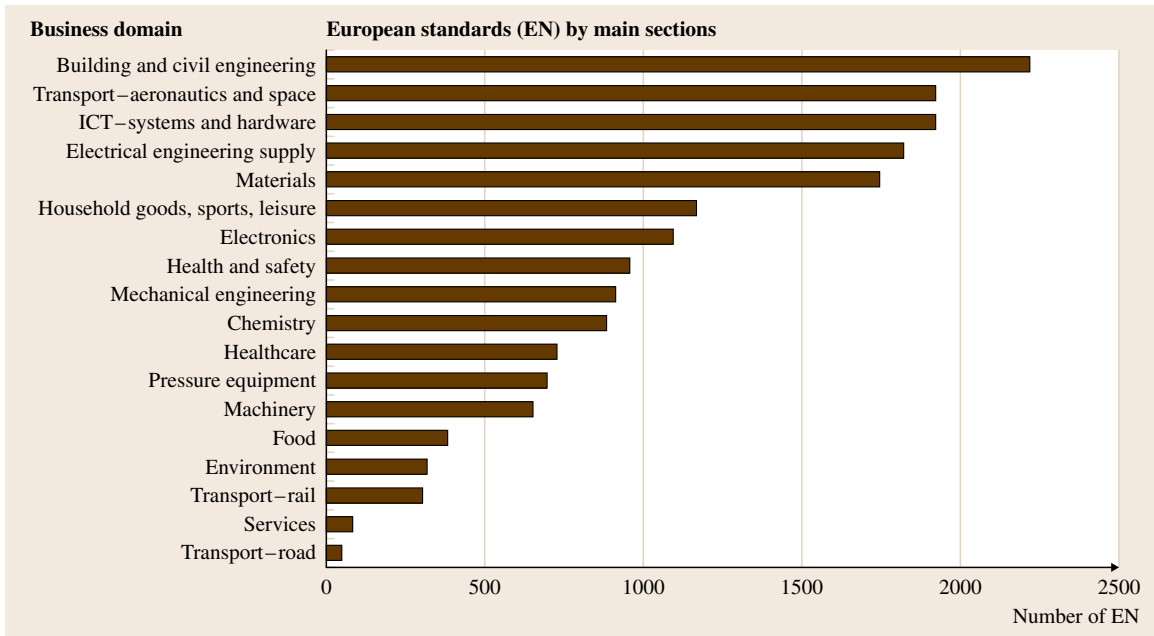


Fig. 3.41 Business domains and number of European standards

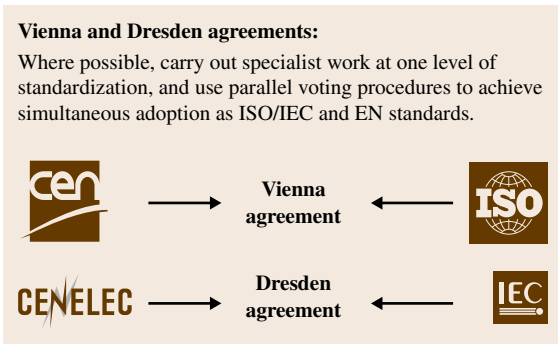


Fig. 3.42 International agreements in standardization

3.10.2 Conformity Assessment

The regulation of international trade is done through the World Trade Organization (WTO) at the global level, and through several other regional arrangements such as MERCOSUR in South America, the North American Free Trade Agreement (NAFTA) between the USA, Canada, and Mexico, and the European Union (EU). International standards have to follow the principles of the World Trade Organization (WTO) Committee on Technical Barriers to Trade, i.e., transparency, openness, impartiality and consensus, effectiveness, and relevance.

Conformity assessment – performed by *conformity assessment bodies (CABs)* – is any activity to determine, directly or indirectly, that a process, product or service meets relevant standards and fulfills relevant re-

quirements. The types of conformity assessment bodies are

- laboratories
 - testing laboratories
 - calibration laboratories
- inspection bodies
- certification bodies for
 - management systems
 - products
 - persons.

The results of conformity assessment activities are, e.g., certificates, (testing) reports, declarations, and marks of conformity. The documents must be correct, valuable, clear, and easy to understand for all participants in the market. The results must be in such a form that participants in the market and authorities are able to use them in their decisions. The requirements written in standards of conformity assessment activities and the requirements for the CABs must give confidence in the results of the conformity assessment bodies. General requirements in all conformity assessment standards are

- organization and structure,
- impartiality, independence,
- competence of personnel and access to competence,
- equipment, procedures, and methods,
- decision on conformity assessment and reporting,
- management system of the CAB.

An overview on the standards of conformity assessment is given in Fig. 3.43 and Table 3.20.

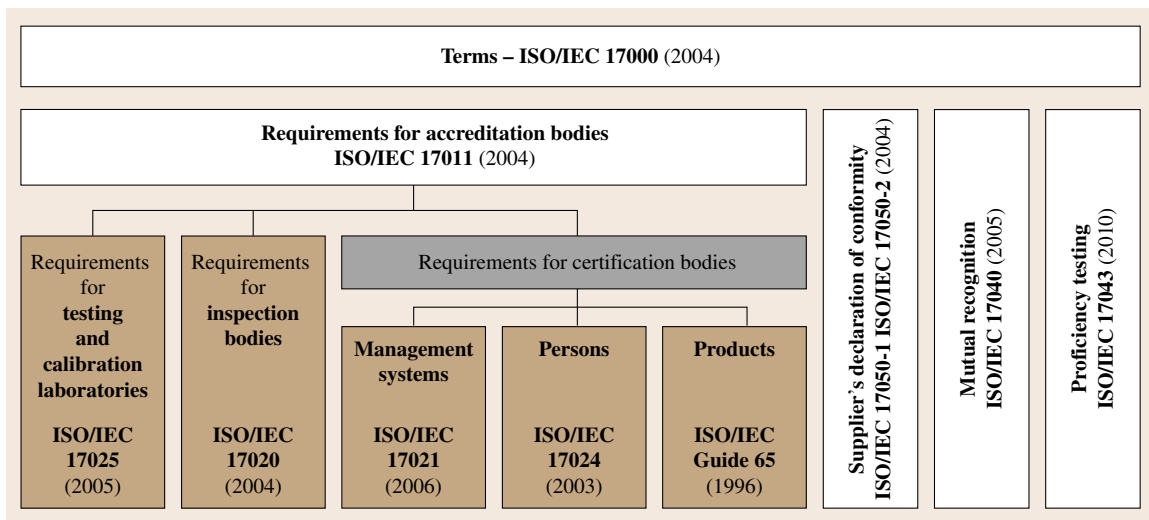


Fig. 3.43 Overview of conformity assessment standards

Table 3.20 Conformity assessment standards

ISO/IEC 17000:2004	Terms, <i>reference document</i>
ISO/IEC 17011:2004	Accreditation bodies
ISO/IEC 17020:2004	Inspection bodies
ISO/IEC 17021:2006	Certification bodies for management systems
ISO/IEC 17024:2003	Certification bodies for persons
ISO/IEC 17025:2005	Laboratories
EN 45011:1998 (EN ISO/IEC 17065)	Certification bodies for products (possibly to be replaced in the future)
ISO/IEC 17040:2005	Peer assessment
ISO/IEC 17050-1:2000	Supplier's declaration of conformity
ISO/IEC 17050-2:2004	

3.11 Human Aspects in a Laboratory

3.11.1 Processes to Enhance Competence – Understanding Processes

Continuous development of the technical competence of all staff necessitates processes that lead to creative and innovative solutions. Such processes must be understood in such a way that continuous progress at all levels and for all functions in an organization is self-evident.

Clients expect from laboratories services and solutions that take into account the latest developments in a respective technical field. Only competent laboratories will be able to perform such services in an economic and reliable way. Materials testing is very seldom based on routine testing. Often, methods have to be developed or adapted to

- new materials,
- new questions to be answered,
- special problems to be solved.

Validation plays a big role, as testing methods must be adapted to given tasks and be proved suitable for these tasks. To prove the fitness for purpose of testing methods in order to achieve highly reliable results, which can in special cases be very complex, requires the continuous development of specialized knowledge. Such knowledge consists not only of the details of the testing methods that one plans to use but also the knowledge about what customers are planning to do with the results and a general knowledge about the materials tested.

In very rare cases the required competence can be organized from outside. Competence must be developed

by all people involved in a laboratory, who are faced with the daily questions and problems. This requires staff who are highly motivated and deeply engaged in their daily tasks.

The long-term safeguarding of competence requires the use of processes at all levels of an organization. This necessitates an organizational structure that enables the development of such processes. Processes involving people consist of a host of small steps with the goal of creating something new. Competence, e.g., according to the spirit of the standards relevant for accreditation, can be assured in the long term only if their implementation is considered as an ongoing learning process. Learning processes are highly dependent on management structures, and on the provisions to make sure that the whole staff can feel full responsibility for their work.

We all undergo processes, whether we want to or not, be it consciously or unconsciously, simply because of all the information that reaches us and daily interactions. It is important for the head of an organization to ask the following questions.

- What kinds of processes are going on in the entire company, in parts of it, and within individual people?
- Which of them are important for me, and how can I recognize them?
- What can I do to support processes leading to engaged staff with good motivation and loyalty?
- What is the driving force for enthusiasm in my organization?

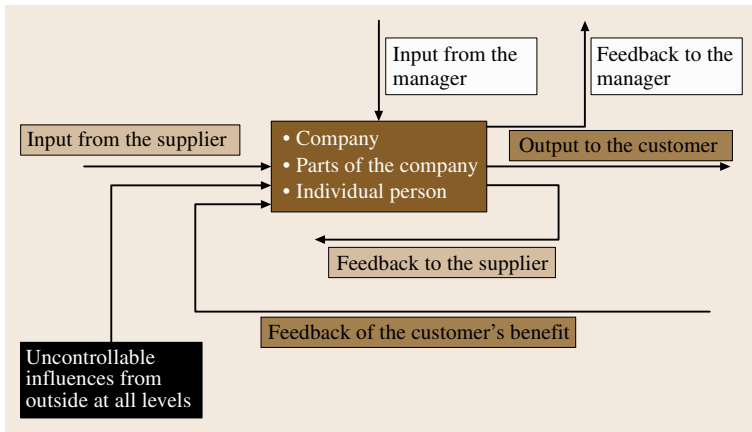


Fig. 3.44 The principle of systematically controlled input and output

To find answers it is important that

- communication principles are discussed regularly,
- conflicts are treated and solved systematically,
- internal audits are carried out in such a way that aspects of the management system and procedures that could hinder learning processes or lead to internal conflicts are discovered.

Being process-orientated means that each staff member may bring in his/her competence and his/her creativity for

- planning procedures
- putting procedures into effect

and therefore participates in the ongoing innovative process.

This is also a reply to those who perceive documented management systems as limiting, restrictive, and conservative, and that, at best, they are able to optimize something already existing, but in no case to create something new and innovative.

Management systems should therefore always, and particularly in the case where the aim is long-term safeguarding of competence and quality, be implemented in such a way that creativity plays an important role. Creativity also depends on how responsibilities are allocated and on the functional behavior of all individuals in an institution; this means that each staff member must have the possibility to take on his or her responsibility fully and be assured of the protection required to provoke unconventional ideas.

3.11.2 The Principle of Controlled Input and Output

Functional behavior therefore necessitates a clear definition of responsibilities. This means that everyone assumes responsibility and respects the responsibility of people who come above or below them in the hierarchy and of colleagues at the same hierarchical level. If this does not happen, good processes will be blocked and creativity cannot arise. Clear structures in a laboratory's management system are therefore an important prerequisite. This structure should ensure that client requests will lead to respective reactions at all levels: the individual staff level, the subunit level, and at the whole organization level. Of course it is important that these reactions are fully controllable and controlled, without taking responsibility away from the individual staff.

The First Control Circle: Input from and Feedback to the Manager (Superior Person)

Input should be given regularly, e.g., by defining targets to be achieved. This can be done on daily, weekly or monthly bases and requires regular feedback from the collaborator. Input and feedback should be systematically planned and given in a structured way. Respected responsibility means that each collaborator has the freedom to organize and to arrange their own activities within his defined frame of responsibility.

The Second Control Circle: Input from and Feedback to the Supplier

All internal and external institutions (parts of a company), and individual people performing the activities

prior to and in support of one's own activities, should be considered as suppliers and treated as such. Input and feedback should be defined, planned, and given in a structured way.

The Third Control Circle:

Input from and Feedback to the Customer

All internal and external institutions (parts of a company) and individual persons benefiting from one own's activities should be considered as customers and treated as such. Output and feedback should be well defined, planned, and given in a structured way.

The principle of systematically controlled input and output should be valid for the whole organization, for parts of it, and for the individual staff. Each element, the whole organization, parts of it or individual staff members have to deal with information from clients, customers, and superiors. If such a system is applied, it will greatly assist the development of staff entrepreneurship. The system will distinguish between those who are prepared to take responsibility as an entrepreneur and those who are not. It is obvious that staff feeling like entrepreneurs will undergo learning processes to develop the technical and personal skills needed to take the responsibility linked to given hierarchical competencies.

The principle of systematically controlled input and output will automatically lead to intensive interaction of the individuals involved, the team, the subject, and the involved environment and therefore provide good bases for implementation of management systems such as that defined in the [ISO/IEC 17025](#) standard.

3.11.3 The Five Major Elements for Consideration in a Laboratory

Quality management starts with the individual. If the principle of systematically controlled input and output is applied strictly, each entrepreneur in the organization will feel responsible for the quality of his or her product or performed service. The following five elements will help to assure reliable performance at all hierarchical levels, the laboratory, the subunits, and the individual staff.

1. Systematic estimation of opportunities and the corresponding risks
2. Leadership and ability to lead at all levels
3. Traceability of all decisions; decisions should be comprehensive
4. Periodic evaluation of the effectiveness of one's own organization, procedures, etc.

5. A general system to limit damage. Corresponding procedures should be laid down in the overall quality management system.

Regardless of the quality system applied, internal audits should preferably be used to monitor how these five elements are implemented at all the hierarchical levels mentioned above.

3.11.4 Internal Audits

Internal audits are a very helpful tool to observe whether good processes are being carried out. However, they should not be used to establish hidden supervision of staff and their activities. To audit means to observe if the structure of the management system is developed in such a way that conscious learning processes at all levels in a company are possible and provide feedback. This means that auditors have to take into account

- the people,
- their processes,
- the structure of the organization and the management system.

Auditors have to respect the functions and the corresponding hierarchical competencies in an organization. The staff should therefore always be included in the audit teams and be responsible for those audits that are performed within their own area of responsibility. Audit teams should include the following team members.

- The individual persons responsible for a given activity or task
- The superior who wants to gain trust in the work of his collaborator
- A person having the necessary communication skills and who is familiar with
 - the quality system,
 - its structure and procedures, and
 - the audit techniques.

To audit an organization, parts of it, or an individual person means to observe and to learn how the management system is implemented, whether it enables conscious processes at all levels in a company, and to give feedback.

The most important point is that auditors are trained to observe learning processes, and to this end they need to know more about human beings and behavior. If

international standards, such as the ISO/IEC 17000 series of standards, are implemented and audits are used to verify if these standards are implemented effectively, auditors should not only look at how these standards are translated into action but if this translation is of benefit to the company, parts of it, and the individual staff. This means that audits must concentrate on the effects of the defined measures, and after an audit the audited organization or persons should be able to explain what they discovered during the audit, e.g., in the audit report, which is – in the best case – provided by the audited people or the people who are responsible for the audited part of the organization.

3.11.5 Conflicts

Conflicts are normal and will occur in all situations. Conflicts result from disagreements or different opinions. Conflicts can occur if engaged people are convinced about their own solutions or ideas. To be in conflict with somebody is not bad behavior; bad behavior is not to solve these conflicts. Unsolved conflicts lead to situations where learning processes are no longer possible and later where cooperation between staff members becomes nearly impossible.

It is therefore good practise to establish a system to solve conflicts, even the smallest one, in *statu nascendi* and in a systematic way. This can, e.g., be done using the following principles.

1. All the staff (including the general manager) are required to declare a conflict (even a possible one) as soon as it is recognized, to the person(s) with whom a potential conflict exists. The person who recognizes the conflict can be considered as the client, and the other conflicting person as the supplier.
2. The client should discuss this potential conflict as soon as possible with the supplier, while this is possible and with the least emotion possible.
3. If the client and the supplier are not able to solve the conflict, it is important that they involve a third person to act as an arbitrator. Arbitration in an organization should not be considered as a tribunal, but as a good way to translate to one another different opinions that obviously cannot be understood. It is important that the arbitrator does not rate the opinions of the conflicting persons. On the other hand, he is obliged to explain what is already fixed,

e.g., in the management system or in technical procedures.

4. Both conflicting people (client and supplier) should afterwards express their wish for future solutions in a comprehensive way such that it is clear what the other person is expecting. The arbitrator ensures that this discussion remains factual.
5. Having learned from each other, both conflicting partners explain to the other person the next steps to realizing good solutions in the future.
6. All three partners explain what they have learned in the process. If one of the partners does not have trust in the solution by the other partner, he will announce this and clarify remaining points immediately.
7. The supplier will minute the discussions, especially the agreed conclusions about the next steps.

It is recommended to lay down such a procedure in the corresponding management system of an organization. This will ensure that conflicts do not remain untouched and that the necessary learning steps are taken; this is an important aspect to maintain the necessary competence of all staff.

3.11.6 Conclusions

The increasing development of globalization, the European and worldwide reduction of technical barriers to trade, and the recognition of conformity certificates worldwide is leading to increasing competition not only between companies, conformity assessment bodies, and laboratories, but also between marketplaces and economic regions. Specialized knowledge, use of modern technologies, and experience and competence in the management and realization of innovative scientific technical solutions are the ways to face this development.

Consideration of human aspects is of utmost important, especially in laboratories where there is a clear need to continuously develop technical competence. Technical competence can only be continuously developed and improved, if the management can base this on engaged staff. There are a few basic principles that must be respected to support the development of engagement. It is highly recommended to invest in these principles. Such investments should be treated in the same way as investments in technical equipment or scientific developments. They are at least of similar importance.

3.12 Further Reading: Books and Guides

The following is a selection of sources and is neither comprehensive nor intended as a recommendation.

Statistics

- NIST/SEMATECH e-Handbook of Statistical Methods, <http://www.itl.nist.gov/div898/handbook/> (last updated June 23, 2010, last accessed June 8, 2011)
- G. W. Snedecor, W. G. Cochran: *Statistical Methods* (Iowa State Univ. Press, Ames 1993)
- R. Caulcott: *Statistics in Research and Development* (Chapman Hall, New York 1983)
- V. Barnett, T. Lewis: *Outliers in Statistical Data*, 3rd edn. (Wiley, New York 1994)
- P.J. Huber: *Robust Statistics* (Wiley, New York 1981)

Experimental Design

- G. M. Clarke: *Statistics and Experimental Design* (Edward Arnold, London 1984)
- S. N. Deming, S. L. Morgan: *Experimental Design: A Chemometric Approach* (Elsevier, Amsterdam 1987)

Quality Control

- J. W. Oakland: *Statistical Process Control* (Heinemann, Oxford 1989)
- ISO 8258:1991: *Shewhart Control Charts* (ISO, Geneva 1991)

Uncertainty Estimation

- S. G. Rabinovich: *Measurement Errors and Uncertainties: Theory and Practice* (Springer, New York 2000)
- ISO: *Guide to the Expression of Uncertainty in Measurement*, 2nd edn. (ISO, Geneva 1995)
- ISO TS 21748:2005: *Guide to the Use of Repeatability, Reproducibility and Trueness Estimates in*

Measurement Uncertainty Estimation (ISO, Geneva 2005)

Free and Open-Source Statistical Software

- R: *A Language and Environment for Statistical Computing* (R Foundation for Statistical Computing, Vienna 2005), <http://www.r-project.org/> (last accessed June 8, 2011)
- NIST Dataplot: <http://www.itl.nist.gov/div898/software/dataplot/homepage.htm> (date created June 5, 2001, last updated May 15, 2010, last accessed June 8, 2011)
- AMC Software Excel add-ins: <http://www.rsc.org/Membership/Networking/InterestGroups/Analytical/AMC/Software/index.asp> (Roy. Soc. Chem., London 2011)

General Statistics

- GenStat (VSN International Ltd.): Video Streaming Network (2011) <http://www.vsn-intl.com/?s=genstat> (last accessed June 3, 2011)
- Minitab (Minitab Inc.): <http://www.minitab.com/en-DE/default.aspx> (Minitab, State College 2011)
- SAS/STAT (SAS Institute Inc.): <http://www.sas.com/> (SAS Institute Inc., Cary 2011)
- TIBCO Spotfire S+: <http://spotfire.tibco.com/products/s-plus/statistical-analysis-software.aspx> (TIBCO, Somerville) (last accessed June 8, 2011)
- SPSS (IBM SPSS Inc.): <http://www.spss.com/> (last accessed June 8, 2011)
- Statistica (Statsoft Inc.): <http://www.statsoft.com/> (last accessed June 8, 2011)

Experimental Design

- Design-Ease (StatEase Inc.): <http://www.statease.com/> (Stat-Ease, Inc., Minneapolis 2011)
- MODDE (Umetrics): <http://www.umetrics.com/> (Umetrics, Andover 2011)

References

- 3.1 P.M. Gy: *Sampling of Particulate Materials, Theory and Practice* (Elsevier, Amsterdam 1979) p. 431
- 3.2 M.H. Ramsey, S.L.R. Ellison (Eds.): *Eurachem/EURO-LAB/CITAC/Nordtest/AMC Guide: Measurement Uncertainty Arising from Sampling: A Guide to Methods and Approaches* (Eurachem, Prague 2007)
- 3.3 ISO: *Guide to the Expression of Uncertainty in Measurement*, 2nd edn. (ISO, Geneva 1995)
- 3.4 U. Kurfürst, A. Desaules, A. Rehnert, H. Muntau: Estimation of measurement uncertainty by the budget approach for heavy metal content in soil under different land use, *Accredit. Qual. Assur.* **9**, 64–75 (2004)

- 3.5 Analytical Methods Committee (AMC): Uncertainty of Measurement: Implications of its Use in Analytical Science, *Analyst* **120**, 2303–2308 (1995)
- 3.6 M.H. Ramsey, A. Argyraki: Estimation of measurement uncertainty from field sampling: Implications for the classification of contaminated land, *Sci. Total Environ.* **198**, 243–257 (1997)
- 3.7 J.A. Lyn, M.H. Ramsey, S. Coad, A.P. Damant, R. Wood, K.A. Boon: The duplicate method of uncertainty estimation: Are eight targets enough?, *Analyst* **132**, 1147–1152 (2007)
- 3.8 M.H. Ramsey: Sampling as a source of measurement uncertainty: Techniques for quantification and comparison with analytical sources, *J. Anal. At. Spectrom.* **13**, 97–104 (1998)
- 3.9 S.L.R. Ellison, M. Roesslein, A. Williams (Eds.): *Eurachem/CITAC Guide: Quantifying Uncertainty in Analytical Measurement* (Eurachem, London 2000), Available from the Eurachem secretariat, or from LGC Limited
- 3.10 M.H. Ramsey, S. Squire, M.J. Gardner: Synthetic reference sampling target for the estimation of measurement uncertainty, *Analyst* **124**(11), 1701–1706 (1999)
- 3.11 S. Squire, M.H. Ramsey, M.J. Gardner, D. Lister: Sampling proficiency test for the estimation of uncertainty in the spatial delineation of contamination, *Analyst* **125**(11), 2026–2031 (2000)
- 3.12 M. Thompson, T. Fearn: What exactly is fitness for purpose in analytical measurement?, *Analyst* **121**, 275–278 (1996)
- 3.13 M.H. Ramsey, P.D. Taylor, J.C. Lee: Optimized contaminated land investigation at minimum overall cost to achieve fitness-for-purpose, *J. Environ. Monit.* **4**(5), 809–814 (2002)
- 3.14 M.H. Ramsey, J.A. Lyn, R. Wood: Optimised uncertainty at minimum overall cost to achieve fitness-for-purpose in food analysis, *Analyst* **126**(10), 1777–1783 (2001)
- 3.15 B. Geelhoed, H.J. Glass: Comparison of theories for the variance caused by the sampling of random mixtures of non-identical particles, *Geostand. Geoanal. Res.* **28**(2), 263–276 (2004)
- 3.16 C.C. Ferguson: The statistical basis for the spatial sampling of contaminated land, *Ground Eng.* **25**, 34 (1992)
- 3.17 International vocabulary of metrology – Basic and general concepts and associated terms (VIM), 3rd edn., JCGM 200:2008 (including Corrigendum of Mai 2010)
- 3.18 BIPM, IEC, IFCC, ISO, IUPAC, IUPAP, OIML: *Guide to the Expression of Uncertainty in Measurement (GUM)*, 1st edn. (BIPM and IEC and IFCC and ISO and IUPAC and IUPAP and OIML, Paris 1993), corrected and reprinted in 1995
- 3.19 ISO: *Guide to the Expression of Uncertainty in Measurement*, 1st edn. (ISO, Geneva 1995)
- 3.20 EUROLAB: *Guide to the Evaluation of Measurement – Uncertainty for Quantitative Test Results*, Tech. Rep. 1/2006 (EUROLAB, Paris 2006), <http://www.eurolab.org/>
- 3.21 EUROLAB: *Measurement Uncertainty Revisited: Alternative Approaches to Uncertainty Evaluation*, Tech. Rep. 1/2007 (EUROLAB, Paris 2007), <http://www.eurolab.org/>
- 3.22 ISO: ISO 5725 (series of standards in 6 parts), Accuracy (trueness and precision) of measurement methods and results (ISO, Geneva 1998–2005)
- 3.23 ISO/TS 21748, Guide to the use of repeatability, reproducibility and trueness estimates in measurement uncertainty estimation (ISO, Geneva 2004)
- 3.24 EURACHEM/CITAC: *Quantifying Uncertainty in Analytical Measurement*, 2nd edn. (EURACHEM/CITAC, Prague 2000)
- 3.25 EUROLAB: *Measurement Uncertainty in Testing*, Tech. Rep. 1/2002 (EUROLAB, Paris 2002)
- 3.26 EA: *Expression of Uncertainty in Quantitative Testing*, Guideline EA-4/16 (EA, Rijswijk 2003), www.european-accreditation.org/content/publications/pub.htm (last accessed 14 April 2011)
- 3.27 B. Magnusson, T. Näykki, H. Hovind, M. Krysell: *Handbook for Calculation of Measurement Uncertainty in Environmental Laboratories*, Tech. Rep. 537 (Nordtest, Espoo 2003)
- 3.28 EA: *Expression of the Uncertainty of Measurement in Calibration*, Guideline EA-4/02 (European Cooperation for Accreditation, Paris 1999)
- 3.29 AFNOR FD X 07-021: Fundamental standards – Metrology and statistical applications – Aid in the procedure for estimating and using uncertainty in measurements and test results (European Diagnostic Manufacturers Association, Brussels 2006)
- 3.30 Supplement No. 1 to the GUM: Propagation of distributions using a Monte Carlo method (ISO/IEC Guide 98-3:2008/Suppl 1:2008) (BIPM, Paris 2008)
- 3.31 ISO 13528: Statistical methods for use in proficiency testing by interlaboratory comparison (ISO, Geneva 2005)
- 3.32 ISO/TS 21749: Measurement uncertainty for metrological applications (ISO, Geneva 2005)
- 3.33 ISO: *ISO 9000, International Consensus on Good Quality Management Practices* (ISO, Geneva 2000)
- 3.34 CITAC/EURACHEM: *Guide to Quality in Analytical Chemistry – An Aid to Accreditation* (CITAC/EURACHEM, Prague 2002)
- 3.35 AOAC International: *AOAC Peerverified Methods Policies and Procedures* (AOAC International, Gaithersburg 1993)
- 3.36 S. Kromidas: *Validierung in der Analytik* (Wiley-VCH, Weinheim 1999), (in German)
- 3.37 W. Wegscheider: Validation of analytical methods. In: *Accreditation of Chemical Laboratories*, ed. by H. Günzler (Springer, Berlin, Heidelberg 1996)

- 3.38 ISO: *ISO Guide 30, Terms and Definitions Used in Connection with Reference Materials* (ISO, Geneva 1992)
- 3.39 B. King: 4E-RM-Guide, Selection and use of reference materials – A basic guide for laboratories and accreditation bodies (EURACHEM, Prague 2002) <http://www.eurachem.ut.pt/>
- 3.40 IAGRM: *Final Third Party Quality Assessment of Producers of Reference Materials* (IAGRM, Bristol 2004)
- 3.41 ISO: *International Vocabulary of Basic and General Terms in Metrology* (ISO, Geneva 1999)
- 3.42 ISO: *ISO Guide 34, General Requirements for the Competence of Reference Materials Producers* (ISO, Geneva 2009)
- 3.43 United Nation: *Glossary of Terms for Quality Assurance and Good Laboratory Practices* (United Nation, New York 1995)
- 3.44 M.J.T. Milton, T.J. Quinn: Primary methods for the measurement of amount of substance, *Metrologia* **38**, 289–296 (2001), <http://www.bipm.org/en/metrologia/> (last accessed 14 April 2011)
- 3.45 BAM: COMAR database (Federal Institute for Materials Research and Testing, Berlin 2011), <http://www.comar.bam.de>
- 3.46 International Atomic Energy Agency (IAEA): *Nuclear Sciences and Applications* (IAEA, Vienna 2011), <http://www-naweb.iaea.org>
- 3.47 Bureau International des Poids et Mesures (BIPM): <http://www.bipm.org/> (BIPM, Paris 2011)
- 3.48 ISO: *ISO Guide 31, Contents of Certificates of Reference Materials* (ISO, Geneva 2000)
- 3.49 A. Zschunke (Ed.): *Reference Materials in Analytical Chemistry* (Springer, Berlin, Heidelberg 2000)
- 3.50 J. Pauwels, A. Lamberty: CRMs for the 21st century new demands and challenges, *Fresenius J. Anal. Chem.* **370**, 111–114 (2001)
- 3.51 M. Parkany, H. Klich, S.D. Rasberry: REMCO, the ISO Council Committee on Reference Materials – its 1st 25 years, *Accredit. Qual. Assur.* **6**, 226–235 (2001)
- 3.52 ISO: *ISO 6506-1, Metallic Materials – Brinell Hardness Test – Part 1: Test Method* (ISO, Geneva 2005)
- 3.53 ISO: *ISO 6507-1, Metallic Materials – Vickers Hardness Test – Part 1: Test Method* (ISO, Geneva 2005)
- 3.54 ISO: *ISO 6508-1, Metallic Materials – Rockwell Hardness Test – Part 1: Test Method* (ISO, Geneva 2005)
- 3.55 ISO: *ISO 6507-2, Metallic Materials – Vickers Hardness Test – Part 2: Verification and Calibration of Testing Machines* (ISO, Geneva 2005)
- 3.56 ISO: *ISO 148-1, Metallic Materials – Charpy Pendulum Impact Test – Part 1: Test Method* (ISO, Geneva 2009)
- 3.57 ISO: *ISO 148-2, Metallic Materials – Charpy Pendulum Impact Test – Part 2: Verification of Testing Machines* (ISO, Geneva 2008)
- 3.58 ISO: *ISO 148-3, Metallic Materials – Charpy Pendulum Impact Test – Part 3: Preparation and Characterization of Charpy V-Notch Test Pieces for Indirect Verification of Pendulum Impact Machines* (ISO, Geneva 2008)
- 3.59 ISO: *ISO Guide 35, Reference Materials – General and Statistical Principles for Certification* (ISO, Geneva 2006)
- 3.60 ISO: *ISO 6892-1, Metallic Materials – Tensile Testing – Part 1: Method of Test at Room Temperature* (ISO, Geneva 2009)
- 3.61 ISO: *ISO 5725-6, Accuracy (Trueness and Precision) of Measurement Methods and Results – Part 6: Use in Practice of Accuracy Values (ISO 5725-6:1994 Including Technical Corrigendum 1:2001)* (ISO, Geneva 2002)
- 3.62 ISO: *ISO/IEC Guide 98-3, Uncertainty of Measurement – Part 3: Guide to the Expression of Uncertainty in Measurement (GUM:1995)* (ISO, Geneva 2008)
- 3.63 JCGM 200: *International Vocabulary of Metrology – Basic and General Concepts and Associated Terms (VIM)* (JCGM, 2008), <http://www.bipm.org/en/publications/guides/vim.html> (identical to ISO Guide 99:2007, VIM, 3rd edn.) (last accessed 14 April 2011)
- 3.64 EUROLAB Position Paper No. 1/2007: Reference laboratories in the field of testing (March 2007) http://www.eurolab.org/pub/i_pub.html (last accessed 14 April 2011)
- 3.65 A. Ono, T. Baba, K. Fujii: Traceable measurements and data of thermophysical properties for solid materials: A review, *Meas. Sci. Technol.* **12**, 2023–2030 (2001), (last accessed 14 April 2011)
- 3.66 ISO: *ISO 14192, Gas Analysis – Conversion of Gas Mixture Composition Data* (ISO, Geneva 1998), (last accessed 14 April 2011)
- 3.67 EURAMET: *EURAMET Guide, Metrology in Short*, 3rd edn. (EURAMET, 2008), <http://www.euramet.org/index.php?id=mis> (last accessed 14 April 2011)
- 3.68 ISO: *ISO 15195, Clinical Laboratory Medicine – Requirements for Reference Measurement Laboratories* (ISO, Geneva 2003)
- 3.69 JCGM 101: Evaluation of measurement data – Supplement 1 to the “Guide to the expression of uncertainty in measurement”, Propagation of distributions using a Monte Carlo method (JCGM, 2008) <http://www.bipm.org/en/publications/guides/gum.html> (last accessed 14 April 2011)
- 3.70 IUPAC: *IUPAC Compendium of Chemical Terminology ('Gold Book')*, 2nd edn. (IUPAC, 1997), <http://www.iupac.org/indexes/books> (last accessed 14 April 2011)
- 3.71 JCGM 100: Evaluation of measurement data – Guide to the expression of uncertainty in measurement (JCGM, 2008) (identical to ISO/IEC Guide 98-3:2008 Uncertainty of measurement – Part 3: Guide to the expression of uncertainty in

- measurement (GUM:1995)) <http://www.bipm.org/en/publications/guides/gum.html> (last accessed 14 April 2011)
- 3.72 International Measurement Evaluation Programme (IMEP) http://irmm.jrc.ec.europa.eu/html/interlaboratory_comparisons/imep/index.htm (last accessed 14 April 2011)
- 3.73 ISO: *ISO 78-2 Chemistry – Layout for Standards – Methods of Chemical Analysis* (ISO, Geneva 1999)
- 3.74 BAM Federal Institute for Materials Research and Testing (Berlin): Catalogue of Reference Procedures <http://www.bam.de/en/fachthemen/referenzverfahren/index.htm> (contact person: M. Hedrich, BAM) (last accessed 14 April 2011)
- 3.75 BIPM: Key comparison database – Appendix B (Key and supplementary comparisons) <http://kcdb.bipm.org/> (contact person: C. Thomas, BIPM) (last accessed 14 April 2011)
- 3.76 BIPM: Key comparison database – Appendix C (Calibration and measurement capabilities) <http://kcdb.bipm.org/> (contact person: C. Thomas, BIPM) (last accessed 14 April 2011)
- 3.77 Versailles Project on Advanced Materials and Standards (VAMAS): <http://www.vamas.org/> (chair person: G. Sims, NPL)
- 3.78 CIPM: 97th Meeting 2008, Report of the CIPM ad hoc Working Group on Materials Metrology (WGMM), CIPM/08-WGMM “Evolving Need for Metrology in Material Property Measurements” <http://www.bipm.org/en/committees/cipm/>
- 3.79 S. Bennett, J. Valdés: *Materials metrology*, *Metrologia* **47**(2), S1–S193 (2010), Special edition on Materials metrology

Chemical Part B

Part B Chemical and Microstructural Analysis

4 Analytical Chemistry

Willie E. May, Gaithersburg, USA
Richard R. Cavanagh, Gaithersburg, USA
Gregory C. Turk, Gaithersburg, USA
Michael Winchester, Gaithersburg, USA
John Travis, Gaithersburg, USA
Melody V. Smith, Gaithersburg, USA
Paul DeRose, Gaithersburg, USA
Steven J. Choquette, Gaithersburg, USA
Gary W. Kramer, Gaithersburg, USA
John R. Sieber, Gaithersburg, USA
Robert R. Greenberg, Gaithersburg, USA
Richard Lindstrom, Gaithersburg, USA
George Lamaze, Gaithersburg, USA
Rolf Zeisler, Gaithersburg, USA
Michele Schantz, Gaithersburg, USA
Lane Sander, Gaithersburg, USA
Karen W. Phinney, Gaithersburg, USA
Michael Welch, Gaithersburg, USA
Thomas Vetter, Gaithersburg, USA
Kenneth W. Pratt, Gaithersburg, USA
John H. J. Scott, Gaithersburg, USA
John Small, Gaithersburg, USA
Scott Wight, Gaithersburg, USA
Stephan J. Stranick, Gaithersburg, USA
Ralf Matschat, Berlin, Germany
Peter Reich, Berlin, Germany

5 Nanoscopic Architecture and Microstructure

Koji Maeda, Tokyo, Japan
Hiroshi Mizubayashi, Tsukuba, Japan

6 Surface and Interface Characterization

Martin Seah, Teddington, UK
Leonardo De Chiffre, Kgs. Lyngby, Denmark

Analytical Chemistry

Measurements of the chemical compositions of materials and the levels of certain substances in them are vital when assessing and improving public health, safety and the environment, are necessary to ensure trade equity, and are required when monitoring and improving industrial products and services. Chemical measurements play a crucial role in most areas of the economy, including healthcare, food and nutrition, agriculture, environmental technologies, chemicals and materials, instrumentation, electronics, forensics, energy, and transportation.

This chapter presents a broad overview of the analytical techniques that can be used to perform the *higher order chemical characterization of materials*. Techniques covered include mass spectrometry, molecular spectrometry, atomic spectrometry, nuclear analytical methods, chromatographic methods and classical chemical methods.

For each technique, information is provided on the principle(s) of operation, the scope of the technique, the nature of the sample that can be used, qualitative analysis, traceable quantitative analysis, and key references. Examples of representative data are provided for each technique, where possible.

4.1	Bulk Chemical Characterization	145
4.1.1	Mass Spectrometry	145
4.1.2	Molecular Spectrometry.....	147

4.1 Bulk Chemical Characterization

4.1.1 Mass Spectrometry

Inductively Coupled Plasma Mass Spectrometry (ICP-MS)

Principles of the Technique. The inductively coupled plasma (ICP) associated with this technique is an atmospheric-pressure argon plasma that is produced

4.1.3	Atomic Spectrometry.....	156
4.1.4	Nuclear Analytical Methods	161
4.1.5	Chromatographic Methods	168
4.1.6	Classical Chemical Methods.....	173
4.2	Microanalytical Chemical Characterization	179
4.2.1	Analytical Electron Microscopy (AEM)	179
4.2.2	Electron Probe X-ray Microanalysis .	180
4.2.3	Scanning Auger Electron Microscopy	183
4.2.4	Environmental Scanning Electron Microscope	185
4.2.5	Infrared and Raman Microanalysis .	186
4.3	Inorganic Analytical Chemistry: Short Surveys of Analytical Bulk Methods	189
4.3.1	Inorganic Mass Spectrometry	190
4.3.2	Optical Atomic Spectrometry	192
4.3.3	X-ray Fluorescence Spectrometry (XRF).....	192
4.3.4	Neutron Activation Analysis (NAA) and Photon Activation Analysis (PAA)	194
4.4	Compound and Molecular Specific Analysis: Short Surveys of Analytical Methods	195
4.5	National Primary Standards – An Example to Establish Metrological Traceability in Elemental Analysis	198
	References	199

in a quartz torch connected to a radiofrequency (RF) generator. Operating RF powers are typically between 1000 and 1500 W. The aqueous liquid sample solution is injected as an aerosol into the axial channel of the ICP, where temperatures on the order of 7000 K prevail. Here the sample is decomposed into its constituent elements, which are ionized. The ions are differentially

pumped into a mass spectrometer (MS) through a sampling cone and skimmer. The relative ion count rates are used to gauge the relative concentrations of the elements in the sample. The most common instruments use quadrupole mass spectrometers with unit mass resolution capabilities. Higher resolution magnetic sector mass spectrometers are also available.

Scope. ICP-MS is used primarily for quantitative elemental analysis, in other words to determine the concentrations of specific elements in a sample. It is also used to measure elemental isotope ratios. It is roughly 1000 times more sensitive than ICP-atomic emission spectrometry (AES), making it very suitable for trace metal analysis at ng/g and even pg/g solution concentrations. It is widely used in the semiconductor industry to test high-purity production chemicals. It is also heavily used for the environmental monitoring of water and soil samples. ICP-MS is used in geological studies, including isotope ratio studies.

Nature of the Sample. In the most common situations, samples are introduced into the ICP as solutions. If the sample being analyzed is a solid, it must first be dissolved. This typically involves dissolving a 0.1 g sample in 100 mL of acidified aqueous solution. Dissolving most samples will require hot concentrated mineral acids.

An alternative sample introduction system uses laser ablation of solid samples to generate an aerosol of sample particles, which can be injected directly into the ICP.

Qualitative Analysis. Specific elements are identified based on the known mass/charge ratios and isotopic patterns of the elements.

Traceable Quantitative Analysis. For systems using solution sample introduction, the ICP-MS instrumentation must be calibrated using solutions containing known concentrations of the analyte elements. Such calibration solutions are available from many commercial suppliers. These solutions are often traceable to one of a set of NIST single-element solution standard reference materials. The analysis of complex samples can be susceptible to matrix effects (the combined effect that all of the species present in the sample have on the mass spectrometric signal of the analyte). This will lead to measurement bias if the calibration solutions are not matched to the matrix of the sample being analyzed. The method of standard additions is an effective

strategy for dealing with matrix effects. Use of an internal standard will also reduce susceptibility to matrix interferences.

For high-accuracy work, quantitation can also be accomplished through isotope dilution. In this procedure the isotope ratio of a pair of analyte isotopes is perturbed by spiking the sample with a known amount of a solution that is enriched in the concentration of an isotope of the element that is naturally not very abundant. The degree of perturbation of the isotope ratio depends on the concentration of the analyte element present in the sample before being spiked, and the concentration can be calculated by measuring the perturbed isotope ratio.

Isobaric interferences occur when two or more ionic species with nominally the same mass-to-charge ratio are present in the ICP. The argon plasma is the source of the most severe of these interferences. For example, ^{40}Ar interferes with ^{40}Ca , and $^{40}\text{Ar}^{16}\text{O}$ interferes with ^{56}Fe in quadrupole systems. The latter example can be resolved with high-resolution systems.

Calibration of systems using sample introduction based on laser ablation is more difficult. The laser ablation process is very matrix-dependent, and calibration requires the use of solid standards that match the characteristics of the sample quite closely.

Certified reference materials are available in a wide variety of sample matrix types from NIST and other sources. These CRMs should be used to validate ICP-MS methods.

Glow Discharge Mass Spectrometry (GD-MS)

Principles of the Technique. A glow discharge is a reduced-pressure, inert gas plasma maintained between two electrodes. Argon is typically used at absolute pressures of a few hundred Pascals or less, and the solid sample serves as the cathode in the circuit. When the discharge is ignited, Ar^+ ions formed in the plasma are accelerated toward the sample surface by means of electrical fields. A substantial fraction of these Ar^+ ions strike the surface of the sample with enough kinetic energy to eject sample atoms from the surface. In this way, the solid sample is directly atomized. Once in the plasma, sputtered atoms may be ionized through collisions with metastable Ar atoms (Penning ionization) or energetic electrons (electron impact ionization). The ions generated are extracted from the plasma and directed into a mass analyzer with one or more detectors. The ions are separated and detected according to the mass-to-charge (m/z) ratios, resulting in a glow discharge mass spectrum.

GD-MS instruments usually employ quadrupole or double-focusing magnetic sector mass analyzers, although other types have also been reported (such as time-of-flight (TOF), ion cyclotron resonance (ICR), and ion traps). To date, there has only been one commercial GD-MS instrument that can truly be said to have been successful in the marketplace. This is the VG-9000 double-focusing glow discharge mass spectrometer (Thermo Elemental, Cambridge, United Kingdom), costing more than \$500 000 (To describe experimental procedures adequately, it is occasionally necessary to identify commercial products by manufacturer's name or labels. In no instance does such identification imply endorsement by the National Institute of Standards and Technology, nor does it imply that the particular products or equipment are necessarily the best available for that purpose). The number of VG-9000 instruments in use around the world is probably somewhere between 40 and 60. Some other double-focusing instruments, as well as quadrupole instruments, often custom-built by the user, are also employed.

Scope. Glow discharge devices used in GD-MS may be powered by either a direct-current (DC) or radiofrequency (RF) power supply. In DC-GD-MS, the sample must be electrically conductive, since current must pass through it. Therefore, DC-GD-MS is applicable to conductive bulk samples. In principle, the technique is also applicable to samples consisting of conductive layered materials (such as thin films on surfaces). In such a case, registration of ion intensities as surface layers are sputtered away results in a *depth profile* of the sample. However, very little work in this area has been reported so far. RF-GD-MS overcomes the restriction to conductive sample types, because in this configuration it is not necessary for net current to flow through the sample. As a result, RF-GD-MS can be applied to electrically insulating bulk solids and coated surfaces with insulating substrates and/or layers.

The greatest strengths of GD-MS, whether DC or RF, are the high sensitivities and low limits of detection available (sub- to low ng/g range directly in the solid state). Owing to these characteristics, the technique has been most widely applied for purity assessments of highly-pure, solid materials, such as those used in the semiconductor industry. The ability to detect H, O and N is also advantageous for this application. Isobaric interferences are not generally problematic in GD-MS, unless low-resolution mass analyzers (such as quadrupoles, which have only unit resolution) are used.

Disadvantages of GD-MS include the fact that matrix effects, while relatively mild compared to many other direct solid techniques, are nonetheless present. Matrix effects manifest themselves mainly as overall sputtering rates that vary from matrix to matrix. Fortunately, even though this is true, once sputtering has reached *steady state* for a given sample, the relative fluxes of sputtered atoms accurately reflects the stoichiometry of that sample. Another disadvantage of GD-MS is that it is inherently a *relative* technique, requiring reference materials for calibration. Unfortunately, reference materials with certified values in the mass fraction range of greatest interest (< 1 mg/g) are rare. As a result, GD-MS calibration can only be accomplished to the degree allowed by available reference materials.

Nature of the Sample. As noted above, samples amenable to GD-MS analysis include bulk solids and layered surfaces. Bulk solids are often machined into pins for analysis, although flat samples can also be employed.

Qualitative Analysis. Calibration of a GD-MS instrument consists of measuring relative sensitivity factors (RSFs) for the analytes. RSFs are generated by measuring the signal levels for suitable reference materials. When suitable reference materials are lacking, GD-MS cannot be calibrated, resulting in qualitative analysis. Nonetheless, given the very low limits of detection, the technique finds much use in this mode.

Traceable Quantitative Analysis. Quantitative GD-MS analysis (with accuracies in the range of $\pm 30\%$ relative, for example) is performed by employing RSFs generated from matrix-matched reference materials. If RSFs must be developed from non-matrix-matched reference materials, then GD-MS becomes a semiquantitative technique (giving accuracies within a factor of 2 for example). In either case, the calibrants constitute the traceability link to the SI.

Several review articles [4.1–8] are available.

4.1.2 Molecular Spectrometry

Traceability in UV/Vis Molecular Absorption Spectrometry

Principles of the Technique. Molecular absorption spectrometry in the ultraviolet and visible spectral region, often simply known as UV/Vis, is one of the oldest and most mature instrumental methods of chem-

ical analysis, with the development of photoelectric detection spectrophotometers dating from the 1920s. Numerous books and review articles have been written on the instrumentation and applications of this mature technology. The present treatment will thus only touch on the bare essentials of the technology as they relate to the subject of assuring traceable measurements at levels of measurement uncertainty that are appropriate to the application, or *fit for purpose*.

The basic measurement of molecular absorption spectrometry is the *absorbance* (A) of a sample, defined as

$$A(\lambda) = \log \frac{I_0(\lambda)}{I(\lambda)}, \quad (4.1)$$

where the numerator of the logarithmic argument is the intensity of light incident on the sample centered at a given wavelength (λ), and the denominator is the reduced intensity of the same distribution as it exits the far side of the absorbing sample. In chemical applications, the sample would normally be a solution containing one or more species that absorb UV/Vis radiation, and the intensity measurements may be made in such a way as to compensate for reflective losses at the faces of the cell containing the solution.

Scope. A plot of A as a function of λ for a known concentration of a neat compound in a transparent solvent, the *absorbance spectrum*, is characteristic of the compound (and sometimes the solvent), and may be employed for qualitative and quantitative analysis. Compounds are frequently characterized by the wavelength and *absorptivity* (absorbance per unit concentration and path length) of the major absorbance bands in the spectrum. Mixtures of absorbing compounds are subject to spectral interference errors during quantitation, since the absorbance bands tend to be relatively broad. Separations and other chemical methods used to avoid these errors are beyond the scope of this article.

Nature of the Sample. The main sample requirement for UV/Vis analyses is at least partial transparency to optical radiation in the range between 200 and 700 nm. Homogeneous, clear solutions are the most usual sample formats for UV/Vis analyses, but there is no requirement that such solutions be liquid, as glasses, polymer mixtures and thin film materials on transparent substrates are also commonly measured. Samples containing dispersed particulates are troublesome for UV/Vis measurements due to photometric errors gen-

erated by reflectance and scattering of the incident light by the particles.

Qualitative Analysis. UV/Vis can be used qualitatively to determine the presence or absence of components in a sample; however, the broad absorbance bands of most samples often limit the utility of this approach. The UV/Vis spectrum of a material combined with its luminescence and reflectance spectra determine the color appearance of the material. This aspect of optical spectroscopy, often referred to as color science, has tremendous commercial utility and implications and has evolved into a nearly separate field from optical spectrometry, which is primarily devoted to the quantitation of materials based on their optical spectra.

Traceable Quantitative Analysis. Most absorbance standards and many UV/Vis *methods* specify wavelength accuracy on the order of ± 1 nm. Rare earth elements in solution or in glass provide sharp absorbance bands appropriate to wavelength standardization, and these are available in a sample geometry that is compatible with the most common chemical sample holder. Traceability of these standards to the meter may derive from the intrinsic properties of the absorbing species in the stated matrix, documented along with all the required uncertainty analysis, or by individual or batch calibration or certification of the artifact by a standards-producing organization.

Because the absorbance scale is based on the ratio of two intensities (4.1), accuracy requires that the combination of the wavelength-selection device and the photoelectric detector yield a signal S that is directly proportional to the light intensity I . Instead, allowing for a background B and an intensity-dependent proportionality between signal and intensity $k(I)$ we may have

$$\frac{S_0}{S} = \frac{k(I_0)I_0 + B}{k(I)I + B}. \quad (4.2)$$

Equation (4.2) may be seen to reduce to the desired ratio I_0/I in the special case for which there is no dark current or stray radiant energy (SRE) ($B = 0$) and for which the proportionality between the light intensity and the detector signal is constant $k(I) = k(I_0) = \text{constant}$. Most research-grade spectrophotometers are designed to render these bias sources negligible over the useful analytical range $0 \leq A \leq 3$, and are frequently employed as *transfer spectrophotometers* to provide absorbance calibrations or absorbance-certified reference materials with traceability to a *reference spectrophoto-*

tometer maintained by a National Metrology Institute (NMI) such as the National Institute of Standards and Technology (NIST) in the USA. Utility instruments used for routine measurement may also exhibit negligible bias, but calibrated or certified artifact standards are typically run periodically to verify the accuracy of the instrument and to provide a record for quality management or regulatory purposes.

An extensive treatment of the history and development of reference materials for spectrophotometry, as well as current recommendations, has been given in the 50th anniversary publication of the UV Spectrometry Group (UVSG) of the United Kingdom. While NMIs may be credited with designing and distributing spectrophotometric certified reference materials (CRMs) for many years, current trends in fit-for-purpose quality management and multinational commerce favor a more distributed model. The infrastructure for leveraging the production of CRMs into the private sector is supported by the concept of *traceability* as defined by the International Organization for Standardization (ISO) and endorsed by NIST and other NMIs. Producers of CRMs may assert traceability by rigorous documentation of adherence to the requirement of *an unbroken chain of comparisons, all having stated uncertainties* relating the certified values to *stated references*.

ISO Guide 34 provides a detailed framework for the production of CRMs. The accreditation of a laboratory to this guide for the production of specified CRMs is recognized by ISO as a necessary and sufficient condition for the assertion of traceability of the certified values for those materials. Similarly, ISO Guide 17025 confers the mantle of traceability on absorbance and wavelength calibration measurements on customer-furnished artifact samples.

Fluorescence/Phosphorescence Spectroscopy

Principles of the Technique. Fluorescence/phosphorescence spectroscopy is the study of UV, visible and near infrared (NIR) light that is emitted by a chemical species after it has absorbed light. This absorption of light puts the species into an electronically excited state. The emission wavelengths are usually longer or less energetic than the excitation wavelength. A fluorescence spectrometer or fluorometer is the instrument that is used to measure the intensity of emitted light, or emission, as a function of wavelength. Fluorescence and phosphorescence are the two types of emission activated by light absorption. Fluorescence has a short lifetime (typically 1–10 ns) and usually arises from an *allowed* transition from an excited singlet state to the ground

electronic state. Phosphorescence has a long lifetime (typically 1 ms–1 s) and usually arises from a *forbidden* transition from an excited triplet state to the ground electronic state. Emission with lifetimes that fall in the range from hundreds of nanoseconds to hundreds of microseconds is not uncommon and may possess characteristics of both fluorescence and phosphorescence. Fluorescence is almost always more intense than phosphorescence, under similar conditions. For the sake of simplicity and space, fluorescence detection will be discussed exclusively in what follows, but much of this discussion also applies to phosphorescence.

Scope and Qualitative Analysis. Fluorescence spectroscopy is a *background-free* technique, meaning that the measured signal should be equal to zero (the lower bound for the signal) if the sample does not fluoresce. The upper bound for the signal is not well-defined, making it very difficult to express fluorescence intensity on a scale that is independent of instrument geometry and excitation intensity (fluorescence intensity is dependent upon the excitation intensity, the absorption coefficient, concentration, quantum yield, and geometry of the sample, the instrument geometry, and the response of the detection system). This is quite different from absorption spectrophotometry, for instance, where the transmittance is measured as the ratio of the light intensity transmitted by the sample versus the light intensity incident upon the sample, the latter intensity being the upper limit. Because of this difficulty in defining the fluorescence intensity scale, few have attempted to compare fluorescence intensities measured by different instruments or even by the same instrument over long periods of time. For most of its history, fluorescence spectroscopy has mainly been used to determine whether or not a particular species is present in an unknown sample. When this technique has been used to quantitate amounts of analyte, it has been done using a calibration curve of fluorescence intensity versus concentration, which is only useful for measuring the particular analyte on the particular instrument on which the curve was obtained. Only in recent years has the need to compare fluorescence intensities and spectral contours taken at different times or on different instruments become crucial in order to ensure compliance with quality and regulatory standards in many key areas where fluorescence detection is used.

Fluorescent species have been detected at low concentrations since the first commercial fluorometers were produced in the 1950s. The high sensitivity of fluorescence detection enables nanomolar concen-

trations of fluorophores to be detected routinely and single molecules to be detected with more difficulty. In the past, fluorometry was primarily viewed as a research technique due to the fact that few naturally occurring compounds fluoresce. This view has changed dramatically over the past 10–15 years due to the synthesis of a long list of fluorescent probes, which have been tailored to bond to an equally large and varied number of analytes. This development has caused fluorescence to become a highly selective detection technique, thereby expanding its scope of use into a broad range of commercial applications. The powerful combination of sensitivity and selectivity of fluorescence-based measurements has fueled the dramatic growth in biotechnology and drug discovery in recent years. Fluorescence detection was used to map the human genome, and is being used to map proteins and the genes of viruses and living organisms. It is also being used by pharmaceutical companies to single out promising drug *leads* in combinatorial chemistry libraries of compounds using microwell plates and microarrays, and in clinical diagnostics to count relative populations of diseased or drug-responsive cells using flow cytometry. In addition, fluorescence detection has important applications in environmental monitoring, where it is used to detect contaminants such as polycyclic aromatic hydrocarbons (PAHs).

Nature of the Sample. The conventional fluorometer is a benchtop instrument with a light source (such as a Xe lamp) and wavelength selector for excitation before the sample, a sample compartment with a mount to hold the sample in the path of the excitation light, and a wavelength selector and detector for emission after the sample. The wavelength selector is usually a monochromator with a range from 200 to 800 nm. Fluorescence from liquid samples is measured at a 90° angle relative to the excitation beam using a rectangular cuvette that holds 3 to 4 mL. Fluorescence from solid samples is typically collected from the same side of the sample as the excitation beam at an angle of 90° or less with respect to the excitation beam. Portable fluorometers are becoming more popular due to their low cost and ease of use in the field. They commonly use a grating to disperse fluorescence onto a linear, charge-coupled device (CCD) array detector, and a fiber optic is often used to both deliver excitation light to and collect fluorescence from the sample. Portable fluorometers have a broad emission range from 200 to 1100 nm, but use a lamp, light-emitting diode (LED) or diode laser with-

out a wavelength selection device for excitation. They are less sensitive and have lower spectral resolutions than benchtop instruments. High-throughput fluorometers – microwell and microarray readers – are designed to measure a large number of samples in a short period of time. Typical sample densities are 1536 wells on a 12.8 cm (L) × 8.5 cm (W) microwell plate and 40 000 spots on a 7.5 cm (L) × 2.5 cm (W) microarray chip. A lamp with a bandpass filter and a monochromatic laser are used for excitation with microwell plate and microarray readers, respectively. Filters with a bandpass of 25 nm or more are used for wavelength selection of emission.

Traceable Quantitative Analysis. Quantitative determinations of fluorescent or fluorescently labeled species are performed most often by first making a plot of fluorescence intensity versus concentration using standard solutions of the species of interest. This plot is typically linear at low concentrations, so it can be fitted to a straight line function. The fitted function can then be used to determine the concentration of an unknown solution by measuring its fluorescence intensity, but a calibration curve of this type is only useful for the instrument on which it was obtained with a fixed set of instrument parameters and for that one particular species used to obtain the curve. In addition, organic dyes, used to make standard solutions, are difficult to acquire with known purity, and their fluorescence intensity is often environment-dependent, making them less than ideal standards for quantifying fluorescent probe concentrations. As fluorescence-based assays become more and more quantitative, particularly in regulated areas such as clinical diagnostics and pharmaceutical quality assurance, it is essential for fluorescence intensities to be comparable between different instruments and laboratories. This requires fluorometers to be rigorously calibrated.

Fluorometers with a wavelength selection device, such as a monochromator, should first be calibrated for wavelength and bandwidth accuracy for emission and excitation. Then, the fluorescence intensity should be calibrated as a function of emission and/or excitation wavelength, depending on whether the intensity is being measured as a function of one or both wavelength axes. Wavelength and bandwidth accuracy are most commonly calibrated using atomic lamps at the sample and/or source positions. The Raman line of water with a Stokes shift of 3382 cm⁻¹ can also be used to calibrate one wavelength axis if the other has already been calibrated.

The fluorescence intensity as a function of wavelength, or the spectral emissivity, can be calibrated relatively (calibrated for spectral shape) or absolutely (calibrated for both shape and absolute intensity). Relative intensity can be calibrated as a function of emission or excitation wavelength using a calibrated light source or a calibrated detector at the sample position, respectively. An absolute calibration is usually done in one of two ways: either by using a calibrated detector at the sample position followed by a calibrated reflector at the sample position, or by using a calibrated light source at the sample position followed by a calibrated reflector at the sample position. The absolute calibration yields a correction factor for intensity as a function of wavelength that enables the bispectral luminescence radiance factor (BLRF) of a fluorescent sample to be determined from its measured fluorescence spectrum. The BLRF is defined as the ratio of the radiance of the fluorescence of a sample versus the excitation irradiance incident on the sample, and is a function of both the excitation and emission wavelengths. A fluorescence spectrum or intensity that is expressed in BLRFs is termed *absolute* because it is not instrument-dependent, only sample-dependent. Material standards supplied with certified values for relative intensity, or better still BLRFs, would greatly simplify the calibration process, enabling non-experts to calibrate their fluorometers with greater ease and at less expense. Several national metrology institutes are developing certified reference materials of this type, but at present, SRM 936a quinine sulfate dihydrate, a relative intensity standard that effectively covers the emission region from 390 to 590 nm, is the only such standard that is commercially available.

Raman Spectroscopy

Principles of the Technique. The Raman effect occurs when a sample is irradiated with intense monochromatic light, usually from a laser. The resulting inelastically scattered light is shifted in frequency due to interactions with the vibrational modes of the chemical sample. Although similar in principle to infrared spectroscopy, quantum mechanical selection rules choose only those vibrational modes that cause the polarizability of the chemical bond to become Raman active. The effectiveness of the bond toward scattering is directly dependent upon the polarizability; polarizability decreases as the electron density increases or the length of the bond decreases. As a result, symmetric vibrational bond stretches are typically Raman active.

The sample to be measured is illuminated with a laser and the resulting scattered light measured with

a spectrometer. Raman spectrometers can be either grating or Fourier transform instruments. Because the scattering is very inefficient, typically less than one photon in 10^6 , very efficient filters are required to separate the laser scatter from the Raman spectrum. The invention of holographic notch filters allowed rejection ratios as great as 10^{12} and enabled the use of optically efficient spectrometers coupled with high quantum efficiency detectors. The net result is that Raman spectroscopy, once a strictly academic technique requiring room-filling instrumentation, is now a real-time, suitcase-portable analytical technique.

Scope and Nature of the Sample. Raman spectroscopy is applicable to gases, liquid, and solid samples, and instruments accommodating microsamples as well as bulk chemical samples have been developed. Because the lasers typically used are visible and diode-based, fiber optic sampling is becoming more common and this is facilitating its use in routine qualitative spectroscopy in nontraditional locations. An example is its use on loading docks at pharmaceutical companies to assure the identity of incoming materials. Raman spectroscopy is predominantly a qualitative technique. That is, many applications capitalize on the unique spectrum that each compound or class of compounds exhibits. It is suitable for the identification of both organic and inorganic materials.

Raman spectroscopy's strengths are that it is non-destructive and requires very minimal, if any, sample preparation. It is also rapid, as the spectra of neat compounds can be acquired in seconds. Water has very weak Raman scatter. Aqueous samples are measurable using Raman in contrast to IR spectroscopy, where water is a major interference. An additional advantage of the technique (over IR) is that very low wavenumber vibrational modes are easily measured. Typical commercial analytical systems allow measurement to 150 cm^{-1} , and some as low as 4 cm^{-1} . IR, in contrast, is limited to at best 500 cm^{-1} . The low-frequency region provides detailed information about crystal structure and is becoming commonly used in the pharmaceutical industry for polymorph characterization.

Raman spectroscopy's weakness is that it is an emission measurement (single beam), and as a result the spectra are highly instrument-dependent. The resulting spectrum is a convolution of the instrument response (due to laser color, optical geometry, fiber optic sampling, and other factors), the scattering characteristics of the sample, and the *true* Raman spectrum of the compound. Because of the complexities of this convolution,

all libraries of Raman spectra today are instrument-dependent. Unfortunately, interpreting Raman spectra from first principles is often difficult for the nonspecialist. In addition, Raman spectroscopy is not a trace quantitative analytical technique. For even strongly scattering samples, such as benzene, quantitation of less than 1% by mass of an analyte is difficult. This is due to the noise characteristics of the measurement and also interference. If a sample or its matrix should fluoresce, this *noise* is several orders of magnitude greater than the Raman signal and may make the measurement impossible. This can be alleviated, in part, by switching to longer wavelength lasers, but at the expense of sensitivity. It should be noted though that microscope-based Raman techniques allow the identification of very small quantities of neat materials. Nanogram quantities of organics can be routinely measured, and submonolayer coverage of chemical vapor deposited (CVD) diamond on silicon is a routine measurement for semiconductor manufacturers.

Qualitative Analysis. Raman spectroscopy is primarily a qualitative technique, useful for identifying compounds by their unique spectral features. Unlike infrared spectroscopy, not many Raman libraries exist due to the instrument-dependent response mentioned previously. Those that have been developed are typically useable at a single excitation wavelength, which to date are predominately Fourier transform (FT) Raman systems operating at 1064 nm. NIST is producing a set of artifact standards that will correct the relative intensity axis of Raman spectrometers operating with a variety of commercially important laser excitation wavelengths.

This will enable the production of instrument-corrected libraries, allowing their use on differing systems.

Traceable Quantitative Analysis. Quantitative analysis by Raman spectroscopy is a growing practice, but still rare compared to its use for qualitative analysis. Similar to absorbance-based techniques, the Raman emission scattering from a vibrational mode is proportional to the concentration of the analyte. Standard addition and internal standard techniques have been used for quantitative analysis. Recently, however, the use of multivariate statistical techniques is becoming more common for quantitative work with Raman. This method uses a series of spectra of known analyte concentrations to *train* a calibration model. The spectrum of an unknown sample is then compared to the training set utilizing a variety of regression-based statistical techniques. Because the full spectrum of the analyte may be used, high precision – and in some cases lower limits of quantitation – may be obtained with these methods than with similar univariate (Beer's law) type calibrations.

Example Spectrum. A Raman spectrum of cyclohexane is shown in Fig. 4.1. The *x*-axis is in Raman shift units, expressed as the difference between the absolute wavenumber frequency of the band and the excitation laser. This practice is observed to make the spectra appear similar to infrared spectra. The upper spectrum was acquired using 785 nm laser excitation and is uncorrected for instrument response. The lower spectrum is corrected for instrument response. As can be seen, the C–H stretching region (3300 to 2600 cm^{-1}) is greatly affected by the system response.

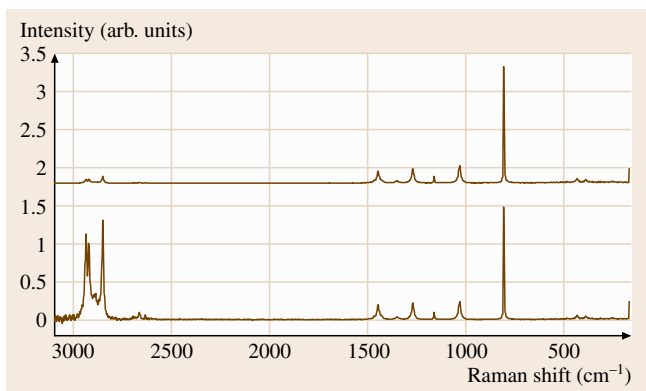


Fig. 4.1 Raman spectroscopy. *Upper:* Raman spectrum of cyclohexane uncorrected for instrument response; *lower:* Raman spectrum of cyclohexane corrected for instrument response

Infrared Spectroscopy

Principles of the Technique. The infrared (IR) region of the spectrum spans from approximately 750 nm to 300 μm , or in wavenumbers roughly from 13 000 to 33 cm^{-1} . Radiation is absorbed in this spectral region when its frequency matches a vibrational mode of the chemical sample. Quantum mechanical selection rules dictate that only those modes of the molecule that undergo a change in dipole moment will absorb in the infrared. Vibrational modes of homonuclear and/or linear molecules such as Cl_2 or N_2 do not show a net change in charge distribution and thus are not IR-absorbing. Molecules that contain heteroatomic substituents or have nonsymmetric vibrational modes are IR active due to the net charge density change. Carbonyl groups are an example.

In IR spectroscopy the sample to be measured is illuminated with a broadband IR source. The resulting IR spectrum is measured with an IR spectrometer. These spectrometers may be either grating-based or Fourier transform (FT) instruments, although in the last ten years FT instruments have all but replaced the dispersive systems due to their many advantages (speed, sensitivity, signal-to-noise ratio, and cost). As the IR range spans a very large wavelength/wavenumber range, material constraints of the optics comprising the spectrometer, such as the beam splitter, detector sensitivity, and so on, limit the range of typical IR spectrometers from 6000 to 660 cm^{-1} . This is not viewed as a major limitation, as this range covers the entire fundamental vibrational mode space for most organic molecules.

Scope and Nature of the Sample. Infrared spectroscopy is applicable to gases, liquids and solid samples. Instruments accommodating microsamples as well as bulk chemical samples have been developed. With the advent of 2-D focal plane detectors, chemical mapping is becoming more widespread. Compositional mapping has applications in analytical chemistry and in health-related areas such as pathology and forensics.

The technique's strengths are many. It is highly sensitive due to the nature of the absorbance, and microgram quantities of neat material are readily measured with excellent sensitivity. The instrumentation is relatively inexpensive and easily used by the non-specialist. Because the technique is absorbance-based (based on a transmittance ratio), all spectra look alike on all spectrometers, unlike emission techniques such as Raman spectroscopy. As a result, a large number of spectral libraries exist. Specialized IR libraries include polymers, pharmaceuticals, forensic materials, drugs, explosives, pesticides, chemical warfare agents – the list is essentially endless. In fact, several commercial libraries comprise more than 220 000 spectra. Arguably, IR is the second most useful identification technique behind mass spectrometry, with much less sample preparation required. It is, in principle, nondestructive to the sample, and has been paired with other analytical techniques to provide additional information. Examples include gas chromatography-infrared (GC-IR) and thermal gravimetric analysis-infrared (TGA-IR).

The weakness of IR spectroscopy is in fact due to the high absorptance of the vibrational modes of chemical bonds. Neat compounds will typically com-

pletely absorb portions of the IR spectrum unless the optical pathlength through the sample is kept below 100 μm . This requires the use of expensive and difficult-to-maintain optical cells, the materials of which are limited to inorganic salts (such as KBr or NaCl) or expensive semiconductor-type materials. Glass or quartz – commonly used for UV/Vis, Raman or fluorescence spectroscopy – are not appropriate as they completely absorb all IR radiation. In addition, water cannot be used as a solvent for similar reasons. Water vapor can be a significant interference, which requires a dry nitrogen purge of the spectrometer. All the above require significant time for sample preparation, and significant skill may be required of the operator.

Qualitative Analysis. IR is most commonly used to identify chemical samples, as the IR spectrum of a compound represents one of its truly unique physical properties. No two compounds have identical IR spectra, with the exception of optical isomers. As mentioned, sample dilution/preparation can be difficult for traditional transmission measurements. However, an array of new sampling techniques enable acquisition of the IR spectra of intact samples. Attenuated total reflectance utilizes the principle of frustrated total internal reflectance to control the depth of penetration into sample. One micrometer sample pathlengths are easily achieved and highly scattering/absorbing samples such as cloth, oil or even foods such as peanut butter are readily measured. New polytetrafluoroethylene (PTFE, teflon) polymer cards allow liquid samples to be smeared onto disposable cards for transmission measurements, eliminating the need for expensive and delicate salt windows.

Traceable Quantitative Analysis. Infrared spectroscopy may be used for quantitative analysis, but it is only infrequently used in this way compared to UV/Vis transmission measurements due to the difficulty in maintaining similar cell pathlengths for the sample and reference cells. The tolerance required would be on the order of 1 μm or less. When IR is used for quantitative analysis, typically the internal standard or standard addition methods are used to relate the sample concentration to the band area (or height). NIST produces one SRM appropriate to IR spectrometry. SRM 1921 is a wavelength calibration standard useful for both dispersive and FT instruments.

Example Spectrum. An example infrared spectrum of benzene is displayed in Fig. 4.2.

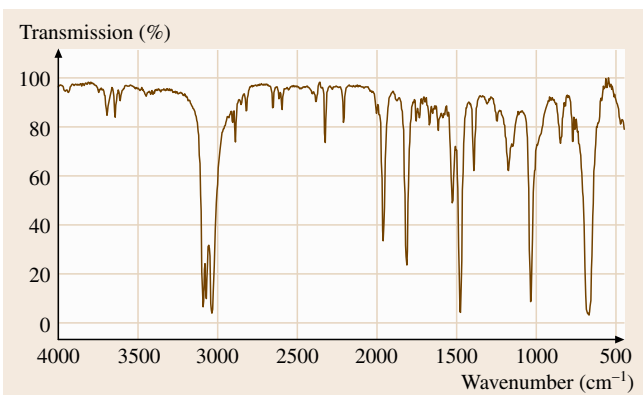


Fig. 4.2 Infrared spectroscopy: IR spectrum of benzene

Quantitative Proton Nuclear Magnetic Resonance Spectroscopy – ^1H QNMR

Principles of the Technique. When a nucleus with a nonzero spin quantum number is placed in a homogeneous external magnetic field, the spin of the nuclear charge creates a magnetic dipole that aligns itself in specific orientations with the external field. The quantum spin number of the nucleus (I) determines the number of these orientations ($2I + 1$), and the energy difference between them is $B_0 h \gamma / 2\pi$, where B_0 is the bulk magnetic field strength, h is Planck's constant, and γ is the magnetogyric ratio, a fundamental constant for each type of magnetically active nucleus. For protons (^1H), $I = \frac{1}{2}$, so there are two states with a slight population excess in the lower state. Transitions between the lower energy state and higher level state can be effected by applying radiofrequency radiation (RF) at the Larmor or resonance frequency equal to $B_0 \gamma / \pi$. At resonance, the nuclei undergoing the transition absorb energy from the RF that is detected and measured. The RF can be introduced either by continuous wave (CW) scanning (holding the bulk field constant and scanning the RF or vice versa) or by applying an RF pulse. At resonance, the magnetic dipoles not only transit from the low to the higher energy state, but also the phases of their spins synchronize (phase-up) to establish a net magnetization. When the resonance condition is removed, the nuclear spin system reverts to its thermodynamically normal state by first-order rate processes. The means by which the energy state population distribution is re-established is called the spin–lattice relaxation, with a rate constant of $1/T_1$, while the spin dephasing mechanism is called spin–spin relaxation, with a rate constant of $1/T_2$.

The magnetic environments of each of the same nuclei in a molecule are often slightly different depend-

ing on the molecular and electronic configurations, and this gives rise to slightly different resonance frequencies and forms the basis for a chemical shift scale that is very useful for identifying the structural environments of atoms in the molecule. Furthermore, the magnetic environment of a given nucleus can be influenced by that of other nearby nuclei, causing a further splitting of the energy levels depending on whether the adjacent dipoles are aligned or opposed. These splitting patterns (or couplings) are used to determine the number and type of the nearest neighbor nuclei in a molecule and their orientations. The resonance frequencies for different types of nuclei are often widely separated (megahertz apart), whereas the chemical shift range for a given nucleus is smaller (kilohertz), and the splitting differences are smaller still (hertz).

Modern NMR spectrometers use superconducting solenoids to provide the bulk magnetic field. While these instruments could be operated in the CW mode, it has proved much more efficient to operate them where the RF is provided through a brief (μs) RF pulse. This excites all of the nuclei simultaneously, and the resulting signals (the free-induction decay or FID) are collected digitally in the time domain (intensity versus time) and then converted to the frequency domain (intensity versus frequency) by Fourier transformation. The signal-to-noise ratios (S/N) of such measurements are improved by collecting and time-averaging multiple FIDs prior to Fourier transformation. The S/N improves by the square root of the number of FIDs collected, provided all of the nuclei have fully relaxed between pulses.

Scope. While there is a wide range of NMR-active nuclei, only a handful are commonly used. Fortunately, isotopes of the most common atoms in organic molecules are in this category. ^1H is the most commonly observed nucleus due to its large natural abundance and high relative sensitivity. Other commonly utilized nuclei are shown in Table 4.1.

Nature of the Sample. High-resolution NMR spectra are most commonly collected from liquid samples or materials in solution. Sample sizes range from micrograms to hundreds of milligrams. NMR spectra of solids can be obtained. However, special techniques involving spinning the sample very rapidly about an axis specifically oriented to the bulk field (at the *magic angle*) are necessary to narrow the lineshapes. The NMR process is nondestructive, so samples can be recovered. To avoid interferences, solvents devoid of the nuclei being ob-

Table 4.1 Properties of commonly observed NMR-active nuclei

Nucleus	Resonance at 14.09 T (MHz)	Spin number (<i>I</i>)	Natural abundance (%)	Relative sensitivity	Abundance × sensitivity
¹ H	599.944	1/2	99.984	1.000	99.984
¹⁹ F	564.511	1/2	100	0.834	83.4
³¹ P	242.862	1/2	100	0.0664	6.64
¹³ C	150.856	1/2	1.108	0.0159	0.018
²⁹ Si	119.192	-1/2	4.7	0.00785	0.037
² H	92.095	1	0.0156	0.00964	0.00015
¹⁵ N	60.815	-1/2	0.365	0.00104	0.00038

served are often employed. For ¹H NMR, deuterated solvents are commonly used. The NMR signals from the deuterium nuclei are also utilized in a separate detection channel to provide a field-frequency lock to stabilize the spectrometer, as it is necessary to maintain the field-frequency ratio to better than 1 part in 10⁹ for modern instruments. Commonly, a small amount of a standard is added along with the solvent to provide a chemical shift reference. Tetramethylsilane (TMS) is often used for this purpose in ¹H, ¹³C and ²⁹Si spectra.

Qualitative Analysis. The chemical shift differences between the various nuclei and the internuclear couplings in a molecule can be used to determine the atomic interconnections in a molecule. The number and chemical type of the observed nuclei can also be determined. Often, only a single structural configuration will fit the spectrum, making it easy to differentiate isomers. Molecular conformations and components of mixtures can also be determined. Even enantiomers can be determined if the molecule of interest interacts with a chiral solvent or another material to form a diastereomer. The direction and extent of chemical reactions can be monitored. Rates of configurational, conformational, or tautomeric interchange in molecules can be studied, providing they fall within the NMR timescale (reciprocal of chemical shift difference in Hz between the signals of the forms).

Traceable Quantitative Analysis. The area under the NMR peaks (the integrated resonance intensity of the NMR signal) is directly proportional to the concentration of the nuclei giving the resonance. If the experiment is done properly, the proportionality constant is the same for each resonance in the spectrum. Therefore, the ratio of peaks due to different materials in a sample gives the molar ratio of the materials once the peak integrals are corrected for the number of equivalent nu-

clei present for each resonance. Relative concentrations can be determined directly from the relative peak areas.

$$\frac{C_t}{C_n} = \frac{\frac{I_t}{N_t}}{\frac{I_n}{N_n}} \quad (4.3)$$

Equation (4.3) describes the determination of relative concentration by QNMR where: *C_t* = concentration of test material; *C_n* = concentration of other material; *I_t* = integral of test material signal; *N_t* = relative number of nuclei responsible for test material signal; *I_n* = integral of other material signal; *N_n* = relative number of nuclei responsible for other material signal.

If each resonance in the spectrum can be accounted for and assigned to a specific molecule, then molar purity can be determined without the need for standards, assuming, of course, that all of the impurities are observable

$$\text{mol\% } P_t = \frac{\frac{I_t}{N_t}}{\sum \frac{I_n}{N_n}} \times 100. \quad (4.4)$$

Here *P_t* = purity of the test material; *I_t* = integral of test material signal; *N_t* = relative number of nuclei responsible for test material signal; *I_n* = integral of other signals; *N_n* = relative number of nuclei responsible for other signals.

If the molecular mass of each material is known, then the molar purities can be converted into the more useful mass-based purities by multiplying each by its molecular mass and dividing by the sum of the respective masses. If this cannot be established for a given mixture, then an internal standard procedure can be utilized to determine absolute purities where a known amount of an internal standard material is added to a solution containing a measured amount of the test material.

$$\text{mass\% } P_t = \frac{I_t}{I_s} \frac{N_s}{N_t} \frac{M_t}{M_s} \frac{W_s}{W_t} P_s \times 100 \quad (4.5)$$

Here: P_t = purity of the test material; I_s = integral of standard; I_t = integral of test material; N_s = relative number of nuclei responsible for standard signal; N_t = relative number of nuclei responsible for test material signal; M_s = molecular mass of standard; M_t = molecular mass of test material; W_s = mass of standard; W_t = mass of test material; P_s = purity of standard.

Several key conditions must be met for accurate QNMR determinations. Spectral signal-to-noise ratio and resolution should be optimized. To avoid effects due to relaxation of the NMR signals, the T_1 of each nucleus in the sample should be known, and either the RF pulse width or delay time between pulses should be adjusted to ensure sufficient time for full relaxation between acquisitions. Since the frequency width covered by the RF pulse is inversely related to the pulse width, care should be taken to ensure that nuclei at the extreme ends of wide spectral widths receive similar excitation intensities. The skirts of Lorentzian-shaped NMR signals extend to infinity, so care must be taken when comparing the integrals of peaks with very different peak widths. ^1H NMR spectra are complicated by signals due to coupling of the proton signals with the 1.1% of ^{13}C nuclei naturally present in organic materials. These signals must be treated consistently – either always integrated with the main signal or always omitted. Spectra acquired at higher fields help in this regard because chemical shifts (expressed in hertz) increase in proportion to the magnitude of the bulk field, whereas coupling constants (also in hertz) remain constant. Sidebands due to modulation caused by spinning the sample tube are best avoided by obtaining the spectrum in non-spinning mode with careful shimming (adjustment of the magnetic field homogeneity) to maintain resolution. For best results, only the highest grade solvents should be used in QNMR, although a spectrum of the solvent only (blank spectrum) can sometimes be used to correct for some solvent impurities. Vigilance in sample preparation is needed to avoid adventitious interferences. Sample tubes should be cleaned, then rinsed with the NMR solvent, and dried at 140 °C overnight prior to use. All transfer tools (pipettes, spatulas, and so on) must be scrupulously clean. At no time should the sample solution come into contact with the NMR tube cap or septum, as just a single contact can result in the extraction of sufficient plasticizers, surfactants and other contaminants from these materials to render a sample useless for QNMR. Similarly, touching a pipette or syringe needle with bare hands can result in the introduction of observable squalene and other components of body oil into the sample. It is common practice to

make up the analytical solution in the NMR tube itself, as this minimizes inadvertent contamination. When this is done, and when accurate weighings are required (such as when using the internal standard method), care must be used to avoid weighing errors due to static charges on the tube. Commercially available radioactive sources can be used to minimize such static effects. Nevertheless, uncertainties in weighing are likely to dominate the error equation. The requirements and attributes of appropriate internal standard materials have been well-documented, but it should be apparent from (4.5) that the purity of the internal standard material and its uncertainty are key parameters. Finally, the NMR signals used for quantitation should be immune to chemical exchange. For ^1H NMR, this often means avoiding signals due to protons bound to oxygen and nitrogen.

With modern NMR spectrometers, optimal ^1H QNMR can be routinely carried out with detection and quantitation down to the 0.01% mass-fraction level with uncertainties (U_{95}) in the 0.5–1.0% range. In many cases, the detection and quantitation limits can be reduced by an order of magnitude by spending additional time on the data collection. High-field, state-of-the-art spectrometers with cryogenically cooled probes and preamplifiers can extend the useable detection and quantitation limits by another factor of four. While these limits do not begin to impinge on the ultimate sensitivities of other analytical techniques, such as mass spectrometry or fluorescence spectrometry, the use of QNMR for moderate trace-level determinations is on the increase. The coupling of NMR with chromatographic separation techniques further increases its utility.

Several review articles [4.9–34] are available.

4.1.3 Atomic Spectrometry

Atomic Absorption Spectrometry (AAS)

Principles of the Technique. The sample being analyzed is decomposed to free atoms and ions in a high-temperature flame or furnace. These atoms absorb light emitted at atomic resonance wavelengths from a hollow cathode discharge lamp with a cathode containing the analyte element. The optical absorbance is measured, and through Beer's law is proportional to concentration.

The most common atomizer is the premixed air-acetylene flame. Measurement of refractory elements requires the use of the hotter N_2O /acetylene flame. Better sensitivity is obtained using an electrically heated furnace referred to as an electrothermal atomizer or

graphite furnace. The longer residence time of atoms within the beam of hollow cathode emission yields improved sensitivity in comparison to flame atomizers.

Scope. AAS is used for quantitative elemental analysis, in other words for the determination of total concentrations of specific elements in a sample. It is commonly used for the analysis of environmental samples, industrial materials such as metal alloys, clinical or industrial hygiene measurements, and others. In general, flame AAS can be used for solution concentrations in the 10–100 mg/L range, and electrothermal AAS in the 1–100 µg/L range. AAS cannot be used for the determination of nonmetallic elements.

The instrumentation is generally less expensive than other forms of elemental analysis. In the vast majority of cases, only a single element can be measured at a time. The hollow cathode lamp must be changed to one of a different element before that element can be detected. Consequently, measurement times can be impractically long if multi-element information is required. Flame instrumentation requires training to use safely, and fumes must be exhausted.

Nature of the Sample. With few exceptions, samples are introduced into the flame or electrothermal atomizer as solutions. If the sample being analyzed is a solid, it must first be dissolved. A typical dissolution will dissolve a gram of sample in 100 mL of acidified aqueous solution. Dissolution of most samples will require hot concentrated mineral acids.

Qualitative Analysis. AAS is not typically used for qualitative analysis. The specificity (or identification) of the analyte element is provided by the atomic resonance wavelength emitted by the hollow cathode lamp.

Traceable Quantitative Analysis. AAS instrumentation must be calibrated using solutions containing known concentrations of the analyte element. Such calibration solutions are available from many commercial suppliers. These solutions are often traceable to one of a set of NIST single-element solution standard reference materials. Many AAS analyses are susceptible to matrix effects (the combined effect that the constituent species present in the sample have on the atomic absorption signal of the analyte). This will lead to measurement bias if the calibration solutions are not matched to the matrix of the sample being analyzed. The method of standard additions is an effective strategy for dealing with matrix effects. Another common source of bias is

broadband molecular absorption resulting from matrix elements that are not fully atomized, or scattering of the hollow cathode beam by small particles. Most instruments utilize one of several background correction procedures to deal with such interferences. Certified reference materials are available in a wide variety of sample matrix types from NIST and other sources. These CRMs should be used to validate AAS methods.

Inductively Coupled Plasma Atomic Emission Spectrometry (ICP-AES)

Principles of the Technique. The inductively coupled plasma (ICP) used in this technique is an atmospheric-pressure argon plasma that is produced in a quartz torch connected to a radiofrequency generator. Operating RF powers are typically between 1000 and 1500 W. The aqueous liquid sample solution is injected as an aerosol into the axial channel of the ICP, where temperatures on the order of 7000 K prevail. Here the sample is decomposed to free atoms and ions, and atomic or ionic emission results as thermally populated excited states of valence electrons of the atoms or ions return to lower energy levels. A suitable optical transfer system, a monochromator or polychromator, and a detector selectively and quantitatively measure the relative emission intensities at specific analytical wavelengths. The emission intensity at an elemental emission wavelength is used as a relative measure of the concentration of that element in the sample. The method is sometimes referred to as inductively coupled plasma optical emission spectrometry (ICP OES).

Scope. ICP-AES is used for quantitative elemental analysis; in other words to determine the total concentrations of specific elements in a sample. Typical application areas include metallurgy, geological measurements, environmental monitoring, food analysis, the measurement of additives or wear metals in oil, and forensics. In general, ICP-AES is used for solution concentrations in the 1–100 mg/L range. Some nonmetallic elements (S, P) can be measured.

The instrumentation is generally more expensive than AAS, but unlike AAS it has the significant advantage of being able to detect multiple elements simultaneously. This results in significant time savings if multielement analysis is required. It is generally less expensive than ICP-MS.

Nature of the Sample. In the most common situations, samples are introduced into the ICP as solutions. If the sample being analyzed is a solid, it must first be dis-

solved. Typically, 1 g of sample is dissolved in 100 mL of acidified aqueous solution. The dissolution of samples often requires hot concentrated mineral acids.

An alternative sample introduction system uses laser ablation of solid samples to generate an aerosol of sample particles, which can be injected directly into the ICP.

Qualitative Analysis. Specific elements are identified via the known wavelengths of atomic emission lines.

Traceable Quantitative Analysis. For systems using solution sample introduction, ICP-AES instrumentation must be calibrated using solutions containing known concentrations of the analyte elements. Such calibration solutions are available from many commercial suppliers. These solutions are often traceable to one of a set of NIST single-element solution standard reference materials. The analysis of complex samples can be susceptible to matrix effects (the combined effect that the constituent species present in the sample has on the atomic emission signal of the analyte). This will lead to measurement bias if the calibration solutions are not matched to the matrix of the sample being analyzed. The method of standard additions is an effective strategy for dealing with matrix effects.

Calibrating systems using laser ablation sample introduction is more difficult. The laser ablation process is very matrix-dependent, and calibration requires the use of solid standards that match the characteristics of the sample quite closely. A measurement of the ratio of the analyte emission relative to a matrix emission line is often used in some form to improve accuracy and precision.

Spectral interference from the argon plasma emission or sample matrix components is another potential source of bias. Most systems utilize some form of spectral background correction to deal with such interferences. Certified reference materials are available in a wide variety of sample matrix types from NIST and other sources. These CRMs should be used to validate ICP-OES methods.

Spark Optical Emission Spectrometry (Spark OES)

Principles of the Technique. A high-voltage spark is generated from a cathode in an argon atmosphere to a conducting sample which acts as the anode. The sample is melted and atomized and the free atoms are excited to yield atomic emission. A suitable optical transfer system, polychromator, and detector selectively

and quantitatively measure the relative emission intensity at specific analytical wavelengths. The emission intensity at an elemental emission wavelength is used as a relative measure of the concentration of that element in the sample. The method is sometimes referred to simply as optical emission spectrometry (OES) or as spark atomic emission spectrometry.

Scope. The analysis of metals is the major application area of spark OES. Tens of thousands of spark OES instruments are installed in large steel mills, aluminum smelters, and casting operations, as well as small forges and small foundries. Measurements are made for quality control, raw material testing and research. Speed of analysis, without the need for sample dissolution, is the major advantage of spark OES over ICP-OES.

Nature of the Sample. Metal samples may need to be ground flat to form a good electrode. Powders can be mixed with graphite and pressed to form a flat surface.

Qualitative Analysis. Specific elements are identified via the known wavelengths of atomic emission lines.

Traceable Quantitative Analysis. The spark sampling and excitation process is very complex and matrix-dependent. Calibration is done using large sets of Certified reference materials selected to match the type of sample to be analyzed.

As with any spectroscopic measurement, spectral interference from the sample matrix components or the spark source is a potential source of bias. Most systems utilize some form of spectral background correction to deal with such interferences.

An individual spark lasts only several microseconds, and will vaporize less than a microgram of sample. Sample inhomogeneity can impede accurate analysis of the bulk sample. Analyses are based on multiple sparks from different locations on the sample.

Glow Discharge Optical Emission Spectroscopy (GD-OES)

Principles of the Technique. A glow discharge is a reduced-pressure inert gas plasma maintained between two electrodes. Argon is typically used at absolute pressures of between a few hundred Pascals and about 2.5 kPa, and the solid sample serves as the cathode in the circuit. When the discharge is ignited, Ar⁺ ions formed in the plasma are accelerated toward the sample surface by means of electric fields. At least a substantial fraction of these Ar⁺ ions strike

the surface of the sample with enough kinetic energy to eject sample atoms from the surface. In this way, the solid sample is directly atomized. Once in the plasma, sputtered atoms may be electronically excited through collisions with energetic electrons and other particles. Some fraction of the excited sputtered atoms will relax to lower electronic energy levels (often the ground state) by means of photon emission. The wavelengths of these photons are characteristic of the emitting species. A grating spectrometer, with either photomultiplier tubes (PMTs) mounted on a Rowland circle, or one or more charge transfer devices (CTDs), is used to measure the intensity of the plasma emission at specific wavelengths. In this way, the elemental constituents of the solid sample can be quantitatively estimated.

A significant number of GD-OES instruments have been available commercially from several manufacturers for many years. The instruments that are currently available vary in both capabilities and costs. An instrument for a specific and routine application can be obtained for as little as \$60 000, whereas a *fully loaded* research instrument may cost in excess of \$200 000. There are currently more than 1000 GD-OES instruments in use around the world.

Scope. Glow discharge devices used in GD-OES may be powered by either a DC or RF power supply. In DC-GD-OES, the sample must be electrically conductive, since current must pass through it. RF-GD-OES overcomes this restriction, because in this configuration it is not necessary for net current to flow through the sample. As a result, RF-GD-OES can be applied to both electrically conductive and insulating samples.

GD-OES has traditionally been applied to bulk analysis of solids, and it is still routinely used for this purpose. More recently, GD-OES *depth profiling* (the determination of elemental composition as a function of depth) has begun to mature. In GD-OES depth profiling, registration of emission intensities over time as surface layers are *sputtered* away produces the *depth profile* of the sample. Algorithms exist to convert the resulting intensity versus time plot into elemental mass fraction versus depth. While much development remains to be done, GD-OES depth profiling is already being fairly widely applied for analyses of both electrically conductive and insulating layers on either electrically conductive or insulating substrates. Probably the widest application to date has been the analysis of galvanized coatings on steel. However, depth profiling of other sample types, such as thin films (< 10 nm thickness)

and organic coatings, is being demonstrated. While bulk analysis will likely remain an important application of GD-OES, the brighter future of the technique lies in the depth profiling arena.

Some strengths of GD-OES include a relative lack of interferences and matrix effects compared to many other direct solid techniques (such as spark OES and secondary ion mass spectrometry, or SIMS). Also, limits of detection are useful for many applications (sub- to low parts per million range directly in the solid state). The ability to detect H, O and N is also an advantage. An important disadvantage is that GD-OES is inherently a *relative* technique, requiring reference materials for calibration.

Nature of the Sample. As described above, GD-OES is applicable to bulk and depth profiling analyses of electrically conductive and insulating solid samples. The RF mode is required when insulating samples are involved. Analyzed surfaces are usually flat, although special sample holders can be used for surfaces of different shapes (such as tubing).

Qualitative Analysis. Calibration of a GD-OES instrument consists of measuring emission intensities for suitable reference materials and calculating a calibration equation. Qualitative analysis can be performed without calibration, simply by noting the elemental wavelengths at which signals exist. Owing to the prominent lack of certified mass fractions for H, O and N in reference materials, GD-OES is often capable of only qualitative determinations of these nonmetallic elements.

Traceable Quantitative Analysis. Quantitative GD-OES analyses are accomplished through calibration with suitable reference materials. Accuracies improve with the level of matrix-matching of the calibrants to the unknowns. Mass fraction biases on the order of 1% relative are usually found for major and minor elements, while those observed at mass fractions below $100 \mu\text{g g}^{-1}$ are normally higher (for example, > 15% relative). The accuracy of the depth axis obtained in GD-OES depth profiling may vary widely, depending upon the circumstances, but can be as good as $\pm 5\%$ relative. Whether bulk analysis or depth profiling is performed, traceability to the SI is accomplished through calibration with reference materials.

X-ray Fluorescence (XRF)

Principles of the Technique. The specimen to be analyzed can be solid (powder or bulk) or liquid (aqueous

or oil-based). It is placed in an instrument and irradiated by a primary x-ray source or a particle beam (electrons or protons). The primary radiation is absorbed and ejects electrons from their orbitals. Relaxation processes fill the holes and result in the emission of characteristic x-ray radiation. The intensity of characteristic radiation that escapes the sample is proportional to the number of atoms of each element present in the specimen. Therefore, XRF is both qualitative, using the *fingerprint* of characteristic x-rays to identify constituent elements, and quantitative, using a counting process to relate the number of x-rays detected per unit time to the total concentration of the element.

X-ray fluorescence spectrometers are available in a number of designs suited for a variety of applications and operating conditions. State-of-the-art laboratory spectrometers are typically designed as wavelength-dispersive spectrometers with a high-power tube source and a high-resolution detection system comprised of collimators or slits, a set of interchangeable crystals to diffract the characteristic x-rays according to Bragg's equation, and two or more detectors mounted on a goniometer with the crystals. Lower-cost, lower-power spectrometers consist of either smaller wavelength-dispersive spectrometers with low-power tube sources or energy dispersive spectrometers using solid-state detectors and low-power tubes or radioisotope sources. Some energy-dispersive spectrometers use beams of electrons or protons as the primary radiation source. There are even handheld units designed for field use. Given the wide variety of instruments, prices range from \$25 000 to \$300 000.

Scope. XRF is used for quantitative elemental analysis, typically without regard to the chemical environment of the elements in the specimen. It is a relative technique that must be calibrated using reference materials. X-rays from one element are absorbed by other elements in the specimen possibly resulting in fluorescence from those other elements. Due to these matrix effects, the best performance is obtained when the calibrant(s) are similar in overall composition to the specimen. A number of sophisticated procedures are available to compensate for matrix effects including empirical and theoretical calibration models. It is possible to obtain composition results using just theory and fundamental parameters (basic physical constants describing the interactions of x-rays with matter); however, the quality of such results varies widely. XRF measurements are also influenced by the physical nature of the specimen including particle size or grain size, mineralogy, sur-

face morphology, susceptibility to damage by ionizing radiation, and other characteristics.

XRF is often referred as being nondestructive because it is possible to present specimens to the instrument with little or no preparation, and with little or no damage resulting from the measurement. However, x-rays cause damage at a molecular level and are not truly nondestructive, especially to organic matrices. Still, in many cases (the best example being alloys), specimens may be analyzed for other properties following XRF analysis.

XRF is at its best for rapid, precise analyses of major and minor constituents of the specimen. Spectrometers can be used for concentrations ranging from ≈ 1 mg/kg to 100% mass fraction. Analyses are accomplished in minutes and overall relative uncertainties can be limited to 1% or less. XRF is widely used for product quality control in a wide range of industries including those involving metals and alloys, mining and minerals, cement, petroleum, electronics and semiconductors.

Trace analysis is complicated by varying levels of spectral background that depend on spectrometer geometry, the excitation source, the atomic number of the analyte element, the average atomic number of the specimen, and other factors. Trace analysis below 1 mg/kg is possible using specially designed spectrometers, such as total reflection XRF, and destructive sample preparation techniques similar to other atomic emission.

Qualitative Analysis. XRF is uniquely suited for qualitative analysis with its (mostly) nondestructive nature and sensitivity to most of the periodic table (Be–U). Characteristic x-rays from each element consist of a family of lines providing unambiguous identification. Energy-dispersive spectrometers are especially well-suited for qualitative analysis because they display the entire spectrum at once. For the purpose of choosing the optimum measurement conditions, qualitative analysis is performed prior to implementation of quantitative analysis methods.

Traceable Quantitative Analysis. XRF spectrometers must be calibrated to obtain optimum accuracy. The choice of calibrants depends on the form of the specimens and the concentration range to be calibrated. Using destructive preparation techniques such as borate fusion, calibrants can be prepared from primary reference materials (elements, compounds and solutions) and the results are traceable to the SI provided the purity and stoichiometry of the reference materials are assured. The caveat is that calibrants and unknowns must

be closely matched in terms of their entire composition. The same can be accomplished for liquid materials when calibrant solutions are sufficiently similar in matrix to the unknowns.

In cases where a variety of calibrants with varying degrees of comparability to the unknowns must be used, it is necessary to apply matrix corrections. The preferred approach is to use theory and fundamental parameters to estimate the corrections. Still, some number of calibrants in the form of reference materials must be used to calibrate the spectrometer. Traceability is established through the set of reference materials to the issuing body or bodies.

Alternatives to matrix correction models are internal standards, internal reference lines and standard additions. Of course, these apply only under the appropriate circumstances in which the material to be analyzed can be prepared in some manner to incorporate the spiking material.

Several review articles [4.35–49] are available.

4.1.4 Nuclear Analytical Methods

Additional discussions of x-ray techniques are described in Sects. 4.1.4 and 4.2 [4.50–72].

Neutron Activation Analysis (NAA)

Neutron activation analysis (NAA) is an isotope-specific, multielemental, analytical method that determines the total elemental content of about 40 elements in many materials. The method is based on irradiating a sample in a field of neutrons, and measuring the radioactivity emitted by the resulting irradiation products. Typically a nuclear reactor is used as the source of neutrons, and germanium-based semiconductor detectors are used to measure the energy and intensity of the gamma radiation, which is then used to identify and quantify the analytes of interest. NAA is independent of the chemical state of the analytes, since all measurement interactions are based on nuclear and not chemical properties of the elements. In addition, both the incoming (excitation) radiation (neutrons) and the outgoing radiation (gamma rays) are highly penetrating. Due to the above characteristics, there are very few matrix effects and interferences for NAA compared to many other analytical techniques. NAA can be applied in nondestructive or *instrumental* (INAA) mode, or in a destructive mode involving dissolution and/or other chemical manipulation of the samples. The most common form of the latter mode is radiochemical NAA (RNAA), where all chemical processing is done

after the irradiation step. Both INAA and RNAA are essentially free from chemical blank, since after irradiation, only the radioactive daughter products of the elements contribute to the analytical signal. In fact, for most RNAA procedures, carriers (stable forms of the elements under investigation) are added to the samples after irradiation to enhance separation and minimize losses. The amount of carrier remaining after separation can be measured to determine the chemical yield of each sample when separations are not quantitative. In other cases, a small amount of a radioactive tracer of an element under investigation can be used to determine the chemical yield.

Principles of the Technique. Most elements have one or more isotopes that will produce a radioactive daughter product upon capturing a neutron. Samples are irradiated for a known amount of time in a neutron field, removed, and then subjected to a series of gamma-ray spectrometry measurements using suitable decay intervals to emphasize or suppress radionuclides with different half-lives. Spectra of gamma-ray intensity versus energy (typically from about 70 keV–3 MeV) are collected. For RNAA measurements, virtually any type of separation procedure can be applied after irradiation. Radionuclides are identified by both their gamma-ray energy (or energies) and approximate half-lives.

Elemental content in a sample is directly proportional to the decay corrected gamma-ray count rate if irradiation and gamma-ray spectrometry conditions are held constant. The decay-corrected count rate A_0 is given

$$A_0 = \frac{\lambda C_x e^{\lambda t_1}}{(1 - e^{-\lambda \Delta})(1 - e^{-\lambda T})}, \quad (4.6)$$

where

- A_0 = decay-corrected count rate,
- λ = decay constant = $\ln 2/t_{1/2}$,
- Δ = live time of count,
- C_x = net counts in γ -ray peak,
- t_1 = decay time to start of count,
- T = irradiation time.

Scope. This method is useful for elements with isotopes that produce radioactive daughter products after neutron irradiation and decay by gamma-ray emission. Although ≈ 75 elements meet these criteria, typically 30–45 elements can be quantified instrumentally in most samples. Low-intensity signals can be lost in the continuum of background noise of the gamma-ray spec-

tra (unless radiochemical separations are employed to isolate elements of interest). Detection limits vary by approximately six orders of magnitude for INAA, and depend mainly on the nuclear properties of the elements, as well as experimental conditions such as neutron fluence rate, decay interval, and detection efficiency of the gamma-rays of interest.

Nature of the Sample. Samples of interest are encapsulated in polyethylene or quartz prior to irradiation. Typical sample sizes range from a few milligrams to about a gram, although some reactor facilities can irradiate kilogram-size samples. Because of the highly penetrating nature of both neutrons and gamma-rays, the effects of sample sizes of up to a gram are minimal unless the sample is very dense (metals) or contains large amounts of elements that are highly neutron-absorbing (B, Li, Cd, and some rare earths). Smaller sample sizes are needed for dense or highly neutron-absorbing samples. The presence of large amounts of elements that activate extremely well, such as Au, Sm, Eu, Gd, In, Sc, Mn or Co, will worsen the detection limits for other elements in the samples.

Qualitative Analysis. Radionuclides are identified by gamma-ray energies and half-lives. ^{51}Ti and ^{51}Cr have identical gamma-ray energies (320.1 keV) since they decay to the same, stable daughter product (^{51}V). However, their half-lives differ greatly: 5.76 min for ^{51}Ti and 27.7 d for ^{51}Cr . Gamma rays with an energy of 320.1 keV observed shortly after irradiation are almost entirely from Ti, while those observed even one day after irradiation are entirely from ^{51}Cr . It is possible to determine Ti in a sample with a high Cr content by first counting immediately after irradiation, counting again under the same conditions one day after irradiation, and then subtracting the ^{51}Cr contribution to the ^{51}Ti peak. In addition, many radionuclides have more than one gamma-ray, and the presence of all the intense gamma-rays can be used as confirmation.

Traceable Quantitative Analysis. Quantification for NAA can be achieved by three basic methods:

1. use of fundamental parameters;
2. by comparing to a known amount of the element under investigation, or
3. some combination of the two previous methods (the k_0 method is the best-known variant of this).

The second method, often called the comparator method, contains the most direct traceability links and

Table 4.2 Prompt gamma activation analysis: approximate detection limits. Data from [4.61]

> 1 μg	B, Cd, Sm, Eu, Gd, Hg
1–10 μg	H, Cl, Ti, V, Co, Ag, Pt
10–100 μg	Na, Al, Si, S, K, Ca, Cr, Mn, Fe, Cu, Zn, As, Br, Sr, Mo, I, W, Au
100–1000 μg	N, Mg, P, Sn, Sb
1–10 mg	C, F, Pb, Bi

will be discussed further. Typically, standards containing known amounts of the elements under investigation are irradiated and counted under the same conditions as the sample(s) of interest. Decay-corrected count rates A_0 are calculated via (4.6), and then the masses of each element in the sample(s) are calculated through (4.7). The R -values account for any experimental differences between standards and sample(s), and are normally very close to unity

$$m_{\text{unk}} = m_{\text{std}} \frac{(A_{0,\text{unk}})}{(A_{0,\text{std}})} R_{\theta} R_{\phi} R_{\sigma} R_{\varepsilon} \quad (4.7)$$

where: m_{unk} = mass of an element in the unknown sample, m_{std} = mass of an element in the comparator standard, R_{θ} = ratio of isotopic abundances for unknown and standard, R_{ϕ} = ratio of neutron fluences (including fluence drop-off, self-shielding and scattering), R_{σ} = ratio of effective cross-sections if neutron spectrum shape differs from unk. to std., R_{ε} = ratio of counting efficiencies (differences due to geometry and γ -ray self-shielding).

Prompt Gamma Activation Analysis (PGAA)
Principles of the Technique. The binding energy released when a neutron is captured by an atomic nucleus is generally emitted in the form of instantaneous gamma-rays. Measuring the characteristic energies of these gamma rays permits qualitative identification of the elements in the sample, and quantitative analysis is accomplished by measuring their intensity. The source of neutrons may be a research reactor, an accelerator-based neutron generator, or an isotopic source. The most sensitive and accurate analyses use reactor neutron beams with high-resolution Ge gamma-ray spectrometers. A sample is simply placed in the neutron beam, and the gamma-ray spectrum is measured during an irradiation lasting from minutes to hours. The method is nondestructive; residual radioactivity is usually negligible. Because PGAA employs nuclear (rather than chemical) reactions, the chemical form of the analyte

is unimportant. No dissolution or other sample pretreatment is required.

Scope. The sensitivity of the analysis depends on experimental conditions and on the composition of the sample matrix. For a neutron beam with a flux of $10^8 \text{ cm}^{-2} \text{ s}^{-1}$ and an irradiation time of several hours, approximate detection limits are given in Table 4.2.

Nature of the Sample. Typical samples are in the range of 100–1000 mg, preferably pressed into a pellet. Samples can be smaller if the elements of interest have high sensitivities, and must be smaller if the matrix is a strong neutron absorber. Large samples may be most accurately analyzed through element ratios.

Qualitative Analysis. The energies of the peaks in the gamma-ray spectrum are characteristic of the elements. Because the spectra of most elements contain numerous peaks, elemental identification is generally positive.

Quantitative Analysis. Standards of known quantities of pure elements or simple compounds are irradiated to determine sensitivity factors. Multiple gamma rays are used for quantitation to verify the absence of interferences.

Example Spectrum. The plot shown in Fig. 4.3 is a PGAA spectrum of a fertilizer reference material. In this material, the elements H, B, C, N, P, S, Cl, K, Ca, Ti, V, Mn, Fe, Cd, Sm and Gd are quantitatively measurable.

Neutron Depth Profiling

Neutron depth profiling (NDP) is a method of near-surface analysis for isotopes that undergo neutron-induced positive Q -value (exothermic) charged particle reactions, for example (n,α) , (n,p) . NDP combines nuclear physics with atomic physics to provide information about near-surface concentrations of certain light elements. The technique was originally applied in 1972 by Ziegler et al. [4.62] and independently by Biersack and Fink [4.63]. Fink [4.64] has produced an excellent report giving many explicit details of the method. The method is based on measuring the energy loss of the charged particles as they exit the specimen. Depending on the material under study, depths of up to $10 \mu\text{m}$ can be profiled, and depth resolutions of the order of 10 nm can be obtained. The most studied analytes have been boron, lithium, and nitrogen in a variety of matrices, but several other analytes can also be measured. Because

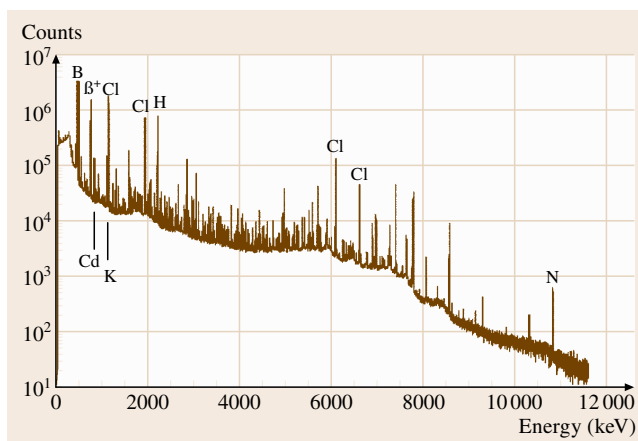


Fig. 4.3 Prompt gamma activation analysis

the incoming energy of the neutron is negligible and the interaction rate is small, NDP is considered a non-destructive technique. This allows the same volume of sample to receive further treatment for repeated analysis, or to be subsequently analyzed using a different technique that might alter or destroy the sample.

Principles of the Technique. Lithium, boron, nitrogen, and a number of other elements have an isotope that undergoes an exoergic charged particle reaction upon capturing a neutron. The charged particles are protons or alpha particles and an associated recoil nucleus. The energies of the particles are determined by the conservation of mass-energy and are predetermined for each reaction (for thermal neutrons, the added energy brought in by the neutron is negligible). As the charged particle exits the material, its interaction with the ma-

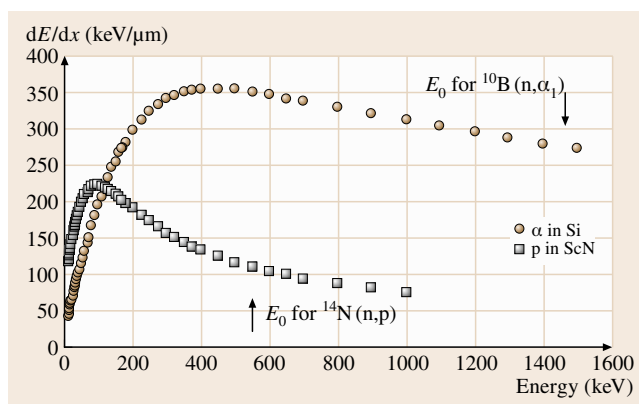


Fig. 4.4 Neutron depth profiling: stopping power for alphas in silicon and protons in ScN

trix causes it to lose energy, and this energy loss can be measured and used to determine the depth of the originating reaction. Because only a few neutrons undergo interactions as they penetrate the sample, the neutron fluence rate is essentially the same at all depths. The depth corresponding to the measured energy loss is determined by using the characteristic stopping power of the material. The chemical or electrical state of the target atoms has an inconsequential effect on the measured profile in the NDP technique. Only the concentration of the major elements in the material is needed to establish the depth scale through the relationship to stopping power.

Mathematically, the relationship between the depth and residual energy can be expressed as

$$x = \int_{E(x)}^{E_0} \frac{dE}{S(E)}, \quad (4.8)$$

where x is the path length traveled by the particle through the matrix, E_0 is the initial energy of the particle, $E(x)$ is the energy of the detected particle, and $S(E)$ is the stopping power of the matrix. Examples of the relationship between x and $E(x)$ are displayed in Fig. 4.4 for $^{10}\text{B}(n,\alpha)$ in silicon and $^{14}\text{N}(n,p)$ in ScN. For the boron reaction, $^{10}\text{B}(n,\alpha)^7\text{Li}$, there are two outgoing alpha particles with energies of 1.472 MeV (93% branch) and 1.776 MeV (7%), and two corresponding recoil ^7Li nuclei with energies of 0.840 and 1.014 MeV. For the nitrogen reaction, $^{14}\text{N}(n,p)^{14}\text{C}$, there is a 584 keV proton and a 42 keV ^{14}C recoil. A silicon surface barrier detector detects particles escaping from the surface of the sample. The charge deposited in the detector is directly proportional to the energy of the incoming particle.

Scope. A principal limitation of the technique is that it can only be applied to a few light elements. The most commonly analyzed are boron, lithium and nitrogen. However, as a result, very few interfering reactions are encountered. Furthermore, since the critical parameters in the technique are nuclear in origin, there is no dependence upon the chemical or optical characteristics of the sample. Consequently, measurements are possible at the outer few atomic layers of a sample or through a rapidly changing composition such as at the interface between insulating and conducting layers, and across chemically distinct interfaces. In contrast, measurement artifacts occur with surface techniques such as secondary ion mass spectrometry and Auger electron

spectrometry when the sample surface becomes charged and the ion yields vary unpredictably.

Nature of the Sample. Samples of interest are usually thin films, multilayers or exposed surfaces. Because of the short range of the charged particles, only depths to about 10 μm can be analyzed. The samples are placed in a thermal neutron beam and the dimensions of the beam determine the maximum area of the sample that can be analyzed in a single measurement. Some facilities have the ability to scan large-area samples. The analyzed surface must be flat and smooth to avoid ambiguities caused by surface roughness. All samples are analyzed in vacuum, so the samples must be nonvolatile and robust enough to survive the evacuation process. Some samples may become activated and require some decay time before being available for further experimentation. The latter condition is the only barrier to the entire process being completely nondestructive.

Qualitative Analysis. Most of the interest in the technique relates to determining the shape of the distribution of the analyte and how it responds to changes in its environment (annealing, voltage gradients and so on). Determining the shape of the distribution involves determining the energy of the particles escaping from the surface and comparing with the full energy of the reaction. The detector can be calibrated for the full energy by measuring a very thin surface deposit of the analyte in question. The detector is typically a surface-barrier detector or another high-resolution charged particle detector. The difference between the initial energy of the particle and its measured energy is equal to the energy loss, and with (4.8) it yields the depth of origin. The depth resolution varies from a few nanometers to a few hundred nanometers. Under optimum conditions the depth resolution for boron in silicon is approximately 8 nm.

Stopping powers for individual elements are given in compilations like that of Ziegler [4.65]. Because the analytic results are obtained in units of areal density (atoms per square centimeter), a linear depth scale can be assigned only if the volume density of the material remains constant and is known. Consequently, the conversion of an energy loss scale to a linear depth axis is only as accurate as the knowledge of the volume density. By supplying a few physical parameters, customized computer programs are used to convert the charged particle spectrum to a depth profile in units of concentration and depth. A Monte Carlo program, SRIM [4.66], can also be used to provide stopping

power and range information. Even if the density is not well-known, mass fraction concentration profiles can be accurately determined even through layered materials of different density. In many cases, it is the mass fraction composition that is the information desired from the analysis.

Traceable Quantitative Analysis. To compare concentration profiles among samples, both the charged particle spectrum and the neutron fluence that passes through each sample are monitored and recorded. The area analyzed on a sample is defined by placing an aperture securely against the sample surface. This aperture need only be thick enough to prevent the charged particle from reaching the detector and can therefore be very thin. Neutron collimation is used to reduce unwanted background, but it does not need to be precise. The absolute area defined by the aperture need not be accurately known as long as the counting geometry is constant between samples. The neutron fluence recorded with each analysis is used to normalize data from different samples. In practice, a run-to-run monitor that has a response proportional to the total neutron fluence rate is sufficient to normalize data taken at differing neutron intensities and time intervals. To obtain a traceable quantitative analysis of the sample, a spectrum should be obtained using a sample of known isotopic concentration, such as the NIST SRM 2137 boron implanted in silicon standard for calibrating concentration in a depth profile. When determining an NDP profile it should be remembered that only the isotopic concentration is actually determined and that the elemental profile is inferred.

Photon Activation Analysis (PAA)

Principles of the Technique. PAA is a variant of activation analysis where photons are used as activating particles. The nuclear reactions depend on the atomic number of the target and on the energy of the photons used for irradiation. The source of photons for PAA is nearly always the bremsstrahlung radiation produced with electron accelerators. The photon energies are commonly 15–20 MeV, predominantly inducing the (γ, n) reaction. Other reactions that can be used include (γ, p) , $(\gamma, 2n)$, and (γ, α) . PAA is very similar to neutron activation analysis (NAA) in that the photons can completely penetrate most samples. Thus procedures and calculations are similar to those used in NAA. The method has constraints due to the stability and homogeneity of the photon beam, with inherent limitations to the comparator method. Recent developments

in bremsstrahlung target technology have achieved improvements in the photon source that greatly benefit the precision and accuracy of the method [4.59]. A detailed discussion of PAA has been given by Segebade et al. [4.67].

Scope. The method is complementary to INAA, and the determination of light elements C, N, O and F are good examples of PAA where detection limits of $< 0.5 \mu\text{g}$ are possible. A few heavy metal elements can be determined in biological and environmental materials with similar sensitivity, such as Ni, As, and Pb; the latter cannot be determined by thermal NAA. One reaction with lower energy photons is the ${}^9\text{Be}(\gamma, n){}^{10}\text{Be} \rightarrow 2 {}^4\text{He} + 2n$ reaction because of the low neutron binding energy of the Be. The reaction can be induced by the 2.1 MeV gamma rays from ${}^{124}\text{Sb}$ and measured through the detection of the neutrons. (The same reaction is also used as a neutron source).

Nature of the Sample. Samples are commonly in solid form, requiring little or no preparation for analysis. Metals, industrial materials, environmental materials and biological samples can be characterized in their original form.

Qualitative Analysis. The (γ, n) reaction leaves the product nucleus proton-rich, consequently the analytical nuclide is frequently a positron emitter. This requires discrimination by half-life or radiochemical separation for element-specific characterization. Heavier elements can form product nuclides which emit their own characteristic gamma rays, rather than just positron annihilation radiation.

Traceable Quantitative Analysis. The comparator method of activation analysis relates directly the measured gamma rays of a sample to the measured gamma rays of a standard with a known element content (4.7). Spectral interferences, fluence differences in sample and standard, and potential isotopic differences must be carefully considered.

Charged Particle (Beam) Techniques

Principles of the Technique. In charged particle activation analysis (CPAA), the activating particles, such as protons, deuterons, tritons, ${}^3\text{He}$, α - and higher atomic number charged particles are generated by accelerators. The type of nuclear reaction induced in the sample nuclei depends on the identity and energy of the incoming charged particle. Protons are selected in many instances

because they can be easily accelerated and have low Coulomb barriers. The (p,n) and (p, γ) reactions result most often with protons up to about 10 MeV in energy. Higher energy protons may also induce (p, α), (p,d) or (p,2n) reactions. Larger incident particles require higher energies to overcome the Coulomb barrier. They then deposit higher energies in the target nucleus during reaction, which leads to a greater variety of pathways for the de-excitation of the activated nucleus. Therefore, a great variety of reactions and measurement options are available to the analyst in CPAA. CPAA has been discussed in more detail by *Strijckmans* [4.68].

Particle-induced x-ray emission (PIXE) is a combined process, in which continuum and characteristic x-rays are generated through the recombination of electrons and electron vacancies produced in ion-atom collision events when a beam of charged particles is slowed down in an object. Usually protons of energies between 0.1–3 MeV are utilized; the energies typically depend on the accelerator type and are selected to minimize nuclear reactions. The target elements emit characteristic x-ray lines corresponding to the atomic number of the element. A detailed introduction to the technique and its interdisciplinary applications is given by *Johansson et al.* [4.69].

Scope. CPAA can be regarded as a good complement to neutron activation analysis (NAA), since elements that are measured well are quite different from those ordinarily determined by NAA. The low Coulomb barriers and low neutron capture cross-sections of light elements make CPAA a good choice for the nuclear analysis of B, C, N, O, and so on. PIXE is generally applicable to elements with atomic numbers $11 \leq Z \leq 92$. Because charged particles may not penetrate the entire sample as neutrons do, CPAA or PIXE is often used for determinations in thin samples or as a surface technique. The ability to focus charged particle beams is widely used in applications for spatial analysis. Elaborate ion-optical systems of particle accelerators composed of focusing and transversal beam scanning elements offer an analytical tool for lateral two-dimensional mapping of elements in micro-PIXE.

Nature of the Sample. Samples are commonly in solid form, requiring no or little preparation for analysis. Metals, industrial materials, environmental materials and biological samples can be characterized in their original solid form. However, many facilities require that the sample is irradiated in a vacuum chamber connected to the accelerator beam line. Samples with

volatile constituents and liquid samples require that the beam is extracted from the beam line through a thin window. Activation and x-ray production in the window and surrounding air significantly increases the background in prompt gamma ray and x-ray spectra. An additional restriction may be imposed on sample materials by the sensitivity of the sample to local heating in the particle beam.

Qualitative Analysis. The selection of nuclear reaction parameters in CPAA permits the formation of rather specific product nuclides which emit their own characteristic gamma rays for unique identification. PIXE offers direct identification of elements via their characteristic *K* and *L* series x-rays.

Traceable Quantitative Analysis. For CPAA, the interaction of the charged particle with the sample requires a modification of the activation equation, introduced in Sect. 4.2.4. The particles passing through a sample lose energy, so the cross-section for the nuclear reaction changes with depth. The expression for the produced activity in NAA has to be modified to account for this effect

$$A(t) = nI \int_0^R \sigma(x) dx . \quad (4.9)$$

Here *I* is the beam intensity (replacing the neutron flux Φ), *n* is the density of target nuclides, and *R* is the penetration range determined by the stopping power of the medium according to Sect. 4.2.4.

As with NAA, the fundamental equation is not used directly in practice, but a relative standardization (comparator) method is used. A working equation for the comparator method is

$$m_x = m_s \frac{A_x I_s R_s}{A_s I_x R_x} . \quad (4.10)$$

Here we have omitted the saturation, decay, and counting factors, which should be applied the same as in the case of NAA (4.7).

Like NAA, PIXE can be described by sets of equations relating to all of the physical parameters applicable in the excitation process. However, accurate calibration of a PIXE system is extremely difficult. The comparator method suffers from the fact that only one sample, either the unknown or the standard, can be irradiated at a given time. Thin target yields for thin homogeneous samples with negligible energy loss of the bombarding particle and no absorption of x-rays in the sample can be calculated and normalized

for standards and unknowns. For a thick homogeneous sample, thick target yields can be calculated if the composition is known. The comparator method is further affected by the problem of insufficient matrix match between unknown and standard sample here. Often internal standards, such as homogeneously mixed in yttrium, provide an experimental calibration method with a potential limit to uncertainties of 3–5%.

Activation Analysis with Accelerator-Produced Neutrons

Principles of the Technique. This nuclear analytical method is based on small, low-voltage (≈ 105 – 200 kV) accelerators producing 3 and 14 MeV neutrons via the ${}^2\text{H}(d,n){}^3\text{He}$ and ${}^3\text{H}(d,n){}^4\text{He}$ reactions, respectively. Principles of operation and output characteristics of these neutron generators have been described in the past [4.70] and were recently updated in a technical document [4.55]. The NAA procedures follow the same principles as those with thermal neutrons. The high-energy neutrons can be used to interact directly with target nuclides in fast neutron activation analysis (FNAA), or they are moderated to thermal energies before interacting with a sample like in conventional NAA. Hence, the principal neutron energies of interest obtained from neutron generators are ≈ 14 MeV, ≈ 2.8 MeV, and ≈ 0.025 eV (thermal). The different nuclear reactions of the generator neutrons are listed here in the approximate order of increasing threshold energy: (n,γ) , (n,n',γ) , (n,p) , (n,α) , and $(n,2n)$. The (n,γ) reaction is exoergic and the cross-section in most cases decreases with increasing neutron energy. Nevertheless, some nuclides have high resonance absorption at certain neutron energies and FNAA is used in their determination. The (n,n',γ) reactions are slightly endoergic; most can be induced by the 3 MeV neutrons. Only a limited number of nuclides, however, have longer lived isomeric states that can be measured after irradiation. The (n,p) , (n,α) , and $(n,2n)$ reactions are predominantly endoergic and generally occur with the 14 MeV neutrons only. With this wide array of selectable parameters, highly specialized applications have been developed.

Scope. The FNAA methods based on small neutron generators play an important role in the development of new technologies in process and quality control systems, exploration of natural resources, detection of illicit traffic materials, transmutation of nuclear waste, fusion reactor neutronics, and radiation effects on biological and industrial materials. A considerable number of systems

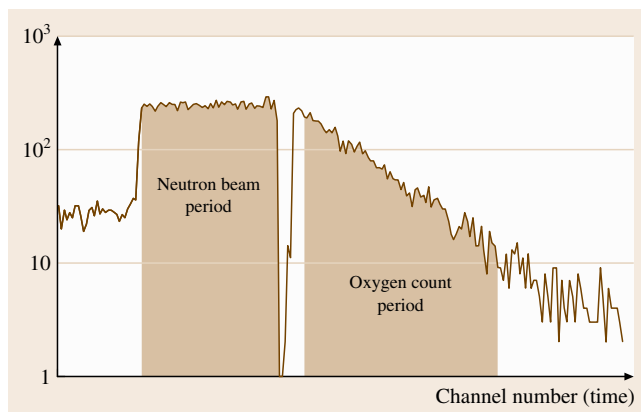


Fig. 4.5 Activation analysis with accelerator-produced neutrons: multiscaling spectrum of neutron beam monitor and oxygen gamma-ray counts in the FNAA of coal

have been specifically tailored to the important application of oxygen determination via the ${}^{16}\text{O}(n,p){}^{16}\text{N}$ ($T_{1/2} = 7.2$ s) reaction. This outstanding analytical application for the direct, nondestructive determination of oxygen is discussed here in more detail. The procedure has been documented in an evaluated standard test method (ASTM).

Nature of the Sample. Samples are in solid or liquid form, requiring little or no preparation for analysis. Metals, industrial materials, environmental materials and biological and other organic samples can be characterized in their original forms. For highly sensitive oxygen determinations, samples are commonly prepared under inert gas protection and sealed in low-level oxygen irradiation containers. Comparator standards are commonly prepared from stoichiometric oxygen-containing chemicals measured directly or diluted with relatively oxygen-free filler materials.

Qualitative Analysis. In general applications of FNAA, the activation products are identified by their unique nuclear decay characteristics. The oxygen analysis commonly utilizes the summation of all gamma rays above ≈ 4.7 MeV; the specificity of the accumulated counts is ascertained by decay curve analysis.

Traceable Quantitative Analysis. FNAA follows the general principles of NAA for quantitative analysis. The specific nature of the neutron flux distributions and intensities during an activation cycle with a generator and the produced nuclides, which are frequently short-lived,

however, require specific measures to control sources of uncertainty.

The 14 MeV *FNAA* method has been used to determine the uptake of oxygen in *SRM 1632c* trace elements in coal (bituminous) [4.71]. In this application it was expected to quantify a relative change of 5% in the oxygen content ($\approx 12\%$ mass fraction) in the *SRM*. Automated irradiation and counting cycles alternate samples and standards and achieve high precision though multiple (ten) passes for each sample and standard. Figure 4.5 illustrates the signals recorded in the analyzer for each pass. The duration of the irradiation and its intensity is recorded from a neutron monitor, while the oxygen gamma rays are obtained from a matched pair of *NaI(Tl)* photon detectors after travel of the sample from the irradiation to the counting position. An on-line laboratory computer controls the process and quantitatively evaluates the data [4.72].

4.1.5 Chromatographic Methods

Gas Chromatography (GC)

Principles of the Technique. Gas chromatography (GC) can be used to separate volatile organic compounds. A gas chromatograph consists of a flowing mobile phase (typically helium or hydrogen), an injection port, a separation column containing the stationary phase, and a detector. The analytes of interest are partitioned between the mobile (inert gas) phase, and the stationary phase. In capillary gas chromatography, the stationary phase is coated on the inner walls of an open tubular column typically comprised of fused silica. The available stationary phases include methylpolysiloxanes with varying substituents, polyethylene glycols with different modifications, chiral columns for separations, as well as other specialized stationary phases. The polarity of the stationary phase can be varied to effect the separation.

The suite of gas chromatographic detectors includes the flame ionization detector (*FID*), the thermal conductivity detector (*TCD* or hot wire detector), the electron capture detector (*ECD*), the photoionization detector (*PID*), the flame photometric detector (*FPD*), the atomic emission detector (*AED*), and the mass spectrometer (*MS*). Except for the *AED* and *MS*, these detectors produce an electrical signal that varies with the amount of analyte exiting the chromatographic column. In addition to producing the electrical signal, the *AED* yields an emission spectrum of selected elements in the analytes. The *MS*, unlike other *GC* detectors, responds to mass, a physical property common to all organic compounds.

Scope. Capillary chromatography has been used for the separation of complex mixtures, components that are closely related chemically and physically, and mixtures that consist of a wide variety of compounds. Because the separation is based on partitioning between a gas phase and stationary phase, the analytes of interest must volatilize at temperatures obtainable by *GC* injection port temperatures (typically 50–300°C) and be stable in the gas phase.

Samples may be introduced using split, splitless or on-column injectors. During a split injection, a portion of the carrier gas is constantly released through a splitter vent located at the base of the injection port, so that the same proportion of the sample injected will be carried out of the splitter vent upon injection. For applications where sensitivity or degradation in the injection port is not an issue, split injections are performed. During a splitless injection, the splitter vent is closed for a specified period of time following injection and then opened. For applications where sensitivity is an issue but degradation in the injection port is not an issue, and there are a lot of coextractables in the sample, splitless injection is used. Inlet liners are used for both split and splitless injections. For on-column injection, the column butts into the injection port so that the syringe needle used for injections goes into the head of the column. In this case, all of the sample is deposited onto the head of the column typically at an injection temperature below the boiling point of the solvent being used. For applications where sensitivity and degradation in the injection port are both issues and there is a limited amount of coextractables in the sample, on-column injection is used.

Nature of the Sample. The samples are introduced into the gas chromatograph as either gas or liquid solutions. If the sample being analyzed is a solid, it must first be dissolved into a suitable solvent, or the analytes of interest in the matrix must be extracted into a suitable solvent. In the case of complex matrices, the analytes of interest may be isolated from some of the coextracted material using various steps, including but not limited to size exclusion chromatography, liquid chromatography and solid-phase extraction.

Qualitative Analysis. Gas chromatography provides several types of qualitative information simultaneously. The appearance of the chromatogram is an indication of the complexity of the sample. The retention times of the analytes allow classification of various components roughly according to volatility. The rate at which

a component travels through the GC system (retention time) depends on factors in addition to volatility, however. These include the polarity of the compounds, the polarity of the stationary phase, the column temperature, and the flow rate of the gas (mobile phase) through the column. GC-AED and GC/MS provide additional qualitative information.

Traceable Quantitative Analysis. Regardless of the detector being used, GC instrumentation must be calibrated using solutions containing known concentrations of the analyte of interest along with internal standards (surrogates) that have been added at a known concentration. The internal standards (surrogates) chosen should be chemically similar to the analytes of interest, and for many of the GC/MS applications are isotopically labeled analogs of one or more of the analytes of interest. Approximately the same quantity of the internal standard should be added to all calibration solutions and unknown samples within an analysis set. Calibration may be performed by constructing a calibration curve encompassing the measurement range of the samples or by calculating a response factor from measurements of calibration solutions that are very similar in concentration to or closely bracket the sample concentration for the analyte of interest. For more detail on quantitative analysis as it relates to chromatography, see the section in this chapter on liquid chromatography.

Certified reference materials are available in a wide variety of sample matrix types from NIST and other sources. These CRMs should be used to validate the entire GC method, including extraction, analyte isolation and quantification.

Liquid Chromatography (LC)

Liquid chromatography (LC) is a method for separating and detecting organic and inorganic compounds in solution. The technique is broadly applicable to polar, nonpolar, aromatic, aliphatic and ionic compounds with few restrictions. Instrumentation typically consists of a solvent delivery device (a pump), a sample introduction device (an injector or autosampler), a chromatographic column, and a detector. The flexibility of the technique results from the availability of chromatographic columns suited to specific separation problems, and detectors with sensitive and selective responses. The goal of any liquid chromatographic method is the separation of compounds of interest from interferences, in either the chromatographic and/or detection domains, in order to achieve an instrumental response proportional to the analyte level.

Principles of the Technique. Retention in liquid chromatography is a consequence of different associations of solute molecules in dissimilar phases. In the simplest sense, all chromatographic systems consist of two phases: a fixed *stationary phase* and a moving *mobile phase*. The diffusion of solute molecules between these phases usually occurs on a time scale much more rapid than that associated with fluid flow of the mobile phase. Differential association of solute molecules with the stationary phase retards these species to different extents, resulting in separation. Retention processes depend on a complex set of interactions between solute molecules, stationary phase ligands and mobile phase molecules; the characteristics of the column (such as the physical and chemical properties of the substrate, the surface modification procedures used to prepare the stationary phase, the polarity, and so on) also provide a major influence on retention behavior. Two modes of operation can be distinguished: reversed-phase liquid chromatography (RPLC) and normal-phase LC. For normal-phase LC, the mobile phase is less polar than the stationary phase; the opposite situation exists with RPLC. Column choice is critical when developing an LC method. Most separations are performed in the reversed-phase mode with C₁₈ (octadecylsilane, ODS) columns. An instrumental response proportional to the analyte level typically results from spectrometric detection, although other forms of detection exist. Common detectors include UV/Vis absorbance, fluorescence (FL), electrochemical (EC), refractive index (RI), evaporative light scattering (ELSD), and mass spectrometric (MS) detection.

Scope. Liquid chromatography is applicable to compounds that are soluble (or can be made soluble by derivatization) in a suitable solvent and can be eluted from a chromatographic column. Accurate quantification requires the resolution of constituents of interest from interferences. Liquid chromatography is often considered a low-resolution technique, since only about 50–100 compounds can be separated in a single analysis; however, selective detection can be implemented to improve the overall resolution of the system. Recent emphasis is on the use of mass spectrometry for selective LC detection. In general, liquid chromatographic techniques are most suited to thermally labile or non-volatile solutes that are incompatible with gas phase separation techniques (such as gas chromatography).

Nature of the Sample. Liquid chromatography is relevant to a wide range of sample types, but in all cases

samples must be extracted or dissolved in solution to permit introduction into the liquid chromatograph. To reduce sample complexity, enrichment (clean-up) of the samples is sometimes carried out by liquid–liquid extraction, solid-phase extraction, or LC fractionation. Sample extracts should be miscible with the mobile phase, and typically small injection volumes (1–20 μL) are employed. Solvent exchange can be carried out when sample extracts are incompatible with the mobile phase composition.

Qualitative Analysis. Liquid chromatography is sometimes used for tentative identification of sample composition through comparison of retention times with authentic standards. Identifications must be verified by complementary techniques; however, disagreement in retention times is usually sufficient to prove the absence of a suspected compound.

Traceable Quantitative Analysis. Liquid chromatography is a relative technique that requires calibration. The processes of calibration and quantification are similar to those used in other instrumental techniques for organic analysis (such as gas chromatography, mass spectrometry, capillary electrophoresis, and related hyphenated techniques). The quantitative determination of organic compounds is usually based on the comparison of instrumental responses for unknowns with calibrants. Calibrants are prepared (usually on a mass fraction basis) using reference standards of known (high) purity. This comparison is made by using any of several mathematical models. Linear relationships between response and analyte level are often assumed; however, this is not a requirement for quantification, and nonlinear models may also be used.

Several approaches to quantification are potentially applicable: the external standard approach, the internal standard approach, and the standard addition approach. The external standard approach is based on a comparison of absolute responses for analytes in the calibrants and unknowns. The internal standard approach is based on a comparison of relative responses of the analytes to the responses of one or more compounds (the internal standard(s)) added to each of the samples and calibrants. The standard addition approach is based on one or more additions of a calibrant to the sample, and may also utilize an internal standard.

The external standard approach is often used when an internal standard is not available or cannot be used, or when the masses of standard and unknown samples can easily be controlled or accounted for. The external stan-

dard approach demands care since losses from sample handling or sample introduction will directly influence the final results. All volumes (or masses) must be accurately known, and sample transfers must be quantitative.

The internal standard approach utilizes one or more constituents (the internal standard(s), not present in the unknown samples) which are added to both calibrants and unknowns. Calculations are based on relative responses of the analytes to these internal standards. The use of internal standards lessens the need for quantitative transfers and reduces biases from sample processing losses. Internal standards should (ideally) have properties similar to the analytes of interest; however, even internal standards with unrelated properties may provide benefits as *volume correctors*. An isotopic form of the analyte of interest is used for isotope dilution methods. A mass difference of at least 2 and substitution at nonlabile atoms is typically required for mass spectrometric methods. Separation of isotopically labeled species (required for non-mass selective detection) is sometimes possible for deuterated species when the number of deuterium atoms is 8–10 or greater. Separation of the internal standard is required when detection is nonselective, as with ultraviolet absorbance detection. For techniques that utilize selective detection (such as mass spectrometry), separation of the internal standard is not required, and often it is desired that the internal standard and analyte coelute for improved precision (as in isotope dilution approaches).

The standard addition approach is based on the addition of a known quantity(s) of a calibrant to the unknown (with or without addition of an internal standard). At least two sample levels must be prepared for each unknown; one sample can be the unspiked unknown. Since separate calibrations are carried out for each unknown sample, this approach is labor-intensive.

Internal and external standard approaches to quantification can utilize averaged response factors, a zero intercept linear regression model, a calculated intercept linear regression model, or another nonlinear model. The responses can be unweighted or weighted. The model utilized should be evaluated as appropriate for the measurement problem.

The number and level of calibrants used depends on the measurement problem. When the level(s) of the unknown can be estimated, calibrants should be prepared to approximate this level(s). Preparation of calibrants in this way minimizes the issue of response linearity. When less is known about the unknowns, or when unknowns are expected to span a concentration range, calibrants should be prepared to span this range. It is un-

desirable to extrapolate to concentrations outside of the calibration interval. When possible, prepare calibrants by independent gravimetric processes and avoid serial dilutions or use of stock solutions.

When internal standards are used as part of the method, levels should be selected to approximate the levels of components being measured. The response for the internal standard should be the same or similar for calibrants and unknowns, and the ratio of internal standard and analyte(s) should be similar. When possible, the absolute response for analytes and internal standards should be significantly greater than the noise level. If the analyte level(s) are low in the unknown samples, the internal standard should be added at higher levels (measurement precision should be enhanced if the internal standard is significantly greater than the noise level).

Capillary Electrophoresis

Principles of the Technique. Capillary electrophoresis (CE) refers to a family of techniques that are based upon the movement of charged species in the presence of an electric field. A simplified diagram of a CE instrument is shown in Fig. 4.6. When a voltage is applied to the system, positively charged species move toward the negatively charged electrode (cathode), while negatively charged species migrate toward the positively charged electrode (anode). Neutral species are not attracted to either electrode.

Separations are typically performed in fused silica capillaries with an internal diameter of 25–100 μm and a length of 25–100 cm. The capillary is filled with a buffer, and the applied voltage generally ranges from 10–30 kV. A number of different detection strategies

are available, including UV absorbance, laser-induced fluorescence, and mass spectrometry.

Scope. CE is applicable to a wide range of pharmaceutical, bioanalytical, environmental and forensic analyses. Various modes of CE are employed depending upon the type of analyte and the mechanism of separation. Capillary zone electrophoresis (CZE) is the most widely used mode of CE and relies upon differences in size and charge between analytes at a given pH to achieve separations. Some of the demonstrated applications of CZE include the analysis of drugs and their metabolites, peptide mapping, and the determination of vitamins in nutritional supplements. Neutral compounds are typically resolved using micelles, through a technique known as micellar electrokinetic capillary chromatography (MECC or MEKC). Both CZE and MEKC have also been utilized for enantioselective separations. Capillary gel electrophoresis (CGE) has been used extensively for the separation of proteins and nucleic acids. The gel network acts as a sieve to separate components based on size. Capillary isoelectric focusing (CIEF) separates analytes on the basis of their isoelectric points and incorporates a pH gradient. This technique is commonly used for the separation of proteins. Capillary isotachopheresis (CITP) utilizes a combination of two buffer systems and is sometimes used as a preconcentration method for other CE techniques.

CE has been viewed as an alternative to liquid chromatography (LC), although CE is not yet as well-established as LC. CE typically provides a higher efficiency than LC and has lower sample consumption. In addition, the various modes of CE offer flexibility in method development. Because CE utilizes a different separation mechanism to LC, it can be viewed as an orthogonal technique that provides complementary information to LC analyses. Currently, the primary limitations of CE involve sensitivity and reproducibility issues, but improvements continue to be made in these areas.

Nature of the Sample. Samples for CE cover a wide range and include matrices such as biological fluids, protein digests and pharmaceutical compounds. Depending on the sample matrix, the sample may be injected directly or may be diluted in water or the run buffer. Certain sample preparation techniques can be utilized to optimize sensitivity. Derivatization of the analytes is often required for laser-induced fluorescence detection.

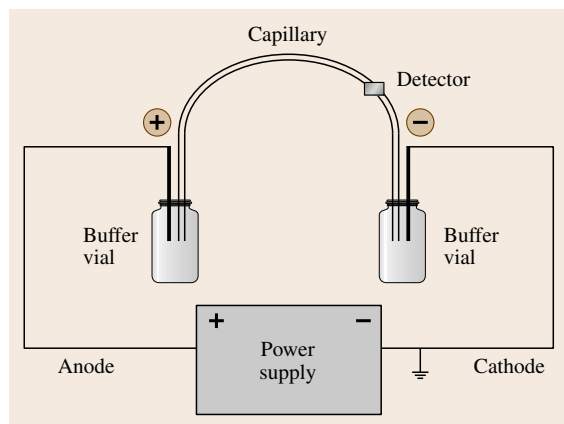


Fig. 4.6 Capillary electrophoresis: diagram of CE instrumentation

Qualitative Analysis. CE is particularly applicable to qualitative analyses of peptides and proteins. The high efficiency of CE yields separations of even closely related species, and the *fingerprints* resulting from the analysis of two different samples can be compared to reveal subtle differences.

Traceable Quantitative Analysis. Quantification in CE is generally performed by preparing calibration solutions of the analyte(s) of interest at known concentrations and comparing the peak areas obtained for known and unknown solutions. Quantification approaches used in CE are generally similar to those used in LC. One unique aspect of CE is the fact that the peak area is related to the migration velocity of the solute. Corrected peak areas, obtained by dividing the peak area by the migration time of the analyte, improve quantitative accuracy in CE.

Liquid Chromatography/Mass Spectrometry (LC/MS) and LC/MS/MS

The combination of liquid chromatography (LC) with mass spectrometry (MS) is a powerful tool for the determination of organic and organometallic species in complex matrices. While LC is sometimes combined with ICP-MS for elemental analysis, this section will focus on combining LC with MS using either electrospray ionization (ESI)¹ or atmospheric pressure chemical ionization (APCI), the most widely used approaches for the determination of organic species. Generally, reversed-phase LC using volatile solvents and additives is combined with a mass spectrometer equipped with either an ESI or an APCI source. ESI is the favored approach for ionic and polar species, while APCI may be preferred for less polar species. If the mass spectrometer has the ability to perform tandem mass spectrometry (MS/MS) using collision-induced dissociation, analysis of daughter ions adds additional specificity to the process.

Principles of the Technique. The principles of liquid chromatography are covered in the liquid chromatography section. For LC/MS, the effluent from the LC column flows into the source of the mass spectrometer. For ESI the effluent is sprayed out of a highly charged orifice, creating charged clusters that lose solvent molecules as they move from the orifice, resulting in charged analyte molecules. For APCI, a corona discharge is used to ionize solvent molecules that act as chemical ionization reagents to pass charges to the analyte molecules. Desolvated ions pass into the MS

vacuum system through a pinhole. The ions may be separated by various devices including quadrupole, ion trap, magnetic sector, time-of-flight, or ion cyclotron resonance devices. The principles of operation of these devices are beyond the scope of this discussion. Ions are generally detected using electron or ion multipliers.

Scope. LC/MS and LC/MS/MS have been used to determine organic species ranging from highly polar peptides and oligonucleotides to low-polarity species such as nitrated polycyclic aromatic hydrocarbons in virtually any matrix imaginable. For many polar substances such as drug metabolites or hormones, LC/MS has largely supplanted GC/MS as the approach of choice for two reasons. Sample preparation is much simpler with LC/MS in that the analyte is generally not derivatized and analyte isolation from the matrix is often faster. Nevertheless, with most complex matrices, some sample processing is generally necessary before the sample is introduced into the LC/MS. Secondly, sensitivity is often greater, resulting in better quantification of very low concentrations. Because both ESI and APCI are soft ionization techniques, there is little fragmentation observed in contrast to what is seen for many analytes in GC/MS. This can be either advantageous or a negative feature. The ion intensity is concentrated in far fewer ions, thus improving sensitivity. However, if there are interferences at the ions being monitored, there are not usually any alternatives ions that can be used for measurement, such as there often are with GC/MS. However, if MS/MS is available, there is usually a parent–daughter combination that is free from significant interference. For both LC/MS and LC/MS/MS, use of an isotope-labeled form of the analyte as the internal standard is the preferred approach for quantification. However, satisfactory results are sometimes possible with a close analog of the analyte, provided that they can be separated.

Qualitative Analysis. LC/MS can be a useful tool for qualitative analysis. With ESI, this approach is widely used for characterizing proteins. LC/MS/MS is also used for protein studies and can be used to determine the amino acid sequence. It is also very useful for drug metabolite studies.

Traceable Quantitative Analysis. Excellent quantitative results can be obtained with these techniques. With an isotope-labeled internal standard, measurement precision is typically 0.5–5%. Accuracy is dependent upon several factors. The measurements must be calibrated

with known mixtures of a pure form of the analyte and the internal standard. Knowledge about the purity of the reference compounds is essential. Other important aspects that must be considered are: liberation of the analyte from the matrix, equilibration with the internal standard, and specificity of the analytical measurements.

Several review articles [4.73–83] are available.

4.1.6 Classical Chemical Methods

Classical chemical analysis comprises gravimetry, titrimetry and coulometry. These techniques are generally applied to assays: analyses in which a major component of the sample is being determined. Classical methods are frequently used in assays of primary standard reagents that are used as calibrants in instrumental techniques. Classical techniques are not generally suited to trace analyses. However, the methods are capable of the highest precision and lowest relative uncertainties of any techniques of chemical analysis. Classical analyses require minimal equipment and capital outlay, but are usually more labor-intensive than instrumental analyses for the corresponding species. Other than rapid tests, such as spot tests, classical techniques are rarely used for qualitative identification.

Kolthoff et al. [4.84] provide a thorough yet concise summary of the classical techniques described in this section.

Gravimetry

Principles of the Technique. Gravimetry is the determination of an analyte (element or species) by measuring the mass of a definite, well-characterized product of a stoichiometric chemical reaction (or reactions) involving that analyte. The product is usually an insoluble solid, though it may be an evolved gas. The solid is generally precipitated from solution and isolated by filtration. Preliminary chemical separation from the sample matrix by ion-exchange chromatography or other methods is often used.

Gravimetric determinations require corrections for any trace residual analyte remaining behind in the sample matrix and any trace impurities in the insoluble product. Instrumental methods, which typically have relatively large uncertainties, can be used to determine these corrections and improve the overall accuracy and measurement reproducibility of the gravimetric analysis, since these corrections represent only a small part of the final value (and its uncertainty).

Scope. Gravimetric determination is normally restricted to analytes that can be quantitatively separated to form a definite product. In such cases, relative expanded uncertainties are in the range of 0.05–0.3%. The applicability of gravimetry can be broadened (at the cost of increased method uncertainty) to cases where the product is a compound with greater solubility and/or more impurities by judicious use of instrumental techniques to determine and correct for residual analyte in the solution and/or impurities in the precipitate. Gravimetry can be labor-intensive and is usually applied to an analytical set of 12 or fewer samples, including blanks.

The advantage of coupling gravimetry with instrumental determination of a residual analyte and contaminants can be demonstrated by the gravimetric determination of sulfate in a solution of K_2SO_4 . In an application of this determination [4.85], sulfate was precipitated from a K_2SO_4 solution and weighed as $BaSO_4$. The uncorrected gravimetric result for sulfate was 1001.8 mg/kg with a standard deviation of the mean of 0.32 mg/kg. When instrumentally determined corrections were applied to each individual sample, the corrected mean result was 1003.8 mg/kg sulfate with a standard deviation of the mean of 0.18 mg/kg. The uncorrected gravimetric determination had a significantly negative bias (0.2%, relative) and a measurement reproducibility that was nearly twice that of the corrected result.

The insoluble product of the gravimetric determination can be separated from the sample matrix in several ways. After any required dissolution of the sample matrix, the analyte of interest can be separated from solution by precipitation, ion-exchange or electrodeposition. Other separation techniques (such as distillation or gas evolution [4.86]) can also be used. The specificity of the separation procedure for the analyte of interest and the availability of suitable complementary instrumental techniques will determine the applicability of a given gravimetric determination.

Separation by precipitation from solution can be accomplished by evaporation of the solution, addition of a precipitating reagent, or by changing the solution pH. After its formation, the precipitate may be filtered, rinsed and/or heated and weighed. The resulting precipitate must be relatively free from coprecipitated impurities. An example is the determination of silicon in soil [4.87]. Silicon is separated from a dissolved soil sample by dehydration with HCl and is filtered from the solution. The SiO_2 precipitate is heated and weighed. HF is added to volatilize the SiO_2 and the mass of the remaining impurities is determined. The

SiO_2 is determined by difference. Corrections for Si in the filtered solution can be determined by instrumental techniques.

With ion-exchange separation of the analyte, the precipitation and filtration step may not be required. After collection of the eluate fraction containing the analyte, if no further precipitation reactions are required, the solution can be evaporated to dryness with or without adding other reagents. Ion-exchange and gravimetric determination is demonstrated by the determination of Na in human serum [4.88]. The Na fraction in a dissolved serum sample is eluted from an ion-exchange column. After H_2SO_4 is added, the Na fraction is evaporated to dryness, heated, and weighed as Na_2SO_4 . Instrumentally determined corrections are made both for Na in the fractions collected before and after the *Na fraction* and also for impurities in the precipitate.

Electrodeposition can be used to separate a metal from solution. The determination of Cu in an alloy can be used as an illustration [4.86]. Copper in a solution of the dissolved metal is plated onto a Pt gauze electrode by electrolytic deposition. The Cu-plated electrode is weighed and the plated Cu is stripped in an acid solution. The cleaned electrode is reweighed so that the Cu is determined by difference. Corrections are made via instrumental determination of residual Cu in the original solution that did not plate onto the electrode and metal impurities stripped from the Cu-plated electrode.

Nature of the Sample. Samples analyzed by gravimetry must be in solution prior to any required separation. Generally, an amount of analyte that will result in a final product weighing at least 100 mg (to minimize the uncertainty of the mass determination) to no more than 500 mg (to minimize occlusion of impurities) is preferred. Potentially significant interfering substances should be present at insignificant levels. Examples of significant interfering substances would be more than trace B in a sample for a determination of Si (B will volatilize with HF and bias results high) or significant amounts of a substance that is not easily separated from the analyte of interest (for example, Na may not be easily separated by ion exchange from a Li matrix). The suitability of the gravimetric quantification can be evaluated by analyzing a certified reference material (CRM) with a similar matrix using the identical procedure.

Qualitative Analysis. Many of the classical qualitative tests for elements or anions use the same precipitate-forming reactions applied in gravimetry. Gravimetry

can also be used to determine the total mass of salt dissolved in a solution (for example, by evaporation with weighing).

Traceable Quantitative Analysis. The mass fraction of the analyte in a gravimetric determination is measured by weighing a sample and the separated compound of known stoichiometry from that sample on a balance that is traceable to the kilogram. Appropriate ratios of atomic weights (gravimetric factors) are applied to convert the compound mass to the mass of the analyte or species of interest. Gravimetry is an absolute method that does not require reference standards. Thus it is considered a direct primary reference measurement procedure [4.89]. Gravimetry can be performed in such a way that its operation is completely understood, and all significant sources of error in the measurement process can be evaluated and expressed in SI units together with a complete uncertainty budget. Any instrumentally determined corrections for residual analyte in the solution or for impurities in the precipitate must rely on standards that are traceable to the SI for calibration. To the extent that the gravimetric measurement is dependent on instrumentally-determined corrections, its absolute nature is debatable.

Titrimetry

Principles of the Technique. The fundamental basis of titrimetry is the stoichiometry of the chemical reaction that forms the basis for the given titration. The analyte reacts with the titrant according to the stoichiometric ratio defined by the corresponding chemical equation. The equivalence point corresponds to the point at which the ratio of titrant added to the analyte originally present (each expressed as an amount of substance) equals the stoichiometric ratio of the titrant to the analyte defined by the chemical equation.

The endpoint (the practical determination of the equivalence point) is obtained using visual indicators or instrumental techniques. Visual indicators react with the added titrant at the endpoint, yielding a product of a different color. Hence, a bias (indicator error) exists with the use of indicators, since the reaction of the indicator also consumes titrant. This bias is evaluated (along with interfering impurities in the sample solvent) in a blank titration. Potentiometric detection generally locates the endpoint as the point at which the second derivative of the potential versus the added titrant function equals zero. Other techniques (amperometry, nephelometry, spectrophotometry, and so on) are also used.

The titrant is typically added as a solution of the given reagent. Solutions are inherently homogeneous and can be conveniently added in aliquots that are not restricted by particle size. The amount of titrant added is obtained from the amount-of-substance concentration (hereafter denoted *concentration*) of the titrant in this solution and its volume (amount-of-substance content and mass, respectively, for gravimetric titrations). The concentration of the solution is obtained by direct knowledge of the assay of the reagent used to prepare the solution, or, more frequently, by standardization. In titrimetry, standardization is the assignment of a value (concentration or amount-of-substance content) to the titrant solution via titration(s) against a traceable standard.

Scope. Titrimetry is restricted to analytes that react with a titrant according to a strict stoichiometric relationship. A systematic bias in the result arises from any deviation from the theoretical stoichiometry or from the presence of any other species that reacts with the titrant. The selectivity of titrimetric analyses is generally not as great as that of element-specific instrumental techniques. However, titrimetric techniques can often distinguish among different oxidation states of a given element, affording information on speciation that is not accessible by element-specific instrumental techniques. Titrimetric methods generally have lower throughput than instrumental methods.

The most commonly encountered types of titrations are acid–base (acidimetric), oxidation–reduction, precipitation, and compleximetric titrations. The theory and practice of each are presented in [4.84]. A detailed monograph [4.90] provides exhaustive information, including properties of unusual titrants.

Titrimetric methods generally have lower throughput than instrumental methods.

Nature of the Sample. Samples analyzed by titrimetry must be in solution or dissolve totally during the course of the given titration. Certain analyses require pretreatment of the sample prior to the titrimetric determination itself. Nonquantitative recovery associated with such pretreatment must be taken into account when evaluating the uncertainty of the method. Examples include the determination of protein using the Kjeldahl titration and oxidation–reduction titrimetry preceded by reduction in a Jones reductor. If possible, a certified reference material (CRM) with a similar matrix should be carried through the entire procedure, including the sample pretreatment, to evaluate its quantitiveness.

Qualitative Analysis. Titrimetry is not generally used for qualitative analysis. It is occasionally used for semiquantitative estimations (for example, home water hardness tests).

Traceable Quantitative Analysis. Titrimetry is considered a primary ratio measurement [4.89], since the measurement itself yields a ratio (of concentrations or amount-of-substance contents). The result is obtained from this ratio by reference to a standard of the same kind. However, titrimetry is different from instrumental ratio primary reference measurements (as in isotope dilution mass spectrometry), in that the standard can be a different element or compound from the analyte. This ability to *link* different chemical standards has been proposed as a basis for interrelating many widely-used primary standard reagents [4.91].

The traceability of titrimetric analyses is based on the traceability to the SI of the standard used to standardize or prepare the titrant. CRMs used as standards in titrimetry are certified by an absolute technique, most often coulometry (see the following section).

Literature references frequently note that certain titrants can be prepared directly from a given reagent without standardization. Such statements are based on historic experience with the given reagent. Traceability for such a titrant rests solely on the manufacturer's assay claim for the given batch of reagent, unless the titrant solution is directly prepared from the corresponding CRM or prepared from the commercial reagent and subsequently standardized versus a suitable CRM. Titrants noted in the literature as requiring standardization (such as sodium hydroxide) have lower and/or variable assays. Within- and between-lot variations of the assays of such reagents are too great for use as titrants without standardization.

The stability and homogeneity of the titrant affect the uncertainty of any titrimetric method in which it is used. The concentration of any titrant solution can change through evaporation of the solvent. A mass log of the solution in its container (recorded before and after each period of storage, typically days or longer) is useful for estimating this effect. In addition, the titrant solution can react during storage, either with components of the atmosphere (for example, O₂ with reducing titrants or CO₂ with hydroxide solutions) or with the storage container (for instance, hydroxide solutions with soda-lime glass or oxidizing titrants with some plastics). Each such reaction must be estimated quantitatively to obtain a valid uncertainty estimate for the given titrimetric analysis.

In titrations requiring ultimate accuracy, the bulk (typically 95–99%) of the titrant required to reach the endpoint is often added as a concentrated solution or as the solid titrant (see the Gravimetric Titrations section). The remaining 1–5% of the titrant is then added as a dilute solution. This approach permits optimal determination of the endpoint, which is further sharpened by virtue of the decreased total volume of solution. Using this approach, a precision on the order of 0.005% can be readily achieved.

Gravimetric Titrations. In traditional gravimetric titrations (formerly called *weight titrations*), the titrant solution is prepared on an amount-of-substance content (moles/kg) basis. The solution is added as a known mass. The amount of titrant added is calculated from its mass and amount-of-substance content.

Gravimetric titrimetry conveys the advantages of mass measurements to titrimetry. Masses are readily measured to an accuracy of 0.001%. Mass measurements are independent of temperature (neglecting the small change in the correction for air buoyancy resulting from the change in air density). The expansion coefficient of the solution ($\approx 0.01\%$ /K for aqueous solutions) does not affect mass measurements.

A useful variation of the dual-concentration approach described above is to add the bulk of the titrant gravimetrically as the solid (provided the solid titrant has demonstrated homogeneity, as in a CRM) or as its concentrated solution. This bulk addition is followed by volumetric additions of the remainder of the titrant (for example, 5% of the total) as a dilute solution for the endpoint determination. The main advantage of this approach is that the endpoint determination can be performed using a commercial titrator. The advantages of gravimetric titrimetry and the dual-concentration approach described above are each preserved. Any effect of variation in the concentration of the dilute titrant is reduced by the reciprocal of the fraction represented by its addition (for example, a 20-fold reduction for 5%).

Coulometry

Principles of the Technique. Coulometry is based on Faraday's Laws of Electrolysis, which relate the charge passed through an electrode to the amount of analyte that has reacted. The amount-of-substance content of the analyte, ν_{analyte} , is calculated directly from the current I passing through the electrode; the time t ; the stoichiometric ratio of electrons to analyte n ; the Faraday constant F ; and the mass of sample m_{sample} . The

limits of integration, t_0 and t_f , depend on the type of coulometric analysis (see below).

$$\nu_{\text{analyte}} = \frac{\int_{t_0}^{t_f} I dt}{n F m_{\text{sample}}} \quad (4.11)$$

Since I and t can be measured more accurately than any chemical quantity, coulometry is capable of the smallest uncertainty and highest precision of all chemical analyses.

Coulometric analyses are performed in an electrochemical (coulometric) cell. The coulometric cell has two main compartments. The sample is introduced into the sample compartment, which contains the working (coulometric) electrode. The other main compartment contains the counter-electrode. These main compartments are connected via one or more intermediate compartment(s) in series, providing an electrolytic link between the main compartments. The contents of the intermediate compartments may be rinsed or flushed back into the sample compartment to return any sample or titrant that has left the sample compartment during the titration.

Coulometry has two main variants, controlled-current and controlled-potential coulometry. Controlled-current coulometry is essentially titrimetry with electrochemical generation of the titrant. Increments of charge are added at one or more values of constant current. In practice, a small amount of the analyte is added to the cell initially. This analyte is titrated prior to introducing the actual sample. The endpoint of this pretitration yields the time t_0 in (4.11). The quantity t_f corresponds to the endpoint of the subsequent titration of the analyzed sample. The majority of the sample (typically 99.9%) is titrated at a high, accurately controlled constant current I_{main} (typically 0.1–0.2 A) for a time t_{main} . Lower values of constant current (1–10 mA) are used in the pretitration and in the endpoint determination of the sample titration. This practice corresponds to the dual-concentration approach used in high-accuracy titrimetry.

Controlled-potential coulometry is based on exhaustive electrolysis of the analyte. A potentiostat maintains the potential of the working electrode in the sample compartment at a constant potential with respect to a reference electrode. Electrolysis is initiated at $t = t_0$. The analyte reacts directly at the electrode at a mass-transport-limited rate. The electrode current I decays exponentially as the analysis proceeds, approaching zero as t approaches infinity. In practice, the electrolysis is discontinued at $t = t_f$, when the current decays

to an insignificant value. A blank analysis is performed without added analyte to correct for any reduction of impurities in the electrolyte.

A survey of coulometric methods and practice through 1986 has been published [4.92].

Scope. Controlled-current coulometry is an absolute technique capable of extreme precision and low uncertainty. Analyses reproducible to better than 0.002% (relative standard deviation) with relative expanded uncertainties of < 0.01% are readily achieved. Standardization of the titrant is not required. Most of the acidimetric, oxidation–reduction, precipitation, and compleximetric titrations used in titrimetry can be performed using controlled-current coulometry. Compared to titrimetry, controlled-current coulometry has the advantage that the titrant is generated and used virtually immediately. This feature avoids the changes in concentration during storage and use of the titrant that can occur in conventional titrimetry.

Controlled-potential coulometry is also an absolute technique. However, in most cases the correction for the background current limits the uncertainty to roughly 0.1%. Controlled-potential coulometry can afford greater selectivity, through appropriate selection of the electrode potential, than either controlled-current coulometry or titrimetry. The analyte must react directly at the electrode, in contrast to controlled-current coulometry or titrimetry, which can determine nonelectroactive species that react with the given titrant.

Compared to titrimetry, both coulometric techniques have lower throughput. A single high-precision controlled-current coulometric titration requires at least an hour to complete, using typical currents and sample masses. The exhaustive electrolysis required in controlled-potential coulometry requires a period of up to 24 h for a single analysis.

Coulometric techniques are well-suited to automation. Automated versions of controlled-current coulometry [4.93, 94] are used to certify the CRMs used as primary standards in titrimetry.

Nature of the Sample. Sample restrictions for coulometry are similar to those of titrimetry noted above. Additionally, electroactive components other than the analyte can interfere with coulometric analyses, even though the corresponding titrimetric analysis may be feasible.

Qualitative Analysis. Coulometric techniques are not used for qualitative analysis.

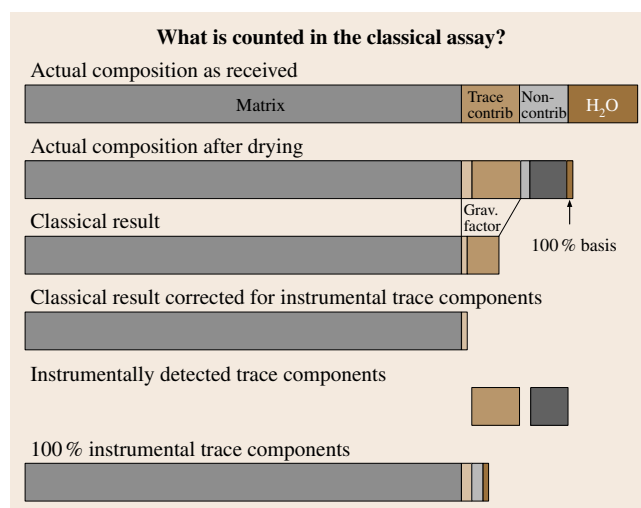


Fig. 4.7 Assay and purity determinations of analytical reagents

Traceable Quantitative Analysis. Traceability for coulometric analyses rests on the traceability of the measured physical quantities I and t and on the universal constant F . In addition, the net coulometric reaction relating electrons to analyte must proceed with 100% current efficiency, so that each mole of electrons that passes through the electrode must react, directly or indirectly, with exactly $1/n$ moles (according to (4.11)) of the added analyte. Interferents or side-reactions that consume electrons yield a systematic bias in the coulometric result. Such interferents must be excluded or taken into account in the uncertainty analysis. The criterion of 100% current efficiency is evaluated by performing trial titrations with different current densities. In controlled-current titrations using an added titrant-forming reagent, its concentration can also be varied to evaluate the generation reaction [4.95].

Coulometry yields results directly as v_{analyte} , as shown in (4.11). Results recalculated from v_{analyte} to a mass fraction basis (% assay) must take into account the uncertainty in the IUPAC atomic weights [4.96] in the uncertainty analysis. In high-precision, controlled-current coulometry, this contribution to the combined uncertainty can be significant.

Assay and Purity Determinations of Analytical Reagents

The purity of an analytical reagent can be determined by two different approaches: direct assay of the matrix species, and purity determination by subtraction of trace impurities. In the first approach, a classical assay

technique directly determines the mass fraction of the matrix species. In the second approach, the sum of the mass fractions of all components of the sample is taken as exactly unity (100%). Trace-level impurities in the reagent are determined using one or more of the instrumental techniques described in this chapter. The sum of the mass fractions of all detected impurities is subtracted from 100% to yield the quoted purity (species that are not detected are taken as present at a mass fraction equal to half the detection limit for the given species, with a relative uncertainty of $\pm 100\%$; the corresponding value and uncertainty are included in the calculation of the purity and its uncertainty). No assay is performed per se.

In principle, both approaches yield the same result. However, difficulties arise in practice owing to the shortcomings of each. In the classical assay, trace impurities can contribute to the given assay, yielding a result greater than the true value. For example, trace Br^- is typically titrated along with the matrix Cl^- in classical titrimetric and coulometric assay procedures. Such trace interferences contribute to the apparent assay to an extent given by the actual mass fraction multiplied by the ratio of the equivalent weight [4.84,90] of the matrix species to that of the actual interferent, analogous to the gravimetric factor in gravimetry. The equivalent weight is given by the molar mass of the given species (calculated from IUPAC atomic weights [4.96]) divided by an integer n . For coulometry, n is that given in (4.11). For other methods, n is defined by the reaction that occurs in the titration or precipitation process.

In the 100% *minus impurities* approach, the result only includes those species that are actually sought. For example, commercial high-purity reagents often state a high purity, such as 99.999%, based on a semiquantitative survey of trace metal impurities. Other species, notably occluded water in high-purity crystalline salts, or dissolved gases in high-purity metals, are not sought, but they may be present at high levels, such as 0.1%. The purity with respect to the stated impurities is valid. However, if the level of unaccounted-for impurities is significant in comparison to the requirements for the calibrant, the stated purity is not valid for use of the reagent as a calibrant.

Figure 4.7 illustrates schematically the contrasting advantages and disadvantages of both approaches

toward the purity of a hypothetical crystalline compound. The total length of each bar corresponds to the purity as obtained by the stated method(s). The matrix compound is shown at the left in gray. Impurities (including water) are denoted by segments of other shades at the right end of each bar. The upper bar shows the true composition as received. The impurities are divided into two classes: those that contribute to the classical assay, and those that do not. The second bar shows the true composition after drying. Each class of impurities is subdivided into a component that is detected instrumentally and one that is not. The two components that are detected instrumentally are shown separately in the second line from the bottom.

The third bar shows the classical assay without any corrections for contributing impurities. The lower bar represents the purity obtained from the 100% *minus impurities* approach. Each value has a positive bias with respect to the true assay, the length of the matrix segment. The gravimetric factor represents the ratio of equivalent weights noted above.

The fourth bar shows the result of the classical assay corrected for instrumentally-determined impurities that also contribute to the classical assay. This bar is closest in length to the true assay, represented by the length of the matrix segment. A small bias remains for impurities that both evade instrumental detection and contribute to the classical assay.

An additional problem with classical assays of ionic compounds is that a single technique generally determines only a component of the matrix compound (such as Cl^- in the assay of KCl by titration with Ag^+). The reported mass fraction of the assay compound is calculated assuming the theoretical stoichiometry. The identity of the counterion (such as K^+ in an argentimetric KCl assay) is assumed.

A more rigorous approach toward a *true* assay of an ionic compound by classical techniques is to perform independent determinations of the matrix components. As an example, K^+ in KCl could be assayed by gravimetry, with Cl^- assayed by titrimetry or coulometry. A rigorous version of each of these assays would include corrections for contributing trace interferences to the respective assays.

Several review articles [4.84–96] are available.

4.2 Microanalytical Chemical Characterization

Establishing the spatial relationships of the chemical constituents of materials requires special methods that build on many of the bulk methods treated in the preceding portion of this chapter. There may be interest in locating the placement of a trace chemical constituent within an engineered structure, or in establishing the extent of chemical alteration of a part taken out of service, or in locating an impurity that is impacting on the performance of a material. When the question of the relative spatial locations of different chemical constituents is at the core of the measurement challenge, methods of chemical characterization that preserve the structures of interest during analysis are critical. Not all bulk analytical methods are suited for surface and/or microanalytical applications, but many are. In the remainder of this chapter, some of the more broadly applicable methods are touched upon, indicating their utility for establishing chemical composition as a function of spatial location, in addition to their use for quantitative analysis.

4.2.1 Analytical Electron Microscopy (AEM)

When a transmission electron microscope (TEM) is equipped with a spectrometer for chemical analysis, it is usually referred to as an *analytical electron microscope*. The two most common chemical analysis techniques employed by far are energy-dispersive x-ray spectrometry (XEDS) and electron energy-loss spectroscopy (EELS). In modern TEMs a field emission electron source is used to generate a nearly monochromatic beam of electrons. The electrons are then accelerated to a user-defined energy, typically in the range of 100–400 keV, and focused onto the sample using a series of magnetic lenses that play an analogous role to the condenser lens in a compound light microscope. After interacting with the sample, the transmitted electrons are formed into a real image using a magnetic objective lens. This real image is then further magnified by a series of magnetic intermediate and projector lenses and recorded using a charged coupled device (CCD) camera.

Principles of the Technique. Images with a spatial resolution near 0.2 nm are routinely produced using this technique. In an alternative mode of operation, the condenser lenses can be used to focus the electron beam into a very small spot (less than 1 nm in diameter) that is rastered over the sample using electrostatic deflection coils. By recording the transmitted intensity at

each pixel in the raster, a *scanning transmission electron microscope (STEM)* image can be produced. After a STEM image has been recorded, it can be used to locate features of interest on the sample and the scan coils can then be used to reposition the electron beam with high precision onto each feature for chemical analysis. As the beam electrons are transmitted through the sample, some of them are scattered inelastically and produce atomic excitations. Using an EELS spectrometer, a spectrum of the number of inelastic scatters as a function of energy loss can be produced. Simultaneously, an XEDS spectrometer can be used to measure the energy spectrum of x-rays emitted from the sample as the atoms de-excite. Both of these spectroscopies can provide detailed quantitative information about the chemical structure of the sample with very high spatial resolution.

In many ways EELS and XEDS are complementary techniques, and the limitations of one spectroscopy are often offset by the strengths of the other. Because elements with low atomic number do not fluoresce efficiently, XEDS begins to have difficulty with elements lighter than sodium and is difficult or impossible to use for elements below carbon. In contrast, EELS is very efficient at detecting light elements. Because EELS has much better energy resolution than XEDS (≈ 1 eV for EELS and 130 eV for XEDS), it is also capable of extracting limited information about the bonding and valence state of the atoms in the analysis region. The two main drawbacks to EELS are that the samples need to be very thin compared to XEDS samples, and that it places greater demands on the analyst, both experimentally during spectrum acquisition and theoretically during interpretation of the results. Because XEDS works well on relatively thick samples and is easier to execute, it enjoys widespread use, while EELS is often considered a more specialized technique.

Nature of the Sample. Perhaps the single most important drawback to AEM is that all samples must be thinned to electron transparency. The maximum acceptable thickness varies with the composition of the sample and the nature of the analysis sought, but in most cases the samples must be less than ≈ 500 nm thick. For quantitative EELS, the samples must be much thinner: a few tens of nanometers thick at most. Another important limitation is that the samples be compatible with the high vacuum environment required by the electron optics. Fortunately, a wide array of sample prepara-

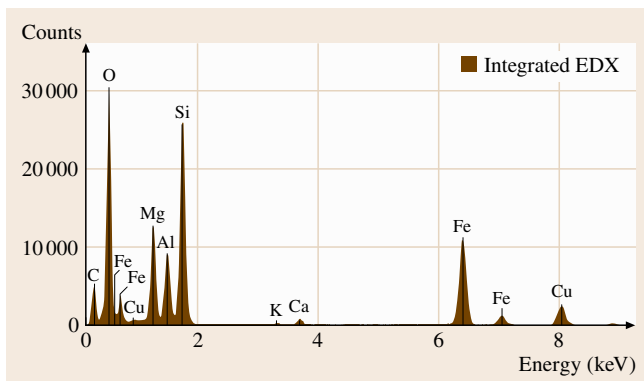


Fig. 4.8 Analytical electron microscopy: example XEDS spectrum from a sample containing C, O, Mg, Al, Si, K, Ca and Fe. The Cu peaks are from the sample mount

tion techniques have been developed over the years to convert macroscopic pieces of (sometimes wet) material into very thin slices suitable for AEM: dimpling, acid jet polishing, bulk ion milling, mechanical polishing, focused ion beam (FIB) processing, and diamond knife sectioning using an ultramicrotome. Preparation of high-quality AEM samples that are representative of the parent material without introducing serious artifacts remains one of the most important tasks facing the AEM analyst.

Qualitative Analysis. The AEM is a powerful tool for the qualitative chemical analysis of nanoscale samples.

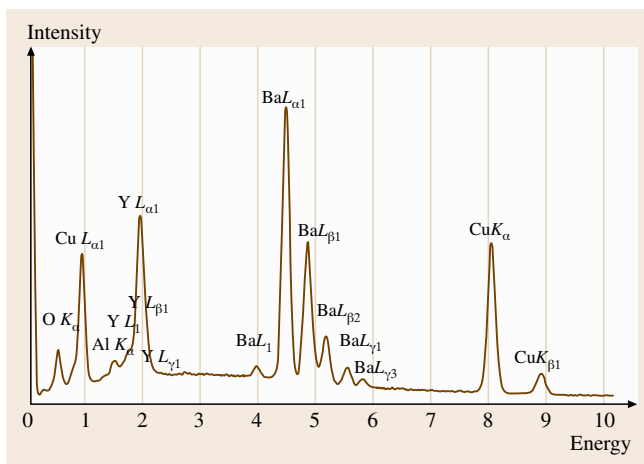


Fig. 4.9 Energy-dispersive spectrometry (EDS) of an $\text{YBa}_2\text{Cu}_3\text{O}_{7-x}$ single crystal with a trace aluminum constituent. Beam energy = 20 keV

The XEDS spectrometer can be used to detect most elements present in the sample at concentrations of 1 mg/g (0.1% mass fraction) or higher (see Fig. 4.8). EELS can be used in many cases down to a detection limit of 100 $\mu\text{g/g}$, depending on the combination of elements present. While these numbers are not impressive in terms of minimum mass fraction (MMF) sensitivity, it should be noted that this performance is available with spatial resolutions measured in nanometers and for total sample masses measured in attograms. In favorable cases, single-atom sensitivity has been demonstrated in the AEM for several elements, thus establishing it as a leader in minimum detectable mass (MDM) sensitivity.

Traceable Quantitative Analysis. Through the use of standards and the measurement of empirical detector sensitivity factors (Cliff–Lorimer k -factors), XEDS measurements in the AEM can be made quantitative. The precision of the measurement is often limited by the total signal available (related to the sample thickness and elemental abundances), while the accuracy is affected by poorly-known sample geometry and absorption effects. Traceability of the results is limited by the extreme rarity of certified reference materials with sufficient spatial homogeneity suitable for the measurement of k -factors. EELS measurements can be quantified by a first-principles approach that does not require standards, but this method is limited in practice by our inability to compute accurate scattering cross-sections and our incomplete understanding of solid-state beam-sample interactions.

Several review articles [4.97–100] are available.

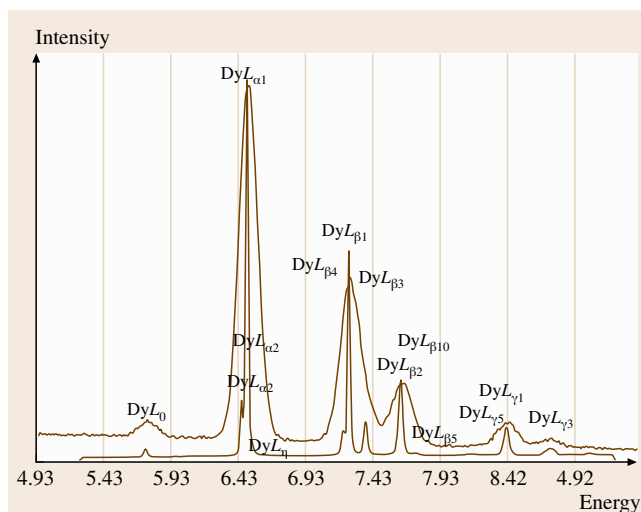
4.2.2 Electron Probe X-ray Microanalysis

Most solid matter is characterized on the microscopic scale by a chemically differentiated microstructure with feature dimensions in the micrometer to nanometer range. Many physical, biological and technological processes are controlled on a macroscopic scale by chemical processes that occur on the microscopic scale. The electron probe x-ray microanalyzer (EPMA) is an analytical tool based upon the scanning electron microscope (SEM) that uses a finely focused electron beam to excite the specimen to emit characteristic x-rays. The analyzed region has lateral and depth dimensions ranging from 50 nm to 5 μm , depending upon specimen composition, the initial beam energy, the x-ray photon energy, and the exact analytical conditions.

Table 4.3 Comparison of the characteristics of EDS and WDS x-ray spectrometers

Feature	EDS (semiconductor)	WDS
Energy range	0.1–25 keV (Si) 0.1–100 keV (Ge)	0.1–12 keV (4 crystals)
Resolution at MnK_{α}	130 eV (Si); 125 eV (Ge)	2–20 eV (E, crystal)
Instantaneous energy coverage	Full range	Resolution, 2–20 eV
Deadtime	50 MS	1 MS
Solid angle (steradian)	0.05–0.2	0.01
Quantum efficiency	$\approx 100\%$, 3–15 keV (Si)	< 30%, variable
Maximum count rate, EDS	≈ 3 kHz (best resolution)	100 kHz (single photon energy)
Maximum count rate, SDD	≈ 30 kHz (mapping)	
	≈ 15 kHz (best resolution) ≈ 400 kHz (mapping)	
Full spectrum collection	10–200 s	600–1800 s
Special strengths	Views complete spectrum for qualitative analysis at all locations	Resolves peak interferences; rapid pulses for composition mapping

Principles of the Technique. The EPMA/SEM is capable of quantitatively analyzing major, minor and trace elemental constituents, with the exceptions of H, He and Li, at concentrations as low as a mass fraction of $\approx 10^{-5}$. The technique is generally considered nondestructive and is typically applied to flat, metallographically polished specimens. The SEM permits application of the technique to special cases such as rough surfaces, particles, thin layers on substrates, and unsupported thin layers. Additionally, the SEM provides a full range of morphological imaging and structural crystallography capabilities that enable characterization of topography, surface layers, lateral compositional variations, crystal orientation, and magnetic and electrical fields over the micrometer to nanometer spatial scales. Two different types of x-ray spectrometers are in widespread use, the energy-dispersive spectrometer (EDS) and the wavelength-dispersive (or crystal diffraction) spectrometer (WDS). The characteristics of these spectrometers are such that they are highly complementary: the weaknesses of one are substantially offset by the strengths of the other. Thus, they are often employed together on the same electron beam instrument. The recent emergence of the silicon drift detector (SDD) has extended the EDS output count rate into the range 100–500 kHz. Figure 4.9 shows a typical EDS spectrum from a multicomponent specimen, $YBa_2Cu_3O_7$, demonstrating the wide energy coverage. Figure 4.10 shows a comparison of the EDS and WDS spectra for a portion of the dysprosium L-series. The considerable improvement in the spectral resolution of WDS compared to EDS is readily apparent. Table 4.3 com-

**Fig. 4.10** Comparison of EDS and WDS for dysprosium L-family x-rays excited with a beam energy of 20 keV

pare a number of the spectral parameters of EDS and WDS.

Qualitative Analysis. Qualitative analysis, the identification of the elements responsible for the characteristic peaks in the spectrum, is generally straightforward for major constituents (for example, those present at concentrations > 0.1% mass fraction), but can be quite challenging for minor (0.01–0.1% mass fraction) and trace constituents (< 0.01% mass fraction). This is especially true for EDS spectrometry when peaks of

minor and trace constituent peaks are in the vicinity ($< 100\text{ eV}$ away) of peaks from major constituents. Such interferences require peak deconvolution, especially when the minor or trace element is a light element ($Z < 18$), for which only one peak may be resolvable by EDS. Automatic computer-aided EDS qualitative analyses must always be examined manually for accuracy. The superior spectral resolution of the WDS can generally separate major/minor or major/trace peaks under these conditions, and is also not susceptible to the spectral artifacts of the EDS, such as pile-up peaks and escape peaks. However, additional care must be taken with WDS to avoid incorrectly interpreting higher order reflections ($n = 2, 3, 4, \dots$ in the Bragg diffraction equation) as peaks arising from other elements.

Quantitative Analysis: Spectral Deconvolution. Quantitative analysis proceeds in three stages:

1. extraction of peak intensities;
2. standardization; and
3. calculation of matrix effects.

For EDS spectrometry, the background is first removed by applying a background model or a mathematical filter. Peak deconvolution is then performed by the method of multiple linear least squares (MLLSQ). MLLSQ requires a model of the peak shape for each element determined on the user's instrument, free from

interferences from other constituents. A peak region from an unknown that consists of contributions from two or more constituents is deconvolved by constructing linear combinations of the reference peak shapes for all constituents. The synthesized peaks are compared with the measured spectrum until the best match is obtained, based upon a statistical criterion such as minimization of chi-squared, determined on a channel-by-channel basis. For WDS spectrometry, the resolution is normally adequate to separate the peak interferences so that the only issue is the removal of background. Because the background changes linearly over the narrow energy window of a WDS peak, an accurate background correction can be made by interpolating between two background measurements on either side of the peak.

Quantitative Analysis: Standardization. The basis for accurate quantitative electron probe x-ray microanalysis is the measurement of the ratio of the intensity of the x-ray peak in the unknown to the intensity of that same peak in a standard, with all measurements made for the same beam energy, known electron dose (beam current \times time), and spectrometer efficiency. This ratio, known as the k -value, is proportional to the ratio of mass concentrations for the element in the specimen and standard

$$\frac{I_{A,\text{spec}}}{I_{A,\text{std}}} = k \approx \frac{C_{A,\text{spec}}}{C_{A,\text{std}}} \quad (4.12)$$

This standardization step quantitatively eliminates the influence of detector efficiency, and reduces the impact of many physical parameters needed for matrix corrections. A great strength of EPMA is the simplicity of the required standard suite. Pure elements and simple stoichiometric compounds for those elements that are unstable in a vacuum under electron bombardment (such as pyrite, FeS_2 for sulfur) are sufficient. This is a great advantage, since making multielement mixtures that are homogeneous on the micrometer scale is generally difficult due to phase separation.

Quantitative Analysis: Matrix Correction. The relationship between k and $C_{A,\text{spec}}/C_{A,\text{std}}$ is not an equality because of the action of matrix or interelement effects. That is, the presence of element B modifies the intensity of element A as it is generated, propagated and detected. Fortunately, the physical origin of these matrix effects is well-understood, and by a combination of basic physics as well as empirical measurements, multiplicative correction factors for atomic number effects Z , absorption

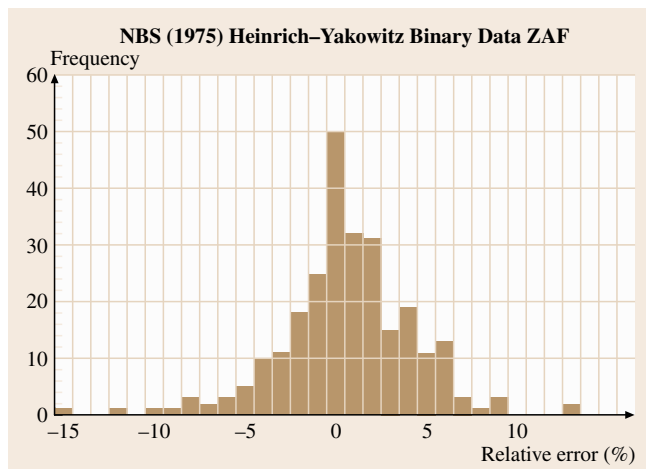


Fig. 4.11 Distribution of analytical relative errors (defined as $100\% \times [\text{measured} - \text{true}]/\text{true}$) for binary alloys as measured against pure element standards. Matrix correction by National Bureau of Standards ZAF; wavelength-dispersive x-ray spectrometry; measurement precision typically 0.3% relative standard deviation (after Heinrich and Yakowitz)

A and fluorescence F have been developed

$$\frac{C_{A,\text{spec}}}{C_{A,\text{std}}} = kZA F. \quad (4.13)$$

From the previous discussion, it is obvious that all three matrix effects – Z , A , and F – depend strongly on the composition of the measured specimen, which is the unknown for which we wish to solve. The calculation of matrix effects must therefore proceed in an iterative fashion from an initial estimate of the concentrations to the final calculated value. The measured k -values are used to provide the initial estimate of the specimen composition by setting the concentrations equal to normalized k -values

$$C_{i,1} = \frac{k_i}{\sum k_i}, \quad (4.14)$$

where i denotes each measured element. The initial concentration values are then used to calculate an initial set of matrix corrections, which in turn are used to calculate predicted k -values. The predicted k -values are compared with the experimental set, and if the values agree within a defined error, the calculation is terminated. Otherwise, the cycle is repeated. Convergence is generally found within three iterations.

This matrix correction procedure has been tested repeatedly over the last 25 years by using various microhomogeneous materials of known composition as test unknowns, including alloys, minerals, stoichiometric binary compounds, and so on. A typical distribution of relative errors (defined as $[\text{measured} - \text{true}]/\text{true} \times 100\%$) for binary alloys analyzed against pure element standards is shown in Fig. 4.11.

Compositional Mapping. A powerful method of presenting x-ray microanalysis information is in the form of compositional maps or images that depict the area distribution of the elemental constituents. These maps can be recorded simultaneously with SEM images that provide morphological information [4.101–103]. The digital output from a WDS, EDS or SDD over a defined range of x-ray photon energy corresponding to the peaks of interest is recorded at each picture element (pixel) scanned by the beam. The most sophisticated level of compositional mapping involves collecting a spectrum, or at least a number of spectral intensity windows for each picture element of the scanned image. These spectral data are then processed with the background correction, peak deconvolution, standardization, and matrix correction necessary to achieve quantitative analysis. The resulting maps are actually records of the

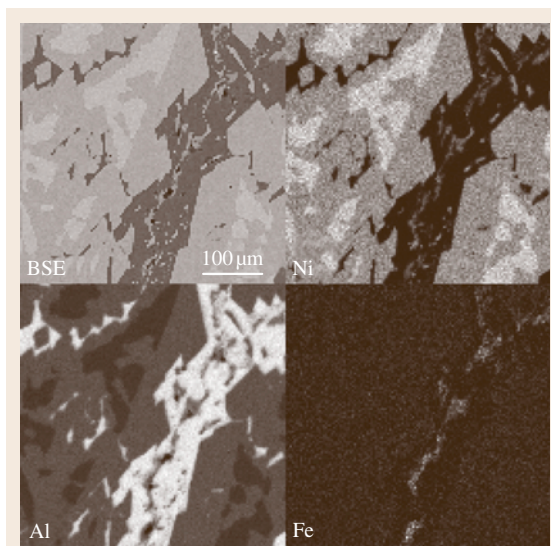


Fig. 4.12 Compositional maps (Ni, Al and Fe) and an SEM image (backscattered electrons, BSE) of Raney nickel (Ni-Al) alloy, showing a complex microstructure with a minor iron constituent segregated in a discontinuous phase

local concentrations, so that when displayed, the gray or color scale is actually related to the concentration. Figure 4.12 shows examples of compositional maps for an aluminum-nickel alloy.

Several review articles [4.104–106] are available.

4.2.3 Scanning Auger Electron Microscopy

Scanning Auger electron microscopy is an electron beam analytical technique based upon the scanning electron microscope. Auger electrons are excited in the specimen by a finely focused electron beam with a lateral spatial resolution of ≈ 2 nm point-to-point in current state-of-the-art instruments. An electron spectrometer capable of measuring the energies of emitted Auger electrons in the range of 1–3000 eV is employed for qualitative and quantitative chemical analysis. As in electron-excited x-ray spectrometry, the positions of the peaks are representative of the chemical composition of the specimen. The inelastic mean free path for Auger electrons is on the order of 0.1–3 nm, which means that only the Auger electrons that are produced within a few nanometers of the specimen surface are responsible for the analytical signal. The current state-of-the-art instruments are capable of providing true surface characterization at ≈ 10 nm lateral resolution.

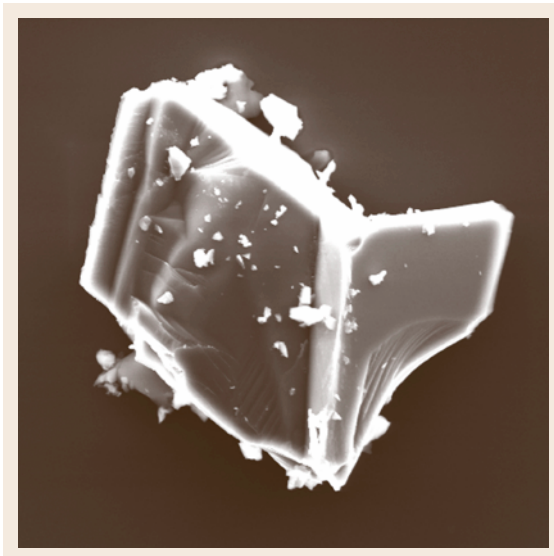


Fig. 4.13 SE image of particle, 25 μm field of view

Principles of the Technique. A primary electron beam interacting with a specimen knocks out a core electron, creating a core level vacancy. As a higher energy level electron moves down to fill the core level vacancy, energy is released in the form of an Auger electron, with the energy corresponding to the difference between the two levels. This is the basis for Auger electron spectroscopy (AES). The core-level vacancy can also be created by an x-ray photon, and this is the basis for x-ray photoelectron spectroscopy. The energy difference between the higher energy electron and the core level can also be released as a characteristic x-ray photon, and this is the basis for electron probe microanalysis.

The primary electron beam in an Auger microscope operates between 0.1 and 30 kV, and beam currents are on the order of nanoamps for analysis. Tungsten and lanthanum hexaboride electron guns can be used for AES, but field emission electron guns are the best choice because of the higher current density. It is desirable for AES to have more electrons in a small spot, and field emission guns deliver the smallest spot sizes normalized to beam current. Auger microscopes are also very good scanning electron microscopes, capable of producing secondary electron images (see Fig. 4.13) of the specimen as well as backscattered electron images if so equipped.

Auger electrons are produced throughout a sample volume defined by the interaction of the primary electron beam and the specimen. Auger electrons are relatively low in energy and so can only travel a small distance in a solid. Only the Auger electrons that are created close to the surface, within a few nanometers, have sufficient mean free path to escape the specimen and be collected for analysis. Since the Auger information only comes from the first few nanometers of the specimen surface, AES is considered a surface-sensitive technique. Several review articles are available.

Nature of the Sample. The surface sensitivity of AES requires the specimen to have a clean surface free of contamination. For this reason, Auger microscopes are ultrahigh vacuum (UHV) in the specimen chamber, which is on the order of 10^{-8} Pa. Steps must be taken to clean specimens prior to introduction into the Auger microscope so that they are free of volatile organic compounds that can contaminate the chamber vacuum. The Auger specimen chamber is equipped with an argon ion gun for sputter cleaning-off the contamination or ox-

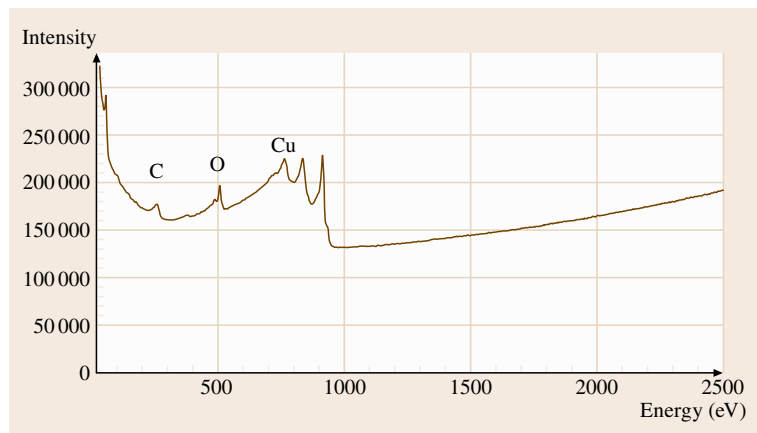


Fig. 4.14 Direct AES of copper with carbon and oxygen

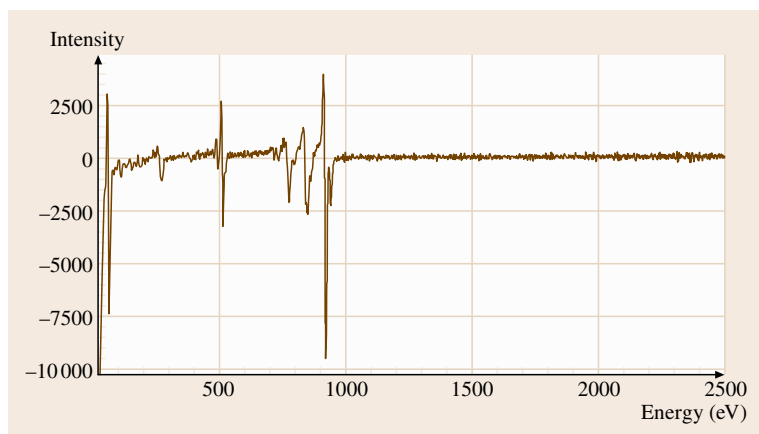


Fig. 4.15 Derivative AES of copper with carbon and oxygen

ide layer that coats specimens as a result of transporting them in air.

Investigation of a buried structure or an interface that is deeper than the Auger escape depth can be accomplished by Auger depth profiling. In Auger depth profiling, the instrument alternates between Ar ion sputtering of the surface and Auger analysis of the surface until, as material is sputtered away, the elemental composition changes with depth.

Qualitative/Quantitative Analysis. Auger electrons are recorded as a function of their energy by the electron spectrometer in the Auger microscope and provide elemental as well as bonding information. There are two

types of electron spectrometer, the cylindrical mirror analyzer (CMA) and the hemispherical analyzer (HSA). The CMA is concentric with the electron beam and has a greater throughput because of its favorable solid angle. The HSA has the higher energy resolution, which is desirable for unraveling overlapped peaks. In the direct display mode (Fig. 4.14), peaks on the sloping background of an Auger spectrum indicate the presence of elements between Li and U. Spectra can also be displayed in the derivative mode (Fig. 4.15), which removes the sloping background and random noise. Auger quantitation is complicated by many instrumental factors and is normally done with sensitivity factors normalized to an elemental silver Auger signal collected under the same instrumental conditions.

Several review articles [4.107–109] are available.

4.2.4 Environmental Scanning Electron Microscope

The environmental scanning electron microscope (ESEM) is a unique modification of the conventional scanning electron microscope (SEM). While the SEM operates with a modest vacuum ($\approx 10^{-3}$ Pa), the ESEM is able to operate with gas pressures ranging between 10 and 2700 Pa in the specimen chamber due to a multistage differential pumping system separated by apertures. The relaxed vacuum environment of the ESEM chamber allows examination of wet, oily and dirty specimens that cannot be accommodated in the higher vacuum of a conventional SEM specimen chamber. Perhaps more significant, however, is the ability of the ESEM to maintain liquid water in the specimen chamber with the use of a cooling stage (Fig. 4.16). The capability to provide both morphological and compo-

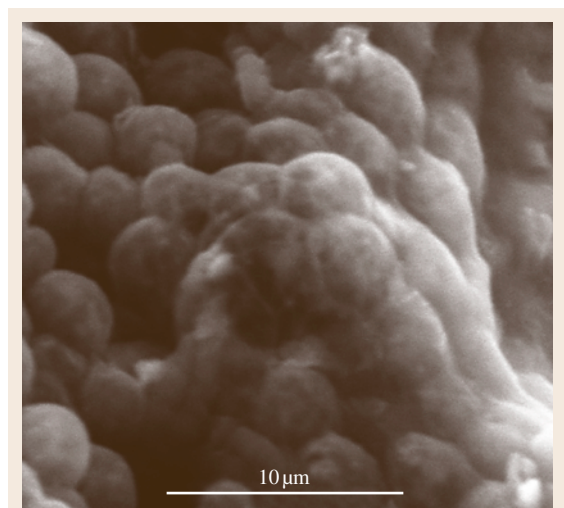


Fig. 4.16 ESEM image of hydrated, freshwater algal surface

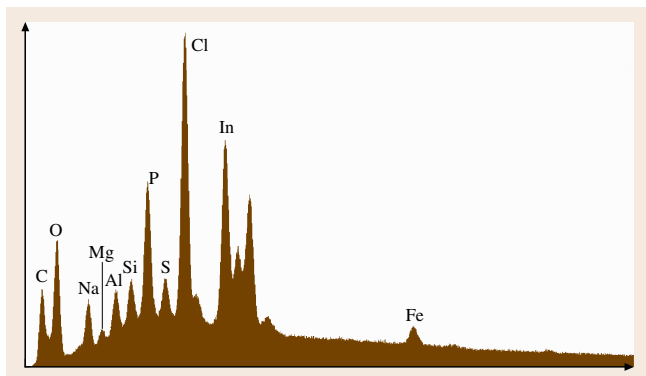


Fig. 4.17 EDS image of biological solids from a wastewater treatment facility. The indium peak is caused by the support stub

sitional analysis of hydrated samples has allowed the ESEM to benefit a number of experimental fields, ranging from material science to biology. Several review articles are available.

Principles of the Technique. The ESEM utilizes a gaseous secondary electron detector (GSED) that takes advantage of the gas molecules in the specimen chamber. The primary electron beam, operating between 10 and 30 kV, are generated from tungsten, lanthanum hexaboride, or field emission electron guns. When a primary electron beam strikes a specimen, it generates both backscattered and secondary electrons. Backscattered electrons are energetic and are collected by a line-of-sight detector. The secondary electrons are low-energy and, as they emerge from the specimen, are accelerated towards the GSED by the electric field set up between the positive bias on the GSED and the grounded specimen stage. These secondary electrons collide with gas molecules, resulting in ionizations and more secondary electrons, which are subsequently accelerated in the field. This amplification process repeats itself multiple times, generating imaging gain in the gas. A byproduct of this process is that the gas molecules are left positively charged and act to discharge the excess electrons that accumulate on an insulating specimen from the primary electron beam. This charge neutralization obviates the need for conductive coatings or low-voltage primary beams, as are often used in conventional SEM to prevent surface charging under the electron beam.

Secondary and backscattered electrons are produced throughout the interaction volume of the specimen, the depth of which is dependent on the energy of the primary electron beam and the specimen composition. The

backscattered electrons contain most of the energy of the primary electron beam and can therefore escape from a greater depth in the specimen. In contrast, secondary electrons are only able to escape from the top 10 nm of the specimen, although backscattered electrons can also create secondary electrons prior to exiting the sample and provide sample depth information to the image. In general, it is possible to routinely resolve features ranging from 10 to 50 nm. However, the primary electron beam can also interact with the gas molecules, resulting in beam electrons being scattered out of the focused electron beam into a wide, diffuse skirt that surrounds the primary beam impact point. Similarly, chamber gas composition can also impact the amplification process and thereby affect image quality.

Qualitative/Quantitative Analysis. In addition to the image-producing backscattered and secondary electrons that are generated when a primary beam strikes a specimen, there are also electron beam interactions that result in the generation of x-rays from the interaction volume. The energy of the resulting x-rays is representative of the chemical composition within the interaction volume and can be measured with an EDS. X-ray counts are plotted as a function of their energy, and the resulting peaks can be identified by element and line with standard x-ray energy tables (Fig. 4.17). EDS in the ESEM is considered a qualitative method of compositional analysis since x-rays may originate hundreds of micrometers from the impact point of the primary electron beam as a result of electrons scattered out of the beam by gas molecules.

Several review articles [4.110–117] are available.

4.2.5 Infrared and Raman Microanalysis

Infrared and Raman microanalysis is the application of Raman and/or infrared (IR) spectroscopies to the analysis of microscopic samples or sample areas. These techniques are powerful approaches to the characterization of spatial variations in chemical composition for complex, heterogeneous materials, operating on length scales similar to those accessible to conventional optical microscopy while also yielding the high degree of chemical selectivity that underlies the utility of these vibrational spectroscopies on the macroscale. Sample analyses of this type are particularly useful in establishing correlations between macroscopic performance properties (such as mechanical and chemical stability, biocompatibility) and material microstructure, and are thus a useful ingredient in the rational design of

high-performance materials. Several review articles are available.

Principles of the Technique. A typical Raman microscope comprises a laser excitation source, a light microscope operating in reflection mode, and a spectrometer. Photons inelastically scatter from the sample at frequencies shifted from that of the excitation radiation by the energies of the fundamental vibrational modes of the material, giving rise to the chemical specificity of Raman scattering. A high-quality microscope objective is used both to focus the excitation beam to an area of interest on the sample and to collect the backscattered photons. In general, the Rayleigh (elastic) scattering of the incident photons is many orders of magnitude more efficient than Raman scattering. Consequently, the selective attenuation of the Rayleigh photons is a critical element in the detection scheme; recent advances in dielectric filter technology have simplified this problem considerably. The attainable spatial resolution is, in principle, limited only by diffraction, allowing sub-micrometer lateral resolution in favorable cases. Fine vertical resolution can also be achieved through the use of a confocal aperture, opening up the possibility of constructing 3-D chemical images through the use of Raman depth profiling. Raman images are usually acquired by raster scanning the sample with synchronized spectral acquisition. Wide-field illumination and imaging configurations have been explored, but they

are generally only useful in limited circumstances due to sensitivity issues. Chemical composition maps can easily be extracted from Raman images by plotting the intensities of bands due to particular material components. Subtle spectral changes (such as band shifts) can also be exploited to generate spatial maps of other material properties, such as crystallinity and strain.

A typical IR microscope system consists of a research-grade Fourier transform (FT) IR spectrometer coupled to a microscope that operates in both reflection and transmission modes. Reflective microscope objectives are widely used due to their uniformly high reflectivity across the broad infrared spectral region of interest and their lack of chromatic aberration. The spectrum of IR light measured upon transmission through or reflection from the sample is normalized to a suitable background spectrum. The normalized spectrum displays attenuation of the IR light reaching the detector due to direct absorption at frequencies resonant with the active vibrational modes of the sample components. The frequencies at which absorption occurs are characteristic of the presence of particular functional groups (such as C=O), resulting in the powerful chemical specificity of the measured spectra (Fig. 4.18). Microscopes employing a sample raster scanning approach to image acquisition were the first available, but have now been joined by those employing a wide-field illumination, array-based imaging detection approach. The spatial resolution attainable with this

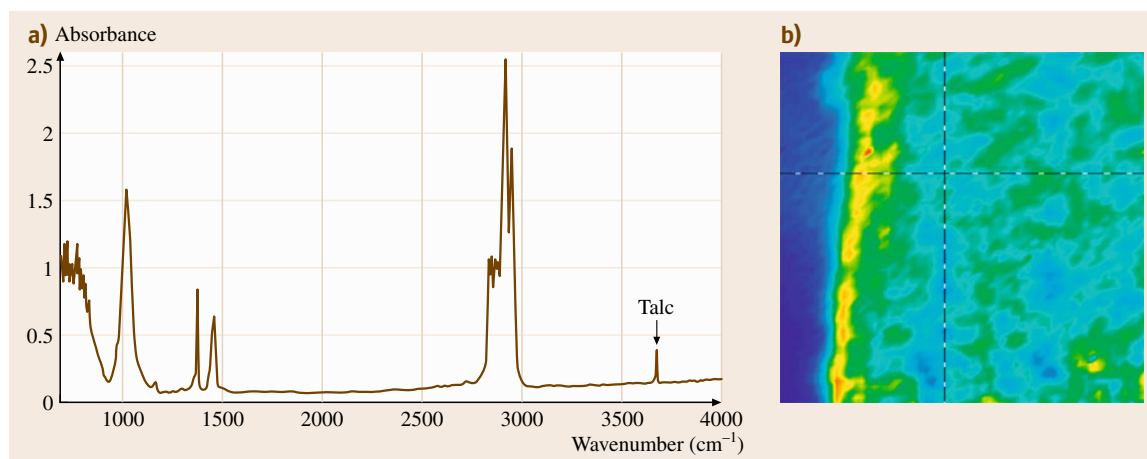


Fig. 4.18 (a) IR microspectrum of a thin film microtome section of injection-molded thermoplastic olefin. The sharp spectral feature at 3700 cm^{-1} is due to the OH stretching vibration of the talc filler (b) $325\text{ }\mu\text{m} \times 325\text{ }\mu\text{m}$ IR image of a thermoplastic olefin cross-section wherein the amplitude of the talc band is plotted on a blue (low amplitude) to red (high amplitude) color scale. The yellow-red band on the left side of the film is due to a talc-rich layer formed near the mold surface

technique is typically on the order of 20–40 μm , and diffraction-limited performance is not achieved due to source brightness limitations. Several alternative sampling techniques that have found widespread utility in IR spectroscopy of macroscopic samples have been successfully adapted on the microscale, including attenuated total reflection (ATR) and grazing incidence reflectivity. Maps of chemical composition can be extracted from IR spectral images in a manner similar to the Raman case, wherein amplitudes of bands due to material components of interest are plotted as a function of position on the sample.

Raman and IR microanalysis are complementary techniques, as is the case for their macroscopic analogs, widely applicable to extended solids, particles, thin films and even these materials under liquid environments. The choice between these analysis techniques is often dictated by the relative strength of the Raman and/or IR transitions that most effectively discriminate among the sample components. Notably, the molecular properties that dictate the strength of these transitions, molecular polarizability in the case of Raman and transition dipole moments for IR, are not generally correlated. In fact, for centrosymmetric molecules the techniques are particularly complementary as IR transitions forbidden by symmetry are by definition Raman active and vice versa. Sample considerations also play a role in this choice, as the nature of the material can preclude the use of one (or both) techniques. Raman microscopy can be used to study a broad array of materials, as the Raman photons are scattered over a wide, often isotropic, distribution of solid angles and are thus easily detected by the same microscope objective used for excitation. In contrast, transmission IR microscopy requires that the sample of interest be mounted on an IR-transparent substrate and that the sample itself be sufficiently thin to avoid saturation effects. Similarly, reflection mode IR microscopy is optimized when the analyte is mounted on a highly reflective substrate; the constraints on sample thickness apply in this configuration as well. However, Raman microscopy suffers from another significant limitation, as background fluorescence precludes the measurement of high signal-to-noise Raman spectra for many materials, particularly for higher-energy excitation wavelengths (for example, 488 and 532 nm). It is often the case that the shot noise present on a large fluorescence background is sufficiently larger than the Raman signal itself such that no amount of signal averaging will yield a high-quality spectrum. Notably, typical cross sections for fluorescence are vastly larger than those of Raman scattering,

so the Raman excitation wavelength need not be in exact resonance with a sample electronic transition to yield an overwhelming fluorescence background. This problem can be mitigated by the use of lower energy excitation wavelengths (for example, 785 and 1064 nm), although the Raman scattering efficiency drops with λ^4 . The cross-sections for Raman scattering are generally much lower than those of IR absorption, and so some materials with low Raman cross-sections are not amenable to Raman microanalysis, simply due to lack of signal, particularly in the microanalysis context. Although the Raman signal does scale with incident intensity, sample damage considerations typically limit this quantity. IR microanalysis often suffers from the opposite problem, wherein even microscopic samples can absorb sufficient radiation to lead to saturation effects in the spectra.

Nature of the Sample. The sample preparation requirements for Raman microscopy are quite modest; the surfaces of most solid materials are easily examined and some depth profiling is also possible depending on the material transparency. The Raman spectra of some materials are dominated by a fluorescent background; this is the most important sample property limiting the application of Raman microscopy. Two factors are critical in sample preparation for IR microscopy: choice of mounting substrate and sample thickness. For transmission microscopy, the substrate is limited to a set of materials that are broadly transparent over the IR (such as CaF_2 or KBr). In reflection microscopy, the substrate is often a metal film that is uniformly reflective across the IR region (such as Au or Ag). The issue of sample thickness is related to the onset of saturation effects in the spectra. The cross-sections for many IR absorption transitions are sufficiently large that samples can absorb nearly all of the resonant incident radiation, leading to spectral artifacts that interfere with both qualitative and quantitative analysis. For example, polymers as thin as 30 μm can show saturation artifacts in the C–H stretching bands. Sample preparation methods such as microtomy and alternative sampling methods such as μ -ATR can be used to address this problem for some classes of samples.

Qualitative Analysis. IR and Raman microspectroscopy are both powerful tools for the qualitative analysis of microscopic samples. The appearance of particular bands in the measured vibrational spectra indicate the presence of specific functional groups, and the chemical structure of the analyte can often be obtained from an analysis of the entire spectrum. Additionally, large libraries of IR and Raman spectra of a wide variety of

materials are now available, greatly facilitating the use of spectral matching algorithms in the identification of materials on the basis of the IR and/or Raman spectrum. The chemical specificity of vibrational spectroscopy is undoubtedly its most powerful characteristic, one that is particularly useful in the identification of various components of complex materials that are compositionally heterogeneous on microscopic length scales. The sensitivity of these techniques is difficult to characterize as cross-sections for these types of transitions generally vary over many orders of magnitude and thus the sensitivity for different analytes varies in a similar manner. However, analytes that occupy the minimum focal volumes attainable in these microscopies (Raman: $1\ \mu\text{m} \times 1\ \mu\text{m} \times 3\ \mu\text{m}$, IR: $25\ \mu\text{m} \times 25\ \mu\text{m} \times 50\ \mu\text{m}$) are generally detectable in both IR and Raman (particularly for strong scatterers).

4.3 Inorganic Analytical Chemistry: Short Surveys of Analytical Bulk Methods

In addition to the description of measurement methods for inorganic chemical bulk characterization (Sect. 4.1) short surveys of analytical methods are summarized in this section, outlining specifications of typical values of sample volume or mass and limits of detection as well as outputs, and relevant examples of applications.

Quite in general, metrology in chemistry and, therefore, in inorganic chemical analysis in special, has its own characteristics and singularities not to be found in this kind or in analogous manner in the field of physical metrology [4.122]. In this context the terms *selectivity* or *qualitative analysis* are essential keywords to characterize the problem. A typical example could arise from spectral interferences, were the characteristic signal of an element A (to be measured) could not only be interfered by that of another element B thus adulterating the result for the mass fraction of the element A, but also a characteristic signal of the element B could be erroneously be interpreted as a characteristic signal of the element A. In other words, in this case one could have tried to measure the mass fraction of e.g. copper in a sample, but in reality he would have measured the mass fraction of iron. Therefore the selectivity of a method is a very important characteristic and may have been one main reason why in the practical everyday work very precise working classical chemical methods of often rather lower selectivity, such as gravimetry, coulometry or titrimetry, were substituted

Traceable Quantitative Analysis. Although traceable quantitative analysis of macroscopic samples with IR spectroscopy is well-established (particularly for gases), extension to the microanalysis of solids is quite challenging. Through the use of well-characterized standard materials, IR microscopy can be used for quantitation, although the accuracy of this approach is often limited by optical effects (such as scattering) due to the complex morphology of typical samples. Estimates of Raman scattering cross-sections can be made in favorable cases, based on the characterization of instrumental factors affecting detection efficiency. However, extension to quantitative analysis is impractical due to a lack of reference materials and difficulties associated with the ab initio calculation of Raman cross-sections for all but the simplest materials.

Several review articles [4.118–121] are available.

on a large scale by modern methods of higher selectivity step by step in the past, even when the results of letter ones showed much lower precision.

Concerning the traceability of results of inorganic chemical analysis to the SI unit (mol or kg of the relevant analyte) for almost all inorganic analytical methods calibration of the analytical instruments is necessary by using solutions or substances of known content of the analyte. *Known content* means: a known mass fraction or concentration of the analyte – at which the specified value of content must include the specified value of its uncertainty according to GUM based on a definite traceability chain.

If methods needing calibration are used for the *analysis of liquid samples* calibration solutions are prepared from basic (*stock*) solutions which either come from commercial suppliers or are prepared in the laboratory by chemical dissolution of a definite mass of a material of definite purity in elemental form or as a compound of definite stoichiometry and purity (e.g. a pure metal or a pure metal salt, respectively), – or such solutions are only used to verify the elemental concentration of a commercial solution which is used as calibration stock solution after verification of its analyte concentration. After all, in all cases high purity substances with well known content of the main component (the respective element to be determined) are the starting materials for preparation of stock solutions and therefore actual

transfer standards directly to the SI unit (mol or kg of the analyte). Without such materials a really complete traceability chain to the SI unit does not exist, because the uncertainty of the final calibration solution would be based on assumptions about the purity of the starting material. An internationally harmonized system of such primary pure transfer standards directly to SI unit does not exist. First international attempts to harmonize measurement results of purity assessment of high-purity materials were made by national metrological institutes in the frame of CCQM by interlaboratory comparisons for the determination of a limited number of analytes in materials of pure nickel [4.123] and of pure zinc [4.124]. For an example of a national attempt to establish a system of primary pure materials as National Primary Standards for Elemental Analysis and of a traceability system based on those standards (Sect. 4.5).

In case of *direct analysis of solid samples* certified matrix reference materials or other appropriate solid materials of similar composition as the sample to be analyzed having known analyte contents must be used for calibration in the majority of cases. In this situation the traceability chain to the SI unit (mol or kg of the analyte) is less direct than for calibration with methods applied to the analysis of liquid samples. This is, because the process of certification of such matrix materials used for calibration commonly includes the calibration of instruments with liquid calibration samples.

The metrological advantage of methods needing calibration by liquid calibration samples over those needing calibration by solid matrix materials is also based on the fact that liquid samples of homogeneously distributed and definite analyte and matrix concentrations can easily be prepared by mixing or diluting of definite volumes or masses of stock solutions of definite concentration of analytes. In most cases an analogy to this fact does not really exist for the direct analysis of solid samples because of problems with losses, contamination or lack of homogeneity when adequate solid calibration samples are prepared. Therefore such solid calibration samples, such as e.g. powder mixtures or samples of metal alloys, normally after their preparation, need a certification of their real mass fractions by either methods not needing a calibration (which normally are not available) or by methods based on instrument calibration with liquids.

As quite explained above, the selectivity of a method is of high importance. The analysis of complex samples can often induce matrix effects as a combination of influences of the other elements in the

sample on the characteristic signal of the analyte to be determined or of chemical or physical differences between calibration sample and measured sample (such as acidity of solutions or grain size of powders). Those effects impair the trueness of results and can be decreased by matching of the composition of calibration samples to the composition of the sample to be analyzed (matrix matching, matrix adaptation) or by application of the method of standard addition. However, the method of standard addition (as mainly used with AAS, see below) is based on the precondition that the measured characteristic signal would be zero if the sample would contain no content of the measured analyte. This cannot be ensured in many cases. Internal standardisation can also be used to reduce matrix effects. In this case it must be assumed that the signal of the internal standard elements reacts with the same quantitative change to matrix influences as the signal of the investigated analyte. However, also this is not always the case.

4.3.1 Inorganic Mass Spectrometry

Today this field is dominated by inductively coupled plasma mass spectrometry (ICP-MS) and by glow discharge mass spectrometry (GD-MS). ICP-MS is mainly used for the analysis of liquid samples while GD-MS is used for direct analysis of solid samples.

ICP-MS

ICP-MS combines the advantages of extremely low detection limits, broad multielement-capability – and (especially in case of using high resolution mass spectrometers) a relatively low number of serious spectral interferences in comparison to ICP OES. ICP-MS spectrometers are latterly combined with chromatographs, especially with GC- or HPLC-chromatographs, to measure the contents of organometallic compounds in the frame of speciation analysis. Thus the high selectivity of chromatography for such species is combined with the extremely high detection power of ICP-MS not to achieve by only using combined methods of organic chemical analysis, such as GC-MS or HPLC-MS. But in the approach of the analysis with ICP-MS, such methods are often used to identify the compounds belonging to the chromatographic peaks.

Isotope Dilution

Isotope dilution in combination with mass spectrometry (TIMS or ICP-MS) offers an enormous advantage because the internal standardization is achieved using the same chemical element as the measured one. Moreover,

there is the advantage, too, of eliminating adulterations of the results arising in the process of chemical sample preparation if the spike can be added to the sample before chemical treatment of the sample. However, the metrological precondition of the highly preferable method of isotope dilution is always the knowledge of the purity of the isotope spike used concerning its total mass fraction of the relevant element.

GD-MS

GD-MS instruments though offering the advantage of rather fast direct solid sample analysis are much less in use than ICP-MS instruments. GD-MS can be powered by either a direct-current (DC) or radiofrequency

(RF) power supply. Up to now the latter option is not available in commercially offered GD-MS instruments, although RF instruments have the advantage that not only electrically conducting but also nonconducting materials can be directly be analyzed. In the past there had been only one commercial GD-MS instrument widespread among a larger number of users, – this was the VG-9000 (Thermo Elemental, UK). Several instruments of this type are still in use. The VG 9000 has not been produced since some years since it was replaced by the new Element GD (Thermo Instr. Corp., USA) which is a double focussing high resolution spectrometer, too. But its GD cell is based on a Grimm type geometry allowing faster sputtering than with the GD

Table 4.4 Inorganic mass spectrometry

Analytical method	Inorganic mass spectroscopy (MS) TIMS, ICP-MS, GD-MS, SS-MS
Measurement principle	Measurement of the mass spectra of ions generated due to the ionisation in an ionization source (thermal-ionization <i>TI</i> , inductively coupled plasma <i>ICP</i> , glow discharge <i>GD</i> , or electrical spark source <i>SS</i> ; – <i>ICP-MS</i> sometimes combined with laser ablation). A mass spectrum consists of peaks of ions of a definite ratio of their atomic masses divided by their charge number (m/z). It results from a stream of gaseous ions with different values of m/z . The intensity of the spectral mass peaks of isotopes corresponds with the concentration of the corresponding element in the plasma
Sample volume/mass	<i>TIMS</i> : wide range depending on sample preparation, (final sub-sample 1–10 μL); <i>ICP-MS</i> : 1–10 mL, <i>GD-MS</i> and <i>SS-MS</i> (direct solid sampling methods): ablated sample mass small, depending on instrument and parameters used: about 1–20 mg
Typical limits of detection	<i>TIMS</i> : pg to ng – absolute (upper ng kg^{-1} to lower $\mu\text{g kg}^{-1}$ range relative) <i>ICP-MS</i> : 0.001–0.1 $\mu\text{g L}^{-1}$ (using high resolution spectrometers and in aqueous solution up to 2 orders of magnitude lower) GDMS, SSMS: 0.1–10 $\mu\text{g kg}^{-1}$
Output, results	Simultaneous and sequential multielement analyses <i>TIMS</i> : high precision, high accuracy, highest metrological level with isotope dilution technique (<i>IDMS</i>), but raw analyte isolation needed. Advantages of <i>ICP-MS</i> : Simultaneous multielement capability, very low limits of detection, very high dynamic range. Combined with laser ablation (<i>LA ICP-MS</i>): for solid samples; combined with isotope dilution technique (<i>ID-ICP-MS</i>): high metrological level results of high accuracy <i>GD-MS</i> : Simultaneous multielement capability, direct sampling without chemical sample handling, very low detection limits, very high dynamic range <i>SS-MS</i> : Not yet widely-used
Typical applications	Qualitative and quantitative elemental and isotopic analysis, e.g. semiconductors, ceramics, pure metals, environmental and biological materials, high purity reagents, nuclear materials, geological samples; Speciation analysis when <i>ICP-MS</i> is combined with chromatographic methods <i>ID-MS</i> : Metrological high level technique for reference values of international comparisons in <i>CCQM</i> and for certification of reference materials

cell of VG 9000 and therefore a distinctly shortened time for one analysis. The Element GD is now getting its global acceptance. GD-MS can also be used for the determination of several nonmetals. This is of special interest because only few methods can be used for this important task. The detection limits can be considerably decreased when mixtures of argon and helium are used instead of argon alone as working gas of GD as it was demonstrated for trace determination of different nonmetals in pure copper samples [4.125].

GD-MS calibration is normally based on the availability of appropriate reference materials which may be a very restricting condition for carrying out quantitative analyses by this method. Because of lack of appropriate reference materials this restriction is especially unfavourable in case of ultra-trace determination. An alternative possibility to achieve a calibration having a shorter traceability chain and being applicable without having appropriate reference materials available was demonstrated in case of analysis of ultra-pure metals using calibration samples made from pure metal powders quantitatively doped with calibration liquids and pressed to pellets under high pressure after drying and homogenization [4.126].

Some relevant information concerning the inorganic mass spectrometry is summarized in Table 4.4.

4.3.2 Optical Atomic Spectrometry

Atomic absorption spectrometry (AAS) is a method of high selectivity mainly applied to the analysis of liquids. The Flame AAS is very robust and still applied in many laboratories although it is increasingly substituted by ICP OES. One reason is the mono-elemental character of one measurement cycle in AAS needing a time consuming change of element-specific radiation source (such as hollow cathode lamp or electrodeless discharge lamp) when another element shall be measured. In the modern high resolution continuum source AAS (HR-CS AAS) [4.127] only one continuous radiation source is used for all elements to be determined in a spectral region of 190–900 nm. The graphite furnace AAS is a very sensitive micro-method. In recent times specific AAS spectrometers for direct electro-thermal evaporation of solid micro-samples are also available. The powdered micro-sample is directly weighed into the sample boat of the graphite furnace of the instrument.

ICP optical emission spectrometry (ICP OES) is now the most widespread method for the multielement determination of liquid samples. The method is

very robust. Most instruments contain compact Echelle-spectrometers with area detectors such as CCD or CID; – or classical spectrometer types (monochromators or polychromators) are used combined with line detectors or PMTs. ICP OES can be combined with devices for electrothermal vaporization of solid micro-samples. In several cases and after checking this possibility, the instrument can even be calibrated by using solutions, thus enabling a short traceability chain to SI unit as demonstrated e.g. in case of analysis of plant materials [4.128].

The spark OES [4.129] is since many years worldwide widespread and the workhorse in metallurgical industry, especially for the direct determination of traces and minor components in production control and in final check of composition of metals and alloys. The method is extremely fast and robust and has the advantage that micro-inhomogeneity of the sample in the spark spot is largely compensated during the pre-spark phase by micro-melting action of many single individual sparks.

The glow discharge OES (GD-OES) can be alternatively applied to the spark-OES for the bulk analysis of metals. It has in some cases the advantage of a higher trueness of results, but it is often less robust and not so fast as the spark-OES. The main area of application of GD-OES is the analysis of layers or surfaces of electrically conducting and (in case of RF-GD cells) also of non-conducting samples.

Some relevant information concerning the optical atomic spectrometry is summarized in Table 4.5 for AAS and in Table 4.6 for OES.

4.3.3 X-ray Fluorescence Spectrometry (XRF)

X-ray fluorescence spectrometry (XRF) in its classical form is an important method used for the direct analysis of solid samples. It is not really a trace method but its applicability reaches from determination of higher trace contents up to the precise measurement of the main matrix component. Depending on counting rate and time the precision of the method can be extremely high; – but it is necessary to use very well matrix matched calibration materials to achieve a high trueness of the results, too. In metallurgical industry XRF and spark-OES are complementary mutually. XRF has the advantage that electrically non-conducting materials can also be analyzed. If direct solid sample technique is used, traceability is achieved via calibration with certified matrix reference materials of a similar composition as the samples to be analyzed. If the borate fusion technique is used, calibration samples can be

Table 4.5 Atomic absorption spectrometry

Analytical method	Atomic absorption spectrometry (AAS) F AAS, GF AAS (ET AAS), HG AAS, SS ET AAS
Measurement principle	Measurement of the optical absorption spectra of atoms based on the absorption of radiation (emitted by a primary (background) radiation source) by the atoms (being mainly) in the ground state in the gaseous volume of the atomized sample. The strength of the line absorption corresponds with the concentration of the element in the absorbing gaseous volume
Sample volume/mass	Flame AAS (<i>F AAS</i>): 1–10 mL graphite furnace (<i>GF AAS</i>) (= electro thermal atomisation AAS, <i>ET AAS</i>): 0.01–0.1 mL hydride generation AAS (<i>HG AAS</i>): 0.5–5 mL solid sampling (<i>SS ET AAS</i>): 0.1–50 mg
Typical limits of detection	<i>F AAS</i> : 1–1000 $\mu\text{g L}^{-1}$, <i>GF AAS</i> : 0.01–1 $\mu\text{g L}^{-1}$, <i>HG AAS</i> : 0.01–0.5 $\mu\text{g L}^{-1}$, <i>SS ET AAS</i> as direct solid sampling method: 0.01–100 $\mu\text{g kg}^{-1}$
Output, Results	Quantitative analysis, sequential multielement analysis possible in separate analytical cycles, with some spectrometers multielement determination possible by new techniques, especially by high-resolution continuum source AAS (<i>HR-CS AAS</i>)
Typical Applications	Quantitative analysis of elements in the trace region. Extremely low detection limits by <i>ET AAS</i> . Environmental samples and samples from technical materials. Combination with hydride generation, flow injection analysis (<i>FIA</i>) and solid sampling possible. <i>F AAS</i> was in the near past certainly the most commonly used method of elemental analysis of liquid samples and is today in many cases alternatively used to <i>ICP OES</i>

Table 4.6 Optical emission spectrometry

Analytical method	Optical emission spectroscopy (OES) (Atomic emission spectroscopy, AES) Flame-OES, ICP OES, arc-OES, spark-OES, glow-discharge-OES (GD-OES)
Measurement principle	Measurement of the optical emission spectra of atoms or ions due to the excitation with flame (<i>Flame-OES</i>), inductively coupled plasma (<i>ICP OES</i> , sometimes combined with laser ablation (<i>LA-ICP OES</i>) or electrothermal vaporisation (<i>ETV-ICP OES</i>)) electrical <i>arc</i> , <i>spark</i> or glow discharge (<i>GD-OES</i>). An emission spectrum consists of lines produced by radiative deexcitation from excited levels of atoms or ions. The intensity of the spectral lines corresponds with the concentration of the element in the plasma
Sample volume/mass	<i>Flame-OES</i> : 5–10 mL, <i>ICP OES</i> : 1–10 mL Arc-, spark- and glow discharge-OES are direct solid sampling methods <i>Arc-OES</i> : 1–50 mg, <i>Spark-OES</i> : 10–30 mg, <i>GD-OES</i> : \approx 10 mg (often used for surface/layer analysis)
Typical limits of detection	<i>Flame-OES</i> : 1–1000 $\mu\text{g L}^{-1}$, <i>ICP OES</i> : 0.1–50 $\mu\text{g L}^{-1}$ <i>Spark-OES</i> , <i>GD-OES</i> : 1–100 mg kg^{-1} <i>Arc-OES</i> , <i>ETV-ICP OES</i> : 0.01–10 mg kg^{-1}
Output, results	Qualitative and quantitative analysis. Determination of traces up to main constituents (depending on the special method). Sequential and simultaneous multielement analysis possible
Typical applications	Qualitative and quantitative elemental analysis of metals and alloys (especially by solid sampling <i>spark-OES</i>), technical materials, environmental, geological and biological samples. <i>ICP OES</i> is the mainly used method for multielement determination in liquid samples

prepared from primary reference materials (elements, compounds and solutions) and the results are directly traceable to the SI provided the purity and stoichiometry of the primary reference materials are assured. With this technique a very high accuracy of the results can be achieved if a multistage process of preparing calibration samples similar to the analyzed sample (this technique of calibration is called *reconstitution analysis*) is carried out [4.130]. Results achieved this way are of high value in metrological interlaboratory comparisons as well as for certification of reference materials.

Total reflection *XRF* is a very special ultra-trace micro-method for the analysis of objects or layers of very low thickness. The calibration can often be carried

out using residues of solutions. The widespreading of the method is not high.

Some relevant information concerning the x-ray fluorescence spectrometry is summarized in Table 4.7.

4.3.4 Neutron Activation Analysis (NAA) and Photon Activation Analysis (PAA)

Both methods are characterized by low blank values, because all kinds of chemical handling (such as sample dissolution or surface cleaning) can be done after the step of irradiation, and only the radioactive daughter products of the elements to be determined deliver the measured characteristic signals.

Table 4.7 X-ray fluorescence spectrometry

Analytical method	X-ray fluorescence spectrometry <i>XRF</i> Total reflection x-ray fluorescence spectrometry <i>TXRF</i>
Measurement principle	The solid (or liquid) sample is irradiated with x-rays or a particle beam. Primary radiation is absorbed ejecting inner electrons. Relaxation processes fill the holes and lead to emission of characteristic fluorescence x-rays. The energies (or wavelengths) of these characteristic x-rays are different for each element. Basis for quantitative analysis is the proportionality of the intensity of characteristic x-rays of a certain element and its concentration, but this relation is strongly influenced by the other constituents of the sample <i>TXRF</i> is based on the effect of total reflection to achieve extremely high sensitivity
Sample volume/mass	<i>XRF</i> : Direct analysis of polished disks of metals or other solid materials or pellets of pressed powders or powders filled into sample cups, thin films, liquids in special sample cells, particulate material on a filter. Typically samples must be flat having surface diameters larger than the diameter of the primary exciting radiation beam. Especially relevant in metrological exercises is the use of fused borate samples in combination with the so-called <i>reconstitution technique</i> for calibration <i>TXRF</i> : direct analysis of thin (thickness < 10 μm) micro-samples or of thin deposits or layers
Typical limits of detection	<i>XRF</i> : Strongly dependent from element and matrix as well as from spectrometer (wave length dispersive or energy dispersive). 1–100 mg kg ⁻¹ for elements with medium atomic number, up to some percent for the lightest measurable elements (B, Be) <i>TXRF</i> : Down to μg L ⁻¹ and below for dried droplets of aqueous solutions
Output, results	Qualitative and quantitative analysis. Semi-quantitative results are easily obtained using special computer programs of the instrument; truly quantitative results require careful sample preparation and calibration of the instrument. Advantages of <i>XRF</i> are high precision and wide dynamic range up to high contents
Typical applications	<i>XRF</i> : Qualitative and quantitative analysis of metals, alloys, cement, glasses, slag, rocks, inorganic air pollutions, minerals, sediments, freeze-dried biological materials <i>TXRF</i> : trace analysis in all kinds of thin micro-samples and residues of solutions for ultra-trace determination

Table 4.8 Neutron and photon activation analysis

Analytical method	Activation analysis <i>NAA, PAA</i>
Measurement principle	Activation analysis is based on the measurement of the radioactivity of indicator radionuclides formed from stable isotopes of the analyte elements by nuclear reactions induced during irradiation of the samples with suitable particles (neutrons: neutron activation analysis <i>NAA</i> , high energy photons: photon activation analysis <i>PAA</i>)
Sample volume/mass	Solid or (dried) liquid samples: ≈ 50 mg to ≈ 2 g, (in some special systems up to 1 kg)
Typical limits of detection	Trace and ultratrace region, strongly depending on element, sample composition, sub-sample mass and parameters of irradiation. Absolute detection limits: <i>NAA</i> 1 pg–10 μ g; for most elements: 100 pg–10 ng <i>PAA</i> for several nonmetals: 0.1–0.5 μ g
Output, results	Qualitative and quantitative analysis. Easy calibration procedure (low matrix influences), high sensitivity and freedom of reagent blanks make in principle the <i>NAA</i> (and <i>PAA</i>) to important methods with partially very low limits of detection and high accuracy. Homogeneity of elemental distribution can be checked by using small sub-samples. They are important complements to other methods, e.g. to check losses or contamination from wet-chemical sample preparation of the other methods <i>PAA</i> is an important complement to <i>NAA</i> , especially in view of determination of nonmetals
Typical applications	<i>NAA</i> : Simultaneous trace and ultratrace multielement determination. Nondestructive analysis for ≈ 70 elements (typically up to about 40 elements in one analysis cycle). In principle accurate determination of higher element contents is possible <i>PAA</i> : Important especially for determination of nonmetallic analytes. Sample surface can be cleaned after sample irradiation, therefore e.g. very low oxygen blanks are possible for determination of real oxygen bulk content in pure materials

Neutron activation analysis (*NAA*) normally needs a special nuclear reactor as neutron source. Primarily therefore, the method is not widespread. In principal, up to 70 elements can be determined, however with strongly differing limits of detection. Enormous advantages of the method are the independence of the results from chemical state of analytes and the fact that other matrix effects are marginal mainly according to the high penetration potential of incoming and outgoing radiation. This causes the high metrological value of the method as one being to calibrate easily by pure substances or dried solutions even when the method is used in direct solid sampling mode in form of instrumental *NAA* (*INAA*). *INAA* is the (quasi) nondestructive direct

sampling mode of *NAA*, in opposite to the destructive mode, mostly used as radiochemical *NAA* (*RNAA*).

The photon activation analysis (*PAA*) is complementary to *NAA*, especially concerning its high sensitivity for light elements, such as nonmetals as C, N, O or F. The method needs a sophisticated device for producing appropriate high energy gamma rays as well as for sample handling and measurement of characteristic signals. Therefore *PAA* is not a widespread method, even though this method can be of very high analytical importance when low contents of non-metals are to measure accurately at high metrological level.

Some relevant information concerning *NAA* and *PAA* is summarized in Table 4.8.

4.4 Compound and Molecular Specific Analysis: Short Surveys of Analytical Methods

Molecular systems can be identified by their characteristic molecular spectra, obtained in the absorption

or emission mode from samples in the gaseous, liquid or solid state. Upon interaction with the appropriate

Table 4.9 Basic features of instrumental analytical methods: optical spectroscopy

Analytical method	Measurement principle	Specimen type	Sample amount	Output results	Applications
UV/Vis spectroscopy	Measurement of absorption of emission in the UV/Vis region due to changes of electronic transitions in π -system	Organic compounds, inorganic complexes, ions of transition elements	Solution in transmission, powder in reflexion	Relations between structure and color Photochemical processes	Qualitative and quantitative analysis of aromatic and olefinic compounds Detector for chromatographic methods
Fluorescence spectroscopy	Measurement of fluorescence emission in relation to the wavelength of the excited radiation	Fluorescent organic compounds, dyes, inorganic complex compounds	Solid, liquid or in solution, $\approx 50 \mu\text{L}$	Structure/fluorescence relations; most sensitive opto-analytical method	Qualitative/quantitative analysis of aromatic compounds with low-energy π - π^* transitions (conjugated chromophors)

Table 4.10 Basic features of instrumental analytical methods: NMR spectroscopy

Analytical method	Measurement principle	Specimen type	Sample amount	Output results	Applications
Nuclear magnetic resonance spectroscopy	Determination of chemical shift and coupling constants due to magnetic field excitation and analysis of RF-emission	Inorganic, organic and organometallic compounds: gaseous, liquid, in solution, solid	Samples in all aggregation states $\approx 100 \mu\text{g}$	Contribution to the molecular structure: bond length, bond angle, interactions about several bonds	Identification of substances in combination with other techniques (MS, IR- and Raman-spectroscopy, chromatography)

Table 4.11 Basic features of instrumental analytical methods: mass spectroscopy

Analytical method	Measurement principle	Specimen type	Sample amount	Output results	Applications
Analytical mass spectroscopy	Generation of gaseous ions from analyte molecules, subsequent separation of these ions according to their mass-to-charge (m/z) ratio, and detection of these ions. Mass spectrum is a plot of the (relative) abundance of the ions produced as a function of the m/z ratio.	Organic and organometallic compounds: quantitative mixture analysis	Samples in all aggregation states; MS is the most sensitive spectroscopic technique for molecular analysis	Determination of the molecular mass and elemental composition; Contribution to the structure elucidation in combination with NMR, IR- and Raman-spectroscopy	Structure elucidation of unknown compounds; MS as reference method and in the quantitation of drugs; Detector for gas (GC) and liquid chromatographic (LC) methods

Table 4.12 Basic features of instrumental analytical methods. by the methods Infrared, Raman, EPR, Mössbauer Spectroscopy

Analytical method	Measurement principle	Specimen type	Sample amount	Output results	Applications
Infrared spectroscopy	Measurement of absorption (extinction) of radiation in the infrared region due to the modulation of molecular dipole moment	Inorganic, organic and organometallic compounds: adsorbed molecules	Samples in all aggregation states; In solution, embedded or in matrix isolation, $\approx 100 \mu\text{mol}$	Contribution to the molecular structure: bond length, bond angle, force constants; Identification of characteristic groups and compounds by means of data bases	Identification of substances in combination with other techniques (Raman, NMR, MS, and chromatography); quantitative mixture analysis; Surface analysis of adsorbed molecules; Detector for chromatographic methods
Raman spectroscopy	Measurement of Raman scattering (in the UV-Vis-NIR region) due to the modulation of molecular polarizability	Inorganic, organic and organometallic compounds, surfaces and coatings	Samples in all aggregation states, in solution and in matrix isolation: $\approx 50 \mu\text{L}$, $\approx 1 \mu\text{g}$	Contribution to the molecular structure; Identification of characteristic groups and compounds in combination with IR-data	Identification of substances; Surface and phase analysis; Detector for thin layer chromatographic methods
Electron paramagnetic resonance spectroscopy	Selective absorption of electromagnetic microwaves due to reorientation of magnetic moments of single electrons in a magnetic field	Organic radicals, reactive intermediates Internal defects in solids in biomatrices	In-situ investigation of organic radicals, oriented paramagnetic single crystals, crystal powders	In-situ detection of organic radicals and their reaction kinetics (time-resolved EPR) Paramagnetic centers of crystals	Studies of photochemical and photophysical processes (requirement: 10^{11} single electrons); Semiconductor studies, trace detection of 3-D-elements in biomaterials
Mössbauer spectroscopy	Measurement of the isomeric shift, line width and line intensity due to the recoil free gamma quantum absorption	Inorganic compounds and phases, organometallic compounds	Samples in the solid state, or as freezing solutions, several mg	Determination of the oxidation number and the spin state of the Mössbauer nuclei	Phase analysis including amorphous phase on glasses, ceramics and catalysts

type of electromagnetic radiation, characteristic electronic, vibrational and rotational energy term schemes can be induced in the sample. These excited states usually decay to their ground states within 10^{-2} s, either by emitting the previously absorbed radiation in all directions with the same or lower frequency, or by radiationless relaxation, thus providing spectral information for chemical analysis. Basic features of instrumental analytical methods are summarized in the overview Tables 4.9–4.12 (compiled by Peter Reich, BAM, Berlin, 2004).

Further complementary structural information about molecular systems may be obtained by investigating

the nuclear magnetic resonance spectroscopy (NMR) of a sample being irradiated with radio frequency in a magnetic field.

Structural information can also be determined by analysing the intensity distribution mass fragments of a sample bombarded with free electrons, photons or ions in the analytical mass spectroscopy (MS).

Additional information on the near neighbour order in the solid state are provided in particular by the methods infrared (IR) and Raman spectroscopy, EPR and Mössbauer spectroscopy. These techniques provide images of the interactions mentioned above and contain analytical information about the sample.

4.5 National Primary Standards – An Example to Establish Metrological Traceability in Elemental Analysis

Chemical measurements in elemental analysis are measurements of contents (e.g. mass fractions) of analytes in the sample to be analyzed, at which the *chemical identity of the analyte* has to be defined as the element to be measured in the sample. For this purpose, a *metrological traceability system to the SI unit (mol or kg of the chemical element to be measured) for measurement results of inorganic chemical analysis* was set up in Germany in cooperation between the National Metrology and Materials Research Institutes PTB and BAM [4.131, 132]. Currently, the system comprises national primary elemental standards for Cu, Fe, Bi, Ga, Si, Na, K, Sn, W, and Pb and the certification of other elements is in preparation. In this system, core components are

- pure substances (Primary National Standards for Inorganic Chemical Analysis) characterised at the highest metrological level [4.133],
- primary solutions prepared from these pure substances, and
- secondary solutions deduced from the primary solutions intended for transfer to producers of commercial calibration stock solutions and for technical applications.

For certifying a material of a Primary National Standard representing one chemical element in the *System of National Standards for Inorganic Chemical Analysis* all impurities in the material, i. e. all relevant trace elements of the Periodic Table have to be metrologically considered and their mass fractions have to be measured by appropriate analytical methods and then subtracted

from 100% mass fraction (= the ideal mass fraction of the investigated element) to establish the real mass fraction of the main component with an uncertainty $< 0.01\%$. This upper limit of the aspired uncertainty is one order of magnitude lower than the lowest uncertainties achieved with direct measurements of the mass fraction of the main component using best metrological methods of elemental analysis, such as IDMS. Even for IDMS measurements the National Standards of Elemental Analysis are intended to be used in the future as instruments of metrological traceability, namely by using them as *natural backspikes for IDMS* of known mass fraction of the main component and therefore as a trustworthy basis to determine the purity of isotopically enriched spike materials. To determine all trace elements in the pure materials different methods of elemental analysis have to be applied. About 70 metallic impurities can be determined using inductively coupled plasma with high-resolution mass spectrometry (ICP-HRMS). For supplementation and validation, inductively coupled optical emission spectroscopy (ICP OES) and atomic absorption spectrometry (AAS) are used. Classical spectrophotometry is applied for the determination of phosphorous, sulphur and fluorine. Carrier gas hot extraction (CGHE) is used to determine oxygen and nitrogen and combustion analysis is used for carbon and sulphur. In addition to C, O and N, chlorine, bromine and iodine are determined using photon activation analysis (PAA). Hydrogen is measured using nuclear reaction analysis (RNA). For comparison and if possible, also direct methods, typically electrogravimetry (e.g. for copper) or coulometry, are applied in order

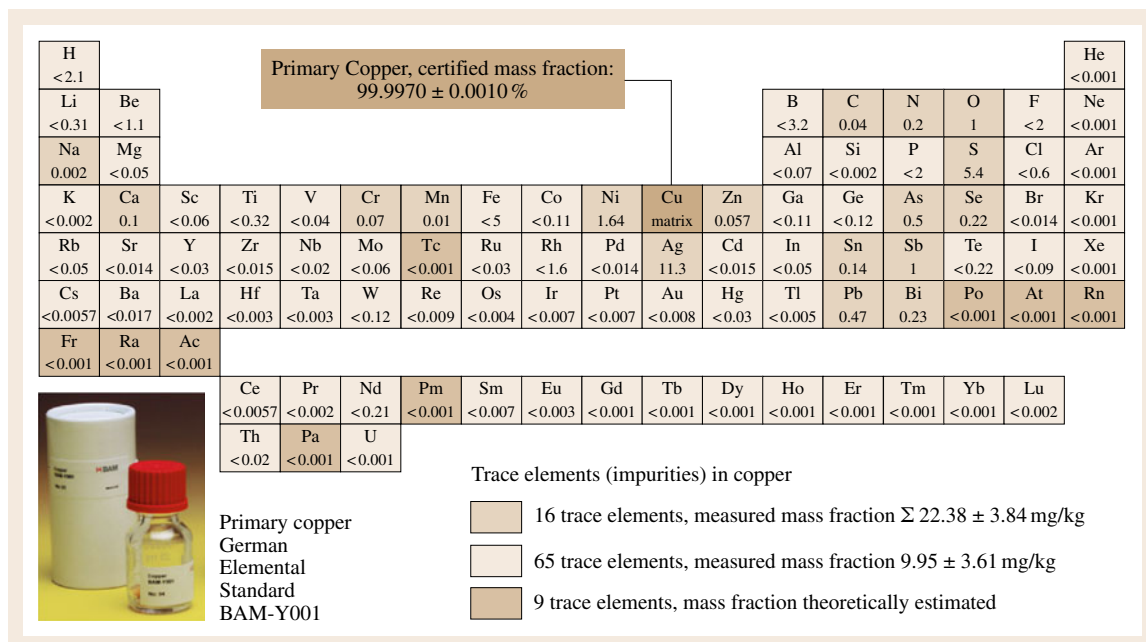


Fig. 4.19 Metrology in elemental analysis. The example of copper as primary standard; mass fractions of trace elements in mg/kg. The expanded uncertainty of matrix element copper has a coverage factor of $k = 2$

to determine the mass fraction of the matrix directly, but of course, with a higher uncertainty.

For those of the high-purity materials, which are most convenient to handle not as pure elements but in the form of salts (alkali metals and alkaline earth metals), additionally to the measurements of the metallic and nonmetallic impurities, the anionic impurities are determined, too. These measurement results are consistent with those of the other element-specific methods for I, Br, S, P or N. For the radioactive elements Tc, Pm, Po, At, Rn, Fr, Ra, Ac and Pa upper limits are estimated from theoretical considerations. For noble gases either measurements are carried out by static mass spectroscopy or limits are estimated from theoretical considerations. All uncertainties are calculated accord-

ing to the *ISO Guide to the Expression of Uncertainty in Measurement (GUM)*.

An example of this metrology-based system for elemental materials characterisation is given in Fig. 4.19, showing the certified mass fraction data of *primary copper* together with the data of all measured trace elements of the Periodic Table of Chemical Elements. The certified mass fraction of Primary Copper results from subtracting the mass fractions of all impurities from 100%. At this, for each of the 65 values measured below limit of determination or of the 9 values estimated from theoretical considerations below a limit value, half of the limit value (having an assumed uncertainty of (\pm half of the limit value)) was subtracted from 100%.

References

- 4.1 A. Montaser, D.W. Golightly (Eds.): *Inductively Coupled Plasmas in Analytical Atomic Spectrometry*, 2nd edn. (Wiley-VCH, Weinheim 1992)
- 4.2 R.K. Marcus (Ed.): *Glow Discharge Spectroscopies* (Plenum, New York 1993) p. 514
- 4.3 R.K. Marcus, J.A.C. Broekaert (Eds.): *Glow Discharge Plasmas in Analytical Spectroscopy* (Wiley, Chichester 2003) p. 482
- 4.4 R.S. Houk, V.A. Fassel, G.D. Flesch, H.J. Svec, A.L. Gray, C.E. Taylor: *Inductively coupled argon*

- plasma as an ion source for mass spectrometric determination of trace elements, *Anal. Chem.* **52**, 2283–2289 (1980)
- 4.5 P. Semeniuk, S. Berman: Analysis of high purity metals and semiconductor materials by glow discharge mass spectrometry, *Spectrochim. Acta Rev.* **13**, 1–10 (1990)
- 4.6 W.W. Harrison, K.R. Hess, R.K. Marcus, F.L. King: Glow discharge mass spectrometry, *Anal. Chem.* **58**, 341A–356A (1986)
- 4.7 W.W. Harrison, B.L. Bentz: Glow discharge mass spectrometry, *Prog. Anal. Spectrosc.* **11**, 53–110 (1988)
- 4.8 M.R. Winchester, R. Payling: Radio-frequency glow discharge spectrometry: A critical review, *Spectrochim. Acta B* **59**, 607–666 (2004)
- 4.9 C. Burgess, T. Frost (Eds.): *Standards and Best Practice in Absorption Spectrometry* (Blackwell Science, Oxford 1999)
- 4.10 G. Wyszecski, W.S. Stiles: *Color Science*, 2nd edn. (Wiley-Interscience, New York 1982)
- 4.11 ISO: *International Vocabulary of Basic and General Terms in Metrology (VIM)*, 2nd ed., (BIPM/IEC/IFCC/ISO/IUPAC/IUPAP/OIML, International Organization for Standardization, Geneva 1993)
- 4.12 ISO: *Guide 34, General Requirements for the Competence of Reference Material Producers*, 2nd ed., (International Organization for Standardization, Geneva 2000)
- 4.13 ISO: *International Standard ISO/IEC 17025, General Requirements for the Competence of Testing and Calibration Laboratories*, 1st ed., (International Organization for Standardization, Geneva 1999)
- 4.14 J.R. Lakowicz: *Principles of Fluorescence Spectroscopy* (Kluwer/Plenum, New York 1999)
- 4.15 ASTM: ASTM Standard E388, Standard test method for wavelength accuracy and spectral bandwidth of fluorescence spectrometers. In: *Annual Book of ASTM Standards*, Vol. 03.06, (ASTM, West Conshohocken 2004)
- 4.16 K.D. Mielenz (Ed.): Optical radiation measurements. In: *Measurement of Photoluminescence*, Vol. 3 (Academic, New York 1982) pp.15–154
- 4.17 J.N. Miller: Techniques in visible and ultraviolet spectrometry. In: *Standards in Fluorescence Spectrometry*, Vol.2, ed. by J.N. Miller (Chapman and Hall, New York 1981)
- 4.18 R.L. McCreery: *Raman Spectroscopy for Chemical Analysis*, Chemical Analysis, Vol. 157 (Wiley, New York 2000)
- 4.19 P.R. Griffiths, J.A. de Haseth: *Fourier Transform Infrared Spectrometry* (Wiley, New York 1986)
- 4.20 P.B. Coleman (Ed.): *Practical Sampling Techniques for Infrared Analysis* (CRC, Boca Raton 1993)
- 4.21 R.M. Silverstein, F.X. Webster: *Spectrometric Identification of Organic Compounds*, 6th edn. (Wiley, New York 1998)
- 4.22 D.L. Rabenstein, D.A. Keire: Quantitative analysis by NMR. In: *Modern NMR Techniques and Their Application in Chemistry*, Vol.11, ed. by A.I. Popov, K. Hallenga (Dekker, New York 1991), Chap. 5, pp. 323–369
- 4.23 F. Kasler: *Quantitative Analysis by NMR Spectroscopy* (Academic, New York 1973)
- 4.24 H. Jancke: NMR spectroscopy as a primary analytical method, *CCQM Report* **98(2)**, 1–12 (1998)
- 4.25 J.P. Heesch: Nuclear magnetic resonance spectroscopy. In: *The Characterization of Chemical Purity Organic Compounds*, ed. by K.L.A. Staveley (International Union of Pure and Applied Chemistry, Butterworth and Co, London 1977) pp.137–147
- 4.26 D. Filmore: Seeing with spectroscopy. In: *Chronicles of Chemistry II: Enterprise of the Chemical Sciences, Supplemental publication of the American Chemical Society*, ed. by J.F. Ryan (ACS, Washington 2004) p. 87
- 4.27 J.C. Travis, J.C. Acosta, G. Andor, J. Bastie, P. Blattner, C.J. Chunnillall, S.C. Crosson, D.L. Duewer, E.A. Early, F. Hengstberger, C. Kim, L. Liedquist, F. Manoocheri, F. Mercader, A. Mito, L.A.G. Monard, S. Nevas, M. Nilsson, M. Noël, A.C. Rodriguez, A. Ruiz, A. Schirmacher, M.V. Smith, G. Valencia, N. van Tonder, J. Zwinkels: Intrinsic wavelength standard absorption bands in holmium oxide solutions for UV/visible molecular absorption spectrophotometry, *J. Phys. Chem. Ref. Data* **34**, 41–56 (2005)
- 4.28 R.A. Velapoldi, K.D. Mielenz: A fluorescence standard reference material: Quinine sulfate dihydrate, US Dept. of Commerce, NBS special publication NIST SP 260-64, 122 pp. (1980)
- 4.29 S.J. Choquette, E.E. Etz, W. Hurst, D. Blackburn: Relative intensity correction standards for Raman spectroscopy for excitation with several common laser wavelengths, *Am. Pharm. Rev.* **6(2)**, 74–80 (2003)
- 4.30 S.J. Choquette, S.N. Chesler, D.L. Duewer, S. Wang, T.C. O'Haver: Identification and quantitation of oxygenates in gasoline ampules using FT-NIR and FT-Raman spectroscopy, *Anal. Chem.* **68(20)**, 3525 (1996)
- 4.31 L. Griffiths, A.M. Irving: Assay by nuclear magnetic resonance spectroscopy: Quantification limits, *Analyst* **123**, 1061–1068 (1998)
- 4.32 National Institute of Standards and Technology (2010), <http://nist.gov/traceability/>
- 4.33 National Institute of Standards and Technology: NIST Physics Laboratory, Optical Technology Division (2011), <http://nist.gov/pml/div685>
- 4.34 National Institute of Standards and Technology: NIST calibration services website (2010), <http://nist.gov/mean-services>
- 4.35 J.D. Ingle Jr., S.R. Crouch: *Spectrochemical Analysis* (Prentice Hall, Englewood Cliffs 1988)
- 4.36 J.R. Dean, D.J. Ando (Eds.): *Atomic Absorption and Plasma Spectroscopy* (Wiley, New York 1997)
- 4.37 A. Montaser, D.W. Golightly (Eds.): *Inductively Coupled Plasmas in Analytical Atomic Spectrometry*, 2nd edn. (Wiley-VCH, Weinheim 1992)

- 4.38 R.D. Sacks: Emission spectroscopy. In: *Treatise on Analytical Chemistry* Vol. 7, 2nd edn., ed. by I.M. Kolthoff, P.J. Elving (Wiley-Interscience, New York 1981) Chap. 6
- 4.39 R.K. Marcus (Ed.): *Glow Discharge Spectroscopies* (Plenum, New York 1993) p. 514
- 4.40 R. Payling, D. Jones, A. Bengtson (Eds.): *Glow Discharge Optical Emission Spectrometry* (Wiley, Chichester 1997) p. 846
- 4.41 R.K. Marcus, J.A.C. Broekaert (Eds.): *Glow Discharge Plasmas in Analytical Spectroscopy* (Wiley, Chichester 2003) p. 482
- 4.42 T. Nelis, R. Payling: *Glow Discharge Optical Emission Spectroscopy: A Practical Guide*, ed. by N.W. Barnett (The Royal Society of Chemistry, Cambridge 2003) p. 211
- 4.43 R. Jenkins: *Practical X-Ray Spectrometry*, 2nd edn. (Springer, Berlin Heidelberg 1970) p. 190
- 4.44 R.E. Van Grieken, A.A. Markowicz (Eds.): *Handbook of X-Ray Spectrometry*, 2nd edn. (Dekker, New York 2002) p. 1016
- 4.45 E.P. Bertin: *Principles and Practice of X-Ray Spectrometric Analysis*, 2nd edn. (Plenum, New York 1975) p. 1079
- 4.46 B. Dziunikowski (Ed.): *Energy Dispersive X-Ray Fluorescence Analysis* (Elsevier, New York 1989) p. 431
- 4.47 A. Walsh: The application of atomic absorption spectra to chemical analysis, *Spectrochim. Acta* **27B**, 108 (1955)
- 4.48 V.A. Fassel, R.N. Kniseley: Inductively coupled plasma-optical emission spectroscopy, *Anal. Chem.* **46A**, 1110 (1974)
- 4.49 M.R. Winchester, R. Payling: Radio-frequency glow discharge spectrometry: A critical review, *Spectrochim. Acta Part B* **59**, 607–666 (2004)
- 4.50 D. De Soete, R. Gijbels, J. Hoste: *Neutron Activation Analysis* (Wiley-Interscience, London 1972)
- 4.51 S.J. Parry: *Handbook of Neutron Activation Analysis* (Viridian, Surrey 2003)
- 4.52 A. Vertes, S. Nagy, Z. Klencsar: *Handbook of Nuclear Chemistry, Chemical Applications of Nuclear Reactions and Radiations*, Vol. 3, ed. by G.L. Molnar (Kluwer, Dordrecht 2003)
- 4.53 G.L. Molnár, Z. Révay (Eds.): *Handbook of Prompt Gamma Activation Analysis with Neutron Beams* (Kluwer, Dordrecht 2004)
- 4.54 Z.B. Alfassi, C. Chung (Eds.): *Prompt Gamma Neutron Activation Analysis* (CRC, Boca Raton 1995)
- 4.55 IAEA: *Use of Accelerator Based Neutron Sources*, IAEA-TECDOC-1153 (International Atomic Energy Agency, Vienna 2000)
- 4.56 R. Paul: The use of element ratios to eliminate analytical bias in cold neutron prompt gamma-ray activation analysis, *J. Radioanal. Nucl. Chem.* **191**(2), 245–256 (1995)
- 4.57 R.R. Greenberg, R.F. Fleming, R. Zeisler: High sensitivity neutron activation analysis of biological/environmental standard reference materials, *Environ. Int.* **10**, 129 (1984)
- 4.58 R.L. Paul, R.M. Lindstrom: Prompt gamma-ray activation analysis: Fundamentals and applications, *J. Radioanal. Nucl. Chem.* **243**, 181–189 (2000)
- 4.59 W. Goerner, A. Berger, K.H. Ecker, O. Haase, M. Hedrich, C. Segebade, G. Weidemann, G.J. Wermann: Broad band application of combined instrumental photon and neutron activation analysis, *Radioanal. Nucl. Chem.* **248**(1), 45–52 (2001)
- 4.60 ASTM: ASTM E 385–90, *Annual Book of ASTM Standards*, Vol. **12.02** (ASTM, West Conshohocken 1990)
- 4.61 C. Yonezawa: Prompt-ray analysis of elements using cold and thermal reactor guided neutron beams, *Anal. Sci.* **9**, 185 (1993)
- 4.62 J.F. Ziegler, G.W. Cole, J.E.E. Baglin: Technique for determining concentration profiles of boron impurities in substrates, *J. Appl. Phys.* **43**, 3809(1972)
- 4.63 J.P. Biersack, D. Fink: Observation of the blocking effect after ${}^6\text{Li}(n, t){}^4\text{He}$ reactions with thermal neutrons, *Nucl. Instrum. Methods* **108**, 397–399 (1973)
- 4.64 D. Fink: Neutron depth profiling, Reports of the Hahn–Meitner Inst. (HMI)–B 539, 307 (1996)
- 4.65 J.F. Ziegler: *The Stopping and Ranges of Ions in Matter* (Pergamon, New York 1977)
- 4.66 J.F. Ziegler: *Public Domain Computer Code, SRIM-2003* (IBM-Research, Yorktown 2003)
- 4.67 C. Segebade, H.P. Weise, G.J. Lutz: *Photon Activation Analysis* (Hawthorne, New York 1987)
- 4.68 K. Strijckmans: *Chemical Analysis by Nuclear Methods*, ed. by Z.B. Alfassi (Wiley, Chichester 1994) Chap. 10, pp. 215–252
- 4.69 S.A.E. Johansson, J.L. Campbell, K.G. Malmqvist: Particle-induced X-ray emission spectroscopy (PIXE). In: *Chemical Analysis: A Series of Monographs on Analytical Chemistry and its Applications*, Vol. 133, ed. by D. Winfordner (Wiley, Chichester 1995)
- 4.70 S.S. Nagolwalla, E.P. Przybylowicz: *Activation Analysis with Neutron Generators* (Wiley, New York 1973)
- 4.71 W.D. James, R. Zeisler: Uptake of oxygen in a coal standard reference material[®] determined by fast (14–MeV) neutron activation analysis, *J. Radioanal. Nucl. Chem.* **248**, 233–237 (2001)
- 4.72 W.D. James, M.S. Akanni: *IEEE Trans. Nucl. Sci.* **NS-30**, 1610–1613 (1983)
- 4.73 H.M. McNair, J.M. Miller: *Basic Gas Chromatography* (Wiley-Interscience, New York 1998)
- 4.74 M.C. McMaster: *GC/MS: A Practical User's Guide* (Wiley-Interscience, New York 1998)
- 4.75 K.J. Hyber (Ed.): *High Resolution Gas Chromatography* (Hewlett-Packard, Wilmington 1989)
- 4.76 L.R. Snyder, J.J. Kirkland: *Introduction to Modern Liquid Chromatography* (Wiley Interscience, New York 1979)
- 4.77 L.R. Snyder, J.J. Kirkland, J.L. Glajch: *Practical HPLC Method Development* (Wiley, New York 1997)

- 4.78 C.F. Poole: *The Essence of Chromatography* (Elsevier, San Diego 2003)
- 4.79 S.F.Y. Li: *Capillary Electrophoresis* (Elsevier, New York 1993)
- 4.80 J.W. Jorgenson, K.D. Lukacs: Zone electrophoresis in open-tubular glass capillaries, *Anal. Chem.* **53**, 1298–1302 (1981)
- 4.81 K.D. Altria: Overview of the status and applications of capillary electrophoresis, *J. Chromatogr. A* **1023**, 1–14 (2004)
- 4.82 J.B. Fenn, M. Mann, C.K. Meng, S.F. Wong, C.M. Whitehouse: Electrospray ionization for mass spectrometry of large biomolecules, *Science* **246**, 64 (1989)
- 4.83 S.S.-C. Tai, M.J. Welch: Development and evaluation of a candidate reference method for the determination of total cortisol in human serum using isotope-dilution liquid chromatography-mass spectrometry and liquid chromatography-tandem mass spectrometry, *Anal. Chem.* **76**, 1008–1014 (2004)
- 4.84 I.M. Kolthoff, E.B. Sandell, E.J. Meehan, S. Bruckenstein: *Quantitative Analysis*, 4th edn. (Macmillan, New York 1969)
- 4.85 T.W. Vetter, K.W. Pratt, G.C. Turk, C.M. Beck II., T.A. Butler: Using instrumental techniques to increase the accuracy of the gravimetric determination of sulfate, *Analyst* **120**, 2025–2032 (1995)
- 4.86 T.R. Dulski: *A Manual for the Chemical Analysis of Metals* (ASTM, West Conshohocken 1996)
- 4.87 C.O. Ingamells: *Applied Geochemical Analysis* (Wiley-Interscience, New York 1986)
- 4.88 J.R. Moody, T.W. Vetter: Development of the ion exchange-gravimetric method for sodium in serum as a definitive method, *J. Res. Natl. Inst. Stand.* **101**(2), 155–164 (1996)
- 4.89 5th CCQM Meeting, p.83, available at http://www.bipm.org/en/committees/cc/ccqm/publications_cc.html
- 4.90 I.M. Kolthoff: *Volumetric Analysis*, Vol. 3, 2nd edn. (Interscience, New York 1942–1957)
- 4.91 Analytical Chemists' Committee of ICI Ltd.: The standardization of volumetric solutions, *Analyst* **75**, 577–604 (1950)
- 4.92 J. Berčík: *Coulometria* (Olomouc, Czechoslovakia 1986)
- 4.93 M. Máriássy, L. Vyskočil, A. Mathiasová: Link to the SI via primary direct methods, *Accredit. Qual. Assur.* **5**(10/11), 437–440 (2000)
- 4.94 K.W. Pratt: High-precision coulometry. 1. Engineering and instrumentation, *Anal. Chim. Acta* **294**, 125–134 (1994)
- 4.95 G. Marinenko, J.K. Taylor: Precise coulometric titrations of potassium dichromate, *J. Res. Natl. Inst. Stand.* **67A**(5), 453–459 (1963)
- 4.96 IUPAC Commission: Atomic weights of the elements 2001, *Pure Appl. Chem.* **75**(8), 1107–1122 (2003)
- 4.97 D.C. Joy, A.D. Romig, J.I. Goldstein (Eds.): *Principles of Analytical Electron Microscopy* (Plenum, New York 1986) pp.1–306
- 4.98 D.B. Williams, B.C. Carter: *Transmission Electron Microscopy: A Textbook for Materials Science* (Kluwer/Plenum, New York 1996) pp.1–306
- 4.99 R.F. Egerton: Electron energy-loss spectroscopy. In: *The Electron Microscope* (Kluwer/Plenum, New York 1996) pp.0–306
- 4.100 L. Reimer: *Transmission Electron Microscopy* (Springer, Berlin Heidelberg 1993) pp.1–387
- 4.101 J.I. Goldstein, D.E. Newbury, D.C. Joy, C.E. Lyman, P. Echlin, E. Lifshin, L. Sawyer, J. Michael: *Scanning Electron Microscopy and X-Ray Microanalysis*, 3rd edn. (Plenum, New York 2003)
- 4.102 D.E. Newbury, C.E. Fiori, R.B. Marinenko, R.L. Myklebust, C.R. Swyt, D.S. Bright: Compositional mapping with the electron probe microanalyzer: Part I, *Anal. Chem.* **62**, 1245A–1254A (1990)
- 4.103 D.E. Newbury, C.E. Fiori, R.B. Marinenko, R.L. Myklebust, C.R. Swyt, D.S. Bright: Compositional mapping with the electron probe microanalyzer: Part II, *Anal. Chem.* **62**, 1159A–1166A (1990)
- 4.104 D.B. Williams, J.I. Goldstein, D.E. Newbury (Eds.): *X-Ray Spectrometry in Electron Beam Instruments* (Plenum, New York 1995)
- 4.105 L. Struder, C. Fiorini, E. Gatti, R. Hartmann, P. Holl, N. Krause, P. Lechner, A. Longoni, G. Lutz, J. Kemmer, N. Meidinger, M. Popp, H. Soltau, C. van Zanthier: High-resolution nondispersive X-ray spectroscopy with state of the art silicon detectors, *Mikrochim. Acta (Suppl.)* **15**, 11 (1998)
- 4.106 J.I. Goldstein, H. Yakowitz, D.E. Newbury, E. Lifshin, J.W. Colby, J.R. Coleman: *Practical Scanning Electron Microscopy* (Plenum, New York 1974)
- 4.107 D. Briggs, J.T. Grant (Eds.): *Surface Analysis by Auger and X-Ray Photoelectron Spectroscopy* (Cromwell, Trowbridge 2003)
- 4.108 D. Briggs, M.P. Seah (Eds.): *Practical Surface Analysis, Vol. 1: Auger and X-Ray Photoelectron Spectroscopy*, 2nd edn. (Wiley, West Sussex 1983)
- 4.109 J.F. Watts, J. Wolstenholme: *An Introduction to Surface Analysis by XPS and AES* (Wiley, West Sussex 2003)
- 4.110 G.D. Danilatos: Foundations of environmental scanning electron microscopy, *Adv. Electron. El. Phys.* **71**, 109–250 (1988)
- 4.111 G.D. Danilatos: Introduction to the ESEM instrument, *Microsc. Res. Tech.* **25**, 354–361 (1993)
- 4.112 S.A. Wight: Experimental data and model simulations of beam spread in the environmental scanning electron microscope, *Scanning* **23**, 320–327 (2001)
- 4.113 S.A. Wight, C.J. Zeissler: Direct measurement of electron beam scattering in the environmental scanning electron microscope using phosphor imaging plates, *Scanning* **22**, 167–172 (2000)
- 4.114 J.I. Goldstein, D.E. Newbury, P. Echlin, D.C. Joy, A.D. Romig Jr, C.E. Lyman, C. Fiori, E. Lifshin: *Scan-*

- ning *Electron Microscopy and X-Ray Microanalysis* (Kluwer/Plenum, New York 2003)
- 4.115 E. Griffith, D.E. Newbury (Eds.): Introduction to environmental scanning electron microscopy issue, *Scanning* **18**(7), 465–527 (1996)
- 4.116 D.E. Newbury, E. Griffith (Eds.): Part II of the special issue on environmental scanning electron microscopy, *Scanning* **19**(2), 70 (1997)
- 4.117 E.M. Griffith, G.D. Danilatos (Eds.): Environmental scanning electron-microscopy, microscopy research and technique, *Microsc. Res. Tech.* **25**(5/6), 353–361 (1993)
- 4.118 J.M. Chalmers, P.R. Griffiths (Eds.): *Handbook of Vibrational Spectroscopy* (Wiley, New York 2002)
- 4.119 I.R. Lewis, H.G.M. Edwards (Eds.): *Handbook of Raman Spectroscopy* (Dekker, New York 2001)
- 4.120 H.J. Humecki: *Practical Guide to Infrared Microspectroscopy* (Dekker, New York 1995)
- 4.121 R.L. McCreery: *Raman Spectroscopy for Chemical Analysis* (Wiley, New York 2000)
- 4.122 H. Kipphardt, R. Matschat, U. Panne: Metrology in Chemistry – A rocky road, *Microchim. Acta* **162**, 35–41 (2008)
- 4.123 H. Kipphardt, R. Matschat: Purity assessment for providing primary standards for elemental determination – A snap shot of international comparability, *Microchim. Acta* **162**, 269–275 (2008), DOI 10.1007/s00604-007-0937-2
- 4.124 H. Kipphardt, R. Matschat, J. Vogl, T. Gusarova, M. Czerwensky, H.-J. Heinrich, A. Hioki, L.A. Konopelko, B. Methven, T. Miura, O. Petersen, G. Riebe, R. Sturgeon, G.C. Turk, L.L. Yu: Purity determination as needed for the realisation of primary standards for elemental determination: status of international comparability, *Accredit. Qual. Assur.* **15**, 29–37 (2010), DOI 10.1007/s00769-009-0557-0
- 4.125 B. Lange, H. Kipphardt, R. Matschat: Enhancement of intensities in glow discharge mass spectrometry by using mixtures of argon and helium as plasma gases, *Anal. Bioanal. Chem.* **389**, 2287–2296 (2007)
- 4.126 R. Matschat, J. Hinrichs, H. Kipphardt: Application of glow discharge mass spectrometry to multielement ultra-trace determination in ultrahigh-purity copper and iron: A calibration approach achieving quantification and traceability, *Anal. Bioanal. Chem.* **386**, 125–141 (2006)
- 4.127 B. Welz, H. Becker-Roß, S. Florek, U. Heitmann: *High-Resolution Continuum Source AAS – The better way to do atomic absorption spectrometry* (Wiley-VCH, Weinheim 2005)
- 4.128 A. Detcheva, P. Barth, J. Haßler: Calibration possibilities and modifier use in ETV-ICP OES determination of trace and minor elements in plant materials, *Anal. Bioanal. Chem.* **394**, 1485–1495 (2009)
- 4.129 K. Slickers: *The automatic atomic emission-spectrometry* (Verlag der Brühlschen Universitätsdruckerei, Lahn-Gießen 1992)
- 4.130 G. Staats, S. Noack: *Qualitätssicherung in der Analytik; Die Rekonstitution – Eine Methode zur Optimierung der Richtigkeit von Analysen* (Verlag Stahleisen GmbH, Düsseldorf 1996)
- 4.131 H. Kipphardt, R. Matschat, O. Rienitz, D. Schiel, W. Gernand, D. Oeter: Traceability system for elemental analysis, *Accredit. Qual. Assur.* **10**, 633–639 (2006)
- 4.132 H. Kipphardt, R. Matschat, U. Panne: Development of SI traceable standards for element determination, *Chimia* **63**, 637–639 (2009)
- 4.133 BAM Federal Institute for Materials Research and Testing, Berlin, http://www.rm-certificates.bam.de/certificates/primary_pure_substances/index.htm

5. Nanoscopic Architecture and Microstructure

The methods compiled in this chapter are important in many areas of materials science and technology because various physical properties of materials (mechanical, thermal, electronic, optical, magnetic, dielectric, biological) depend on their geometric architecture, on scales ranging from the atomic or nanoscopic to the semimicroscopic. Some of the properties are governed only by an elementary atomic group in the structural hierarchy while others are brought about by cooperative functioning of multiple phases or microscopic structures in different dimensions. Corresponding to the vast variety of materials and their properties, a wide range of experimental techniques are available, so that the choice of which technique to employ on starting a study may not be clear. In this respect one should also bear in mind that some of the techniques presented in this chapter are based on physical principles, which are also relevant to the measurement methods compiled in Chaps. 6 and 11.

5.1	Fundamentals	211
5.1.1	Diffraction and Scattering Methods	211

5.1.2	Microscopy and Topography	215
5.1.3	Spectroscopy	226
5.2	Crystalline and Amorphous Structure Analysis	232
5.2.1	Long-Range Order Analysis	232
5.2.2	Medium-Range Order Analysis	235
5.2.3	Short-Range Order Analysis	237
5.3	Lattice Defects and Impurities Analysis ...	239
5.3.1	Point Defects and Impurities	240
5.3.2	Extended Defects	252
5.4	Molecular Architecture Analysis	258
5.4.1	Structural Determination by X-Ray Diffraction	258
5.4.2	Nuclear Magnetic Resonance (NMR) Analysis	259
5.4.3	Chemophysical Analysis	267
5.5	Texture, Phase Distributions, and Finite Structures Analysis	269
5.5.1	Texture Analysis	269
5.5.2	Microanalysis of Elements and Phases	271
5.5.3	Diffraction Analysis of Fine Structures	273
5.5.4	Quantitative Stereology	274
	References	277

Following the preceding chapter on the measurement of chemical composition, this chapter focuses on the characterization of the *nanoscopic architecture and microstructure of materials*. Surface and interface characterization methods are treated in the next chapter.

To support the selection of the most appropriate method for a given problem, all readers are recommended to read Sect. 5.1 before proceeding to the relevant subsequent section. Table 5.1 may help you to select applicable methods. If you are interested in, for example, the structure of macromolecules, you go to the *Molecular architecture* column under *Subject under consideration*. You will find ◦ symbols in the rows of that column that express an applicable methodology, indicated in the first and second columns. If you find

the line (method) *NMR* interesting, you may check the *Material type* and *Atom arrangement* sections on the same line to the right, to find that the method is applicable to amorphous samples as well as crystals as long as the sample is nonmetallic. Special requirements, if any, are noted in the column on the far right. The third column indicates the section(s) describing the detail of the method or literature to which the interested reader should refer. You may then proceed to each section or subsection for further details.

The organization of the chapter is as follows. After a concise review of the necessary fundamentals – diffraction and scattering methods, microscopy and topography, spectroscopy – the presentation of *Measurement Methods for Nanoscopic Architecture*

and *Microstructure* is structured into four parts, relating to

- crystalline and amorphous structures analysis
- lattice defects and impurities analysis
- molecular architecture analysis

- phase distributions, texture and finite structures analysis.

For the reader's convenience, Table 5.2 lists sample requirements for the representative techniques described in this chapter.

Table 5.1 Methodology selection table

Methodology			Subject under consideration				Material type				Atom arrangement		Requirements
Category	Method	Ref. ¹	Structural order	Defects and impurities	Molecular architecture ²	Microstructure ³ / Finite structures ⁴	Metal	Semiconductor	Insulator	Others ⁵	Crystalline	Amorphous	
Diffraction													
	Selected area electron diffraction	5.1.1, 5.2.1	○	○		○	○	○	○	○	○	○	HV ⁶
	RHEED	6	○				○	○			○		UHV ⁷
	Convergent electron beam diffraction	5.2.2	○	○		○	○	○	○	○	○		
	LEED	6	○				○	○			○		UHV
	Single-crystal X-ray diffraction	5.1.1, 5.2.1	○	○	○	○	○	○	○	○	○	○	
	Powder x-ray diffraction	5.1.1, 5.2.1	○		○		○	○	○	○	○		
	Small-angle scattering	5.5.3	○	○		○	○	○	○	○	○	○	
	Stokes–Wilson scattering	5.3.1	○	○			○	○	○	○	○		
	Neutron diffraction ⁸	5.1.1, 5.5.1	○		○	○	○	○	○	○	○		
	Rutherford back scattering	5.3.1	○	○		○	○	○	○	○	○	○	
Microscopy													
	TEM ⁹	5.1.2, 5.2.2, 5.3.2, 5.5.2, 5.5.3	○	○		○	○	○	△	○	○		HV, thin sample
	STEM ¹⁰	5.1.2, 5.3.1, 5.3.2, 5.5.2	○	○		○	○	○	△	○	○		HV, thin sample
	SEM ¹¹	5.1.2, 5.3.1, 5.3.2, 5.5.1	○	○		○	○	○	△	○	○	○	HV
	OM ¹²	5.1.2, 5.3.2	○	○		○	○	○	○	○	○	○	
	LSCM ¹³	5.1.2, 5.4.3, 5.5.3			○	○	○	○	○	○	○	○	
	TIRFM ¹⁴	5.1.2			○	○		○	○	○	○	○	
	X-ray topography	5.1.2, 5.3.2	○	○		○	○	○	○	○	○		
	X-ray phase contrast imaging	5.5.3	○			○	○	○	○	○	○	○	
	SNOM	5.1.2		○	○	○	○	○	○	○	○	○	

Table 5.1 (continued)

Methodology			Subject under consideration				Material type				Atom arrangement		Requirements
Category	Method	Ref. ¹	Structural order	Defects and impurities	Molecular architecture ²	Microstructure ³ / Finite structures ⁴	Metal	Semiconductor	Insulator	Others ⁵	Crystalline	Amorphous	
Microscopy													
	STM	5.1.2, 5.3.1, 6	○	○	○	○	○	○	○	○	○	△	Atomically flat surface
	AFM	5.1.2, 6	○	○	○	○	○	○	○	○	○	△	
	FIM	5.1.2, 5.5.3	○	○		○	○	○			○		UHV
	Scanning acoustic microscopy	Briggs ¹⁵				○	○	○	○	○	○	○	
Spectroscopy													
	Positron annihilation	5.3.1		○			○	○	○	○	○	○	
	Photoabsorption ¹⁶	5.1.2, 5.3.1, 11	○	○	○	○		○	○	○	○	○	
	Photoluminescence	5.1.2, 5.3.1, 11	○	○	○	○		○	○	○	○	○	
	Raman	5.1.2, 5.3.1, 5.5.2, 11	○	○	○	○		○	○	○	○	○	
	FT-IR	5.1.2, 5.3.1	○	○	○	○		○	○	○	○	○	
	IRAS ¹⁷	5.3.1		○	○			○	○	○	○	○	
	Surface plasmon resonance	5.5.2				○	○						
	Capacitance spectroscopy ¹⁸	5.3.1		○				○			○	○	Metal contact
	ESR ¹⁹	5.1.2, 5.3.1		○	○			○	○	○	○	○	Paramagnetic center
	Circular dichroism ²⁰	5.4.3	○	○	○			○	○	○	○		
	Nuclear magnetic resonance	5.1.2, 5.3.1, 5.4.2, 5.5.3	○	○	○			○	○	○	○	○	Limited nuclear species, diamagnetic molecules
	ENDOR ²¹	5.3.1		○	○			○	○	○	○	○	
	μSR	5.3.1		○			○	○	○	○	○		Limited nuclear species
	X-ray fluorescence	5.5.2		○	○	○	○	○	○	○	○	○	
	EXAFS ²²	5.3.1	○	○	○	○	○	○	○	○	○	○	
	Photoemission electron spectroscopy ²³	6		○	○		○	○	△	○	○	○	
	Perturbed angular correlation	5.3.1		○			○	○	○	○	○	○	Limited nuclear species

Table 5.1 (continued)

Methodology			Subject under consideration				Material type				Atom arrangement		Requirements
Category	Method	Ref. ¹	Structural order	Defects and impurities	Molecular architecture ²	Microstructure ³ / Finite structures ⁴	Metal	Semiconductor	Insulator	Others ⁵	Crystalline	Amorphous	
Spectroscopy													
	Möbbauser spectroscopy	5.3.1		○		○	○	○	○	○	○	○	Limited nuclear species
	Mechanical Spectroscopy ²⁴	5.1.2, 5.3.1, 5.3.2	○	○		○	○	○	○	○	○	○	
	Noise Spectroscopy	5.3.1	○	○			○	○	○	○	○	○	
	DSC/DTA	4.1, 8	○	○		○	○	○	○	○	○	○	
Microanalysis													
	EDX ²⁵	5.5.2		○		○	○	○	○	○	○	○	Heavy elements
	TEM-EELS ²⁶	5.5.2	○	○		○	○	○	○	○	○	○	HV, thin sample
	Micro-Auger	5.5.2, 6		○		○	○	○	○	○	○	○	Intermediate elements
	EPMA ²⁷	5.5.2		○	○	○	○	○	○	○	○	○	UHV
	X-ray diffraction	5.5.1				○	○	○	○	○	○		
	SEM-electron channeling pattern	5.5.1	○	○		○	○	○	Δ		○		HV
	Scanning tunneling spectroscopy	5.3.1	○	○	○	○	○	○		○	○	○	UHV
	SPM-nanospectroscopy	5.5.2	○	○	○	○	○	○	○	○	○	○	
	Nano-indenter	5.5.2				○	○	○	○	○	○	○	
	Fluorescence microscopy ²⁸	11		○	○	○		○	○	○	○	○	
	Micro-Raman	5.5.2	○		○	○		○	○	○	○	○	
Stereology													
	Stereogram	5.5.3		○	○		○	○	○	○	○		
	LSCM	5.5.3				○		○	○		○	○	Transparent sample
	Light scattering tomography	Ogawa ²⁹		○		○		○	○	○	○	○	
	Nonlinear microscopy ³⁰	5.5.3				○		○	○	○	○	○	
	3D-SEM	5.5.3				○	○	○	○	○	○	○	
	3D-TEM	5.5.3	○	○		○	○	○	○	○	○	○	HV
	3D atom probe	5.5.3	○	○		○	○	○		○			UHV
	Micro-XCT	5.5.3				○	○	○	○	○	○	○	Light elements

Table 5.1 (continued)

Methodology			Subject under consideration				Material type				Atom arrangement		Requirements
Category	Method	Ref. ¹	Structural order	Defects and impurities	Molecular architecture ²	Microstructure ³ / Finite structures ⁴	Metal	Semiconductor	Insulator	Others ⁵	Crystalline	Amorphous	
Miscellaneous													
	Density measurements	Gupta ³¹		o		o	o	o	o	o	o	o	
	Quartz crystal microbalance	Gupta ³¹			o	o	o	o	o	o	o	o	
	Radioactivation analysis	Alfassi ³²		o	o		o	o	o	o	o	o	Limited nuclear species
	SIMS Profile	6		o	o	o	o	o	o	o	o	o	UHV
	Q-Mass	4		o	o	o	o	o	o	o	o	o	UHV
	LC-MS ³³	5.4.3, 4.1			o		o	o	o	o	o	o	
	GC-MS ³⁴	5.4.3, 4.1			o		o	o	o	o	o	o	
	GPC/GFC ³⁵	5.4.3, 4.1			o		o	o	o	o	o	o	
	ICP ³⁶	4.2		o	o		o	o	o	o	o	o	
	AAS/AES ³⁷	6		o	o		o	o		o	o	o	UHV
	Electrophoresis	5.4.3			o		o	o		o	o	o	
	Electron Holography	Tonomura ³⁸		o			o	o	o	o	o		
	FRET ³⁹	5.4.3		o	o	o		o	o	o	o	o	
	Pump & Probe	Shah ⁴⁰ , 11		o	o	o		o	o	o	o	o	Ultrafast pulse laser

¹ Chapter(s) and section(s) describing the detail or literature to which the interested readers should refer

² Including macromolecules

³ Including phase distribution and texture

⁴ e.g., dendrites, cells, bones, fibres, nanoparticles, device structures etc.

⁵ Isolated molecules and molecular solids

⁶ High vacuum

⁷ Ultrahigh vacuum

⁸ Including anomalous

⁹ Including HRTEM

¹⁰ Including HAADF-STEM

¹¹ Including back scattering EM, SEM-EBIC, SEM-CL, scanning reflection electron microscopy

¹² Including etch pits observation

¹³ Laser scanning confocal microscopy

¹⁴ Total internal reflection fluorescence microscopy

¹⁵ [5.1]

¹⁶ Including photoacoustic spectroscopy, resonance-enhanced multiphoton ionization

¹⁷ Including pure rotation spectroscopy

Table 5.1 (continued)

¹⁸ Including DLTS, phot capacitance
¹⁹ Including optically-detected magnetic resonance
²⁰ Including optical rotary dispersion and magnetic circular dichroism
²¹ Electron nuclear double resonance
²² Extended x-ray absorption fine structure
²³ Including XPS, UPS
²⁴ Including internal friction, anelasticity
²⁵ Including SEM-based and (S)TEM-based
²⁶ Including EXELFS (extended energy loss fine structure)
²⁷ Electron probe micro analyzer
²⁸ Fluorimetry
²⁹ [5.2]
³⁰ Including nonlinear fluorescence (two-photon) microscopy and second-harmonic generation microscopy
³¹ [5.3]
³² [5.4]
³³ Liquid chromatography-mass spectroscopy
³⁴ Gas chromatography-mass spectroscopy
³⁵ Gel permeation (filtration) chromatography
³⁶ Including flame photometry (FAAS/FAES/FAFS (flame atomic absorption (emission, fluorescence) spectrometry))
³⁷ Atomic absorption (emission) spectrometry
³⁸ [5.5]
³⁹ Fluorescence resonance energy transfer
⁴⁰ [5.6]

Table 5.2 Sample requirements in some common methods in their conventional form

Method	Minimum center density	Minimum sample amount	Maximum molecular size ^a
Element analysis			
GC-MS	10 ppb	≈ 1 ml	Boiling temperature < 400 °C
Radioactivation analysis	0.1 ppb	0.01 ng	—
X-ray fluorescence	10 ppm	100 mg ^b	—
Structure analysis			
Single crystal XRD	—	0.1 mm ^c	< 100 atoms ^d , > 600 atoms or 10 ⁶ in molecular weight ^e
Powder XRD	—	0.2–0.5 mm	Several 10 ³ atoms
NMR	≈ 1%	1 mM, several mg	3 × 10 ⁴ in molecular weight
Defect analysis			
ESR ^f	10 ¹² –10 ¹³ cm ^{-3g} or 10 ¹⁴ –10 ¹⁶ cm ^{-3h}	< cavity size	—
Positron annihilation	5 × 10 ¹⁵ –5 × 10 ¹⁸ cm ⁻³ⁱ	No serious limitation	≈ 10 vacancies ^j
Raman scattering	0.01–1% (several ppb ^k)	Several μl (liquid)	—
FT-IR	0.01%	sub μg ^l	—
PL	0.1 ppm	> mg	—
Capacitance spectroscopy	10 ¹⁴ cm ⁻³	1 mm	—

^a In crystal structure analysis, the size of atom assembly (*molecule*) occupying a lattice point

^b Reduced by orders of magnitude when a synchrotron radiation source is used

^c 0.02 mm when a synchrotron radiation source is used

Table 5.2 Sample requirements in some common methods in their conventional form, cont.

^d	When direct method is used
^e	When heavy atoms substitution method works
^f	The sensitivity is quite dependent on what signal is detected. Here the signal is microwave absorption. Even a single spin can be detected if a special technique is used [5.7]
^g	In insulators
^h	In semiconductors
ⁱ	For negatively charged vacancies at room temperature no serious limitation
^j	Above which the vacancy clusters become indistinguishable from the surface
^k	When resonant Raman scattering is employed
^l	When combined with a chromatographic separation preprocess

5.1 Fundamentals

This section deals with the fundamental (minimum) knowledge that the reader should have in advance. This section is also intended to guide the reader to be able to select properly the appropriate techniques for their purpose by overviewing the range of energy, the length scale, the spatial resolution and the time scale that are covered by the entire range of these respective techniques. Since it appears that diffraction methods are not well covered in other parts of this handbook, the basic physics of diffraction and the principles of microscopic techniques (mainly TEM) based on beam diffraction will be described in some depth. We leave most of the basics of spectroscopic techniques to Chap. 11.

5.1.1 Diffraction and Scattering Methods

The scattering of particles by an interacting target is a common phenomenon usually interpretable in terms of classical mechanics with a minor correction. Generally, the waves (electromagnetic, de Broglie, vibrational, etc.) are scattered with an efficiency that can vary widely depending on the nature and the size of the scatterers and the wavelength. The diffraction of waves is a term used to describe the constructive interference of waves coherently scattered by multiple scatterers. Scattering and diffraction are, thus, inseparable concepts that are sometimes treated together in textbooks. Absorption is an apparently different aspect of waves in which some wave energy is consumed by excitation of a quasiparticle of different nature. In some cases, however, absorption is an aspect of wave scattering in which the excited state is derived from the interference of the scattered waves. The wavelength dependence of absorption is the central subject of various schemes of spectroscopy, which are addressed mainly in Sect. 5.1.2.

The scatterers of electromagnetic waves from the visible light to the x-ray regime are electrons, and those in the infrared regime are phonons or molecular vibrations. Although the penetration of electromagnetic waves through solids can vary significantly from material to material due to the wavelength dependence of the absorption coefficient, hard x-rays have a relatively high penetrability through solids as long as the constituent elements are light. In contrast, since electrons have a negative electric charge, they interact so strongly with matter that they practically cannot penetrate even thin solids unless the energy is higher than 100 keV. On the contrary, neutrons have no electric charge and so can penetrate deeply into solids. Neutrons have a spin magnetic moment and therefore interact with electrons, which also have a magnetic moment. This fact provides unique experimental approaches for studies of magnetism in solids. Furthermore, neutrons also interact with nuclei with scattering cross sections that are quite different from those of x-rays and electrons; for example, the detection of protons that are difficult to detect with x-rays and electrons but that are detectable by neutrons due to the large scattering cross section.

The physical parameter of fundamental importance in scattering and diffraction of waves or quantum beams is the wavelength or wave number. Figure 5.1 shows the wavelength of various beams plotted as a function of the quantum energy of the beam, the energy quantum $h\nu$ of a photon and the kinetic energy of an electron and of a neutron. Since, as explained later, diffraction occurs most significantly when the wavelength is close to the separation of the scatterers, particle beams with a wavelength of the order of 0.1 nm are most suitable for diffraction studies of atomic arrangement. Among electromagnetic waves, x-rays of 10 keV

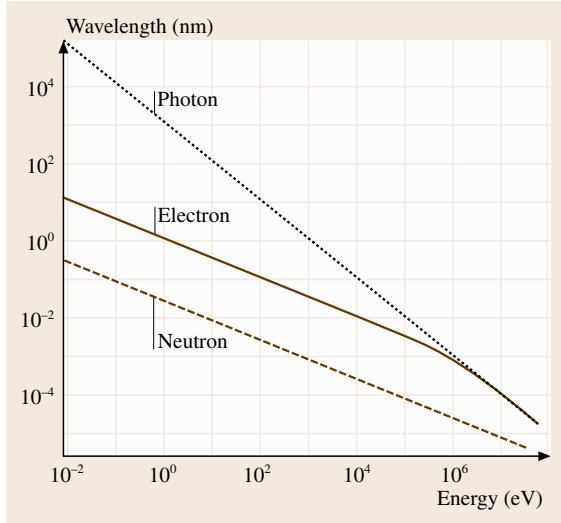


Fig. 5.1 Wavelength versus energy relations in various quantum beams

are in this range, whereas electrons of 100 eV also have such a wavelength. The fast neutrons emitted from nuclear reactors or accelerator targets have energies of the order of MeV but can be slowed down to energies below 1 keV after passing through a moderator consisting of materials such as water and graphite. Among the slow neutrons, those whose energy is near room temperature (0.025 eV) and those below room temperature are called thermal neutrons and cold neutrons, respectively. These are the neutrons used for diffraction studies. Neutron diffraction can be an alternative to x-ray diffraction when x-rays do not detect low- Z elements well, to distinguish near- Z elements or to penetrate thick samples.

Since a comprehensive description of the fundamentals of crystal diffraction is found in many good textbooks [5.8–12], only the essence is summarized here so that the reader may understand the principles of the experimental techniques described in later sections.

In cases in which the interaction of waves with matter is weak (typically in x-ray and neutron diffraction), it is a good approximation to use the kinematical theory which assumes that the wave can be scattered only once in the matter. However, when the matter is crystalline and the crystal is thick and nearly perfect, diffraction may have to be treated by the dynamical theory that rigorously takes into account multiple diffractions in the crystal. The same situation also arises in the diffraction of charged particles such as electrons that interact very

strongly with solids. Nevertheless, although the quantitative interpretation of some phenomena requires the dynamical theory, many of the phenomena encountered in experiments can be understood in the framework of the kinematical theory. For the dynamical theory, the minimum knowledge is given in Sects. 5.1.2 and 5.3.2 where it is required.

In real space, a strong diffraction of a wave of wavelength λ is induced by a set of net planes (Note that atoms on each net plane do not have to be regularly arrayed.) regularly separated by a distance a (Fig. 5.2) when the wave is incident on the net planes at an angle θ satisfying the Bragg condition

$$2a \sin \theta = n\lambda \quad (n : \text{integer}). \quad (5.1)$$

In the reciprocal space, the Ewald sphere is the most commonly used graphical construction of wave diffraction, whether for x-ray or de Broglie waves. Precisely, the sphere of radius $1/\lambda$ is three-dimensional but usually represented in two dimensions by a circle touching the origin of the reciprocal lattice, as shown in Fig. 5.3. The Bragg condition is satisfied when the sphere passes through a reciprocal lattice point other than the origin. The wave vector of the incident wave \mathbf{k}_0 and that of the diffracted wave \mathbf{k} are indicated by the arrows drawn

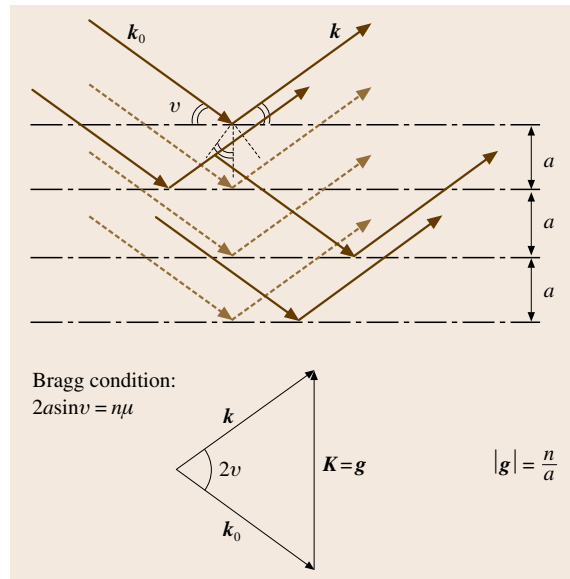


Fig. 5.2 Diffraction by a set of net planes periodically separated by a distance a . Constructive interference takes place under the Bragg condition. Note that atoms on each net plane are not necessarily periodic for specular reflection to occur

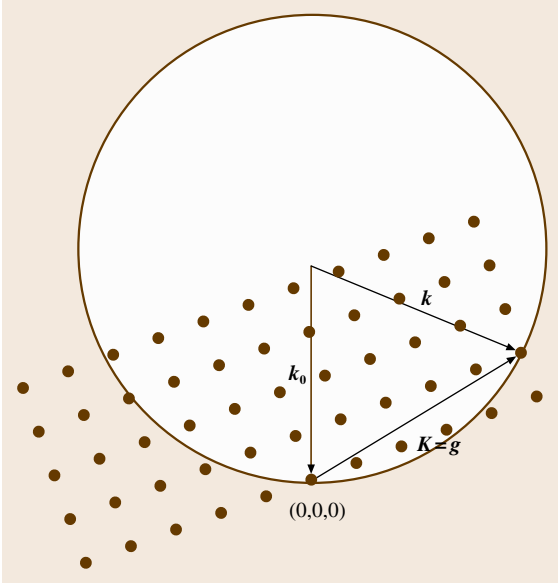


Fig. 5.3 Graphical reconstruction of wave diffraction by Ewald sphere in the reciprocal lattice. $\mathbf{K} = \mathbf{g}$ corresponds to the Bragg condition

from the center of the sphere to the origin and to the reciprocal lattice point, respectively. Thus, the Bragg condition (5.1) is equivalent to

$$\mathbf{K} = \mathbf{g}, \quad (5.2)$$

where $\mathbf{K} \equiv \mathbf{k} - \mathbf{k}_0$ is called the scattering wave vector, and \mathbf{g} ($|\mathbf{g}| = n/a$) is the reciprocal lattice vector normal to the net planes. (Throughout this chapter, we follow the convention that the factor 2π is not included in the definition of reciprocal vectors \mathbf{g} and wave vectors \mathbf{k} .)

In x-ray diffraction, the entities that scatter x-rays in matter are electrons. Electrons forced to oscillate by the alternating electric field of the electromagnetic wave emit an electromagnetic wave of the same photon energy (elastic scattering or Thomson scattering) or of a slightly reduced energy (inelastic scattering or Compton scattering), the latter constituting the background for the coherent interference of the former, elastically scattered, waves. Generally, waves incident with intensity I_e and wave vector \mathbf{k}_0 are scattered by a collection of electrons or an electron cloud of density $\rho(\mathbf{r})$ to interfere to yield a far-field electromagnetic wave with a wave vector \mathbf{k} and intensity

$$I(\mathbf{K}) = I_e \left| \int \rho(\mathbf{r}) \exp(2\pi i \mathbf{K} \cdot \mathbf{r}) d\mathbf{v} \right|^2. \quad (5.3)$$

If the scatterers are electrons only in a single atom, the scattering intensity is given by

$$I_a(\mathbf{K}) = I_e |f(\mathbf{K})|^2, \quad (5.4)$$

with the atomic scattering factor defined by

$$f(\mathbf{K}) \equiv \int \rho_a(\mathbf{r}) \exp(2\pi i \mathbf{K} \cdot \mathbf{r}) d\mathbf{v}, \quad (5.5)$$

the magnitude of which is determined by the atomic electron density $\rho_a(\mathbf{r})$ and hence specific for the atomic element. The atomic scattering factor is a complex quantity and may also vary depending on the beam energy, bringing about the anomalous dispersion effect (Sects. 5.2.1 and 5.2.3).

In the Born approximation, or the kinematical theory, in which a *crystal* is thin enough for x-ray scattering to take place at most once in the solid, the intensity of the x-ray scattered by the assembly of atoms is simply given by

$$\begin{aligned} I(\mathbf{K}) &= I_e \left| \sum_{n,j} f_j(\mathbf{K}) \exp[2\pi i \mathbf{K} \cdot (\mathbf{R}_n + \mathbf{r}_j)] \right|^2 \\ &\equiv I_e \cdot G(\mathbf{K}) \cdot |F(\mathbf{K})|^2. \end{aligned} \quad (5.6)$$

Here, as shown in Fig. 5.4, $\mathbf{R}_n = n_1 \mathbf{a} + n_2 \mathbf{b} + n_3 \mathbf{c}$ denotes the position of the n th crystalline unit cell (the vectors \mathbf{a} , \mathbf{b} and \mathbf{c} are the unit-cell translations while n_1 , n_2 and n_3 are integers), \mathbf{r}_j is the relative position of the j th atom within the unit cell, and f_j is the atomic scattering factor of the j th atom. The factor

$$F(\mathbf{K}) \equiv \sum_j^{\text{unit cell}} f_j(\mathbf{K}) \exp(2\pi i \mathbf{K} \cdot \mathbf{r}_j) \quad (5.7)$$

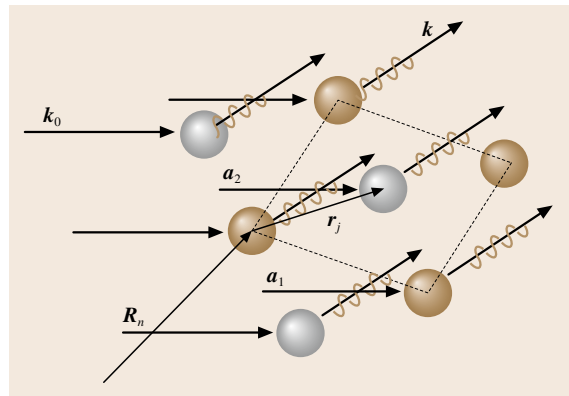


Fig. 5.4 X-ray diffraction by a crystal lattice the unit cell of which is indicated with a parallelogram

is called the structure factor and characterizes the atomic arrangement in the unit cell. Another factor

$$\begin{aligned}
 G(\mathbf{K}) &\equiv \left| \sum_n \exp(2\pi i \mathbf{K} \cdot \mathbf{R}_n) \right|^2 \\
 &= \left| \sum_{n_1} \exp(2\pi i k_1 n_1 a) \sum_{n_2} \exp(2\pi i k_2 n_2 b) \right. \\
 &\quad \left. \times \sum_{n_3} \exp(2\pi i k_3 n_3 c) \right|^2 \quad (5.8)
 \end{aligned}$$

is called the interference function, which is written in the second formula in terms of the components of the vector $\mathbf{K} = (k_1, k_2, k_3)$ projected onto the unit-cell translation vectors. In diffraction of a monochromatic wave from a sufficiently large single crystal (n_1, n_2 and n_3 are all large), $G(\mathbf{K})$ is nonzero ($n_1 \cdot n_2 \cdot n_3$) only when

$$k_1 a = h, \quad k_2 b = k \quad \text{and} \quad k_3 c = \ell, \quad (5.9)$$

for integers h, k and ℓ . This is again equivalent to the Bragg condition (5.2), the condition for constructive interference. In such cases, the diffraction intensity is

simply given by $|F(\mathbf{g})|^2$ times the number of unit cells in the sample. In small crystals, however, diffraction also occurs in directions other than those satisfying (5.2) with intensities that depend on the interference function, $G(\mathbf{K})$, which reflects the size and external shape of the crystal.

Thus, we have to consider two cases: the case of large crystals for which the effects of $G(\mathbf{K})$ can be neglected, and the case of small crystals for which the morphological information contained in $G(\mathbf{K})$ is our main concern.

Combining (5.5) and (5.7) we find that $F(\mathbf{K})$ is related to the electronic density $\rho(\mathbf{r})$ through a Fourier transformation. This means that for large crystals we could deduce the electronic density $\rho(\mathbf{r})$ or the atomic arrangement in the crystalline unit cell by inverse Fourier transformation of the structure factors that can be found from the experimental scattering intensity. This forms the basis of structural determination by x-ray diffraction from crystalline samples (Sects. 5.2.1 and 5.4.1).

For small crystals, we have broadening of diffraction spots as happens in the diffraction of light by an optical grating of finite size (Fig. 5.5a). This diffraction broadening could be regarded as due to the aug-

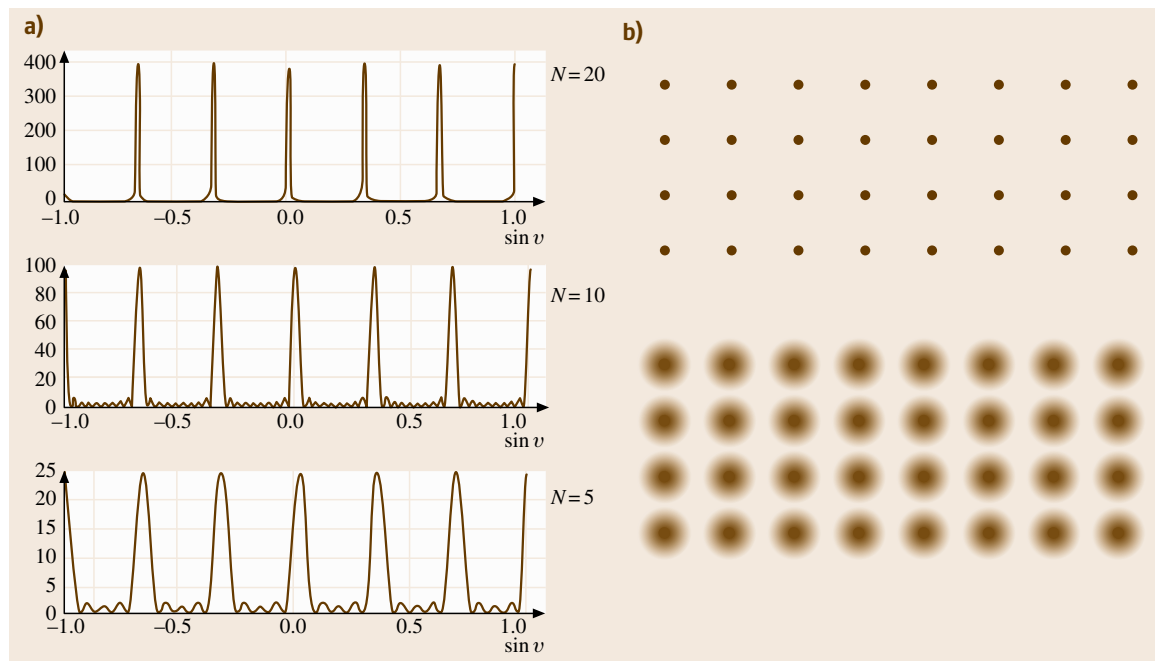


Fig. 5.5a,b As the sharpness of diffraction decreases with the decreasing size of a grating in a monochromator (a), diffraction peaks in small crystals show broadening, which is represented by the diffuseness of reciprocal lattice points (b)

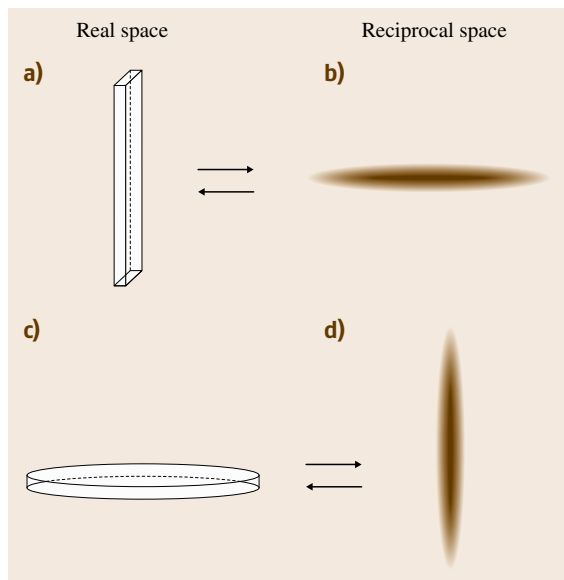


Fig. 5.6a–d Broadening and sharpening of reciprocal lattice points (b),(d) due to the external shape of the crystals (a),(c)

mentation of the reciprocal lattice points (Fig. 5.5b). Mathematically, $G(\mathbf{K})$ is again the Fourier transform of the external shape of the crystal, so thin crystals elongated in one direction, as shown in Fig. 5.6a, yield sharpening of the reciprocal lattice points along that direction but broadening perpendicular to it, as shown in Fig. 5.6b. Similarly, plate-like flat crystals (Fig. 5.6c) broaden the diffraction peaks along the surface normal, as shown in Fig. 5.6d. This fact makes it possible to analyze the medium-range order (Sect. 5.2.2), to determine experimentally the small particle size (Sect. 5.5.3), and to conduct high-resolution TEM observations (Sect. 5.1.2).

5.1.2 Microscopy and Topography

Microscopy allows one to study material structures with spatial resolution. The resolving power of microscopes depends on the *beam* that is used to construct images. Most microscopic methods may be grouped into one of two types: ordinary microscopy, which uses certain waves for sample *illumination* and a set of lenses for construction of an image; and scanning microscopy, which uses a tiny *probe* that is scanned over the sample to construct a microscopic image synchronously displayed on a two-dimensional screen. In the former type of microscopes, the dominant factor governing the

spatial resolution is the wavelength of the wave or the aberration of the objective lens (the convex lens nearest to the object being observed). Even if the lens is free of aberration, its focus is not a perfect *point* but is blurred by the effect of wave diffraction due to the finite lens diameter (Fig. 5.7). Owing to the parallel imaging capability in the former type of microscopes, one may observe *in situ* the dynamic change or motion of objects, which could be recorded by a video camera, although the same may also be possible in the latter type if the scanning rate is high enough to follow the events. Figure 5.8 shows the range of scales that is covered by various microscopes. The lower limit and the upper limit of the lateral scale indicate the lateral resolution and the maximum size of the specimen that can be surveyed, respectively. The lower and upper limits of the vertical scale indicate the sample thinness required for microscopic observations and the sample thickness allowed for experiments, respectively. Other features of microscopic techniques are also summarized in Table 5.3.

Optical Microscopy (OM)

We mention here only briefly three types of optical microscopy (OM): interference microscopy, which is mature but plays important roles in the assessment of material microstructures; laser scanning confocal

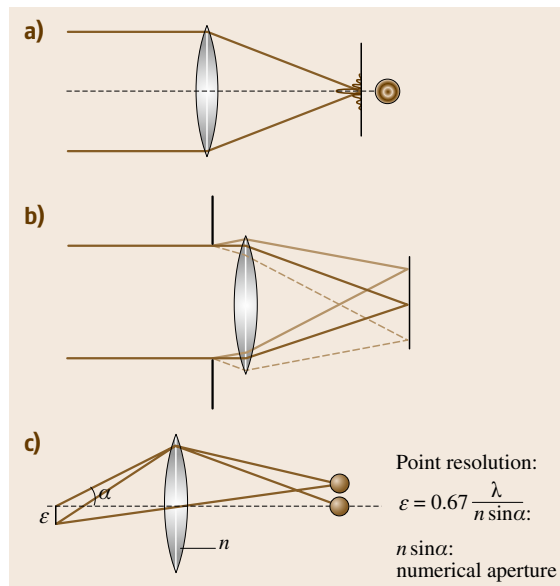


Fig. 5.7a–c Point resolution in microscopes limited by wave diffraction. In lenses of finite size, even if aberration-free, the focal point is blurred due to the diffraction effect. (a) is equivalent to (b); (c) defines the point resolution

Table 5.3 Comparison of various microscopic techniques

Method	Operation mode	Object	Resolution	Sample requirement	Test environment	Merit	Demerit
Optical microscopy	Interference microscopy	Steps	< 1 μm	Transparent or reflective	Ambient, liquid	Easy operation, wide survey range, dynamic observation	Limited magnification
	LSCM TIRFM	Light scatterers, fluorochromes fluorochromes					
X-ray topography		Internal architecture	< a few μm^a	High quality single crystal	Ambient, gaseous, vacuum	Applicable to bulky samples	Low magnification
TEM	Two-wave diffraction	Dislocations, planar defects	Several tens nm	Thickness < 1 μm^a	Vacuum	Crystallographic analysis, dynamic observation	Narrow survey range
	Weak beam HRTEM	Dislocations Extended defects, layer stacking	0.5 nm 0.2 nm	Thickness < 1 μm^a Thickness < 100 nm ^a	Vacuum Vacuum	Atomic-level resolution, dynamic observation	Critical sample preparation
STEM	HAADF	Extended defects, impurities	< 0.2 nm	Thickness < several tens nm ^a	Vacuum	Insensitivity to focusing and sample thickness	Slow image acquisition
SEM	SEM-SE	Surface morphology	< 1 nm	High SE efficiency, electrically conductive	Vacuum, gas	Easy operation, wide survey range, dynamic observation	Little information on material substance
	SEM-EBIC	Recombination centers in semiconductors	$\approx 1 \mu\text{m}^a$	Semiconductors with electrodes	High Vacuum (HV)	High sensitivity	Needs electrical contacts
	SEM-CL	Cathodo-luminescent/nonradiative centers	$\approx 1 \mu\text{m}^a$	Luminescent semiconductors	HV	Nondestructive spectroscopic	Limited to luminescent materials
	EPMA	Element analysis	$\approx 1 \mu\text{m}$	X-ray fluorescence	HV, Ultra-High Vacuum (UHV)	Established	Vulnerable to contamination
FIM		Surface atoms	< 0.1 nm	Electrically conductive thin needles	UHV	Atomic resolution	Difficult sample preparation
STM	Constant current	Surface LDOS, subsurface defects	< 0.1 nm	Electrically conductive clean surface	Ambient, UHV, liquid	Affinity with various micro-spectroscopic techniques	Limited imaging speed, difficulty in reproducible tip preparation
AFM	Noncontact	Surface atoms, surface morphology	$\approx 0.2 \text{ nm}$ (depends)	Roughness < 1 μm^a	Ambient, UHV, liquid	Applicable to nonconductive samples	Limited imaging speed
SNOM	Variable	Variable	Several tens nm	Optically active	Ambient, UHV, liquid	Many potential applications	Limited imaging speed

^a Variable depending on the material and experimental conditions

microscopy (LSCM) of the scanning type; and total internal reflection fluorescence microscopy (TIRFM), a relatively new technique with expanding applications particularly to biological substances. For the principles of conventional OM, the interested reader should refer to [5.13].

Interference microscopy is based on the phase shifts of the illuminating light that take place when the light passes through a transparent sample with different refraction indices or when it is reflected at a surface with steps of different heights. The interference of this light with a reference light forms interference fringes or, in differential interference Nomarski microscopes (Fig. 5.9), the interference of two slightly displaced beams is converted to different colors with high spatial resolution, which allows the measurement of step heights with a precision of 20 nm.

LSCM is classified as a scanning microscope, using a laser beam as a probe. The principle is shown in

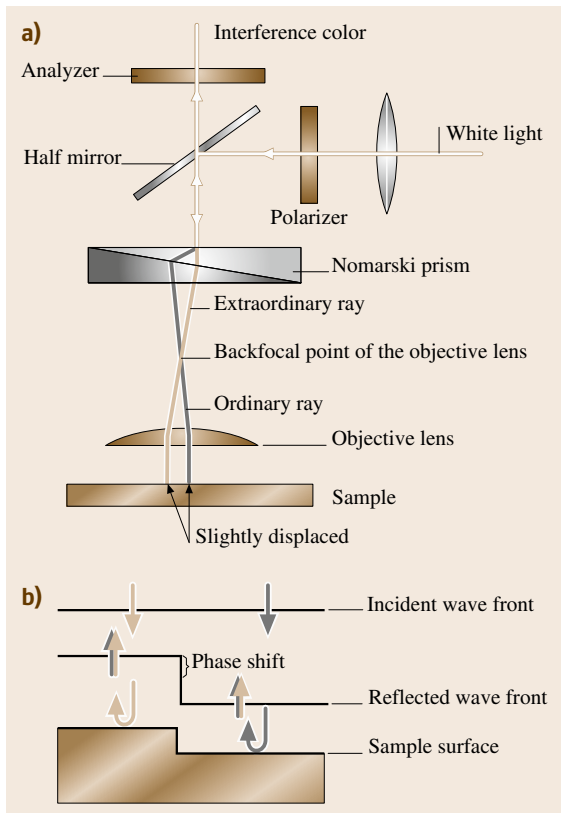


Fig. 5.9 (a) The principle of differential interference optical (Nomarski) microscopy. (b) Phase shift that occurs in reflecting waves at a step edge

Fig. 5.10, where a parallel laser beam focused at an entrance aperture is further focused by an objective lens to a small spot in the sample and the scattered light is

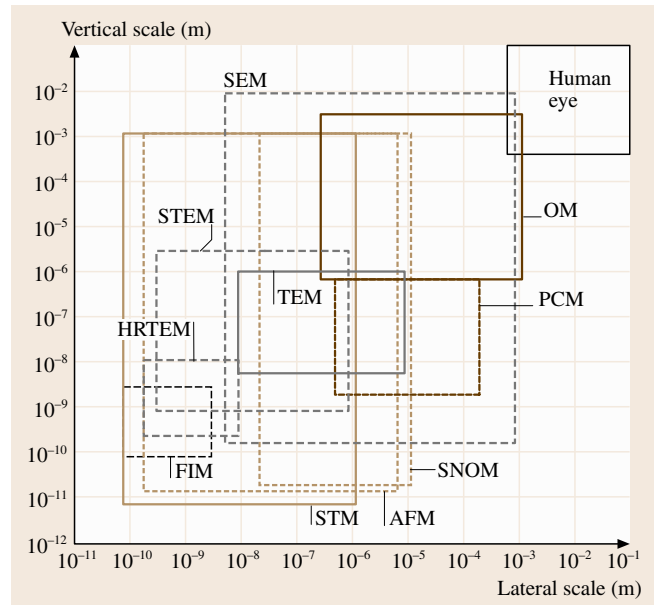


Fig. 5.8 Scale range covered by various types of microscopic techniques. For the meaning of the horizontal and vertical axes, see the text

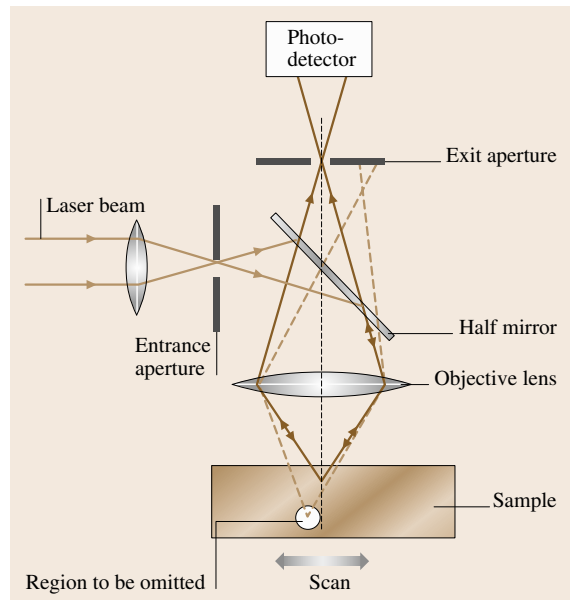


Fig. 5.10 The principle of laser scanning confocal microscopy

collected by the same objective lens and focused again but now at an exit slit that is placed at the confocal position of the entrance aperture. The light passing through the confocal aperture is detected by a photosensor. The light from the sample may be luminescence from a substance at the focal spot. The important point is that light from points on the sample other than the focal spot are rejected by the confocal exit aperture, thereby greatly reducing stray background light. If we scan the sample laterally with respect to the objective lens, we obtain a two-dimensional image on the screen. It should be pointed out that, although the point resolution is limited to a subwavelength (a few hundred nanometers) due to the effect of light diffraction, tiny objects much smaller than the resolution limit may be viewed as bright spots when they scatter or emit light visible to the human eye or detectable by a photosensor. This means that signals from even a single molecule can be detected if their separation from other molecules is large enough. A disadvantage of LSCM is the long image acquisition time due to its scanning nature.

TIRFM is based on the evanescent waves generated when light is incident onto an interface between two optical media of different refractive indices. It uses an ordinary fluorescence microscope equipped with a sample illumination system, as shown in Fig. 5.11. Samples attached to the surface of a glass plate are labeled by fluorescent molecules (fluorochromes). The back of the glass surface is illuminated with light at an angle smaller than the critical angle for total internal reflection, so that only fluorochromes within the small extension distance ($<$ light wavelength) of the evanescent wave are illuminated to induce fluorescence, which is imaged by the objective lens. The sample may be immersed in a liquid whose refractive index is smaller than

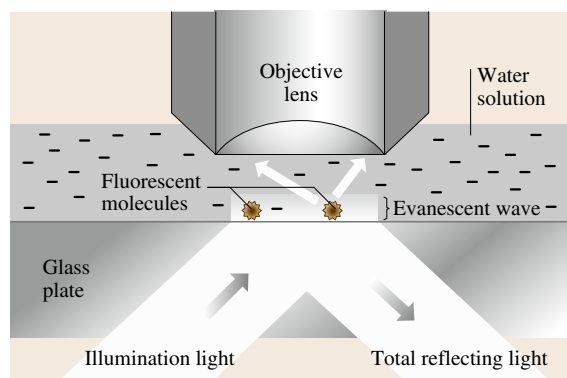


Fig. 5.11 The principle of total internal reflection fluorescence microscopy

that of glass, so the magnification can be increased up to $\times 100$ by immersion, and biomolecules can be investigated in vivo in water solutions. TIRFM is superior to LSCM in its high speed of image acquisition.

Transmission Electron Microscopy (TEM) [5.14]

Electrons interact so strongly with solids that they cannot penetrate thick solids. Figure 5.12 shows the dependence of the electronic absorption cross section on the electron energy. Electrons lose their energy most efficiently by exciting plasmons in the low energy range (10–30 eV), but the cross section governed by electronic excitations decreases with increasing kinetic energy of electrons except at core excitation edges that are specific to the elements contained in the sample until it increases due to the start of Bremsstrahlung radiation loss. Therefore, if the sample thickness is smaller than $\approx 1 \mu\text{m}$, electrons of energies higher than $\approx 100 \text{ keV}$ can penetrate the film sample to some extent. A key issue for TEM studies is how to prepare samples thin enough for observation. The most common method is chemical thinning by using a chemical etchant after a prior mechanical thinning process, though a suitable etchant cannot always be found. The advent of the ion milling method using an accelerated Ga ion beam for sputtering, however, has relieved the common difficulty in sample preparation and so widens the range of materials that may be studied by TEM.

A great advantage of TEM over other microscopic techniques is its ability to switch operation between the imaging and diffraction modes very easily, thereby investigating in situ the crystallographic properties of a specific sample area just being observed in the image.

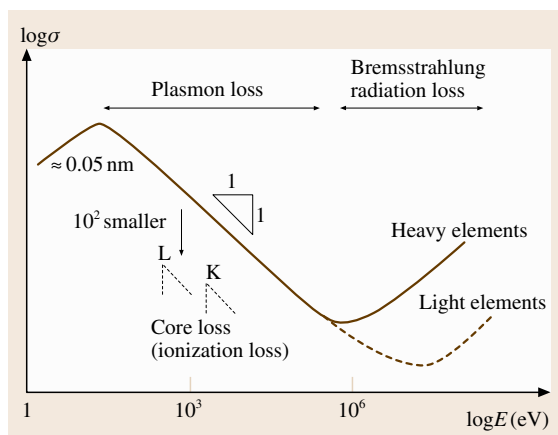


Fig. 5.12 Energy dependence of the absorption cross section of electrons

Figure 5.13 illustrates the electron optics of ordinary TEM in the two modes. Essentially, in the imaging mode, the image in the real space formed on the image plane of the objective lens is projected onto the fluorescence screen, whereas in the diffraction mode the diffraction pattern formed on the back focal plane is projected onto the screen just by changing the focal length of the intermediate electromagnetic lens. Usually, for observations of inhomogeneities in samples, to obtain an image arising from a specific diffraction an (objective) aperture is inserted at the back focal plane where a diffraction pattern is being formed. To obtain a diffraction pattern from a specific area of the sample, an aperture for selected area diffraction (SAD) is inserted at the image plane of the objective lens. Usually the objective aperture selects only the direct beam, so the images obtained generally look bright (contrasted against a gray background due to absorption) with varying contrast due to inhomogeneities, and are therefore called bright-field (BF) images. Occasionally, a diffracted beam can be selected to brighten the images of the imperfections responsible for the diffraction against the dark background, leading to a dark-field (DF) image.

In most cases, a TEM image is an interference pattern of the electron waves diffracted by a crystalline sample. Therefore, no correct interpretation of a TEM image is possible until one carefully compares images acquired under various diffraction conditions. Although the quantitatively precise interpretation of TEM images requires the dynamical theory, the images in many cases can be understood rather intuitively in the framework of the kinematical theory. Nevertheless, in some important cases, dynamical effects or multiple reflection effects must be taken into account. As illustrated in Fig. 5.14,

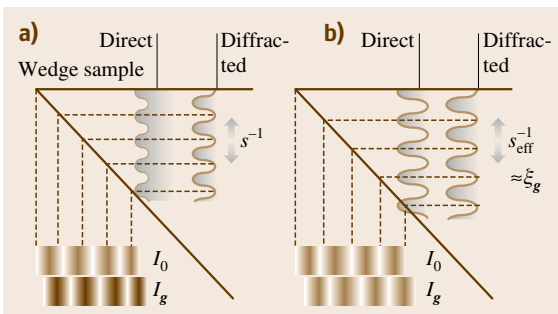


Fig. 5.14a,b Periodic exchange of electron energy between direct and diffracted waves. (a) kinematical case $|\xi_g|^{-1} \ll |s|$ and (b) dynamical case $|\xi_g|^{-1} \gg |s| \approx 0$. After [5.16]

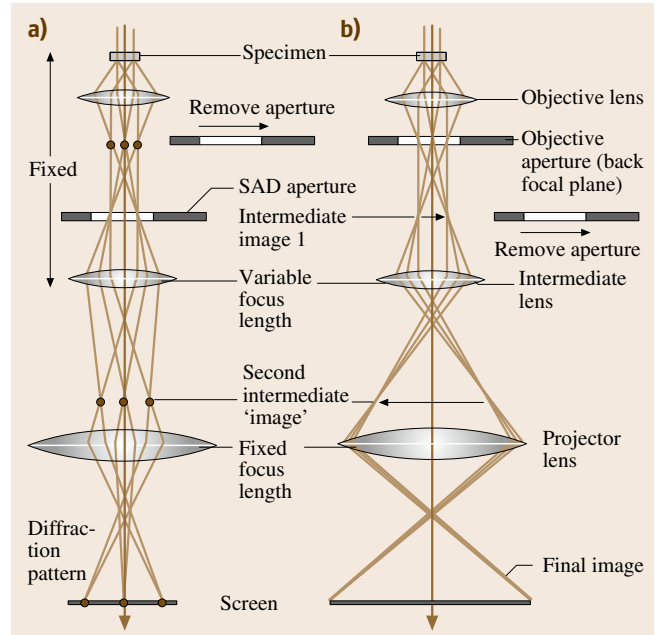


Fig. 5.13a,b Electron optics of transmission electron microscope in the diffraction mode A and in the imaging mode B. After [5.15, p. 144]

a beam incident with a Bragg angle of θ_B onto a set of net planes is reflected to give rise to a diffraction beam which may be reflected again by the reverse side of the same net planes returning to the primary beam direction. If the crystal is thick, this process is repeated with the electron energy being interchanged periodically between the direct beam and the diffracted beam. When only one diffraction \mathbf{g} is excited, a detailed analysis [5.16] shows that the intensity of the direct wave and that of the diffracted wave emanating from a sample of thickness t are given by

$$I_0 = \cos^2(\pi s_{\text{eff}} t) + \left[(s_{\text{eff}} \xi_g)^2 - 1 \right] \left(\frac{\pi t}{\xi_g} \right)^2 \frac{\sin^2(\pi s_{\text{eff}} t)}{(\pi s_{\text{eff}} t)^2} \quad (5.10)$$

and

$$I_g = \left(\frac{\pi t}{\xi_g} \right)^2 \frac{\sin^2(\pi s_{\text{eff}} t)}{(\pi s_{\text{eff}} t)^2}, \quad (5.11)$$

respectively, where ξ_g , the so-called extinction distance (The terms extinction distance or extinction effects often used in textbooks originate from the fact that, due to the diffraction effect, within the distance ξ_g the primary beam intensity decays, or is extinguished, more rapidly

than expected from the energy absorption effect), is defined as

$$\xi_g \equiv \frac{\pi \Omega \cos \theta_B}{\lambda F_g}, \quad (5.12)$$

where Ω is the volume of the unit cell, θ_B is the Bragg angle, λ is the electron wavelength, and F_g is the structure factor for \mathbf{g} . The parameter s_{eff} is

$$s_{\text{eff}} \equiv \sqrt{s^2 + \xi_g^{-2}}, \quad (5.13)$$

where s denotes the deviation from the Bragg condition in reciprocal space. Figure 5.14 shows schematically how the two intensities vary with the thickness of a wedge-shaped sample. When $|\xi_g|^{-1} \ll |s|$ (Fig. 5.14a) or $t \ll \xi_g$, we could apply the kinematical theory, in which the thickness dependence is determined by s . On the other hand, when $|\xi_g|^{-1} \gg |s| \approx 0$ (Fig. 5.14b) or $t > \xi_g$, the transmission intensity must be treated rigorously by the dynamical theory, where $s_{\text{eff}} \rightarrow \xi_g^{-1}$ and the two beams exchange their intensities, alternating with a period of ξ_g , not s^{-1} . One should note that $I_0 + I_g = 1$ throughout the sample. For its resemblance to the behavior of two coupled pendulums, this effect that gives rise to thickness fringes is referred to as Pendellösung, which forms the basis of similar fringe contrasts not only in TEM but also in x-ray topography. In imperfect crystals, the argument is modified by introducing an additional phase shift due to the presence of defects. The consequence is described in Sect. 5.3.

The Pendellösung effect embodies the presence of two dispersion branches at the zone boundary corresponding to the Bragg diffraction at $\mathbf{K} = \mathbf{g}$. It may be regarded as a consequence of beating between the two Bloch waves on the two branches. They have amplitudes

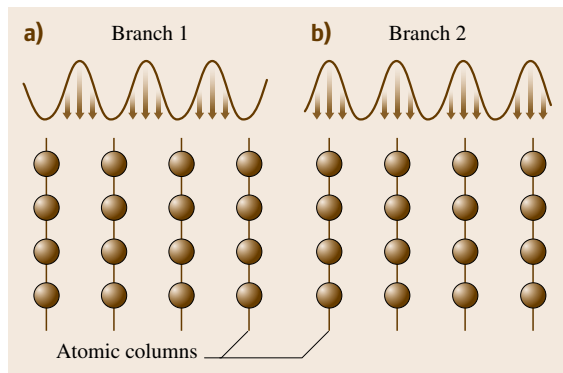


Fig. 5.15a,b Bloch waves on two dispersion branches. Waves (a) and (b) are absorbed less and more, respectively

at different column positions as shown in Fig. 5.15: The wave (a) has its amplitude in between the atomic columns whereas the wave (b) along the columns. Since the interaction of the waves with the atoms is weak in (a) but strong in (b), the waves (a) and (b) are absorbed by the crystal to a lesser and greater extent, respectively. This causes the effects of anomalous absorption (Kikuchi patterns in electron diffraction, Sect. 5.5.1) or anomalous transmission (Electron channeling, Sect. 5.5.1) for electrons and the Borrmann effect for x-rays, Sect. 5.3.2) propagating in particular directions.

The Ewald sphere in the diffraction of TEM electrons of energy ≈ 100 keV is large compared with the reciprocal lattice parameter. The reciprocal lattice points are broadened perpendicular to the sample surface due to the small thickness of the sample in TEM. As a consequence, if the thickness is smaller than ≈ 100 nm, the electron diffractions practically occur in many \mathbf{g} vectors, as shown in Fig. 5.16. This makes it possible to form an image by collecting many diffraction beams, including those of large $|\mathbf{g}|$ values that contain information of small-scale structures in the sample. This is the basis of high-resolution transmission electron microscopy (HRTEM) which is now a standard installation in modern TEM microscopes owing to the technological progress in the improvement of spherical aberration of the objective lens. Under a special defocusing condition, called

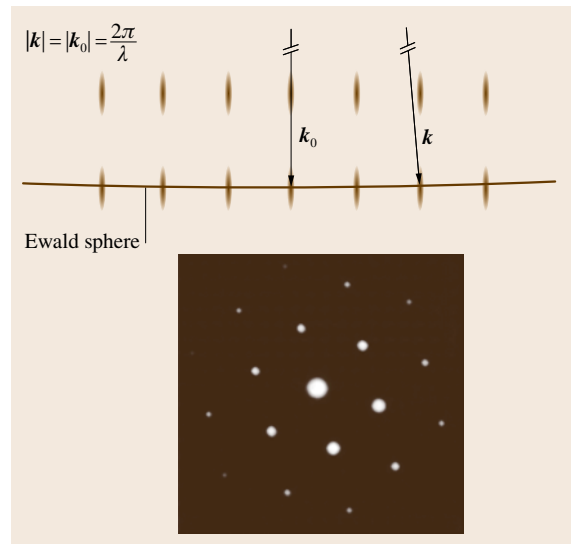


Fig. 5.16 Ewald construction of electron diffraction in TEM. The reciprocal lattice points are elongated normal to the surface of thin specimens, so that many diffractions can be excited

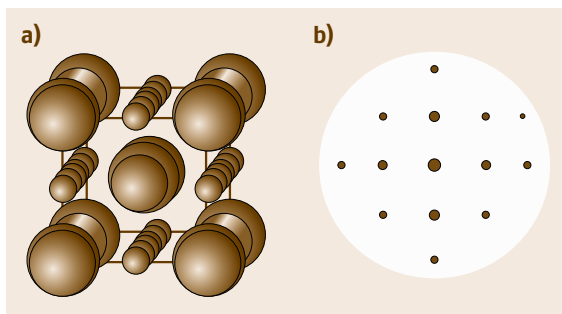


Fig. 5.17a,b The principle of high-resolution TEM. (a) A perspective view of a schematic crystal along an axis along which the electron beam is incident to obtain a symmetric diffraction pattern, as schematically shown in (b). Diffracted beams with large wave numbers are collected to form a high-resolution TEM image that represents, under the Scherzer defocus condition, approximately the projection of the atomic columns viewed along the direct beam

the Scherzer defocus, the HRTEM images represent approximately the arrangement of atomic rows viewed along the direction of the electron beam, as illustrated in Fig. 5.17. HRTEM images depend sensitively on the defocus condition, the sample thickness, and the depth of the object in the films. The true atomic arrangements can be deduced only by careful comparison of experimental images taken under various defocusing conditions other than the Scherzer defocus and theoretical images simulated for model structures using the dynamical theory. The routine resolution (point resolution) of HRTEM is ≈ 0.2 nm.

X-Ray Topography (XRT)

As with transmission electron microscopy, x-ray diffraction may be used to image crystallographic inhomogeneities in crystalline samples. A significant difference from TEM, however, is the lack of good lenses for x-rays so images cannot easily be magnified as in OM and TEM. The best resolution is determined by the particle size of the emulsion in x-ray films, typically around 2–3 μm , which may be reduced to ≈ 1 μm by the use of synchrotron radiation. The simplest setup for x-ray topography (XRT) is one devised by Lang shown in Fig. 5.18. A version using reflected beams for imaging (the Berg-Barrett method) is also used, particularly when the sample is not transparent to x-rays. XRT images are obtained by recording diffracted beams of a certain g vector, equivalent to dark-field images in TEM. An advantage of XRT over TEM is that it can examine rather bulky samples in a gaseous atmo-

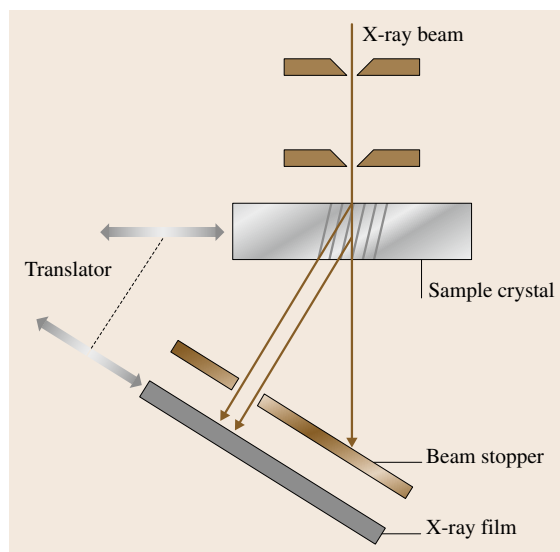


Fig. 5.18 Lang camera for transmission x-ray topography. The crystal and the x-ray film are simultaneously translated to record a topographic image consisting of sample sections

sphere. Owing to this fact, together with the higher accuracy in the detection of strains, XRT is suitable for studies of phenomena in which the stress state is of primary importance (e.g., fracture). A judicious choice of diffraction geometry as well as x-ray wavelength and sample thickness allows high topographic contrast. Applications of XRT are described in Sect. 5.3.2.

High-Angle Annular Dark-Field STEM (HAADF-STEM)

In scanning transmission electron microscopy (STEM), an electron beam focused to a small size is raster scanned in parallel across a sample surface and a detector collects some signal arising from the interaction of the electrons with the sample solid. The signal intensity, which may vary over the sample position depending on the crystal structure, orientation, composition, etc., is used to construct two-dimensional maps of the material properties in each pixel. The spatial resolution of STEM is limited by the size of the focused probe beam. The advantage of STEM is that it does not need imaging lenses that inevitably have some chromatic aberration and limit the resolution of TEM images, and the sample thickness may be relatively thick in comparison with TEM samples. A demerit of STEM is the lower speed of image acquisition (seconds to minutes for a single image) due to the serial recording of the signal.

In bright-field (BF) STEM, the signal collected is the directly transmitted electrons that are not diffracted by the crystallographic sample. Similarly, dark-field (DF) STEM images can be obtained by collecting only diffracted electrons. Although the imaging principle of STEM is different from that of TEM, the two microscopic techniques could be viewed as equivalent if one regards the electron detector in STEM as the objective aperture in TEM, both of which are (not physically as for the detector in STEM) placed at the back focal plane of the objective lens.

High-angle annular dark-field STEM (HAADF-STEM) allows one to observe STEM images with higher resolution and compositional information. As shown in Fig. 5.19, HAADF-STEM images are formed by collecting high-angle scattered electrons with an annular dark-field detector placed at the back focal plane of the objective lens. The image formation mechanism is based on the fact that a fraction of electrons incident on a crystalline sample along a channeling direction are diffusely scattered by thermal vibrations of atoms at relatively high angles ($\gtrsim 70$ mrad) when the beam scans over the atomic columns. Therefore, in HAADF-STEM images, the positions of atoms are observed as bright contrasts depending strongly on the average atomic number of the atoms in the column. Owing to this feature, HAADF-STEM, otherwise called Z-contrast imaging, is a powerful technique for composition analysis especially for elements of large atomic numbers. The spatial resolution in HAADF-STEM is limited by the size of the focused probe beam as in or-

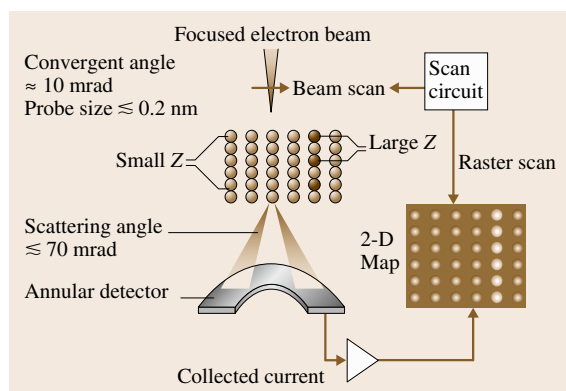


Fig. 5.19 Setup of high-angle annular dark-field scanning transmission electron microscopy (HAADF-STEM). Electrons diffusely scattered by thermal vibrations of atoms with relatively high angles are collected by an annular detector to form a scan image

dinary STEM. Under good conditions, an atomic-level spatial resolution can be achieved, although such samples must be thin enough (usually thinner than several tens of nanometers) for beam broadening to be avoided. The advantage of HAADF-STEM over HRTEM is the insensitivity to focusing conditions and sample thickness variations, both of which very substantially affect the phase sensitive contrast of HRTEM images.

Scanning Electron Microscopy (SEM). The representative microscope of the scanning type is the scanning electron microscope (SEM) [5.17], in which the scanning probe is a finely focused electron beam. Figure 5.20 shows various forms of signals generated by incidence of electrons onto solid samples. Some of the incident electrons lose most of their initial energy and are emitted from the surface with a low energy (\approx a few tens of eV). These electrons are called secondary electrons, which can escape only from very shallow depths of the solid due to their large absorption cross section (Fig. 5.12). Without losing much energy, other electrons are either reflected backward as back-scattered electrons or absorbed into the solid as a drain current. On the loss of electron energy, x-ray fluorescence or Auger electron emission occur, which are very useful for element analysis. In semiconductor samples, the electron energy may be converted to a luminescence (cathodoluminescence, CL) or an electron-beam-induced current (EBIC) when an electric field separating electron-hole pairs is built up in the surface layer. Depending on the detected signal, SEM has several operation modes. The most common mode is secondary electron SEM (SEM-SE), in which the difference in the escape probability of secondary electrons depending on the direction relative to the surface normal produces surface roughness contrast observed from an oblique angle when the electron detector is placed as shown in Fig. 5.21.

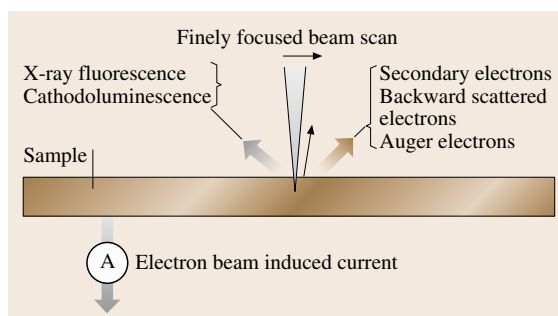


Fig. 5.20 Signals generated in scanning electron microscopy

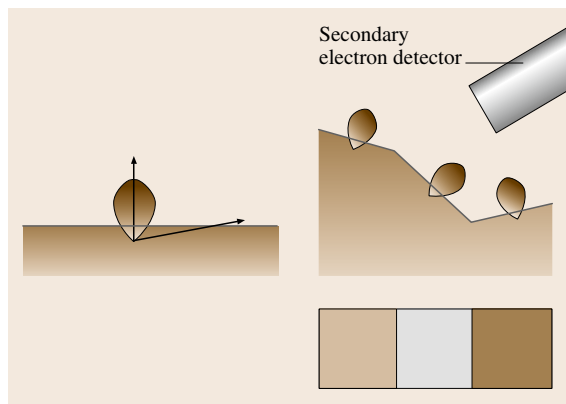


Fig. 5.21 Escape probability of secondary electrons (SE) with its maximum in the surface normal direction rendering the morphological contrasts in SEM-SE

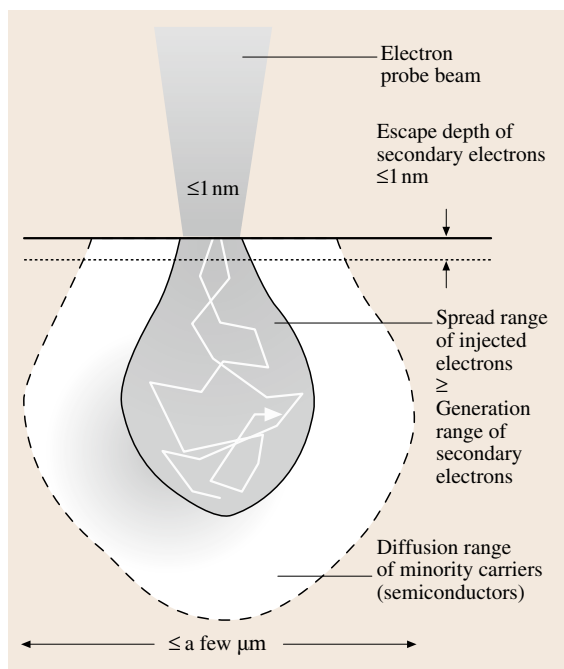


Fig. 5.22 Factors governing the spatial resolution in SEM

The spatial resolution depends on what signal is used and how large the signal is. As illustrated in Fig. 5.22, incident electrons are spread by a random walk on the nanometer range that increases in depth with increasing acceleration voltage. For the primary beam size to dominate the resolution in SEM-SE, we should choose an accelerating voltage at a medium value to reduce the lateral spreading of electrons. In

commercial SEM-SE operated at 5 keV, subnanometer resolution is achievable by the use of a field emission gun, the high brightness of which allows extremely fine focusing of the probe beam. The resolution in SEM-SE is determined by the spread range, while the resolution in SEM-CL and SEM-EBIC is worsened by the diffusion of the carriers generated by the electrons. The samples for SEM observations must be more or less electrically conductive to avoid charging effects. If they are not metals or semiconductors, precoating the samples with Au films may work.

For samples which are too thin for the fast electrons to excite secondary electrons for SEM-SE observations, the use of low-energy electrons ($< 1\text{ keV}$) or inactive light He^+ ions for the probe beam enables studies for such samples as single-walled carbon nanotubes.

Scanning Probe Microscopy. Since the advent of scanning tunneling microscopy (STM) [5.18–20], the use of extremely sharp tips controlled by a piezo-actuator as shown in Fig. 5.23 opened fascinating opportunities to study materials on the nanometer scale. To date, many schemes of scanning probe (tip) microscopy (SPM) have been devised, though some of them are still under development at present.

Scanning Tunneling Microscopy (STM). The STM is based on the fact that a quantum mechanical tunneling current flows between two electrically conductive solids closely spaced within a distance of $\approx 1\text{ nm}$ under an electric bias voltage, with a very sensitive dependence on the separation. Figure 5.24a–c illustrates the situation for a combination of metallic tip and a semiconductor sample. If the probe tip, usually an electrochemically etched tungsten needle, is sharp enough, the tunneling current is confined to a very narrow region

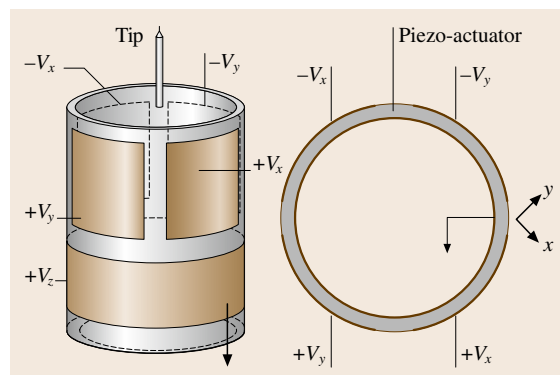


Fig. 5.23 Piezo-actuator (tube scanner) for tip scanning

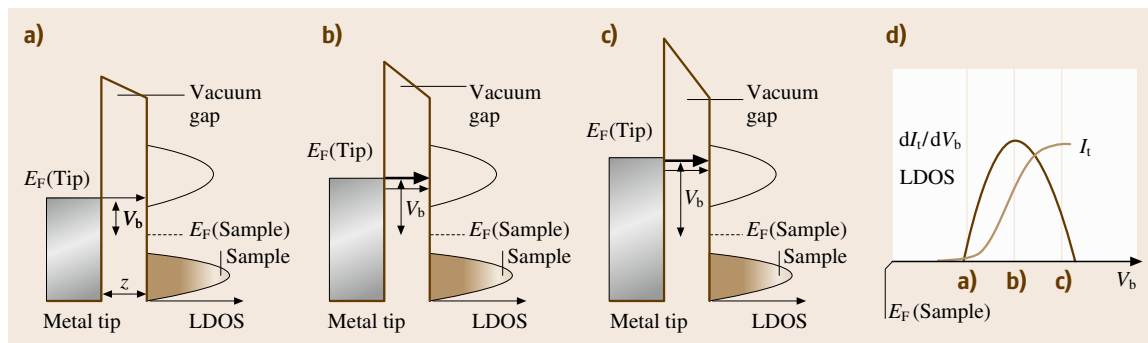


Fig. 5.24a–d Vacuum tunneling between a metallic tip and a semiconducting sample, also illustrating the principle of scanning tunneling spectroscopy

(< 0.1 nm) beneath the tip. Scanning a sample surface with such a sharp tip and recording as a signal the voltage applied to the piezo-actuator that acts to keep the tip–sample distance (more precisely the tunneling current) constant, we can obtain a two-dimensional image of the surface topography, as shown in Fig. 5.25.

STM images generally reflect very strongly the local density of states (LDOS) of surface electrons on which the tunneling current is also dependent. This fact provides a unique method, scanning tunneling spectroscopy (STS), for the assessment of local electronic properties of the samples. Figure 5.24 illustrates the principle of STS, which is based on the fact that most of the external bias voltage is applied across the vacuum gap and that electron tunneling occurs from electronic filled states to empty states conserving energy. The tunneling current I_t varies with the bias voltage V_b as in Fig. 5.24d with its derivative with respect to V_b approximately representing the LDOS.

In principle, STM experiments could be conducted in ambient environments as long as the current is confined beneath the tip, but in most cases clean surfaces are investigated in ultra-high vacuum to obtain reproducible results. Preferably, the surface should be atomically flat with steps in atomic heights; otherwise in rough surfaces, the tip shape is convoluted with the image giving a spurious surface morphology.

Atomic Force Microscopy (AFM). Atomic force microscopy (AFM) uses a sharp probe tip mounted on a cantilever, as shown in Fig. 5.26 [5.21, 22]. When the sample and the tip are close enough, the sample exerts a short-range force on the cantilever, an attractive force originating from the van der Waals interaction, a repulsive force due to the Pauli exclusion principle, and a variable force of chemical origin. The force may also

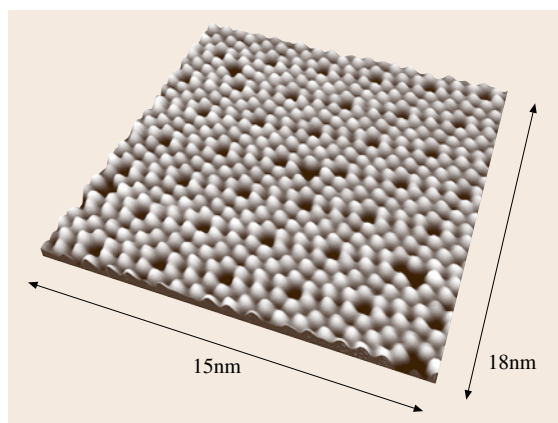


Fig. 5.25 STM image of Si(111)-7×7 surface

be long-ranged, arising from a Coulombic interaction. The simplest AFM with the tip in mechanical contact with the sample surface detects a force-induced deviation of the cantilever by an optical or electronic method. Recently, noncontact AFM has made great progress in imaging solid surfaces at atomic resolution comparable with STM. The common technique used for the detection of atomic force is to measure the shift of the resonance frequency of the cantilever that is caused by a nonlinear force operating between the sample and the tip (Fig. 5.26). In the current state-of-the-art instruments, the lateral and vertical resolutions are 10 pm and one to several pm, respectively. Figure 5.27 shows a set of noncontact AFM images of a GaAs surface. An atomic resolution is achieved when the closest distance z between the sample and the cantilever tip is shorter than ≈ 0.1 nm (b and c). The blurred contrast in (a), obtained at a slightly large closest approach, is considered to indicate the presence of charged defects beneath the sample surface.

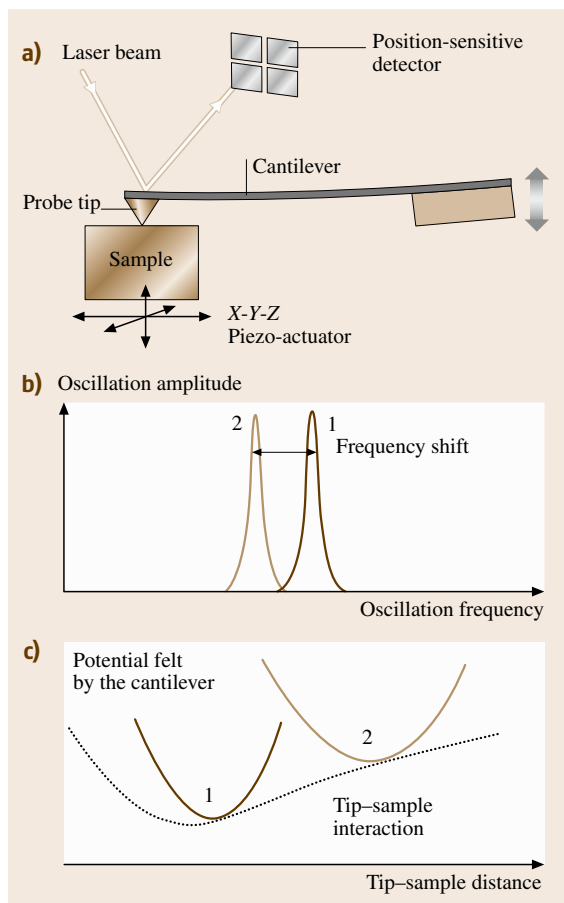


Fig. 5.26a–c The principle of noncontact atomic force microscopy (AFM). (a) The sample exerts a force on the probe tip on top of a cantilever whose deflection is detected, in this case, by an optical lever method. The cantilever is forced to oscillate at the resonance frequency (b) which changes with the tip–sample distance due to the nonlinear interaction between the tip and the sample (c)

Scanning Near-Field Optical Microscopy (SNOM). Scanning near-field optical microscopy (SNOM) [5.23] overcomes the diffraction-imposed resolution limit of OM by exploiting an evanescent field that is generated and/or detected by a probe tip that is brought very close to the sample. Usually, the tip is made of metal-coated optical fiber with a tiny aperture at the apex. The tip–sample distance may be controlled by the same technique used in STM and AFM. There are many SNOM schemes, only two of which are illustrated in Fig. 5.28. In Fig. 5.28a, the light guided by an optical fiber illuminates the sample in a region that is

highly localized by the aperture, and the light scattered or emitted by the object is collected by the probe itself or detected as a far-field light by a photosensor. In the setup in Fig. 5.28b, the sample on an optically flat glass is illuminated with an evanescent wave of a total internal reflecting light. The probe collects secondary light, or a photodetector senses a change to the total reflected light intensity caused by the presence of the tip in close vicinity to the object. More recently, attempts at apertureless SNOM using a metallic tip illuminated with a macroscopic light to exploit the metal–tip-enhanced optical field have been reported. In any case, the spatial resolution at present is limited to tens of nanometers. SNOM is a rapidly growing technique because of the wide applicability to materials, regardless of sample properties such as electrical conductivity, and the flexible test environments. Interested readers should refer to most contemporary articles for the latest progress.

Field Ion Microscopy (FIM). The field ion microscope (FIM) [5.24] is a type of microscope based on a principle completely different from those described so far. In the basic setup, illustrated in Fig. 5.29, the sample is a metallic needle the apex of which is atomically sharpened with an end radius of 50–100 nm so that an electric field applied to the sample is concentrated on the atomic step edges. The sample faces a phosphor screen placed at a distance of ≈ 5 cm from the needle tip. To obtain images, a small amount ($\approx 10^{-3}$ Pa) of an inert gas, usually helium, is introduced into the ultra-high-vacuum chamber in which the sample and the screen are accommodated, and a positive (with respect to the screen) bias voltage is then applied to the sample. The inert gas atoms polarized by the electric field are electrostatically attracted to the tip and migrate further to the step edges where a high electric field is concentrated. When the bias voltage is high enough (a few tens of V/nm), an electron in the inert gas atom tunnels quantum mechanically to the tip resulting in the formation of a positively charged ion at the step edges. The ion formed is immediately repelled by the strong electric field present between the sample and the screen, and starts to be accelerated towards the screen along the direction of the electric field. Since the electric field emanates radially from the tip apex, the distribution of the ion impinging spots on the screen, as shown in Fig. 5.30, represents a highly magnified image of the atoms at the step edges on the sample tip. Usually, a multichannel plate is placed in front of the phosphor screen for signal enhancement. The sample may be cooled to a low temperature to suppress thermal atomic motion on the

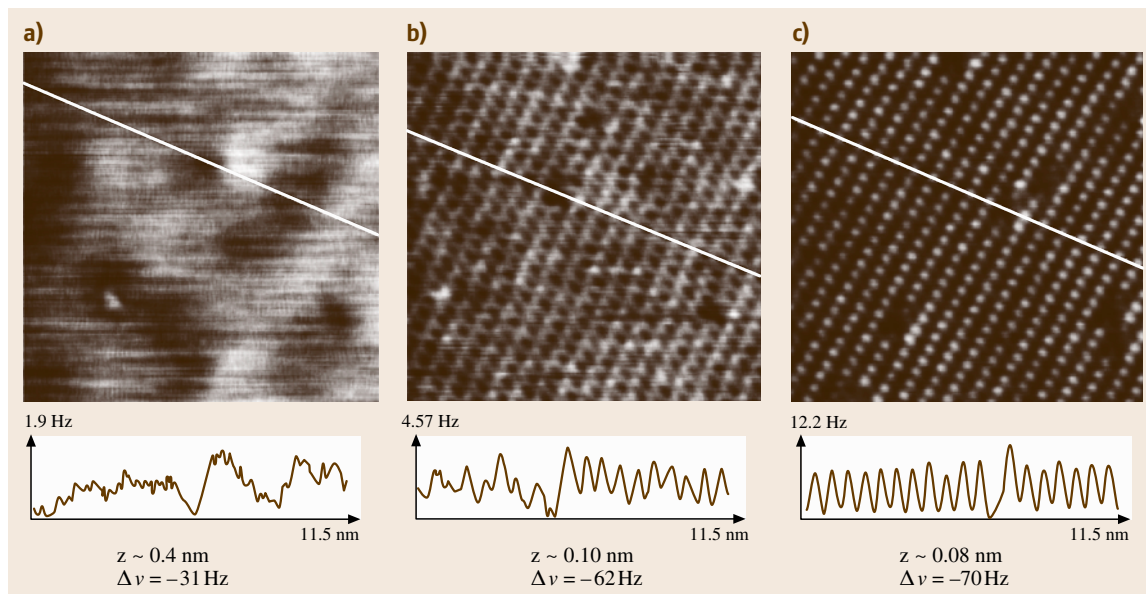


Fig. 5.27a–c Noncontact AFM images of a p-GaAs(110) surface. z denotes the closest distance between the sample and the tip, and $\Delta\nu$ the shift of the cantilever resonance frequency. p-GaAs(110) $N_A = 1.4 \times 10^{19} \text{ cm}^{-3}$ (after [5.25])

surface. FIM is useful for three-dimensional microanalysis of element distribution if combined with an atom probe method (Sect. 5.5.3).

5.1.3 Spectroscopy

Optical Spectroscopy

The physical property of primary importance in optical spectroscopy is the energy of the photons. Figure 5.31 summarizes the main optical spectroscopic methods arranged according to the range of photon energies, and the corresponding wavelengths and frequencies. Although electromagnetic waves in general range from radio frequency (RF) waves to γ -rays, we first confine ourselves in traditional optical spectroscopy, which is usually limited to a range from infrared to ultraviolet light (It should be noted that, owing to the development of more intense light sources and more sensitive light detectors, the techniques now mostly applied to this range are being extended, based on essentially the same principle, to regions down to THz waves and up to x-rays. For recent development in the range of extreme violet (30–250 eV) to soft x-rays (250 eV–several keV) see [5.26]). The interaction of light in this range of photon energies with matter has different origins depending on which quasiparticles (quanta) are excited: electronic, vibrational, or

both coupled (vibronic). In the bottom of Fig. 5.31, the quanta that can be studied are shown. In this section, we touch only on matters relevant to this chapter.

Infrared Absorption Spectroscopy (IRAS)

Fourier transform (FT) spectroscopy has advantages over spectroscopic measurements using a dispersive

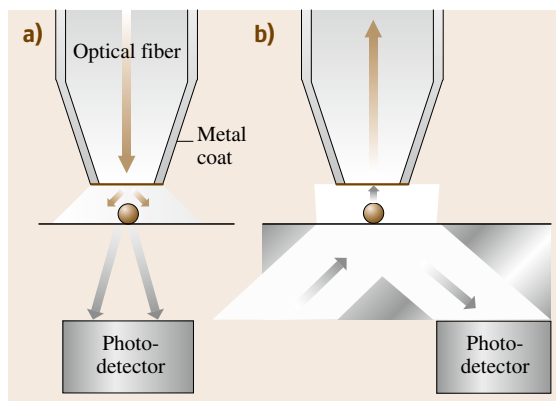


Fig. 5.28a,b Two representative setups of scanning near-field optical microscopy (SNOM) using evanescent waves (a) from an optical fiber tip and (b) from the surface of a glass plate internally total reflecting light

monochromator (e.g., a grating monochromator), in which spectral signals are detected sequentially with a single detector, under certain conditions. For FT measurements we use, instead of a dispersive monochromator, an interferometer such as a Michelson-type device shown in Fig. 5.32. The output of the interferometer fed with light of wavelength λ and intensity I_λ^0 is variable depending on Δx , the displacement of the movable

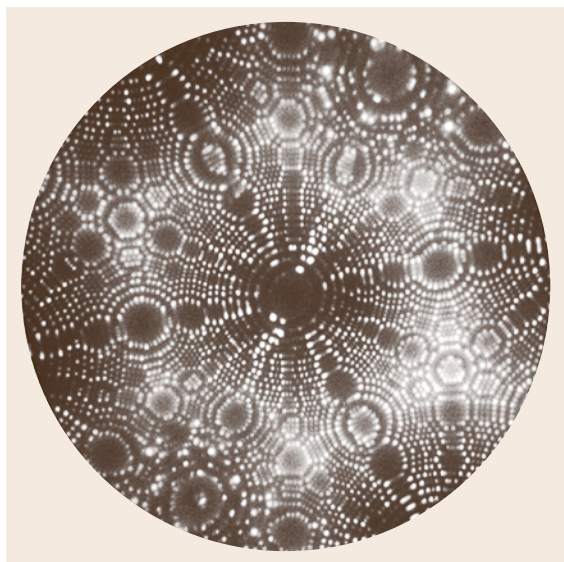


Fig. 5.30 FIM Image of a W tip (Courtesy of Dr. K. Hono)

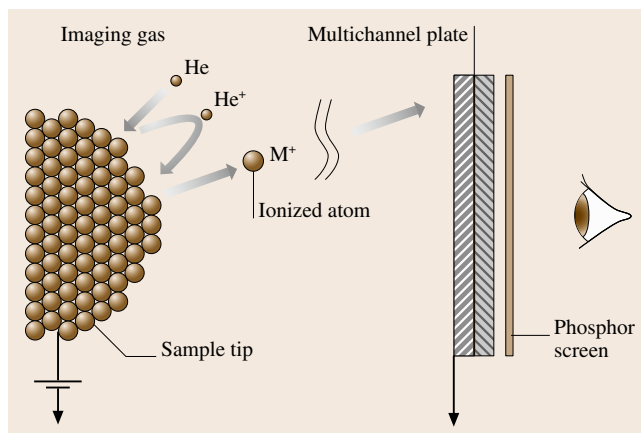


Fig. 5.29 The principle of field ion microscopy (FIM). Inert imaging gas atoms arriving at the field-concentrated atoms at step edges are ionized and repelled towards a phosphor screen to project the atomic image at high resolution

mirror, through

$$I_\lambda(\Delta x) = I_\lambda^0 \sin\left(2\pi \frac{2\Delta x}{\lambda}\right). \quad (5.14)$$

If the movable mirror is displaced at a constant velocity v , then $\Delta x = vt$ at time t , and hence

$$I_\lambda(t) = I_\lambda^0 \sin\left(\frac{4\pi v}{\lambda}t\right) = I_\lambda^0 \sin(\omega_\lambda t). \quad (5.15)$$

Equation (5.15) indicates that light of intensity I_λ^0 is sinusoidally modulated at a frequency given by

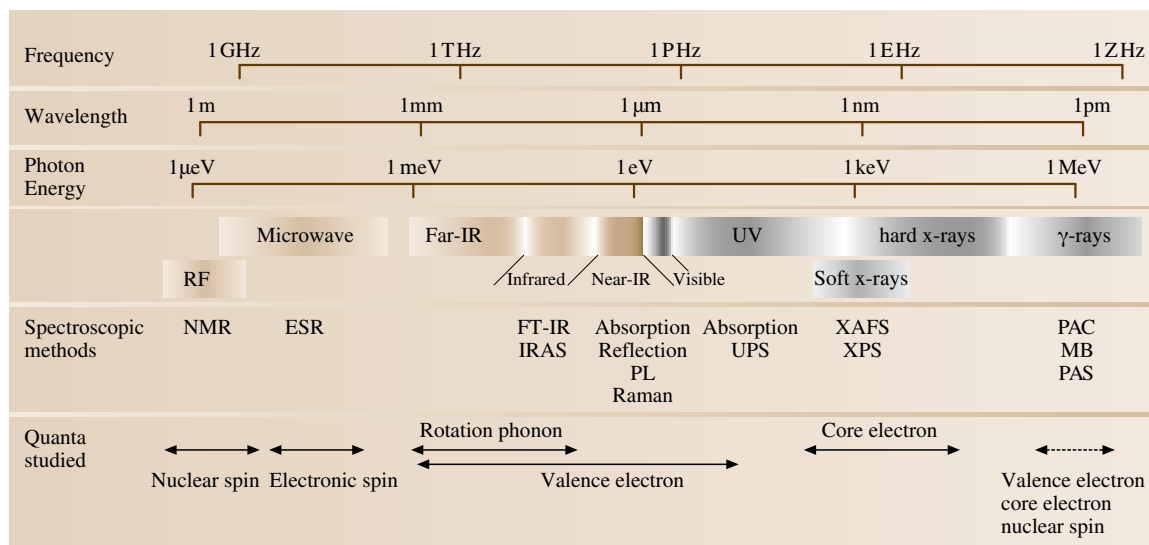


Fig. 5.31 The energy of photons used for optical spectroscopic measurements of various quanta

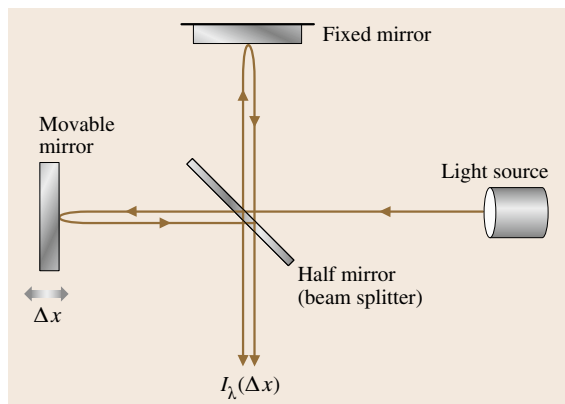


Fig. 5.32 Michelson-type interferometer used in Fourier transform infrared (FT-IR) spectroscopy

the wavelength λ . In other words, when the light input to the interferometer contains different spectral components, the interference fringes or interferogram (Fig. 5.33a), the temporal superposition of the modulated signals, constitutes the Fourier transform of the whole spectrum. Conversely, the inverse Fourier transform of the experimentally measured interferogram provides the spectrum (Fig. 5.33b) without any spectral dispersive apparatus. The FT spectroscopy is advantageous in terms of the signal-to-noise ratio when the detector noise is large and we need high spectral resolution. The infrared (IR) spectroscopy is a typical case to which the FT scheme is most efficiently applied.

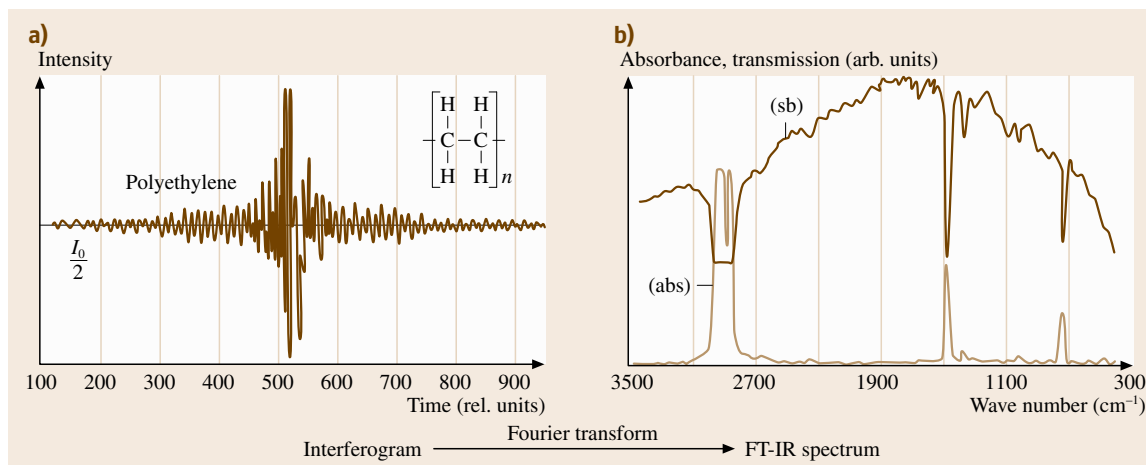
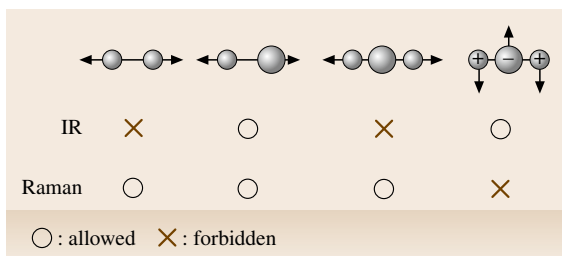


Fig. 5.33a,b An example of FT-IR absorption spectroscopy. (a) An interferogram of transmission through a polyethylene sample, (b) (sb) Fourier transform of the interferogram and (abs) the absorbance spectrum corrected for the instrumental background (after [5.27])

Raman Scattering

Raman scattering is a generic term for inelastic scattering of light but in most cases it refers to inelastic scattering brought about by optical phonons (quantized vibrations) in molecules and solids. While infrared absorption originates from the polarization of the substance, Raman scattering originates from a modulation of optical polarizability of the substance by phonons. Therefore, the selection rule is different for the two phenomena. In molecules, infrared absorption occurs when the molecules have an electric dipole transition moment in the polarization direction of the incident light, as in the cases shown in Fig. 5.34. Raman scattering occurs when a molecular vibration in a certain mode alters the electronic distribution of the molecule (Fig. 5.34) and consequently the optical polarizability for the incident light. In solids, although the selection rules are not as intuitive as for molecules, the principles are the same. Due to this difference in the selection rules, infrared spectroscopy and Raman scattering spectroscopy are complementary in studies of atomic vibrations in matter.

In the energy diagram, the sequential two-photon process in Raman scattering is depicted in Fig. 5.35, which shows only the case of the Stokes shift, in which a phonon mode of energy $h\Omega$ is excited and as a result the photon energy is decreased on scattering by this amount. The broken line in Fig. 5.35a indicates an intermediate virtual electronic state via which the system evolves in the sequence of photon absorption and emission. In contrast to infrared absorption, Raman



IR	×	○	×	○
Raman	○	○	○	×

○ : allowed × : forbidden

Fig. 5.34 Selection rules of infrared absorption and Raman scattering illustrated for molecules in various vibration modes

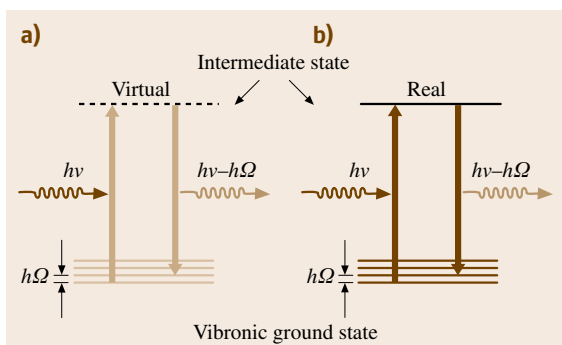


Fig. 5.35a,b Raman scattering process: (a) nonresonant, (b) resonant, shown for the Stokes shift by exciting a single phonon. $h\nu$ and $h\Omega$ are the energy of the incident photon and the phonon energy, respectively

scattering is a two-photon process and the scattering signal is generally very weak. However, when the intermediate electronic state is not virtual but really present (Fig. 5.35b), Raman scattering occurs in a resonant manner with the scattering intensity being substantially enhanced (resonant Raman scattering). The minimum content of Raman-active centers required is 0.01–1% or $> 10^{19} \text{ cm}^{-3}$ in nonresonant cases. When the centers to be detected are present in the surface layer of samples, the sensitivity is further enhanced (up to 10^6 times) by employing the scheme of surface-enhanced Raman scattering [5.28, 29], which exploits a dramatic increase of the optical electric field in the vicinity of metallic nanoparticles such as Ag and Au.

Magnetic Resonance Spectroscopy

Experimental methods based on magnetic resonance of nuclear or electronic spins are applied to the investigation of defects and impurities in solids, structural analysis of molecules, and in some cases, microstructure analysis.

When electrons and nuclei have an angular momentum $\hbar S$ (where \hbar is Planck's constant), a magnetic moment

$$\mu = \gamma \hbar S \quad (5.16)$$

is associated with it. S stands for $s = 1/2$ for electronic spins, for j for electronic orbital angular momenta, and for I , various multiples of $1/2$, for nuclear spins. The coefficient γ is called the magnetogyric ratio defined by

$$\gamma \equiv \frac{ge}{2mc}, \quad (5.17)$$

where g and m are the g -factor (a numeric constant in the range 1–3 depending on the origin of the angular momentum) and the mass of the particle, respectively, and e is the electronic charge, and c the speed of light.

Quantum mechanically, a spin or a magnetic moment under a static magnetic field of intensity B_0 (magnetic flux density) has discrete eigenstates. For the simplest case of $S = 1/2$, the spin has two states, as shown by the energy level diagram in Fig. 5.36a, sep-

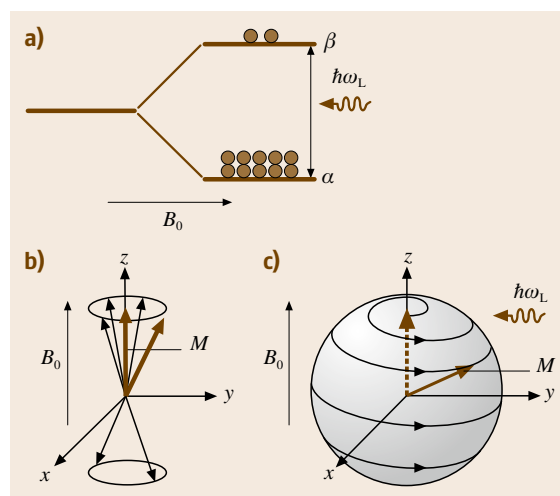


Fig. 5.36a–c Quantum-mechanical picture (a) and classical vector model (b,c) of magnetic resonance illustrated for an $S = 1/2$ system. In (a), since the Zeeman-split lower spin state α , is more occupied than the higher state β , in thermal equilibrium, the application of a resonant electromagnetic wave causes transitions between the two states, resulting in a net energy absorption. Classically, (b) the macroscopic magnetization M is the average of the spin magnetizations precessing with random phase in thermal equilibrium. (c) On resonance the spin magnetizations are bunched and the resultant magnetization starts to flip its head down, tracing a spiral trajectory in real space

arated by an energy $\hbar\omega_L$ where

$$\omega_L = \gamma B_0 \quad (5.18)$$

is called the Larmor angular frequency. In magnetic resonance experiments, the sample is further subject to a small magnetic field perpendicular to the static field and alternating at the Larmor frequency, which resonantly induces transitions between the two states. In Fig. 5.36a, the number of filled circles indicates the population of the respective states. Since, in thermal equilibrium, the lower energy state (up-spin state) is more occupied than the higher energy state (down-spin state), the spin system absorbs a net energy from the electromagnetic oscillations.

Classically, a magnetic moment under a static magnetic field precesses around the axis of the static magnetic field (normally taken as the z -axis) at the Larmor frequency, as shown schematically in Fig. 5.36b. In thermal equilibrium, however, the precession of the spins cannot be detected because each precession is random (incoherent) and hence, in macroscopic samples containing many spins, the magnetization of the spin assembly is averaged out leaving only the z -axis component, due to the excess population of up spins. An intuitive picture of magnetic resonance is such that the spins become bunched coherently under a resonant microwave and the resultant magnetization, represented by a vector shown in Fig. 5.36c, flips its head down drawing a spiral trajectory. Although this classical vector model is rarely used in electron spin resonance (ESR) or electron paramagnetic resonance (EPR), it is repeatedly applied to interpretation of nuclear magnetic resonance (NMR). (Although ESR and EPR are often used interchangeably in textbooks, the term ESR in this chapter refers to a generic methodology including EPR.)

What makes magnetic resonance informative for structural studies of materials is the interactions of various origins operating between spins. The magnetic moments associated with spins exert an effective magnetic field on the dipole moment of other spins (classical dipole–dipole interaction). The Pauli principle gives rise to a quantum-mechanical interaction between two electronic spins (exchange interaction). The behavior of a general system consisting of electron spins and nuclear spins interacting with each other is described by the effective spin Hamiltonian formally written as

$$H = B_0\gamma_e' S - 2S\mathbf{J}_e' S + S\mathbf{A}I - B_0\gamma_n I + \mathbf{I}\mathbf{J}_n\mathbf{I} + \mathbf{I}\mathbf{Q}\mathbf{I} + \dots \quad (5.19)$$

Here S and I are now quantum operators of total electronic spins and nuclear spins, respectively. The tensorial magnetogyric ratios γ_e' [slightly modified from (5.17) by spin–orbit coupling, the detail of which is given in Sect. 5.4.2] and γ_n or the corresponding tensorial g -factors describe the Zeeman splitting, respectively, \mathbf{J}_e' the direct exchange interaction between spins (slightly modified by spin–orbit coupling), \mathbf{J}_n the nuclear spin–spin indirect interaction, \mathbf{A} the effect of the environment of the spins (e.g., anisotropic crystal field), \mathbf{Q} the nuclear quadrupole interaction between the electric quadrupole moment associated with $I > 1/2$ nuclei and an electric field gradient at the nuclear position. Due to the large difference between the particle mass of electrons and nuclei, $\gamma_e' \gg \gamma_n$. Therefore, electron spins feel only small perturbations by nuclear spins, but the EPR spectra exhibit quite informative fine structures arising mainly from the third term of (5.19). On the contrary, since the presence of electronic spins has enormous effects on the nuclear spin states, NMR spectra become complicated in paramagnetic samples.

In the absence of electronic spins, the interaction of nuclear spins with the environment is so weak that the nuclei have a long spin lifetime, a quantity expressing how long the spin coherence once established is maintained as long as the nuclei are stationary in space. In other words, the decrease of nuclear spin lifetime with dynamic motion of the nuclei gives ample information of the dynamics. This unique feature of NMR provides the basis of NMR studies of impurity diffusion in solids (Sect. 5.3.1) and of molecular architecture (Sect. 5.4.2).

There are many other experimental methods that may be classified as magnetic resonance spectroscopy. Optically detected magnetic resonance (ODMR) (Sect. 5.3.1), magnetic circular-polarized emission (MCPE) (Sect. 5.3.1), and magnetic circular dichroic absorption (MCDA) (Sect. 5.3.1) are optical spectroscopic versions of EPR. Muon spin resonance (μ SR) (Sect. 5.3.1) and perturbed angular correlation (PAC) (Sect. 5.3.1) may be regarded as NMR of exotic or radioactive particles. However, these techniques will be described in a more relevant section (Sect. 5.3.1).

Electron Spectroscopy
Electron Energy–Loss Spectroscopy (EELS). Nowadays, transmission electron microscopes are often equipped with an electron energy spectrometer for routine analysis of electron energy loss. Like photons, electrons injected into solid samples lose their energy by ex-

citing quanta of various forms, but the main loss arises from excitation of other electrons. Among them, the excitation of plasmons with a loss energy of ≈ 20 eV is the most efficient process, whereas this is not the case in photoabsorption, determining the limited penetration power of the electrons through the sample. The plasmon energy is not sufficiently sensitive to the material, so the plasmon loss does not give significant information other than the thickness of the thin samples used for TEM observations. If the energy of incident electrons exceeds the energy necessary for a core electron excitation, another energy-loss mechanism takes place. Since the electron energy used in TEM is high enough, the corresponding thresholds are observed in the EELS spectrum, which is a common technique for element analysis by TEM.

X-Ray Electron Spectroscopy. On core excitations by x-rays, electrons may be emitted from the solid via two different mechanisms. Direct photoelectron emission occurs when the x-ray photon energy is high enough to excite the core electrons to vacuum levels (electronic energy levels just outside the solid surface). The energy of the photoelectrons measured relative to the Fermi level of the sample, therefore, directly reflects the energy of the core electrons. Another mechanism is Auger electron emission that occurs when a hole generated at the core level is annihilated with an electron in an upper level. The energy released on the electron-hole annihilation is spent either by creation of a photon (x-ray fluorescence) or an excitation of another electron (Auger electron) to a vacuum level. The processes are competitive but the Auger process dominates in elements lighter than $Z \approx 30$. Whether through direct photoelectron emission or Auger emission, when the energy of the electrons is of the order of 10 eV, the electronic mean free path is so short due to the plasmon loss that they cannot escape from deep positions in the sample. For this reason, x-ray photoemission spectroscopy (XPS) and Auger electron spectroscopy (AES) are surface-sensitive techniques, being powerful for studies of surfaces but not suitable for bulk samples.

Mechanical Spectroscopy

Mechanical spectroscopy [5.30] is the generic term for characterization methods of anelastic behavior such

as elastic aftereffect, internal friction and ultrasonic attenuation. Anelastic spectroscopy is a synonym of mechanical spectroscopy. In the elastic range, the strain response to applied stress is composed of the (instantaneous) elastic strain ε_e and the (delayed) anelastic strain ε_a , where the ratio $\varepsilon_a/\varepsilon_e$ is indicative of anelasticity. The measurement time scale is quasistatic for elastic after effect, below $\approx 10^4$ Hz for internal friction and above $\approx 10^4$ Hz for ultrasonic attenuation. Interaction of acoustic waves with phonons is out of the present scope. Thermoelastic relaxation is associated with the adiabatic temperature change induced by application of a stress and can be commonly observed in solid materials, but its magnitude is negligibly small except in the vicinity of the resonant condition. Mechanical spectroscopy can be applied to detect the recoverable motions of/in atoms, lattice defects, interfaces, magnetic domain walls and so on when they modify the strain response. The value of $\varepsilon_a/\varepsilon_e$ is a function of the anelastic strain for each process and the concentration of participating agents, which may be a function of the strain amplitude ε , frequency f and temperature T . For example, the value of $\varepsilon_a/\varepsilon_e$ at room temperature is of the order of 10^{-7} in silicon single crystals, 10^{-1} in highly damping metals and more than unity in polymers.

The anelastic relaxation is characterized by the relaxation time τ and $\varepsilon_a/\varepsilon_e$, where the relaxation peak exhibits a maximum at $\omega\tau = 1$ ($\omega = 2\pi f$). Thermally activated anelastic relaxation is studied as a function of temperature or frequency. The elastic aftereffect is isothermally measured as a function of elapsed time, where τ and $\varepsilon_a/\varepsilon_e$ at a given temperature are found directly. In subresonance measurements, internal friction is isothermally measured as a function of frequency, e.g., in the range between 10^{-3} and 10 Hz. These methods are applicable for $\varepsilon_a/\varepsilon_e > 10^{-5}$ because of limitations on experimental accuracy. It is emphasized that these methods can also be applied to materials with $\varepsilon_a/\varepsilon_e > 1$. The resonance methods are applicable to cases of $\varepsilon_a/\varepsilon_e < 10^{-1}$, where internal friction is measured as a function of temperature. These methods are applicable to thin plates or rod specimens. Ultrasonic attenuation is applicable to bulky specimens, where the specimen length should be longer than the pulse length. In Sects. 5.3.1 and 5.3.2, some more detail of internal friction is described.

5.2 Crystalline and Amorphous Structure Analysis

The subject covered in this section will be structural analysis of ordinary metallic and nonmetallic crystalline solids, molecular crystal, liquid crystals, amorphous solids, and quasicrystals. The subsections are divided according to the extent of structural order in space. Surface-specific problems are beyond the scope of this chapter.

5.2.1 Long-Range Order Analysis

Single Crystal Analysis

As mentioned in Sect. 5.1.1, the structure factor $F(\mathbf{K})$ in wavenumber space is related to the electronic density $\rho(\mathbf{r})$ in real space through a Fourier transformation. Since the electrons are concentrated at the atomic positions, knowing the electronic density $\rho(\mathbf{r})$ is to know the crystal structure. In principle, therefore, the crystal structure can be deduced by the inverse Fourier transformation of the structure factors if known experimentally. In practice, however, the only quantities we can measure in experiments are not $F(\mathbf{g}) = F_{\mathbf{g}} \exp(i\phi_{\mathbf{g}})$ but $|F(\mathbf{g})|^2$ (hereafter, reciprocal lattice vectors \mathbf{g} in structure factors implicitly indicate the structure factors integrated over the broadening width), which means that we lack the knowledge of the phase factors $\phi_{\mathbf{g}}$ to calculate the electronic distribution immediately. This phase problem is the main difficulty in structural analysis of x-ray diffraction, to which much effort has been devoted. The standard analytical methods to tackle this problem are the direct method, the heavy atom method and the anomalous dispersion method.

The direct method is based on a general relation (Sayre's formula)

$$F(\mathbf{h}) = a \sum_{\mathbf{g}} F(\mathbf{g})F(\mathbf{h} - \mathbf{g}) \quad a: \text{ a real coefficient} \quad (5.20)$$

which holds for arbitrary structure factors. In many practical cases, diffraction intensities are concentrated in a limited number of diffraction spots. In the simplest case, where a single term containing a specific \mathbf{g} predominates in the sum,

$$F(\mathbf{h}) \approx aF(\mathbf{g})F(\mathbf{h} - \mathbf{g}), \quad (5.21)$$

we have a phase relationship of

$$\phi_{\mathbf{h}} \approx \phi_{\mathbf{g}} + \phi_{\mathbf{h} - \mathbf{g}} \quad (5.22)$$

approximately. Thus, having assumed two phase values, one could evaluate the other and so on, successively. In

the actual procedure, starting with an initial set of phase values for dominant diffractions, one repeats an iterative procedure to recalculate the phase values until convergence is achieved. Such procedures are attempted for many initial sets of $F(\mathbf{g}) = F_{\mathbf{g}} \exp(i\phi_{\mathbf{g}})$, or model structures that yield the sets, until the best fit with experiment is achieved.

The heavy atom method is based on the fact that the atomic scattering factor $f(\mathbf{K})$ increases with the number of electrons in the atom and hence the atomic number. This method can be efficient in those crystals containing metal complexes in which the structure factors are determined mainly by the arrangement of the heavy metal atoms. Exploiting this situation, we could estimate the approximate positions of the heavy atoms in the unit cell. The experimentally measured inverse Fourier transform of $|F(\mathbf{g})|^2$ is called the Patterson function, the autocorrelation function of the electron density $\rho(\mathbf{r})$,

$$P(\mathbf{u}) = \int \rho(\mathbf{r})\rho(\mathbf{r} + \mathbf{u}) d\mathbf{v}. \quad (5.23)$$

Therefore, the Patterson function has strong peaks at relative positional vectors connecting two heavy atoms in real space. From these peaks one could deduce the real positions of only the heavy atoms in the unit cell (for more details, see the relevant textbooks [5.8]). The heavy atoms may be intentionally introduced in the process of crystal growth or in the synthesis of chemicals for macromolecules that are to be grown into crystalline samples. Chemical substitution is a method commonly used in structural analysis of biomolecules (Sect. 5.4.1).

Instead of substituting atoms, in some cases the anomalous dispersion effect can be used. Anomalous dispersion is a phenomenon in which the complex atomic structure factor changes considerably at wavelengths around the core excitation edge. Therefore, if we use x-rays of an appropriate wavelength, we can effectively *substitute* atoms with different atomic scattering factors. Since the advent of synchrotron radiation sources, it has become possible to use strong monochromatic x-rays tunable to a specific wavelength so that the anomalous dispersion method now constitutes a powerful technique applicable to many materials.

In addition to the phase problem, measurements of $F_{\text{obs}}(\mathbf{K})$ for only a limited number of \mathbf{K} vectors could lead to spurious results due to a cut-off effect in the inverse Fourier transformation. These difficulties are now being overcome by the application of the maxi-

imum entropy method (MEM) [5.31], a state-of-the-art technique that allows very precise analysis of diffraction data based on the method of least presumption and structural models of the crystal.

Regarding the sample, the availability of a single crystal is an essential prerequisite. As shown in (5.8), the intensity of the diffracted x-rays depends linearly on the number of atoms or the sample volume, in other words, it decreases rapidly as the third power of the sample dimension. If we use a conventional sealed x-ray tube, the size of single crystals must be larger than 0.1 mm, but if a synchrotron radiation source is available, the sample size may be reduced by one order of magnitude. The crystal quality must be high enough that peak broadening due to imperfections is small enough to allow peak separation. This is of particular importance in molecular crystals because the lattice constant of molecular crystals is likely to be so large that the diffraction peaks crowded one another.

The samples are mounted on a goniometer as shown in Fig. 5.37 and rotated around three Eulerian axes. Usually the ω - 2θ (θ - 2θ) scan scheme is employed: the angles ϕ and χ are adjusted so that the sample can be rotated around a zone axis coincident with the ω -axis by increasing the incidence angle θ step by step while simultaneously rotating the detector by 2θ so as to maintain specular reflection conditions.

Powder Diffraction

Single crystal diffraction experiments using a relatively large crystal give a data set from which we could deduce the crystal structure with high accuracy. However, since most materials of technical interest cannot grow to large single crystals, one has to resort to the use of powder samples consisting of small crystallites. At this point, one might suspect that, instead of using crystalline sam-

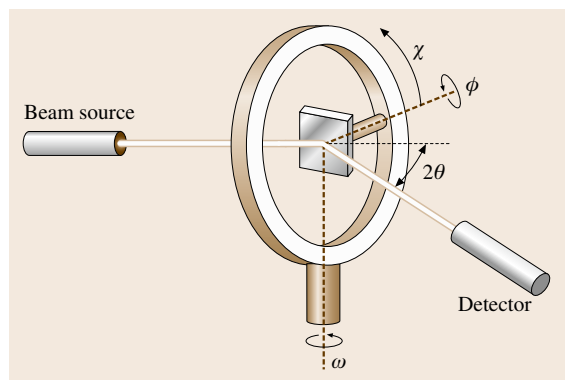


Fig. 5.37 Rotation angles in a four-circle goniometer

ples, one could use amorphous samples as the extreme of small crystallites. This view is totally wrong because for the Bragg diffraction, which is a consequence of constructive interference, to occur, the crystal must have a finite size. For crystal structure determination by powder diffraction, the crystallite size should preferably be larger than the micron scale. X-ray analysis of short-range order in amorphous solids will be described in Sect. 5.2.3.

In powder diffraction, the reciprocal lattice is randomly oriented with respect to the incident x-ray beam and the Ewald sphere. As a consequence, the x-ray diffraction by crystallographically equivalent lattice planes occurs in directions forming a cone with a common diffraction angle 2θ , as illustrated in Fig. 5.38a. The diffraction pattern thus obtained consists of rings (Debye rings) of different diameters the values of which are related to the interplanar spacings in the Bragg condition (5.1). The historical method of studying the Debye rings is to use a Debye-Scherrer camera (Fig. 5.38b) in which a slice of Debye rings is recorded on a strip of x-ray film placed around the sample. In modern experiments, the x-ray film is replaced with an x-ray detector turning on a diffractometer (Fig. 5.38c). If the Debye rings or diffraction peaks are properly in-

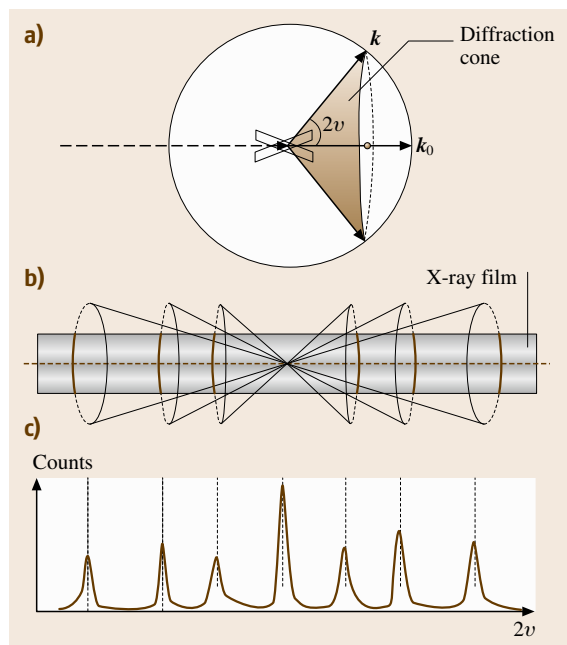


Fig. 5.38 (a) Ewald construction for powder diffraction, (b) Debye-Scherrer camera and (c) diffraction profile recorded by a diffractometer

dexed with knowledge of the crystal structure and the extinction rule, the lattice parameter of the crystal can be determined with accuracy higher than 10^{-6} .

The sample requirements for powder diffraction measurements are as follows.

1. The sample must be an assembly of crystallites each smaller than $\approx 10 \mu\text{m}$ (ideally $\approx 3 \mu\text{m}$).
2. Individual crystallites must be oriented randomly.

Condition 1 is important because, if exceptionally large crystallites are present, they introduce bright spots in the Debye rings (as exemplified in Fig. 5.99), which introduces a spurious diffraction profile. Similarly, if the orientational randomness is lost, it is impossible to measure correct profiles. In such cases, the sample must be rotated to remove such artifacts. For assessment of orientationally textured materials see Sect. 5.5.1.

The main drawback of the powder diffraction method compared to methods using single crystals is the overlap of diffraction peaks that prevents the accurate determination of the integrated intensity of each reflection and hence the structure factor. The Rietveld method, which allows an effective separation of these overlapping peaks, is a standard technique routinely used nowadays in the analysis of powder diffraction data. For the phase problem, the power of MEM (Sect. 5.2.1) in the analysis of x-ray powder diffraction, combined with the Rietveld method, has also been progressively discovered [5.33]. Using powder diffraction, one can determine the structures of considerably large molecules such as metmyoglobin, the single crystal unit cell of which contains two molecules (≈ 5000 atoms) and ≈ 800 waters [5.34].

Selected Area Diffraction (SAD)

The general merit of using TEM is that one can investigate solid structures at a medium-scale range, but most of this matter is more relevantly addressed in the section on microstructure analysis (Sect. 5.5). Selected area diffraction in TEM corresponds to single crystal diffraction of monochromatic x-rays, displaying a two-dimensional projection of the reciprocal lattice in the zeroth-order Laue zone (ZOLZ). In this regard, there is no great difference in principle between x-ray diffraction and SAD. Nevertheless, the real-time graphic presentation of the reciprocal lattice in SAD may give us more chance to notice subtle changes in crystal ordering visually. Figure 5.39a shows a SAD pattern of an CuAu stoichiometric alloy ordered with a superperiodicity (b). The SAD pattern is characterized by satellite spots which are absent when the crystal is

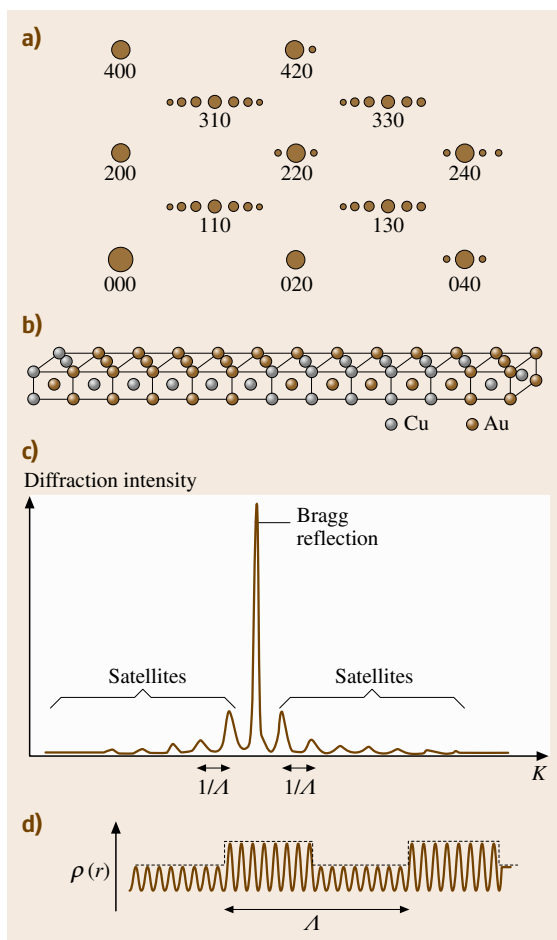


Fig. 5.39a–d Superlattice reflections (a) in the superperiodic ordered phase of CuAu stoichiometric alloy. (b) After [5.32] and Fourier transform (c) of a periodically modulated sinusoidal wave (d)

ordered but not in the long range. The origin of the satellites may be understood by examining Fig. 5.39c, which illustrates the Fourier transform of a periodically modulated sinusoidal wave (d) that mimics the superperiodic structure.

Similar satellites can be observed by x-ray diffraction of artificial superlattice thin films grown by the molecular beam epitaxial method. For the superlattice spots to be observed, x-ray diffraction experiments are conducted in a reflection configuration, where the x-rays incident to the front side of the films are Bragg reflected by lattice planes that are parallel to the film surface, as shown schematically in Fig. 5.2 (Sect. 5.1.1).

5.2.2 Medium-Range Order Analysis

Convergent Beam Electron Diffraction (CBED)

Although the selected area diffraction (SAD) (Sects. 5.1.2 and 5.2.1) in TEM gives us structural information of the local parts ($> 0.5 \mu\text{m}$ in size) of the sample selected by the objective aperture, the crystallographic information is limited compared with x-ray diffraction. The convergent beam electron diffraction (CBED) is even more informative than x-ray diffraction in some cases. In contrast to the parallel electron beam used in SAD, the electron beam used in CBED is focused onto a sample with a convergence semi-angle $\alpha > 10 \text{ mrad}$. Figure 5.40 illustrates how CBED patterns are formed in reciprocal space (a) and in real space (b). The beam convergence not only improves the spatial resolution down to tens of nanometres but also changes substantially the information contained in the diffraction patterns if the sample thickness t is larger than the extinction distance ξ_g , the case in which the dynamical effect (Sect. 5.1.2) must be taken into account. Figure 5.41 shows a schematic CBED pattern: the zero-order Laue zone (ZOLZ) diffraction spots in SAD are observed as disks in CBED. If the convergence angle 2α is large enough, diffraction is also excited from higher-order Laue zones (HOLZ) outside of the ZOLZ disks (HOLZ is the general term for the first-order Laue zone (FOLZ), the second-order Laue zone (SOLZ), and so on). An effect of multiple reflections in CBED is the characteristic dynamical contrasts *within* the disks that are absent when $t < \xi_g$. In kinematical x-ray diffraction, centrosymmetric crystals and noncentrosymmetric ones cannot be distinguished because (h, k, ℓ) and $(\bar{h}, \bar{k}, \bar{\ell})$ diffraction spots are, in any case, observed with the same intensity. In CBED, however, the diffraction pattern exhibits the same symmetry as the point group of the crystal due to the dynamical effect, so that one may fully determine the point group symmetry from a set of CBED patterns obtained for different zone axes.

Measurements of lattice parameter by SAD is not as accurate ($\approx 2\%$) as in x-ray diffraction even if the camera length, which directly affects the diameter of the diffraction rings on the screen, is calibrated carefully by using a reference crystalline powder (e.g., Au). However, the accuracy could be enhanced to $\approx 0.2\%$ by measuring the positions of sharp CBED Kikuchi lines, another effect of dynamical diffraction in CBED. When the convergence semi-angle α is larger than the Bragg angle θ_B (Fig. 5.40c), some electrons in the beam may already satisfy the Bragg condition and hence be reflected by the net planes to form Kikuchi lines sim-

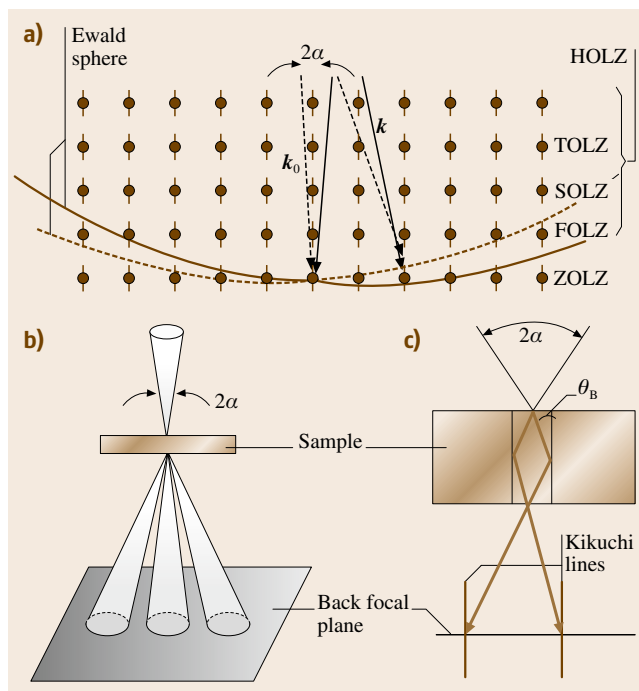


Fig. 5.40a–c Convergent beam electron diffraction (CBED) in reciprocal space (a) and in real space (b). If $\alpha > \theta_B$ (Bragg angle), CBED Kikuchi lines are formed (c)

ilar to those also observed in SAD. However, while the Kikuchi lines in SAD originate from inelastic scattering of incident electrons, the CBED Kikuchi lines are formed by elastically scattered electrons. There are two types of CBED Kikuchi lines, those bisecting each ZOLZ disk (ZOLZ Kikuchi lines) and those arising from HOLZ diffractions (Fig. 5.41). The Kikuchi lines of particular importance here are the deficient (dark) Kikuchi lines observed within the direct $(0, 0, 0)$ disk, which have their origins in the HOLZ Kikuchi lines. The positions of the HOLZ Kikuchi lines are more sensitive to lattice strain than ZOLZ Kikuchi lines because the larger $|g| = 1/d$ (d : interplanar spacing), the larger its shift $\Delta|g| = -(\Delta d/d)|g|$, which means the higher sensitivity to strain $\Delta d/d$. The sharpness of the CBED Kikuchi lines due to the smallness of the sampled area also serves to enhance the strain sensitivity.

Methods for Paracrystalline Solids

The term paracrystal is used as a model of disorder in crystalline solids. In this chapter, we use this term in a broader sense to mean materials that are intermediate between three-dimensionally periodic crystals and com-

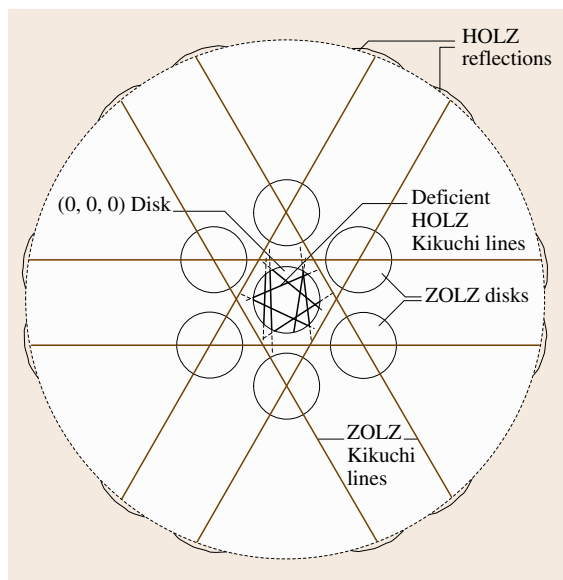


Fig. 5.41 A schematic CBED pattern featured by zero-order Laue zone (ZOLZ) disks, deficient HOLZ Kikuchi lines in the direct (0, 0, 0) disk, and reflections from higher-order Laue zones (HOLZ)

pletely amorphous structures. Most of the largest size macromolecules are polymers which are formed by the linear repetition of a group of atoms called a monomer. A polymer has no fixed configuration but takes an almost infinite variety of forms. Due to the flexibility of

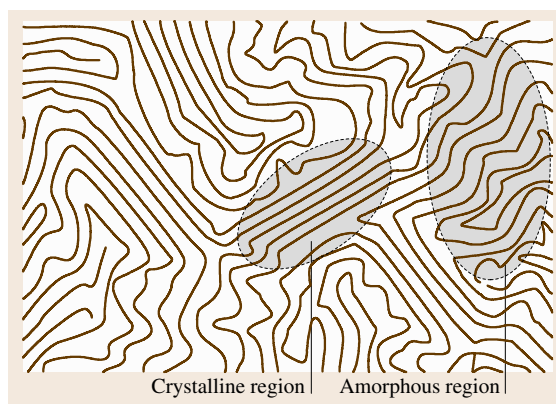


Fig. 5.42 Structure of polymer solid with coexisting crystalline and amorphous domains

polymeric chains and the tendency for mutual entanglement, polymers are likely to solidify in an amorphous or glassy form and are difficult to crystallize perfectly. So it is common that the ordered structure, if present, extends only to a limited range, as illustrated in Fig. 5.42. For the assessment of the medium-range order, one of the most common methods is to use interference optical microscopes, in which phases having different optical properties in terms of refractive index, birefringency, the rotary power, etc. are imaged as different contrasts or colors.

Between completely three-dimensional crystals and glasses, some molecular solids have structures in which

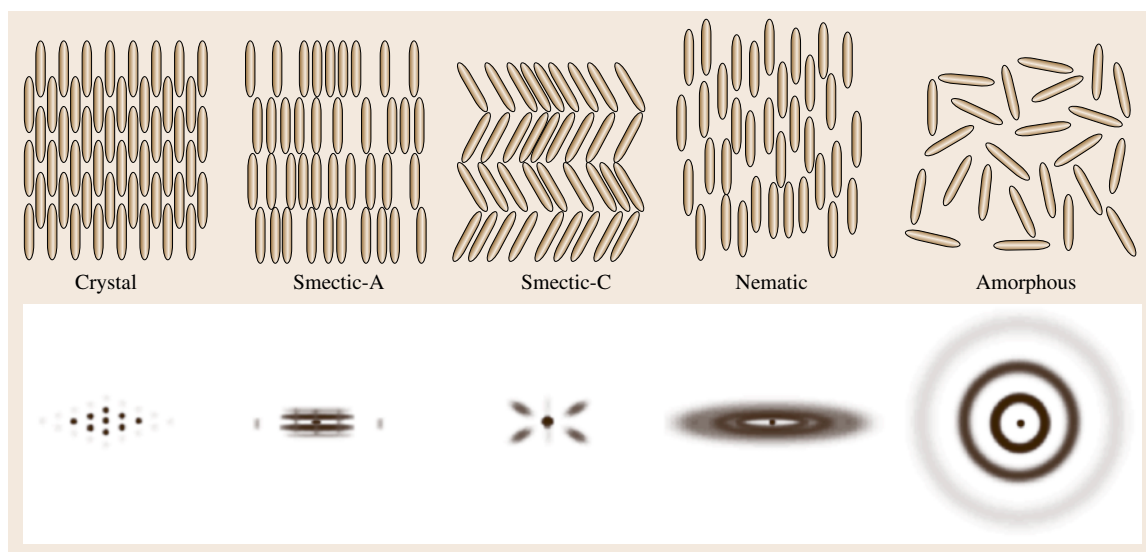


Fig. 5.43 Liquid crystal phases and their diffraction patterns (schematic)

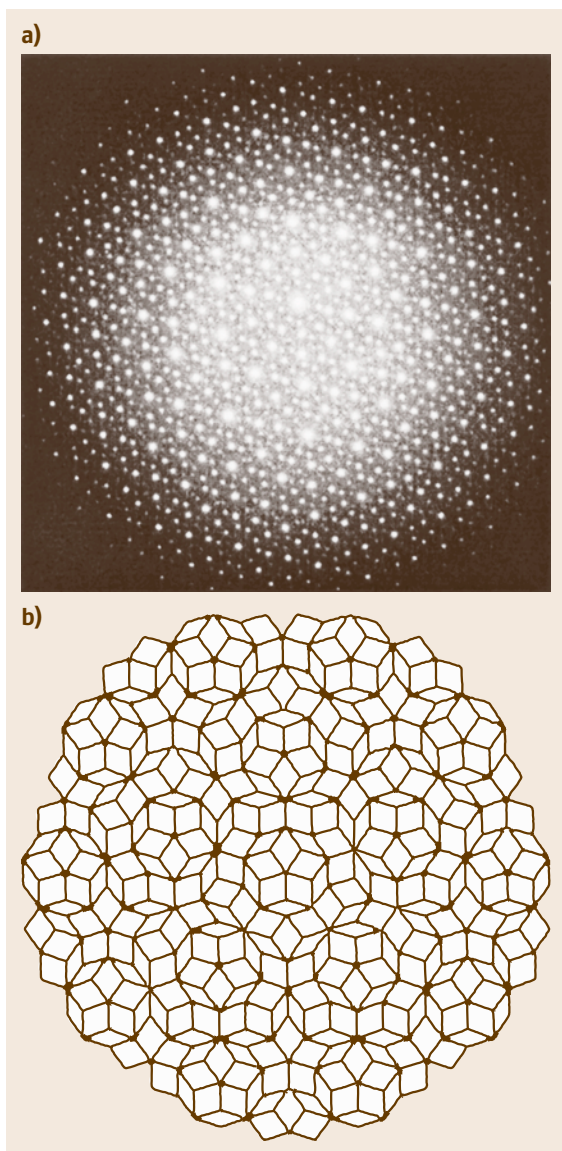


Fig. 5.44a,b SAD pattern of a quasicrystal (a) and the model structure (b). Courtesy of Dr. K. Suzuki

the crystalline order is lost in some dimensions. Solids belonging to this category are called liquid crystals. The molecules in liquid crystals are commonly elongated rigid rods with a typical length of ≈ 2.5 nm and a slightly flattened cross section of $0.6 \text{ nm} \times 0.4 \text{ nm}$. The upper drawings in Fig. 5.43 show various forms of liquid crystals in different degrees of order. The crystalline phase on the left and the amorphous phase on the right are completely ordered and disordered,

respectively, in terms of both molecular position and orientation. In the so-called nematic phase in between, the molecules are orientationally ordered but positionally disordered, and in smectic phases, the molecules are orientationally ordered forming layers but the molecular positions are random within each layer. The lower drawings in Fig. 5.43 illustrate the schematic x-ray diffraction patterns of the aforementioned phases. Thus, we may judge the phase from its characteristic diffraction pattern.

Quasicrystals are noncrystalline solids condensed with no periodicity that are not amorphous but that have regularity different from crystals. Quasicrystals consist of unit cells with five-fold symmetry which is incompatible with any crystalline long-range order. In spite of the absence of crystalline order, however, quasicrystals exhibit clear diffraction, as demonstrated by the SAD pattern in Fig. 5.44a. This is due to the fact that, even if the crystalline periodicity is absent, there are atomic net planes regularly spaced as one may find in the model structure of a two-dimensional quasicrystal shown in Fig. 5.44b.

5.2.3 Short-Range Order Analysis

Diffraction Methods

Although the atomic arrangement in amorphous solids is extremely disordered, it is not completely random as in a gas phase but preserves a short-range order to some extent. This is evidenced by halo diffraction rings from amorphous solids, as shown in Fig. 5.45. For amorphous solids, the intensity of the diffracted wave is simply given by (5.6) where the unit cell extends over the whole solid. Hence

$$\begin{aligned} I(\mathbf{K}) &= I_e \left| \sum_j f_j(\mathbf{K}) \exp(i\mathbf{K} \cdot \mathbf{r}_j) \right|^2 \\ &= I_e \sum_{m,n} f_m(\mathbf{K}) f_n(\mathbf{K}) \exp[i\mathbf{K} \cdot (\mathbf{r}_m - \mathbf{r}_n)]. \end{aligned} \quad (5.24)$$

For single component solids ($f_m = f_n \equiv f$) consisting of N atoms, some calculations show that

$$K \frac{I(K)/N - f^2}{f^2} = 4\pi \int_0^\infty r [\rho(r) - \rho_0] \sin Kr \, dr, \quad (5.25)$$

where $\rho(r)$ is the radial distribution function, which is defined as the mean density of atoms located at distance r from an atom, and ρ_0 denotes the average density of atoms. The above equation means that the

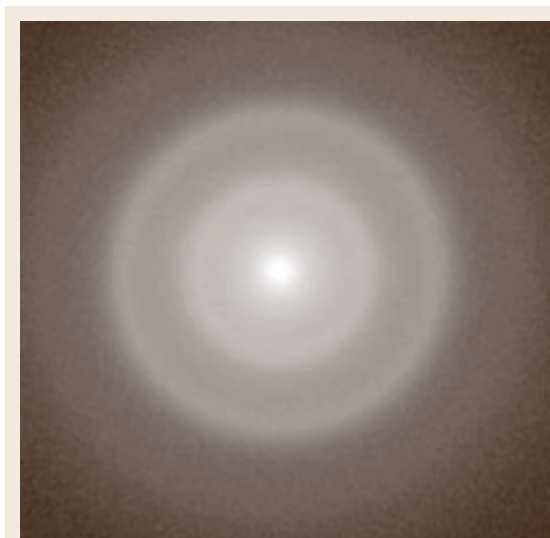


Fig. 5.45 Halo pattern of selected area electron diffraction from an amorphous carbon film

quantity $r[\rho(r) - \rho_0]$ is given by the inverse Fourier transformation of the quantity on the left, which is measurable in diffraction experiments.

For multicomponent solids, the similarly defined partial distribution functions are deduced from diffraction patterns if one uses techniques such as anomalous dispersion that allow one to enhance the atomic scattering factor f_j of only a specific element by tuning

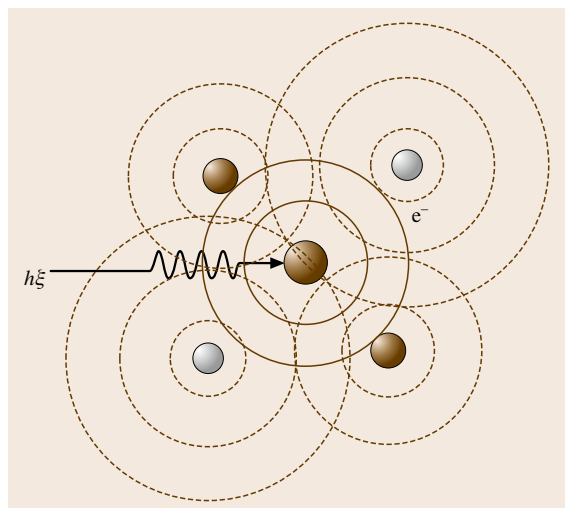


Fig. 5.46 Interference of core-excited electron waves scattered by surrounding atoms giving rise to EXAFS

the wavelength of the x-rays. The atomic scattering factor for neutrons is generally quite different from that for x-rays (Sect. 5.1.1). So coupling neutron diffraction with x-ray diffraction, we could extend the range of elements that can be studied by using diffraction methods.

Extended X-Ray Absorption Fine Structure (EXAFS)

X-ray absorption occurs when the photon energy exceeds the threshold for excitations of core electrons

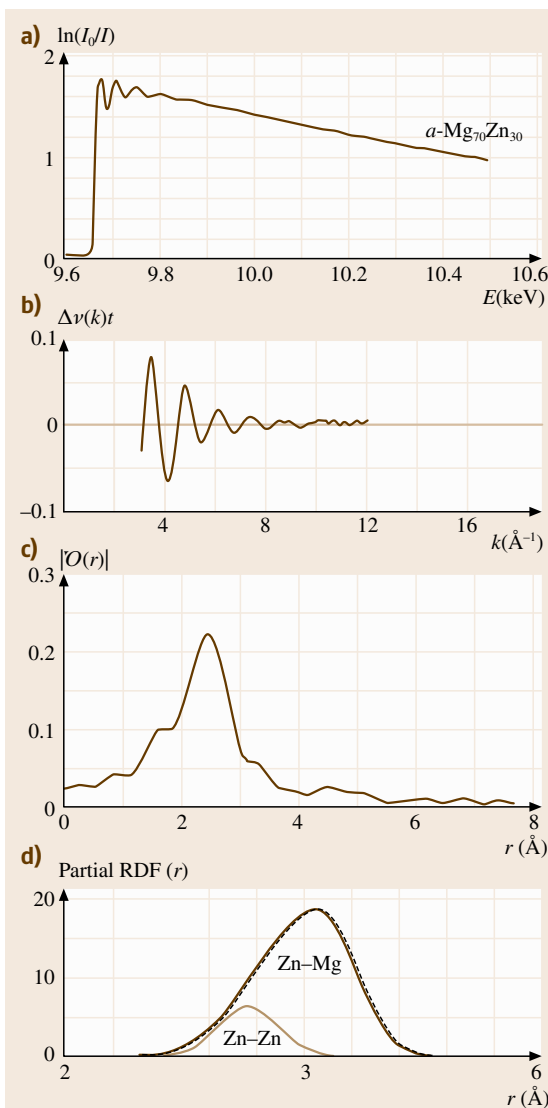


Fig. 5.47a-d Analysis of short-range order by extended x-ray absorption fine structure. After [5.35]

to unoccupied upper levels. The core absorption spectrum has a characteristic fine structure extending over hundreds of eV above the absorption edge. The undulating structures within ≈ 50 eV of the edge is referred to as x-ray absorption near-edge structures (XANES) or near-edge x-ray absorption fine structures (NEXAFS), whereas the fine structures beyond ≈ 50 eV are called the extended x-ray absorption fine structures (EXAFS). The EXAFS is brought about by interference of the excited electron wave primarily activated at a core with the secondary waves scattered by the surrounding atoms (Fig. 5.46). Therefore, the EXAFS contains information on the local atomic arrangement, neighbor distances and the coordination numbers, around the atoms of a specific element responsible for the core excitation absorption. Figure 5.47a shows an experimental x-ray absorption spectrum near the zinc K-edge of an amorphous $\text{Mg}_{70}\text{Zn}_{30}$ alloy, and Fig. 5.47b the oscillatory part of the EXAFS obtained by subtracting the large monotonic background in (a). Assuming appropriate phase shifts on electron scattering, we obtain Fig. 5.47c, a Fourier transform of a function modified from (b), from which we deduce Fig. 5.47d, the partial distribution function around Zn atoms. The area of deconvoluted peaks in (d) gives the coordination number for the respective atom pair. The element-selectivity of the EXAFS method provides a unique tool that enables one to investigate the local order for different atomic species in alloys, regardless of the long-range order or the crystallinity and amorphousness of the sample.

X-Ray Photoemission Spectroscopy (XPS)

Though x-ray photoemission spectroscopy (XPS) is surface sensitive, it may be used for studies of very short-range order around atoms. The energy of the pho-

toelectrons measured relative to the Fermi level of the sample directly reflects the energy of the core electrons. The core level is slightly affected by how much electronic charge is distributed on the nucleus in the solid (chemical shift): the more negatively charged, the higher the core level and hence the smaller the photoelectron energy. The spectral peak position and its intensity in XPS thus indicate the character of chemical bonding or the degree of chemisorption to the selectively probed atoms.

Raman Scattering

Since the principle of Raman scattering has been described already (Sect. 5.1.2), we only mention an application of Raman scattering to studies of structural order in crystalline and amorphous solids. From the energy of Raman-active optical phonons, the material phases present in the sample can be determined. The selection rule in infrared absorption based on the translational symmetry of the crystal allows only optical modes near $k \approx 0$ in the Brillouin zone. Similarly the translational symmetry restricts the Raman scattering to limited modes. The presence of defects or disorder in crystals breaks the translational symmetry of the lattice, so that translationally forbidden Raman modes become active and detectable as an increase of the extended lattice phonon signal. Raman scattering is one of the standard methods for structural assessment of graphitic or amorphous carbon [5.36]. This is owing to the fact that the visible spectral region, the most widely used for Raman scattering experiments, is electronically resonant with graphitic crystals, enhancing the scattering signals. Two broad spectral bands, called G and D, respectively corresponding to crystalline and disordered graphitic phases are well separated for quantitative analysis of disorder.

5.3 Lattice Defects and Impurities Analysis

This section deals with methods for the study of atomistic structural defects and impurities in regular lattices. Section 5.3.1 covers point defects including vacancies, interstitial atoms, defect complexes, defect clusters, and impurities. Section 5.3.2 deals with extended defects including dislocations, stacking faults, grain boundaries, and phase boundaries.

The sensitivity (or field of view) of the methods described here is not necessarily high (wide) enough for detecting a low density of defects, so in many cases the

defects must be intentionally introduced into the sample by some means. For intrinsic point defects such as vacancies and self-interstitials, the most common method is to irradiate the sample with high energy particles such as MeV electrons and fast neutrons. For dislocations, the sample may have to be deformed plastically. However, one should always pay careful attention to the possibility that the primary defects may react to form complexes with themselves or impurities and the plastically deformed samples may contain point defects as well.

5.3.1 Point Defects and Impurities

Diffraction and Scattering Methods

X-Ray Diffuse Scattering. The lattice distortion induced by the presence of point defects and impurities, as illustrated in Fig. 5.48a, causes a diffuse scattering in x-ray diffraction as well as a shift of the diffraction peaks. The diffuse scattering from such imperfect crystals generally has two components (Fig. 5.48b): Huang scattering, which appears near the diffraction peaks and represents a long-range strain field around the defects and impurities, and Stokes–Wilson scattering, which extends the between diffraction peaks and represents a short-range atomic configuration and hence its distribution in the reciprocal space reflects the symmetry of the strain field associated with the defect and impurity. Figure 5.49 shows the Stokes–Wilson scattering from an electron-irradiated Al sample [5.37] experimentally deduced by carefully subtracting a background of different origins one or two orders of magnitude larger than the signal. The experimental profiles measured along different trajectories in the reciprocal space agree most with the theoretical curves predicted by self-interstitials split along the $\langle 100 \rangle$ direction.

Rutherford Back Scattering. When light ions such as H^+ and He^+ in energy of a few MeV are incident on a solid, some of them are classically scattered by atoms in the solid, reflected backward and emitted from the sample, which is called Rutherford back scattering (Fig. 5.50a). These backscattered ions lose an energy

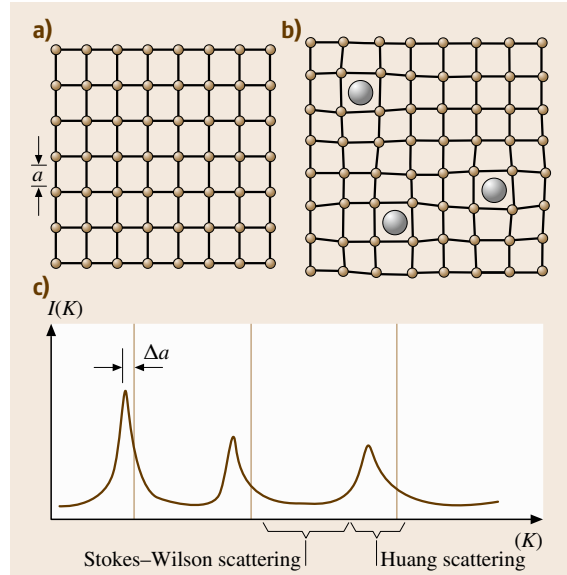


Fig. 5.48 (a) A perfect lattice and (b) a lattice distortion induced by point defects reflected in the x-ray diffraction (c) as shifts of Bragg peaks, Stokes–Wilson scattering for the short-range elastic fields and Huang scattering for the long-range fields

depending on the atoms with which the ions collide and the collision parameters: the heavier the atoms, the larger the energy loss in an elastic collision. Figure 5.50b shows a schematic diagram of the energy distribution of the backscattered ions. If the sample con-

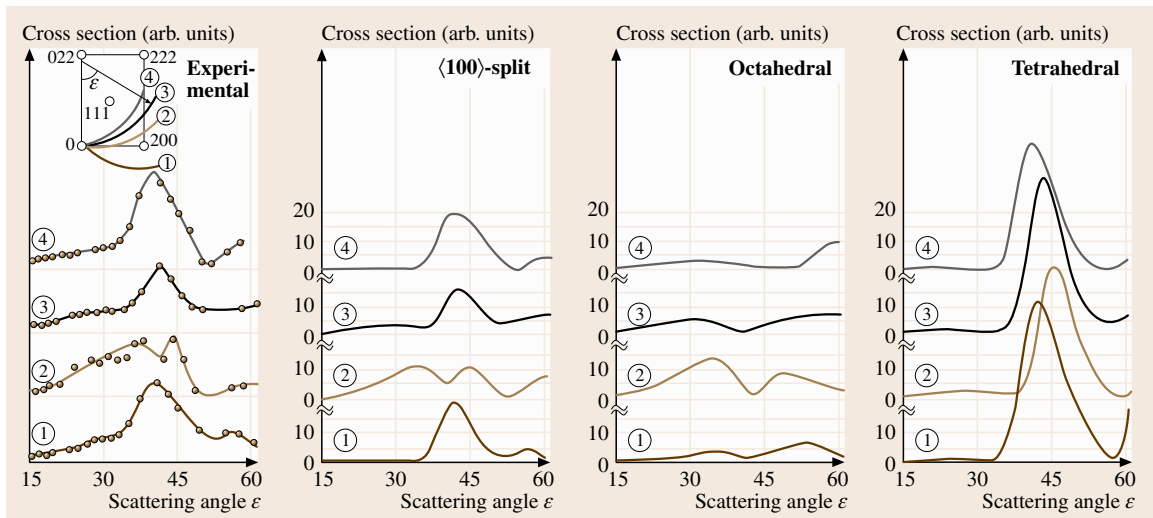


Fig. 5.49 Structural determination of selfinterstitial in Al by x-ray diffuse scattering (after [5.37, p. 87])

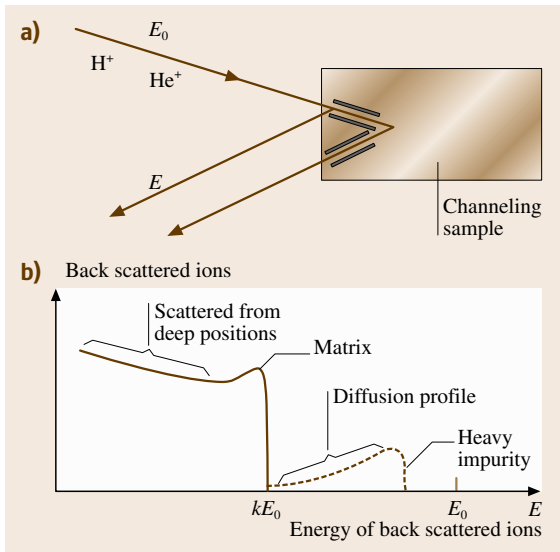


Fig. 5.50 (a) Light ions with primary energy E_0 are incident along a channel direction and inelastically scattered backward (Rutherford back scattering) with a reduced energy E . (b) The energy distribution of backscattered ions. When heavy impurities are present in the channels, a distribution arises for smaller losses

tains impurity atoms much heavier than the atoms in the matrix, an additional component due to these impurities appears between the primary ion energy E_0 and the energy kE_0 ($k < 1$) representing the energy of an ion that has collided only once with a matrix atom. This provides a means to measure the depth profile of diffusant atoms from the surface. Furthermore, in single crystal samples, ions can penetrate, without scattered, over an anomalously large distance along specific crystallographic directions called channels. If an interstitial atom is present in the channel, the number of backscattered ions incident in the channeling directions is increased. The out-going backscattered ions also may feel the channeling effect, which enables the method of double channeling that allows determination of the crystallographic position of the interstitial atoms in the lattice.

Microscopic Methods

Scanning Tunneling Microscopy (STM). One of the microscopic methods currently available for direct observations of point defects is scanning tunneling microscopy (STM). As explained in Sect. 5.1.2, the tunneling current reflects the local density of states (LDOS) of electrons at the tip position above the surface. Therefore, if the wave functions associated with defects even

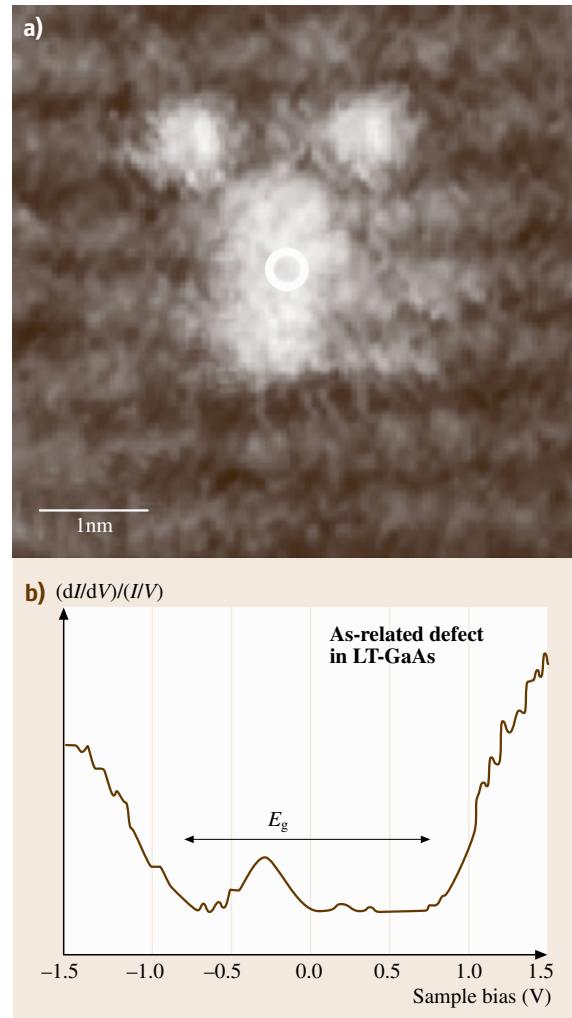


Fig. 5.51 (a) Scanning tunneling microscopic image of an arsenic-related point defect beneath the surface and (b) the local density of states measured at the defect position [5.38]

beneath the surface extend out of the surface, we can image the defect contrasts using STM. Figure 5.51 shows an STM image obtained for an arsenic-related point defect located below the surface [5.38]. Defect studies by STM are in the early stages of promising applications for various material systems.

High-Angle Annular Dark-Field STEM (HAADF-STEM). An ambitious approach for rather indirect observations of point defects is high-angle annular dark-field STEM (HAADF-STEM). The progress of improve-

ment of spherical aberration has achieved successful atomic-scale imaging of impurity atoms [5.39] and vacancies [5.40] in each atomic column. Nevertheless, elaborate image simulations are necessary for decisive conclusions to be drawn.

Spectroscopic Methods

Relaxation Spectroscopy.

Mechanical Spectroscopy. When the lattice distortion induced by defects and impurities is anisotropic, such as the strain ellipsoid depicted in Fig. 5.52a, the stress-induced reorientation (ordering) of the anisotropic distortion centers can be detected as the Snoek relaxation (peak), which allows one to evaluate the λ tensor (Fig. 5.52a) and the relaxation time. The equilibrium anelastic strain $\varepsilon_a^{(eq)}$ is given by

$$\varepsilon_a^{(eq)} = \frac{C_0 v_0 \sigma}{3kT} \left[\sum_p (\lambda^{(p)})^2 - \frac{1}{3} \left(\sum_p \lambda^{(p)} \right)^2 \right] \quad (5.26)$$

with

$$\lambda^{(p)} = (\alpha_1^{(p)})^2 \lambda_1 + (\alpha_2^{(p)})^2 \lambda_2 + (\alpha_3^{(p)})^2 \lambda_3, \quad (5.27)$$

where C_0 is the concentration of the anisotropic distortion centers, v_0 is the molar volume, and $\alpha_1^{(p)}$, $\alpha_2^{(p)}$ and $\alpha_3^{(p)}$ are the direction cosines between the stress axis and the three principal axes of the λ tensor. A typical application is to carbon, nitrogen and oxygen interstitial atoms in bcc metals which occupy one of three equivalent interstitial sites (octahedral sites) inducing tetragonal distortions in different crystallographic directions. The concept of the Snoek relaxation is also applied to the hydrogen internal friction peak in amorphous alloys.

A pair of differently sized solute atoms in the solid solution in the nearest-neighbor configuration can be an

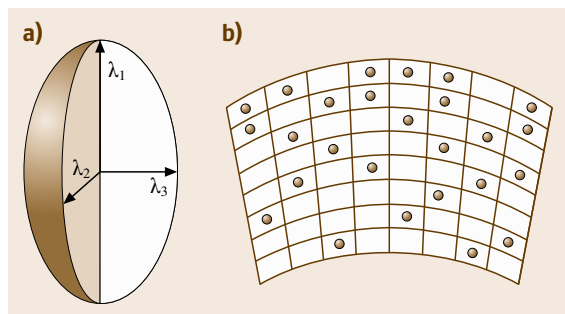


Fig. 5.52 (a) The strain ellipsoid, (b) hydrogen atoms in a bent specimen

anisotropic distortion center. For such cases, the anelastic relaxation (peak) associated with the stress-induced reorientation (ordering) of the anisotropic distortion centers is referred to as the Zener relaxation (peak). The Zener relaxation provides a tool for the study of atomic migration in substitutional alloys, without radioisotopes, at temperatures much lower than in conventional diffusion methods.

When the lattice distortion induced by an applied stress is not homogeneous, a stress-induced redistribution of interstitial impurities takes place resulting in an anelastic strain (Fig. 5.52b). Such relaxation is referred to as the Gorsky relaxation and provides a tool for the study of long-range migration of interstitial impurities. The relaxation time τ and the relaxation strength Δ_E for a specimen of rectangular section are given by

$$\tau = d^2 / \pi^2 D \quad (5.28)$$

and

$$\Delta_E = (C_0 v_0 E / 9kT \beta) (\text{tr } \lambda)^2, \quad (5.29)$$

where D is the diffusion coefficient of the impurity, β is the number of interstitial sites per host atom, and d and E are the thickness and the Young's modulus of the specimen, respectively. This method is applied to hydrogen diffusion because of the rapid diffusion rate.

Dielectric or Magnetic Relaxation. Quite similar relaxation processes occur in the dielectric or magnetic response of defects and impurities. Tightly bound pairs in ionic crystals have in some cases, such as in F_A centers (pairs of anion vacancy and isovalent cation impurity atom) in alkali halides, an electric dipole moment along the bond orientation [5.41]. Therefore, responding to the application and the removal of an electric field, the dipole moment reorients by a movement of constituent atoms, which is detected as a dielectric relaxation. Magnetic aftereffects are also brought about by movements of point defects and impurities. Since interstitial atoms in bcc metals diffuse in response to an external magnetic field through magnetostriction, essentially by the same mechanism as the Snoek effect, the Snoek relaxation can be studied by measurements of the magnetic relaxation.

Noise Spectroscopy. Relaxation and fluctuation represent two aspects of statistical behaviors of a physical quantity q that is under stochastic random forces [5.42, 43]. Debye-type relaxation behavior, which is characterized by a time constant τ_r with which the quantity

responds to a stepwise stimulation, is described by an autocorrelation function

$$\varphi_q(\tau) = \langle q(t)q(t+\tau) \rangle \propto \exp(-\tau/\tau_r) . \quad (5.30)$$

Generally, the autocorrelation function in the time domain is related to the fluctuation power spectrum $S_q(\omega)$ in the frequency domain through the Wiener–Khinchine theorem

$$S_q(\omega) = 4 \int_0^{\infty} \varphi_q(\tau) \cos \omega\tau \, d\tau . \quad (5.31)$$

Therefore, from measurements of the fluctuation power spectrum without intentional stimulation, we can deduce the relaxation time. The fluctuations may be detected in the form of electrical noise. The source of the noise varies from case to case. In semiconductors containing impurities or defects forming deep levels in the band gap, we may observe a generation–recombination (g–r) noise arising from the fluctuations of carrier density on random exchange of carriers between the deep levels and the band states. Since the fluctuation or relaxation time constant is determined, in many cases, by the rate of thermal activation of carriers from the deep level to the band, measurements of the noise intensity as a function of temperature give spectroscopic information about the depth of the deep level from the relevant band edge. Since such noise becomes more significant as the number of carriers becomes smaller, noise spectroscopy is useful for studies of small systems such as nanostructures.

Infrared Absorption Spectroscopy (IRAS). The optical photon energy that IRAS detects is determined by the atomic mass and the strength of the bonds with the surrounding atoms. Therefore, the local vibrational frequency of impurity atoms of mass similar to the matrix easily overlap with the lattice phonon band and form a resonance mode that is hard to detect in IRAS due to the strong background. Since the local vibrational modes (LVM) associated with intrinsic point defects behave similarly, few studies have been reported for IRAS experiments of LVM of intrinsic point defects. (This is also due to the fact that simple intrinsic point defects are usually easily reconstructed to secondary defects such as complexes with impurities.) Instead, IRAS experiments on light elements such as oxygen in Si have been intensively carried out and the experimental data documented. Hydrogen is an exceptionally light element which is used indirectly to detect point defects,

such as self-interstitials and vacancies in Si for example [5.44], through the LVM associated with hydrogen defect complexes. The detection limit of impurities by IRAS is $\approx 0.01\%$.

Raman Spectroscopy. Since Raman scattering is a two-photon process, the scattering signal is generally very weak, as mentioned in Sect. 5.1.2. Therefore, Raman scattering has so far rarely been used for studies of local vibrations associated with defects at low density. However, when resonant Raman scattering is used, the detection limit could be reduced down to several ppb under good conditions if the fluorescence or luminescence background is low. Figure 5.53 demonstrates the power of resonant Raman scattering, which enables detection of the LVM of As-related point defects in GaAs [5.45]. Generally, for LVM to be detected clearly by Raman scattering, the vibrational energy of the LVM must be well separated from those of the resonance modes (the local mode in resonance with the lattice phonon bands) which have relatively large intensities. The F-center (a neutral anion vacancy trapping an electron) in KI [5.46] is such an exceptional case in which the masses of potassium and iodine are so different that the gap between the acoustic and the optic bands is wide enough to accommodate the gap mode induced by defects.

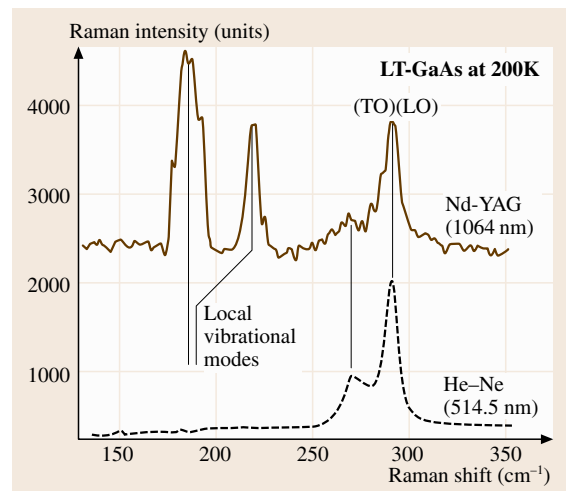


Fig. 5.53 Defect-selective resonant Raman spectra of a low-temperature grown GaAs crystal measured at 200 K by using two different excitation lasers. The wavelength of the Nd:YAG laser (1064 nm) is resonant with the intra-center electronic excitation of the As-related EL2 centers. (Courtesy of Dr. A. Hida)

Visible Photoabsorption and Photoluminescence (PL). In contrast to IRAS and Raman scattering, photoabsorption and photoluminescence (PL) in the visible to near-infrared region are widely used for studies of defects in nonmetallic solids. If the sample yields strong PL, the sensitivity can be as high as ≈ 0.1 ppm. The spectrum of PL is complementary to the photoabsorption spectrum, with both representing electronic dipolar transitions. Defects in semiconductors and insulators often introduce electronic states in the band gap. The classic examples are color centers in alkali halides. When the electronic state is deep in the gap, the electronic wave function tends to be localized in space. In such cases, the electronic energy is sensitive to the local arrangement of atoms at the defect. This effect is referred to as strong electron lattice coupling, the degree of which is reflected in the optical transition spectra. Figure 5.54a,b illustrates the situations by using configuration coordinate diagrams: each curve indicates the (adiabatic) potential energy of the system, consisting of the electronic energy and the nuclear potential energy, drawn as a function of the nuclei positions in the system that are expressed by one-dimensional coordinate

(configuration coordinate). The lower curves represent the adiabatic potentials for the electronically ground state while the upper curves the adiabatic potentials for an electronically excited state. The ladder bars indicate the vibrational states in each electronic state. If the electron–lattice coupling is weak (Fig. 5.54a), the stable configurations do not differ much between the ground state and the excited state. In this case, the optical transitions take place with spectra characterized by a sharp zero-phonon line reflecting transitions with no phonon involved, as shown in Fig. 5.54c. If the electron–lattice coupling is strong (Fig. 5.54b), the stable configurations differ considerably between the ground state and the excited state. The consequences are a broad bandwidth and a large Stokes shift (red shift) as shown in Fig. 5.54d.

Generally, the dipolar optical transition is not as efficient as competitive nonradiative processes, including Auger processes, multiphonon emission processes, and thermally activated opening of different recombination channels. The last process is common in many systems, so samples for PL measurements must usually be cooled to a low temperature (≤ 20 K) to obtain a detectable

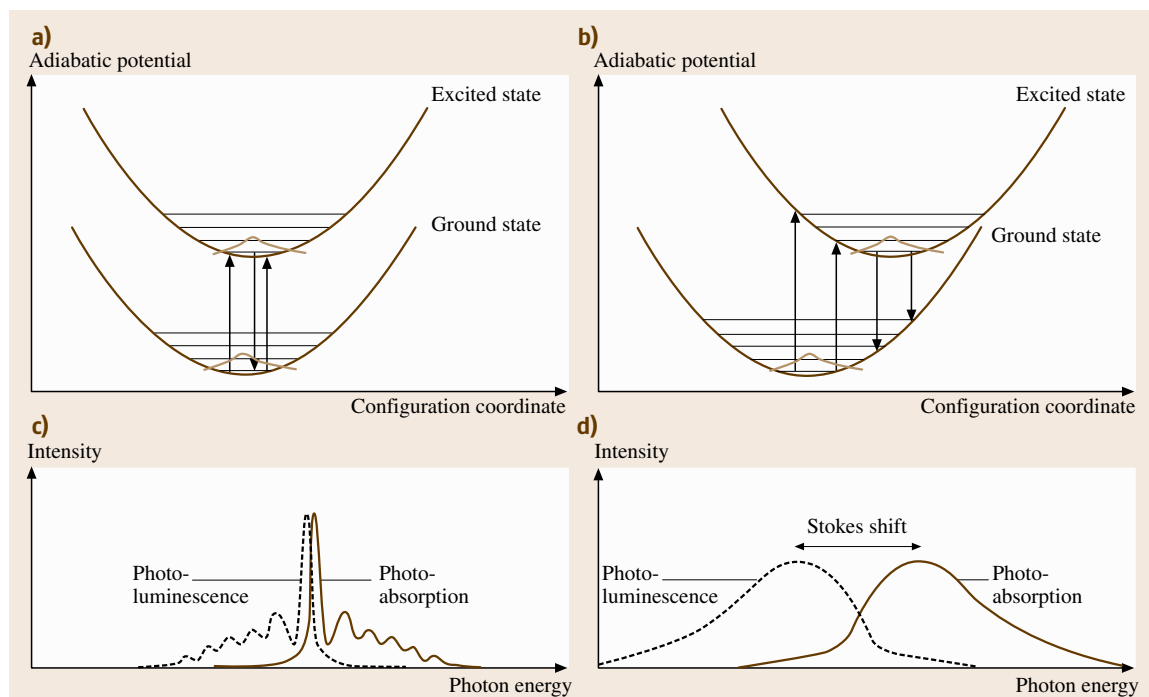


Fig. 5.54a–d Configuration coordinate diagrams and corresponding spectra of photoabsorption and photoluminescence (PL) for two cases in which electron–lattice coupling is weak (a),(c) and strong (b),(d). Note that the absorption and PL spectra are almost mirror symmetric, regardless of the electron–lattice coupling

PL intensity. The sample cooling is also beneficial for both photoabsorption and PL measurements to resolve the spectral fine structures.

Scanning electron microscopy using cathodoluminescence as the signal (SEM-CL) allows one to observe the distribution of radiative centers in semiconducting crystals. Figure 5.55 shows monochromatic SEM-CL images of semiconductor quantum dots [5.47] from which we can determine from where in the dots each luminescence arises. Similar images can be obtained by STEM equipped with a light collecting system. An advantage of STEM-CL is that one can also obtain crystallographic information about the defect.

Electron Paramagnetic Resonance (EPR). The second term $-2S\mathbf{J}'_e\mathbf{S}$ in (5.19) represents the spin–spin exchange interaction that is of fundamental importance in magnetic (ferromagnetic and antiferromagnetic) materials. In paramagnetic substances where the exchange interaction is absent, the effective spin Hamiltonian relevant to electron paramagnetic resonance (EPR) is

$$H = B_0\gamma'_e S - \lambda^2 \mathbf{S}\mathbf{A}\mathbf{S} + \mathbf{S}\mathbf{A}\mathbf{I}. \quad (5.32)$$

Here the term $-\lambda^2 \mathbf{S}\mathbf{A}\mathbf{S}$, though formally similar to $-2S\mathbf{J}'_e\mathbf{S}$, now represents the magnetic dipole interaction between electronic spin \mathbf{S} and orbital momentum \mathbf{L} (spin–orbit coupling) of magnitude $\lambda(\mathbf{L} \cdot \mathbf{S})$. For the systems with $S = 1/2$ encountered in most cases, this term is absent. Still, however, the effective magnetogyric ratio $\gamma'_e \equiv \gamma_e(1 - \lambda\mathbf{A})$ is modified from that of an isolated electronic spin $\gamma_e = \mu_B g_e$ ($\mu_B \equiv e/2m_e c$: Bohr magneton) to

$$\gamma'_e \equiv \gamma_e(1 - \lambda\mathbf{A}) = \mu_B g_e(1 - \lambda\mathbf{A}) \equiv \mu_B g. \quad (5.33)$$

Since a static magnetic field B_0 induces a Zeeman splitting of unpaired electrons much larger than that of nuclear spins, a measurable microwave absorption is observed when the microwave frequency becomes resonant with the Larmor frequency. Unlike Fourier-transform NMR (Sect. 5.4.2), an EPR spectrum is measured by sweeping the external magnetic field applied to the sample placed in a microwave cavity resonant at a fixed frequency of ≈ 10 GHz. Usually the signal is detected by a magnetic field modulation technique so that the resonance field is accurately determined as the fields at which the signal crosses the zero base line (Fig. 5.56a).

The symmetry of the defect can be determined by the dependence of the electronic g -tensor or the corresponding resonance field on the direction of the

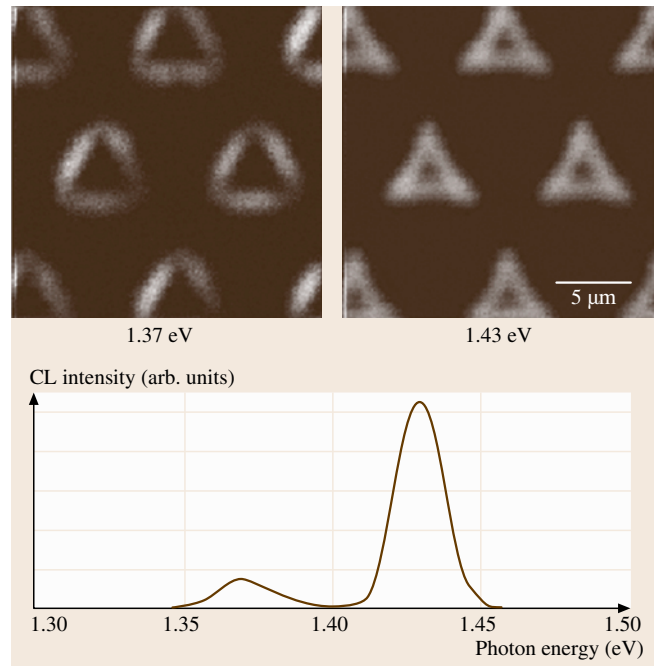


Fig. 5.55 Monochromatic SEM-CL images of semiconductor quantum dots and the CL spectrum (after [5.47])

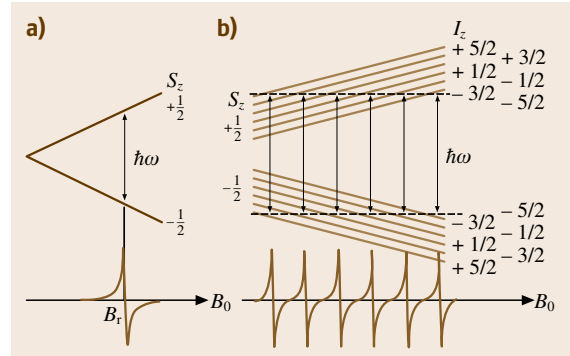


Fig. 5.56a,b Spin resonance of isolated electrons (a) and electrons interacting at the hyperfine level with a nucleus with $I = 5/2$ (b)

crystallographic axis with respect to the direction of the external magnetic field. Some point defects in semiconductors form electronic levels in the band gap and could change their charge states according to the Fermi level. If the levels are degenerate with respect to the orbitals due to the point symmetry of the center, a symmetry-breaking lattice distortion (Jahn–Teller distortion) may occur depending on the charge state so as to lift the degeneracy and consequently lower the electronic en-

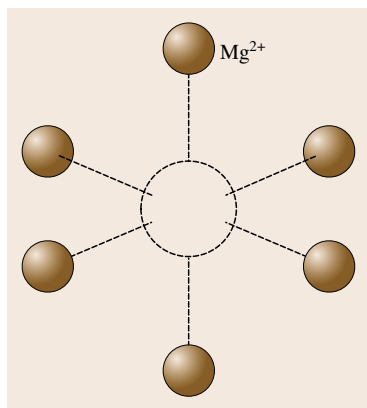


Fig. 5.57
Oxygen vacancy
in MgO

ergy. An historical example in which the EPR method shows its power is seen in structural determination of vacancies in Si in different charge states [5.48].

The chemical environment of the center or the lattice position of the defect can be identified from the knowledge of hyperfine structures arising from the last term \mathbf{SAI} in (5.32) that originates in the magnetic dipole–dipole interaction between the electronic spin and the nuclear spins over which the electron cloud is mostly distributed. Figure 5.56b illustrates how the hyperfine structure is brought about by the interaction of the electron with a nucleus of $I = 5/2$. As a concrete example [5.49], we consider oxygen vacancies in ionic MgO crystals as shown in Fig. 5.57. The vacancy of the oxygen ion O^{2-} is double-positively charged and EPR insensitive because all the electrons are paired. But if it traps an electron and becomes single-positively charged, EPR signals arise from the unpaired $S = 1/2$ spin. Since no nucleus is present at the center of the vacancy, the hyperfine interaction is due only to the surrounding six equidistant Mg^{2+} ions. Among abundant isotopes, only the ^{25}Mg nucleus (10.11% abundance) has nonzero nuclear spin of $I = 5/2$. Therefore, the relative intensity of hyperfine signals is determined by the occupation probability of ^{25}Mg ions among the six Mg ion sites. For example, the probability that all the Mg sites are not occupied by ^{25}Mg ions is $(0.8989)^6 = 52\%$, so 52% of the vacancies should show no hyperfine splitting, as shown in Fig. 5.56a. Similarly the probability of finding one ^{25}Mg ion ($I = 5/2$) in the neighborhood is $6 \times (0.8989)^5 \times (0.1011) = 35.6\%$, so that 35.6% of vacancies should exhibit $(2I + 1) = 6$ hyperfine splitting signals, as illustrated in Fig. 5.56b following the selection rule in EPR $\Delta s_z = \pm 1$ and $\Delta I_z = 0$. The probability of finding two ^{25}Mg ions ($I = 5$) is $(6!/4!2!) \times (0.8989)^4 \times (0.1011)^2 = 10\%$, so

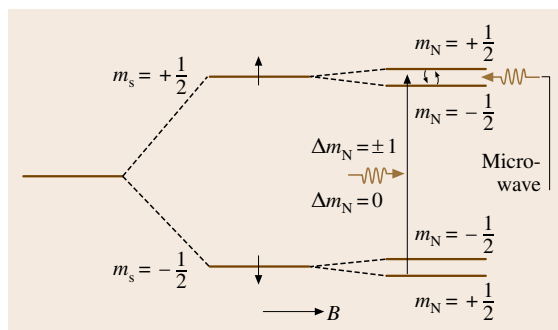


Fig. 5.58 Electron nuclear double resonance (ENDOR) in $I = 1/2$ nuclei

that 10% of vacancies should exhibit $(2I + 1) = 11$ hyperfine splitting signals. The intensity of the hyperfine signals in this case differs depending on the degeneracy of the spin configurations: only one configuration $(5/2, 5/2)$ contributes to the $I_z = 5$ signal, two configurations, $(5/2, 3/2)$ and $(3/2, 5/2)$, to the $I_z = 4$ signal, three configurations, $(5/2, 1/2)$, $(3/2, 3/2)$ and $(1/2, 5/2)$, to the $I_z = 3$ signal, and so on, resulting in the relative intensity ratio 1 : 2 : 3 : 4 : 5 : 6 : 5 : 4 : 3 : 2 : 1, which is verified experimentally.

The electron–nuclear interaction represented by the term \mathbf{SAI} in (5.32) can be extended to include indirect interactions $\sum_k \mathbf{SA}_k \mathbf{I}_k$ with nuclei k beyond the nearest neighbors, giving rise to the super-hyperfine structures around each hyperfine signals. One major drawback of EPR spectroscopy is the low resolution ($\Delta\nu \approx 10$ MHz) compared to NMR ($\Delta\nu \approx 50$ kHz), which is a disadvantage in the analysis of crowded or overlapped signals. Due to the electron–nuclear interaction, the EPR intensity of each super-hyperfine structure changes when nuclear magnetic resonance occurs in the nucleus responsible for the super-hyperfine EPR signal (Fig. 5.58). This EPR-detected NMR spectroscopy is called electron nuclear double resonance (ENDOR) [5.50] which also improves the low sensitivity of conventional NMR [5.51]. ENDOR is used to investigate the spatial extent of the electron cloud probed by EPR.

In semiconductors, unpaired spins as sparse as 10^{14} to 10^{16} cm^{-3} can be detected by EPR provided that the density of free carriers is below 10^{18} cm^{-3} so that the microwave can penetrate the sample well. In metals, the presence of free electrons limits the penetration depth below the sample surface due to the skin effect. It should be stressed that EPR signals can be detected only when unpaired electrons are present.

Optically Detected Magnetic Resonance (ODMR).

Optically detected magnetic resonance (ODMR) is applicable to studies of electronic states in which a magnetic field lifts the degeneracy of energy levels differing only in magnetic spin. ODMR is a double resonance technique that allows highly sensitive EPR measurements and facilitates the assignment of the spin state responsible for the magnetic resonance. The most common experimental schemes are either detecting circular polarized photoluminescence (PL) or magnetic circular dichroic absorption (MCDA) in response to magnetic resonance. Figure 5.59 illustrates a simple case in which the ground state and an excited state are spin degenerate in the absence of a magnetic field. When a static magnetic field is applied, these states are split to Zeeman levels. Due to the selection rule, optical transitions (PL and photoabsorption) occur either between the excited down-spin state and the ground up-spin state with a right-hand circular polarization (σ^+), or between the excited up-spin state and the ground down-spin state with a left-hand circular polarization (σ^-). In the relaxed excited state in which the occupancy of the up-spin level is higher than that of the down-spin level, the σ^- PL is stronger in intensity than σ^+ PL. However, if we apply an electromagnetic field in resonance with a spin flip transition between the excited Zeeman levels, the occupancy of the down-spin excited state becomes somewhat increased, which is detected by an increase of the σ^+ emission at the expense of the σ^- emission. Thus, the PL-detected magnetic resonance or magnetic circular polarized emission (MCPE) measurements (Fig. 5.59a) allow the detection of EPR in the electronically relaxed excited state. MCPE is also possible when the nonradiative recombination is spin-dependent. An example is found in studies of dangling bonds in amorphous Si : H solids [5.52] and of relaxed excited state of F-centers in alkali halides [5.50]. MCPE can be more sensitive than ordinary EPR as long as the PL intensity is high. However, the concentration of the centers studied successfully by MCPE is limited by the concentration quenching effect, a decrease of PL intensity due to an energy transfer mechanism (cross relaxation) starting to operate between nearby centers in close proximity (Sect. 5.4.3).

Similarly, ODMR based on magnetic circular dichroic absorption (MCDA) shown in Fig. 5.59b facilitates the assignment of the ground state spin. MCDA has advantages over MCPE in its applicability to non-luminescent samples. Other signals used in ODMR include such spin-dependent quantities as spin-flip Raman scattering light, resonant changes of electric

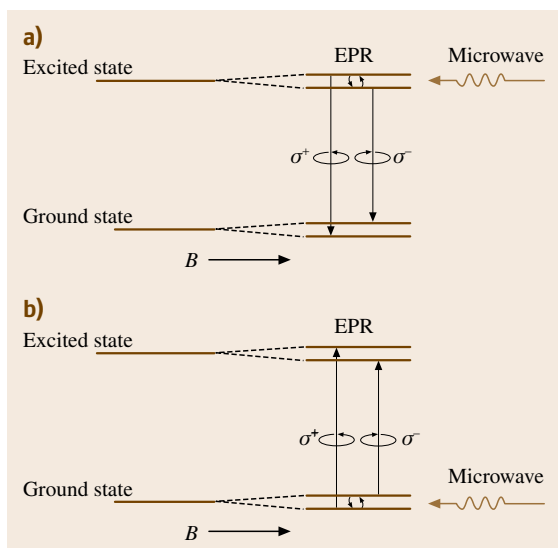


Fig. 5.59 (a) Magnetic circular polarized emission (MCPE) and (b) Magnetic circular dichroic absorption (MCDA)

current affected by the spin state of the defect centers that determines the carrier lifetime. Especially the last electrically detected magnetic resonance (EDMR) technique allows one to detect selectively a very few paramagnetic centers that are located along the narrow current path [5.7].

Muon Spin Rotation (μ^+SR). A muon is a mesonic particle which is created during the decay of a π -meson generated by a high energy particle accelerator. The muon is a Fermion having spin 1/2, whose mass is 207 times the electron mass. There are two types of muon, μ^+ and μ^- , differing in the electric charge $+e$ and $-e$, respectively. The muon disintegrates to an electron (or positron) and two neutrinos in a mean lifetime of $\approx 2 \mu\text{s}$ emitting a γ -ray with a characteristic angular distribution relative to the spin direction, as shown in Fig. 5.60a. Therefore, the rotation of spins under a static magnetic field during the lifetime can be observed as a signal oscillating at the Larmor frequency detected by a γ -ray counter placed in an appropriate direction (Fig. 5.60b). Since the negatively charged μ^- are strongly attracted to nuclear ions, they behave as if forming a nucleus of atomic number $Z - 1$. In contrast, since the positively charged μ^+ are repelled by nuclear ions in solids, they migrate along interstitial sites or become trapped at vacancies, behaving like a light isotope of protons. In ferromagnetic solids, μ^+ feel an internal magnetic field specific to the site on which the μ^+ spend their

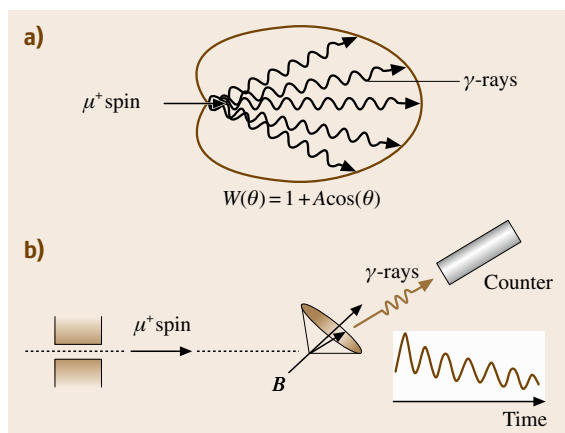


Fig. 5.60 (a) Directional emission of γ -rays from μ^+ spin and (b) a setup of μ^+ SR experiments

lifetime. This provides a means to detect the diffusion of vacancies introduced by irradiation with high energy particles [5.53]. At low temperatures, the diffusion of μ^+ along interstitial sites is so slow that they exhibit a characteristic rotation frequency corresponding to the internal magnetic field at the interstitial site. As the temperature increases, however, μ^+ become mobile, and once trapped by a vacancy, show a different rotation frequency. At temperatures where the vacancies are annihilated, the signal then disappears again. Thus, detecting the change of the μ^+ SR signal with temperature, one could study the recovery process of point defects.

Perturbed Angular Correlation (PAC). Some radioactive nuclei such as ^{111}Ag and ^{111}In emit two γ -rays (or particles) successively in the nuclear transformation process (Fig. 5.61a). If the lifetime of the intermediate state is short ($<$ hundreds ns), there exists an angular correlation between the two rays. In the absence of external fields such as a magnetic field and an electric field gradient, the direction of the second γ -ray is oriented principally in the direction of the nuclear spin at the time of the first γ -ray emission. As illustrated in Fig. 5.61b, when an external field is present as a perturbation and if the intermediate nuclei have a magnetic moment, the spins rotate during the intermediate lifetime. This is detected as a signal oscillating at the Larmor frequency by a counter for the second γ -rays emitted in coincidence with the first ones (Fig. 5.61c). This perturbed angular correlation (PAC) method allows one to study the recovery process of point defects in a manner similar to μ^+ SR.

Solid-State NMR. A famous example of applications of NMR spectroscopy to solids is the measurement of the diffusion rate of atoms. Nuclei feel a local magnetic field of various origins (Sect. 5.4.2) other than a large external magnetic field. The fluctuations of the local magnetic field due to the motion of nuclei in solids gives rise to lateral alternating fields with a frequency component that causes resonant transitions between Zeeman levels. This fluctuation-induced transition results in an energy relaxation of the spin system and shortening of the spin–lattice relaxation time T_1 . The reduction of T_1 occurs most efficiently when the correlation time of fluctuations τ satisfies $\omega_L \tau \approx 1$, where ω_L denotes the Larmor frequency. The fluctuation time constant τ represents the time constant of atomic jumps and therefore depends on temperature if the atomic jumps are thermally activated. So, if one measures T_1 as a function of temperature, one finds that T_1 becomes minimum at a certain temperature Θ_{\min} . Since ω_L can be varied by changing the external magnetic field, the activation energy and the frequency prefactor of atomic jumps

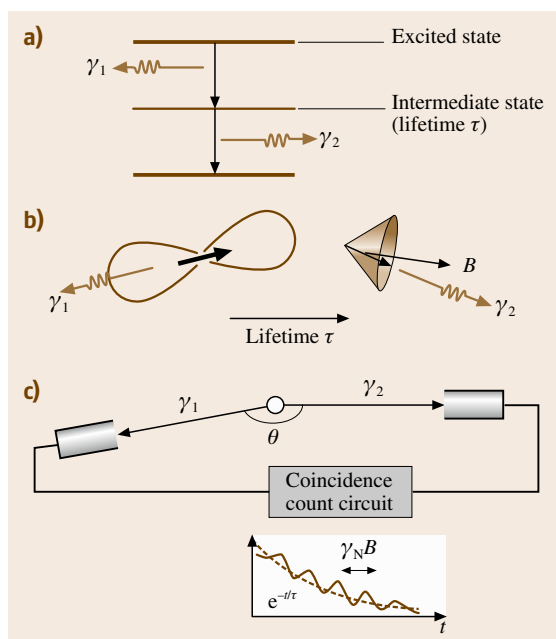


Fig. 5.61a–c In perturbed angular correlation (PAC) experiments, each direction of two γ -rays successively emitted (a) indicates the direction of the intermediate nuclear spin, which may rotate under an internal magnetic field (b). The spin rotation during the lifetime is detected by coincident count electronics (c)

could be evaluated from an Arrhenius plot of $\omega_L (= \tau^{-1})$ versus Θ_{\min} obtained for various magnetic fields. In ordinary measurements, however, the jump rate τ^{-1} is limited to the narrow range of Larmor frequencies $\omega_L \approx 10^6 - 10^8 \text{ s}^{-1}$. Experimentally this range can be expanded down to 1 s^{-1} by employing the rotating field method [5.54] in which the effective field is given by a rotating magnetic field with a small amplitude which is resonant with the Larmor frequency. The range of the jump rate τ^{-1} covered by such NMR measurements may be further reduced to $10^{-3} - 10^{-2} \text{ s}^{-1}$ in ionic crystals due to the absence of the free electrons that would induce additional relaxation in metals limiting the correct measurement of T_1 .

Positron Annihilation Spectroscopy (PAS). The positron is the antiparticle of the electron with the same mass as the electron but an electric charge of $+e$ [5.61, 62]. Positrons are created as a decay product of some radioactive isotopes such as ^{22}Na , ^{58}Co and ^{22}Cu . For the case of the parent nucleus being ^{22}Na shown in Fig. 5.62, a positron e^+ is emitted from the source with an energy of hundreds of keV on the β^+ decay of the ^{22}Na to an intermediate nucleus of $^{22}\text{Ne}^*$ (* indicates that the nucleus is in an excited state). The unstable $^{22}\text{Ne}^*$ immediately, within 0.3 ps, relaxes to the stable ^{22}Ne by emitting a γ -ray of 1.28 MeV in energy. The generated positron, if injected into a solid, loses its energy rapidly within $\approx 1 \text{ ps}$ by inelastic collision with the lattice (thermalization), and after some duration (100–500 ps) is annihilated with an electron in the solid. On this positron annihilation, two γ -rays of 0.511 MeV are emitted in almost opposite directions.

Among various schemes of positron annihilation spectroscopy (PAS), the simplest is the positron lifetime measurement. The lifetime can be measured as the time difference between the emission of the 1.28 MeV γ -ray, that indicates the time of the introduction of a thermalized positron into the sample, and the emission of the 0.511 MeV γ -rays that indicates the occurrence of an annihilation event. The positron lifetime reflects the density of the electrons with which they are annihilated. Since e^+ is positively charged, if the crystalline sample contains no imperfections, they migrate along interstitial sites until they are annihilated with electrons along the diffusion path. However, if the crystal contains vacant defects (vacancies, microvoids, dislocation cores etc.), the positrons are trapped by them because the missing ions form an attractive potential for positrons. Once the positron is trapped at a vacant site, it has less chance of being annihilated with an electron and as a re-

sult the lifetime is elongated significantly. Figure 5.63 shows the positron lifetime calculated for multiple vacancies of various sizes. From comparison of the experimental value of positron lifetime with the theoretical predictions, one can reliably infer the number of vacancies if it is smaller than ≈ 10 . When vacancies of different sizes coexist in the sample, the positron lifetime has a spectrum consisting of components each representing one type of vacancies of a different size. A successful example of positron lifetime spectroscopy is its application to measurements of thermal vacancy concentration as a function of temperature [5.63]. When the sample contains only monovacancies, the component with long lifetime increases proportionally with the increasing va-

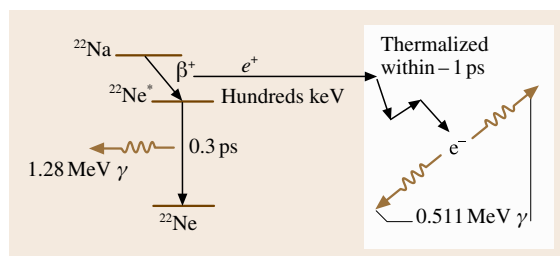


Fig. 5.62 Generation of a positron and its annihilation with an electron in solids

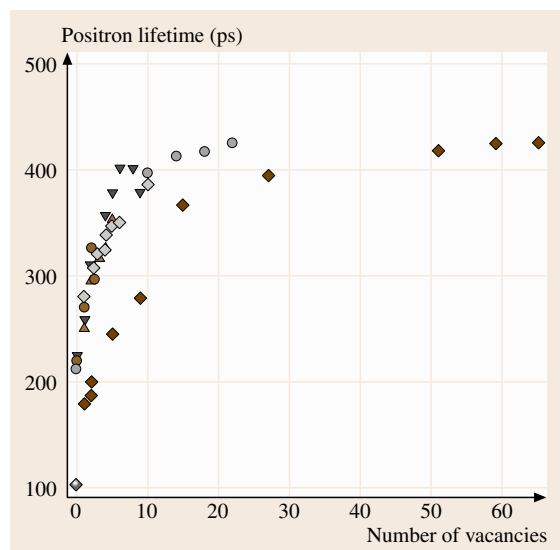


Fig. 5.63 Calculated positron lifetime for vacancies of various sizes. Experimental data for Si are collected from literature [5.55–57]. Theoretical values for vacancies in Si calculated [5.58, 59] are indicated with open marks. Experimental data for Fe [5.60] are also shown (solid diamonds) for comparison. Courtesy of Prof. M. Hasegawa

cancy concentration, as long as the vacancies are not saturated with positrons. Owing to the preferential trapping of positrons to vacancies, the detection limit of vacancy concentrations is enhanced by 2–3 orders of magnitude compared to the dilatometric method [5.64]. Since PAS experiments can be conducted irrespective of sample temperature, the vacancy concentration can be measured in thermal equilibrium, which is an advantage over the resistometric techniques that need sample quenching from various annealing temperatures.

The directions of the two γ -rays emitted on positron annihilation are not completely opposite due to the fact that the electrons to be annihilated have a finite momentum whereas the momentum of thermalized positrons is negligible: the larger the electron momentum, the larger the correlation angle (Similarly, the energy of γ -rays emitted on positron annihilation reflects the kinetic energy of the electrons through a Doppler effect. The Doppler shift measurements provide information similar to that given by the γ - γ angular correlation. The coincident Doppler broadening technique is found to be useful for the identification of impurities bound to vacancy defects [5.65].) Figure 5.64 illustrates a schematic γ - γ angular correlation curve which consists of a parabolic component, which arises from annihilation with conduction electrons whose momentum is relatively small, and a Gaussian component, which is due to annihilation with core electrons whose momentum extends to larger values. The potential felt by conduction electrons at vacancy sites is shallower and the electron momentum is smaller than the perfect sites. So, if the positrons are trapped by vacancy-type defects, the parabolic component becomes sharper and increases its intensity at the expense of the core

component. Various line shape parameters have been proposed to quantify this curve shape change and used to investigate, for example, the agglomeration of vacancies in electron-irradiated crystal upon isochronal annealing [5.66]. Nowadays, γ - γ angular correlation experiments are conducted in two-dimensions by using two position-sensitive detectors in a coincidence arrangement. The 2-D-angular correlation of annihilation radiation (2-D-ACAR) is a modern method that allows one to investigate nanosize crystalline phases such as G-P zones enriched with transition metals in noble metals such as Cu and Ag [5.67].

The detection limit of vacancies by PAS is usually around 10^{-6} in metals. In semiconducting materials, it may be enhanced by two orders of magnitude at low temperatures when the vacancies are negatively charged. Since the positrons initially emitted from the positron source (e.g., ^{22}Na) have an energy of the order of hundreds of keV, they can penetrate deep into the sample (≈ 1 mm in Si, ≈ 0.2 mm in Fe), so the thickness of the samples must be of the order of 1 mm. The use of slow positron beams, with energy ranging between a few eV and several tens of keV, enables one to study the depth profile of point defects, a problem of particular importance in semiconductor device technology.

Mössbauer Spectroscopy. The Mössbauer spectroscopy is based on the recoil-less radiation and absorption of γ -rays by Mössbauer nuclei embedded in solids with an extremely narrow natural width ($\approx 5 \times 10^{-9}$ eV). Semi-classically, the conservation of the momentum and the energy of the emitted (or absorbed) γ -ray and the solid suspending the nucleus requires that a part of the γ -ray energy

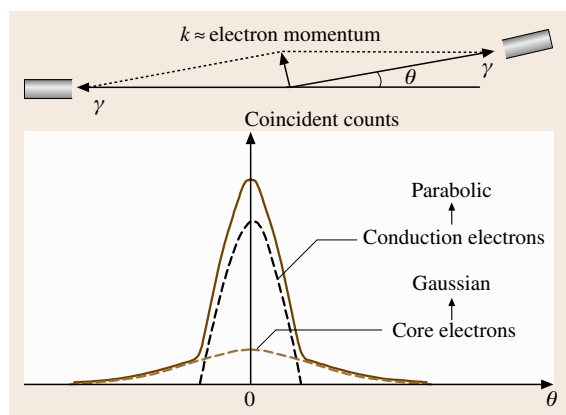


Fig. 5.64 Setup of γ - γ angular correlation experiments and a schematic correlation spectrum

$$E_R = \frac{E_\gamma^2}{2Mc^2} \quad (5.34)$$

must be transferred to the nucleus as a recoil energy. Here E_γ is the energy of the γ -ray, M the nuclear mass, and c the light velocity. Quantum mechanically, however, the motion of nuclei is quantized in the form of phonons, so if $E_R < \hbar\Omega$ (phonon energy), the emission and absorption of γ -rays occurs free of recoil. The condition for this recoil-less radiation and absorption is $k_B\theta_D > E_\gamma^2/Mc^2$, where k_B is the Boltzmann constant, and θ_D the Debye temperature of the crystal. The most common combination of an emitter and an absorber satisfying this condition is ^{57}Co (half life = 270 d) and ^{57}Fe (natural abundance = 2.17%) between which 14.413 keV γ -rays are transferred.

Figure 5.65 shows a typical setup for Mößbauer experiments. The γ -ray source (e.g., ^{57}Co) is mounted on a stage that can be moved with various velocities (0 to \pm several mm/s) so as to change the γ -ray energy by the Doppler effect. A sample containing the γ -ray absorber (^{57}Fe for ^{57}Co source) is irradiated with the γ -rays and the absorbance is measured by a γ -ray detector as a function of the Doppler-shifted γ -ray energy. Although the experiments are applicable only to limited stable isotopes (^{40}K , ^{57}Fe , ^{61}Ni , ^{67}Zn , ^{73}Ge , ^{119}Sn , ^{121}Sb , ^{184}W) Mößbauer spectroscopy places no severe restrictions on the temperature and the environment of the samples, other than that the sample thickness should be in the range 2–50 μm depending on the concentration of the absorber.

The degeneracy of the states of a nucleus in a solid is lifted under the influence of the local environment. For absorber nuclei having a nuclear spin, the internal magnetic field, if present, can be evaluated by measuring the nuclear Zeeman splitting, which is more than one order

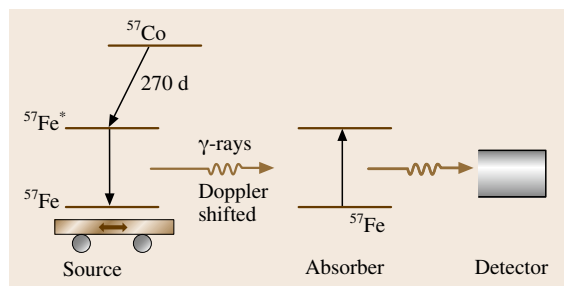


Fig. 5.65 Experimental setup for Mößbauer spectroscopy

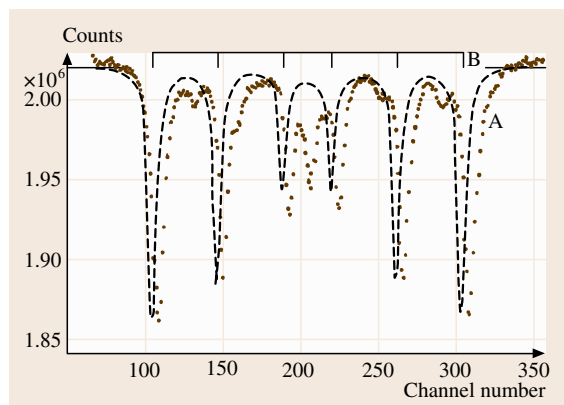


Fig. 5.66 Mößbauer spectra of iron-4.2% carbon martensite (dots A) and of pure α -iron (broken line B). The central peak is due to the presence of paramagnetic austenite phase (after [5.68])

of magnitude larger than the natural width of the γ -rays. This provides a good probe of ferromagnetic phases, which is demonstrated for the case of quenched iron steel ([5.68]) in Fig. 5.66. For absorber nuclei having a quadrupole moment ($I > 1/2$), the Mößbauer spectroscopy allows one to assess the electric field gradient at the nuclei by measuring the quadrupole splitting. This can be applied to the detection of symmetry breaking of crystal field by the presence of point defects in the vicinity of the absorber nuclei. Since the thermal motion of absorber nuclei causes a Doppler shift, a careful analysis of the spectral line shape gives us information on the lattice vibrations that may be affected by lattice defects.

Deep-Level Transient Spectroscopy (DLTS). Point defects in semiconductors often form deep levels in the band gap. Deep-level transient spectroscopy (DLTS) allows quantitative measurements of the density and the position of the gap levels with respect to the relevant band edge. The charge state of deep-level centers can be changed by various means such as impurity doping, electronic excitations, and carrier injection. The thermal occupation of a deep level, once disturbed by some means, is recovered by a thermally activated release of the carriers trapped at the centers by the disturbance. The recovery rate is determined by the depth of the electronic level from the relevant band edge (the conduction band edge for electron traps or the valence band edge for hole traps). In standard DLTS experiments, the objects to be measured are deep-level centers located in the depletion layer beneath a metal–semiconductor contact fabricated on the sample surface. The change of the electronic occupancy of the centers is detected by the change of the electrostatic capacitance associated with the contact, and the electronic disturbance is caused by carrier injection through the contact or photocarrier generation. From the temperature dependence of the rate of capacitance recovery, we can evaluate the energy depth of the gap level, and from the amount of recovery, we can measure the density of the center. An advantage of DLTS over optical spectroscopic methods is that, from the sign of the capacitance change, we can determine which carriers (electrons or holes) are transferred between the gap level and the related band, and therefore can definitely know from which band edge the level depth is measured. The capacitance spectroscopic methods including DLTS have a sensitivity as high as $\approx 10^{14} \text{ cm}^{-3}$ in moderately doped samples.

5.3.2 Extended Defects

For extended defects, most diffraction methods are coupled with microscopic methods based on crystal diffraction. Also, spectroscopic methods are not specific to extended defects, other than that the number of the *centers* in extended defects to be studied is generally too small unless the sample is prepared by intentionally introducing the defects at a high density. The description in this subsection, therefore, is limited to microscopic methods.

Chemical Etching

A simple method for direct observation of extended defects is chemically etching the sample surface to reveal the defects as etch pits, hillocks, and grooves that develop according to the difference in the chemical reactivity at the defect sites. Figure 5.67 demonstrates an example of such etching patterns observed by optical microscopy on a chemically etched surface of a plastically deformed CdTe crystal. The left diagram shows the traces of the pits positions tracked by successive removal of the surface. The linear nature of the traces proves that these defects are dislocations. The chemical etching method is also applicable to planar defects, such as grain boundaries and stacking faults that intersect the surface. The resolution may be enhanced by the use of

SEM-SE if etching is stopped before etching patterns overlap.

Transmission Electron Microscopy (TEM)

Dislocations. Among extended defects, dislocations are the most common objects, for which TEM displays its full capability. A standard scheme for observations of dislocations is to employ a two-beam condition in which the sample crystal is tilted in such orientations that only one diffraction g is strongly excited, as shown schematically in Fig. 5.68. For plan-view imaging an edge dislocation lying nearly in parallel to the sample surface (Fig. 5.69a), we tilt the sample to the direction parallel to the Burgers vector b so as to bring the sample to a two-beam condition. Then, we tilt the sample slightly further away from the Bragg condition, so that we allow lattice planes *only near* the dislocation to satisfy the Bragg condition. In this configuration, the primary (direct) beam is diffracted strongly near the dislocation, and as a result, if we are looking at the bright field image, the dislocations are observed as dark lines as shown in Fig. 5.70. For screw dislocations (Fig. 5.69c), since the lattice planes normal to the dislocation line and hence the Burgers vector b are inclined near the core, the plan-view dislocation contrast arises from the same mechanism. Thus, regardless of whether dislocations are of edge or screw type, the dislocation

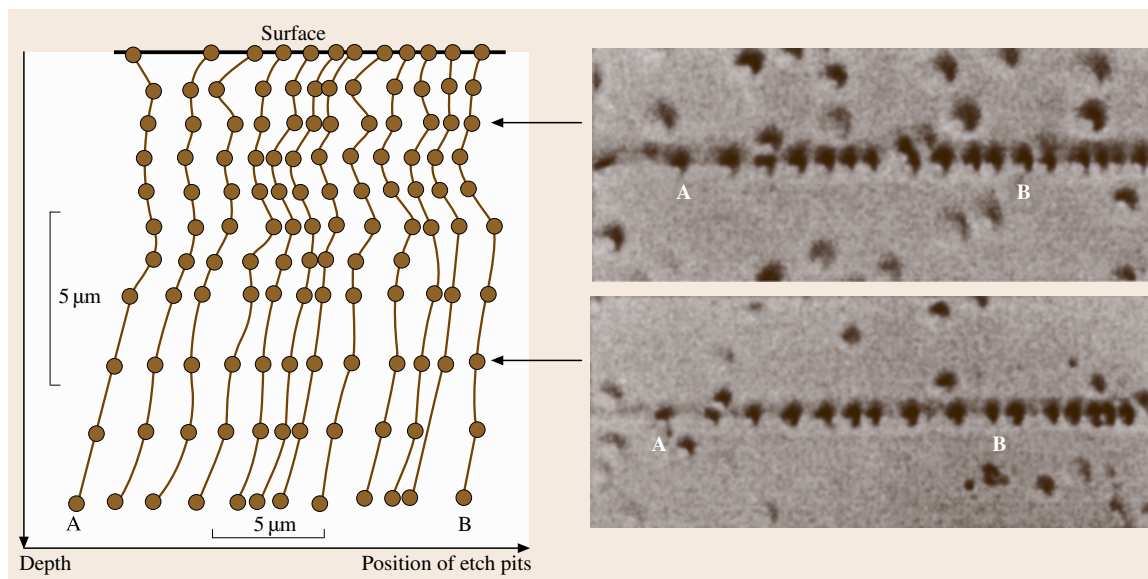


Fig. 5.67 Optical microscopic images of dislocation etch pits revealed on a plastically deformed CdTe surface by wet chemical etching (after [5.69])

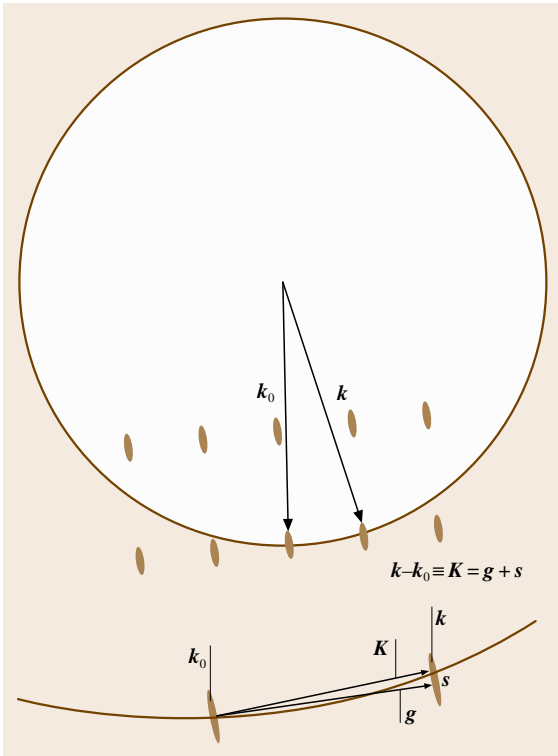


Fig. 5.68 Two-beam diffraction condition; s denotes the deviation from the Bragg condition

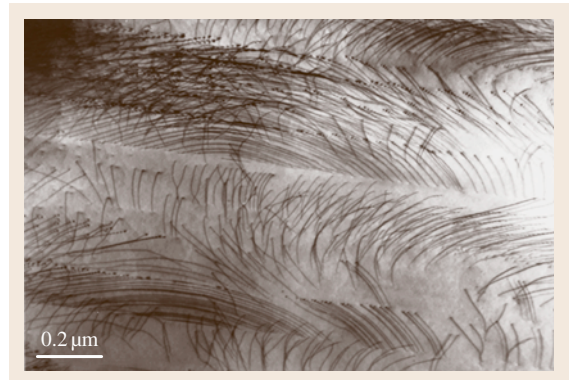


Fig. 5.70 TEM image of dislocations in plastically deformed 6H-SiC

contrasts are obtained when $(\mathbf{g} \cdot \mathbf{b}) \neq 0$. In other words, when

$$(\mathbf{g} \cdot \mathbf{b}) = 0 \tag{5.35}$$

the dislocation contrasts diminish, as demonstrated in Fig. 5.71. More precisely, dislocations are not necessarily invisible even if $(\mathbf{g} \cdot \mathbf{b}) = 0$ when $(\mathbf{g} \cdot \mathbf{b} \times \mathbf{u}) = 0$, where \mathbf{u} denotes the unit vector parallel to the dislocation line. Examining this invisibility criterion for various \mathbf{g} vectors, one can determine the direction of the Burgers vector. It should be noted that, for determi-

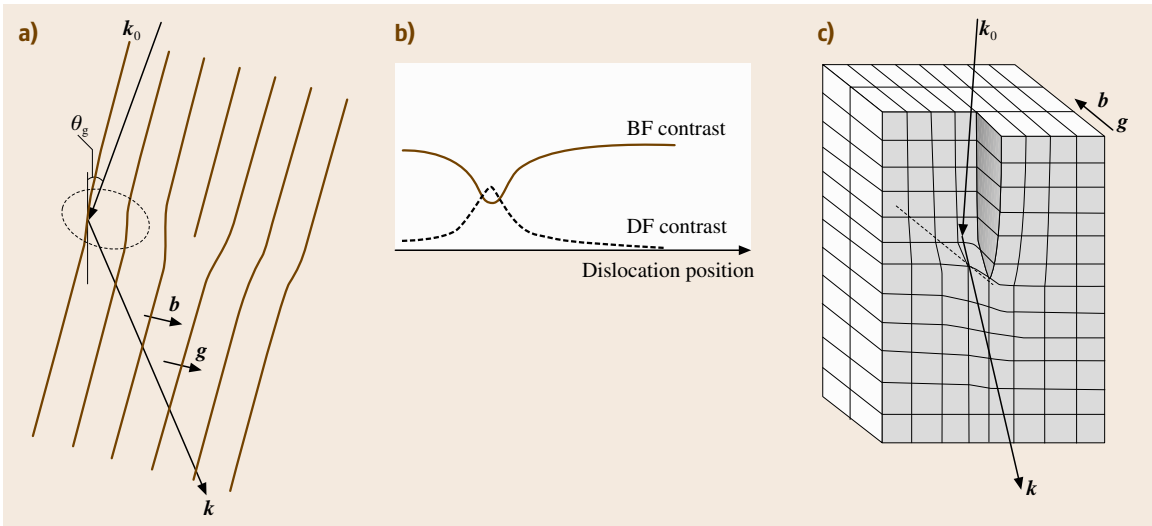


Fig. 5.69a-c Imaging dislocations (a) edge, (c) screw under two-beam conditions. The diffraction is locally enhanced at a position near the dislocation core where the lattice planes are tilted so that the Bragg condition is locally satisfied. The Burgers vector can be determined by the invisibility criterion $(\mathbf{g} \cdot \mathbf{b}) = 0$

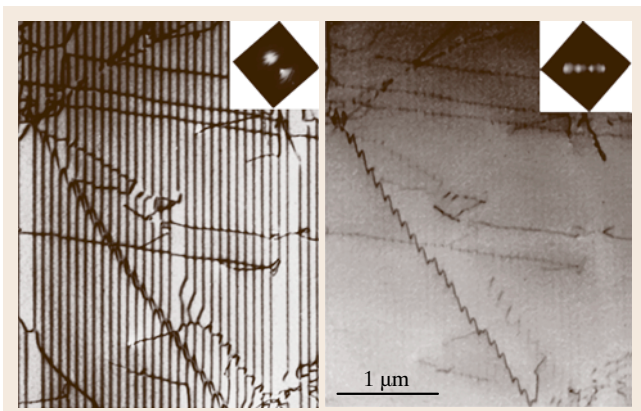


Fig. 5.71 TEM images of dislocation lines in Mo acquired for two different diffraction conditions. The invisibility criterion is used to determine the Burgers vector (after [5.70])

nation of the sense and the magnitude of the Burgers vector, we need some additional information [5.14].

When the dislocations are dissociated into partial dislocations separated by a narrow stacking fault, imaging in the normal two-beam condition is enough neither to resolve each partial dislocation nor give the correct position of the cores. In such cases, the weak-beam dark-field method is useful for imaging dislocation lines with a width of ≈ 1.5 nm and a positional deviation of only ≈ 1 nm from the real core. Figure 5.72 demonstrates a weak-beam image of dissociated dislocations in a CoSi_2 single crystal.

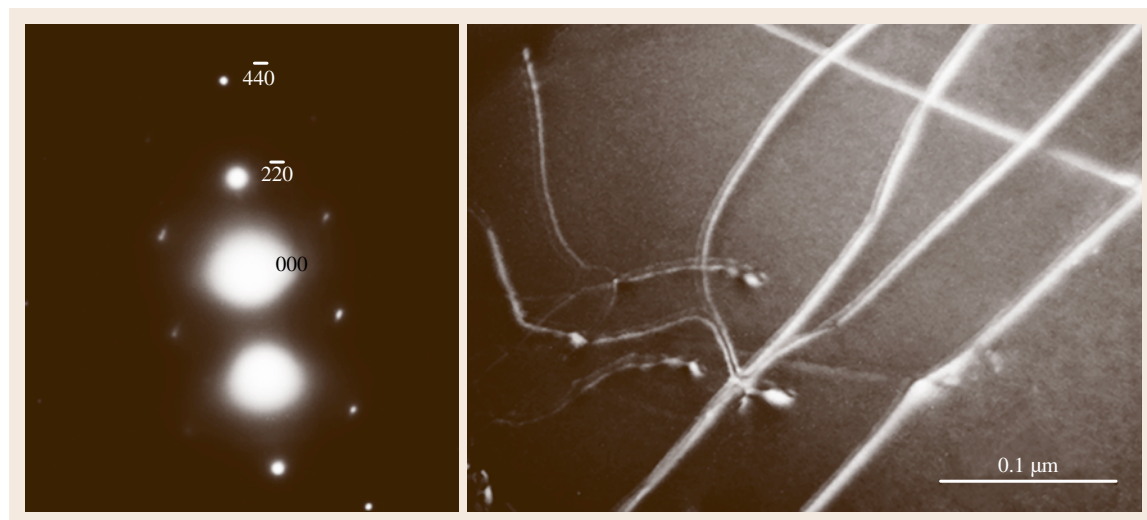


Fig. 5.72 A weak-beam TEM image of dissociated dislocations in CoSi_2 (Courtesy of M. Ichihara)

High-resolution transmission electron microscopy (HRTEM) is applicable to imaging edge dislocations. As explained in Sect. 5.1.2, under an appropriate (Scherzer) defocus condition, HRTEM images approximately represent the arrangement of atomic rows viewed along the beam direction. Figure 5.73a shows an HRTEM lattice image of an end-on edge dislocation penetrating a ZnO sample film. The presence of the dislocation can be recognized by tracing a Burgers circuit drawn around the dislocation core. One should note that the HRTEM is not applicable to imaging screw dislocations, because screw dislocations would not be visible as such a topological defect in the end-on configuration. A modern HRTEM technique has been shown to be able to visualize the strain field around a single dislocation [5.71].

Planar Defects. There are many types of planar defects, stacking faults, antiphase boundaries, inversion domain boundaries, twin boundaries, grain boundaries, and phase boundaries, each of which is characterized by a translation vector \mathbf{R} , a crystal rotation, lattice misfit and so on by which the crystal on one side of the boundaries is displaced relative to the other. In this subsection, we confine ourselves mainly to stacking faults (SFs), representative planar defects in crystals, which are characterized by only a constant translation vector \mathbf{R} .

As mentioned in Sect. 5.1.2, the dynamical theory in perfect crystals under two-beam conditions may be extended to imperfect crystals by introducing an addi-

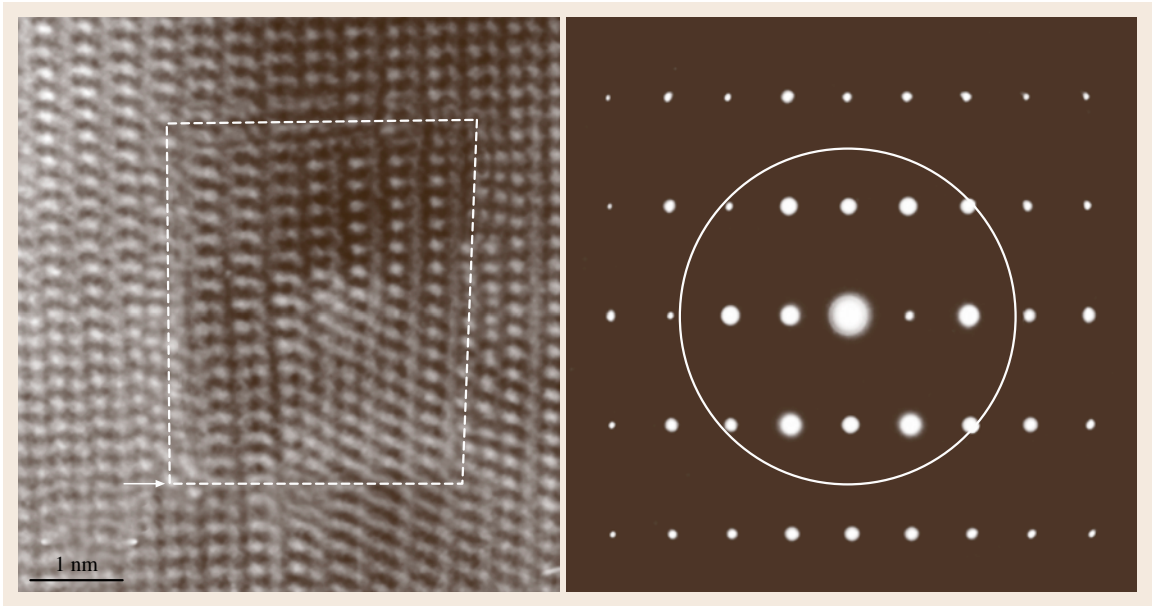


Fig. 5.73 (a) HREM image of an edge dislocation in ZnO (b) the diffraction spots encircled were used for HREM imaging (Courtesy of M. Ichihara)

tional phase shift

$$\alpha = 2\pi \mathbf{g} \cdot \mathbf{R} \tag{5.36}$$

into the arguments. Here $\mathbf{R}(\mathbf{r})$ is the displacement of atoms from the perfect positions \mathbf{r} due to the presence of the defects. Therefore, quite generally, if $\alpha = 0$, there arises no TEM contrast of the defects. Also as mentioned in Sect. 5.1.2, the Pendellösung effect is a consequence of beating between the two Bloch waves excited on the two dispersion branches. Arriving at a planar defect, the two Bloch waves each generates two other Bloch waves with a phase shift interfering with the other. A detailed analysis (see for example [5.15, p. 381]) shows that fringe contrasts as illustrated in Fig. 5.74 should be observed by TEM with a period that is half of the thickness (Pendellösung) fringe expected for a wedge-shaped sample of the upper part of the crystal above the SF plane.

Stacking faults are grouped into two types, intrinsic SFs, which are formed by interplanar slips of lattice planes with a translation vector (\neq lattice periodicity) parallel to the SF planes or by coalescence of vacancies with a translation vector normal to the SF planes, and extrinsic stacking faults, which are formed by coalescence of self-interstitial atoms with a translation vector normal to the SF planes. All types of SFs, if closed in a crystal, are bounded by a loop of partial dislocation.

In fcc crystals, the so-called sessile (unable to glide) Frank partial dislocations bounding the vacancy-type and the interstitial-type SFs have Burgers vectors \mathbf{R} of $\pm 1/3[111]$ equal in magnitude but opposite in direction, while the so-called glissile Shockley partial dislocations bounding the other type of intrinsic SFs have a Burgers vector \mathbf{R} of $1/6[11\bar{2}]$. The invisibility criterion is, therefore, different for the Shockley-bounded SFs and

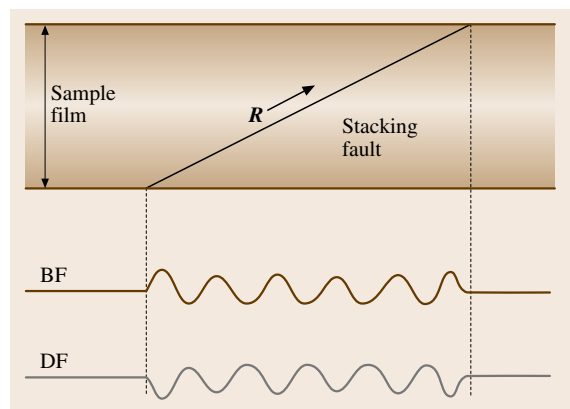


Fig. 5.74 TEM fringe contrasts of a stacking fault when absorption is neglected. The period is half that expected from the thickness fringe. The contrast is reversed in x-ray topography

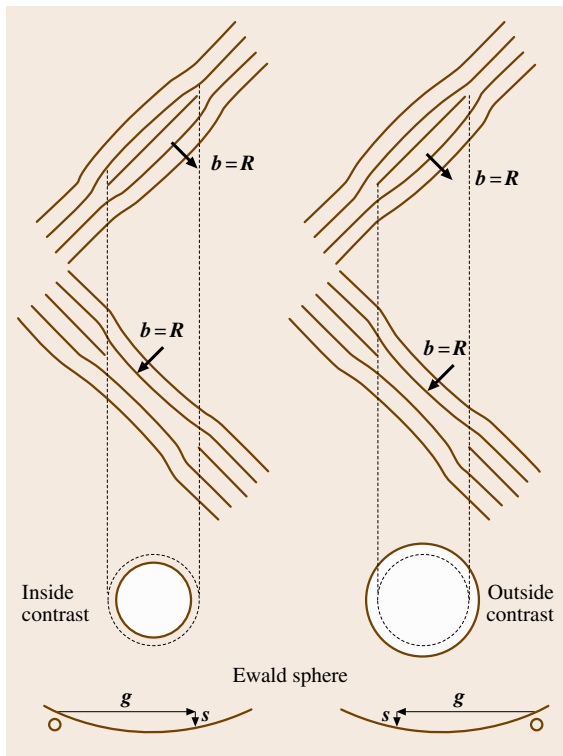


Fig. 5.75 Inside–outside contrast method for distinguishing interstitial- (upper) and vacancy-type (lower) stacking faults

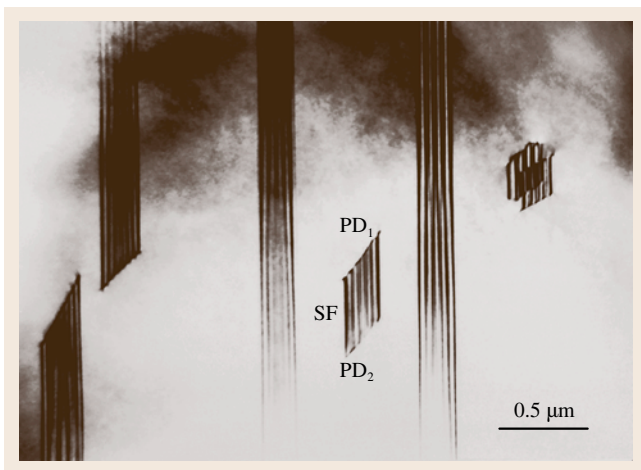


Fig. 5.76 TEM image of intrinsic stacking faults bounded by Shockley partial dislocations (PD_1 and PD_2). The sample is a plastically deformed 6H-SiC single crystal

the others. To determine experimentally whether the SFs are interstitial loops or vacancy loops and the sense of inclination of SF planes in the sample, the inside–outside contrast method illustrated in Fig. 5.75 is used [5.15, p. 410]. The same method is also useful for determining the sense of the Burgers vectors of general dislocations. Figure 5.76 shows a TEM image of intrinsic stacking faults in a 6H-SiC crystal in which the formation energy of SF is so low that wide SFs are observed after plastic deformation.

Small-angle grain boundaries are imaged by TEM as a densely arrayed dislocations. In some cases, grain boundaries are visible as Moiré patterns of two overlapping crystals. Modern TEM studies of planar defects, however, are often conducted by imaging end-on the defects by HRTEM. Recently, for example, cross-sectional HRTEM imaging of epitaxial thin films (a kind of phase boundaries) has become a standard routine in assessment of these materials. Cross-sectional HRTEM not only presents straightforward pictures for nonspecialists but also provides quantitative information that cannot be collected with conventional TEM. In particular, atomic arrangements at grain boundaries can be directly deduced by comparing end-on HRTEM images and simulations. The density of stacking faults can be evaluated by cross-sectional HRTEM even if the density is too high for plan-view observations to be possible.

X-Ray Topography (XRT)

Dislocations and stacking faults are observable also by x-ray topography (XRT) based on essentially the same principle in TEM, although there is some difference due to differences in the optical constants between electrons and x-rays. Roughly speaking, XRT images correspond to dark-field images in TEM. Figure 5.77 shows a transmission XRT image of dislocations in a Si ingot crystal introduced in the seeding process. Here the dislocations are imaged as white contrasts. The important parameter to be considered in interpretation of XRT images is the product μt , where t is the sample thickness and μ is the absorption coefficient. If $\mu t \gg 1$, we need the dynamical theory to understand images correctly, but if μt is of the order of unity or less, the kinematical theory is sufficient, which is the case in Fig. 5.77 ($\mu t \approx 1$ for $t = 0.6$ mm). The mechanism of white dislocation contrasts in Fig. 5.77 is essentially the same as that of dark contrasts in TEM bright-filled images due to the kinematical effect that the diffraction beam is

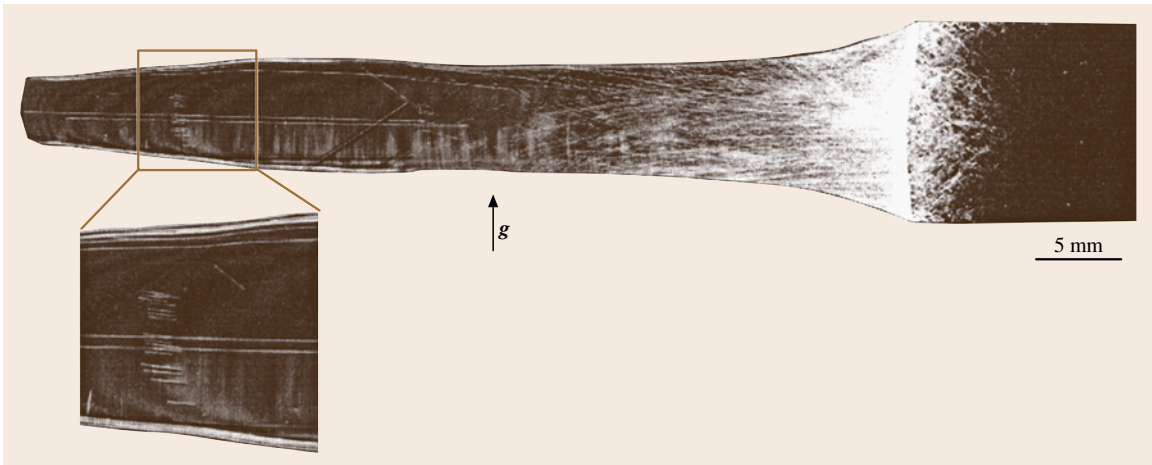


Fig. 5.77 A transmission x-ray-topographic image of dislocations in a Si ingot crystal introduced in the seeding process. The sample thickness is 0.6 mm. (Courtesy of Dr. I. Yonenaga)

directly reflected from the close vicinity of the dislocation cores where the Bragg condition is locally satisfied. Figure 5.78 shows another transmission XRT image of dislocations now in a plastically deformed GaAs crystal. In this case, the dislocations are imaged as dark contrasts. Though the sample thickness is 0.5 mm, even smaller than the case of Fig. 5.77, the absorption coefficient is much larger and as a result $\mu t \approx 10$. The anomalous transparency despite the large μt is owing to a dynamical effect (Borrmann effect), the anomalous transmission of the channeling Bloch wave. Although the quantitative interpretation of the image needs the dynamical theory, the origin of the dark dislocation contrasts in this case is the loss of crystallinity in the severely deformed regions that results in the reduction of the diffraction intensity.

Scanning Electron Microscopy in Cathodoluminescence Mode (SEM-CL)

Dislocations in semiconductors in many cases act as efficient nonradiative recombination centers. In such cases, they are observed as dark spots or lines in SEM-CL images when the matrix emits luminescence. Figure 5.79 shows an SEM-CL image of an indented CdTe surface and an OM image of the same area of the surface of which was chemically etched to reveal dislocations after the SEM-CL image was acquired. In some exceptional cases, the dislocations themselves emit light which gives rise to bright contrasts. TV scanning allows one to observe in situ the dynamical motion of dislocations. Similar images may be obtained by using OM if the defect density is sufficiently low.



Fig. 5.78 An anomalous transmission x-ray topographic image of dislocations in GaAs introduced by plastic deformation. The sample thickness is 0.5 mm (Courtesy of Dr. I. Yonenaga)

X-Ray Diffraction Analysis of Planar Defects

The density of planar defect such as stacking faults can be assessed by quantitative analysis of the x-ray diffraction profile with proper corrections for instrumental and particle size broadening. The presence of planar defects introduces phase shifts of scattering

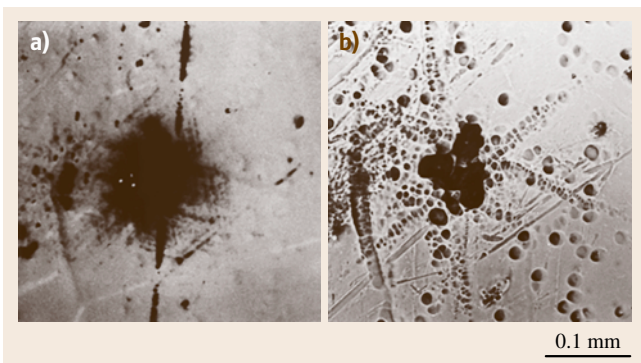


Fig. 5.79a,b Dislocation contrasts observed in an indented CdTe surface. (a) SEM-CL image showing dislocations in dark contrast and (b) OM image showing dislocation etch pits developed after (a) was recorded

waves resulting in diffraction peak broadening and peak shifts along the direction normal to the defect planes. Analogously to the effect of finite crystal size on diffraction, the peak broadening width is inversely proportional to the mean distance between adjacent

5.4 Molecular Architecture Analysis

The materials in the scope of this section include simple molecules, polymers, macromolecules (super-molecules) as well as biomolecules such as proteins. The rapidly advancing techniques relating to DNA analysis are out of the scope of this section. Molecules on large scales can have higher-order structures that perform important functions, especially in biopolymers. The primary structure of proteins, for example, is a sequence of amino acids (peptide) that constitutes secondary structures in forms such as helices and sheets. The secondary structures linked in a protein are usually folded to tertiary structures that may further become associated to a quaternary structure that brings about such bioactivity as allosteric effects. This section addresses mainly nuclear magnetic resonance (NMR) in considerable detail for its unique power in the analysis of the architecture of macromolecules. Although single crystal x-ray diffraction is another important technique for structural determination of macromolecules, we only briefly mention some points specific to macromolecular samples. The large molecules may be pretreated by chromatographic techniques to separate or decompose them into constituents or smaller fragments that can be analyzed by simpler methods. After the preprocess-

ing, the molecules or the fragments may be subjected to standard analysis such as FT-IR, Raman scattering, and fluorescence spectroscopy for identification of the constituent bases, as described in other sections (Sects. 5.1.2 and 5.2.3). In this section, we mention only optical techniques based on the circular dichroism exhibited by helix molecules and the fluorescence resonant energy transfer (FRET) that provides information on the proximity of two stained molecules.

Mechanical Spectroscopy

Internal friction (Sects. 5.1.2 and 5.3.1) provides a sensitive tool to study the motion of dislocations at very low stresses. A typical application is to elementary processes of dislocation motion in metals and ionic crystals. Dislocation pinning is applied to detect the migration of defects and impurities.

Recoverable atomic motion in grain boundaries can be studied by means of mechanical spectroscopy (Sect. 5.1.2), e.g., the anelastic relaxation of grain boundaries is observed above room temperature in coarse-grained fcc metals but below room temperature in nanocrystalline fcc metals.

ing, the molecules or the fragments may be subjected to standard analysis such as FT-IR, Raman scattering, and fluorescence spectroscopy for identification of the constituent bases, as described in other sections (Sects. 5.1.2 and 5.2.3). In this section, we mention only optical techniques based on the circular dichroism exhibited by helix molecules and the fluorescence resonant energy transfer (FRET) that provides information on the proximity of two stained molecules.

5.4.1 Structural Determination by X-Ray Diffraction

The principle of structural analysis by x-ray diffraction in macromolecules is essentially the same as that of single crystal diffraction and powder diffraction already described in Sect. 5.1.1. For the growth of molecular crystals, the synthesis of the material molecules is necessary. Thanks to progress in genetic engineering such as the advent of the polymerase chain reaction (PCR) technique, even large biomolecules such as proteins can be synthesized in sufficient amounts. However, macromolecules and polymers tend to be condensed to amorphous or very disordered aggregates (Sect. 5.2.2);

the growth of single crystals at high quality is generally difficult for such materials. The direct method is applicable only to molecules of 100 or fewer atoms because, as molecular size increases, the ambiguity in phase determination rapidly increases. The heavy atoms substitution method works for molecules larger than 600 atoms. So a gap is present for molecules in the intermediate size range. In principle, as long as a good single crystal sample is obtained, there is no limitation on the molecular size. The maximum size so far achieved by making full use of up-to-date methods is as large as that of ribosome (4×10^6 in molecular weight), though normally, the maximum size subject to routine analysis is $\approx 10^4$ in molecular weight. The powder diffraction technique is also applicable to large molecules, but the accuracy is limited due to the difficulty in separation of diffraction peaks, which are more crowded than from small molecules. The maximum molecular size is several thousands of atoms. For more details on x-ray structural analysis of macromolecules, see [5.73].

5.4.2 Nuclear Magnetic Resonance (NMR) Analysis

Standard structural analysis by NMR proceeds following (1) sample preparation, (2) NMR spectra measurements, (3) spectral analysis to assign NMR signals to the responsible nuclei and find the connectivity of the nuclei through bonds and space, (conventionally the term *signals* is used rather than *peaks* because NMR resonances are not always observed as peaks.) and finally (4) the deduction of structural models using the knowledge obtained in (3) as well as information from other chemical analyses as a constraint in the procedure of fitting model to experiment. The final step (4) is like forming a chain of metal rings of various shapes (e.g., amino acid residues in proteins) on a frame having knots in some places linked to others on the chain. For this reason, particularly for macromolecules such as proteins, it is difficult to determine the complete molecular structure uniquely from NMR analysis alone. Since we can only deduce possible candidates for the structure, it is better to refer to *models* rather than *structures*. This is in marked contrast to structural analysis by x-ray diffraction in which the crystal structure is more or less *determined* from the diffraction data alone. Nevertheless, NMR has advantages over x-ray diffraction methods in many respects such as

1. Single crystal samples are *not* needed. The samples may be amorphous or in solution.

2. Effects of intermolecular interactions, that may change the molecular structure, can be avoided by dispersing samples in suspending solution.
3. Dynamic motion of molecules can be detected.
4. A local structure can be selectively investigated without knowing the whole structure.
5. Fatal damage due to intense x-ray irradiation, that is likely to happen in organic molecules, can be avoided.

Points 2–4 are of particular importance for proteins that function in solution, changing their local conformational structure dynamically.

In this chapter, we will describe only steps (2) and (3) in some detail, leaving (1) and (4) to good textbooks [5.74–76] except for a few words on step (1). Before proceeding to the experimental details, we briefly summarize the information that NMR spectra contain.

Information Given by NMR Spectra

Nuclei other than those containing both an even number of protons and neutrons (such as ^{12}C and ^{16}O) have a nonzero nuclear spin I . The magnetogyric ratio γ_n giving the nuclear magnetic moment (Sect. 5.1.2) is a natural constant specific to the nuclear species. Table 5.4 lists isotopic nuclei commonly contained in organic molecules having hydrocarbons in the backbones. Among them, proton ^1H , carbon ^{13}C and nitrogen ^{15}N are characterized by the smallest nuclear spin $1/2$. As explained later, this fact, together with the fact that ^1H in very high natural abundance has a large γ_n value, provides the reason why mainly these isotopes are used for high-resolution NMR measurements. As far as stated in the following, we consider only the case of $I = 1/2$ for simplicity. The values of the Larmor (not angular) frequency at a typical magnetic field of 2.35 T are listed in the fifth column in Table 5.4 for various isolated nuclei. It should be noted that, with increasing γ_n , the energy difference of the two spin states, and hence the population difference and the magnetization to be detected in experiments, increase, so the sensitivity of NMR is high particularly for protons that have a large γ_n value.

The magnetic field B_0 felt by the nuclear spins may differ from the external field due to many causes.

Chemical Shift. The external magnetic field is shielded by the diamagnetic current of s electrons or enhanced by the paramagnetic current of p and d electrons surrounding the nucleus. In contrast to the shielding field

Table 5.4 Properties of nuclear species commonly used for NMR analysis of macromolecules. After [5.77]

Nuclear species	Nuclear spin I (\hbar)	Magnetogyric ratio γ_n ($10^8 \text{ rad s}^{-1} \text{ T}^{-1}$)	Natural abundance (%)	Larmor frequency (MHz) ^a
¹ H	1/2	18.861	99.985	100.000
² H	1	2.895	0.015	15.351
³ H	1/2	20.118	Radioactive	106.663
¹² C	0	—	98.0	—
¹³ C	1/2	4.743	1.1	25.144
¹⁴ N	1	1.363	99.634	7.224
¹⁵ N	1/2	−1.912	0.366	10.133
¹⁶ O	0	—	99.762	—
¹⁷ O	5/2	−2.558	0.038	13.557
¹⁸ O	0	—	0.200	—

^aNMR resonance frequency of isolated nuclei at a typical magnetic field of 2.35 T

from s electrons (Fig. 5.80a), which is isotropic in the sense that it is directed along the magnetic field due to the isotropic nature of s electrons, the shielding field is anisotropic when the electrons are, e.g., π electrons in double bonds (Fig. 5.80b). In all these cases, the applied magnetic field induces a screening current of electrons surrounding the nucleus which exerts an additional local field on that nucleus. Since the degree of screening depends on the chemical environment of the nucleus, the difference in the nuclear environment

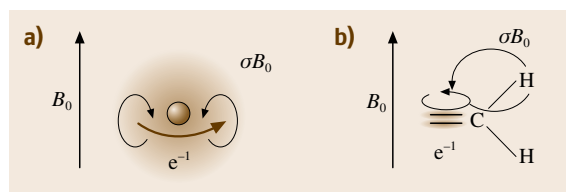


Fig. 5.80a,b The magnetic shielding by electrons inducing the chemical shifts in NMR. (a) Isotropic shielding by s electrons, (b) anisotropic shielding by π electrons

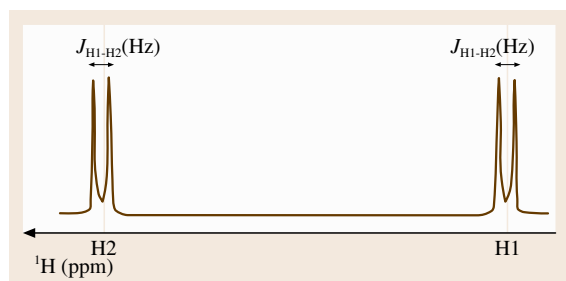


Fig. 5.81 Chemical shifts and J -coupling in molecules containing two protons in different environments (schematic)

results in a small shift, called the chemical shift δ , of the resonance frequency. As illustrated by a schematic NMR spectrum in Fig. 5.81 of protons in a molecule which contains two protons at different positions, the chemical shift can differ depending on the chemical environment. Thus, the chemical shift is used to discriminate the position in a molecule at which the probed nuclei are situated. Since the chemical shift increases proportionally with the external field, the shift is usually expressed by a fraction (in unit of ppm) of the Larmor frequency of the nucleus, which also increases linearly with the field.

Spin–Spin Coupling (Connection Through Bonds). In Fig. 5.81, the two sets of spectral signals corresponding to different chemical shifts further splits to two signals with small separations. This is due to the spin–spin coupling mediated by electrons contributing chemical bonds linking the two spins: as shown in the top left illustration in Fig. 5.82, a nuclear spin interacts with electrons surrounding the nucleus, then the spins of the electrons interact with other electrons through an exchange interaction when chemical bonds are formed, and the latter electrons interact with another nuclear spin. Unlike the direct dipole–dipole interaction between magnetic moments that operates only in a small distance, such indirect spin–spin coupling extends to a larger distance of up to 3–4 bonds. In contrast to the chemical shift, the magnitude of the spin–spin coupling is independent of the external magnetic field and therefore the splits of the resonance frequency due to the spin–spin coupling are expressed by a coupling constant J scaled in units of microwave frequency. Due to the origin of the spin–spin coupling (hereafter called

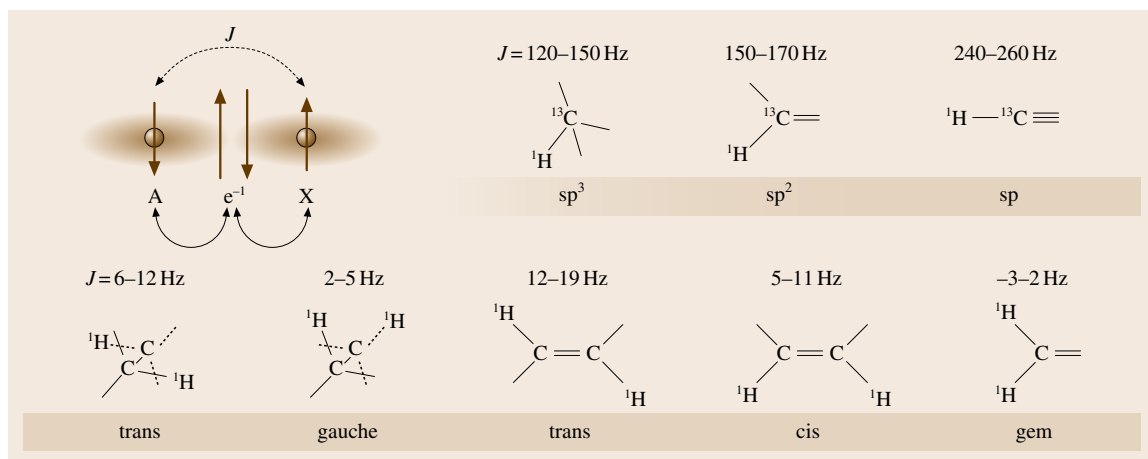


Fig. 5.82 J -coupling in various bases

J -coupling), the value of J can vary and even change its sign depending on the character and the number of chemical bonds intervening between the two spins. Some typical values of J are indicated in Fig. 5.82 between two ^1H nuclei or ^1H and ^{13}C connected with different types of chemical bonds. Thus, the value of the spin coupling constant J reflecting the *interaction through bonds* provides information of the steric local configuration of the molecule.

Nuclear Overhauser Effect (Connection Through Space). In contrast to the spin–spin interaction mediated by electrons, the magnetic moments associated with two nuclei can directly interact through the classical dipole–dipole interaction. Since the strength of the dipole–dipole interaction depends quadratically on the product of the magnetogyric ratios and decays rapidly with the internuclear distance d as d^{-3} , the dipole–dipole interaction acts virtually only between two proton nuclei within a distance of $\approx 5 \text{ \AA}$ in diamagnetic molecules. Since electrons inducing paramagnetism have a large magnetogyric ratio, they in-

teract so strongly with nuclear spins that NMR becomes very broad or unobservable.

The dipole–dipole interaction gives rise to the following nuclear Overhauser effect (NOE) that provides powerful methods for structural determination. Generally, systems of nuclear spins, once disturbed, attempt to recover their equilibrium state. The recovery or relaxation takes place via two different processes: the spin–lattice relaxation in which the excited energy is released to the heat bath (usually lattice) by flipping of spins, and the spin–spin relaxation in which only the coherence of spins is lost without energy dissipation. The relaxation processes are characterized by first-order time constants, called the vertical time constant T_1 for the former and the transverse time constant T_2 for the latter.

As an illustrative relevant example, we consider two protons, I and S, that are supposed not to be J -coupled, for simplicity. The energy level diagram of the two-spin system in thermal equilibrium is shown in Fig. 5.83a, in which the state $\alpha_I\beta_S$, for example, indicates that the spin of I is up (α) while the spin of S is down (β). In

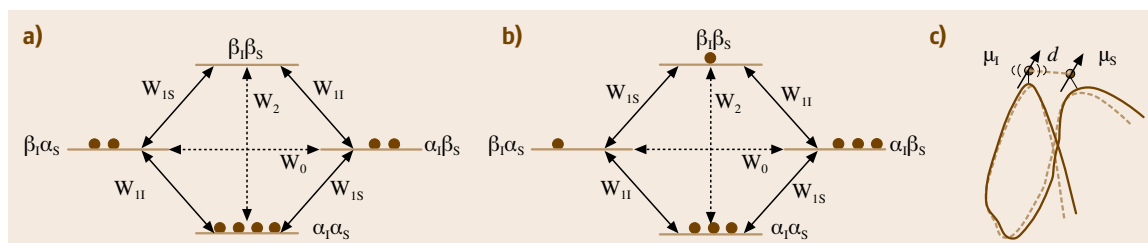


Fig. 5.83a–c Level diagrams illustrating the nuclear Overhauser effect (NOE), which operates between nuclei close in space. For details, see the text

the absence of J -coupling, the levels $\alpha_I\beta_S$ and $\beta_I\alpha_S$ are nearly degenerate with a small difference due to possible chemical shifts in I and S. The number of dots on each level indicates the level population. Now, we assume that, as shown in Fig. 5.83b, the S spins are selectively irradiated with microwaves at the resonance frequency so that the populations are equalized between the levels linked by W_{1S} , called single-quantum processes, achieved by the flipping of a single spin. Once the populations are disturbed this way, spin–lattice relaxation occurs via single-quantum transitions between $\alpha_I\alpha_S$ and $\beta_I\alpha_S$, $\alpha_I\beta_S$ and $\beta_I\beta_S$ for I, and between $\alpha_I\alpha_S$ and $\alpha_I\beta_S$, $\beta_I\alpha_S$ and $\beta_I\beta_S$ for S, both observable as singlet NMR spectra. The spin–lattice relaxation may also occur by transitions between $\alpha_I\alpha_S$ and $\beta_I\beta_S$, called double-quantum processes W_2 , that correspond to simultaneous flipping of both spins. The populations may also be recovered by the transition between $\beta_I\alpha_S$ and $\alpha_I\beta_S$, called a zero-quantum process W_0 , which causes spin–spin relaxation. The relaxation through W_0 and W_2 are normally forbidden but becomes allowed when there are magnetic field fluctuations that act as an alternating field at various frequencies, which induces spin flipping. The field fluctuations are generated by the diffusional or rotational motion of nuclei and molecules (Fig. 5.83c) that cause fluctuations in the local field affected by the dipole–dipole interaction. Generally, the fluctuation-induced relaxation rate becomes maximum when the resonance condition $\omega_0\tau_c \approx 1$ is satisfied, where τ_c is the correlation time of the fluctuation and $\hbar\omega_0$ is the relevant transition energy. Since $\omega_0 = \omega_L$ for W_1 and $\omega_0 = 2\omega_L$ for W_2 , normally $\omega_0\tau_c \gg 1$ in large molecules or molecules in viscous solution for which τ_c is large, and hence relaxation through W_1 and W_2 is inefficient in such systems. For the process W_0 , however, the two levels are close in energy ($\omega_0 \approx 0$) so that relaxation through W_0 can be efficient when $\omega_0\tau_c \approx 1$ is satisfied, thereby dominating the spin–spin relaxation. In any cases, the excited spin systems recover their thermal populations with a rate affected by the cross relaxation processes W_0 and W_2 due to the dipole–dipole interaction, if present. This NOE effect, originating from an *interaction through space*, is exploited for determination of the conformation of macromolecules.

Experimental Methods

Vector Model in Rotating Frame. In modern NMR experiments, we do not anymore measure the absorption of a continuous microwave, but instead measure a response of the spin system to a sequence of microwave pulses and Fourier transform the oscillatory current sig-

nal response to the pulses to obtain an NMR spectrum. Experimentally, in addition to the static magnetic field along the z -axis, we apply another magnetic field to the spins with a small intensity $2B_1$ alternating at an angular frequency ω with a coil (transmitter) that is wound around the sample with its axis (taken as x -axis) normal to the z -axis. One of the circularly rotating fields of intensity B_1 gives rise to two effects: it forces the precession of the spins to synchronize and to tip away from the z -axis. A simple calculation shows that, if one views the precessing spin from the coordinate system $O-x'y'z$ rotating around the z -axis at the alternating frequency ω , the spin feels an effective magnetic field composed of a static field B_1 directing along the x' -axis and a constant field $B_0 - \omega/\gamma_n$ along the z -axis. Therefore, if we prepare spins under a static field B_0 and at time $t = 0$ we apply a rotating field B_1 that satisfies the resonance condition $\omega = \omega_L (= \gamma_n B_0)$, only the field B_1 remains and causes the spins to turn coherently around the x' -axis at a small angular frequency of $\gamma_n B_1$. Therefore, if we focus on the magnetization, the average of the magnetic moments associated with spins rather than the spins themselves, we can draw pictures like Fig. 5.36a–c, in which the magnetization is represented by a thick vector. Hereafter we will repeatedly use such classical vector models in rotating frames for intuitive interpretation.

High-Resolution NMR. As mentioned already, the absolute magnitude of chemical shifts becomes larger as the external magnetic field B_0 is increased while the fine structure due to J -coupling is fixed in magnitude. Therefore, the use of a higher magnetic field allows one to resolve overlapping signals closely split with very small differences in chemical shifts (Fig. 5.84). Espe-

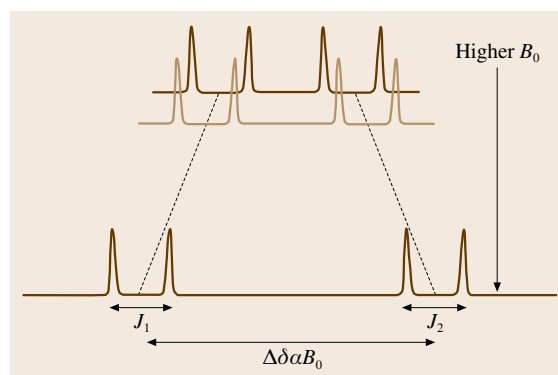


Fig. 5.84 Chemical shifts $\Delta\delta$ increasing with magnetic field and invariable spin–spin couplings J_1 and J_2 . The use of high field enhances the resolution of NMR

cially in macromolecules such as proteins, substantial overlapping of NMR spectra are common and the removal of the overlaps is requisite. One experimental solution is to use an extremely high-field (superconducting) magnet the strength of which being, in terms of the equivalent ^1H resonance frequency, as high as, e.g., 800 MHz.

One-Dimensional (1-D) NMR. Free Induction Decay (FID). An extensive range of modern techniques developed for NMR experiments are solely devoted to separate complicated signals, such as shown in Fig. 5.85, without artifacts. Some of the tasks can be solved, as well as through the use of high-field magnets, by one-dimensional NMR (1-D-NMR) schemes that are illustrated by pulse sequence diagrams. The simplest case, though rarely encountered in practice, is illustrated by a vector model shown in Fig. 5.86a–c. In the initial state (Fig. 5.86a) the magnetization vector is aligned along the z -axis, and in the second step (Fig. 5.86b) we apply a rotating field at a reference frequency ω for a duration Δt that just satisfies $\gamma_{\text{n}} B_1 \Delta t = \pi/2$ so that the magnetization is tipped onto the y' axis. We may not be able a priori to set the reference frequency ω identical to the resonance Larmor frequency ω_{r} to be measured. In such off-resonance cases, the magnetization vector in the rotating frame would rotate with a rate $\omega_{\text{r}} - \omega$. In the third step (Fig. 5.86c), since the rotating field is switched off (free), the coherent magnetization remains in the y' axis. This means that the magnetization starts to rotate in the laboratory frame with the Larmor frequency ω_{r} and can be detected as an oscillatory induction current flowing the transmitter coil, now acting as a receiver coil, as illustrated in Fig. 5.86d, with a decay due to relaxation processes. When the nuclei are isolated such that they have a single Larmor frequency,

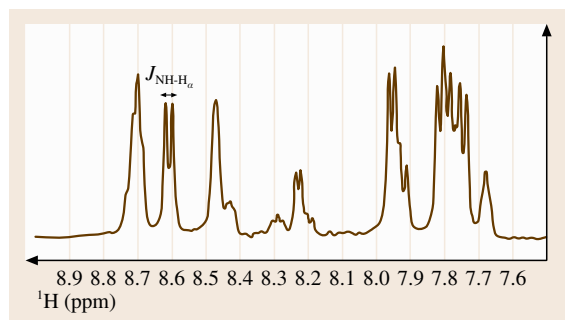


Fig. 5.85 NMR spectrum showing chemical shifts and J -coupling in cyclic-GRGDSPA peptides (Courtesy of Prof. I. Shimada)

the Fourier transform of the free induction decay (FID) curve has a signal at the Larmor frequency, as shown in Fig. 5.87a, which represents the NMR spectrum of the nuclei.

When multiple resonance signals coexist, the duration of the $\pi/2$ pulse Δt should be short enough ($\approx 10 \mu\text{s}$, with B_1 being correspondingly large) for the alternating frequency to spread over a range covering the chemical shifts of the nuclei concerned, so that all the nuclei can be tipped nonselectively with a single pulse. Such pulses are called hard pulses. In contrary, the longer and weak pulses, called soft pulses, tip a specific nucleus selectively. The FID and NMR spectrum in Fig. 5.87b are those obtained by using a hard $\pi/2$ pulse. Conventionally NMR spectra are displayed with the frequency axis increasing to the left.

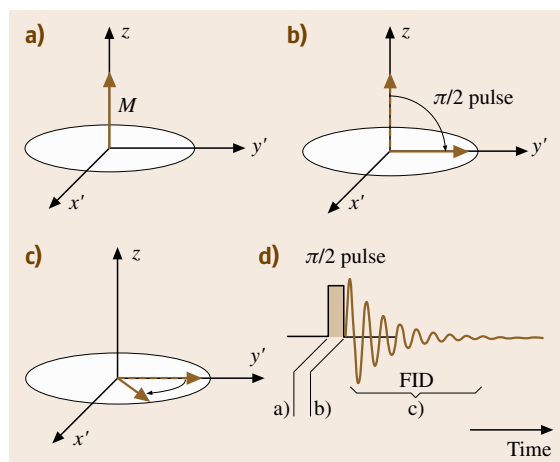


Fig. 5.86 (a–c) The magnetization response in vector model in the rotation frame and (d) free induction decay (FID)

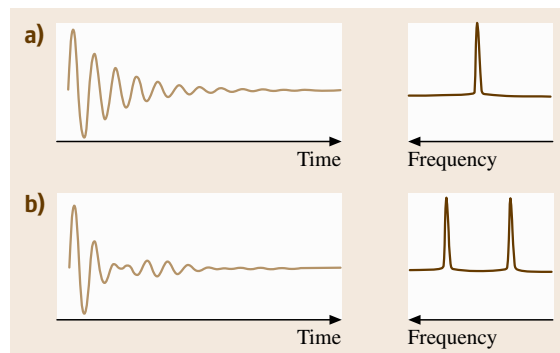


Fig. 5.87a,b Fourier transform NMR spectra (right) obtained from FID curves (left)

More general procedures of 1-D-NMR consist of first to perturb the spin system from equilibrium somehow (preparation), to allow it to evolve after the perturbation for various periods (evolution), and then to detect what has happened in the evolution period by collecting the subsequent FID (detection). If the evolution is spin relaxation, we can measure the spin relaxation time. In practice, however, the FID decays more rapidly than expected from the true spin relaxation time. The main cause is the spatial inhomogeneity of the external magnetic field. In this case, the spin echo technique allows us to avoid the artifact. The idea of spin echoes is embedded in various schemes of pulse NMR experiments. Since there are too many variations of 1-D-NMR having their own acronyms, only two schemes are presented here to touch on some of the ideas.

Spin Decoupling. If we can determine whether or not a pair of neighboring signals are really coupled to each other, this method allows the assignment of the signals. Also if the doublet splitting can be suppressed, it allows the simplification of complex spectra. Consider two spins A and X that are J -coupled with a coupling constant J . If the spin X is irradiated selectively but strongly with a microwave pulse at the resonance frequency, the resonance A loses its doublet splitting (spin decoupled) because the spin X flips so rapidly that the A spin feels only the average of the spin states of X. If we examine the presence or the absence of such spin decoupling effects for pairs of doublets in a complex NMR spectrum, we can identify J -coupled pairs within a distance of 3–4 bonds in the molecular network.

Selective Polarization Inversion (SPI). Another example is given by again considering a J -coupled pair of spins, A and X, but in this case, the pair is supposed to be heteronuclear, e.g., A is ^{13}C and X is ^1H , as illustrated by an energy level diagram in Fig. 5.88a. The level notation $\beta\alpha$, for example, indicates that the A (^{13}C) spin is down (β) while the X (^1H) spin is up (α). Due to the large difference in γ values between A and X, the level population in thermal equilibrium differs considerably. The bottom diagram in Fig. 5.88a shows the schematic NMR spectrum with the vertical bars representing the intensity. Now, consider that the resonance between $\alpha\alpha$ and $\alpha\beta$ is selectively excited by a soft pulse so as to invert the populations, as shown in Fig. 5.88b. Then the NMR signals are drastically changed, as illustrated by the bottom spectrum, because the signal intensity is determined by the population difference. The negative signal means that the FID component is out of phase by π with the positive signal. Such changes would not be observed if A and X are completely

independent, which signifies that the two spins are coupled somehow. Unlike the NOE effect, the change is immediate in the case of J -coupling, so we can distinguish whether they are dipole-coupled or J -coupled. A subsidiary merit of polarization transfer techniques is that weak NMR signals, such as that of ^{13}C , can be enhanced.

Two-Dimensional (2-D) NMR. In small molecules, signal assignment may be possible through 1-D-NMR experiments, but in large molecules such as proteins that yield bewilderingly complex spectra, we need more sophisticated NMR measurement schemes. Two-dimensional NMR (2-D-NMR) is a successful solution to this problem. The idea is to sort out crowded NMR signals in a two-dimensional map according to which pairs of signals are coupled to each other. The methods may be regarded as double resonance techniques that can be extended to multidimensional NMR by using ap-

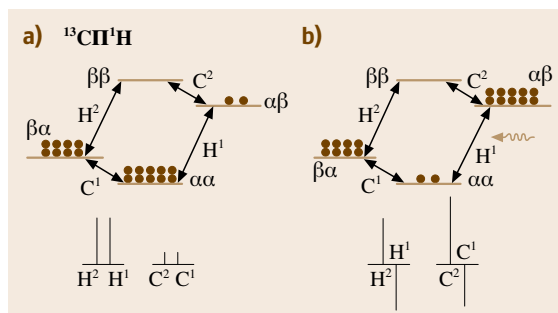


Fig. 5.88a,b Heteronuclear selective polarization inversion (SPI). (a) In thermal equilibrium, (b) when ^1H is selectively excited

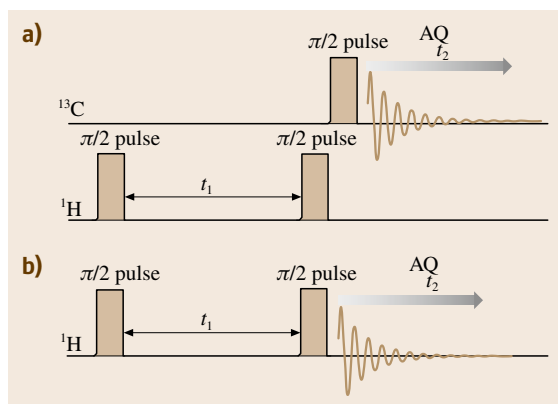


Fig. 5.89a,b Pulse sequences for 2-D-NMR; (a) heteronuclear 2-D-NMR, (b) homonuclear 2-D-NMR (COSY)

appropriate relays of pulse sequences. Two representative schemes that are most commonly used are explained briefly.

An example of pulse sequence diagram for 2-D-NMR experiments is shown in Fig. 5.89a, in which two heteronuclear spins of ^{13}C and ^1H are assumed to be J -coupled. Before FID is detected for ^{13}C spins, two $\pi/2$ pulses separated by a time t_1 are applied to the ^1H spins. Figure 5.90 depicts what happens in the vector model. After the magnetization of ^1H is turned to the y' -axis by the first $\pi/2$ pulse, the ^1H spins start to rotate in the rotating frame at a rate $\Omega_{\text{H}} = \delta_{\text{H}} \pm J_{\text{CH}}/2$, where δ_{H} is the chemical shift of the ^1H spins and J_{CH} is the constant of J -coupling with ^{13}C , provided that the reference frequency is set at the Larmor frequency of the isolated ^1H . The diagrams in the second column indicate this rotation at time t_1 increasing downward. By the second $\pi/2$ pulse, the ^1H spins have turned further around the x' -axis, as shown in the third column. At this moment, the FID of ^{13}C spins, not of ^1H , is acquired by applying a $\pi/2$ pulse on ^{13}C . When $t_1 = 0$, the magnetization of ^1H is inverted, so the ^{13}C signal changes drastically reflecting the inverted population of ^1H , as in the case of SPI experiments in Fig. 5.88 (the x' -component, not turned by the second $\pi/2$ pulse, does not affect the J -coupling). At the arbitrary time t_1 , the magnetization of ^1H after the second $\pi/2$ pulse on ^1H has a z -component of magnitude $M \cos \Omega_{\text{H}} t_1$, as shown in the second line of the third column in Fig. 5.90, so the ^{13}C signal intensity (schematically shown in the right column) is modulated accordingly. Since the ^{13}C signal modulation has a period of $2\pi\Omega_{\text{H}}^{-1}$, if we repeat such measurements systematically changing the time t_1 , the Fourier transform of the ^{13}C signal intensity with respect to t_1 gives the NMR spectrum of the ^1H spins with a chemical shift δ_{H} and the doublet splitting magnitude J_{CH} . This may be regarded as a double resonance or ^{13}C -NMR-detected NMR of ^1H spins. In other words, the ^{13}C resonance signal acts as though it is labeled with the resonances of the ^1H spins that are J -coupled to the ^{13}C . If the $\pi/2$ pulses on ^1H are hard and hence nonselective, we will obtain an NMR spectrum in two dimensions for frequency ν_1 (corresponding to t_1) and for frequency ν_2 (corresponding to t_2), as illustrated in Fig. 5.91. The signals on the diagonal line (diagonal peaks) are always present, but the off-diagonal signals (cross peaks) indicate the presence of J -coupling between the corresponding ^{13}C nuclei and ^1H nuclei. It is obvious that, even if the 1-D spectra are complicated, the connectivity through J -coupling is more easily resolved in such 2-D spectrum.

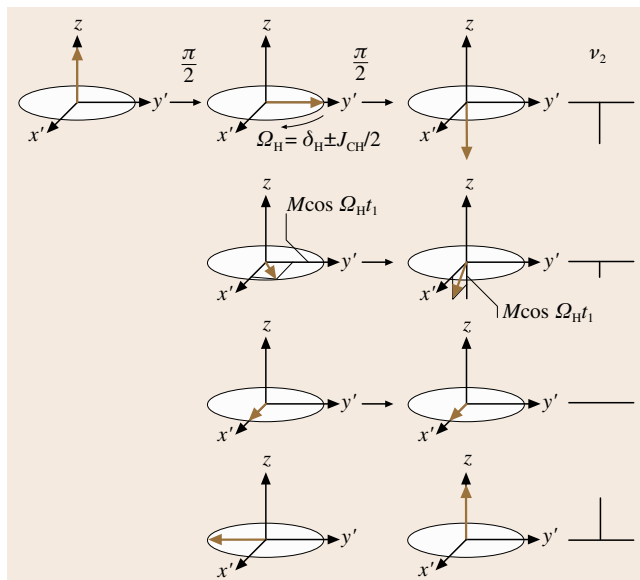


Fig. 5.90 Vector model for heteronuclear 2-D-NMR. For details, see the text

The homonuclear version of the above scheme is called correlated spectroscopy (COSY) and is widely used to find J -couplings between ^1H nuclei. The pulse sequence, shown in Fig. 5.89b, is similar to that in Fig. 5.89a, except that the FID measured is now for ^1H itself. Although the precise interpretation needs a quantum mechanical description, the cause of the cross peaks may be inferred by analogy to the heteronuclear case above. Figure 5.92 shows an example of COSY

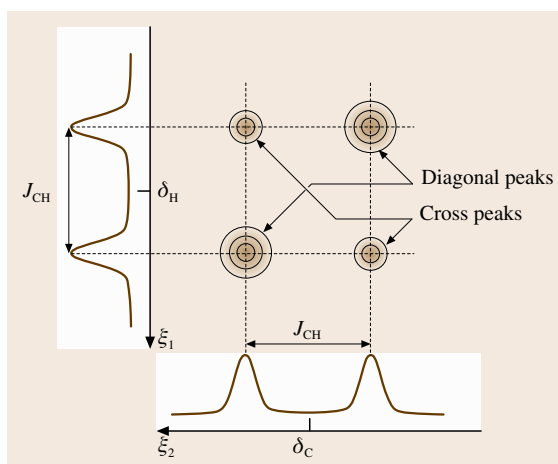


Fig. 5.91 Schematic 2-D-NMR spectrum of ^{13}C and ^1H J -coupled with each other

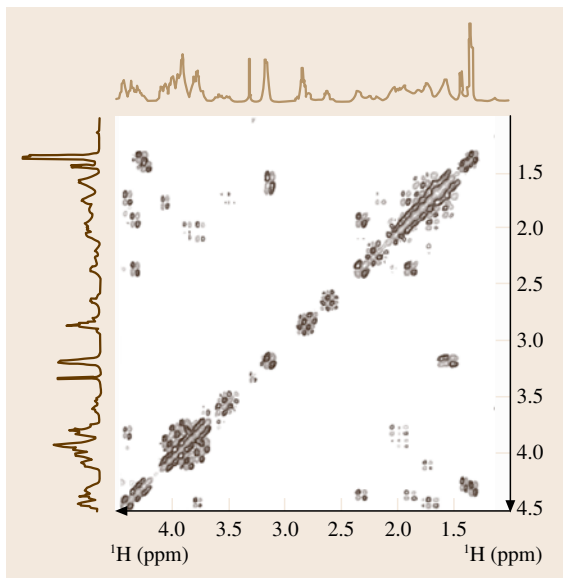


Fig. 5.92 DQF (double quantum-filtered)-COSY spectrum of cyclic-GRGSPA peptides (Courtesy of Prof. I. Shimada)

(a more sophisticated double-quantum-filtered COSY) spectrum obtained for the same peptide molecules whose 1-D spectrum was shown in Fig. 5.85.

In the 2-D-NMR experiments discussed so far, the pulse sequence generally consists of preparation, evolution and detection stages. In Fig. 5.89a, the first $\pi/2$ pulse corresponds to preparation, the duration t_1 until the second $\pi/2$ pulse to evolution, and the acquisition of FID to detection. In more sophisticated schemes

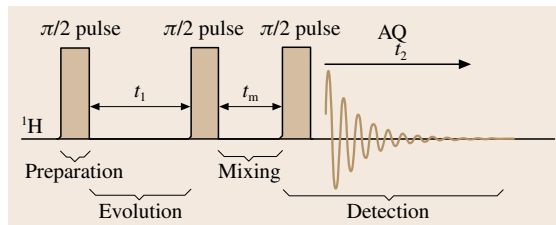


Fig. 5.93 The pulse sequence for NOESY experiments

of 2-D-NMR, we add another stage, mixing, following evolution. Figure 5.93 shows the pulse sequence in NOESY (NOE spectroscopy) extensively used for analysis of macromolecules. The corresponding vector model is shown in Fig. 5.94. The sequence of the first $\pi/2$ pulse (Fig. 5.94a,b), an evolution time t_1 (Fig. 5.94b,c), and the second $\pi/2$ pulse (Fig. 5.94c,d) is the same as in Fig. 5.90 except that we consider two spins, I and S, having different resonance frequencies but coupled through a dipole-dipole interaction. During the mixing stage, which lasts for t_m (Fig. 5.94e,f), the z -components of the magnetization (the x' -components have no effect and are not shown), which arise from the population difference of the spin states, exchange their populations due to the NOE effect. Thus, the intensity of the NMR signals measured in the detection stage (Fig. 5.94f,g) tells us how rapidly the relaxation has occurred. Similarly to the COSY spectrum, the NOESY spectrum is displayed with one axis representing the frequencies of the I spin and another axis the frequencies of the S spin. The cross peaks indicate that the two nuclei giving the signals are closer than $\approx 5 \text{ \AA}$ in space so that they are dipole-dipole coupled.

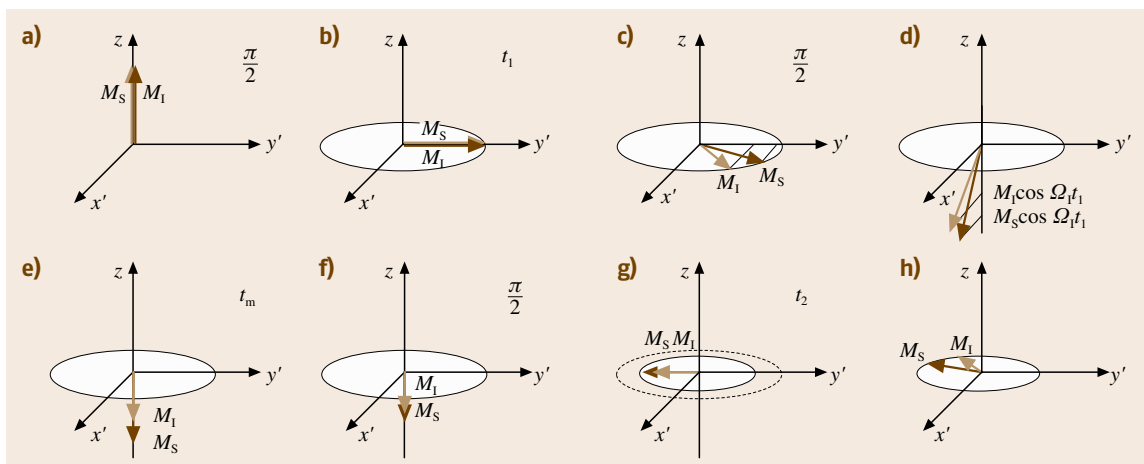


Fig. 5.94a-h Vector model of NOESY

Sample Requirements. Finally, some comments are added on the requirements for samples. Since NMR signals are proportional to the number of spins, for a sufficiently high signal-to-noise ratio to be achieved, the sample amount must usually be greater than several milligrams or 1 mM, which may be difficult. As mentioned before, nuclei with spin $I > 1/2$ are not very suitable for NMR experiments because the spectrum broadens due to the strong quadrupole interaction (Sect. 5.1.2). Even if we confine ourselves to $I = 1/2$ nuclei, however, there are other causes of spectral broadening that prohibit us from conducting high-resolution NMR measurements. In actual experiments, an inhomogeneity in the external magnetic field induces an apparently rapid decay in the FID or a broadening of the NMR spectra. Although the effect of magnetic field inhomogeneity could be removed by the spin echo technique, there still remains a cause of spectral broadening due to the variation of molecular orientations, which gives rise to different degrees of anisotropic shielding and as a result continuously varying chemical shifts. When the molecules are so small that they rotate rapidly in the medium, the variation of chemical shifts is averaged and consequently the NMR spectral signals become sharpened. While small molecules in solution benefit from this motional narrowing effect, large molecules cannot do so if their rotation rate is too small. Thus, NMR analysis generally becomes difficult for large molecules that lack mobility. Although many techniques, such as sorting signals according to intentionally controlled spin relaxation lifetime, have been developed to escape the difficulty, an upper limit exists around 3×10^4 in molecular weight for which structural analysis by NMR is practically possible. This is in great contrast to x-ray diffraction methods in which much larger molecules, such as ribosome (4×10^6 in molecular weight), can in principle be analyzed if single crystals can be grown.

5.4.3 Chemophysical Analysis

Chromatography

Chromatography is a generic term for techniques that separate complex mixtures into their components, which are distributed with a variable probability between a stationary and a mobile phase; the methods are based on the percolation of the mobile phase through the solid phase in what is known as a column. The mobile phase is gaseous in gas chromatography (GC) and is liquid in liquid chromatography (LC). There are various schemes for chromatography further depending on

the type of stationary phase (solid or liquid) and hence on the principle of molecular separation (ion exchange, affinity difference, gel-filtration, hydrophobic interaction etc.).

As illustrated in Fig. 5.95, chromatographic measurements are conducted by constantly injecting into a column a sample mixture carried by a mobile phase and recording a chromatogram, a chart that plots the amount of an analyte reaching a detector placed at the outlet of the column versus the time t starting from the sample injection. The retention time, t_r , is the time between sample injection and a peak in the chromatogram, while t_m is the time taken for the mobile phase just to pass through the column. The molecular species can be identified from their retention time and their total amount is measured from the integrated area of the corresponding peak. Among the various types of detectors, the most common are thermal conductive detectors, which are sensitive to any species. Using a mass spectrometer as the detector, one can obtain more structural information of the separated molecular species. GC is suitable for routine analysis and has high resolution, short measurement time, low cost, and requires a small amount of sample (1–10 μl in a liquid sample and 0.2–10 ml in a gaseous sample) as long as the boiling temperature of the sample is below 300 °C; LC is applicable to multicomponent, less volatile or pyrolytic (thermally decomposable) samples that are not covered by GC. The limitation of ordinary chromatography is that peaks in chromatograms have no significant structure, unlike those observed in photospectroscopy methods that provide detailed information on the possible variety of each component. Nevertheless, there is room for further improvements in detection techniques

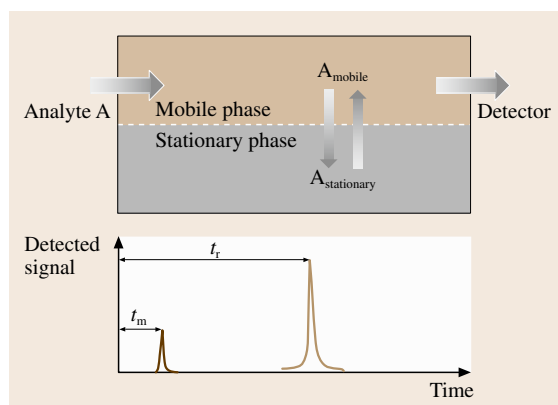


Fig. 5.95 General experimental configuration of chromatography

that allow chromatography to become useful as a pre-process for more sophisticated analysis.

Electrophoresis utilizes the difference in the drift mobility of ionic molecules in a stationary phase under an electric field. Electrophoresis using gel as the stationary phase is called gel electrophoresis (GE), and that using aqueous solution in a capillary is called capillary electrophoresis (CE). CE has advantages over GE because of reduced problems with Joule heating and the action of the capillary itself as the pumping system.

Circular Dichroism (CD)

Circular dichroism (CD) arises from the helicity or chirality of molecules that exhibit optical absorption due to electronic excitations at ultraviolet to visible wavelengths. CD spectra of chiral proteins, peptides and nucleic acids have distinct structures and are sensitive to conformational changes. Figure 5.96 shows a schematic diagram of experimental setup. Linearly polarized light can be regarded as a superposition of left- and right-hand circularly polarized light. Optically active substances such as chiral molecules transmit the opposite circularly polarized light with slightly different absorption coefficients. As a consequence, the linearly polarized light incident on the sample becomes elliptically polarized light without changing the main polarization axis. The degree of ellipticity (CD) depends on the difference in the absorption coefficients.

In contrast, optical rotation arises from differences in the index of refraction that cause a difference of the rotation angle between the opposite components of circularly polarized light. The optical rotary dispersion (ORD) spectrum, the dependence of rotation angle on wavelength, is related to the CD spectrum by a Kramers–Kronig transformation. The ORD curve changes sign at the extremum peak of the CD spectrum, known as the Cotton effect, as illustrated in Fig. 5.97.

Owing to the fact that CD/ORD curves exhibit features that are characteristic to the molecular structures, CD/ORD measurements provide structural information about the molecule. In proteins, for example, CD sig-

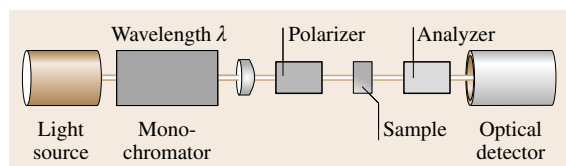


Fig. 5.96 Experimental setup of circular dichroism (CD) and optical rotary dispersion (ORD) measurements

nals are more sensitive to α -helical residues than those of random coils and β -sheets. Experimental data are fitted to reference model spectra to determine the amounts (composition) of the constituent secondary structure of proteins. The reliability of composition analysis is enhanced by the use of proteins of known structure as the basis set. More sophisticated analysis of molecular positions, conformation and absolute configuration can be conducted with detailed knowledge of the influence of these factors on the Cotton effect.

Samples are usually prepared as a solute in an optically nonactive solution. CD/ORD measurements allow quantitative analysis since the signal intensity is proportional to the molecular density in the solution. Structural analysis, however, is only possible at densities that yield an optical absorbance of 1–2 at the absorption maximum, where the Cotton effect is observed, in order to avoid signal weakening due to excessive absorption.

Although simple CD and ORD are observed only in optically active molecules, similar dichroic effects are also induced in achiral substances under a magnetic field applied parallel to the measuring light beam. Magnetic circular dichroism (MCD) combined with photoabsorption measurements is most commonly used to analyze chromophoric groups in which the magnetic field lifts the degeneracy of optically excited energy levels differing only in magnetic spin (Sect. 5.3.1). In biology, MCD is also applicable to metalloproteins, pro-

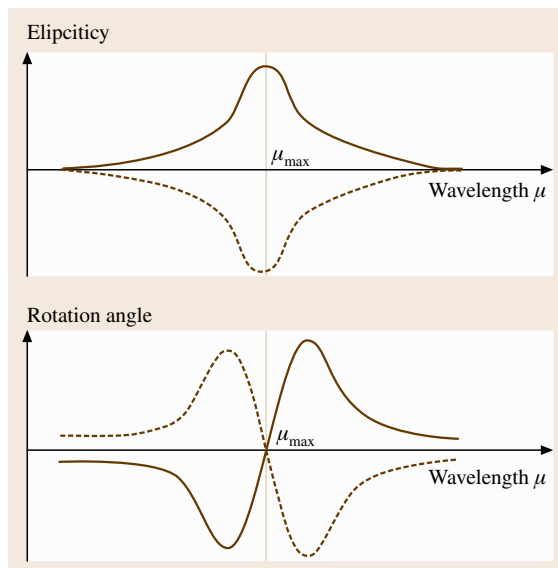


Fig. 5.97 Schematic spectra of circular dichroism (CD) and optical rotary dispersion (ORD)

tein molecules that contain a metal substance necessary for a certain reaction to take place.

Fluorescence Resonant Energy Transfer (FRET)

Fluorescence resonant energy transfer (FRET) occurs when the distance between a fluorescent donor dye molecule and a photoabsorbing acceptor dye molecule is close enough for the electronic excited energy of the donor molecule to be transferred to the acceptor molecule nonradiatively. Since the efficiency of FRET depends on the inverse sixth power of the intermolecular distance, it is useful for determining the proximity of the two molecules within 1–10 nm, which is a distance range of particular importance in biological macromolecules. For FRET to take place, the fluorescence spectrum of the donor and the absorption spectrum of the acceptor must overlap, as shown in Fig. 5.98. Based on this technique, the approach of two molecules can be detected by quenching the donor fluorescence, and

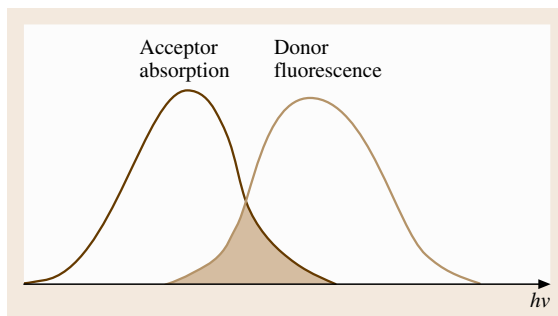


Fig. 5.98 Spectral overlap necessary for fluorescence resonant energy transfer (FRET)

one can study the conformation change of a single molecule by detecting FRET under a laser scanning confocal microscope (LSCM) (Sect. 5.1.2) or a total internal reflection fluorescence microscope (TIRFM) (Sect. 5.1.2) [5.78].

5.5 Texture, Phase Distributions, and Finite Structures Analysis

This section deals with materials that are inhomogeneous on a relatively large scale with respect to their composition, structure, and physical properties. Polycrystals are said to have a texture when they have a nonrandom distribution of grain orientations. The phase distribution or element distributions may play an important role in the macroscopic properties of the material. Another issue addressed is solid structures with finite three-dimensional size that may have their own functions, such as biological cells, nanoparticles, etc. In the last subsection, we describe some of the recent progress in stereology, an emerging field of three-dimensional analysis of materials.

5.5.1 Texture Analysis

Textures evolve by various mechanisms. Plastic deformation of crystals by glide motion of dislocations proceeds on preferential crystallographic slip planes, usually low-index planes with the largest spacing. If polycrystalline wires are drawn through a die, the wires have a texture (wire texture) such that the slip planes tend to align parallel to the wire axis, because otherwise each grain would be subject to further deformation. The texture of polycrystalline materials is of technological importance for various physical properties, mechanical properties such as strength and elastic constants, mag-

netic permeability, flux pinning in superconductors of the second kind, and so on.

Texture Analysis by X-Ray Diffraction

The best established technique for assessing textures is x-ray diffraction. In powder diffraction, each diffraction ring consists of fine spots which correspond to crystallites in different orientations. If the crystallites are randomly oriented, the spots or the diffraction intensity is uniformly distributed around the circle. If textures are present, however, one observes an inhomogeneous distribution of diffraction spots or diffraction arcs, as shown in Fig. 5.99. In modern experiments, the data are collected by using a diffractometer equipped with a four-circle goniometer (Fig. 5.37) that scans all orientations by a combinatorial rotation around the Eulerian ω - ϕ - χ axes. For thick or large-grained samples, neutron diffraction may offer an alternative to x-ray diffraction, if a facility is accessible. The merit of diffraction techniques is the ease with which good statistical data can be acquired.

The texture of materials is expressed by several different representations. The pole figure (Fig. 5.100) presents the orientational distribution of a specific pole (crystallographic (0001) axis in Fig. 5.100a) with respect to the sample orientation, which is displayed on a stereographic projection with the surface normal at

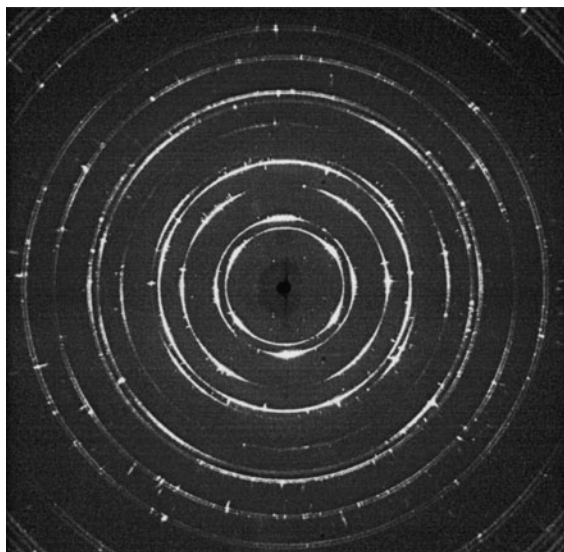


Fig. 5.99 X-ray diffraction pattern from a mechanically drawn Al wire. Exposure time 30 s using x-ray source $\text{Mo } K_{\alpha}$ (50 kV, 40 mA) recorded on an imaging plate placed 10 cm from the sample (Courtesy of Rigaku Co)

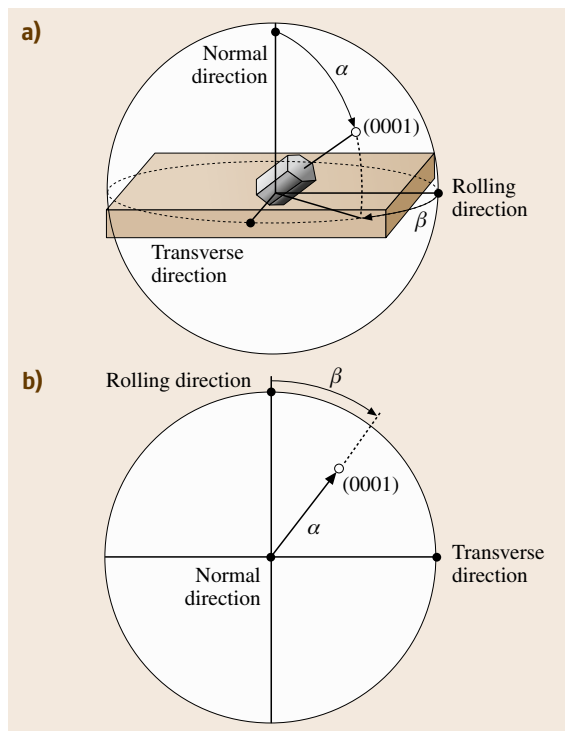


Fig. 5.100a,b A presentation of the texture (a) by the stereographic pole figure in (b)

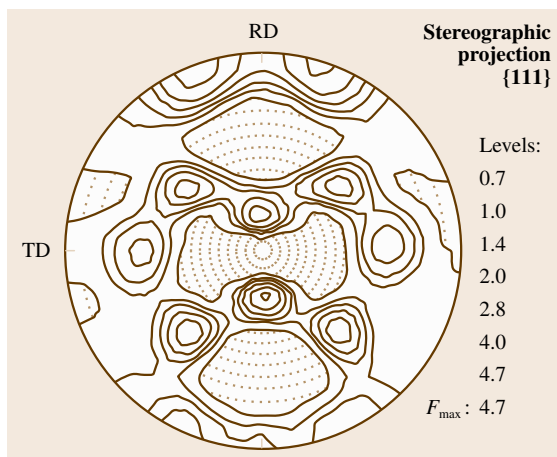


Fig. 5.101 An experimental pole figure of an aluminum sheet rolled and annealed. After [5.79]

the origin, a specific direction along the sample surface (e.g., the rolling direction in rolled metals) at the north pole, and the transverse direction in the horizontal direction. Figure 5.101 shows an experimental pole figure of an aluminium sheet thermally annealed after mechanical rolling [5.79, p. 102]. The four crystallographically equivalent (111) poles are distributed in some dominant directions. Also widely used is the inverse pole figure that presents the orientation distribution of the specimen coordinate system with respect to the crystal coordinate system, the latter being reduced to a standard stereographic triangle. Whichever the case, however, the projection of the three-dimensional orientation distribution onto a two-dimensional figure causes a loss of information. The orientation distribution function (ODF) is a three-dimensional presentation thus devised for a full description of texture. The ODF can only be obtained by calculations from a data set of several pole figures. For details, see the textbook by *Randle and Engler* [5.79].

Texture Analysis by SEM Electron Channeling Pattern (ECP)

The disadvantage of diffraction techniques for the analysis of texture is the lack of direct information about the grain size. Local crystal orientations may be determined by microscopic techniques that also reveal the dimension of each grain directly [5.80]. TEM is a routine method to conduct such measurements, but the samples are limited to thin films. The electron channeling pattern (ECP), which can be obtained by scanning electron microscopy (SEM), is a more convenient approach for studies of texture using bulk samples.

SEM-ECP corresponds to the Kikuchi lines (Sect. 5.1.2) or bands observed in **TEM**. Figure 5.102a illustrates how the Kikuchi lines are formed. As mentioned in Sect. 5.1.2, the Bloch wave with its largest amplitude on the atomic column (Fig. 5.102b) interacts more strongly with the atoms and is more likely to be scattered inelastically, losing coherency with the direct wave. As shown in Fig. 5.102a, some of the electrons thus inelastically scattered in various directions will be reflected by lattice planes satisfying the Bragg condition and, if the specimen is moderately thick, propagate along the *channel* direction with an anomalously small absorption coefficient. The electrons are projected onto the back focal plane of the objective lens as a pair of traces of the diffraction cones. Line pairs (Kikuchi lines) or bands formed in this way indicate the orientation of the crystal. In a similar way to the Kikuchi lines in **TEM**, if the electron beam in **SEM** is incident to a crystalline sample in an orientation along a channeling direction (Fig. 5.102b), the electrons penetrate deeply into the sample and have less chance to be back scattered and detected by a back-scattering electron detector. If one rocks the beam direction as in Fig. 5.102b and synchronously displays a two-dimensional map of the intensity of back-scattered electrons in the **SEM** screen as a function of the beam orientation, one obtains patterns as shown in Fig. 5.103a,b. Since the **SEM-ECP** pattern reflects the crystalline orientation of the sample position at which the beam is rocked, beam scanning with the beam direction fixed gives

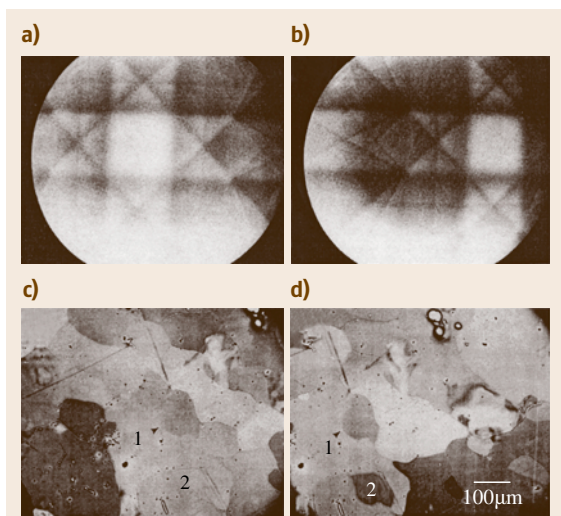


Fig. 5.103a–d Electron channeling patterns (a),(b) and images (c),(d) at different tilt angles. After [5.17]

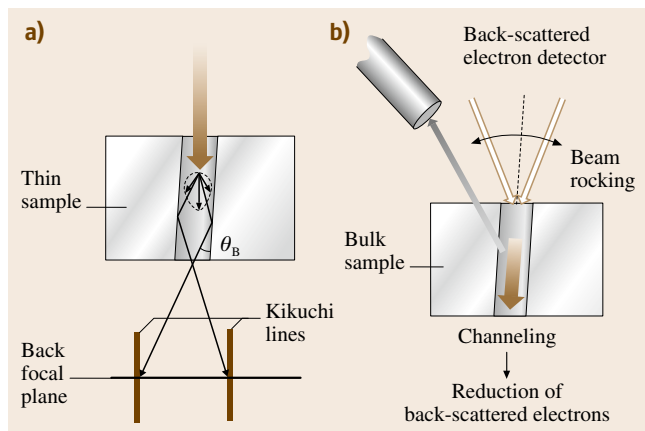


Fig. 5.102a,b Formation of Kikuchi lines in **TEM** (a) and electron channeling pattern in **SEM** (b)

ECP images, as shown in Fig. 5.103c,d. From such crystallographic orientation contrasts, one can determine the orientation distribution and the size of each grain.

5.5.2 Microanalysis of Elements and Phases

Dark-Field TEM Imaging

Dark-field (**DF**) **TEM** images (Sect. 5.1.2) formed by a diffracted beam of a specific diffraction vector provide the most standard technique for microscopic analysis of coexisting multiphases. Figure 5.104 shows a bright-field image of a metallic compound of Nb_3Te_4 and the corresponding **DF** images obtained for two different diffraction vectors. The lateral resolution is similar to that of **BF-TEM** images as long as the sample is thin enough for the overlap of different phases to be avoided.

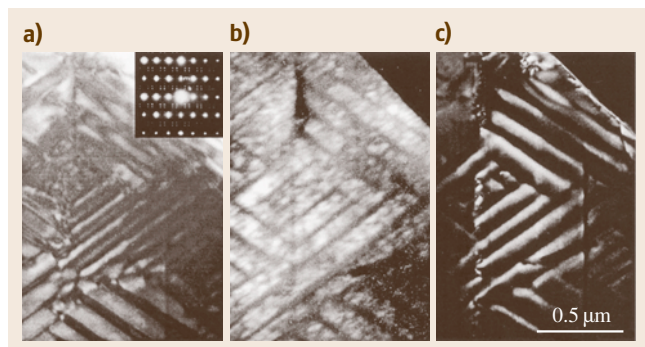


Fig. 5.104 (a) Bright-field and (b),(c) dark-field images of multiphase Nb_3Te_4 (courtesy of M. Ichihara)

Electron Probe Microanalysis (EPMA)

Another common method to investigate element distribution in solid materials is scanning electron microscopy operated in the x-ray fluorescence mode, usually referred to as an electron probe microanalyzer (EPMA). On the impingement of electrons in the energy range of 1–40 keV, the samples emit x-rays at wavelengths characteristic of the elements contained. The emitted x-ray is usually detected with an energy dispersive x-ray (EDX) solid-state detector placed above the specimen (Fig. 5.105). Scanning the beam gives us a map of the element distribution with a spatial resolution of a few nm to 100 μm . The technique becomes more sensitive as the mass number increases.

Similar measurements could be conducted using TEM. In ordinary SAD, however, it is difficult to reduce the size of a selected area to smaller than several tens of nm, whereas in CBED the beam size can be reduced down to a subnanometer scale. The best choice is to use a focused beam in STEM that allows one to conduct CBED analysis as well as mapping element distribution over the scanned area. For heavy elements, STEM-EDX has advantages over the following techniques, though there are technical problems with the energy resolution ($\approx 150\text{ eV}$) and the time for data acquisition.

Electron impingements induce the emission of Auger electrons whose energies are characteristic of specific elements (Fig. 5.67). Since the energy of Auger electrons is so small that the escape distance is as short as $\approx 1\text{ nm}$ (Fig. 5.59), Auger electron spectroscopy (AES) is overly sensitive to the surface.

Energy Loss Analysis

Energy filtering TEM (EFTEM) is a TEM or STEM equipped with an energy filter passing only electrons of a specific energy that are used to construct an image of the spatial distribution of the corresponding elements. The energy filter may be placed inside the optical column of the TEM (in-column type) or in front of the camera chamber (post-column type). EFTEM al-

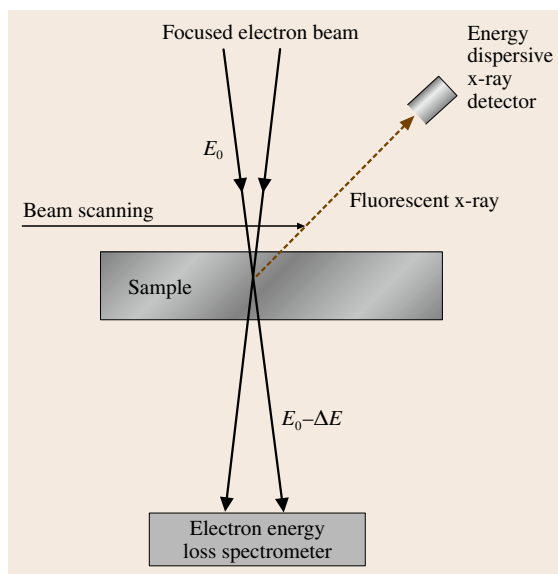


Fig. 5.105 Element analysis by an electron probe

lows spectrum imaging of the element distribution with an energy resolution of $\approx 30\text{ eV}$ and a spatial resolution of down to $\approx 1\text{ nm}$ at 200 kV and $\approx 0.5\text{ nm}$ at 300 kV.

In contrast to EFTEM, the spatial resolution in STEM-EELS, if equipped with a field emission gun, is much higher owing to the fact that STEM generally does not need an objective lens to image the aberration that governs the spatial resolution of TEM micrographs. A disadvantage of STEM-EELS is the long acquisition time due to the scanning nature of the microscopy, but the use of a parallel EELS (PEELS) detector and the great assistance of a computer have advanced the progress of STEM-EELS as a tool able to identify even a single atom in small molecules [5.81], as demonstrated in Fig. 5.106. STEM-EELS has advantages over STEM-EDX for light elements.

Micro-Raman Scattering

Raman scattering measurements (Sects. 5.1.2, 5.2.3, and 5.3.1) can be coupled with optical microscopes to investigate the local distribution of particular phases with a spatial resolution of $\approx 1\text{ }\mu\text{m}$. The diffraction limit of OM is now overcome by the use of scanning near-field optical microscopy (SNOM) (Sect. 5.1.2), in which the enhancement of the optical field by surface plasmon resonance at the metallic tip allows the detection of Raman spectra for even a single molecule [5.82] under good conditions.



Fig. 5.106 STEM-EELS image of Gd (white) atoms in a carbon (gray) nanotube. Scale bar = 3 nm. After [5.81]

Scanning Nano-Indenter

Materials often encountered may be in the form of thin films or nanoscale complexes of multiple phases. One may need to conduct mechanical tests for very thin films grown on a substrate. The difference in material phase may reflect the mechanical strength. The scanning nano-indenter is a modern version of the micro-hardness tester with which the local mechanical strength of crystallites smaller or thinner than $\approx 1 \mu\text{m}$ can be measured with a lateral resolution of several hundreds nanometres from the indent size in situ observed by a microscope similar to an AFM and STM. The extremely tiny indenter can be driven into and retracted from the sample surface at a controlled rate, so that one can also deduce the local elastic modulus.

5.5.3 Diffraction Analysis of Fine Structures

Tiny objects such as precipitates, crystallites, and fine particles smaller than $\approx 100 \text{ nm}$ can be investigated by not only microscopic but also diffraction and spectroscopic techniques.

Small-Angle Scattering Analysis of Tiny Phases

The Guinier–Preston (GP) zone, an extremely tiny precipitate with a thickness of only one atomic layer and lateral size of several atomic distances, is directly observable by HRTEM at present; it was originally discovered in x-ray diffraction as a source of diffuse scattering. In Guinier's approximation, in which a particle is a Gaussian sphere

$$\rho(\mathbf{r}) = \rho_0 \exp\left(-\frac{r^2}{a^2}\right) \quad (5.37)$$

with a representing the particle size, the diffraction intensity or the Fourier transform of (5.37) will be

$$I(\mathbf{K}) = \rho_0^2 a^2 \pi \exp\left(-\frac{a^2}{2} K^2\right). \quad (5.38)$$

The magnitude of (5.38) is small except for small $|\mathbf{K}|$ values or small scattering angles, which means that the primary beam is diffusely scattered within a small angle. In terms of the radius of gyration R_g , the root mean square of the mass-weighted distances of all subvolumes in a particle from the center of mass,

$$I(\mathbf{K}) \propto \exp\left(-R_g^2 K^2/3\right). \quad (5.39)$$

Thus, from the slope of the so-called Guinier plot, $\log I(\mathbf{K})$ versus K^2 , we can evaluate a measure of the particle radii R_g experimentally.

Line-Broadening Analysis of Crystallite Size and Stress

The broadening of x-ray beams occurs not only in the primary beam but also in diffracted beams when the crystallites or domains are small [5.83]. This arises from the fact that the diffraction intensity depends on the interference function, which reflects the external shape of the crystal (Sect. 5.1.1).

More generally, the line broadening is induced by causes other than the finite crystal size. The main causes are instrumental errors and the strain distribution. The instrumental broadening due to spatial, angular and wavelength distribution of the incident x-ray beam is experimentally evaluated by using a standard sample, usually a large and perfect single crystal such as Si. The line broadening due to lattice strain is in most cases due to lattice defects such as dislocations.

As a measure of the line broadening, we conveniently employ the integral breadth β , which is defined as the width of a rectangle having the same area A and height I_0 as the line profile of interest, or $\beta \equiv A/I_0$. For Gaussian broadening, the relevant breadth β_s of sample origin in our concern is estimated by

$$\beta_s^2 = \beta_m^2 - \beta_i^2, \quad (5.40)$$

where β_m and β_i are the experimental and instrumental breadths, respectively. The separation of the lattice strain component is achieved by plotting β_s versus $\sin \theta$ for various diffractions. From the Bragg condition (5.1), the line broadening in terms of the diffraction angle 2θ due to a distribution of net-plane spacing Δd is given by

$$\Delta\theta = \tan \theta \frac{\Delta d}{d}. \quad (5.41)$$

When there is another contribution from the finite crystal, the experimentally measured integral breadth β_s is generally given by

$$\beta_s(\mathbf{g}) = a\varepsilon \tan \theta_g + \beta_p \quad (5.42)$$

where $\varepsilon \equiv \Delta d/d$ represents the strain and β_p the size contribution in our concern. Since the integral breadth β_p is related to the average size of crystallites L by Scherrer's formula [5.84, p. 102]

$$\beta_p(\mathbf{g}) = \frac{\lambda}{L \cos \theta_g}, \quad (5.43)$$

(5.43) is written as

$$\beta_s(\mathbf{g}) \cos \theta_g = a\varepsilon \sin \theta_g + \frac{\lambda}{L}. \quad (5.44)$$

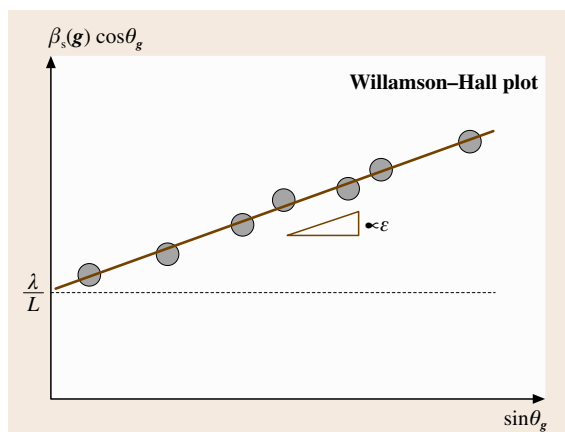


Fig. 5.107 A schematic Williamson–Hall plot for line broadening analysis

Thus, by plotting $\beta_s(\mathbf{g}) \cos \theta_g$ versus $\sin \theta_g$ (the so-called Williamson–Hall plot), as shown in Fig. 5.107, we can evaluate the average size L of the crystallites from the θ_g -independent level.

Thus, the analysis of line broadening simultaneously enables evaluation of lattice strain ϵ or the internal stress in the crystallites. With access to costly facilities such as synchrotron radiation sources (for x-ray diffraction) or nuclear reactors (for neutron diffraction), one is able to conduct experiments with great advantages for probing the stress state deep into the sample [5.85].

Light Scattering Analysis of Particle Shape

The cloudy or milky appearance of latex and solid polymer reflects a heterogeneous structure with two coexisting phases [5.29] (colloid particles and liquid in latex; crystalline and amorphous domains in solid polymer) (Fig. 5.42). This is due to the high-angle scattering of light over a wide range of wavelength, called Mie scattering in contrast to the wavelength-dependent Rayleigh scattering. When the particle size is smaller than the light wavelength, we enter to a regime of surface plasmon resonance. The resonance frequency

depends on the dielectric function of the particle material and the shape of the particle. As the particle is elongated in one direction, the resonance is shifted to longer wavelengths, so measuring the resonant wavelength of the scattering, we can determine how the particles are distorted from a sphere.

5.5.4 Quantitative Stereology

The great increase of computer power and resources has made it possible to process the enormous amount of data necessary for three-dimensional reconstruction of a sample structure. There are various types of stereological techniques, as listed in Table 5.5, differing in the reconstruction method.

Stereogram

Two micrographs are acquired for a sample that is tilted by $\pm 1-10^\circ$ in an eucentric way about a tilting axis at the center of the sample. If one views two such images placed side by side with an appropriate separation distance, three-dimensional stereovision of the object is obtained, as demonstrated in Fig. 5.108.

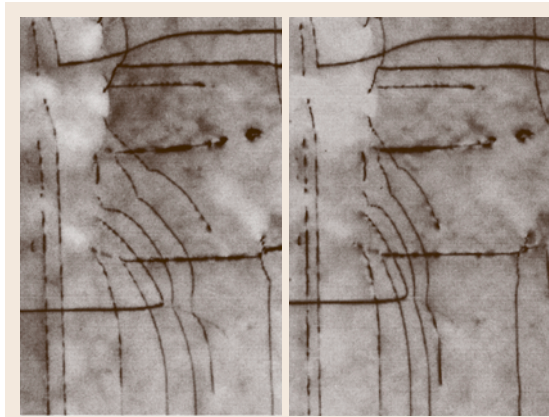


Fig. 5.108 A set of TEM stereograms showing dislocations in $\text{Si}_{0.87}\text{Ge}_{0.13}/\text{Si}(100)$

Table 5.5 Comparison of various stereology methods

Method	3-D reconstruction	Resolution	Test environment
3-D-SEM	Stereogram	< 10 nm	Vacuum
LSCM+ nonlinear optical microscopy	Stacked tomographs	lateral $\approx 1 \mu\text{m}$ depth $\approx 1 \mu\text{m}$	Ambient, liquid, vacuum
3-DAP-FIM	Stacked tomographs	< 0.2 nm	UHV
X-CT	Computed tomography	$\approx 1 \mu\text{m}$	Ambient, vacuum
X-PCI	Computed tomography	a few μm	Ambient
3-D-TEM	Computed tomography	< 10 nm	Vacuum

The three-dimensional vision could also be provided by an anaglyph image, an overlaid image of the two micrographs that are superimposed with different colors, when viewed with red–blue glasses. Quantitatively, the surface profile is calculated from the disparity in the stereo image pairs. The reconstruction of three-dimensional structure is possible from such stereograms acquired in TEM and SEM.

Stacked Tomographs

Laser Scanning Confocal Microscopy (LSCM). The high depth resolution of $\approx 1 \mu\text{m}$ in laser scanning confocal microscopy (LSCM) enables reconstruction of 3-D images from successively acquired optical images of optically sliced layers by changing the focal position. The great advantage of LSCM is that there are no special requirements for the test environment except that the sample medium must be optically transparent.

Ordinary LSCM is based on one-photon processes such as scattering or fluorescence of light. In thick samples, however, remaining light scattering deteriorates the spatial resolution. Nonlinear fluorescent microscopy uses an intense laser light whose photon energy is too small for a one-photon excitation of a fluorochrome but is large enough for a two-photon excitation. Due to the quadratic dependence of the fluorescence intensity on the intensity of excitation laser, the focal point is effectively reduced so that the spatial resolution is enhanced whereas the background fluorescence is removed. Two-photon microscopy has the merit of avoiding photobleaching or optical damage that would be caused when excitation lights of higher photon energy in the ultraviolet range is used for one-photon excitation. Similar benefits are obtained in second-harmonic generation microscopy in which the dielectric response of the sample is nonlinear.

Three-Dimensional Atom Probe (3-DAP) Microanalysis. As described in (Sect. 5.1.2), the field ion microscope (FIM) [5.86] is an atom-resolving microscope in which an imaging gas projects the positions of step-edge atoms on a phosphor screen without destroying the surface. If the applied voltage is high enough, the step-edge atoms themselves evaporate due to the field. The field-evaporating atoms (positively charged ions) are conveyed by the bias field to the screen to form a direct image of the atomic distribution on the tip, now destructively. As illustrated by Fig. 5.109, this field evaporation can be induced by a pulse bias voltage applied to the sample that is triggered as the starting signal for time of flight (TOF) measurements of the evaporated ions.

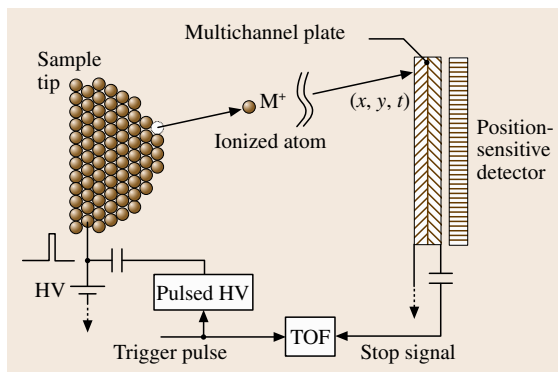


Fig. 5.109 Experimental setup of 3-D atom-probe FIM

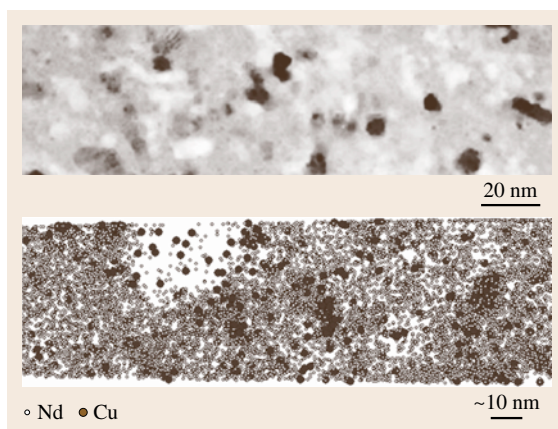


Fig. 5.110 Elemental mapping of Cu and Nd in $\text{Nd}_{4.5}\text{Fe}_{75.8}\text{B}_{18.5}\text{Cu}_{0.2}\text{Nb}_1$ alloy imaged by 3-D atom-probe FIM (Courtesy of Dr. K. Hono)

The use of a multichannel plate in front of the phosphor screen and a gated acquisition of the ion signal allows one to detect specific element atoms sorted by the TOF. Since the field evaporation takes place exclusively at step edges, the evaporation processes are repeated as if the atomic layers are being peeled back one by one. The layer-by-layer acquisition of such atom probe signals are used to reconstruct a three-dimensional map of elements in the sample tip. Figure 5.110 shows an example of three-dimensional atom probe (3-DAP) images obtained for a multicomponent alloy. The lateral and depth resolution of 3-DAP microanalysis is $\approx 0.2 \text{ nm}$, the best among the stereological methods developed so far.

Computed Tomography (CT)

Computed tomography is based on mathematical transformations that enable reconstruction of the two-

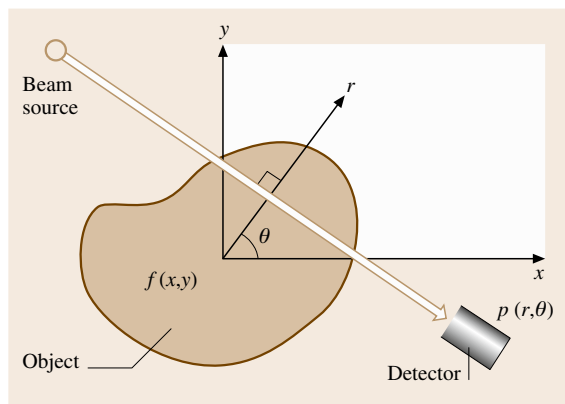


Fig. 5.111 Geometry in computed tomography

dimensional distribution function $f(x, y)$ (e.g., of the absorption coefficient) of an object from a set of one-dimensional intensity profiles $p(r, \theta)$ detected by the detector of a transmitted beam that is emitted from a source in various directions θ , as illustrated in Fig. 5.111. The computed tomographs obtained for successive cross sections of the object are further stacked to form a three-dimensional reconstruction of the whole body.

X-Ray Computed Tomography (XCT). X-ray computed tomography (XCT) using an x-ray for the source beam is common equipment for clinical diagnosis, but can also be used for materials analysis. In XCT, the beam is fanned to scan an angle θ rather than scan position r . The resolution of recent x-ray CT is $\approx 1 \mu\text{m}$, comparable with that of OM.

Magnetic Resonance Imaging (MRI). Magnetic resonance imaging (MRI) or NMR-CT is also now common for clinical diagnosis. MRI is based on the principle that when the applied magnetic field in NMR has an intentional gradient (i.e., varies with position), the resonance frequency of an NMR signal becomes dependent on the position of the nucleus. The positional r -dependent NMR signal frequency constitutes the profile function $p(r, \theta)$ in which the angle θ is given by the direction of the magnetic field gradient.

Three-Dimensional TEM (3-D-TEM). Although x-ray crystallography can provide structural information at atomic resolution, its application depends on whether we can obtain crystalline arrays of the molecules with good quality and analyze the diffraction data in light of relevant phase information [5.87]. Further-

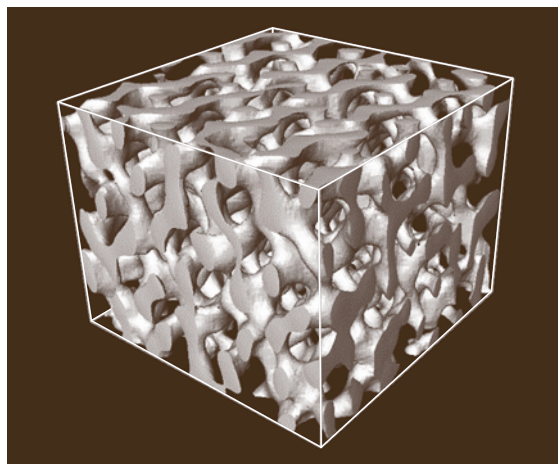


Fig. 5.112 A 3-D-TEM image of a selfassembled triblock copolymer, poly(styrene-block-isoprene-block-styrene). The box size is $270 \text{ nm} \times 270 \text{ nm} \times 210 \text{ nm}$. 120 digital images were acquired at tilt angles ranging from -60° to 60° with 1° steps on a computer-controlled JEOL JEM-2200FS operated at 200 kV (Courtesy of Dr. H. Jinnai)

more, a serious problem especially in biomolecules is that crystallization may alter the conformation of the molecules that could differ significantly from that in which the molecules function in the natural environment. In single-particle electron microscopy, the 3-D structure of a single macromolecule ($\text{MW} > 250\,000 \text{ Da}$) is reconstructed at a resolution of 1–2.5 nm from a set of TEM images obtained in many different sample orientations. In practice, sample damage due to electron irradiation is reduced by the use of cryo-microscopes and simultaneous observations of many sample molecules (usually embedded in ice for biomolecules) to overcome signal-to-noise problems. Figure 5.112 shows a graphical rendering of 3-D-TEM image obtained for a selfassembled polymer material. 3-D-TEM is applicable to amorphous solids, but not suitable for crystalline samples in which the TEM images are too sensitive to diffraction conditions for a simple three-dimensional reconstruction to be carried out.

X-Ray Phase Contrast Imaging (PCI)

The contrast of conventional x-ray transmission images, except for x-ray topography, is based on the positional difference of the absorption coefficient [5.88]. For materials consisting of light elements such as biological tissues and polymers, conventional x-ray transmission microscopy, unless staining with heavy elements is

possible, is not efficient enough. Phase contrast imaging (PCI), as in optical microscopy (Sect. 5.1.2), is an approach to overcome this problem also in x-ray regions, though there is a difficulty due to the small size of the phase shift in light elements. However, in the soft x-ray region, the phase shift can be 10^3 times larger than in the hard x-ray region, so x-ray PCI has been introduced. Among the four schemes so far attempted, interferometric imaging, holography-like imaging, diffraction enhancement imaging, and Zernike-type microscopy, the interferometric method is most sensitive for acquiring phase contrasts. The method uses a Mach-Zehnder x-ray interferometer cut out of a large Si single crystal ingot which is mounted on a multi-axis goniometer set in the beam line of a synchrotron radiation source. X-ray phase shift computed tomography [5.89] exploiting the ability of phase retrieval allows one to reconstruct 3-D images such as those shown in Fig. 5.113.

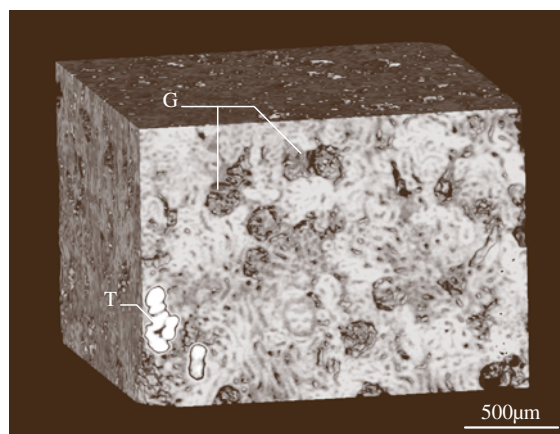


Fig. 5.113 X-ray phase image of a tissue of a rat kidney. Tubules in the tissue, a part of which was clogged by protein (T), were depicted. Glomeruli (G) were also revealed (Courtesy of Drs. A. Momose, J. Wu, and T. Takeda)

References

- 5.1 A. Briggs, W. Arnold: *Advances in Acoustic Microscopy* (Plenum, New York 1995)
- 5.2 K. Sakai, T. Ogawa: Fourier-transformed light scattering tomography for determination of scatterer shapes, *Meas. Sci. Technol.* **8**, 1090 (1997)
- 5.3 S.V. Gupta: *Practical Density Measurement and Hydrometry* (IOP, Bristol 2002)
- 5.4 Z. Alfassi: *Activation Analysis*, Vol. I&II (CRC, Boca Raton 1990)
- 5.5 A. Tonomura: *Electron Holography* (Springer, Berlin, Heidelberg 1999)
- 5.6 J. Shah: *Ultrafast Spectroscopy of Semiconductors and Semiconductor Nanostructures* (Springer, Berlin, Heidelberg 1996)
- 5.7 T. Wimbauer, K. Ito, Y. Mochizuki, M. Horikawa, T. Kitano, M.S. Brandt, M. Stutzmann: Defects in planar Si pn junctions studied with electrically detected magnetic resonance, *Appl. Phys. Lett.* **76**, 2280 (2000)
- 5.8 L.V. Azároff: *Elements of X-ray Crystallography* (McGraw-Hill, New York 1968)
- 5.9 J.M. Cowley: *Diffraction Physics* (North-Holland, Amsterdam 1975)
- 5.10 B.D. Cullity: *Elements of X-ray Diffraction* (Addison-Wesley, Reading 1977)
- 5.11 A. Guinier: *X-ray Diffraction in Crystals and Imperfect Crystals, Amorphous Bodies* (Dover, New York 1994)
- 5.12 G. Rhodes: *Crystallography Made Crystal Clear* (Academic, San Diego 2000)
- 5.13 S. Bradbury: *An Introduction to the Optical Microscope* (Oxford Sci. Publ., Oxford 1989)
- 5.14 P.B. Hirsch, A. Howie, R.B. Nicholson, D.W. Pashley, M.J. Whelan: *Electron Microscopy of Thin Crystals* (Butterworths, London 1965)
- 5.15 D.B. Williams, C.B. Carter: *Transmission Electron Microscopy* (Plenum, New York 1996)
- 5.16 M.J. Whelan: Dynamical Theory of Electron Diffraction. In: *Modern Diffraction and Imaging Techniques in Materials Science*, ed. by S. Amelinckx, R. Gevers, G. Remaut, J. Van Landuyt (North-Holland, Amsterdam 1970) p. 35
- 5.17 C.E. Lyman, D.E. Newbury, J.I. Goldstein, D.B. Williams, A.D. Romig Jr., J.T. Armstrong, P. Echlin, C.E. Fiori, D.C. Joy, E. Lifshin, K. Peters: *Scanning Electron Microscopy, X-ray Microanalysis and Analytical Electron Microscopy* (Plenum, New York 1990)
- 5.18 D. Bonnell (Ed.): *Scanning Probe Microscopy and Spectroscopy* (Wiley, Weinheim 2001)
- 5.19 B. Bhushan, H. Huchs, S. Hosaka (Eds.): *Applied Scanning Probe Methods* (Springer, Berlin, Heidelberg 2004)
- 5.20 K.S. Birdi: *Scanning Probe Microscopes* (CRC, Boca Raton 2003)
- 5.21 V.J. Morris, A.R. Kirby, A.P. Gunning: *Atomic Force Microscopy for Biologists* (Imperial College Press, London 1999)
- 5.22 S. Morita, R. Wiesendanger, E. Meyer: *Noncontact Atomic Force Microscopy* (Springer, Berlin, Heidelberg 2002)

- 5.23 M. Ohtsu: *Near-Field Nano-Atom Optics and Technology* (Plenum, New York 1999)
- 5.24 M.K. Miller, G.D.W. Smith: *Atom Probe Microanalysis* (Materials Research Society, Pittsburgh 1989)
- 5.25 S. Morita, N. Oyabu: Atom selective imaging and mechanical atom manipulation based on noncontact atomic force microscope method, *e-J. Surf. Sci. Technol.* **1**, 158 (2003)
- 5.26 D. Attwood: *Soft X-rays and Extreme Ultraviolet Radiation* (Cambridge Univ. Press, Cambridge 1999)
- 5.27 H. Kusmany: *Solid State Spectroscopy* (Springer, Berlin, Heidelberg 1998) p. 210
- 5.28 M. Fleischman, P.J. Hendra, A.J. McQuillan: Raman-spectra of pyridine adsorbed at a silver electrode, *Chem. Phys. Lett.* **26**, 163 (1974)
- 5.29 D.L. Feldheim, C.A. Foss Jr.: *Metal Nanoparticles* (Marcel Dekker, New York 2002)
- 5.30 A.S. Nowick, B.S. Berry: *Anelastic Relaxation in Crystalline Solids* (Academic, New York 1972)
- 5.31 G. Bricogne: Maximum-entropy and the foundations of direct methods, *Acta Cryst. A* **40**, 410 (1984)
- 5.32 S. Ogawa, M. Hirabayashi, D. Watanabe, H. Iwasaki: *Long-period Ordered Alloys* (Agne Gijutsu Center, Tokyo 1997)
- 5.33 R. Kitaura, S. Kitagawa, Y. Kubota, T.C. Kobayashi: Formation of a one-dimensional array of oxygen in a microporous metal-organic solid, *Science* **298**, 2358 (2002)
- 5.34 R.B. Von Dreele: Combined Rietveld and stereochemical restraint refinement of a protein crystal structure, *J. Appl. Cryst.* **32**, 1084 (1999)
- 5.35 M. Ito, H. Narumi, T. Mizoguchi, T. Kawamura, H. Iwasaki, N. Shiotani: Structural change of amorphous Mg₇₀Zn₃₀ alloy under isothermal annealing, *J. Phys. Soc. Jpn.* **54**, 1843-1854 (1985)
- 5.36 S.R.P. Silva: *Properties of Amorphous Carbon* (INSPEC, London 2003)
- 5.37 P. Ehrhart, H.G. Haubold, W. Schilling: Investigation of Point Defects and Their Agglomerates in Irradiated Metals by Diffuse X-ray Scattering. In: *Festkörperprobleme XIV/Advances in Solid State Phys.*, ed. by H.J. Queisser (Vieweg, Braunschweig 1974)
- 5.38 A. Hida, Y. Mera, K. Maeda: Identification of arsenic antisite defects with EL2 by nanospectroscopic studies of individual centers, *Physica B* **308-310**, 738 (2001)
- 5.39 P.M. Voyles, D.A. Muller, J.L. Grazul, P.H. Citrin, H.-J.L. Gossmann: Atomic-scale imaging of individual dopant atoms and clusters in highly n-type bulk Si, *Nature* **416**, 826 (2002)
- 5.40 D.A. Muller, N. Nakagawa, A. Ohtomo, J. Grazul, H.Y. Hwang: Atomic-scale imaging of nanoengineered oxygen vacancy profiles in SrTiO₃, *Nature* **430**, 657 (2004)
- 5.41 F. Lüty: FA centers in alkali halide crystals. In: *Physics of Color Centers*, ed. by W.B. Fowler (Academic Press, New York 1968) p. 181
- 5.42 A. van der Ziel: *Noise in Solid State Devices and Circuits* (Wiley, New York 1986)
- 5.43 N.B. Lukyanchikova: *Noise Research in Semiconductor Physics* (Gordon Breach, Amsterdam 1996)
- 5.44 N. Fukata, T. Ohori, M. Suezawa, H. Takahashi: Hydrogen-defect complexes formed by neutron irradiation of hydrogenated silicon observed by optical absorption measurement, *J. Appl. Phys.* **91**, 5831 (2002)
- 5.45 A. Hida: unpublished
- 5.46 J.P. Buisson, S. Lefrant, A. Sadoc, L. Taureland, M. Billardon: Raman-scattering by KI containing F-centers, *Phys. Status Solidi (b)* **78**, 779 (1976)
- 5.47 T. Sekiguchi, Y. Sakuma, Y. Awano, N. Yokoyama: Cathodoluminescence study of InGaAs/GaAs quantum dot structures formed on the tetrahedral-shaped recesses on GaAs (111)B substrates, *J. Appl. Phys.* **83**, 4944 (1998)
- 5.48 G.D. Watkins: *Radiation Damage in Semiconductors* (Dunod, Paris 1964) p. 97
- 5.49 B. Henderson: *Defects in Crystalline Solids* (Arnold, London 1972)
- 5.50 L.F. Mollenauer, S. Pan: Dynamics of the optical-pumping cycle of F centers in alkali halides-theory and application to detection of electron-spin and electron-nuclear-double-spin resonance in the relaxed-excited state, *Phys. Rev. B* **6**, 772 (1972)
- 5.51 S.E. Barrett, R. Tycko, L.N. Pfeiffer, K.W. West: Directly detected nuclear-magnetic-resonance of optically pumped GaAs quantum-wells, *Phys. Rev. Lett.* **72**, 1368 (1994)
- 5.52 K. Morigaki: Spin-dependent radiative and nonradiative recombinations in hydrogenated amorphous silicon: Optically detected magnetic resonance, *J. Phys. Soc. Jpn.* **50**, 2279 (1981)
- 5.53 A. Möslang, H. Graf, G. Balzer, E. Recknagel, A. Weidinger, T. Wichert, R.I. Grynszpan: Muon trapping at monovacancies in iron, *Phys. Rev. B* **27**, 2674 (1983)
- 5.54 C.P. Slichter, D. Ailion: Low-field relaxation and the study of ultraslow atomic motions by magnetic resonance, *Phys. Rev.* **135**, A1099 (1964)
- 5.55 M.J. Puska, C. Corbel: Positron states in Si and GaAs, *Phys. Rev. B* **38**, 9874 (1988)
- 5.56 M. Hakala, M.J. Puska, R.M. Nieminen: Momentum distributions of electron-positron pairs annihilating at vacancy clusters in Si, *Phys. Rev. B* **57**, 7621 (1998)
- 5.57 M. Hasegawa: private communication
- 5.58 M. Saito, A. Oshiyama: Lifetimes of positrons trapped at Si vacancies, *Phys. Rev. B* **53**, 7810 (1996)
- 5.59 Z. Tang, M. Saito, M. Hasegawa: unpublished
- 5.60 H. Ohkubo, Z. Tang, Y. Nagai, M. Hasegawa, T. Tawara, M. Kiritani: Positron annihilation study of vacancy-type defects in high-speed deformed Ni, Cu and Fe, *Mater. Sci. Eng. A* **350**, 95 (2003)
- 5.61 P. Hautojärvi: *Positrons in Solids* (Springer, Berlin, Heidelberg 1979)

- 5.62 R. Krause-Rehberg, H.S. Leipner: *Positron Annihilation in Semiconductors* (Springer, Berlin, Heidelberg 1999)
- 5.63 W. Triftshäuser, J.D. McGevey: Monovacancy formation energy in copper, silver, and gold by positron-annihilation, *Appl. Phys.* **6**, 177 (1975)
- 5.64 R.O. Simmons, R.W. Balluffi: Measurements of equilibrium vacancy concentrations in aluminum, *Phys. Rev.* **117**, 52 (1960)
- 5.65 M. Hasegawa, Z. Tang, Y. Nagai, T. Nonaka, K. Nakamura: Positron lifetime and coincidence Doppler broadening study of vacancy-oxygen complexes in Si: Experiments and first-principles calculations, *Appl. Surf. Sci.* **194**, 76 (2002)
- 5.66 S. Mantl, W. Triftshäuser: Defect annealing studies on metals by positron-annihilation and electrical-resistivity measurement, *Phys. Rev. B* **17**, 1645 (1978)
- 5.67 M. Hasegawa, Z. Tang, Y. Nagai, T. Chiba, E. Kuramoto, M. Takenaka: Irradiation-induced vacancy and Cu aggregations in Fe-Cu model alloys of reactor pressure vessel steels: State-of-the-art positron annihilation spectroscopy, *Philos. Mag.* **85**, 467 (2005)
- 5.68 T. Moriya, H. Ino, F.E. Fujita, Y. Maeda: Mössbauer effect in iron-carbon martensite structure, *J. Phys. Soc. Jpn.* **24**, 60 (1968)
- 5.69 K. Nakagawa, K. Maeda, S. Takeuchi: Observation of dislocations in cadmium telluride by cathodoluminescence microscopy, *Appl. Phys. Lett.* **34**, 574 (1979)
- 5.70 L.N. Pronina, S. Takeuchi, K. Suzuki, M. Ichihara: Dislocation-structures in rolled and annealed (001) [110] single-crystal molybdenum, *Philos. Mag. A* **45**, 859 (1982)
- 5.71 M.J. Hÿtch, J. Putaux, J. Pénisson: Measurement of the displacement field of dislocations to 0.03 by electron microscopy, *Nature* **423**, 270-273 (2003)
- 5.72 R.L. Snyder, J. Fiala, H.J. Bunge: *Defect, Microstructure Analysis by Diffraction* (Oxford Univ. Press, Oxford 1999)
- 5.73 G. Rhodes: *Crystallography: A Guide for Users of Macromolecular Models*, 2nd edn. (Academic, San Diego 2000)
- 5.74 K. Wüthrich: *NMR of Proteins and Nucleic Acids* (Wiley, New York 1986)
- 5.75 J.K.M. Sanders, B.K. Hunter: *Modern NMR Spectroscopy* (Oxford Univ. Press, Oxford 1993)
- 5.76 T.D.W. Claridge: *High Resolution NMR Techniques in Organic Chemistry* (Elsevier, Oxford 1999)
- 5.77 Y. Arata: *NMR in Proteins* (Kyoritsu, Tokyo 1996)
- 5.78 S. Weiss: Measuring conformational dynamics of biomolecules by single molecule fluorescence spectroscopy, *Nat. Struct. Biol.* **7**, 724 (2000)
- 5.79 V. Randle, O. Engler: *Introduction to Texture Analysis* (Taylor Francis, London 2000)
- 5.80 D.C. Joy, D.E. Newbury, D.L. Davidson: Electron channeling patterns in the scanning electron-microscope, *J. Appl. Phys.* **53**, R81 (1982)
- 5.81 K. Suenaga, T. Tence, C. Mori, C. Colliex, H. Kato, T. Okazaki, H. Shinohara, K. Hirahara, S. Bandow, S. Iijima: Element-selective single atom imaging, *Science* **290**, 2280 (2000)
- 5.82 N. Hayazawa, A. Tarun, Y. Inouye, S. Kawata: Near-field enhanced Raman spectroscopy using side illumination optics, *J. Appl. Phys.* **92**, 6983 (2002)
- 5.83 R. Snyder, J. Fiala, H.J. Bunge: *Defect and Microstructure Analysis by Diffraction* (Oxford Univ. Press, Oxford 1999)
- 5.84 B.D. Cullity: *Elements of X-ray Diffraction*, 2nd edn. (Addison-Wesley, Reading 1978)
- 5.85 M.E. Fitzpatrick, A. Lodini: *Analysis of Residual Stress by Diffraction Using Neutron and Synchrotron Radiation* (CRC, Boca Raton 2004)
- 5.86 K. Hono: Nanoscale microstructural analysis of metallic materials by atom probe field ion microscopy, *Prog. Mater. Sci.* **47**, 621 (2002)
- 5.87 H. Jinnai, Y. Nishikawa, T. Ikehara, T. Nishi: Emerging technologies for the 3D analysis of polymer structures, *Adv. Polym. Sci.* **170**, 115 (2004)
- 5.88 A. Momose: Phase-contrast X-ray imaging based on interferometry, *J. Synchrotron Rad.* **9**, 136 (2002)
- 5.89 A. Momose: Demonstration of phase-contrast X-ray computed tomography using an X-ray interferometer, *Nucl. Instrum. Methods A* **352**, 622(1995)

6. Surface and Interface Characterization

While the *bulk material properties* treated in Part C of this handbook are obviously important, the surface characteristics of materials are also of great significance. They are responsible for the appearances of materials and surface phenomena, and they have a crucial influence on the interactions of materials with gases or fluids (in corrosion, for example; Chap. 12), contacting solids (as in friction and wear; Chap. 13) or biospecies (Chap. 14), and materials–environment interactions (Chap. 15). Surface and interface characterization have been important topics for very many years. Indeed, it was known in antiquity that impurities could be detrimental to the quality of metals, and that keying and contamination were important to adhesion in architecture and also in the fine arts. In contemporary technologies, surface modification or functional coatings are frequently used to tailor the processing of advanced materials. Some components, such as quantum-well devices and x-ray mirrors, are composed of multilayers with individual layer thicknesses in the low nanometer range. Quality assurance of industrial processes, as well as the development of advanced surface-modified or coated components, requires chemical information on material surfaces and (buried) interfaces with high sensitivity and high lateral and depth resolution. In this chapter we present the methods applicable to the chemical and physical characterization of surfaces and interfaces.

This chapter covers the three main techniques of surface chemical analysis: Auger electron spectroscopy (AES), x-ray photoelectron spectroscopy (XPS), and secondary ion mass spectrometry (SIMS), which are all still rapidly developing in terms of instrumentation, standards, and applications. AES is excellent for elemental analysis at spatial resolutions down to 10 nm, and XPS can define chemical states down to 10 μm . Both analyze the outermost atom layers and, with sputter depth profiling, layers up to 1 μm thick.

Dynamic SIMS incorporates depth profiling and can detect atomic compositions significantly

6.1	Surface Chemical Analysis	282
6.1.1	Auger Electron Spectroscopy (AES) ...	285
6.1.2	X-ray Photoelectron Spectroscopy (XPS)	294
6.1.3	Secondary Ion Mass Spectrometry (SIMS)	298
6.1.4	Conclusions	307
6.2	Surface Topography Analysis	308
6.2.1	Stylus Profilometry	312
6.2.2	Optical Techniques	316
6.2.3	Scanning Probe Microscopy	318
6.2.4	Scanning Electron Microscopy	320
6.2.5	Parametric Methods	321
6.2.6	Applications and Limitations of Surface Measurement	322
6.2.7	Traceability	322
6.2.8	Summary	325
	References	326

below 1 ppm. Static SIMS retains this high sensitivity for the surface atomic or molecular layer but provides chemistry-related details not available with AES or XPS. New reference data, measurement standards, and documentary standards from ISO will continue to be developed for surface chemical analysis over the coming years.

The chapter also discusses surface physical analysis (topography characterization), which encompasses measurement, visualization, and quantification. This is critical to both component form and surface finish at macro-, micro-, and nanoscales. The principal methods of surface topography measurement are stylus profilometry, optical scanning techniques, and scanning probe microscopy (SPM). These methods, based on acquiring topography data from point-by-point scans, give quantitative information on surface height with respect to position. The integral methods, which are based on a different approach, produce parameters that represent some average property of the surface under examination. Measurement methods, as well as their application and limitations, are briefly reviewed, including standardization and traceability issues.

6.1 Surface Chemical Analysis

The principal methods of surface chemical analysis are Auger electron spectroscopy (AES), x-ray photoelectron spectroscopy (XPS), and secondary ion mass spectrometry (SIMS). These three methods provide analyses of the outermost atomic layers at a solid surface, but each has distinct attributes which lead to each having dominance in different sectors of analysis. Additionally, each may be coupled with ion sputtering, to erode the surface whilst analyzing, in order to generate a composition depth profile. These profiles may typically be over layers up to 100 nm thick or, when required, up to 1 μm thick or more. The depth resolutions can approach atomic levels. Useful figures to remember are that an atomic layer is about 0.25 nm thick and contains about 1.6×10^{19} atoms m^{-2} or 1.6×10^{15} atoms cm^{-2} . All of the above methods operate with the samples inserted into an ultrahigh vacuum system where the base pressure is designed to be 10^{-8} Pa (10^{-10} Torr) but that, with fast throughputs or gassy samples, may degrade to 10^{-5} Pa (10^{-7} Torr). Thus, all samples need to be vacuum-compatible solids.

We shall describe the basics of each of the methods later, but it is useful, here, to outline the attributes of the methods so that the reader can focus early on their method of choice.

In Auger electron spectroscopy (AES), the exciting radiation is a focused electron beam, and in the latest instruments, resolutions ≤ 5 nm are achieved. This provides elemental analysis with detectabilities reaching 0.1%, but not at the same time as very high spatial resolution. Additionally, the higher the spatial resolu-

tion, the more robust the sample should be, since the electron beam fluence on the sample is then very high. Thus, metals, oxides, semiconductors or some ceramics are readily analyzed, although at the highest flux density the surface of compounds may be eroded. In AES, there is chemical information, but it is not as easily observed as in XPS. In XPS, the peaks are simpler and so quantification is generally more accurate, the chemical shifts are clearer, detectability is similar to in AES, but the spatial resolution is significantly poorer. Typically, ≤ 5 μm spatial resolution is the best achieved in the latest instruments. In XPS, with a lower flux of charged particles, ceramics and other insulators may be analyzed more readily than with AES, although if spatial resolution ≤ 5 μm is required, AES must generally be used, and efforts then need to be taken to avoid any charging or damage problems.

For layers with compositions that change within the outermost 8 nm, information on the layering may be obtained by XPS or angle-resolved XPS. If the compositions vary over greater depths, sputter depth profiling is used, generally with AES or, if more convenient or for particular information, with XPS. The sputtering is usually conducted in situ for AES and may be in situ or in a linked vacuum vessel for XPS.

Where greater detectability is required, as for studying dopant distributions in semiconductor device fabrication, SIMS is the technique of choice. Modern SIMS instruments have resolutions of around 100 nm, but critical to semiconductor work is the ability to detect levels as low as 0.01 ppm. In SIMS, the ion intensities

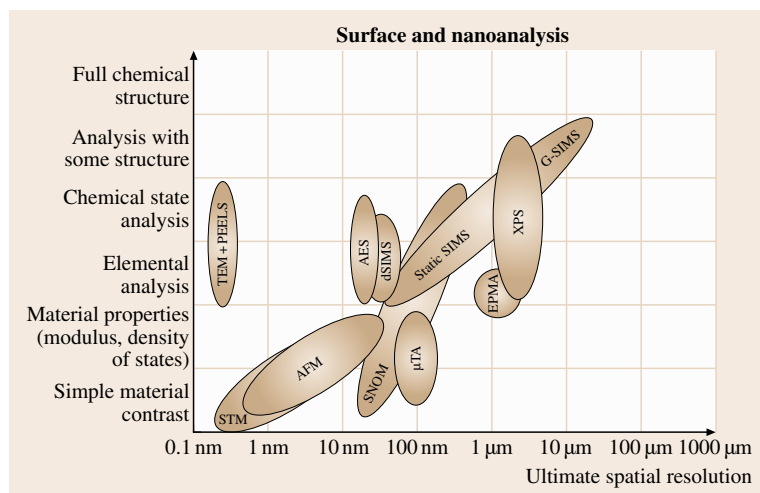


Fig. 6.1 The resolution and information content of a range of analytical methods (STM = scanning tunneling microscopy, AFM = atomic force microscopy, TEM = transmission electron microscopy, PEELS = parallel electron energy loss spectroscopy, SNOM = scanning near-field optical microscopy, μTA = microthermal analysis, EPMA = electron probe microscopy) that can be used at surfaces (after Gilmore et al. [6.1])

Table 6.1 Methodology selection table for surface analysis

Method	AES		XPS		Dynamic SIMS		Static SIMS	
	Traditional	High-energy resolution	Traditional	Imaging	Imaging	Depth profiling	Gas source	Liquid metal ion source
Configuration								
Section	Sect. 6.1.1		Sect. 6.1.2		Sect. 6.1.3		Sect. 6.1.3	
Best spatial resolution	5 nm	5 nm	20 μm	2 μm	50 nm	50 μm	5 μm	80 nm
Best depth resolution	0.3 nm	0.3 nm	0.3 nm	1.5 nm	3 nm	0.3 nm	0.3 nm	0.3 nm
Approx. sensitivity	0.5%	1%	1%	3%	0.01 ppm	0.01 ppm	0.01%	0.01%
Typical information depth	10 nm	10 nm	10 nm	10 nm	3 nm	3 nm	0.5 nm	0.5 nm
Elements not analyzed	H, He	H, He	H, He	H, He				
Information								
Elemental	✓	✓	✓	✓	✓	✓	✓	✓
Isotopic					✓	✓	✓	✓
Chemical		✓	✓	✓			✓	✓
Molecular			✓				✓	✓
Material								
Metal	✓	✓	✓	✓	✓	✓	✓	✓
Semiconductor	✓	✓	✓	✓	✓	✓	✓	✓
Insulator or ceramic			✓	✓	✓	✓	✓	✓
Polymer, organic or bio			✓	✓			✓	✓

depend sensitively on the matrix, and so quantification is difficult for concentration levels above 1%, but in the more dilute regime the intensity is proportional to the composition. SIMS has thus found a dominant role here. The use of a mass spectrometer in SIMS allows isotopes to be separated, and this leads to a useful range of very precise diffusion studies with isotopic markers. The above considerations for SIMS cover the technique that is often called dynamic SIMS (d-SIMS). Another form of SIMS, static SIMS (SSIMS), is used to study the outermost surface, and here detailed information is available to analyze complex molecules that is not available in XPS. This is less routine but has significant promise for the future.

Figure 6.1 [6.1] shows a diagram of the spatial resolution and information content of these and other techniques, which helps to place the more popularly used methods in context. Additional information is given in Table 6.1. These analytical techniques have all been in use in both industry and the academic sector since the end of the 1960s, but it is only more recently that fast throughput, highly reliable instruments have become available and also that good infrastructures have been developed to support analysts generally. Documentary standards for conducting analysis were started early by ASTM [6.2]. In 1993, international activity started in the ISO in technical committee TC201 on surface

chemical analysis. Details may be found at the website given in reference [6.3] or on the National Physical Laboratory (NPL) website [6.4], following the route *International Standardisation and Traceability*. Table 6.2 shows the titles of ISO standards published to date, and Table 6.3 the standards currently in draft. One-page articles on most of the published standards are given in the journal *Surface and Interface Analysis*. The relevant references are listed in the final column in Table 6.2.

Whilst consistent working depends on documentary standards, much quantitative measurement depends on accurate data and traceable measurement standards. This requires reference data, reference procedures, and certified reference materials. Some of these are available at the NPL website [6.4], some on the website of the US National Institute of Standards and Technology (NIST) [6.5], and reference materials may be found from several of the national metrology institutes and independent suppliers. Further assistance can be found in essential textbooks [6.6–8] or online at usergroups [6.9]. We shall cite these as appropriate in the text below. Of particular importance is ISO 18115 and the amendments in which ≈ 800 terms used in surface analysis and scanning probe microscopy are defined. Relevant terms are used and defined here, consistent with that international standard. We first consider issues for measurement by AES and XPS and then for dynamic and static SIMS.

Table 6.2 Published ISO Standards from ISO TC201

No.	ISO standard	Title (SCA = surface chemical analysis)	Title and author
1	14237	SCA – Secondary ion mass spectrometry – Determination of boron atomic concentration in silicon using uniformly doped materials	[6.10]
2	14606	SCA – Sputter depth profiling – Optimization using layered systems as reference materials	[6.11]
3	14975	SCA – Information formats	[6.12]
4	14976	SCA – Data transfer format	[6.13]
5	15470	SCA – X-ray photoelectron spectroscopy – Description of selected instrumental performance parameters	
6	15471	SCA – Auger electron spectroscopy – Description of selected instrumental performance parameters	
7	15472	SCA – X-ray photoelectron spectrometers – Calibration of energy scales	[6.14]
8	TR 15969	SCA – Depth profiling – Measurement of sputtered depth	[6.15]
9	TR 16268	SCA – Proposed procedure for certifying the retained areic dose in a working reference material produced by ion implantation	
10	17560	SCA – Secondary ion mass spectrometry – Method for depth profiling of boron in silicon	[6.16]
11	17973	SCA – Medium-resolution Auger electron spectrometers – Calibration of energy scales for elemental analysis	[6.17]
12	17974	SCA – High-resolution Auger electron spectrometers – Calibration of energy scales for elemental and chemical-state analysis	[6.18]
13	18114	SCA – Secondary ion mass spectrometry – Determination of relative sensitivity factors from ion-implanted reference materials	[6.19]
14	18115	SCA – Vocabulary	[6.20]
15	18115Amd1	SCA – Vocabulary	[6.21]
16	18115Amd2	SCA – Vocabulary	[6.22]
17	18116	SCA – Guidelines for preparation and mounting of specimens for analysis	
18	18117	SCA – Handling of specimens prior to analysis	
19	18118	SCA – Auger electron spectroscopy and x-ray photoelectron spectroscopy – Guide to the use of experimentally determined relative sensitivity factors for the quantitative analysis of homogeneous materials	[6.23]
20	TR 18392	SCA – X-ray photoelectron spectroscopy – Procedures for determining backgrounds	[6.24]
21	18394	SCA – Auger electron spectroscopy – Derivation of chemical information	[6.25]
22	18516	SCA – Auger electron spectroscopy and x-ray photoelectron spectroscopy – Determination of lateral resolution	[6.26]
23	19318	SCA – X-ray photoelectron spectroscopy – Reporting of methods used for charge control and charge correction	[6.27]
24	TR 19319	SCA – Auger electron spectroscopy and x-ray photoelectron spectroscopy – Determination of lateral resolution, analysis area, and sample area viewed by the analyzer	[6.28]
25	20341	SCA – Secondary ion mass spectrometry – Method for estimating depth resolution parameters with multiple delta-layer reference materials	[6.29]
26	20903	SCA – Auger electron spectroscopy and x-ray photoelectron spectroscopy – Methods used to determine peak intensities and information required when reporting results	[6.30]
27	21270	SCA – X-ray photoelectron and Auger electron spectrometers – Linearity of intensity scale	[6.31]
28	22048	SCA – Information format for static secondary ion mass spectrometry	[6.32]
29	TR 22335	SCA – Depth profiling – Measurement of sputtering rate: mesh-replica method using a mechanical stylus profilometer	
30	23812	SCA – Secondary ion mass spectrometry – Method for depth calibration for silicon using multiple delta-layer reference materials	
31	23830	SCA – Secondary ion mass spectrometry – Repeatability and constancy of the relative-intensity scale in static secondary ion mass spectrometry	
32	24236	SCA – Auger electron spectroscopy – Repeatability and constancy of intensity scale	[6.33]
33	24237	SCA – X-ray photoelectron spectroscopy – Repeatability and constancy of intensity scale	[6.34]
34	29081	SCA – Auger electron spectroscopy – Reporting of methods used for charge control and charge correction	

Table 6.3 ISO standards from ISO TC201 for AES, SIMS, and XPS in draft

No.	ISO std.	Title ^a
1	10810	SCA – X-ray photoelectron spectroscopy – Guidelines for analysis
2	12406	SCA – Secondary ion mass spectrometry – Method for depth profiling of arsenic in silicon
3	13084	SCA – Secondary ion mass spectrometry – Calibration of the mass scale for a time-of-flight secondary ion mass spectrometer
4	13424	SCA – X-ray photoelectron spectroscopy – Reporting of results for thin-film analysis
5	TR 14187	SCA – Characterization of nanostructured materials
6	14237	SCA – Secondary ion mass spectrometry – Determination of boron atomic concentration in silicon using uniformly doped materials
7	14701	SCA – X-ray photoelectron spectroscopy – Measurement of silicon oxide thickness
8	16242	SCA – Recording and reporting data in Auger electron spectroscopy (AES)
9	16243	SCA – Recording and reporting data in x-ray photoelectron spectroscopy (XPS)
10	18115-1	SCA – Vocabulary – Part 1: General terms and terms used in spectroscopy
11	18115-2	SCA – Vocabulary – Part 2: Terms used in scanning probe microscopy
12	TR 19319	SCA – Determination of lateral resolution in beam-based methods

^a ISO titles spell out the acronyms in full but are abbreviated here for reasons of space:
 AES = Auger electron spectroscopy or spectrometer(s)
 SCA = Surface chemical analysis
 SIMS = Secondary ion mass spectrometry or spectrometer(s)
 TR = Technical report
 XPS = X-ray photoelectron spectroscopy or spectrometer(s)

6.1.1 Auger Electron Spectroscopy (AES)

General Introduction

In AES, atoms in the surface layers are excited using an electron beam of typically 5 or 10 keV energy, but generally in the range 2–20 keV. In modern instruments this will typically be of 5–50 nA beam current, giving a spatial resolution in the range 20 nm–2 μm and, in carefully designed instruments, below 5 nm. The surface atoms lose an electron from an inner shell and the atoms then de-excite either by an Auger transition – emitting an Auger electron – or by filling with an outer shell electron and emitting an x-ray that would be detected in the complementary technique of electron probe microanalysis (EPMA). In the Auger process, an electron from a higher level E_2 fills the vacant inner shell level E_1 , and the quantum of energy liberated is removed by a third electron from a level E_3 that is emitted with a characteristic energy E_A , defined approximately by

$$E_A = E_2 + E_3 - E_1. \quad (6.1)$$

In (6.1), the energies of the bound levels E_1 , E_2 , and E_3 are taken to be negative quantities. This is shown in Fig. 6.2a. Relaxation effects add small additional energy terms of the order of 5–10 eV, but (6.1) allows us to identify the characteristic peaks in the emitted electron energy spectrum and hence all the elements present except H and He. Core levels deeper

than about 2.5 keV have weak ionization cross sections, and so Auger electrons with emitted energies greater than 2.5 keV are weak and are rarely analyzed. Additionally, Auger electrons with energies below 50 eV are superimposed on the large secondary-electron emission background. Thus, the peaks used for analysis generally lie in the kinetic energy range 50–2500 eV, and this conveniently covers all of the elements except H and He.

The reason why AES is both surface specific and surface sensitive lies in the range of the Auger electrons be-

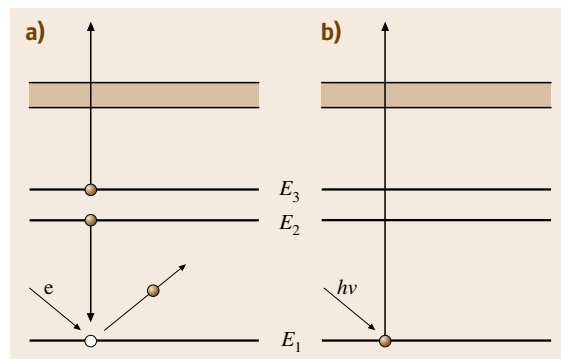


Fig. 6.2a,b Energy level diagram showing emission processes: (a) Auger electrons, (b) photoelectrons. The shaded region shows the conduction or valence bands to which the energy levels are referenced

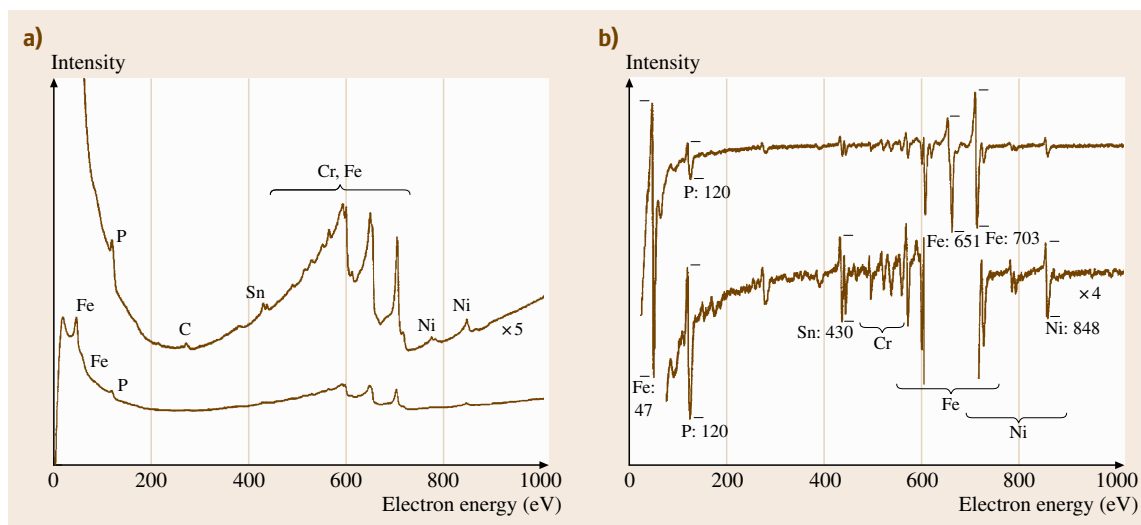


Fig. 6.3a,b Auger electron spectra from the grain boundary fracture surface of a low alloy steel with 0.056 wt % added phosphorus after a temper brittling heat treatment and analyzed using a cylindrical mirror analyzer: **(a)** direct mode presentation, with the *lower curve* magnified five times, and **(b)** differential mode presentation, with the *lower curve* magnified four times (after *Hunt and Seah* [6.36]). The fracture is made, in situ, usually by impact, in ultrahigh vacuum to stop the oxidation that would otherwise occur upon air exposure. Oxidation would remove the interesting elements from the spectra

fore inelastic scattering causes them to be lost from the peak and merged with the background. In early work, this electron attenuation length L is given by [6.35]

$$L = \frac{538}{E_A^2} + 0.41 (aE_A)^{0.5} \text{ monolayers}, \quad (6.2)$$

where a^3 is the atomic volume in nm^3 . A typical value of a is 0.25 nm, so that L ranges from one monolayer at low energies to ten monolayers at high energies.

Figure 6.3 shows a typical Auger electron spectrum from studies to characterize material used to aid quantification when analyzing the grain boundary segregation of phosphorus in steel. To obtain this spectrum, the material is fractured, in situ, in the spectrometer, to present the grain boundary surface for analysis. The peaks are labeled for both the direct mode and the differential mode of analysis. Historically, spectra were only presented in the differential mode so that low-energy peaks such as those of P and minor constituents such as Cr, which occur on steeply sloping backgrounds, could be reliably measured. Simple methods of valid background subtraction are not generally available, so even though spectra may be recorded today in the direct mode, they are often subsequently differentiated using a mathematical routine with a function of 2–5 eV width [6.37, 38].

The shapes of the spectra and the positions of the peaks may be found in relevant handbooks [6.39–43]. The transitions in AES are usually written using x-ray nomenclature so that, if the levels 1, 2, and 3 in (6.1) are the $2p_{3/2}$, $3p_{3/2}$, and $3d_{5/2}$ subshells, the transition would be written $L_3M_3M_5$ and, for the metals Ca to Cu, since M_5 is in the valence band, this is often written L_3M_3V . Auger electron peaks involving the valence band are usually broader than those only involving core levels, and those involving two electrons in the valence band can be broader still. The precise energies and shapes of the peaks change with the chemical state. The transitions involving the valence band are the ones most affected by the chemical state and can show peak splitting and shifts of up to 6 eV upon oxidation [6.44]. The three large Fe peaks in Fig. 6.3 are LCC, LCV, and LVV at 600, 651, and 700 eV, respectively, where C represents a core level. The LVV transition is the most strongly affected by oxidation in the series from Ti to Cu, with the effect strongest at Cr [6.44].

For quantitative analysis, many users apply a simple equation of the form

$$X_A = \frac{I_A/I_A^\infty}{\sum_i I_i/I_i^\infty}, \quad (6.3)$$

where X_A is the atomic fraction of A, assumed to be homogeneous over the 20 or so atom layers of the

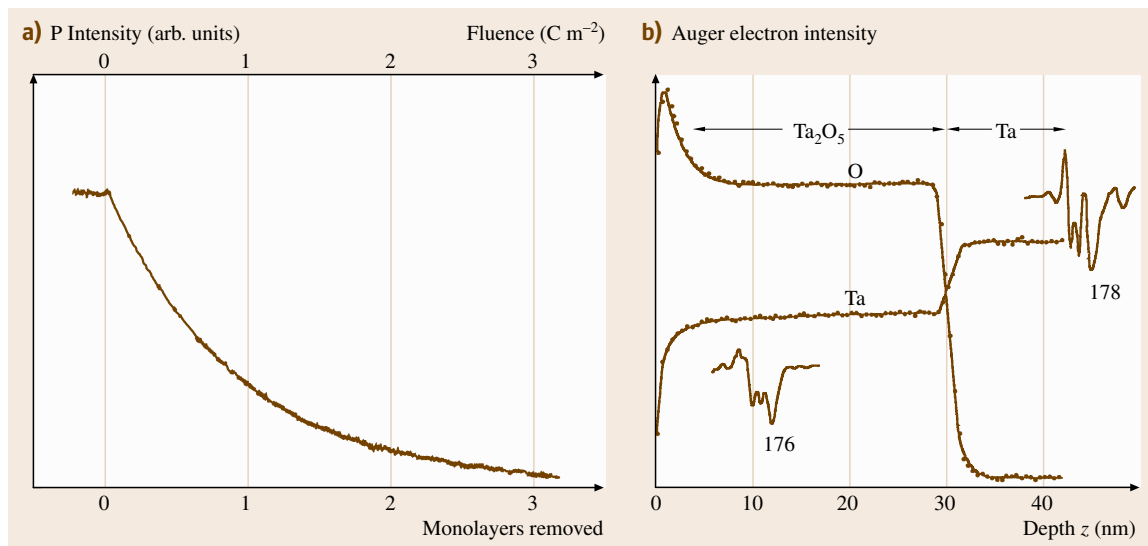


Fig. 6.4a,b Sputter depth profiles for differential signals in AES using argon ions: (a) P signal at 120 eV from the low alloy steel in Fig. 6.3b using 3 keV ions (after [6.36]), (b) O and Ta signals from a 28.4 nm-thick Ta₂O₅ layer using 2 keV ions (after *Seah and Hunt* [6.45]). The steel sample is profiled after fracture, in situ, and so is not air exposed, whereas the Ta₂O₅ layer had been prepared 6 months earlier and kept in laboratory air

analysis. In (6.3), the I_i^∞ are pure element relative sensitivity factors taken from handbooks [6.39–43]. This gives an approximate result but suffers from three major deficiencies that may be resolved reasonably easily. We shall return to this later but will continue, for the present, to deal with the general usages of AES.

Two major uses that developed early concerned imaging and composition depth profiling using inert gas ion sputtering. Generally, in imaging, most analysts were content to use the peak intensity from the direct spectrum and then to remove an extrapolated background so that the brightness of each point in the image was proportional to the peak height. This is quick and easy in modern multidetector systems. Earlier systems used the signal at the negative peak of the analog differential spectrum. These approaches are simple and practical and can rapidly define points for subsequent analysis, but interpretation of the contrast for samples with significant surface topography or for thin layers with underlying materials with different atomic numbers can be very complex.

Generally, in composition depth profiling, argon ions in the energy range 1–5 keV are used with current density of 1–30 $\mu\text{A}/\text{cm}^2$. Profiles could either be for monolayers, as exemplified in Fig. 6.4a by the profile for the segregated phosphorus shown in Fig. 6.3b, or for thicker layers, as exemplified in Fig. 6.4b for

the tantalum pentoxide certified reference material (CRM) BCR 261 [6.45–48]. The quantification of the depth and the depth resolution are the critical factors here, and these we shall discuss *Sputter Depth Profiling*.

Handling of Samples

In many applications of AES, the samples are prepared in situ in the ultrahigh vacuum of the instrument, and the user will be following a detailed protocol evaluated already in their laboratory or in the published literature. However, where samples have been provided from elsewhere or where the item of interest is the overlayer that is going to be depth-profiled, the samples will usually arrive with surface contamination. This contamination is usually from hydrocarbons, and it attenuates all of the signals to be measured. It is useful to remove these hydrocarbons unless they are the subject of analysis, and for most materials, high-performance liquid chromatography (HPLC)-grade isopropyl alcohol (IPA) is a very effective [6.49] contamination solvent unless dealing with polymers or other materials soluble in IPA. This makes analysis of the surface both clearer and more accurate and, for sputter depth profiling, removes much of the low sputter yield material that may cause loss of depth resolution in the subsequent profile. Samples can then either be stored in

Table 6.4 Kinetic energies, $E_{\text{ref } n}$, for reference to the vacuum level. Values in parenthesis are referenced to the Fermi level

Peak number n	Assignment	Kinetic energy, $E_{\text{ref } n}$ (eV)	
		Direct spectra	Differential spectra
1	Cu M _{2,3} VV	58 (62)	60 (64)
2	Cu L ₃ VV	914 (919)	915** (920**)
3	Al KL _{2,3} L _{2,3}	1388 (1393)	1390** (1395**)
4	Au M ₅ N _{6,7} N _{6,7}	2011* (2016*)	2021 (2026)

* For beam energies below 6 keV and for $0.25\% < R \leq 0.5\%$ add 1 eV
 ** For $0.27\% < R \leq 0.5\%$ add 1 eV
 This table is derived from work in [6.50–52]

clean glass containers [6.49] until needed or analyzed directly.

Details on how samples should be collected and supplied to the analyst are given in ISO 18117 and for mounting them for analysis in ISO 18116, listed in Table 6.2. The guiding principle for mounting the sample is to reduce the presence of any material that causes gases in the vacuum system, contamination of the surface to be analyzed or local charging of insulating material.

We are now ready for analysis and need to consider the spectrometer.

Calibrating the Spectrometer Energy Scale

Depending on the type of spectrometer and its intended use, there are two ISO standards that provide procedures for calibrating the spectrometer energy scale. ISO 17973 is for medium-resolution systems designed for elemental analysis and is suitable for instruments with a relative resolution R of $\leq 0.5\%$, used in either the direct mode or the differential mode with a peak-to-peak differentiation of 2 eV. ISO 17974 is for high-resolution spectrometers intended for both elemental and chemical state analysis. With both standards, high-purity metal foils of the appropriate elements are used with their surfaces cleaned by a light ion sputtering. The exact peak energies are defined by a simple, accurate protocol [6.54], and those are then compared with tabulated values obtained from traceable measurements.

For medium-resolution spectrometers, the peak energies are given in Table 6.4, and for most spectrometers, only Cu and Au foils are required. Note that values are given referenced to both the vacuum level and, in brackets, the Fermi level. In principle, energies can only be accurately referenced to the Fermi level, since the vacuum level – the level in the vacuum of the spectrometer at which a stationary electron exists – varies from point to point in the spectrometer. This will change

after bake-out, and depends on local surface work functions. This level generally exists at 4–5 eV above the Fermi level, and for convenience, a value of 4.5 eV is used in these ISO standards and elsewhere. The vacuum level is used here, since all early work and the handbooks [6.39–43] use the vacuum level reference.

A few spectrometers do not measure kinetic energies above 2 keV, and for these, an alternative energy peak is provided in Table 6.4 using Al.

For high-resolution spectrometers, the vacuum level is too vague, and data are Fermi level referenced. High-resolution spectrometers are often also used for XPS, where only Fermi level referencing is used, and this enhances consistency. For high-resolution spectrometers, Cu and Au are again used, except in the exceptional circumstances where the spectrometer scale is limited to 2 keV, in which case Au must again be replaced by Al, as shown in Table 6.5.

To obtain the necessary level of accuracy, either where the resolution R is poorer than 0.07% and when Au is used, or where R is poorer than 0.04% and when Al is used, a correction is required to the tabulated values such that the peaks are located at $E_{\text{ref } n}$, where

$$E_{\text{ref } n} = E_{\text{ref } n}^0 + cR + dR^2. \quad (6.4)$$

Table 6.5 Reference values for the peak positions on the kinetic energy scale [6.52] $E_{\text{ref } n}^0$ for $R < 0.04\%$ if Al is used, or $R < 0.07\%$ if Au is used

Peak number n	Assignment	$E_{\text{ref } n}^0$ (eV)
1	Cu M _{2,3} VV	62.37
2	Cu L ₃ VV	918.69
3	Al KL _{2,3} L _{2,3}	1393.09
4	Au M ₅ N _{6,7} N _{6,7}	2015.80

These kinetic energies are referenced to the Fermi level.
 This table is a refinement of earlier tables (after [6.50,51,53])

Table 6.6 Corrections to the reference kinetic energies for resolutions poorer than 0.07% when Au is used, or poorer than 0.04% when Al is used

Peak number <i>n</i>	Assignment	<i>c</i> (eV)	<i>d</i> (eV)
1	Cu M _{2,3} VV	0.0	0.0
2	Cu L ₃ VV	0.2	-2.0
3	Al KL _{2,3} L _{2,3}	-0.3	-1.8
4	Au M ₅ N _{6,7} N _{6,7} : 5 keV <i>n</i> (<i>E</i>) 5 keV <i>En</i> (<i>E</i>) 10 keV <i>n</i> (<i>E</i>) 10 keV <i>En</i> (<i>E</i>)	0.0	0.0
		-0.3	4.4
		-0.2	0.0
		-0.1	0.0

This table is a simplification of a more complex table (after [6.51]) and is consistent with the more complex table for relative resolutions in the range $0\% < R < 0.2\%$ to within 0.015 eV

The values of the coefficients *c* and *d* are given in Table 6.6, where the resolution *R*, given by $\Delta E/E$, is expressed in percent.

In these ISO standards, detail is provided of the signal levels to use, the contributions leading to uncertainties in the final calibration, and methods to ensure, as far as is reasonable, that the instruments are kept in calibration within their stated tolerance limits in order to be fit for purpose.

Repeatability of the Intensity Scale

All electron spectrometers use electron multiplier detectors, and these, unfortunately, age with use. Thus, even though the analyst may use consistent spectrometer settings each time, the absolute intensity of the measured spectrum will slowly reduce. This reduction may be offset by increasing the detector multiplier voltage. However, then the user may observe that the relative intensities of peaks in the spectrum have changed, and if we quantify a spectrum via equations such as (6.3), the calculated value of *X* – the measured composition – will appear to have changed. These effects mean that the analyst needs to understand the behavior of the multiplier detector [6.55] in order to maintain long-term repeatability of measurements. Indeed, a failure to understand detector behavior can lead to gross spectral distortion [6.56].

With many pulse-counting systems, the electron multiplier is designed to give a sufficiently large output pulse that the detection electronics receives that pulse well separated in magnitude from the ambient noise in the system. However, the pulses from the multiplier have a distribution of intensities, and so it is necessary to increase the multiplier gain until all of the pulses are clearly separated from the background noise. The gain is set by the multiplier voltage, and the separation point is defined by a discriminator in the detector electronics.

As the multiplier voltage is increased from a low level, at a voltage usually in the range 1800–2400 V, the count rate suddenly starts to rise, reaching 90% of its maximum over a range of about 250 V. The count rate then rises more slowly to a saturation maximum value [6.57]. The transition from zero to the maximum count rate occurs rapidly except at high count rates [6.57]. At high count rates, the pulse height distribution broadens and the transition occupies a wider voltage range. NPL has adopted a procedure, for single-channel electron multipliers, of setting the multiplier voltage at 500 V more positive than the voltage required to observe 50% of the saturation count rate when set to measure around 100 kc/s. These values are not critical but do lead to precise setting of the multiplier voltage. This gives a reliable result and allows the user to track the multiplier behavior as it ages in order to replace the multiplier at a convenient time. If a significantly lower multiplier voltage than this setting is used, the count rates are lowered and the system becomes very nonlinear. If higher multiplier voltages are used, the linear counting range extends to higher counting rates but this occurs at the expense of the multiplier life [6.58].

In their normal use, all counting systems suffer some loss of counts at high counting rates arising from the counting electronics' dead time. Information on dead time may be found in references [6.57, 58] as well as ISO 21270. ISO 21270 also deals with the diagnoses of the gross nonlinearities that have been seen in the intensity scales of certain designs of detector [6.59, 60].

If the detector is correctly set, it is important to establish the constancy and repeatability of the instrument's intensity response. For AES, the ratio of the intensity of the Cu L₃VV peak to that of the M_{2,3}VV peak is a useful measure, particularly using the peak-to-peak differential heights. Providing that sufficient intensities are acquired to be statistically meaningful,

seven repeat measures of one peak followed by seven of the other allows the trend in the ratio during acquisition to be evaluated as well as the intensity ratio repeatability standard deviation. With around 2 M counts per channel at the peaks, ISO 24236 shows how repeatability standard deviation of better than 0.5% may be attained if the data are recorded at 0.1 eV energy intervals and specific Savitzky and Golay smoothing [6.37] is used. Any drift in the absolute intensities or of the ratio between measurements may indicate a source, analyzer or detector instability that then needs to be investigated.

Calibrating the Intensity Scale

Interlaboratory studies to compare the shapes of spectra obtained in different laboratories unfortunately show that there are marked differences [6.61] that can lead to variations of a factor of two in quantification if the same relative sensitivity factors are to be used in all laboratories. These differences exist between similar models of spectrometer from the same manufacturer and arise mainly from the age dependence of the detector efficiency $D(E)$. $D(E)$ exhibits a curve that rises with the detected electron kinetic energy E from zero at $E = 0$ to a maximum in the energy range 200–600 eV and then to a slow decline at higher energies. In addition to the detector efficiency, there are electron optical terms to describe the spectrometer transmission function $T(E)$. These need to be combined to give the total instrumental response.

Formally, one may write the intensity–energy response function (IERF) as

$$\text{IERF} = T(E) D(E), \quad (6.5)$$

with additional terms, omitted here, that may arise from stray electron or magnetic fields [6.62]. The term $T(E)$ is usually approximately proportional to E for spectrometers operated in the constant $\Delta E/E$ mode, and proportional to E^{-n} , where n ranges from 0 to 1, as the energy increases in the constant ΔE mode. In the constant $\Delta E/E$ mode, all voltages on electron optical elements of the spectrometer are scanned so that they remain in fixed proportion to each other. The resolution then deteriorates as the energy increases. This is the mode generally used for AES, unless high-resolution spectra are required, since very simple spectrometers may then be used with high efficiency and with high intensities at the high energies where the peaks are weak. On the other hand, the constant ΔE mode is used for high-resolution analysis so that ΔE , the spectrometer energy resolution, is maintained at, say, 0.25 eV at all energies. This is usually achieved by setting the pass

element of the spectrometer to detect, say, 25 eV electrons, and then scanning this through the spectrum. If we know the IERF, the true spectrum that we need, $n(E)$, is given by

$$n(E) = \frac{I(E)}{\text{IERF}}, \quad (6.6)$$

where $I(E)$ is the measured spectrum.

In order to calibrate spectrometers for their absolute or relative IERFs, a series of studies were made using different configurations of an instrumented spectrometer with a Faraday cup detector to measure absolute reference spectra [6.61–64]. These spectra were measured for Cu, Ag, and Au polycrystalline foil samples using a 5 keV electron beam at 30° to the surface normal. Using these spectra, the absolute IERF may be determined for any spectrometer. To facilitate this, a software system has been designed for users to self-calibrate their instruments based on their own measurements for these foils [6.65]. The reason for using three foils when, in principle, one would suffice, is to evaluate the scatter between the three independent IERF derivations in order to calculate the repeatability of the average IERF derivation. These derivations can be consistent to < 1%. In the calibration, certain other diagnostics are important. For instance, internal scattering [6.66] may occur in some spectrometers, and if this has any significant intensity, it leads to uncertainty in the derived IERF. The above-mentioned software diagnoses the extent of the internal scattering using the rules established in [6.66] with the Cu and Ag samples.

The true spectral shape obtained in this way will not change significantly with time provided the IERF is determined at appropriate time intervals. Being absolute, use may then be made of an extremely large volume of theoretical knowledge as well as background removal procedures based on physically meaningful algorithms [6.67, 68] in order to interpret different aspects of the spectra.

As noted earlier, many analysts do not use any significant theoretical evaluation of the spectra and simply use the peak-to-peak differential intensity. Relative sensitivity factors for (6.1) are available from several handbooks [6.39–43], but analysis shows that the lack of control of the IERF leads to significant variability. Additionally, different choices of modulation energy for the differentiation increase that variability from source to source [6.69], so that half of the published sensitivity factors for each element differ from the average by more than a factor of 1.5. These issues are addressed below.

Quantitative Analysis of Locally Homogeneous Solids

It is useful to consider the basic derivation of sensitivity factors so that the user appreciates why things are done in certain ways and can link this text with older texts.

The Auger electron intensity per unit beam current into a small solid angle $d\Omega$ for a sample of pure element A involving the XYZ transition I_{AXYZ} may be calculated from the relation for homogeneous systems [6.70].

$$I_{\text{AXYZ}}^{\infty} = \gamma_{\text{AXYZ}} n_{\text{AX}} \sigma_{\text{AX}}(E_0) \sec \alpha \times [1 + r_{\text{A}}(E_{\text{AX}}, E_0, \alpha)] N_{\text{A}} Q_{\text{A}}(E_{\text{AXYZ}}) \times \lambda_{\text{A}}(E_{\text{AXYZ}}) \cos \theta \left(\frac{d\Omega}{4\pi} \right), \quad (6.7)$$

where γ_{AXYZ} is the probability that the ionized core level X in element A is filled with the ejection of an XYZ Auger electron, $\sigma_{\text{AX}}(E_0)$ is the ionization cross section of the core level X in element A for electrons of energy E_0 , n_{AX} is the population of the level X, α is the angle of incidence of the electron beam from the surface normal, $r_{\text{A}}(E_{\text{AX}}, E_0, \alpha)$ is the additional ionization of the core level X with binding energy E_{AX} arising from backscattered energetic electrons, $Q_{\text{A}}(E_{\text{AXYZ}})$ is a term discussed later in this section, N_{A} is the atomic density of the A atoms, $\lambda_{\text{A}}(E_{\text{AXYZ}})$ is the inelastic mean free path (IMFP) for the XYZ Auger electrons with energy E_{AXYZ} in sample A, and θ is the angle of emission of the detected electrons from the surface normal.

The inner shell ionization cross section is often calculated using *Gryzinski's* formula [6.71], but a detailed analysis [6.72] shows that the formula of *Casnati* et al. [6.73] is significantly more accurate. Plots of these cross sections may be found in [6.72].

The parameter γ_{AX} allows for the competing process of x-ray emission, where

$$\gamma_{\text{AX}} = 1 - \frac{Z^4}{Z^4 + Z_0^4}, \quad (6.8)$$

with $Z_0 = 32.4$ [6.74] for $X = K$, 89.4 [6.74] for $X = L$, 155.9 [6.75] for $X = M$, and 300 for $X = N$ shell [6.76].

The next term is the backscattering factor $r_{\text{A}}(E_{\text{AX}}, E_0, \alpha)$, and this is taken from the work of *Shimizu* [6.77]. General plots of this function may be found in [6.70]. Figure 4 in [6.78] shows the Z dependence of $[1 + r_{\text{A}}(E_{\text{AX}}, 5000, 30^\circ)]$ for various $E_{\text{AX},i}$, where the backscattering enhancement may reach over a factor of two. N_{A} values are evaluated from published data for elements [6.79, 80]. Figure 5 in [6.78] shows a plot of N_{A} versus Z. This is strongly periodic and spans

a range of values with a factor of eight between the maximum and minimum values. The weak correction factor $Q_{\text{A}}(E_{\text{AXYZ}})$ is a term allowing for the reduction in overall escape probability of electrons from the solid arising from elastic scattering [6.81]. This parameter ranges from 0.9 to 1.0 and depends on the element and the electron energy. Values of Q may be taken from the plots of *Seah* and *Gilmore* [6.82]. The inelastic mean free path, $\lambda_{\text{A}}(E)$, can be taken from the TPP-2M formula [6.83] given by

$$\lambda_{\text{A}}(E) = \frac{E}{E_{\text{p}}^2 [\beta \ln(\gamma E) - (C/E) + (D/E^2)]} \quad [\text{\AA}], \quad (6.9)$$

where

$$E_{\text{p}} = 28.8 \left(\frac{\rho N_{\text{v}}}{A} \right)^{0.5} \quad [\text{eV}], \quad (6.10)$$

$$\beta = -0.10 + 0.944(E_{\text{p}}^2 + E_{\text{g}}^2)^{-0.5} + 0.069\rho^{0.1}, \quad (6.11)$$

$$\gamma = 0.191\rho^{-0.50}, \quad (6.12)$$

$$C = 1.97 - 0.91W, \quad (6.13)$$

$$D = 53.4 - 20.8W, \quad (6.14)$$

$$W = \frac{\rho N_{\text{v}}}{A}. \quad (6.15)$$

In these equations, ρ is the density (in g cm^{-3}), N_{v} is the number of valence electrons per atom, and A is the atomic weight. For metals, the value of E_{g} , the band gap, is zero. Recommended values for N_{v} have recently been published by *Tanuma* et al. [6.84]. Free software is available to facilitate this process [6.5, 85].

The above formulae allow us to calculate the intensity for a pure element, and I_{A}^{∞} (for simplicity, we now omit to define the particular transition XYZ) may be considered as a pure element relative sensitivity factor (PERSF). These are what one would obtain by measuring spectra in the reference handbooks [6.39–43], after correcting for the IERF. To compute the composition, one then needs to use not (6.2), but [6.70]

$$X_{\text{A}} = \frac{F_{\text{AM}}(I_{\text{AM}}/I_{\text{A}}^{\infty})}{\sum_i F_{i\text{M}} I_{i\text{M}}/I_i^{\infty}}, \quad (6.16)$$

where the $I_{i\text{M}}$ are the intensities for the elements i measured in the matrix M of the sample. The matrix elements $F_{i\text{M}}$ are given by [6.70]

$$F_{i\text{M}} = \frac{N_i}{N_{\text{M}}} \frac{Q_i(E_i)}{Q_{\text{M}}(E_i)} \frac{[1 + r_i(E_i)]}{[1 + r_{\text{M}}(E_i)]} \frac{\lambda_i(E_i)}{\lambda_{\text{M}}(E_i)}. \quad (6.17)$$

The difficulty of calculating the F_{iM} when the matrix is not known until the X_A are calculated leads most analysts to ignore the F_{iM} and effectively replace them by unity. The F_{iM} vary from 0.1 to 7 in different systems [6.78], and so this is the error involved by ignoring them.

Seah and Gilmore [6.78] show that (6.2) is in fact valid if the $PERSF$, I_A^∞ , is replaced by the average matrix relative sensitivity factor ($AMRSF$) I_A^{Av} , given by

$$I_A^{Av} = \gamma_A n_A \sigma_A \sec \alpha [1 + r_{Av}(E_A)] N_{Av} Q_{Av}(E_A) \times \lambda_{Av}(E_A) \cos \theta \left(\frac{d\Omega}{4\pi} \right). \quad (6.18)$$

In this equation, the items concerning effects inside the atom retain their original element A specificity and subscript (“A”), but those outside, such as the number density, become that for an average matrix (“Av”). Appropriate equations for the average matrix terms are given in references [6.78, 86] and may also be found in ISO 18118.

Many of the above numbers are difficult to calculate, and so experimental databases are often used. However, we may now see why lack of calibration of the spectrometers and use of the wrong measures can lead to significant errors. Tables of data for $AMRSFs$ and their constituent parts are available on the [NPL](#) website [6.4] for the convenience of analysts.

Quantification of Inhomogeneous Samples

The general quantification of inhomogeneous layers that vary over the outermost 8 nm is a complex issue dealt with in detail elsewhere [6.87, 88]. However, for AES there is a special case of particular interest to metallurgists and those studying catalysts: the case of the segregated layer one atom thick with partial coverage. Expressed as a fraction of a monolayer at the packing density of the substrate s , the fraction of the monolayer is given by θ_A , where [6.70]

$$\theta_A = X_A \frac{L_s(E_A)}{a_s} \cos \theta, \quad (6.19)$$

where a_s^3 is the atomic volume of the substrate atoms and $L_s(E_A)$ is the attenuation length of electrons of energy E_A in the overlayer. $L_s(E_A)$ is related to $\lambda_s(E_A)$ [6.82], as discussed later at (6.21). In (6.19), θ_A is unity at a_s^{-2} atoms per unit area. Much early and some recent AES work in this area ignores the difference in concept between θ_A and X_A , leading to confusion and errors in the range 1–10.

Sputter Depth Profiling

The basic principle of sputter depth profiling is that one removes the surface layer by layer using inert gas ion sputtering, in situ, usually with 1–5 keV argon ions, whilst monitoring the remaining surface by AES . For samples with air-exposed surfaces there will be a level of hydrocarbon contamination that is first removed, and during this short period, the signals from the underlying material rise rapidly, as seen in Fig. 6.4b. This effect is not seen in Fig. 6.4a, as the surface there is not air exposed. For elemental solids, the signal then remains constant until the layer is removed. The signal then falls to an appropriate level or zero for the next layer. If the layer is a compound, one element may be preferentially sputtered so that the quantified signal no longer reflects the composition prior to sputtering. For the Ta_2O_5 layer in Fig. 6.4b, we see the composition fall from Ta_2O_5 to approximately TaO as the oxygen is depleted. The compound is not stoichiometric TaO but a distribution of chemical states [6.89–91] over a thin layer of the order of the projected range [6.92] of the sputtering ion. This range is typically slightly more than the analysis depth [6.93].

The preferential sputtering of compounds has been a long and rather frustrating area of research where theoretical models have been proposed [6.90, 94–97] but predicting the effect in any quantitative way is currently not possible. To quantify a profile involving a compound, the best approach is to sputter a reference layer of the compound under identical conditions to the sample in order to evaluate the spectral intensities expected. Generally, those who conduct such profiles are less interested in quantifying compound layers that they know are there, and are more interested in changes in the layers as a result of, say, a heat treatment that leads to changes in the interface shape. Thus there is already a built-in reference layer. To measure changes at the interfaces, good depth resolution is required.

In early studies of sputtered metallic layers, the depth resolution Δz deteriorated roughly according to

$$\Delta z = kz^{0.5}, \quad (6.20)$$

where for Δz and z in units of nm, k is approximately unity [6.90, 98]. This was caused by the development of topography, which can be measured by scanning electron microscopy (SEM ; Sect. 6.2.4) or atomic force microscopy (AFM ; Sect. 6.2.3). For single-crystal wafer studies, it was found that the depth resolution, which starts as an exponential decay of one monolayer (≈ 0.26 nm) for a submonolayer film, as

shown in Fig. 6.4a, degrades and saturates at approximately 1 nm [6.98, 99] for thicker films.

A major development was made by Zalar [6.101], who suggested rotating the sample whilst sputtering in the same manner as when preparing samples for transmission electron microscopy (TEM). With rotation speeds of about 1 rpm, excellent results of 5 nm resolution are obtained, even for the difficult polycrystalline metallic layers [6.102]. It is essential that the electron and ion beams are properly aligned to the same point on the sample surface, irrespective of the use of rotation or not, in order to obtain the best depth resolution [6.103].

In the above, we have used the term depth resolution without clearly defining it. In ISO 18115 it is defined as the depth range over which a signal changes by a specified quantity when reconstructing the profile of an ideally sharp interface between two media or a delta layer in one medium. In an attached note it adds that, for routine analytical use, a convention for the specified levels is 16–84% for layers such as those shown in Fig. 6.4b. These levels arise from the standard deviation points when the interface resolution is described by a Gaussian function. For very high-resolution profiles, the interface shape is described by exponentials [6.45, 102] and the above convention, although useful, then has no specific correlation with a physical model.

Above, we have considered Δz , but also critical is the measurement of the absolute depth z . Measurement of the sputtered depth is covered in the ISO technical report ISO/TR 15969. Usually, a stylus profilometer is

used (Sect. 6.2.1), but certain laboratories prefer optical techniques (Sect. 6.2.2) or AFM (Sect. 6.2.3). AFM can be particularly useful for small, shallower craters where the roughness of the crater base is also of interest. There are several issues that analysts need to be aware of that are of increasing importance at shallower depths. At the start of sputtering, some contamination is removed. This takes a brief time. Next, the incident ions are implanted, causing a slight swelling. As the beam particles build up in the sample, the sputtering yield changes until, after sputtering for approximately 1 nm, an equilibrium is established. After this, the system remains constant if rotation is used; if not, a surface topography may develop that slowly reduces the sputtering rate. For sputtering with argon ions, the build-up of argon is typically 2.5% [6.104] and so these effects are small and are generally ignored. A further effect, seen for samples that react with air, is that the crater base will swell as it oxidizes on air exposure prior to the depth measurement. If a correlation of time and depth is made for many craters, a straight line correlation should be found, but it may not pass through the origin. Typically, the offset may be up to 1 nm for Si wafers.

Where a system comprises layers of different types, the sputtering rate will change from layer to layer, and an elapsed time to depth conversion cannot be made with one sputtering rate. Figure 6.5 shows the sputtering yield for argon incident at 45° for several energies and many elements. The rates for different elements clearly vary enormously. The rate then needs to be evaluated for

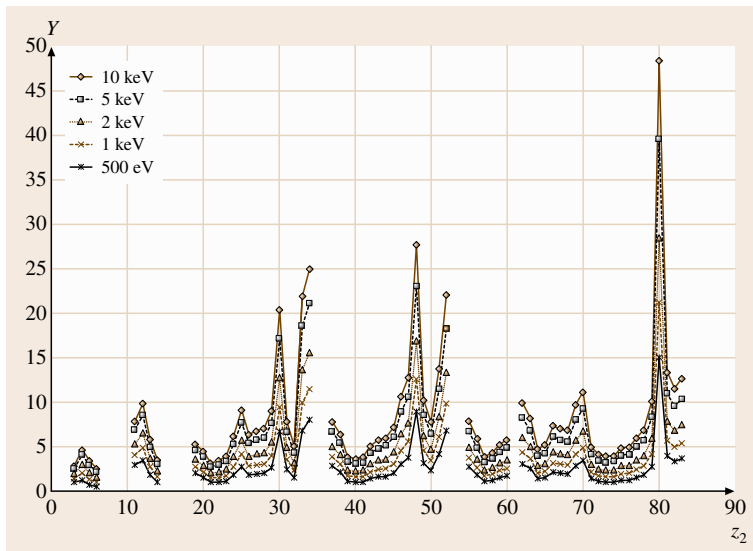


Fig. 6.5 Calculated sputtering yields of elements using argon ions at 45° to the sample surface for several energies as a function of the atomic number of the sample, Z_2 (after [6.3, 93, 100])

each layer separately or evaluated through calculation of the relevant sputtering yields Y and a measurement of the ion beam current density J at the AES measurement point

$$d = \frac{JtYa^3}{e}, \quad (6.21)$$

where t is the time for sputtering that layer, e is the electronic charge, and a^3 is the atomic volume deduced from

$$1000\rho Na^3 = A. \quad (6.22)$$

Ion beam currents generally need to be measured using a screened Faraday cup, but focused ion beam currents may be measured using an appropriately drilled hole in a sample or the sample stage [6.105]. In (6.22), ρ is the density of the element (kg/m^3) of atomic weight A , and N is Avogadro's number. Thus, d may be determined if Y is known. Values of Y have been tabulated for many elements and some compounds. Recent work has led to significant improvements in the accuracy of calculating Y for elements for Ne, Ar, and Xe bombarding ions at 0° and 45° angles of incidence [6.93, 104], with a typical uncertainty, for the calculations shown in Fig. 6.5, of 10%. The equations are rather complicated, and so plots of the yields may also be found as tables on the NPL website [6.100]. The uncertainty from this convenient route, however, means that it is not as accurate as a direct measurement of depth.

For sputter depth profiling, Ar is most popular. Occasionally, if the argon AES peaks interfere with the peaks to be measured, Ne or Xe may be used [6.104]. Some analysts prefer Xe, as the depth resolution is then improved sometimes.

6.1.2 X-ray Photoelectron Spectroscopy (XPS)

General Introduction

XPS has a considerable base in physics, in common with AES, and is often conducted using the same instrument. XPS uses characteristic x-rays to excite electrons that are energy-analyzed by the same spectrometer that is used for high-energy-resolution AES analysis. Thus, XPS instruments often have an added electron gun for AES. The x-ray source is generally of Mg or Al K_α x-rays or, in many modern instruments, monochromated Al K_α x-rays. As shown in Fig. 6.2b, the x-rays of energy $h\nu$ directly eject core electrons from the solid with kinetic energy E given by

$$E = h\nu - E_1, \quad (6.23)$$

where it is these E_1 values, the core level binding energies, that are required in XPS. Thus, the E_1 values are usually taken to be positive values, unlike (6.1), and the binding energy scale is usually used directly rather than the Fermi level referenced kinetic energy E . The values of E_1 provide information about the chemical state of the element analyzed. Tabulated binding energies for the elements may be found in Bearden and Burr [6.106] and for elements and compounds in handbooks [6.107–109], textbooks [6.110], and websites [6.111]. Note that, whilst Bearden and Burr use the x-ray nomenclature for energy levels, as is common for AES, this is rarely used in XPS. Here, the level number and subshell letter with the spin-orbit coupling number are given, so that M_V or M_5 translates to $3d_{5/2}$. After the initial excitation, the atom is left with a core hole that can be filled by an Auger process ejecting an Auger electron. This electron also appears in the measured spectrum. Figure 6.6 shows a photoelectron spectrum for copper with the photoelectron and Auger electron peaks labeled.

The photoelectrons are mostly in the kinetic energy range 500–1500 eV, and so XPS is similar to AES in its surface sensitivity. For a few (often important) elements, the characteristic peaks may have kinetic energies as low as 200 eV.

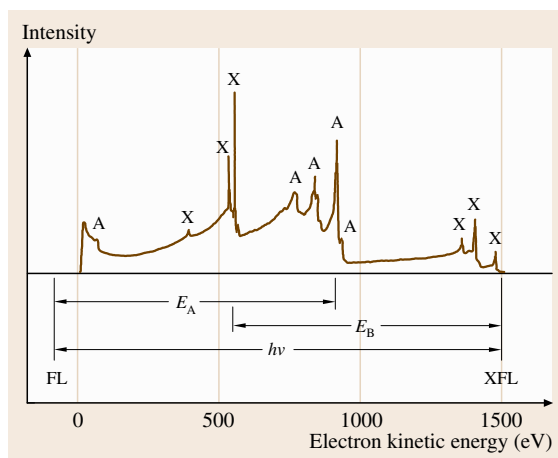


Fig. 6.6 X-ray photoelectron spectrum for Cu using an unmonochromated Al x-ray source. The photoelectron peaks are labeled “X” and the Auger electron peaks “A”. The positions of the Cu Fermi level (FL) and the photoemitted Fermi level electrons (XFL) are indicated (after [6.53]). The vacuum level, indicated by the start of the spectrum, is 4.5 eV above the Fermi level (FL) and is shown exaggerated here for illustrative purposes

Handling of Samples

The handling of samples for XPS is generally the same as that for AES, except that the types of sample tend to be rather different. Environmental contaminants such as poly(dimethyl siloxane) (PDMS) and similar materials are often analyzed, and so it is rare for samples to be cleaned. More samples are insulating, and so greater consideration needs to be given to charge control and charge correction. Information on most of the important methods for these is given in ISO 19318, but what is achievable often depends on the specific instrumental setup. Samples can be in the form of polymer films or powders generally not studied by AES.

In some instruments, mounting the sample under a grid or aperture works well for charge control, but in others this leads to broader peaks. With monochromated x-rays, an electron flood gun or very low-energy ion flux may be required for charge control. Whatever is used, the analyst should ensure that the sample is not exposed to unnecessary levels of radiation, since most of these samples are easily degraded by heat, electrons or ions [6.115, 116].

Calibrating the Spectrometer Energy Scale

As for AES, Cu and Au samples set with their angle of emission $\leq 56^\circ$ are sputtered clean, and the measured energies of the peaks listed in Table 6.7 are compared with the energy values given there. As for AES, the peak energy for the calibration is evaluated from the top of the peak without background subtraction [6.54]. In Table 6.7, peak number 3 is an Auger electron peak, and whilst this works well for unmonochromated x-rays, it cannot be used accurately with a monochromator. The lineshapes and energies of the K_{α_1} and K_{α_2} x-rays that characterize $h\nu$ in (6.23) appear to be the same in all unmonochromated instruments. However, the lineshapes and energies of the K_α x-rays, when monochromated, vary significantly and depend on the setup of the monochromator and its thermal stability. By altering the monochromator settings, the measured

energies of the peak may be moved over a kinetic energy range of 0.4 eV without too much loss of intensity [6.113]. Thus, for monochromated systems, in Table 6.7 the Cu Auger electron peak is replaced by the $3d_{5/2}$ photoelectron peak from Ag. This action requires the cleaning of an additional sample.

In ISO 15472, the calibration given in Table 6.7 is included into a full protocol that includes methods of conducting the calibration, assessing the uncertainties, establishing tolerance limits, and evaluating a calibration schedule. For laboratories operating under a quality system [6.117], and for analysts trying to ensure the validity of their data, these are essential. Use of the standard with a modern, well-maintained spectrometer should result in calibration within tolerance limits of ± 0.2 eV over 4 months or ± 0.1 eV over 1 month before recalibration is required. For many purposes ± 0.2 eV is satisfactory.

Repeatability of the Intensity Scale

For XPS, the evaluation of the repeatability of the intensity scale is similar to that for AES in Sect. 6.1.1. Of critical importance are the comments made there in relation to detectors and especially ISO 21270 on the linearity of the intensity scale. For XPS, the intensity ratio is determined from cleaned copper using the Cu 3p and Cu $2p_{3/2}$ peak areas after subtracting a Shirley background [6.118]. Smoothing of the end-points for establishing the Shirley background can improve the precision and enable repeatabilities as good as 0.2% to be achieved in a series of measurements. ISO 24237 describes the signal levels and procedures needed to get the best quality data from a sample of copper, how to build that into a monitoring protocol, and how to set up tolerance limits for a control chart to try to ensure that the intensity measurements remain fit for purpose.

Calibrating the Intensity Scale

Interlaboratory studies to compare the shapes of spectra obtained in different laboratories unfortunately show

Table 6.7 Reference values for peak positions on the binding energy scale [6.113, 114] $E_{\text{ref } n}$

Peak number n	Assignment	$E_{\text{ref } n}$ (eV)		
		Al K_α	Mg K_α	Monochromatic Al K_α
1	Au $4f_{7/2}$	83.95	83.95	83.96
2	Ag $3d_{5/2}$	—	—	368.21
3	Cu L_3VV	567.93	334.90	—
4	Cu $2p_{3/2}$	932.63	932.62	932.62

This table is a refinement of earlier tables (after [6.53, 112])

that there are marked differences [6.63]. These lead to variations of a factor of two in quantification if the same relative sensitivity factors were to be used in all laboratories.

The situation here and the rationale and protocol for evaluating and using the IERF are precisely the same as in *Calibrating the Intensity Scale* for AES, except that, instead of measuring the spectra from the Cu, Ag, and Au reference foils using 5 keV electrons, we use the Al or Mg x-rays at incident angles in the range 0–50° from the surface normal.

Relative sensitivity factors for (6.3) are available from several handbooks [6.107–109], textbooks [6.119], and publications [6.69, 120]. Early sensitivity factors varied significantly [6.69], and it is not clear if these later values are consistent for the instruments intended or if significant uncertainties still persist. An analysis has not been made since the assessment in 1986 [6.69] showed that the sensitivity factor datasets were very variable. This partly arose because the IERFs of the instruments used were not measured in these handbooks. In the next section we address the basic concept of the peak intensities.

Quantitative Analysis of Locally Homogeneous Solids

Following the procedure for AES, the x-ray photoelectron intensity per photon of energy $h\nu$ into a small solid angle $d\Omega$ for a pure element A from the subshell X_i is

given by

$$I_{AX_i}^{\infty} = n_{AX_i} \sigma_{AX_i} \sec \alpha N_A Q_A(E_{AX_i}) \lambda_A(E_{AX_i}) \times \left[1 + \frac{1}{2} \beta_{\text{effAX}} \left(\frac{3}{2} \sin^2 \gamma - 1 \right) \right] \times \cos \theta \left(\frac{d\Omega}{4\pi} \right), \quad (6.24)$$

where n_{AX_i} is the population of electrons in the subshell i of the core level shell X of element A, σ_{AX_i} is the ionization cross section for that core level for photons of energy $h\nu$, α is the angle of incidence of the x-ray beam from the surface normal, γ is the angle between the incident x-ray beam and the direction of the photoemitted electrons, and the other terms are as for AES. Values of the product of n_{AX_i} and σ_{AX_i} are taken from the data of Scofield [6.121]. Other cross sections exist but have been shown to be less accurate [6.122].

At the magic angle, where $\gamma = 54.7^\circ$, the final term in square brackets in (6.14) is unity. However, at other angles this function is generally higher than unity for $\gamma > 54.7^\circ$. The values of β are tabled by Yeh and Lindau [6.123] and by Reilman et al. [6.124] as well as others. The parameter β is valid for gas-phase work, but in solids Jablonski [6.81] has shown that β is reduced to β_{eff} by elastic scattering. Seah and Gilmore [6.82] reduce Jablonski's Monte Carlo data to sets of equations

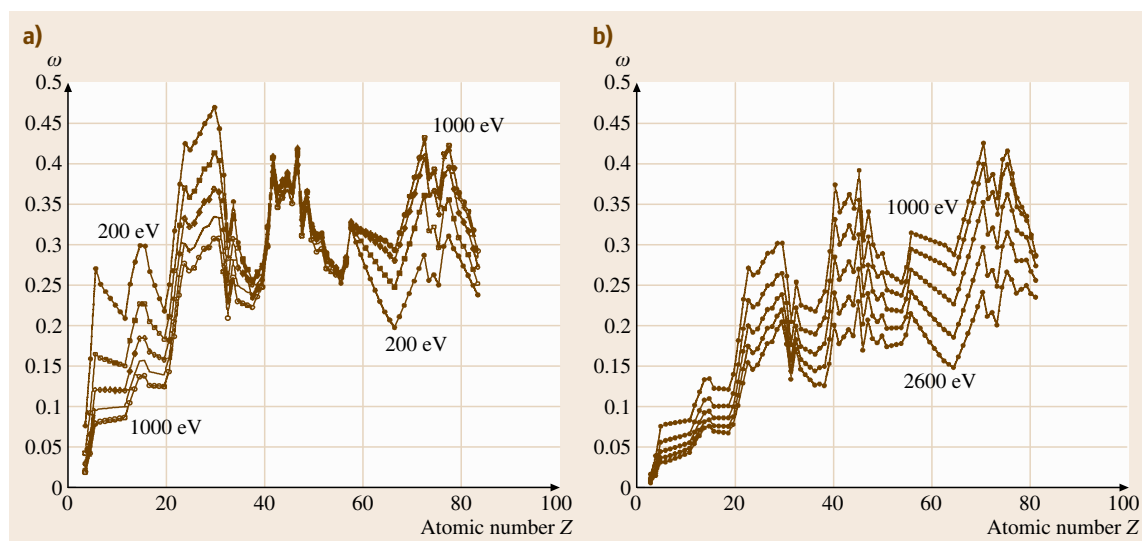


Fig. 6.7a,b Dependence of ω on Z for various electron kinetic energies: (a) at 200 eV intervals from 200 to 1000 eV and (b) at 400 eV intervals from 1000 to 2600 eV (after [6.82])

such as

$$\beta_{\text{eff}}(\theta) = \beta_{\text{eff}}(0)(1.121 - 0.208 \cos \theta + 0.0868 \cos^2 \theta), \quad (6.25)$$

where

$$\frac{\beta_{\text{eff}}(\theta)}{\beta_{\text{eff}}} = 0.876[1 - \omega(0.955 - 0.0777 \ln Z)], \quad (6.26)$$

where the value of ω may be read from graphs [6.82] or Fig. 6.7.

The above calculation gives the **PERSFs** for **XPS**. However, for quantification, as discussed above for **AES**, we really need **AMRSFs** and so may use (6.3). If we use **PERSFs** in (6.3) and effectively ignore the relevant matrix factors, the errors involved range from 0.3 to 3 [6.86]. Using **PERSFs** we obtain (6.16) and (6.17), except that the $[1 + r(E)]$ term is replaced by the term $[1 + 1/2\beta_{\text{eff}}(3/2 \sin^2 \gamma - 1)]$. Then [6.86, 125]

$$I_{\text{A}}^{\text{AV}} = n_{\text{AX}_i} \sigma_{\text{AX}_i} N_{\text{AV}} Q_{\text{AV}}(E_{\text{AX}_i}) \lambda_{\text{AV}}(E_{\text{AX}_i}) \times G_{\text{AV}}(E_{\text{AX}_i}), \quad (6.27)$$

where [6.125]

$$G_{\text{AV}}(E_{\text{AX}_i}) = 1 + \frac{1}{2}\beta_{\text{effAVAX}_i}(\theta) \left(\frac{3}{2} \sin^2 \gamma - 1\right). \quad (6.28)$$

Here, β_{eff} is calculated via (6.25) and (6.26) with $Z_{\text{AV}} = 41$ and ω_{AV} deduced from Fig. 6.7 or the **NIST** databases [6.5, 126].

In the past, the differences between the **PERSFs** and **AMRSFs** have not been recognized, and in general, the experimental data have been for compounds and not elements and so relate more closely to **AMRSFs**. However, these had no spectrometer calibration and furthermore were often blended with **PERSF** calculations, leading to parameters that were ill defined but which were adjusted by manufacturers to give valid results on their equipment when tested against certain reference compounds. As noted in Sect. 6.1.1, tables of data for **AMRSFs** and their constituent parts are on the **NPL** website [6.3] under *Reference data* for the convenience of analysts.

Quantification of Thin Homogeneous Overlayers

An important use of **XPS** is the measurement of overlayer thicknesses of up to 8 nm. The intensities of a pure layer of A of thickness d on a substrate of B are given by

$$I_{\text{A}} = I_{\text{A}}^{\infty} \left\{ 1 - \exp \left[-\frac{d}{L_{\text{A}}(E_{\text{A}}) \cos \theta} \right] \right\} \quad (6.29)$$

and

$$I_{\text{B}} = I_{\text{B}}^{\infty} \exp \left[-\frac{d}{L_{\text{A}}(E_{\text{B}}) \cos \theta} \right]. \quad (6.30)$$

In the approximation of no elastic scattering, the L_{A} values would be the **IMFPs** λ_{A} . However, in the presence of elastic scattering, *Cumpson and Seah* [6.127] showed that λ_{A} should be replaced by the attenuation length L_{A} and that (6.29) and (6.30) were valid for $\theta \leq 58^\circ$. *Seah and Gilmore* [6.82] analyze these data to show, as an analog to (6.16), that elastic scattering leads to

$$\frac{L}{\lambda} = 0.979[1 - \omega(0.955 - 0.0777 \ln Z)]. \quad (6.31)$$

More detailed calculations by *Jablonski and Powell* [6.128] give similar results.

For general films, (6.29) and (6.30) are not easy to solve for d from values of I_{A} and I_{B} , since if $E_{\text{A}} \neq E_{\text{B}}$, the analysis must become iterative. For this reason, *Cumpson* devised the *Thickogram* to help solve this problem [6.129]. For metals and their oxides as overlayers, (6.29) and (6.30) can be used for the oxygen peak and the substrate in the metallic form. However, any adsorbed moisture on the surface adds to the oxygen peak [6.130], and a better method is to use the substrate metal intensities in the oxide (o) and elemental (e) states using **XPS** with peak synthesis. This has the advantage that $E_{\text{A}} = E_{\text{B}}$ sufficiently closely that their difference may be ignored. Thus, in **XPS**,

$$d = L_{\text{O}} \cos \theta \ln(1 - R_{\text{expt}}/R_{\text{O}}), \quad (6.32)$$

where $R_{\text{expt}} = I_{\text{o}}/I_{\text{e}}$ and $R_{\text{O}} = I_{\text{o}}^{\infty}/I_{\text{e}}^{\infty}$. The value of R_{O} may be calculated, but for accurate measurements of d , it is recommended that R_{O} is measured experimentally using the same peak fitting as will be used for the analysis. If the samples can be reasonably cleaned, and if there is a significant range of thicknesses, a plot of I_{o} versus I_{e} gives the sought-after I_{o}^{∞} and I_{e}^{∞} as the intercepts of the axes, since from (6.29) and (6.30),

$$\frac{I_{\text{o}}}{I_{\text{o}}^{\infty}} + \frac{I_{\text{e}}}{I_{\text{e}}^{\infty}} = 1. \quad (6.33)$$

The use of (6.32) to quantify the thicknesses of thermal SiO_2 layers on Si wafers has been evaluated in a major international study [6.130, 131] involving comparison with medium-energy ion scattering (**MEIS**), Rutherford backscattering spectrometry (**RBS**), elastic backscat-

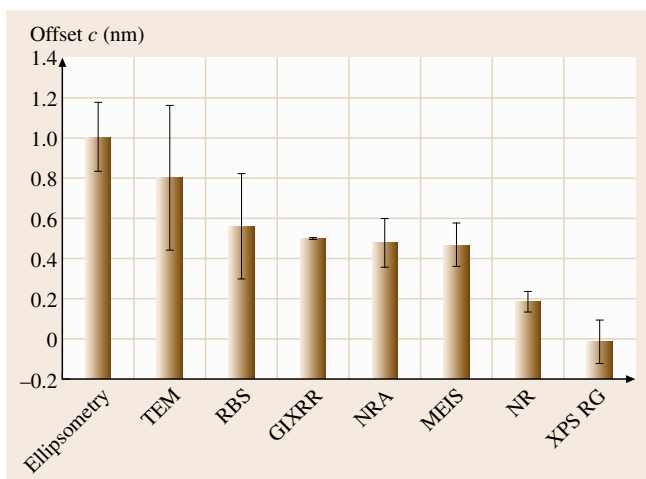


Fig. 6.8 The offsets c measured for various techniques, shown by their averages and standard deviations when compared with XPS (after [6.130]), updated for data in [6.134]. Note that one atomic layer is approximately 0.25 nm thick

tering spectrometry (EBS), nuclear reaction analysis (NRA), secondary ion mass spectrometry, ellipsometry, grazing-incidence x-ray reflectance (GIXRR), neutron reflectance (NR), and transmission electron microscopy (TEM). The thicknesses were in the range 1.5 nm to 8 nm to cover the range for ultrathin gate oxides. In order to use (6.32) reliably in XPS, the diffraction or forward-focusing effects of the crystal substrate need to be averaged or avoided [6.132]. To do this, a reference geometry (RG) is used with the emission direction at 34° to the surface normal in an azimuth at 22.5° to the [011] direction for (100) surfaces, and 25.5° from the surface normal in the [101] azimuth for (111) surfaces [6.132]. If these orientations are not chosen, R_o tends to be smaller and (6.32) gives a result that is progressively in error for thinner layers. Using the above approach, excellent linearity is obtained [6.133], and excellent correlations with the other methods show that L_o can be calibrated to within 1%, allowing XPS to be used with very high accuracy. Care needs to be taken, when working at this level, to ensure that the angles of emission are accurately known [6.134].

In the study, when matched against the XPS thickness d_{XPS} , most of the other methods lead to offsets c in the relation

$$d = md_{\text{XPS}} + c. \quad (6.34a)$$

These offsets c are shown in Fig. 6.8 [6.130]. For MEIS, NRA, and RBS, the offset represents the thickness of

the adsorbed oxygen-containing species, such as water, since these methods measure the total oxygen thickness rather than oxygen in SiO_2 . An offset of 0.5 nm represents between one and two monolayers of water. For ellipsometry, where the measurements are in air, there is a further layer of hydrocarbon and physisorbed water that builds this up to around 1 nm. The offset for TEM is not understood and may arise from progressive errors in defining the thicknesses of thinner films. The offsets for GIXRR and NR also arise from the contaminations but are weaker in NR and may, in the future, be fully removed by modeling.

For quantitative measurement of the thicknesses of organic layers A, Seah and Spencer [6.135] use (6.30) where the attenuation length $L_A(E_B)$ is given by

$$L_A(E_B) = 0.00837E_B^{0.842}. \quad (6.34b)$$

The analyses of more complex profiles are discussed by Cumpson [6.87] and by Tougaard [6.88].

Sputter Depth Profiling

There is essentially very little difference between sputter depth profiling using XPS and that using AES except concerning certain practical issues. Firstly, if unmonochromated sources are used, the larger area analyzed requires a larger area to be sputtered and generally a poorer depth resolution is obtained. This arises from the difficulty in retaining a flat, uniform depth over a larger area. With focused monochromators this should not be a problem, but the depth resolution is rarely as good as for AES. Secondly, the need to maintain a good vacuum environment around the x-ray source discourages the use of in situ, large-area ion guns with their higher gas loads.

Much of the advantage of XPS – of measuring the chemical state – is lost as a result of the changes in composition brought about by preferential sputtering by the ion beam. Thus, XPS depth profiling has been less popular than AES, but recent work has shown that, in organic materials, the chemical state may be retained if the primary sputtering ions are C_{60} [6.136] or argon clusters [6.137]. These have excellent promise for XPS and SIMS [6.138].

6.1.3 Secondary Ion Mass Spectrometry (SIMS)

General Introduction

In secondary ion mass spectrometry, atoms and molecules in the surface layers are analyzed by their removal using sputtering and subsequent mass analysis

in a mass spectrometer. The majority of emitted ions come from the outermost atom layer. Unfortunately, most of the particles are emitted as neutral atoms and only 10^{-4} – 10^{-2} are emitted as ions. Nevertheless, the detection capability of SIMS is generally far superior to those of AES or XPS. A second problem is that the intensity of the ion yield is extremely matrix sensitive, and there are, as yet, no methods for calculating this effect accurately [6.139]. These properties have led to SIMS becoming very important in two major fields and being used in two distinct ways.

Historically, the most important approach has been that of dynamic SIMS, and this has found major use in characterizing wafers for the semiconductor industry. It is here that measurement issues are critical, and so it is here that we shall focus. More recently, the second approach – that of static SIMS – has been able to provide unique information concerning complex molecules at surfaces. Static SIMS has been in use for more than 30 years, but recent instrumental developments have made the method reliable and more straightforward for industrial analysts to use. We shall treat these fields separately below, but note that their separation is reducing. In a recent analysis of publications for the biennial SIMS conferences [6.141], the historical dominance of dynamic SIMS has disappeared, and research effort is currently slightly biased in favor of static SIMS.

Dynamic SIMS

In dynamic SIMS, the use of well-focused ion beams or imaging mass spectrometers allows submicrome-

ter images of the surface to be obtained with very high sensitivity and facilitated isotope detection. At present, 50 nm spatial resolution can be achieved. High-resolution imaging is usually achieved with the removal of a significant amount of the surface material, which is why it is called dynamic SIMS or (historically) just SIMS. The dynamic removal of material allows composition depth profiles to be measured, and it is these profiles for the semiconductor industry that account for much of the routine industrial analysis. All of the ISO standards in this area (Tables 6.2, 6.3), certified reference materials, and two-thirds of the dynamic SIMS applications at meetings [6.141] concern depth profiling with semiconductors. There are two essential measurement issues that require quantification in sputter depth profiles for dopants in semiconductors: the composition and the depth scale. However, these cannot be evaluated in many cases without considering the depth resolution. SIMS is very powerful when studying dopants, since the method has the high sensitivity required for the low concentrations, as shown in Fig. 6.9. Fortunately, the peak concentration levels are still sufficiently low that linearity of composition and signal can still, generally, be assumed. We shall start by considering the depth resolution.

Depth Resolution. In AES and XPS, we have defined the depth resolution from the profile width of a sample characterized by a step-function composition. This is very useful for the small dynamic range of those spectroscopies, but in SIMS it is more useful to char-

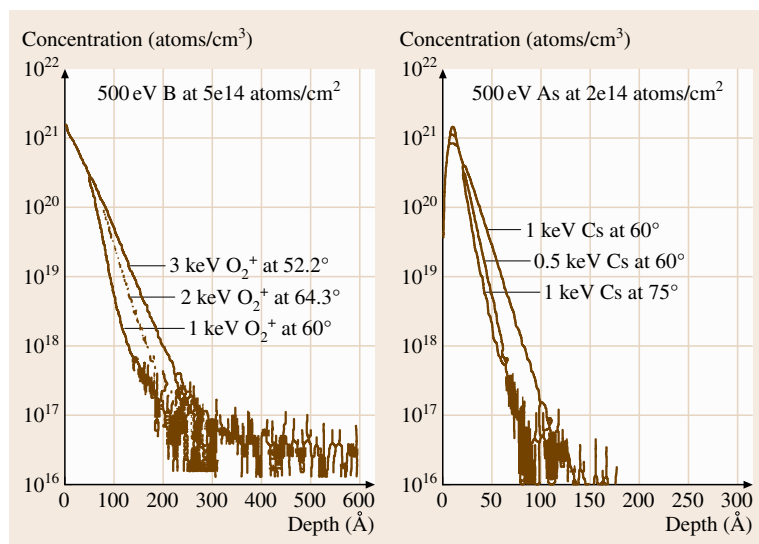


Fig. 6.9 Profiles of 500 eV boron and 500 eV arsenic implants in silicon using O_2^+ and Cs^+ ion beams (after Hitzman and Mount [6.140]). These show the benefit of very low-energy primary ion beams

acterize the resolution by the slope of the exponentials describing the up or down slopes as the new region is entered or exited. These slopes are termed the leading edge decay length λ_c and the trailing edge decay length λ_t in ISO 18115, and are defined as the characteristics of the respective exponential functions. These have a physical basis, unlike the descriptions used for AES or XPS. Since one is often dealing with dilute levels, the depth resolution is best characterized by the up and down slopes from delta layers. The method for estimating depth resolution in this way is described in ISO 20341, based on the analytical description of Dowsett et al. [6.142] and illustrated, with detailed data, by Moon et al. [6.143] using five GaAs delta layers in Si at approximately 85 nm intervals.

In Fig. 6.9, one clearly sees that the ion beam species, angle of incidence, and energy all affect the depth resolution, and that this affects the tail of the dopant distribution, its half-width, and the position and magnitude of the peak. It is generally also true that, the lower the beam energy and more grazing the incidence angle, the better the depth resolution. In many mass spectrometers, a high extraction field is used to focus all of the ions ejected from the sample into the mass spectrometer, and the consequent field around the sample effectively limits the choice of energy and angle of incidence. To avoid this limitation, the traditional quadrupole mass spectrometer has retained its popularity. With these mass spectrometers, the low extraction field allows very low-energy ion guns to be utilized [6.144, 145]. For instance, Bellingham et al. [6.146] show that, for a 1 keV ^{11}B implant, the trailing edge decay length λ_t , when profiled using O_2^+ at normal incidence, increased with the beam energy E approximately as

$$\lambda_t = 0.13 + 0.1E, \quad (6.35)$$

where λ_t is in nm and E is in keV. The lowest value, 0.14 nm, was obtained using a 250 eV O_2^+ beam (125 eV per atom). For delta layers, the trailing edge decay length is always greater than the leading edge decay length as a result of the forward projection of the dopant atoms. Therefore, attention is directed above to λ_t .

Considerable effort is expended designing focused ion beams that work at these low energies and yet still have sufficient current density to be able to profile significant depths in a reasonable time for practical analysis. Use of more grazing incidence angles is also beneficial [6.145, 146], but this can usually only be achieved by tilting the sample, and this generally detrimentally affects the ion collection efficiency. The

choice of ion species also affects the depth resolution, and in general, the larger the incident ion cluster, the lower the energy per constituent atom and the shorter the trailing edge decay lengths. Thus, *Illgen* et al. [6.147] show that, when profiling delta layers of B in Si with 1 keV ions and with O_2 flooding of the sample, SF_5^+ is better than O_2^+ , which in turn is better than Xe^+ , Kr^+ , Ar^+ , and Ne^+ .

Recognizing the limitation of λ_t for shallow implants being affected by the atomic mixing, many authors [6.148–150] now experiment with removing the substrate chemically and profiling the critical layer from the backside. This reduces the atomic mixing and should improve the detection limit, but issues then arise from the flatness of the substrate removal.

Depth. The depth scale may be obtained by using the signal from a marker layer at a known depth, or by measuring the depth of the crater after profiling, or by calculating from the sputtering yield. The latter route [6.93, 104] is very convenient but only accurate, as noted earlier, to some tens of percent. The usual route is to use a stylus depth-measuring instrument, as described in Sect. 6.2.1, to define the crater depth in the region from which the signal is obtained. Alternatively, as discussed in ISO 17560, optical interferometry, as described in Sect. 6.2.2, may be used. Both of these give an accurate measurement of the crater depth d_0 at the end of the profile at time t_0 . Analysts then generally scale the depth d at time t according to

$$d = \frac{d_0}{t_0} \quad (6.36)$$

using the assumption that the sputtering yield or sputtering rate is constant. Unfortunately, this is only true once equilibrium is established.

At the present time, we cannot accurately calculate how the sputtering rate changes as the surface amorphizes and the incident ions dynamically accumulate in the eroding surface layer, but the effect can be measured. *Moon* and *Lee* [6.151] show, for instance, that the sputtering yield of Si falls from 1.4 to 0.06 as a result of 3.5×10^{16} 500 eV O_2^+ ions cm^{-2} incident normally on an amorphous Si layer. *Wittmaack* [6.152] finds that the rate for O_2^+ ions at 1 and 1.9 keV, at 55–60° incidence, falls to 40% after sputtering 2–5 nm. In more recent work studying thermal SiO_2 films, *Seah* et al. [6.130] find that the rate, when using 600 eV Cs^+ , falls similarly by a factor of two over the initial 1.5 nm.

In a recent study by *Homma* et al. [6.153] using multiple BN delta layers in Si with pitches of 2 or 3 nm,

it is shown that the sputtering rate for 250 eV O_2^+ ions falls by a factor between 1.2 and 1.43, depending on the delta layer pitch and the ion beam angle of incidence. At 1000 eV, a factor of 3.5 is seen for the 3 nm pitch delta layers. In an interlaboratory study of seven laboratories profiling these samples, this effect has been further studied by *Toujou et al.* [6.154]. *Homma et al.*'s data were repeated but, with the addition of O_2 flooding, the effect could be largely removed.

In addition to the nonlinearity occurring whilst the equilibrium is being established, a longer-term nonlinearity arising from the development of surface topography also occurs. This occurs when using O_2^+ bombardment to enhance the ion yields and to homogenize the matrix. It has been found for both Si and GaAs [6.155]. The surface starts smooth, but at a critical depth, ripples develop on the surface, orientated across the incident beam azimuth [6.156]. The critical depth for the onset of roughening has been reviewed by *Wittmaack* [6.157], who shows that, in vacuum without O_2 flooding, the critical depth for impact angles in the range $38\text{--}62^\circ$ falls from $10\ \mu\text{m}$ at 10 keV approximately linearly with energy to $1\ \mu\text{m}$ at 3 keV, but then approximately as $E^{4.5}$ to 15 nm at 1 keV beam energy. Once roughening has been established, the Si^+ and other signal levels used to normalize the sputtering rate change and, at the same time, the sputtering rate reduces. In many studies, O_2 flooding is used, but *Jiang and Alkemade* [6.158] show that this causes the roughening to occur more rapidly, such that, for a 1 keV beam at 60° incidence and intermediate O_2 pressures, the erosion rate had fallen after a critical depth of 50 nm and, above 3×10^{-5} Pa, the critical depth reduces to 20 nm. Use of other ion sources, such as Cs^+ , does not improve things [6.159].

The final issue that affects the measured rate of sputtering is that the crater depth only measures the thickness of material removed for deep craters. For shallow craters, as noted for AES, there will be some swelling of the crater floor resulting from implanted primary ions as well as postsputtering oxidation when the sample is removed from the vacuum system for measurement. For inert gas sputtering, the swelling should be small, since the take-up of inert gas is only some 2–3% over the projected range of the ion [6.104]. Similarly, on exposure to air, for Si, approximately 1 nm of oxide will be formed, which will cause a net swelling of around 0.6 nm. The whole swelling, therefore, may be 1 nm, and this is generally ignored for craters with depths greater than 100 nm. For other ion beams, the swelling arising from implantation may well be signifi-

cantly higher than this, but data do not exist to estimate the effect, except for, say, O_2^+ , where if a zone 1 nm thick is converted to SiO_2 , we get the above 0.6 nm swelling but nothing further upon air exposure.

Even if we have the correct depth scale, there is a final issue that profiles appear to be shifted from their true positions, since the atoms of a marker layer of interest are recoiled to a different depth from that of the matrix atoms [6.160]. Further shifts in the centroids and the peaks of delta layers arise from the atomic mixing and interface broadening terms as well as the effects of nearby delta layers [6.161]. The shifts seen by *Dowsett et al.* [6.161] were all less than 3 nm and arise from the overall asymmetry of the measured profile for each delta layer.

Thus, obtaining a repeatable depth scale with modern instruments when profiling dopants in Si is relatively simple. The ion beam sources are reasonably stable, and that stability may be monitored in situ via a matrix signal such as Si^+ . However, translating that to an accurate depth scale, particularly for ultrashallow depth profiles, is currently not routine and (depending on the sample) may involve significant errors.

Quantification. Quantification in dynamic SIMS is very important for semiconductor studies. Equations such as (6.3) can be used, but it is found that the sensitivity factors cannot really be used from lookup tables, since the factors vary too much from instrument to instrument and condition to condition. However, by using a reference material, this may be overcome. Two types of reference material are employed: bulk doped and ion implanted. Either type of sample may be used just prior to or following the sample to be analyzed with identical analytical conditions. If these analyses occur regularly, the data from the reference material may be used in statistical process control procedures to underpin a quality system and ensure consistent instrument operation.

ISO 18114 shows how to deduce relative sensitivity factors (RSFs) from ion-implanted reference materials. At the present time, not many of these exist at the certified reference material level. NIST sells ^{75}As -, ^{10}B -, and ^{31}P -doped Si as SRMs 2134, 2137, and 2133, respectively, with levels of around 10^{15} atoms/cm² but certified with 95% confidence limits ranging from 0.0028×10^{15} atoms/cm² for As to 0.035×10^{15} atoms/cm² for B. KRISS also provides B-doped Si thin films as KRISS CRM 0304-300. Using an implanted material, one measures the implant signal I_i^X as a function of the depth d through the profile until the implant or dopant signal has reached the back-

ground noise level I_{∞}^x . From the total implanted dose N (atoms/m²), the sensitivity factor S_x may be calculated as

$$S_x = \frac{Nn}{d \sum_{i=1}^n \left(\frac{I_i^x - I_{\infty}^x}{I_i^m} \right)}, \quad (6.37)$$

where I_i^m is a normalizing matrix signal and n cycles of measurement are required to reach the crater depth d , which must be measured after the profile using a profilometer or other calibrated instrument.

The concentration C_i^x at any point is then given by

$$C_i^x = S_x \frac{I_i^x - I_{\infty}^x}{I_i^m}. \quad (6.38)$$

Bulk-doped reference materials are also useful, and here, if the concentration of the reference material is K^x ,

$$S_x = \frac{K^x}{\left(\frac{I_i^x - I_{\infty}^x}{I_i^m} \right)}. \quad (6.39)$$

The background level I_{∞}^x in this case must be determined from a sample with a very low level, which may occur, for example, in part of the sample to be analyzed. In all of these situations, one must be aware that one is only measuring the intensity of one isotope and that the reference sample may have a different isotope ratio from that of the sample to be analyzed. If this is the case, corrections will be needed in (6.37–6.39) to allow for the relevant fractions. These issues are dealt with in detail for B in Si using bulk-doped material and ion-implanted reference materials in ISO 14237 and ISO 18114, respectively.

A number of interlaboratory studies have been carried out on these materials, and it is useful to summarize the results here so that users can see the level of agreement possible. In very early studies for B in Si, Clegg and coworkers [6.162] showed very good results for a 70 keV ¹¹B ion-implanted wafer between ten laboratories using either O₂⁺ or Cs⁺ ion sources in the range 2–14.5 keV. For this relatively broad profile, the average standard deviation of the widths at concentrations equal to 10⁻¹, 10⁻², 10⁻³, and 10⁻⁴ of the maximum concentration was 2.8%, the depth typically being 500 nm. Later work [6.163] using ⁶⁶Zn, ⁵²Cr, and ⁵⁶Fe sequentially implanted into GaAs showed slightly poorer results. That work also showed that elements accumulating near the surface, where the sputtering equilibrium is being established, would lead to variable results. A later study by *Mieth*

and *Cirlin* [6.164] analyzing Si delta-doped layers in GaAs found good results but that, to obtain meaningful depth resolution, laboratories at that time needed both better control of their scanning systems for the flat-bottomed crater, and to use sample rotation to avoid the degrading effects of developing sample topography.

To cover a wider range of dopant concentrations, *Okamoto* et al. [6.165] analyzed 50 keV ¹¹B⁺-implanted wafers with doses from 3 × 10¹⁴ to 1 × 10¹⁷ ions/cm². Eighteen laboratories profiled these samples using ¹¹B⁺ and ²⁷BO⁺ when using positive ion detection with O₂⁺ incident ions, or ³⁹BSi⁻ and ¹¹BO⁻ when using negative ion detection with Cs⁺ incident ions. The signals are, of course, ratioed to those of the relevant matrix ions. These results showed good consistency but that the RSFs for ¹¹B⁺ and ¹¹B⁻ were affected by the matrix for the two higher B implant levels, the RSFs being slightly reduced. In an extension of this work for shallow implants for ultralarge-scale integration (ULSI) devices, *Toujou* et al. [6.166] note that, at 1 × 10¹⁶ ions/cm², the peak B concentration is over 10²¹ atoms/cm², in other words over 1% atomic fraction. They find that, for 4 keV O₂⁺ at impact angles $\theta > 30^\circ$, the B and Si ion yields increased for concentrations > 10²¹ atoms/cm³, but, under 4 keV Cs⁺ bombardment, no increase occurred up to 60°. They therefore recommend using O₂⁺ at $\theta < 20^\circ$ or Cs⁺ at $\theta < 60^\circ$ incidence angle to avoid the nonlinearity at high concentrations. These angle issues are not discussed in the relevant standards ISO 14237 and ISO 17560, but there it is recommended to measure both ¹⁰B⁺ and ¹¹B⁺ when using an oxygen beam and ¹⁰B²⁸Si⁻ and ¹¹B²⁸B⁻ with a cesium ion beam. The ²⁸Si ion or its molecular ions should be used as the matrix ion, and the ratios of the dopant and matrix ions are determined for each cycle of measurement as in (6.36–6.38).

In more recent work for the draft ISO 12406, *Tomita* et al. [6.167] have studied the depth profiling of 100 keV ⁷⁵As⁺ implants in Si for doses between 3 × 10¹⁴ and 3 × 10¹⁶ ions/cm² with peak concentrations up to 5.8 × 10²¹ atoms/cm³ (12 at. %). They find that, for Cs⁺ incident ions, use of the ion intensity ratios AsSi⁻/Si₂⁻ or As⁻/Si⁻ as the measured intensities, with point-by-point normalization, leads to constant RSFs for all doses and for angles of incidence in the range 24–70°. However, use of the intensity ratios AsSi⁻/Si⁻ or As⁻/Si₂⁻ led to 10% changes in the RSF at arsenic doses of 10¹⁶ ions/cm² and above and were not recommended. It is likely that these issues will be included in a future ISO standard.

Static SIMS

In dynamic SIMS, with the use of low energies and high incidence angles, many uncertainties are focused into the first 1 nm of depth, during which the sputtering process comes to equilibrium. In static SIMS, it has traditionally been suggested that the upper limit of fluence should be restricted to about 0.1% of this, and early work suggested that it should be less than 10^{13} ions/cm² for molecular analysis. The intensities of certain peaks may be expressed as

$$I = I_0 \exp(-N\sigma t), \quad (6.40)$$

where N is the number of ions/(m² s) arriving at the surface, t is the time, and σ is a damage cross section. For I to represent I_0 to within 10%, and for a sputtering yield in the range 1–10, one can see that elements at the surface can only be analyzed using fluences up to 10^{13} ions/cm². However, Gilmore and Seah [6.168] showed that, the larger the fragment studied, clearly the larger the physical cross section of the molecular fragment and the higher the value of σ , so that a 10% loss of intensity of the group C₁₀H₉O₄ from poly(ethylene terephthalate) occurred at an argon fluence of 10^{12} ions/cm². For the smaller C₆H₄ ion, 5×10^{12} argon ions/cm² could be tolerated.

Today, molecules of very much larger physical sizes are analyzed with concomitantly lower damage thresholds, but fortunately, modern time-of-flight mass spectrometers used for SIMS studies only need a total of 10^9 ions, and with a useful ion yield of 10^{-4} , the spectrum has an excellent 10^5 ions. This may be achieved in typical systems using a pulsed ion source delivering 600 ions per pulse every 100 μ s for a total spectrum acquisition time of 3 min. If this dose is spread out over a raster area of 300 μ m by 300 μ m, the fluence is just at the 10^{12} cm⁻² static limit. However, for spatially resolved data this is no longer possible, and damage becomes an important issue. This needs consideration in order to generate reliable and repeatable data. The next important issue is to interpret that data, and we shall deal with these aspects in the next sections.

Control of Damage. Two sources of damage arise in static SIMS: the primary ions, and the electrons from the electron flood neutralizing system for discharging insulators for analysis. As noted earlier, most analysts keep the ion fluence below 10^{12} ions/cm² to avoid damage, although for the study of larger molecules, such as proteins, which may have a cross-sectional area of 20 nm², one may expect 20% to be damaged at this dose and 2×10^{11} ions/cm² may be a safer limit. This leads

to an optimum spatial resolution of 0.7 μ m for spectra with 10^5 counts.

Depending on the information required, one can, of course, work at much better spatial resolution, as shown in Fig. 6.10. In the study in Fig. 6.10, it is known that there are essentially two regions, since the sample was made to be a polymer blend of polyvinylchloride (PVC) and polycarbonate (PC) that are phase separated but may be partially miscible. Here, one can work to lower signal levels per pixel and then sum pixels to obtain low-noise spectra. One may also use a higher dose to consume more of the material. Thus, for PVC one may use the Cl⁻ signal, and for PC the sum of the O⁻ and OH⁻ signals. In Fig. 6.10, the images comprise 256 \times 256 pixels with a dose per pixel of 10^4 ions, giving a total of 6×10^8 ions into the 50 \times 50 μ m² area and a fluence of 2.5×10^{13} ions/cm². For a good static SIMS spectrum at the 10^{12} ions/cm² level, we must analyze 150 \times 150 μ m² using a total number of 2.25×10^8 ions, as shown in Fig. 6.11. Fortunately, here we have a useful ion yield in the negative ions of 10^{-3} – 10^{-2} , so that each pixel of the left-hand image of Fig. 6.10 contains 10–100 Cl⁻ ions. We can see patterns of dark dots within the bright zones. These are not noise, but can be shown by AFM to be 200 nm-diameter pools of PC [6.1]. The SIMS is just resolving these generally as single pixels, indicating a static SIMS resolution, in a near-static mode, of 200 nm.

Figures 6.10 and 6.11 show typical analyses of materials using a modern time-of-flight SIMS system. The samples are insulating and need electron flooding to remove charge. This is relatively easy, but in practice we have found that many users ensure charge neutralization

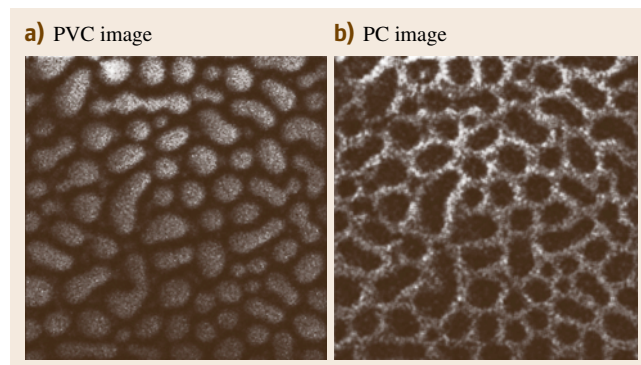


Fig. 6.10a,b Static SIMS negative ion images for a total fluence of 2.5×10^{13} ions/cm² of a PVC and PC polymer blend: (a) Cl⁻ for PVC and (b) OH⁻ + O⁻ for PC; field of view 50 \times 50 μ m² (after Gilmore et al. [6.1])

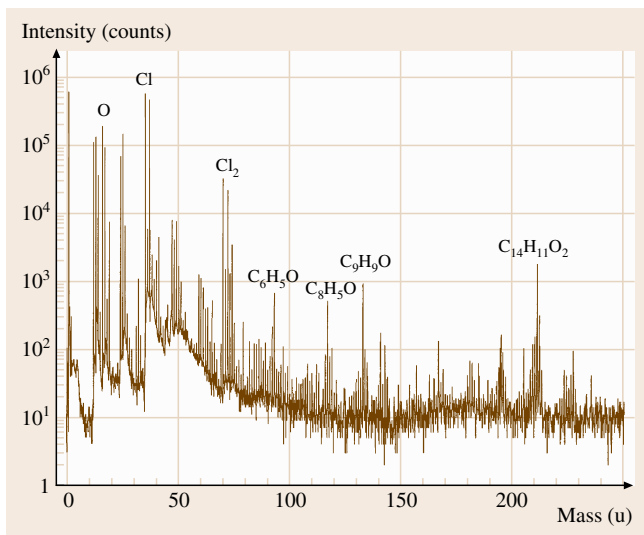


Fig. 6.11 Static SIMS negative ion spectrum for 10^{12} ions/cm² on a fresh $150 \times 150 \mu\text{m}^2$ area of material as in Fig. 6.10 (after Gilmore et al. [6.1])

by using an electron flux density that is far too high. This ensures that there is no charging, but it damages the sample at about the same rate as the ions. Low-energy electrons have a very high cross section for bond dissociation. Gilmore and Seah [6.169] find that, at electron fluences of 6×10^{14} electrons/cm², polymers such as PS, PVC, poly(methyl methacrylate) (PMMA), and polytetrafluoroethylene (PTFE) are damaged, whereas some instruments have been set well above this limit. The avoidance of electron flood damage typically limits the electron flood current to 100 nA, but as a minimum, the sample needs about 30 electrons per incident ion to stop significant charging.

Identifying Materials. In static SIMS we cannot identify materials, beyond elemental species, simply by observing the masses of the peaks. For the molecules generally studied, there are very many mass peaks of high intensity in the 12–100 u range and often series of peaks at masses up to and beyond 1000 u. The unit u here is the unified atomic mass unit, often also called the dalton. The peaks mainly correspond to highly degraded fragments of the original molecules or material at the surface. This degradation is such that many organic materials look broadly similar, and experts develop their own schemes of selected significant peaks in order to measure intensities. Thus, much information is rejected. In order to identify materials in

this way, static SIMS libraries have been developed. The first two libraries [6.170, 171] were in a print-on-paper format, effectively using unit mass resolution since they arose from very careful data compilations using the earlier quadrupole mass spectrometers. Despite the care, contamination and damage effects are more likely in these data. These libraries contain 81 materials and 85 polymers, respectively. The more recent library by Vickerman et al. [6.172] extends the earlier library [6.170] by including spectra for the higher mass resolution, early time-of-flight instruments so that the combined library now covers 519 materials. The fourth library [6.173] is for consistent high-resolution data, is available digitally, and is for calibrated, later generation time-of-flight instruments. This contains data for 147 compounds. These libraries form an invaluable resource to which analysts may add their own data. For quantification, analysts typically select one or two major characteristic peaks and simply use equations such as (6.3). Individual research groups use much more sophisticated analyses, but these are not applicable for general analysis.

The modern time-of-flight mass spectrometer should be able to determine mass to better than the 10 ppm needed to be able to associate each peak with the correct number of C, O, N, H, and so on, atoms. However, a recent interlaboratory study [6.174] shows that, even having calibrated the scale on appropriate masses, a lack of understanding of the issues involved [6.175] leads to a standard deviation of scatter of 150 ppm for the protonated Irgafos peak at 647.46 u [6.174]. Thus, at the present time, the lack of an appropriate procedure means that analysts need to check a range of possibilities to identify each peak.

The spectrum measured in a laboratory may differ from that shown in a database library for one or more of several reasons. Even when using reference samples to generate a library, great care needs to be taken to avoid contaminants, for example poly(dimethyl siloxane) (PDMS). Secondly, in the first static SIMS interlaboratory study [6.176], it was shown that, whilst some laboratories could repeat data at a 1% level, 10% was more typical and 70% occurred in some cases, indicating that some laboratories/instruments could not really generate repeatable data. In that work the 18 analysts used 21 instruments and their preferred ion sources ranged from Ar⁺ and Ga⁺ to Cs⁺ and O₂⁻ with primary ion beam energies from 2.5 to 25 keV. In a more recent study [6.169], improvements in practice and equipment have led to a general improvement in repeatability, but the issue of different sources remains.

To study larger molecules, a range of new ion sources has been developed to provide a higher yield of large fragments compared with the sources listed above. *Benninghoven et al.* [6.177] show that the yields of all fragments increase through the primary ion series Ar^+ , Xe^+ , SF_5^+ , $\text{C}_{10}\text{H}_8^+$, C_6F_6^+ , $\text{C}_{10}\text{F}_8^+$ when analyzing Irganox 1010 at the surface of polyethylene. These results, for 11 keV ions, covered the mass range 50–1000 u and indicated a simple increase above 100 u of 0.3, 1, 4, 6, 7, and 12, respectively, when normalized to the Xe^+ data. Below 150 u the increases were stronger. For matrix-isolated biomolecules, a change from Ar^+ to SF_5^+ led to yield increases of characteristic peaks above 1000 u of 6–32 times. *Schneiders et al.* [6.178] show that, for molecular overlayers of adenine and β -alanine on Ag or Si, SF_5^+ gives significantly higher yields than Xe^+ and that this is, in turn, better than Ar^+ . These overall results are nicely summarized in the studies of *Kersting et al.* [6.179, 180], who look at both the yield increase and the damage effects, as shown in Fig. 6.12, where they call σ in our (6.40) the disappearance cross section. They define the ratio of the yield to the damage cross section as the efficiency E . Clearly, if the yield doubled at the expense of twice the rate of damage, there would be no real improvement for the analyst and this would be reflected in an unchanged value of the efficiency E . However, in Fig. 6.12 it is clear, where data are given for C_{60}^+ , Au_3^+ , Au_2^+ , Au^+ , SF_5^+ , Cs^+ , and Ga^+ , that they are 2000, 500, 200, 33, 45, and 6 times better than Ga, respectively. It seems that higher mass ions are better than low mass, and polyatomic ions are better than monatomic ions of the same beam energy.

Earlier studies of polyatomic ions identified C_{60}^+ as an interesting candidate. *Wong et al.* [6.181] have designed a suitable ion gun and show significant yield enhancements compared with Ga^+ at 15 keV. The total yield increase for the polypeptide gramicidin, spin-cast onto copper, is 41 and, in the 200–1000 u range, rises to 50. For the molecular ion, a strong signal is observed for C_{60}^+ but not at all for Ga^+ . The results for bulk polyethylene terephthalate (PET) were around 60 for most of the mass range for equivalent doses of both ions. The damage rates were not measured, but the very strong result for the gramicidin molecular ion showed significant promise. More recently, *Weibel et al.* [6.182] extended this work and measured the Y , σ , and E values to show that E for masses above 250 u would range from 60 to 15 000 times higher for C_{60}^+ than for Ga^+ when analyzing thick polymer or Irganox 1010 layers.

In recent analysis of the data for Fig. 6.12, *Seah* [6.183] shows that there is a clear improvement in both sensitivity and efficiency through the series and that the larger clusters are very beneficial in studying organic materials.

To increase the mass of the projectile for the liquid metal ion gun structures used for high-resolution imaging, *Davies et al.* [6.184] have used a gold ion source. Using a gold-germanium eutectic alloy as the source for a liquid metal ion gun, they could generate Ge^{2+} , Ge^+ , Au^{2+} , Au^+ , Au_2^+ , and Au_3^+ beams all at around the 1 pA needed. The results, compared with Ga^+ for the gramicidin and PET analyzed with the C_{60}^+ , show that Au^+ gives typically a fourfold improvement and that Au_3^+ gives a tenfold improvement, except for the gramicidin

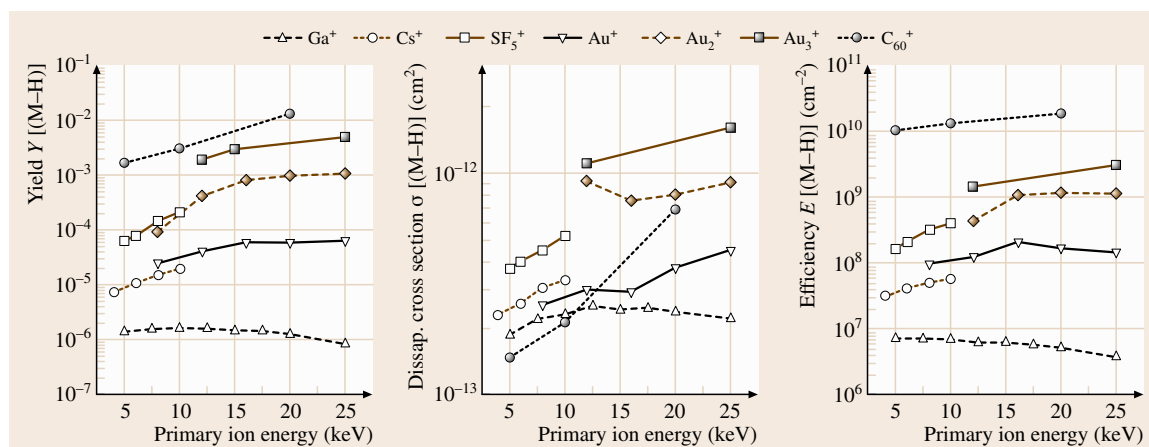


Fig. 6.12 Secondary ion yields, damage or disappearance cross section σ , and efficiency E measured for the Irganox 1010 quasimolecular ion $(\text{M}-\text{H})^-$ as a function of the primary ion energy and type (after *Kersting et al.* [6.180])

molecular ion where the improvement is 64 times. It appears that Au_3^+ is less effective at generating the molecular ions for gramicidin than C_{60}^+ , but no data are available for the damage rates to evaluate the efficiencies. Clearly, the liquid metal ion source approach will continue to provide better spatial resolution, and so we expect that there will be further new sources in the future. This does not help the analyst trying to use the spectral libraries, since the relative intensities of the peaks depend on the ion source. For the analyst there is an urgent need for

1. a routine to treat spectra so that they may be related from one source to another,
2. a procedure for accurate mass calibration, and
3. a chemometrics platform to be able to apply reliable algorithms to extract chemical information directly from the spectra.

To aid this process in static SIMS, two standards, ISO 14976 and ISO 22048, as shown in Table 6.2, have been designed to allow export and import of spectral data files so that new software may be developed to do this processing.

In recent years a variant of static SIMS has been developed called G-SIMS. This spectroscopy uses the ratio of two static SIMS spectra to generate a new spectrum called the G-SIMS spectrum that contains peaks far less degraded in the fragmentation process. As a result of the characterization for the static SIMS interlaboratory study [6.174], it was shown that the ratio of the spectrum obtained for 4 keV argon to that for 10 keV argon exhibited clusters of results near unity but with fragments of the type C_xH_y having the highest ratio for the least degradation [6.186]. The G-SIMS spectrum I_x for the mass x is given by

$$I_x = F_x^g N_x M_x, \quad (6.41)$$

where the ratio of the 4 and 10 keV spectra is F_x , g is the G-SIMS index, N_x is the 4 keV static SIMS spectrum, and M_x is a linear mass term. In practice, for 4 and 10 keV argon, a useful value of g is found to be 13. Tests with other sources shows that, whilst 4 and 10 keV argon is convenient and is an easy choice to be able to align the beams on the same area, SF_5^+ , Cs, and Xe may be ratioed to Ar or Ga and a stronger effect obtained [6.186]. An example of G-SIMS is shown in Fig. 6.13 for poly-L-lysine [6.185]. Figure 6.13a is the static SIMS spectrum where the poly-L-lysine structure is shown. The spectrum is, as usual, dominated by the low mass fragments. In Fig. 6.13b is a G-SIMS spectrum using the ratio of 10 keV Cs to 10 keV Ar and a g index of 13 [6.185]. The intense double peak in the center arises from a separate

bromide compound as the material is supplied as a salt. The G-SIMS peaks show a clear dimer with an added NH and a peak defining the amino acid side-chain. A number of polymers [6.186] and organics [6.185] have been studied, and each time the information can be related to unfragmented parts of the molecule.

In a test of the capability of G-SIMS, investigations of a small brown stain on paper identified oil of bergamot from the molecular peak that was not noticeable in the static SIMS spectrum. Identifying species from the molecular weight is thus possible using G-SIMS and, possibly, Au_3^+ or C_{60}^+ . This frees the analyst from the limit of fewer than 800 materials defined by the spectra available in libraries of static SIMS spectra [6.170–

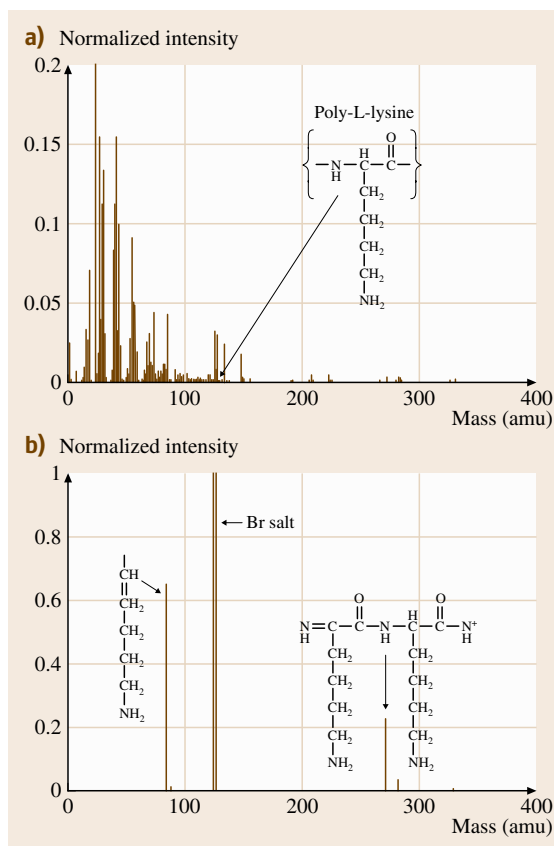


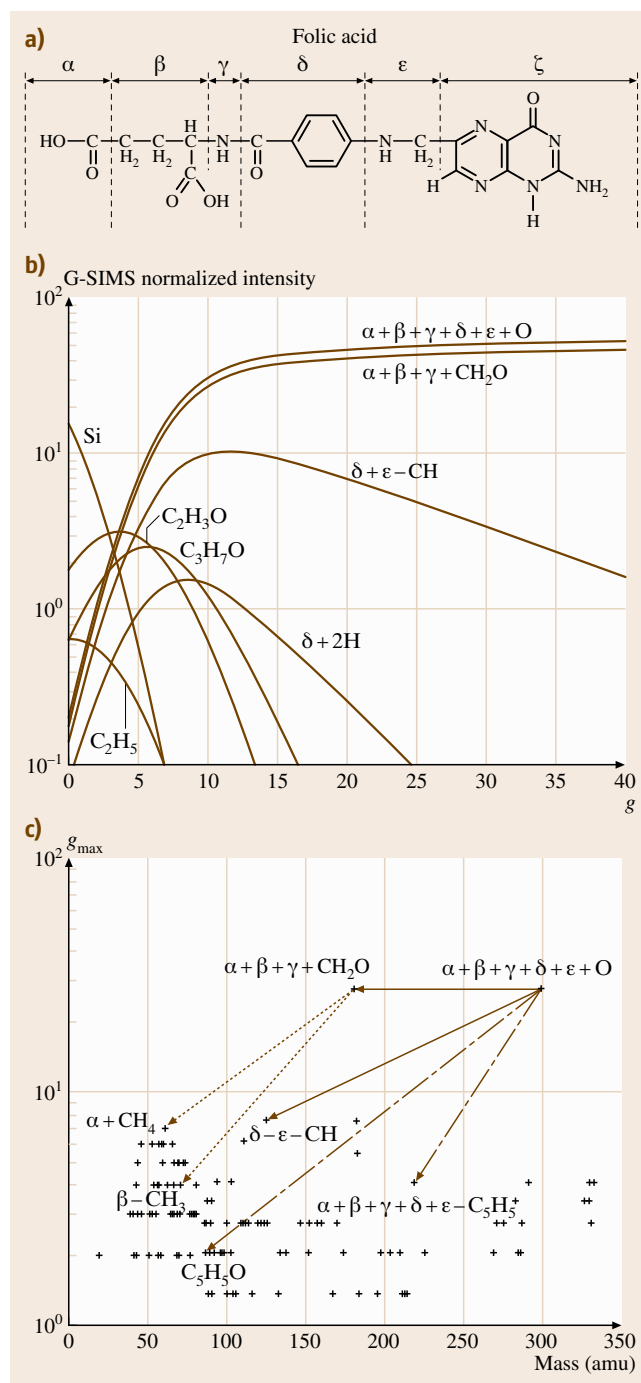
Fig. 6.13a,b Spectra for poly-L-lysine: (a) 10 keV Cs^+ static SIMS spectrum showing strong fragments at low mass and no peak at the repeat unit of 128 u, and (b) G-SIMS using the ratio of 10 keV Cs^+ to Ar^+ with strong intensity at 84.1 u for the side-chain and 271.2 u for a dimer repeat with an extra NH from the backbone (after Gilmore and Seah [6.185])

Fig. 6.14a–c G-SIMS-FPM for folic acid: (a) the molecular structure of folic acid identifying six subunits, (b) the change in relative intensities of G-SIMS peaks with g index showing the peak g values, g_{\max} , and (c) the reassembly plot showing fragmentation pathways (after *Gilmore and Seah* [6.187]) ▶

173] and opens up the method to the life sciences and other areas where the libraries would need to run to hundreds of thousands of spectra. Unfortunately, in the life sciences and similar areas, the molecular weight may not be adequate to identify a molecule and knowledge is required about its structure. An extension of G-SIMS called G-SIMS with fragmentation pathway mapping (G-SIMS-FPM) shows how this may be done [6.187]. By altering the index g in (6.41), we may view spectra that move progressively from the highly fragmented static SIMS ($g = 0$) to the unfragmented G-SIMS with $g = 40$. During this process, we can see higher mass peaks being built up and parts of the molecule being reassembled in the spectra. With accurate mass calibration, the composition of each fragment may be evaluated. Figure 6.14 shows how this works for folic acid. To the left in Fig. 6.14b we see the intensities of certain peaks. As g increases, these either grow or die. Those that grow may peak at a certain g value, g_{\max} , and this value is then plotted as the ordinate value in Fig. 6.14c. Molecules or large fragments to the right in Fig. 6.14b or the top in Fig. 6.14c are split into smaller mass fragments, peaking further to the left in Fig. 6.14b or down and to the left in Fig. 6.14c. Unfortunately, not all fragments are emitted as ions and so the plots are not complete, but they do add sufficient dimension to the information to permit identification where the static SIMS or G-SIMS data are insufficient. The use of cluster primary ions is important here for analyzing the larger molecules [6.188].

6.1.4 Conclusions

In Sect. 6.1, we have presented the measurement status of surface chemical analysis. The three main techniques of AES, XPS, and SIMS are all still rapidly developing in both instrumentation and applications. The spatial and spectral resolutions are still improving, and signal levels are increasing. AES, XPS, and dynamic SIMS are all relatively mature with extensive procedural standards available from ISO [6.3, 4] and ASTM [6.2]. This area is also highly active, and both these and research results also feed back into the hardware and software of the commercial instruments. Static SIMS, which has very strong development potential, is be-



ing increasingly used in industrial laboratories to obtain levels of detail and sensitivity not available with AES or XPS. The latest generation of time-of-flight (TOF)-

SIMS instruments and their new ion sources make this a very fast developing and fruitful area. New standards

in ISO are expected to be developed over the coming years.

6.2 Surface Topography Analysis

The topography of a surface is the set of geometrical details that can be recorded through a measurement. Most commonly, topography is either related to the mechanical nature of the surface, typically involved in contact situations, or to its electromagnetic nature, typically involved in optical effects. Topography is of paramount importance for the functional behavior of a surface, strongly interplaying with material properties and operating conditions.

Surface topography characterization is a powerful tool in connection with design, manufacture, and function. As schematically illustrated in Fig. 6.15, it allows one to link the functional behavior of a surface to the microgeometry obtained from its generation. The three main phases of surface topography characterization are measurement, visualization, and quantification. These phases encompass a number of basic steps, nowadays prevalently involving digital techniques and extensive use of computers: data acquisition, conditioning, visualization, elaboration, and quantification. In particular, quantification typically concerns the geometry of single surface features at micrometer or nanometer scale, being based on the extraction of parameters, curves, functions or basic geometrical features from a representative profile or area on the surface. Quantifying the microgeometries of surfaces after they

have been measured is important in all applications of process control, quality control, and design for functionality.

The principal methods of surface topography measurement are stylus profilometry, optical scanning techniques, and scanning probe microscopy (SPM). These methods, based on acquisition of topography data from point-by-point scans, give quantitative information on heights with respect to position. Other methods such as scanning electron microscopy (SEM) can also be used. Based on a different approach, the so-called integral methods produce parameters representing some average property of the surface under examination. A further classification distinguishes between contacting and noncontacting instruments. While stylus instruments are inherently contacting methods and optical instruments noncontacting methods, scanning probe microscopes can be both contacting and noncontacting. We shall describe the basics of each of the methods later, but it is useful to outline the attributes of the methods here so that the reader can focus early on their method of choice.

In a stylus profilometer, the pick-up draws a stylus over the surface at a constant speed, and an electric signal is produced by the transducer. This kind of instrument can produce very accurate measurements in the laboratory as well as in an industrial environment, covering vertical ranges up to several millimeters with resolutions as good as nanometric, with lateral scans of up to hundreds of millimeters being possible. The stylus is typically provided with a diamond tip with a cone angle (total included angle) of 60° or 90° and a tip radius in the range 1–10 μm. The maximum detectable slopes using a stylus instrument are, respectively, 60° or 45°. The spatial resolution achieved by this method, generally in the range 2–20 μm, is limited by the tip geometry, and depends on the actual surface slopes and heights in the neighborhood of the point of contact. Moreover, the force applied by the stylus on the surface can generate plastic deformation on the surface, making this method inapplicable to surfaces that are soft or where even light scratches cannot be accepted.

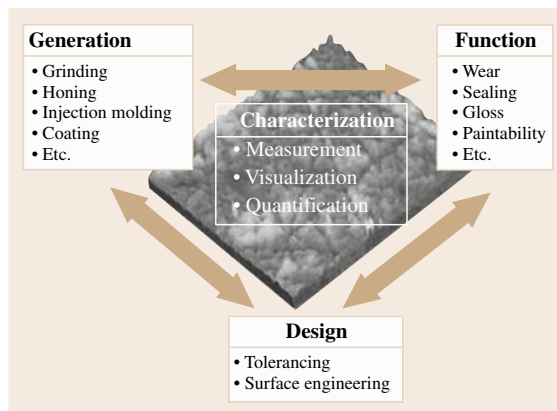


Fig. 6.15 Surface topography characterization links design, generation, and function (after [6.189])

Optical scanning techniques encompass most typically optical profilometers, confocal microscopes, and interferometers. The optical methods are noncontacting, which allows measurements on soft surfaces. However, this kind of instrument is subject to measurement errors related to achieving a useful reflection signal from surfaces that are shiny or transparent to the light source. Optical styli for profilometry can be based on the autofocusing signal of a laser beam detector. The beam has a spot diameter of about $1\ \mu\text{m}$, and this kind of instrument is similar in use to conventional stylus instruments, with vertical resolution of approximately $5\ \text{nm}$. The maximum detectable slope using an autofocusing stylus instrument is approximately 15° . Laser scanning confocal microscopy is another optical technique based on the focus detection principle, where one surface picture element (pixel) is imaged at a time. Topography is reconstructed as a stack of vertical optical sections, in a fashion similar to computer tomography. Confocal microscopes allow steep surface details to be assessed, the maximum detectable slope being up to 75° . Confocal microscopes have limited lateral resolution, and some commercially available instruments even have limited vertical resolution. Interference microscopy combines an optical microscope and an interferometer objective into a single instrument. These optical methods allow fast noncontacting measurements on essentially flat surfaces. Interferometric methods offer subnanometer vertical resolution, being employed for surfaces with average roughnesses down to $0.1\ \text{nm}$ and peak-to-valley heights up to several millimeters. Interferometric microscopes are all limited with respect to the surface slopes from the finite numerical apertures. Moreover, the lateral resolution is limited by diffraction. The maximum detectable slope using interferometry amounts to about 30° .

Scanning probe microscopy, including atomic force microscopy (AFM) and scanning tunneling microscopy (STM), is based on a powerful class of tools for subnanometric acquisition of topography data on very fine surfaces. SPM uses a sharp probe scanning over the surface while maintaining a very close spacing to the surface. SPM allows measurements on surfaces with an area up to approximately $100 \times 100\ \mu\text{m}^2$ and that have local variations in surface height which are less than approximately $10\ \mu\text{m}$. SPM is a three-dimensional (3-D) microscopy technology in which the resolution is not limited by the diffraction of light. The vertical resolution of SPM is about $0.1\ \text{nm}$, while the horizontal

resolution for most AFM devices is typically $2\text{--}10\ \text{nm}$, but it can be atomic. SPM requires minimal sample preparation.

Scanning electron microscopy (SEM) can also be used for qualitative surface topography analysis, primarily based on the fact that SEM allows excellent visualization achieved through the very high depth of focus of this technique. However, SEM photographs are still inherently two-dimensional (2-D), and no height information can be extracted directly from the images. The 3-D achieved by reconstructing from stereo pairs or triplets can be used to evaluate surface topography, but it is limited by a number of factors.

Figure 6.16 [6.190] shows a diagram of the spatial resolutions of the different techniques that helps to place the more popularly used methods in context. Additional information is given in Table 6.8. Documentary standards covering surface topography are published by ISO. Updated information regarding the ISO standards for surface texture can be found on the www.iso.org website and by searching in the ISO catalogue under 17.040.20 *Properties of surfaces* and 17.040.30 *Measuring instruments*. Surface texture is a topic covered by the technical committee TC213 Geometrical Product Specifications under the ISO, the homepage of which can be found through the above-mentioned website. Table 6.9 lists the titles of ISO standards published

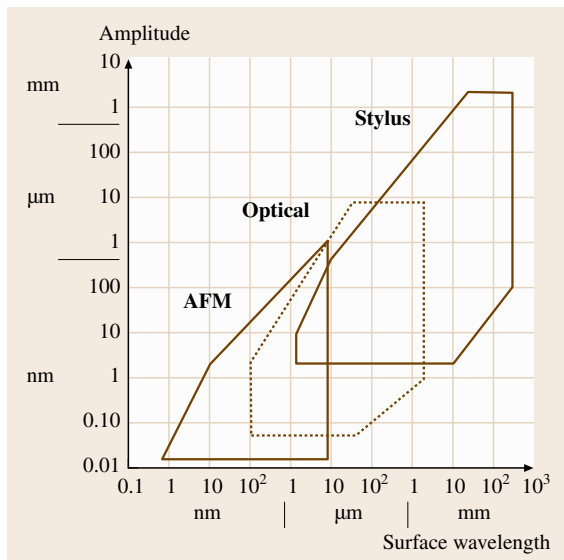


Fig. 6.16 Diagram showing the vertical and horizontal resolution achievable with different instruments for surface topography measurements (after *Stedman* [6.190])

Table 6.8 Resolutions and ranges of some techniques for surface topography analysis

Instrument	Vertical axis		Horizontal axes	
	Resolution (nm)	Range (mm)	Resolution (nm)	Range (mm)
Stylus	< 1	10	2000	> 100
Auto-focus	< 5	1	1000	> 100
WLI	0.1	1	500	< 10
SEM	1	1	2	1
AFM	< 0.1	0.01	1	0.1

WLI – white-light interferometry
SEM – scanning electron microscopy
AFM – atomic force microscopy

in the field of surface texture. Most standards cover 2-D profiling techniques, but also standards for 3-D areal measurements are currently under publication by

ISO. Table 6.10 presents a list of ISO standards under development related to surface topography. Essential textbooks covering the area are [6.191–193].

Table 6.9 Published standards from ISO TC213 for surface texture

No.	ISO standard	Title [reference]
1	ISO 1302:2002	Geometrical product specifications (GPS) – Indication of surface texture in technical product documentation [6.194]
2	ISO 3274:1996, (*)	Geometrical product specifications (GPS) – Surface texture: Profile method – Nominal characteristics of contact (stylus) instruments [6.195]
3	ISO 4287:1997, (*)	Geometrical product specifications (GPS) – Surface texture: Profile method – Terms, definitions, and surface texture parameters [6.196]
4	ISO 4287:1997Amd 1:2009, (*)	Peak count number [6.197]
5	ISO 4288:1996, (*)	Geometrical product specifications (GPS) – Surface texture: Profile method – Rules and procedures for the assessment of surface texture [6.198]
6	ISO 5436-1:2000, (*)	Geometrical product specifications (GPS) – Surface texture: Profile method; Measurement standards – Part 1: Material measures [198]
7	ISO 5436-2:2002, (*)	Geometrical product specifications (GPS) – Surface texture: Profile method; Measurement standards – Part 2: Software measurement standards [6.199]
8	ISO 8785:1998	Geometrical product specification (GPS) – Surface imperfections – Terms, definitions, and parameters [6.200]
9	ISO 11562:1996, (*)	Geometrical product specifications (GPS) – Surface texture: Profile method – Metrological characteristics of phase-correct filters [6.201]
10	ISO 12085:1996, (*)	Geometrical product specifications (GPS) – Surface texture: Profile method – Motif parameters [6.202]
11	ISO 12179:2000	Geometrical product specifications (GPS) – Surface texture: Profile method – Calibration of contact (stylus) instruments [6.203]
12	ISO 13565-1:1996, (*)	Geometrical product specifications (GPS) – Surface texture: Profile method; Surfaces having stratified functional properties – Part 1: Filtering and general measurement conditions [6.204]
13	ISO 13565-2:1996, (*)	Geometrical product specifications (GPS) – Surface texture: Profile method; Surfaces having stratified functional properties – Part 2: Height characterization using the linear material ratio curve [6.205]
14	ISO 13565-3:1998	Geometrical product specifications (GPS) – Surface texture: Profile method; Surfaces having stratified functional properties – Part 3: Height characterization using the material probability curve [6.206]
15	ISO/TS 16610-1:2006	Geometrical product specifications (GPS) – Filtration – Part 1: Overview and basic concepts [6.207]
16	ISO/TS 16610-20:2006	Geometrical product specifications (GPS) – Filtration – Part 20: Linear profile filters: Basic concepts [6.208]

Table 6.9 (continued)

No.	ISO standard	Title [reference]
18	ISO/TS 16610-22:2006	Geometrical product specifications (GPS) – Filtration – Part 22: Linear profile filters: Spline filters [6.209]
19	ISO/TS 16610-28:2010	Geometrical product specifications (GPS) – Filtration – Part 28: Profile filters: End effects [6.210]
20	ISO/TS 16610-29:2006	Geometrical product specifications (GPS) – Filtration – Part 29: Linear profile filters: Spline wavelets [6.211]
21	ISO/TS 16610-30:2009	Geometrical product specifications (GPS) – Filtration – Part 30: Robust profile filters: Basic concepts [6.212]
22	ISO/TS 16610-31:2010	Geometrical product specifications (GPS) – Filtration – Part 31: Robust profile filters: Gaussian regression filters [6.213]
23	ISO/TS 16610-32:2009	Geometrical product specifications (GPS) – Filtration – Part 32: Robust profile filters: Spline filters [6.214]
24	ISO/TS 16610-40:2006	Geometrical product specifications (GPS) – Filtration – Part 40: Morphological profile filters: Basic concepts [6.215]
25	ISO/TS 16610-41:2006	Geometrical product specifications (GPS) – Filtration – Part 41: Morphological profile filters: Disk and horizontal line-segment filters [6.216]
26	ISO/TS 16610-49:2006	Geometrical product specifications (GPS) – Filtration – Part 49: Morphological profile filters: Scale space techniques [6.217]
27	ISO 25178-6:2010	Geometrical product specifications (GPS) – Surface texture: Areal – Part 6: Classification of methods for measuring surface texture [6.218]
29	ISO 25178-601:2010	Geometrical product specifications (GPS) – Surface texture: Areal – Part 601: Nominal characteristics of contact (stylus) instruments [6.219]
30	ISO 25178-602:2010	Geometrical product specifications (GPS) – Surface texture: Areal – Part 602: Nominal characteristics of noncontact (confocal chromatic probe) instruments [6.220]
31	ISO 26178-701:2010	Geometrical product specifications (GPS) – Surface texture: Areal – Part 701: Calibration and measurement standards for contact (stylus) instruments [6.221]

Note (*): Standard amended by technical corrigendum. Published corrigenda are: ISO 3274:1996/Cor 1:1998; ISO 4287:1997/Cor 1:1998; ISO 4287:1997/Cor 2:2005; ISO 4288:1996/Cor 1:1998; ISO 5436-2:2001/Cor 1:2006; ISO 5436-2:2001/Cor 2:2008; ISO 11562:1996/Cor 1:1998; ISO 12085:1996/Cor 1:1998; ISO 13565-1:1996/Cor 1:1998; ISO 13565-2:1996/Cor 1:1998

Table 6.10 Standards under development

No.	ISO standard	Title [reference]
1	ISO 1302:2002/DAMd 2	Indication of material ratio requirements [6.222]
2	ISO/DIS 16610-21	Geometrical product specifications (GPS) – Filtration – Part 21: Linear profile filters: Gaussian filters [6.223]
3	ISO/CD 25178-1	Geometrical product specifications (GPS) – Surface texture: Areal – Part 1: Indication of surface texture [6.224]
4	ISO/DIS 25178-2	Geometrical product specifications (GPS) – Surface texture: Areal – Part 2: Terms, definitions, and surface texture parameters [6.225]
5	ISO/DIS 25178-3.2	Geometrical product specifications (GPS) – Surface texture: Areal – Part 3: Specification operators [6.226]
6	ISO/DIS 25178-7	Geometrical product specifications (GPS) – Surface texture: Areal – Part 7: Software measurement standards [6.227]
7	ISO/DIS 25178-603	Geometrical product specifications (GPS) – Surface texture: Areal – Part 603: Nominal characteristics of noncontact (phase-shifting interferometric microscopy) instruments [6.228]
8	ISO/DIS 25178-604	Geometrical product specifications (GPS) – Surface texture: Areal – Part 604: Nominal characteristics of noncontact (coherence scanning interferometry) instruments [6.229]
9	ISO/CD 25178-605	Geometrical product specifications (GPS) – Surface texture: Areal – Part 605: Nominal characteristics of noncontact (point autofocusing) instruments [6.230]

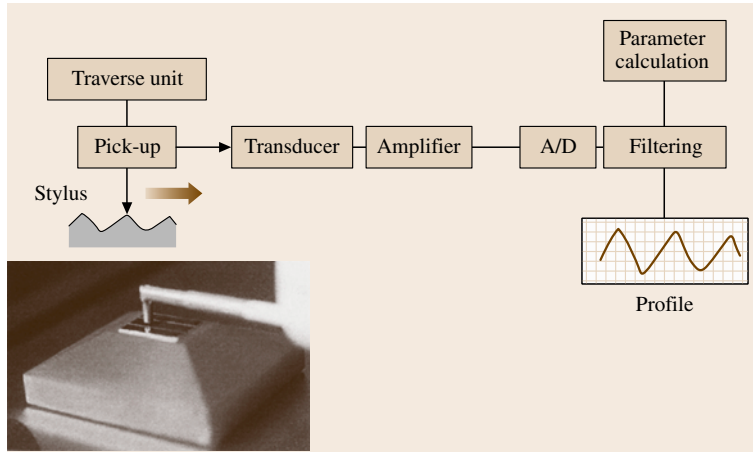


Fig. 6.17 Operational scheme for a stylus profilometer; A/D = analog-to-digital converter

6.2.1 Stylus Profilometry

General Introduction

The most well-known surface profilometer in the manufacturing industry is the stylus instrument used for conventional two-dimensional roughness measurements. This kind of instrument, shown in Fig. 6.17, has existed for over 60 years, and it yields a high degree of accuracy, robustness, and user-friendliness. In a typical surface tester, the pick-up draws the stylus over the surface at a constant speed, and an electrical signal is produced by the transducer, which can be piezoelectric, inductive or laser interferometric. The signal is amplified and digitized for subsequent data processing such as filtering and parameter calculation. In a more comprehensive laboratory stylus system, parallel tracings can be made over the workpiece, allowing reconstruction of a whole surface area, in order to perform so-called three-dimensional surface topography characterization. The versatility of the stylus instrument is underlined by the ability to use this instrument on

all kinds of items, irrespective of orientation, and to mount the pick-up on other machines, such as a coordinate measuring machine or a form tester, to achieve measurement of the surface topography over complex workpieces. The stylus is provided with a diamond tip with a total cone angle of 60° or, more commonly, 90° . Standardized values for the tip radius are 2, 5, and $10\ \mu\text{m}$, but other values are also used. Stylus instruments feature vertical ranges of up to several millimeters, with best resolutions at nanometric level and scans of up to hundreds of millimeters possible. The standardized values for the maximum load corresponding to the above-mentioned radii are 0.7, 4, and 16 mN, respectively. In many cases, a tracing speed of 0.5 mm/s is used.

Measurement and Filtering

When tracing a surface profile, a stylus instrument works as schematically shown in Fig. 6.17. Filters are used to separate roughness from waviness and form. ISO operates with three different types of profile that can be extracted from the acquired profile through filtering: primary P-profile, waviness W-profile, and roughness R-profile. Filters are useful in that they permit the user to focus on wavelength components that are important from a functional point of view. Modern filter definitions introduced in ISO standards are based on digital Gaussian cut-off filters characterized by being phase-correct and robust to single features such as scratches. Referring to Fig. 6.18 and [6.196], ISO operates with cut-off filters with nominal wavelengths λ_s , λ_c , and λ_f , where the index “s” refers to sampling, “c” to cut-off, and “f” to form. An ISO filter is characterized by the wavelength at which it transmits 50% of

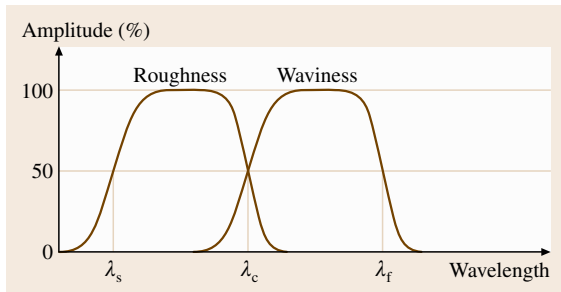


Fig. 6.18 Transmission characteristic of roughness and waviness profiles using ISO filters (after [6.196])

the amplitude. As illustrated in Fig. 6.18, the three filters λ_s , λ_c , and λ_f delimit the wavelength intervals for the roughness and waviness profiles by creating two filter windows. As an alternative, parameters can be calculated on the basis of the so-called primary profile, which results from eliminating the short-wave components only, by using the λ_s filter (λ_s is used to eliminate high-frequency components along with the mechanical filtering effect from the stylus tip radius). As indicated on the figure, the filters are not sharp but instead produce a progressive damping of the signal.

The data obtained from a measured surface are typically processed as follows.

1. A form fit, such as a least-squares arc or line (best fit), is applied to the data in order to remove the form.
2. The ultrashort-wave components are removed using a λ_s filter. The result is the primary profile, from which P-parameters can be calculated.
3. The primary profile is passed through a λ_c filter with a specific cut-off value that separates waviness from roughness.
4. The resultant roughness or waviness profile is then processed to calculate the roughness or waviness parameters.

The result of filtering is illustrated in Fig. 6.19. ISO 4287 operates with a number of standardized elements used for parameter calculations: the *mean line*, which is the reference line from which the parameters are calculated, such as the *mean line for the roughness profile*, which is the line corresponding to the longwave profile component suppressed by the profile filter λ_c ; the *sampling length* l_P , respectively l_W and l_R , which is the length in the direction of the X-axis used to identify the irregularities characterizing the profile; and the *evaluation length* l_n , generally defined by ISO as five times the sampling length (P_t , W_t , and R_t shown in Fig. 6.19 are calculated over the evaluation length). More advanced methods of filtering are described in the new series of ISO 16610 standards [6.207–217].

Visualization

The very first step in surface topography analysis consists of a visualization of the microgeometry, either as single profiles or as surface areas, to provide realistic representations of the surface. The usefulness of such an approach for qualitative characterization is well recognized: often the image inspection, possibly aided by some enhancement techniques, can be assumed as the

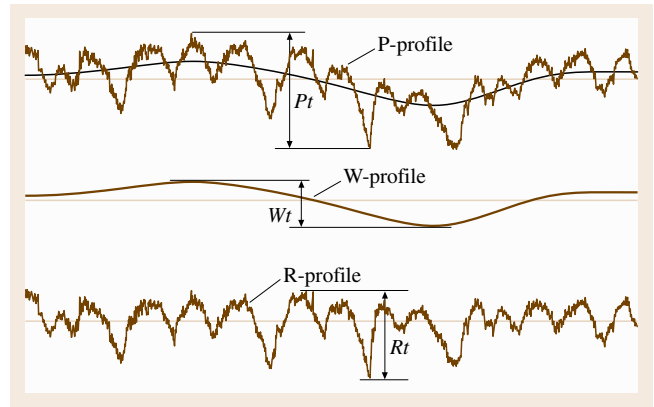


Fig. 6.19 Primary P-profile, waviness W-profile, and roughness R-profile

only aim of the analysis. Indeed, the image conveys a vast amount of information, which can be easily interpreted by an experienced observer; even a single profile contains a large amount of relevant information, and moreover in a condensed way by adopting different scales for the horizontal and vertical axes. The passage from profile two-dimensional analysis to surface three-dimensional analysis enlarges the possibilities for gaining knowledge and representing the surface texture. Many techniques have been developed to display the sampled data, with the possibility of enhancing some particular features, such as

- contour plots, color plots, and grayscale mapping, techniques borrowed from soil cartography to represent the surface heights,
- isometric and dimetric (as in Fig. 6.15) projections, where the single data points are interconnected with all the neighboring points by straight or curved lines. Projections can be modified by the scales and projection angles, for enhancement of amplitudes, texture, etc.,
- inversion and truncation techniques, whereby the visual interpretation of the projections is enhanced through data manipulation. Other manipulation techniques are used, for example, to emphasize surface slopes.

Quantification of Surface Texture

Quantitative assessment of surface texture can be very useful in relation to process control, tolerance verification, and functional analysis. Nevertheless, it must be undertaken with care, since interpretation of mere parameters can lead to wrong conclusions. Unless the

topographic nature of the surface under consideration is known, it is strongly recommended that quantitative characterization should only be used in connection with a visual examination of the surface topography, as described above.

2-D Parameters Covered by ISO Standards. Conventional roughness parameters, which are those most commonly known to quantify surface texture, are often referred to as 2-D parameters, since they are computed on the basis of single profiles containing information in two dimensions (horizontal and vertical). The 2-D surface texture area has been totally revised by ISO, with the introduction of several new international standards [6.189, 194, 195, 198–206, 231]. According to current ISO terminology, as mentioned in connection with filters, the concept of surface texture encompasses roughness, waviness, and the primary profile. In the following, an overview is presented of the existing ISO parameters for surface texture. Only ISO parameters are considered here, since they adequately cover what can be quantified through 2-D parameters. A more complete review of parameters can be found in the monographs [6.187–189]. Conventional 2-D parameters are described in the current ISO standard ISO 4287 [6.197], while other 2-D parameters are covered by ISO 12085 [6.202] and ISO 13565 [6.204–206]. ISO 1302 [6.194] prescribes a detailed indication of surface texture tolerances on technical drawings, with indication of the measurement specifications to follow when verifying tolerances.

Conventional 2-D Parameters. ISO 4287 defines three series of 14 parameters each: P-parameters for the unfiltered profile, R-parameters for the roughness profile, and W-parameters for the waviness profile; see Table 6.11 and [6.197]. Filtering to obtain the R and W profiles is introduced in the same standard and specified in [6.201]. Only examples of some parameters are given in this section. The reader should refer to the standard for complete definitions of each parameter.

Conventional 2-D surface texture parameters are defined in ISO 4287, but their value ranges are addressed in ISO 4288 [6.198]. ISO 4288 uses five sampling lengths as default for roughness profile parameters, indicating how to recalculate their upper and lower limits based on other numbers of sampling lengths. It should be noted that the same terminology is used in ISO 4287 and ISO 4288 to indicate the parameters computed over one sampling length and over five sampling lengths, respectively. It should be also noted that wavelengths under 13 μm and amplitudes of less than 25 nm are not covered by existing ISO standards, which therefore disregard typical ranges of interest in usual AFM metrology. However, since the ranges of definition seem to be dictated by the physical possibilities of existing stylus instruments, it can be assumed that the definitions can also be extended to values below those, but this must be investigated.

- *Ra* is the most widely used quantification parameter in surface texture measurement. It has also been known in the past as the center line average (CLA) or, in the USA, as the arithmetic average (AA). *Ra* is the arithmetic average value of the profile departure from the mean line within a sampling length, which can be defined as

$$Ra = \frac{1}{L} \int_0^L |z(x)| dx \approx \frac{1}{n} \sum_{i=1}^n |z_i| \quad (6.42)$$

Here, *z* is the height from the mean line defined in Fig. 6.19.

- *Rq*, corresponding to the root mean square (RMS), is preferred to *Ra* for modeling purposes. *Rq* is the geometric average value of the profile departure from the mean line within a sampling length, which can be defined as

$$Rq = \sqrt{\frac{1}{L} \int_0^L [z(x)]^2 dx} \approx \sqrt{\frac{1}{n} \sum_{i=1}^n (z_i)^2} \quad (6.43)$$

Table 6.11 Profile parameters defined by ISO 4287 (1997)

	Amplitude parameters					Distance parameters				Hybrid parameters	Curves and related parameters			
	Top-valley					Mean value					<i>RSm</i>	<i>RΔq</i>	<i>Rmr(c)</i>	<i>Rδc</i>
Roughness parameters	<i>Rp</i>	<i>Rv</i>	<i>Rz</i>	<i>Rc</i>	<i>Rt</i>	<i>Ra</i>	<i>Rq</i>	<i>Rsk</i>	<i>Rku</i>	<i>RSm</i>				
Waviness parameters	<i>Wp</i>	<i>Wv</i>	<i>Wz</i>	<i>Wc</i>	<i>Wt</i>	<i>Wa</i>	<i>Wq</i>	<i>Wsk</i>	<i>Wku</i>	<i>WSm</i>	<i>WΔq</i>	<i>Wmr(c)</i>	<i>Wδc</i>	<i>Wmr</i>
Structure parameters	<i>Pp</i>	<i>Pv</i>	<i>Pz</i>	<i>Pc</i>	<i>Pt</i>	<i>Pa</i>	<i>Pq</i>	<i>Psk</i>	<i>Pku</i>	<i>PSm</i>	<i>PΔq</i>	<i>Pmr(c)</i>	<i>Pδc</i>	<i>Pmr</i>

- R_p is the maximum height of the profile above the mean line within a sampling length.
- R_v is the maximum depth of the profile below the mean line within a sampling length.
- R_z is the maximum peak-to-valley height of the profile within the sampling length.
- R_t is a parameter which basically has the same definition as R_z but the definition of which is based on the total assessment, or evaluation, length (l_n). The evaluation length covers by default five sampling lengths, see ISO 4288 [6.198].
- R_{Sm} (mean spacing) is the mean width of the profile elements at the mean line within the sampling length.

Other Parameters Defined by ISO. Other parameters defined by ISO standards are the motif parameters and the bearing curve parameters. ISO 12085 [6.202] concerns parameters calculated through profile evaluation using the motif method, so far only used by the French motor industry. The method is based on dividing the unfiltered profile into geometrical features, characterized by peaks, that may merge or remain unaltered depending on their relative magnitudes, and thus calculating a number of roughness and waviness parameters. It should be noted that waviness and roughness in ISO 12085 do not refer to the same definitions used for the conventional parameters defined in ISO 4887. ISO 13565 describes two sets of parameters extracted from the bearing curve, and was specifically developed to characterize stratified surfaces with different functional properties at different depths. ISO 13565-1 [6.204] describes filtering. Parameters developed by the German motor industry are defined in ISO 13565-2 (Fig. 6.20 and [6.178]), while ISO 13565-3 describes the parameter set developed by the US engine manufacturer Cummins [6.195, 198, 199, 201, 203, 206, 231, 232].

3-D Parameters. Parameters calculated over an area are referred to as areal, or 3-D, parameters. Currently,

3-D surface texture measurement is the object of a number of ISO standards currently under development. Based on the research carried out within the European Program [6.233], a set of 3-D parameters has been proposed [6.234, 235]. These parameters are denoted by S instead of R to indicate that they are calculated over a surface. Table 6.12 gives an overview of the so-called field parameters currently under consideration by ISO. Most of the parameters of the set are derived from the corresponding 2-D parameters, while three are uniquely devised for surfaces. For example, the parameters S_a and S_q are calculated using equations similar to, respectively, (6.42) and (6.43). The reader should refer to the ISO documents or to the above-mentioned research reports for complete definitions of each parameter. Note that in ISO 25178 [6.236] conventional profilometry is referred to as line-profiling methods, while 3-D surface characterization is called areal-topography methods.

Table 6.12 3-D Parameters by ISO – Field parameters

Height parameters	Arithmetical mean height S_a (μm)
	Root-mean-square height of the scale-limited surface S_q (μm)
	Skewness of the scale-limited surface S_{sk}
	Kurtosis of the scale-limited surface S_{ku}
	Maximum peak height S_p (μm)
	Maximum pit height S_v (μm)
	Maximum height of the scale-limited surface S_z (μm)
Spatial parameters	Autocorrelation length S_{al} (μm)
	Texture aspect ratio S_{tr}
Hybrid parameters	Root-mean-square gradient of the scale-limited surface S_{dq}
	Developed interfacial area ratio of the scale-limited surface S_{dr}
Other parameters	Texture direction of the scale-limited surface S_{td} (deg)

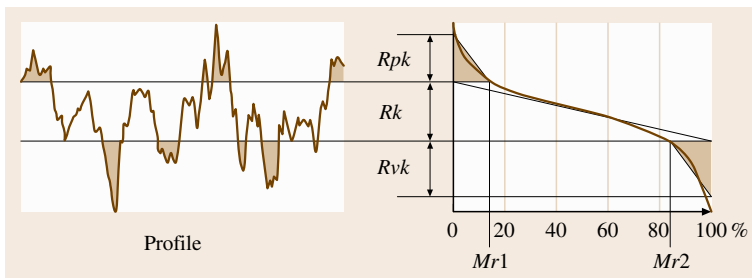


Fig. 6.20 Definition of bearing curve parameters according to ISO 13565-2:1996 (after [6.205]). Vertically, the bearing curve is divided into three zones, each described by a parameter: R_{pk} (peaks), R_k (core), and R_{vk} (valleys). Horizontally, two parameters are defined: Mr_1 and Mr_2 (material portions)

6.2.2 Optical Techniques

Many different measuring instruments based on optical techniques exist [6.191, 193, 237, 238]. In this section, the three most important ones are described: optical stylus profilometry, confocal microscopy, and interferometry. Some issues are of importance to all optical microscopy methods [6.239].

- Material response: optical probing is only possible when a signal above the detector threshold is received, which is determined by the material's reflectivity.
- Lateral resolution: this is limited by light diffraction. For an instrument numerical aperture NA and a light wavelength λ , the limit d is given by [6.196]

$$d = \frac{1.22\lambda}{NA} \quad (6.44)$$

- Maximum detectable slope: this depends on the kind of reflection (specular or diffused), which in turn depends on the surface topography and material, as well as on the objective working distance and numerical aperture.
- Wavelength of full-amplitude modulation: this quantity is intended as the maximum aspect ratio of a measurable surface structure.

Optical Stylus Profilometry

Optical styli for profilometry can be based on the autofocusing signal of a laser beam detector. A laser beam with a spot diameter of about $1\ \mu\text{m}$ is focused onto a point on the surface through a lens characterized by a high numerical aperture (NA). The scattered light is collected by the same lens on a focus detector, which operates a control system. When the detector moves horizontally, the controller, normally piezoelectric, modifies the distance of the lens from the surface so as to keep the beam focused. Consequently, the movement

of the lens follows the surface at a constant separation distance, and its trajectory describes the surface profile, as shown in Fig. 6.21. This kind of instrument is similar in use to conventional stylus instruments, with vertical resolution of approximately 5 nm. The optical method is noncontacting, which allows measurements on soft surfaces. However, this kind of instrument is connected to some problems related to achieving a useful reflection signal from surfaces that are shiny or transparent to the laser beam. The measurements obtained with the autofocusing method do not always correlate very well with those obtained with the stylus method [6.235, 237], as the optical method tends to overestimate the peak heights and the stylus method to underestimate the valley heights of the surface. The optical stylus method was found to work well on very flat samples, but when measuring roughnesses below $1\ \mu\text{s}$ it was very prone to error. The maximum detectable slope using an autofocusing stylus instrument is approximately 15° .

Confocal Microscopy

Confocal microscopy is an optical technique based on the focus detection principle. It is routinely applied in biological sciences, where relatively thick biological samples, such as cells in tissue, are investigated using fluorescence. However, it is also suitable for 3-D topography assessment, when the reflected light is detected rather than the emitted fluorescence. Here, the technique is presented with reference to the reflection mode of operation with a laser light source. The working principle is easily seen by referring to Fig. 6.22, where key components and optical ray diagrams are sketched (the scanner which moves the laser spot on the surface is not shown) [6.239].

Confocality consists in that both the light source pinhole P1 and the detector pinhole P2 are focused on the specimen. In laser scanning confocal microscopy one surface picture element (pixel) is imaged at a time. The final image is therefore built up sequentially. This has relevant consequences for the application of this technique to topography measurement; the measurement time is negatively affected while the maximum detectable surface slope is increased. Topography is reconstructed as a stack of vertical optical sections, in a fashion similar to computer tomography. In other words, it is built by overlapping a number of optical slices with normal vectors aligned with the optical axis. A single optical slice contribution to the final topography is given by all of the pixels where reflection occurs. The two pinholes shown in Fig. 6.22 allow, in principle, the detection of light back from

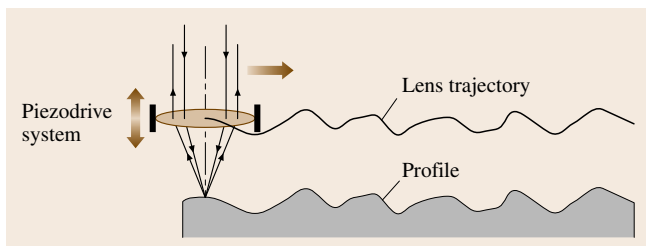


Fig. 6.21 Operating principle of the autofocusing method (after [6.237])

the focal plane. Stray light should be stopped here and should not reach the detector. This would be strictly true for an infinitesimally small pinhole, but the finite size always allows some amount of out-of-plane light to be collected by the photodetector. The pinhole diameter can be adjusted by the operator; practical values for the diameter in reflection-mode confocal microscopy go down to the diffraction limit given by (6.44). As a consequence, optical slices have a finite thickness. As regards the designs of confocal microscopes, some systems are provided with monochromatic (laser) illumination; others are based on xenon lamps which emit white light. The latter source allows detection by means of a charge-coupled device (CCD) sensor, with no scan being required in the lateral plane. As concerns laser scanners, galvanometric scanning mirrors are used to move the laser spot laterally, without physical table motion. The drive of the vertical axis determines the vertical resolution. With a piezo actuator, ranges of a few hundred microns are possible with resolution of a few nanometers. When a direct-current (DC) motor drives the objective, a range of up to 100 mm can be covered with resolution of about 100 nm. Confocal microscopes allow steep surface details to be assessed, the maximum detectable slope being up to 75° . Confocal microscopes have limited lateral resolution, and some commercially available instruments even have limited vertical resolution [6.239].

Interference Microscopy

Interference microscopy combines an optical microscope and an interferometer objective into a single instrument. Interferometric methods offer subnanometer vertical resolution, and are employed for surfaces with average roughnesses down to 0.1 nm and peak-to-valley heights of up to several millimeters.

Interferometry is a well-known optical principle that is widely used in metrology, which has recently also been applied to surface metrology [6.237]. Basically, interferometric systems are derived from the Fizeau interference microscope, as shown in Fig. 6.23. A light beam is sent through a microscope objective onto the sample surface. A part of the incident beam is reflected back by a semitransparent reference surface. The beams coming from the sample surface and the reference surface are projected onto the CCD detector, where they interfere. A piezoelectric transducer moves the objective and the interferometer vertically, causing fringe modulation. The intensity at each point of the interference pattern is proportional

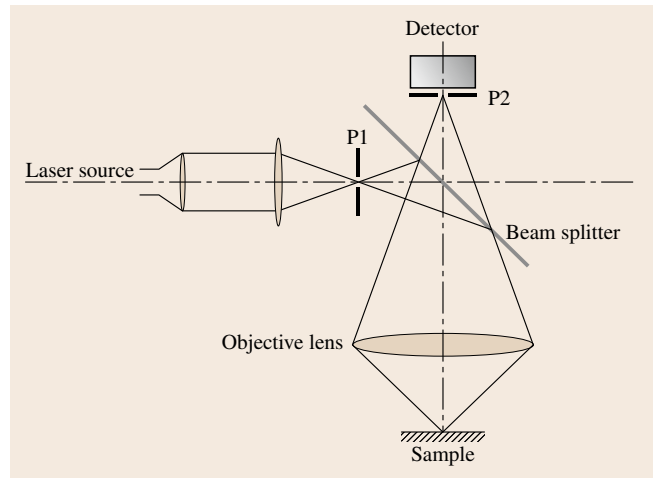


Fig. 6.22 Confocal principle

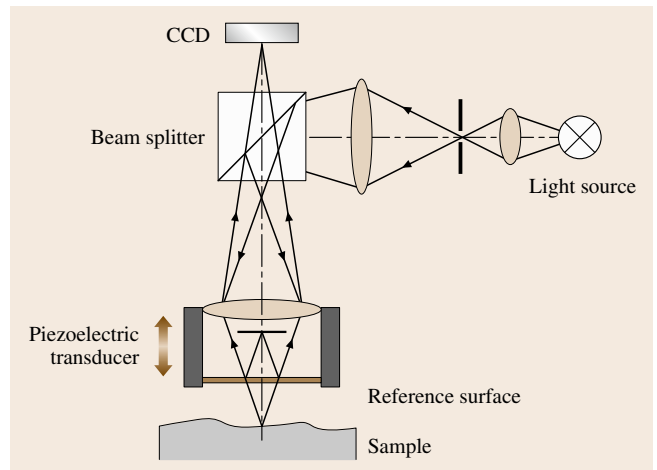


Fig. 6.23 Optical layout of an interferometric measuring system (after [6.237])

to

$$I(x, y) = \cos[\varphi(x, y) + \alpha(t)], \quad (6.45)$$

where $\varphi(x, y)$ is the initial phase and $\alpha(t)$ is the time-varying phase. The initial phase at each point is calculated from the fringe modulation, and the corresponding height is obtained using

$$z(x, y) = \frac{\varphi(x, y)\lambda}{4\pi}, \quad (6.46)$$

where λ is the wavelength of the light source. Two main interferometric techniques are commonly used in connection with surface measurements [6.239]

- phase-shift interferometry (PSI),
- scanning white-light interferometry (SWLI).

In **PSI**, the illumination is from a monochromatic light source (laser interferometry); this technique is characterized by the highest resolving power, while the dynamic range (maximum detectable depth difference between two neighboring pixels) is limited to $\lambda/4$, typically about 150 nm. A clear interference pattern can only be observed on smooth surfaces, while the interference fringes are corrupted by speckle effects when the roughness is larger than $\lambda/4$.

SWLI can be regarded as an extension of the **PSI** method, where a broadband frequency (instead of a single frequency) contributes to topography measurement. With white light, the dynamic range is no longer limited to $\lambda/4$. This is explained, referring to the frequency-domain analysis technique (**FDA**), by the fact that an interval of wavelengths, rather than a single one, is used to evaluate the slope. **FDA** implementation in **SWLI** is based on the discrete Fourier transform (**DFT**).

PSI is used mainly for testing optical components and silicon wafers with high accuracy and short measuring times (below 1 s), while most technical surfaces can be inspected by **SWLI**. Regardless of the category, the lateral resolution is always worse than $0.3\ \mu\text{m}$, due to the diffraction limit stated in (6.44). These microscopes are all limited with respect to the surface slopes from the finite numerical apertures. The maximum detectable slope using interferometry amounts to about 30° . These optical methods allow fast noncontacting measurements on essentially flat surfaces.

6.2.3 Scanning Probe Microscopy

General Introduction

Scanning probe microscopy, including atomic force microscopy (**AFM**) and scanning tunneling microscopy

(**STM**), provides a powerful tool for subnanometric acquisition of topographical data on very fine surfaces. Since the invention in 1986 of the scanning tunneling microscope [6.240], **SPM** and especially **AFM** have developed very rapidly, from scientific instruments used for basic research to their use in quality control in manufacturing [6.191, 241].

Measurement and Data Processing

In an **SPM**, as illustrated in Fig. 6.24a, a sharp tip with a radius of approximately 5–20 nm (the original contact-mode tip and cantilever are made out of silicon nitride using photolithography and preferential etching) is scanned over the surface by an xyz actuator with resolution of much less than a nanometer and a dynamic range on the order of $10\ \mu\text{m}$ in the z -direction and up to $100\ \mu\text{m}$ in the x - and y -directions. Alternatively, as shown in Fig. 6.24b, the tip is stationary while the sample is moved. The probe records a control signal; in the atomic force microscope this signal is the nondestructive force exerted by the surface on the tip; in the scanning tunneling microscope the control signal is a small current flowing from the tip into the sample. The tip is moved relative to the surface, raster-scanning over a number of nominally parallel lines; in the **AFM** the height of the probe as a function of the x and y position is recorded as an image and the topography of the surface is built up into a three-dimensional image. The tip is mounted on a very soft cantilever with spring constant k in the range of $1\ \text{N/m}$ – so soft that the scanning probe will not move the atoms around on the surface. At the start of a measurement, the cantilever is positioned towards the sample. When the tip touches the sample, the cantilever begins to bend proportionally to the force exerted by the tip on the surface. The tip, ideally terminated by a single atom, traces the contours of the surface and is actually touching the sample surface with a very low force – so low that the atomic structures

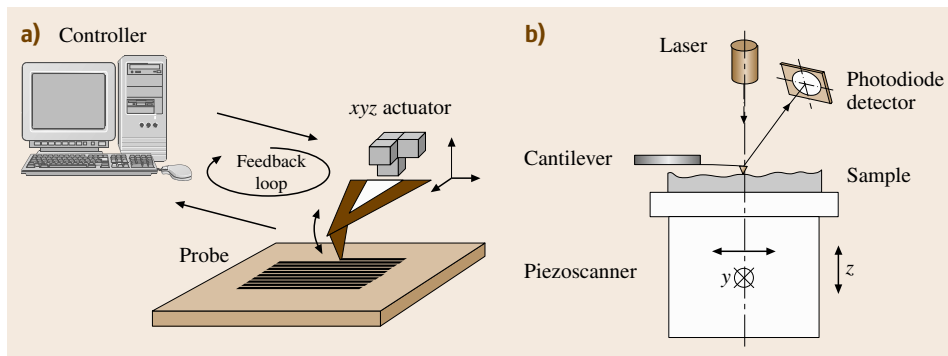


Fig. 6.24a,b Principle of a **SPM**: (a) raster-scanning the tip over a surface, (b) optical force detection with the sample scanned in an **AFM**

are unaltered – both on the sample as well as on the tip. The low force between the tip and sample is kept at a constant level during scanning, being typically lower than 10 nN in contact-mode atomic force microscopy. The most accurate and commonly used principle of detection of the cantilever deflection is optical: a focused laser beam, typically from a laser diode, is reflected from the back of the cantilever towards a photodiode with two or four segments, as illustrated in Fig. 6.24b. When the cantilever is bent, the laser spot at the photodiode will move; in other words, the relative intensity of light hitting the segments will change and produce a signal.

AFM Operation Modes

Different modes of AFM operation exist. The simplest mode of operation for an atomic force microscope is the contact mode, where the probing tip senses the small repulsive force occurring from constantly touching the sample surface. The signal from the detector is used to vertically adjust the tip position with respect to the sample surface, so as to eliminate the deflection of the cantilever. For most applications, resonant vibrating cantilever modes are preferred, although they are more complicated to understand. In the noncontact mode, the cantilever is forced to vibrate a little *above* its resonant frequency. When the vibrating tip comes so close to the surface that it begins to feel the attractive van der Waals forces, the amplitude of the vibration will become smaller. It is this (decreased) amplitude which is kept constant during scanning in noncontact mode. In intermittent contact mode, the cantilever is forced to vibrate a little *below* its resonant frequency, far away from the sample surface. When the vibrating tip comes so close to the surface that it begins to touch the sample surface during a fraction of the vibration cycle, the amplitude of the vibration, as in noncontact mode, becomes smaller relatively to the free amplitude. It is this (decreased) amplitude that is kept constant during scanning in the intermittent mode. Figure 6.25 summarizes the different modes of operation discussed above.

The atomic force microscope can be operated in several other modes than those described above, for example with the purpose of, at least qualitatively, differentiating material properties. During scanning, the tip can tilt, caused by friction between tip and sample surface. The tip also suffers from friction when it passes a ridge and, unfortunately, the friction and topography signal often become mixed. It is possible to give the tip a permanent charge that makes it sensitive to charged areas on the sample when it scans over the

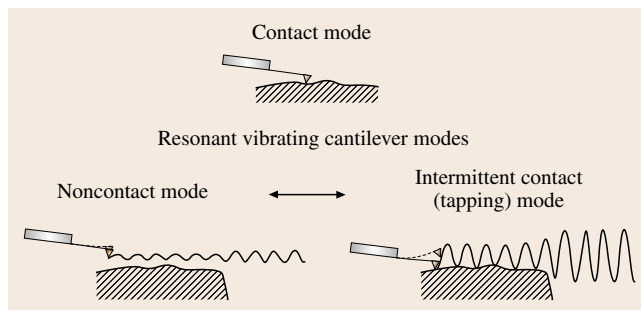


Fig. 6.25 Different operating modes of an AFM

surface without touching it. It is also possible to have the tip covered with a permanent magnetic material. If the sample has domains with different magnetic magnitudes, the tip can detect that. In a force modulation microscope, the tip is scanned in contact with the sample and the cantilever, or sample, is forced to swing periodically by a constant control signal. The actual amplitude of the cantilever changes according to the elastic properties of the sample. Atomic force microscopy can be performed in many environments, including ultrahigh vacuum, ambient conditions, and liquids. If the atomic force microscope works in ultrahigh vacuum, it can resolve not only single atoms but also single atom defects on, say, the surface of silicon. Working in air, AFM can only resolve the unit cell structure. It is yet to be demonstrated that it can resolve single atom defects when working in ambient air.

AFM Scanners

In many commercial microscopes, the movement of the tip is performed by a scanner tube, which is a hollow cylinder made out of a piezoelectric material that will change its linear dimensions when subjected to an electric field, and wag in the x - y -plane like a dog's tail. By raising the voltage on the inner electrode, or by mounting a separate piezo element on top of the tube, one can generate movement in the z -direction. This construction has the advantage of being simple and rigid, since all three movements are performed by the same elements. The disadvantage is that the movement is not very accurate. Piezo materials have a number of undesirable properties. First of all, they are intrinsically nonlinear, and what is worse, piezoelectric materials also suffer from hysteresis. Another problem is creep, which means that, when a voltage is applied, the extension or contraction of the piezo material will not reach its final state instantly. Another problem when generating the movement is the coupling between the x - and

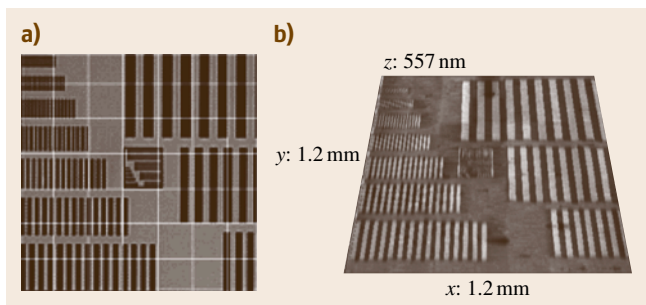


Fig. 6.26 (a) Scanning strategy; (b) 3-D plot of AFM image composed of 49 single scans stitched together (after [6.239])

the y -motion. Generally speaking, whenever the tip or the sample is moving in one direction, it will unintentionally also move a little bit in other directions. This is particularly bad for movement in the x -direction, since the associated small movement in the z -direction will make a flat surface look curved [6.231]. For smooth surfaces, this curvature can easily dominate the roughness. Over a side length of $100\ \mu\text{m}$, the peak-to-peak values for the image bow range from a few nanometers for high-quality flexure stages to more than $100\ \text{nm}$ for some commonly used tube scanners. Part of the non-linearity and the hysteresis can be corrected off-line by image processing software. In the x - and y -directions, correction methods can lead to an accuracy of 1–2% under optimum conditions. For the z -direction, unfortunately, it is very difficult – if not impossible – to make a model correction, because the history is generally not known. Using the most linear piezo material, which means trading away some scan range in the z -direction, an accuracy that reaches down to 1% can also be achieved in this direction. The way to overcome the nonlinearity of the piezo material is to use linear distance sensors that independently measure the movement of either the sample or the tip, as used in so-called metrology AFMs.

Large-Range AFM

An AFM allows measurement of the surface topography with very high resolution, but over a limited range. In a specially made instrument, an AFM probe is mounted on a coordinate-measuring machine (CMM), achieving free positioning of the AFM in the space covered by the CMM [6.242, 243]. In particular, this integrated system can be used for surface mapping [6.242–247]. The CMM is used to reposition the AFM probe in-between surface roughness measurements to stitch together different areas covering continuous regions larger than the

range scanned by the probe. Correct stitching independently of the positioning errors of the CMM is obtained through optimization of the cross-correlation between two adjacent overlapping surface areas. A maximum uncertainty of 0.8% was achieved for the case of surface mapping of $1.2 \times 1.2\ \text{mm}^2$, consisting of 49 single AFM images, as shown in Fig. 6.26 [6.239]. Another example of large-range AFM, developed by Physikalisch-Technische Bundesanstalt (PTB), is described in [6.248].

6.2.4 Scanning Electron Microscopy

Scanning electron microscopy (SEM) can be used for qualitative surface topography analysis, primarily based on the fact that SEM allows excellent visualization. As regards topography, SEM has some unique properties that, combined together, are not matched by any other microscopy technique. These are listed below [6.239].

- Possible magnification levels from less than $100\times$ up to $100\,000\times$. This means that the imaged range can either be on the order of $1\ \text{mm}^2$ or just $1\ \mu\text{m}^2$. SEM is in fact a multiscale technique. There is no other microscopy method as flexible as SEM in terms of the range of scalability.
- At high magnification, the ultimate resolution is as good as about $2\ \text{nm}$ on conductive surfaces. SEM metrology is not limited by light diffraction. Such high resolving power can only be achieved by scanning probe microscopes that, on the other hand, are limited in terms of measurable range.
- Large depth of field. In a SEM, features lying at different depths can be kept simultaneously in focus.
- Long usable working distance. High-magnification images, say at $1000\times$ or more, can easily be taken with working distances of several millimeters (ten or even more). This feature allows the development of measuring strategies based on multiple positioning. Moreover, commercially available SEMs are provided with moveable sample stages, with some degrees of freedom for observing features from different viewpoints.

Although SEM images obtained by detecting secondary electrons have a striking three-dimensional appearance (due to the shadowing effects), they are still inherently 2-D. No height information can be extracted directly from the images, and measurements in the x - and y -dimensions are only correct in a single plane. In order to reconstruct the third dimension of surface features,

photogrammetry methods can be used [6.249–255]. A specimen is imaged in the SEM under two different perspectives. Surface features of different heights on the specimen surface differ in their lateral displacement in the two images. The disparities between projections of the surface features in the two images are used to derive quantitative surface topography. A fundamental prerequisite for successful calculation is the correct matching of single surface features in the two images. In most SEMs, it is possible to take the two different stereo viewpoints by tilting the specimen about a horizontal axis.

Three-dimensional data achieved by reconstructing stereo pairs or triplets can be used to evaluate surface topography, but they are limited by a number of factors. First of all, SEM measurements require conductive sample materials, or sample preparation through deposition of a gold layer on the surface. A major limitation is that roughness parameters should be calculated over a relatively large area, while, in the case of large magnifications, the area is relatively small. Another limitation is that smooth surfaces are reconstructed with high uncertainty [6.239].

An investigation was carried out at Danmarks Tekniske Universitet (DTU) on the traceability of surface texture measurements using stereo-pair SEM. A positioning procedure that realizes pseudo-eucentric tilting was developed. A model for calculating the accuracy of topography calculation was given, based on an existing theory adapted to comply with the hypothesis of eucentric tilting [6.256, 257]. A novel design for a calibration artefact, suited for testing the performance of a three-dimensional SEM at high magnifications, was proposed [6.239].

6.2.5 Parametric Methods

Besides the above methods, which produce height scans over the surface, a number of techniques exist that produce measurable parameters representing some averaged property of the surface topography. All of the phenomena related to the interaction between a light wave and a surface are affected by the microgeometry of the surface, and methods based upon specular or diffuse reflectance, speckle, and polarization have been developed. A review by *Vorburger* and *Teague* [6.258] discusses these techniques, considering potentialities and limits. The so-called integral methods, by which surface roughness is measured and quantified as a whole, operate with parameters based on surface statistics, correlation, and frequency analysis. The main

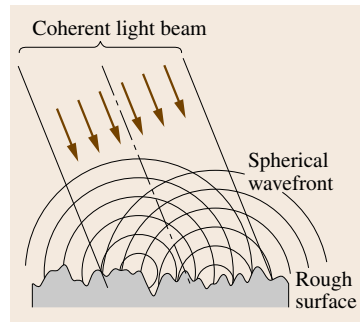


Fig. 6.27 The Huygens–Fresnel principle as the basis of light scattering from rough surfaces (after [6.218])

advantage of statistical surface description is that it describes a profile or surface with a minimum number of parameters, which enables a characterization of the profile or surface [6.259]. The statistical analysis of surface topography leads to a broad variety of parameters, which are not covered by ISO standards in general. In addition to pure statistical properties, further information can be obtained from autocorrelation and autocovariance functions of a given surface $h(x)$ (ACF and ACVF), which are identical for functions with zero mean, as well as from the power spectral density function (PSDF). These are described mathematically in (6.47) and (6.48). A simplified theoretical treatment of light scattering from rough surfaces is based on the Huygens–Fresnel principle, as shown in Fig. 6.27. Here, it may be helpful to emphasize that, irrespective of the method, data cannot be influenced by any property of the sample that is outside the sensing regime of the measuring instrument as defined in the Stedman diagram of Fig. 6.2. Thus, the data from instruments may not agree, even if they are fully calibrated according to the best procedures.

$$\text{PSDF}(k_x) = L^{-1} \left| \int_0^L h(x) \exp(-ik_x x) dx \right|^2, \quad (6.47)$$

$$\begin{aligned} \text{ACF}(\tau) &= L^{-1} \int_0^L h(x)h(x+\tau) dx \\ &= \frac{1}{2\pi} \int_{-\infty}^{\infty} \text{PSDF}(k_x) \exp(ik_x \tau) dk_x. \end{aligned} \quad (6.48)$$

Parametric methods based on capacitive and other methods exist as well, but are not relevant to the present chapter. Parametric methods are called area-integrating methods in ISO 25178 [6.128].

6.2.6 Applications and Limitations of Surface Measurement

Visualization of the surface profile, or surface area, is perhaps the most powerful tool associated with topographic surface analysis. Significant information can be drawn directly from the plots, especially when investigating surface functionality. When quantitative information is required, the adoption of parameters becomes essential; for instance, peaks are important when considering friction and wear properties, as the interaction between surfaces concentrates around them. Valleys are important for the retention of lubrication. At the same time, fracture propagation and corrosion start in valleys. The R_z parameter can be useful where components are subjected to high stresses; any large peak-to-valley value could be associated with areas which are likely to suffer from crack propagation. For both qualitative as well as for quantitative characterization, 3-D analysis is a powerful tool which can give much more information compared with conventional 2-D methods. In [6.260], a method for identifying different wear mechanisms by measuring surface texture alterations was proposed and applied to deep drawing dies. Using a combination of the areal bearing curve parameters Spk and Svk , adhesive, abrasive, and fatigue wear as well as plowing and pick-up could be recognized. An important application of areal analysis concerns the quantification of 3-D features such as dominant texture direction, shape of contact asperities, lubricant reservoirs, and valley connectivity.

It cannot be emphasized strongly enough that single parameters, which are inherently synthetic, cannot completely describe the complex reality of a surface. Each parameter can only give information about some specific features of the microgeometrical texture, and this requires a sound interpretation. For example, the R_a parameter on its own does not tell us anything about the

functional behavior of a component, and many existing surfaces can be characterized by the same values of R_a but are extremely different with respect to functionality, as clearly illustrated by Fig. 6.28. R_a can be used as a process control parameter, since changes in R_a value may indicate that some process conditions have changed, such as cutting tool geometry, cutting speed, feed or cutting fluid action. However, being an average value, R_a cannot be used to control processes involving stratified surfaces, such as plateau honing. As a general rule, it is strongly recommended that parameters should only be used in connection with a visual examination of the surface topography. An example of extracting comprehensive information using commercial software (SPIP [6.218]) in connection with surface topography analysis is shown in Fig. 6.29.

Other limitations are related to error sources from the measurement; for instance, roughness parameters can be subject to large variations arising from their definitions and can also be unstable due to spurious features such as dust, burrs or scratches. A metrological limitation in stylus profilometry is that the geometry of the tip acts like a mechanical filter that cannot reproduce smaller details. The resolution achieved by the stylus method depends on the actual surface slopes and heights in the neighborhood of the point of contact, as illustrated in Fig. 6.16. Some parameters describing the shape of the surface are directly influenced by the geometry of the stylus; for example, the tip radius R is added to the radii of peaks and subtracted from the radii of valleys. Moreover, the force applied by the stylus on the surface can generate plastic deformation of the surface and affect the measurement. Also, in AFM there are limitations on resolution imposed by the geometry of the probing tip and error sources related to instrument and measuring conditions. No existing instrument can be regarded as truly 3-D: stylus instruments, SPMs, and optical instruments can be considered, at most, as $2\frac{1}{2}$ dimensional. More typically, the vertical range is limited to about one-tenth of the lateral ones. No commercially available instrument is suitable for measuring deep cavities, pores or reentrances, not to mention hidden details. The need for true 3-D characterization of surface details has been addressed in [6.261].

6.2.7 Traceability

Traceability is defined as the property resulting from measuring to the value of a standard whereby it can be related to stated references, usually national or international standards, through an unbroken chain of

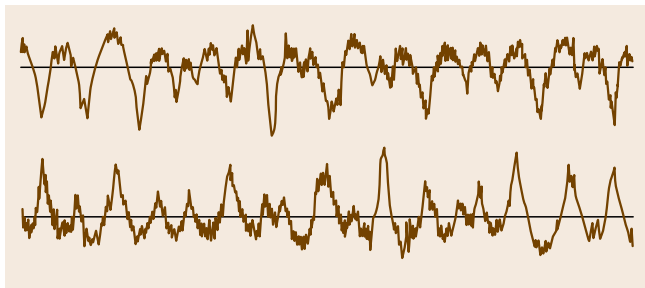


Fig. 6.28 Two profiles with the same R_a (and R_z) value but with very different functional behaviors

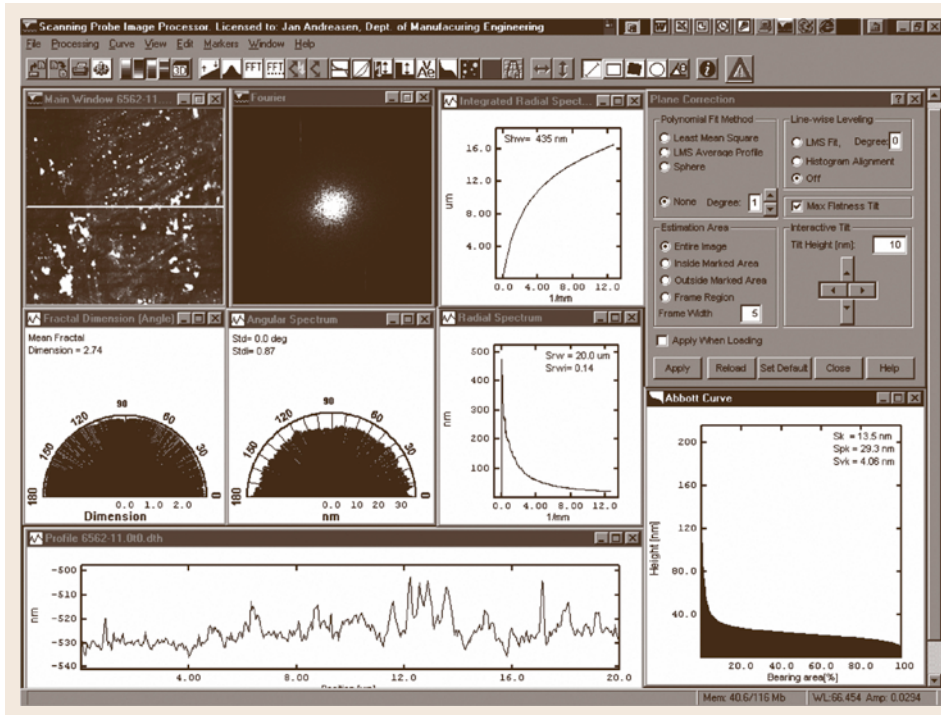


Fig. 6.29
Example of comprehensive information associated with surface analysis using SPIP (after [6.236])

comparisons, all with stated uncertainties [6.261, 262]. In the case of surface roughness measurements, several factors influence this property, for example, the measurement principle, the characteristics of the instrument, the measurement procedure, and the data evaluation [6.263]. Calibration, traceability, and uncertainty issues in surface texture metrology are addressed in a NPL report by Leach [6.264]. A recent international comparison regarding surface texture traceability is reported in [6.265].

Calibration of Instruments

Standards and procedures for the verification of the entire measurement system are described in international standards [6.231, 266]. These standards cover the most conventional uses of the instruments and the most common parameters. The verification of algorithms for the calculation of surface roughness parameters can be carried out by means of software gages, thereby establishing traceability for the data evaluation or software. This principle is described in [6.199]. In the case of new methods for the characterization of surface texture (for example, integral methods), new approaches have to be taken in order to establish traceability. Here, the measurement principle, including the physical principle as

well as the data evaluation method, must be taken into account, and the procedure and principle are essential to the result. An example is the common effort to establish traceability for atomic force microscopy, where not only the physical principle of the instrumentation but also the data evaluation methods are investigated [6.267–269].

Some examples of 2-D surface texture calibration standards described by ISO are shown in Fig. 6.30. These calibration standards can be purchased from roughness instrument manufacturers, and their accredited calibration is provided by a large number of laboratories. Methods and standards for 3-D instrument calibration are currently under standardization by ISO TC213 (Table 6.10).

The minimum necessary equipment for calibration of a stylus instrument for general industrial use is an optical flat to check the background noise and an ISO type C or D standard with a known parameter value (R_a or R_z). The background noise, which originates from the electrical and mechanical parts in the instrument, results in a systematic error. As a main rule, the roughness measuring instrument should only be used for measurements of specimens with parameter values higher than five times the background noise. Typical background noise levels are

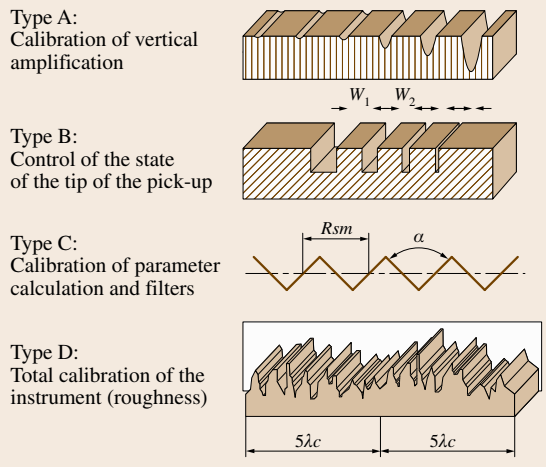


Fig. 6.30 Examples of surface texture calibration standards described by ISO 5436 (after [6.199, 231])

1. portable roughness measuring instruments Ra : 0.02–0.05 μm ,
2. stationary roughness measuring instruments Ra : 0.002–0.01 μm .

The magnifications of instruments with external pick-up data can be calibrated using an ISO type A standard. It is customary to use calibration standards frequently, in connection with the use of the instruments.

Calibration of optical instruments is not as well established as calibration of stylus instruments [6.238, 258, 270, 271]. A proposal for a guideline to calibrate interference microscopes using the same artifacts and procedures that are used for stylus instruments is presented in [6.271].

Calibration of SPMs, currently still under development, encompasses scaling, nonlinearity, hysteresis, and orthogonality of x - y - z -axes, as well as shape, size, and dynamics of the probe [6.239, 267–269]. Transfer standards designed for certification are available through the instrument manufacturers, while their certification can be obtained from major national metrological institutes (PTB, NPL, NIST, etc.).

Uncertainty Budgeting

Upon calibration using a transfer standard, it is possible to produce an uncertainty budget for measurements with a stylus instrument. An example of an uncertainty budget for the calibration of an instrument using an ISO type C standard with a certified uncertainty U_n fol-

lows. The budget contains three components that can be calculated from knowledge about

1. reference uncertainty,
2. background noise level, and
3. measurement repeatability.

Following a convention, u indicates the standard uncertainty at the 1σ level, while U is for the 95% confidence level at a coverage factor of 2.

- Uncertainty of the calibration standard from certificate: $u_n = U_n/2$
- Uncertainty in the transfer of traceability (repeatability of the instrument): $u_r = \text{STD}_r/\sqrt{n}$, where n is the number of measurements in the same track with the standard deviation STD_r ;
- Uncertainty caused by the background noise: $u_b = \frac{1}{2}R_x0/\sqrt{3}$, where R_x0 is the measured background noise (average $Ra0$ or $Rz0$ value measured on an optical flat, assuming rectangular noise distribution);
- Total uncertainty: $U_{\text{inst}} = 2\sqrt{u_n^2 + u_r^2 + u_b^2}$.

If the same instrument is used for measurements on a workpiece, the resulting uncertainty increases with the variation in roughness of the workpiece, which is determined by taking measurements at different locations. It shall be noted that this component (estimated as u_s) depends on whether or not the measurement result is used for tolerance verification.

- u_s is the uncertainty caused by variations in the roughness of the specimen at different locations (n is the number of measurements carried out on the specimen with corresponding standard deviation STD_s)
- General (without tolerance verification): $u_s = \text{STD}_s/\sqrt{n}$;
- Verification after the 16% rule (ISO 4288): $u_s = 1/2\text{STD}_s/\sqrt{n}$;
- Verification after the max rule (ISO 4288 [6.198]): $u_s = 0$ (single measurements);
- Total uncertainty: $U_{\text{tot}} = 2\sqrt{u_n^2 + u_r^2 + u_b^2 + u_s^2}$.

It may be worth reminding the reader that the uncertainties only refer to the properties of the sample within the zone defined on the Stedman plot in Fig. 6.2; they are not necessarily the true uncertainties.

Current Situation and Future Developments

The present situation concerning surface metrology can be illustrated with respect to the traceability of surface

topography measurements. Figure 6.31 shows the range of different calibration standards currently available. Comparing the present possibilities with the measurement ranges covered by existing instruments (Fig. 6.16), and with the requirements from production [6.261], the need for developments in the nanometer range is clear. Traceable calibration of optical surface roughness instruments is also challenging [6.270–272]. Another clear challenge is the true three-dimensional characterization of surface details involving reentrances, as discussed in [6.241, 261, 272].

6.2.8 Summary

Surface topography characterization encompasses measurement, visualization, and quantification. The principal methods of surface topography measurement are stylus profilometry, optical scanning techniques, and scanning probe microscopy (SPM). These methods, based on the acquisition of topography data from point-by-point scans, give quantitative information on heights with respect to position. Based on a different approach, the so-called integral methods produce parameters representing some average property of the surface under

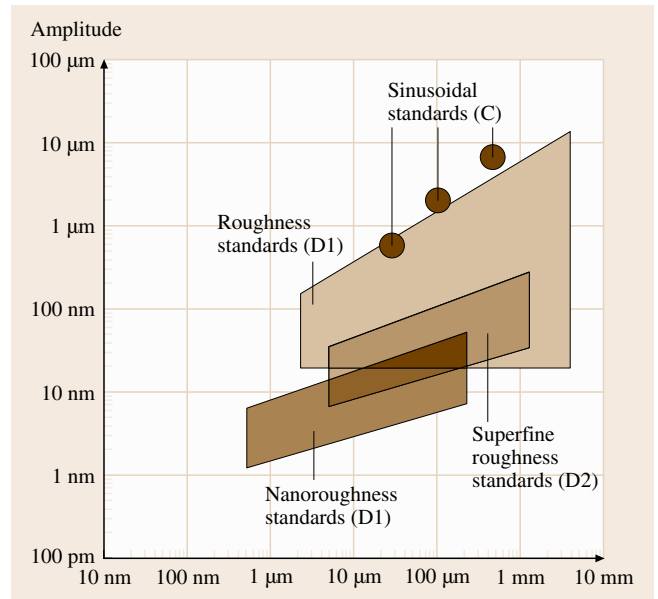


Fig. 6.31 Diagram of wavelength versus amplitude for different surface roughness calibration standards (courtesy of the PTB from [6.261])

Table 6.13 Merits, limitations, and applications of some techniques for surface topography analysis

Technique	Merits	Limitations	Applications
Stylus profilometry	Large vertical and lateral range Slopes up to 60° Robust Universally applicable externally as well as for internal measurements	Micrometer resolution Scratches soft surfaces	All kinds of industrial surfaces
Autofocus profilometry	Noncontact	Maximum slope 15° Signal problems on shiny or transparent materials	Soft as well as hard surfaces
White-light interferometry	Fast method High vertical resolving power (down to 0.1 nm)	Limited lateral resolution Maximum detectable slope up to about 30°	Roughness of flat surfaces Film thickness Low-aspect-ratio MST components (MST: Micro Systems Technologies)
Confocal microscopy	High-aspect-ratio structures Maximum detectable slope up to 75°	Limited lateral resolution Limited vertical resolution in some commercially available instruments	Dimensions of high-aspect-ratio MST components
Scanning electron microscopy	Wide range of operation, from less than 100× up to 100 000× Nanometer resolution Large depth of field Large working distance	Requires conductive sample material or preparation Small area for calculation of roughness parameters	Nanotechnology All kinds of material
Scanning probe microscopy	Nanometer/subnanometer resolution	Slow method Limited lateral and vertical range	Nanotechnology Nanoroughness

examination. Measurement methods, as well as their application and limitations, have been briefly reviewed, including standardization and traceability issues. Ta-

ble 6.13, adapted from [6.239], gives an overview of the merits, limitations, and typical applications of different techniques for surface topography measurements.

References

- 6.1 I.S. Gilmore, M.P. Seah, J.E. Johnstone: Quantification issues in ToF-SIMS and AFM coanalysis in two-phase systems, exemplified by a polymer blend, *Surf. Interface Anal.* **35**, 888 (2003)
- 6.2 ASTM: *Annual Book of ASTM Standards*, Vol. 03.06 (ASTM, West Conshohocken 2003)
- 6.3 ISO: *List of Technical Committees* (International Organization for Standardization, Geneva)
http://www.iso.org/iso/standards_development/technical_committees/list_of_iso_technical_committees.htm
- 6.4 NPL: *Surface and Nano-Analysis* (National Physical Laboratory, Teddington)
<http://www.npl.co.uk/nanoanalysis>
- 6.5 NIST: *Surface Data*, NIST Scientific and Technical Data Base (NIST, Gaithersburg)
<http://www.nist.gov/srdsurface.cfm>
- 6.6 D. Briggs, M.P. Seah (Eds.): *Practical Surface Analysis. Auger and X-ray Photoelectron Spectroscopy*, Vol. 1 (Wiley, Chichester 1990)
- 6.7 D. Briggs, M.P. Seah (Eds.): *Practical Surface Analysis. Ion and Neutral Spectroscopy*, Vol. 2 (Wiley, Chichester 1992)
- 6.8 D. Briggs, J.T. Grant (Eds.): *Surface Analysis by Auger and X-ray Photoelectron Spectroscopy* (IM Publications and Surface Spectra, Manchester 2003)
- 6.9 S. Morton: UK Surface Analysis Forum
<http://www.uksaf.org/home.html>
- 6.10 Y. Homma: Summary of ISO/TC 201 Standard, II ISO14237:2000 – SCA – Secondary-ion mass spectrometry – Determination of boron atomic concentration in silicon using uniformly doped materials, *Surf. Interface Anal.* **33**, 361 (2002)
- 6.11 K. Kajiwara: Summary of ISO/TC 201 Standard, IV ISO14606:2000 – SCA – Sputter depth profiling – Optimization using layered systems as reference materials, *Surf. Interface Anal.* **33**, 365 (2002)
- 6.12 K. Yoshihara: Summary of ISO/TC 201 Standard, V ISO14975:2000 – SCA – Information formats, *Surf. Interface Anal.* **33**, 367 (2002)
- 6.13 M.P. Seah: Summary of ISO/TC 201 Standard, I ISO14976:1998 – SCA – Data transfer format, *Surf. Interface Anal.* **27**, 693 (1999)
- 6.14 M.P. Seah: Summary of ISO/TC 201 Standard, VII ISO15472:2001 – SCA – X-ray photoelectron spectrometers – Calibration of energy scales, *Surf. Interface Anal.* **31**, 721 (2001)
- 6.15 S. Hofmann: Summary of ISO/TC 201 Standard, IX ISOTR15969:2000 – SCA – Depth profiling – Measurement of sputtered depth, *Surf. Interface Anal.* **33**, 453 (2002)
- 6.16 Y. Homma: Summary of ISO/TC 201 Standard, X ISO17560:2002 – SCA – Secondary-ion mass spectrometry – Method for depth profiling of boron in silicon, *Surf. Interface Anal.* **37**, 90 (2005)
- 6.17 M.P. Seah: Summary of ISO/TC 201 Standard, XII ISO17973:2002 – SCA – Medium-resolution Auger electron spectrometers – Calibration of energy scales for elemental analysis, *Surf. Interface Anal.* **35**, 329 (2002)
- 6.18 M.P. Seah: Summary of ISO/TC 201 Standard, XI ISO17974:2002 – SCA – High-resolution Auger electron spectrometers – Calibration of energy scales for elemental and chemical-state analysis, *Surf. Interface Anal.* **35**, 327 (2003)
- 6.19 D.S. Simons: Summary of ISO/TC 201 Standard: XIII, ISO 18114:2003 – SCA – Secondary-ion mass spectrometry – Determination of relative sensitivity factors from ion-implanted reference materials, *Surf. Interface Anal.* **38**, 171 (2006)
- 6.20 M.P. Seah: Summary of ISO/TC 201 Standard, VIII ISO18115:2001 – SCA – Vocabulary, *Surf. Interface Anal.* **31**, 1048 (2001)
- 6.21 M.P. Seah: Summary of ISO/TC 201 Standard: XXVIII, ISO 18115:2001/Amd.1:2006 – SCA – Vocabulary – Amendment 1, *Surf. Interface Anal.* **39**, 367 (2007)
- 6.22 M.P. Seah: Summary of ISO/TC 201 Standard: XXXIII, ISO 18115:2001/Amd.2:2007 – SCA – Vocabulary – Amendment 2, *Surf. Interface Anal.* **40**, 1500 (2008)
- 6.23 S. Tanuma: Summary of ISO/TC 201 Standard: XX, ISO 18118:2004 – SCA – Auger electron spectroscopy and x-ray photoelectron spectroscopy – Guide to the use of experimentally determined relative sensitivity factors for the quantitative analysis of homogeneous materials, *Surf. Interface Anal.* **38**, 178 (2006)
- 6.24 L. Kövér: Summary of ISO/TC 201 Standard: XXV, ISO 18392:2005 – SCA – X-ray photoelectron spectroscopy – procedures for determining backgrounds, *Surf. Interface Anal.* **38**, 1173 (2006)
- 6.25 L. Kövér: Summary of ISO/TC 201 Standard: XXX, ISO TR18394:2006 – SCA – Auger electron spectroscopy – Derivation of chemical information, *Surf. Interface Anal.* **39**, 556 (2007)
- 6.26 J. Wolstenholme: Summary of ISO/TC 201 Standard: XXXI, ISO 18516:2006 – SCA – Auger electron spectroscopy and x-ray photoelectron spectroscopy – Determination of lateral resolution, *Surf. Interface Anal.* **40**, 966 (2008)

- 6.27 D.R. Baer: Summary of ISO/TC 201 Standard: XVIII, ISO 19318:2004 – SCA – X-ray photoelectron spectroscopy – Reporting of methods used for charge control and charge correction, *Surf. Interface Anal.* **37**, 524 (2005)
- 6.28 C.J. Powell: Summary of ISO/TC 201 Standard, XIV ISOTR19319:2003 – SCA – Auger electron spectroscopy and x-ray photoelectron spectroscopy – Determination of lateral resolution, analysis area, and sample area viewed by the analyser, *Surf. Interface Anal.* **36**, 666 (2004)
- 6.29 D.W. Moon: Summary of ISO/TC 201 Standard, XV ISO20341:2003 – SCA – Secondary-ion mass spectrometry – Method for estimating depth resolution parameters with multiple delta-layer reference materials, *Surf. Interface Anal.* **37**, 646 (2005)
- 6.30 C.J. Powell: Summary of ISO/TC 201 Standard: XXIX, ISO 20903:2006 – SCA – Auger electron spectroscopy and x-ray photoelectron spectroscopy – Methods used to determine peak intensities and information required when reporting results, *Surf. Interface Anal.* **39**, 464 (2007)
- 6.31 M.P. Seah: Summary of ISO/TC 201 Standard, XXI. ISO21270:2004 – SCA – X-ray photoelectron and Auger electron spectrometers – Linearity of intensity scale, *Surf. Interface Anal.* **36**, 1645 (2004)
- 6.32 I.S. Gilmore, M.P. Seah, A. Henderson: Summary of ISO/TC 201 Standard, XXII ISO22048:2004 – SCA – Information format for static secondary ion mass spectrometry, *Surf. Interface Anal.* **36**, 1642 (2004)
- 6.33 M.P. Seah: Summary of ISO/TC 201 Standard: XXIII, ISO 24236:2005 – SCA – Auger electron spectroscopy – Repeatability and constancy of intensity scale, *Surf. Interface Anal.* **39**, 86 (2007)
- 6.34 M.P. Seah: Summary of ISO/TC 201 Standard: XXIV, ISO 24237:2005 – SCA – X-ray photoelectron spectroscopy – Repeatability and constancy of intensity scale, *Surf. Interface Anal.* **39**, 370 (2007)
- 6.35 M.P. Seah, W.A. Dench: Quantitative electron spectroscopy of surfaces – A standard data base for electron inelastic mean free paths in solids, *Surf. Interface Anal.* **1**, 2 (1979)
- 6.36 C.P. Hunt, M.P. Seah: A submonolayer adsorbate reference material based on a low alloy steel fracture sample for Auger electron spectroscopy, I: Characterisation, *Mater. Sci. Technol.* **8**, 1023 (1992)
- 6.37 A. Savitzky, M.J.E. Golay: Smoothing and differentiation of data by simplified least squares procedures, *Anal. Chem.* **36**, 1627 (1964)
- 6.38 J. Steiner, Y. Termonia, J. Deltour: Comments on *Smoothing and differentiation of data by simplified least squares procedures*, *Anal. Chem.* **44**, 1906 (1972)
- 6.39 L.E. Davis, N.C. MacDonald, P.W. Palmberg, G.E. Riach, R.E. Weber: *Handbook of Auger Electron Spectroscopy*, 2nd edn. (Physical Electronics Industries, Eden Prairie 1976)
- 6.40 G.E. McGuire: *Auger Electron Spectroscopy Reference Manual* (Plenum, New York 1979)
- 6.41 Y. Shiokawa, T. Isida, Y. Hayashi: *Auger Electron Spectra Catalogue: A Data Collection of Elements* (Anelva, Tokyo 1979)
- 6.42 T. Sekine, Y. Nagasawa, M. Kudoh, Y. Sakai, A.S. Parkes, J.D. Geller, A. Mogami, K. Hirata: *Handbook of Auger Electron Spectroscopy* (JEOL, Tokyo 1982)
- 6.43 K.D. Childs, B.A. Carlson, L.A. Lavanier, J.F. Moulder, D.F. Paul, W.F. Stickle, D.G. Watson: *Handbook of Auger Electron Spectroscopy* (Physical Electronics Industries, Eden Prairie 1995)
- 6.44 M.P. Seah, I.S. Gilmore, H.E. Bishop, G. Lorang: Quantitative AES V, Practical analysis of intensities with detailed examples of metals and their oxides, *Surf. Interface Anal.* **26**, 701 (1998)
- 6.45 M.P. Seah, C.P. Hunt: Atomic mixing and electron range effects in ultra high resolution profiles of the Ta/Ta₂O₅ interface by argon sputtering with AES, *J. Appl. Phys.* **56**, 2106 (1984)
- 6.46 J. Pauwels: Institute of Reference Materials and Measurements (IRMM), Retieseweg, 2440 Geel, Belgium
- 6.47 C.P. Hunt, M.P. Seah: Characterisation of high depth resolution tantalum pentoxide sputter profiling reference material, *Surf. Interface Anal.* **5**, 199 (1983)
- 6.48 M.P. Seah, S.J. Spencer, I.S. Gilmore, J.E. Johnstone: Depth resolution in sputter depth profiling – Characterisation of a tantalum pentoxide on tantalum certified reference material, *Surf. Interface Anal.* **29**, 73 (2000)
- 6.49 M.P. Seah, S.J. Spencer: Ultra-thin SiO₂ on Si, I: Quantifying and removing carbonaceous contamination, *J. Vac. Sci. Technol. A* **21**, 345 (2003)
- 6.50 M.P. Seah, G.C. Smith, M.T. Anthony: AES – Energy calibration of electron spectrometers. I: An absolute, traceable energy calibration and the provision of atomic reference line energies, *Surf. Interface Anal.* **15**, 293 (1990)
- 6.51 M.P. Seah, I.S. Gilmore: AES – Energy calibration of electron spectrometers. III: General calibration rules, *J. Electron Spectrosc.* **83**, 197 (1997)
- 6.52 M.P. Seah: AES – energy calibration of electron spectrometers. IV: A re-evaluation of the reference energies, *J. Electron Spectrosc.* **97**, 235 (1998)
- 6.53 M.P. Seah, G.C. Smith: Spectrometer energy scale calibration. In: *Practical Surface Analysis. Auger and X-ray Photoelectron Spectroscopy*, Vol. 1, ed. by D. Briggs, M.P. Seah (Wiley, Chichester 1990) p. 531, Appendix 1
- 6.54 P.J. Cumpson, M.P. Seah, S.J. Spencer: Simple procedure for precise peak maximum estimation for energy calibration in AES and XPS, *Surf. Interface Anal.* **24**, 687 (1996)
- 6.55 M.P. Seah: Channel electron multipliers: Quantitative intensity measurement – Efficiency, gain, linearity and bias effects, *J. Electron Spectrosc.* **50**, 137 (1990)

- 6.56 M.P. Seah, C.S. Lim, K.L. Tong: Channel electron multiplier efficiencies – The effect of the pulse–height distribution on spectrum shape in Auger electron spectroscopy, *J. Electron Spectrosc.* **48**, 209 (1989)
- 6.57 M.P. Seah, M. Tosa: Linearity in electron counting and detection systems, *Surf. Interface Anal.* **18**, 240 (1992)
- 6.58 M.P. Seah: Effective dead time in pulse counting systems, *Surf. Interface Anal.* **23**, 729 (1995)
- 6.59 M.P. Seah, I.S. Gilmore, S.J. Spencer: Signal linearity in XPS counting systems, *J. Electron Spectrosc.* **104**, 73 (1999)
- 6.60 M.P. Seah, I.S. Gilmore, S.J. Spencer: Method for determining the signal linearity in single and multidetector counting systems in XPS, *Appl. Surf. Sci.* **144/145**, 132 (1999)
- 6.61 M.P. Seah, G.C. Smith: AES – Accurate intensity calibration of spectrometers – Results of a BCR interlaboratory comparison cosponsored by the VAMAS SCA TWP, *Surf. Interface Anal.* **17**, 855 (1991)
- 6.62 M.P. Seah: A system for the intensity calibration of electron spectrometers, *J. Electron Spectrosc.* **71**, 191 (1995)
- 6.63 M.P. Seah: XPS – Reference procedures for the accurate intensity calibration of electron spectrometers – Results of a BCR intercomparison cosponsored by the VAMAS SCA TWP, *Surf. Interface Anal.* **20**, 243 (1993)
- 6.64 M.P. Seah, G.C. Smith: Quantitative AES and XPS determination of the electron spectrometer transmission function and the detector sensitivity energy dependencies for the production of true electron emission spectra in AES and XPS, *Surf. Interface Anal.* **15**, 751 (1990)
- 6.65 NPL: *Systems for the Intensity Calibration of Auger and X-ray Photoelectron Spectrometers, A1 and X1* (National Physical Laboratory, Teddington 2005), see <http://www.npl.co.uk/nanoanalysis/a1calib.html> and follow links
- 6.66 M.P. Seah: Scattering in electron spectrometers, diagnosis and avoidance. I: Concentric hemispherical analysers, *Surf. Interface Anal.* **20**, 865 (1993)
- 6.67 S. Tougaard: X-ray photoelectron spectroscopy peak shape analysis for the extraction of in-depth composition information, *J. Vac. Sci. Technol. A* **5**, 1275 (1987)
- 6.68 S. Tougaard, C. Jannsson: Comparison of validity and consistency of methods for quantitative XPS peak analysis, *Surf. Interface Anal.* **20**, 1013 (1993)
- 6.69 M.P. Seah: Data compilations – Their use to improve measurement certainty in surface analysis by AES and XPS, *Surf. Interface Anal.* **9**, 85 (1986)
- 6.70 M.P. Seah: Quantitative AES and XPS. In: *Practical Surface Analysis. Auger and X-ray Photoelectron Spectroscopy*, Vol. 1, ed. by D. Briggs, M.P. Seah (Wiley, Chichester 1990) p. 201, Chap. 5
- 6.71 M. Gryzinski: Classical theory of atomic collisions. I: Theory of inelastic collisions, *Phys. Rev. A* **138**, 336 (1965)
- 6.72 M.P. Seah, I.S. Gilmore: Quantitative AES. VII: The ionisation cross section in AES, *Surf. Interface Anal.* **26**, 815 (1998)
- 6.73 E. Casnati, A. Tartari, C. Baraldi: An empirical approach to K-shell ionization cross section by electrons, *J. Phys. B* **15**, 155 (1982)
- 6.74 E.H.S. Burhop: *The Auger Effect and Other Radiationless Transitions* (Cambridge Univ. Press, Cambridge 1952)
- 6.75 J.I. Goldstein, H. Yakowitz (Eds.): *Practical Scanning Electron Microscopy* (Plenum, New York 1975)
- 6.76 M.P. Seah, I.S. Gilmore: A high resolution digital Auger database of true spectra for AES intensities, *J. Vac. Sci. Technol. A* **14**, 1401 (1996)
- 6.77 R. Shimizu: Quantitative analysis by Auger electron spectroscopy, *Jpn. J. Appl. Phys.* **22**, 1631 (1983)
- 6.78 M.P. Seah, I.S. Gilmore: Quantitative AES. VIII: Analysis of Auger electron intensities for elemental data in a digital auger database, *Surf. Interface Anal.* **26**, 908 (1998)
- 6.79 G.W.C. Kaye, T.H. Laby: *Tables of Physical and Chemical Constants*, 15th edn. (Longmans, London 1986)
- 6.80 D.R. Lide (Ed.): *CRC Handbook of Chemistry and Physics*, 74th edn. (CRC, Boca Raton 1993)
- 6.81 A. Jablonski: Database of correction parameters for elastic scattering effects in XPS, *Surf. Interface Anal.* **23**, 29 (1995)
- 6.82 M.P. Seah, I.S. Gilmore: Simplified equations for correction parameters for elastic scattering effects for Q , β and attenuation lengths in AES and XPS, *Surf. Interface Anal.* **31**, 835 (2001)
- 6.83 S. Tanuma, C.J. Powell, D.R. Penn: Calculations of electron inelastic mean free paths (IMFPs). V: Data for 14 organic compounds over the 50–2000 eV range, *Surf. Interface Anal.* **21**, 165 (1994)
- 6.84 S. Tanuma, C.J. Powell, D.R. Penn: Calculations of electron inelastic mean free paths. VII: Reliability of the TPP-2M IMFP predictive equation, *Surf. Interface Anal.* **35**, 268 (2003)
- 6.85 NIST: *SRD 71 Electron Inelastic Mean Free Path Database, Version 1.1* (NIST, Gaithersburg 2001)
- 6.86 M.P. Seah, I.S. Gilmore, S.J. Spencer: Quantitative XPS. I: Analysis of x-ray photoelectron intensities from elemental data in a digital photoelectron database, *J. Electron. Spectrosc.* **120**, 93 (2001)
- 6.87 P.J. Cumpson: Angle-resolved x-ray photoelectron spectroscopy. In: *Surface Analysis by Auger and X-ray Photoelectron Spectroscopy*, ed. by D. Briggs, J.T. Grant (IM Publications and Surface Spectra, Manchester 2003) p. 651, Chap. 23
- 6.88 S. Tougaard: Quantification of nanostructures by electron spectroscopy. In: *Surface Analysis by Auger and X-ray Photoelectron Spectroscopy*, ed. by D. Briggs, J.T. Grant (IM Publications and Surface Spectra, Manchester 2003) p. 295, Chap. 12
- 6.89 S. Hofmann, J.M. Sanz: Quantitative XPS analysis of the surface layer of anodic oxides obtained during

- depth profiling by sputtering with 3 keV Ar⁺ ions, *J. Trace Microprobe Tech.* **1**, 213 (1982)
- 6.90 S. Hofmann: Depth profiling in AES and XPS. In: *Practical Surface Analysis. Auger and X-ray Photoelectron Spectroscopy*, Vol.1, ed. by D. Briggs, M.P. Seah (Wiley, Chichester 1990) p.143, Chap. 4
- 6.91 J.M. Sanz, S. Hofmann: Quantitative evaluation of AES-depth profiles of thin anodic oxide films (Ta₂O₅/Ta, Nb₂O₅/Nb), *Surf. Interface Anal.* **5**, 210 (1983)
- 6.92 J.F. Ziegler: *The Stopping and Range of Ions in Matter SRIM-2003*, SRIM-2003 v.02 SRIM code (IBM, Yorktown Heights 2005), available for download from <http://www.SRIM.org>
- 6.93 M.P. Seah, F.M. Green, C.A. Clifford, I.S. Gilmore: An accurate semi-empirical equation for sputtering yields. I: For argon ions, *Surf. Interface Anal.* **37**, 444 (2005)
- 6.94 O. Auciello, R. Kelly (Eds.): *Ion Bombardment Modifications of Surfaces* (Elsevier, Amsterdam 1984)
- 6.95 R. Kelly: On the role of Gibbsian segregation in causing preferential sputtering, *Surf. Interface Anal.* **7**, 1 (1985)
- 6.96 J.B. Malherbe, R.Q. Odendaal: Models for the sputter correction factor in quantitative AES for compound semiconductors, *Surf. Interface Anal.* **26**, 841 (1998)
- 6.97 T. Wagner, J.Y. Wang, S. Hofmann: Sputter depth profiling in AES and XPS. In: *Surface Analysis by Auger and X-ray Photoelectron Spectroscopy*, ed. by D. Briggs, J.T. Grant (IM Publications and Surface Spectra, Manchester 2003) p. 619, Chap. 22
- 6.98 M.P. Seah, C.P. Hunt: The depth dependence of the depth resolution in composition-depth profiling with auger electron spectroscopy, *Surf. Interface Anal.* **5**, 33 (1983)
- 6.99 M.P. Seah, J.M. Sanz, S. Hofmann: The statistical sputtering contribution to resolution in concentration-depth profiles, *Thin Solid Films* **81**, 239 (1981)
- 6.100 NPL: *Sputtering Yields for Neon, Argon and Xenon Ions* (National Physical Laboratory, Teddington 2005), available for download from <http://www.npl.co.uk/nanoscience/surface-nanoanalysis/products-and-services/sputter-yield-values>
- 6.101 A. Zalar: Improved depth resolution by sample rotation during Auger electron spectroscopy depth profiling, *Thin Solid Films* **124**, 223 (1985)
- 6.102 S. Hofmann, A. Zalar, E.-H. Cirlin, J.J. Vajo, H.J. Mathieu, P. Panjan: Interlaboratory comparison of the depth resolution in sputter depth profiling of Ni/Cr multilayers with and without sample rotation using AES, XPS, and SIMS, *Surf. Interface Anal.* **20**, 621 (1993)
- 6.103 C.P. Hunt, M.P. Seah: Method for the alignment of samples and the attainment of ultra-high resolution depth profiles in Auger electron spectroscopy, *Surf. Interface Anal.* **15**, 254 (1990)
- 6.104 M.P. Seah: An accurate semi-empirical equation for sputtering yields. II: For neon, argon and xenon ions, *Nucl. Instrum. Methods B* **229**, 348 (2005)
- 6.105 I.S. Gilmore, M.P. Seah: Fluence, flux, current, and current density measurement in faraday cups for surface analysis, *Surf. Interface Anal.* **23**, 248 (1995)
- 6.106 J.A. Bearden, A.F. Burr: X-ray wavelengths and x-ray atomic energy levels, *Rev. Mod. Phys.* **31**, 49 (1967)
- 6.107 C.D. Wagner, W.M. Riggs, L.E. Davis, J.F. Moulder, G.E. Muilenberg: *Handbook of X-ray Photoelectron Spectroscopy* (Physical Electronics Industries, Eden Prairie 1979)
- 6.108 N. Ikeo, Y. Iijima, N. Niimura, M. Sigematsu, T. Tazawa, S. Matsumoto, K. Kojima, Y. Nagasawa: *Handbook of X-ray Photoelectron Spectroscopy* (JEOL, Tokyo 1991)
- 6.109 J.F. Moulder, W.F. Stickle, S.E. Sobol, K.D. Bomben: *Handbook of X-ray Photoelectron Spectroscopy* (Perkin Elmer/Physical Electronics Division, Eden Prairie 1992)
- 6.110 C.D. Wagner: Photoelectron and Auger energies and the Auger parameter – A data set. In: *Practical Surface Analysis. Auger and X-ray Photoelectron Spectroscopy*, Vol.1, ed. by D. Briggs, M.P. Seah (Wiley, Chichester 1990) p. 595, Appendix 5
- 6.111 C.D. Wagner, A.V. Naumkin, A. Kraut-Vass, J.W. Allison, C.J. Powell, J.R. Rumble: *NIST XPS Database* (NIST, Gaithersburg 2005), <http://srdata.nist.gov/xps/>
- 6.112 M.P. Seah: Post-1989 calibration energies for x-ray photoelectron spectrometers and the 1990 Josephson constant, *Surf. Interface Anal.* **14**, 488 (1989)
- 6.113 M.P. Seah, I.S. Gilmore, S.J. Spencer: XPS – Energy calibration of electron spectrometers 4 – An assessment of effects for different conditions and of the overall uncertainties, *Surf. Interface Anal.* **26**, 617 (1998)
- 6.114 M.P. Seah, I.S. Gilmore, G. Beamson: XPS – Binding energy calibration of electron spectrometers 5 – A re-assessment of the reference energies, *Surf. Interface Anal.* **26**, 642 (1998)
- 6.115 G. Beamson, D. Briggs: *High-Resolution XPS of Organic Polymers – The Scienta ESCA300 Database* (Wiley, Chichester 1992)
- 6.116 M.P. Seah, S.J. Spencer: Degradation of poly(vinyl chloride) and nitrocellulose in XPS, *Surf. Interface Anal.* **35**, 906 (2003)
- 6.117 ISO 17025: *ISO: General Requirements for the Competence of Testing and Calibration Laboratories* (ISO, Geneva 2000)
- 6.118 D.A. Shirley: High-resolution x-ray photoemission spectrum of the valence bands of gold, *Phys. Rev. B* **5**, 4709 (1972)
- 6.119 C.D. Wagner: Empirically derived atomic sensitivity factors for XPS. In: *Practical Surface Analysis. Auger and X-ray Photoelectron Spectroscopy*, Vol.1, ed. by D. Briggs, M.P. Seah (Wiley, Chichester 1990) p. 635, Appendix 6

- 6.120 C.D. Wagner, L.E. Davis, M.V. Zeller, J.A. Taylor, R.M. Raymond, L.H. Gale: Empirical atomic sensitivity factors for quantitative analysis by electron spectroscopy for chemical analysis, *Surf. Interface Anal.* **3**, 211 (1981)
- 6.121 J.H. Scofield: Hartree–Slater subshell photoionization cross-sections at 1254 and 1487 eV, *J. Electron Spectrosc.* **8**, 129 (1996)
- 6.122 M.P. Seah, I.S. Gilmore, S.J. Spencer: Quantitative AES IX and quantitative XPS II: Auger and x-ray photoelectron intensities from elemental spectra in digital databases reanalysed with a REELS database, *Surf. Interface Anal.* **31**, 778 (2001)
- 6.123 J.J. Yeh, I. Lindau: Atomic subshell photoionization cross sections and asymmetry parameters: $1 \leq Z \leq 103$, *At. Data Nucl. Data Tables* **32**, 1 (1985)
- 6.124 R.F. Reilman, A. Msezane, S.T. Manson: Relative intensities in photoelectron spectroscopy of atoms and molecules, *J. Electron Spectrosc.* **8**, 389 (1970)
- 6.125 M.P. Seah: Quantification in AES and XPS. In: *Surface Analysis by Auger and X-ray Photoelectron Spectroscopy*, ed. by D. Briggs, J.T. Grant (IM Publications Surface Spectra, Manchester 2003) p. 345, Chap. 13
- 6.126 NIST: *SRD 64 Electron Elastic Scattering Cross-Section Database* (NIST, Gaithersburg 2002), Version 2.0
- 6.127 P.J. Cumpson, M.P. Seah: Elastic scattering corrections in AES and XPS II – Estimating attenuation lengths, and conditions required for their valid use in overlayer/substrate experiments, *Surf. Interface Anal.* **25**, 430 (1997)
- 6.128 A. Jablonski, C.J. Powell: The electron attenuation length revisited, *Surf. Sci. Rep.* **47**, 33 (2002)
- 6.129 P.J. Cumpson: The thickogram: A method for easy film thickness measurements in XPS, *Surf. Interface Anal.* **29**, 403 (2000)
- 6.130 M.P. Seah, S.J. Spencer, F. Bensebaa, I. Vickridge, H. Danzebrink, M. Krumrey, T. Gross, W. Oesterle, E. Wendler, B. Rheinländer, Y. Azuma, I. Kojima, N. Suzuki, M. Suzuki, S. Tanuma, D.W. Moon, H.J. Lee, M.C. Hyun, H.Y. Chen, A.T.S. Wee, T. Osipowicz, J.S. Pan, W.A. Jordaan, R. Hauert, U. Klotz, C. van der Marel, M. Verheijen, Y. Tamminga, C. Jeynes, P. Bailey, S. Biswas, U. Falke, N.V. Nguyen, D. Chandler–Horowitz, J.R. Ehrstein, D. Muller, J.A. Dura: Critical review of the current status of thickness measurements for ultra-thin SiO₂ on Si: Part V Results of a CCQM pilot study, *Surf. Interface Anal.* **36**, 1269 (2004)
- 6.131 M.P. Seah: Intercomparison of silicon dioxide thickness measurements made by multiple techniques – The route to accuracy, *J. Vac. Sci. Technol. A* **22**, 1564 (2004)
- 6.132 M.P. Seah, S.J. Spencer: Ultra-thin SiO₂ on Si, II: Issues in quantification of the oxide thickness, *Surf. Interface Anal.* **33**, 640 (2002)
- 6.133 M.P. Seah, S.J. Spencer: Ultra-thin SiO₂ on Si, IV: Thickness linearity and intensity measurement in XPS, *Surf. Interface Anal.* **35**, 515 (2003)
- 6.134 M.P. Seah, S.J. Spencer: Ultrathin SiO₂ on Si, VII: Angular accuracy in XPS and an accurate attenuation length, *Surf. Interface Anal.* **37**, 731 (2005)
- 6.135 M.P. Seah, S.J. Spencer: Attenuation lengths in organic materials, *Surf. Interface Anal.* **43**, 744 (2011)
- 6.136 N. Sanada, Y. Yamamoto, R. Oiwa, Y. Ohashi: Extremely low sputtering degradation of polytetrafluoroethylene by C₆₀ ion beam applied in XPS analysis, *Surf. Interface Anal.* **36**, 280 (2004)
- 6.137 T. Miyayama, N. Sanada, M. Suzuki, J.S. Hammond, S.–Q.D. Si, A. Takahara: X-ray photoelectron spectroscopy study of polyimide thin films with Ar cluster ion depth profiling, *J. Vac. Sci. Technol. A* **28**, L1 (2010)
- 6.138 A.G. Shard, F.M. Green, P.J. Brewer, M.P. Seah, I.S. Gilmore: Quantitative molecular depth profiling of organic delta-layers by C60 ion sputtering and SIMS, *J. Phys. Chem. B* **112**, 2596 (2008)
- 6.139 K. Wittmaack: Physical and chemical parameters determining ion yields in SIMS analyses: A closer look at the oxygen-induced yield enhancement effect, *Proc. 11st Int. Conf. Second. Ion Mass Spectrom.*, SIMS XI, ed. by G. Gillen, R. Lareau, J. Bennett, F. Stevie (Wiley, Chichester 1998) p. 11
- 6.140 C.J. Hitzman, G. Mount: Enhanced depth profiling of ultra-shallow implants using improved low energy ion guns on a quadrupole SIMS instrument, *Proc. 11st Int. Conf. Second. Ion Mass Spectrom.*, SIMS XI, ed. by G. Gillen, R. Lareau, J. Bennett, F. Stevie (Wiley, Chichester 1998) p. 273
- 6.141 I.S. Gilmore: Private communication (2004)
- 6.142 M.G. Dowsett, G. Rowland, P.N. Allen, R.D. Barlow: An analytic form for the SIMS response function measured from ultra-thin impurity layers, *Surf. Interface Anal.* **21**, 310 (1994)
- 6.143 D.W. Moon, J.Y. Won, K.J. Kim, H.J. Kang, M. Petravic: GaAs delta-doped layers in Si for evaluation of SIMS depth resolution, *Surf. Interface Anal.* **29**, 362 (2000)
- 6.144 M.G. Dowsett: Depth profiling using ultra-low-energy secondary ion mass spectrometry, *Appl. Surf. Sci.* **203/204**, 5 (2003)
- 6.145 K. Wittmaack: The “Normal Component” of the primary ion energy: An inadequate parameter for assessing the depth resolution in SIMS, *Proc. 11st Int. Conf. Second. Ion Mass Spectrom.*, SIMS XII, ed. by A. Benninghoven, P. Bertrand, H.–N. Migeon, H.W. Werner (Wiley, Chichester 2000) p. 569
- 6.146 J. Bellingham, M.G. Dowsett, E. Collart, D. Kirkwood: Quantitative analysis of the top 5 nm of boron ultra-shallow implants, *Appl. Surf. Sci.* **203/204**, 851 (2003)
- 6.147 K. Itgen, A. Benninghoven, E. Niehius: TOF-SIMS depth profiling with optimized depth resolution, *Proc. 11st Int. Conf. Second. Ion Mass Spectrom.*, SIMS XI, ed. by G. Gillen, R. Lareau, J. Bennett, F. Stevie (Wiley, Chichester 1988) p. 367
- 6.148 C. Hongo, M. Tomita, M. Takenaka, M. Suzuki, A. Murakoshi: Depth profiling for ultrashallow implants using backside secondary ion mass spectrometry, *J. Vac. Sci. Technol. B* **21**, 1422 (2003)

- 6.149 J. Sameshima, R. Maeda, K. Yamada, A. Karen, S. Yamada: Depth profiles of boron and nitrogen in SiON films by backside SIMS, *Appl. Surf. Sci.* **231/232**, 614 (2004)
- 6.150 F. Laugier, J.M. Hartmann, H. Moriceau, P. Holliger, R. Truche, J.C. Dupuy: Backside and frontside depth profiling of B delta doping, at low energy, using new and previous magnetic SIMS instruments, *Appl. Surf. Sci.* **231/232**, 668 (2004)
- 6.151 D.W. Moon, H.J. Lee: The dose dependence of Si sputtering with low energy ions in shallow depth profiling, *Appl. Surf. Sci.* **203/204**, 27 (2003)
- 6.152 K. Wittmaack: Influence of the depth calibration procedure on the apparent shift of impurity depth profiles measured under conditions of long-term changes in erosion rate, *J. Vac. Sci. Technol. B* **18**, 1 (2001)
- 6.153 Y. Homma, H. Takenaka, F. Toujou, A. Takano, S. Hayashi, R. Shimizu: Evaluation of the sputter rate variation in SIMS ultra-shallow depth profiling using multiple short-period delta-layers, *Surf. Interface Anal.* **35**, 544 (2003)
- 6.154 F. Toujou, S. Yoshikawa, Y. Homma, A. Takano, H. Takenaka, M. Tomita, Z. Li, T. Hasegawa, K. Sasakawa, M. Schuhmacher, A. Merkulov, H.K. Kim, D.W. Moon, T. Hong, J.-Y. Won: Evaluation of BN-delta-doped multilayer reference materials for shallow depth profiling in SIMS: Round robin test, *Appl. Surf. Sci.* **231/232**, 649 (2004)
- 6.155 F.A. Stevie, P.M. Kahora, D.S. Simons, P. Chi: Secondary ion yield changes in Si and GaAs due to topography changes during O_2^+ or Cs^+ ion bombardment, *J. Vac. Sci. Technol. A* **6**, 76 (1988)
- 6.156 Y. Homma, A. Takano, Y. Higashi: Oxygen-ion-induced ripple formation on silicon: Evidence for phase separation and tentative model, *Appl. Surf. Sci.* **203/204**, 35 (2003)
- 6.157 K. Wittmaack: Artifacts in low-energy depth profiling using oxygen primary ion beams: Dependence on impact angle and oxygen flooding conditions, *J. Vac. Sci. Technol. B* **16**, 2776 (1998)
- 6.158 Z.X. Jiang, P.F.K. Alkemade: Erosion rate change and surface roughening in Si during oblique O_2^+ bombardment with oxygen flooding, *Proc. 11st Int. Conf. Second. Ion Mass Spectrom., SIMS XI*, ed. by G. Gillen, R. Lareau, J. Bennett, F. Stevie (Wiley, Chichester 1998) p. 431
- 6.159 K. Kataoka, K. Yamazaki, M. Shigeno, Y. Tada, K. Wittmaack: Surface roughening of silicon under ultra-low-energy cesium bombardment, *Appl. Surf. Sci.* **203/204**, 43 (2003)
- 6.160 K. Wittmaack: Concentration-depth calibration and bombardment-induced impurity relocation in SIMS depth profiling of shallow through-oxide implantation distributions: A procedure for eliminating the matrix effect, *Surf. Interface Anal.* **26**, 290 (1998)
- 6.161 M.G. Dowsett, J.H. Kelly, G. Rowlands, T.J. Ormsby, B. Guzman, P. Augustus, R. Beanland: On determining accurate positions, separations, and internal profiles for delta layers, *Appl. Surf. Sci.* **203/204**, 273 (2003)
- 6.162 J.B. Clegg, A.E. Morgan, H.A.M. De Grefte, F. Simondet, A. Huebar, G. Blackmore, M.G. Dowsett, D.E. Sykes, C.W. Magee, V.R. Deline: A comparative study of SIMS depth profiling of boron in silicon, *Surf. Interface Anal.* **6**, 162 (1984)
- 6.163 J.B. Clegg, I.G. Gale, G. Blackmore, M.G. Dowsett, D.S. McPhail, G.D.T. Spiller, D.E. Sykes: A SIMS calibration exercise using multi-element (Cr, Fe and Zn) implanted GaAs, *Surf. Interface Anal.* **10**, 338 (1987)
- 6.164 K. Miethe, E.H. Cirlin: An international round robin exercise on SIMS depth profiling of silicon delta-doped layers in GaAs, *Proc. 9th Int. Conf. Second. Ion Mass Spectrom., SIMS IX*, ed. by A. Benninghoven, Y. Nihei, R. Shimizu, H.W. Werner (Wiley, Chichester 1994) p. 699
- 6.165 Y. Okamoto, Y. Homma, S. Hayashi, F. Toujou, N. Iso-mura, A. Mikami, I. Nomachi, S. Seo, M. Tomita, A. Tamamoto, S. Ichikawa, Y. Kawashima, R. Miori, Y. Mitsuoka, I. Tachikawa, T. Toyoda, Y. Ueki: SIMS round-robin study of depth profiling of boron implants in silicon, *Proc. 11st Int. Conf. Second. Ion Mass Spectrom., SIMS XI*, ed. by G. Gillen, R. Lareau, J. Bennett, F. Stevie (Wiley, Chichester 1998) p. 1047
- 6.166 F. Toujou, M. Tomita, A. Takano, Y. Okamoto, S. Hayashi, A. Yamamoto, Y. Homma: SIMS round-robin study of depth profiling of boron implants in silicon, II Problems of quantification in high concentration B profiles, *Proc. 12nd Int. Conf. Second. Ion Mass Spectrom., SIMS XII*, ed. by A. Benninghoven, P. Bertrand, H.-N. Migeon, H.W. Werner (Wiley, Chichester 2000) p. 101
- 6.167 M. Tomita, T. Hasegawa, S. Hashimoto, S. Hayashi, Y. Homma, S. Kakehashi, Y. Kazama, K. Koezuka, H. Kuroki, K. Kusama, Z. Li, S. Miwa, S. Miyaki, Y. Okamoto, K. Okuno, S. Saito, S. Sasaki, H. Shichi, H. Shinohara, F. Toujou, Y. Ueki, Y. Yamamoto: SIMS round-robin study of depth profiling of arsenic implants in silicon, *Appl. Surf. Sci.* **203/204**, 465 (2003)
- 6.168 I.S. Gilmore, M.P. Seah: Static SIMS: A study of damage using polymers, *Surf. Interface Anal.* **24**, 746 (1996)
- 6.169 I.S. Gilmore, M.P. Seah: Electron flood gun damage in the analysis of polymers and organics in time of flight SIMS, *Appl. Surf. Sci.* **187**, 89 (2002)
- 6.170 D. Briggs, A. Brown, J.C. Vickerman: *Handbook of Static Secondary Ion Mass Spectrometry (SIMS)* (Wiley, Chichester 1989)
- 6.171 J.G. Newman, B.A. Carlson, R.S. Michael, J.F. Moulder, T.A. Honit: *Static SIMS Handbook of Polymer Analysis* (Perkin Elmer, Eden Prairie 1991)
- 6.172 J.C. Vickerman, D. Briggs, A. Henderson: *The Static SIMS Library* (Surface Spectra, Manchester 2003), version 2
- 6.173 B.C. Schwede, T. Heller, D. Rading, E. Niehius, L. Wiedmann, A. Benninghoven: *The Münster High*

- Mass Resolution Static SIMS Library* (ION-TOF, Münster 2003)
- 6.174 I.S. Gilmore, M.P. Seah: Static TOF-SIMS – A VAMAS interlaboratory study, Part I: Repeatability and reproducibility of spectra, *Surf. Interface Anal.* **37**, 651 (2005)
- 6.175 F.M. Green, I.S. Gilmore, M.P. Seah: TOF-SIMS: Accurate mass scale calibration, *J. Am. Mass Spectrom. Soc.* **17**, 514 (2007)
- 6.176 I.S. Gilmore, M.P. Seah: A static SIMS interlaboratory study, *Surf. Interface Anal.* **29**, 624 (2000)
- 6.177 A. Benninghoven, D. Stapel, O. Brox, B. Binkhardt, C. Crone, M. Thiemann, H.F. Arlinghaus: Static SIMS with molecular primary ions, *Proc. 12nd Int. Conf. Second. Ion Mass Spectrom., SIMS XII*, ed. by A. Benninghoven, P. Bertrand, H.-N. Migeon, H.W. Werner (Wiley, Chichester 2000) p. 259
- 6.178 A. Schneiders, M. Schröder, D. Stapel, H.F. Arlinghaus, A. Benninghoven: Molecular secondary particle emission from molecular overlayers under SF_5^+ bombardment, *Proc. 12nd Int. Conf. Second. Ion Mass Spectrom., SIMS XII*, ed. by A. Benninghoven, P. Bertrand, H.-N. Migeon, H.W. Werner (Wiley, Chichester 2000) p. 263
- 6.179 R. Kersting, B. Hagenhoff, P. Pijpers, R. Verlack: The influence of primary ion bombardment conditions on the secondary ion emission behaviour of polymer additives, *Appl. Surf. Sci.* **203/204**, 561 (2003)
- 6.180 R. Kersting, B. Hagenhoff, F. Kollmer, R. Möllers, E. Niehuis: Influence of primary ion bombardment conditions on the emission of molecular secondary ions, *Appl. Surf. Sci.* **231/232**, 261 (2004)
- 6.181 S.C.C. Wong, R. Hill, P. Blenkinsopp, N.P. Lockyer, D.E. Weibel, J.C. Vickerman: Development of a C_{60}^+ ion gun for static SIMS and chemical imaging, *Appl. Surf. Sci.* **203/204**, 219 (2003)
- 6.182 D.E. Weibel, N. Lockyer, J.C. Vickerman: C_{60} cluster ion bombardment of organic surfaces, *Appl. Surf. Sci.* **231/232**, 146 (2003)
- 6.183 M.P. Seah: Cluster ion sputtering: Molecular ion yield relationships for different cluster primary ions in static SIMS of organic materials, *Surf. Interface Anal.* **39**, 890 (2007)
- 6.184 N. Davies, D.E. Weibel, P. Blenkinsopp, N. Lockyer, R. Hill, J.C. Vickerman: Development and experimental application of a gold liquid metal ion source, *Appl. Surf. Sci.* **203/204**, 223 (2003)
- 6.185 I.S. Gilmore, M.P. Seah: G-SIMS of crystallisable organics, *Appl. Surf. Sci.* **203/204**, 551 (2003)
- 6.186 I.S. Gilmore, M.P. Seah: Static SIMS: Towards unfragmented mass spectra – The G-SIMS procedure, *Appl. Surf. Sci.* **161**, 465 (2000)
- 6.187 I.S. Gilmore, M.P. Seah: Organic molecule characterisation – G-SIMS, *Appl. Surf. Sci.* **231/232**, 224 (2004)
- 6.188 M.P. Seah, F.M. Green, I.S. Gilmore: Cluster primary ion sputtering: Secondary ion intensities in static SIMS of organic materials, *J. Phys. Chem. C* **114**, 5351 (2010)
- 6.189 L. De Chiffre, P. Lonardo, H. Trumpold, D.A. Lucca, G. Goch, C.A. Brown, J. Raja, H.N. Hansen: Quantitative characterisation of surface texture, *CIRP Ann.* **49(2)**, 635–652 (2000)
- 6.190 M. Stedman: Basis for comparing the performance of surface measuring machines, *Precis. Eng.* **9**, 149–152 (1987)
- 6.191 D.J. Whitehouse: *Handbook of Surface and Nanometrology*, 2nd edn. (CRC, Boca Raton 2011)
- 6.192 T.R. Thomas: *Rough Surfaces*, 2nd edn. (Imperial College Press, London 1999)
- 6.193 K.J. Stout, L. Blunt: *Three-Dimensional Surface Topography* (Penton, London 2000)
- 6.194 ISO 1302:2002 Geometrical Product Specifications (GPS) – Indication of surface texture in technical product documentation (ISO, Geneva 2002)
- 6.195 ISO 3274:1996 Geometrical Product Specifications (GPS) – Surface texture: Profile method – Nominal characteristics of contact (stylus) instruments (ISO, Geneva 1996)
- 6.196 ISO 4287:1997 Geometrical Product Specifications (GPS) – Surface texture: Profile method – Terms, definitions and surface texture parameters (ISO, Geneva 1997)
- 6.197 ISO 4287:1997/Amd1:2009 Peak count number (ISO, Geneva 1997)
- 6.198 ISO 4288:1996 Geometrical Product Specifications (GPS) – Surface texture: Profile method – Rules and procedures for the assessment of surface texture (ISO, Geneva 1996)
- 6.199 ISO 5436-2:2001 Geometrical Product Specifications (GPS) – Surface texture: Profile method; Measurement standards – Part 2: Software measurement standards (ISO, Geneva 2001)
- 6.200 ISO 8785:1998 Geometrical Product Specification (GPS) – Surface imperfections – Terms, definitions and parameters (ISO, Geneva 1998)
- 6.201 ISO 11562:1996 Geometrical Product Specifications (GPS) – Surface texture: Profile method – Metrological characteristics of phase correct filters (ISO, Geneva 1996)
- 6.202 ISO 12085:1996 Geometrical Product Specifications (GPS) – Surface texture: Profile method – Motif parameters (ISO, Geneva 1996)
- 6.203 ISO 12179:2000 Geometrical Product Specifications (GPS) – Surface texture: Profile method – Calibration of contact (stylus) instruments (ISO, Geneva 2000)
- 6.204 ISO 13565-1:1996 Geometrical Product Specifications (GPS) – Surface texture: Profile method; Surfaces having stratified functional properties – Part 1: Filtering and general measurement conditions (ISO, Geneva 1996)
- 6.205 ISO 13565-2:1996 Geometrical Product Specifications (GPS) – Surface texture: Profile method; Surfaces

- having stratified functional properties – Part 2: Height characterization using the linear material ratio curve (ISO, Geneva 1996)
- 6.206 ISO 13565-3:1998 Geometrical Product Specifications (GPS) – Surface texture: Profile method; Surfaces having stratified functional properties – Part 3: Height characterization using the material probability curve (ISO, Geneva 1998)
- 6.207 ISO/TS 16610-1:2006 Geometrical product specifications (GPS) – Filtration – Part 1: Overview and basic concepts (ISO, Geneva 2006)
- 6.208 ISO/TS 16610-20:2006 Geometrical product specifications (GPS) – Filtration – Part 20: Linear profile filters: Basic concepts (ISO, Geneva 2006)
- 6.209 ISO/TS 16610-22:2006 Geometrical product specifications (GPS) – Filtration – Part 22: Linear profile filters: Spline filters (ISO, Geneva 2006)
- 6.210 ISO/TS 16610-28:2010 Geometrical product specifications (GPS) – Filtration – Part 28: Profile filters: End effects (ISO Geneva 2010)
- 6.211 ISO/TS 16610-29:2006 Geometrical product specifications (GPS) – Filtration – Part 29: Linear profile filters: Spline wavelets (ISO, Geneva 2006)
- 6.212 ISO/TS 16610-30:2009 Geometrical product specifications (GPS) – Filtration – Part 30: Robust profile filters: Basic concepts (ISO, Geneva 2009)
- 6.213 ISO/TS 16610-31:2010 Geometrical product specifications (GPS) – Filtration – Part 31: Robust profile filters: Gaussian regression filters (ISO, Geneva 2010)
- 6.214 ISO/TS 16610-32:2009 Geometrical product specifications (GPS) – Filtration – Part 32: Robust profile filters: Spline filters (ISO, Geneva 2009)
- 6.215 ISO/TS 16610-40:2006 Geometrical product specifications (GPS) – Filtration – Part 40: Morphological profile filters: Basic concepts (ISO, Geneva 2006)
- 6.216 ISO/TS 16610-41:2006 Geometrical product specifications (GPS) – Filtration – Part 41: Morphological profile filters: Disk and horizontal line-segment filters (ISO, Geneva 2006)
- 6.217 ISO/TS 16610-48:2006 Geometrical product specifications (GPS) – Filtration – Part 49: Morphological profile filters: Scale space techniques (ISO, Geneva 2006)
- 6.218 ISO 25178-6:2010 Geometrical product specifications (GPS) – Surface texture: Areal – Part 6: Classification of methods for measuring surface texture (ISO, Geneva 2010)
- 6.219 ISO 25178-601:2010 Geometrical product specifications (GPS) – Surface texture: Areal – Part 601: Nominal characteristics of contact (stylus) instruments (ISO, Geneva 2010)
- 6.220 ISO 25178-602:2010 Geometrical product specifications (GPS) – Surface texture: Areal – Part 602: Nominal characteristics of noncontact (confocal chromatic probe) instruments (ISO, Geneva 2010)
- 6.221 ISO 26178-701:2010 Geometrical product specifications (GPS) – Surface texture: Areal – Part 701: Calibration and measurement standards for contact (stylus) instruments (ISO, Geneva 2010)
- 6.222 ISO 1302:2002/DAMd 2 Indication of material ratio requirements (ISO, Geneva 2002)
- 6.223 ISO/DIS 16610-21 Geometrical product specifications (GPS) – Filtration – Part 21: Linear profile filters: Gaussian filters
- 6.224 ISO/CD 25178-1 Geometrical product specifications (GPS) – Surface texture: Areal – Part 1: Indication of surface texture
- 6.225 ISO/DIS 25178-2 Geometrical product specifications (GPS) – Surface texture: Areal – Part 2: Terms, definitions and surface texture parameters
- 6.226 ISO/DIS 25178-3.2 Geometrical product specifications (GPS) – Surface texture: Areal – Part 3: Specification operators
- 6.227 ISO/DIS 25178-7 Geometrical product specifications (GPS) – Surface texture: Areal – Part 7: Software measurement standards
- 6.228 ISO/DIS 25178-603 Geometrical product specifications (GPS) – Surface texture: Areal – Part 603: Nominal characteristics of noncontact (phase-shifting interferometric microscopy) instruments
- 6.229 ISO/DIS 25178-604 Geometrical product specifications (GPS) – Surface texture: Areal – Part 604: Nominal characteristics of noncontact (coherence scanning interferometry) instruments
- 6.230 ISO/CD 25178-605 Geometrical product specifications (GPS) – Surface texture: Areal – Part 605: Nominal characteristics of noncontact (point autofocusing) instruments
- 6.231 ISO 5436-1:2000 Geometrical Product Specifications (GPS) – Surface texture: Profile method; Measurement standards – Part 1: Material measures (ISO, Geneva 2000)
- 6.232 M.C. Malburg, J. Raja: Characterization of surface texture generated by plateau honing process, CIRP Ann. **42**(1), 637–639 (1993)
- 6.233 K.J. Stout, P.J. Sullivan, W.P. Dong, E. Mainsah, N. Luo, T. Mathia, H. Zahouani: *The Development of Methods for the Characterisation of Roughness in Three Dimensions, Report EUR 15178 EN* (European Commission, Brussels 1993)
- 6.234 K.J. Stout: *Three Dimensional Surface Topography, Measurement, Interpretation and Applications* (Penton, London 1994)
- 6.235 L. Blunt, X. Jiang: *Advanced Techniques for Assessment Surface Topography* (Penton, London 2003)
- 6.236 Image Metrology AIS: *Scanning Probe Image Processor (SPIP)* (Image Metrology AIS, Lyngby 2010), www.imagemet.com
- 6.237 P.M. Lonardo, L. De Chiffre, A.A. Bruzzone: Characterisation of functional surfaces, Proc. Int. Conf. Tribol. Manuf. Processes, ed. by N. Bay (IPL/Technical University of Denmark, Lyngby 2004)
- 6.238 R. Hillmann: Surface profiles obtained by means of optical methods – Are they true representa-

- tions of the real surface?, CIRP Ann. **39**(1), 581–583 (1990)
- 6.239 P. Bariani: Dimensional metrology for microtechnology. Ph.D. Thesis (Technical University of Denmark, Lyngby 2004)
- 6.240 G. Binnig, C.F. Quate, C. Gerber: Atomic force microscope, Phys. Rev. Lett. **56**, 930–933 (1986)
- 6.241 P.M. Lonardo, D.A. Lucca, L. De Chiffre: Emerging trends in surface metrology, CIRP Ann. **51**(2), 701–723 (2002)
- 6.242 N. Kofod: Validation and industrial application of AFM. Ph.D. Thesis (Technical University of Denmark and Danish Fundamental Metrology, Lyngby 2002)
- 6.243 L. De Chiffre, H.N. Hansen, N. Kofod: Surface topography characterization using an atomic force microscope mounted on a coordinate measuring machine, CIRP Ann. **48**(1), 463–466 (1999)
- 6.244 H.N. Hansen, P. Bariani, L. De Chiffre: Modelling and measurement uncertainty estimation for integrated AFM–CMM instrument, CIRP Ann. **54**(1), 531–534 (2005)
- 6.245 J.C. Wyant, J. Schmit: Large field of view, high spatial resolution, surface measurements, Int. J. Mach. Tools Manuf. **38**(5/6), 691–698 (1998)
- 6.246 K. Yanagi, M. Hasegawa, S. Hara: A computational method for stitching a series of 3–D surface topography data measured by microscope–type surface profiling instruments, Proc. 3rd EUSPEN Int. Conf. 2, ed. by F.L.M. Delbressine, P.H.J. Schellekens, F.G.A. Homburg, H. Haitjema (TU Eindhoven, Eindhoven 2002) pp. 653–656
- 6.247 S.H. Huerth, H.D. Hallen: Quantitative method of image analysis when drift is present in a scanning probe microscope, J. Vac. Sci. Technol. **21**(2), 714–718 (2003)
- 6.248 G. Dai, F. Pohlenz, H.U. Danzebrink, M. Xu, K. Hasche, G. Wilkening: A novel metrological large range scanning probe microscope applicable for versatile traceable topography measurements., Proc. 4th EUSPEN Int. Conf. (euspen, Glasgow 2004) pp. 228–229
- 6.249 A. Boyde: Quantitative photogrammetric analysis and qualitative stereoscopic analysis of SEM images, J. Microsc. **98**, 452–471 (1973)
- 6.250 W. Hillmann: Rauheitsmessung mit dem Raster-Elektronenmikroskop (REM), Tech. Mess. **47**, V9116–6 (1980), in German
- 6.251 G. Piazzesi: Photogrammetry with the scanning electron microscope, J. Phys. E **6**(4), 392–396 (1973)
- 6.252 O. Kolednik: A contribution to stereo-photogrammetry with the scanning electron microscope, Pract. Metallogr. **18**, 562–573 (1981)
- 6.253 S. Scherer: 3–D surface analysis in scanning electron microscopy, G.I.T Imaging Microsc. **3**, 45–46 (2002)
- 6.254 M. Schubert, A. Gleichmann, M. Hemmleb, J. Albertz, J.M. Köhler: Determination of the height of a microstructure sample by a SEM with a conventional and a digital photogrammetric method, Ultramicroscopy **63**, 57–64 (1996)
- 6.255 Alicona Imaging: *MeX Software* (Alicona Imaging, Graz 2008)
- 6.256 P. Bariani: *Investigation on Traceability of 3–D SEM based on the Stereo–Pair Technique*, IPL Internal Report (Technical University of Denmark, Lyngby 2003)
- 6.257 P. Bariani, L. De Chiffre, H.N. Hansen, A. Horsewell: Investigation on the traceability of three dimensional scanning electron microscope measurements based on the stereo–pair technique, Precis. Eng. **29**, 219–228 (2005)
- 6.258 V.T. Vorburger, E.C. Teague: Optical techniques for on–line measurement of surface topography, Precis. Eng. **3**, 61–83 (1981)
- 6.259 G. Stauffert, E. Matthias: Kennwerte der Oberflächenrauigkeit und ihre Aussagekraft hinsichtlich der Charakterisierung bestimmter Oberflächentypen, CIRP Ann. **25**(1), 345–350 (1977), in German
- 6.260 S. Christiansen, L. De Chiffre: Topographic characterisation of progressive wear on deep drawing dies, Tribol. Trans. **40**, 346–352 (1997)
- 6.261 L. De Chiffre, H. Kunzmann, G.N. Peggs, D.A. Lucca: Surfaces in precision engineering, microengineering and nanotechnology, CIRP Ann. **52**(2), 561–577 (2003)
- 6.262 ISO: *International Vocabulary of Basic and General Terms in Metrology* (ISO, Geneva 1993)
- 6.263 H. Haitjema, M. Morel: Traceable roughness measurements of products, Proc. 1st EUSPEN Top. Conf. Fabr. Metrol. Nanotechnol., Vol.2, ed. by L. De Chiffre, K. Carneiro (IPL/Technical University of Denmark, Lyngby 2000) pp. 373–381
- 6.264 R. Leach: *Calibration, Traceability and Uncertainty Issues in Surface Texture Metrology*. NPL report CLM 7 (National Physical Laboratory, Teddington 1999)
- 6.265 L. Koenders, J.L. Andreasen, L. De Chiffre, L. Jung, R. Krüger–Sehm: Supplementary comparison e-romet, L–S11 comparison on surface texture, Metrologia **41**, 04001 (2004)
- 6.266 EAL G20: *Calibration of Stylus Instruments for Measuring Surface Roughness*, 1st edn. (European Cooperation for Accreditation, Paris 1996) pp.1–9
- 6.267 N. Kofod, J. Garnaes, J.F. Jørgensen: Calibrated line measurements with an atomic force microscope, Proc. 1st EUSPEN Topical Conf. Fabrication and Metrology in Nanotechnology, Vol. 2 (2000) pp. 373–381
- 6.268 N. Kofod, J.F. Jørgensen: Methods for lateral calibration of Scanning Probe Microscopes based on two–dimensional transfer standards, Proc. 4th Semin. Quant. Microsc. (QM), Semmering, ed. by K. Hasche, W. Mirandé, G. Wilkening (PTB, Braunschweig 2000) pp. 36–43
- 6.269 J. Garnaes, L. Nielsen, K. Dirscherl, J.F. Jørgensen, J.B. Rasmussen, P.E. Lindelof, C.B. Sørensen: Two–

- dimensional nanometre-scale calibration based on one-dimensional gratings, *Appl. Phys. A* **66**, S831–S835 (1998)
- 6.270 R. Leach, A. Hart: *A comparison of stylus and optical methods for measuring 2-D surface texture*, *NPL Report CBTLM 15* (National Physical Laboratory, Teddington 2002)
- 6.271 R. Krüger-Sehm, J.A. Luna Perez: Proposal for a guideline to calibrate interference microscopes for use in roughness measurement, *Mach. Tools Manufact.* **41**, 2123–2137 (2001)
- 6.272 P.M. Lonardo, H. Trumpold, L. De Chiffre: Progress in 3-D surface microtopography characterization, *CIRP Ann.* **45**(2), 589–598 (1996)

Materials

Part C

Part C Materials Properties Measurement

7 Mechanical Properties

Sheldon M. Wiederhorn, Gaithersburg, USA
Richard J. Fields, Gaithersburg, USA
Samuel Low, Gaithersburg, USA
Gun-Woong Bahng, Daejeon, South Korea
Alois Wehrstedt, Berlin, Germany
Junhee Hahn, Daejeon, South Korea
Yo Tomota, Hitachi, Japan
Takashi Miyata, Nagoya, Japan
Haiqing Lin, Menlo Park, USA
Benny D. Freeman, Austin, USA
Shuji Aihara, Chiba, Japan
Yukito Hagihara, Tokyo, Japan
Tetsuya Tagawa, Nagoya, Japan

8 Thermal Properties

Wolfgang Buck, Berlin, Germany
Steffen Rudtsch, Berlin, Germany

9 Electrical Properties

Bernd Schumacher, Braunschweig, Germany
Heinz-Gunter Bach, Berlin, Germany
Petra Spitzer, Braunschweig, Germany
Jan Obrzut, Gaithersburg, USA
Steffen Seitz, Braunschweig, Germany

10 Magnetic Properties

Joachim Wecker, Erlangen, Germany
Günther Bayreuther, Regensburg, Germany
Gunnar Ross, Köln, Germany
Roland Grössinger, Vienna, Austria

11 Optical Properties

Tadashi Itoh, Osaka, Japan
Tsutomu Araki, Osaka, Japan
Masaaki Ashida, Osaka, Japan
Tetsuo Iwata, Tokushima, Japan
Kiyofumi Muro, Chiba, Japan
Noboru Yamada, Moriguchi, Japan

Mechanical

7. Mechanical Properties

Materials used in engineering applications as structural components are subject to *loads*, defined by the application purpose. The mechanical properties of materials characterize the *response* of a material to loading.

The mechanical loading action on materials in engineering applications may be static or dynamic and can basically be categorized as tension, compression, bending, shear, and torsion. In addition, thermomechanical loading effects can occur (Chap. 8). There may also be *gas loads* from the environment, leading to *gas/materials interactions* (Chap. 6) and to *transport phenomena* such as permeation and diffusion.

The mechanical loading action and the corresponding response of materials can be illustrated by the well-known *stress-strain curve* (for definition see Sect. 7.1.2). Its different regimes and characteristic data points characterize the mechanical behavior of materials treated in this chapter in terms of *elasticity* (Sect. 7.1), *plasticity* (Sect. 7.2), *hardness* (Sect. 7.3), *strength* (Sect. 7.4), and *fracture* (Sect. 7.5). Methods for the determination of permeation and diffusion are compiled in Sect. 7.6.

7.1	Elasticity	340
7.1.1	Development of Elasticity Theory.....	340
7.1.2	Definition of Stress and Strain, and Relationships Between Them ..	341
7.1.3	Measurement of Elastic Constants in Static Experiments.....	344
7.1.4	Dynamic Methods of Determining Elastic Constants	349
7.1.5	Instrumented Indentation as a Method of Determining Elastic Constants	352
7.2	Plasticity	355
7.2.1	Fundamentals of Plasticity	355
7.2.2	Mechanical Loading Modes Causing Plastic Deformation	357
7.2.3	Standard Methods of Measuring Plastic Properties	358
7.2.4	Novel Test Developments for Plasticity	365
7.3	Hardness	366
7.3.1	Conventional Hardness Test Methods (Brinell, Rockwell, Vickers and Knoop)	368
7.3.2	Selecting a Conventional Hardness Test Method and Hardness Scale	374
7.3.3	Measurement Uncertainty in Hardness Testing (HR, HBW, HV, HK)	376
7.3.4	Instrumented Indentation Test (IIT)	378
7.4	Strength	388
7.4.1	Quasistatic Loading	389
7.4.2	Dynamic Loading	398
7.4.3	Temperature and Strain-Rate Effects	401
7.4.4	Strengthening Mechanisms for Crystalline Materials	402
7.4.5	Environmental Effects.....	404
7.4.6	Interface Strength: Adhesion Measurement Methods ...	405
7.5	Fracture Mechanics	408
7.5.1	Fundamentals of Fracture Mechanics	408
7.5.2	Fracture Toughness.....	410
7.5.3	Fatigue Crack Propagation Rate.....	419
7.5.4	Fractography	424
7.6	Permeation and Diffusion	426
7.6.1	Gas Transport: Steady-State Permeation	427
7.6.2	Kinetic Measurement.....	429
7.6.3	Experimental Measurement of Permeability	431
7.6.4	Gas Flux Measurement.....	433
7.6.5	Experimental Measurement of Gas and Vapor Sorption.....	436
7.6.6	Method Evaluations.....	440
7.6.7	Future Projections	442
	References	442

7.1 Elasticity

Elastic properties of materials must be obtained by experiment methods. Materials are too complicated and theories of solids insufficiently sophisticated to obtain accurate theoretic determinations of elastic constants. Usually, simple static mechanical tests are used to evaluate the elastic constants. Specimens are either pulled in tension, squeezed in compression, bent in flexure or twisted in torsion and the strains measured by a variety of techniques. The elastic constants are then calculated from the elasticity equation relating stress to strain. From these measurements, Young's modulus, Poisson's ratio and the shear modulus are determined. These are the moduli commonly used for the calculation of stresses or strains in structural applications. More accurate than the static method of determining the elastic constants are the dynamic techniques that have been developed for this purpose. In these techniques a bar is set into vibration and the resonant frequencies of the bar are measured. A solution of the elastic equations for the vibration of a bar yields a relationship between the elastic constants, the resonant frequencies and the dimensions of the bar. These techniques are about five times as accurate as the static techniques for determining the elastic constants. Elastic constants can also be measured by determining the time of flight of an elastic wave through a plate of given thickness. Because there are two kinds of waves that can traverse the plate (longitudinal waves and shear waves), the two elastic constants required for structural calculations can be determined independently. Finally, the newest advances in techniques for measuring the elastic constants of materials have their origins in the need to measure these constants in thin films, or parts too small to be determined independently. The development of nanoindentation devices proves to be ideal for the measurement of elastic constants in these kinds of materials. Each of these techniques is discussed in terms of standard American Society for Testing and Materials (ASTM) and international test methods that were developed to assure repeatability and reliability of testing. This discussion serves as a primer for engineers and scientists wanting to determine the elastic constants of materials.

7.1.1 Development of Elasticity Theory

The design of new components for structural applications usually includes an analysis of stress and strain to assure structural reliability. Two general kinds of practical problems are encountered: the first in which all

of the forces on the surface of a body and the body forces are known; the second in which the surface displacements on the body are prescribed and the body forces are known [7.1]. In both cases, calculation of the stresses and displacements throughout the body and at the body surface is the objective. Within the limits of an elastic material, i. e., a material in which the displacements and stresses completely disappear once all of the constraints are removed, the theory for solving such problems was completely developed by the end of the 19th century. There are many methods of solving such problems, especially with the development of finite element analysis. All such problems require the elastic constants of the material of interest as an input in order to obtain a solution. The description of experimental techniques of measuring the elastic constants of engineering materials are the main subject of this chapter, but before describing the experimental techniques, we first give a brief history of the development of the theory of elasticity. We then go on to describe the theory of elasticity in order to put our later discussion of experimental techniques into context. There are several good books or chapters in books that give a history of the theory of elasticity [7.1–3], and there are many excellent texts that describe the theory [7.1, 4]. The discussion given below rests heavily on [7.1–4].

The first scientist to consider the strength of materials was *Galileo* in 1638 with his investigation of the strength of a rigid cantilever beam under its own weight, the beam being imbedded in a wall at one end [7.5]. He treated the beam as a rigid solid and tried to determine the condition of failure for such a beam. The concepts of stress and strain were not yet developed, nor was it known that the neutral axis should be in the middle of the beam. The solution he obtained was not correct; nevertheless, his worked stimulated other scientists to work on the same problem.

The next important contributor to the theory of elasticity was *Hooke* in 1678, when he discovered the law that has been subsequently named after him [7.6]. He found that the extension of a wide variety of springs and spring-like materials was proportional to the forces applied to the springs. This finding forms the basis of the theory of elasticity, but Hooke did not apply the discovery to material problems. A few years later (1680), *Mariotte* announced the same law and used it to understand the deformation of the cantilever beam [7.7]. He argued that the resistance of a beam to flexural forces should result from some of the *filaments* of the beam

being put into tension, the rest being put into compression. He assigned the neutral axis to one-half the height of the beam and used this assumption to correctly solve the force distribution in the cantilever beam. *Young* further developed Hooke's law in 1807 by introducing the idea of a modulus of elasticity [7.8,9]. Young's modulus was not expressed simply as a proportionality constant between tensile stress and tensile strain. Instead, he defined the modulus as the relative diminution of the length of a solid at the base of a long column of the solid. Nevertheless, his contribution was used in the development of general equations of the theory of elasticity.

The first attempt to develop general equations of elastic equilibrium was by *Navier*, whose model was based on central-force interactions between molecules of a solid [7.10]. He developed a set of differential equations that could be used to calculate internal displacements in an isotropic body. The form of the equations was correct, but because of an oversimplification of the force law, the equations contained only one elastic constant.

Stimulated by the work of Navier, Cauchy in 1822 developed a theory of elasticity that contained two elastic constants and is essentially the one we use today for isotropic solids (presented to the French Academy of Sciences on Sept. 30, 1822; Cauchy published the work in his *Exercices de mathématique*, 1827 and 1828. See footnote 32 in the first chapter of [7.3]). For nonisotropic solids, many more elastic constants are needed, and for a long time an argument raged over whether the number of constants for the most general type of anisotropic material should be 15 or 21. The controversy was settled by experiments that were carried out on single crystals with pronounced anisotropy, which showed that 21 is the correct number of constants in the most anisotropic elastic case. This number is also supported by crystal symmetry theory.

Once the theory of elasticity was completely developed, equations could then be derived for experimental measurement of the elastic constants. This has now been done quite generally so that the techniques that have been developed have a good scientific basis in the theory of elasticity. Elastic constants can be measured statically (tension, compression, torsion or flexure), or dynamically through the study of vibrating bars, or by measuring the velocity of sound through the material. Most of these measurements are made on materials that are isotropic, so that only two constants are determined; however, with the development of composite materials for structural members, isotropy is lost and other constants have to be considered.

7.1.2 Definition of Stress and Strain, and Relationships Between Them

The theory of linear elasticity begins by defining stress and strain [7.1, 3, 4]. Stress gives the intensity of the mechanical forces that pass through the body, whereas strain gives the relative displacement of points within the body. In the theory of linear elasticity, stress and strain are related by the elastic constants, which are material properties. In this section we define and discuss stress and strain and show how they are related through the elastic constants. It is these elastic constants that must be determined in order to evaluate stress distributions in structural components.

Stresses

When a body is under load by external forces, internal forces are set up between different parts of the body. The intensities of these forces are usually described by the force per unit area on the test surface through which they act. One can imagine cutting a small test surface within a material and replacing the material on one side of the surface by forces that would maintain the position of the surface in exactly the same position as it was before the cut was made. As the size of the test surface is diminished to zero, the sum of the forces on the surface divided by the area of the surface is defined as the magnitude of the stress on the surface. The direction of the stress is given by the direction of the force on the surface and need not be normal to the surface.

From the definition of stress, it is clear that the stress on a surface will vary with orientation and position of the surface within the solid. It is also usual to break down the components of stress into stresses normal and parallel to the surface. The stresses parallel to the surface are called shear stresses. Because stress depends on both the orientation of the surface, and the direction of the forces on the surface, the symbol indicating stress will have two subscripts attached to it, the first indicating the surface normal, the second indicating the direction of the forces on the surface. Consider a Cartesian coordinate system with three mutually perpendicular axes, x_1 , x_2 , and x_3 . A test surface normal to the x_1 -axis will have stresses, σ_{11} , σ_{12} , and σ_{13} , where σ is the symbol for stress. The force indicated by the stress σ_{11} is on the x_1 -surface, and its orientation is parallel to the x_1 -axis. The stress σ_{11} is either a tensile stress (positive sign by convention), or a compressive stress (negative sign). The stresses, σ_{12} and σ_{13} , are shear stresses: σ_{12} being on the x_1 -surface and oriented in the x_2 -direction; σ_{13} being on the x_1 -surface and oriented in the x_3 -direction.

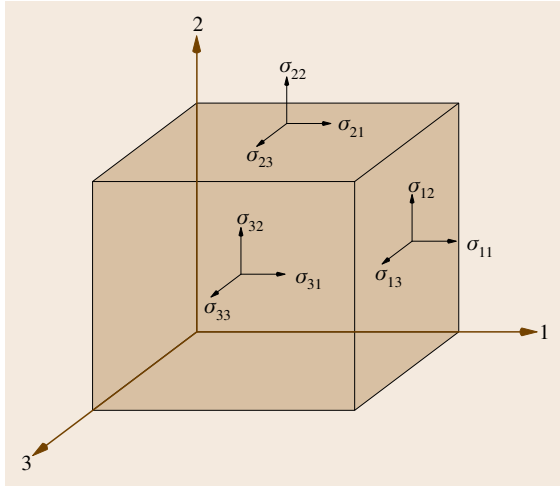


Fig. 7.1 Illustration of the two-index notation of stress. Stresses on the negative side of the cube have the opposite direction to those on the front side. Stresses in the figure are all positive

An example of the stresses oriented around a small cube is shown in Fig. 7.1. From the fact that the cube is in equilibrium, the equation of equilibrium can be determined. Summing up the forces in the x_1 -direction, the following equation is obtained

$$\frac{\partial \sigma_{11}}{\partial x_1} + \frac{\partial \sigma_{12}}{\partial x_2} + \frac{\partial \sigma_{13}}{\partial x_3} + F_1 = 0, \quad (7.1)$$

where F_1 are the body forces in the x_1 -direction. Similar equations are found for the x_2 - and x_3 -axes.

A convenient shorthand representation has been developed for equations similar to (7.1). The subscripts of (7.1) are indicated by lower-case letters, usually i , j , and k . A partial derivative is indicated by a comma; a repeated index indicates a summation. Thus, (7.1) can be

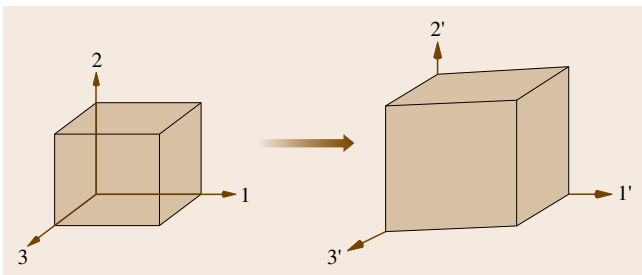


Fig. 7.2 On deformation, the size of the box has increased and the angles between the sides are no longer right angles, indicating both a tensile and a shear strain

represented by

$$\sigma_{ij,j} + F_i = 0. \quad (7.2)$$

Assignment of the value of 1, 2 and 3 for i yields three independent equations for equilibrium. The body forces F_i may be constant, or a function of space and time.

The state of equilibrium for the cube in Fig. 7.1 can also be used to prove that $\sigma_{ij} = \sigma_{ji}$. Taking the moment of the forces about a cube corner parallel to the x_1 -axis, $\sigma_{23} \sigma dx_2(dx_1 dx_3) = \sigma_{32} \sigma dx_3(dx_2 dx_1)$, which yields $\sigma_{23} = \sigma_{32}$. Similar equations are obtained around the x_2 - and x_3 -axis, proving the assertion that $\sigma_{ij} = \sigma_{ji}$. Therefore, of the nine possible stress components at any point within a body that is subjected to external forces, only six of them are independent.

Strains

Strains are determined by the relative displacements of points within a body that has been subjected to external forces. Imagine a volume within the body that was a cube prior to deformation, but has now been deformed into a general hexahedron, the axes of which may not be of equal length, or the angles between them right angles (Fig. 7.2). Two types of strain can be defined from this figure: tensile strain, in which the length of the axes of the cube have been changed by deformation, and a shear strain, in which the angle between the axes of the cube have been changed by the deformation. If u represents the displacement in the x_1 -direction of any point within the body due to the application of a set of forces, then the displacement of an adjacent point a distance dx_1 away from the first in a direction defined by the x_1 -axis is given by $u + (\partial u / \partial x_1) dx_1$. The relative change between the two points in the x_1 -direction is $\partial u / \partial x_1$, which is defined as the tensile strain in the x_1 -direction, ϵ_{11} . Similar definitions are used for the tensile strain in the x_2 - and x_3 -directions: ϵ_{22} and ϵ_{33} . In this case, v and w are the displacements in the y - and z -directions, respectively.

The shear strains are defined by the change in angle of the cube corners. Projecting the cube onto an x_2 - x_3 plane (Fig. 7.3), the change in the angle of the cube is given by $\partial v / \partial x_3 + \partial w / \partial x_2$, where v and w are the displacements in the x_2 - and x_3 -direction, respectively. The strain ϵ_{23} is defined by $\epsilon_{23} = (\partial v / \partial x_3 + \partial w / \partial x_2) / 2$. Similar equations are obtained for ϵ_{12} and ϵ_{13} . As with the shear components of the stress tensor $\epsilon_{ij} = \epsilon_{ji}$, as can be seen from the definition of shear strain.

Some other properties of stress and strain are commented on without proof. Both stress and strain are tensor quantities and transform as tensors with the rota-

tion of system axes. Consider a transformation of axes from x_i, x_j, x_k to $x_\alpha, x_\beta, x_\gamma$, then the stresses will transform according to the following equation

$$\sigma_{\alpha\beta} = l_{\alpha i} l_{\beta j} \sigma_{ij}, \quad (7.3)$$

where $l_{\alpha i}$ and $l_{\beta j}$ are the cosines of the angles between x_α and x_i , and x_β and x_j , respectively. Once the σ_{ij} are obtained at a point for a given set of axes, they can be obtained for any other set of axes using this simple transformation.

Stress–Strain Relations

Finally we arrive at the set of equations that relate stress and strain. Since there are six independent components to the stress tensor and six independent components to the strain tensor, there will be 36 constants of proportionality connecting the two

$$\sigma_{ij} = C_{ijkl} \varepsilon_{kl}. \quad (7.4)$$

The coefficients C_{ijkl} are the elastic stiffness constants. The repeat of the index kl in the subscripts on the right-hand side of this equation indicate by convention a summation over these subscripts for $k = 1, 2$ and 3 and similarly for l . Thus, for each of the six stress components on the left-hand side of the equation, there are six terms on the right-hand side and six coefficients C_{ijkl} . Of the 36 constants, it can be shown by strain-energy considerations that only 21 are independent. This number is reduced further by the symmetry of the solid. For a cubic material, the number of elastic constants is reduced from 21 to three. For an isotropic material, the

number of elastic constants is two. Equation (7.4) may be rewritten so that strain is expressed as a function of stress, in which case the two tensors are related by a set of constants S_{ijkl} known as the elastic compliances. The stiffness C_{ijkl} and the compliance S_{ijkl} are both fourth-order tensors that depend on the axis orientation for their values. They both transform as fourth-order tensors

$$C_{\alpha\beta\gamma\delta} = l_{\alpha i} l_{\beta j} l_{\gamma k} l_{\delta l} C_{ijkl} \quad (7.5)$$

with a similar equation for the compliances.

Since most engineering materials are isotropic, it is worth expanding the stress–strain equation (7.4) into a form that has more practical significance. The elastic constants that are most commonly used are the Young’s modulus E (the ratio of the tensile stress to the tensile strain), the shear modulus μ (the ratio of the shear stress to the shear strain), and the Poisson’s ratio ν (the ratio of the strain parallel to the tensile axis to the strain normal to the tensile axis). Since only two of these are independent for an isotropic material, it can be shown that the following relationship between the three exists

$$\mu = \frac{E}{2(1 + \nu)}. \quad (7.6)$$

Strain can be expressed in terms of stress for an isotropic material, by the following equation

$$\varepsilon_{ij} = \frac{1 + \nu}{E} \sigma_{ij} - \frac{\nu}{E} \delta_{ij} \Theta, \quad (7.7)$$

where δ_{ij} is the Kronecker delta; it equals one for $i = j$ and zero otherwise. The term Θ is equal to σ_{ii} , which indicates the sum over the subscript ($\sigma_{ii} = \sigma_{11} + \sigma_{22} + \sigma_{33}$). When expanded (7.7) yields six equations, one for each of the strain terms.

A similar equation can be written for stresses in terms of strains; in which case, the most appropriate elastic constants are the shear modulus μ and the Lamé constant λ

$$\sigma_{ij} = \lambda \varepsilon_{kk} \cdot \delta_{ij} + 2\mu \varepsilon_{ij}. \quad (7.8)$$

The Lamé constant can be expressed in terms of the other elastic constants by

$$\lambda = \frac{E\nu}{(1 + \nu)(1 - 2\nu)}. \quad (7.9)$$

Most of this article deals with the evaluation of Young’s modulus, the shear modulus, and Poisson’s ratio, since these are the ones most often used in practical applications, and hence, are the ones for which the standards are written.

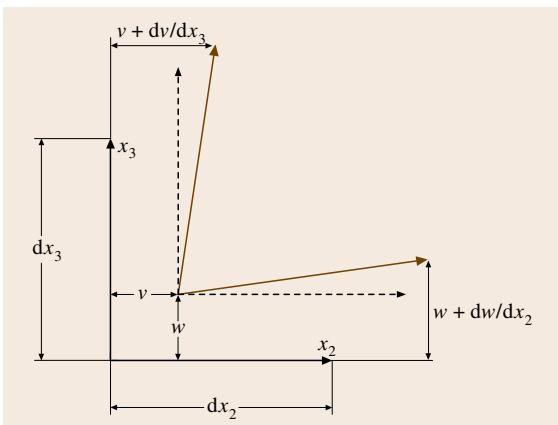


Fig. 7.3 As can be seen from the figure, the angle between the x_2 - and the x'_2 -axes is $1/2(dw/dx_2 + dv/dx_3)$, as for the x_3 - and x'_3 -axes. This angle is defined as the shear strain $\varepsilon_{23} = \varepsilon_{32}$ (after [7.2])

Linear elastic solutions of boundary problems can be obtained using the relationships between stress and strain (7.7) or its inverse (7.8) and the equations of equilibrium (7.2) subject to the conditions at the boundary. The solutions must satisfy a set of six equations known as the compatibility relations. These equations assure that solutions obtained yield valid displacement fields, i.e. fields in which the body contains no voids or overlapping regions after deformation.

The experimental configurations normally used to determine the elastic constants are cylinders of circular or rectangular cross sections, which are loaded in tension, flexure or torsion. Under static loading, elastic moduli are calculated from the load on the specimen, a measurement of specimen displacement and an elastic solution for the particular specimen. Measurements can also be made by dynamic techniques that involve resonance, or the time of flight of an elastic pulse through the material. In general, the static technique yielded results that are not as accurate as those obtained dynamically, differing by about -5 to $+7\%$ of the mean value of the dynamic technique [7.11]. The difference may be due to a combination of effects (adiabatic versus isotropic conditions, dislocation bowing, other sources of inelasticity, and different levels of accuracy and precision). This is discussed in Sect. 7.1.4.

In the remainder of this chapter, the techniques for determining the elastic constants for isotropic materials are discussed. The most recent *ASTM* recommended tests will form the basis of the discussion. The standards that are currently in use will be described and their application to a given material will be discussed. Since materials have a wide range of values for their elastic properties, given standards are not suitable for all materials. So, in the course of the discussion, the standards will be discussed with reference to the different classes of materials (polymers, ceramics, and metals) and recommendations will be made as to which technique is preferred for a given material. The relative error of each standard measurement will also be discussed with reference to the various materials.

Although *ASTM* tests are used in our discussions, we recognize that these standards are not universal. Other countries use different sets of standards. Nevertheless, the standards for elastic constants are all based on the same set of elastic equations and the same physical principals. So, regardless of which standard is used, the investigator should obtain identical results within experimental scatter. Furthermore, the same material considerations have to be taken into account in es-

tablishing a standard measurement technique. So here too, the standard tests will have to be similar to obtain a given accuracy. A list of European standards is given in the appendix for those readers who prefer to use standards other than *ASTM*.

Five general tests are used to determine the elastic constants of materials. Tensile testing employing a static load is used to measure Young's modulus, and Poisson's ratio. Torsion testing of tubes or rods is used to determine the shear modulus. Flexural testing under a static load is used to determine Young's modulus. Various geometries are used for the flexural tests. Finally, resonant vibration of long thin plates and the time of flight of sonic pulses are both used to measure Young's modulus and the shear modulus.

7.1.3 Measurement of Elastic Constants in Static Experiments

In principal the simplest test geometry for determining elastic constants is the tensile test. A fixed load is placed on the ends of the specimen and the displacement over a fixed portion of gage section is measured. The load divided by the cross-sectional area gives the stress and the displacement divided by the length over which displacement was measured gives the strain. The Young's modulus is then given by the stress divided by the strain. Often, the Young's modulus is measured as part of a test carried out to determine the plastic properties of the metal. In such a test, a stress-strain curve is obtained on the metal, and the linear portion of the curve at the beginning of the test is used to calculate the Young's modulus. At the same time, if the lateral dimensions of the specimen are measured during the test, the test results can be used to determine Poisson's ratio as a function of strain.

Test Specimens

Tensile tests are generally carried out on a universal test machine. The precautions needed to achieve high measurement accuracy include alignment of the test machine, calibration of the load cell, firm attachment of the extensometers used to measure strain, and accurate measurement of the dimensions of the specimen cross section. Examples of specimen types and shapes, and methods of gripping used in these machines are shown in Fig. 7.4 [7.12]. The type of specimen depends on the stock from which the specimen is taken. Sheet materials are usually tested in the form of flat specimens that are clamped with wedge grips on their ends. The flat specimens may also be pinned as well as be-

ing clamped. Round stock is tested with threaded-end or shoulder-end specimens that have matching shoulders or threads on the gripping device. Wires are tested using special snubbing devices in which the wire is wound around a mandrel to add the load gradually to the wire and thus prevent stress concentrations that will reduce the measured strength (in a strength test). In all specimens but the wires, the gage section is reduced to decrease the stress at the gripping points. Finally, the grips are usually attached to the testing machine through universal joints that prevent bending of the specimen during loading. Specific criteria for specimen dimensions and shapes are given in *ASTM E 8* [7.12].

Test Forces

Forces are determined by electronic load cells that attach to the testing machine and these can be calibrated through dead-weight testing through the use of elastic proving rings, or by the use of calibration strain-gage load cells following the recommendations of *ASTM E 74* [7.13]. To assure that the load cell is operating correctly calibrations should be done periodically. Proving rings and load cells are both portable, however the latter tend to be smaller, especially for large-scale loads and so are often preferred. Regardless which device is used, they in turn should be calibrated according to the procedures in *ASTM E 74*. The calibration of load cells on universal test machines should be checked each time

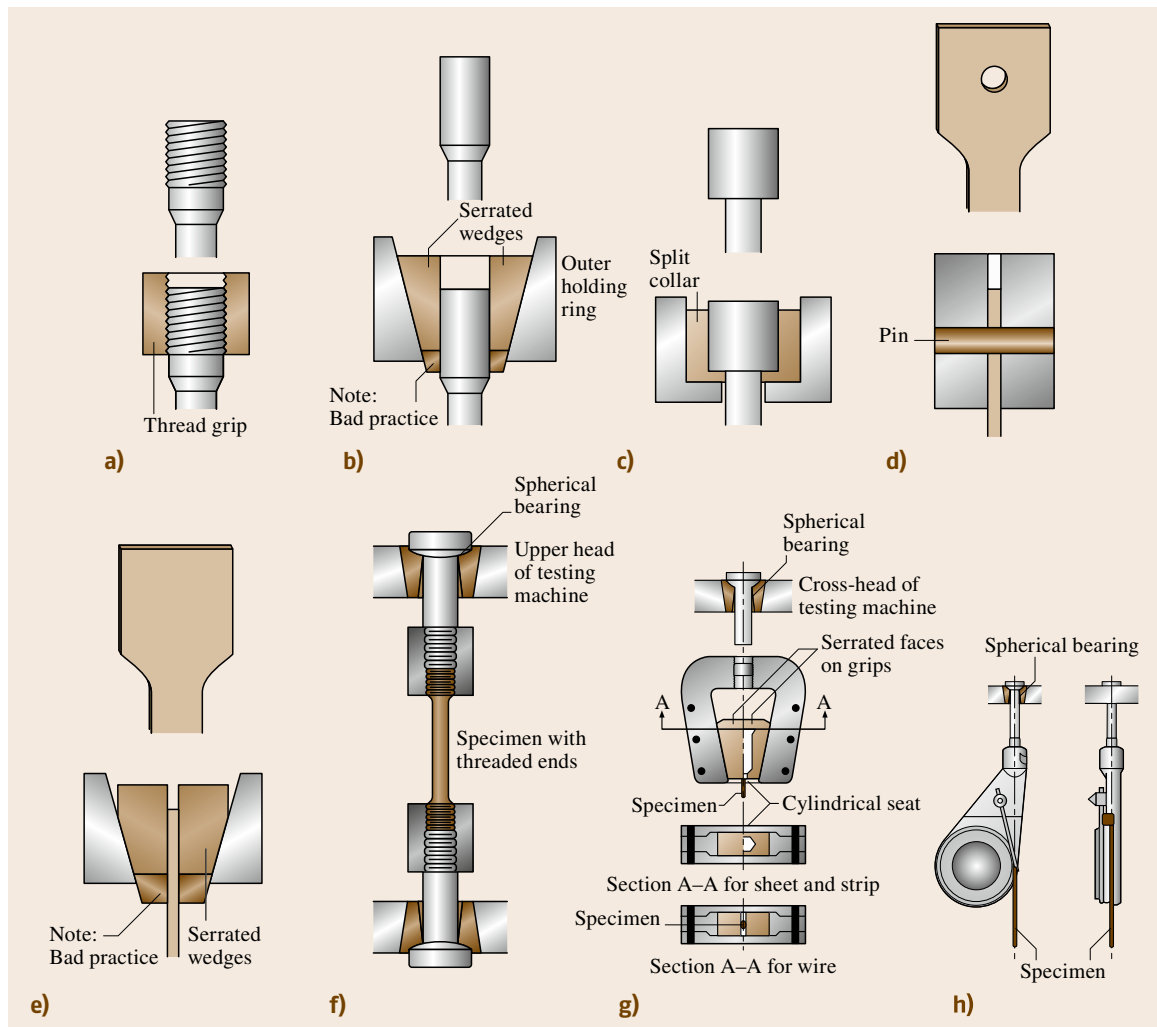


Fig. 7.4a–h Specimen types and shapes, and methods of gripping specimens in a universal testing machine (after [7.12])

the machine is run, and periodic verifications of the load system should be carried out using ASTM E 4 [7.14]. The required practice is to verify the test system one year after the first calibration and after that a minimum of once every 18 months.

Strain Measurement

Strain on tensile specimens can be measured by the use of extensometers that attach directly to the gage section of the test specimen, by the use of strain gages that are mounted directly to the specimen, or by the use of optical systems, which directly sense the motion of marks on the gage section or flags attached to the gage section of the tensile specimen. Clip-on extensometers have knife-edges that press into the specimen surface and clearly define the length of the gage section. They are inherently more accurate than other techniques and hence are used in standard methods for determining the elastic constants [7.18].

Two basic kinds of clip-on extensometers are used to detect strain. One contains a linear variable differential transformer (LVDT) that moves as a consequence of specimen deformation and produces an electrical signal that is proportional to the motion. These are small, lightweight instruments that have knife-edges to define the exact points of contact. They can be used over a wide range of gage lengths (10–2500 mm) and can be modified to operate over a wide range of temperatures, –75 to 1205 °C [7.18].

The second type of extensometer uses strain gages to measure the deformation. The strain gage is usually mounted on a beam within the extensometer that deforms elastically as the tensile specimen is deformed. The strain gage is a wire grid that changes its resistance as the beam is deformed elastically. To detect the

strain, the gage is connected to a bridge that measures the resistance of the gage. The signal from the bridge is conditioned and amplified before going to a digital read out device. Using strain-gage extensometers, the amplification of the original displacement can be as high as 10 000 to 1 [7.18]. Strain gage extensometers are also light and are easily attached onto the gage sections with knife-edge clips.

Strain gages may be attached directly to the gage section of the test specimen, in which case the strain measured over a nominal gage length rather than the more precise length typical of extensometers. Since the calibration of individual strain gages and the integrity of their attachment are often deduced by measuring a material with a known elastic modulus, strain gages cannot be used to certify a measurement of elastic modulus. For noncritical applications, however, they are often the simplest approach to acquiring elastic properties and usually provide satisfactory results.

In ASTM E 83 [7.19], strain extensometers are classified into six classes according to their accuracy. Only the three most accurate classes, class A, class B1 and sometimes class B2, can be used for evaluation of the Young's modulus of materials. To evaluate the performance of a strain extensometer, verification procedures have been put forth by various standards organizations [7.18]. Class A extensometers show the highest accuracy for strain measurements, but are generally not available commercially [7.18]. Class B1 extensometers are available commercially and are the ones most commonly used for elastic constant measurement. Class B2 can also be used for elastic constant determination on plastics, which are high-compliance materials.

Test Procedures

Quasistatic tests to evaluate the elastic constants should be carried out according to the procedures outlined in the standard shown in Table 7.1.

These tests vary according to the materials tested and the constant being determined. For metals the Young's modulus is determined by applying a tensile load to the specimen following the procedure given in ASTM E 111. The specimen is loaded uniaxially and strain is obtained as a function of load. Stress is calculated from the load; the linear portion of a plot of stress versus strain is used to determine the Young's modulus. The linear section of the plot is fitted by the method of least squares and the Young's modulus is given by the slope of the plot. The coefficient of determination r^2 and the coefficient of variation V_1 are reported to give a measure of the goodness of the fit.

Table 7.1 Standard quasistatic tests for elastic constants

Specification number	Specification title
ASTM E 111-04 [7.15]	Standard Test Method for Young's Modulus, Tangent Modulus, and Chord Modulus
ASTM E 132-04 [7.16]	Standard Test Method for Poisson's Ratio at Room Temperature
ASTM E 143-02 [7.17]	Standard Test Method for Shear Modulus at Room Temperature

The test can be carried out either with calibrated dead weights or, more often, by using a universal test machine. Class B1 extensometers are specified for the test, and an averaging extensometer, or the average of at least two extensometers arranged at equal angles around the test specimen are recommended. The standard points out that for many materials, Young's modulus determined in tension and compression are not the same, so that separate determinations for each mode of loading are recommended. Finally, the standard notes that some materials loaded in the elastic range exhibit some curvature and so should not be fitted by a straight line. For these materials, a tangent modulus or a chord modulus are recommended for practical applications.

The determination of Poisson's ratio at room temperature is described in ASTM E 132. Tests are carried out on a universal test machine using the same sort of specimens described in ASTM E 111. Average longitudinal and transverse strains ϵ_l and ϵ_t are measured as a function of applied load P . Two plots of strain versus load are obtained. The data are fitted to a linear equation by the method of least squares and the slopes of the data are determined. Poisson's ratio ν is calculated from the ratio of the two slopes

$$\nu = -(d\epsilon_t/dP)/(d\epsilon_l/dP) . \quad (7.10)$$

As with the standard for determining Young's modulus, class B1 extensometers are specified for this test.

The determination of Young's modulus and Poisson's ratio on polymeric materials differs somewhat from the same tests carried out on metals. Because the Young's modulus of polymers is only one hundredth that of metals, strains are much higher than those for metals. Hence, class B2 extensometers are adequate for the determination of elastic constants of polymers. Also, because of the high degree of sensitivity of many plastics to the rate of straining and to environment conditions these parameters must be controlled and specified for each test. Furthermore, according to statements in ASTM D 638 [7.21], the standard test method for tensile properties of plastics, *data obtained by this test method cannot be considered valid for applications involving load time scales or environments widely different from those of this test method.* In ASTM D 638, tests are carried out on dumbbell-shaped specimens or on tubes specified. The test speeds and the test conditions are specified and the specimen is loaded in a universal test machine. For polymers that exhibit an elastic region of behavior, calculations for determining Young's modulus and

Poisson's ratio are the same as for metals. In case the material exhibits no elastic behavior, a secant modulus is suggested to approximate the elastic behavior of the polymer.

Polymeric sheets are tested in tension according to the procedures given in ASTM D 882 [7.22]. The modulus of elasticity determined by this test is an index of stiffness of the plastic sheet. Specimens are sheets of polymers at least 5 mm wide, but no greater than 25.4 mm wide. A length of 250 mm is considered standard. Because of the sensitivity of polymeric sheets to environment, the sheets have to be conditioned to the laboratory test environment prior to testing. Strain rates are specified within the test procedure. The elastic modulus is determined from the linear portion of the stress-strain curve, or where the curve is nonlinear, a secant modulus is determined as in ASTM D 638.

The Young's moduli of ceramic materials, concretes or stones are not determined in tension. Because of the high value of the elastic constants and the weakness of these materials in tension, the kinds of loads needed for accurate strain measurements cannot be applied without rupture of these materials. The exception to this statement is the testing of high-strength glass or ceramic fibers, which tend to be very strong and so, can be subjected to sufficiently high loads for accurate measurement of displacements. The tensile strength and Young's modulus of the fiber are calculated from load-elongation and cross-sectional-area measurements on the fiber. ASTM D 3379-75 [7.20] gives a procedure that can be followed to test ceramic fibers. Fibers are glued onto a mounting tab that is gripped by the test machine (Fig. 7.5). As shown in the figure, the gage length is set by the tab. After the specimen has been

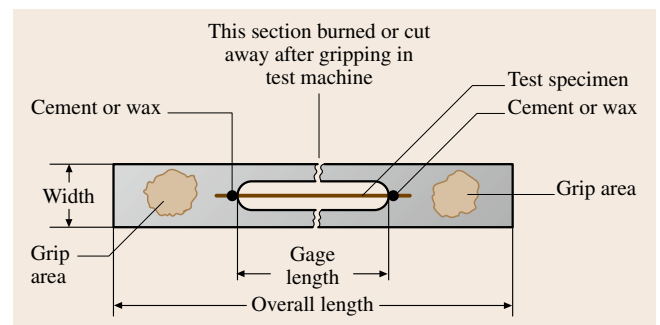


Fig. 7.5 Method of mounting high-strength ceramic fibers onto a universal testing machine. The fibers are glued onto a mounting tab that is gripped by the test machine. After the specimen has been mounted in the test machine, a section of the tab is cut or burned away, leaving the specimen free to be tested (after [7.20])

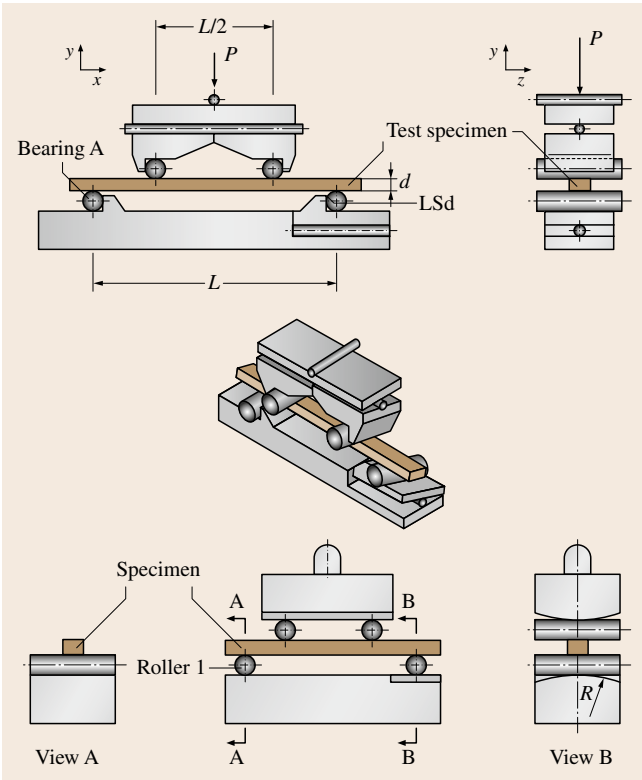


Fig. 7.6 Examples of fully articulating bearing in test fixtures in test fixtures designed to test advanced ceramic composite materials (after [7.23]) ◀

Table 7.2 Relation between strain rate and displacement rate for flexure testing in ASTM C 1341-00 [7.23]

Test geometry I (3-point)	$\dot{D} = 0.167\dot{\epsilon}L^2/d$
Test geometry IIA (4-point; 1/4 point)	$\dot{D} = 0.167\dot{\epsilon}L^2/d$
Test geometry IIB (4-point; 1/3 point)	$\dot{D} = 0.185\dot{\epsilon}L^2/d$

For bulk-size ceramics, or for other materials such as stones or concretes, the Young’s modulus can be measured from the displacement of a beam tested in three- or four-point bending. To assure that the specimen is loaded evenly, ASTM C 1341-00 [7.23] recommends the use of fully articulating bearing in the test fixtures (Fig. 7.6). In these test fixtures, one of the bearings is fixed to stabilize the specimen. The other bearings can both roll and rock to keep in full contact with the specimen cross section. Using a constant displacement rate, load is measured as a function of displacement. The Young’s modulus E is obtained from the linear portion of the stressing rate – straining rate equation

$$\dot{\epsilon} = d\epsilon/dt = \dot{\sigma}/E . \tag{7.11}$$

mounted in the test machine, a section of the tab is cut or burned away, leaving the specimen free to be tested. Strains are estimated by the machine displacement, or are measured optically from the edges of the mounting tab.

In this test configuration, the strain rate is directly proportional to the rate of cross-head displacement. For the geometries shown in Fig. 7.7, Table 7.2 gives the relation between the strain rate and the displacement rate.

Here \dot{D} is the rate of crosshead motion in mm/s, L is the outer support span in mm, d is the specimen thickness in mm. A similar technique is described in ASTM C 674-88 (1999) [7.24].

In addition to tension or compression tests to determine Young’s modulus and Poisson’s ratio, the shear modulus μ can be determined directly through torsion tests on tubes or solid round bars, ASTM E 143 [7.17]. The angle of twist in radians θ is measured as a function of applied torque T and a shear stress is calculated from the appropriate equation. The shear modulus μ is given by

$$\mu = TL/J\theta , \tag{7.12}$$

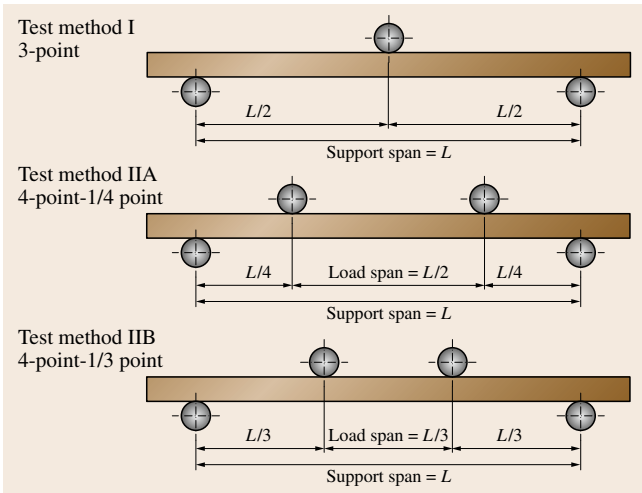


Fig. 7.7 Specimen geometries for flexure testing (after [7.23]) ◀

where L is the gage length and J is the polar moment of inertia of the section about its center. For a cylinder

$$J = \pi(D_o^4 - D_i^4)/32, \quad (7.13)$$

where D_o is the external diameter of the cylinder and D_i is the internal diameter. For a solid cylinder, D_i equals zero.

7.1.4 Dynamic Methods of Determining Elastic Constants

Dynamic methods of measuring the elastic constants of materials are the most commonly used for all kinds of materials. They were first introduced in the mid 1930s [7.33, 34]. These techniques have the advantage that the stresses used to measure the moduli are far below those at the elastic limit. They therefore do not give rise to complex creep effects or elastic hysteresis. Because the stresses are infinitesimal, the specimens are not altered by the stresses so that repeated measurements can be made on the same sample. A single specimen can, therefore, be used to obtain the elastic moduli as a function of temperature, or pressure. Specimens are small and simple compared to those used to determine elastic constants in static tests.

Ultrasonic Pulse Technique

Two types of dynamic tests are commonly conducted to measure the elastic constants. In one an ultrasonic pulse

is sent through the specimen and its time of flight measured. The elastic constant determined by this technique depends on the kind of pulse used for the measurement. If a longitudinal pulse is used, then the Young's modulus is defined by the density of the specimen ρ and the longitudinal velocity of the pulse v_l [7.2]

$$E = \rho v_l^2. \quad (7.14)$$

The velocity of the pulse is measured directly from the time to transit a fixed distance in the specimen. For a specimen of a well-defined thickness L the distance traveled by the wave is usually $2L$, when the pulse-echo techniques is used to measure the velocity.

If an ultrasonic shear pulse v_s is used for the measurement then the shear modulus μ can be obtained from the density and the velocity measurement [7.2]

$$\mu = \rho v_s^2 \quad (7.15)$$

where v_s is the velocity of the shear pulse.

The accuracy of these measurement techniques depends on the dimensions of the specimen and on the end-face parallelism, the coupling technique and the signal-to-noise ratio. The accuracy of these techniques is typically $\pm 0.1\%$ of the mean measurement. Despite its accuracy and simplicity, the material test community has not adapted this technique. It is used, however, in ASTM C 1419-99a [7.35] as a standard method of obtaining approximate values of Young's modulus in refractory materials at room temperature.

Table 7.3 ASTM standard test methods employed to determine elastic constants by the resonance technique

Specification number	Specification title
ASTM C 215 [7.25]	Test method for fundamental transverse, longitudinal and torsional frequencies of concrete specimens
ASTM C 623 [7.26]	Test method for Young's modulus, shear modulus and Poisson's ratio for glass and glass-ceramics by resonance
ASTM C 747-93 (1998) [7.27]	Test method for moduli of elasticity and fundamental frequencies of carbon and graphite materials by sonic resonance
ASTM C 848-88 (1999) [7.28]	Standard test method for Young's modulus, shear modulus, and Poisson's ratio for ceramic whitewares by resonance
ASTM C 885-87 (2002) [7.29]	Standard test method for Young's modulus of refractory shapes by sonic resonance
ASTM C 1198-01 [7.30]	Standard test method for dynamic Young's modulus, shear modulus and Poisson's ratio for advanced ceramics by sonic resonance
ASTM E 1875 [7.31]	Standard test method for dynamic Young's modulus, shear modulus, and Poisson's ratio by sonic resonance
ASTM E 1876-01 [7.32]	Standard test method for dynamic Young's modulus, shear modulus, and Poisson's ratio by impulse excitation of vibration

Free-Vibration Techniques

The second type of dynamic test employs freely vibrating rods to determine the elastic constants. The rods can have a rectangular or circular cross section. Specimens are excited mechanically, either by an impulse or continuously through the rod supports. Then, the resonant frequency for the rod is measured and the density ρ or mass m and the specimen dimensions are used to determine the elastic constants. The bars can be excited in such a way as to favor measurement of the shear modulus or the Young's modulus; equations have been developed to calculate both these quantities. The derivations of these equations are complex, especially the equation for standing flexural vibrations, and so are not addressed in this review. A discussion of the equations used in the resonance techniques and references to the earlier work in this field can be found in the article by *Tefft* [7.36]. The impulse technique and the continuous resonance technique have both been adapted by a number of *ASTM* committees for the purpose of measuring

elastic constants (Table 7.3). The techniques proposed by these committees are very similar to one another.

Free Resonance by Impulse Excitation

A full description of this technique is given in *ASTM* designation E 1876-01. The following brief description has been abstracted from the designation. A schematic diagram of the kind of specimen used to measure elastic moduli by free resonance is shown in Fig. 7.8. The ratio of the specimen length to the minimum cross-section dimension should be 20–25 for ease of calculation. For shear modulus measurement on rectangular bars, a width-to-thickness ratio of five or greater is recommended. The specimen supports should be located at the fundamental nodal points $0.224L$ from each end. The specimen is then impacted with a small impuler, such as that shown in Fig. 7.9. The vibration is then picked up by a microphone sensor located at the antinode. Alternatively, a contact sensor located near the node lines can also be used to pick up the vibration. The impact sites and the location of the sensors are indicated in Fig. 7.8.

The Young's modulus is calculated from the fundamental vibrational frequency f_f , the specimen mass m , width b , length L , and thickness t , and a correction factor T_1 [7.32]

$$E = 0.9465(m f_f^2 / b)(L^3 / t^3) T_1 . \quad (7.16)$$

The correction factor is a complex algebraic term that depends on the Poisson's ratio, the thickness and length of the test specimen. For specimen lengths 20 times greater than the thickness, T_1 is independent of the Poisson's ratio to a good approximation. In this limit, the following equation may be used for T_1 [7.32]

$$T_1 = 1.000 + 6.585(t/L)^2 . \quad (7.17)$$

The procedure for determining the Young's modulus from rods with circular cross sections is similar to those

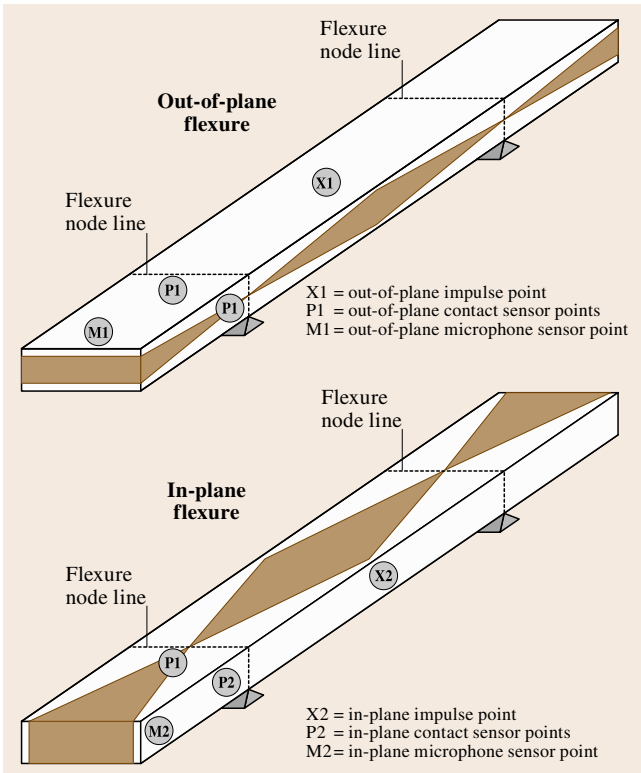


Fig. 7.8 A schematic diagram of the kind of specimen used to measure elastic moduli by the free-resonance technique (flexure testing) (after [7.32])

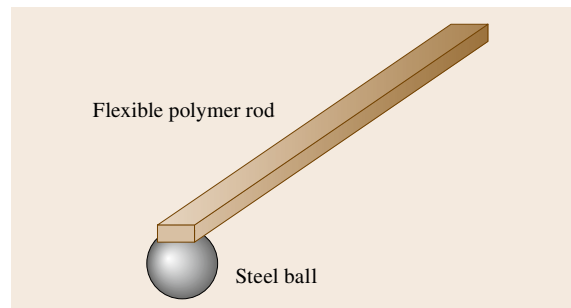


Fig. 7.9 A typical impuler for small specimens (after [7.32])

for rectangular cross sections, but the equations used are different. These may be found in [ASTM E 1876 \[7.32\]](#). Young's modulus can also be obtained from rectangular specimens subjected to longitudinal vibrations. Here the specimen is impacted on one end and the vibrations are picked up from the other. The equations for the calculation and the details of the procedure are given in [ASTM E 1876](#).

The dynamic shear modulus can be obtained from rectangular specimens of a similar geometry to that used to obtain the Young's modulus. As with the flexural specimens, the specimen supports are placed along the node lines, but the location of these lines, [Fig. 7.10](#), differ substantially from those of the flexural tests. The location of the support lines, the impulse point and the sensor points are shown in [Fig. 7.10](#). Once the fundamental torsional resonant frequency f_t is determined, the dynamic shear modulus can be determined from the following equation [7.32]

$$G = \frac{4Lm f_t^2}{bt} [B/(1 + A)], \quad (7.18)$$

where B and A are correction factors that can be found in [ASTM E 1876](#).

Free Resonance by Continuous Excitation

The continuous resonance technique differs from the impulse technique only in the way the resonant frequencies are excited. Therefore, the equations used to calculate the shear modulus and Young's modulus are identical to those used for the impulse technique. One configuration of test specimen is shown in [Fig. 7.11](#). A rectangular specimen is suspended with two loops of thread or fine wire. The exciting transducer sends a sonic vibration down one of the supports and the signal is detected through the other support. The resonant vibration is detected as an enhancement of the signal as the frequency of the input signal is varied. Care has to be taken to separate the flexural resonant modes from the torsional resonant modes and the various resonant harmonics from each other. Suggestions as to how this can be achieved are given in [ASTM E 1875](#). A second configuration for specimen support is shown in [Fig. 7.12](#). Locating the supports at the flexural or torsional nodes tends to favor the primary harmonic for each of these modes. Nevertheless, a proper identification of the resonant frequencies requires movement of the transducers along the total specimen length to identify the nodes and antinodes. The suspension method has been used to determine the elastic moduli as a function of temperature, from cryogenic [7.37] to high temperatures [7.38].

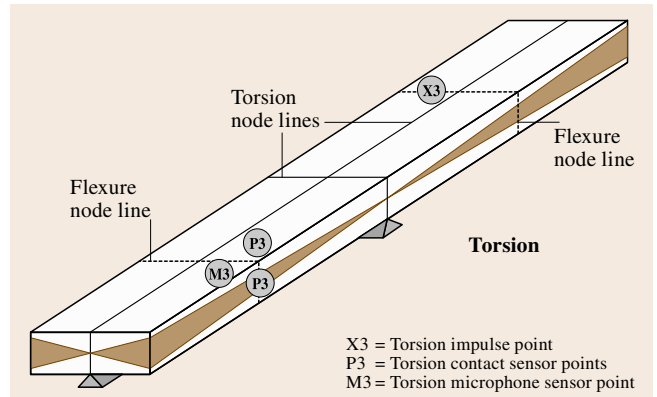


Fig. 7.10 A schematic diagram of the kind of specimen used to measure elastic moduli by the free resonance technique (torsion testing) (after [7.32])

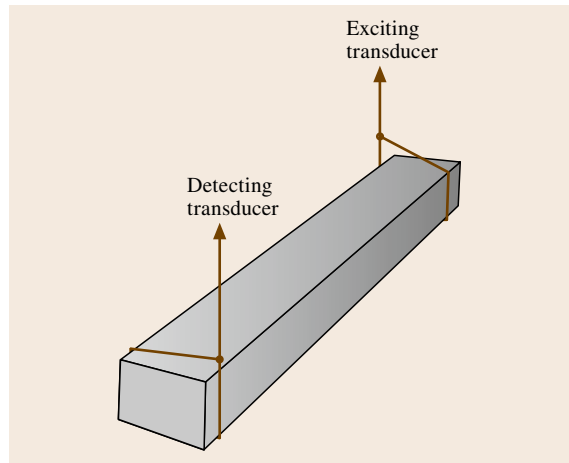


Fig. 7.11 A schematic diagram of the kind of experimental set up used to determine elastic moduli by the continuous resonance technique (after [7.31])

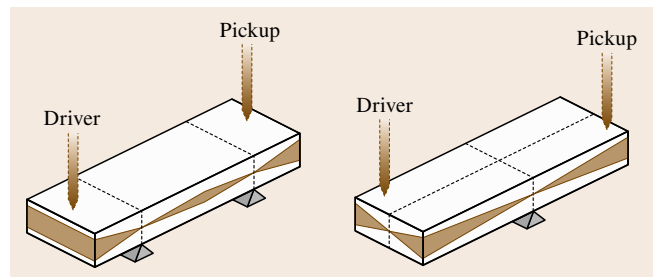


Fig. 7.12 An alternate configuration for determining the elastic moduli by the continuous resonance technique. Here the supports are directly under the resonance nodes (after [7.31])

Comparing the Static and Dynamic Methods

From a historical perspective, the static methods of determining elastic constants were the first to be developed. Dynamic methods were only discovered in the 1930s [7.33, 34] and required some time to become known and then popular. Standards for the static methods of determining elastic constants were developed in the 1950s. For example, ASTM E 111 was first issued in 1955. The dynamic techniques required a rather complex theoretical analysis and a numerical evaluation in order to know the resonant frequencies as a function of specimen shape, density and dimensions. Also, modern electronics had to have been developed before the measurements could be made to determine resonant frequencies. It was not until the late 1950s that progress was sufficient that the dynamic techniques could be developed in such a way as to be easy to use and useful. The first ASTM designation for measurement of elastic constants by resonance was C 623 in 1969, i. e., about 10 years after the technique was developed.

Ide [7.33] recognized the advantages of dynamic techniques over static techniques of determining elastic constants as early as 1935. He stated,

Dynamic methods for measuring Young's modulus of elasticity possess advantages over the usual static methods. The dynamic modulus is obtained for minute alternating stresses far below the elastic limit, which do not give rise to complex creep effects or to elastic hysteresis. This accurately fulfills the assumptions of the mathematical theory.

This opinion about the inherent superiority is still held today. In a study by *Smith* et al. [7.11], the authors used dynamic test techniques to determine the Young's modulus of an Inconel alloy to an accuracy of better than 1% of the mean value. The static techniques could only achieve an accuracy of between 5 and 7% on the same alloy. These authors recommend one of the dynamic techniques (impulse excitation) for routine quality-control work because of their accuracy and simplicity. The continuous excitation method was recommended for more complete elastic characterization studies of materials. A major advantage of the impulse technique is that a nodal analysis is not required to determine the resonance frequencies. They feel that the static method is not desirable for quality-control work, because it is a labor-intensive technique that is time-consuming.

There are fundamental reasons for differences between the dynamic and static techniques [7.39]. Static

tests are isothermal because there is plenty of time for heat conduction during the test. Ultrasonic tests take place so fast that the conditions are adiabatic and the sample's temperature actually changes during the test. Resonant tests are usually adiabatic, but this depends on the resonant frequency and the size of the specimen. Dislocation bowing and other sources of internal friction always take place during static tests and never during ultrasonic tests. Again, resonant tests may or may not be affected by these phenomena. In fact, tests in which the frequency is changed are used to characterize these effects. Static tests tend to explore higher stresses than dynamic tests. Therefore, higher-order elastic behavior is implicitly included in static measurements.

If the application is highly loaded and static in nature, such as in a building, ship, or bridge, the static methods for measuring modulus are more appropriate despite the uncertainty levels mentioned above. If the application is dynamic in nature, such as ballistic penetration or elastic wave propagation, one should use dynamic methods to evaluate the elastic constants.

7.1.5 Instrumented Indentation as a Method of Determining Elastic Constants

Up to this point, the discussion has involved what may be regarded as standard test methods. The methods are standard in the sense that they were developed to evaluate the elastic constants of materials that are of a macroscopic size. The materials are uniform and can be considered to behave as a continuum. Chemically and microstructurally the materials are uniform throughout. Most standard materials are first manufactured and then are machined to the size and shape of the part. The elastic constants of the materials are the same in the part as in the bulk. In the case of materials that are manufactured directly into parts (H-beams, motor castings, etc.), the parts are large enough that pieces can be removed to measure their property, and the property measured in this way is assumed to be identical to the property in the part. For certain applications, however, removal of pieces from the part is not an easy option; the parts may be too small to have pieces removed from them in such a way as to be representative of the part on the whole. Also, the piece removed may be too small to be tested by standard means. Materials that fit this category include multilayers, and interlayers in electronic components, component parts of microelectromechanical systems (MEMS), and ther-

mal barrier coatings in the stators and blades of gas turbines. For these components, the elastic constants of the materials that make up the part have to be measured by techniques that are not the standard techniques discussed earlier in this paper. Often, the properties of the materials have to be measured in situ, that is, while the material is still in place in the part. (Materials scientists are currently developing small test fixtures and methods of testing specimens μm in size. The specimens are obtained directly from components, so that the properties measured will be representative of those components.) Instrumented indentation testing is a technique that offers the possibility of determining the elastic constants in situ and currently is being used extensively for this purpose. In the rest of this section, this technique is briefly reviewed and the advantages and disadvantages of the technique are discussed. A good review article for the instrumented indentation apparatus may be found in [7.40]. The technique is discussed in greater detail in [7.41] and in Sect. 7.3.4 of this volume.

Instrumented Indentation Test Apparatus

A schematic diagram of an instrumented indentation apparatus is shown in Fig. 7.13. The apparatus consists of three parts: a force actuator to apply the load, a displacement sensor to measure the depth of penetration and an indenter to penetrate the solid. Forces for these instruments have been generated electromagnetically, electrostatically or piezoelectrically [7.40] and the level of force is often determined by the voltage or current used to generate the force. Displacements are measured by a variety of gages: capacitive sensors, linear variable differential transformers and laser interferometers.

The indenters are generally made of diamond, having several geometries. In general, four-sided pyramidal indenters are not used for nanoindenters, because they usually end in a flat-ended chisel edge that interferes with the method at very light loads. Three-sided indenters are used since they can be sharpened to a point. The most common three-sided indenter is the Berkovich indenter, which has the same depth to area as the commonly used Vickers hardness indenter. The centerline to face angle for the Berkovich indenter is 65.3° . A cube-corner pyramidal indenter, so called because the three faces of the indenter are at 90° to one another, is also commonly used for nanoindentation studies (Sect. 7.3.4). The centerline to face angle for the cube-corner indenter is 35.3° . This indenter angle is more acute than that for the Berkovich indenter. Hence, the stresses at the tip of the indenter are much higher than

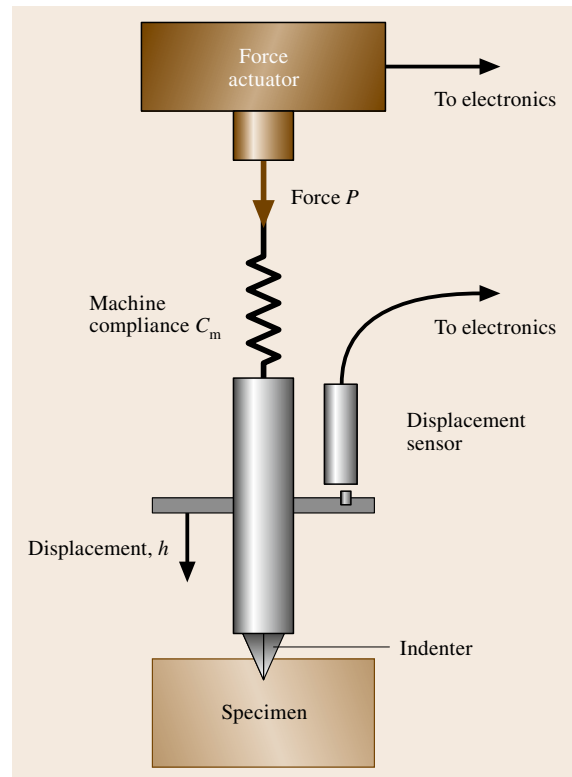


Fig. 7.13 A schematic diagram illustrating the parts to an instrumented indentation tester (after [7.40])

the stresses at the tip of the Berkovich indenter and the tendency for crack formation is greater. The third type of indenter used for instrumented indentation studies is the spherical indenter. This has the advantage over the others that the initial contact of the indenter to the solid is elastic, which would make it ideal for the determination of elastic constants. Unfortunately, small spherical indenters – a micron or less in diameter – are difficult to make, which is why the Berkovich indenter is the indenter of choice for most small-scale testing [7.40].

Determining the Elastic Modulus by Indentation

A schematic representation of the indentation load P as a function of displacement h is shown in Fig. 7.14. The loading of the indenter is due to a mixture of elastic and plastic deformation. The initial portion of the loading is primarily due to elastic deformation in the vicinity of the indentation [7.41]. As the penetration increases, so does the plastic contribution to the deformation. An

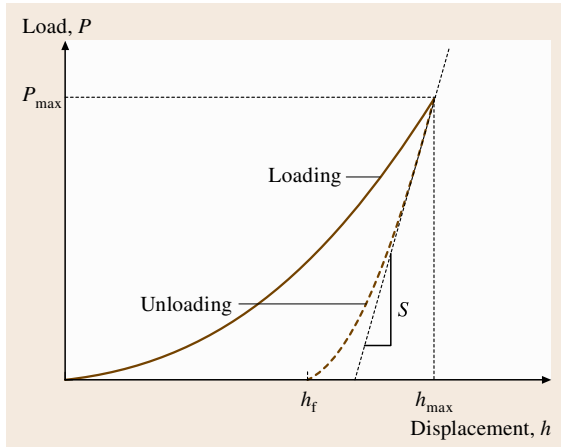


Fig. 7.14 An illustration of a load displacement curve for a single loading cycle on an instrumented indentation tester (after [7.40])

estimate for the Young's modulus is obtained from the slope of the unloading curve S , at the point of maximum load using the following formula, which is founded in elastic contact theory [7.40, 42, 43]

$$E_r = \frac{\sqrt{\pi}}{2\beta} \frac{S}{\sqrt{A}}, \quad (7.19)$$

where A is the area of contact β is a constant that depends on the geometry of the indenter [7.44], and E_r is the reduced elastic modulus. The reduced elastic modulus is used to take account of the fact that deformation occurs in both the target material and the indenter. To calculate the Young's modulus of the target material, an estimate of the Poisson's ratio of the material must be made. This estimate results in an error of only 5% in the determination of E . The value of β for the Berkovich and the cube-corner indenters is 1.034 [7.40].

The slope of the unloading curve S is known as the contact stiffness, and can be obtained by using a power relation of the load P to the penetration depth h devel-

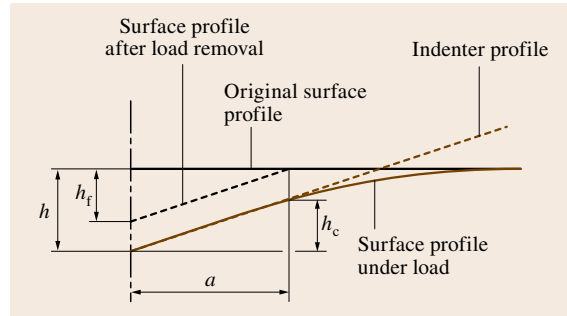


Fig. 7.15 A schematic representation of a section through a conical indentation illustrating the various parameters used to obtain (7.18) through (7.21) (after [7.40])

oped by *Oliver and Pharr* [7.45]

$$P = BA(h - h_f)^m, \quad (7.20)$$

where B and m are empirical fitting parameters and h_f is the final displacement after complete unloading. The contact stiffness is determined by differentiating (7.20) with regard to h and evaluating the result at $h = h_{\max}$

$$S = Bm(h_{\max} - h_f)^{m-1}. \quad (7.21)$$

Equation (7.21) does not always provide an adequate description of the unloading curve in which case a fit is usually applied just to the upper 25% to 50% of the data [7.40].

All that is needed to characterize Young's modulus by (7.19) is the contact area A at maximum load P_{\max} . The contact area is usually expressed in terms of the depth of the circle of contact h_c which defines the depth of contact for a conical indentation (Fig. 7.15). The geometry of the area of contact is discussed in [7.41] with regard to the penetration depth h_c and the area of contact A . For a Berkovich indenter, the two are related by the following equation

$$A = 24.5h_c^2. \quad (7.22)$$

Standard	Current stage	Purpose
ISO 14577-1:2002 Ed. 1	Published	Test method
ISO 14577-2:2002 Ed. 1	Published	Verification and calibration of testing machines
ISO 14577-3:2002 Ed. 1	Published	Calibration of reference blocks
ISO 14577-4 Ed. 1	Under development	Test methods for coatings
ISO 14577-5 Ed. 1	Under development	Indentation tensile properties

Table 7.4 International Organization for Standardization ISO 14577, Metallic materials – Instrumented indentation test for hardness and materials parameters. Work is also underway in the ASTM on similar standards

The parameter h_c is given by the following formula

$$h_c = h - \varepsilon \frac{P}{S}. \quad (7.23)$$

The parameter ε is a constant that depends on the indenter geometry. Its value can be obtained through elastic or elastic–plastic analyses of the indentation process. For the Berkovich indenter, the parameter ε has a value of about 0.75 [7.45].

7.2 Plasticity

Plasticity, or permanent deformation, is one of the most useful mechanical properties of materials. It permits forming of parts, and provides a significant degree of safety in use. The ability to specify plastic properties measured by the standard methods described in this chapter provides industry with a valuable means of controlling the manufacture of materials. These measures also provide the analyst with data for prediction and modeling. However, the current phenomenological basis for plasticity requires a large number of measurements and the development of a more physical basis is badly needed. In this chapter, we briefly discuss the physical basis for plasticity and then describe at length standard methods for measuring plastic properties. Although most industrial needs are being met by existing standards, the appearance of new materials and extreme applications of traditional materials are driving the development of new standard measurement methods.

In the context of this section, plasticity refers to the permanent strain that occurs after the elastic limit and before the onset of localization that determines a material's ultimate strength. Plasticity in materials is known to be due to the creation, movement, and annihilation of defects (dislocations, vacancies, etc.) while the forces between atoms remain elastic in nature. It is also well known that these defects often move at stresses below the elastic limit, a process called microplasticity, and that the ultimate strength can be determined by purely plastic processes. Nevertheless, from an engineering point of view, it is entirely appropriate to consider elasticity (Sect. 7.1), plasticity (Sect. 7.2), and ultimate strength (Sect. 7.4) as separate phenomena.

7.2.1 Fundamentals of Plasticity

The onset of plasticity at the yield strength signals an end to purely elastic deformation, i. e., the elastic limit.

With the determination of the area of contact, all of the parameters in (7.17) are known and the Young's modulus can in principle be calculated. In 2002, the technique was issued as a test standard by the International Organization for Standardization (ISO): ISO 14577-1 through ISO 14577-3 (Metallic materials – Instrumented indentation test for hardness and materials parameters). Two additional parts to the standard are still under consideration. The parts of this standard and their purpose are listed in Table 7.4.

Many designs are elastic and the maximum working (or allowable) load may be chosen as the load when the yield strength is reached in some part of the design. Plasticity may also be viewed as a margin of safety before the ultimate strength has been reached. For this reason, the maximum plastic strain or ductility may assure the user of a certain level of safety if the yield strength is exceeded by accident. Ductility also permits the manufacturer to form materials without failure, and workhardening (the increase in stress with plastic strain needed to continue plastic deformation) assures that the part will be even stronger when it is finished. The standards that exist today were created in an effort to standardize the meaning and measurement of these important plastic properties.

These standards now also serve the analytical community that seeks to predict plastic behavior under conditions of use, forming, accidents, etc. This community uses the theory of plasticity to make its predictions. While there is elastic strain proportional to applied pressure (through the bulk modulus) and the fracture strength depends on the applied pressure, plastic deformation is practically independent of the applied pressure. There is also little or no volume change associated with plasticity. The plastic behavior depends strongly on the deviatoric or shear components of the stress tensor and results in a shape change rather than a volume change. These observations have led to the development of the mathematical or phenomenological theory of plasticity. In this theory, plastic yielding begins at a critical value of the second invariant of the stress tensor (von Mises criterion) or at the maximum shear stress (Tresca criterion). If the von Mises criterion is plotted in a space of principal stresses, it appears as a cylinder whose axis lies along the $\sigma_1 = \sigma_2 = \sigma_3$ locus. In the σ_1/σ_2 plane, perpendicular to the σ_3 -axis, the cut through the cylinder appears as an ellipse and is

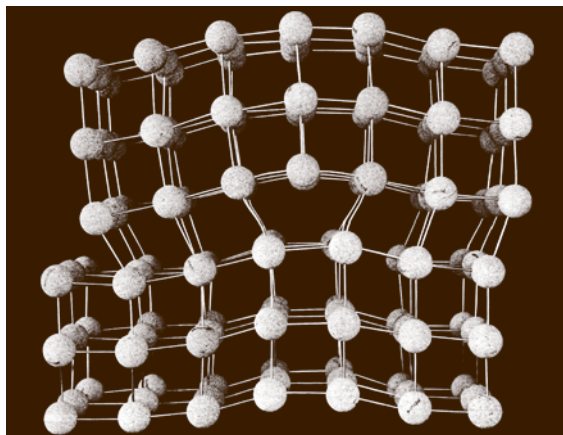


Fig. 7.16 Model of an edge dislocation oriented so that the atoms are viewed parallel to the dislocation line (CD) in Fig. 7.18. (Model courtesy of R. deWit [7.48])

known as the von Mises ellipse. Inside the ellipse, all strain is assumed to be elastic. When the combination of stresses touches the ellipse, plastic deformation begins to take place. Plastic strain usually results in strain hardening and this may change the size, shape, or position of the von Mises ellipse. After yielding, it may no longer be elliptical. The description of this theory in any more detail is beyond the scope of this article. The reader is directed to one of the earliest and most important treatise on this subject [7.46] and to one of the most recent texts [7.47]. The theory of plasticity has had great success in the prediction of plastic deformation

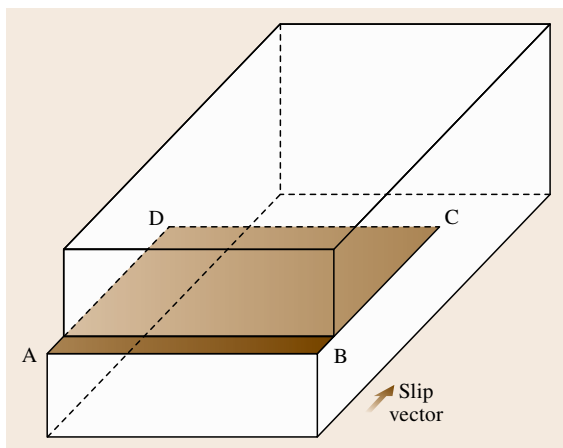


Fig. 7.18 The slip that produces an edge dislocation has occurred over the area ABCD. The boundary CD of the slipped area is the dislocation; it is perpendicular to the slip vector

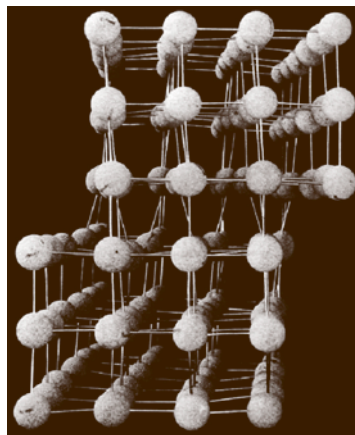


Fig. 7.17 Model of a screw dislocation viewed perpendicular to the dislocation line CD in Fig. 7.19. (Model courtesy of R. deWit [7.48])

of materials. However, because of its phenomenological basis, it requires an extensive number of measurements and assumptions to accurately describe the behavior of real materials undergoing complex deformation paths.

There are several physical phenomena that result in plasticity: movement of dislocations [7.49], movement of atoms (Nabarro–Herring creep or Coble creep) [7.50], phase transformations (TRIP) [7.51], twinning (TWIP) [7.52], or clay plasticity [7.53]. The predominant mechanism is movement of dislocations and a brief description of how this results in plastic behavior is appropriate here.

Dislocations as a source of plastic deformation in crystals were postulated in the 1930s independently by Taylor, Orowan, and Polanyi [7.54]. Quantum mechanics was being developed at that time and at least one of these three was searching for a *quantum* of plastic deformation [7.55]. They sought something that could explain the low yield strength as compared to the high theoretical stress to slide a whole atomic plane over another. It also had to be consistent with the behavior of slip steps and etch pits with increasing plastic strain. They proposed new kinds of crystal defects in the crystal lattice, edge and screw dislocations (Figs. 7.16 and 7.17) [7.48], that could concentrate the applied stress on a row of atoms.

Under the action of a stress much less than the theoretical shear stress, dislocations could move (Figs. 7.18 and 7.19), resulting in plastic deformation of a crystal and the formation of slip steps.

The evidence supporting this at the time was etch pits which resulted from stress-enhanced dissolution around the dislocation. Transmission electron microscopy has now well established dislocations as the primary source of plasticity (Fig. 7.20).

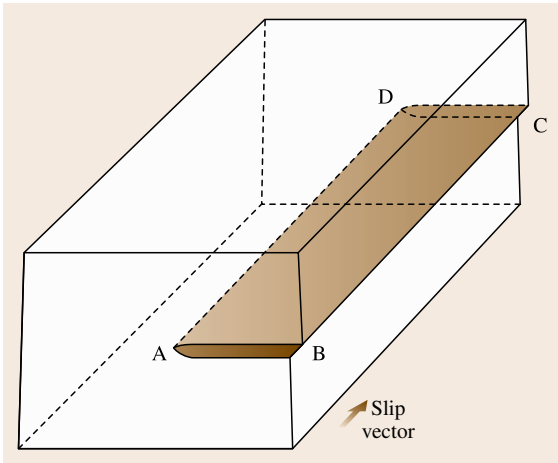


Fig. 7.19 The slip that produces a screw dislocation has occurred over ABCD. The screw dislocation AD is parallel to the slip vector

For significant plasticity to occur in a crystal, the movement and interaction of 10^1 – 10^4 km of dislocation length must take place in every cubic millimeter of material [7.56]. Furthermore, most materials of commercial importance are polycrystalline and contain enormous numbers of crystals that may be randomly or nonrandomly oriented. Thus, the quantitative prediction of plastic behavior in commercial materials based on an understanding of dislocation mechanics is a difficult problem and has not yet been successful enough to replace the phenomenological approach described previously and embodied in current analytical schemes.

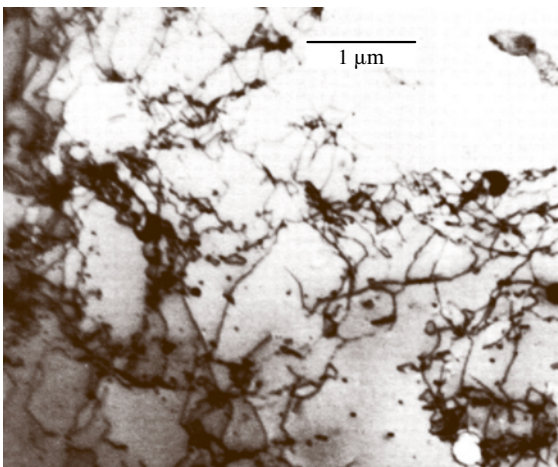


Fig. 7.20 Dislocations in niobium as viewed in the transmission electron microscope

This situation is beginning to change [7.57–60] and may ultimately lead to great simplifications in what actually must be measured.

7.2.2 Mechanical Loading Modes Causing Plastic Deformation

As noted in the previous section, plasticity is extremely insensitive to the mean stress (hydrostatic tension or pressure). Thus, there is no test using purely hydrostatic tension or pressure to measure plasticity. That is not to say there is no interest in the effect of superimposed hydrostatic tension or pressure. This invariant of the stress tensor will greatly affect the fracture behavior of most materials. *Bridgman* used superimposed hydrostatic pressure to suppress fracture in tensile bars and achieve much larger elongations to fracture and reductions in area [7.61]. He noted that plastic yielding in tension occurred at roughly the same value of shear stress as yielding in compression. Furthermore, workhardening behavior was unaffected by pressure. Since the effect of hydrostatic tension or pressure is mainly on the factors that determine strength, it will not be discussed in this section on plasticity.

Due to the fact that plasticity responds to the deviatoric components of the stress tensor, most tests are designed to develop significant levels of shear stress. In Fig. 7.21, commonly used mechanical modes of loading are shown that may be used to measure the plastic properties of materials. There are standard test methods

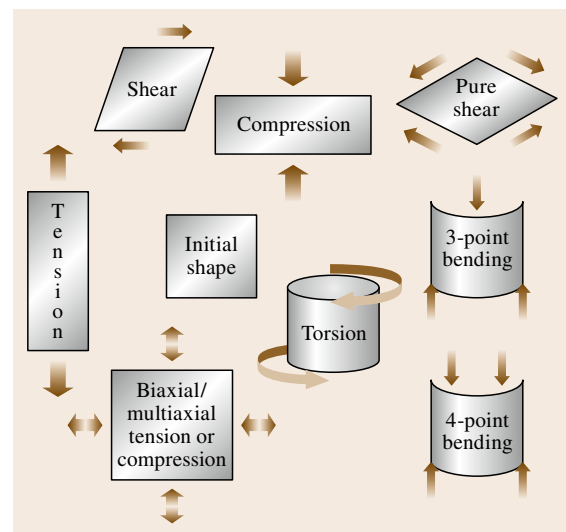


Fig. 7.21 Modes of mechanical loading used to measure plastic properties of materials

for plastic behavior that employ each of these loading modes and are the subject of this section on plasticity.

In uniaxial *tension*, a bar or sheet is pulled along its long axis. The stress in the bar is calculated by dividing the applied force by the cross-sectional area of the bar. The strain is determined from the change in length of an initial, fiducial length. In uniaxial *compression* a bar is subject to compressive loading along one axis and the stress and strain are determined in much the same way as for tension. Both tension and compression have components of hydrostatic tension or pressure which may affect the ultimate behavior, but not the yielding or workhardening behavior. One of the great values of tension and compression testing arises from the fact that the stress and strain are uniform and simply calculated from applied forces, displacements, and specimen dimensions.

In practice, *shear* results in some bending and *bending* results in some shear loading. The shear stress is the tangential surface force divided by the surface area. The shear strain is defined as the change in angle that results. Bending develops additional tensile and compressive loading away from the neutral axis resulting in mean stress effects. *Pure shear* and *torsion* (which generates pure shear) do not develop any significant level of mean stress.

Lastly, combinations of loading modes are used to assess the effect of complex stress or strain states on plasticity and ultimate behavior. Bulge testing or cup testing is largely a *biaxial tension* test for sheet material with a small component of bending. The ratio of the stress or strain in the two orthogonal directions can be adjusted by cut outs or specimen shape. One of the most popular tests for plasticity, the hardness test, is a complex *multiaxial compression* test with a high, superimposed pressure (Sect. 7.3).

7.2.3 Standard Methods of Measuring Plastic Properties

This section lists and briefly describes standard tests used to measure plastic behavior. Some of the most critical features of each method and their limitations are discussed. As noted above, plasticity is highly sensitive to the stress and strain state. Thus, the methods are classified according to loading mode and listed in order of importance or frequency of performance.

Hardness Tests

Whereas hardness is treated in detail in the next section, Sect. 7.3, a glimpse of plasticity in hardness is also

made here. The hardness of a material as measured by the indentation test methods quantifies a material's resistance to plastic flow. By definition, a soft material deforms plastically more easily than a hard material. Indentation tests are used industrially for quality control. They are the most frequently performed mechanical tests because of their simplicity, rapidity, low cost, and usually nondestructive nature. In the indentation test, a spherical or pointed indenter is pressed into the surface of a material by a predetermined force. The depth of the resulting indentation or the force divided by the area of the resulting indentation is a measure of the hardness. However, these tests measure the resistance to plastic deformation in complex, multiaxial, and nonuniform stress and strain fields at varying strain rates. Thus, the interpretation of these tests in terms of more common concepts is difficult. The yield strength, workhardening, or ultimate tensile strength can only be estimated by empirical correlation. The ductility cannot be estimated by any means. It is extremely difficult to use the results from these tests analytically to accurately describe plastic deformation in other applications. This drawback is being addressed by instrumented indentation test standards (ISO 14577 [7.62] and efforts underway at ASTM). The commercial importance of hardness testing cannot be underestimated and justifies an entire Sect. 7.3 devoted entirely to hardness.

Tension Tests

The uniaxial tension test is the most important test for measuring the plastic properties of materials for specification and analytical purposes. It provides well-defined measures of yielding, workhardening, ultimate tensile strength, and ductility. It is also used to measure the temperature dependence and strain rate sensitivity of these quantities. Versions of the tension test provide important parameters for predicting forming behavior. The tension test is carried out on a bar, plate, or strip of material that has a region of reduced cross-sectional area, the gage section (Fig. 7.22). The reduced area causes all plastic deformation to occur in the gage section. The unreduced ends are held in grips (Fig. 7.4 of Sect. 7.1) and the specimen is elongated parallel to its long axis. Initially, the sample deforms elastically, as described in Sect. 7.1, and in linear proportion to the applied stress as shown schematically in Fig. 7.23. At some applied force, nonlinear and unrecoverable deformation, i.e., plasticity begins. The proportional limit is the force at the onset of plasticity divided by the initial cross-sectional area of the sample.

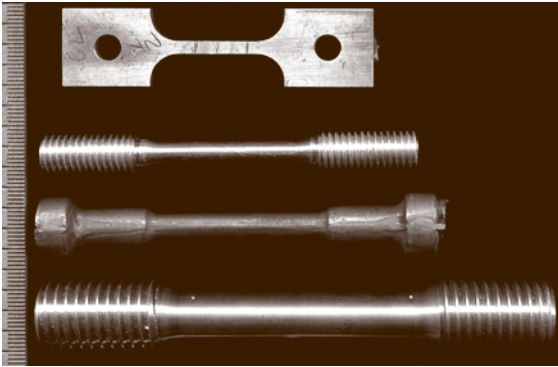


Fig. 7.22 Examples of tensile test specimens used to measure plastic behavior of metals

Various definitions of yielding are used. In the figure, the 0.2% offset (plastic) yield stress is shown. As the sample continues to elongate, it workhardens. At the ultimate tensile strength (UTS), it breaks or becomes unstable to continued uniform deformation. A region of localized thinning or necking characterizes the latter instability (Fig. 7.24). This ultimate behavior is covered in Sect. 7.4 on strength.

There are many standards for performing uniaxial tensile tests. Some standards are widely used: [ASTM E 8 \[7.63\]](#), [ISO 6892 \[7.64\]](#), [DIN EN 10002-1 \[7.65\]](#), [JIS Z 2241 \[7.66\]](#), and [BS 18 \[7.67\]](#). Other standards are modeled after these or are based in some way on them. For example, [ASTM E 8M \[7.68\]](#) is a metric version of [ASTM E 8 \[7.63\]](#), [SAE J416 \[7.69\]](#) provides some guidance in sample geometry for testing according to [ASTM E 8 \[7.63\]](#), [ASTM A 370 \[7.70\]](#) describes tensile testing of steel products, and [ASTM B 557 \[7.71\]](#) provides for tensile testing lightweight metals, but all reference [ASTM E 8 \[7.63\]](#). [ASTM E 345 \[7.72\]](#) also refers to [ASTM E 8 \[7.63\]](#) when testing metallic foils. [ASTM E 646 \[7.73\]](#), [ISO 10275 \[7.74\]](#), and [NF A03-659 \[7.75\]](#) refer to [ASTM E 8 \[7.63\]](#) or [ISO 6892 \[7.64\]](#) compliant tensile tests to measure workhardening behavior. [ASTM E 517 \[7.76\]](#) and [NF A03-658 \[7.77\]](#) also require adherence to one of the standard tensile test methods to measure the r -ratio. Frequently used fastener test standards (e.g., [SAE J429 \[7.78\]](#), [ASTM F 606 \[7.79\]](#), and [ISO 898 \[7.80\]](#)) refer to [ASTM E 8 \[7.63\]](#) or [ISO 6892 \[7.64\]](#) for details of tensile testing fasteners and fastener materials. While the [ASTM](#) tensile tests for plastics ([ASTM D 638 \[7.81\]](#), [ASTM D 882 \[7.82\]](#), and [ASTM D 1708 \[7.83\]](#)) do not reference [ASTM E 8 \[7.63\]](#); the actual performance of the test is very similar to that in [ASTM](#)

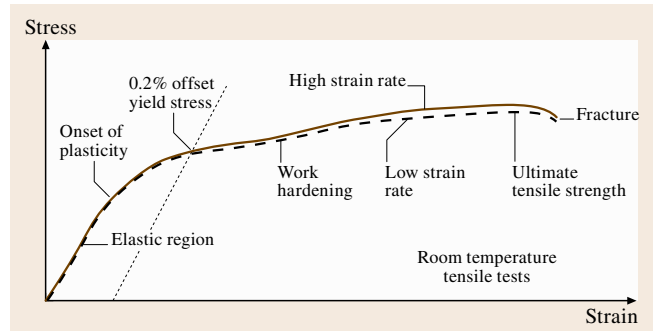


Fig. 7.23 Uniaxial engineering stress versus engineering strain curves at two strain rates, showing elastic region, onset of plasticity (proportional limit), offset yield stress, workhardening, ultimate tensile strength, and fracture

[E 8 \[7.63\]](#). The interpretation of results is somewhat different.

In principle, all standards for tensile testing are fairly similar, so only [ASTM E 8 \[7.63\]](#) will be described in detail here. This standard first discusses the following acceptable testing apparatus: testing machines and by reference [ASTM E 4 \[7.84\]](#), gripping devices, dimension-measuring devices, and extensometers, which measure sample displacement for monitoring strain within the gage section, by reference to [ASTM E 83 \[7.85\]](#). Acceptable test specimen details are then presented. These cover size, shape, location from product, and machining. Testing procedure is described in detail:

- (1) preparation of test machine
- (2) measurement of specimen dimensions
- (3) gage length marking of specimens
- (4) zeroing of the test machine
- (5) gripping of the test specimen
- (6) speed of testing

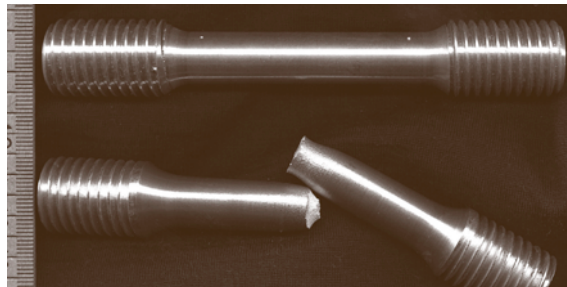


Fig. 7.24 Broken tensile specimen showing necking prior to fracture

- (7) determination of yield strength
- (8) yield point elongation
- (9) uniform elongation
- (10) tensile strength
- (11) elongation
- (12) reduction of area
- (13) rounding reported test data, and
- (14) replacement criteria for unsatisfactory specimens or tests.

Of these, (6) speed of testing and (7) method of determining yield strength have the most significant effect on the actual measurement of plastic properties. Speed of testing is defined in terms of:

- (a) rate of straining of the specimen
- (b) rate of stressing of the specimen
- (c) rate of separation of the two crossheads of the testing machine during the test
- (d) the elapsed time for completing part or all of the test, or
- (e) free-running crosshead speed.

Speed of testing can affect all test values because of the strain-rate sensitivity of materials. Ideally, the actual strain rate experienced by the gage section should be known and reported. All other speed of testing measures are relevant only so far as they affect this strain rate. Unless the strain rate is controlled, two laboratories may get significantly different results even when following the standard method.

According to [ASTM E 8 \[7.63\]](#), the yield strength can be determined by:

- (a) the offset method
- (b) the extension under load method
- (c) the autographic diagram method, or
- (d) the halt-of-the-beam method. These methods may produce different results with different uncertainties, yet all are equally valid at this time.

In general, the quantities reported from this test are yield point or yield strength, ultimate tensile strength (UTS), elongation to fracture (total elongation divided by initial gage length), and reduction in area (area decrease in the fracture plane divided by initial gage area). It is not uncommon to find data with no record of testing speed or initial gage length. This is unfortunate since the speed of testing (as noted above) can significantly affect the yield strength and the other properties to a lesser extent. The initial gage length can affect the elongation

due to the nonuniform deformation that occurs in the necked region.

Other important quantities, such as workhardening, strain-rate sensitivity, and temperature effects, can also be determined in a tensile test. The measurement of these is left to other standards that will be discussed next.

Workhardening Behavior. After yielding, the stress-strain curves of many materials exhibit workhardening, that is, an increased stress to achieve additional plastic strain. This is usually due to the increased concentration of dislocations and their complex interactions. Various standards address the measurement of workhardening

- [ASTM E 646 \[7.73\]](#)
- [ISO 10275 \[7.74\]](#)
- [NF A03-659 \[7.75\]](#)

to mention a few. In general, a uniaxial tensile test is performed according to [ASTM E 8 \[7.63\]](#) with some added constraints with regard to rate of testing and collection of data. The true stress/true strain (that is, the applied force or elongation divided by the current, instead of the initial, area or gage length) curve is determined from the raw data. In [ASTM E 646 \[7.73\]](#), the curve is fit by the equation

$$\sigma = N\varepsilon^n$$

to find n , the strain hardening exponent, where σ is the true stress, ε is the true strain, and n is a constant. The method is appropriate for materials whose stress-strain curve can be reasonably fit by the equation above. For the most important exception, i.e., steel, which may have a discontinuous stress-strain curve, it is recommended that only the region that can be fit reasonably be used. In general, n is probably a function of strain. This possibility is not covered in [ASTM E 646 \[7.73\]](#).

Strain-Rate Sensitivity. The only standard addressing the measurement of this property is European Structural Integrity Society (ESIS) designation P7-00.2000, Procedure for Dynamic Tensile Tests. (European Structural Integrity Society documents may be obtained from Professor K.-H. Schwalbe, GKSS-Forschungszentrum Geesthacht, 21502 Geesthacht, Germany.) Here the tensile test data (σ and true strain rate, $d\varepsilon/dt$, both measured at the same strain ε) are fit to an equation of the form

$$\sigma = M(d\varepsilon/dt)^m$$

to find m , the strain-rate sensitivity. This procedure is relatively new. In time, this approach may be accepted by other standards development organizations (SDOs). The only issue may be that the form of the equation has little physical basis. There are other fits to strain-rate-dependent plastic properties, e.g., the Johnson–Cook model [7.86] or the Bodner–Partom model [7.87].

Temperature Effects on Plasticity. The movement of dislocations and vacancies is strongly temperature-dependent and, thus, so is plasticity [7.88]. It is important to characterize this behavior for any application that occurs at low or high temperatures. Examples of such applications are cryogenic tanks, pipelines operating in the arctic, steam plant components, nuclear power generators, jet engines, structures that might be exposed to fires – the list is a long one. Some standards addressing tensile tests at low and high temperatures are

- ASTM E 1450 [7.89]
- ISO/DIN 19819 [7.90]
- ISO 15579 [7.91]
- ASTM E 21 [7.92]
- DIN EN 10002-5 [7.93]
- JIS G 0567 [7.94].

These standard tests are essentially the same as the room-temperature ones, but have or refer to extensive requirements related to controlling and/or determining the temperature at which the test is performed (see, for example, ASTM E 633 [7.95]). Additionally, in elevated-temperature tests, the speed of testing is more tightly controlled than in room-temperature tests. This additional control is necessary because the plastic behavior becomes strongly time- or rate-dependent at high temperatures due to the significant amount of creep strain that can accrue even in a short-term tensile test.

Time-Dependent Plasticity. Time-dependent plasticity is called creep. This mode of plasticity is important in any part or structure that is exposed to temperatures above about 1/3 of its melting temperature, especially if it must resist permanent deformation for significant lengths of time. Creep may also be noticed at room temperature in very long, highly stressed components such as bridge cables. The loosening of bolts is also due to creep, but under a decreasing stress. This effect is called stress relaxation.

The importance of time dependent plasticity, i. e., creep and stress relaxation, has necessitated the development of many standard tests for metals

- ASTM E 139 [7.96]
- ASTM E 328 [7.97]
- DIN EN 10291 [7.98]
- DIN EN 10319 [7.99]
- ISO 204 [7.100]
- JIS Z 2271 [7.101].

At elevated temperatures, brittle materials that normally exhibit extremely limited or no plasticity at room temperature, begin to deform plastically by creep. For this reason, there are tensile creep standards, similar to those for metallic materials that apply to ceramics, composites, and plastics

- ASTM C 1337 [7.102]
- ASTM C 1291 [7.103]
- ISO 899-1 [7.104]
- JIS K 7115 [7.105].

Creep tests are performed by loading a standard uniaxial tensile sample with a constant force or stress and measuring the tensile strain that occurs with time. Stress-relaxation tests apply a constant strain and measure the relaxation of stress with time. Both tests are measures of time-dependent plasticity.

These tests are usually done at an elevated temperature, but the term elevated is quite relative to the material being tested. Significant time-dependent plasticity is usually observed at or above one-third of the melting temperature of most materials. For solder alloys, this is below room temperature. For structural ceramics, industrially relevant creep and stress relaxation rates require temperatures in excess of 1000 °C.

For metals and alloys, it is usually found that creep rates increase exponentially with temperature. They are often modeled using an Arrhenius (or other thermal activation) law [7.88]. Therefore, it is important to know and tightly control the temperature to about ± 1 °C if 1% accuracy is desired. Furthermore, this temperature must be applied uniformly to the gage section of the test piece. The various standard methods require accurate and uniform temperature environments for the test.

Another important parameter is the load. Since a constant force, that may be greater than 10^4 N, is generally required for a long time (up to 100 000 h or more), it is customary to use dead or static loads. These are most frequently applied by a complicated system of levers, knife-edges, and weights. It is essential to confirm that the applied load is correct. This is dealt with in the standards, see for example ISO 7500-2 [7.106] or ASTM E 4 [7.84].

As the creep sample elongates under load, its cross-sectional area usually decreases. Thus, a constant applied force leads to an increasing stress on the sample. Loading systems have been designed that reduce the load as the sample creeps to maintain a constant stress [7.107, 108]. These are not covered by any standard. While this might seem to be an oversight, most applications of creep-resistant materials can only tolerate a few percent strain. For these, the difference between constant load and constant stress is negligible. However, if one is interested in creep forming or superplastic forming (SPF) where large plastic strains are required, the differences between the two loading systems can be quite large [7.109].

Superplasticity. Superplasticity in metals is characterized by extraordinarily large ductilities. It is not uncommon to observe strains of 1000 to 3000%. While at first a laboratory curiosity, superplasticity is now used to form complex and highly deformed shapes like small boat hulls, fuel tanks, spare tire wells, aircraft doors, to mention a few. Superplastic behavior is exhibited by a number of alloys under particular conditions of microstructure, temperature, and strain rate. Any test for superplasticity is chiefly for the purpose of characterizing this processing window. An ASTM standard method of characterizing superplastic behavior in uniaxial tension has been recently approved. A draft ISO tensile test has also been proposed based on JIS H 7501 [7.110]. This Japanese standard specifies the test specimen geometry, the apparatus, and the procedure for the evaluation of tensile properties of metallic superplastic materials. In particular, it specifies how the stress-strain curves and the strain rate sensitivity are to be determined. It has been noticed for some time that superplastic materials have a strain rate sensitivity m near unity. Some researchers have claimed that an m near unity implies superplastic behavior despite limited ductility in the actual test. Superplasticity, by definition, requires very large ductilities, so these claims would seem incorrect.

The main feature of any standard for measuring superplasticity would be specifications to perform the test over a range of temperatures, perform the test over a range of commercially useful strain rates, and apply and measure the large strains that will necessarily occur.

Plastic Strain Ratio r for Sheet Metal. Another important plastic property that can be obtained from the tension test is the plastic strain ratio r . It is defined as the ratio of the true plastic width strain to the true

plastic thickness strain at some level of plastic tensile strain in the length direction (usually 15 to 20%). The plastic strain ratio quantifies the ability of a sheet metal to resist plastic thinning when subjected to tensile strains in the plane of the sheet. It is a consequence of plastic anisotropy and is related to the preferred crystallographic orientations within a polycrystalline metal. This resistance to thinning contributes to the forming of shapes, such as cylindrical flat-bottomed cups, by the deep-drawing process. The r -value, therefore, may be considered an indicator of sheet metal drawability. Three standards for measuring the plastic strain ratio are

- ASTM E 517 [7.76]
- ISO 10113 [7.111]
- NF A03-658 [7.77].

Basically, a tensile test is run according to one of the tensile test standards mentioned previously. In addition to measuring the gage length, the width of the gage is measured. While the thickness can be measured directly, the changes in thickness are very small, especially in thin sheets. The standard permits calculating the thickness from the width and length assuming constant volume. These measurements should be done in the unloaded condition as the definition of r is in terms of true plastic strains, not total strains. Otherwise, some adjustment for the elastic strains must be made.

Since r is strongly dependent on the crystallographic texture, it may depend on the direction within the sheet the tensile sample was taken. The standards have procedures for assessing this effect.

Compression Tests

Compression testing, like tension testing, is uniaxial. It provides similar data on plasticity of materials: initial plastic behavior, such as yield strength and workhardening. It is sensitive to alignment and buckling can be a problem. Friction between the sample and compression platens may also affect the results. Barreling, i. e., nonuniform changes in the cross sectional area along the length also causes deviations from uniaxiality and ambiguities in the measurement of stress and strain. If not for these effects, the compression test could be carried out to very high strains in a plastic material. Instead, it is usually limited to about the same amount of strain as the tensile test, or less. Standard methods for performing compression tests are

- ASTM E 9 [7.112]
- ASTM E 209 [7.113]

- DIN 50106 [7.114]
- DIN EN 12290 [7.115]
- ISO 604 [7.116]
- JIS K 7132 [7.117]
- JIS K 7135 [7.118].

The samples are typically short cylinders (height-to-diameter ratios between 2 and 3) or plates. If the plates are thin, anti-buckling guides are required. An increasing axial compressive force loads the specimen and the mechanical properties (mainly yield strength and workhardening) in compression are determined. There is much more attention paid to axial alignment issues in these standards compared to those for tension. This is because load alignment will only get worse as compression increases whereas it usually improves with tensile strain. If one wishes to achieve as large a strain as possible in these tests, it is essential to provide lubrication throughout the test. Some experimentalists machine shallow, concentric grooves in the top and bottom of the sample and fill them with lubricant. This provides a reservoir of lubricant throughout the test and has met with a fair degree of success.

ASTM E 209 [7.113] is interesting because it provides guidance for performing compression tests under a wide range of temperatures, strain rates, and heating rates. This provides the basic data for determining, for example, the strain-rate sensitivity or the temperature-dependence of workhardening, but the standard does not favor any one model for interpreting the results. This approach permits one to use or compare any of the many constitutive laws that might apply.

Standard Tests Employing Other Loading Modes

As we shall see, standard tests for plasticity employing modes of loading other than tension and compression have been used chiefly as measures of ultimate strength or ductility. This may be due to stress concentrations obscuring the early yield behavior, poorly defined gage section to calculate the strain, difficulty determining the stress directly from the applied load, or a combination of these. The fact that these tests do provide certain important plastic properties and are easy to perform often outweighs their other limitations.

Shear. Shear loading is applied as single shear or double shear as shown in Fig. 7.25. In single shear, pulling the ends of the sheet specimen in tension generates a state of shear between the two slot tips. The slots are at 45° to the tensile axis and the radius of the slot tips are tightly controlled. Yielding is very sensitive to the details of the

slot tip curvatures and the gage length for shear is not well defined.

In double shear, a bar of material is inserted in a clevis grip and pull (or push) rod having close-tolerance holes. The pull or push rod and clevis may be pulled in tension or compressed to generate two regions of shear (i. e., double shear) in the specimen. Again, the gage length for the shear is poorly defined. The onset of yielding is also sensitive to the radius of curvature of the edges of the holes in the pull/push rod and the clevis.

Standards for measuring plastic properties in shear are

- ASTM B831 [7.119]
- ASTM B769 [7.120]
- ASTM B565 [7.121]
- DIN 50141 [7.122]
- DIN EN 4525 [7.123]
- DIN EN 28749 [7.124]
- ISO 7961 [7.125]
- ISO 84749 [7.126].

ASTM B 831 [7.119] is carried out in the single-shear mode (Fig. 7.25a), while ASTM B 565 [7.121] is in double-shear tension, and ASTM B 769 [7.120], DIN 50141 [7.122], and ISO 7961 [7.125] are in double-shear compression. All of the standard shear tests are used mainly to measure the ultimate shear strength. This is due to the fact that load fixture or specimen stress concentrations limit their usefulness in accurately measuring the early yield behavior and the poorly defined gage section over which the shear acts means that the shear strain is not well defined. These tests provide a shear stress that can be used to assure that a compo-

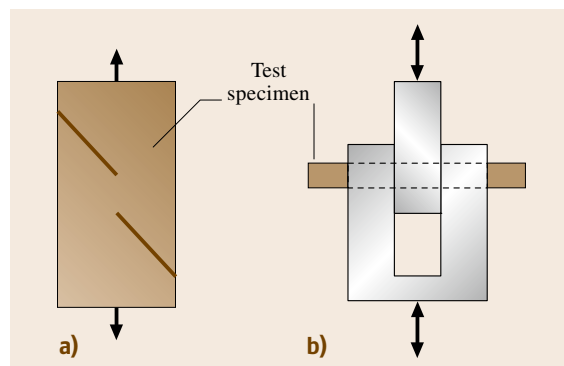


Fig. 7.25a,b Shear loading modes. (a) single shear, in tension only for sheet and plates, and (b) double shear, in tension or compression, for bars

ment does not fail plastically in shear even if the yield stress in shear is exceeded.

Torsion. Torsion loading is generated by twisting a bar that is usually round in cross section around its long axis (Fig. 7.21). Torsion provides a pure shear loading with principal stresses $\sigma_1 = -\sigma_2$ and $\sigma_3 = 0$. Therefore, the hydrostatic tension is zero throughout the test and does not increase as it does in a tension test. Consequently, the processes responsible for ductile fracture are greatly reduced. When a solid bar is tested in torsion, very large ductilities are possible if the material is inherently ductile. No instabilities will intervene as occur in tension and compression testing. If a tube is tested in torsion, however, buckling will occur and end the test prematurely.

There are standards for torsion testing to measure the shear modulus and standards to measure the ductility of wires in pure shear

- ASTM E 143 [7.127]
- ASTM A 938 [7.128]
- ISO 7800 [7.129]
- ISO 9649:1990 [7.130].

There are published procedures used by individual researchers, notably *Nadai* [7.131], who developed an analysis to obtain the shear stress/shear strain curve from torsion tests on bars. Without such an analysis, the stress in a solid bar cannot be determined. For this reason, some researchers use tubes. As noted above, tubes have a limited strain before buckling occurs.

At this time, the only standard torsion test that provides shear stress/shear strain data in the plastic region is ASTM F 1622 [7.132]. This standard is not only limited to a narrow range of materials and components, but it only determines the torsional yield strength. Nevertheless, since the entire plot of torque versus angle of rotation is recorded, the data obtained by this method could be analyzed to give the shear stress/shear strain curve.

Bending. Bending, like torsion, requires an analysis to convert the load–displacement or moment–curvature data to stress–strain curves when more than a few tenths of 1% plastic strain has accrued. The standards that use bending to characterize room-temperature plasticity are only for determining the ductility or resistance to cracking under this mode of loading. No other data are obtained. Room-temperature bend test standards include

- ASTM E 290 [7.133]
- ASTM E 190 [7.134]
- ASTM E 796 [7.135]
- ISO 7438 [7.136]
- ISO 7799 [7.137]
- ISO 7801 [7.138]
- ISO 7802 [7.139]
- ISO 8491 [7.140].

There are more international standards that refer to these and many more national standards that use bending as a means of determining plastic ductility of a variety of materials and welds in various shapes. They are all variations on the above methods. In ASTM E 290 [7.133], ISO 7438 [7.136], and ISO 8491 [7.140], the sample is bent monotonically either in three- or four-point bending, or as a cantilever. In ASTM E 796 [7.135], ISO 7799 [7.137], and ISO 7801 [7.138], the bending is carried out by cumulative cyclic, reversed bending. If the sample cracks, the amount of cumulative cyclic strain in bending to achieve cracking is reported. Other requirements might be that the sample be bent to a certain level without cracking, such as in ASTM E 190 [7.134] and ISO 7802 [7.139]. In this case, the method is a pass or fail test.

Bending is a favorite testing mode for brittle materials because of the simplicity of sample fabrication and not having to grip the sample in any way. For this reason, ceramics are often tested in bending. Bending is also one of the customary ways to test ceramics and brittle plastics at temperatures where they do exhibit creep. As long as the creep strain is small, the elastic stress analysis is approximately correct and there are standards for these tests

- DIN V ENV 820-4 [7.141]
- ISO 899-2 [7.142]
- JIS K 7116 [7.143].

It is important to note here that ceramics are well known to have different creep behavior in tension and compression. An added complication of using bending to characterize creep in ceramics is the fact that it convolutes compression and tension behavior. Thus, bending obscures some important features in the plastic behavior of ceramics at high temperature.

Ball Punch Deformation of Sheet Materials. These tests are used to determine the ductility of materials under a particular biaxial strain state. In this test,

a spherical punch is pressed into a sheet of material that is held in a hold-down assembly. The ball is pressed into the sheet forming a cup until the sheet fails in some way. Ball punch tests tend to be equi-biaxial, that is $\varepsilon_1 = \varepsilon_2$ in the plane of the sheet. Due to conservation of volume, $\varepsilon_3 = -(\varepsilon_1 + \varepsilon_2)$. Exhaustion of ductility is defined at the onset of severe localization, cracking, or drop in load on the punch. Standard methods for this test are

- ASTM E 643 [7.144]
- ASTM E 2218 [7.145]
- ISO 20482 [7.146]
- ISO 12004 [7.147].

ASTM E 2218 [7.145] and ISO 12004 [7.147] provide directions for achieving other states of plastic strain by testing strips of different widths instead of square or round sheets. The state of strain is determined from the distortion of an array of squares, circles, or both printed onto the surface of the sheet specimens. While the load on the punch or the hold-down force may be measured in these tests, the stress in the sheet is unknown. Furthermore, only the endpoint condition is reported. In the case of ASTM E 643 [7.144] and ISO 20482 [7.146], it is the limiting dome height. In the case of ASTM E 2218 [7.145] and ISO 12004 [7.147], it is the principal in-plane strains ε_1 and ε_2 at failure.

Other Loading Modes. There are applications in which highly complex plastic straining is required to make important parts or assure safe performance. The ability of a material to sustain these modes of loading is so important that standards have been developed just for them. The following standard test methods are mainly to determine the ductility of various materials under a particular complex strain history which is usually indicated by the name of the test

- ISO 8492 [7.148]
- ISO 8493 [7.149]
- ISO 8494 [7.150]
- ISO 8495 [7.151]
- ISO 8496 [7.152]
- ISO 11531 [7.153]
- ISO 15363 [7.154]
- ISO/TS 16630 [7.155].

These tests are in some ways like the hardness test: they are so specific and involve such a complex strain path that no extended meaning in terms of more fundamental quantities can be easily deduced from them. Neverthe-

less, they have significant industrial and commercial importance. The reader is referred to the standards themselves for more information.

7.2.4 Novel Test Developments for Plasticity

Motivation for the development of new standards for measuring plasticity may be better appreciated after a brief discussion of the industrial needs in this area that are not being met by existing standards.

Now, one can specify the yield strength in tension or compression, the ultimate tensile strength, the elongation at fracture, and the reduction in area at fracture. The workhardening exponent and the r -ratio can be specified. The creep rate and stress relaxation behavior can be specified. The critical plastic strain for localization or fracture can be specified under a variety of strain states. All these specifications can be checked by standardized tests. Are there material properties associated with plasticity that industry needs to specify that are *not* covered by standard tests? As will be shown below, there are unsatisfied needs for standards to measure plastic properties.

Data for New Forming Processes

New forming methods drive a need for specification of materials with particular properties. An example mentioned previously was superplastic forming (SPF). Currently, industry cannot specify the material for an SPF operation by some standard means of testing to determine whether it is superplastic enough for a particular application. User and supplier can easily end up at odds. That is what is driving the development of standards in this area.

Another issue stems from the desire to reduce the weight of automobiles and other products. This has driven industry to use high-strength steel and aluminum alloys. An impediment to the wider use of these materials is that they do not form like the traditional automotive alloys. One particular problem is that, during certain forming operations, they spring back so much that conventional die-design methods do not work. This problem, known as springback, arises from a complex interaction of the elastic and plastic strain, the residual stress, and the complicated shape of the workpiece. Two standards for characterizing the tendency for materials to springback are currently under consideration – one by ISO, and another by ASTM. The ISO document is based on JIS H 7702 [7.156] while the ASTM standard is based on extensive industrial experience [7.157] has just been approved.

Data for Crashworthiness and Fire-Resistive Steel

Another driving force for the development of standards for characterizing plastic behavior arises when materials are used under extreme conditions that can be reasonably expected to occur. Two examples are: (1) automotive materials involved in high-speed collisions, and (2) structural steel exposed to a fire.

In case (1), an extensive topic called crashworthiness has grown up in the last decade. Automobiles are now designed to remain as safe as possible under accident conditions. Their materials of manufacture are expected to behave reproducibly in a certain way at the high rates encountered under such conditions. A review of existing standards for acquiring data needed to predict structural behavior in an accident [7.158] identified the need for tests to measure high-rate plastic-deformation properties. This need has motivated the European Structural Integrity Society (ESIS) to develop its procedure for high-rate tensile tests mentioned previously. (European Structural Integrity Society documents may be obtained from Professor K.-H. Schwalbe, GKSS-Forschungszentrum Geesthacht, 21502 Geesthacht, Germany.) Recently, Japan has developed methods based on the Kolsky bar to provide this sort of rate-dependent plastic data [7.159]. It will not be long before these methods are proposed to standards development organizations (SDOs).

In the case of steel used in buildings, bridges, or other structures subject to fires, the reduction in yield strength with increasing temperature and the onset of creep result in large plastic strains that endanger the load-carrying capacity of the structure. Japanese and German steelmakers have begun making and selling steel claimed to be fire-resistive [7.160]. By this they mean that the yield strength retains 2/3 of its room temperature value at 600°C. ASTM has now convened a working group to decide what is meant by fire-resistive: is the arbitrary definition above satisfactory, or should some combination of standard or modified hot tensile and creep tests be used to define fire resistive,

or, lastly, should a new type of standard test, such as a tensile creep test conducted with a temperature ramp, be developed? Other possibilities are also being considered.

Finite Element Analysis

The impact of complex computer codes and powerful computers has made the accurate prediction of forming and performance possible if the needed inputs of material properties are available. These programs accept plastic properties in a variety of forms from raw stress-strain curves in tabular form to evaluated constitutive laws such as the Voce equation [7.161]. The traditional data provided by existing standards is barely adequate for these analyses. One real problem that frequently arises is the need for true stress/true strain data well beyond the onset of necking and fracture in tension tests, or beyond buckling and barreling instabilities in compression tests. The current solution to the lack of data is to make some simplistic assumptions, such as arbitrarily extending the stress-strain curve as required. This need could be better filled by data obtained in the torsion test [7.162], which can probe these high strains easily. As mentioned earlier in this chapter, torsion standards have been developed for shear modulus measurements, fatigue testing, and ductility testing. It should not be difficult to go this next step.

The other area that is left to assumption in these advanced analyses is the multiaxial workhardening behavior. Most often, the yield surface is assumed to expand in a self-similar way with strain (isotropic hardening) [7.47]. However, it is known that, in many cases, it is better to assume that the origin of the yield surface moves in stress space (kinematic hardening) [7.47]. Improved prediction would be possible if there were a standard method for measuring exactly what does happen. There have been developments recently in measuring the stress during cup deformation tests that would permit this to happen [7.163]. It may take a decade or more for these developments to reach the standards development organizations (SDOs).

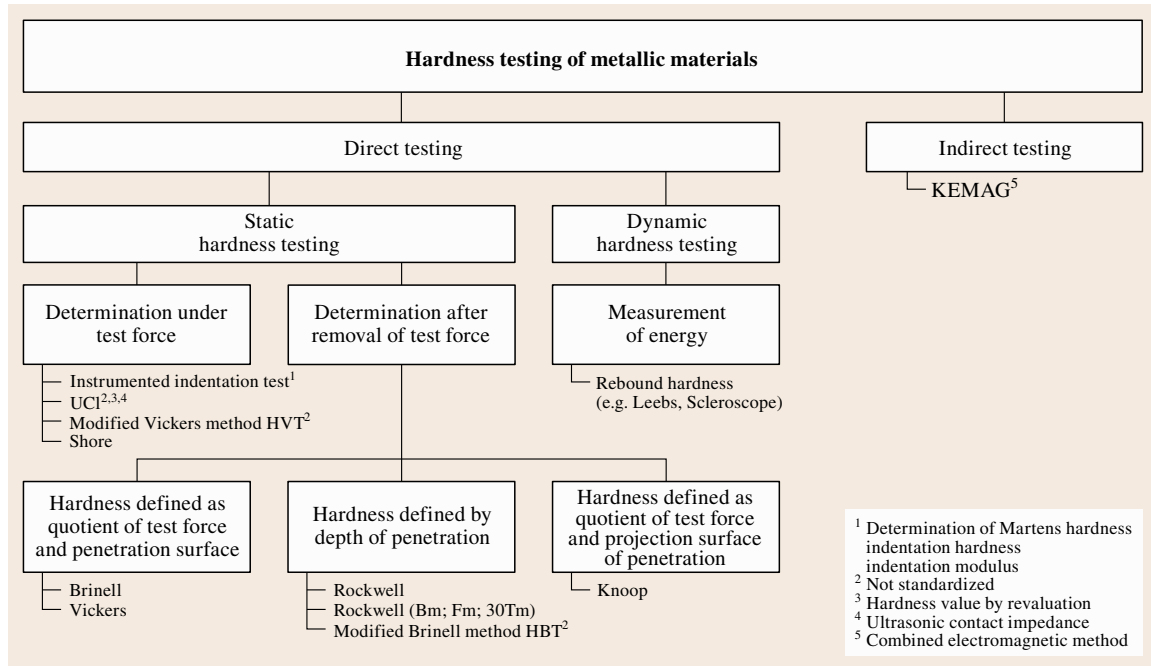
7.3 Hardness

Hardness may be defined as the resistance of a material to permanent penetration by another material. A hardness test is generally conducted to determine the suitability of a material to fulfill a certain pur-

pose [7.164]. Conventional types of static indentation hardness tests, such as the Brinell, Vickers, Rockwell, and Knoop hardness, provide a single hardness number as the result, which is most useful as it correlates to

Table 7.5 First publications of hardness testing standards in different countries

Test method	Germany	UK	USA	France	ISO	Europe
Brinell (1900)	1942	1937	1924	1946	1981	1955
Rockwell (1919)	1942	1940	1932	1946	1986	1955
Vickers (1925)	1940	1931	1952	1946	1982	1955
Knoop (1939)			1969		1993	


Fig. 7.26 Overview of the hardness testing methods (after [7.165])

other properties of the material, such as strength, wear resistance, and ductility. The correlation of hardness to other physical properties has made it a common tool for industrial quality control, acceptance testing, and selection of materials.

With the rising interest in the testing of thin coatings and in order to obtain more information from an indentation test, the instrumented indentation tests have been developed and standardized. In addition to obtaining conventional hardness values, the instrumented indentation tests can also determine other material parameters such as Martens hardness, indentation hardness, indentation modulus, indentation creep and indentation relaxation.

Hardness testing is one of the longest used and well-known test methods not only for metallic materials, but for other types of material as well. It has special

importance in the field of mechanical test methods, because it is a relative inexpensive, easy to use and nearly nondestructive method for the characterization of materials and products. In order to work with comparable measured values, standards of hardness testing methods have been developed. This work started in the 1920s (Table 7.5). In some cases, national, regional and international standards specify different requirements; however, it is generally accepted to aim at the complete alignment of hardness standards at all standardization levels [7.166, 167].

Hardness data are test-system dependent and not fundamental metrological values. For this reason, hardness testing needs a combination of certified reference materials (reference blocks) and certified calibration machines to establish and maintain national and worldwide uniform hardness scales. Therefore, all hardness

testing standards related to a specific hardness test include different parts specifying requirements for the

1. Test method
2. Verification and calibration of testing machines
3. Calibration of reference blocks.

An overview of the different well-known conventional methods of hardness testing is given in Fig. 7.26.

7.3.1 Conventional Hardness Test Methods (Brinell, Rockwell, Vickers and Knoop)

The most commonly used indentation hardness tests used today are the Brinell, Rockwell, Vickers, and Knoop methods. Beginning with the introduction of the Brinell hardness test in 1900, these methods were developed over the next four decades, each bringing an improvement to testing applications. The Rockwell method greatly increased the speed of testing for industry, the Vickers method provided a continuous hardness scale from the softest to hardest metals, and the Knoop method provided greater measurement sensitivity at the lowest test forces. Since their development, these methods have been improved and their applications expanded, particularly in the cases of the Brinell and Rockwell methods.

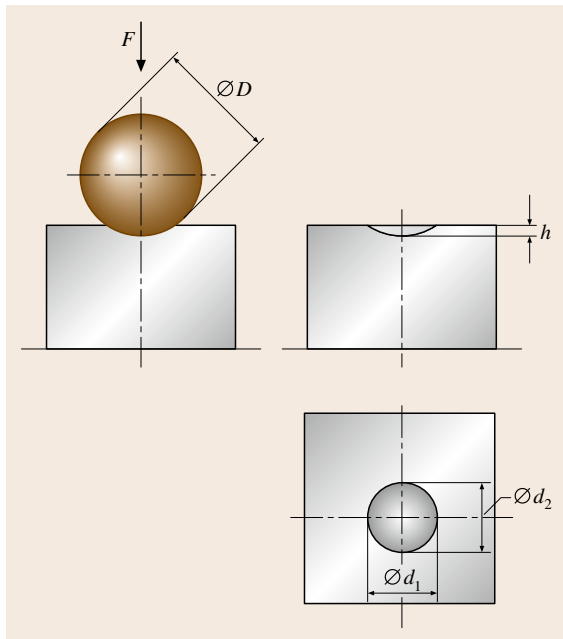


Fig. 7.27 Principle of the Brinell hardness test

Many manufactured products are made of different types of materials, varying in hardness, strength, size and thickness. To accommodate the testing of these diverse products, each conventional hardness method has defined a range of standard force levels to be used in conjunction with several different types of indenters. Each combination of indenter type and applied force level has been designated as a distinct hardness scale of the specific hardness test method.

Brinell Hardness Test (HBW)

Principle of the Brinell Hardness Test [7.168, 169].

An indenter (hardmetal ball with diameter D) is forced into the surface of a test piece and the diameter of the indentation d left in the surface after removal of the force F is measured (Fig. 7.27). The Brinell hardness is proportional to the quotient obtained by dividing the test force by the curved surface area of the indentation. The indentation is assumed to be spherical with a radius corresponding to half of the diameter of the ball

$$\begin{aligned} \text{Brinell hardness HBW} &= \text{Constant} \times \frac{\text{Test force}}{\text{Surface area of indentation}} \\ &= 0.102 \times \frac{2F}{\pi D(D - \sqrt{D^2 - d^2})}, \end{aligned} \quad (7.24)$$

where F is in N and D and d are in mm.

Designation of the Brinell Hardness Test. The Brinell hardness is denoted by **HBW** followed by numbers representing the ball diameter, applied test force, and the duration time of the test force. Note that, in former standards, in cases when a steel ball had been used, the Brinell hardness was denoted by **HB** or **HBS**.

Example. 600 HBW 1/30/20

600 Brinell hardness value

HBW Brinell hardness symbol

1/ Ball diameter in mm

30 Applied test force (294.2 N \cong 30 kgf)

/20 Duration time of test force (20 s) if not indicated in the designation (10–15 s)

Application of the Brinell Hardness Test. For the application of the Brinell hardness test, the most commonly used Brinell scales for different testing conditions are given in Table 7.6. Other combinations of test forces and ball sizes are allowed, usually by special agreement.

Table 7.6 Standard test forces for the different testing conditions

Hardness symbol	Ball diameter D (mm)	Force : diameter ratio $0.102F/D^2$ (N/mm ²)	Nominal value of test force F (kN)
HBW 10/3000	10	30	29.42
HBW 10/1500	10	15	14.71
HBW 10/1000	10	10	9.807
HBW 10/500	10	5	4.903
HBW 10/250	10	2.5	2.452
HBW 10/100	10	1	0.9807
HBW 5/750	5	30	7.355
HBW 5/250	5	10	2.452
HBW 5/125	5	5	1.226
HBW 5/62.5	5	2.5	0.6129
HBW 5/25	5	1	0.2452
HBW 2.5/187.5	2.5	30	1.839
HBW 2.5/62.5	2.5	10	0.6129
HBW 2.5/31.25	2.5	5	0.3065
HBW 2.5/15.62	2.5	2.5	0.1532
HBW 2.5/6.25	2.5	1	0.06129
HBW 1/30	1	30	0.2942
HBW 1/10	1	10	0.09807
HBW 1/5	1	5	0.04903
HBW 1/2, 5	1	2.5	0.02452
HBW 1/1	1	1	0.009807

Advantages of the Brinell Hardness Test.

- Suitable for hardness tests even under rough workshop conditions if large ball indenters and high test forces are used.
- Suitable for hardness tests on inhomogeneous materials because of the large test indentations, provided that the extent of the inhomogeneity is small in comparison to the test indentation.
- Suitable for hardness tests on large blanks such as forged pieces, castings, hot-rolled or hot-pressed and heat-treated components.
- Relatively little surface preparation is required if large ball indenters and high test forces are used.
- Measurement is usually not affected by movement of the specimen in the direction in which the test force is acting.
- Simple, robust and low-cost indenters.

Disadvantages of the Brinell Hardness Test.

- Restriction of application range to a maximum Brinell hardness of 650 HBW.
- Restriction when testing small and thin-walled specimens.

- Relatively long test time due to the measurement of the indentation diameter.
- Relatively serious damage to the specimen due to the large test indentation.
- Measurement of many indentations can lead to operator fatigue and increased measurement error.

Rockwell Hardness Test (HR)

Principle of the Rockwell Hardness Test [7.170, 171]. The general Rockwell test procedure is the same regardless of the Rockwell scale or indenter being used. The indenter is brought into contact with the material to be tested and a preliminary force is applied to the indenter. The preliminary force is held constant for a specified time duration, after which the depth of indentation is measured. An additional force is then applied at a specified rate to increase the applied force to the total force level. The total force is held constant for a specified time duration, after which the additional force is removed, returning to the preliminary force level. After holding the preliminary force constant for a specified time duration, the depth of indentation is measured for a second time, followed by removal of the indenter from

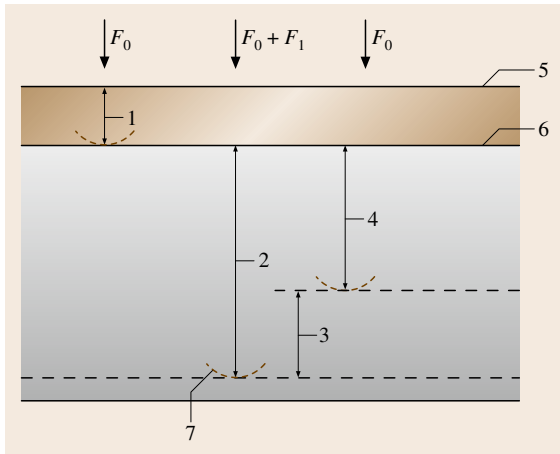


Fig. 7.28 Rockwell principle diagram (Key: 1 – Indentation depth by preliminary force F_0 ; 2 – Indentation depth by additional test force F_1 ; 3 – Elastic recovery just after removal of additional test force F_1 ; 4 – Permanent indentation depth h ; 5 – Surface of test piece; 6 – Reference plane for measurement; 7 – Position of indenter)

the test material (Fig. 7.28). The difference in the two depth measurements is calculated as h in mm. From the value of h and the two constant numbers N and S (Table 7.7), the Rockwell hardness is calculated following the formula

$$\text{Rockwell hardness} = N - \frac{h}{S}. \quad (7.25)$$

Designation of the Rockwell Hardness Test. The Rockwell hardness is denoted by the symbol **HR**, followed by a letter indicating the scale, and either an S or W to indicate the type of ball used (S = steel; W = hardmetal, tungsten carbide alloy) (Table 7.7).

Example. 70 HR 30N W

70 Rockwell hardness value

HR Rockwell hardness symbol

30N Rockwell scale symbol (Table 7.7)

W Indication of type of ball used, S = steel, W = hardmetal

Application of the Rockwell Hardness Test. For the application of the Rockwell hardness test, the indenter types and specified test forces, as well as, typical applications for the different scales are given in Table 7.7.

ASTM International defines thirty different Rockwell scales [7.170] while the **ISO** [7.171] defines a subset of these scales (Table 7.7).

Advantages of the Rockwell Hardness Test.

- Relatively short test time because the hardness value is automatically displayed immediately following the indentation process.
- The test may be automated.
- Relatively low procurement costs for the testing machine because no optical measuring device is necessary.
- No operator influence of evaluation because the hardness value is displayed directly.
- Relatively short time needed to train operator.

Disadvantages of the Rockwell Hardness Test.

- Possibility of measurement errors due to movement of the test piece and poorly seated or worn machine components during the application of the test forces.
- Less possibility of testing materials with surface layer hardening as a consequence of relatively high test forces.
- Sensitivity of the diamond indenter to damage, thus producing a risk of incorrect measurements
- Relatively low sensitivity on the difference in hardness.
- Significant influence of the shape of the conical diamond indenter on the test result (especially of the tip).

Vickers Hardness Test (HV)

Principle of the Vickers Hardness Test [7.172–174]. A diamond indenter in the form of a right pyramid with a square base and with a specified angle between opposite faces at the vertex is forced into the surface of a test piece followed by measurement of the diagonal length of the indentation left in the surface after removal of the test force F (Fig. 7.29).

Designation of the Vickers Hardness Test. The Vickers hardness is denoted by the symbol **HV** followed by numbers representing the applied test force, and the duration time of the test force.

Example. 640 HV 30/20

640 Vickers hardness value

HV Hardness symbol

30 Applied test force (294.2 N $\hat{=}$ 30 kgf)

/20 Duration time of test force (20 s) if not indicated in the designation (10–15 s)

Application of the Vickers Hardness Test. **ISO** [7.174] specifies the method of Vickers hardness test for the three different ranges of test force for metallic mater-

Table 7.7 Rockwell hardness scales and typical applications [7.175]

Scale symbol	Indenter type (ball dimensions indicate diameter)	Preliminary force (N)	Total force (N)	Typical applications	HR calculation	
					N	S
HRA	Spheroconical diamond	98.07	588.4	Cemented carbides, thin steel, and shallow case hardened steel	100	0.002
HRB	Ball – 1.588 mm	98.07	980.7	Copper alloys, soft steels, aluminum alloys, malleable iron, etc.	130	0.002
HRC	Spheroconical diamond	98.07	1471	Steel, hard cast irons, pearlitic malleable iron, titanium, deep case hardened steel, and other materials harder than HRB 100	100	0.002
HRD	Spheroconical diamond	98.07	980.7	Thin steel and medium case hardened steel, and pearlitic malleable iron	100	0.002
HRE	Ball – 3.175 mm	98.07	980.7	Cast iron, aluminum and magnesium alloys, and bearing metals	130	0.002
HRF	Ball – 1.588 mm	98.07	588.4	Annealed copper alloys, and thin soft sheet metals	130	0.002
HRG	Ball – 1.588 mm	98.07	1471	Malleable irons, copper-nickel-zinc and cupro-nickel alloys	130	0.002
HRH	Ball – 3.175 mm	98.07	588.4	Aluminum, zinc, and lead	130	0.002
HRK	Ball – 3.175 mm	98.07	1471	Bearing metals and other very soft or thin materials, use smallest ball and heaviest load that does not give anvil effect	130	0.002
HRL ^a	Ball – 6.350 mm	98.07	588.4		130	0.002
HRM ^a	Ball – 6.350 mm	98.07	980.7		130	0.002
HRP ^a	Ball – 6.350 mm	98.07	1471		130	0.002
HRR ^a	Ball – 12.70 mm	98.07	588.4		130	0.002
HRS ^a	Ball – 12.70 mm	98.07	980.7		130	0.002
HRV ^a	Ball – 12.70 mm	98.07	1471		130	0.002
HR15N	Spheroconical diamond	29.42	147.1		Similar to A, C and D scales, but for thinner gage material or case depth	100
HR30N	Spheroconical diamond	29.42	294.2	100		0.001
HR45N	Spheroconical diamond	29.42	441.3	100		0.001
HR15T	Ball – 1.588 mm	29.42	147.1	Similar to B, F and G scales, but for thinner gage material	100	0.001
HR30T	Ball – 1.588 mm	29.42	294.2		100	0.001
HR45T	Ball – 1.588 mm	29.42	441.3		100	0.001
HR15W ^a	Ball – 3.175 mm	29.42	147.1	Very soft material	100	0.001
HR30W ^a	Ball – 3.175 mm	29.42	294.2		100	0.001
HR45W ^a	Ball – 3.175 mm	29.42	441.3		100	0.001
HR15X ^a	Ball – 6.350 mm	29.42	147.1		100	0.001
HR30X ^a	Ball – 6.350 mm	29.42	294.2		100	0.001
HR45X ^a	Ball – 6.350 mm	29.42	441.3		100	0.001
HR15Y ^a	Ball – 12.70 mm	29.42	147.1		100	0.001
HR30Y ^a	Ball – 12.70 mm	29.42	294.2		100	0.001
HR45Y ^a	Ball – 12.70 mm	29.42	441.3		100	0.001

^a These scales are defined by ASTM International, but are not included in the ISO standards

ials, whereas ASTM International [7.172, 173] divides the Vickers test into two ranges (Table 7.8).

The Vickers hardness test is specified in ISO to apply to lengths of indentation diagonals of

0.020–1.400 mm, whereas ASTM International [7.173] allows indentation diagonals below 0.020 mm.

Although, for the application of the Vickers hardness test, any force level is allowed between the

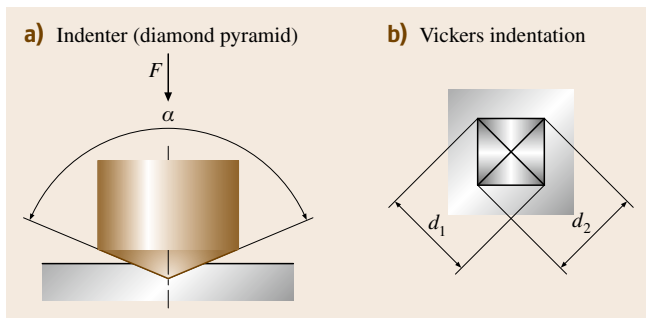


Fig. 7.29a,b Principle of the Vickers hardness test

specified limits, traditionally used and recommended test forces for different testing conditions are given in Table 7.9.

Table 7.8 Ranges of Vickers hardness tests

ISO		
Vickers range (ISO 6507-1)	Nominal ranges of test force, F (N)	Hardness range
Vickers hardness	$F \geq 49.03$	$\geq \text{HV } 5$
Low force Vickers hardness	$1.961 \leq F < 49.03$	$\text{HV } 0.2$ to $\text{HV } 5$
Vickers microhardness	$0.09807 \leq F < 1.961$	$\text{HV } 0.01$ to $\text{HV } 0.2$

ASTM International		
Vickers range	Nominal ranges of test force F (N)	Hardness range
Vickers hardness (ASTM E 92)	$9.807 \leq F < 1177$	$\text{HV } 1$ to $\text{HV } 120$
Vickers micro-indentation hardness (ASTM E 384)	$0.0098 \leq F < 9.807$	$\text{HV } 0.001$ to $\text{HV } 1$

Table 7.9 Recommended test forces

Hardness test ^a		Low-force hardness test		Microhardness test	
Hardness symbol	Nominal value of the test force F (N)	Hardness symbol	Nominal value of the test force F (N)	Hardness symbol	Nominal value of the test force F (N)
HV 5	49.03	HV 0.2	1.961	HV 0.01	0.09807
HV 10	98.07	HV 0.3	2.942	HV 0.015	0.147
HV 20	196.1	HV 0.5	4.903	HV 0.02	0.1961
HV 30	294.2	HV 1	9.807	HV 0.025	0.2452
HV 50	490.3	HV 2	19.61	HV 0.05	0.4903
HV 100	980.7	HV 3	29.42	HV 0.1	0.9807

^a Nominal test forces greater than 980.7 N may be applied

Advantages of the Vickers Hardness Test.

- Practically no limit to the use of the method due to the hardness of the test piece.
- Testing thin sheets, small test pieces or test surfaces, thin-walled tubes, thin, hard and plated coatings is possible.
- In most cases, the small indentation has no influence on the function or appearance of tested materials or products.
- The hardness value is usually independent of the test force in the range of HV 0.2 and above.
- No incorrect measurement if the test piece yields to a limited extent in the direction of the test force.
- Can be reported in terms of stress values.

Disadvantages of the Vickers Hardness Test.

- High effort in preparing a suitable test surface.
- Relatively long test time due to the measurement of the diagonal lengths.
- Sensitivity of the diamond indenter to damage.
- If the test indentations are small, dependence of the hardness on the shape deviations of the indenter and the preparation of the test surfaces.
- Very sensitive to effects of vibration, especially in the microhardness range.
- Relatively large variation in measurement depending on the operator of microscope. Especially for low force hardness testing.

For the application of the Vickers hardness test for the different ranges of test force see [7.176–179].

Knoop Hardness Test (HK)

Principle of the Knoop Hardness Test [7.173, 180]. A diamond indenter, in the form of a rhombic-based pyramid with specified angles between opposite faces at the vertex, is forced into the surface of a test piece followed by measurement of the long diagonal of the in-

dentation remaining in the surface after removal of the test force F (Figs. 7.30, 7.31, Table 7.10).

The Knoop hardness is proportional to the quotient obtained by dividing the test force by the projected area of the indentation, which is assumed to be a rhombic-based pyramid, and having at the vertex the same angles as the indenter.

Designation of the Knoop Hardness. The Knoop hardness is denoted by the symbol **HK** followed by numbers representing the applied test force, and the duration time of the test force.

Example. 640 HK 0.1/20

640 Knoop hardness value

HK Hardness symbol

0.1 Applied test force (0.9807 N \cong 0.1 kgf)

/20 Duration time of test force (20 s) if not indicated in the designation (10–15 s)

Application of the Knoop Hardness Test. For the application of the Knoop hardness test, traditionally used and recommended test forces for different testing conditions are given in Table 7.11.

Advantages of the Knoop Hardness Test.

- Particularly suitable for narrow test pieces, such as wire, due to the large diagonal length ratio of approximately 7 : 1.
- Better suited to thin test pieces or platings than the Vickers test method because the indentation depth is smaller by a factor of four for the same diagonal length.

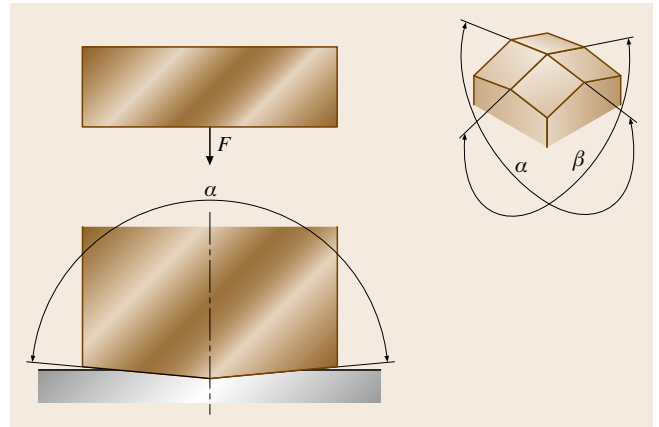


Fig. 7.30 Symbols and designations for the Knoop hardness test

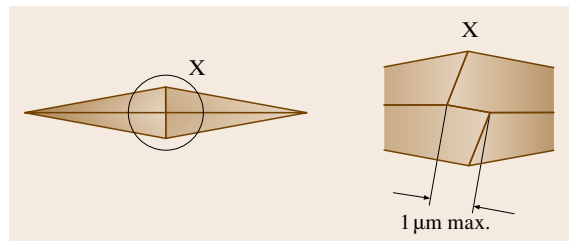


Fig. 7.31 Symbols and designations for the Knoop hardness test

- Particularly suitable for brittle materials because of lower tendency to cracking.
- Particularly suited to investigating the anisotropy of a material because the Knoop test is dependent on

Table 7.10 Symbols and designations for the Knoop hardness test

Symbol	Designation
F	Test force (N)
d	Length of the long diagonal (mm)
c	Indenter constant, relating projected area of the indentation to the square of the length of the long diagonal Indenter constant, $c = \frac{\tan \frac{\beta}{2}}{2 \tan \frac{\alpha}{2}}$, ideally $c = 0.07028$, where α and β are the angles between the opposite edges at the vertex of the diamond pyramid (Fig. 7.30)
HK	Knoop hardness = Gravitational constant ^a $\times \frac{\text{Test force}}{\text{Projected area of indentation}}$ $= 0.102 \times \frac{F}{cd^2} = 1.451 \frac{F}{d^2}$

^a: Gravitational constant = $\frac{1}{g_n} = \frac{1}{9.80665} \approx 0.102$, where g_n is the acceleration of gravity

Table 7.11 Recommended test forces

Hardness Symbol	Nominal value of the test force F (N)
HK 0.01	0.09807
HK 0.02	0.1961
HK 0.025	0.2452
HK 0.05	0.4903
HK 0.1	0.9807
HK 0.2	1.961
HK 0.3	2.942
HK 0.5	4.903
HK 1	9.807

the direction selected for the long diagonal in such cases.

- In most cases, the small indentation has no influence on the function or appearance of tested materials or products.
- Practically no limit on the application of the method from the hardness of the material tested.

Disadvantages of the Knoop Hardness Test.

- Time effort to achieve a sufficiently fine test surface.
- Considerable dependency of the hardness on the test force, with an especially strong influence of the preparation of the test surface.
- Sensitivity to damage of the diamond indenter.
- Expensive alignment of the test surface to achieve symmetrical test indentations.
- Relatively long test time due to the measurement of the diagonal length.
- Measurement of the diagonal length is more difficult than in the Vickers test method as a consequence of the indenter geometry.

7.3.2 Selecting a Conventional Hardness Test Method and Hardness Scale

The selection of a specific hardness testing method is substantially influenced by many factors as discussed below. Unfortunately, there is no one hardness test that meets the optimum conditions for all applications. Although the Brinell, Rockwell, Vickers and Knoop hardness testing methods have been developed to be capable of testing most materials, in many testing circumstances the size or depth of the indentation is generally the primary consideration when choosing the appropriate test forces and type of indenter to be utilized by the hardness test method. The combinations of test forces and indenter types are known as a hardness

method's specific hardness scales. The hardness scales have been defined to provide suitable measurement sensitivity and indentation depths that are appropriate for different materials, strengths and dimensions of test pieces. The largest and deepest indentations are generally obtained from the heavy-force Brinell scales, followed by the commonly used heavy-force Rockwell and Vickers scales, while small to extremely small indentations can be obtained from the commonly used lower-force Rockwell, Vickers and Knoop scales.

Strength of the Test Piece

A material's resistance to penetration or its strength is of primary importance when selecting a hardness method or hardness scale. An appropriate test force and indenter must be chosen to produce a large enough indentation in the test material to enable the hardness testing machine's measuring system to resolve and measure the depth or size of the indentation with sufficient sensitivity to produce a meaningful hardness result, but at the same time to not penetrate too deeply beyond the indenter's useful depth. On the other hand, a suitable indenter of the appropriate material, size and shape must be chosen to prevent the indenter from being damaged when testing high-strength materials. For example, hardened and tempered steel material generally requires hardness methods that employ higher test forces and a pointed or conical diamond indenter, whereas testing cemented carbides with high forces could lead to the diamond being fractured.

Test-Piece Size, Shape, Weight, Accessibility, Dimensions, and Thickness

The choice of a hardness test method may be influenced by the size, shape or weight of the test piece. The designs of some typical standard hardness testing machines may prevent the testing of very large and heavy test pieces or unusually shaped test pieces, and may require special machine designs, special designs of indenters or additional test piece support fixtures. These types of designs are usually limited to the Brinell, Rockwell and heavy-force Vickers machines. In contrast, small sample sizes may require mounting in a support material which is generally only suitable for the Knoop and low-force Vickers hardness methods.

The dimensions of the test piece may also have to be considered for another reason. As a hardness measurement is being made, the material surrounding the indentation is plastically deformed, with the deformation extending well to the sides and below the indentation. If a hardness measurement is made too near the edge of the

test material, the deformation surrounding the indentation may extend to the edge and push out the material, thus affecting the measured hardness value. Similarly, if the deformation extends completely through the thickness of thin test material, then the deformed material may flow at the interface with the supporting anvil, or the anvil material may contribute to the hardness measurement. These problems can influence the deformation process likely causing the test to give erroneous hardness results. Consequently, in cases where a hardness test is to be made on narrow-width or thin material or material having a small area, an appropriate hardness test and scale must be chosen that produces indentations small enough to prevent this edge interaction. Also keep in mind that the area surrounding a previously made indentation may also affect a new hardness test due to induced residual stress and areas of workhardening surrounding the indentation. Therefore, the number of indentations that will be made must be taken into consideration when small test areas are involved.

Material Composition and Homogeneity

The size and location of metallurgical features within the test material should be considered when choosing the hardness test method and hardness scale. For materials that are not homogeneous, an appropriate hardness test and scale should be chosen that will produce a sufficiently large indentation representative of the material as a whole. For example, forgings and cast iron are typically tested using the Brinell method. If the subject of interest is a material artifact, such as a decarburization zone or a thin material layer, then a hardness test and scale should be chosen that produces a small or shallow indentation. In an analogous way to the issues of test-piece size, the closeness to adjacent regions of a differing hardness, such as the heat-affected zone of a weld, should also be considered. If the deformation zone surrounding an indentation extends into these regions, the test measurement may be influenced. In such cases, an appropriate hardness test and scale should be chosen that uses test forces and indenter that produce a small enough indentation to avoid the influence of these areas.

Permissible Damage

One of the greatest attributes of a hardness test is that it is essentially a nondestructive test, leaving only a small indentation which usually does not detract from a product's function or appearance. However, there are some applications for which a hardness indentation of a certain size could be detrimental to a product's service or appearance. For example, it is possible that an inden-

tation could act as an initiation point for a fracture in a part subjected to cyclic loading, or a large visible indentation could affect the appearance of a product. In these cases, smaller indentations may be the solution.

Test Surface Preparation

When the ability to prepare the testing surface is not possible or practical or is limited, a hardness method and hardness scale must be chosen that is less sensitive to the level of surface preparation. The degree of surface roughness that can be tolerated by the different hardness testing methods is generally dependent on the force levels to be applied, indenter size and resultant indentation size. In general, the larger the indentation size and depth, the less sensitive is the hardness test to the level of surface roughness and imperfections, and the more likely the measurement will represent the true hardness value of a material. This is particularly true for the Brinell, Vickers and Knoop methods because of the need to accurately resolve and measure the resultant indentation. The larger the sizes of surface anomalies with respect to the indentation size, the more likely it becomes that errors in the indentation measurement and the hardness result will increase.

An important feature of the Rockwell test method, which bases the hardness result on depth measurement rather than indentation size, is the use of the preliminary force as part of the testing cycle. Application of the preliminary force acts to push the indenter through minor surface imperfections and to crush residual foreign particles present on the test surface. By establishing a reference beneath the surface prior to making the first depth measurement, it allows testing of materials with slight surface flaws while maintaining much of the test accuracy.

As a general guide, the high-force scales of the Brinell test method requires the least surface preparation, such as a surface that has been filed, ground, machined or polished with no. 000 emery paper. Material tested by the Rockwell test method usually does not need to be polished, but should be smooth, clean and free of scale. The Brinell test method and the heavy-force Vickers scales producing small indentations are likely to require polished surfaces to allow accurate measurement of the indentation sizes.

Permissible Measurement Uncertainty

The measurement uncertainty of a hardness test is influenced by many factors, including, among others, the operator, the machine's repeatability and reproducibility, and the testing environment (Sect. 7.3.3). With

respect to choosing a hardness test method, the number of different operators that would potentially use the hardness machine should be considered. Two of the larger sources of hardness measurement error are related to the operator's measurement of an indentation, such as is the case for Brinell, Vickers and Knoop methods, and the operation of manually controlled hardness testers. The variability between operators contributes to the measurement uncertainty by increasing the lack of repeatability and reproducibility in the measurement system. If a low measurement uncertainty is of high concern, then it may be beneficial to use automatically controlled hardness machines or automated indentation measuring systems, or to use the Rockwell hardness method, which lessens the influence of the operator by basing the hardness result on indentation depth as measured by the machine.

Speed of Testing Desired

For many industrial processes, time is one of the most important parameters. In circumstances where hardness testing is an integral part of a process and many tests must be performed, the time required to complete each test becomes an extremely important consideration. For a hardness test, the time required for each step of a measurement must be considered from the preparation of the test piece, to the indentation process, to the measurements needed to determine the hardness result, and finally to the calculation of the hardness value. The Brinell, Vickers and Knoop methods are two-step processes: (1) the indentation process, followed by (2) measurement of the indentation. The Rockwell hardness method was specifically designed to reduce the time needed for a hardness test by eliminating the second step of having to measure the size of the indent after the indentation process. The Rockwell hardness method quickly and automatically calculates and displays the hardness result based on the machine's measurement of indentation depth. Instrumented indentation testing is likely to take the longest time to complete due to the care and time required for preparing the test sample, running the indentation cycle, and analyzing the data.

Economic Viability and the Availability of Machines and Equipment

Other nontechnical but nevertheless important considerations in choosing a hardness method are the economics and practicality of the selection. Economic limitations often drive the choice of which hardness method is chosen for use. It may be a difficult choice in weighing the benefits of the best hardness method for an appli-

cation against its cost. This may be particularly true when existing hardness equipment currently exists in-house. Finally, the volume of testing and the necessary training of operators should be taken into account when selecting a test.

Guidance on selecting hardness test methods is given in international hardness test method standards, such as those published by ISO and ASTM International. When several hardness methods are acceptable for testing a material, generally, the most commonly used method for the type of material or product should be chosen. In circumstances where the user wants to compare measurements with previously obtained hardness data, the same hardness test method and scale should be chosen as was used for the previous testing as long as a valid test can be obtained. This is preferred to testing with one hardness test method and scale and then converting the data to another hardness scale by way of published conversion tables. Converted data is never as accurate as the original measurement. This also holds true when the hardness method and scale is specified in a product specification or contract. The specified hardness method or scale should be used whenever possible as long as a valid test can be obtained.

7.3.3 Measurement Uncertainty in Hardness Testing (HR, HBW, HV, HK)

The concept of measurement uncertainty is relatively new to users of hardness testing, particularly as applied to the conventional hardness tests, Rockwell, Brinell, Vickers and Knoop. Historically, industry has relied on limiting hardness measurement error by adhering to error tolerances specified by national and international hardness test method standards. Test method standards specify tolerances for components of the hardness machine, such as the allowed error when applying the test forces and the error in measuring the indentation size or penetration depth. Tolerances are also specified for the performance of the hardness machine limiting the machine's measurement error with respect to the certified values of hardness block reference standards.

Hardness measurement uncertainty is very different from the tolerances specified by test method standards. Uncertainty does not limit measurement error. It provides an estimation of the error in a hardness measurement value with respect to the true hardness of the tested material. In recent years, with the advent of accreditation programs for testing and calibration laboratories, measurement uncertainty has gained increasing importance for hardness laboratories since most accred-

itation programs require a laboratory to determine their own measurement uncertainty.

Estimating Hardness Uncertainty – Direct Approach

The Guide to the Expression of Uncertainty in Measurement (GUM) [7.181] provides guidance for estimating the uncertainty in a measurement value. One procedure is a direct approach to quantify the significant influence quantities of the test (for example: force error, test speed, indenter shape, etc.), determine the biases and uncertainties of each influence quantity, correct for the biases, determine and evaluate sensitivity coefficients to convert from the units of the input quantity to the units of the measurand, and finally combine the uncertainties to provide an overall uncertainty in the resultant measurement value.

A hardness test involves the time-dependent application of forces to specifically shaped indenters, and, for some types of harness tests, simultaneously measuring the resultant indentation depths. This is done using machines that can range from entirely mechanical to various combinations of electronic and mechanical components. As a result, it is often difficult to identify all of the significant influence quantities that contribute to the measurement uncertainty. For example, error sources may exist due to the internal workings of the mechanical components of the hardness machine or the indenter, which are not easily measurable. Complicating this, the determination of some sensitivity coefficients is a lengthy and difficult undertaking since these conversion factors may be dependent on the hardness scale and the material being tested which can only be determined by experimental testing. An additional complication is that the accepted practice for calibrating a hardness machine is to not correct for biases in the operational components of the machine as long as they are within the specified tolerance limits.

Although this technique of assessing the separate parameters of the hardness testing machine for their individual error contributions is an effective method for determining hardness measurement uncertainty, it may be best applied at the highest calibration levels, such as by National Metrology Institutes, which have the time and resources to assess each of the sources of error. However, it may present an overwhelming challenge to many industrial hardness laboratories using the conventional hardness tests. Detailed procedures for calculating uncertainty by this method are too involved to be described here; however, recommended procedures have been published as a document of the

European Cooperation for Accreditation of Laboratories (EAL) [7.182].

Estimating Hardness Uncertainty – Indirect Approach

A second procedure for determining hardness uncertainty is an indirect approach based on familiar procedures and practices of hardness testing facilities and laboratories. Most of the contributions of uncertainty can be estimated from the results of hardness tests on reference materials and the material under test. Hardness reference materials provide traceability to the national hardness standards maintained by the world's National Metrology Institutes (NMIs) and are necessary to establish a starting point for the uncertainty analysis as per the GUM. In some cases, where reference materials are not available from a NMI, suitable reference materials may be obtained from a secondary reference source.

This indirect approach views the hardness machine and indenter as a single measuring device, and considers uncertainties associated with the overall measurement performance of the hardness machine. It may be more applicable for industrial laboratories in determining the measurement uncertainty for the conventional types of hardness tests. It is important to understand that this procedure is appropriate only when a hardness machine is operating within all operational and performance tolerances to ensure that a large error in one machine component is not being offset by another large, but opposite, error in a second component. These opposite errors could then combine to produce satisfactory hardness results when testing reference blocks even when the machine is not operating properly.

This approach considers uncertainties due to the lack of repeatability of the hardness machine, the reproducibility of the hardness measurement over time, the resolution of the hardness machine display or indentation measuring instrument, the nonuniformity of the material under test, the uncertainty of the certified value of the reference standards, and the measurement bias as compared to reference standards.

- The repeatability of the hardness machine is its ability to continually produce the same hardness value each time a measurement is made over a short time period and under constant testing conditions, including the same operator. All testing instruments, including hardness machines, exhibit some degree of a lack of repeatability.

- The reproducibility of a hardness machine can be thought of as how well the hardness values agree under changing testing conditions. Influences such as different machine operators and changes in the test environment often affect the performance of a hardness machine.
- The finite resolution of devices that display the hardness value or that measure the size of indentations prevents the determination of an absolutely accurate hardness value. Devices such as a dial display on a Rockwell hardness machine or a portable handscope for measuring Brinell hardness indents may have a low resolution which can contribute a significant level of uncertainty to the hardness value.
- When reported measurement values are based on the average of multiple hardness tests, the nonuniformity of the material under test contributes a component of uncertainty in the hardness value, such as would occur in the calibration of a reference block.
- Reference test blocks provide the link to the hardness standard to which traceability is claimed. All reference hardness blocks should have a reported uncertainty in the certified hardness value. This uncertainty contributes to the measurement uncertainty of hardness machines calibrated or verified with the reference test blocks.

The general approach of this procedure is to calculate a combined standard uncertainty u_c by combining the contributing components of uncertainty u_1, u_2, \dots, u_n , for the applicable sources of error discussed above, such that

$$u_c = \sqrt{u_1^2 + u_2^2 + \dots + u_n^2} . \quad (7.26)$$

The appropriate contributing components of uncertainty to combine for this calculation are dependent on what the uncertainty value represents. For example, a combined uncertainty may be calculated for a single hardness value, an average of multiple hardness values, a hardness machine's error determined as part of an indirect verification, or the certified value resulting from a reference block calibration.

Measurement uncertainty is usually expressed and reported as a combined expanded uncertainty U_c , which is calculated by multiplying the combined standard uncertainty u_c by a numerical coverage factor k , such that

$$U_c = k u_c . \quad (7.27)$$

A coverage factor is chosen that depends on how well the standard uncertainty was estimated (number of measurements), and the level of uncertainty that is desired.

The measurement bias b of the hardness machine is the difference between the expected hardness measurement results and the true hardness of a material. When test systems are not corrected for measurement bias, the bias then contributes to the overall uncertainty in a measurement. Ideally, measurement biases should be corrected; however, in practice, this is commonly not done for traditional types of hardness tests. There are a number of possible methods for incorporating uncorrected biases into an uncertainty calculation, each of which has both advantages and disadvantages. A simple and conservative method is to combine the bias with the expanded uncertainty as

$$U = k u_c + |b| , \quad (7.28)$$

where $|b|$ is the absolute value of the bias.

Discussions of the calculations for each of the uncertainty components, which uncertainty components should be combined, and how they should be combined for all types of hardness measurements are too involved to be described in detail here. Guidance on this approach can be found in newly developed recommended procedures recently added to the international hardness test method standards of ISO and ASTM for the specific conventional hardness tests.

Reporting Uncertainty

Ideally, an individual measurement uncertainty should be determined for each hardness scale and hardness level of interest since the contributing components of uncertainty may vary depending on the scale and hardness level. In practice, this may not be practical. In many cases, a single uncertainty value may be applied to a range of hardness levels based on the laboratory's experience and knowledge of the operation of the hardness machine. Also, because several approaches may be used to evaluate and express measurement uncertainty, a brief description of what the reported uncertainty value represents should be included with the reported uncertainty value.

7.3.4 Instrumented Indentation Test (IIT)

Principle of the Instrumented Indentation Test [7.183]

The continuous monitoring of the force and the depth of indentation can allow the determination of hardness values equivalent to traditional hardness values. More significantly, additional properties of the material, such as its indentation modulus and elasto-plastic hardness, can also be determined. All these values can be calcu-

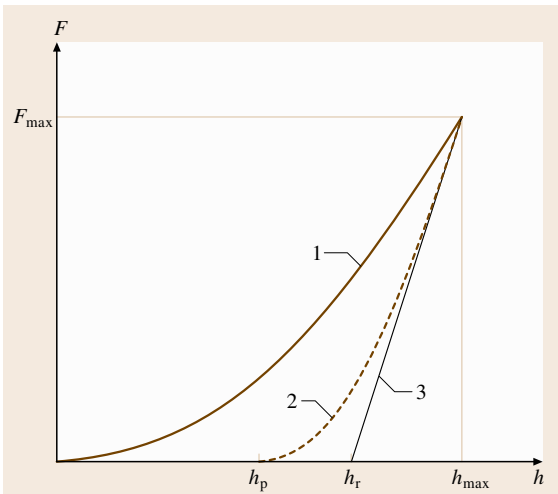


Fig. 7.32 Schematic representation of test procedure (Key: 1 – Application of the test force; 2 – Removal of the test force; 3 – Tangent to curve 2 at F_{\max})

lated without the need to measure the indent optically (Figs. 7.32, 7.33). An indenter consisting of a material harder than the material tested with the following shapes can be used.

1. Diamond indenter shaped as an orthogonal pyramid with a square base and with an angle $\alpha = 136^\circ$ between the opposite faces at the vertex (Vickers pyramid)
2. Diamond pyramid with triangular base (e.g., Berkovich pyramid)
3. Hardmetal ball (especially for the determination of the elastic behavior of materials)
4. Diamond spherical indenter.

For tests at indentation depths of less than $1\ \mu\text{m}$, the mechanical deformation strongly depends on the real shape of indenter tip and the calculated materials parameters are significantly influenced by the contact area function of the indenter used in the testing machine. Therefore careful calibration of both instrument and indenter shape is required in order to achieve an acceptable reproducibility of the material parameters determined with different machines.

At high contact pressures, damage to the indenter is possible. For this reason in the force range higher than 2 N, hardmetal indenters are often used. For test pieces with very high hardness and modulus of elasticity the influence of indenter deformation on test result should be taken into account.

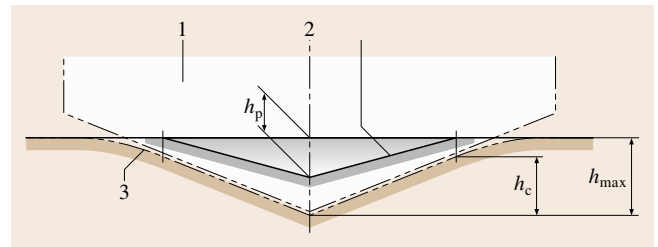


Fig. 7.33 Schematic representation of a cross section through indentation (Key: 1 – Indenter; 2 – Surface of residual plastic indentation in test piece; 3 – Surface of test piece at maximum indentation depth and test force)

The test procedure can either be force-controlled or displacement-controlled. The test force F , the corresponding indentation depth h and time are recorded during the whole test procedure. The result of the test is the data set of the test force and the relevant indentation depth as a function of time (Fig. 7.32). For a reproducible determination of the force and corresponding indentation depth, the zero point for the force/indentation depth measurement must be assigned individually for each test.

Where time-dependent effects are being measured

1. using the force-controlled method, the test force is kept constant over a specified period and the change of the indentation depth is measured as a function of the holding time of the test force,
2. using the indentation-depth-controlled method the indentation depth is kept constant over a specified period and the change of the test force is measured as a function of the holding time of the indentation depth.

For references for the application of the instrumented indentation test, see [7.184–202].

Table 7.12 gives the symbols and designations used for the instrumented indentation test.

Table 7.13 gives an overview about the parameters of the instrumented indentation test and additional influence factors on the test result.

Martens Hardness (HM)

Determination of Martens Hardness. Martens hardness is measured under an applied test force. Martens hardness is determined from the values given by the force/indentation depth curve during the increasing of the test force, preferably after reaching the specified test force. Martens hardness includes the plastic and elastic

Table 7.12 Symbols and designations

Symbol	Designation	Unit ^{a,b}
α	Angle, specific to the shape of the pyramidal indenter	°
r	Radius of spherical indenter	mm
F	Test force	N
F_{\max}	Maximum test force	N
h	Indentation depth under applied test force	mm
h_{\max}	Maximum indentation depth at F_{\max}	mm
h_T	Point of intersection of the tangent to curve 2 at F_{\max} with the indentation depth axis (Fig. 7.32)	mm
h_p	Permanent indentation depth after removal of the test force	mm
h_c	Depth of the contact of the indenter with the test piece at F_{\max}	mm
$A_s(h)$	Surface area of the indenter at distance h from the tip	mm ²
$A_p(h_c)$	Projected area of contact of the indenter at distance h_c from the tip	mm ²
HM	Martens hardness	N/mm ²
HM _s	Martens hardness, determined from the slope of the increasing force/indentation depth curve	N/mm ²
H_{IT}	Indentation hardness	N/mm ²
E_{IT}	Indentation modulus	N/mm ²
C_{IT}	Indentation creep	%
R_{IT}	Indentation relaxation	%
W_{total}	Total mechanical work of indentation	Nm
W_{elast}	Elastic reverse deformation work of indentation	Nm
η_{IT}	Relation $W_{\text{elast}}/W_{\text{total}}$	%

^a To avoid very long numbers multiples or sub-multiples of the units may be used

^b 1 N/mm² = 1 MPa

deformation, thus this hardness value can be calculated for all materials.

Martens hardness is defined for both pyramidal indenters. It is not defined for the Knoop indenter or for ball indenters.

Martens hardness is defined as the test force F divided by $A_s(h)$ the surface area of the indenter penetrating beyond the zero point of the contact and is expressed in N/mm².

The relationship between Martens hardness, indentation depth and test force is given in Fig. 7.34.

$$\begin{array}{ll} \text{(a) Vickers indenter} & \text{(b) Berkovich indenter} \\ \text{HM} = \frac{F}{A_s(h)} = \frac{F}{26.43h^2} & \text{HM} = \frac{F}{A_s(h)} = \frac{F}{26.44h^2} \end{array} \quad (7.29)$$

$$\begin{array}{ll} A_s(h) = \frac{4 \sin(\frac{\alpha}{2})}{\cos^2(\frac{\alpha}{2})} h^2 & A_s(h) = \frac{3\sqrt{3} \tan \alpha}{\cos \alpha} h^2 \end{array} \quad (7.30)$$

Designation of the Martens Hardness [7.184]. The Martens hardness is denoted by the symbol HM.

Example. HM 0.5/20/20 = 8700 N/mm²

HM 0.5 Test force in N
/20 Application time of test force in s
/20 Duration time of test force in s
= 8700 N/mm² Hardness value

Indentation Hardness (H_{IT})

Determination of the Indentation Hardness. The indentation hardness H_{IT} is a measure of the resistance to permanent deformation or damage.

$$H_{IT} = \frac{F_{\max}}{A_p}, \quad (7.31)$$

where F_{\max} is the maximum applied force, A_p is the projected (cross-sectional) area of contact between the indenter and the test piece determined from the force–displacement curve and a knowledge of the area function of the indenter, see 4.5.2 of ISO 14577-2.

Equation (7.31) defines hardness as the maximum applied force, divided by the projected (cross-sectional) contact area of the indenter with the test piece. This def-

Table 7.13 Parameters of the instrumented indentation test and additional influence factors on the test result

	Martens hardness HM	Martens hardness HM_s	Indentation hardness H_{IT}	Indentation modul. E_{IT}	Indentation creep C_{IT}	Indentation relax. R_{IT}	Indentation work η_{IT}
Applied test force	×	×	×	×	×		×
Applied indentation depth						×	□
Duration of test force	×		×	×	×	×	×
Application time of test force		×					
Holding time at constant test force			×	×	×		□
Holding time at constant indentation depth						×	□
Time of removal of test force in the curve-fitting range			×	×			□
Material and shape of the indenter	□	□	□	□	□	□	□
Mode of control (test force or indentation depth)	□	□	□	□	□	□	□
Approach speed of the indenter	□		□				□
Speed of application of the test force	□	□	□				□
Speed of application of the indentation depth	□	□	□				□
Position and duration of additional holding periods	□	□	□				□
Temperature	□	□	□	□	□	□	□

× Expressed with the test result
 □ Additional factors that influences the test result

initiation is in accord with that generally agreed and first proposed by *Meyer* [7.185].

For indentation depths $< 6 \mu\text{m}$ the area function of the indenter cannot be assumed to be that of the theoretical shape, since all pointed indenters will have some degree of rounding at the tip and spherically ended indenters (spherical and conical) are unlikely to have a uniform radius. The determination of the exact area function for a given indenter is required for indentation depths $< 6 \mu\text{m}$, but is beneficial for larger indentation depths (see 4.2.1 and 4.6 of ISO 14577-2).

For indentation depths $> 6 \mu\text{m}$ a first approximation to the projected area A_p is given by the theoretical shape of the indenter.

For a perfect Vickers indenter

$$A_p = 24.5h_c^2.$$

For a perfect Berkovich indenter

$$A_p = 23.96h_c^2.$$

For a modified Berkovich indenter

$$A_p = 24.5h_c^2,$$

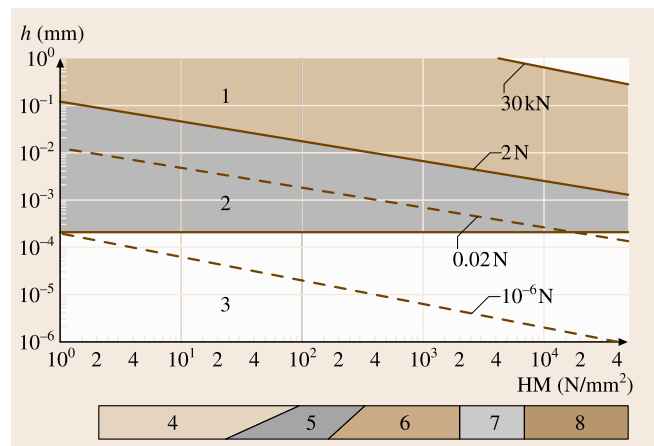


Fig. 7.34 Relationship between Martens hardness, indentation depth and test force (Key: 1 – Macro range; 2 – Micro range; 3 – Nano range; 4 – Rubber; 5 – Plastics; 6 – Nonferrous metals; 7 – Steel; 8 – Hardmetals, ceramics) ►

where h_c is the depth of contact of the indenter with the test piece calculated as

$$h_c = h_{\max} - \varepsilon(h_{\max} - h_r) .$$

Figures 7.32 and 7.33 schematically show the different depths monitored during an indentation test. The theoretical basis of the method for the determination of contact depth is given in [7.203]. The contact depth is derived from the force removal curve using the tangent depth h_r and the maximum displacement h_{\max} correcting for elastic displacement of the surface according to *Sneddon's* analysis [7.186], where ε depends on the indenter geometry (Table 7.14).

h_r is derived from the force–displacement curve and is the intercept of the tangent to the unloading cycle at F_{\max} with the displacement axis.

Designation of Indentation Hardness H_{IT} . The indentation hardness is denoted by the symbol H_{IT} .

Example. $H_{IT} 0.5/10/20/30 = 11\,300\text{ N/mm}^2$
 $H_{IT} 0.5/$ Test force in N
 10/ Application time of test force in s
 20 Duration time of test force in s
 /30 Time taken to remove the test force during the fitted portion of the test force removal curve in s
 = 11 300 N/mm² Hardness value

Indentation Modulus (E_{IT})

Determination of Indentation Modulus. The indentation modulus E_{IT} can be calculated from the slope of the tangent for the calculation of indentation hardness H_{IT} and is comparable with the Young's modulus of the material

$$E_{IT} = \frac{1 - (\nu_s)^2}{\frac{1}{E_r} - \frac{1 - (\nu_i)^2}{E_i}} , \tag{7.32}$$

$$E_r = \frac{1}{\beta} \frac{\sqrt{\pi}}{2} \frac{1}{\sqrt{A_p}} \frac{1}{C_s} , \tag{7.33}$$

Table 7.14 Correction factor ε for different indenter geometries

Indenter geometry	ε
Flat punch	1
Conical	$2(\pi - 2)/\pi = 0.73$
Paraboloid of revolution (includes spherical)	3/4
Berkovich, Vickers	3/4

where

- ν_s is the Poisson's ratio of the test piece;
- ν_i is the Poisson's ratio of the indenter (for diamond 0.07) [7.187];
- E_r is the reduced modulus of the indentation contact;
- E_i is the modulus of the indenter (for diamond $1.14 \times 10^6\text{ N/mm}^2$) [7.187];
- C_s is the compliance of the contact, i.e. dh/dF of the (frame stiffness corrected) test force removal curve evaluated at the maximum test force;
- β is the correction factor for different tip geometry (Table 7.15).

Designation of Indentation Modulus. The indentation modulus is denoted by the symbol E_{IT} .

Example. $E_{IT} 0.5/10/20/30 = 222\,000\text{ N/mm}^2$
 $E_{IT} 0.5/$ Test force in N
 10/ Application time of test force in s
 20 Duration time of test force in s
 /30 Time taken to remove the test force during the fitted portion of the test force removal curve in s
 = 222 000 N/mm² Indentation modulus

Nanoindentation Method

The elastic and plastic properties of a coating are critical factors determining the performance of the coated product. Indeed many coatings are specifically developed to provide wear resistance that is usually conferred by their high hardness. Measurement of coating hardness is often used as a quality-control tool. Young's modulus becomes important when calculation of the stress in a coating is required in the design of coated components. For example, the extent to which coated components can withstand external applied forces is an important property in the capability of any coated system.

It is relatively straightforward to determine the hardness and indentation modulus of bulk materials using instrumented indentation. However, when measurements are made normal to a coated surface, depending

Table 7.15 Correction factor β for different indenter geometries [7.195]

Indenter geometry	β
Axis symmetric (e.g. conical, spherical)	1
Berkovich	1.034
Vickers	1.012

on the force applied and the thickness of the coating, the substrate properties influence the result.

The purpose of this part of handbook is to provide guidelines for conditions where there is no significant influence of the substrate and, where such influence is detected, to provide possible analytical methods to enable the coating properties to be extracted from the composite measurement.

The analysis used here does not make any allowances for pile-up of indents. Use of atomic force microscopy (AFM) to assess the indent shape allows the determination of possible pile-up of the surface around the indent. This surface effect results in an underestimate of the contact area in the analysis and hence may influence the measured results. Pile-up generally occurs for fully workhardened materials. Pile-up of soft, ductile materials is more likely for thinner coatings due to the constraint of the stresses in the zone of plastic deformation in the coating. It has been reported that the piled-up material results in an effective increase of the contact area for the determination of hardness, while the effect is less pronounced for the determination of indentation modulus, since the piled-up material behaves less rigidly [7.197].

Verification and Calibration of Testing Machines. The instrument shall be calibrated according to the procedures set out in ISO 14577-2 [7.204].

Indirect verification using a reference material shall be made to ensure the direct calibration is valid and that no damage or contamination has occurred to the indenter tip. If the results of these initial indentations indicate the presence of contamination or damage then the indenter should be cleaned using the procedure recommended in ISO 14577-1 before further trial indents are made. If indentation into the reference material still indicates the presence of contamination or damage after cleaning, inspection with an optical microscope at a magnification of 400× is recommended. Detection of submicroscopic damage or contamination is possible using appropriate microscopy of indents or the indenter. Where damage is detected the indenter shall be replaced.

The machine compliance C_f and the area function $A_p(h_c)$ calibration/verification shall be implemented before a new indenter is used, see subclause *Procedures for determination of machine compliance and indenter area function*.

The instrumented indentation instrument shall achieve the required mechanical and thermal stability before starting an indentation cycle, see subclause *Measurement procedure*.

Indentation experiments may be performed with a variety of differently shaped indenters, which should be chosen to optimize the plastic and elastic deformation required for a given coating substrate system. Typical indenter shapes are Vickers, Berkovich, conical, spherical and corner cube. For the determination of coating plastic properties, pointed indenters are recommended. The thinner the coating, the sharper the indenter should be. For the determination of coating elastic properties, spherical indenters are recommended. Ideally, a large-radius sphere is used, which enables indentation in the fully elastic regime over a reasonable indentation displacement. If the radius is too large, the surface effects (roughness, surface layers etc.) will dominate the uncertainties. And if the radius is too small, the maximum force or displacement before plastic deformation begins will be very low. The optimum radius can be identified by preliminary experiments or modeling.

Test Piece. Generally surface preparation of the test piece should be kept to a minimum, and if possible, the test piece should be used in the as-received state if surface flatness is consistent with the criteria given in ISO 14577-1.

The test piece shall be mounted using the same methods as employed for determination/verification of the instrument frame compliance, and shall be such that the test surface is normal to the axis of the indenter and such that the local surface at the proposed indentation site is less than $\pm 5^\circ$ from perpendicular to the indentation axis. Perpendicularity can be checked in practice by imaging the indent made by a nonaxisymmetric indenter.

Indentation into rough surfaces will lead to an increased scatter in the results with decreasing indentation depth. Clearly when the roughness value R_a approaches the same value as the indentation depth the contact area will vary greatly from indent to indent, depending on its position relative to peaks and valleys at the surface. Thus it is recommended that the final surface finish shall be as smooth as available experience and facilities permit. The R_a value should be less than 5% of the maximum penetration depth whenever possible.

It has been shown that, for a Berkovich indenter, the angle that the surface normal presents to the axis of indentation has to be greater than 7° for significant errors to result [7.198]. The important angle is that between the indentation axis and the local surface normal at the point of contact. This angle may be significantly different to the average surface plane for rough surfaces.

While R_a has been recommended as a practical and easily understood roughness parameter, it should be borne in mind that this is an average, and thus single peaks and valleys may be greater than this, as defined by the R_z value, although the likelihood of encountering the maximum peak, for example, on the surface is small. Modeling to investigate the roughness of the coating surface has concluded that there are two limiting situations for any R_a value. When the *wavelength* of the roughness (in the plane of the coating surface) is much greater than the indenter tip radius, the force–penetration response is determined by the local coating–surface curvature, but when the wavelength is much less than the tip radius, asperity contact occurs and the effect is similar to having an additional lower-modulus coating on the surface.

In cases where coatings are used in the as-received condition, nevertheless, random defects occur such as nodular growths or scratches and where an optical system is included in the testing machine, it is recommended that flat areas away from these defects are selected for measurement.

The roughness profilometer probe radius should be comparable to the indenter radius. If the roughness parameter R_a is determined with an AFM on a scan area, the size of this area should be agreed upon between the customer and the measurement laboratory. A scan area of 10 μm by 10 μm is recommended.

It should be appreciated that mechanical polishing of surfaces may result in a change in the workhardening and/or the residual stress state of the surface and consequently the measured hardness. For ceramics this is less of a concern than for metals, although surface damage may occur. Grinding and polishing shall be carried out such that any stress induced by the previous stage is removed by the subsequent stage and the final stage shall be with a grade of polishing medium appropriate to the displacement scale being used in the test.

Many coatings replicate the surface finish of the substrate. If it is acceptable to do so, surface-preparation problems can be reduced by ensuring that the substrate has an appropriate surface finish, thus eliminating the need to prepare the surface of the coating. In some cases, however, changing the substrate surface roughness may affect other coating properties; therefore, care should be taken when using this approach.

In coatings it is common for there to be relatively large residual stresses e.g. arising from thermal expansion coefficient mismatch between the coating and the substrate and/or stress induced by the coating deposition process. Thus, a stress-free surface would not normally

be expected. Furthermore, stress gradients in coatings are not uncommon, so that removal of excessive material during a remedial surface preparation stage may result in a significant departure from the original surface state.

Polishing reduces the coating thickness and so the effects of the substrate will be enhanced. Where the data analysis requires an accurate knowledge of the coating thickness indented, polishing will require remeasurement of the coating thickness. This again emphasizes the need to carry out minimum preparation.

Generally, provided the surface is free from obvious surface contamination, cleaning procedures should be avoided. If cleaning is required, it shall be limited to methods that minimize damage, e.g.

- application of a dry oil-free filtered gas stream
- application of subliming particle stream of CO_2 (avoiding surface temperatures below the dew point)
- application of ultrasonic methods
- rinse with a solvent (which is chemically inert to the test piece) and then dry.

If these methods fail and the surface is sufficiently robust, the surface may be wiped with a lintless tissue soaked in solvent to remove trapped dust particles and the surface shall be rinsed in a solvent as above. Ultrasonic methods may not be used as these are known to create or increase damage to coatings.

Test Conditions. Indenter geometry, maximum force and/or displacement and force displacement cycle (with suitable hold periods) shall be selected by the operator to be appropriate to the coating to be measured and the operating parameters of the instrument used.

It is important that the test results are not affected by the presence of an interface, free surface or by any plastic deformation introduced by a previous indentation in a series. The effect of any of these depends on the indenter geometry and the materials properties of the test piece. Indentations shall be at least three times their indentation diameter away from interfaces or free surfaces and, where multiple indentations are planned, the minimum distance between indentations shall be at least five times the largest indentation diameter.

The indentation diameter is the in-plane diameter at the surface of the test piece of the circular impression of an indent created by a spherical indenter. For noncircular impressions, the indentation diameter is the diameter of the smallest circle capable of enclosing the indentation. Occasional cracking may occur at the corners

of the indentation. When this occurs, the indentation diameter should enclose the crack.

The minimum distances specified are best applicable to ceramic materials and metals such as iron and its alloys. For other materials it is recommended that separations of at least ten indentation diameters be used. If in doubt, it is recommended that the values from the first indentation are compared with those from subsequent indentations in a series. If there is a significant difference, the indentations may be too close and the distance should be increased. A twofold increase is suggested.

The following parameters of coating/substrate influencing the measurement result should be considered.

1. Substrate hardness, Young's modulus and Poisson's ratio
2. Coating thickness
3. Surface roughness
4. Adhesion of the coating to the substrate.

All these parameters should be kept constant if a direct comparison is to be made between two or more test pieces.

The time dependence of the materials parameter should be taken into account.

Variations in test-piece parameters other than hardness or modulus can affect measurement of these quantities. If the indentation depth is a sufficiently small fraction of the coating thickness, or the coating

thickness is well known, it is possible to compare coatings of different thickness. The exact limits depend on the ratio of properties of coating and substrate. It is recommended that methods for normalizing results to determine coating properties from coatings of different thickness always be used.

Measurement Procedure. Introduce the prepared test piece and position it so that testing can be undertaken at the desired location. Carry out the predetermined number of indentation cycles using the selected test conditions.

A single force application and removal cycle shall be used. A decision tree to assist in estimating the thermal drift during the experiment is shown in Fig. 7.35. If the drift rate is significant the displacement data shall be corrected by measuring the drift rate during a hold at as close to zero force as is practicable or at 90% removed force. The hold period shall be sufficient to allow determination of the drift in displacement due to temperature fluctuations. Drift (as opposed to noise) in displacement values determined during the hold period at 90% force removal or at close to zero is believed to result from temperature changes, and, a linear correction should be applied such that

$$\begin{aligned} & \text{(corrected displacement)} \\ & = (\text{displacement}) - (\text{thermal drift rate}) \times \text{time} . \end{aligned}$$

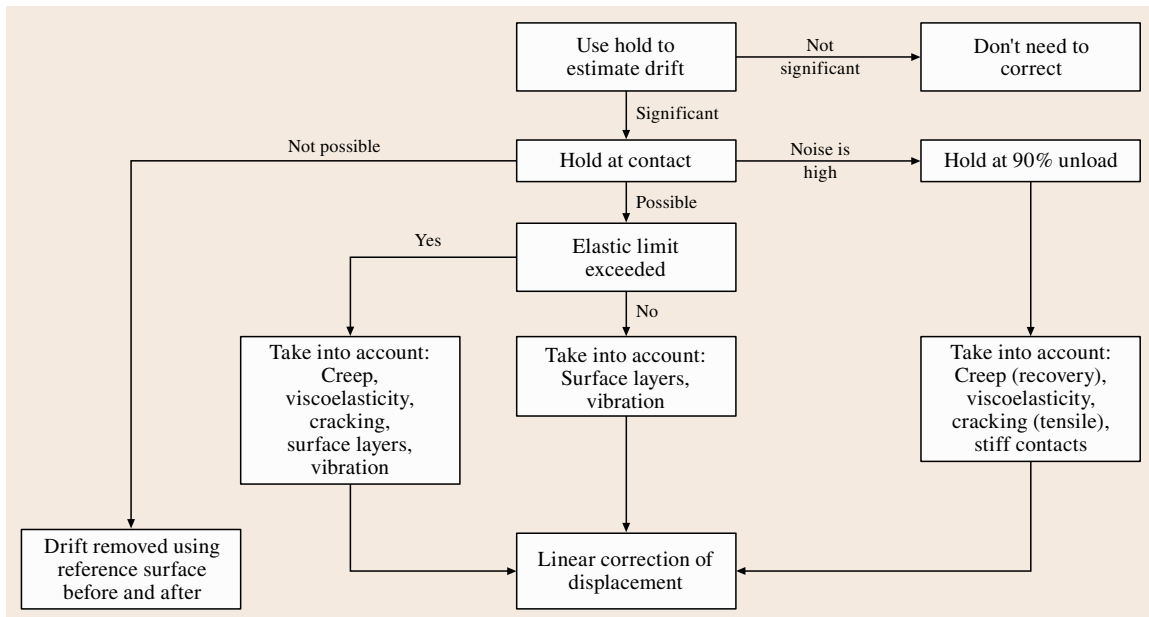


Fig. 7.35 Decision tree to assist in estimating the drift during a force-controlled experiment

If a contact in the fully elastic regime can be obtained, a hold at initial contact is preferred. In this way, material influences (creep, viscoelasticity, cracking) can be avoided. If no elastic contact can be obtained, depending on the material under investigation, a hold at initial force (e.g. viscoelastic material) or at 90% removed force (e.g. soft material) may be preferred. For difficult materials, a hold period at both ends of the indentation cycle may be included. It is recommended that the first 10–20 s of the hold data should be discarded for the analysis since these initial data may be significantly influenced by time-dependent effects (material time-dependent deformation, formation of capillary surface layers) [7.199, 200].

A further hold period shall be performed at maximum force to allow for completion of any time-dependent deformation. In all cases this hold period shall be long enough to reduce the error in the slope of the force removal curve to less than 1%. The minimum hold-period length is therefore dependent on the instrument capability and the material being tested. The hold period shall be long enough and/or the time to remove force shall be short enough such that

$$\begin{aligned} &(\text{creep rate}) \times (\text{time to remove force}) \\ &< F_{\max} / S / 100 . \end{aligned}$$

Force application and removal rates may be the same but it is recommended that the removal rate should be higher than the application rate (if possible) to minimize the influence of creep. Slower force application reduces the hold period length required at F_{\max} to achieve the necessary reduction in creep rate.

The influence of the material creep behavior on hardness and modulus results has been reported [7.199]. The results show that, especially for materials with low hardness-to-modulus ratio (among them most metals), the modulus results are not reliable if the hold period is too short. A modulus error, due to creep, of more than 50% may arise. The variation of the hold period produced a hardness change of up to 18%. Reference [7.199] proposes hold periods dependent on the material type that range from 8 s for fused quartz to 187 s for aluminum. The criterion used was that the creep rate should have decayed to a value where the depth increase in one minute is less than 1% of the indentation depth. It is recommended that the creep rate be assessed in preliminary experiments.

Data Analysis and Evaluation of Results. The hardness and indentation modulus of the test piece can be calculated using (7.31)–(7.33). The properties thus calculated

are composite properties for the coating/substrate combination. This clause provide methods for extracting the indentation modulus of the coating from the composite properties measured, assuming that the coating properties are constant with depth.

For hardness measurement of electroplated coatings on steels [7.201], it is recommended that the indentation depth does not exceed one tenth the thickness of the coating, while for paint films [7.202] penetration of up to one third the coating thickness may be allowed. These approximations can be unsatisfactory in many cases. Test parameters for ductile and brittle coatings need to be considered separately.

For in-plane indentation, elastic deformation of the substrate will mostly occur for all coatings, even though this could be negligibly small for a thick compliant coating on a stiff substrate. Thus the measured modulus will be the composite modulus of the coating and substrate and the value obtained will be a function of indentation depth.

For hardness measurement it is recommended to use as small a radius indenter (i.e. as sharp) as possible to limit the plastic deformation to be within the coating. A measurement of the uncoated substrate hardness is a useful guide to the appropriate choice of analysis (soft versus hard). In some circumstances it is possible to identify a range of indentation depth over which the measured hardness is constant (i.e. before the onset of substrate plastic deformation) and then carry out indentation experiments within this range.

Estimates of coating hardness and modulus may be extracted from the composite values E_{IT} , H_{IT} obtained from in-plane indentation by expressing those composite values as a function of the contact radius a or indentation depth h_c normalized to the coating thickness. Measurement of the coating thickness t_c is recommended for reproducible measurement of coating properties. For indenters of different geometries (e.g., Berkovich, Vickers, spherical, cone, etc.), a is approximated by the radius of a circle having the same area as the projected area of contact with the indenter

$$a = \sqrt{\frac{A_p}{\pi}} . \quad (7.34)$$

This value has exact equivalence for a spherical or conical indenter but becomes increasingly less physically meaningful as the axial symmetry of the indenter reduces, i.e. cone = sphere > Vickers > Berkovich.

It is relatively easy to measure the hardness of ductile coatings or the elastic modulus of brittle coatings. It is more difficult to determine the hardness of brittle or

hard coatings or the elastic modulus of ductile coatings. Where t_c is not measured, nominal values of t_c may be used but comparison between coatings of different thicknesses will be less accurate.

In the case of force-controlled cycles and test pieces of unknown indentation response, a set of trial indentations shall be performed (e.g. at two widely spaced forces) and analyzed to enable estimates of the test force required for the range of a/t_c specified below.

In the case of soft/ductile coatings indentation force or displacement and indenter geometry shall be chosen such that data shall be obtained in the region where $a/t_c < 1.5$. The coating indentation modulus E_{IT}^* is obtained by taking a series of measurements at different indentation depths and extrapolating a linear fit to indentation elastic modulus versus a/t_c to zero (Fig. 7.36).

A linear fit to indentation elastic modulus versus a/t_c to zero is a first approximation in the range $a/t_c < 2$. However, in general, a nonlinear relationship appears and can be reproduced by finite element analysis (FEA). The exact nature of this nonlinear relation is not known and so a linear fit over the restricted range indicated is a robust first approximation but is not applicable over a range wider than this.

For the determination of coating indentation hardness, it is recommended that an elastic stress analysis of the coating/substrate system be undertaken using the approximation of a spherical indenter of a radius equivalent to the tip radius of the self-similar-geometry indenter. This will determine whether the coating or the

substrate will yield first during indentation and therefore whether it is possible to determine the coating hardness at all. It is recommended that hardness values for the substrate be obtained for comparison, by testing if necessary. Delamination or fracture of the coating can be recognized by the hardness values obtained, clustering at the substrate value, even at low h_c/t_c . Note that sharper indenters may cause fracture at lower forces than blunter indenters.

In the case of hard coatings on a softer substrate, the indentation force or displacement and indenter geometry shall be chosen such that h_c/t_c (or $\approx a/t_c$) is in a range where H_{IT} is a maximum. Commonly, the range is $0 < h_c/t_c < 0.5$. If a constant maximum value of H_{IT} (a plateau) is observed over this range, this is the coating indentation hardness. If only a maximum in H_{IT} occurs and indentation of a thicker coating yields the same value, then this is a strong indicator that this is the value for the coating. Otherwise this is only the minimum estimate of the coating indentation hardness.

The extent of substrate plastic deformation will depend upon a number of factors, including the relative difference in hardness and modulus between the coating and the substrate, adhesion, the coating thickness, the indenter radius of curvature (sharpness) and the maximum force.

To measure the coating hardness the coating must yield sufficiently before the substrate yields. The best conditions for this are when the maximum of the von Mises stress is inside the thickness of the coating and causes plastic deformation whilst the stress in the substrate below does not exceed the substrate yield stress. In a spherical contact, the maximum of the von Mises stress is approximately $0.47\times$ (mean pressure) at $0.5a$ below the surface.

Procedures for Determination of Machine Compliance and Indenter Area Function. The calibration procedures detailed below require the use of reference materials (see ISO 14577-3 [7.205]) which shall be isotropic and homogeneous. The Young's modulus and Poisson's ratio are assumed to be independent of the indentation depth. Some procedures need reference materials of known Young's modulus and Poisson's ratio.

Currently recommended materials are freshly polished tungsten and fused silica. The forces used should not exceed the threshold at which cracking occurs ($\approx 80\text{--}100\text{ mN}$ for an average radius Berkovich tip indenting fused silica).

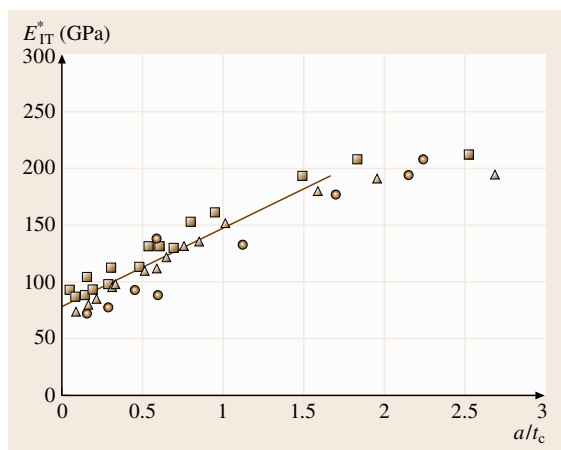


Fig. 7.36 Indentation reduced elastic modulus versus normalized contact radius Au on Ni, selected data for spherical (filled circle), Berkovich (filled triangle) and Vickers (filled square) indenter

Principle. The total measured compliance C_T is the sum of contact compliance C_s and the machine compliance C_f thus

$$C_T = C_s + C_f, \quad (7.35)$$

where C_T is derived from the derivative of the (uncorrected) test force removal curve at maximum force

$$C_T = \left(\frac{dF}{dh} \right)^{-1} \quad (7.36)$$

and C_s is the contact compliance of the specimen material

$$C_s = \frac{\sqrt{\pi}}{2E_r} \cdot \frac{1}{\sqrt{A_P(h_c)}} \quad (7.37)$$

with

$$\frac{1}{E_r} = \frac{1 - \nu_s}{E_{IT}} + \frac{1 - \nu_i}{E_i} \quad (7.38)$$

and

$$h_c = h_{\max} - \varepsilon F_{\max} C_T, \quad (7.39)$$

where E_i and ν_i are, respectively, the Young's modulus and the Poisson number of the indenter.

Thus the total compliance is

$$C_T = C_f + \frac{\sqrt{\pi}}{2E_r} \frac{1}{\sqrt{A_P(h_c)}}. \quad (7.40)$$

If it can be assumed that the elastic modulus is constant and independent of indentation depth, a plot of C_T versus $A^{-1/2}$ is linear for a given material and the intercept of the plot is a direct measure of the machine

load-frame compliance. The best values of C_f are obtained when the second term on the right-hand side of (7.39) is small, i. e., for large indentations. In addition, the largest indentations are advantageous to find area function. A perfect modified Berkovich indenter, for instance

$$A(h_c) = 24.5h_c^2 \quad (7.41)$$

can be used to provide a first estimate of the contact area. Initial estimations of C_f and E_r are thus obtained by plotting C_T versus $A^{-1/2}$ for the two largest indentations in the reference block. Using these values, contact areas are computed for all, at least six, indentation sizes by rewriting (7.39) as

$$A_P = \frac{\pi}{4} \frac{1}{E_r^2} \frac{1}{(C - C_f)^2}, \quad (7.42)$$

from which an initial guess at the area function is made by fitting A_P versus h_c data to the relationship

$$A(h_c)_P = 24.5h_c^2 + C_1h_c^1 + C_2h_c^{1/2} + C_3h_c^{1/4} + \dots + C_8h_c^{1/128}, \quad (7.43)$$

where C_1 – C_8 are constants. The lead term describes a perfect modified Berkovich indenter; the others describe deviations from the Berkovich geometry due to blunting of the tip.

The procedure is not complete at this stage because the exact form of the area function influences the values of C_f and E_r , so using the new area function the procedure shall be applied again and iterated several times until convergence is achieved.

7.4 Strength

The strength of materials is influenced by the strain rate, temperature, loading manner and chemical environment. The conventional test for the examination of the strength of materials is tension testing with a slow strain rate of around 10^{-3} s^{-1} at room temperature. Tensile properties obtained using this test are widely used in engineering practices such as mechanical design, fabrication and maintenance of products. In the case of brittle materials, compression or bending tests are frequently used to examine their strength. These tests are done under so-called quasistatic-loading conditions. Tests at very slow strain rates are performed to examine creep or stress-relaxation behavior. To consider automobile collision, earthquakes etc., strength at

a high strain rate such as 10^3 s^{-1} is required; impact or high-speed deformation testing, such as a Hopkinson pressure-bar test, is employed. Resistance to fracture under cyclic loading is called fatigue strength. Strength is also influenced by temperature as well as the environment accompanied by chemical reactions such as corrosion, or radiation damage. Fracture is frequently found to occur under combined conditions of stress, microstructural change and chemical reaction. In some cases, high-temperature strength or low-temperature toughness are of importance for engineering application of materials, so that the meaning of the strength of materials is not unique but depends on the conditions of their use.

7.4.1 Quasistatic Loading

Strength

According to their loading speed, tests are classified as quasistatic (or simply static) or dynamic. The most common quasistatic measurement of the strength of materials is tension testing. The strength of a material has three different meanings, which it is important not to confuse. First, when the applied load is small, deformation is reversible, that is, elastic deformation occurs. Stresses are proportional to elastic strains and the so-called Hooke's law holds. The slope between tensile stress and tensile elastic strain is called the Young's modulus, as was explained in Sect. 7.1. A material with high Young's modulus is strong, or rigid to elastic deformation. Secondly, when the applied stress becomes higher, materials usually show plastic deformation. The stress at the onset of plastic flow is called the *yield strength*, which has no direct relation with the Young's modulus. The yield strength indicates resistance against plastic flow. In the case of engineering materials, it is necessary to define how to determine the yield strength for mechanical design. Usually, 0.2% proof stress or lower yield strength is employed. Thirdly, materials show fracture under applied stress. Since there are many fracture mechanisms, the strength against fracture is different from the yield strength. Ductile materials show workhardening with plastic deformation and plastic instability, i. e., necking in the case of tension, resulting in dimple fracture. Frequently fracture occurs after a considerable amount of plastic flow, but fracture takes place with little or no plastic deformation. This is called *brittle fracture*, so that the resistance to brittle fracture is another aspect of strength. Fracture is also strongly dependent on the chemical environment.

Tension Test

This test is usually performed at room temperature with a strain rate of 10^{-4} – 10^{-1} s $^{-1}$. The testing procedure and the shape and dimensions of a tensile specimen should be taken from the ISO or other related standards, depending on the materials and products under consideration. The loading speed, or extending speed, should be controlled within the above strain-rate range using a gear-driven type or servo-hydrostatic-type tester. During testing, the applied load and displacement of a gage length of a tensile specimen should be recorded. Then, the load–displacement diagram can be obtained. The curve is converted to a nominal stress–strain curve and sometimes further to a true stress–strain curve. Typical tensile properties such as the yield strength,

tensile strength, uniform elongation, total elongation, workhardening exponent (n -value), r -value etc., can be obtained from the results of the tension test.

Stress–Strain Curves of Ductile Materials

An example of the standard tension specimens is shown in Fig. 7.37. Depending on the purpose, a strain gage or extensometer is attached to monitor the change in gage length (ΔL), while the load (F) is measured simultaneously with a load cell. Based on the initial area (A_0) and gage length (L_0), the nominal stress (σ) and nominal strain (ε) are obtained by the following equations

$$\sigma = F/A_0, \quad (7.44)$$

$$\varepsilon = \Delta L/L_0. \quad (7.45)$$

Here, the units for F and ε are Pa ($=\text{N/m}^2$) and m/m (nondimensional), respectively. In Fig. 7.38, two typical examples of nominal stress–strain curves are presented; one shows the case of discontinuous yielding (a) and the other shows continuous yielding (b). Most metals and alloys show the type of yielding shown in (b). However, annealed mild steels, which are widely used, show the type shown in (a). As can be seen, these curves are divided into three regions.

1. A linear elastic region at the beginning, where stress is proportional to strain and the deformation is reversible.
2. After the onset of plastic flow, the curve deviates from the elastic line. The flow stress increases with increasing strain, meaning that the material is strengthened by plastic deformation; this is called

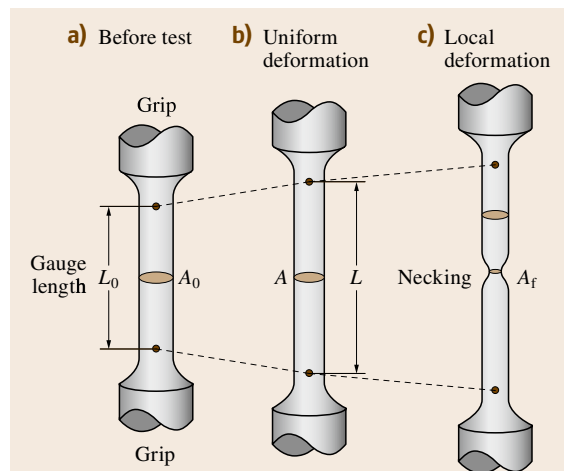


Fig. 7.37a–c Tension specimen and macroscopic tensile deformation behavior

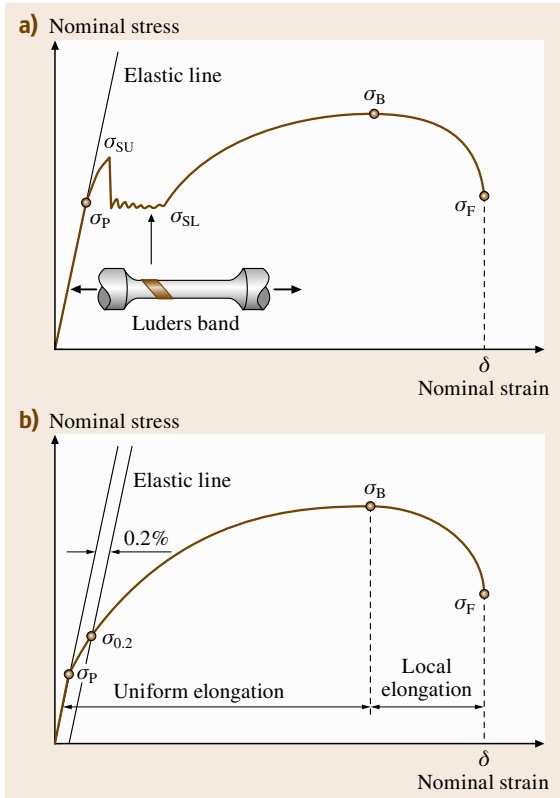


Fig. 7.38a,b Nominal stress–strain curves: (a) discontinuous yielding and (b) continuous yielding

workhardening. When unloaded, only the elastic strain is recovered but a permanent deformation, i. e., plastic strain, remains. In this region, uniform plastic deformation occurs. For plastic strains, the condition of *constant volume* is often assumed (Fig. 7.37b [7.206]).

3. After reaching the maximum stress, which is called the *ultimate tensile strength (UTS)* or simply the *tensile strength (TS)*, a lower stress is enough to

continue to deform the material plastically because necking occurs (Fig. 7.37c). After the onset of necking, deformation is localized to a necked region in which the stress condition is no longer uniaxial but is triaxial. Microvoids form inside the necked region, grow, connect to each other and lead to slip-off of the remaining, outside ring region. Thus, the view after fracture looks like a cup and a cone and hence is called *cup-and-cone fracture*. This phenomenon is typical of ductile fracture. The inner, flat area consists of dimples; the dimple pattern observed on the fracture surface is shown in Fig. 7.39a.

4. When a material is brittle, as is the case for ceramics, necking is not observed and the flow curve stops suddenly at the fracture stress, often within the elastic regime. In such a case, the fracture surface consists of cleavage or transgranular facets. Examples of the fracture surface are presented in Fig. 7.39b and 7.39c,

True Stress–Strain Curves and the Workhardening Exponent (n -Value)

Within the uniformly elongated regime in Fig. 7.38, the assumption of constant volume for plastic strains holds approximately. This means that the cross section in the gage volume in Fig. 7.37 decreases with increasing tensile strain. Hence, the area (A) to support the applied stress decreases with deformation so that the stress per unit area is given by

$$\sigma^* = F/A \quad (7.46)$$

instead of (7.44); σ^* is called the *true stress*. Similarly to σ^* , the gage length l_0 changes continuously with deformation. Then, the *true strain* (ε^*) is defined by

$$\varepsilon^* = \int_{l_0}^l dl/l = \ln(l/l_0). \quad (7.47)$$

One of the merits of using ε^* is its additive nature. For instance, when a length changes from L_A to L_B ,

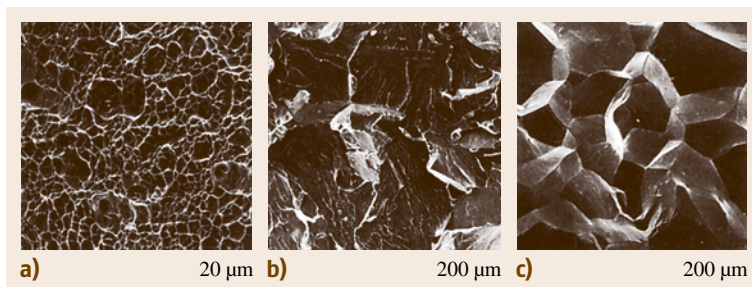


Fig. 7.39a–c Fracture surface: (a) dimple, (b) cleavage and (c) intergranular fracture

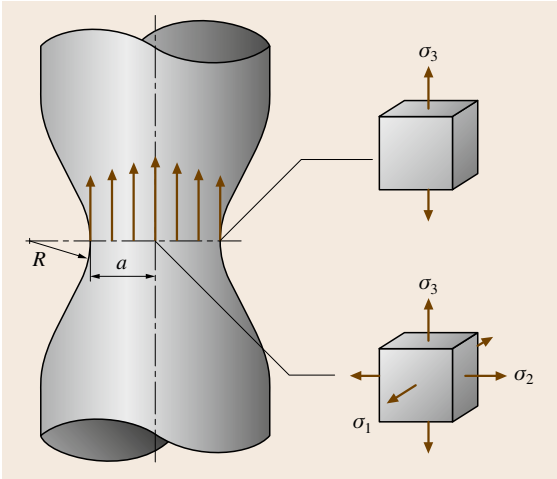


Fig. 7.40 Stress condition in a necked region in tension test

and then to L_C , the true strain from L_A to L_B is $\ln(L_B/L_A)$ and from L_B to L_C is $\ln(L_C/L_B)$. Therefore, $\ln(L_B/L_A) + \ln(L_C/L_B) = \ln(L_C/L_A)$ holds. In contrast, in the case of nominal strain, we have $(L_B - L_A)/L_A + (L_C - L_B)/L_B \neq (L_C - L_A)/L_A$, and hence this property is not additive. Taking the assumption of constant volume ($A_0L_0 = AL$) we obtain the following conversion from nominal stress and strain to true stress and strain. Thus, we find the relation for true stress versus true strain starting from Fig. 7.38 by using

$$\sigma^* = F/A_0 = \sigma(1 + \epsilon), \quad (7.48)$$

$$\epsilon^* = \ln(L/L_0) = \ln(1 + \epsilon). \quad (7.49)$$

After the onset of necking, the specimen geometry changes and the stress condition is also altered. As shown in Fig. 7.37c and Fig. 7.40, the stress condition in a necked region is not uniform but is a complicated triaxial stress condition. According to *Bridgman's* analysis [7.207], the tensile stress at the surface of the smallest cross section, σ_0 (Fig. 7.40), is given by

$$\sigma_0 = \frac{F/A}{(1 + 2R/a) \ln(1 + a/2R)}, \quad (7.50)$$

where R and a are given in Fig. 7.40. Microvoids form in the center of the necked region under triaxial stresses, as explained above, leading to cup-and-cone fracture.

An example of curves of true stress versus true strain converted from the nominal stress–strain curve by using (7.49) and (7.50) is shown in Fig. 7.41. This shows that workhardening continues even in local deforma-

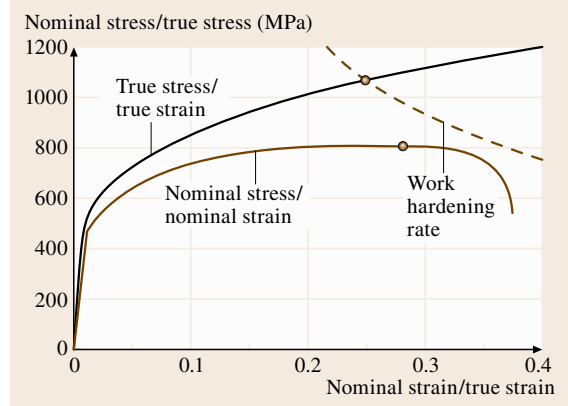


Fig. 7.41 True stress–strain curve in which the workhardening rate is plotted to indicate the onset of necking

tion; the necking is caused from the balance between cross-sectional area reduction and workhardening with increasing tensile plastic strain. Hence, the crossing point of the true stress σ^* and the workhardening rate $d\sigma^*/d\epsilon^*$ shows the onset of necking (Fig. 7.41).

Tensile Properties

Tension testing is simple and gives us lots of useful information on mechanical properties. So, this test is the most basic and popular to understand the mechanical behavior of materials. Several parameters for engineering use obtained by tension testing are explained below.

Elastic Limit and Proportional Limit

Most mechanical products are designed to be used within the regime of elastic deformation. The rigorous limit of elastic deformation is determined by the elastic limit or proportional limit on the stress–strain curve. The proportional limit is the point of deviation from the linear relationship between stress and strain. On the other hand, the elastic limit is found as the maximum stress without permanent strain after unloading. These stresses are very sensitive to the method used to measure strain. Within the linear stress–strain regime, as was explained in details in Sect. 7.1, the Young's modulus (E) is determined from the slope, while the Poisson's ratio (ν) is determined by the absolute ratio between the transverse strain and tensile strain. When the tensile direction is taken as the x_3 -axis, these are determined by

$$E = \sigma_{33}/\epsilon_{33}, \quad (7.51)$$

$$\nu = |\epsilon_{11}/\epsilon_{33}| = |\epsilon_{22}/\epsilon_{33}|. \quad (7.52)$$

In the case of steel, E is nearly 200 GPa and ν is approximately 0.3. The elastic strain in steels is usually less than 1%, which is very small compared with the uniform elongation of the order of 10%. We note here that the constant-volume assumption is not applicable to elastic deformation.

Yield Strength

Special measurements such as those based on strain gages are required for the measurement of elastic strains less than 0.01 so that the yield strength (YS) is determined for mechanical design using the conventional tensile test. In the case of discontinuous yielding observed in mild steel, as shown in Fig. 7.38a, the upper or lower yield point is observed on the stress–strain curve and used as the yield strength in engineering. After the upper yield point, a plastic-deformation regime called the *Luders band* appears and spreads within the specimen gage volume under the lower yield stress. Since the upper yield strength is strongly dependent on the tensile speed, i. e., the strain rate, the lower yield strength is more popularly used. The strain during this heterogeneous deformation is called the Luders elongation, which is also dependent on grain size.

On the other hand, Fig. 7.38b shows the case of continuous yielding, which is observed in many metals and alloys such as aluminum, austenitic stainless steel etc. 0.2% proof stress is usually employed, which means a plastic (permanent) strain of 0.2% remains after unloading. Usually the elastic linear line is shifted by 0.2% and the intersection with the stress–strain curve is found. Macroscopic yielding can be observed to take place at this point. Although 0.2% strain is the choice for engineering, other strains, for instance 0.1%, are employed in other industrial fields.

Tensile Strength

The maximum stress appearing in Fig. 7.38 is determined by the tensile strength (TS), frequently called the ultimate tensile strength (UTS). In the case of an extreme design that allows plastic flow, TS is employed as the design strength.

Ductility

Parameters to describe the ductility includes uniform elongation, total elongation and reduction in area after fracture. Uniform elongation is important for plastic forming etc. and is determined as the strain at the tensile strength. After the tensile strength, local deformation, i. e. necking, starts. The total strain is given as the strain to fracture in Fig. 7.41. It should be noted that the to-

tal elongation is dependent on the gage length adopted. Therefore, fracture strain (ϵ_f) is sometimes used, which is defined as $\ln(A_0/A_f)$, where A_f refers to the smallest area in the necked region after fracture. Conventionally, the reduction in area (φ) defined by $[(A_0 - A_f)/A_0] \times 100\%$ is used. The extreme case observed in a pure metal is a point fracture, where $A_f = 0$.

Workhardening Exponent (n -Value)

The true stress–strain curve shown in Fig. 7.41 is often fitted by using the following Hollomon's equation

$$\sigma^* = K(\epsilon^*)^n, \quad (7.53)$$

where K and n stand for the strengthening factor and the workhardening exponent (n -value), respectively. By taking two measuring points or by using the least-squares method for $\ln \sigma^*$ versus $\ln \epsilon^*$ within an appropriate strain regime, these K and n values are determined. The n -value is important because it is equivalent with uniform elongation. The plastic instability condition, i. e., the onset of necking can be given by

$$dF = \sigma^* dA + A d\sigma^* = 0, \quad (7.54)$$

where F is the applied tensile load. This equation is rewritten by $\sigma^* = d\sigma^*/d\epsilon^*$ under the assumption of constant volume and therefore $\epsilon^* = n$ is obtained. A large n -value means excellent plastic formability.

Rankford Value (Plastic Anisotropy: r -Value)

Another parameter that indicates the plastic formability, and which is also obtained by the tension test for sheet metals and alloys, is the r -value. When tensile strain reaches 10–20%, the strain for a thickness of ϵ_t and the strain for a width of ϵ_w are measured and the r -value is determined by

$$r = \epsilon_w / \epsilon_t. \quad (7.55)$$

If the assumption of constant volume is used, this becomes

$$r = \ln(W_0/W) / \ln(LW/L_0W_0), \quad (7.56)$$

where W_0 , L_0 and W , L refer to the width and gage length in the tensile direction before and after the tension test, respectively. These values are much more easily measured precisely than the thickness because most cases use thin sheets. In an isotropic material, the r -value equals unity. Commercially available materials generally show anisotropic feature in plastic flow because of their texture. Materials with high r -values are desirable

for heavy drawing because the thickness change is small. To achieve this, texture control is important.

The Compression Test

The compression test looks like the reverse of the tension test, but more skill is required to obtain reliable stress–strain curves. A schematic illustration of compression of a round column is presented in Fig. 7.42, where the top and bottom surfaces of the specimen should be maintained with good parallelism. Friction between the specimen and the anvil must be minimized using an appropriate lubricant such as graphite or Mo₂S powder otherwise bulging, shown in Fig. 7.42b, becomes serious and leads to constrained deformation. If the compression alignment is not satisfactory with respect to the specimen axis, buckling or bending occurs easily at small strains. To avoid such buckling, the length of the specimen should be designed taking

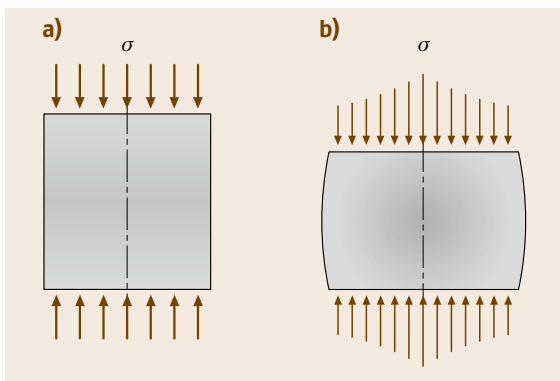


Fig. 7.42a,b Compression test where bulging is illustrated

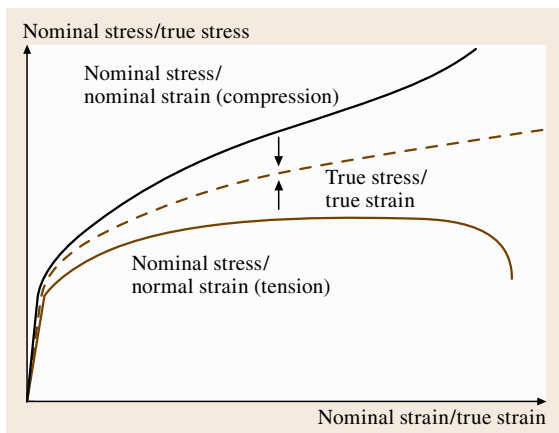


Fig. 7.43 Compression flow curve compared with that in tension

the cross-sectional area into consideration. Usually, the ratio of the diameter of the cross-sectional area d_0 to the length h_0 is chosen as 1.0–3.0. When the top and bottom of a specimen are plastically constrained by an anvil, the stress distribution within the cross section is not uniform and plastic deformation occurs in an inhomogeneous manner within the specimen.

The nominal stress–strain curve obtained by the compression test is higher than that obtained by the tension test because the cross-sectional area increases with deformation. Hence, flow curves measured by the tension test and the compression test should be compared in terms of true stress–strain curves. If a material shows isotropic plastic deformation, these two flow curves (the true stress–strain curves) coincide, as shown in Fig. 7.43. However, if a material contains phase or intergranular residual stress, so-called second-type residual stresses, the yield strength will differ between compression and tension, which is called the *strength difference (SD)* effect. The SD effect is also caused by crystallographic features in plastic flow or stress-induced martensitic transformations.

In general, the flow stress (true stress) in compression after some amount of tensile plastic deformation is smaller than that for continuous tension, as shown in Fig. 7.44. This is called the Bauschinger effect (BE). As seen in Fig. 7.44, the magnitude of the BE is often expressed by the BE stress or BE strain (Fig. 7.44). Generally speaking, the flow stress becomes smaller when the strain path changes, even under biaxial or triaxial stresses. In a stress space (the general stress condition is described by six components, as will be described later), the yield condition is shown using

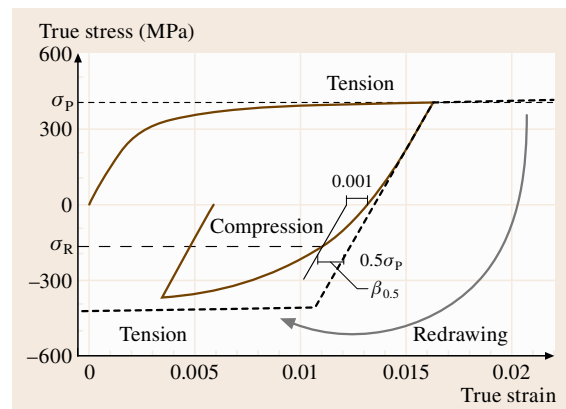


Fig. 7.44 Tension-compression test to examine the Bauschinger effect (BE) in which the parameters of BE stress ($\sigma_p - \sigma_R$) and BE strain $\beta_{0.5}$ are defined

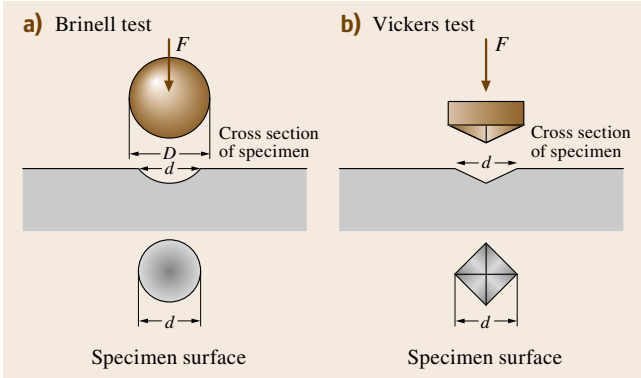


Fig. 7.45a,b Hardness tests by indenting deformation

the yielding surface. When a material is plastically deformed and thus workhardened, the yielding stress surface expands and moves in the stress space. Hence, the yield strength after plastic deformation depends on the loading conditions. Typical cases are: (1) isotropic hardening, where the yield surface expands homogeneously, and (2) kinematic hardening, where the surface moves without changing its shape and size. The BE is important in order to understand plastic forming, which is used to make mechanical parts. In addition, the BE behavior is closely related to low-cycle fatigue behavior. In the case of brittle materials such as concrete, in which the SD effect for fracture is remarkable, the compressive fracture strength is much higher than the tensile value.

Hardness Test and Strength/Hardness Relations

In addition to the treatment of hardness measurements methods given in Sect. 7.3, relations between strength

and hardness are briefly considered. The most popular measurement is a kind of compression test with an indenter. The indenter is made from a hard material such as diamond or high-carbon martensite steel. As explained above and shown again in Fig. 7.45 an indenter is pressed on the surface of a testing material, and the indentation after unloading is measured. Since the Vickers hardness test employs a pyramidal diamond indenter, the applied stress is almost proportional to the area, which means that the Vickers hardness number is insensitive to the applied load. As is estimated in Fig. 7.45, the deformation zone is limited to just underneath of the indenter and is complicated. According to an elasto-plastic analysis, the representative plastic strain in the plastic zone is about 8%, so that the hardness number should correspond to 8% flow stress in the simple tension or compression test [7.208, 209]. Figure 7.46 shows the relationship between the hardness and tensile properties, the yield strength or tensile strength (8% proof stress is usually not recorded). Excellent correspondence is found between the yield or tensile strength and hardness. The experimental relationship of (7.57) is used to connect the Vickers hardness number (HV) to the yield or tensile strength (Y)

$$HV = cY, \quad (7.57)$$

where the coefficient c is 2.9–3.0. Therefore, the hardness test is a convenient way to check the strength of materials, particularly for engineering products.

Supplementing the discussion of nanohardness measurements given in Sect. 7.3.4, strengthening mechanisms will be considered briefly. In most cases, the

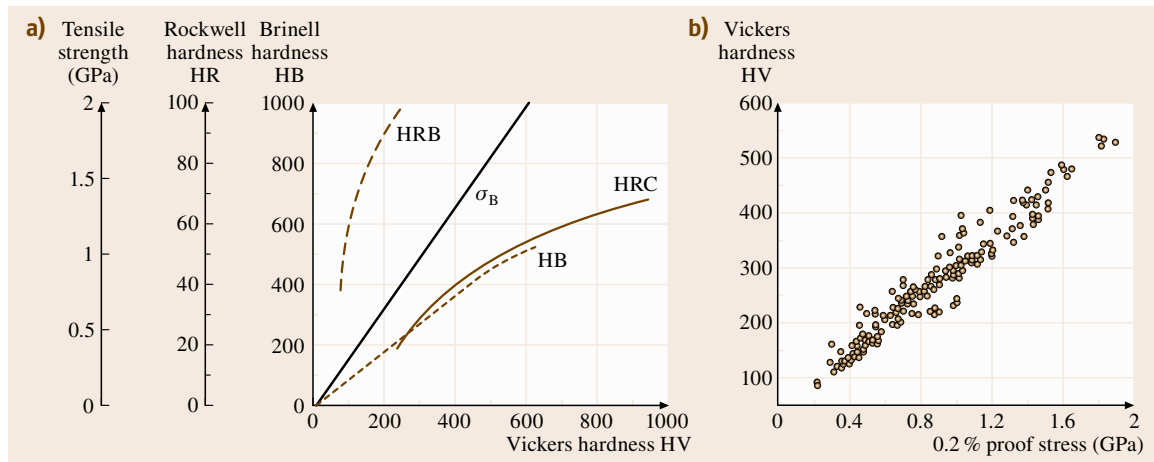


Fig. 7.46a,b Relationship between hardness and tensile properties

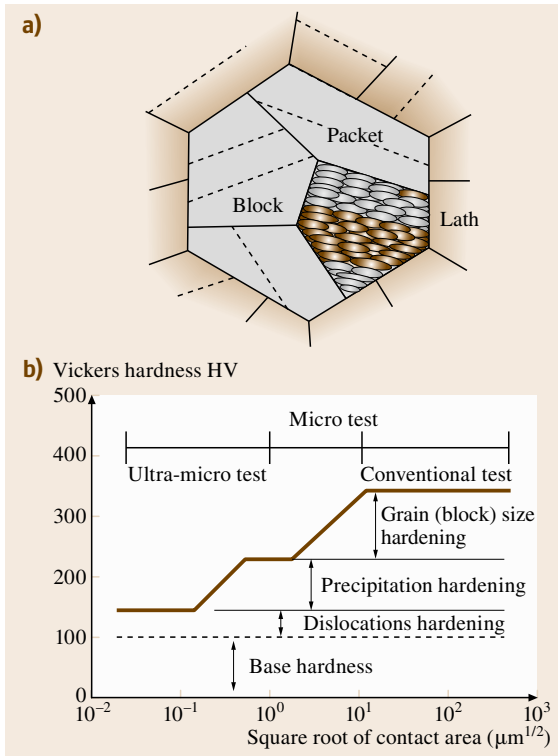


Fig. 7.47a,b Hardness with various loads to examine the strengthening mechanism in a tempered martensite steel

shape of a diamond indenter is triangle pyramid because the tip of square pyramid is difficult to make precisely. The test is performed under very small loads, such as a few grams, and is widely used for thin-film or electronics devices. One of the recent application [7.210] is summarized in Fig. 7.47, where the hardness was measured using a wide range of applied loads for a tempered martensite steel. Because an engineering material shows multiscale heterogeneous microstructure that brings the multiscaled heterogeneous plastic deformation. For example, the tempered martensite is composed of laths, blocks and packets as shown in Fig. 7.47a and hence the strengthening mechanisms due to grain refinement, dislocation density, carbon solid solution and carbide precipitation overlap. By examining the hardness with various loads, using three kinds of hardness testers, the contribution of individual strengthening mechanism can be found separately, as illustrated in Fig. 7.47b.

The Bending Test

Schematic illustration of the bending test is presented in Fig. 7.48. This test is frequently used to measure the

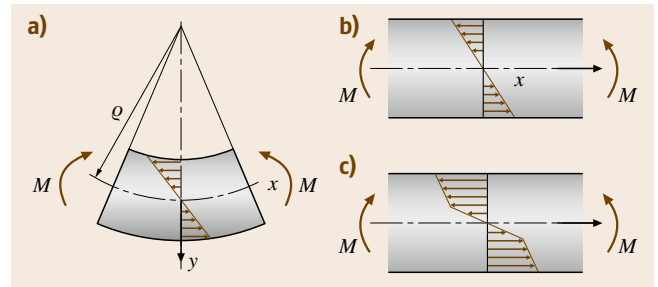


Fig. 7.48a–c Bending test: (a) deformation aspect, (b) stress distribution in elastic deformation and (c) that in elasto–plastic deformation

strength of brittle materials or the bending formability of ductile materials. As shown in Fig. 7.48, two kinds of tests, three- and four-point bending are used. three-point bending is easy to carry out. However, four-point bending is preferable because the bending moment M is then constant in the central part of the specimen. When a rectangular specimen is bent, as shown in Fig. 7.48a, strain and stress distribution occurs in the cross section, where the upper surface is in compression and the lower surface is under tension. There exists a neutral stress-free plane, which is denoted by the x -axis. If the curvature is expressed by ρ , the normal strain under elastic deformation is given by

$$\varepsilon = y/\rho. \quad (7.58)$$

The normal stress is proportional to the strain, and hence we obtain the maximum stress by

$$\sigma = 6M/(bh^2), \quad (7.59)$$

where b and h refer to the width and thickness of the specimen, respectively. The stress distribution is shown in Fig. 7.48b.

After yielding at $M = \sigma_s bh^2/6$, the stress distribution changes from Fig. 7.48b–c, where σ_s stands for the yield strength. When M is further increased, the boundary between the elastic region and the elasto–plastic region moves towards the neutral plane. The stress or strain distribution in the plastic region is dependent on the workhardening of a material. A schematic illustration is given in Fig. 7.48c. When the applied moment is removed, the residual stress distribution remains: tensile stress at the upper surface and compression at the bottom surface.

The Torsion Test

Shear deformation is related to the combination of biaxial deformation of tension and compression. This

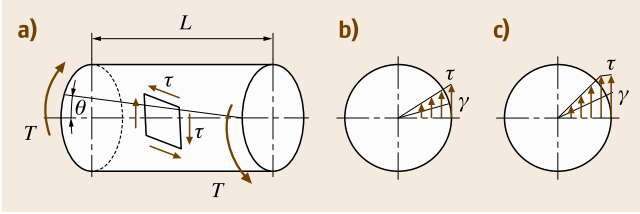


Fig. 7.49a–c Torsion test: (a) deformation aspect, (b) stress distribution in elastic deformation and (c) that in elasto–plastic deformation

conversion is achieved by rotating the coordinate system by 45° . In particular, the torsion test is used for wires and bars. Figure 7.49 shows a schematic illustration of torsion (a) and the shear stress distribution (b) in the cross section of a round bar with radius r . The engineering shear strain γ is related to the shearing angle θ and the bar length L by

$$\gamma = r\theta/L. \quad (7.60)$$

Considering the stress equilibrium, the torsion moment (for torque T) is given by

$$\tau = 16T/\pi d^3, \quad (7.61)$$

where d refers to the diameter of the round bar specimen. Similarly to the bending test depicted in Fig. 7.48, the stress distribution changes after yielding, as represented in Fig. 7.49c. Fracture usually takes place perpendicularly to the specimen axis in ductile fracture while along 45° direction in case of brittle fracture. In some cases, fracture along the longitudinal direction occurs, which is called delamination. Delamination fracture has to be avoided for practical application of wires.

Yielding Criteria under Multiaxial Stresses

Tension and compression tests are performed with uniaxial loading. The general stress condition is a triaxial stress, which is described by six components

$$\begin{pmatrix} \sigma_{11} & \tau_{12} & \tau_{31} \\ \tau_{12} & \sigma_{22} & \tau_{23} \\ \tau_{31} & \tau_{23} & \sigma_{33} \end{pmatrix}.$$

When a special coordinate related to the principal stresses, $\sigma_i(\sigma_1, \sigma_2, \sigma_3)$ is employed, the shear stress components all become zero. For instance, in the case of the tension test along the tensile direction of the x_3 -axis, the six stress components or three principal stresses are

written as

$$\begin{aligned} \sigma_{33} = \sigma_3, \quad \sigma_{11} = \sigma_1 = 0, \quad \sigma_{22} = \sigma_2 = 0, \\ \tau_{23} = \tau_{31} = \tau_{12} = 0. \end{aligned} \quad (7.62)$$

The yield strength σ_s is determined by σ_{33} at 0.2% plastic strain, or the Luders deformation. In the case of the general stress condition, the stresses are converted to principal stresses by changing the coordinate system. For example, in the torsion test, $\tau = 16T/\pi d^3$ and the other stresses are zero at the surface of a bar specimen from (7.61). Rotating the coordinate by 45° gives $\sigma_1 = -\sigma_2 = 16T/\pi d^3$ and the other stress components are zero.

Two of the most popular criteria for yielding under general stress conditions are the Tresca and von Mises criteria. The Tresca criterion is based on the maximum shear stress theory. When $\sigma_3 > \sigma_2 > \sigma_1$, the maximum shear stress is given by $|\sigma_3 - \sigma_1|/2$. Therefore, the yielding criterion is written by

$$|\sigma_3 - \sigma_1| = 2k, \quad (7.63)$$

where k is a constant and is given by $\sigma_s/2$ for the tension test.

On the other hand, the von Mises criterion is based on the theory of shear strain energy. The shear strain energy per unit volume is given by

$$\frac{1+\nu}{6E} [(\sigma_1 - \sigma_2)^2 + (\sigma_2 - \sigma_3)^2 + (\sigma_3 - \sigma_1)^2].$$

Using the results of the tension test, the criterion can be written as

$$[(\sigma_1 - \sigma_2)^2 + (\sigma_2 - \sigma_3)^2 + (\sigma_3 - \sigma_1)^2] = 2\sigma_s^2. \quad (7.64)$$

In general, yielding is found to occur at a stress condition between these two criteria. Hence, the general stress condition is projected to the case of the tension test and the equivalent stress is then determined. For instance, in the case of the von Mises criterion, the equivalent stress σ_{eq} is given by

$$\sigma_{eq} = [(\sigma_1 - \sigma_2)^2 + (\sigma_2 - \sigma_3)^2 + (\sigma_3 - \sigma_1)^2]^{1/2}$$

or more generally,

$$\begin{aligned} \sigma_{eq} = [(\sigma_{11} - \sigma_{22})^2 + (\sigma_{22} - \sigma_{33})^2 + (\sigma_{33} - \sigma_{11})^2 \\ + 6(\sigma_{23}^2 + \sigma_{31}^2 + \sigma_{12}^2)]^{1/2}. \end{aligned} \quad (7.65)$$

Another interpretation of the von Mises criterion is the maximum shear stress acting on the pyramidal plane in the principal stress space.

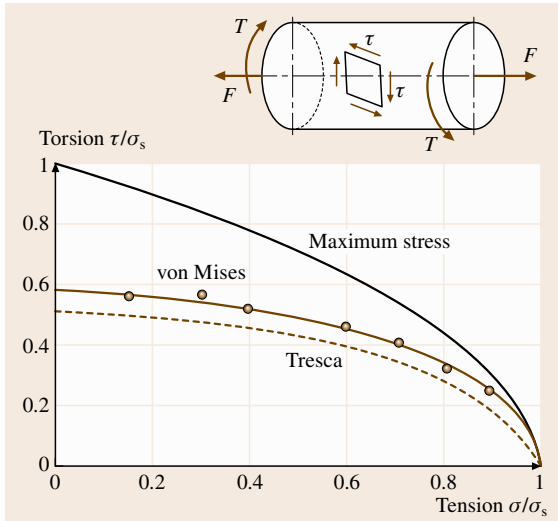


Fig. 7.50 Yielding under combined tension and torsion stresses

A schematic illustration of the yielding surface under combined torsion and tension loads [7.211, 212] is shown in Fig. 7.50. Such a yielding condition under general stress conditions is given by the yielding surface in the stress space (six-dimensional or principal stress space (three dimension)), which changes with plastic deformation. This is called workhardening, which includes isotropic hardening and kinematic hardening. The Baushinger effect in Fig. 7.44 is an example of kinematic workhardening, as already mentioned.

The Creep Test

Plastic deformation and fracture usually show time dependence. When an external load is kept constant, a specimen deforms plastically gradually, which is called creep deformation. This is clearly observed at high temperatures ($T > 0.3T_m$), where T_m denotes the melting temperature of a material. In general, creep deformation at constant temperature is divided into three stages in the creep curve, as shown in Fig. 7.51.

Here, after the initial strain that occurs during loading to a certain fixed stress, plastic strain initially increases gradually, which is called *transient creep*. The rate of increase of the strain in transient creep saturates to a constant rate in the second regime. This is called *steady creep*. The third regime, called *tertiary* or *accelerated creep*, leads to the rupture of the specimen. This effect is important, but it is not clear why and when this acceleration from steady to tertiary creep takes place. When the external load is small, tertiary

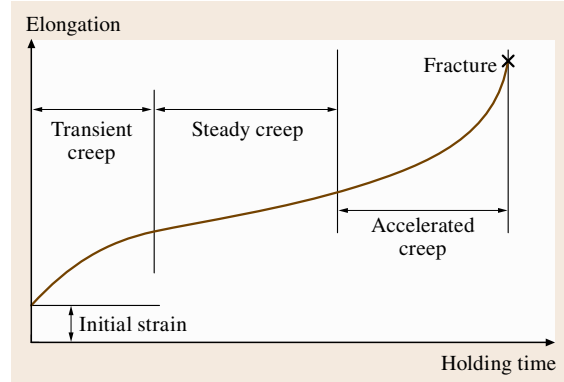


Fig. 7.51 General creep deformation behavior under constant load and temperature

creep is not observed and hence the specimen does not fracture.

The experimental methods to examine creep behavior include the constant-stress creep test, the torsion creep test, the tension-torsion combined test, cyclic loading creep, and the creep crack-propagation test. A tester with an electric furnace and a lever-type loading system for a round bar specimen is popular. In general, creep rupture requires a long time, so that many testers are used simultaneously. A dial gage or differential transducer with a high sensitivity is also required for strain measurement. When the experimental data obtained at various temperatures are summarized by employing the following Larson–Miller parameter,

$$\lambda = T(20 + \log t_r) \times 10^{-3}, \quad (7.66)$$

where t_r stands for the rupture time, the experimental data for applied stress (σ) versus t_r are well summarized by a σ – λ master curve. The master curve is influenced by strengthening mechanisms such as solid solution hardening, grain refinement, precipitation, etc. The speed of crack growth is evaluated from the viewpoint of fracture mechanics as will be explained in Sect. 7.4.

Stress Relaxation

Plastic deformation shows time dependence, as explained for creep where the external stress is kept constant. On the other hand, when a specimen is pulled to induce plastic flow and then kept at a constant total strain, plastic flow occurs with holding time and hence stress (elastic strain) decreases, which is called stress relaxation. To measure relaxation behavior,

a high-sensitivity strain detector is necessary because the change in the elastic strain is very small. In other words, this is a tensile test with extremely low strain rates, and the strain rate decreases continuously while the stress is held.

7.4.2 Dynamic Loading

Dynamic means that the loading or deformation speed is high compared with the quasistatic case. Several kinds of dynamic loading are found. These include high-speed tension or compression tests such as the Hopkinson split-bar method, impact tests, and fatigue tests. These three tests are explained below.

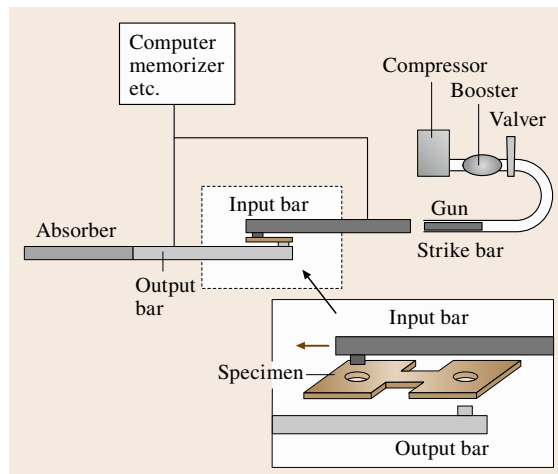


Fig. 7.52 Schematic illustration of a high-speed tension test using the Hopkinson split-bar method

High-Speed Tension or Compression Tests

These testing methods include the split pressure-bar tester, the one-bar method, the load-sensing block-type tester, and the servo-hydrostatic loading machine. The most popular method is the Hopkinson split-bar method in which either tension or compression impact deformation can be carried out. The outline of the test is shown in Fig. 7.52, where the input bar and the output bar are pictured. A specimen is set between them. To avoid the reflected stress pulse, the specimen gage length should be sufficiently short. Examples of flow curves obtained at a strain rate of $2 \times 10^3 \text{ s}^{-1}$ are presented in Fig. 7.53 [7.213, 214]. As seen, the flow stress becomes higher at a high speed, similarly to the case of lowering test temperature. Very-high-speed deformation occurs almost under adiabatic conditions, so that the temperature of a specimen increases with plastic deformation. Hence workhardening decreases in a low carbon steel with a large temperature dependence of flow stress. Such workhardening behavior is the difference between the deformation at lower temperature with a low strain rate and that at room temperature with a high strain rate. These data are useful for the safety design of automobiles with respect to traffic collisions or the safety of infrastructures such as buildings with respect to the occurrence of earthquakes.

The dislocation structure that evolves during plastic deformation is strongly dependent on the test temperature and strain rate. As shown in Fig. 7.54 [7.213] for the case of a low-carbon steel, the dislocation cell structure evolves at room temperature under a low-strain-rate deformation. However, planar dislocation arrays are observed either during low-temperature deformation with a low strain rate or at room temperature with a high strain rate.

Impact Test

Impact testing is performed to evaluate the toughness of materials. There are several loading methods, including tension, compression, bending, and torsion. The typical test is the Charpy impact test in which three-point bending is employed. As shown in Fig. 7.55, a hammer is dropped to hit a rectangular specimen. A V- or U-type notch is introduced to allow easy fracture due to stress concentration for ductile materials. In the case of brittle materials such as ceramics, cast iron etc., a notch is not introduced. Parts of the hammer before and after hitting (breaking) a specimen are compared. The balance is considered to show the resistance to fracture, and the energy needed to bend and fracture the specimen. The impact tester can impart 300 J for metallic materials use,

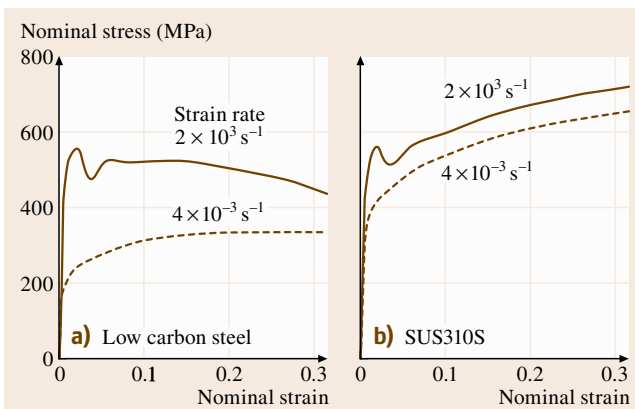


Fig. 7.53a,b Flow curves observed under high-speed deformation (the Hopkinson split-bar tension test): (a) low-carbon steel and (b) austenitic steel

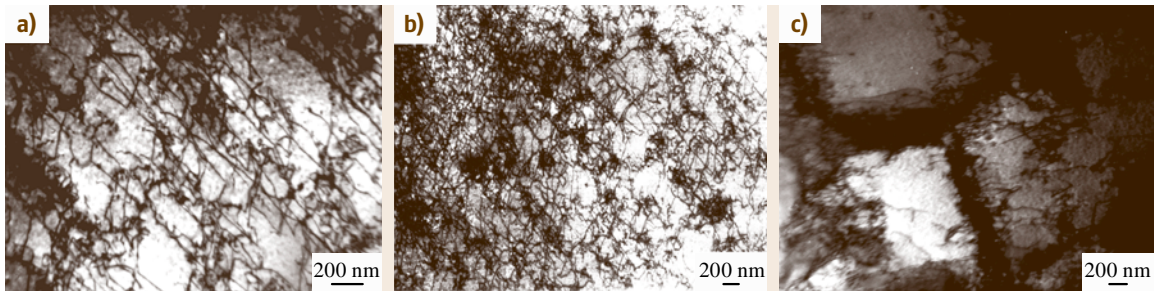


Fig. 7.54a-c Dislocation structures evolved by tensile deformation (10%) in ferritic steels: (a) 77 K, $3.3 \times 10^{-3} \text{ s}^{-1}$, (b) 295 K, $2 \times 10^3 \text{ s}^{-1}$ and (c) 295 K, $3.3 \times 10^{-3} \text{ s}^{-1}$

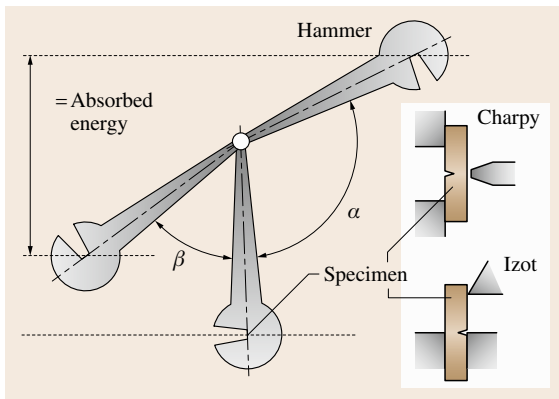


Fig. 7.55 Outline of impact testing: Charpy and Izot tests

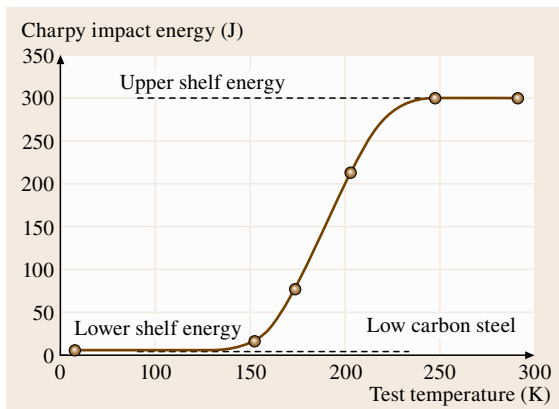


Fig. 7.56 Ductile-to-brittle transition behavior observed by the Charpy impact test

and 3 J for resin or plastics. The Izot tester is another typical device but is now rarely used. The specimen is held in a different way, as shown in Fig. 7.55. The absorbed energy K is calculated from the angle of the hammer and the starting (α) and maximum (β) height

after hitting,

$$K = WR(\cos \beta - \cos \alpha), \quad (7.67)$$

where W and R refer to the weight and the arm length, respectively.

Some materials fracture in a ductile manner under quasistatic testing but fracture in a brittle manner under impact testing. As the fracture mode is strongly dependent on the testing temperature, the Charpy impact test is carried out at a variable test temperature. The absorbed energy is then plotted as a function of the test temperature, as presented in Fig. 7.56 [7.208]. In the case of ferrite steel, for example, the energy changes at a certain temperature, known as the *ductile-to-brittle transition temperature (DBTT)*. At higher temperatures, specimens fracture in a ductile mode so that the fracture surface exhibits a dimple pattern. However, intergranular or cleavage (transgranular) fracture facets are observed in specimens fractured at lower temperatures. The DBTT is determined either from the absorbed energy or the percentage of dimple facet on the fracture surface. The results of impact tests are often used for material selection. It is difficult to use the results quantitatively for machine design, e.g., for the determination of design stress. On the other hand, the quantitative resistance to fracture is determined by other tests using precracked specimens based on fracture mechanics (see Sect. 7.4 for details).

Fatigue

Several fatigue testing methods have been utilized to date.

Rotating (four-point) bending has been used to simulate a wheel axis, where a tension-compression stress wave is repeated on the surface. The results are summarized in a diagram of stress amplitude versus number of cycles to fracture ($S-N$). As shown in Fig. 7.57, the applied stress amplitude is plotted as a function of the

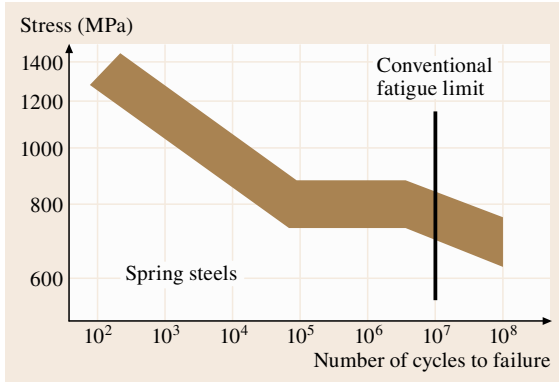


Fig. 7.57 Stress amplitude versus number of cycles to failure ($S-N$) curve for fatigue fracture

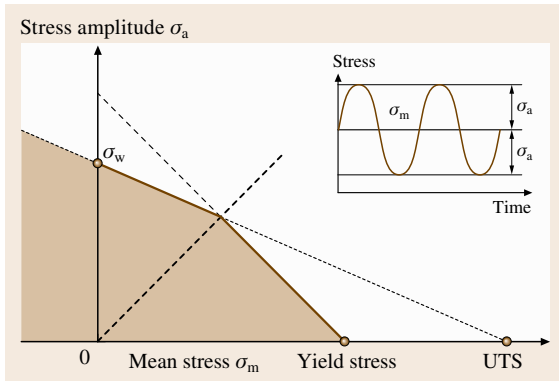


Fig. 7.58 Fatigue endurance-limit diagram where the influence of mean stress is given

number of cycles to failure [7.215]. As can be seen, the relationship is almost linear in the beginning and tends to saturate at a certain stress level near 10^6-10^7 cycles. In general, the stress at 10^7 cycles is called the fatigue strength or endurance limit σ_w . At stresses higher than σ_w , the number determines the time to fracture and is called fatigue life. Thus, the fatigue strength and fatigue life are utilized for the design of machines or structures.

Recent studies on very-long-life fatigue reveal that some materials fracture even at stresses below the conventional σ_w . In the case of aged materials, this should also be taken into consideration.

The influence of the mean stress on the fatigue stress (stress amplitude) is discussed using the fatigue-limit diagram shown in Fig. 7.58 where the stress amplitude at 10^7 cycles is plotted as a function of the mean applied stress. The diagram is constructed with consideration of the yield strength σ_s , tensile strength σ_B , and the

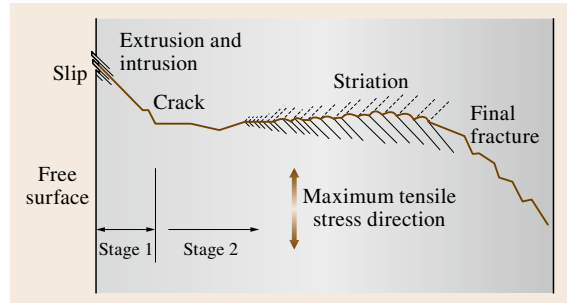


Fig. 7.59 Schematic illustration on fatigue fracture; crack initiation, growth and final fracture

true fracture strength, σ_f , obtained by tension testing that corresponds to a quarter cycle of the fatigue test. A hatched area is evaluated to be safe for both fatigue fractures and macroscopic yielding (failure of elasticity).

The mechanism for fatigue fracture is illustrated schematically in Fig. 7.59. In the usual case, a fatigue crack is initiated on the surface or a stress-concentrated region such as a flaw, brittle inclusions etc. If a material is nearly free from such defects, slip deformation occurs preferentially near the surface. Because of cyclic loading of small stress below the yield strength, slip occurs locally and repeatedly, resulting in intrusion and extrusion at the surface. Since the intrusion is a kind of micro-crack at which stress is concentrated (the first stage of fatigue cracking), plastic flow occurs locally at the tip of the micro-crack. The growth direction along the maximum shear stress then changes to be perpendicular to the applied tensile stress. This crack-propagating regime is called stage 2. When the crack length has increased enough to satisfy the final fracture condition given by the fracture mechanics approach (a detailed explanation of which is given in Sect. 7.4)

$$K_{\max} \geq K_{\text{th}}^F, \tag{7.68}$$

then final fracture takes place. Here, the left-hand side of (7.68) is the maximum stress-intensity factor K_{\max} ($= \alpha \sigma_{\max} \sqrt{\pi c}$), where α , σ_{\max} , and c refer to a constant related to the specimen's geometry, the maximum stress applied to the specimen and the crack length, respectively, and K_{th}^F is the fracture toughness against fatigue.

The crack growth speed during stage 2 is measured using a prepared specimen in which a sharp prenotch is introduced. With repeated application of the stress, the length of the crack is measured and the growth rate is then plotted as a function of the amplitude of the stress-intensity factor ΔK ($= \Delta \sigma \sqrt{\pi c}$), as shown in Fig. 7.60.

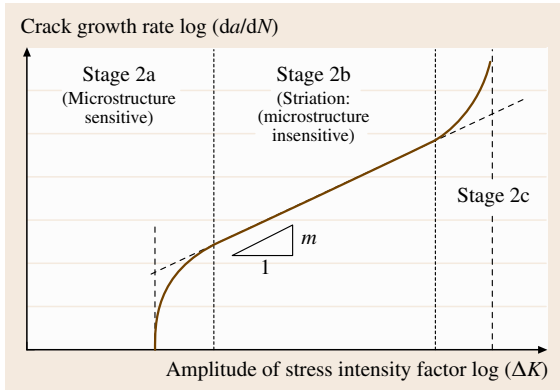


Fig. 7.60 Fatigue crack growth rate as a function of stress-intensity amplitude

The growth rate in the low- ΔK region can be measured by decreasing $\Delta\sigma$ continuously. Here, the engineering lower limit for crack growth is determined as the threshold intensity factor ΔK_{th} , which is sensitive to microstructural parameters. In the middle of the curve, it is approximated by a linear relationship described by Paris' equation [7.216, 217]

$$dc/dN = C \Delta K^m, \quad (7.69)$$

where C and m are constants. The crack growth rate during this stage 2 is insensitive to microstructure.

If the initial crack length c_i in a material is known, for example, by using nondestructive inspection such as x-ray transmission, the fatigue life N_f of the material can be predicted by combining (7.68) and (7.69). That is, by integrating (7.68), we obtain,

$$N_f = \int_{c_i}^{c_f} \frac{dc}{C(\alpha \Delta \sigma \sqrt{\pi c})^m}, \quad (7.70)$$

where c_f can be calculated by (7.68). In ductile materials, the fracture surface during stage 2 consists of striation, which is caused by repeated loading. Hence, the crack growth speed is estimated from fractography.

7.4.3 Temperature and Strain-Rate Effects

Flow stress is influenced by the test temperature mainly due to thermal activation mechanisms for dislocation motion. The thermal vibration of atoms leads to the vibration of the dislocation line. Therefore, the possibility per second of achieving a certain thermal activation energy is proportional to the Boltzmann probability. This means that the influence of temperature and strain rate on strength should be understood simultaneously; to achieve this, the *deformation mechanism map* has been constructed for various materials [7.218]. As an example, the deformation map for iron is presented in Fig. 7.61. Because iron shows ferrite-to-austenite and then austenite-to-ferrite transformations when heated,

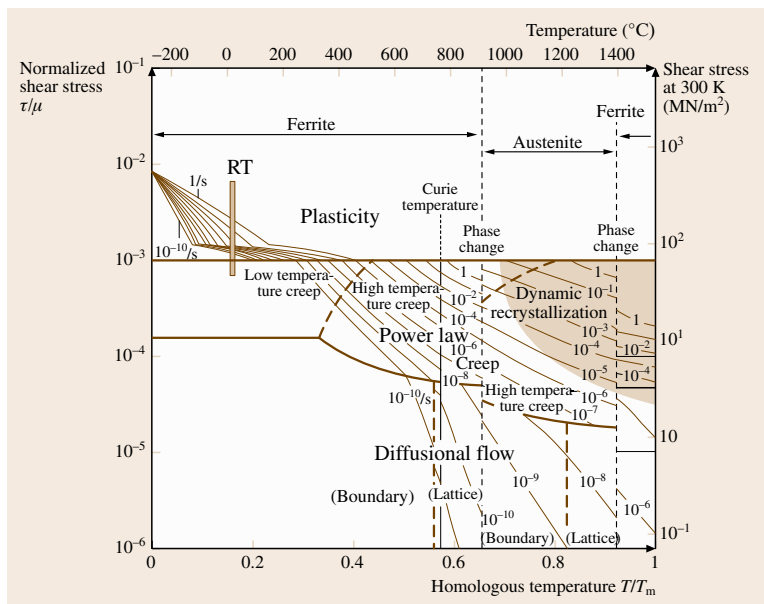


Fig. 7.61 Deformation map for iron ($d = 0.1$ mm)

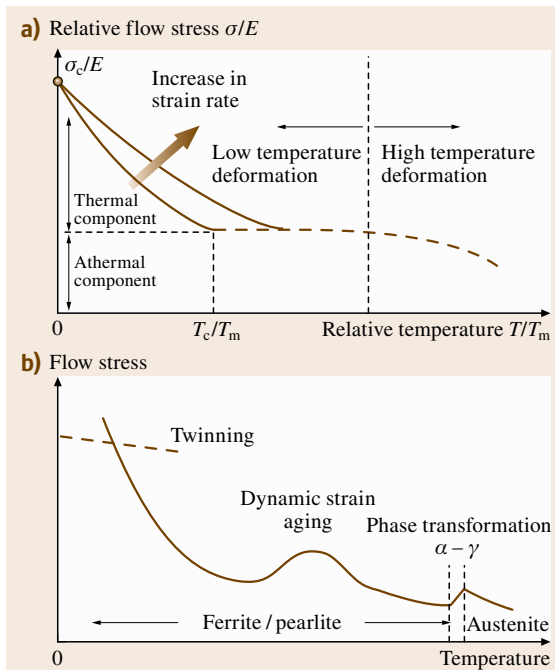


Fig. 7.62a,b Effect of temperature on the yield strength (schematic illustration): (a) general case and (b) mild steel

the curves for body-centered cubic (BCC, ferrite) is interrupted by a face-centered cubic (FCC, austenite) regime. Depending on the temperature and strain rate, various deformation mechanisms become dominant. Taking a look at the map near room temperature with a strain rate of $10^0-10^{-5} \text{ s}^{-1}$, the dominant mechanism is slip, i. e. dislocation motion. A simpler illustration to explain the effect of temperature on the yield strength is given in Fig. 7.62. At 0 K, the enhancement by thermal activation disappears and the strength corresponds to the theoretical strength. At a certain temperature, the strength is decreased through due to thermal activation of dislocation motion. At higher temperatures near $T_m/2$, all the short-range barriers for dislocation motion can be overcome, but some long-range barriers remain. The stresses related to overcoming these two kinds of barriers are called thermal stress (or effective stress) and athermal stress (internal stress), respectively. Thus, as shown in Fig. 7.62a, thermal stress becomes zero at T_0 . Below T_0 the temperature dependence of the yield strength is ascribed to thermal activation mechanisms for dislocation motion. Therefore, if the strain rate is increased, its effect is equivalent to decreasing temperature. The influence of strain rate on the yield

strength is also drawn schematically in Fig. 7.62a. Flow stress can also be discussed using this approach, although the evolution of the dislocation structure must also be taken into account. With increasing of plastic strain, the dislocation density (ρ) increases by ρ^+ and then workhardening occurs. At the same time, dislocations are annihilated with recovery to be decreased by ρ^- , which is influenced by temperature. Therefore, the total dislocation density ($\rho^+ + \rho^-$) is determined as a function of the strain as well as temperature and time, i. e., strain rate. The flow curve obtained at high strain rate is therefore influenced by two thermal activation mechanisms: dislocation motion and dynamic recovery.

When the test temperature is higher than T_0 , the microstructure itself changes obviously during deformation, for example exhibiting to grain growth, dynamic recovery and/or recrystallization. Such a region, as shown in Fig. 7.62a, is called high-temperature deformation. As observed in Fig. 7.61, creep deformation occurs strongly at high temperatures with small strain rates.

The behavior of a real material is complicated in comparison with that of the pure metal in Fig. 7.62a. The example of mild steel is presented in Fig. 7.62b [7.219]. The curve in the lower-temperature region corresponds to the deformation of the BCC ferrite phase, while that in the higher-temperature region corresponds to FCC austenite. Moreover, due to the intrusion of deformation twinning at cryogenic temperatures and dynamic strain aging caused by solute carbon and nitrogen atoms in the region slightly above room temperature, the typical behavior explained in Fig. 7.62a is not easy to discern.

7.4.4 Strengthening Mechanisms for Crystalline Materials

As described above, flow stress is controlled by the motion of dislocations. Hence, there are two ways to strengthen a material: remove dislocations thoroughly or introduce a large number of obstacles to prevent dislocation motion. The former approach has been achieved in the form of single-crystal whiskers. When the diameter of the whisker increases, the strength decreased rapidly due to the inevitable introduction of defects including dislocations. The latter approach has been used widely, including solid-solution hardening, precipitation hardening or dispersion particles hardening, workhardening, grain-refinement hardening and the duplex structure (composite) hardening. These mechanisms to prevent dislocation motion are described below.

Solid-Solution Hardening

The interstitial or substitutional solute atoms hinder the motion of dislocations due to the size effect and/or the effect of an inhomogeneous elastic modulus. These are elastic interactions and hence can be overcome by thermal activation for dislocation motion. The amount of hardening is given by

$$\Delta\sigma = Ac^n, \quad (7.71)$$

where A and c refer to a material constant and the concentration of solute atoms, respectively. The constant n is about 0.5–1.0 from experimental or theoretical considerations.

Workhardening

As explained in the previous sections, the dislocation density is increased by plastic deformation and mobile dislocations have to pass through the resulting dislocation structure. There are two types of dislocation–dislocation interactions: short-range interactions, including elastic interactions, cutting, reactions etc., and long-range interaction due to internal stresses caused by the dislocation structure. The back-stress caused by piled-up dislocations is a typical example. Either model gives strengthening according to

$$\Delta\sigma = B\sqrt{\rho}, \quad (7.72)$$

where B is constant. This equation was firstly proposed by *Bailey and Hirsch* [7.220].

Precipitation or Dispersion Hardening

When small precipitates are dispersed in a matrix, a dislocation line interacts with them. When the particle is weak, the dislocation line cuts through such particles and passes through, as shown in Fig. 7.63. The threshold con-

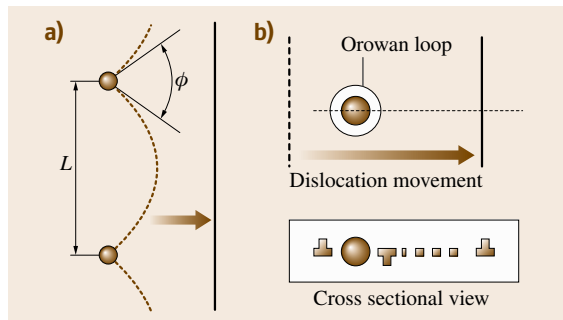


Fig. 7.63a,b Strengthening mechanisms for obstacles dispersion; (a) cut-through mechanism and (b) Orowan bypass mechanism

dition is given by the following equation

$$\Delta\sigma = (a\mu b/\lambda) \cos(\phi/2), \quad (7.73)$$

where a is a constant, μ is the shear modulus, b is the magnitude of the Burgers vector of a dislocation, λ is the average distance between particles, and ϕ is the critical angle to cut the particle. If ϕ is 0° , a dislocation line passes through the particle, leaving a dislocation loop known as an Orowan loop (Fig. 7.63b). This is the case of a strong particle, leading to the following equation for dispersion hardening (using $\phi = 0$ and $a \approx 2$ in (7.73))

$$\Delta\sigma = 2\mu b/\lambda. \quad (7.74)$$

Grain-Refinement Hardening

When a dislocation moves towards a grain boundary, it is stopped and induces internal stress, as is shown in Fig. 7.64. When dislocations pile up at the grain boundary, the back-stress generated hinders the further motion of dislocations, as described for the case of workhardening. Because the number of piled-up dislocations depends on the applied stress and slip distance, i. e., grain diameter (d), the amount of strengthening ($\Delta\sigma$) is given by theoretical relations such as

$$\Delta\sigma = kd^{-1/2}. \quad (7.75)$$

Other interpretations have been proposed for the effect of grain size in this mechanism. For instance, the dislocation density is increased due to the occurrence of many

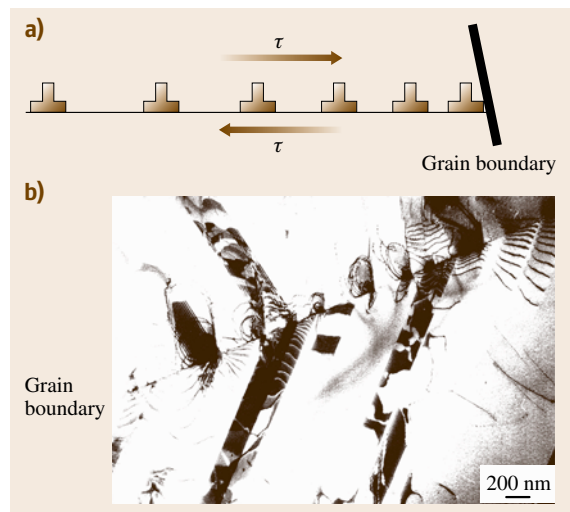


Fig. 7.64a,b Strengthening mechanism for grain boundary or interface: (a) dislocation pile-up model and (b) TEM micrograph for a high-nitrogen-bearing austenitic steel

slip systems in the vicinity of a grain boundary due to high local internal stresses. The amount of strengthening is given by the Bailey–Hirsch relation (7.72). Because the increase in the dislocation density is proportional to the grain diameter d , the resultant equation exhibits the same form as (7.75). Another interpretation for grain-refinement hardening is that new dislocations are emitted from a grain boundary in the neighboring grain to relax high local internal stresses. As (7.75) was first proposed by Hall and Petch [7.221–223] based on experimental data, it is called the Hall–Petch relation. In fact, several phenomena must be overlapping in this mechanism, but the increase in strength can be expressed roughly by (7.75).

Duplex Structure (Coarse Multiphase) Hardening

When the grain diameter of the second phase is comparable to that of the matrix, the mechanism for dispersion hardening such as the Orowan bypass model is no longer applicable. Plastic flow takes place preferentially in the soft phase, resulting in stress partitioning between the constituents, known as phase stress or averaged internal stress. Such strengthening is similar to that for composite materials. Many engineering materials such as ferrite–pearlite steel, dual-phase steels, $\alpha - \beta$ Cu–Zn alloys etc., belong to this category. Although micromechanics models have been developed to express the deformation of a multiphase material, flow stress is described roughly by a kind of mixture rule. In the case of a two-phase alloy,

$$\sigma = \sigma_1(1 - f) + \sigma_2 f, \quad (7.76)$$

where σ_1 , σ_2 , f refer to the strength of the matrix, the strength of the second phase and the volume fraction of the second phase, respectively.

Usually the above strengthening mechanisms are superposed. Hence, a suitable superposition rule has to be used for real engineering materials. This may be simply described by

$$\sigma = \sum_{i=1}^n \sigma_i^N. \quad (7.77)$$

In the case of superposition of strong and weak obstacles, the value of N is believed to be nearly unity but is less than unity in other cases where both obstacles are strong.

7.4.5 Environmental Effects

The environment where a material is used influences its strength. Such influences include chemical reactions

such as corrosion and radiation damage in a nuclear furnace. Here, two examples are explained because the social impact of these fracture is serious: hydrogen embrittlement and stress corrosion cracking.

Hydrogen-Induced Embrittlement

The most difficult barrier to the use of high-strength steels is hydrogen embrittlement, or so-called delayed cracking. Hydrogen atoms invade not only during the processing of products but also during service. Current topics in this area include the interaction of mobile dislocation and hydrogen atoms and the diffusion of hydrogen atoms within materials. The fracture mechanism is, however, not yet clear.

Figure 7.65 shows the fracture strength after 100 h in water for various kinds of steels [7.224]. The fracture strength is plotted as a function of the tensile strength obtained using the conventional tension test. It is clear the fracture strength increases with increasing tensile strength up to approximately 1.0 GPa. However, steels in the 1.5 GPa (tensile strength) class exhibit a large scatter in their fracture strength; some remain strong while others can drop below 1.0 GPa. Therefore, the strengthening in a mild environment is not necessarily valid under different environmental conditions. The occurrence of fracture depends strongly on the microstructure, i.e., strengthening mechanism.

Another fracture mechanism caused by hydrogen atoms is *hydrogen attack* which is observed for materials subjected to high temperatures in chemical

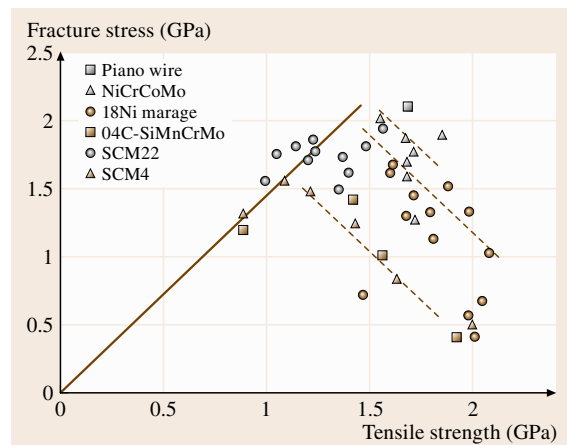


Fig. 7.65 Hydrogen-induced embrittlement observed in various kinds of steels. (Fracture stress at 100 h in water for a notched specimen with a stress concentration factor of 10 versus tensile strength)

atmospheres such as that in an oil plant. In the case of carbon steel, the invading hydrogen atoms react with cementite particles to produce methane gas, resulting in the formation of blisters that lead to rupture. The critical condition for hydrogen attack is summarized by the so-called Nelson diagram, in which the dangerous conditions are summarized in terms of temperature and partial pressure of hydrogen.

Stress Corrosion Cracking

Stress corrosion cracking (SCC) is observed in many alloys (not in pure metals) under certain combined conditions of stress, chemical environment and microstructure, as shown in Fig. 7.66a. For instance, SCC has been found for Al alloys in air and sea water, Mg alloys in sea water, Cu alloys in water or ammonium atmosphere, carbon steels in NaOH solution, austenitic stainless steels in hot water, and so on. External or

residual tensile stress always plays an important role in fracture. Stress accelerates local corrosion (anode solution) and amplifies the stress at crack tips, leading to fracture. SCC fracture occurs along either certain crystal planes in grains or grain boundaries. Macroscopic crack propagation is summarized by using the stress intensity factor K , as shown in Fig. 7.66b. The threshold K is defined as K_{ISCC} , which is dependent on the materials's microstructure. In general, the stronger the yield strength, the lower the value of K_{ISCC} , so that the balance between strength and toughness is important.

When an austenitic stainless steel is exposed to a high-temperature atmosphere, Cr carbide precipitates along the grain boundaries, leading to the formation of a low-Cr zone. Corrosion then concentrates in such low-Cr zone in the vicinity of the grain boundary and cracks are initiated along the grain boundary, influenced by local corrosion and local stress concentration. The concentration of carbon is, therefore, extremely reduced in steel-making for this use; in a nuclear reactor, it is known that stress corrosion cracking is a key problem for safe operation. Thus, extensive investigations have been made on SCC for austenitic stainless steels. It is also known that radiation damage accelerates SCC cracking. However, recent results have indicated that stress corrosion cracking on shroud plates in a nuclear reactor starts in the interior of grains at the surface, although the reason for this is not clear.

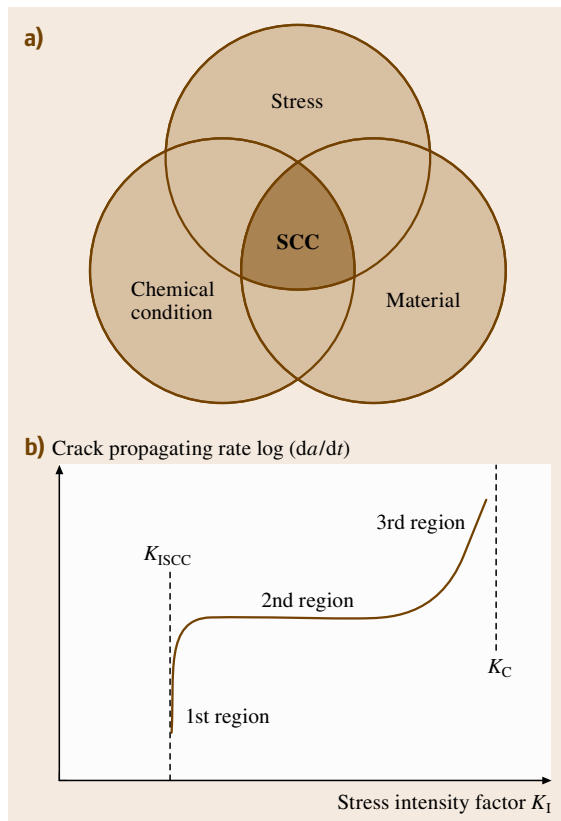


Fig. 7.66a,b Stress corrosion cracking: (a) influential factors of stress, microstructure and chemical environment for stress corrosion cracking and (b) crack-propagation rate as a function of stress-intensity factor

7.4.6 Interface Strength: Adhesion Measurement Methods

Most engineering materials consist of multiple phases. For instance, inclusions or precipitates are usually introduced into engineering materials, whether intentionally or not. Some of these are harmful to the material properties but others are useful for improving properties such as material strength. A typical example is a composite material. In the case of electronics packaging, interfaces between different materials are very important. In particular, for nanosized devices, performance is strongly dependent on the situation of interfaces. To examine the strength of an interface experimentally, several methods are employed depending on the requirements. The tests are not easy and require careful analysis, sometimes with the help of FEM calculations. The strength of an interface is theoretically predicted by means of the molecular dynamics method, which is helpful for understanding the mechanism as well as interface design.

Tensile Strength

The fracture strength perpendicular to the interface is tested in a similar method to tension test. Figure 7.67 shows the tension test used to measure the interface strength [7.225]. Here, one should note the inclination of the interface with respect to the tensile direction. If the interface is inclined, even at an angle less than 1° , the shear stress component appears to influence the fracture mode. The normal to the interface should be carefully adjusted to be parallel to the tensile direction. This test is quite simple and easy to apply to some artifi-

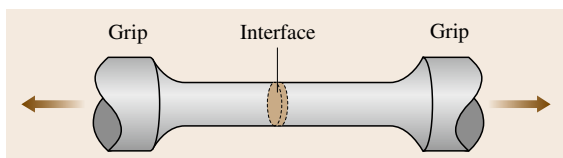


Fig. 7.67 Tension test to measure the normal separation at the interface

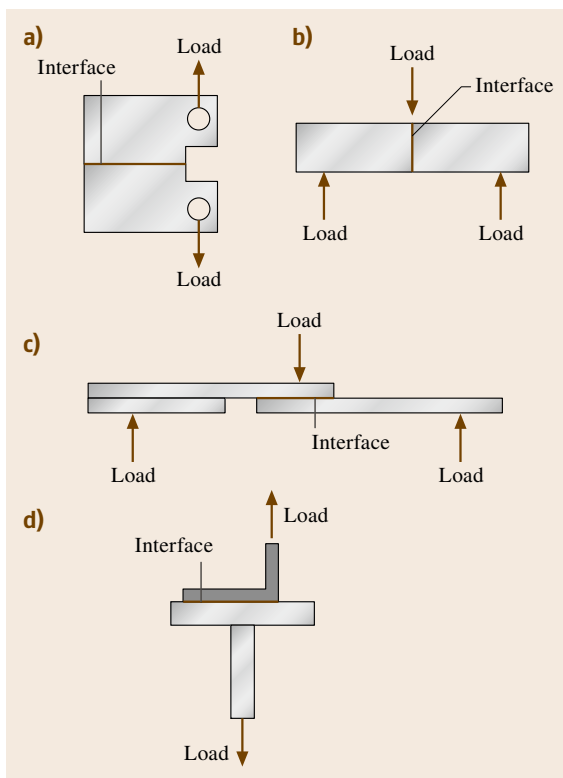


Fig. 7.68a–d Bending test to evaluate cleaving stress at the interface: (a) compact tension test, (b) three-point bending loading parallel to the interface, (c) three-point bending loading perpendicular to the interface and (d) peel-off test

cially bonded parts but is not easy to apply to multiphase alloys.

Cleavage Strength (Bending)

Similar to fracture toughness testing, compact tension testing, using a specimen shown in Fig. 7.68a, is employed to examine the cleaving features of the interface where the fracture mode is tensile [7.225]. Simpler methods based on three- or four-point bending are shown in Fig. 7.68b and c. The strength for the decohesion can be evaluated by these tests, while Fig. 7.68d shows the peeling test. Some modifications of these tests are also used.

Shear Strength (Adhesive Strength)

The evaluation of shear strength at the interface, which is a key issue for composite strengthening and several mechanically bonded parts, is an interesting measurement. To measure the adhesive shear strength, the most popular test is shown in Fig. 7.69a [7.225]. The thickness of the grip is the same as that of the specimen containing the interface, so that a bending moment can be avoided. Figure 7.69b exhibits the compression-type shearing test, which is frequently employed to evaluate the strength of wire bonding in electric devices. As shown in Fig. 7.69c, a special tool is prepared to push the bonded wire to measure the decohesion stress [7.226].

The interface strength between inclusions or precipitated particles and the matrix in engineering materials cannot be measured directly. In the case of fiber-reinforced materials, methods to measure the shear strength between the reinforcement and the matrix based on pulling or pushing the fiber have been attempted. To realize such a test, a small jig to grip the fiber or a small

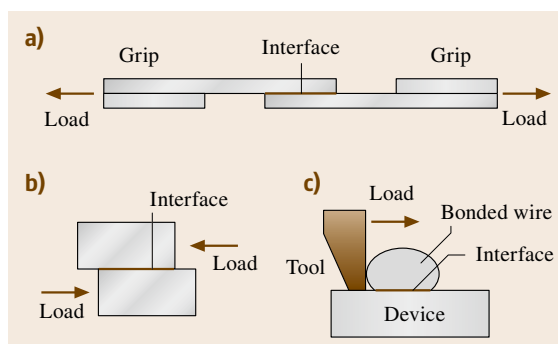


Fig. 7.69a–c Shearing tests: (a) tension-type test for shearing the interface, (b) compression-type test, (c) shearing test for wire bonding

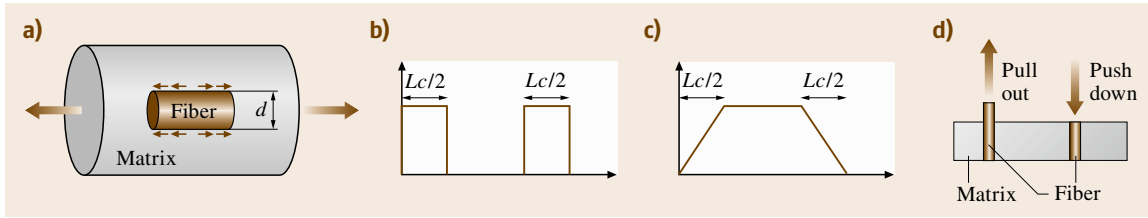


Fig. 7.70a–d Shear strength of interface in a composite material: (a) model of short fiber-reinforced composite, (b) shear stress distribution under the applied stress when the matrix is yielded, (c) tensile stress distribution corresponding to (b) and (d) pull-out and push-down tests to evaluate the shear strength of the interface

indenter with a tiny tip must be prepared. The schematic testing arrangement is illustrated in Fig. 7.70 [7.227]. The simple shear-lag model for composite strengthening is shown in Fig. 7.70a. When the matrix yields under the external tensile stress, the load transfer from the matrix to a fiber, i. e., the shear stress τ_c , can be roughly described as in Fig. 7.70b. Within a limited length L_c , shear stress is generated and the integrated tensile stress inside the fiber is shown in (b). If the fiber is short, a pull-out phenomenon occurs, but if the fiber is long enough, the tensile stress reaches the fracture strength σ_f . Hence, in order to use the strength of fiber efficiently, the length should be larger than $\sigma_f d / (2\tau_c)$, where d is the fiber diameter. This is called the critical length $L_{c_{max}}$. When a fiber is shorter than $L_{c_{max}}$, fracture does not take place. Figure 7.70d presents mechanical tests to measure the decohesion shear strength at the interface. If the length of the fiber is shorter than $L_{c_{max}}$, it can be pulled out or pushed down and the interface strength can be evaluated from the relevant load–displacement curve. However, in most cases, the fiber fractures during pulling, and suitable modeling has to be considered to estimate the shear stress. When a brittle phase is formed at the interface, fracture occurs easily and the cracking of the brittle layer plays the part of a notch in reducing the fiber strength.

Scratch Test for Thin-Film Coatings

The decohesion strength of thin or thick films is frequently of concern for surface modification. Various surface treatment such as chemical vapor deposition (CVD), physical vapor deposition (PVD) etc. have been developed. For rough testing to evaluate the interface strength, adhesive tape is stuck onto the film and pulled quickly, as shown in Fig. 7.71a. If the interface strength

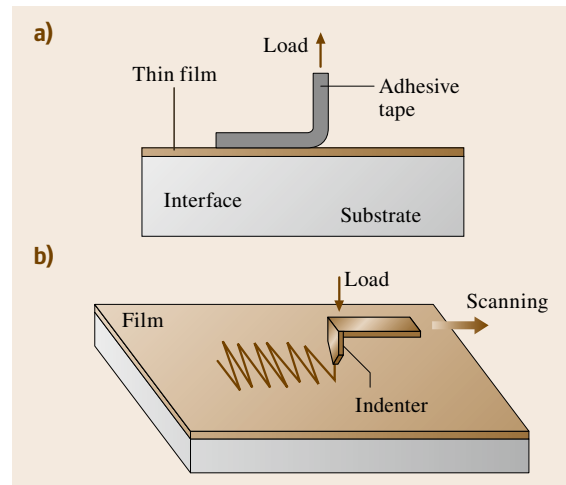


Fig. 7.71a,b Tests to evaluate the strength of interface between the deposited film and substrate: (a) peel-off test using adhesive tape and (b) scratching test for thin film on a substrate to examine decohesion behavior, where a diamond indenter with a tip radius of several μm is used

is weak, the film can be removed easily. However, this test is not sufficient to evaluate the reliability of bonding and hence more quantitative tests are used. Figure 7.71b shows a schematic illustration of such a test [7.226]. An indenter is pressed into the film and pulled along to scratch a zigzag route, during which the applied stress is increased gradually. After this test, the position where separation starts can be determined by observation with a scanning electron microscope (SEM) and the applied stress at that point can then be found. Sometimes, the test is performed inside a SEM.

7.5 Fracture Mechanics

In materials that are components of large engineering structures the presence of fabrication flaws and their development during operational service should be anticipated. It is rational to assume that flaws exist and that countermeasures against the fracture and fatigue that develop from them should be taken.

In the 1920s, A. A. Griffith conducted a series of experiments to determine the fracture strength of glass components that contained small flaws. From this experiments, he concluded that for *brittle materials* the stress required to cause failure decreased as the size of the flaw increased, even after correction is made for the reduced cross section of good material. Extending these findings to other types of materials, it was generally found that the strength of a structural component that contains a crack or crack-like flaw decreases with increasing crack size and cannot be deduced from the mechanical properties obtained in conventional tensile tests (Sect. 7.3.1) or other mechanical tests using smooth specimens. The combined mathematical–experimental approach employed in the evaluation of the strength of cracked components is called *fracture mechanics*; it provides a methodology to determine the amount of crack growth and the residual strength of cracked components during operational service.

7.5.1 Fundamentals of Fracture Mechanics

The fundamental principle of fracture mechanics is that the stress and strain field ahead of a sharp crack can be characterized in terms of a single parameter, such as the stress intensity factor K , that is a function of the applied stress, crack size and geometrical boundary conditions. Crack growth or fracture initiation from a precrack must be controlled by the stress or strain state at the crack–tip region. This implies that the fracture behavior from a crack can be described by the fracture mechanics pa-

rameter, as an analogy with the plastic yielding behavior of materials described in the form of σ_{eq} (equivalent stress) = σ_{ys} (yield strength of the material). The crack–tip stress–strain similarity anticipates to result in the same type of fracture under the same environmental condition. Once the fracture resistance of a material is described in terms of its fracture mechanics parameter in laboratory tests, one can deduce its fracture behavior under different applied stresses, crack sizes and geometrical boundary conditions without any discussion of the mechanisms of fracture concerned. The fracture mechanics approach has three variables for the evaluation of strength, as shown in Fig. 7.72.

Fracture mechanics can be subdivided into two general categories, namely linear elastic and elastic–plastic. Materials with relatively low fracture resistance fail under small-scale yielding at the crack tip and can be analyzed through linear-elastic fracture mechanics (LEFM), in which the stress intensity factor, K , is based on the elastic stress analysis. Metallic materials often show large-scale plastic yielding preceding crack growth or fracture initiation from the crack. Elastic–plastic fracture mechanics (EPFM) is applied for these large-scale yielding conditions. The J integral and the crack–tip opening displacement (CTOD) can be used as alternative fracture mechanics parameters to K .

Linear Fracture Mechanics

Consider an elastic body of arbitrary configuration with an ideally sharp crack, subjected to arbitrary external forces. There are three types of relative movements of the two crack surfaces, as Fig. 7.73 illustrates. The opening mode, mode I, is the most popular displacement mode in practical components, and is characterized by opening displacements in the direction of the principal load. Mode II and mode III correspond to in-plane shear loading and out-of-plane shear load-

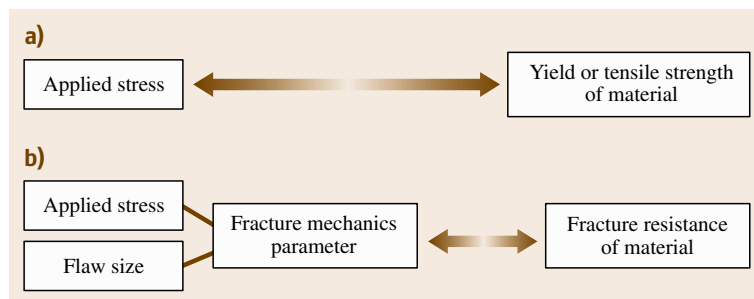


Fig. 7.72a,b Comparison of the fracture mechanics approach (b) to design with the (a) traditional design approach

ing, respectively. In any problem a cracked body can be treated as one or a combination of these three modes.

The theory of elasticity derives closed-form expressions for the stresses around the crack tip for each of these modes of deformation, assuming isotropic linear elastic material behavior [7.228–230]. For a polar coordinate axis as shown in Fig. 7.74, the stress field in any cracked body is given by

$$\sigma_{ij}(r, \theta) = \left(k \sqrt{\frac{a}{r}} \right) f_{ij}(\theta) + \sum_{n=0}^{\infty} A_n \left(\sqrt{\frac{r}{a}} \right)^n g_{ij,n}(\theta), \quad (7.78)$$

where σ_{ij} is the stress tensor, k and A_n are constants, and f_{ij} and g_{ij} are functions of θ . The higher-order terms depend on the geometrical boundary conditions. The first leading term approaches infinity as r reaches 0, but the other terms remain finite. Thus, the stress at the crack–tip region has a singularity of order $1/\sqrt{r}$, regardless of the configuration of the cracked body. The stress fields ahead of a crack tip, where r is sufficiently small compared with the crack length a , can be rewritten as

$$\sigma_{ij, I} = \frac{K_I}{\sqrt{2\pi r}} f_{ij, I}(\theta), \quad (7.79a)$$

$$\sigma_{ij, II} = \frac{K_{II}}{\sqrt{2\pi r}} f_{ij, II}(\theta), \quad (7.79b)$$

$$\sigma_{ij, III} = \frac{K_{III}}{\sqrt{2\pi r}} f_{ij, III}(\theta), \quad (7.79c)$$

for modes I, II, and III, respectively. These field equations show that the magnitude of the elastic stress field can be described by the single-term parameters K_I , K_{II} , and K_{III} . The stress intensity factor K , given a subscript to denote the mode of crack deformation, is a function of the applied force, the crack shape and size, and the structural configuration. However, since mode I cracking is often question in practical constructions, the subscript I is usually abbreviated for the mode I.

The general form of the stress intensity factor is given by

$$K = F\sigma\sqrt{\pi a}, \quad (7.80)$$

where F is a parameter that depends on the geometry of the specimen or component with a crack. For an infinite plate subjected to uniform tensile stress σ containing a through-thickness crack of length $2a$, the stress intensity factor is

$$K = \sigma\sqrt{\pi a}. \quad (7.81)$$

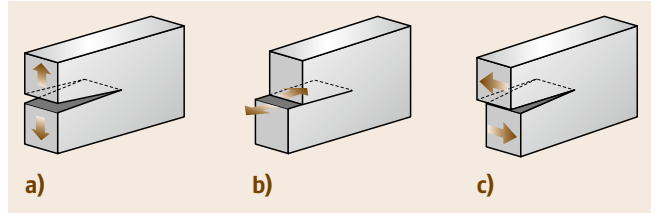


Fig. 7.73a–c Three modes of crack deformation. (a) Mode I (opening) (b) Mode II (in-plane shear) (c) Mode III (out-of-plane shear)

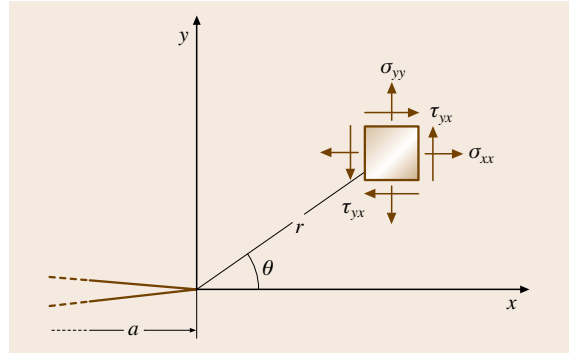


Fig. 7.74 Crack–tip stresses in polar coordinate

Equations (7.79aa–c) show the elastic stress field in the singularity zone ahead of the crack for an idealized crack model. In real materials, the stresses at the crack tip do not take an infinite value because the crack–tip radius must be finite, and the metallic material in this region undergoes plastic deformation and leads to further relaxation of the crack–tip stress. However, the size of the plastic zone or the ambiguity zone that surrounds the crack tip is so small compared with the singularity zone (for small-scale yielding) that the stresses in the surrounding zone still take the form (7.79a). Thus, the stress intensity factor K is still a representative parameter for the stress field at the crack tip, although the crack–tip stresses are devoured in black box.

The small-scale yielding condition is given by the ASTM [7.231] as

$$a \geq 2.5 \left(\frac{K}{\sigma_{ys}} \right)^2, \quad (7.82)$$

which gives one of the limitations for linear elastic fracture mechanics.

Elastic–Plastic Fracture Mechanics

Under the large-scale yielding condition, where (7.82) is not satisfied, the stress intensity factor loses its physical basis as a fracture mechanics parameter. An al-

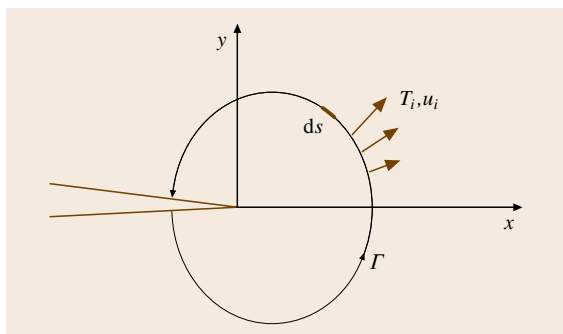


Fig. 7.75 Contour integral around the crack tip

ternative parameter for a nonlinear elastic material is the J integral. Rice [7.232] presented a path-independent contour integral, which is called J , for a cracked body. The J integral is given by

$$J = \int_{\Gamma} \left[W(\varepsilon_{ij}) dy - T_i \frac{\partial u_i}{\partial x} ds \right] \quad (7.83)$$

where $W(\varepsilon_{ij})$ is the strain energy density, T_i are the components of the traction vector, u_i are the components of the displacement vector, and ds is a length increment along the contour Γ , as illustrated in Fig. 7.75.

The value of the J integral is independent of the path of integration and is equivalent to the energy-release rate for a nonlinear elastic material. It can be shown that the J integral characterizes the crack-tip stress field in a nonlinear elastic material (the Hutchinson–Rice–Rosengren (HRR) stress field) [7.233, 234] as well as the stress intensity factor in a linear elastic material. Under the large-scale yielding condition, the size of the HRR stress field depends on the magnitude of the plastic yielding scale and the plastic constraint of a specimen. Whether the HRR stress field exists or not gives a limitation on the J integral approach for large-scale yielding [7.235].

Another parameter in elastic–plastic fracture mechanics is the crack-tip opening displacement (CTOD), the plastic deformation blunted an initially sharp crack, as illustrated in Fig. 7.76. Wells [7.236] proposed the opening at the crack tip as a measure of fracture toughness. The CTOD can be related to the stress intensity factor and the J integral under the small-scale yielding condition as given by

$$J = m\delta\sigma_{ys} = \frac{K^2}{E(1-\nu^2)}, \quad (7.84)$$

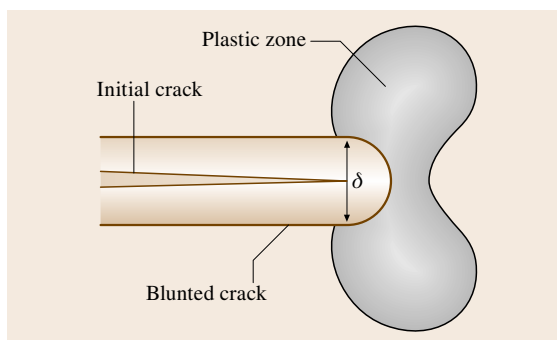


Fig. 7.76 Crack-tip blunting and CTOD

where δ is the CTOD, m is a dimensionless constant that depends on material properties and stress triaxiality, and E and ν are the elastic modulus and Poisson's ratio, respectively.

Details of the J integral and CTOD are well described in [7.235]. To evaluate the J integral according to (7.83), numerical analysis with a constitutive equation for the material (relationship between plastic strain and stress) is needed. The CTOD has an ambiguity in its definition for numerical analysis. Thus, the evaluation of parameters during the application of the elastic–plastic fracture mechanics for actual structures is difficult. For a deeply cracked specimen subjected to bending load, simple experimental procedures have been proposed to evaluate the J integral and CTOD [7.235, 237, 238].

7.5.2 Fracture Toughness

The fracture mechanics parameter uniquely stipulates the stress and strain state at the crack tip provided that the constraint in a direction parallel to the crack front is the same. The constraint on deformation in the crack-tip region is closely related to the triaxial stress state and depends on the geometry of the specimen, the scale of plastic yielding, and strain hardening of the material.

Linear elastic fracture mechanics describes unstable fracture as fracture occurs when the stress intensity factor K reaches a critical value K_c . The fracture toughness, K_c for mode I deformation under small-scale yielding and plane-strain stress state (sufficient constraint), is designated K_{Ic} [7.231]. The toughness in terms of the J integral is designated by J_{Ic} and J_c [7.237]. J_{Ic} is the toughness for onset of slow crack growth from a crack and J_c is the toughness for unstable fast fracture. It should be noted that there is no harmonization in terminology of K_{Ic} and J_{Ic} . The

CTOD criterion is also applied to evaluate the fracture toughness under large-scale yielding. Historically, the cleavage fracture toughness of structural steels has often been evaluated in terms of the critical CTOD δ_c .

In the standards for toughness testing, several specifications are prescribed so that the constraint effect can be negligible. Single-parameter fracture mechanics breaks down in the presence of excessive plasticity, or for specimens with too shallow a notch, and fracture toughness depends on the size and geometry of the test specimen.

K_{Ic} Testing

The standard test methods for determining plane-strain fracture toughness (K_{Ic}) of metallic materials are specified in several standards [7.231, 238, 239]. In these standards, ASTM E399-90 [7.231], which was originally published as E399-70, is widely used.

For the standard K_{Ic} test, a single-edge notched (SEN) bend specimen or a compact test (CT) specimen is used; these standard geometries are shown in Figs. 7.77 and 7.78, respectively. The standard bend specimen has a rectangular cross section ($B \times 2B$, $W = 2B$, where B is the specimen thickness and W is the specimen width). Alternative a specimen geometry with square cross section ($B \times B$, $W = B$) can also be used for the bend test. However, the size requirement for

the plane-strain fracture toughness test, which will be described later, should be satisfied. In the CT specimen, $W = 2B$ is recommended.

The fatigue precrack is introduced at the notch tip by cyclic loading and the recommended value for the total crack length (machined notch plus fatigue crack) is $0.45\text{--}0.55W$. The fatigue precracking load can affect the fracture toughness results, so the cyclic loading conditions are strictly limited. The stress ratio (minimum load to maximum load) of cyclic loading is between -1 and 0.1 . The maximum fatigue stress intensity (K_{max}) does not exceed 80% of the K_{Ic} value of the material. For the final stage of fatigue crack extension, K_{max} must not exceed 60% of the K_{Ic} value, and the ratio of K_{max} to the Young's modulus of the material K_{max}/E should not exceed $0.00032\text{ m}^{1/2}$. Usually, the number of cycles for fatigue precracking is $10^4\text{--}10^6$. Normally, as the temperatures of the fatigue cracking and fracture toughness tests are different, the effect of temperature should be taken into account. When fatigue cracking is conducted at temperature T_1 and the fracture testing at a different temperature, T_2 , K_{max} must not exceed $0.6(\sigma_{ys1}/\sigma_{ys2})K_{Ic}$, where σ_{ys1} and σ_{ys2} are the yield stress at the respective temperatures T_1 and T_2 . It is recommended that the length of the fatigue crack be larger than 1.3 mm and 2.5% of W for a straight-through notch.

The single-edge notched specimen is loaded in three-point bending with a support span S , which is normally equal to $4W$, that is $S = 4W$. The bend testing fixture is designed to minimize friction effects by allowing the support rollers to rotate and move apart slightly when the specimen is loaded. The compact specimen is loaded in tension through pins by allowing the specimen to rotate during the test.

Fracture tests are conducted with a static loading with a rate of increase of stress intensity of $0.55\text{--}2.75\text{ MPa m}^{1/2}$. The test temperature is controlled within 3°C [7.237] and the specimen should be kept at the test temperature for 1.2 min/mm of specimen thickness before testing [7.238]. During testing, continuous measurement of load versus crack mouth opening displacement is required. The displacement is measured by a double-cantilever displacement gage or a ring-type displacement gage.

After fracture testing, the crack length is measured at the following three positions: at the crack front, and midway between the center of the crack front and the end of the crack front on each surface of the specimen. The average of these three measurements is the crack length and is used to calculate the stress intensity.

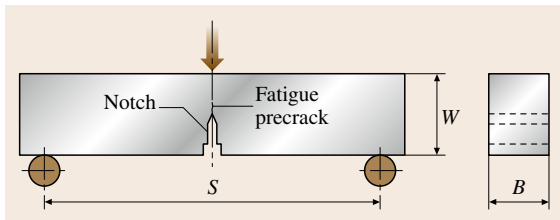


Fig. 7.77 Single-edge notched (SEN) bend specimen

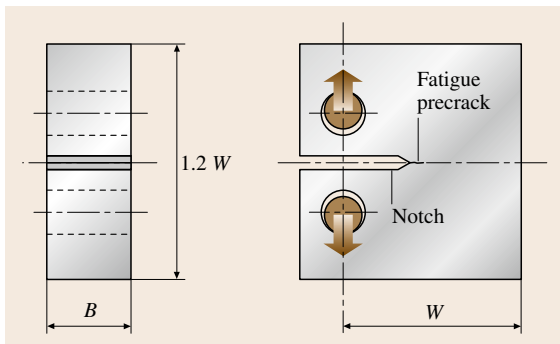


Fig. 7.78 Compact test (CT) specimen

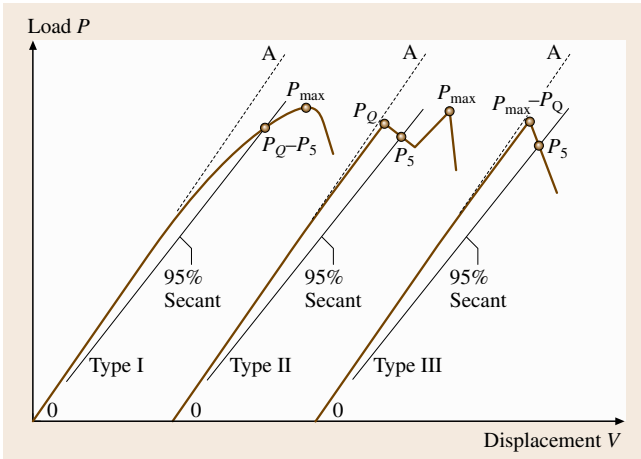


Fig. 7.79 Principal types of load–displacement records

The maximum difference between these measurements is specified in the standards.

Based on the test record of load versus crack mouth opening displacement, it is first necessary to calculate a conditional result K_Q , using which the size requirement for the plane–strain condition is judged. When the size requirement is satisfied K_Q becomes K_{Ic} . The procedure is as follows

1. Draw the secant line OP_5 from the origin of the record with the slope $(P/V)_5 = 0.95(P/V)_0$, where $(P/V)_0$ is the slope of the tangent OA to the initial linear part of the test record, as shown in Fig. 7.79. The load P_Q is then defined as follows: if the load at every point on the record which precedes P_5 is lower than P_5 , then P_5 is P_Q (Fig. 7.79, type I); if, however, there is a maximum load preceding P_5 that exceeds it, then this maximum load is P_Q (Fig. 7.79, types II and III).
2. Calculate the ratio P_{\max}/P_Q , where P_{\max} is the maximum load of the record. If this ratio does not exceed 1.10, that is,

$$\frac{P_{\max}}{P_Q} \leq 1.10 \quad (7.85)$$

then, proceed to calculate K_Q .

For an SEN bend specimen,

$$K = \frac{PS}{BW^{1.5}} f\left(\frac{a}{W}\right),$$

$$f(x) = \frac{3x^{0.5}}{2(1+2x)(1-x^{1.5})} \times (1.99 - 2.15x + 6.08x^2 - 6.83x^3 + 2.07x^4),$$

$$x = \frac{a}{W}. \quad (7.86)$$

For a CT specimen,

$$K = \frac{P}{(BW^{0.5})} f\left(\frac{a}{W}\right),$$

$$f(x) = \frac{2+x}{(1-x)^{1.5}} \times (0.886 + 4.64x - 13.32x^2 + 14.72x^3 - 5.60x^4),$$

$$x = \frac{a}{W}. \quad (7.87)$$

3. Calculate $2.5(K_Q/\sigma_{ys})^2$, where σ_{ys} is the yield stress of the material at the test temperature. If the following is satisfied, then K_Q is equal K_{Ic} .

$$B, a \geq 2.5 \left(\frac{K_Q}{\sigma_{ys}}\right)^2. \quad (7.88)$$

4. If the test results fails to meet the requirements in (7.80) or in (7.81), or both, it is necessary to use a larger specimen to determine K_{Ic} .

J_c, J_u Testing

When the specimen size is inadequate to meet the requirement given by (7.88), a valid K_{Ic} value is not obtained. The reason for this is that the plastic deformation in the specimen is too large to meet the plane–strain condition. In such case, an alternative method is to use elastic–plastic fracture mechanics. The J integral is one such parameters, which is a line or surface integral enclosing the crack front from one crack surface to the other, and is used to characterize the local stress–strain field around the crack tip. The method for determining fracture toughness at the fracture instability based on the J integral is described in the standards [7.237, 238, 240], of which ASTM E1820-01 [7.237] covers the procedures and guidelines for the determination of the fracture toughness using fracture parameters such as K , J , CTOD (δ). The original J_{Ic} and $J-R$ test methods were developed in the original ASTM E813-81 [7.241] and E1152-87 [7.242], respectively. These test methods are now unified in E1820.

When fracture instability occurs before stable tearing the fracture toughness, labeled J_c , is obtained. When the instability occurs after stable tearing the fracture toughness is denoted by J_u . In J_c and J_u testing, the standard specimen for K_{Ic} testing is applicable. However, in order to calculate J , it is necessary to record the curves of load versus load-line displacement. For

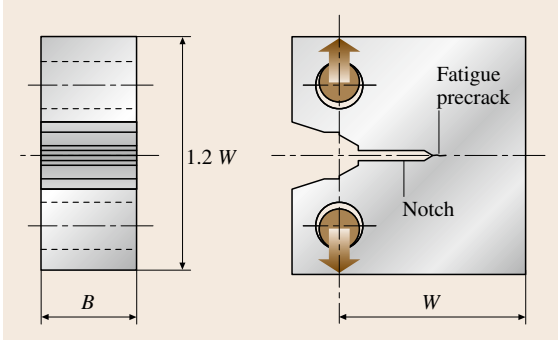


Fig. 7.80 Compact test (CT) specimen for the J integral test

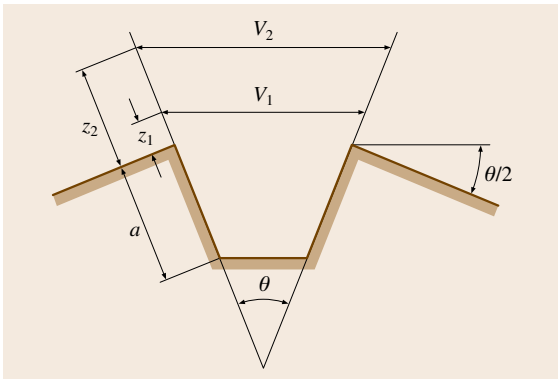


Fig. 7.81 Double-clip gage method for determining load-line displacement of the SEN bend test

CT test, the load-line displacement is directly measured by using the specimen shown in Fig. 7.80. For the SEN bend test, special care must be paid to indentation of the specimen by the loading jig. One possible method for measuring the load-line displacement is to use double clip gages. The load-line displacement V_L may be calculated by (Fig. 7.81) [7.238]

$$V_L = \frac{W(V_2 - V_1)}{z_2 - z_1} \quad (7.89)$$

For fatigue precracking, the maximum load should be less than

$$P_{\max} \leq P_f \quad (7.90)$$

P_f is given by

$$P_f = \frac{0.5Bb_o\sigma_Y}{S} \quad (7.91)$$

for the SEN bend specimen. For the CT specimen,

$$P_f = \frac{0.4Bb_o\sigma_Y}{2W + a_o} \quad (7.92)$$

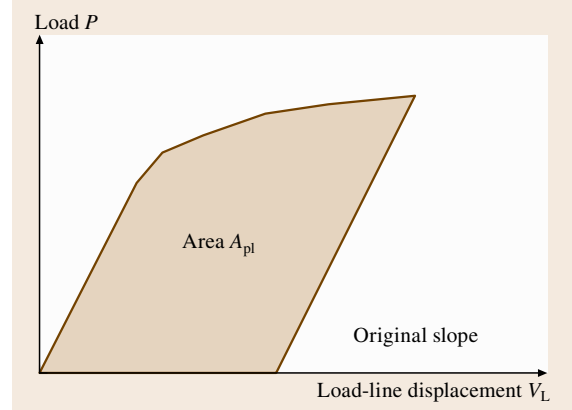


Fig. 7.82 Definition of area for the J calculation

where, $b_o = W - a_o$ (initial ligament depth) and σ_Y is the flow stress given as the average of the yield stress, σ_{ys} and the tensile strength σ_{uts} . The condition (7.90) is equivalent to limiting the maximum stress intensity, K_{\max} of fatigue precracking, according to

$$K_{\max} \leq 0.47\sigma_Y B^{0.5} \quad (7.93)$$

From the fracture instability point, the critical load P_Q is determined. The J -integral value J_Q corresponding to P_Q is calculated using

$$J = J_{el} + J_{pl} \quad (7.94)$$

where J_{el} is the elastic component of J and J_{pl} is the plastic component of J . At a point corresponding to V_L and P on the specimen load versus load-line displacement, J is calculated through

$$J = \frac{K^2}{E'} + \eta \frac{A_{pl}}{Bb_o} \quad (7.95)$$

where, $\eta = 2$ for the SEN bend, and $\eta = 2 + 0.522b_o/W$ for the CT method. $E' = (1 - \nu^2)/E$, and A_{pl} is the area shown in Fig. 7.82.

After testing, along the front of the fatigue crack and the front of the stable crack extension (if it exists), measure the size of the original crack and the final physical crack size at nine equally spaced points centered about the specimen centerline and extending to $0.005W$ from the specimen surface. The original crack size a_o and the physical crack size a_p are calculated by averaging the two near-surface measurements and the remaining seven crack-length measurements. The crack extension, Δa_p is calculated as $a_o - a_p$.

If $\Delta a_p < 0.2 \text{ mm} + J_Q/2\sigma_Y$, the fracture instability point corresponds to instability before stable tearing.

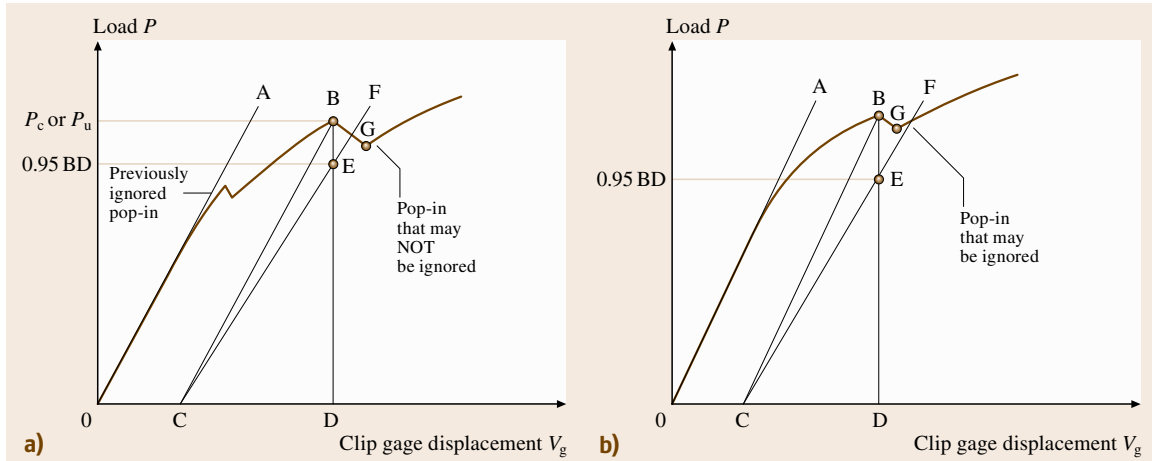


Fig. 7.83a,b Procedure for evaluating the significance of pop-in

For a ferritic steel with $250 \text{ MPa} < \sigma_{ys} < 725 \text{ MPa}$ and $250 \text{ MPa} < \sigma_{uts} < 725 \text{ MPa}$ for the room temperature strength of the material,

$$B, b_o \geq 50 \frac{J_Q}{\sigma_Y}, \quad (7.96)$$

and for other metallic materials,

$$B, b_o \geq 100 \frac{J_Q}{\sigma_Y}, \quad (7.97)$$

where J_Q becomes J_c . It should be noted that, even if these conditions are met, J_c might depend on thickness.

If $\Delta a_p > 0.2 \text{ mm} + J_Q/2\sigma_Y$, the fracture instability point corresponds to instability after stable tearing and J_Q becomes J_u . This is a characteristic of the material and specimen geometry and size.

When the material is heterogeneous, pop-ins are sometimes observed in the record. If the pop-in is attributed to an arrested fracture instability in the plane of the fatigue crack, the result is considered to be a characteristic of the material tested. Pop-in can be assessed by a specific change in compliance, and also post-test examination of the fracture surfaces. Pop-ins are only evaluated when the load rises with increasing displacement after pop-in, otherwise it is considered to be a fracture instability.

The following procedure is used to assess the significance of pop-ins when post-test examination indicates that they are associated with arrested fracture instability in the plane of the fatigue precrack. As shown in Fig. 7.83: (1) draw a line CB which is parallel to the initial slope OA and passes through the pop-in point under consideration. (2) Draw a line CF with a slope 5%

less than the line CB. (3) Mark the point G, corresponding to the load and displacement at pop-in. (4) When the point G is within the angle BCF, the pop-in is judged to be insignificant (Fig. 7.83b). (5) When the point G is outside the angle BCF, the pop-in is significant (Fig. 7.83a). The judgment of (4) and (5) is whether the arrested crack is more than 0.02 of the crack length or not.

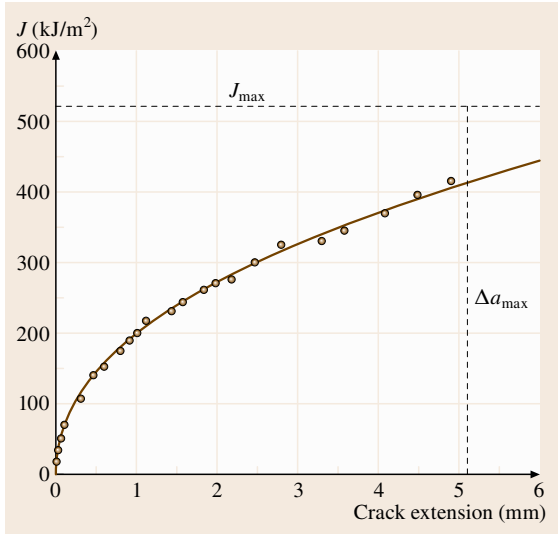
J-R Curve Testing

The J - R curve shows resistance of a material to stable crack extension in terms of the J integral and consists of a plot of J versus crack extension. The standard test method of ASTM E1820-01 [7.237] is to use a single-specimen technique with partial unloading using an elastic-compliance method to determine the stable crack extension. The maximum J integral capacity of a specimen J_{\max} and the maximum crack extension capacity for a specimen Δa_{\max} are given by the following

$$J_{\max} = \min \left(\frac{b\sigma_Y}{20}, \frac{B\sigma_Y}{20} \right), \quad (7.98)$$

$$\Delta a_{\max} = 0.25b_o. \quad (7.99)$$

In J - R testing, SEN and CT specimens are used, usually with side groove. Here, the net thickness is denoted by B_N and the effective thickness is expressed by $B_e = B - (B - B_N)^2/B$. The J - R curve is constructed by plotting J integral values versus the corresponding crack extension values, as shown in Fig. 7.84. The unload/reload sequences are spaced at load-line displacement intervals of about $0.005W$. The J integral


Fig. 7.84 Typical J - R curve

values are calculated by

$$J_i = \frac{K_i^2}{E'} + J_{pl,i}, \quad (7.100)$$

$$J_{pl,i} = \left(J_{pl,i-1} + \frac{\eta_{i-1}}{b_{i-1}} \frac{A_{pl,i} - A_{pl,i-1}}{B_N} \right) \times \left(1 - \gamma_{i-1} \frac{a_i - a_{i-1}}{b_{i-1}} \right), \quad (7.101)$$

$$A_{pl,i} - A_{pl,i-1} = (P_i + P_{i-1}) \frac{V_{pl,i} - V_{pl,i-1}}{2}, \quad (7.102)$$

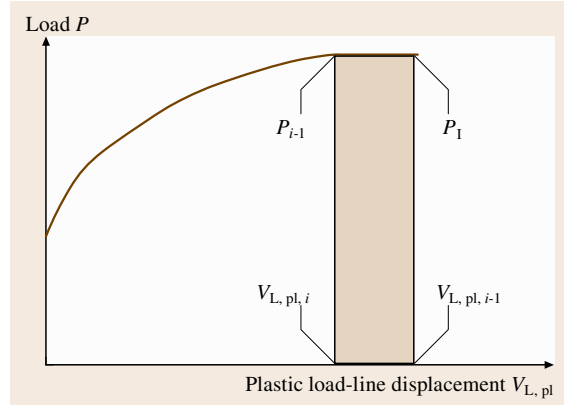
where, for **SEN** specimens $\eta_i = 2$ and $\gamma_i = 1$, and for **CT** specimens $\eta_i = 2.0 + 0.522b_{i-1}/W$ and $\gamma_i = 1.0 + 0.76b_{i-1}/W$. The quantity $A_{pl,i} - A_{pl,i-1}$ in (7.102) is the increment of plastic area under the load versus load-line displacement record between lines of constant displacement at points $i-1$ and i , as shown in Fig. 7.85.

Using an elastic-compliance technique on an **SEN** specimen with crack mouth opening displacement the crack length is given as

$$\frac{a_i}{W} = 1.000 - 3.950u + 2.982u^2 - 3.214u^3 + 51.52u^4 - 113.0u^5, \quad (7.103)$$

where

$$u = \frac{1}{\left(\frac{B_e W E C_i}{S/4} \right)^{0.5} + 1}. \quad (7.104)$$


Fig. 7.85 Definition of area for the J calculation

For **CT** specimens, the crack length is determined using the load-line displacement as

$$\frac{a_i}{W} = 1.000 + 4.063u + 11.24u^2 - 106.0u^3 + 464.3u^4 - 650.7u^5, \quad (7.105)$$

$$u = \frac{1}{(EC_i B_e)^{0.5} + 1}. \quad (7.106)$$

J_{Ic} Testing

The property J_{Ic} characterizes the toughness of a material near the onset of crack extension from a fatigue precrack. Originally, the J_{Ic} test was specified in **ASTM E813** [7.241] and is now unified in **ASTM E1820** [7.237]. E1820-01 gives two methods to determine J_{Ic} : the basic procedure and the resistance curve procedure. The basic procedure involves physical marking of the crack extension and multiple (more than five) specimens, which are used to develop a plot from which an initiation toughness value is evaluated. The resistance curve procedure is to determine the J_{Ic} value from the J - R curve, which is an elastic-compliance method where multiple points are determined from a single specimen.

In the basic procedure, five or more specimens are used. After unloading the specimen, the crack is marked by heat-tinting at about 300 °C (for steels and titanium alloys) or fatigue cracking, and then, cooling and breaking the specimen. The physical crack size a_p is then measured at nine equally spaced points along the front of the marked region of stable crack extension. The crack extension Δa is calculated with

$$\Delta a = a_p - a_o. \quad (7.107)$$

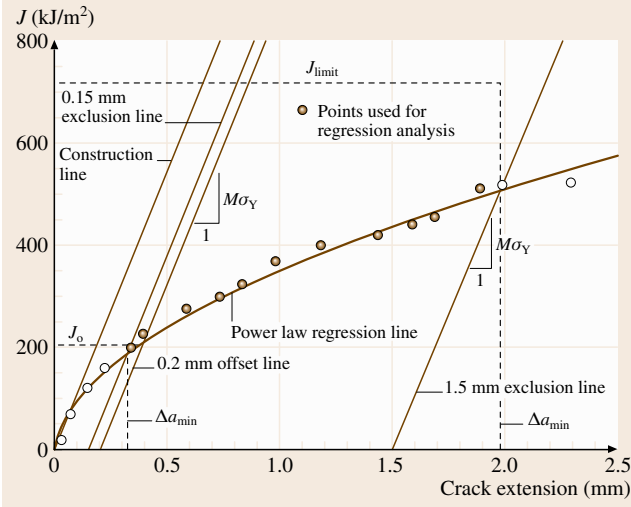


Fig. 7.86 Definition of construction line for data qualification

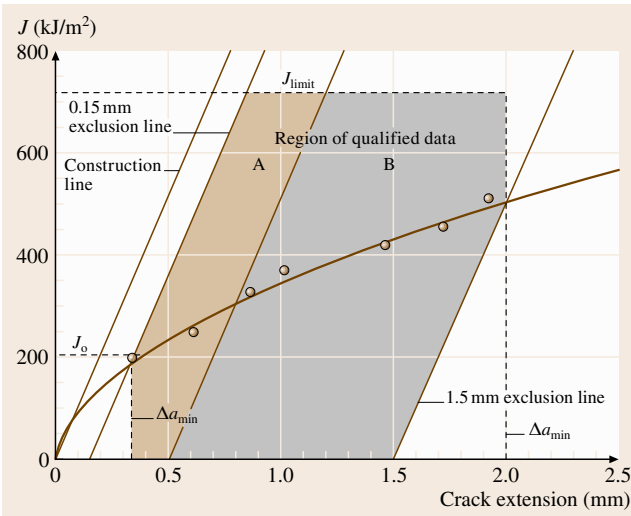


Fig. 7.87 Definition of regions for data qualification

The J value is calculated using (7.95) at the point where unloading was conducted.

In the resistance curve procedure, a correction is applied to the estimated Δa_i data to obtain an improved original crack size, a_{oq} from the compliance. Using the data set of J_i and a_i , a_{oq} is calculated from

$$a = a_{oq} + \frac{J}{2\sigma_Y} + BJ^2 + CJ^3. \quad (7.108)$$

The coefficients B and C in this equation are determined using a least-square fit procedure. In this procedure,

it is necessary that there are more than eight data and that three of the eight are between $0.4J_Q$ and J_Q . Moreover, the correlation coefficient of this fit should be more than 0.96 and the difference between the optically measured crack length, a_o and a_{oq} should be less than $0.01W$. For each a_i value, the crack extension is calculated by

$$\Delta a_i = a_i - a_{oq}. \quad (7.109)$$

The J_i values are determined from (7.100–7.102).

The next step is to plot J versus Δa , as shown in Fig. 7.86. Draw a construction line in accordance with

$$J = M\sigma_Y \Delta a, \quad (7.110)$$

where $M = 2$. Then, draw exclusion lines parallel to the construction line intersecting the abscissa at 0.15 mm and 1.5 mm, as shown in Fig. 7.87. These lines give the minimum and maximum Δa values (Δa_{min} , Δa_{max}). At least one J - Δa point should lie between the 0.15 mm exclusion line and the 0.5 mm offset line, and one point should also lie between the 0.5 mm offset line and the 1.5 mm exclusion line. Next we draw the regression line with

$$\ln(J) = \ln(C_1) + C_2 \ln(\Delta a). \quad (7.111)$$

The J_Q value is determined as the intersection of the regression line of (7.111) and the 0.2 mm offset line. If the following size requirements are satisfied, J_Q becomes J_{Ic} ,

$$B, b_o > 25J_Q/\sigma_Y. \quad (7.112)$$

CTOD Testing

The CTOD test is especially appropriate for materials that exhibit a change from ductile to brittle behavior with decreasing temperature. Typical standards of CTOD testing method are specified in [7.238, 243, 244].

The method uses fatigue precracked specimens. A rectangular- or square-cross-sectioned three-point bend specimen or compact specimen is used. The configurations of the specimens are similar to those for K_{Ic} testing (Figs. 7.77 and 7.78). A fatigue precrack is introduced half way along the specimen width, 0.45–0.55 times the specimen width. In order to expedite fatigue precracking, a machined notch is produced by milling, sawing or disc grinding. A chevron notch may be machined if fatigue precracking is difficult to control. The fatigue precrack is introduced by repeated loading at room temperature. The maximum fatigue precracking load should be lower than a prescribed value. This restriction is to limit the plastic zone size at the fatigue

precrack tip. Excessive plastic deformation at the crack tip may influence the critical **CTOD** value.

The specimens are tested in displacement-controlled and quasistatic monotonic loading. The machine for load application should be capable of applying load at a rate of stress intensity factor within the range $0.5\text{--}3.0\text{ MPa m}^{1/2}\text{ s}^{-1}$. A typical set up of a specimen is shown in Figs. 7.77 and 7.78.

The notch opening displacement is measured by a displacement gage attached to the edge of the notch. Knife-edges are attached at the notch edge. Alternatively, integral knife-edges are used. A record of load versus notch opening displacement is made. Characteristic types of load versus displacement records in the test are shown in Fig. 7.88. Note that P_c is the applied load at the onset of brittle crack extension or pop-in when the average stable crack extension (Δa), including the stretched zone width (**SZW**), is less than 0.2 mm; P_u is the applied load at the onset of brittle crack extension or pop-in when the event is preceded by Δa of at least 0.2 mm; and P_m is the applied load at the first attainment of a maximum load plateau for fully plastic behavior. If the specimen fractures by brittle crack extension prior to the first attainment of a maximum load plateau (type (4)), the fracture surface is examined for evidence of stable crack extension in the region between the fatigue precrack front and the start of brittle crack extension. When an initiated brittle crack is arrested after a short extension, the load versus notch opening record exhibits pop-in, see types (3) and (5) in Fig. 7.88. Pop-ins giving both a load drop, y , and displacement increase, x , of less than 1% are ignored.

The types and the amount of Δa are recorded. The critical values of the load and notch opening displacement of F_c and V_c , or F_u and V_u , are measured at points corresponding to

1. Fracture, when there are no significant pop-ins: record types (1), (2) and (4);
2. The earliest significant pop-in prior to fracture: record types (3) and (5);
3. Fracture, when all significant pop-ins prior to fracture give values of $d\%F$ that are less than 5%, where

$$d\%F = 100 \left[1 - \frac{D}{F} \left(\frac{F-y}{D+x} \right) \right] \% . \quad (7.113)$$

Values of P_m and V_m are measured at points corresponding to

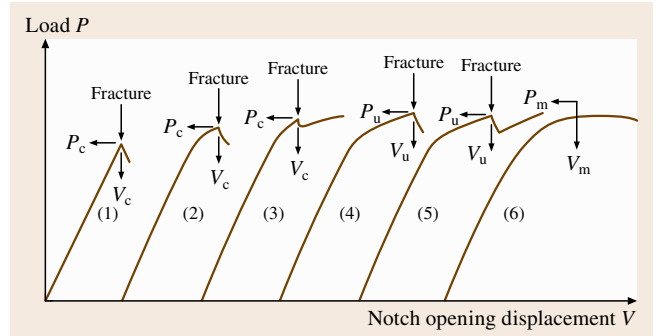


Fig. 7.88 Characteristic types of load-displacement records in a **CTOD** testing (after [7.238])

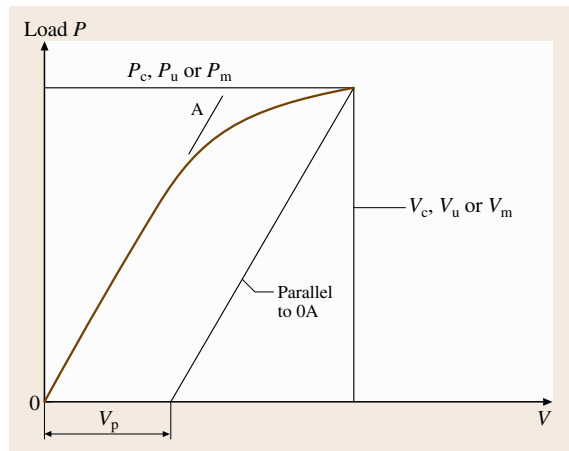


Fig. 7.89 Definition of V_p for determining the **CTOD** (after [7.238])

- First attainment of the maximum load plateau, when there is no fracture or pop-ins prior to the first attainment of the maximum load plateau: record type (6).

Critical **CTOD** values, δ_c , δ_u , δ_m , corresponding to P_c and V_c , P_u and V_u , or P_m and V_m , respectively, are calculated by

$$\delta = \left[\frac{PS}{BW^{1.5}} \times f\left(\frac{a_o}{W}\right) \right]^2 \frac{(1-\nu^2)}{2\sigma_{ys}E} + \frac{0.4(W-a_o)V_p}{0.4W+0.6a_o+z} , \quad (7.114)$$

where, P is the critical value of the applied load, S is the bending span, B and W are the thickness and width of the specimen, respectively (Fig. 7.77), a_o is average original crack length, f is a mathematical function of a_o/W (7.86) [7.238], σ_{ys} is 0.2% of the proof strength at

the temperature of fracture test, z is distance of the notch opening gage location above the surface of the specimen and V_p is the plastic component of critical notch opening displacement, as defined by Fig. 7.89.

CTOD Testing of Welds

Fracture toughness evaluation of welds is more complicated than that of base metal because the welds have heterogeneities in terms of microstructure and toughness. Therefore, toughness values of welds inherently show large scatter. The existence of local brittle zones (LBZ) in the heat-affected zone (HAZ) sometimes gives extremely low toughness values. From this viewpoint, special attention should be paid to CTOD testing for welds.

Figure 7.90 shows the variation of critical CTOD values of high-strength-steel weld HAZ as a fraction of the coarse-grained (CG) HAZ along the fatigue precrack front in the thickness direction [7.245]. This result indicates that at least 15% of the CG HAZ should be sampled by the fatigue precrack to assess the lower-bound CTOD value; see below for the definition of %CG HAZ. Most of the CTOD testing standards of weld HAZ specify the %CG HAZ for this reason. Typical standards of for CTOD testing method for welds are specified in [7.246, 247]. Among these, API RP 2Z [7.246] was the first to specify a CTOD testing method for weld HAZ. Other standards follow the same concept. The API RP 2Z standard is intended for preparing and certifying fabrication welding procedures and assuring that the steel to be supplied is inherently suitable for welding.

API RP 2Z refers to BSI 7448 part 1 [7.238] and ASTM E 1290-02 [7.243] for the CTOD testing method. Additional requirements are specified regarding the notch positioning in the weld and post-test examinations for sampling the CG HAZ regions, which is thought to have lower-bound toughness. Figure 7.91 shows the HAZ regions in a multipass weld. Because of the multi-thermal cycles induced by multipass welding, the HAZ has an extremely complex microstructure distribution. It is intended that the fatigue precrack certainly samples the CG HAZ. For this purpose, the fatigue precrack should be carefully introduced. Welding should be made carefully so that the fusion line of the weld is straight enough to sample as much CG HAZ as possible. It should be noted that proper welding consumables and welding procedures should be adopted to maintain a certain level of critical CTOD value for the weld metal. In addition, welding residual stress may be relieved prior to fatigue precracking to promote crack-front straightness. This is done by lateral compression (Fig. 7.92) [7.248].

API RP 2Z requires three levels of weld heat inputs. At least five or eight, depending on the heat input, CTOD tests should be conducted for each welding condition. At least three specimens aim to sample the CG HAZ regions close to the fusion line and at least two specimens aim to sample the boundary region between the HAZ and base metal.

Post-test metallographic examinations are specified. Figure 7.93 shows the sectioning method for this purpose. The broken half of the specimen is sectioned at the fatigue precrack front, etched and its microstructure is revealed. The CG HAZ regions sampled by the fatigue precrack tip is measured (Fig. 7.94), and the %CG is calculated as

$$\%CG = \frac{100 \sum_i^n L_i}{B}, \quad (7.115)$$

where L_i is length of the i -th CG region sampled by the crack front and B is the plate thickness. The CG regions need not be continuous. The value of %CG should be at least 15% for the three specimens. For the other two specimens, the crack front should sample at least 50% of the boundary region between the HAZ and the base metal.

The CTOD toughness values are influenced by many other factors than the local brittle zones. One is the degree of strength matching, i. e. the ratio of yield strength of the weld metal to that of base metal. An overmatch may cause excessive constraint in the HAZ, which may cause unexpectedly low critical CTOD values.

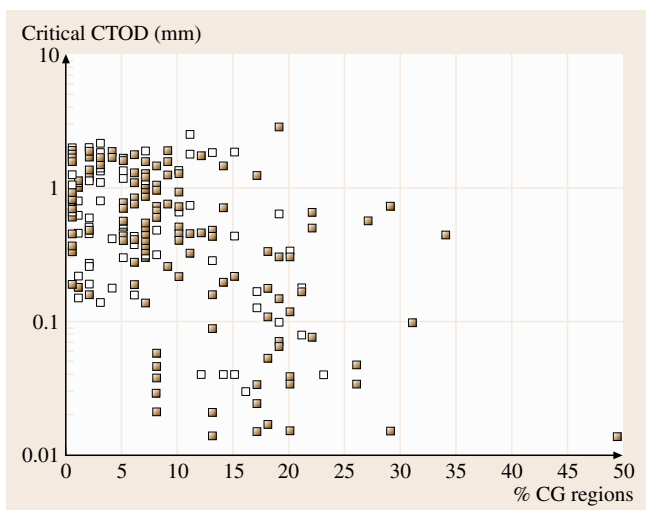


Fig. 7.90 Critical CTOD values versus % CG regions for steels showing some LBZ behavior (after [7.245])

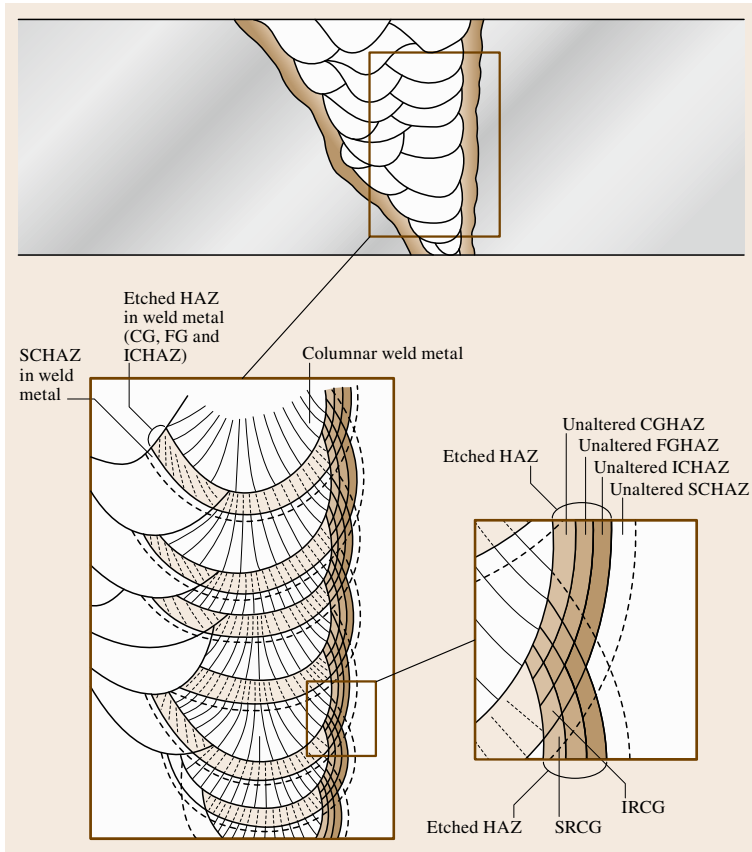


Fig. 7.91 Schematic of microstructures in HAZ of a multi-pass welding (after [7.246])

7.5.3 Fatigue Crack Propagation Rate

Fatigue crack propagation results from the cyclic plastic strain cumulation at the crack tip, especially in stable crack propagation. It is expected that the crack propagation rate da/dN can be related to the stress-intensity factor range ΔK ($= K_{\max} - K_{\min}$). Since Paris et al. [7.249, 250] first demonstrated the characterization of crack growth by fatigue in the early 1960s, a considerable number of works have covered the determination of crack growth behaviors using fracture mechanics. Figure 7.95 shows typical fatigue crack growth behavior in metallic materials, which is expressed in a schematic log-log relationship between da/dN and ΔK ; ΔK is usually defined as the positive component of the total stress-intensity factor range, which is

$$\begin{aligned} \Delta K &= K_{\max} - K_{\min} = (1 - R)K_{\max} \quad \text{for } R \geq 0 \\ \Delta K &= K_{\max} \quad \text{for } R \leq 0 \end{aligned} \quad (7.116)$$

where R is the stress ratio ($= \sigma_{\min}/\sigma_{\max} = K_{\min}/K_{\max}$). The sigmoidal curve in Fig. 7.95 can be divided into three regions. Region I is a lower bound against crack growth, which is characterized by a threshold value ΔK_{th} . Below ΔK_{th} , there is no observable fatigue crack growth. In region II, for intermediate ΔK values, the re-

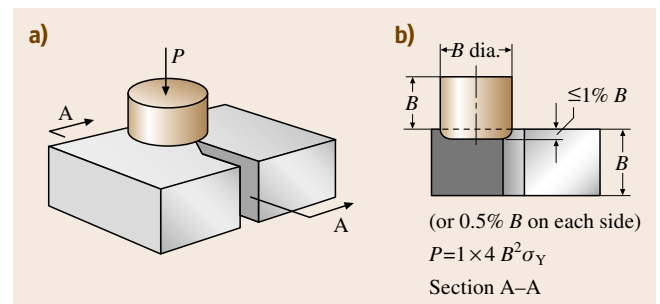


Fig. 7.92a,b Lateral compression prior to fatigue precracking, for relieving welding residual stress (after [7.248])

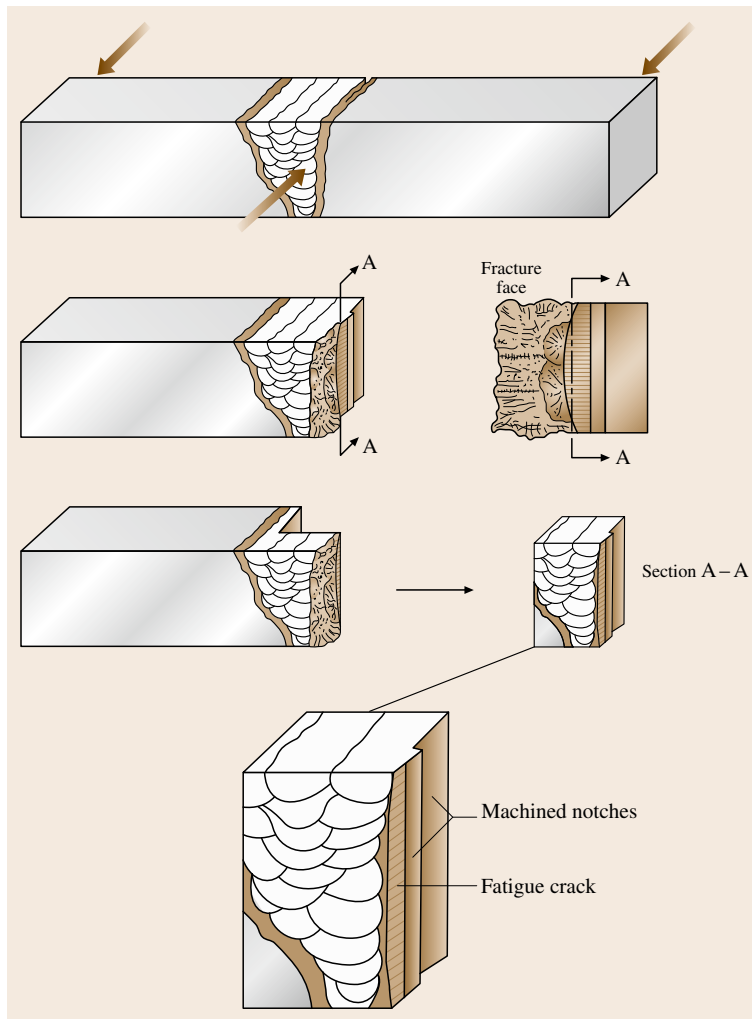


Fig. 7.93 Sectioning the weld half of a CTOD specimen for post-test metallographic examination (after [7.246])

relationship in Fig. 7.95 can be fitted with a linear line, which is formulated as

$$da/dN = C(\Delta K)^m, \quad (7.117)$$

where C and m are both materials constants, which should be determined experimentally. The fatigue crack growth rate in region II is mainly controlled by ΔK , and is insensitive to the R ratio. This power-law relationship for fatigue crack growth in region II was first proposed by *Paris and Erdogan* [7.250] and (7.117) is often referred to as *Paris' law*. In region III, crack growth is accelerated. Even if the applied stress amplitude $\Delta\sigma$ is constant, ΔK shows a rapid increase due to fast crack extension and the increased ΔK enhances the acceleration in crack growth. When the

$K_{\max} [= \Delta K/(1-R)]$ reaches the fracture toughness of the material K_c , the crack growth transforms into instability, which corresponds to an infinite value in da/dN .

The *ASTM* has standardized the measurement methodology for the fatigue crack propagation rate based on fracture mechanics since 1978 [7.251]. The following is a summary of the *ASTM* standard E 647. The compact tension C(T) specimen with a side-edge crack and the middle tension specimen M(T) with a center crack are prescribed. The configurations of the C(T) and M(T) specimens are shown in Figs. 7.96 and 7.97, respectively. The C(T) specimen is recommended only for tension–tension loading while the M(T) specimen can be loaded in either tension–tension

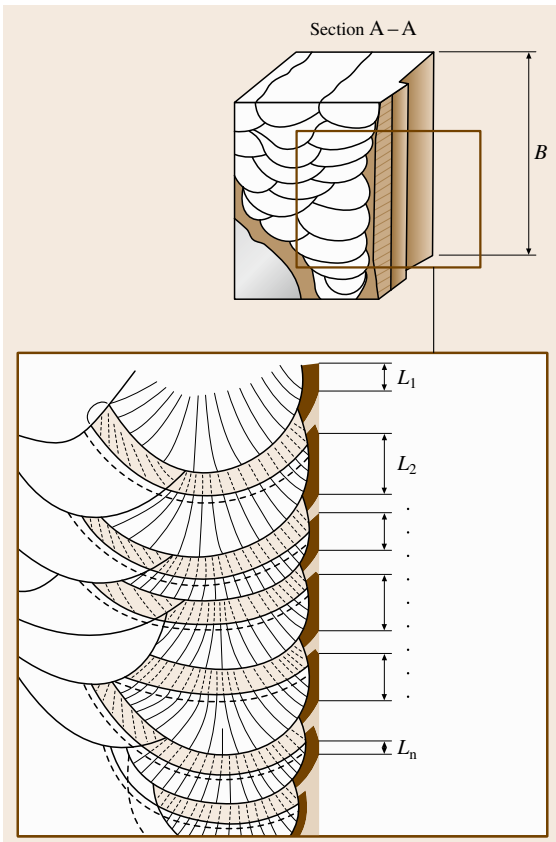


Fig. 7.94 Calculation of %CG HAZ sampled by the fatigue precrack tip (after [7.246])

or tension-compression. The configurations of both specimens are given with proportional dimensions of the specimen width W . The C(T) specimen prescribed here has the same configuration as the C(T) specimen in the toughness measurement except for the specimen thickness B . It is not necessary to adopt a large thickness in the fatigue crack growth, because the plane-strain concept is not required in the da/dN measurement. Small specimen thicknesses are rather better because a thumbnail crack front possibly enhances the uncertainty in the measurement of the crack length. From these points of view, the specimen thickness requirement in a fatigue crack growth measurement can be flexibly chosen within the recommended range.

The formula for the stress-intensity factor K for each type of specimen is given in the standard, being a function of the specimen dimensions and applied load P . It is the ΔK that is calculated from the positive component

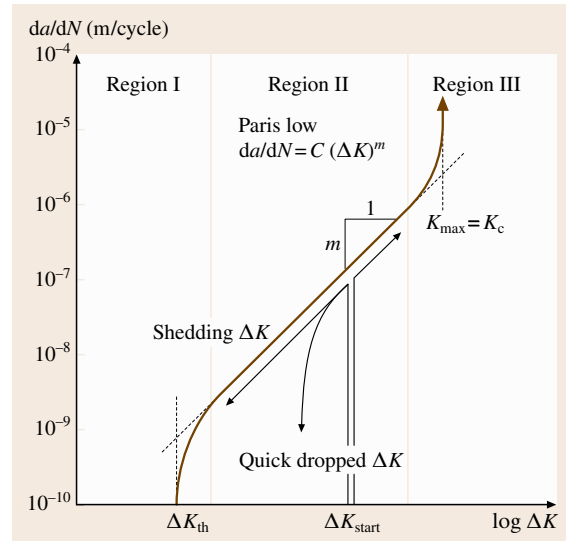


Fig. 7.95 Schematic relation between stress intensity range ΔK and crack growth rate da/dN

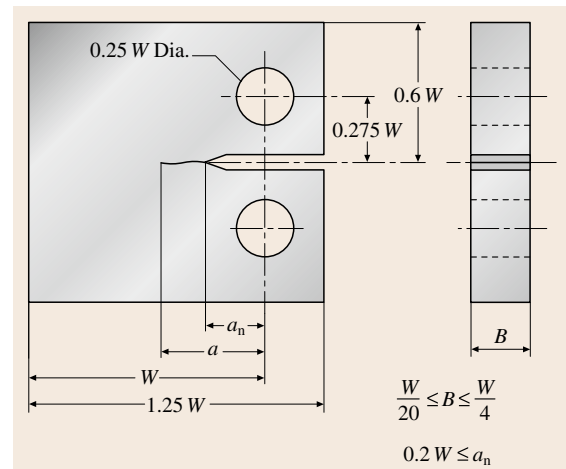


Fig. 7.96 Compact tension C(T) specimen

of an applied load amplitude ΔP (referring to (7.116)) and an extending crack length $a (= a_0 + \Delta a)$.

A sharpened starter crack must be introduced by fatigue from a machined notch. Sufficient size and straightness of a fatigue crack must be kept to eliminate the effect of the machined starter notch on the K calibration and the effect of the crack-front shape on the subsequent crack growth rate data. The machined notch outline must lie within the 30° angled lines whose apex is at the end of the fatigue precrack shown in Fig. 7.98. The length of the precrack should

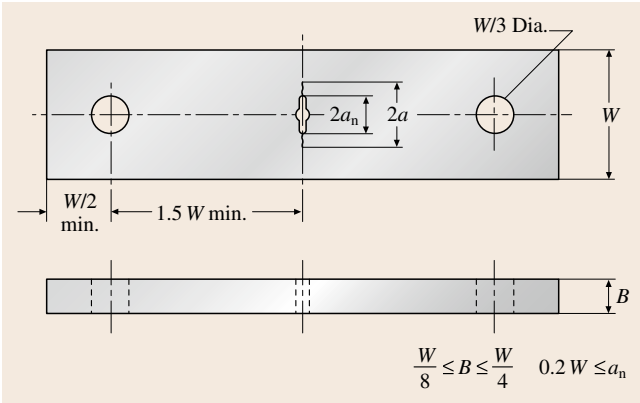


Fig. 7.97 Middle tension M(T) specimen

not be less than $0.1B$, h or 1 mm, whichever is greater. The K_{\max} value during the fatigue loading for precracking must be suppressed below the initial K_{\max} value for which the da/dN data are of interest. Precracking growth rates less than 10^{-8} m/cycle are suggested, especially when near-threshold growth rates are to be obtained. The precrack sizes measured on the front and back surfaces must not differ by more than $0.25B$.

In da/dN measurements, the crack extension should be measured as a function of elapsed cycles under a controlled load amplitude. The crack can be visually measured with a traveling microscope. The compliance variation that is the crack opening displacement response for a specified load and the electric potential difference can be also used to estimate the crack growth, similarly to the detection of the J_{Ic} test methodology prescribed in ASTM E 1820 [7.237]. Bisual measurement is recommended, together with either the compliance technique or the electric potential-difference technique. In all methods, a minimum resolution below 0.1 mm or $0.002W$ (whichever is greater) is required. Crack size extension is measured at a Δa interval larger than 0.25 mm. However, the Δa measurement in each crack extension of 0.25 mm is sometimes difficult in near-threshold (ΔK_{th}) testing, where it is required that there are at least five da/dN data points despite the fact that crack extension has almost stopped. In this case, the measuring interval Δa can be reduced by ten times the crack size measurement precision.

A loading procedure with either ΔK increasing or ΔK decreasing must be selected, depending on the da/dN value that is to be measured. The ΔK -increasing procedure is well suited to fatigue crack growth rates above 10^{-8} m/cycle. However, it becomes gradually

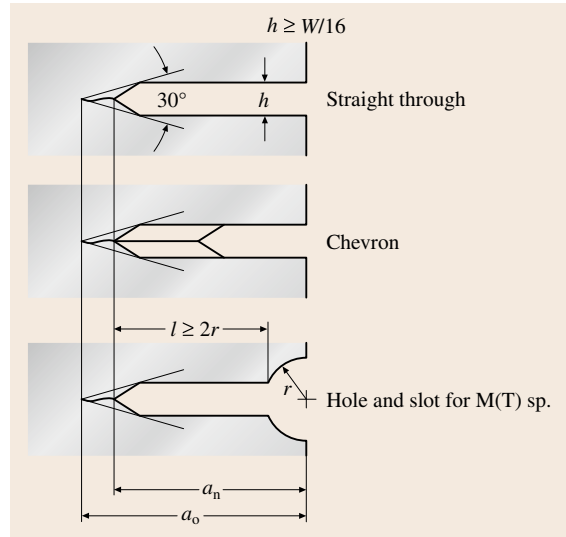


Fig. 7.98 Examples of fatigue precrack from machined notch

more difficult for small initial da/dN values because the applied ΔK should be smaller than that in the precracking.

The ΔK -decreasing test procedure can be conducted for rates below 10^{-8} m/cycle. In the ΔK -increasing test procedure, an applied load range (ΔP) and other loading variables (stress ratio and frequency) are fixed constant. The schematic variation of the ΔK value and the crack growth Δa as a function of elapsed cycles are shown in Fig. 7.99a.

In the ΔK -decreasing test procedure for da/dN measurements below 10^{-8} m/cycle, ΔK and K_{\max} must start from a level equal to or greater than the terminal precracking values. Subsequently, the load ΔP is shed as the crack grows, until the lowest ΔK or crack growth rate of interest is reached. Load shedding is usually performed as decreasing load steps at specified crack size intervals, as shown in Fig. 7.99b. The shedding of load should be gradual enough to preclude anomalous data resulting from sudden reductions in the stress-intensity range. The load reduction in each shedding step should not exceed 10% of the maximum load P_{\max} in the previous load step. After a step reduction, a minimum crack extension of 0.5 mm is recommended. The da/dN measured using these shedding rules sometimes shows a trace different from the true material properties, as shown in Fig. 7.95. This mainly results from strain hardening and compressive residual stress in the crack-tip

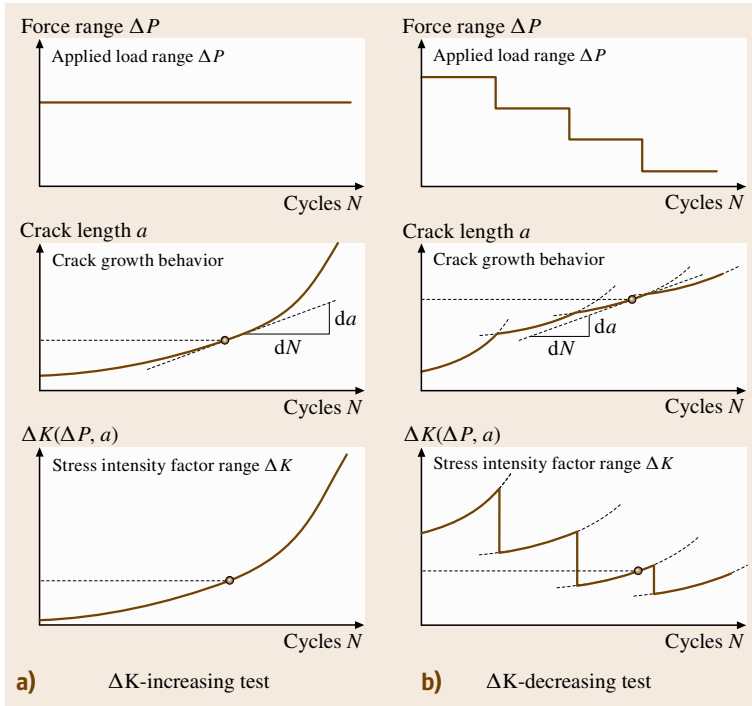


Fig. 7.99a,b Correspondences of applied load with crack growth and stress-intensity factor range. (a) ΔK -increasing test, (b) ΔK -decreasing test

plastic zone formed in the previous load step. This mis-measured da/dN - ΔK relation usually gives an overestimation in the fatigue crack growth resistance of the materials.

The crack growth rate is determined from the crack size versus elapsed cycles data (a - N curve). The secant and incremental polynomial methods are recommended. Both methods are suitable for the ΔK -increasing test. For the ΔK -decreasing tests, where load is shed in decremented steps, the secant method is recommended. A crack growth rate determination should not be made over any increment of crack extensions that include a load step. The secant method simply involves a calculation of the slope of the straight line joining two adjacent data points on the a - N curve. It is formally expressed as follows

$$(da/dN)_{\bar{a}} = (a_{i+1} - a_i) / (N_{i+1} - N_i). \quad (7.118)$$

Since the da/dN value calculated in this way is an average rate over the $a_{i+1} - a_i$ increment, the average crack size $\bar{a} = (a_{i+1} + a_i) / 2$ is used to calculate ΔK . On the other hand, the incremental polynomial method involves fitting a second-order polynomial to a set of $(2n + 1)$ successive data points, where n is usually taken to be 1–4. The form of the equation for the local fit is

as follows

$$\hat{a}_i = b_0 + b_1(N_i - C_1) / C_2 + b_2 \left[(N_i - C_1) / C_2 \right]^2, \quad (7.119)$$

where $-1 \leq (N_i - C_1) / C_2 \leq +1$ and b_0 , b_1 , and b_2 are the regression parameters that are determined by the least-square approximations over the range $a_{i-n} \leq a \leq a_{i+n}$. The value \hat{a}_i is the fitted value of the crack size at N_i . The parameters $C_1 = (N_{i-n} + N_{i+n})$ and $C_2 = (N_{i-n} - N_{i+n})$ are used to scale the input data. The crack growth rate da/dN at N_i is calculated from the derivative of the parabola above, as follows

$$(da/dN)_{\hat{a}_i} = b_1 / C_2 + 2b_2(N_i - C_1) / C_2^2. \quad (7.120)$$

The ΔK value associated with this da/dN value is calculated using the fitted crack size \hat{a}_i corresponding to N_i .

Both recommended methods can give the same average da/dN response. However, the secant method often results in increased scatter in da/dN relative to the incremental polynomial method, since the latter numerically smoothes the data.

The K_{\max} value of all data must be examined within the linear elastic fracture mechanics. When the data

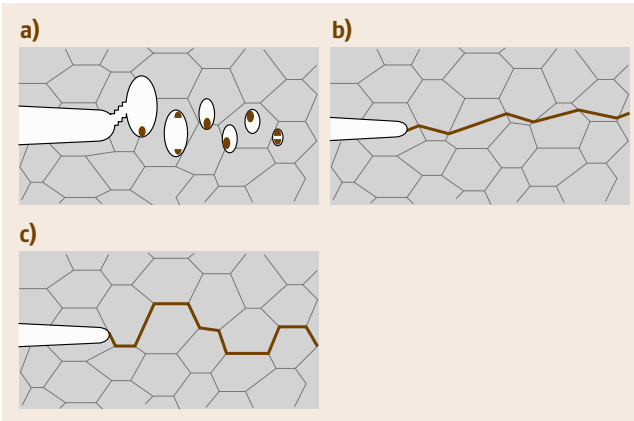


Fig. 7.100a–c Three of the most common fracture mechanisms: (a) microvoid coalescence fracture; (b) cleavage fracture; (c) intergranular fracture

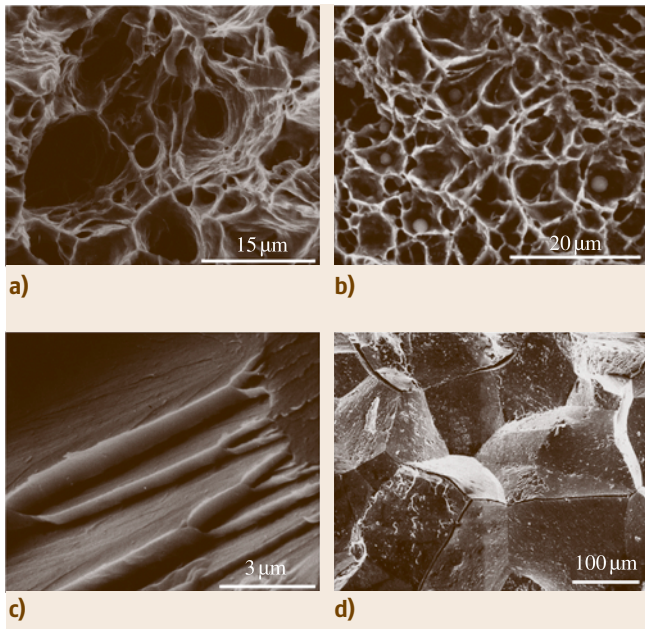


Fig. 7.101a–d SEM micrographs for most common fracture appearances: (a) microvoid coalescence fracture/dimple pattern; (b) microvoid coalescence fracture/dimple pattern; (c) cleavage fracture/river pattern; (d) intergranular fracture

satisfy the specimen size requirements below, the specimen can be predominantly identified as elastic.

$$W - a \geq (4/\pi)(K_{\max}/\sigma_Y)^2 \text{ for a C(T) specimen,}$$

$$W - 2a \geq 1.25 P_{\max}/(B\sigma_Y) \text{ for an M(T) specimen.}$$

(7.121)

This specimen size requirement here is rather more relaxed than that in the fracture toughness K_{Ic} for unstable fracture prescribed in ASTM E-399 [7.231].

The relation as shown in Fig. 7.95 appears on the log–log graph plots between da/dN and valid ΔK . At least five data points of approximately equal spacing at growth rates 10^{-9} – 10^{-10} m/cycle are needed to determine the threshold value of ΔK , denoted by ΔK_{th} .

The best-fit straight line from a linear relation of $\log da/dN$ versus $\log \Delta K$ using a minimum of five data points of approximately equal spacing at growth rates of 10^{-9} – 10^{-10} m/cycle. The ΔK_{th} value is determined from the ΔK that corresponds to a growth rate of 10^{-10} m/cycle on the fitted line.

The da/dN – ΔK relation and/or the ΔK_{th} value, which are measured with laboratory specimens, can be applied to the crack growth assessment of the structures. As ΔK is a function of both an applied stress range and a crack length, an integration of the da/dN – ΔK relation or (7.117) with an assumed initial crack size predicts the crack growth for a elapsed loading cycles in service. When the calculated ΔK for a stress range in service and an initial crack size is smaller than the ΔK_{th} value, no crack growth is predicted.

However, it is necessary to examine the crack closure effect in testing. Compressive residual stress and/or crack deflection often suppress crack–tip opening in spite of the applied tensile load. The effective stress-intensity factor range for a crack–tip opening of ΔK_{eff} is smaller than the apparent value, which enhances the overestimation in the ΔK_{th} value of the material. The da/dN – ΔK_{eff} relation is sometimes evaluated using the compliance variation procedure or the high-stress-ratio loading.

The effect of small cracks in practical applications should also be considered. When an initial crack in a structure is smaller than a certain crack size, the crack sometimes behaves differently from Fig. 7.95. Even for smaller values of ΔK than ΔK_{th} , small cracks can grow. da/dN for a small crack is generally faster than the value of da/dN estimated using the long-crack method, even for the same ΔK . This small-crack effect may result from both the effect of discontinuities in the microstructure and limitations of fracture mechanics.

7.5.4 Fractography

Important information can be obtained from microscopic examination of the fractured surface. This study is usually called fractography. The scanning electron microscope (SEM) is commonly employed in fractog-

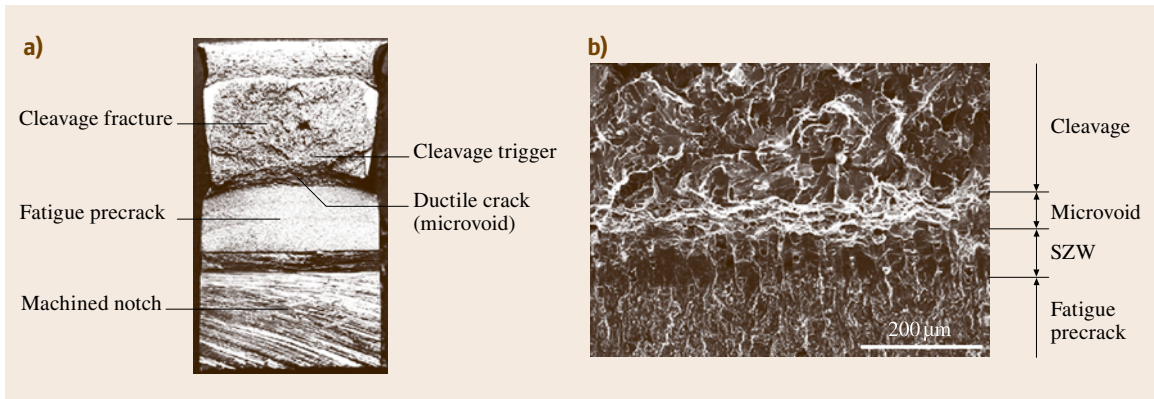


Fig. 7.102a,b Fracture appearance of toughness specimen in low carbon steel: (a) macroscopic observation, and (b) microscopic observation

raphy because of its large depth of focus. Fractography is sometimes applied in order to find the cause of accidental failures.

Figure 7.100 shows schematically three of the most common fracture mechanisms, which are caused by monotonic tension in metallic engineering materials.

Ductile materials usually show microvoid coalescence type of fracture, shown in Fig. 7.100a. Microvoids nucleate at second-phase particles or inclusions due to either interface decohesion or particle cracking. After growth of the voids, adjacent voids coalesce due to ligament fracture. The appearance of the fracture is characterized by the *dimples* shown in Fig. 7.101a. In material with many inclusions, the dimple size on the fracture surface is small because they coalesce easily (Fig. 7.101b).

The BCC and hexagonal close-packed (HCP) crystalline systems have cleavage planes along specific crystallographic planes. Once cleavage fracture is triggered, a crack along a cleavage plane propagates unstably. The propagating crack changes its direction each time it crosses a grain boundary, as shown in Fig. 7.100b. Figure 7.101c shows the appearance of the fracture, observed by an SEM. The fracture surface consists of several flat facets. The facet edges converge to a single line like tributaries of a river. When a propagating cleavage crack encounters a grain boundary, the nearest cleavage-plane angle in the adjacent grain is often oriented at a twist angle to the current cleavage plane. Cracking in a number of parallel cleavage planes just beyond a grain boundary accommodates the twisted-angle mismatch. This river pattern is caused by the convergence of multiple cracks into a single crack during its propagation within a grain.

Under special circumstances, cracks can propagate along grain boundaries, as shown in Fig. 7.100c. This intergranular fracture sometimes appears when the strength of the grain boundary is weakened by the following mechanisms: segregation of embrittling elements or precipitation of a brittle phase on the grain boundary, grain-boundary cavitation at elevated temperature, or attack of the grain boundary by corrosion or hydrogen. The grain boundary, which looks like rock candy, is shown under SEM observation in Fig. 7.101d.

The macroscopic appearance of fractures such as the ductile and brittle types described do not necessarily correspond to the microscopic fracture. In low-carbon steels, however, ductile fracture is generally caused by microvoid coalescence, and cleavage fracture leads to brittle fracture with less ductility.

In fracture toughness tests for low-carbon steels, cleavage fracture is often triggered after a certain crack extension due to microvoid coalescence. Figure 7.102a shows the macroscopic appearance of a fracture toughness specimen obtained at the ductile–brittle transition temperature. The dark thumbnail area following the fatigue precrack shows stable crack extension due to microvoid coalescence. A triggered cleavage crack at the ductile crack tip propagates unstably. Figure 7.102b shows the fracture appearance transition observed by SEM. The stretched zone (SZ) can be observed between the fatigue precrack and the ductile crack. The SZ is not caused by fracture, but by a blunting deformation of the fatigue precrack. The stretched zone (SZ) conceptually corresponds to the crack–tip opening displacement CTOD. The fracture toughness of material can be estimated from the depth and/or the width of the stretched zone on the fracture surface.

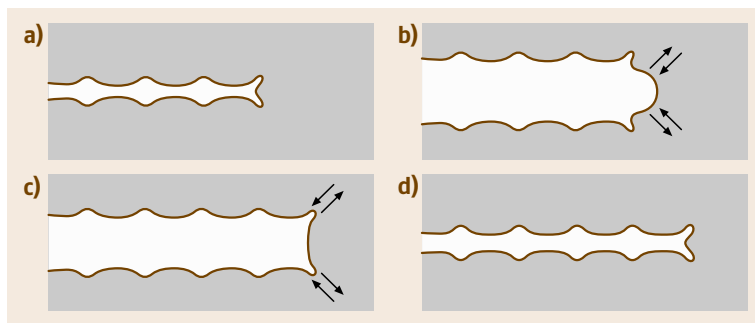


Fig. 7.103a–d Plastic blunting process for striation formation (after [7.252])

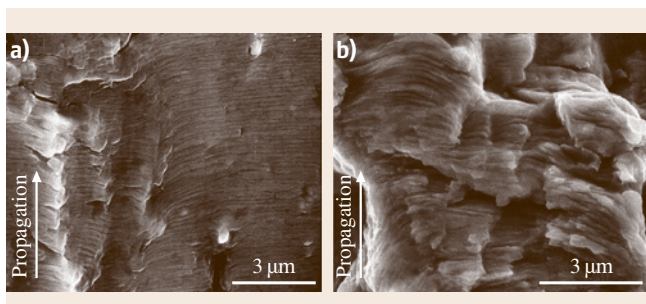


Fig. 7.104a,b Fatigue striations in: (a) aluminum alloy, and (b) steel

Fatigue crack propagation often produces *striations* on the fractured surface. Figure 7.103 shows one of the

proposed mechanisms for striation formation [7.252]. When the tensile stress is applied, the crack tip is blunted due to the concentrated slip deformation (Fig. 7.103b). The fatigue crack incrementally extends as a result of the formation of this stretched zone. When the stress changes to compression, the slip direction at the crack tip is reversed (Fig. 7.103c). This process causes the buckling to form a resharpened crack tip. The ripples left by these process above can be observed as striations.

Figure 7.104 shows typical striations for aluminum alloy and steel. Striations are formed in a similar manner in materials with plasticity. According to the mechanism in Fig. 7.103, the striation spacing is equal to the crack growth rate da/dN .

7.6 Permeation and Diffusion

The diffusion of small molecules in materials has attracted significant interest, primarily because it is of great significance to many applications in the chemical, petrochemical and medical industries [7.253, 254]. For example, a polymer matrix has the ability to exhibit different permeation rates for various chemical species, thus providing the basis for separation [7.253]. Current applications include water desalination, gas and vapor purification, and medical applications such as controlled-release devices and the artificial kidney [7.253, 254]. Separations using membranes have inherent advantages over conventional separation technologies, including low energy cost (since no phase transition is involved in the separation), high reliability (no moving parts) and small footprint [7.255]. Of particular interest are gas separations, where polymeric membranes behave as molecular filters. For example, an O_2/N_2 selectivity of 5.9 can be achieved in polymeric membranes such as polysulfone, even though the

kinetic diameter difference between O_2 and N_2 is only 0.018 nm [7.256]. Additionally, if a polymeric material is not very permeable to penetrants such as O_2 and H_2O , it acts as a barrier, which can be useful for packaging applications [7.257].

This section reviews experimental techniques used to study gas and vapor sorption, diffusion and permeation in polymeric films. The more detailed fundamental theory and industrial applications pertinent to gas transport in polymers are available in several books [7.258–261] and review articles [7.262–264]. Specific reviews of experimental methods to measure gas transport properties are also available [7.265–268]. In particular, *Felder* and *Huvar* reviewed experimental methods from a historical perspective and critically evaluated the strengths and weaknesses of the various techniques in 1980 [7.265]. Without intending to review the subjective exhaustively, the main objective of this section is to provide readers with a self-

consistent set of manual-like instructions to choose and design the most suitable and reliable experimental techniques for specific systems based on our laboratory's experience.

7.6.1 Gas Transport: Steady-State Permeation

Gas transport through a dense or nonporous polymeric film is often described by the solution–diffusion mechanism [7.269]. As illustrated in Fig. 7.105, feed gas at a high (i. e., upstream) pressure p_2 dissolves into the feed-side surface of the film, diffuses through the film due to a concentration gradient, and finally desorbs from the permeate-side surface at the downstream (i. e., low pressure) face of the film. In the absence of chemical reaction between the gas and polymer, the diffusion of dissolved penetrant is the rate-limiting step in this process. The one-dimensional flux of gas A through the film in the x -direction (i. e., N_A) can be described by Fick's Law [7.264, 270]

$$N_A = -D \frac{dC_A}{dx} + w_A(N_A + N_p), \quad (7.122)$$

where D is the gas diffusion coefficient in the film, C_A is the local concentration of dissolved gas and w_A is the weight fraction of gas A in the film; N_p is the flux of the membrane, which is typically taken to be zero. Consequently, (7.122) reduces to [7.264]

$$N_A = -\frac{D}{1 - w_A} \frac{dC_A}{dx} \quad (7.123)$$

Steady-State Permeation

The steady-state permeability of gas A, P_A , through a film of thickness l is defined as [7.262, 264, 271]

$$P_A \equiv \frac{N_A l}{p_2 - p_1}, \quad (7.124)$$

where p_2 and p_1 are the upstream (i. e., high) and downstream (i. e., low) pressures, respectively. Permeability coefficients are commonly expressed in Barrers, where $1 \text{ Barrer} = 1 \times 10^{-10} \text{ cm}^3(\text{STP}) \text{ cm/cm}^2 \text{ s cm Hg}$. Combining (7.123) and (7.124) and integrating from $x = 0$ ($C = C_2$) to $x = l$ ($C = C_1$), one obtains

$$P_A = D_A \frac{C_2 - C_1}{p_2 - p_1}, \quad (7.125)$$

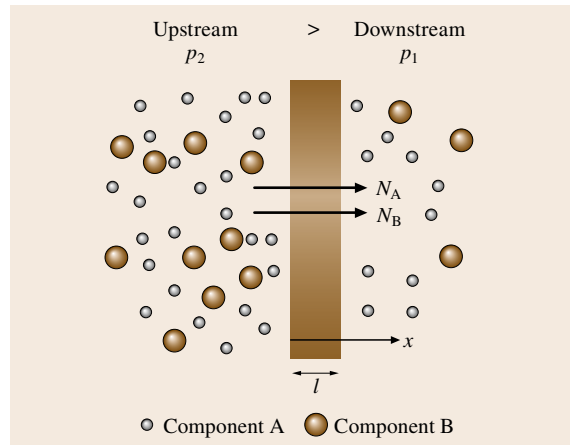


Fig. 7.105 Transport of gases A and B across a membrane

where D_A is the concentration-averaged effective diffusion coefficient in the range C_1 – C_2

$$\begin{aligned} D_A &= \frac{1}{C_2 - C_1} \int_{C_1}^{C_2} \frac{D}{1 - w_A} dC \\ &= \frac{1}{C_2 - C_1} \int_{C_1}^{C_2} D_{\text{eff}} dC, \end{aligned} \quad (7.126)$$

where D_{eff} is the local effective diffusion coefficient.

In general, it can be challenging to measure the average gas diffusivity directly. Instead, gas permeability and gas solubility are often measured independently, and gas diffusivity is inferred from these measurements, as described below. For simplicity, experiments are often designed so that $p_1 \ll p_2$ and, consequently, $C_1 \ll C_2$. In this limit, (7.125) reduces to

$$P_A = D_A \times S_A, \quad (7.127)$$

where $S_A = C_2/p_2$ is the apparent sorption coefficient or solubility of penetrant A in the polymer. Therefore, by measuring the gas permeability at an upstream pressure of p_2 and solubility at a pressure of p_2 , one can calculate the average gas diffusivity D_A . As indicated in (7.126), this diffusion coefficient is an average over the concentration range 0 – C_2 . The local effective diffusion coefficient D_{eff} , characterizing the penetrant diffusivity in the polymer at a penetrant concentration of C_2 , can be evaluated using an equation obtained by taking the derivative of both sides of (7.125) with respect

to C [7.272]

$$D_{\text{eff}}(C_2) = \left(P_A + p \frac{dP_A}{dp} \right)_{p_2} \left(\frac{dp}{dC_2} \right)_{p_2}, \quad (7.128)$$

which requires the pressure dependence of the permeability and solubility to calculate D_{eff} . Methods to measure pressure dependence of permeability and solubility are discussed in this chapter.

Gas sorption isotherms in polymers are typically described using simple models, such as Henry's law, the Flory–Huggins theory or the dual-mode sorption model [7.264]. These models have been extensively investigated in the literature [7.273] and, therefore, will only be briefly introduced. Once the gas sorption in a polymer has been measured, values of dp/dC_2 can be easily calculated for use in (7.128).

Henry's law corresponds to a linear relationship between C and p [7.274]

$$C = k_D p, \quad (7.129)$$

where k_D is the solubility coefficient, or Henry's law constant. This equation is typically valid for light gas sorption in rubbery polymers at low concentrations, such as $1 \text{ cm}^3(\text{STP})/\text{cm}^3$ polymer. For example, N_2 and O_2 sorption in poly(dimethylsiloxane) (PDMS) at 35°C obey Henry's law over a rather wide pressure range [7.272].

For highly sorbing penetrants in rubbery polymers, such as organic vapors, penetrant concentration in the polymer is often described using the Flory–Huggins model [7.274]

$$\ln a = \ln \phi_2 + (1 - \phi_2) + \chi(1 - \phi_2)^2, \quad (7.130)$$

where a is the penetrant activity, χ is the Flory–Huggins interaction parameter, and ϕ_2 is the volume fraction of penetrant dissolved in the polymer matrix. For ideal gases, the activity is equal to p/p_0 , where p_0 is the penetrant vapor pressure at the experiment temperature. The volume fraction ϕ_2 is given by [7.274].

$$\phi_2 = \frac{(C/22\,414)V_2}{1 + (C/22\,414)V_2}, \quad (7.131)$$

where V_2 is the partial molar volume (cm^3/mol) of the penetrant in the polymer, and C has units of $\text{cm}^3(\text{STP})/(\text{cm}^3 \text{ polymer})$. For low concentrations of sorbed gas, $\phi_2 \ll 1$, (7.130) and (7.131) reduce to Henry's law [7.275]. For high concentrations of sorbed gas, this model predicts an increasing value of solubility (i. e., C/p) as pressure increases. Equation (7.130)

successfully describes the sorption of strongly sorbing penetrants in rubbery polymers, such as CO_2 in poly(ethylene oxide) at 35°C [7.275].

The dual-mode sorption model was originally used to describe gas sorption in glassy polymers, which contain both equilibrium volume (i. e., Henry's law sorption sites) and nonequilibrium excess volume (i. e., microvoids or Langmuir sorption sites). The model is expressed as follows [7.276]

$$C = C_D + C_H = k_D p + \frac{C'_H b p}{1 + b p}, \quad (7.132)$$

where C_D and C_H are the gas concentrations in the Henry's law sorption sites and Langmuir sites, respectively, b is the Langmuir affinity constant, which characterizes the affinity between penetrants and microvoids, and C'_H is the Langmuir capacity constant [$\text{cm}^3(\text{STP})/\text{cm}^3$ polymer], which characterizes the maximum sorption capacity of the nonequilibrium excess volume. This model has also been applied to describe the gas sorption in hybrid systems such as blends of rubbery polymers and additives [7.277, 278]. These additives could be fillers that physically adsorb the gas or dissolved species that chemically interact with the gas.

The dependence of permeability on pressure is often described using empirical equations. For example, the following equation is often used to describe the pressure dependence of gas permeability in rubbery polymers [7.272, 275]

$$P_A = P_{A0}(1 + m \Delta p), \quad (7.133)$$

where P_{A0} and m are constants, and $\Delta p = p_2 - p_1$. For glassy polymers at $p_1 = 0$ (or, equivalently, $\Delta p = p_2$), the following equation, based on the dual-mode model, has been used [7.279]

$$P_A = k_D D \left(1 + \frac{FK}{1 + b p_2} \right), \quad (7.134)$$

where $K = C'_H b/k_D$, and D and F are constants obtained by fitting the model to experimental sorption and permeation data. For example, Koros and coworkers obtained k_D , b and C'_H by fitting gas sorption isotherms to (7.132) and then fitting the permeability data at various upstream pressures to (7.134) to obtain D and F [7.279]. Equation (7.133) or (7.134) can be used to calculate dP_A/dp , which can be substituted into (7.128) along with dp/dC_2 to calculate D_{eff} .

The ideal selectivity of a membrane for gas A over gas B (i. e., $\alpha_{A/B}$) is the ratio of their pure-gas perme-

abilities [7.262]

$$\alpha_{A/B} = \frac{P_A}{P_B} = \left(\frac{D_A}{D_B} \right) \times \left(\frac{S_A}{S_B} \right), \quad (7.135)$$

where D_A/D_B is the diffusivity selectivity, which is the ratio of the diffusion coefficients of gases A and B. The ratio of the solubility coefficients of gases A and B, S_A/S_B , is the solubility selectivity. For a binary gas mixture, the selectivity of gas A to gas B ($\alpha_{A/B}^*$) is defined as

$$\alpha_{A/B}^* \equiv \frac{y_A/y_B}{x_A/x_B} = \alpha_{A/B} \frac{\Delta p_A/x_A}{\Delta p_B/x_B}, \quad (7.136)$$

where y_i and x_i are the mole fractions of component i in the upstream and downstream gas phases, respectively, and Δp_i is the partial pressure difference of component i across the membrane. When the downstream pressure is much less than the upstream pressure, $\alpha_{A/B}^*$ approaches the ideal separation factor $\alpha_{A/B}$.

7.6.2 Kinetic Measurement

The kinetics of gas transport through a thin uniform film have been modeled, and such measurements can yield solubility, diffusivity and permeability in a single experiment. The penetrant concentration as a function of time and position in the film is given by Fick's second law [7.270]

$$\frac{\partial C}{\partial t} = \frac{\partial}{\partial x} \left(D_{\text{eff}} \frac{\partial C}{\partial x} \right). \quad (7.137)$$

The analytical solution of (7.137) depends on initial conditions, boundary conditions and the concentration dependence of the diffusion coefficient, if any. The diffusion coefficient could be a function of concentration, which makes the solution to (7.137) more complex [7.261]. However, *Crank* and *Park* have shown that solutions to (7.137) assuming constant D_{eff} values are also applicable when the diffusion coefficient depends on concentration [7.268]. In general, this approximation is sufficiently accurate to model experimental data [7.268], except that the diffusion coefficient obtained from such an analysis should be interpreted as an average effective diffusion coefficient as defined in (7.126).

Constant Diffusion Coefficient

In the simplest scenario, the gas diffusion coefficient is constant over the concentration range of interest. This assumption is usually valid for low-sorbing penetrants in rubbery polymers. However, care must be taken

since gas diffusion coefficients can exhibit concentration dependence at concentrations where gas sorption still obeys Henry's law, i. e., when gas solubility is independent of pressure [7.280]. Nevertheless, in a typical experiment, initially (i. e., at $t = 0$) the membrane is at a uniform concentration C_0 . At $t > 0$, one face ($x = 0$) of the membrane is exposed to a constant concentration C_2 by changing the gas pressure in contact with the membrane, and the other face at $x = l$ is exposed to C_1 [7.261]. The analytical solution to (7.137) under these conditions is [7.261]

$$\begin{aligned} C = & C_2 + (C_1 - C_2) \frac{x}{l} \\ & + \frac{2}{\pi} \sum_{n=1}^{\infty} \frac{C_1 \cos n\pi - C_2}{n} \\ & \times \sin \left(\frac{n\pi x}{l} \right) \exp(-Dn^2\pi^2 t/l^2) \\ & + \frac{4C_0}{\pi} \sum_{m=0}^{\infty} \frac{1}{2m+1} \sin \left(\frac{(2m+1)\pi x}{l} \right) \\ & \times \exp[-D(2m+1)^2\pi^2 t/l^2]. \end{aligned} \quad (7.138)$$

The direct measurement of penetrant concentration in the film as a function of position and time is very difficult and is usually not done. Instead, a much more straightforward experiment, measurement of the gas flux out of the film is usually performed. Two methods are typically used to monitor this kinetic process: (1) transient permeation, and (2) sorption (or desorption).

In a transient permeation study, C_0 and C_1 are zero. The gas molecules diffusing out of the membrane at $x = l$ (i. e., the downstream side) are collected in a closed volume of known size. The gas flux [i. e., $-D(\partial C/\partial x)_{x=l}$] can be easily calculated from the rate of gas accumulation in the closed volume. The total amount of gas transported across the membrane at time t , Q_t , is given by

$$\begin{aligned} Q_t = & \int_0^t -D \left(\frac{\partial C}{\partial x} \right)_{x=l} dt \\ = & \frac{DtC_2}{l} - \frac{lC_2}{6} - \frac{2lC_2}{\pi^2} \\ & \times \sum_{n=1}^{\infty} \frac{(-1)^n}{n^2} \exp(-Dn^2\pi^2 t/l^2), \end{aligned} \quad (7.139)$$

which reduces to the following equation when the gas flux reaches a steady state or, equivalently, as $t \rightarrow \infty$

$$Q_t = \frac{DC_2}{l} \left(t - \frac{l^2}{6D} \right). \quad (7.140)$$

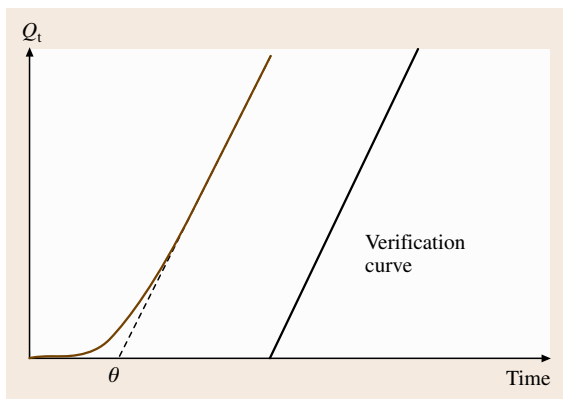


Fig. 7.106 A typical curve for the amount of accumulated permeate Q_t as a function of time in a transient permeation experiment

A typical curve for the amount of accumulated gas as a function of time appears in Fig. 7.106. The intercept of the steady-state region of Q_t with the time axis (i. e., $l^2/6D$) is defined as the time lag θ . The diffusion coefficient is given by

$$D = l^2/6\theta. \quad (7.141)$$

The above theoretical analysis was developed by *Daynes* in 1920 [7.281]. In 1939, *Barrer* and coworkers reported a system to measure the time lag and steady-state flow in polymers. Using this instrument, permeability, diffusivity and solubility can be estimated from a single experiment [7.282].

In a kinetic sorption or desorption study, the migration of gas into or out of a film is monitored by measuring the weight change of the polymer film containing the sorbed gas as a function of time. Typically, a polymer film with an initial gas concentration C_0 is suddenly exposed to an environment with a constant gas pressure p_2 , i. e., at $t > 0$, $C = C_2$ at $x = 0$ and l . C_2 is the concentration of gas in the polymer in equilibrium with the applied gas pressure p_2 . When $C_2 > C_0$, sorption occurs, and penetrant diffuses into the film. Desorption happens when $C_2 < C_0$. The kinetics of these processes are given by [7.261]

$$\begin{aligned} \frac{M_t}{M_\infty} &= 1 - \frac{8}{\pi^2} \sum_{n=0}^{\infty} \frac{1}{(2n+1)^2} \exp[-D(2n+1)^2\pi^2 t/l^2], \end{aligned} \quad (7.142)$$

where M_t and M_∞ denote the total amount of penetrant sorbed or desorbed in the film at time t and at equilib-

rium, respectively. For a film of cross-sectional area A and thickness l , M_t is given by

$$M_t = \left| A \int_0^l C(x, t) dx - C_0 Al \right| \quad (7.143)$$

and M_∞ is given by

$$M_\infty = |C_2 - C_0| Al. \quad (7.144)$$

Therefore, by determining the weight change of the sample with time, diffusion coefficients can be obtained by fitting the experimental data to (7.142). When $M_t/M_\infty > 0.7$, all terms with $n > 0$ in (7.142) can be neglected, and (7.142) becomes

$$\frac{M_t}{M_\infty} = 1 - \frac{8}{\pi^2} \exp(-D\pi^2 t/l^2), \quad (7.145)$$

which can be rearranged to [7.261]

$$\ln(1 - M_t/M_\infty) = \ln \frac{8}{\pi^2} - \frac{D\pi^2}{l^2} t. \quad (7.146)$$

In this way, the diffusion coefficient can be easily obtained by fitting the experimental data to (7.146).

Another way to analyze kinetic sorption data is based on an alternative analytical solution to (7.138), which is [7.261]

$$\begin{aligned} \frac{M_t}{M_\infty} &= 4 \left(\frac{Dt}{l^2} \right)^{1/2} \left[\pi^{-1/2} \right. \\ &\quad \left. + 2 \sum_{n=1}^{\infty} (-1)^n i \operatorname{erfc} \frac{nl}{2\sqrt{Dt}} \right]. \end{aligned} \quad (7.147)$$

The above solution can be simplified to the following equation at short times (i. e., $M_t/M_\infty < 0.6$)

$$\frac{M_t}{M_\infty} = \left(\frac{16D}{\pi l^2} \right)^{1/2} t^{1/2}. \quad (7.148)$$

Equation (7.148) predicts that the amount of penetrant sorbed or desorbed exhibits a linear dependence on $t^{1/2}$, and the diffusion coefficient can be calculated from the slope of the fractional uptake (or desorption) kinetics versus $t^{1/2}$.

In general, penetrant solubility can be derived from M_∞ and the initial concentration C_0

$$S_A = \frac{1}{p_2} \left(C_0 \pm \frac{M_\infty}{Al} \right), \quad (7.149)$$

where p_2 is the gas-phase pressure at equilibrium. The + sign is for sorption, and the - sign is for desorption.

Variable Diffusion Coefficient

In many situations, penetrant diffusion coefficients vary with concentration [7.261]. For example, strongly

sorbing penetrants in rubbery or glassy polymers often swell the polymer at sufficiently high activity, leading to changes in polymer properties (e.g., glass-transition temperature, fractional free volume, etc.) and penetrant diffusion coefficients [7.264]. *Frisch* developed an explicit expression for the time lag when the diffusion coefficient is concentration-dependent [7.283]. *Crank* treated this subject in detail using both analytical and numerical methods [7.261]. Strictly speaking, most of these treatments require knowledge of the functional form of the relationship between diffusion coefficient and concentration [7.261]. In contrast, the steady-state measurements discussed in Sect. 7.6.1 can provide a reliable way to evaluate diffusion, solubility and permeability coefficients without making a priori assumptions regarding the concentration dependence of the diffusion coefficient.

Various experimental approaches have been reported to measure gas transport through polymeric films. In principle, most of the techniques directly measure gas flux through the film or gas uptake by the film (i.e., solubility). Diffusion coefficients are typically derived indirectly from permeability and solubility measurements based on the theory introduced earlier. In the following sections, general strategies are described for measuring gas transport properties in polymers.

7.6.3 Experimental Measurement of Permeability

Film Preparation

The measurement of gas flux requires the successful preparation of a uniform, nonporous thin film. In general, polymer films for permeation testing have thicknesses of less than 250 μm , unless special situations require a thicker film. For example, thicker films may make it easier to prepare nonporous specimens for study, or they may be used to increase the time lag when studying penetrants with high diffusion coefficients (e.g., He or H_2). Uniformity of thickness is important for reducing the uncertainty in permeability, as illustrated in (7.124). A nonporous film is required if one wishes to determine the inherent properties of the material under study, because gas flow through a pinhole obeying Knudsen diffusion can be orders of magnitude faster than that through a dense film obeying the solution–diffusion mechanism [7.258]. Thus, any pinhole defects in a sample can compromise the accurate measurement of gas flux through a polymer film. The first challenge in successfully measuring gas per-

meation properties typically lies in the ability to prepare uniform, pinhole-free films.

Polymer films are typically prepared in the laboratory by melt-pressing and solvent-casting [7.284, 285]. Melt-pressing is used less often than solvent-casting to prepare films for study. In melt-pressing, one applies heat to melt a polymer powder, and then a film is made by pressing the molten polymer under high pressure. Solvent-casting is a widely used method to prepare films. In this method, solid polymer is dissolved in a solvent, the resulting solution is cast on a leveled support, and the solvent is allowed to evaporate slowly, leaving a solid film behind.

Gas permeation properties of films are often influenced by many processing factors. One critical factor is the solvent used in preparing the film, which can strongly affect polymer morphology and, in turn, gas permeation properties. For example, poly(4-methyl-1-pentene) films were prepared by solvent-casting using chloroform and carbon tetrachloride [7.285]. The N_2 permeability at 35 $^\circ\text{C}$ and 2 atm is 1.1 Barrers for a film prepared from chloroform solution, but it is 6.0 Barrers for a similar film prepared from carbon tetrachloride solution, even though the two films exhibit almost the same crystallinity values (i.e., 57% and 56%, respectively) [7.285]. Other possible factors influencing gas transport properties include polymer concentration, evaporation temperature, annealing conditions, etc. Pinholes in a solid film can be introduced during the solvent-casting process by bubbles present in the solution before casting, the presence of insoluble impurities in the solution (such as dust), and very rapid solvent evaporation. Typically, before casting, the solution is filtered to remove any impurities, and the solvent evaporation rate is controlled during film drying. For highly crystalline polymers such as poly(ethylene oxide), thermal annealing above the melting temperature could be critical to form defect-free films, although the reason for this is not clear [7.275].

Uniform thickness films can be obtained by spreading the solution onto a support using tools such as a Gardner knife or a doctor blade, which controls the liquid film thickness [7.284]. Alternatively, the solution may be poured into a glass ring resting on a flat solid support. The glass ring is typically stuck to the support using silicon caulk to achieve a leak-free boundary. The film thickness is controlled by the amount of liquid solution added and its concentration. The solid support needs to be leveled to obtain films of uniform thickness. The choice of the support material can be important. If the solution cannot wet the support, the liquid polymer

solution will bead up, and it will not form a continuous film. If the solid film adheres too strongly to the support, it can be difficult or impossible to remove the film intact from the support. Common supports are glass plates, Teflon plates, metal plates, plastic plates (which do not interact with the solvent) and even liquid surfaces such as water and mercury [7.284].

Permeation Cell

Gas permeability is the steady-state flux through a film normalized by the pressure difference and film thickness, as indicated in (7.124). Pressure is measured using commercial sensors or gauges with high precision in different pressure ranges. For example, Dresser Instruments (Shelton, USA) provides a digital indicator for pressure measurement with an accuracy of 0.025% of full scale over the pressure range 0–20 atm. Film thickness can be measured using a digital micrometer (Mitutoyo Corp., Japan), which can measure thickness to the nearest micrometer. To measure the thickness of rubbery polymers, the film should be covered with a uniform thin plate (quartz, glass or other flat, rigid materials) to prevent direct contact of the measuring tip of the digital micrometer with the soft film. The measurement tip can press into flexible films or even penetrate them; in either case, the thickness value provided by the micrometer is an underestimate of the true film thickness.

The gas flux through the film, which is the key parameter for permeability measurements, is typically measured from the permeate side ($x = l$) using a permeation cell. Figure 7.107a–c presents schematics of typical permeation cell designs for constant-pressure variable-volume, constant-volume variable-pressure and mixed-gas systems, respectively. These cells are com-

mercially available from Millipore Corporation (Billerica, USA) under the tradename of high-pressure filter holder. A flat polymer film with the same size as the inner diameter of the cell is placed on a sintered-metal support inside the cell, dividing the system into upstream (i. e., above the film) and downstream (i. e., below the film) compartments. A silicon or Viton O-ring is often used to prevent gas leakage at the film edge from the upstream (i. e., high-pressure) to the downstream (i. e., low-pressure) side of the cell and to avoid gas exchange between the upstream portion of the cell and the exterior atmosphere. In this way, only the feed gas permeating through the film is collected in the downstream section of the cell. For a pure-gas study, the upstream portion of the cell can be designed as a dead end, and gas permeating into the downstream side of the film will be collected as illustrated in Fig. 7.107a and b. For mixed-gas studies, the gas flow pattern requires a special cell design to minimize gas composition changes in the upstream and downstream chambers of the permeation cell. The upstream gas enters the cell at the center of the film, flows radially to the film edge and then flows out of the cell, which eliminates any trapped gas or dead zones in the cell [7.286]. Typically, trapped gas does not mix well with the entering feed gas, which results in gas concentration variations across the film and, therefore, errors in estimating the partial pressure that the film experiences during the measurement. The design of the permeate side follows similar principles. Additionally, to reduce the change of feed gas composition during flow from the film center to the edge, due to the preferential permeation of a gas component, the gas flow rate in the upstream is much higher than the gas flow rate due to permeation through the film. Typically, the ratio of the permeate gas

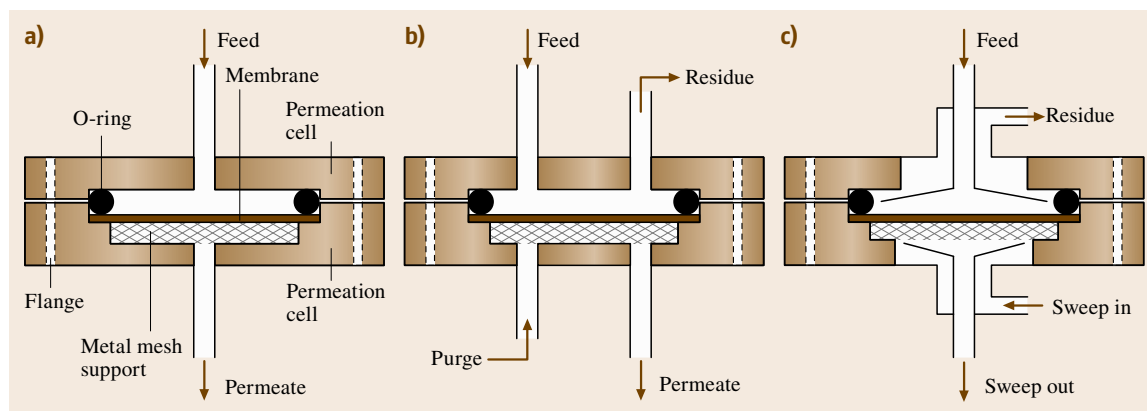


Fig. 7.107a–c Schematic of a typical permeation cell (a) for pure-gas measurements using the continuous flow method; (b) for pure-gas measurements using the constant-volume variable-pressure method and (c) for mixed-gas measurements

flow rate to feed gas flow rate (the so-called stage cut) would be 1% or less.

Films are typically supported on filter paper and then on a sintered-metal support. In general, the mass transfer resistance of the paper and the metal support should be negligible relative to that of the polymer film so that the measured gas flux reflects only the inherent properties of the film. The practical film area available for gas diffusion is not the same as the area of the entire film, because the contact area between the O-ring and the film area is not accessible to gas diffusion. Typically, after the cell is clamped in place for measurements, the O-ring would leave an imprint on the film. The inside diameter of the imprint is often used to calculate the active test area. In many cases (for example, films that are too soft or viscous or when the area of the films is smaller than the cell size), films need to be partially masked using impermeable aluminum tape so that there is no direct contact of the O-ring with the films [7.275, 287, 288].

Temperature Control

Thermal uniformity is an important factor since gas permeability can depend strongly on temperature [7.265]. Two typical media are used as temperature-control fluids: air and liquids. An air bath can conveniently provide operational temperatures above room temperature. Such a system includes a fan to circulate air past a heating element and the permeation instrumentation, a heater element (which can be as simple as a light bulb for temperatures near ambient or commercially available heating elements from, for example, Omega Engineering Inc. (Stamford, USA)) and a temperature control system. Commercially available temperature controllers, such as a CN76000 microprocessor-based temperature/process controller made by Omega Engineering, work well for this purpose. A liquid bath, such as a mixture of methanol and water (50/50 by weight) can provide temperatures as low as -30°C . For low-temperature operations, cooling is typically accomplished using a chiller. Generally, good circulation in the bath is required to achieve a uniform temperature around the cell and other components of the measurement system.

7.6.4 Gas Flux Measurement

Gas flux is commonly measured using one of the following three methods: (1) constant-pressure variable-volume, (2) constant-volume variable-pressure and (3) a method using a special sensor for mixed-gas permeation measurements. These techniques are discussed below.

Constant-Pressure Variable-Volume Method

A schematic of a constant-pressure variable-volume (or continuous flow) permeation system is shown in Fig. 7.108. A schematic of a typical cell for such a system is given in Fig. 7.107b. The feed gas enters the cell and leaves in the residue stream, and the downstream is typically purged using the feed gas before beginning measurements to remove any impurities from the downstream. This apparatus operates by applying a target gas at a constant pressure to the upstream face of the film and measuring the resulting steady-state gas flux on the downstream side of the film or membrane being tested using a flow meter. Electronic flow meters are commercially available, such as the Agilent model ADM1000 (Wilmington, USA). However, a simple and convenient device is a soap-bubble flow meter (Alltech Associates, Inc. Deerfield, USA). By timing the movement of the soap film in a graduated capillary tube, the steady-state permeability (cm^3 (STP) cm/cm^2 s cmHg) is given by

$$P_A = \frac{l}{p_2 - p_1} \frac{273 p_{\text{atm}}}{TA 76} \left(\frac{dV}{dt} \right), \quad (7.150)$$

where the downstream pressure p_1 is atmospheric pressure (cmHg) in this case, p_{atm} is the atmospheric pressure (cmHg), T is the absolute temperature of the gas in the bubble flow meter (K), and dV/dt is the steady-state volumetric displacement rate of the soap film (cm^3/s). The accuracy of this method depends on the sensitivity of the bubble flow meter. Typically, the accuracy of the bubble flow meter becomes higher as the capillary tube diameter decreases. This method is typically used to study polymeric films with high gas fluxes, such as poly(dimethylsiloxane) (PDMS), poly(1-trimethylsilyl-1-propyne) (PTMSP) and compos-

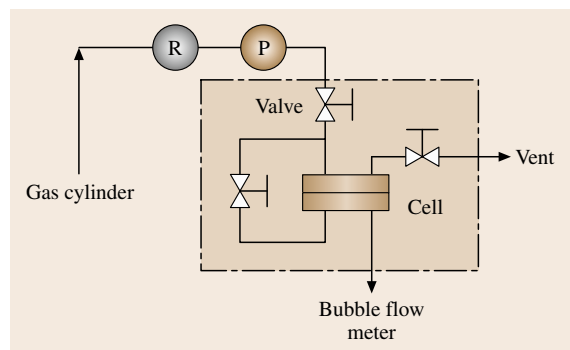


Fig. 7.108 Schematic of a constant-pressure variable volume apparatus for gas permeability measurements (R: regulator; P: pressure transducer). The parts within the *dashed box* are in a temperature-controlled chamber

ite membranes with very thin polymer coatings on porous membrane supports [7.289]. The authors have good experience with such materials and bubble flow meters with ranges such as 0–1.0 ml, 0–10 ml and 0–100 ml, which are made by Alltech Associates, Inc. (Deerfield, USA).

Constant-Volume Variable-Pressure Method

As illustrated in Fig. 7.109, a constant-volume variable-pressure system measures permeate flux by monitoring the pressure increase of collected permeate gas in a closed volume using a pressure transducer. A typical cell is presented in Fig. 7.107a. Unlike the cell used for the continuous-flow method, the cell used here does not require a residue or purge stream since any volatile impurities or air gases can be removed from the sample by exposing the whole system to vacuum prior to beginning a measurement. The apparatus operates by initially evacuating the upstream and downstream volumes to degas the film. Then, the valve connecting the permeation cell to the vacuum pump is closed, and a slow pressure rise in the downstream volume (i.e., the leak rate of the system) is observed. This rate of pressure rise should be at least ten times less than the estimated steady-state rate of pressure rise due to permeation to obtain accurate permeability estimates. The feed gas is then introduced to the upstream side of the membrane, and the pressure rise in the downstream volume is recorded as a function of time. Gas permeability ($\text{cm}^3(\text{STP}) \text{ cm}/(\text{cm}^2 \text{ s cmHg})$) is calculated from the

following expression [7.275, 290]

$$P_A = \frac{V_d l}{p_2 A R T} \left[\left(\frac{dp_1}{dt} \right)_{\text{ss}} - \left(\frac{dp_1}{dt} \right)_{\text{leak}} \right], \quad (7.151)$$

where V_d is the downstream volume (cm^3), l is the film thickness (cm), p_2 is the upstream absolute pressure (cmHg), A is the film area available for gas transport (cm^2), the gas constant R is $0.278 \text{ cmHg cm}^3/(\text{cm}^3(\text{STP}) \text{ K})$, T is absolute temperature (K) and $(dp_1/dt)_{\text{ss}}$ and $(dp_1/dt)_{\text{leak}}$ are the steady-state rates of pressure rise (cmHg/s) in the downstream volume at fixed upstream pressure and under vacuum, respectively. The downstream pressure must be kept much lower than the upstream pressure to maintain an effectively constant pressure difference across the membrane. In our laboratory, the downstream pressure is typically lower than 0.03 atm, compared with a typical upstream pressure of 4.4 atm or more. If steady-state permeation cannot be achieved before the downstream pressure increases to a significant value, the downstream should be evacuated using the vacuum pump, and the recording of the pressure rise in the downstream volume is restarted. Additionally, the design of the downstream in Fig. 7.109 allows one to choose a suitable downstream volume to achieve a reasonable rate of pressure rise for films of different fluxes. If the flux is low, the smallest volume (i.e., the volume of the downstream tubing only) can be used to observe the pressure rise. On the other hand, one or two additional volumes can be used if the flux is high.

In this method, the upstream and downstream pressures can be accurately measured using commercially available pressure gauges or transducers. The key parameter to be measured is the downstream volume, for example V_0 (defined as the tubing volume), which includes part of the permeation cell (i.e., beneath the film), tubing, tubing connections and valves, as illustrated in Fig. 7.109. The direct measurement of V_0 is impossible. One way to circumvent this issue is to measure volume 1, V_1 , including a short section of tubing and a vessel (as illustrated in Fig. 7.109) first by liquid filling followed by Burnett gas expansion [7.291]. Volume 1 is filled with a volatile liquid, such as methanol, and the value of V_1 equals the volume of the liquid required to completely fill volume 1. To obtain the value of V_0 , an impermeable aluminum foil film is installed in the permeation cell to isolate the downstream from the upstream. Initially, V_0 and V_1 are under vacuum (i.e., the pressure is 0 cmHg). Volume 1 is isolated from V_0 by turning off valve 1, and gas is introduced into the tubing at a pressure of p_0 (which is typically much lower

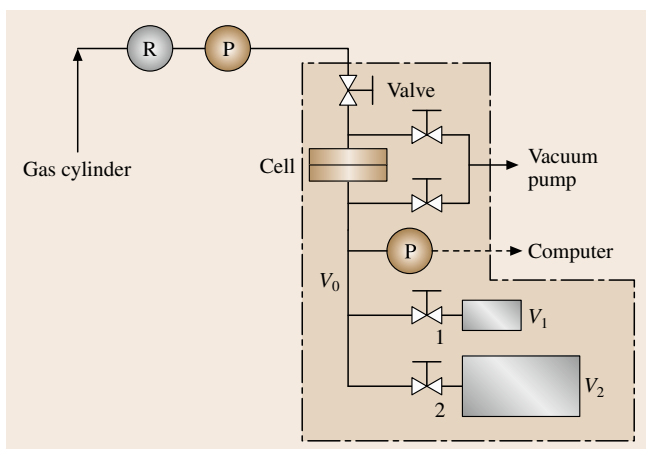


Fig. 7.109 Schematic of a constant-volume variable-pressure apparatus for gas permeability measurements (R: regulator; P: pressure transducer; V_0 , V_1 and V_2 : tubing volume, volumes 1 and 2, respectively). The parts within the dashed box are in a temperature-controlled chamber

than 1 atm). Light gases such as N_2 and He are typically used since they exhibit ideal gas behavior at subatmospheric pressure. After the value of p_0 stabilizes, the valve is opened, and the gas expands into volume 1; the pressure reaches p_f in both volumes. Assuming ideal gas behavior, the ratio of the two volumes is given by

$$V_1/V_0 = p_0/p_f - 1, \quad (7.152)$$

which permits one to obtain an accurate value of the tubing volume. Following the same procedure, V_2 can be estimated. V_2 can also be estimated using the liquid-filling method.

To simplify the data acquisition process, automatic recording of the downstream pressure can be employed. Typically, transducers (such as those from MKS Instruments, Wilmington, MA, USA) used in the downstream sense the pressure and give an analog voltage output signal. The pressure is typically linearly related to the transducer output voltage, and this relationship can be obtained by calibrating the transducer using a standard pressure indicator. The voltage signal can be recorded using a chart recorder. More conveniently, the signal can be digitized and monitored using a computer via data-acquisition programs such as Labtech Notebook (Laboratory Technologies Corp., Andover, MA, USA) or Labview (National Instruments Corp., Austin, TX, USA), which show and record the pressure in real time and allow one to analyze the data with widely used software such as Microsoft Excel. The required hardware, including computer boards, terminals, readouts etc., is provided by commercial sources, such as Measurement Computing Corp. (Middleboro, MA, USA).

Due to the ability to measure pressure accurately, the constant-volume variable-pressure system is able to measure a wide range of flux values, including materials exhibiting flux values too low to be measured by a constant-pressure variable-volume system.

Mixed-Gas Permeability Measurement

The measurement of mixed-gas permeability coefficients follows principles similar to those used for pure-gas permeability measurements, except that the mixed-gas measurement requires a sensor to detect gas concentration in the feed, residue and permeate streams. A gas chromatograph (GC) is the most widely used concentration detection method [7.290, 292]. A schematic of a mixed-gas permeation instrument is provided in Fig. 7.110 [7.289]. In general, the permeate is swept away from the membrane surface using a carrier gas (e.g., He, H_2 or N_2) at a pressure of about 1 atm. The preferred carrier gas should have a thermal conductivity

that is very different from that of the permeate gas, since thermal conductivity detectors are widely used for concentration detection in the GC. Consequently, helium or hydrogen is often used as the carrier gas [7.293]. By measuring the permeate gas concentration in the sweep gas and the sweep gas flow rate (i. e., S), permeability can be calculated as follows [7.289]

$$P_A = \frac{x_{1A} S_F l}{x_{He}^P A (p_2 x_{2A} - p_1 x_{1A})} \quad (7.153)$$

where x_{1A} and x_{He}^P are the mole fractions of component A and helium in the permeate stream, respectively; x_{2A} is the mole fraction of component A in the feed gas.

Mixed-gas measurements require a specially designed permeation cell, as illustrated in Fig. 7.107c, to ensure good mixing in the gas phase above and below the membrane. Low stage-cut values (the stage cut is the ratio of the permeate gas flow rate to the feed gas flow rate) are used to improve mixing efficiency on the feed side of the membrane. Typically, the stage cut is set to be less than 1%; that is, the permeate flow rate is less than 1% of the feed flow rate. Additionally, this method can be used for pure-gas studies. Compared with the continuous flow system described earlier (i. e., constant pressure/variable volume system), this apparatus is able to measure low permeate flux, mainly because of the high sensitivity of GC for gas composition detection and the ease of measurement of the high sweep gas flux using a bubble flow meter.

An alternative technique can also be used for mixed-gas permeability measurement [7.294]. Instead of using a carrier gas on the permeate side of the membrane, a closed downstream volume is used. When the gas flux

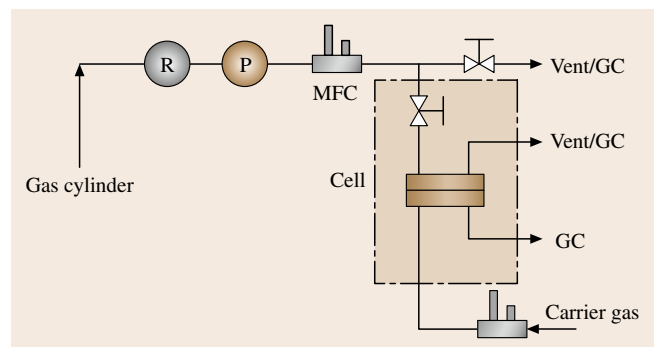


Fig. 7.110 Schematic of a mixed-gas permeability apparatus for gas permeability measurements using a gas chromatograph for concentration detection (R: regulator; P: pressure transducer; MFC: mass-flow controller; GC: gas chromatograph). The parts within the dashed box are in a temperature-controlled chamber

reaches steady state, as detected by monitoring the rate of downstream pressure rise, the downstream is evacuated to remove the gas accumulated during nonsteady-state permeation. Afterwards, the downstream volume is isolated, and pressure in this volume increases. Then, a valve is opened, and the gas expands into an evacuated line connecting the gas chromatograph to the downstream volume. The gas permeability can be calculated from the steady-state rate of pressure rise in the downstream volume and the corresponding composition of the permeate gas determined using the GC.

Besides GC, other sensors have been employed for gas permeation studies. For example, oxygen transmission across films is an important property in food packaging, since the exposure of food and beverages to oxygen can significantly influence their shelf life [7.257]. The American Society for Testing and Materials (ASTM) standard F1307 describes a constant-volume variable-pressure system which employs an oxygen sensor to detect the oxygen concentration in the downstream volume [7.295]. Coupled with the rate of pressure rise in the downstream volume, O_2 permeability can be easily calculated using (7.151). This method is particularly convenient for mixed gas feeds containing O_2 and other species, where only the O_2 permeability is of interest.

Transient Transport Measurement

Based on the pioneering work by *Daynes* and *Barber* [7.281, 282], transient transport measurements (time lag) have come to be widely practised. The most common system used to detect the time lag is the constant-volume variable-pressure system [7.266], although systems employing a gas chromatograph have also been reported [7.292]. As illustrated in Fig. 7.106, the time lag is defined as the intercept of the extrapolated linear pseudo-steady-state region of the downstream pressure rise back to the time axis. A key issue is to ensure that the experiment has reached steady

state. *Koros* and *Zimmerman* proposed a procedure illustrated in Fig. 7.106 [7.266]. The experiment is run for a period that is approximately five to six time lags, then the downstream volume is evacuated, and the measurement is restarted. If the slope of the downstream pressure rise versus time is consistent with the rate of downstream pressure rise measured before evacuation, then the experiment is considered to be at steady state.

This technique requires films having good mechanical properties to sustain the pressure difference across the sample and a leak-free downstream volume. To increase the sensitivity of this technique, i. e., to increase the time lag, thicker films can be used. As illustrated in (7.141), time lag increases with the square of the film thickness. This strategy is especially useful for studies of small penetrants such as hydrogen and helium, which typically have high diffusion coefficients and, therefore, exhibit time lag values that are often too short to be detected. On the other hand, (7.141) suggests that film thickness uniformity is very important for reducing the uncertainty of this measurement.

7.6.5 Experimental Measurement of Gas and Vapor Sorption

The sorption of gas in a polymer film is usually detected by either a decrease of gas pressure (i. e. gas-phase concentration) in the environment surrounding a polymer in a closed chamber or the weight increase of a polymer film due to gas sorption. An apparatus is typically designed to measure changes in either the amount of gas in the gas phase or the weight change of the polymer film due to the sorption or desorption of the penetrant. In the following section, common methods of measuring gas sorption are described. They include the dual-volume, pressure-decay method, the gravimetric method, and inverse gas chromatography.

The Dual-Volume Pressure-Decay Method

The dual-volume pressure-decay method employs dual transducers and dual cells, and is widely used to determine pure-gas solubility in polymeric samples [7.296, 297]. A schematic diagram of such a system is shown in Fig. 7.111. The system consists of a sample cell containing a polymer sample and a charge cell connected to a gas cylinder. In the first step, the sample cell is evacuated and then isolated from the charge cell, which is subsequently charged with a target gas at a known pressure. The valve between the charge and sample cells is opened briefly to introduce gas to the sample cell. The valve between the sample and charge cells is closed, and

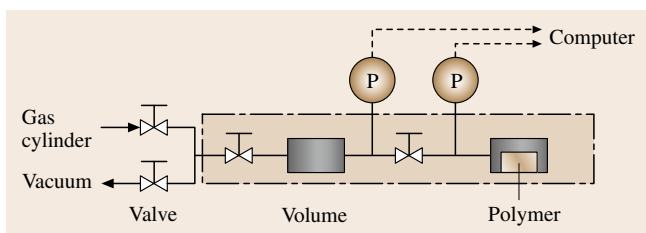


Fig. 7.111 Schematic of a barometric pressure decay apparatus for gas sorption measurement (dual-volume dual-transducer system) (P: pressure transducer). The parts within the dashed box are in a temperature-controlled chamber

the pressure in the sample cell is monitored as a function of time. The difference between the initial and final pressure in the charge cell can be used to calculate the number of moles of gas admitted into the sample cell. As the polymer sample sorbs gas, the pressure in the gas phase of the sample cell decreases. When the sample cell pressure reaches a stable value, the polymer has sorbed all of the gas that it can at the final pressure in the sample cell (i. e., equilibrium is achieved). From the final pressure in the sample cell, the number of moles of gases in the gas phase of the sample cell can be calculated. The difference between the moles of gas admitted to the sample cell from the charge cell and the final number of moles of gas in the gas phase of the sample cell is the number of moles of gas sorbed by the sample at the final pressure of the sample cell. The second step is to add more gas to the charge cell and repeat the procedure outlined above to obtain a data point at a higher pressure. At step m , the number of moles of gas sorbed in the polymer $n_{p,m}$ is given by [7.296]

$$n_{p,m} = n_{p,m-1} + \left(\frac{p_{c,m-1} V_c}{RTZ_{c,m-1}} + \frac{p_{s,m-1} (V_s - V_p)}{RTZ_{s,m-1}} \right) - \left(\frac{p_{c,m} V_c}{RTZ_{c,m}} + \frac{p_{s,m} (V_s - V_p)}{RTZ_{s,m}} \right), \quad (7.154)$$

where V_c is the volume of the charge cell, V_s is the volume of the sample cell, and V_p is the volume of polymer sample. $Z_{c,m}$, $Z_{s,m}$, $Z_{c,m-1}$ and $Z_{s,m-1}$ are the compressibility factors of gas in the charge cell at step m , sample cell at step m , charge cell at step $(m-1)$ and sample cell at step $(m-1)$, respectively. The subscripts m and $m-1$ represent the properties at step m and step $(m-1)$, respectively. For example, $n_{p,m-1}$ is the number of moles of gas sorbed in the polymer at step $(m-1)$. In the first step (i. e., $m=1$), the sample cell is under vacuum, and $n_{p,0}$ is zero. From these sequential measurements, the gas sorption isotherm in the polymer can be obtained, and the gas solubility as a function of gas pressure can be calculated based on the definition of solubility: $S = C/p$.

Compressibility factors are related to pressure by [7.298]

$$Z = 1 + B^* p + C^* p^2, \quad (7.155)$$

where B^* and C^* are virial coefficients which depend on temperature. They have been compiled by *Dymond* and *Smith* for a large number of gases at various temperatures [7.298]. Virial coefficients are also available for some gas mixtures from the same source [7.298].

In general, the amount of gas in the gas phase is much greater than that sorbed in the polymer, i. e., the values of the two terms in brackets on the right-hand side of (7.154) are much larger than $n_{p,m}$ or $n_{p,m-1}$. In this sense, the value of $n_{p,m}$ is the result of a subtraction between two much larger numbers. Therefore, the accuracy of $n_{p,m}$ is sensitive to the calibration of the pressure transducers and volumes. A typical transducer used for such studies is the Super TJE model (Sensotec, Columbus, OH, USA), which measures a pressure range of 0–34 atm with an uncertainty as low as $\pm 0.05\%$ of full scale (i. e., ± 0.017 atm). It is one of the most accurate transducers commercially available. Generally, the transducers sense pressure and provide an analog signal such as a voltage, which can be related to the pressure measured by a standard pressure gauge (such as the **PM** indicator made by Dresser Instruments, Shelton, CT, USA) using a linear or polynomial equation. The volume calibration can be performed by a two-step Burnett expansion process [7.291]. In the first step, gas (typically helium) in the charge cell at a pressure p_0 is expanded to the empty sample cell, which is kept under vacuum before the expansion. The pressure in both cells reaches a stable value of p_f . Based on a mass balance, the following equation can be derived

$$\frac{p_0 V_c}{RTZ_0} = \frac{p_f (V_c + V_s)}{RTZ_f}, \quad (7.156)$$

where Z_0 and Z_f are compressibility factors at pressures of p_0 and p_f , respectively. Substituting (7.155) into (7.156) and letting the third virial coefficient, C^* , equal zero (since C^* is a very small number for helium [7.298] and $C^* p^2$ is typically negligible for helium), yields

$$\frac{p_0}{p_f} = \frac{B^* V_s}{V_c} p_0 + \frac{V_c + V_s}{V_c}. \quad (7.157)$$

By varying p_0 , one can generate data to prepare a plot of p_0/p_f as a function of p_0 . The resulting line intersects the p_0/p_f axis at $(1 + V_s/V_c)$. The second step is to vary the volume of the sample cell by inserting some nonsorbing solid of known volume V_m , such as stainless-steel spheres, into the sample cell. Repeating the Burnett expansion step outlined above, the following equation is obtained

$$\frac{p_0}{p_f} = \frac{B^* (V_s - V_m)}{V_c} p_0 + \frac{V_c + V_s - V_m}{V_c}. \quad (7.158)$$

Again, one can perform gas expansions as a function of pressure to fit this model and determine $(V_s - V_m)/V_c$,

which can be coupled with the value of V_s/V_c to calculate V_s and V_c .

As discussed above, the accuracy of gas solubility measurements depends strongly on the calibration of the transducers and the volumes, especially for low-sorbing materials. Since the true volume of the sample cell in the measurement is the difference between the sample cell volume and the polymer sample volume, the accurate measurement of gas solubility depends sensitively on the measurement of polymer sample volume and, therefore, polymer density, which is used to calculate polymer sample volume. The following procedure has been developed in our laboratory to estimate the effect of these uncertainties on solubility values. After the volume calibration, a standard sorption experiment (i. e., a blank experiment) is performed using the gases of interest while still keeping the nonsorbing volume (e.g., stainless-steel spheres) in the sample cell. Ideally, the gas solubility estimated from this experiment should be zero since these nonporous spheres sorb a negligible amount of gas. However, due to the uncertainties in the pressure and volume values, a small nonzero sorption value is typically obtained. In studying gas sorption in polymers, the sample should have a volume similar to V_m , and the pressure decay sequence is kept similar to that in the blank experiments. The solubility values obtained in this experiment are compared with those obtained from blank experiments. The difference between these two series of results is regarded as the true gas sorption in the polymer samples. A principal rule of thumb to judge the validity of the data is that the gas solubility values obtained using the polymer samples need to be much larger (such as ten times larger) than the values from the blank experiments. In general, the polymer sample volume (V_m) or the added volume should be as

large as possible so that the gas pressure change in the sample cell during each sorption step will be very pronounced, which reduces the uncertainty in the solubility values. In our laboratory, this technique has been used to measure solubility as low as $0.10 \text{ cm}^3(\text{STP})/(\text{cm}^3 \text{ atm})$ with a standard deviation of less than 10%.

Koros and coworkers have used data from the transient region of the pressure decay experiments to obtain gas diffusion coefficients in polymers. They monitored the pressure change in the sample cell as a function of time and interpreted the results using an analytical solution to (7.138) [7.299]. However, this method is not commonly used for kinetic studies, partially because the polymer sample is typically stacked in the small sample cell, and a uniform boundary condition during the transient sorption process for the entire polymer sample might be difficult to achieve.

Gravimetric Technique

Unlike the barometric technique described above, which is used mainly for high-pressure gas sorption measurements, the gravimetric technique is often used at subatmospheric pressures [7.265]. Lately, this technique has been extended for use at high pressures. For example, ISOSORP, a commercial apparatus made by Rubotherm (Bochum, Germany) and designed based on the gravimetric method, can be operated at pressures as high as 100 MPa. The basic principle is to monitor the weight change of a polymer film due to penetrant uptake. Typically, the results yield information about transient sorption kinetics and equilibrium sorption. From these data, solubility, diffusivity and permeability can be calculated using a proper model. This section focuses on the McBain spring balance apparatus, the Cahn electrobalance, and the quartz-crystal microbalance techniques.

A McBain spring balance is commonly used to track the kinetics of mass uptake in a thin polymer film, as illustrated in Fig. 7.112. The polymer sample is suspended from a calibrated quartz spring in a water-jacketed glass chamber, where the temperature is controlled by circulation of water from a temperature bath [7.265, 300]. The quartz spring typically obeys Hook's law over a wide range of loading

$$M = kx, \quad (7.159)$$

where M is the weight, x is the spring extension, and k is the spring constant. Generally, the spring constant is calibrated by measuring the spring extension when loaded with a series of known weights. Thus, the penetrant uptake as a function of time can be ob-

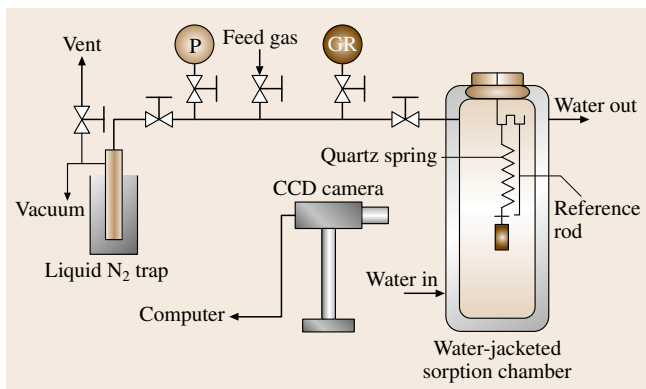


Fig. 7.112 Schematic of a McBain spring system for sorption measurements (P: pressure transducer; GR: gas/vapor reservoir)

tained by monitoring the spring extension with time, which is typically measured as the displacement of a certain point on the spring relative to the end of a reference rod using a cathetometer or a camera [7.300]. The experiment begins by degassing the polymer sample and then exposing the film to a large amount of gas or vapor at a fixed pressure. The spring extension is monitored until the sorption reaches equilibrium (i. e., until there is no further spring extension). The pressure in the chamber can be increased sequentially, and gas sorption isotherms can be obtained from such data. Additionally, gas diffusion coefficients can be obtained from kinetic sorption data. One key design element of this apparatus is to make the sorption chamber large enough so that the change in gas pressure during the sorption or desorption process is negligible, and thus the boundary condition remains $C = C_2$ at $x = 0$ and l .

Care must be taken to eliminate any external interference of the spring operation, which is very sensitive to vibrations. For example, the system needs to be fixed in an area free of vibration, and the introduction of gas or vapor into the chamber to start the experiment needs to be slow.

One limitation of conventional McBain spring balance systems is that the penetrant needs to have vapor pressure values high enough so that the pressure can be measured using a pressure transducer. For example, a pressure of 0.1 mmHg is probably the lowest practical value that could be achieved using a system such as the one in Fig. 7.112 [7.301]. However, the performance of food packaging materials can depend upon the sorption and diffusion of flavor compounds (e.g., higher hydrocarbons, benzaldehyde, benzyl alcohol, etc.), which are typically not very volatile (i. e., they have very low vapor pressure values). Additionally, these flavor compounds may be present at low thermodynamic activity, which requires the study of transport properties of these compounds at very low pressure [7.301]. In our laboratory, we have modified a McBain system to avoid the requirement of low-pressure measurement by employing gas chromatography to measure penetrant activity [7.301]. A light gas such as helium (which is essentially nonsorbing in the polymer at pressures of one atmosphere or less) is bubbled through the liquid penetrant at a controlled temperature and introduced into the sample chamber. The concentration of liquid penetrant in the gas phase can be adjusted by controlling the temperature of the liquid or by diluting the gas mixture with another stream of light gas. The concentration of the penetrant in helium is

measured using a gas chromatograph. Since the light gas essentially does not sorb into the film, the polymer weight change is due only to the sorption or desorption of the penetrant. In this way, the sorption of penetrants with very low vapor pressure can be studied.

Instead of a spring, other devices have been used to monitor the weight change of a polymer sample during sorption or desorption. Examples of such devices include the Cahn electrobalance [7.302], the magnetic suspension balance [7.303] and the quartz-crystal microbalance [7.304]. These systems have been tested at high pressure, for example, up to 200 atm [7.304], and at temperatures from room temperature to 120 °C [7.302]. The first two balances are commercially available.

A quartz-crystal microbalance contains a piezoelectric crystal which oscillates at its characteristic frequency when an alternating current is applied to it. By coating a polymer layer on the crystal and exposing the polymer coatings to gas, the crystal oscillating frequency changes as a result of the weight change by the polymer due to penetrant sorption. The mass of gas sorbed or desorbed (i. e., the mass change of the crystal, Δm) is given by [7.305]

$$\Delta m = -\Delta f/G, \quad (7.160)$$

where Δf is the frequency change due to sorption or desorption, and G is a constant determined by the vibrational frequency, frequency constant of the crystal, density of the quartz, and the effective area of the vibrating plate [7.305]. Special care is required for calibration of the quartz-crystal microbalance, since the surface properties of the coated crystal can significantly affect the frequency, thus introducing errors into the mass calculation [7.304].

Inverse Gas Chromatography

Inverse gas chromatography (IGC) has been used to measure gas sorption, though it is less widely used. IGC is an indirect method, which uses a gas chromatograph containing a solid support coated with a polymer material of interest as the stationary phase [7.306]. The penetrant of interest is introduced as the mobile phase, and its passage through the GC column depends on its interaction with the polymer. Typically, gas sorption in the polymer is related to the gas's retention time on the polymer-coated column. IGC can easily be used to study gas sorption as a function of temperature even up to high temperatures. However, the column cannot withstand high pressures.

Mixed-Gas Sorption Measurement

Mixed-gas sorption measurements are rarely reported, partly due to the complexity of these measurements. Additionally, gas sorption in polymers is often low, so the mixed-gas sorption is typically assumed to be the sum of the amounts of the components sorbed based on pure-gas sorption measurements. In some cases, however, competitive sorption is expected, and the mixed-gas sorption level could deviate from those estimated based on pure-gas sorption. CO₂ and C₂H₄ sorption in glassy poly(methyl methacrylate) (PMMA) is an example of such a system [7.314]. To understand the effect of sorbing of one penetrant on the other in PMMA, Sanders et al. designed a mixed-gas sorption system based on barometric pressure decay principles such as those described in Sect. 7.6.3. The design is similar to the pure-gas measurement, except that the gas compositions must be determined before and after the gas is introduced into the sample cell using a gas chromatograph [7.314]. For details regarding the apparatus design and operation, readers should consult [7.314].

Special Techniques

Advances in analytical equipment can potentially improve methods to measure gas transport properties in polymer films. In addition to the more typical systems discussed above, there are special techniques available for certain situations. Crank and Park reviewed various techniques to measure penetrant concentration directly as a function of time and position [7.268]. These techniques include refractive-index measurements, radiation absorption methods and radiotracer methods [7.268]. From these techniques, small-molecule transport properties such as solubility,

diffusivity and permeability can be obtained when these results are combined with flux measurements. Fieldson and Barbari applied Fourier-transform infrared (FTIR-ATR) spectroscopy to study small-molecule diffusion in polymers [7.315]. Assink used nuclear magnetic resonance (NMR) techniques to study ammonia sorption in glassy polystyrene [7.316]. As discussed in Sect. 7.6.2, glassy polymers exhibit two distinct sorption sites, Henry's law sites and Langmuir sites. It is commonly assumed that gas sorbed into these two populations of sorption sites can exchange rapidly (i.e., the local equilibrium hypothesis), and gas sorbed into the Langmuir sites is typically less mobile than that in Henry's law sites [7.316, 317]. To test that assumption, Assink determined gas concentration in the film using NMR and obtained the relative concentration by fitting the data to (7.132). Based on the characteristic exponential decay of the nuclear magnetization, he was able to verify the validity of the local equilibrium hypothesis [7.316].

7.6.6 Method Evaluations

In the USA, the American Society for Testing and Materials (ASTM) has published guidelines for many of the measurement techniques discussed above. Table 7.16 provides a synopsis of relevant ASTM standards. Interested readers should consult the original ASTM documents, which discuss equipment design, operating procedures, and application of the techniques. Some commercial instruments used for gas transport property measurement are listed in Table 7.17.

In general, it is important to plan the experiments needed to understand the transport of particular

Table 7.16 A list of some ASTM International standards related to the measurement of gas transport properties in polymer films

Document number ^a	Measurement	Method	Ref.
D1434-82	Gas permeability	Constant-pressure variable-volume, constant-volume variable-pressure	[7.307]
D3985-02	Dry O ₂ permeability	Continuous flow with a coulometric detector	[7.308]
F1307-02	Dry O ₂ permeability	Continuous flow with a coulometric detector	[7.295]
F1927-98	Humidified O ₂ permeation	Continuous flow with a coulometric detector	[7.309]
E96-00	Water vapor permeance	Gravimetric cup method (desiccant method and water method)	[7.310]
E398-03	Water vapor permeance	Relative humidity measurement	[7.311]
F1770-97	Water permeability, solubility and diffusivity	Continuous flow with a water-concentration-dependent sensor; time lag	[7.312]
F1769-97	Vapor permeability, solubility and diffusivity	Continuous flow with a flame ionization detector; time lag	[7.313]

^a The numbers after the dash indicate the year of original adoption or last revision

Table 7.17 Some representative commercially available instruments

Model	Measurement	Method	Company
OX-TRAN Model 2/21	O ₂ permeability	ASTM D3985	MOCON Inc., Minneapolis, MN, USA
PERMATRAN-W Model 3/33	Water permeability	ASTM F1249	
PERMATRAN-C Model 4/41	CO ₂ permeability	Constant volume with an infrared detector	
ISOSORP 2000	Gas or vapor sorption	Gravimetric method	Rubotherm, Bochum, Germany
L100-5000	Gas permeability	ASTM D1434	Lyssy AG, Rütli, Switzerland
OPT-5000	O ₂ permeability	Continue flow with a sensor	Illinois Instruments, Inc., Johnsburg, IL, USA
L80-5000	Water vapor permeability		
Model 8500	O ₂ permeability		
Model 7000	Water vapor permeability		
No. 869 Frazier-type permeator	Air permeability		Toyo Seiki Seisaku-Sho, Ltd., Tokyo, Japan

penetrants in a polymer. Permeability and selectivity represent the inherent separation performance of a material and are often of interest industrially. Pure-gas studies are much easier to organize and perform than mixed-gas measurements. However, mixed-gas transport properties can, in some cases, yield results that are different from the pure-gas results, especially when one of the penetrants can interact strongly with the polymer. For example, in studies of CO₂ and CH₄ permeation through cellulose acetate, CO₂ plasticizes the cellulose acetate, leading to an increase in the polymer free volume, chain flexibility and CH₄ mixed-gas permeability. At 35 °C, pure-gas CH₄ permeability is about 0.12 Barrers at a pressure of 10 atm, but it is 0.32 Barrers when the feed gas to the membrane is a mixture of CO₂ and CH₄ with CH₄ and CO₂ partial pressures of about 10 atm and 24 atm, respectively. Thus, the mixed-gas CO₂/CH₄ selectivity was 20 while the pure gas selectivity was approximately 80 [7.318].

Gas permeability must be decoupled into solubility and diffusivity components to understand the fundamentals of gas transport in polymers and polymer-based materials of interest. For new materials, equilibrium sorption and steady-state permeation are often studied independently to determine the transport parameters [7.319]. Transient transport or sorption studies (i.e., the time-lag method or McBain spring system) depend on specific assumptions of diffusion models, which cannot always be judged a priori for new materials. The following sections give some general guidelines regarding the selection of a proper method.

A. Permeation

1. Pure-gas permeation is commonly measured using a constant-volume variable-pressure or a constant-pressure variable-volume device. The latter is suitable for polymers when the permeate gas flow is greater than 0.3 cm³/min. At this and higher flows, the gas flow can be accurately measured by a bubble flow meter. Otherwise, a constant volume/variable pressure device can be used for a wide range of flux values, as long as an appropriate downstream volume is chosen.
2. The time-lag method is most useful when the concentration dependence of the diffusion coefficient is known. In this way, both permeability and diffusivity can be obtained in one single experiment. From measurements of permeability and diffusivity, solubility can be estimated according to $S = P/D$.

B. Sorption

1. The most common devices for sorption measurements include the barometric pressure-decay apparatus for high-pressure studies and the McBain spring system for low-pressure studies (i.e., for condensable vapors). The pressure-decay method requires equation of the state information for the desired gas (e.g., the second and third virial coefficients), while the McBain spring system does not.
2. Diffusion coefficient can be obtained from transient studies only when the dependence of the diffusion coefficient on penetrant concentration is known or an assumption is made, as discussed in Sect. 7.6.1. The McBain spring system is most widely used in low-pressure studies.

3. If defect-free polymer films are very difficult to prepare for permeation studies, a transient sorption study could be very useful to obtain gas solubility and diffusion coefficients, and these can be used to estimate permeability. Solubility and diffusivity values obtained from kinetic sorption studies are virtually insensitive to pinhole defects in samples.

7.6.7 Future Projections

This chapter reviews basic models of gas transport in polymer films and measurement techniques to determine transport parameters. Guidelines for choosing one method over another are provided. Although phenomena such as non-Fickian diffusion are not discussed, the basic principles of equipment design still apply, except that the data analysis would be different [7.265]. Additionally, some polymers exhibit special properties which need to be considered in the experimental design. For example, poly(1-trimethylsilyl-1-propyne) (PTMSP) ages rapidly (i.e., polymer films become denser, which decreases gas diffusion coefficients over time) during the measurement, so a standardized sample-pretreatment protocol is required to obtain reproducible results, along with rapid permeation tests and frequent confirmation of the polymer properties by measuring the permeability of a marker penetrant.

The development of experimental techniques for gas transport property measurement has benefited from other fields, such as gas absorption in liquids [7.320] and adsorption [7.321]. For example, the dual-volume

pressure-decay method used to determine gas sorption in polymers at high pressures is based upon a similar principle as the one developed for gas sorption in liquids [7.296, 320]. Similarly, the principles introduced here can also be found in other applications, such as H₂ storage (or H₂ sorption in solids) [7.322]. It might be fair to predict that the future development of measurement methods would rely on knowledge transfer from related fields and advancement in sensors such as those for pressure and gas concentration measurements. Recently, molecular simulations have been extensively investigated to calculate gas solubility, diffusivity and permeability in polymers [7.323, 324]. This approach often offers a detailed description of complex polymer structure and transport mechanism, although quantitative agreement between simulated and experimental results is not always obtained [7.324]. Further information can be found in the following additional references [7.238, 239, 241–244, 246, 247, 251, 325, 326].

There is a growing interest in mixed gas solubility measurements. Mixed gas solubility data are rarely reported in the literature, probably due to the complexity of such experiments. However, in many scenarios (such as at high pressures, with highly sorbing penetrants, etc.), mixed gas solubility can deviate substantially from pure gas solubility [7.327, 328]. The capability of measuring mixed gas solubility and calculating mixed gas diffusivity is very valuable for developing a more informed and fundamental understanding of the transport of gas mixtures in polymers.

References

- 7.1 I.S. Sololnikoff: *Mathematical Theory of Elasticity* (McGraw-Hill, New York 1956)
- 7.2 S.P. Timoshenko: *History of Strength of Materials* (Dover, New York 1983)
- 7.3 A.E.H. Love: *A Treatise on the Mathematical Theory of Elasticity* (Dover, New York 1944)
- 7.4 S.P. Timoshenko, J.N. Goodier: *Theory of Elasticity*, 3rd edn. (McGraw-Hill, London 1982)
- 7.5 G. Galilei: *Discorsi e Dimostrazioni Matematiche* (Elsevier, Leiden 1636)
- 7.6 R. Hooke: *De Potentia Restitutiva* (Martyn, London 1678)
- 7.7 E. Mariotte: *Traité du Mouvement des Eaux* (Michallet, Paris 1686)
- 7.8 T. Young: *A Course of Lectures on Natural Philosophy and the Mechanical Arts*, Vol. 1 (Johnson, London 1807)
- 7.9 T. Young: *A Course of Lectures on Natural Philosophy and the Mechanical Arts*, Vol. 2 (Johnson, London 1807)
- 7.10 C.L.M.H. Navier: *Résumé des Leçons sur l'Application de la Mécanique*, Vol. 3 (Carilian-Goeury, Paris 1864)
- 7.11 J.S. Smith, M.D. Wyrick, J.M. Poole: An evaluation of three techniques for determining the Young's modulus of mechanically alloyed materials. In: *Dynamic Elastic Modulus Measurements in Materials*, ASTM STP, Vol. 1045, ed. by A. Wolfenden (American Society Testing and Materials, Philadelphia 1990) pp. 195–206
- 7.12 ASTM E 8–01: Standard test methods for tension testing of metallic materials, Annual Book of ASTM Standards (ASTM Int., West Conshohocken 2003)
- 7.13 ASTM E 74: Standard practice of calibration of force-measuring instruments for verifying the force

- indication of testing machines, Annual Book of ASTM Standards, Vol. 03.01 (ASTM, West Conshohocken 1995)
- 7.14 E4-03: Standard practices for force verification of testing machines, Annual Book of ASTM Standards, Vol. 03.01 (ASTM, West Conshohocken 1995)
- 7.15 ASTM E 111-04: Standard test method for Young's modulus, tangent modulus and chord modulus, Annual Book of ASTM Standards, Vol. 03.01 (ASTM, West Conshohocken 1995)
- 7.16 ASTM E 132-04: Standard test method for Poisson's ratio at room temperature, Annual Book of ASTM Standards, Vol. 03.01 (ASTM, West Conshohocken 1995)
- 7.17 ASTM E 143-02: Standard test method for shear modulus at room temperature, Annual Book of ASTM Standards, Vol. 03.01 (ASTM, West Conshohocken 1995)
- 7.18 J.W. House, P.P. Gillis: Testing machines and strain sensors. In: *ASM Handbook, Mechanical Testing and Evaluation*, Vol. 8, ed. by H. Kuhn, D. Medlin (ASM Int., Materials Park 2000)
- 7.19 ASTM E 83: Practice for verification and classification of extensometers, Annual Book of ASTM Standards, Vol. 03.01 (ASTM, West Conshohocken 1995)
- 7.20 ASTM D3379-75: Standard test method for tensile strength and Young's modulus for high-modulus single-filament materials, Annual Book of ASTM Standards, Vol. 15.01 (ASTM, West Conshohocken 2005)
- 7.21 ASTM D 638-03: Standard test method for tensile properties of plastics, Annual Book of ASTM Standards, Vol. 08.01 (ASTM, West Conshohocken 2005)
- 7.22 ASTM 882-02: Standard test method for tensile properties of thin plastic sheeting, Annual Book of ASTM Standards, Vol. 08.01 (ASTM, West Conshohocken 2005)
- 7.23 ASTM C 1341-00: Standard test method for flexural properties of continuous fiber-reinforced advanced ceramic composites, Annual Book of ASTM Standards, Vol. 15.01 (ASTM, West Conshohocken 2005)
- 7.24 ASTM C674-88: Standard test methods for flexural properties of ceramic whiteware material, Annual Book of ASTM Standards, Vol. 15.02 (ASTM, West Conshohocken 2006)
- 7.25 STM C 215-02: Standard test method for fundamental transverse, longitudinal, and torsional frequencies of concrete specimen, Annual Book of ASTM Standards, Vol. 04.02 (ASTM, West Conshohocken 2005)
- 7.26 ASTM 623-92: Standard test method for Young's modulus, shear modulus, and Poisson's ratio for glass and glass-ceramics by resonance, Annual Book of ASTM Standards, Vol. 15.02 (ASTM, West Conshohocken 2006)
- 7.27 ASTM C 747-93: Test method for moduli of elasticity and fundamental frequencies of carbon and graphite materials by sonic resonance, Annual Book of ASTM Standards, Vol. 05.01 (ASTM, West Conshohocken 1998)
- 7.28 ASTM C 848-88: Test method for Young's modulus, shear modulus, and Poisson's ratio for glass and glass-ceramics by resonance, Annual Book of ASTM Standards, Vol. 15.02 (ASTM, West Conshohocken 2006)
- 7.29 ASTM C 885-87: Standard test method for Young's modulus of refractory shapes by sonic resonance, Annual Book of ASTM Standards, Vol. 15.01 (ASTM, West Conshohocken 2005)
- 7.30 ASTM C 1198-01: Standard test method for dynamic Young's modulus, shear modulus, and Poisson's ratio for advanced ceramics by sonic resonance, Annual Book of ASTM Standards, Vol. 15.01 (ASTM, West Conshohocken 2005)
- 7.31 ASTM E 1875: Standard test method for dynamic Young's modulus, shear modulus, and Poisson's ratio by sonic resonance, Annual Book of ASTM Standards, Vol. 03.01 (ASTM, West Conshohocken 1995)
- 7.32 ASTM E 1876-01: Standard test method for dynamic Young's modulus, shear modulus, and Poisson's ratio by impulse excitation of vibration, Annual Book of ASTM Standards, Vol. 03.01 (ASTM, West Conshohocken 1995)
- 7.33 J.M. Ide: Some dynamic methods of determination of Young's modulus, *Rev. Sci. Instrum.* **6**, 296-298 (1935)
- 7.34 F. Forster: Ein neues Messverfahren zur Bestimmung des Elastizitätsmoduls und der Dämpfung, *Z. Metallkd.* **29**, 109-115 (1937)
- 7.35 C1419-99a: Standard test method for sonic velocity in refractory materials at room temperature and its use in obtaining an approximate Young's modulus, Annual Book of ASTM Standards, Vol. 15.01 (ASTM, West Conshohocken 2005)
- 7.36 W.E. Tefft: Numerical solution of the frequency equations for the flexural vibration of cylindrical rods, *J. Res. NBS* **64b**, 237-242 (1960)
- 7.37 R.E. Smith, H.E. Hagy: A low temperature sonic resonance apparatus for determining elastic properties of solids, *Int. Rep.*, Vol. 2195 (Corning Glass Works, Corning 1961)
- 7.38 J.B. Wachtman Jr., W.W. Tefft, D.G. Lam Jr., C.S. Apstein: Exponential temperature dependence of Young's modulus for several oxides, *Phys. Rev.* **122**, 1754 (1961)
- 7.39 A.H. Cottrell: *Mechanical Properties of Matter* (Wiley, New York 1964)
- 7.40 J.L. Hay, G.M. Pharr: Instrumented indentation testing. In: *ASM Handbook, Mechanical Testing and Evaluation*, Vol. 8, ed. by H. Kuhn, D. Medlin (ASM Int., Materials Park 2000)
- 7.41 A.C. Fischer-Crips: *Nanoindentation* (Springer, Berlin Heidelberg 2002)
- 7.42 A.E.H. Love: Boussenisq's problem for a rigid cone, *J. Math.* **10**, 161-175 (1939)

- 7.43 I.N. Sneddon: The relation between load and penetration in the axisymmetric Boussinesq problem for a punch of arbitrary profile, *Int. J. Eng. Sci.* **3**, 47–56 (1965)
- 7.44 S.I. Bulychev, V.P. Alekhin, M.K. Shorshorov, A.P. Ternovskii, G.D. Shnyrev: Determining Young's modulus from the indenter penetration diagram, *Zavod. Lab.* **41**, 1137–1140 (1975)
- 7.45 W.C. Oliver, G.M. Pharr: An improved technique for determining hardness and elastic modulus using load and displacement sensing indentation experiments, *J. Mater. Res.* **7**, 1564–1583 (1992)
- 7.46 R. Hill: *The Mathematical Theory of Plasticity* (Oxford Univ. Press, Oxford 1950)
- 7.47 W.F. Chen, D.J. Han: *Plasticity for Structural Engineers* (Gau Lih, Taipei 1995)
- 7.48 R. deWit: Theory of dislocations: An elementary introduction. In: *Mechanical Behavior of Crystalline Solids*, NBS Monogr., Vol. 59, ed. by R. deWit (US Printing Office, Washington 1962) pp. 13–34
- 7.49 E.R. Parker: Plastic flow and fracture of crystalline solids. In: *Mechanical Behavior of Crystalline Solids*, NBS Monogr., Vol. 59, ed. by R. deWit (US Printing Office, Washington 1962) pp. 1–12
- 7.50 H.J. Frost, M.F. Ashby: *Deformation-Mechanism Maps: The Plasticity and Creep of Metals and Ceramics* (Pergamon, New York 1982)
- 7.51 F.D. Fischer, G. Reisner, E. Werner, K. Tanaka, G. Cailletaud, T. Antretter: A new view on transformation induced plasticity (TRIP), *Int. J. Plast.* **16**(7), 723–748 (2000)
- 7.52 O. Grassel, L. Krüger, G. Frommeyer, L.W. Meyer: High strength Fe–Mn–(Al,Si) TRIP/TWIP steel development – properties – applications, *Int. J. Plast.* **16**(10), 1391–1409 (2000)
- 7.53 K.H. Roscoe, J.H. Burland: On the generalized stress strain behavior of wet clay. In: *Engineering Plasticity*, ed. by J. Heyman, F.A. Leckie (Cambridge Univ. Press, Cambridge 1968) pp. 585–609
- 7.54 A.H. Cottrell: *Dislocations and Plastic Flow in Crystals* (Oxford Univ. Press, London 1965)
- 7.55 E. Orowan: Private communication (1972)
- 7.56 R.W.K. Honeycomb: *The Plastic Deformation of Metals* (Edward Arnold, London 1968)
- 7.57 L.E. Levine (Ed.): Dislocations 2000: An international conference on the fundamentals of plastic deformation, *Mater. Sci. Eng. A* **309**, 1–284 (2001)
- 7.58 L.E. Levine (Ed.): Dislocations 2000: An international conference on the fundamentals of plastic deformation, *Mater. Sci. Eng. A* **310**, 285–567 (2001)
- 7.59 A.S. Khan (Ed.): *Dislocations, Plasticity, and Metal Forming: Proc. 10th Int. Symp. Plasticity and Its Current Applications* (Neat, Fulton 2003)
- 7.60 L.E. Levine, R. Thomson: The statistical origin of bulk mechanical properties and slip behavior of fcc metals, *Mater. Sci. Eng. A* **400**, 202 (2005)
- 7.61 P.W. Bridgman: *Studies in Large Plastic Flow and Fracture* (McGraw–Hill, New York 1952)
- 7.62 ISO 14577: *Metallic Materials – Instrumented Indentation Test for Hardness and Materials Parameters* (International Organization for Standardization (ISO), Geneva 2002)
- 7.63 ASTM E 8: *Standard Test Methods of Tension Testing Metallic Materials* (ASTM Int., West Conshohocken 2004)
- 7.64 ISO 6892: *Metallic Materials – Tensile Testing at Ambient Temperatures* (International Organization for Standardization (ISO), Geneva 1998)
- 7.65 DIN EN 10002-1: *Metallic Materials – Tensile Testing – Part 1: Method of Testing at Ambient Temperature* (Deutsches Institut für Normung (DIN), Berlin 2001)
- 7.66 JIS Z 2241: *Method of Tensile Test for Metallic Materials* (Japanese Standards Association, Tokyo 1998)
- 7.67 BS 18: *Methods for Tensile Testing of Metallic Materials* (British Standards Institute (BSI), London 1987)
- 7.68 ASTM E 8M: *Standard Test Methods for Tension Testing of Metallic Materials* (ASTM Int., West Conshohocken 2004)
- 7.69 SAE J416: *Tensile Test Specimens* (Society for Automotive Engineers (SAE International), Warrendale 1999)
- 7.70 ASTM A 370: *Standard Test Methods and Definitions for Mechanical Testing of Steel Products* (ASTM Int., West Conshohocken 2005)
- 7.71 ASTM B557: *Standard Test Methods of Tension Testing Wrought and Cast Aluminum- and Magnesium-Alloy Products* (ASTM Int., West Conshohocken 2002)
- 7.72 ASTM E 345: *Standard Test Methods of Tension Testing of Metallic Foil* (ASTM Int., West Conshohocken 2002)
- 7.73 ASTM E 646: *Standard Test Method for Tensile Strain-Hardening Exponents (n-Values) of Metallic Sheet* (ASTM Int., West Conshohocken 2000)
- 7.74 ISO 10275: *Metallic Materials – Sheet and Strip – Determination of Tensile Strain Hardening Exponent* (International Organization for Standardization (ISO), Geneva 1993)
- 7.75 NF A03-659: *Method of Determination of the Coefficient of Work Hardening N of Sheet Steels* (Association Francaise de Normalisation (AFNOR), Saint-Denis La Plaine Cedex 2001)
- 7.76 ASTM E 517: *Standard Test Method for Plastic Strain Ratio r for Sheet* (ASTM Int., West Conshohocken 2000)
- 7.77 NF A03-658: *Method of Determination of the Plastic Anisotropic Coefficient R of Sheet Steels* (Association Francaise de Normalisation (AFNOR), Saint-Denis La Plaine Cedex 2001)
- 7.78 SAE J429: *Mechanical and Material Requirements for Externally Threaded Fasteners* (Society for Automotive Engineers (SAE International), Warrendale 1999)
- 7.79 ASTM F 606: *Standard Test Methods for Determining the Mechanical Properties of Externally and Internally Threaded Fasteners, Washers, and Rivets* (ASTM Int., West Conshohocken 2002)

- 7.80 ISO 898: *Mechanical Properties of Fasteners* (International Organization for Standardization (ISO), Geneva 1999)
- 7.81 ASTM D638: *Standard Test Method for Tensile Properties of Plastics* (ASTM Int., West Conshohocken 2003)
- 7.82 ASTM D882: *Standard Test Method for Tensile Properties of Thin Plastic Sheeting* (ASTM Int., West Conshohocken 2002)
- 7.83 ASTM D1708: *Standard Test Method for Tensile Properties of Plastics By Use of Microtensile Specimens* (ASTM Int., West Conshohocken 2002)
- 7.84 ASTM E 4: *Standard Practices for Force Verification of Testing Machines* (ASTM Int., West Conshohocken 2003)
- 7.85 ASTM E 83: *Standard Practice for Verification and Classification of Extensometers* (ASTM Int., West Conshohocken 2002)
- 7.86 G.R. Johnson, W.H. Cook: A constitutive model and data for materials subjected to large strains, high strain rates, and high temperatures, Proc. 7th Int. Symp. Ballistics (1983) p. 541
- 7.87 S.R. Bodner, Y. Partom: Constitutive equations for elasto-viscoplastic strain-hardening materials, ASME J. Appl. Mech. **42**, 385 (1975)
- 7.88 U.F. Kocks, A.S. Argon, M.F. Ashby: *Thermodynamics and Kinetics of Slip* (Pergamon, Oxford 1975)
- 7.89 ASTM E 1450: *Standard Test Method for Tensile Testing of Structural Alloys in Liquid Helium* (ASTM Int., West Conshohocken 2003)
- 7.90 ISO/DIN 19819: *Metallic Materials – Tensile Testing in Liquid Helium* (International Organization for Standardization (ISO), Geneva 2004)
- 7.91 ISO 15579: *Metallic Materials – Tensile Testing at Low Temperatures* (International Organization for Standardization (ISO), Geneva 2000)
- 7.92 ASTM E 21: *Elevated Temperature Tension Testing of Metallic Materials* (ASTM Int., West Conshohocken 2005)
- 7.93 DIN EN 10002-5: *Tensile Testing of Metallic Materials, Method of Testing at Elevated Temperature* (Deutsches Institut für Normung (DIN), Berlin 2001)
- 7.94 JIS G 0567: *Method of Elevated Temperature Tensile Test for Steels and Heat-Resisting Alloys* (Japanese Standards Association, Tokyo 1998)
- 7.95 ASTM E 633: *Standard Guide for the Use of Thermocouples in Creep and Stress Rupture Testing to 1800 °F 1000 °C* (ASTM Int., West Conshohocken 2005)
- 7.96 ASTM E 139: *Conducting Creep, Creep Rupture, and Stress Rupture Tests of Metallic Materials* (ASTM Int., West Conshohocken 2000)
- 7.97 ASTM E 328: *Stress Relaxation for Materials and Structures* (ASTM Int., West Conshohocken 2002)
- 7.98 DIN EN 10291: *Metallic Materials – Uniaxial Creep Testing in Tension – Method of Test* (Deutsches Institut für Normung (DIN), Berlin 2005)
- 7.99 DIN EN 10319: *Metallic Materials – Tensile Stress Relaxation Testing* (Deutsches Institut für Normung (DIN), Berlin 2005)
- 7.100 ISO 204: *Metallic Materials – Uninterrupted Uniaxial Creep Testing in Tension – Method of Test* (International Organization for Standardization (ISO), Geneva 1997)
- 7.101 JIS Z 2271: *Method of Creep and Creep Rupture Testing for Metallic Materials* (Japanese Standards Association, Tokyo 1999)
- 7.102 ASTM C 1337: *Standard Test Method for Creep and Creep Rupture of Continuous Fiber-Reinforced Ceramic Composites under Tensile Loading at Elevated Temperatures* (ASTM Int., West Conshohocken 2005)
- 7.103 ASTM C 1291: *Standard Test Method for Elevated Temperature Tensile Creep Strain, Creep Strain Rate, and Creep Time-to-Failure for Advanced Monolithic Ceramics* (ASTM Int., West Conshohocken 2005)
- 7.104 ISO 899-1: *Plastics – Determination of Creep Behavior – Part 1. Tensile Creep* (International Organization for Standardization (ISO), Geneva 2003)
- 7.105 JIS K 7115: *Plastics – Determination of Creep Behavior – Part 1. Tensile Creep* (Japanese Standards Association, Tokyo 1999)
- 7.106 ISO 7500-2: *Metallic Materials – Verification of Static Uniaxial Testing Machines – Part 2: Tension Creep Testing Machines – Verification of the Applied Load* (International Organization for Standardization (ISO), Geneva 1996)
- 7.107 L.M.T. Hopkin: A simple constant stress apparatus for creep testing, Proc. R. Soc. **B63**, 346–349 (1950)
- 7.108 R.B. Grishaber, R.H. Lu, D.M. Farkas, A.K. Mukherjee: A novel computer controlled constant stress lever arm creep testing machine, Rev. Sci. Instrum. **68**(7), 2812–2817 (1997)
- 7.109 A.K. Mukherjee: Deformation mechanisms in superplasticity, Annu. Rev. Mater. Sci. **9**, 191–217 (1979)
- 7.110 JIS H 7501: *Method for Evaluation of Tensile Properties of Metallic Superplastic Materials* (Japanese Standards Association, Tokyo 2002)
- 7.111 ISO 10113: *Metallic Materials – Sheet and Strip – Determination of Plastic Strain Ratio* (International Organization for Standardization (ISO), Geneva 1991)
- 7.112 ASTM E 9: *Standard Test Methods for Compression Testing of Metallic Materials at Room Temperature* (ASTM Int., West Conshohocken 2000)
- 7.113 ASTM E 209: *Standard Practice for Compression Tests of Metallic Materials at Elevated Temperatures with Conventional or Rapid Heating Rates and Strain Rates* (ASTM Int., West Conshohocken 2005)
- 7.114 DIN 50106: *Testing of Metallic Materials – Compression Test* (Deutsches Institut für Normung (DIN), Berlin 2005)
- 7.115 DIN EN 12290: *Advanced Technology Ceramics – Mechanical Properties of Ceramic Composites at High Temperature in Air at Atmospheric Pressure – Determination of Compressive Properties* (Deutsches Institut für Normung (DIN), Berlin 2005)

- 7.116 ISO 604: *Plastics – Determination of Compressive Properties* (International Organization for Standardization (ISO), Geneva 2002)
- 7.117 JIS K 7132: *Cellular Plastics, Rigid – Determination of Compressive Creep under Specified Load and Temperature Conditions* (Japanese Standards Association, Tokyo 1999)
- 7.118 JIS K 7135: *Cellular Plastics, Rigid – Determination of Compressive Creep* (Japanese Standards Association, Tokyo 1999)
- 7.119 ASTM B831: *Standard Test Method for Shear Testing of Thin Aluminum Alloy Products* (ASTM Int., West Conshohocken 2005)
- 7.120 ASTM B769: *Standard Test Method for Shear Testing of Aluminum Alloys* (ASTM Int., West Conshohocken 2000)
- 7.121 ASTM B565: *Standard Test Method for Shear Testing of Aluminum and Aluminum-Alloy Rivets and Cold-Heading Wire and Rod* (ASTM Int., West Conshohocken 2004)
- 7.122 DIN 50141: *Testing of Metals: Shear Test* (Deutsches Institut für Normung (DIN), Berlin 2005)
- 7.123 DIN EN 4525: *Aerospace Series – Aluminium and Aluminium Alloys – Test Method; Shear Testing* (Deutsches Institut für Normung (DIN), Berlin 2005)
- 7.124 DIN EN 28749: *Determination of Shear Strength of Pins* (Deutsches Institut für Normung (DIN), Berlin 1986)
- 7.125 ISO 7961: *Aerospace – Bolts – Test Methods* (International Organization for Standardization (ISO), Geneva 1994)
- 7.126 ISO 84749: *Pins and Grooved Pins – Shear Test* (International Organization for Standardization (ISO), Geneva 2005)
- 7.127 ASTM E 143: *Standard Test Method for Shear Modulus at Room Temperature* (ASTM Int., West Conshohocken 2002)
- 7.128 ASTM A 938: *Standard Test Method for Torsion Testing of Wires* (ASTM Int., West Conshohocken 2004)
- 7.129 ISO 7800: *Metallic Materials – Wire – Simple Torsion Test* (International Organization for Standardization (ISO), Geneva 2003)
- 7.130 ISO 9649: *Metallic Materials – Wire – Reverse Torsion Test* (International Organization for Standardization (ISO), Geneva 1990)
- 7.131 A. Nadai: *Theory of Flow and Fracture of Solids*, Vol. 1, 2nd edn. (McGraw-Hill, New York 1950) pp.347–349
- 7.132 ASTM F 1622: *Standard Test Method for Measuring the Torsional Properties of Metallic Bone Screws* (ASTM Int., West Conshohocken 2005)
- 7.133 ASTM E 290: *Standard Test Method for Bend Testing of Materials for Ductility* (ASTM Int., West Conshohocken 2004)
- 7.134 ASTM E 190: *Standard Test Method for Guided Bend Test for Ductility of Welds* (ASTM Int., West Conshohocken 2003)
- 7.135 ASTM E 796: *Standard Test Method for Ductility Testing of Metallic Foils* (ASTM Int., West Conshohocken 2000)
- 7.136 ISO 7438: *Metallic Materials – Bend Test* (International Organization for Standardization (ISO), Geneva 2005)
- 7.137 ISO 7799: *Metallic Materials – Sheet and Strip 3mm Thick or Less – Reverse Bend Test* (International Organization for Standardization (ISO), Geneva 1985)
- 7.138 ISO 7801: *Metallic Materials – Wire – Reverse Bend Test* (International Organization for Standardization (ISO), Geneva 1984)
- 7.139 ISO 7802: *Metallic Materials – Wire – Wrapping Test* (International Organization for Standardization (ISO), Geneva 1983)
- 7.140 ISO 8491: *Metallic Materials – Tube (in full section) – Bend Test* (International Organization for Standardization (ISO), Geneva 1998)
- 7.141 DIN V ENV 820-4: *Advanced Technical Ceramics – Monolithic Ceramics; Thermo-mechanical Properties – Part 4: Determination of Flexural Creep Deformation at Elevated Temperatures* (Deutsches Institut für Normung (DIN), Berlin 2005)
- 7.142 ISO 899-2: *Plastics – Determination of Creep Behaviour – Part 2: Flexural Creep by Three-Point Loading* (International Organization for Standardization (ISO), Geneva 2003)
- 7.143 JIS K 7116: *Plastics – Determination of Creep Behaviour – Part 2: Flexural Creep by Three-Point Loading* (Japanese Standards Association, Tokyo 1999)
- 7.144 ASTM E 643: *Standard Test Method for Ball Punch Deformation of Metallic Sheet Materials* (ASTM Int., West Conshohocken 2003)
- 7.145 ASTM E 2218: *Standard Test Method for Determination of Forming Limit Diagrams* (ASTM Int., West Conshohocken 2002)
- 7.146 ISO 20482: *Metallic Materials – Sheet and Strip – Erichsen Cupping Test* (International Organization for Standardization (ISO), Geneva 2003)
- 7.147 ISO 12004: *Metallic Materials – Guidelines for the Determination of Forming-Limit Diagrams* (International Organization for Standardization (ISO), Geneva 1997)
- 7.148 ISO 8492: *Metallic Materials – Tube – Flattening Test* (International Organization for Standardization (ISO), Geneva 1998)
- 7.149 ISO 8493: *Metallic Materials – Tube – Drift-expanding Test* (International Organization for Standardization (ISO), Geneva 1998)
- 7.150 ISO 8494: *Metallic Materials – Tube – Flanging Test* (International Organization for Standardization (ISO), Geneva 1998)
- 7.151 ISO 8495: *Metallic Materials – Tube – Ring-Expanding Test* (International Organization for Standardization (ISO), Geneva 1998)
- 7.152 ISO 8496: *Metallic Materials – Tube – Ring Tensile Test* (International Organization for Standardization (ISO), Geneva 1998)

- 7.153 ISO 11531: *Metallic Materials – Earing Test* (International Organization for Standardization (ISO), Geneva 1994)
- 7.154 ISO 15363: *Metallic Materials – Tube Ring Hydraulic Pressure Test* (International Organization for Standardization (ISO), Geneva 2000)
- 7.155 ISO/TS 16630: *Metallic Materials – Method of Hole Expanding Test* (International Organization for Standardization (ISO), Geneva 2003)
- 7.156 JIS H 7702: *Method for Springback Evaluation in Stretch Bending of Aluminium Alloy Sheets for Automotive Use* (Japanese Standards Association, Tokyo 2003)
- 7.157 M.Y. Demeri, M. Lou, M.J. Saran: *A Benchmark Test for Springback Simulation in Sheet Metal Forming*, SAE Techn. Paper No. 2000-01-2657 (Society Automotive Engineers (SAE Int.), Warrendale 2000)
- 7.158 R.J. Fields, T.J. Foecke, R. deWit, G.E. Hicho, L.E. Levine: *Standard Test Methods and Data for Modeling Crashworthiness*, NIST Rep. No. NISTIR 6236 (US National Institute of Standards and Technology, Gaithersburg 1998)
- 7.159 A. Uenishi, H. Yoshida, Y. Kuriyama, M. Takahashi: Material characterization at high strain rates for optimizing car body structures for crash events, *Nippon Steel Tech. Rep.* **88**, 22–26 (2003)
- 7.160 Y. Sakumoto, T. Yamaguchi, M. Ohashi, H. Saito: High-temperature properties of fire-resistant steel for buildings, *ASCE J. Struct. Eng.* **118**(2), 392–407 (1992)
- 7.161 U.F. Kocks: Laws for work-hardening and low-temperature creep, *J. Eng. Mater. Technol.* **98**, 76–85 (1976)
- 7.162 U.F. Kocks, M.G. Stout: Torsion testing for general constitutive relations, Gilles Canova's Master's Thesis, *Model. Simul. Mater. Sci. Eng.* **7**, 675–682 (1999)
- 7.163 T. Foecke, M.A. Iadicola: Direct measurement of multiaxial yield loci as a function of plastic strain, *Am. Inst. Phys. Conf. Proc.*, Vol. 118 (2005) p. 388
- 7.164 V.E. Lysaght: *Indentation Hardness Testing* (Reinhold, New York 1949)
- 7.165 VDI/VDE 2616: *Hardness Testing of Metallic Materials, Part 1* (VDI, Düsseldorf 2002)
- 7.166 A. Wehrstedt: Situation of standardization in the field of hardness testing of metals, *ASTM J. Test. Eval.* **23**(6), 405–407 (1998)
- 7.167 A. Wehrstedt: Situation of standardization in the field of hardness testing of metals, *Proc. Int. Symp. Adv. Hardness Meas.*, ed. by Standard's Press of China (IMEKO, Beijing 1998)
- 7.168 ASTM E 10-01: *Standard Test Method for Brinell Hardness of Metallic Materials* (ASTM, West Conshohocken 2003)
- 7.169 ISO 6506-1: *Metallic Materials – Brinell Hardness Test – Part 1, Test Method* (ASTM International Organization for Standardization, Geneva 2005)
- 7.170 ASTM E 18-03: *Standard Test Methods for Rockwell Hardness and Rockwell Superficial Hardness of Metallic Materials* (ASTM Int., West Conshohocken 2003)
- 7.171 ISO 6508-1: *Metallic Materials – Rockwell Hardness Test – Part 1, Test Method (Scales A, B, C, D, E, F, G, H, K, N, T)* (International Organization for Standardization, Geneva 2005)
- 7.172 ASTM E 92-82: *e2 Standard Test Method for Vickers Hardness of Metallic Materials* (ASTM Int., West Conshohocken 2003)
- 7.173 ASTM E 384-99: *e1 Standard Test Method for Microindentation Hardness of Materials* (ASTM Int., West Conshohocken 2003)
- 7.174 ISO 6507-1: *Metallic Materials – Vickers Hardness Test – Part 1, Test Method* (International Organization for Standardization, Geneva 2005)
- 7.175 S. Low: *Rockwell Hardness Measurement of Metallic Materials* (NIST, Gaithersbourg 2001) pp. 960–965
- 7.176 H. Bückle: *Mikrohärteprüfung und ihre Anwendung* (Berliner Union, Stuttgart 1965), (Note: very extensive), (in German)
- 7.177 H. Bückle: Echte und scheinbare Fehlerquellen bei der Mikrohärteprüfung: Ihre Klassifizierung und Auswirkung auf die Messwerte, *VDI Ber.* **11**, 29–43 (1957), (Note: extensive), (in German)
- 7.178 D. Dengel: Wichtige Gesichtspunkte für die Härtemessung nach Vickers und nach Knoop im Bereich der Kleinlast- und Mikrohärte, *Z. Werkstofftech.* **4**, 292–298 (1973), (Note: short extract), (in German)
- 7.179 E. Matthaei: *Härteprüfung mit kleinen Prüfkräften und ihre Anwendung bei Randschichten* (DGM-Informationsgesellschaft, Oberursel 1987), (Note: overall view of sources), (in German)
- 7.180 ISO 4545-1: *Metallic Materials – Knoop Hardness Test* (International Organization for Standardization, Geneva 2005)
- 7.181 ISO: *Guide to the Expression of Uncertainty in Measurement* (International Organization for Standardization, Geneva 1993)
- 7.182 EA 10-16: *Guidelines on the Estimation of Uncertainty in Hardness Measurements* (European Cooperation for Accreditation of Laboratories, Paris 2001)
- 7.183 ISO 14577-1: *Metallic Materials – Instrumented Indentation Test for Hardness and Materials Parameters – Part 1: Test Method* (International Organization for Standardization, Geneva 2002)
- 7.184 H.-R. Wilde, A. Wehrstedt: Martens hardness HM – An international accepted designation for Hardness under test force, *Z. Materialprüf.* **42**, 468–470 (2000), (in German)
- 7.185 E. Meyer: Untersuchungen über Härteprüfung und Härte, *Z. Ver. Dtsch. Ing.* **52**, 645–654 (1908), (in German)
- 7.186 I.N. Sneddon: The relation between load and penetration in the axisymmetric Boussinesq problem for a punch of arbitrary profile, *Int. J. Eng. Sci.* **3**, 47–57 (1965)

- 7.187 J.E. Field, R.H. Telling: *The Young Modulus and Poisson Ratio of Diamond* (PCS Cavendish Lab., Cambridge 1999)
- 7.188 C. Heermant, D. Dengel: Zur Abschätzung 'klassischer' Werkstoffkennwerte mittels Universalhärteprüfung, *Z. Materialprüf.* **38**, 374–378 (1996), (in German)
- 7.189 H.-H. Behncke: Bestimmung der Universalhärte und anderer Kennwerte an dünnen Schichten, insbesondere Hartstoffschichten, *Härt.-Tech. Mitt. HTM* **48**, 3–10 (1993), (in German)
- 7.190 P. Grau, C. Ullner, H.-H. Behncke: Uncertainty of depth sensing hardness, *Z. Materialprüf.* **39**, 362–367 (1997)
- 7.191 M.F. Doerner, W.D. Nix: A method for interpreting the data from depth sensing indentation instruments, *J. Mater. Res.* **1**, 601–609 (1986)
- 7.192 M. Petzold, C. Hagendorf, M. Fütting, J.M. Olaf: Scanning force microscopy of indenter tips and hardness indentations, *VDI Ber.* **1194**, 79 (1995)
- 7.193 C. Trindade, A. Cavaleiro, J.V. Fernandes: Estimation of Young's modulus and of hardness by ultra-low load hardness tests with a Vickers indenter, *ASTM J. Test. Eval.* **22**, 365–369 (1994)
- 7.194 K. Hermann, N.M. Jennett, W. Wegener, J. Meneve, K. Hasche, R. Seemann: Progress in determination of the area function of indenters used for nanoindentation, *Thin Solid Films* **377/378**, 394–400 (2000)
- 7.195 R.B. King: Elastic analysis of some punch problems for a layered medium, *Int. J. Solids Struct.* **23**, 1657–1664 (1987)
- 7.196 A. Wehrstedt, C. Ullner: Standardization of the instrumented indentation test – Historical development and comments, *Z. Materialprüf.* **46**, 106–112 (2004)
- 7.197 A. Bolshakov, G.M. Pharr: Influences of pile-up and the measurement of mechanical properties by load and depth sensing indentation techniques, *J. Mater. Res.* **13**, 1049–1058 (1998)
- 7.198 N.J. McCormick, M.G. Gee, D.J. Hall: The calibration of the nanoindenter, *Mater. Res. Soc. Symp. Proc.* **308**, 195–200 (1993)
- 7.199 T. Chudoba, F. Richter: Investigation of creep behaviour under load during indentation experiments and its influence on hardness and modulus results, *Surf. Coat. Technol.* **148(2/3)**, 191–198 (2001)
- 7.200 N. Schwarzer, F. Richter, G. Hecht: Elastic field in a coated half space under Hertzian pressure distribution, *Surf. Coat. Technol.* **114**, 292 (1999)
- 7.201 ISO 4516: *Metallic and Other Inorganic Coatings – Vickers and Knoop Microhardness Tests* (International Standardization Organisation, Geneva 2002)
- 7.202 ASTM D-1474: *Indentation Hardness of Organic Coatings* (ASTM Int., West Conshohocken 2003)
- 7.203 W.C. Oliver, G.M. Pharr: An improved technique for determining hardness and elastic modulus using load and displacement sensing indentation experiments, *J. Mater. Res.* **7(6)**, 1564–1583 (1992)
- 7.204 ISO 14577-2: *Metallic Materials – Instrumented Indentation Test for Hardness and Materials Parameters – Part 2: Verification and Calibration of Testing Machines* (International Organisation for Standardization, Geneva 2002)
- 7.205 ISO 14577-3: *Metallic Materials – Instrumented Indentation Test for Hardness and Materials Parameters – Part 3: Calibration of Reference Blocks* (International Organisation for Standardization, Geneva 2002)
- 7.206 Y. Tomota: *Ferrum* **4**, 536–542 (1999), (in Japanese)
- 7.207 P.W. Bridgeman: *Studies in Large Plastic Flow and Fracture* (Harvard Univ. Press, London 1964)
- 7.208 D. Tabor: *The Hardness of Metals* (Clarendon, Oxford 1951)
- 7.209 T. Yoshizawa: *Hardness Test and Application* (Shokabo, Tokyo 1967), (in Japanese)
- 7.210 K. Hirukawa, S. Matuoka, Y. Furuya, K. Miyahara: Nano-scaled strength analysis of a tempered martensite, *Trans. Jpn. Soc. Mech. Eng. A* **68**, 1473–1478 (2002)
- 7.211 G.I. Taylor, H. Quinney: The plastic deformation of metals, *Philos. Trans. R. Soc. A* **230**, 323–362 (1931)
- 7.212 Y. Murakami: *Strength of Materials* (Morikita Syuppan, Tokyo 1994)
- 7.213 C.-H. Park: Effect of solution hardening on high speed deformation for ferritic steels, *Z. Metallkd.* **94**, 53–59 (2003)
- 7.214 Y. Tomota: *Deformation and Fracture at High Strain Rates for Aluminum Alloys*, Seminar Textbook (Inst. Light Metals, Toyohashi 2003), (in Japanese)
- 7.215 T. Abe, Y. Furuya, S. Matuoka: 10^{10} cycles fatigue properties for a series of SUP 7 spring steels, *Trans. Jpn. Soc. Mech. Eng. A* **696**, 1050–1059 (2004)
- 7.216 F. Erdogan: *Materials for Mechanical Engineering* (Soc. Mater. Sci. Jpn., Kyoto 1993)
- 7.217 P.C. Paris, F. Erdogan: A critical analysis of crack propagation laws, *Trans. ASME D* **85**, 528–534 (1963)
- 7.218 H.J. Frost, M.F. Ashby: *Deformation Mechanism Map* (Pergamon, New York 1982)
- 7.219 Y. Tomota: Strength of steels at room temperature, *Bull. Iron Steel Inst. Jpn. (Ferrum)* **4**, 536–542 (1999)
- 7.220 J.E. Bailey, P.B. Hirsch: The dislocation distribution, flow stress, and stored energy in cold-worked polycrystalline silver, *Philos. Mag.* **4**, 85 (1960)
- 7.221 W.C. Leslie: *The Physical Metallurgy of Steels* (McGraw-Hill, New York 1985)
- 7.222 E.O. Hall: The deformation and aging of mild steel, *Proc. R. Soc. Lond. B* **64**, 47–53 (1951)
- 7.223 N.J. Petch: The cleavage strength of polycrystals, *J. Iron Steel Inst.* **174**, 25–28 (1953)
- 7.224 T. Fujita, Y. Yamada: SCC and HE of iron base alloys. In: *Stress Corrosion Cracking and Hydrogen Embrittlement of Iron Base Alloys NACE-5*, ed. by R.W. Staehle, J. Hochmann, R.D. McCright, J.E. Slater (Nat. Assoc. Corrosion Engineers, Houston 1977) p. 736

- 7.225 JIS Standard: *Testing Methods of Bonding Strength of Adhesive* (Japanese Standards Association, Tokyo 1999)
- 7.226 J. Onuki: *Semiconductor Materials* (Uchidaroho, Tokyo 2004), (in Japanese)
- 7.227 Jpn. Soc. Composite Materials (Ed.): *Handbook of Composite Materials* (Kohichido, Tokyo 1989)
- 7.228 H.M. Westergaard: Bearing pressures and cracks, *J. Appl. Mech.* **6**, 49–53 (1939)
- 7.229 G.R. Irwin: Analysis of stresses and strains near the end of a crack traversing a plane, *J. Appl. Mech.* **24**, 361–364 (1957)
- 7.230 M.L. Williams: On the stress distribution at the base of a stationary crack, *J. Appl. Mech.* **24**, 109–114 (1957)
- 7.231 ASTM E 399–90: *Standard Test Method for Plane Strain Fracture Toughness of Metallic Materials* (American Society for Testing and Materials, Philadelphia 1990)
- 7.232 J.R. Rice: A Path Independent Integral and the Approximate Analysis of Strain Concentration by Notches and Cracks, *J. Appl. Mech.* **35**, 379–386 (1968)
- 7.233 J.W. Hutchinson: Singular behavior at the end of a tensile crack tip in a hardening material, *J. Mech. Phys. Solids* **16**, 13–31 (1968)
- 7.234 J.R. Rice, G.F. Rosengren: Plane strain deformation near a crack tip in a power-law hardening material, *J. Mech. Phys. Solids* **16**, 1–12 (1968)
- 7.235 T.L. Anderson: *Fracture Mechanics – Fundamentals and Applications*, 2nd edn. (CRC, Boca Raton 1995)
- 7.236 A.A. Wells: Application of fracture mechanics at and beyond general yielding, *Br. Weld. J.* **10**, 563–570 (1963)
- 7.237 ASTM E 1820–99: *Standard Test Method for Measurement of Fracture Toughness* (American Society for Testing and Materials, Philadelphia 1990)
- 7.238 BS 7448–1997: *Fracture Mechanics Test, Part 1: Method for Determination of K_{Ic} , Critical CTOD and Critical J Values of Metallic Materials* (British Standard Institution, London 1997)
- 7.239 ISO 12737: *Metallic Materials – Determination of Plane-Strain Fracture Toughness* (International Organization for Standardization, Geneva 1996)
- 7.240 ISO 12135: *Metallic Materials – Unified Method of Test for the Determination of Quasistatic Fracture Toughness* (International Organization for Standardization, Geneva 1996)
- 7.241 ASTM E 813–81: *Standard Test Method for J_{Ic} , A Measure of Fracture Toughness* (American Society for Testing and Materials, Philadelphia 1981)
- 7.242 ASTM E 1152–87: *Standard Test Method for Determining J–R Curves* (American Society for Testing and Materials, Philadelphia 1987)
- 7.243 ASTM E 1290–02: *Standard Test Method for Crack-Tip Opening Displacement (CTOD) Fracture Toughness Measurement* (American Society for Testing and Materials, Philadelphia 2002)
- 7.244 WES 1108–1995: *Standard Test Method for Crack-Tip Opening Displacement (CTOD) Fracture Toughness Measurement* (Japan Welding Engineering Society, Tokyo 1995)
- 7.245 D.P. Fairchild: Fracture toughness testing of weld heat-affected zones in structural steel, ASTM STP, Vol. 1058 (American Society of Testing and Materials, Philadelphia 1990) pp. 117–141
- 7.246 API RP 2Z: *Recommended Practice for Preproduction Qualification for Steel Plates for Offshore Structures* (American Petroleum Institute, Washington 1998)
- 7.247 WES 1109–1995: *Guidance for Crack-Tip Opening Displacement (CTOD) Fracture Toughness Test Method of Weld Heat-Affected Zone* (Japan Welding Engineering Society, Tokyo 1995)
- 7.248 M.G. Dawes, H.G. Pisarski, S.J. Squirrell: Fracture mechanics tests on welded joints, ASTM STP, Vol. 995 (American Society of Testing and Materials, Philadelphia 1989) pp. 191–213
- 7.249 P.C. Paris, M.P. Gomez, W.P. Anderson: A rational analytic theory of fatigue, *Trend Eng.* **13**, 9–14 (1961)
- 7.250 P.C. Paris, F. Erdogan: A critical analysis of crack propagation laws, *J. Basic Eng.* **85**, 528–534 (1960)
- 7.251 ASTM E 647–00: *Standard Test Method for Measurement of Fatigue Crack Growth Rates* (American Society of Testing and Materials, Philadelphia 2004)
- 7.252 C. Laird: The influence of metallurgical structure on the mechanisms of fatigue crack propagation. In: *Fatigue Crack Propagation*, ASTM STP, Vol. 415, ed. by J. Grosskreutz (American Society of Testing and Materials, Philadelphia 1967) pp. 131–167
- 7.253 R.W. Baker: *Membrane Technology and Application*, 2nd edn. (Wiley, New York 2004)
- 7.254 S.P. Nunes, K.-V. Peinemann: *Membrane Technology in the Chemical Industry* (Wiley-VCH, New York 2001)
- 7.255 B.D. Freeman, I. Pinnau: Gas and liquid separations using membranes: An overview. In: *Advanced Materials for Membrane Separations*, ACS Symp., Vol. 876, ed. by B.D. Freeman, I. Pinnau (American Chemical Society, Washington 2004) pp. 1–23
- 7.256 K. Ghosal, R.T. Chern, B.D. Freeman, W.H. Daly, I.I. Negulescu: Effect of basic substituents on gas sorption and permeation in polysulfone, *Macromolecules* **29**, 4360–4369 (1996)
- 7.257 S.N. Dhoot, B.D. Freeman, M.E. Stewart: Barrier polymers. In: *Encyclopedia of Polymer Science and Technology*, Vol. 5, ed. by J.I. Kroschwitz (Wiley Interscience, New York 2003) pp. 198–262
- 7.258 M. Mulder: *Basic Principles of Membrane Technology* (Kluwer Academic, Dordrecht 1996)
- 7.259 W.S.W. Ho, K.K. Sirkar: *Membrane Handbook* (Chapman Hall, New York 1992)
- 7.260 J. Crank, G.S. Park: *Diffusion in Polymers* (Academic, New York 1968)
- 7.261 J. Crank: *The Mathematics of Diffusion*, 2nd edn. (Oxford Univ. Press, New York 1995)

- 7.262 W.J. Koros, G.K. Fleming: Membrane-based gas separation, *J. Membr. Sci.* **83**, 1–80 (1993)
- 7.263 S.A. Stern: Polymers for gas separations: The next decade, *J. Membr. Sci.* **94**, 1–65 (1994)
- 7.264 K. Ghosal, B.D. Freeman: Gas separation using polymer membranes: An overview, *Polym. Adv. Technol.* **5**, 673–697 (1994)
- 7.265 R.M. Felder, G.S. Huvard: Permeation, diffusion and sorption of gases and vapors. In: *Methods of Experimental Physics*, Vol. 16C, ed. by R. Fava (Academic, New York 1980) p. 315
- 7.266 W.J. Koros, C.M. Zimmerman: Transport and barrier properties. In: *Comprehensive Desk Reference of Polymer Characterization and Analysis*, ed. by R.F. Brady (Oxford Univ. Press, Washington 2003)
- 7.267 B. Flaconneche, J. Martin, M.H. Klopffer: Transport properties of gases in polymers: Experimental methods, *Oil Gas Sci. Technol.–Rev. IFP* **56**, 245–259 (2001)
- 7.268 J. Crank, G.S. Park: Methods of measurement. In: *Diffusion in Polymers*, ed. by J. Crank, G.S. Park (Academic, New York 1968) pp. 1–39
- 7.269 T. Graham: On the absorption and dialytic separation of gases by colloid septa part I: Action of a septum of caoutchouc, *Philos. Mag.* **32**, 401–420 (1866)
- 7.270 R.B. Bird, W.E. Stewart, E.N. Lightfoot: *Transport Phenomena*, 2nd edn. (Wiley, New York 2002)
- 7.271 R.R. Zolanz, G.K. Fleming: Gas permeation. In: *Membrane Handbook*, ed. by W.S.W. Ho, K.K. Sirkar (Chapman Hall, New York 1992) pp. 17–102
- 7.272 T.C. Merkel, V.I. Bondar, K. Nagai, B.D. Freeman, I. Pinnau: Gas sorption, diffusion, and permeation in poly(dimethylsiloxane), *J. Polym. Sci. B* **38**, 415–434 (2000)
- 7.273 J.H. Petropoulos: Mechanisms and theories for sorption and diffusion of gases in polymers. In: *Polymeric Gas Separation Membranes*, ed. by D.R. Paul, Y.P. Yampolskii (CRC, Boca Raton 1994)
- 7.274 B.D. Freeman: Mutual diffusion in polymeric systems. In: *Comprehensive Polymer Science: First Supplements*, ed. by S.L. Aggarwal, S. Russo (Pergamon, New York 1992)
- 7.275 H. Lin, B.D. Freeman: Gas solubility, diffusivity and permeability in poly(ethylene oxide), *J. Membr. Sci.* **239**, 105–117 (2004)
- 7.276 W.J. Koros, D.R. Paul: CO₂ sorption in poly(ethylene terephthalate) above and below the glass transition, *J. Polym. Sci. B* **16**, 1947 (1978)
- 7.277 E.L. Cussler: Facilitated and active transport. In: *Polymeric Gas Separation Membranes*, ed. by D.R. Paul, Y.P. Yampol'skii (CRC, Boca Raton 1994) pp. 273–300
- 7.278 D.R. Paul, D.R. Kemp: The diffusion time lag in polymer membranes containing adsorptive fillers, *J. Polym. Sci. Symp.* **41**, 79–93 (1973)
- 7.279 W.J. Koros, D.R. Paul, A.A. Rocha: Carbon dioxide sorption and transport in polycarbonate, *J. Polym. Sci. B* **14**, 687–702 (1976)
- 7.280 S.A. Stern, J.T. Mullhaupt, P.J. Gareis: The effect of pressure on the permeation of gases and vapors through polyethylene. Usefulness of the corresponding states principle, *AIChE Journal* **15**, 64–73 (1969)
- 7.281 H.A. Daynes: The process of diffusion through a rubber membrane, *Proc. R. Soc. A* **97**, 286–307 (1920)
- 7.282 R.M. Barrer: Permeation, diffusion and solution of gases in organic polymers, *Trans. Faraday Soc.* **35**, 628–643 (1939)
- 7.283 H.L. Frisch: The time lag in diffusion, *J. Phys. Chem.* **61**, 93–95 (1957)
- 7.284 E.B. Mano, L.A. Durao: Review of laboratory methods for the preparation of polymer films, *J. Chem. Educ.* **50**, 228–232 (1973)
- 7.285 J.M. Mohr, D.R. Paul: Effect of casting solvent on the permeability of poly(4-methyl-1-pentene), *Polymer* **32**, 1236–1243 (1991)
- 7.286 S.J. Metz: Water vapor and gas transport through polymeric membranes. Ph.D. Thesis (University of Twente, Enschede 2003)
- 7.287 Z. Mogri, D.R. Paul: Membrane formation techniques for gas permeation measurements for side-chain crystalline polymers, *J. Membr. Sci.* **175**, 253–265 (2000)
- 7.288 T.T. Moore, S. Damle, P.J. Williams, W.J. Koros: Characterization of low permeability gas separation membranes and barrier materials; Design and operation considerations, *J. Membr. Sci.* **245**, 227–231 (2004)
- 7.289 T.C. Merkel, R.P. Gupta, B.S. Turk, B.D. Freeman: Mixed-gas permeation of syngas components in poly(dimethylsiloxane) and poly(1-trimethylsilyl-1-propyne) at elevated temperatures, *J. Membr. Sci.* **191**, 85–94 (2001)
- 7.290 D.G. Pye, H.H. Hoehn, M. Panar: Measurement of gas permeability of polymers. I. Permeabilities in constant volume/variable pressure apparatus, *J. Appl. Polym. Sci.* **20**, 1921–1931 (1976)
- 7.291 E.S. Burnett: Compressibility determinations without volume measurements, *J. Appl. Mech.* **3**, 136–140 (1936)
- 7.292 H. Yasuda, K.J. Rosengren: Isobaric measurement of gas permeability of polymers, *J. Appl. Polym. Sci.* **14**, 2839–2877 (1970)
- 7.293 D.G. Pye, H.H. Hoehn, M. Panar: Measurement of gas permeability of polymers. II. Apparatus for determination of permeabilities of mixed gases and vapors, *J. Appl. Polym. Sci.* **20**, 287–301 (1976)
- 7.294 K.C. O'Brien, W.J. Koros, T.A. Barbari, E.S. Sanders: A new technique for the measurement of multi-component gas transport through polymeric films, *J. Membr. Sci.* **29**, 229–238 (1986)
- 7.295 ASTM Standards F 1307: *Standard Test Method for Oxygen Transmission Rate Through Dry Packages Using a Coulometric Sensor* (ASTM, West Conshohocken 2002)

- 7.296 W.J. Koros, D.R. Paul: Design considerations for measurement of gas sorption in polymers by pressure decay, *J. Polym. Sci. B* **14**, 1903–1907 (1976)
- 7.297 V.I. Bondar, B.D. Freeman, I. Pinnau: Gas sorption and characterization of poly(ether-*b*-amide) segmented block copolymers, *J. Polym. Sci. B* **37**, 2463–2475 (1999)
- 7.298 J.H. Dymond, E.B. Smith: *The Virial Coefficients of Pure Gases and Mixtures: A Critical Compilation* (Oxford Univ. Press, New York 1980)
- 7.299 C.M. Zimmerman, A. Singh, W.J. Koros: Diffusion in gas separation membrane materials: A comparison and analysis of experimental characterization techniques, *J. Polym. Sci. B* **36**, 1747–1755 (1998)
- 7.300 C.C. McDowell, D.T. Coker, B.D. Freeman: An automated spring balance for kinetic gravimetric sorption of gases and vapors in polymers, *Rev. Sci. Instrum.* **69**, 2510–2513 (1998)
- 7.301 S.N. Dhoot, B.D. Freeman: Kinetic gravimetric sorption of low volatility gases and vapors in polymers, *Rev. Sci. Instrum.* **74**, 5173–5178 (2003)
- 7.302 B. Wong, Z. Zhang, Y.P. Handa: High-pressure gravimetric technique for determining the solubility and diffusivity of gases in polymers, *J. Polym. Sci. B* **36**, 2025–2032 (1998)
- 7.303 S. Areerat, E. Funami, Y. Hayata, D. Nakagawa, M. Ohshima: Measurement and prediction of diffusion coefficients of supercritical CO₂ in molten polymers, *Polym. Eng. Sci.* **44**, 1915–1924 (2004)
- 7.304 Y. Wu, P. Akoto-Ampaw, M. Elbaccouch, M.L. Hurrey, S.L. Wallen, C.S. Grant: Quartz crystal microbalance (QCM) in high-pressure carbon dioxide (CO₂): Experimental aspects of QCM theory and CO₂ adsorption, *Langmuir* **20**, 3665–3673 (2004)
- 7.305 R. Zhou, D. Schmeisser, W. Gopel: Mass sensitive detection of carbon dioxide by amino group-functionalized polymers, *Sens. Actuators B* **33**, 188–193 (1996)
- 7.306 A.Y. Alentiev, V.P. Shantarovich, T.C. Merkel, V.I. Bondar, B.D. Freeman, Y.P. Yampolskii: Gas and vapor sorption, permeation, and diffusion in glassy amorphous teflon AF1600, *Macromolecules* **35**, 9513–9522 (2002)
- 7.307 ASTM Standards D 1434: *Standard Test Method for Determining Gas Permeability Characteristics of Plastic Film and Sheeting* (ASTM, West Conshohocken, Pennsylvania 2003), Originally Approved in 1982
- 7.308 ASTM Standards D 3985: *Standard Test Method for Oxygen Gas Transmission Rate Through Plastic Film and Sheeting Using a Coulometric Sensor* (ASTM, West Conshohocken 2002)
- 7.309 ASTM Standards F 1927: *Standard Test Method for Determination of Oxygen Gas Transmission Rate, Permeability and Permeance at Controlled Relative Humidity Through Barrier Materials Using a Coulometric Detector* (ASTM, West Conshohocken 2004), Approved in 1998
- 7.310 ASTM Standards E 96: *Standard Test Methods for Water Vapor Transmission of Materials* (ASTM, West Conshohocken 2002)
- 7.311 ASTM Standards E 398: *Standard Test Method for Water Vapor Transmission Rate of Sheet Materials Using Dynamic Relative Humidity Measurement* (ASTM, West Conshohocken 2003)
- 7.312 ASTM Standards E 1770: *Standard Practice for Optimization of Electrothermal Atomic Absorption Spectrometric Equipment* (ASTM, West Conshohocken 2001), Approved in 1995
- 7.313 ASTM Standards F 1769: *Standard Test Method for Measurement of Diffusivity, Solubility, and Permeability of Organic Vapor Barriers Using a Flame Ionization Detector* (ASTM, West Conshohocken 2004), Approved in 1997
- 7.314 E.S. Sanders, W.J. Koros, H.B. Hopfenberg, V. Stannett: Mixed gas sorption in glassy polymers: Equipment design considerations and preliminary results, *J. Membr. Sci.* **13**, 161–174 (1983)
- 7.315 G.T. Fieldson, T.A. Barbari: Analysis of diffusion in polymers using evanescent field spectroscopy, *AIChE Journal* **41**, 795–804 (1995)
- 7.316 R.A. Assink: Investigation of the dual mode sorption of ammonia in polystyrene by NMR, *J. Polym. Sci. B* **13**, 1665–1673 (1975)
- 7.317 W.J. Koros, A.H. Chan, D.R. Paul: Sorption and transport of various gases in polycarbonate, *J. Membr. Sci.* **2**, 165–190 (1977)
- 7.318 S.Y. Lee, B.S. Minhas, M.D. Donohue: Effect of gas composition and pressure on permeation through cellulose acetate membranes, *AIChE Symp. Ser.* **84**, 93–101 (1988)
- 7.319 D.R. Paul, D.R. Kemp: The diffusion time lag in polymer membranes containing adsorptive fillers, *J. Polym. Sci. Symp.* **41**, 79–93 (1973)
- 7.320 H.W. Clever, R. Battino: The solubility of gases in liquids, *Tech. Chem.* **8**, 379–441 (1975)
- 7.321 R.T. Yang: *Gas Separation by Adsorption Processes* (Butterworths, Boston 1987)
- 7.322 N.L. Rosi, J. Eckert, M. Eddaoudi, D.T. Vodak, J. Kim, M. O’Keeffe, O.M. Yaghi: Hydrogen storage in microporous metal-organic frameworks, *Science* **300**, 1127–1129 (2003)
- 7.323 X. Wang, K.M. Lee, Y. Lu, M.T. Stone, I.C. Sanchez, B.D. Freeman: Modeling transport properties in high free volume glassy polymers, *New Polymeric Materials, ACS Symp. Ser.* **916**, 187 (2004)
- 7.324 E. Tocci, D. Hofmann, D. Paul, N. Russo, E. Drioli: A molecular simulation study on gas diffusion in a dense poly(ether-ether-ketone) membrane, *Polymer* **42**, 521–533 (2001)
- 7.325 EN 10225:2001: *Annex E, Weldability Testing for Steels of Groups 2 and 3 and Mechanical Testing of Butt Welds* (CEN, Brussels 2001)

- 7.326 BS 7448-1997: *Fracture Mechanics Toughness Tests, Part II: Method for Determination of K_{Ic} , Critical CTOD and Critical J Values of Welds in Metallic Materials* (British Standard Institution, London 1997)
- 7.327 R.D. Raharjo, B.D. Freeman, E.S. Sanders: Pure and mixed gas CH₄ and *n*-C₄H₁₀ sorption and dilation in poly(dimethylsiloxane), *J. Membr. Sci.* **292**, 45–61 (2007)
- 7.328 C.P. Riberiro, B.D. Freeman: Carbon dioxide/ethane mixed-gas sorption and dilation in a cross-linked poly(ethylene oxide) copolymer, *Polymer* **51**, 1156–1168 (2010)

Thermal Properties

8. Thermal Properties

If materials – solids, liquids or gases – are heated or cooled, many of their properties change. This is due to the fact that thermal energy supplied to or removed from a specimen will change either the kinetic or the potential energy of the constituent atoms or molecules. In the first case, the temperature of the specimen is changed, since temperature is a measure of the average kinetic energy of the elementary particles of a sample. In the second case, e.g. the binding energy of these particles is altered, which may cause a phase transition.

Thermal properties are associated with a material-dependent response when heat is supplied to a solid body, a liquid, or a gas. This response might be a temperature increase, a phase transition, a change of length or volume, an initiation of a chemical reaction or the change of some other physical or chemical quantity.

Basically, almost all of the other materials properties treated in *Part C*, namely mechanical, electrical, magnetic, or optical properties, are temperature-dependent (except a material that is especially designed to be resistant to temperature variations). For example, temperature influences mechanical hardness, electrical resistance, magnetism, or optical emissivity. Temperature is also of importance to the characterization of material performance (*Part D*) as it influences materials integrity when subject to corrosion, friction and wear, biogenic impact or material–environment interactions. Temperature effects related to these areas are dealt with in the other chapters of this book dedicated to those topics. Only if those properties are needed to explain measuring methods within this chapter are they outlined in the following sections.

In this chapter, a number of materials properties are selected and called *thermal properties*, where the effect of thermal energy treatment plays the major role compared to electrical, magnetic, chemical or other effects. The presentation

of *measurement methods for thermal properties* is organized into five parts, referring to:

1. Thermal transport properties, such as thermal conductivity, thermal diffusivity or specific heat capacity, characterizing the ability of materials to conduct, transfer, store and release heat.
2. Phase transitions and chemical reactions of materials. Various calorimetric methods are presented, which are used to investigate e.g. phase transitions, adsorption, and mixing processes. Typical examples are first-order transitions such as boiling and melting, but also combustion and solution processes.
3. Physical properties, which are affected when heat is supplied to a body. The determination of the temperature dependence of these quantities requires knowledge of thermal measurement methods. Among the many different physical quantities the most important for applications in materials science and engineering are length and its relation to thermal expansion.
4. Thermogravimetry, which is important in chemical analysis, see Chap. 4.
5. Temperature measurement methods, since these techniques are essential for all the other measurements described above. Temperature scales and the principles, types and applications of temperature sensors are compiled.

8.1	Thermal Conductivity and Specific Heat Capacity	454
	8.1.1 Steady-State Methods	456
	8.1.2 Transient Methods.....	458
	8.1.3 Calorimetric Methods.....	461
8.2	Enthalpy of Phase Transition, Adsorption and Mixing	462
	8.2.1 Adiabatic Calorimetry	464
	8.2.2 Differential Scanning Calorimetry ...	465

8.2.3	Drop Calorimetry	466	8.5	Temperature Sensors	471
8.2.4	Solution Calorimetry	467	8.5.1	Temperature	
8.2.5	Combustion Calorimetry	468		and Temperature Scale	471
8.3	Thermal Expansion		8.5.2	Use of Thermometers	474
	and Thermomechanical Analysis	469	8.5.3	Resistance Thermometers	475
8.3.1	Optical Methods	469	8.5.4	Liquid-in-Glass Thermometers	477
8.3.2	Push Rod Dilatometry	470	8.5.5	Thermocouples	478
8.3.3	Thermomechanical Analysis	470	8.5.6	Radiation Thermometers	479
8.4	Thermogravimetry	471	8.5.7	Cryogenic Temperature Sensors	480
			References		482

8.1 Thermal Conductivity and Specific Heat Capacity

There are two main material properties (thermophysical properties) associated with heat transfer in materials. These are the ability of a material to store heat and the ability to transfer heat by conduction. If a specific amount of heat dQ is supplied to a thermally isolated specimen of mass m the relationship between heat and temperature increase dT is given by

$$dQ = mc_p dT . \quad (8.1)$$

Consequently the ability of a material to store heat is characterized by the specific heat capacity at constant pressure c_p . If two equal volumes of different materials are compared to each other, the ability to store heat is described by the product of density and specific heat capacity ρc_p . This product is used if simultaneous heat conduction and storage processes are investigated by means of the transient heat conduction equation. In many cases the density of a material or the mass of a specimen is well known or can be easily determined with sufficient accuracy. Therefore, the problem is reduced to the determination of the specific heat capacity. For gases and some liquids a distinction between the specific heat capacity at constant pressure c_p and at constant volume c_v is made. This is due to the work required for the thermal expansion of the gas or liquid. For solids this contribution is very small in comparison to the measurement uncertainty and can be neglected.

The thermal conductivity λ is the material property associated with heat conduction and is defined by Fourier's law

$$q = -\lambda \frac{\partial T}{\partial x} = -\lambda \frac{\Delta T}{d} = \frac{\Delta T}{R_{th}} . \quad (8.2)$$

Here, q is the heat flux, the heat conducted during a unit time through a unit area, driven by a temperature

gradient $\partial T/\partial x$. In practice, for thermal conductivity measurements the temperature difference ΔT between two opposite surfaces of a sample with a separation of d is determined. The quotient of distance and thermal conductivity is the thermal resistance R_{th} . In contrast to the storage of heat, conduction is considered as a steady-state process, i. e. the temperature field and the heat flux within heat-conducting materials are not a function of time.

But, in most cases both heat conduction and heat storage are simultaneously occurring processes. This is taken into account by the transient heat conduction equation. The temperature field $T(x, t)$ in one dimension is dependent on the location x and time t

$$\frac{\partial T}{\partial t} = a \frac{\partial^2 T}{\partial x^2} . \quad (8.3)$$

The thermal diffusivity a is given as the ratio of the thermal conductivity and the product of density and specific heat capacity

$$a = \frac{\lambda}{\rho c_p} . \quad (8.4)$$

From its physical meaning thermal diffusivity is associated with the speed of heat propagation. In analogy to Einstein's relation, which connects random walks and diffusion, the mean square displacement $\langle r^2 \rangle$ of a thermal pulse is proportional to the observation time t (one-dimensional diffusion)

$$a = \frac{\langle r^2 \rangle}{2t} . \quad (8.5)$$

A further thermal property is the thermal effusivity e . The thermal effusivity is a measure of a material's abil-

ity to exchange heat with the environment (thermal impedance) and is defined according to

$$e = \sqrt{\lambda \rho c_p}. \quad (8.6)$$

Knowing the thermal diffusivity and thermal effusivity, other complementary materials properties, e.g. λ and ρc_p , can be calculated.

Based on the fundamental laws of heat conduction and storage three different attempts to measure these thermophysical properties can be distinguished. The first one is the steady-state approach using (8.2) in order to determine the thermal conductivity. Steady-state conditions mean that the temperature at each point of the sample is constant, i. e. not a function of time. The determination of the thermal conductivity is based on the measurement of a heat flux and a temperature gradient, i. e. mostly a temperature difference between opposite surfaces of a sample. If the specific heat capacity is the property of interest, a calorimetric method

based on (8.1) is used. In this case, heat is supplied to a sample that is isolated from the surroundings, and the change of the (mean) sample temperature is measured. The third approach is the simultaneous determination of both properties by a transient technique. For that purpose numerous solutions of the transient heat conduction equation based on one-, two-, or three-dimensional geometries have been derived.

The main experimental problem for all methods for the determination of thermal properties is that ideal thermal conductors or insulators do not exist. In comparison to electrical transport the ratio of thermal conductivities of the best conductors and the best insulators is many orders of magnitudes smaller. Therefore, instruments for the determination of thermal properties are often optimized or restricted for a specific class of materials or temperature range [8.1]. Table 8.1 gives an overview of the most important methods used for the measurement of thermal conductivity and thermal diffusivity.

Table 8.1 Comparison of measurement methods for the determination of thermal conductivity and thermal diffusivity

Method	Temperature range	Uncertainty	Materials	Merit	Demerit
Guarded hot plate	80–800 K	2%	Insulation materials, plastics, glasses	High accuracy	Long measurement time, large specimen size, low conductivity materials
Cylinder	4–1000 K	2%	Metals	Temperature range, simultaneous determination of electrical conductivity and Seebeck-coefficient possible	Long measurement time
Heat flow meter	–100–200 °C	3–10%	Insulation materials, plastics, glasses, ceramics	Simple construction and operation	Measurement uncertainty, relative measurement
Comparative	20–1300 °C	10–20%	Metals, ceramics, plastics, plastics	Simple construction and operation	Measurement uncertainty, relative measurement
Direct heating (Kohlrausch)	400–3000 K	2–10%	Metals	Simple and fast measurements, simultaneous determination of electrical conductivity	Only electrically conducting materials
Pipe method	20–2500 °C	3–20%	Solids	Temperature range	Specimen preparation, long measurement time
Hot wire, hot strip	20–2000 °C	1–10%	Liquids, gases, low conductivity solids	Temperature range, fast, accuracy	Limited to low conductivity materials
Laser flash	–100–3000 °C	3–5%	Solids, liquids	Temperature range, most solids, liquids and powders, small specimen, fast, accuracy at high temperatures	Expensive, not for insulation materials
Photothermal photoacoustic	30–1500 K	Not sufficiently known	Solids, liquids, gases, thin films	Usable for thin films, liquids and gases	Nonstandard, knowledge about accuracy

8.1.1 Steady-State Methods

The principle of (one-dimensional) steady-state methods for the determination of the thermal conductivity is derived from (8.2) and based on the measurement of a heat flux and a temperature difference according to

$$\lambda = \frac{qd}{T_2 - T_1} = \frac{Pd}{A(T_2 - T_1)}. \quad (8.7)$$

In many cases the heat flux q is determined by the measurement of a power P released in an electrical heater divided by the area A of the sample. The temperature difference $T_2 - T_1$ is determined between two opposite surfaces of the specimen having a separation of d .

The typical sample geometry and the configuration of a measurement system for thermal conductivity measurements depend most strongly on the magnitude of the thermal conductivity. When the thermal conductivity of a material is low, the samples are usually flat disks or plates. In the case of a high thermal conductivity the sample geometry is formed by a cylinder or rod. According to the relationship between the sample geometry (assumed to be cylindrical) and the direction of the heat flow, axial and radial heat flow methods of measuring the thermal conductivity are distinguished.

Guarded Hot Plate and Cylinder Method

The guarded hot plate method can be used for the determination of the thermal conductivity of nonmetals such as glasses, ceramics, polymers and thermal insulation materials but also for liquids and gases in the temperature range between about 80 K and 800 K. The geometry of the sample or sample chamber is a plate or a cylinder with axial heat flow. Depending on the thermal conductivity and homogeneity of the material under investigation, the sample thickness varies between a few millimeters and a few decimeters. There are two different types of guarded hot plate instruments: the

two-specimen and the single-specimen apparatus shown in Fig. 8.1.

Guarded hot plate instruments consist of one or two cold plates, a hot plate and a system of guard heaters and thermal insulation. The cold plates are liquid-cooled heat sinks, the hot plate is electrically heated. To make sure that the heat released in the hot plate is passed only through the sample, the hot plate is surrounded by guard heaters and thermal insulation. This minimizes the heat losses from the hot plate and ensures the high accuracy of this method. With guarded hot plate instruments relative expanded uncertainties of thermal conductivity measurements of about 2% can be achieved. There are two main sources of uncertainty in thermal conductivity measurements: the heat flux and the temperature difference determination. The major contributions to heat flux errors are heat losses from the hot plate and the heat exchange between the sample and the surrounding medium. With increasing thermal resistance of the sample (insulation materials) these sources of uncertainty become dominant.

The advantage of the two-specimen apparatus is that heat losses from the hot plate can be controlled more effectively because of the symmetric specimen arrangement. In contrast to the single-specimen method, only solid materials can be investigated. This is because of the influence of convection on thermal conductivity measurements. In order to avoid convection, the sample must be heated from the top.

The cylinder method with axial heat flow can be used for thermal conductivity measurements of metals with thermal conductivities up to $500 \text{ W m}^{-1} \text{ K}^{-1}$ in a temperature range between about 4 K and 1000 K. Comparing the principle of operation and the mathematical model, the cylinder method and the guarded hot plate method fully agree. The most important difference is the sample geometry, which is a flat plate or disk for the guarded hot plate method and a long cylinder or rod for the cylinder method. This is due to the fact that the main difficulty for measurements of materials with high thermal conductivity (e.g. metals) is the determination of the temperature difference. In this case the contact resistances between the sample and the heater and between the sample and the cold plate must be considered. The minimization and determination of the resulting temperature drop across these thermal contact resistances is the most important criterion for the optimization of this type of instrument.

Therefore, guarded hot plate and cylinder method are realizations of the same measurement principle optimized for different ranges of thermal conductivity.

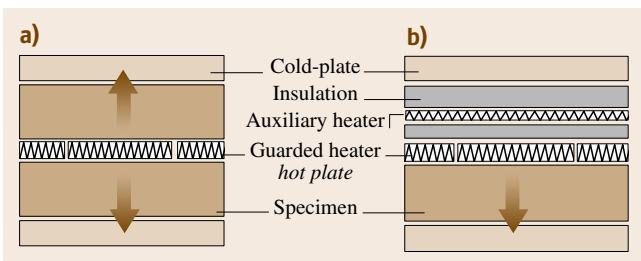


Fig. 8.1a,b Principle of the guarded hot plate method. (a) two-specimen apparatus. (b) single-specimen apparatus

Heat Flow Meter and Comparative Method

The main disadvantage of steady-state methods is that they are very time consuming. This is because the whole system of specimen and guard heaters must reach thermal equilibrium in order to avoid unaccounted heat losses and deviations from steady-state conditions. The basic idea of the heat flow meter and the comparative method is the determination of the (axial) heat flux by means of the measurement of a temperature drop across a thermal resistor. This is in analogy to the determination of a current by the measurement of a voltage drop across an electrical resistor. The implementation of this idea for heat flux measurements is carried out either by the use of a reference sample with well-known (certified) thermal resistance or by means of a heat flux sensor. Most heat flux sensors consist of a series connection of thermocouples across a thermal resistor, e.g. a thin ceramic or plastic plate. The measured signal is a thermovoltage proportional to the temperature drop across the plate. Usually a heat flux sensor is calibrated in a steady-state temperature field with well-known heat flux, e.g. in a guarded hot plate apparatus.

The design of a heat flow meter apparatus is very similar to that of the single-specimen guarded hot plate instrument. Instead of the main heater a heat flux sensor is used. In some cases a second heat flux sensor at the cold plate is applied to determine radial heat losses and to reduce the measurement duration. This is of particular advantage for measurements of insulation materials. To avoid radial heat losses the lateral surfaces of the sample are surrounded by thermal insulation or additional guard heaters.

If a reference sample for heat flux measurements is used, the sample and reference samples are piled upon one another in a temperature field (series connection of thermal resistors). The temperature drops across both sample and reference sample are measured and compared (comparative method). To correct for radial heat losses two reference samples are mostly used and the investigated sample is sandwiched between them. Under steady-state conditions the heat flux at each point of the stack is the same. In that case the ratio of the thermal resistances of the sample and reference sample is equal to the ratio of the corresponding temperature drops. In contrast to the guarded hot plate method the heat flow meter and the comparative method are relative and not absolute methods. The heat flow meter method is mostly used for insulation materials and polymers ($\lambda < 0.3 \text{ W m}^{-1} \text{ K}^{-1}$), in some cases for glasses and ceramics, i. e. for materials with thermal conductivities less than about $5 \text{ W m}^{-1} \text{ K}^{-1}$. In contrast, the typical

application range of the comparative technique is the investigation of metals, ceramics and glasses having thermal conductivities above $1 \text{ W m}^{-1} \text{ K}^{-1}$. Typical upper temperature limits are about 200°C for the heat flow meter method and about 1300°C for the comparative method. The measurement uncertainties are about 3% for insulation materials near room temperature and between 10 and 20% at high temperatures.

Direct Heating (Kohlrausch) Method

The disadvantages of steady-state thermal conductivity measurement methods are the long equilibration time needed to reach steady-state conditions and the difficult quantification of heat losses, in particular at high temperatures. These can be avoided using the direct heating method, although this can only be used for materials with sufficiently high electrical conductivity, such as metals. Typically samples are wires, pipes or rods with a diameter d between 0.5 and 20 mm and a length l between 50 and 500 mm. Figure 8.2 shows the schematic of the most popular design of the direct heating method.

The sample is placed in a vacuum chamber, clamped between two liquid-cooled heat sinks and heated by a sufficiently high electrical current I_h to achieve sample temperatures in the range 400–3000 K. Temperatures and voltage drops are measured at three positions; one position is in the middle of the rod, while the oth-

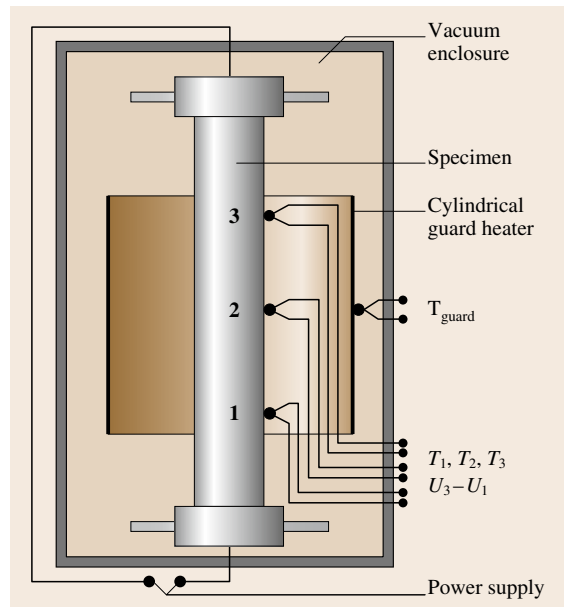


Fig. 8.2 Principle of the direct heating method

ers are placed symmetrically at equal distances from the middle position. In most cases thermocouples are used because of their dual usability as temperature sensors and for voltage-drop measurements. The result of measurements by the direct heating method is the product of the thermal conductivity and the specific electric resistivity $\lambda\rho_{el}$.

$$\lambda\rho_{el} = \frac{(U_3 - U_1)^2}{4[2T_2 - (T_1 + T_3)]} \quad (8.8)$$

The specific electrical resistivity can be determined from the length l and cross-sectional area A of the sample, heating current I_h and voltage drop U_h according to

$$\rho_{el} = \frac{U_h A}{I_h l} \quad (8.9)$$

Pipe and Hot Wire Method

The characteristic of this class of methods is radial heat flow in a cylindrical sample (diameter d_1 , length l). Figure 8.3 shows the principle of the pipe method.

A hole on the central axis of the sample contains the core heater (diameter d_2), which is a rod,

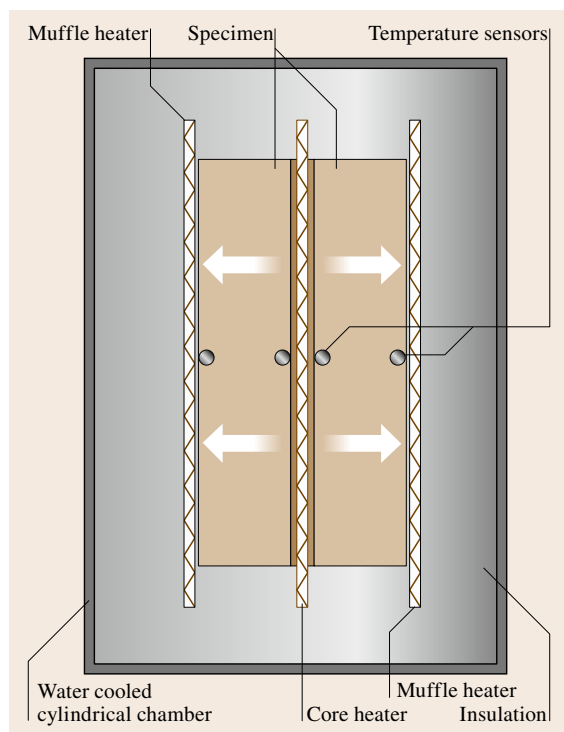


Fig. 8.3 Principle of the pipe method

tube or wire. Depending on the temperature range of interest the sample is surrounded by a liquid-cooled heat sink or a combination of muffle heater and water jacket. Axial heat losses can be minimized by additional end guard heaters or a special sample geometry, i. e. a large length-to-diameter ratio. The thermal conductivity is determined by the measurement of the radial heat flow Φ and the temperature difference between the inner and the outer surface of the sample according to

$$\lambda = \frac{\Phi \ln\left(\frac{d_2}{d_1}\right)}{2\pi l (T_1 - T_2)} \quad (8.10)$$

Because of its simple design modified versions of this technique have been used for solids covering the thermal conductivity range between insulation materials ($20 \text{ mW m}^{-1} \text{ K}^{-1}$) and metals ($200 \text{ W m}^{-1} \text{ K}^{-1}$) for temperatures between room temperature and 2770 K . Transient modifications to this technique for the simultaneous determination of thermal conductivity and thermal diffusivity are of increasing interest (Sect. 8.1.2).

8.1.2 Transient Methods

With the availability of modern computers and data acquisition systems transient methods have become increasingly popular. The advantages of transient methods are that much less time is needed for the experiments and that various thermal properties can be determined in the same measurement cycle. A typical measurement duration of one hour for steady-state methods is reduced to a few minutes or to a subsecond interval for transient methods. In many cases the temperature measurement at two opposite surfaces of the sample is replaced by a temperature measurement as a function of time at only one position. This makes the design of instruments for transient measurements straightforward in comparison to steady-state methods and can improve the accuracy of the results.

Transient Hot Wire and Hot Strip Method

Most thermal conductivity measurements of liquids, gases and powders are carried out by means of the transient hot wire method, a modification of the steady-state pipe method with a cylindrical specimen geometry and radial heat flow. The pipe is replaced by a thin platinum wire or nickel strip [8.2,3]. For measurements on solids the wire is embedded in grooves between two equally sized specimens. Considerable care is needed in the sample preparation to achieve sufficiently low thermal contact resistances between solid samples and the heating wire. Therefore, the use of a thin metal foil strip (hot

strip method) instead of the heating wire has become increasingly popular for measurements on solids. In this case the sample preparation is simplified by the use of a heat sink compound. The disadvantage of deviations from the radial symmetric temperature field in comparison to the wire method is compensated by an adequate mathematical model and evaluation procedure [8.2,4,5].

In the standard transient hot wire technique (Fig. 8.4) the platinum wire has two functions, as a heater and as a temperature sensor.

The heat source is assumed to have a constant output, which is ensured by a stabilized electrical power supply. From the slope of the resulting linear temperature rise as a function of elapsed time the thermal conductivity λ of the specimen is determined. The thermal diffusivity a can be found from the intercept of this linear temperature dependence. To eliminate the effect of axial conduction via the large-diameter current supply leads attached to the ends of the hot wire, two hot wires of differing lengths are often operated in a differential mode. Further modifications of this technique are the cross-wire and the parallel-wire techniques, where the heater and temperature sensor are separated from each other. For the cross-wire technique,

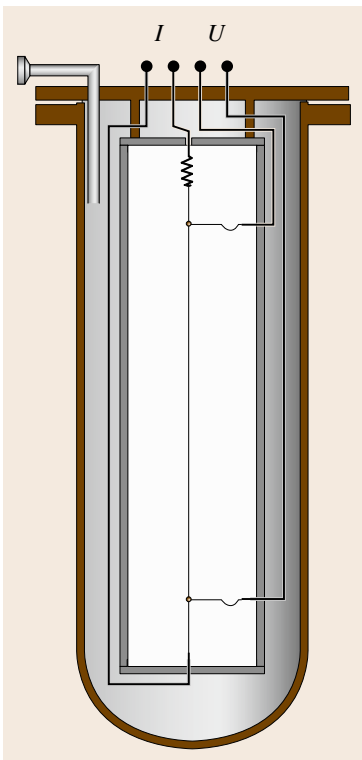


Fig. 8.4 Principle of the hot wire method

the heating wire and legs of a thermocouple are in direct contact with each other and form a cross. The advantage of the parallel wire method is that it can be used for anisotropic materials and for materials having a thermal conductivity above $2 \text{ W m}^{-1} \text{ K}^{-1}$. Further developments are the use of modulated heat input, e.g. pulse or sinusoidal modulation.

Relative expanded ($k = 2$) uncertainties of the measured values of 0.38% for thermal conductivity and 1.7% for thermal diffusivity (resp. ρc_p) of liquids have been achieved [8.5].

Laser Flash Method

The most frequently used method for the determination of thermal transport properties of solids is the laser flash method. The main reason is that it can be used in a wide temperature and thermal diffusivity range. Measurements in a temperature range between -100°C and about 3000°C are possible. In contrast to most other methods different material classes, such as polymers, glasses, ceramics and metals, can be investigated without significant limitations on the achievable measurement uncertainty.

Using this method the thermal diffusivity a is determined. If the specific heat capacity and the density of a material are known, the thermal conductivity can be calculated by using (8.4). Therefore, thermal diffusivity measurements are often supplemented by calorimetric measurements for the determination of the specific heat capacity.

The principle of the laser flash method is based on the heating of a specimen by a short laser pulse on the front side of the specimen and the detection of the temperature increase at its rear side (Fig. 8.5).

If the laser pulse can be considered to be instantaneous and if the sample is kept at adiabatic conditions, the thermal diffusivity a can be calculated according to

$$a = 0.1388 \frac{d^2}{t_{1/2}} \quad (8.11)$$

The thermal diffusivity is calculated from the thickness d of the specimen (typically 2 mm) and the time $t_{1/2}$. This is the time needed for the temperature of the rear specimen surface to reach half its maximum value. Several improvements of the evaluation methods have been developed since the introduction of this method by *Parker et al.* in 1961 [8.6]. These are the consideration of three-dimensional heat flow, heat losses, finite pulse duration, nonuniform heating, composite structures and radiation contributions to the heat transfer. In addition several modifications, e.g. for the

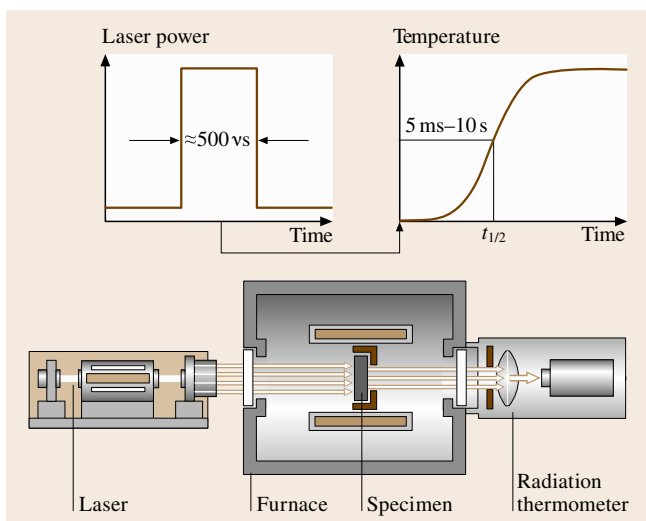


Fig. 8.5 Principle of the laser flash method

measurement of the specific heat capacity or for the direct determination of the thermal conductivity, have been developed.

The most important advantage of the laser flash method is that, for the determination of a thermal property, neither absolute temperatures nor heat measurements are necessary. The thermal diffusivity measurement is carried out by determination of the relative temperature change as a function of time only. This is the main reason why relative measurement uncertainties in the 3–5% range can be achieved even at high temperatures [8.7–9].

Photothermal Methods

The principle of these methods is based on the investigation of a light-induced change in the thermal state of a material in solid, liquid or gaseous state. If light is absorbed by a sample, subsequent changes in temperature, pressure or density are detected. There are methods in which the sample is in contact with the detection system and others that involve remote, noncontact detection systems.

Photothermal and photoacoustic methods for the determination of optical absorption and thermal properties of materials can be classified according to the detection technique used. These are based on the measurement of changes in:

- Temperature: Changes in temperature are usually investigated by means of contact thermometry (e.g.

the photopyroelectric technique), radiation thermometry or calorimetric methods.

- Pressure: Pressure changes are determined via acoustic methods.
- Density: The investigation of density changes include the detection of refractive index variations or of surface deformations. The most important techniques are the thermal lens method, thermal wave technique, beam deflection, refraction or diffraction methods.

The general idea of thermal diffusivity measurement by photothermal methods is modulated heating of a sample surface and detection of the amplitude and phase of the temperature at the opposite sample surface as a function of modulation frequency. This technique can be modified by simultaneous heating of both surfaces with a single modulation frequency and measurement of the phase difference between both surface signals.

Photoacoustic Technique. Typically the sample is placed in an acoustically sealed cell containing a contact gas and a microphone. A monochromatic light source periodically heats the sample and the resulting expansion causes a pressure wave which is sensed with the microphone pressure transducer. Liquid or solid samples can be measured either by direct coupling of the acoustic wave to the microphone or via a gas (coupling fluid). A great variety of photoacoustic configurations have been developed depending on the aggregate state of the sample, the property to be measured (e.g. thermal diffusivity, effusivity, optical properties) or the temperature and pressure range of interest.

Optical Beam Deflection Technique. An excitation beam heats the material periodically while a continuous wave (cw) probe beam is used either in order to detect density changes of the gas near the sample surface or to probe the sample directly. Depending on the relative position between excitation and probe beam, collinear and perpendicular configurations are distinguished. If the sample surface temperature is different from that of the surrounding gas, this results in a temperature gradient between the gas near the sample surface and the bulk gas. Since the density of a gas is temperature dependent, a gradient of the refractive index of the gas is observed. This method, also known as the *optical mirage* technique, is based on the refraction of the probe beam caused by the dependence of the speed of light on the gas temperature.

Thermal Lens Technique. This method is of particular interest for the determination of thermal properties of transparent liquids and solids, such as glasses, polymers or liquid crystals. The photothermal lens is created through the temperature dependence of the refractive index of the sample resulting from the heating of the sample by an excitation laser beam. Typically the lens causes a laser beam divergence which is detected as a time-dependent decrease in power at the center of the beam.

Thermal Wave Technique. The principle of the thermal wave technique is based on measurements of temperature fluctuations in a (gaseous) sample following the absorption of intensity-modulated light. The thermal diffusivity is determined from frequency- and time-domain behavior of a thermal wave in a fixed volume. An improvement of this technique is the development of the thermal wave resonant cavity, which has been used for the measurement of the thermal diffusivity of gases with very high precision. A thermal wave cavity consists of two parallel walls. One wall is fixed and periodically heated by a laser beam or resistive heating. The other one consists of a pyroelectric thin-film transducer, which is used to monitor the spatial behavior of the thermal wave by means of cavity-length scans. By this method the thermal conductivity and thermal diffusivity of the gas in the cavity can be measured.

For a more detailed discussion we refer to [8.10].

8.1.3 Calorimetric Methods

The general principle of all calorimetric methods for the determination of the specific heat capacity is based on (8.1), i. e. the measurement of a specific amount of heat dQ and the resulting temperature increase dT . In most cases two experiments are necessary, a first one with the empty calorimeter in order to determine the instrument's heat capacity and for the correction of the remaining heat losses and a second one with the filled calorimeter including the sample.

Numerous types of calorimeters have been developed for the determination of specific heat capacities of materials. Table 8.2 shows the most important of these and their typical application range.

The most accurate methods for specific heat capacity measurements are *adiabatic calorimetry* and *drop calorimetry* (for details see Sect. 8.2). Construction of these high-precision instruments, which are not commercially available, requires considerable effort and

money, while their operation demands substantial experience and time.

Therefore, probably more than 90% of specific heat capacity measurements of solids and liquids are carried out by means of a *differential scanning calorimeter* (DSC, for a detailed description see Sect. 8.2.2). A DSC is operated in dynamic mode, which means that the furnace is heated or cooled with a constant scanning rate of, typically, 20 K/min. The measured quantities are the heat flow rate $\Phi = dQ/dt$ and the corresponding sample temperature T . Usually, three experiments are necessary: the measurement of the empty calorimeter, the sample measurement and the calibration sample measurement.

A calibration is needed because differential scanning calorimetry is a relative method. There are two materials that are considered as standards for the test or calibration of calorimeters used for the determination of specific heat capacities of solids. These are copper for the temperature range 20–320 K [8.11] and synthetic sapphire for the temperature range 10–2250 K [8.12]. The relative measurement uncertainties are less than 0.1% for copper, and less than 0.1% for sapphire in the temperature range 100–900 K and in the range 1–2% at higher temperatures.

In many cases a certified reference material such as synthetic sapphire (e.g., SRM 720 from the National Institute of Standards and Technology, Gaithersburg, USA) is used as the calibration material.

If the heating rates of the sample (s), calibration sample (cal) and empty (0) measurement are identical, the specific heat capacity of the sample $c_{p,s}$ is given by

$$c_{p,s} = \frac{m_{\text{cal}} c_{p,\text{cal}}}{m_s} \frac{\Phi_s - \Phi_0}{\Phi_{\text{cal}} - \Phi_0}. \quad (8.12)$$

Here m_s and m_{cal} are the masses of the sample and calibration sample and the corresponding heat flow rates are Φ_s and Φ_{cal} . There are several commercially available instruments that can be used in different temperature ranges between 100 K and 1900 K. For most DSCs disk-typed samples with diameters of about 6 mm and heights of 1 mm are used. But there are also cylinder-type DSCs (known as Calvet-type devices) having sample container volumes in the range 1.5–150 ml. For measurements on liquids a measurement or control of the vapor pressure and of the sample volume is necessary. This is carried out by special sample cells in cylinder-type instruments or DSCs specially developed for the purpose.

The typical measurement uncertainties of specific heat capacity measurements of solids by means of DSCs

Table 8.2 Different types of calorimeters used for the determination of specific heat capacities

Type of calorimeter	Quantities	Typical temperature range (K)	Uncertainty (%)	Merit	Demerit
Differential scanning calorimeter	Specific heat capacity, enthalpy of phase transition of solids and liquids	100–1900	1.5–10	Standardized, easy to use, fast	Relative method
Adiabatic calorimeter	Specific heat capacity, enthalpy of phase transition of solids, liquids and gases	1–1900	0.05–2	High accuracy	Long measurement time, expensive
Drop calorimeter	Specific heat capacity, enthalpy of phase transition of solids and liquids	273–3000	0.1–2	High accuracy	Expensive
Pulse calorimeter	Specific heat capacity, enthalpy of phase transition of solids and liquids	600–10 000	2–3	Fast, high temperature	Only electrically conducting materials, expensive
Flow calorimeter	Specific heat capacity and enthalpy measurements of liquids and gases	100–700	0.05	–	–
Bomb calorimeter	Heat of combustion of solids, liquids and gases	300	0.01	Standard method for solids, liquids	Low accuracy for gases
Gas calorimeter	Heat of combustion of gases	300	0.03–0.5	Standard method for gases	–

are about 5% below 700 °C and up to 10% at high temperatures. A higher accuracy requires considerable more time and effort to be spent on a proper calibration and evaluation procedure. In those cases a relative uncertainty of about 1.5% is achievable using this technique [8.13].

At high temperatures there are considerable problems with most calorimetric techniques due to heat losses by thermal radiation, mechanical, electrical or chemical properties of the sample and the construction material of the calorimeters. Therefore, for measurement at temperatures above 2000 K, *pulse calorimetry* is advantageous [8.1, 14], but can only be used for materials having a sufficiently high electrical conductivity. The principle of the pulse method is based on a rapid re-

sistive self-heating of a rod- or wire-type specimen by the passage of an electrical current pulse through it. For the determination of the specific heat capacity measurements of the current through the specimen (typically in the range 100–10 000 A), the voltage drop across the specimen and of the specimen temperature with submillisecond resolution are necessary. If the heating rate is sufficiently large, investigations in the liquid state are possible. Modifications of this technique allow the additional determination of the emissivity, the electrical and thermal conductivity and of the enthalpy of fusion.

The temperature range of this technique is approximately 600–10 000 K. For specific heat capacity measurements by pulse calorimetry relative uncertainties of 2–3% can be achieved.

8.2 Enthalpy of Phase Transition, Adsorption and Mixing

According to the first law of thermodynamics the change in the internal energy of a thermodynamic system dU is equal to the difference between the heat transfer into the system dQ and the mechanical work done by the system dW (other energy forms are neglected here).

$$dU = dQ + dW = dQ - p dV \quad (8.13)$$

The enthalpy of a thermodynamic system is defined according to $H = U + pV$ and the resulting enthalpy change dH is

$$dH = dU + p dV + V dp = dQ + V dp. \quad (8.14)$$

Equation (8.14) describes the relationship between the measured quantity, the exchanged heat dQ , and the quantity assigned to the material, the enthalpy

change dH . The relationship between these quantities as a function of the variables of state, namely pressure p , temperature T and composition ξ , is given by:

$$dQ = \left[\left(\frac{\partial H}{\partial p} \right) - V \right]_{T,\xi} dp + \left(\frac{\partial H}{\partial T} \right)_{p,\xi} dT + \left(\frac{\partial H}{\partial \xi} \right)_{T,p} d\xi. \quad (8.15)$$

In many cases the pressure change is very small and the first term of (8.15) is negligible. The second term is the heat capacity at constant pressure of nonreacting systems. The third term describes the isothermal and isobaric enthalpy change due to phase transitions, mixing or chemical reactions. At constant pressure and in the absence of other energy conversions (e.g. deformation, oxidation or surface energy transformation) the enthalpy of transition of a material $\Delta_{\text{trs}}H$ is equal to the heat of transition Q_{trs} .

To understand the general principles of calorimetric measurements it is helpful to separate a calorimeter into three parts: (a) the calorimeter vessel with sample, crucible, thermometer and additional equipment for heat measurement, (b) the immediate surroundings of the calorimeter vessel, e.g. a temperature-controlled liquid bath or metal block and (c) a means for initiation chemical reactions, mixing, solution or adsorption processes. Often a calorimeter is characterized according to its mode of operation, being either adiabatic, isothermal or isoperibol. Adiabatic means that the heat exchange between calorimeter vessel and surroundings is considered to be zero. In isothermal mode the temperature of the calorimeter vessel remains constant. In isoperibol mode the temperature of the surroundings is kept constant.

There are numerous types of calorimeters in use and, as a consequence, several classification systems have been proposed. Typical criteria for the classification are the following:

Principle of (Heat) Measurement.

- *Heat-compensation calorimeters*
The heat to be measured is determined, e.g., by Joule heating, Peltier cooling or by means of the latent heat of a phase transition (e.g., Bunsen ice calorimeter). The measurements are mostly carried out under isothermal or quasi-isothermal conditions.
- *Heat-accumulation calorimeters*
The heat is determined by means of a temperature change measurement. It is based on the fact that the temperature increase of a calorime-

ter is proportional to the amount of heat added. The proportionality factor must be determined by calibration with a known amount of heat. This principle of measurement requires the minimization of heat losses. Therefore, measurements are preferably carried out under adiabatic or quasi-adiabatic conditions.

- *Heat-conduction calorimeters*

In this type of calorimeter the heat is exchanged between the calorimeter and its surroundings via a well-defined heat conduction path. The corresponding heat flow rate (with dimensions of power) is measured, e.g., by means of heat flux sensors (thermopiles). Heat is determined by integration of the measured heat flow rate as a function of time. Instruments of that type are often operated at isoperibol conditions, i. e. the temperature of the surroundings remains constant.

Mode of Operation.

- *Static mode*
This mode includes adiabatic, isothermal or isoperibol operation.
- *Dynamic mode*
Either the temperature of the calorimeter vessel or that of the surroundings is changed. The linear scanning mode (constant heating rate) is most often used, i. e. the temperature of the calorimeter vessel is a linear function of time. During recent years an increasing number of variable heating rate techniques was developed. Typical modes of operation are stepwise heating or the superposition of a constant heating rate by sinusoidal or sawtooth temperature changes.

Construction Principles. These are single, twin or differential calorimeters.

Methods of Reaction, Solution, Mixing or Adsorption Initiation. Examples are continuous (e.g. flow calorimeters), discontinuous or incremental working instruments (e.g. incremental titration).

The use of certified reference materials or pure substances with well-known thermodynamic properties [8.15–18] to check the proper functioning of a calorimeter, the calibration of the instrument, and for validation of the reliability of the measurement uncertainty budget is highly recommended. Certified reference materials for calorimetry are available from the National Institute of Standards and Technology (NIST, USA), the Physikalisch-Technische Bundes-

anstalt (PTB, Germany) and the Laboratory of the Government Chemist (LGC, UK).

8.2.1 Adiabatic Calorimetry

Adiabatic calorimetry is one of the most accurate thermal methods. Relative uncertainties of less than 0.1% for enthalpy of fusion or specific heat capacity measurements can be achieved. To reach this level, substantial expenditure on the construction, measurement and control of the system is required [8.19, 20]. Typically an adiabatic calorimeter can be divided into three parts: a cylindrical inner part surrounded by a system of adiabatic shields and a furnace (Fig. 8.6).

The inner part of the calorimeter consists of a thermometer, crucible(s), sample, heater and inner radiation shields. In contrast to other calorimeters standard platinum resistance thermometers are mostly used. This allows the determination of transition temperatures with the highest accuracy ($\Delta T \approx 1$ mK).

For the realization of adiabatic measurement conditions (prevention of heat exchange with the surroundings) the inner sample part of the calorimeter is enclosed by a heated adiabatic shield, controlled to the same temperature as the inner part. For proper control of the adiabatic conditions and to ensure sufficient temperature homogeneity further guard and radiation shields

are concentrically arranged around the adiabatic shield. The outer part of an adiabatic calorimeter is the furnace (or cryostat) and an enclosure for measurements in vacuum or at controlled inert gas flow. To minimize heat losses and temperature gradients within the calorimeter, construction materials must have a very high thermal conductivity and low emissivity in the infrared range (e.g. silver).

The basic principle of adiabatic calorimetry is the measurement of the temperature increase of the sample due to the supply of a known amount of heat. Therefore, the typical mode of operation consists of alternating heating and equilibration periods, but there are also several adiabatic calorimeters that operate in scanning mode at very low scanning rates. Under adiabatic conditions the enthalpy increment is equal to the supplied heat, which is determined by an electrical energy measurement of high accuracy ($P_{el}t = Q$, P_{el} : power, t : time). Determination of the specific heat capacity of a material is reduced to the basic relation

$$c_p = \frac{Q}{m \Delta T} = \frac{P_{el}t}{m \Delta T} \quad (8.16)$$

In real measurements very small heat losses remain, which can be determined and corrected by means of additional experiments. For that purpose in a first empty run the heat capacity of the calorimeter without a sample is measured. In a properly designed adiabatic calorimeter the heat losses are equal in the empty and filled state. Therefore, the empty measurement is also the basis for the correction of the remaining heat losses.

A measurement procedure for the determination of the enthalpy of fusion also consists of different runs and again a step heating procedure with alternating heating and equilibration periods is used. For experimental reasons each fusion experiment starts below and stops above the fusion temperature. Therefore, the heat capacity contributions of the (filled) calorimeter must be considered. Further experiments are needed to determine the fusion temperature of the material. For that purpose the method of fractional fusion is used.

Adiabatic calorimeters are used from temperatures below 1 K up to about 1900 K [8.21]. At high temperatures the main problems are deviations from adiabatic conditions because of thermal radiation. This results in measurement uncertainties of a few percent for enthalpy of fusion and specific heat capacity measurements at temperatures above 1000 K. In the low-temperature range the specific heat capacity of materials and the sensitivity of most high-precision thermometers rapidly decrease as a function of temperature. This leads to the

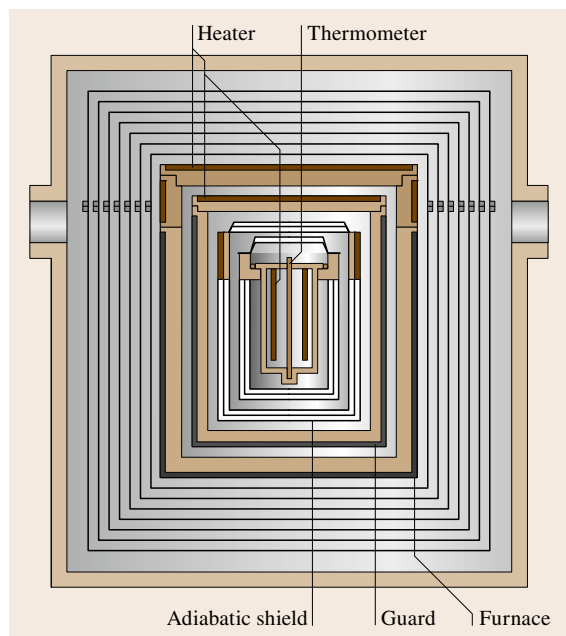


Fig. 8.6 Principle of an adiabatic calorimeter

requirement for considerable effort for the measurement of the temperature difference of the sample and for the control of the adiabatic shield. The lowest uncertainties for enthalpy of fusion measurements of less than 0.1% are achieved in the 100–900 K range.

8.2.2 Differential Scanning Calorimetry

Differential scanning calorimeters (DSCs) are twin-type systems consisting of identical measuring systems for the sample and a reference sample [8.22]. These are mounted in the same furnace and commonly subjected to a controlled temperature program (heating or cooling). During heating or cooling heat is exchanged between the furnace and sample part of the calorimeter (corresponding heat flow rate Φ_{FS}) and in the same manner between the furnace and reference part of the calorimeter (corresponding heat flow rate Φ_{FR}). The difference between these heat flow rates ($\Delta\Phi = \Phi_{FS} - \Phi_{FR}$) is measured and used for the determination of the quantity of interest, e.g. the enthalpy of fusion of the sample. A differential scanning calorimeter measures two quantities, the heat flow rate $\Delta\Phi$ (with dimensions of power) and the corresponding sample temperature. For the measurement of temperatures either platinum resistance thermometers or thermocouples are used. Heat flow rates are measured either by direct electrical power measurements or by means of thermocouples or thermopiles. The use of thermocouples or thermopiles is based on the determination of a temperature drop across a thermal resistor, in analogy to the determination of electrical currents by the measurement of the voltage drop across an ohmic resistor.

Using DSC, both the determination of a transition temperature and the determination of a heat of transition is possible. The transition temperature is determined from the extrapolated peak onset temperature T_e and the transition enthalpy from the peak area of the heat flow rate curve (Fig. 8.7).

To determine the peak area the baseline must be subtracted. The proper choice of the baseline has a major influence on the measurement uncertainty of the transition enthalpy.

A further feature of differential scanning calorimetry is the dynamic mode of operation. Typically a temperature program consists of three segments: an initial isothermal segment, followed by a scanning segment (heating or cooling) with a constant rate and a final isothermal segment. Scanning rates in the range ± 0.1 –500 K/min in a temperature range between -150°C and 1600°C are used for the determination

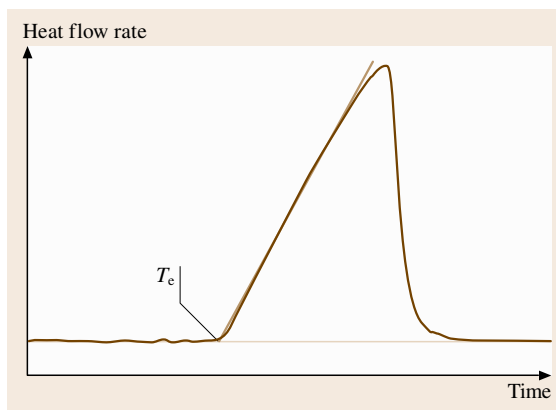


Fig. 8.7 Heat flow rate signal of a DSC during a transition in heating mode with extrapolated peak onset temperature T_e

of enthalpies of phase transitions and specific heat capacities.

A further development is the variable heating rate DSC, where a temperature modulation is superimposed on the constant heating or cooling rate of a conventional DSC. The simplest and most commonly used modulation type is periodic, e.g. sinusoidal, sawtooth or stepwise heating. This technique has been successfully applied for the separation of superimposed effects such as glass transitions and enthalpy relaxations or the determination of specific heat capacities during phase transitions.

There are two basic types of DSCs, the heat flux DSC and the power compensation DSC. The principle of the heat flux type of DSC is based on the measurement of the difference of the heat flow rates $\Delta\Phi$ as described above. The heat flux within the DSC takes place via a well-defined heat conduction path with low thermal resistance. There are two different principles of construction of heat flux DSCs, namely disk-type and cylinder-type systems (Fig. 8.8).

A power compensation DSC consists of two identical microfurnaces (for sample and reference sample) which are heated separately according to a prescribed temperature program. The temperature difference between the two microfurnaces is measured and controlled to achieve the same program of temperature versus time for the sample and reference sample. The compensating heating power is a measure of the heat flow rate difference $\Delta\Phi$.

Several modified DSCs have been developed for special applications. Among these are the high-pressure DSC [8.23], photo DSCs for the investigation of light-

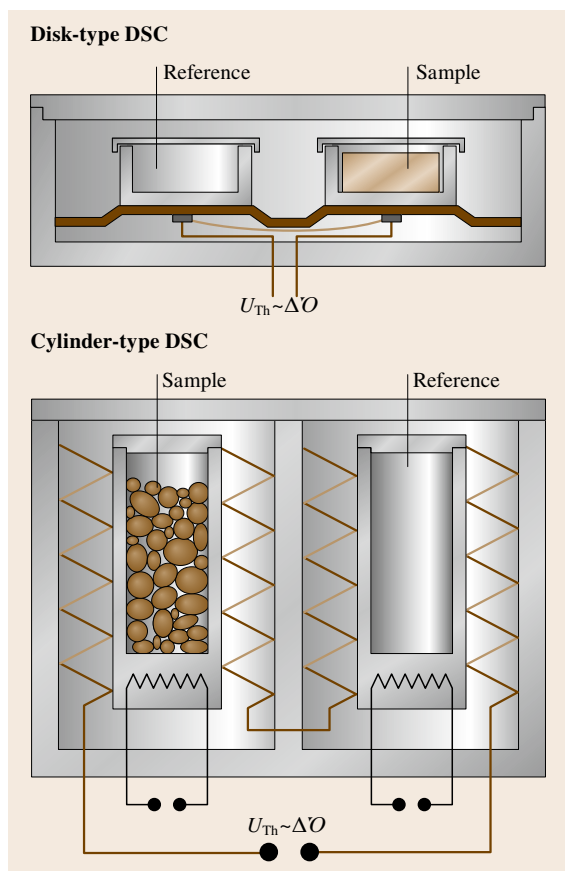


Fig. 8.8 Different types of heat flux DSCs

induced reactions [8.24] and DSCs for measurements on fluids [8.25, 26]. Cylinder-type instruments can be modified to investigate mixing, solution or adsorption processes.

The basic requirement for reliable measurements by means of DSC is the calibration of the instrument, for several reasons. These are the possible drift of sensors and other parts of the measuring system but more importantly the dependence of the calibration on temperature, heating rates, sample holder and crucible or sample properties, e.g. mass, thermal conductivity. It is generally recommended that the calibrations be carried out at conditions similar to those of the actual measurement. A typical example is the heat flow rate calibration. In principle, a cylinder-type DSC could be calibrated using a number of methods, e.g. electrically by means of a calibration heater, by means of a reference material with known specific heat capacity or by means of a material with known enthalpy of fusion. One

would expect it to be sufficient to calibrate the instrument by any of these methods. But, depending on the actual measurement problem, very different measurement uncertainties would be achieved. Therefore, the German Society for Thermal Analysis (GEFTA) recommends [8.15, 27] to distinguish between the heat and the heat flow rate calibration of a DSC, even though the same sensor and electronics are used for both types of measurement. As an example, if the enthalpy of fusion of an unknown material is measured, a heat calibration of the DSC by means of a reference material with known enthalpy of fusion at a temperature close to the fusion temperature of the unknown material is recommended.

A metrologically flawless calibration of a DSC is very time consuming but can improve the accuracy of results by about one order of magnitude. Basic requirements for DSC calibrations are given by international standards and more detailed procedures have been published by GEFTA or the International Confederation for Thermal Analysis and Calorimetry.

With carefully calibrated instruments relative measurement uncertainties of about 1% for enthalpy of fusion measurements and 1.5% for specific heat capacity measurements can be achieved. For routine work relative uncertainties in the 5–10% range are more typical.

8.2.3 Drop Calorimetry

Drop calorimeters are used for the determination of enthalpy increments and specific heat capacities of solid or liquid materials in a temperature range between room temperature and more than 3000 K. The only requirements are that the sample should be nonreactive with its container and have a low vapor pressure to avoid mass loss and significant contributions from heat of reaction or vaporization.

The basic principle of a drop calorimeter is the rapid translation (drop) of a sample from some exterior, temperature-controlled zone (furnace) with temperature T_1 into a calorimeter with temperature T_2 , which is used for the measurement of the heat transferred.

If the instrument is properly designed then the heat loss during the translation from the furnace to the calorimeter is negligible and relative measurement uncertainties of less than 0.1% are possible [8.28]. A disadvantage of that technique is that an initial cooling rate of the sample of up to 2000 K/s is possible. In that case the sample might become frozen in a metastable state.

The calorimeter is typically an adiabatic, isoperibol or isothermal instrument. These can be considered as consisting of two parts: the central measuring part and its enclosing surroundings. In adiabatic calorimeters at any time the temperature of the surroundings is controlled to the same value as that of the central (sample) measuring part. Consequently, no heat losses occur (adiabatic conditions), and adding of heat results in a temperature increase that is used as a measure of that heat. The relationship between heat and temperature increase and the heat capacity of the empty calorimeter are determined by electrical calibrations.

An isoperibol mode of operation means that the temperature of the surroundings is kept constant. In that case two processes occur, if heat is added, firstly the temperature of the calorimeter is increased (heat is stored) and secondly heat is exchanged with the surroundings. The lowest measurement uncertainties are achieved if the amount of stored heat is considerably larger than the exchanged heat.

Several methods are in use for the determination of the heat loss correction. These are based on the validity of Newton's law of cooling [$dT_2/dt = -k(T_2 - T_1)$]. The basic idea of most methods for the correction of heat losses in adiabatic and isoperibol calorimeters is the back and forward extrapolation of the final and initial temperatures over time (Fig. 8.9). This allows the determination of the adiabatic temperature difference ΔT_{adiab} (without heat losses) at the time where areas A_1 and A_2 are equal.

In a calorimeter working in isothermal mode, both the temperature of the surroundings T_s and the temperature of the central measuring part T_m remain constant. This is achieved by using a thermostat to keep the tem-

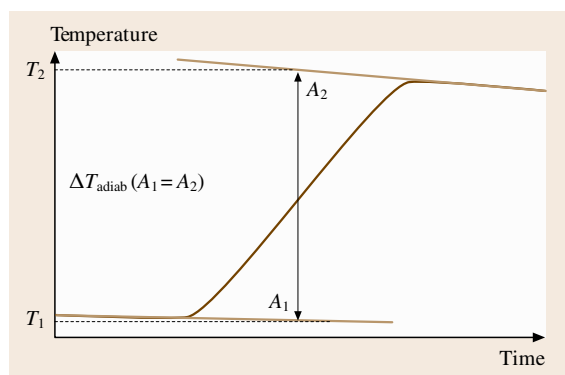


Fig. 8.9 Principle of the heat loss correction based on Newton's law of cooling

perature of the surroundings constant and a two-phase system as the working substance for the measuring part. Using a two-phase system (usually a solid–liquid phase transition) for temperature control means that adding heat to the measuring part of a calorimeter results in a change of the phase distribution (melting of some material) at constant temperature. The amount of melted material is determined either by weighing or by a volume change measurement. The volume change measurement is based on density differences of the working substance between its solid and liquid state (e.g. Bunsen ice calorimeter). On this basis heat measurements with relative uncertainties of 0.02% have been made.

8.2.4 Solution Calorimetry

The determination of heat of solution, mixing, or adsorption [8.29] is of interest in different fields of materials research, e.g. for investigation of polymers, pharmaceutical products or ceramics. Differences in the heat of solution between different batches of a material can reflect variations in polymorphism, moisture content, degree of crystallinity, surface area or surface energy. Instruments can be classified according to the state of aggregation of the interacting materials or whether a continuous (flow calorimeters) step mode (e.g. titration) or discontinuous mode of operation is used.

A further classification scheme is the mode of operation resulting from the coupling between the central part of the calorimeter, which is used for the calorimetric measurements, and the surroundings. Solution calorimeters are operated either in adiabatic, isothermal or isoperibol mode.

Specific problems are the separation and the temperature control of the components before the start, complete mixing over the course of the investigations and the change in the vapor pressure during mixing. Calorimeters for discontinuous operation consist of a reaction vessel, a thermometer, a mixing unit or ampoule-breaking system, the stirrer and a resistance heater for electrical calibration. Typically thermometers are thermistors, platinum resistance (Sect. 8.5) or quartz thermometers. The principle of a quartz thermometer is based on the resonant frequency dependence of a quartz oscillator as a function of temperature. Often one of the samples is sealed in a thin-walled glass ampoule. After the system is in thermal equilibrium, the solution or reaction process under study is started by breaking the glass ampoule.

Adiabatic and some isoperibol instruments work as heat-accumulation calorimeters, i. e. the heat to be measured is detected via the temperature change of the calorimeter. The calibration of the instrument is determined either by electrical calibration or by the use of reference materials with well-known heat of solution, reaction or adsorption.

A further method is to suppress the temperature change by measuring the required compensating heat, e.g. by means of electric energy (Joule heating or Peltier cooling). In this case only a sensitive temperature sensor (no calibration is required) with sufficient long-term stability is needed because the calorimeter operates in the isothermal mode. The thermometer is used only for the control of the compensation power, so that the temperature remains constant.

A third method of heat measurement is the determination of heat exchanged between the reaction vessel and the (isothermal) surroundings by means of heat flux sensors (Sect. 8.1.1). The vapor pressure of a mixture depends on its composition. Heats of vaporization are usually larger than heats of mixing. Therefore, the determination and correction of the influence of the vapor pressure change during the experiment is very important. Measurement uncertainties of about 0.25% can be achieved [8.30].

The advantages of continuously working flow calorimeters [8.31] are that the measurements can be carried out in a shorter period of time and that less material is needed. Measurements of heat of mixing in a temperature range of 273–479 K and a pressure range between 0.1 MPa and 40.5 MPa with relative uncertainties of 0.5% being possible [8.32].

8.2.5 Combustion Calorimetry

The most common device for measuring the heat of combustion or calorific value of a solid or liquid material is the bomb calorimeter [8.33–36].

A sample is contained under a pressure (about 3 MPa) of pure oxygen in a pressure-tight stainless-steel container (bomb, $V \approx 300$ ml) and is burned under standardized conditions. During recent years several new micro-bomb calorimeters ($V < 100$ ml) have been developed. All instruments are provided with an electrical system for the ignition of the combustion process. The determination of the heat of combustion is based on the observed temperature rise, which is measured with high-precision temperature sensors such as standard platinum resistance thermometers, thermistors or quartz thermometers. Adiabatic, isoperibol or aneroid

instruments are commercially available. In most cases a correction of the measured temperature increase is needed to consider the heat exchange with the surrounding. Furthermore, the calibration factor (energy equivalent) of the calorimeter must be determined. For that purpose a reference material with a well-known heat of combustion is needed. Benzoic acid is the preferred material for that purpose. With well-designed bomb calorimeters relative measurement uncertainties of less than 0.01% can be achieved [8.37] with highly purified materials containing C, H, and O. If other elements are present, the accuracy is limited by the extent to which the stoichiometry of the combustion process can be controlled and determined. Systematic deviations can arise from incomplete combustion or from the lack of a well-defined final state.

Calorimeters for the determination of the calorific value of gases can be subdivided into three different groups [8.38]:

- combustion of the gas inside of a bomb calorimeter (isochoric combustion)
- combustion without a flame on a catalyst (isobaric combustion)
- combustion of the gas in an open flame of a gas burner (isobaric combustion)

The first two groups of methods are used only in rare cases for very specific applications, e.g. investigations on fluorochlorohydrocarbons.

Calorimetric methods in the third group are based on the combustion of the gas at constant pressure and flow rate (flow calorimeter) with an open flame. A heat exchanger is used to transfer the combustion heat to a heat-absorbing fluid (air or water). The temperature increase of the heat-absorbing fluid is a measure of the calorific value. For the calibration of these calorimeters various methods can be applied: the use of gases with well-known calorific values, electrical calibration techniques and methods based on the determination of temperature increase, volume flows and the knowledge of the heat capacity of the heat absorbing fluid. There are several gas calorimeters commercially available, e.g. the Junkers calorimeter, the Reinecke calorimeter, the Thomas–Cambridge calorimeter, or the Cutler–Hammer calorimeter. The typical relative measurement uncertainty of these instruments is about 0.5%.

A high-precision constant-pressure gas-burning calorimeter has been used for the determination of the heat of combustion of methane [8.39]. The resulting combined standard uncertainty was 0.21 kJ/mol which corresponds to a relative uncertainty of 0.024%.

8.3 Thermal Expansion and Thermomechanical Analysis

Thermomechanical analysis (TMA) measures the change in dimension (deformation) of a sample under constant (static force) compressive, tensile, or flexural loads as the temperature of the sample is changed. The special case with negligible force is called dilatometry or thermodilatometry. Typical applications of TMA are the determination of the coefficient of thermal expansion, glass-transition temperatures, softening or shrinkage behavior or the investigation of changes in dimension caused by sintering or chemical reactions. There are several instruments commercially available covering the temperature range between -260°C and 2400°C .

In dynamic mechanical analysis DMA a dynamic force is applied to the sample and the resulting displacement is measured as a function of temperature, frequency or time. A special case is the application of an oscillating force. Dynamic mechanical analysis is used for the determination of the modulus of elasticity (stiffness), viscous modulus and damping coefficient ($\tan \delta$) of materials (for details see Chap. 7). In addition, DMA measurements give insight into the temperature and frequency dependence of molecular mobility and can be used for the determination of glass-transition temperatures.

Thermal expansion is the change of the length of a specimen ΔL as a function of the temperature change ΔT

$$\Delta L = L - L_0 = L_0 \alpha \Delta T. \quad (8.17)$$

This behavior is described by the coefficient of (linear) thermal expansion (CTE)

$$\alpha = \alpha_L = \frac{1}{L_0} \frac{dL}{dT} \quad (8.18)$$

and is a function of temperature $\alpha = \alpha(T)$. The reference length L_0 of the specimen is generally given either at a temperature of 0°C or at 20°C . In crystalline anisotropic solids the coefficient of thermal expansion is direction dependent and may have up to six different contributions.

The change of the volume of a body as a function of temperature is described by the volumetric coefficient of thermal expansion

$$\alpha = \alpha_V = \frac{1}{V_0} \frac{dV}{dT}. \quad (8.19)$$

In most cases the volumetric coefficient of thermal expansion can be determined from the linear coefficient of thermal expansion with sufficient accuracy by means of $\alpha_V \approx 3\alpha_L$.

There are several different descriptions of thermal expansion in use. In the definition according to (8.18) α is often called the physical or differential coefficient of thermal expansion. Furthermore, in some cases a so called mean or technical coefficient of thermal expansion according to

$$\alpha_m = \frac{1}{L_0} \frac{L(T_2) - L(T_1)}{T_2 - T_1} = \frac{1}{L_0} \frac{\Delta L}{\Delta T} \quad (8.20)$$

is used. The third kind is the specification of a relative length change $\Delta L/L_0$ at a (mean) temperature T .

The coefficient of thermal expansion of a sample is usually determined according to its definition (8.18) by the measurement of the reference (initial) length L_0 at the temperature T_0 , and the change of the length ΔL as a result of a temperature change ΔT at different (mean) temperatures.

The shape of the samples is typically a cylindrical rod with a diameter in the range 5–10 mm and a length in the range 25–50 mm. Depending on the temperature range of interest, cryostats, liquid baths, multizone or heat pipe furnaces with excellent temperature stability and homogeneity are used. These are operated either by stepwise heating or by scanning at low rates. Thermocouples or radiation thermometers are mostly used for the temperature measurements. More information can be found in [8.40].

8.3.1 Optical Methods

For measurements of length changes with highest accuracy, e.g., for the certification of reference materials, for materials with very low coefficients of thermal expansion (Zerodur, Invar) and for cases when only small samples are available, optical methods are chosen. Relative measurement uncertainties of the certified values of α_L of high-purity synthetic Al_2O_3 of 0.18–1% were achieved in a temperature range between -180°C and $+400^{\circ}\text{C}$ [8.41].

The optical methods can be divided into three main types. The first one is based on the creation of an image of a sample and the determination of the spatial movement of the ends or other marks along the length. In this case the optical path is perpendicular to the displacement direction. The image is formed either by background illumination to give a silhouette effect or by the radiant light emitted from the specimen itself. These techniques are known as optical imaging, optical comparator or twin telemicroscopy.

The second type is based on interferometry. Here the displacement is determined by the measurement of the path difference of beams reflected from opposite surfaces of the sample. Because the refractive index of air or inert gases is not known with sufficient accuracy most measurements are carried out in vacuum.

In the third method speckle interferometry is used to determine the displacement by means of changes in the interference pattern on the surface of the sample.

There are further specialized techniques which do not fall into the above categories. Details can be found in [8.42].

For the certification of reference materials instruments based on Fizeau and Michelson interferometers have been used [8.43, 44]. At temperatures above 800 K several problems lead to a decrease in the accuracy of this method. Therefore, instruments based on optical heterodyne interferometers for absolute measurements at temperatures of 300–1300 K [8.45] and 1300–2000 K [8.46] have been developed. For measurements with these instruments combined standard uncertainties of $1.1 \times 10^{-8} \text{ K}^{-1}$ [0.26% for $100(\Delta\alpha/\alpha)$] at 900 K and of 1.3% in the range 1300–2000 K have been claimed.

The highest accuracies are achieved around room temperature. Measurement results on ceramic and steel gauge blocks with uncertainties of $1 \times 10^{-9} \text{ K}^{-1}$ in a temperature range between -10°C and 60°C have been published [8.47].

8.3.2 Push Rod Dilatometry

The most common method of measuring thermal expansion is push rod dilatometry. Several instruments are commercially available for the temperature range between -260°C and 2800°C .

A sample is heated in a furnace or other temperature-controlled environment and the displacement of the ends is mechanically transmitted to a displacement sensor (e.g. a linear variable differential transformer, (LVDT)) by means of push rods. There are several possible arrangements of the push rods. The first is the parallel arrangement of two push rods, the double push rod system. This arrangement can be modified by simultaneous use of sample and reference samples, known as the differential method. A further arrangement is for one of the rods to be in the form of a closed tube. The sample and the other push rod are located along the central axis of the tube. In this case the sample is clamped between the central push rod and the closed end of the other tube-shaped push rod.

The displacement sensor is maintained in a controlled-temperature environment close to room temperature. Therefore, the most critical part is the push rod, which transmits the expansion signal from the sample to the displacement sensor. The resulting temperature difference between opposite ends of push rods can be more than 2000 K. Therefore, the homogeneity of the temperature field in the furnace, the repeatability of a temperature program and the material used for the push rods are of critical importance for high-quality measurements.

The main criterion for the choice of a material used for push rods is a low, reproducible, and accurately known coefficient of thermal expansion. At low temperatures vitreous silica is the preferred material. There are very different recommendations for the upper temperature for the use of vitreous silica for this purpose, ranging from the temperature of the α - β transition of about 550°C to 1000°C as the maximum temperature to avoid devitrification, i. e. the transition from the glassy state to a crystalline structure. For temperatures up to 1600°C push rods are made from silica, either in single-crystal form (sapphire) or sintered (polycrystalline) state, at higher temperatures rods consisting of isotropic graphite are used.

Dilatometers are often operated in a dynamic mode by temperature scanning with a constant rate of typically less than 5 K/min. Depending on the method of construction more than one measurement may be necessary to determine the correction for the thermal expansion of the push rods and to calibrate both the displacement- and the temperature sensor. For this purpose certified reference materials are necessary. High-purity materials such as silicon, tungsten, platinum, copper, aluminum, sapphire or vitreous silica are mostly used for displacement calibration. The calibration of the temperature sensor is carried out by the measurement of the dimensional change of a high-purity metal during melting.

With careful work relative measurement uncertainties for the CTE of 2% at temperatures between room temperature and 973°C have been achieved [8.48].

8.3.3 Thermomechanical Analysis

The basic difference between thermomechanical analysis (TMA) and dilatometry is that for TMA a load (static force) is applied to the sample. As a consequence instruments for TMA are operated with vertical sample orientation. This is different from most dilatometers, where horizontal sample and furnace orientation is cho-

sen as this gives better temperature uniformity. There are several modes of force control and sample configuration for **TMA**. At negligible load the thermal expansion measurements are carried out in a very similar manner to dilatometry. In the compression mode a rod with well-known cross section or geometry presses with a known force on the sample and the compression, penetration or bending is determined as a function of force, temperature or time. From these

8.4 Thermogravimetry

Thermogravimetry (**TG**) is a method of thermal analysis in which the mass of a sample is measured as a function of temperature whilst the sample is subjected to a controlled temperature program. In many cases the reaction products are analyzed by supplementary investigations. As for most other methods of thermal analysis the typical temperature program is a linear scan, i.e. the temperature changes linearly in time. During recent years so called controlled-rate thermal analysis has been increasingly used. This means that the scanning rate can vary as a function of time depending on the magnitude of the measured quantity; for example, the scanning rate of a thermogravimetric instrument is controlled as a function of the measured mass change of the sample or the amount of a specific evolved gas.

Typical applications are the evaluation of the thermal decomposition kinetics of materials such as rubbers or polymers, the investigation of processes such as sintering, drying, oxidation or reduction. There are several instruments for investigations in a temperature range between -150°C and 2400°C commercially available. Typical sample masses are in the range 5–25 mg. Mass changes can be detected with resolutions in the range 0.1–10 μg . Most **TG** instruments can be combined

kinds of measurements elastic modulus, creep or cure behavior, softening temperatures or phase transition are determined. This is also of advantage for the investigation of transitions in thin films such as polymer coatings or lacquers. Further applications are measurements in tension mode and investigations of the viscous properties or gelation of fluids. There are instruments commercially available for a temperature range between -160°C and 2400°C .

with calorimetric detection systems for simultaneous differential thermal analysis or differential scanning calorimetry. Thermogravimetry is performed in a controlled atmosphere including oxygen, nitrogen, helium or argon with adjustable flow rates.

A mass spectrometer (**MS**) or a Fourier-transform infrared (**FTIR**) spectrometer can be coupled to most **TG** instruments for continuous, online identification and analysis of the evolved gases during heating of the sample. To avoid a separation or loss of evolved gases by condensation these are routed to the **MS** via a heated capillary or a system of orifices held at the same temperature as the sample (Skimmer coupling).

A recent extension of **TG** systems is pulse thermal analysis [8.49]. This is based on the injection of a specific amount of liquid or gaseous reactant into the inert carrier gas stream and monitoring of the changes in the mass, enthalpy, and/or gas composition. By this method gas–solid reactions, adsorption or catalytic processes can be studied. A further application is the direct calibration of the mass spectrometer or **FTIR** spectrometer by injecting a known amount of substance into the inert carrier gas stream and relating it to the spectrometer signal. For more information the reader is referred to [8.50].

8.5 Temperature Sensors

Temperature sensors are needed for the measurement of thermal properties of materials, of course, but they are used in a much larger field of applications, since temperature is the quantity measured most frequently in science, industry, and daily life. In the following chapter a selected number of temperature sensors of sufficient reliability for scientific and industrial measurements is described as well as the temperature scale against which they should be calibrated.

8.5.1 Temperature and Temperature Scale

Temperature characterizes the thermal state of matter independently of the nature of the substance. It is an intensive quantity, not depending on the addition or reduction of the amount of matter concerned, but changed by supplying or removing heat or mechanical work. Classically, the definition of temperature is derived from the thermodynamic description of a Carnot engine re-

versibly driven in a thermodynamic cycle, the efficiency of which depends only on temperature. The ratio of the heat Q_1 fed to the engine isothermally at high temperature to the heat Q_2 removed at low temperature to get back mechanical work was found to be identical to the ratio of the temperatures T_1 and T_2 at both isothermal parts of the cycle by William Thomson, the later Lord Kelvin:

$$Q_1/Q_2 = T_1/T_2. \quad (8.21)$$

From this definition of temperature he could derive the equation of state for an ideal gas to be

$$pV = \text{const } T. \quad (8.22)$$

This states that the product of the gas pressure p and the volume V filled with the gas is proportional to the absolute temperature. The constant in (8.22) turned out to be equal to nR , the product of the number n of moles involved and the gas constant R .

By statistical methods it was shown during the second half of the 19th century that the average kinetic energy of a molecule of an ideal gas amounts to

$$pV = \text{const} \left(mv^2/2 \right), \quad (8.23)$$

a fact, which demonstrates that temperature is a measure of the averaged internal energy of the gas molecules, which are ascribed a mass m and a velocity v .

An apparatus built to determine the pressure and the volume of a known number of moles of an ideal gas can be used to measure the temperature of the gas according to (8.22). Such a gas thermometer is called a primary thermometer, since there is no need to calibrate it against another thermometer and it is based on a fundamental physical law including the thermodynamic temperature. There are several other primary thermometers based on different fundamental laws listed in Table 8.3.

Since these primary thermometers are usually complicated and difficult to handle, a temperature scale was introduced for practical purpose and refined over the years. Such a scale consists of temperature fixed points, the temperature values of which are determined with great effort by comparison with primary thermometers, and of interpolating instruments, which are calibrated at those fixed points and define the temperature in between. After some early attempts such a scale was adopted in 1927 following a suggestion by Callendar

Table 8.3 Primary thermometers and the fundamental relations on which they are based

Thermometer	Fundamental relation
Constant-volume gas thermometer (ideal gas) pressure p , volume V , number of moles n , molar gas constant R , temperature T	$pV = nRT$
Acoustic gas thermometer (ideal gas) speed of sound c_s , ratio γ of specific heat capacities at constant pressure and constant volume, gas constant R , temperature T , molar mass M	$c_s = (\gamma RT/M)^{1/2}$
Dielectric-constant gas thermometer (ideal gas) pressure p , Boltzmann constant k_B , temperature T , dielectric constant ϵ , electric constant ϵ_0 , static electric dipole polarisability of a gas atom α_0	$p = k_B T (\epsilon - \epsilon_0) / \alpha_0$ (Clausius–Mosotti equation)
Total radiation thermometer total radiance L , Boltzmann constant k_B , temperature T , speed of light in vacuum c , Planck constant h	$L = (2\pi^5 k_B^4 T^4) / (15c^2 h^3)$ (Stefan–Boltzmann law)
Spectral band radiation thermometer spectral radiance L_ν , Planck constant h , frequency of light in vacuum ν , speed of light in vacuum c , Boltzmann constant k_B , temperature T	$L_\nu = 2h\nu^3/c^2 [\exp(h\nu/k_B T) - 1]^{-1}$ (Planck's Law)
Noise thermometer mean square noise voltage $\langle V^2 \rangle$, Boltzmann constant k_B , temperature T , resistance R , bandwidth Δf	$\langle V^2 \rangle = 4k_B TR \Delta f$ (Nyquist formula)

from 1899. The actual revision of the temperature scale dates from 1990. It is called the International Temperature Scale of 1990, ITS-90. It is based on 14 fixed points from the triple point of hydrogen (13.8033 K) to the freezing point of copper (1357.77 K) and the vapor pressure of the stable helium isotopes below.

One of these fixed points is the triple point of water, the value of which is fixed to 273.16 K, as the defining point of the temperature unit kelvin. This definition states: the kelvin is the fraction $1/273.16$ of the thermodynamic temperature of the triple point of water.

Interpolating instruments are the vapor pressure thermometer with ^3He or ^4He as the working gas from 0.65 K to 5 K, which is part of the scale's definition as well, an interpolating gas thermometer with the same gases up to 25 K and standard platinum resistance thermometers (SPRTs) above. From the freezing point of silver (1234.93 K) to the highest temperatures to be reached the relative spectral radiance thermometer is used, being calibrated at the Ag, Au or Cu fixed point, respectively. Table 8.4 includes the temperature fixed points and indicates the uncertainty ΔT_{90} of the realization of the ITS-90.

In 2000 the CIPM (Comité International des Poids et Mesures) adopted an extrapolation of the temperature scale to subkelvin temperatures. This scale, called the Provisional Low Temperature Scale of 2000, PLTS-2000, is based on magnetic and superfluid phase

transitions in ^3He and the minimum of its melting pressure as fixed points and the ^3He melting curve thermometer as the interpolating instrument.

The national metrological systems, often divided into legal and industrial branches, provide national temperature standards and calibration facilities for science and industry to trace back the readings of thermometers of individual users. The lowest uncertainty is available from those national metrological institutes, which compare their particular representations of ITS-90 from time to time by means of so called key comparisons to guarantee the uniformity of temperature measurements throughout the world. The definition of temperature, the development of temperature scales and the principles of thermometry are extensively explained in the monograph [8.52].

Very recently, efforts have been started by several national metrological institutes to replace the dependence of the kelvin on a material property, namely the already mentioned triple point of water. Instead, it is suggested that the kelvin should be based on a fundamental constant as is done with other SI units, which are already related to a fundamental constant, such as the meter to the speed of light in vacuum, or are in the process of being related, like the kilogram. In the case of the kelvin the appropriate constant would be the Boltzmann constant k_B . If its value is determined with sufficient accuracy – about one order of magnitude bet-

Table 8.4 The defining fixed points of ITS-90 (after [8.51])

No.	T_{90} (K)	t_{90} ($^{\circ}\text{C}$)	ΔT_{90} (mK)	Substance	State
1	3–5	–270.15 to –268.15	0.1	^3He and ^4He	Vapor pressure
2	13.8033	–259.3467	0.1	e- H_2^{a}	Triple point
3	≈ 17	≈ -256.15	0.2	e- H_2	Vapor pressure ≈ 33.3213 kPa
4	≈ 20.3	≈ -252.85	0.2	e- H_2	Vapor pressure ≈ 101.292 kPa
5	24.5561	–248.5939	0.2	Ne	Triple point
6	54.3584	–218.7916	0.1	O_2	Triple point
7	83.8058	–189.3442	0.1	Ar	Triple point
8	234.3156	–38.8344	0.05	Hg	Triple point
9	273.16	0.01	0.02	H_2O	Triple point
10	302.9146	29.7646	0.05	Ga	Melting point
11	429.7485	156.5985	0.1	In	Freezing point
12	505.078	231.928	0.1	Sn	Freezing point
13	692.677	419.527	0.1	Zn	Freezing point
14	933.473	660.323	0.3	Al	Freezing point
15	1234.93	961.78	1–10	Ag	Freezing point
16	1337.33	1064.18	10	Au	Freezing point
17	1357.77	1084.62	15	Cu	Freezing point

^a e- H_2 is hydrogen at the equilibrium concentration of the ortho and para molecular forms

ter than now – and then fixed by definition, temperature could be traced back to the internal energy $k_B T$, the quantity to which it is proportional in the microscopic view, as mentioned at the beginning of this section.

8.5.2 Use of Thermometers

Strictly speaking, a thermometer never measures the temperature of the sample of interest, but always its own. To get an indication of the sample's temperature its temperature and the temperature of the thermometer should agree within the requested uncertainty of the measurement. To meet this requirement within a finite amount of time heat should easily be able to flow between them. If the heat flow has approached zero, so called thermal equilibrium is reached between sample and thermometer, and the thermometer is ready to indicate the sample's temperature. In the case of contact thermometry the thermal resistance between the sample and the thermometer should be low. Thermal conductivity should be high within the sample and within the thermometer to provide thermal equilibrium within both. A small heat capacity of the thermometer is advantageous, since then only a small amount of heat is forced to flow in order to reach thermal equilibrium. Small heat capacity, good thermal contact and large internal thermal conductivity make the thermometer fast.

A thermometer gives an indication of its temperature by measuring some other property that is somehow dependent on temperature. With a constant-volume gas thermometer the pressure is the quantity that measures temperature, with a resistance thermometer it is the electrical resistance of the sensor. Usually some energy is needed to read the thermometer on the display. This energy is fed to the sensor and, in principle, due to the permanent heat flow, keeps the thermometer out of equilibrium. Therefore, the measuring energy must be reduced to a value that does not disturb the result. Since thermal conductivity, thermal contact resistance and heat capacity change with temperature, the measuring energy must also be changed in most cases over the temperature range.

In the following, we will consider some frequently appearing errors in the use of thermometers, which are discussed in [8.53] in great detail.

- *Electromagnetic interference*
Since the energy flowing between sample and thermometer is not limited to the measuring energy, other energy contributions coupled into the system, such as heat leaks, must be kept under control

during the measurement. If electromagnetic energy from radio and television broadcasts irradiates the thermometer and is fed in by the wiring, or if the electromagnetic radiation emitted from hot surfaces nearby is absorbed by the thermometer, the measuring result can be significantly affected. Electromagnetic shielding of the thermometric sensors and electronics, filtering circuits in the sensor wiring and radiation shields are necessary tools when the amount of irradiated external energy can not be tolerated. In extreme situations the whole measurement should be located in an electromagnetically shielded room.

- *Immersion error*
Immersion error is an issue for liquid-in-glass thermometers and others that are usually not fully immersed in the liquid to be measured. In this case, heat is permanently flowing through the stem of the thermometer from the bath to the surrounding air. This is a typical nonequilibrium situation inappropriate for an exact result. As a rule of thumb a thermometer should be immersed into the bath by more than ten diameters of the thermometer (that means 40 mm beyond the sensing element with a sensor diameter of 4 mm) to limit the error to 0.01%.
- *Heat capacity error*
If the heat capacity of the thermometer is not negligible compared to the heat capacity of the sample and the sample is more or less thermally isolated, a certain amount of heat flows between them when the starting temperatures are different. After reaching thermal equilibrium both temperatures have changed to a common value somewhere between their initial temperatures. This means that, if the sample's temperature was, e.g. much hotter than that of the thermometer, the finally indicated temperature of the sample would be less than its value before the measurement. This difference is called the heat capacity error.
- *Time constant*
Even if the sample's heat capacity is large enough to avoid the heat capacity error it may take a significant time to replace the heat in the sample that has flown into the thermometer while thermal equilibrium was established. Therefore, the reading of the thermometer approaches its final value following an exponential trend with a time constant τ_0 . If insufficient time is given to the system, a settling response error is arising. If the temperature of a sample is changing at a certain rate, and the settling rate of

the thermometer is too slow compared to the temperature variation rate, a lag between the real and the measured temperature will develop. This can be avoided either by slowing down the rate of temperature change or by a constructive improvement of the thermal coupling between the parts of the system.

- *Environmental irradiation*

According to the Stefan–Boltzmann law (see Table 8.3) all material surfaces emit electromagnetic radiation proportional to T^4 . Therefore, all radiating sources in the environment should be removed, if possible, or at least shielded, since thermometers should not see surfaces at temperatures very different from their own. In addition, thermometers show significantly different readings up to the order of some kelvin depending on their surface emissivity. This fact recommends proper shielding, as well.

To clarify the different influences on thermometers during the measurement of temperature it is helpful to use *analogue electrical modeling*. Since thermal conductivity can be described in a similar way as its electrical correspondent, one can derive analogue relations. Heat Q corresponds to electrical charge Q_{el} , heat flux q to electrical current I , temperature difference ΔT to voltage V , thermal resistance R_{th} to electrical resistance R_{el} , and heat capacity c_p to electrical capacitance C . Thus, Ohm's law can be applied in analogy to heat flow processes in the following form:

$$\Delta T = T_2 - T_1 = qR_{\text{th}}. \quad (8.24)$$

If the heat flow crosses several materials with different thermal conductivities and thermal contact resistances in between, the thermal resistances can be added like electrical resistances in series. If there are several heat flows from different sources to one thermometer, such as heat conduction from the sample and from the surroundings and thermal radiation from other nearby objects, the inverse of the thermal resistances can be added again. Within this electrical analogue picture one can state that a thermometer measures the correct sample temperature when the thermal resistance between them goes to zero, whereas the thermal resistances to other objects such as the surroundings tend to infinity by screening or shielding measures.

If temperature measurements are performed in a way that excludes all errors, most of which are mentioned above, the result is reliable only with the correct calibration of the instrument. This means, that its indicated result must be traced to the SI unit kelvin by linking it to the international temperature scale. Further-

more, the uncertainty of the calibration caused by the number of steps or the special way of this trace back must be known or investigated, and the reliability of the instrument over a longer period of time should be proven. The last requirement can be met by repeated calibrations from time to time, depending on the frequency and intensity of the thermometer's use.

8.5.3 Resistance Thermometers

The type of thermometers most frequently found in scientific and technical equipment is the resistance thermometer, since it is easily read by electronics and can simply be used for temperature control cycles. The most widespread type among the resistance thermometers is the platinum resistance thermometer, which at the same time is the interpolating instrument of the ITS-90 at the highest level of accuracy. In the latter case it is called the standard platinum resistance thermometer (SPRT) and is used in different forms between the triple point of hydrogen at 13.8033 K and the freezing point of silver at 1234.93 K.

The electrical resistance of metallic samples comes from the scattering of the conduction electrons at the atoms or molecules of the solid lattice. There is a temperature-dependent part of the resistance R_t due to lattice vibrations, which increases with increasing internal energy, and a temperature-independent part R_0 caused by impurities and by lattice defects. The total sample resistance arises as the sum of both

$$R(T) = R_t(T) + R_0. \quad (8.25)$$

This equation, in the literature called Mathiessens's rule, can be reformulated as

$$R(T) = R(0^\circ\text{C})(1 + \alpha t), \quad (8.26)$$

where α is the temperature coefficient of resistance. Fewer impurities or defects reduce R_0 or R at 0°C and increase α . Therefore, the metals that should be used for resistance thermometers are those that can be purified to the highest values and effectively annealed. High-purity platinum most closely obeys Mathiessen's rule with small deviations found by Callendar and later by van Dusen. Finally, (8.26) is modified to the Callendar–van Dusen equation

$$R(T) = R(0^\circ\text{C}) \left[1 + At + Bt^2 + C(t - 100)t^3 \right], \quad (8.27)$$

with coefficients of the order: $A = 4 \times 10^{-3} \text{ }^\circ\text{C}^{-1}$, $B = -6 \times 10^{-7} \text{ }^\circ\text{C}^{-2}$, and $C = 4 \times 10^{-12} \text{ }^\circ\text{C}^{-3}$.

This ideal behavior of platinum thermometers is only true, if no other effects influence its resistance. Such disturbing effects to be avoided are strain, mechanical shock, vibration, pressure, humidity, and corrosion. Some of them, such as strain, are caused by temperature changes in an uncontrolled manner. Others can be reduced by careful handling. Further ones must be minimized by using a sealed and shielded construction.

Standard platinum resistance thermometers for ITS-90 realization are manufactured in three different types, as listed in Table 8.5.

SPRTs are usually constructed of high-purity coiled platinum wire within a sheath of glass or quartz embedded in a platinum tube. This is a setup free of strain and danger of contamination, but extremely sensitive to shock, vibrations or other mechanical stress. Therefore, SPRTs are, on one hand, temperature standards with high stability and an uncertainty of less than 1 mK, but on the other not suitable for rough industrial environments. To obtain a more robust device, the support of the platinum wire should be improved. This inevitably causes more strain during temperature variations and increases the uncertainty to about 10 mK. A further disadvantage of all wire-made devices is the poor thermal contact only made by the gas in the capsule and the leads, resulting in time constants of several seconds. As an alternative solution, thick-film thermometers are available, which can be glued to the sample of interest and have improved thermal contact and time constant. They mostly have a nominal resistance of 100 Ω and are well suited as sensors for rough environments and temperature control circuits, but they feel much more strain and contamination effects and suffer from a larger uncertainty of about 100 mK. All of these devices are available commercially and should not be fabricated by the user except for very special needs. Some of them are shown in Fig. 8.10.

For the *electronics of resistance thermometers* two different concepts are in use: the potentiometric method and the resistance bridge (Fig. 8.11). The first is the most common concept, especially since precise electronic devices appeared on the market. A reference resistor is placed in series with the temperature sensor and the voltage drop across each of the resistors

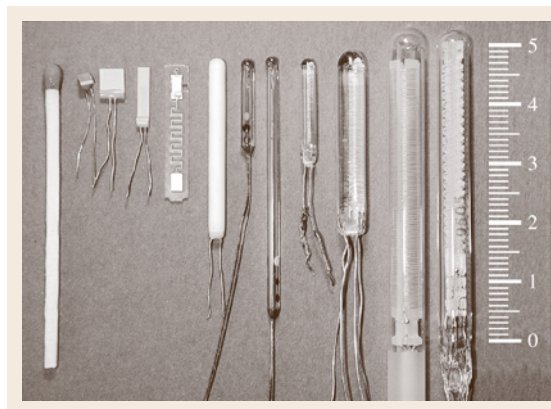


Fig. 8.10 (from left to right) three thick-film Pt-100 resistors; Pt-500 chip resistor prepared for SMD mounting; Pt-100 resistor in ceramics; two NTC thermistors in glass; Pt-100 resistor in glass; double Pt-100 resistors in glass; long-stem SPRT (Pt-25); capsule SPRT (Pt-25)

is determined when a constant current is applied. The voltage drop across the known reference resistor R_{ref} yields the current I through the sensor. Using the voltage drop $V(T)$ measured across the sensor, the resistance $R(T)$ can be calculated using Ohm's law again.

The use of bridge circuits is an alternative method. These circuits rely on the principle of the Wheatstone bridge. The design consists of two parallel branches of two resistors in series, e.g. R_1 and the sensor $R(T)$ in one branch and R_2 and R_3 in the other. In the balanced bridge mode, the resistor R_3 is adjusted so that the voltage between the centers of the two branches is zero. This adjustment has to be done for each temperature T . $R(T)$ is then given by

$$R(T) = R_1 (R_3 / R_2) . \quad (8.28)$$

If this balancing is performed at only one temperature, say T_0 , the bridge output $V_1 - V_2$ differs from zero at other temperatures and is proportional to the measured temperature in the linear range of the bridge around T_0 .

When measuring the temperature sensor's resistance one has to consider that there always is a lead resistance in series. The best method to avoid this error is to measure with a four-lead arrangement, where the

Table 8.5 Types of standard platinum resistance thermometers

Type of thermometer	Temperature range	Typical resistance
Capsule thermometers, 50–60 mm long	13.8–430 K	25.5 Ω
Long-stem thermometers, 450 mm long	84–933 K	25.5 Ω
High-temperature long-stem thermometers	0.01–962 $^{\circ}\text{C}$	0.25 Ω

two voltage probe leads are fixed as close to the sensor as possible. If the voltmeter's internal resistance is close to infinity, only a negligible current flows through the voltage leads and their voltage drop can be neglected. If four leads are too expensive and less accuracy is sufficient, a two-lead arrangement can be used. For the lead wires, materials with a low temperature coefficient of electrical resistance are preferred. Furthermore, the wiring should be performed such that the temperature along these leads will not change during the measurement to keep their resistance constant. There is also a third method, which is a sort of compromise in expense and accuracy between both methods described: the three-lead concept. Here only one voltage lead is connected close to the sensor. Thus, one can measure the voltage drop across the sensor and one current lead in series and subtract the voltage drop of the other current lead measured separately.

There are further sources of errors not dealt with up to now, the thermoelectric effect at connections of different materials along the leads and the input offset voltage of the voltmeter. By reversing the direction of the measuring current those errors can be averaged out. If this is done systematically by applying alternating current for the measurement, one can remove these errors quantitatively. In addition, the resolution of the measurement can be improved by the application of lock-in techniques.

Electromagnetic interference (EMI) can be a problem in particular with alternating current (AC) measurements, if the filtering of, e.g., the power lines is not adequate in the electronics. In addition, the sensor leads should be protected from extra currents induced by changing external magnetic fields. This could be achieved using the twisted-pair design or by coaxial cable to minimize the loop area between the lead wires. The heating of the sensor by captured radio and television frequencies should be prevented by appropriate shielding of the whole measuring arrangement. Other errors are primarily due to the handling of the measurement and the methods of avoiding these are described in the previous section.

A different type of resistance thermometer is the rhodium–iron thermometer (0.5% Fe in Rh). Its merits are at the low temperature range between 0.5 K and 30 K, where it is more sensitive than the platinum thermometer, but it is still useful up to room temperature. Besides the wire-type device with a resistance in the range 20–50 Ω , thick-film versions are commercially available. For very low temperatures different resistance materials are used and described in the last section.

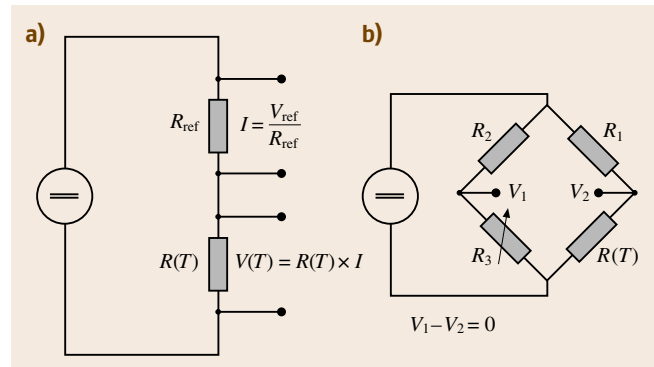


Fig. 8.11a,b Resistance measurement circuits (a) potentiometric type. (b) bridge type

There are also resistance thermometers made from semiconducting materials, known as negative temperature coefficient (NTC) or positive temperature coefficient (PTC) thermistors. The temperature dependence of the resistance of NTCs obeys an exponential law

$$R(T) = A \exp(B/T). \quad (8.29)$$

Compared to platinum resistance thermometers, NTCs show more than 100 times the sensitivity (3–6%/°C) in the temperature range from –100 °C to +150 °C as well as being smaller and faster. Two such devices are shown in Fig. 8.10. However, they are significantly less stable than PRTs and their temperature resistance relation is extremely nonlinear (8.29) and difficult to fit accurately over a wide range. They are ideal for use in control circuits and for differential temperature measurements.

8.5.4 Liquid-in-Glass Thermometers

A liquid-in-glass thermometer, the oldest type of thermometer, is based on the thermal expansion of a liquid as a function of temperature. It consists of a glass bulb connected to a capillary containing the sensing liquid – in most cases mercury or an organic liquid. Attached to it is a scale scratched on a flat glass strip along the capillary or on the capillary itself. The bulb, capillary, and scale are placed in a slightly wider glass tube as a protective container.

In spite of the image of simplicity that liquid-in-glass thermometers have obtained, they are more complicated to understand and to handle than is commonly recognized. Such a thermometer is a system with strong interference between its components. The liquid is the temperature sensor and its indicator at the same time, which means that the volume of the

bulb that contains the sensing liquid should be much larger (by a factor of at least 1000) than the volume of the indicating capillary due to the small relative expansion coefficients (mercury: $0.00016\text{ }^{\circ}\text{C}^{-1}$; ethanol: $0.00104\text{ }^{\circ}\text{C}^{-1}$). The bulb and capillary are the container for the sensing liquid but, as they have a temperature coefficient different from zero, they are an integral part of the sensor and are the origin of nonlinearities in the reading. Finally, the scale, which is needed for the user to read the indicated temperature by comparison with the liquid level in the capillary, shows a temperature-dependent length dilatation. It can easily be seen, that this complicated temperature dependence causes uncertainties, especially due to the level of immersion of the thermometer in the bath to be measured. Therefore, the depth of immersion during calibration is usually marked on the thermometer and should preferably be used again when measurements are made.

There are other sources of errors, some of which are similar to issues in other thermometers. Thermal contact through the glass walls and the heat capacity of the liquid in the bulb lead to time-constant effects and errors if there is not enough time for the system to equalize. Particular errors of liquid-in-glass thermometers result from pressure effects. High external pressure may change the bulb volume and consequently the level of the liquid in the capillary. The gas in the capillary, which should compensate for the vapor pressure of the liquid at higher temperatures to avoid interruptions of the liquid column and the formation of bubbles, will affect the indication. Linearization of the scale may not be perfect or the scale may be misplaced or misaligned. Also, parallax errors may occur due to refraction by the glass tubes if the reading is not taken exactly perpendicular to the surface.

The advantages of liquid-in-glass thermometers remain their immunity to chemical attack and electromagnetic interference and their low cost. Instruments are available with a maximum error of $0.1\text{ }^{\circ}\text{C}$ in the range from the ice point to about $50\text{ }^{\circ}\text{C}$. This error increases to $1\text{ }^{\circ}\text{C}$ or $2\text{ }^{\circ}\text{C}$ near the limits of the application range at $-80\text{ }^{\circ}\text{C}$ and $500\text{ }^{\circ}\text{C}$.

8.5.5 Thermocouples

Thermocouples nowadays have the widest field of application of all temperature sensors. They generate an electrical readout similar to resistance thermometers, but the measuring principle is quite different. In resistance thermometers a sensor's property, namely the temperature-dependent resistance of the material, is

measured at the location of the sensor. With thermocouples, their basic principle, the Seebeck effect (one of the thermoelectric effects, discovered in 1821), is a property of the whole wiring between the measuring and the reference junction. The principle circuit of a thermocouple is presented in Fig. 8.12.

The Seebeck effect means that within a conducting wire exposed to a temperature gradient a voltage difference is generated between its ends depending on their temperature difference. The simplified picture considering the electrons within the conductor as free particles explains that they tend to move to the low-temperature side because on the high-temperature side the electron gas contains more kinetic energy and expands to the other end of the wire. This expansion causes a negatively charged low-temperature end. The voltage difference generated in this way finally stops the electron motion at an equilibrium state. If the conductor, named A for distinction, is homogeneous along its length with respect to its geometrical cross section, chemical composition, and lack of defects, the Seebeck voltage depends only on the temperature difference between the ends. To measure this voltage one connects a second wire B of a different material to the temperature-measuring end of wire A and leads it, via a contact stabilized to a reference temperature, to the other input terminal of a voltmeter. Due to the fact that disturbing effects can only be excluded from the temperature measurement for homogeneous parts of the circuit, all inhomogeneous parts of the wiring, such as the measuring junction, the reference junction and other contacts within the measuring voltmeter circuit, should be strictly kept isothermal. Consequently, the number of junctions in the wiring should be reduced to an absolute minimum. In addition, current-induced voltage drops along the leads should be excluded by the use of a high-impedance voltmeter.

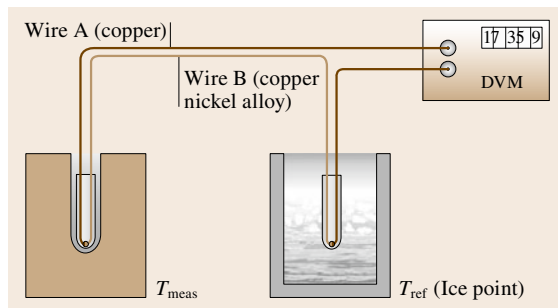


Fig. 8.12 Principle design of a thermocouple

Table 8.6 The eight internationally adopted types of thermocouples

Type	Materials	max. Temp. (°C)	Sensitivity ($\mu\text{V}/^\circ\text{C}$) at		
			20 °C	100 °C	500 °C
B	Platinum 30% rhodium/platinum 6% rhodium	1700	0	0.9	5.1
E	Nickel-chromium alloy/copper-nickel alloy	870	60.5	67.5	81.0
J	Iron/another slightly different copper-nickel alloy	760	51.5	54.4	56.0
K	Nickel-chromium alloy/nickel-aluminium alloy	1260	40.3	41.4	42.7
N	Nickel-chromium alloy/nickel-silicon alloy	1300	26.6	29.6	38.3
R	Platinum 13% rhodium/platinum	1400	5.9	7.5	10.9
S	Platinum 10% rhodium/platinum	1400	5.9	7.4	9.9
T	Copper/copper-nickel alloy	370	40.3	46.7	

For the temperature of the reference junction in most cases the ice point is used, since it can be realized simply and provides sufficient temperature stability and homogeneity. Alternatively, an isothermal reference junction at a stabilized temperature different from 0 °C can be applied, if its temperature is accurately measured and the Seebeck voltage of the reference-junction temperature read from standard tables (see below) is used for correction.

For different measuring purposes, different materials are used for thermocouples. In Table 8.6 standard commercially available devices are listed including their maximum temperature.

There are mathematical definitions for the response of each leg material or material composition to temperature changes. Manufacturers guarantee tolerance classes 1 to 3 for the agreement of their products with those formula-based tables (class 1: 0.4%; class 2: 0.75%; class 3: 1.5% within certain temperature limits).

Most errors when using thermocouples are similar to those with other thermometers concerning heat capacity, time constants, immersion and radiation. Particular errors due to material properties or construction principles are avoided by obtaining the instrument from a well-known supplier.

The type of thermocouple appropriate for a certain application should be selected first according to the temperature range specified by the manufacturer. For low-accuracy demands in industrial environment uncertainties of 1% are reached with standard devices. For higher demands, rare-metal thermocouples such as type B, R and S should be chosen because of their improved uncertainty of 0.1%.

8.5.6 Radiation Thermometers

Radiation thermometers determine the surface temperature of an object by measuring its temperature-

dependent radiation. They are noncontact thermometers and are suitable for remote sensing. This makes them a superior or even only choice, if the objects are far away, moving fast or if they are too hot or dangerous to achieve direct contact, e.g. hot furnaces, the blades of a spinning turbine or the sun and other stars in the universe.

Radiation thermometers rely on fundamental thermodynamic physical laws, e.g. Planck's law, and they can easily be modeled in great detail. A measurement at a certain temperature can be related to the measurement of the temperature of the triple point of water or another temperature fixed point by direct comparison and is, by this means, directly traceable to the ITS-90. The measured radiance has to be corrected, however, due to the quality of the sample's surface, characterized by its spectral emissivity and the stray light reflected into the detector from the surroundings.

A radiation thermometer observes only the temperature of the object's surface, which may even be considered as the sensing element of the method, and not the sample's temperature deep in the bulk. This is a disadvantage for the determination of bulk temperatures, but it turns out to be an exclusive advantage if the surface temperature is the quantity of interest.

The most common type of radiation thermometers are *spectral band radiation thermometers* (for the design principle and a photograph, see Fig. 8.13). The main components are focusing optics with a set of two apertures defining the observed part of the target surface and the field of view. Within the optical path a band filter selects the wavelengths of interest. Finally a radiation detector converts the collected light flux into an electrical current which is amplified and indicated on the display.

Although everything radiates, only for certain geometric configurations can the radiance be calculated ab initio, so that they can be used for calibration

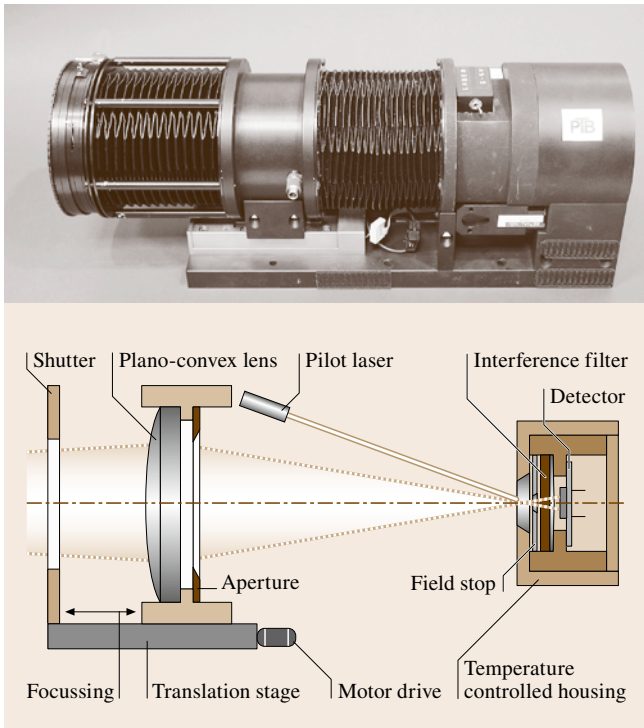


Fig. 8.13 Principle design and photograph of a radiation thermometer

of electromagnetic radiation detectors, especially for radiation thermometers. Those calculable sources are blackbodies, which radiate according to Planck's law (Table 8.3), and electron storage rings, which deliver synchrotron radiation at higher energies following the Schwinger formula. Because the wavelengths used in radiation thermometry mainly coincide with the regime of Planck's law, blackbodies operating at the fixed point temperatures of ITS-90 are the natural devices for temperature calibrations.

The spectral radiance L_{meas} measured by a spectral-band radiation thermometer is given by (8.30) for sample temperatures higher than 200 °C

$$L_{\text{meas}} = \varepsilon(\lambda)L_{\text{bb}}(\lambda, T_s) . \quad (8.30)$$

This is the spectral radiance of a blackbody $L_{\text{bb}}(\lambda, T_s)$ at the sample temperature T_s corrected by the emissivity $\varepsilon(\lambda)$ of the sample surface. Applying Wien's radiation law

$$L_{\text{bb}}(\lambda, T) = (c_1/\lambda^5) \exp(-c_2/\lambda T) \quad (8.31)$$

as a valid approximation for the blackbody radiation at the wavelengths shorter than λ_{max} commonly used in radiation thermometry the true temperature of the sample

surface T_s can be estimated from the measured radiance temperature T_{meas} according to

$$1/T_s = 1/T_{\text{meas}} + (\lambda/c_2) \ln[\varepsilon(\lambda)] . \quad (8.32)$$

T_{meas} is the temperature derived from the spectral radiance L_{meas} by Wien's law. If the sample temperature is below 200 °C, the detector's own radiance must be compensated.

Calibration of a radiation thermometer is performed by comparison with a source of known radiance. This can be done by measuring the emission of a tungsten strip lamp or, as mentioned, of a blackbody at a certain temperature known from a calibrated, e.g., platinum thermometer or preferably of a temperature fixed point blackbody. If only an uncalibrated light source is available, one may compare the thermometer under test with a reference radiation thermometer when they both observe the radiance of a light source with stable emission.

There are several other types of radiation thermometers, such as the disappearing-filament thermometer, the ratio thermometer, and the multispectral radiation thermometer, which are not described here [8.53]. Based on a different physical law, the Stefan–Boltzmann law (Table 8.3), *total radiation thermometers* measure a signal proportional to T^4 . They often collect the radiation of the target incident on a hemisphere. Therefore, the distance to the object has to be quite short. Further thermometers use optical fibres to conduct the light to their detector. In some cases the other end of the fibre is covered by a sort of small blackbody, the temperature of which is changed by thermal contact with the target. Its temperature is then determined from its spectral radiance as described above.

8.5.7 Cryogenic Temperature Sensors

Temperatures near absolute zero seem to be of interest only to specialists in ultra-low temperature physics. However, a lot of important material properties, which are of increasing interest for technical applications, change with decreasing temperature, superconductivity and superfluidity being the most prominent examples. There are further macroscopic quantum phenomena, such as the Josephson effect, that are essential for the highest sensitivity magnetic-field sensors (superconducting quantum interference devices or **SQUIDS**) or the quantum Hall effect as basis for the international standard for the resistance unit ohm. As a consequence the **CIPM** recently adopted an extension of the international temperature scale from the lower end of ITS-90 near 1 K down to below 1 mK, the Provisional

Low Temperature Scale of 2000 (PLTS-2000). It is given by the definition of the relation between pressure and temperature along the melting curve of ^3He . This solid–liquid phase transition can be described by the Clausius–Clapeyron equation in principle. But, since the molar volumes and entropies of the solid and the liquid phase are not known with sufficient accuracy, a polynomial with internationally agreed coefficients is used [8.54].

Before cooling the sample and the thermometer ^3He is filled from the gas-handling system into the measuring cell (Fig. 8.14) via a capillary. The pressure in the cell at low temperatures varies within the range 2.9–4.0 MPa and is determined capacitively. One of the cell walls is shaped as a membrane and responds to pressure changes by changing the distance between the moving plate glued to it and the fixed counter plate (center plate). The center plate and the reference plate represent a stable reference capacitor at low temperatures. The resolution of the capacitance bridge indicates distance changes between the plates of the order of only fractions of an atomic diameter, which yields a temperature resolution of some μK at 1 mK up to some 100 μK at 1 K.

The temperature values related to the ^3He pressure were determined by primary thermometry based on a noise thermometer with a resistive SQUID as the temperature-sensitive element (Table 8.3). It was cross-checked by several magnetic thermometers described later on. Nuclear orientation thermometry is a further primary method at millikelvin temperatures. It relies on the temperature-dependent ordering of the magnetic moments of radioactive nuclei indicated by the anisotropy of their emitted γ radiation. The prob-

lem of this thermometer is its narrow temperature range depending on the activation of the sensor. There is a danger of overheating at low temperatures with high activities, and of insufficient sensitivity at high temperatures with low activities.

For practical temperature measurements, different resistance thermometers are used. The principle of these measurements is described in Sect. 8.5.3. The RhFe resistors mentioned there are suitable for temperatures down to 1 K. Below that, germanium and carbon resistors have been the favourites for a long time. These are semiconducting materials with a temperature-dependent resistance caused by the carriers being frozen with falling temperature. Over recent years further types of resistors have been developed by different manufacturers (carbon-glass resistors, carbon-ceramic resistors, ruthenium-oxide sensors).

Magnetic thermometers show a temperature-dependent magnetization. If the magnetic moments of either the electronic shell of the thermometer's atoms or of their nuclei are exposed to a homogeneous and static magnetic field, they order to a certain extent depending on the lattice or nuclear temperature according to the Boltzmann distribution. The resulting macroscopic magnetization is inversely proportional to temperature (Curie or Curie–Weiss law) and can be probed by susceptibility or magnetic resonance measurements. The first case is realized with the electronic moment of, e.g., cerium magnesium nitrate (CMN), which is a useful thermometric substance and workhorse from above 1 K to about 10 mK. For the measurement of temperatures from about 30 mK down to the μK region pulsed NMR with pure platinum (Pt-NMR) is the standard method. For both thermometers a precise calibration at

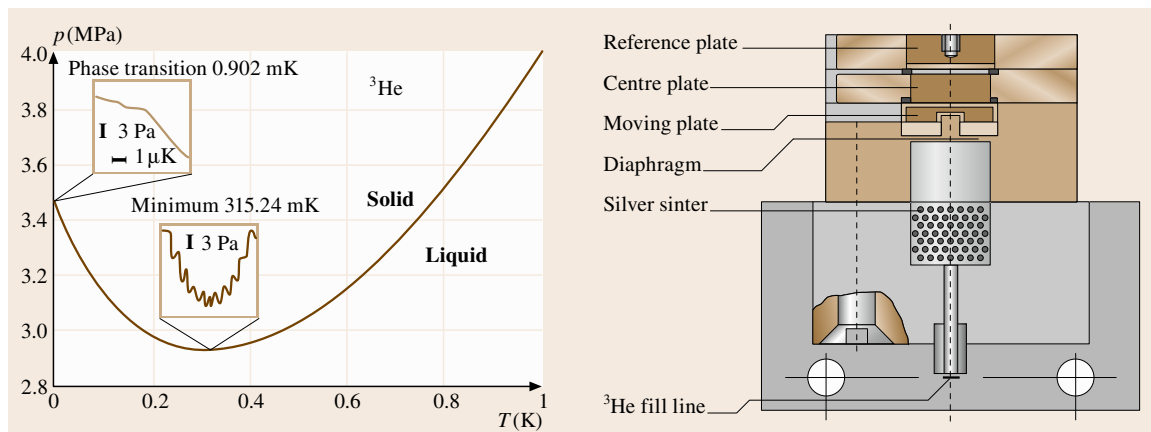


Fig. 8.14 The melting pressure of ^3He and the capacitive pressure sensor to measure it

their high-temperature end is essential, where the signal amplitude unfortunately is low. In addition, both the construction of the device and the purity of the sensing substance should produce a strictly linear behavior,

because only extrapolation to their respective lowest temperatures is possible. A detailed description how to generate very low temperatures and how to measure them is given in [8.55] and [8.56].

References

- 8.1 K. Maglič, A. Cezairliyan, V. E. Peletsky (Eds.): *Compendium of Thermophysical Property Measurement Methods*, Vol. 1: *Survey of Measurement Techniques* (1984), Vol. 2: *Recommended Measurement Techniques and Practices* (1992) (Plenum, New York 1984/1992)
- 8.2 M.J. Assael, M. Dix, K. Gialou, L. Vozár, W.A. Wakeham: Application of the transient hot-wire technique to the measurement of the thermal conductivity of solids, *Int. J. Thermophys.* **23**, 615–633 (2002)
- 8.3 S.E. Gustafsson, E. Karawacki, M.N. Khan: Transient hot-strip method for simultaneous measuring thermal conductivity, thermal diffusivity of solids, liquids, *J. Appl. Phys.* **12**, 1411–1421 (1979)
- 8.4 U. Hammerschmidt, W. Sabuga: Transient hot strip (THS) method: Uncertainty assessment, *Int. J. Thermophys.* **21**, 217–248 (2000)
- 8.5 H. Watanabe: Further examination of the transient hot-wire method for the simultaneous measurement of thermal conductivity, thermal diffusivity, *Metrologia* **39**, 65–81 (2002)
- 8.6 W.J. Parker, J.R. Jenkins, P.C. Butler, B.L. Abbott: Flash method of determining heat capacity, thermal conductivity, *J. Appl. Phys.* **32**, 1679–1684 (1961)
- 8.7 M. Ogawa, K. Mukai, T. Fukui, T. Baba: The development of a thermal diffusivity reference material using alumina, *Meas. Sci. Technol.* **12**, 2058–2063 (2001)
- 8.8 B. Hay, J.-R. Filtz, J. Hameury, L. Rongione: Uncertainty of thermal diffusivity measurements by laser flash method, *Tech. Dig. 15th Symp. Thermophys. Prop.*, Boulder (2003)
- 8.9 L. Vozár, W. Hohenauer: Uncertainty of the thermal diffusivity measurement using the laser flash method, *Tech. Dig. 15th Symp. Thermophys. Prop.*, Boulder (2003)
- 8.10 D.P. Almond, P.M. Patel: *Photothermal Science and Techniques* (Kluwer, Dordrecht 1996)
- 8.11 D.L. Martin: "Tray" type calorimeter for the 15–300 K temperature range: Copper as a specific heat standard in this range, *Rev. Sci. Instrum.* **58**, 639–646 (1987)
- 8.12 D.A. Ditmars, S. Ishihara, S.S. Chang, G. Bernstein, E.D. West: Enthalpy, heat-capacity standard reference material: Synthetic sapphire (α -Al₂O₃) from 10 to 2250 K, *J. Res. Natl. Bur. Stand.* **87**, 159–163 (1982)
- 8.13 S. Rudtsch: Uncertainty of heat capacity measurement with differential scanning calorimeters, *Thermochim. Acta* **382**, 17–25 (2002)
- 8.14 F. Righini, G.C. Bussolino: Pulse calorimetry at high temperatures, *Thermochim. Acta* **347**, 93–102 (2000)
- 8.15 S.M. Sarge, G.W.H. Höhne, H.K. Cammenga, W. Eysel, E. Gmelin: Temperature, heat, heat flow rate calibration of scanning calorimeters in the cooling mode, *Thermochim. Acta* **361**, 1–20 (2000)
- 8.16 D.G. Archer, D.R. Kirklin: NIST, standards for calorimetry, *Thermochim. Acta* **347**, 21–30 (2000)
- 8.17 S. Stølen, F. Grønvold: Critical assessment of the enthalpy of fusion of metals used as enthalpy standards at moderate, high temperatures, *Thermochim. Acta* **327**, 1–32 (1999)
- 8.18 R. Sabbah, X.-W. An, J.S. Chickos, M.V. Roux, L.A. Torres: Reference materials for calorimetry, differential thermal analysis, *Thermochim. Acta* **331**, 93–204 (1999)
- 8.19 J.P. McCullough, D.W. Scott (Eds.): *Calorimetry of Nonreacting Systems*, Vol. 1 (Butterworth, London 1968)
- 8.20 B. LeNeindre, B. Vodar (Eds.): *Experimental Thermodynamics of Nonreacting Fluids*, Vol. II (Butterworth, London 1975)
- 8.21 M. Braun, R. Kohlhaas, O. Vollmer: Zur Hochtemperatur-Kalorimetrie von Metallen, *Z. Angew. Phys.* **25**, 365–372 (1968)
- 8.22 G.W.H. Höhne, W. Hemminger, H.-J. Flammersheim: *Differential Scanning Calorimetry*, 2nd edn. (Springer, Berlin, Heidelberg 2003)
- 8.23 G.W.H. Höhne, K. Blankenhorn: High pressure DSC investigations on *n*-alkanes, *n*-alkane mixtures and polyethylene, *Thermochim. Acta* **238**, 351–370 (1994)
- 8.24 G.R. Tryson, A.R. Shultz: A calorimetric study of acrylate photopolymerization, *J. Polym. Sci.: Polym. Phys. Ed.* **17**, 2059–2075 (1979)
- 8.25 P.L. Privalov, V.V. Plotnikov: Three generations of scanning microcalorimeters for liquids, *Thermochim. Acta* **139**, 257–277 (1989)
- 8.26 V.V. Plotnikov, J.M. Brandts, L.N. Liu, J.F. Brandts: A new ultrasensitive scanning calorimeter, *Anal. Biochem.* **250**, 237–244 (1997)
- 8.27 S.M. Sarge, W. Hemminger, E. Gmelin, G.W.H. Höhne, H.K. Cammenga, W. Eysel: Metrologically based procedures for the temperature, heat, heat flow rate calibration of DSC, *J. Therm. Anal.* **49**, 1125–1134 (1997)

- 8.28 D.A. Ditmars, T.B. Douglas: Measurement of the relative enthalpy of pure α -Al₂O₃ (NBS heat capacity, enthalpy standard reference material No. 720) from 273 to 1173 K, J. Res. Natl. Bur. Stand. **75**, 401–420 (1971)
- 8.29 K.N. Marsh, P.A.G. O'Hare: *Solution Calorimetry*, Vol. IV (Blackwell Science, Oxford 1994)
- 8.30 R. Anderson, J.M. Prausnitz: High precision, semimicro, hydrostatic calorimeter for heats of mixing of liquids, Rev. Sci. Instrum. **32**, 1224–1229 (1961)
- 8.31 P. Picker, C. Jolicoeur, J.E. Desnoyers: Differential isothermal microcalorimeter: Heats of mixing of aqueous NaCl, KCl solutions, Rev. Sci. Instrum. **39**, 676–680 (1968)
- 8.32 J.J. Christensen, D.L. Hansen, R.M. Izatt, D.J. Eatough, R.M. Hart: Isothermal, isobaric, elevated temperature, high-pressure, flow calorimeter, Rev. Sci. Instrum. **52**, 1226–1231 (1981)
- 8.33 F.D. Rossini (Ed.): *Measurement of Heats of Reaction*, Vol. 1 (Interscience, New York 1956)
- 8.34 H.A. Skinner (Ed.): *Experimental Thermochemistry*, Vol. II (Interscience, New York 1962)
- 8.35 J.D. Cox, G. Pilcher: *Thermochemistry of Organic and Organometallic Compounds* (Academic Press, London 1970)
- 8.36 S. Sunner, M. Månsson: *Combustion Calorimetry*, Vol. 1 (Pergamon, Oxford 1979)
- 8.37 D.R. Kirklin: Enthalpy of combustion of acetylsalicylic acid, J. Chem. Thermodyn. **32**, 701–709 (2000)
- 8.38 P. Ulbig, D. Hoburg: Determination of the calorific value of natural gas by different methods, Thermochim. Acta **382**, 27–35 (2002)
- 8.39 A. Dale, C. Lythall, J. Aucott, C. Sayer: High precision calorimetry to determine the enthalpy of combustion of methane, Thermochim. Acta **382**, 47–54 (2002)
- 8.40 R.E. Taylor, C.Y. Ho (Ed.): *Thermal Expansion of Solids* (ASM International, Materials Park 1998)
- 8.41 W. Gorski: Interferometrische Bestimmung der thermischen Ausdehnung von synthetischem Korund und seine Verwendung als Referenzmaterial, PTB-Bericht, W–59 (1994)
- 8.42 J.D.J. James, J.A. Spittle, S.G.R. Brown, R.W. Evans: A review of measurement techniques for the thermal expansion coefficient of metals, alloys at elevated temperatures, Meas. Sci. Technol. **12**, R1–R15 (2001)
- 8.43 T.A. Hahn: Thermal expansion of copper from 20 to 800 K – standard reference material 736, J. Appl. Phys. **41**, 5096–5101 (1970)
- 8.44 A.P. Miiller, A. Cezairliyan: Thermal expansion of molybdenum in the range 1500–2800 K by a transient interferometric technique, Int. J. Thermophys. **6**, 695–704 (1985)
- 8.45 H. Watanabe, N. Yamada, M. Okaji: Development of a laser interferometric dilatometer for measurements of thermal expansion of solids in the temperature range 300 to 1300 K, Int. J. Thermophys. **26**, 543–554 (2002)
- 8.46 H. Watanabe, N. Yamada, M. Okaji: Laser interferometric dilatometer applicable to temperature range from 1300 to 2000 K, Int. J. Thermophys. **22**, 1185–1200 (2001)
- 8.47 M. Okaji, N. Yamada, H. Moriyama: Ultra-precise thermal expansion measurements of ceramic, steel gauge blocks with an interferometric dilatometer, Metrologia **37**, 165–171 (2000)
- 8.48 N. Yamada, R. Abe, M. Okaji: A calibration method for measuring thermal expansion with a push-rod dilatometer, Meas. Sci. Technol. **12**, 2121–2129 (2001)
- 8.49 M. Maciejewski, C.A. Müller, R. Tschan, W.-D. Emmerich, A. Baiker: Novel pulse thermal analysis method, its potential for investigating gas–solid reaction, Thermochim. Acta **295**, 167–182 (1997)
- 8.50 M. Brown (Ed.): *Handbook of Thermal Analysis and Calorimetry*, Vol. 1 (Elsevier, Amsterdam 1998)
- 8.51 Bureau International des Poids et Mésures (BIPM): *Supplementary Information for the International Temperature Scale of 1900* (BIPM, Sèvres 1997) pp. 92–822
- 8.52 T.J. Quinn: *Temperature*, 2nd edn. (Academic Press, London 1990)
- 8.53 J.V. Nicholas, D.R. White: *Traceable Temperatures* (Wiley, Chichester 2001)
- 8.54 Comité International des Poids et Mésures (CIPM): *Report on the 89th meeting* (BIPM, Sèvres October 2000)
- 8.55 F. Pobell: *Matter and Methods at Low Temperatures* (Springer, Berlin, Heidelberg 1992)
- 8.56 R.C. Richardson, E.N. Smith (Eds.): *Experimental Techniques in Condensed Matter Physics at Low Temperatures* (Addison-Wesley, Reading 1988)

Electrical Properties

Electronic materials – conductors, insulators, semiconductors – play an important role in today's technology. They constitute *electrical and electronic devices*, such as radio, television, telephone, electric light, electromotors, computers, etc. From a materials science point of view, the electrical properties of materials characterize two basic processes: electrical energy conduction (and dissipation) and electrical energy storage.

- Electrical conductivity describes the ability of a material to transport charge through the process of conduction, normalized by geometry. Electrical dissipation comes as the result of charge transport or conduction. Dissipation or energy loss results from the conversion of electrical energy to thermal energy (Joule heating) through momentum transfer during collisions as the charges move.
- Electrical storage is the result of charge storing energy. This process is dielectric polarization, normalized by geometry to be the material property called dielectric permittivity. As polarization occurs and causes charges to move, the charge motion is also dissipative.

In this chapter, the main methods to characterize the electrical properties of materials are compiled. Sections 9.2 to 9.5 describe the measuring methods under the following headings

- Electrical conductivity of metallic materials
- Electrolytical conductivity
- Semiconductors
- Dielectrics.

As an introductory overview, in Sect. 9.1 the basic categories of electrical materials are outlined in adopting the classification and terminology of the chapter *Electronic Properties of Materials of Understanding Materials Science* by Hummel [9.1].

9.1	Electrical Materials	486
9.1.1	Conductivity and Resistivity of Metals	486
9.1.2	Superconductivity	487
9.1.3	Semiconductors	488
9.1.4	Conduction in Polymers	490
9.1.5	Ionic Conductors	490
9.1.6	Dielectricity	491
9.1.7	Ferroelectricity and Piezoelectricity	492
9.2	Electrical Conductivity of Metallic Materials	493
9.2.1	Scale of Electrical Conductivity; Reference Materials	493
9.2.2	Principal Methods	494
9.2.3	DC Conductivity, Calibration of Reference Materials	496
9.2.4	AC Conductivity, Calibration of Reference Materials	496
9.2.5	Superconductivity	497
9.3	Electrolytic Conductivity	498
9.3.1	Scale of Conductivity	498
9.3.2	Basic Principles	499
9.3.3	The Measurement of the Electrolytic Conductivity	501
9.4	Semiconductors	507
9.4.1	Conductivity Measurements	507
9.4.2	Mobility Measurements	510
9.4.3	Dopant and Carrier Concentration Measurements	513
9.4.4	I - V Breakdown Mechanisms	518
9.4.5	Deep Level Characterization and Minority Carrier Lifetime	519
9.4.6	Contact Resistances of Metal-Semiconductor Contacts ...	523
9.5	Measurement of Dielectric Materials Properties	526
9.5.1	Dielectric Permittivity	527
9.5.2	Measurement of Permittivity	529
9.5.3	Measurement of Permittivity Using Microwave Network Analysis .	532
9.5.4	Uncertainty Considerations	536
9.5.5	Conclusion	537
	References	537

9.1 Electrical Materials

One of the principal characteristics of materials is their ability (or lack of ability) to conduct electrical current. According to their conductivity σ they are divided into conductors, semiconductors, and insulators (dielectrics). The inverse of the conductivity is called resistivity ρ that is $\rho = 1/\sigma$. The resistance R of a piece of conducting material is proportional to its resistivity and to its length L and is inversely proportional to its cross-sectional area A : $R = L\rho/A$. To measure the electrical resistance, a direct current is applied to a slab of the material. The current I through the sample (in ampere), as well as the voltage drop V on two potential probes (in volt) is recorded as depicted in Fig. 9.1.

The resistance (in ohm) can then be calculated by making use of Ohm's law $V = RI$. Another form of Ohm's law $j = \sigma E$ links current density $j = I/A$, that is, the current per unit area (A/cm^2), with the conductivity σ ($\Omega^{-1}cm^{-1}$ or siemens per centimeter) and the electric field strength $E = V/L$ (V/cm).

The conductivity σ of different materials at room temperature spans more than 25 orders of magnitude as depicted in Fig. 9.2. Moreover, if one takes the conductivity of superconductors, measured at low temperatures, into consideration, this span extends to 40 orders of magnitude (using an estimated conductivity for superconductors of about $10^{20} \Omega^{-1}cm^{-1}$). This is the largest known variation in a physical property.

9.1.1 Conductivity and Resistivity of Metals

For metallic materials it is postulated that they contain *free electrons* which are accelerated under the influence of an electric field maintained, for example, by a battery. The drifting electrons can be considered, in a preliminary, classical description, to occasionally collide (that is, electrostatically interact) with certain lattice atoms, thus losing some of their energy. This constitutes the electrical resistance.

Semiconductors or insulators which have only a small number of free electrons (or often none at all) display only very small conductivities. The small number of electrons results from the strong binding forces between electrons and atoms that are common for insulators and semiconductors. Conversely, metals which contain a large number of free electrons have a large conductivity. Further, the conductivity is large when the average time between two collisions τ is large. Obviously, the number of collisions decreases (i. e.,

τ increases) with decreasing temperature and decreasing number of imperfections. The simple *free electron model* describes the electrical behavior of many materials reasonably well.

Electron Band Model

Electrons of isolated atoms (for example in a gas) can be considered to orbit at various distances about their nuclei. These orbits constitute different energies. Specifically, the larger the radius of an orbit, the larger the excitation energy of the electron. This fact is often represented in a somewhat different fashion by stating that the electrons are distributed on different energy levels, as schematically shown in Fig. 9.3.

These distinct energy levels, which are characteristic for isolated atoms, widen into energy bands when atoms approach each other and eventually form a solid as depicted on the left-hand side of Fig. 9.3. Quantum mechanics postulates that the electrons can only reside within these bands, but not in the areas outside of them. The allowed energy bands may be noticeably separated from each other. In other cases, depending on the material and the energy, they may partially or completely overlap. In short, each material has its distinct electron energy band structure. Characteristic band structures for the main classes of materials are schematically depicted in Fig. 9.4.

The band structures shown in Fig. 9.4 are somewhat simplified. Specifically, band schemes actually possess a fine structure, that is, the individual energy states

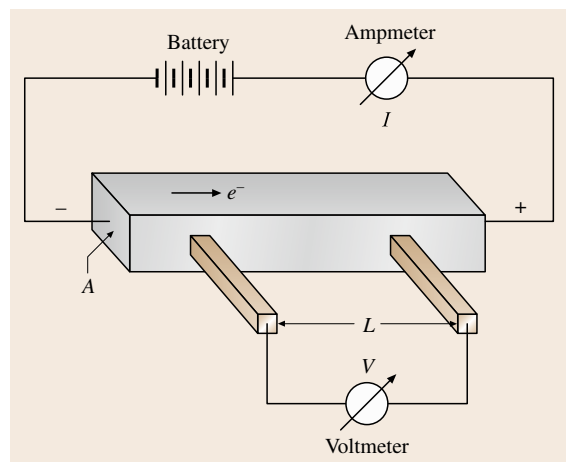


Fig. 9.1 Principle of the measurement of the resistance of a conductor

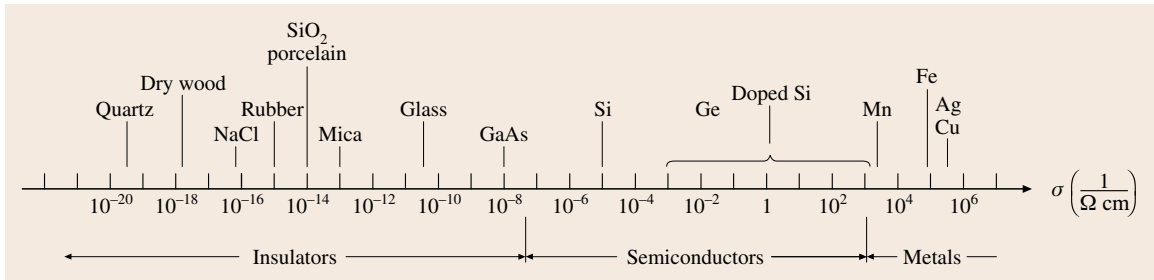


Fig. 9.2 Conductivity scale of materials

(i. e., the possibilities for electron occupation) are often denser in the center of a band (Fig. 9.5).

Some of the bands are occupied by electrons while others remain partially or completely unfilled. The degree to which an electron band is filled by electrons is indicated in Fig. 9.4 by shading. The highest level of electron filling within a band is called the Fermi energy E_F . Some materials, such as insulators and semiconductors, have completely filled electron bands. (They differ, however, in their distance to the next higher band.) Metals, on the other hand, are characterized by partially filled electron bands. The amount of filling depends on the material, that is, on the electron concentration and the amount of band overlap.

According to quantum theory, first only those materials that possess partially filled electron bands are capable of conducting an electric current. Electrons can then be lifted slightly above the Fermi energy into an allowed and unfilled energy state. This permits them to be accelerated by an electric field, thus producing a current. Second, only those electrons that are close to the Fermi energy participate in the electric conduction. Third, the number of electrons near the Fermi energy depends on the density of available electron states (Fig. 9.5). The conductivity in quantum mechanical terms yields the following equation: $\sigma = 1/3e^2v_F^2 \tau N(E_F)$, where v_F is the velocity of the electrons at the Fermi energy (called the Fermi velocity) and $\tau N(E_F)$ is the density of filled electron states (called the population density) at the Fermi energy. Monovalent metals (such as copper, silver, and gold) have partially filled bands, as shown in Fig. 9.4. Their electron population density near the Fermi energy is high which results in a large conductivity. Bivalent metals, on the other hand, are distinguished by overlapping upper bands and by a small electron concentration near the bottom of the valence band. As a consequence, the electron population near the Fermi energy is small which leads to a comparatively low conductivity. For alloys, the residual resistivity increases with increasing amount of

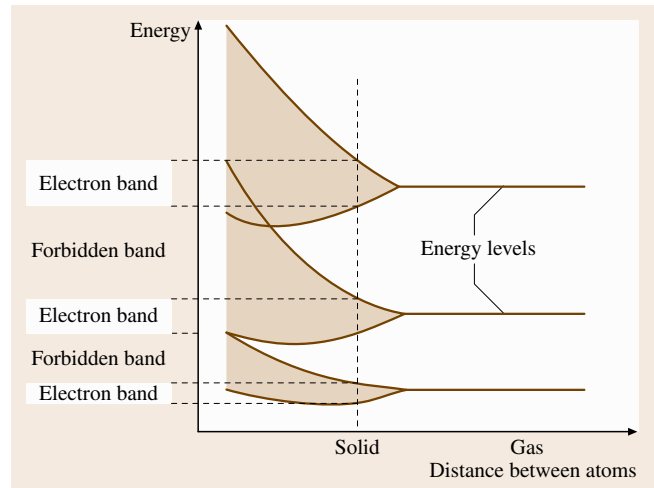


Fig. 9.3 Schematic representation of electron energy levels in materials

solute content. Finally, insulators have completely filled (and completely empty) electron bands which results in a virtually zero population density as shown in Fig. 9.4. Thus, the conductivity in insulators is virtually zero.

9.1.2 Superconductivity

The resistivity in superconductors becomes immeasurably small or virtually zero below a critical temperature T_c . About 27 elements, numerous alloys, ceramic materials (containing copper oxide), and organic compounds (based, e.g., on selenium or sulfur) have been found to possess this property (Table 9.1).

It is estimated that the conductivity of superconductors below T_c is about $10^{20} \Omega^{-1}\text{cm}^{-1}$. The transition temperatures where superconductivity starts range from 0.01 K (for tungsten) up to about 125 K (for ceramic superconductors). Of particular interest are materials with T_c above 77 K, that is, the boiling point of liquid nitro-

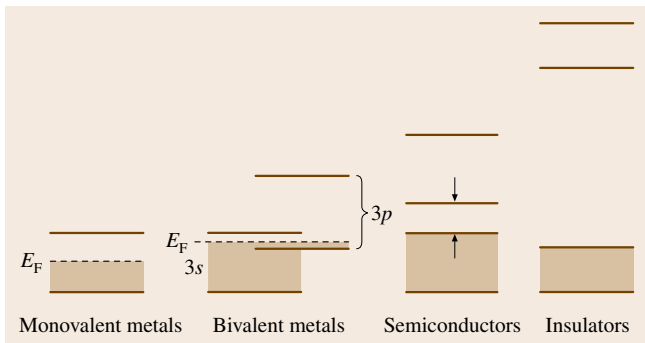


Fig. 9.4 Electronic energy-band representation

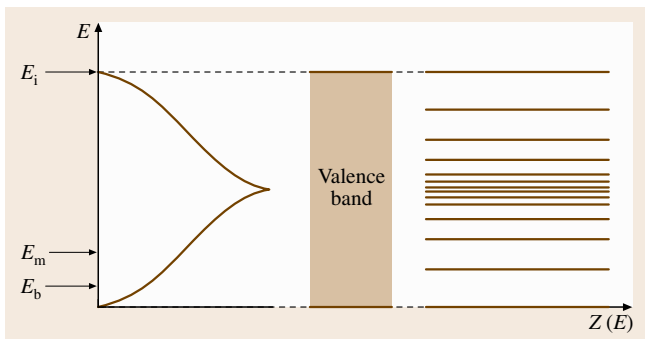


Fig. 9.5 Schematic representation of the density of electrons within an electron energy band

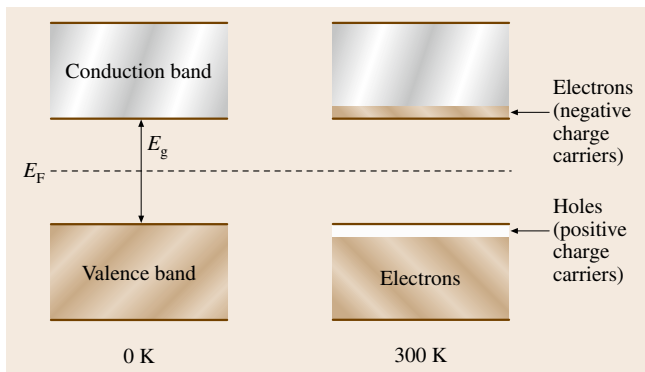


Fig. 9.6 Simplified band diagrams for an intrinsic semiconductor

gen which is more readily available than other coolants. Among the so-called high- T_c superconductors are the 1-2-3 compounds such as $\text{YBa}_2\text{Cu}_3\text{O}_{7-x}$, where molar ratios of rare earth to alkaline earth to copper relate as 1 : 2 : 3. Their transition temperatures range from 40 to 134 K. Ceramic superconductors have an orthorhombic, layered, perovskite crystal structure which contains

Table 9.1 Critical temperatures of some superconducting materials (R = Gd, Dy, Ho, Er, Tm, Yb, Lu)

Materials	T_c (K)
Tungsten	0.01
Mercury	4.15
Sulfur-based organic superconductor	8
Nb_3Sn and Nb-Ti	9
V_3Si	17.1
Nb_3Ge	23.2
La-Ba-Cu-O	40
$\text{YBa}_2\text{Cu}_3\text{O}_{7-x}$	≈ 92
$\text{RBa}_2\text{Cu}_3\text{O}_{7-x}$	≈ 92
$\text{Bi}_2\text{Sr}_2\text{Ca}_2\text{Cu}_3\text{O}_{10+\delta}$	113
$\text{Tl}_2\text{CaBa}_2\text{Cu}_2\text{O}_{10+\delta}$	125
$\text{HgBa}_2\text{Ca}_2\text{Cu}_3\text{O}_{8+\delta}$	134

two-dimensional sheets and periodic oxygen vacancies. (The superconductivity exists only parallel to these layers, that is, it is anisotropic.) The first superconducting material was found by Kammerlingh Onnes in 1911 in mercury which has a T_c of 4.15 K. Methods to measure superconductivity are described in Sect. 9.2.5.

9.1.3 Semiconductors

The electrical properties of semiconductors are commonly explained by making use of the electron band structure model which is the result of quantum-mechanical considerations. In simple terms, the electrons are depicted to reside in certain allowed energy regions.

Figure 9.6 depicts two electron bands, the lower of which, at 0 K, is completely filled with valence electrons. This band is appropriately called the valence band. It is separated by a small gap (about 1.1 eV for Si) from the conduction band which contains no electrons at 0 K. Further, quantum mechanics stipulates that electrons essentially are not allowed to reside in the gap between these bands (called the forbidden band). Since the filled valence band possesses no allowed empty energy states in which the electrons can be thermally excited (and then accelerated in an electric field), and since the conduction band contains no electrons at all, silicon is an insulator at 0 K. The situation changes decisively once the temperature is raised. In this case, some electrons may be thermally excited across the band gap and thus populate the conduction band (Fig. 9.6). The number of these electrons is extremely small for statistical reasons. Specifically, about one out of every 10^{13} atoms contributes an electron at room temperature. Nev-

ertheless, this number is large enough to cause some conduction. The number of electrons in the conduction band N_e increases exponentially with temperature T but also depends, of course, on the size of the gap energy. The conductivity depends naturally on the number of these electrons but also on their mobility. The latter is defined to be the velocity v per unit electric field E that is $\mu = v/E$. All taken, the conductivity is $\sigma = N_e \mu e$, where e is the charge of an electron. The mobility of electrons is substantially impaired by interactions with impurity atoms and other lattice imperfections (as well as with vibrating lattice atoms). It is for this reason that silicon has to be extremely pure and free of grain boundaries which requires sophisticated and expensive manufacturing processes called zone refining or Czochralski crucible pulling.

The conductivity for semiconductors increases with rising temperature. This is in marked contrast to metals and alloys, for which the conductivity decreases with temperature. The thermal excitation of some electrons across the band gap has another important consequence. The electrons that have left the valence band leave behind some empty spaces which allow additional conduction to take place in the valence band. The empty spaces are called defect electrons or electron holes. These holes may be considered to be positively charged carriers similarly as electrons are defined to be negatively charged carriers. In essence, at elevated temperatures, the thermal energy causes some electrons to be excited from the valence band into the conduction band. They provide there some conduction. The electron holes which have been left behind in the valence band cause a hole current which is directed in the opposite direction compared to the electron current. The total conductivity, therefore, is a sum of both contributions $\sigma = N_e \mu_e e + N_h \mu_h e$, where the subscripts e and h refer to electrons and holes, respectively. The process is called intrinsic conduction and the material involved is termed an intrinsic semiconductor since no foreign elements are involved. The Fermi energy of intrinsic semiconductors can be considered to be the average of the electron and the hole Fermi energies and is therefore situated near the center of the gap as depicted in Fig. 9.6.

The number of electrons in the conduction band can be considerably increased by adding, for example, to silicon small amounts of group-V elements called donor atoms. Dopants such as phosphorous or arsenic are commonly utilized which are added in amounts of, for example, 0.0001%. These dopants replace some regular lattice atoms in a substitutional manner (Fig. 9.7). Since phosphorous has five valence electrons, that is,

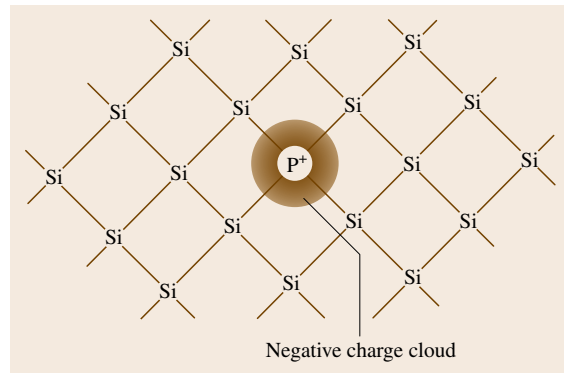


Fig. 9.7 Two-dimensional representation of a silicon lattice (covalent bonds) with a phosphorus atom substituting a regular lattice atom

one more than silicon, the extra electron called the donor electron is only loosely bound. The binding energy of phosphorous donor electrons in a silicon matrix is about 0.045 eV. Thus, the donor electrons can be dissociated from their nuclei by only a slight increase in thermal energy. At room temperature all donor electrons have already been excited into the conduction band.

Near room temperature, only the majority carriers need to be considered. For example, at room temperature, all donor electrons in an n-type semiconductor have been excited from the donor levels into the conduction band. At higher temperatures, however, intrinsic effects may considerably contribute to the conduction. Compounds made of group-III and group-V elements, such as gallium arsenide, have similar semiconducting properties as the group-IV materials silicon or germanium. GaAs is of some technical interest because of its above-mentioned wider band gap and because of its larger electron mobility which aids in high-speed applications. Further, the ionization energies of donor and acceptor impurities in GaAs are one order of magnitude smaller than in silicon which ensures complete electron (and hole) transfer from the donor (acceptor) levels into the conduction (valence) bands even at relatively low temperatures. However, GaAs is about ten times more expensive than Si and its heat conduction is smaller. Other compound semiconductors include II–VI combinations such as ZnO, ZnS, ZnSe, or CdTe, and IV–VI materials such as PbS, PbSe, or PbTe. Silicon carbide, a IV–IV compound, has a band gap of 3 eV and can thus be used up to 700 °C before intrinsic effects set in. The most important application of compound semiconductors is, however, for optoelectronic purposes (e.g. for light-emitting diodes and lasers).

9.1.4 Conduction in Polymers

Materials that are electrical (and thermal) insulators are of great technical importance and are, therefore, used in large quantities in the electronics industry. Most polymeric materials are insulating and have been used for this purpose for decades. It came, therefore, as a surprise when it was discovered that some polymers and organic substances may have electrical properties which resemble those of conventional semiconductors, metals, or even superconductors. Historically, transoidal polyacetylene (Fig. 9.8) has been used as a conducting polymer.

It represents what is called a conjugated organic polymer, that is, it has alternating single and double bonds between the carbon atoms. It is obtained as a silvery, flexible, and lightweight film which has a conductivity comparable to that of silicon. Its conductivity increases with increasing temperature similarly as in semiconductors. The conductivity of trans-polyacetylene can be made to increase by up to seven orders of magnitude by doping it with arsenic pentafluoride, iodine, or bromine, which yields a p-type semiconductor. Thus, σ approaches the lower end of the conductivity of metals as shown in Fig. 9.9.

Among other dopants are *n*-dodecyl sulfonate (soap). However, the stability of this material is very poor; it deteriorates in hours or days. This very drawback which it shares with many other conducting polymers nevertheless can be profitably utilized in special devices such as remote gas sensors, biosensors, and other remotely readable indicators which detect changes in humidity, radiation dosage, mechanical abuse, or chemical release. Other conducting polymers include polypyrrole and polyaniline. The latter has a reasonably good conductivity and a high environmental stability. It has been used for electronic devices such as field-effect transistors, electrochromic displays, as well as for rechargeable batteries.

In order to better understand the electronic properties of polymers by means of the electron theory

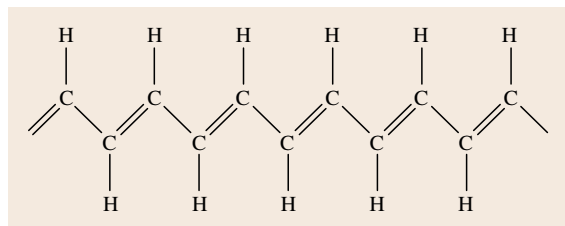


Fig. 9.8 Transoidal isomer of polyacetylene

and the band structure concept, one needs to know the degree of order or the degree of periodicity of the atoms because only ordered and strongly interacting atoms or molecules lead to distinct and wide electron bands. It has been observed that the degree of order in polymers depends on the regularity of the molecular structure. One of the electrons in the double bond of a conjugated polymer can be considered to be only loosely bound to the neighboring carbon atoms. Thus, this electron can be easily disassociated from its carbon atom by a relatively small energy which may be provided by thermal energy. The delocalized electrons behave like free electrons and may be accelerated as usual in an electric field. It should be noted in closing that the interpretation of conducting polymers is still in flux and future research needs to clarify certain points.

9.1.5 Ionic Conductors

Electrical conduction in ionically bonded materials, such as the alkali-halides, is extremely small. The reason for this is that the atoms in these chemical com-

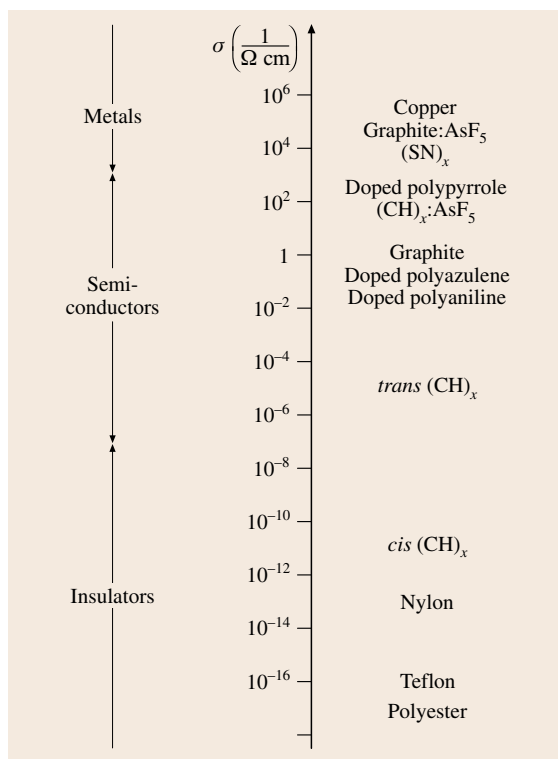


Fig. 9.9 Conductivity of various polymeric materials

pounds strive to assume the noble gas configuration for maximal stability and thus transfer electrons between each other to form positively charged cations and negatively charged anions. The binding forces between the ions are electrostatic in nature, that is, they are very strong. Essentially no free electrons are therefore formed. As a consequence, the room temperature conductivity in ionic crystals is about 22 orders of magnitude smaller than that of typical metallic conductors (Fig. 9.2). The wide band gap in insulators allows only extremely few electrons to become excited from the valence into the conduction band (Fig. 9.4 right).

The main contribution to the electrical conduction in ionic crystals (as little as it may be) is due to ionic conduction. Ionic conduction is caused by the movement of some negatively (or positively) charged ions which *hop from lattice site to lattice site* under the influence of an electric field. The ionic conductivity $\sigma_{\text{ion}} = N_{\text{ion}}e\mu_{\text{ion}}$ is the product of three quantities. In the present case, N_{ion} is the number of ions per unit volume which can change their position under the influence of an electric field whereas μ_{ion} is the mobility of these ions. In order for ions to move through a crystalline solid they must have sufficient energy to pass over an energy barrier. Further, an equivalent lattice site next to a given ion must be empty in order for an ion to be able to change its position. Thus, N_{ion} depends on the vacancy concentration in the crystal (i. e., on the number of Schottky defects).

In short, the theory of ionic conduction contains essential elements of diffusion theory. Diffusion theory links the mobility of the ions with the diffusion coefficient D through the Einstein relation $\mu_{\text{ion}} = De/(k_{\text{B}}T)$.

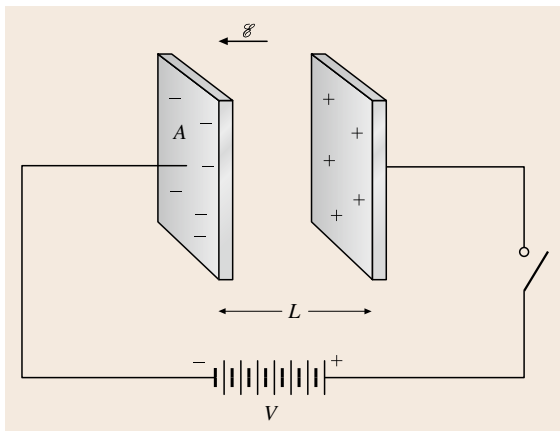


Fig. 9.10 Principle of storing electric energy in a dielectric capacitor

The diffusion coefficient varies with temperature by an Arrhenius equation $D = D_0 \exp[-Q/(k_{\text{B}}T)]$, where Q is the activation energy for the process under consideration and D_0 is a preexponential factor which depends on the vibrational frequency of the atoms and some structural parameters. Combining the equations yields $\sigma_{\text{ion}} = [N_{\text{ion}}e^2 D_0/(k_{\text{B}}T)] \exp[Q/(k_{\text{B}}T)]$. This equation is shortened by combining the preexponential constants into σ_0 : $\sigma_{\text{ion}} = \sigma_0 \exp[Q/(k_{\text{B}}T)]$.

In summary, the ionic conduction increases exponentially with increasing temperature (as in semiconductors). Further, σ_{ion} depends on a few other parameters such as the number of ions that can change their position, the vacancy concentration, as well as on an activation energy.

9.1.6 Dielectricity

Dielectric materials, that is, insulators, possess a number of important electrical properties which make them useful in the electronics industry.

When a voltage is momentarily applied to two parallel metal plates which are separated by a distance L as shown in Fig. 9.10, the resulting electric charge essentially remains on these plates even after the voltage has been removed (at least as long as the air is dry).

This ability to store an electric charge is called the capacitance C which is defined to be the charge q per applied voltage V that is $C = q/V$, where C is given in coulombs per volt or farad. The capacitance is higher, the larger the area A of the plates and the smaller the dis-

Table 9.2 DC dielectric constants of some materials

Barium titanate	4000	Ferroelectric
Water	81.1	Dielectric
Acetone	20	
Silicon	11.8	
GaAs	10.9	
Marble	8.5	
Soda-lime-glass	6.9	
Porcelain	6.0	
Epoxy	4.0	
Fused silica	4.0	
Nylon 6.6	4.0	
PVC	3.5	
Ice	3.0	
Amber	2.8	
Polyethylene	2.3	
Paraffin	2.0	
Air	1.000576	

tance L between them. Further, the capacitance depends on the material that may have been inserted between the plates. The experimental observations lead to $C = \epsilon\epsilon_0 (A/L)$, where $\epsilon = C/C_{\text{vac}}$ determines the magnitude of the added storage capability. It is called the (unitless) dielectric constant (or occasionally the relative permittivity ϵ_r). ϵ_0 is a universal constant having the value of 8.85×10^{-12} F/m (farad per meter) or A s/(V m) and is known by the name permittivity of empty space (or of vacuum).

Some values for the dielectric constant are given in Table 9.2. The dielectric constant of empty space is set to be 1 whereas ϵ of air and many other gases is nearly 1.

The capacitance increases when a piece of a dielectric material is inserted between two conductors. Under the influence of an external electric field, the negatively charged electron cloud of an atom becomes displaced with respect to its positively charged core. As a result, a dipole is created which has an electric dipole moment $p = qx$, where x is the separation between the positive and the negative charge. (The dipole moment is generally a vector pointing from the negative to the positive charge.) The process of dipole formation (or alignment of already existing dipoles) under the influence of an external electric field that has an electric field strength E , is called polarization. Dipole formation of all involved atoms within a dielectric material causes a charge redistribution so that the surface which is nearest to the positive capacitor plate is negatively charged. As a consequence, electric field lines within a dielectric are created which are opposite in direction to the external field lines. Effectively, the electric field lines within a dielectric material are weakened due to polarization. The electric field strength $E = V/L = E_{\text{vac}}/\epsilon$ is reduced by inserting a dielectric between two capacitor plates. Within a dielectric material the electric field strength E is replaced by the dielectric displacement D (also called the surface charge density), that is, $D = \epsilon\epsilon_0 E = q/A$. The dielectric displacement is the superposition of two terms: $D = \epsilon_0 E + P$, where P is called the dielectric polarization, that is, the induced electric dipole moment per unit volume. The units for D and P are C/m². The polarization is responsible for the increase in charge density (q/A) above that for vacuum.

The mechanism just described is known as electronic polarization. It occurs in all dielectric materials that are subjected to an electric field. In ionic materials, such as the alkali halides, an additional process may occur which is called ionic polarization. In short, cations and anions are somewhat displaced from their equilib-

rium positions under the influence of an external field and thus give rise to a net dipole moment. Finally, many materials already possess permanent dipoles which can be aligned in an external electric field. Among them are water, oils, organic liquids, waxes, amorphous polymers, polyvinylchloride, and certain ceramics such as barium titanate (BaTiO₃). This mechanism is termed orientation polarization or molecular polarization. All three polarization processes are additive if applicable.

Most capacitors are used in electric circuits involving alternating currents. This requires the dipoles to reorient quickly under a rapidly changing electric field. Not all polarization mechanisms respond equally quick to an alternating electric field. For example, many molecules are relatively sluggish in reorientation. Thus, molecular polarization breaks down already at relatively low frequencies. In contrast, electronic polarization responds quite rapidly to an alternating electric field even at frequencies up to 10^{16} Hz. At certain frequencies a substantial amount of the excitation energy is absorbed and transferred into heat. This process is called dielectric loss. It is imperative to know the frequency for dielectric losses for a given material so that the device is not operated in this range.

9.1.7 Ferroelectricity and Piezoelectricity

Ferroelectricity is the electric analogue to ferromagnetism (Chap. 10). Ferroelectric materials, such as barium titanate, exhibit spontaneous polarization without the presence of an external electric field. Their dielectric constants are orders of magnitude larger than those of dielectrics (Table 9.2). Thus, they are quite suitable for the manufacturing of small-sized, highly efficient capacitors. Most of all, however, ferroelectric materials retain their state of polarization even after an external electric field has been removed. Specifically, if a ferroelectric is exposed to a strong electric field E , its permanent dipoles become increasingly aligned with the external field direction until eventually all dipoles are parallel to E , and saturation of the polarization P_S has been achieved as depicted in Fig. 9.11.

Once the external field has been withdrawn a remanent polarization P_r remains which can only be removed by inverting the electric field until a coercive field E_c has been reached. By further increasing the reverse electric field, parallel orientation of the dipoles in the opposite direction is achieved. Finally, when reversing the field once more, a complete hysteresis loop is obtained as depicted in Fig. 9.11. Therefore, ferroelectrics can be utilized for memory devices in computers, etc.

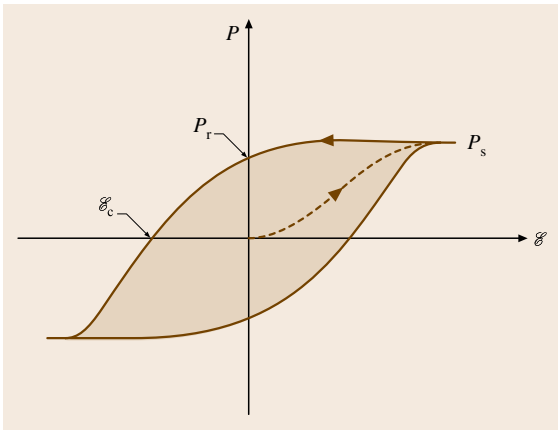


Fig. 9.11 Schematic representation of a hysteresis loop for a ferroelectric material in an electric field

The area within a hysteresis loop is proportional to the energy per unit volume that is dissipated once a full field cycle has been completed.

A critical temperature, called the Curie temperature, exists above which the ferroelectric effects are destroyed and the material becomes dielectric. Typical Curie temperatures range from -200°C for strontium titanate to at least 640°C for NaNbO_3 . By heating BaTiO_3 above its Curie temperature (120°C), the tetragonal unit cell transforms to a cubic cell whereby the ions now assume symmetric positions. Thus, no

spontaneous alignment of dipoles remains and BaTiO_3 becomes dielectric.

If pressure is applied to a ferroelectric material such as BaTiO_3 , a change in the polarization may occur which results in a small voltage across the sample. Specifically, the slight change dimensions causes a variation in bond lengths between cations and anions. This effect is called piezoelectricity. It is found in a number of materials such as quartz (however, much weaker than in BaTiO_3), in ZnO , and in complicated ceramic compounds such as PbZrTiO_6 . Piezoelectricity is utilized in devices that are designed to convert mechanical strain into electricity. Those devices are called transducers. Applications include strain gages, microphones, sonar detectors, and phonograph pickups, to mention a few.

The inverse mechanism, in which an electric field produces a change in dimensions in a ferroelectric material, is called electrostriction. An earphone utilizes such a device. Probably the most important application, however, is the quartz crystal resonator which is used in electronic devices as a frequency selective element. Specifically, a periodic strain is exerted to a quartz crystal by an alternating electric field which excites this crystal to vibrations. These vibrations are monitored in turn by piezoelectricity. If the applied frequency coincides with the natural resonance frequency of the molecules, then amplification occurs. In this way, very distinct frequencies are produced which are utilized for clocks or radio frequency signals.

9.2 Electrical Conductivity of Metallic Materials

9.2.1 Scale of Electrical Conductivity; Reference Materials

Precise measurements of the electrical conductivity date back to the end of the 19th century. With the development of the electrical industry it became important to check the quality of the copper used in electrical machines. The Physikalisch-Technische Reichsanstalt in Berlin, Germany, for instance, was strongly supported by Werner von Siemens, head of the Siemens company. Nowadays, copper is still an important part where conductivity measurements are applied. Furthermore, the aircraft manufacturing industry uses conductivity measurements for the quality assurance of aluminum alloys. Recently, it became also important for the coin manufacturing industry. With the introduction of the Euro, these coins are produced all over Europe, but have to

meet strong criteria in conductivity, on the one hand to protect the consumers from fraud, on the other hand for the acceptance of coins in vending machines.

Conductivity is usually measured in the unit MS/m , or $\mu\Omega\text{ m}$. In practice, the values are commonly given in so-called % IACS, which stands for *Percent International Annealed Copper Standard*. This standard is a hypothetical copper bar of 1 m in length and 1 mm^2 in area having a resistance of $1/58\ \Omega$.

Typical values for some metals and alloys are listed in Table 9.3. Generally there are three main areas for conductivity measurements, conductors (copper) at 100% IACS, aluminum alloys at 50% IACS and alloys for coins at 10% IACS. Instruments for the measurement of conductivity operate either with direct current methods (DC) or alternating current methods (AC). The DC methods usually is a voltage-current method,

Table 9.3 Typical values for the conductivity of metals and alloys

Metal/alloy	Conductivity at 20 °C	
	(MS/m)	(% IACS)
Copper (soft)	59.9	103.3
Copper (annealed)	58	100.0
Aluminum (soft)	35.7	61.6
E-AlMgSi (Aldrey)	30.0	51.7
Brass (CuZn40)	15.0	25.9
Bronze (CuSn6)	9.1	15.7
Titanium	2.4	4.1

whereas the AC methods make use of the eddy current principle. Details are described in Sect. 9.2.2 and for the calibration of reference standards in Sects. 9.2.3 and 9.2.4.

For precise measurements of conductivity reference materials are needed. Commonly these reference materials are pure metals and alloys of known composition. Due to the size of the material samples, these materials must have a high homogeneity. Another prerequisite for precise measurement of reference standards for conductivity is the precise knowledge of the dimensions as well as the geometry of the material under test. Typical shapes for a reference material are bars or blocks and the dimensions range from 30 to 80 mm in width, 200–800 mm in length, and 3–10 mm in thickness for bars and 80 mm × 80 mm × 10 mm for blocks. Opposite sides of the blocks and bars have to be parallel and the surface should have mirror finishing. Furthermore, an important issue is the temperature. The resistivity of pure metals strongly depends on temperature. Typical temperature coefficients are of the order of $1 \times 10^{-3} \text{ K}^{-1}$.

For AC measurements of the electrical conductivity based on the eddy current method it is important that the magnetic susceptibility of the material is less than 1.001. Magnetic impurities in the metal influence the conductivity as well as the accuracy of the measurement.

The following section describes the principal methods for the determination of the electrical conductivity of metals.

9.2.2 Principal Methods

In principal, the measurement methods for electrical conductivity can be divided in to two sections, direct current (DC) and alternating current (AC) measurement methods. Applications are found in several fields of

material testing as there are air craft industry, coin manufacturing, and pure metal manufacturing (e.g. copper, aluminum). A more qualitative aspect of conductivity measurements is the nondestructive material testing. Cracks and voids in the material lead to a local change in conductivity which can be detected by conductivity probes. In contrast to the determination of conductivity, in this case the metals may also be magnetic.

The determination of conductivity with DC is made by measuring the resistance R and the dimensions of the conductor (length l , width w , and thickness d , Fig. 9.12). From these measurements, the conductivity σ is calculated (9.1)

$$\sigma = \frac{l}{Rwd} . \quad (9.1)$$

The resistance R is usually determined by a voltage–current method. A current I of known value is fed into the sample and the voltage U is measured via point or blade contacts. Since the resistance of metals is typically very low, even for currents of 10 A the voltage drop is of the order of some μV up to several mV. This means high sensitive nanovoltmeters have to be used. The resistance is then calculated according to Ohm's law

$$R = U/I . \quad (9.2)$$

This method can only be applied to materials of particular shape like rods or bars. For more complex

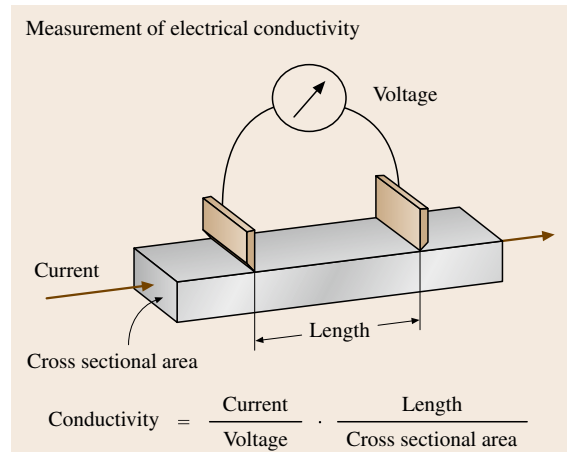


Fig. 9.12 Principle of conductivity measurements. The sample under test is of bar shape with known cross sectional area. A current is passed through the sample in the direction of its longitudinal axis. The voltage drop is measured with two contacts, either point or blade type, at a known distance

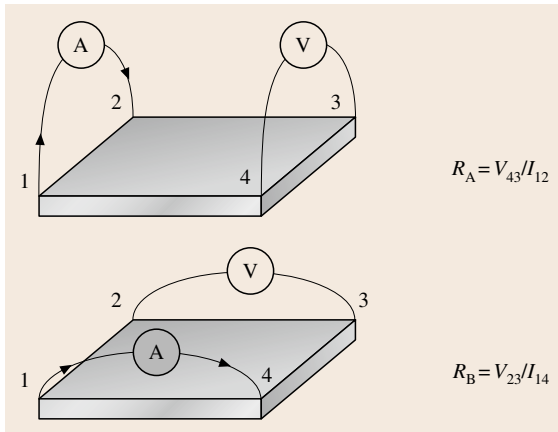


Fig. 9.13 Principle of the van der Pauw measurement. The van der Pauw method requires two measurements. First the current is passed into contacts 1 and 2 and the voltage is measured at contacts 4 and 3, then the current is passed into contacts 2 and 3 and the voltage is measured at contacts 1 and 4. These two voltage–current measurements together with the measurement of the thickness of the device under test allow for the determination of the conductivity

$$R_A = V_{43}/I_{12}$$

$$R_B = V_{23}/I_{14}$$

geometries, like, for instance, the surface of an aeroplane, other methods have been developed.

A local determination of the DC conductivity can be obtained by the so-called four-point probe. Four-point electrodes are pressed on the material and a special sequence of voltage–current measurements is made. The basic principle of this method is the van der Pauw method (Fig. 9.13) [9.3, 4]. The van der Pauw method consists of two measurements of resistance, R_A and R_B

$$R_A = V_{43}/I_{12}, \quad R_B = V_{23}/I_{14}. \quad (9.3)$$

From these two measurements and the knowledge of the thickness of the sample under test, the conductivity can be determined by the solution of the following equation

$$e^{-\pi R_A/R_S} + e^{-\pi R_B/R_S} = 1, \quad (9.4)$$

where R_S is the resistance to be determined. If R_A and R_B are similar, (9.3) can be simplified and solved for the conductivity σ as follows

$$\frac{1}{\sigma} = \frac{\pi d}{\ln 2} \frac{(R_A + R_B)}{2}, \quad (9.5)$$

where d is the thickness of the sample. The precision of such a van der Pauw measurement depends on the flatness and parallelism of the surfaces of the sample and on the fact that the contacts are point contacts. An error ε

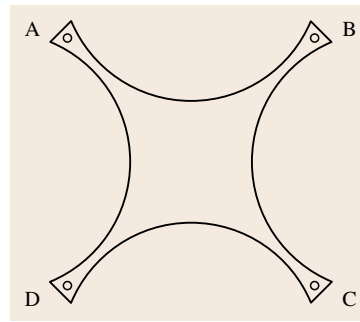


Fig. 9.14 Cross-conductivity standard (after [9.2]). Similar as in Fig. 9.13, the current is either fed into pairs of contact A–B and A–D, and the voltages are measured at contact pairs D–C and B–C

caused by nonideal point contacts can be estimated by

$$\varepsilon = 2.05\lambda^4, \quad (9.6)$$

where, for a sample with square geometry, λ is the ratio of the width of the contact and the length of one side of the square. Such small contact areas lead to the problem of local heating since the current density in these contacts becomes significantly high. On the other hand a reduction of the current will lead to loss of sensitivity. A different approach to this problem is the so-called cross-conductivity standard. If one considers a perfect square and transforms this via conform transformation into a star shaped sample (Fig. 9.14) [9.2]. The conductivity σ is also calculated by (9.4).

DC measurements require a good contact between material and electrodes. In practice, the surface of a metal is covered by a thin oxide layer. For a correct DC measurement this layer has to be penetrated. This problem can be overcome by the AC measurement method. The basic principle of AC measurement methods makes use of eddy currents. Alternating magnetic fields induce currents in conducting materials. If the alternating magnetic fields are induced by a pair of coils, the second coil in turn picks up the magnetic field produced by the eddy current. A probe of such a construction acts as a mutual inductor. The magnetic field, induced in the second coil is a function of the magnitude of the eddy current which in turn depends on the conductivity of the material.

Making conductivity measurements with this method, the skin effect has to be taken into consideration. The skin effect limits the penetration of the eddy currents into the material. The higher the conductivity of the material the smaller is the penetration depth. The penetration depth δ is approximately

$$\delta = \sqrt{\frac{2}{\omega\sigma\mu_0}}, \quad (9.7)$$

where ω is the angular frequency ($2\pi f$) and μ_0 the vacuum permittivity.

9.2.3 DC Conductivity, Calibration of Reference Materials

The DC conductivity is given by a simple model

$$\sigma = ne\mu, \quad (9.8)$$

where n is the number of electrons, e is the charge of an electron and μ is its mobility. The number of electrons is nearly the same for all metals, e is constant, but the mobility depends on the lattice parameters of the material.

The basic principles and requirements for the measurement of DC conductivity have been laid out in DIN/IEC 768, *Measurement of Metallic Conductivity* [9.5]. The standard to be measured must fulfil certain criteria regarding its geometry. The length of the sample has to be at least 0.3 m. A DC current is fed in to the end sections and the voltage drop is measured with either sharp point contacts or blade contacts. The distance between these contacts and the current contacts has to be at least 1.5 times the circumference ($2(t + w)$) of the device under test to allow for uniform current distribution between the contact electrodes.

The latest practical approach of this method is shown in Fig. 9.15. The current is fed into the sample via the clamps at the ends and the potential is measured at the knife edge blade contacts. The blades are mounted on a precisely machined stainless steel bar. This method has the advantage that the distance of the blade contacts has only to be determined once and is the same for a whole set of measurements. Also the parallelism of the contacts is assured by this method.

A principal drawback of the DC method is its sensitivity to oxide layers on certain materials (e.g. aluminum). Since a precise knowledge of the thickness of the sample under test is essential, it is practically im-

possible to gain full knowledge of the thickness of an aluminum sample without knowing the thickness of the oxide layer. A consequence of this problem is the possibility of differences in conductivity values for the same material determined with the DC method compared to that determined with the AC method. This problem was subject of an intensive study [9.6, 7]. Although the relative uncertainties for conductivity calibrations are of the order of 0.5% for the AC method and of the order of 0.1% for the DC method, differences between the values could be up to 1%.

9.2.4 AC Conductivity, Calibration of Reference Materials

In principle, one could think of measuring the AC conductivity in the same way as the DC conductivity. But the problem of current displacement at AC current is much more pronounced. Depending on the conductivity and the measuring frequency, the current flows in a thin layer at the surface of the material. The thickness of this layer can be estimated by (9.5). So it is not possible to exactly determine the AC conductivity by a simple current–voltage measurement since one dimension, the thickness, is not known without knowledge of the conductivity. On the other hand, most commercial conductivity meters measure with an AC method. To meet the demand of AC conductivity calibration, a suitable method has been developed at the National Physics Laboratory Teddington, UK (NPL) [9.8].

Alternating electromagnetic fields can penetrate metallic materials and so generate an eddy current in the material. This effect is used in a way that the material under test is induced into a nearly ideal inductor. Due to the eddy currents, the inductor is no longer ideal but shows magnetic loss. This loss can be measured as the resistive part of the inductor and from that resistance the conductivity can be calculated according to (9.9). From two-dimensional theory this resistance R_m can be deduced which is not a real resistance but a process of energy loss modelled by a resistance

$$\sigma = \frac{2\omega(b+d)^2\mu_0 N^4}{R_m^2 l^2}. \quad (9.9)$$

The measurement system used is the so-called Heydweiller bridge (Fig. 9.16). The bridge consists of the mutual inductor M with N windings, two fixed resistors R_1 and R_4 , and the balancing circuit R_{21} , R_{22} , C , and R_v . The mutual inductor is of toroidal shape. It can be opened and a specimen of annular shape of width $b = 80$ mm, thickness $d = 10$ mm, and central circum-

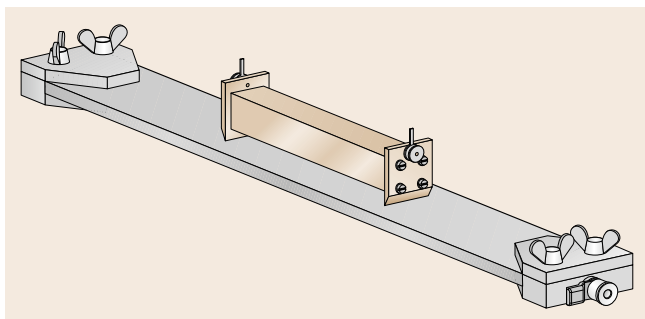


Fig. 9.15 Measurement setup for the determination of the DC conductivity of bar-shaped samples. The potential contacts are of knife edge type

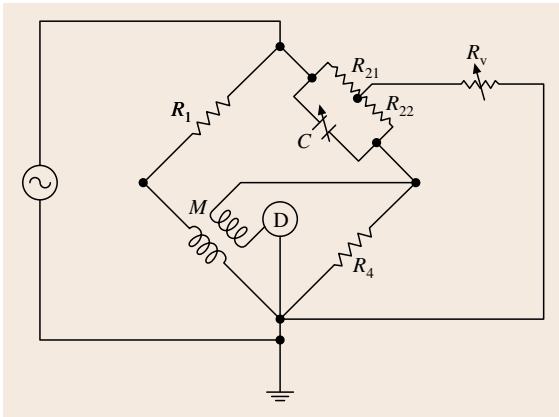


Fig. 9.16 Heydweiller bridge for measuring NPL primary conductivity standards at frequencies from 10 to 100 kHz. The standard under test is brought into the mutual inductor M . From the change in R_v , necessary to balance the bridge, the conductivity can be calculated (R_v = variable resistor, C = variable capacitor, $R_{21} = R_{22} = 10\text{ k}\Omega$, $R_1 = 1\text{ k}\Omega$, $R_4 = 10\ \Omega$, M = inductor)

ference $l = 320\ \pi\ \text{mm}$, can be inserted. From the change in resistance R_v necessary to balance the bridge, R_m is determined and the conductivity can be calculated.

Since the annulus is of considerable size (0.4 m in diameter), the conductivity value of a selected segment that represents the average value of conductivity of the specimen is transferred to a block shaped sample of size 80 mm \times 80 mm \times 10 mm. The system used for this transfer is the same bridge system, the mutual inductor is a coil of approximately 80 mm in diameter which can be placed on the annulus as well as on the block. These blocks then can be used as reference material.

9.2.5 Superconductivity

Some metals, alloys, compounds and ceramic materials lose their resistance, if they are cooled down to very low temperatures of some K [9.9]. The physical principle is that in these materials electrons of opposite spin and of opposite momentum form pairs. As these pairs have no spin, they can occupy the same lowest energy state. This state allows dissipation free transport of electrical energy since the pairs are not scattered by the surrounding lattice that means an electrical current is carried without measurable resistivity [9.10]. The transition into this state occurs at a critical temperature T_c and varies with the type of material. For so-called low-temperature superconductors (LTS) the critical temperature is in the range up to 30 K, for high-temperature superconduc-

tors (HTS) T_c can be even higher than 100 K. LTS are typically pure metals or alloys, like e.g. lead (Pb), niobium (Nb), tin (Sn), or Nb_3Sn . The HTS are perovskite crystals of mixed copper oxides. This class of material has been discovered in the mid 1980, first by *Bednorz* and *Müller* [9.11]. From that time on, various compositions of copper oxides with rare-earth metals have been investigated [9.12]. The first reproducible composite was barium-lanthanum-copper-oxide (BaLaCuO) which showed a critical temperature of 40 K. For tellurium-barium-calcium-copper-oxide (TBCCO) a T_c of as high as 125 K was observed [9.13].

Superconductors of either type are used for several purposes, as there are

- the transport of electrical energy,
- the generation of high magnetic fields,
- sensitive measurements of small magnetic fields with superconducting quantum interference devices (SQUID) [9.14],
- recently quantum computing, based on QUBITs,
- arrays of superconducting contacts are used as voltage standards.

The first two are DC or low-frequency applications, the other applications make use of the so-called Josephson effect (at radio/microwave frequencies) which is described in detail in [9.15, 16].

Superconductors need low temperatures so applications using LTS are typically operated at the temperature of liquid helium (4.2 K), whereas HTS can be operated at the temperature of liquid nitrogen (77 K). The latter is becoming more and more of interest for industrial applications, since on the one hand it is possible to produce mechanically stable ceramic components (e.g. of YBaCuO), and on the other hand the effort for cooling and thermal isolation is less than that for LTC.

The use of superconductors for the generation of high magnetic fields requires to pay attention to their behavior in magnetic fields. This behavior can be di-

Table 9.4 Some typical values for superconductors

Metal/alloy/material	T_c (K)	B_c (T) at 4.2 K
Tin (Sn)	3.7	0.03
Lead (Pb)	7.3	0.08
Niobium (Nb)	9.2	0.2
Nb_3Sn	19	24
Nb_3Ge	23	38
YBaCuO	93	55
BSCCO	110	29

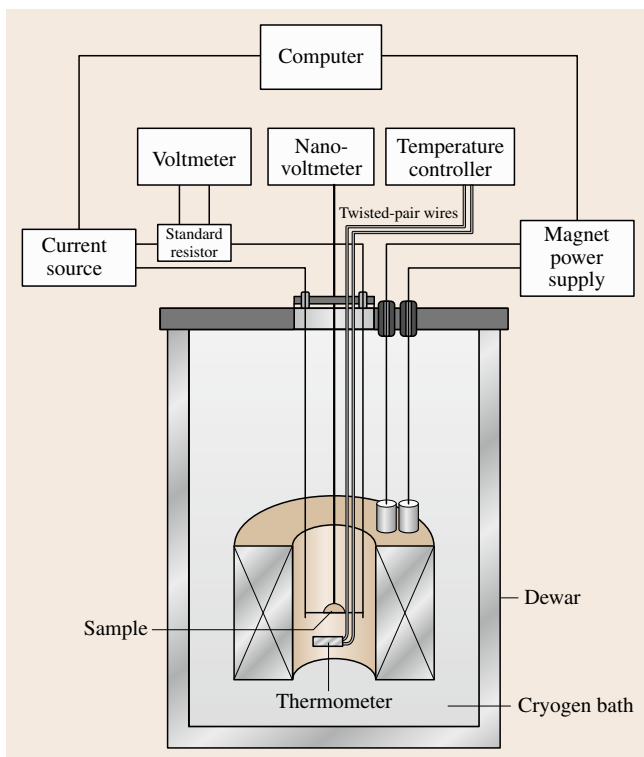


Fig. 9.17 Measurement setup for the characterization of superconductors (after [9.18]). The resistance of the superconductor is determined by a voltage–current measurement. The apparatus allows for the variation of temperature and magnetic field to determine T_c and B_c

vided into so-called type-I and type-II superconductors. If a superconductor of type-I is kept at a temperature $T < T_c$ and the magnetic induction B is increased there is a critical magnetic induction B_c , where the superconductor becomes normal conducting. Below this B_c ,

9.3 Electrolytic Conductivity

The electrolytic conductivity is a measure of the amount of charge transport of ions in solution. While in metals the current is carried by electrons in metals, in electrolyte solutions, molten salts and ionic solids the charge carriers are ions. The extent to which current flows through an electrolyte solution depends on the concentration, charge and mobility of the dissolved ions present.

The SI derived unit of conductivity is siemens per meter (S/m). The symbol for electrolytic conductivity

screening currents on the surface of the superconductor compensate the magnetic field inside. This means that a type-I superconductor behaves like a perfect diamagnet, $\mu_r = 0$ [9.17]. Since this effect is also observed for a volume surrounded by a superconductor, these type-I superconductors allow perfect shields for magnetic fields at low temperatures.

Superconductors of type-II show a different behavior. With increasing magnetic induction B , the transition from the superconducting state to the normal conducting state occurs continuously with two critical inductions B_{c1} and B_{c2} . Below B_{c1} , a type-II superconductor behaves as one of type-I. At the critical induction B_{c1} , the magnetic field starts to penetrate the conductor creating flux vortices. At the critical induction B_{c2} no more vortices can be created and the magnetic field can completely penetrate the superconductor and it becomes normal conducting. The critical induction B_{c2} is typically much higher than B_{c1} or the B_c of a type-I superconductor. Some properties (T_c and B_c) of typical superconductors are listed in Table 9.4.

The measurement of these parameters are carried out in an apparatus allowing for control of both, temperature and magnetic field by measuring the voltage as a function of current through the superconductor (Fig. 9.17) [9.18].

Similar to the determination of the DC conductivity the voltage drop over a short length of a superconducting strand is measured, passing a DC current I . At constant temperature T and magnetic induction B the current I is varied to determine the critical current density of the material under test. Other possible measurements are the determination of T_c as a function of B or of B_c as a function of T with I kept constant. With these measurements it is possible to characterise a superconductor. Standardized methods for the determination of parameters are described in [9.19].

is κ in chemistry, σ or γ in solid-state physics. Very low conductivity values are often expressed in terms of resistivity ($\rho = 1/\kappa$) in the unit ohm meter (Ωm).

9.3.1 Scale of Conductivity

Electrolytic conductivity is a nonspecific sum parameter reflecting the concentration and mobility of all ions dissolved in a solution. Since the mobility of the ions is temperature dependent, the conductivity also depends on

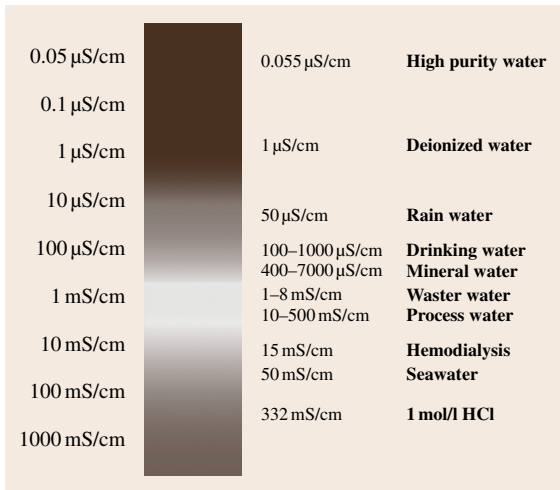


Fig. 9.18 The scale of conductivity with examples of various aqueous solutions at 25 °C

temperature. Sometimes the term *specific conductance* is used to describe conductivity. Since electrolytic conductivity is nonspecific this expression is misleading and should be avoided. Figure 9.18 shows the electrolytic conductivity of different aqueous media at 25 °C.

The measurement of conductivity ranges from quality control of high purified water to waste water treatment monitoring and process control in chemical industry. Electrolytic conductivity can also be used to determine the relative ionic strength of solutions and as a detection technique in ion chromatography.

Electrolytic conductivity is in fact the most widely used parameter to monitor the overall ionic purity of water and it is considered the major parameter defining and ranking grades of purified water, e.g., in pharmaceutical, semiconductor and power plant industries. Electrolytic conductivity measurements are used for the evaluation of water quality under regulations and standard practices, e.g., drinking water and water used in food industry. Important parameters in specific areas as, for instance, the measurement of the amount of total dissolved solids (TDS) and the salinity of sea water are also related to conductivity measurements. Furthermore, electrolytic conductivity is also measured in nonaqueous or mixed solutions like fuels and paints and varnishes, respectively for quality control purposes.

9.3.2 Basic Principles

In a volume, in which a homogeneous electric field is present, the conductivity κ is given as the ratio of the

current density j , generated by the field, and by the electric field strength E

$$\kappa E = j. \quad (9.10)$$

Figure 9.19 schematically shows such a volume with respect to an electrolyte solution. Two parallel electrodes are immersed into the solution and connected to a voltage source. The applied voltage generates a homogeneous electric field in the volume. Positive ions move constantly towards the cathode, while the negative ions move towards the anode.

Ion Mobility

For a volume of a constant cross sectional area A , electrode distance l and with a homogeneous, constant electric field of strength E , the voltage U across the sample between the electrodes is given by

$$U = lE. \quad (9.11)$$

The field exerts a force F on an ion of charge ze according to (9.12), where z is the signed charge number of the ion and e the elementary charge

$$F_z = zeE. \quad (9.12)$$

This force (9.12) accelerates the cations in the direction of the cathode and anions towards the anode. An ion moving through the solvent experiences also a frictional force F_R proportional to its velocity. Assuming Stoke's law of friction is applicable [9.20], the frictional force is given by (9.13) and where r is the radius of

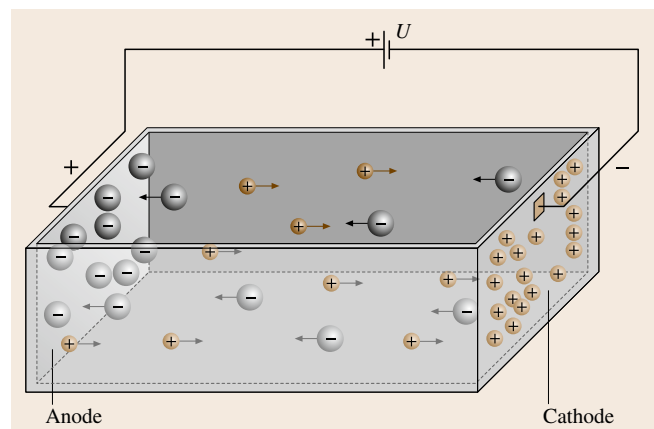


Fig. 9.19 Ions in solution conduct the electric current. The positive ions (cations) constantly move towards the negative electrode (cathode), while the negative ions (anions) move towards the positive electrode (anode)

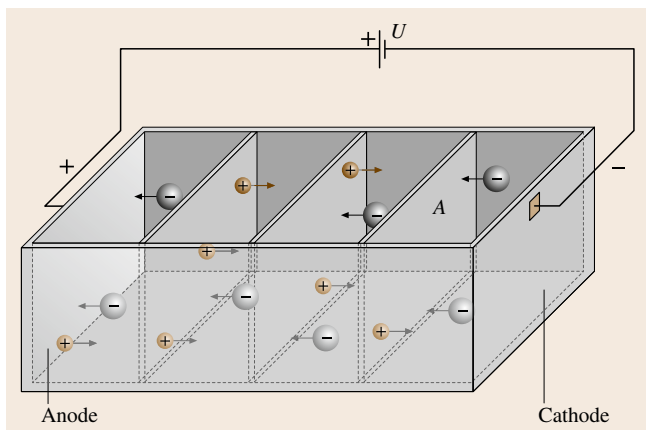


Fig. 9.20 The charge carried per time Δt period through the area A results in the current I_+ and I_- , respectively

the ion, which includes the radius of its solvate shell, η is the viscosity of the solvent and w the speed of ion motion

$$F_R = 6\pi r\eta w. \quad (9.13)$$

The two forces act in opposite direction. After a short time the speed of ion motion reaches a steady state (9.14) and (9.15)

$$F_Z = -F_R, \quad (9.14)$$

$$w = E \frac{ze}{6\pi r\eta}. \quad (9.15)$$

Note that the direction of the movement is determined by the sign of z and that the speed of motion is proportional to the field strength. From (9.15) a field independent quantity for the speed of ions, the ion mobility u_i can be derived

$$u = \frac{ze}{6\pi r\eta}, \quad (9.16)$$

with

$$w = uE. \quad (9.17)$$

A strong electrolyte i.e. potassium chloride (KCl), $A_{v+}B_{v-}$ dissociates into v_+ cations A and v_- anions B carrying the charge z_+e and z_-e , respectively. Lets assume the amount of substance concentration of an electrolyte solution is c , then the concentration of cations is v_+c and of anions is v_-c . The number of cations and anions, respectively, per volume is v_+cN_A and v_-cN_A . N_A is Avogadro's constant. In the electric field, cations and anions move with speed w_+ and

w_- in opposite direction. Hence, during a time period Δt a positive charge of $\Delta Q_+ = N_A v_+ c z_+ e w_+ \Delta t$ and a negative charge of $\Delta Q_- = N_A v_- c z_- e w_- \Delta t$ pass an area A as shown in Fig. 9.20.

The charge carried per time period through the area A results in the current $I_+ = \Delta Q_+ / \Delta t$ and $I_- = \Delta Q_- / \Delta t$, respectively [9.21]. Inserting Faraday constant F (9.18) and using (9.15) and (9.11) gives I_+ (9.19) and I_- (9.20) depending of the applied voltage U

$$F = N_A e, \quad (9.18)$$

$$I_+ = F v_+ z_+ c u_+ \left(\frac{A}{l} \right) U, \quad (9.19)$$

$$I_- = F v_- z_- c u_- \left(\frac{A}{l} \right) U. \quad (9.20)$$

According to (9.19) and (9.20) an electrolyte solution shows the same electric behaviour as an ohmic resistor $R = \rho(A/l)$, where ρ is the resistivity of the conducting material.

Molar Ionic Conductivity

With Ohm's law (9.21), we find for the conductivity κ_+ (the reciprocal of resistivity) of the cations (9.22),

$$I = \frac{U}{R}, \quad (9.21)$$

$$\kappa_+ = \frac{l}{A} \frac{1}{R_+} = \frac{l}{A} \frac{I_+}{U}. \quad (9.22)$$

Inserting (9.19) into (9.22) yields (9.23) for the molar ionic conductivity λ_{m+} of the cations.

$$\frac{\kappa_+}{v_+ c} = z_+ u_+ F = \lambda_{m+}. \quad (9.23)$$

The molar ionic conductivity λ_{m-} of the anions is derived similarly.

Since the conductivity depends on concentration of all mobile ions, measured values for different solutions are not directly comparable. For this reason the molar conductivity Λ_m of electrolytes (9.24) as the sum of the molar ionic conductivities of anions and cations has been introduced. Equations (9.23) and (9.24) applied to the anions and cations in the solution yield (9.25). The molar conductivity is expressed in $\text{S m}^2 \text{mol}^{-1}$

$$\Lambda_m = v_+ \lambda_{m+} + v_- \lambda_{m-}, \quad (9.24)$$

$$\kappa = c \Lambda_m. \quad (9.25)$$

For strong electrolytes, Kohlrausch's law empirically relates the molar conductivity with concentration according to (9.26) meaning that the molar conductivity

decreases with increasing concentration due to ionic interaction

$$\Lambda_m = \Lambda_m^0 - K\sqrt{c}, \quad (9.26)$$

where λ_m^0 is the limiting molar conductivity of an electrolyte at infinite dilution, K is a (typically small) constant and depends primarily on the type of electrolyte and on the solvent. In an aqueous solution the ions arrange in a way that on a time average each ion is surrounded by a sphere of counter ions. As a consequence two main effects lead to a decrease of the molar conductivity with increasing electrolytic concentration. When the ions move in an applied electric field they permanently try to rebuild the ionic sphere, which results in a restoring force and lowers their mobility. This effect is called the relaxation or asymmetry effect. The so called electrophoretic effect is a result of the ionic sphere influencing the friction force which a solvated ion experiences when moving through the solution. For a detailed description of the classical Debye–Hückel–Onsager theory and further sophisticated quantitative treatment of the concentration dependence of the conductivity see [9.22, 23]. If the sample contains only the species of interest and if the concentration dependence of this species is known, conductivity measurement can be used to estimate concentration.

Weak electrolytes dissociate only to a certain degree, which depends on the concentration of the weak electrolyte. Therefore the molar conductivity is mainly determined by the nonlinear dependence of the dissociation constant α (9.27) on the electrolyte concentration

$$\alpha = \frac{\Lambda_m}{\Lambda_m^0}. \quad (9.27)$$

The limiting molar conductivity for any electrolyte solution can be expressed in terms of the limiting molar conductivities of the anions and cations (9.28). This relation is known as Kohlrausch's law of the independent motion of ions in electrolyte solutions at infinite dilution

$$\Lambda_m^0 = \nu_+ \lambda_{m+}^0 + \nu_- \lambda_{m-}^0. \quad (9.28)$$

Limiting conductivities of cations and anions in various solvents are listed in [9.23]. The ion mobilities and therefore the limiting ionic molar conductivities of the hydronium and of the hydroxyde ions are much larger than for other ions due to a different transport mechanism. Hydronium and hydroxyde ions are not transported through the solution but protons are transferred by a sequential von Grotthuss type proton-hopping mechanism through water bridges [9.24].

9.3.3 The Measurement of the Electrolytic Conductivity

Basic Measurement Principle

An equipment to measure the electrolytic conductivity consists of a cell, mostly with built-in temperature probe and a measurement device to determine the resistance (and the temperature) of the cell (conductivity meter). The conductivity cannot be measured directly. According to (9.22) the conductivity $\kappa = \kappa_+ + \kappa_-$ of a solution under investigation is evaluated from the measurement of the resistance R of a sample in the cell and the geometric cell dimensions. In case of two parallel electrodes opposite to each other the geometric parameters in (9.22) are combined in terms of the cell constant K (9.29).

$$K = \frac{l}{A}. \quad (9.29)$$

K is equal to 1.0 cm^{-1} if the current flow contained within 1 cm^3 of sample solution is between the two electrodes of 1 cm^2 area and in a distance of 1 cm . The so-called standard cell is shown in Fig. 9.21.

The cells shown in Figs. 9.19 and 9.21 are idealized. In practice, side effects must be taken into account. These effects in particular include effects at the electrode–solution interface: electrode polarisation, i. e. accumulation of ions at the electrodes (so-called double layer capacitance), charge transfer across the electrodes (polarization resistance) and adsorption/desorption phenomena. Additionally, fringing electric fields at the

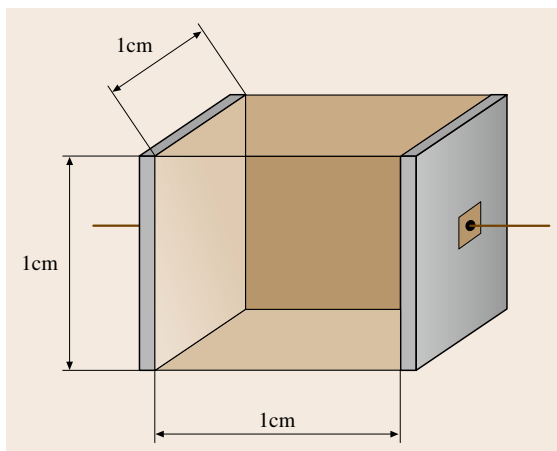


Fig. 9.21 For a standard cell, the volume of the sample solution is the area of the electrode times the distance between the electrodes

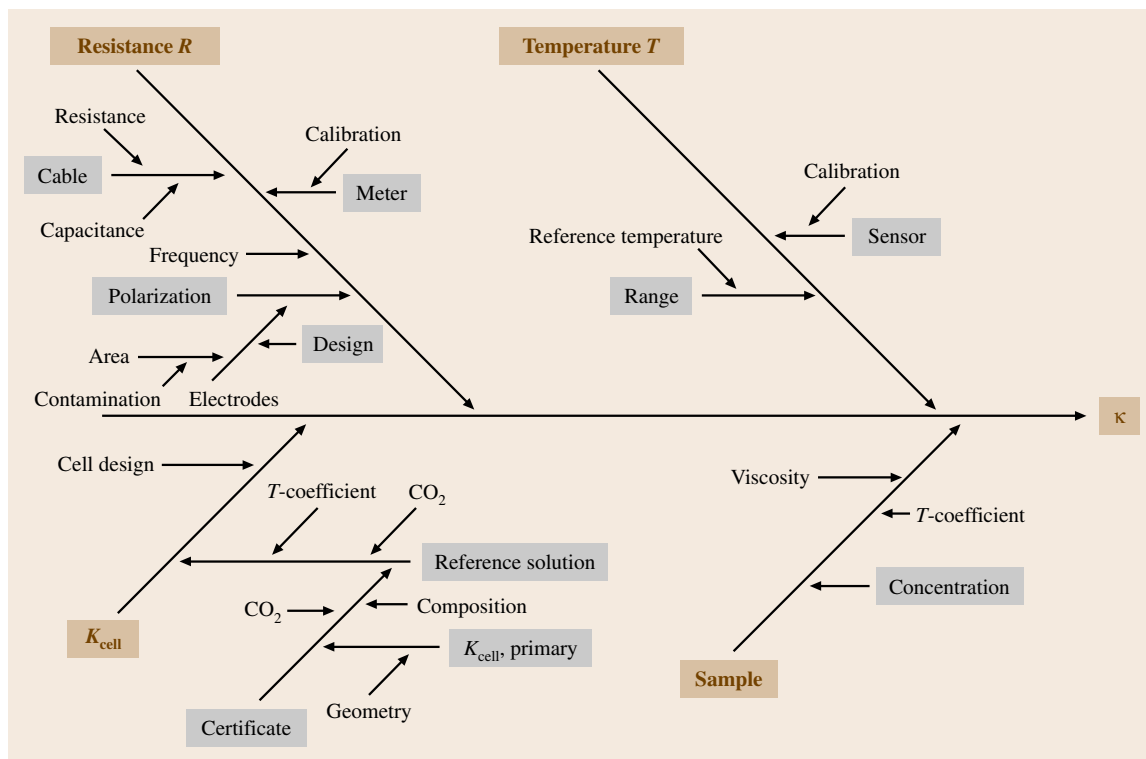


Fig. 9.22 The relevant uncertainty sources and their relationship are shown in a cause and effect diagram (fishbone)

cell margin and the geometric capacitance of the two electrodes affect the measured resistance. The solution resistance is therefore typically determined from impedance measurements $Z_i(f_i)$ at various frequencies f_i rather than a DC measurement of U and I . Depending on the electrode design, electrode effects affect the measured impedance spectrum at low frequencies, typically up to a few kHz, while the influence of the (rather small) geometric capacitance shows up at frequencies in the upper kHz range. The resistance R of the solution therefore can be derived from an extrapolation (9.30) of the real part of the impedances measured in the low frequency range [9.25]

$$R = \lim_{(1/f) \rightarrow 0} \operatorname{Re}\{Z_i(f_i)\}. \quad (9.30)$$

Furthermore, the cell design must be optimized to permit minimization the influence of fringing electrical fields. For this purposes a confinement of the current path to a defined volume having a large cross section A , and a small electrode distance is desirable. On the other hand this reduces the measured resistance. This is of disadvantage for the conductivity measurement of solu-

tions having large conductivities, since the uncertainty of resistance measurements increases for resistances in the ohm and milliohm region. Hence, geometric and electric properties of a conductivity cell are typically optimised for a conductivity range of interest.

If the cell constant K is determined from the geometric dimensions of the cell and if the resistance is measured traceable back to the SI, such as outlined above, the resulting conductivity of a solution is traceable to the SI unit S m^{-1} . Such *primary cells* are used to measure the conductivity of primary reference solutions (primary standards). Aqueous solutions of potassium chloride are usually used for this purpose. In a traceability chain, the known electrolytic conductivity of primary standard is used to calibrate conductivity cells of unknown cell constant. These cells are then used together with properly calibrated conductivity meters for routine measurements the results of which are traceable to the SI unit S m^{-1} [9.26]. Calibration and measurements of such devices are usually performed at a single frequency. On a worldwide scale the equivalence of the existing national primary measurement standards are ensured by means of international comparison measurements.

The best way to obtain all information on possible sources of uncertainty on the resulting conductivity of the sample is a cause and effect diagram shown in Fig. 9.22. This fishbone visualizes the relationship of the uncertainty sources. The main sources of uncertainty are the measurement of the resistance of the sample, the sample temperature, the cell constant and the stability of the sample.

Temperature Influence on Electrolytic Conductivity

The conductivity of a solution depends on temperature. Consequently, only conductivity values obtained at the same measurement temperature can be compared. The concept of reference temperatures (mostly 25 °C) was introduced to solve this problem. A temperature correction function allows the conductivity meter to convert the actually measured conductivity to that of the reference temperature.

There are three ways to deal with the temperature dependence of conductivity

- No correction (according to the specification of the United States Pharmacopeia (USP) [9.27] for water used in pharmaceutical industry, like water for injection (WFI);
- Linear correction to a reference temperature, which is, depending on the target uncertainty, appropriate for small deviations of up to 1 °C;
- Nonlinear correction (e.g. for natural waters according to ISO 7888 [9.28]).

The standard uncertainty of the temperature should be $u = 0.1$ K or better. For low target uncertainty it is recommended to thermostat the sample so that the same temperature is used for calibration and measurement.

Primary Cells

The conductivity of primary reference solutions are measured by means of conductivity cells with cell constants, which are determined by geometric measurements. Various cell types have been tested in the past on their ability to avoid or minimize fringe effects and stray fields typical for two-electrode cells as seen from Fig. 9.22. Two common models are shown in Figs. 9.23 and 9.24.

The cell type schematically shown in Fig. 9.24 was developed at the National Institute of Standards and Technology (NIST, Gaithersburg) [9.29]. The so-called Jones cell [9.30] is based on the principle of a geometrically measured, removable center section. The cell constant is primarily determined by the cross sec-

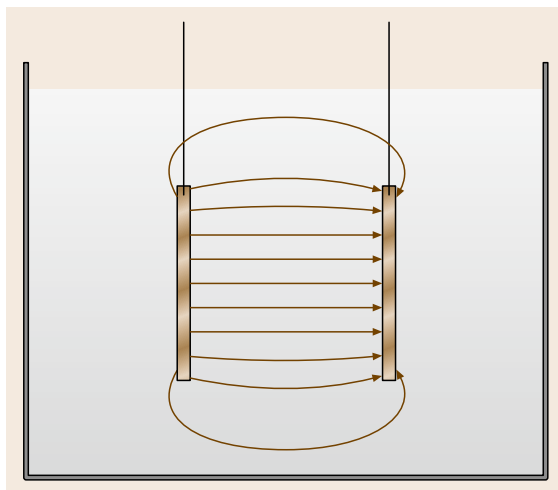


Fig. 9.23 Fringe effects occur on the edge of a two-electrode cell. If the field is not homogeneous it is not possible to determine the cell constant by a geometrical approach

tional area and length Δl of the glass tube separating the platinum electrodes rather than by the size of the electrodes themselves. In this primary cell the resistance of the solution can be reduced by removing the center section. The difference in the measured resistances is therefore correlated to the length of the removable center section. The conductivity of the sample can

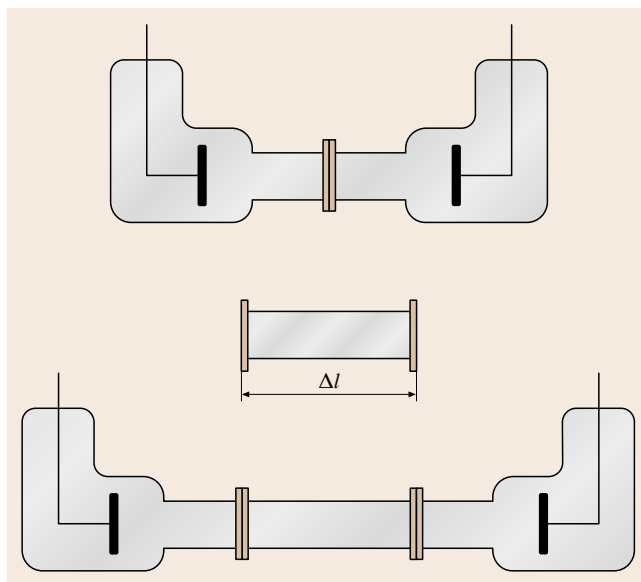


Fig. 9.24 Jones-type primary cell with removable center section

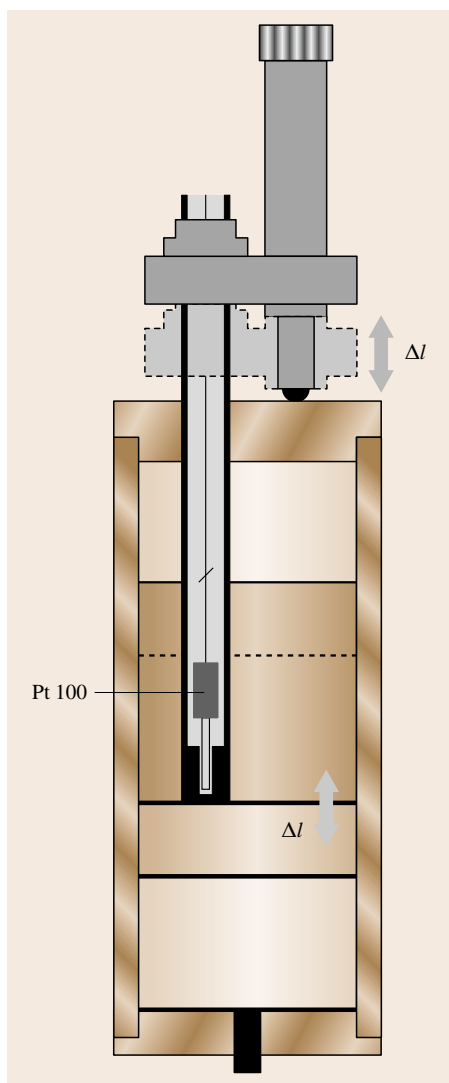


Fig. 9.25
Primary differential cell with adjustable electrode distance

therefore be determined from Δl and the differential resistance.

The disadvantage of this cell design is that the cell must be disassembled and cleaned between measurements with and without the center section which enhances the risk of contamination. The relatively expanded uncertainty (coverage factor $k = 2$) e.g. for the conductivity of a 0.01 mol/kg potassium chloride solution with nominal conductivity of 1.41 mS/cm (at 25 °C) is of the order of 0.03%.

A different approach of a two-electrode cell with well-known geometry developed at the Physikalisch-Technische Bundesanstalt (PTB, Braunschweig) [9.31]

goes back to *Saulnier* [9.32,33]. In this design one electrode is mounted on a movable piston. The distance between the two electrodes can be adjusted very precisely without the cell being disassembled. The cell design is shown in Fig. 9.25. The cross-sectional area is constant and is determined by the internal diameter of the cylindrical tube. The two electrodes are made of Pt, directly vapour deposited onto the electrode bodies [9.34]. If the spacing between the two electrodes is large enough, the distribution of the electric field in the bulk solution is not influenced by the movement. Therefore the difference in the measured resistances then can be attributed to the change Δl of the distance between the electrodes, so that conductivity can be calculated from the differential values, quite similar to the Jones cell.

Four-Terminal DC Cell

Conductivity measurements of a primary reference solution can also be performed using a four-electrode DC cell [9.35]. This method can be applied at higher conductivities, i. e. at low resistances. It has the advantage [9.26] to avoid the reactive effects typical of AC circuits. Measurements are effected by two outer Pt current electrodes, which imprint a constant current to cell, and two inner electrodes to measure the voltage drop across a portion of the cell. The current has to be kept relatively low to avoid heating the solution and electrolysis. Reversible potential electrodes are required to eliminate any polarization effect. The traceable value of the cell constant is directly determined through the geometry of a center glass tube precisely bored at which ends the potential electrodes are located.

Commercial Conductivity Cells – Two-Electrode Cell

The two-electrode cell as shown in Fig. 9.26 is the classical conductivity cell sometimes called Kohlrausch cell.

The two-electrode cell consists of two parallel electrodes immersed in the sample solution. An AC current

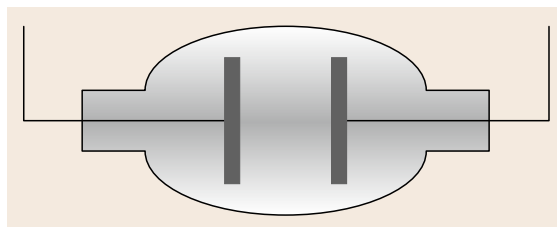


Fig. 9.26 Classical two-electrode conductivity cell

at a single frequency is typically applied and the resulting voltage is measured. Stray field and polarization effects influence the measurement. These effects must be kept under control in order to measure only the bulk resistance of the sample. Polarization is a side effect of the contact of electronically conducting electrodes with a solution showing ionic conduction. A charge buildup occurs at the electrical double layer at the electrode–solution interface and causes a voltage drop across the electrode surface. As a consequence, the measurements can, in general, not be performed with DC but have to be carried out with AC in the frequency range of typically up to 5 kHz.

The deposition of a platinum black layer on a platinum electrode (platinization) also reduces the polarization effect by increasing the electrode surface [9.36]. This increases the double layer capacitance so that the measured impedance is virtually resistive.

It is important to choose the right frequency for the respective application, which significantly depends on the cell design and the solution under investigation. In general, low frequencies in the sub-kHz region can be applied at low conductivities. In this range the polarization is negligible compared to the bulk resistance of the sample. Frequencies in the low kHz region must be applied at high conductivities in order to minimize the influence of electrode polarization.

A disadvantage of the two-electrode cells is that any changes of the electrode surface such as corrosion or coatings influence the measurement result. If the electrodes are covered by platinum black any scratch or other damage would change the surface and therefore the cell constant.

Four-Electrode Cell

The four-electrode cell reduces the problem of polarization effects. Changes of the electrode surface like blocking and coating do not influence the measurement result. A typical four-electrode cell as oversimplified shown in Fig. 9.27 consists of four concentric rings. One outer pair of current electrodes and one inner pair of voltage electrodes. A constant AC current is applied to the outer pair of rings. The voltage is measured on

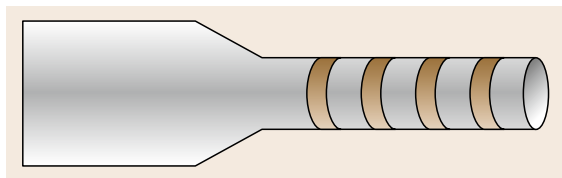


Fig. 9.27 Oversimplified four-electrode cell

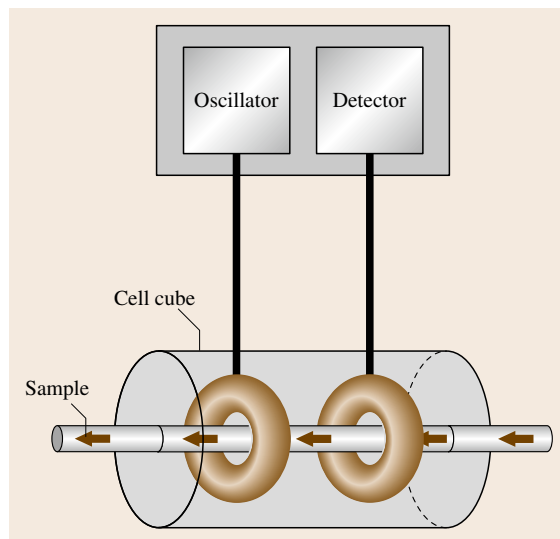


Fig. 9.28 Toroidal inductive conductivity cell

the inner rings with a large input impedance of the impedance meter to reduce polarization effects.

Three-Electrode Cells

The three-electrode cell type is nowadays almost completely replaced by the four-electrode cell. In a three-pole cell a third pole is connected to one electrode of a two electrode cell, which serves to guide the electrical field. In this way the stray-field can be reduced [9.37].

Electrodeless Conductivity Measurements – Toroidal Inductive Conductivity

In a toroidal conductivity measurement cell as shown in Fig. 9.28, the electrodes are located outside the solution being investigated. An oscillating potential is applied to the first electrode, which induces a current in the solution. Inversely the induced current is measured with the second toroidal coil [9.38]. A main field of application is the process control, e.g., in food industry.

Monitoring the Purity of Water

Since electrolytic conductivity is a sensitive measure for the amount of ions dissolved in the solution, a threshold for conductivity is a clear and simple specification for the quality and purity of water in general but also for high-purity water. The relevant measuring range is below 0.1 mS/m (0.06–1 μ S/cm at 25 °C). The US Pharmacopoeia [9.27] as well as the European one [9.39] have specified the standard

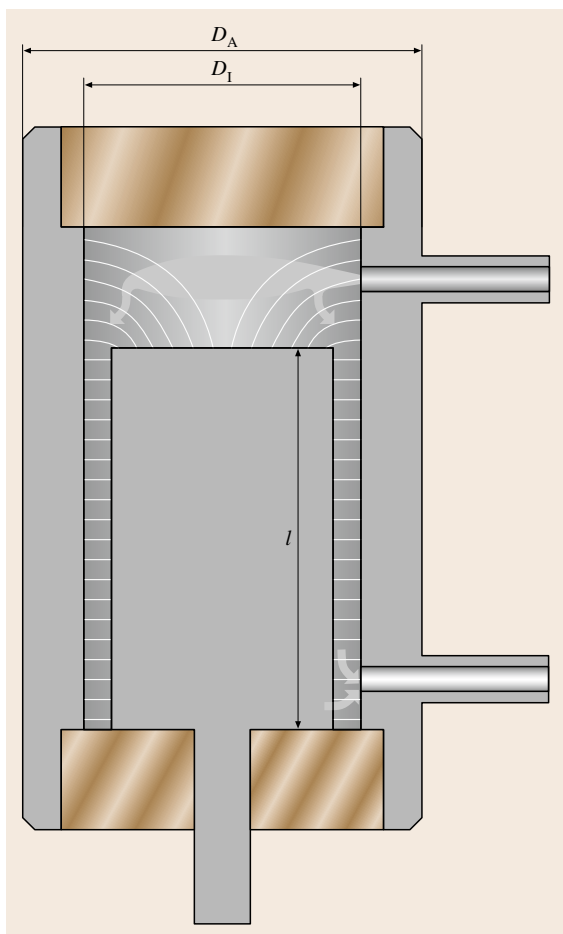


Fig. 9.29 Flow-through cell for the low conductivity range. For this closed cell type the influence of air-borne contaminations like carbon dioxide on the measurement result can be avoided

for purified water, highly purified water and water for injection for the pharmaceutical industry based on conductivity measurements. Sectors that also use conductivity thresholds for water purity are electrical power plants, food industry, electronic industry and analytical laboratories.

In the sub-mS/m region no certified aqueous reference solutions are available, because the conductivity of aqueous solutions is not stable due to the influence of atmospheric carbon dioxide (CO_2). CO_2 dissolves in water and partly forms carbonic acid. By that it contributes to the measured conductivity value in the order of 0.1 mS/m, depending on the partial CO_2 pressure present during the measurement. To compensate for the

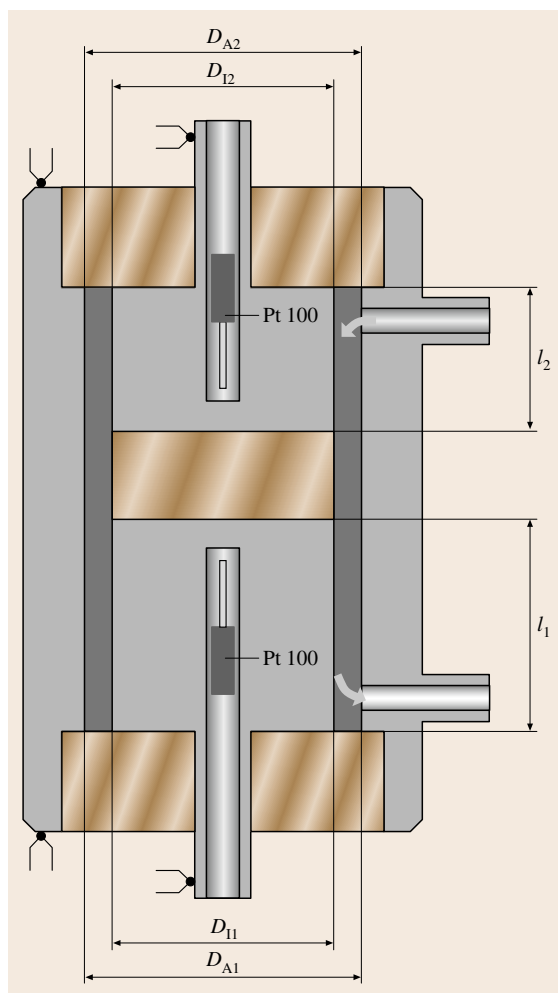


Fig. 9.30 Primary flow-through cell for in-line conductivity measurements in the high-purity water range. The concentric cell consists of two inner electrodes of different length and one outer electrode. The gap between the inner electrodes is filled with inert material

absence of certified reference solutions, a calibration method based on high-purity water as a standard has become widely accepted by the users of low conductivity measuring devices [9.40]. For this purpose it is necessary to determine the conductivity of high-purity water traceable to the SI unit S/m.

Flow-Through Cell for the Low-Conductivity Range

The most common cell design for in-line applications in the high-purity water range is shown in Fig. 9.29. The

concentric design minimizes electromagnetic interference [9.41] and is suitable for integration of the cell into a closed loop. Contamination with atmospheric carbon dioxide from surrounding air is avoided for this type of cell. For calibration it is integrated into a closed loop of purified water together with a reference cell of known cell constant, which is used to measure the conductivity of the purified water. In this way the purified water in the loop is used as a *transient* reference material to calibrate the commercial cell in-line and at the same temperature.

The principle of a primary reference flow-through cell [9.42] is shown in Fig. 9.30. It consists of two inner cylindrical electrodes of different lengths l_1 and l_2 and an concentric outer electrode, which herby form two conductivity measurement cells. The gap between the inner electrodes is filled with inert, nonconducting material. Platinum resistance temperature sensors are mounted in each inner electrode. The cell constant of each cell can be calculated from the inner and outer diameter D_i and D_o , respectively, and from the lengths of the inner electrodes according to (9.31). Fringe effects at the holes and at the end of the electrodes are considered in terms of an effective stray

length a

$$\begin{aligned} K_1 &= \frac{\ln(D_o/D_i)}{2\pi(l_1+a)}, \\ K_2 &= \frac{\ln(D_o/D_i)}{2\pi(l_2+a)}. \end{aligned} \quad (9.31)$$

Since the two cells just defer in length, a can be assumed equal for both cells. Using $\kappa = K_1/R_1 = K_2/R_2$ (9.22) the effective stray length can be calculated from the measured resistances R_1 and R_2 of the pure water in the two cells. The cell constants are of the order of 1 m^{-1} with a relative expanded target uncertainty ($k = 2$) smaller than 0.5%. Because cell dimensions, resistance and temperature measurements are measured traceable to the SI unit, the conductivity of the high-purity water can thus be determined in the SI unit S/m.

Another promising design of a primary flow-through cell is based on the on the so-called van der Pauw principle which is used extensively in solid-state physics to measure surface resistivity. The principle is based on a theorem similar to that of Lambert used for the determination of the capacitance unit. The theorem can be applied to a cell with constant cross section and with four electrodes at the edges [9.43].

9.4 Semiconductors

Semiconductor materials offer a wide range of conductivity according to their free carrier concentration, starting from the intrinsic conductivity (10^{-8} S/cm) up to 10^5 S/cm by controlling the doping concentration from 10^{12} up to 10^{21} cm^{-3} . Thus, the determination of the conductivity, conductivity type (n- or p-doped), and the related majority carrier mobility are the most important characterizations, especially in the case of newly developed materials.

After these majority carrier properties are known, minority carrier properties come into consideration, which are mainly related to lattice defects (vacancies and interstitials), but also to chemical impurities, which produce (deep) electron or hole states within the band gap. The most important parameter is the minority carrier lifetime which is applied to describe leakage currents of p-n junctions, charge storage times in dynamic memory cells or sensitivity of charge-coupled device light sensors.

With respect to high-speed devices, like e.g. bipolar transistors or photodiodes, saturated drift velocity values are needed to estimate the high-speed performance.

Many semiconductor devices reach their operating limits with respect to some breakdown mechanisms, like the onset of tunneling currents or impact ionization.

Table 9.5 gives a selected list on semiconductor properties and related methods to determine their values. The following paragraphs give some guidance to determine the most relevant parameters useful for device simulation, device design, and device analyses.

As all semiconductor devices need a more or less ideal contacting of their active regions via metallization of ohmic contacts, the final section collects measurements methods for specific contact resistances.

9.4.1 Conductivity Measurements

Conductivity measurements on semiconductors are predominantly related to bulk material, e.g. semiconductor wafers and epitaxial layers or layer stacks. The conductivity σ (S/cm) is related to the specific resistance ρ ($\Omega \text{ cm}$)

$$\sigma = \frac{1}{\rho}. \quad (9.32)$$

Table 9.5 Overview on selected semiconductor properties and related characterization methods

Property	Symbol	Characterization method
Specific resistance	ρ	Four-point probe, van der Pauw method
Conductivity type	(n- or p-type)	Thermoprobe, Hall effect
Carrier concentration	n, p	Hall effect, capacitance–voltage (C–V)
Carrier mobility	μ_n, μ_p	Hall effect with resistivity
Compensation ratio	$N_A/N_D, N_D/N_A$	Temperature dependence of Hall coefficient
In-depth doping profile	$N(x)$	Capacitance–voltage (C–V), Hall effect with selective layer removal, spreading resistance on beveled samples
Diffusion length	L_n, L_p	Junction photocurrent, electron beam induced currents (EBIC)
Saturated drift velocities	$v_{n,sat}, v_{p,sat}$	I–V analysis (Kelvin method)
Ionization rates by electrons or holes (impact ionization)	α_n, α_h	Temperature resolved I–V analyses
Minority carrier lifetime	τ_n, τ_p	I–V analysis, photoconductivity
Deep states (traps): density, thermal emission rates, capture cross sections, energy level	N_t $e_n, e_p, \sigma_n, \sigma_p$ E_t	Deep level transient spectroscopy (DLTS)

The conductivity can be calculated from basic semiconductor properties in case of dominating electron conduction

$$\sigma = q\mu n, \quad (9.33)$$

with the elementary charge q (1.602×10^{-19} A s), the carrier mobility μ (unit $\text{cm}^2/(\text{V s})$), and the carrier density n (unit cm^{-3}).

If both carrier types (electrons and holes) are concerned, the conductivity is deduced from

$$\sigma = q\mu_n n + q\mu_p p. \quad (9.34)$$

The standard method for measuring the specific resistance of bulk materials and thin layers is the four-point probe [9.44]. This method is well established for silicon and germanium but works as well on GaAs, InP, and other III–V compound materials. By applying the method to beveled surfaces, in-depth resistivity profiles can be deduced (spreading resistance method [9.45]).

The basic measurement setup of the four-point probe (c.f. e.g. DIN Norm 50431) is depicted in Fig. 9.31. A measurement head comprising four spring-loaded needles with equal distances s (e.g. $s = 1$ mm), is pressed onto the semiconductor sample with a pressure ensuring good near-ohmic contacts, but soft enough not

to produce visible damage. The measurement current I is fed via the outer needles through the sample. The voltage V is measured between the inner needles. Assuming a constant current source with nearly infinite source impedance and a voltage meter with nearly infinite input resistance, possible contact voltages at the needles due to the current flow can be neglected in this Kelvin-like setup. The specific resistance of the sample is

$$\rho = \frac{V}{I} c, \quad (9.35)$$

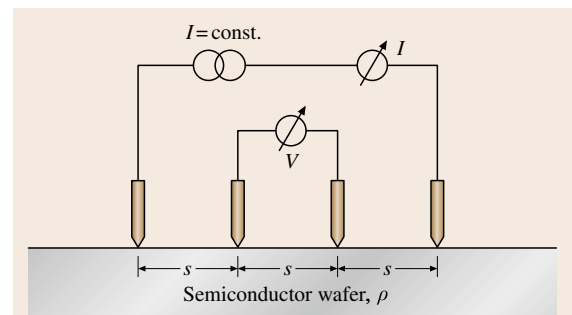


Fig. 9.31 Four-point probe on a semiinfinite semiconductor wafer with specific resistance ρ

with c denoting a geometry dependent correction factor, depending on the sample dimensions and the needle distances. The following constraints have to be fulfilled in all sample configurations for accurate measurement within inaccuracies below 1%

- nearly ohmic contacts between the needles and the semiconductor,
- negligible heating of the sample due to the measurement current I (mA range),
- no excess injection of carriers, which would lead to excess conduction (dark measurement),
- no extreme surface potential induced surface band bendings; otherwise leading to stronger surface accumulation or surface inversion layers which would affect the bulk conduction.

In the following sections the correction factor c is given for different samples geometries.

Conductivity of Thin Layer Samples

The measurement setup of the four-point probe applied to a laterally infinitely extended thin layer of thickness d and specific resistance ρ , grown on a semiinsulating wafer is depicted in Fig. 9.32. The specific resistance (unit Ω cm) of the layer can be deduced from the measured voltage V , induced by the current I using

$$\rho = \frac{V}{I} d \frac{\pi}{\ln 2}. \quad (9.36)$$

An error in the evaluation of the specific resistance approaches 1%, if the layer thickness d would be one half of the needle distance s . This error would increase to 8%, if the layer thickness d would equal the needle distance s . Normally, needle distances of 1 mm are used, thus, for layer thickness values in the 1–10 μm range this systematic error can be neglected easily. This solution is also applicable in all cases, where the lateral dimensions of the sample are much larger than the threefold measurement–tip distance. If the latter condition cannot be met a setup as in Fig. 9.33 has to be used.

Conductivity of Semiinfinite Bulk Samples

The measurement setup of the four-point probe applied to a semiinfinitely extended bulk sample with a specific resistance ρ , is depicted in Fig. 9.34. The specific resistance of the semiinfinite bulk sample can be deduced from the measured inner voltage V induced by the outer current I by

$$\rho = \frac{V}{I} s 2\pi. \quad (9.37)$$

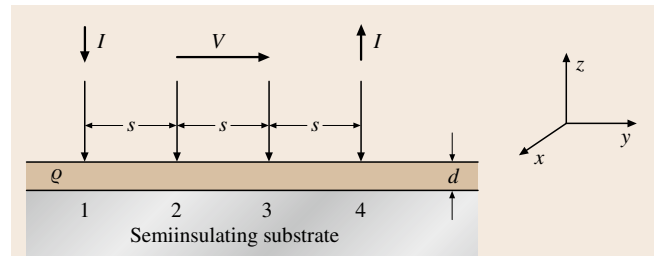


Fig. 9.32 Four-point probe applied to a thin, infinitely extended layer of thickness d and specific resistance ρ ; the measured layer is isolated by a semiinsulating substrate

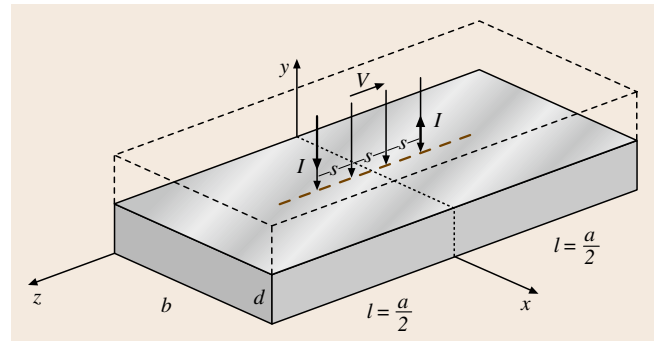


Fig. 9.33 Four-point probe on a thin, rectangular shaped layer of dimensions $a \times b \times d$ with a specific resistance ρ ; the measured layer may be isolated by an underlying semiinsulating substrate or a pn-isolation

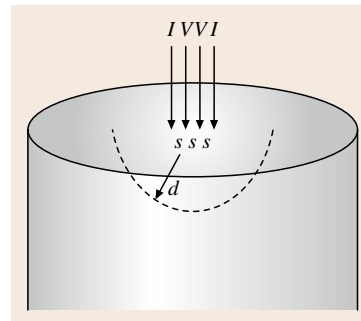


Fig. 9.34 Four-point probe on a semi-infinitely extended bulk sample with a specific resistance ρ ; the radius of the measured volume is defined roughly by $d > 3.5s$

This is valid under the assumption, that the radius of the measurement volume $d > 3.5s$, with s denoting the equal spaces s of the needle setup.

Conductivity of Rectangular Shaped Small Samples

In some cases, the samples to be characterized exhibit neither the shape of a semiinfinitely extended bulk sample nor the structure of a laterally infinitely extended thin

layer. Thus, a further solution is given for the case of a rectangular shaped sample of finite dimensions a and b (Fig. 9.33).

The solution of this problem can be obtained by several approaches, like finite difference methods. Here, an analytical approach of Hansen [9.46] may be mentioned which can be easily implemented on desktop computers. The Laplace equation is solved using a separation of variables and applying standard boundary conditions on the doubled sample (see dotted lines in Fig. 9.33) without changing the field and current line conditions in the original sample. A series expansion is developed in [9.46] to deduce the specific resistance ρ from measured I - V values and the sample geometry data a , b , and d as well as the probe head tip distances s

$$\rho = \frac{V}{I} \left(\frac{s}{bd} + \frac{8}{bd} \times \sum_{m=0}^{\infty} \sum_{n=0}^{\infty} \frac{\cosh \beta (l - 3s/2) \sinh (\beta s/2)}{(1 + \delta_{0,m}) (1 + \delta_{0,n}) \beta \cosh (\beta l)} \right)^{-1} \quad (9.38)$$

with (m, n) unequal to $(0, 0)$ and

$$\beta = \frac{2\pi}{b} \left[m^2 + \left(\frac{nb}{2d} \right)^2 \right]^{1/2} \quad (9.39)$$

and $\delta_{r,s}$ = Kronecker's delta ($\delta_{0,m} = 1$ ($m = 0$) or 0 ($m > 0$)).

A general remark for all four-point probe configurations: the four-point probe can be applied to silicon and germanium using pressures of the needles of approximately up to 50 p; in case of more sensitive III-V materials like InP, the pressure of the probe needles has to be reduced to around 5 p.

Conductivity of Isotype 2-Layer Stacks

If there are two adjacent layers (1, 2) with isotype conduction type with individual sheet carrier concentrations $n_{1,2}$ (unit cm^{-2}) and mobilities $\mu_{1,2}$ (unit cm^2/Vs), contributing to the total sheet conductance δ_s , the resulting mixed conductance in terms of the effective sheet carrier density n_s and effective mobility μ_s can be calculated from the conductances of the single layers according to [9.47]

$$n_s = \frac{(\mu_1 n_1 + \mu_2 n_2)^2}{\mu_1^2 n_1 + \mu_2^2 n_2}, \quad (9.40)$$

$$\mu_s = \frac{\mu_1^2 n_1 + \mu_2^2 n_2}{\mu_1 n_1 + \mu_2 n_2}. \quad (9.41)$$

It is assumed that the adjacent isotype layers are grown either on a semiinsulating buffer layer or together being isolated by a pn-junction from the substrate. Thus, the substrate or buffer conductance should be negligible in this two-layer mixed conduction model.

9.4.2 Mobility Measurements

The mobility μ of the majority carriers is extracted by a two-step procedure applying van der Pauw test structures [9.48]. Firstly, the specific resistance ρ is measured, secondly the carrier concentration n is determined. Both measurement setups use the same test structure but apply different schemes for contacting to feed the measurement current into the sample and to measure the resulting voltages. In a final step the mobility is deduced from the equation $\sigma = q\mu n$ solved for μ

$$\mu = \frac{\sigma}{qn} = \frac{1}{qn\rho}. \quad (9.42)$$

The term $|1/(qn)|$ is the Hall constant, which is indicative of the carrier concentration n within the test sample. Thus, the mobility can also be written as

$$\mu = \frac{R_H}{\rho} = R_H \sigma. \quad (9.43)$$

Due to the fact that the Hall effect is polarity sensitive with respect to the conduction type, the sign of the Hall constant comprises the information of the dominating carrier type: negative sign – n-type, positive sign – p-type. In the following, the Hall effect is explained in more detail and some van der Pauw test structures will be discussed.

Hall Effect, van der Pauw Structures

The Hall effect after Hall (1879) denotes the onset of a voltage V_H at a long thin sample of length a , where a current I is driven through the long axis and a magnetic field \mathbf{B} is applied perpendicular to the sample (Fig. 9.35). Due to the balance of the Lorentz force $\mathbf{F} = q\mathbf{v} \times \mathbf{B}$ and the electric field force due to E_H of the Hall voltage, the Hall voltage for an n-type sample can be deduced after integrating over the transverse field E_H

$$V_H = -\frac{1}{nq} \frac{1}{d} IB. \quad (9.44)$$

The term $-1/(nq)$ is known as the Hall constant R_H of the sample, the sign of which depends on the carrier type. In case of a p-type sample, the Hall constant has a positive sign.

Thus, the Hall effect can be used to determine the dominant carrier or conduction type of an unknown semiconductor sample.

The Hall voltage of either type can be written as

$$V_H = R_H \frac{1}{d} IB, \quad (9.45)$$

with voltage signs $+/- \leftrightarrow$ p/n-type conduction.

When Hall's constant R_H is determined, the carrier concentration can be deduced

$$n, p = \frac{1}{qR_H} \quad (9.46)$$

(with n, p due to a negative, positive sign, respectively)

In principle, the mobility value can now be calculated from (9.43) assuming that the conductivity of the sample was determined by the four-point probe before. This method applying two different test samples would work but it is rather unpractical. A more convenient way was published in [9.48], where a disk of arbitrary shape can be used for both types of measurement. In practice, later a rectangular sample is preferred. The original van der Pauw sample type is shown in Fig. 9.36; the sample must not contain any holes. The van der Pauw sample is used in two measurement configurations

1. *For the measurement of the specific resistance.*

The current I is fed into contacts M, N and the voltage V is taken at contacts P, O. This I - V configuration can be cycled around 90° , and the voltage at M, P taken, too. Thus, two resistances are built: $R_{MN,OP}$ and $R_{NO,PM}$. In [9.48], it is shown by a conformal mapping method that the sample's specific resistance obeys van der Pauw's equation

$$e^{[-(\pi d/\rho)R_{MN,OP}]} + e^{[-(\pi d/\rho)R_{NO,PM}]} = 1. \quad (9.47)$$

The specific resistance can be solved from (9.47) graphically or numerically, e.g. by a Newton method. For the practically preferred rectangular sample geometry the specific resistance can be deduced from

$$\rho = \frac{\pi d}{\ln 2} R_{MN,OP}. \quad (9.48)$$

In this symmetrical case, the I - V configuration can be rotated four times by 90° and the resulting four voltage values can be averaged. Additionally, the current polarity can be reversed and the resulting voltages averaged again. Thus small asymmetries of the sample can be averaged by taking the mean value of eight measurements. More elaborate evaluation procedures in cases of asymmetric I - V measurements in the van der Pauw configuration are given in [9.44].

2. *For measurement of the carrier concentration.*

For the determination of the carrier concentration

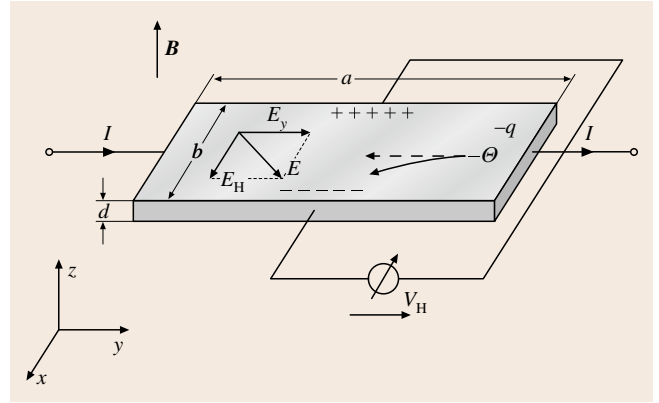


Fig. 9.35 Hall effect at a long sample with dimensions $a \times b \times d$, where a measurement current I is driven along a , and a magnetic field is applied perpendicular to a, b in z -direction

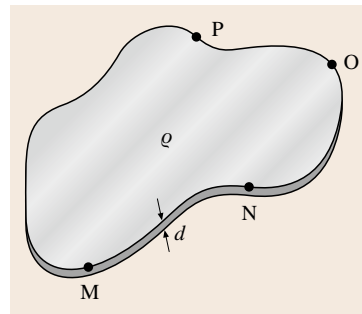


Fig. 9.36 van der Pauw test sample of specific resistance ρ , disc of arbitrary shape of thickness d with infinitesimal small contacts M, N, O, P at its periphery

from a Hall measurement at the van der Pauw sample, the I - V setup is modified in which the current and voltage contacts are now crossed. The Hall constant is determined in this case by forming the average out of two measurements

$$R_H = \frac{d}{B} \left(\frac{R_{NP,OM} + R_{OM,PN}}{2} \right). \quad (9.49)$$

This scheme can also be improved by averaging over eight Hall resistance terms, as given in [9.44]. The carrier mobility is now deduced using (9.43), (9.49) together with (9.48).

Van der Pauw Test Structures

It was mentioned before, that a rectangular test sample with quite small contacts at the corners can be used favorably for the van der Pauw measurements (Fig. 9.37). The ideal infinitesimally small contacts can be approached by soldering $500 \mu\text{m}$ Sn balls into the corners of the sample while using sample sizes of, e.g. $> 5 \times 5 \text{ mm}^2$.

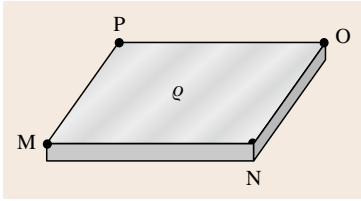


Fig. 9.37 Quadratic van der Pauw test sample with ideal infinitesimally small contacts in the four corners



Fig. 9.38a–e van der Pauw test samples with nonideal finite contact sizes (after [9.44])

However, real samples suffer from different nonidealities of the sample preparation; the contacts are not small enough compared to the sample's edge length or the contacts are not correctly deposited at the sample's corners. Respective correction terms can be found in [9.44]. To overcome the distorting effects of finitely extended contacts, a lot of alternative test samples are in use. Figure 9.38 gives an overview of common van der Pauw test sample geometries [9.44]. Very popular is the clover-leaf structure (e), which can be fabricated by ultrasonic cutting and which does not need further electrical corrections even in the presence of finite contacts. Very precise results can also be obtained from the greek cross structure (b). Many discussions concerning ease of fabrication, fragility, heat dissipation, and needs of correction factors can be found in [9.44].

Temperature Dependent Carrier Concentration and Compensation

The carrier concentration determined by the standard Hall technique described so far is assumed to represent the value of the dopant concentration as well. This is valid when a complete dopant ionization can be assumed. In practice, at least two additional aspects have to be considered.

Temperature Dependent Carrier Concentration (Dopant Ionization <100%)

The mobile carrier concentration $n(p)$ follows the dopant concentration $N_D(N_A)$ up to concentration values of the order of the effective density of states (N_c or N_v , for n- or p-type conduction, respectively). The effective density of states depends, besides the sample temperature ($\propto T^{3/2}$), on the effective mass of the

carrier, e.g. for the conduction band E_c

$$N_c = 2 \left(\frac{2\pi m_0 m_e k_B T}{h^2} \right)^{3/2}, \quad (9.50)$$

with m_0 denoting the free electron mass and m_e the effective mass of the electrons; the other constants have their usual meanings. Normally, electron effective masses m_e are smaller than hole effective masses m_h . Thus, the density of states in the conduction band is smaller than in the valance band (for a first very rough orientation take $N_c = 10^{18} \text{ cm}^{-3}$ and $N_v = 10^{19} \text{ cm}^{-3}$ for E_c and E_v , respectively). The free carrier concentration n is regulated by the position of the Fermi level E_F with respect to the band edges E_c and E_v . Although the Fermi distribution [9.49] gives the correct Fermi level and carrier concentration, often Boltzmann's approximation is used for nondegenerate semiconductors ($E_c - E_F > 3k_B T$), again denoted for the electron concentration: $n = N_c \exp[-(E_c - E_F)/(k_B T)]$ (for holes: $p = N_v \exp[(E_v - E_F)/(k_B T)]$). The Fermi level E_F adjusts itself in relation to the band edges to provide overall charge neutrality for the sum of fixed and mobile charges, i.e. for the charge sum of ionized impurities and electron and hole densities (for the n-type semiconductor: $N_D^+ = n - p$). The ionized impurity concentration N_D^+ is given by the Fermi level position with respect to the impurity level energy E_D

$$N_D^+ = N_D \frac{1}{1 + g \exp[-(E_D - E_F)/(k_B T)]} \quad (9.51)$$

with g denoting the ground-state degeneracy of the donor level ($g = 2(4)$ for electrons (holes)), E_D usually is some (ten) meV below the conduction band edge energy. This equation shows that complete ionization can be achieved at Fermi level positions well below E_D , i.e. for doping concentrations below the effective density of states N_c . The charge neutrality equation together with Boltzmann's approximations for the free carrier concentrations and the before mentioned ionization relation for the dopant N_D fixes the Fermi energy and the free carrier concentrations for a given temperature. For incompletely ionized donors, i.e. for lower temperatures (below 100 K) the carrier freeze-out range begins. This means that only a certain percentage of the donor concentration results in free electrons in the conduction band. Thus, also the Hall technique will measure a reduced carrier density towards decreasing temperatures. Fitting the free carrier concentration given by the above

equations to a temperature-resolved Hall measurement, e.g. within a range from 77 up to 400 K, allows the determination of the dopant ionization energy E_D .

Compensation Effects

In semiconductors there may also coexist a smaller amount of the adverse dopant type of opposite charge polarity besides the dominating one which determines the sign of the Hall constant and the conduction type (n- or p-type). This adverse dopant type tends to partially compensate the effectiveness of the major dopant and results in a pronounced temperature behavior of the free charge concentration in excess of that of an uncompensated semiconductor. At normal (room) temperatures, the free carrier concentration is given by $n = N_D - N_A$, while at reduced temperatures, the free carrier concentration diminishes much more pronounced due to the compensation and incomplete ionization of the majority carrier dopant type. The charge neutrality equation is now replaced by $N_D^+ - N_A^- = n - p$. Applying again Boltzmann's approximations for the free carrier concentrations and the noted ionization relation for the dopants N_D and N_A , the free electron concentration in case of a partially compensated n-type semiconductor can be deduced

$$\frac{n}{N_D} = -\frac{1}{2} \left(\frac{n_1}{gN_D} + \frac{N_A}{N_D} \right) + \sqrt{\frac{1}{4} \left(\frac{n_1}{gN_D} + \frac{N_A}{N_D} \right)^2 + \frac{1}{g} \left(1 - \frac{N_A}{N_D} \right) \frac{n_1}{N_D}}, \quad (9.52)$$

with $n_1 = N_c \exp[-(E_c - E_D)/(k_B T)]$. This equation can be related again to a temperature-resolved Hall measurement $n(T)$. The fit allows to determine, besides the donor ionization energy E_D , also the compensation ratio N_A/N_D . In dominating p-type semiconductors, the compensation ratio is defined as $N_D/N_A (< 1)$.

In all cases of compensated semiconductors, the Hall mobility is more or less lower than in the uncompensated cases because the additional ionized impurity scattering effects at the compensating centers lead to reduced mobility values. This effect can be even more pronounced at low temperatures when carrier scattering effects by lattice vibrations are negligible, i. e. when the Hall mobility is only affected by free carrier or ionized impurity scattering. Thus, the maximum mobility values of low-doped semiconductors achievable at e.g. 77 K give invaluable information on the purity of the material.

Hall Mobility and Drift Mobility

Deducing from the Hall effect, the carrier velocity was orientated solely along the y -direction of the constant current fed through the long test sample. In practice, the electrons (or holes) are moving not with a linear translation but they are moving on cycloid-type paths due to the two forces of the electric field in y -direction and to Lorentz's force in x -direction. These cycloid-type curves are interrupted by scattering events of the carriers at lattice vibrations and (ionized) impurities depending on the impurity density. A result of these combined movements of the carriers in x - and y -directions under the combined electrical (E_y) and magnetic (Hall) field (E_H) forces are trajectories, where the carriers feel the crystallographic properties of the semiconductor crystal in both directions x and y . Consequently, the Hall mobilities $\mu_{H,n,p}$ may deviate from the drift mobilities $\mu_{n,p}$. The newly introduced Hall factor $r_{H,n}$ denotes the ratio of $\mu_{H,n}/\mu_n$; in the case of a p-type semiconductor, $r_{H,p}$ denotes the ratio of $\mu_{H,p}/\mu_p$. The Hall factor modifies the formerly Hall constants for an n-type semiconductor $R_{H,n} = -r_{H,n}1/(qn)$ and for the p-type semiconductor $R_{H,p} = -r_{H,p}1/(qp)$. The Hall factors depend slightly on the magnetic field, the crystal structure, and the measurement temperature. For high magnetic fields, the Hall factor tends to unity. In practice, due to often unknown precise values of the Hall factors, a unity value is assumed for material quality comparisons of different epitaxial approaches or annealing conditions.

Field-Effect Mobility (FET Transistor)

In devices like field-effect transistors (FET), the conducting channel is controlled by gate electrode applying an electrical field perpendicular to the current path. The channel can be either located at the surface of the device, like in a MISFET (metal-insulator-semiconductor FET) or the channel may be buried, like in HFET/HEMT (hetero structure/high-electron mobility FET) transistors. For these large variety of devices, the Hall effect can be applied to measure the channel mobility which can be either enhanced by two-dimensional electron gas effects or be reduced due to surface scattering effects between the insulating gate oxide and the surface conducting channel, compared to bulk conduction in thicker epitaxial layers.

9.4.3 Dopant and Carrier Concentration Measurements

The measurement of the dopant and carrier concentration is mainly done by capacitance-voltage ($C-V$)

analyses because this method delivers not only averaged carrier concentrations but provides the in-depth carrier concentration profiles, too. Capacitance–voltage (C – V) analyses are predominantly executed applying LCR-meters, which can measure the sample's AC conductance besides the capacitance. C – V analyses should be evaluated under the assumption that the loss tangent ($G/\omega C$) of the sample does not exceed some percent proving that the capacitance for a given measurement frequency is dominating the conductance contribution. If sufficiently low values of the loss tangent cannot be achieved for a standard frequency of e.g. 1 MHz, then higher frequencies should be chosen in case of parallel conductance leakage, or lower frequencies should be used in cases of high series resistances of the samples under test. A rule of thumb is to choose the measurement frequency according to the minimum of the loss tangent. If stray capacitances in parallel to the sample are present, then those should be determined by applying adequate test structures and subtracting them before conducting further C – V analyses.

The C – V method can be most simply explained applying a Schottky contact, i. e., a metal contact on an n-type semiconductor. Firstly, the doping profile analysis is explained under the assumption of the depletion approximation. Secondly, some limitations of the C – V method with respect to in-depth resolution limitations due to Debye length effects are discussed. Thirdly, correction procedures are explained for the most important cases of near-surface doping profiles in metal–insulator–semiconductor (MIS) structures and in-depth implantation profiles as well as high-low doping profiles.

Capacitance–Voltage (C – V) Analyses

The basic capacitance–voltage (C – V) evaluation with respect to semiconductor in-depth doping profiling is based on the depletion approximation, i. e. on the assumption of an abrupt space charge edge in conjunction with complete dopant ionization. A suitable sample test structure is shown in Fig. 9.39. A Schottky contact metal with defined area A is evaporated on top of the semiconductor, while ohmic metallization is provided at the back side. Due to the work function difference of the metal to the electron affinity of the semiconductor, a space charge region of depth w is formed. The depth of the space charge region can be controlled by a reverse biased voltage applied to the top gate electrode. Within the depletion approximation, the capacitance of the space charge region (neglecting side wall effects and other stray capacitances) is given by the plate capacitor

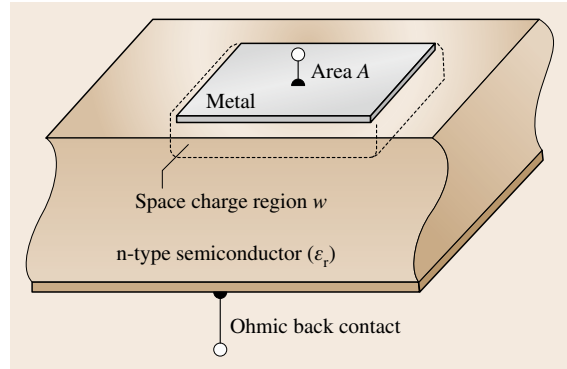


Fig. 9.39 Schottky metal contact (area A) on top of an n-type semiconductor with space charge region depth w

model

$$C_{sc} = \epsilon_0 \epsilon_r \frac{A}{w_0}, \quad (9.53)$$

with ϵ_r being the dielectric constant of the semiconductor, ϵ_0 the vacuum permittivity, and w_0 the space charge width at zero bias. Figure 9.40 shows the related band diagram at zero bias. The Schottky barrier height Φ_{Bn} induces a band bending within the semiconductor of qV_{bi} , with V_{bi} being the built-in voltage of the Schottky diode. E_c , E_v and E_F are the conduction, valence band edges, and the Fermi level, respectively. The Fermi level at equilibrium is constant throughout the whole metal–semiconductor structure indicating the absence of current flow at zero bias conditions. If an external reverse voltage is applied to the left-sided metal electrode, the band bending of the semiconductor increases and the width of the space charge region increases, too. Consequently, the resulting capacitance is reduced, according to (9.53). The depletion approximation model can be seen in Fig. 9.41, where the in-depth free electron

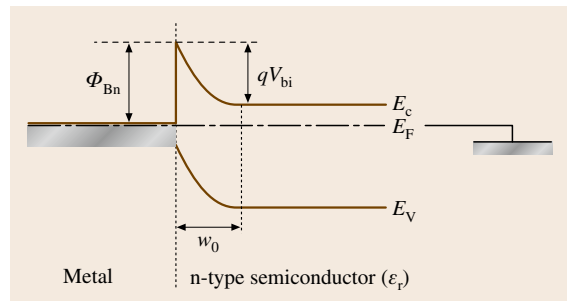


Fig. 9.40 Band diagram of a metal–semiconductor Schottky contact in thermal equilibrium at zero bias

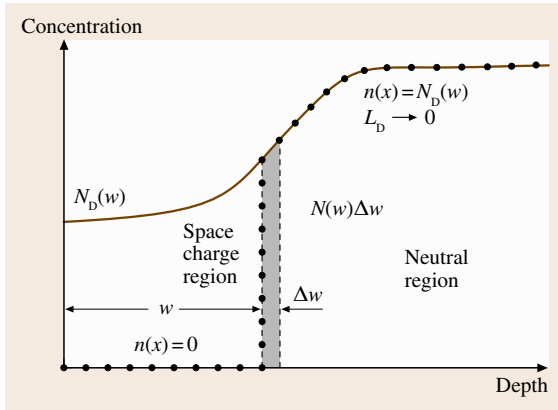


Fig. 9.41 Arbitrary in-depth doping profile $N_D(w)$ and resulting in-depth free electron concentration profile $n(x)$, described according to the depletion approximation

concentration $n(x)$ is shown in idealized form compared to an arbitrarily assumed in-depth doping concentration profile $N_D(w)$. In the neutral region, the free carriers (here electrons) compensate the ionized donor atoms [$N_D^+(w) = N_D(w) = n(x)$]. Depletion approximation means that the free carrier concentration at the edge of the space charge region makes an abrupt transition down towards zero concentration inside the space charge region. This corresponds to a zero Debye length. The Debye length $L_D = \sqrt{\epsilon_0 \epsilon_r k_B T / (q^2 n)}$ denotes a typical screening length depending on the square root of temperature T compensating space charge distortions from thermal equilibrium of the carrier concentration n .

By solving Poisson's equation $\text{div } \mathbf{D} = \rho$ and integrating twice over the space charge region, the total band bending potential V depending on the space charge region depth w , can be deduced: $V = \frac{1}{2} q N_D w^2 / (\epsilon_0 \epsilon_r)$ (so far a constant dopant profile N_D is assumed). By combining this equation with the plate capacitor equation, solving for an expression of $1/C^2(V)$ and differentiating $1/C^2(V)$ versus the external voltage, an expression for a nonconstant in-depth carrier concentration profile $n(x)$ (identified equal to $N_D(x)$) due to the depletion approximation can be found

$$N_D(x) = \frac{1}{q \epsilon_0 \epsilon_r} \frac{1}{A^2} \frac{C^3(V)}{dC(V)/dV} \quad \text{for an n-type semiconductor,} \quad (9.54)$$

$$N_A(x) = -\frac{1}{q \epsilon_0 \epsilon_r} \frac{1}{A^2} \frac{C^3(V)}{dC(V)/dV} \quad \text{for a p-type semiconductor.} \quad (9.55)$$

In both cases, the depth x is calculated from the plate capacitor model $x = \epsilon_0 \epsilon_r A / C(V)$.

The accuracy of the C - V method is mainly determined by the known accuracy of the gate electrode area, e.g. an accuracy of the area A within 1% gives an accuracy of the doping profile of 2%. Further, the spatial variation of the doping profile should be small within a Debye length to assure the validity of local charge neutrality during in-depth profiling.

Limitations on C - V Analyses, Applying the Depletion Approximation

The in-depth resolution of doping profiles determined by the C - V profiling method is limited by the Debye length. The finite Debye length leads to a smear out of the abrupt space charge edge over roughly 2–3 Debye lengths. This phenomenon is shown in Fig. 9.42. Two effects may result: first, in the case of abrupt steps within the doping profile, the equilibrium carrier profile will not follow the doping step with the same abruptness (local neutrality is not fulfilled); second, in the case of near-surface profiling, the free carrier tail of the space charge edge will touch the interface region even if a certain space charge region is still opened. In both cases profiling errors will arise. In the first case, the abruptness of real doping profiles cannot be measured adequately; in the second case the apparent carrier profile (from which the user concludes the doping profile) will increase artificially towards the interface when the space charge region is smaller than about two Debye lengths.

The Debye length can be reduced by lowering the measurement temperature ($L_D \sim \sqrt{T}$), but for very low

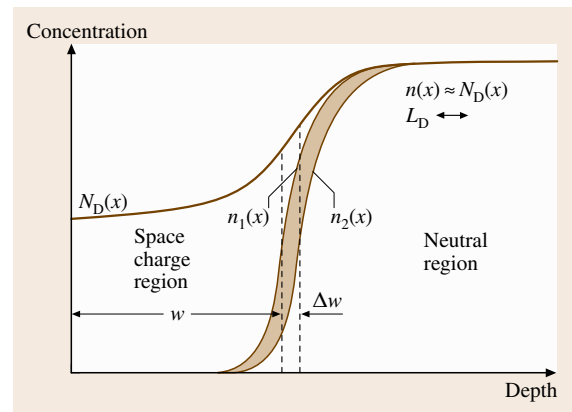


Fig. 9.42 Arbitrary in-depth doping profile $N_D(x)$ and more realistic in-depth free electron concentration profile $n(x)$ in presence of Debye length smearing of the space charge edge

temperatures, the dopant ionization is diminished, too. Thus, the measured carrier concentration would underestimate the true dopant concentration and this approach was limited to very shallow donor levels.

These further aspects of finite Debye length problems during doping profiling will be discussed in the next section.

Debye Length Corrections for Near-Surface Doping Profiles in MOS/MIS Structures and for Ion-Implanted In-Depth Profiles

In this section two correction procedures will be described which help to improve approximations of the true doping profiles while the apparent $C-V$ (carrier) profiles are affected by Debye length broadening effects.

Near-Surface Doping Profiles in MOS Structures MOS (metal-oxide-semiconductor) or MIS (metal-insulator-semiconductor) structures play an important role in all CMOS based devices, like CMOS transistors or (B)CCD ((buried) charge-coupled device) focal plane arrays. The surface doping profile, i. e. the doping profile in the direct vicinity of the dielectric-semiconductor interface needs to be known very accurately because the value and homogeneity of the threshold voltage depends on it. MIS structures isolate quite well any current flow due to the high specific resistivity of the dielectric/oxide. This allows to solve Poisson's equation while neglecting any current flow and to consider the additional contribution of mobile carriers in the space charge region [9.50]. By applying this analytical approach Ziegler et al. [9.50] extended the range of the depletion approximation till up to the flatband point of MIS capacitors which means up to the semiconductor surface. They developed an analytic tabular correction algorithm for the apparent carrier profile, which is calculated from the depletion approximation and they avoid any artificial increase of the apparent carrier profile towards the surface, even when the profiling depth is lower than two Debye lengths. Figure 9.43 shows a typical comparison of uncorrected concentration profiles (dash-dotted lines) with the corrected ones (circles). In both cases of boron and phosphorus doping of the MIS capacitor, the correction algorithm delivers relatively flat profiles. Without this correction pile-up effects of the dopants were assumed due to annealing and segregation effects. The precise determination of the flatband point and the surface inversion point were greatly improved by applying the Ziegler-Klausmann-Kar profile correction [9.50]. The method is applicable

for quasi-static RF measured MIS $C-V$ curves as well as to pulsed RF $C-V$ curves which avoid the surface inversion of MIS structures during the short (ms) measurement windows.

Measurement of Ion Implanted Profiles

In-depth profiling of ion implanted semiconductors is a special challenge for the application of the depletion approximation because a Gaussian-like implantation profile has more or less steep edges around the maximum, i. e. around the average projected range of deposited atoms. Furthermore, implantation profiles are used, compared to diffusion doping profiles, to achieve more abrupt doping transitions when scaling devices or to achieve low-ohmic contacts. Thus, the steepness of profile edges may occur easily within a Debye length, especially for lower implantation doses.

The discussed correction algorithm of Ziegler et al. [9.50] cannot be applied for smaller depth than two Debye lengths. For larger depths this algorithm exhibits

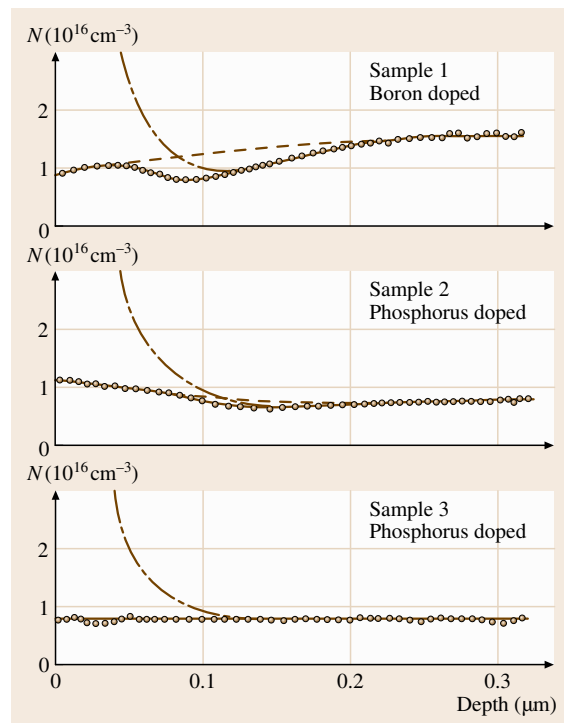


Fig. 9.43 Examples for doping profiles in silicon MIS capacitors. The *steeply uprising curves* show the apparent doping profiles using the uncorrected depletion approximation; the *circles* show the Debye-length corrected measurements (after [9.50])

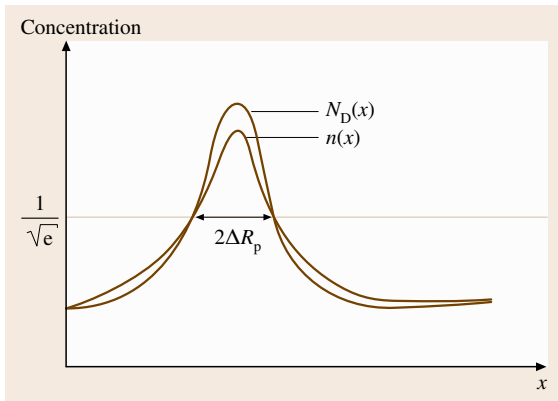


Fig. 9.44 In-depth profiles of implanted dopants $N_D(x)$ and free carrier concentration $n(x)$: near the peak is $N_D(x) > n(x)$ and far away from the peak is $n(x) > N_D(x)$

a smooth transition into the standard depletion approximation. Quite a lot of implanted profiles show their projected ranges are quite deeper than several Debye lengths.

The same problem arises during profiling of high–low or low–high doping transitions of the same doping type, e.g. in varactor diodes. In all these cases, local charge neutrality is not fulfilled, especially in the vicinity of the steepest doping gradient. This typical situation is explained in Fig. 9.44 using the example of an implantation profile $N_D(x)$ with a Gaussian-like shape of its edges. The mobile carrier concentration $n(x)$ deviates typically from the dopant distribution due to spreading diffusion effects and repelling electrical field forces, i. e. at the maximum, free carriers are missing and in the edges the mobile carriers produce longer tails of the apparent concentration. This can be proved by comparing SIMS (secondary ion mass spectroscopy) measured implantation profiles with their C – V evaluated counterparts. The C – V technique is based on the signal from the mobile carriers ($C = dQ/dV$), thus the apparent doping profile lacks the abruptness of the real profile. Unfortunately SIMS cannot replace the C – V evaluation because SIMS cannot measure the electrically active concentration which is relevant for the device function. It determines only the atom concentration without information with respect to electrical activation. Thus, an effort is needed to improve the C – V evaluation in these applications. This improvement was done by Kennedy et al. [9.51, 52]. They developed a correction of the apparent depletion approximation profiles assuming that the free carrier concentration is known. Therefore, they solved Poisson’s equation considering

additionally the charge contributions of the majority carriers and neglecting current flow in the reverse direction of Schottky- or pn-junction contacts. They deduced (9.56) which extracts the dopant profile $N_D(x)$ from the mobile carrier profile $n(x)$

$$N(x) = n(x) - \frac{\varepsilon_0 \varepsilon_r k T}{q^2} \frac{d}{dx} \left(\frac{1}{n(x)} \frac{dn(x)}{dx} \right), \quad (9.56)$$

where $n(x)$ is obtained by evaluation of the standard depletion approximation (9.54), (9.55) evaluation from a C – V measurement. This extraction is valid if the true mobile carrier profile would be known exactly. Unfortunately, the C – V measurement determines only an approximation to this true mobile carrier profile because the space charge edge is smeared out over about two Debye lengths. Thus, the Kennedy correction [9.51, 52] is a useful improvement to obtain a more realistic shape of implanted profiles but it cannot, in principle, provide the true physical profile again caused by Debye length reasons. A good rule of thumb in case of implanted profiles, not to be affected too much by Debye length distortions (error < 1%), is the relation $\Delta R_p \geq 10L_D$, with ΔR_p being the half width of the implanted profile and L_D the Debye length for a given doping. This means in practice that high-dose implanted profiles suffer much less from Debye length distortions applying the C – V technique.

Applying (9.56) for the improvement of step-like high–low doping profiles, it is recommended (if possible) to provide the depletion from the highly doped side because the Debye length is shorter at the begin of the measurement which helps the accuracy of the profile reconstruction [9.53].

Electron and Hole Effective Masses

The effective masses of mobile carriers in semiconductors reflect the curvatures of the band structure in the $E(k)$ diagrammes. The effective mass is of a tensorial type with components: $1/m_{ij}^* \equiv 1/(h/2\pi)^2 [\partial^2 E(k)/(\partial k_i \partial k_j)]$ with E denoting the band energy and k ($= 2\pi/\lambda$) the wavevector of the carrier related to its moment $p = (h/2\pi)k$. The band structure of semiconductors is described by Schrödinger’s equation which is based on the wave nature of electron propagation in crystals. Tabulated values of effective masses of common semiconductors can be found in [9.49]. Effective masses can be measured by cyclotron resonance and by angle-resolved photoemission spectroscopy (ARPES) [9.54]. III–V semiconductors with their low effective electron masses (≈ 0.07) provide high carrier velocities within short acceleration

times and thus a very high speed potential of electronic circuits.

9.4.4 I - V Breakdown Mechanisms

Electrical breakdown in semiconductors is characterized in terms of the electrical field strength (unit kV/cm) in regions of the I - V curve, where the current increases to a much higher extent than for slightly reduced field strength below. Electrical breakdown, indicated by a steep current increase versus voltage, is mainly related to two mechanisms: impact ionization (avalanche) breakdown and tunneling (internal field emission). Both mechanisms can be distinguished by investigating the temperature behavior of the current-voltage (I - V) curves. For a certain constant voltage in the breakdown region a positive temperature coefficient of the current is indicative for tunneling breakdown, while a negative temperature coefficient indicates impact ionization breakdown. Both mechanisms are discussed in more detail in the following two subsections.

Impact Ionization Breakdown Field Strength

Impact ionization is a bulk controlled current flow mechanism induced by a carrier multiplying band-band process. Carriers are accelerated by an high electrical field, that they can induce electron-hole pair ionization due to their high energy. The resulting additional electrons and holes are accelerated in opposite directions, until they gain and overcome their specific ionizing energy ($\gg kT$); thus, the whole process produces an avalanche-like increase of the current after an only small voltage increase. Impact ionization breakdown can be concluded from a negative temperature coefficient of the current at a high fixed reverse voltage. Increasing temperature causes more lattice vibrations, which hinder carriers, to gain directed acceleration; thus higher electrical fields are needed at elevated temperatures, to produce the same current. Small effective masses ease the ionization process due to higher carrier mobility in the accelerating field. Impact ionization is a band-band pair generation process, thus the breakdown electric field strength increases with increasing bandgap of the semiconductor. The avalanche process is described by the ionization rates α_n and α_h (unit 1/cm) for electron or hole induced electron-hole pairs, respectively. The ionization rates $\alpha_{n,h}$ depend largely on the electrical field strength E

$$\alpha(E) = \alpha_\infty e^{[-(E_0/E)^m]} \quad (9.57)$$

with α_∞ , E_0 , and m being a temperature dependent material constant. Graphs of ionization rates of several semiconductors can be found in [9.49] ranging up to values of $\alpha_{n,h}$ of 10^5 /cm.

Tunneling (Internal Field Emission) Breakdown Field Strength

Tunneling or internal field emission is a quantum mechanical process, where carriers penetrate through thin energy barriers when the barrier thicknesses approach the value of the de Broglie wavelength (a few nm). During the quantum mechanical tunneling process their energy is conserved. Carrier tunneling is a barrier-controlled current flow mechanism. Tunneling is observed in highly doped pn junctions, where narrow barriers are favored by the high doping and the resulting small space charge regions. The de Broglie wavelength $\lambda_{e,h}$ is given by

$$\lambda_{e,h} = \frac{h}{\sqrt{2 * m_0 m_{e,h} E}} \quad (9.58)$$

with m_0 denoting the free electron mass, $m_{e,h}$ the effective mass of electrons or holes, and E the energy of the carrier. For, e.g. InP with an electron effective mass of 0.07 and an electron energy of kT ($T = 300$ K) λ_e amounts to 29 nm, while for $E = 1$ eV, λ_e reduces to 4.64 nm.

The barrier to be penetrated by the carrier should be narrower than de Broglie's wavelength for the relevant carrier's energy. The probability for tunneling increases considerably for electrical field strength in the range of 10^6 V/cm, i. e. 1 (e)V/10 nm, where the effective barrier width for band-band tunneling is reduced to 10 nm, being in the range of the aforementioned de Broglie wavelength. For this nonthermal process, the thermal energy of the carrier (electron) is most often neglected.

Temperature Dependent Reverse Current I - V Analysis

According to the explanations given in the two subsections before, the dominating mechanism for breakdown in pn-diodes or transistors can be identified by measuring the reverse I - V characteristics for various temperatures. A recommended temperature range extends, e.g. from 0 to 80 °C in steps of 20 °C, which can be controlled by Peltier cooling or heating. Much wider temperature ranges can be achieved in cryostats, where electrical heating in conjunction with liquid nitrogen cooling can provide a temperature range between 77 and 420 K. Because generation currents in pn-junctions are increasing proportional to the intrinsic concentration

n_i , which itself increases exponentially over temperature in half of a given bandgap; an even moderate temperature spacing within a set of I - V curves results in a current spread over about two orders of magnitude in the low-field generation current regime. The current versus voltage in this low-field generation regime increases quite moderately with the square root of the voltage. At the onset of either tunneling or avalanche breakdown a much steeper increase of current is observed. The following two figures of pn-diodes show typical characteristics of either tunneling or avalanche breakdown.

Figure 9.45 shows for a GaInAs homojunction photodiode the typical band-band tunneling behavior for voltages above of 15 V, where the remaining temperature dependence stems from the decreasing bandgap with increasing temperature. Thus, a positive temperature coefficient of the current for fixed voltage is present in the tunneling region. Typical at the onset of tunneling is a pronounced reduction of the temperature sensitivity at the transition from the generation regime below 15 V to the tunneling regime above 15 V.

Figure 9.46 presents the typical reverse current characteristics of a silicon p^+n diode [9.56] dominated by avalanche breakdown above 27 V. Again, in the lower field regime, the I - V characteristics show typical Shockley-Read-Hall generation behavior exhibiting a pronounced temperature sensitivity according to the higher bandgap of silicon (compared to Fig. 9.45) comprising a GaInAs photodiode. The onset of impact ionization is characterized by a much steeper increase of the current versus voltage compared to the tunneling breakdown in Fig. 9.45. Furthermore, the temperature coefficient is reversed compared to the tunneling case before. In the impact ionization regime, a higher voltage is needed for constant current with higher temperature, due to increasing lattice vibrations which hinder the electrons from being accelerated due to a higher collision rate. Thus, the I - V characteristics exhibit a typical crossing behavior when the generation regime is taken over by impact ionization.

In conclusion, the temperature resolved I - V characteristics can clearly distinguish between generation, tunneling and impact ionization regimes.

9.4.5 Deep Level Characterization and Minority Carrier Lifetime

Deep levels in semiconductors heavily affect the forward and reverse current curves they increase the noise in photodiodes and transistors, reduce the minority

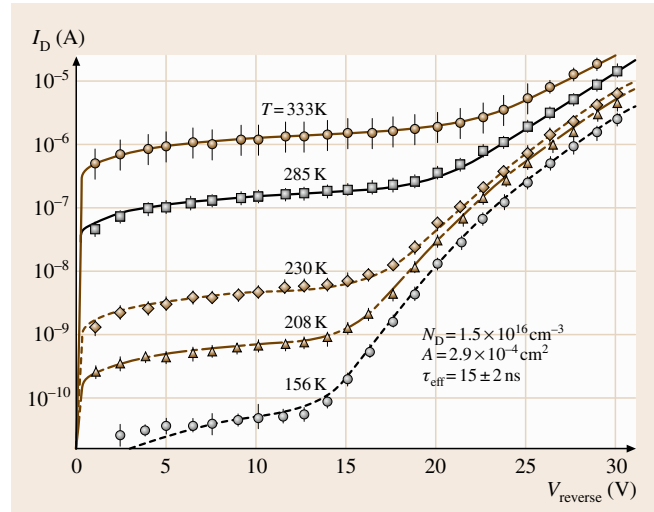


Fig. 9.45 Dark current of a GaInAs homojunction photodiode (after [9.55]) dominated by tunneling breakdown above 15 V

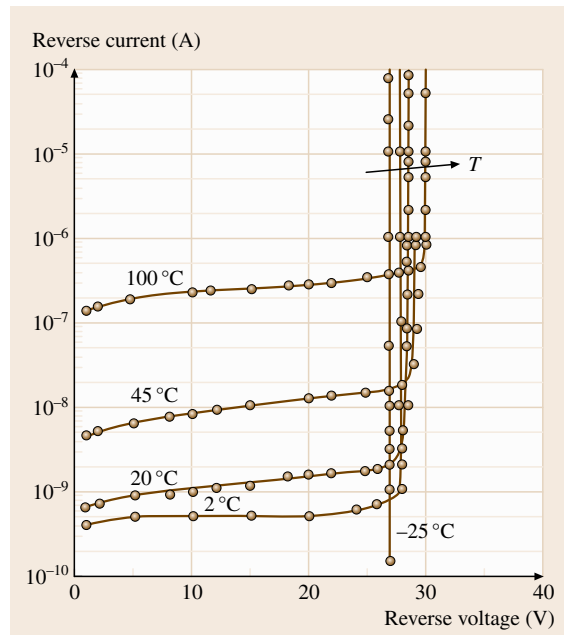


Fig. 9.46 Reverse current of a silicon p^+n diode (after [9.56]), dominated by avalanche breakdown above 27 V

carrier lifetime, or quench the storage time in charge-coupled devices or CMOS focal plane arrays. One of the most sensitive methods to determine a comprehensive set of deep level or trap parameters is the DLTS (deep level transient spectroscopy) technique.

Definition and Role of Trap Parameters

There is a common basis for the description of donor or acceptor states and the so called deep levels or traps. Donor or acceptor states are situated very closely to the respective band edges in the band diagram (some tens meV), while deep levels or traps have an energy position more or less close to the midgap band energy, i.e. they are located deeper than 200 meV. The equations for deep and shallow level ionization, which are given in Sect. 9.4.2 are valid for dopants as well as for deep levels or traps. The difference between deep levels and traps is mainly attributed to their different interaction rates with both bands. While deep levels often may interact with the conduction and valence bands with comparable probabilities, traps are exchanging their carriers dominantly on with one band. This behavior is reflected by differences in energetic positions: deep levels are close to the midgap energy while traps are located near to one of the bands, but considerably deeper than shallow donors or acceptors. Thus, deep levels often function as recombination centers to extract electrons and holes from the bands under nonequilibrium excitation conditions, while traps capture carriers from one of the bands within a very short time constant (capture time constant in the ns range) and emit these carriers back to the same band after some delay (emission time constant in the ms range). The temporal change of the total charge (ionized dopants and deep levels) in the depletion region of a Schottky diode affects the space charge capacitance, which can be measured versus time to monitor trap recharging processes. This field is called capacitance spectroscopy [9.57], or more detailed deep level transient spectroscopy (DLTS) [9.58].

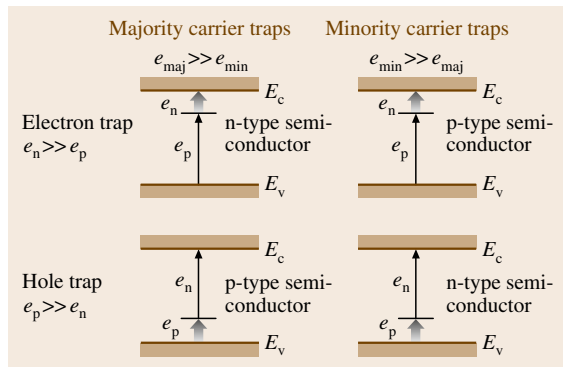


Fig. 9.47 Energetic location and main interactions of majority carrier traps and minority carrier traps in n- and p-type semiconductors

Figure 9.47 shows the principal possibilities for locating traps in the band diagrams of n- and p-type semiconductors. The thick arrows indicate the dominant interaction paths. If a trap is located much closer to the conduction band than to the valence band (see the electron traps in the upper parts of Fig. 9.47), then their electron emission rates e_n (unit s^{-1}) are considerably larger than their hole emission rates e_p (unit s^{-1}). This situation reverses for hole traps located near to the valence band. A trap interacting dominantly with the majority (minority) carrier band is called a majority (minority) carrier trap. A trap interacting dominantly with the conduction (valence) band is called an electron (hole) trap.

Traps are characterized by several parameters. The first is the concentration N_T (unit cm^{-3}), the second is the energetic distance from the corresponding energy band edge $E_c - E_T$ ($E_T - E_v$) (unit eV). The capture of carriers represented by the capture rates c_n, c_p (unit s^{-1}) into traps from the bands is normally a very fast process, the time constant of which is in the ns range

$$c_n = \sigma_n v_{th} n \quad \text{and} \quad c_p = \sigma_p v_{th} p, \quad (9.59)$$

with σ_n, σ_p denoting the capture cross sections (unit cm^2 , for orientation purposes $10^{-15} cm^2$), v_{th} denoting the carrier thermal velocity ($10^7 cm/s$) and n, p the carrier concentrations in the corresponding bands. After the capture process the subsequent emission rate e_n (unit s^{-1}) is driven exponentially by the trap activation energy $E_c - E_T$ given here for an electron trap

$$e_n = \sigma_n v_{th} N_c g \exp\left(-\frac{E_c - E_T}{k_B T}\right). \quad (9.60)$$

Equation (9.60) is the basis for the Arrhenius plot which allows the extraction of the trap activation energy by plotting $\log(e_n/T^2)$ versus $1000/T$ (Fig. 9.48). The prefactor T^2 stems from the joined temperature behavior of the effective density of states N_c in conjunction with the thermal velocity v_{th} .

The minority carrier lifetime τ_{eff} (s) can be deduced from the generation rate U ($cm^{-3}s^{-1}$) from the trap parameters according to the theory of *Shockley, Read, and Hall* [9.59, 60].

$$\tau_{eff} = \frac{n_i}{U} \quad (9.61)$$

with n_i denoting the intrinsic carrier concentration of the semiconductor material [9.49] and

$$U = \frac{\sigma_p \sigma_n v_{th} N_T}{\sigma_n \exp\left(\frac{E_{trap}}{k_B T}\right) + \sigma_p \exp\left(-\frac{E_{trap}}{k_B T}\right)} n_i. \quad (9.62)$$

Here, E_{trap} is the trap energy position with respect to the intrinsic energy E_i ($E_i \approx (E_c + E_v)/2$) of the semi-

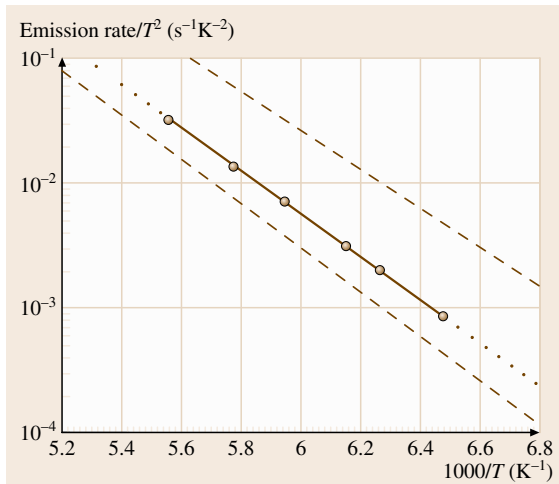


Fig. 9.48 Arrhenius plot of the DLTS spectrum in Fig. 9.49 for Au in n-type silicon; the measurement is shown as *full line*, the *dashed lines* represent comparison data from a trap library to assess the measured Arrhenius data compared to known data for easier identification. The measured activation energy is 340 meV. The *dotted line* is used for extrapolation of the capture cross section for $1000/T \rightarrow 0$

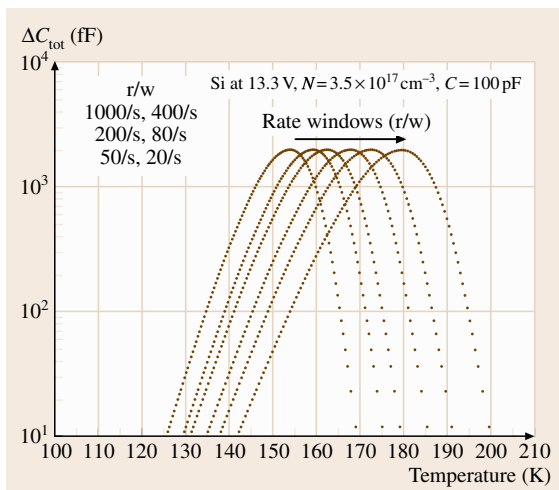


Fig. 9.49 DLTS measurement of the Au trap in n-type silicon doped with $3.5 \times 10^{17} \text{ cm}^{-3}$, reverse pulse: 13.3 V. The rate windows r/w are from *left to right*: 20/s, 50/s, 80/s, 200/s, 400/s, and 1000/s. The depletion capacitance is 100 pF

conductor. It can be seen from this equation that deep levels near midgap are most effective for generation and recombination because they lead to the largest generation or recombination rates U and thus give the lowest minority carrier lifetime according to (9.61). Thus, it is an important task of semiconductor materials quality assessment to determine the trap parameters N_T , E_T (respectively E_{trap}), σ_n , and σ_p to deduce all further generation and recombination statistics.

The DLTS Technique

The DLTS technique is based upon repetitive pulsing the bias of a Schottky diode or pn-diode from slight forward bias conditions (short pulse, some μs) into deep depletion for a considerably longer time (ms to s) and observe the resulting capacitance transient which stems from the charging and emptying of traps. During these repetitive measurements which also allow averaging of the mostly relatively small capacitance transients, the measurement temperature of the sample is varied over a large range, e.g. from 77 to 400 K. The development of this temperature dependent capacitance transient which is directly indicative for trap charging and emission is shown in more detail in this section.

Figure 9.50 shows the typical capacitance transient for the emission phase 3 of a majority carrier trap, i. e. a donor-like trap which is neutral in the electron occupied or filled state and positively charged in the empty state.

The process starts after phase (1), the empty (positively charged) state of all traps in reverse bias of the sample (not shown in Fig. 9.50, this corresponds to $C(t) \rightarrow \infty$), with a short filling pulse at $t < 0$, which is in the range of some μs . The time period 2 is long enough so that all majority carrier traps capture electrons from the conduction band because in the forward biased filling phase all traps are pulsed below the Fermi energy E_F . The traps are now neutrally filled at the end of phase (2). The emission phase (3) is started by pulsing the sample into deep depletion and the capacitance drops to a minimum $C(t=0) = C_0$. The resulting

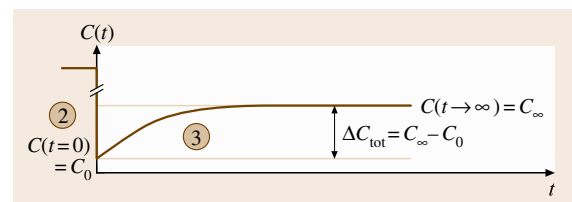


Fig. 9.50 Transient capacitance during majority carrier emission (3) after trap filling phase (2) of a donor-like trap

space charge depth is given by the bias voltage and the depleted donor charge of the shallow doping level. The traps are neutral at the beginning of the emission phase (3) and thus they do not contribute to the depleted space charge. Due to the high reverse bias V_r in phase (3) all traps are pushed above the Fermi energy and they are switched to emission. The capacitance transient $C(t)$ in the emission phase can be calculated with (9.63)

$$C(t) = A \sqrt{\frac{q\epsilon_0\epsilon_r}{2(V_{bi} + V_r)}} \left\{ N_D^+ + N_T [1 - \exp(-e_n t)] \right\} \quad (9.63)$$

with A denoting the area of the Schottky diode and V_{bi} representing the built-in voltage of the test diode. Towards the end of the emission phase (3) all traps are empty, i. e. after losing their electrons to the conduction band, the traps now contribute to the space charge of the shallow donors $N_D^{(+)}$ with concentration $N_T^{(+)}$. The transient capacitance thus changes by an amount $\Delta C_{tot} = C_\infty - C_0$. From the amplitude ΔC_{tot} of this transient, the trap concentration N_T can be deduced. For large trap concentrations and thus large capacitance transients, it may be practical to fit (9.63) with a transient capacitance measurement to extract the trap concentration. In practice, this direct way is difficult when the trap concentration falls below the shallow doping level by orders of magnitude. The transient will be buried within the noise of the measurement. In 1974 *Lang* published a procedure to detect very small capacitance transients out of the noise even when the trap concentration falls by 4–5 orders of magnitude below the shallow doping level: the **DLTS** technique [9.58].

Two aspects are important. First, according to the **DLTS** technique, the biasing sequence between filling (slight forward direction) and emptying (reverse voltage V_r) of the traps is applied repeatedly to the sample, thus averaging of the transient can be reached. Second, due to (9.60), the emission rate covers a very large range of more than 10 orders of magnitude if all possible trap positions between conduction band and midgap are considered. This implies too much problems for standard electronics in covering this large emission time range to measure the capacitance transient with sufficient resolution. Thus, the capacitance transient is observed by sampling within a given time window called the rate window rw . The measurement temperature is scanned such that the maximum of the transient amplitude can be easily observed for any given

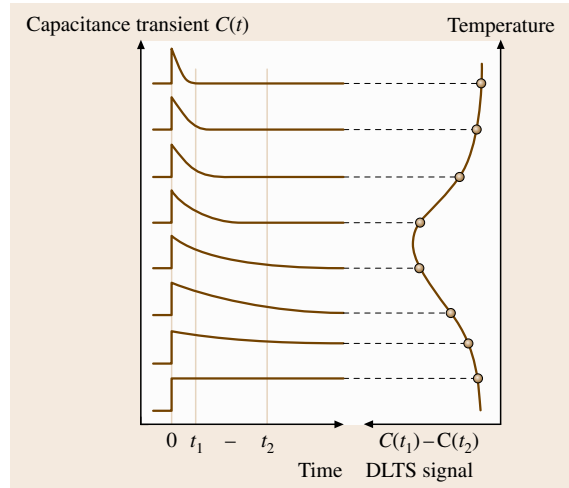


Fig. 9.51 Construction of a **DLTS** signal ($C(t_1) - C(t_2)$) by observing the temperature dependent transient capacitance within an observation time window ($t_2 - t_1$)

rate window rw . Figure 9.51 elucidates the principle of *Lang's DLTS* technique. For deep temperatures, the emission process is very slow, thus the capacitance stays practically constant over the observation time window $t_2 - t_1$. For high temperatures, the transient has occurred completely even before the first sampling time t_1 , thus the observed capacitance difference over $t_2 - t_1$ is again a constant. For a certain intermediate temperature, where the trap emission rate fits the observation time window, a maximum transient will be measured. The **DLTS** signal ($C(t_1) - C(t_2)$) (right) is the difference capacitance over the rate window rw , according to $t_2 - t_1$. If a trap is very shallow, i. e. located energetically near to the band edge, quite deep temperatures are needed to obtain the maximum of the **DLTS** signal.

The sign of the **DLTS** signal allows to determine the trap type, $\Delta C_{tot} > 0$: majority trap and $\Delta C_{tot} < 0$: minority carrier trap. Minority carrier traps in Schottky diodes can be excited by applying pulsed optical illumination (*optical DLTS*); in pn-diodes a sufficient forward biasing is necessary to inject minority carrier, to be trapped.

A typical **DLTS** measurement of the Au donor trap in n-type silicon is shown in Fig. 9.49. The shift of the **DLTS** peak to higher temperatures with increasing rate window can be observed i. e. the emission rate increases with increasing temperature. The trap concentration can be determined from the amplitude of the **DLTS** signal. For extracting the trap activation energy, the emission rates need to be plotted in an Arrhenius plot over the in-

verse of the temperature $1000/T$. From the same plot, the capture cross section for $T \rightarrow \infty$ can be extracted by extrapolating the emission rate for $1000/T \rightarrow 0$. A corresponding Arrhenius plot of the measurement in Fig. 9.49 is shown in Fig. 9.48. The measurement of the emission rate, deduced from the DLTS signal maxima for the different rate windows is shown in full line, the dashed lines represent comparison data from a trap library to assess the measured Arrhenius data compared to known data for easier identification. The measured activation energy is 340 meV. The dotted line is used for extrapolation of the capture cross section for $1000/T \rightarrow 0$.

The DLTS method cannot identify the physical nature of a trap or a deep level, e.g. if the level originates from a crystal defect or from an impurity. The big advantage of DLTS is its impressive sensitivity of N_T/N_D down to 10^{-6} , unsurpassed by other physical analyses. Trap concentrations as low as $< 10^{10} \text{ cm}^{-3}$ can be detected, this is 13 orders of magnitude below the crystals atomic concentration. Therefore electronic averaging of the sampled small capacitance transients applying boxcar or lock-in techniques are necessary. DLTS delivers fingerprints of deep levels, which should be compared to trap libraries of known defects, concerning activation energy and capture cross section. DLTS is spectroscopic, because traps with different activation energies appear with their maxima at different temperatures. If the spectra of two traps are overlapping, subtraction methods can be applied by simulating and approximating the DLTS maxima by Gaussian curves with different slopes and subtracting the leading peak from the rest of the spectrum until all traps have been identified.

A lot of extensions of the DLTS technique have been published. One important evaluation is the determination of the temperature dependence of the capture cross section of a deep level [9.61], having in mind that the standard DLTS technique allows only to measure the extrapolated capture cross section for $T \rightarrow \infty$. The method of Partin et al. is based on varying the width of the filling pulse to very short times until the traps cannot capture anymore carriers in the filling phase.

The Surface Recombination Velocity

Mesa diodes and also planar pn-diodes sometimes suffer from additional leakage currents across the surface or perimeter of the sample. Thus analyses of the bulk currents are impeded by surface currents, which are induced by additional surface recombination. The surface recombination is described by the surface recombi-

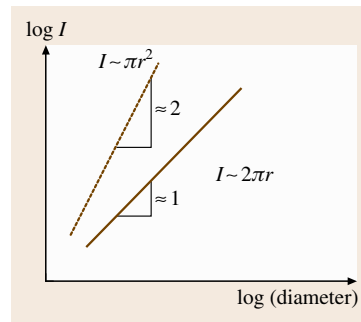


Fig. 9.52 Measured current of a test diode in double logarithmic plot versus diode diameter

nation velocity S_0 (cm/s). Surface recombination or generation occurs during nonequilibrium conditions, e.g. under reverse bias of a pn-junction. A surface recombination current j_s (A/cm^2) is directed perpendicular to the semiconductor surface

$$j_s = -qS_0\Delta n, \quad (9.64)$$

Δn is the deviation of the carriers from the equilibrium value. The surface recombination velocity S_0 can be expressed by surface state parameters, like the capture cross section of the surface state σ_0 (cm^2) and the concentration N_{st} (cm^{-2}).

$$S_0 = \sigma_0 v_{th} N_{st}. \quad (9.65)$$

To identify whether a measured current of a test sample is dominated by bulk or by surface conduction, a double logarithmic plot of the current versus the diameter of the samples under test is helpful (Fig. 9.52). If the current increases linearly with the diameter, then surface recombination is dominant. If the current increases quadratically with the diameter, bulk conduction is dominant.

Bulk conduction should be proved before current conduction mechanisms or parameters are extracted from I - V measurements, like Schottky barriers, ideality factors, Shockley-Read-Hall trap parameters, or reverse current analyses are done with respect to tunneling or impact ionization.

9.4.6 Contact Resistances of Metal-Semiconductor Contacts

Ohmic contacts at semiconductor devices are mandatory to connect the inner active regions to the outside circuitry or other devices. Ideal ohmic contacts may be described by several views of physicists or engineers on the idealization of the tasks of ohmic contacts, i. e. ohmic contacts should provide

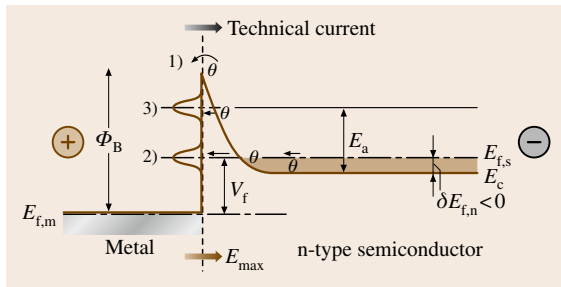


Fig. 9.53 Band diagram of a highly doped, degenerated metal–semiconductor contact under forward bias conditions (metal is positive with respect to the grounded n-type semiconductor)

- a bipolar linear I – V characteristics,
- an unlimited high recombination rate for minority carriers,
- negligible voltage decay compared to that of the active regions,
- no minority carrier injection.

Basic work on the description and technology of ohmic contacts to semiconductors can be found in [9.62, 63]. The main current conduction mechanisms in ohmic contacts are elucidated in Fig. 9.53. A metal is evaporated onto an n-type semiconductor. The work function difference to the electron affinity of the n-type semiconductor should be well chosen to induce at best either an accumulation region at the semiconductor side or at least a small barrier height Φ_B . This has to be surmounted or penetrated by electrons from the semiconductor, e.g. here under forward biasing conditions. A more or less small barrier is a usual case for a lot of metals to semiconductors. If the barrier cannot be avoided principally, it should be only a small obstacle to be surmounted or penetrated. Three current conduction mechanisms should be mentioned here which help electrons to cross the interface into the metal.

1. Thermal emission: electrons have to surmount the barrier V_{bi} ($\approx \Phi_B$) which is only possible for a few electrons with enough energy compared to the thermal energy kT . Consequently, thermal emission results into bad ohmic contacts. Mostly, these contacts exhibit rectifying characteristics at room temperature. Thermal emission is favored exponentially at high temperatures (thermal process).
2. Field emission or tunneling: this quantum mechanical process allows electrons, due to their wave-like nature, to penetrate the barrier without energy loss if the barrier width is small compared to the de

Broglie wavelength (9.58). This process is likely at very high degenerate doping levels ($\gg 10^{18} \text{ cm}^{-3}$) which induce very narrow space charge regions ($< 10 \text{ nm}$) and consequently very narrow tunneling barrier widths. This process is nearly temperature independent and useful even at very low temperatures because no thermal activation is needed for quantum mechanical tunneling.

3. Thermal field emission or thermally activated tunneling: A certain part of the electrons are thermally activated to penetrate the barrier at an enhanced energy position by tunneling but below the peak of the barrier.

Both current conduction mechanisms 1. and 3. contribute in series to the conduction *over* the barrier. Compared to the aforementioned processes the electrons *see* a smaller and narrower barrier. This mechanism is likely for intermediate doping levels.

Figure 9.54 depicts the behavior of the contact resistance of different metals on n-type silicon versus the silicon doping level [9.63]. The contact resistance ($\Omega \text{ cm}^2$) strongly decreases with increasing doping level when thermionic conduction is taken over by tunneling or field emission.

Technically useful contact resistances should be below $10^{-5} \Omega \text{ cm}^2$. Thus, doping levels in excess of 10^{19} cm^{-3} are needed here to guarantee clear predominance of tunneling over thermionic emission. Values of contact resistances lower than $10^{-7} \Omega \text{ cm}^2$ are achievable today.

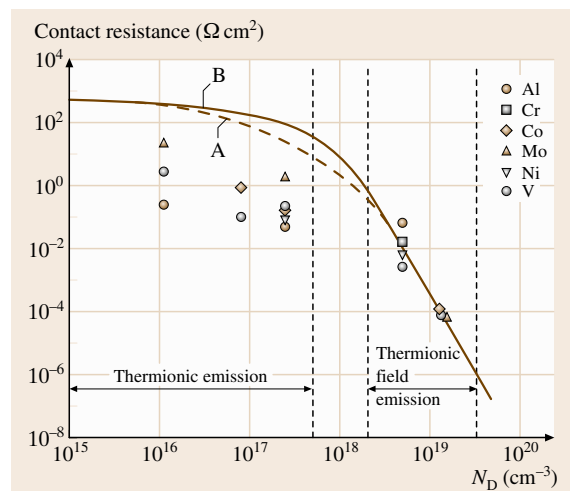


Fig. 9.54 Contact resistance of various metals on n-type silicon depending on doping N_D (after [9.18])

The more exactly termed specific contact resistance $R_{c,\text{spec.}}$ ($\Omega \text{ cm}^2$) is solely the contact resistance in the interface between metal and semiconductor, while the (total) contact resistance R_c (Ω) comprises additional contributions of the spreading resistance of the semiconductor which is depending on the current field lines and thus on the geometry of the ohmic contact: distinguish contacts with vertical current spreading (e.g. top contacts to lasers or emitter contacts to bipolar transistors) and contacts with lateral current spreading (e.g. base contacts in bipolar transistors or source/drain contacts to field-effect transistors). The latter contact type exhibits a strong inhomogeneous current density over the contact length compared to the former contact type, which has a better homogeneous current distribution over its contact area.

Measurement techniques for contact resistances may be attributed to the aforementioned contact geometry. They should allow to extract the (low) specific contact resistance from the (somewhat higher) total contact resistance to provide information for optimizing the contact resistance, e.g. by annealing procedures.

Measurements on ohmic contacts should be done applying a Kelvin contact configuration which means to feed a constant current via two terminals (needles) to the pads of the contacts to be characterized and using two different terminals (needles) to measure the resulting (small) voltage between the contact pads. In this way, distorting effects of additional contact resistances between the measurement needles and the contact pads can be eliminated.

A method for characterizing contact resistances of contacts with nearly homogeneous current flow into vertical contacts uses contact dots of different diameters on the semiconductor, to distinguish between the specific contact resistance and the spreading resistance contributions. This method by *Cox* and *Strack* is described in [9.65].

A more versatile method which is mainly applied to lateral contacts to thin semiconductor layers with strongly inhomogeneous current flow, is the transmission line method by *Berger* [9.64]. Figure 9.55 shows the current distribution in this lateral contact type. The semiconductor layer is assumed with a specific resistance ρ_s ($\Omega \text{ cm}$) and its sheet resistance R_s (Ω/\square): $R_s = \rho_s/h$. For technically relevant contacts, the semiconductor sheet height h is often quite less than the contact length d . For this configuration, the following equivalent circuit can be derived (Fig. 9.56). The resistance of the epitaxial layer is described by the sum of its differential elements dR_1 .

The specific contact resistance $R_{c,\text{spec.}}$ ($= \rho_c$) is represented by the distributed vertical elements dR_2 . The total contact resistance R_c is the ratio of the voltage at the left beginning of the contact region and the total constant current I fed into the structure. According to the transmission line nature of such a structure [9.64], the specific contact resistance ρ_c may be extracted from the measurement of the total contact resistance R_c . For that purpose differential equations are formulated [9.64] which can be solved giving a relation between total and specific contact resistance in an implicit equation (9.66)

$$R_c = \frac{1}{w} \sqrt{R_s (\rho_c + 0.2 R_s h^2)} \times \coth \left(\sqrt{\frac{R_s}{\rho_c + 0.2 R_s h^2}} d \right). \quad (9.66)$$

This implicit equation allows the extraction of ρ_c after R_c has been measured and the geometrical constants w , h , and d of the test structure have been determined. The sheet resistance R_s of the epitaxial layer between two contact stripes has also to be measured before.

The measurement of R_s and R_c can be done with a setup of three contact stripes in a Kelvin contact configuration with two distances l_1 and l_2 between two contacts (Fig. 9.57).

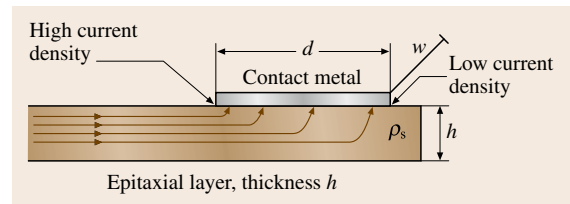


Fig. 9.55 Lateral contact of width w and of length d on a thin epitaxial layer of thickness h (after [9.64])

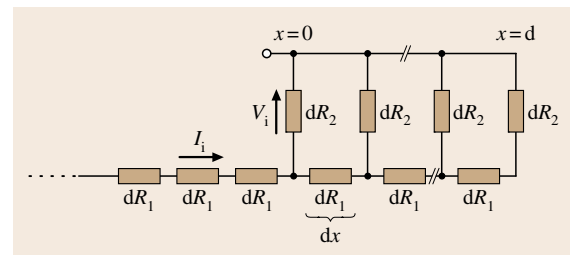


Fig. 9.56 Equivalent circuit diagram of a lateral ohmic contact according to the current distribution in Fig. 9.55 for the contact resistance of a metal on a thin semiconductor layer

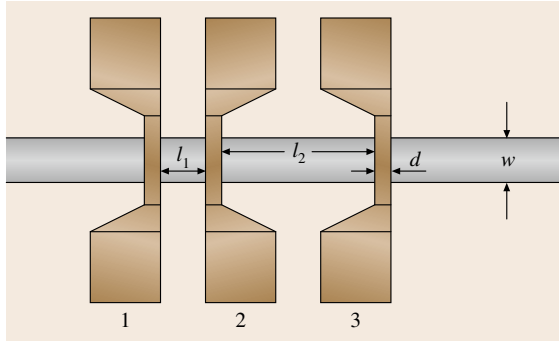


Fig. 9.57 TLM mask for the determination of the sheet resistance R_s and total contact resistance R_c from which the specific contact resistance ρ_c can be extracted (TLM: transmission line model)

Two measurements need to be taken: first, the current I (mA range) is fed through the epitaxial layer stripe of width w by using the two left-hand contacts 1, 2 with distance l_1 and measuring the voltage V_1 ; second, the two contacts 2, 3 with distance l_2 are used to measure the respective voltage V_2 by driving the same amount of current through the epitaxial layer.

From these two voltage values V_1 and V_2 together with the constant current I the sheet resistance R_s and

the total contact resistance R_c under each contact can be calculated by

$$R_s = \frac{V_1 - V_2}{I} \frac{w}{l_1 - l_2}, \quad \text{and}$$

$$R_c = \frac{1}{2} \left(\frac{V_1}{I} - l_1 \frac{R_s}{w} \right). \quad (9.67)$$

With these two terms now (9.66) can be used to extract the specific contact resistance ρ_c . The contact distances l_1 and l_2 (1–100 μm) need to be determined with high precision (submicrometer range) because otherwise larger errors would result for ρ_c , especially when ρ_c falls below $10^{-6} \Omega \text{cm}^2$.

For electrically long contacts (e.g. $d = 40 \mu\text{m}$) the transfer length L_T is defined as $L_T = \sqrt{\rho_c / R_s}$. The transfer length illustrates the typical length for the current to pass from the epitaxial layer into the metal contact. Practical contacts do not need to be designed longer than about three transfer lengths.

The transfer resistance R_T is defined as $R_T = \sqrt{R_s \rho_c}$ (Ωmm). The transfer resistance characterizes the lowest contact resistance which can be achieved for an electrically long contact of a given width w . Transfer resistance values for e.g. FETs should be lower than $0.2 \Omega \text{mm}$.

9.5 Measurement of Dielectric Materials Properties

Dielectric materials are the building blocks of functional electronic circuits, capacitors, gate dielectrics, transmission lines are essential as electrical insulators for power distribution. Molecular solids, organic polymer resins, ceramic glasses and composites of organic resins with ceramic fillers represent typical dielectrics. The dielectric properties of materials are used to describe electrical energy storage, dissipation and energy transfer. Electrical storage is the result of *dielectric polarization*. Dielectric polarization causes charge displacement or rearrangement of molecular dipoles. Electrical energy dissipation or *loss* results from

1. electrical charge transport or *conduction*,
2. *dielectric relaxation*,
3. *resonant transitions* and
4. *nonlinear dielectric* effects.

Energy loss is eventually related to scattering, radiation or conversion of electrical energy into thermal energy (Joule heating). Energy transfer is related to propagation of electromagnetic waves in dielectric media,

transmission lines and waveguides, where the dielectric permittivity determines the velocity of wave propagation, attenuation and ultimately the dimensions of the devices.

It is important to understand the basic characteristics of these processes because they determine the optimal approach to measurement.

Interaction of electromagnetic radiation with materials at frequencies of about 10^{12} Hz and above gives rise to quantized transitions between the electronic, vibrational and rotational molecular energy states, which can be observed by using appropriate quantum spectroscopy techniques. By contrast, the dielectric properties are governed by reorientational motions of molecular dipoles (dipolar relaxation) and motions of electrical charge carriers (electrical conduction), which leads to continuous dielectric dispersion and absorption that is observed in the frequency range of 10^{-6} – 10^{12} Hz.

The dielectric relaxation [9.66] describes the dispersion of real permittivity ϵ' and the occurrence of dielectric absorption ϵ'' . Permittivity measurements

allows for the determination of molecular dipole moments and, subsequently, can link the relaxation process with molecular dynamics and structure. The dielectric absorption (loss) spectra as a function frequency and temperature [9.67, 68], can be used to characterize molecular dynamics in dipolar liquids (polar solvents and solutes), rotator-phase crystals, nonpolar and polar polymers (polyethylene, polyacrylates, epoxy resins, polyimides). Research on dielectric relaxation in molecular liquids and solids was pioneered by Fröhlich [9.69], Hill et al. [9.70], Bottcher and Bordewijk [9.71], and for macromolecules by McCrum et al. [9.72], and Runt and Fitzgerald [9.73]. Selected developments in dielectric and related molecular processes were reviewed by Davies [9.74]. Since 1954, the most widely known and comprehensive work on dielectric materials and corresponding measurements has been that of von Hippel [9.75]. Measurement of RF properties of materials were surveyed by Bussey [9.76]. Broadband waveguiding and free-space measurement methodologies for the agriculture industry were developed by Nelson and coworkers [9.77, 78]. Extensive dielectric data were obtained recently for ferroelectric ceramics (barium titanate), inorganic and organic semiconductors and photoconductors, for ultra thin dielectrics films, which have important applications in solid-state electronic circuits and devices. Recent advances in the theory of dielectric relaxation and the corresponding experimental methodologies were reviewed by Kremer and Schönhals [9.79].

9.5.1 Dielectric Permittivity

The interaction of electromagnetic fields with matter is described by Maxwell's equations [9.80]. The polarization \mathbf{P} describes the dielectric displacement \mathbf{D} which originates from the response of the material to an external electric field \mathbf{E}

$$\mathbf{P} = \mathbf{D} - \varepsilon_0 \mathbf{E} = (\varepsilon_r^* \varepsilon_0 - \varepsilon_0) \mathbf{E}, \quad (9.68)$$

where ε_0 is the dielectric permittivity of free space ($\varepsilon_0 = 8.854 \times 10^{-12}$ F/m), and $\varepsilon^* = \varepsilon_0 \varepsilon_r^* = \varepsilon' - i\varepsilon''$ is the complex permittivity tensor, which depends on temperature, frequency, and in the case of anisotropic materials, on the direction of the electric field vector \mathbf{E} . The frequency dependence of the permittivity is illustrated in Fig. 9.58.

Relative permittivity ε_r^* is a dimensionless ratio of complex permittivity to the permittivity of free space $\varepsilon_r^* = \varepsilon^*/\varepsilon_0 = \varepsilon_r' - i\varepsilon_r''$. The dielectric constant is the real part of the relative permittivity. The symbol used in this

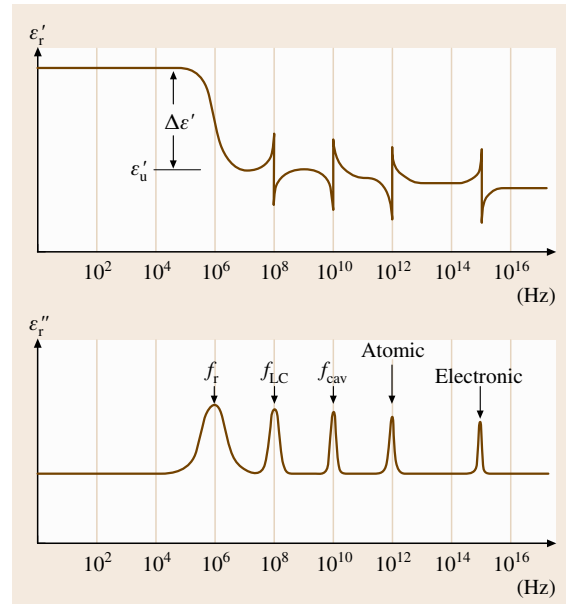


Fig. 9.58 Frequency dependence of the real ε_r' , and imaginary ε_r'' parts of the complex permittivity with a single relaxation process at the relaxation frequency f_r

document is ε_r' (other symbols such as K , k , K' , k' , ε_r and ε' are used in the technical literature). Dielectric loss tangent $\tan(\delta)$ is a dimensionless ratio of the dielectric loss ε_r'' to the dielectric constant ε_r' , $\tan(\delta) = \varepsilon_r''/\varepsilon_r'$. Figure 9.58 illustrates that the real part of dielectric permittivity decreases by $\Delta\varepsilon_r'$ at a certain frequency f_r which gives rise to a corresponding peak of the dielectric loss ε_r'' . Such frequency dependence of the complex permittivity indicates a *dielectric relaxation*. A dielectric material may exhibit several dielectric relaxation processes, each associated with its characteristic $\Delta\varepsilon_r'$, ε_r'' and f_r depending on the molecular mechanism involved.

The dielectric relaxation should not be confused with resonant transitions between vibrational and electronic states and those that originate from a resonant behavior of the electrical measurement circuit.

Dielectric Relaxation

Unlike *electrical conduction* in which charge carriers (electrons, ions and holes) move physically through the material under the influence of an electric field, the *dielectric relaxation* originates from reorientational responses of electric dipoles to the applied electric field. Materials in which the dipoles are induced only by the application of an electric field are nonpolar mater-

ials. Polar materials, on the other hand, have permanent molecular dipoles which may exhibit a number of different relaxation processes, each having a characteristic strength measured by $\Delta\epsilon'_r$, and a characteristic relaxation frequency f_r . In the simplest case with a single relaxation time τ_r the dielectric relaxation function may be described by Debye's model [9.66], shown by (9.69). Here ϵ'_u is the dielectric constant at high frequencies, which does not contain a permanent dipole contribution ($\epsilon'_r = \epsilon'_u$ when $f \gg f_r$, Fig. 9.58)

$$\frac{\epsilon^*}{\epsilon_0} = \epsilon'_u + \frac{\Delta\epsilon_r}{1 + i\omega\tau_r}. \quad (9.69)$$

Cooperative distortional polarization, local rotational polarization and interfacial polarization are the most commonly observed relaxation processes. In a composite material, many or all of these processes may be present and give rise to a very complex relaxation behavior, which can be modeled as a superposition of several relaxations. The Havriliak–Negami (HN) relaxation function, defined below, has often been found to provide a good phenomenological description of dielectric relaxation data in molecular liquids, solids and glass formers [9.81, 82]

$$\frac{\epsilon^*}{\epsilon_0} = \sum_k \left(\epsilon'_u + \frac{\Delta\epsilon_r}{[1 + (i\omega\tau_r)^\alpha]^\gamma} \right), \quad k = 1, 2, 3, \dots \quad (9.70)$$

The parameters α and γ describe the extent of symmetric (α) and asymmetric (γ) broadening of the complex dielectric function, where α and γ are ($0 < \alpha \leq 1$ and $0 < \alpha\gamma \leq 1$). Equation (9.70) reduces to the well-known Debye expression when $\alpha = \gamma = 1$. While the HN equation is often referred to as an *empirical* relaxation function, recent modeling has linked the parameters α and γ to the degree of intermittency in molecular movement and long-lived spatial fluctuations in local material properties (*dynamic heterogeneity*) [9.83], which gives some insight into the meaning of the fitted parameters. In this view, the exponent α is related to the temporal intermittency of molecular displacements while γ corresponds to long-lived *dynamic heterogeneities* (or dynamic clusters). It is beyond the scope of this chapter to explain the theory of these processes and the reader is advised to consult references [9.84–87].

Regardless of the particular molecular mechanism of the dielectric relaxation, the phenomenological dependence of ϵ'_r on frequency, as shown in Fig. 9.58, can be used as a guide to select an appropriate measurement method, and then be applied to describe and analyze the dielectric properties of most dielectric materials.

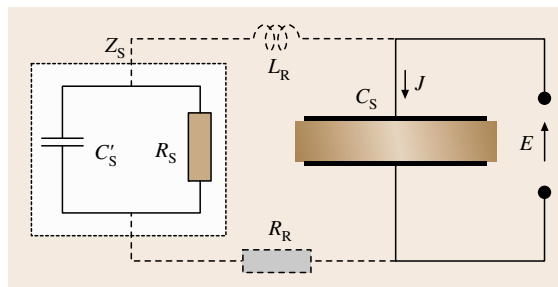


Fig. 9.59 Equivalent electrical circuit of a dielectric material

According to Fig. 9.58, the frequency spectrum can be divided into several regions, each corresponding to a characteristic dielectric response.

1. At low frequencies, well below f_r , dipoles easily respond and align with the applied alternating E -field without a time lag. The dielectric loss is negligibly small and the polarization as measured by ϵ'_r can achieve the maximum value, which depends on the statistical distribution of thermally induced molecular orientations and the amplitude of the applied field. At higher fields, polarization saturation may occur, where all the dipoles are aligned. The E -field induced polarization dominates over the thermal effects, giving rise to a *nonlinear dielectric response*.
2. At frequencies close to f_r , the molecular dipoles are too slow to reorient in phase with the alternating electric field. They lag behind and their contribution to ϵ'_r is smaller than that at low frequencies. This time lag or phase difference between E and P gives rise to the dielectric loss which peaks at f_r .
3. At frequencies above f_r the particular molecular dipoles cannot follow the electric field and do not contribute to ϵ'_r and ϵ''_r , and $\epsilon'_r = \epsilon'_u$.

It is important to note that the relaxation process always leads to a decrease of ϵ'_r with increasing frequency. Dipolar relaxation can be adequately described by an electrical equivalent circuit consisting of a capacitance C_s connected in parallel with resistance R_s which is illustrated in Fig. 9.59. Both, C_s and R_s can be experimentally measured and related to the material's dielectric properties ϵ'_r and ϵ''_r .

Resonant Transitions

The rapid oscillations of ϵ'_r shown in Fig. 9.58 at frequencies above f_r indicate a resonance. Similarly to relaxation, the resonance transitions are associated with the dielectric loss peak. However, the distinguished fea-

ture of a resonance transition is a singular behavior of ϵ_r' at the resonant frequency. From the dielectric metrology viewpoint, the most important resonances are the series resonance and the cavity resonance. These transitions are typically observed in the radio-frequency range and at microwave frequencies, respectively.

Series Inductance–Capacitance Circuit Resonance

Every electrical circuit consists of interconnecting leads that introduce finite residual inductance L_R . Therefore, when measuring a capacitance C_s there will be a certain frequency $f_{LC} = 1/(2\pi\sqrt{L_R C_s})$ at which a series resonance occurs. The equivalent electrical circuit for the series resonance consists of C_s in series with L_R . The residual resistance R_R is due to finite conductivity of the interconnects (Fig. 9.59). Since at f_{LC} the energy is concentrated in the magnetic field (or current) of the inductive component L_R rather than in the electric field in C_s , these resonance conditions generally are not useful in measurement of the dielectric permittivity. The phenomenon is a common source of systematic errors in dielectric metrology unless the inductance is known or introduced purposely [9.88] to determine the capacitance from the resonant frequency. The characteristic feature of the series resonance is a rapid decrease in the measured complex impedance which reaches the value of R_R when the frequency approaches f_{LC} . The drop in the impedance is associated with an abrupt change of phase angle from $-\phi$ to ϕ . The C_s value appears very large near f_{LC} when L_R is neglected in the equivalent circuit (Fig. 9.59), and consequently, it can be incorrectly interpreted as an apparent increase in the dielectric constant (Fig. 9.58).

Dielectric Resonance

When the dimensions (l) of the dielectric specimen are comparable with the guided wavelength $\lambda_g = \lambda_0/\sqrt{\epsilon_r'}$ a superposition of the transmitted and reflected waves leads to a standing wave called cavity or dielectric resonance. At the resonant frequency, the electromagnetic energy is concentrated in the electric field inside the dielectric. Therefore the measurement techniques that are based on the dielectric resonators are the most accurate methods for determining the dielectric permittivity of low loss materials.

Infrared and Optical Transitions

Interaction of electromagnetic radiation with materials at frequencies of about 10^{12} Hz and above gives rise to quantized resonant transitions between the elec-

tronic, vibrational and rotational molecular energy states. These transitions are responsible for a singular behavior of the dielectric permittivity and the corresponding absorption, which can be observed by using appropriate quantum spectroscopy techniques. These quantum spectroscopies form a large part of modern chemistry and physics. At optical frequencies the materials dielectric properties are described by complex optical indices, $n^* = \sqrt{\epsilon^*}$, rather than permittivity.

9.5.2 Measurement of Permittivity

Techniques for complex permittivity measurement may be subdivided into two general categories [9.75].

1. The frequency range, typically below 1 GHz, over which the dielectric specimen may be treated as a circuit of lumped parameter components. Because the mathematical manipulations are relatively simple, the lumped parameter circuit approximate equations can always be used when they yield the required accuracy over sufficiently broad frequency range.
2. The high frequency range where the wavelength of the electric field is comparable to the physical dimensions of the dielectric specimen and, as a consequence, it is often referred as a distributed parameter system. Distributed parameter analysis based on the exact relations obtained from Maxwell's equations, is necessary when the effective values of circuit elements change rapidly with frequency, or when the highest accuracy is needed.

In the low frequency range, where the wave propagation effects can be neglected, the equivalent complex impedance Z_s of the relaxation circuit shown in Fig. 9.59 can be measured to determine the complex capacitance C_s and then the material's relative complex permittivity ϵ_r^* . In the following discussion complex impedance $Z_s = Z_s' - iZ_s''$ is considered to be a constant proportionality of sinusoidal voltage and current. Parameters shown in bold face indicate complex (vector) quantities.

When a capacitor is filled with a dielectric material (Sect. 9.1.6) the resulting capacitance is C_s and the dielectric permittivity is defined by (9.71)

$$\epsilon_r^*(\omega) = \epsilon_r'(\omega) - i\epsilon_r''(\omega) = \frac{C_s(\omega)}{C_0}, \quad (9.71)$$

where C_0 is the capacitance of the empty cell and ω is the angular frequency ($\omega = 2\pi f$).

If the sinusoidal electric field $E(\omega) = E_0 \exp(i\omega t)$ is applied to C_s then the dielectric permittivity can be de-

terminated by measuring the complex impedance Z_s of the circuit.

$$\frac{1}{Z_s(\omega)} = i\omega C_s, \quad (9.72)$$

$$\epsilon_r^*(\omega) = \frac{1}{i\omega Z_s C_0}, \quad (9.73)$$

Consistent with the electrical equivalent circuit of the real capacitance C'_s in parallel with a resistance R_s the impedance is given by

$$\frac{1}{Z_s(\omega)} = \frac{1}{R_s} + i\omega C'_s \quad (9.74)$$

and the direct expressions for ϵ'_r and ϵ''_r are

$$\epsilon'_r = \frac{C'_s}{C_0}, \quad (9.75)$$

$$\epsilon''_r = \frac{1}{\omega R_s C_0}. \quad (9.76)$$

The capacitance of the empty cell C_0 (cell constant) is typically determined from the specimen geometry or measurements of standard materials with known dielectric permittivity. Commercially available dielectric test fixtures have the cell constant and error correction formulas provided by their manufacturers [9.89, 90].

Impedance Measurement Using a Four-Terminal Method

In the frequency range of up to about 10^8 Hz, a four terminal (4T) impedance analyzer can be employed to measure complex impedance of the capacitance C_s and then the permittivity can be calculated from (9.74–9.76). The 4T methodology refers to the direct phase sensitive measurement of the sample's current and voltage. Systems combining Fourier correlation analysis with dielectric converters and impedance analysis have recently become commercially available [9.79]. The

recently developed dielectric instrumentation incorporates into one device a digital synthesizer-generator, sine wave correlators and phase sensitive detectors, capable of automatic impedance measurements from 10^{-2} to 10^{13} Ω . The broad impedance range also allows a wide capacitance measurement range with resolution approaching 10^{-15} F. The instrumentation should be calibrated against appropriate impedance standards using methods and procedures recommended by their manufacturers.

The dielectric samples typically utilize a parallel-plate or cylindrical capacitor geometry [9.75, 91] having capacitances of about 10 pF to several hundred pF. The standard measurement procedures [9.91] recommend a three-terminal (3T) cell configuration with a guard electrode (G), which minimizes the effect of the fringing and stray electric fields on the measurements. The optimal method for connecting a 3T circular cell to a 4T impedance analyzer is shown in Fig. 9.60.

The *high* current on voltage terminals should be connected via coaxial cables directly to the unguarded electrode H , while the *low* current and voltage should be connected to the electrode that is surrounded by the guard electrode. Note that the return current loop of coaxial shields connections S should be short and connected to G at a single common point. The return current loop S is absolutely necessary for accurate impedance measurements, especially above 1 MHz. In a two terminal configuration (2T) without the guard electrode, the connections S should be simply grounded together.

The dielectric constant, dielectric loss and the relaxation frequency are temperature dependent. Therefore, it is essential to measure the specimen temperature and to keep it constant (isothermal conditions) during the measurements.

Impedance Measurements Using Coaxial Line Reflectometry

In the 4T configuration the residual inductance L_R of interconnecting cables contributes to the circuit impedance creating conditions for the series resonance at $f_{LC} \approx 1/(2\pi\sqrt{L_R C'_s})$, which limits the usable frequency range. Typically, the series resonance occurs above about 30 MHz. Impedance at higher frequencies may be determined from the reflection coefficient using microwave techniques with precision transmission lines. In these techniques the reference plane can be set up right at the specimen section which largely eliminates propagation delay due to L_R . When a dielectric specimen of impedance Z_s terminates a transmission line that has a known characteristic impedance Z_0 and known wave

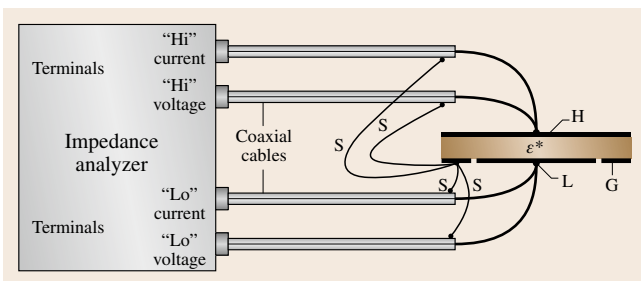


Fig. 9.60 A 3T cell to an 4T impedance analyzer. H and L are the high and low potential electrodes respectively; G is the guard electrode; S are the return current loops of coaxial shield connections

propagation characteristic, the impedance mismatch between the line and the specimen results in reflection of the incoming wave. The relation between Z_s and complex reflection coefficient Γ is given by (9.77) [9.92,93]

$$\Gamma = \frac{Z_s - Z_0}{Z_s + Z_0} \quad (9.77)$$

It follows from (9.77) that when the line is terminated with a *short* ($Z_{\text{short}} = 0$) then $\Gamma = -1$. For an *open* termination ($Z_{\text{open}} = \infty$) $\Gamma = 1$, while in the case of a matched load, when $Z_s = Z_0$, $\Gamma = 0$, which results in no reflection. These three terminations, i. e. *short, load and open*, are used as calibration standards for setting-up the reference plane and proper measurement conditions of the reflection coefficient $|\Gamma|$ and the phase angle ϕ .

Many coaxial line configurations are available in the RF and microwave ranges, each designed for a specific purpose and application. The frequency range is limited by the excitation of the first circular waveguide propagation mode in the coaxial structure [9.92]. Decreasing the diameter of the outer and inner conductors increases the highest usable frequency. The following is a brief review of coaxial line configurations, having Z_0 of 50 Ω , most commonly used for microwave testing and measurements [9.94].

Precision APC-7 mm Configuration

The APC-7 (Amphenol Precision Connector-7 mm) utilizes air as a dielectric medium between the inner and outer conductors. It offers the lowest reflection coefficient and most repeatable measurement from DC to 18 GHz, and is the preferred configuration for the most demanding applications, notably metrology and calibration. The diameter of the inner conductor $d = 3.02$ mm and the diameter of the outer conductor $D = 7.00$ mm (Fig. 9.61) determines the characteristic impedance value of 50 Ω [9.92].

Precision APC-3.5 mm Configuration

The 3.5 mm configuration also utilizes air as a dielectric medium between the inner and outer conductors. It is mode free up to 34 GHz.

Precision-2.4 mm Configuration

The 2.4 mm coaxial configuration was developed by Hewlett Packard and Amphenol for use up to 50 GHz. It can mate with the APC 3.5 mm connector through appropriate adapters. The 2.4 mm coaxial line is offered in three quality grades: general purpose, instrument, and metrology. The general purpose grade is intended for economy use on components and cables. Instrument

grade is best suited for measurement applications where repeatability and long life are primary considerations. Metrology grade is best suited for calibration applications where the highest performance and repeatability are required.

1.85 mm Coaxial Configuration

The 1.85 mm configuration was developed in the mid-1980s by Hewlett Packard, now Agilent Technologies, for mode-free performance to about 65 GHz. HP offered their design to the public domain in 1988 to encourage standardization of this connector types. Nevertheless, few devices and instrumentation are available today from various manufacturers, mostly for research work. The 1.85 mm connector mates with the 2.4 mm connector.

1.0 mm Coaxial Configuration

Designed to support transmission all the way up to 110 GHz, approaching optical frequencies. This 1.0 mm coaxial configuration, including the matching adapters and connectors, is a significant achievement in precision microwave component manufacturing.

Coaxial Test Fixtures

There is a large family of coaxial test fixtures designed for dielectric measurements.

Open-ended coaxial test fixtures (Fig. 9.61a) are widely used for characterizing thick solid materials and liquids [9.95], and are commercially available (Agilent, Novocontrol Dielectric Probes) [9.96]. The measurements are conveniently performed by contacting one flat surface of the specimen or by immersing the probe in the liquid sample.

Short-terminated probes (Fig. 9.61b) are better suited for thin film specimens. Dielectric materials of

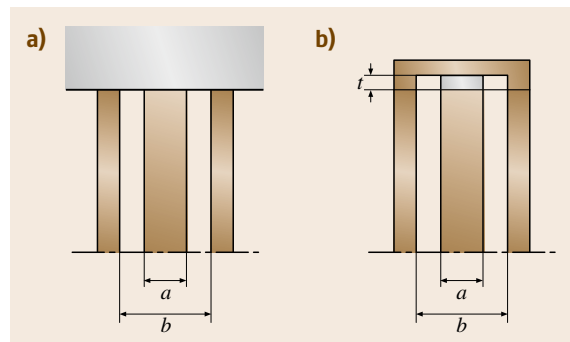


Fig. 9.61 (a) Open-ended, and (b) short terminated coaxial test fixture with a film specimen of thickness t

precisely known permittivity (air, water) are often used as a reference for correcting systematic errors in measuring $|\Gamma|$ and the phase angle ϕ , that are due to differences between the measurement and the calibration configurations. If the relaxation circuit satisfies the lumped parameters, then ε'_r and ε''_r can be obtained by combining (9.73) and (9.77) [9.97, 98]

$$\varepsilon'_r = \frac{-2|\Gamma| \sin \phi}{\omega Z_0 C_0 (1 + 2\Gamma \cos \phi + |\Gamma|^2)}, \quad (9.78)$$

$$\tan \delta = \frac{\varepsilon''_r}{\varepsilon'_r} = \frac{1 - |\Gamma|^2}{-2|\Gamma| \sin \phi}. \quad (9.79)$$

In practice, the conventional lumped parameter formulas (9.78, 9.79) and the corresponding test procedures are accurate up to a frequency at which the impedance of the specimen decreases to about one tenth (0.1) of the characteristic impedance of the coaxial line. Since the standard characteristic impedance of coaxial configuration listed above is 50Ω , the lowest usable impedance value of lumped-parameter circuits is about 5Ω , hence, $f_{\max} \approx 1/(10\pi C'_s)$ [9.99]. Depending on the specimen permittivity and thickness, this upper frequency limit in the APC-7 configuration is typically below 5 GHz. At frequencies $f > f_{\max}$, wave propagation causes a spatial distribution of the electric field inside the specimen section which can no longer be treated as a lumped capacitance and has to be analyzed as a microwave network.

9.5.3 Measurement of Permittivity Using Microwave Network Analysis

Microwave network analyzer terminology describes measurements of the incident, reflected, and transmitted electromagnetic waves [9.100]. The reflected wave can be, for example, measured at the Port 1, and the transmitted wave is measured at Port 2 (Fig. 9.62).

If the amplitude and phase of these waves are known, then it is possible to quantify the reflection and transmission characteristics of a material under test (MUT) with its dielectric permittivity and the dimensions of the test fixture. The reflection and transmission parameters can be expressed as vector (magnitude and phase), scalar (magnitude only), or phase-only quantities. In this notation, impedance Z , reflection coefficient Γ and complex wave amplitudes a_i , b_i are vectors. Network characterization at low frequencies is usually based on measurement of complex voltage and current at the input or output ports (terminals) of a device. Since it is difficult to measure total current or voltage at high frequencies, complex scattering parameters, S_{11} ,

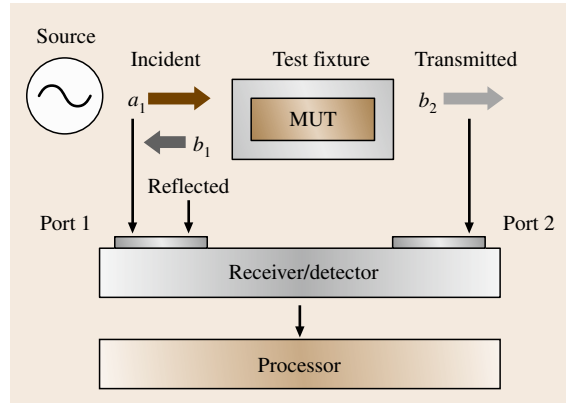


Fig. 9.62 Block diagram of a network analyzer

S_{12} , S_{21} and S_{22} are generally measured instead [9.101, 102]. Measurements relative to the incident wave allow normalization and quantification the reflection and transmission measurements to obtain values that are independent of both, absolute power and variations in source power versus frequency. The scattering parameters (S -parameters) are defined by (9.80) [9.101]

$$\begin{aligned} b_1 &= S_{11}a_1 + S_{12}a_2, \\ b_2 &= S_{21}a_1 + S_{22}a_2. \end{aligned} \quad (9.80)$$

A general signal flow graph of a two-port network with the corresponding scattering parameters is shown in Fig. 9.63a. Here a_1 and a_2 are the complex amplitudes of the waves entering the network, while b_1 and b_2 are complex amplitudes of the outgoing waves.

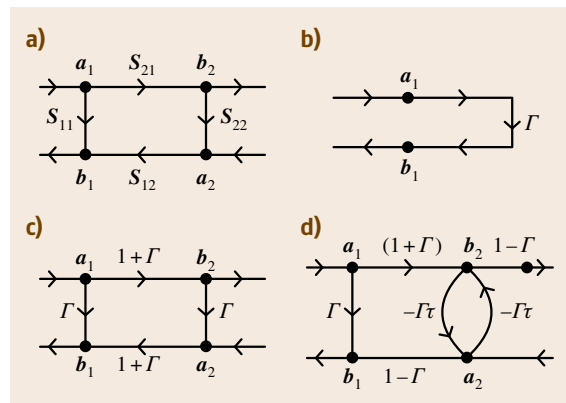


Fig. 9.63a–d Scattering parameters signal flow diagrams: (a) two-port network, (b) load termination, (c) shunt admittance, (d) transmission line partially filled with a dielectric specimen of a transmission coefficient τ

The number of S -parameters for a given device is equal to the square of the number of ports. For example, a two-Port device has four S -parameters. The numbering convention for S -parameters is that the first number following the S is the Port at which energy emerges, and the second number is the port at which energy enters. S_{21} is a measure of power emerging from Port 2 as a result of applying an RF stimulus to Port 1. Same numbers (e.g. S_{11} , S_{22}) indicate a reflection measurement. The measured S -parameters of multiple devices can be cascaded to predict the performance of more complex networks. Figure 9.63b shows a termination or load with a reflection coefficient Γ . Since there is no transmitted wave to Port 2, $b_2 = 0$, $\Gamma = b_1/a_1 = S_{11}$. Figure 9.63c is a shunt discontinuity, such as the junction of two lines or impedance mismatch, for which $S_{11} = S_{22} = \Gamma$, while $S_{12} = S_{21} = 1 + \Gamma$ [9.101]. Figure 9.63d shows the flow diagram for a transmission line, which is partially filled with a dielectric material of finite length l [9.103]. This network has a practical application in the dielectric measurements.

Network Calculations by Using Scattering Parameters and Signal-Flow Graphs

Scattering parameters are convenient in many calculations of microwave networks and they form a natural set for use with signal-flow graphs. In S -parameter signal-flow graphs, each port is represented by two nodes a_k and b_k (Fig. 9.63). Node a_k represents a complex wave entering the network at port k , while node b_k represents a complex wave leaving the network at port k . The complex scattering parameters are represented by multipliers on directed branches connecting the nodes within the network. The transfer function between any two nodes in the network can be determined by using topological flow graph rules [9.101, 104]. The Mason's nontouching-loop rule provides a method for solving a flow-graph by inspection [9.104]. The flow graph consists of branches, paths and loops. A path is a continuous succession of branches. A forward path connects an input node and an output node, where no node is encountered more than once. A first-order loop is a path that originates and terminates on the same node, and no node is encountered more than once. A second order loop is the product of three nontouching first-order loops that have no branches or nodes in common. A third order loop is the product of three nontouching first-order loops, etc. The loop value is the product of the branch multipliers around the loop. The path value is the product of all the branch multipliers along the path. The solution T of the flow-graph is the ratio of

the output variable to the input variable, and is given by

$$T = \frac{\sum_k T_k \Delta_k}{\Delta}, \quad (9.81)$$

where T_k is the path gain of k -th forward path, $\Delta = 1 - (\text{sum of all first-order loop gains}) + (\text{sum of all second-order loop gains}) - (\text{sum of all third-order loop gains})$, and $\Delta_k = 1 - (\text{sum of all first-order loop gains not touching the } k\text{-th forward path}) + (\text{sum of all second-order loop gains not touching the } k\text{-th forward path}) - \dots$

In Fig. 9.63d, the transmission line outside the specimen section has a real characteristic impedance Z_0 , while within the specimen section the network assumes a new (complex) impedance Z_s to be determined from the solution of the flow graph. The complex amplitude of the waves entering the network are a_1 and a_2 , while b_1 and b_2 are the complex amplitudes of the outgoing waves.

If the length l of the specimen were infinite then the reflection of a wave incident on the interface from the reference line, would be given simply by $S_{11} = b_1/a_1$.

In the case of a finite propagation length the amplitude of the wave transmitted depends on the complex transmission coefficient $\tau = e^{-\gamma l}$ where γ is the complex propagation constant. The signal flow in Fig. 9.63d can be solved for the scattering parameters S_{11} and S_{21} of the network by executing the rules of algebra of the flow graphs [9.101, 104]. Accordingly, from nodes a_1 to b_2 there are two first order paths with the following coefficients: $a_1 \rightarrow b_1 = \{\Gamma\}$, $\{(1 + \Gamma)e^{-\gamma l}, -\Gamma e^{-\gamma l}, (1 - \Gamma)\}$. Similarly, the path $a_1 \rightarrow b_2 = \{(1 + \Gamma)e^{-\gamma l}, (1 - \Gamma)\}$. The flow graph contains one loop: $\{-\Gamma e^{-\gamma l}, -\Gamma e^{-\gamma l}\}$ that represents the wave multiple reflection and phase change at each of the two interfaces $Z_0 - Z_s$ and $Z_s - Z_0$. The value of the path is the product of all coefficients encountered in the route. Thus, the network determinant Δ according to the graph algebra rules, equals $\Delta = 1 - \Gamma^2 e^{-2\gamma l}$. Consequently, the relative complex amplitudes of the waves at nodes b_1 and b_2 are given by (9.82) and (9.83) respectively

$$S_{11} \equiv \frac{b_1}{a_1} = \frac{a_1 \rightarrow b_1}{\Delta} = \frac{\Gamma(1 - e^{-\gamma l})(1 + e^{-\gamma l})}{1 - \Gamma^2 e^{-2\gamma l}}, \quad (9.82)$$

$$S_{21} \equiv \frac{b_2}{a_1} = \frac{a_1 \rightarrow b_2}{\Delta} = \frac{e^{-\gamma l}(1 - \Gamma)(1 + \Gamma)}{1 - \Gamma^2 e^{-2\gamma l}}, \quad (9.83)$$

where, S_{11} and S_{21} are the measured complex scattering parameters, γ is the complex propagation constant ($\gamma = \alpha + j\beta$), l is the propagation length, and Γ is the complex reflection coefficient [9.92, 93]. From (9.83) one can find

$$e^{-\gamma l} = \left[\frac{1 - (S_{11}/\Gamma)}{1 - S_{11}\Gamma} \right]^{1/2} \quad (9.84a)$$

and then substituting (9.84a) to (9.82) yields $1/2\Gamma - 1/2\Gamma b + 1/2 = 0$, from which

$$\Gamma = b \pm \sqrt{b^2 - 1}, \quad b = \frac{S_{11}^2 - S_{21}^2 + 1}{2S_{11}} \quad (9.84b)$$

and

$$Z_s = Z_0 \frac{1 + \Gamma}{1 - \Gamma} \quad (9.84c)$$

In order to determine the values of the complex γ , and Z_s , from (9.84), the measured complex S_{11} and S_{21} parameters should be returned by the network analyzer in complex coordinates form i. e. $S_{ij} = (\text{Re}S_{ij}, \text{Im}S_{ij})$. If polar notation is used then the phase angle needs to be converted to the true value of the measured phase (β) in radians rather than the cyclically mapped phase angle $\pm 180^\circ$. Results that indicate no physical meaning such as negative attenuation constant (α) need to be corrected by selecting an appropriate solution of (9.84a) and (9.84b). Equation (9.84) are general and applicable to network configurations consisting of a transmission line with impedance discontinuity Z_0 - Z_s - Z_0 , which is inserted between two reference transmission lines of the characteristic impedance Z_0 . Once γ and Z_s are obtained then the circuit distributed parameters, the corresponding materials electrical characteristics can be determined by using the conventional transmission line relations. The following sections describe application of (9.84) to measurements of the broadband dielectric permittivity of bulk materials and thin films.

Two-Port Transmission-Reflection Method

Figure 9.64 shows a testing configuration where the dielectric specimen of length l partially fills a precision coaxial air-line of characteristic impedance Z_0 .

The impedance in the specimen section changes from Z_0 to Z_s , and thus, this network can be represented by the flow-graph shown in Fig. 9.64. The scattering parameters S_{11} and S_{21} are measured at the reference planes A and B, and then the complex reflection coefficient Γ and the propagation constant γ are determined from (9.84). In the case of nonmagnetic media the dielectric permittivity ϵ_r^* can be obtained by simultaneously

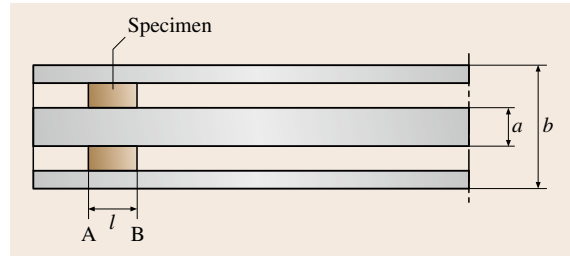


Fig. 9.64 Coaxial air-line partially filled with a dielectric slab of length l . The scattering parameters S_{11} and S_{21} are measured at the reference planes A and B, where the line assumes impedance Z_s

solving (9.85a) and (9.85b)

$$\Gamma = \frac{Z_s - Z_0}{Z_s + Z_0} = \frac{1 - \sqrt{\epsilon_r^*}}{1 + \sqrt{\epsilon_r^*}} \quad (9.85a)$$

$$\gamma = \frac{i\omega}{c\sqrt{\epsilon_r^*}} \quad (9.85b)$$

Using an APC-7 precision bead-less coaxial air line as a sample holder with $a = 3.02$ mm and $b = 7.0$ mm, the dielectric permittivity can be measured at frequencies of up to 18 GHz [9.105–107]. However, multiple wave reflections at the Z_0 - Z_s - Z_0 interfaces cause interference that may result in a singular behavior of Z_s at certain frequencies.

The dielectric specimen for the transmission-reflection method described above must be machined precisely to fit dimensions of the inner (a) and outer conductors (b) of the coaxial line (Fig. 9.64). A more detailed description of the measurement and analysis of this testing procedure can be found in [9.107, 108].

One-Port Reflection Method

An important application of network analysis to the high frequency dielectric metrology is the measurement of dielectric permittivity of thin films in a short-terminated coaxial test fixture (Fig. 9.61b).

In order to extend the measurements to the microwave range, a thin-film capacitance terminating a coaxial line is treated as a distributed network [9.109]. The wave enters the specimen from the coaxial-air line of characteristic impedance Z_0 , propagates along the diameter (a) of the specimen, and returns back to the coaxial line. The specimen represents a transmission line of impedance Z_s and propagation length l , which corresponds to the diameter of the specimen rather than to its thickness [9.109]. The wave propagation and reflection at the Z_0 - Z_s - Z_0 interfaces can be rep-

represented by the flow-graph shown in Fig. 9.63d. Here, the measured scattering parameter S_{11} is a sum of normalized incoming and outgoing waves $S_{11} = b_1/a_1 + b_2/a_1$, which are given by (9.82) and (9.83) respectively

$$\begin{aligned} S_{11} &= \frac{b_1}{a_1} + \frac{b_2}{a_1} \\ &= \frac{\Gamma(1 - e^{-\gamma l})(1 + e^{-\gamma l})}{1 - \Gamma^2 e^{-2\gamma l}} \\ &\quad + \frac{e^{-\gamma l}(1 - \Gamma)(1 + \Gamma)}{1 - \Gamma^2 e^{-2\gamma l}}, \end{aligned} \quad (9.86)$$

which simplifies to (9.87)

$$S_{11} = \frac{\Gamma + e^{-\gamma l}}{1 + \Gamma e^{-\gamma l}}. \quad (9.87)$$

The corresponding expression for the impedance is given by (9.88) [9.110]

$$Z_s = \frac{x \cot(x)}{i\omega C_s} + i\omega L_s, \quad (9.88)$$

where, x is the wave propagation parameter $x = \omega l \sqrt{\epsilon_r^*}/2c$, C_s is the capacitance of the specimen $C_s = C_0 \epsilon_r^*$, ω is the angular frequency, l is the propagation length ($l = 2.47$ mm in the APC-7 configuration), and L_s is the residual inductance of the specimen of thickness t [9.110]

$$L_s = 1.27 \times 10^7 [\text{H/m}] \cdot t [\text{m}]. \quad (9.89)$$

The resulting expression for the relative complex permittivity ϵ_r^* is given by (9.90)

$$\epsilon_r^* = \frac{x \cot(x)}{i\omega C_0(Z_0 l + S_{11}/1 - S_{11} - i\omega L_s)}. \quad (9.90)$$

Equation (9.90) eliminates the systematic uncertainties of the lumped element approximations [9.97] and is suitable for high-frequency characterization of dielectric films of low and high permittivity values. Equations (9.88)–(9.90) have been validated numerically and experimentally up to the first cavity resonance

$$f_{\text{cav}} = \frac{c}{l \text{Re}(\sqrt{\epsilon_r^*})}, \quad (9.91)$$

where Re indicates the real part of complex square root of permittivity and $l = 2.47$ mm, which is the propagation length for the APC-7 test fixture presented in Fig. 9.61b [9.110]. For example, in the case of a specimen with a dielectric constant of 100, f_{cav} is about 12 GHz. Since the propagation term x depends on permittivity, (9.90) needs to be solved iteratively. At low frequencies, where the electrical length of the specimen

is small in comparison to the wavelength, $x \cot(x) \approx 1$, L_s can be neglected and (9.90) simplifies to the conventional (9.78) and (9.79) for a transmission line terminated with a lumped shunt capacitance. A detailed description of the measurement procedure and the calculation algorithm can be found in the reference [9.111].

Resonant Cavity Methods

Resonant measurement methods are the most accurate in determining the dielectric permittivity. In order to excite a resonance the materials must have a low dielectric loss ($\epsilon_r'' < 10^{-3}$). The measurements are usually limited to the microwave frequency range. A fairly simple and commonly used resonant method for measurement of microwave permittivity is the resonant cavity perturbation method [9.112]. Figure 9.65 illustrates a cavity test fixture which is a short section of rectangular waveguide. Conducting plates bolted or soldered to the end flanges convert the waveguide into a resonant box. A small iris in each end plate feeds microwave energy into and out of the cavity. Clearance holes centered in opposite walls are provided for a dielectric specimen, which is placed into region of maximum electric field. The measurement frequency is limited to few values corresponding to the fundamental mode and few higher order modes. Typically standard rectangular waveguide for the X-band [9.106] is used as a test fixture that covers the frequency range from 8 to 12 GHz. The test specimen may have the shape of a cylindrical rod, sphere or a rectangular bar [9.112].

The test fixture is connected to a network analyzer (Fig. 9.62) by using appropriate adapters and waveguide

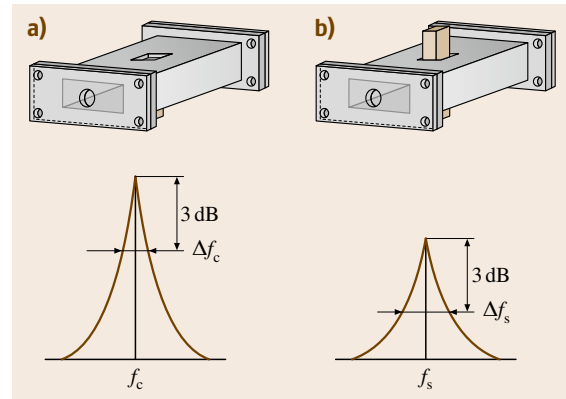


Fig. 9.65a,b Scattering parameter $|S_{21}|$ measured for (a) an empty test fixture and (b) for test fixture with a specimen inserted

uides. The resonance is indicated by a sharp increase in the magnitude of the $|S_{21}|$ parameter, with a peak value at the resonant frequency. When the dielectric specimen is inserted to the empty (air filled) cavity the resonant frequency decreases from f_c to f_s while the bandwidth Δf at half power, i. e. 3 dB below the $|S_{21}|$ peak, increases from Δf_c to Δf_s (see illustration in Fig. 9.65). A shift in resonant frequency is related to the specimen dielectric constant, while the larger bandwidth corresponds to a smaller quality factor Q , due to dielectric loss. The cavity perturbation method involves measurement of f_c , Δf_c , f_s , Δf_s , and volume of the empty cavity V_c and the specimen volume V_s .

The quality factor for the empty cavity and for the cavity filled with the specimen is given by (9.92)

$$Q_c = \frac{f_c}{\Delta f_c}, \quad Q_s = \frac{f_s}{\Delta f_s}. \quad (9.92)$$

The real and imaginary parts of the dielectric constant are given by (9.93) and (9.94), respectively

$$\epsilon'_r = \frac{V_c(f_c - f_s)}{2V_s f_s}, \quad (9.93)$$

$$\epsilon''_r = \frac{V_c}{4V_s} \left(\frac{1}{Q_s} - \frac{1}{Q_c} \right). \quad (9.94)$$

The resonant cavity perturbation method described above requires that the specimen volume be small compared to the volume of the whole cavity ($V_s < 0.1V_c$), which can lead to decreasing accuracy. Also, the specimen must be positioned symmetrically in the region of maximum electric field. However, compared to other resonant test methods, the resonant cavity perturbation method has several advantages such as overall good accuracy, simple calculations and test specimens that are easy to shape. Moreover, circular rods, rectangular bars or spheres are the basic designs that have been widely used in manufacturing ceramics, ferrites and organic insulating materials for application in the microwave communication and electric power distribution.

There is a large number of other resonant techniques described in the technical and standard literature, each having a niche in the specific frequency band, field behavior and loss characteristic of materials. Some of these are briefly described below.

Sheet low loss materials can be measured at X-band frequencies by using a split cavity resonator [9.113]. The material is placed between the two sections of the splittable resonator. When the resonant mode is ex-

cited the electric field is oriented parallel to the sample plane.

The split-post dielectric resonator technique [9.114] is also suitable for sheet materials. The system is excited in the transfer electromagnetic azimuthal mode. A useful feature of this type of resonant cavity is the ability to operate at lower frequencies without the necessity of using large specimens.

Parallel-plate resonators [9.115] with conducting surfaces allow measurements at lower frequencies since the guided wavelength λ_g inside the dielectric is smaller than in the air-filled cavities by a factor of approximately $\sqrt{\epsilon'_r}$. The full-sheet resonance technique [9.116] is commonly used to determine the permittivity of copper clad laminates for printed circuit boards.

9.5.4 Uncertainty Considerations

With increasing frequency, the complexity of the dielectric measurement increases considerably. Several uncertainty factors such as instrumentation, dimensional uncertainty of the test specimen geometry, roughness and conductivity of the conduction surfaces contribute to the combined uncertainty of the measurements. The complexity of modeling these factors is considerably higher within the frequency range of the LC resonance. Adequate analysis can be performed, however, by using the partial derivative technique [9.97, 107] and considering the instrumentation and the dimensional errors. Typically, the standard uncertainty of S_{11} can be assumed to be within the manufacturer's specification for the network analyzer, about ± 0.005 dB for the magnitude and $\pm 0.5^\circ$ for the phase. The combined relative standard uncertainty in geometrical capacitance measurements is typically smaller than 5%, where the largest contributing factor is the uncertainty in the film thickness measurements. Equation (9.90), for example, allows evaluation of systematic uncertainty due to residual inductance. It has been validated empirically for specimens 8–300 μm thick for measurements in the frequency range of 100 MHz to 12 GHz. These are reproducible with relative combined uncertainty in ϵ'_r and ϵ''_r of better than 8% for specimens having $\epsilon'_r < 80$ and thickness $t < 300 \mu\text{m}$. The resolution in the dielectric loss tangent measurements is < 0.005 . Additional limitations may arise from the systematic uncertainty of the particular instrumentation, calibration standards and the dimensional imperfections of the implemented test fixture [9.106]. Furthermore, the results of impedance measurements may not be reliable at frequencies, where $|Z|$ decreases below 0.05Ω .

9.5.5 Conclusion

In summary, one technique alone is typically not sufficient to characterize dielectric materials over the entire frequency range of interest. The lumped parameter approximate equations (9.72)–(9.76) can be utilized when they yield the required accuracy. The upper frequency limit for lumped parameter techniques is typically in the range of 100–300 MHz. Precision coaxial test fixtures can extend the applicability of the lumped parameter measurement techniques into the microwave range (9.78)–(9.79). When the effective values of circuit elements change with frequency due to wave propagation effects, it is necessary to use the distributed circuit analysis (9.84) along with the corresponding microwave network measurement methodology. The microwave broad-band one-port reflection method

(9.88)–(9.90) is most suitable for thin high dielectric constant films that are of interest to electronics, bio- and nano-technologies. For bulk anisotropic dielectrics, the microwave two-port transmission reflection method (9.85) is probably the most accurate broad-band measurement technique. The resonant cavity method (9.92)–(9.94) is best for evaluating low-loss solid dielectric materials that have the standard shapes used in manufacturing ceramics, ferrites, and organic insulating materials for application in microwave communication and electric power distribution.

In order to avoid systematic errors and obtain the most accurate results, it is important that the proper method is used for the situation at hand. Therefore measurements of dielectric substrates, films, circuit board materials, ceramics or ferrites always present a metrological challenge.

References

- 9.1 R.E. Hummel: Electrical properties of materials. In: *Understanding Materials Science*, ed. by R.E. Hummel (Springer, New York, Berlin 2004) pp.185–222, Chap. 11
- 9.2 C.H. He, Z. Lu, S. Liu, R. Liu: Cross-conductivity standard for nonferrous metals, *IEEE Trans. Instrum. Meas.* **44**, 181–183 (1995)
- 9.3 G. Rietveld, C.V. Kojimans, L.C.A. Henderson, M.J. Hall, S. Harmon, P. Warnecke, B. Schumacher: DC conductivity measurements in the van der Pauw geometry, *IEEE Trans. Instrum. Meas.* **52**, 449–453 (2003)
- 9.4 L.J. van der Pauw: A method of measuring specific resistivity and Hall effect of discs of arbitrary shape, *Philips Res. Rep.* **13**, 1–9 (1958)
- 9.5 DIN IEC 468: *Method of Measurement of Resistivity of Metallic Materials* (Beuth, Berlin 1981)
- 9.6 NPL Report DEM-ES 001: Techniques and materials for the measurement of DC and AC conductivity of non-ferrous metals and alloys, *Conductivity*, May 2004, the *Conductivity* project is (has been) financially supported by an EU grant (contract No. G6RD-CT-2000-00210) under the EU Growth programme, part of the 5th Framework programme
- 9.7 M.J. Hall, L.C.A. Henderson, G. Ashcroft, S. Harmon, P. Warnecke, B. Schumacher, G. Rietveld: Discrepancies between the DC and AC measurement of low frequency electrical conductivity, *Dig. Conf. Proc. Electrom. Meas. CPEM 2004*, London (2004) pp.34–35
- 9.8 A.C. Lynch, A.E. Drake, C.H. Dix: Measurement of eddy-current conductivity, *IEE Proc. Sci. Meas. Technol.* **130**, 254–260 (1983)
- 9.9 H. Kamerlingh Onnes: The superconductivity of mercury, *Commun. Phys. Lab. Univ. Leiden* **122b**, 13–15 (1911)
- 9.10 J. Bardeen, L.N. Cooper, J.R. Schrieffer: Theory of superconductivity, *Phys. Rev.* **108**, 1175–1204 (1957)
- 9.11 J.G. Bednorz, K.A. Müller: Possible high- T_c superconductivity in the Ba-La-Cu-O system, *Z. Phys. B* **64**, 189–193 (1986)
- 9.12 M.K. Wu, J.R. Ashburn, C.J. Torng, P.H. Hor, L.R. Meng, L. Gao, Z.J. Huang, Y.Q. Wang, C.W. Chu: Superconductivity in a new mixed phase Y-Ba-Cu-O system at ambient pressure, *Phys. Rev. Lett.* **58**, 908–910 (1987)
- 9.13 C.N.R. Rao, R. Nagarajan, R. Vijayaraghavan: Synthesis of cuprate superconductors, *Supercond. Sci. Technol.* **6**, 1–22 (1993)
- 9.14 J. Clarke, A.I. Braginski: *The SQUID Handbook, Fundamentals and Technology of SQUIDS and SQUID Systems*, Vol.1 (Wiley, New York 2004)
- 9.15 B.D. Josephson: Possible new effects in superconductive tunneling, *Phys. Lett.* **1**, 251–253 (1962)
- 9.16 R. Pöpel: The Josephson effect and voltage standards, *Metrologia* **29**, 153–174 (1992)
- 9.17 W. Meissner, R. Ochsenfeld: Ein neuer Effekt bei Eintritt der Supraleitfähigkeit, *Naturwissenschaften* **21**, 787 (1933), (in German)
- 9.18 S.A. Keys, D.P. Hampshire: Characterization of the transport critical current density for conductor applications. In: *Handbook of Superconducting Materials. II: Characterization, Applications and Cryogenics*, ed. by D.A. Cardwell, D.S. Ginley (IOPP, London 2003) p.1297
- 9.19 DIN EN IEC 61788-1: *Superconductivity – Critical, Current Measurement – DC Critical Current of Cu/Nb-Ti Composite Superconductors* (Beuth, Berlin 1999)
- 9.20 P.W. Atkins: *Physikalische Chemie*, 3rd edn. (VCH, Weinheim 1990) pp.3834–3846, (German transl.)

- 9.21 C.H. Hamann, W. Vielsich: *Elektrochemie*, 3rd edn. (VCH, Weinheim 1998), (in German)
- 9.22 J.M.G. Barthel, H. Krienke, W. Kunz: *Physical Chemistry of Electrolyte Solutions – Modern Aspects*, Top. Phys. Chem., Vol. 5 (Springer, Berlin, Heidelberg 1998)
- 9.23 J.O.M. Bockris, A.K.N. Reddy, K.N. Amly: *Modern Electrochemistry 1, Ionics*, 2nd edn. (Springer, Berlin, Heidelberg 1989) p. 379
- 9.24 O.F. Mohammed, D. Pines, J. Dreyer, E. Pines, E.T.J. Nibbering: Sequential proton transfer through water bridges in acid–base reactions, *Science* **310**, 83–86 (2005)
- 9.25 S. Seitz, A. Manzin, H.D. Jensen, P.T. Jakobsen, P. Spitzer: Traceability of electrolytic conductivity measurements to the International System of Units in the sub mS m^{-1} region and review of models of electrolytic conductivity cells, *Electrochim. Acta* **55**, 6323–6331 (2010)
- 9.26 F. Brinkmann, N.E. Dam, E. Deák, F. Durbiano, E. Ferrara, J. Fükö, H.D. Jensen, M. Máriássy, R.H. Shreiner, P. Spitzer, U. Sudmeier, M. Surdu: Primary methods for the measurement of electrolytic conductivity, *Accredit. Qual. Assur.* **8**, 346–353 (2003)
- 9.27 United States Pharmacopeia: USP 27–NF 22 (US Pharmacopeia, Rockville 2004)
- 9.28 ISO 7888: 1985 Water Quality: Determination of electrical conductivity (ISO, Geneva 1985)
- 9.29 Y.C. Wu, K.W. Pratt, W.F. Koch: Determination of the absolute specific conductance of primary standard KCl solutions, *J. Solut. Chem.* **18**, 515–528 (1989)
- 9.30 G. Jones, S.M. Christian: The measurement of the conductance of electrolytes. VI. Galvanic polarization by alternating current, *J. Am. Chem. Soc.* **57**, 272–284 (1935)
- 9.31 P. Spitzer, U. Sudmeier: Electrolytic conductivity – A new subject field at PTB, Report on the 146 PTB Semin. *Electrolytic Conduct.*, PTB–ThEx–15, ed. by P. Spitzer, U. Sudmeier (Physikalisch–Technische Bundesanstalt, Braunschweig 2000) pp. 39–47
- 9.32 P. Saulnier: Absolute determination of the conductivity of electrolytes. Double differential cell with adjustable constant, *J. Solut. Chem.* **8**, 835–845 (1979)
- 9.33 P. Saulnier, J. Barthel: Determination of electrolytic conductivity of a 0.01 M aqueous potassium chloride solution at various temperatures by an absolute method, *J. Solut. Chem.* **8**, 847–851 (1979)
- 9.34 F. Löffler: Design and production of the electrical conductivity cell, Report on the 146 PTB Semin. *Electrolytic Conduct.*, PTB–ThEx–15, ed. by P. Spitzer, U. Sudmeier (Physikalisch–Technische Bundesanstalt, Braunschweig 2000) pp. 49–64
- 9.35 Y.C. Wu, W.F. Koch, D. Feng, L.A. Holland, A.E. Juhász, A. Tomek: A DC method for the absolute determination of conductivities of the primary standard KCl solutions from 0 °C to 50 °C, *J. Res. Natl. Inst. Stand. Technol.* **99**, 241–246 (1994)
- 9.36 D.F. Evans, M.A. Matesich: The measurement and interpretation of electrolytic conductance. In: *Techniques of Electrochemistry*, Vol. 2, ed. by E. Yeager, A.J. Salkind (Wiley, New York 1973)
- 9.37 T.S. Light: Temperature dependence and measurement of resistivity of pure water, *Anal. Chem.* **56**, 1138–1142 (1994)
- 9.38 F. Oehme: *Chemische Sensoren. Funktion, Bauformen, Anwendungen* (Vieweg, Braunschweig 1991), p. 39
- 9.39 European Pharmacopeia: *Conductivity* (European Pharmacopeia, Strasbourg 2004), EP 4, 2.2.38, <http://www.pheur.org/>
- 9.40 W.L. Marshall: Electrical conductance of liquid and supercritical water evaluated from 0 °C and 0.1 MPa to high temperatures and pressures. Reduced–state relationships, *J. Chem. Eng. Data* **32**, 221–226 (1987)
- 9.41 R.D. Thornton, T.S. Light: A new approach to accurate resistivity measurement of high purity water, *Ultrapure Water* **7**, 14–21 (1989)
- 9.42 P. Spitzer, B. Rossi, Y. Gignet, S. Mabic, U. Sudmeier: New approach to calibrating conductivity meters in the low conductivity range, *Accredit. Qual. Assur.* **10**, 78–81 (2005)
- 9.43 H.D. Jensen, J. Sørensen: Electrolytic conductivity at DFM – results and experiences, Report on the 146 PTB Semin. *Electrolytic Conduct.*, PTB–ThEx–15, ed. by P. Spitzer, U. Sudmeier (Physikalisch–Technische Bundesanstalt, Braunschweig 2000) pp. 153–213
- 9.44 D.C. Look: *Electrical Characterization of GaAs Materials and Devices* (Wiley, Chichester 1989)
- 9.45 P. Blood, J.W. Orton: *The Electrical Characterization of Semiconductors: Majority Carriers and Electron States* (Academic, New York 1992)
- 9.46 E.B. Hansen: On the influence of shape and variations in conductivity of the sample on four-point measurements, *Appl. Sci. Res. B* **8**, 93–104 (1960)
- 9.47 R.L. Petritz: Theory of an experiment for measuring the mobility and density of carriers in the space-charge region of a semiconductor surface, *Phys. Rev.* **110**, 1254–1262 (1958)
- 9.48 L.J. van der Pauw: A method of measuring specific resistivity and Hall effect of discs of arbitrary shape, *Philips Res. Rep.* **13**, 1–9 (1958)
- 9.49 S.M. Sze: *Physics of Semiconductor Devices* (Wiley, Chichester 1981)
- 9.50 K. Ziegler, E. Klausmann, S. Kar: Determination of the semiconductor doping profile right up to its surface using the MIS capacitor, *Solid–State Electron.* **18**, 189–198 (1975)
- 9.51 D.P. Kennedy, P.C. Murley, W. Kleinfelder: On the measurement of impurity distributions in silicon by the differential capacitance technique, *IBM J. Res. Dev. Sept.*, 399–409 (1968)

- 9.52 D.P. Kennedy, R.P. O'Brian: On the measurement of impurity atom distributions by the differential capacitance technique, IBM J. Res. Dev. **March**, 212–214 (1969)
- 9.53 W.C. Johnson, P.T. Panousis: The influence of Debye length on the C - V -measurement of doping profiles, IEEE Trans. Electron Devices **18**, 956–973 (1971)
- 9.54 W.A. Harrison: *Electronic Structure and the Properties of Solids: The Physics of the Chemical Bond* (Dover, New York 1989)
- 9.55 S.R. Forest, R.F. Leheny, R.E. Nahory, M.A. Pollack: $\text{In}_{0.53}\text{Ga}_{0.47}\text{As}$ photodiodes with dark current limited by generation-recombination and tunneling, Appl. Phys. Lett. **37**(3), 322–325 (1980)
- 9.56 A. Goetzberger, B. McDonald, R.H. Haitz, R.M. Scarlett: Avalanche effects in silicon p-n junction. II. Structurally perfect junctions, J. Appl. Phys. **34**, 1591–1601 (1963)
- 9.57 G.L. Miller, D.V. Lang, L.C. Kimerling: Capacitance transient spectroscopy, Annu. Rev. Mater. Sci. **7**, 377–448 (1977)
- 9.58 D.V. Lang: Deep-level transient spectroscopy, J. Appl. Phys. **45**(7), 3023–3032 (1974)
- 9.59 R.N. Hall: Electron-hole recombination in germanium, Phys. Rev. **87**, 387 (1952)
- 9.60 W. Shockley, W.T. Read: Statistics of the recombinations of holes and electrons, Phys. Rev. **87**, 835–842 (1952)
- 9.61 D.L. Partin, J.W. Chen, A.G. Milnes, L.F. Vassamillet: J. Appl. Phys. **50**(11), 6845 (1979)
- 9.62 E.H. Rhoderick: *Metal-Semiconductor Contacts* (Clarendon, Oxford 1980)
- 9.63 A. Piotrowska, A. Guivarc'h, G. Pelous: Ohmic contacts to III-V compound semiconductors: A review of fabrication techniques, Solid-State Electron. **26**(3), 179–197 (1983)
- 9.64 H.H. Berger: Models for contacts to planar devices, Solid-State Electron. **15**, 145–158 (1972)
- 9.65 R.H. Cox, H. Strack: Ohmic contacts for GaAs devices, Solid-State Electron. **10**, 1213–1218 (1967)
- 9.66 P.W. Debye: *Polar Molecules* (Chemical Catalog, New York 1927)
- 9.67 C.P. Smyth: *Dielectric Behavior and Structure* (McGraw Hill, New York 1955)
- 9.68 K.S. Cole, R.H. Cole: Absorption in dielectrics dispersion, J. Chem. Phys. **9**, 341 (1941)
- 9.69 H. Fröhlich: *Theory of Dielectrics* (Oxford Univ. Press, Oxford 1949)
- 9.70 N. Hill, W.E. Vaughan, A.H. Price, M.M. Davies: *Dielectric Properties and Molecular Behavior* (Van Nostrand Reinhold, New York 1969)
- 9.71 C.J.F. Bottcher, P. Bordewijk: *Theory of Electric Polarization* (Elsevier, New York 1996)
- 9.72 N.G. McCrum, B.E. Read, G. Williams: *Anelastic and Dielectric Effects in Polymeric Solids* (Wiley, New York 1967)
- 9.73 J.P. Runt, J.J. Fitzgerald: *Dielectric Spectroscopy of Polymeric Materials* (Am. Chem. Soc., Washington 1997)
- 9.74 D.W. Davies: *The Theory of the Electric and Magnetic Properties of Molecules* (Wiley, New York 1969)
- 9.75 A.R. von Hippel (Ed.): *Dielectric Materials Applications* (Wiley, New York 1954)
- 9.76 H.E. Bussey: Measurement of RF properties of materials, A survey, Proc. IEEE **55**(5), 1046–1053 (1967)
- 9.77 S.O. Nelson: Dielectric properties of agricultural products, IEEE Trans. Electr. Insul. **26**, 845–869 (1991)
- 9.78 A.W. Kraszewski, S. Trabelsi, S.O. Nelson: Broadband microwave wheat permittivity measurements in free space, J. Microw. Power Electromag. Energy **37**, 41–54 (2002)
- 9.79 F. Kremer, A. Schönhals: *Broadband Dielectric Spectroscopy* (Springer, Berlin, Heidelberg 2003)
- 9.80 J.C. Maxwell: *An Elementary Treatise on Electricity*, 2nd edn. (Clarendon, Oxford 1888)
- 9.81 S. Havriliak, S.J. Negami: A complex plane analysis of α -dispersions in some polymer systems, J. Polym. Sci. C Polym. Symp. **14**, 99 (1966)
- 9.82 D.W. Davidson, R.H. Cole: Dielectric relaxation in glycerine, J. Chem. Phys. **18**, 1417–1418 (1950)
- 9.83 V.V. Novikov, V.P. Privalko: Temporal fractal model for the anomalous dielectric relaxation of inhomogeneous media with chaotic structure, Phys. Rev. E **64**, 031504 (2001)
- 9.84 V.V. Daniel: *Dielectric Relaxation* (Academic, London 1967)
- 9.85 A.K. Jonscher: *Dielectric Relaxation in Solids* (Chelsea Dielectrics, London 1983)
- 9.86 F. Alvarez, A. Alegria, J. Colmenero: A new method for obtaining distribution of relaxation times from frequency relaxation spectra, J. Chem. Phys. **103**, 798–806 (1995)
- 9.87 H. Schäfer, E. Sternin, R. Stannarius, M. Arndt, F. Kremer: Novel approach to the analysis of broadband dielectric spectra, Phys. Rev. Lett. **76**, 2177–2180 (1996)
- 9.88 L. Hartshorn, W.H. Ward: The measurement of the permittivity and power factor of dielectrics from 10^4 to 10^8 cycles per second, J. Inst. Electr. Eng. **79**, 567–609 (1936)
- 9.89 Agilent Technologies: *Accessories Selection Guide For Impedance Measurements, Dielectric Test Fixtures* (Agilent Technologies, Palo Alto 2001) p.38, <http://www.agilent.com/>
- 9.90 Application Note 1369-1: *Agilent Solutions for Measuring Permittivity and Permeability with LCR Meters and Impedance Analyzers* (Agilent Technologies, Palo Alto 2001), <http://www.agilent.com/>
- 9.91 ASTM D 150-98: *Standard Test Method for AC Loss Characteristics and Permittivity of Solid Electrical Insulating Materials* (ASTM, West Conshohocken 1998), <http://www.astm.org/>

- 9.92 D.A. Gray: *Handbook of Coaxial Microwave Measurements* (General Radio, West Concord 1968)
- 9.93 S. Ramo, J.R. Whinnery, T. Van Duzer: *Fields and Waves in Communication Electronics* (Wiley, New York 1994)
- 9.94 Agilent Technologies: *RF and Microwave Test Accessories* (Agilent Technologies, Palo Alto 2006), <http://www.agilent.com/>
- 9.95 J.P. Grant, R.N. Clarke, G.T. Symm, N. Spyrou: A critical study of the open-ended coaxial line sensor technique for RF and microwave complex permittivity measurements, *J. Phys. E Sci. Instrum.* **22**, 757–770 (1989)
- 9.96 Agilent Technologies: *85070C Dielectric Probe Kit* (Agilent Technologies, Palo Alto 2005), <http://www.agilent.com/>
- 9.97 S.S. Stuchly, M.A. Rzepecka, M.F. Iskander: Permittivity measurements at microwave frequencies using lumped elements, *IEEE Trans. Instrum. Meas.* **23**, 5662 (1974)
- 9.98 M.A. Stuchly, S.S. Stuchly: Coaxial line reflection methods for measuring dielectric properties of bio-logical substances at radio and microwave frequencies: A review, *IEEE Trans. Instrum. Meas.* **29**, 176183 (1980)
- 9.99 M.F. Iskander, S.S. Stuchly: Fringing field effect in the lumped-capacitance method for permittivity measurements, *IEEE Trans. Instrum. Meas.* **27**, 107109 (1978)
- 9.100 R.J. Collier, A.D. Skinner (Eds.): *Microwave Measurements* (The Institution of Engineering Technology, Stevenage 2007)
- 9.101 J.K. Hunton: Analysis of microwave techniques by means of signal flow graphs, *IRE Trans. Microw. Theory Tech.* **8**, 206212 (1960)
- 9.102 K. Kurokawa: Power waves and the scattering matrix, *IEEE Trans. Microw. Theory Tech.* **13**, 194202 (1965)
- 9.103 A.M. Nicolson: Broad-band microwave transmission characteristics from a single measurement of the transient response, *IEEE Trans. Instrum. Meas.* **19**, 337382 (1970)
- 9.104 J. Mason: Feedback theory, *Proc. IRE* **44**, 920–926 (1956)
- 9.105 S.S. Stuchly, M. Matuszewski: A combined total reflection-transmission method in application to dielectric spectroscopy, *IEEE Trans. Instrum. Meas.* **27**, 285288 (1978)
- 9.106 Product Note 8510-3: *Measuring the Dielectric Constant of Solids with the HP Network Analyzer* (Hewlett Packard, Palo Alto 1985)
- 9.107 J. Baker-Jarvis, E.J. Vanzura, W.A. Kissick: Improved technique for determining complex permittivity with the transmission/reflection method, *IEEE Trans. Instrum. Meas.* **38**, 10961103 (1990)
- 9.108 J. Baker-Jarvis, R.G. Geyer, P.D. Domich: A nonlinear least-squares with causality constraints applied to transmission line permittivity, *IEEE Trans. Instrum. Meas.* **41**, 646652 (1992)
- 9.109 J. Obrzut, N. Noda, R. Nozaki: Broadband characterization of high dielectric constant films for power – Ground decoupling, *IEEE Trans. Instrum. Meas.* **51**, 829–832 (2002)
- 9.110 J. Obrzut, A. Anopchenko: Input impedance of a coaxial line terminated with a complex gap capacitance numerical experimental analysis, *IEEE Trans. Instrum. Meas.* **53**, 11971202 (2004)
- 9.111 IPC: Standard test methods, IPC TM-650, Method 2.5.5.10: High frequency testing to determine permittivity and loss tangent of embedded passive materials (IPC, Bannockburn 2005) http://www.ipc.org/4.0_Knowledge/4.1_Standards/test/2-5-5-10.pdf
- 9.112 ASTM D2520-01: *Standard Test Methods for Complex Permittivity (Dielectric Constant) of Solid Electrical Insulating Materials at Microwave Frequencies and Temperatures to 1650 °C, Test Method B – Resonant Cavity Perturbation Method* (ASTM, West Conshohocken 1998), <http://www.astm.org/>
- 9.113 G. Kent: Nondestructive permittivity measurements of substrates, *IEEE Trans. Instrum. Meas.* **45**, 102106 (1996)
- 9.114 S. Maj, M. Pospieszalski: A composite multilayered cylindrical dielectric resonator, *Microwave Symposium Digest, 1984 IEEE MTT-S Int.* (IEEE, San Francisco 1984) pp. 190–191
- 9.115 J. Krupka, K. Derzakowski, A. Abramowicz, M.E. Toobar, R.G. Geyer: Use of whispering-gallery modes for complex permittivity determinations of ultra-low-loss dielectric materials, *IEEE Trans. Microw. Theory Tech.* **47**, 752759 (1999)
- 9.116 G.I. Woolaver: Accurately measure dielectric constant of soft substrates, *Microwave RF* **24**, 153158 (1990)

Magnetic Properties

10. Magnetic Properties

Magnetic materials are one of the most prominent classes of functional materials, as introduced in Sect. 1.3. They are mostly inorganic, metallic or ceramic in nature and typically multicomponent when used in applications (e.g. alloys or inter-metallic phases). Their structure can be amorphous or crystalline with grain sizes ranging from a few nanometers (as in high-end nanocrystalline soft magnetic materials) to centimeters (as in grain-oriented transformer steels). They are available as powders, cast, sintered or composite materials, ribbons or even thin films and find a huge variety of applications in transformers, motors, generators, medical system sensors, and microelectronic devices.

The aim of this chapter is to give advice as to which methods are most applicable to determine the characteristic magnetic properties of any of the materials mentioned above. Magnetic thin-film structures have recently gained significant scientific and economic importance. Not only can their properties deviate from the respective bulk materials but novel phenomena can also occur, such as giant and tunnel magneto-resistance, which lead to their application in read heads and their likely future application to nonvolatile magnetic solid-state memory (MRAM). Therefore, we have added a section that explains the important peculiarities special to thin films, in which we summarize the most relevant measurement techniques.

Section 10.1 will give a short overview to enable the reader to differentiate between the various manifestations of magnetism, different materials and their related properties. For a deeper understanding, of course, textbooks should be used (see the references given in Sect. 10.2). Section 10.2 covers the standard measurement techniques for soft and hard magnetic materials. The tables at the beginning of Sect. 10.2.1 are a valuable guide to choose the best technique for any given property to be measured. It is anticipated that this chapter will cover the

overwhelming needs for a routine characterization of soft and hard magnetic materials in their various forms. Section 10.3 introduces an elegant, novel and extremely fast technique, the so-called pulse field magnetometer, to measure the hysteresis loop of hard magnetic materials and thereby to determine the remanent magnetization, the anisotropy field and coercivity, respectively. This method has been developed only recently and is not yet comprehensively covered in textbooks. It is therefore described in more detail with a critical discussion of possible measurement errors and calibration requirements. Finally, as mentioned above, Sect. 10.4 addresses features peculiar to magnetic thin films and recommends techniques for their magnetic characterization. It comprises an overview of magneto-resistive effects occurring in magnetic thin films or multilayers where the electrical resistivity depends on external magnetic fields. These devices find important applications as read heads in hard-disc drives and as sensors in the automotive and automation industries. The standard measurement to determine the field response (change in resistance within a given field range) is simply a resistivity measurement, as described in Chap. 9, except that it needs to be done in an external magnetic field. These electrical techniques are therefore not covered in this chapter.

In bulk and thin-film ferromagnets properties such as remanent magnetization and coercivity often depend on the time scale used in the measurement (Sects. 10.1.6, 10.3.3). Time-dependent measurements needed, e.g., to predict the stability of the material in applications are not explicitly described in this chapter since, in principle, any sensitive magnetometer can be used for these measurements. In research, sophisticated methods are used to resolve magnetization dynamics on pico- or even femtosecond time scales. A detailed description of these more specialized methods is beyond the scope of this handbook.

10.1	Magnetic Materials	542	10.2.3	Properties of Soft Magnetic Materials	555
10.1.1	Diamagnetism, Paramagnetism, and Ferromagnetism	542	10.3	Magnetic Characterization in a Pulsed Field Magnetometer (PFM)	567
10.1.2	Antiferromagnetism, Ferrimagnetism and Noncollinear Magnetism	543	10.3.1	Industrial Pulsed Field Magnetometer	568
10.1.3	Intrinsic and Extrinsic Properties	544	10.3.2	Errors in a PFM	569
10.1.4	Bulk Soft and Hard Materials	544	10.3.3	Calibration [10.1]	573
10.1.5	Magnetic Thin Films	544	10.3.4	Hysteresis Measurements on Hard Magnetic Materials	575
10.1.6	Time-Dependent Changes in Magnetic Properties	545	10.3.5	Anisotropy Measurement	576
10.1.7	Definition of Magnetic Properties and Respective Measurement Methods	545	10.3.6	Summary: Advantages and Disadvantages of PFM	579
10.2	Soft and Hard Magnetic Materials: (Standard) Measurement Techniques for Properties Related to the $B(H)$ Loop ..	546	10.4	Properties of Magnetic Thin Films	579
10.2.1	Introduction	546	10.4.1	Saturation Magnetization, Spontaneous Magnetization	579
10.2.2	Properties of Hard Magnetic Materials	549	10.4.2	Magneto-Resistive Effects	583
			References	585

10.1 Magnetic Materials

Empirically, materials are classified according to their response to an applied magnetic field, i.e. the magnetization induced by the external field. A more fundamental understanding results from considering the microscopic mechanisms that determine the behavior of materials in the magnetic field.

10.1.1 Diamagnetism, Paramagnetism, and Ferromagnetism

Diamagnetism is a property of all materials. It results from an additional orbital angular momentum of electrons induced in a magnetic field. In analogy to the induction of eddy currents in a conductor it manifests itself as a magnetization oriented in the opposite direction to the external field; by definition this is equivalent to a negative susceptibility (definitions are given below).

Paramagnetism means a positive magnetic susceptibility, i.e. the induced magnetization is along the direction of the external magnetic field. It is observed in materials which contain atoms with nonzero angular momentum, e.g. transition metals. The susceptibility scales with $1/T$ (Curie's law). Paramagnetism is also found in certain metals (e.g. aluminum) as a consequence of the spin of conduction electrons (Pauli spin susceptibility). The related susceptibility is essentially independent of temperature. The paramagnetic

susceptibility is generally several orders of magnitude larger than the diamagnetic component; therefore, diamagnetism is not observable in the presence of paramagnetism.

Ferromagnetism describes the fact that certain solid materials exhibit a *spontaneous magnetization*, M_S , even in the absence of an external magnetic field. It is a collective phenomenon resulting from the spontaneous ordering of the atomic magnetic moments due to the *exchange interaction* among the electron spins. It is observed in a few transition metals (e.g. 3d, 4f) where itinerant electrons play the essential role for the exchange coupling mechanism, but also in their oxides, halides etc., where the exchange interaction is mediated by localized electrons of oxygen, sulfur etc. atoms located between neighboring metal atoms (*indirect exchange*, *superexchange*). Recently ferromagnetism has been observed in semiconductors (e.g. GaAs, TiO₂) doped with a few percent of a transition element like Mn, Fe or Co which provides localized magnetic moments and free charge carriers which mediate the exchange interaction among the localized moments. If ferromagnetic order in these materials can be maintained above room temperature (which is currently not certain) they might become useful for future electronic devices based on the spin of electrons besides their charge (*spintronics*).

Many ferromagnetic objects do not show a net magnetization without an external magnetic field. This is a consequence of magnetic domains, which are formed to reduce the energy connected with the dipolar fields (the stray field and demagnetizing field). When an external magnetic field is applied domains gradually vanish due to the motion of domain walls and rotation of the magnetization inside the domains. These processes are partly reversible and irreversible. In sufficiently high fields *technical saturation* is achieved. The corresponding *saturation magnetization*, however, must not be mistaken for the *spontaneous magnetization*. The reason is that, at any temperature $T > 0$, an external field will increase the magnetization above the spontaneous value inside the domains (i. e. M_S at $H = 0$) by suppression of spin waves (the *para-process*). Hence, the experimental determination of the spontaneous magnetization in general requires a specific extrapolation of high-field data to zero field.

Spin-wave excitations are the reason for the decrease of the spontaneous magnetization with increasing temperature, which in general follows Bloch's law, i. e. the decrease of the spontaneous magnetization from its ground-state value at $T = 0$ is proportional to $T^{3/2}$. The phase transition from long-range ferromagnetic order to the paramagnetic state at a critical temperature (the *Curie temperature*, T_C) is governed by power laws for the spontaneous magnetization close to T_C , $M_S = A(1 - T/T_C)^\beta$, for the magnetic susceptibility, $\chi = \chi_0(1 - T/T_C)^{-\gamma}$ and for other quantities. The *critical exponents* (β and γ) are of universal character and depend only on the dimensionality of the sample in real space (e.g. 3-D for a bulk material, or 2-D for ultrathin films) and in spin space (e.g. 3-D if all orientations of the magnetization are allowed, 2-D if the magnetization vector is confined to a plane, and 1-D in the case of extremely strong uniaxial anisotropy).

In general, the magnetization of a ferromagnetic object is preferentially oriented along certain axes that correspond to an *energy minimum*, which are known as *easy axes* of magnetization. The directions of the respective *energy maxima* are called *hard axes* or *hard directions*. This property, *magnetic anisotropy*, is the key to many technical applications of ferromagnetic materials; e.g. a binary memory element requires a *uniaxial anisotropy* characterized by two stable states. The strength of the anisotropy is expressed by anisotropy constants K_i ; it can be measured by the external field required to rotate the magnetization from an easy direction to a hard one. Materials with small/large anisotropy constants are called *magnetically soft/hard*.

Two interactions are responsible for magnetic anisotropies: *dipolar interactions* between atomic moments are directly connected with the shape of a given ferromagnetic body (*shape anisotropy*), while *spin-orbit interaction* is the origin of all other anisotropies: magneto-crystalline, magneto-elastic, surface/interface anisotropies, which are intimately related to the local symmetry of the atomic configuration.

10.1.2 Antiferromagnetism, Ferrimagnetism and Noncollinear Magnetism

In certain materials atomic moments are strictly ordered without showing any resulting magnetization. This happens if neighboring magnetic moments are antiparallel to each other due to a *negative exchange interaction* between the spins; this phenomenon is called *antiferromagnetism* and is mainly found in transition-metal oxides, halides etc. (MnO, CoO, NiO, α -Fe₂O₃ etc.), but also in metal alloys such as FeMn or IrMn. Antiferromagnetism vanishes above a critical temperature called the Néel temperature. Due to their zero net magnetic moment, antiferromagnets are hardly affected by external magnetic fields. This has recently led to technical applications in so-called *spin-valves* where the antiferromagnet pins the magnetization of an adjacent ferromagnetic layer in a magneto-resistive sensor.

A special form of antiferromagnetism is observed in metallic chromium: the local magnetization varies sinusoidally along certain lattice directions. This is called a *spin-density wave* and is not always commensurate with the crystal lattice.

Ferrimagnetism is a more general version of antiferromagnetism: neighboring moments are antiparallel but of different sizes, resulting in a finite net magnetization. It is found in compounds of 3d transition metals and rare-earth elements (e.g. ferrites, garnets, amorphous 3d-4f alloys and multilayers).

Other forms of magnetic order are found mainly in rare-earth compounds: magnetic moments can form helical structures (*helimagnetism*) and even more complex structures giving rise to noncollinear magnetism meaning that magnetic moments are not aligned along a defined axis. Such a magnetic order can result from different or competing exchange interactions and very strong magnetic anisotropies.

Competing ferromagnetic and antiferromagnetic coupling between neighboring moments in a crystalline lattice or purely antiferromagnetic interactions on a triangular lattice can lead to *frustration*; this means that the individual spins cannot follow the exchange cou-

pling to all neighbors simultaneously. The consequence is a spin configuration similar to a *frozen paramagnet* called a *spin-glass* state. It manifests itself by thermal hysteresis below the freezing temperature and pronounced relaxation effects, indicating the presence of highly degenerate states. Typical materials showing such behavior are dilute alloys of 3d metals (Mn, Fe, Co) in a nonmagnetic matrix (Au, Cu).

10.1.3 Intrinsic and Extrinsic Properties

Intrinsic magnetic properties are those characteristic of a given material (e.g. spontaneous magnetization, magneto-crystalline anisotropy constant etc.), while extrinsic properties are strongly affected by the specific shape and size of the magnetic object as well as by their microstructure. The most important example is the *magnetic shape anisotropy* caused by the dipolar energy via the demagnetizing field: for a three-dimensional ferromagnetic object characteristic quantities such as the remanent magnetization and saturation field are mainly determined by the shape and much less by the intrinsic magnetic anisotropy.

Another *extrinsic* effect is the role of mechanical strain in a specimen; this may be introduced during the production process. Stress and strain may significantly alter the shape of the magnetization loop via magnetostrictive effects.

10.1.4 Bulk Soft and Hard Materials

The *magnetic softness* or *magnetic hardness* of a material is a key factor for many applications. For instance, *magnetically soft* materials are needed for transformers, motors and sensors, i. e. where the magnetization should fully align with even very small external magnetic fields. This requires very low coercivity and the highest possible susceptibility (or permeability), which is equivalent to weak anisotropy and large magnetization. Also, very low magnetostriction is needed to prevent mechanical strain from building up magneto-elastic anisotropies. As an example, in some specific binary or ternary alloys of 3d metals the magneto-crystalline anisotropy can be very close to zero, making them magnetically very soft. In particular, $\text{Ni}_{81}\text{Fe}_{19}$ (*permalloy*) has nearly zero magneto-crystalline anisotropy and very weak magnetostriction. A large number of special alloys of Fe, Co and Ni with the addition of Cr, Mn, Mo, Si and other elements have been developed that allow for a compromise between high permeability (e.g. 78 permalloy = $\text{Fe}_{21.2}\text{Ni}_{78.5}\text{Mn}_{0.3}$,

supermalloy = $\text{Fe}_{15.7}\text{Ni}_{79}\text{Mn}_{0.3}\text{Mo}_5$, mu-metal = $\text{Fe}_{18}\text{Ni}_{75}\text{Cr}_2\text{Cu}_5$) and high magnetization (e.g. permendur = $\text{Fe}_{49.7}\text{Co}_{50}\text{Mn}_{0.3}$). For all these alloys proper heat treatment is essential for optimum soft magnetic properties.

For high-frequency applications soft magnetic ferrites still play an important role.

Magnetically hard materials, in turn, are needed for permanent magnets, magnetic information-storage media (memories) and other applications. They should possess strong anisotropies and large coercivity so their magnetic state cannot be easily altered by external magnetic fields. Besides high coercivity and large remanent magnetization their maximum energy product $(\text{BH})_{\text{max}}$ is a key quantity. While alloys of 3d metals with aluminum dominated the market until 1975 (e.g. Alnico V = $\text{Al}_8\text{Ni}_{14}\text{Co}_{24}\text{Fe}_{51}\text{Cu}_3$) they have gradually been replaced by materials based on intermetallic rare-earth cobalt compounds (e.g. SmCo_5 , $\text{Sm}_2(\text{Co}, \text{Fe})_{17}$) and more recently by $\text{Nd}_2\text{Fe}_{14}\text{B}_1$, which does not contain relatively expensive cobalt. The magnetic properties of these materials critically depend on the metallurgical production process, which affects the granular structure needed for high coercivity and large energy product; the latter has increased by more than an order of magnitude since the development of rare-earth-containing permanent magnets. For less-demanding applications ferrite magnets are still in use.

For magnetic recording media (mainly hard-disk drives) somewhat different requirements have to be met. Here alloys of the type CoCrPt in the form of thin films are mainly used today.

10.1.5 Magnetic Thin Films

For several reasons ferromagnetic thin films constitute a special class of magnetic materials.

1. The reduced dimensionality of a thin film makes the axis perpendicular to the film plane a natural symmetry axis, which gives rise to specific magnetic anisotropies, e.g. the so-called shape anisotropy with an easy plane and a perpendicular hard axis.
2. The reduced dimensionality also causes modifications of fundamental magnetic properties such as the saturation magnetization, its temperature dependence, the Curie temperature and others. These *size effects* become more pronounced with decreasing film thickness.
3. Magnetic properties at surfaces and interfaces are generally different from the corresponding bulk

properties. These *surface effects* become more influential with decreasing film thickness and may even become dominant for *ultrathin* films, i.e. films of only a few atomic layers. Indeed, new materials with a combination of properties that does not occur in nature can be created in this way, e.g. multilayers or superlattices of a ferromagnetic and a nonmagnetic component.

4. Certain magneto-transport phenomena such as the *giant magneto-resistance (GMR)* or *tunnel magneto-resistance (TMR)* effects can best be observed and exploited in very thin films. As these effects find more practical applications (e.g. in hard-disk read heads) thin and ultrathin magnetic films receive increasing attention.

The growing interest in magnetic films and their technical application naturally increases the demand for methods and instruments to characterize their magnetic properties as completely as possible. Established instruments suitable for the study of bulk magnetic materials are of limited value because of the high sensitivity required for measurements of the small material quantities typical for thin films. Suitable methods will be described in Sect. 10.4.

10.1.6 Time-Dependent Changes in Magnetic Properties

Ferromagnetic materials frequently show a continuous change of their macroscopic magnetization in the course of time even in a constant or zero applied magnetic field. This is usually termed the *magnetic aftereffect* or *magnetic viscosity* and may occur on a time scale of seconds, minutes or even thousands of years. The underlying physical reason is that a ferromagnetic object with a net magnetic moment in the absence of an external magnetic field is generally in a thermodynamically metastable state. This is indicated by the presence of hysteresis. The equilibrium state will be asymptotically approached by domain nucleation and wall motion. Domain-wall motion is a relatively slow process due to the effective mass or inertia that can be attributed to a magnetic wall; since it is thermally activated it also depends strongly on temperature. For the same reason the coercivity of a sample depends on the measurement time if magnetization reversal occurs via domain walls. This needs to be taken into account when comparing data obtained by quasistatic measurements with those extracted from high-speed measurements (Sect. 10.3.3).

In the absence of domains walls and for a uniformly magnetized sample the magnetization responds to the torque exerted by an external magnetic field by a precession of the magnetization vector around the effective field, which is well described by the Landau–Lifschitz–Gilbert equation. As a consequence, in these cases the maximum rate of change of the magnetization is limited by the precession frequency of the magnetization vector, which for common materials like Fe, Co, Ni and their alloys is between 1 GHz and 20 GHz in moderate applied magnetic fields. It is evident that magnetization dynamics on a timescale of nanoseconds and below is relevant for magnetic devices in high-frequency applications.

10.1.7 Definition of Magnetic Properties and Respective Measurement Methods

The most important magnetic quantities are defined in the following in conjunction with their primary measurement methods.

The *magnetic field* H , or *flux density* B , (which are equivalent in free space) are measured with Hall probes, inductive probes (e.g. flux-gate magnetometers for very low fields) or nuclear magnetic resonance (NMR) probes for very high accuracy.

Magnetic moments are measured by different types of magnetometers.

- Via the force exerted by a magnetic field gradient (e.g. Faraday balance, or alternating gradient magnetometer (AGM))
- Via the voltage induced in a pickup coil by the motion of the sample, e.g. the vibrating-sample magnetometer (VSM, Fig. 10.7) is a widely used standard instrument, or a superconducting quantum interference device (SQUID, Figs. 10.48, 10.49) magnetometer for highest sensitivity

Quantity	Symbol	Unit
Magnetic field	H	[A/m]
Magnetic flux density, magnetic induction	B	[T]
Magnetic flux	Φ	[Wb]
Magnetic moment	m	[A m ²]
Magnetization (= m/V)	M	[A/m]
Magnetic polarization (= $\mu_0 M$)	J	[T]
Susceptibility (= M/H)	χ	[–]

The (average) *magnetization* of a magnetic object is usually determined by dividing the magnetic moment by the volume of the sample. Care must also be taken concerning the vector component of the magnetic moment that is detected. This is crucial in the case of samples with a significant magnetic anisotropy which can even result from the shape of the specimen (Sect. 10.1.1).

All these instruments need careful calibration. This is important because the effective calibration factors depend more or less on the size and shape of the specimen.

Magnetic moments related to different chemical elements in a specimen can be measured selectively by means of magnetic x-ray circular dichroism (MXCD) or XMCD based on the absorption of circularly polarized x-rays from a suitable synchrotron radiation source. In principle, this method allows the separation of orbital and spin magnetic moments.

If only the relative value of the magnetization is of interest and not its absolute value, then a number of different methods can be used to measure, for instance, M as a function of temperature or of the applied magnetic field. Such methods include magneto-optic effects (e.g. the magneto-optic Kerr effect (MOKE)) or the magnetic hyperfine field measured by using the Mößbauer effect, perturbed angular correlations (PAC) of gamma emission, or nuclear magnetic resonance (NMR). While MOKE is frequently used for characterizing magnetic materials, nuclear methods due to their relative complexity are restricted to special applications where standard techniques do not provide adequate information. NMR is widely exploited in magnetic resonance imaging (MRI) as a diagnostic tool in medicine.

The methods most commonly used for characterizing different magnetic materials are discussed in the following sections.

10.2 Soft and Hard Magnetic Materials: (Standard) Measurement Techniques for Properties Related to the $B(H)$ Loop

10.2.1 Introduction

During the past 100 years many different methods have been developed for the measurement of magnetic material properties and sophisticated fixtures, yokes and coil systems have been designed. Many of them vanished when new materials required extended measuring conditions. With progress in electronic measuring techniques other instruments were superseded. Fluxmeters and Hall-effect field-strength meters, for example, replaced ballistic galvanometers and rotating coils. Comprehensive explanations of the older methods can be found in [10.2]. New methods are ready to enter magnetic measuring technique. One new opportunity is for the pulse field magnetometer (PFM), which is discussed in Sect. 10.3. This device can complement the capabilities of a hysteresisgraph for hard magnetic materials, although it should be mentioned that the instrumentation is not less demanding. The difficulties involved require a careful interpretation of the results.

Table 10.1 gives an overview of the measuring methods described in the subsequent chapters. The techniques are classified according their main application for hard or soft magnetic materials, although some of them may also be applicable in the other group.

Table 10.2 compares the capabilities of various methods. Of course, it can only cover typical configura-

tions and applications and give rough indications. In many cases, the measuring conditions may be adjusted to meet special demands. The magnitude of the quantities, which limit the measuring ranges, can either be determined by the instrumentation or by the requirements resulting from the specimen properties.

The tables can certainly not give a complete survey of all requested quantities and methods that are used today. The selected techniques are common in industrial and scientific research or in quality control.

Some basic methods in magnetic measurement are taken as known. Fluxmeters are used in many measuring set ups to integrate voltages that are induced in measuring coils to obtain the magnetic flux. Today various analog or digital integration methods are used. A discussion of them can be found in [10.3].

The same applies for field-strength meters that use the Hall effect. These instruments, usually called Gauss- or Teslameters, are widespread. A description of their working principle is given in many educational books.

In many cases it is impossible to determine the material properties of components in a shape that is defined by the production conditions or application. In these cases, relative measuring methods are often applied. These usually compare measurable properties or combinations of properties with those of a reference sample.

Sections 10.2.2 and 10.2.3 focus on methods that provide directly material properties, allow traceable

Table 10.1 Measuring methods for properties of magnetic materials

Measuring method	Soft/hard	Quantities
Hysteresisgraph for hard magnetic materials	H	$J(H), B(H), B_r, H_{cJ}, H_{cB}, (BH)_{\max}, \mu_{\text{rec}}$
Vibrating-sample magnetometer (VSM)	H, (S)	$J_s, J(H), B_r, H_{cJ}, H_{cB}, (BH)_{\max}, \mu_{\text{rec}}, J(T), T_C$
Torque magnetometer	H, (S)	Anisotropy constants
Moment-measuring coil (Helmholtz)	H	J (at working point)
Pulse field magnetometer (PFM) (Sect. 10.4)	H	$J_s, J(H), B(H), B_r, H_{cJ}, H_{cB}, (BH)_{\max}$
DC hysteresisgraph for soft magnetic materials – ring method	S	$J_s, B(H), B_r, H_{cB}, \mu(H), \mu_i, \mu_{\max}, P$
DC hysteresisgraph (permeameter) for soft magnetic materials – yoke methods	S	$J_s, J(H), B(H), B_r, H_{cJ}, H_{cB}, \mu_i, \mu_{\max}, P$
Coercimeter	S, (H)	H_{cJ}
AC hysteresisgraph – ring method	S	$B(H), B_r, H_{cB}, \mu_a, P_w, \mu_a(H), \mu_a(B), P_w(H), P_w(B), P_w(f), J_s$
Epstein frame	S	$P_w, J(H), B_r, H_{cJ}, \mu_a$
Single-sheet tester (SST)	S	$P_w, J(H), B_r, H_{cJ}, \mu_a$
Wattmeter method	S	P_w
Voltmeter–ammeter method	S	P_w, μ_a
Saturation coil	S	J_s, μ_r
Magnetic scales (Faraday, Gouy)	S	$\mu(H), \mu_i, \mu_{\max}, \chi(H), \chi_i, \chi_{\max}, J_s, T_C$
Impedance bridges	S	$\underline{\mu} = \mu' - i\mu'', Q, \tan \delta$

$J_s = \mu_0 M_s$ saturation polarization; T_C : Curie temperature; $B_r = J_r$: remanence; H_{cJ} : coercivity (coercive field strength) for $J(H)$ hysteresis loop; H_{cB} : coercivity (coercive field strength) for $B(H)$ hysteresis loop; $(BH)_{\max}$: maximum energy product; $\mu = \mu_0 \mu_r$: permeability; $\chi = \mu - 1$: susceptibility; μ_r : relative permeability; μ_i, χ_i : initial permeability/susceptibility; μ_{\max}, χ_{\max} : maximum permeability/susceptibility; μ_{rec} : recoil permeability; μ_a : amplitude permeability; $\underline{\mu} = \mu' - i\mu''$: complex permeability; P : hysteresis loss; P_w : total loss; Q : Q -factor, quality factor; δ : loss angle; f : frequency

Table 10.2 Characteristics of measuring methods for magnetic materials

Measurement principle	Measurement range (limiting quantities)	Measurement sensitivity	Measurement reproducibility range (%)	Materials specimen type	Specimen geometry, dimensions	Methods merit	Methods demerit
Hysteresisgraph for hard magnetic materials	H_{\max} : 1.6–2.4 MA/m J_{\max} : 1.2–1.5 T	H : 0.1 kA/m J : 1 mT	H : 1–3 J : 0.5–2	Bulk permanent magnets	Cylinders, blocks, segments, (large) rings	Many quantities, standardized, easy operation	Restricted for non-plane-parallel specimens
Vibrating-sample magnetometer (VSM)	H_{\max} : 1.2–4 MA/m m_{\max} : 1 A m ² j_{\max} : 10 ⁻⁶ V s m	H : 0.1 kA/m m : 10 ⁻⁹ A m ² , j : 10 ⁻¹⁵ V s m	H, J : 1–3	Ferro- and paramagnetic material, amorphous or nanocrystalline alloys	Powders, thin films, ribbons, small massive samples	High sensitivity, wide specimen temperature range	Demagnetization factor to be considered
Torque magnetometer	H_{\max} : 0.8–10 MA/m L : 10 ⁻⁴ –10 ⁻² N m	1) L : 10 ⁻⁹ –10 ⁻⁷ N m	1) L : 1–5	Ferro- and paramagnetic material	Discs, spheres, small particles, films, single crystals	High sensitivity, low temperatures possible	Restricted specimen shape, sometimes delicate instrumentation

Table 10.2 (continued)

Measurement principle	Measurement range (limiting quantities)	Measurement sensitivity	Measurement reproducibility range (%)	Materials specimen type	Specimen geometry, dimensions	Methods merit	Methods demerit
Moment-measuring coil	\hat{J}_{\max} : 10^{-4} – 10^{-2} V s m	j : 10^{-10} V s m	j : 0.5–1	Bulk permanent magnets	Cylinders, blocks, rings, segments	Fast and accurate, standardized	Only for two pole magnets, one quantity
Pulse field magnetometer (PFM)	H_{\max} : 4–8 MA/m	H : 1 kA/m J : 1 mT	H, J : 1–3	Bulk permanent magnets	Cylinders, blocks, segments	High field strength, fast	Demagnetization factor, eddy currents to be considered
DC hysteresis-graph – ring method	H_{\max} : 10–20 kA/m	H : 0.01 A/m	H : 1 J : 1–2	Ferromagnetic, sintered or powder compacted rings, wound ring cores	Rings (geometries with closed magnetic path), stamped stacks of sheet	Many quantities, very low field strength possible, standardized	Requires specimen winding
DC hysteresis-graph – yoke methods	H_{\max} : 50–200 kA/m	H : 1 A/m	H : 2–3 J : 1–2	Ferromagnetic steel	Bars, strips of sheet	Many quantities, standardized	Restricted specimen dimensions and shapes
Coercimeter	H_{\max} : 20–200 kA/m	H : 0.5–1 A/m	H_c : 2–5	Ferromagnetic steel	Components of various shapes	Various specimen shapes, standardized	Only one quantity (H_c)
AC hysteresis-graph – ring method	f : 10 Hz–1 MHz	H : 0.01 A/m	J : 1–10 H : 1–2	Ferromagnetic materials	Rings (geometries with closed magnetic path), stamped stacks of sheet	Many quantities, standardized	Restricted specimen shape, requires specimen winding
Epstein frame	f : \leq 400 Hz \hat{J}_{\max} : 1.5–1.7 T	J : 1 mT	J : 2–3 P_w : 2–7	Ferromagnetic (electric) steel	Strips of sheet	Standardized, widespread method	Demanding specimen preparation, systematic error
Single-sheet tester (SST)	f : 50–400 Hz \hat{H}_{\max} : 1–10 kA/m \hat{J}_{\max} : 0.8–1.8 T	J : 1 mT	J, H : 2–3 P_w : 1–2	Ferromagnetic (electric) steel	Sheet	Standardized, simple specimen preparation	Large specimens in standardized version, systematic error
Wattmeter method	\hat{H}_{\max} : 1–10 kA/m	2)	2)	Ferromagnetic (electric) steel	Rings, sheet using fixtures	Standardized method	Few quantities
Voltmeter–ammeter method	\hat{H}_{\max} : 1–10 kA/m	2)	2)	Ferromagnetic (electric) steel	Rings, sheet using fixtures	Fast, standardized method, common instrumentation	Few quantities

Table 10.2 (continued)

Measurement principle	Measurement range (limiting quantities)	Measurement sensitivity	Measurement reproducibility range (%)	Materials specimen type	Specimen geometry, dimensions	Methods merit	Methods demerit
Saturation coil	H : 100–900 kA/m j_{\max} : 10^{-4} – 10^{-2} V s m	j : 10^{-10} V s m	j : 1–2	Nickel, Ni alloys, Co content in hard metals	Discs, wire, cylinders, small components	Fast, standardized method	Only one quantity, J_s limit depends on shape
Faraday scale	H : 800–1600 kA/m	1)	1)	Ferro-, para- and diamagnetic materials	Small massive samples, powders, films	High sensitivity, wide temperature range, small samples	Delicate, costly instrumentation
Gouy scale	H : 800–2400 kA/m	1)	1)	Para- and diamagnetic materials	Bars, vessels with liquids or gasses	High sensitivity, wide temperature range	Often delicate instrumentation, large specimen volume
Impedance bridges	f : 1 Hz–100 MHz	2)	2)	Ferro- and ferri-magnetic materials	Rings, components	Component testing close to electrical application	Require specimen winding

1) mostly research instruments with differing ranges, sensitivities and reproducibility
2) strongly depending on capabilities of standard electrical instrumentation

calibrations and are widespread in application. The information is selected to allow an evaluation of the methods. More details are given where errors are liable to be introduced.

Section 10.2.3 is completed by a short description of measuring methods for magnetostriction and, provided by Grössinger, nonstandard testing methods for soft magnetic materials that are used in scientific research laboratories.

10.2.2 Properties of Hard Magnetic Materials

Hysteresisgraph for Hard Magnetic Materials

A very important instrument for the characterization of bulk permanent magnets is the hysteresisgraph. It is mainly used to record the second-quadrant hysteresis loop. From this, material parameters such as the remanence B_r , the maximum energy product $(BH)_{\max}$ and the coercive field strengths (coercivities) H_{cJ} and H_{cB} , can be determined. A measurement of recoil loops allows the calculation of the recoil permeability μ_{rec} .

The main components are an electromagnet to magnetize and demagnetize the specimen, measuring coils for the field strength H and the polarization J and

two electronic integrators (fluxmeters) to integrate the voltages induced in the coils. A typical configuration of a computer-controlled hysteresisgraph is shown in Fig. 10.2.

An electromagnet with a vertical magnetic-field direction is used. The magnet specimen is placed on the pole cap of the lower pole. The upper pole can be lowered to close the magnetic circuit.

While recording the hysteresis loop, high flux densities are only required for relatively short time periods. Therefore it is possible to avoid active cooling of the electromagnet coils up to a peak electric power of approximately 3 kW. If the electromagnet is designed carefully, maximum flux densities of 1500–2400 kA/m can be achieved for specimen heights of several millimeters. Beyond this point, the steel parts of the electromagnet frame become saturated. For a further increase of the field strength significantly higher electric power and water cooling become necessary.

The measuring principle is based on the fact that the poles of the electromagnet form faces of equal magnetic potential. It is only under this condition that the specimen is homogeneously magnetized and the field strength that is measured next to the magnet is equal to its inner field strength. The pole materials (soft mag-



Fig. 10.2 Hysteresisgraph for hard magnetic materials. The cabinet contains two fluxmeters for H and J measurement and the electromagnet power supply. The specimen and surrounding coil are placed between the poles of the electromagnet (Permagraph C Magnet-Physik Dr. Steingroever GmbH, Köln)

netic steel or iron-cobalt alloy) and the polarizations of permanent-magnet specimens limit the measuring range of the method to about $H < 800$ kA/m in the first quadrant and $|H| < 2400$ kA/m in the second quadrant of the hysteresis loop.

As it is impossible to saturate rare-earth permanent magnets (Sm-Co, Nd-Fe-B) in an electromagnet, it is necessary to saturate them in a pulsed magnetic field prior to the measurement. Depending on the recoil permeability, the polarization will be lower than the remanence after the specimen has been inserted into the electromagnet and the magnetic circuit has been closed. However, a magnetization in the electromagnet allows full remanence to be achieved again.

Measuring Coils. Two types of measuring coils are used: the J -compensated surrounding coil and the pole-coil measuring system.

The J -compensated surrounding coil (Fig. 10.1) is suitable for all kinds of permanent-magnet materials. For the measurement it is placed around the specimen. It consists of the following windings.

One winding with area-turns of $N_1 A_1$ encloses the inner hole of the coil that accepts the specimen during the measurement. This senses the magnetic flux pene-

trating the magnet specimen,

$$\Phi_M = B_M N_1 A_M, \quad (10.1)$$

where B_M is the flux density and A_M is the cross-sectional area of the magnet specimen. If the coil is not completely filled by the specimen, the air flux between the specimen and the winding,

$$\Phi_{A_1} = \mu_0 H N_1 (A_1 - A_M), \quad (10.2)$$

is also detected, where H is the field strength in air next to the specimen.

A second coil with area-turns $N_2 A_2$ also surrounds the specimen but does not enclose it. This senses only the air flux,

$$\Phi_{A_2} = \mu_0 H N_2 A_2. \quad (10.3)$$

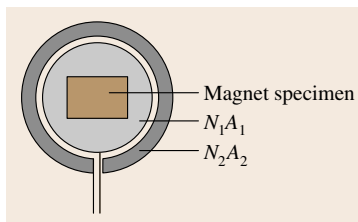


Fig. 10.1 Area-turns of a J -compensated surrounding coil

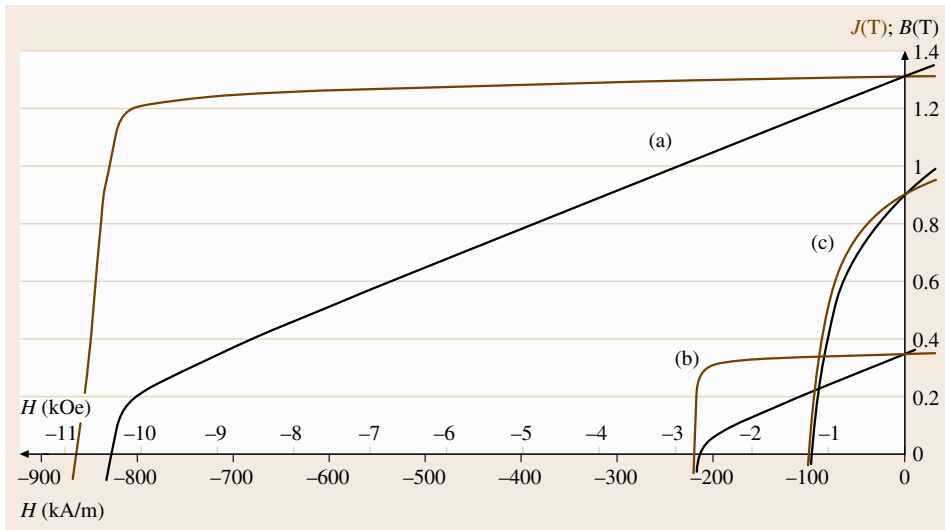


Fig. 10.3 Surrounding coil measurements on (a) NdFeB 320/86, (b) hard ferrite 24/23 and (c) AlNiCo 38/10 permanent magnets

The area-turns of the two coils are adjusted to be equal

$$N_1 A_1 = N_2 A_2 . \quad (10.4)$$

Both coils are connected in series opposition to a fluxmeter integrator. If the inner of the first coil is partially filled by a specimen, the magnetic flux measured is

$$\begin{aligned} \Phi &= \Phi_M + \Phi_{A_1} - \Phi_{A_2} = (B_M - \mu_0 H) N_1 A_M \\ &= J N_1 A_M , \end{aligned} \quad (10.5)$$

where J is the polarization of the specimen, which is connected to the magnetization M by $J = \mu_0 M$. In the absence of a specimen the resulting flux Φ is zero.

Usually the surrounding coil system contains a third coil that senses the magnetic field strength H . It is connected to a second fluxmeter integrator. In this way the $J(H)$ hysteresis loop can be measured directly using one combined-coil system that can be made 1 mm thin. The $B(H)$ hysteresis loop can be derived from the $J(H)$ loop. Figure 10.3 shows the demagnetization curves of different permanent-magnet materials measured using surrounding coils.

Instead of the field measuring coil a Hall probe can also be placed next to the specimen to sense H . This requires additional space for the probe and an additional measuring instrument. Because of the linearity error and the temperature dependence of the sensitivity of a Hall sensor, suitable corrections are necessary. Additional errors can arise from the facts that the Hall probe always has to be aligned truly perpendicular to the magnetic-field direction and that it is, due to the small active area, more sensitive to local field-strength variations.

The second coil system that is used in hysteresis-graphs is the pole-coil measuring system [10.4]. It is used mainly for hard ferrite magnets. The pole-coil system consists of two coils that are embedded into one pole of the electromagnet (Fig. 10.4). One coil is completely covered by the specimen. The other coil remains free.

The first coil senses the flux density B at the surface of the specimen. The second coil measures the magnetic field strength H . Both coils are connected in series opposition. In this way the polarization, $J = B - \mu_0 H$, is obtained directly. This compensation also cancels out the residual field of the poles before the specimen is inserted.

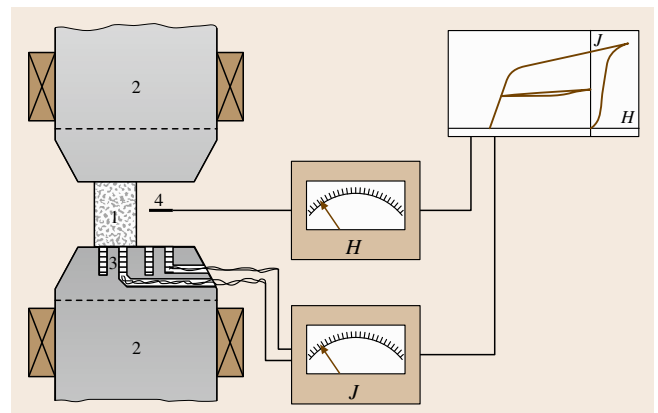


Fig. 10.4 Hysteresis measurement with pole coils (1 – magnet specimen, 2 – electromagnet poles, 3 – pole coils, 4 – field-strength sensor)



Fig. 10.5 Segment poles with pole coils

The surrounding coil measures the whole magnetic flux penetrating the specimen. The pole-coil system only senses the flux in a small area (typically with a diameter of 3–6 mm) on the surface. Therefore it is suitable for the detection of nonhomogeneities in different regions. Especially for anisotropic ferrite magnets it is usual to carry out measurements on both sides of a magnet to quantify differences caused by the production process.

Pole-coil systems are also made arc-shaped for measurements on segment magnets for motor applications. They must be machined to match the radii of the segments exactly. Both the upper and the lower pole contain a pair of pole coils.

Measurements at Elevated Temperatures. For measurements at temperatures up to 200 °C pole caps with built-in heating (Fig. 10.6) can be used. A hole in the pole cap accepts a thermocouple for temperature meas-

urement and control. Prior to the measurement the specimen must remain between the poles for a sufficient time to reach the desired temperature. The surrounding coil needs to be temperature-proof. Hysteresis measurement is carried out in the same way as at room temperature.

Measurements on Powders. Powder samples can be measured in the same way as solid magnets if the powder is filled into a nonmagnetic container, for example a brass ring that is sealed with a thin adhesive foil at the bottom. As the measured polarization depends on the apparent density, it may be more feasible to regard the specific polarization. The coercivity H_{CJ} however can be measured directly.

Vibrating Sample Magnetometer (VSM)

The VSM is used to measure the magnetic moment m and the magnetic dipole moment $j = \mu_0 m$ in the presence of a static or slowly changing external magnetic field [10.5]. As the measurement is carried out in an open magnetic circuit the demagnetization factor of the specimen must be considered.

Most instruments use stationary pickup coils and a vibrating specimen but arrangements with vibrating coils and rigidly mounted specimens have also been proposed. The drive is either carried out by an electric motor or by a transducer similar to a loudspeaker system.

The specimen is suspended between the poles of the electromagnet and oscillates vertically to the field direction; it must be carefully centered between the pickup coils.

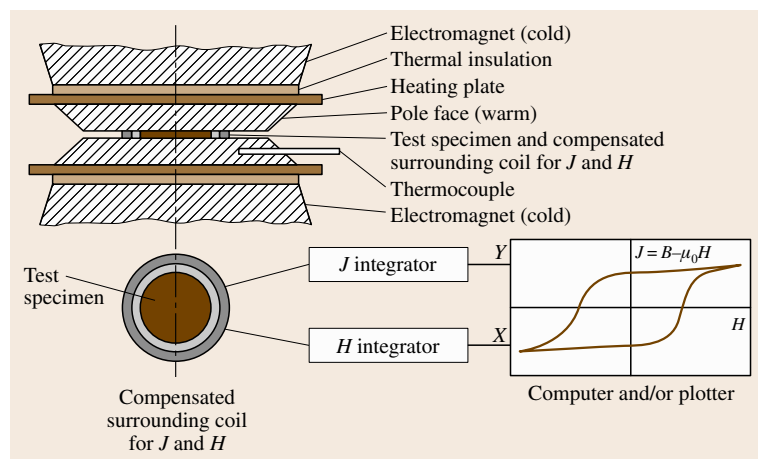


Fig. 10.6 Heating poles for measurements at elevated temperatures

In the pickup coils a signal at the vibration frequency is induced. This signal is proportional to the magnetic dipole moment of the specimen but also to vibration amplitude and frequency. The coil design ensures that it is independent of variations in the field generated by the electromagnet.

The amplitude and frequency can be measured separately, for example using

- a capacitor with one set of fixed plates and one set of movable plates (Fig. 10.7),
- a pickup coil and a permanent magnet,
- an electrooptical sensing system.

The signals are fed to a differential amplifier, so that changes of oscillation amplitude and frequency can be compensated. A synchronous detector (lock-in amplifier) followed by a low-pass filter produces a direct-current (DC) output signal that only depends on the magnetic moment.

For the generation of the outer magnetic field a strong electromagnet is required; the field direction is horizontal. Water-cooled magnets are mostly used but superconducting magnets are also common. The power required is even higher than for a hysteresisgraph as the volume between the pole caps is quite large. The specimen rod must be able to oscillate, and sufficient space for a pickup coil system is required between the specimen holder and the pole caps.

Usually a distance that is sufficient for an optional oven or a cryostat to heat or cool the specimen is chosen. Ovens, LN₂ or helium cryostats that are shaped to fit between electromagnet poles are available. Care must be taken to avoid errors due to magnetic components or electrical supply lines. In this way the determination of Curie temperatures and the observation of other phase transitions become possible.

Figure 10.8 shows measurements on nanocrystalline specimens. Measurement below room temperature was carried out using an LN₂ cryostat. Above room temperature a tubular oven was used; it had a water-cooled outer wall to avoid heating of the pickup coils and electromagnet poles. The oven can be evacuated or filled by an inert gas to avoid specimen oxidation.

For practical purposes and to separate the mechanical system from building oscillations it is usually mounted onto the electromagnet. This offers a stable base due to its large mass. For high sensitivity the transfer of oscillations from the drive to the pickup coils through the electromagnet should be avoided; a mechanical resonator can achieve this. In this case the drive frequency must be matched to the resonant frequency.

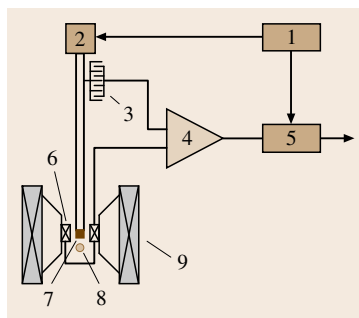


Fig. 10.7 Vibrating-sample magnetometer: 1 – oscillator, 2 – transducer, 3 – capacitor for frequency and amplitude measurement, 4 – differential amplifier, 5 – synchronous detector, 6 – pickup coils, 7 – specimen, 8 – H field sensor, e.g. Hall probe, 9 – electromagnet poles and coils (frame not shown)

A VSM is mostly used for measurements on magnetically hard or semi-hard materials. Specimen forms include small bulk samples, powders, melt-spun ribbons and thin films. The VSM can also be used for measurements on soft magnetic materials. In this case the electromagnet can be replaced by a Helmholtz-coil system.

VSMs are very sensitive instruments. Commercial systems offer measuring capabilities down to approximately 10^{-9} A m². A system that used a SQUID sensor instead of pickup coils achieved a resolution of 10^{-12} A m² [10.6].

Closely related to the VSM is the alternating gradient field magnetometer (AGM). As it is typically

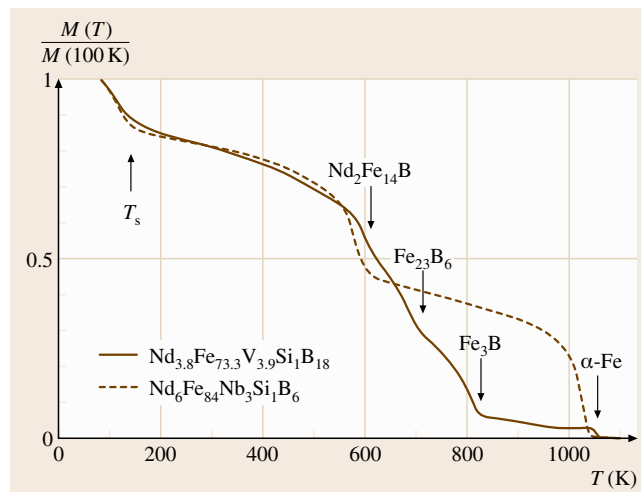


Fig. 10.8 VSM measurement of the temperature dependence of the magnetization M of nanocrystalline melt-spun samples. The curve shows the spin-reorientation temperature T_s of Nd₂Fe₁₄B and the Curie temperatures of the comprised phases (heating curves, $dT/dt = 45$ K/min)

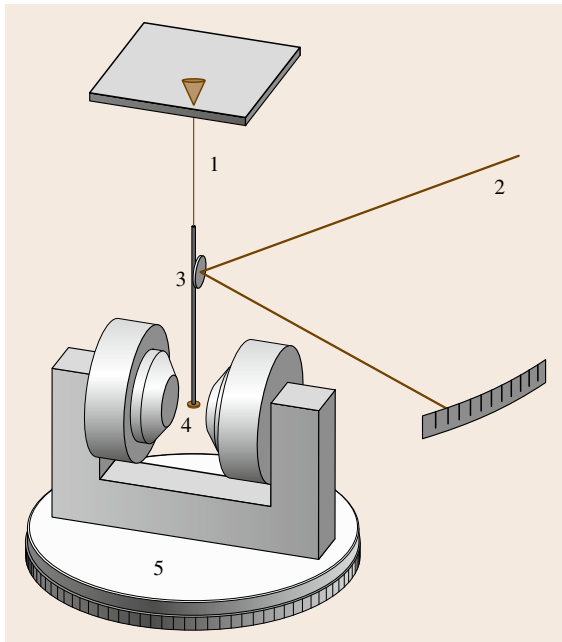


Fig. 10.9 Torque magnetometer: 1 – torsion wire, 2 – light beam, 3 – specimen rod with mirror attached, 4 – specimen, 5 – electromagnet on rotating base

used for measurements on thin films, it is discussed in Sect. 10.4.

Torque Magnetometer

If the magnetization energy of a freely rotating specimen depends on direction, the specimen aligns with its axis of easy magnetization parallel to a magnetic field. The axis of easy magnetization is determined by the magnetocrystalline anisotropy energy E_a if the specimen has rotational symmetry.

If the magnetic field is rotated out of the preferred direction by an angle α , the vector of polarization J_s will point in the direction of H , if the field strength is sufficiently large to saturate the specimen. If H is smaller, the direction of J_s is rotated only by an angle $\varphi < \alpha$.

For a material showing uniaxial anisotropy, the anisotropy energy is assumed to be

$$E_a = K_1 \sin^2 \varphi, \quad (10.6)$$

where K_1 is the uniaxial anisotropy constant. The magnetizing energy is

$$E_H = HJ_s \cos(\alpha - \varphi), \quad (10.7)$$

which leads to the torque

$$L = -\frac{d(E_a + E_H)}{d\varphi} = -K_1 \sin 2\varphi - HJ_s \sin(\alpha - \varphi). \quad (10.8)$$

Therefore the determination of anisotropy constants requires high field strengths or suitable extrapolation. A broad discussion of the anisotropy energy for different crystal symmetries can be found in [10.7, Chap. 5].

The specimen is attached to a rod that is suspended between torsion wires, and is located between the poles of an electromagnet. The electromagnet is mounted to a base plate that can be rotated by 360°. The rotation angle can be measured and recorded.

The excitation of the specimen is measured by the deflection of a light beam from a mirror that is attached to the specimen rod.

Automated systems use an electrodynamic compensation of the torsion, which is measured by an optical system consisting of a mirror attached to the specimen rod, a light beam and photosensors to detect the excitation. The excitation is compensated by an electromagnetic system that is located outside the stray field of the electromagnet. The current in the compensating coil is proportional to the torque.

The main application of the torque magnetometer is the determination of anisotropy field constants of hard magnetic materials, including small particles and thin films. Other applications are the determination of texture on grain-oriented electrical sheet and strip and the determination of the anisotropy of susceptibility of paramagnetic materials with noncubic structure.

Moment-Measuring Coils

Helmholtz-coil configurations [10.8] are very common for the measurement of the magnetic dipole moment of permanent magnets. They provide a large region with

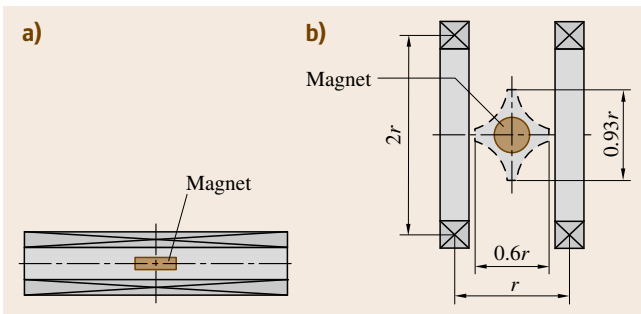


Fig. 10.10a,b Moment-measuring coils: solenoid (a) and Helmholtz coil. (b) The dashed line in the Helmholtz coil marks the cross section of the measuring space for 1% accuracy

uniform sensitivity that can be easily accessed from all sides. Long solenoids can also be used (Fig. 10.10). The installation of the coil must be carried out with care. No magnetic or magnetizable parts are allowed in the vicinity of the coil as they would affect the measurement result.

The measuring coil is connected to a fluxmeter. The magnet specimen is placed in the center of the coil so that the vector of polarization is aligned with the coil axis. The fluxmeter is set to zero and the magnet is withdrawn from the coil as long as the reading of the fluxmeter changes. Alternatively the magnet can be rotated by 180° so that the vector of polarization points in the opposite direction. If the rotation method is used, the fluxmeter reading must be divided by 2.

The magnetic dipole moment j of the specimen is proportional to the measured magnetic flux Φ ,

$$j = k\Phi . \quad (10.9)$$

The measuring constant k can be calculated from the dimensions and the number of turns n of the coil. For a Helmholtz coil, k is approximately $1.4r/n$, where r is the coil radius. In practice, k is obtained by calibration.

From the dipole moment, the magnetic polarization J in the working point of a magnet with the volume V can be calculated using

$$J = j/V . \quad (10.10)$$

This allows the determination of the working point if the demagnetization curve of the material is known.

For an anisotropic magnet, the polarization in the working point is typically only 1–3% lower than the remanence B_r . This fact is used in the main application of the method: a fast and repeatable test for B_r . This makes it popular in industrial quality control if a measurement of the demagnetization curve is too time-consuming or expensive.

The method can also be used for radially anisotropic, arc-shaped magnets that are common in motor applications (Fig. 10.11). As the coil only detects

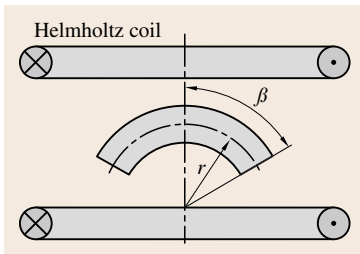


Fig. 10.11 Measurement of the magnetic dipole moment of a radially anisotropic segment magnet

the magnetic moment parallel to the coil axis, a correction must be applied.

The measured magnetic dipole moment is

$$j' = 2JA r \int_0^\beta \cos \beta d\beta . \quad (10.11)$$

Here A is the cross-sectional area of the specimen. The volume of the magnet,

$$V = 2Ar\beta , \quad (10.12)$$

leads to the polarization

$$J = \frac{j'}{V} \frac{\beta}{\sin \beta} . \quad (10.13)$$

Another application is the determination of the anisotropy direction of block magnets. The magnetic dipole moment is measured in the direction of one geometrical symmetry axis (j_x) and in two perpendicular directions (j_y, j_z).

The angle α between the geometrical symmetry axis and the axis of anisotropy is

$$\alpha = \arccos \frac{j_x}{\sqrt{j_x^2 + j_y^2 + j_z^2}} . \quad (10.14)$$

10.2.3 Properties of Soft Magnetic Materials

DC Hysteresisgraph – Ring Method

The basic method for the measurement of quasistatic hysteresis loops mostly uses ring-shaped specimens (Fig. 10.12). Other specimen shapes providing a closed magnetic circuit with constant cross section may also be appropriate. The specimen is equipped with a primary winding and a secondary winding.

Usually the bipolar current source is computer-controlled and the fluxmeter and ammeter are also integrated into a data-acquisition system.

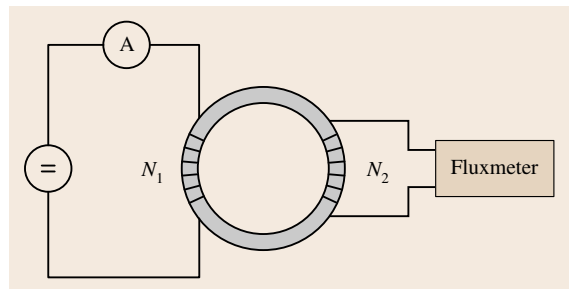


Fig. 10.12 Circuit of the ring method

The magnetizing current I is applied to the primary winding. The magnetic field strength H is calculated from

$$H = \frac{N_1 I}{l_m}, \quad (10.15)$$

where N_1 is the number of turns of the primary winding. The mean magnetic path length l_m is usually obtained from

$$l_m = \pi \frac{D+d}{2}, \quad (10.16)$$

where D is the outside diameter and d is the inside diameter of the ring.

The radial variation of H must be kept small. Therefore the ratio between the outer diameter and inner diameter should not exceed 1.4. Thinner rings are often impracticable, especially for fragile sintered specimens. If this condition cannot be met for any reason, l_m can better be calculated with respect to the average field strength,

$$l_m = \pi \frac{D-d}{\ln\left(\frac{D}{d}\right)}. \quad (10.17)$$

The voltage that is induced into the secondary winding must be integrated to obtain the magnetic flux Φ . Therefore a fluxmeter is used. From the flux Φ , the flux density B is calculated as

$$B = \frac{\Phi}{N_2 A}. \quad (10.18)$$

Here N_2 is the number of turns of the secondary winding and A is the cross-sectional area of the specimen. For a massive ring of rectangular cross section and height h , the area is calculated from

$$A = \frac{D-d}{2} \cdot h. \quad (10.19)$$

If the ring consists of stacked sheets or wound ribbons, the area must be calculated from

$$A = \frac{2m}{\rho\pi(d+D)}, \quad (10.20)$$

where m is the mass and ρ is the density of the specimen material.

Prior to the measurement the specimen is demagnetized. An alternating current with decreasing amplitude is applied to the primary winding. The frequency and decay rate of this current can be preset. The measurement can then be started with the initial magnetization curve. The hysteresis loop is either excited up

to the maximum current provided by the current source or to a preset limit of H or B .

Often the measuring speed is controlled so that a constant rate of change of the flux density with time, dB/dt , is achieved. This allows the steep parts of the loop to be passed slowly to avoid errors due to eddy currents. The flat parts of the curves can be passed faster as eddy currents do not affect the magnetization. However, the instrument must also have the possibility to run curves at constant speed, for instance in the case that control is not possible, e.g. for a high squareness loop. The typical time to trace a hysteresis loop is of the order 1 min.

Quasistatic measurement allows one to obtain magnetic material properties independently of the influence of eddy currents. In this way the hysteresis loss can be obtained directly by integrating the area of the hysteresis loop

$$P = \oint B dH. \quad (10.21)$$

Coercivities of soft magnetic ring specimens range from less than 0.1 A/m for ring cores made of wound ribbons of amorphous alloys up to several 100 A/m for rings made of solid steel or sintered material. Depending on the ring dimensions, current and number of primary turns, typically maximum field strengths up to approximately 10 kA/m can be achieved.

The permeability curve $\mu_r(H)$ can be created by dividing the corresponding values of B and $\mu_0 H$, which are usually taken from the initial magnetization curve. The highest point of the $\mu_r(H)$ curve, the maximum permeability μ_{\max} , is typically stated in measurement reports.

Figure 10.13 shows some sample measurements on different materials. The field-strength excitation is 5 kA/m for the Fe-Si and 60 A/m for the Fe-Ni specimen.

Winding a Ring Specimen. In schematic drawings such as Fig. 10.12 primary and secondary windings are usually shown on opposite sides of the ring. This configuration produces a high stray field if the permeability decreases while approaching saturation. Therefore, both windings are often equally distributed around the circumference if the number of turns is sufficiently large. To avoid air flux between the ring and the secondary winding, this winding is wound directly onto the ring. The primary winding is wound onto the secondary winding.

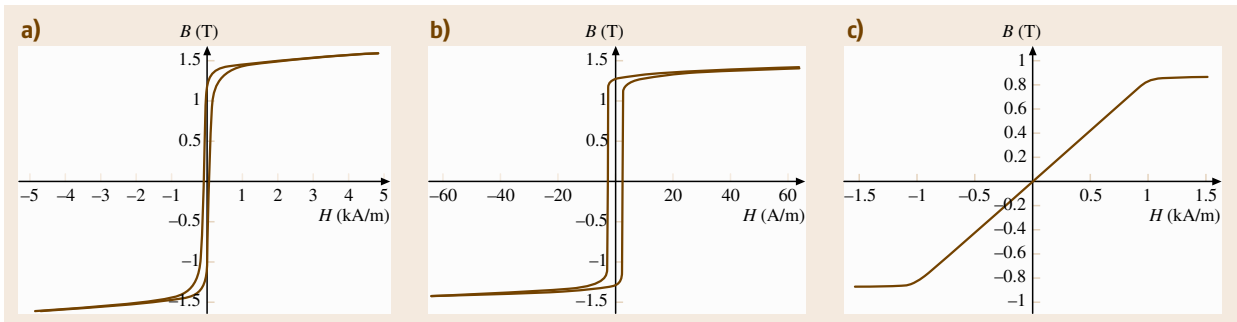


Fig. 10.13a–c Hysteresis loops of ring specimens measured by the DC ring method, (a) Fe-Si alloy with round (R-)hysteresis loop, (b) Fe-Ni alloy with high squareness (Z-)loop, (c) amorphous cobalt alloy with flat (F-)loop

Each of the equally distributed windings produces an effective circular turn with a diameter equal to the mean diameter of the ring. In this way the primary winding produces a magnetic field in the direction of the ring axis. This can be avoided by winding the turns in pairs of layers that are wound alternating clockwise and counterclockwise around the ring.

This also reduces the error arising from the effective mutually inductive coupling between the two windings in the axial direction. To minimize this error, the wire of the secondary winding can also be led back along the mean diameter of the ring.

After winding, the specimen should be checked for short circuits between the windings and core.

Specimens for ring-core testing include wound ribbons of amorphous alloys and iron-nickel alloys. If the magnetic properties can easily be altered by mechanical stress, the windings cannot be applied to the cores directly. The cores can be coated or placed in plastic core boxes that are wound afterwards. Prefabricated windings with multipole connectors are also used.

Depending on the field-strength range, the air flux between the measuring winding and specimen must be considered. The flux density must then be calculated from

$$B = \frac{\Phi}{N_2 A} - \mu_0 H \frac{A_2 - A}{A}, \quad (10.22)$$

where A_2 is the cross-sectional area of the secondary winding and A is the area of the specimen.

DC Hysteresisgraph – Yoke Methods

The DC hysteresisgraph or permeameter is used for quasistatic hysteresis measurements on soft magnetic materials. The specimen can either be a bar with round or rectangular cross section or a strip of flat material.

The choice of the method depends on the shape and magnetic properties of the specimen. Yoke methods are generally used instead of the ring method if the coercivity of the specimen material is larger than 50–100 A/m. Maximum field strengths range from 50–200 kA/m.

The most widespread yoke configurations today are the permeameter yokes type A and type B according to [S-10-31] and the Fahy permeameter [10.9] (Fig. 10.14). Many other, often similar, configurations have been designed. A larger collection can be found in [10.10].

For the measurement of the flux density B , a coil that is directly wound onto the specimen can be used. In everyday use J -compensated coils are often preferred. They can be made sturdier and can be used for specimens with various diameters and shapes.

The measurement of the field strength H can be carried out by a Hall probe or a field-measuring coil (search coil) next to the specimen. Due to the restricted space, this approach is used with the type A permeameter. Another way is a c-shaped potential-measuring coil, as shown in Fig. 10.14b for the type B permeameter. It is placed directly onto the specimen surface and senses the magnetic potential difference P between its ends. The magnetic field strength is obtained by $H = P/s$, where s is the distance between the ends of the potential coil. A straight potential-measuring coil can be used with the Fahy permeameter.

In the type A permeameter, the specimen is surrounded by the magnetizing coil. This configuration generates relatively high field strengths. However, specimen and field strength sensor are heated directly by the power dissipation in the coil. If the field strength is increased above approximately 50 kA/m, forced air or even water cooling becomes necessary. The minimum specimen length for the type A permeameter is 250 mm.

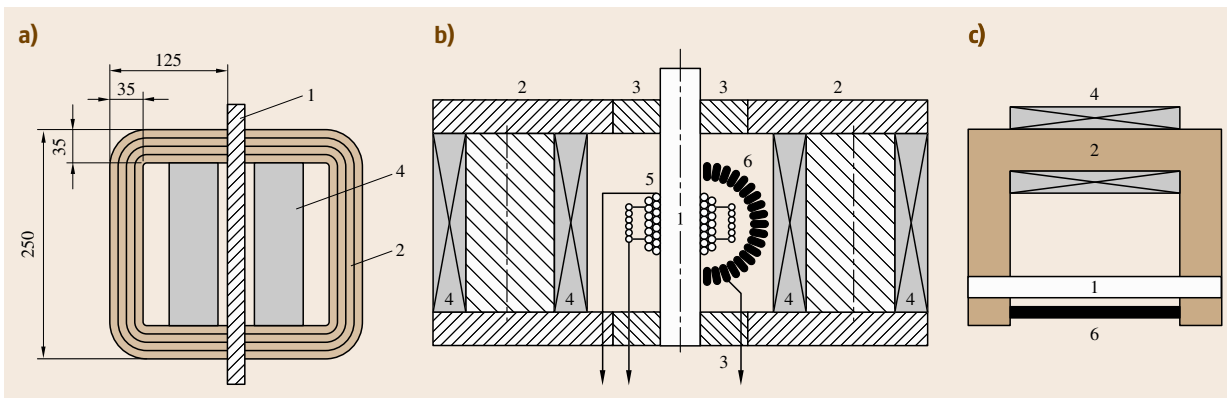


Fig. 10.14a–c Permeameters: IEC Type A (a), IEC Type B (b), Fahy Simplex (c). 1 – specimen, 2 – yoke frame, 3 – exchangeable pole pieces, 4 – field-generating coils, 5 – surrounding coil for B or J, 6 – sensor for H

The type B permeameter uses specimens that are only 90 mm long, but the maximum field strength is limited to 50–60 kA/m as the yoke frame saturates above.

Like in the DC ring method, the measuring speed is often controlled to $dB/dt = \text{const.}$ to minimize the influence of eddy currents on the measurement results.

Coercimeter. The size and shape of soft magnetic components often makes it impossible to measure the complete hysteresis loop. In this case a coercimeter can be used to determine the coercivity H_{cJ} . As this quantity depends sensitively on the microstructure, it is a good indicator of successful material heat treatment. The measurement is carried out in an open magnetic circuit.

A solenoid is used to magnetize and demagnetize the specimen. The maximum field strength must be sufficient to achieve technical saturation, beyond which the coercivity would remain constant if the magnetizing field strength were further increased. This can be tested by a series of measurements with increasing magnetizing field strengths. The required field strength depends on the specimen material and shape. Commercial solenoids provide up to 100–200 kA/m. Sometimes an additional higher-field pulse is used for saturation.

After the specimen has been saturated and the polarity is reversed, the field strength must be increased slowly to avoid errors due to eddy currents in the specimen. A field sensor detects the stray field. For a homogeneously magnetized specimen the stray field vanishes at H_{cJ} . Fluxgate probes, Hall probes or compensated coils can be used as zero-field-strength detectors. The arrangement of the sensors in

Fig. 10.15 ensures that only the stray field of the specimen and not the field generated by the solenoid is measured.

Formerly it was usual to align the instrument with respect to the Earth's magnetic field. Today shielded systems are preferred as they are easier to install and also dynamic noise fields are suppressed.

It is often claimed that coercimeters allow measurement of the coercivity independently of the specimen shape. For machined components such as parts of relays the coercivity is not uniform due to mechanical or heat treatment. Complex-shaped parts are not uniformly magnetized. In these cases the coercimeter provides only an integral value given by the vanishing stray field at the sensor position.

AC Hysteresisgraph. An AC hysteresisgraph is mainly used for ring specimens but also sometimes with fixtures that allow measurements of strips. In these cases

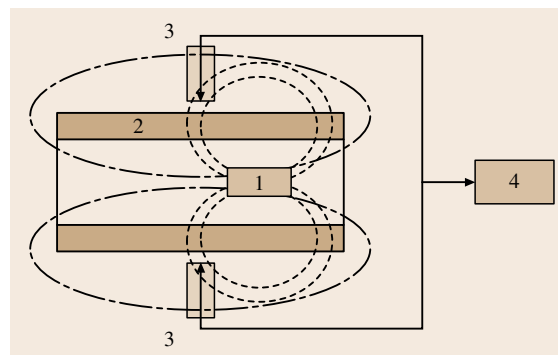


Fig. 10.15 Coercimeter: 1 – specimen, 2 – field-generating solenoid, 3 – field sensors, 4 – zero detector

the feedback yoke, e.g. a C-core, must be laminated to avoid eddy currents. The permeability should be high compared with the permeability of the specimen.

For the winding of the ring specimen the same considerations as for the DC ring method apply.

The simplest version of an AC hysteresisgraph uses an oscilloscope. The secondary induced voltage is integrated using a resistor–capacitor (RC) circuit. The output is displayed as a function of the primary current. Today this method is mainly used for demonstration purposes. For material testing, digital data-acquisition systems are more suitable.

Figure 10.16 shows the operating principle. A programmable function generator controls a power amplifier that supplies a current I to the primary winding of the specimen. The current is measured using a shunt with negligible inductance. From the current and the magnetic path length l_m the field strength H can be calculated. The secondary induced voltage is digitized and integrated to obtain the flux density B .

The measuring conditions have to be defined to achieve comparable results. Programmable function generators allow the waveform of B to be defined as sinusoidal [10.11]. A sinusoidal H can be easier achieved using a current output amplifier. Systems with digital control for B are available up to frequencies of several kHz, while uncontrolled systems can reach several 100 kHz or even a few MHz.

Due to an increase of applications for soft magnetic materials using pulse-width modulation (PWM), the interest in measuring systems that allow measurements in the presence of higher harmonics is growing [10.12]. Function generators with arbitrarily programmable waveforms can meet these requirements.

After $U_1(t)$ and $U_2(t)$ have been recorded, various evaluations can be carried out. The hysteresis loop and the total loss can be calculated.

The AC hysteresisgraph can also measure the curve of normal magnetization, also called commutation curve. Therefore the amplitude of the magnetizing current is successively increased and corresponding peak values of the field strength and flux density, \hat{H} and \hat{B} , are recorded. The amplitude permeability $\mu_a(H)$ or $\mu_a(B)$ can be calculated from these.

Epstein Frame. The Epstein frame is mainly used by producers and users of electrical sheet and strip. Many consignments in industry are based on Epstein values. The main disadvantage of the method is the demanding specimen preparation and the large quantity of specimen material. The classical Epstein frame had a width

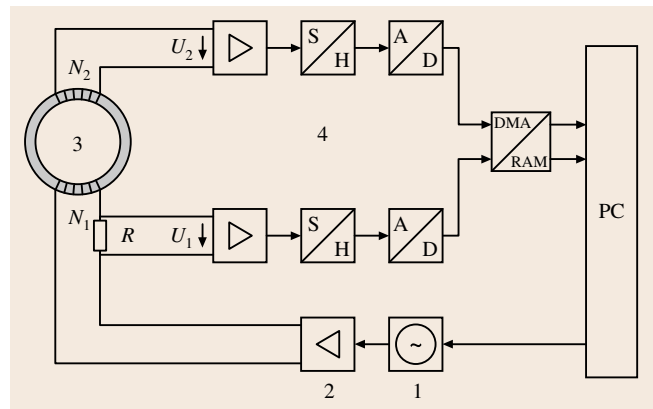


Fig. 10.16 AC hysteresisgraph: 1 – programmable frequency generator, 2 – power amplifier, 3 – specimen, 4 – transient recorder with preamplifier and analog-to-digital conversion

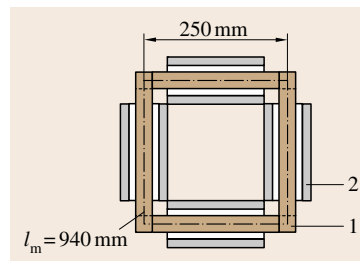


Fig. 10.17 25 cm Epstein frame: 1 – specimen, 2 – magnetizing and measuring coils

of 50 cm and required about 10 kg specimen mass. It has been nearly completely replaced by the 25 cm frame (Fig. 10.17).

Four coil sets form the frame. Each of them contains two windings: an inner flux measuring winding and an outer winding to magnetize specimen. The specimen must be cut into strips that are between 280 mm and 320 mm long and 30 mm \pm 0.2 mm wide. These are stacked into the frame so that they overlap alternately in the corners.

For nonoriented material, one half of the strips is cut in the rolling direction and the other half perpendicular to it. The strips cut perpendicular to the rolling direction must be placed at opposite sides.

Measurements are mainly carried out at power-line frequencies (50–400 Hz). Rarely the Epstein frame is also used for quasistatic measurements or up to the kHz range. Normally the measurements are carried out under the condition of sinusoidal flux density B . The excitation is typically limited to $\hat{B} = 1.5$ T for nonoriented and $\hat{B} = 1.8$ T for oriented material. At higher excitations, digital or analog feedback control becomes necessary.

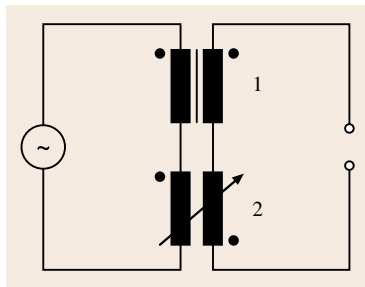


Fig. 10.18 Air-flux compensation using an adjustable mutual inductor: 1 – Epstein frame, 2 – mutual inductor

To calculate the magnetic field strength H from the magnetizing current I , the magnetic path length l_m is required (10.11). Due to the overlapping edges, l_m cannot be determined exactly. Therefore it is set by definition to 94 cm for the 25 cm frame.

To obtain the polarization J , the air flux that is generated in the measuring coils must be compensated. A mutual inductor is the conventional solution (Fig. 10.18). It is adjusted so that the output of the measuring winding is canceled out if no specimen is inserted in the frame.

Today the Epstein frame is mostly connected to a data-acquisition system, as shown in Fig. 10.16 for the AC hysteresisgraph. Then the air-flux correction can also be carried out by calculating the difference between a measurement with an empty frame and the measurement on the specimen.

The Epstein frame is not always used to measure the complete hysteresis loop. If only loss or permeability data are required, the wattmeter method or the voltmeter-ammeter method can be applied to the Epstein frame.

Single-Sheet Tester. The single-sheet tester (SST) uses a yoke to close the magnetic circuit (Fig. 10.19). The specimen is placed between the two halves of the yoke inside a set of coils that consists of an inner measuring coil and an outer coil that applies the magnetizing field.

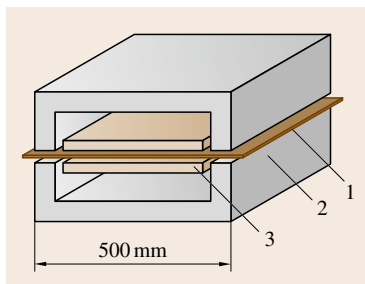


Fig. 10.19 Single-sheet tester: 1 – specimen, 2 – yoke frame, 3 – magnetizing and measuring coils

The standardized SST yoke is 500 mm long and wide. It is designed for sheets with a minimum length of 500 mm. A square specimen allows measurement in and perpendicular to the rolling direction. Narrower specimens can also be measured. For a sufficient measuring signal, they should cover at least 60% of the yoke width. In practice down-scaled frames for smaller specimen sizes are also used.

To minimize the influence of eddy currents, the frame must be made of strip-wound cut cores or stacked isolated sheets. The magnetic losses of the yoke must be much smaller than the losses of the specimen. Therefore high-quality electrical steel or iron-nickel alloy is used.

The main advantages compared to the Epstein frame are lower specimen mass and easier specimen preparation and installation. The SST allows the measurement of the same quantities and curves as the Epstein frame. The electronic part of the instrumentation is principally the same.

For comparing Epstein frame to SST measurements, it is essential to explore the relationship between the two methods [10.13]. The results of an extended comparison for grain-oriented steel are compiled in [10.14]. Unfortunately a single correlation factor for all material grades could not be established.

Normally the field strength is calculated from the magnetizing current. In this case the magnetic losses of the yoke and in the gaps to the specimen must be minimized. An uncertainty also exists in the determination of the magnetic path length. To overcome these difficulties, a measurement of the field strength has been proposed, among others by [10.15], but attempts in this direction have shown poor reproducibility.

Wattmeter Method. The wattmeter method is used to measure the specific total loss (power loss) on ring specimens at a given alternating-current (AC) excitation. The measurement is carried out under condition of sinusoidal magnetic flux density. For some specimens this may require digital control of the magnetizing current waveform or an analog feedback control of the power amplifier.

The circuit of the wattmeter method is shown in Fig. 10.20. Three instruments are necessary: a voltmeter V_1 displaying the average rectified value (sometimes scaled to 1.111 times the rectified value), a voltmeter V_2 displaying the root mean square (rms) voltage and a wattmeter. All instruments must have high input impedances and the wattmeter must have a low power factor.

Prior to a measurement the specimen must be demagnetized. Therefore the amplitude of the magnetizing alternating current is slowly reduced from its maximum value to zero. The current is then increased to generate the desired flux density \hat{B} in the specimen. This is determined via the average rectified voltage

$$\overline{|U_1|} = 4fN_2A\hat{B}. \quad (10.23)$$

The form factor of the secondary waveform must be verified to ensure a sinusoidal flux density. This is determined by the ratio of the rms voltage U_2 to the average rectified voltage U_1 . Additionally an oscilloscope can be used to monitor the waveform.

For the calculation of the total loss of the specimen, the power P_i consumed by the instruments connected to the secondary winding must be taken into account. As the voltage shall be sinusoidal it is, to a first approximation, equal to

$$P_i = \frac{(1.111 \cdot \overline{|U_2|})^2}{R_i}, \quad (10.24)$$

where R_i is the combined input resistance of all the instruments connected to the secondary winding. The total loss P of the specimen is calculated from the reading P_m of the wattmeter using

$$P = \frac{N_1}{N_2} P_m - P_i. \quad (10.25)$$

The specific total loss is obtained by dividing P by the mass of the specimen.

Voltmeter–Ammeter Method. The voltmeter–ammeter method allows the determination of the normal magnetization curve and the amplitude permeability. The circuit of the method is shown in Fig. 10.21. The instruments needed are an average-type voltmeter, a root-mean-

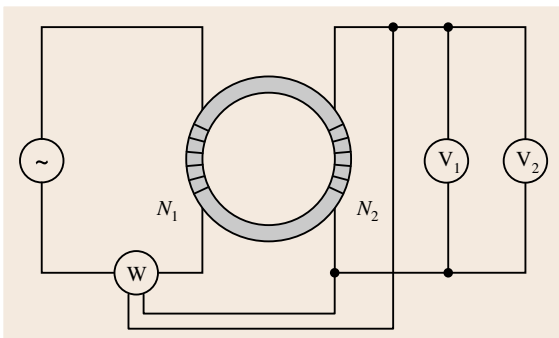


Fig. 10.20 Circuit diagram of the wattmeter method. V_1 is an average-type voltmeter, V_2 is an rms voltmeter

square-type (rms) voltmeter and an rms or peak-reading ammeter or a noninductive resistor and appropriate voltmeter. The voltmeters must have high input impedances. An oscilloscope can be helpful to monitor the secondary induced waveform.

If comparable results are desired, either the waveform of the primary current or of the secondary voltage must be kept sinusoidal. Depending on the excitation and the shape of the hysteresis loop control can be necessary. A sinusoidal H waveform can be achieved by a current-controlled power amplifier or by a feedback using a noninductive resistor in the primary circuit. This can be the resistor used for current measurement. A sinusoidal secondary voltage can be achieved by analog or digital control. The form factor can be determined by the ratio of the rms voltage to the average rectified voltage.

The excitation field strength \hat{H} is calculated from the current I using (10.15). If I is sinusoidal it can be measured by multiplying the rms value by the square root of 2. If the primary waveform is significantly non-sinusoidal a peak-reading instrument would be required. In practice this is often ignored and an effective excitation field strength that is lower than the real field strength is used instead.

Prior to the measurement the specimen is demagnetized. Then I is successively increased and the average rectified value of the secondary voltage is measured. The flux density \hat{B} is calculated from (10.23). The normal magnetization curve can be obtained by plotting corresponding values of \hat{H} and \hat{B} .

The relative amplitude permeability μ_a can be calculated from

$$\mu_a = \frac{\hat{B}}{\mu_0 \hat{H}} \quad (10.26)$$

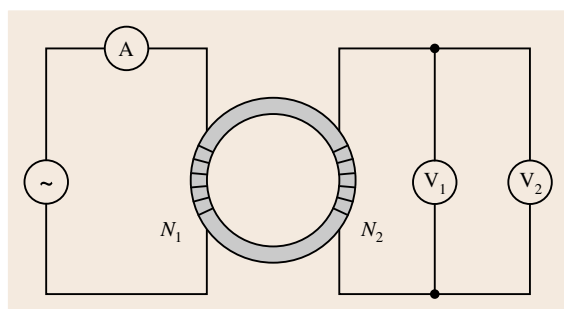


Fig. 10.21 Circuit diagram of the voltmeter–ammeter method. V_1 is an average-type voltmeter, V_2 is an rms voltmeter

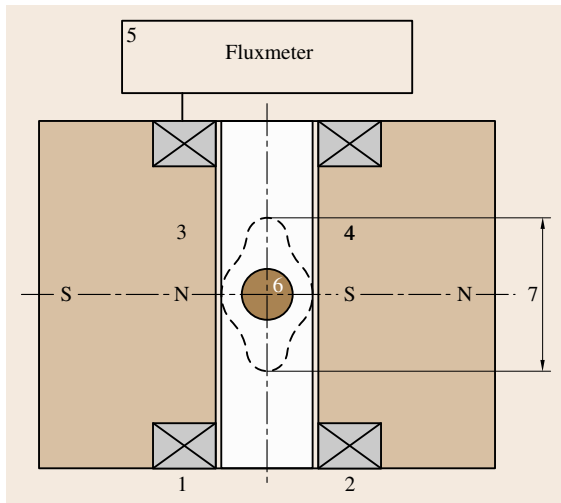


Fig. 10.22 Saturation coil: 1, 2 – windings of a Helmholtz coil, 3, 4 – permanent magnet material, 5 – fluxmeter, 6 – specimen; the dashed line (7) marks the maximum specimen volume for 1% accuracy

and the rms amplitude permeability from

$$\mu_{a,rms} = \frac{\hat{B}}{\mu_0 \sqrt{2} \tilde{H}}, \quad (10.27)$$

where \tilde{H} is the rms value of the field strength.

Saturation Coil. The saturation coil, sometimes also called J_S -coil or saturation magnetometer, combines the moment-measuring coil with a permanent-magnet system that magnetizes soft magnetic specimens [10.16]. The measuring coil, usually a Helmholtz coil, is connected to a fluxmeter.

When a specimen with volume V is inserted into the coil, it is magnetized and the magnetic dipole moment j can be obtained from the flux measurement using (10.9). If the field strength is sufficiently high, the

saturation polarization can be determined through

$$J_S = \frac{j}{V}. \quad (10.28)$$

Of course the specimen can also be withdrawn from the coil for measurement, but the rotation method, which is frequently used with the moment-measuring coil, cannot be used.

For lower field strength the relative permeability can be calculated using

$$\mu_r = 1 + \frac{J}{H_i}. \quad (10.29)$$

The inner field strength H_i of the specimen must be determined from the magnetizing field strength, taking into account the demagnetization factor.

The main applications of the method are the determination of the saturation polarization of specimens made of nickel or nickel alloys and the determination of the cobalt content in hard metal specimens.

Magnetic Scales. Magnetic scales or balances measure the force that acts on a magnetic specimen in a nonhomogeneous field [10.17]. From this force the following quantities can be determined

- magnetic moment m and magnetic dipole moment $j = \mu_0 m$,
- magnetic permeability μ and magnetic susceptibility $\chi = \mu - 1$.

As the specimens can be easily heated or cooled, the methods can also be used to measure the temperature dependencies of the properties. This includes the determination of Curie and Néel temperatures and the observation of other phase transitions.

Faraday Method. The force acting on a small specimen with volume V in a magnetic field with gradient dH/dy is

$$F = j \frac{dH}{dy} = V \chi H \frac{dH}{dy}. \quad (10.30)$$

The specimen is suspended from the scale so that it is located between the poles of an electromagnet (Fig. 10.23). The pole caps are shaped such that the product $H(dH/dy)$ is constant over the whole volume (gradient pole caps), so that the force is proportional to the susceptibility χ . The Faraday method is suitable for all kind materials, especially ferro- and ferrimagnetic specimens. It allows the determination of the saturation polarization J_S for soft magnetic materials if the specimen shape is appropriate.

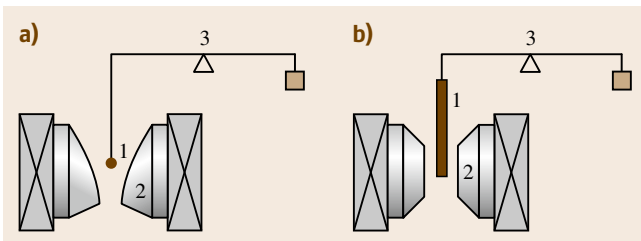


Fig. 10.23 (a) Faraday method and (b) Gouy method, 1 – specimen, 2 – electromagnet poles, 3 – balance

Gouy Method. A long bar-shaped specimen is suspended from the scale so that one end is located between the poles of an electromagnet generating a field strength H . The other end outside the poles is only affected by the stray field strength $H_s \ll H$. The force acting on the whole sample is

$$F = \frac{1}{2} A \chi (H^2 - H_s^2) \approx \frac{1}{2} A \chi H^2, \quad (10.31)$$

where A is the cross-sectional area of the specimen. The Gouy method is mainly used for para- and diamagnetic materials including liquids and gases.

Impedance Bridges. If an alternating current is supplied to a coil that contains a ferromagnetic core, a phase shift between magnetic field strength and flux density occurs. The magnetic material can be characterized by the complex permeability

$$\underline{\mu} = \mu' - i\mu'' . \quad (10.32)$$

The impedance of the filled coil is

$$\underline{Z} = R + i\omega L = \omega\mu'' L_0 + i\omega\mu' L_0 \quad (10.33)$$

if losses and additional phase shifts that are not caused by the core material are neglected. L_0 is the inductance of the measuring winding without the magnetic core. For a cylindrical specimen, it can be calculated as

$$L_0 = \frac{\mu_0}{2\pi} \ln\left(\frac{D}{d}\right) h N^2, \quad (10.34)$$

where D is the outer diameter, d is the inner diameter and h the height of the coil, and N is the number of turns of the winding.

The loss angle δ and the Q -factor can be determined from

$$\tan \delta = \frac{R}{\omega L} = \frac{1}{Q} = \frac{\mu''}{\mu'} . \quad (10.35)$$

For the determination of \underline{Z} , various impedance bridges are available from electrical measuring techniques; they differ in sensitivity and frequency range. For the characterization of magnetic components, suitable circuits are used in a frequency range of approximately 1 Hz to 100 MHz. A basic circuit is the Maxwell–Wien bridge shown in Fig. 10.24. It can be used from about 50 Hz to 100 kHz.

The specimen, a ring core that is uniformly wound with a single winding, is defined by its equivalent circuit diagram consisting of R_x and L_x . The bridge is balanced if

$$R_x = \frac{R_1 R_2}{R_v} \quad (10.36)$$

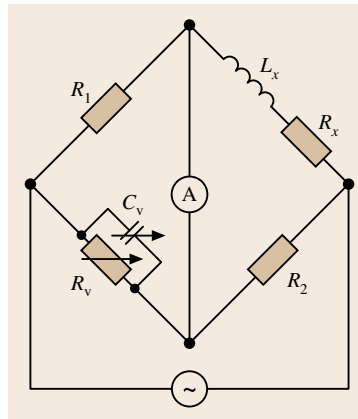


Fig. 10.24
Maxwell–Wien
bridge

and

$$L_x = R_1 R_2 C_v . \quad (10.37)$$

R_x consists of the loss R caused by the magnetic core and the loss in the winding

$$R_x = R + R_0 . \quad (10.38)$$

The loss in the winding R_0 is basically the DC resistance if the frequency is not too high, and can be obtained from a resistance measurement.

The inductance L_x is composed of the leakage inductance L_σ and the inductance of the specimen L

$$L_x = L_\sigma + L = L_\sigma + \mu' L_0 . \quad (10.39)$$

For large permeabilities the leakage inductance L_σ can be neglected and μ' can be calculated to

$$\mu' = \frac{L}{L_0} \approx \frac{L_x}{L_0} . \quad (10.40)$$

Otherwise the real inductance L'_0 of the winding should be considered. L'_0 can be measured on an air-core coil: a winding that is wound on a nonmagnetic core and that has the same dimensions as the measuring winding. It can be assumed for small permeabilities that the stray field would be the same, regardless whether there is a core or not. With

$$L'_0 \approx L_\sigma + L_0, \quad (10.41)$$

it follows that

$$\mu' \approx 1 + \frac{L_x - L'_0}{L_0} . \quad (10.42)$$

At higher frequencies the resistance of the winding differs from the DC resistance due to the skin effect. In this case mutual inductance bridges provide more accurate results, as in these circuits the resistance of the wire does not enter the measuring result. The specimens must be equipped with two windings. Suitable circuits are the Wilde [10.18] and Hartshorn bridges. Further methods are compiled in [10.19].

Measurement of Magnetostriction. Magnetostriction comprises all dimensional changes of a specimen that are caused by changes in magnetization. For both the volume-invariant shape effect and the volume magnetostriction, a measurement of a change of the specimen length in one or more dimensions can be carried out.

The specimen is placed in the center of a solenoid, which generates the magnetic field required. The change in length is transferred via a rod to a displacement transducer that is located outside the stray field of the solenoid. The material of the rod must be properly chosen to keep the outer force acting on the specimen as small as possible and to avoid errors due to temperature-induced changes in length. Capacitive, inductive or optical sensors are used to measure the displacement.

Another method uses strain gauges that are directly attached to the specimen. To cancel out errors due to the magnetic and thermal properties of the strain-sensing element, a second element of the same type can be attached to a substrate that shows no magnetostriction but is exposed to the same environment. The two sensing elements can be connected to opposite paths of a bridge circuit.

A third method uses a single-mode optical fiber attached to the specimen. The fiber is part of an interferometer. The change in length is detected as a phase shift in the electromagnetic wave propagating in the fiber [10.20].

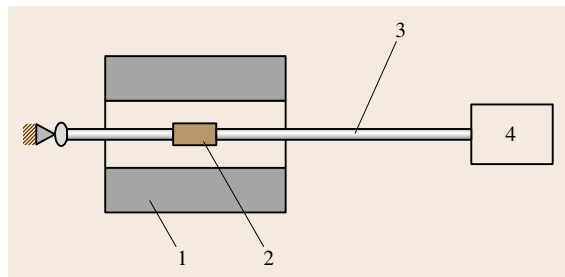


Fig. 10.25 Magnetostriction measurement: 1 – solenoid, 2 – specimen, 3 – specimen rod, 4 – displacement transducer

The volume magnetostriction can also be measured by the conventional measuring method for volumetric content. The specimen, immersed in a liquid, is exposed to the magnetic field.

Magnetostriction is an important parameter in many applications of electrical steel. A comprehensive description of magnetostriction measuring methods for these materials can be found in [10.21].

Measurement of the Hysteresis Loop of Amorphous or Nanocrystalline Ribbons

Sample Shape. In the case of soft magnetic ribbons the hysteresis loop can be measured on

1. open ribbons, in which case the demagnetizing factor has to be considered,
2. toroids.

The temperature the loop is measured is also important. In the case of low- or high-temperature measurements the system has to withstand the desired temperature.

In principle, magnetic measurements should always be carried out on a toroid instead of open ribbons because only then is a closed magnetic circuit realized. For ribbons this method has the disadvantage that the material is not in a stress-free state – there is a tensile stress on the outer surface and compressive stress on the inner surface. Another possibility is to use a single straight ribbon but then the demagnetizing field has to be considered.

Hysteresis Loop on a Single Ribbon. When hysteresis is measured on a single open ribbon a well-defined external stress can be applied. Temperature-dependent measurements are possible, although technically more complex. The facilities necessary for measuring the hysteresis loop are field coils, a compensated pickup coil, a current source, an ammeter and an integrator (fluxmeter). For the measurement of coercivity a Helmholtz coil is mainly used, and for the measurement of saturation magnetization the field is applied by a cylindrical coil producing a sufficient high field. The coils are energized by a computer-controlled power supply.

The devices are connected and controlled by a data-acquisition and control unit, forming a full automatic hysteresis-loop system. Figure 10.26 shows as an example a set up for such a hysteresis measurement on single strip ribbons.

In this case a compensated pickup system has to be used. When the pickup and the compensation coils are connected, so that the induction signals due to the field

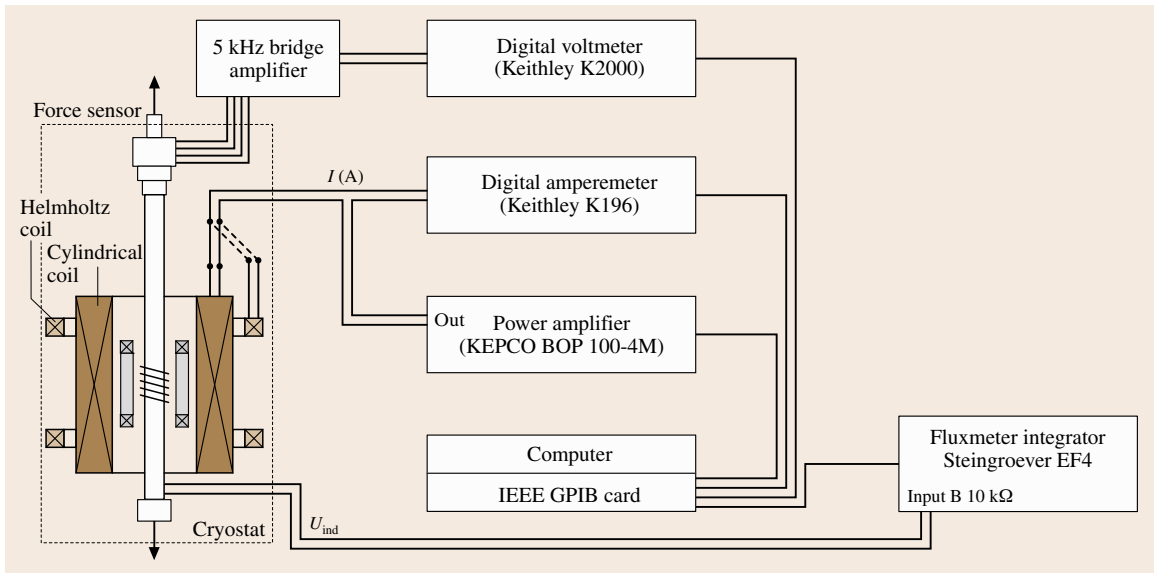


Fig. 10.26 Hysteresisgraph for a quasistatic hysteresis measurements and devices for force measurement for single ribbons

are subtracted, the remaining signal will be proportional to the magnetization M

$$u_{\text{ind}} = u_{\text{pick}} - u_{\text{comp}} = -N_{\text{pick}}\mu_0 A_{\text{rib}} \frac{dM}{dt}. \quad (10.43)$$

Magnetostriction. Magnetostriction on thin ribbons can be measured by direct and indirect methods. Direct methods are, for example, measurements with strain gauges, capacitance transducers or interferometers. All these methods have the disadvantage that sample preparation is difficult. Strain gauges are limited in sensitivity ($\Delta\lambda/\lambda_0 = \pm 1 \times 10^{-6}$). Additionally the saturation magnetostriction constant has to be determined from measurements parallel and perpendicular to the external field.

Indirect methods are the Becker–Kersten method [10.22] and the small-angle magnetization-rotation (SAMR) method [10.23]. With the Becker–Kersten method the magnetostriction is determined from the stress dependence of the hysteresis loop. The SAMR method was developed by Narita et al., especially for ribbon shaped materials with a small magnetostriction constant.

The SAMR Method. First of all a DC field is applied in the ribbon axis. This field should magnetically saturate the sample. Then a smaller AC field (with frequency f)

is applied perpendicular to the ribbon axis. This causes a small rotation (small angle) of the magnetization vector out of the ribbon axis. A small induction signal with double the frequency of the AC field is now detected by a pickup coil (Fig. 10.27a) and measured by a lock-in amplifier. Applying an external stress to the ribbon causes, for ribbons with positive magnetostriction, a decrease in the deflection angle, whereas for samples with negative magnetostriction the angle increases (Fig. 10.27b). Now the DC field H_{DC} is changed in such a way that the deflection angle and therefore

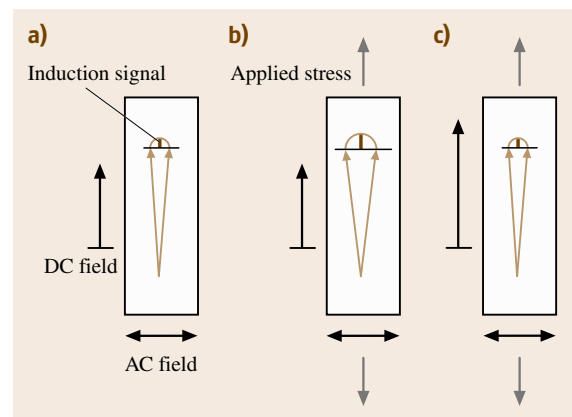


Fig. 10.27a–c Magnetostriction measurement by the SAMR method

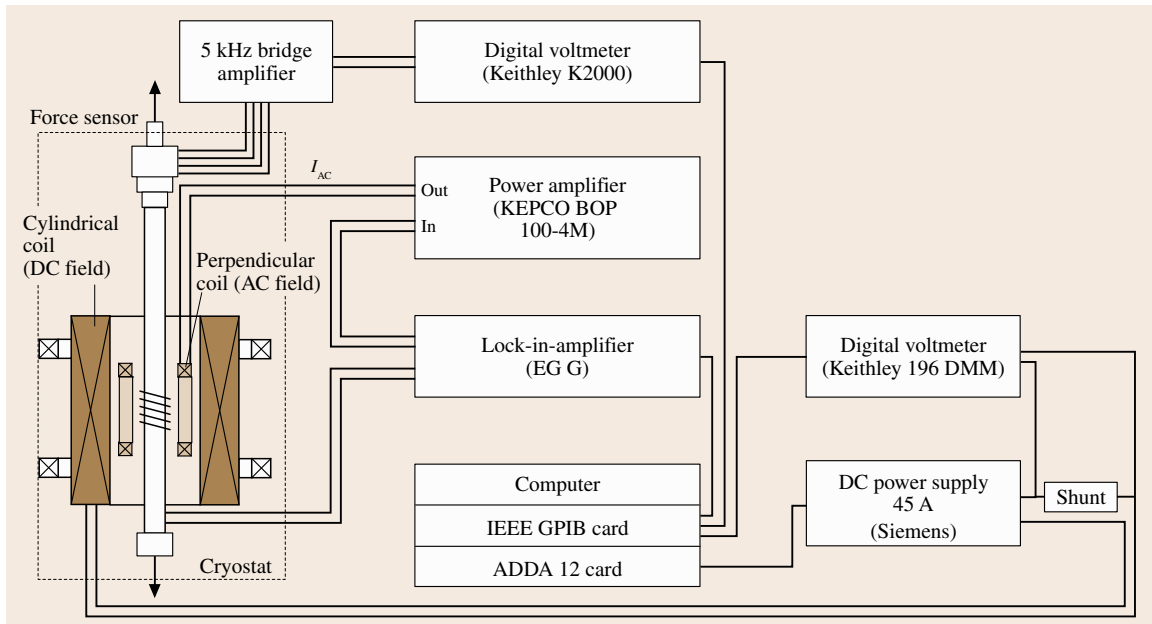


Fig. 10.28 Experimental set up for magnetostriction measurement by SAMR method

also the induction signal go back to their initial value (Fig. 10.27c). The variation of the DC field ΔH_{DC} and the variation of the external stress $\Delta\sigma$ determine the magnetostriction constant. To get an accurate value this procedure has to be repeated step by step with increasing stress. From the balance of the magnetic and the magnetoelastic energy one can calculate the saturation magnetostriction as

$$\begin{aligned}\lambda_s &= -\frac{1}{3} J_s \left(\frac{\Delta H_{DC}}{\Delta\sigma} \right) \Big|_f = -\frac{1}{3} \frac{\Phi_{sat}}{A_{rib}} \left(\frac{\Delta H_{DC}}{\Delta F/A_{rib}} \right) \\ &= -\frac{1}{3} \Phi_{sat} \left(\frac{\Delta H_{DC}}{\Delta F} \right),\end{aligned}\quad (10.44)$$

where J_s is the saturation polarization of the ribbon at a certain temperature. The polarization J_s is proportional to α/A_{rib} , where α is the output value of the fluxmeter and A_{rib} is the cross section of the sample. The value of $\Delta\sigma$ is given by $\Delta F/A_{rib}$. According to the equation above the magnetostriction then becomes completely independent of the cross section. The magnetostriction then depends only on the exact measurement of the magnetic flux (saturation value Φ_{sat}), on the measurement of the force F ($\Delta F = F_1 - F_2$, by the force-sensor bridge) and on the measurement of the magnetic field H_{DC} ($\Delta H_{DC} = H_{DC1} - H_{DC2}$). Figure 10.28 shows as an example a possible set up

for magnetostriction measurements using the SAMR method.

This method was used successfully to determine the magnetostriction of many amorphous materials [10.24]. It delivers comparable results and achieves a sensitivity in the magnetostriction constant of up to 10^{-9} [10.25].

Magnetoimpedance. Relevant information about transversal magnetization processes in magnetic materials can be obtained from the field H and frequency f dependence of the complex impedance ($Z = R + iX$). In soft magnetic high-permeability materials, large variations of Z (for current frequencies larger than 100 kHz) have been observed upon the application of relatively small magnetic fields, the so-called giant magnetoimpedance effect (GMI) [10.26–28]. Generally magnetoimpedance is based on the application of an AC field caused by an inhomogeneous field distribution in a conducting material with a high permeability. This effects depends therefore on the frequency, and on the applied field, but also on material parameters such as the conductivity as well as the permeability – which depends additionally on the applied DC field – of the material. Additionally the sample geometry (ribbons, wires) as well as local fluctuations of material parameters have to be considered.

For these measurements one needs: a digital lock-in amplifier working over a broad frequency range, a power supply, a dynamic signal analyzer, some form of digital multimeter, and a computer with an interface for the data acquisition. The lock-in amplifier supplies the AC signal and is also employed to read the real and imaginary voltage drop across the sample. In GMI measurements, a constant-current source supplies a constant AC current flowing along the sample in order to assure a constant circular magnetic field. As the generator of the lock-in works generally as a constant-voltage source, either one uses an external constant-current source or one measures the AC voltage drop across a resistor R , which determines the actual current through the sample as shown in Fig. 10.4. In this experiment not only the AC current has to be controlled but also the phase signal. In order to do this a two-position relay controlled by a computer can be used; the two positions correspond to calibration and measurement. In the calibration position (Fig. 10.29), the signal is applied to the sample, which is in series with a grounded resistor and the lock-in measures the voltage across the resistor, which can be controlled to maintain a constant intensity value. In the measurement position (Fig. 10.29), the relay inverts the ground and signal position so that the signal is applied to the resistor, and the sample is grounded. The lock-in thus measures the sample's signal. The voltage over the sample is measured in a four-probe configuration and the contacts with the sample are made using silver conducting ink.

The magnetic DC field, which is applied along the sample's length, is supplied by a pair of Helmholtz

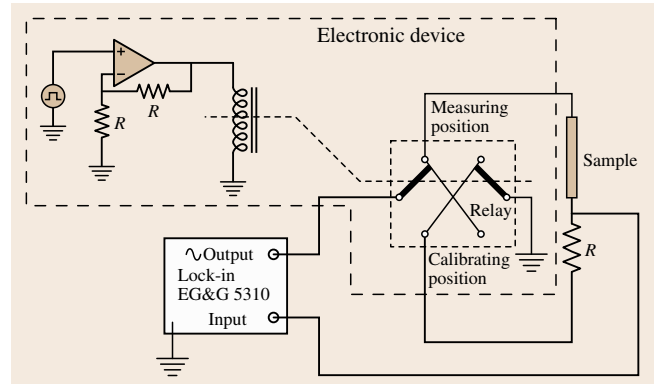


Fig. 10.29 Schematic diagram of the electric necessary to measure the magneto-impedance

coils connected to a power supply, which operates as a current source. The current passing through the coils is measured by a multimeter. With this equipment the magnetoimpedance as a function of frequency and external DC field can be measured. Furthermore, the experimental set up can be completed by a dynamic signal analyzer, which allows one to follow the time dependence of the impedance after a sudden rearrangement of the domain configuration [10.29]. After the magnetic field is switched off ($t = 0$), it is possible to measure both R and X from t_0 up to t_1 by connecting the DC output of the lock-in to one of the inputs of the signal analyzer. The sensitivity is high enough to notice relative variations as low as 0.1%. With this extension magnetic disaccommodation of the magnetoimpedance can also be measured.

10.3 Magnetic Characterization in a Pulsed Field Magnetometer (PFM)

Industrial producers and consumers of magnets are increasingly demanding systems which allow fast and reliable online tests of the hysteresis properties of magnets. High-quality permanent magnets based on rare-earth intermetallic compounds such as Sm-Co and Nd-Fe-B exhibit coercivities of 2 T and sometimes even higher, which are too high for Fe-yoke-based systems [10.7, 30].

The current conventional methods, namely vibrating-sample magnetometers (VSMs) and permeameters have limiting physical constraints. Fe-yoke-based VSMs and permeameters offer only a limited field strength (max-

imum 1.5 T). Permeameters are used for measuring the second quadrant of the hysteresis loop and need careful sample preparation (cutting, polishing). VSMs that use a superconducting solenoid require liquid helium for cooling and are generally expensive; additionally standard magnetometers are currently only available for relatively small samples (mm sizes). Additionally superconducting solenoids allow only limited field-sweep rates (dH/dt rates) which are of the order of T/min . Generally all these systems need special sample preparation and measurement times that are unacceptable for industrial purposes. It will be shown that a PFM is

a new instrument that is well suited for fast and reliable measurement of the hysteresis loops of hard magnetic materials.

10.3.1 Industrial Pulsed Field Magnetometer

A short-pulse system (typical pulse duration 1–50 ms) has a condenser battery as an energy source, which has a certain size given in kJ (typical values are 10–100 kJ). The available power determines the time constant of the total system.

Figure 10.30 shows a block diagram of a pulsed field magnetometer (PFM) [10.10, 31]. A pulsed field magnetometer consists of

1. the energy source, generally a capacitor battery; the stored energy is given by $CU^2/2$. The maximum charging voltage can be 1–30 kV. The capacitance determines the costs of such a system, the maximum sample size and the time constant. For a magnetometer that can measure the full loop, voltage reversal on the battery must be allowed.
2. charging unit, which should generate a reproducible and selectable charging voltage; it determines the repeatability of the achieved field in the pulse magnet.
3. pulse magnet: for an existing energy, the pulse magnet determines, via its inductivity, the pulse duration. Additionally the volume (diameter, homogeneity) limits the dimensions of the experiment inside of the magnet. Heating during a pulse may be also a problem when high repetition rates are desired.

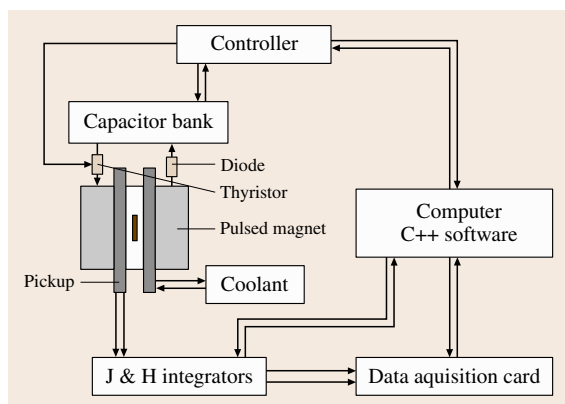


Fig. 10.30 Block diagram of a typical capacitor-driven industrial PFM

4. measuring device: this consists of the pickup system and the measuring electronics (amplifiers, integrators, PCs, data storage). A careful design of the pickup system is very important in order to achieve a high degree of compensation and consequently a good sensitivity.
5. electronics: this consists either of a digital measuring card or of a storage oscilloscope which is connected to a modern data-acquisition system on a standard PC, which allows a software-supported operation of the PFM (charging, discharging and the measurement with an evaluation of the resulting loop). In order to obtain a reasonable accuracy the analog-to-digital converters (ADCs) of the storage oscilloscope (measuring card) should have a resolution of at least 12 bit.

High-Field Magnets

The pulse magnet has to be optimized with respect to the available power, the heating of the magnet and the stresses. The field homogeneity over the desired length of the experiment should be better than 1%. In systems where the hysteresis loop is measured, the pulse magnet has to be optimized with respect to low damping and also for a certain measuring task (maximum field, pulse duration, pulse shape, sample volume).

Pickup Systems

Generally the magnetization is measured using a pickup coil system, which has to be compensated in order to measure the magnetization M instead of the induction B . For this purpose different arrangements of pickup coils have been developed (Fig. 10.31). It was found that a coaxial system based on Maxwell coils is best suited to this purpose [10.32]. The main idea of constructing a pickup system is that the space distribution of the field around the sample is first developed into a dipole (and quadrupole) contribution. These contributions should be compensated in order to cancel the effect of the external field. Therefore such systems consist of at least two coils (Fig. 10.31c). The induced voltages can be written as

$$u_1(t) = -\mu_0 N_1 K_1 \left(R_1^2 \pi \right) \left(\frac{dH}{dt} + \frac{dM}{dt} \right),$$

$$u_2(t) = -\mu_0 N_2 K_2 \left(R_2^2 \pi \right) \left(\frac{dH}{dt} \right); \quad (10.45)$$

where u_i , N_i , $K_i R_i$ ($i = 1, 2$) are the induction voltage, number of windings, coupling factor, radius of the outer ($i = 1$) and inner ($i = 2$) pickup coil, respectively.

Dipole compensation is fulfilled when $R_1^2 N_1 = R_2^2 N_2$ is valid. The coupling factor with respect to the field H is the same for both coils, but not with respect to the sample. It is assumed that for the outer coil the voltage due to the magnetization can be neglected (in reality there exists a small induction voltage due to M which only reduces the calibration factor). Subtracting now the signal of the two antiparallel-wound coils causes a cancelling of the effect of the field, which yields the dipole compensation. Also higher multipoles can be compensated, which leads to a more complex pickup system for which more space is necessary. Therefore for pulsed field systems usually only the dipole compensation is used.

For some applications the pickup system should be cooled in order to hold a stable temperature, which is especially important for a room-temperature system with a high repetition rate. The details of such a pickup system as well as electronic balancing are described in [10.33].

For an industrial system a reasonable sample size is important; typical values are samples up to 30 mm in diameter and 10 mm in length within a $\pm 1\%$ pickup homogeneity range. For magnetic measurements exact positioning (reproducibility better than 0.1 mm) in the PFM is necessary.

10.3.2 Errors in a PFM

The Demagnetizing Factor

In a magnetically open circuit the correction for the demagnetizing factor N is a very important step to get the true hysteresis loop as a function of the internal field H_{int} . For ellipsoids and spheres the demagnetizing field H_d is simply written

$$\begin{aligned} H_{\text{int}} &= H_{\text{ext}} - NM, \\ H_d &= NM. \end{aligned} \quad (10.46)$$

The demagnetizing factor N is just a number $0 < N < 1$ for a sphere ($N = 1/3$) or an ellipsoid. In all other cases the demagnetizing field H_d is no longer constant.

Important points such as the remanence and the working point, but also the energy product $(BH)_{\text{max}}$, depend strongly on N . Unfortunately in industry more complex shapes, such as cylinders, cylinders with holes and even arc segments, are used. In this case N can become a tensor according to the symmetry of the sample. For complex shapes a finite-element package has to be used in order to calculate the stray field.

In order to investigate the effect of N for simple shapes in Fig. 10.32 the demagnetizing curves in the

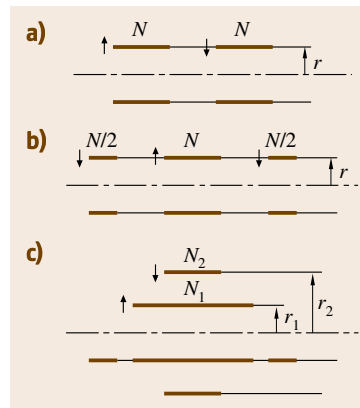


Fig. 10.31a–c Scheme of a coaxial pickup system for measuring the magnetization

second quadrant for an anisotropic ferrite HF 24/16 are drawn. The two samples were from the same batch, one was a cylinder and one a sphere. The shape of the loops agrees very well. This means that in this special case the use of a constant number for N even for the cylinder is sufficient for the correction.

Figure 10.33 shows the hysteresis loop as measured on a cylindrical sample with a hole (outer diameter 19 mm, hole: 3.17 mm; $h = 2$ mm) of plastic-bonded Nd-Fe-B-type material. Assuming $N = 0.45$ gives a remanence of 0.666 T, whereas assuming $N = 0.55$ delivers a remanence of 0.682 T. The static value measured with an electromagnet was 0.682 T. This demonstrates the problem of such an unknown demagnetizing factor. It is impossible to say what the correct value is really.

Finally it should be mentioned that the problem discussed here of an unknown demagnetizing factor is not only a problem for the PFM; this is a general problem

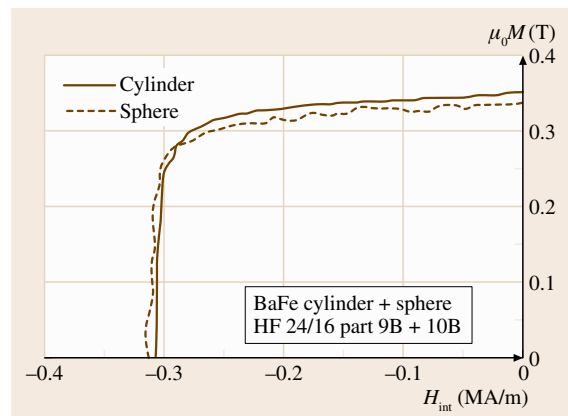


Fig. 10.32 Demagnetizing curve as obtained for a spherical and a cylindrical anisotropic Ba-ferrite (HF 24/16)

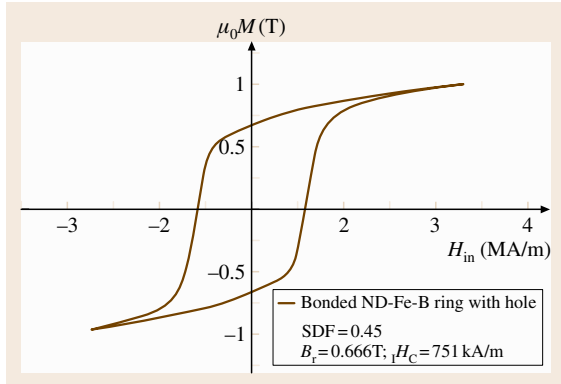


Fig. 10.33 Hysteresis loop of a cylindrical sample with a hole of plastic-bonded Nd-Fe-B-type material

for all magnetometers using a magnetically open circuit, such as e.g. in a **VSM** or also in a **SQUID**.

Transient-Field Errors

The application of transient fields causes errors, which have to be considered. Two possible errors may arise in pulsed field measurements due to the field sweep rate dH/dt

- Eddy current errors,
- Magnetic viscosity effects.

Eddy Currents and Their Solution [10.34]

A time-dependent external magnetic field in a metallic conducting sample causes, according to Maxwell equations, currents (*eddy currents*), which create a dynamic magnetic moment that is antiparallel to the external field, as is demonstrated in Fig. 10.34. The time behavior is exponential: $I(t) = I_{\text{eddy}} \exp(-r/M)t$, where M is a dynamic mutual inductance and r is also a differential resistance due to the path of the eddy currents.

It can be shown [10.34] by solving the Maxwell equations for an electrical conducting material (without considering the permeability) that the dynamic magne-

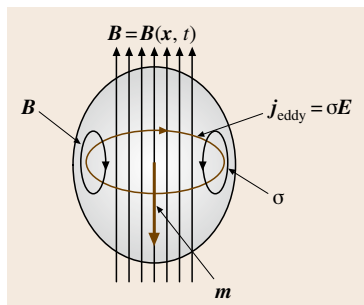


Fig. 10.34 The principle of eddy currents in a metallic sample

tization due to eddy currents can be written as

$$\mathbf{M} = \text{curl} \mathbf{j} = -\sigma \frac{\partial}{\partial t} (\text{curl} \mathbf{A}) = \sigma \frac{\partial \mathbf{B}}{\partial t} = \frac{\mu}{\rho} \frac{\partial \mathbf{H}}{\partial t}. \quad (10.47)$$

This means that plotting the magnetization m due to eddy currents versus dH/dt of a conducting sample delivers a linear relation where the slope is proportional to σ (specific electrical conductivity) which is equal to $1/\rho$ (specific electrical resistivity), as is also found experimentally.

The maximum eddy-current density ($J_{\text{max}} = J(r_{\text{sample}}, z = 0)$) of all samples with different pulse duration and their magnetic moment m_{FEMM} , m_{FEMM} can also be calculated using a finite element package such as FEMM by *Meeker* [10.35] (2-D finite-element software). For samples that are not large and frequencies that are not high a linear relation between the eddy-current density and the radius r holds, which gives a rather simple solutions for calculating the dynamic eddy-current magnetization, as follows.

The magnetization for a cylinder is

$$M = \frac{j_{\text{max}} r_s}{4}. \quad (10.48)$$

Hence, the magnetization is independent of the height of the cylinder.

A similar calculation delivers the magnetization for a sphere

$$M = \frac{j_{\text{max}} r_s}{5}. \quad (10.49)$$

To prove the assumption that the magnetization due to the eddy-current density increases linear with the radius but stays constant with the height of the sample, several cylindrical and spherical samples of Cu were studied [10.34]. It was demonstrated that the measured maximum magnetization can be fitted with a function $f = Cr^2$, where r is the radius of the sample, which gives, as theoretically expected, a quadratic dependence as shown in Fig. 10.35.

On the experimental side, in agreement with the formulas above, the eddy currents were found to be independent of the height of the sample [10.36].

Conducting, Magnetic Samples – $f/2f$ Method [10.37, 38]

In a magnetic material the eddy currents are determined by the electrical conductivity σ but also by the perme-

ability μ , where the latter is also a nonlinear function of the external field. In this case the eddy-current problem cannot be solved analytically. Here, numerical methods are the only possible way. However in some cases simplifications are possible. In order to correct the hysteresis loop of a hard magnetic material as measured in a PFM for the eddy-current error a special method was developed. The hysteresis loop of each sample is measured with two different pulse durations, f and $2f$, which generate the same J signal with respect to the applied field but with the addition of different dynamic magnetizations due to eddy-current distributions. The eddy currents are related to the frequency; the eddy-current magnetization is approximately proportional to dH/dt , as was shown already. By processing the two measurements it is possible to remove the error due to eddy currents, producing the direct equivalent of a static hysteresis plot; this approach is known as the $f/2f$ method [10.37, 38]. This method is based on the following equations

$$H_m = H_{\text{ext}} - H_{\text{eddy}} + H_d, \quad (10.50)$$

where H_{ext} is the external field applied by the pulse, H_{eddy} is the dynamic field caused by the eddy currents, and H_d is the demagnetizing field.

The polarization J appearing in a pulse-field experiment consists of two components, the true polarization $J_{\text{DC}}(H_{\text{DC}})$ as measured as a function of a DC field H_{DC} and the apparent polarization due to eddy currents J_{eddy} . Now performing two experiments, one with a short pulse (described by “s”) and one with a long pulse (described by “l”) one gets a set of field data and polarization data

$$H_{\text{ext},s} + \frac{J_{\text{eddy},s}}{\mu_0} = H_{\text{ext},l} + \frac{J_{\text{eddy},l}}{\mu_0}. \quad (10.51)$$

Based on these equations a mathematical procedure was developed which delivers the so-called $f/2f$ correction. This method can be applied under the general assumption of a sufficiently small eddy-current error, which means less than 20%. The validity and the limits of the $f/2f$ method were investigated and proofed by a three-dimensional (3-D) finite-element calculation [10.39]. Therefore, this so-called $f/2f$ method seems to be a good way to correct eddy-current errors in the measured hysteresis loop.

Application of the $f/2f$ Correction to a Magnet

To test the $f/2f$ correction a large cylindrical commercial Nd-Fe-B magnet from VAC (Vacodym 510, Charge

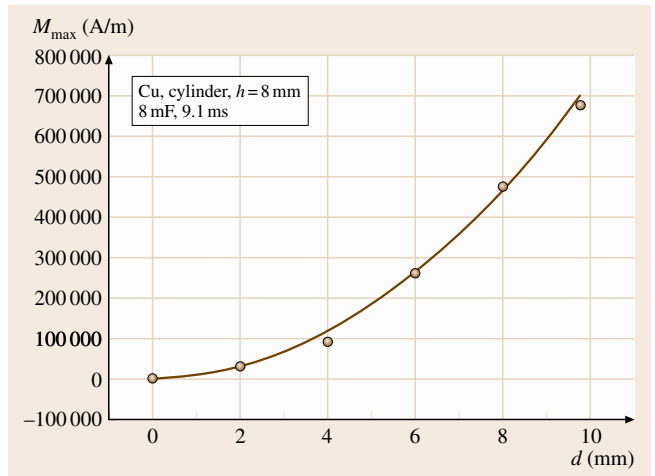


Fig. 10.35 Dependence of the maximum eddy-current magnetization on the radius

210105) was measured (Fig. 10.36). This cylinder had a diameter of $d = 20$ mm, and a height of 6.9 mm. The static data measured by VAC were: remanence $B_R = 1.296$ T, and coercivity ${}_1H_C = 1255$ kA/m.

The $f/2f$ -corrected coercivity value was found to be 1275 kA/m, which is 2% too high. The measured remanence value of 1.25 T is about 2% too low. This is experimental proof of the validity of this $f/2f$ correction.

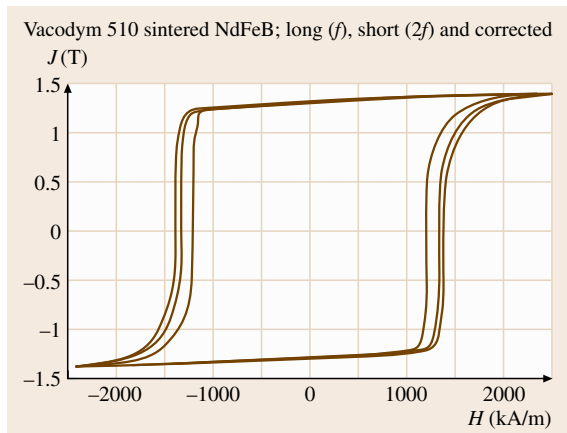


Fig. 10.36 Room-temperature hysteresis loop as obtained on a large (20 mm diameter) sintered Vacodym 510 magnet. One loop was measured with a long pulse (time duration of 57 ms) and one with a short pulse (time duration of 40 ms) (outer loop). The inner lying loop represents the corrected hysteresis

Magnetic Viscosity

The magnetic viscosity can influence the shape of a in a PFM-measured hysteresis loop. This leads especially to higher coercivity values measured in a transient field. The general questions are: how large is this error, when is this error not negligible, what is the origin of this error, and can this error be corrected?

The effect of magnetic viscosity has been well known for many years and has been investigated for many hard magnetic materials [10.40, 41]. It has also been shown that the magnetic viscosity coefficient S_v can be used to determine the activation volume, an important parameter for the understanding of the coercivity mechanism [10.42]. The viscosity coefficient is usually determined by static field measurement. One measures the loop $M(H)$ and stops in the second quadrant with this measurement at a certain field H . There under the condition $H = \text{const.}$ the time dependence of M is measured, from which the magnetic relaxation coefficient $S = dM/d \ln t$ can be determined. For calculating S_v one needs also the irreversible susceptibility χ_{irr} . One has to consider that the typical field sweep rate in pulsed field experiments dH/dt is approximately 1000 T/s, which is 10^6 orders of magnitude larger than the field sweep rate dH/dt that can usually be achieved in VSMs using an electromagnet or a superconducting coil. Generally, the viscosity coefficient (S_v) determined from static field measurements (denoted by S_{v1}) is much smaller than that obtained from PFM measurements (denoted as S_{v2}). However, it may be of great importance that the time windows in these two experiments are completely different.

Experimental Method to Determine Viscosity

In order to obtain the coercive field of the specimen under fields with different sweep rates, hysteresis loops of the samples are recorded at a fixed temperature by using a pulse field magnetometer (PFM) applying a sufficiently high maximum field. The sweep rate dH/dt can be changed either by varying the capacitance of the condenser battery or by changing the amplitude of the field or both; with this method field sweep ranges from about 0.5 up to 20 GA $\text{m}^{-1} \text{s}^{-1}$ and even higher are possible. The dependence of the coercivity on the field sweep rate dH/dt can be used to estimate the viscosity S_v (10.52)

$$S_{vp} = \frac{H_{C1} - H_{C2}}{\ln \left[(dH_1/dt) / (dH_2/dt) \right]} \quad (10.52)$$

This method and its limitation were recently demonstrated on the model material $\text{SmCo}_{5-x}\text{Cu}_x$ and related compounds [10.43].

The Magnetic Viscosity in $\text{SmCo}_{5-x}\text{Cu}_x$ Alloys [10.43]

SmCo_5 is nowadays a standard permanent-magnet material. However, substituting Co by Cu causes a change of the coercivity mechanism from nucleation to pinning. Additionally it was found that in $\text{Sm}(\text{Co}, \text{Cu})_5$ a large magnetic-viscosity effect appears. Therefore this is also a model material in order to investigate viscosity effects in a PFM. In Fig. 10.37 the coercive field as a function of dH/dt , as measured in as-cast and annealed $\text{SmCo}_{5-x}\text{Cu}_x$ magnets, is presented. The coercivity increases with dH/dt , providing evidence for the existence of a strong magnetic aftereffect.

Conclusion

a) *Eddy-current errors.* The application of a transient field causes eddy currents in metallic samples which lead to a dynamic magnetization M_{eddy} that is proportional to dH/dt [10.34]; the proportionality factor is the specific electrical conductivity. Additionally, M_{eddy} scales with R^2 (R is the radius of a rotational symmetrical sample), which means that the error increases quadratically with increasing sample diameter [10.34]. Fortunately most of the metallic permanent magnets are sintered materials where the specific resistivity (typically $2 \times 10^{-4} \Omega \text{ m}$) is generally a factor 50–100 higher

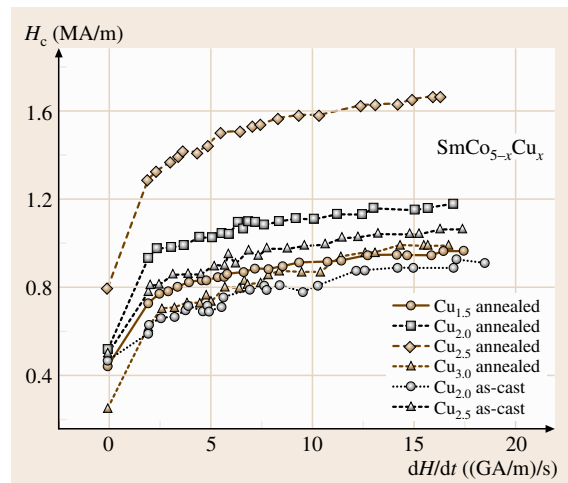


Fig. 10.37 Coercive field as a function of the sweep rate dH/dt measured in as-cast and annealed $\text{SmCo}_{5-x}\text{Cu}_x$ alloys

that of Cu. Therefore the error in magnetization measurements due to eddy currents is rather small. These considerations have led to the development of eddy-current correction for hysteresis loops measured in pulsed fields, which is called the $f/2f$ method. In this case one measures the loop with two different pulse durations and calculates the corrected loop point by point, applying an extrapolation procedure [10.37, 38]. It was shown by finite-element calculations that for eddy-current errors that were not too large (less than 20%) the corrected loop agrees with the true loop within 2%. This means that the effect of eddy currents is understood and can be corrected in most cases [10.39].

b) Magnetic viscosity effects. When the hysteresis loop of hard magnetic materials is measured in transient fields the so-called magnetic viscosity causes a difference between the measured loop and the true loop. The magnetic viscosity is also observed in nonconducting materials (e.g., ferrites), therefore it is not due to eddy currents. It has to be mentioned that the time constant of the exponential decay of eddy currents (in metallic samples) is of the order of typical values of microseconds, whereas that of the logarithmic decay of the viscosity lies between milliseconds and seconds. Additionally eddy currents depend on the geometry of the sample whereas this is not the case for the viscosity.

10.3.3 Calibration [10.1]

Field Calibration

The field is calibrated using a small pickup coil whose effective winding area is known from an NMR calibration. The induced voltage $u(t)$ is then fitted using (10.53), in order to determine the field calibration factor k , the damping factor and the pulse duration (including the effect of the damping)

$$\begin{aligned} H &= H_0 \exp(-at) \sin \omega t, \\ u_i(t) &= -NA \frac{dB}{dt} \\ &= -NA\mu_0 H_0 \frac{d}{dt} [\exp(-at) \sin \omega t]. \quad (10.53) \end{aligned}$$

The damping factor a determined in this way can be compared with the value given by a PFM circuit using $a \approx R/2L$ (where R is the resistivity of the pulse magnet, and L is the inductivity of the pulse magnet).

The calibration factor k is also determined as a function of the gain (integrator gain and the gain of preamplifier). The calibration factor k gives a relation between the induced voltage and the field at the search coil. At the same time the integrated voltage (using different gain factors) of the H -measuring coil (which is located at the pickup rod) on the magnetometer system is recorded.

It was shown that the calibration factor k was also determined as a function of the gain using an analogue integrator [10.1]. The scattering of the k factor was below $\pm 1\%$. This indicates that the linearity of the gain is better than 1%. Using such a procedure, an absolute field calibration of better than 1% is achieved, including the time constants (gain) of the integrator.

Magnetization Calibration

The magnetization is calibrated using well-known materials such as Fe and Ni (in which the eddy-current error causes an uncertainty) or preferably a nonconducting sample such as Fe_3O_4 or a soft magnetic ferrite, such as 3C30 (Philips). All calibration measurements are performed at room temperature. The results of the magnetization calibration measurements are summarized in Table 10.3. To check the reproducibility all measurements were repeated 10 times to give an average value (M). Additionally measurements using a shorter pulse duration (40 ms) were performed, which were generally in good agreement with that of the long pulse. For the metallic samples an error of 1–2% due to the eddy currents occurs.

The mean value of the deviations $D_{mv} = 1.6\%$ is higher than the true values. It should be mentioned that no significant differences in the measured magnetization values were obtained, when different pulse duration were employed.

The mean value of the deviations $D_{mv} = 1.6\%$ has a standard deviation of 0.95%. The standard deviations concerning the reproducibility gave a mean value of

Table 10.3 Summary of calibration results

Sample	Shape	$\mu_0 H_{\max}$ (T) $t = 57$ ms	$\langle \mu_0 M \rangle$ (T)	$\mu_0 M_{\text{literature}}$ (T)	Error (%)	$\mu_0 M$ (T) $t = 40$ ms
Fe_3O_4	Sphere $2r = 5.5$ mm	1.5	0.5787 ± 0.001	0.569 [10]	+1.6	0.5782
Ni	Cylinder $D = 4; h = 8$ mm	1.5	0.6259 ± 0.0008	0.610 [11]	+2.6	0.6322
Fe	Cylinder $D = 4; h = 8$ mm	4.5	2.1525 ± 0.0051	2.138 [12]	+1.4	2.1826

0.19%. Therefore, the deviation is, in the worst case, 1.14%. This means that the magnetization value could be calibrated with an absolute accuracy of $\pm 1.14\%$.

Reliability of Calibration

For testing the reliability of the calibration procedure a *calibrated sample* from the Physikalisch-Technische Bundesanstalt (PTB) in Braunschweig, Germany was measured. This sample was an anisotropic barium-ferrite from Magnetfabrik Schramberg with a cylindrical shape, with a height of 10 mm and a diameter of 6 mm. The mass was 1.417 g. The hysteresis measurement was performed by applying an external field of 2 T and a pulse duration of 56 ms. In order to reduce the statistical error the measurement was repeated 7 times.

The mean value of the remanence magnetization determined in this way is $B_r = (0.3644 \pm 0.0002)\text{T}$, which corresponds to an error of $\pm 0.05\%$. PTB gave a remanence value of $B_r = (0.3625 \pm 0.0044)\text{T}$. So the difference between the PFM and the PTB value is about 0.5%, which is smaller than the given calibration error.

In order to test the effect of pulse duration, the PTB-calibrated sample was measured under the same conditions but with different pulse durations (56 ms and

40 ms) (Fig. 10.38). The difference in the remanence magnetization is below 1%. It should be noted that also the measured coercivity is only 2% higher, than the PTB value, which strongly supports the reliability of our field calibration.

Influence of Sample Geometry on Magnetization Values

In order to investigate the effect of the sample geometry on the accuracy of the magnetization measurements in the PFM, a set of industrial soft magnetic ferrites with different shapes were used (Philips (3C30)). All samples were from one batch. This material has a magnetization at room temperature of about 0.55 T, whilst the Curie temperature was about 240 °C. The density is 4800 kg/m³. Since this material is an insulator, there are no eddy-current effects. The chosen shapes are given in Table 10.5.

The samples were measured in an external field with an amplitude of 2 T and a pulse duration of 56 ms. All samples were measured at room temperature ($21\text{ °C} \pm 1\text{ °C}$) using the same amplification factor and the same mechanical adjustments. Small deviations are visible in the shape of the hysteresis loops, especially where the saturation enters the high-permeability region (Fig. 10.39). This is due to the fact that the mean

Table 10.4 Summary of calibration measurement

Sample	$\mu_0 M_{\text{meas}}$ (T)	S (%)	$\mu_0 M_{\text{literature}}$ (T)	Deviation (%)
Fe ₃ O ₄	0.5787	0.2	0.569	+1.6
Nickel	0.6259	0.13	0.610	+2.6
Iron	2.1525	0.24	2.138	+0.7

Table 10.5 Shapes and masses of the 3C30 samples

Sample (mm)	Size	Mass (g)
Sphere	$d = 9.1$	$m = 1.9065$
Small cube	$11.2 \times 11 \times 0.8$	$m = 0.5226$
Medium cube	$11.9 \times 11.9 \times 3$	$m = 1.9316$
Big cube	$21 \times 14.6 \times 11.9$	$m = 17.3848$

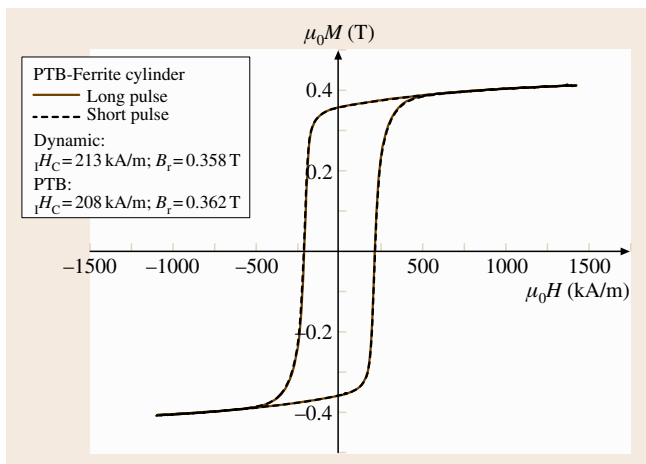


Fig. 10.38 Comparison of the on the PTB-magnet measured magnetization for a short and long pulse

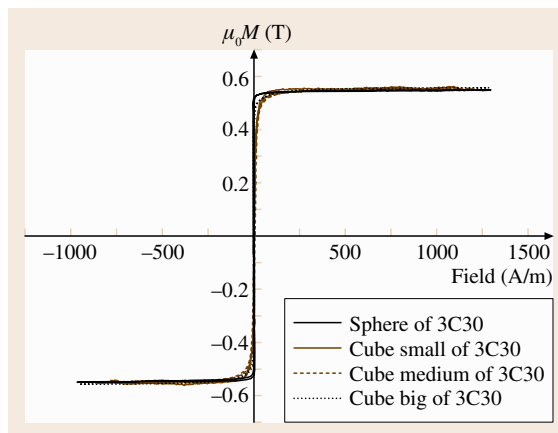


Fig. 10.39 Hysteresis measurements on 3C30 samples with different shapes

Table 10.6 Magnetization at $H = 2$ T of 3C30 samples

Sample	Magnetization (T)
Sphere	0.550
Small cube	0.558
Medium cube	0.555
Big cube	0.557

demagnetization factor causes an error, which becomes especially significant in this part of the loop.

The results are summarized in Table 10.6: The magnetization values of the three different cubes show a difference of up to 0.6% (Table 10.6). The value for the sphere exhibits the largest difference of 2% with respect to the average value of the cubes. (This may be a result of the grinding process in an air-pressure-driven mill. The sample is forced to rotate rapidly in a container of corundum.) It is possible that the surface structure of the sample may have been destroyed. If a disturbed surface layer of $40\ \mu\text{m}$ is assumed, this could account for the deviation of the magnetization value.

Discussion of the Calibration Procedure

The field of a PFM is calibrated using a small pickup coil, where the effective winding area is known from NMR calibration. Using such a procedure allows an absolute field calibration of better than 1%, including the time constants (gain) of the integrator. The obtained field calibration also agrees within 2% with that of the PTB-calibrated magnet coercivity value.

In principle, nonconducting materials, such as Fe_3O_4 or a soft magnetic ferrite like 3C30, are better

suitable for this calibration. Unfortunately, the temperature dependence of the magnetization of the industrially available ferrite 3C30 is much worse than that of Fe_3O_4 (Fig. 10.40).

The calibration constants using Fe_3O_4 , Fe and Ni agree within 1.6%. The reproducibility of the different magnetization measurements – especially using Fe or Ni samples – was better than 0.3%. The error due to eddy currents in the rather long pulse duration (56 ms) is negligible. The zero signal of the system is less than 10% of the Fe_3O_4 sample signal, which has the smallest sample signal. According to these considerations, one can conclude that the sensitivity of the PFM investigated here is high enough to measure Nd-Fe-B magnet samples as small as 0.3 g mass, which corresponds to a cube of $3\ \text{mm} \times 3\ \text{mm} \times 3\ \text{mm}$. Such a PFM is, however, also capable of measuring samples with diameters up to 30 mm. It has to be mentioned that the sensitivity for a certain sample size depends mainly on the coupling between the sample and the pickup system. Therefore the sensitivity can be improved by adjusting the pickup system to a certain sample dimension.

If one works very carefully, an absolute magnetization calibration within $\pm 1\%$ is possible. Due to the good linearity of the analogue measuring electronics available nowadays and the high resolution of ADC cards (14 bit), a relative measurement – which is most important for a quality-control system – with a relative accuracy better than 0.5% is possible.

10.3.4 Hysteresis Measurements on Hard Magnetic Materials

Comparison Static Measurement – Dynamic Measurement

For testing a PFM system a set of commercial permanent-magnet samples was chosen: isotropic and anisotropic barium ferrite, anisotropic low- and high-coercivity Nd-Fe-B magnets. The shape of the samples was cylindrical: diameter 4 mm, length 5 mm; a demagnetizing factor of 0.255 was used. In order to allow a comparison between static hysteresis and dynamic hysteresis measurements a set of spheres (from the same batch of samples) were produced at the Technical University (TU) of Vienna.

In order to test the reliability of dynamic measurements pulsed field hysteresis loops were compared with static loops. In Fig. 10.41 the hysteresis loop as measured on an isotropic barium ferrite obtained in the static system at the Centre National de la Recherche Scientifique (CNRS) in Grenoble is compared with that

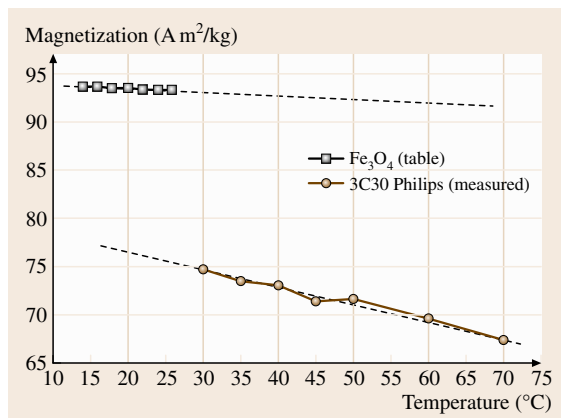


Fig. 10.40 Temperature dependence of the saturation magnetization of 3C30 compared with that of Fe_3O_4

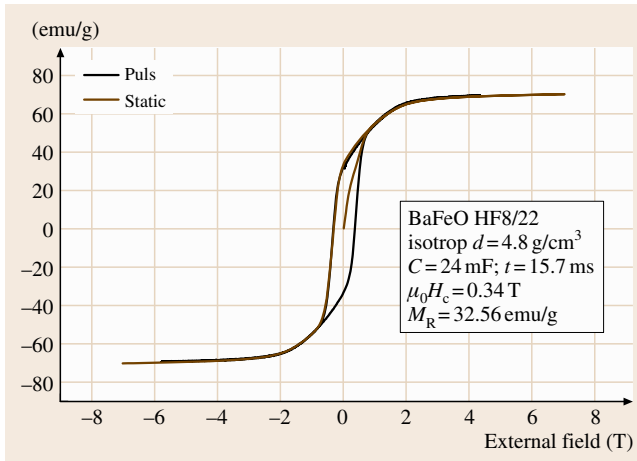


Fig. 10.41 Hysteresis loop as measured on the isotropic BaFeO HF 8/22 spherical sample

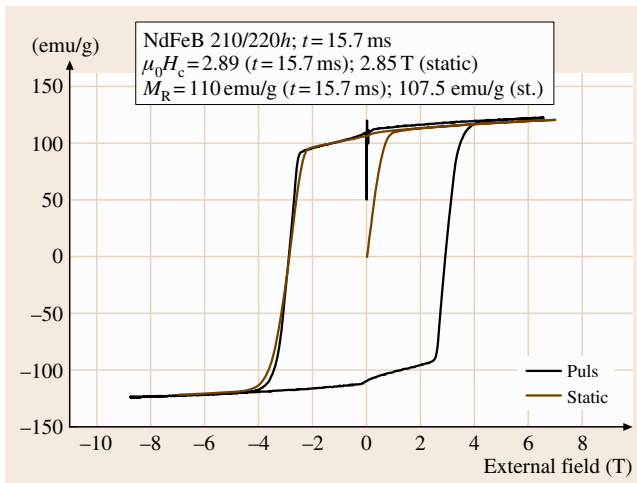


Fig. 10.42 Room-temperature hysteresis loop of a spherical Nd-Fe-B 210/220 magnet measured in a static magnetometer and in the pulsed field magnetometer

measured in the **TU PFM**. The use of barium ferrite has the advantage that there are no eddy currents because this material is an insulator. The difference is within the line thickness.

Figure 10.42 also shows for comparison hysteresis measurements on a Nd-Fe-B magnet as performed in the **PFM** (TU Vienna) and in the static magnetometer (CNRS Grenoble). There are differences in the slope of the $M(H)$ curve close to the coercivity. It is believed that this is due to small differences in the sphericity of the samples. This cannot be due to eddy currents

in the sample because the coercivity value is the same. This shows that, for sample sizes below 10 mm, and for the pulse duration here used (15.7 ms) the eddy-current effects are negligible.

Rare-Earth-Based Magnets

For the following discussion of different types and shapes of rare-earth-based industrial magnets the room-temperature hysteresis loops were measured in the industrial **PFM** located at TU Vienna.

Figures 10.43 and 10.44 show such a loop as obtained from Vacodym 510 (a Nd-Fe-B magnet); the agreement between the static and pulsed data is very good. The applied field, especially in the second half wave, is not sufficient.

10.3.5 Anisotropy Measurement

Generally the magnetocrystalline anisotropy constants are determined from measurements on a single crystal in a torque magnetometer or similar device. Unfortunately single crystals are not available from many materials. In this case, polycrystalline material can sometimes be aligned in an external field and then the magnetization $M(H)$ is measured parallel and perpendicular to the external field. Curves determined in this way can be fitted, which also allows an estimate of the magnetocrystalline anisotropy to be made.

Another, sometimes better, possibility is to determine the magnetocrystalline anisotropy field H_a using the so-called singular point detection (**SPD**) technique [10.44]. The principle of the **SPD** method is shown in Fig. 10.45. Single crystals are not necessary for the **SPD** method, and it allows the determination of the physically relevant anisotropy field even for polycrystalline samples. This is especially important when investigating technically relevant compositions, which often consist of many phases and exhibit rather complex compositions, such as e.g. $\text{Sm}(\text{Co}, \text{Fe}, \text{Cu}, \text{Zr})_{7.5}$ which is typical for a so-called 2/17-based technical magnet [10.45]. Additionally many new technologies, such as rapidly quenching, hydrogenation disproportionation desorption recombination (**HDDR**), nitrogen loading or even thin films, lead to isotropic material, where single crystals are not possible in principal. In this case the **SPD** technique is the only possibility to determine the anisotropy field. Up to now this method was restricted to uniaxial systems. Recently it was extended to easy plane systems [10.46], which is essentially for many 3-D-dominated compounds.

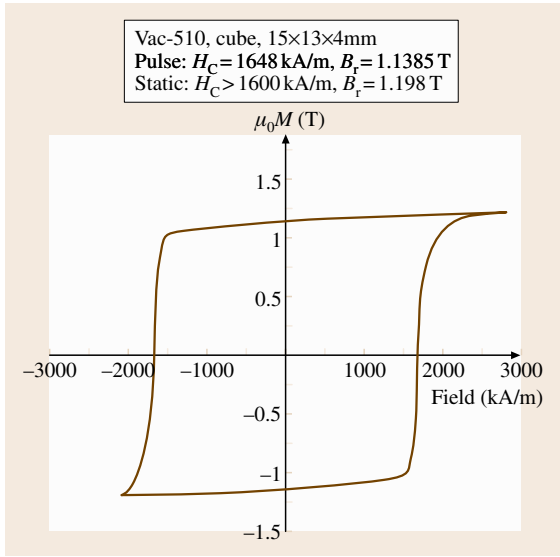


Fig. 10.43 Room-temperature hysteresis loop as obtained on a cube of Vacodym 510 (an Nd-Fe-B magnet)

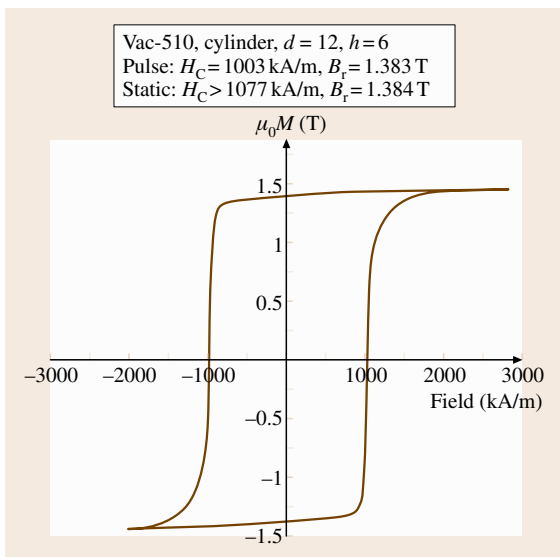


Fig. 10.44 Room-temperature hysteresis loop as obtained on a cylinder of Vacodym 510 (an Nd-Fe-B magnet)

Limitations of the SPD Method

The **SPD** method delivers only the anisotropy field H_a . This is technically relevant, but it is not sufficient for a deeper analysis based on the anisotropy constants. At least the anisotropy energy and its temperature dependence have to be known. If the real saturation magnetization can be determined the anisotropy energy

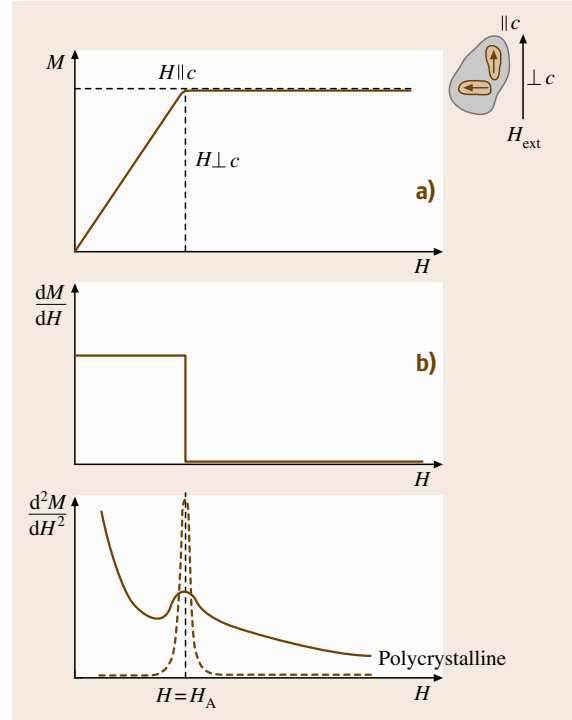


Fig. 10.45a–c The principle of the **SPD** measurement for determining the anisotropy field

can be calculated from H_a . Unfortunately an accurate determination of the saturation magnetization is not simple in hard magnetic compounds, because insufficiently high fields are available in usual magnetometers. For this purpose accurate magnetization measurements up to fields which are comparable to H_a (or larger) are necessary, and at different temperatures. When the temperature dependence of the anisotropy energy and that of the magnetization is known, various types of analysis such as scaling laws can be used in order to come to an understanding of these data. From such an analysis, information about the origin of the anisotropy can be deduced.

Studies performed in existing pulsed field systems (in Vienna and Parma) showed that the **SPD** method works well for anisotropy fields up to about 20 T. The reason for this limitation is that the maximum external field has to be at least 50% higher than H_a in order to make the singularity visible. Another limitation comes from the fact that at higher fields (above approximately 25 T) the vibrations and consequently the noise of the high-field system increases drastically, although this is not yet fully understood. Because the **SPD** method is

based on a differentiating technique ($d^2M(t)/dt^2$) the noise appearing at higher fields limits the measurable H_a values.

One of the basic problems here is that using a differentiating technique greatly increases all type of noise; and the high-frequency noise in particular increases with ω^2 .

In the meantime the SPD method has been used to investigate the anisotropy field of many hard magnetic materials [10.47–49]. Some materials of interest recently where the measurement of the anisotropy field is only possible using the SPD method are the exchange coupled nanocrystalline hard magnetic materials.

The Anisotropy Field of Nanocrystalline Materials

It is not an easy task to determine the anisotropy field in these intrinsic isotropic samples. In addition, the strong magnetic exchange interaction among nanocrystallites makes measurements even more difficult. In this respect, singular point detection (SPD) provides a unique method for the direct determination of the anisotropy field of isotropic samples. In Fig. 10.46 the temperature dependencies of the anisotropy field measured for mechanically alloyed, nanocrystalline $\text{Pr}_9\text{Fe}_{85}\text{B}_6$, $\text{Pr}_{11.76}\text{Fe}_{82.36}\text{B}_{5.88}$ and $\text{Pr}_{18}\text{Fe}_{76}\text{B}_6$ is shown [10.50]. Here the sample $\text{Pr}_9\text{Fe}_{85}\text{B}_6$ represents a nanocomposite with $\text{Pr}_2\text{Fe}_{14}\text{B}$ and $\alpha\text{-Fe}$; the $\text{Pr}_{11.76}\text{Fe}_{82.36}\text{B}_{5.88}$ should be single phase containing only $\text{Pr}_2\text{Fe}_{14}\text{B}$ grains whereas the $\text{Pr}_{18}\text{Fe}_{76}\text{B}_6$ should contain $\text{Pr}_2\text{Fe}_{14}\text{B}$ grains that are decoupled by an excess of Pr.

It is worth noting that the anisotropy field measured by using the SPD technique corresponds only to that of the hard magnetic phase. In the case of $\text{Pr}_9\text{Fe}_{85}\text{B}_6$ which consists of $\text{Pr}_2\text{Fe}_{14}\text{B}$ and $\alpha\text{-Fe}$, that is the $\text{Pr}_2\text{Fe}_{14}\text{B}$ phase. The reduction of the anisotropy field in the nanocrystalline $\text{Pr}_{12}\text{Fe}_{14}\text{B}$ grains is a strong indication of the presence of magnetic exchange interactions. In the case of microcrystalline sintered Pr-Fe-B magnets the magnetic exchange interaction among the micro-sized grains is insignificant to influence the easy magnetization direction (EMD) of the grains. Thus the anisotropy field measured in the microcrystalline magnets corresponds to the anisotropy field of isolated $\text{Pr}_2\text{Fe}_{14}\text{B}$ grains. However, when the average grain size is reduced to nanometer size ($D_V < 50\text{ nm}$), the exchange interaction among the hard magnetic grains may become so strong that the EMDs of the nanocrystallites can be slightly tilted without the presence of external fields. The actual direction of the final EMD could be an energetic compromise of the surrounding

nanocrystallites. This slightly tilted EMD gives a naturally reduction of the anisotropy field. This reduction of H_a also becomes visible in the SPD peak of the measurement of d^2M/dt^2 versus H , where the peak indicates the position of H_a (Fig. 10.47). From Fig. 10.46 a systematic decrease of $H_a(T)$ with increasing coupling between the grains going from excess Pr content (18% Pr) to a stoichiometric sample (12% Pr) to a low-Pr-content material (9% Pr) becomes clearly visible for higher temperatures. For lower temperatures, because of the increasing anisotropy, a decoupling of the grains occurs that causes equal values of H_a for all three samples.

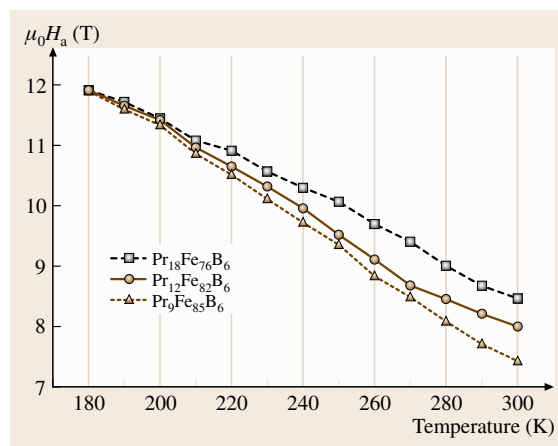


Fig. 10.46 The temperature dependence of the anisotropy field for hot-pressed mechanically alloyed Pr-Fe-B

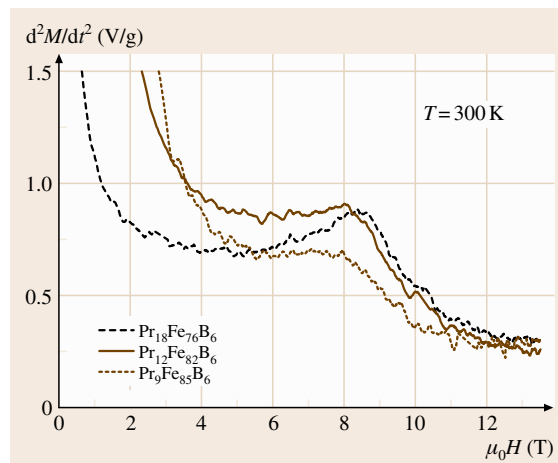


Fig. 10.47 The SPD peak measured at 300 K for mechanical alloyed hot-pressed Pr-Fe-B samples with nanosized grains

10.3.6 Summary: Advantages and Disadvantages of PFM

A PFM generally allows fast magnetization measurements in sufficiently high magnetic fields. Reproducible, nondestructive fields up to 40 T are nowadays the state of the art. Using a capacitor bank as an energy store allows the generation of a pulsed magnetic field in a volume that is best suited to solve a technical task. Therefore for many applications a PFM is much better suited than a standard static magnetometer, which is less flexible.

Comparison with static hysteresis loops demonstrated that, if both systems are calibrated carefully, PFM measurements of hard magnetic materials are reliable and achieve a similar accuracy to that of a static system.

In terms of the demagnetizing field, correction for industrial shapes is not simple. For shapes like cylinders or cubes that are not too complex the use of a single factor is sufficient, but for other shapes this problem is still open. This is not only a problem for PFM, but occurs in all magnetic open circuits.

A general understanding of eddy currents now exists. The $f/2f$ method is a good fast method to correct for eddy-current errors in PFM measurements.

In principle magnetic viscosity causes an error in all hard magnetic materials. However, it seems that pinning-type materials exhibit a larger magnetic viscosity. The magnetic viscosity generally increases with the magnetocrystalline anisotropy. Therefore for room-temperature measurements on nucleation-type materials (ferrites, Nd-Fe-B, SmCo₅-based) this effect seems to be sufficient small.

To summarize, PFMs can be constructed that show better results than many static hysteresis graphs however with the advantage that in a PFM higher fields are available, a faster measurement is possible and no special sample preparation is generally necessary. For ferrites and Nd-Fe-B-based magnets, fields up to 5 T are necessary, whereas for materials such as SmCo₅-based magnets, fields of approximately 10 T are necessary.

Beside the possibility of measuring a magnetization (hysteresis loop) a PFM can also be used to determine the anisotropy field using the SPD method, as was shown. This method is unique because it works even for polycrystalline materials.

10.4 Properties of Magnetic Thin Films

Magnetic thin films are receiving growing interest both from a fundamental scientific point of view and because of a variety of novel applications, in particular for magnetic-field sensors and information storage. Some of their specific properties relating to new technologies have already been mentioned in Sect. 10.1.5. In the present section the most important magnetic properties of magnetic thin films are discussed together with the most suitable methods of measuring the related quantities.

10.4.1 Saturation Magnetization, Spontaneous Magnetization

Phenomena

The saturation magnetization of a material M_{sat} , defined as the magnetic moment per volume, is of great technical interest because it determines the maximum magnetic flux that can be produced for a given cross section. However, M_{sat} as the *magnetization at technical saturation* is not a well-defined quantity because a large enough external magnetic field must be applied to pro-

duce a uniform magnetization by eliminating magnetic domains and aligning the magnetization along the field against magnetic anisotropies; however, at the same time the magnetization at any finite temperature $T > 0$ will continue to increase with increasing applied field (*high-field susceptibility*). The only well-defined quantity, hence, is the spontaneous magnetization M_S i. e. the uniform magnetization inside a magnetic domain in zero external field.

In practice, M_S is determined by measuring the magnetization as a function of the external field, $M(H)$ (which means the magnetization component parallel to the applied field) up to technical saturation, with a linear extrapolation of the data within the saturated region back to $H = 0$. A linear fit is a good approximation for temperatures well below the Curie temperature of the ferromagnetic material.

The method proposed above works best by applying the external field along an easy axis of magnetization and is especially well suited for thin films because of the absence of a demagnetizing field for in-plane magnetization; usually a relatively small field is sufficient

for saturation and the extrapolation to $H = 0$ is not required. Of course, higher fields are required for magnetically hard materials. In films having a dominating intrinsic anisotropy with a perpendicular easy axis the measurement should be done along the film normal.

When comparing the magnetization of a thin film to the value of the corresponding bulk material two different effects can be important.

1. The magnetization or the magnetic moment per atom in the ground state, i. e. at absolute zero temperature, might be enhanced. Depending on the specific combination of ferromagnetic material and substrate the enhancement may reach 30% for a single atomic layer (e.g. Fe on Ag or Au), but will disappear 3–4 atomic layers away from the interface. Depending on the band structure of the materials the magnetic moments at the interface may also be reduced in some cases (e.g. for Ni on Cu);
2. Thermal excitations which result in a decrease of M_S with increasing temperature are more pronounced in thin films compared to bulk material. In a film of 10 atomic layers of Fe on Au, M_S at room temperature is reduced by about 10% compared to bulk Fe. The origin of this effect is the reduced (magnetic) coordination at surfaces and interfaces, which leads to an enhanced excitation of spin waves; for the same reason the Curie temperature is reduced in ultrathin films compared to the bulk material.

Measurement Techniques and Instruments

A variety of methods are used to measure the magnetic properties of thin films. In many cases, especially for relatively thick films, the techniques used for bulk material can be applied as well (see the overview in Sect. 10.1.6). Here, the emphasis is put on the high sensitivity required for films thinner than about 100 nm and for ultrathin films with thicknesses down to 1 nm or less.

Magnetic moments m in terms of absolute values are determined with a suitable magnetometer from the field dependence of the moment, the so-called magnetization loop $m(H)$. The magnetization $M(H)$, i. e. magnetic moment per volume, is found by dividing the moment by the magnetic volume. For ultrathin films the main uncertainty on M often comes from the determination of the volume rather than from the magnetic moment itself.

Vibrating-Sample Magnetometer (VSM)

The vibrating-sample magnetometer (VSM) is probably the most widely used standard instrument. The princi-

ple of operation is described in Sect. 10.2 (Fig. 10.7). When the specimen oscillates between a set of pickup coils with a frequency of several 10 Hz to a few 100 Hz, the amplitude of the AC voltage induced in the pickup coils is proportional to the magnetic moment of the specimen and the vibration amplitude of the sample. The factor of proportionality depends on the entire geometry including the shape and size of the sample. This must be taken into account when an absolute calibration is carried out. The principle of measurement can be combined with an iron core electromagnet, or with air coils for low-field operation, or with a superconducting magnet for high-field applications. The VSM allows relatively fast measurements (1–10 min for a complete $M(H)$ loop, depending on the type of magnet and the required sensitivity), is flexible and easy to use. In particular, measurements at various angles can be made with the great precision required for the determination of magnetic anisotropies. The sensitivity attainable depends largely on the geometry and position of the pickup coils. Standard versions are useful for magnetic moments corresponding to Fe or NiFe films more than 5 nm thick (assuming a lateral size of 1–2 cm). Thinner films of 1 nm or less can be measured with an optimized VSM. The sensitivity is generally reduced for variable-temperature measurements when a cryostat or oven must be mounted.

The SQUID Magnetometer

The SQUID magnetometer is based on the same principle as the VSM but with a superconducting pickup coil circuit and a superconducting quantum interference device (SQUID) as the flux detector. The structure of a commercial SQUID magnetometer is schematically shown in Fig. 10.48 [10.51].

The sample executes a periodic linear motion with a vibration frequency of 0.1–5 Hz. This causes a change of magnetic flux in the pickup coils, which are part of the totally superconducting circuit outlined in Fig. 10.49.

The SQUID itself is operated in a constant-flux mode and serves as an extremely sensitive zero-detector in the feedback loop outlined in Fig. 10.49. The output signal of the magnetometer is proportional to the current in the feedback coil required to compensate the flux change sensed by the pickup coils.

The detection limit of the SQUID magnetometer for magnetic moments is about 1000 times lower than that of the VSM, i. e. about 10^{-9} Gcm³ or 10^{-18} V s m. It is usually combined with a superconducting magnet

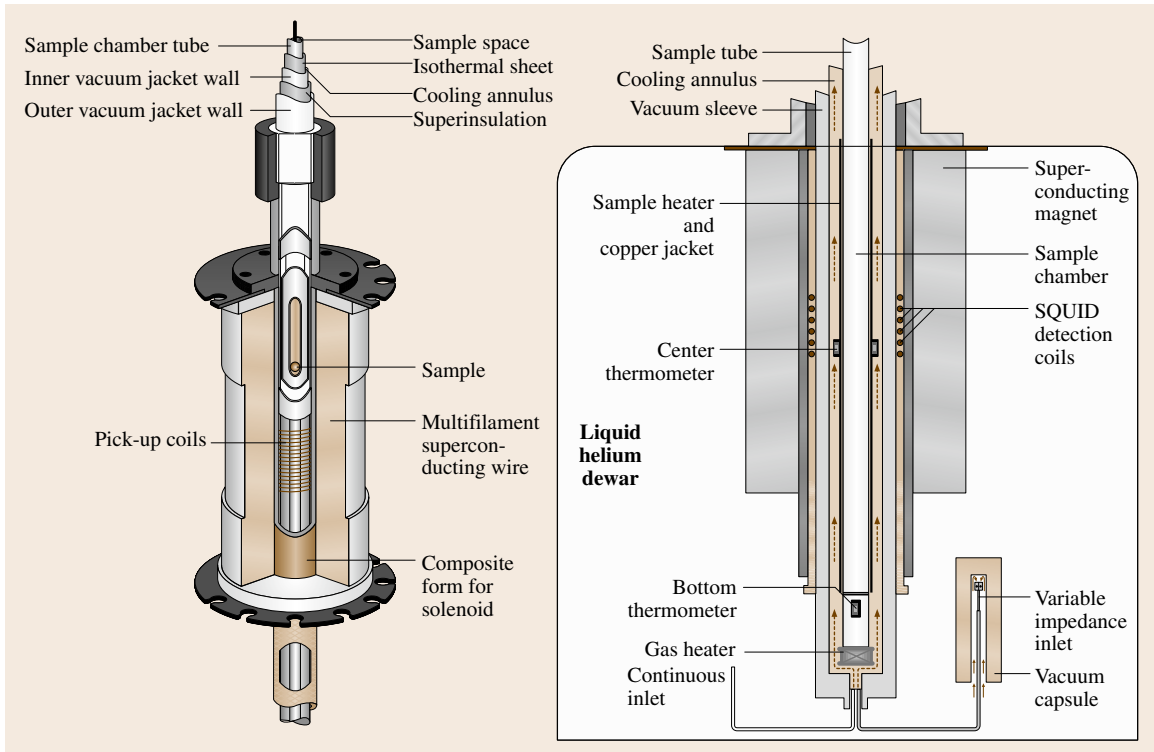


Fig. 10.48 Schematic view of a commercial **SQUID** magnetometer consisting of a liquid-He cryostat, a superconducting magnet, the variable-temperature sample chamber with thermometers and the detection coils close to the sample position. After [10.51]

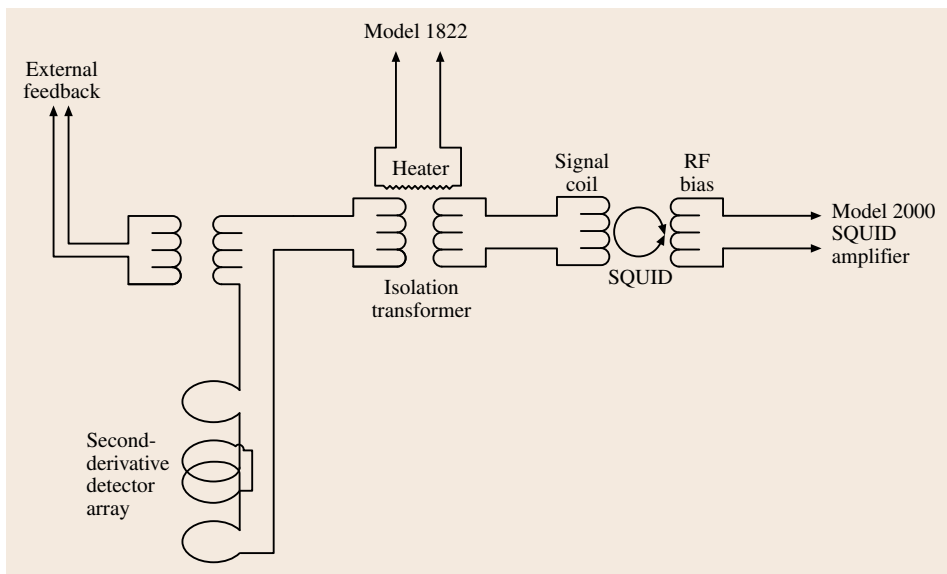


Fig. 10.49 Schematic diagram of the circuit of a commercial **SQUID** magnetometer (Quantum Design Inc.). All the coils are superconducting. The **SQUID** amplifier transforms any flux change sensed by the detector coils into a current, which is fed to the feedback coils such that this flux change is exactly compensated. This compensating current at the same time constitutes the output signal of the magnetometer. After [10.51]

and a variable-temperature He cryostat, which allows for measurements in high fields (3–7 T for commercial instruments) and at low temperatures. The biggest challenge is to make use of the high sensitivity of the SQUID in the presence of unavoidable fluctuations of the field from the external magnet. The most efficient solution is to use carefully balanced pickup coils in the form of a gradiometer of first or second order (e.g. a second-order gradiometer is shown in Fig. 10.49).

Typical measuring times for a complete magnetization loop may range from 30 min up to a full day depending on the field range and number of data points. For precision measurements a careful calibration that takes into account the specific sample geometry is necessary. For most purposes the SQUID magnetometer is the most suitable and versatile instrument for measuring extremely thin films in a wide range of temperatures (typically 2–400 K) and applied magnetic fields (up to 7–9 T).

The Alternating (Field) Gradient Magnetometer

The alternating (field) gradient magnetometer (AGM or AFGM) is a modification of the well-known Faraday balance that determines the magnetic moment of a sample by measuring the force exerted on a magnetic dipole by a magnetic field gradient. The principle of the instrument [10.52] is sketched in Fig. 10.50. The force is measured by mounting the sample on a piezoelectric bimorph, which creates a voltage proportional to the elastic deformation and, hence, to the force acting on the sample. By driving an alternating current through the gradient coils, with lock-in detection of the piezo voltage and by tuning the frequency of the field gradient to the mechanical resonance of the sample mounted on the piezoelectric element by a glass capillary a very high sensitivity can be achieved that approaches that of a SQUID magnetometer under favorable conditions. The main advantage of the AGM is its relative immunity to external magnetic noise and the resulting high signal-to-noise ratio and short measuring time. A major disadvantage is the difficulty in obtaining an absolute calibration of the magnetic moment because the signal is not only proportional to the sample magnetic moment but also to the Q -factor of the sample-capillary-piezo system, which varies with sample mass and temperature. This problem can be overcome by inserting a small calibration coil close to the sample position. Also, difficulty in obtaining an exact angular orientation of the sample relative to the external magnetic field is a drawback of this instrument. An AGM is relatively easy to build, but is also commer-

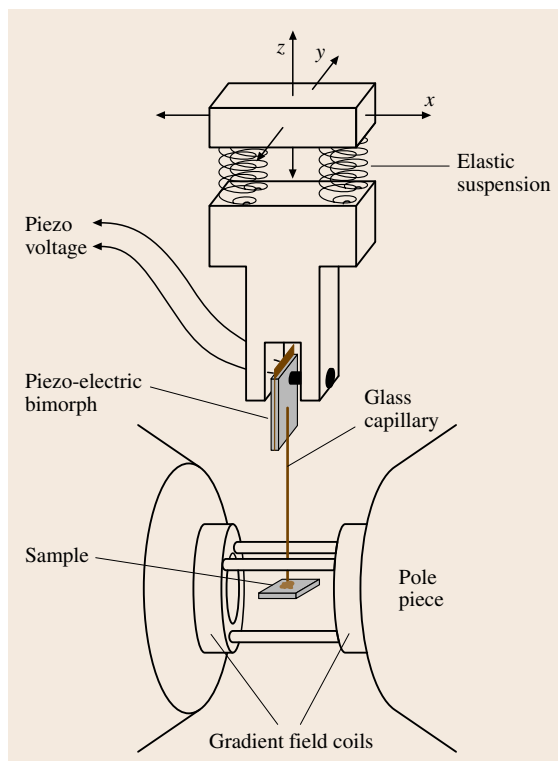


Fig. 10.50 Principle of the alternating (field) gradient magnetometer (AGM/AFGM); the gradient field coils are fed with an alternating current with a frequency tuned to the mechanical resonance of the sample-capillary-piezo system. The sample and gradient coils are mounted between the pole pieces of an electromagnet

cially available. It can be equipped with a cryostat or oven for variable-temperature measurements.

Torque Magnetometers

Torque magnetometers in the form of a torsion pendulum (Sect. 10.2.2) have been successfully used for ultrathin films due to the high sensitivity attainable [10.53]. However, they measure the effective magnetic anisotropy of the sample; therefore, the different contributions to the anisotropy of the given sample must be known in order to determine the magnetic moment. This is further discussed in the next section.

Magneto-optic Techniques

When only the shape of the magnetization loop, or the relative variation of the magnetization with temperature, orientation of the external field or another external parameter is of interest, *magneto-optic effects*

(magneto-optic Faraday effect or Kerr effect, **MOKE**) are very useful. Because of the limited penetration depth of light magneto-optic techniques only probe the first 10–50 nm below the surface of a metallic sample and are therefore well suited for the fast characterization of magnetic thin films. For these, **MOKE** is a particularly powerful technique [10.54].

A typical arrangement is sketched in Fig. 10.51.

Upon reflection from a magnetic surface a beam of linearly polarized light in general will change its state of polarization depending on the relative orientation of the magnetization of the sample and the polarization axis. Both the ellipticity ε_K and Kerr rotation angle of the polarization δ_K occurring due to reflection can be used to measure a certain magnetization component defined by the specific arrangement. Basically, there are three different arrangements: i) the polar Kerr effect is measured with (nearly) perpendicular incidence of the light beam; the magnetizing field is applied perpendicular to the film plane and δ_K is proportional to the perpendicular component of the magnetization; ii) the longitudinal Kerr effect is observed with the light beam at oblique incidence and the in-plane magnetization component parallel to the plane of incidence is measured; iii) the transverse Kerr effect, which is observed in the same geometry as the longitudinal **MOKE**, produces a change of the intensity of the reflected beam and is proportional to the magnetization component perpendicular to the plane of incidence.

Gas lasers like He-Ne or laser diodes are equally used for **MOKE** measurements provided that the intensity and polarization are sufficiently stable. Various modulation techniques in combination with synchronous detection have been used to enhance the signal-to-noise ratio. A careful arrangement allows for very high sensitivity that is sufficient to measure the magnetization loops of films of less than a single atomic layer [10.55].

A major advantage of the **MOKE** technique is the possibility to focus the laser spot at the sample surface to less than 1 μm and thus measure magnetic properties with high lateral resolution. This is especially useful when the thickness dependence of properties is investigated by producing wedged samples with a lateral thickness variation. Another characteristic feature is the limited penetration depth of visible light of a few 10 nm in typical metal films; this allows measurements with a certain depth resolution, which is especially interesting for investigating multilayer structures. This can be further enhanced by choosing an appropriate wavelength for the light source according to the materials

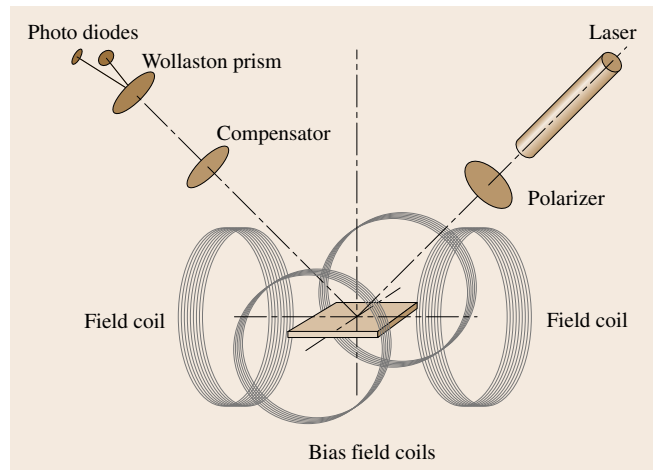


Fig. 10.51 Outline of a set up for magneto-optic Kerr-effect (**MOKE**) measurements (see text)

of interest, because the Kerr angle δ_K and Kerr ellipticity ε_K vary with the material and wavelength of the light.

MOKE, on the other hand, does not allow for a quantitative measurement of the absolute value of the magnetization. However, it is one of the most useful tools to investigate magnetic anisotropies, temperature dependence of magnetization and fast magnetization dynamics in magnetic films.

Magneto-optic effects in the (soft) x-ray energy range, in particular x-ray circular magnetic dichroism (**XMCD**), offer a unique potential: by tuning the photon energy to a core-level absorption edge it is possible to measure magnetic moments in an element-specific way. Furthermore, orbital and spin magnetic moments of electrons can be separately determined via so-called sum rules. This technique requires a synchrotron radiation source with circular polarization.

10.4.2 Magneto-Resistive Effects

Magneto-resistance means that the electric resistance of a material changes upon the application of a magnetic field. All conductive materials show magneto-resistive effects. However, here the discussion is restricted to magneto-resistance of ferromagnetic materials based on several different mechanisms.

Anisotropic Magneto-Resistance (AMR)

The dependence of the electric resistance on the angle θ between the magnetization and the current in a ferromagnetic material is called anisotropic magneto-

resistance (AMR) and can be described by

$$R(\theta) - R_0 = a \cos^2 \theta . \quad (10.54)$$

The relative resistance change amounts to a fraction of a percent in most materials, up to 3% in permalloy films. The AMR effect has proved to be very useful for magnetic sensors.

Giant Magneto-Resistance (GMR)

The giant magneto-resistance effect is observed in layered magnetic film systems consisting of at least two ferromagnetic layers separated by a nonmagnetic metallic interlayer. When the magnetization in neighboring magnetic layers is switched from an antiparallel to a parallel configuration the electric resistance changes by an amount ranging from a few percent for two ferromagnetic layers to about 200% in special multilayer stacks. The GMR effect results from the spin-dependent scattering of electrons inside the layers and at the interfaces. For most materials the overall scattering rate is stronger for the antiparallel configuration, making it the high resistance state. In principle, the GMR can be observed both with the current flowing in the film plane (current-in-plane (CIP) configuration) or perpendicular (current-perpendicular-to-plane (CPP) configuration). However, measurement of the CPP-GMR due to the small junction resistance requires either the use of superconducting leads or restricted lateral junction dimensions of 100 nm or less.

An obvious application of GMR junctions is for magnetic-field sensors. The most suitable configuration is the so-called spin valve, which consists of a free magnetic layer that is easily magnetized along a small external field, a nonmagnetic metallic interlayer (Cu in most cases) and a hard magnetic layer with its magnetization pinned to a fixed direction by exchange coupling to an antiferromagnetic layer. The resistance R of such a device varies with the angle θ of the free layer magnetization as

$$R(\theta) - R_{\min} = c \cos \theta . \quad (10.55)$$

Compared to the characteristics of an AMR element it is obvious that GMR is more useful as an angle sensor, and this is indeed an attractive application of this effect. The most successful application, however, is still in read

heads for hard-disc drives, where it has contributed to the steady increase in areal storage density.

Tunnel Magneto-Resistance

The tunnel magneto-resistance (TMR) is observed in ferromagnetic double-layer structures with an intermediate insulating layer. If the insulator is very thin, i. e. typically 1–2 nm, and a small voltage is applied between the two magnetic metallic contacts then a current will flow by a quantum-mechanical tunneling process. Similarly to the GMR effect the current depends on the relative orientation of the magnetization in both layers, with a large current flowing in the parallel configuration. The magnetization in one of the layers is frequently pinned by exchange coupling to an antiferromagnet (*exchange bias*) as in a spin-valve. As a consequence, the tunnel resistance varies with the angle of the magnetization of the free layer in the same way as for GMR as discussed above. Over the years the TMR ratio at room temperature in state-of-the-art tunnel junctions of FeCo layers and Al-oxide tunnel barriers has been increased to about 50% in moderate external fields, which makes them a very attractive field sensor. It should be noted, however, that the TMR ratio decreases strongly with increasing bias voltage and tunneling current. This has to be taken into account when different magnetic tunnel junctions (MTJs) are compared.

The most spectacular application of MTJs – besides hard disk read heads – is in all-solid-state fast magnetic random-access memories (MRAMs), which are now in an early state of production. A very promising recent achievement is a room-temperature TMR ratio of 500% and more obtained in junctions with a MgO tunnel barrier. This opens the way to an even brighter future for devices based on the TMR effect.

Colossal Magneto-Resistance

Extremely large magneto-resistance effects of more than 10 000% have been observed in certain compounds, especially in manganites with a perovskite structure. This effect is related to a metal–insulator transition which can be driven by a magnetic field. However, the largest effects are only observed at low temperatures and in very high fields, making these materials of limited technical value.

References

- 10.1 R. Grössinger, M. Taraba, A. Wimmer, J. Dudding, R. Cornelius, P. Knell, P. Bissel, B. Enzberg-Mahlke, W. Fernengel, J.C. Toussaint, D. Edwards: Calibration of an industrial pulsed field magnetometer, *IEEE Trans. Magn.* **38**(5), 2982–2984 (2002)
- 10.2 E.P. Wohlfarth: *Experimental Methods in Magnetism* (North-Holland, Amsterdam 1967)
- 10.3 E. Steingroever, G. Ross: *Magnetic Measuring Techniques* (Magnet-Physik Dr. Steingroever, Cologne 2009)
- 10.4 E. Steingroever: Some measurements of inhomogeneous permanent magnets by the pole-coil method, *J. Appl. Phys.* **37**, 1116–1117 (1966)
- 10.5 S. Foner: Versatile and sensitive vibrating-sample magnetometer, *Rev. Sci. Instrum.* **30**, 548–557 (1959)
- 10.6 R. Beranek, C. Heiden: A sensitive vibrating sample magnetometer, *J. Magn. Magn. Mater.* **41**, 247–249 (1984)
- 10.7 H. Zijlstra: Measurement of magnetic quantities. In: *Experimental Methods in Magnetism*, Vol. 2, ed. by E.P. Wohlfarth (North-Holland, Amsterdam 1967) pp. 168–203
- 10.8 S.R. Trout: Use of Helmholtz coils for magnetic measurements, *IEEE Trans. Magn.* **24**, 2108–2111 (1988)
- 10.9 B.D. Cullity: *Introduction to Magnetic Materials* (Addison-Wesley, Reading 1972) pp. 72–73
- 10.10 L.R. Moskowitz: *Permanent Magnet Design and Application Handbook* (Cahners Books International, Boston 1976) pp. 128–131
- 10.11 G. Bertotti, E. Ferrara, F. Fiorillo, M. Pasquale: Loss measurements on amorphous alloys under sinusoidal and distorted induction waveform using a digital feedback technique, *J. Appl. Phys.* **73**, 5375–5377 (1993)
- 10.12 D. Son, J.D. Sievert, Y. Cho: Core loss measurements including higher harmonics of magnetic induction in electrical steel, *J. Magn. Magn. Mater.* **160**, 65–67 (1996)
- 10.13 H. Ahlers, J.D. Sievert, Q. Qu: Comparison of a single strip tester and Epstein frame measurements, *J. Magn. Magn. Mater.* **26**, 176–178 (1982)
- 10.14 J. Sievert, H. Ahlers, P. Brosin, M. Cundeve, J. Luedke: Relationship of Epstein to SST. Results for grain-oriented steel, *Proc. 9th ISEM Conf.*, Vol. 18, ed. by P. di Barba, A. Savini (IOS, Amsterdam 2000) pp. 3–6
- 10.15 H. Pfützner, P. Schönhuber: On the problem of the field detection for single sheet testers, *IEEE Trans. Magn.* **27**, 778–785 (1991)
- 10.16 E. Steingroever: A magnetic saturation measuring coil system, *IEEE Trans. Magn.* **14**, 572–573 (1978)
- 10.17 H. Ahlers: Polarization. In: *Units in Physics and Chemistry*, Landolt-Börnstein: Numerical Data and Functional Relationships in Science and Technology – New Series, Vol. Subvol. a, ed. by O. Madelung (Springer, Berlin, Heidelberg 1991) pp. 2–288–2–294
- 10.18 H. Wilde: Die Vorteile der Gegeninduktivitätsmeßbrücke bei ferromagnetischen Messungen, *Int. J. Electron. Commun. (AEÜ)* **6**, 354–357 (1952), (in German)
- 10.19 E. Blechschmidt: *Präzisionsmessungen von Kapazitäten, Induktivitäten und Zeitkonstanten* (Vieweg, Braunschweig 1956), (in German)
- 10.20 K.P. Koo, F. Bucholtz, A. Dandridge, A.B. Tveten: Stability of a fiber-optic magnetometer, *IEEE Trans. Magn.* **22**, 141–143 (1986)
- 10.21 IEC/TR 62581: Electrical steel – Methods of measurement of the magnetostriction characteristics by means of single sheet and Epstein test specimens (IEC, 2010)
- 10.22 R. Becker, M. Kersten: Die Magnetisierung von Nickeldraht unter starkem Zug, *Z. Phys.* **64**, 660 (1930), (in German)
- 10.23 K. Narita, J. Yamasaki, H. Fukunaga: Measurement of saturation magnetostriction of a thin amorphous ribbon by means of small-angle magnetization rotation, *IEEE Trans. Magn.* **16**, 435–439 (1980)
- 10.24 R. Grössinger, G. Herzer, J. Kerschhagl, H. Sassik, H. Spindler: *An. Fis. B* **86**, 85–89 (1990)
- 10.25 C. Polak, R. Grössinger, G. Vlasak, L. Kraus: *J. Appl. Electromagn. Mater.* **5**, 9–17 (1994)
- 10.26 K. Mohri, T. Kohzawa, K. Kawashima, H. Yoshida, L.V. Panina: *IEEE Trans. Magn.* **28**(5), 3150–3152 (1992)
- 10.27 R.S. Beach, A.E. Berkowitz: *Appl. Phys. Lett.* **64**(26), 3652–3654 (1994)
- 10.28 F.L.A. Machado, C.S. Martins, S. Rezende: *J. Phys. Rev. B* **51**(6), 3926–3929 (1995)
- 10.29 M. Knobel, M.L. Sartorelli, J.P. Sinnecker: *Phys. Rev. B* **55**, R3362–R2265 (1997)
- 10.30 R. Grössinger, X.C. Kou, M. Katter: *Physica B* **177**, 219–222 (1992)
- 10.31 R. Grössinger, M. Taraba, A. Wimmer, J. Dudding, R. Cornelius, P. Knell, B. Enzberg-Mahlke, W. Fernengel, J.C. Toussaint: *Proc. 17th Int. Workshop Rare-Earth Magn. Appl.* (Newark 2002) pp. 18–22
- 10.32 R. Gersdorf, F.A. Müller, L.W. Roeland: *Colloq. Int. CNRS No. 166* (1967)
- 10.33 D. Eckert, R. Grössinger, M. Doerr, F. Fischer, A. Handstein, D. Hinz, H. Siegel, P. Verges, K.-H. Müller: *Physica B* **294/295**, 705–708 (2001)

- 10.34 R. Grössinger, M. Küpferling, P. Kasperkovitz, A. Wimmer, M. Taraba, W. Scholz, J. Dudding, P. Lethuillier, J.C. Toussaint, B. Enzberg-Mahlke, W. Fernengel, G. Reyne: *J. Magn. Magn. Mater.* **242–245**, 911–914 (2002)
- 10.35 D. Meecker: *Finite Element Method Magnetism* (Foster-Miller, Waltham 2004), <http://femm.berlios.de/>
- 10.36 M. Küpferling: Diploma Thesis (TU Vienna, Vienna 2001)
- 10.37 G.W. Jewell, D. Howe, C. Schotzko: *IEEE Trans. Magn.* **28**, 3114–3116 (1992)
- 10.38 R. Grössinger, G.W. Jewell, J. Dudding, D. Howe: *IEEE Trans. Magn.* **29**, 29080–29082 (1993)
- 10.39 C. Golovanov, G. Reyne, G. Meunier, R. Grössinger, J. Dudding: *IEEE Trans. Magn.* **36(4)**, 1222–1225 (2000)
- 10.40 D. Givord, M.F. Rossignol, V. Villas-Boas, F. Cebollada, J.M. Gonzales: In: *Rare Earth Transition Metal Alloys*, ed. by F.P. Missel (World Scientific, Sao Paulo 1996)
- 10.41 R. Street, R.K. Day, J.B. Dunlop: *J. Magn. Magn. Mater.* **69**, 106 (1987)
- 10.42 D. Givord, P. Tenaud, T. Vadiou: *IEEE Trans. Magn.* **24**, 19 (1988)
- 10.43 J.C. Téllez-Blanco, R. Sato Turtelli, R. Grössinger, E. Estévez-Rams, J. Fidler: *J. Appl. Phys.* **86**, 5157 (1999)
- 10.44 G. Asti: *J. Appl. Phys.* **45**, 3600 (1974)
- 10.45 X.C. Kou, E.H.C.P. Sinnecker, R. Grössinger, P.A.P. Wendhausen: *IEEE Trans. Magn.* **31(6)**, 3638–3640 (1995)
- 10.46 X.C. Kou, E.H.C.P. Sinnecker: *J. Magn. Magn. Mater.* **157/158**, 83–84 (1996)
- 10.47 R. Grössinger, R. Krewenka, H. Kirchmayr, S. Sinnema, F.M. Yang, Y.K. Huang, F.R. de Boer: *J. Less Common Met.* **132**, 265 (1987)
- 10.48 R. Grössinger, X.C. Kou, T.H. Jacobs: *J. Appl. Phys.* **69(8)**, 5596–5598 (1991)
- 10.49 J.C. Téllez-Blanco, X.C. Kou, R. Grössinger, E. Estevez-Rams, J. Fidler, B.M. Ma: *Proc. 14th Int. Workshop Rare-Earth Magn. Appl.*, ed. by F.P. Missel, V. Villas-Boas, H.R. Rechenberg, F.J.G. Landgraf (World Scientific, Sao Paulo 1996) pp. 707–716
- 10.50 M. Dahlgren, X.C. Kou, R. Grössinger, J. Wecker: *Proc. 9th Int. Symp. Magn. Anisotropy Coerc.*, ed. by F.P. Missel, V. Villas-Boas, H.R. Rechenberg, F.J.G. Landgraf (World Scientific, Sao Paulo 1996) pp. 307–316
- 10.51 Quantum Design, San Diego 1996
- 10.52 P.J. Flanders: *J. Appl. Phys.* **63**, 3940 (1988)
- 10.53 U. Gradmann, W. Kümmerle, R. Tham: *Appl. Phys.* **10**, 219 (1976)
- 10.54 J.F. Dillon Jr.: In: *Magnetic Properties of Materials*, ed. by J. Smit (McGraw-Hill, New York 1971) p. 149
- 10.55 S.D. Bader, E.R. Moog, P. Grünberg: *J. Magn. Magn. Mater.* **53**, L295 (1986)

Optical Properties

11. Optical Properties

At present, optical measurement methods are the most powerful tools for basic and applied research and inspection of the characteristic properties of a variety of materials, especially following the development of lasers and computers. Optical measurement methods are widely used for optical spectroscopy including linear and nonlinear optics and magneto-optics, conventional and unconventional optical microscopy, fiber optics for passive and active devices, optical recording for CD/DVD and MO disks, and various kinds of optical sensing.

In this chapter, as an introduction to the following sections, the concept and fundamentals of optical spectroscopy are described in Sect. 11.1, including optical measurement tools such as light sources, detectors and spectrometers, and standard optical measurement methods such as reflection, absorption, luminescence, scattering, etc. A short summary of laser instruments is also included. In Sect. 11.2 the microspectroscopic methods that have recently become quite useful for nano-science and nano-technology are described, including single-dot/molecule spectroscopy, near-field optical spectroscopy and cathodoluminescence spectroscopy using scanning electron microscopes. In Sect. 11.3 magneto-optics such as Faraday rotation is introduced and the superlattice of semi-magnetic semiconductors is applied for the imaging measurement of magnetic flux patterns of superconductors as an example of spintronics. Section 11.4 is devoted to fascinating subjects in laser spectroscopy, such as nonlinear spectroscopy, time-resolved spectroscopy and THz spectroscopy. In Sect. 11.5 fiber optics is summarized, including transmission properties, nonlinear optical properties, fiber gratings, photonic crystal fibers, etc. In Sect. 11.6 optical recording technology for high-density storage is described in detail, including the measurement methods for the characteristic properties of phase-change and magneto-optical materials. Finally, in Sect. 11.7 a variety of optical sensing methods are described, including the measurement of distance, displacement, three-

dimensional shape, flow, temperature and, finally, the human body for bioscience and biotechnology.

This chapter begins with a section on basic technology for optical measurements. Sections 11.2–11.4 deal with advanced technology for optical measurements. Finally Sects. 11.5–11.7 discuss practical applications to photonic devices.

11.1 Fundamentals of Optical Spectroscopy	588
11.1.1 Light Source	588
11.1.2 Photosensors	590
11.1.3 Wavelength Selection	592
11.1.4 Reflection and Absorption	594
11.1.5 Luminescence and Lasers	598
11.1.6 Scattering.....	602
11.2 Microspectroscopy	605
11.2.1 Optical Microscopy.....	605
11.2.2 Near-field Optical Microscopy	606
11.2.3 Cathodoluminescence (SEM-CL)	607
11.3 Magneto-optical Measurement	609
11.3.1 Faraday and Kerr Effects	609
11.3.2 Application to Magnetic Flux Imaging	610
11.4 Nonlinear Optics and Ultrashort Pulsed Laser Application	614
11.4.1 Nonlinear Susceptibility	614
11.4.2 Ultrafast Pulsed Laser	618
11.4.3 Time-Resolved Spectroscopy.....	620
11.4.4 Nonlinear Spectroscopy.....	623
11.4.5 Terahertz Time-Domain Spectroscopy	624
11.5 Fiber Optics	626
11.5.1 Fiber Dispersion and Attenuation ...	627
11.5.2 Nonlinear Optical Properties	630
11.5.3 Fiber Bragg Grating	632
11.5.4 Fiber Amplifiers and Lasers.....	635
11.5.5 Miscellaneous Fibers.....	638
11.6 Evaluation Technologies for Optical Disk Memory Materials	641
11.6.1 Evaluation Technologies for Phase-Change Materials.....	641
11.6.2 Evaluation Technologies for MO Materials.....	647

11.7 Optical Sensing.....	649	11.7.4 Flow Measurement.....	652
11.7.1 Distance Measurement.....	649	11.7.5 Temperature Measurement.....	653
11.7.2 Displacement Measurement.....	651	11.7.6 Optical Sensing for the Human Body	655
11.7.3 3-D Shape Measurement.....	651	References	656

11.1 Fundamentals of Optical Spectroscopy

11.1.1 Light Source

There are many light sources for use in scientific and industrial measurements [11.1–4]. This subsection deals with the features of various light sources. For source selection, various characteristics should be considered, such as wavelength range, radiant flux, directionality, stability in time and space, lifetime, area of emission, and temporal behavior. Spectral output, whether it is a continuum, a line, or a continuum-plus-line source, should also be considered. No light source covers all wavelengths simultaneously from the ultraviolet (UV) to infrared (IR) wavelength region. Although a blackbody with extremely high temperature could realize such an ideal light source, the melting point of the materials that form the electrodes must be extremely high,

and it is impossible to construct it. We, therefore, should select an adequate source that covers the required wavelength region from the UV to the IR region. In general, we use a gas discharge lamp for the UV region and a radiation source from a solid for the visible and the IR region. At present, many kinds of light sources covering each wavelength region, as shown in Fig. 11.1, are available. Those can be broadly classified into: 1) thermal radiation sources such as a tungsten filament lamp (W lamp) and an incandescent lamp in the IR region such as a Nernst glower and a glouber, 2) arc lamps such as a high-pressure xenon arc lamp (Xe lamp), a high- or low-pressure mercury lamp, a hydrogen and a deuterium-hydrogen arc lamp (D₂ lamp) based on electrical discharge in gas, 3) a light-emitting diode (LED) or a laser diode (LD) basing on emission from

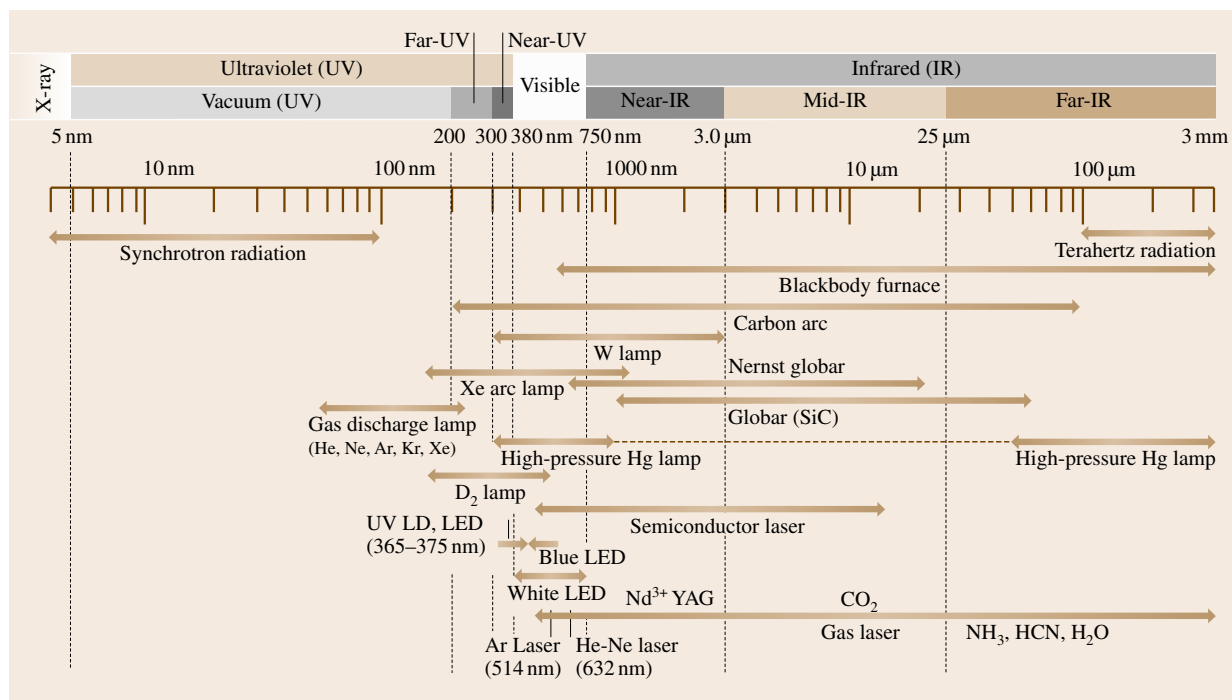


Fig. 11.1 Wavelength regions of various light sources

the pn junction of a semiconductor, and 4) narrow-line sources using an atomic or molecular transition lines such as a hollow cathode discharge tube and an electrodeless discharge lamp, including many kinds of lasers. Recently, synchrotron radiation and terahertz emission in the far-UV and submillimeter wavelength regions, respectively, have become available, mainly for research purposes.

Among those light sources, one of the most stable, well-known, and intensively characterized in the visible and the near-IR region is the W lamp (or tungsten-filament white bulb). Although the spectral emissivity of tungsten is about 0.5 in the visible region and about 0.25 in the near-IR region, its spectral distribution of emission agrees relatively well with that of Planck's blackbody radiation. The W lamp can be used in an arbitrary color temperature up to 3100 K. However, more than 90% of the total emission energy is distributed in the IR wavelength region and less than 1% in the UV region below 400 nm. Therefore, it cannot be used in the UV region. The UV region, however, is especially important in the field of spectrochemical analysis. To cover the lower energy in the UV region, the D₂ lamp is used in combination with the W lamp, although the D₂ lamp has some problems in terms of emission stability and ease of operation.

For the tungsten white bulb, a vacuum bulb is used for color temperatures up to 2400 K. A gas bulb sealed in nitrogen, argon, or krypton gas at around 1 atm is used for color temperatures between 2000 and 2900 K. For color temperatures around 3100 K, a tungsten-halogen bulb is used. In order to prevent deposition of tungsten atoms onto the inner surface of the bulb, the pressure of argon or krypton gas is maintained at several atmospheres and the bulb is made mechanically rigid by using quartz. Furthermore, by mixing a small amount of halogen molecules such as I₂, Br₂, or Cl₂ into the gas, the decrease in transmittance due to the deposition of tungsten atoms on the inner surface of the bulb is effectively prevented. This process is known as a halogen cycle. To make the process effective, the bulb temperature must be kept relatively high. The lifetime of the lamp is extended by about two times compared to a lamp that does not benefit from this process.

One of the most significant developments in light sources during the last 15 years is blue or UV LEDs. Blue and UV LDs have even appeared. The blue LED is used mainly for traffic signals and the blue and UV LD as recording or read-out light sources for circular discs and digital videodiscs. However, they also have great potential as light sources for scientific measurement. At

present, UV LEDs and UV LDs with an emission wavelength around 365–375 nm are commercially available. Such LEDs and LDs are based on emission from gallium nitride (GaN) materials. GaN is a direct-transition-type semiconductor and has an energy gap of about 3.44 eV at room temperature, which corresponds to the UV emission wavelength. By adding indium (In) and aluminum (Al) to the GaN, one can obtain blue emission. When using gallium phosphorus (GaP) instead of GaN materials, and when adding In and Al, one can obtain green emission. When adding only In, one can obtain red emission. Another light source to be noted is the white LED, which has been commercialized rapidly as a back-illumination light source for liquid crystal displays. The white LED consists of a blue or UV LED and fluorescent materials deposited onto the LED in the same package. The blue or UV LED is used as an excitation light source for the fluorescent materials, which may be yttrium aluminum garnet (YAG) materials or some kinds of rare-earth compounds. The excitation light and fluorescence together make the white light. A high-power white LED exceeding 5 W has been developed. Figure 11.2 shows typical emission spectra of such LEDs and that of the UV LD.

For scientific measurements or for spectrochemical analyses, a pulsed light source in the UV wavelength region is important, for example, for distance measurements, fluorescence lifetime measurements, and so on. For such requirements, a picosecond light pulsar with a pulse duration around 60 ps, a wavelength of 370 nm, and a repetition frequency of 100 MHz has appeared on the market. However, in general, such a laser has a problem in wavelength selection and cost. To solve such problems, a technique to drive the Xe lamp in

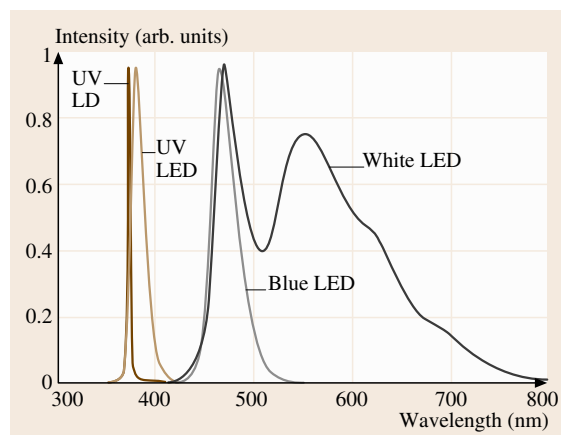


Fig. 11.2 Emission spectra of a blue, UV, and white LED, and that of a UV LD

a nanosecond pulsed mode has been developed [11.5–7]. A technique to modulate the Xe lamp sinusoidally has also been developed so that it can be used in combination with a lock-in light-detection scheme. The UV or the blue LED also can be driven with a large current pulse, resulting in a pulse duration less than 1.5 ns [11.8–10].

11.1.2 Photosensors

This subsection deals with sensing features of various photosensors [11.1–4]. The photosensor is the terminology used for a photodetector when used for a sensing purpose. Photodetectors can be broadly classified into quantum-effect (QE) detectors (or photon detector) and thermal detectors. The QE detector can be subdivided into an external and an internal type, as shown in Table 11.1. Furthermore, the internal type is subdivided into a photoconductive (PC) detector, a photovoltaic (PV) detector, and a photoelectromagnetic (PEM) detector. Figure 11.3 shows the spectral response of each photodetector.

The operating principle of the external QE detector is based on the photoelectron emissive effect of a metal. Representative detectors are a phototube (PT) and a photomultiplier tube (PMT). A variety of photosensitive cathodes, having different spectral responses, are available from the UV to the near-IR wavelength region. A photocathode whose principal component is gallium arsenic (GaAs) gives high quantum efficiency and has sensitivity at longer wavelengths exceeding 1 μm . The

PT consists of two electrodes sealed in a vacuum tube: a photocathode and an anode. The PT had been used for light sensing at relatively high powers. At present, it is mainly used for measuring ultra-short light pulses by taking advantage of its simple structure. Such a special PT is known as a biplaner type. The PMT consists of the photocathode, the anode, and 6–12 stages of dynodes aligned between the two electrodes. The role of each dynode is to emit a larger number of secondary electrons than are incident on it. The total amplification factor is typically 10^6 , depending on the number of dynodes and the applied voltage. Because of its stability, wide dynamic range, and large specific detectivity D^* , the PMT is widely used for precise light detection. The PMT can be considered as a constant-current source with high impedance. Therefore, the intensity of the output signal is mainly determined by a value of the load resistor. The response time is determined by a time constant calculated from the load resistor and an output capacitance. By cooling the photocathode and adopting a photon counting technique, shot-noise-limited weak-light measurement is possible. Recently, a small type of a metal-packaged PMT has become available [11.11]. By taking advantage of its shorter electron-transit time and smaller time spread of secondary electrons, a new gating technique with a resolution time of less than 0.3 ns has been proposed [11.12].

The operating principle of the PC detector is based on the photoconductive effect of a semiconductor. The electric conductivity of materials, especially semi-

Table 11.1 Classification of photosensors

Type	D^* ($\text{cm Hz}^{1/2} \text{W}^{-1}$)	Spectral range (nm)	Linear range (decades)	Rise time (ns)
External quantum-effect detector (photon detector)				
Phototube (PT)	$10^8 - 10^{10}$	200–1000	4.5–5.5	0.3–10
Photomultiplier tube (PMT)	$10^{12} - 10^{18}$	200–1000	5.0–6.0	0.3–15
Internal quantum-effect detector				
Photoconductive detector (PC) (PbS, InSb, Ge)	$10^9 - 10^{12}$	750–6000	5.0–6.0	$50 - 10^6$
Photovoltaic detector (PV) (Si photodiode)	$10^8 - 10^{12}$	400–5000	3.0–4.0	$10^3 - 10^6$
Photoelectromagnetic detector (PEM) (InSb)				
	D^* ($\text{cm Hz}^{1/2} \text{W}^{-1}$)	Spectral range (μm)	Linear range (W)	Time constant (ms)
Thermal detector				
Thermocouple	$10^8 - 10^9$	0.8–40	$10^{-10} - 10^{-8}$	10–30
Thermistor (Bolometer)	$10^8 - 10^9$	0.8–40	$10^{-6} - 10^{-1}$	10–30
Pneumatic detector (Golay cell)	$10^8 - 10^9$	$0.8 - 10^3$	$10^{-6} - 10^{-1}$	2–50
Pyroelectric detector TGS, PZT	$10^7 - 10^8$	$0.3 - 10^3$	$10^{-6} - 10^{-1}$	5–1000

conductors, varies depending on the intensity of the incident light. For **UV** and visible wavelength regions, intrinsic semiconductors are used. For the **IR** region, impurity semiconductors are used. The upper limit on wavelength sensitivity for intrinsic semiconductors is determined by the band gap energy (E_g) and that for impurity semiconductors by the ionized potential of the impurities. Generally, CdS ($E_g = 2.4$ eV) and CdSe are ($E_g = 1.8$ eV) used in the **UV** and the visible region. For the **IR** region, PbS, PbSe, PbTe, and $Hg_{1-x}Cd_xTe$ are used, where a cooling procedure is often required to suppress noise.

The operating principle of the **PV** detector is based on the photovoltaic effect. When a light flux whose energy is larger than the energy gap of the pn junction of a semiconductor is incident, a photoinduced voltage proportional to the incident light intensity is generated. Silicon detectors are popular and can be used from the visible to the near-**IR** region. The dynamic range for the incident intensity is more than 10^5 . To achieve sensitivity in the **UV** region, detectors with a processed surface or made from GaAsP have been devised; commercially these are known as blue cells. Compared to **PC** detectors, the **PV** detector gives a faster response time. Another advantage is that it requires no power supply. The **PV** detector has two operation modes: the photovoltaic mode and photoconductive mode (or photodiode mode). In the photovoltaic mode, the detector is used with zero bias voltage and the detector is considered as a constant-voltage source with low internal resistance. In the photoconductive mode, the detector is used with a reverse

bias voltage and can be considered as a constant-current source with high impedance. The photoconductive mode gives a wide dynamic range and a fast response. When one needs a high-speed subnanosecond response, use of a pin photodiode or an avalanche photodiode (**APD**) should be considered [11.13, 14].

The **PEM** detector utilizes contributions of an electron-hole pair to the photovoltage. The electron-hole pair is generated on the surface of an intrinsic semiconductor such as InSb. By applying the external magnetic field to the semiconductor during a diffusion process, the pair is divided in opposition directions, each contributing to the voltage. This type of detector is, however, not commonly used now.

In a thermal detector, optical power absorbed on the surface of the detector is converted to thermal energy and a temperature detector measures the resulting change of temperature. A variety of techniques have been developed to attain high-speed response and high sensitivity, which is a tradeoff. Although, in principle, an ideal thermal detector does not have a wavelength-dependent sensitivity, one cannot realize such an ideal detector. Typical thermal detectors are thermocouples, thermopiles, pneumatic detectors, Golay cells, pyroelectric detectors etc.

A multichannel (**MD**) detector has been developed that integrates many internal **QE** detectors onto a silicon substrate. Electric charges produced by the incident light, usually in the **UV** and visible range, are

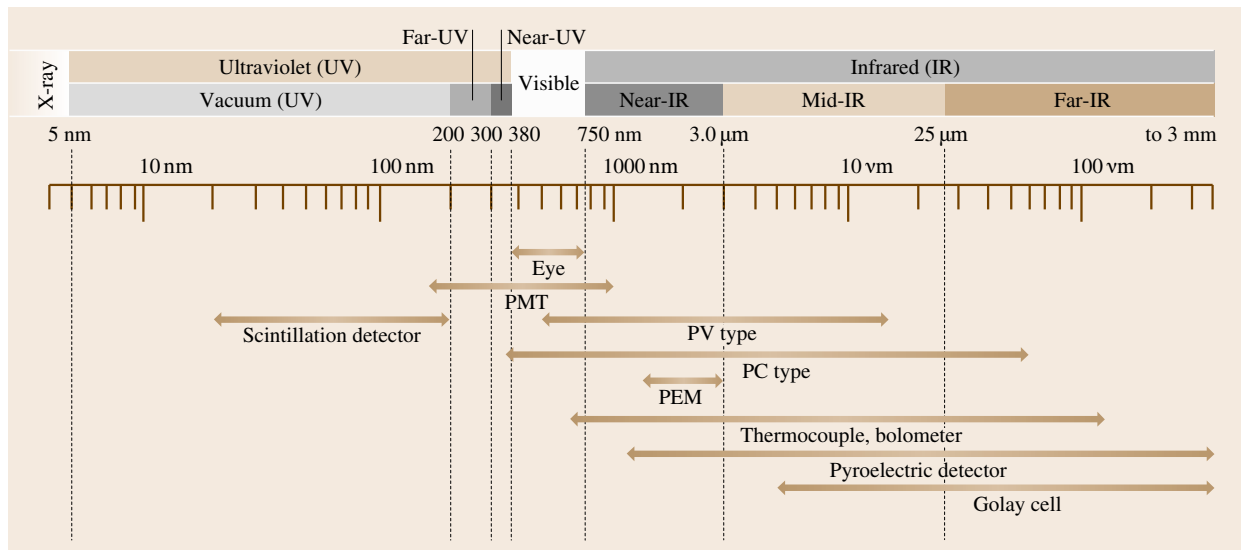


Fig. 11.3 Applicable wavelength regions of various photodetectors

accumulated on individual detectors. A metal–oxide–semiconductor-type (MOS) detector employs electric switches to read out the electric charge. A charge-coupled device (CCD) has a larger integration density than the MOS type because of the simplicity of the process of charge accumulation and transfer. The sensitivity is 10^7 – 10^8 photons/cm² and the dynamic range is 10^3 – 10^4 . Recently, infrared image sensors using HgCdTe have appeared in the market. This MD can be used not only as a spectral photosensor but also as a position sensor.

To select the optical detector, the fundamental issues to be considered are: 1) spectral response, 2) sensitivity, 3) detection limit, and 4) time response. Concerning the spectral response, spectral matching with the light source should be considered. The spectral distribution of the background light also should be taken into account. The sensitivity of the detector is defined by the ratio of the intensity of the output signal to that of the incident light. Generally, overall (or all-spectral) sensitivity is employed. To determine the sensitivity, a standard light source whose spectral distribution is known is used as the incident light: a tungsten lamp of 2856 K for the UV and the visible region and a pseudo-blackbody furnace of 500 K for the IR region. The detection limit is usually represented by the noise-equivalent power (NEP) or

the specific detectivity D^* , where $\text{NEP} = PV_n/V_s$ and $D^* = \sqrt{A\Delta f}/\text{NEP}$, where P is the radiation flux, V_s is the output signal, V_n is the root mean squared value of output noise, A is area of the detector, and Δf is the noise-equivalent frequency bandwidth. The time response is represented by a step response or a steady-state frequency response. The step response is represented by a rise time or a fall time, which are used especially for detectors with a nonlinear response. For high-speed detectors, the time constant is important; this is calculated by the internal resistance of the detector and the parallel output capacitance. Impedance matching with the following electronics is also important.

11.1.3 Wavelength Selection

In a practical measurement, it is often necessary to select a suitable wavelength from the light source. This section deals with some wavelength-selection techniques [11.1–4]. In order to select the monochromatic or quasi-monochromatic light, we usually use a dispersion element, such as an optical filter, a prism, and a diffraction grating. Generally, the diffraction grating is installed in a monochromator (MON). To gather all spectral information simultaneously, one uses a polychromator (POL) in combination with a multichannel detector

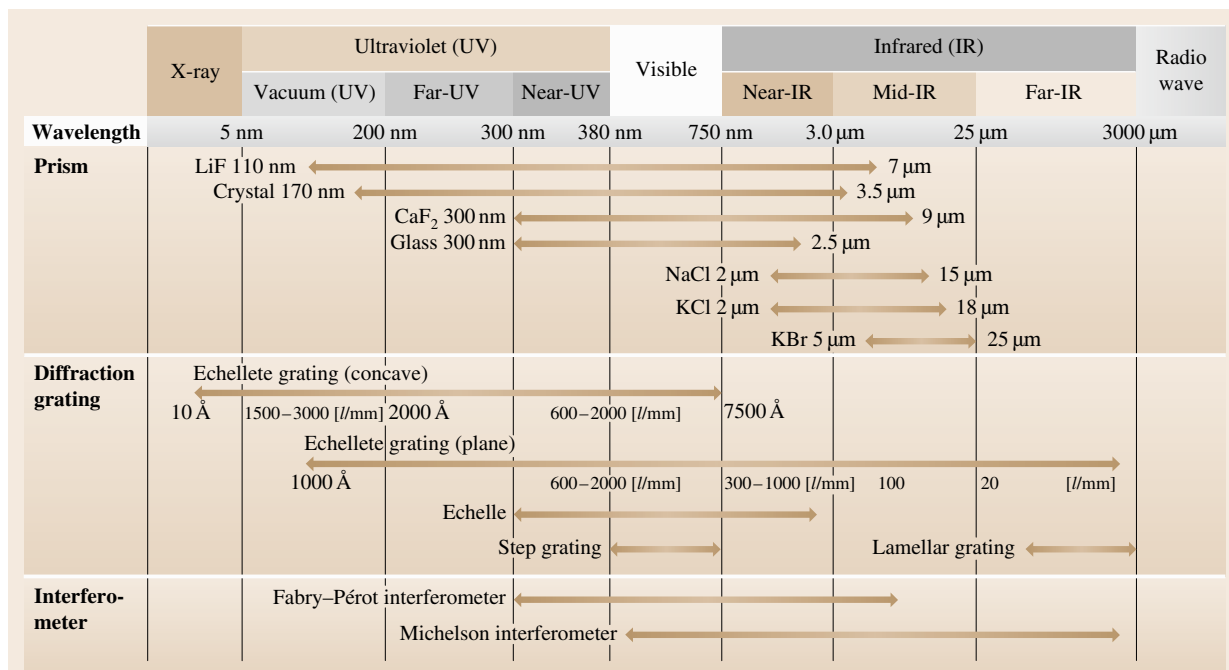


Fig. 11.4 Wavelength regions of various wavelength-selection elements and devices

(MD). In the IR region, a Michelson-type interferometer is sometimes used for a Fourier-transform spectrometer (FTS) [11.15]. For extremely high spectral-resolution measurements, a Fabry–Pérot interferometer should be considered. [11.16] Figure 11.4 shows various elements, devices, systems applicable in each wavelength region.

The prism has been used as the main dispersion element. Dispersion occurs in the prism primarily because of the wavelength dependence of the refractive index of the prism material. Many materials for the prism have been used, for example, glass (350 nm–1 μ m), quartz (185 nm–2.7 μ m), CaF (125 nm–9 μ m), NaCl (200 nm–17 μ m), KCl (380 nm–21 μ m). When the wavelength is λ (or $\lambda + \Delta\lambda$) and the angle between the incident beam and the deviated monochromatic ray is θ (or $\theta + \Delta\theta$), the angular dispersion, $\Delta\theta/\Delta\lambda$, is given by $\Delta\theta/\Delta\lambda = \Delta\theta/\Delta n \cdot \Delta n/\Delta\lambda = 2 \sin(\alpha/2) / \sqrt{1 - n^2 \sin^2(\alpha/2)} \Delta n/\Delta\lambda$, where n and α are the refractive index and the apex angle of the prism, respectively. In order to increase the spectral resolution, $\lambda/\Delta\lambda$, we should use a prism with a long base L because $\lambda/\Delta\lambda = L \cdot (\Delta n/\Delta\lambda)$.

A plane diffraction grating is made by ruling parallel closely spaced grooves on a thin metal layer deposited on glass. When collimated light flux strikes the grating in a plane perpendicular to the direction of the grooves, different wavelengths are diffracted and constructively interfere at different angles. Although there are two types of gratings, transmission and reflection, the reflection type is invariably used for wavelength selection. If the incident angle is α and the diffraction angle is β , measured from the normal to the grating plane, and the groove interval is d , the following grating formula holds, $d(\sin \alpha + \sin \beta) = m\lambda$, where m is the order of diffraction. In the formula, the order m as well as the diffraction angle β is taken as positive for diffraction on the same side of the grating normal as the incident ray and negative on the opposite side. Then, the angular dispersion is given by $\Delta\beta/\Delta\lambda = m/(d \cos \beta)$ and the resolution power is given by $\lambda/\Delta\lambda = mN$, where N is the total number of grooves. From the formula, we can understand that many wavelengths are observed for a specified diffraction angle β for a given α and d . This phenomenon is known as overlapping orders. From the following two equations, $d(\sin \alpha + \sin \beta) = m\lambda = (m+1)(\lambda - \Delta\lambda)$, we can obtain $\Delta\lambda = \lambda/(m+1)$; the value $\Delta\lambda$ is called the free spectral range. The overlapping orders are usually separated by limiting the source bandwidth with a broadband filter, called the order sorter, or with a predisperser.

Figure 11.5 shows a typical shape of the cross section of the groove. When the angle between the grating plane and the long side of the groove is γ so that $\gamma - \alpha = \beta - \gamma$, the incident and the diffracted light satisfy the relation for specular reflection on the long side of the triangle. Then, we obtain the relation $2d \sin \gamma \cos(\alpha - \gamma) = m\lambda$. When, we put $\alpha = \beta = \gamma$ and $m = 1$, then $2d \sin \gamma = \lambda$. Such a wavelength λ and angle γ are called the blaze wavelength and angle, respectively. The blazed grating is often called an echelle. In this situation, the maximum diffraction efficiency is obtained. For high-resolution spectral measurements, an echelle grating is used, which is a relatively coarse grating with large blaze angles. The steep side of the groove is employed at very high orders.

A concave grating is the same as a plane grating but the grooves are ruled on a concave mirror so that the grooves become a series of equally spaced straight lines when projected onto a plane perpendicular to the straight line connecting the center of the concave shape and a center of its curvature. A circle, whose diameter is equal to the radius of the curvature and which is on a plane perpendicular to the grooves, is called the Rowland circle. Rays starting from a point on the Rowland circle and diffracted by the grating are focused onto a point on the same circle. The two points form an optical conjugate pair with respect to each other. Usually, an entrance and an exit slit are placed on the two points. A problem concerning the concave grating is the presence of relatively large astigmatism. It is, however, used for the UV region because no additional reflection optical element that introduces reflection energy loss is necessary. Recently, various kinds of holographic gratings have been developed to solve the problem of aberration, including astigmatism.

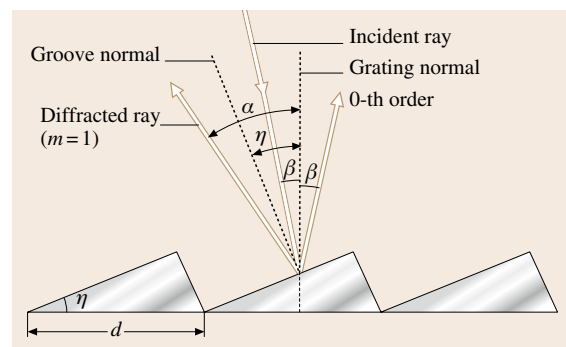


Fig. 11.5 Cross section of a blazed grating. By tilting the groove facet by an angle γ , the zeroth-order ray does not correspond to the specularly reflected ray from the groove surface

When choosing a wavelength-selection method, significant parameters to be considered are the dispersion characteristics, resolution power, solid angle and F -number (or optical throughput factors), degree of stray light, and optical aberration. One of the most convenient and simplest ways is to use a spectroscopic filter such as a color glass filter or an interference filter. However, those lack versatility. The **MON** is a multipurpose apparatus, which has a grating, an entrance, an exit slit, additional optics, and a wavelength-selection mechanism in one box, by which monochromatic light can be extracted. Many types of mounting and optical arrangement of the optics including the grating, have been proposed.

Although the dispersion-type **MON** is widely used for the purpose of wavelength selection, it has some drawbacks. In principle, its optical throughput is not large because of the presence of the entrance slit. Furthermore, because of the requirement of the wavelength-scanning mechanism for measuring a continuum spectrum, the total number of wavelength elements limits the signal-gathering time allocatable to a unit wavelength element, resulting in lowering signal-to-noise (**SNR**) ratio. On the contrary, the **FTS** has optical throughput and multiplex advantages over the dispersion-type **MON**. This is because the **FTS** requires no entrance slit and the entire spectrum is measured simultaneously in the form of an interferogram. However, the multiplex advantage is given only when the detector noise is dominant, such as for an **IR** detector. Nevertheless, it is sometimes used in the visible region. This is because of the presence of the optical throughput advantage, high precision in wavenumber, and the possibility of realizing extremely high spectral resolution. However, even for the dispersion-type **MON**, when used in a form of a **POL** together with the **MD**, the multichannel advantage is generated. Table 11.2 summarizes the **SNR** of the **FTS**, $(\text{SNR})_{\text{FTS}}$, and that of the **POL** with an **MD**, $(\text{SNR})_{\text{POL}}$, over that of the dispersion **MON** with a single detector, $(\text{SNR})_{\text{MON}}$, for cases of when the detector noise, the shot

noise, and the scintillation noise is dominant. In the table, n is the total number of spectral elements.

11.1.4 Reflection and Absorption

Reflection or absorption spectra provide rich information on the energy levels of the material, such as inner or valence electrons, vibrations or rotations of molecules or defects in condensed matters, a variety of energy gaps and elementary excitations, e.g. phonons and excitons.

Reflection and Transmission

When a light beam incident on a material surface passes through the material, some of the light is reflected at the surface, while the rest propagates through the material. During the propagation the light is attenuated due to absorption or scattering. The coefficients of *reflectivity* R and *transmittance* T are defined as the ratio of the reflected to the incident power and the transmitted to the incident power, respectively. If there is no absorption or scattering, $R + T = 1$. A schematic diagram for measuring R or T is shown in Fig. 11.6. A tunable light source, a combination of a white light (Sect. 11.1.1) and a monochromator (Sect. 11.1.3) or a tunable laser (Sect. 11.1.5), is used here. Details of detectors are reviewed in Sect. 11.1.2. Changing the wavelength λ of the tunable light source, one can obtain a reflectivity spectrum $R(\lambda)$ or a transmittance spectrum $T(\lambda)$. For convenience the white light directly irradiates the sample and the reflected or transmitted light is detected with a combination of a spectrometer and an array detector, e.g. **CCD**, if the luminescence from the sample caused by the white light is negligible.

If the beam propagates in the x direction, the intensity $I(x)$ at position x satisfies the following relation

$$\begin{aligned} \Delta I(x) &= I(x + dx) - I(x) = -\alpha I(x) dx, \\ \therefore \frac{dI(x)}{dx} &= -\alpha I. \end{aligned}$$

Table 11.2 Comparisons of the **SNR** of the **FTS**, $(\text{SNR})_{\text{FTS}}$, and that of the **POL** with a **MD**, $(\text{SNR})_{\text{POL}}$, over that of the **MON** with a **SD**, $(\text{SNR})_{\text{MON}}$, for cases when the detector noise, the shot noise, and the scintillation noise are dominant, where n is the total number of spectral elements

Noise	Detector noise	Shot noise	Scintillation noise
SNR			
$\frac{(\text{SNR})_{\text{FTS}}}{(\text{SNR})_{\text{MON}}}$	$\frac{\sqrt{n}}{2}$	$\frac{1}{\sqrt{2}}$	$\frac{1}{n}$
$\frac{(\text{SNR})_{\text{POL}}}{(\text{SNR})_{\text{MON}}}$	\sqrt{n}	\sqrt{n}	1

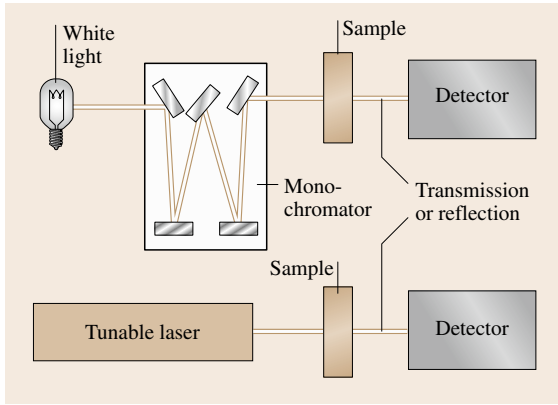


Fig. 11.6 Schematic diagram of reflection or transmission measurement

Here α is called the *absorption coefficient*. The integrated form is

$$I(x) = I_0 \exp(-\alpha x), \quad (11.1)$$

where I_0 is the intensity of the incident light. The position at $x = 0$ corresponds to the surface of the material. This relation is called *Beer's law*. If the scattering is negligible, the transmittance T is described by

$$T = (1 - R_1) \exp(-\alpha l)(1 - R_2), \quad (11.2)$$

where R_1 and R_2 are the reflectivities of the front and back surfaces, respectively, and l is the sample thickness.

Optical Constants

If the light propagates in the x direction, the electric field is described by

$$E(x, t) = E_0 \exp[i(kx - \omega t)], \quad (11.3)$$

where k is the wavevector of the light and ω is an angular frequency. In a transparent material with refractive index n , k and the wavelength in vacuo λ are related each other through

$$k = \frac{2\pi}{\lambda/n} = \frac{n\omega}{c}. \quad (11.4)$$

This formula can be generalized to the case of an absorbing material by introducing the *complex refractive index* [11.17]

$$\tilde{n} = n + i\kappa, \quad (11.5)$$

$$k = \frac{\tilde{n}\omega}{c}, \quad (11.6)$$

where κ is called the *extinction coefficient*. The imaginary part of \tilde{n} leads to an exponential decay of the electric field; the absorption coefficient can be described by

$$\alpha = \frac{2\kappa\omega}{c} = \frac{4\pi\kappa}{\lambda}. \quad (11.7)$$

The *amplitude reflectivity* r , the ratio of the electric field of the incident light to that of the reflected light, in the case of normal incidence is described by [11.18]

$$r = \frac{\tilde{n} - 1}{\tilde{n} + 1}. \quad (11.8)$$

If we define the real and imaginary part of r by

$$r \equiv R \exp(i\theta), \quad (11.9)$$

then the (intensity) reflectivity can be described by

$$R = \left| \frac{\tilde{n} - 1}{\tilde{n} + 1} \right|^2 = \frac{(n - 1)^2 + \kappa^2}{(n + 1)^2 + \kappa^2}, \quad (11.10)$$

and conversely, n and k are written as

$$n = \frac{1 - R}{1 + R - 2\sqrt{R} \cos \theta}, \quad (11.11)$$

$$\kappa = \frac{2\sqrt{R} \sin \theta}{1 + R - 2\sqrt{R} \cos \theta}. \quad (11.12)$$

Ellipsometry enables us to obtain the amplitude reflectivity [11.19]. Thus one can obtain the complex refractive index by measuring the reflectivity.

The optical response of the material, e.g. light propagation described in the complex refractive index, originates from the polarization induced by the incident light. If the electric field E of the light is weak and within linear regime (cf. Sect. 11.4), the polarization P is given by

$$P = \varepsilon_0 \chi E, \quad (11.13)$$

where ε_0 and χ are the vacuum dielectric constant and the *electric susceptibility*, respectively. The electric displacement is

$$\begin{aligned} D &= \varepsilon_0 E + P, \\ &\equiv \varepsilon_0 \varepsilon E. \end{aligned} \quad (11.14)$$

where ε is the *complex dielectric constant*;

$$\varepsilon = \varepsilon_0(1 + \chi), \quad (11.15)$$

$$= \varepsilon_1 + i\varepsilon_2, \quad (11.16)$$

where ε_1 and ε_2 are the real and imaginary parts of ε . From the Maxwell equation [11.1],

$$\begin{aligned} \frac{\varepsilon}{\varepsilon_0} &= \tilde{n}^2, \\ \frac{\varepsilon_1}{\varepsilon_0} &= n^2 - \kappa^2, \end{aligned} \quad (11.17)$$

$$\frac{\varepsilon_2}{\varepsilon_0} = 2n\kappa, \quad (11.18)$$

and conversely,

$$n = \sqrt{\frac{\varepsilon_1 + \sqrt{\varepsilon_1^2 + \varepsilon_2^2}}{2}}, \quad (11.19)$$

$$\kappa = \sqrt{\frac{-\varepsilon_1 + \sqrt{\varepsilon_1^2 + \varepsilon_2^2}}{2}}. \quad (11.20)$$

Kramers–Kronig Relations

The Kramers–Kronig relations allow us to find the real (imaginary) part of the response function of a linear passive system, if one knows the imaginary (real) part at all frequencies. The relations are derived from the principle of causality [11.17]. In the case of the complex refractive index, the relations are written as

$$n(\omega) = 1 + \frac{2}{\pi} \text{P} \int_0^{\infty} \frac{\omega' \kappa(\omega')}{\omega'^2 - \omega^2} d\omega', \quad (11.21)$$

$$\kappa(\omega) = -\frac{2}{\pi\omega} \text{P} \int_0^{\infty} \frac{\omega'^2 [n(\omega') - 1]}{\omega'^2 - \omega^2} d\omega', \quad (11.22)$$

where P indicates the Cauchy principal value of the integral. Using these relations one can calculate n from κ , and vice versa. The θ in (11.9) is calculated from the reflectivity R using the following formula

$$\theta(\omega) = -\frac{\omega}{\pi} \text{P} \int_0^{\infty} \frac{\ln \left[\frac{R(\omega')}{R(\omega)} \right]}{\omega'^2 - \omega^2} d\omega', \quad (11.23)$$

thus n and κ are determined using (11.11, 11.12) from the reflectivity spectrum. This analysis is very useful for materials with strong absorption in which only the reflectivity is measurable. The Kramers–Kronig analysis of reflection spectra with synchrotron radiation, which covers extremely wide wavelength regions from the far-IR to x-rays, reveals the electronic structures of a huge number of materials [11.20].

The Lorentz Oscillator Model (Optical Response of Insulators)

The responses of bound (valence) electrons in insulators can be written by the equation of motion of a damped harmonic oscillator

$$m \frac{d^2 x}{dt^2} = -m\gamma \frac{dx}{dt} - m\omega_0^2 x - eE_0 \exp(-i\omega t), \quad (11.24)$$

where m and e are the mass and charge of the electron, γ is the damping constant, ω_0 is the resonant frequency,

E_0 is the amplitude of the electric field of the light. If we assume $x(t) = x_0 \exp(-i\omega t)$,

$$x_0 = \frac{-eE_0}{m(\omega_0^2 - \omega^2 - i\gamma\omega)}. \quad (11.25)$$

Thus the *polarization* is given by

$$P_{\text{resonant}} = \frac{ne^2}{m(\omega_0^2 - \omega^2 - i\gamma\omega)}, \quad (11.26)$$

where n is the number of electrons per unit volume. Now we can write the electric displacement

$$\begin{aligned} D &= \varepsilon_0 E + P_{\text{background}} + P_{\text{resonant}}, \\ &= \varepsilon_0 E + \varepsilon_0 \chi_{\text{background}} E + P_{\text{resonant}}, \end{aligned}$$

where the electric susceptibility $\chi_{\text{background}}$ accounts for all other contributions to the polarization. Using (11.15, 16), we obtain the following equations

$$\varepsilon(\omega) = 1 + \chi + \frac{ne^2}{\varepsilon_0 m(\omega_0^2 - \omega^2 - i\gamma\omega)}, \quad (11.27)$$

$$\varepsilon_1(\omega) = 1 + \chi + \frac{ne^2(\omega_0^2 - \omega^2)}{\varepsilon_0 m[(\omega_0^2 - \omega^2)^2 + (\gamma\omega)^2]}, \quad (11.28)$$

$$\varepsilon_2(\omega) = n \frac{e^2 \gamma \omega}{\varepsilon_0 m[(\omega_0^2 - \omega^2)^2 + (\gamma\omega)^2]}. \quad (11.29)$$

The dielectric constants in the low and high frequency limit are defined as

$$\varepsilon(0) \equiv \varepsilon_{\text{ST}}, \quad \varepsilon(\infty) \equiv \varepsilon_{\infty}.$$

Figure 11.7 shows the frequency dependence of the optical constants introduced in this section.

Typical Absorption Spectrum of Insulators

A schematic plot of a typical absorption spectrum of insulators is shown in Fig. 11.8. There are sharp absorption lines due to *phonons* in the far-infrared region and due to *excitons* in the visible or ultraviolet region; a phonon is a quantized lattice vibration and an exciton is a bound state of an electron and hole like a hydrogen atom. The shape of the absorption or reflection spectra of phonons or excitons can be analyzed by using the Lorentz oscillator model. If the coupling between the photon and the phonon (exciton) is strong, we have to introduce a coupled mode of a photon and a phonon (exciton), *phonon–polariton* (*exciton–polariton*) [11.21]. Phonon sidebands usually accompany the exciton absorption lines and provide information on the phonons and excitons [11.22].

Above the exciton lines, strong interband absorption is observed. The absorption edge is caused by the onset of the interband transition, in which free electrons and free holes are created simultaneously across the band gap of the insulator. We can obtain a variety of information on the band structure of the material from the interband absorption spectra. Between the phonon and exciton lines there are two weak bands: the multiphonon absorption band due to the combination of several phonons lies around the mid-infrared region and the Urbach tail appears as the onset of optical absorption in the near-infrared or visible region at finite temperature. The shape of the Urbach tail is expressed as [11.21]

$$\alpha(\omega) \propto \exp \left[-\sigma \frac{\hbar(\omega_0 - \omega)}{k_B T} \right], \quad (\omega < \omega_0), \quad (11.30)$$

where σ is an empirical steepness parameter. The σ indicates the strength of the exciton–phonon coupling, because the Urbach tail is caused by phonon-assisted processes. Generally, there is a minimum in the absorption coefficient between the multiphonon region and the Urbach tail. In the case of SiO₂ glasses this minimum lies in the near-infrared region around 1 eV. Thus optical fibers operate between 1.2–1.6 μm (Sect. 11.1.5).

Drude Model (Optical Response in Metals)

The responses of free electrons in metals can be written by the equation of motion (11.24) without a restoring force

$$m \frac{d^2 x}{dt^2} = -m\gamma \frac{dx}{dt} - eE_0 \exp(-i\omega t). \quad (11.31)$$

If we assume $x(t) = x_0 \exp(i\omega t)$,

$$x_0 = \frac{eE_0}{m(\omega^2 + i\gamma\omega)}. \quad (11.32)$$

Thus the polarization is given by

$$\begin{aligned} P &= -nex, \\ &= \frac{-ne^2 E}{m(\omega^2 + i\gamma\omega)}. \end{aligned} \quad (11.33)$$

$$\begin{aligned} D &= \epsilon_0 E + P \\ &\equiv \epsilon_0 \epsilon E, \\ \therefore \epsilon &= 1 - \frac{ne^2}{\epsilon_0 m (\omega^2 + i\omega/\tau)} \\ &= 1 - \frac{\omega_p^2}{\epsilon_0 m (\omega^2 + i\omega/\tau)}. \end{aligned} \quad (11.34)$$

$$\begin{aligned} \tau &\equiv \frac{1}{\gamma}, \\ \omega_p &= \left(\frac{ne^2}{\epsilon_0 m} \right)^{1/2}, \end{aligned} \quad (11.35)$$

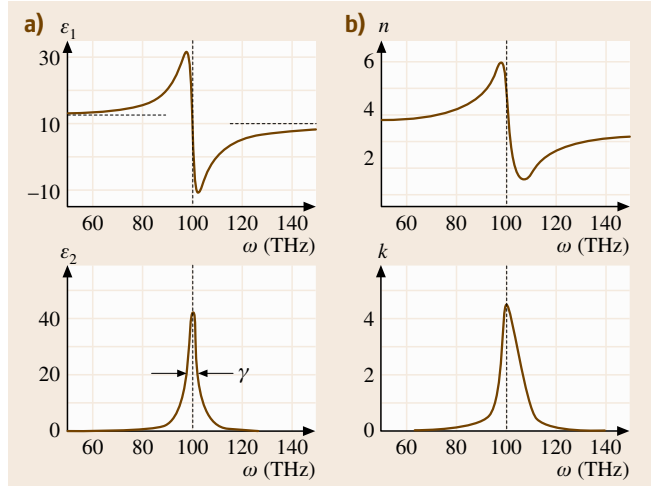


Fig. 11.7 (a) Frequency dependence of the real and imaginary parts of the dielectric constant, and (b) frequency dependence of the complex refractive index, calculated in the case of $\omega_0 = 100$ THz, $\gamma = 5$ THz, $\epsilon_{ST} = 12$ and $\epsilon_\infty = 10$ using (11.28, 29)

where τ is the relaxation time and ω_p is called the *plasma frequency*. Figure 11.9 shows the reflectivity R in the case of $\gamma = 0$ using (11.10). Perfect reflection occurs for $\omega \leq \omega_p$, and then R decreases for $\omega > \omega_p$, approaching zero.

Electric conductivity can be generalized to the optical frequency region. The current density \mathbf{j} is related to the velocity of free electrons and the electric field through

$$\mathbf{j} \equiv -Ne \frac{dx}{dt} = \sigma \mathbf{E}, \quad (11.36)$$

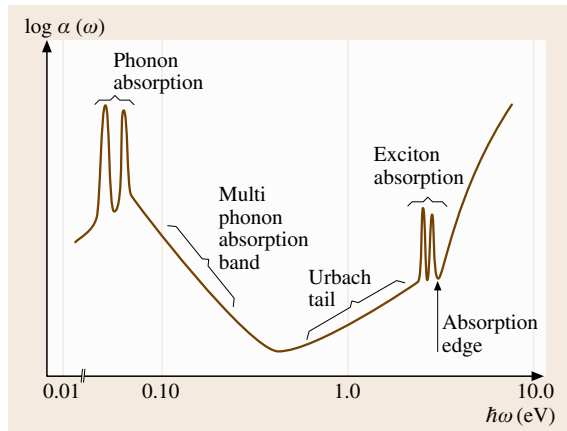


Fig. 11.8 Schematic illustration of the absorption spectrum of insulators

where σ is called the *optical conductivity*. From (11.23) and (11.27),

$$\sigma(\omega) = \frac{\sigma_0}{1 - i\omega\tau}, \quad (11.37)$$

where

$$\sigma_0 \equiv \frac{ne^2\tau}{m}. \quad (11.38)$$

σ_0 corresponds to the DC conductivity. Thus the DC conductivity can be estimated by purely optical measurements without electrical contacts. Optical conductivity is written in terms of the dielectric function as follows

$$\sigma(\omega) = -i\varepsilon_0\omega[\varepsilon(\omega) - 1]. \quad (11.39)$$

The Kramers–Kronig relations of the optical conductivity are as follows

$$\sigma_1(\omega) = \frac{2}{\pi} P \int_0^\infty \frac{\omega' \sigma_2(\omega')}{\omega'^2 - \omega^2} d\omega', \quad (11.40)$$

$$\sigma_2(\omega) = \frac{-2\omega}{\pi} P \int_0^\infty \frac{\sigma_1(\omega')}{\omega'^2 - \omega^2} d\omega', \quad (11.41)$$

where $\sigma_1(\sigma_2)$ is the real (imaginary) part of the σ .

Optical Conductivity of Superconductors

Superfluid electrons in superconductors can move without dissipation, therefore one can take the limit $\tau^{-1} \rightarrow 0$ in (11.37),

$$\sigma(\omega) \rightarrow -\frac{ns_S e^2}{i\omega m},$$

where n_S corresponds to the superfluid electron density. Accordingly, the real part σ_1 for the superfluid electrons is zero unless $\omega = 0$. Using (11.40), σ_1 is expressed by a delta function,

$$\sigma_1(\omega) = \frac{\pi ns_S e^2}{m} \delta(\omega). \quad (11.42)$$

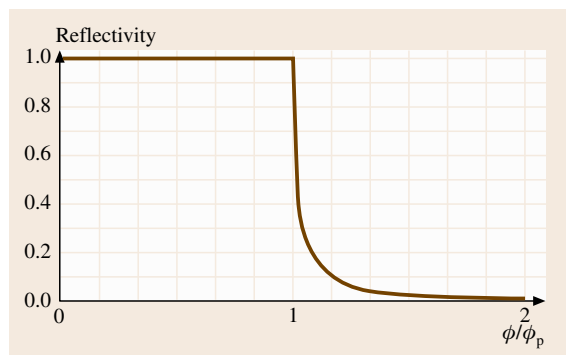


Fig. 11.9 The reflectivity of free electrons in the case of $\gamma = 0$

Finally, the optical conductivity of superfluid electrons is given by

$$\sigma(\omega) = \frac{\pi ns_S e^2}{m} \delta(\omega) - \frac{ns_S e^2}{i\omega m}. \quad (11.43)$$

Superconductivity originates from the formation of Cooper pairs. In the higher-frequency region above the binding energy of the Cooper pair, σ_1 should be finite. A schematic illustration of optical conductivity spectrum in superconductors is depicted in Fig. 11.10. Here Δ is called the Bardeen–Cooper–Schrieffer (BCS) gap parameter and 2Δ corresponds to the energy gap in the superconductor [11.17]. Thus we can measure the superconducting gap by optical spectroscopy in the infrared region.

11.1.5 Luminescence and Lasers

Materials emit light by *spontaneous emission* when electrons in the excited states drop to a lower level. The emitted light is called *luminescence*. Such materials with excited electrons can amplify the incident light via *stimulated emission*, which is utilized in *lasers*, an acronym for light amplification by stimulated emission of radiation.

Emission and Absorption of Light

The processes of spontaneous emission, stimulated emission and absorption are illustrated in Fig. 11.11 in the case of a two-level system.

The rate equations are as follows

$$\frac{dN_2}{dt} = -A_{21} N_2, \quad (11.44)$$

$$\frac{dN_2}{dt} = -B_{21} N_2 \rho(\nu), \quad (11.45)$$

$$\frac{dN_1}{dt} = -B_{12} N_1 \rho(\nu), \quad (11.46)$$

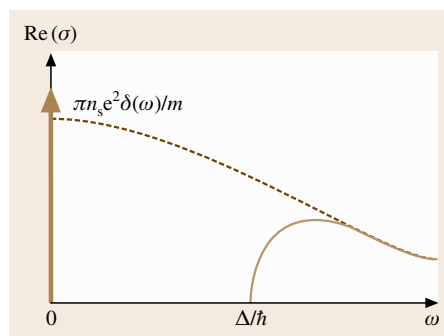


Fig. 11.10 Optical conductivity of a normal metal (*dashed line*) and a superconductor (*solid line*)

where N_1 and N_2 are the populations of a ground state $|1\rangle$ and an excited state $|2\rangle$, respectively, $\rho(\nu)$ is an energy density of the incident light, and A_{21} , B_{21} and B_{12} are Einstein coefficients. The right-hand side of (11.44) shows spontaneous emission (Fig. 11.11a) of a photon with the energy $h\nu = E_2 - E_1$. A radiative lifetime τ_R of the excited state is defined by

$$\tau_R = \frac{1}{A_{21}}. \quad (11.47)$$

The right-hand side of (11.45) shows stimulated emission (Fig. 11.11b) from $|2\rangle$ to $|1\rangle$. The rate is proportional to the energy density at the resonant frequency ν . Equation (11.46) represents absorption (Fig. 11.11c) from $|1\rangle$ to $|2\rangle$. As seen in the derivation of Beer's law, (11.1), the rate of absorption is proportional to the energy density of the incident light. Combining (11.44–11.46), we obtain the rate equation

$$\frac{dN_2}{dt} = -A_{21}N_2 - B_{21}N_2\rho(\nu) + B_{12}N_1\rho(\nu). \quad (11.48)$$

In the steady state, $N_1/dt = N_2/dt = 0$, then

$$A_{21}N_2 + B_{21}N_2\rho(\nu) = B_{12}N_1\rho(\nu). \quad (11.49)$$

In thermal equilibrium, the Planck distribution for cavity radiation is

$$\rho(\nu) = \frac{8\pi h\nu^3}{c^3} \frac{1}{\exp\left(\frac{h\nu}{k_B T}\right) - 1}, \quad (11.50)$$

and the Boltzmann distribution between two levels is

$$\frac{N_2}{N_1} = \exp\left(-\frac{E_2 - E_1}{k_B T}\right) = \exp\left(-\frac{h\nu}{k_B T}\right). \quad (11.51)$$

From (11.49–11.51) we obtain the *Einstein relations*

$$\frac{A_{21}}{B_{21}} = \frac{8\pi h\nu^3}{c^3}, \quad (11.52)$$

$$B_{21} = B_{12}. \quad (11.53)$$

Luminescence

Luminescence is categorized as follows

1. **Photoluminescence (PL)**
The reemission of light after absorbing an excitation light. Details are described in this section.
2. **Electroluminescence (EL)**
The emission of light caused by an electric current flowing through the material. This is utilized in op-

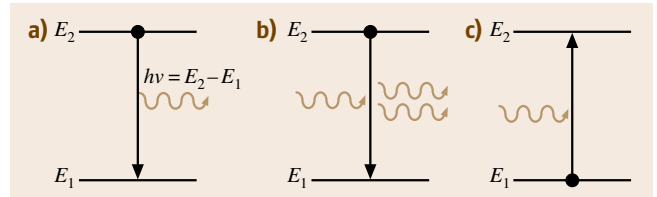


Fig. 11.11a–c Transition processes in a two-level system: (a) spontaneous emission, (b) stimulated emission, and (c) absorption

toelectronic devices: the light emitting diode (LED) and the laser diode (LD).

3. **Cathodoluminescence (CL)** The emission of light due to irradiation by an electron beam. Details are explained in Sect. 11.2.
4. **Chemiluminescence**
The emission of light caused by a chemical reaction. Bioluminescence which originates in an organism belongs to chemiluminescence.

The process involved in luminescence does not simply correspond to the reverse process of absorption in condensed matter. Nonradiative processes, e.g. a phonon-emission process, compete with the radiative process. Hence the decay rate of an excited state $1/\tau$ is described by

$$\frac{1}{\tau} = \frac{1}{\tau_R} + \frac{1}{\tau_{NR}}, \quad (11.54)$$

where the two terms on the right-hand side represent the radiative and nonradiative decay rates, respectively. The luminescence efficiency or quantum efficiency η is defined by

$$\eta = \frac{1/\tau_R}{1/\tau_R + 1/\tau_{NR}}. \quad (11.55)$$

If the radiative lifetime τ_R is faster than the nonradiative lifetime τ_{NR} , luminescence is a main de-excitation process and luminescence spectroscopy is a powerful method for the investigation of the excited state. Time-resolved measurements introduced in Sect. 11.4.3 provide direct information on $1/\tau_R$. In many cases, nonradiative decay processes give rise to heating of the material. Therefore, photocalorimetric or photoacoustic spectroscopy is utilized to obtain the information on the nonradiative decay processes [11.23].

PL Spectroscopy

The experimental set-up for the PL measurement is shown in Fig. 11.12. The sample is excited with a laser or a lamp. The PL spectrum is obtained by using array detectors, e.g. a CCD, or by scanning the wavelength

of the spectrometer with a **PMT**. The sample is usually mounted in a cryostat to cool it to liquid nitrogen or helium temperatures, because the nonradiative process is activated at higher temperature. Conversely, the temperature dependence of **PL** gives information on the nonradiative decay mechanism. The spectra obtained should be corrected to take into account the sensitivity of the detection system (the spectrometer and the **CCD** or **PMT**), while this correction is not required in the case of reflection and absorption measurements, in which the response function of the detection system is canceled in the calculation of I/I_0 (see (11.1)). Reabsorption effects should also be taken into account [11.22] if the frequency region of the luminescence overlaps that of the absorption. Time-resolved **PL** spectroscopy provides the radiative decay time and direct information on the relaxation process in the excited states. The experimental set-up will be reviewed in Sect. 11.4.3.

PL excitation spectroscopy (**PLE**) in which the detection wavelength is fixed and the excitation wavelength is scanned allows the absorption spectrum to be measured in the case that direct transmission measurements are impossible because of very weak absorption or an opaque surface of the material. **PLE** spectroscopy is similar to ordinary absorption measurements but is subject to the condition that there exists a relaxation channel from the (higher) excited state to the emission state being monitored. *Fluorescence line narrowing (FLN)* or *luminescence line narrowing* is a high-resolution spectroscopic technique that uses laser excitation to selected specific subpopulations optically from the inhomogeneously broadened absorption band of the sample, as

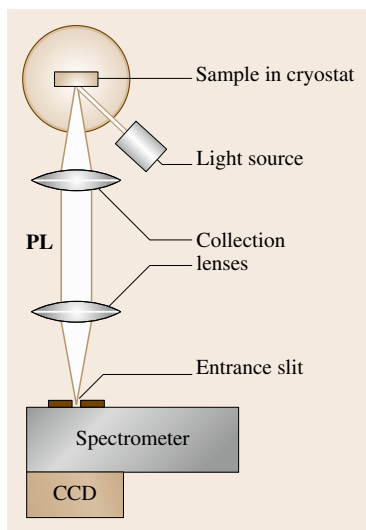


Fig. 11.12 Experimental setup for **PL** measurement

shown in Fig. 11.23a,b [11.24]. One can obtain the homogeneous width using **FLN** spectroscopy (Sect. 11.2).

Optical Gain

Laser action arises from stimulated emission, while spontaneous emission prevents lasing. Using (11.44, 11.45, 11.52) the ratio between the rates of stimulated emission and spontaneous emission is calculated as

$$\frac{N_2 B_{21} \rho(\nu)}{N_2 A_{21}} = \frac{1}{\exp\left(\frac{h\nu}{k_B T}\right) - 1}. \quad (11.56)$$

This ratio is less than unity if T is positive. Hence a *negative temperature* is required for the lasing. From (11.51) this negative temperature corresponds to $N_2 > N_1$, which is called *population inversion*.

If population inversion is realized, the incident light, called *seed light*, is amplified by stimulated emission. In the case that the seed light originates from the luminescence of the material itself, *amplified spontaneous emission (ASE)* appears, as shown in Figure 11.13.

Optical gain is calculated using (11.45, 11.46) as an extension of Beer's law (11.1)

$$\frac{dI(x)}{dx} = (B_{21} N_2 - B_{12} N_1) \frac{g(\nu) h\nu I(x)}{c}, \quad (11.57)$$

where $g(\nu)$ is a spectral function which describes the frequency spectrum of the spontaneous emission. Then, using the Einstein relation (11.52), we obtain

$$I(x) = I_0 \exp[G(\nu)x], \quad (11.58)$$

$$G(\nu) = \frac{(N_2 - N_1) A_{21} c^2 g(\nu)}{8\pi\nu^2}, \quad (11.59)$$

where I_0 and I are the input and output light intensities, respectively. $G(\nu)$ is called the *gain coefficient*.

The population inversion can be obtained in the following ways

1. **Optical pumping**
This method is used in solid-state lasers (except **LDs**) and dye lasers.
2. **Electric discharge**
Gas lasers and flash lamps which are used for the optical pumping of solid state lasers, e.g. **Nd:YAG** laser.
3. **Electron beam**
Large excimer lasers are pumped with a large-volume electron beam.
4. **Current injection**
This method allows compact, robust and efficient laser device (**LDs**).

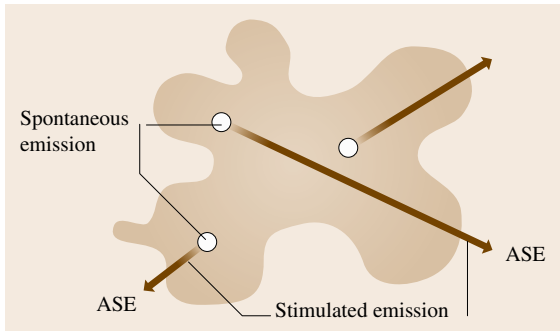


Fig. 11.13 Schematic illustration of amplified spontaneous emission. The shaded area shows an excited volume where population inversion is established

Laser Configuration

A combination of the population-inverted medium and the optical cavity which gives optical feedback provides the laser oscillation, which is like an electronic oscillator. Thus the laser consists of a laser medium, a pumping source and an optical cavity. Figure 11.14 shows a schematic arrangement of a laser. ASE with the correct frequency and direction of propagation is reflected back and forth through the laser medium. One of the mirrors, called the *output coupler*, is partially transparent to extract the light within the cavity. The cavity acts as a Fabry–Pérot resonator, so that the cavity modes are formed inside the cavity. The mode separation is expressed by

$$\Delta\nu = c/2l, \quad (11.60)$$

where l is a cavity length. We see lasing in the frequency region in which the intensity is above the threshold, as shown in Fig. 11.15. As seen in the figure, several modes oscillate simultaneously, which is called *multi-mode operation*. The random phases between these laser modes may cause a chaotic behavior of the output power. To avoid this effect, there are two solutions: *single-mode operation* in which a single cavity mode is selected by introducing another interferometer within the cavity and *mode-locked operation*, which is introduced in Sect. 11.4.2. The former operation achieves very narrow line widths down to 1 Hz.

Typical Lasers

Typical lasers are concisely summarized in the following. The lasers are classified depending on the laser media: gas, liquid and solid. Solid-state lasers are categorized into rare-earth metal lasers, transition-metal lasers

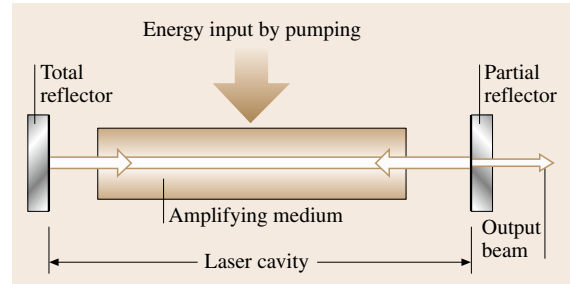


Fig. 11.14 Schematic arrangement of a laser. The partial reflector corresponds to the output coupler

and semiconductor lasers (LD). There are two laser operation modes: continuous wave (CW) and pulsed.

Gas lasers utilize atomic or molecular gases, as shown in Table 11.3. Though they are fixed-wavelength lasers in principle, multiple lines exist in molecular gas lasers and tunable operation is possible in CO₂ lasers. Excimer lasers utilize an excited diatomic molecule *excimer*, which is unstable in the ground state, and provide high-intensity pulses at UV wavelengths.

Dye lasers provide tunable operation, because dyes are organic molecules and have broad vibronic emission bands due to interaction with the solvent. Figure 11.16 shows the tuning range of typical dye lasers.

Solid-state lasers with transition-metal ions, as summarized in Table 11.4, also show broad emission bands (except the ruby laser) caused by the strong interac-

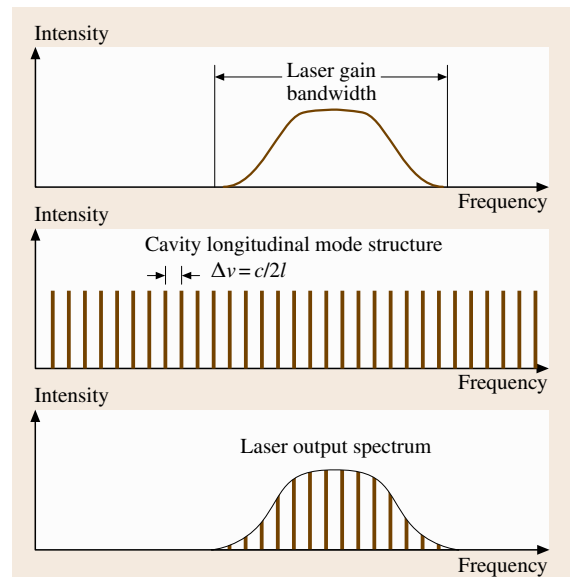


Fig. 11.15 Schematic illustration of laser output spectrum

Table 11.3 Typical gas lasers

Laser media	Oscillation wavelength (μm)	Notes
He-Ne	0.6328, 1.15/1.52/3.39, 0.604/0.612, 0.594, 0.543	CW, used in metrology (length standard) and in optical alignment
He-Cd	0.636, 0.538, 0.442, 0.325	Typical CW laser in UV region
Cu (vapor)	0.511, 0.578	Pulse operation with 10 kHz repetition in visible region
Ar ion	0.275–1.09 (discrete), 0.515, 0.488 (typical lines)	Typical CW laser in visible region
CO ₂	9–11 (tunable), 10.6	CW or pulse operation, giant pulse in infrared region, used in material processing
N ₂	0.337	Compact pulsed laser
XeCl	0.308	Used in pumping for dye lasers
KrF	0.248	Highest power among excimer lasers
ArF	0.193	LSI fabrication
F ₂	0.157	Commercially shortest wavelength

tion between 3d electrons and phonons, e.g. the Ti ion in sapphire provides very wide tuning range shown in Fig. 11.16 and are widely used, in particular, as ultra-fast pulsed lasers (Sect. 11.4.2).

Solid-state lasers with rare-earth ions, as summarized in Table 11.5, work as fixed-wavelength lasers because of the narrow emission lines due to the weak interaction between 4f ions and their environments. They are pumped with flash lamps or LDs and, are themselves used for the optical pumping of tunable lasers.

Finally, semiconductor diode lasers, as summarized in Fig. 11.17, are nowadays most widely applied in tiny light sources for optical fiber communication, optical recording of CDs, DVDs, MOs, etc. Current injection is used for the laser pumping, which makes their combination with electronic circuitry feasible.

11.1.6 Scattering

Scattering is the phenomenon in which the incident light changes its wavevector or frequency. Scattering is called *elastic* if the frequency is unchanged, or *inelastic* if the frequency changes.

Elastic Scattering

This phenomenon occurs due to variation of the refractive index of the material. The scattering can be classified into two types depending on the size of the variation a as follows [11.18]

1. Rayleigh scattering: in the case of $a \ll \lambda$
The probability (cross section) of Rayleigh scattering is proportional to $1/\lambda^4$.
2. Mie scattering: in the case of $a \geq \lambda$
The size dependence of the probability of the Mie scattering is not simple but is approximately proportional to $1/\lambda^2$ in the case of $a \approx \lambda$. This phenomenon enables us to monitor the sizes of the particles in the air or in transparent liquid.

Inelastic Scattering

This phenomenon occurs due to fluctuation of the electric susceptibility of electrons or lattices in a material. The electric field E of the incident light and the polarization P of the material are described by (Sect. 11.1.4)

$$E = E_0 \cos \omega t ; \quad P = P_0 \cos \omega t . \quad (11.61)$$

If the fluctuation of the electric susceptibility can be written by

$$\chi = \chi_0 + \chi' Q \cos \Omega t , \quad (11.62)$$

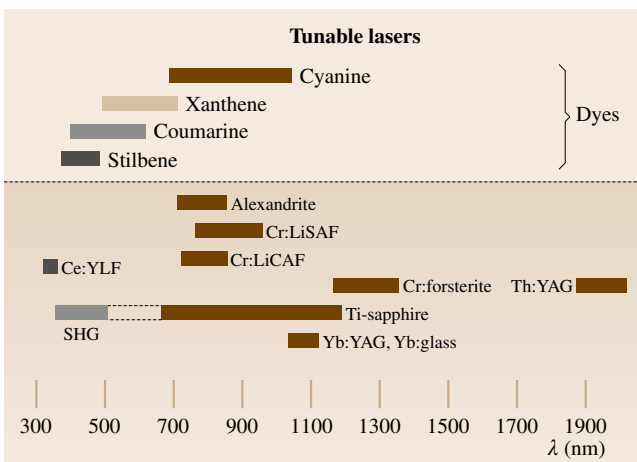


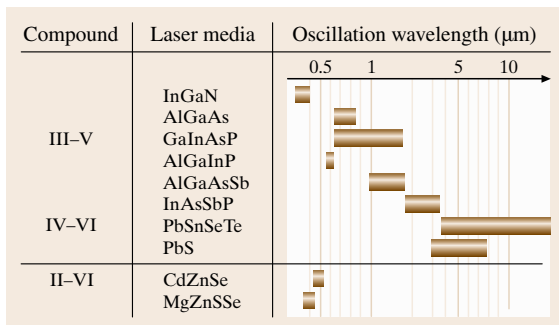
Fig. 11.16 Tuning range of typical dye and solid-state lasers

Table 11.4 Typical transition-metal-ion lasers

Laser media	Oscillation wavelength (μm)	Notes
Ruby (Cr:sapphire (Al ₂ O ₃))	0.6943	Pulse, the first laser invented in 1960
Ti:sapphire (Al ₂ O ₃)	0.65–1.1	CW or pulse, ultrafast pulse generation (Sect. 11.4.2)
Alexandrite (Cr:BeAl ₂ O ₄)	0.70–0.82	CW or pulse, removal of hair, tattoos, and visible leg veins
Cr:LiSAF (LiSrAlF ₆)	0.78–1.01	Pumped with LD, medical imaging and remote sensing
Cr:forsterite (Mg ₂ SiO ₄)	1.13–1.35	Frequency-doubled range located at missing region covered with Ti:sapphire laser

Table 11.5 Typical rare-earth-ion lasers

Laser media	Oscillation wavelength (μm)	Notes
Nd:YAG	1.064	CW or pulse, used in material processing. SHG, THG and FHG are also used.
Nd:glass	1.062 (SiO ₂ glass), 1.054 (PO glass)	CW or pulse, very strong pulse operation
Nd:YLF	1.053, 1.047, 1.323, 1.321	CW or pulse, good thermal stability
Nd:YVO ₄	1.065	CW, pump source for Ti:sapphire laser
Yb:YAG	1.03	CW, used in a disk laser
Er:glass	1.54	CW, fiber laser, optical communication
Ce:LiSAF	0.285–0.299	UV operation


Fig. 11.17 Typical laser diodes

the polarization of the material is described as

$$\begin{aligned}
 P &= \varepsilon_0 \chi E_0 \cos \omega t + \varepsilon_0 \chi' E_0 Q \cos \Omega t \cos \omega t \\
 &= \varepsilon_0 \chi E_0 \cos \omega t + \frac{1}{2} \varepsilon_0 \chi' E_0 Q \\
 &\quad \times [\cos(\omega + \Omega)t + \cos(\omega - \Omega)t] . \quad (11.63)
 \end{aligned}$$

The first term corresponds to the Rayleigh scattering and the second term means that new frequency components with $\omega \pm \Omega$, called *Raman scattering*, arises from the fluctuation. The down- and upshifted components are called the *Stokes scattering* and the *anti-Stokes scattering*, respectively.

In the case of the Raman scattering due to phonons, the Stokes (anti-Stokes) process corresponds to a phonon emission (absorption), as shown in Fig. 11.19. The scat-

tering caused by acoustic phonons has a special name: *Brillouin scattering*. The frequency shift with respect to the incident light is called the *Raman shift*, and is determined by the phonon energy. In other words, the energy of the phonons or other elemental excitations can be obtained by Raman spectroscopy. Nowadays Raman spectroscopy is indispensable for material science and is applied to a huge number of materials [11.25].

Selection Rules for Raman Scattering

In the case of Raman or Brillouin scattering of phonons in crystals, energy and momentum conservation rules hold

$$\omega_i = \omega_s \pm \Omega , \quad (11.64)$$

$$k_i = k_s \pm K , \quad (11.65)$$

where ω_i and k_i (ω_s , k_s) are the frequency and wavevector of the incident (scattered) photon and Ω and K are those of the phonon. The plus sign corresponds to the Stokes process, which is shown in Fig. 11.20 and the minus sign corresponds to the anti-Stokes process.

If the incident light is in the optical region (from IR to UV), the wavevector is negligibly small in comparison with the Brillouin zone of the crystal. Hence, phonons with $q \approx 0$ are usually observed in the Raman scattering.

In a crystal with inversion symmetry, the phonon modes which are observed in the Raman scattering, called *Raman-active modes*, are not *infrared active* (not

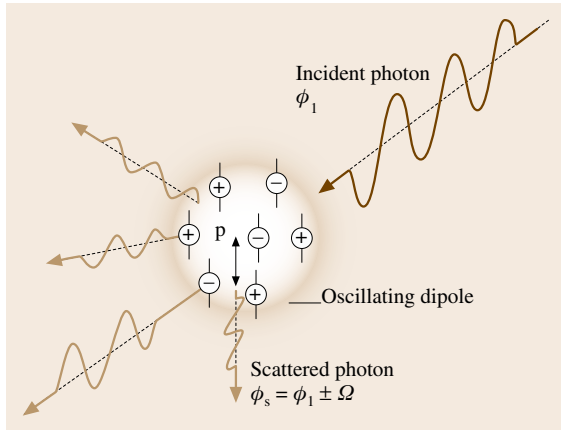


Fig. 11.18 Oscillator model for light scattering

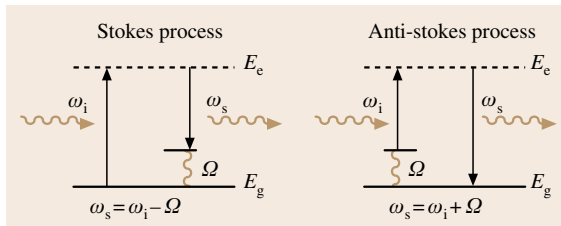


Fig. 11.19 Energy-level diagram of the Raman processes. Stokes and anti-Stokes processes are illustrated

observed in the infrared absorption), and vice versa. This is called the *rule of mutual exclusion* [11.26].

In general, the coefficient χ' of the Raman scattering term in (11.62) is a tensor and is related to a Raman tensor \mathbf{R} , which is determined by the symmetry of the crystal or molecule. The intensity of the Raman scattering I is proportional to

$$I \propto |\mathbf{e}_i \mathbf{R} \mathbf{e}_s|, \quad (11.66)$$

where \mathbf{e}_i and \mathbf{e}_s are the polarization vectors of the incident and scattered light, respectively. The configuration for Raman spectroscopy is specified as $\mathbf{k}_i(\mathbf{e}_i; \mathbf{e}_s)\mathbf{k}_s$ and the allowed combination of the polarizations are found if the Raman tensor \mathbf{R} is given. This is called the *polarization selection rule* [11.26].

Electronic Raman Scattering

An electronic transition as well as a phonon is observed in the Raman scattering. This is called *electronic Ra-*

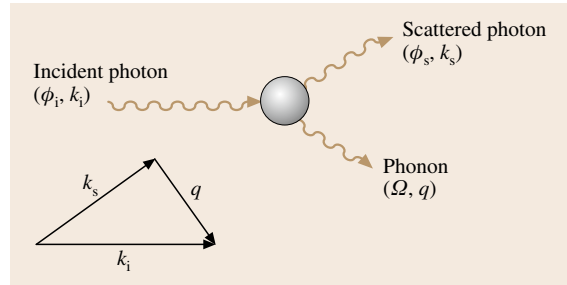


Fig. 11.20 Schematics of the Stokes scattering process. The wavevector conservation rule is also depicted

man scattering. This is a very useful probe for plasmons in semiconductors, magnons in magnetic materials, or in determining the superconducting gap and the symmetry of the order parameter of superconductors, in particular, strongly correlated electron systems; a new type of elementary excitation was found by this technique [11.27].

Resonant Raman Scattering

If the frequency of the incident light ω_i approaches the resonance of the material ω_0 , the scattering probability is enhanced and the process is called *resonant Raman scattering*. In this case violation of the selection rules and multiple-phonon scattering occur. In the just-resonant case ($\omega_i \approx \omega_0$), the discrimination between the scattering, which is a coherent process, and the luminescence, an incoherent process, is a delicate problem. The time-resolved measurement of resonant Raman scattering reveals the problem and provides information on the relaxation process of the material [11.28].

Experimental Set-up

The configuration for Raman spectroscopy is similar to that used for luminescence spectroscopy, but a spectrometer with less stray light is required, because strong incident laser or Rayleigh scattering is located near the signal light. A double or triple spectrometer instead of a single spectrometer is usually used in Fig. 11.12 to reduce the stray light. An alternative method is to cut the laser light with a very narrow-line sharp-cut filter placed just in front of the entrance slit of a single spectrometer. This kind of filter is called a *notch filter*, which is a kind of dielectric multilayer interference filter.

11.2 Microspectroscopy

In nanoscience and nanotechnology the optical spectroscopic study of the individual properties of nanostructured semiconductor materials or biomolecules with ultrahigh spatial resolution is useful. This is achieved by avoiding the inhomogeneity caused by differences in the size, shape or surrounding environment. This kind of spectroscopy is called *single-quantum-dot or single-molecule spectroscopy*. In this section, we will introduce the principles and the application of three kinds of microspectroscopic methods based on conventional microscopy, near-field optical microscopy and cathodoluminescence spectroscopy with the use of scanning electron microscopy.

11.2.1 Optical Microscopy

Since light has a wave nature and suffers from diffraction, the spatial resolution of an optical microscope cannot go below approximately a half of the optical wavelength: the so-called diffraction limit. The typical set-up of microphotoluminescence spectroscopy is illustrated in Fig. 11.21. A laser beam for the photoexcitation source is focused on a sample surface with a spot diameter of about $1\ \mu\text{m}$ through an objective lens with a high magnification factor. The luminescence from the sample is collected by the same objective lens and passed through an achromatic beam splitter to separate the luminescence from the scattered light of the excitation laser, and the luminescence image is focused onto a CCD camera or the luminescence spectrum is analyzed through the combination of spectrometer and intensified CCD camera.

The principle of single-quantum-dot or single-molecule spectroscopy is illustrated in Fig. 11.22. For example, the luminescence from the ensemble of quantum dots of semiconductors having a size distribution shows the inhomogeneous spectral broadening due to the size-dependent luminescence peak energy, as shown in Fig. 11.22a. If the spot size of the focused point is comparable to the mean separation distance between the quantum dots, the number of quantum dots detected by the objective lens is limited and the sharp luminescence lines with discrete photon energies are detected, as shown in Fig. 11.22c. If the distribution of the dots is dilute enough, one can detect a single dot, as shown in Fig. 11.22b where the line width is limited by intrinsic homogeneous broadening corresponding to the inverse of the phase relaxation time of the excited state.

As an example of laser microphotoluminescence spectroscopy, Fig. 11.23 shows the result of the ZnCdSe quantum dots grown on a ZnSe substrate [11.29]. Although the diameter of the quantum dots is 10 nm on average and has a wide size distribution, the microphotoluminescence spectra show the spiky structures that critically depend on the spot position of observation. From the top to the bottom spectra, the spot position is shifted successively by $10\ \mu\text{m}$ distance. The bottom spectrum is taken at the original position to check the reproducibility, from which one notes that the change in the spectra comes from fluctuation not in time but in position.

As another example of single-molecule spectroscopy, Fig. 11.24 illustrates the microluminescence excitation spectroscopy for light-harvesting complexes LH2 acting as an effective light antenna in photosynthetic purple bacteria at 2 K [11.30]. The complexes contain two types of ring structure of bacteriochlorophyll molecules (BChl a) with 9 and 18 molecules stacked against each other. Since the 9- and 18-molecule rings have their absorption bands at 800 and 860 nm, respectively, the ensemble of LH2 complexes, as illustrated in curve (a), shows two broad peaks with inhomogeneous broadening caused by different surrounding environment. On the other hand, when the complexes are dilutely dispersed in polyvinyl acetate (PVA) polymer film, individual complexes are found to show different spectra, as illustrated in curves (b)–(f). Here sharp structures are found around

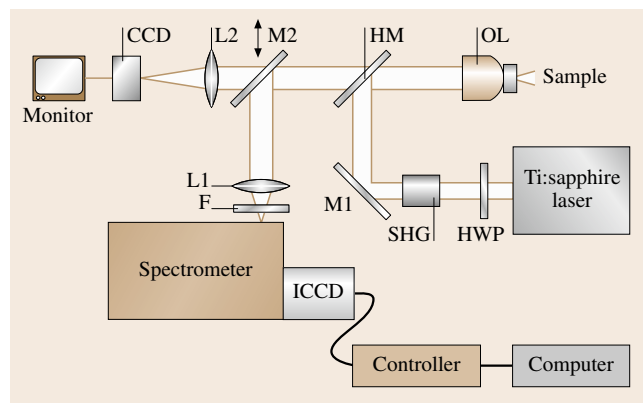


Fig. 11.21 Experimental set-up of microphotoluminescence spectroscopy. HM – dichroic reflection mirror for excitation light; OL – objective lens; HWP – half-wave plate; F – laser-blocking filter or linear polarizer

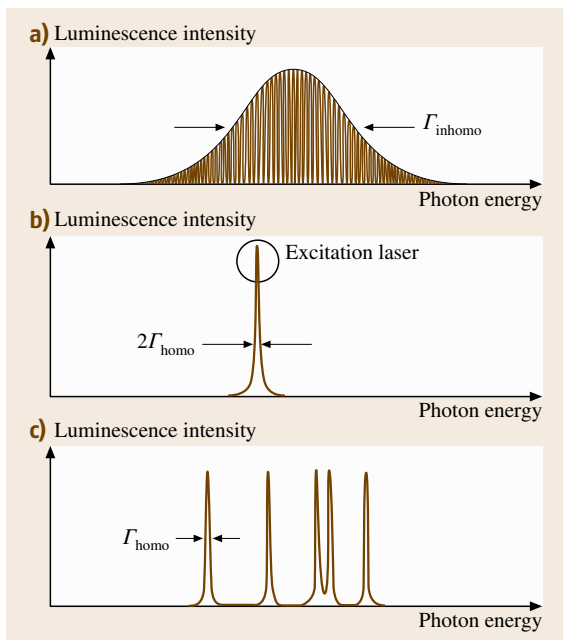


Fig. 11.22a–c Schematic drawing of luminescence spectra for samples with inhomogeneous broadening observed by: (a) broadband excitation, (b) site- or size-selective excitation, and (c) single-molecule/particle spectroscopy

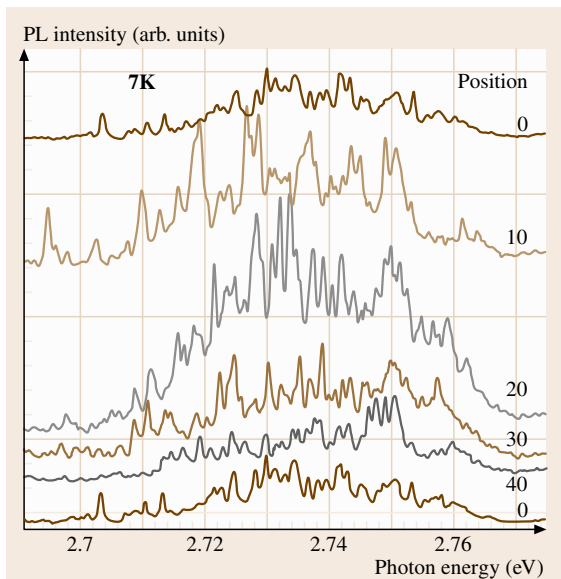


Fig. 11.23 Focussed position dependence of exciton luminescence of ZnCdSe quantum dots observed at 2 K by microphotoluminescence spectroscopy. The positions moved on a straight line are given in units of μm (after [11.29])

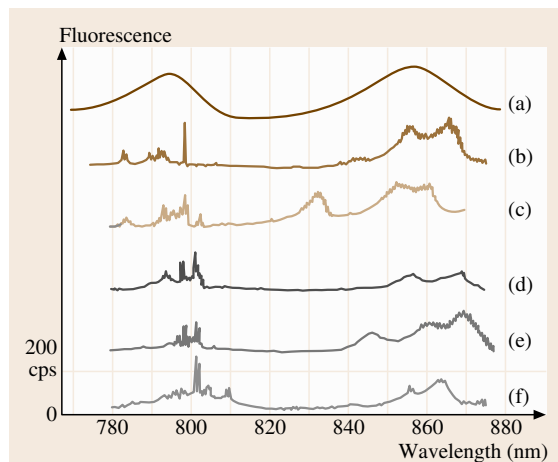


Fig. 11.24 Comparison of fluorescence-excitation spectra for an ensemble of LH2 complexes (a), and for several individual LH2 complexes (b–f) of photosynthetic bacteria at 1.2 K (after [11.30])

800 nm, while still broad structures around 860 nm. The former result indicates the localization of photoexcitation energy at one molecule, while the latter, indicates delocalization over the ring.

11.2.2 Near-field Optical Microscopy

In order to realize the spatial resolution beyond the diffraction limit, one can illuminate the sample with an extremely close light source of evanescent wave having large wavevectors produced from an aperture smaller than the wavelength of light. Here, the lateral resolution is mainly limited by the aperture size of the light source, if the distance between the light source and the sample surface is much smaller than the wavelength of light. Such a microscopy is called near-field optical microscopy. A schematic diagram of near-field microscope is illustrated in Fig. 11.25. One end of the optical fiber is sharpened by melting or chemically etching and used as a microprobe tip not only for the optical tips but also for atomic-force tips. To avoid the leakage of the light from the side of the tip end, the tip end is coated with Al or Au. The distance of the probe tip end from the surface of the sample is kept constant to within a few tens of nanometers using the principle of the atomic-force microscope (AFM). Laser light is sent through the optical fiber and the light emitted from the ultra-small aperture that illuminates the sample surface with a spot size similar to the aperture size (illumination mode). The transmitted or luminescent light from the sample is

collected by an objective lens and detected by a photodetector such as photomultiplier. For luminescence measurements a band-pass filter or a monochromator is placed before the photodetector. In some case to improve the spatial resolution the reflected or luminescence light is again collected by the same probe tip (illumination/collection mode). The lateral position of the tip end or the sample is scanned on the X - Y plane and the two-dimensional intensity image of the optical response of the sample can be recorded together with the topographical image of the sample surface. The minimum spatial resolution using the optical fiber tip end is considered practically to be a few tens of nanometers.

Figure 11.26 illustrates the example of images of the double monolayer of a self-organized array of polystyrene microparticles with a diameter of $1\ \mu\text{m}$ on a glass substrate [11.31]. Figure 11.26a shows the AFM image of the sample surface where the close packed hexagonal array is observed. The near-field transmission image using light from a $514.5\ \text{nm}$ Ar ion laser is shown in Fig. 11.26b. Inside one microparticle indicated by a white circle, one can see seven small bright spots with a characteristic pattern. The spot size is about $150\ \text{nm}$, which is restricted by the aperture size. Since the distance between these spots depends on the wavelength of light, the pattern represents nanoscale field distribution of a certain electromagnetic wave mode standing inside the particle double layer.

Another example of monitoring the spatial distribution of the wave function of electronic excited states is shown in Fig. 11.27 [11.32]. The near-field luminescence images of confined excitons and biexcitons in GaAs single quantum dots are observed using the illumination/collection mode with a probe tip with an aperture size of less than $50\ \text{nm}$. The size of the image of the exciton is found to be larger than that of the biexciton, reflecting the difference in effective sizes for the translational motion of the electronically excited quasi-particles.

11.2.3 Cathodoluminescence (SEM-CL)

Cathodoluminescence (CL) spectroscopy is one of the techniques that can be used to obtain extremely high spatial resolution beyond the optical diffraction limit. Cathodoluminescence refers to luminescence from a substance excited by an electron beam, which is usually measured by means of the system based on a scanning electron microscope (SEM), as illustrated in Fig. 11.28. The electron beam is emitted from an electron gun of the SEM, collected by electron lenses and

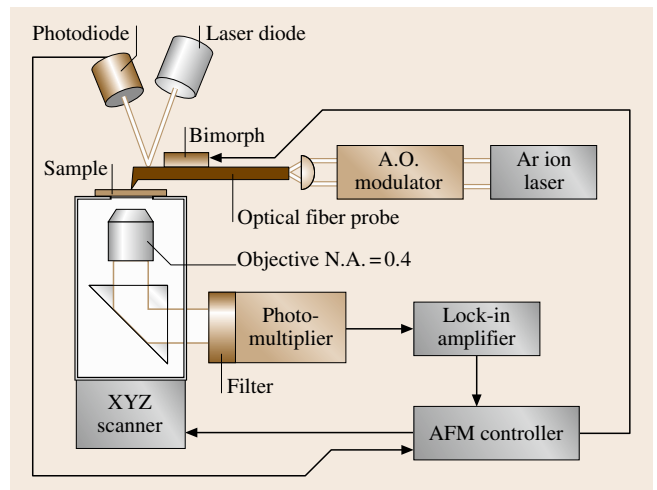


Fig. 11.25 Schematic diagram of a scanning near-field optical microscope (SNOM) in illumination mode. Near-field light coming out from a fiber probe illuminates a sample. Transmitted light is collected by an objective lens and fed to a photomultiplier

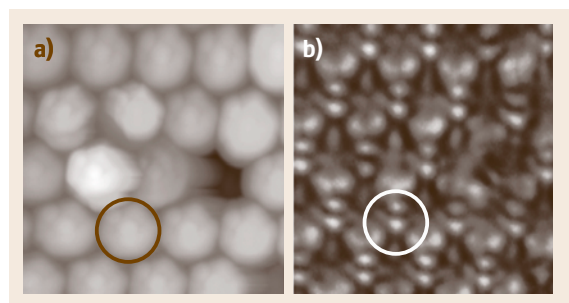


Fig. 11.26a,b $4.5\ \mu\text{m} \times 4.5\ \mu\text{m}$ images of a double monolayer film of self-organized $1.0\text{-}\mu\text{m}$ polystyrene spherical particles on a glass substrate: (a) AFM topographic image, and (b) SNOM optical transmission image (after [11.31])

focused on a sample surface. The luminescence from the sample is collected by an ellipsoidal mirror, passed through an optical fiber and sent to a spectrometer equipped with a CCD camera. Lateral resolutions less than $10\ \text{nm}$ are available in CL measurement, since the de Broglie wavelength of electrons is much shorter than light wavelengths. Moreover, energy- and wavelength-dispersive x-ray spectroscopy can be carried out simultaneously due to the high energy excitation of the order of keV. However, there are some difficulties in CL spectroscopy that are common to the observation of SEM images. A tendency toward charge accumulation at the irradiated spot requires that specimens have an elec-

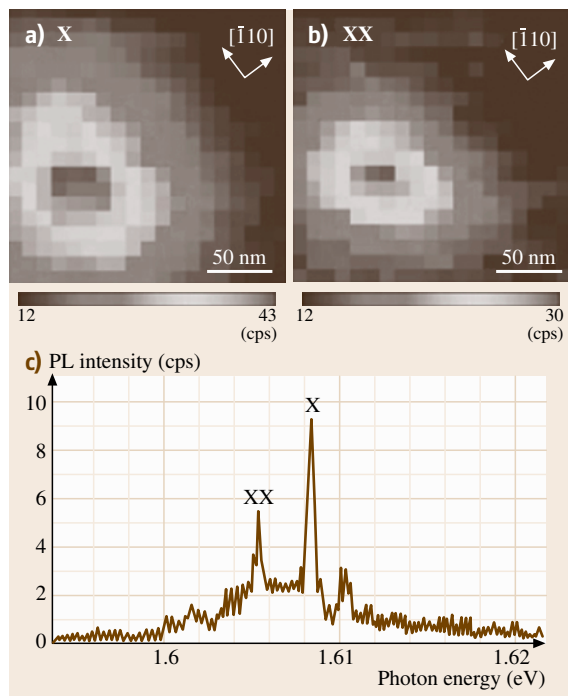


Fig. 11.27a–c High-resolution photoluminescence SNOM images of (a) X – exciton state, and (b) XX – biexciton state for a single GaAs quantum dot. The corresponding photoluminescence spectrum is also shown in (c) (after [11.32])

tric conductivity, since it induces an electric field which disturbs the radiative recombination of carriers. In addition, incident electrons with high kinetic energy often give rise to degradation of the sample. In CL spectroscopy, it is important to recognize those properties and to treat samples with a metal coating if needed.

Figure 11.29 illustrates an example of CL measurement on a system based on SEM. Spatial distribution of spectrally integrated CL intensity as well as SEM image is obtained, as shown in Fig. 11.29a,b. The sample is ZnO:Zn which corresponds to ZnO with many oxygen vacancies near the surface, and is a typical green phosphor. The CL image consists of 100×100 pixels, and the brightness of each pixel shows the CL intensity under the excitation within an area of $63 \times 63 \text{ nm}^2$. The CL intensity is different among spatial positions at the nanoscale. The CL spectrum for each pixel can also be derived from this measurement, and the feature varies according to positions.

The penetration depth of incident electrons under electron-beam excitation is controllable by changing the accelerating voltage [11.33]. Electrons with high ki-

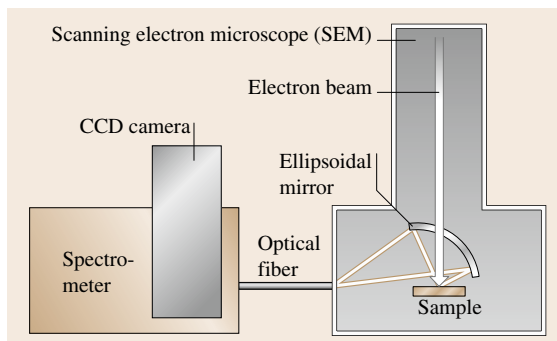


Fig. 11.28 Configuration of the CL measurement system based on SEM

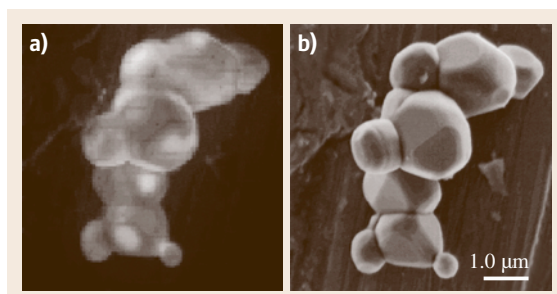


Fig. 11.29 (a) Spectrally integrated CL image of ZnO:Zn particles, and (b) SEM image at the same position

netic energy are able to penetrate deeper than photons which penetrate at most up to the depth corresponding to the reciprocal of the absorption coefficient, and therefore internal optical properties of substances can be examined in CL measurement. An example of accelerating voltage dependence of CL spectra is illustrated in Fig. 11.30. The sample is once again ZnO:Zn, in which free-exciton luminescence by photoexcitation is not observed at room temperature, since excitons are separated into electrons and holes due to the electric field in the surface depletion layer [11.34]. For an accelerating voltage of 2 kV, at which the penetration depth of incident electrons is comparable to the reciprocal of the absorption coefficient of photons, the CL spectrum does not show any structure in the exciton resonance region. On the other hand, the free exciton luminescence appears for an accelerating voltage of 5 kV, at which the penetration depth of the incident electrons is estimated to be about five times larger than that of photons. The luminescence is highly enhanced for an accelerating voltage of 10 kV, at which incident electrons are considered from the estimation of the penetration depth to spread throughout the electron-injected

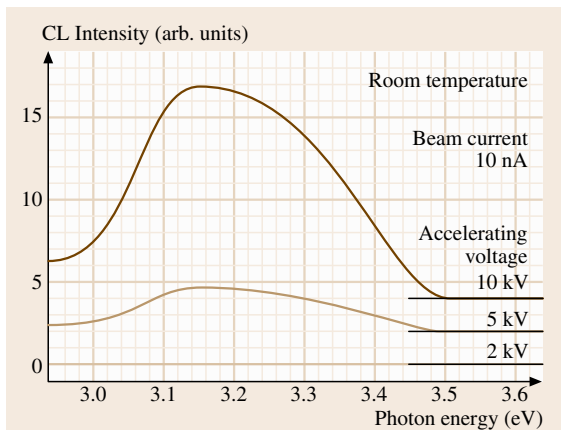


Fig. 11.30 Accelerating-voltage dependence of CL spectra in the exciton-resonance region at room temperature

ZnO:Zn particle. Although the total number of carriers in the particle increases with the accelerating voltage, the change in carrier density should be small because of the increase in excitation volume, i.e. nonlinear enhancement of the luminescence is not attributed to any high density effects. These facts indicate that injected

electrons penetrate into the internal region where many excitons can recombine radiatively due to the lower concentration of oxygen vacancies, and the width of the depletion layer in the particle is of the order of the reciprocal of the absorption coefficient.

The electric field in the depletion layer can be screened by increasing the density of photoexcited carriers. However, photoexcitation with high carrier density also induces strong nonlinear optical response near the exciton resonance region, such as exciton–exciton scattering and electron–hole plasmas [11.35]. In CL measurements, nonlinear effects do not appear in ZnO:Zn, since the carrier density under electron-beam excitation in the system based on SEM is much lower than that under photoexcitation using pulsed lasers. The free exciton luminescence does not appear with low accelerating voltage and low beam current, as shown in Fig. 11.30, whereas it can be observed with larger beam current. In CL spectroscopy, the internal electric field in the depletion layer is weakened with high efficiency and the free exciton luminescence near the surface can be observed without high density effects, since electrons are directly supplied into the oxygen vacancies, which are a source of the internal field.

11.3 Magneto-optical Measurement

11.3.1 Faraday and Kerr Effects

It is well known in magneto-optical effect that the polarization plane of an electromagnetic wave propagating through matter is rotated under the influence of a magnetic field or the magnetization of the medium [11.36]. This effect is called the Faraday effect, named after the discoverer *Michael Faraday* [11.37]. This effect is phenomenologically explained as the difference of the refractive index between right and left circular polarizations. In this effect the angle of optical rotation is called the Faraday rotation angle. In the case of low applied magnetic field the Faraday rotation angle θ_F is proportional to the sample thickness l and the applied magnetic field H . Thus θ_F is written as

$$\theta_F = VH, \quad (11.67)$$

where V is called the Verdet constant. The Faraday effect appears even without a magnetic field in an optically active medium, e.g. saccharide, etc. Furthermore, the magnetic Kerr effect is the Faraday effect for reflected light [11.38]. This effect is ascribed to the phase difference between right and left circular polarizations

when the electromagnetic wave is reflected on the surface of a magnetic material.

For practical use the Faraday effect is utilized for imaging of magnetic patterns. These magnetic patterns have been experimentally studied by various techniques,

1. moving a tiny magnetoresistive or Hall-effect probe over the surface,
2. making powder patterns with either ferromagnetic or superconducting (diamagnetic) powders (Bitter decoration technique),
3. using the Faraday magneto-optic effect in transparent magnetic materials in contact with the surface of a superconducting film as a magneto-optic layer (MOL).

In order to get a high-resolution image of the magnetic pattern, one of these methods, Faraday microscopy (3 above), is the most useful [11.39, 40]. A schematic drawing of the Faraday imaging technique is shown in Fig. 11.31.

The linearly polarized light enters the MOL, in which the Faraday effect occurs and is reflected at the mirror layer. In areas without flux, no Faraday rotation

takes place. This light is not able to pass through the analyzer that is set in a crossed position with respect to the polarizer, hence the superconducting regions stay dark in the image. On the other hand, in regions where flux penetrates, the polarization plane of the incident light is rotated by the Faraday effect so that some light passes through the crossed analyzer, thus the normal areas will be brightly imaged.

Figure 11.31 shows the case of nonzero reflection angle, whereas in the experiment perpendicular incident light is normally used (Faraday configuration).

The Faraday rotation angle is transformed into light intensity levels. The sample surface is imaged onto a CCD detector array. In the case of crossed polarizer and analyzer the intensity of the signal from the CCD detector is

$$I(r, \lambda, B) = I_0(r, \lambda) \sin^2[\theta_F(r, \lambda, B)] + I_1(r, \lambda), \quad (11.68)$$

where r is the spatial coordinate on the CCD surface, λ is the wavelength of the incident light, B is the applied magnetic field, θ_F is the Faraday angle, and I_0 is the light intensity reflected by the sample. I_1 is the background signal ascribed to the dark signal of the CCD and residual transmission through the crossed polarizer and analyzer. When the analyzer is uncrossed by an angle θ ,

$$I(r, \lambda, B) = I_0(r, \lambda) \sin^2[\theta + \theta_F(r, \lambda, B)] + I_1(r, \lambda). \quad (11.69)$$

The angular position θ of the analyzer should be adjusted to obtain the best contrast between superconducting ($\theta_F = 0$) and normal ($\theta_F \neq 0$) areas. By changing the sign of θ , normal areas can appear brighter or darker than superconducting areas. In our experiment the angle

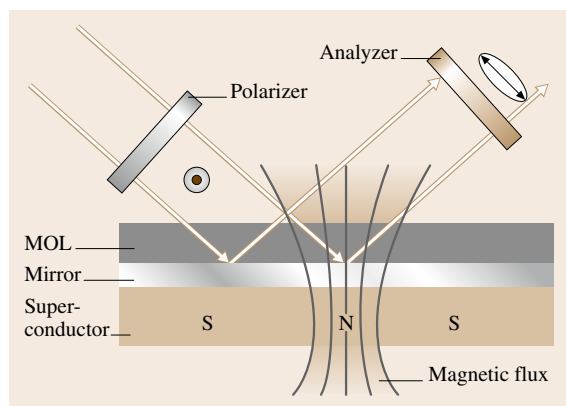


Fig. 11.31 Schematic drawing of the Faraday effect

θ is set to yield black in normal areas and gray in superconducting areas.

11.3.2 Application to Magnetic Flux Imaging

Experimental Set-up

Magneto-optical imaging is performed using a pumped liquid-helium immersion-type cryostat equipped with a microscope objective. This objective, with a numerical aperture of 0.4, is placed in the vacuum part of the cryostat and can be controlled from outside. The samples are studied in a magnetic field applied from exterior coils. The optical set-up is similar to a reflection polarizing microscope as shown in Fig. 11.32. Before measurement the samples are zero-field cooled to 1.8 K. The indium-with-QWs sample is illuminated with linearly polarized light from a Ti:sapphire laser, through a rotating diffuser to remove laser speckle. In the case of a lead-with-EuS sample a tungsten lamp with an interference filter is used the light source. Reflected light from the sample passes through a crossed or slightly uncrossed analyzer and is focused onto the CCD camera. The spatial resolution of $1 \mu\text{m}$ is limited by the numerical aperture of the microscope objective.

Magneto-optic Layers

Conventional magneto-optic layers. As for typical conventional MOLs, essentially, thin layers of Eu-based MOL (Eu chalcogenides, e.g. EuS and EuF_2 mixtures, EuSe) and doped yttrium iron garnet (YIG) films have been used [11.41]. These are usable up to the critical temperature of the ferromagnetic-paramagnetic transition ($\approx 15\text{--}20$ K) because their Verdet constants decrease with increasing temperature.

Since EuS undergoes ferromagnetic ordering below $T_c \approx 16.3$ K, a mixture of EuS with EuF_2 is better used. EuF_2 stays paramagnetic down to very low temperatures, therefore the ordering temperature of the mixture can be tuned by the ratio EuS : EuF_2 . But there are several problems; difficulty of preparation due to difference of melting temperatures, and the need for a coevaporation technique.

Then the single-component EuSe layer has been further used because, even in the bulk, EuSe is paramagnetic down to 4.6 K and has a larger Verdet constant. Below 4.6 K, EuSe becomes metamagnetic, however, the reappearance of magnetic domains in the EuSe layers is not seen down to 1.5 K. However, there is also a problem owing to the toxicity of Se compounds.

On the other hand, due to their high transition temperature (Curie temperature), bismuth- and gallium-

doped yttrium-iron garnets (YIG) have been developed and used for the study of high- T_c superconductors. They are disadvantageous since they show ferrimagnetic domains, however, these MOLs are developed further by the introduction of ferrimagnetic garnet films with in-plane anisotropy. Using such films, the optical resolution is about $3\ \mu\text{m}$, but a direct observation of the magnetic flux patterns is possible and the advantages of the garnet films, i.e. high magnetic field sensitivity, large temperature range, are retained.

Generally this kind of MOL often has the demerit of poor spatial resolution because of their thickness of several micrometers. Furthermore, self-magnetic ordering that may modify the flux distributions in superconducting samples may limit their use. However, it was recently reported that an optimized ferrite garnet film allowed the observation of single flux quanta in superconducting NbSe_2 [11.42].

Novel magneto-optic layers. In this section we refer to an alternative type of MOL [11.39, 40] based on semimagnetic semiconductor (SMSC) $\text{Cd}_{1-x}\text{Mn}_x\text{Te}$. It consists of SMSC (also called diluted magnetic semiconductor (DMS)) $\text{Cd}_{1-x}\text{Mn}_x\text{Te}$ quantum wells (QWs) embedded in a semiconductor-metal optical cavity. It is well-known that SMSCs exhibit a large Faraday rotation mainly due to the giant Zeeman splitting of the excitonic transition ascribed to sp-d exchange interactions between spins of magnetic material and band electron spins. The most advantageous point is no self-magnetic ordering due to paramagnetic behavior of Mn ions. Therefore, it is very convenient since there is no possibility to modify the magnetic flux patterns of intermediate

state of type-I superconductors. There are several other advantages of this MOL. It is easy to increase Faraday rotation by making an optical cavity (metal/semiconductor/vacuum) with a thickness of $= (2n + 1)\lambda/4$. Multiple reflections of light take place inside the cavity. Moreover, in order to adjust the cavity thickness at the desired wavelength, a wedged structure is constructed. The highest spatial resolution is obtained when the superconducting film is evaporated directly onto the MOL. This is because, the smaller the distance between the MOL and the sample, the better the magnetic imaging becomes since there is little stray-field effect.

In addition to these ideas already proposed for conventional MOL (EuSe) [11.41], there is another strong point. Using QWs is also interesting due to low absorption, easy adjustment of the balance between absorption and Faraday rotation by choosing the number of QWs, and the possibility to have a thin active layer (QWs) in a thick MOL in order to keep good spatial resolution. When a $\text{Cd}_{1-x}\text{Mn}_x\text{Te}$ QW is inserted in an optical cavity the Faraday rotation can be further increased by using a Bragg structure, that is, placing the QWs at antinodes of the electric field in the optical cavity.

In order to make an optical cavity Al, or the superconductor itself if it is a good reflector, should be evaporated on top of the cap layer as a back mirror. In order to obtain the largest Faraday rotation, a minimum of the reflectivity spectrum has to be matched with the QWs transition. This is the resonance condition. However, the reflectivity, which decreases at the QW transition when the resonance condition is fulfilled, has to be kept to a reasonable level that is compatible with a good signal-to-noise ratio. Therefore an

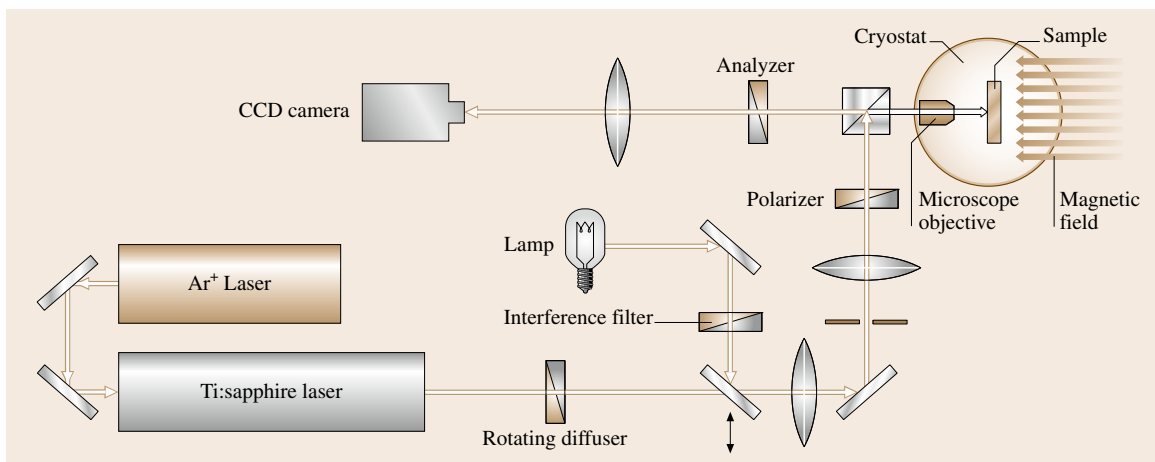


Fig. 11.32 Experimental set-up for the Faraday imaging technique

optimum number of QWs has to be found in multi-quantum-well structures. The Mn composition of the QWs also has to be optimized. It governs not only the Zeeman splitting of the excitonic transition but also the linewidth.

The time decay of the magnetization of the Mn ions in SMSC is known to be fast, in the subnanosecond range, since it is governed by spin–spin relaxation rather than by spin–lattice relaxation [11.43, 44]. This opens the way for time-resolved imaging studies with good temporal resolution, e.g. the study of the dynamics of flux penetration. On the other hand, there are also problems in fabrication. It is troublesome to remove the GaAs substrate by chemical etching while retaining fragile layers. Furthermore, the chemical etching solution strongly reacts with some metals e.g. lead.

Lead with europium sulfide magneto-optic layers. Since lead reacts strongly with the chemical etching solution used to remove the GaAs substrate from the

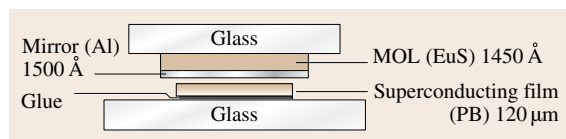


Fig. 11.33 Schematic drawing of Pb with EuS sample. The thickness of EuS, Al, and Pb are 145, 150 nm, and 120 μm , respectively. EuS is fabricated by Joule-effect evaporation. The EuS MOL is fixed on the Pb by pressing overnight

SMSC sample, we tried to use EuS as a MOL. The sample is shown in Fig. 11.33.

The thickness of the EuS MOL fabricated by Joule-effect evaporation on a 0.4 mm glass substrate is 145 ± 15 nm, hence it is thin enough for good spatial resolution. A 150-nm-thick Al layer is evaporated on the EuS MOL as a mirror in order to get high reflectivity. The EuS MOL is pressed onto Pb with a weight and left overnight.

A typical reflectivity spectrum and Faraday angle curve of EuS MOL are displayed in Fig. 11.34. The Ti:sapphire laser is tuned to 700 nm to get good reflected light and large Faraday rotation angle from the sample. Indeed EuS MOL may be expected to disturb the flux pattern, but no self-magnetic domain could be observed in this EuS sample, probably because the layer consists of a mixture of EuS and EuO. Figure 11.35 shows the images of the magnetic flux pattern at the surface of a 120- μm -thick superconducting lead film for magnetic field values of 20 mT. The temperature is 2 K, that is, much lower than the critical temperature of lead (7.18 K). The critical field of lead at 2 K is $H_c(2 \text{ K}) = 74.1$ mT.

The raw image has to be processed in order to correct the intensity fluctuations of the reflected light for thickness fluctuations in the MOL and for the sensitivity of CCD detector. In order to obtain an intensity level proportional to the Faraday angle, the gray level of each pixel should be calculated as

$$I' = I_H^\alpha / I_{H=0}^\alpha \quad (11.70)$$

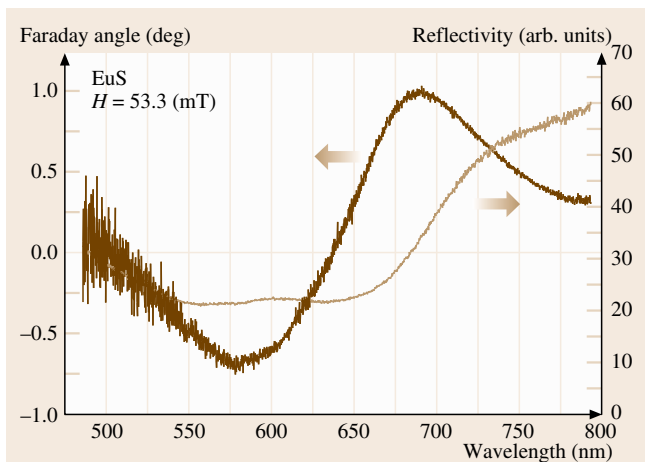


Fig. 11.34 Right scale: light reflection spectrum for zero applied magnetic field $H = 0$ mT at $T = 2$ K. Left scale: Faraday rotation-angle spectrum for $H = 53.3$ mT (after T. Okada, unpublished)

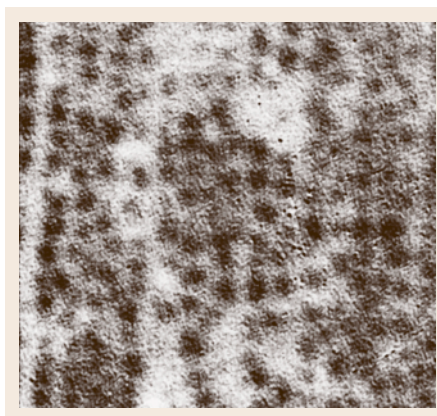


Fig. 11.35 The image of the magnetic flux patterns at the surface of 120- μm -thick superconducting Pb revealed with an EuS magneto-optical layer in an applied magnetic field of 20 mT ($h = 0.270$). Normal and superconducting domains appear in black and gray, respectively. The image size is $233 \mu\text{m} \times 233 \mu\text{m}$. The temperature is $T = 2$ K (after T. Okada, unpublished)

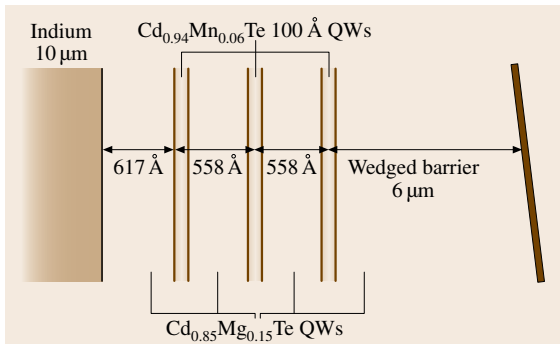


Fig. 11.36 Schematic representation of the sample composition (not to scale) after the etching of the GaAs substrate

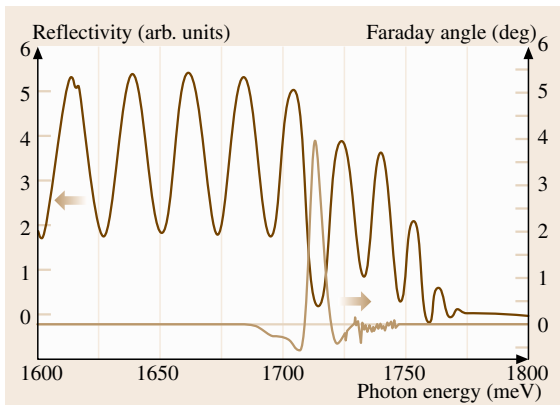


Fig. 11.37 *Left scale:* light reflection spectrum for zero applied magnetic field $H = 0$ mT at $T = 2$ K. *Right scale:* Faraday rotation-angle spectrum for $H = 56$ mT

where I_H^α is the raw gray level obtained for an applied field H and an analyzer angle α and θ is the Faraday angle. The quality of the image is further improved by Fourier-transform filtering, but the magnetic contrast is not very good because the contact between lead and the MOL may not be as good as for an evaporated metallic sample.

Indium with quantum-well magneto-optical layers.

The sample consists of an indium layer as the superconducting material and a $\text{Cd}_{1-x}\text{Mn}_x\text{Te}/\text{Cd}_{1-y}\text{Mg}_y\text{Te}$ heterostructure as the MOL. The structure is sketched in Fig. 11.36 [11.40].

The semiconductor heterostructure was grown by molecular beam epitaxy. The $\text{Cd}_{0.85}\text{Mg}_{0.15}\text{Te}$ buffer was deposited on (001)GaAs substrate without rotation of the sample holder, resulting in a slight gradient of both the thickness of the buffer and its refrac-

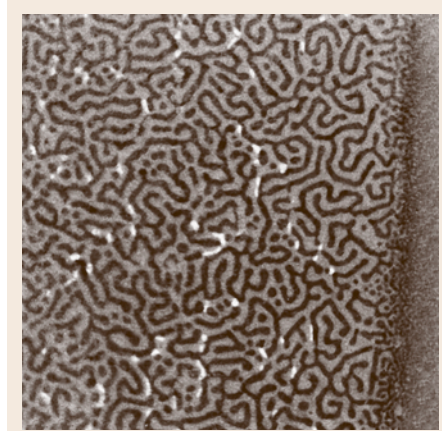


Fig. 11.38 The image of the magnetic flux patterns at the surface of 10- μm -thick superconducting In film revealed with the $\text{Cd}_{1-x}\text{Mn}_x\text{Te}$ QWs structure as the magneto-optical layer in an applied magnetic field of 6.3 mT ($h = 0.325$). Normal and superconducting domains appear in black and gray, respectively. The edge of the indium film can be seen on the right-hand side of images where the flux pattern disappears. The image size is $527 \mu\text{m} \times 527 \mu\text{m}$. The analyzer was uncrossed by $\alpha = 20^\circ$ with respect to the polarizer. The temperature is $T = 1.9$ K (after T. Okada, unpublished)

tive index. The buffer was followed by three 10-nm $\text{Cd}_{0.94}\text{Mn}_{0.06}\text{Te}$ QWs separated by $\text{Cd}_{0.85}\text{Mg}_{0.15}\text{Te}$ barriers that were 55.8 nm thick. A 10- μm -thick indium layer was then evaporated directly on top of the 61.7-nm $\text{Cd}_{0.85}\text{Mg}_{0.15}\text{Te}$ cap layer. The MOL is designed as an optical cavity and indium serves both as the superconducting layer and the cavity back mirror. The first and third QWs are nearly located at antinodes of the electric field in the cavity in order to enhance Faraday rotation. The indium-covered side was glued onto a glass plate and the GaAs substrate was removed by mechanical thinning and selective chemical etching. For the Faraday microscopy the spatial resolution was checked as $1 \mu\text{m}$, with a magnetic resolution of 10 mT; the range of temperature for use should be up to 20 K.

A typical reflectivity spectrum and Faraday angle curve are displayed in Fig. 11.37. The reflectivity spectrum presents an interference pattern associated with the metal/semiconductor/vacuum optical cavity. This pattern shows a spectral shift when the illuminating spot is scanned along the sample surface, according to the thickness variation of the cavity. The maximum Faraday angle is observed when a minimum of reflect-

tivity is matched with the QW transition energy (the cavity resonance condition). The peak Faraday angle was found to vary linearly with the applied magnetic field H . The measured slope equals 54.4°T^{-1} at the QWs (e1-hh1) exciton transition. Fig. 11.38 shows an intermediate state structure at the surface of the indium superconducting layer obtained at $T = 1.9 \text{ K}$ at magnetic field values 6.3 mT . The critical field of indium at 1.9 K is 19.4 mT .

Black and gray areas are normal and superconducting state, respectively. The intricate flux pattern

results from the competition between long-range repulsive magnetic interactions between normal zones and short-range interactions due to the positive interfacial energy between normal and superconducting areas [11.45, 46].

In the same way as for the lead sample, the raw images were processed in order to eliminate intensity fluctuations of the reflected light due to thickness inhomogeneities of the MOL and the sensitivity of CCD detector. The quality of the image is further improved compared with Fig. 11.35.

11.4 Nonlinear Optics and Ultrashort Pulsed Laser Application

Nonlinear optical effects with lasers are utilized in frequency conversion, optical communication (Sect. 11.5) and spectroscopy of materials. This chapter deals with nonlinear optics and its application to pulsed lasers.

11.4.1 Nonlinear Susceptibility

Definition of Nonlinear Susceptibility and Symmetry Properties

Nonlinear optical phenomena originate from nonlinearity of materials. Linear and nonlinear polarization induced in the material is expressed as follows

$$P_i = \chi_{ij} E_j + \chi_{ijk}^{(2)} E_j E_k + \chi_{ijkl}^{(3)} E_j E_k E_l + \dots, \quad (11.71)$$

where i, j, k and l represent x, y , or z and $\chi^{(n)}$, which is an $(n+1)$ -th-rank tensor, is called the n -th-order *nonlinear optical susceptibility*. Each term corresponds to the n -th order polarization

$$P_{i_1}^{(n)} = \chi_{i_1 i_2 \dots i_{n+1}}^{(n)} \overbrace{E_{i_2} E_{i_3} \dots E_{i_{n+1}}}^n, \quad (11.72)$$

where i_1, i_2, \dots , or i_{n+1} represents x, y , or z . The second-order nonlinearity in the argument ω is described by

$$P_i^{(2)}(\omega_1 + \omega_2) = \chi_{ijk}^{(2)}(\omega_1 + \omega_2; \omega_1, \omega_2) \times E_j(\omega_1) E_k(\omega_2). \quad (11.73)$$

The $\chi^{(2)}$ tensor has the following symmetry properties [11.47].

1. Intrinsic permutation symmetry

$$\chi_{ijk}^{(2)}(\omega_1 + \omega_2; \omega_1, \omega_2) = \chi_{ikj}^{(2)}(\omega_1 + \omega_2; \omega_2, \omega_1) \quad (11.74)$$

2. Permutation symmetry for materials without losses

$$\begin{aligned} \chi_{ijk}^{(2)}(\omega_1 + \omega_2; \omega_1, \omega_2) &= \chi_{jki}^{(2)}(\omega_1; -\omega_2, \omega_1 + \omega_2) \\ &= \chi_{kij}^{(2)}(\omega_2; \omega_1 + \omega_2, -\omega_1) \end{aligned} \quad (11.75)$$

3. Kleinman's relation (for the nonresonant case $\chi^{(2)}$ is independent of the frequency ω)

$$\chi_{ijk}^{(2)} = \chi_{jki}^{(2)} = \chi_{kij}^{(2)} = \chi_{ikj}^{(2)} = \chi_{jik}^{(2)} = \chi_{kji}^{(2)}, \quad (11.76)$$

where the arguments are $(\omega_1 + \omega_2; \omega_1, \omega_2)$. A consideration of crystal symmetry allows us to reduce the number of elements of the $\chi^{(n)}$ tensor of the material [11.47, 48]. A typical example is as follows.

If the material has inversion symmetry,

$$\begin{aligned} -P_i^{(2)} &= \chi_{ijk}^{(2)}(-E_j)(-E_k), \\ P_i^{(2)} &= 0. \end{aligned}$$

In the same way, we obtain

$$P^{(2n)} = 0 \quad (n : \text{integer}).$$

Then if the material has inversion symmetry,

$$\chi^{(2n)} = 0 \quad (n : \text{integer}). \quad (11.77)$$

Oscillator Model Including Nonlinear Interactions

The nonlinear optical susceptibility can be calculated quantum mechanically using the density matrix formalism [11.47]. Here we use a classical model [11.49], modifying the Lorentz oscillator model (11.15) to include nonlinear interactions of light and matter as follows

$$\begin{aligned} m \frac{d^2 x}{dt^2} &= -m\gamma \frac{dx}{dt} - m\omega_0^2 x - amx^2 \\ &\quad - bmx^3 + eE(t), \end{aligned} \quad (11.78)$$

where the third and fourth terms on the right-hand side correspond to the second- and third-order anharmonic potentials, respectively. Here we assume that the driving term can be expressed by

$$E(t) = \{E_1[\exp(-i\omega_1 t) + \exp(i\omega_1 t)] + E_2[\exp(-i\omega_2 t) + \exp(i\omega_2 t)]\}/2. \quad (11.79)$$

We can solve (11.78) by perturbative expansion of $x(t)$ in powers of the electric field $E(t)$,

$$x(t) \equiv x^{(1)} + x^{(2)} + x^{(3)} + \dots,$$

where $x^{(i)}$ is proportional to $[E(t)]^i$. Then we get the successive equations as follows

$$\frac{d^2 x^{(1)}}{dt^2} + \gamma \frac{dx^{(1)}}{dt} + \omega_0^2 x^{(1)} = \frac{eE(t)}{m}, \quad (11.80)$$

$$\frac{d^2 x^{(2)}}{dt^2} + \gamma \frac{dx^{(2)}}{dt} + \omega_0^2 x^{(2)} = a(x^{(1)})^2, \quad (11.81)$$

$$\frac{d^2 x^{(3)}}{dt^2} + \gamma \frac{dx^{(3)}}{dt} + \omega_0^2 x^{(3)} = 2ax^{(1)}x^{(2)} + b(x^{(1)})^3. \quad (11.82)$$

If we define a common denominator

$$D(\omega) \equiv \frac{1}{\omega_0^2 - \omega^2 - i\gamma\omega}, \quad (11.83)$$

the solution of (11.80) is expressed by

$$x^{(1)} = [E_1 D(\omega) \exp(-i\omega_1 t) + E_2 D(\omega) \exp(-i\omega_2 t)] \times e/(2m) + \text{c.c.}, \quad (11.84)$$

where c.c. means complex conjugate. This is just a superposition of (11.95). Then we substitute this result for the right-hand side of (11.81). The solution consists of five groups as follows

$$x^{(2)}(2\omega_1) = -[E_1^2 D(2\omega_1) D(\omega_1)^2 \times \exp(-2i\omega_1 t)] a e^2 / (4m^2) + \text{c.c.}, \quad (11.85)$$

$$x^{(2)}(2\omega_2) = -[E_2^2 D(2\omega_2) D(\omega_2)^2 \times \exp(-2i\omega_2 t)] a e^2 / (4m^2) + \text{c.c.}, \quad (11.86)$$

$$x^{(2)}(\omega_1 + \omega_2) = -\{E_1 E_2 L(\omega_1 + \omega_2) D(\omega_1) D(\omega_2) \times \exp[-i(\omega_1 + \omega_2)t]\} a e^2 / (2m^2) + \text{c.c.}, \quad (11.87)$$

$$x^{(2)}(\omega_1 - \omega_2) = -\{E_1 E_2^* D(\omega_1 - \omega_2) D(\omega_1) D(\omega_2)^* \times \exp[-i(\omega_1 - \omega_2)t]\} \frac{a e^2}{2m^2} + \text{c.c.}, \quad (11.88)$$

$$x^{(2)}(0) = -[|E_1|^2 D(\omega_1) + |E_2|^2 D(\omega_2)] \times \frac{a e^2}{2m^2}. \quad (11.89)$$

These equations indicate that new frequency components arise from the second-order nonlinearity. These components are used in frequency conversion. Details are discussed in the following subsection.

Next, the third-order nonlinearity is treated similarly, assuming three frequency components

$$E(t) = [E_1 \exp(-i\omega_1 t) + E_2 \exp(-i\omega_2 t) + E_3 \exp(-i\omega_3 t)]/2 + \text{c.c.} \quad (11.90)$$

Then using (11.82–11.89) for all combinations of ω_1 , ω_2 and ω_3 , we finally obtain 22 groups

$$x^{(3)} \text{ for } \omega_1 + \omega_2 + \omega_3, \omega_1 + \omega_2 - \omega_3, \omega_1 - \omega_2 + \omega_3, \\ -\omega_1 + \omega_2 + \omega_3, 2\omega_1 \pm \omega_2, 2\omega_1 \pm \omega_3, \\ 2\omega_2 \pm \omega_3, 2\omega_2 \pm \omega_1, 2\omega_3 \pm \omega_1, 2\omega_3 \pm \omega_2, \\ \omega_1, \omega_2, \omega_3, 3\omega_1, 3\omega_2 \text{ and } 3\omega_3.$$

For example,

$$x^{(3)}(\omega_1, \omega_2, -\omega_2) = -E_1 E_2 E_2^* D(\omega_1)^2 D(\omega_2) D(\omega_2)^* \exp(-i\omega_1 t) + \text{c.c.}, \quad (11.91)$$

$$x^{(3)}(\omega_1, \omega_1, -\omega_2) = -E_1^2 E_2^* D(2\omega_1 - \omega_2) D(\omega_1)^2 D(\omega_2)^* \times \exp[-i(2\omega_1 - \omega_2)t] \left[\frac{3b}{2} - 2a^2 D(\omega_1 - \omega_2) - a^2 D(2\omega_1) \right] \frac{e^2}{4m^3} + \text{c.c.} \quad (11.92)$$

The i -th-order polarization is given by

$$P^{(i)} = -n e x^{(i)}. \quad (11.93)$$

Then from (11.72), (11.91) we obtain a frequency component of the third-order polarization

$$P^{(3)}(\omega_1) = n e D(\omega_1)^2 |D(\omega_2)|^2 |E(\omega_2)|^2 E(\omega_1) \equiv \chi^{(3)}(\omega_1; \omega_1 + \omega_2 - \omega_2) \times |E(\omega_2)|^2 E(\omega_1). \quad (11.94)$$

This term means that the optical constant, e.g. refractive index n for the ω_1 light, can be controlled by the other light of ω_2 .

Table 11.6 Values of $\chi^{(2)}$ for typical nonlinear crystals

Material	Maximum value of $\chi^{(2)}$ (10^{-8} esu)	Fundamental wavelength (μm)
α -SiO ₂	0.19	1.06
Te	2.5×10^3	10.6
BaNaNb ₅ O ₁₅	9.6	1.06
LiNbO ₃	19	1.06
BaTiO ₃	-8.5	1.06
ADP (NH ₄ H ₂ PO ₄)	0.24	0.694
KDP (KH ₂ PO ₄)	0.25	1.06
β -BBO (BaB ₂ O ₄)	0.98	1.06
ZnO	-3.3	1.06
LiIO ₃	-2.8	1.06
CdSe	26	10.6
GaAs	95	10.6
GaP	18	3.39

Estimation of Nonlinear Susceptibility

We can estimate the value of $\chi^{(2)}$ using the anharmonic oscillator model, e.g. in the case of (11.84) as follows

$$P^{(2)}(\omega_1 + \omega_2) = -n\epsilon\chi^{(2)}(\omega_1 + \omega_2, \omega_1, \omega_2)E(\omega_1)E(\omega_2), \quad (11.95)$$

if we neglect the complex conjugate term,

$$\begin{aligned} \chi^{(2)}(\omega_1 + \omega_2, \omega_1, \omega_2) &= \frac{D(\omega_1 + \omega_2)D(\omega_1)D(\omega_2)nae^3}{m^2} \\ &= \frac{\chi^{(1)}(\omega_1 + \omega_2)\chi^{(1)}(\omega_1)\chi^{(1)}(\omega_2)ma}{N^2e^3}. \end{aligned}$$

Then we obtain *Miller's rule*

$$\chi^{(2)} \frac{\omega_1 + \omega_2, \omega_1, \omega_2}{\chi^{(1)}(\omega_1 + \omega_2)\chi^{(1)}(\omega_1)\chi^{(1)}(\omega_2)} = \frac{ma}{n^2e^3} (\text{const.}). \quad (11.96)$$

The density is estimated approximately

$$n \approx \frac{1}{d^3},$$

where d is a lattice constant. If we assume $m\omega_0^2d = mad$,

$$a = \frac{\omega_0^2}{d}.$$

In the nonresonant case, the denominator is approximated by

$$D(\omega) \approx \frac{1}{\omega_0^2}.$$

Table 11.7 Second-order nonlinear effects

Name of frequency conversion	Conversion process
Second harmonic generation (SHG)	$\omega \rightarrow 2\omega$
Sum frequency generation (SFG)	$\omega_1, \omega_2 \rightarrow \omega_1 + \omega_2$
Difference frequency generation (DFG)	$\omega_1, \omega_2 \rightarrow \omega_1 - \omega_2$
Optical rectification (OR)	$\omega \rightarrow 0$ (DC)
Optical parametric generation (OPG)	$\omega \rightarrow \omega_1, \omega_2$ ($\omega = \omega_1 + \omega_2$)

Finally we can estimate the value of $\chi^{(2)}$

$$\begin{aligned} \chi^{(2)} &\approx \frac{e^3}{m^2\omega_0^4d^4} \\ &\approx 10^{-8} \text{ esu}, \end{aligned} \quad (11.97)$$

if we assume $\omega_0 \approx 10^{16} \text{ s}^{-1}$ and $d \approx 0.1 \text{ nm}$. Table 11.6 shows values of $\chi^{(2)}$ for typical nonlinear crystals.

Frequency Conversion

As seen in (11.85–11.89), second-order nonlinearity enables frequency conversion by mixing of two photons. Frequency conversion processes using $\chi^{(2)}$ are summarized in Table 11.7.

Second-harmonic generation (SHG), expressed by (11.85), is widely used for generation of visible or ultraviolet lights, because most solid-state lasers including LDs deliver infrared or red lights; e.g. a green line at 532 nm is the SH of a Nd:YAG laser (1064 nm) and near-UV region (350–500 nm) is covered by the SH of a Ti:sapphire laser (Fig. 11.16). The SHG is also used to measure the pulse width of an ultrashort pulsed laser (Sect. 11.4.3).

Sum-frequency generation (SFG) in (11.87) is also used for the generation of the higher frequency region from the lower frequency region; the third-harmonic generation (THG) at 355 nm is achieved by SFG of the SH and fundamental of the Nd:YAG laser. The SFG provides up-conversion spectroscopy (Sect. 11.4.3).

Difference-frequency generation (DFG) in (11.88) is used for generation of infrared light. A combination of DFG and OPO enables us to tune the frequency in the infrared region (3–18 μm) with AgGaS₂ or GaSe crystals. *Optical rectification (OR)* in (11.89) is a special case of DFG and provides ultra-broadband infrared pulse generation by using femtosecond lasers (Sect. 11.4.5).

Optical-parametric generation (OPG) is the reverse process of SFG; one photon is divided into two pho-

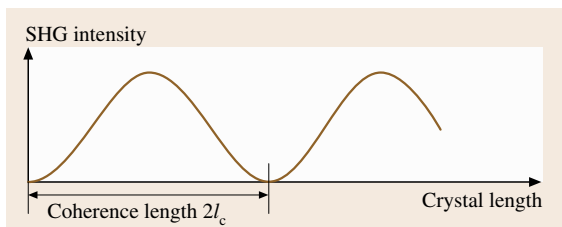


Fig. 11.39 SHG intensity with respect to crystal length

tons. This process is utilized in a tunable laser, *optical-parametric oscillator (OPO)*, pumped with a fixed-frequency laser.

Phase-matching condition is crucial for efficient frequency conversion [11.47]. The wavevector should be conserved in the frequency conversion processes; in the SHG case the phase-matching condition is described by

$$k(2\omega) = 2k(\omega), \quad (11.98)$$

where $k(\omega)$ is the wavevector at frequency ω . In other cases, the converted component 2ω and the incident component ω interfere with each other destructively, as seen in Fig. 11.39. Here the *coherence length* l_c is defined by

$$l_c = \frac{\pi c}{2} [\omega |n(\omega) - n(2\omega)|], \quad (11.99)$$

where $n(\omega)$ is the refractive index at frequency ω . The condition in (11.98) means that l_c becomes infinity. The phase-matching condition can be achieved using birefringence of a nonlinear crystal [11.47].

Third-order Nonlinear Effects

The third-order nonlinearity causes a variety of effects, which are summarized in Table 11.8.

Though the *third-harmonic generation (THG)* is used in frequency conversion, this process is useful for obtaining the spectroscopic information on the magnitude of $\chi^{(3)}$ or electronic structures, which is called *THG spectroscopy* [11.50].

Refractive index of the material depends on the intensity of the incident light as follows

$$n = n_0 + n_2 I, \quad (11.100)$$

where n_2 is nonlinear refractive index and I is the intensity of the light. As already seen in (11.94), the n_2 is proportional to $\chi^{(3)}$

$$n_2 = \frac{\chi^{(3)}}{n_0^2 c \epsilon_0}. \quad (11.101)$$

This refractive index change that is dependent on the light intensity is called the *optical Kerr effect (OKE)*, and

Table 11.8 Third-order nonlinear effects

The third-order effect	Notes
Third-harmonic generation (THG)	$\omega \rightarrow 3\omega$
Optical Kerr effect (OKE)	$n \rightarrow n_0 + n_2 I$
Two-photon absorption (TPA)	$\alpha \rightarrow \alpha_0 + \beta I$
Four-wave mixing (FWM)	$\omega_1, \omega_2, \omega_3 \rightarrow \omega_4$

produces a nonlinear phase shift $\Delta\Phi$

$$\Delta\Phi = \frac{2\pi}{\lambda} n_2 l I, \quad (11.102)$$

where l is the sample length. The nonlinear phase shift is utilized in optical switching (Sect. 11.5). The OKE gives rise to transverse variations of a light beam which cause the wavefront distortion that leads to *self-focusing* [11.47], used in Kerr lens mode-locking (Sect. 11.4.2) or Z-scan measurement (Sect. 11.4.4). The OKE also leads to temporal variations of the phase of the light pulse, called *self-phase modulation (SPM)*, which cause frequency shift, called *frequency chirp* [11.51], shown in Fig. 11.40. If a strong beam is focused on a material with large nonlinearity, *white-light continuum* can be generated via the SPM. This phenomenon is widely used in spectroscopy (Sect. 11.4.4).

The imaginary part of the complex refractive index also depends on the intensity of the incident light due to the third-order nonlinearity. Thus the absorption coefficient is defined by

$$\alpha(I) = \alpha + \beta I, \quad (11.103)$$

where β is called the *two-photon absorption (TPA) coefficient*. TPA is explained in Sect. 11.4.4. We apply the Kramers–Kronig relation (11.21) to the nonlinear optical constants

$$n_2(\omega) = \frac{c}{\pi} \int_0^\infty \frac{\beta(\omega')}{\omega'^2 - \omega^2} d\omega'. \quad (11.104)$$

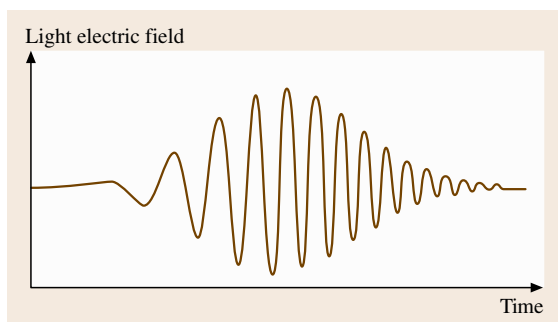


Fig. 11.40 Schematic illustration of a frequency chirp. The instantaneous frequency changes from red to blue

Four-wave mixing (FWM) is a general name for the third-order nonlinear optical processes and has a number of variations. Its spectroscopic application is introduced in Sect. 11.4.4.

11.4.2 Ultrafast Pulsed Laser

Properties of Ultrashort Pulses [11.51]

The relationship between a temporal profile (envelope of the electric power $|E(t)|^2$) and a spectral shape is illustrated in Fig. 11.41. A CW laser, in particular a single-mode laser, delivers monochromatic light and the envelope is independent of time, as shown in Fig. 11.41a. On the other hand, a pulsed laser produces a pulsed light which consists of a number of frequency components; the pulse duration Δt and spectral width $\Delta \nu$ are finite in Fig. 11.41b. The relation between them is determined by the Fourier transformation

$$\Delta \nu \Delta t \geq K, \quad (11.105)$$

where K is a constant determined by the pulse shape function, as shown in Table 11.9. The equal sign is valid only for pulses without frequency modulation and such pulses are called *Fourier-transform-limited*. This inequality corresponds to the uncertainty relation between energy and time in quantum mechanics.

The temporal shape of the ultrashort pulses with very broad spectral width is easily distorted by *group velocity dispersion*, $dv_g/d\omega$ [11.51], where v_g is a group velocity; the red component propagates through the material normally faster than the blue component. If the original pulse envelope is described by a Gaussian $\exp(-t^2/\tau_0^2)$,

the pulse width broadens as

$$\tau = \tau_0 \sqrt{1 + \left(\frac{|\text{GDD}|}{\tau_0^2}\right)^2}, \quad (11.106)$$

where the *group delay dispersion* (GDD) is written as

$$\text{GDD}(\omega) = l \frac{d^2}{d\omega^2} \left[\frac{\omega}{c} n(\omega) \right], \quad (11.107)$$

where l is the sample length. The GDD is related to the group velocity dispersion as follows

$$\text{GDD}(\omega) = \frac{d}{d\omega} \left(\frac{l}{v_g} \right). \quad (11.108)$$

The compensation of the pulse broadening in (11.106) is crucial when dealing with ultrashort pulses.

The time width of the ultrashort pulses is determined by an *auto-correlator* in Fig. 11.42. The incoming pulse is divided in a beam splitter; a part of the light passes through a fixed delay line, while the other part passes through a variable delay line. They overlap on the non-linear crystal surface and SHG occurs. The intensity of the SH light with respect to the time delay τ corresponds to the *autocorrelation function* $I_A(\tau)$ of the input pulse $I(t)$ as follows

$$I_A(\tau) = \int I(t)I(t - \tau) dt. \quad (11.109)$$

The pulse width of the input pulse $I(t)$ is estimated from the width of the autocorrelation function $I_A(\tau)$ using Table 11.9, if the pulse shape function is known (or assumed).

Q-Switching

A *Q-switch*, which controls the Q value of a cavity, provides a short and very intense laser pulse. The Q value

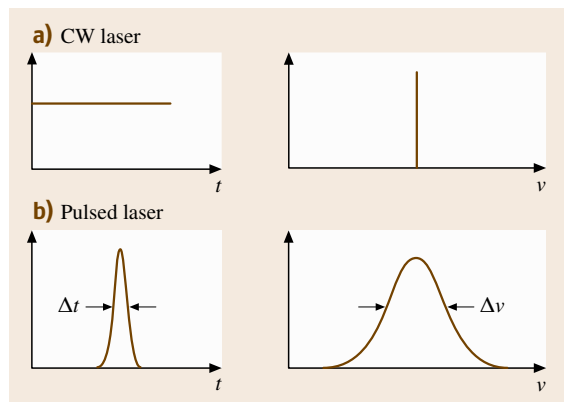


Fig. 11.41a,b Relationship between temporal profile and spectral shape

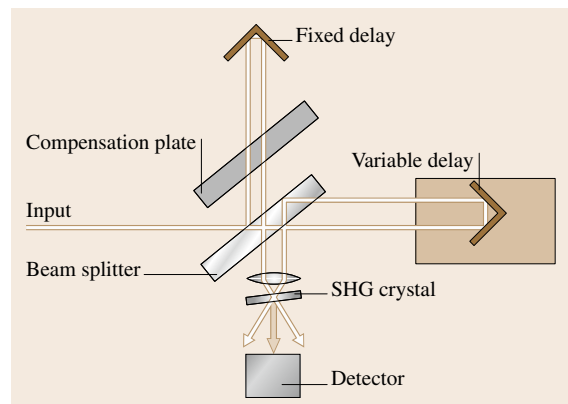


Fig. 11.42 Set-up of auto-correlator

Table 11.9 Calculated results of K , the relation between Δt , τ_A which is the width of the autocorrelation function for typical functions

Pulse shape function	K	$\Delta t/T$	τ_A/T	$\Delta t/\tau_A$
Gaussian: $\exp(-t^2/T^2)$	0.441	$2\sqrt{\ln 2}$	$2\sqrt{2 \ln 2}$	0.707
Diffraction function: $\sin^2(t/T)$	0.886	2.78	3.71	0.751
Hyperbolic square: $\text{sech}^2(t/T)$	0.315	1.76	2.72	0.648
Lorentzian: $[1 + (t/T)^2]^{-1}$	0.221	2	4	0.500
One-sided exponential: $\exp(-t/T)$ ($T > 0$)	0.110	$\ln 2$	$2 \ln 2$	0.500

is a measure of how much light from the laser medium is fed back into itself by the cavity resonator. A high Q value corresponds to low resonator losses per round trip. A schematic description of Q-switching is illustrated in Fig. 11.43. Without a Q-switch, the laser delivers pulses with a moderate intensity and pulse width, shown in Fig. 11.43a, according to the pumping condition, e.g. optical pumping with a flash lamp. With the Q-switch (off), initially the laser medium is pumped, while the Q-switch, producing the resonator with low Q , prevents feedback of light into the medium as shown in Fig. 11.43b. This produces population inversion; the amount of energy stored in the laser medium will increase, and finally reach some maximum level, as shown in Fig. 11.44, due to losses from spontaneous emission and other processes. At this point, the Q-switch is quickly changed from low to high Q , allowing feedback

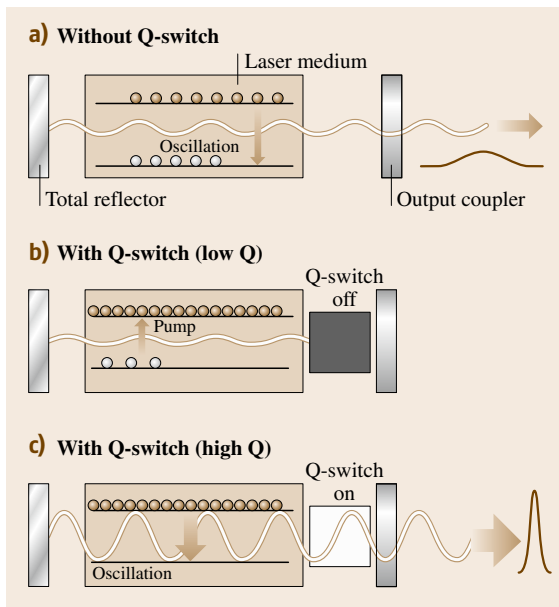


Fig. 11.43a–c Schematic illustration of Q-switching

and the process of optical amplification by stimulated emission to begin, as shown in Fig. 11.43c. Because of the large amount of energy already stored in the laser medium, the intensity of light builds up very quickly; this also causes the energy stored in the medium to be exhausted quickly, as seen in Fig. 11.44. The net result is a short pulse with a width of 1–100 ns, which may have a very high peak intensity. The typical example is a Q-switched Nd:YAG laser, which can deliver 1 MW.

Mode-Locking

If all modes shown in Fig. 11.15 operate with fixed phases among them, the laser output in a simple case is described by

$$\begin{aligned}
 E(t) &= \sum_{m=-N}^N E_0 \exp[i(\omega_0 + m \Delta\omega)t + m\theta_0], \\
 &= E_0 \frac{\sin[(2N+1)(\Delta\omega t + \theta_0)/2]}{\sin[(\Delta\omega t + \theta_0)/2]} \exp(i\omega_0 t),
 \end{aligned}
 \tag{11.110}$$

where ω_0 is the center frequency of the laser spectrum, $\Delta\omega = \pi(c/l)$ from (11.60) and we assume that $2N+1$ modes with the same amplitude E_0 exist and that the phase difference between adjacent modes is constant θ_0 .

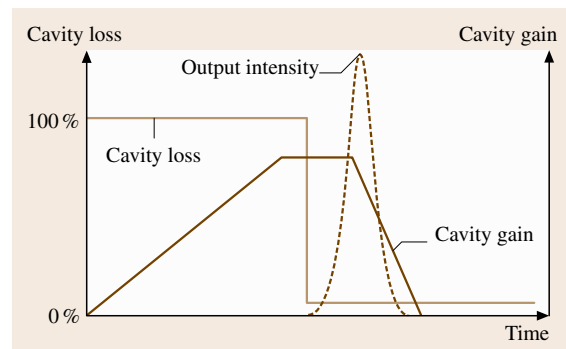


Fig. 11.44 Time evolution of cavity loss caused by the Q-switch, optical gain due to the pumping and laser intensity

The calculated envelope $|E(t)|^2$ is plotted in Fig. 11.45. The time interval between the strong peaks Δt is

$$\Delta t = \frac{2\pi}{\Delta\omega} = \frac{2l}{c}, \quad (11.111)$$

which corresponds to the round-trip time of the laser pulse inside the cavity. The pulse width of the peak δt is

$$\delta t = \frac{2\pi}{(2N+1)\Delta\omega}. \quad (11.112)$$

This means that a broader spectral width results in a shorter pulse width, as expected from the energy–time uncertainty relation.

Mode-locking is achieved by modulation of the resonator loss synchronized to the round-trip time of the

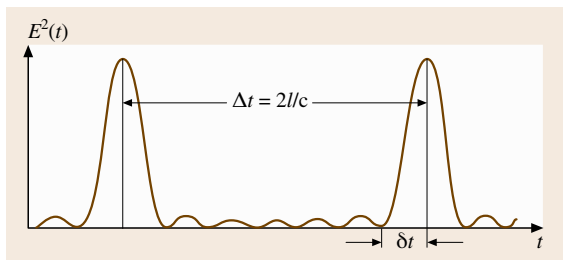


Fig. 11.45 A temporal profile of $|E(t)|^2$ in the case $N = 7$ in (11.105)

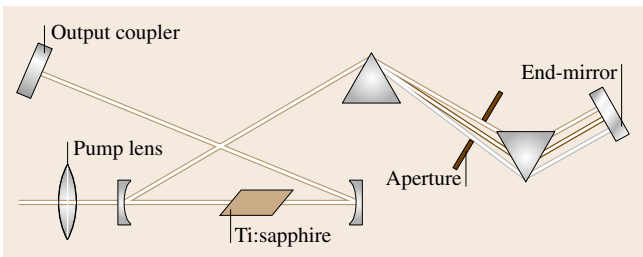


Fig. 11.46 Schematic construction of a mode-locked Ti:sapphire laser

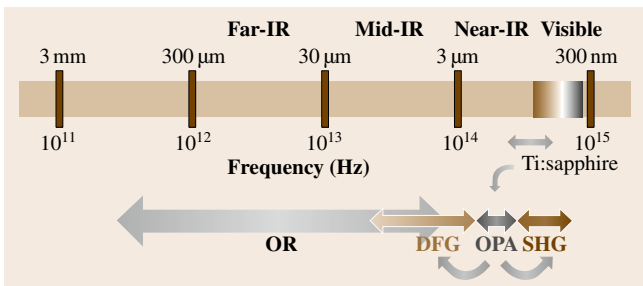


Fig. 11.47 Frequency map covered by the OPA system

laser pulse. There are two types: *active mode-locking* and *passive mode-locking*. The former uses an AOM which acts as a shutter that is open during a certain duration separated by the round-trip time; a typical example is a mode-locked Nd:YAG laser. The most successful method for the passive mode-locking is *Kerr-lens mode-locking (KLM)*, which manifests itself in a mode-locked Ti:sapphire laser. KLM is based on the optical Kerr effect of the laser medium, Ti:sapphire itself.

Figure 11.46 shows a schematic configuration of a Ti:sapphire laser. An intense pulse which experiences large refractive index due to the n_2 is focused within the Ti:sapphire rod, so the diameter of the pulse is reduced. Only the intense pulse can pass through the aperture inside the cavity with less loss and be amplified further. The very broad gain spectrum of the Ti:sapphire crystal allows the formation of ultrashort pulses with 10-fs duration. The group velocity dispersion is compensated with the prism pair, which introduces different delays for the different frequency components. The repetition rate of the mode-locked lasers is determined by the cavity length, typically 80 MHz. Generation of more intense pulses is possible by reducing the repetition rate; a *regenerative amplifier* delivers intense pulses with energy of ≈ 1 mJ and repetition frequency of ≈ 1 kHz [11.51]. Such pulses bring a variety of nonlinear phenomena; an *optical parametric amplifier (OPA)* which utilizes parametric process in Sect. 11.4.1 boosts a seed light of white-light continuum and works as a tunable light source. Thus the OPA system with additional frequency converters in Fig. 11.47 pumped with a regenerative amplifier based on a Ti:sapphire oscillator provides tunable light pulses with fs duration from the far-IR to UV region. This is a powerful tool for time-resolved and/or nonlinear spectroscopy.

11.4.3 Time-Resolved Spectroscopy

Time-resolved spectroscopy enables us to obtain the dynamics of electrons, phonons, spins, etc. in the materials in timescales down to femtoseconds. Pulsed lasers introduced in the last section are usually utilized as light sources, while many detection techniques are used depending on the timescale or the repetition rate of events. The techniques for time-resolved spectroscopy are classified into electrical methods with electronic apparatus and optical methods using nonlinear optics. Time-resolved measurements for the luminescence are reviewed in this section.

Electrical Methods

The electric signal from a photosensor, e.g. a PMT or PD (Sect. 11.1.2), is registered with electrical apparatus shown in Table 11.10 (except a streak camera). Their principles are illustrated in Fig. 11.48.

1. A *digital storage oscilloscope* with sample rates higher than 1 GS/s makes it possible to follow the electric signal with a time resolution of nanoseconds [11.52].
2. A *boxcar integrator* stores the signal during a time window whose position and duration (wider than ns) can be set arbitrarily [11.52]. Though temporal profiles can be obtained by sweeping the time window, this apparatus is mainly used for the gating of the temporal signal with a low repetition rate of up to 1 kHz, e.g. in pump-probe experiments using a regenerative amplifier (Sect. 11.4.4).
3. A *time-to-amplitude converter (TAC)* is used with a multichannel analyzer (MCA) to perform *time-correlated single-photon counting (TCSPC)*.

A schematic diagram of the TCSPC method is depicted in Fig. 11.49. Here CFD is an abbreviation of *constant fraction discriminator* which discriminates a signal pulse from a noise as follows. The CFD produces an output electric pulse when the input voltage exceeds a preset threshold value; the time delay between the input and output pulses does not depend on the input electric pulse height or shape. Very weak light behaves as a photon, which can be counted as an electric pulse from a PMT or APD. The time interval between the excitation pulse and the luminescence pulse from the sample reflects the decay time statistically; the accumulation of a number of such events reproduces the decay curve. The TAC produces an electronic pulse with a height which is proportional to the time difference between the start pulse triggered by the excitation pulse and the stop pulse from the detector. The MCA receives the electronic pulse from the TAC and converts the voltage into a channel address number of a storage memory. A histogram, which corresponds to the decay curve, is built up in the MCA with increasing numbers of events. The counting rate should be smaller than $\approx 1\%$, so that the probability

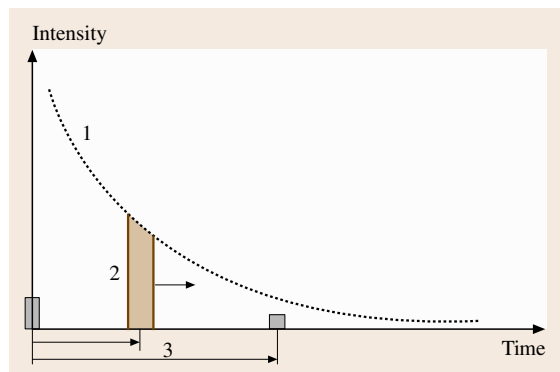


Fig. 11.48 Illustration of the principles for detecting transient electric signals

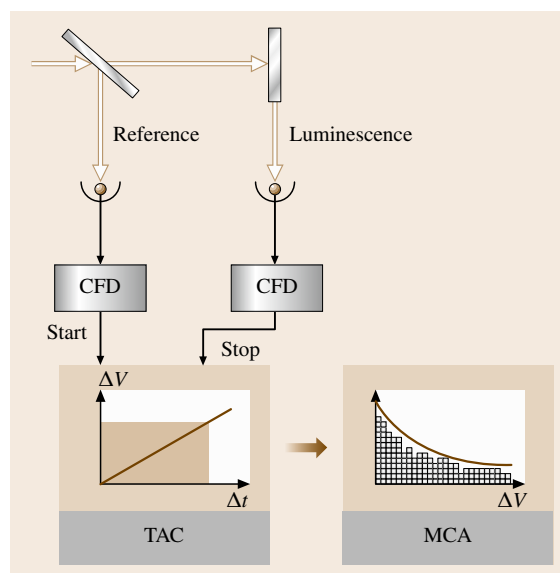


Fig. 11.49 Schematic diagram of the time-correlated single-photon counting method

of a simultaneous arrival of two photons is negligible ($< 0.01\%$). Thus a light source with a high repetition rate, e.g. a mode-locked laser, is required [11.53]. The time resolution of this technique is determined by the jit-

Table 11.10 Comparison between four electric methods

Apparatus	Time resolution	Features
Digital storage oscilloscope	\approx ns	Single-shot or repetitive events
Boxcar integrator	\approx sub-ns	Repetitive events
Time-to-amplitude converter (TAC)	\approx 10 ps	Repetitive events, single photon counting
Streak camera	\approx ps	Single-shot or repetitive events

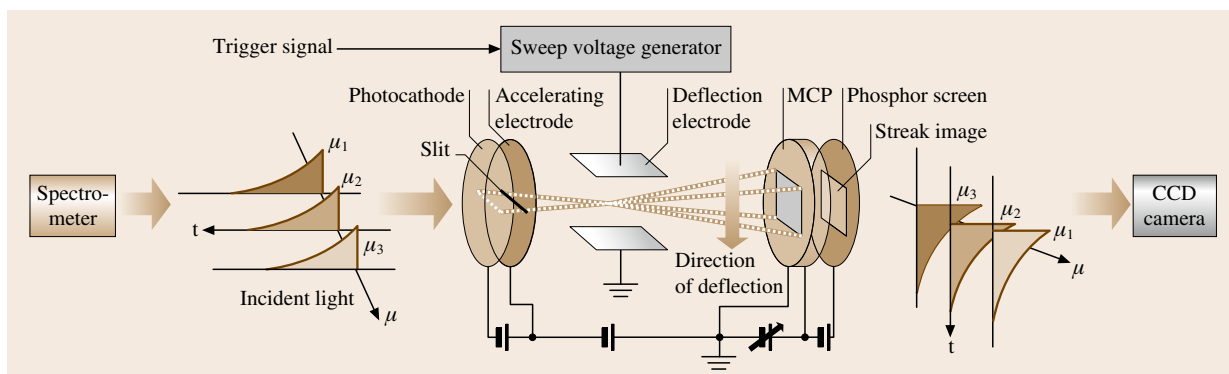


Fig. 11.50 Schematic construction of the streak camera

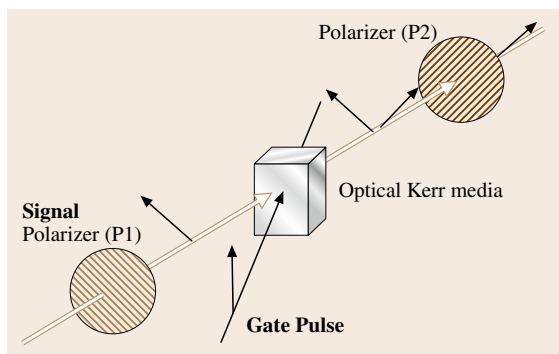


Fig. 11.51 Schematic illustration of the Kerr shutter

ter of the electric circuit, not by the width of the electric signal from the photosensors. Therefore, time resolution of tens of picoseconds can be achieved with a specially designed PMT or APD. Very accurate data can be obtained because of no linearity problems in the detector, but *convolution analysis* is usually required in sub-ns region, because an artifact, called *after-pulse*, due to the photosensors distorts the signal.

A *streak camera* is widely used in time-resolved spectroscopy, because it enables us to obtain temporal and spectral information simultaneously. A schematic construction of the streak camera is illustrated in Fig. 11.50. A spectrometer is usually installed before the streak camera in order to disperse the incoming light horizontally. The spectrally dispersed light impinges on a photocathode from which photoelectrons are emitted. The electrons are accelerated and temporally dispersed by deflection electrodes subjected to a rapidly changing sweep voltage in the vertical direction. Then the spectrally and temporally dispersed electrons hit a *microchannel plate* (MCP) which multiplies electrons while keeping their spatial distribution. The multiplied

electrons irradiate a phosphor screen on which a so-called streak image appears. The image is recorded with a CCD camera. A time-resolved spectrum can be obtained even for a single event, if the incident light is strong. This feature enables us to study a phenomenon which shows substantial shot-by-shot fluctuations [11.54]. Time resolution of 200 fs is achieved in single-shot detection. Usually repetitive events are integrated on a CCD chip. In this case, the electronic jitter of the trigger signal synchronized to the incident light trigger pulse determines the time resolution of the streak camera. A synchroscan streak camera used for mode-locked lasers with high repetition rates of ≈ 100 MHz achieves picosecond time resolution [11.55]. In the case of very weak light, single-photon counting detection is possible using a fast-readout CCD camera, because the MCP has a large multiplication factor.

Optical Methods (Using Nonlinear Optics)

Optical Kerr shutters (OKS) utilize the optical Kerr effect (Sect. 11.4.1); a Kerr-active medium with large $\chi^{(3)}$ works as an optical gate. The schematic configuration of the OKS is depicted in Fig. 11.51. A strong laser pulse induces birefringence in the Kerr medium, so that the plane of the polarization of the incident light determined by a polarizer P1 is rotated. Thus the incident light, normally blocked by a crossed polarizer P2, can pass through the P2. This configuration is inserted between the collection lenses and the spectrometer in Fig. 11.12. The time-resolved spectrum is then obtained by changing the delay between the gate and incident pulses [11.56]. The extinction ratio of the crossed polarizers determines the background of this technique, while the time response of the Kerr medium determines the time resolution of the OKS.

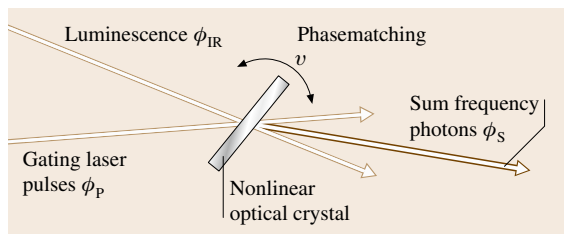


Fig. 11.52 Principle of up-conversion spectroscopy

Table 11.11 Comparison between the Kerr shutter and up-conversion

Method	Time resolution	Features
Kerr shutter	sub-ps	Strong gating pulse is required
Up-conversion	≈ 100 fs	Wavelength scanning is required

Up-conversion spectroscopy is based on SFG (Sect. 11.4.1); the up-converted photon ω_s from IR luminescence ω_{IR} is emitted when the gating laser pulse ω_p irradiates the nonlinear crystal, as shown in Fig. 11.52. A combination of the pump pulse and the nonlinear crystal acts as an optical gate like a boxcar integrator. By sweeping the delay time of the pump pulse, a temporal profile of the luminescence is obtained. A time-resolved spectrum is obtained by scanning the crystal angle (and monochromator) for the phase-matching condition [11.57]. Down-conversion for UV luminescence is also possible.

11.4.4 Nonlinear Spectroscopy

Nonlinear spectroscopy reveals electronic structures, relaxation processes in various materials and provides us rich information on the materials which cannot be supplied by linear spectroscopy. Though the application of nonlinear spectroscopy is very wide, this section focuses on the topics for time-resolved measurements.

Pump-Probe Experiment

In the *pump-probe experiment*, a pump pulse causes the absorption or reflection change of the material, which is observed in a probe pulse. This technique enables us to obtain a temporal evolution of an optical response of the material with ultrafast time resolution (shorter than 10 fs) by sweeping the time delay between pump and probe pulses. A schematic experimental set-up is shown in Fig. 11.53. Two laser beams are focused on the same spot of the sample. A delay line with vari-

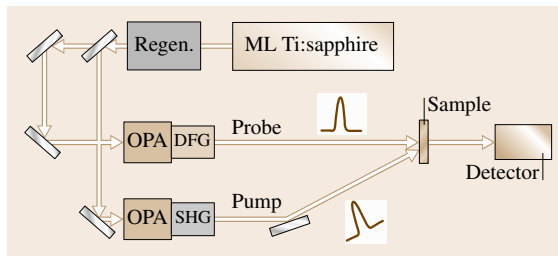


Fig. 11.53 Typical experimental set-up for the pump-probe transmission measurement. ML: mode-locked laser; Regen.: regenerative amplifier

able length is used to change the optical path difference between pump and probe paths. In the case of transmission pump-probe measurement, differential transmission change is defined as

$$\frac{\Delta T}{T} = \frac{I_{\text{on}} - I_{\text{off}}}{I_{\text{off}}}, \quad (11.113)$$

where I_{on} and I_{off} are the intensities of the probe pulses passing through the sample with and without the pump pulse, respectively. Pump-induced absorption change $\Delta\alpha$ is expressed by

$$\Delta\alpha l = \ln \left(1 + \frac{\Delta T}{T} \right), \quad (11.114)$$

where l is the sample thickness.

By scanning the probe frequency the spectrum of the absorption change can be obtained. A combination of white-light continuum in Sect. 11.4.1, which is available in the visible region, as a probe pulse and an array detector reduces the acquisition time remarkably. In this case, the frequency chirp of the white-light continuum should be corrected.

Transient Absorption and Two-Photon Absorption

A schematic diagram for transient absorption is illustrated in Fig. 11.54. If nonradiative processes is dominant and luminescence cannot be observed, the transient absorption measurement provides decay process of the excited state $|e_1\rangle$. In addition, the higher excited state $|e_2\rangle$, which cannot be observed in the linear (one-photon) absorption, may be found in the transient absorption. Here materials with inversion symmetry have a selection rule

$$\langle g|r|e_1\rangle \neq 0, \langle e_1|r|e_2\rangle \neq 0, \langle g|r|e_2\rangle = 0, \quad (11.115)$$

if $|g\rangle$ and $|e_2\rangle$ are even, $|e_1\rangle$ is odd. Absorption decrease called *bleaching*, corresponding to a negative signal of

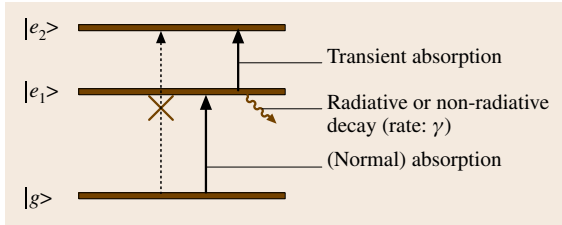


Fig. 11.54 Schematic diagram for transient absorption

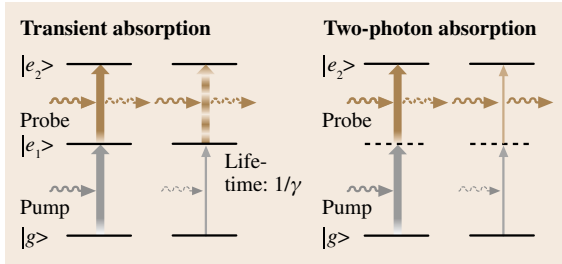


Fig. 11.55 Comparison between transient absorption and two-photon absorption

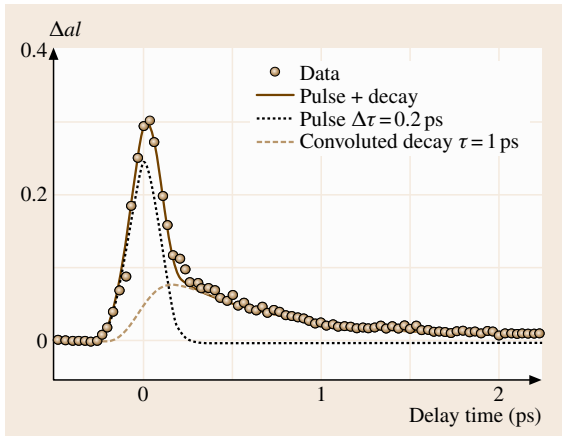


Fig. 11.56 Typical example of the absorption change

Δal , shows population decrease in the ground state $|g\rangle$. This signal reflects a process of ground-state recovery.

The transient absorption shows an exponential decay profile, while *two-photon absorption (TPA)* in which pump and probe pulses absorbed simultaneously results in an instantaneous response following the temporal profile of the pump pulse, as illustrated in Fig. 11.55. The TPA reveals hidden electronic levels which are not detectable in linear spectroscopy.

Example of Pump-Probe Measurement

A typical example of the absorption change is shown in Fig. 11.56 [11.58]. The signal consists of two components: a Gaussian pulse with 0.2-ps width which is determined by the pulse duration of the laser and an exponential decay with decay constant $\tau = 1$ ps. The former is caused by the TPA. Changing the pump and probe frequencies, we can obtain a TPA spectrum directly [11.59]. The latter arises from the transient absorption from the excited state $|e_1\rangle$ to the higher excited state $|e_2\rangle$ in Fig. 11.55. Its decay constant reflects the decay time of the excited state $|e_1\rangle$. It is noted that convolution analysis is required in this case in which the decay time is comparable to the pulse duration. Here we calculated a convolution of Gaussian shape with 0.2-ps width and a single exponential decay with a 1-ps decay constant, shown in the figure by a broken line.

Z-scan

This simple technique allows us to measure both the sign and magnitude of the nonlinear refractive index n_2 . A schematic set-up is shown in Fig. 11.57. A laser beam with a Gaussian spatial beam profile is focused at $z = 0$ and the sample position is varied. The intensity transmitted through the aperture is measured as a function of the sample position z shown in Fig. 11.57b. Here the sample acts as a lens whose focal length depends on the position z . Numerical calculation shows [11.60]

$$\Delta T \approx 0.4 \Delta \Phi, \tag{11.116}$$

where (11.102) is used. Thus we can obtain n_2 directly.

Four-Wave Mixing

There are many variations of four-wave mixing (FWM) with two or three beams, which have the same frequency (degenerate) or different frequencies (nondegenerate). This phenomenon is based on the interference between several beams inside the material [11.61]. FWM spectroscopy generally provides information on

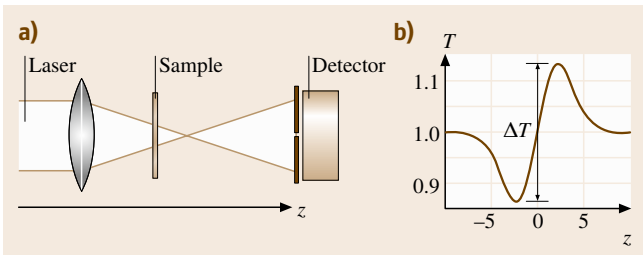


Fig. 11.57 (a) Schematic illustration of Z-scan measurement, and (b) normalized transmission against z

coherent processes in the excited states. This technique is also used to estimate the value of $\chi^{(3)}$.

11.4.5 Terahertz Time-Domain Spectroscopy

As a unique application of ultrashort pulsed lasers, terahertz (THz) time-domain spectroscopy (TDS) is introduced in this section. The THz region is located between microwave radiation and infrared light. Due to the lack of a suitable light source and detector, spectroscopy in this region was difficult and tedious. After the development of the mode-locked Ti:sapphire laser, THz TDS is intensively applied to many materials, e.g. doped semiconductors, superconductors, biomaterials [11.62]. The TDS enables us to obtain a waveform of the THz electric field $E(t)$ itself, not $|E(t)|^2$ as in conventional spectroscopy. This provides us a lot of advantages, e.g. simultaneous determination of real and imaginary parts of the dielectric function.

A schematic illustration of the generation and detection method for a THz pulse using a photoconductive antenna is depicted in Fig. 11.58 [11.63]. The antenna structure is fabricated on a substrate of semi-insulating semiconductors, e.g. low-temperature grown (LT)-GaAs. As an emitter, the antenna is subjected to a DC voltage and irradiated with a femtosecond laser around the gap between the dipoles, as illustrated in Fig. 11.58a. Then the mono-cycle THz pulse $E(t)$ is emitted according to the simple formula

$$E(t) \propto \frac{\partial j_e}{\partial t}, \quad (11.117)$$

where j_e is the surge current due to photocarriers created by the irradiation of the laser pulse. Over 30 THz generation has been reported by using 15-fs pulses. The alternative method is OR (Sect. 11.4.1) of ultrashort pulses; generation of ultra-broadband infrared pulse beyond 100 THz by using 10-fs pulses and GaSe crystals has also been demonstrated [11.64].

The antenna is also used as a receiver; photocarriers created by the pulse irradiation provide a transient current $j_d(t)$ which is proportional to the instantaneous THz electric field $E(\tau)$ as follows:

$$j_d(t) \propto \int E(\tau)N(t-\tau)d\tau, \quad (11.118)$$

where $N(t)$ is the number of photocarriers created by the laser pulse. If the pulse duration and the decay time of the $N(t)$ is negligibly short, $N(t) = N_0\delta(t)$, then

$$j_d(t) \propto E(t). \quad (11.119)$$

Thus the THz electric field can be reproduced by sweeping the time delay between the laser pulse and the THz

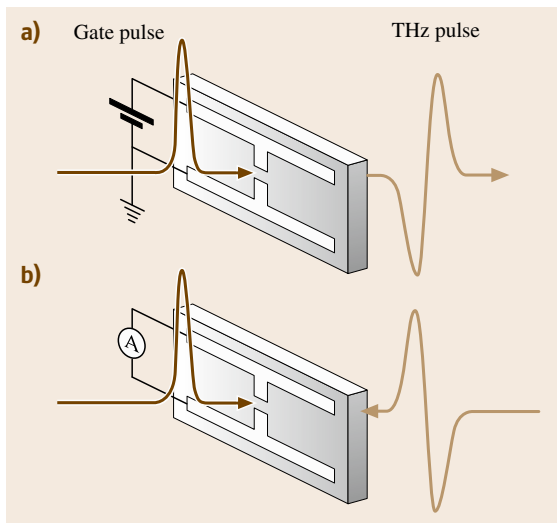


Fig. 11.58a,b Schematic illustration of (a) the generation and (b) the detection method for THz time-domain spectroscopy

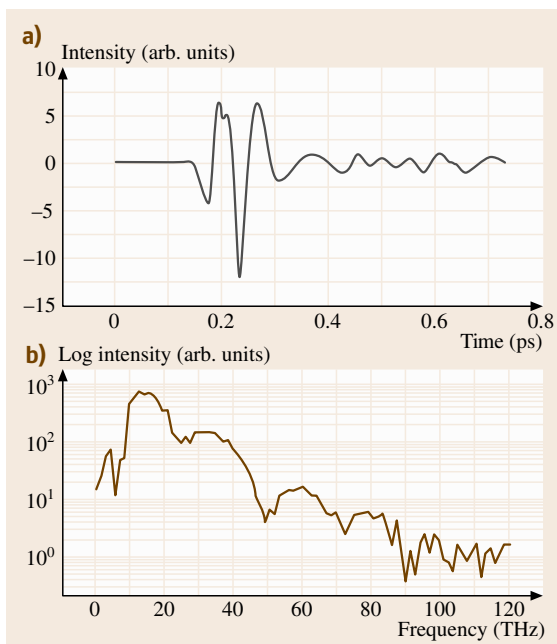


Fig. 11.59 (a) Temporal waveform of ultra-broadband THz radiation detected with a PC antenna. (b) Fourier-transformed electric-field spectrum of (a)

pulse. Figure 11.59a shows a typical example of temporal waveform of the ultra-broadband THz emission by OR with a 10-fs laser and a thin GaSe crystal detected

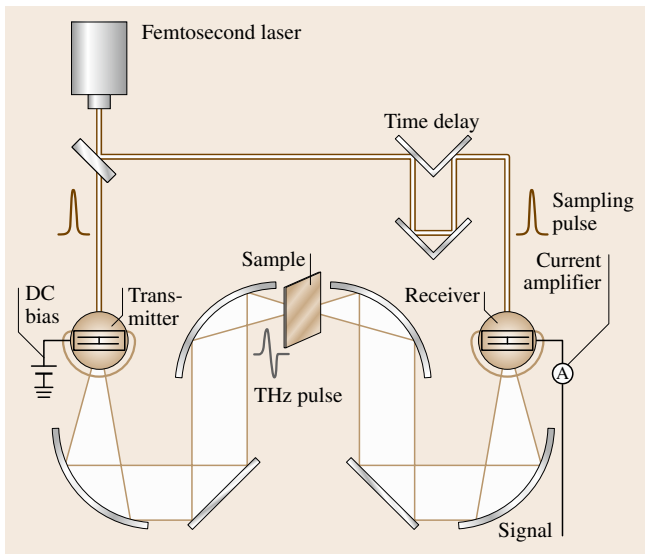


Fig. 11.60 Experimental set-up for THz TDS

with a PC antenna [11.65]. Its Fourier-transformed spectrum is also shown in Fig. 11.59b. The high-frequency region beyond 80 THz is detectable using a PC antenna. The alternative method is to use electrooptic sam-

pling, which achieves ultra-broad-band detection beyond 120 THz [11.66].

An experimental set-up is shown in Fig. 11.60. Parabolic mirrors are used for focusing light in the far- and mid-IR region.

The complex Fourier transformation of $E(t)$ is defined by

$$E(\omega) = \frac{1}{2\pi} \int E(t) \exp(-i\omega t) dt. \quad (11.120)$$

In the transmission measurement, the complex refractive index n can be obtained using

$$\frac{E(\omega)}{E_0(\omega)} = \exp \left\{ -i[n(\omega) - 1] \frac{L\omega}{c} \right\}, \quad (11.121)$$

where L is the sample thickness and $E(\omega)$ and $E_0(\omega)$ are Fourier transformations of the transmitted and incident waveform, respectively. Thus the real and imaginary parts are determined simultaneously without complex analyses such as the Kramers–Kronig transformation or the ellipsometry introduced in Sect. 11.1.4.

THz waves penetrate dry materials such as paper, ceramics and plastics but are strongly absorbed in water. Recently *terahertz imaging* has been used for drug detection, luggage inspection and integrated circuit inspection [11.67].

11.5 Fiber Optics

Optical fiber technology has developed rapidly during the last 30 years under the demands of the telecommunication network. Today a variety of commercial and laboratory applications of fiber optics are going on because of the excellent properties of optical fiber, e.g. flexibility and compactness. This section summarizes the unique properties of fibers and their characterization methods.

In its simplest form an optical fiber consists of a central glass core surrounded by a cladding layer whose refractive index n_1 is lower than the core index n_0 .

Figure 11.61 shows schematically the cross section and path of a ray propagating via total internal reflection in a step-index fiber. The critical angle for the total internal reflection at the interface is expressed as

$$\theta_c = \sin^{-1} \left(\frac{n_1}{n_0} \right)$$

The fiber numerical aperture (NA), which is defined as the sine of the half-angle of acceptance, is given by

$$NA = \sin(\theta_{\max}) = \sqrt{n_0^2 - n_1^2}.$$

Two parameters that characterize the step-index fiber are the normalized core–cladding index difference

$$\Delta = \frac{n_0 - n_1}{n_1}$$

and the so-called V parameter defined as

$$V = \frac{2\pi a}{\lambda} \sqrt{n_0^2 - n_1^2},$$

where a is the radius of core and λ is the wavelength of light.

The V parameter determines the number of modes supported by the fiber. A step-index fiber supports a single mode if $V < 2.405$. Fibers with a value of V greater than this are multimodal. More sophisticated index profiles were developed to modify the mode profile and dispersion. Detailed analysis of fiber modes in various structures is described in the textbook [11.68].

A common material for optical fiber is silica glass synthesized by chemical vapor deposition. The refractive index difference between the core and cladding is introduced by selective doping during the fabrication process. Dopants such as GeO_2 and P_2O_5 increase the

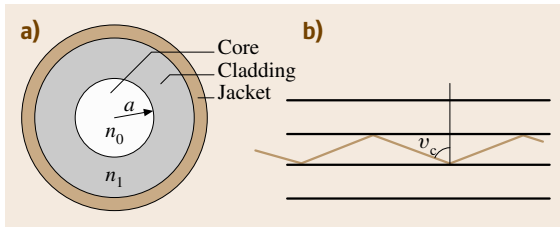


Fig. 11.61a,b Cross section of a step-index fiber (a) and the path of a ray propagating via total internal reflection (b)

refractive index of silica and are used for the core, while materials such as boron and fluorine decrease the refractive index of silica and are used for the cladding.

The fabrication process for optical fibers involves two stages: the formation of a preform and drawing into a fiber. A cylindrical preform with the desired index profile and relative core-cladding dimensions is fabricated through chemical vapor deposition. The preform is then drawn into a fiber using a precision-feed mechanism into a furnace. The fabrication methods for optical fibers are described in [11.69].

11.5.1 Fiber Dispersion and Attenuation

Chromatic dispersion and attenuation of the optical signal are the most important fiber parameters for telecommunications.

Optical Attenuation in Fibers

If P_i is the incident power introduced into a fiber of length L , the transmitted power P_t is expressed by

$$P_t = P_i \exp(-\alpha L),$$

where α is the conventional attenuation constant. Customarily, α is expressed in the unit of dB/km using the following definition.

$$\alpha_{\text{dB}} = -\frac{10}{L} \log \left(\frac{P_t}{P_i} \right).$$

There are three principal attenuation mechanisms in fibers: absorption, scattering and radiative loss. Radiation losses are generally kept small enough by using thick cladding.

Figure 11.62 shows the measured loss spectrum of a typical low-loss silica fiber [11.69]. Silica suffers from absorption due to electronic transitions in the ultraviolet region below 170 nm and absorption due to vibrational transitions in the infrared beyond 2 μm , but is highly transparent in the visible and near-infrared. In this region the fundamental attenuation mechanism is

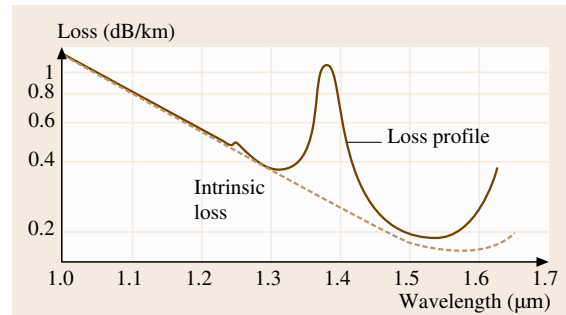


Fig. 11.62 Measured loss spectrum of a single-mode silica fiber. The *dashed curve* shows the contribution resulting from Rayleigh scattering (after [11.69])

Rayleigh scattering due to the irregular glass structure. Intrinsic losses in silica fiber due to Rayleigh scattering is estimated to be

$$\alpha_R = \frac{C_R}{\lambda^4},$$

where the constant C_R is in the range 0.7–0.9 dB/km μm^4 depending on the constituents of the fiber core. Typical losses in modern fibers is around 0.2 dB/km near 1.55 μm . Conventional silica fiber has absorption peaks at 1.4, 2.2 and 2.7 μm due to OH vibration modes and these absorption peaks are sensitive to water contamination.

Attenuation Measurement

There are two general methods for the measurement of fiber loss; the cut-back method and optical time-domain reflectometry (OTDR). In any scheme special attention must be paid to uncertainty arising from the source-to-fiber coupling. The cut-back method is a destructive evaluation which neatly avoids the difficulty [11.70]. It operates in the following way.

- Couple the light from the source into a long length of fiber.
- Measure the light output with a large-area detector.
- Cut the fiber back by a known length and measure the change in the light output.

The change in the output is considered to arise from the attenuation in the cut fiber.

In the case of a single-mode fiber, the fiber may be cut back to a relatively short length (several meters) where the cladding modes are effectively removed. However, if the higher mode is near or just beyond the cut-off, we may need a sufficiently long length of

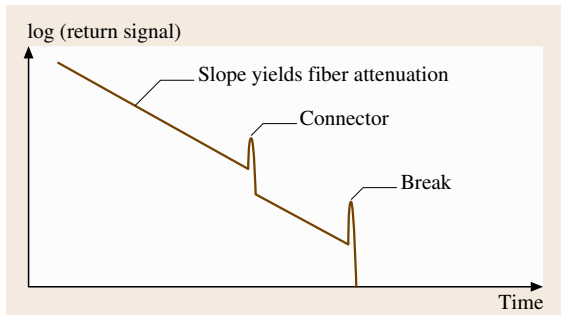


Fig. 11.63 Typical OTDR signal. OTDR can be used for attenuation measurement, splice and connector loss

fiber to strip off the unfavorable lossy modes [11.71]. In the case of multimode fiber the situation becomes more delicate because the attenuation depends on the modes, i. e. higher-order modes have higher losses. So, we should try to excite modes evenly and wait until the mode equilibrium is established through mode conversion. This may need a considerable length of fiber, typically ≈ 1 km.

Nondestructive loss measurement has now become possible with the technological advancement of low-loss single-mode splices or connectors, simply by assuring that the connector loss is much smaller than the fiber loss.

Optical time-domain reflectometry (OTDR) is another nondestructive evaluation method for attenuation. In this method the fiber is excited with a narrow laser pulse and a continuous backscattering signal from the fiber is recorded as a function of time. Assuming a linear and homogeneous backscattering process the decrease in backscattered light with time reflects the round-trip attenuation as a function of distance.

Figure 11.63 shows a typical OTDR signal. The linear slope yields the fiber attenuation and the sudden drop in intensity represents the splice loss; the narrow peak indicates a reflection. The OTDR method enables the evaluation of the loss distribution along the fiber including splice loss even in the deployed fiber. OTDR is also very sensitive to the excitation condition into the fiber, so control of the launch condition is the key for all attenuation measurement of fibers.

Chromatic Dispersion

The refractive index of every material depends on the optical frequency; this property is referred to as chromatic dispersion. In the spectral region far from absorption the index is well-approximated by the Sellmeier equation. For bulk fused silica $n(\lambda)$ is expressed

by the equation,

$$n(\omega)^2 = 1 + \sum_{j=1}^m \frac{B_j \omega_j^2}{\omega_j^2 - \omega^2},$$

where ω_j is the resonance frequency and B_j is the strength of the j th resonance. For bulk fused silica, these parameters are found to be $B_1 = 0.6961663$, $B_2 = 0.4079426$ and $B_3 = 0.8974794$, $\lambda_1 = 0.0684043 \mu\text{m}$, $\lambda_2 = 0.1162414 \mu\text{m}$, and $\lambda_3 = 9.896161 \mu\text{m}$ [11.72], where $\lambda_j = 2\pi c/\omega_j$ and c is the speed of light.

Dispersion plays a critical role in the propagation of short optical pulses because the different spectral components propagate with different speeds, given by $c/n(\omega)$. This causes dispersion-induced pulse broadening, which is detrimental for optical communication systems. The effect of chromatic dispersion can be analyzed by expanding the propagation constant β in a Taylor series around the optical frequency ω_0 on which the pulse spectrum is centered.

$$\beta(\omega) = n(\omega) \frac{\omega}{c} = \beta_0 + \beta_1(\omega - \omega_0) + \frac{1}{2} \beta_2(\omega - \omega_0)^2 + \dots,$$

where

$$\beta_m = \left(\frac{d^m \beta}{d\omega^m} \right)_{\omega=\omega_0} \quad (m = 0, 1, 2, 3, \dots).$$

The parameter β_1 and β_2 are related to the refractive index n through the relations

$$\beta_1 = \frac{1}{v_g} = \frac{1}{c} \left(n + \omega \frac{dn}{d\omega} \right),$$

$$\beta_2 = \frac{1}{c} \left(2 \frac{dn}{d\omega} + \omega \frac{d^2 n}{d\omega^2} \right),$$

where v_g is the group velocity. The envelope of the optical pulse moves at the group velocity. The parameter β_2 , which is a measure of the dispersion of group velocity, is responsible for the pulse broadening. This phenomenon is known as group velocity dispersion (GVD). In bulk fused silica, the GVD parameter β_2 decreases with increasing wavelength, vanishes for wavelengths of about $1.27 \mu\text{m}$ and becomes negative for longer wavelengths. This wavelength is referred to as the zero-dispersion wavelength, denoted by λ_D .

The dispersion behavior of actual silica fiber deviates from the bulk fused silica case for the following two reasons. First, the fiber core usually has small

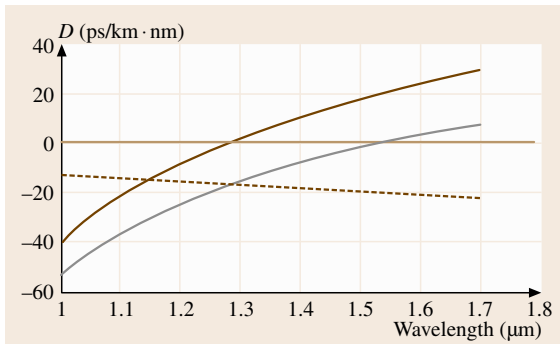


Fig. 11.64 Wavelength dependence of the dispersion parameter D for dispersion-shifted fiber (brown line). Brown curve and dotted line represent D for silica bulk material and wave-guide dispersion, respectively

amounts of dopants such as GeO_2 and P_2O_5 . In this case, we should use the Sellmeier equation with parameters appropriate to the amount of doping [11.73]. Second, because of dielectric waveguiding, the effective mode index reflects the field distribution in the core and cladding and is slightly lower than the material index $n(\omega)$ of the core. The field distribution itself depends on ω , and this results in what is commonly termed waveguide dispersion [11.74]. Waveguide dispersion is relatively small except near the zero-dispersion wavelength λ_D , so the main effect of the waveguide contribution is to shift λ_D toward longer wavelengths; $\lambda_D = 1.31 \mu\text{m}$ for standard single-mode fiber.

The dispersion parameter D (ps/km · nm) is commonly used in fiber optic literature in place of β_2 . D is related to β_2 by the relation.

$$D = \frac{d\beta_1}{d\lambda} = -\frac{2\pi c}{\lambda^2} \beta_2 \approx \frac{\lambda}{c} \frac{d^2 n}{d\lambda^2}$$

An important aspect of waveguide dispersion is that the contribution to D depends on design parameters such as the core radius a and the core-cladding index difference Δ . As shown in Fig. 11.64 this feature was used to shift the zero-dispersion wavelength λ_D in the vicinity of $1.55 \mu\text{m}$ where the fiber loss is at its minimum [11.74]. Such dispersion-shifted fibers, called zero- and nonzero-dispersion shifted fibers, depending on whether $D = 0$ at $1.55 \mu\text{m}$ or not, play an important role in optical communication network systems.

Dispersion Measurements

Optical pulse method is a simple time-domain measurement. Pulse delay through an optical fiber is directly measured as a function of wavelength [11.75]. This

system usually consists of a fast optical pulse generator with a tunable laser source and a fast waveform monitor system, which are common to instruments characterizing optical transmission lines. However, the accuracy is limited by optical pulse distortion due to dispersion and the time resolution of the waveform monitor.

Phase shift method is the prevailing method because higher time-domain resolution can be obtained with a relatively low frequency modulation ($< 3 \text{ GHz}$) [11.76]. The measurement scheme is shown in Fig. 11.65.

A tunable light source like an external cavity laser is usually used as the light source. The light is modulated by a sinusoidal wave at a frequency of f_m with a LiNbO_3 Mach-Zender modulator. The optical signal propagated through a test fiber is converted to an electrical signal and then compared with the reference signal using a phase comparator. The phase difference $\phi(\lambda)$ is measured as a function of the wavelength λ . The group velocity delay $\tau(\lambda)$ (s/km) for an optical fiber of length L (km) is obtained by the equation

$$\tau(\lambda) = \frac{\phi(\lambda)}{f_m L},$$

where $\tau(\lambda)$ is supposed to be approximated by a three-term Sellmeier equation

$$\tau(\lambda) = A\lambda^2 + B + \frac{C}{\lambda^2}.$$

Usually, the A , B and C parameters are determined from the delay data and the GVD value is then obtained by differentiating the curve with respect to λ .

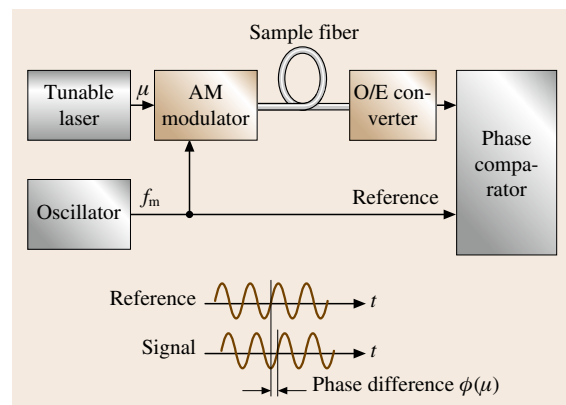


Fig. 11.65 Diagram for dispersion measurement by the phase-shift method

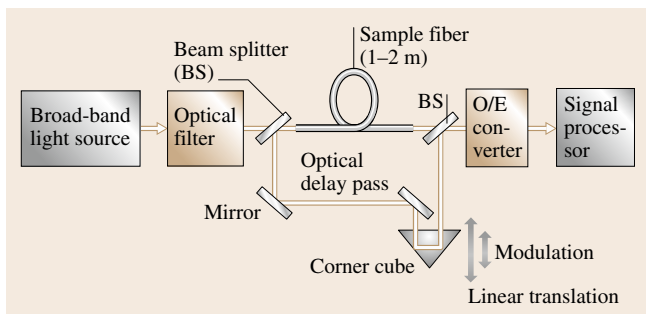


Fig. 11.66 Measurement scheme for the interference measurement method

Interference measurement method is appropriate for short fiber lengths, and allows a detailed and direct comparison of the optical phase shifts between a test fiber and a reference arm. This measurement scheme is illustrated in Fig. 11.66 [11.77].

A broadband light source like white light or an LED is used as the light source in order to reduce the coherence length. Typically, a tunable optical filter with a bandwidth of around 10 nm is introduced in front of the interferometer. A free-space delay line or optical fiber of which the GVD is well-known is utilized as the reference arm. By moving the modulated corner cube, the position d corresponding to the zero-pass interference peak is detected. The group velocity delay $\tau(\lambda)$ for the test fiber is expressed by

$$\tau(\lambda) = \frac{2(d - d_0)}{c},$$

where d_0 is the zero-pass difference position at the reference wavelength and c is the velocity of light. The GVD is also estimated by differentiating the smoothed $\tau(\lambda)$ curve with respect to λ .

11.5.2 Nonlinear Optical Properties

This subsection deals with the nonlinear optical properties of fiber. The low loss and long interaction length of optical fibers make nonlinear processes significant. Stimulated Raman and Brillouin scattering limits the power-handling ability of fibers. Four-wave mixing presents an important limit on the channel capacity in wavelength division multiplexing (WDM) systems. Soliton formation and nonlinear polarization evolution are also summarized.

The small cross section and long interaction length of optical fiber make nonlinear optical process significant even at modest power levels. Recent developments

in fiber amplifiers have increased the available power level drastically. Optical nonlinearities are usually detrimental to optical communication networks and put some limits on the power-handling ability of fibers in medical and industrial applications. On the other hand, these optical nonlinearities are utilized in the generation of ultra-short pulse, soliton-based signal transmission, and Raman amplifiers.

As SiO_2 is a symmetric molecule, the second-order nonlinear susceptibility $\chi^{(2)}$ vanishes for silica glasses. So, nonlinear effects in optical fibers originate from the third-order susceptibility $\chi^{(3)}$, which is responsible for phenomena such as third-harmonic generation, four-wave mixing and nonlinear refraction.

In the simplest form, the refractive index can be written as

$$n(\omega, I) = n(\omega) + n_2 I.$$

Self-phase modulation (SPM) is the most important phenomena among the various nonlinear effects arising from the intensity dependence of the refractive index. The self-induced phase shift experienced by an optical field during its propagation is

$$\phi = (n + n_2 I) k_0 L,$$

where $k_0 = 2\pi/\lambda$ and L is the length of the fiber.

The measured n_2 value for bulk silica at $1.06 \mu\text{m}$ is $2.7 \times 10^{-20} \text{ m}^2/\text{W}$ [11.78]. Measured values for various silica optical fibers are found to be in the range $2.2\text{--}3.9 \times 10^{-20} \text{ m}^2/\text{W}$ [11.79]. The scatter of the data may be partly ascribed to the difference of the doping in the core materials of the fibers.

Pulse Compression and Solitons

Figure 11.67 illustrates what happens to an optical pulse which propagates in a nonlinear optical medium. The local index change raises so-called self-phase modulation. Since n_2 is positive, the leading edge of the pulse produces a local increase in refractive index. This results in a red shift in the spontaneous frequency. On the other hand, the pulse experiences a blue shift on the trailing edge.

If the fiber has a normal dispersion at the central wavelength of the optical pulse, the red-shifted edge will advance and the blue-shifted trailing edge will retard, resulting in pulse spreading in addition to the normal chromatic dispersion. However, if fiber exhibits anomalous dispersion, the red-shifted edge will retard and the optical pulse will be compressed. Near the dispersion minimum, the optical pulse is stabilized and

propagates without changing shape at a critical shape. This optical pulse is called a soliton [11.80]. A soliton requires a certain power level in order to maintain the necessary index change. The record for soliton transmission is now well over 10 000 km, which was achieved by utilizing the gain section of a stimulated Raman amplifier or a rare-earth-doped fiber amplifier. In the laboratory, optical fiber nonlinearity is used in the mode-locked femtosecond laser [11.81, 82] and the generation of white continuum [11.83].

Third-harmonic generation and the four-wave mixing effect are based on the same $\chi^{(3)}$ nonlinearity but they are not efficient in optical fibers because of the difficulty in achieving the phase-matching condition. However, WDM signal transmission systems encounter serious cross-talk problems arising from four-wave mixing between the WDM channels near the zero-dispersion wavelength of 1.55 μm [11.85].

The nonlinear optical effects governed by the third-order susceptibility are elastic, so no energy is exchanged between the electromagnetic field and the medium. Another type of nonlinear effect results from stimulated inelastic scattering, in which the optical field transfers part of its energy to the nonlinear medium. Two such scattering processes are important in optical fiber: 1) stimulated Raman scattering (SRS), and 2) stimulated Brillouin scattering (SBS).

The main difference between the two is the phonon participating in the process; optical phonons participate in SRS while acoustic phonons participate in SBS. In optical fiber SBS occurs only in the backward direction while SRS can occur in both directions. The equation governing the growth of the Raman-shifted mode is as follows

$$\frac{dI_S}{dz} = \frac{g_R}{a_{\text{eff}}} I_P - \alpha I_S,$$

where I_S is the Stokes intensity, I_P is the pump intensity and a_{eff} is the effective area of the modes. g_R is Raman gain coefficient. The same equation holds for SBS by replacing g_R with the Brillouin gain coefficient g_B . The Raman gain spectrum in fused silica is shown in Fig. 11.68.

The Raman gain spectrum of silica fiber is broad, extending up to 30 THz [11.84] and the peak gain $g_R = 10^{-13}$ m/W occurs for a Stokes shift of ≈ 13 THz for a pump wavelength near 1.5 μm . In contrast to Raman scattering, Brillouin gain is extremely narrow with a bandwidth < 100 MHz and the Stokes shift is ≈ 1 GHz close to 1.5 μm .

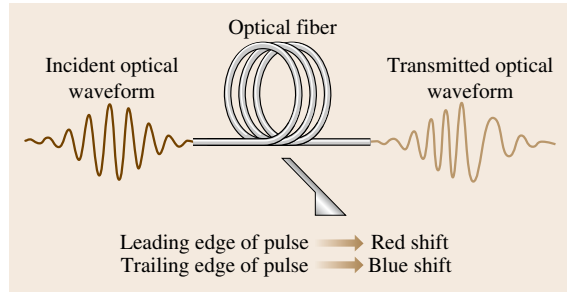


Fig. 11.67 Pulse evolution in a nonlinear medium

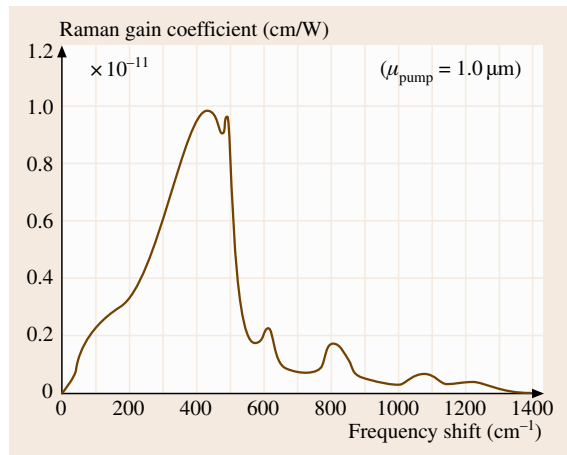


Fig. 11.68 Raman gain spectrum in fused silica (after [11.84])

SRS and SBS exhibit a threshold-like behavior against pump power. Significant conversion of pump energy to Stokes radiation occurs only when the pump intensity exceeds a certain threshold level. For SRS in a single mode fiber with $\alpha L \gg 1$, the threshold pump intensity is given by [11.86]

$$I_P^{\text{th}} = 16\alpha \frac{a_{\text{eff}}}{g_R}.$$

SRS can be observed at a power level of ≈ 1 W. Similarly, the threshold pump intensity for SBS is given by [11.86]

$$I_P^{\text{th}} = 21\alpha \frac{a_{\text{eff}}}{g_R}.$$

The Brillouin gain coefficient $g_B = 6 \times 10^{-11}$ m/W and is larger by three orders of magnitude compared with g_R . So, SBR threshold is ≈ 1 mW for CW narrow-bandwidth pumping.

Silica fibers with large effective cross section and short length have a significantly higher power-handling

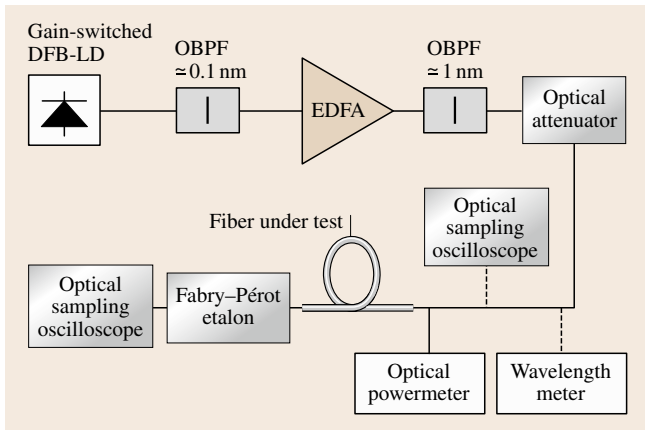


Fig. 11.69 Schematic diagram of the measurement of optical non-linearity of fiber based on the self-phase modulation method

ability and the broad-spectrum operation helps to increase the power-handling ability of the fiber.

Measurement of Nonlinear Refractive Index n_2

The nonlinear refractive index is expressed by the equation,

$$n(\omega, E^2) = n(\omega) + n_2 E^2,$$

In order to characterize the nonlinearity of the fiber, it is more practical to use the following equation.

$$n(\omega, P) = n(\omega) + \frac{n_2}{A_{\text{eff}}} P$$

where P is the power propagating in the fiber and A_{eff} is the effective area of fiber defined by the equation, [11.80]

$$A_{\text{eff}} = \frac{2\pi \left[\int_0^\infty |E(r)|^2 r dr \right]}{\int_0^\infty |E(r)|^4 r dr},$$

where $E(r)$ presents the field distribution in the fiber; A_{eff} is approximately related to the mode field diameter (MFD) by the following equation

$$A_{\text{eff}} \approx \pi \left(\frac{\text{MFD}}{2} \right)^2.$$

For reliable evaluation of the nonlinearity of fiber, a variety of methods have been developed based on self-phase modulation [11.87–89], cross-phase modulation [11.90], four-wave mixing [11.91] and interferometry.

Figure 11.69 shows a measuring system based on self-phase modulation developed by *Namihira* et al. [11.87]. The output of a gain-switched DFB-LD with

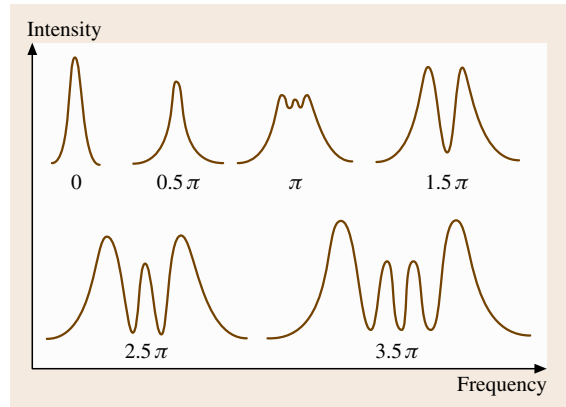


Fig. 11.70 Spectral evolution due to the self-phase modulation as a function of incident power (after [11.87])

a pulse width of 26.5 ps is filtered by a narrow-band filter with a bandwidth of 0.1 nm to get a nearly transformation-limited beam. The beam is amplified by an Er-doped fiber amplifier (EDFA), and is introduced into a test fiber through a variable optical attenuator. The optical spectra of the fiber output are measured by a Fabry-Pérot interferometer. The observed output spectra from the fiber for various input powers is shown in Fig. 11.70 [11.87]. The number of observed spectral peaks M is related to the maximum phase shift, Φ_{max} by the equation

$$\Phi_{\text{max}} = \left(M - \frac{1}{2} \right) \pi,$$

Φ_{max} is also related to (n_2/A_{eff}) by the equation

$$\Phi_{\text{max}} = \left(\frac{2\pi}{\lambda} \right) \left(\frac{n_2}{A_{\text{eff}}} \right) L_{\text{eff}} P_0,$$

where P_0 is the incident power into the test fiber and L_{eff} is the effective length of fiber and expressed by the equation,

$$L_{\text{eff}} = \frac{1 - e^{-\alpha L}}{\alpha},$$

where α is the absorption coefficient and L is the length of the test fiber. (n_2/A_{eff}) can be estimated from the slope of Φ_{max} against P_0 .

11.5.3 Fiber Bragg Grating

The photosensitivity of silica fiber was discovered in 1978 by *Hill* et al. at the Communications Research Center in Canada [11.92]. Fiber Bragg grating (FBG) devices based on these phenomena allow the integration of sophisticated filtering and dispersion functions into

a fiber and have many applications in optical fiber communication and optical sensor systems. This subsection summarizes FBG technology and their properties. More information on FBGs can be found in the following references [11.93–95].

Photosensitivity

When ultraviolet light radiates an optical fiber, the refractive index is changed permanently; this effect is called photosensitivity. The change in refractive index is permanent if the fiber is annealed appropriately. These phenomena were first discovered in a fiber with a germanium-containing core, and have been observed in a variety of different fibers. However, optical fiber with germanium-containing core remains the most important material for FBG devices. 248 and 198 nm radiation from KrF and ArF lasers with a pulse width of ≈ 10 ns at a repetition rate of ≈ 100 pps are most commonly used. Typically fibers are exposed to laser light for a few minutes at irradiation levels in the range 100–1000 mJ/cm². Under these conditions, the index change Δn of fibers with germanium-containing cores is in the range between 10^{-5} – 10^{-3} . Irradiation at higher intensities introduces the onset of different kinds of photosensitive processes, leading to a physical damage. The index change can be enhanced by processing fibers prior to irradiation with hydrogen-loading [11.96] and flame-brushing [11.97] techniques. (Photoinduced index changes up to 100 times greater are obtained by hydrogen loading for a Ge-doped core fiber, and a ten times increase in the index change can be achieved using flame brushing.) The physical

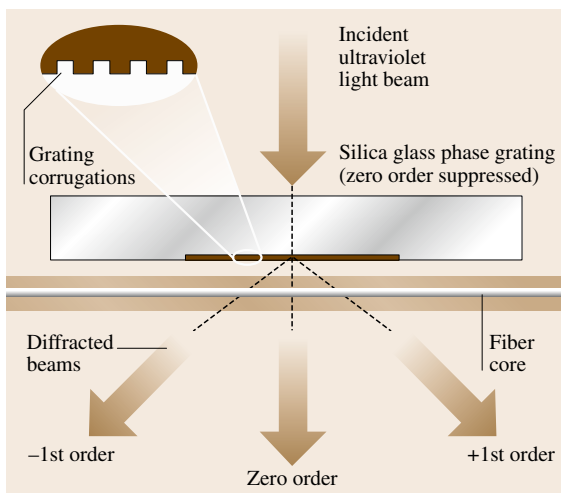


Fig. 11.71 FBG fabrication with phase mask technique

process underlying photosensitivity is not completely understood, however it is believed to be related to the bleaching of the color centers in the ultraviolet spectral range.

Fabrication Techniques

Many techniques have been developed for the fabrication of FBG, e.g. the transverse holographic technique [11.98], the phase mask technique [11.99] and the point-by-point technique [11.100]. The phase mask technique is the most common because of its simple manufacturing process, high performance and great flexibility.

Figure 11.71 shows a schematic diagram of the phase mask technique for the manufacture of FBGs. The phase mask is made from a flat silica-glass slab with a one-dimensional periodic structure etched using photolithography techniques.

The phase mask is placed almost in contact with the optical fiber at a right angle to the corrugation and the ultraviolet light is incident normal to the phase mask. Most of the diffracted light is scattered in the +1 and -1 orders because the depth of the corrugation is designed to suppress diffraction into the zeroth order. If the period of the phase mask grating is Λ , the period of the photoimprinted FBG is $\Lambda/2$, which is independent of the wavelength of the irradiated ultraviolet. The phase mask technique greatly simplifies the manufacturing process and its low coherence requirement on the ultraviolet beam permits the use of a conventional excimer laser. The phase mask technique not only yields high-performance devices, but is very flexible, i. e. apodization and chirping techniques are easily introduced to control the spectral response characteristics of the FBGs [11.101].

Another approach to the manufacture of FDB gratings is the point-by-point technique, in which each index perturbation is written point by point. This technique is useful for making long-period FBG devices that are used for band-rejection filters and fiber-amplifier gain equalizers.

Properties of FBGs

Light propagating in an FBG is backscattered by Fresnel reflection from each successive index change. The back reflections add up coherently in the region of the Bragg wavelength, λ_B and cancel out in the other wavelength regions.

The reflectivity of strong FBGs can approach 100% at the Bragg wavelength, whereas the light in the other spectral region passes through the FBG with negligible

loss. The Bragg wavelength λ_B is given by

$$\lambda_B = 2N_{\text{eff}}\Lambda,$$

where N_{eff} is the modal index of the fiber and Λ is the grating period.

The Bragg grating can be described theoretically by using coupled-mode equations [11.102]. Here important properties are summarized for the tightly bound single-mode propagation through a uniform grating. The grating is assumed to have a sinusoidal index profile with amplitude Δn . The reflectivity R of the grating at the Bragg wavelength is expressed by the simple equation, $R = \tanh^2(\kappa L)$ where $k = (\pi/\lambda)\Delta n$ is the coupling coefficient and L is the length of the grating. The reflectivity is determined by κL , and a grating with a κL greater than one is termed a strong grating whereas a weak grating has a κL less than one. Figure 11.72 shows the typical reflection spectra for weak and strong gratings.

The other important property of FBGs is the reflection bandwidth. In the case of weak coupling ($\kappa L < 1$), the $\Delta\lambda_{\text{FWHM}}$ is approximated by the spectral distance from the Bragg wavelength, λ_B to the neighboring dip wavelength, λ_D ; $\Delta\lambda_{\text{FWHM}} \approx (\lambda_0 - \lambda_B) = \lambda_B^2/(2N_{\text{eff}}L)$. The bandwidth of a weak grating is inversely proportional to the grating length and can be very narrow for a long grating. On the other hand, in the case of strong coupling ($\kappa L > 1$), $\Delta\lambda_{\text{FWHM}}$ is approximated by the wavelength difference between the adjacent re-

flexion dips across the Bragg wavelength, $\Delta\lambda_{\text{FWHM}} = 4\lambda_B^2\kappa/(\pi N_{\text{eff}})$. The bandwidth is directly proportional to the coupling coefficient κ .

The bandwidth of the FBG is limited by the attainable values of the index perturbation, Δn , of the photosensitivity, and several nanometers is the actual limit corresponding to $\Delta n \approx 0.001$ at wavelengths used for optical fiber telecommunications, 1.5 μm .

A chirped or aperiodic grating has been introduced in order to broaden the spectral response of FBGs.

The spectral response of a finite-length grating with a uniform index modulation has secondary maxima on either side of the main reflection peak, as shown in Fig. 11.72 [11.95]. This kind of response is detrimental to applications such as wavelength division multiplexing. However, if the index modulation profile Δn along the fiber length is apodized, these secondary peaks can be suppressed. Using the apodization technique, the side lobes of the FBG have been suppressed down to 30 \approx 40 dB.

Another class of grating, termed the long-period grating, was proposed by Vengsarkar et al. [11.103]. Gratings with longer periods, ranging into the hundreds of micrometers, involves coupling of a guided mode to forward-propagating cladding modes; the cladding modes are attenuated rapidly due to the lossy cladding coating. FBGs with a long-period grating act as transmission filters with rather broad dips and are utilized as band-rejection filters and fiber amplifier gain equalizers [11.104].

Measurement of FBG Performance

Narrow-band filters with high dynamic range are the key components for dense WDM fiber optic network systems.

However, their characterization was not easy until ultra-high resolution optical spectral analyzers became available. Q8384 (Advantest LTd.) and AQ6328C (Ando Co.) with a folded-beam four-grating configuration have a 0.01-nm resolution and 60-dB dynamic range at 0.2 nm away from the central wavelength. By using such a high-performance spectrometer together with a fiber-coupled broadband light source, characterization of FBGs is no longer difficult.

Applications of FBGs

Many potential applications of FBGs in optical fiber communication and optical sensor systems are reviewed in the reference [11.102]. FBG devices have many excellent properties for fiber optic communication systems, i. e., narrow-band and high-dynamic-range fil-

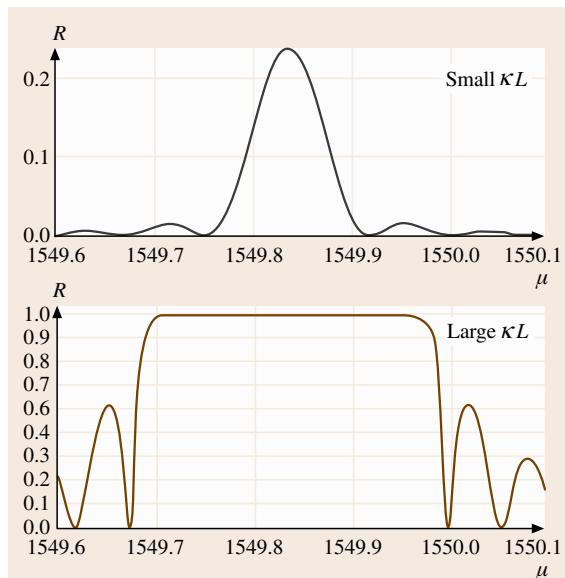


Fig. 11.72 Typical reflection spectra of weak and strong FBGs (after [11.95])

tering, low insertion loss, low back reflection and so on. So, FBG devices acquired a lot of applications in the fiber optic communication system in a short period, e.g., add-drop filtering devices, dispersion-compensation devices, gain-equalizing filters in fiber amplifiers, and wavelength locking of pump lasers.

Figure 11.73 shows some examples of FBG applications in optical fiber communication network systems. Figure 11.73a presents a schematic diagram of a multichannel dispersion compensator. FBG devices are inherently reflection filtering function whereas a transmission device is usually desired. A narrow-band transmission filtering function is commonly realized with the aid of an optical circulator. Figure 11.74b shows the wavelength locking of pump lasers for Er-doped optical amplifiers. Feedback of the weakly reflected light from FBG locks the lasing wavelength of diodes to λ_B . The temperature coefficient of the fractional change of Bragg wavelength, $\Delta\lambda_B/\lambda_B$ is $\approx 10^{-5}$ due to the very stable thermal properties of silica glass. This value is one order of magnitude lower than the temperature stability of the wavelength of DFB lasers, and is two orders of magnitude smaller than the gain peak shift of conventional laser diodes. So, wavelength locking of the pump laser stabilizes the properties of Er-doped fiber amplifiers against temperature shifts and aging effects.

A change of the in the value of L and N_{eff} causes a shift of the Bragg wavelength, and the fractional change, $\Delta\lambda_B/\lambda_B$ is given by the equation [11.106]

$$\frac{\Delta\lambda_B}{\lambda_B} = \frac{\Delta L}{L} + \frac{\Delta N_{\text{eff}}}{N_{\text{eff}}},$$

where $\Delta L/L$ and $\Delta N_{\text{eff}}/N_{\text{eff}}$ the fractional changes of the period and effective modal index, respectively. An axial change results in a shift of the Bragg wavelength given by the equation

$$\frac{1}{\lambda_B} \left(\frac{\Delta\lambda_B}{\varepsilon} \right) = \frac{1}{L} \frac{\Delta L}{\varepsilon} + \frac{1}{N_{\text{eff}}} \left(\frac{\Delta N_{\text{eff}}}{\varepsilon} \right).$$

The first term on the right is unity by definition and the second term, which is approximately -0.27 for silica fiber, represents the change due to the photoelastic effect. So, the fractional change of the Bragg wavelength due to axial strain is 0.73ε . This property of FBGs can be used in strain sensors [11.106].

11.5.4 Fiber Amplifiers and Lasers

Fiber amplifiers are key components in the current dense wavelength-division multiplexed (DWDM) telecommunication system. Er-doped fiber amplifiers (EDFA),

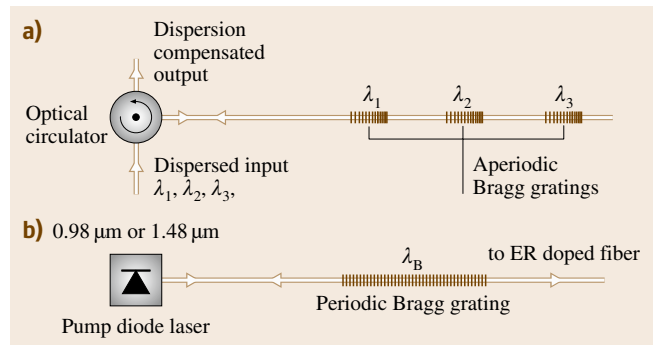


Fig. 11.73a,b Some applications of fiber Bragg gratings

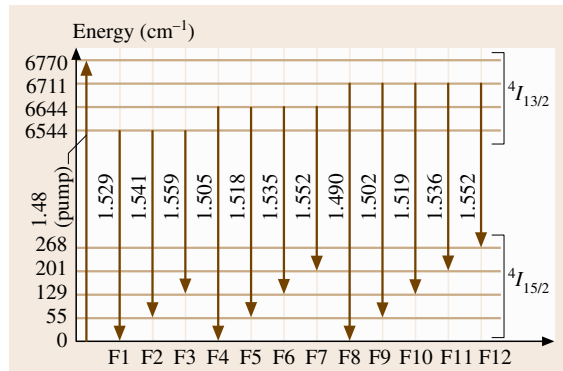


Fig. 11.74 Energy-level diagram for erbium. Optical gain occurs in the vicinity of $1.53 \mu\text{m}$ under pumping at a wavelength of 0.98 or $1.48 \mu\text{m}$ (after [11.105])

which have a stimulated emission band in the vicinity of $1.53 \mu\text{m}$, are most widely used as repeaters in the optical network. Fiber amplifiers and lasers have many excellent properties, e.g. high efficiency, compactness, thermal and mechanical stability, and so are used in many scientific, medical and industrial applications.

This subsection summarizes Er-doped fiber amplifiers and briefly introduces some recent advancements in femtosecond fiber lasers and high-power fiber lasers with a double-cladding structure.

Er-doped Fiber Amplifiers (EDFAs)

Energy Levels of Er. Figure 11.74 shows an energy diagram for erbium. Gain in EDFAs occurs in the vicinity of $1.53 \mu\text{m}$ when an inversion population exists between the $^4I_{13/2}$ and $^4I_{15/2}$ states; this is realized by optical pumping at the wavelengths of $0.98 \mu\text{m}$ (pumping to $^4I_{11/2}$) or $1.48 \mu\text{m}$ (pumping to $^4I_{13/2}$) [11.105, 107].

When Er ions are incorporated into the fiber core, each ion level, $^{2S+1}J_J$ presents Stark splitting due to

the interaction between the ion and host matrix. Other mechanisms, thermal fluctuation and inhomogeneous environments in the glass matrix further broaden the emission spectrum. Figure 11.75 shows the absorption and emission spectra for erbium in silica with aluminum and phosphorous codoping [11.108]. The spectrum is constructed from the superposition of the transitions between the Stark levels and is sensitive to the host material. Considerable effort has been devoted to obtaining broadened shapes for the emission spectra for a broadband amplifier. Use of alumino-silicate glass ($\text{SiO}_2\text{-Al}_2\text{O}_3$) results in slight broadening and smoothing over the pure SiO_2 . The use of fluoride-based glasses such as ZBLAN provides significant improvements on spectral width and smoothness [11.109, 110].

EDFA configuration. A general fiber amplifier configuration is shown in Fig. 11.76. A typical Er-doped

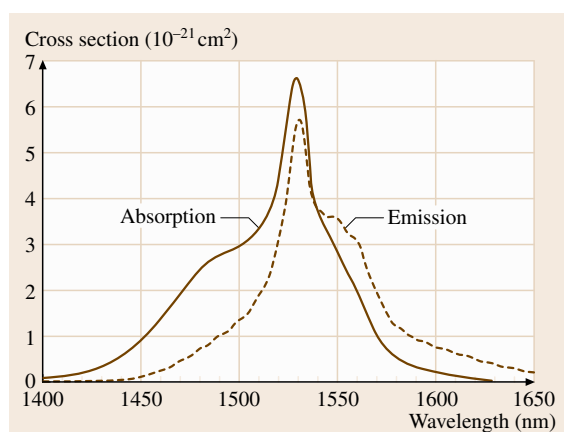


Fig. 11.75 Absorption and emission spectra for erbium in silica with aluminum and phosphorous codoping. Spectrum associated with the transition in Fig. 11.73 (after [11.108])

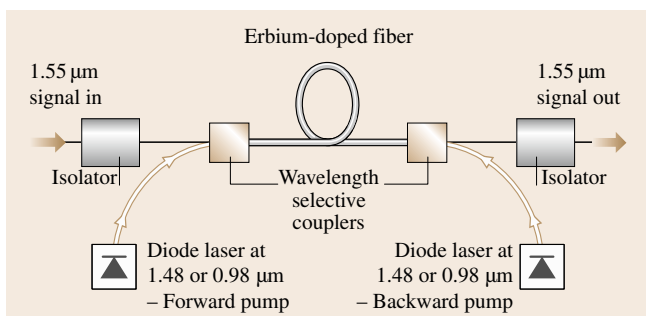


Fig. 11.76 Er-doped fiber amplifier configuration with bidirectional pumping

amplifier consists of an Er-doped fiber positioned between optical isolators. Pump light is introduced into the Er-doped fiber through a wavelength-selective coupler, which can be configured for either forward or backward pumping, or for bidirectional pumping. In either case, pump power is absorbed over the amplifier length, such that the population inversion varies with position along the fiber. To get the highest overall effect, the fiber length is chosen so that the length the fiber is transparent to the signal at the point of minimum pump power, i. e., the fiber end opposite to the pump laser for unidirectional pumping and at the midpoint for bidirectional pumping. Other factor like gain saturation and amplified spontaneous emission (ASE) may modifies the optimum length of fiber amplifier [11.111]. Optical isolators are usually positioned at the entrance and exit to avoid gain quenching, noise enhancement or possibly parasitic lasing due to the unfavorable backscattering or reflected light.

Operating regime. There are three operating regimes, which depend on the use intended for the amplifier [11.112]: 1) small-signal, 2) saturation and 3) deep saturation regimes. In the small-signal regime, a low input signal ($< 1 \mu\text{W}$) is amplified with negligible saturation. Small-signal gains of EDFAs range between 25 and 35 dB. The gain efficiency is defined as the ratio of the maximum small-signal gain to the input pump power. Gain efficiencies of well-designed EDFA are $\approx 10 \text{ dB/mW}$ for pumping at $0.98 \mu\text{m}$ and $\approx 5 \text{ dB/mW}$ for pumping at $1.48 \mu\text{m}$. In the saturation regime, the output power is reduced significantly from the power expected in the small-signal regime. Input saturation power is defined as the input signal power required to reduce the amplifier gain by 3 dB. Alternatively, saturation output power is defined as the amplifier output when the gain is reduced by 3 dB. For the power amplifier applications, where the amplifiers operate in the deep saturation regime, the power conversion efficiency between pump and signal is important.

However, to achieve deep saturation the input signal must be high enough, so the more important situation is the saturation regime, where the choice of pumping configuration and pump power can substantially influence the performance [11.112].

Noise and gain flattening. Noise is a very important factor in telecommunication applications and is quantified using the noise figure. The noise figure of an EDFA is defined in a manner consistent with the IEEE standard definition for a general amplifier. For a shot-noise-limited input signal, the noise figure is defined

as the signal-to-noise ratio of the input divided by the signal-to-noise ratio of the output. The most serious noise source of EDFA is amplified spontaneous emission (ASE), which can be reduced by ensuring that the population inversion is as high as possible. With 0.98 μm pumping theoretically limited noise figures of about 3 dB have been obtained, while the best results for 1.48 μm pumping have been around 4 dB because of the difference in the pump scheme [11.113].

DWDM systems need a flattened gain spectra for all wavelength channels. Gain-flattening techniques are classified into three categories. First, use of aluminosilicate glass or fluoride-based glass with smoother and broader gain spectra. Second, spectral filtering at the output of an amplifier or between the cascaded amplifiers. Third, hybrid amplifiers with different gain media in cascaded and parallel configurations. Flattened gain spectra of EDFA have been extended in the range 12 to 85 nm.

For more details of Er-doped amplifiers, excellent reviews and text books are available [11.111, 112, 115].

Other Fiber Amplifiers

EDFAs have excellent performances within the conventional gain band (1530–1560 nm) and recent efforts have resulted in the extension of EDFA gain into the longer wavelength range (1565–1625 nm). Other rare-earth dopants or dopant combinations have been used to produce fiber amplifiers that have gain at other wavelength regions. These include praseodymium-doped fiber amplifiers, which have gain at 1300 nm and are pumped at 1020 nm [11.116]. Thulium-doped fibers have been developed for amplification at 1480 nm [11.117, 118] and 1900 nm [11.119]. Ytterbium-doped fibers amplify radiation in the wavelength range from 975–1150 nm with the pump wavelengths between 910 and 1064 nm. Erbium-ytterbium codoped fibers provide gain around 1550 nm with the pumping sources, similar to ytterbium-doped fibers [11.120]. Neodymium-doped fiber amplifiers work in the wavelength range 1064–1088 nm under pumping at 810 nm.

Raman amplifiers have also been developed by using the fiber transmission line as a gain media to increase the bandwidth and flexibility of the optical network. Raman amplifiers need multiple high-power pump sources at different wavelengths to realize broadband amplification [11.121].

Fiber Lasers

Fiber lasers are configured by replacing the isolators at both ends of fiber amplifiers by fiber Bragg gratings or making a closed loop with couplers. In the case of

a ring laser one needs a coupler for the output. Fiber lasers are inherently compact, lightweight and maintenance-free, and also do not require any water cooling. So, fiber lasers have already been deployed in some industrial applications.

Er fiber lasers can be pumped with telecom-compatible pump diodes and allow for the straightforward excitation of soliton pulses using standard optical fibers. Figure 11.77 shows a configuration of the passively mode-locked all-fiber laser, which is referred to as a figure-of-eight laser because of its layout [11.114]. Nonlinear all-optical switch including a nonlinear amplifying loop mirror allows self-starting mode-lock operation for femtosecond pulses. Current passive mode-locking lasers are usually based on the nonlinear polarization evolution in a slightly birefringent fiber because they require the least number of optical components [11.122]. Currently, mode-locked fiber lasers which generate pulses with width from 30 fs to 1 ns at repetition rates ranging from 1 MHz to 200 GHz have been developed in a variety of technologies. Details of these ultrafast lasers can be found in the textbook [11.123].

Conventional fiber lasers as well as EDFAs have simple structures with a single core for guiding both the signal and the pumped light, implying that single-mode pump diodes must be used.

The limited available power of single-mode diode-pumped sources has limited the output power to ≈ 1 W. Cladding pumping has been developed as a method to overcome this situation using the so-called double-clad fiber shown in Fig. 11.78. Double-clad fiber has a rare-earth-doped core for guiding the single-mode output beam, surrounded by a lower-index inner cladding. The inner cladding also forms the core for a secondary waveguide that guides the pumped light. The inner cladding is surrounded by an outer cladding of lower refractive index material to facilitate waveguiding.

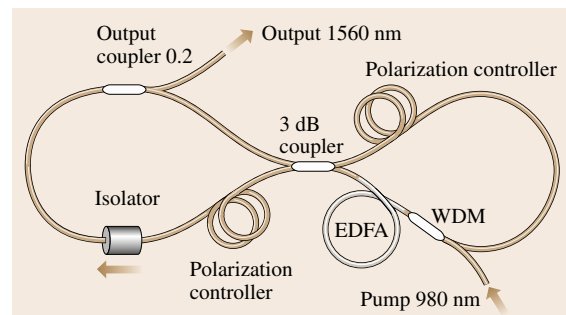


Fig. 11.77 Set-up of passively mode-locked figure-of-eight laser (after [11.114])

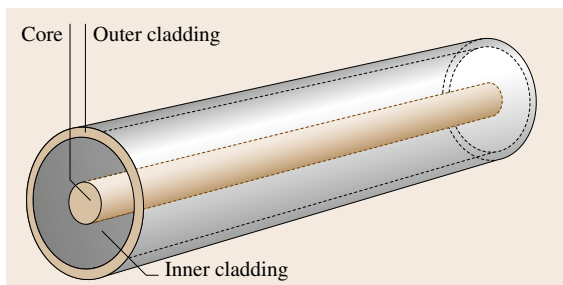


Fig. 11.78 Schematic drawing of a double-clad fiber

Cladding-pumped fiber lasers accommodate high-power multimode pump sources, but can still produce a single-mode output. In the last decade various pumping schemes, such as star-coupler pumping [11.124], V-groove pumping [11.125] and side-coupler pumping [11.126, 127], have been developed to increase the available count of multimode pump sources in addition to the simple end-pumping approach [11.128, 129]. Cladding-pump technology has drastically increased the output power of fiber lasers to well over 100 W even in single-mode operation and seems likely to surpass bulk lasers in many industrial application areas.

11.5.5 Miscellaneous Fibers

In addition to silica-glass-based fibers, many kinds of optical fibers have been developed for various applications, such as local area networks, laser power delivery and optical sensing. In this section, most viable and commercially available fibers are reviewed.

Infrared Fibers

Infrared fibers, defined as fiber optics transmitting radiation with wavelengths greater than $2\ \mu\text{m}$ are divided into three categories, i. e., glass, crystalline, and hollow waveguides. Figure 11.79 shows the optical loss for the most common infrared fibers [11.135]. In general, both the optical and mechanical properties of infrared lasers are inferior to those of silica-based fibers, and the use of infrared fibers is still limited to applications in laser power delivery, thermometry, and chemical sensing.

HMFG Fibers. Heavy-metal fluoride glass (HMFG), most commonly, $\text{ZrF}_4\text{-BaF}_2\text{-LaF}_3\text{-NaF}$ (fluorozirconate, ZBLAN) and $\text{AlF}_3\text{-ZrF}_4\text{-BaF}_2\text{-CaF}_2\text{-YF}_4$ (fluoroaluminate) presents a low optical loss around $2.5\ \mu\text{m}$ [11.130]. The attenuation in HMFG fiber is predicted to be about ten times less than that for

silica fibers based on extrapolations of the intrinsic losses resulting from Rayleigh scattering and multi-phonon absorption [11.136]. ZBLAN is also a candidate host material for various fiber amplifiers because of the smoothed broadened spectra. However, their low durability against moisture attack and poor mechanical strength prevent their widespread use. The losses of fluoroaluminate fibers are not as low as for the ZBLAN, but fluoroaluminate fibers have the advantage of higher glass-transition temperatures and therefore are more promising for the power delivery of Er:YAG laser wavelength of $2.94\ \mu\text{m}$.

Germanate fibers. Heavy-metal-oxide glass fibers based on GeO_2 are an alternative candidate to HMFG fibers for $3\ \mu\text{m}$ laser power delivery because of a higher glass-transition temperature (680°C) and excellent durability [11.137]. These fibers have a higher damage threshold and can deliver laser powers over 20 W from Er:YAG lasers.

Chalcogenide fibers. Chalcogenide glass fibers are classified into three categories: sulfide, selenide, and telluride. One or more chalcogen elements are mixed with one or more elements such as As, Ge, P, Sb, Ga to form a glass. Chalcogenide glasses are stable, durable, and insensitive to moisture. Generally, the glasses have a low softening temperature and a rather large value of dn/dT . This fact limits their laser power-handling capability, and the fibers are considered to be a promising candidate for evanescent-wave fiber sensors and in-

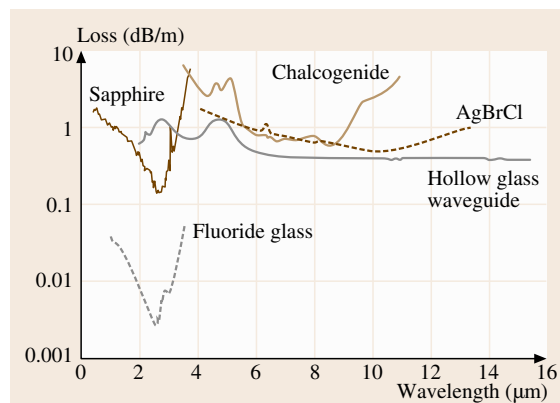


Fig. 11.79 Loss spectra for some common infrared fiber optics: ZBLAN fluoride glass [11.130], single-crystal sapphire [11.131], chalcogenide glass [11.132], polycrystalline AgBrCl [11.133], and a hollow-glass waveguide [11.134] (after [11.135])

frared fiber image bundles. The loss spectra for the most important chalcogenide fibers, AsGeSeTe [11.132] are shown in Fig. 11.79.

Crystalline fibers. Sapphire is an extremely hard, robust and insoluble material with an infrared transmission region from 0.5 to 3.2 μm and a melting point of over 2000 $^{\circ}\text{C}$. These superior physical properties make sapphire the ideal infrared fiber candidate for applications at wavelengths less than 3.2 μm . The disadvantage of sapphire single-crystal fiber is fabrication difficulties. Fiber diameters range from 100 to 300 μm and lengths are generally less than 2 m. The loss spectra of sapphire fiber [11.131] are shown in Fig. 11.79. Fiber loss is less than 0.3 dB/m at the Er:YAG laser wavelength of 2.94 μm , and the fibers are used to deliver over 10 W of average power. Sapphire fiber can be used at temperatures up to 1400 $^{\circ}\text{C}$ without any change in transmission.

Halide crystals have excellent infrared transmission, especially in the longer wavelength region. However, only the silver and thallium halides have been successfully fabricated into fiber optics, using a hot extrusion technique. In the hot extrusion process, a single-crystal perform is placed in a heated chamber at a temperature equal to about half the melting point, and the fiber is extruded to a fiber shape through a diamond or tungsten carbide die. The fibers are usually 900–500 μm in diameter. The loss spectra of polycrystalline AgBrCl fiber [11.133] are shown in Fig. 11.79. The loss at 10.6 μm can be as low as 0.2 dB/m and the transmission band extends up to about 20 μm .

Hollow glass waveguides. Previously, hollow waveguides were formed using metallic and plastic tubing. Today, the most popular structure is the hollow glass waveguide (HGW). The advantage of glass tubing is that it is much smoother than either metal or plastic tubing. HGWs are fabricated using a conventional wet process first to deposit a layer of Ag film on the inside of silica glass tubing, and then a dielectric layer of AgI is formed over the metallic film by converting some of the Ag to AgI. The thickness of the AgI is optimized to give high reflectivity at a particular laser wavelength [11.138]. The spectral loss for an HGW with a 530 μm bore, which is optimized for a wavelength of 10 μm [11.134], is shown in Fig. 11.79. HGWs have been used successfully in infrared laser-power delivery and some sensor applications. CO₂ and Er:YAG laser power below about 80 W can be delivered without difficulty. Employment of water-cooling jackets fur-

ther increased the handleable laser power up to about 1 kW [11.139].

More detailed information on infrared fibers can be found in the literature [11.140].

Plastic optical fiber. Plastic optical fibers are commercially available for local-area networks, sensing use, and illumination. Conventional plastic optical fibers are multimode fibers with a large core diameter of about 1000 μm and are made of polymethyl methacrylate (PMMA). Figure 11.80 shows the transmission loss of the plastic optical fibers as a function of wavelength [11.141]. The transmission loss reaches a minimum value of about 100 dB/km around the spectral region between 500 and 600 nm. Usually, signal transmission lines of plastic optical fibers use 650 nm light-emitting diodes and the transmission distance is limited to 50 m because of the relatively high transmission loss (160 dB/km).

Recent development of perfluorinated plastic optical fibers significantly improved the transmission characteristics of plastic optical fibers in the spectral region from visible to 1300 nm because the perfluorinated polymer has no C–H bond in its chemical structure. The specific loss at a wavelength of 850 nm is 17 dB/km. Signal transmission at 2.5 Gb/s was conducted over 144 m perfluorinated graded-index plastic optical fiber with an 850 nm vertical-cavity surface-emitting laser (VCSEL) transceiver [11.142].

Photonic Crystal Fibers

The photonic band gap concept triggered the development of photonic crystal fibers [11.143, 144]. Since the first fabrication of photonic crystal fiber (PCF) in 1995 [11.145], a sequence of innovations has been

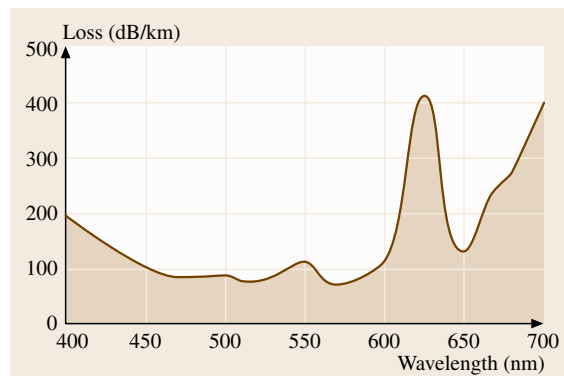


Fig. 11.80 Transmission loss in plastic optical fiber

achieved in fiber optics technology. The remarkable properties of PCF have overturned many of the key precepts of textbook fiber optics. The enormous potential offered by this new structure may make current fiber optic technology obsolete.

PCFs are optical waveguides in which a microstructured cladding confines light to the fiber core. Unlike conventional all-solid fibers, which guide light by the total internal reflection at the core-clad interface, the new structures provide great freedom to control the characteristics of the fibers.

PCFs are divided into two categories based on the principal mechanism by which light is confined to the core. One of these is a species of total reflection, and the other is a new physical effect – the photonic band gap. Those typical structures are shown in Fig. 11.81.

The first type of PCF usually has a silica core surrounded by the air hole, as shown in Fig. 11.81a. Optical confinement is achieved when the effective (area-averaged) refractive index is lower in the cladding region than in the core.

Figure 11.81b shows the structure of the photonic band gap and hollow-core PCF. The guiding mechanism relies on the coherent backscattering of light into the core. This effect, which is based on the photonic band gap (PBG), allows fiber to be made with hollow core.

PCF can be made by stacking tubes and rods of silica glass into a structure that is a macroscopic preform of the pattern of holes required in the final fiber. The typical dimension of this preform is 1 m long and 20 mm in diameter. The preform is then introduced into the furnace of a fiber-drawing tower.

Index-Guiding PCF

Large core. Light can be guided in PCFs by embedding a region of solid glass enclosed by an array of air holes. This approach has several important applications, and an excellent introduction is available in the review [11.146]. Index-guiding PCF provides new opportunities that stem from the special properties of the photonic crystal cladding, which are caused by the large refractive index contrast and the 2-D nature of the microstructure. These affect the dispersion, smallest attainable core size, the number of guided mode and the birefringence in a different way to conventional silica fiber.

For example, endlessly single-mode PCF can be made with a very large core area [11.147, 148]. In contrast with conventional fibers, single-mode operation is guaranteed in solid-core PCF whatever the overall size of structure – in particular for large core – provided that

the ratio of hole-diameter to spacing is small enough. Ultra-large mode area PCF may have applications in high-power transmission and high-power lasers and amplifiers [11.149].

Small core. In contrast, if the holes are enlarged and the overall scale of the structure reduced so that the solid core is $\approx 0.8 \mu\text{m}$ in diameter (ultra-small mode), the zero-dispersion wavelength can be 560 nm in the green. This is quite different from the zero-dispersion wavelengths in conventional silica fibers. In fact, the group velocity dispersion can be radically affected by pure waveguide dispersion in fibers with small cores and large air holes in the cladding [11.150]. Another feature of fibers with ultra-small mode area is that the intensity of light attainable for a given launched power is very high, so nonlinear optical effects can be easily obtained. With a fiber with a small core and a zero-dispersion wavelength around 800 nm, femtosecond pulses from a Ti:sapphire laser was efficiently converted to a single-mode broadband optical continuum [11.151], which is already being used in frequency metrology [11.152], optical coherence tomography [11.153] and spectroscopy. Enormous birefringence that exceeds values attained in conventional fibers by an order of magnitude, have already been achieved in PCFs [11.154].

Hollow-Core Photonic Band Gap Fibers

In 1999, the first hollow-core photonic band gap fiber was drawn from a stack of thin-wall silica capillaries with an extra large hole in the center, which was formed by omitting seven capillaries from the stack [11.155]. The strong wavelength dependence of guiding indicated a photonic band gap effect: only certain wavelength

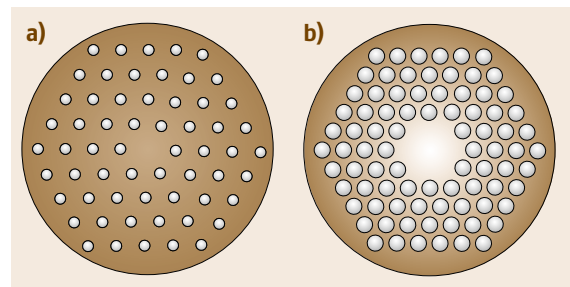


Fig. 11.81a,b Two different designs of PCF. (a) shows a single-mode fiber with a pure silica core surrounded by a reduced-index photonic-crystal cladding material, (b) is an air-guiding fiber in which the light is confined to a hollow core by the photonic-band-gap effect

ranges fall within the band gaps and are guided, while other light quickly leaks out of the hollow core.

The most important factor for any fiber technology is loss. Loss in conventional fibers has been reduced over the past 30 years and seems to be approaching the material limit. However, losses in hollow-core photonic band gap fibers might be reduced below the levels found in conventional fibers because the majority of the light travels in the hollow core, in which scattering and absorption could be very low. Confinement losses can be eliminated by forming a sufficiently thick cladding. However, increased scattering at the many surfaces is a potential problem. The lowest attenuation reported to date for hollow-core photonic band gap fiber is 1.7 dB/km [OFC-PD] [11.156], and is still an order of magnitude higher than that of conventional state-of-the-art silica fibers, 0.15 dB/km [11.157]. The dramatic reduction of loss over the past few years suggests that it will be reduced still further. Dispersion is far lower than in solid-core fibers. Group velocity dispersion (GVD) in these

fibers – a measure of their tendency to lengthen a short pulse during propagation – crosses zero within the low-loss window, and is anomalous over much of the wavelength band. This implies that these fibers could support short-pulse propagation as optical solitons. The Kerr nonlinearity of the hollow-core fiber was low because it was filled with gas, whereas the effects of Raman scattering were eliminated by filling the fiber with xenon. Hollow-core fibers exhibited a substantially higher damage threshold than conventional fibers [11.158], making them suitable for delivery of high-power beams for laser machining and welding. 200-fs 4-nJ pulses from a Ti:sapphire laser have been transmitted through 20 m of hollow-core fibers with a zero-GVD wavelength of 850 nm, and the autocorrelation width of the output pulse was broadened to roughly 3.5 times the input pulse, partly due to the modest spectral deformation [11.159]. Further improvement is expected by working away from the zero-GVD wavelength. Hollow-core fibers seem to have massive potential.

11.6 Evaluation Technologies for Optical Disk Memory Materials

Two types of rewritable optical disks are well-known today. One is a phase-change optical disk that utilizes the phenomenon of optical changes that accompany the reversible phase transitions between amorphous and crystalline states. Utilizing phase-change materials, various rewritable optical disks such as DVD-RAM, DVD-RW, CD-RW and blu-ray discs have been commercialized. The other is a magneto-optical (MO) disk that utilizes the polar Kerr effect. It is known that the polarization plane of linearly polarized light revolves slightly when it is reflected from a perpendicularly magnetized magnetic film. MO disks have also been commercialized as various office tools and as the Mini-Disc (MD) for audio use. In this section, the evaluation technologies for a phase-change material are first explained, and those for an MO material follow. For each case, evaluation technologies are mainly described from two points of view: the material property itself and the device property that uses the memory material. As described below, the properties of the two materials are very different, while the second aspect is generally common. Strictly speaking, various drive technologies such as servo technology and optics etc. are necessary to carry out sufficiently precise evaluations. However, the essence of them will be understood by the descriptions here.

11.6.1 Evaluation Technologies for Phase-Change Materials

To evaluate phase-change memory materials, knowing their thermal and optical characteristics is essential. This is because i) the optical change is dominantly and directly determined by the change of optical properties of the phase-change films, and ii) the phase-change mechanism is typically a thermal process. It is also very important to examine the thermal and optical properties of additional layers such as transparent protection layers composed of dielectric materials and reflection layers composed of metallic materials. The typical layer structure of a phase-change optical disk is shown in Fig. 11.82. Accordingly, practical optical disk characteristics can be estimated by knowing the thermal and optical characteristics of all these films. However, the evaluation technology is limited to the phase-change materials themselves due to space restriction.

Research and Development History of Phase-Change Materials

Today, many phase-change optical disks have been put to practical use. Without exception, they have adopted chalcogenide films for their memory layers. Study of chalcogenide alloys started in Russia in the 1950s.

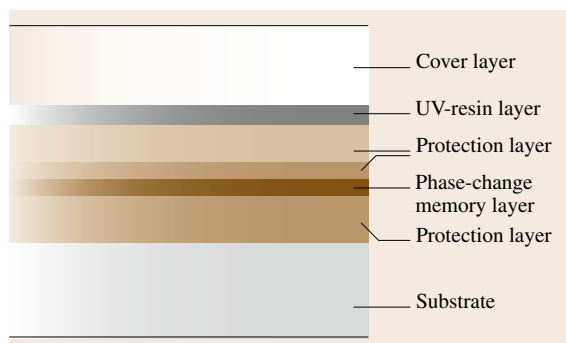


Fig. 11.82 Cross section of a typical layer structure of phase-change optical disk with four layers

Kolomiets et al. found that various chalcogenide alloys, such as Tl–Te and Tl–Se, could be easily vitrified and the obtained glassy substance showed semiconductor properties [11.160]. These new glass materials were named *dark glass* in contrast to the conventional transparent oxide glasses, and they were generically called chalcogenide glass semiconductor in the 1960s.

Ovshinsky's group first demonstrated the great potential of these glass materials as optical memories. In 1971, *Feinleib* et al. reported that a short laser pulse induced instant and reversible phase changes on a chalcogenide glass semiconductor thin film, representatively $\text{Te}_{81}\text{Ge}_{15}\text{Sb}_2\text{S}_2$ [11.161]. This result aroused large research and development (R&D) activities all over the world at the beginning of the 1980s, and various materials, especially Te-based eutectic alloys, were studied towards the beginning of the 1980s [11.162–165].

However, these Te-based eutectic compositions have not ultimately resulted in practical use, and R&D activities on phase-change optical memories declined in the mid-1980s. This is because conventional chalcogenide glass materials had several fatal problems, such as data rewriting speed and cyclability, for a rewritable optical memory.

Under these circumstances, *Yamada* et al. proposed the $\text{GeTe} - \text{Sb}_2\text{Te}_3$ pseudo-binary material system (hereinafter denoted by GeSbTe) based on a novel concept [11.166]. The largest difference between GeSbTe and the conventional materials is that GeSbTe is no longer a chalcogenide glass but just a chalcogenide while the conventional materials have characteristics suitable for the name of chalcogenide glasses [11.167]. GeSbTe has solved the fundamental problems and realized a very short crystallization time of several tens of nanoseconds, more than 100 000 cycles of data rewriting, and tens of years of estimated life. It can be said

that this material created a new era for the R&D of phase-change optical memories. The basic concept of GeSbTe has been succeeded by other materials such as AgInSbTe and $\text{Ge}(\text{Sb}_{75}\text{Te}_{25}) - \text{Sb}$ etc. Those are generically named $\text{Sb} - \text{Te}$ [11.168, 169]. The latest compositions being studied are Sb-based compositions including Te [11.170].

Principle of Phase-Change Recording

The phase-change principle is explained in Fig. 11.83, which shows the relation between the temperature and free energy of a substance. Molten substance crystallizes at the melting temperature (T_m) when it is gradually cooled down while maintaining thermal equilibrium. However, the molten substance sometimes does not crystallize even though it is cooled below T_m when the cooling speed is sufficiently large. This is a supercooled state and it is frozen into a noncrystalline solid called an amorphous state at a certain temperature (T_g) that is intrinsic to a substance. Conversely, the amorphous solid can be transformed into a crystalline solid by heating it above T_g for a period of time. The amorphous solid then becomes a supercooled liquid and crystallization occurs abruptly.

In order to achieve recording and erasing, it is necessary to undergo the above thermal process on a revolving optical disk. For this requirement, a well-focused laser beam is utilized. Figure 11.84 shows the heat profile of a phase-change recording film of an optical disk while the optical disk is passing through the laser beam. In the figure, two curves show the temperature at the center part of the track. When the laser power is strong enough to melt the phase-change film instantly (a), the temperature increases above T_m as the disk approaches

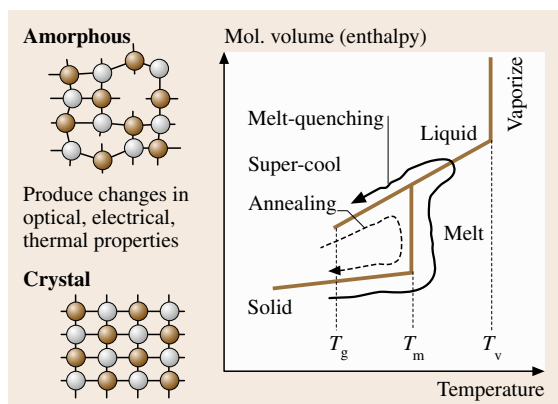


Fig. 11.83 Thermodynamical explanation of a phase-change process

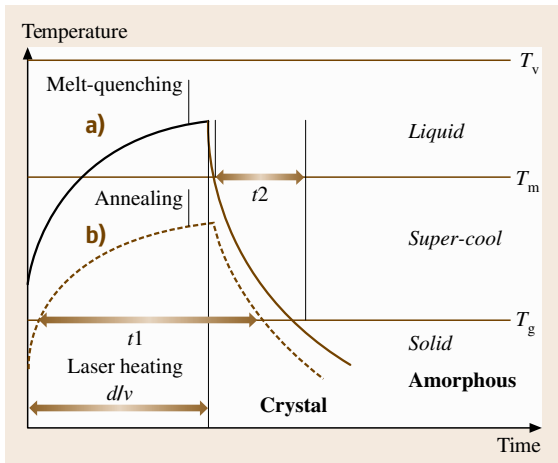


Fig. 11.84a,b Schematic view of the thermal profile of a laser-exposed area on an optical disk while it passes through the laser spot

the laser beam, and decreases as the disk goes away from the laser beam. By designing the heat capacity of the recording film to be sufficiently small, and the thermal diffusion rate from the recording film to the adjacent films to be sufficiently large, the molten area can be transformed into an amorphous state. On the contrary, when the laser power is not high enough to elevate the film temperature over T_m but high enough to elevate it over T_g (b), it is seen from the figure that the period when the temperature is between T_g and T_m (t_1) becomes rather longer than the case of (a). Thus, the exposed area is re-transformed into a crystalline state.

Fundamental Properties of Phase-Change Materials

For the recording film of a phase-change optical disk, optical and thermal properties are very important factors. The former is tightly related to the quality of the recording signal itself and the latter relates to the recording sensitivity or thermal reliability. At first, the technologies for obtaining the basic physical properties are described.

Melting Temperature T_m , Glass Transition Temperature T_g , and Crystallization Temperature T_x . It is widely known that the temperatures T_m , T_g , and T_x are measured using differential scanning calorimetry (DSC) or differential thermal analysis (DTA). It is generally said that measurement results by DSC have higher accuracy than with DTA. DTA is suitable for a measurement under rather high-temperature conditions. For a preparation of the specimens, phase-change films are deposited on

a glass substrate, scratched off and powdered. T_m and T_g are observed as endothermic peaks by these machines; however, it is difficult to observe T_g in the case of recent high-speed phase-change materials. It is said that T_g does not appear for those materials since T_g is higher than T_x . T_x is observed as an exothermic peak. Because T_x shows a distinct dependence on the heating rate, the activation energy can be obtained based on Kissinger's equation (11.122) as shown in Fig. 11.85.

$$\ln \frac{\alpha}{T_x^2} = \frac{\Delta E}{R} \frac{1}{T_x} + \text{const.}, \quad (11.122)$$

where α , R , E and T_x are the heating rate, gas constant, activation energy and crystallization temperature, respectively.

Therefore, by plotting $\ln \alpha/T_x^2$ versus $1/T_x$, an activation energy E can be obtained from the slope of the graph [11.171, 172]. Each value of T_m , T_x , and E closely relates to recording sensitivity, thermal resistance of the amorphous state, and crystallization speed under high-temperature conditions.

There is another, optical method to measure T_x , which is shown in Fig. 11.86. In the case of a phase-change material, phase-change phenomenon naturally accompany distinct optical properties. Accordingly, crystallization temperatures can be measured by detecting the temperature at which the optical properties, such as transmittance and reflectivity, drastically change when elevating the temperature of the film sample at a constant heating rate. Optical changes can be detected for example using a He-Ne laser. The greatest advantage of the optical method is that a film sample can be used instead of a powdered sample. Though it is reported that T_x abruptly increases as the film thickness becomes thinner, practical T_x of an optical disk can be measured by this optical method. Additionally, it is very important that

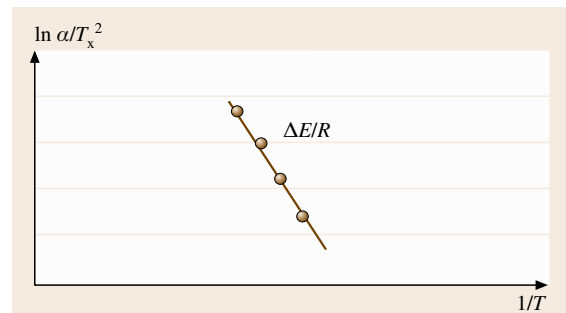


Fig. 11.85 Schematic of a Kissinger plot from which the activation energy E can be obtained as the gradient of the line

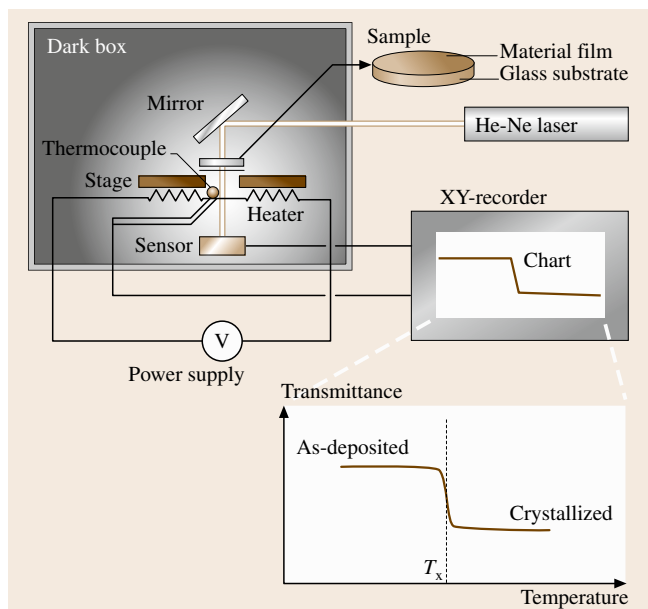


Fig. 11.86 Optical method for evaluating the crystallization temperature T_x of a phase-change thin film. The *upper* figure shows the set-up and the *bottom* shows the obtained chart

this method drastically saves time for a sample preparation.

Optical Constants. It is intrinsically important for phase-change optical materials to obtain their optical constants: n (refractive index) and k (extinction coefficient). Especially, obtaining them for wavelengths λ around 300–1000 nm is very important since laser diodes exist in the range. With the constants both in the amorphous and crystalline states, we can simulate the optical characteristics when the materials are applied as the memory layer of optical disks. They are, for example, reflectivity, absorbance, transmittance and variations of these before and after recording. To obtain these optical constants, we can adopt a commercial ellipsometer. Since it is difficult to obtain a large laser-quenched amorphous film, an as-deposited film is usually substituted for an amorphous sample. A crystalline sample is prepared by annealing the as-deposited film in an Ar or N₂ gas atmosphere.

Optical constants can also be obtained by a calculation method. Firstly, optical reflectivity parameters (from both the film and substrate sides), transmittance and film thickness are experimentally measured using a spectrometer and a step-meter called a DEKTAK or α -step, respectively. Secondary, sets of optical parameters are calculated by assuming values for the optical

constants n and k based on the matrix method [11.173]. The measured and the calculated parameters are compared, and the assumed optical constants giving the smallest error are selected as the real values.

Crystallization Speed. Data-rewriting speed is as important a factor as recording capacity for memory devices. In the case of phase-change memory, data-rewriting speed is dominated by the crystallization speed. Since it is difficult to measure the crystallization speed directly, the evaluation of the crystallization speed is usually substituted by the required laser exposure duration that causes crystallization. The laser exposure duration can be calculated from the disk revolving speed v and the laser beam size d (laser wavelength and NA of the objective lens) on a real dynamic tester as d/v ; however, a static tester is applied in order to simulate the response under a wider range of laser exposure conditions.

Figure 11.87 shows a representative set-up of a static tester and a coupon-size specimen [11.174]. On the static tester, laser exposure from a laser diode (LD) is carried out with varying laser power and exposure duration on the coupon specimen. For a detection of the exposure results, a sufficiently weakened laser beam is re-exposed and the variations are observed as the reflectivity changes. Here, it is very important that the specimen has a similar layer structure as the practical optical disks. Accordingly, dynamic properties such as crystallization time and amorphization sensitivity can be simulated on the static tester. For example, we can determine whether the materials are applicable to DVD-RAM by investigating whether their crystallization times are faster than 80 ns. The recording-erasing conditions of DVD-RAM are: revolving speed $v = 8.2$ m/s, laser beam size $d = 0.66$ μm ($1/e$), calculated effective exposure duration of $d/v = 80$ ns. In the case of the GeTe–Sb₂Te₃ pseudo-binary system, one of the most well-known materials, the obtained crystallization time is as short as 30 ns, and it is known that this material system can be used as a memory layer for DVD-RAM [11.175].

Instrumental Analyses. For characterization of phase-change materials, various instrumental analyses are utilized. Firstly, averaged film compositions are examined using an x-ray micro analyzer (XMA), an electron-probe microanalyzer (EPMA) and inductively coupled plasma (ICP). XMA and EPMA can detect the contained elements in a microscopic area on a film sample, although the accuracy is not as high as for ICP. On the other hand, ICP can obtain very precise composition values. The weak points of ICP are that it is not suitable for detecting

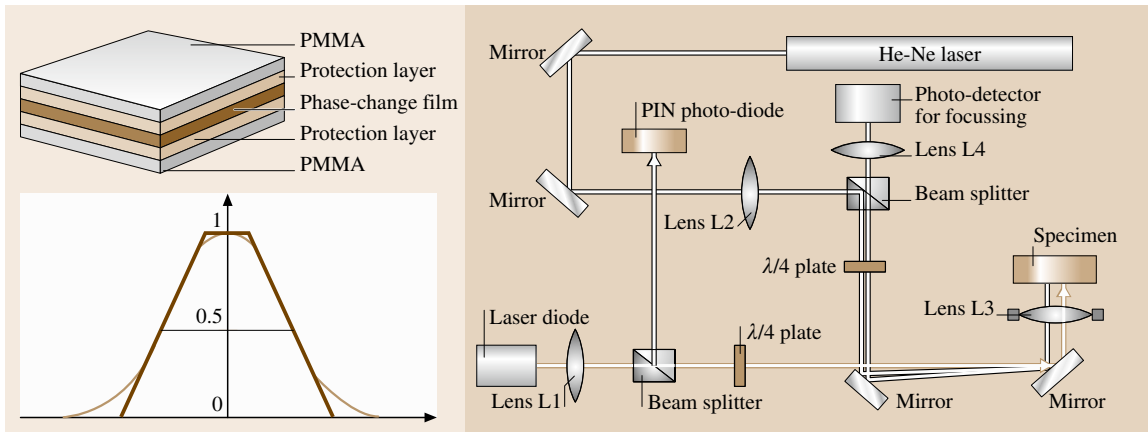


Fig. 11.87 Optical set-up and a specimen to evaluate phase-change process such as crystallization rate and crystallization-amorphization sensitivity etc.

light elements such as O and N and for detection on a limited area. In order to detect light elements, Rutherford back scattering (RBS) can be adopted.

When a depth profile of the film composition is necessary, Auger electron spectroscopy (AES) and secondary ion mass spectrometry (SIMS) are adopted. Quantitative evaluation is not possible for each method, but it is possible by comparison with reference samples whose compositions are known beforehand. To examine chemical bonding between each element, x-ray photoelectron spectroscopy (XPS) has conventionally been adopted. Recently, thermal desorption mass spectrometry (TDS) has also been developed.

For the observation of crystallization condition and shape of recording marks, transmission electron microscope (TEM) has been exclusively utilized; however, some new methods such as the scanning electron microscope (SEM) and surface potential microscope (SPOM) have become important in recent years. This is because the thickness of the memory film has become thinner and observation by TEM is becoming increasingly difficult.

To investigate the structures of memory materials, diffraction studies such as x-ray diffraction (XRD), electron diffraction (ED) and neutron diffraction (ND) are very effective. Precise structure can be obtained, for example, by applying the *Rietvelt* method to XRD results [11.176].

Dynamic Properties of a Phase-Change Optical Disk

In this part, some dynamic properties of an optical disk will be explained. Though this handbook does not cover practical devices, it is very important for us to

understand how the material characteristics relate to device performance under the practical conditions. Here, carrier-to-noise ratio (C/N), erasability, jitter, and bit error rate (BER) are explained as technologies for evaluating dynamic properties.

C/N and Erasability. C/N and erasability are the most basic items for evaluating the potential of phase-change optical disks. To measure the C/N of an optical disk, a monotone signal with a frequency f_1 is first recorded on an optical disk revolving at a constant linear velocity. Generally, f_1 corresponds to the minimum mark length (i.e., the highest recording density) to evaluate the resolution of the disk. Here, the exposed laser power is modulated between a peak power level P_p for amorphization and a bias power level for crystallization P_b (Fig. 11.88). The DC laser beam is shone on the recorded track at low power to read-out the recorded signal. The reflectivity of the optical disk dif-

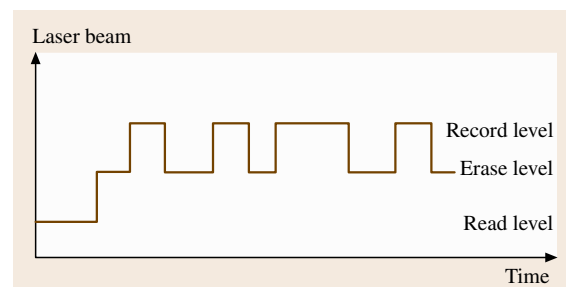


Fig. 11.88 Representative laser-modulation scheme for overwriting on a phase-change optical disk using only one laser beam

fers between the amorphous and crystalline portions; accordingly, the recorded signals are detected as the variation of the reflection light intensity from the optical disk. The C/N ratio is determined by the ratio of the averaged signal amplitude and the noise floor at the frequency f_1 , as shown in Fig. 11.89. Usually, the above operations are carried out using a spectrum meter by stepping up the exposed laser powers, and the saturated value is determined as the C/N ratio of the optical disk. It is said that 45 dB is the usual minimum limit for a digital recording. The laser power to achieve saturation is determined by the recording power, as shown. To rewrite the data, another monotone signal with a frequency f_2 is overwritten on the recorded signal track, and the attenuation ratio of the signal amplitude of f_1 is determined to be the erasability. It is generally said that the erasability should be at least 20–26 dB to avoid influencing the quality of the overwritten signal.

The signal amplitude, noise level, and erasability are tightly related to the optical changes of the material, film quality such as surface flatness and grin size, and crystallization properties such as the crystallization rate, respectively.

Jitter and BER. In recent optical disks, signal marks with various lengths, for example from 1.5 to 4 T with a resolution of 0.5 T (where T is the clock period) are recorded as digital signals on an optical disk, and information is put at every distance from a certain mark-edge to the neighboring mark-edges. Figure 11.90 shows a schematic model of the digital recording signals. As can be seen from the figure, inhibition of the mark-edge deviation is important for increasing signal quality; an error occurs if the deviation becomes over half of the clock period T . To increase the record-

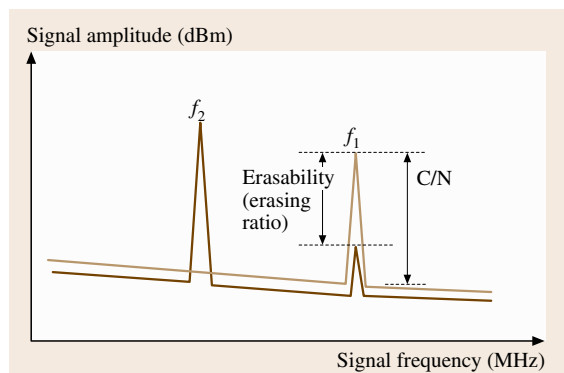


Fig. 11.89 Measurement scheme of C/N using spectrum analyzer

ing density, the mark length and space length has to be as short as possible. However, this is thermally restricted since the phase-change mechanism is a heat-mode process. This means that the desired thermal conductivity of phase-change films is lower than that of metals. Jitter is measured using a time-interval analyzer.

BER is the most important index to evaluate the disk performance for digital recording. It is measured by comparing the source signal and readout signal one by one. In the case of computer uses, an error rate of 10^{-3} – 10^{-4} is the minimum level.

Reliability

Reliability is naturally one of the most important factors for industrial materials. In particular, the highest level of reliability is intrinsically required for memory devices. In the case of phase-change optical memory, reliability includes the thermal stability of the amorphous state and the chemical stability of the material itself. Both factors are usually evaluated through accelerated environmental tests based on Arrhenius's equation (11.123).

$$K = A \exp\left(-\frac{E}{RT}\right) \quad \text{or}$$

$$\ln(k) = -\frac{E}{R} \frac{1}{T} + \ln A, \quad (11.123)$$

where K , A , E , R and T are the reaction rate constant, frequency factor, activation energy, gas constant and environmental temperature, respectively.

The equation gives an estimation of the chemical reaction speed at a certain temperature. It is seen that the rate of chemical reaction becomes large as the temperature increases. The right-hand side of the equation means that the logarithm of K varies lin-

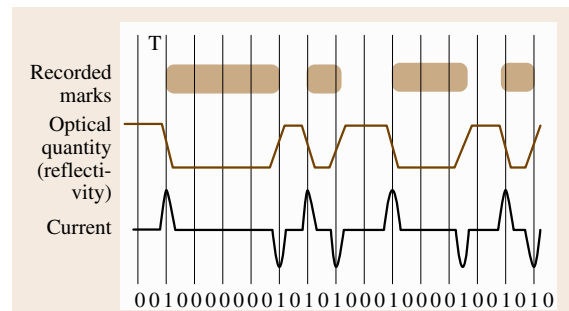


Fig. 11.90 Schematic of the mark-edge recording-reproducing method. Signal 1 is applied on positions where reflectivity drastically changes

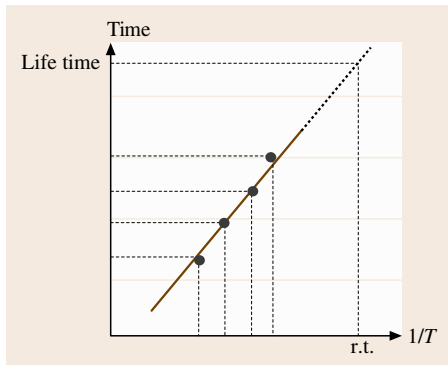


Fig. 11.91 Schematic of Arrhenius plot for obtaining an estimated life at room temperature (r.t.) based on the Arrhenius equation

early with $1/T$ on a logarithmic graph. Accordingly, it is possible to obtain the activation energy for the chemical reaction as the gradient of the straight line. The straight line is drawn based on the least-squares method by plotting the test results at various temperatures. By extrapolating the relation to room temperature, an estimated life under practical conditions can be obtained.

Figure 11.91 shows a schematic example of an Arrhenius plot. In the figure, the vertical axis shows the time for -3 dB of C/N . By extrapolating the straight line to 30°C , the estimated life of this optical disk is determined to be more than 50 years. The vertical axis can be arbitrarily selected to BER, reflectivity, amplitude and noise level etc. as required. The acceleration condition can also be selected in a number of ways. In the case of optical disks, the acceleration test is usually carried out under high-humidity conditions such as 70 or 80% RH in order to evaluate moisture resistance.

11.6.2 Evaluation Technologies for MO Materials

To evaluate magneto-optical memory materials, the investigation of their magnetic characteristics is the most important. Of course, thermal and optical properties are not disregarded; however, broadly speaking, these parameters are only important in relation to the magnetic properties. Items that are common to the phase-change technologies are omitted here.

R&D History of MO Materials

Research into MO recording was started by Williams in 1957 [11.177]. He recorded a signal on an MnBi

magnetic film using a magnetic pen and observed the recorded magnetic domain based on the MO effect. The following year, Mayer formed similar magnetic domains using a thermal pen. This fact became the origin of so-called thermal-magnetic recording [11.178]. There was a short break before Chang first reported thermal-magnetic recording using a laser beam in 1965. This became the prototype of present MO recordings [11.179]. From that point, various studies have been carried out to search for memory materials suitable for MO recording. Finally, in 1973, Chaudhari et al. found a good MO material based on the rare-earth transition-metal (RE-TM) system [11.180]. It is known that the RE-TM material system has the following superior characteristics

1. the film noise is intrinsically low since the film is used in its amorphous state,
2. the perpendicular magnetization is easily formed, and a large MO effect is obtained,
3. a plastic substrate can be adopted since it does not require thermal treatment, and
4. the recording properties can be freely optimized since it is a ferrimagnetic material.

Today, various RE-TM materials are formed combining from heavy-earth elements such as Ge, Tb and Dy and the transition-metal elements Co and Fe. These have been adopted for the memory layer of all the commercialized MO disks without exception. RE-TM materials are characterized by their magnetically continuous structure, as opposed to the gradual structure of usual magnetic materials used in their crystal state.

Evaluation and measurement methods for MO technology are described below, as relevant to their application to RE-TM materials for memory layers.

Principle of MO Recording

The principle of MO recording is explained using Fig. 11.92. Before recording, the direction of the perpendicular magnetization is aligned to one direction by globally applying an intense magnetic field. At this time, the film is instantly heated, which is usually achieved with a flash lamp. The MO film has a large coercive force and a very intense magnetic field is necessary to change the direction of the magnetic field at room temperature. However, the coercive force of a magnetic material is lowered when the film temperature is increased.

Utilizing this phenomenon, we use both a laser beam and an external magnetic field for recording. One

method is optical modulation. Here, the laser power is modulated according to the recording data under a constant magnetic field. Since the laser beam instantly heats the magnetic film to the Curie point, the heated areas change their magnetization direction. When erasing the data, DC laser exposure is applied to align the magnetization in the same direction. A second method is magnetic-field modulation. Here, a magnetic coil is used to make a modulation field while DC laser exposure is applied. In this case, the direction of the magnetization is changed according to the magnetic field formed by the magnetic coil. In this case, recording and erasing is carried out simultaneously and the erase process is not necessary.

For both cases, the Kerr effect is used to read the recorded data. When polarized light is incident on a polarized magnetized film, the polarization plane of the reflected light is slightly revolved from that of the incident light, and the revolution direction changes with the magnetization direction.

Fundamental Magnetic Properties

The most fundamental and important parameters for evaluating MO films are the dependence of the magnetization and magneto-optical effects on the magnetic field. Though the size of the magnetization itself is not a parameter that directly influences the record-reproduce characteristics, the value of the magnetization is indispensable for the analysis of the mechanism of magnetic reversal. On the other hand, the size of the magneto-optical effect, which is the reproducing mechanism itself, directly impacts on the record-reproduce characteristics.

Magnetization. There are various types of magnetometers, a device that measures magnetization directly. For example, i) those that observe the temporal variation of the magnetic flux produced by a magnetic body, ii) those which measure the force applied to a magnetic body placed in a magnetic field gradient, iii) those which measure the alternating force applied to a magnetic body placed in an alternating magnetic field, and iv) vibrating sample magnetometers (VSM), which measure the electromotive force produced in a detection coil placed beside a vibrating sample in a magnetic field. The last of these has become the standard method and almost all magnetic-film institutes provide this measurement equipment. Nowadays, various types are commercially available and the fundamental procedures for gathering data, analysis and the sweeping of the magnetic field are built into a microcomputer as a measuring program and measurements are automated.

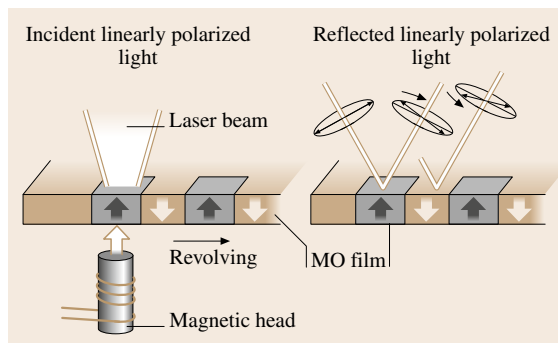


Fig. 11.92 Recording (left) and read (right) principle of MO disk

MO Effect and the Curie Point. As described above, the Kerr effect is a very important property for MO recording materials. For the evaluation of the magneto-optical effect, we measure the angle through which the polarization plane of linearly polarized light is turned on vertical incidence to a specimen in a magnetic field. In the practical polar Kerr magnetometer, a hysteresis loop is drawn by sweeping the magnetic field. Various types of this magnetometer have been commercialized, and the fundamental procedures of data gathering, analyses and the sweeping mode of the magnetic field are automatized. It is known that the magneto-optical effect depends strongly on the optical wavelength. For the evaluation of the wavelength dependence, equipment that can cover a wide wavelength range from the ultraviolet to the infrared has been developed and commercialized [11.181].

The Curie point is an important factor that is closely relating to the recording sensitivity of MO disks. This value can be obtained by measuring the thermal dependence of the magnetization and the Kerr rotation angle at temperatures varying from the ferromagnetic to the paramagnetic state. The measurements are carried out using the VSM and a Kerr magnetometer with a heating mechanism and thermal monitoring capability.

Perpendicular Magnetic Anisotropy. It is also important to measure a perpendicular magnetic anisotropy, K_u , in order to discuss the magnetic reversal phenomenon. K_u is calculated from the contortion value of a wire that supports the sample in the revolving magnetic field. The contortion is calibrated to the torque produced in the sample. The torque-meter is usually equipped with an VSM. The fundamental evaluation methods for the magnetic characteristics are overviewed above. However, in recent years, several new technolo-

gies have been proposed. These include, for example, laser-modulation overwrite technologies [11.182, 183] and magnetic super-resolution technologies [11.184–189] utilizing the mutual interaction between a number of magnetic films with deferent thermal properties. In order to evaluate the new technologies, the magnetic cohesion between layers become an important parameter in addition to the aforementioned material properties. An effective method is to compare the hysteresis curves among stacked layers and each layer separately, and observe the magnetic field change required for magnetic reversal [11.188].

Observation of Magnetic Domains. Polarized optical microscopes were used for the observation of magnetic domains until the 1980s, but since then the magnetoforce micrometer (MFM) has been used to meet this demand [11.190–197]. This is because the polarized microscope is not good at observing with at higher resolving powers. Additionally, the polarization plane becomes unaccepted as the reflectance of the p-polarized and s-polarized light starts to differ with increasing objective-lens curvature.

Dynamic Recording Properties

The same set-up as a commercial MO disk drive is applied for evaluating the recording–reproducing properties of MO materials. Here, C/N, jitter and BER are measured as for the aforementioned phase-change materials.

Reliability

In order to evaluate the lifetime of MO materials, a similar method as for phase-change materials is applicable. Accelerated environmental tests are performed at several temperatures around 60–90 °C, and the lifetime at room temperature can be estimated based on the Arrhenius plot. This method has frequently been used at the first stage of MO disk development, and has resulted in an ideal structure using SiN protective layers on both sides of MO layer. Almost all commercial MO disks have adopted a multilayer structure today. Of course, it is natural that this evaluation procedure should be performed when a new MO disk utilizing new materials is developed.

Another important item is the read-power tolerance. Firstly, this is because the magnetic domain size tends to be smaller in recent high-density MO disks. In addition, new super-resolution technologies such as domain-wall displacement detection (DWDD) [11.198] and the magnetic amplifying magneto-optical system (MAM-MOS [11.199]) require high temperatures (i.e., high read powers) to produce the super-resolution mechanism. It is generally known that the coercive force decreases as the magnetic domain size becomes smaller or as the temperature of the magnetic domain becomes higher. To measure the read stability, it is necessary to examine the relation between read laser power and read cycle number and experimentally determine the read power that does not produce degradation. It is said that tolerance to at least one million passes is necessary.

11.7 Optical Sensing

11.7.1 Distance Measurement

Distance is defined as *the length of the space between two points* and sometimes means simply *the full length*. The optical distance meter is mainly based on: 1) triangulation measurement, 2) pulse time-of-flight, or 3) amplitude modulation telemetry. The performance of these methods are summarized in Table 11.12.

Triangulation

Let us observe a target from two points that are d apart, as shown in Fig. 11.93. Then the distance L can be calculated as

$$L = \frac{d}{\tan \theta}, \quad (11.124)$$

where θ is the tilt angle. This method has been applied to measurements ranging from millimeters to hundreds of kilometers. Our vision system senses a distance from the body to the target by the same method, where d corresponds to a distance between the two eyeballs. The change of θ is detected by a strain gauge namely the *muscle spindle* that is mounted in the eyeball control muscles, as shown in Fig. 11.94.

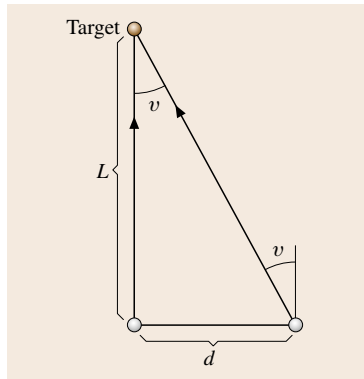
Time-of-Flight Measurement

The round-trip transit time (Δt) for a very short high-power pulsed light from a device such as a Q-switched solid-state laser is measured. The distance L from the light source to the target is given by

$$L = \frac{c\Delta t}{2}, \quad (11.125)$$

Table 11.12 Comparison of the performance of triangulation measurements, pulse time-of-flight, and amplitude-modulation telemetry

Method	Typical light source	Typical range	Typical accuracy	Applications
Triangulation	Passive light, light source unnecessary	mm to hundreds of km	10^{-6}	Auto-focusing camera, survey
Time-of-flight	Q-switched laser, pulsed diode laser	mm to km	10^{-5}	Military range finding, satellite ranging
Amplitude modulation	He-Ne laser, diode laser	sub-mm to km	10^{-6}	Survey

**Fig. 11.93** Triangulation distance measurement

where c is the light speed in the measurement medium. In the actual measurement, the transit time (Δt) is measured with a time-base counter or a time-to-amplitude converter. A time resolution better than 6 ps is required to resolve 1 mm in length. A distance meter that can resolve 1 mm is achieved using a conventional time-base instrument and a pulse-driven diode laser [11.200]. Although the resolution of time-of-flight method is somewhat low, measurement is rapid. Therefore this method is usually applied to military range-finding in combination with a laser radar.

Amplitude Modulation

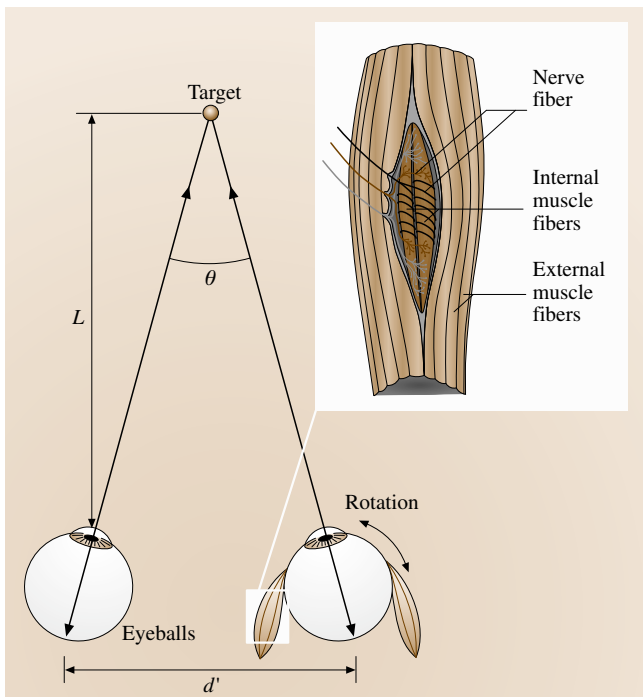
The amplitude of a stationary light source is sinusoidally modulated by modulation of the driving current with frequency of f (Hz). The wavelength of the modulation (Λ) is

$$\Lambda = \frac{c}{f}. \quad (11.126)$$

The distance L is given by

$$L = \frac{\Lambda}{2} \left(N + \frac{\phi}{2\pi} \right), \quad (11.127)$$

where ϕ (rad) is the phase difference between the light source and the detected light (see Fig. 11.95), and N is an integer ($N = 0, 1, 2, 3, \dots$). The value of L is simply determined by ϕ when Λ is smaller than $L/2$, but several possible values exist when Λ is larger than $L/2$. In that case, light with different modulation frequencies is additionally used to determine N . An optical laser distance meter using a variable frequency, a sinusoidally modulated He-Ne laser and a precision phasemeter enables measurement distances of as much as 50 km. A portable version with a diode laser and a photodiode as the light source and detector, respectively, can measure distances of up to a few kilometers with an error of 5 mm. Precise distance measurement requires high-frequency no-distortion sinusoidally modulated light. For this purpose, an intermode beat signal of 1 GHz

**Fig. 11.94** Triangulation distance sensing by human eyes

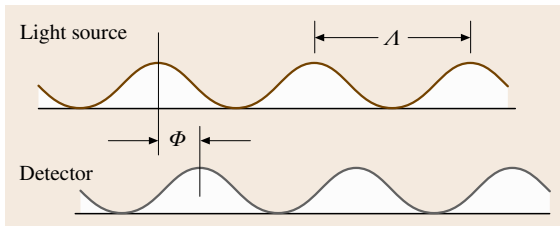


Fig. 11.95 Distance measurement by amplitude modulation

generated in a frequency stabilized two-mode He–Ne laser has been utilized [11.201].

11.7.2 Displacement Measurement

A displacement measurement means the measurement of the movement of a point from one position to another, and often requires very accurate length measurement. There are various types of optical instruments, i.e., microscope-based measurement, an optical lever in combination with a mechanical measurement, and triangulation-based methods. In consideration of the very accurate noncontact displacement measurement, a light interferometer is commonly used. A typical set-up called a Michelson interferometer is shown in Fig. 11.96a. Monochromatic light of wavelength λ from a light source such as a laser is collimated onto the beam splitter BS that reflects half of the light towards the flat mirror M and allows transmission of the other half toward the work piece W. Both beams are recombined at BS and transmitted to the screen, resulting in the formation of interference fringes. Fringes appear and disappear when the optical path length of the two beams Δ is an even and odd multiple of $\lambda/2$, respectively, as shown in Fig. 11.96b. There are several variations of the interferometer optics configuration such as the Fizeau interferometer, Twyman–Green interferometer, Kösters interferometer, Mach–Zehnder interferometer, and Dyson interferometer [11.202].

A simple combination of fiber optics and photodetector depicted in Fig. 11.97 can be applied effectively to displacement measurements from the submicrometer range to several tens of centimeters. Such equipment is commercially available, and its typical sensitivity and resolution are 13 nm/mV and tens of nanometers, respectively, up to 60 μm .

11.7.3 3-D Shape Measurement

For noncontact profile measurement, photographs using an electric imaging device such as a CCD camera are

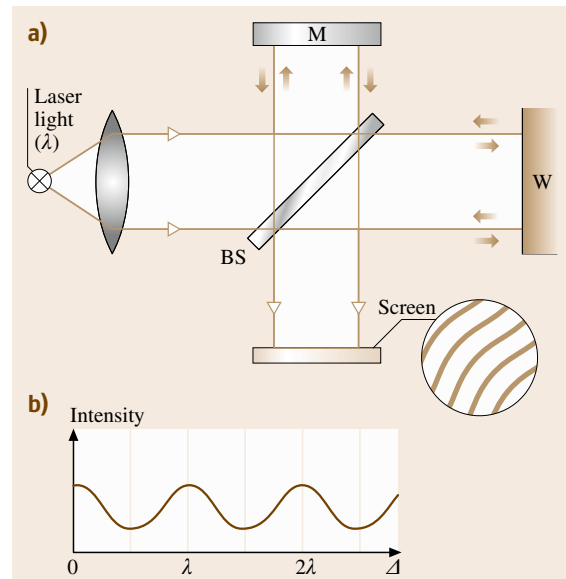


Fig. 11.96a,b Schematic of Michelson interferometer: (a) optics configuration and typical fringe profile on the screen, (b) change of fringe brightness with respect to the optical path length between the two beams

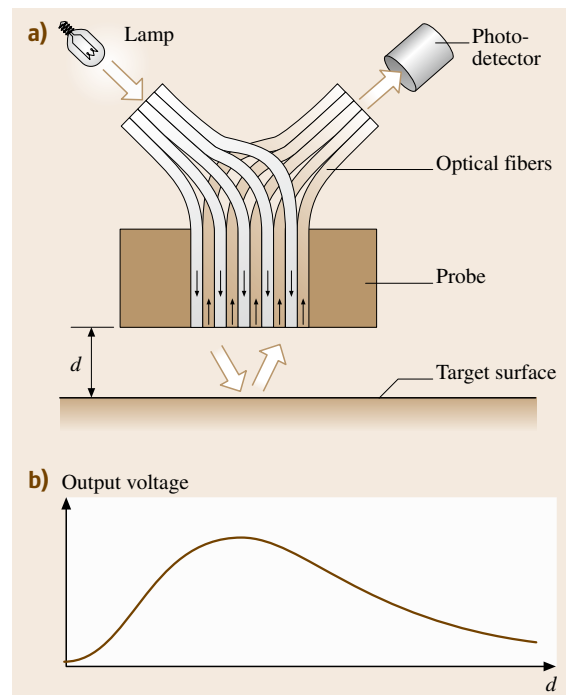


Fig. 11.97a,b Fiber-optic displacement transducer: (a) optics configuration, (b) typical output profile

Table 11.13 Comparison of the performance of typical 3-D measurement methods

Method	Features	Applications
Stereo-photograph	High accuracy, for large scale object, expensive	Map, large building, survey
Optical sectioning	Simple construction, enable from small size to large size object, changeable sensitivity	Car body, industrial parts
Moiré topography	Simple construction, high reliability, moderate sensitivity	Car body, human body
Holograph	High sensitivity, for small size object	Small parts

still dominant. The 3-D measurement can be done with the use of two cameras taking stereo images. Accurate 3-D measurement is made simply by combination of a light sheet and a CCD camera, as shown in Fig. 11.98. This method is one application of the triangulation measurement and is called optical sectioning. To reconstruct the 3-D profile, scanning of the light sheet and/or irradiation of a grating sheet light with an adequate binary (black and white) data treatment by the signal level discrimination are combined. A moiré topography and holographic technique are also widely applied. The features and typical applications of these methods are summarized in Table 11.13.

11.7.4 Flow Measurement

Flow visualization are based on two basic schemes: a) association of tracer particles and b) detection of changes in fluid optical properties caused by flow change.

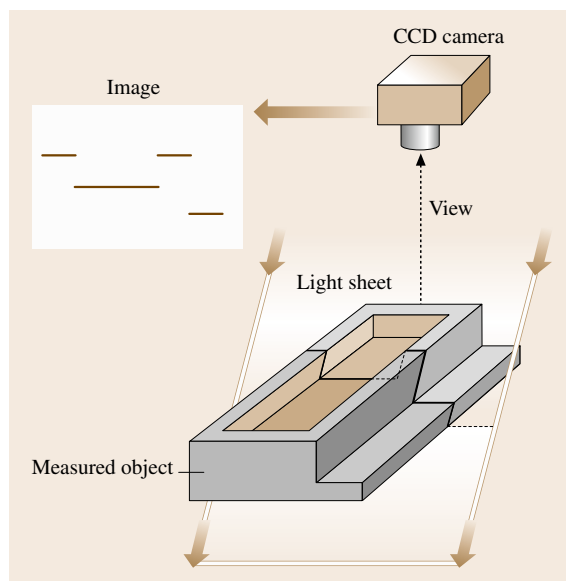


Fig. 11.98 Optical sectioning by light sheet and CCD camera

Tracer-Particle Image Velocimeter

The flow direction and the velocity of each tracer particle in the liquid can be informed by applying a repetitive stroboscopic light illumination for photographic measurement. Colored dyes and gas bubbles are the common tracers and this technique is known as tracer-particle image velocimetry. When the color of the tracer particle changes with temperature, both temperature and velocity mapping are completed simultaneously. For this purpose, a temperature-sensitive liquid crystal is used as the tracer.

Laser Doppler Velocimeter

For tracer-particle associated flow measurement, a laser Doppler velocimeter (LDV) based on the Doppler shift plays an important role. The frequency of light scattered by a moving object changes depending on the velocity of the object and the scattering geometry. Advantages of LDV are the very high-frequency response (to MHz range) and sensing of very small measurement volumes (smaller than 0.1 mm^3), while disadvantages are the point nature of the measurement, the requirement for tracer particles, and the high cost and complexity of the apparatus. The particles are not always necessary, because microscopic particles are normally contained in the measurement liquid, e.g., corpuscles in blood. However, gas flow often needs to be seeded. Figure 11.99a shows a popular dual-beam (or differential Doppler) configuration. Though the relationship between the velocity V of the particle moving and the frequency f of the electric signals is introduced by the Doppler shift, the interference fringe explanation depicted in Fig. 11.99b is rather useful in this case. The two crossing light beams form the fringe pattern with a fringe interval of

$$\delta = \frac{\lambda}{2 \sin\left(\frac{\theta}{2}\right)}, \quad (11.128)$$

where λ is the wavelength of the light in the fluid and θ is the angle between the two converging beams. A moving particle crossing the dark and light fringe pattern produces a sinusoidally modulated electric signal with

a modulation frequency f given by

$$f = \frac{V}{\delta} = \frac{2V \sin\left(\frac{\theta}{2}\right)}{\lambda} \quad (11.129)$$

Flow Visualization

The density of the fluid varies with velocity, resulting in a variation in its refractive index. Shadowgraph and schlieren techniques employ this variation in the refractive index. In these methods, light and dark patterns related to the velocity are made by the bending of light rays as they pass through a region of varying density. Because the optical set-ups of these two methods are simple, they are widely utilized for qualitative studies. For quantitative measurement, the Mach–Zehnder interferometer shown in Fig. 11.100a is advantageous. The light and fringe patterns (Fig. 11.100b) are formed by the interference between the reference beam and the measured beam. The regular light/dark fringes are displayed even for no flow. The fringe profile partially distorts according to the change of the optical length caused by changes in the refractive properties of the fluid medium when appreciable flow occurs. The appearance of fringes on the screen can then be directly related to changes in density in the flow field. The features of these three methods are summarized in Table 11.14.

11.7.5 Temperature Measurement

Temperature measurement is based on the following three methods: 1) blackbody radiation, 2) temperature-dependent-color material, and 3) other spectroscopic methods.

Blackbody Radiation

Any substance at a temperature above 0 K emits radiation. The theory of this radiation is well explained using an ideal emitter called a blackbody. Figure 11.101 shows the change of the emission profile of the blackbody as a function of wavelength λ and temperature T (K). This profile follows the Planck distribution equation,

$$L_{\lambda,T} = \frac{C_1}{\lambda^5} \left(\frac{1}{e^{C_2/\lambda T} - 1} \right), \quad (11.130)$$

where $L_{\lambda,T}$ is the emitted monochromatic blackbody power, and C_1 and C_2 are the Planck emission constants. As one can see, the wavelength corresponding to the maximum energy moves both toward higher energies and shorter wavelengths with increasing temperature.

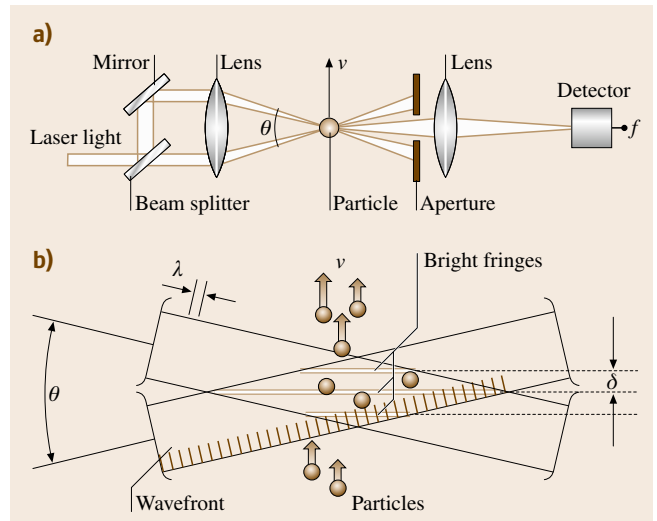


Fig. 11.99a,b Dual-beam laser Doppler velocimeter: (a) schematic of configuration, (b) interference fringes formed by the two beams

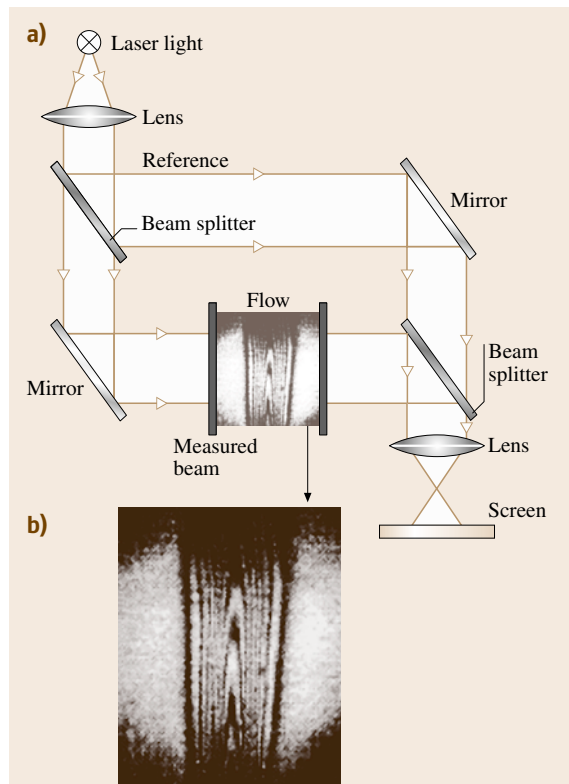


Fig. 11.100a,b Mach–Zehnder interferometer for flow visualization: (a) optics configuration, (b) example of the visualized flow (thanks to Prof. H. Kimoto, Osaka Univ.)

Table 11.14 Comparison of performance of shadowgraph, the schlieren technique and a Mach–Zehnder interferometer for flow visualization

Method	Light source	$\Delta I/I$ is proportional to
Shadowgraph	Continuous wavelength light, CW laser	Gradient of dp/dy
Schlieren	Continuous wavelength light, CW laser	Gradient of p
Mach–Zehnder	Monochromatic light is necessary, e.g., CW laser	Fluid density p

The total thermal radiation power E (W) emitted by a blackbody with unit surface area (1 m^2) at a temperature T is given by the integration of $L_{\lambda,T}$ over λ , resulting in

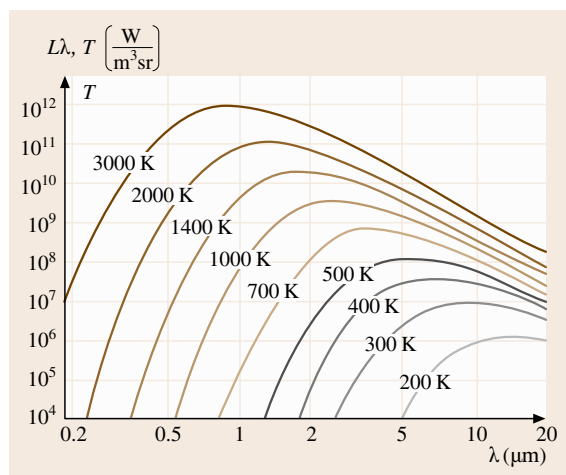
$$E = \sigma T^4, \quad (11.131)$$

where σ is the Stefan–Boltzmann constant ($5.6704 \times 10^{-8} \text{ W}/(\text{K}^4 \text{ m}^2)$).

The wavelength at the maximum emitted power λ_{max} can be obtained by derivation of $L_{\lambda,T}$ by λ . The relationship between λ_{max} (μm) and T is given by Wien's law as

$$\lambda_{\text{max}} T = 2897.6 \mu\text{m K}. \quad (11.132)$$

However, spectral profiles of the actual materials may vary from that of a blackbody (they may exhibit lower emission in some wavelength), and these are called graybodies. The temperature of the blackbody can thus be estimated by the measurement of either the total emitted thermal energy, the wavelength of maximum emitted power, or the spectral profile of the emission. Several methods are available to measure the emitted energy and/or spectral profiles with appropriate optical sensors.

**Fig. 11.101** Emission profile of a blackbody as a function of wavelength and temperature

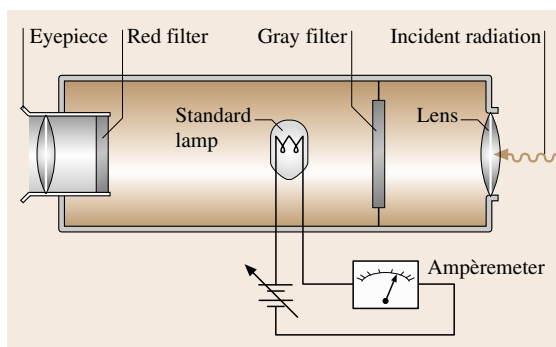
These methods are called optical pyrometry. A typical scheme for the pyrometer is shown in Fig. 11.102, where the standard lamp is placed in the optical path of the incident radiation. By adjusting the lamp current, the color of the filament is made the same as that of the incident radiation. Because the temperature is calibrated via the lamp heating current, the temperature of the radiation can then be estimated from the lamp current.

Temperature-Dependent-Color Material

Microcapsules that envelope temperature-depend-color liquid crystals are prepared. Because the color of the capsule changes with temperature, the surrounding temperature can be determined by the color of the capsule. The merit of this method is that it allows the simultaneous determination of both the temperature and its distribution (see the tracer-particle image velocimeter). However, the measurable temperature range is fairly narrow, i.e., from room temperature to 50°C . A laser-induced fluorescence (LIF) method extends the measurable temperature to 1000°C [11.203]. In LIF, an appropriate fluorescent material whose fluorescence intensity and/or fluorescence lifetime change with temperature is used.

Coherent Anti-Stokes Raman Spectroscopy

The infrared light region reflects the state of the molecular vibration energy. Because the population of the molecular vibrational and rotational states depends on

**Fig. 11.102** Scheme for optical pyrometer

temperature, the temperature of a gas molecule can be determined directly by appropriate infrared spectroscopy. Among the various spectroscopic techniques, a coherent anti-Stokes Raman spectroscopy (CARS) is attractive and has been applied to gas temperature monitoring [11.204].

Another advantageous application of CARS is the identification of analytical molecules. For this purpose, a CARS microscope has been proposed [11.205].

11.7.6 Optical Sensing for the Human Body

The important features of the optical method are that it is rapid, noninvasive and safe. These features are useful for measurements in health care and for medical examination of the human body.

Body Temperature and Thermograph

Body temperature monitoring is the most essential examination in health care. It can typically be monitored within 0.1–0.3 s using an infrared ear thermometer, which measures the infrared energy emitted from the eardrum. A short tube with a protective sleeve is inserted into the ear, and a shutter is opened to allow in radiation from the tympanic membrane.

A thermograph is a picture of the heat levels in the body. It is measured with an infrared imaging system that detects infrared radiation from the body's surface. Since some disorders such as breast cancer or soft-tissue injuries have a very high metabolism, they are slightly hotter than the surrounding normal tissues and can therefore be detected by the thermograph. The other technique is based on liquid crystal (LC) technology. It provides a color map of temperature. Spraying or painting the skin with LC materials displays temperature as different color bands.

Body Contours

Optical sectioning and moiré topography are widely employed to body shape measurement. In clinical applications, spinal faults and progress of their treatment is monitored by so-called moiré contourography, which highlights body contours [11.206]. The moiré contours are obtained by passing angled light through a grid onto the surface of the body.

Retina Examination

Optical coherent tomography (OCT) is a noncontact, noninvasive imaging technique used to obtain high-resolution cross-sectional images of optically transparent materials [11.207]. OCT achieves much greater

longitudinal resolution (approximately 10 μm) than ultrasonic examination, and is thus clinically useful for local imaging of selected macular diseases including macular holes, macular edema, age-related macular degeneration, central serous chorioretinopathy, epiretinal membranes, schisis cavities associated with optic disc pits, and retinal inflammatory diseases. In addition, OCT has the capability of measuring the retinal nerve fiber layer thickness in glaucoma and other diseases of the optic nerve. LDV [11.208] (Sect. 11.7) and laser-speckle flowgraphy [11.209] are also applied for blood-flow determination in the retina.

Pulse Oximetry

Pulse oximetry is an optical method to monitor the hemoglobin (Hb) concentration of arterial blood that is saturated with oxygen [11.210]. The absorption profiles of oxy-Hb and deoxy-Hb show absorption peaks at around 920 and 750 nm, respectively. Therefore, the relative amount of oxy-Hb can be determined by measurement of light absorption in the near-infrared region. The pulse oximeter consists of an optical probe attached to the patient's finger or ear lobe which outputs an absorption signal corresponding to Hb and a computerized signal-processing unit. The unit displays the percentage of Hb saturated with oxygen together with an audible signal for each pulse beat. A reflection-type pulse oximeter that increases the flexibility of installation has been developed [11.211].

Brain Optical Topography

As described in the former section, the concentration of Hb in the artery can be determined optically. Since near-infrared light is transmitted through biological tissues including bones easily, local Hb concentration topography has been achieved optically to analyze functions of the brain [11.212]. To achieve brain topography, multiple pairs of light sources and a detector are placed around the head.

Skin Spectroscopy

Skin spectroscopy provides useful information for skin diagnosis. For example, the oxygen saturation of blood and melanin in the skin can be determined by the measurement of a skin spectral reflectance image and the application of component analysis [11.213]. LDV is also applied to skin diagnosis, for example, burn depth has been determined by a laser Doppler imager [11.214]. Second-harmonic generation (SHG) occurs at appreciable levels when collagen is irradiated with intense short-duration pulsed light if the polarization direction of the

incidence light wave is consistent with the collagen fiber orientation [11.215]. This feature has been applied effectively to the determination of collagen fiber orientation in the human dermis [11.216]. The characteristics of a terahertz electromagnetic wave (THz wave) are situated at the boundary between light and radio waves, and these features of THz waves has been applied to the detection of skin cancer and hydration level [11.217]. We recommend the articles on optics of the human skin published in 2004 for further study [11.218].

Glucose Monitoring

Noninvasive, in vivo optical glucose monitoring is one of the most important measurements to be achieved for human health care and diagnosis. However, the analytical probe light is strongly scattered by the skin and blood cells, resulting in a decrease in measurement reliability. This noninvasive measurement is successful at present only when applied to aqueous humor, which the probe light can reach through the cornea without unwanted scattering [11.219].

References

- 11.1 A.P. Thone: *Spectrophysics*, 2nd edn. (Chapman Hall, New York 1988)
- 11.2 J.D. Ingle Jr., S.R. Crouch: *Spectrochemical Analysis* (Prentice Hall, Piscataway 1988)
- 11.3 H.H. Willard, L.L. Merritt Jr., J.A. Dean, F.A. Settle Jr.: *Instrumental Methods of Analysis*, 7th edn. (Wadsworth Publishing, Belmont 1988)
- 11.4 G.W. Ewing: *Instrumental Methods of Chemical Analysis*, 4th edn. (McGraw-Hill, Tokyo 1975)
- 11.5 T. Iwata, T. Tanaka, T. Araki, T. Uchida: Externally-controlled nanosecond Xe discharge lamp equipped with a synchronous high-voltage power supply using an automobile ignition coil, *Rev. Sci. Instrum.* **73**(9), 3165–3169 (2002)
- 11.6 T. Iwata, T. Tanaka, T. Komatsu, T. Araki: An externally-controlled nanosecond-pulsed, Xe lamp using a high voltage semiconductor switch, *Rev. Sci. Instrum.* **71**, 4045–4049 (2000)
- 11.7 E. Miyazaki, S. Itami, T. Araki: Using a light-emitting diode as a high-speed, wavelength selective photodetector, *Rev. Sci. Instrum.* **69**, 3751–3754 (1998)
- 11.8 T. Araki, H. Misawa: LED-based nanosecond UV-light source for fluorescence lifetime measurements, *Rev. Sci. Instrum.* **66**, 5469–5472 (1995)
- 11.9 T. Araki, Y. Fujisawa, M. Hashimoto: An ultraviolet nanosecond light pulse generator using a light emitting diode for test of photodetector, *Rev. Sci. Instrum.* **68**, 1365–1368 (1997)
- 11.10 T. Iwata: Proposal for Fourier-transform phase-modulation fluorometer, *Opt. Rev.* **10**(1), 31–37 (2003)
- 11.11 T. Iwata, T. Takasu, T. Miyata, T. Araki: Combination of a gated photomultiplier tube and a phase sensitive detector for use in an intensive pulsed background situation, *Opt. Rev.* **9**, 18–24 (2002)
- 11.12 T. Iwata, T. Takasu, T. Araki: Simple photomultiplier-tube internal-gating method for use in sub-nanosecond time-resolved spectroscopy, *Appl. Spectrosc.* **57**, 1145–1150 (2003)
- 11.13 T. Miyata, T. Araki, T. Iwata: Correction of the intensity-dependent phase delay in a silicon avalanche photodiode by controlling its reverse bias voltage, *IEEE J. Quantum Electron.* **QE-39**, 919–923 (2003)
- 11.14 T. Miyata, T. Iwata, T. Araki: Construction of a pseudo-lock-in light detection system using a gain-enhanced gated silicon avalanche photodiode, *Meas. Sci. Technol.* **16**, 2453–2458 (2005)
- 11.15 P. Griffiths, J.A. de Haseth: *Fourier Transform Infrared Spectrometry* (Wiley, New York 1986)
- 11.16 J.M. Chalmers, P.R. Griffiths (Ed.): *Handbook of Vibrational Spectroscopy*, Vol.1 (Wiley, New York 2002)
- 11.17 M. Dressel, G. Grüner: *Electrodynamics of Solids* (Cambridge Univ. Press, Cambridge 2002)
- 11.18 M. Born, E. Wolf: *Principles of Optics: Electromagnetic Theory of Propagation, Interference and Diffraction of Light* (Cambridge Univ. Press, Cambridge 1999)
- 11.19 R.M.A. Azzama, N.M. Bashara: *Ellipsometry and Polarized Light* (North-Holland, Amsterdam 1977)
- 11.20 S. Uchida, T. Ido, H. Takagi, T. Arima, Y. Tokura, S. Tajima: Optical spectra of $\text{La}_{2-x}\text{Sr}_x\text{CuO}_4$: Effect of carrier doping on the electronic structure of the CuO_2 plane, *Phys. Rev. B* **43**, 7942–7954 (1991)
- 11.21 Y. Toyozawa: *Optical Processes in Solids* (Cambridge Univ. Press, Cambridge 2003)
- 11.22 M. Ashida, Y. Kawaguchi, R. Kato: Phonon sidebands of ν_{00} line in absorption and luminescence spectra of NaNO_2 : Spatial dispersion of ν_{00} exciton, *J. Phys. Soc. Jpn.* **58**, 4620–4625 (1989)
- 11.23 Y. Kondo, T. Noto, S. Sato, M. Hirai, A. Nakamura: Hot luminescence and non-radiative transition of F centers in KCl and NaCl crystals, *J. Lumin.* **38**, 164–167 (1987)
- 11.24 I. Akimoto, M. Ashida, K. Kan'no: Luminescence from C_{60} single crystals in glassy phase under site-selective excitation, *Chem. Phys. Lett.* **292**, 561–566 (1999)
- 11.25 M. Cardona, G. Güntherrodt (Eds.): *Light Scattering in Solids I–VIII* (Springer, Berlin, Heidelberg 2000)
- 11.26 W. Hayes, R. Loudon: *Scattering of Light by Crystals* (Wiley, New York 1987)

- 11.27 E. Saitoh, S. Okamoto, K.T. Takahashi, K. Tobe, K. Yamamoto, T. Kimura, S. Ishihara, S. Maekawa, Y. Tokura: Observation of orbital waves as elementary excitations in a solid, *Nature* **410**, 180–183 (2001)
- 11.28 A. Kato, M. Ashida, R. Kato: Temperature dependence of resonant secondary emission in NaNO_2 crystals, *J. Lumin.* **66/67**, 264–267 (1996)
- 11.29 B.P. Zhang, T. Yasuda, W.X. Wang, Y. Segawa, K. Edamatsu, T. Itoh, H. Yaguchi, K. Onabe: A new approach to ZnCdSe quantum dots, *Mater. Sci. Eng. B* **51**, 127–131 (1998)
- 11.30 A.M. van Oijen, M. Ketelaars, J. Koehler, T.J. Aartsma, J. Schmidt: Unraveling the electronic structure of individual photosynthetic pigment-protein complexes, *Science* **285**, 400–402 (1999)
- 11.31 T. Fujimura, K. Edamatsu, T. Itoh, R. Shimada, A. Imada, T. Koda, N. Chiba, H. Muramatsu, T. Ataka: Scanning near-field optical images of ordered polystyrene particle layers in transmission and luminescence excitation modes, *Opt. Lett.* **22**, 489–491 (1997)
- 11.32 K. Matsuda, T. Saiki, S. Nomura, M. Mihara, Y. Aoyagi, S. Nair, T. Takagahara: Near-field optical mapping of exciton wave functions in a GaAs quantum dot, *Phys. Rev.* **91**, 177401 (2003)
- 11.33 H.C. Ong, A.S.K. Li, G.T. Du: Depth profiling of ZnO thin films by cathodoluminescence, *Appl. Phys. Lett.* **78**, 2667–2669 (2001)
- 11.34 K. Vanheusden, W.L. Warren, C.H. Seager, D.R. Tal-lant, J.A. Voigt, B.E. Gnade: Mechanisms behind green photoluminescence in ZnO phosphor powders, *J. Appl. Phys.* **79**, 7983–7990 (1996)
- 11.35 D.M. Bagnall, Y.F. Chen, Z. Zhu, T. Yao, S. Koyama, M.Y. Shen, T. Goto: Optically pumped lasing of ZnO at room temperature, *Appl. Phys. Lett.* **70**, 2230–2232 (1997)
- 11.36 K. Shinagawa: Faraday and Kerr effects in ferromagnets. In: *Magneto-Optics*, Vol.128, ed. by S. Sugano, N. Kojima (Springer, Berlin, Heidelberg 2000) p.137
- 11.37 M. Faraday: On the magnetization of light and the illumination of magnetic lines of force, *Philos. Trans. R. Soc.* **136**, 104–123 (1846)
- 11.38 J. Kerr: On rotation of the plane of polarization by reflection from the pole of a magnet, *Philos. Mag.* **3**, 321 (1877)
- 11.39 C. Gourdon, G. Lazard, V. Jeudy, C. Testelin, E.L. Ivchenko, G. Karczewski: Enhanced Faraday rotation in CdMnTe quantum wells embedded in an optical cavity, *Solid State Commun.* **123**, 299–304 (2002)
- 11.40 C. Gourdon, V. Jeudy, M. Menant, A.T. Le, E.L. Ivchenko, G. Karczewski: Magneto-optical imaging with diluted magnetic semiconductor quantum wells, *Appl. Phys. Lett.* **82**, 230–232 (2003)
- 11.41 M.R. Koblischka, R.J. Wijngaarden: Magneto-optical investigations of superconductors, *Superconduct. Sci. Technol.* **8**, 199–213 (1995)
- 11.42 P.E. Goa, H. Hauglin, M. Baziljevich, E. Il'yashenko, P.L. Gammel, T.H. Johansen: Real-time magneto-optical imaging of vortices in superconducting NbSe_2 , *Superconduct. Sci. Technol.* **14**, 729–731 (2001)
- 11.43 M.A. Butler, S.J. Martin, R.J. Baughman: Frequency-dependent Faraday rotation in CdMnTe , *Appl. Phys. Lett.* **49**, 1053–1055 (1986)
- 11.44 D. Scalbert, J. Cernogora, C. Benoit à la Guillaume: Spin-lattice relaxation in paramagnetic CdMnTe , *Solid State Commun.* **66**, 571–574 (1988)
- 11.45 V. Jeudy, C. Gourdon, T. Okada: Impeded growth of magnetic flux bubbles in the intermediate state pattern of type I superconductors, *Phys. Rev. Lett.* **92**, 147001 (2004)
- 11.46 A. Cebers, C. Gourdon, V. Jeudy, T. Okada: Normal-state bubbles and lamellae in type-I superconductors, *Phys. Rev. B* **72**, 014513 (2005)
- 11.47 Y.R. Shen: *The Principles of Nonlinear Optics* (Wiley, New York 1984)
- 11.48 S.V. Popov, P.Y. Svirko, N.I. Zheludev: *Susceptibility Tensors for Nonlinear Optics* (Inst. Physics, London 1995)
- 11.49 D.L. Mills: *Nonlinear Optics Basic Concepts* (Springer, Berlin, Heidelberg 1998)
- 11.50 H. Kishida, M. Ono, K. Miura, H. Okamoto, M. Izumi, T. Manako, M. Kawasaki, Y. Taguchi, Y. Tokura, T. Tohyama, K. Tsutsui, S. Maekawa: Large third-order optical nonlinearity of Cu-O chains investigated by third-harmonic generation spectroscopy, *Phys. Rev. Lett.* **87**(4), 177401 (2001)
- 11.51 C. Rulliere (Ed.): *Femtosecond Laser Pulses* (Springer, Berlin, Heidelberg 2003)
- 11.52 M. Ashida, R. Kato: Resonant emission under excitation of isotopic level in NaNO_2 , *J. Phys. Soc. Jpn.* **63**, 2808–2817 (1993)
- 11.53 A. Kato, M. Ashida, R. Kato: Time-resolved study of exciton thermalization in NaNO_2 , *J. Phys. Soc. Jpn.* **66**, 2886–2892 (1997)
- 11.54 M. Ashida, H. Arai, O. Morikawa, R. Kato: Luminescence and superfluorescence-like emission from a thin layer of O_2^- centers in KBr crystal, *J. Lumin.* **72–74**, 624–625 (1997)
- 11.55 M. Kuwata, T. Kuga, H. Akiyama, T. Hirano, M. Matsuoka: Pulsed propagation of polariton luminescence, *Phys. Rev. Lett.* **61**, 1226–1228 (1988)
- 11.56 S. Kinoshita, H. Ozawa, Y. Kanematsu, I. Tanaka, N. Sugimoto, S. Fujiwara: Efficient optical Kerr shutter for femtosecond time-resolved luminescence spectroscopy, *Rev. Sci. Instrum.* **71**, 3317–3322 (2000)
- 11.57 T. Matsuoka, S. Saito, J. Takeda, S. Kurita, T. Sue-moto: Overtone modulation and anti-phasing behavior of wave-packet amplitudes on the adi-

- abatic potential surface of self-trapped excitons, *Nonlinear Opt.* **29**, 587–593 (2002)
- 11.58 M. Ashida, T. Ogasawara, N. Motoyama, H. Eisaki, S. Uchida, Y. Taguchi, Y. Tokura, H. Ghosh, A. Shukla, S. Mazumdar, M. Kuwata-Gonokami: Interband two-photon transition in Mott insulator as a new mechanism for ultrafast optical nonlinearity, *Int. J. Mod. Phys. B* **15**, 3628–3632 (2001)
- 11.59 M. Ashida, T. Ogasawara, Y. Tokura, S. Uchida, S. Mazumdar, M. Kuwata-Gonokami: One-dimensional cuprate as a nonlinear optical material for ultrafast all-optical switching, *Appl. Phys. Lett.* **78**, 2831–2833 (2001)
- 11.60 M. Sheik-Bahae, A.A. Said, T.-H. Wei, D.J. Hagan, E.W. Van Stryland: Sensitive measurement of optical nonlinearities using a single beam, *IEEE J. Quantum Electron.* **QE-26**, 760–769 (1990)
- 11.61 N. Peyghambarian, S.W. Koch, A. Mysyriwicz: *Introduction to Semiconductor Optics* (Prentice Hall, Piscataway 1993)
- 11.62 B. Ferguson, X.C. Zhang: Materials for terahertz science and technology, *Nat. Mater.* **1**, 26–33 (2002)
- 11.63 K. Sakai (Ed.): *Terahertz Optoelectronics* (Springer, Berlin, Heidelberg 2005)
- 11.64 R. Huber, F. Tauser, A. Brodschelm, M. Bichler, G. Abstreiter, A. Leitenstorfer: How many-particle interactions develop after ultrafast excitation of an electron-hole plasma, *Nature* **414**, 286–289 (2001)
- 11.65 M. Ashida: Ultra-broadband terahertz wave detection using photoconductive antenna, *Jpn. J. Appl. Phys.* **47**, 8221–8225 (2008)
- 11.66 C. Kübler, R. Huber, S. Tübel, A. Leitenstorfer: Ultrabroadband detection of multi-terahertz field transients with GaSe electro-optic sensors: Approaching the near infrared, *Appl. Phys. Lett.* **85**, 3360–3362 (2004)
- 11.67 K. Kawase: Terahertz imaging for drug detection and large-scale integrated circuit inspection, *Opt. Photon. News* **15**, 34–39 (2004)
- 11.68 J.A. Buck: *Fundamentals of Optical Fibers* (Wiley, New York 1995), Chap. 3
- 11.69 T. Li (Ed.): *Optical Fiber Communications: Fiber Fabrication*, Vol. 1 (Academic, San Diego 1985)
- 11.70 TIA-455-78: Spectral Attenuation Cutback Measurement for Single Mode Optical Fibers (Electronic Industries Association, Washington 2002)
- 11.71 TIA/EIA-455-50: Light Launch Conditions for Long-Length, Graded-Index Optical Fiber Spectral Attenuation measurements, Procedure B (Electronic Industries Association, Washington 2001)
- 11.72 I.H. Maliston: Interspecimen comparison of the refractive index of fused silica, *J. Opt. Soc. Am.* **55**, 1205–1209 (1965)
- 11.73 M.J. Adams: *An Introduction to Optical Waveguides* (Wiley, New York 1981), Chap. 7
- 11.74 B.J. Ainslie, C.R. Day: A review of single-mode fibers with modified dispersion characteristics, *J. Lightwave Technol.* **4**, 967–979 (1986)
- 11.75 L.G. Cohen, C. Lin: Pulse delay measurements in the zero material dispersion wavelength region for optical fibers, *Appl. Opt.* **16**, 3136–3139 (1977)
- 11.76 B. Costa, D. Mazzoni, M. Puleo, E. Vezzoni: Phase shift technique for the measurement of chromatic dispersion in optical fibers using LEDs, *IEEE J. Quantum Electron.* **QE-18**, 1509–1515 (1982)
- 11.77 M. Takeda, N. Shibata, S. Seikai: Interferometric method for chromatic dispersion measurement in a single-mode optical fiber, *IEEE J. Quantum Electron.* **QE-17**, 404–407 (1981)
- 11.78 D. Milam, M.J. Weber: Measurement of nonlinear refractive-index coefficients using time-resolved interferometry: Application to optical materials for high-power neodymium lasers, *J. Appl. Phys.* **47**, 2497–2501 (1976)
- 11.79 A. Fellegara, M. Artiglia, S.B. Andreasen, A. Melloni, F.P. Espunes, M. Martinelli: COST 241 intercomparison of nonlinear refractive index measurements in dispersion shifted optical fibres at $\lambda = 1550$ nm, *Electron. Lett.* **33**, 1168–1170 (1997)
- 11.80 G.P. Agrawal: *Nonlinear Fiber Optics* (Academic, New York 1989)
- 11.81 M.E. Fermann, A. Galvanauskas, G. Sucha, D. Harter: Fiber-lasers for ultrafast optics, *Appl. Phys. B* **65**, 259–275 (1997)
- 11.82 L.E. Nelson, D.J. Jones, K. Tamura, H.A. Haus, E.P. Ippen: Ultrashort-pulse fiber ring lasers, *Appl. Phys. B* **65**, 277–294 (1997)
- 11.83 J.K. Ranka, R.S. Windeler, A.J. Stentz: Visible continuum generation in air-silica microstructure optical fibers with anomalous dispersion at 800 nm, *Opt. Lett.* **25**, 25–27 (2000)
- 11.84 R.H. Stolen: Nonlinearity in fiber transmission, *Proc. IEEE* **68**, 1232–1236 (1980)
- 11.85 D. Marcuse, A.R. Chraplyvy, R.W. Tkach: Effect of fiber on long distance transmission, *IEEE J. Lightwave Technol.* **9**, 121–128 (1991)
- 11.86 R.G. Smith: Optical power handling capacity of low loss optical fibers as determined by stimulated Raman and Brillouin scattering, *Appl. Opt.* **11**, 2489–2494 (1972)
- 11.87 Y. Namihara, M. Miyata, N. Tanahashi: Nonlinear coefficient measurements for dispersion shifted fibres using self-phase modulation method at 1.55 μm , *Electron. Lett.* **30**, 1171–1172 (1994)
- 11.88 A. Boskovic, S.V. Chernikov, J.R. Taylor, L. Gruner-Nielsen, O.A. Levring: Direct continuous-wave measurement of n_2 in various types of telecommunication fiber at 1.55 μm , *Opt. Lett.* **21**, 1966–1968 (1996)
- 11.89 R.H. Stolen, C. Lin: Self-phase-modulation in silica fibers, *Phys. Rev.* **17**, 1448–1454 (1978)
- 11.90 T. Kato, Y. Suetsugu, M. Takagi, E. Sasaoka, M. Nishimura: Measurement of the nonlinear refractive index in optical fiber by the cross-phase-modulation method with depolarized pump light, *Opt. Lett.* **20**, 988–990 (1995)

- 11.91 L. Prigent, J.P. Hamaide: Measurement of fiber nonlinear Kerr coefficient by four-wave mixing, *IEEE Photon. Technol. Lett.* **5**, 1092–1095 (1993)
- 11.92 K.O. Hill, Y. Fujii, D.C. Johnson, B.S. Kawasaki: Photosensitivity in optical fiber waveguides: Application to reflection filter fabrication, *Appl. Phys. Lett.* **32**, 647–649 (1978)
- 11.93 K.O. Hills, B. Malo, F. Bilodeau, D.C. Johnson: Photosensitivity in optical fibers, *Annu. Rev. Mater. Sci.* **23**, 125–157 (1993)
- 11.94 I. Bennion, J.A.R. Williams, L. Zhang, K. Sugden, N. Doran: Tutorial review, UV-written in-fibre Bragg gratings, *Opt. Quantum Electron.* **28**, 93–135 (1996)
- 11.95 M. Bass, E.W. Van Stryland: *Fiber Optics Handbook, Fiber, Devices and Systems for Optical Communications* (McGraw-Hill, New York 2002), Chap. 9
- 11.96 P.J. Lemaire, R.M. Adkins, V. Mizrahi, W.A. Reed: High pressure H₂ loadening as a technique for achieving ultrahigh UV photosensitivity in GeO₂ doped optical fibers, *Electron. Lett.* **29**, 1191–1193 (1993)
- 11.97 F. Bilodeau, B. Malo, J. Albert, D.C. Johnson, K.O. Hill, Y. Hibino, M. Abe, M. Kawachi: Photosensitization of optical fiber and silica-on-silicon/silica waveguides, *Opt. Lett.* **18**, 953–955 (1993)
- 11.98 G. Meltz, W.W. Morey, W.H. Glenn: Formation of Bragg gratings in optical fibers by a transverse holographic method, *Opt. Lett.* **14**, 823–825 (1989)
- 11.99 K.O. Hill, B. Malo, F. Bilodeau, D.C. Johnson, J. Albert: Bragg gratings fabricated in monomode photosensitive optical fiber by UV exposure through a phase mask, *Appl. Phys. Lett.* **62**, 1035–1037 (1993)
- 11.100 K.O. Hill, B. Malo, K.A. Vineberg, F. Bilodeau, D.C. Johnson, I. Skinner: Efficient mode conversion in telecommunication fiber using externally written gratings, *Electron. Lett.* **26**, 1270–1272 (1990)
- 11.101 B. Malo, S. Theriault, D.C. Johnson, F. Bilodeau, J. Albert, K.O. Hill: Apodised in-fibre Bragg grating reflectors photoimprinted using a phase mask, *Electron. Lett.* **31**, 223–225 (1995)
- 11.102 K.O. Hill, G. Metz: Fiber Bragg grating technology fundamentals and overview, *J. Lightwave Technol.* **15**, 1263–1276 (1997)
- 11.103 A.M. Vengsarkar, P.J. Remaire, J.B. Judkins, V. Bhatia, T. Erdogan, J.E. Sipe: Long-period fiber gratings as a band-rejection filters, *J. Lightwave Technol.* **14**, 58–65 (1996)
- 11.104 A.M. Vengsarkar, J.R. Pedrazzani, J.B. Judkins, P.J. Lemaire, N.S. Bergano, C.R. Davidson: Long-period fiber-grating-based gain equalizers, *Opt. Lett.* **21**, 336–338 (1996)
- 11.105 E. Desurvire: *Erbium-Doped Fiber Amplifiers, Principles and Applications* (Wiley-Interscience, New York 1994) p. 238
- 11.106 M. Bass, E.W. Van Stryland: *Fiber Optics Handbook, Fiber, Devices, and Systems for Optical Communications* (McGraw-Hill, New York 2002), Chap. 15
- 11.107 S. Sudo: Outline of optical fiber amplifiers. In: *Optical Fiber Amplifiers: Materials, Devices, and Applications*, ed. by S. Sudo (Artech House, Boston 1997) pp. 81–83
- 11.108 W.J. Miniscalco: Erbium-doped glasses for fiber amplifiers at 1500 nm, *IEEE J. Lightwave Technol.* **9**, 234–250 (1991)
- 11.109 T.J. Whitley, R. Wyatt, D. Szebesta, S. Davey, J.R. Williams: Quarter-Watt output at 1.3 μm from a praseodymium-doped fluoride fiber amplifier pumped with a diode-pumped Nd:YLF laser, *IEEE Photon. Technol. Lett.* **5**, 399–401 (1993)
- 11.110 T.J. Whitley: A review of recent system demonstrations incorporating 1.3 μm praseodymium-doped fluoride fibre amplifiers, *IEEE J. Lightwave Technol.* **13**, 744–760 (1995)
- 11.111 P.C. Becker, N.A. Olsson, J.R. Simpson, A.A. Olsson: *Erbium-Doped Fiber Amplifiers, Fundamentals and Technology* (Academic, San Diego 1999) pp. 139–140
- 11.112 E. Desurvire: *Erbium doped Fiber Amplifiers, Principles and Applications* (Wiley-Interscience, New York 1994) pp. 339–340
- 11.113 H.A. Haus: The noise figure of amplifiers, *IEEE Photon. Technol. Lett.* **10**, 1602–1606 (1998)
- 11.114 I.N. Duling: All-fiber ring soliton laser mode locked with a non-linear mirror, *Opt. Lett.* **16**, 539–541 (1991)
- 11.115 M. Bass, E.W. Van Stryland: *Fiber Optics Handbook* (McGraw-Hill, New York 2002), Chap. 5
- 11.116 S.T. Davey, P.W. France: Rare-earth-doped fluorozirconate glass for fiber devices, *Br. Telecom Technol. J.* **7**, 58 (1989)
- 11.117 F. Roy, D. Bayart, A. Le Sauze, P. Baniel: Noise and gain band management of thulium doped fiber amplifier with dual-wavelength pumping schemes, *Photon. Technol. Lett.* **13**, 788–790 (2001)
- 11.118 T. Karamatsu, Y. Yano, T. Ono: Laser-diode pumping (1.4 and 1.56 μm) of gain-shifted thulium-doped fiber amplifier, *Electron. Lett.* **36**, 1607–1609 (2000)
- 11.119 R.M. Percival, D. Szebesta, C.P. Seltzer, S.D. Perlin, S.T. Davey, M. Louka: A 1.6 μm pumped 1.9 μm thulium-doped fluoride fiber laser and amplifier of very high efficiency, *IEEE J. Quantum Electron.* **QE-31**, 498–493 (1995)
- 11.120 S. Sudo: Progress in Optical Fiber Amplifiers. In: *Current Trends in Optical Amplifiers and their Applications*, ed. by P.T. Lee (World Scientific, Teaneck 1996) pp. 19–21
- 11.121 S. Namiki, Y. Emori: Ultra-broadband Raman amplifiers pumped and gain equalized by wavelength-division-multiplexed high-power diode, *IEEE J. Sel. Quantum Electron.* **7**, 3–16 (2001)
- 11.122 M.E. Fermann: Nonlinear polarization evolution in passively modelocked fiber laser. In: *Compact Ul-*

- trafast Pulse Sources*, ed. by I.N. Duling (Cambridge Univ. Press, Cambridge 1995)
- 11.123 M.E. Fermann, A. Galvanauskas, G. Sucha: *Ultra-fast Lasers: Technology and Applications* (Marcel Dekker, New York 2003)
- 11.124 D.J. DiGiovanni, A.J. Stentz: Tapered fiber bundles for coupling light into and out of cladding-pumped fiber lasers, US Patent 5864644 (1999)
- 11.125 L. Goldberg, P. Koplow, D.A.V. Kliner: Highly efficient 4-W Yb-doped fiber amplifier pumped by a broad-stripe laser diode, *Opt. Lett.* **24**, 673–675 (1999)
- 11.126 V.P. Gapontsev, I. Samartsev: Coupling arrangement between a multi-mode light source and an optical fiber through an intermediate optical fiber length, US Patent 5999673 (1999)
- 11.127 N.S. Platonov, V.P. Gapontsev, O. Shkurihin, I. Zaitsev: 400 W low-noise single-mode CW ytterbium fiber laser with an integrated fiber delivery, *Conf. Lasers Electro-Opt.* (Optical Society of America, Washington 2003), postdeadline paper CThPDB9
- 11.128 V. Dominic, S. MacCormack, R. Waarts, S. Sanders, S. Bicknese, R. Dohle, E. Wolak, P.S. Yeh, E. Zucker: 110 W fibre laser, *Electron. Lett.* **35**, 1158–1160 (1999)
- 11.129 J. Nilsson, J.K. Sahu, W.A. Clarkson, R. Selvas: High power fiber lasers: New developments, *Proc. SPIE* **4974**, 50–59 (2003)
- 11.130 S.F. Carter, M.W. Moore, D. Szebesta, D. Ransom, P. France: Low loss fluoride fibre by reduced pressure casting, *Electron. Lett.* **26**, 2115–2117 (1990)
- 11.131 R. Nubling, J.A. Harrington: Optical properties of single-crystal sapphire fibers, *Appl. Opt.* **36**, 5934–5940 (1997)
- 11.132 J. Nishii, S. Morimoto, I. Inagawa, R. Iizuka, T. Yamashita, T. Yamagishi: Recent advances and trends in chalcogenide glass fiber technology, A review, *J. Non-Cryst. Solids* **140**, 199–208 (1992)
- 11.133 V. Artjushenko, V. Ionov, K.J. Kalaidjian, A.P. Kryukov, E.F. Kuzin, A.A. Lerman, A.S. Prokhorov, E.V. Stepanov, K. Bakhshpour, K.B. Moran, W. Neuberger: Infrared fibers: Power delivery and medical applications, *Proc. SPIE* **2396**, 25–36 (1995)
- 11.134 Y. Matsuura, T. Abel, J.A. Harrington: Optical properties of small-bore hollow glass waveguides, *Appl. Opt.* **34**, 6842–6847 (1995)
- 11.135 E.W. Van Stryland, M. Bass: *Fiber Optics Handbook* (McGraw-Hill, New York 2002), Chap. 14
- 11.136 P.W. France, S.F. Carter, M.W. Moore, C.R. Day: Progress on fluoride fibres for optical communications, *Br. Telecom Technol. J.* **5**, 28–44 (1987)
- 11.137 S. Kobayashi, N. Shibata, S. Shibata, T. Izawa: Characteristics of optical fibers in infrared wavelength region, *Electr. Commun. Lab. Rev.* **26**, 453–467 (1978)
- 11.138 T. Abel, J. Hirsch, J.A. Harrington: Hollow glass waveguides for broadband infrared transmission, *Opt. Lett.* **19**, 1034–1036 (1994)
- 11.139 R.K. Nubling, J.A. Harrington: Hollow-waveguide delivery systems for high-power, industrial CO₂ lasers, *Appl. Opt.* **35**, 372–380 (1996)
- 11.140 J. Sanghera, I. Aggarwal: *Infrared Fiber Optics* (CRC, Boca Raton 1998)
- 11.141 A. Weinert: *Plastic Optical Fibers: Principle, Components, Installation* (VCH, Weinheim 1999)
- 11.142 Y. Watanabe, C. Tanaka: Current status of perfluorinated GI-POF and 2.5 Gbps data transmission over it, *Proc. OFC, Los Angeles* (2003) pp. 12–13
- 11.143 E. Yablonovitch: Photonic band-gap structures, *J. Opt. Soc. Am. B* **10**, 283–295 (1993)
- 11.144 T.A. Birks, R.J. Robert, P.S.J. Russell: Full 2-D photonic band gaps in silica/air structures, *Electron. Lett.* **31**, 1941–1943 (1995)
- 11.145 J.C. Knight, T.A. Birks, D.M. Adkin, P.S.J. Russell: Pure silica single mode fiber with hexagonal photonic crystal cladding, *Proc. OFC, San Jose* (1996), PD3
- 11.146 P. Russell: Photonic crystal fibers, *Science* **299**, 385–362 (2003)
- 11.147 T.A. Birks, J.C. Knight, P.S.J. Russell: Endlessly single-mode photonic crystal fibers, *Opt. Lett.* **22**, 961–963 (1997)
- 11.148 J.C. Knight, T.A. Birks, P.S.J. Russell, D.M. Atkin: All-silica single-mode optical fiber with photonic crystal cladding, *Opt. Lett.* **21**, 1547–1549 (1996)
- 11.149 J. Limpert, T. Schreiber, S. Nolte, H. Zellmer, T. Tunnermann, R. Iliw, F. Lederer, J. Broeng, G. Vienne, A. Petersson, C. Jakobsen: High-power air-clad large-mode-area photonic crystal fiber laser, *Opt. Express* **11**, 818–823 (2003)
- 11.150 J.C. Knight, J. Arriaga, T.A. Birks, A. Ortigosa-Blanch, W.J. Wadsworth, P.S.J. Russell: Anomalous dispersion in photonic crystal fiber, *IEEE Photon. Technol. Lett.* **12**, 807–809 (2000)
- 11.151 J.K. Ranka, R.S. Windeler, A.J. Stentz: Visible continuum generation in air-silica microstructure optical fibers with anomalous dispersion at 800 nm, *Opt. Lett.* **25**, 25–27 (2000)
- 11.152 T. Udem, R. Holzwarth, T.W. Hänsch: Optical frequency metrology, *Nature* **416**, 233–237 (2002)
- 11.153 B. Povazy, K. Bizheva, A. Unterhuber, B. Hermann, H. Sattmann, A.E. Fercher, W. Drexler, A. Apolonski, W.J. Wadsworth, J.C. Knight, P.S.J. Russell, M. Vetterlein, E. Scherzer: Submicrometer axial resolution optical coherence tomography, *Opt. Lett.* **27**, 1800–1802 (2002)
- 11.154 A. Ortigosa-Blanch, J.C. Knight, W.J. Wadsworth, J. Arriaga, B.J. Mangan, T.A. Birks, P.S.J. Russell: Highly birefringent photonic crystal fibers, *Opt. Lett.* **25**, 1325–1327 (2000)
- 11.155 R.F. Cregan, B.J. Mangan, J.C. Knight, T.A. Birks, P.S.J. Russell, P.J. Roberts, D.C. Allan: Single-mode photonic bandgap guidance of light in air, *Science* **285**, 1537–1539 (1999)
- 11.156 B.J. Mangan, L. Farr, A. Langford, P.J. Roberts, D.P. Williams, F. Cony, M. Lawman, M. Ma-

- son, S. Coupland, R. Flea, H. Sabert, T.A. Birks, J.C. Knight, P.S.J. Russell: Low loss (1.7 dB/km) hollow core photonic bandgap fiber, Proc. Opt. Fiber Commun. Conf., Vol. 2 (Optical Society of America, Los Angeles 2004) p. 3, (post deadline paper)
- 11.157 K. Nakayama: Ultra-low loss (0.151 dB/km) fiber and its impact on submarine transmission system, Proc. OFC (Anaheim 2002), FA10-1
- 11.158 J.D. Shephard, J. Jones, D. Hand, G. Bouwmans, J. Knight, P. Russell, B. Mangan: High energy nanosecond laser pulses delivered single-mode through hollow-core PBG fibers, Opt. Express **12**, 717-723 (2004)
- 11.159 G. Bouwmans, F. Luan, J. Knight, P.S.J. Russell, L. Farr, B. Mangan, H. Sabert: Properties of a hollow-core photonic bandgap fiber at 850 nm wavelength, Opt. Express **13**, 1613-1620 (2003)
- 11.160 B.T. Kolomiets: Chalcogenide alloy vitreous semiconductor physicochemical, optical, electrical, photoelectric and glass crystal transition properties, Phys. Status Solidi (b) **7**, 359-372 (1964)
- 11.161 J. Feinleib, J. deNeufville, S.R. Ovshinsky: Rapid reversible light-induced crystallization of amorphous semiconductors, Appl. Phys. Lett. **18**, 254-257 (1971)
- 11.162 A.W. Smith: Injection laser writing on chalcogenide films, Appl. Opt. **13**, 795-798 (1974)
- 11.163 N. Yamada, S. Ohara, K. Nishiuchi, M. Nagashima, M. Takenaga, S. Nakamura: Erasable optical disc using TeO_x thin film, Proc. 3rd Int. Display Res. Conf., Japan Display, Kobe, ed. by F.J. Kahn, T. Yoshida (Society for Information Display and Institute of Television Engineers of Japan, 1983) pp. 46-48
- 11.164 M. Chen, K.A. Rubin, V. Marrello, U.G. Gerber, V.B. Jipson: Reversibility and stability of tellurium alloys for optical data storage applications, Appl. Phys. Lett. **46**, 734-736 (1985)
- 11.165 M. Terao, T. Nishida, Y. Miyauchi, T. Nakao, T. Kaku, S. Horigome, M. Ojima, Y. Tsunoda, Y. Sugita, Y. Ohta: Sn-Te-Se phase change recording film for optical disks, Proc. SPIE **529**, 46 (1985)
- 11.166 N. Yamada, E. Ohno, K. Nishiuchi, N. Akahira, M. Takao: Rapid-phase transitions of GeTe-Sb₂Te₃ pseudobinary amorphous thin films for an optical disk memory, J. Appl. Phys. **69**, 2849-2856 (1991)
- 11.167 N. Yamada: Erasable phase-change optical materials, MRS Bulletin **21**(9), 48-50 (1996)
- 11.168 H. Iwasaki, Y. Ide, M. Harigaya, Y. Kageyama, I. Fujimura: Completely erasable phase change optical disk, Jpn. J. Appl. Phys. **31**(2), 461-465 (1992)
- 11.169 M. Horie, N. Nobukuni, K. Kiyono, T. Ohno: High-speed rewritable DVD up to 20 m/s with nucleation-free eutectic phase-change material of Ge(Sb₇₀Te₃₀)+Sb, Proc. SPIE **4090**, 135-143 (2001)
- 11.170 H. Tashiro, M. Harigaya, K. Ito, M. Shinkai, K. Tani, N. Yiwata, A. Watada, N. Toyoshima, K. Makita, A. Kitano, K. Kato: Phase-change material for high-speed rewritable media, Proc. E*PCOS2003, Lugano, ed. by I. Satoh (2003), (online publication http://www.epcos.org/pdf_2003/Tashiro.pdf)
- 11.171 H.E. Kissinger: Variation of peak temperature with heating rate in differential thermal analysis, J. Res. Nat. Bur. Stand. **57**, 217-221 (1956)
- 11.172 H.E. Kissinger: Reaction kinetics in differential thermal analysis, Anal. Chem. **29**(11), 1702-1706 (1957)
- 11.173 H. Kubota: *Hadou-kougaku* (Iwanami, Tokyo 1971), (in Japanese)
- 11.174 K. Nishiuchi, N. Yamada, N. Akahira, M. Takenaga: Laser diode beam exposure instrument for rapid quenching of thin-film materials, Rev. Sci. Instrum. **63**(6), 3425-3430 (1992)
- 11.175 I. Satoh, N. Yamada: DVD-RAM for all audio/video, PC, and network applications, Proc. SPIE **4085**, 283-290 (2001)
- 11.176 H.M. Rietveld: A profile refinement method for nuclear and magnetic structures, J. Appl. Crystallogr. **2**, 65-71 (1969)
- 11.177 H.J. Williams, R.C. Sherwood, F.G. Foster, E.M. Kelley: Magnetic writing on thin films of MnBi, J. Appl. Phys. **28**(10), 1181-1184 (1957)
- 11.178 L. Mayer: Curie-point writing on magnetic films, J. Appl. Phys. **29**(6), 1003 (1958)
- 11.179 J.T. Chang, J.F. Dillon Jr., U.F. Gianola: Magneto-optical variable memory based upon the properties of a transparent ferrimagnetic garnet at its compensation temperature, J. Appl. Phys. **36**, 1110-1111 (1965)
- 11.180 P. Chaudhari, J.J. Cuomo, R.J. Gambino: Amorphous metallic films for magneto-optic, Appl. Phys. Lett. **22**, 337-339 (1973)
- 11.181 W.P. Van Drent, T. Suzuki: A new ultra-violet magneto-optical spectroscopic instrument and its application to Co-based multilayers and thin films, IEEE Trans. Magn. **33**(5), 3223-3225 (1997)
- 11.182 J. Saito, M. Sato, H. Matsumoto, H. Akasaka: Direct overwrite by light power modulation on magneto-optical multi-layered media, Jpn. J. Appl. Phys. **26**(Suppl. 4), 155-159 (1987)
- 11.183 T. Fukami, Y. Kawano, T. Tokunaga, Y. Nakaki, K. Tsutsumi: Direct overwrite technology using exchange-coupled multilayer, J. Magn. Soc. Jpn. **15**(Suppl. 1), 293-298 (1987)
- 11.184 M. Kaneko, K. Aratani, M. Ohta: Multilayered magneto-optical disks for magnetically induced super resolution, Jpn. J. Appl. Phys. Ser. **6**, 203-210 (1991)
- 11.185 K. Aratani, A. Fukumoto, M. Ohta, M. Kaneko, K. Watanabe: Magnetically induced super resolution in a novel magneto-optical disk, Proc. SPIE **1499**, 209-215 (1991)
- 11.186 M. Ohta, A. Fukumoto, M. Kaneko: Read out mechanism of magnetically induced super resolution, J. Magn. Soc. Jpn. **15**(Suppl. 1), 319-322 (1991)

- 11.187 A. Takahashi, M. Kaneko, H. Watanabe, Y. Uchihara, M. Moribe: 5 Gbit/inch² MO technology, *J. Magn. Soc. Jpn.* **22**(Suppl. 2), 67–70 (1998)
- 11.188 K. Shono: 3.5-inch MO disk using double-mask MSR Media, *J. Magn. Soc. Jpn.* **23**, 177–180 (1999)
- 11.189 M. Birukawa, K. Uchida, N. Miyatake: Reading a 0.2 μm mark using the MSR method, *J. Magn. Soc. Jpn.* **20**(Suppl. S1), 103–108 (1996)
- 11.190 E. Betzig, J.K. Trautman, R. Wolfe, E.M. Gyorgy, P.L. Finn, M.H. Kryder, C.-H. Chang: Near-field magneto-optics and high density data storage, *Appl. Phys. Lett.* **61**, 142–144 (1992)
- 11.191 V. Kottler, N. Essaidi, N. Ronarch, C. Chappert, Y. Chen: Dichroic imaging of magnetic domains with a scanning near-field optical microscope, *J. Magn. Mater.* **165**(1–3), 398–400 (1997)
- 11.192 S. Sato, T. Ishibashi, T. Yoshida, J. Yarnamoto, A. Iijirna, Y. Mitsuoka, K. Nakajima: Observation of recorded marks of MO disk by scanning near-field magneto-optical microscope, *J. Magn. Soc. Jpn.* **23**(Suppl. 1), 201–204 (1999)
- 11.193 Y. Martin, D. Rugar, H.K. Wickramasinghe: High-resolution magnetic imaging of domains in TbFe by force microscopy, *Appl. Phys. Lett.* **52**, 244–246 (1988)
- 11.194 P. Grutter, D. Rugar, T.R. Albrecht, H.J. Mamin: Magnetic force microscopy—recent advantages and applications to magneto-optic recording, *J. Magn. Soc. Jpn.* **15**(Suppl. S1), 243–244 (1991)
- 11.195 H.W. van Kesteren, A.J. den Boef, W.B. Zeper, J.H.M. Spruit, B.A.J. Jacobs, P.F. Garcia: Scanning magnetic force microscopy on Co/Pt magneto-optical disks, *J. Magn. Soc. Jpn.* **15**(Suppl. S1), 247–250 (1991)
- 11.196 P. Giljer, J.M. Sivertsen, J.H. Judy, C.S. Bhatia, M.F. Doerner, T. Suzuki: Magnetic recording measurements of high coercivity longitudinal media using magnetic force microscopy (MFM), *J. Appl. Phys.* **79**(8), 5327–5329 (1996)
- 11.197 M. Birukawa, Y. Hino, K. Nishikiori, K. Uchida, T. Shiratori, T. Hiroki, Y. Miyaoka, Y. Hozumi: Two-inch-diameter magneto-optical disk system with 3 GB capacity and 24 Mbps data transfer rate using a red laser, *Trans. Magn. Soc. Jpn.* **2**, 273–278 (2002)
- 11.198 H. Awano, S. Ohnuki, H. Shirai, N. Ohta, A. Yamaguchi, S. Sumi, K. Torazawa: Magnetic domain expansion readout for amplification of an ultra high density magneto-optical recording signal, *Appl. Phys. Lett.* **69**, 4257–4259 (1996)
- 11.199 T. Shiratori, E. Fujii, Y. Miyaoka, Y. Hozumi: High-density magneto-optical recording with domain displacement detection, *J. Magn. Soc. Jpn.* **22**(Suppl. 2), 47–50 (1998)
- 11.200 T. Araki: Optical distance meter developed using a short pulse width laser diode, a fast avalanche photodiode, *Rev. Sci. Instrum.* **66**, 43–47 (1995)
- 11.201 T. Araki, S. Yokuyama, N. Suzuki: Simple optical distancemeter using an intermode-beat modulation of He-Ne laser and an electrical heterodyne technique, *Rev. Sci. Instrum.* **65**, 1883–1888 (1994)
- 11.202 M. Born, E. Wolf: *Principle of Optics*, 7th edn. (Cambridge Univ. Press, Cambridge 1997)
- 11.203 S. Alaruri, A. Brewington, M. Thomas, J. Miller: High-temperature remote thermometry using laser induced fluorescence decay lifetime measurements of Y₂O₃:Eu and YAG:Tb, *IEEE Trans. Instrum. Meas.* **42**, 735–739 (1993)
- 11.204 A.C. Eckbreth, G.M. Dobbs, J.H. Stufflebeam, P.A. Tellex: CARS temperature and species measurements in augmented jet engine exhausts, *Appl. Opt.* **23**, 1328–1339 (1984)
- 11.205 M. Hashimoto, T. Araki, S. Kawata: Molecular vibration imaging in the fingerprint region by use of coherent anti-Stokes Raman scattering microscopy with a collinear configuration, *Opt. Lett.* **25**, 1768–1770 (2000)
- 11.206 N. Brand, C. Gizoni: Moiré contourography and infrared thermography; Changes resulting from chiropractic adjustments, *J. Manip. Physiol. Ther.* **5**, 113–116 (1982)
- 11.207 D. Huang, E.A. Swanson, C.P. Lin, J.S. Schuman, W.G. Stinson, W. Chang, M.R. Hee, T. Flotte, K. Gregory, C.A. Puliafito, J.G. Fujimoto: Optical coherence tomography, *Science* **254**, 1178–1181 (1991)
- 11.208 Y. Aizu, T. Asakura: Coherent optical techniques for diagnostics of retinal blood flow, *J. Biomed. Opt.* **4**, 61–75 (1999)
- 11.209 N. Konishi, H. Fujii: Real-time visualization of retinal microcirculation by laser flowgraphy, *Opt. Eng.* **34**, 65–68 (1995)
- 11.210 J.G. Webster: *Design of Pulse Oximeter* (IOP, Bristol 1997)
- 11.211 K. Matsushima, K. Aoki, Y. Yamada, N. Kakuta: Fundamental study of reflection pulse oximetry, *Opt. Rev.* **10**, 482–487 (2003)
- 11.212 H. Koizumi, Y. Yamashita, A. Maki, T. Yamamoto, Y. Itoh, H. Itagaki, R. Kennan: Higher-order brain function analysis by trans-cranial dynamic near-infrared spectroscopy imaging, *J. Biomed. Opt.* **4**, 403–413 (1999)
- 11.213 M. Okuyama, N. Tsumura, Y. Miyake: Evaluating a multi-spectral imaging system for mapping pigments in human skin, *Opt. Rev.* **10**, 580–584 (2003)
- 11.214 S.A. Pape, C.A. Skouras, P.O. Byrne: An audit of the use of laser Doppler imaging (LDI) in the assessment of burns of intermediate depth, *Burns* **27**, 233–239 (2001)
- 11.215 S. Roth, I. Freund: Second harmonic generation in collagen, *J. Chem. Phys.* **70**, 1637–1643 (1979)
- 11.216 T. Yasui, Y. Tohno, T. Araki: Characterization of collagen orientation in human dermis by two-

- dimensional second-harmonic-generation polarimetry, *J. Biomed. Opt.* **9**, 259–264 (2004)
- 11.217 R.M. Woodward, B.E. Cole, V.P. Wallace, R.J. Pye, D.D. Arnone, E.H. Linfield, M. Pepper: Terahertz pulse imaging in reflection geometry of human skin cancer and skin tissue, *Phys. Med. Biol.* **47**, 3853–3863 (2002)
- 11.218 J.S. Nelson: Special section on optics of human skin, *J. Biomed. Opt.* **9**, 247–420 (2004)
- 11.219 C. Chou, C. Han, W. Kuo, Y. Huang, C. Feng, J. Shyu: Noninvasive glucose monitoring in vivo with an optical heterodyne polarimeter, *Appl. Opt.* **37**, 3553–3557 (1998)

Materials

Part D

Part D Materials Performance Testing

12 Corrosion

Bernd Isecke, Berlin, Germany
Michael Schütze, Frankfurt am Main,
Germany
Hans-Henning Strehblow, Düsseldorf,
Germany

13 Friction and Wear

Ian Hutchings, Cambridge, UK
Mark Gee, Teddington, UK
Erich Santner, Bonn, Germany

14 Biogenic Impact on Materials

Ina Stephan, Berlin, Germany
Peter D. Askew, Hartley Wintney, UK
Anna A. Gorbushina, Berlin, Germany
Manfred Grinda, Berlin, Germany
Horst Hertel, Berlin, Germany
Wolfgang E. Krumbein, Berlin-Lichterfelde,
Germany
Rolf-Joachim Müller, Braunschweig,
Germany
Michael Pantke, Berlin, Germany
Rüdiger (Rudy) Plarre, Berlin, Germany
Guenter Schmitt, Iserlohn, Germany
Karin Schwibbert, Berlin, Germany

15 Material-Environment Interactions

Franz-Georg Simon, Berlin, Germany
Oliver Jann, Berlin, Germany
Ulf Wickström, Borås, Sweden
Anja Geburtig, Berlin, Germany
Peter Trubiroha, Berlin, Germany
Volker Wachtendorf, Berlin, Germany

16 Performance Control: Nondestructive Testing and Reliability Evaluation

Uwe Ewert, Berlin, Germany
Gerd-Rüdiger Jaenisch, Berlin, Germany
Kurt Osterloh, Berlin, Germany
Uwe Zscherpel, Berlin, Germany
Claude Bathias, Paris, France
Manfred P. Hentschel, Berlin, Germany
Anton Erhard, Berlin, Germany
Jürgen Goebbels, Berlin, Germany
Holger Hanselka, Darmstadt, Germany
Bernd R. Müller, Berlin, Germany
Jürgen Nuffer, Darmstadt, Germany
Werner Daum, Berlin, Germany
David Flaschenträger, Darmstadt, Germany
Enrico Janssen, Darmstadt, Germany
Bernd Bertsche, Stuttgart, Germany
Daniel Hofmann, Stuttgart, Germany
Jochen Gäng, Stuttgart, Germany

Corrosion

12. Corrosion

Corrosion is defined as the interaction between a metal and its environment that results in changes in the properties of the metal, and which may lead to significant impairment of the function of the metal. In most cases the interaction between the metal and the environment is an electrochemical reaction where thermodynamic and kinetic considerations apply. Depending on the characteristics of the corrosion system various types of corrosion occur.

In this chapter all test methods available today are described. For scientific purposes as well as investigations in the laboratory so called conventional electrochemical test methods with direct current are primarily used (Sect. 12.1). In addition, newer techniques have been proposed (Sect. 12.1) that are based on dynamic system analysis (Sect. 12.2.1) or that allow study of corrosion processes in situ with spatial resolution down to 20 μm (Sects. 12.2.2 and 12.2.3). In the following sections a distinction has been made between testing for performance of corrosion protection measures such as inhibitors (Sect. 12.8) and testing that focuses on specific types of corrosion. In this context it is advisable to differentiate between corrosion without (Sect. 12.4) and with mechanical loading (Sect. 12.5) including hydrogen-assisted cracking (Sect. 12.8) which has some similarities to stress corrosion. High-temperature corrosion (Sect. 12.6) has a different mechanistic background than electrolytic corrosion because it is a corrosion process at a metal/gas or metal/salt interface. Exposure and on-site testing (monitoring) require specific considerations in the design of test facilities, probes and the interpretation of results (Sect. 12.4).

Another important source of information regarding corrosion testing is that edited by *Baboian* [12.1].

12.1	Background	668
12.1.1	Classification of Corrosion.....	669
12.1.2	Corrosion Testing.....	670
12.2	Conventional Electrochemical Test Methods	671
12.2.1	Principles of Electrochemical Measurements and Definitions	671
12.2.2	Some Definitions.....	673
12.2.3	Electrochemical Thermodynamics..	674
12.2.4	Complex Formation	676
12.2.5	Electrochemical Kinetics.....	676
12.2.6	The Charge-Transfer Overvoltage ...	676
12.2.7	Elementary Reaction Steps in Sequence, the Hydrogen Evolution Reaction ..	679
12.2.8	Two Different Reactions at One Electrode Surface	681
12.2.9	Local Elements.....	683
12.2.10	Diffusion Control of Electrode Processes.....	684
12.2.11	Rotating Disc Electrode (RDE) and Rotating Ring-Disc Electrode (RRDE).....	686
12.2.12	Ohmic Drops	689
12.2.13	Measurement of Ohmic Drops and Potential Profiles Within Electrolytes	690
12.2.14	Nonstationary Methods, Pulse Measurements.....	692
12.2.15	Concluding Remarks	695
12.3	Novel Electrochemical Test Methods	695
12.3.1	Electrochemical Noise Analysis.....	695
12.4	Exposure and On-Site Testing	699
12.5	Corrosion Without Mechanical Loading ...	699
12.5.1	Uniform Corrosion	700
12.5.2	Nonuniform and Localized Corrosion	701
12.6	Corrosion with Mechanical Loading	705
12.6.1	Stress Corrosion.....	706
12.6.2	Corrosion Fatigue	709

12.7	Hydrogen-Induced Stress Corrosion Cracking	714	12.8.3	Mass Change Measurements	721
12.7.1	Electrochemical Processes	715	12.8.4	Special High-Temperature Corrosion Tests	729
12.7.2	Theories of H-Induced Stress Corrosion Cracking	716	12.8.5	Post-Test Evaluation of Test Pieces	731
12.7.3	Environment and Material Parameters	717	12.8.6	Concluding Remarks	732
12.7.4	Fractographic and Mechanical Effects of HISSC	717	12.9	Inhibitor Testing and Monitoring of Efficiency	732
12.7.5	Test Methods	718	12.9.1	Investigation and Testing of Inhibitors	733
12.8	High-Temperature Corrosion	718	12.9.2	Monitoring of Inhibitor Efficiency ..	734
12.8.1	Main Parameters in High-Temperature Corrosion	718	12.9.3	Monitoring Inhibition from Corrosion Rates	736
12.8.2	Test Standards or Guidelines	719	References	738

12.1 Background

According to ISO 8044 [12.2] corrosion is defined as an interaction between a metal and its environment that results in changes in the properties of the metal, and which may lead to significant impairment of the function of the metal, the environment, or the technical system, of which these form a part. This definition has solved a conflict because previously the term corrosion had been used to mean the process, results of the process and damage caused by the process. In most cases the interaction between the metal and the environment is an electrochemical reaction where thermodynamic and kinetic considerations apply. From a thermodynamic point of view the driving force as in any electrochemical reaction is a potential difference between anodes and cathodes in a short-circuited cell.

The result of corrosion is a corrosion effect which is generally detrimental and may lead to loss of material, contamination of the environment with corrosion products or impairment of a technical system. It is important to notice that corrosion damage resulting from an attack to the metal has to be distinguished from corrosion failure which is characterized by the total loss of function of the technical system. Corrosion protection measures are available to influence corrosion process with the objective of avoiding corrosion failures.

Corrosion and protective measures against corrosion result in costs. Many attempts have been made to estimate the financial expenditure to the community caused by corrosion. These include the costs which can arise in the form of corrosion protection measures, through replacement of corrosion-damaged parts or through different effects deriving from corrosion, such as shut-down of production or accidents which

lead to injuries or damage to property. Several estimations have arrived at the conclusion that the total annual corrosion costs in the industrialized countries amount to about 4% of the gross national product. Part of these costs is unavoidable since it would not be economically viable to carry out the necessary precautions to eliminate completely corrosion damage. It is, however, certain that one can reduce losses considerably solely by better exploiting the knowledge we have today and, according to one estimate, about 15% of corrosion costs are of this type [12.3].

Due to the technical, scientific and economic importance of the problem numerous textbooks [12.1, 4–18] and publications in journals or proceedings from conferences are available. As mentioned before the corrosion reaction is in most cases of electrochemical nature. Therefore many of the published information deal with the electrochemical reactions and especially the kinetics of the corrosion process. For the engineer durability aspects in a technical plant or equipment or the safety of a process play a more important role. However, both approaches follow the same route in yielding information about the corrosion rate of a material in a specific environment [12.4].

The schematic diagram in Fig. 12.1 [12.4] shows the various reactions that can occur sequentially and simultaneously in the corrosion process. Material transport and chemical reactions can supply or remove important reaction components. In addition to adsorption or desorption, a phase-boundary reaction occurs which mostly involves electrochemical reactions and which can be affected by external currents. An example is the formation of hydride on lead where the partner to the

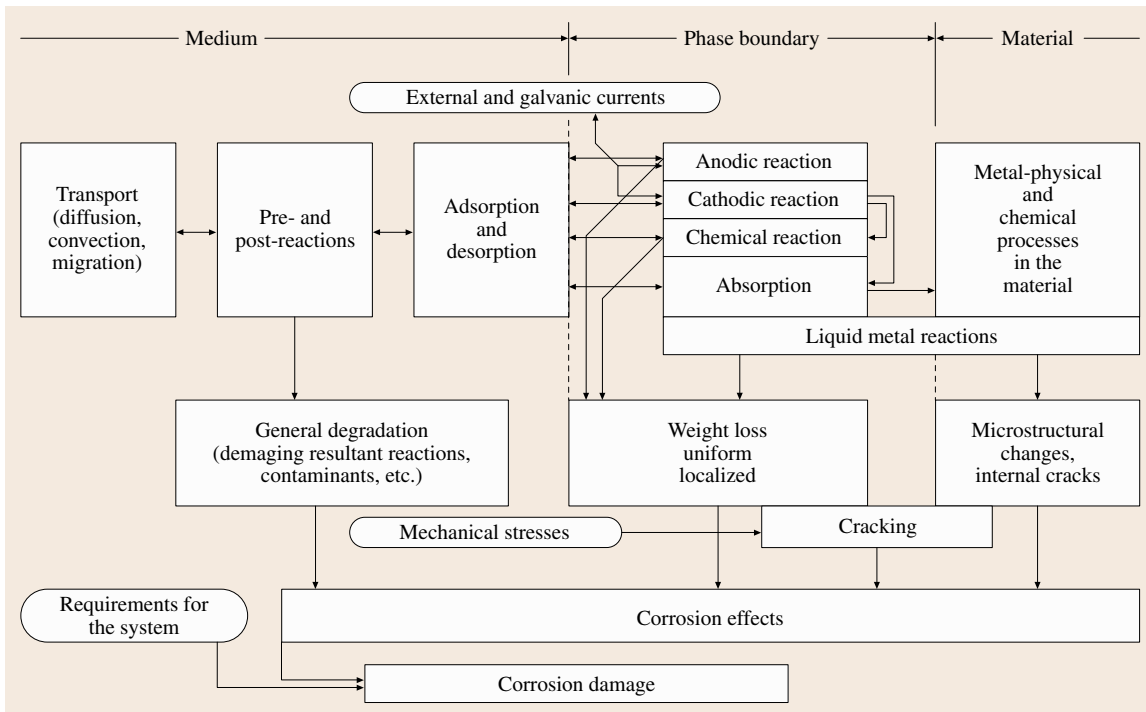


Fig. 12.1 Flow diagram of corrosion processes and types of damage (after [12.4])

hydrogen reaction can arise from the cathodic process. Hydrogen can also penetrate the metal microstructure, where it can have a physical or chemical effect, causing a degradation of the mechanical properties of the material. In this type of corrosion cracks can form during mechanical testing, leading to fracture without the loss of any metal.

12.1.1 Classification of Corrosion

Numerous concepts have been applied to classify corrosion into categories. Due to the complex interaction between a material and its environment different classification schemes have developed to classify corrosion by the type of attack, the rate of attack, the morphology of the attack, or the properties of the environment, which may change in the ongoing corrosion process.

Type of damage have been predominantly used. This can be classified as uniform or localized metal removal, corrosion cracking or detrimental effects to the environment. Local attack can take the form of shallow pits, pitting, selective dissolution of small microstructure regions or cracking. It is usual, where different results of reactions lead to definite forms of corrosion

effects, to classify them as particular types of corrosion. The most important are uniform corrosion, pitting corrosion, crevice corrosion, intergranular corrosion, and those with accompanying mechanical-stress corrosion and corrosion fatigue. The two latter are most feared. Most failures arise from pitting corrosion. Uniform corrosion almost always occurs in practice but seldom leads to failure.

From [12.19] it can be taken that there are generally eight forms of corrosion.

1. General (uniform) corrosion;
2. Localized corrosion;
3. Galvanic corrosion;
4. Cracking phenomena;
5. Intergranular corrosion;
6. Dealloying;
7. High-temperature corrosion.

The eight forms of corrosion can be divided into three categories.

Group I Those readily identified by visual examination (forms 1, 2 and 3);

- Group II Those which may require supplementary means of examination (forms 5, 6 and 7);
- Group III Those which usually should be verified by microscopy, optical or scanning electron microscope, although they are sometimes apparent to the naked eye.

The individual phenomena are illustrated in Fig. 12.2.

12.1.2 Corrosion Testing

The safe use of materials in technical plants, structures or equipment requires sufficient information for assessing corrosion risks – especially if mechanical stresses are superimposed on the electrolytic load and failure of components due to stress corrosion cracking (SCC)

cannot be excluded. If sufficient knowledge about the corrosion behavior is not available then tests to determine this under practical conditions will be required. In this context a distinction must be made between the terms corrosion investigation and corrosion test. According to the International Standards Organization (ISO) standard ISO 8044 [12.2] a corrosion investigation includes corrosion tests and their evaluation and is directed towards the following objectives.

- The explanation of corrosion reactions,
- Obtaining knowledge on corrosion behavior of materials under corrosion load,
- Selecting measures for corrosion protection.

This enables statements about the properties of a corrosion system to be made. A corrosion test is a special

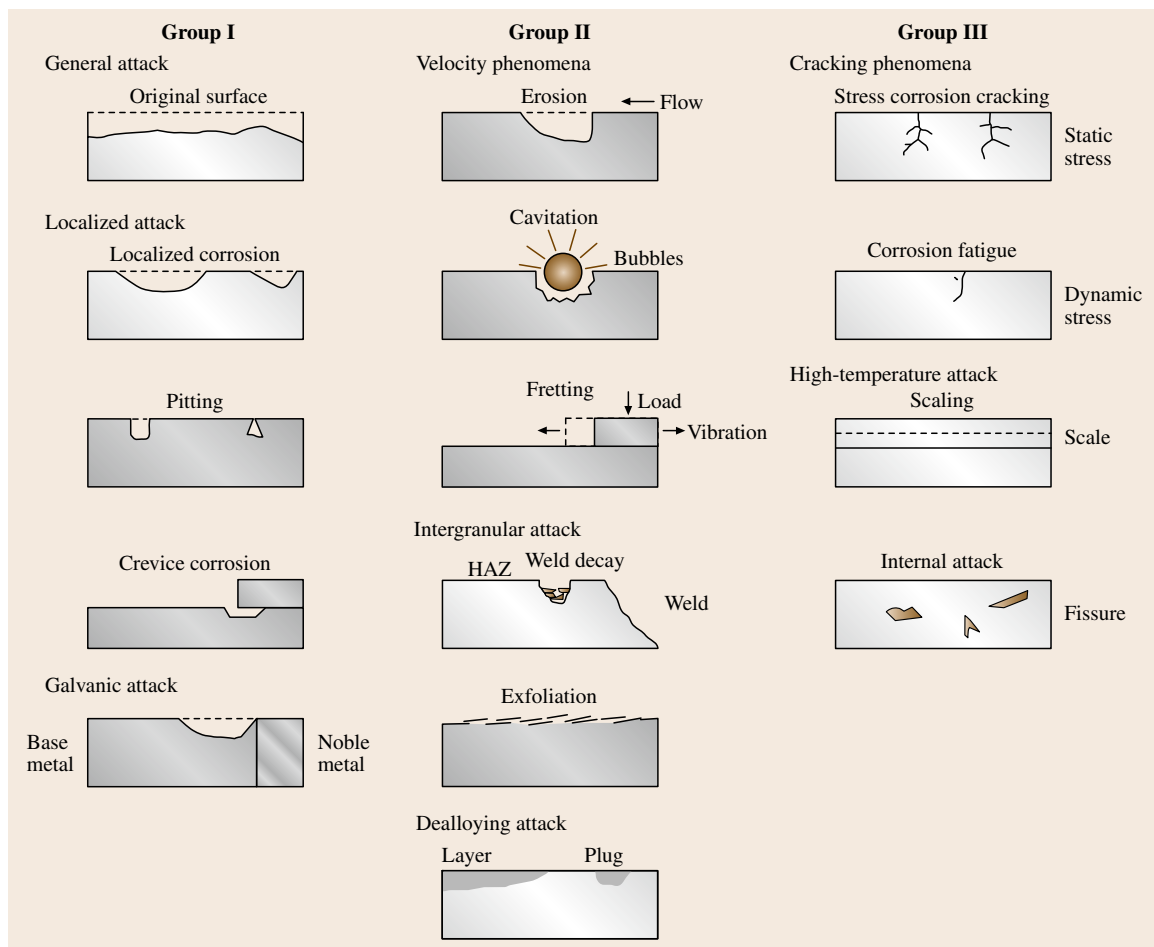


Fig. 12.2 Types of corrosion

case of a corrosion investigation; the corrosion load and the assessment of the results being prescribed by certain regulations (standards, test sheet) and/or agreements such as, for example, delivery conditions.

Corrosion tests mainly help in quality control during production and further treatment of materials as well as for the assessment of corrosion protection measures. The significance of the corrosion tests selected for an investigation differs. While corrosion tests under loads that are characteristic of service conditions give the best

estimation of the real corrosion behavior, tests with increased corrosion load or accelerated corrosion tests are less suitable to give a reliable prognosis of behavior in practice as the corrosion mechanism could differ from that under practical conditions. Nevertheless, accelerated corrosion tests are more suitable for determining certain material properties (e.g. resistance to intergranular corrosion or stress corrosion cracking) although they can be reliably used only if sufficient experience exists for the transfer of the test results to practical situations.

12.2 Conventional Electrochemical Test Methods

Corrosion is the degradation of materials by gaseous or liquid environments. Atmospheric corrosion involves the influence of both media on the surface of a solid, often with alternating wet and dry periods. Any kind of materials may be attacked, including metals, semiconductors and insulators as well as organic polymers. This chapter describes corrosion of metals in electrolytes and therefore some fundamentals of electrochemistry and related test methods are discussed.

Large losses are caused by corrosion in modern industrial societies. One estimate is that 4.0% of the gross national product is lost by corrosion, a third of which may be avoided if all knowledge is taken into account. Traditionally corrosion is subdivided into attack by dry and hot gases and by electrolytes. In this section corrosion in aqueous electrolytes only is described, although solutions with organic solvents may play an important role in praxis. Corrosion is a reaction at the metal/electrolyte phase boundary. Although the bulk properties of the solid and the solution may play an important role for the degradation of the materials, the properties of the metal surface and the reactions at the solid/electrolyte interface are most important. Therefore corrosion science and corrosion engineering apply the concepts of electrochemistry and electrode kinetics. In Sect. 12.2.1 a basic introduction to the equipment and experimental procedures is given. Corrosion involves electrode processes which are ruled by the electrode potential and thermodynamic and kinetic factors. For this reason the equilibria and the related thermodynamic properties of the metal/electrolyte interface and their electrode kinetics are discussed. In Sect. 12.2.3 a short introduction to electrochemical thermodynamics and equilibrium is given followed by an introduction to electrode kinetics in Sect. 12.2.5. Finally this chapter is completed by a description of the application of

electrochemical transient measurements and some electroanalytical methods.

12.2.1 Principles of Electrochemical Measurements and Definitions

Electrochemical measurements are performed in an electrochemical cell, which contains a three-electrode arrangement in its most simple form Fig. 12.3. The

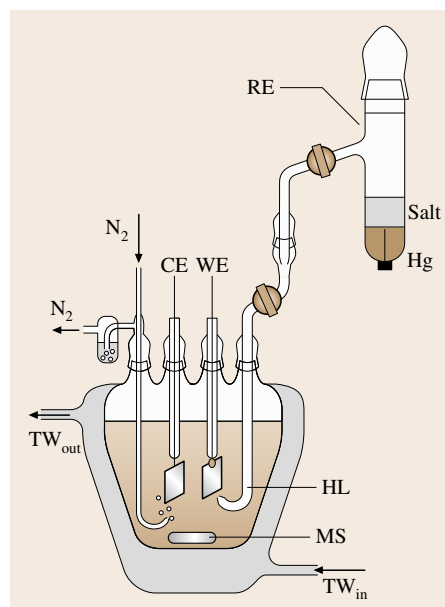


Fig. 12.3 Standard electrochemical cell with working electrode (WE), counter-electrode (CE), reference electrode (RE), Haber–Luggin capillary (HL), magnetic stirring (MS), water jacket with thermostat water (TW) and nitrogen inlet

Table 12.1 Some commonly used reference electrodes and their related standard potential E^0 from [12.20]

Electrode	E^0/V	Nernst equation
Calomel electrode: $\text{Hg}/\text{Hg}_2\text{Cl}_2/\text{Cl}^-$	0.268	$E = E^0 - 0.059 \log [\text{Cl}^-]$
Hg_2SO_4 electrode: $\text{Hg}/\text{Hg}_2\text{SO}_4/\text{SO}_4^{2-}$	0.615	$E = E^0 - 0.059 \log [\text{SO}_4^{2-}]$
HgO electrode: $\text{Hg}/\text{HgO}/\text{OH}^-$	0.926	$E = E^0 - 0.059 \log [\text{OH}^-]$
AgCl electrode: $\text{Ag}/\text{AgCl}/\text{Cl}^-$	0.222	$E = E^0 - 0.059 \log [\text{Cl}^-]$
PbSO_4 electrode: $\text{Pb}/\text{PbSO}_4/\text{SO}_4^{2-}$	-0.276	$E = E^0 - 0.029 \log [\text{SO}_4^{2-}]$

working electrode (WE) of the material under study, the counter electrode (CE) of a metal which is not attacked by the electrolyte, in most cases a platinum or gold electrode, and finally the reference electrode (RE) with an electrolytic contact to the bulk electrolyte via the Haber–Luggin (HL) capillary. Usually such an electrochemical cell contains an inlet for protective gases such as nitrogen or argon, a stirrer for the electrolyte and a water jacket to keep the electrolyte at the desired temperature using a thermostat. Numerous special designs for electrochemical cells have been applied depending on the special problem under study. In some cases small electrolyte vessels are used as e.g. for microscopic in situ investigations or in situ measurements with a scanning tunneling microscope (STM). Another approach is cells that restrict the investigated surface area to the size of droplets in the μm range. In all these cases a three-electrode set up is used with the exception of in situ STM investigations. Here two working electrodes are required, the material under study and the STM tip. The potentials of both electrodes have to be set independently and therefore a bipotentiostat is required. A similar situation with two or even more working electrodes exists for a rotating ring-disc electrode. This analytical method will be described in Sect. 12.2.11. The reference electrode is usually an electrode of the second kind. Its potential is fixed by a weakly soluble compound of the metal and an anion of the solution. Table 12.1 gives some examples of mercury and silver

electrodes [12.20]. These reference electrodes are easy to prepare and to handle and their electrode potential is very stable.

For most experiments the electrode potential is fixed by an electronic potentiostat and the current is measured. Potentiodynamic polarization curves involve a linear change of the electrode potential with time. Potentiostatic measurements keep the potential constant. Potentiostatic transients require its rapid change. With a fast potentiostat and some precautions a potential change can be achieved in a few microseconds so that fast electrode processes can be followed with a high time resolution starting in the μs range. In most cases of corrosion studies a ms resolution of the current measurement is sufficiently fast.

Figure 12.4 explains with a simple block diagram the characteristics of a potentiostat built with an operational amplifier (OA). The reference electrode, RE, is given directly to the inverting input of OA and the desired electrode potential is determined by the setting of the voltage ΔU from a power source fed into the noninverting input. The working electrode WE is set to common. The high gain of the operational amplifier (factor 10^5) ensures a negligibly small deviation of both inputs. Thus RE has a potential difference ΔE to WE equal to ΔU . The input resistance is very high ($10^7 \Omega$) so that almost no current flow occurs into the OA. Its output resistance is very low so that it may supply a sufficiently high current I_C to WE via CE and the electrolyte which may be required for the rate of the electrode processes related to the chosen potential. I_C is measured via its ohmic drop RI_C at the resistor R . This simple electronic circuit stabilizes the chosen electrode potential automatically, independent of the required current density I_C . However, a good potentiostat contains additional booster units to provide high currents and to improve the setting of potential changes with a fast response. Usually potentiostats contain additional circuits built with operational amplifiers for necessary options such as, e.g., an adder which permits the addition of various potentials forming a potential program with ramps and pulses for potentiostatic transients. A special circuit

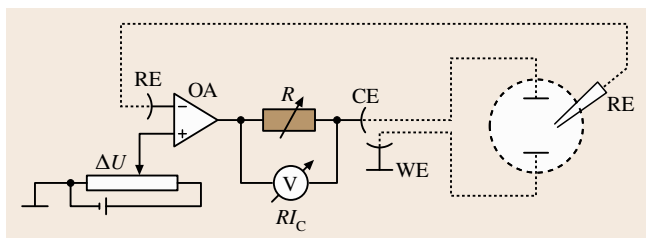


Fig. 12.4 Block diagram of potentiostat with operational amplifier (OA), potential setting ΔU , resistance R for current measurement I_C as RI_C and connections to working electrode (WE), counter-electrode (CE) and reference electrode (RE)

compensates for ohmic drops within the electrolyte between WE and HL which may occur in the case of high-current densities and electrolytes with low conductivity.

Galvanostatic measurements require the setting of a current I_C while the change of the electrode potential ΔE is followed with time. This is achieved by a galvanostat (constant-current source) depicted as a simple block diagram in Fig. 12.5. I_C is set via a proportional voltage ΔU from a built-in power source. ΔU is given to the noninverting input of the operational amplifier OA, which is compared to the ohmic drop RI_C across the resistor R at the output. This voltage drop passes a differential amplifier (DA), which avoids the setting of a second point of the circuit to common. As both inputs of OA have to be at the same potential as a consequence of its high magnification, I_C is adjusted to the desired value $RI_C = \Delta U$. Usually galvanostats are built in to potentiostats. Appropriate voltages ΔU may be given to the input with specific time characteristics to permit also galvanodynamic measurements including galvanostatic transients controlled by appropriate voltage pulses given to OA.

12.2.2 Some Definitions

An electrochemical cell usually consists of two electrodes. Figure 12.6 gives as an example an iron electrode in a Fe^{2+} solution in contact with a hydrogen electrode via a diaphragm. The H^+/H_2 electrode consists of a platinum electrode in a solution of a given pH with the introduction of pure hydrogen. If the solution is 1 M for the H^+ concentration, i. e. if pH is 0, and the gas pressure of H_2 is 1 atm = 1.013 bar, this is the standard hydrogen electrode (SHE). Potential drops at the electrode–electrolyte interface cannot be measured separately in principle. The contact of a voltmeter to the electrolyte introduces automatically a second interface so that the measured voltage necessarily includes the potential drop of two electrodes. The potentials of any electrode is therefore given relative to the SHE. The electrode potential of the standard hydrogen electrode is thus set to 0 V by definition. Its value relative to the zero point of the potential scale in physics, i. e. the charge-free vacuum level, has been determined to -4.6 V [12.21, 22], so that both scales may be converted to each other.

There are two main kinds of electrodes, metal/metal-ion electrodes and redox electrodes. For the first case the electrode reaction requires the transfer of metal ions across the electrode–electrolyte interface. The Fe/Fe^{2+} electrode is an example. Redox electrodes involve the

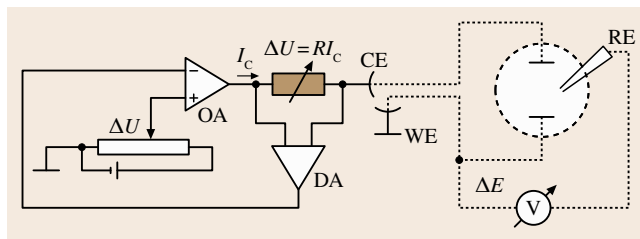


Fig. 12.5 Block diagram for galvanostat with operational amplifier (OA), differential amplifier (DA), voltage supply ΔU for current setting I_C and connections to working electrode (WE), counter-electrode (CE) and reference electrode (RE)

transfer of electrons, which is the case for the hydrogen electrode. A Pt electrode within a solution of Fe^{2+} and Fe^{3+} ions or $\text{Fe}(\text{CN})_6^{4-}$ and $\text{Fe}(\text{CN})_6^{3-}$ are other examples. If no reaction occurs, the electrode is in electrochemical equilibrium, i. e. both reactions – Fe^{2+} dissolution or Fe deposition – compensate each other. The same is the case for the redox reaction.

One has to distinguish anodic and cathodic processes. An anodic process involves the transfer of positive charge from the electrode to the electrolyte, such as Fe dissolution to Fe^{2+} , or the transfer of negative charge in the opposite direction, e.g. the oxidation of Fe^{2+} to Fe^{3+} . A cathodic process involves the transfer of positive charge from the electrolyte to the electrode, such as the deposition of Fe^{2+} from the solution as Fe metal or the transfer of negative charge in the opposite direction, e.g. the reduction of Fe^{3+} to Fe^{2+} . The currents of anodic processes get a positive

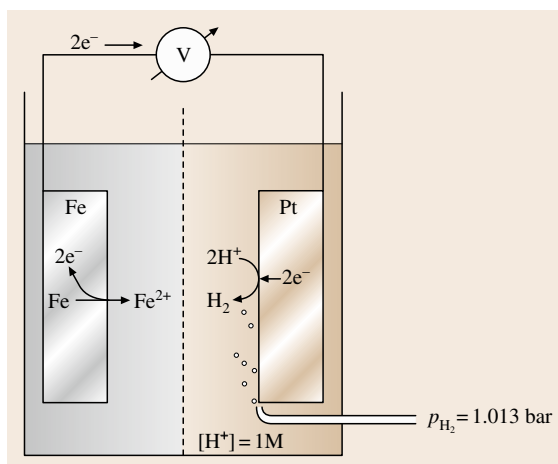


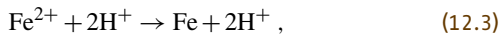
Fig. 12.6 Electrochemical cell with an Fe/Fe^{2+} and H_2/H^+ electrode

sign, those for cathodic reactions a negative sign. In conclusion, it is the kind of process which determines whether an electrode acts as an anode or a cathode. Depending on the applied electrode potential and further electrochemical conditions an electrode may be either an anode or a cathode.

If anodic and cathodic currents of a redox or a metal/metal-ion electrode compensate each other the electrochemical equilibrium is established at the equilibrium potential E_0 . A positive deviation $\eta = E - E_0$ leads to an anodic current. η is called the overvoltage. A deviation in the negative direction with a negative overvoltage $\eta = E - E_0 < 0$ causes a cathodic reaction. If two *different* electrode processes compensate each other, such as an anodic Fe dissolution and cathodic hydrogen evolution with vanishing current in the external circuit, the electrode is at its rest potential E_R . A positive deviation $\pi = E - E_R > 0$ is called a positive polarization and $\pi = E - E_R < 0$ a negative polarization.

12.2.3 Electrochemical Thermodynamics

The equilibrium potential E_0 is related to the change of the Gibbs free energy for standard conditions ΔG_0^0 of the related electrode process, i. e. for activities of solutes of $a = 1$ M and gas pressures of $p = 1.013$ bar. As all electrode potentials are referred to the standard hydrogen electrode its reaction has been chosen as a compensating process for thermodynamic calculations. Equations (12.1, 12.2) describe the process of an electrochemical cell with the Fe/Fe²⁺ and the H₂/H⁺ electrode; (12.3) describes their combination. ΔG_0^0 for the electrode process of interest has to be calculated for the cathodic direction and the compensating process of the reference electrode in the anodic direction to avoid mistakes in the sign (12.4). The relation between ΔG_0^0 and the electrode potential is given by (12.5). The concentration dependence of the equilibrium potential E_0 is given by the Nernst equation (12.6, 12.7) for both electrodes. Equation (12.7) describes the pH dependence of the hydrogen electrode



$$\Delta G_{298}^0 = \sum_i \nu_i G_{i,i}^0 = -G_{\text{Fe}^{2+}}^0 = 78.9 \text{ kJ mol}^{-1}, \quad (12.4)$$

$$\Delta G_{298}^0 = -nFE_0, \quad (12.5)$$

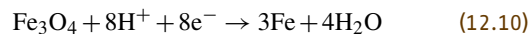
$$E^0 = -\frac{\Delta G_{298}^0}{2F} = -\frac{78.94 \times 10^3}{2F} = -0.409 \text{ V}, \quad (12.6)$$

$$E_0 = E^0 + \frac{RT}{nF} \ln a(\text{Fe}^{2+}) = -0.409 + \frac{0.059}{2} \lg a(\text{Fe}^{2+})/\text{V}, \quad (12.7)$$

$$E_0 = 0 + \frac{RT}{2F} \ln \left(\frac{a(\text{H}^+)^2}{p(\text{H}_2)} \right) = -0.059 \text{ pH}/\text{V}, \quad (12.8)$$

$$\text{with } \text{pH} = -\lg [a(\text{H}^+)]. \quad (12.9)$$

Electrode reactions that involve solid compounds are treated in a similar way. As an example the equilibrium of Fe with Fe₃O₄ is given in (12.10–12.13). This equilibrium describes the electrochemical formation of an oxide layer at the metal surface. These equilibria are important for the calculation of potential–pH diagrams, so called Pourbaix diagrams, which will be discussed in the next section.



$$\Delta G_{298}^0 = 1013.23 - 4(237.13) = 64.71 \text{ kJ/mol} \quad (12.11)$$

$$E^0 = -\frac{64.71 \times 10^3}{8F} = -0.084 \text{ V} \quad (12.12)$$

$$E_0 = -0.084 + \frac{0.059}{8} \lg [a(\text{H}^+)^8] = -0.084 - 0.059 \text{ pH}/\text{V} \quad (12.13)$$

Thermodynamic data and especially standard Gibbs free energies ΔG_f^0 for the formation of compounds from the elements are listed in special publications for $T = 298$ K, but also for other temperatures [12.23, 24]. They permit the calculate of data for electrochemical equilibria as shown for (12.1–12.13). For most equilibria the standard electrode potentials E^0 are listed. Their dependence on the concentrations of the reacting species, i. e. their Nernst equations, are used to calculate potential–pH diagrams [12.25]. Figure 12.7 shows the diagram for iron, which is a very important example in corrosion. The horizontal line (1) at $E = -0.589$ V describes the pH-independent Fe/Fe²⁺ equilibrium with a 10⁻⁶ M, i. e. a negligibly small concentration of Fe²⁺. At $E = 0.771$ V the Fe²⁺/Fe³⁺ equilibrium is given as a further horizontal line (2). Line (3) depicts the pH-dependent formation of Fe₃O₄ according to (12.10–12.13). Line (4) corresponds to the Fe₃O₄/Fe₂O₃ equilibrium. Lines (5) and (6) refer to the oxidation

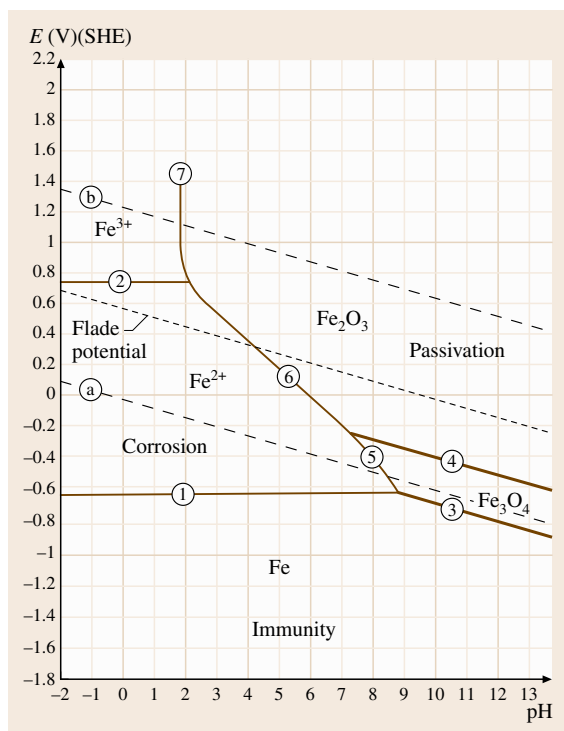


Fig. 12.7 Potential–pH diagram of Fe with equilibria (1–7) and (a) and (b) and domains of corrosion, immunity and passivation, as described in the text, Flade potential describing passivation in acidic electrolytes

of soluble Fe^{2+} to Fe_3O_4 and Fe_2O_3 respectively. The vertical line (7) describes the potential-independent dissolution equilibrium of $\text{Fe}_2\text{O}_3/\text{Fe}^{3+}$ that is related to a specific pH. According to this diagram one has to distinguish three main fields. Corrosion, i. e. metal dissolution, should occur where soluble products are stable, i. e. at the upper left end of the diagram Fig. 12.7. At the lower end of the diagram one has the field of immunity where Fe is the stable species. In the upper right part the surface should be protected by anodic oxide layers. Here thin anodic films should form at the metal surface, which block further oxidation and lead to passivity. The lines (a) and (b) describe the equilibrium potential of the hydrogen and oxygen electrode, which are important redox systems for aqueous corrosion. These diagrams have been calculated at 298 K for all elements, metals, semiconductors and elements with insulating properties [12.26, 27]. More recently they have also been calculated for elevated temperatures. They provide an excellent possibility to get a first idea of the corrosion properties of a metal. However, one should

always keep in mind that they are calculated on the basis of thermodynamic data only. Any kinetic properties are not included. This means that conclusions on the basis of these diagrams may be misleading. Pourbaix diagrams tell us whether a reaction may occur or not. Whether the predictions really happen or not depends on the kinetic parameters of the related reactions. A typical exception is the passive behavior of iron in strongly acidic electrolytes such as 0.5 M H_2SO_4 or 1 M HClO_4 . Iron should dissolve at potentials above $E = -0.409$ V. However, passivation occurs when the potential gets above $E = 0.58 - 0.059 \text{ pH}[\text{V}]$. This condition is depicted as a dashed line in Fig. 12.7. Surface analytical investigations have shown that Fe forms a poreless few-nm-thick layer of Fe_2O_3 a spinell-type oxide which is very slowly dissolving in these acidic electrolytes. Detailed electrochemical studies come to the conclusion that the transfer of Fe^{3+} cations from the oxide surface to the electrolyte is an extremely slow process, although the oxide layer is far from its dissolution equilibrium. As a consequence this surface film passivates the metal underneath. It has been shown that the passivation potential may be explained by the thermodynamic data for the anodic oxidation of Fe_3O_4 to Fe_2O_3 [12.28]. Apparently the structure and the electrochemical properties of Fe_2O_3 provide sufficient stability for dissolution, i. e. the activation energy to transfer Fe^{3+} ions from the potential well of the O^{2-} matrix of an oxide is very high. Similar arguments hold for passive layers on Cr. Here a Cr_2O_3 film of only 1–2 nm thickness dissolves in acidic solutions so extremely slowly that Cr is protected very effectively against corrosion in strongly acidic electrolytes [12.29–31]. This is also the case for Cr-containing alloys, such as Ni/Cr or Fe/Cr. The strong bonds between Cr^{3+} ions and its ligands in its complexes are well known from inorganic chemistry. The exchange of ligands is so slow that many of these Cr^{3+} compounds are almost insoluble, although this description is misleading; they dissolve extremely slowly, which has the same effect. As an example the extremely slow dissolution of CrCl_3 should be mentioned, which leads to its description as an insoluble compound. However, this behavior is only caused by an extremely slow dissolution rate [12.31]. This becomes faster at elevated temperatures when the related high activation energy for the exchange of ligands has been overcome.

In conclusion the Pourbaix diagrams provide excellent initial information on the corrosion behavior of metals on the basis of thermodynamic data. However, a reliable discussion has to include kinetic parameters

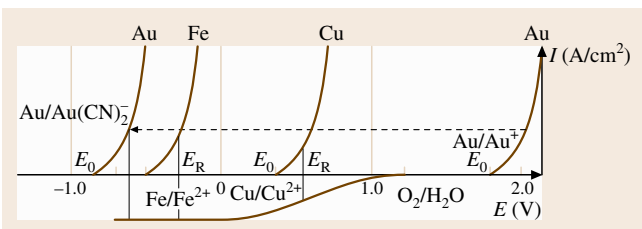


Fig. 12.8 Schematic diagram of E_0 , E_R , and anodic dissolution of Fe, Cu and Au and the shift of E_0 of Au by complexation with cyanide with oxygen reduction as counter-reaction

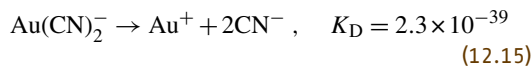
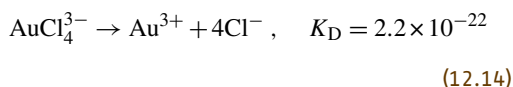
Diffusion	Diffusion overvoltage η_D
Preceding reaction	Reaction overvoltage η_r
Adsorption	
Charge transfer reaction	Charge transfer overvoltage η_d
Desorption	
Following reaction	Reaction overvoltage η_r
Diffusion	Diffusion overvoltage η_D
$\eta = \eta_D + \eta_r + \eta_d$	

Fig. 12.9 Elementary reaction steps of an electrode process with related overvoltages

in order to avoid misleading conclusions which might contradict experimental results.

12.2.4 Complex Formation

The formation of strong complexes of dissolved cations with anions has an important influence on the dissolution of metals; they shift the concentration of free cations to very small values and thereby shift the equilibrium potential of the related metal/metal-ion electrode to very negative values [12.20, 32, 33] (Fig. 12.8). A well-known effect is the strong complexation of Au^{3+} by Cl^- or of Au^+ by CN^- as depicted in (12.14, 12.15). The standard potential of Au dissolution is shifted by Cl^- from 1.42 V to 0.994 V or by CN^- from 1.68 V to -0.60 V, which is a consequence of the small value of the dissociation constant $K_D = 2.2 \times 10^{-22}$ of the AuCl_4^- and $K_D = 2.3 \times 10^{-39}$ for the $\text{Au}(\text{CN})_2^-$ complex. Therefore Au dissolution occurs in a 1 : 3 mixture of HCl and HNO_3 (aqua regia) whereas pure HNO_3 does not attack. Similarly Au may be dissolved in CN^- -containing solution by air oxidation (Fig. 12.8). The latter example is shown by (12.16, 12.17) in detail, and has been applied for extraction of Au from minerals.



$$a(\text{Au}^+) = K_D \frac{a(\text{Au}(\text{CN})_2^-)}{a^2(\text{CN}^-)} \quad (12.16)$$

$$\begin{aligned} E &= E_{\text{Au}}^0 + \frac{RT}{F} \ln a(\text{Au}^+) \\ &= 1.68 + 0.059 \log K_D \\ &\quad + 0.059 \log \frac{a[\text{Au}(\text{CN})_2^-]}{a^2(\text{CN}^-)} \end{aligned} \quad (12.17)$$

$$\begin{aligned} E_{\text{AuCN}}^0 &= 1.68 - 0.059 \log 2.3 \times 10^{-39} \\ &= 1.68 - 2.28 = -0.60 \text{ V} \end{aligned} \quad (12.17a)$$

Complexation of cations also plays a role in the enhanced dissolution of passivating layers. The formation of complexes of cations with halides has been proposed as a mechanism for the breakdown of passivity and localized corrosion [12.29–31].

12.2.5 Electrochemical Kinetics

The kinetics of electrode processes influence decisively corrosion phenomena. As usual in kinetics the rate of a chemical reaction at the electrode surface is ruled by the activation energy of the slowest of a sequence of elementary reaction steps. This could be the charge-transfer process or any preceding or following reaction step. Any electrode process requires the transport of the reacting species to the electrode surface, a possible chemical reaction within the solution in front of the electrode, the charge-transfer process, a possible following chemical reaction and finally the transport of the product from the electrode to the bulk electrolyte. In addition adsorption and desorption processes may be involved. Any of those steps may be the slowest and thus may be rate-determining for the overall reaction. Figure 12.9 describes the sequence of elementary reaction steps, including the charge-transfer reaction, that together form the overall reaction. Each of these steps may contribute with its special overvoltage η_i to the total overvoltage $\eta = \sum \eta_i$ of the whole reaction (Fig. 12.9). Usually one reaction step is the slowest and thus rate-determining for the overall reaction. Its overvoltage η_i dominates η .

12.2.6 The Charge-Transfer Overvoltage

If the charge transfer is rate-determining the related current density follows an exponential relationship, the Butler–Volmer equation. As mentioned earlier an ion or

an electron may be the transferred species. This process occurs within the Helmholtz layer, i.e. within a distance of the radius of solvated ions of typically less than 1 nm. The charge transfer of (12.18) occurs via a tunneling process that is seriously influenced by the potential drop $\Delta\phi = \phi_M - \phi_S$ within this layer. Combining the usual rate equation with Faraday's law one obtains a redox process (12.19) which includes the two opposite parts due to the anodic and the cathodic reactions. At the equilibrium potential these are equal and compensate each other. F is the Faraday constant and n is the number of charges transferred for this reaction, which is usually 1 and may be larger if several one-electron processes occur in a sequence, k_+ and k_- are the rate constants for the anodic and cathodic reaction steps and $c(\text{Red})$ and $c(\text{Ox})$ are the concentrations of the oxidized and reduced species of the redox system involved. For metal dissolution equivalent (12.20, 12.21) hold where Θ_{Me} is the surface coverage for metal atoms which is proportional to their surface concentration, and $c(\text{Me}^{z+})$ is the concentration of the cations within the electrolyte. One has to distinguish in general between the charges n which are involved in the total electrode reaction of (12.18, 12.20), and the charge z of the species which is transferred across the electrode–electrolyte interface during the charge-transfer process. In the case of a simple metal dissolution, according to (12.20) n equals z . If the dissolving cation forms a complex with anions from the solution in a reaction before the charge-transfer step these number may be quite different. For a redox reaction z equals 1. If however, more than one electron is transferred in a fast sequence of several steps, i.e. in the case of a charge-transfer reaction with more electrons n will be larger



$$i = nF \left(\frac{-dc(\text{Red})}{dt} - \frac{-dc(\text{Ox})}{dt} \right) \\ = nF [k_+c(\text{Red}) - k_-c(\text{Ox})], \quad (12.19)$$



$$i = nFk_+\Theta_{\text{Me}} - nFk_-c(\text{Me}^{z+}). \quad (12.21)$$

The rate equations of both types of charge-transfer processes may contain the concentration of additional species that are involved in their mechanisms. An example is the catalysis of active Fe dissolution by OH^- ions. The exponent of the concentrations of OH^- , i.e. its electrochemical reaction order, is 1.5 [12.34]. Reaction orders may be any number for a given reaction depending on the details of its mechanism.

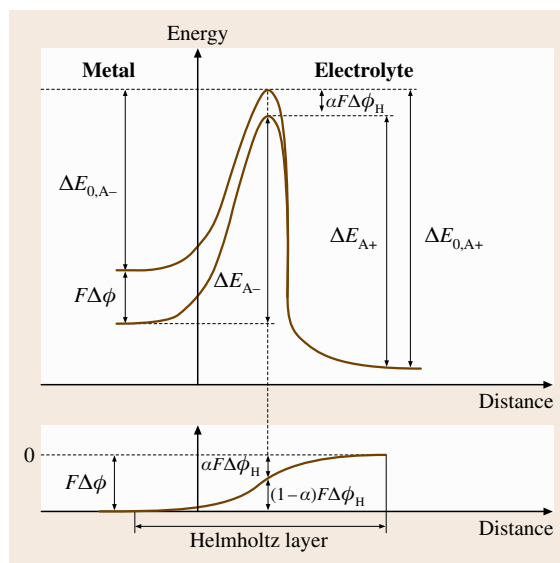


Fig. 12.10 Activation energy $\Delta E_{0,A}$ and its change to ΔE_A for the anodic (+) and cathodic reaction (–) due to the potential drop $\Delta\phi$ across the electrode–electrolyte interface

As usual, both rate constants k_+ and k_- depend exponentially on their activation energy $\Delta E_{0,A,+}$ and $\Delta E_{0,A,-}$ (12.22, 12.23). According to Fig. 12.10 the activation energies $\Delta E_{A,+}$ and $\Delta E_{A,-}$ for the transfer of charged species across the electrode–electrolyte interface are influenced by the potential drop $\Delta\phi$. However, only a fraction of $\Delta\phi$ will modify $\Delta E_{0,A,+}$. The part α takes into account the fraction of $\Delta\phi$ which is kinetically effective, i.e. which part will act on the species up to the maximum of the energy–distance curve; α usually has a value of 0.2–0.8. If α refers to the anodic process $1 - \alpha$ will hold for the cathodic reaction. Thus the activation energy $\Delta E_{A,+}$ will change by $-\alpha z F \Delta\phi$ for the anodic and $\Delta E_{A,-}$ by $+(1 - \alpha) z F \Delta\phi$ for the cathodic process, respectively; z is the charge of the species which is transferred across the double layer, where $z = 1$ for electrons, i.e. for charge-transfer processes, and z may be larger for metal ions, e.g. $z = 2$ for Fe^{2+} . Equations (12.22, 12.23) describe the influence of $\Delta\phi$ on the rate constants of both processes and (12.24) gives the full kinetic equation for a redox reaction. An equivalent equation is obtained for a metal/metal-ion electrode. The unknown potential drop $\Delta\phi$ within the double layer is replaced by the electrode potential E and the drop $\Delta\phi_H$ within the double layer of the SHE ($\Delta\phi = E - \Delta\phi_H$). As $\Delta\phi_H$ is constant, any changes of $\Delta\phi$ will equal that of the electrode

potential E

$$\begin{aligned}
 k_+ &= k_{0+} \exp \frac{-(E_{0,A+} - \alpha z F \Delta \phi)}{RT} \\
 &= k'_{0+} \exp \frac{\alpha z F \Delta \phi}{RT} \\
 &= k'_{0+} \exp \frac{-\alpha z F \Delta \phi_H}{RT} \exp \frac{\alpha z F E}{RT}, \quad (12.22) \\
 k_- &= k_{0-} \exp \frac{-[E_{0,A-} + (1-\alpha)zF\Delta\phi]}{RT} \\
 &= k'_{0-} \exp \frac{-(1-\alpha)zF\Delta\phi}{RT} \\
 &= k'_{0-} \exp \frac{-(1-\alpha)zF\Delta\phi_H}{RT} \exp \frac{-(1-\alpha)zFE}{RT}. \quad (12.23)
 \end{aligned}$$

The introduction of (12.22, 12.23) into (12.19) yields (12.24). For the conditions of electrochemical equilibrium, i.e. for $E = E_0$ and $i = 0$, one obtains the expression for the exchange current density i_0 of (12.25). Introducing the overpotential $\eta = E - E_0$ and (12.25) for i_0 in (12.24) one obtains the Butler–Volmer equation (12.26)

$$\begin{aligned}
 i &= n F k'_{0+} c(\text{Red}) \exp \left(\frac{\alpha z F (E + \Delta \phi_H)}{RT} \right) \\
 &\quad - n F k'_{0-} c(\text{Ox}) \exp \left(-\frac{(1-\alpha)zF(E + \Delta \phi_H)}{RT} \right) \quad (12.24)
 \end{aligned}$$

for $E = E_0, i = 0$,

$$\begin{aligned}
 i_0 &= n F k'_{0+} c(\text{Red}) \exp \left(\frac{\alpha z F (E_0 + \Delta \phi_H)}{RT} \right) \\
 i_0 &= n F k'_{0-} c(\text{Ox}) \exp \left(-\frac{(1-\alpha)zF(E_0 + \Delta \phi_H)}{RT} \right), \quad (12.25)
 \end{aligned}$$

$$\begin{aligned}
 i &= i_+ + i_- = i_0 \left[\exp \left(\frac{\alpha z F \eta}{RT} \right) \right. \\
 &\quad \left. - \exp \left(\frac{-(1-\alpha)zF\eta}{RT} \right) \right]. \quad (12.26)
 \end{aligned}$$

For large positive overpotentials $\eta \gg RT/F$ the cathodic current density may be neglected and for large negative overpotentials with $\eta \ll RT/F$ the anodic current density is vanishingly small. Taking the logarithm of (12.26) one obtains the η -log i equations, (12.27) and (12.28), for both cases. The appropriate semi-logarithmic presentation yields the so-called Tafel

plot

$$\eta = -\frac{RT}{\alpha z F} \ln i_0 - \frac{RT}{\alpha z F} \ln i_+ = a + b \log i_+, \quad (12.27)$$

$$\begin{aligned}
 \eta &= \frac{RT}{(1-\alpha)zF} \ln i_0 - \frac{RT}{(1-\alpha)zF} \ln |i_-| \\
 &= a + b \log |i_-|. \quad (12.28)
 \end{aligned}$$

Figure 12.11 gives an example of a dimensionless $\log |i|/i_0 - \eta$ presentation for different charge-transfer coefficients α with an anodic and a cathodic branch. For $\alpha = 0.5$ both branches are symmetrical to each other and for $\alpha \neq 0.5$ they are asymmetric. The measured current densities i deviate from the Tafel lines for $\eta \leq 0.1$ V and $\eta \geq -0.1$ V due to the influence of the corresponding counter-reaction. Extrapolation of the Tafel lines meet at the equilibrium potentials with $\eta = 0, i = i_0$ and $\log |i|/i_0 = 0$. The constants a and b of a Tafel plot are important kinetic parameters for an electrode process. The b factor contains the value of α and constant a the exchange current density i_0 . According to (12.22–12.25) i_0 depends on the activation energy and the electrochemical reaction order for those species that influence the rate law. The same equations (12.22–12.28) hold for redox reactions as well as for anodic metal dissolution and cathodic metal deposition, when the concentrations of the cations are introduced. The evaluation of the kinetics of a redox process or metal dissolution requires Tafel plots, which then yield data from the slope and the intersection with the ordinate.

An alternative approach requires the determination of the slope of the polarization curve at $E = E_0$ only. For small overpotentials the development of the i - η relation (12.26) in a MacLaurin series with only the linear terms for η yields (12.29). Its reverse slope for $\eta \rightarrow 0$ V yields the charge-transfer resistance R_T of (12.30). According to this equation only the reciprocal slope of the polarization curve has to be determined for $\eta \rightarrow 0$ to get the exchange current density i_0 . Thus the determination of the total polarization curve is not required. A similar situation holds for the rest potential E_R when two different reactions compensate each other, as will be shown in the following section (12.36, 12.37)

$$i = i_0 \left(1 + \frac{\alpha z F \eta}{RT} - \frac{[(1-\alpha)zF\eta]}{RT} \right) = \frac{i_0 z F \eta}{RT}, \quad (12.29)$$

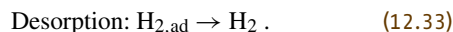
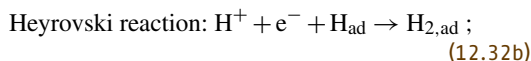
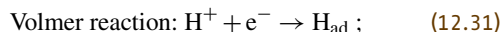
$$R_T = \left(\frac{d\eta}{di} \right)_{\eta \rightarrow 0} = \frac{RT}{z F i_0}. \quad (12.30)$$

12.2.7 Elementary Reaction Steps in Sequence, the Hydrogen Evolution Reaction

Electrochemical processes often consist of a sequence of elementary reaction steps. This situation is treated similarly to the general rules of chemical kinetics. The slowest step in a sequence determines the total rate. Any preceding process is submitted to stationary conditions or chemical equilibrium may even be established. Any fast following step does not affect the rate of the overall process. In this section the possible mechanisms of cathodic hydrogen evolution and its influence on the rate equation and cathodic current density are described. This relatively complicated electrochemical process is presented as an example for the treatment of a sequence of elementary reaction steps. Furthermore it is a very important reaction for corrosion processes.

Two possible reaction paths are discussed, the Volmer–Tafel and the Volmer–Heyrovski mechanism. In both cases the process starts with the oxidation of hydrogen ions to atoms H_{ad} adsorbed at the electrode surface according to the Volmer reaction of (12.31). The

following Tafel reaction (12.32a) involves the combination of two H_{ad} to $H_{2,ad}$, which is then finally transferred to the electrolyte by desorption and diffusion to the bulk electrolyte. At high negative overvoltages hydrogen formation is fast enough to form gas bubbles. An alternative is the Heyrovski reaction (12.32b), a second charge-transfer step which involves the reduction of a hydrogen ion in the vicinity of H_{ad} to form $H_{2,ad}$ that then again desorbs and diffuses to the bulk.



With the Volmer reaction as a rate-determining step one obtains for the cathodic current density of hydrogen evolution i_H the Butler–Volmer equation as described by (12.26). For sufficiently large cathodic overvoltages i_H is described by (12.28). A Tafel plot of (12.28) yields, with $z = 1$ and $\alpha = 0.5$, a slope $b = \frac{d\eta}{d \log |i_H|} = \frac{RT \cdot 2.303}{(1-\alpha)F} = \frac{0.059}{0.5} = -0.120 \text{ V}$. Figure 12.12 presents the Tafel plot for cathodic hydrogen evolution at various metals [12.35]. From the slope $1/b$ of this $\log |i_H| - \eta$ presentation one obtains for most metals a factor $b = -0.12 \text{ V}$. The Tafel lines for the metals are shifted relative to each other, which proves the strong influence of the kind and surface condition of the electrode materials on the electrode kinetics. The parallel shift of these lines is caused by the specific values of the exchange current density $i_{H,0}$ for the different metals, i. e. of the constant a of (12.28). Pt is a metal with a small overvoltage whereas Pb and Hg have large overvoltages. The very fast kinetics on Pt are very useful for water electrolysis to produce hydrogen as fuel with optimized energy input. On the contrary Pb and Hg electrodes are well suited to the suppression of hydrogen evolution when other cathodic reactions are of interest, such as the reduction of organic compounds or electrolysis of NaCl or KCl solutions, which yield Cl_2 gas at the anode and K or Na amalgam at the cathode. Hg electrodes are also well suited for polarography. Here again the large overvoltage suppresses hydrogen evolution and permits the analysis of cations of very reactive metals such as Zn^{2+} and Cd^{2+} by their cathodic reduction.

If the Heyrovski reaction of (12.32b) is the rate-determining step it will lead to the kinetic equation (12.34). Here Θ_H is the surface coverage of hydrogen atoms which is proportional to their surface concentration. Assuming electrochemical equilibrium for the

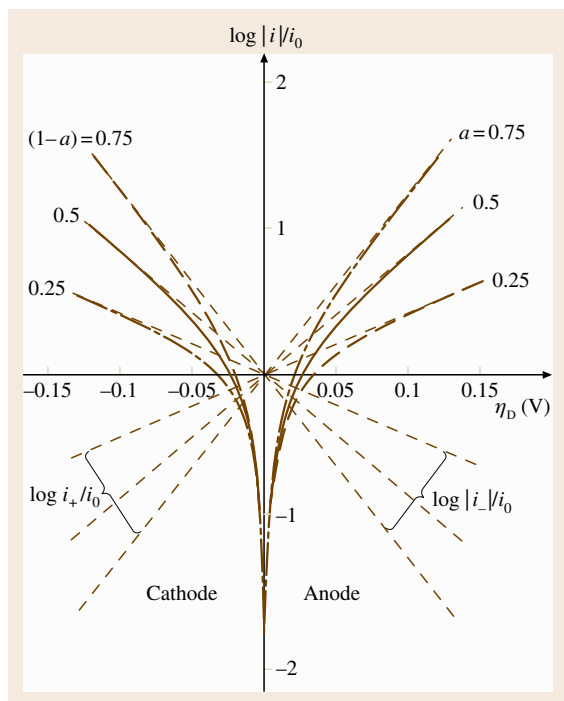


Fig. 12.11 Tafel plot for a charge-transfer-controlled reaction and its dependence on the charge-transfer coefficient α (after [12.35])

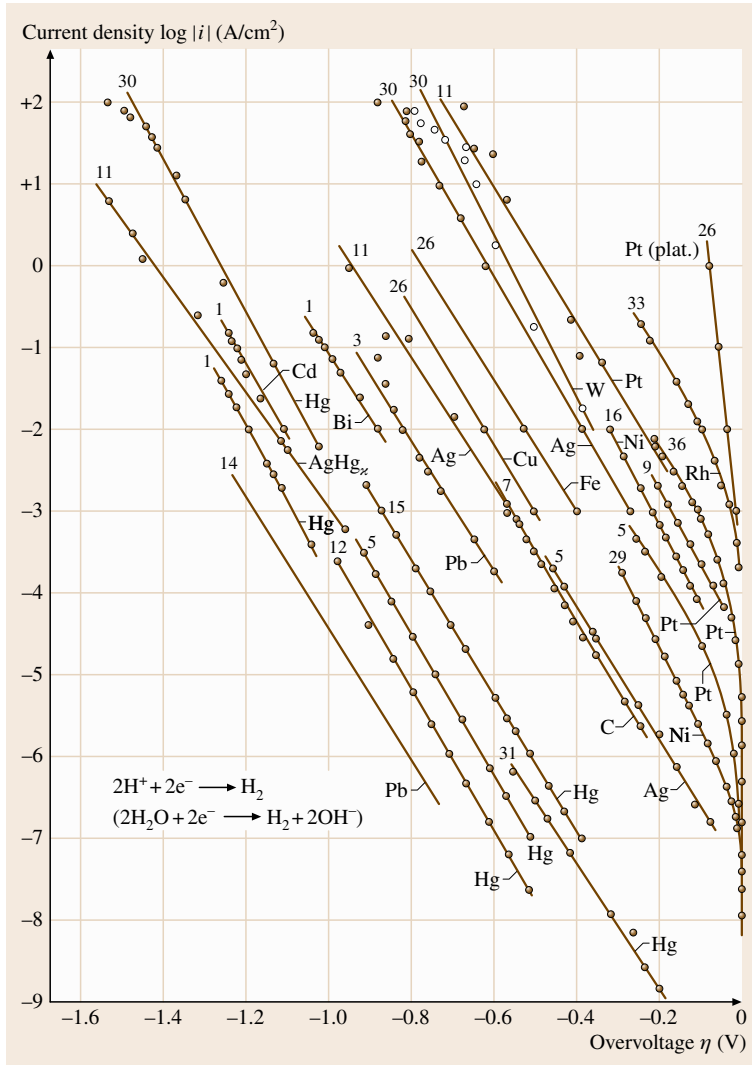


Fig. 12.12 Tafel plot of cathodic hydrogen evolution for different electrode metals (after [12.35])

preceding Volmer reaction one obtains from the related Nernst equation (12.35) which allows the replacement of Θ_H with (12.36) in (12.34). Equation (12.37) then contains $c^2(H^+)$, i.e. the electrochemical reaction order of H^+ is 2. It also contains a modified exponential term. Replacing $E = E^0 + \eta$ one obtains the related Tafel (12.38) which yields with $\alpha = 0.5$ a slope $b = 0.40$

$$i_H = -k_- \Theta_{HC} (H^+) \exp\left(-\frac{(1-\alpha) F}{RT} E\right), \tag{12.34}$$

$$E = \text{const}' + \frac{RT}{F} \ln \frac{c(H^+)}{\Theta_H}, \tag{12.35}$$

$$\Theta_H = \text{const } c(H^+) \exp\left(-\frac{F}{RT} E\right), \tag{12.36}$$

$$\begin{aligned} i_H &= -k_- c^2(H^+) \exp\left(-\frac{(2-\alpha) F}{RT} E\right) \\ &= -k_- c^2(H^+) \exp\left[-\frac{(2-\alpha) F}{RT} (E^0 + \eta)\right], \end{aligned} \tag{12.37}$$

$$\begin{aligned} \eta &= \frac{RT2.303}{(2-\alpha) F} \log |i_{0,H}| - \frac{RT2.303}{(2-\alpha) F} \log |i_H| \\ &= a + b \log |i_H|. \end{aligned} \tag{12.38}$$

If the Tafel reaction (12.32a) is the rate-determining step one starts with (12.39) and (12.40) for i_H and Θ_H and $i_{0,H}$ and $\Theta_{H,eq}$ respectively. Assuming electrochemical equilibrium for the Volmer reaction (12.31) yields the Nernst equation for this charge-transfer step and consequently (12.41a) for the electrode potential E and for the overvoltage η . η is thus a consequence of the varying surface coverage Θ_H with i_H . For this discussion diffusion control of H^+ ions from the bulk to the electrode surface is excluded and therefore the same concentration $c(H^+)$ is present within the bulk and at the electrode–electrolyte interface. In consequence the Tafel plot according to (12.40) yields a slope $d\eta/d \log i_H = b = -0.29$ V if the Tafel reaction is the rate-determining step

$$|i_H| = kF\Theta_H^2, \quad \Theta_H = \sqrt{\frac{|i_H|}{kF}}, \quad (12.39)$$

$$|i_{H,0}| = kF\Theta_{H,eq}^2, \quad \Theta_{H,eq} = \sqrt{\frac{|i_{H,0}|}{kF}}, \quad (12.40)$$

$$E - E_0 = \eta = \frac{RT}{F} \ln \frac{\Theta_{H,eq}}{\Theta_H} = \frac{RT}{F} \ln \sqrt{\frac{|i_{H,0}|}{|i_H|}}; \quad (12.41a)$$

$$\eta = \frac{0.059}{2} \log |i_{H,0}| - \frac{0.059}{2} \log |i_H| \\ = a + b \log i_H. \quad (12.41b)$$

12.2.8 Two Different Reactions at One Electrode Surface

The corrosion rate may be ruled by metal dissolution or by a compensating cathodic reaction of a redox system. Metal dissolution by hydrogen evolution or oxygen reduction are important examples. In acidic electrolytes hydrogen evolution is the favored counter-reaction for dissolution of reactive metals such as iron and will be discussed as an example. The equilibrium potential of the hydrogen electrode $E_0 = -0.059$ pH is much more positive than the standard potential $E^0 = -0.409$ V for the Fe/Fe^{2+} electrode, which is a necessary requirement for an efficient metal dissolution. However in addition the kinetics of both processes determine the shape of their polarization curves and thus have a strong influence on the overall process. Figure 12.13 presents schematically the anodic and cathodic reactions of both electrodes in the vicinity of their equilibrium potentials $E_0(Me/Me^{z+})$ and $E_0(H_2/H^+)$. The rest potential E_R is found between both values where anodic metal dissolution and cathodic hydrogen evolution compensate

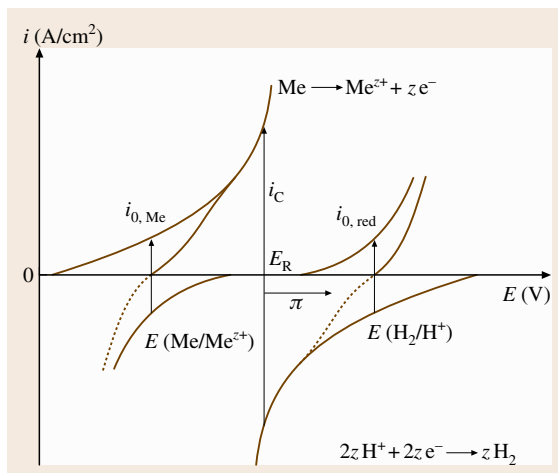


Fig. 12.13 Schematic diagram of metal dissolution and hydrogen evolution as cathodic counter-reaction with rest potential E_R

each other. E_R is sufficiently distant from both equilibrium potentials so that only Fe dissolution and hydrogen evolution have to be taken into account. For a positive polarization $\pi = E - E_R > 0$ metal dissolution exceeds hydrogen evolution with a total anodic current i and for the opposite case hydrogen evolution is larger with a total cathodic current i . Both partial reactions may be described by a Butler–Volmer equation and their sum leads to a similar expression (12.42) as discussed before when opposite partial reactions of the same electrode process compensate each other as described by (12.26). For a vanishing total current density i , i.e. for $\pi = 0$, one obtains (12.43) for the corrosion current density i_C . Its application to (12.42) yields (12.44) which has a similar form as (12.26)

$$i = i_{Me} + i_H = i_{0,Me} \exp\left(\frac{\alpha_{Me} z_{Me} F (E - E_{0,Me})}{RT}\right) \\ - i_{0,H} \exp\left(-\frac{(1 - \alpha_H) F (E - E_{0,H})}{RT}\right), \quad (12.42)$$

$$i_C = i_{0,Me} \exp\left(\frac{\alpha_{Me} z_{Me} F (E_R - E_{0,Me})}{RT}\right) \\ = i_{0,H} \exp\left[-\frac{(1 - \alpha_H) F (E_R - E_{0,H})}{RT}\right], \quad (12.43)$$

$$i = i_C \left[\exp\left(\frac{\alpha_{Me} z_{Me} F \pi}{RT}\right) \right. \\ \left. - \exp\left(-\frac{(1 - \alpha_H) F \pi}{RT}\right) \right]. \quad (12.44)$$

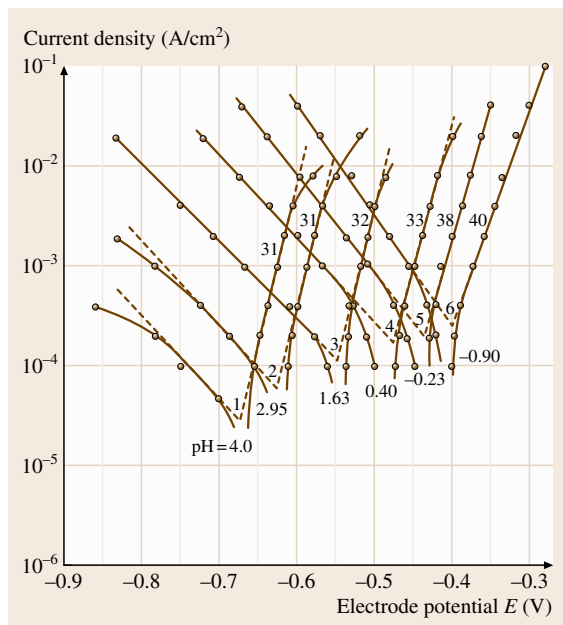


Fig. 12.14 Tafel plot for Fe^{2+} dissolution and hydrogen evolution of an Fe electrode in solutions of $\text{H}_2\text{SO}_4/\text{Na}_2\text{SO}_4$ mixtures: 0.482 M/1 M, pH 4.0, 0.00482 M/1 M, pH 2.95, 0.0965 M/0.9 M, pH 1.63, 0.75 M/0.75 M, pH 0.40, 2 M/0, pH -0.23, 5 M/0 M, pH -0.90 (after [12.36])

For large polarizations i. e. $\pi \gg RT/\alpha_{\text{Me}}z_{\text{Me}}F$ or $\pi \ll RT/(1-\alpha_{\text{H}})F$ the anodic or cathodic current density dominates the overall process, so that i equals the first or second term of (12.44), respectively. These conditions yield (12.45) and (12.46), which describe Tafel plots for metal dissolution and hydrogen evolution. The extrapolation of the lines intersect at $\pi = 0$ and $E = E_{\text{R}}$ with $i = i_{\text{C}}$. An example for iron dissolution and hydrogen evolution is presented in Fig. 12.14 as a function of pH [12.36]. With increasing pH the Tafel lines of hydrogen evolution are shifted to negative potentials. This is a consequence of the -0.059 pH dependence of the equilibrium potential of the H^+/H_2 electrode, but also of the decrease of the kinetics of H_2 evolution. At pH 4.0 and 3.0 the start of diffusion control may be seen by the deviation of the current density from the Tafel line for large cathodic overvoltages. In addition Fe dissolution is pH-dependent; its Tafel lines shift to more negative potentials with increasing pH. This is a consequence of the aforementioned OH^- catalysis of iron dissolution [12.34]. Iron dissolution occurs with a dissolution current density $\log i \propto 1.5 \log c(\text{O}^-)$. Thus the electrochemical reaction order for OH^- ions is 1.5, i. e.

$\log i$ increases by 1.5 orders when the pH increases by one unit. Both effects lead to the observed negative shift of E_{R} with increasing pH but they compensate each other partially with an only moderate decrease of the corrosion current density i_{C} at the rest potential. i_{C} may be determined by the evaluation of the Tafel lines but also by a direct measurement of metal dissolution. The related data may be obtained by analysis of the concentration of metal ions within the electrolyte but also by the weight loss of metal specimens. These independent data should match each other

$$\log i = \log i_{\text{C}} + \frac{\alpha_{\text{Me}}z_{\text{Me}}F}{RT}\pi \quad \text{for } \pi > 0, \quad (12.45)$$

$$\log i = \log i_{\text{C}} - \frac{(1-\alpha_{\text{H}})F}{RT}\pi \quad \text{for } \pi < 0. \quad (12.46)$$

A third possibility uses the inverse polarization resistance $1/R_{\text{p}} = (di/d\pi)_{\pi \rightarrow 0}$ similar to the discussion of the charge-transfer resistance of (12.30). The development of (12.44) by a MacLaurin series for $\pi \rightarrow 0$ yields (12.47) and (12.48) which may serve to determine the missing kinetic parameters α_{Me} and α_{H} . With known charge-transfer coefficients α one may determine i_{C} . Similar relations hold with z_{Red} as a factor of the second term of (12.47) for the case of other redox systems such as the reduction of dissolved oxygen or Fe^{3+} ions taking over the counter-reaction for metal dissolution

$$i = i_{\text{C}} \left(\frac{\alpha_{\text{Me}}z_{\text{Me}}F\pi}{RT} + \frac{(1-\alpha_{\text{H}})F\pi}{RT} \right), \quad (12.47)$$

$$\left(\frac{di}{d\pi} \right)_{\pi \rightarrow 0} = \frac{i_{\text{C}}F}{RT} [\alpha_{\text{Me}}z_{\text{Me}} + (1-\alpha_{\text{H}})]. \quad (12.48)$$

Hydrogen evolution by water decomposition is an important cathodic process for neutral and alkaline solutions. In these cases the concentration of H^+ ions is too small to contribute to the cathodic reduction. Hydrogen evolution by water reduction has a large overpotential and thus relatively negative potentials are required to start this reaction. The cathodic polarization curves for different pH merge at very negative potentials all in one line because it is not the H^+ but the high and pH-independent water concentration that enters the rate equation for these conditions. Figure 12.15 compares the hydrogen evolution on Fe in HCl solution with 4% NaCl [12.37, 38]. In acidic electrolytes a linear part for $\log i/E$ is found, corresponding to charge-transfer control of H^+ reduction. The deviation in the vicinity of E_{R} is caused by compensating Fe dissolution. At large cathodic polarization the current density enters a plateau which is caused by diffusion control. Its value

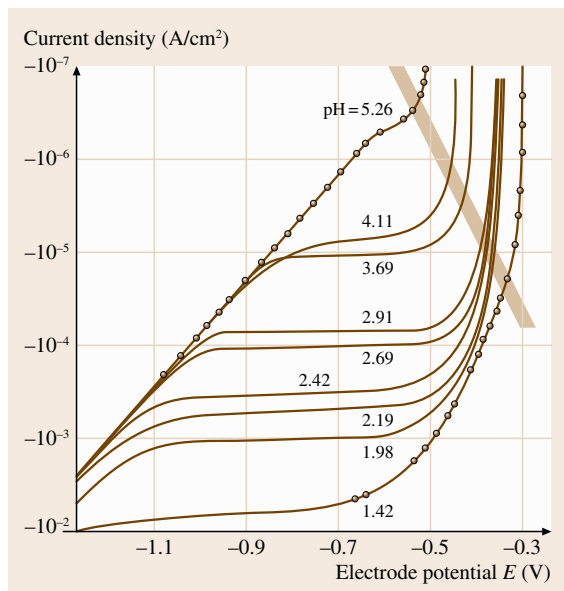


Fig. 12.15 Hydrogen evolution on Fe in HCl + 4% with pH as indicated (after [12.37, 38])

is proportional to $c(\text{H}^+)$. This situation with dominating diffusion overvoltage will be discussed in Sect. 12.2.11. Finally all cathodic current densities merge in one line corresponding to hydrogen evolution by water decomposition. No limiting current is achieved for very high cathodic overvoltages due to the high water concentration as reacting species of 55.56 M. For $\text{pH} > 4$ no hydrogen evolution by H^+ reduction is possible due to its very small bulk concentration and the plateau of a diffusion-limited process of H^+ reduction is missing.

12.2.9 Local Elements

The above discussion assumes a homogeneous electrode with the same reactivity all over the surface. If an electrode is composed of physically or chemically different areas A and B with varying electrochemical activity their cathodic and anodic reaction rates and related current densities i_A and i_B will follow the same behavior as described above. i_A and i_B are the polarization curves that could be measured for the pure surfaces A and B. They differ from each other in shape and position on the potential scale and thus have different rest potentials $E_{R,A}$ and $E_{R,B}$. The combination of A and B in one surface causes a potential shift of A and B to a new value $E_{R,AB}$ in between both. At $E_{R,AB}$ the anodic current i_A on A and a cathodic current

i_B on B will compensate each other. As a consequence a net current $|i_A(E_{R,AB})| = |i_B(E_{R,AB})|$ will flow from A to B within the electrolyte and thus will lead to local elements at the metal surface. If the electrolyte in front of the electrode is sufficiently conductive and does not allow an ohmic drop, A and B will assume the same electrode potential Fig. 12.16. In the example of Fig. 12.16, A will be dissolved at a higher rate than B and the reduction of hydrogen will occur at a higher rate on B. Therefore the A sites are the local anodes and the B sites are the local cathodes. The application of a polarization $\pi = E - E_{R,AB}$ via an external supply, such as a potentiostat, allows the determination of the polarization curve. One measures the current density $i = i_A + i_B$ as a function of the polarization π of a metal surface with local anodes A and cathodes B. Low conductivity of the electrolyte may cause a potential drop in front of the electrode between sites A and B due to the local current densities between both. This situation will be discussed in Sects. 12.2.12 and 12.2.13.

These local elements frequently lead to a pronounced increase of the corrosion rate. A well-known example is the increase of Zn dissolution by small deposits of copper at its surface for open-circuit conditions. Hydrogen evolution on the Cu deposits occurs at

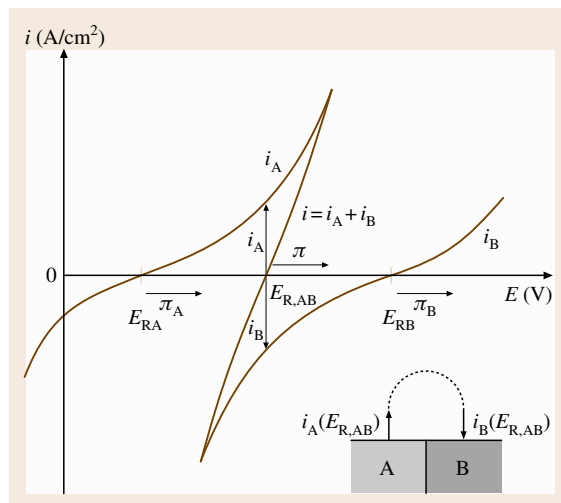


Fig. 12.16 Polarization curve of a metal surface with sites A and B with different electrochemical properties. Rest potentials $E_{R,A}$ and $E_{R,B}$ of pure sites and $E_{R,AB}$ of mixed electrode. Polarization π for the sites A and B and mixed surface AB. i_A , i_B are current densities of sites A and B which compensate each other at $E_{R,AB}$. Inset shows local elements with current flow from A to B at rest potentials $E_{R,AB}$

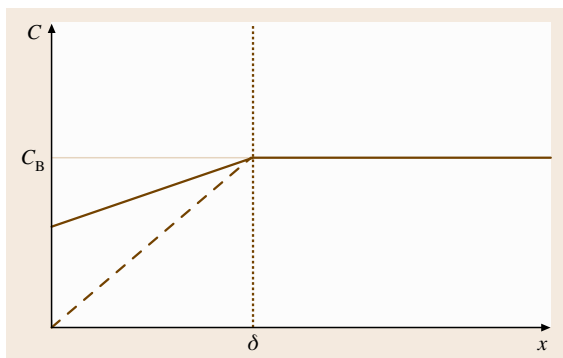


Fig. 12.17 Concentration profile in front of an electrode with Nernst diffusion layer of thickness δ , maximum current density i_D for $c = 0$

much higher rates, thus promoting zinc dissolution. The common rest potential is positive when compared to that of pure zinc. These local elements often cause serious corrosion damage. Another well-known example is the corrosion of Cu-containing commercial aluminum. Cu inclusions prevent the total protection of the Al surface by a passivating Al_2O_3 film. Cu acts as a local cathode, which compensates the dissolution of Al by local oxygen reduction. Well-passivated Al does not permit the reduction of redox systems such as oxygen due to the isolating electronic properties of the pure protecting Al_2O_3 film. For similar reasons one should not combine reactive metals such as Fe with Cu in water-containing supplies. The close vicinity of both metals and some Cu dissolution and its redeposition on a reactive metal surface will cause local elements. Effective oxygen reduction at these Cu deposits causes increased Fe dissolution, as described above.

12.2.10 Diffusion Control of Electrode Processes

In many cases metal corrosion and the compensating redox process may be under diffusion control, which leads to a diffusion overvoltage η_D . Diffusion of H^+ ions in weakly acidic electrolytes during Fe dissolution is one example that was discussed in the last section. Oxygen diffusion within electrolytes is another. Low oxygen concentration in solution and thick layers of electrolyte are a frequent situation that causes diffusion overvoltage. In all these cases the concentration of the oxidizing species reduces at the metal surface due to its intense consumption by the reduction process, leading to a concentration profile. Similarly high dissolution

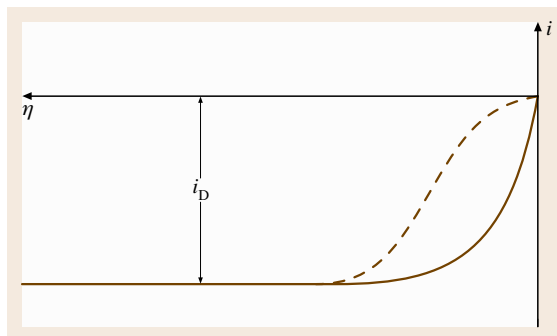


Fig. 12.18 i/η dependence for a cathodic reaction under diffusion control without (*solid*) and with additional charge-transfer control (*dashed line*)

rates of a metal cause the accumulation of its cations at the metal surface and a related increase of its concentration. As a consequence a concentration profile builds up which may cause locally saturated or supersaturated solutions and even the precipitation of corrosion products, such as the formation of salt films.

Figure 12.17 presents the concentration profile of the oxidized component Ox in front of an electrode within the Nernst diffusion layer of thickness δ . The dashed line refers to the maximal concentration gradient when the concentration of Ox at the surface approaches zero. For a diffusion-controlled electrode process the transfer of Ox equals the current density i according to (12.49) which is a combination of Fick's first diffusion equation and Faraday's law with Faraday's constant F , the diffusion constant D , the concentration of Ox at the surface c_S and within the bulk c_B , the thickness of the diffusion layer δ and the number of electrons for the charge-transfer process n . For vanishing concentration $c_S = 0$ one obtains the maximum diffusion current density i_D according to (12.50). The combination of (12.49) and (12.50) yields (12.51). If the charge-transfer reaction is fast with respect to diffusion the electrochemical equilibrium is established with an electrode potential $E = E_0 + \eta_D$. η_D is given by the difference of the electrode potentials for the concentrations c_S and c_B according to the Nernst equation, which yields (12.52). Introducing the current densities i and i_D with (12.49) and (12.50) one obtains (12.53). Figure 12.19 depicts the change of the current density with η for a cathodic process which approaches i_D for large overvoltages. For small η the reaction becomes charge-transfer controlled, which results in the dashed curve of Fig. 12.18. Similarly metal dissolution for large positive polarizations becomes diffusion con-

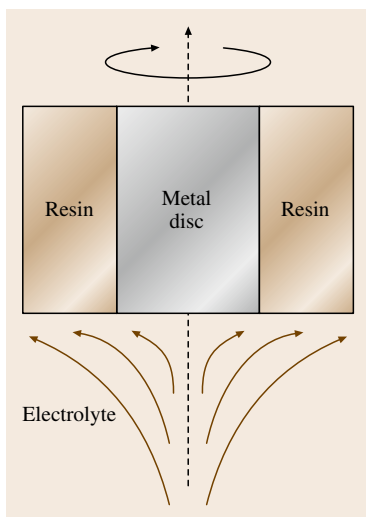


Fig. 12.19
Rotating disc electrode with electrolyte convection in front

$$i = i_D - \frac{nFDc_S}{\delta}, \quad (12.51)$$

$$\eta_D = \frac{RT}{nF} \ln \left(\frac{c_S}{c_B} \right), \quad (12.52)$$

$$\eta_D = \frac{RT}{nF} \ln \left(\frac{i_D - i}{i_D} \right). \quad (12.53)$$

trolled and the current density becomes independent of the electrode potential. For large positive overvoltages the accumulation of cations at the electrode surface yields precipitation of corrosion products and salt films may form, which slow down the metal dissolution rate. In many cases the growth of oxides films at the metal surface causes a much more pronounced decrease of its dissolution current density. These processes may lead to thin passive layers that act as a barrier to the transfer of cations from the metal to the electrolyte, thus effectively protecting even very reactive metals against corrosion.

$$i = -\frac{(c_B - c_S)nFD}{\delta}, \quad (12.49)$$

$$i_D = -\frac{nFDc_B}{\delta}, \quad (12.50)$$

Diffusion of oxygen to a corroding metal surface is frequently the rate-determining step for corrosion processes. This is a consequence of its limited dissolution in water and the presence of thick water layers, which act as a diffusion barrier. For very thin water layers the access of oxygen is less hindered and sufficiently fast, yielding high corrosion rates. This is often the case under atmospheric corrosion. As an estimate i_D of oxygen reduction is calculated using the first diffusion law according to (12.50) with $n = 4$ for oxygen reduction to H_2O . With a diffusion constant $D_{\text{O}_2} = 10^{-5} \text{ cm}^2/\text{s}$ the thickness of the Nernst diffusion layer $\delta = 5 \times 10^{-3} \text{ cm}$ and a concentration of saturation for oxygen at 25°C $c_B = 2 \times 10^{-4} \text{ M} = 2 \times 10^{-7} \text{ mol/cm}^3$, a value of $i_D = 1.6 \times 10^{-4} \text{ A/cm}^2 = 0.16 \text{ mA/cm}^2$ is obtained. This value is relatively large and will also disturb electrochemical studies in the laboratory as a cathodic background current. It may be suppressed effectively by purging of electrolytes with nitrogen or argon.

Diffusion may be enhanced by microelectrodes with a small radius a . According to Fig. 12.20 the diffusion in front of a hemispherical electrode follows the current lines, which follow the direction of its radius. The concentration gradient is given by the density of the hemispheres of constant concentration surrounding the electrode surface (dashed circles). Most variation is located close to the surface due to the divergence of the current lines. According to the hemispherical shape of

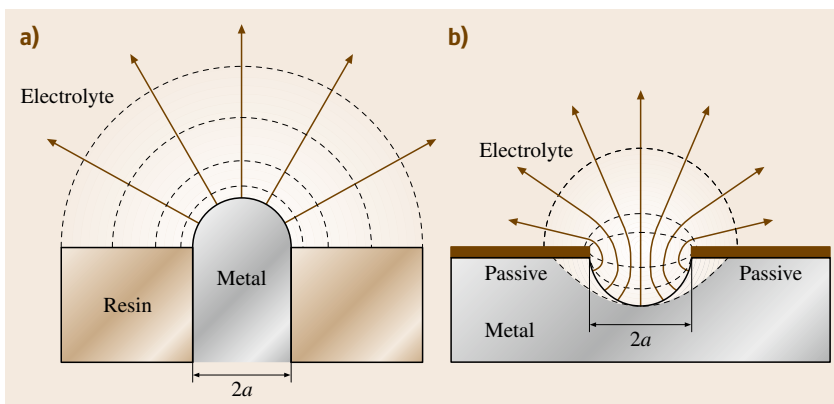


Fig. 12.20a,b Cross section of a convex hemispherical electrode/electrolyte combination (a) and a concave hemisphere (b) with diffusion lines or current lines (solid) and curves of equal concentration or potential (dashed) respectively; a is the radius of the electrode

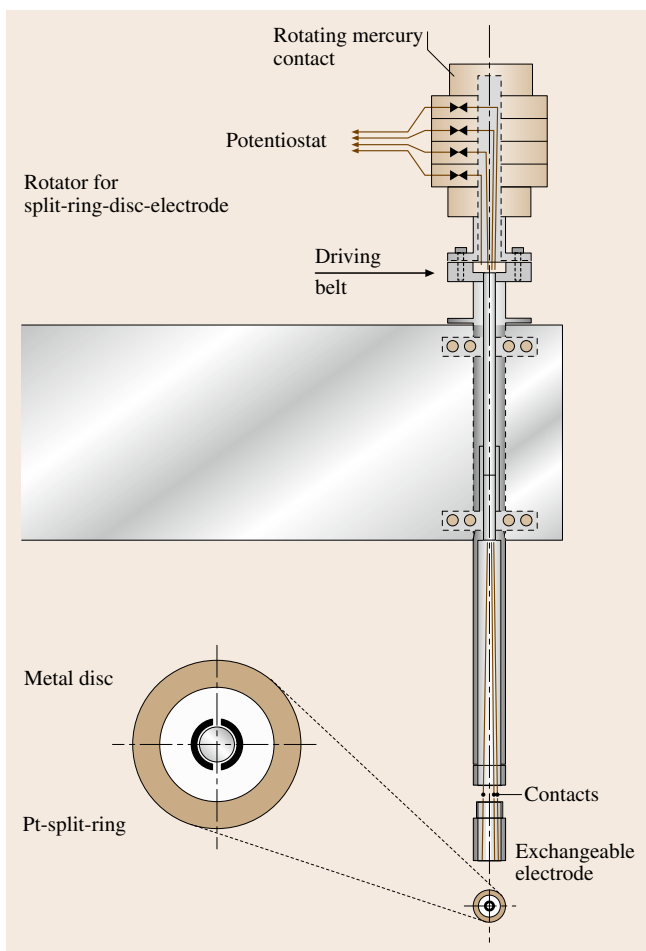


Fig. 12.21 Disc rotator with an exchangeable RRDE with a split ring

this transport the current density $i(r)$ decreases with the distance $a+r$ from the surface according to (12.54) with the radius a for the metal electrode and the current density $i(a)$ at its surface. Integration of the first diffusion law (12.55) for these conditions in the range $r = 0$ to $r = \infty$ yields (12.56) for i and the limiting current density i_D

$$i(r) = i(a) \frac{a^2}{(a+r)^2}, \quad (12.54)$$

$$i = nFD \frac{(a+r)^2}{a^2} \frac{dc}{dr}, \quad (12.55)$$

$$i = nFD \frac{c^S - c^B}{a}; \quad i_D = -nFD \frac{c^B}{a}. \quad (12.56)$$

If the radius a becomes small, i_D may achieve large values. For $c_B = 1 \text{ M} = 10^{-3} \text{ mol/cm}^3$, $n = 1$

and $D = 5 \times 10^{-6} \text{ cm}^2/\text{s}^1$ and an ultramicroelectrode with a radius $a = 1 \mu\text{m} = 10^{-4} \text{ cm}$ one obtains $i_D = 5 \text{ A/cm}^2$. This value will be even higher for electrodes of nm dimensions. In contrast using (12.50) for a planar electrode with a well-stirred electrolyte and a diffusion-layer thickness of $\delta = 5 \times 10^{-3} \text{ cm}$, one obtains $i_D = 0.1 \text{ A/cm}^2$. This is one reason why such small electrodes are used for electroanalytical purposes. For similar reasons a small radius leads to small ohmic voltage drops in front of an ultramicroelectrode which will be discussed in the next section.

Small active areas on a metal surface of this size may occur during localized corrosion of a passivated metal surface. In these cases extremely high local corrosion current densities may be measured within corrosion pits of up to several 10 A/cm^2 , whereas the rest of the surface shows extremely small dissolution currents in the range of $\mu\text{A/cm}^2$. The concentration gradient is about three times larger in this case due to the concave geometry when compared to a convex hemisphere (Fig. 12.21b) [12.39]. This more complicated transport problem has been solved numerically [12.40]. An analytical solution does not exist. Effective hemispherical transport will delay the accumulation of corrosion products for high dissolution rates, at least for some time before they precipitate. The precipitation of salt films will decrease the local current density and change the shape of growing pits from a polygonal shape to hemispheres due to the electropolishing effect of the precipitates [12.29, 30, 39].

12.2.11 Rotating Disc Electrode (RDE) and Rotating Ring-Disc Electrode (RRDE)

Diffusion control of electrode processes has been applied to various polarographic methods to analyze qualitatively and quantitatively the composition of electrolytes or the products formed at an electrode surface. The rotating disc electrode (RDE) and rotating ring-disc electrode (RRDE) are special arrangements to measure qualitatively and quantitatively the amount and composition of corrosion products. A disc that rotates with moderate speed has a laminar flow of the front electrolyte. Its flow is perpendicular and parallel to the rotating disc, as shown in Fig. 12.19. On one hand metal dissolution causes an increase of the concentration of the corrosion products during the outward flow of the electrolyte film parallel to the surface. On the other hand the income of fresh electrolyte from the bulk perpendicular to the surface yields a decrease of the concentration. Both effects compensate

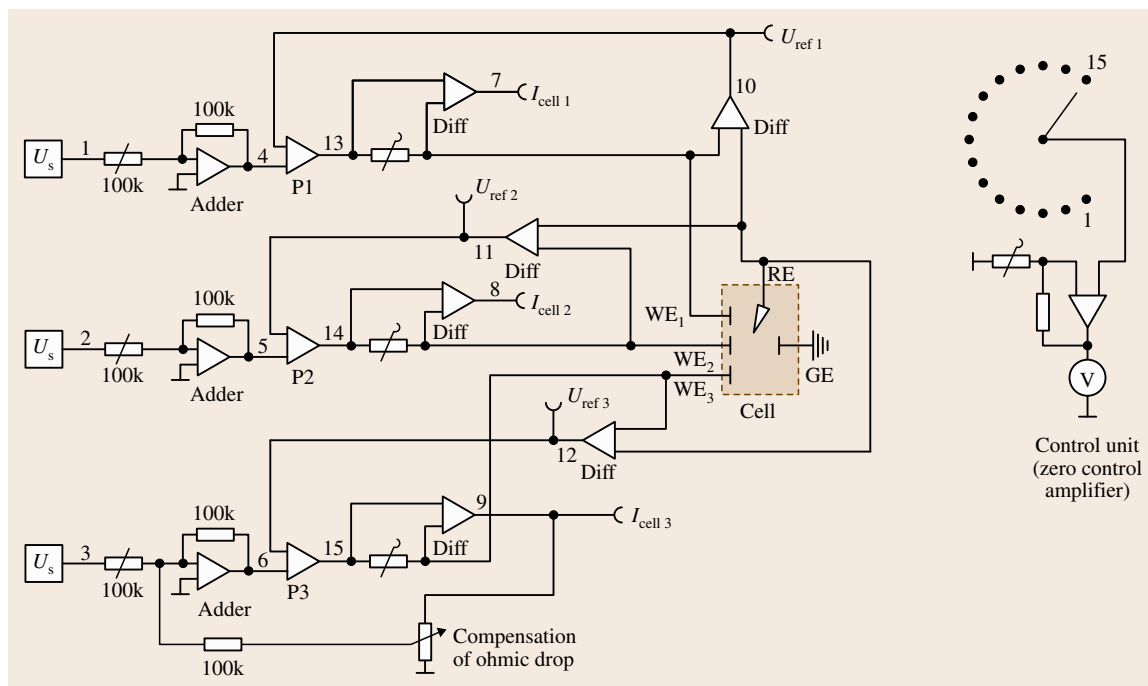


Fig. 12.22 Tripotentiostat for potentiostatic RRDE studies

each other, so that one may calculate diffusion to the bulk with a constant thickness of the Nernst diffusion layer and a constant concentration profile independent of the location at the disc surface. The quantitative treatment of this problem yields the Levich equation (12.57) [12.41] for the thickness of the diffusion layer δ , with the rotation speed $\omega = 2\pi f$, the frequency f , $\nu = \nu'/\rho$, i.e. the viscosity ν' divided by the density ρ of the electrolyte and the diffusion coefficient D . With $\nu = 10^{-2} \text{ cm}^2/\text{s}$ for water, $D = 5 \times 10^{-6} \text{ cm}^2/\text{s}$ and $\omega = 63 \text{ s}^{-1}$ one obtains $\delta = 1.6 \times 10^{-3} \text{ cm}$. Introducing this value in (12.50) yields with $n = 1$ and $c_B = 10^{-3} \text{ M}$ for the limiting disc current density of a species which is consumed at the disc surface $i_D = 300 \mu\text{A}/\text{cm}^2$. Another example is i_D of a rotating iron disc in $0.5 \text{ M H}_2\text{SO}_4$. With a saturation concentration of $c = 0.56 \text{ M}$ for FeSO_4 and its bulk concentration $c_B = 0$ one calculates, for all other conditions the same, $i_D = 0.336 \text{ A}/\text{cm}^2$. Continued Fe dissolution causes accumulation of corrosion products and leads finally to a precipitated salt film which restricts the dissolution to the calculated value. This is close to the experimental maximum $i_D = 200 \text{ mA}/\text{cm}^2$ of dissolution of a flat iron electrode with moderate agitation of the electrolyte. A better coincidence cannot be expected due to

the difference in hydrodynamic flow between the two electrodes

$$\delta = 1.61\omega^{-1/2}\nu^{1/6}D^{1/3}. \quad (12.57)$$

The RRDE consist of a central disc with a surrounding analytical ring electrode, usually made of a noble metal such as gold or platinum (Fig. 12.21). The products of the central disc are transported parallel to the electrode surface and finally pass the ring surface where they undergo an electrochemical process with a diffusion-limited maximum current density. The transfer efficiency N from the disc to the ring may be calculated from the dimensions of both electrodes [12.42] or may be determined experimentally. Values of $N > 30\%$ may be achieved easily. The disc current I_{D_i} and the ring current I_R are correlated by (12.58), which takes into account the number of exchanged charges n_{D_i} and n_R at both electrodes. With (12.58) one may calculate I_{D_i} and the formation of soluble products at the ring from measured I_R values. A reaction well suited to the experimental calibration of a RRDE and the determination of N is the redox reaction of $[\text{Fe}(\text{CN})_6]^{3-/4-}$ with an oxidation of $[\text{Fe}(\text{CN})_6]^{4-}$ at the disc and the related reduction of

$[\text{Fe}(\text{CN})_6]^{3-}$ at the ring or vice versa

$$N = \frac{n_{\text{Di}} I_{\text{R}}}{I_{\text{Di}} n_{\text{R}}} \quad (12.58)$$

RRDE with different metal discs and even brittle semiconductor electrodes have been formed. Usually the disc is embedded in a thin layer of resin with a cylinder of Au or Pt glued by resin to its surface. The total set is then surrounded by resin within a cylinder of a polymer and the electrodes are contacted from the rear side. This exchangeable **RRDE** may then be attached to a disc rotator with rotating contacts for a reliable connection of the rotating electrodes to a potentiostat (Fig. 12.22) [12.43]. Frequently two isolated half cylinders are used instead of a full cylinder, which

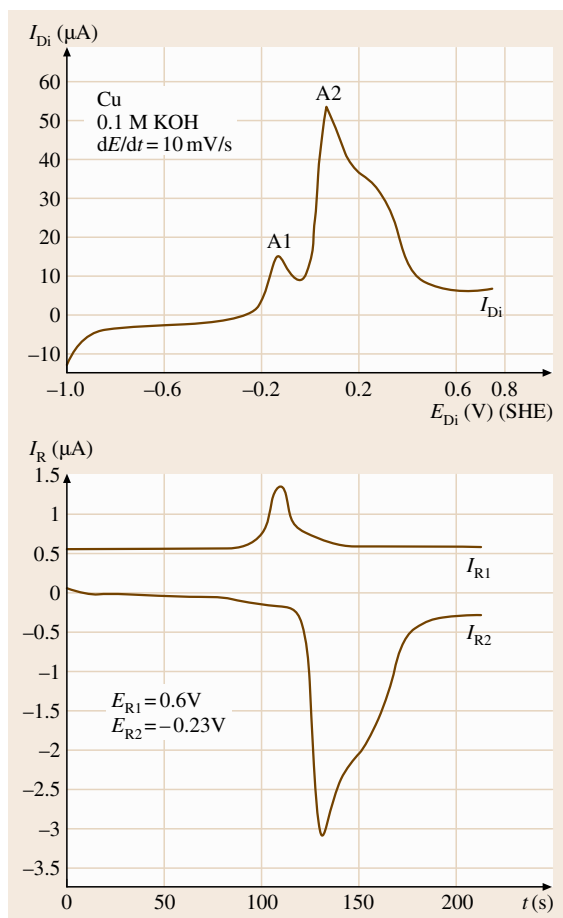


Fig. 12.23 Current of a copper disc I_{Di} and ring currents I_{R1} and I_{R2} of a split **RRDE** in 0.1 M KOH for a potentiodynamic scan of the disc potential $dE_{\text{Di}}/dt = 10 \text{ mV/s}$

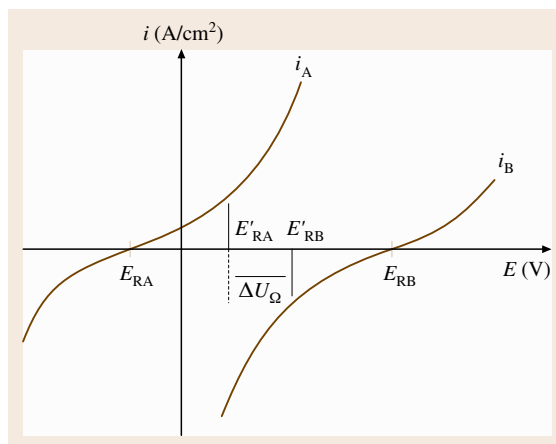


Fig. 12.24 Current densities i_{A} and i_{B} of two surface sites A and B with an ohmic drop ΔU_{Ω} within the electrolyte in front and related rest potentials E'_{RA} and E'_{RB}

opens the possibility to measure the formation of two products simultaneously at the split ring. The **RRDE** requires a bipotentiostat to set the potential of two working electrodes independently from each other. An **RRDE** with a split ring needs a tripotentiostat. The related block diagram is depicted in Fig. 12.22. The three working electrodes WE_1 , WE_2 and WE_3 (disc, ring 1 and ring 2) are connected via a differential amplifier to avoid grounding problems. The three circuits have one common reference electrode, **RE**, and one counter-electrode, **CE**, which is grounded. Further details are similar to those discussed for the block diagram of

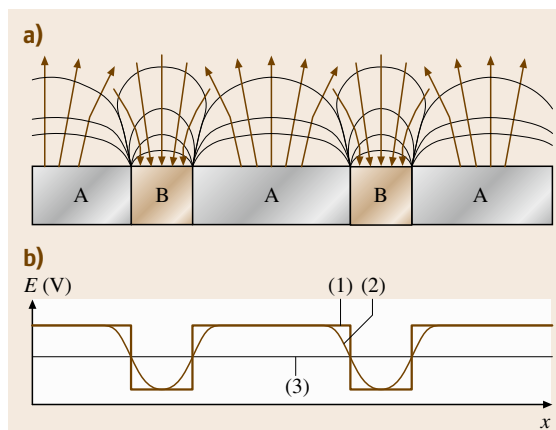


Fig. 12.25 (a) Current lines (arrows) and curves of equal potential in the presence of local elements with surface sites A and B. (b) potential profile with very low (1), low (2), and very high conductivity (3) of the electrolyte

Fig. 12.4. Figure 12.23 presents as an example the I_D of the polarization curve of a Cu disc in 0.1 M KOH. Cu forms a passivating oxide layer at sufficiently positive potentials at the anodic peaks A1 and A2. Figure 12.23 depicts I_{R1} and I_{R2} of the two analytical ring electrodes, which are set to appropriate potentials $E_{R1} = 0.6$ V and $E_{R2} = -0.23$ V, respectively. These potentials are suited to oxidize soluble Cu(I) ions to Cu(II) ions and to reduce Cu(II) to Cu(I) ions respectively. Thus the measured analytical ring currents permit the determination of the kind and the amount of soluble corrosion products from the disc. The calculation of the related disc currents $I_{Di}(\text{CuI})$ and $I_{Di}(\text{CuII})$ of soluble products with (12.58) and their comparison with the measured total current I_{Di} allow the determination of the charge which is stored as a passivating oxide film on the copper electrode. Thus these measurements with RRDE allow the determination of the efficiency of layer formation and dissolution. Figure 12.23 shows the close relation of the current peaks A1 and A2 of I_{Di} for Cu(I) oxide and Cu(II) oxide formation and the dissolution of the related ions. Even the dissolution of weakly soluble Cu(I) ions may be detected by I_{R1} in 0.1 M KOH.

A further development of the RRDE is its hydrodynamical modulation of the rotation speed ω . Here the thickness δ of the Nernst diffusion layer is modulated according to (12.57) and thus the diffusion of corrosion products and their transfer to the rings. With a hydrodynamical square-wave modulation one may even distinguish quantitatively between species of the same kind from the bulk electrolyte and those formed at the disc. A detailed description of this method and its application to corrosion is beyond the scope of this chapter and the reader is referred to the literature. An example of its application to the dissolution and film formation has been described for Fe in 1 M NaOH [12.44]. The agreement of experiments and calculation is shown in [12.45].

12.2.12 Ohmic Drops

High current densities cause ohmic drops within the electrolyte. For a planar electrode with a current density i the voltage drop ΔU_Ω changes according to (12.59) with the electrolyte resistance R_Ω , the specific conductivity κ of the electrolyte, and the distance d from the electrode surface. The ohmic drop ΔU_Ω in front of a hemispherical electrode of radius a at distance r is given by (12.60). For $r \rightarrow \infty$, ΔU_Ω obtains a maximum value $\Delta U_{\Omega, \max}$ related to the maximum ohmic resistance $R_{\Omega, \max}$. Similar to the concentration gradient

related to diffusion in front of a hemispherical electrode a small radius a reduces $R_{\Omega, \max}$ and $\Delta U_{\Omega, \max}$ to very small values. For $i = 1$ A/cm² a distance of $d = 5$ mm, and $\kappa = 22$ Ω^{-1} cm⁻¹ for an electrolyte with good conductivity such as 0.5 M H₂SO₄, one obtains for a planar electrode at a distance $d = 0.5$ cm, a value of $\Delta U_\Omega = 0.023$ V = 23 mV (12.59). ΔU_Ω will be much larger for less-conducting electrolytes and higher current densities. These values are characteristic of the ohmic drop between the Haber–Luggin capillary of a reference electrode and the working electrode of a potentiostatic circuit. It may be compensated automatically to about 90% by an electronic feedback loop, a unit built into potentiostats. However, this may still be a problem for electrochemical measurements at very high current densities of $i \geq 10$ A/cm² or electrolytes with low conductivity. Large electrodes will also be submitted to a nonhomogeneous potential distribution due to the presence of large local differences of the ohmic drops.

In the case of a microelectrode with a radius of $a = 10^{-4}$ cm one obtains $\Delta U_{\Omega, \max} = 4.5 \times 10^{-3}$ mV for conditions otherwise the same as given above (12.60). Furthermore the potential will be uniform in front of its surface even for high current densities. Similar conditions will hold for concave hemispherical surfaces such as small corrosion pits with μm dimensions. Here again the potential drop will be three times larger, i.e. 13.5×10^{-3} mV for $a = 1$ μm , due to the concave geometry

$$\Delta U_\Omega = iR_\Omega \quad \text{with} \quad R_\Omega = \frac{d}{\kappa}, \quad (12.59)$$

$$\Delta U_\Omega = iR_\Omega, \quad R_\Omega = \frac{ra}{\kappa(r+a)};$$

$$R_{\Omega, \max} = \frac{a}{\kappa} \quad \text{for} \quad r \rightarrow \infty. \quad (12.60)$$

Microelectrodes are of increasing interest. Many processes occur on a very small scale so that micro- and nanoelectrochemistry are actively developing branches in electrochemistry. These fields are also important for corrosion studies. Many corrosion processes occur on a small scale and still cause huge damage. Mechanistic studies of localized corrosion of passive metal electrodes may follow the formation and growth of corrosion pits to micrometer and nanometer scales with appropriate methods such as scanning force microscopy (SFM) and scanning tunneling microscopy (STM). These methods use very sharp tips that may also be seen as ultramicroelectrodes. Another important example is corrosion of integrated circuits, which is a serious problem for their life time and reliability. There are al-

ways electrolyte residues on metallic connections on chips and the encapsulant gives imperfect protection against the ingress of moisture. The voltage supply of 5 or 15 V is large for any electrochemical process and thus dissolution of metal at positive potentials and its re-deposition at negative potential causes disconnection of vapor-deposited metal connections with μm dimensions and short circuits by the deposition of dendrites. The investigation of biological processes and the development of sensors also need electrochemistry on a micrometer scale. Further miniaturization pushes electrochemistry to a nanometer scale. Thus micro- and nanotechnology require studies of electrochemical processes with the help of micro- and ultramicroelectrodes. Corrosion research necessarily has to address these small and extremely small scales. Modern electroanalytical chemistry uses these micro- and ultramicroelectrodes for scanning electrochemical microscopes (SECM). It should also be mentioned that the tip of an STM or an SFM may be used for highly localized electrochemical studies and surface structuring in combination with the imaging of the electrode surface with mesoscopic and atomic resolution. One possible application of these ultramicroelectrodes is the structuring of metal surfaces by dissolution and deposition of metal on a submicrometer and nanometer scale.

12.2.13 Measurement of Ohmic Drops and Potential Profiles Within Electrolytes

The ohmic drop in front of an electrode may be used as a measure of localized electrochemical processes, as e.g. in the case of local elements and other localized corrosion phenomena. For an electrolyte with good conductivity the potential in front of an electrode does not change if the current densities assume moderate values, although the rate of electrode reactions change locally with the surface sites A and B due to their physical or chemical differences. This leads to local anodes A and cathodes B as discussed in Sect. 12.2.9 with no potential drop between them (Fig. 12.16). However for a low-conductivity electrolyte large potential drops ΔU_{Ω} may occur, which shift the rest potentials of these sites to the values E'_{RA} and E'_{RB} apart from each other (Fig. 12.24). For a vanishingly small conductivity κ the potential profile parallel to the electrode surface within the electrolyte follows the shape of the related areas A and B with steep changes at their contact (Fig. 12.25). For $0 < \kappa < \infty$ a smoothed profile is found which disappears for $\kappa \rightarrow \infty$. Thus the potential in close vicinity to the electrode surface will change within the electrolyte

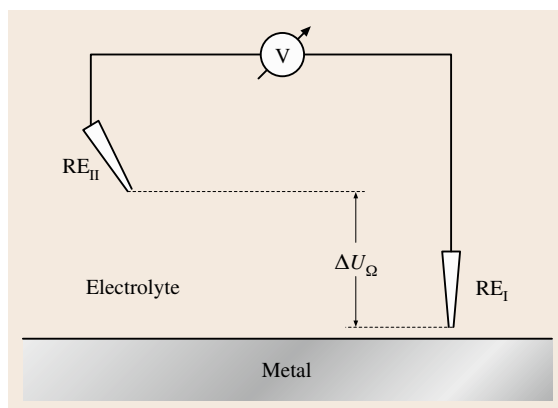


Fig. 12.26 Measurement of the potential profile ΔU_{Ω} within the electrolyte with two reference electrodes RE_I and RE_{II}

with location. However, these differences will smear out with increasing distance from the electrode due to the spread of the current lines.

The related ohmic potential drop ΔU_{Ω} may be measured with two reference electrodes, e.g. two calomel electrodes, one close to the surface moving to the locations of interest (RE_I) and the other at large distance within the bulk electrolyte (RE_{II}). This arrangement measures the total drop ΔU_{Ω} with superimposed changes when moving the sampling electrode parallel to the surface (Fig. 12.26). More sensitive measurements of small changes of ΔU_{Ω} are performed when two reference electrodes are fixed with their Haber-Luggin capillaries close to each other (Fig. 12.27). If they are moved together across the metal surface one measures the potential difference referring to their close

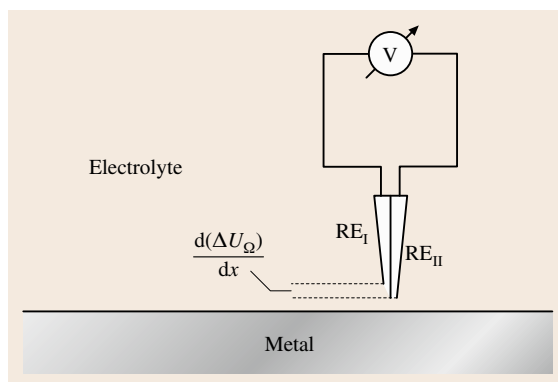


Fig. 12.27 Measurement of the profile of the potential gradient $d(\Delta U_{\Omega})/dx$ within the electrolyte with two close reference electrodes RE_I and RE_{II}

distance as a function of position. Their potential difference changes with their common position in front of the electrode surface and thus samples local potential gradients without a large background voltage. In conclusion, with the second electrode separation within the bulk electrolyte one measures the integral potential drop ΔU_{Ω} whereas with two closely interconnected reference electrodes, i.e. with the so called scanning reference electrode technique (SRET) [12.46–48], the local potential gradient $d\Delta U_{\Omega}/dx$ is obtained. One may improve the spatial resolution with two small platinum tips that are isolated at their sides and which may be arranged closer to each other.

An even better arrangement works with a vibrating reference electrode, i.e. the scanning vibrating electrode technique (SVET) [12.46, 47]. Here one uses a small vibrating metal tip and a second reference electrode far away in the bulk electrolyte. The small amplitude of vibration measures the related local potential gradient corresponding to the small local changes during vibration. The measurement of the related small potential changes may be improved by a lock-in technique that separates the signal from the background and disturbing signals of different frequencies from other sources. With an applied scan of the vibrating electrode parallel to the electrode surface one samples the related potential profile and thus images the sites of different electrochemical activity. The potential change may also be investigated perpendicular to the surface and thus three-dimensional potential profiles may be obtained. Useful SVET equipment is available commercially. One may even calculate from these potential gradients the local current densities when the size of the surface sites of different activity and a possible change of the conductivity of the electrolyte in front are taken into account. At present the vibrating electrode is used mainly to map surface sites of different activity. Examples of frequent interest are local elements on a corroding metal surface with cathodic and anodic areas, inclusions at a metal surface causing localized corrosion or corrosion pits with high metal dissolution rates within a passivated metal surface.

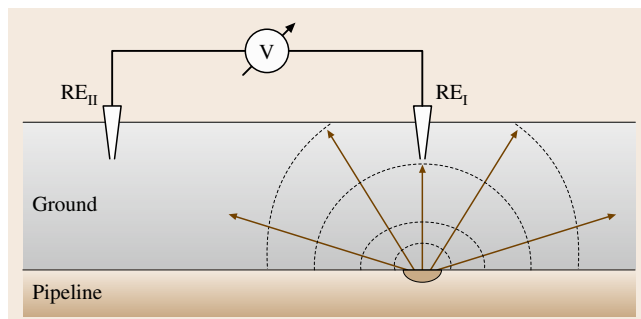


Fig. 12.28 Detection of localized corrosion sites on under ground pipelines by measurement of potential profiles with two reference electrodes (RE)

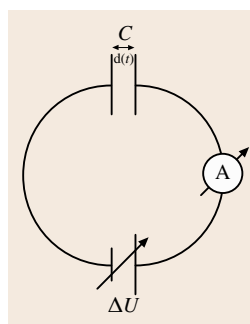


Fig. 12.29 Equivalent circuit of a Kelvin probe with the capacity C of the vibrating tip/specimen combination, the compensation voltage ΔU and current measurement A

In industry the investigation of local corrosion damage by potential measurements is a very important method. Corrosion damage of metal constructions under ground may be detected by screening with two reference electrodes (Fig. 12.28). Similarly to the above discussion, localized corrosion of a pipeline will cause a spread of currents and related potential drops within the ground. The center of the damage may be found by two references which are in contact with the ground. One of these will be placed at different sites, thus measuring the potential difference as a function of location. The position of large potential differences should be close to the site of active corrosion damage.

The scanning Kelvin probe provides another possibility to investigate surface sites with varying elec-

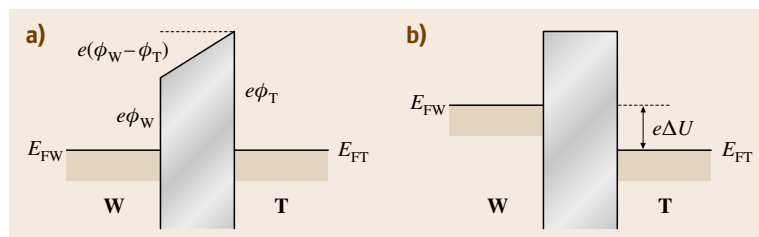


Fig. 12.30a,b Contact of specimen W and tip T with work functions $e\Phi_W$ and $e\Phi_T$ and (a) the resulting contact potential difference $e(\Phi_W - \Phi_T)$, (b) compensation of $e(\Phi_W - \Phi_T)$ by $e\Delta U$. E_{FW} and E_{FT} are the Fermi levels of the specimen and the tip

trochemical activity. Its application to surface studies is complementary to the two aforementioned methods for corrosion studies. Its advantage is that it enables a potential measurement without direct contact with the medium of interest. Two different metals, the working electrode W and a vibrating tip T in its vicinity, form a condenser (Fig. 12.29). Their direct contact in the outer circuit produces a contact potential difference which equals the difference of the work functions $e_0(\Phi_W - \Phi_T) = e_0\Delta\Phi$ of both metals (Fig. 12.30a). This potential difference $\Delta\Phi$ causes a small alternating current during the vibration of the tip to the surface of the working electrode due to the change of the capacity $C = \frac{\varepsilon\varepsilon_0 A}{d}$ with distance d according to (12.62). This current disappears when an externally applied voltage ΔU compensates $\Delta\Phi = (\Phi_W - \Phi_T)$ ((12.61), Figs. 12.29, 12.30b). Thus the difference of the work functions is measured by a disappearing current density i of a Kelvin probe. The work function is closely related to the energy of the Fermi level of a metal, which changes with the potential drop within the electrolyte in front of an electrode, i. e. due to charging of its dou-

ble layer. Any change of the potential drop across the electrode–electrolyte interface affects the work function and thus the compensating voltage of the Kelvin probe. With a vibrating small metal electrode T one may scan the electrode surface and thus measure the changes of the difference of the work functions of W and T as a function of its position and consequently the potential distribution in front of a corroding metal. The main advantage is the measurement of potential differences without making contact with the electrolyte in front of the electrode. This may be very important when the electrode–electrolyte interface is buried below a layer of polymer. For these cases the Kelvin probe allows one to follow electrochemical reactions and corrosion processes, including the delamination of polymer layers on metals via potential measurements that otherwise would not be accessible [12.49, 50]. Another example is atmospheric corrosion when only a very thin film of electrolyte covers the surface, to which one cannot easily make a conducting contact via the Haber–Luggin capillary of a reference electrode.

$$\Delta U_{\text{tot}} = e_0\Delta\Phi - \Delta U = e_0(\Phi_W - \Phi_T) - \Delta U = 0, \quad (12.61)$$

$$\frac{dC}{dt} = \frac{\varepsilon\varepsilon_0 A}{dd} = \frac{\frac{dQ}{dt}}{\Delta U_{\text{tot}}} = \frac{i}{\Delta U_{\text{tot}}}, \quad (12.61a)$$

$$i = \frac{dC}{dt} \Delta U_{\text{tot}} = \frac{\varepsilon\varepsilon_0 A}{dd} \Delta U_{\text{tot}} = 0. \quad (12.62)$$

12.2.14 Nonstationary Methods, Pulse Measurements

The sequence of several elementary reaction steps and their influence on the overall electrochemical corrosion process requires their separation. This could be done by electrochemical transient measurements. A very rapid change of the electrode potential leads to a sequence of reaction steps (Fig. 12.31) that may be separated in the time domain. The ohmic drop within the electrolyte between the reference electrode and the working electrode is established within less than a microsecond. This may be measured with fast galvanostatic transients. For this discussion a useful equivalent circuit for an electrode within the electrolyte consists of a capacity C in parallel to a charge-transfer resistance R_{CT} . A resistance R_Ω in series to this combination takes care of the electrolyte resistance between the Haber–Luggin capillary and the working electrode (Fig. 12.31). A galvanostatic pulse with a rise time in the range of about 100 ns may easily be applied between working and counter-electrode. As

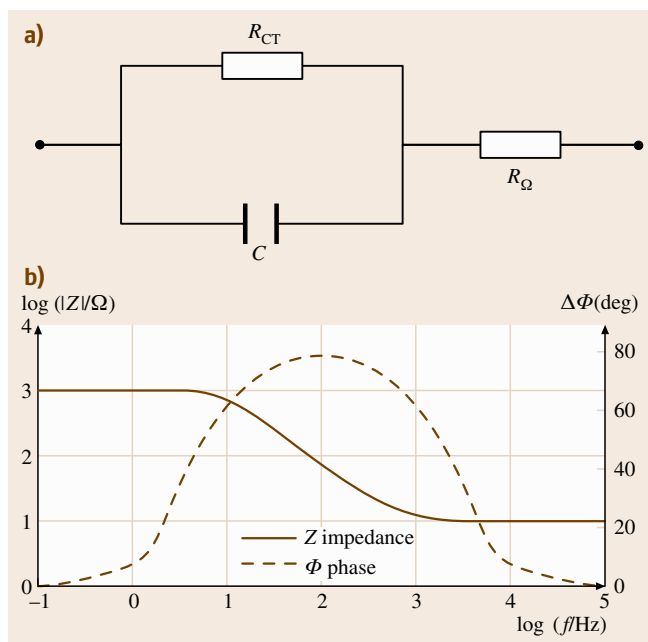


Fig. 12.31 (a) Equivalent circuit of an electrode surface with a double-layer capacity $C = 10 \mu\text{F}$, a charge-transfer resistance $R_{CT} = 1 \text{ k}\Omega$ and an ohmic resistance $R_\Omega = 10 \Omega$ within the electrolyte. (b) Bode diagram of the impedance Z in dependence on the frequency of the added alternating voltage (*solid*) and the related phase shift $\Delta\Phi$ (*dashed*)

a consequence the ohmic drop will be detected immediately, within less than $1 \mu\text{s}$. The subsequent charging of the double layer, i. e. of the capacity C with time causes an increase of the measured voltage across the equivalent circuit. Extrapolation of this voltage increase back to $t = 0$ yields at the intersection the ohmic drop ΔU_{Ω} , which should increase linearly with the galvanostatically applied current density i . The thus measured ohmic drop $\Delta U_{\Omega} = R_{\Omega}i$ may be used for an appropriate setting of the resistance R_{Ω} at the compensation unit of a potentiostat. Thus one may compensate ΔU_{Ω} automatically during potentiostatic transients, which increase proportionally to the current density i .

The electronic properties of the electrode–electrolyte interface and its related equivalent circuit may be determined by measurement of the impedance and its dependence on frequency, which is presented in Fig. 12.31 as a so-called Bode plot. For impedance measurements the electrode potential is varied by a small superimposed amplitude of a few mV in order to justify the approximation of the electrochemical system by the proposed equivalent circuit. A linear i – E relation in the sense of Ohm’s law is valid for small potential changes only. In general the i – E relation is exponential according to the Butler–Volmer equation of (12.26). Figure 12.31 also contains the phase shift $\Delta\Phi$. For the presented example $R_{\text{CT}} = 1 \text{ k}\Omega$, $R_{\Omega} = 10 \Omega$ and $C = 10 \mu\text{F}$ are chosen. These values are reasonable for the electrode–electrolyte interface. At low frequency ($\omega = 2\pi f$), i. e. below 1 Hz, the current passes the ohmic resistances leading to approximately $Z = R_{\text{CT}} + R_{\Omega}$ because the parallel capacitive resistance $1/\omega C$ becomes very large. The phase shift is vanishingly small. At very high frequencies of $f = 100 \text{ kHz}$ the capacitive resistance is very low with a short circuit across C . In this case the impedance equals R_{Ω} with $\Delta\Phi = 0$. At intermediate frequencies of $f = 100 \text{ Hz}$, $Z = 1/\omega C$ will hold approximately with a maximum of $\Delta\Phi$. In the example of Fig. 12.31a,b one obtains $1/\omega C = 100 \Omega$ for $f = 158 \text{ Hz}$, which refers to the maximum of the phase shift $\Delta\Phi$.

For potentiostatic transients one has to discuss a sequence of time ranges. Figure 12.32 presents an example for a rotating Au disc electrode in a solution of $0.5 \times 10^{-3} \text{ M}$, $\text{K}_3[\text{Fe}(\text{CN})_6]$ and $\text{K}_4[\text{Fe}(\text{CN})_6]$, which are dominated by the following processes: (1) charging of the double layer, (2) charge-transfer control of the electrode process (3) increasing diffusion control and (4) full diffusion control. This charge-transfer process of a redox system does not involve complicating chemical reaction steps within the electrolyte and adsorption

and desorption at the electrode surface (Fig. 12.11). Therefore it is still a relatively simple situation.

1. The charging of the double layer via the R_{Ω} – C combination in series occurs according to (12.63, 12.64). The total applied voltage is the sum of the potential drop at the ohmic resistance R_{Ω} and the capacity C of the double layer i. e. $\Delta U = \Delta U_{\Omega} + \Delta E$. With a typical capacity of $20 \mu\text{F}/\text{cm}^2$ for a free metal surface and a resistance of $R_{\Omega} = 0.1 \Omega \text{ cm}^2$ for a well conducting electrolyte at the short distance between the metal surface and the Haber–Luggin capillary of the reference electrode the charging of the double layer occurs with a time constant of $R_{\Omega}C = 2 \times 10^{-6} \text{ s} = 2 \mu\text{s}$. For potentiostatic transients the measured current density drops according to (12.63) and the voltage across the double layer, i. e. across the capacitance C , increases according to (12.64). After about $8 \mu\text{s}$ the electrode potential ΔE should be fully established. A larger R_{Ω} value will increase the time constant. This is the case for low-conductivity electrolytes. However in most cases the charging time for the double layer is short enough to follow corrosion processes with a sufficient time resolution

$$i = \frac{\Delta U}{R_{\Omega}} \exp\left(-\frac{t}{R_{\Omega}C}\right), \quad (12.63)$$

$$\Delta E = \Delta U \left[1 - \exp\left(-\frac{t}{R_{\Omega}C}\right)\right]. \quad (12.64)$$

2. After about $10 \mu\text{s}$ of double-layer charging one may measure the electrode reaction under charge-transfer control with the related charge-transfer overvoltage η_d . For these conditions the electrode process is ruled by the Butler–Volmer equation (12.26). If the current density is small enough no further complications are involved. This situation refers to the plateau currents in time range 2 of Fig. 12.32. The current density assumes a constant value of $10^{-2} \text{ A}/\text{cm}^2$ for about 0.3 ms , which corresponds to a charge of $3 \mu\text{C}/\text{cm}^2$ and thus to $3 \times 10^{-11} \text{ mol}/\text{cm}^2$ of $\text{K}_3[\text{Fe}(\text{CN})_6]$. For the $5 \times 10^{-4} \text{ M}$ solution this amount of reacting ions is within a layer of 600 nm . This distance is close to the mean diffusion path $\bar{x} = \sqrt{2Dt} = \sqrt{2 \times 5 \times 10^{-6} \times 3 \times 10^{-4}} = \sqrt{30 \times 10^{-10}} = 5.5 \times 10^{-5} \text{ cm} = 550 \text{ nm}$ of dissolved ions within the electrolytes.
3. If diffusion becomes rate-determining for a sufficiently large current density the change of the electrolyte composition immediately at the elec-

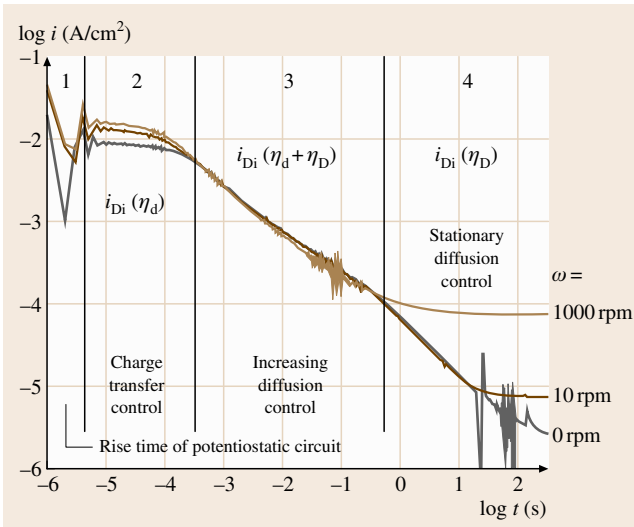


Fig. 12.32 Potentiostatic transient for an Au RDE, with the different time domains, change of i with the frequency of rotation $\omega = 2\pi f/(\text{min}^{-1})$

trode surface leads to a diffusion overvoltage η_D . Consequently the reaction rate becomes determined by the diffusion overvoltage after some time when the concentrations of the reacting species at the electrode surface deviate from their bulk values. If only the diffusion overvoltage is effective, Cottrell derived the current density as a function of time, as shown in (12.65) [12.51]. i depends exponentially on the diffusion overvoltage η_d and (12.65) is similar to (12.53), which holds for stationary conditions. For a potentiostatic transient i also depends on time with $1/\sqrt{t}$. The bulk concentration c_B and the diffusion constant D refer to a species that is involved in the electrode process and which causes diffusion overvoltage by its limited transport. It could be a reduced or oxidized species and the current density then refers to the anodic or cathodic process, respectively. Equation (12.65) is not valid for $t = 0$ because i goes to infinity for this condition. However, charge-transfer overvoltage cannot be excluded, which limits the current density for short times. This however, is not included in this treatment.

$$i = nF\sqrt{\frac{D}{\pi}}c_B \left[\exp\left(\frac{nF}{RT}\eta_D\right) - 1 \right] \sqrt{\frac{1}{t}}. \quad (12.65)$$

If both, charge transfer and diffusion are rate-determining the total overvoltage equals $\eta = \eta_d + \eta_D$. For these conditions the change of the current density for potentiostatic transients has been deduced as (12.66) [12.52, 53]. $i(0)$ is the current density for $t \rightarrow 0$ when the double-layer charging is finished and the concentration of any reacting species is still unchanged. This corresponds to (12.26) when diffusion control is still not effective. For short times, i. e. for $\lambda\sqrt{t} \ll 1$, the approximation of (12.67) has been derived which may be used to determine $i(0)$ from $i-\sqrt{t}$ plots of the current values of potentiostatic transients. Thus $i(0)$ is obtained by extrapolation of $i-\sqrt{t}$ plots to $\sqrt{t} \rightarrow 0$ for each electrode potential. The $i(0)$ values may then be compared to the polarization curve for pure charge-transfer control. For $\lambda\sqrt{t} \gg 1$ the approximation of (12.68) has been derived with a $t^{-0.5}$ dependence of i . This condition corresponds to dominant diffusion control. The double logarithmic plot of the current transient of Fig. 12.32 shows a slope $d \log i / d \log t = -0.5$. This result is expected for the $t^{-0.5}$ dependence of (12.65). A slope of -0.5 is also expected from the approximation of (12.68) for $\lambda\sqrt{t} \gg 1$

$$i = i(0) \exp(\lambda^2 t) \operatorname{erfc}(\lambda\sqrt{t}), \quad (12.66)$$

$$\lambda = \frac{i_0}{zF} \left[\frac{1}{c_{B,\text{Red}}\sqrt{D_{\text{Red}}}} \exp\left(\frac{\alpha z F}{RT}\eta\right) + \frac{1}{c_{B,\text{Ox}}\sqrt{D_{\text{Ox}}}} \exp\left(-\frac{(1-\alpha)zF}{RT}\eta\right) \right], \quad (12.66a)$$

$$i(0) = i_+ + i_- = i_0 \left[\exp\left(\frac{\alpha z F \eta}{RT}\right) - \exp\left(-\frac{(1-\alpha)zF\eta}{RT}\right) \right], \quad (12.26)$$

$$i = i(0) \left(1 - \frac{2}{\sqrt{\pi}} \lambda\sqrt{t} \right) \quad (\text{for } \lambda\sqrt{t} \ll 1), \quad (12.67)$$

$$i = i(0) \frac{1}{\sqrt{\pi} \lambda\sqrt{t}} \quad (\text{for } \lambda\sqrt{t} \gg 1). \quad (12.68)$$

- For times longer than 0.5 s the transients of Fig. 12.32 are in the regime of total diffusion control with a current density which depends on the rotation speed of the RDE. In this time range the current densities follow the $\sqrt{\omega}$ dependence according to the Levich equation (12.57) demonstrating the full diffusion control of the process.

12.2.15 Concluding Remarks

Corrosion within electrolytes or under the influence of thin electrolyte films is an electrochemical process. For an understanding of its leading mechanisms the application of electrochemical methods is a necessary requirement. They allow the simulation of corrosion phenomena under well-controlled electrochemical conditions with a systematic variation of the related parameters. For a detailed understanding of the mechanisms and the condition of the metal surfaces one needs additional information, which is obtained through the application of surface analytical methods. For a chemical analysis of corroding surfaces and surface films methods working in the ultrahigh vacuum such as x-ray photoelectron spectroscopy (XPS) [12.54, 55] or Auger electron spectroscopy (AES) [12.56] are valuable analytical tools that provide qualitative and quantitative information. The structure of surfaces and surface layers may be investigated with synchrotron methods such as x-ray diffraction (XRD) and x-ray absorption spec-

troscopy (XAS), which yield the parameters of the long- or short-range order of surfaces or surface films, respectively [12.57]. A direct image of surface structures even down to atomic resolution is obtained by the in situ application of scanning methods such as scanning force microscopy (SFM) and scanning tunneling microscopy (STM). There are numerous other in situ methods such as infrared (IR) or laser Raman spectroscopy, each of them having its specific advantages and providing some insight into a corroding system. All these methods together give information on the chemical composition, structure and the properties of surfaces and surface films. Electrochemistry remains incomplete and rather arbitrary without the surface methods, whereas these analytical tools without a detailed understanding of the electrochemical reactions and a well-controlled electrochemical specimen preparation give no reliable results. One therefore has to apply many of these methods in combination in order to get reliable results without too much speculation for the usually complicated systems in corrosion, whether in theory or practice.

12.3 Novel Electrochemical Test Methods

During the last 30 years new electrochemical techniques have arisen which give more and faster information about corrosion reactions and also provide data on corrosion in geometric orders at the nanoscale. Analyzing the dynamic behavior of a corrosion system requires special techniques, which are essentially different from conventional direct-current (DC) techniques (Sect. 12.1), such as measurement of the open-circuit potential, polarization curves, weight loss, or other physicochemical parameters. Based on linear system theory (LST), electrochemical impedance spectroscopy (EIS) is one of the most powerful techniques.

Electrochemical noise analysis (ENA) is a relatively new method. Stochastic fluctuations of the electrode potential or the cell current are often referred to as electrochemical noise, analogous to the word *noise*, indicating random fluctuations of incoherent acoustic or electrical signals. Noise analysis is a well-developed technique in many fields, and it is being applied increasingly to electrochemical systems, in particular in corrosion science and engineering.

Another important and widely used tool for corrosion investigations is the scanning electrode technique. The inherent advantage of scanning reference electrodes is the possibility to measure the initiation, distribution,

and rate of local corrosion processes in situ with spatial resolution down to 20 μm .

12.3.1 Electrochemical Noise Analysis

Within corrosion research, the analysis of electrochemical noise offers a simple, sensitive and virtually nondestructive measuring technique for assessment of the corrosion susceptibility of metallic materials and for the investigation of corrosion processes. The present status of knowledge concerning noise diagnostics in corrosion processes permits the application of this method not only to experimental tasks in the laboratory, but also to special problems in the context of practical corrosion monitoring. Furthermore, specific advantages of the technique enable its use to an increasing extent in supporting or improving conventional corrosion testing. The advantages here include obtaining additional information and shortening testing times, thus resulting in state-of-the-art corrosion testing.

ENA is an electrochemical method that offers great potential for measuring and monitoring localized corrosion. This technique needs no external signal to obtain corrosion data. The principle is based on the fact that two identical electrodes exposed to the same medium

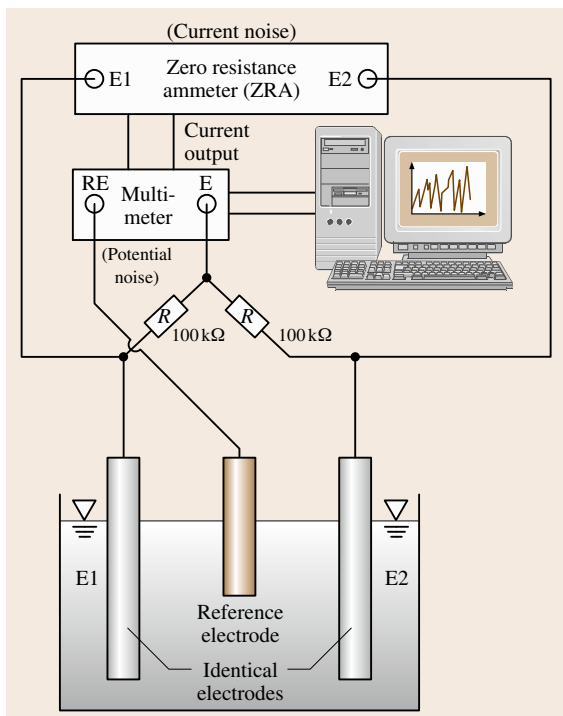


Fig. 12.33 Experimental set up for potential and current noise measurements

(environment) under free corrosion conditions show stochastic fluctuations of the open-circuit potential in the μV range and of the galvanic coupling current in the nA range, generated by corrosion reactions on the electrode surfaces [12.58–61]. These potential and current fluctuations are known as electrochemical noise.

The experimental set up for measuring electrochemical noise is relatively simple (Fig. 12.33). The two identical electrodes (made, e.g., from mild steel) are connected over a zero-resistance ammeter (ZRA), which feeds the current output (current noise) via a multimeter into a computer. The two electrodes can be connected over two ultraaccurate metal resistors ($100\text{ k}\Omega$ each) in series to provide an average potential point: since the resistance of the two resistors is much larger than the solution resistance (generally not more than $100\ \Omega$) no measurable disturbance is introduced into the system by the potential and current measurements. The potential between this average point and the reference electrode (e.g. Saturated Calomel Electrode (SCE)) is sampled. For potential and current measurements a 2 points/s sampling rate for 500 s (8.3 min) of mea-

suring time is sufficient. For corrosion monitoring this procedure will be repeated in appropriate time intervals.

Figure 12.34 shows potential and current noise versus time plots of mild steel in two cooling waters with different salt concentration [12.61]. Cooling water 2 contained higher chloride and sulfate levels, which obviously resulted in a significantly different fluctuation pattern of the electrochemical noise at mild steel in these two waters. The electrochemical noise signals can be processed in a digital or analogue manner. The digital signal-processing technique involves the acquisition of raw data and their subsequent numerical analysis, while the analog processing method produces an output signal proportional to the root mean square (RMS) of the noise using electronic filters and amplifiers. From these data the noise resistance R , can be defined as

$$R_n = \delta V / \delta I, \quad (12.69)$$

where δV is the RMS of the corrosion potential fluctuation and δI is the RMS of the current fluctuation [12.62, 63].

Data processing can also include transformation in the frequency-domain (spectral density) curves using the maximum-entropy method (MEM) or fast Fourier transformation (FFT). The MEM inherently produces smoother spectra without apparent loss of information [12.64] and is simpler to use when the number of data points is not a power of two. Analysis in the frequency domain needs simultaneous collection of potential and current noise data.

With FFT the spectral noise response $R_{sn}(f)$ can be calculated at each frequency f by

$$R(f) = V(f)/I(f) \quad \text{and} \quad (12.70)$$

$$R_{sn} = |R(f)| = \left[R(f)_{re}^2 + R(f)_{im}^2 \right]^{1/2}, \quad (12.71)$$

where $V(f)$ and $I(f)$ are complex numbers obtained from the FFT. The spectral noise resistance R_{sn} is defined as the value of

$$R_{sn}(f) \quad \text{at} \quad f = 0, \quad (12.72)$$

$$R_{sn}^0 = \lim_{f \rightarrow 0} [R_{sn}(f)]. \quad (12.73)$$

An analysis in the frequency domain can yield information on the type of corrosion at the electrodes.

The electrochemical current-noise power-spectral density [PSD(I)] at high frequencies (100–1000 MHz) can be indicative for general corrosion while the shape and the repetition rate of transients of the electrochemical potential and current determine the type of corrosion [12.61]. The slope of the power-spectrum den-

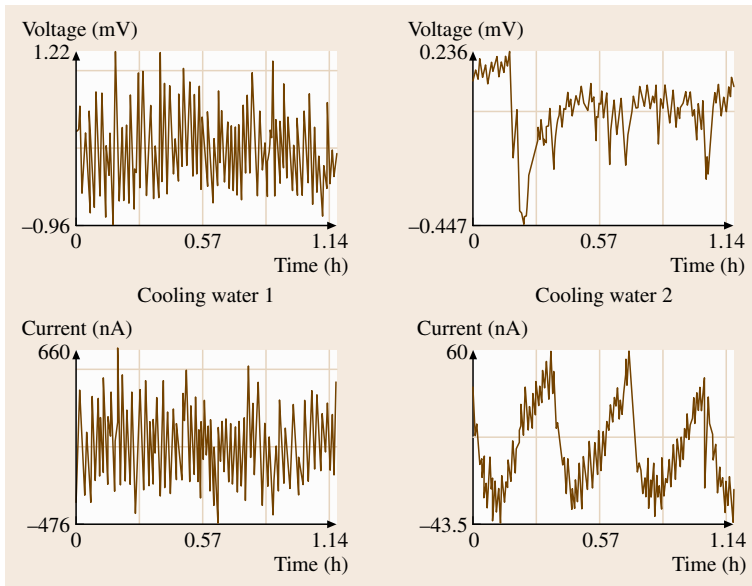


Fig. 12.34 Potential and current noise at mild steel in different cooling waters (after [12.61])

sity of the electrochemical voltage-noise relationship [PSD(U)] after the removal of the linear trend was recognized as a significant parameter for distinguishing between uniform and local corrosion. The electrochemical noise generated by uniform corrosion is, white noise, and therefore the slope is close to zero. Electrochemical noise generated by localized corrosion consists of

exponentially decreasing transients and the slope of the PSD(U) curve is higher ($> 12 \text{ dB (V}^2 \text{ Hz}^{-1}) \text{ decade}^{-1}$). Figure 12.35 shows PSD(U) graphs that, for the uniformly corroding steel in cooling water 1, the slope is $6.3 \text{ dB (V}^2 \text{ Hz}^{-1}) \text{ decade}^{-1}$, while the slope is $15.3 \text{ dB (V}^2 \text{ Hz}^{-1}) \text{ decade}^{-1}$ at the locally corroding steel in cooling water 2.

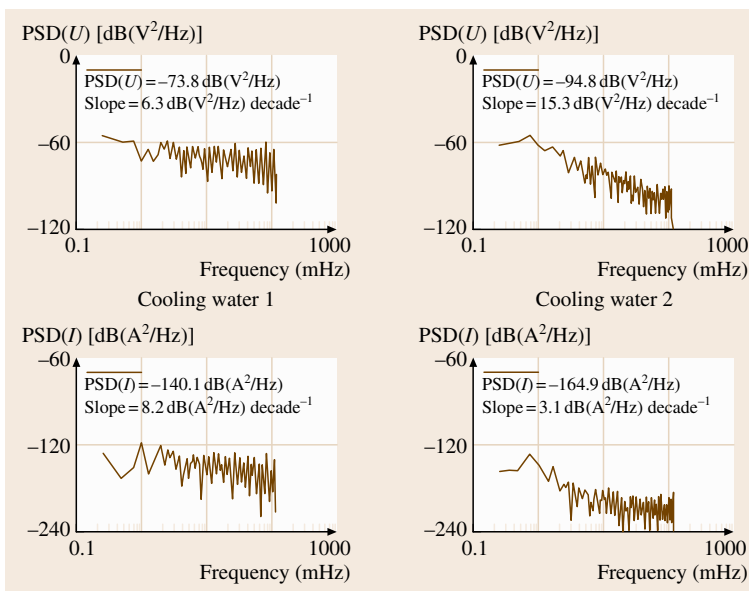


Fig. 12.35 Power-spectral density (PSD) for potential and current noise at mild steel in different cooling waters (after [12.61])

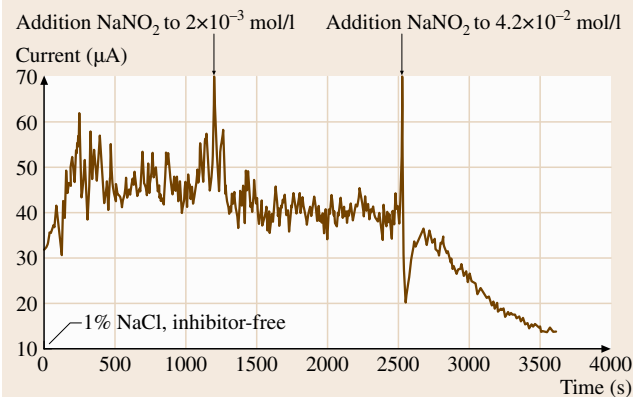


Fig. 12.36 Current noise plot of mild steel in air saturated 1 mass % NaCl solution. Effect of NaNO₂ concentration

Similar results were obtained with Admiralty brass, which generally showed only localized corrosion but with a higher initiation rate of pits in cooling water 2.

These and other results reported in the literature allow one to conclude that ENA can be used for corrosion monitoring with the possibility of distinguishing between uniform and local corrosion.

However, it has been shown [12.65–67] that measuring only potential noise can be misleading in cases where small fluctuations in mass-transport control can produce large changes in the corrosion potential U . Such is the case for metals and alloys that are immune to corrosion such as Pt or are passive, such as stainless steel in neutral, aerated aqueous solutions; e.g. it was found that potential noise plots, as analyzed with the use of power-spectral density (PSD), were similar for Pt and for an Al/SiC metal matrix composite, which pits severely in aerated 0.5 N NaCl. However, the current-noise PSD plots were very different for the two materials. The explanation is that mass transport of oxygen can play a large role in potential noise.

For corrosion monitoring, specifically large-scale corrosion monitoring and field testing, the statistical analysis of noise data resulting in RMS values has many advantages over spectral analysis by FFT or MEM which requires expensive equipment and/or complicated analysis programs. It was shown [12.65] that the noise resistance R_n and the polarization resistance R_p have similar values and trends; therefore theoretical relationships between R_n and R_p are currently investigated. Thus for cases where only qualitative results are needed in a fast, simple and inexpensive way, collection and evaluation of R_n data is sufficient. However, a quan-

titative understanding of electrochemical noise and its relationship to corrosion, specifically to localized corrosion phenomena, can only be achieved through spectral analysis of noise data, leading to the determination of the spectral noise resistance R_{Sn} which shows very strong relations between R_n and R_p [12.66, 67]. The pitting index (PI) defined as

$$PI = \delta I / I_{\text{mean}}, \quad (12.74)$$

where δI is the RMS current noise and I_{mean} the mean coupling current [12.63], appeared not to be applicable for all corrosion systems for the determination of the nature of the corrosion mechanism, specifically localized corrosion; e.g. for the system steel/aqueous salt solution the PI gave misleading results [12.66, 67]. This can be understood considering that I_{mean} in the above definition equation should be close to zero for all cases of uniform corrosion. PI can therefore show large fluctuations independent of the actual corrosion mechanism.

ENA seems to be very useful for investigation of corrosion-inhibitor performance. The great advantage is that only two metal electrodes are necessary to measure a current signal, which indicates high or low general corrosion rates and susceptibility to pitting and other localized corrosion. Figure 12.36 gives an example how in a very short time the critical concentration of a dangerous anodic inhibitor (NaNO₂) for steel corrosion in aerated 1% NaCl solution can be evaluated. In this example two identical mild-steel electrodes were placed in the inhibitor free brine. In the first 20 min considerable current fluctuation indicates typical oxygen corrosion of the steel electrodes. Addition of 2×10^{-3} mol/l NaNO₂ reduces the noise, however, the noise level indicates insufficient inhibition. After another 20 min more NaNO₂ is added to make a NaNO₂ concentration of 4.2×10^{-2} mol/l, which is above the critical concentration of NaNO₂. Consequently the current noise ceases nearly completely, indicating complete inhibition. ENA technology today is advanced enough to be used as a monitoring device for critical inhibitor concentration and the start of localized corrosion.

ENA can also be applied in media with low conductivity and also in multiphase media because, in contrast to other electrochemical methods, it needs no reference electrode which could give measuring problems due to high IR drops and – specifically in oil/water mixtures – plugging or sealing of the diaphragm. In technical systems the life of the reference electrode is also determined by the tendency of the test media to contaminate the electrolyte in the electrode.

12.4 Exposure and On-Site Testing

There is a considerable number of sources of material testing data that have been accumulated over the years and are available to process plant designers to assess the most suitable materials selection for a particular plant and operating conditions. However, many of the factors involved in the selection of an optimum choice are subject to variability, and this makes the choices more complex.

The ranking of the most valuable corrosion data for plant designers is generally understood to be as follows.

1. Operating experience on full-scale equipment under the actual process environment.
2. Operating experience on a pilot plant with similar feedstock and operating conditions.
3. Sample tests in the field, coupons, electrical resistance (ER) probes, or stressed samples exposed to the process environment.
4. Laboratory evaluations on actual plant fluids, or simulated environments.
5. Materials and corrosion database.

It should also be recognized that the economics of the various material selection choices is not constant. A decision that makes economic sense at the design time, or at the materials selection time, may not make sense by the time the plant is actually built or operating. In addition, the economics of plant shutdowns due to failure can depend on the market for the product being generated by the plant, although these costs are generally always upward.

The balance between choice of a more-expensive corrosion-resistant alloy versus the cost of subsequent chemical treatment costs to inhibit corrosion is also subject to change, due to changes in the raw material costs of chromium, nickel, and other constituents in corrosion-resistant alloys. Sometimes a less-expensive

material that would otherwise be unacceptable due to low corrosion resistance can still be the best choice when used with chemical corrosion inhibitors.

Corrosion testing may be conducted in the laboratory, pilot plant, or field. Systems that are either in the design phase or operating benefit from laboratory and pilot plant testing. In situ testing is useful for pilot plant testing and for providing information for systems that are currently operating.

Laboratory tests should simulate the water chemistry and operating conditions of the freshwater system. A sample of water from the system may be used if it is available. Immersion testing and electrochemical testing (Sect. 12.1) are commonly used for laboratory tests.

In situ testing is commonly conducted in pilot plants. This testing is useful in evaluating or monitoring a water-treatment system or the effects of varying operating parameters such as flow rate and temperature. In addition, the performance of different alloys in a system may be studied by in situ testing. In situ testing provides information on uniform corrosion rate, types of corrosion, and pitting tendencies (Sect. 12.4).

In situ testing is also performed in the field to determine the effectiveness of a water treatment system, the performance of different alloys, and the effects of varying operating parameters such as flow rate and temperature. Uniform corrosion rates, types of corrosion, and pitting tendencies are identified with in situ testing.

Another form of testing the corrosion behavior especially for coatings is atmospheric exposure under various climatic conditions. This type of testing yields more reliable information on the corrosion behavior than testing in climatic chambers. A disadvantage is the long duration of such tests. For reasons of practicability a mixture of laboratory testing and exposure under natural environmental conditions is recommended.

12.5 Corrosion Without Mechanical Loading

By taking into consideration the different causes of corrosion and their mechanisms, as well as the appearance of the attack, one can differentiate between several types of corrosion. A common approach is to distinguish between corrosion systems with or without mechanical loading. In the latter case the result of corrosion is the initiation and propagation of cracks. If only corrosion takes place and there is

no conjoint action of mechanical loading the various forms of corrosion occurring in such systems can either be described as local or uniform. Also corrosion testing is different if mechanical loads have to be included in the test set up. Therefore this section is specifically dedicated to types of corrosion where mechanical loading is unavailable in the system.

Table 12.2 Corrosion rate conversion

	mA/cm²	mm year⁻¹	mpy	g m⁻² day⁻¹
mA/cm ²	1	3.28 <i>M/nd</i>	129 <i>M/nd</i>	8.95 <i>M/n</i>
mm year ⁻¹	0.306 <i>nd/M</i>	1	39.4	2.74 <i>d</i>
mpy	0.00777 <i>nd/M</i>	0.0254	1	0.0694 <i>d</i>
g m ⁻² day ⁻¹	0.112 <i>n/M</i>	0.365/ <i>d</i>	14.4/ <i>d</i>	1

where: mpy = milliinch per year

n = number of electrons freed by the corrosion reaction

M = atomic mass

d = density

Note: you should read the table from left to right, i. e.:

$$1 \text{ mA/cm}^2 = (3.28M/nd) \text{ mm year}^{-1} = (129M/nd) \text{ mpy} = (8.95M/n) \text{ g m}^{-2} \text{ day}^{-1}$$

For example, if the metal is steel or iron (Fe), *n* = 2, *M* = 55.85 g and *d* = 7.88 g cm⁻³ and the table of conversion becomes

	mA/cm²	mm year⁻¹	mpy	g m⁻² day⁻¹
mA/cm ²	1	11.6	456	249
mm year ⁻¹	0.0863	1	39.4	21.6
mpy	0.00219	0.0254	1	0.547
g m ⁻² day ⁻¹	0.00401	0.0463	1.83	1

Note: you should read the table from left to right, i. e.: 1 mA/cm² = 11.6 mm y⁻¹ = 456 mpy = 249 g m⁻² day⁻¹

12.5.1 Uniform Corrosion

Uniform corrosion is given when a metal is corroding with the same rate over the whole surface of the metal exposed to the corrosive environment. The extent can be given by the weight loss per unit area or the average penetration, which is the average of the corrosion depth. This can be determined by direct measurement or by calculation from the weight loss per unit area when the density of the material is known. Uniform corrosion takes place as a rule via the effect of corrosion cells without clearly defined anode and cathode surfaces. A prominent case for uniform corrosion is the rusting of railways due to atmospheric exposure. From a technical standpoint uniform corrosion is quite easy to handle because the design engineer must only include an additional thickness to the material which equals the loss due to corrosion over the life time of the structure.

Uniform corrosion rates may be determined by weight loss or electrochemical methods. Both methods average a specimen's corrosion rate over its surface area. Corrosion rates calculated from weight-loss data also average the loss over the exposure period. Electrochemical methods may yield instantaneous or time-averaged corrosion rates. Weight-loss testing is performed by immersing a coupon in a test solution either in the laboratory or in situ. Another method is

exposing a metal or a coated specimen to a specific environment (atmosphere) or a climatic chamber and measure the corrosion loss over a certain period of time. It should be noted that measurements carried out in climatic chambers very rarely correspond to the behavior of a material under practical conditions. Therefore investigations in the laboratory are mostly advisable for comparing different materials and give a ranking on their sensitivity to corrosion in a laboratory environment than to get reliable information on their performance in service.

There is a correlation between the electrical parameters and the weight loss of the material. Table 12.2 yields information how the values correspond. The following charts provide a simple way to convert data between the most common corrosion units in usage, i. e. corrosion current (mA/cm²), mass loss (g/(m² day)) and penetration rates (mm/y or mpy) for all metals or for steel.

Another important factor for determining uniform corrosion and its rate of corrosion is the removal of corrosion products from the surface to measure the corrosion loss in weight units.

There are a large number of chemical solutions available for the different materials used in practice to remove oxide layers from surfaces. Table 12.3 yields information on typical solutions for various materials.

Table 12.3 Some solutions used to remove corrosion products from metals

Metal	Corrosion products	Reagents and temperature
Iron and steel	FeO; Fe ₂ O ₃ × H ₂ O; Fe ₃ O ₄ × H ₂ O	1. HCl (20–25%) + 0.8–1% PB-5 inhibitor 2. 0.151 H ₂ SO ₄ (specific gravity 1.84) + 0.85 IH ₂ O + 1% PB-5 or PB-8 inhibitor 3. 10% ammonium tartrate + NH ₄ OH, 25–70 °C 4. 10% ammonium citrate + NH ₄ OH, 25–70 °C 5. 10% H ₂ SO ₄ + 1% As ₂ O ₃ , 25 °C 6. 5% NaOH + Zn (granulated or turnings), 80–90 °C, 30–40 min
Zinc-coated iron, zinc	Zn(OH) ₂ ; ZnCO ₃ ; ZnO; ZnCO ₃ × 2ZnO × 3H ₂ O; ZnCO ₃ × 3Zn(OH) ₂	1. 10% ammonium persulfate 2. Saturated CH ₃ COO(NH ₄)
Lead	PbO; PbSO ₄ ; Pb(OH) ₂ 2PbCO ₃ × Pb(OH) ₂	1. Saturated CH ₃ COO(NH ₄) 2. 1% CH ₃ COOH, boiling 3. 80 g/l NaOH + 50 g/l mannite + 0.62 g/l hydrazine sulfate
Tin	SnO ₂ ; SnO	1. 5% HCl 2. 15% solution of neutral sodium phosphate
Copper and its alloys	Cu ₂ O; CuO; Cu(OH) ₂ CuSO ₄ × 3Cu(OH) ₂ ; CuCO ₃ × Cu(OH) ₂	1. 5% solution of H ₂ SO ₄ 2. 18% HCl
Aluminum and its alloys	Al ₂ O ₃ ; Al(OH) ₃	1. 5% HNO ₃ 2. 5% HNO ₃ (specific gravity 1.4) + 1% H ₂ Cr ₂ O ₇ 3. 65% HNO ₃ 4. 20% orthophosphoric acid + 8% CrO ₃
Magnesium	MgO; MgCO ₃	1. 20% CrO ₃ + 1% AgNO ₃ , boiling solution, 1 min

12.5.2 Nonuniform and Localized Corrosion

In contrast to uniform corrosion nonuniform or localized corrosion is corrosion attack that is preferentially concentrated on discrete sites of the metal surface exposed to the corrosive environment. Localized corrosion can result in, for example, pits, cracks, grooves or scars. In any case it is the occurrence of a local nonuniform attack due to the build up of corrosion cells over the metal, which means a local and uneven distribution of anodic and cathodic sites over the metal surface. What makes the case worse is the comparatively high corrosion rate at the anodic sites and, especially in pitting or crevice corrosion, self-accelerating processes occur in the course of the corrosion process. Therefore pitting and crevice corrosion are the most prominent and dangerous forms of corrosion attack as well as intercrystalline corrosion which can be encountered along or in the vicinity of grain boundaries.

Pitting

Pitting is localized corrosion which results in pits in the metal surface (Fig. 12.37). This type of corrosion gener-

ally takes place in corrosion cells with clearly separated anode and cathode surfaces. The anode is situated in the pit and the cathode usually on the surrounding surface (Fig. 12.38). Pitting usually results in worse damage than uniform corrosion because it can lead to perforation in a very short period of time.

When evaluating attack caused by pitting the following should be taken into account

- the number of pits per unit area,
- the diameter of the pits, and
- the depth of the pits.

The number of pits per unit area and the pit diameter are easily determined by comparison with a pictorial standard. In the case of pit depth it is usually the maximum depth that is determined. In some cases this means the depth of the deepest pit observed on the sample examined, but in others the mean value of, for example, the five deepest pits. The depth of the pits can be measured with a microscope by focusing first on the bottom of the pit and then on the surface of the uncorroded metal. In this way the distance between the two focusing levels is obtained. The depth of pitting can also be determined

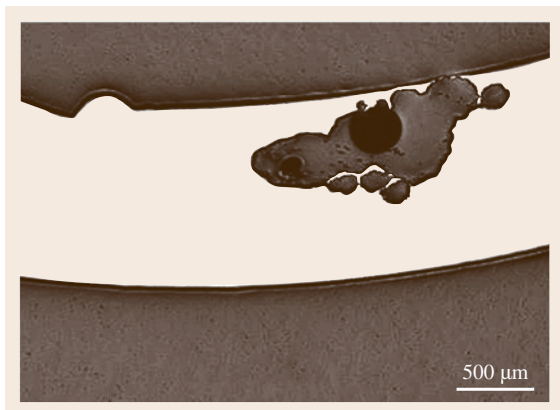


Fig. 12.37 Pitting in stainless steel

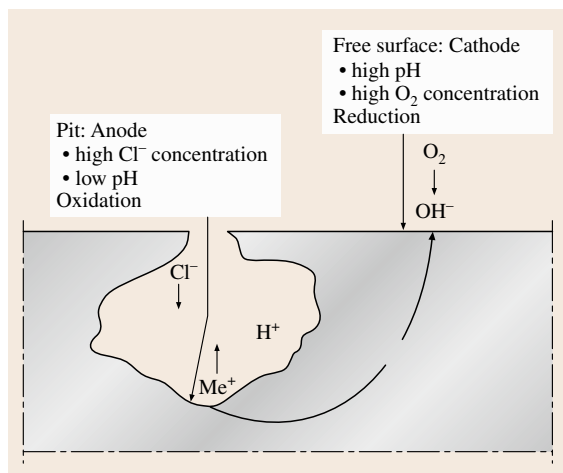


Fig. 12.38 Principle of pitting corrosion

with a micrometer or by cutting a cross section through the pit followed by direct measurement – possibly with the aid of a microscope.

The ratio of the maximum pit depth (P_{\max}) and the average penetration (P_{aver}) is called the *pitting factor* (F) (Fig. 12.39)

$$F = \frac{P_{\max}}{P_{\text{aver}}} \quad (12.75)$$

Pitting can occur in most metals. Amongst passivated metals this type of corrosion is initiated only above a certain electrode potential, the *pitting potential*.

Especially stainless steels where the protective effect results from passivation of the steel are prone to pitting under certain environmental conditions. Stainless steels are iron-based alloys in which chromium is the main alloying additive at a concentration of at least

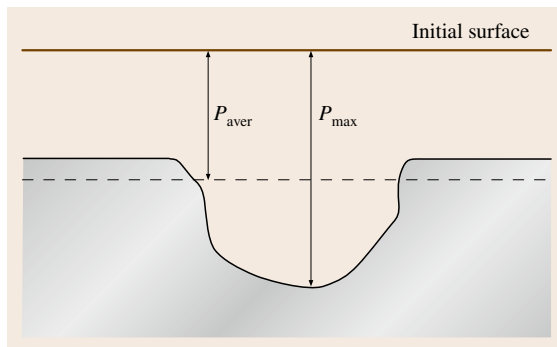


Fig. 12.39 Pitting factor $F = P_{\max}/P_{\text{aver}}$ (after [12.10])

12%. Because of the chromium content, stainless steels are easily passivated and hence have good corrosion resistance in many of the more common environments. In unfavorable conditions, however, even stainless steels can be subject to, for example, uniform corrosion, pitting, crevice corrosion, intergranular corrosion or stress corrosion cracking.

One can distinguish between different types of stainless steels depending on their structure, e.g. ferritic, austenitic and ferritic–austenitic steels. Differences in structure convey differences in corrosion characteristics and even differences in weldability, hardening capacity and magnetic properties. Ferritic and ferritic–austenitic steels are magnetic in contrast to pure austenitic steels.

The Active and Passive States

The conditions for passivation are shown in the anodic polarization curves of the steels. If, in the case of a stainless steel in sulphuric acid solution, the electrode potential is increased then the current density rises to a maximum, with dissolution of the metal taking place in the *active state*; the current density is an expression of the dissolution rate. At a certain potential, the *passivation potential*, the corrosion current density is drastically reduced and the metal surface becomes *passivated*. Passivation is associated with the formation of a thin, protective coating which largely consists of a mixed iron–chromium oxide and hydroxide. If the potential is further increased to very high values the current density will increase again as a result of, so-called, *transpassive corrosion*.

Mechanism of Pitting and Crevice Corrosion

When using stainless steel in an environment with a high chloride content, such as sea water or the bleaching liquors used in the pulp industry, *localized corrosion* will often occur in the form of pitting – which can some-

times result in perforation of pipe walls – or in the form of *crevice corrosion*, e.g. in flanged joints. These two corrosion types are related.

Stainless steels are sensitive to localized corrosion, especially in the presence of halogen ions. Amongst these the chloride ion is the most corrosive and also of greatest practical importance.

Addition of sulphide considerably increases the corrosiveness of the environment and may take place, e.g. due to the dissolution of sulphide inclusions in the steel surface.

Pitting in stainless steel also affects the shape of the anodic polarization curve. Thus, if the potential is increased above a certain critical value, referred to as the breakdown potential, the current density will begin to increase and the curve often shows thereafter a series of current peaks. Since this rise marks the beginning of pitting the breakdown potential is in this case called the *pitting potential*. If the potential is then decreased, passivation is achieved again, but only when a *protection potential*, which is a little below the pitting potential, is reached. A similar development occurs with corrosion in crevices or under surface deposits. The existence and value of the pitting potential can be demonstrated by using an auxiliary electrode and an applied voltage. In practice, the presence of an oxidizing agent, e.g., oxygen, chlorine or peroxide, in the solution is often sufficient to raise the potential to the pitting value with consequent attack. The breakdown potential is not a well-defined constant but depends to a large extent on conditions such as chloride concentration, temperature and the method of measurement.

Localized corrosion is observed only after a certain incubation time during which the initiation of the attack takes place. This is followed by the propagation stage and the growth of the pit. Both initiation and propagation take place by a mechanism which involves electrochemical corrosion cells.

Many mechanisms have been proposed for the *initiation stage*. In some the initiation can consist of a new, unpassivated metal surface being created as a result of the dissolution of sulphide or sulphide/oxide inclusions in the surface. This could then lead to an acidic solution containing a high sulphide content developing in the incipient cavities; these conditions would not allow passivation of the stainless-steel surface to occur at these sites. In other cases, initiation can be associated with depletion of oxygen in a crevice or under a deposit. This would give rise to an oxygen concentration cell with the anode in the crevice or under the deposit, and the cathode outside these regions. Hydrolysis of an-

odically dissolved metal ions in the various situations gives rise to acidic, unpassivating conditions at anodes.

When localized attack has been initiated and the growth has reached steady-state conditions then the process can be said to have reached the *propagation stage*. Certain characteristic conditions now prevail in the pit, as detailed below.

The pH value is lower than in the bulk of the solution because anodically dissolved metal ions, such as Fe^{2+} and Cr^{3+} have been hydrolyzed with the formation of oxides, hydroxides or hydroxide salts, thus releasing hydrogen ions. The actual pH value will depend on the composition of the steel and will be lower the more corrosion resistant the steel. Often a pH value of 0–1 can arise.

The solution in the pit has a higher chloride concentration than the bulk of the solution. This is because chloride ions migrate against the electric current in through the mouth of the pit. In practice a chloride concentration as high as 5 M can occur in the pit.

The resistance of stainless steels towards localized corrosion can be *evaluated* by

- determination of the breakdown potential, i.e. the pitting potential or crevice corrosion potential; this can be done by recording the anodic polarization curve in a solution of chloride (American Society for Testing and Materials (ASTM) G 61),
- determination of the critical pitting temperature (*cpt*) and the critical crevice corrosion temperature (*cct*); the *cpt* or *cct*, is the lowest temperature at which attack takes place, while maintaining the stainless steel at a constant potential.
- total immersion testing in a suitable corrosive agent, e.g. ferric chloride solution (ASTM G 48), followed by measurement of the maximum pit depth; in this type of test an elastic string or plastic disc is pressed against the test piece and the depth of attack is measured at the points of contact after the exposure period.

Crevice Corrosion

Corrosion which is associated with a crevice and which takes place in or immediately around the crevice, is called *crevice corrosion*. In some cases crevice corrosion can simply be caused by corrosive liquid being held in the crevice, while surrounding surfaces dry out. If the crevice and the surrounding metal surfaces are in a solution, the liquid in the crevice can be almost stagnant. As a result of corrosion in the crevice the conditions there can be changed; for example, the pH value can decrease

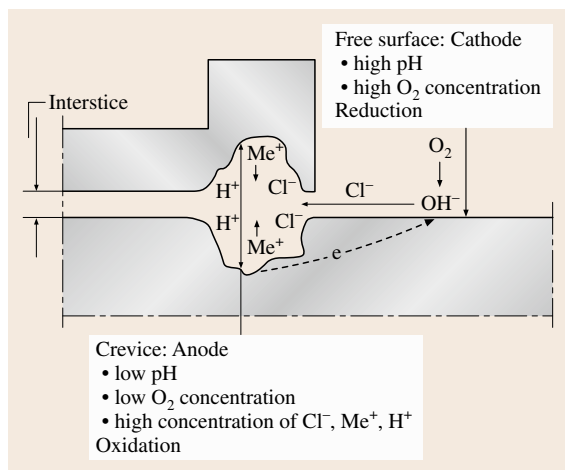
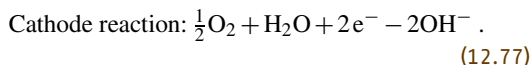


Fig. 12.40 Principle of crevice corrosion

and the concentration of chloride increase, and as a consequence the corrosiveness can be higher in the crevice than outside (Fig. 12.40).

When stationary conditions have been established, anodic attack of the metal usually takes place near the mouth of the crevice, while cathodic reduction of oxygen from the surroundings takes place on the metal surfaces outside



Crevice corrosion can take place in most metals. The risk of crevice corrosion should be especially heeded with passive metals, e.g. stainless steel.

Crevice corrosion not only takes place in the crevices between surfaces of the same metal, but also when the metal is touching a nonmetallic material. A combination of crevice corrosion and bimetallic corrosion can take place when two different metals form a crevice. The presence of Cl⁻, Br⁻ or I⁻ ions generally accelerates this type of corrosion. As in the case of pitting, crevice corrosion is initiated only above a certain electrode potential.

Deposit Corrosion

Corrosion which is associated with a deposit of corrosion products or other substances and which takes place under or immediately around the deposit is called *deposit corrosion*.

This type of corrosion is caused by moisture being held in and under the deposit. Because the movement of water is poor, corrosive conditions can be created under the deposit in a similar way to that described in crevice corrosion. The result is that a corrosion cell is formed with the anode under the deposit and the cathode at, or just outside, the edge.

Deposit corrosion is found, for example

- under the road-mud in the wheel arch of a car,
- under leaves which have collected in guttering, and
- under fouling on ships' hulls and in sea-water-cooled condensers.

Selective Corrosion

Selective corrosion can be found in alloys and results from the fact that the components of the alloy corrode at different rates.

The most well-known example of selective corrosion is the *dezincification* of brass. During dezincification the zinc is dissolved selectively, while the copper is left as a porous mass having poor structural strength. Similar corrosion processes are the *dealuminization* of aluminum bronze and the *selective dissolution of tin* in phosphor bronze.

Graphitic corrosion in grey cast iron provides another example of selective corrosion where the metallic constituents of the iron are removed. The remaining graphite allows the object concerned to maintain its shape but its strength and weight are severely reduced.

Intergranular Corrosion

Intergranular corrosion means corrosion in or adjacent to the grain boundaries of the metal. Metals are usually built of crystal grains. When a metal solidifies or is heat treated, several processes take place which cause the grain-boundary region to take on other corrosion characteristics than the main mass of the grain.

Intergranular corrosion can occur in most metals under unfavorable conditions. Most well known is intergranular corrosion in stainless steel (Fig. 12.41) as a consequence of chromium carbide formation when the carbon concentration is too high and unfavorable heat treatment has occurred, e.g. in the heat-affected zone along a weld.

Intergranular corrosion can occur in certain types of stainless steel which have a high carbon content (0.05–0.15% C). This can take place if the stainless steel is heat treated so that chromium carbide precipitates in the grain boundaries and the material is subsequently

exposed to an acidic solution or sea water. The precipitation of chromium carbide takes place only under certain conditions, for austenitic steel this is in the temperature range 550–850 °C. The steel is then said to be *sensitized*. The carbide precipitation results in a narrow zone near the grain boundaries becoming so depleted in chromium that the steel loses its stainless character.

Sensitization is not restricted to manufacturing heat-treatment processes. It can also occur as a result of welding, since a region of the metal near the weld will pass through the above temperature range. On exposure to a corrosive environment the chromium-depleted zones, together with the remaining parts of the grains, form corrosion cells. In these the chromium-depleted metal acts as the anode and is attacked, resulting in intergranular corrosion.

Intergranular corrosion does not usually influence the shape of the object but the strength characteristics can be catastrophically reduced. In a chloride environment, e.g. sea water, the attack can be visible as pitting. Intergranular corrosion also results in the loss of metallic sound when the affected component is struck.

Countermeasures are designed so as to counteract the precipitation of chromium carbide, which is the cause of the sensitization. The following possibilities exist.

- The choice of stainless steel with a low carbon content ($< 0.05\%$ or preferably $< 0.03\%$),
- The choice of steel which has been *stabilized* by the addition of titanium or niobium, which bind the carbon as carbides so that the formation of chromium carbide is prevented,
- The shortest possible time at 550–850 °C and
- *Solution heat treatment*; the material is heated to about 1050 °C to dissolve precipitates of chromium carbide that have formed, followed by subsequent rapid cooling so that new chromium carbide precipitates have no time to form.

The resistance of stainless steel to intergranular corrosion can be evaluated through

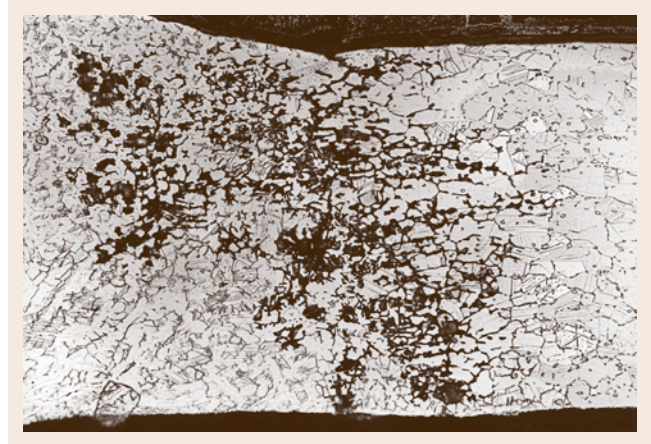


Fig. 12.41 Intercrystalline corrosion

- *Strauss test* (ASTM A 262 practice E); the test piece is exposed to a boiling copper sulphate solution containing sulphuric acid and metallic copper; after exposure the test piece is deformed by bending, and the surface is then examined for cracks,
- *Streicher test* (ASTM A 262 practice B); the test piece is exposed to a boiling ferric sulphate-sulphuric acid solution for 120 h; after the exposure the weight loss of the test piece is determined, and
- *Huey test* (ASTM A 262 practice C); the test piece is exposed to a boiling 65% nitric acid solution; evaluation consists of determining weight loss; Huey testing is particularly significant for material that is to be used in strongly oxidizing media.

Layer Corrosion

With *layer corrosion* the attack is localized to internal layers in wrought metal. As a rule the layer is parallel to the direction of processing and usually to the surface. The attack can result in the unattacked layers becoming detached and looking like the pages in a book. But the result can also be the formation of blisters swelling the metal surface, because of the voluminous corrosion products. Layer corrosion is rather unusual. It is best known amongst certain aluminum alloys.

12.6 Corrosion with Mechanical Loading

When investigating corrosion systems it is advisable to distinguish between corrosion systems where no external mechanical load is applied or residual stresses are present and systems which include influences of me-

chanical stresses. The distinction is useful because the forms of corrosion involved are different from their appearance as well as their mechanistic background. The same considerations apply for the test methods. Testing

of corrosion systems where mechanical stress is part of the environmental conditions the metal is subjected to means to study the influence of additional parameters, e.g. mechanical stress or strain, which may be supplied to the material in a static or dynamic regime. In summary this requires the study of the interaction of all parameters involved and very often the mechanical parameters are of higher importance with respect to the corrosion behavior than the electrolytic conditions.

There is also completely different equipment and evaluation of test data. The introduction of mechanical stresses into the test system needs an apparatus to supply stresses or strains to the system in a static or dynamic manner and the type of specimen may be smooth, notched or precracked, depending on the specific parameter to be studied (crack initiation or propagation).

12.6.1 Stress Corrosion

General

Stress corrosion cracking means crack initiation and propagation in the presence of certain corrosive media under static tensile stresses. In some cases residual stresses within the material are sufficient to initiate this form of corrosion. Contrary to most other manifestations of corrosion, the failure, due to a sudden brittle fracture, often occurs without formation of detectable corrosion products and is not necessarily characterized by any previously occurring visible damage.

For assessing the corrosion, parameters of the medium as well as of the material are important. In practice, where complex corrosion conditions often exist, adequate knowledge of the corrosion process is therefore required in the evaluation of failures. Stress corrosion cracking can be subdivided into an initiation and a propagation process. In theory, such a differentiation is possible, but experimentally it is very difficult to detect as the two processes overlap during the stepwise progress of the cracking [12.68]. Furthermore, metal surfaces often have incipient cracks and crevices already present in the as-delivered state which could act as crack nuclei, which means that crack initiation in such cases is not necessary at all.

Considerable differences can be found when comparing experimentally determined crack-growth rates of various metal/environment systems. This immediately indicates that stress corrosion cracking cannot be explained satisfactorily by only one theoretical model. The spectra of the proposed mechanisms range from models where crack growth is regarded as a very fast local metal dissolution at the crack tip to models that

assume that the adsorption of certain species of the medium at the metal surface weakens the binding forces between the metal atoms and favors brittle fracture along the cleavage planes. A comparison of both mechanisms shows that in the first case hydrogen-induced and in the second case brittle fracture is the predominant factor. Between both cases various transitions are possible which means that the degree of the corrosion effect is also different [12.68].

When discussing stress corrosion cracking a differentiation has to be made between an anodic and a cathodic mechanism. Stress corrosion cracking is usually described as anodic when the propagation rate is equivalent to the anodic metal dissolution rate at the crack tip. Cathodic stress corrosion cracking (HISCC) results from the embrittlement of the material due to hydrogen, which is generated by cathodic hydrogen evolution at the metal surface. Although the external appearance of the damage in both cases shows similarities, the mechanisms responsible for the failure are different.

Anodic Stress Corrosion Cracking

Anodic stress corrosion cracking requires several preconditions: (i) the electrolyte must have a specific effect on the material, (ii) the material itself has to be susceptible to stress corrosion cracking, and (iii) the tensile stresses have to be sufficiently high. The stress corrosion cracking susceptibility of a material is not a material property comparable to the tensile strength but a manifestation which the material shows under specific conditions. It is based on a three-component system consisting of the material (strength, microstructure, surface condition), mechanical stresses (external stresses, residual stresses) and a specific electrolyte. Furthermore the existence of protecting layers on the metal surface is a necessary but not sufficient prerequisite for initiation of stress corrosion cracking. Local damage of this surface layer – which could result from chemical as well as mechanical effects – provides starting points for crack formation. The mechanisms of crack propagation can be subdivided into two groups. The first group considers stress corrosion cracking as selective electrochemical metal dissolution at the crack tip while the other group supposes that the reduction of binding forces of the atoms at the crack tip in the presence of specific ions or molecules is responsible [12.37].

Test Methods for Stress Corrosion Cracking

Corrosion systems with simultaneous corrosion load and mechanical stresses are very complex as the condi-

tions change with time and the changes resulting from the parameter interactions are often difficult to interpret. It is therefore necessary to set up stress corrosion cracking tests in such a way that the main parameters are clearly defined and measured during the test. The existing literature provides standards [12.69, 70] and summaries [12.71] in which all relevant aspects are presented and discussed. In the next section the main parameters will be discussed on the basis of these references as these provide a basis for a practice-related test method for assessing the susceptibility of prestressing steels. Nearly all mechanical types of stress have been used for investigating prestressed steels.

Aim of Stress Corrosion Test

From the definition of stress corrosion it is clear that stress corrosion cracking is a special case of stress corrosion and that under certain circumstances corrosion will not lead to the formation of cracks.

Although there is an agreement that crack formation is the normal test result, other manifestations have also been found like intergranular corrosion or elongated fine cracks which are intensified in the presence of stresses.

There is a large variety of methods to assess the stress corrosion cracking properties of metals. Each of them has its specific advantages and disadvantages.

It is important to recall that the term test in connection with the resistance or susceptibility to stress corrosion cracking has a special meaning. Whether stress corrosion cracking occurs in a certain case or not depends on the environmental and mechanical conditions as well as the material properties of the material. The word susceptibility does not describe a material property or quality which can be related to an overall valid scale as the ranking of a series of alloys can be very different depending on the exposure conditions.

In an ideal case for a given application the likelihood of occurrence of stress corrosion cracking can only be determined by carrying out simulation tests under all possible exposure conditions. In practice this is difficult and sometimes even impossible. Therefore, on the basis of practical experience, a certain number of standard test methods have been developed which give useful guidance for the likely practical behavior in specific cases of application. These laboratory standard test methods are only suitable for such practical conditions if they are based on experience or where relevant relations exist, even if they are only empirical.

The fact that a given material may or may not pass a test which was previously useful for another material may not be significant and, similarly, a test which

correctly distinguishes between two materials for one application does not necessarily provide reliable evidence when exposure conditions are different. Therefore the use of a standard test for conditions outside the scope of the test requires validation.

Selection of the Test Method

Prior to starting a programme for stress corrosion cracking testing it is necessary to decide which kind of test is suitable. Such a decision mainly depends on the purpose of the test and the type of information to be obtained. While some test methods try to simulate practical conditions as far as possible, this being of great value to plant engineers, other tests are directed towards evaluating certain mechanistic effects of failure. In the first case limitations with respect to e.g. material, space, time etc. can lead to relatively simple test methods while under different conditions refined methods are necessary. For example, investigations on the crack growth rate can require the use of cracked specimens, but these are unsuitable for evaluating the effects of surface treatments. Although improved techniques are available the use of a simple test can be valuable for conditions where the more complicated techniques cannot be used.

In selecting a test method which only gives a failure/nonfailure result it is important to ensure that it is not so severe that it leads to rejection of a material which has already proven its suitability in a special practical application. On the other hand it must not be so mild that it encourages the use of a material under conditions which could lead to rapid failure.

In general the aim of a stress corrosion cracking test is to obtain quicker information on the prediction of practical behavior than is possible from practical experience. There are various possibilities to achieve this, such as using higher stresses, continuous slow straining, cracked specimens, higher concentration of certain substances in the test environment and higher temperatures, i.e. compared to service conditions, and also electrochemical stimulation. However, it is very important that the methods used and parameters selected do not change the details of the failure mechanism.

Loading Systems

General. The methods for loading the specimens (smooth, notched or cracked) are usually classified as follows

- constant strain,
- constant load,
- slow strain rate.

In the case of cracked specimens the limiting conditions are defined by the critical threshold stress intensity factor K_{Isc} .

Tests with Constant Strain

The various types of bending tests that are in use often belong to this category. These can simulate stresses from production which are often the cause for failures in service conditions.

The advantage of bending tests is the use of simple and hence often cheap specimens and clamping devices. Problems with this kind of tests usually result from the low reproducibility of the stress level – if indeed this can be measured at all. Tests to improve this situation have led to refined types of bending tests, e.g. four-point loading instead of three-point loading. But the limitations of the simple bending theory which is usually used to calculate the stress level can lead to errors, especially if straining beyond the elastic limit is necessary. The application of strain gauges to measure the stresses at the surface can be useful. The preparation of bend-shaped parts for U-formed bending specimens introduces significant plastic deformation which could affect crack initiation.

Tensile tests with constant strain are sometimes preferred to bending tests as the application and calculation of the stress is simplified. However, more massive stressing frames are required than for bending specimens of similar cross section.

Apart from affecting the value of the maximum initial load the stiffness of the frame can also affect the time to failure of the specimen. In most of the tests with constant strain, especially when testing ductile materials, the initial elastic elongation is partly converted into plastic deformation as the crack formation proceeds.

The magnitude of any loading relaxation can differ from specimen to specimen and can affect the time to failure of the specimen depending on the number of pits or cracks that are present. In the case of specimens with many cracks or pits considerable relaxation can be observed while in the presence of only a few cracks little relaxation can be observed. Thus if only one single crack occurs it does not necessarily have to grow to a considerable size for sudden failure (fracture) of the specimen to occur as the applied load will remain high. On the other hand the significant relaxation of the loading that takes place in the presence of many stress corrosion cracks means that these cracks have to proceed further to reach a size that will be sufficient to generate stress conditions for a sudden fracture to occur at relatively low loading.

Tests with Constant Load

These tests are more suitable for simulating failures due to stress corrosion cracking brought about by loads or stresses occurring in practice. As the effective cross section of a specimen is reduced by propagating crack formation tests with constant load include an intensified stress situation. Hence, it is more probable that such tests will lead to an earlier failure or fracture compared to tests with constant total elongation.

Tests with constant load lead to an increasing stress situation as the initiated cracks continue to grow and therefore it is more unlikely that cracks, once started, will be arrested in these tests than those in a constant strain test below the critical stress threshold. As a consequence, in any particular system the value for the critical stress threshold is probably lower when determined under constant load than under constant strain.

Tests with Slow Strain Rate

The application of dynamic slow straining, which originally was only employed as a quick selection test, has now become more important for simulating conditions in practice.

This method includes a relatively slow strain or deformation rate (e.g. 10^{-6} s^{-1}) of a specimen under defined environmental conditions, which is continued until fracture occurs.

For stress corrosion cracking, crack propagation rates are generally in the range of 10^{-3} to $10^{-6} \text{ mm s}^{-1}$ which means that in laboratory tests under constant total strain or constant loading failure of specimens with usual dimensions will take place within a few days. This has also been observed in practice in those systems where stress corrosion cracking can easily be initiated. On the other hand it is common experience that specimens do not fail even after very long testing times; for such situations the test will be stopped after an arbitrary time period.

The first applications of this test procedure were aimed at getting data to compare the effects of such variables as material composition and microstructure or the addition of inhibitors to stress corrosion cracking initiating environments. It was also used to initiate stress corrosion cracking for material/environment combinations which did not show crack formation under constant load or constant total strain in the laboratory. This means that this test is relatively severe as it often initiates failure of the specimen due to stress corrosion cracking where other types of loading of smooth specimens did not lead to crack formation. In view of that it must be classified in the same category as tests with

precracked specimens where the failure of the specimen is also inherent to the test.

Composition of Test Solution

Although it is unavoidable that the medium is a very important factor for SCC tests, some of the solutions are often used in combination with special alloys. Two examples are boiling MgCl solution for stainless steels and boiling nitrate solutions for carbon steels. Such solutions have been criticized for various reasons; most importantly because they do not represent practical service conditions. This can be very significant, because relative susceptibilities of a series of materials are not always the same in different media.

The effect of a change in the pH value is well known in the case of general corrosion in electrolytes, and as far as corresponding experiments exist, such effects are no less obvious with SCC. Changes of media pH value during a test can be as important as the initial pH value. Any change of pH value during a test will depend on solution volume, surface area of exposed specimen and time. Use of a relatively large solution volume combined with a small surface area of the metal or replenishment or exchange of solution during the test is likely to lead to a smaller pH change and therefore a different time to failure of the test specimen than would be the case with a small solution volume and large metal surface.

Small changes of O concentration can have significant influence where oxygen plays an important role in corrosion reactions causing crack initiation.

Electrochemical Aspects

Free corrosion experiments, i. e. at the free corrosion potential, can be used for reference and serial experiments. They are always problematic if the corrosion medium does not contain a defined redox system with enough redox capacity since electrochemical reactions can change with time. Controlled electrochemical experiments can be used to determine the dependence of SCC on potential and to obtain information on the effect of system parameters on the potential. These parameters include, for instance, the redox systems of aggressive environments and, under special circumstances, the alloying components of the metal. Controlled electrochemical experiments have been used to achieve a reduction in the time to failure of the specimen by setting the test electrochemical conditions to give maximum susceptibility to SCC. In such cases care has to be taken that the corrosion type and mechanism do not change. This can be examined by metallographic analysis.

Discussion and Evaluation of Results

In tests under constant load, the SCC sensitivity of different materials can only be assessed by determination of the following values.

- Fracture: yes/no;
- Cracks: yes/no;
- Depth and amount of cracks.

An assessment of relative resistance to SCC of different materials based only on the time to failure is not possible, for the reasons given above. Tests with slow strain rate provide the following evaluation possibilities for determining SCC susceptibility. For experiments continued until fracture

- (a) depth of secondary cracks;
- (b) elongation after fracture;
- (c) reduction of area;
- (d) breaking load.

For experiments finished before fracture

- (e) experimental duration and measured crack depth.

Evaluation regarding (a) and (e) is usually more sensitive than (b–d). Information regarding the SCC behavior of a system can more easily be obtained if the mechanical values (b–d) are related to values measured in an inert environment (air, oil).

In general, a metallographic evaluation of the specimen following the experiment is necessary to determine reliably the resistance to SCC of metallic materials using the slow-strain-rate test method. For other types of tests metallography is also in many cases the only method for the reliable detection of SCC and for distinguishing different types of SCC. The average or maximum depth of secondary cracks and resulting crack growth rates can be used as the basis for comparison tests.

12.6.2 Corrosion Fatigue

Corrosion fatigue is a process which involves conjoint corrosion and alternating straining of the metal, often leading to cracking. It may occur when a metal is subjected to cyclic straining in a corrosive environment. Corrosive or otherwise chemically active environments can promote the initiation of fatigue cracks in metals and alloys and increase the rate of fatigue crack propagation. Corrosion fatigue processes are not limited to specific metal/environment systems and reliable estimates of fatigue life for all combinations of loading and environment cannot be made without data from laboratory tests.

Regarding the parameters involved in the process there are some similarities between stress corrosion cracking and fatigue but especially the mechanical loading is different. For testing a metal's resistance to corrosion fatigue in general two types of test have been developed: cycles to failure testing (ISO 11782-1) and crack propagation testing (ISO 11782-2).

Cycles to Failure Testing

In the presence of an aggressive environment the fatigue strength of a metal or alloy is reduced to an extent which depends on the nature of the environment and the test conditions. For example, the well-defined fatigue strength limit observed for steels in air may no longer be evident as illustrated in Fig. 12.42. Interpretation of results is then based on the assumption of an acceptable life of the component.

The test involves subjecting a series of specimens to the number of stress cycles required for a fatigue crack to initiate and grow large enough to cause failure during exposure to a corrosive or otherwise chemically active environment at progressively smaller alternating stresses in order to define either the fatigue strength at N

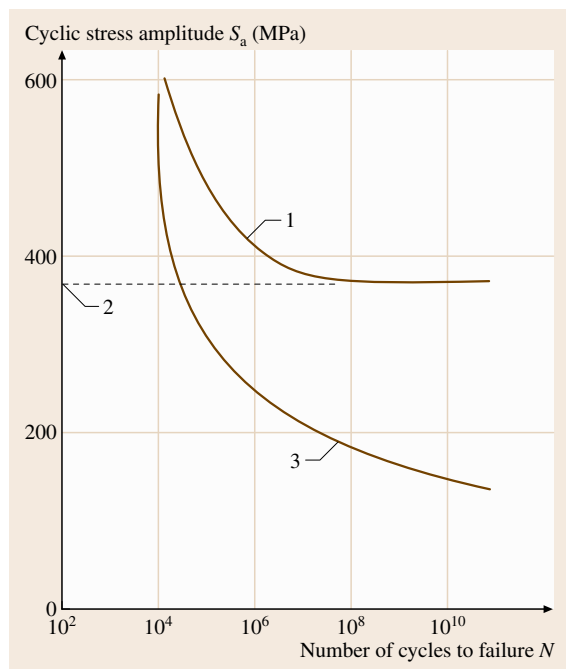


Fig. 12.42 Schematic comparison of $S-N$ behavior during fatigue and corrosion fatigue for steel. Key: 1 fatigue in air, 2 fatigue limit in air, 3 corrosion fatigue (no fatigue limit)

cycles, S_N , from an $S-N$ diagram or the fatigue strength limit as the fatigue life becomes very large.

The test is used to determine the effect of environment, material, geometry, surface condition, stress, etc., on the corrosion fatigue resistance of metals or alloys subjected to applied stress for relatively large numbers of cycles. The test may also be used as a guide to the selection of materials for service under conditions of repeated applied stress under known environmental conditions.

Specimens

The design and type of specimen used depends on the fatigue testing machine used, the objective of the fatigue study and the form of the material from which the specimen is to be made. Fatigue test specimens are designed according to the mode of loading, which can include axial stressing, plane bending, rotating beam, alternate torsion or combined stress.

Specimens may have circular, square, rectangular, annular or, in special cases, other cross sections.

The gripped ends may be of any shape to suit the holders of the test machine. Problems may arise unless the gripped portion of the specimen is isolated from the corrosive test environment.

The test section of the specimen shall be reduced in cross section to prevent failure in the grip ends and should be of such a size as to use the middle to upper ranges of the load rating of the fatigue machine to optimize the sensitivity and response of the system. The transition from the gauge section to the gripped ends of the specimen shall be designed to minimize any stress concentration. It is recommended that the radius of the blending fillet should be at least eight times the specimen test section diameter or width. The cross-sectional area of the gripped ends should, where possible, be at least four times that of the test section area. The test section length should be greater than three times the test section diameter or width.

For tests run in compression, the length of the test section shall be less than four times the test section diameter or width in order to minimize buckling. For the purposes of calculating the load to be applied to obtain the required stress, the dimensions from which the area is calculated shall be measured to within 0.02 mm. Specimens should be identified by an indelible marking method, such as stamping, on surface areas, preferably on the plain ends, without having an influence on the test results. Specimens should be stored after appropriate cleaning under desiccated conditions prior to testing in order to avoid corrosion which may influence the test results.

Cylindrical Specimens

Two types of specimens with circular cross section are frequently used for corrosion fatigue tests.

1. Specimens with tangentially blending fillets between the test section and the grip ends; these are suitable where axial loading is employed;
2. Specimens with a continuous radius between the grip ends with the minimum diameter at the center; these are suitable for rotating bend tests.

A minimum cross-sectional diameter of 5 mm is preferred.

Flat Sheet or Plate Specimens

Flat specimens for fatigue tests are reduced in width in the test section and may have thickness reductions.

If the specimen thickness is less than 2.5 mm, and the tests are performed in compression, provisions for lateral support should be made to prevent buckling without affecting the applied load by more than 5%.

The most commonly used types include

1. specimens with tangentially blending fillets between the test section and the grip ends;
2. specimens with a continuous radius between the grip ends.

Notched Specimens

The effect of machined notches on corrosion fatigue strength can be determined by comparing the $S-N$ curves of notched and unnotched specimens.

The data for notched specimens are usually plotted in terms of nominal stress based on the net cross section of the specimen.

The effectiveness of the notch in decreasing the fatigue limit is expressed by the fatigue notch factor K_f (the ratio of the fatigue limit of unnotched specimens to the fatigue limit of notched specimens).

The notch sensitivity of a material in fatigue is expressed by the notch sensitivity factor q

$$q = \frac{K_f - 1}{K_t - 1}, \quad (12.78)$$

where K_t is the stress concentration factor; $q = 0$ for a material that experiences no reduction in fatigue limit due to a notch; $q = 1$ for a material where the notch exerts its full theoretical effect.

If the standard size cannot be met other specimen configurations can be used with appropriate caution.

Specimen Size Effects, Surface Condition and Environmental Considerations

Size effects can be important in fatigue for several reasons, including residual stress distribution, variations in the stress gradient across the diameter (plain or notched specimens in bending or tension and notched specimens in axial tension–compression loading), variations in surface area, variations in hydrogen concentration gradient (in appropriate environmental conditions). There is a tendency for the fatigue strength to decrease as the specimen size increases but this may not always be the case. The size effect means that it can be difficult to predict the fatigue performance of large components directly from the results of laboratory tests on small specimens.

Corrosion fatigue properties can be very sensitive to surface condition since fatigue cracks usually initiate at the surface. In general, fatigue life increases as the magnitude of the surface roughness decreases. Therefore, attention must be paid to the surface preparation of corrosion fatigue test specimens. Unless it is required to investigate the behavior of an as-manufactured surface, it is recommended that a metallographically polished surface free of machining grooves and scratches should be used. The direction of polishing can be important and in axial loading the final surface preparation should involve grinding, or polishing in the longitudinal direction, i. e. in the same direction as the applied stress.

Other important parameters which must be considered in the test design and evaluation include surface and residual stress and microstructural surface effects. More detailed information on these topics is given in the relevant standards. For environmental factors all considerations presented in Sect. 12.5.1 on stress corrosion cracking apply.

Stressing Considerations

Cyclic Frequency. Cyclic frequency is of far greater importance when cycles to failure tests are conducted in aggressive environments rather than in air, where cyclic frequency usually has little, if any, effect. This sensitivity to frequency is due to time-dependent processes associated with the material–environment interaction. In a narrow context this may simply reflect the timescale of overall testing for significant pit development but more broadly the cycle period affects the extent of reaction or transport during a load cycle and consequently the extent of crack advance.

In the presence of an aggressive environment the fatigue strength of a metal or alloy generally decreases as the cyclic frequency is reduced. It is important, there-

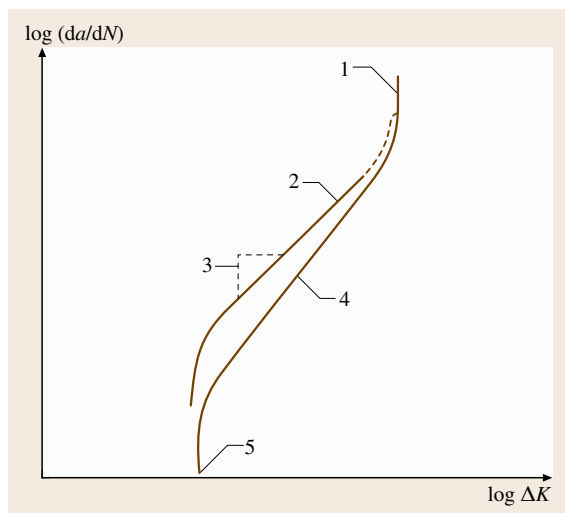


Fig. 12.43 Corrosion fatigue crack propagation rate as a function of the range of the stress intensity factor ◀

fore, that a cyclic frequency relevant to the service application be used during testing.

Waveform

In some cases, corrosion fatigue strength is strongly affected by the waveform of the loading cycle. This is particularly so where the cycle incorporates hold times during which time-dependent corrosion or stress corrosion processes may influence crack initiation and growth.

The rate of loading and unloading may also influence environmental effects if these involve, for example, diffusion or repassivation processes. It can be important, therefore, to employ a waveform representative of that encountered during service. Sinusoidal, triangular, sawtooth and square waveforms are often employed to simulate service loading conditions and, where appropriate, hold times can be imposed during the cycle.

Variable-Amplitude Loading Patterns

Some practical applications involve exposure to random loading cycles or to well-defined periodic changes in the cyclic loading conditions. While some insight into

the influence of these fluctuations may be gained by the summation of the effects observed during a series of tests under different loading conditions, it is preferable to simulate the service conditions by computer control using block or random loading programs.

Test Report

The test report should include the following information.

1. Specimen design, dimension, machining processes and surface condition;
2. For notched specimens, details of the notch and its stress concentration factor;
3. Description of the test machine, including the method of verification of dynamic load monitoring;
4. Test material characterization in terms of, for example, chemical composition, melting and fabrication process, heat treatment, microstructure, grain size, nonmetallic inclusion content and mechanical properties; product size and form shall also be identified; the method of stress relief, if applicable;
5. Specimen orientation and its location with respect to the parent product from which it was removed;
6. Test loading variables, including stress amplitude and stress ratio, fatigue life or cycles to end of test, cyclic frequency and waveform for each specimen;
7. The initial solution composition, pH, degree of aeration (or concentration of other relevant gases), flow conditions, temperature and electrode potential; specification of flow rate should be in terms of approximate linear rate past the specimen if determined by the recirculation rate; the reference electrode used shall be indicated; the potential shall be reported and referred to an appropriate standard electrode (for example, the standard hydrogen electrode or saturated calomel electrode at 25 °C);

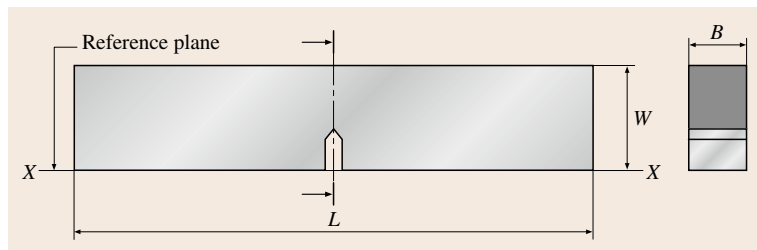


Fig. 12.44 Three or four-point single-edge notch bend specimen (SEN3)

8. The starting procedure for the test, for example any change in initial electrode potential;
9. Transients in the environment or in the loading (including test interruptions) during testing, noting the nature and duration;
10. Description of the environmental chamber and all equipment used for environmental monitoring or control;
11. Failure criterion;
12. An $S-N$ diagram plotting the maximum stress, minimum stress, stress range or alternating stress against the number of cycles to failure; it is conventional to plot fatigue life, N , in cycles logarithmically on the abscissa while stress is plotted arithmetically or logarithmically on the ordinate; all data should be plotted in the $S-N$ diagram along with a best-fit regression analysis line; this procedure develops the $S-N$ diagram for 50% probability of survival when the logarithms of the lives are described by normal distribution.

Crack Propagation Testing Using Precracked Specimens

This part describes the fracture mechanics method of determining the crack growth rates of preexisting cracks under cyclic loading in a controlled environment and the measurement of the threshold stress intensity factor for crack growth below which the rate of crack advance falls below some defined limit agreed between parties.

Principle of Corrosion Fatigue Crack Propagation Testing

A fatigue precrack is induced in a notched specimen by cyclic loading. As the crack grows the loading conditions are adjusted until the values of AK and R are appropriate for the subsequent determination of AK_{th} or

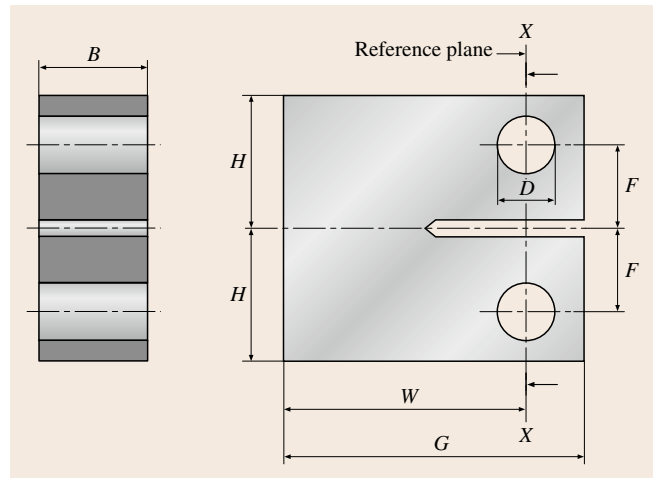


Fig. 12.45 Compact tension (CT) specimen

crack growth rates and the crack is of sufficient length for the influence of the notch to be negligible.

Corrosion fatigue crack propagation tests are then conducted using cyclic loading under environmental and stressing conditions relevant to the particular application. During the test, crack length is monitored as a function of elapsed cycles. These data are subjected to numerical analysis so that the rate of crack growth, da/dN , can be expressed as a function of the stress-intensity factor range AK .

Crack growth rates presented in terms of AK are generally independent of the geometry of the specimen used. The principle of similitude allows the comparison of data obtained from a variety of specimen types and allows da/dN versus AK data to be used in the design and evaluation of engineering structures provided that appropriate mechanical, chemical and electrochemical test conditions are employed. An important deviation from the principle of similitude can occur in relation

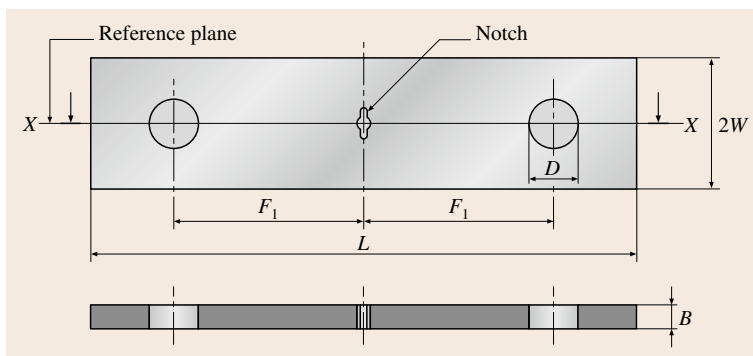


Fig. 12.46 Center-cracked tension specimen (CCT)

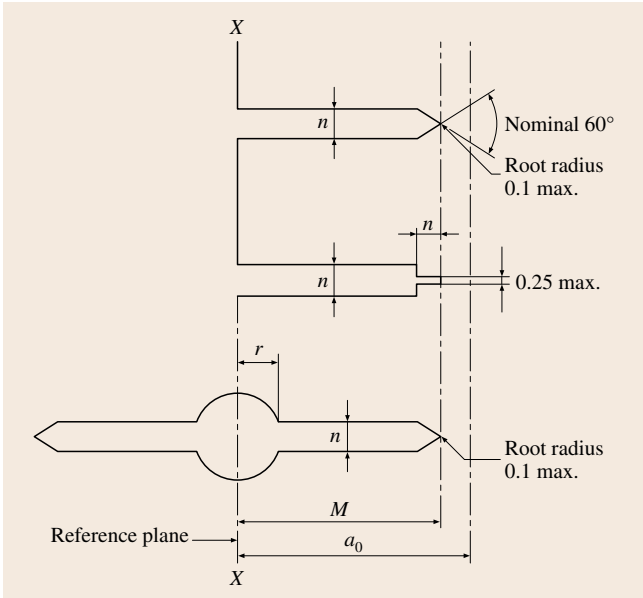


Fig. 12.47 Permitted notch geometry

to short cracks because of crack-tip chemistry differences, microstructurally sensitive growth and crack-tip shielding considerations.

The threshold stress-intensity factor range for corrosion fatigue, AK_{th} may be higher or lower than the threshold in air depending on the particular metal/environment conditions. It may be determined by a controlled reduction in load range until the rate of growth becomes insignificant for the specific application. Practically, from a measurement perspective it is necessary to assign a value to this.

Results of corrosion fatigue crack growth-rate tests for many metals have shown that the relationship between da/dN and AK can differ significantly from the three-stage relationship usually observed for tests in air, as shown in Fig. 12.43. The shape of the curve depends on the material/environment system and for some cases time-dependent (as distinct from cycle-dependent) cracking modes can ensue which can enhance crack growth producing frequency-dependent growth-rate plateaux as shown in Fig. 12.43.

12.7 Hydrogen-Induced Stress Corrosion Cracking

Hydrogen-induced stress corrosion cracking or hydrogen embrittlement is a process where the uptake of

Specimen Design

A wide range of standard specimen geometries of the type used in fracture toughness testing may be used (see ISO 11782-2). The particular type of specimen selected will be dependent upon the form of the material to be tested and the conditions of test. Pin-loaded specimens such as compact tension (CT) specimens are not suitable for tests with R values of zero or less than zero because of backlash effects. For such purposes four-point single-edge notch bend (SENB4) or center-cracked tension (CCT) specimens loaded by friction grips are suitable.

A basic requirement is that the dimensions of the specimens be sufficient to maintain predominantly triaxial (plane strain) conditions in which plastic deformation is limited in the vicinity of the crack tip. Experience with fracture toughness testing has shown that for a valid K_{Ic} measurement a , B and $(W - a)$ should not be less than

$$2.5 \left(\frac{K_{Ic}}{\sigma_y} \right)^2, \quad (12.79)$$

where σ_y is the yield strength.

It is recommended that a similar criterion be used to ensure adequate constraint during corrosion fatigue crack growth testing where K_{max} is substituted for K_{Ic} in the above expression.

Specimen geometries which are frequently used for corrosion fatigue crack growth rate testing include the following.

1. Three-point single-edge notch bend (SENB3)
2. Four-point single-edge notch bend (SENB4)
3. Compact tension (CT)
4. Center-cracked tension (CCT).

Details of standard specimen designs for each of these types of specimen are given in Figs. 12.44–12.46 and permitted notch geometries are given in Fig. 12.47.

ISO 11782-2 is recommended for specific and detailed information regarding test procedure, determination of corrosion fatigue crack propagation rates and stress intensity factor range where an overview on methods for measuring crack lengths is also available.

hydrogen into a material leads to brittle cracking of the material under nominally uncritical loads. Its display

has many similarities in comparison to stress corrosion cracking but there are also certain differences, namely that it most frequently in high-strength materials and the brittle fracture must be traced back to a different mechanism.

12.7.1 Electrochemical Processes

In the case of hydrogen-induced stress corrosion cracking or hydrogen embrittlement the adsorbed hydrogen at the steel surface is responsible for the crack growth. As hydrogen is mostly generated by the cathodic partial reaction of the corrosion process this kind of corrosion mechanism is also called cathodic stress corrosion cracking. A prerequisite for the absorption of hydrogen into the metal is that the hydrogen is present in a dissociated form. The practical importance of hydrogen-induced stress corrosion cracking lies in the fact that, even under otherwise harmless humidity conditions (condensation) on the steel surface, minor corrosion reactions could provide sufficient hydrogen to initiate crack growth. Experimentally determined crack growth of stressed high-strength steels in low-aggressive media such as humid air or distilled water have shown that even small amounts of hydrogen are sufficient to embrittle these steels [12.72].

For high-strength steels this type of corrosion does not require a specific medium. Only a sufficient amount of atomic hydrogen capable of adsorption is necessary and this can be formed by the Volmer reaction in acid and neutral media or by water dissociation in alkaline media. In both cases the hydrogen evolution is quantitatively coupled to the anodic partial reaction (iron dissolution) of the corrosion process even though a considerable metal loss does not necessarily take place. Often pitting corrosion due to chlorides and subsequent acidification of the electrolyte within the corrosion pits is the cause for hydrogen evolution (pitting-induced stress corrosion cracking). In this case there is an overlapping of local acid corrosion with local cathodic hydrogen evolution and anodic metal dissolution. This has led to the idea of anodic hydrogen embrittlement. During anodic crack growth hydrogen evolution takes place in the electrolyte at the crack tip and atomic hydrogen could then enter the metal lattice leading to embrittling processes [12.73, 74].

In fracture mechanics investigations too it has been observed that hydrogen-induced fracture mechanisms exist not only with cathodic polarization but also with anodic polarization [12.75]. Even with passive steels in aqueous alkaline solutions hydrogen evolution has

been proved experimentally to be the result of the cathodic partial reaction of the dissolution of passive iron [12.76]. On the other hand, the free corrosion potential is strongly dependent on the aeration conditions. Measurements of the free corrosion potential of prestressing steel in saturated $\text{Ca}(\text{OH})_2$ solution gave values between -0.79 V normal hydrogen electrode (NHE) with nitrogen saturation and -0.03 V (NHE) with aeration. In oxygen-free solutions the range of free corrosion potentials and the range of cathodic hydrogen evolution potentials overlap and hydrogen can consequently also be generated at prestressing steels in alkaline solutions. Even small amounts of cathodically evolved hydrogen have resulted in strong changes of the fracture properties determined in constant-extension-rate tests (CERT) [12.77].

The hydrogen reduction reaction can be split into different steps. In the first step protons are discharged at the phase boundary



H atoms adsorbed at the metal surface recombine in a second step according to the Tafel equation



or the Heyrovsky reaction



H_2 molecules formed by this reaction can escape to the atmosphere. With kinetic inhibition of the recombination adsorbed hydrogen atoms build up near the surface and can lead to high H activities, resulting in the penetration of hydrogen into the metal



An equilibrium exists between the concentration of adsorbed hydrogen at the surface and dissolved H atoms in the metal matrix. With an increasing degree of coverage by adsorbed atomic hydrogen the probability of H absorption increases.

For hydrogen-induced corrosion the activity of the adsorbed hydrogen and not the evolution rate of hydrogen is the main determining factor. Hydrogen only leads to a chemical reaction with the material, or to a metal-physical hydrogen absorption if additional critical conditions exist with respect to the state and type of material, environment, electrochemical conditions and mechanical loading.

12.7.2 Theories of H-Induced Stress Corrosion Cracking

From the metal physics point of view there are four main theories of H-induced corrosion [12.78]. The basic principles of these different mechanisms will be briefly described below.

Pressure Theory

The first theory to explain the mechanisms of H-induced corrosion was the pressure theory [12.79]. It is based on the recombination of atomic hydrogen at internal surfaces of the metal especially at sharp-edged inclusions. This results in high pressure, which can initiate pore formation or microcracks. The pressure theory is able to explain the formation of blisters and H-induced internal cracks.

Adsorption Model

The basic idea of the adsorption model is that, as a result of the adsorption of certain species, e.g. atomic hydrogen, at the crack tip the surface energy is reduced [12.80]. The reduction of the surface energy lowers the critical stress which is necessary for crack propagation. An improvement of this model that is mainly based on thermodynamical considerations was achieved using an atomistic point of view. According to this, the binding energy of the atoms forming the crack tip is reduced by adsorption of certain species; brittle fracture is favored when the cohesive strength of the lattice drops below the critical shear stress at the crack tip. But the applicability of this model to explain H-induced material fracture is limited as H-induced crack nuclei are not formed at the surface of the crack tip itself but within the material in the vicinity of the crack tip due to the concentration of stresses there.

Dislocation Theory

Today it is well accepted that atomic hydrogen is enriched in areas of high dislocation densities and can be transported together with the dislocations through the metal lattice when tensile loading of the metallic material is present [12.81]. A possible cause of H-induced material damage arising from the interaction of hydrogen and dislocations could be the diffusion of hydrogen into the dilatation zone of the dislocation and, by forming a Cottrell cloud, restraining the dislocation mobility, changing the gliding mechanisms and handicapping the deformation behavior, especially the deformation ability in front of the crack tip due to strengthening and thus favoring brittle fracture.

The interaction of dissolved hydrogen and dislocations is often taken either as the only cause or in combination with other mechanisms of H-induced corrosion to explain H-induced material fractures. The increased hydrogen mobility due to the transport via dislocations is especially important for face-centered-cubic metals due to the low diffusion rate of the interstitially dissolved hydrogen atoms in these lattice structures.

As a result of tests with high-strength martensitic steels which indicated an increased dislocation mobility after hydrogen uptake the slip softening model was developed. According to this model the preferential crack growth of high-strength steels is explained by the increased dislocation mobility resulting from hydrogen uptake, which facilitates the deformation ability.

Decohesion Theory

The decohesion theory proposed by *Troiano* [12.82] and further improved by *Oriani* [12.83] differs from the adsorption model in that it considers the formation of fracture nuclei in the vicinity of the crack tip within the bulk metal. The basic idea of this model is that the binding force of the metal atoms in the metal lattice can be reduced as a result of interactions with atomic hydrogen and then, in combination with high mechanical stresses, result in pure elastic rupture of the material. Hydrogen absorbed by the metallic material diffuses to areas of high stresses which are present at notches and therefore also in front of the crack tip because of the multiaxial state of stress. The area with the highest stresses is the boundary between the plastically deformed skin layer and the elastically deformed center. With sufficient hydrogen concentration the cohesion forces between the single atomic layers in the lattice are reduced so that crack initiation and crack growth are possible. Crack initiation occurs near the surface but contrary to anodic stress corrosion cracking not at the surface in contact with the medium. Critical hydrogen contents are most likely to occur in areas of high lattice defect density, i. e. at dislocation pile-ups, and at phase or especially grain boundaries vertically oriented to the acting stress. The crack propagation develops stepwise. For each propagation step enough hydrogen must be accumulated through diffusion into the region of the highest triaxial state of stress that occurs at the transition from the plastically deformed zone at the crack tip to the elastically stressed center. This produces an additional crack which then grows and coalesces with the initial crack. The decohesion theory enables material ruptures to be explained even with low hydrogen absorption. Among the

different hypotheses put forward to explain hydrogen-induced embrittlement, the decohesion theory seems to be the most reasonable for high-strength prestressing steels.

12.7.3 Environment and Material Parameters

Since hydrogen is adsorbed in the atomic and not the molecular form its uptake will be substantially increased by the presence of agents (promoters) which hinder the recombination of hydrogen atoms to hydrogen molecules by reaction [12.80]. Effective promoting agents are certain compounds of the fifth and sixth main groups of the periodic system, e.g. As, S, Se and Te compounds. Sulfides and thiocyanates have been identified as technically relevant substances in connection with prestressing steels. Even small amounts of contaminants or other active substances in building materials can substantially accelerate stress corrosion cracking of susceptible steels [12.84].

Because of its low atomic diameter hydrogen forms an interstitial solid solution with iron, the hydrogen atom releasing its electron to the electron gas of the metal and so remaining present as a proton. The low diameter and the interstitial position of the hydrogen atoms as well as the high mobility of protons lead to a high diffusibility of hydrogen within the iron lattice. The dissolved hydrogen can interact with itself, with dislocations and with other lattice defects and thus influence the mobility of the dislocations in the metal which, in turn, can change the deformability of the material. For the damage mechanism of hydrogen-induced stress corrosion cracking the actual source of the hydrogen is of minor importance. The damage probably proceeds via a two-step process. In the first step hydrogen can be picked up from the material in the absence of mechanical loading, and then, in a second step, failure occurs after stress is applied. The extent of the corrosion damage is determined by the hydrogen activity.

Hydrogen solubility depends on lattice structure, amount of internal surfaces and temperature. Internal surfaces are interfaces of cracks, pores and other voids as well as phase boundaries [12.85]. More hydrogen can be dissolved in face-centered-cubic lattices (by a factor of about three) than in body-centered-cubic lattices. This results in a lower hydrogen susceptibility for austenitic steels. The diffusion coefficient is also dependent on the lattice structure. At a certain temperature in a body-centered-cubic lattice it is from 3–6 orders of

magnitude higher than in a face-centered-cubic lattice. Therefore under critical conditions there is a higher risk of hydrogen-induced stress corrosion cracking for ferritic and martensitic steels. Those structural anomalies of a perfect iron lattice with which hydrogen can react are often called traps. These are disturbances of the lattice which can trap hydrogen and hold it for a certain period of time.

As well as the parameters mentioned above hydrogen-induced stress corrosion cracking and propagation also depend on hydrogen concentration and tensile stresses. With high tensile stresses susceptible steels require only very low hydrogen activity, to initiate crack growth [12.86].

Hydrogen-induced stress corrosion cracking of high-strength steels of the quenched and tempered type is characterized by cracks with intergranular corrosion along the former austenite grain boundaries.

12.7.4 Fractographic and Mechanical Effects of HISC

The process of hydrogen-induced brittle fracture can be described as follows. Initially, the change of tensile stress immediately in the crack initiation zone is so slow that hydrogen can diffuse to the crack tip and act decohesively. The consequence is to produce a stable intergranular fracture along the grain boundaries which act as weak spots of the microstructure. Ductile regions and micropits can be observed at the grain surfaces. With increasing crack propagation rate hydrogen cannot diffuse sufficiently to the crack tip and an area with a dimple fracture appearance is formed. As the fracture develops unstable crack propagation takes place with the formation of a radial structure (quasi-cleavage fracture area) and finally, when the monoaxial state of stress is reached, the formation of a shear stress lip, which is characterized by the appearance of a fracture with fine dimples.

The effect of hydrogen is mainly to reduce the binding energy of the metallic atoms thus favoring crack initiation and propagation. When the crack growth has reached a level where the diffusion of hydrogen to the crack tip is no longer possible the further crack progress is similar to a nonembrittled sample. In some cases in the area of the radial structure hydrogen can also influence the structure of the fracture surface, i. e. sometimes the cleavage fracture will show clear signs of intergranular components.

When assessing hydrogen embrittlement of prestressing steels the type of mechanical loading has

to be considered in addition to the hydrogen content. A tensile test cannot always prove the embrittling effects of hydrogen caused by diffusion processes. With high strain rates hydrogen-charged samples show nearly the same reduction of area as samples free of hydrogen. It is only at very low straining rates that hydrogen results in brittle behavior. The reason for this phenomenon is that with high deformation rates not enough hydrogen can be provided to cause a brittle fracture. Ductile behavior can be observed, i.e. a minimum time period is necessary for crack initiation and crack propagation of a critical length [12.74, 86]. Fractography can provide proof of hydrogen embrittlement even in those cases where there are only slight changes in mechanical properties. Undeniable indications can be found in the surface area of the crack breakthrough. Hydrogen-embrittled quenched and tempered steels always have an intergranular crack zone. This is clearly different from the behavior of notch-

based brittle fractures or ductile spontaneous fractures. Apart from the crack area the other parts of the fracture surface could look like notch-based brittle fractures.

12.7.5 Test Methods

For testing the susceptibility of a material against hydrogen-induced stress corrosion cracking or determining the effect of specific environmental conditions on a metal with regard to hydrogen embrittlement all test methods previously described in Sects. 12.5 and 12.6 are applicable. In addition to these tests also the uptake of hydrogen in an electrochemical cell which has been proposed by Devanathan can be investigated and the data evolved may be used for determining the diffusion coefficient of hydrogen in a metal or, if the diffusion coefficient is known, provide data on hydrogen activity at the surface of the metal.

12.8 High-Temperature Corrosion

In industrial high-temperature applications corrosion is a major life-limiting factor for in-service components. Such applications are e.g. fossil-fuel power stations, petrochemical and chemical plants, exhaust ducts, land based gas turbines and jet engines, etc. There exist a number of tests aiming at evaluating the effect of the high-temperature environment on material performance for the different applications that in most cases are laboratory tests, although some field testing may also be performed. In the laboratory tests it is usually intended to simulate conditions which are close to the industrial situation with regard to environment, temperature and mechanical stresses. As the situation in high-temperature applications in most cases is very complex it is, however, not easy to simulate the actual conditions on a one-to-one basis. Therefore most of the high-temperature corrosion tests in the laboratory are based on a simplification of the practical conditions or on conditions leading to an acceleration of the test. In the latter case it should, however, be kept in mind that accelerated testing may lead to a change in the corrosion mechanism and, thus, possibly to misinterpretation of the data for the material performance under practical conditions. Furthermore extreme care should be taken if the results of such accelerated laboratory tests are taken for life time extrapolation.

12.8.1 Main Parameters in High-Temperature Corrosion

Corrosion Testing

The basic principles for high-temperature corrosion testing are relatively easy. Actually there are *two types* of parameters which are usually measured. The first is parameters related to mass change that results from the reaction of the material with its environment by which either a mass gain or a mass loss can take place. A mass gain will occur if the reaction leads to the formation of a solid corrosion product on the surface and/or in the metal subsurface zone. Mass losses will occur when either the solid corrosion product spalls from the surface (e.g. oxide bits flake off the sample) or if volatile corrosion products are formed which evaporate. Since the mass change is proportional to the amount of species from the environment taken up by the material in the oxidation reaction or to the amount of material evaporated by formation of volatile corrosion products the high-temperature corrosion kinetics can easily be determined by continuous or discontinuous measurements of the specimen weight or mass in tests. Such mass measurements can of course also be performed with specimens from field exposure so that it becomes possible to determine corrosion kinetics also in field testing.

In combination with mass measurements it is beneficial and even necessary to characterize additional damage parameters resulting from the corrosion process. These parameters are determined by post-experimental sectioning of the specimens in the metallography and measurement of geometrical data on surface scale thickness and on internal corrosion depth. Again this method can also be applied to specimens from field testing. In the present chapter it is intended to focus on laboratory testing. Actually many of the aspects dealing with laboratory testing (especially those on the evaluation of the corrosion data) can also be applied to field testing. With regard to the specific aspects of field testing, please refer to [12.87].

12.8.2 Test Standards or Guidelines

Although high-temperature corrosion testing has been performed in industry and scientific laboratories now for almost a century there are very few guidelines or standards describing the test procedures. In the following the more important of these standards or guidelines are listed.

- **ASTM G 54** *Practice for simple static oxidation testing* [12.88]:
This standard covers the determination of the relative growth, scale, and microstructural characteristics of an oxide on the surface of a pure metal or alloy under isothermal condition in still air. This standard was later withdrawn but is still regarded as useful.
- **ASTM B 76** *Method for accelerated life test of nickel-chromium and nickel-chromium-iron alloys for electrical heating* [12.89]:
This standard covers the determination of the resistance to oxidation of nickel-based electrical heating alloys at elevated temperatures under intermittent heating using a constant-temperature cycle test. This test method is used for comparative purposes only.
- **ASTM B 78** *Method for accelerated life test of iron-chromium-aluminum alloys for electrical heating* [12.90]:
This standard covers the determination of the resistance to oxidation of iron-chromium-aluminum alloys for electrical heating at elevated temperatures under intermittent heating similar to ASTM G 76. This test is again used for comparative purposes only.
- **ASTM G 79** *Practice for evaluation of metals exposed to carburization environments* [12.91]:
This standard covers procedures for the identification and measurement of the extent of carburization in a metal sample and for the interpretation and evaluation of the effects of carburization. It applies mainly to iron- and nickel-based alloys for high-temperature applications.
- Draft code of practice: **TESTCORR – Discontinuous corrosion testing in high-temperature gaseous environment** (ERA report 2000-0546) [12.92]:
This draft code of practice, which is the result of a research programme supported by the CEC standards, measurements and testing programme describes in detail the procedures for the determination of specimen wastage using mass and dimensional change. A major consideration is the traceability of the measurements and the validity of the statistical treatment of the data generated. These procedures have been developed in conjunction with specimen preparation guidelines and recommendations for a statistical analysis of the data.
- **JIS** (Japanese Institute of Standards) **Z 2281-1993** *Test method for continuous oxidation test at elevated temperatures for metallic materials* [12.93]:
This Japanese standard covers one of the most often-used tests in high-temperature corrosion. A tentative translation from the Japanese manuscript into English is available from JIS.
- **JIS Z 2282-1996** *Method of cyclic oxidation testing at elevated temperatures for metallic materials* [12.94]:
This standard covers another most often used high-temperature corrosion test in industry and is also available as a tentative translation from Japanese into English.
- EFC publication no. 14 *Guidelines for methods of testing and research in high temperature corrosion* [12.95]:
This publication contains the papers of a workshop on this topic organized by the working party on corrosion by hot gases and combustion products of the European Federation of Corrosion where all major aspects of high-temperature corrosion testing were addressed.
- EFC publication no. 27 *cyclic oxidation of high temperature materials – mechanisms, testing methods, characterization and life time estimation* [12.96]:

This publication is based on the papers presented at a workshop of the same title again organized by the aforementioned working party of the European Federation of Corrosion. The workshop was solely devoted to thermal cycling oxidation testing.

Especially at the last mentioned workshop with strong international participation from around the world it was stated that the situation with regard to standardization of high-temperature corrosion testing is rather unsatisfactory at present. As a consequence two initiatives were started. One was in the form a European research project named COTEST [12.97] which aimed at the development of a code of practice for a test method for thermal cycling oxidation testing. The results of this work have been published as a book [12.98]. The second initiative was started by Japanese industrial researchers aiming at the development of an ISO standard based on the existing Japanese standards mentioned above. A workgroup was formed in the ISO technical committee 156 (corrosion of metals and alloys) which has the designation WG 13, high-temperature corrosion. The aim of this work group is to develop ISO standards in the following fields.

- Thermogravimetric testing:
ISO work group definition: in situ mass measurements at elevated temperatures on a single specimen without intermediate cooling.
- Continuous isothermal exposure testing:
ISO work group definition: single post-exposure

mass measurement on a series of specimens without intermediate cooling.

- Discontinuous isothermal exposure testing:
ISO work group definition: series of mass measurements on a single specimen with intermediate cooling at predetermined times not necessarily regular.
- Thermal cycling oxidation testing:
ISO work group definition: series of mass measurements on a single specimen with repeated, regular and controlled temperature cycles.
- General guidelines for a post-exposure examination:
No definition by the ISO work group.

In the development of these work items the knowledge existing in the form of the national standards and European guidelines mentioned above is being used. This particularly concerns the results from the TEST-CORR document and the COTEST document as well as the Japanese standards. These ISO standards are expected to be the first documents with international acceptance in the field of high-temperature corrosion testing. The current documents of ISO WG13 are listed in Table 12.4. As these documents are still under development, in the present chapter the most recent situation with regard to the working drafts of these standards will be taken into account. This chapter on high-temperature corrosion testing, therefore, cannot yet rely on generally accepted existing standards but the content will be presented in a way which is supposed to be compatible with the future ISO standards.

Table 12.4 Draft documents of ISO TC 156 WG 13 on high temperature corrosion testing to become international standards

Title	Voting Stage (as of July 2010)
ISO/NP 21608: Corrosion of metals and alloys – Test method for isothermal exposure oxidation testing under high temperature corrosion conditions for metallic materials	30.99 (CD approved for registration as DIS)
ISO/CD 13573: Corrosion of metals and alloys – Test method for thermal cycling exposure testing under high temperature corrosion conditions for metallic materials	30.20 (CD study/ballot initiated)
ISO/CD 26146: Corrosion of metals and alloys – Method for metallographic examination of samples after exposure to high temperature corrosive environments	30.20 (CD study/ballot initiated)
New documents (under work as of July 2010):	
1 Corrosion of Metals and Alloys Test method for high-temperature corrosion testing of metallic materials by <i>fully embedding</i> in salt, ash, or other inorganic solids	
2 Corrosion of Metals and Alloys Test method for high-temperature corrosion testing of metallic materials by <i>partially embedding</i> in salt, ash, or other inorganic solids	
3 Corrosion of Metals and Alloys Test method for high-temperature corrosion testing of metallic materials by <i>immersing</i> in molten salt or other inorganic liquids	
4 Corrosion of Metals and Alloys Test method for high-temperature corrosion testing of metallic materials by <i>coating</i> with salt, ash, or other inorganic solids	

12.8.3 Mass Change Measurements

Principles

The basic idea behind the mass change measurements is to have an easy method providing information about the oxidation or corrosion kinetics. This kinetics allow an assessment of materials performance from the viewpoint of oxidation or corrosion resistance according to the schematic representation in Fig. 12.48. The ideal situation with regard to high-temperature corrosion resistance is the formation of a very thin and dense protective oxide scale on the surface of the material. This behavior is usually characterized by parabolic kinetics with slow scale growth rates, i. e. the mass increase or the increase of the oxide scale thickness follow a parabolic time law

$$(\Delta m/A)^2 = k_p t, \quad (12.84)$$

where Δm is the mass increase, A is the specimen surface area, k_p is the parabolic oxidation rate constant and t is oxidation time. A slow oxidation rate means that k_p has a very low value. Equation (12.84) can also be written in terms of the increase of the oxide scale thickness according to

$$x^2 = k'_p t, \quad (12.85)$$

where x is the oxide scale thickness. As in many cases oxidation does not strictly follow a parabolic rate law, (12.84) and (12.85) can also be written in the more general form including the temperature dependence [12.99]

$$\Delta m/A = [k(T)]^{1/n} \left(\frac{t}{t_0} \right)^{1/n}, \quad (12.86)$$

$$k(T) = k^0 e \left(\frac{-E_A}{RT} \right) \quad (12.87)$$

with $k(T)$ as a temperature-dependent oxidation rate constant (for the parabolic case $k(T) = k_p$), t_0 as the time basis (e.g. 1 s if seconds are used for t), k^0 as the general oxidation rate constant, E_A as the activation energy, T as temperature and R as the general gas constant. The exponent n characterizes the type of rate law, e.g. $n = 2$ for the parabolic case. If oxidation or high-temperature corrosion occur only via the formation of a surface layer the mass change results can be converted into scale thickness data by

$$\Delta m/A = x f_z \quad (12.88)$$

$$\text{with } f_z = \rho_{\text{MeX}} \frac{z M_X}{M_{\text{MeX}}} \quad (12.89)$$

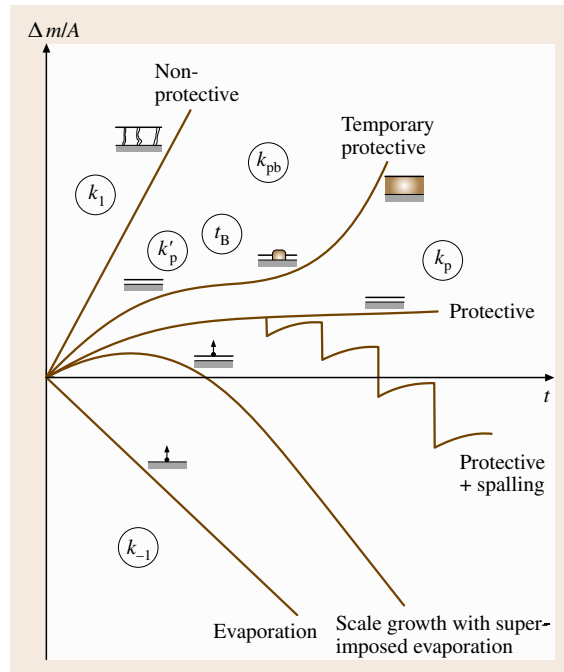


Fig. 12.48 Schematic of the most common types of oxidation/corrosion kinetics at high temperature

with ρ_{MeX} being the density of the compound MeX and M_{MeX} being the molar mass of the same compound. M_X and z are the molar mass and a stoichiometric factor, respectively, of the reacting species of the environment. For several oxides the values of f_z are given in tables [12.100]. This estimation, however, requires that the surface scales are single phase and practically fully dense and do not show any significant degree of porosity. Furthermore internal corrosion is neglected by this conversion.

In the following, Fig. 12.48 shall be discussed in some more detail as this schematic shows all the potential results which may come out of the mass change measurements. The following situations can be encountered.

Nonprotective Oxidation Behavior. In this case oxidation/corrosion occurs at a very high rate, i. e. rapid conversion of metal into the corrosion product layer on top of the specimen is observed. This surface layer does not have any protective character, which can be due to cracks or pores in the scale or due to high diffusion rates in the scale lattice. In most cases the corrosion kinetics are linear ($n = 1$) but can also be of the parabolic type ($n = 2$) with a high k_p value if the growth of the corro-

sion product layer is diffusion controlled. This case is undesired in material service.

Temporary Protective Oxidation Behavior. In many practical applications at the beginning of oxidation or life time of the component a protective situation is observed following slow parabolic kinetics or sometimes even cubic kinetics ($n = 3$) which also points towards a protective behavior of the oxide scale formed. However, after a certain period of time it may happen that, due to scale cracking and/or depletion processes in the oxide/subsurface-metal system, so-called break-away oxidation starts, i. e. the formerly protective oxide scale is converted into a nonprotective type that ends up in a significant increase of the oxidation rate (acceleration of oxidation). The characteristic values of this type of curve are k_p for the protective region, t_B for the moment at which accelerated oxidation starts (break-away time) and k_{pb} for the oxidation rate constant in the nonprotective post-breakaway time range. It should be pointed out here that many laboratory tests for technical materials ended before t_B had been reached so that protective behavior of the material was assumed. However, under industrial application oxidation times are usually much longer than laboratory tests so that t_B may easily be exceeded. Therefore laboratory results may sometimes be questionable, which also illustrates the problems which may arise from short-time accelerated testing.

Protective Oxidation Behavior. This is the ideal situation which guarantees resistance of the material against high-temperature corrosion and which is usually observed when a thin and dense protective slowly growing oxide scale is formed. In this case oxidation kinetics can often be described by (12.88) and (12.89) with k_p having very low values. The value k_p is therefore the key value that characterizes the oxidation resistance and is therefore determined in the oxidation tests.

Protective Oxidation Behavior but Spalling of the Protective Scale. In particular when temperature changes occur during oxidation, the protective oxide scale may crack and spall due to different values of the coefficients of thermal expansion (CTE) of the oxide scale and the substrate. As a consequence, starting from a certain point of time, a sudden decrease in mass occurs, followed by an increase of mass due to ongoing oxidation. During the next spalling period mass decreases again and increases by oxidation until a further spalling period starts, leading to a repeated sequence of

spalling and scale growth. Unless healing of the spalled oxide occurs, and thus a restoration of the protective effect becomes possible, spalling usually leads to a non-protective situation.

Oxide Scale Growth with Superimposed Evaporation at Corrosion Products. If a solid corrosion product scale is formed during high-temperature corrosion, accompanied by the formation of a volatile corrosion species, then after an initial mass increase a continuous mass decrease will occur. As an example such situations can be encountered in oxidizing/chloridizing environments where the oxide scale is reduced or destroyed by the formation of volatile metal chlorides [12.101]. A similar situation may also occur with other metal halogen compounds. Kinetics in this case can be described by

$$\Delta m/A = [k(T)]^{1/n} \left(\frac{t}{t_0}\right)^{1/n} - k_{-l} \left(\frac{t}{t_0}\right) \quad (12.90)$$

where k_{-l} is the negative linear rate constant.

Corrosion only by Evaporation of Volatile Corrosion Products. If neither solid nor liquid corrosion products are formed but only gaseous species result from the corrosion reaction then a continuous linear decrease in mass will be observed. This linear decrease is characterized by $n = 1$ and a linear negative rate constant of k_{-l} .

Summarizing Fig. 12.48, it is actually only the protective case that can be accepted for industrial use of the materials. For most technical materials the exponent n in this case usually ranges between 2 and 3 and $k(T)$ takes low values. The temporary protective case can be accepted if t_B is not much shorter than the expected exposure time in service and the spallation case can be accepted if the amount of spalling is relatively small. The same is valid for scale growth with superimposed evaporation but all other cases lead to severe problems in practical use.

The test methods described in the following serve for the quantitative determination of the parameters of Fig. 12.48 and also for the qualitative characterization of oxidation/high-temperature corrosion behavior according to these systematic cases. For further illustration in Fig. 12.49 examples of values of the parabolic rate constant are given for protective oxides scales and a temperature range 800–1400 °C [12.102]. This figure shows that alumina surface scales are superior to chromia surface scales with regard to the protective effect. Figure 12.49 furthermore can serve for orientation

Fig. 12.49 Oxidation rate constants k_p for the alloy groups Al_2O_3 -scale formers and Cr_2O_3 -scale formers (after [12.102]) ▶

whether the measured values determined in the experiments characterize protective or nonprotective behavior of the materials.

Thermogravimetric Testing. Mostly in scientific laboratories the thermogravimetric method is a widely used type of test to investigate the oxidation kinetics and other types of high-temperature corrosion continuously in situ. The principles of the equipment are given in Fig. 12.50. The weight of the specimen is continuously recorded by a laboratory balance, which usually sits on top of a laboratory furnace. To hang the specimen platinum wires or silica strings, which are supposed to be inert in most environments, are normally used. (It should however be mentioned here that under certain conditions even platinum and silica may evaporate and, thus, lead to a decrease in weight of the string which is also measured by the balance.) The specimen and the weighing system are usually encapsulated in a retort to allow the use of defined gas compositions. The interior of the laboratory balance should be shielded against penetration of the reactive gas in the furnace by counterflow of inert gas (e.g. Ar). The gas entrance should be opposite to the gas exit. In most cases the retort is manufactured from quartz. Especially at very high temperatures, alumina retorts are also used. For accelerated testing the measurements are sometimes performed under thermal cycling conditions (see later). The same equipment can be used with a moveable furnace, the movement of which is controlled by an electronic device that allows defined temperature cycles. The temperature at the specimen is monitored by a thermocouple, which is placed close to the specimen, although no friction between the thermocouple and the specimen should occur. Furthermore any friction between the quartz string or the platinum wire leading to the balance and the retort or tube walls should be avoided. Further recommendations for the thermogravimetric tests are given below in the section on continuous and discontinuous isothermal exposure testing.

As indicated in Fig. 12.50 it is also possible to combine this type of measurement, especially in the case of thermal cycling testing, with acoustic emission measurements. In this case the platinum wire that is connected to the specimen can be used simultaneously as an acoustic waveguide. Acoustic emission signals

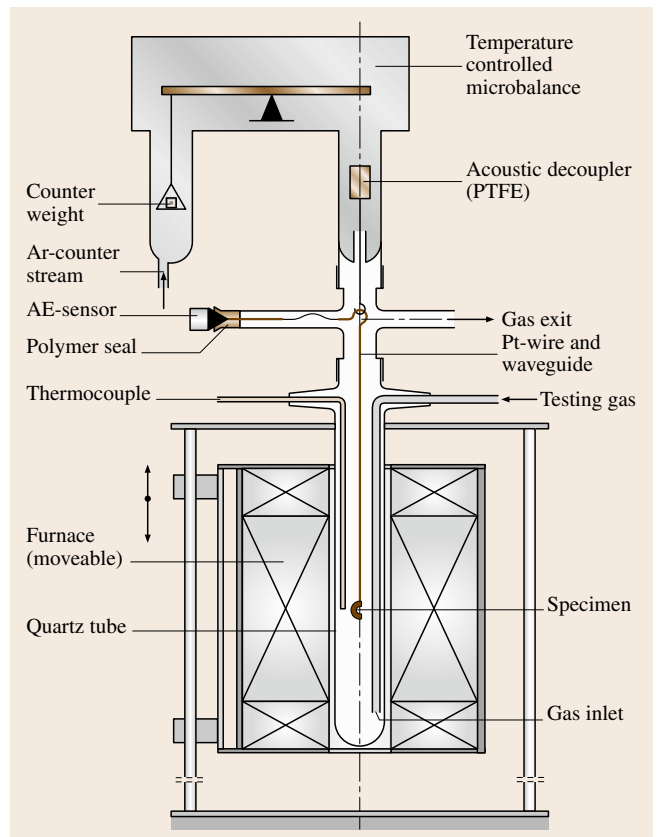
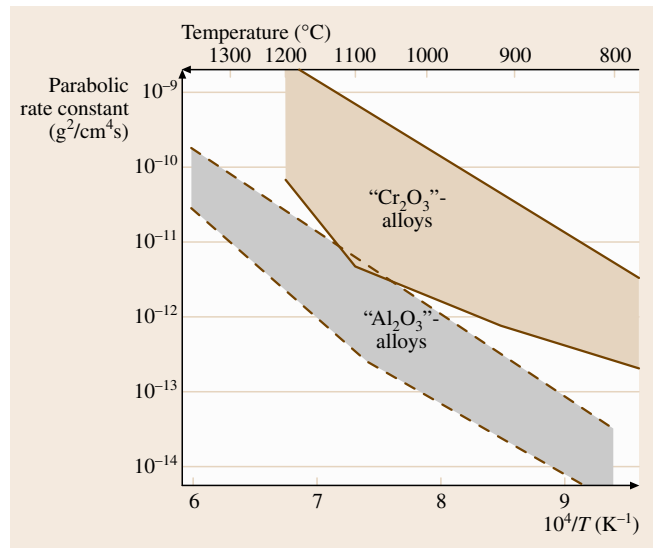


Fig. 12.50 Schematic of a thermobalance for continuous in situ mass measurements

can reveal the extent to which cracking or spalling of the oxide scale occurs either during isothermal or during cyclic oxidation. The results of the thermogravimetric measurements are the curves shown schematically in Fig. 12.48. However, a major disadvantage of this method is that only one sample can be tested at a time so that generating a large number of comparative data for different materials is a lengthy process. This is the main reason why industrial laboratories prefer to test multiple samples simultaneously. This issue will be addressed in the next section.

Continuous and Discontinuous Isothermal Exposure Testing

To accommodate a larger number of specimens in one furnace a special arrangement of equipment is necessary, as shown schematically in Fig. 12.51. This equipment is again composed of a temperature-regulating device for heating the test piece(s) uniformly at a constant temperature and, ideally, a testing portion capable of separating the test piece(s) from the outside air (i. e., a closed system). Since for many materials humidity in the test environment may have a significant effect on oxidation behavior, a humidifying regulator should be used to continuously supply a gas kept at a constant humidity, which should be monitored with a hygrometer. As for all closed systems, including those for thermogravimetric testing, the gas supply should be

controlled by a gas-flow meter. It is important that the test-piece chamber is not composed of a material that reacts with the test environment during the test to a degree that changes the composition of the atmosphere. If closed systems with a test-piece chamber cannot be used, then tests may also be performed in an open system with laboratory air. In this case it is recommended that the humidity of the air should be recorded and that the laboratory should be kept free from temperature changes and the influence of weather conditions as far as possible.

The furnace has to be characterized prior to testing to determine the length of the isothermal zone inside the furnace and the set point of the apparatus. A common method is by the use of an independent movable thermocouple. The draft of the present ISO work item recommends that the temperature-regulating device should be capable of guaranteeing that the temperature of the test piece is kept within a permissible range, given in Table 12.5. The material of the thermocouples has to withstand this test temperature. The temperature has to be measured by a suitable device according to ASTM E 633-00 [12.103]. Thermocouples of type S (Pt-10% Rh/Pt), type R (Pt-Pt/13% Rh) up to 1000 °C or type B (Pt/30% Rh-Pt/6% Rh) up to 1700 °C are preferred. A thermocouple should be positioned close to the test-piece surface and must be calibrated in accordance with standards ASTM E 220-

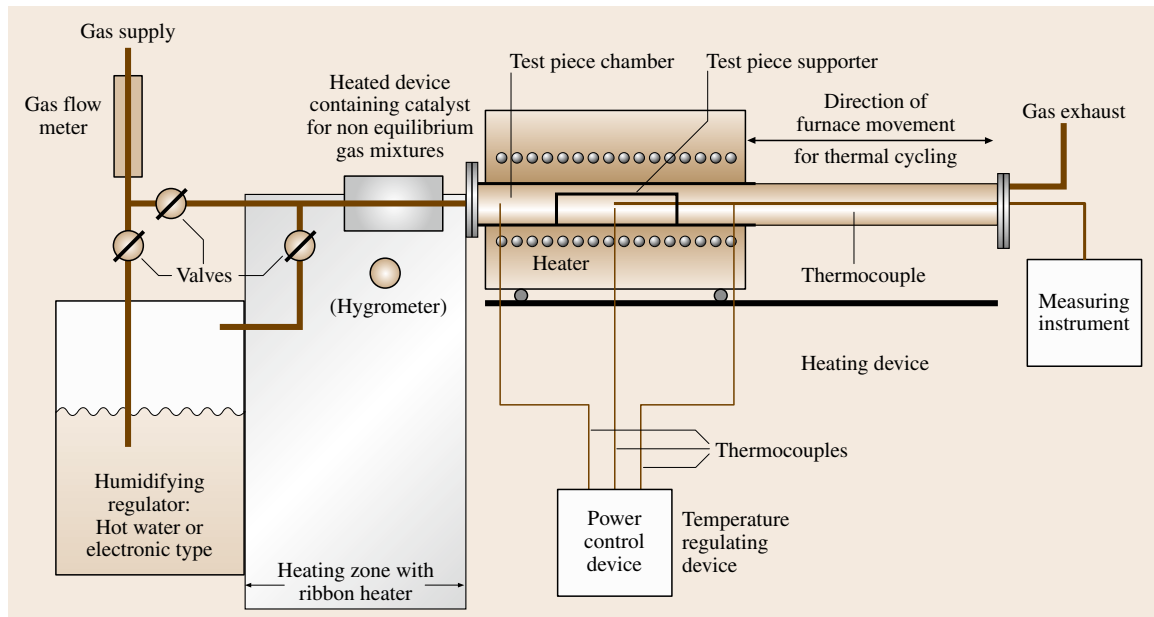


Fig. 12.51 Basic design of a horizontal exposure furnace for discontinuous oxidation/corrosion testing

Table 12.5 Permissible tolerance of temperature of test piece [12.97]

$T \leq 573 \text{ K}$	$573 \text{ K} < T \leq 873 \text{ K}$	$873 \text{ K} < T \leq 1073 \text{ K}$	$1073 \text{ K} < T \leq 1273 \text{ K}$	$T > 1273 \text{ K}$
$\pm 2 \text{ K}$	$\pm 3 \text{ K}$	$\pm 4 \text{ K}$	$\pm 5 \text{ K}$	$\pm 7 \text{ K}$

02, ASTM E 230-02 and ASTM E 1350-97 [12.104–106]. If, however, the environment does not allow the use of such thermocouples in this way the test-piece temperature has to be deduced from the furnace calibration using dummy test pieces and appropriate thermometry in an inert environment. The thermocouple should be capable of confirming that the test temperature is within the range given in Table 12.5. It should be located at a defined, fixed position as close to the test pieces as possible.

When a humidifying regulator is used it should be capable of adjusting to the desired humidity and the space between the humidifying regulator and the test-piece chamber should be kept above the dew point to avoid condensation. The water-vapor content should be measured, which can be achieved by, e.g., the use of a hygrometer before the test-piece chamber or measuring the amount of water after condensation of the exhaust gases. The gas flow has to be high enough to ensure that no depletion of the reacting species will occur. At the same time the gas flow must be slow enough to allow the gas mixture to preheat and in some applications to reach reaction equilibrium. The TESTCORR document recommends 1–10 mm/s.

It is recommended that the test pieces have a minimum surface area of 500 mm² [12.92]. Their shape can be a rectangular plate, a disc or a cylinder. Final surface finishing of the test pieces should be 1200 grit according to the Federation of European Producers of Abrasives (FEPA) standard 43-1984 R 1993 [12.107] and ISO 6344 [12.108]. Deformation by marking, stamping or notching of the surface should be avoided. Identification of the test pieces should be solely on the basis of recording their relative position within the test chamber. In particular for hanging specimens, e.g. for the thermogravimetric test, holes for the test-piece support are permissible. The test pieces must be dried after degreasing in an ultrasonic bath using isopropanol or ethanol. Before exposure the mass of the test pieces $m_T(t_0)$ has to be determined by three independent measurements with the difference between the measurements not exceeding 0.05 mg.

Several test pieces exposed for different times are necessary to define the oxidation kinetics of the material. Therefore it is recommended that duplicate test pieces are used with (at least four) exposure times in-

creasing progressively (e.g., 10 h, 30 h, 100 h, 300 h, ...). The material used for the test-piece supports should not react at the test temperature neither with the environment nor with the specimen. Examples of recommended test-piece supports are shown in Fig. 12.52. Where the possibility of depletion of active species in the test atmosphere is a concern, the exchange of the test atmosphere can be improved by the use of holes or slots in the bottom part of the side walls of the test-piece support. To remove volatile compounds it is furthermore recommended that new test-piece supports should be baked for at least 4 h at 1000 °C in air. In addition to the mass of the test pieces, that of the test-piece supports $m_s(t_0)$ should be determined prior to exposure.

Thermal Cycling Oxidation Testing

In the majority of industrial applications temperatures are never constant. Therefore temperature cycling oxidation/corrosion tests are most often used in industry. The test equipment is rather similar to that for isothermal testing, with the major difference that either the specimen or the furnace can be moved so that temperature cycles are possible in the test. In Figs. 12.50 and 12.51 the test equipment shown for isothermal testing already allowed for the possibility of moving the furnace, so that in the same equipment cyclic oxidation testing would also be possible. The advantage of the equipment shown in Figs. 12.50 and 12.51 is that these tests can be performed in a defined environment. In some of the more traditional thermal cycling oxidation test rigs the specimens are moved by some device out of and into the furnace, which usually requires that these tests are performed in an open system. As mentioned above, closed systems with defined environments are preferred over open systems with laboratory air.

For completeness it should be mentioned that, as well as tests with small laboratory specimens, component tests, e.g. with complete heat-exchanger tubes, can even be performed under thermal cycling conditions, as shown by the schematic in Fig. 12.53. In this case the furnace consists of two half shells that can be moved apart on a rail system so that the test-piece chamber is at ambient temperature when the furnace is open. The test piece, which in this example is a heat-exchanger

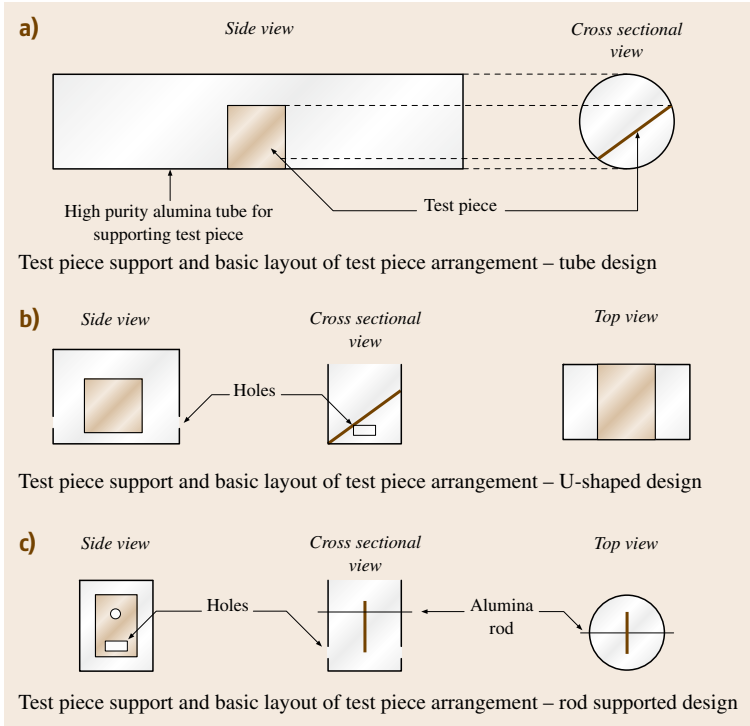


Fig. 12.52 (a) Test-piece support and basic layout of test-piece arrangement – tube design; (b) Test-piece support and basic layout of test-piece arrangement – U-shaped design; (c) Test-piece support and basic layout of test-piece arrangement – rod-supported design

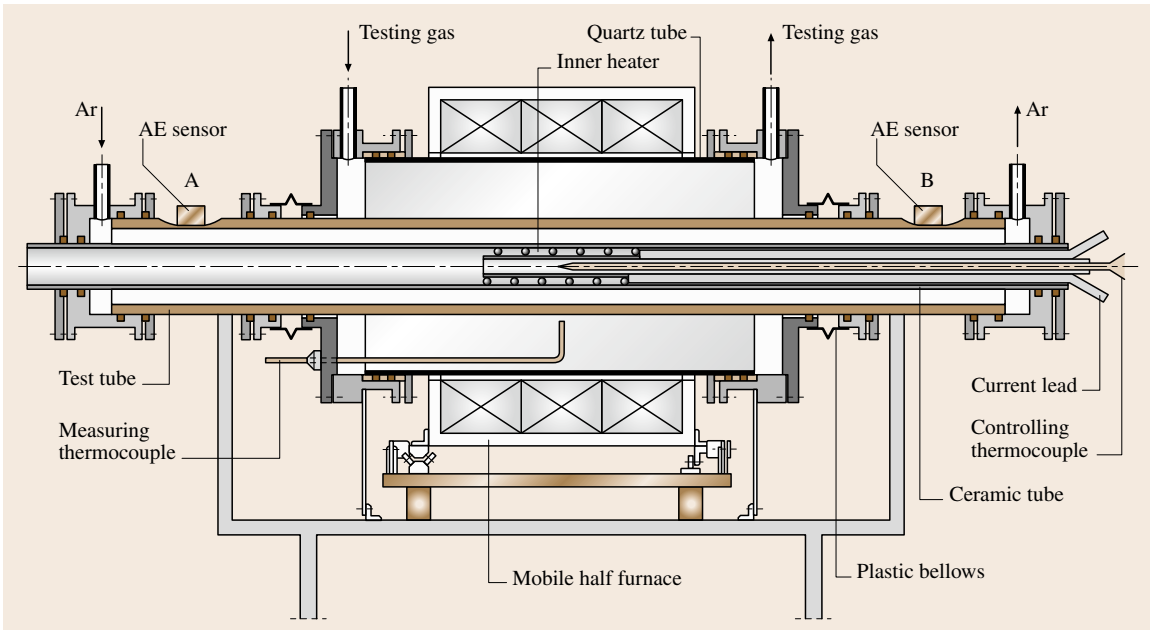


Fig. 12.53 Equipment for thermal cyclic testing of heat-exchanger tubes (after [12.109])

tube, is placed inside a quartz tube and sealed at the ends with flanges. This design allows the possibility of having defined environments on the outer surface of the tube as well as on the inner surface. These two environments can even be different from each other, e.g. combustion gas on the outside and steam on the inside of the tube. Component tests as in this example are always desirable when geometrical effects of these components on the oxidation behavior are to be investigated. Figure 12.53 again includes the possibility of using the acoustic emission technique for the detection of failure of the protective oxide scales due to thermal cycling and spalling.

Generally all the recommendations given in the continuous and discontinuous isothermal exposure testing section are also applicable to thermal cycling testing. The difference compared to discontinuous isothermal testing is that in thermal cycling testing the temperature cycles always have the same shapes. Based on a detailed scientific model calculation the parameters characterizing such a thermal cycle have been determined as follows [12.110, 111]. The heating period of the cycle starts when the test piece enters the furnace and ends with the beginning of the hot dwell time. The latter is defined as the time when the actual temperature exceeds 97% of the desired hot dwell temperature measured in kelvin. The hot dwell time ends and the cooling time starts when the heating of the test piece is stopped, e.g. by the removal of the test piece from the furnace. The end of the cooling time is defined as when the actual test-piece temperature falls below 50 °C. The cold dwell time starts after the test pieces have cooled below 50 °C and ends when the test pieces are heated again. The characteristic parameters of a thermal cycle are summarized in Fig. 12.54.

Depending on the type of industrial application, *three* general types of thermal cycles are regarded as typical. The *first* type is long-dwell-time testing, which aims to simulate conditions in large-scale industrial facilities encountered in applications such as power-generation plants, waste-incineration plants or chemical industry. In these applications the metallic components are designed for extremely long-term operation, e.g. typically for up to 100 000 h. Thermal cycling of the materials occurs due to plant shutdowns, e.g. for regular maintenance, or due to unplanned shutdowns as a result of offset conditions. Therefore, the time intervals between various thermal cycles are relatively long and the number of cycles is (related to the long operation time of the components) relatively small, e.g. typically around 50 cycles. A recommended test cycle

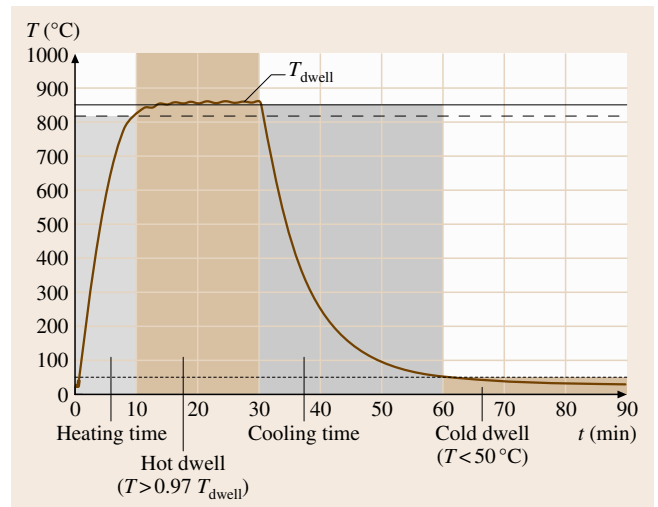


Fig. 12.54 Schematic of a temperature cycle in thermal cycling oxidation testing

for this application consists of an overall time of 24 h with a 20 h hot dwell time and 4 h period, which includes the cooling time, the cold dwell time and the heating time.

The *second* type is thermal cycling with short dwell times, which is typically experienced in applications such as jet engines, automotive parts, and heat-treatment facilities. The intervals between start and shutdown of the facilities are generally much shorter than in applications with long dwell times. Also the life times and/or the times until complete overhaul/repair (typically 3000–30 000 h) are shorter and, depending on the specific practical application, the number of cycles is much higher than in the cases above. The recommended testing cycle in this case consists of one hour hot dwell time and 15 min cold dwell time.

The *third* type of testing has ultrashort dwell times and mainly addresses applications of high-temperature alloys as heating elements in the form of wires or foils. Another typical application in which such ultrashort cycles prevail is catalyst foil carriers, e.g. in cars. In such applications the number of cycles is related to the overall design life (typically several hundred to a few thousand hours) and can be extremely high, and the time intervals between heating and cooling can be as low as minutes or even seconds. Such conditions are commonly also encountered in a number of other industrial applications such as burners and hot gas filters, as well as in a large variety of domestic applications where metallic heating elements are used e.g. in cooking plates, toasters, boilers, dryers, and fryers. The

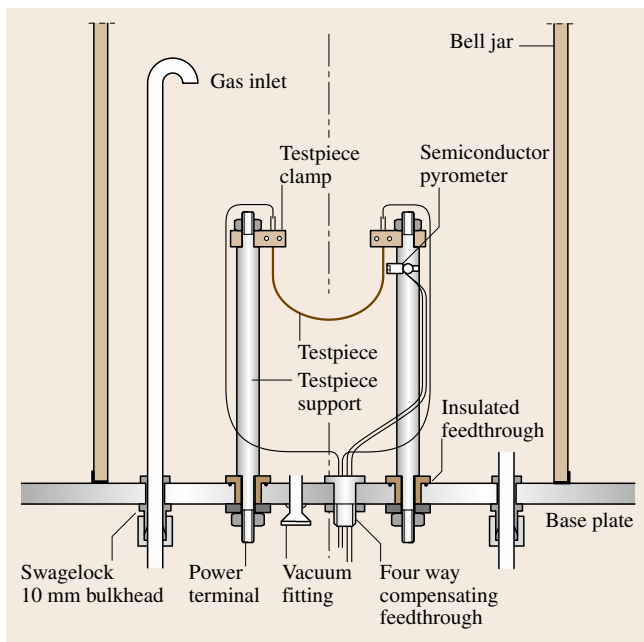


Fig. 12.55 Schematic of a test rig for thermal cycling oxidation testing using ultrashort temperature cycles

recommended test cycle for ultrashort-dwell-time testing consists of 5 min hot dwell and 2 min cold dwell. For this specific type of test a special test rig is needed, as described in detail in [12.112]. A schematic of this rig is shown in Fig. 12.55.

Generally the test duration in thermal cycling testing should be at least 300 h of accumulated hot dwell time to allow significant oxidation or corrosion of the test pieces. For more reliable results it is however recommended to extend the accumulated hot dwell time to at least 1000 h.

Evaluation of the Mass Change

After the tests, or during the tests at intervals when the specimens are cold, the mass has to be determined to quantify the corrosion kinetics. For this weighing procedure the specimens have to be taken out of the equipment but they should never be touched with hands, to eliminate any contamination (grease, salts). Generally the use of tweezers is recommended. After removing from the furnace the test-piece supporters containing the test pieces should be settled in the weighing room for 15 min to allow them to acclimatize. The test pieces should not be descaled unless specified. For each mass-change determination the sum m_{ST} of the mass of the test-piece support (m_S) contain-

ing one test piece (m_T) and the spalled scales (m_{sp}), i. e. $m_{ST} = m_S + m_T + m_{sp}$, the mass $m_S + m_{sp}$ of the test-piece support including the spalled scales, and the mass m_T of the test piece including the adherent scales should be measured. The following values have to be determined.

1. Gross mass change Δm_{gross} , i. e. mass change of test piece after cooling including collected spall

$$\Delta m_{\text{gross}} = m_{ST} - [m_S(t_0) + m_T(t_0)]; \quad (12.91)$$

2. Mass of spalled oxide Δm_{sp} , i. e. scale flaked from the test piece

$$\Delta m_{\text{sp}} = m_S - m_S(t_0); \quad (12.92)$$

3. Net mass change Δm_{net} , i. e. mass change of test piece after cooling without spall

$$\Delta m_{\text{net}} = m_T - m_T(t_0). \quad (12.93)$$

The net mass-change results of the test pieces from these measurements are plotted against time, as shown in Fig. 12.56. To determine the quantitative key parameters characterizing the corrosion behavior of the material a double logarithmic plot (log net mass change versus log time) as shown in Fig. 12.57 is used. From the y-axis intercept the oxidation rate constant $k(T)$ can be calculated as

$$\begin{aligned} a &= \log k(T)^{1/n} \rightarrow a = 1/n \log k(T) \rightarrow k(T) \\ &= 10^{an}. \end{aligned} \quad (12.94)$$

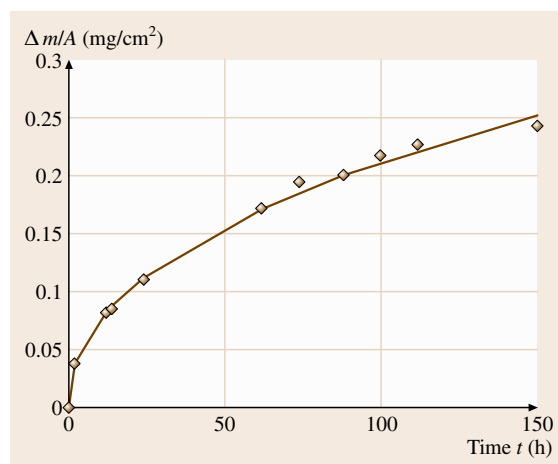


Fig. 12.56 Example of a plot of net mass change versus time as a direct plot

If spalling or breakaway oxidation occur, the time at the beginning of these mechanisms can also be of significant interest. In [12.109] a detailed procedure is described that allows the quantitative determination of these parameters.

12.8.4 Special High-Temperature Corrosion Tests

Burner Rig Tests

In addition to the standard tests described so far several special tests have also been developed that try to take the specific loading situation under practical conditions into account. Especially in the gas-turbine manufacturing industries the so-called burner rig test has become of some importance. In this test the test environment is produced by combustion of fuel with air (Figs. 12.58 and 12.59). In Fig. 12.58 a schematic of the so-called *high-velocity burner rig* is shown, where the gas stream on the specimen surface can reach velocities of up to mach 0.3. In the case of a *low-velocity burner rig*, combustion in a zone in the vicinity of the specimen supporter produces the test gas, which flows at a relatively low rate through a large tube to the specimens (Fig. 12.59). Especially in the case of a low-velocity burner rig, impurities are often added to the combustion environment, first of all in the form of salt water [12.87].

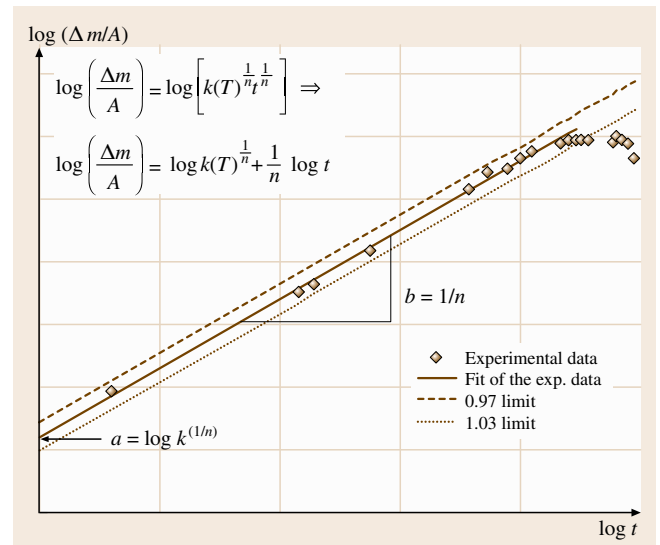


Fig. 12.57 Double logarithmic plot of the data of Fig. 12.56 for the evaluation of the parameters $k(T)$ and n

Typical test specimens have the shape of a rod with a rotating specimen carousel in the test rig carrying a larger number of these rods. Using this carousel, corrosion of rotating parts in engines is simulated. Furthermore all specimens are subjected to the same test conditions. In most cases with the burner rig test a ther-

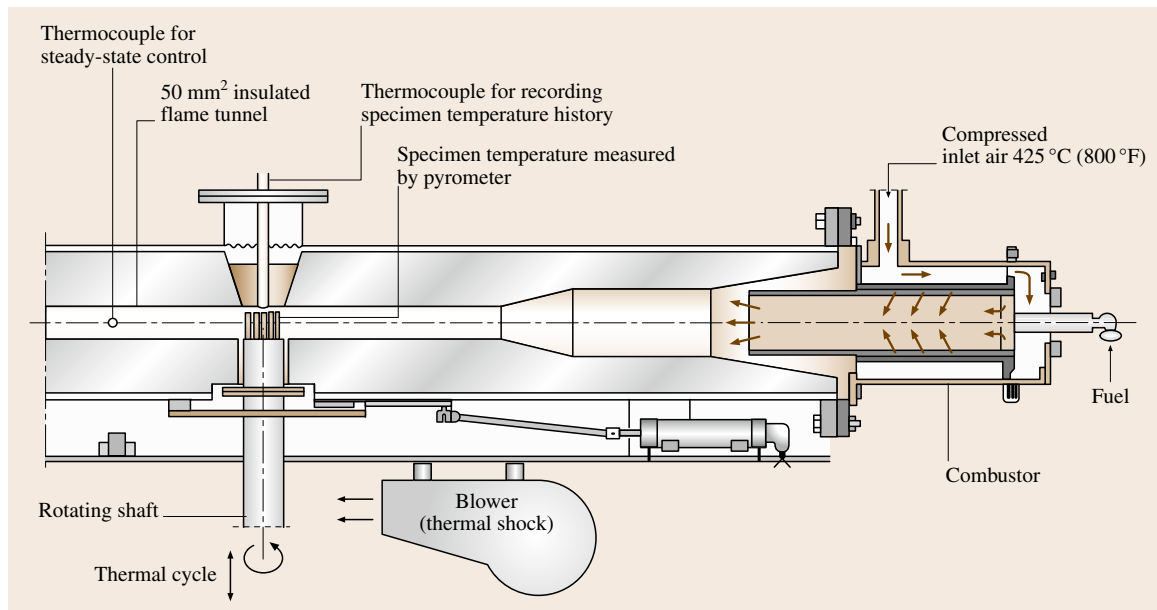


Fig. 12.58 Schematic of a high-velocity burner rig (after [12.87])

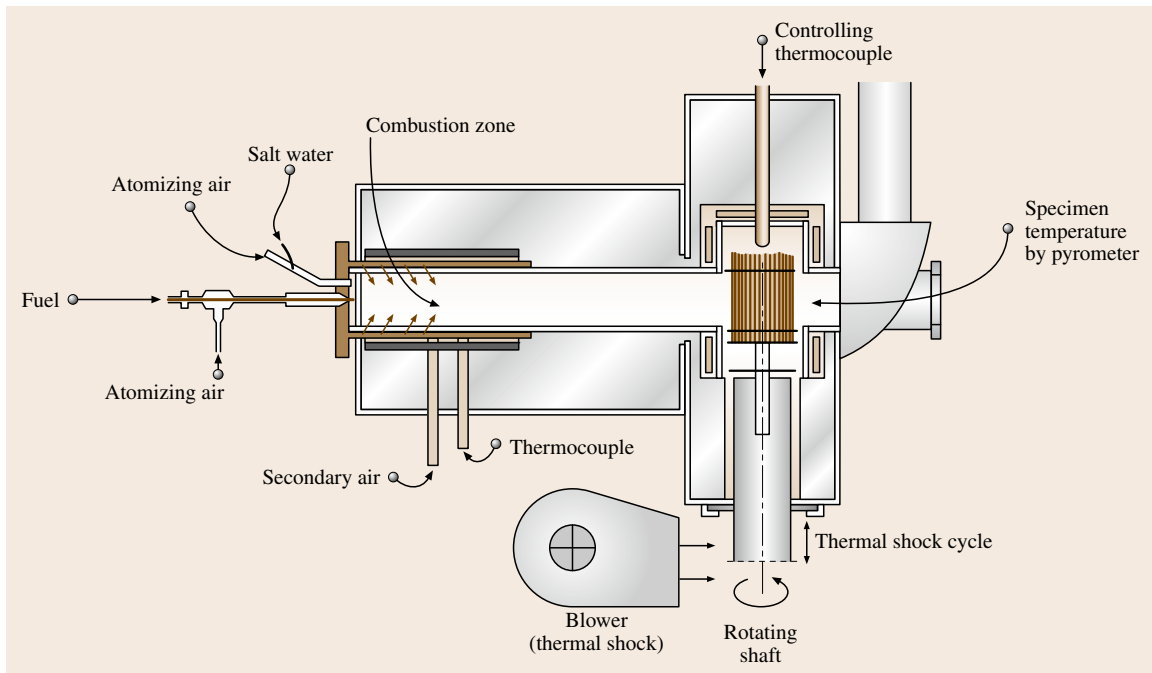


Fig. 12.59 Schematic of a low-velocity burner rig (after [12.87])

mal cycling test is performed, where the carousel with the specimens is automatically moved out of the hot zone once every 30 or 60 min and then cooled before reinsertion.

Corrosion with Mechanical Loading

A parameter which is neglected in standard high-temperature corrosion tests is the role of mechanical stresses, which are omnipresent in practical operation. Their role has been investigated extensively over the past two decades and it turned out that significant effects on the life time of high-temperature components can be possible [12.109, 113–115]. For this reason different types of tests have also been developed that combine mechanical stresses with attack by high-temperature corrosion. In most cases the equipment for such kinds of tests is basically the same as for the determination of the mechanical properties of materials at high temperatures. In other words, standard creep test [12.116] or constant-strain-rate test [12.117] as well as low cycle fatigue (LCF) and high cycle fatigue test (HCF) [12.118] rigs have been used. In some cases even creep fracture mechanics approaches have been combined with high-temperature corrosion investigations [12.119, 120]. For these mechanical high-temperature corrosion tests the standard

mechanical test rigs were equipped with an environmental chamber that can hold different types of test gases. Examples of the design of such environmental chambers are shown in Figs. 12.60 and 12.61, where Fig. 12.61 shows the environmental equipment to be inserted into a constant-load creep testing machine with two separate specimens, where the strain can be monitored by either mechanical or electronic strain gages. Figure 12.60 shows the schematic of a creep fracture mechanics environmental equipment for CT specimens where ceramic pull rods had been used. The information received from these experiments is the mechanical properties under the influence of corrosive attack, i. e. strain versus time, strain rate versus time, or stress versus strain curves. In the LCF and HCF test rigs it is usually the number of cycles to failure and the cyclic deformation curve that are measured. There are also examples in the literature where crack growth rates at high temperatures have been measured under corrosive conditions [12.119–121].

An important aspect of these tests is post-test evaluation by metallographic sectioning and microanalysis of the corrosion products. The results from such investigations can reveal whether internal formation of corrosion products at grain boundaries or at crack tips can significantly reduce the life time of components

by corrosion-assisted crack initiation and crack growth. A number of examples have been studied in the literature [12.113].

12.8.5 Post-Test Evaluation of Test Pieces

Macroscopic Evaluation

The macroscopic appearance of the surface of the test piece should be photographed if necessary using a low magnification. Color photographs are preferred over black and white photographs since coloring may already give some information about the type of oxidation/corrosion of the surface.

Metallographic Cross Section

For scale thickness measurements by metallographic cross sections it is recommended that the recommendations in [12.88] and the new draft ISO document ISO/CD 26146 (Table 12.4) be followed. Care has to be taken in mounting the specimen orthogonally to the primary axis of the test piece. The cross section of the test pieces is analyzed using conventional light microscopy. The measurements consist of

- deposit thickness,
- scale thickness,
- depth of internal penetration inside the grains and at grain boundaries,
- depth of any depleted zone,
- remaining cross section of unaffected material.

A minimum of eight measurements per test piece should be taken. In addition the position of maximum attack is measured.

Reporting

The report of each test should contain the following information.

- Test material: manufacturer, name of the material (manufacturer designation, ASTM designation, Deutsches Institut für Normung (DIN) designation, etc.), grade or symbol, heat number/batch number, chemical composition, processing conditions, heat-treatment conditions.
- Test piece: designation of test piece, dimensions and surface area of test piece, surface finish condition of test piece, degreasing method of test piece, method of test-piece support, initial mass.
- Temperature and testing environments: test temperature (and maximum and minimum temperatures

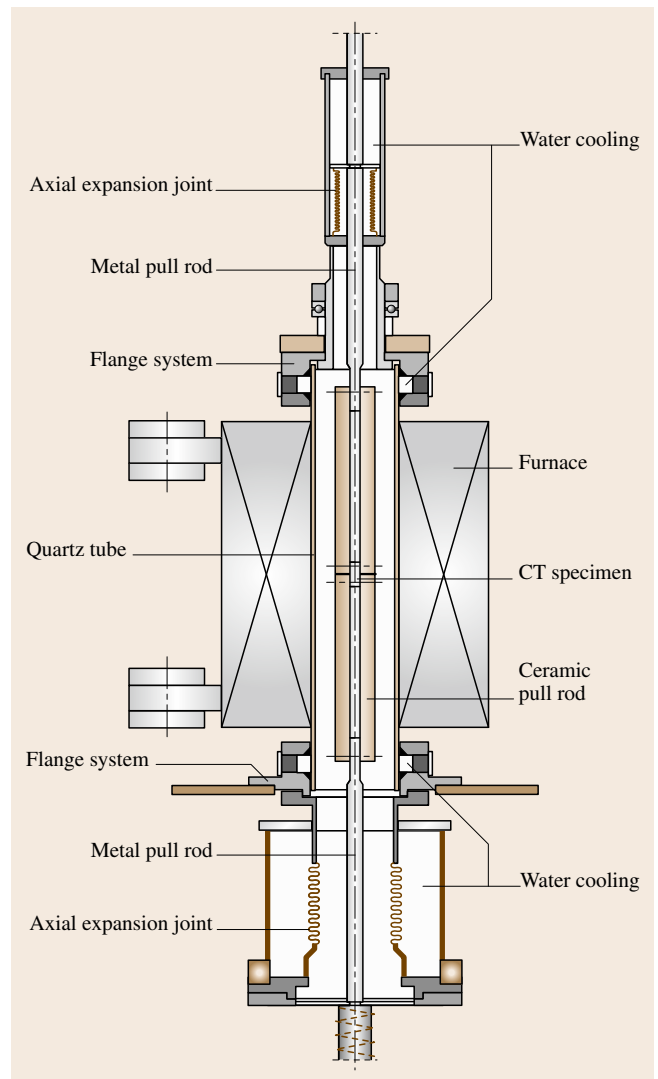


Fig. 12.60 Schematic of a closed system for crack growth measurements in high-temperature corrosion environments (after [12.119])

during the test), test duration, hot dwell time, cold dwell time, heating time, cooling time, dew point temperature of humidified test gas or humidity of laboratory air, flow rate of the test gas, type of system (open or closed).

- Test results: plot of net mass change per area $\Delta m_{\text{net}}/A$ in mg/cm^2 versus time t , results of any metallographic investigations, amount of spalled scale Δm_{sp} in mg, photograph of appearance after testing, photograph of the metallographic section

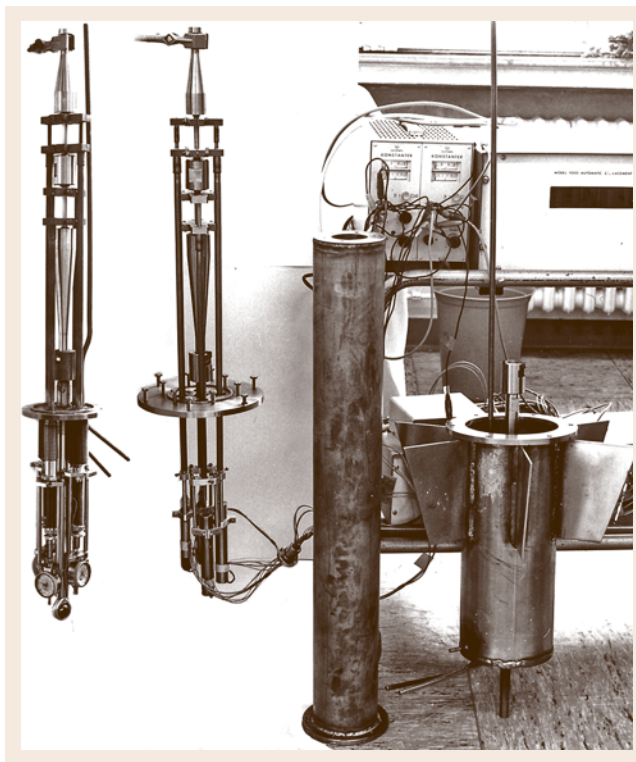


Fig. 12.61 Two examples of closed systems for constant load creep testing in high-temperature corrosion environments (after [12.122]) ◀

the accumulated hot dwell time t_B that correspond to the onset of spallation or breakaway oxidation. If existing the report should also contain analytical results from scanning electron microscopy/EDS (Energy Dispersive Spectrometer), electron probe microanalysis/WDS (Wavelength Dispersive Spectrometer) or x-ray diffraction.

12.8.6 Concluding Remarks

The aim of this section has been to provide a concise and informative overview of the measurement methods used today in high-temperature corrosion testing. Two of the more commonly used test methods were described in some detail while the others were only discussed very briefly. For more detailed information it is recommended to read the literature given in the list of references. It should, however, be pointed out that there is still significant development work going on in these test methods. A certain settlement of this situation will be reached after finalization of the present work items of work group 13 in ISO technical committee 156. In the meantime it is recommended to follow the work of this work group closely when planning the set up of new high-temperature corrosion testing facilities.

of the test piece including the surface layer after testing, oxidation rate constant $k(T)$, exponent of growth law n , the number of cycles N_B and

12.9 Inhibitor Testing and Monitoring of Efficiency

The addition of small amounts of chemicals capable of reducing corrosion of the exposed metal is a preventative measure known as corrosion inhibition. According to the ISO 8044 definition corrosion inhibitors are chemical substances that decrease the corrosion rate when present in the corrosion system in sufficient concentration, without significantly changing the concentration of any corrosive agent.

Inhibitors may act on both cathodic and anodic partial reactions and are termed accordingly either cathodic or anodic inhibitors. A cathodic inhibitor shifts the corrosion potential in a negative direction, while the anodic inhibitor causes a positive change; in both cases the corrosion rate decreases.

Investigating corrosion inhibitor efficiency aims to gather information on the profile of the functional additive, including its inhibition mechanism. Corrosion

experiments as well as electrochemical and surface analytical methods are the major tools in such investigations. In this context it is of utmost importance to note that electrochemical measurements are not corrosion experiments and cannot replace real corrosion experiments. On the other hand, testing tries to find out if and how well a functional substance performs under specific experimental conditions. Performance in a test may not correlate with performance under service conditions. There are numerous examples where functional compounds have been developed and designed to pass specific tests but have failed in service application. *Monitoring* in this context intends to create online information on the time-related status of the corrosion intensity of an inhibited corrosion system. Appropriate correlation between monitoring data and the real corrosion status of a system

needs a detailed knowledge of the corrosion system itself.

12.9.1 Investigation and Testing of Inhibitors

As corrosion inhibitors are active at the electrified interface their performance can be investigated by electrochemical means.

Various electrochemical measuring methods have been developed and applied for investigations of inhibited systems. The questions arise: which method gives which information and what are the application limits of the methods? Before applying any of the methods one has to consider the actual task of the investigation. Is it aimed mainly at scientific research or is information needed on the performance of inhibitors under service conditions.

In scientific research it is important, which of the two partial reactions (Fig. 12.62), the *anodic metal dissolution*,



or the cathodic reduction of an oxidizing agent,



is influenced by the inhibitor. Is it an anodic, cathodic or anodic–cathodic inhibitor (Fig. 12.63a–c)? Is the cor-

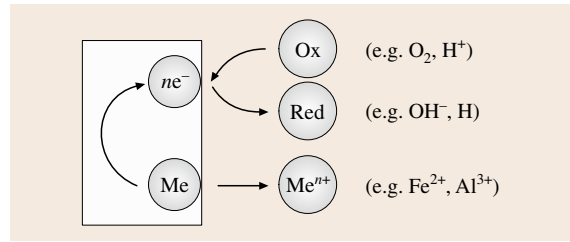


Fig. 12.62 Schematic representation of electrochemical corrosion

rosion rate controlled by charge transfer or by mass transport (Fig. 12.64a–c)? Is the inhibition effect due to the formation of films, adsorption on metal surfaces (e.g. in corrosion product pores) or incorporation in corrosion product layers? (Fig. 12.64c)?

For practical applications information is needed on the effect of inhibitors on, e.g.,

- the reduction of metal loss in corrosive environments,
- the influence of hydrogen uptake of the metal (in systems with hydrogen formation in the cathodic partial reaction),
- the likelihood of localized corrosion.

Before starting any investigation the corrosion system must be carefully studied in terms of the appearance of

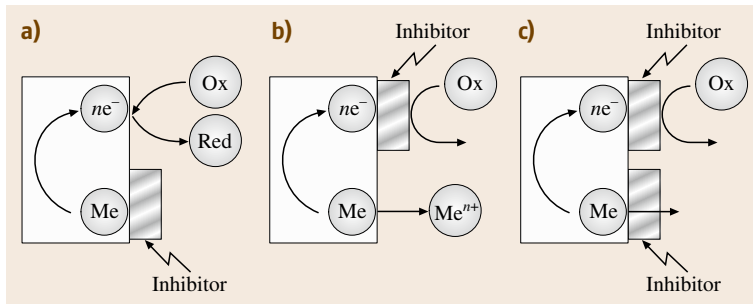


Fig. 12.63a–c Schematic representation of inhibitor action on bare metal surface: (a) anodic inhibition, (b) cathodic inhibition, (c) anodic–cathodic inhibition

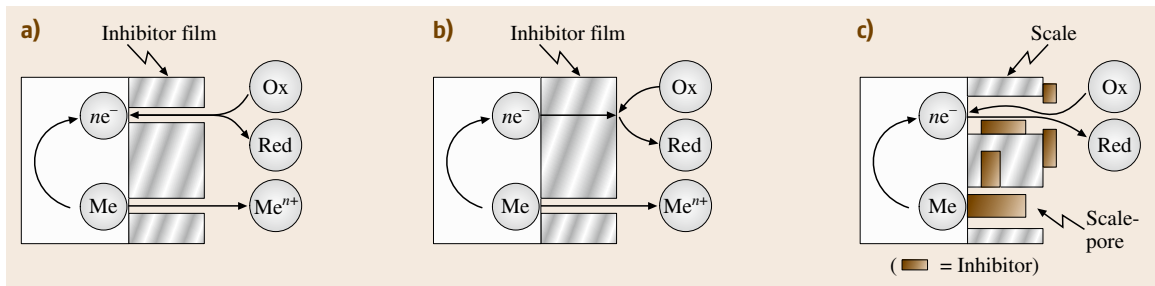


Fig. 12.64a–c Schematic representation of inhibitor action: (a) mass transport control at films (b) charge-transfer control at films (c) inhibitor action on scaled surfaces

corrosion (uniform, local, ability to passivation, character of layers developed by corrosion, scaling etc.) and the rate-determining step of the corrosion process. Particularly in exposure testing the analysis of the electrolyte over the period of testing can play an important role.

The methods of investigation were generally outlined in Sects. 12.1 and 12.2. All conclusions regarding the applicability and interpretation of such tests also apply for testing of inhibitors. Special care has to be taken if results from laboratory testing are transferred into practice. In any case it is advisable to carry out performance monitoring during service. The aim of this section primarily focuses on performance of systems affected by corrosion. Therefore monitoring of efficiency will be the main focus of this publication.

12.9.2 Monitoring of Inhibitor Efficiency

General Remarks

It is important to monitor the effectiveness of a corrosion-inhibitor treatment. It is even more important to ensure that the conditions under which the monitoring is carried out are representative and relevant to the operational conditions. Monitoring should ideally be carried out under the worst conditions that are likely to be encountered (e.g. stagnant areas or very high flow rates etc.), otherwise failures may occur while the monitoring process indicates that inhibition is effective.

Variables that need to be considered when monitoring include

- environment – both normal and extraordinary conditions fluid flow conditions, including multiphase flow patterns,
- temperature,
- fluid velocity chemical analysis – to cover seasonal variations,
- type of system – closed, open evaporative cooling, once-through.

Application of Monitoring Data

The broad objective of carrying out monitoring is to manage the corrosion problem, in this case to control the corrosion-inhibitor treatment so that it works properly. The management process thus requires objectives to be set, and measurements to be made that can be compared with these objectives, so that adjustments to the treatment can be made as necessary to achieve the required performance. The objectives may include one or more of the following, depending upon the corrosion management philosophy

- to achieve a specified degree of corrosion protection (corrosion rates), to correlate with previous experience or tests (corrosion rates, inhibitor concentrations),
- to achieve a required inhibitor efficiency E_i

$$E_i = 100(w_o - w_{inh}/w_o);$$

where w_o = weight loss or corrosion rate without inhibitor, w_{inh} = weight loss or corrosion rate with inhibitor.

It is important that the type of measurement made provides the data required. Thus, if the objective is to maintain a specified inhibitor concentration, corrosion rate measurements will be of little value.

Measurement of Inhibition Parameters to be Measured

A number of parameters relevant to corrosion inhibition may be measured.

- Actual inhibitor concentration,
- Inhibitor efficiency by corrosion monitoring,
- Operational parameters in the plant that may affect inhibitor performance,
- Chemical composition of the fluid containing the inhibitor.

Frequency of Measurement

The frequency of measurement may depend upon corrosion monitoring practice. In general it is important to monitor immediately after the first addition of the inhibitor, and then at least daily until the level has stabilized, since some of the inhibitor will be removed from the fluid by adsorption on surfaces within the system.

Open systems are more likely to suffer unplanned upsets than closed ones, and therefore should be monitored more frequently. For critical systems online measurements are useful. Online measurement systems have other advantages.

- They allow more rapid detection of changes or trends in corrosion, and data can be continually analyzed to reveal longer-term trends.
- They eliminate variations associated with sampling processes.

Chemical Analysis of Inhibitor Concentration Sampling Techniques. It is essential to take as representative a sample of the fluid as possible. The location of sampling points is important.

- Avoid dead legs,
- If possible, use isokinetic sampling techniques,

- Avoid long sampling lines with high surface : volume ratios.

When taking a sample

- always run a volume of the fluid to be sampled to waste before taking a sample,
- wash out the container with fluid before filling with the sample,
- observe sample preservation requirements (e.g. air exclusion, cool in ice).

Measurement of Inhibitor Concentration

The efficiency of an inhibitor is usually closely dependent upon its concentration in solution, since it is assumed that there is an equilibrium of the form: dissolved inhibitor + surface → inhibited surface.

Measurement of the concentration of the inhibitor does not give direct information about its efficiency. A minimum concentration is usually specified for the inhibitor to provide the required performance, and this depends upon the conditions. Changes in operating conditions may therefore require adjustments to be made in inhibitor concentration to maintain the same performance.

Allowing the concentration to fall below the specified level can be very dangerous with anodic inhibitors, since partial failure of anodic inhibition can lead to a high-cathode-area low-anode-area situation, and induce rapid localized corrosion.

Characteristics of Commercial Inhibitors

Measuring the concentrations of commercial inhibitors may not be straightforward as

- commercial inhibitors are rarely pure analytical-grade chemicals,
- they may be formulated with other chemicals to improve their performance (solvents, surfactants),
- their specification may allow a range of compositions.

The variability in concentration and composition may make it desirable to analyze the product before use,

unless a quality-assurance scheme is in operation. The supplier's recommendations for the concentrations to be used should be adhered to; this avoids complications if problems or failure occurs.

Laboratory Methods of Analysis

These have a number of advantages.

- They are very versatile.
- They can be very sensitive.
- High selectivity is possible.

A wide range of techniques is available. Separation and detection techniques are combined to increase sensitivity. Particularly useful are

- ICPS – inductively coupled plasma spectrometry;
- MS – mass spectrometry;
- HPLC – high-performance liquid chromatography;
- IC – ion chromatography.

The disadvantages are

- they require special, usually expensive, equipment,
- good performance requires well-trained operators,
- samples have to be returned to the laboratory, resulting in a time delay.

Field Methods of Analysis

These have a number of common features.

- They give almost instant results.
- They employ preprepared and prepacked reagents (the sell-by date should not be exceeded).
- They usually involve color formation reactions.
- They compare color to intensity scale or use a battery-operated photometer.

Some common methods are specified in Table 12.6.

Some disadvantages are

- individual kits cover limited concentration ranges; choose the one you need,
- look out for possible interferences (other colored species present),

Table 12.6 Field methods of analysis

Species	Semiquantitative method	Quantitative
CrO ₄ ⁻	Diphenylcarbazone complex	Photometry of diphenylcarbazone complex
NO ₂	Magenta azo dye	(a) Photometry of magenta azo dye; (b) Acidimetric titration with sulfamic acid
PO ₄ ³⁻	Phosphomolybdenum blue	Photometry of molybdenum-vanadate – phosphoric acid
SiO ₂ /silicate	Silicomolybdenum blue	Photometry of silicomolybdenum blue
Zn	Zn-thiocyanate-brilliant green	Atomic absorption spectroscopy

Table 12.7 Summary of techniques

Technique type	Information	Time for measurement	Response to change	Corrosion type	Application interpretation
Optical	Distribution of attack	Fast, if, accessible	Slow	Localized	Simple
Analytical methods	Corrosion state, total	Fairly fast	Fairly fast	General	Relatively easy, needs knowledge of corrosion in system, inhibitor present
Corrosion coupons	Average rate of corrosion and form	Long exposure	Poor	General or localized	Easy, simple
Polarisation resistance	Corrosion rate	Immediate	Fast	General, localized	Simple to complex
Electrical resistance	Integrated corrosion	Immediate	Moderate	General	Relatively simple
Corrosion potential	Corrosion state	Immediate	Fast	General or localized	Easy to apply, needs knowledge and experience to interpret
ZRA = zero-resistance ammetry	Corrosion state	Immediate	Fast	Bimetallic galvanic corrosion	Fairly easy, needs corrosion knowledge
Ultrasonics	Thickness of metal left cracks, pits	Fast	Fairly poor	General or localized	Easy to apply, care with sensitivity
Eddy currents	Cracks, pits	Immediate	Fairly poor	Localized	Easy
Acoustic emission	Propagation of cracks, leak detection, cavitation	Immediate	Fast	Cracking, leaks	Expensive, needs specialist
Hydrogen probe	Total corrosion	Fast	Poor	General	Easy, only in acid
Sentinel holes	Go/no go for slow remaining thickness		Poor	General	Easy, relatively simple
Thin-layer activation (TLA)	Integrated material removal	Slow	Variable	General, localized	Simple, special equipment

- color intensity may vary with time, may bleach in sunlight,
 - the number of species that can be detected is limited (pH, nitrite, chromate).
- Interpretation: Inhibitor Loss Processes**
Lower than expected concentrations of inhibitor may be the result of a number of processes.
- Precipitation, which may depend on temperature, solution composition,
 - Chemical reaction with other species, e.g. oxygen,
 - Adsorption on surfaces (metals, solids in suspension, corrosion products, precipitates),
 - Degradation by microorganisms,
 - Thermal degradation.
- Mass balance: gross check of concentration – chemicals used, make-up water volume,
 - System features
 - concentration of atmospheric impurities in open systems,
 - process-side leaks,
 - inefficient blow-down microbiological activity,
 - fouling of surfaces, including heat transfer surfaces.
 - Operational parameters
 - fluid temperature surface temperature, including hot-spots,
 - flow velocities – periods of shut-down.

12.9.3 Monitoring Inhibition from Corrosion Rates

General

The main objective of using inhibitors is to control corrosion, therefore a measurement of the corrosion rate can be the most direct way of assessing the effectiveness of a corrosion control programme. However, a number of points need to be borne in mind.

To assist in finding the reason for the loss of inhibitor, measurements of other fluid chemistry parameters may be useful, as suggested below.

Additional Measurements

- Water chemistry: including pH, dissolved species – chloride, iron etc.,

- The technique must replicate the type of corrosion (general, localized etc.).
- The results must be presented simply and be easy to interpret.
- Some techniques are real-time online measurements, others are not.
- Most rates are measured with samples in the form of a probe or coupon; the results will depend on the geometry (flush, cylindrical, crevice etc.).

Electrical Techniques

Polarization Resistance.

- These are based on the rates of cathodic and anodic electrochemical corrosion reactions.
- They may be difficult to interpret if protective layers are formed.
- Other redox reactions may occur at the same time as the corrosion reaction.
- Bimetallic and selective corrosion processes cannot be detected.

Electrical Resistance.

- This depends upon the change in resistance of a wire or thin plate due to corrosion and/or erosion,
- It can be very sensitive: 1–1000 mpy,
- The metallurgical state of probe may be very unrepresentative of the real material; geometry may be important (e.g., flush, intrusive).

FSM – Electrical Fingerprint.

- This is similar to electrical resistance in principle.
- It uses the actual vessel, pipe.
- It provides nonintrusive, real-time, on-line wall thickness data.
- It allows multiple (96) measurements at different locations e.g. in multiphase flow.
- Changes in thickness are measured from voltage changes when current passed.
- Computer display is provided.
- It is relatively expensive.

Corrosion Coupons. These are the most widely used means of monitoring corrosion. Their advantages are

- cheap to buy,
- available with standard finish, weighed, degreased,

- can give information about localized corrosion,
- bimetallic and welded coupons can be prepared,
- effects of stress can be reproduced in C-rings or four-point load probes can be inserted and retrieved during operation through access fittings.

The measurements that can be made with coupons include

- weight determination after drying (look out for spalling of deposits, corrosion product),
- weight loss after pickling,
- percent area of localized corrosion,
- pit depth by sectioning, grinding,
- analysis of corrosion products,
- optical, SEM metallography of corroded surface.

They have a number of limitations.

- They must be electrically insulated from plant components they only provide integrated measurements of corrosion;
- They must be of reasonable area (1500–2000 mm²) to avoid cut-edge effects;
- The extent of localized corrosion may depend on area;
- The surface finish and material should be the same as for components to be tested;
- There is no standard precorroded surface;
- The location of the coupon is important (fluid flow, temperature effects).

A special type of corrosion coupon is required for measurements under heat-transfer conditions. Such specimens usually have tubular geometries. A number of features have to be considered in choosing and setting up such specimens

- choice of electrical or sensible fluid heating,
- electrical control is most convenient, and easiest,
- most industrial heat transfer involves fluids,
- conditions at the surface depend on the heat-transfer coefficient,
- the heat-transfer coefficient depends on the fluid and the flow conditions, surface temperature or heat flux control.

Table 12.7 provides information on techniques used in the field and their most important features.

References

- 12.1 R. Baboian: *Corrosion Tests and Standards* (ASTM, Philadelphia 1995)
- 12.2 DIN EN ISO 8044: Corrosion of Metals and Alloys – Basic Terms and Definitions (ISO 8044:1999) Trilingual version EN ISO 8044:1999
- 12.3 National Bureau of Standards: *Economic Effects of Metallic Corrosion in the United States*, Special Publication, Vol. 511 (NBS, Gaithersburg 1978)
- 12.4 W. von Baeckmann, W. Schwenk, W. Prinz (Eds.): *Handbook of Cathodic Protection* (Gulf, Houston 1997)
- 12.5 R.G. Kelly, J.R. Scully, D.W. Shoesmith, R.G. Buchheit: *Electrochemical Techniques in Corrosion Science and Engineering* (Dekker, New York 2003)
- 12.6 H. Kaesche: *Corrosion of Metals* (Springer, Berlin, Heidelberg 2003)
- 12.7 M. Schütze (Ed.): *Corrosion and Environmental Degradation*, Vol. I/II (Wiley–VCH, Weinheim 2000)
- 12.8 R.N. Parkins: *Corrosion Processes* (Applied Science, London 1982)
- 12.9 J.E. Strutt, J.R. Nicholls: *Plant Corrosion* (Ellis Horwood, Chichester 1987)
- 12.10 E. Mattson: *Basic Corrosion Technology for Scientists and Engineers* (Ellis Horwood, Chichester 1989)
- 12.11 N. Sridhar, G. Cragnolino (Eds.): *Application of Accelerated Corrosion Tests to Service Life Prediction of Materials*, Vol. 1194 (ASTM STP, Philadelphia 1994)
- 12.12 V. Romanov: *Corrosion of Metals* (US Department of Commerce, Springfield 1969)
- 12.13 P. Dillon: *Corrosion Control in the Chemical Process Industry* (McGraw–Hill, New York 1986)
- 12.14 D. Donovan: *Protection of Metals from Corrosion in Storage and Plants* (Ellis Horwood, Chichester 1986)
- 12.15 P. Marcus, J. Udar: *Corrosion Mechanisms in Theory and Practice* (Dekker, New York 1995)
- 12.16 G. Fontana, N.D. Greene: *Corrosion Engineering* (McGraw–Hill, New York 1987)
- 12.17 C. Scully: *The Fundamentals of Corrosion* (Butterworth Heinemann, Oxford 1990)
- 12.18 L. Shreir, R.A. Jarman, G.T. Burstein: *Corrosion*, Vol. 2, 3rd edn. (Butterworth Heinemann, Oxford 1994)
- 12.19 P. Dillon (Ed.): *Corrosion Handbook, No. 1, The Forms of Corrosion Recognition and Prevention* (NACE, Houston 1982)
- 12.20 R.C. Weast: *Handbook of Chemistry and Physics* (CRC, Cleveland 1977), D 141
- 12.21 S. Trasatti: *J. Electroanal. Chem.* **52**, 313 (1974)
- 12.22 R. Gomer, S. Tryson: *J. Chem. Phys.* **66**, 4413 (1977)
- 12.23 R. Gomer, S. Tryson: *J. Chem. Phys.* **66**(D61), 4413 (1977)
- 12.24 I. Barin, O. Knacke: *Thermodynamic Properties of Inorganic Substances* (Springer, Berlin 1973)
- 12.25 R. Gomer, S. Tryson: *J. Chem. Phys.* **66**(D111), 4413 (1977)
- 12.26 M. Pourbaix: *Atlas d'Equilibres Electrochimiques* (Guthiers Villars and Cie, Paris 1963)
- 12.27 M. Pourbaix: *Atlas of Electrochemical Equilibria in Aqueous Solutions* (Pergamon, Oxford 1966)
- 12.28 K.J. Vetter: *Electrochemical Kinetics. Theoretical Aspects* (Academic, New York 1967)
- 12.29 H.–H. Strehblow: Mechanisms of pitting corrosion. In: *Corrosion Mechanisms in Theory and Praxis*, ed. by P. Marcus (Dekker, New York 2002) p. 258
- 12.30 H.–H. Strehblow: Phenomenological and electrochemical fundamentals of corrosion. In: *Corrosion and Environmental Degradation*, ed. by M. Schütze (Wiley–VCH, Weinheim 1999) p. 59
- 12.31 H.–H. Strehblow: Pitting corrosion. In: *Encyclopedia of Electrochemistry, Corrosion and Oxide Films*, Vol. 4, ed. by A.J. Bard, M. Stratmann, G.S. Frankel (Wiley–VCH, Weinheim 2003) p. 337
- 12.32 R. Christen, G. Baars: *Chemie* (Sauerländer, Aarau 1977) p. 778, (in German)
- 12.33 H.–H. Strehblow: Phenomenological and electrochemical fundamentals of corrosion. In: *Corrosion and Environmental Degradation*, ed. by M. Schütze (VCH, Weinheim 1999) p. 1
- 12.34 E. Heusler: OH Katalyse, *Z. Elektrochem.* **62**, 582 (1958), (in German)
- 12.35 K.J. Vetter: *Elektrochemische Kinetik* (Springer, Berlin 1961) p. 432, (in German)
- 12.36 H. Kaesche: *Die Korrosion der Metalle* (Springer, Berlin 1979), (in German)
- 12.37 H. Kaesche: *Die Korrosion der Metalle*, 3rd edn. (Springer, Berlin 1990), (in German)
- 12.38 M. Stern: *J. Electrochem. Soc.* **102**, 609 (1955)
- 12.39 K.J. Vetter, H.–H. Strehblow: *Ber. Bunsenges. Phys. Chem.* **74**, 1024 (1970), (in German)
- 12.40 J. Newman, D.N. Hansen, K.J. Vetter: *Electrochim. Acta* **22**, 829 (1974)
- 12.41 W.G. Levich: *Physicochemical Hydrodynamics* (Prentice Hall, New York 1962)
- 12.42 W.J. Albery, M.L. Hitchman: *Ring Disc Electrodes* (Clarendon, Oxford 1971)
- 12.43 B.P. Löchel, H.–H. Strehblow: *Werkst. Korros.* **31**, 353 (1980), (in German)
- 12.44 S. Haupt, H.–H. Strehblow: *Langmuir* **3**, 873 (1987)
- 12.45 G. Engelhardt, T. Jabs, H.–H. Strehblow: *J. Electrochem. Soc.* **139**, 2176 (1992)
- 12.46 R.S. Lillard: Scanning electrode techniques for investigating near surface solution current densities in analytical methods. In: *Corrosion Science and Engineering*, ed. by P. Marcus, F. Mansfeld (CRC Taylor Francis, Boca Raton 2006) p. 571
- 12.47 H.S. Isaacs: *J. Electrochem. Soc.* **138**, 722 (1991)
- 12.48 H.S. Isaacs, B. Vyas: *ASTM–STP* **727**, 3–33 (1981)
- 12.49 M. Rohwerder, M. Stratmann, P. Leblanc, G.S. Frankel: Application of scanning kelvin probe

- in corrosion science. In: *Analytical Methods in Corrosion Science and Engineering*, ed. by P. Marcus, F. Mansfeld (CRC Taylor Francis, Boca Raton 2006) p. 605
- 12.50 M. Stratmann, K.T. Tim, H. Streckel: *Z. Metallkd.* **81**, 715 (1990)
- 12.51 F.G. Cottrell: *Z. Phys. Chem.* **42**, 385 (1903)
- 12.52 K.J. Vetter: *Electrochemical Kinetics* (Academic, New York 1967)
- 12.53 H. Gerischer, W. Vielstich: *Z. Phys. Chem.* **3**, 16 (1955)
- 12.54 H.-H. Strehblow, P. Marcus: X-ray photoelectron spectroscopy in corrosion research. In: *Analytical Methods in Corrosion Science and Engineering*, ed. by P. Marcus, F. Mansfeld (CRC Taylor Francis, Boca Raton 2006) p.1
- 12.55 H.-H. Strehblow: Passivity of metals. In: *Advances in Electrochemical Science and Engineering*, ed. by R.C. Alkire, D.M. Kolb (Wiley-VCH, Weinheim 2003) p. 272
- 12.56 J. Castle: Auger electron spectroscopy. In: *Analytical Methods in Corrosion Science and Engineering*, ed. by P. Marcus, F. Mansfeld (CRC Taylor Francis, Boca Raton 2006) p. 39
- 12.57 D. Lützenkirchen-Hecht, H.-H. Strehblow: Synchrotron methods for corrosion research. In: *Analytical Methods in Corrosion Science and Engineering*, ed. by P. Marcus, F. Mansfeld (CRC Taylor Francis, Boca Raton 2006) p.169
- 12.58 J.L. Dawson, K. Hladky: The measurement of localized corrosion using electrochemical noise, *Corros. Sci.* **21**, 317–322 (1981)
- 12.59 J.L. Dawson, K. Hladky: The measurement of corrosion using $1/f$ noise, *Corros. Sci.* **22**, 231–237 (1982)
- 12.60 J.L. Dawson, J. Uruchurtu: Electrochemical methods in corrosion research, *Mater. Sci. Forum* **8**, 436 (1986)
- 12.61 A. Legat: Electrochemical noise as the basis of corrosion monitoring, 12th Int. Corros. Congr., Vol. 3A (1993) pp. 1410–1419
- 12.62 B. Lumsden, M.W. Kendig, S. Jeanjaquet: *Electrochemical noise for carbon steel in sodium chloride solutions. – Effect of chloride and oxygen activity*, Vol. CORROSION/92 (National Association of Corrosion Engineers (NACE), Houston/Tx 1992), Paper 224
- 12.63 N. Rothwell, D.A. Eden: *Electrochemical noise techniques for determining corrosion rates and mechanisms*, Vol. CORROSION/92 (National Association of Corrosion Engineers (NACE), Houston/Tx 1992), Paper 223
- 12.64 A. Cottis, C.A. Loto: Electrochemical noise generation during SCC (stress corrosion cracking) of high strength carbon steel, *Corrosion* **46**, 12–19 (1990)
- 12.65 H. Xiao, F. Mansfeld: Development of electrochemical test methods for the study of localized corrosion phenomena in biocorrosion, ACS Symp. (Washington 1992)
- 12.66 H. Xiao, F. Mansfeld: Electrochemical noise analysis of iron exposed to NaCl solutions of different corrosivity, *J. Electrochem. Soc.* **140**, 2205–2209 (1993)
- 12.67 H. Xiao, F. Mansfeld: Electrochemical noise analysis of iron exposed to NaCl solutions of different corrosivity, 12th Int. Corros. Congr., Vol. 3A (Houston 1993) pp. 1388–1402
- 12.68 H. Böhni: *Schweiz. Bauztg.* **93**, 603 (1975), (in German)
- 12.69 DIN 50922: *Korrosion der Metalle, Untersuchung der Beständigkeit von metallischen Werkstoffen gegen Spannungsrissskorrosion* (1985), (in German)
- 12.70 DIN EN ISO 7539: Teil 1 bis 7, *Korrosion der Metalle und Legierungen, Prüfung der Spannungsrissskorrosion* (1995), (in German)
- 12.71 N. Parkins, F. Mazza, J.J. Royuela, J.C. Scully: *Br. Corros. J.* **7**, 154–167 (1972)
- 12.72 B. Stellwag, H. Kaesche: *Werkst. Korros.* **33**, 274–323 (1982), (in German)
- 12.73 H. Kaesche: *Bruchvorgänge*, Vortr. 20. Sitz. DVM-Arbeitskr. (Frankfurt am Main 1988) pp. 9–45, (in German)
- 12.74 H. Böhni: *Werkst. Korros.* **26**, 199 (1975), (in German)
- 12.75 F. Kuster, K. Bohnenkamp, H.-J. Engell: *Werkst. Korros.* **29**, 792 (1978), (in German)
- 12.76 R. Grauer, B. Knecht, P. Kreis, J.R. Simpson: *Werkst. Korros.* **42**, 637 (1991), (in German)
- 12.77 F. Stoll: *Spannungsrissskorrosion von Spannstählen*. Ph.D. Thesis (Universität Erlangen-Nürnberg, Erlangen 1982), (in German)
- 12.78 E. Wendler-Kalsch: *Grundlagen und Mechanismen der H-induzierten Korrosion metallischer Werkstoffe*. In: *Wasserstoff und Korrosion*, ed. by D. Kuron (Verlag I. Kuron, Bonn 1986), (in German)
- 12.79 C.A. Zapffe, C.E. Sims: *Trans. AIME* **145**, 225 (1941)
- 12.80 N.J. Petch, P. Stables: *Nature* **169**, 842 (1952)
- 12.81 J.K. Tien, A.W. Thompson, J.M. Bernstein, R.J. Richards: *Metall. Trans. A* **7**, 821 (1976)
- 12.82 R. Troiano: *Trans. ASM* **52**, 54 (1960)
- 12.83 R.A. Oriani: *Ber. Bunsenges. Phys. Chem.* **76**, 848 (1972), (in German)
- 12.84 U. Nürnberger: *Korrosion und Korrosionsschutz im Bauwesen*, Vol.1 (Bauverlag, Wiesbaden, Berlin 1995), (in German)
- 12.85 E. Riecke: *Arch. Eisenhüttenwes.* **49**, 509 (1978), (in German)
- 12.86 E. Riecke: *Arch. Eisenhüttenwes.* **44**, 647 (1973), (in German)

- 12.87 J.R. Davies (Ed.): *Heat-Resistant Materials* (ASM International, Materials Park (Ohio) 1997) pp. 31–66
- 12.88 ASTM G54–84: *Standard Practice for Simple Static Oxidation Testing* (ASTM International, Philadelphia 1996), (Withdrawn 2002)
- 12.89 ASTM B76–90: *Standard Test Method for Accelerated Life of Nickel–Chromium and Nickel–Chromium–Iron Alloys for Electrical Heating* (ASTM International, Philadelphia 2001)
- 12.90 ASTM B78–90: *Standard Test Method of Accelerated Life of Iron–Chromium–Aluminum Alloys for Electrical Heating* (ASTM International, Philadelphia 2001)
- 12.91 ASTM G79–83: *Standard Practice for Evaluation of Metals Exposed to Carburization Environments* (e1, ASTM International, Philadelphia 1996)
- 12.92 A.B. Tomkings, J.R. Nicholls, D.G. Robertson: *EC Report, EUR 19479 EN, Discontinuous Corrosion Testing in High Temperature Gaseous Atmospheres* (TEST-CORR, London 2001)
- 12.93 JIS Z 2281: *Test Method for Continuous Oxidation Test at Elevated Temperatures for Metallic Materials* (Japanese Standards Association, Tokio 1993)
- 12.94 JIS Z282: *Method of Cyclic Oxidation Testing at Elevated Temperatures for Metallic Materials* (Japanese Standards Association, Tokio 1996)
- 12.95 H.J. Grabke, D.B. Meadowcroft (Eds.): *Guidelines for Methods of Testing and Research in High Temperature Corrosion*, European Federation of Corrosion Publications, Vol. 14 (The Institute of Materials, London 1995)
- 12.96 M. Schütze, W.J. Quadackers (Eds.): *Cyclic Oxidation of High Temperature Materials – Mechanisms, Testing Methods, Characterisation and Life Time Estimation*, European Federation of Corrosion Publications, Vol. 27 (The Institute of Materials, London 1999)
- 12.97 M. Malessa, M. Schütze: *COTEST – Cyclic Oxidation Testing – Development of a Code of Practice for the Characterisation of High Temperature Materials Performance* (EC Final Report, Brussels 2005)
- 12.98 M. Schütze, M. Malessa (Eds.): *Standardisation of Thermal Cycling Exposure Testing*, European Federation of Corrosion Publications, Vol. 53 (Woodhead, Cambridge 2007)
- 12.99 H. Echsler: *Oxidationsverhalten und mechanische Eigenschaften von Wärmedämmschichten und deren Einfluss auf eine Lebensdauervorhersage*. Ph.D. Thesis (RWTH, Aachen 2002), (in German)
- 12.100 A. Rahmel, W. Schwenk: *Korrosion und Korrosionsschutz von Stählen* (Verlag Chemie, Weinheim 1977), (in German)
- 12.101 M.J. McNallan, W.W. Liang, S.H. Kim, C.T. Kang: *Acceleration of the high temperature oxidation of metals by chlorine*. In: *High Temperature Corrosion*, ed. by R.A. Rapp (NACE, Houston 1983) pp. 316–321
- 12.102 H. Hindam, D.P. Whittle: *Oxid. Met.* **83**, 245 (1982)
- 12.103 ASTM E633–00: *Standard Guide for Use of Thermocouples in Creep and Stress–Rupture Testing to 1800 °F (1000 °C) in Air* (ASTM International, Philadelphia 2000)
- 12.104 ASTM E220–02: *Standard Test Method for Calibration of Thermocouples by Comparison Techniques* (ASTM International, Philadelphia 2002)
- 12.105 ASTM E230–03: *Standard Specification and Temperature–Electromotive Force (EMF) Tables for Standardized Thermocouples* (ASTM International, Philadelphia 2003)
- 12.106 ASTM E1350–97: *Standard Test Methods for Testing Sheathed Thermocouples Prior to, During, and After Installation* (ASTM International, Philadelphia 2001)
- 12.107 FEPA 42–GB–1984 R: *FEPA–Standard for bonded abrasive grains of fused aluminium oxide and silicon carbide* (Federation of European Producers of Abrasives, Paris 1993)
- 12.108 ISO 6344: *Coated Abrasives – Grain Size Analysis* (International Organisation for Standardization, Geneva 1998)
- 12.109 M. Schütze: *Protective Oxide Scales and Their Breakdown* (Wiley, West Sussex 1997)
- 12.110 G. Strehl, G. Borchardt: *Materials at high temperatures*. In: *Standardisation of Thermal Cycling Exposure Testing*, European Federation of Corrosion Publications, Vol. 53, ed. by M. Schütze, M. Malessa (Woodhead, Cambridge 2007) pp. 49–67
- 12.111 M. Malessa, M. Schütze: *Development of guidelines for Cyclic Oxidation Testing of High Temperature Materials* (EUROCORR, Budapest 2003)
- 12.112 M. Schütze: *Test method for thermal cycling oxidation testing*. In: *Standardisation of Thermal Cycling Exposure Testing*, European Federation of Corrosion Publications, Vol. 53, ed. by M. Schütze, M. Malessa (Woodhead, Cambridge 2007) pp. 212–247
- 12.113 V. Guttman, M. Schütze: *Interaction of corrosion and mechanical properties*. In: *High Temperature Alloys for Gas Turbines and Other Applications*, ed. by W. Betz, R. Brunetaud, D. Coutsouradis, H. Fischmeister, T.B. Gibbons, I. Kvernes, Y. Lindblom, J.B. Mariott, D.B. Meadowcroft (Reidel, Dordrecht 1986) p. 293
- 12.114 V. Guttman, M. Merz: *Corrosion and Mechanical Stress at High Temperatures* (Applied Science, London 1981)
- 12.115 S.R.J. Saunders, H.E. Evans, J.A. Stringer (Eds.): *Materials at High Temperatures*, Vol. 12 (Special Issue Mechanical Properties of Protective Oxide Scales, Springer, Netherlands 1994) pp. 83–256, also: 1995, 13, 75–80; 195, 13, 181–195

- 12.116 V. Guttman: Environmental creep testing
<http://ie.jrc.cec.eu.int/facilities.html>
- 12.117 M. Schütze: Deformation and cracking behaviour of protective oxide scales on heat-resistant steels under tensile strain, *Oxid. Met.* **24**, 199 (1985)
- 12.118 S.R. Holdsworth, W. Hoffelner: Fracture mechanics and crack growth in fatigue. In: *High Temperature Alloys for Gas Turbines*, ed. by R. Brunetaud, D. Coutsouradis, T.B. Gibbons, Y. Lindblom, D.B. Meadowcroft, R. Stickler (Springer, Netherlands 1982) p. 345
- 12.119 M. Welker, A. Rahmel, M. Schütze: Investigations on the influence of internal nitridation on creep crack growth in alloy 800 H, *Metall. Trans. A* **20**, 1553 (1989)
- 12.120 M. Schütze, B. Glaser: The influence of Cl-containing atmospheres on creep crack growth at 800 °C. In: *Heat-Resistant Materials II*, ed. by K. Natesan, D. Ganesan, G. Lai (ASM International, Materials Park (Ohio) 1995) pp. 343–351
- 12.121 M. Schütze: Anrißentstehung und Anrißwachstum unter korrosiven Bedingungen bei hohen Temperaturen. In: *Korrosion und Bruch*, ed. by C. Berger (DVM, Berlin 1988) p. 279, (in German)
- 12.122 K.-H. Döhle, A. Rahmel, M. Schmidt, M. Schütze: Two different test rigs for creep experiments in aggressive environments. In: *Corrosion and Mechanical Stress at High Temperatures*, ed. by V. Guttman, M. Merz (Applied Science, London 1981) p. 441

Friction and Wear

13. Friction and Wear

Almost all mechanical systems, artificial or natural, involve the relative motion of solid components. Wherever two surfaces slide or roll against each other, there will be frictional resistance, and wear will occur. The response of materials to this kind of interaction, often termed *tribological*, depends not only on the precise nature of the materials, but also on the detailed conditions of the contact between them and of the motion. Friction and wear are system responses, rather than material properties. The measurement of tribological behavior therefore poses particular challenges, and a keen awareness of the factors that influence friction and wear is essential.

This chapter provides definitions of the key concepts in Sect. 13.1, and provides a rationale for the design and selection of test methods in Sect. 13.2. Various standard and other tribological test methods are comprehensively reviewed in Sect. 13.3, which is followed by descriptions of methods used for the quantitative assessment of both friction (Sect. 13.4) and wear (Sect. 13.5). Methods used for characterizing worn surfaces and wear debris are addressed in Sect. 13.6.

13.1	Definitions and Units	743
13.1.1	Definitions	744
13.1.2	Types of Wear	744
13.1.3	Units for Wear.....	745
13.2	Selection of Friction and Wear Tests	747
13.2.1	Approach to Tribological Testing.....	747
13.2.2	Test Parameters	748
13.2.3	Interaction with Other Degradation Mechanisms	750
13.2.4	Experimental Planning and Presentation of Results	750
13.3	Tribological Test Methods	751
13.3.1	Sliding Motion	751
13.3.2	Rolling Motion	751
13.3.3	Abrasion	752
13.3.4	Erosion by Solid Particles.....	753
13.3.5	Scratch Testing.....	753
13.4	Friction Measurement	754
13.4.1	Friction Force Measurement.....	754
13.4.2	Strain Gauge Load Cells and Instrumentation	754
13.4.3	Piezoelectric Load Sensors	755
13.4.4	Other Force Transducers	755
13.4.5	Sampling and Digitization Errors....	756
13.4.6	Calibration	756
13.4.7	Presentation of Results	758
13.5	Quantitative Assessment of Wear	759
13.5.1	Direct and Indirect Quantities	759
13.5.2	Mass Loss	759
13.5.3	Dimensional Change.....	759
13.5.4	Volume Loss	760
13.5.5	Other Methods	762
13.5.6	Errors and Reproducibility in Wear Testing.....	762
13.6	Characterization of Surfaces and Debris ..	764
13.6.1	Sample Preparation	764
13.6.2	Microscopy, Profilometry and Microanalysis	765
13.6.3	Wear Debris Analysis.....	767
	References	767

13.1 Definitions and Units

Tribology is the science and technology of interacting surfaces in relative motion, which includes the study of friction, wear and lubrication. Friction and wear represent two key aspects of the tribological behavior of materials. Like other measurements of material perfor-

mance, such as corrosion or biodegradation, both friction and wear result from exposure of the material to a particular set of conditions. They do not therefore represent intrinsic material properties, but must be measured and defined under well-characterized test conditions.

13.1.1 Definitions

Wear can be defined as damage to a solid surface, generally involving progressive loss of material, due to relative motion between that surface and a contacting substance or substances [13.1]. Materials in contact are subjected to relative motion in many different applications. In some cases this motion is intentional: for example in rotating plain bearings, pistons sliding in cylinders, automotive brake disks interacting with brake pads, or in the processing of material by machining, forging or extrusion. It may also be unintentional, as in the small cyclic displacements known as fretting which can cause wear in certain structural joints under oscillating loading. If hard particles are present, for example as contamination in a lubricant, or intentionally as in abrasive machining, then these particles will have a profound influence on the resulting wear process.

The friction force is defined as the force acting tangentially to the interface resisting motion, when, under the action of an external force, one body moves or tends to move relative to another. The friction force F may be associated with sliding motion or with pure rolling motion of the bodies; in some practical engineering applications such as the contact between ball and track in a ball-bearing or between a pair of mating gear teeth, there may be more complex motion involving both sliding and rolling.

The coefficient of friction μ is a dimensionless number, defined as the ratio F/N between the friction force F and the normal force N acting to press the two bodies together. The kinetic coefficient of friction μ_k is the coefficient of friction under conditions of macroscopic relative motion between the two bodies, while the static coefficient of friction μ_s is the coefficient of friction corresponding to the maximum friction force that must be overcome to initiate macroscopic motion between the two bodies. The coefficient of friction is a convenient method for reporting friction force, since in many cases F is approximately linearly proportional to N over quite large ranges of N . The equation

$$F = \mu N \quad (13.1)$$

is sometimes called *Amontons Law*.

The value of μ can be expected to depend significantly on the precise composition, topography and history of the surfaces in contact, the environment to which they are exposed, and the precise details of the loading conditions. Although tables of coefficients of friction have been published, they should not be regarded as anything more than general indications of relative values

under the specific conditions of measurement. The coefficient of friction usually lies in the range from 0 to 1, although there is no fundamental reason why it need do so. Negative values of μ may be thought of as being rather artificial, since they result from adhesive forces between the bodies involved which result in a tangential force while the bodies are subjected to a tensile normal force, and *friction* is perhaps not a helpful term to describe this phenomenon; but values of μ greater than 1 are physically quite reasonable, and can be encountered, for example, in the interaction between a car tire and a dry road surface, or in the sliding of certain ductile metals in the absence of oxygen.

A large number of specialist terms used in tribology have been formally defined, most recently by ASTM [13.1]. An earlier compilation including many other terms, as well as their translations into French, German, Italian, Spanish, Japanese, Arabic and Portuguese, was published by an international group [13.2]. A particularly useful term is *triboelement*, defined as one of the two or more solid bodies involved in a tribological contact.

13.1.2 Types of Wear

It is important, especially when describing wear, to distinguish clearly between the nature of the relative motion responsible for the wear and the physical mechanisms by which the material is removed or displaced in wear. Wear tests are designed to produce specific types of relative motion, which can often lead to different mechanisms of wear in different materials, or at different loads or speeds. Methods that can be used to distinguish between wear mechanisms are discussed in Sect. 13.6.

Figure 13.1 illustrates some common types of relative motion that can result in wear. These represent idealized examples and can be further subdivided. For example, sliding and rolling motions may be either continuous or interrupted, and may occur along the same track on a rotating counterbody or on a continuously fresh track. They may involve constant relative velocity (continuous sliding), or varying velocity (such as reciprocating motion with perhaps sinusoidal or linear velocity variation).

When analyzing the motion in a tribological contact, the nature of the contact must also be examined. It is helpful to consider how the contact region moves with respect to the surfaces of the bodies in contact. For example, in the simple example of a small block sliding on a larger counterbody shown in Fig. 13.1, the contact region is fixed relative to the block, which is in continuous

contact, whereas it moves along the larger triboelement, so areas of this experience contact only for a certain period. In the case of simple rolling shown in Fig. 13.1, the contact region moves relative to the surfaces of both triboelements, and areas on both of these surfaces are therefore in intermittent contact.

In many practical situations there is a lubricant film present, but in some others, as well as in many laboratory studies, the sliding or rolling occurs unlubricated in air.

Relative motion normal to the surface of a triboelement may result in impact. Repeated impact by a large counterbody on an essentially single-contact region can lead to wear, as can impact by a large number of small particles or even liquid droplets, in which case the impact sites are usually distributed over an area of the surface. Wear can also result from the collapse close to a solid surface of vapor or gas bubbles produced by local pressure fluctuations in a cavitating liquid.

The presence of small particles in the contact region, usually harder and thus less deformable than one of the moving bodies, leads to a significantly different wear process to that for plain sliding. The most common types of wear associated with hard particles in a sliding contact are illustrated in Fig. 13.2. If the particles are attached to one of the sliding bodies, either forming part of it (for example, as hard discrete phases in a softer matrix, or as particles fixed to the surface, as in abrasive paper) or embedded in the surface, then they

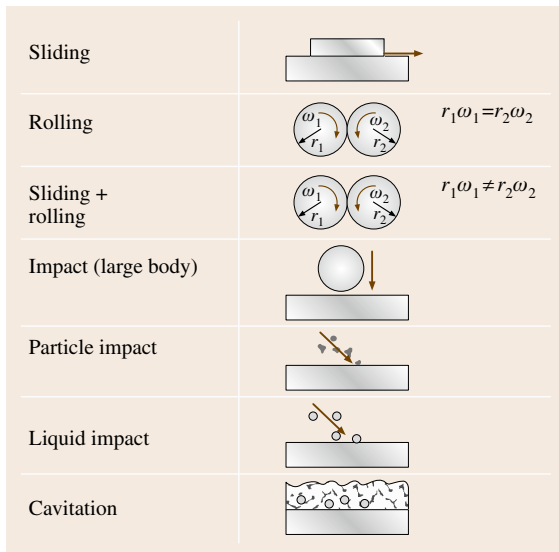


Fig. 13.1 Examples of tribological contacts involving relative motion of triboelements, as well as erosion by particle impact, liquid impact or cavitation in a liquid

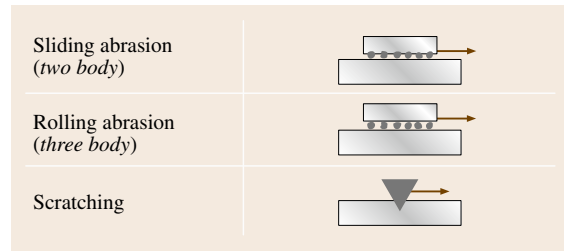


Fig. 13.2 Examples of abrasive wear due to the presence of hard particles in a sliding contact, and scratch damage

will be dragged over the counterbody in a process described as sliding abrasion. This type of abrasion is often termed *two-body* abrasion, since the particles effectively form part of one of the two triboelements. If the particles are free, and roll between the sliding bodies, then their interaction with them is different and can be described as rolling abrasion; this is also known as *three-body* abrasion, since the particles form a distinct *third body* which moves with respect to the two sliding bodies. The terms *two-body* and *three-body* can lead to confusion, since the motion of free particles in a sliding contact will depend on the relative hardnesses of the surfaces and on the applied pressure, and can vary between sliding and rolling even in different regions of the contact. The conditions of abrasive wear are sometimes described as either *low-stress*, in which the abrasive particles themselves are relatively undamaged in the wear process, or *high-stress*, where the particles experience extensive fracture.

If surface damage results from the action of a single hard asperity, or a small number of relatively large asperities, then it is often termed *scratching*, and scratch testing can be used to characterize the response of a material to this type of deformation (see Sect. 13.3.5). Scratching is also shown schematically in Fig. 13.2.

13.1.3 Units for Wear

Since wear is often associated with the removal of material from a surface, it is usually quantified in terms of the volume of material removed, the mass removed, or the change in some linear dimension after wear. All three can be used as primary measurements. For example, the volume of material worn from the end of a spherically-ended pin to form a flat area on the pin may be calculated from a measurement of the diameter of the flat area; volume changes in more complex geometries may be derived computationally from the difference between profile traces recorded before and after wear.

Measurement of mass loss is in principle comparatively straightforward, although great care must be taken in the experimental technique to reduce errors. Linear changes in dimensions (for example, the reduction in length of a pin specimen, or the change in clearance in a bearing) are also in principle straightforward to measure, but are prone to error and so careful experimental procedures are needed. Measurements of mass change can be affected by material transfer and oxidation; dimensional changes can also be influenced by thermal expansion. These and other aspects of experimental techniques are discussed in Sect. 13.5.

In some cases material may be lost from both triboelements, or significant transfer of material may occur between the triboelements, and particular care is then needed in both measuring and describing the magnitude of wear. If wear is associated with the movement of material within the surface of a single triboelement, it will lead to changes in the topography of the surface which can be detected by profilometry, as discussed in Sect. 13.6.2.

The amount of wear that occurs when two surfaces slide over each other tends to increase with sliding distance, and hence with time. The wear rate can then be defined as the rate of material removal or dimensional change per unit time, or per unit sliding distance. Because of the possibility of confusion, the meaning of the term *wear rate* must always be defined, and its units stated. In the case of erosion the wear rate is usually quoted as the mass or volume loss per unit time; for erosion by solid particle impact, it may also be expressed

as the volume or mass loss per unit mass of impinging particles.

Many quantitative models for sliding wear have been developed, but one of the simplest, due to Archard, is useful for comparing wear rates and material behavior under different conditions. The Archard model leads to the equation

$$Q = KW/H, \quad (13.2)$$

where Q is the volume of material removed from the surface by wear per unit sliding distance, W is the normal load applied between the surfaces, and H is the indentation hardness of the softer surface. Many sliding systems do show a dependence of wear on sliding distance which is close to linear, and under some conditions also show wear rates which are roughly proportional to normal load. The constant K , usually termed the Archard wear coefficient, is dimensionless and always less than unity. The value of K provides a means of comparing the severities of different wear processes. Equation (13.2) can be applied to abrasive wear as well as to sliding wear; an analogous equation can also be developed for erosion by solid particle impact, from which a value of K can be derived.

Figure 13.3 shows, very approximately, the range of values of K seen in various types of wear. Under unlubricated sliding conditions (so-called dry sliding), K can be as high as 10^{-2} , although it can also be as low as 10^{-6} . Often two distinct regimes of sliding wear are distinguished, termed *severe* and *mild*. Not only do these correspond to quite different wear rates (with K often above and below 10^{-4} respectively), but they also involve significantly different mechanisms of material loss. In metals, *severe* sliding wear is associated with relatively large particles of metallic debris, while in *mild* wear the debris is finer and formed of oxide particles. In the case of ceramics, the *severe* wear regime is associated with brittle fracture, whereas *mild* wear results from the removal of reacted (often hydrated) surface material.

When hard particles are present and the wear process involves abrasion (by sliding or rolling particles) or erosion (by the impact of particles), then the highest values of K occur; the relatively high efficiency of the removal of material by abrasive or erosive wear explains why these processes can also be usefully employed in manufacturing.

The values of K that occur for unlubricated sliding, or for wear by hard particles, are generally intolerably high for practical engineering applications, and in most tribological designs lubrication is used to reduce

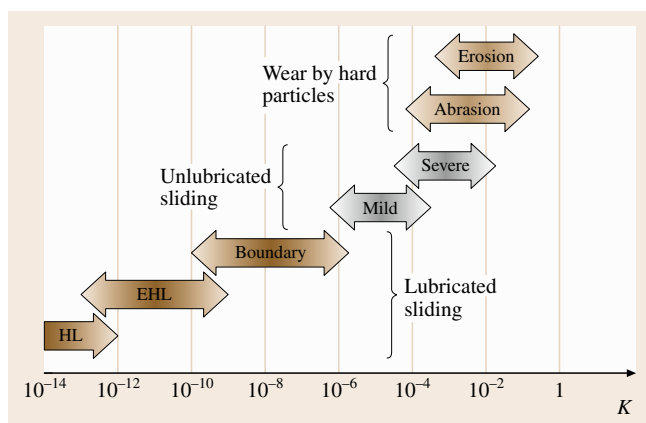


Fig. 13.3 Typical ranges of wear coefficient K exhibited under various tribological conditions: hydrodynamically lubricated (HL); elastohydrodynamically lubricated (EHL); lubricated by a boundary film; unlubricated sliding; abrasive wear; and erosive wear

the wear rate; the effect of lubrication in reducing wear is far more potent than its effect on friction, and the increase in life which results from the reduction of wear is generally much more important than the increase in efficiency from the lower frictional losses. As Fig. 13.3 shows, even the least effective lubrication can reduce the wear rate by several orders of magnitude, and as the thickness of the lubricant film is increased in the progression from boundary, to elastohydrodynamic (EHL) and then to hydrodynamic lubrication (HL), the value of K falls rapidly. In the hydrodynamically lubricated components of a modern automotive engine, values of K as low as 10^{-19} are achieved.

The quantity $Q/W (= K/H)$, given the symbol k , and sometimes termed *specific wear rate* (UK) or *wear factor* (USA), is also useful. The units in which k is expressed are usually mm^3/Nm , representing the volume

lost (mm^3) per unit sliding distance (m) per unit normal load on the contact (N). These units are commonly used when quoting experimentally measured rates of wear. It is useful to note that for a material with a Vickers hardness H of 1 GPa ($\approx 100 \text{ HV}$), then the numerical value of K (dimensionless) is the same as that of k (in units of mm^3/Nm).

Although k (or K) is effectively constant over quite large ranges of load or sliding speed in many cases of sliding wear, in some instances sharp transitions can occur, and k may change by a factor of 100 or even 1000 for a relatively small change in the conditions. This behavior is associated with a change in the predominant mechanism of material removal; for this reason it is always dangerous to extrapolate wear data to predict the likely rate of wear in a system from data obtained under different conditions.

13.2 Selection of Friction and Wear Tests

Friction and wear testing is often carried out to ensure that good tribological performance is achieved from materials. This information is required at different times in the life cycles of products. Designers require data that will enable them to design products that will not wear out or have unacceptably low efficiency, or even fail to function, due to frictional losses; process engineers need equipment to make the products that will function cost-effectively without premature failure from wear; and those marketing the products need to know that they will have good tribological performance. Other tests are performed for more fundamental reasons to investigate wear mechanisms or material performance, perhaps as part of a program of material development.

Friction and wear are important in most industrial sectors, but there is now also increasing attention paid to the application of tribological testing to societal needs. Traditionally, the evaluation of friction and wear has been of major concern in areas such as mining and drilling, transport power plant, power generation and machine tools. Now there is increasing attention to areas such as the tribological performance of biomedical implants and the degradation of decorative finishes. In recent years there has also been much attention given to the design and development of microelectromechanical systems (MEMS) where friction and wear are strongly influenced by the scale of these small components, hampering the development of new devices.

13.2.1 Approach to Tribological Testing

There are many different approaches to friction and wear testing, illustrated schematically in Fig. 13.4, that differ in the scale and complexity of the element that is being tested. Ultimately field testing of the final product will always be required for final proof of effectiveness, but it can often be prohibitively expensive to evaluate several different alternative materials or design variations by this method. It also suffers from a lack of control of the parameters that define the wear processes that are occurring, so that an understanding of the dependence of wear mechanisms on important factors such as load and speed cannot be developed.

As Fig. 13.4 demonstrates, it is possible to break down the complete product into its functional elements. The final stage of this process of abstraction is to use laboratory tests that simulate a particular tribological element of the complete product. Moving away from field trials towards laboratory testing, in general, reduces the costs of testing and increases the ability to control the important factors that affect the magnitude of friction and wear. This enables programs of testing to be designed that allow for the cost-effective development of materials and tribological systems through better understanding of the tribological processes.

There are two main situations for which laboratory tests are required. The first is to provide information on

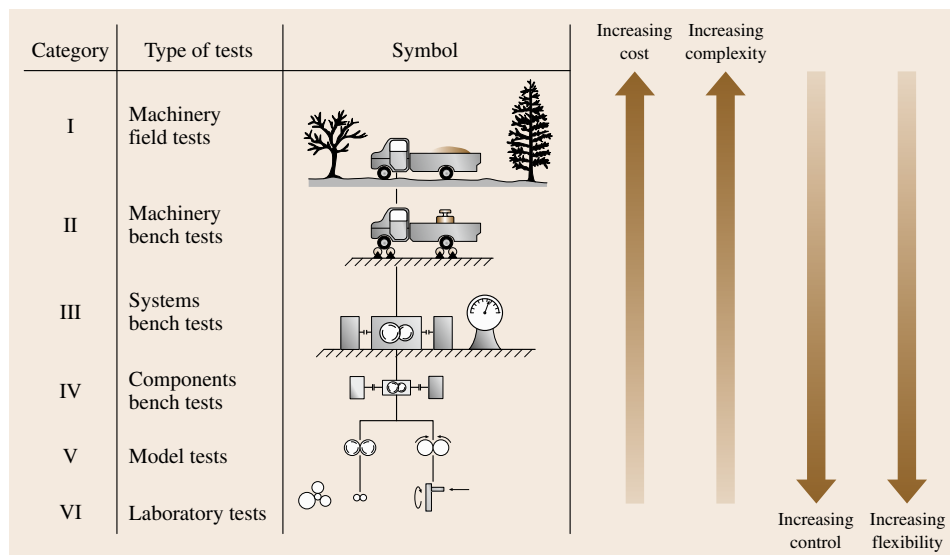


Fig. 13.4
Schematic illustration of types of tribological test (after [13.3])

the tribological performance of materials when they are being developed or selected for a general field of application, but when the specific conditions that will be applied are not well-defined. In this case there is little information to guide the specification of the test parameters to be used in any test program, and indeed the specific test that should be used is not always clear. However, it is important to consider carefully how the materials will be used in order to eliminate inappropriate tests that will only lead to misleading results. Thus, for materials that are being developed for applications where abrasion is extremely likely to occur, sliding wear tests cannot be expected to give relevant data. Nevertheless, so long as the likely mode of wear can be predicted, useful information can be obtained on the likely performance of the materials in practice.

The second situation is where there is a requirement to simulate a specific application. Here the conditions that are operating in the tribological contact should be better defined, so that the design of a program of laboratory wear tests reduces to choosing the appropriate test and test parameters to achieve the correct simulation of the practical application. Although in some cases the best approach is to design and manufacture a specific rig that is intended to reproduce the conditions in the application precisely, in most cases a well-established test can be used, perhaps with some adjustment of the test parameters, to provide a reasonable match with the application. The selection of these parameters is the key to generating a valid test.

As it is often difficult to achieve an exact simulation in the laboratory, it is always important to check that the same mechanisms of wear occur in the laboratory test as in the real application. When this is achieved, the laboratory test is likely to give results that will reliably predict performance in the application. Figure 13.5 shows an example of such a comparison, from tests performed to simulate the abrasion of cemented carbide extrusion tools used to form ceramic roof tiles. The features of the worn surfaces of the cermets were very similar in both laboratory tests and the samples recovered from the practical application, and subsequent field trials showed an excellent match between the results of the laboratory tests and the lifetimes of the components in service.

13.2.2 Test Parameters

Many parameters control and define the conditions in a tribological contact, and hence influence the resulting wear and friction. Important examples are listed in Table 13.1. Some of these parameters are only applicable to specific types of wear; for example the shapes of abrasive or erodent particles are relevant only to the processes of abrasion or erosion.

A full description of the effects of these test parameters is well beyond the scope of this chapter. The reader should refer to other sources for a fuller description [13.4, 5], but some aspects are discussed briefly here.

Table 13.1 List of some important parameters that influence tribological processes

Parameter	Units or type of information
Normal load	N
Sliding speed	m/s
Materials of triboelements	All aspects of composition and microstructure, at surface as well as sub-surface
Test environment (including any lubricant present)	Composition, chemical and physical properties of gas and/or liquid surrounding tribological contact
Temperature	°C
Type of relative motion between surfaces	Trajectory: sliding, rolling, impact etc.
Contact geometry (form)	Shapes of surfaces
Contact geometry (local)	Roughnesses of surfaces
Abrasive/erosive particles	Material, shape (and distribution), size (and distribution)
Contact dynamics	Stiffness, damping, inertial mass

In laboratory testing it is normal to positively control only a few test parameters such as the applied normal load, relative speed and contact geometry. Other

parameters that can have a major effect on the resulting wear and friction are the presence of lubrication, the environment and atmosphere of the test (including the air humidity), the bulk temperature of the samples, and the mechanical dynamics of the test system. These parameters are normally held constant from one test to another, either by the application of a specific control methodology, or simply by using the same test system for the whole sequence of tests in the program.

The contact geometry is a crucial parameter in the design of a wear test where two bulk surfaces are in moving contact, as in sliding. The ideal situation, in which the nominal contact area, and hence nominal contact pressure, would not vary during the test, would be to achieve self-aligning conformal contact between the test samples. This can be achieved in some cases by careful design of the samples and their holders, but often it cannot be achieved, and then high initial contact stresses occur at the edges of the misaligned contacts. To avoid this uncontrolled nonconformal geometry, it is common to use a controlled nonconformal geometry with one triboelement in the form of a ball or spherically-ended pin loaded against a flat sample. A ball diameter of about 10 mm is typically used. The disadvantage of this approach is that although the initial contact geometry is well controlled, the initial contact stresses are high. The ball or pin then wears rapidly until a larger contact area is produced, resulting in a substantially lower contact pressure. This change may lead to a change in

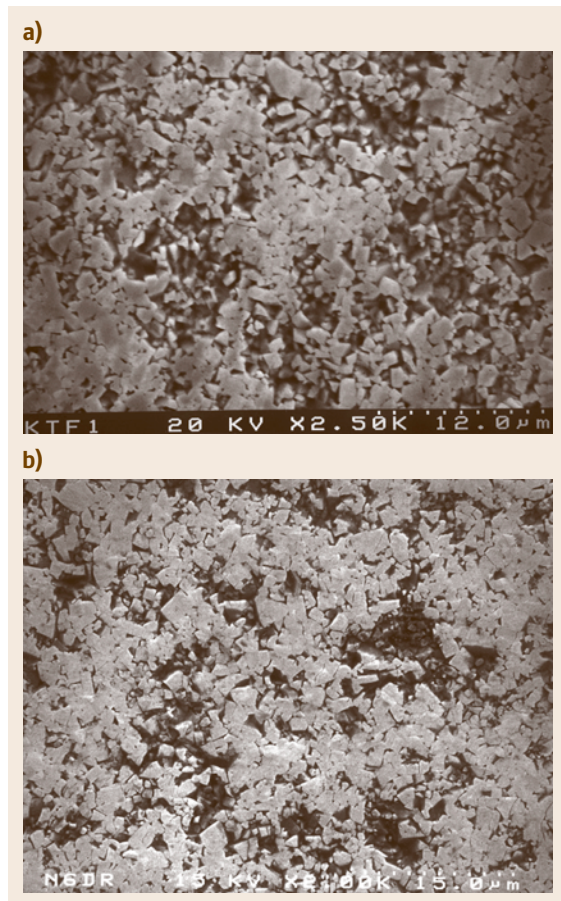


Fig. 13.5a,b Example of comparison of worn surfaces from a laboratory simulation and a practical application. The SEM images show WC/Co tools used to manufacture concrete tiles: (a) worn surface from production tool; (b) worn surface of sample after laboratory wear testing ◀

wear mechanism from the initial high-stress regime to a subsequent low-stress, larger contact area regime. An approach that reduces this effect is to use one triboelement with a large contact radius so that although the initial contact geometry is still well defined, the initial contact pressure is lower, and changes in mechanism are less likely.

The temperatures of the contacting triboelements can affect the tribological behavior through changes in their mechanical and chemical properties. As well as these bulk effects, the areas of the samples in contact become hotter through frictional heating; the power dissipated in the contact is given by μNv where μ is the friction coefficient, N is the normal load, and v is the relative sliding velocity. The local temperatures at the contact areas can therefore become much higher than the bulk temperatures [13.6]. This factor needs to be taken into account when designing wear tests or interpreting test results.

As outlined in Sect. 13.1.3, lubrication of the contacts will also affect the wear, often in terms of mechanism as well as amount. Under certain conditions of sliding speed, load and lubricant viscosity, the two surfaces become separated by a continuous, hydrodynamically-generated lubricant film, and the wear rate can fall to a very low level, as indicated in Fig. 13.3. Hydrodynamic lubrication (a thick lubricant film) is favored by low normal pressure, high lubricant viscosity, and high sliding speed. For conditions where the lubricant film thickness becomes comparable with the roughness of the triboelements, elastic deformation of these bodies becomes important and the pressure in the lubricant is high enough to cause a significant local increase in viscosity; this is the regime of elastohydrodynamic lubrication (EHL). For even thinner films (at low speeds or high contact pressure), the system enters the regime of boundary lubrication, where appreciable interaction occurs between asperities on the two surfaces. Here the chemical composition of the lubricant has a major effect on the nature and properties of the chemically formed surface films and on the wear that occurs.

13.2.3 Interaction with Other Degradation Mechanisms

Other degradation mechanisms such as chemical reaction and fatigue can also make a major contribution to the overall loss of material from moving contacting surfaces. Interactions often occur with the test environment through chemical reactions of the test materials. In wear

corrosion, the triboelements are exposed to an aqueous medium, and corrosion of the materials acts in conjunction with mechanical processes to alter the amount of material lost. There is positive synergy in most cases, so that the mass loss is greater than the sum of the contributions expected from pure corrosion or pure wear alone. Exceptionally, in negative synergy, corrosion can form a mechanically stronger layer on the surface which acts to protect the surface and thus reduce the total wear rate. Tribochemical reactions of materials may also occur; ceramics, for example, can react with water vapor to form hydroxides that reduce friction and protect the wearing surface.

When metals are heated, either through a bulk increase in temperature or by frictional heating, considerable oxidation can occur. At first this may reduce wear, as seen in the mild wear of steels, but as the temperature increases further, the production of weak oxide may increase to such an extent that the wear rate increases once more [13.4].

In many tribological systems, the surfaces of the contacting materials are subjected to alternating stresses. These stresses may be high enough to initiate and grow fatigue cracks in the material that may contribute to the material loss caused by other wear processes. Rolling contact fatigue is an important degradation mechanism in certain applications of materials, but lies outside the scope of this chapter.

13.2.4 Experimental Planning and Presentation of Results

When planning a program of tribological tests, the choice of test conditions must be determined, either by the relevant engineering application, or in order to achieve the appropriate mechanism of wear in more fundamental studies. In the development of materials, a range of conditions can be chosen to represent those likely to occur during actual use of the material.

There are many test factors that need to be controlled during a test. These can be grouped into those concerned with the mechanical test conditions (such as contact load or pressure, speed, motion type and test environment), and sample parameters (such as material composition, microstructure and the initial surface finish of the samples). A full program of testing under all combinations of these factors would be time-consuming and costly, and may not be required. Often a single factor can be identified as *key* to the material response, and in this case a good approach is to set all the other factors at constant values and

vary the chosen factor in a controlled way in a series of tests. This approach is termed a parametric study. More complex statistical, experimental design procedures can be used, but care needs to be taken in the design of experiments to account for the variability that is normally observed in the results of wear tests.

Mapping techniques can be used where two (or more) factors are changed in a controlled way (normally more coarsely than in parametric studies), with the friction and wear results plotted either as individual points or as contours. Regions on the map are then delineated on a mechanistic basis, with the region boundaries

either defined by identifying the wear mechanism by microstructural techniques, or by identifying transitions in friction and wear behavior as sudden changes in wear rate or friction coefficient. The mapping procedure is a very efficient way of determining the overall behavior of a material because it provides useful information about the position of transitions in wear behavior in a systematic and controlled way. This comes at the expense of a reduction in the detailed knowledge of the variation of friction and wear with any one factor, but once the regime of interest is better defined through the use of mapping studies, then a more detailed parametric study can be conducted.

13.3 Tribological Test Methods

This section gives some information on the tribological tests that are in common usage, and which have in many cases been standardized, particularly through the American Society for Testing and Materials (ASTM). Due to constraints on space, only a brief description can be given. Further information can be obtained from other sources [13.5, 7–12]. The main test parameters, the measurements that can be made, and the standards associated with each type of test are listed.

13.3.1 Sliding Motion

Wear tests for materials in sliding contact are characterized by continuous contact between the two samples in tribological contact. There are two distinctly different types of test.

In many tests, the extent of relative movement is sufficiently large (typically greater than 300 μm) so that all contact points on at least one of the bodies are out of contact for some of the test period. This is in contrast to the case of fretting, where at least part of the contact area on both samples is always in contact. In fretting tests, the debris is trapped at the interface between the two samples, leading to different behavior from that in tests involving larger extents of movement, in which the debris is more readily lost from the contact region.

Common tribological test geometries involving sliding motion are shown in Fig. 13.6. Pin-on-disc and reciprocating geometries are used most often, but pin-on-disc testing with continuous rotary motion is often not appropriate since many applications involve reciprocating motion. This difference is important, as it affects the retention of debris at the wear interface and the stress history on the surfaces. Fretting tests are always

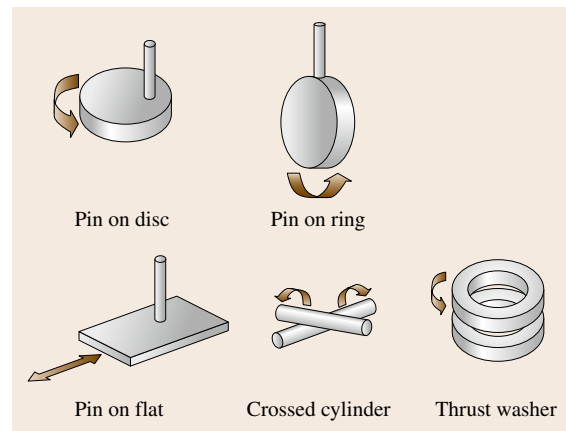


Fig. 13.6 Examples of test geometries used for tribological tests involving sliding motion

carried out with a reciprocating geometry; particular care is needed in apparatus design as the elastic deformation of the test system can be similar in magnitude to the required sample motion, leading to difficulties controlling and measuring sample displacement.

Often balls are used instead of pins, and in some cases blocks (with large contact areas) are also used. The choice of a conformal or nonconformal contact geometry and the frictional generation of heat are factors that need to be carefully considered.

13.3.2 Rolling Motion

Tribological contacts often involve rolling motion. Suitable test geometries are shown in Fig. 13.7. If the application is concerned with bearing races, then this is

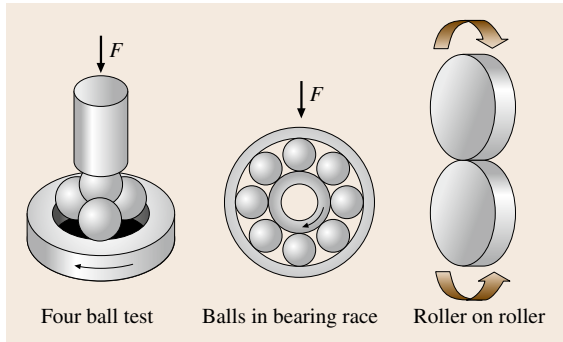


Fig. 13.7 Examples of test geometries used for tribological tests involving rolling motion

one situation where laboratory tests can be carried out relatively easily on the components themselves. This is clearly appropriate for roller bearing applications, but the complexity of the test geometry means that it is often difficult to develop a fundamental understanding of the wear and friction processes that occur.

The four-ball test has been popularly used for many years to test, in particular, the maximum load and speed for failure at the contact points in this test geometry, from mechanisms such as scuffing and seizure. However, results from this test, which can involve very high contact pressures and frictional power dissipation, are not readily extended to practical applications, and the method also suffers from a lack of control of the detailed motion of the balls during the test.

In two-roller testing, on the other hand, there is independent control of the motion of the rollers, and it is possible to adjust the amount of relative sliding between

them as well as the rolling speed. The cylindrical edge of the rollers sometimes has a flat cross-section, but is also commonly crowned.

13.3.3 Abrasion

Abrasion testing can be carried out with a range of tests, as shown in Fig. 13.8. The simplest type of testing is carried out by loading a sample pin against abrasive-coated paper supported on a solid backing. As well as using a rotating abrasive-covered disc, tests can also be carried out with abrasive paper held on to a drum, or with a belt of abrasive paper. An important issue with these tests is that, as abrasion of the test sample takes place, the abrasive paper degrades by clogging with wear debris and due to damage to the contacting regions of the abrasive particles, so that the wear of the test sample will typically decrease as the test progresses; in extreme cases the wear mechanism may change as sliding then occurs predominantly against debris rather than against the abrasive particles. The use of a spiral track on the abrasive paper can achieve a steady process of wear by ensuring abrasion against fresh particles.

In another common type of abrasion test, a sample is pressed against a rotating wheel in the presence of a continuous supply of free abrasive particles. An important parameter in these tests is the stiffness of the wheel or other counterbody. Tests can also be carried out dry or in fluids of different types, allowing tests to be made in the presence of corrosive media. Some tests with rotating wheels involve the recirculation of abrasive during a single test (ASTM B 611 [13.8]), while in others a continuous stream of

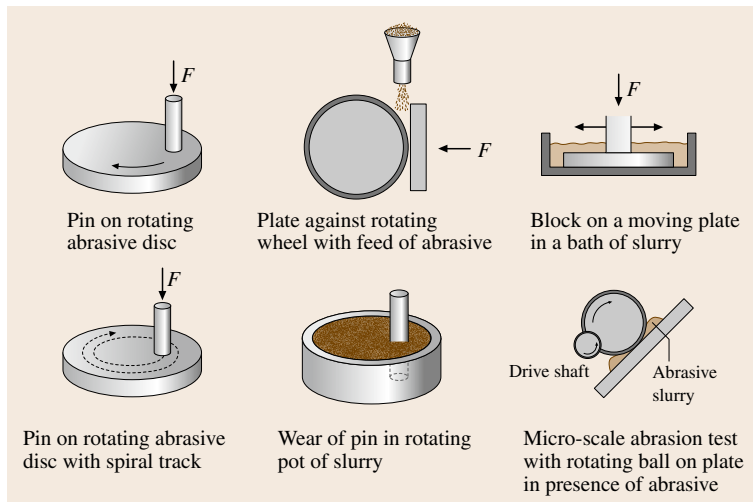


Fig. 13.8 Examples of test geometries involving abrasion

abrasive passes through the wear interface and is not reused (such as the dry sand rubber wheel abrasion test, ASTM G 65 [13.8]).

A test that has received some prominence recently is the microscale abrasion test, in which a ball is rotated against a flat sample in the presence of abrasive. This test is particularly suited to determining the abrasion rate of a coating.

13.3.4 Erosion by Solid Particles

There are two main groups of particulate erosion tests, in which the particles either strike the sample in a gas (usually air), or are transported in a liquid, which is usually termed slurry erosion. Examples are shown in Fig. 13.9.

In the centrifugal accelerator, the erodent particles are accelerated along radial tubes in a rotor so that a stream of erodent particles emerges at some angle to the rotor periphery (which depends on the detailed design) to strike one or more samples located in a ring around the rotor. This test has the advantage that several different samples can be tested simultaneously, but there is usually some uncertainty in the angle with which the particles strike the samples, and only a fraction of the particles fed into the apparatus actually strike the samples. Some designs of centrifugal accelerator impart significant rotation to the particles, which may influence the resulting erosion rate. In the gas-blast test a compressed gas stream (usually air) accelerates the erodent particles along a nozzle towards the sample, which is held at a controlled angle to the stream. In this case only one sample can be tested at a time.

In slurry erosion testing a pump can be used to generate liquid flow through a nozzle. Eroder particles are incorporated into the jet, being either picked up through a venturi system or suspended in the erodent slurry. The resulting jet of slurry is directed against the test sample held at a controlled angle.

In all erosion tests the particle impact speed and the angle of impingement of the erodent stream against the sample are the most important variables.

13.3.5 Scratch Testing

Scratch testing was originally developed to evaluate the adhesion of coatings. In the scratch test an indenter of well-defined geometry is pressed onto and moves relative to a sample under a fixed or increasing normal load. The tangential force resisting the motion (usually described as the friction force) and acoustic emission

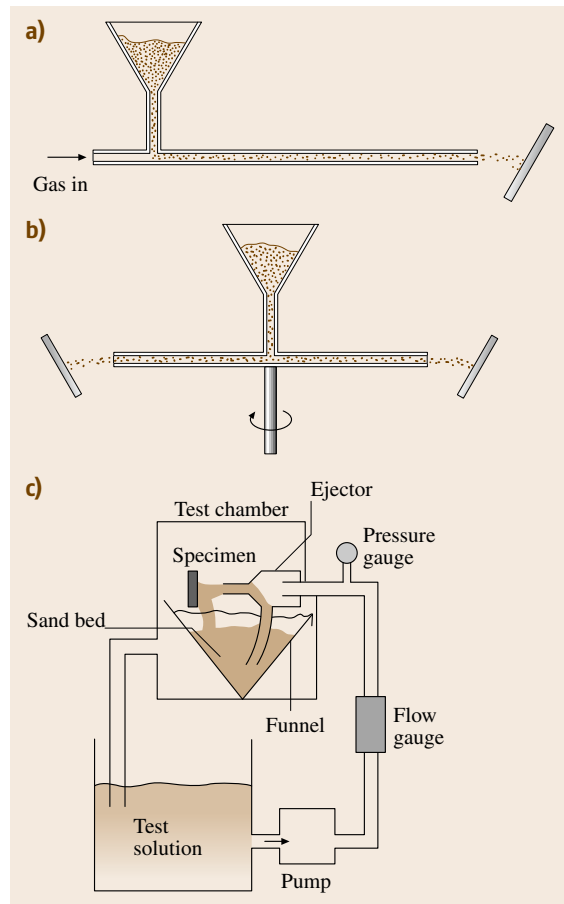


Fig. 13.9a–c Examples of tests involving erosion by solid particles: (a) gas-blast test; (b) centrifugal accelerator; (c) fluid jet rig

from the sample are often both measured continually. The acoustic emission signal typically increases sharply when a brittle coating is cracked, or the coating delaminates from the substrate.

When the test was developed, the adhesion of typical engineering coatings was quite poor and the scratch test provided reasonable results, representative of the adhesion of the coating. More recent coatings are much more adherent, and although the scratch test remains an extremely valuable test for coatings, the results are more difficult to interpret, giving information on the complex response of the coating–substrate composite system to the movement of the indenter.

In the context of wear testing, scratch testing can be used as a model abrasion test; the response of a material to the scratching of the indenter is treated as

an analog of its response to a hard asperity or abrasive particle. Parameters such as the frictional force generated and the scratch width can be measured.

13.4 Friction Measurement

As discussed in Sect. 13.1.1, the measurement of friction involves the measurement of the friction force. For a rotating component it may be useful to define the friction torque, the measurement of which also involves a force measurement combined with a length measurement.

13.4.1 Friction Force Measurement

A friction force measurement system is made up of one or more force transducers mounted between one of the triboelements and the base frame of the tribometer, and their associated instrumentation. A practical force transducer usually consists of a chain of several transducers. For example, the force may act upon and bend a metal beam, and the bending then alters the electrical resistance of a strain gauge bonded to the surface of the beam by an amount proportional to the force. For many types of force measurement system, the term *load cell* is commonly used in place of *force transducer*.

Most force transducers employ some type of elastic load-bearing element or combination of elements. Application of force to the elastic element causes it to deflect, and this deflection is then sensed by a secondary transducer which converts it to an output. The output may be in the form of an electrical signal (as from a strain gauge or LVDT, a linear variable differential transformer), or a mechanical indication (as in proving rings and spring balances). However, the most common method is for longitudinal and lateral strains to be sensed, and when this is done by electrical resistance strain gauges the transducer is known as a *strain gauge load cell*.

13.4.2 Strain Gauge Load Cells and Instrumentation

A strain gauge load cell is based on an elastic element to which a number of electrical resistance gauges are bonded. The geometric shape and elastic modulus of the element determines the magnitude and distribution of the strain field produced by the force to be measured. Each strain gauge responds to the local strain at its location, and the measurement of force

Multiple scratches can be made both in the same position or intersecting one another to extend the model range.

is determined from the combination of these individual measurements of strain. Each elastic element is designed to measure the force acting in a particular direction, and not to be affected by other components such as side loads. The material used for the elastic elements is usually tool steel, stainless steel, aluminum or beryllium–copper. The material should exhibit a linear relationship between the stress (proportional to the force applied) and the strain (output), with low hysteresis and creep in the working range. A further requirement is a high repeatability between force cycles, with no fatigue effects.

The most common materials used for strain gauges are copper–nickel, nickel–chromium, nickel–chromium–molybdenum and platinum–tungsten alloys. The foil strain gauge is the most widely-used type because it has significant advantages over the other types and is employed in the majority of precision load cells. A foil strain gauge consists of a metal foil pattern supported on an electrically insulating backing of epoxy, polyimide and glass-reinforced epoxy phenolic resin. It is constructed by bonding a sheet of thin rolled metal foil, 2–5 μm thick, on a backing sheet 10–30 μm thick. The measuring grid pattern including the terminal tabs is produced by photoetching, in a process similar to that used in the production of printed circuit boards.

Semiconductor strain gauges are manufactured from n-type or p-type silicon. The output from a semiconductor gauge is about 40 to 50 times greater than that from a metal foil gauge. While the output is not linear with strain, they do exhibit essentially no creep or hysteresis and have an extremely long fatigue life. Because of their high temperature sensitivity, careful matching of the gauges and a high level of temperature compensation is required.

Thin film strain gauges are produced by sputtering or evaporation of thin films of metals onto an elastic element. Wire strain gauges are used mainly for high-temperature transducers. The wire is typically 20 to 30 μm in diameter and is bonded to the elastic element with ceramic material.

The rated capacities of strain gauge load cells range from 0.1 N to 50 MN, at a typical total uncertainty of

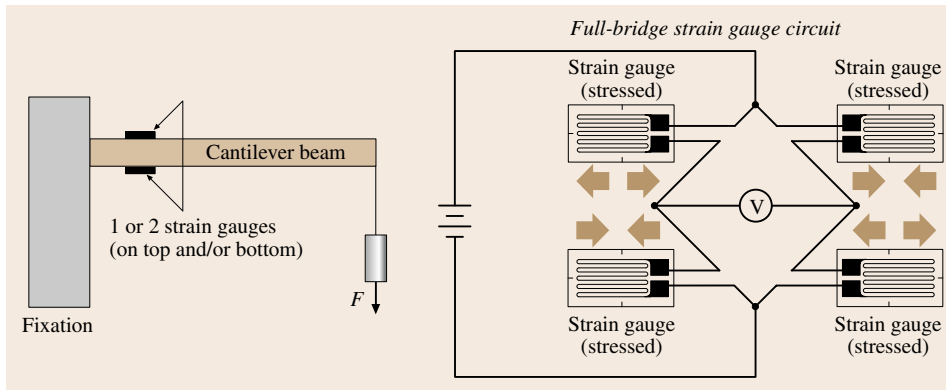


Fig. 13.10
Example of strain gauges connected into a full-bridge circuit

0.02–1% of full scale. The range of capacity depends on the type of gauges, with thin film gauges having the highest sensitivity (typically 0.1–100 N), followed by semiconductor gauges (1 N–10 kN), and foil gauges (5–50 MN).

The response of a load cell can be maximized using one or more strain gauges aligned to respond to a longitudinal strain and another set aligned either to a longitudinal strain of the opposite sign or to the transverse strain. When connected electrically in a Wheatstone bridge configuration, this has the additional advantage of minimizing temperature effects that act equally on all gauges. The resistance change is detected by measuring the differential voltage across the bridge (see for example Fig. 13.10). The load cell forms part of the measurement chain and requires an ac or dc excitation voltage to be supplied, and amplification and conditioning of the output signal, before it can be used. The whole chain must be incorporated into the calibration procedure.

13.4.3 Piezoelectric Load Sensors

Another commonly used type of force measurement transducer is based on the piezoelectric phenomenon exhibited by certain crystalline materials, in which an electric field is generated within a crystal which is proportional to the applied stress. To make use of the device, a charge amplifier is required to provide an output voltage signal that is proportional to the applied force and large enough to measure. Piezoelectric crystal sensors are different from most other sensing techniques in that they are active sensing elements. No power supply is needed for the sensor (although it will be for the amplifier) and the mechanical deformation needed to generate the signal is very small, which gives

a stiff sensor and the advantage of a high-frequency response in the measuring system without introducing geometric changes to the force measuring path. To enable measurement of both tension and compression, piezoelectric force sensors are usually pretensioned by a bolt.

A typical piezoelectric transducer deflects by only 0.001 mm under a force of 10 kN. The high frequency response, typically up to 100 kHz due to the high stiffness, makes piezoelectric crystal sensors very suitable for dynamic measurements. The typical range of rated capacities for piezoelectric crystal force transducers is from a few N to 100 MN, with a typical total uncertainty of 0.3–1% of full scale. While piezoelectric transducers are ideally suited to dynamic measurements, they cannot perform truly static measurements because there is a small leakage of charge inherent in the charge amplifier, which causes a drift of the output voltage even with a constant applied force.

Piezoelectric sensors are suitable for measurements in laboratories as well as in industrial settings because of their small dimensions, the very wide measuring range, rugged packaging, and their insensitivity to overload (typically by > 100% of full scale). They can operate over a wide temperature range (up to 350 °C), and can be packed to form multicomponent transducers (dynamometers) to measure forces in two or three orthogonal directions.

13.4.4 Other Force Transducers

Interesting but less commonly-used examples of force measurement transducers are the *vibrating-wire transducer* and the *gyroscopic load cell*. The first uses a taut ferromagnetic wire which is excited to resonate in transverse vibration. The resonant frequency is a measure of

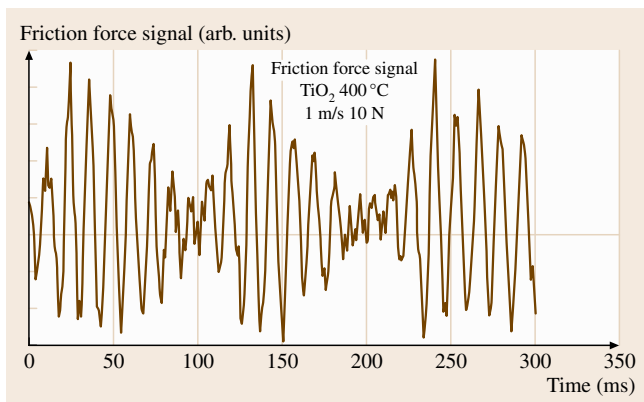


Fig. 13.11 Friction force signal from a load cell recorded with high time resolution, showing vibration at its resonant frequency superimposed on the more slowly varying friction force

the wire's tension and hence the applied force at that instant. The advantage is its direct frequency output, which can be handled by digital circuitry, eliminating the need for analog-to-digital conversion.

Gyroscopic load cells exploit the force-sensitive property of a gyroscope mounted in a gimbal or frame system. The force to be measured is applied to the lower swivel and a couple is produced on the inner frame, causing the gimbals to precess. The time taken for the outer gimbal to complete one revolution is then a measure of the applied force. The gyroscopic load cell is essentially a rapidly responding digital transducer and is inherently free of hysteresis and drift.

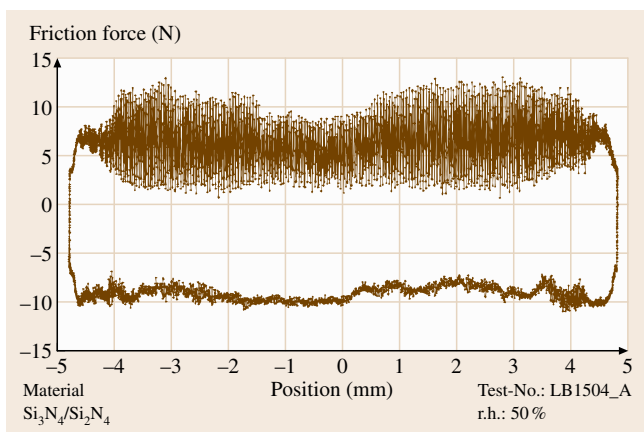


Fig. 13.12 Friction force signal for one sliding cycle of a silicon nitride couple in reciprocating sliding, showing asymmetric behavior due to differences in the stiffness of the system in the two sliding directions (after [13.13]) (r.h. = relative humidity)

13.4.5 Sampling and Digitization Errors

In the case of a strain gauge load cell, the output signal from the whole force measurement chain depends on the mechanical properties of the elastic element to which the strain gauges are bonded and on the electronic circuitry used to convert the resistance changes in the strain gauges (caused by the bending force applied to the elastic element) into a recordable electrical signal proportional to the force. Similar considerations apply to other types of load cell. The design of the elastic element defines the resonance frequency of the load cell. If the dynamic properties of the force to be measured excite this natural frequency, then the output signal will no longer be proportional to the applied force.

Figure 13.11 shows the output signal from a strain gauge load cell, recorded with a high sampling rate; the friction force was generated between a pair of titanium specimens sliding at 1 m/s at a temperature of 400 °C. The dominant component of the alternating signal occurs at the natural resonant frequency of the load cell, due to vibration induced by the friction between the triboelements. Derivation of a friction force from such a signal will clearly lead to error. Such effects will still occur but not be obvious if the sampling rate is too low or if the electronic circuitry used has a long time constant, integrating over the rapid signal variations. Recording the output from a load cell with an analog chart recorder usually filters out such fast signal changes and integrates them.

Another example of a dynamic friction signal is presented in Fig. 13.12. The friction signal, measured with a piezoelectric sensor, for one sliding cycle of a silicon nitride couple exhibits different extents of variation for the two half-cycles, indicating that the sliding couple under these test conditions tends to stick/slip motion. The difference in behavior is caused by the difference in the stiffness of the construction elements in the two directions. For such a system it is not possible to define a quantitative friction level because the measured signals are dominated by the vibrations of the elastic sensor element and are thus not proportional to the friction forces. Results of this type only allow the tendency to stick/slip motion to be deduced.

13.4.6 Calibration

Even with good transducers and a good overall system design, measurements of forces cannot be relied upon without calibration. Instruments capable of performing force calibrations are known as *force standard*

Table 13.2 Types of force standard machine

Type	Principle	Uncertainty attainable	Category
Deadweight machines	A known mass is suspended in the Earth's gravitational field and generates a force on the support	< 0.001%	Primary or secondary
Hydraulic amplification machines	A small deadweight machine applies a force to a piston-cylinder assembly and the pressure thus generated is applied to a larger piston-cylinder assembly	< 0.02%	Secondary
Lever amplification machines	A small deadweight machine with a set of levers which amplify the force	< 0.02%	Secondary
Strain-gauged hydraulic machines	The force applied to an instrument is reacted against strain-gauged columns in the machine's framework	< 0.05%	Secondary
Reference force transducer machines	A force transfer standard is placed in series with the instrument to be calibrated	< 0.05%	Secondary

machines. Primary standards in force measurement are machines whose uncertainty can be verified directly through physical principles to the fundamental base units of mass, length and time. Secondary standards can be compared with primary standards through the use of a force transfer standard, which is a calibrated force transducer, frequently a strain gauge load cell. Standards document ISO 376 describes the calibration and classification of transfer standards.

Table 13.2 lists types of force standard machines that have been developed for the calibration of static forces acting along a single well-defined axis. The principles used for the calibration of multicomponent force sensors remain the same, but cross-talk between the different axes must also be considered. For the measurement of dynamic forces it is assumed that the statically-derived force transducer sensitivities are applicable, but attention must also be paid to the natural frequencies of the load cell.

The calibration of a force transducer can be performed with the transducer in its permanently installed position by using a transfer standard, or prior to its installation and by removal as required for further calibration.

More information on force measurement and calibration can be found elsewhere [13.14, 15].

For very small forces, as measured with an atomic force microscope (AFM), special calibration procedures are needed. An AFM can be used to measure friction forces in the nN range. The calibration methods used for this force-measuring machine also use known masses under gravity, but the lowest attainable uncertainty is much greater than that described above for macroscopic forces. The AFM scans a probe tip over the surface under examination. It operates like a stylus profilometer with constant contact force, which is

maintained by steering the bending of the cantilever beam carrying the probe tip using a piezoelectric element (Fig. 13.13). The bending of the cantilever is sensed by a segmented photodiode which measures the intensity of laser light reflected from the back of the cantilever. The piezoelectric driving voltage is adjusted during the scan over the surface to hold the resulting difference in photocurrent between segments (1 + 2) and segments (3 + 4) constant. A constant photocurrent implies constant beam deflection, which is equivalent to a constant force. The piezoelectric voltage needed to hold the photocurrent constant is thus a measure of the topographical height at the instantaneous position of the tip. The height resolution of an AFM is in the range of atomic dimensions.

If the direction of scanning is perpendicular to the axis of the cantilever, the torsion of the cantilever provides a measure of the friction force between the tip and the sample. The torsion is measured by the difference between the photocurrents from segments (1 + 3) and

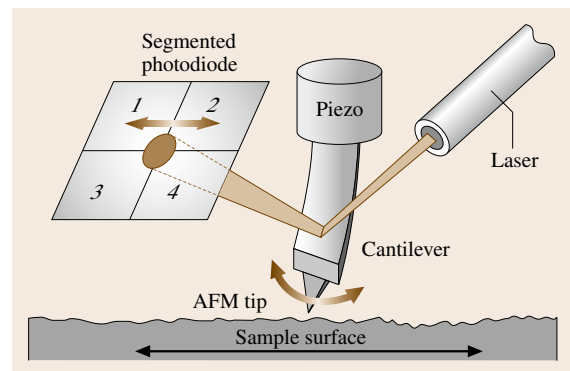


Fig. 13.13 Principle of friction measurement with an AFM (atomic force microscope)

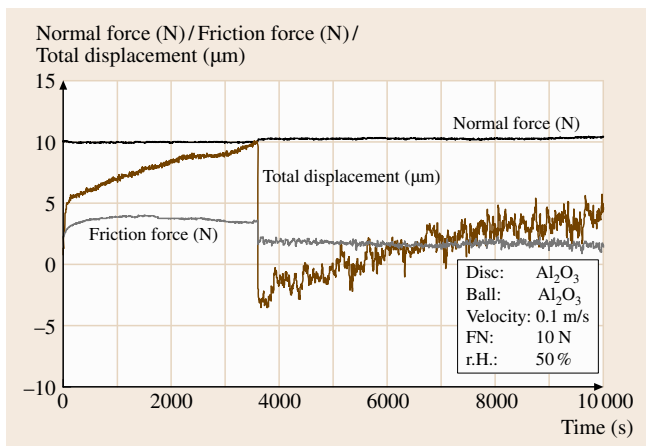


Fig. 13.14 Example of online measurement of linear wear (total displacement of ball relative to disc) and friction force for continuous sliding of an alumina ceramic ball on an alumina disc ◀

Table 13.3 Tribological tests involving sliding motion

Test Parameters
Materials composition and microstructure
Load
Speed
Temperature
Surface condition
Environment
Lubrication
Contact time and interval between loading of contact areas on two samples
Measurements
Direct change of dimension
Volume (usually via weight loss and density)
Profilometry
Friction
Continuous measurement of wear during test
Examination of worn surface
Examination of wear debris
Standards
ASTM G 99
ASTM G 133
ISO 20808

segments (2 + 4). The calibration of the relevant spring constants of the cantilever (in bending and torsion) is not a trivial procedure [13.16–18].

A technique known as *triboscopy* monitors the evolution of time-dependent local phenomena with a spatial

Table 13.4 Tribological tests involving rolling motion

Test Parameters
Materials composition and structure
Load
Relative slip of rolling elements
Rolling speed
Temperature
Surface condition
Environment
Lubrication
Measurements
Direct change of dimension
Volume (usually via weight loss and density)
Profilometry
Torque
Continuous measurement of wear during test
Examination of worn surface
Examination of wear debris

resolution limited by contact size. With this technique, complementary images of the friction force can be obtained by simultaneously recording spatially-resolved electrical contact resistance and friction measurements. The technique provides information about the history of friction and wear processes [13.19]. When measuring the electrical contact resistance, care must be taken that the electrical sensing current remains low, because otherwise the wear process may be influenced.

13.4.7 Presentation of Results

In most cases the specification of a single coefficient of friction is not adequate. This can be seen from the examples in Figs. 13.12 and 13.14, depicting the evolution of friction during individual experimental runs. At the very least, all relevant test and system parameters should be specified. The list in Table 13.1 provides a general guide, and is supplemented by the more specific lists of parameters in Table 13.3 and Table 13.4.

13.5 Quantitative Assessment of Wear

13.5.1 Direct and Indirect Quantities

The amount of wear can be specified in terms of direct or indirect quantities.

Indirect quantities are often used in technical assessments of the lives of machinery and in practical engineering. Examples include

- wear-limited service life (used for cutting tools for example: h , d , number of parts)
- wear-limited throughput (used for the flow of abrasive materials or objects through pipelines for instance: number of parts, m^3 , kg).

Direct wear quantities specify the change in mass, geometrical dimensions or volume of the wearing body. Examples include

- wear amount:
 - mass loss (kg)
 - linear dimensional change (m)
 - volume loss (m^3)
- wear resistance = $1/(\text{wear amount})$ (m^{-1} , m^{-3} , kg^{-1})
- wear rate = $(\text{wear amount})/(\text{sliding distance or time})$ (m/m , m^3/m , kg/m , m/s , m^3/s , kg/s)
- wear coefficient, or specific (or normalized) wear rate (also sometimes called wear factor) = $(\text{wear rate})/(\text{normal force})$ ($m^3 N^{-1} m^{-1}$).

The primary measurement from which these quantities are derived is usually mass loss, dimensional change or volume loss, although other methods can also be used (see Sect. 13.5.5).

13.5.2 Mass Loss

The loss of substance from the surface of a triboelement can be determined by weighing it before and after wear. Continuous sensing of the wear process in terms of mass loss is usually not possible. Mass loss measurement at defined intervals, to obtain information about the development of wear (and hence to investigate running-in, stability of wear rate, and so on), require the test to be halted and the triboelement(s) removed for weighing. In this process the danger exists that the microcontact geometry will be changed on reassembly. Such a change in microgeometry can influence the wear rate. Debris present in the contact region is also likely to be disturbed, and often removed. The most important period in the development of the wear rate may be missed, and

the act of interrupting the test in order to weigh the specimen may alter the progress and even the predominant mechanism of wear.

The sensitivity of this method of wear quantification is relatively low. The method is applicable only for wear rates high enough that a significant mass loss (typically of the order of at least 1 mg) is reached after a reasonable time for a test sample not heavier than about 0.5 kg. For materials which experience significant mass changes from other causes, such as the absorption or loss of water by certain polymers, or the oxidation of metals at high temperatures, special care must be taken to ensure that the mass changes measured are genuinely associated with tribological processes and are not due to other phenomena. Suitable control specimens, not subjected to wear but otherwise exposed to the same conditions as the triboelements, may be helpful for eliminating such effects and also for correcting for any long-term drift in the calibration of the balance.

The accuracy of weighing may be limited by the accuracy or sensitivity of the balance (especially in the case of heavy triboelements), by changes in humidity between the two weighings, or by particle or debris attachment or detachment. Material transfer and oxidation during the wear process often complicate the interpretation of the measured mass values and can sometimes lead to erroneous interpretation of the wear behavior.

Wear is sometimes expressed in units of volume, and in order to convert mass loss to volume loss, the density of the worn material must be known. For a homogeneous bulk material this will usually pose no problems, but if wear is occurring from a coating or treated surface layer then the relevant density may not be accurately known.

13.5.3 Dimensional Change

Changes in linear dimensions due to wear are frequently measured on-line (continuously) during friction tests. This has advantages over making measurements by interrupting the test, because one can then get information about the continuous evolution of wear during the test and, by detecting transitions in the measured linear wear rate, about changes in the dominant wear mechanism.

In most cases a change in the distance between the mounting fixtures of the two triboelements is measured. This implies that only the sum of the linear wear contributions from both elements can be obtained. Material transfer from one triboelement to the other may

lead to misinterpretation. For example, in the frequently used test arrangement with a ball or pin sliding continuously on a disc surface, transfer of material from the disc to the ball will change the distance between them. Depending on the amount of wear of the disc or the ratio of wear to transfer, the measured distance can be reduced, eliminated or increased. This last case may occur if much of the material worn from the larger wear scar on the disc is transferred to the smaller wear area on the ball or pin. Figure 13.14 shows an example of such behavior for an alumina ball sliding on an alumina disc. For up to about 3500 s of sliding, the displacement of the sample increases steadily, with the system apparently showing *negative* wear. The reason for this is that wear debris is accumulating in the contact region. The agglomerated particles of worn material then suddenly detach, leading to a negative total displacement, which is then followed by further accumulation of debris. The friction force also changes, which is associated with a change in the nature of the surface interaction.

In some cases wear of one or both triboelements leads to a significant change in the local geometry of the contact. An example of this behavior is shown in Fig. 13.15. As wear occurs on the steel ball the contact area progressively increases, and the wear rate detected in terms of a change in the distance between the two triboelements falls rapidly with time, although the associated volume wear rate varies much less. In

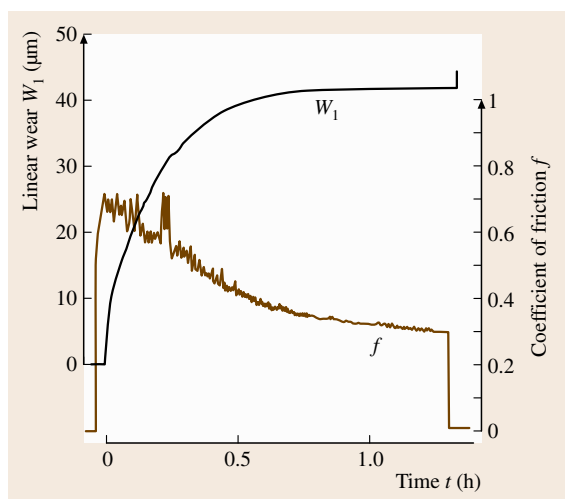


Fig. 13.15 Example of online measurement of linear wear (total displacement of ball relative to disc W_1) and friction force (f) for reciprocating steel ball on a diamond-coated disc (courtesy of D. Klaffke)

this experiment there was also a substantial change in friction force.

For on-line measurements of the changes in linear dimensions or displacements, inductive or capacitive sensors are frequently used. Inductive sensors can attain a resolution down to 1 μm , and capacitive sensors can reach a resolution in the nanometer range. Both types of sensors and their associated electronic circuits exhibit some temperature drift and a limited bandwidth (frequency range over which the defined specification of repeatability, resolution and accuracy is achieved). However, in most cases, the dimensional changes due to temperature variations in the test samples, their fixtures, and the mechanical construction of the apparatus induce greater measurement errors than those of the sensor system itself. Capacitive displacement sensors require a relatively clean environment: dirt, dust, water, oil or other dielectric media in the measuring gap will influence the measurement signal. Inductive sensor systems are generally less expensive and also less sensitive to environmental influences.

13.5.4 Volume Loss

The volume loss from a specimen in a tribological test can be derived from the mass loss if the density of the material is known. As indicated in Sect. 13.5.2, there may however be uncertainty in the density, especially in the case of a coated or surface-treated sample. In principle, the volume loss can also be derived from measured dimensional changes. In many cases this method will be more accurate than weighing a sample before and after testing.

For tests such as the ball-on-disc, pin-on-disc or block-on-ring geometries, this is particularly true for the two limiting cases when the wear occurs on only one of the triboelements. For example, for reciprocating sliding tests with the ball-on-plate configuration, relatively simple equations for the wear volume can be deduced.

If wear occurs only on the ball, then the wear volume of the ball $W_{v,b}$ is given by

$$W_{v,b} \approx (\pi d_a^2 d_p^2 / 64R) . \quad (13.3)$$

The total linear wear is given by

$$W_1 \approx d_a^2 / (8R) \quad (13.4)$$

and therefore

$$W_{v,b} = W_{v,tot} \approx \pi R W_1^2 , \quad (13.5)$$

where the symbols are defined below.

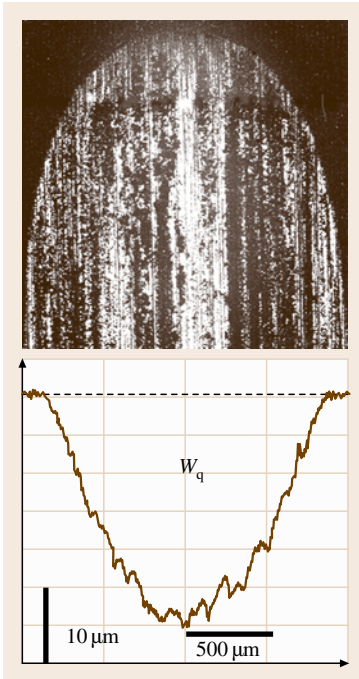


Fig. 13.16 Example of determination of wear volume for a flat specimen after a sliding test with ball-on-flat geometry, by measurement of the cross-section of the wear scar on the flat. The *upper image* shows the end of a linear wear scar produced by reciprocating sliding, and the *lower graph* shows a profilometer trace across it at a representative position

If wear occurs only on the plate (so the ball wear volume is zero), then the wear volume for the plate $W_{v,d}$ is given by

$$W_{v,d} \approx (\pi d_a^2 d_p^2 / 64R) + \Delta x W_q. \quad (13.6)$$

The planimetric wear is

$$W_q \approx d_a^3 / 12R \quad (13.7)$$

and therefore

$$W_{v,d} = W_{v,tot} \approx (\Delta x d_a^3 / 12R) + (\pi d_a^2 d_p^2 / 64R) \quad (13.8)$$

$$\approx \Delta x d_a^3 / 12R \quad (13.8a)$$

since the second term in (13.8) is small compared with the first one in the case of reciprocating sliding, where Δx is large compared with d_a and

$W_{v,d}$ wear volume of the plate,
 $W_{v,b}$ wear volume of the ball,

$W_{v,tot} = W_{v,d} + W_{v,b}$ total wear volume,
 d_p diameter of the wear scar on the ball, parallel to the sliding direction,
 d_a diameter of the wear scar on the ball, perpendicular to the sliding direction,
 W_q planimetric wear (plate),
 W_l total linear wear,
 Δx stroke of motion,
 R radius of the ball.

Combining (13.4), (13.5), and (13.8a) leads to

$$W_{v,d} = W_{v,tot} \approx (4/3)\Delta x(2R)^{1/2} W_l^{3/2}. \quad (13.9)$$

This equation allows the evolution of the volumetric wear to be related to the evolution of the continuously measured linear wear.

Usually, however, wear occurs on both bodies. In this case a *rule of mixtures* can be used

$$W_{v,tot} = \alpha \pi R W_l^2 + \beta (4/3)\Delta x(2R)^{1/2} W_l^{3/2}, \quad (13.10)$$

where α and β describe the contribution of ball and plate to the wear, respectively.

However, the values of α and β are not known beforehand, and can change during the test. Therefore, the determination of the wear volume offline from the dimensions of the wear scars is usually more accurate than online determination from the measurement of the change in linear dimensions during the test.

Measurements of volumetric wear from topographic changes determined with a stylus profilometer, laser profilometer or white light interferometer in most cases deliver more accurate results than online measurement of dimensional changes. With these methods, the three-dimensional profiles before and after the test are determined and the wear volume derived by subtracting one from the other. A precondition for this method is the ability to align the two profiles correctly. With wear scars which are extended in one direction (such as scars formed in linearly reciprocating or rotating triboelements), line scans can be performed across the wear scars and the wear volume calculated from the resulting two-dimensional cross-section profile and the length of the wear scar (Fig. 13.16). This method may, however, lead to large errors if the depth of the wear scar is not much greater than the roughness of the surface.

If the cross-sectional area W_q of a wear scar is measured by profilometry after a ball-on-flat test with reciprocating sliding, the wear volume of the ball can be calculated from

$$W_{v,b} = (\pi d_a^2 d_p^2 / 64) \cdot [(1/R) - (1/R^*)], \quad (13.11)$$

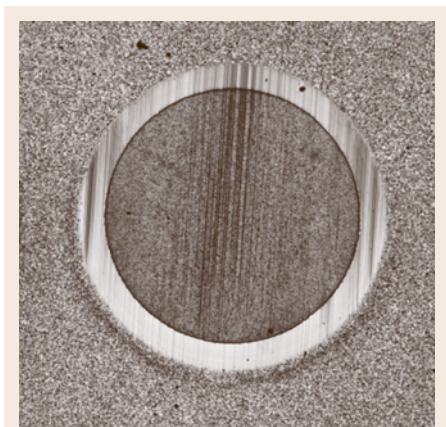


Fig. 13.17 Example of wear scar produced by a ball cratering test on a coated sample (optical micrograph); the boundary between the titanium nitride coating and the steel substrate is clearly seen. Typical wear scar diameter is 1–2 mm

where R^* is the radius of the wear area of the ball. This value can be calculated from the profile of the wear scar on the flat

$$R^* = d_a^3 / (12W_q) \quad (13.12)$$

The wear volume of the flat is given by

$$W_{v,d} \approx (\pi d_a^2 d_p^2 / 64)(1/R^*) + \Delta x W_q \quad (13.13)$$

In the case of well-defined wear scars of known geometry, for example those produced in ball-cratering abrasion tests (Fig. 13.17), the volume of wear can also

be calculated from the diameter of the wear scar and the radius of the ball, the change in which during the test can usually be assumed to be negligible. The diameter of the wear scar may be measured with a stylus profilometer or an optical microscope.

13.5.5 Other Methods

Very small amounts of wear can be determined in real time, for example during the operation of internal combustion engines, by radionuclide (or radioactive tracer) techniques [13.20, 21]. Before starting the wear test, a very thin layer at the surface of one or both triboelements (such as the piston ring and cylinder liner in an internal combustion engine) is activated by irradiation with heavy ions from a particle accelerator. Since only a thin layer is activated, only rudimentary radiation precautions are required. The wear debris from the activated triboelements during the operation of the engine are radioactive and are transported within the oil circuit to a filter. A γ -ray detector close to the filter measures the radiation activity, as shown in Fig. 13.18. The increase in this activity with test duration is proportional to the amount of wear. If the two triboelements (such as the piston ring and cylinder liner) contain different alloying elements, the activation will lead to radioactive isotopes of these elements which emit γ -rays with different characteristic energies. In this case, the wear of each triboelement, and not only the sum of both, can be separately measured online.

Measurement of the electrical contact resistance during a friction test between metallic triboelements, with one contact partner insulated, can provide information about the formation and removal of reaction layers, such as oxides. Special arrangements involving insulation and embedded conductive wires or sensors in a test sample can be used to detect a wear limit [13.22–24].

13.5.6 Errors and Reproducibility in Wear Testing

As mentioned above in Sect. 13.4, the filtering effect of the electronic circuits used for signal recording, as well as the sampling rate in digital signal recording, may introduce errors into measurements of dynamic friction force signals. Vibrations excited at the resonant frequency of the sensor system may be superimposed on the friction force signal, leading to variations in the measured friction force which would not be present in the absence of the sensor system. These vibrations can also influence the wear rate of the system. In the case of

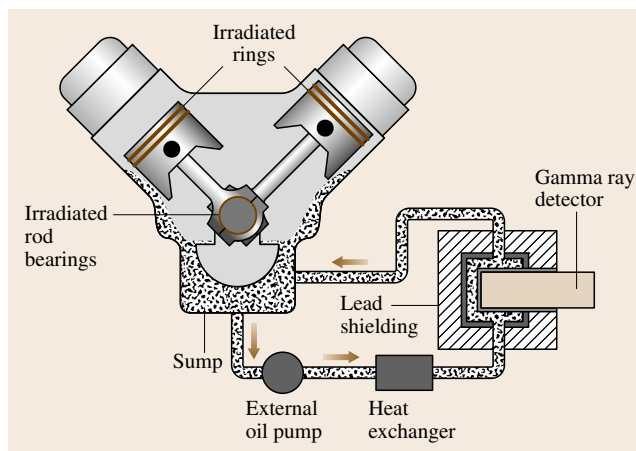


Fig. 13.18 Principle of wear determination in an internal combustion engine by the radionuclide measurement method (courtesy of Southwest Research Institute, USA)

a very unsteady friction signal, friction force measurements must be interpreted with care; it is problematic to deduce a unique coefficient of friction from such tests. Use of a bandwidth that is too low in the electronic recording system can mask the dynamic properties of friction forces resulting, for example, from stick/slip behavior.

The processes involved in sample preparation, especially cleaning of the test specimens, can have a major influence on friction and on the wear of triboelements. Surface machining and polishing often involve the use of cutting fluids or lubricants in contact with the sample, which must be removed by a thorough cleaning procedure. Ultrasonic cleaning with a sequence of suitable solvents is often necessary to obtain acceptably clean surfaces.

In friction measurements with very low external loads, *intrinsic* adhesion forces such as van der Waals or capillary forces must be taken into account in the interpretation of measured friction force.

Material transfer during a tribological test can also lead to erroneous interpretation of the results, for friction as well as for wear. It is therefore important to analyze the worn areas to examine the processes which have occurred. The example shown in Fig. 13.14 involved transfer, agglomeration and compaction of wear particles, which affected not only the wear rate but also the friction.

The wear rate measured in a tribological test will usually be highly specific to the mechanical design of the apparatus used and its applicability to other tribological systems may be doubtful. Measurements derived from a test may be misleading if they are obtained after an inappropriate test duration. An example is shown in Fig. 13.19 for a steel/steel sliding couple. If the tests had been stopped after 100 000 cycles, the wear rates deduced from the tests would have been the same for the dry (7% r.h.) and the humid ($\approx 100\%$ r.h.) conditions. Only longer term tests reveal that in this system the wear rate in fact depends strongly on the humidity of the surrounding atmosphere. Atmospheric humidity is a parameter which is often not controlled in tribological tests, even though it is known to affect the tribological behavior of some systems, especially ceramics, very strongly. Figure 13.20 shows an example of the influence of humidity on tribological behavior for two ceramics, with very different results for tests under *winter* (low humidity) and *summer* (high humidity) conditions.

The specific wear rate of the steel/silicon carbide couple under *winter* conditions was more than twelve

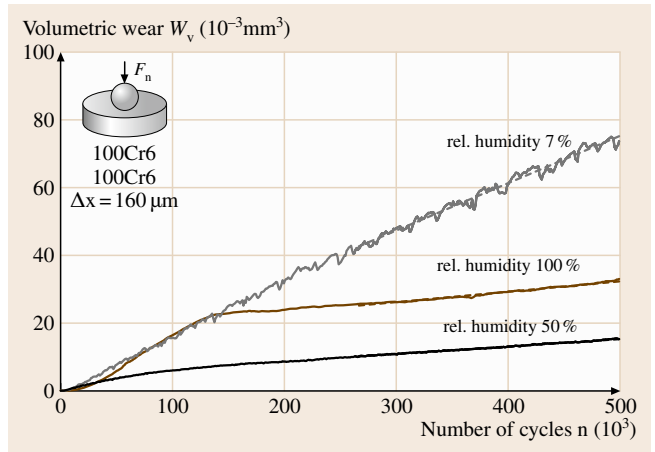


Fig. 13.19 Example showing development of wear volume for a steel/steel couple with the number of sliding cycles (reciprocating), for different relative humidities of the surrounding air

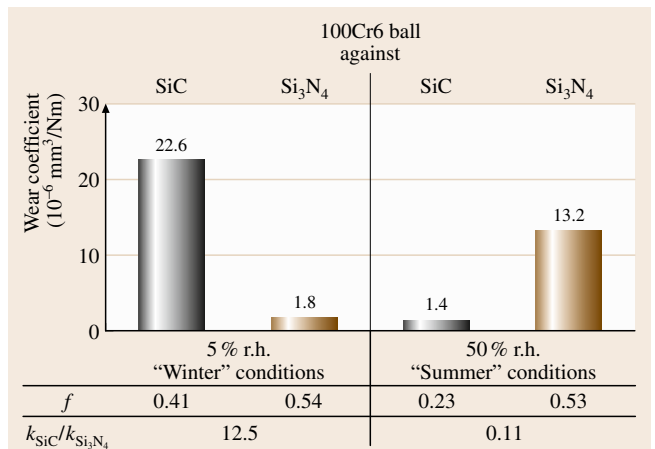


Fig. 13.20 Example showing the strong effect of atmospheric humidity on tribological behavior for two ceramic materials. Specific wear rates and mean coefficients of friction for reciprocating sliding of a 100Cr6-steel ball on SiC and Si₃N₄ discs in air with relative humidities of 5 and 50%

times that of the steel/silicon nitride couple, whereas with the higher *summer* humidity the specific wear rate of the steel/silicon carbide couple was about one tenth of that of the steel/silicon nitride couple. The differences in friction coefficient, in contrast, were quite small.

In a reciprocating sliding test the length of the stroke and the period of each cycle can influence the wear rates if reactions with the environment, for example with oxygen or water vapor, occur. Similar effects may

also occur in continuous sliding on a rotating disc or ring. For these types of test, the time for which the wear scar surface is exposed to the atmosphere, out of contact with the other triboelement, depends on the detailed geometry of the triboelements and the kinematics of their relative motion.

The interpretation of the specific wear rate k derived from a tribological test also needs care. This quantity is defined as the wear volume divided by the sliding distance and the normal force (Sect. 13.1.3). Specific wear rates at higher normal forces can therefore be lower than those at low normal forces, despite the total wear being the same or higher. This may happen if a system can sustain loads up to a certain limit without any change in damage or wear rate.

Accelerated tribological tests, achieved by increasing the load (or pressure) or velocity, for example in order to estimate component life-time, run the danger of encountering a transition in the wear mechanism,

which may be from a relatively low-wear to a high-wear regime. Predicting system wear behavior based on such an accelerated test can lead to errors of one or even two orders of magnitude. Much more reliable information can be provided by *wear mapping*, as described in Sect. 13.2.4.

One reason for variability in friction and wear results is inhomogeneity of the test samples. Material properties can vary between positions on a test sample, and a test which involves a large area of the triboelement will generally be more reproducible than one which samples only a small area. Fretting tests, for example, typically show lower reproducibility than tests involving continuous sliding, since a fretting test with a ball on a flat, with a very small amplitude of motion, may be located close to a flaw in the material, or on an essentially flaw-free region. In a continuous sliding test, however, the response of the material will tend to be averaged over a much larger region.

13.6 Characterization of Surfaces and Debris

Worn surfaces, and the debris resulting from wear, may be examined for several reasons.

- To study the evolution of wear during an experiment, or during the life of a component in a practical application
- To compare features produced in a laboratory test with those observed in a practical application
- To identify mechanisms of wear
- (by studying debris) To identify the source of debris in a real-life application.

13.6.1 Sample Preparation

Samples for surface examination may vary greatly in cleanliness. At one extreme are those which have been prepared and tested under very clean laboratory conditions, perhaps even in ultrahigh vacuum, and at the other extreme, those which have been salvaged from field trials on heavy machinery operating under dirty conditions.

After tribological testing under vacuum conditions, or in a controlled atmosphere, the specimen may be moved directly through a transfer port into a vacuum chamber for instrumental examination (for example by SEM or the various surface analytical techniques described in Sect. 13.6.2 below) without being exposed

to air. In some experiments, the tribological tests may be performed within a vacuum system so that imaging and surface analysis can be carried out during or immediately after the experiment.

However, most tribological tests (and most tribological applications of materials) occur in air, and the presence of atmospheric oxygen and sometimes humidity often plays an important role in the wear process. Further exposure of the specimen to dry air will probably have little effect on the surface film, although any significant corrosion that might occur in steel samples should be avoided by keeping them dry (for example in a desiccator).

Test samples are often contaminated with lubricant. Wear debris may be present, as may corrosion products and, in the case of samples retrieved from field trials or components exposed to wear in service, even extraneous dirt introduced while dismantling the machine and extracting the sample to be studied. These features pose particular challenges, since on the one hand they may obscure or confuse the examination of the worn surface, but on the other hand, as in the case of wear debris, they may be valuable in providing extra information about the wear process. Although each case may present individual problems, it is possible to provide some general guidelines. The sample should be removed as soon as possible after the test apparatus or machine has

stopped, to avoid possible additional corrosion, which might for example be enhanced by the condensation of water in a system which cools below the dew point after running at a higher temperature. Organic lubricants can be removed with organic solvents, and visual and low-magnification optical inspection should reveal the presence of any gross solid contaminants. Corrosion products may not be readily distinguishable from wear debris, and indeed in many cases the wear debris will result from chemical reaction of the substrate material with the environment; but any debris which is localized in and around the worn region is more likely to result from the wear process than material which is more widely distributed on the sample and thus probably a product of general corrosion. When preparing the surface, a balance must be struck regarding the amount of debris to remove to allow the material surface to be studied. Solvent cleaning in a gentle ultrasonic bath, for example with ethanol, isopropanol or propanone, followed by hot-air drying, should produce a surface which is clean enough for microscopic examination, but such a process may remove debris, which can provide valuable information about the wear mechanism. It is sometimes possible to retrieve such debris by careful filtration of the solvent, and to examine the debris on the filter, or to further classify it, for example by ferrography.

Replication involves the preservation of the sample's surface topography by casting or molding a replicating medium against the surface, and then removing it. Careful experimental technique and the use of an appropriate replicating medium can lead to excellent results, and the reproduction of surface features on a submicrometer scale. Replication allows techniques such as SEM and profilometry to be applied to regions of large tribological contacts in the field from which conventional samples cannot be cut, or to which access is very difficult. It also allows a sequence of records to be made from a single specimen at intervals during a wear test, showing the evolution of surface features, since it is a nondestructive technique. The ability to build up a *library* of replicas of the same region of the specimen during a test allows the investigator to subsequently study in detail the evolution of features which only become known to be of particular interest at the end of the test sequence.

Control experiments can be valuable in providing assurance that the observations on the specimen are not associated with artefacts introduced by the method of specimen preparation.

In some cases, examination of the surface of a sample does not provide sufficient information about the

processes involved in wear, and the subsurface material, very close to the worn surface, must be studied. It may also be valuable to measure mechanical properties by micro- or nanoindentation in this region. Cross-sections of samples can be prepared for microscopy by conventional metallographic or ceramographic techniques, but since the regions of interest in the tribological context will be at or very close to the surface, special attention must be paid to retaining features in this region, and to avoiding the introduction of damage during preparation. The surface can be protected by applying metallic coatings (such as electroplated nickel) to metal specimens, or by using a hard embedding resin, preferably containing a hard filler (such as carbon or glass fibers, or ceramic particles), before the sample is cut perpendicularly to the worn surface and then ground and polished. Similar grinding and polishing rates should be aimed for in the protective material and in the worn sample itself, to achieve a perfectly plane cross-sectional surface for examination. Ceramics are particularly difficult to protect in this way, but edge protection may be achieved by clamping two samples of the same ceramic together, with the worn surface at the interface, before embedding and sectioning the composite sample.

Taper sectioning may also be used to study near-surface microstructure and reduce the effect of polishing artefacts close to the surface. This technique involves the examination of a section cut and polished at a shallow angle to the surface. For example, on a section cut at an angle of 5.7° to the surface, a distance of $10\ \mu\text{m}$ normal to the edge of the sample corresponds to a depth beneath the surface of only $1\ \mu\text{m}$ (since $\tan(5.7^\circ) \approx 0.1$).

Focused ion beam (FIB) milling provides a powerful technique to make cuts perpendicular to a worn surface, either for subsequent examination of the near-surface regions by SEM, or as a first step in the production of a sample for TEM. Since it is carried out on a fine scale and in regions which can be examined in detail by SEM before the milling takes place, it is possible to study the subsurface features associated with specific surface areas of interest.

13.6.2 Microscopy, Profilometry and Microanalysis

Worn surfaces are often imaged in order to characterize their surface topography and provide information about the wear mechanism. In many cases, accurate diagnosis of wear mechanism may not be possible from imaging alone, since information on the local chemical composi-

tion and microstructure of the near-surface material, as well as subsurface defects such as cracks or pores, may be required. Thus a wide range of techniques may be employed to study tribological surfaces and subsurface regions. These vary in the information they provide, the accuracy of that information, and the dimensional scale (in both lateral extent and depth into the surface) over which they provide information.

Table 13.5 summarizes commonly used techniques and their attributes. These include imaging techniques and methods of microstructural and compositional analysis. Resolution and sensitivity figures are approximate guides to relative performance, and there is often a trade-off between resolution and sensitivity. Further information on methods of surface chemical analysis can be found in Sect. 6.1 of this volume, and information on surface topography analysis in Sect. 6.2.

Scanning electron microscopy is very widely used to examine worn surfaces and, through the use of different imaging modes, can provide both topographic

(for example, from secondary electron detection) and compositional (such as the mean atomic number from back-scattered electrons) information. Stereo imaging, which involves the capture of two images of the same area of the surface tilted relative to each other by a small angle, can be used to provide qualitative information on topography, and the images can also be processed by suitable software to yield quantitative topographic maps. This method supplements the more traditional methods of profilometry, which use a stylus or optical means to map the surface heights (Sect. 13.6.2). Atomic force microscopy can be used to explore topography at the very finest level.

Low-vacuum and environmental SEMs can be especially valuable for studying some of the contaminated and poorly conducting (such as polymer and ceramic) samples encountered in tribological investigations. Ion channeling contrast can be used in a focused ion beam (FIB) microscope to reveal phase distributions and deformed microstructures, and as mentioned

Table 13.5 Surface examination techniques

Technique	Spatial resolution	Depth resolution	Analytical sensitivity (Z is average atomic number)	Applicability (Z is atomic number of element)
OM	0.2 μm	–	–	–
SEI (SEM)	1.5 nm	–	–	–
NCOP	1 μm	3 nm	–	Topography
CP	0.5 μm	1 nm	–	Topography, but may damage soft samples
XRD	10 mm	10 μm	5%	Crystal phase, lattice strain, particle/grain size
XRF	10 mm	10 μm	1–10 ppm	Z > 4
XPS	5 μm	3 monolayers	0.3%	Z > 2
LIMA	2 μm	1–2 μm	10–100 ppm	All Z
EDS (SEM)	1 μm	1 μm	0.1%	Z > 4
WDS (SEM)	1 μm	1 μm	100 ppm	Z > 4
BEI (SEM)	50 nm	50 nm	0.1 Z	
SSIMS	1 μm	2 monolayers	0.01%	All Z
DSIMS	20 nm	10 monolayers	<1 ppm	All Z
SAM	5 nm	3 monolayers	0.3%	Z > 2
EDS (STEM)	10 nm	20 nm	0.1%	Thin foil, Z > 4 peak overlap
EELS (STEM)	10 nm	20 nm	1%	Thin foil, Z > 3
APFIM	1 nm	1 monolayer	0.1–1%	All Z
EBSP	100 nm	50 nm	–	Crystal phase, orientation

Key: OM = optical microscopy; SEI = secondary electron imaging; BEI = back-scattered electron imaging; XRD, XRF, XPS = x-ray diffractometry, fluorescence and photoelectron spectroscopy; LIMA = laser-induced mass spectroscopy; EDS = energy-dispersive x-ray analysis; WDS = wavelength-dispersive spectrometry; SEM = scanning electron microscopy; SSIMS, DSIMS = static and dynamic secondary ion mass spectrometry; SAM = scanning Auger spectrometry; STEM = scanning transmission electron microscopy; APFIM = atom probe field ion microscope; EBSP = electron back-scattered diffraction pattern; EELS = electron energy loss spectrometry; NCOP = noncontact optical profilometer; CP = contact profilometer

in Sect. 13.6.1 the FIB can also be used to cut sections beneath the specimen surface for microscopy.

13.6.3 Wear Debris Analysis

Debris poses special problems in examination; the first challenge is to obtain a representative sample. In a lubricated system the technique of ferrography can be used to separate and grade magnetic debris. In ferrography, a suspension of wear debris flows through a magnetic field gradient and the particles become separated and

distributed according to size. Filtration can be used to separate nonmagnetic particles. The particles can then be examined (for example by optical or scanning electron microscopy), chemically analyzed, and their sizes and shapes characterized. Optical methods (such as laser light scattering) are commonly used to determine particle size distributions. Automated systems exist to evaluate and describe particle shapes in wear debris, and link them to wear mechanisms [13.25]. The methods of microscopy and microanalysis outlined in Sect. 13.6.2 can be used for debris as well as for worn surfaces.

References

- 13.1 American Society for Testing and Materials: *Standard G40: Standard terminology relating to wear and erosion* (ASTM International, West Conshohocken 2005)
- 13.2 M.B. Peterson, W.O. Winer (Eds.): Glossary of terms and definitions in the field of friction, wear and lubrication: Tribology. In: *Wear Control Handbook*, ed. by M.B. Peterson, W.O. Winer (Eds.) (Am. Soc. Mechanical Engineers, New York 1980) pp.1143–1303
- 13.3 DIN standard 50322: *Wear: Classification of categories in wear testing* (DIN, Berlin 1986)
- 13.4 I.M. Hutchings: *Tribology: Friction and Wear of Engineering Materials* (Arnold, London 1992)
- 13.5 M.J. Neale, M.G. Gee (Eds.): *Guide to Wear Problems and Testing for Industry* (William Andrew, Norwich 2001)
- 13.6 V.V. Dunaevsky: Friction temperatures. In: *Tribology Data Handbook*, ed. by E.R. Booser (CRC, Boca Raton 1997) pp. 462–473
- 13.7 R. Divakar, P.J. Blau (Eds.): *Wear Testing of Advanced Materials, ASTM STP1167* (Am. Soc. Testing Materials, West Conshohocken 1992)
- 13.8 Am. Soc. for Testing and Materials: *ASTM Annual Book of Standards*, Vol. 03.02 (ASTM International, West Conshohocken 2005)
- 13.9 M.G. Gee, M.J. Neale: General approach and procedures for unlubricated sliding wear tests. In: *NPL Good Practice Guide*, Vol. 51 (National Physical Laboratory, Teddington 2002)
- 13.10 M.G. Gee, A. Gant, I.M. Hutchings: Rotating wheel abrasive wear testing. In: *NPL Good Practice Guide*, Vol. 55 (National Physical Laboratory, Teddington 2002)
- 13.11 M.G. Gee, I.M. Hutchings: General approach and procedures for erosive wear testing. In: *NPL Good Practice Guide*, Vol. 56 (National Physical Laboratory, Teddington 2002)
- 13.12 M.G. Gee, A. Gant, I.M. Hutchings, R. Bethke, K. Schiffmann, K. Van Acker, S. Poulat, Y. Gachon, J. von Stebut: Ball cratering or micro-abrasion wear testing of coatings. In: *NPL Good Practice Guide*, Vol. 57 (National Physical Laboratory, Teddington 2002)
- 13.13 D. Klaffke, M. Hartelt: Stick-Slip Untersuchungen an keramischen Werkstoffen, Mater. Wiss. Werkstofftech. **31**, 790–793 (2000)
- 13.14 The Institute of Measurement and Control: *Guide to the Measurement of Force* (The Institute of Measurement and Control, London 1998)
- 13.15 Information on force measurement and calibration of force transducers on the NPL web page at <http://www.npl.co.uk/force/> (National Physical Laboratory, Teddington, 2006)
- 13.16 J.E. Sader, E. White: Theoretical analysis of the static deflection of plates for atomic force microscope applications, J. Appl. Phys. **74**(1), 1–9 (1994)
- 13.17 J.E. Sader, I. Larson, P. Mulvaney, L.R. White: Method for the calibration of atomic force microscope cantilevers, Rev. Sci. Instrum. **66**(7), 3789–3798 (1995)
- 13.18 J.P. Cleveland, S. Manne, D. Bocek, P.K. Hansma: A nondestructive method for determining the spring constant of cantilevers for scanning force microscopy, Rev. Sci. Instrum. **64**(2), 403–405 (1993)
- 13.19 K.J. Wahl, M. Belin, I.L. Singer: A triboscopic investigation of the wear and friction of MoS₂ in a reciprocating sliding contact, Wear **214**, 212–220 (1998)
- 13.20 M. Scherge, K. Pöhlmann, A. Gervé: Wear measurement using radionuclide-technique (RNT), Wear **254**, 810–817 (2003)
- 13.21 D.C. Eberle, C.M. Wall, M.B. Treuhaft: Applications of radioactive tracer technology in real-time measurement of wear and corrosion, Wear **259**, 1462–1471 (2005)
- 13.22 American Society for Testing and Materials: *Standard B794–97: Standard Test Method for Durability Wear Testing of Separable Electrical Connector*

- Systems using Electrical Resistance Measurements* (ASTM International, West Conshohocken 2005)
- 13.23 I. Buresch, P. Rehbein, D. Klaffke: Possibilities of fretting corrosion model testing for contact surfaces of automotive connector, Proc. 2nd World Tribol. Congr., ed. by F. Franek, W.J. Bartz, A. Pauschitz (The Austrian Tribology Society ÖTG, Vienna 2001)
- 13.24 D. Klaffke, M. Hartelt: Influence of electrical voltages on friction and wear in water lubricated sliding of SiC/SiC-TiC, Proc. 2nd World Tribol. Congr., ed. by F. Franek, W.J. Bartz, A. Pauschitz (The Austrian Tribology Society ÖTG, Vienna 2001)
- 13.25 S. Raadnui: Wear particle analysis – utilization of quantitative computer image analysis: a review, Tribol. Int. **38**, 871–878 (2005)

Biogenic Imp

14. Biogenic Impact on Materials

Materials as constituents of products or components of technical systems rarely exist in isolation and many must cope with exposure in the natural world. This chapter describes methods that simulate how a material is influenced through contact with living systems such as microorganisms and arthropods. Both unwanted and desirable interactions are considered. This biogenic impact on materials is intimately associated with the environment to which the material is exposed (Materials-Environment Interaction, Chap. 15). Factors such as moisture, temperature and availability of food sources all have a significant influence on biological systems. Corrosion (Chap. 12) and wear (Chap. 13) can also be induced or enhanced in the presence of microorganisms. Section 14.1 introduces the categories between desired (biodegradation) and undesired (biodegradation) biological effects on materials. It also introduces the role of biocides for the protection of materials. Section 14.2 describes the testing of wood as a building material especially against microorganisms and insects. Section 14.3 characterizes the test methodologies for two other groups of organic materials, namely polymers (Sect. 14.3.1) and paper and textiles (Sect. 14.3.2). Section 14.4 deals with the susceptibility of inorganic materials such as metals (Sect. 14.4.1), concrete (Sect. 14.4.2) and ceramics (Sect. 14.4.3) to biogenic impact. Section 14.5 treats the testing methodology concerned with the performance of coatings and coating materials. In many of these tests specific strains of organisms are employed. It is vital that these strains retain their ability to utilize/attack the substrate from which they were isolated, even when kept for many years in the laboratory. Section 14.6 therefore considers the importance of maintaining robust and representative test

14.1 Modes of Materials – Organisms Interactions	770
14.1.1 Biodeterioration/Biocorrosion.....	770
14.1.2 Biodegradation.....	771
14.1.3 Summary	771
14.1.4 Role of Biocides	771
14.2 Biological Testing of Wood	774
14.2.1 Attack by Microorganisms.....	776
14.2.2 Attack by Insects	781
14.3 Testing of Organic Materials	789
14.3.1 Biodeterioration	789
14.3.2 Biodegradation.....	791
14.3.3 Paper and Textiles.....	803
14.4 Biological Testing of Inorganic Materials	811
14.4.1 Inorganic Materials Subject to Biological Attack.....	811
14.4.2 The Mechanisms of Biological Attack on Inorganic Materials	813
14.4.3 Organisms Acting on Inorganic Materials.....	814
14.4.4 Biogenic Impact on Rocks.....	818
14.4.5 Biogenic Impact on Metals, Glass, Pigments.....	823
14.4.6 Control and Prevention of Biodeterioration.....	824
14.5 Coatings and Coating Materials	826
14.5.1 Susceptibility of Coated Surfaces to Fungal and Algal Growth.....	826
14.6 Reference Organisms	833
14.6.1 Chemical and Physiological Characterization.....	833
14.6.2 Genomic Characterization	834
References	838

organisms that are as capable of utilizing a substrate as their counterparts in nature such that realistic predictions of performance can be made.

14.1 Modes of Materials – Organisms Interactions

A number of interactions result from the contact between living systems and materials some of which result in either biodeterioration or biodegradation. The word *deteriorate* comes directly from Latin and means *to make worse*. The term biodeterioration was adopted in the late 1950s to early 1960s for the study of the deterioration of materials of economic importance by organisms. However, this definition should probably be expanded to include not only the deterioration of materials, but also of constructions (e.g. structural timber as part of a building) or processes (e.g. a paper mill) of economic importance.

Of course, the interaction between biological systems and materials is not always undesirable. In contrast to the above, the word *degrade* also comes directly from Latin and means *to step down*. Thus, biodegradation could mean activities of organisms which result in the breakdown of materials either to man's detriment or benefit. Many essential geochemical cycles (e.g. the nitrogen and carbon cycles) are almost wholly dependent on biological (indeed microbiological) processes and of course in current times the term *biodegradable* is considered an essential property of many manufactured materials to ensure that they can be recycled effectively at the end of their service life. So, although biodegradation may be seen by man as a direct opposite to biodeterioration, it is actually biologically exactly the same process and it is impossible to make a scientific distinction between them. Indeed, they are usually the same processes, changed in meaning and significance solely by human need.

A subdivision of the manifold effects of a *biogenic impact* on materials may either be made according to materials or to organisms. Changes of materials or their service properties may be caused by microorganisms, higher plants as well as by insects and other animals. Among the microorganisms bacteria, yeasts and algae play an important role as do many molds and higher fungi and basidiomycetes. The dominating animal species that impact on materials are among the insects with termites and members of the orders coleoptera and lepidoptera having an especially great destructive potential. But higher animals such as rats, mice and birds also have a significant impact on the service life of many materials. In the marine environment molluscs and crustaceans are usually considered the main deteriorating organisms. Although studies on the interaction between material and biological systems need to be holistic in their approach whether this be to determine the degree

of protection required by a material in service or to examine the impact of a material on an ecosystem, they are usually subdivided into specific areas to afford a more manageable route to their execution.

Materials primarily of natural origin, such as timber, pulp, paper, leather and textiles are particularly susceptible to deterioration by biological systems. However, many modern materials such as paints, adhesives, plastics, plasters, lubricating materials and fuels, technical liquids, waxes etc. can support microbial growth. Even the properties of inorganic products, such as concrete, glass, minerals and metals may suffer from biological attack. There are also many examples which demonstrate that not all breakdown of materials is undesirable as particular microorganisms are used for beneficial purposes, e.g., in extracting and processing raw materials such as alcoholic fermentation, antibiotics, flax retting, leaching etc. and even in extracting certain minerals in mining operations (e.g., bioextraction of uranium from mining residues).

14.1.1 Biodeterioration/Biocorrosion

A natural phenomenon of organisms, especially of microorganisms, is adhesion to surfaces of materials. For example, in the course of their proliferation a slimy matrix is produced by microbial communities at the interface with a material called a biofilm. In technical systems *biofouling* occurs. Drinking or process waters become contaminated, often by biofilms, and further propagation of biomass results in blockages of filter systems, pipings and heat exchangers. Economic damage results from the decrease in performance of technical processes (such as loss of efficiency in a heat exchanger) and can even result in equipment or facilities coming to a complete standstill. Losses amounting to billions of Euros every year are attributable to the effects of unwanted biofilms.

Another prominent example of the impact of biological systems on materials can be seen in the interaction between the organisms employed in a process with the materials used to contain it in the microbial deterioration of concrete in sewage systems caused by acidic fungal excretions. The same mechanism is also responsible for the deterioration of historic frescos and monuments. Even seemingly inert materials, such as the glass in optical devices, for instance binoculars and microscopes, are susceptible to etching which impairs and ultimately destroys their optical properties.

Biological processes may also produce discoloration and bad odors of liquids such as paints, glues, lubricating and technical liquids without actually affecting the performance of the material. Of course, they may also induce changes in consistency and impair the serviceability of such products or result in complete failure of the material. With plastics, biodeterioration can result in loss of mass and changes of technical characteristics, such as elasticity and tensile strength.

Effects of biodeterioration produced by organisms can range from damage caused by inorganic or organic acids, complexation, organic solvents, salt stress, influence of H₂S, NO₃, and NO₂ as well as enzymatic alterations or degradation. Biocorrosion of metals and metal alloys is also known to occur under a wide variety of conditions. The first reports on the corrosive properties of sulfate-reducing bacteria date back to the middle of the past century. Corrosion failures in oil refineries, pipelines and harbor facilities induced intensive research and investigations of the damage mechanisms. Spectacular accidents, such as the crash of a jet airplane due to corrosion of its aluminum fuel tanks illustrated the dangers of *microbially induced corrosion* (MIC). In most cases both bacteria and fungi were found to be responsible for such damage. The corrosion processes were induced either by their metabolites, such as acids, ammonia and hydrogen sulfide or by electrochemical circuits associated with the terminal electron acceptors of anaerobic metabolism. The capability of these microorganisms to form adhesive films on the surface of metals exacerbated the problem as below such films, anaerobic conditions prevail where corrosion-inducing oxygen concentration cells are produced. Similarly, hydrogen embrittlement may be also attributed to the production of hydrogen by microorganisms and its uptake by the metal surface.

14.1.2 Biodegradation

The manifold metabolic processes of organisms have been utilized by man in the course of his evolution. Long before the term biotechnology was coined, people knew how to produce foods by exploiting microbial processes. Agricultural applications included fish retting and waste straw upgrading. Important medical applications such as the production of antibiotics emerged. For a number of microbiological metabolic processes the following synonyms for biodegradation became established; biotransformation/bioconversion, implying the biological transformation of materials as an alternative to chemical processes. Bioleaching: metal

extraction (especially of copper and uranium) from poor ores and mining spoil, the extraction of which would not be profitable by metallurgical processes. Biotreatment, for example, kaolin for producing porcelain but stained by iron oxides may be successfully bleached by reducing or complex-forming metabolites of microorganisms. Bioremediation, for example, TNT and a number of other explosives may be reduced to harmless substances and microbial processes are being used increasingly to decontaminate toxic substances in the environment.

14.1.3 Summary

As discussed above, biodeterioration can be defined as a decrease in the economic value of materials caused by biological organisms. From a physical point of view, biodeterioration can be defined as the transition of a material from a higher to a lower energy level or (chemically) from a more to a less complex state. From a biological point of view it is important to be able to relate biodeterioration and biodegradation events to the cycle of changes of materials which characterize the natural world. Thus, a material may be required to be stable towards biological attack while in service but needs to degrade in the environment to substances that are harmless to and totally integrated with the environment once the service cycle has ended. Many materials, constructions and processes must therefore be looked at in a true *cradle to grave* context to ensure that the economic benefits at one point do not lead to adverse environmental (and economic) impact at a later stage in the cycle of that material's *lifespan*.

14.1.4 Role of Biocides

Many methods exist worldwide for examining the relationship between organisms and both man-made and natural materials. Much of the emphasis of these methods is related to the spoilage, deterioration or defacement of materials whether these are foodstuffs, structural woodwork or water-based coatings [14.1]. Most of the testing technology is focussed on determining both the susceptibility of materials to attack and to the efficacy of agents intended to either prevent or limit this attack. In many cases, these tests are used to form the basis of claims about how well a certain material, additive or technology may be expected to perform when exposed to biological challenges. Often this information is used to make commercial comparisons between either different final products or additives as

well as to attempt to predict whether a material will comply with a certain specification (e.g. service life).

Biocides

Much of the technology mentioned above depends on the use of biocidal agents to prevent growth in association with the material to be protected. In other disciplines, such agents are employed to either limit the growth of or kill organisms within a process, possibly to prevent them from impacting on materials they may come in contact with. A good example of such agents is the additives employed in the water treatment industry. These agents are used in applications such as cooling and humidification systems and paper mills [14.1]. They are introduced to both eliminate health risks associated with the uncontrolled growth of microorganisms (e.g., prevention of the growth of *Legionella* spp. in calorifiers) and limit the impact that they may have on structural components within the process (e.g. corrosion, loss of heat transfer efficiency) and the products of the process (e.g. foul odor in air handling systems, defects in paper resulting from bacterial slimes).

Biocides are also employed to remove populations from either within the matrix of a material or on the surfaces of a material. These agents are often applied as washes or rinses and are used to either sterilize/disinfect or at least reduce either part or all of any population that may be present [14.2]. Such disinfection processes can also take the form of an addition of a biocidal agent to a matrix which contains a population (e.g., the reduction of microbial contamination in metal working lubricolants, the treatment of timber infected with eggs/larvae of wood-boring beetles). Often this will be combined with the introduction of protection against further growth [14.3].

Biocidal agents may also be incorporated into a material to protect it in service. For example, preservatives are used in coating systems to protect the material from spoilage while in its wet state (so-called in-can protection) as well as to exhibit a biocidal effect in the finished film, preventing mold and/or algal growth on the surface of the coating once applied. Similarly, plasticized polyvinyl chloride (PVC) may be formulated with the addition of a fungicide to protect it from attack by microfungi and so protect the plasticizer and prevent loss of elasticity in service [14.4]. Wood may be impregnated with fungicides and insecticides prior to sale for structural applications.

In most of the situations described above, the treatment of a material is intended to either prevent deterioration of it, maximize the protection of the ma-

terial or remove a population from a system prior to its use. The biocides employed for such purposes and the approaches taken to achieve effective disinfection and preservation have been reviewed extensively elsewhere [14.1, 5]. However, in recent years a new form of interaction between a formulated material and biological populations has emerged. In part, this can be viewed as either an extension of the degree of protection provided to a material by the inclusion of a biocidal agent into it or as the transfer of the properties of external treatments of a material into the material itself. The inclusion of the biocidal agent is not simply to protect the material from deterioration but to exert a biological effect either to the immediate surroundings of that material or to items that come into contact with it. These effects may range from the prevention of growth of undesirable microbial populations on a material to which they pose no physical, chemical or biological threat, the immediate destruction of individual microbial cells as they come into close association with a surface (possibly without even coming into direct physical contact) or to the inclusion of insecticidal agents into netting intended as a barrier to mosquitos [14.6]. In all cases the effect is external to the material from which the article is constructed and is not merely present to protect either the material or the item itself. However, it is possible that the effect may take place within an item constructed from a modified/treated material. For example, one can imagine an air filter constructed of paper into which antimicrobial properties have been introduced which is intended to kill bacteria pathogenic to man which impact on it [14.7]. Similarly, a polyethylene foam sponge may be impregnated with an antimicrobial agent which is intended to prevent the growth of bacteria associated with food poisoning in man. This sponge may not be intended to disinfect surfaces on which it is used but simply to prevent it from becoming a reservoir of such bacteria in a food preparation environment.

Clearly, there are some complex situations when the effects intended by treated articles/treated materials are to be considered and this will impact on the suitability of the methods used to measure them. In general however, the effect of a treated item/treated material can be considered to be external to it. The effect is not concerned with either preservation or protection of the material/item itself and is not achieved by the application of a disinfecting agent after the material has entered service.

Finally, when considering suitable test methodologies, the scale and duration of the effect may need to be considered with respect to the claim made. For

example, will the material/item be able to exert the effect claimed for the effect to have any realistic benefit? Similarly, will the scale of the effect be sufficient to provide the benefit either claimed or implied? It is unlikely that data to support such claims would be available from a single test and it is likely that ageing and weathering studies would be needed in addition to tests which provide basic proof of principle and demonstrate performance under conditions which simulate actual use.

Biocidal Activity

Biocidal activity is a generic term but in the context of this chapter we are essentially considering microbiocidal, insecticidal, acaricidal and molluscicidal activity and is considered in more detail in [14.5]. In actual use this activity is further subdivided to represent activity against one or more groups within the various classes. For example, in the case of microorganisms, this will be impacted on by the microbial types/species which are employed in testing and, to a certain extent, the type of test required and this is considered in detail in other chapters in this section. The scale of the effect will often be important in some applications but the outcome of biocidal activity will result in a reduction in the number of test microorganisms as a result of an interaction with the material through an irreversible, killing effect. Such effects may be described as

1. *Bactericidal*: the effect is limited to a reduction in the size of a vegetative bacterial population.
2. *Fungicidal*: the effect is limited to fungi. This effect may be attributed to activity against vegetative growth, spores/dormant structures or both and may require clarification depending on the intended use of the product.
3. *Sporicidal*: the effect is against the spores/dormant structures of bacteria.
4. *Virucidal*: the effect is limited to virus particles.
5. *Protistocidal*: the effect is exhibited against protozoa and their dormant stages.
6. *Algicidal*: the effect is exhibited against algae and their dormant stages.

Biostatic Activity/Repellency

In many of the cases of the protection/preservation of materials the effects required are not associated with killing a population but of either preventing its growth or preventing it coming into contact with the material. In this context most interactions between a *biocide* and microbial populations are biostatic ones. As with bio-

cidal activity, this will be impacted on by the species which are employed in testing and, to a certain extent, the type of test required but obviously, the prevention of growth/metabolism/colonization of/by the target species should be demonstrated. It may be sufficient to demonstrate that growth is either slower or reaches a lower level than on an equivalent control material to either substantiate a claim or demonstrate a benefit. In many cases chemical microbicides exhibit both biostatic and biocidal activity with the initial impact on a microbial population being biostatic and sustained contact resulting in biocidal action. Similar relationships are found with molluscicides where presence of a toxic agent is sufficient to deter attack. In some cases limits to the efficacy of biostatic and repellency action are not related to the potency of the agent but to the durability of the effect in combination with a material (e.g., leach resistance of a fungicide preventing the germination of fungal spores that have alighted on a coating applied to the facade of a building). As with biocidal activity an equivalent subdivision of the type of activity exists, e.g.

1. *Bacteriostatic*: the effect is limited to the prevention of growth/metabolism of bacteria and possibly the germination of bacterial endospores and other dormant structures.
2. *Fungistatic*: the effect is limited to the prevention of growth of fungi and possibly the germination of fungal spores and other dormant structures.
3. *Algistatic*: the effect is limited to the prevention of growth of algae and possibly the germination of dormant structures.

Summary

Although the intrinsic activity of biocidal agents is important, of more concern is the interaction between them and the material/system which they are designed to protect. The spectrum of activity must be appropriate to the challenge the materials is likely to endure and the biocide must be compatible with the material as well as be able to provide protection for a suitable period of service. Although many of the tests described in this section are designed to examine the susceptibility of materials to biological attack, many can be adapted to examine the impact a biocidal treatment can have on that attack. With careful consideration, reliable prediction of the performance of a material equipped with a biocide can be made and this is often the main challenge when considering the negative interaction of biological systems with materials.

14.2 Biological Testing of Wood

Section 14.2 deals with the degradation of wood, wood products and wood treated with preservatives, by insects and microorganisms. It introduces the test methodology used to simulate such attack and how to estimate its impact on the material. The approach to testing differs in detail throughout the world. However, certain basic principles are commonly accepted. The approach taken in Europe will mainly be used to illustrate these principles.

Before elaborating on the specifics of attack by microorganisms (Sect. 14.2.1) and insects (Sect. 14.2.2) some general aspects concerning the testing of wooden materials will be considered.

Wood is one of the oldest construction materials. Its natural availability and omnipresence had made it the most obvious choice to build bridges, houses, ships etc. for millenia. It is relatively easy to process, has good insulating properties, has a high elasticity (compared e.g. to concrete, steel, stone) and wood with a high density is amazingly fire resistant (e.g. oak, teak).

Wood can be cut and bent to the desired size and shape. However, as a typical organic matter, its basic components and its constituents provide a nutrient source for microorganisms, molluscs, insects and other arthropods. Because of this, many species have developed natural defence systems. For example, some tree species (e.g. bongossi, teak) often produce phenolic substances which are deposited in the cells of the heartwood. These substances can considerably delay the attack by microorganisms and lend the material a degree of natural durability. Laboratory and outdoor tests have been developed to assess this natural durability for the commercially most interesting wood species used in Europe (see later: European Standard EN 350, Durability of wood and wood based products). In contrast, other wood species (e.g. pine, beech) can be rapidly degraded. To make long-term use of them in construction etc. they have to be preserved chemically with a wood-protecting biocide. Therefore, the test standards described in the following mainly deal with preservative-treated wood/wooden materials to determine the efficacy and performance of this material.

However, to determine the virulence of the microorganisms used in the different test setups, untreated wood is always incorporated. Some methods also employ so-called *reference products* which include preservatives that have shown their preserving effects on wood for decades. With the help of a reference product the severity of a method can be estimated and the results for a new preservative under test can be put into context.

Ideally, methods for determining the protective efficacy and the performance of treated or untreated timber should

- Reflect the environmental conditions to which the treated timber is subjected in service;
- Cover all relevant organisms and their succession during the time of use of the wooden commodity or construction;
- Take into account the possible methods of treatment for the wood preservative;
- Provide reproducible results rapidly;
- Be uncomplicated and easy to handle;
- Involve minimal costs.

Obstacles are

- The environmental conditions and the decaying organisms to which the timber is subjected are extremely diverse,
- The sensitivity of the decay organisms is different towards different biocides,
- The biocides applied are stressed not only by physical factors like evaporation, leaching and diffusion but;
- In the case of organic biocides, these compounds can also be utilized by organisms that are not the target of the chemical wood preservation and which may deteriorate the biocides or even use them as a nutrient source;
- Not all timber species are equally treatable.

Therefore it is necessary to simplify and to develop methods which nevertheless give sufficient certainty for the assessment of treated and untreated wood under test.

General Requirements for Resistance Against Biological Attack

More general requirements for testing procedures are outlined in the European Standard EN 350 for a natural resistance against wood-destructing organisms and in EN 599 for a wood preservative derived resistance.

- European Standard EN 350-1: Durability of wood and wood-based products – Natural durability of solid wood – Part 1: Guide to principles of testing and classification of the natural durability.
- European Standard EN 350-2: Durability of wood and wood-based products – Natural durability of solid wood – Part 2: Guide to

natural durability and treatability of selected wood species of importance in Europe.

- European Standard EN 599-1: Durability of wood and wood-based products – Performance of wood preservative as determined by biological tests – Part 1: Specification according to use class.
- European Standard EN 599-2: Durability of wood and wood-based products – Performance of wood preservative as determined by biological tests – Part 2: Classification and labelling.

The likelihood for a biological attack of wooden materials also strongly depends on the environment in which the material is used. These potential environments can be categorized into use classes, formerly known as hazard classes, according to the European Standard EN 335.

- European Standard EN 335-1: Durability of wood and wood-based products – Definition of use classes of biological attack – Part 1: General.
- European Standard EN 335-2: Durability of wood and wood-based products – Definition of use classes of biological attack – Part 2: Application to solid wood.
- European Standard EN 335-3: Durability of wood and wood-based products – Definition of use classes of biological attack – Part 3: Application to wood-based panel.

EN 335-1 defines the environmental compartments in which wood can be used and describes the main hazards

wood is exposed to. The standard defines five use classes (Table 14.1). The European standard EN 335 is currently under review. The aim of the review is to combine all three parts to one comprehensive standard. Other countries developed similar classifications. An ISO standard titled *Durability of wood and wood based products – Definition of use classes* is basically following the same principle.

Preconditioning Methods Before Durability Testing of Treated and Untreated Wood

In order to evaluate the effectiveness of a wood preservative over time, artificial ageing of protected wood is performed before a standard test method against microorganisms or insects is carried out.

- European Standard EN 73: *Accelerated ageing tests of treated wood prior to biological testing – Evaporative ageing procedure* describes an evaporative ageing procedure, applicable to test specimens of wood which have previously been treated with a preservative, in order to evaluate any loss in effectiveness when these test specimens are subsequently subjected to biological tests, as compared with test specimens which have not undergone any evaporative ageing procedure.
- European Standard EN 84: *Accelerated ageing tests of treated wood prior to biological testing – Leaching procedure* describes an ageing procedure by leaching, applicable to test specimens of wood which have previously been treated with a preservative, in order to evaluate any loss in effectiveness when these test specimens are subsequently subjected to biological tests, as com-

Table 14.1 European Standard EN 335 *Durability of wood and wood based products – use classes: definitions, application to solid wood and wood based panels*

Use classes	General use situation	Description of expose to wetting in service	Fungi	Beetles ¹	Termites	Marine borers
1	Interior (dry)	None	–	U	L	–
2	Interior, or under cover, not exposed to the weather (risk of condensation)	Occasionally	U	U	L	–
3	Exterior, above ground, exposed to the weather	Frequently	U	U	L	–
4	Exterior in ground contact and/or fresh water	Permanently	U	U	L	–
5	Permanently or regularly submerged in salt water	Permanently	U	U	L	U

U = Universally present within Europe.

L = Locally present within Europe.

¹ The risk of attack can be insignificant according to the specific service situation.

pared with test specimens which have not undergone any ageing procedure by leaching.

- European Technical Report CEN/TR 15046 *Wood preservatives – Artificial weathering of treated wood prior to biological testing – UV-radiation and water-spraying procedure*: This method describes an ageing procedure which simulates intervals of rain and UV-radiation. Because it works with elevated temperatures, to some extent also evaporation is included with this method. The method combines the main stresses by physical factors on the wood preservative in treated wood specimens prior to fungal or insect tests.

Modern organic fungicides and insecticides are susceptible to microbiological degradation. Therefore, the above-mentioned ageing standards are not always sufficient to determine the longevity of wood preservatives formulated with these biocides. A European technical Specification (CEN/TS 15397) titled *Wood preservatives – Method for natural preconditioning out of ground contact of treated wood specimens prior to biological laboratory tests* exists. This method combines natural physical stress factors with the possible succession of naturally occurring microorganisms. This technical specification is intended to overcome the difficulties caused by the nontarget microorganisms at least for wood exposed to the general service situations defined for European use class 3.

14.2.1 Attack by Microorganisms

Microorganisms can only attack wood when water is present in its cell lumina. This state is described as *wood moisture above the fiber-saturation-point*. As a rule of thumb this state is reached at about 30% wood moisture content (related to the dry weight of the wood). Dry wood cannot be metabolized by microorganisms and needs no preservatives to protect it against them.

Above fiber saturation the main components of wood – cellulose, hemicelluloses and lignin – can be degraded by a vast number of microorganisms.

Wood-destroying fungi are the most evident and powerful wood degraders. Their species belong to the

- basidiomycetes, causing brown rot or white rot,
- ascomycetes and fungi imperfecti, causing soft rot and stains.

Wood-destroying bacteria can be present in extremely wet environments, but the speed at which they

degrade wood is normally very slow and they can be neglected as metabolizing organisms of wood components. Nevertheless, with wood preservation moving away from inorganic, undegradable components towards organic compounds, the deterioration of these substances might be influenced by bacteria, leading to a failure of the wood preservative and therefore opening pathways for wood-metabolizing organisms to attack.

In relation to wood destruction mass loss and therefore strength loss of the wood are the primary issues. However, wood can also lose value through discoloration by microorganisms through molds and blue-staining fungi that cause no loss of cellulose, hemicellulose or lignin.

Detecting Wood-Destroying Fungi by Visual Means

The above-mentioned types of rot cause different appearances of the attacked wood. In many cases this can even be detected by the bare eye and can be confirmed by microscopic work. For macroscopic evaluation the wood should be dry, because checks and cracks become more obvious this way. For cutting sections to be analyzed microscopically the wood moisture should be above the fiber saturation point (above 30% wood moisture), because all strength properties of wood decrease with increasing moisture content of the wood until the fiber saturation point is reached. In other words: cutting becomes easier.

Visual Distinction of the Main Types of Wood Decay

Figures 14.2a and 14.3a show brown rot and white rot on wood macroscopically (here the wood has been cut longitudinally). Figure 14.1a shows undecayed, Figs. 14.2b and 14.3b decayed cross sections of wood as it can be seen under the microscope at a magnification of 150× to 200×. Further macroscopic and microscopic examples of wood decay can be found in [14.8].

Soft Rot. These fungi degrade cellulose and hemicelluloses. Macroscopically they cause a greyish-black rot with small cubicle cracks. Microscopically this form of decay is characterized by cavity formation inside the cell wall (Fig. 14.1b).

Blue Stains. Blue stains do not degrade lignin, cellulose or hemicelluloses and therefore cause no loss in mass or stability of the timber. They metabolize sugars deposited in the parenchymatic tissue of the wood. Blue stain fungi grow through the parenchymatic cells and spread in the

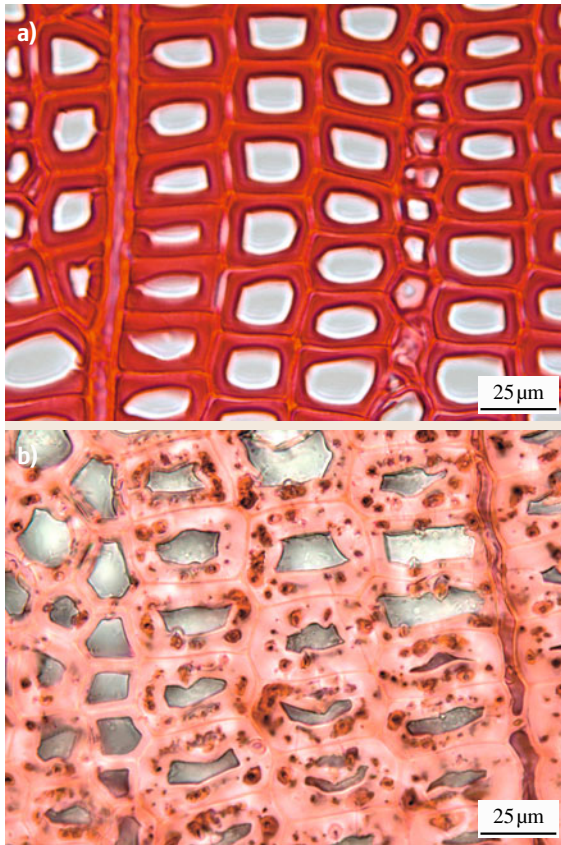


Fig. 14.1 (a) Cross section of sound undecayed wood (*Picea* sp.). (b) Cross section of wood (*Picea* sp.) decayed by soft rot causing cavity formation in the cell wall (Courtesy of Swedish University of Agricultural Science, Uppsala, Sweden)

wood. They stain the wood through their black-bluish hyphae and spores.

Brown Rot Fungi. Brown rot fungi metabolize cellulose and hemicellulose of the wood. Lignin can not be degraded by these fungi. The rot leaves behind cubic cracks (Fig. 14.2a) and a dark brownish tinge to the wood. The microscopic features are shown in Fig. 14.2b.

White Rot Fungi. White rot fungi metabolize all three main components of wood: lignin, cellulose and hemicelluloses.

Macroscopically white rot fungi generally lighten the color of the wood. Two types of white rot can be distinguished: a) simultaneous rot, where in pockets of decay the cellulose, hemicelluloses and lignin are

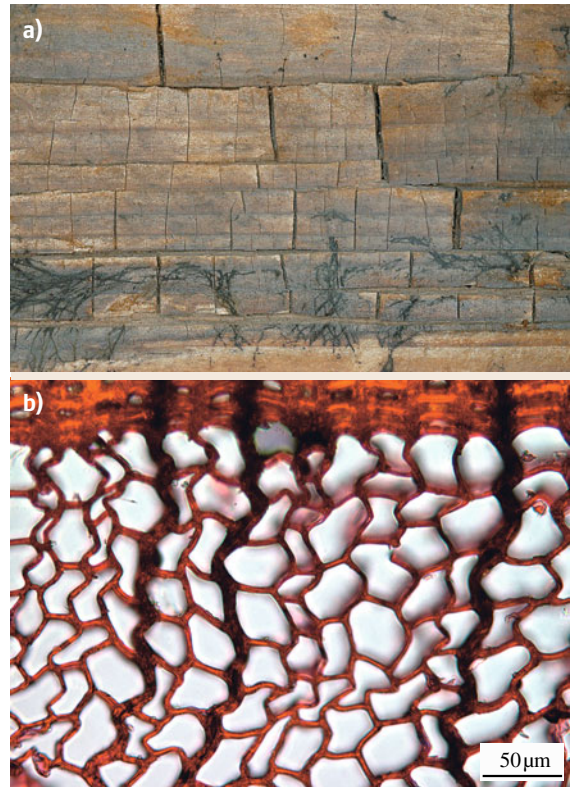


Fig. 14.2 (a) Longitudinal cut of wood (*Picea* sp.) decayed by brown rot causing fungi; wood surface shows cubicle cracks in wood decayed by brown rot, in the lower part of the picture mycelium of the brown rot causing fungus can be seen. (b) Cross section of wood (*Picea* sp.) decayed by brown rot causing fungi (Courtesy of Swedish University of Agricultural Science, Uppsala, Sweden)

completely degraded and b) the selective lignin degradation. Whereas the pockets of decay can be easily detected (Fig. 14.3a) the selective degradation of lignin, which is the more common form of white rot, can not be determined by changes of the wood surface like cracks or holes. Mass loss and change to a lighter color of the wood compared to the undecayed timber are the first signs of such an attack. The microscopic features for lignin degraders are shown in Fig. 14.3b.

Lignin-degrading fungi can be detected by the presence of a phenolic oxidase enzyme based on the Barendam-test. This test allows to biochemically distinguish brown from white rot fungi.

Sap Stains. Fungi grow only on the surface of freshly cut timber. They do not metabolize the wood itself, but

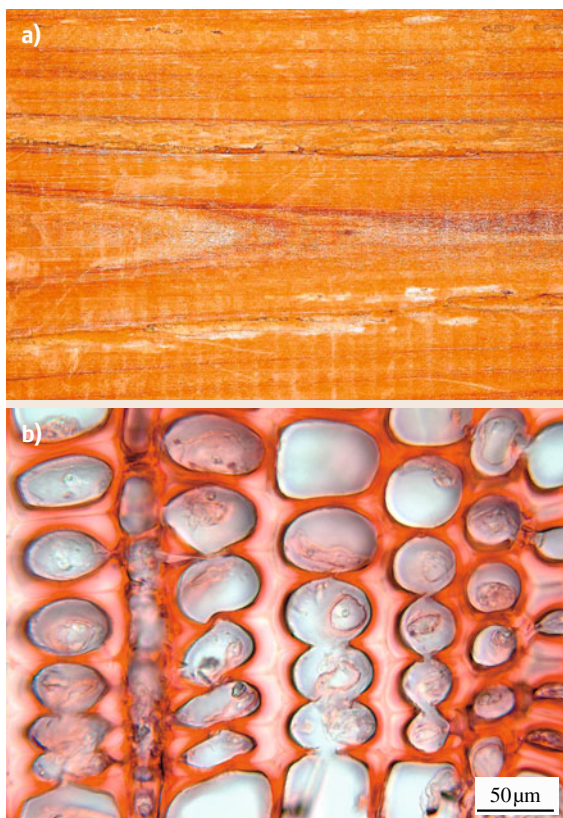


Fig. 14.3 (a) Longitudinal cut of wood (*Picea* sp.) decayed by white rot causing fungi; this picture shows an example for so called *pocket rot*, because white pockets of decay can be seen on the wood surface. (b) Cross section of wood (*Picea* sp.) decayed by white rot causing fungi (Courtesy of Swedish University of Agricultural Science, Uppsala, Sweden)

the sugars deposited in the parenchymatic tissue of the wood. The fungi can access these sugars only in cells that have been damaged (by force: felling or processing). By their metabolic products and colored spores they stain the wood and lead to loss in value.

A good overview on different forms of decay is also given by *Wilkinson* [14.9], and a more detailed description of macro- and microscopic observations can be found, e.g., in *Anagnost* [14.10].

As outlined above (see on *sap stain*, *blue stain*) some microorganisms cause only discoloration of wood while others also lead to mass loss of the wooden substance. Mass loss and therefore density loss is the more critical parameter since it is related to strength loss [14.11] which

is especially undesirable for a construction and building material. Therefore laboratory methods determine the mass of a wooden specimen before and after exposure to fungi which have been selected as aggressive wood-deteriorating organisms under laboratory conditions.

To measure mass loss at a set point in time requires the drying of the wooden material to 0% wood moisture content. This drying process kills living fungal cells and can lead to severe cracking of the wood structure. The rheological properties of the wood also lead to irreversible physicochemical changes while drying. Therefore the determination of mass loss by weighing is not a non-destructive method.

Nondestructive Testing Methods to Detect Fungal Decay

Nondestructive methods are required when the changes of wood structure have to be monitored over a longer time period or when the timber to be tested is already part of a construction. *Bodig* [14.12] listed the following nondestructive methods as examples.

- **Sonic stress wave**
Stress waves are generated either through an impact or by a forced vibration. Usually, with this method either the speed of sound or the vibration spectrum is measured. The dynamic modulus of elasticity (**MOE**) can be calculated from these measurements.
- **Deflection method (static bending technique)**
The deflection is measured at a safe load level which does not lead to rupture of the test piece. The static **MOE** can be calculated from these measurements.
- **Electrical properties**
The products of fungal metabolism are carbon dioxide and water of which the latter leads to a higher moisture content in the wood. This method is based on the relationship between moisture content and electrical resistance of wood.
- **Gamma radiation**
is tool for quantifying decay. It is also employed as a tracing method for quantifying the distribution of preservatives in wood. One of the limitations of this method is the regulations associated with the use of a radioactive source.
- **Penetrating radar**
This method is currently being developed for wood products. The method bears the potential to detect and quantify degradation at inaccessible locations.

- X-ray method
is mostly used in the laboratory or in production lines due to the bulky nature of the x-ray source and the measuring equipment.

Similar techniques (transverse vibration techniques, static bending techniques) are listed in a review on nondestructive testing for assessing timbers in structures by *Ross and Pellerin* [14.13].

Also infrared, x-ray and gamma-ray computerized tomography have been employed to visualize microbiological attack in timber. However, the techniques are mostly very cost intensive.

The oldest nondestructive test method is the visual estimation with the bare eye followed by rating the decay or discoloration of the specimens. This inexpensive method provides the expert with a lot of information. It is mainly applied when large numbers of specimens in a test field have to be assessed. An experienced evaluator will be able to rate the intensity of decay as well as to determine which type of decay has infested the wood.

Testing Wood for Different Use Classes

While the environmental conditions in use classes 1 and 2 do not provide the necessary amount of water to allow growth of microorganisms, the use classes 3 and 4 are the more relevant for testing microbiological decay above ground and in ground contact.

Testing Wood for Use Class 3.

Field Tests. Use class 3 is a very complex class. Depending on the local climatic conditions, the dimensions of the cross section of construction parts and their actual location (near to the ground, mostly covered under a roof etc.) it may reach from nearly use class 2 to use class 4. Many test methods have been developed for use class 3, intended to accelerate the attack by microorganisms and thus to give results in relatively short times. Some of them even use additional artificial wetting regimes. But all of them are simply reflecting different situations in use class 3. They are not accelerated test methods, except when they are used under extremely severe tropical conditions.

Three of these methods shall be described exemplarily.

- EN 330: *Wood preservatives – Field test method for determining the relative protective effectiveness of a wood preservative for use under a coating and exposed out of ground contact: L-joint method.*

With slight modifications the AWP A E9-06 *Standard Field Test for the Evaluation of Wood Preservatives to be Used in Non-Soil Contact* is comparable to this method. Stylized corners of window frames with mortise and tenon (L-joints) are treated with a wood preservative by a method recommended by the supplier of the preservative (double vacuum, dipping or others). After drying of the preservative the mortise members are sealed at the cross section opposite to the mortise and the whole L-joints are coated with an alkyd reference paint or a paint system provided by the supplier of the preservative. Then the specimens are exposed in the field on racks in a position slightly leaned backwards. Prior to exposure the top coat will be broken at the joint by opening and reclosing the joint. In at least annually intervals the L-joints are visually examined for occurrence of wood-disfiguring and wood-destroying fungi. For the assessments the joints are taken apart in order to check the situation within the joint. The fungal attack is rated according to a 5-step rating scale reaching from 0 (sound) to 4 (failure). After 3 and 5 years of exposure additionally exposed specimens are assessed destructively by cutting the joint members lengthwise as to detect interior rot in the wood. The mean service-life of a series of L-joints will be determined by adding the service-life of the individual members of the series after the last member is rated *failure* and dividing that number by the number of parallels in the test.

- ENV 12037: *Wood preservatives – Field test method for determining the relative protective effectiveness of a wood preservative exposed out of ground contact – Horizontal lap-joint method.* AWP A E16-09 *Field Test for Evaluation of Wood Preservatives to be Used Out of Ground Contact: Horizontal Lap-Joint Method* uses the same method with only slight modifications. Objective of the method is to evaluate the relative effectiveness of the preservative, applied to jointed samples of pine sapwood by a treatment method relevant to its intended practical use. In contrast to the L-joint method, the wood preservative is applied without subsequent surface coating. Bound together with cable straps the jointed specimens are exposed on racks outdoors not touching the ground. The joint functions as a water trap, thus providing optimal wood moisture conditions for the attack by wood-destroying fungi for relatively long periods. Again the specimens are examined visually at least annually using a rating scale for the fungal attack.
- AWP A E18-06 *Standard field test for evaluation of wood preservatives intended for use in category 3B*

applications exposed, out of ground contact – Uncoated ground proximity decay method. Test specimens of pine or other softwood species, measuring $125 \times 50 \times 19 \text{ mm}^3$ are treated with a wood preservative according to the recommendation of the supplier of the preservative. After drying of the preservative the specimens are exposed outdoors, lying horizontally on concrete blocks measuring $40 \times 20 \times 10 \text{ cm}^3$ which are placed on the ground. The arrangement is covered by an open frame with a horticultural shade cloth on top. The distance between specimens and cloth is about 3 cm. The cloth is intended to protect the specimens from direct sunlight. It also reduces the drying of the specimens and provides an increased relative humidity within the frame. The specimens are checked for fungal attack at fixed intervals. The attack is rated according to a rating scale.

The purpose of these methods is to expose the treated specimens to the complete range of microorganisms occurring under natural conditions. That means, all possible microorganisms, like bacteria, yeasts and fungi get to attack the wood. According to the local climatic conditions the specimens are subjected to changing temperatures, precipitations and relative humidity. All microorganisms metabolizing wood have their specific optimum temperatures and wood moisture content. Therefore a natural succession of microorganisms occurs which cannot be achieved in the laboratory. To some of the organisms the active ingredients of the wood preservatives may be poisonous, while other microorganisms may detoxify them or in the case of organic substances may even use them as a nutrient source.

All these methods provide data on the performance of wood preservatives. But as the local conditions of temperature and precipitation of the exposure sites can be extremely different even at relatively small distances, the performance data can also vary extremely. As experiments in a European research project (FACT project) have shown, even untreated lap-joints may not be attacked in Northern Europe within three years but be heavily attacked within one year in the tropics. And because it is more or less accidental which decay organism attacks the specimens at which time, the tests are not sufficiently reproducible. Therefore the results cannot be used for approvals of wood preservatives, where reproducible efficacy data are needed which give a certain overall reliability for the consumer [14.14–16].

Laboratory Tests.

- EN 113 *Wood preservatives – Method of test for determining the protective effectiveness against wood destroying basidiomycetes – Determination of the toxic values* works with pure cultures of different basidiomycetes that cause brown or white rot. The preservatives are incorporated into the wood at different concentrations under vacuum conditions. The treated specimens are then exposed to the fungi for 16 weeks at an optimum temperature. The mass loss (%) is determined at the end of the test.
- CEN/TS 839 *Wood preservatives – Determination of the protective effectiveness against wood destroying basidiomycetes – Application by surface treatment* is designed to assess whether a wood preservative is suitable to protect the surface of timber constructions from decay and to prevent the penetration of fungi into the interior parts of timber which are not impregnated with the wood preservative.
- EN 152-1 *Test methods for wood preservatives; laboratory method for determining the protective effectiveness of a preservative treatment against blue stain in service; part 1: brushing procedure* and
- EN 152-2 *Test methods for wood preservatives; laboratory method for determining the protective effectiveness of a preservative treatment against blue stain in service; part 2: application by methods other than brushing* are methods that are applied partly in the field as well as in the laboratory. After a natural weathering period of 6 months (between April to October) on outdoor racks the timber specimens are taken into the laboratory where they are inoculated with blue stain fungi. After 6 weeks of incubation the discoloration of the brushed/coated timber surfaces is evaluated. Optionally the outdoor weathering can be replaced by an artificial weathering in a weathering device with UV-light, condensation and rain periods (see: Preconditioning methods before durability testing of treated and untreated wood).

Testing Wood for Use Class 4.

Field Tests. While in use class 3 the local climates play the decisive role in start and progression of microbial attack of wood, the type of soil is the decisive factor in use class 4.

An example for a test method for this use class is

- EN 252 *Field test method for determining the relative protective effectiveness of a wood preservative in*

ground contact. The AWWA E7-07 *Standard method of evaluating wood preservatives by field tests with stakes* follows the same principle.

EN 252 uses stakes of Scots pine sapwood (dimensions: $500 \times 50 \times 25 \text{ mm}^3$) which are treated with the preservative under test by a vacuum-pressure process. The stakes are exposed in the test field, buried half of their length in the ground. Annually the stakes are examined visually for fungal decay using a rating scale. In addition, the remaining strength of the stakes is probed by a gentle kick against the stakes when still buried in the ground. Stakes treated with a well-known reference preservative are exposed simultaneously. The efficacy of the test preservative is determined by comparing the performance of the test preservative with the performance of the reference preservative.

Methods of nondestructive testing (see above) can also be applied at this point. For instance, measuring the MOE in a static or dynamic manner of the wooden stakes before they are exposed in the field and once every year does give an indication of the performance of the preserved or unpreserved material over time [14.17].

Laboratory Tests.

- Prestandard ENV 807 *Wood preservatives – Determination of the effectiveness against soft rotting micro-fungi and other soil inhabiting microorganisms* gives a basis for assessing the effectiveness of a wood preservative against soft rot-causing fungi. The source of infection is the natural micro-flora of biologically active soil, which may also contain other microorganisms such as bacteria and other fungi. The data obtained from this test provides information by which the value of a preservative can be assessed. Nevertheless it has to be supplemented with other test data for use class 4 to provide a more complete picture.

Testing Wood in Aquatic Environments (Part of Use Class 4 and Use Class 5). The fresh water (use class 4) or marine (use class 5) environment, is a very complex environment in which bacteria, fungi and molluscs can lead to wood destruction. Other organisms like algae might settle on the wood and will help to establish a biofilm on the wood that enhances fouling. Standardized laboratory methods for wood treated with preservatives or tested for their natural resistance against decay are not known to the author. The methods known are all field

tests, which implies the setup of the test specimens into open waters.

Only a few marine organisms shall be mentioned in this context specifically: The mollusc borers *Toredo navalis*, and *Bankia* sp., commonly called *shipworms* and the crustacean borers *Limnoria*, *Cherula* and *Sphaeroma*. These organisms actively bore into the wood and therefore affect wood stability.

14.2.2 Attack by Insects

Several industrial and household materials and construction devices of organic matter, especially those of biogenic origin, are endangered by pest insects. Susceptible to insect attack are mainly materials of plant origin made up of lignin and cellulose, namely wood, or products of wood origin [14.8]. These materials provide a habitat with shelter, food, and breeding sites for a manifold of different pest insect species [14.18]. Most are beetles (*Coleoptera*) (Figs. 14.4 and 14.5) and termites (Fig. 14.6). In most cases the developmental stages of the pests feed on the materials causing their destruction or contaminate it in such a way that their intended function is irreversibly altered.

The rate of destruction caused by insects is strongly influenced by various factors like climate, moisture content of the material, its nutritional value, and the infestation density. Additionally, the respiratory activity of a heavy insect infestation generates heat and moisture and affects the microclimate, favoring the growth of fungi, yeasts, and bacteria which further increase the overall decay rate of the material.

Preventive protection and, more important, regular inspections of potentially endangered materials are essential to guarantee the safety and the serviceability of, for example, wooden constructions, paper-based insulation materials, tools, furniture, and historic artefacts. The sooner an infestation is detected, the better is the chance for a remedial measure. The signs of destruction are generally material specific but may also be pest specific, allowing target-specific corrective and control actions.

However, the degree of damage, especially the one caused by wood-destructing insects, can easily be overseen, for larvae of wood-boring beetles and some termite species excavate wood only from the inside and leave a shallow surface layer fully intact. Nevertheless, a number of indices may point to a pest infestation, and no particular equipment for the detection is necessary.

Preventative control action against material insect pests is usually achieved through the application of

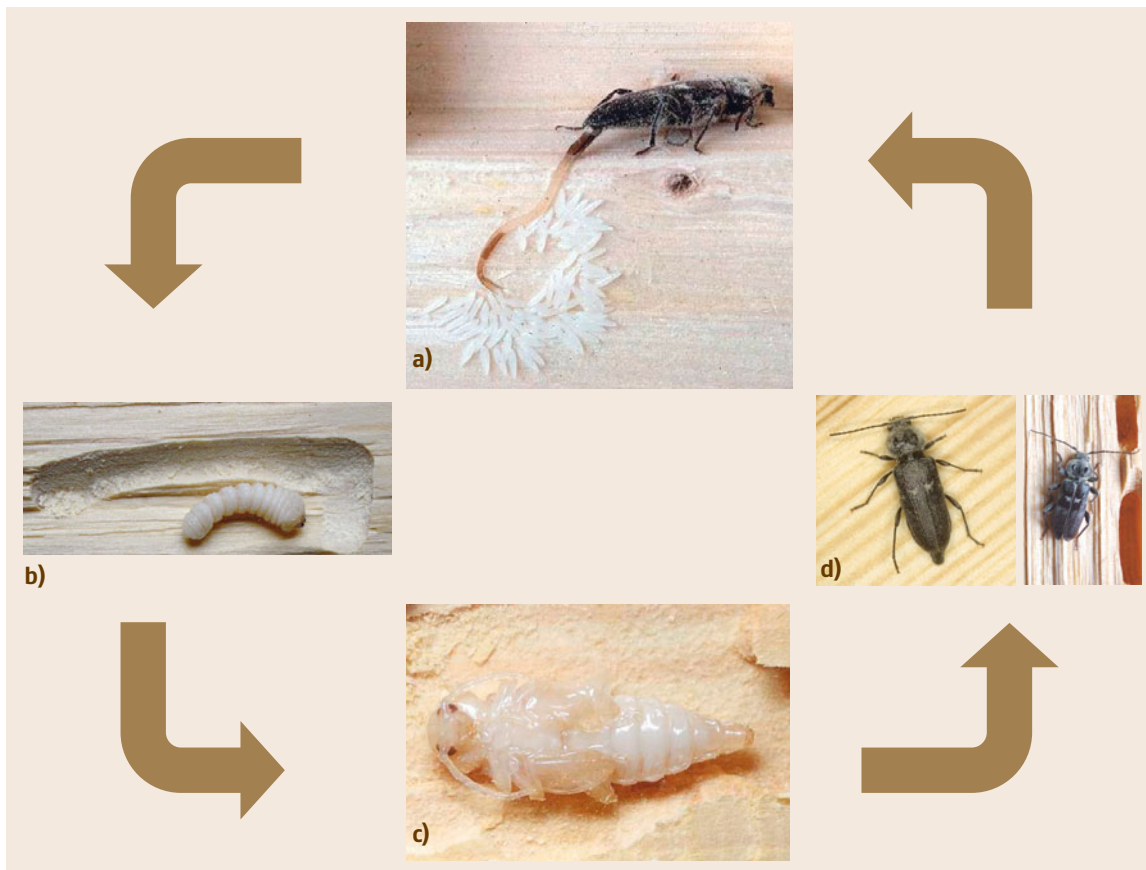


Fig. 14.4a–d Development stages of wood boring beetle using the old house borer *Hylotrupes bajulus* as an example. All stages except adult beetles are inside the wood and usually not visible from the outside. (a) Egg laying female; (b) full grown larva (3 to 6 years old) (c) pupa; (d) adult beetles (female left, male right)

residual pesticides. The effectiveness of these insecticides can be evaluated in several laboratory test methods.

Methods for Detecting Insect Attack

The most important types of insects that attack constructive timber are beetles and termites. Occasionally, a few ant species, wood wasps or horntails, wood-boring moths and a solitary bee may be of some relevance. Numerous indices on the surface wood may directly point to an attack by wood-feeding insects. Prominent signs allow differentiating between the possible pests.

Various inspection methods are available to check for the presence of wood-boring insects: visual, auditory, x-ray, infrared, and even the use of tracker dogs.

Visual Inspection. The simplest check-up of materials potentially endangered by insect attack is visual inspec-

tion of the material's surface, streaming debris from the material and all signs of insect presence (Table 14.2).

Flight holes: Flight or emergence holes are the exit sites of emerged adult insects after having completed their larval stage inside the wood. They appear round or oval and sharp-edged, not to be confused with screw- or nail holes. Broadly oval holes are characteristic for cerambycid beetles, whereas a round shape of these holes points to powder-post or anobiid beetles. However, the mere existence of flight holes is no final proof for an ongoing attack, since the completion of beetle development and the infestation may have occurred a long time previous. Additional information is required. New emergence holes appear bright to light yellow in color, like freshly-sawed wood, and indicate recently emerged beetles with possibly more larvae in the material to complete their development. The longer an infestation is extinct



Fig. 14.5 Wood boring beetles *Anobium punctatum* adult

the more dust is accumulated and oxidation processes darken the powdery inner edges of the holes over time. Paint sealed holes from a previous coating may also indicate an already extinct infestation when no fresh holes are evident. In case of doubt, existing emergence holes should be marked and the material be rechecked after time for additional holes to have occurred. The material may also be tightly wrapped or sealed with paper, for new emerging beetles will penetrate the wrap and indicate developmental activity by leaving their exit holes in the wrap.

The flight holes of dry-wood termites, which may be confused with the exit holes of anobiid beetles, are first signs of their presence. They live in small colonies of up to some hundred individuals entirely in wood that is moderately to extreme dry. They require no contact with the soil. Because of their concealed life, colonies can go undetected for many years inside timber. Often it



Fig. 14.6 Termite *Mastotermes darwiniensis*; 2 worker termites at the bottom and 3 soldier termites at the top

becomes visible only when already considerable damage was produced.

Big round holes, 12 mm wide, mainly outdoors, are the nest entrances of carpenter bees. The wood below the hole often shows yellowish fecal streaks. The entrance is usually guarded by the female bee, giving a humming sound.

Horntails also emerge through round-shaped flight holes. Their size can vary between 4 to 6 mm in cross section and fresh holes occur exclusively in recent cut and build-in timber during the first three years. This is because development is completed from eggs which had been laid by female horntails in the forest on trees declining or dying from fire, disease or insect damage or other natural causes. They also infest newly felled and freshly sawed lumber. Reinfestation of dry structural timber is most unlikely.

Appearance of the wood surface: The larvae of wood-boring insects usually start their tunnelling in the most peripheral parts, leaving a paper-thin layer of the wood surface untouched. The frass produced by growing larvae occupies a greater volume than the wood from which it was produced, and this causes the surface of the infested wood to have a blistered or rippled appearance. Occasionally the surface will break, and frass may fall out through the fine cracks and accumulate on the floor beneath.

Little mud tubes, so-called galleries, extending from the ground over exposed surfaces to a wooden food source are good indicators of the presence of subterranean termites. The tubes are either round or flat and usually measure at least 8 mm. These termites live in colonies which can contain thousands to millions of individuals and are closely associated with the soil habitat where they tunnel to locate water and food, namely wood.

Termites excavate galleries or tunnels in wood as they consume it, leaving nothing more than a thin wooden layer. These areas are easily crushed with a hard object (knife, hammer or screwdriver). In the case of extreme damage partly collapsed wood at bearing points may pinpoint to internal excavation. Noninfested wood gives a sound resonance when pounding the surface, damaged wood sounds hollow.

Slitlike openings called *windows* with some frass directly beneath are positive signs for carpenter ant activity. Usually this frass contains fragments of ants and other insects mixed with the wood fibers, because unlike termites that consume wood, carpenter ants scavenge on dead insects, insect honeydew and other materials.

Table 14.2 Characteristics damage by wood infesting insects (modified from [14.18])

Infested material	Signs of infestation frass	Signs of infestation		Most likely pest
		holes	galleries, tunnels, feeding tubes	
Seasoned sapwood of hardwoods or softwoods (rarely in heartwoods)	Fine powder with elongate lemon-shaped pellets, loosely packed	Exit holes circular 1.6 to 3 mm	Up to 3 mm circular in cross section, numerous and random	Anobiid powderpost beetle
Sapwood of hardwoods primarily, minor in softwoods	Fine to coarse powder, tightly packed, tend to stick together	Exit holes circular 2.5 to 7 mm	1.6 to 10 mm circular in cross section numerous and random	Bostrichid powderpost beetle
Sapwood of ring and diffuse porous hardwoods only	Fine flour-like, loosely packed in tunnel	Exit holes circular 0.8 to 1.6 mm	1.6 mm circular in cross section, numerous, random	Lyctid powderpost beetle
Seasoned sapwood of softwoods	Very fine powder and larger cylindrical pellets, tightly packed in tunnels	Exit holes oval 6 to 10 mm	10 mm oval in cross section, numerous in outer sapwood, ripple marks on walls	Hylotrupes bajulus
Unseasoned wood under bark only, inner bark and surface of sapwood only	Coarse to fine powder, bark coloured, tightly packed	Exit holes circular 1.6 to 2.5 mm	Up to 2.5 mm circular in cross section, random	Bark beetles
Seasoned dry soft- or hardwood	Hard elongate pellets of uniform size, less 1 mm, six flattened or concavely depressed sides	None	Hollow tunnels beneath a thin wooden layer, sometimes filled with fine frass	Dry wood termites
Wood coated with mud galleries	Fine lamellae of late wood remain intact	None	Hollow tunnel beneath a thin wooden layer, mud tubes leading to the wood	Subterranean termites
Seasoned wood	Piles of coarse wood shavings with insect parts	Slitlike windows	Clean smooth galleries	Ants, carpenter ants
Softwood or softer hardwood with no bark	Fine wooden debris with yellowish faecal streaks	Entrance holes large and circular 12 mm	Smooth walled 12 mm circular in cross section, very regular	Carpenter bees
Fresh to slightly seasoned softwood, very rarely hardwood	Fine coarse, usually not outside the wood	Exit holes circular 4 to 6 mm	Strong variation in size, circular in cross section, tightly packed with frass	Horntails
Unseasoned wood or occasionally damp	Fine in texture with granules being circular	Narrow oval ragged margins	Indistinct, less than 3 mm in cross section	Weevils
Unseasoned wood with bark or occasionally damp	Fine, stacked between bark and sapwood	Numerous small entrance and larger exit holes	Bark is lifted up by frass deposits	Warf beetles

Lamellar degradation of the cut end of foundation beams point to the activity of the wood ant *Lasius fuliginosus*. This small ant in general starts to attack wood at the ground level, where it is in contact with moisture and therefore is susceptible for fungus decay. This is a precondition for an initial attack. Later, by autonomous moisture intake, together with this symbiotic fungus the ants progress deeper into the wood thus possibly causing substantial damage.

Occurrence of frass (bore dust): While feeding, beetles often push out powdery frass from holes which they have constructed in the infested wood. The frass is piled below the holes or in cracks of the structures. However,

those piles are not indicative of an active attack, as concussions can cause a release, after an infestation has already ceased. Furniture or other wooden objects with past infestations will sometimes be suspected to be reinfested when frass or insect parts fall out in the process of handling or moving. By placing a dark paper beneath nonmoved objects to detect the appearance of fresh frass will clarify whether the infestation is active or not.

If the wood surface is probed where tunnelling is suspected, the powdery borings may be located. The consistency of the frass ranges from very fine to coarse, depending on the pest. The size and shape of larval frass are often species specific. Larger cylindrical frass pellets

like those produced by the old house borer, *Hylotrupes bajulus*, are typical for cerambycid beetles, whereas round frass pellets with tip-point edges indicate the presence of anobiid larvae like *Anobium punctatum* for example. Flour or talc-like frass points to the presence of powderpost beetles. This will fall out of the emergence holes while tapping the wood with a hammer. A magnifying lens should be used for a reliable inspection of frass pellets.

Small fecal pellets generally found in the close vicinity of their wooden habitat are good indicators for the presence of drywood termites. The pellets can vary in color, depending on the wood that has been consumed. They appear hard, elongate, of uniform size, less than 1 mm in length, with round ends and six flattened or concavely depressed sides. The piles do not contain any other debris such as insect parts or fiber.

A pile of wood shavings outside a hole or opening is a hint for the presence of carpenter ants. The wood shavings are coarse and insect parts and bits of insulation will be mixed among them. These shavings may also be found in spider webs and window sills close to the nest site.

The frass produced by carpenter bees is very similar to those of carpenter ants regarding color and size. It usually lacks insect fragments.

Damaged wood: The larvae of most wood-boring beetles develop for several years inside the inner portion of seasoned wood. Tunnelling is most extensive in sapwood, but it may extend into the heartwood, especially when it is partly decayed. The size and shape of feeding tunnels may be a good indication for the causing pest. However, small tunnels produced by young larvae of cerambycid beetles at an incipient decay can easily be confused with those from an old infestation by anobiid beetles. Therefore, other indices like the shape of frass pellets are needed for a final proof. The frass in the tunnels may be loosely to tightly packed and does not tend to fall out freely from the wood. Some wood-boring species only attack softwoods, like the old houseborer, others specifically infest hardwoods like most bostrichid and lyctid beetles. Some anobiid species will attack both hardwoods and softwoods. Defrassing of suspected infested timber may expose the feeding tunnels and thus ease inspection.

Unseasoned hardwood with bark or wood in damp environments like pit-shafts or seashores may be attacked by wood-boring weevils or wharf beetles (also known as wharf borers). Weevil infestation can be differentiated from those of anobiids by the bore dust and frass which are finer in texture and the individual granules be-

ing more circular. The feeding tunnels are smaller and the exit holes are narrow oval with ragged or indistinct margins. Wharf beetles usually deposit the frass between the bark and the outer sapwood portion, which lifts and loosens the bark. The larval feeding tunnels are covered with ambrosia fungi staining the wood slightly dark. The wood surface may be covered with circular small larval entrance and larger adult emergence holes. Warf beetles are, next to submerged marine wood degraders like shipworms and certain crustaceans (which do not belong to the insects and are therefore dealt with elsewhere), economically the most important pests in the ship-building industry.

Wood damaged by carpenter ants (*Camponotus* spp.) contains galleries that are very clean and smooth. Ants do not eat wood, but tunnel into wood to make a nest. Wood ants like *Lasius* spp. preferentially excavate the early wood layers, leaving a lamellar set of late wood untouched.

Some soil-inhabiting termites (e.g., those of the genus *Coptotermes*) decay wood from the surface (erosive decay). They coat it with wide mud galleries usually underneath and feed on the early wood. Fine lamellae of the late wood remain almost untouched. Others (e.g., of the genus *Reticulitermes*) intrude into the wood and hollow out all but a thin surface layer. Drywood termites simply excavate tunnels and chambers within the timber, which can be filled with frass. They prefer softwoods and the sapwood of hardwoods, but they have been recorded to attack heartwoods as well.

Technical devices can assist in the inspection of possible infestation sites: the use of an endoscope supplies additional information about the degree of damage; a moisture-meter is especially useful for detecting termites in their cavities.

Insects, insect parts: Occasionally, the obvious presence of adult beetles, wasps, bees or termites will be noted. As adult beetles emerge in confined structures, they often are attracted to lights or windows. Membranous insect wings in great number around windows or beneath lamps are an indication for termite activity. Insect manuals and determination keys may allow the identification of the pest. Sometimes insect fragments found in the tunnelled wood or in the frass (wings, legs, cuticle fractions) may be sufficient for identification, however, professional entomological education and good magnifying devices are required.

X-ray and infrared: Hidden infestations inside the wood or concealed parts of a building may be recorded with x-ray machines or infrared cameras. However, the use of x-ray is very limited due to the lack of safe-

to-use portable x-ray devices and the high costs of this technique when applied stationary. Infrared cameras record the heat generated by living organisms. They may be very useful to pinpoint large cryptic infestation hotspots by termites. The accuracy of the recording, however, depends on the building insulation and other potential heat sources. In most cases, cost-benefit considerations do not justify the use of the infrared technique.

Auditory Inspection. Sounds, generated by the insects' interactions with their substrate, may be a hint for an active infestation. Under certain circumstances, especially during the quiet nightly hours, auditory inspection and acoustic detection of wood-infesting insects is possible. Computer-based devices have been developed to facilitate the prospect of success [14.19, 20].

Gnawing sounds of beetle larvae: Even in the early stages of an infestation, the rasping or ticking sounds made by the larvae while boring can be heard. This sound may be detected from a distance of 1–2 m, day and night, at infrequent intervals. The amplitude and frequency spectra of the feeding sound appear to be species specific.

Tapping sounds of adult beetles: Adult beetles of the death-watch beetle tap their heads on the wood as mating signals. The tapping noise is made by both sexes and can be heard unaided. It can be imitated tolerably well, at least to the extent of stimulating surrounding beetles to themselves start tapping.

Running termites: With the help of high-resolution contact microphones attached to the wood to be tested the sound of termites running in their tunnels may be detected.

Alarm signals of carpenter ants: An active colony may produce a dry rustling sound, similar to the crinkling of cellophane. After identifying a potential nest site, tapping against it with a screwdriver may cause a response clicking of alarmed ants. A listening device, such as a stethoscope, may be useful when conditions are quiet and outside noises are at a minimum.

Swarmers. The occurrence of swarming insects is evidence for the presence of ants or termites. Because of the consequences for possible remedial action, it is essential to know the major differences between those two insect groups. Ants, like most hymenoptera, have much larger forewings than hind wings. Termite wings all are of the same size; they break off easily. The antennae of ants are kinked, those of termites are straight. The thorax including the first abdominal segment (first abdominal tergum)

and the rest of the abdomen in ants are joined by a narrow waist, while the thorax of termites is broadly joined to the abdomen.

Swarming termites in the exterior only indicate a termite infested area and not necessarily a termite attack. If, however, the swarmers are observed flying out of the structure from around windows, doors, porch columns or other wood constructions, then there might be some concern. Indoor swarmers point to the presence of either soil-inhabiting termites underneath the structure or drywood termites, which live in the house framework or in wooden furniture. An entomologist should be consulted for identification of the pest species, because control measures are specific for the different insect groups.

Termite Dog. Specialized dogs, trained to smell the trail odors of termites, are used to detect termites in- and outside of properties. According to an investigation at the University of Florida, the success rate is up to 96% [14.21].

Sticky Traps. Sticky traps, baited with the female sex pheromone, mostly used for detecting and monitoring beetle populations, are marketed for *Anobium punctatum*. It only has limited use for mass-trapping by setting out large numbers of traps in infested areas to catch a large number of beetles and thus reduce the population. As the traps only attract males and trap attractiveness has to compete with the natural pheromone of female beetles, the number caught may be too low to prevent mating. Therefore, pheromone traps are mostly used for detecting and monitoring beetle populations only.

Control. Knowledge about the particular insect species responsible for the impact may determine the control measure. Even prior to a thorough investigation of the dwelling and probable consequent treatments, the significance of a possible infestation has to be considered. A differentiation between wood-feeding and wood-breeding insects can assist in estimating the degree of a damage.

The impact on timber by wood-breeding insects can mostly be neglected, as they only attack wood for completing their development. They are only active in green timber. Debarked wood and seasoned lumber is never infested. Prominent examples are the following.

- **Green wood beetles:** Their larvae feed in the cambium, the thin layer of plant tissue between bark and wood. They usually groove the sapwood. At

the end of their development, old larvae tunnel into the wood and pupate. The emerging beetles leave through those tubes. On the surface of plane timber the flight holes may be visible, which can be confused with those from wood-feeding species.

- Bark beetles: Their larvae also feed in the cambium zone of living trees, fallen trees and logs. They excavate a characteristic tunnel called a gallery usually parallel to the grain and may penetrate superficially into the sapwood. Timber is not attacked unless of a high moisture content.
- Wood wasps: Wood wasps, also known as horntails, are capable of penetrating solid wood, especially of debilitated, dying and freshly felled trees, in which the eggs are laid. The damage is characterized by round boreholes densely packed with frass. Emergence holes are circular in cross section and up to 8 mm in diameter.

Methods for Testing Insect Resistance

The resistance of wooden materials against insect attack can be material-specific or generated through the modification of the wooden matrix or the application of wood preservatives, namely insecticides. Several general and specific standard testing procedures are available which allow resistance data obtained in the laboratory to be transferred to field situations. Specific standards may differ for either preventive or curative measures. The test organisms used in these testing standards represent the economically most important pests. *Hylotrupes bajulus* represents a softwood-infesting cerambycid beetle, *Lyctus brunneus* an exclusively hardwood-infesting beetle, and *Anobium punctatum* an opportunist. Tests with termites are usually carried out with subterranean species like *Reticulitermes santonensis* or *Coptotermes formosanus* or others.

Specific Tests for Resistance Against Wood-Boring Beetles (Preventive Measures). The eggs of wood-boring beetles are deposited in cracks and crevices of the wood. Larvae of wood-boring beetles therefore hatch inside the wood and begin tunnelling immediately. This fact was generally taken into account when test procedures were designed. The natural resistance of wood against insect attack may also be tested applying the following standards.

- European Standard EN 20: Determination of the preventive action against *Lyctus brunneus* (Stephens) – Part 2: Preservatives application fully impregnated wood treatment (laboratory method).
- European Standard EN 21: Determination of toxic values against *Anobium punctatum* (De Geer) by larval transfer (laboratory method). This standard describes a laboratory test method which gives a basis for assessment of the effectiveness of a wood preservative against *Anobium punctatum*. It allows the determination of the concentration at which the product prevents the survival of *Anobium punctatum* larvae in impregnated wood of a susceptible species. Although an infestation normally starts from egg-laying, a larval transfer test is applicable when considering the situation of treated wood being put into contact, during repair work, with wood that might be infested.
- European Standard EN 46-1 and EN 46-2: Wood preservatives – determination of the preventive action against recently hatched larvae of *Hylotrupes bajulus* (Linnaeus) (laboratory method). These standards make it possible to determine whether recently hatched larvae are capable of boring through the treated surface of a susceptible wood species and of surviving in the untreated part of the test specimen. For this purpose, the procedure seeks to reproduce normal egg-laying conditions existing in cracks in the wood, which provide the principal egg-laying sites. It takes account of the fact that, if larvae pass through the treated surface, they will then tunnel in the direction of the least protected regions of the wood.
- European Standard EN 47: Determination of the toxic values against recently hatched larvae of *Hylotrupes bajulus* (Linnaeus) (laboratory method). This standard specifies a laboratory test method which gives a basis for the general assessment of the effectiveness of a wood preservative against *Hylotrupes bajulus* by determination and comparison of the concentration at which the product prevents their survival in totally impregnated wood of a susceptible species.
- European Standard EN 49-1: Determination of the protective effectiveness against *Anobium punctatum* (De Geer) by egg-laying and larval survival – Part 1: Application by surface treatment (laboratory method). This part of EN 49 describes a laboratory test method which gives a basis for assessment of the effectiveness of a wood preservative, when applied as a surface treatment, against *Anobium punctatum*. It allows the determination of the concentration at which the product prevents the development of infestation from egg laying. The method simulates conditions which can occur in practice on timber

which has been treated some time previously with wood preservative applied by dip, brush or spray and on which eggs of *Anobium punctatum* are laid.

- European Standard EN 49-2: Determination of the protective effectiveness against *Anobium punctatum* (De Geer) by egg-laying and larval survival – Part 2: Application by impregnation (laboratory method). In contrast to part 1 of this standard, this method simulates conditions which can occur in practice on timber which has been treated some time previously with a deeply penetrating wood preservative and on which eggs of *Anobium punctatum* are laid.

Specific Tests for Resistance Against Wood-Boring Beetles (Curative Control Measures). When susceptible wood is infested with beetle larvae at low density, the infestation can be cured before structural damage occurs. This work requires to be done by experts only. The wood preservative is usually applied by surface application through brushing or spraying and has to penetrate deep enough for contact with tunnelling larvae.

- European Standard EN 1390: Determination of the eradicator action against *Hylotrupes bajulus* (Linnaeus) larvae (laboratory method). This standard describes a laboratory test method which gives a basis for assessment of the eradicator action of a wood preservative against *Hylotrupes bajulus*. It allows determination of the lethal effect of a surface application of a preservative product on a population of large larvae previously introduced into the test specimens. The method simulates conditions in practice where a stake is treated which is only slightly attacked and where insect tunnels have been exposed by cutting away. This represents a valid test of the product.
- European Standard EN 48: Determination of the eradicator action against larvae of *Anobium punctatum* (De Geer) (laboratory method). This standard describes a laboratory test method which gives a basis for assessment of the eradicator action of a wood preservative against *Anobium punctatum*. It allows the determination of the lethal effect of a surface application of the preservative on a population of larvae already established in the test specimens. The method simulates conditions which can occur in practice where a length of wood such as an affected stair tread is treated, which is still free from exit holes and in which certain of the faces are inaccessible, thus constituting valid test conditions.

- European Standard EN 370: Determination of eradicator efficacy in preventing emergence of *Anobium punctatum* (De Geer). This standard describes a laboratory test method which gives the basis for the assessment of the eradicator efficacy of a wood preservative in preventing emergence of *Anobium punctatum*. It determines the lethal effects, on beetles attempting to emerge through treated wood surfaces, of an insecticidal product deposited by surface application.

Specific Test for Resistance Against Termites. Termite control is not achievable by curative treatment of infested wood. Usually, the damage caused by termites is already too severe by the time termite-infested wood is detected. Wood preservative action against termites focuses on preventive treatment of the endangered material or the creation of biocidal or physical soil barriers. The test species may vary depending on the geographical situation.

- European Standard EN 117: Determination of toxic values against European *Reticulitermes* species (laboratory method). This standard describes a laboratory test method which gives a basis for assessment of the effectiveness of a wood preservative against *Reticulitermes* species. It allows the determination of the concentration at which the product completely prevents the attack by this insect of impregnated wood of a susceptible species.
- European Standard EN 118: Determination of preventive action against European *Reticulitermes* species (laboratory method). This standard describes a laboratory test method which gives a basis for assessment of the effectiveness of a wood preservative, when applied as a surface treatment, against *Reticulitermes* species.
- American Society for Testing and Materials ASTM D 3345: Laboratory evaluation of wood and other cellulosic materials for resistance to termites. This method covers the laboratory evaluation of treated or untreated cellulosic material for its resistance to subterranean termites. This test should be considered as a screening test, for treated material and further evaluation by field methods is required.
- American Wood-Preservers' Association Standard E1-72: Standard method for laboratory evaluation to determine resistance to subterranean termites. This method provides for the laboratory evaluation of treated or untreated cellulosic material for its resistance to subterranean termites. This test should be

considered as a screening test for treated material and further evaluation by field methods is required.

- Australian Standard 2178: Protection of buildings from subterranean termites – detection and treatment of infestation in existing buildings. This standard sets out methods for the detection and treatment of subterranean termite infestation in existing buildings and also sets out methods for the prevention of reinfestation.
- Japan Wood Preserving Association Standard 11(2): Method for testing the effectiveness of surface treatments of timber (brushing, spraying and dipping) with termiticides against termites (2) field test. This standard describes a field test method for evaluating effectiveness of surface treatments of timber such as brushing, spraying and dipping with termiticides against termites.
- Japan Wood Preserving Association Standard 12: Method for testing the effectiveness of pressure treatment of timber with termiticides against termites. This standard describes laboratory and field test methods for evaluating effectiveness of pressure treatment of timber with termiticides against termites.
- Japan Wood Preserving Association Standard 13: Method for testing the effectiveness of soil treatment with termiticides against termites. This standard describes a test method for evaluating effectiveness of soil treatment with termiticides against termites.
- Japan Wood Preserving Association Standard 14: Qualitative standards for termiticides, preservative/termiticides and soil-poisoning termiticides. This standard describes qualitative standards for termiticides, preservative/termiticides and termiticides for soil treatment.

14.3 Testing of Organic Materials

Polymeric materials (plastics) are used in all sectors of life as very durable products with tailor-made properties. They provide a combination of easy thermoforming (most plastics, if not cross-linked) and excellent use properties. For some applications, such as paints, items in the automobile industry or for use in buildings, they have to maintain their properties for a long period of time, often decades. The long-lasting exposure to environmental factors often results in a change of material properties such as roughening of the surface, embrittlement, a loss in mechanical strength or just a discoloration. It has been observed in some cases that also the presence of microorganisms such as bacteria, fungi or algae can cause or enhance changes in plastics, although most plastics are supposed to be inert to attacks of microorganisms (*they do not rot*). All these effects usually are not desired and are denoted generally as biocorrosion or as biodeterioration, if the material falls apart due to the ageing process. A number of test methods have been developed to characterize these phenomena.

However, the increasing stability of many plastics against environmental ageing in combination with the intense use of modern plastics generated serious problems with plastic waste in the last decade, especially from plastic packaging. Alternative waste management strategies to landfilling such as incineration or plastics recycling are not always optimal and the subject of very controversial discussions. On this background intensive

attempts were made since the early nineties to develop novel plastics which combine a good performance, comparable to conventional polymers, with a controlled susceptibility to microbial degradation. This new class of materials is usually called *biodegradable plastics*. Applications of these materials are, e.g., bags for collecting biowaste, packaging (disposed via composting), or mulch films in agriculture.

For these novel materials which are claimed to be environmentally friendly, it is demanded to prove their environmentally safe biodegradation using scientifically based and generally accepted methods. Concerning the parameters used for monitoring biodegradation, the testing procedures applied and the evaluation criteria for biodegradability of plastics significantly differ from testing biocorrosion phenomena of plastics. Hence, an own system of test methods and evaluations criteria is being developed for this kind of materials.

14.3.1 Biodeterioration

In contrast to the biodegradation of plastics, where a near complete conversion of the material components into naturally occurring metabolic products of microorganisms (e.g., water, carbon dioxide, methane, biomass etc.) occurs (see later), for biocorrosion or biodeterioration processes only a change in the polymer structure or the plastics composition is observed in many cases [14.22].

General Mechanism of Biodeterioration

Since usually mechanical properties of plastics are predominantly determined by the length of the polymer chains in the material, scission of polymer chains (reduction of the average molar mass) is one major reason for changes in mechanical properties. This effect is especially dramatic if the cleavage of the polymers occurs statistically along the chains (endo-degradation) and not at the ends (exo-degradation). Even just a single endocleavage in a polymer chain can reduce the molar mass to 50%, and hence cause significant changes in mechanical properties.

Embrittlement (= loss in elasticity), however, can also occur when plasticizers are removed from the plastic materials by microorganisms. Especially for polyvinylchlorides (PVC), which in some cases contain high amounts of plasticizers (e.g., low-molecular-weight esters), biocorrosion due to this phenomenon has been reported in earlier times [14.23–25]. A similar effect is observed in polymer blends or (block)-copolymers when single components are selectively degraded by microorganisms. An example for this mechanisms of biodeterioration are mixtures of (unmodified) polyethylene and starch. Here the starch basically can be metabolized by microorganisms, leading to a weakening of the entire material and finally result in fragmentation [14.26].

If the attack of microorganisms only concerns side groups attached to the polymer main chains, this usually results in a change of the chemical characteristic and hence, in the material properties. The cleavage of ester bonds in side chains of cellulose esters (e.g., cellulose acetate) results in the formation of charged chemical groups (at suitable pH values) increasing the

hydrophilicity of the material (this can be followed by an increased water uptake and swelling of the material). If a sufficiently high amount of esters has been transformed into hydroxyl groups the entire material can become accessible to direct microbial attack [14.27,28]. Similar effects can be caused by oxidation phenomena, where new polar carbonyl and carboxyl groups are formed in the polymer (or at the surface of the polymer).

Coloring of plastics can be caused due to the formation of new chromophoric chemical groups, but also the release of pigments from microorganisms can cause changes in the color of plastic materials.

Strictly speaking, real biodegradation involves the direct action of enzymes (biocatalysts) on the plastic material itself. The hydrolysis of ester bonds in polyesters by hydrolases is such a case [14.29–31]. However, in biodeterioration processes microorganisms mostly indirectly contribute to changes in the plastic materials. During microbially induced oxidative degradation of plastics (in nature, for instance present in degradation of lignin or latex [14.32]), the oxidative enzymes do not directly act on the polymers, but produce low-molecular-weight oxygen compounds which diffuse into the polymer material and there cause chemical reactions. Microorganisms can also indirectly induce hydrolytic degradation processes by changing the pH in a microenvironment at the surface of the material (e.g. in biofilms, see below) or through the excretion, e.g., of organic acids such as lactic acid or acetic acid as products of their metabolism.

In real environments, however, corrosion phenomena of plastics are often a mixture of physical, chemical and biological processes. Chemical hydrolysis caused by water which has been diffused into the polymer and oxidation induced by light (photo-oxidation) or by increased temperatures (*thermal oxidation*) in many cases play an important role during biocorrosion and biodeterioration. In fact, the expression *environmental corrosion* would be an expression, better meeting the point than *biocorrosion*.

The mechanism and the impact on the plastics differ basically between chemical or physically processes and the direct action of enzymes on the polymer. While water and oxygen are small molecules which are in principle able to penetrate into the entire plastic material, enzymes are too large to diffuse into the polymer bulk, and thus, can only act at the surface, causing a typical erosion process, where the material is affected layer by layer from the surface. This is illustrated in Fig. 14.7 for the chemical (bulk degradation) and enzymatic hydrolysis (surface erosion) of e.g. a polyester.

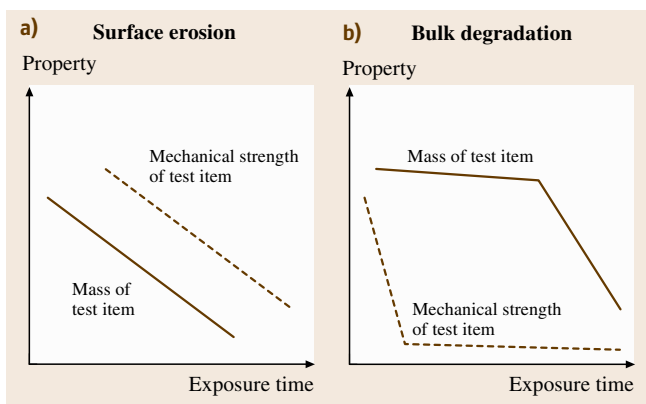


Fig. 14.7a,b Influence of surface erosion (a) and bulk degradation (b) on the material properties of plastics

While for the enzymatic action only a small part of the material at the surface *knows* about the degradation which proceeds slowly from the surface, chemical hydrolysis caused from water contained in the plastics, affects the entire material right from the beginning. As a consequence, changes in mechanical properties and mass loss due to degradation run in parallel for the enzymatic degradation. In contrast, chemical hydrolysis causes chain scissions in all polymer chains simultaneously, resulting in an instant decrease in mechanical strength, while a mass loss of the material is only observable at a later stage of degradation, where polymer chains become so short to be water soluble.

Biofilms

One important phenomenon in correlation with biodeterioration and biocorrosion is the forming of biofilms on material surfaces, also known as biofouling [14.22]. Formation of biofilms is not only restricted to polymer materials, but also plays a central role in corrosion of, e.g., concrete, stones (buildings) and metals. Such biofilms consist of a combination of various microorganisms which is highly complex and variable in time and includes the microorganisms themselves and additionally a number of extracellular polymeric substances, e.g., polysaccharides. Biofilms represent an own microenvironment at the surface of the materials providing optimal living conditions (humidity, pH, nutrient concentrations) for the microorganisms inhabiting the biofilm and protecting them from external attacks, e.g., from other bacteria or fungi, and also to a certain extent from biocides.

In biofilms the concentration of polymer-degrading enzymes, but also, e.g., of oxidating agents formed by the microorganisms can substantially be higher than in a liquid environment, where such substances can diffuse away from the surface. Also concerning the pH value, biofilms can present totally different conditions to the material surface than be measured in the liquid environment. Thus, the presence of such biofilms on polymer surfaces can substantially influence biodeterioration phenomena of plastics.

Standards for Evaluation of Biodeterioration

As mentioned above biodeterioration is usually a very complex process, involving the direct or indirect action of diverse microorganisms forming often a biofilm on the material surfaces and also including in many cases nonbiotic actions such as irradiation or thermal oxidation. As a consequence, the corresponding standard procedures for testing biodeterioration and biocorrosion

phenomena of plastics are correlated to different topics. On the one hand, a number of materials different from plastics such as steel, concrete, textiles or paints are covered, on the other hand, also nonbiotic factors (light, heat, oxygen, moisture, chemicals) are regarded in such tests exclusively or in combination with biotic influences. Thus, only a limited number of tests strictly deal with *pure* biocorrosion or biodeterioration mechanisms of plastics. Those tests, only focussing on biotic effects usually use a number of defined test organisms (Table 14.3). However, in many cases simulation or field tests are used which combine the action of biotic and nonbiotic factors. These standards often are correlated with the expression *weathering* – a selection of such standards is also included in Table 14.3.

14.3.2 Biodegradation

At the beginning of the nineties a novel group of polymers were developed which were intended to be degradable by microorganisms in a controlled manner, but at the time were no adequate methods and criteria available to evaluate the property of biodegradability. First tests carried out at that time (e.g., by using the growth of microorganisms on the surface or a certain loss in mechanical properties such as the tensile strength as indicators for biodegradation) originated from the field of plastics biocorrosion and biodeterioration (see above). However, these evaluation methods proved to be unsuitable to characterize biodegradable materials. A first generation of modified polyethylenes, claimed to be biodegradable based on these tests, did not meet the expectations of the users and caused to some extent a general negative image of biodegradable plastics at the time. As a consequence, the development of suitable testing methods and evaluation criteria for biodegradable plastics started and resulted in a number of standards of various national and international standardization agencies during the past 15 years. This process still continues, since the number of different environments, where plastics can be degraded, make it necessary to establish a quite complex and extended system of testing methods and evaluation criteria for biodegradable plastics.

General Mechanism of Biodegradation

When talking about biodegradation of plastics usually one is referring to the attack of microorganisms on water-insoluble polymer-based materials (plastics). Because of the lack of water-solubility and the length of the polymer molecules, microorganisms are not able to

Table 14.3 Standard test methods for biocorrosion phenomena on plastics

Action of microorganisms on plastics	
ISO 846 – 1997	Plastics – Determination of behaviour under the action of fungi and bacteria. Evaluation by visual examination or measurement of changes in mass or physical properties
ISO 16869 – 2001	Plastics – Assessment of the effectiveness of fungistatic compounds in plastics formulations
EN ISO 846 – 1997	Plastics – Evaluation of the action of microorganisms
ASTM G21-96	Standard practice for determining resistance of synthetic polymer materials to fungi
ASTM G29-96	Standard practice for determining algal resistance of plastic films
DIN IEC 60068-2-10 – 1991	Elektrotechnik; Grundlegende Umweltprüfverfahren; Prüfung J und Leitfaden: Schimmelwachstum; (Identical with IEC 60068-2-10:1988)
IEC 60068-2-10 – 1988	Elektrotechnik; Grundlegende Umweltprüfverfahren; Prüfung J: Schimmelwachstum
Weathering of polymers	
ISO 877:1994	Plastics – Methods of exposure to direct weathering, to weathering using glass-filtered daylight, and to intensified weathering by daylight using Fresnel mirrors
ISO/AWI 877-1	Plastics – Methods of weathering exposure – Part 1: Direct exposure and exposure to glass-filtered daylight
ISO/AWI 877-2	Plastics – Methods of weathering exposure – Part 2: Exposure to concentrated solar radiation
ISO 2810:2004	Paints and varnishes – Natural weathering of coatings – Exposure and assessment
ISO 4582:1998	Plastics – Determination of changes in color and variations in properties after exposure to daylight under glass, natural weathering or laboratory light sources
ISO 4665:1998	Rubber, vulcanized and thermoplastic – Resistance to weathering
ASTM D1435-99	Standard practice for outdoor weathering of plastics
ASTM D4364-02	Standard practice for performing outdoor accelerated weathering tests of plastics using concentrated sunlight

transport the polymers directly through their outer cell membranes into the cells where most of the biochemical processes take place. To be able to use such materials as a carbon and energy source, microorganisms have developed a special strategy. The microbes excrete extracellular enzymes which depolymerize the polymers outside the cells. This means that biodegradation of plastics in its first step is usually a heterogeneous process.

If the molar mass of the polymers has been sufficiently reduced and water-soluble intermediates have been generated, these small molecules can be transported into the microorganisms and introduced there into the metabolic pathways. As a final result new biomass and natural metabolic end-products such as water, carbon dioxide and methane (for degradation processes in the absence of oxygen = anaerobic degradation) are formed.

The excreted extracellular enzymes usually have a molar mass of some ten-thousand Daltons and hence, are to large to penetrate deeper into the polymer material. In consequence, the enzymes only can act on the polymer surface of the plastics and erodes the material layer by layer – biodegradation of plastics is usually a surface erosion process, only affecting a relative small fraction of the entire polymer material at one time. In many cases the enzymatic catalyzed chain length reduc-

tion of the polymers is the process in biodegradation determining the rate of the entire process.

In parallel to the enzymatic attack, nonbiotic chemical and physical processes such as oxidation, irradiation (photodegradation), thermal degradation or chemical hydrolysis can affect the polymer and contribute to the degradation process. In some cases an abiotic degradation mechanism is exclusively responsible for the first step of molar mass reduction.

Some materials, claimed to be biodegradable, directly used such effects to induce the biodegradation process. For instance, poly(lactic acid) is at first hydrolyzed into oligomeric esters by an autocatalytic chemical hydrolysis or sunlight in combination with heat then generates in pro-oxidant-modified polyethylene short hydrophilic intermediates which are considered to be assimilated by microorganisms. Because of the coexistence of biotic and nonbiotic processes in many cases the entire mechanism of polymer degradation could also be called an environmental degradation. Both, biotic and abiotic processes have to be considered in tests evaluating biodegradation of polymers.

Environmental factors do not only influence the plastics themselves, but have also a crucial impact on the microbial population and on the activity of the different microorganisms involved in the polymer

degradation. Parameters such as humidity, temperature, pH, concentration of salts, the presence or absence of oxygen and the supply with different nutrients have an important effect on the microbial degradation of polymers and must be adequately considered when testing the biodegradability of plastics.

A further complicating factor when dealing with biodegradation of plastics is the complexity of plastic materials with regard to their possible compositions, structures and morphologies (Fig. 14.8).

Different monomers can be combined in one polymer chain, where these elements can be distributed statistically along the polymer chains (random copolymers), strictly alternate (alternating copolyesters) or build longer blocks of each structure (block copolymers). Different polymers can be mixed physically in the melt or solution forming polymer blends. Depending on the chemical structure of the components and the formation process, mixtures of different characteristics can be formed (e.g., homogeneous mixtures for miscible polymers, small domains of component A in a continuous phase of component B or penetrating networks of both components). Furthermore, in many cases low-molecular-weight additives (e.g., plasticizer, antiblock agents, nucleation agents) are added to a polymer to adjust properties such as flexibility or processibility.

Different structures, even with the same overall composition of a polymer, can directly influence the accessibility of the material to the enzymatically catalyzed polymer chain cleavage significantly. Another important structural characteristics of polymers are their

average molar mass, their molar mass distribution and possible branching of the chains or the presence of networks (crosslinked polymers).

The structural characteristics of the polymer have a crucial impact on higher ordered structures of the material (crystallinity, crystal morphology, melting temperature or glass transition temperature) which in some cases have been shown to control predominately the degradation behavior of many polymers [14.30, 31]. Finally, the crystallinity and crystal morphology depends on the processing conditions and can change with storage time of the material.

All these factors described above have to be taken into account when measuring biodegradation of plastics and interpreting the results. This makes testing of biodegradable plastics a typical interdisciplinary work. General statements such as *polymer xyz is biodegradable* can not be made since the specific properties of the polymer have to be taken into account. Thus, a detailed description and identification of a material to be tested must be a basic prerequisite for any testing protocol.

Definitions

Standardized evaluations of biodegradable plastics must always be based on definitions as to the meaning of the term biodegradation with regard to plastics. The various national and international standardization agencies and organizations have published a number of different definitions (Table 14.4) which vary significantly. While the definition for *biodegradable plastics* established by the ISO only refers to a chemical change

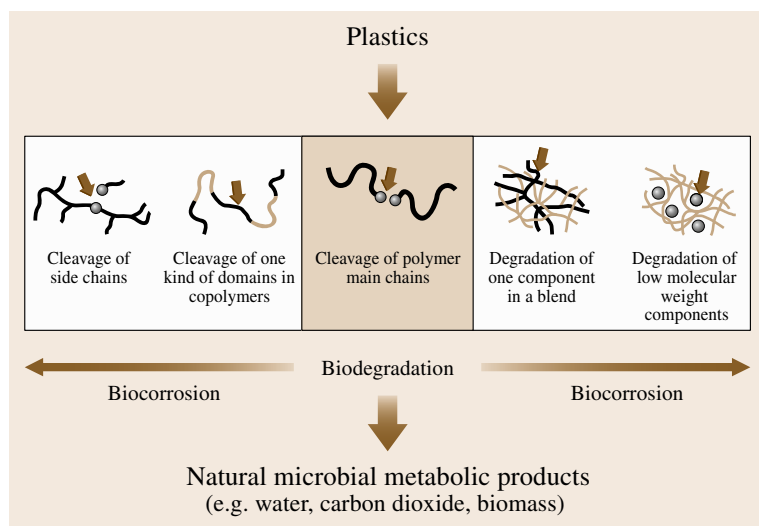


Fig. 14.8 Biodegradation- and biocorrosion phenomena in plastics

Table 14.4 Biodegradation and biodegradable plastics – definitions established by different standardization organizations

Definitions of Biodegradation	
DIN	Biodegradation is a process, caused by biological activity, which leads under change of the chemical structure to naturally occurring metabolic products
CEN	Biodegradation is a degradation caused by biological activity, especially by enzymatic action, leading to a significant change in the chemical structure of a material
Definitions of Biodegradable plastics	
DIN	A plastic material is called biodegradable if all its organic compounds undergo a complete biodegradation process. Environmental conditions and rates of biodegradation are to be determined by standardized test methods
ASTM	A degradable plastic in which the degradation results from the action of naturally occurring microorganisms such as bacteria, fungi and algae
JBPS	Polymeric materials which are changed into lower molecular weight compounds where at least one step in the degradation process is through metabolism in the presence of naturally occurring organisms
CEN	A degradable material in which the degradation results from the action of microorganisms and ultimately the material is converted to water, carbon dioxide and/or methane and a new cell biomass
ISO	A plastic designed to undergo a significant change in its chemical structure under specific environmental conditions resulting in a loss of some properties that may vary as measured by standard test methods appropriate to the plastic and the application in a period of time that determines its classification. The change in the chemical structure results from the action of naturally occurring microorganisms
Definition of Inherent biodegradability	
CEN	The potential of a material to be biodegraded, established under laboratory conditions
Definition of Ultimate biodegradability	
CEN	The breakdown of an organic chemical compound by microorganisms in the presence of oxygen to biodegradability carbon dioxide, water and mineral salts of any other elements present (mineralization) and new biomass or in the absence of oxygen to carbon dioxide, methane, mineral salts and new biomass
Definition of Compostability	
CEN	Compostability is a property of a packaging to be biodegraded in a composting process. To claim compostability it must have been demonstrated that a packaging can be biodegraded in a composting system as can be shown by standard methods. The end product must meet the relevant compost quality criteria

of the material (e.g. oxidation) by microorganisms, the European Standardisation Organisation CEN and the German DIN, in contrast, consider biodegradation of plastics as a final conversion of the material into microbial metabolic products. Other definitions listed in Table 14.4, such as *inherent biodegradability* or *ultimate biodegradability*, are adapted from according considerations for the degradation of low-molecular-weight chemicals, but can also be applied for polymers. Generally, the definitions do not specify any particular environment nor time frames; these are defined in corresponding standards specifying different degradation environments and processes.

Additional definitions have been set up for plastics classified as *compostable*. In the definition of *compostability* biodegradation of the polymeric material is only one requirement and further demands such as a sufficient compost quality after the composting process with plastics are included in the definition.

However, despite of the quite inconsistent definitions the different standards and evaluation schemes are surprisingly congruent.

General Test Methods for Biodegradable Plastics

The evaluation of the degradability of chemicals in the environment has become important as one crucial aspect of their ecological impact. First regulations and according test methods were established for products reaching the wastewater and for pesticides. In this respect a large number of standardized tests have been developed for different environments applying different analytical methods [14.33]. Nowadays, the evaluation of biodegradability, as one aspect of an environmental risk assessment, has become a standard procedure for any new chemical product intended to be marketed. However, testing methods developed for this purpose do not consider the special features (see above) of plastics materials.

Testing methods focussed on the effect of microorganisms on polymers already existed long time before biodegradable plastics started to be developed. It had been shown that conventional plastics, although they are quite resistant to environmental influences, can be attacked in some cases by microorganisms, causing un-

desired changes in their material properties, e.g. in the color or in mechanical properties such as flexibility or mechanical strength and according tests were developed [14.34, 35]. However, for these biocorrosion phenomena a generally different question underlies the corresponding test compared to the process of real biodegradation (as e.g. defined in CEN definitions listed in Table 14.4). While biocorrosion tests aim to characterize changes in the material properties (which can even be caused by minor chemical changes in the polymers such as extraction of plasticizer or oxidation, etc.), biodegradation tests for plastics have to prove that the plastic material is finally transformed into natural biological products.

Despite the large number of standardized degradation tests it turned out to be necessary to develop special testing methods when dealing with biodegradable plastics.

The testing methods published for biodegradable plastics during the last decade [14.36] are predominantly based on principles used for the evaluation of low-molecular-weight substances, but have been modified with respect to the particular environments that biodegradable plastics are exposed to and with respect to the fact that plastics are often complex materials and degrade mainly by a complicated surface mechanism.

The Dilemma in Choosing the Right Degradation Test

When testing degradation phenomena of plastics in the environment one has to face a general problem concerning the kind of tests applied and the conclusions which can be drawn. In principle the degradation tests can be

classified into three categories: field tests, simulation tests and laboratory tests (Fig. 14.9).

Field tests such as burying plastic samples in soil, to place samples in a lake or river, or full-scale composting performed with the biodegradable plastics represent ideal practical environmental conditions, but there are some serious disadvantages of such kinds of tests. One is that environmental conditions such as temperature, pH, or humidity, can not be efficiently controlled in nature and secondly, analytical methods for monitoring the degradation process are very limited. In most cases it is only possible to evaluate visible changes of the polymer samples or to determine the disintegration by measuring the weight loss, and even that may not be feasible if the materials disintegrates into small fragments which have to be quantitatively recovered from the soil, the compost or the water. Analysis of residues and intermediates is complicated due to the complex and undefined environment. Since a pure physical disintegration of a plastic material is not regarded as biodegradation in the sense of most definitions (see above), these tests alone are not suitable to prove whether a material is biodegradable or not.

To overcome these problems at least partially, various laboratory simulation tests have been developed. Here, the degradation takes place in a real environment (e.g. compost, soil or sea water), but the exposure to the environment is performed in a laboratory reactor. This environment is still very close to reality, but important external parameters which can affect the degradation process (e.g. temperature, pH, humidity, etc.) can here be controlled and adjusted, and analytical tools are better than in field tests (analysis of residues and intermediates, determination of CO₂ production or O₂

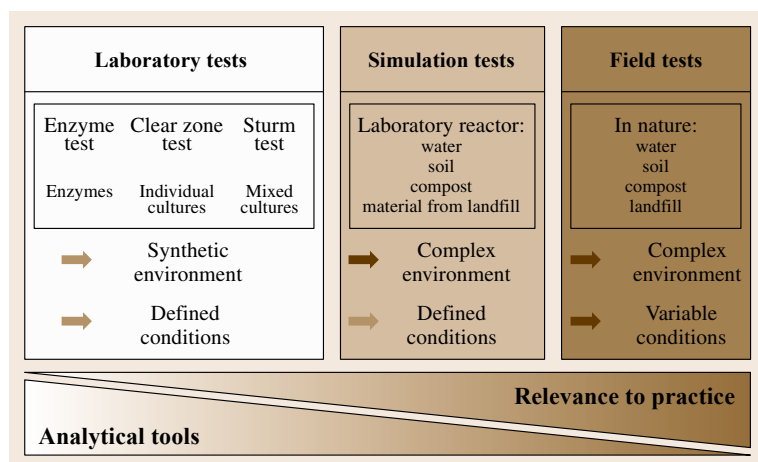


Fig. 14.9 Classification of test methods for biodegradable plastics

consumption). Examples for such tests are the soil burial test [14.37], the so-called controlled composting test [14.38–42], test simulating landfills [14.43–45], or aqueous *aquarium tests* [14.46]. To increase the microbial activity, nutrients are sometimes added in these tests with the aim to accelerate degradation and to reduce the duration of the degradation tests.

The most reproducible biodegradation tests are laboratory tests, where defined (often synthetic) media are used which then are inoculated with a mixed microbial population (e.g., from waste water or compost eluate). In some cases individual microbial strains or mixtures of some strains are used for inoculation. The organisms sometimes have been especially screened for the degradation of the particular polymer. Such tests often take place under conditions optimized for the activity of the particular microorganisms (e.g. temperature, pH etc.) with the effect, that polymers often exhibit a much higher degradation rate in laboratory tests than observed under natural conditions.

The most reproducible degradation tests directly use the isolated extracellular enzymes of the microorganisms which are responsible for the first step of the degradation process, the molar mass reduction of the polymers by depolymerization [14.29–31, 47, 48]. Also with this system it is not possible to prove biodegradation in terms of metabolization by microorganisms.

However, the shorter test durations and the reproducible test conditions make laboratory tests especially useful for systematic investigation when studying basic mechanisms of polymer biodegradation. However, conclusions on the absolute degradation rate in a natural environment can only be drawn to a limited extent.

Besides reproducibility, the shortening of test durations and minimization of the material needed is a crucial point when performing extended systematic investigations or for biodegradation testing as a tool for supporting the development of an industrial material. While degradation experiments in compost or soil often take up to one year, tests with especially screened organisms may only require several weeks and enzymatic degradation can be performed even within a few hours or days. Recent reports applying polymer nanoparticles (increased surface area) indicate that enzymatic degradation tests with polyesters can be performed within seconds [14.49, 50].

As a consequence of the principle discrepancy between the analytical tools applicable in the different tests and the relevance of the test to practical degradation conditions, it will be in most cases necessary to combine different tests to completely evaluate

the biodegradation behavior of a plastic in a certain environment.

Analytical Methods to Monitor Biodegradation

The analytical tools used to follow the degradation process depend on the aim of the work and the test environment used. In the following, some analytical methods are presented.

Visual Observations. The observation of visible changes of plastics can be performed in many tests. Effects which were used to describe degradation are, e.g., the formation of biofilms on the surface, changes in the material color, roughening of the surface, formation of holes or cracks or the occurrence of defragmentation. As already mentioned, these changes do not prove a biodegradation process in terms of conversion of the polymer mass into biomass and natural metabolic products (see definitions), but the parameter of visual changes can be used as a first indication of a microbial attack. More detailed information on the degradation process can be obtained from SEM- or AFM-techniques [14.51]. An example is presented in Fig. 14.10, showing SEM micrographs of a surface of a poly(β -hydroxy butyrate) (PHB) film before and after incubation in an anaerobic environment [14.52]. In the course of the degradation crystalline spherulites appear on the surface. This is caused by a preferential degradation of the amorphous polymer fraction, etching the slower degrading crystalline parts out of the material.

Especially recent developments of the AFM technique allow very detailed investigations on the degradation mechanism of polymers [14.53].

Changes in Polymer Chain Length and Mechanical Properties.

Comparable to visual observations changes in material properties do not allow an evaluation of polymer degradation, since these measurements do not directly prove the metabolization of the plastic material. However, changes in mechanical properties are often used when only small effects on the material due to the degradation process have to be monitored. Properties such as tensile strength are very sensitive to changes in the molar mass of the polymers which is also often directly taken as an indicator for degradation [14.54]. While for an enzymatic attack at the surface, material properties only change if a significant loss of mass is observed (the specimen become thinner because of the surface erosion process; the inner part of the material is not affected by the degradation process) the situation is usually opposite for abiotic degradation

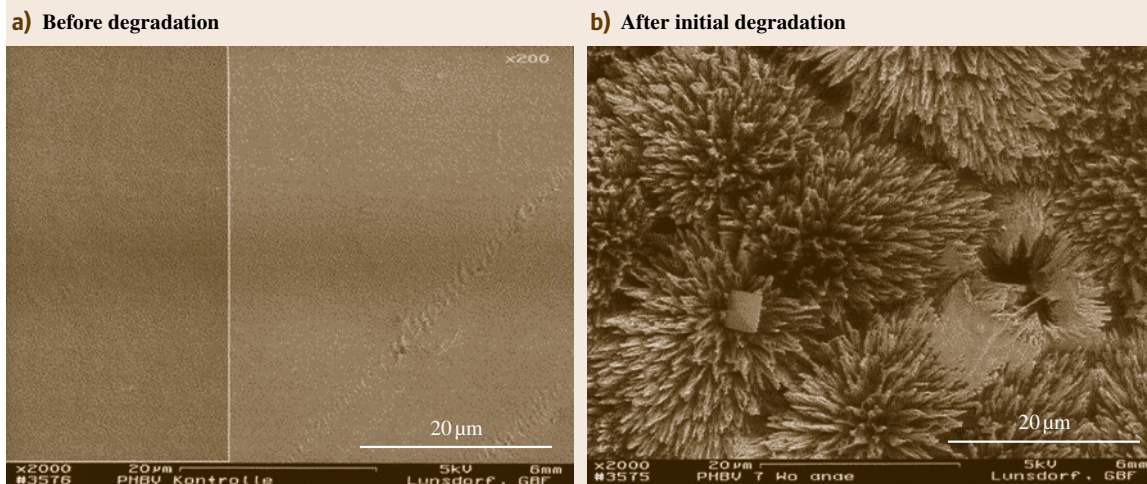


Fig. 14.10a,b Scanning electron micrographs of poly(β -hydroxybutyrate) films before (a) and after (b) incubation in an anaerobic sewage sludge. Amorphous material is degraded preferentially and spherulites of crystalline regions become visible

processes. They often take place throughout the entire material (e.g., hydrolysis of polyester or oxidation of polyethylene) and the mechanical properties of the plastics already change significantly before a loss of mass due to solubilization of degradation intermediates is observed (Fig. 14.4).

Accordingly, this kind of measurement is often used for materials where abiotic processes are responsible for the first degradation step, e.g., for the chemical hydrolysis of poly(lactic acid) or oxidation of modified polyethylenes [14.55, 56].

Weight Loss Measurements/Determination of Residual Polymer. Measuring the mass loss of test specimen (films, test bars or whole items) is often applied, especially in field- and simulation tests. However, again no direct proof of biodegradation is possible from these data. Problems can arise with proper cleaning of the specimen or when the material strongly disintegrates. In the latter case the samples can be placed in small nets to facilitate recovery, a method which is for instance applied in the full-scale composting procedure of ISO 16929. A sieving analysis of the matrix surrounding the plastic samples allows for a better and more reproducible quantitative determination of the disintegration process.

The degradation of finely distributed polymer samples (e.g. powder) can be determined by an adequate separation or extraction technique (polymer separated from biomass or polymer extracted from soil or com-

post). This procedure always has to be carefully adapted and verified for each specific system. Together with a structural analysis of the residual material and low-molecular intermediates a detailed insight into the degradation process can be gained [14.57].

Determination of CO₂ Production and O₂ Consumption. Under aerobic conditions microbes use oxygen to oxidize carbon and form carbon dioxide as one major metabolic end-product. The determination of the oxygen consumption (respirometric test) [14.46, 58] or of the carbon dioxide formation (so-called *Sturm-test*) are good indicators for polymer degradation and the most often used methods to monitor biodegradation processes in laboratory tests. In laboratory tests using synthetic mineral media, the polymer represents the major source of carbon in the system, and only a low background respiration has to be faced. Accordingly, the accuracy of the tests is usually good. Such kinds of tests already have been used to evaluate the degradability of low-molecular-weight chemicals in water (e.g., in OECD guidelines) and now have been modified for biodegradable plastics to take into consideration the special characteristics of usually hydrophobic, nonwater-soluble materials. Also, more sophisticated experimental methods for the determination of CO₂ have been introduced to the standards. Beside the conventional entrapping of CO₂ in Ba(OH)₂-solution in combination with manual titration, the detection of O₂ and CO₂ concentrations in the air stream for aeration

with infrared detectors and paramagnetic O₂-detectors are often used for such experiments.

However, besides of the advantage of an automated and continuous measurement, this kind of measurements harbor also some disadvantages. The exact air flow must be known and the signals of the detectors must be stable for weeks and month. If slow degradation processes have to be monitored, the CO₂-concentration or the drop in the O₂-concentration is very low, increasing the possibility of systematic errors during such long-lasting experiments. Here, entrapping CO₂ in a basic solution (\approx pH 11.5) with continuous titration or detection of the dissolved inorganic carbon [14.59] are useful alternatives. Other attempts to solve the problems with CO₂ detection use noncontinuously aerated, closed systems. Sampling techniques of the gas in combination with an infrared gas-analyzer [14.60] or a titration system [14.61] have been reported in the literature. An additional closed system with a discontinuous titration method has been described by *Solaro* et al. [14.62]. Tests using small closed bottles as degradation reactors and analyzing the CO₂ in the head space [14.63] or by the decrease in dissolved oxygen (so-called *closed bottle test*) [14.64] are simple and quite insensitive to leakage etc., but may cause problems due to the merely low amounts of material and inoculum which can be used.

The method of CO₂-determination to monitor polymer degradation was also adapted to tests in solid matrices such as compost [14.38]. Such methods are now standardized under the name *controlled composting test* (ASTM D 5338-98e1, ISO 14855, JIS K 6953). Actually the *controlled composting test* does not simulate a composting process, since in this test mature compost is used instead of fresh biowaste as a matrix. Biowaste contains large amounts of easily degradable carbon and, hence, would cause a high background CO₂-development, too high for an accurate measurement. Thus, already converted biowaste (= mature compost) is used instead of fresh biomaterials.

Monitoring polymer degradation in soil via carbon dioxide detection turned out to be more complicated than in compost. The usually significantly slower degradation rates causing on the one side very long test durations (up to two years) and a quite low CO₂ evolution compared to the background CO₂ formation in soil. Recent test developments in this area have been published by *Solaro* et al. [14.62]. Despite of the problems mentioned above, standardized methods for testing plastics degradation in soil are currently under development (ISO/PRF 17556).

In order to avoid problems with a high background CO₂ formation from the natural matrices of compost or soil, an inert, carbon-free and porous matrix has been used instead of soil or compost. The inert matrix is then wetted with a synthetic medium and inoculated with a mixed microbial population. This method turned out to be practical for simulating compost conditions (degradation at \approx 60°C) [14.65, 66] but could not be optimized sufficiently for soil conditions up to now.

Measurement of Biogas. Analogous to the formation of CO₂ in the presence of oxygen by aerobic organisms, anaerobic microorganisms produce predominantly a mixture of carbon dioxide and methane (called *biogas*) as the major end-product of their metabolic reactions. The amount and the composition of the biogas can be theoretically calculated from the material composition with the so-called *Buswell* equation [14.67]. The biogas production is mainly used for monitoring biodegradation of plastics under anaerobic conditions [14.68–71] and also standards dealing with the anaerobic biodegradation of plastics are based on such measurements (ISO/DIS 15985, ASTM D 5210, ASTM D 5511). The biogas volume can easily be determined by a manometer method or a simple replacement of water. Additionally, the biogas composition can be analyzed, e.g., by sampling the produced gas and analysis by gas chromatography [14.72].

As discussed for the carbon dioxide evolution, the basic problem is biogas formation from the inoculum. Especially for slow degradation processes this problem affects the accuracy of the testing method. Attempts to reduce the background biogas evolution were made by *Abou-Zeid* [14.68] diluting the anaerobic sludges with a synthetic mineral medium.

¹⁴C-labeling. Applying biodegradable polymers which are radio-labelled with ¹⁴C can avoid many of the problems mentioned above. Already very low concentrations of ¹⁴CO₂ can be detected even if carbon dioxide from other carbon sources (e.g., biowaste) is produced simultaneously. Thus, radio-labelling is used especially when slowly degradable materials are investigated in a matrix containing other carbon sources than the plastics [14.73, 74]. However, in many cases there is a problem with producing the ¹⁴C-labelled materials and carrying out work with radioactive substances from the experimental point of view.

Clear-Zone Formation. The so-called *Clear-Zone test* is a very simple semi-quantitative method. In this test

the polymer is dispersed as very fine particles in a synthetic medium agar, resulting in a opaque appearance of this agar. When inoculated with microorganisms able to degrade the polymer the formation of a clear halo around the colony (Fig. 14.11) indicates that the organisms are at least able to depolymerize the polymer, which is the first step of biodegradation. The test is often used for screening of organisms which can degrade a certain polymer [14.68, 75] but also semiquantitative results can be obtained by analyzing the growth of the clear zones' diameters [14.76].

Other Methods. Some other analytical methods for monitoring biodegradation processes, especially in degradation experiments with depolymerizing enzymes have been described in the literature.

- Analysis of the amount of dissolved organic carbon (DOC) in the medium around the plastics [14.77].
- Monitoring the decrease in optical density of small polymer particles dispersed in water [14.78].
- Analysis of decrease in particle size of small polymer particles using light-scattering [14.49].
- Determination of the free acids formed in enzymatic polyester cleavage applying a pH-stat-titration [14.30, 47, 50].

Standards for Biodegradable Plastics

At the beginning of the nineties demands were stated namely by the industry to establish suitable and reliable standardized testing procedures to evaluate the biodegradability of plastics. Most of the new standards developed were based on existing tests for the biodegradation of low-molecular-weight chemicals. An overview of standard test methods for biodegradable plastics is given in Table 14.5.

First standards, mainly focused on water- and landfill environments, were published by the ASTM. A test system to evaluate the compostability of plastics was first developed by the German DIN (DIN V 54900). This standard did not only specify testing procedures, but defined also limit values for the evaluation. Other international standards from ISO, CEN and ASTM generally followed the testing strategy given by DIN V 54900, which has meanwhile been substituted by the according European standard (EN 13432).

Currently, the development of standards is focussed on degradation in soil, since there is a great interest for applications of biodegradable plastics in

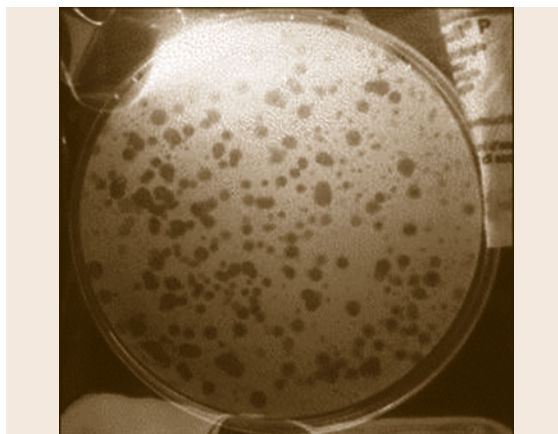


Fig. 14.11 Clear-zone-test: Fine dispersed polymer (β -hydroxybutyrate) in an microbiological agar plate results in a turbid occurrence of the agar. Microorganisms growing on the agar form clear halos (zones) if they are able to depolymerize the polymer

agriculture, e.g., as nonrecoverable mulching films or as matrices for controlled release of nutrients or pesticides etc. Compared to degradation in a compost environment, tests to evaluate degradation in a soil environment proved to be much more complex (e.g., due to different soils or wide variations in external conditions).

In the following, standardization agencies are listed which are involved in the development of standards for biodegradable plastics.

International: ISO TC61/C5/WG22 *Biodegradability*
Europe: CEN TC 261/SC4/WG2 *Biodegradability and organic recovery of packaging and packaging waste*
 CEN TC249/WG9 *Characterization of degradability*

National:

France: AFNOR
 Germany: DIN FNK 103.3 *Bioabbaubare Kunststoffe* (This group has been liquidated in 2002)
 Italy: UNI
 Japan: MITI/JIS
 USA: ASTM D20.96 *Environmentally degradable plastics*

A number of reviews dealing with standard testing methods for biodegradable plastics have been published during the last years [14.36, 79–81]. For some particular

Table 14.5 Standards related to biodegradable plastics

Biodegradability in different environments/simulation tests	
ISO 14851 – 1999	Determination of the ultimate aerobic biodegradability of plastic materials in an <i>aqueous medium</i> – Method by measuring the oxygen demand in a closed respirometer
ISO 14852 – 1999	Determination of the ultimate aerobic biodegradability of plastic materials in an <i>aqueous medium</i> – Method by analysis of evolved carbon dioxide
ISO/DIS 14853 – 1999	Determination of the ultimate anaerobic biodegradability of plastic materials in an aqueous system – Method by measurement of biogas production
ISO 14855 – 1999	Determination of the ultimate aerobic biodegradability and disintegration of plastic materials under controlled <i>composting conditions</i> – Method by analysis of evolved carbon dioxide
ISO 14855/DAMd 1	Use of a mineral bed instead of mature compost
ISO/AWI 14855-2	Determination of the ultimate aerobic biodegradability and disintegration of plastic materials under controlled composting conditions – Part 2: Gravimetric measurement of carbon dioxide evolved in a laboratory-scale test
ISO/DIS 15985 – 1999	Plastics – Determination of the ultimate anaerobic biodegradability and disintegration under high-solids anaerobic-digestion conditions – Method by analysis released biogas
ISO 17556 – 2003	Plastics – Determination of the ultimate aerobic biodegradability in <i>soil</i> by measuring the oxygen demand in a respirometer or the amount of carbon dioxide evolved
CEN TC 249 WI 240509	Plastics – Evaluation of degradability in soil – Test scheme for final acceptance and specifications
ASTM D 5210-92(2000)	Standard method for determining the anaerobic biodegradability of degradable plastics in the presence of <i>municipal sewage sludge</i>
ASTM D 5271-02	Standard test method for assessing the aerobic biodegradation of plastic materials in an <i>activated-sludge-wastewater-treatment system</i>
ASTM D 5338-98e1	Standard test method for determining the aerobic biodegradation of plastic materials under controlled <i>composting conditions</i>
ASTM D 5511-94	Standard test method for determining anaerobic biodegradation of plastic material under <i>high solid anaerobic digestion conditions</i>
ASTM D 5525-94a	Standard practice for exposing plastics to a simulated <i>landfill</i> environment
ASTM D 5526-94(2002)	Standard test method for determining anaerobic biodegradation of plastic materials under accelerated <i>landfill conditions</i>
ASTM D 5988-96	Standard test method for determining aerobic biodegradation in <i>soil</i> of plastic materials or residual plastic materials after composting
ASTM D 6340-98	Standard test methods for determining aerobic biodegradation of radio-labelled plastic materials in an aqueous or <i>compost environment</i>
ASTM D 6691-01	Standard test method for determining aerobic biodegradation of plastic materials in the <i>marine environment</i> by a defined microbial consortium
ASTM D 6692-01	Standard test method for determining the biodegradability of radiolabeled polymeric plastic materials in <i>seawater</i>
ASTM D 6776-2002	Standard test method for determining anaerobic biodegradability of radiolabelled plastic materials in a laboratory-scale simulated <i>landfill environment</i>
JIS K 6950 – 2000	Determination of ultimate aerobic biodegradability of plastic materials in an <i>aqueous medium</i> – Method by measuring the oxygen demand in a closed respirometer
JIS K 6951 – 2000	Determination of the ultimate aerobic biodegradability of plastic materials in an <i>aqueous medium</i> – Method by analysis of evolved carbon dioxide
JIS K 6953 – 2000	Determination of the ultimate aerobic biodegradability and disintegration of plastic materials under controlled <i>composting conditions</i> – Method by analysis of evolved carbon dioxide liquidate
PR NF U 52-001PR	Matériaux de <i>paillage biodégradables pour l'agriculture</i> – Exigences, méthodes d'essais et marquage
Compostability	
ISO 16929 – 2002	Plastics – Determination of the degree of disintegration of plastic materials under defined composting conditions in a pilot-scale test
ISO 20200 – 2004	Plastics – Determination of the degree of disintegration of plastic materials under simulated composting conditions in a laboratory-scale test
EN 13432 – 2000	Packaging – Requirements for packaging recoverable through composting and biodegradation – Test scheme and evaluation criteria for the final acceptance of packaging

Table 14.5 (continued)

ASTM D 5509-96	Standard practice for exposing plastics to a simulated compost environment
ASTM D 5512-96	Standard practice for exposing plastics to a simulated compost environment using an externally heated reactor
ASTM D 6002-96	Guide to access the compostability of environmentally degradable plastics
ASTM D 6400-99e1	Standard specification for compostable plastics
UNI 10785-1999	Compostilità dei materiali plastici – Requisiti e metodi di prova
Polyethylene degradation and photodegradation	
ASTM D 3826-98	Standard practice for determining end point in degradable polyethylene and polypropylene using a tensile test
ASTM D 5071-99	Standard practice for operating xenon arc-type exposure apparatus with water and exposure of photo degradable plastics
ASTM D 5208-01	Standard practice for operating fluorescent ultraviolet and condensation apparatus for exposure of photo degradable plastics
ASTM D 5272-99	Standard practice for outdoor exposure testing of photo degradable plastics
ASTM D 5510-94(2001)	Standard practice for heat ageing of oxidatively degradable plastics
Other tests	
ASTM D 5951-96(2002)	Standard practice for preparing residual solids obtained after biodegradability methods for toxicity and compost quality testing
ASTM D 6003-96	Standard test method for determining weight loss from plastic materials exposed to simulated municipal solid waste (MSW) aerobic compost environment

environments standards for biodegradable plastics will be discussed more in detail in the following.

Compostability of Plastics. The treatment of biodegradable plastics in composting processes is discussed as an alternative to plastics recycling or incineration. A number of standards for the evaluation of the compostability of plastics have been published, which all are, in major respects, congruent (ASTM D 6002-96/ASTM D 6400 99e1, EN 13432 2000); an international norm (ISO CD 15986) is currently under development. Generally, demands for compostability exceed those for biodegradability; compostability usually comprises four demands [14.82].

- The organic fraction of the material must be completely biodegradable;
- The material must disintegrate sufficiently during the composting process;
- The composting process should not negatively be affected by the addition of the plastics;
- The compost quality should not be negatively influenced and no toxic effects should occur.

Taking account of this spectrum of criteria and the principle problems in testing biodegradability in complex (natural) environments discussed above, all test schemes follow for a successive, multistep evaluation strategy.

1. Chemical characterization of the test material
These data serve for the identification of the mater-

ial, provide important data for the following tests (e.g., carbon content, composition, content on inorganic components etc.) and especially give information on toxic substances such as heavy metals.

2. Evaluation of biodegradability
The biodegradability is evaluated by laboratory testing methods monitoring the metabolization of the material by CO₂ formation or O₂ consumption. Two test methods use synthetic aqueous media (ISO 14851, ISO 14852) and allow to establish a carbon balance (besides carbon dioxide, newly built biomass is regarded as *degraded* carbon). The preferred testing method, however, is the so-called controlled composting test [14.38, 41, 42, 83, 84] with mature compost at a temperature of around 60 °C as matrix. The relevance of aquatic tests in a test scheme pertaining to a compost environment has been discussed critically [14.85]. However, disadvantages of the controlled composting test are the relatively high background CO₂ formation, which can be affected by the presence of plastics (*priming effect*) and difficulties in determining a carbon balance with sufficient accuracy. To overcome these problems, the biodegradation is calculated relative to the CO₂-release of a degradable reference substance (e.g. cellulose) or an inert solid matrix inoculated with an eluate from compost is used instead of mature compost [14.65, 66].
In the test schemes, also limit values are given for the evaluation [14.86]. The maximum test duration is usually 6 month (1 year for radio-labelled materials

in ASTM D6400) and the degrees of degradation requested are 60% and 90% relative to the reference. The value of 60% CO₂ formation originates from the OECD guidelines which were developed for low-molecular, chemically homogeneous materials. The figure takes into account that a part of the carbon is converted to biomass. Plastics, however, are complex in their composition (blends, copolymers, additives) and, thus, the limit value of 90% had been set to ensure a complete degradability of the entire material (a 10% error range was assumed for the degradation tests). In aqueous media this limit usually can only be achieved including the biomass formed (carbon balance). In mature compost less new biomass is formed and CO₂ levels of more than 90% are observed for many polymers.

3. Characterization of disintegration in compost

Since in real biowaste respirometric measurements are not possible with a sufficient accuracy, in a real compost environment only disintegration of the materials is evaluated. Disintegration testing can be performed in laboratory tests using controlled reactors of some hundred liters content [14.87] or tests in a real composting plant. The degree of disintegration is determined by sieving the compost and analyzing polymer fragments larger than 2 mm (in all standards a maximum fraction of 10% is allowed).

4. Compost quality/toxicity

The quality of the final compost should not negatively be affected when plastics are composted. Tests to evaluate this requirement are defined by established national testing methods ensuring compost quality. Criteria for compost quality are, for instance, maturity, visual impurities, density, pH, content of nutrients, salts, heavy metals etc. Additionally, ecotoxicity tests focused on plant growth are part of the compost quality characterization (e.g., plant tests according to OECD guidelines (OECD 208)).

Additional toxicity tests (e.g., tests with earthworm, luminicent bacteria, *Daphnia magna*, fish) were discussed during the development of the standards [14.41, 57, 88, 89], but due to the limited experiences with these tests in combination with compost, these tests were not generally included in the test schemes for compostability (ASTM includes earth worm test according to OECD guideline OECD 207).

Anaerobic Biodegradability. Beside normal composting, the treatment of biowaste by anaerobic digestion (anaerobic composting) is becoming more and more

widespread. It has been demonstrated that the anaerobic biodegradation behavior of plastics can differ significantly from that under aerobic conditions [14.68, 69]. Thus, separate tests must become established in order to also include these conditions for biodegradation of plastics. Some standard methods for monitoring the anaerobic degradation via biogas formation do already exist (ASTM D 5511-94, ISO/DIS 14853 1999, ISO/DIS 15985 1999), based on testing protocols designed for low-molecular substances [14.90]. However, the evaluation schemes for biodegradable plastics do not mandatorily demand the proof of anaerobic degradability up to now (in EN 13432 anaerobic tests are mentioned, but are optional).

Biodegradation in Soil Environment. After focusing on degradation in landfills and then on composting processes at the first stage of standardization efforts, currently the characterization of the evaluation of plastics biodegradation in soils has become important since there is now a growing interest in applications of biodegradable plastics in agriculture (e.g., as mulching films or as matrix for controlled release of fertilizers and pesticides).

Compared to the evaluation of the compostability, standardization of testing methods focused on soil degradation face some serious problems.

- Composting is a technical process where parameters such as pH, temperature, humidity and biowaste composition are kept in certain limits to guarantee an optimal composting process. In soil, the kind of environment and the environmental conditions can vary significantly and usually can not be controlled in nature. Standards have to take these variations into account somehow.
- The higher temperatures and activity of the microorganisms involved, causes biodegradation of plastics during composting to usually be faster than in a natural soil environment.

It is much more difficult to monitor the slow degradation processes of some plastics in soil with a sufficient accuracy. Slow degradation sometimes causes extremely long test periods (>1 y).

Currently the CEN working group CEN TC249/WG9 *Characterization of degradability* is developing an evaluation scheme for soil degradation of plastics. The structure of this scheme very likely will be generally similar to that for composting including the different aspects mentioned above. However, due to the

variability in conditions and the differences in applications the test scheme will be more complex than the standards for compostability.

First standards describing the experimental conditions for testing biodegradation of plastics in soil have been established (ISO/PRF 17556-2002). A method for CO₂ detection in a closed system with minimized amount of soil was proposed by *Solaro et al.* [14.62]; *Albertsson et al.* [14.73] published a work based on ¹⁴C-labelled samples. Additionally to possible low carbon dioxide evolution rates, the determination of a carbon balance in soil is problematic and effects of the polymer added on the background CO₂ evolution have been observed [14.91] (*priming effect*). As proposed for the controlled composting test, the use of an inert matrix such as vermiculite is investigated, too.

Problems arise also for the evaluation of the disintegration behavior in soil. The influence of the soil characteristics and the environmental conditions on plastics degradation has been examined in some publications [14.92–96]. To solve this problem, degradation tests in a whole set of different selected soils or a test with a soil mixture are being discussed.

14.3.3 Paper and Textiles

Susceptibility of Paper and Textiles to Biodeterioration

Paper and textiles have been produced and used by humans for millennia. Until relatively recently the composition of both have been dominated by natural materials whether cellulose and plant fibers in the case of paper – or fibers derived from either plants or animals in the case of textiles. In the last 100 years, natural fibers have been mixed with man-made materials created either from polyolefins such as nylon or modified natural materials such as viscose and rayon and in some instances been completely replaced by them. In more recent times, synthetic materials have been used either to add new properties to paper or in some cases even replace paper in its traditional applications (e.g., tear- and water-resistant notepaper). In many cases, man-made fibers have either replaced traditional natural fibers in modern textiles or added properties which could not previously be obtained (e.g. a high degree of elasticity). Despite this, natural fibers play an important role in both paper based and textile products.

Although it has been recognized that paper and textiles derived from natural materials can be damaged by the action of biological systems, i.e., rats and mice, insects or microorganisms, for almost as long as they

have been used, it was only in the 1940s that the study of the biodeterioration of these materials really became a scientific discipline in its own right [14.97]. Various armed conflicts in tropical regions of the Far East resulted in premature failure of items of military clothing (e.g. boots) and equipment (tents and tarpaulins) and attempts were made to predict the performance of materials under such conditions and identify treatments to prevent failure. A variety of standard tests began to emerge [14.98], mainly as part of military specifications, and many of these approaches are still used to this day. Despite the emergence of many man-made materials, the biodeterioration of textiles and paper remains a problem with microorganisms causing discoloration of/odor in finished goods and loss of functionality (e.g., destruction of plasticizers and loss of elasticity following microbial metabolism of critical components of the composition [14.99]). Similarly, microbial action in textile and paper manufacturing processes causes losses in productivity (e.g., microbial slimes resulting in defects in paper and rupturing in the manufacture) as well as function (e.g., blockage of applicators of spin finishes/weaving ancillaries by microbial growth/detached microbial biofilms resulting in either yarn being produced without antistatic agents/lubricants or areas of localized damage due to overheating on the loom).

Microbial attack of finished paper and textiles is most usually associated with fungi although a wide range of microorganisms cause problems in the manufacturing environment [14.100]. Growth occurs on the finished goods when the material is exposed to either high humidity or free water during use and storage. The resultant growth causes either marking/discoloration (Fig. 14.12) or, eventually, physical damage (Fig. 14.13). Such discoloration/spoilage might range from the small blemishes or foxing on historic documents [14.101] to the severe staining/musty odors associated with mildew on tents that have been stored without being dried properly first [14.98]. Growth of microorganisms is usually prevented by ensuring that insufficient moisture is present. In document archives, the humidity is strictly controlled to either prevent growth or to prevent further growth on material that already has some microbial damage. Not only does this ensure that the documents remain stable but also that growth of fungi and the production of fungal spores do not have a negative impact on the health of people who work in the archives [14.102]. Similarly, textiles that have heritage value are also conserved in controlled environments. Growth on other more utilitar-

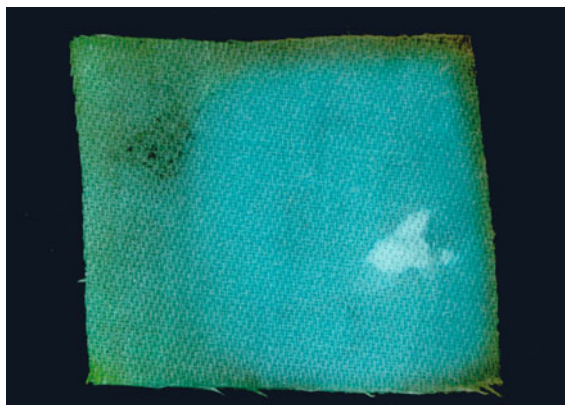


Fig. 14.12 Staining due to mould growth on a cotton based textile

ian goods (e.g., tents and tarpaulins) can be prevented by ensuring that they are dry prior to storage and that they are stored in an environment which limits the availability of moisture. Where exposure to moisture is expected during service or where less than ideal storage conditions prevail, goods can be treated to prevent growth/spoilage [14.103].

The tests used to determine both the susceptibility of materials to microbial biodeterioration and to determine the efficacy of treatments intended to prevent it range from simple agar plate bioassays through cabinet-based tests intended at simulating conditions of exposure in a more realistic manner to field exposure/soil burial trials. A range of such tests is given in Tables 14.6–14.8. The choice of test will depend upon the type of information required and the speed with which that data is needed as well as the importance of the accuracy of any predictions that are being made from it. Combined with some form of simulation of durability (e.g., leaching in water), simple plate assays can be used to screen a range of treatments to select one or two that are likely to function in service. However, such assays should be treated with caution as they do not always provide a realistic simulation of the inherent susceptibility of a material to spoilage (especially where the supporting media contain a source of nutrients) and can underpredict the protective capacity of treatments. For this reason, cabinet-based simulations (e.g. BS2011 Part 2J) and field trials should always be considered when more critical end uses are involved.

It can be seen from Table 14.6 that there is a relatively large number of tests developed to examine the resistance of textiles to fungal growth. The majority of these tests are agar plate based but some use cabi-



Fig. 14.13 Microbial deterioration of a water damaged book

nets. In the case of the agar plate methods they range from simple single species tests performed with samples being placed on a complete nutrient medium and then inoculated to multispecies tests performed on minimal media. While the former can be used to examine the dose response of a number of treatments used to prevent growth, the latter is more suited to gaining information about the inherent susceptibility of a material to microbial spoilage. The cabinet-based tests all take a similar format in which materials are inoculated with the spores of a range of fungi known to grow on textiles and are then incubated under conditions which stimulate fungal growth. Various soiling agents can be employed to increase the degree of severity of the simulation and the incubation period can be extended to simulate the durability required. In all cases growth similar to that experienced/expected under conditions of actual use should be demonstrated on an appropriate control material (in the case of BS2011 Part 2J a paper control is specified, however, the relevance of this to the material under test should be considered and an additional, relevant control included wherever possible). A similar range of fungal tests exists for paper (Table 14.7) but relatively few tests exist to simulate spoilage/biodeterioration by bacteria (BS 6085: 1992). In most instances, biodeterioration by bacteria is encompassed by soil burial trials but there are circumstances where this might be considered as too severe and work is required to develop suitable protocols in this area. In other applications, e.g. geotextiles, soil burial is probably the only sensible manner to attempt to simulate their performance in practice.

A number of tests have also been developed for materials/processes used in the manufacture of paper and textiles. For example, ASTM E1839-07 (2007)

Table 14.6 Methods used to examine the resistance of textiles to biodeterioration

Reference	Title	Description	Major principle
prEN 14119	Testing of textiles – Evaluation of the action of microfungi	The test is designed to determine the susceptibility of textiles to fungal growth. Assessment is by visual rating and measurement of tensile strength	Agar plate test
AATCC 30-1998	Antifungal activity, assessment on textile materials: mildew and rot resistance of textile materials	The two purposes of the test are to determine the susceptibility of textiles to microfungi and to evaluate the efficacy of fungicides on textiles	Agar plate test
DIN 53931	Testing of textiles; determination of resistance of textiles to mildew; growth test	The test determines the efficacy of treatments for prevention of fungal growth on/in textiles. It also allows the performance testing of a treatment after UV irradiation, leaching etc.	Agar plate test
MIL-STD-810F	Environmental engineering considerations and laboratory tests; Method 508.5 FUNGUS	The purpose of the method is to assess the extent to which a material will support fungal growth and how performance of that material is affected by such growth	Humid chamber test (90 to 99% humidity)
BS 6085 :1992	Determination of the resistance of textiles to microbial deterioration	The purpose of the method is to assess the extent to which a material will support fungal/bacterial growth and how performance of the material is affected by such growth Visual Assessment and measurement of tensile strength	a) Soil burial test, b) Agar plate test, c) Humid chamber test
EN ISO 11721-1	Textiles – Determination of resistance of cellulose-containing textiles to microorganisms – Soil burial test – Part 1: Assessment of rot retarding finishing	The test is designed to determine the susceptibility of cellulose containing textiles against deterioration by soil microorganisms. Preserved and unpreserved textiles are compared. Visual Assessment and measurement of tensile strength	Soil burial test
prEN ISO 11721-2	Textiles – Determination of resistance of cellulose-containing textiles to microorganisms – Soil burial test – Part 2: Identification of long-term resistance of a rot retardant finish	The test identifies the long-term resistance of a rot-retardant finish against the attack of soil inhabiting microorganisms. It allows to make a distinction between regular long-term resistance and increased long-term resistance. Visual Assessment and measurement of tensile strength	Soil burial test
BS 2011: Part 2.1J (IEC 68-2-10)	Basic environmental testing procedures	Mould growth test to show the susceptibility of a material towards colonization by fungi	Humid chamber test (90 to 99% humidity)
AS 1157.2 – 1999	Australian standard – Methods of testing materials for resistance to fungal growth Part 2: Resistance of textiles to fungal growth. Section 1 – Resistance to surface mould growth	Test specimens are inoculated with a suspension of spores of <i>Aspergillus niger</i> and then incubated on the surface of a mineral salts based agar for 14 d and then assessed for growth. Both leached and unleached specimens are examined. Glass rings are employed to hold the specimens in intimate contact with agar when necessary. Specimens are examined for the presence of surface mould growth	Agar plate test
AS 1157.4 – 1999	Australian standard – Methods of testing materials for resistance to fungal growth Part 2: Resistance of textiles to fungal growth. Section 2 – Resistance to cellulolytic fungi	Test specimens are inoculated with a suspension of spores of <i>Chaetomium globosum</i> and then incubated on the surface of a mineral salts based agar for 14 d and then assessed for growth. Both leached and unleached specimens are examined and exposed samples are subjected to a tensile strength test. Glass rings are employed to hold the specimens in intimate contact with agar when necessary	Agar plate test
AS 1157.3 – 1999	Australian standard – Methods of testing materials for resistance to fungal growth Part 2: Resistance of cordage and yarns to fungal growth	Test specimens are inoculated with a suspension of spores of <i>Chaetomium globosum</i> and then incubated on the surface of a mineral salts based agar for 14 d and then assessed for growth. Both leached and unleached specimens are examined and exposed samples are subjected to a tensile strength test	Agar plate test (other vessels containing media are employed for large specimens)

describes a standard test method for efficacy of slimicides used in the paper industry and E875-10 (2010) describes a standard test method for determining the efficacy of fungal control agents used as preservatives for

aqueous-based products employed in the paper industry. Work is also in progress on methods to determine the performance of spin finishes and textile ancillaries by the Functional Fluids Group of the International

Table 14.7 Methods used to examine the resistance of paper to biodeterioration

Reference	Title	Description	Major principle
DIN EN 1104	Paper and board intended to come into contact with food-stuffs Determination of transfer of antimicrobial constituents	A minimum of 20 replicates subsamples (each 10–15 mm in diameter) taken from 10 samples of a batch of paper are placed in intimate contact with nutrient agar plates inoculated with either <i>Bacillus subtilis</i> or <i>Aspergillus niger</i> and incubated at 30 °C for 7 d and at 25 °C for 8–10 d respectively	Zone Diffusion Assay
ASTM D 2020-2003	Standard test methods for mildew (fungus) resistance of paper and paperboard – direct inoculation	Replicate samples (3) are inoculated with a suspension of fungal spores and then incubated on the surface of a minimal mineral salts medium to determine if they support fungal growth	Biodeterioration Test
ASTM D 2020-2003	Standard test methods for mildew (fungus) resistance of paper and paperboard – Soil Burial	Replicate samples (5) are buried in soil for 14 d and then examined for the deterioration compared with unburied samples for both physical deterioration and loss of tensile strength	Biodeterioration/ Biodegradation Test
AS 1157.7 – 1999	Australian standard – methods of testing materials for resistance to fungal growth Part 6: Resistance of papers and paper products to fungal growth	Test specimens are placed on the surface of a mineral salts based agar and then both the specimen and the agar are inoculated with a suspension of spores of a range of fungi. They are then incubated for 14 d and then assessed for growth. Growth on the specimen is assessed	Agar plate test
AS 1157.5 – 1999	Australian standard – methods of testing materials for resistance to fungal growth Part 5: Resistance of timber to fungal growth	Test specimens are placed on the surface of a mineral salts based agar and then both the specimen and the agar are inoculated with a suspension of spores of a range of fungi. They are then incubated for 14 d and then assessed for growth. Growth on the specimen is assessed	Agar plate test
AS 1157.6 – 1999	Australian standard – Methods of testing materials for resistance to fungal growth Part 6: Resistance of leather and wet <i>blue</i> hides to fungal growth	Test specimens are placed on the surface of a mineral salts based agar and then both the specimen and the agar are inoculated with a suspension of spores of a range of fungi. They are then incubated for 14 d and then assessed for growth. Both leached and unleached specimens are examined Growth on specimens is assessed. Sucrose containing media is employed where true controls cannot be obtained	Agar plate test

Table 14.8 Methods used to examine the resistance of geotextiles to biodeterioration

Reference	Title	Description	Major principle
EN 12225	Geotextiles and geotextiles-related products – Method for determining the microbiological resistance by a soil burial test	The test is designed to determine the susceptibility of geotextiles and related products to deterioration by soil microorganisms. Visual Assessment and measurement of tensile strength	Soil burial test

Table 14.9 Methods under development to examine the preservation of wipes and moist nonwoven textiles

Reference	Title	Description	Major principle
EDANA Antibacterial Preservation V8	Recommended test method: Nonwovens – Antibacterial preservation	Test designed to determine the efficacy of preservation in non-woven textiles against bacterial contamination	Agar plate test
Publication by A. Crémieux, S. Cupferman, C. Lens	Method for evaluation of the efficacy of antimicrobial preservatives in cosmetic wet wipes	Efficacy of preservative against fungi and bacteria is tested A dry inoculum is placed into the original packaging among the wet wipes. The package is then re-sealed and assessed for growth over time	Bacterial/fungal challenge test

Biodeterioration Research Group (IBRG). A number of specialized tests have also emerged in recent years to address problems that have resulted from the development of new materials. Nonwoven *textiles* have

been developed to produce moist hygienic wipes for clinical and personal care (e.g., infant sanitary wipes). These products are supplied in multipacks and contain premoistened wipes. However, in some instances these

have proven susceptible to fungal growth in storage and in use and methods have been developed to both simulate the problem and help predict the performance of preservatives intended to prevent growth (Table 14.9).

Antimicrobial Textiles and Paper

Recently a number of both textile- and paper-based goods have been produced which include antimicrobial

properties which are not intended merely to prevent deterioration in service but to provide an antimicrobial function in use [14.104]. These articles include items of clothing fortified with microbicides to prevent odors from being formed from human perspiration or prevent cross-infection in clinical environments.

It can be seen from Table 14.10 that there are two major forms of test for microbiological effects of

Table 14.10 Methods used to examine the antimicrobial activity of textiles (fabric, yarn or pile/wadding)

Reference	Title	Description	Major principle
ASTM E2149-10	Standard test method for determining the antimicrobial activity of immobilized antimicrobial agents under dynamic contact conditions	Dynamic shake flask test. Test material is suspended in a buffer solution containing a known number of cells of <i>klebsiella pneumoniae</i> and agitated efficacy is determined by comparing the size of the population both before and after a specified contact time	Relies on either diffusion of antimicrobial mater from treated material into the cell suspension. Some activity may be due to interaction between the population and the surface of the material in suspension
AATCC 147-2004	Antibacterial activity assessment of textile materials: Parallel streak method	Agar plates are inoculated with 5 parallel streaks (60 mm long) of either <i>Staphylococcus aureus</i> or <i>K pneumoniae</i> . A textile sample is then placed over the streaks and in intimate contact with the surface of the agar and incubated. Activity is assessed based on either the mean zone of inhibition over the 5 streaks or the absence of growth behind the test specimen	Zone diffusion assay
AATCC 100-2004	Antibacterial finishes on textile materials	Replicate samples of fabric are inoculated with individual bacterial species (e.g. <i>Staph aureus</i> and <i>K pneumoniae</i>) suspended in a nutrient medium. The samples are incubated under humid conditions at 37 °C for a specified contact time. Activity is assessed by comparing the size of the initial population with that present following incubation. A neutralizer is employed during cell recovery	Cell suspension intimate contact test
XP G 39-010	Propriétés des étoffes – Étoffes et surfaces polymériques à propriétés antibactériennes	Four replicate samples of test material are placed in contact with an agar plate that has been inoculated with a specified volume of a known cell suspension of either <i>Staph aureus</i> and <i>K pneumoniae</i> using a 200 g weight for 1 min. The samples are then removed. Duplicate samples are analysed for the number of viable bacteria both before and after incubation under humid conditions at 37 °C for 24 h. A neutralizer is employed during cell recovery	Cell suspension intimate contact test
JIS L 1902: 1998	Testing method for antibacterial activity of textiles Qualitative Test	Three replicate samples of fabric, yarn or pile/wadding are placed in intimate contact with the surface of agar plates that have been inoculated with a cell suspension of either <i>Staph aureus</i> or <i>K pneumoniae</i> and incubated at 37 °C for 24–48 h. The presence of and size of any zone of inhibition around the samples is then recorded	Zone diffusion assay
JIS L 1902: 1998	Testing method for antibacterial activity of textiles Quantitative Test	Replicate samples of fabric (6 of the control and 3 of the treated) are inoculated with individual bacterial species (e.g. <i>Staph aureus</i> and <i>K pneumoniae</i>) suspended in a heavily diluted nutrient medium. The samples are incubated under humid conditions at 37 °C for a specified contact time. Activity is assessed by comparing the size of the initial population in the control with that present following incubation. No neutraliser is employed during cell recovery	Cell suspension intimate contact test

Table 14.10 (continued)

Reference	Title	Description	Major principle
EN ISO 20645	Textile fabrics – Determination of the antibacterial activity – Agar plate test (ISO 20645:2004)	Four replicate samples of fabric (25 ± 5 mm) are placed in intimated contact with a solid nutrient medium in a petri dish. The samples are then overlaid with molten solid nutrient media which has been inoculated with a cell suspension of either <i>Staph aureus</i> , <i>Escherichia coli</i> or <i>K pneumoniae</i> . The plates are then incubated for between 18 and 24 h and the plates are then assessed for growth based on either the presence of a zone of inhibition of > 1 mm or the absence/strength of the growth in the media overlaying the test specimen	Zone diffusion assay
ISO 20743	Textiles – Determination of antibacterial activity of antibacterial finished products: Absorption method	Replicate (6) samples of textile are inoculated with a standardised broth culture of either <i>staph aureus</i> or <i>K pneumoniae</i> in individual tubes and then incubated at 37°C for 18–24 h in closed containers. Samples are analysed for the presence of viable bacteria both before and after incubation by either total viable count or the determination of total ATP. Samples are sterilised prior to testing and a neutraliser is employed during recovery. The test is validated by growth of 1 order of magnitude during the incubation period	Cell suspension intimate contact test
ISO 20743	Textiles – Determination of antibacterial activity of antibacterial finished products: Transfer method	Replicate (6) samples of test material are placed in contact with an agar plate that has been inoculated with a specified volume of a known cell suspension of either <i>staph aureus</i> and <i>K pneumoniae</i> using a 200 g weight for 1 min. The samples are then removed. Replicate (3) samples are analysed for the either the number of viable bacteria or the total ATM content both before and after incubation under humid conditions at 37°C for 24 h. Samples are sterilised prior to testing and a neutraliser is employed during cell recovery. The test is validated by either growth of 1 order of magnitude during the incubation period or by a measure of the variability of the data obtained	Cell suspension intimate contact test
ISO 20743	Textiles – Determination of antibacterial activity of antibacterial finished products: Printing method	Replicate (6) samples of test material are either <i>staph aureus</i> and <i>K pneumoniae</i> by printing cells collected on a membrane filter onto their surface in a standardised manner. The samples are then incubated under humid conditions for 18–24 h at 20°C for a specified contact time(s). Replicate (3) samples are analysed for the either the number of viable bacteria or the total ATM content both before and after incubation. Samples are sterilised prior to testing and a neutraliser is employed during cell recovery. The test is validated by either determining the survival of the inoculum on the control material	Dry inoculum intimate contact test
SN 195920	Examination of the antibacterial effect of impregnated textiles by the agar diffusion method	Four replicate samples of fabric (25 ± 5 mm) are placed in intimated contact with a solid nutrient medium in a petri dish. The samples are then overlaid with molten solid nutrient media which has been inoculated with a cell suspension of either <i>staph aureus</i> or <i>E. coli</i> . The plates are then incubated for between 18 and 24 h and the plates are then assessed as described in prEN ISO 20645 above	Zone diffusion assay
SN195924	Textile fabrics – Determination of the antibacterial activity: Germ count method	Fifteen replicate samples (each replicate is comprised of sufficient specimens of 25 ± 5 mm to absorb 1 ml of test inoculum) are inoculated with cells of either <i>E. coli</i> or <i>staph aureus</i> suspended in a liquid nutrient medium and incubated in sealed bottles for up to 24 h at 27°C . After 0, 6 and 24 h, 5 replicate samples are analysed for the size of the viable population present. A neutraliser is employed. An increase of 2 orders of magnitude of the population exposed to a control sample is required to validate the test. The method defines a textile as antibacterial if no more than a specified minimum level of growth is observed after 24 h in 4 of the 5 replicate groups of samples	Cell suspension intimate contact test
SN195921	Textile fabrics – Determination of antimycotic activity: Agar diffusion plate test		Zone diffusion assay

Table 14.11 Methods used to examine the antimicrobial activity of carpets

Reference	Title	Description	Major principle
AATCC 174-2007	Antimicrobial Activity Assessment of Carpets Qualitative Antibacterial Activity	Petri dishes with nutrient media are inoculated with a single, diagonal streak (≈ 7.5 cm) of either <i>staph aureus</i> or <i>K pneumoniae</i> . An unsterilized test specimen (25 mm \times 50 mm) is placed in intimate contact and transversely across the inoculum on the agar surface. The plates are then inoculated at 37 °C for 18–24 h. The front and back of the carpet are tested separately. After incubation, the plates are inspected for the presence of growth both below the specimens and for any zone of inhibition caused by the specimen is recorded. The test can also be used to test the effect of cleaning regimes. An untreated control is optional	Qualitative assessment of rate of kill and zone diffusion test
AATCC 174-2007	Antimicrobial Activity Assessment of Carpets Quantitative Antibacterial Activity	Unsterilized specimens of carpet are pre-wetted with either sterile water or a wetting agent before being inoculated with individual suspensions of either <i>staph aureus</i> or <i>K pneumoniae</i> in either a low or a high nutrient solution. The samples are then incubated in a tightly closed jar at 37 °C for a specified contact time. Cells are recovered in 100 ml of a neutraliser after 0 and 6–24 h of incubation. Activity is assessed by comparing the size of the initial population in the control (if used) with that present following incubation. A control is optional. When not employed, viable counts following incubation of the treated specimens alone are considered. The test can also be used to test the effect of cleaning regimes	Cell suspension intimate contact test

treated textiles which are not related to the prevention of biodeterioration. In the first, typified by AATCC 147, samples of textiles are placed onto agar plates which have been inoculated with bacteria and then incubated. The intention is that intimate contact between the textile and the bacteria/growth medium will result in the inhibition of growth either immediately adjacent to the textile or in an area around the textile, in case any antimicrobial agents that have been employed become dissolved in the growth medium. These methods are generally acknowledged as being nonquantitative although they can be employed as assays of certain antimicrobial products in the same manner that such techniques are used for certain antibiotics [14.105]. As with some of the biodeterioration tests described above, this could be useful as a screening tool and for investigating the effect of wash cycles etc. These methods are widely employed in the textile industry as they provide a highly graphic representation of antimicrobial activity although this can lead to misunderstandings of either the scale of effect seen (bigger zones of inhibition looking better) and the implications that mobility of active ingredient could have on service life. Although these techniques are considered to be unsuitable for *quantifying* the effect of the antimicrobial effects of treated textiles there are some

disciplines in which they may provide data which is more relevant to the effect claimed than that delivered by a fully quantitative technique (e.g., predicting the effect/durability of bandages intended for use of suppurating wounds).

From Table 14.10 it can be seen that there are at least four techniques which provide quantitative data on the effect of treated textiles on bacteria. These are typified by the method described in AATCC 100-2004 in which samples are inoculated with suspensions of bacteria and then incubated for a specified time before being examined for the size of the population present (Fig. 14.14). The methods differ in the form of the suspension medium, number of replicates examined, test species and, to a certain extent, conditions for incubation. Methods AATCC-100 and JIS L 1902 appear to be the most commonly employed. The Swiss Standard SN195924 was based on AATCC 100 but was apparently modified to improve reproducibility and repeatability [14.106]. These methods show a clear potential as being suitable to determine both inherent bactericidal and bacteriostatic properties of textiles. Although primarily developed for examining effects against bacteria, they can be extended to the investigation of the impact on yeasts, fungal spores and mycelial fragments. The impact on other species of

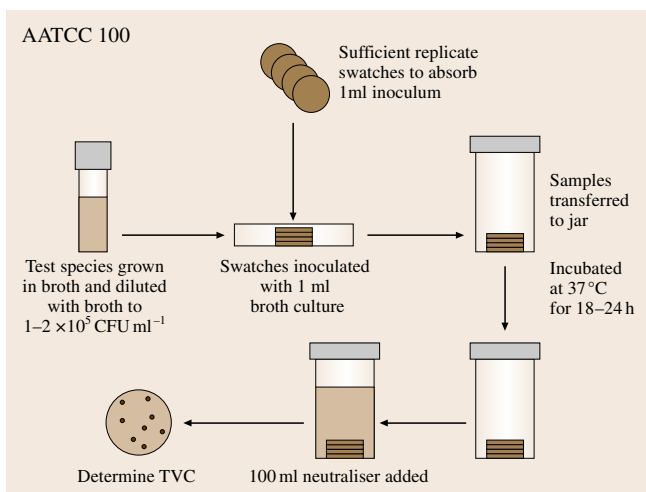


Fig. 14.14 Schematic representation of AATCC 100

bacteria can also be investigated. It is possible to envisage the method being extended to the examination of viral particles, algae and protozoa. In addition, such protocols can be combined with studies on ageing (e.g., the impact of washing cycles) to begin to satisfy at least some of the aspects associated with service life.

It can also be seen from Table 14.10 that no fully quantitative methods exist for the examination of treated textiles on fungi. All of the protocols described are zone diffusion assays of one form or another. As with antibacterial properties, these may be sufficient to substantiate certain claims (e.g., that certain fungi significant to infections on the human skin cannot germinate and grow on the textile) and methods designed for the measurement of the potential for/prevention of biodeterioration could be employed dependent on the claim being made (e.g., EN 14119: 2003 – Table 14.10) as well.

In addition to the truly microbiological methods described above, at least three methods exist which describe the performance of woven textiles [14.107] and nonwoven textiles [14.108, 109] to penetration by bacteria under wet and dry conditions. Further information is required to determine whether these have any use in evaluating treated textiles.

Although no specific standards exist for the examination of antimicrobial effects on paper and board, in many cases the tests intended for textiles can be employed. One method (DIN EN 1104) uses a zone diffusion assay to look for the presence of antimicrobial agents in paper destined for food contact applications, the intention here being to prevent the transfer of any

antimicrobial agents used in both the production of and to prevent the biodeterioration of the paper/board being transferred to food.

Selection of Test Method

For assessing potential biodeterioration and the efficacy of treatments intended to prevent it, the choice of methodology is relatively straightforward and is driven either by a specification to be matched (e.g., a military specification) or by the need to simulate an effect observed in service. In some cases, microorganisms that have caused failure in the field can be isolated and utilized in laboratory tests although care should be taken to use sufficient species/strains to measure an adequate spectrum of activity. Selecting a method to simulate a nonbiodeterioration-related effect is, however, more problematic. Although many of the methods described above and in the tables below can be used to give a measure of an antimicrobial effect, it is important to ensure that this effect and the method used to measure it, is relevant to the application. For example, it may be sufficient to merely slow bacterial growth in a application intended to reduce the generation of odorous compounds from human perspiration. In this instance a test such as that described in AATCC 100 may be modified using species known to biotransform compounds in human sweat to odor-forming molecules. The presence of moisture in the system could be considered as a reasonable model of certain items of sports clothing (e.g. socks) and the temperature used/contact time employed could be altered if necessary to bring the test closer to reality. However, in many other applications such tests provide a poor simulation of the end use. For example, a method that uses a cell suspension to saturate a sample which is then incubated at 37 °C for 24 h cannot be considered as a suitable simulation of textiles used for soft furnishings and the uniforms of medical staff. In normal use these materials would be dry or at worst occasionally splashed with water/fluids containing microorganisms. Not only do the test conditions not simulate the normal environment of the textile in use, but they may artificially predict an effect where none would result in practice. Many antimicrobial agents require free water to facilitate their transfer from a material in which they are contained to a microbial cell that comes in contact with the material. Similarly, all microbial cells require free water to grow and many also require it to survive for any length of time. If either no or insufficient free water is present in an application then it is unlikely that an antimicrobial agent would migrate from a material to a cell or

that the cell would be in a suitable metabolic state to interact with the active ingredient. In some instances, the inclusion of an active ingredient might be to add potential activity which would provide function if suitable conditions were to arise (in a similar manner to the use of a fungicide in a textile intended to prevent mold growth should conditions suitable for growth occur – i. e., keeping the item dry would have the same function in most cases). In this instance care needs to be taken to understand what the effect one is trying to simulate is. If for example, it is to prevent cross infection from one patient to another by contact with the uniform of medical staff, the speed of action will be a critical factor. Not only will the level of moisture need to be selected to simulate the conditions (e.g., moisture

from hand contact, a splash with a body fluid such as sputum) but the contact time will need to reflect the interval in which cross contamination might occur (potentially very short intervals in a busy clinical unit). In some circumstances, a significant level of moisture may simply never be present (e.g., during the settlement of airborne bacteria onto curtains). Methods are being developed which attempt to simulate such conditions (e.g., the printing method stage of ISO 20743) although care must be taken to ensure no artifacts are introduced in the recovery phase of such techniques. Considerable work is still required before many of the claims made for treated textiles/paper can be substantiated and their true benefit be assessed in a robust manner.

14.4 Biological Testing of Inorganic Materials

Ageing applies more or less to all materials. This natural decay process is ruled by physical and chemical interactions with the environment and can be considerably accelerated and in some special cases slowed down by the interaction with organisms and especially microorganisms. The microbes involved are wide-ranging in speciation and at the same time often very specialized in their nutritional and environmental adaptations. Adhesion to surfaces and resistance to stressed conditions are of importance as well as special biochemical pathways to furnish energy, electrons, water and mineral matter to the microbes living on and in inorganic materials. In order to understand detrimental functions and reaction chains, new methods of study and differentiation of physical, chemical and biologically induced or accelerated processes had to be developed. Quantitative data on mere physical and chemical attack in comparison to biologically induced and catalyzed biotransformations and biotransfer processes had to be compared in laboratory and field experiments. Methods of curing, protection, sterilization, biocide treatments had to be especially conceived and tested. Studies on the speed of physical/chemical deterioration as compared to biodeterioration were undertaken. In conclusion it can be stated that all inorganic materials exposed to surface conditions are more rapidly transferred and cycled biologically than under conditions of a sterile environment and atmosphere. Although water plays an eminent role in all biotransfer processes, it is shown that biologically induced accelerations of decay and ageing of materials

takes place in practically all objects of industry, daily use, and of the cultural heritage. Examples of sub-aquatic and subaerial biofilms on inorganic surfaces and microbial networks (biodictyon) inside porous or damaged materials are given as well as the techniques to study them and eventually prevent their damaging potential.

14.4.1 Inorganic Materials Subject to Biological Attack

Generally, the decomposition of inorganic materials is related to empirical observations and even to subjective impressions. The physical, chemical and biological processes are usually not well understood. Thus everybody expects that granite, for example (or any stone) is more durable than tissue (or any other organic material). Some tombstones, however, decay so fast that the son may survive the inscriptions made to commemorate his own parents. Thus in an exclusively physical environment, it is evident that the decomposition of rock and the dissolution of rock-forming minerals proceeds much faster than the physical decay of a protein or carbohydrate. We can state that practically all materials used in the production of objects, buildings and machines will ultimately decay. Biologically induced or accelerated decay processes are, however, often underestimated. Acceleration rates of up to 10 000× have been found in comparative laboratory experiments and field observations. The physical and chemical environment and conditioning of all objects of commercial and

cultural value will determine (1) the longevity of any object and (2) the chances of biological attack and biological catalysis of the natural physical decomposition processes. One simple example is the aggressiveness of water on a marble statue. Distilled pure water has an extremely low dissolution capacity as only a minimal amount of protons are available. Marble in the vicinity of a bakery or a restaurant, however, absorbs volatile organic compounds, which – humidity given – will be transformed to carbonic acid by ubiquitous microbes. The aggressive action of water is modified through various biological processes. Therefore, a durability scale of materials will largely depend on the environmental and biological conditions. However, we can now say more specifically which inorganic materials are more susceptible to biological attack and biodeterioration as compared to others. In the following pages we will, after a short introduction on materials, focus mainly on the organisms and biological phenomena and processes involved in the deterioration of objects made of inorganic materials. We will introduce some modern terminology, describe methods of study and ways for protection of the inorganic materials from biological hazards.

Mineral Materials

Most buildings, sculptures and objects of use are produced from rock types found and procured locally. Since the Egyptian, Greek, Hellenistic and Roman times, however, international trading of beautiful and often most durable rock types is documented and the multiple use and transfer of materials such as Pentelic and Carrara marble, Egyptian porphyry and granite stones and objects is well documented, with famous examples of porphyry columns transferred from Egypt to Rome and from Rome to Provence etc. or Egyptian obelisks being transferred to modern cities such as Paris and London. Vitruvius in his time made a survey on their durability and thus, with the exclusion of cases where cheap materials were used, the more impervious rocks were traditionally used in production of objects if the future owner was ready to pay enough money.

Calcareous Materials. Calcium carbonate is a mostly biologically deposited mineral. It is produced by skeletal macroorganisms or from the byproduct of bacterial-, fungal- and algal metabolic activities. The so-called structure-less carbonate rocks and carbonate cements of sandstones are usually biologically catalyzed deposits. Marble is a pressure-temperature metamorphosis

of limestone. Traditionally, travertines and carbonate tuffs (fresh-water deposits of calcium carbonate produced by carbon dioxide uptake through algae and/or by equilibration of water highly enriched with carbon dioxide) are regarded as high quality materials because it is very easy to cut and treat them in a wet state, while they harden when drying. Many colored marbles (carbonate breccia) are of Alpine Triassic origin. The yellow to brown color of many limestone-derived marbles comes from small amounts of iron oxide admixed. These are especially susceptible to the formation of brown or red films and crusts often called *scialbatura* or oxalate films. Since Roman times, calcium carbonate has also been used as a compound in the production of mortar, stucco and mural paintings. Because the physical and biological mechanisms of decay are practically the same, we shall include carbonate-cemented sandstones in the list of calcareous materials.

Siliceous Materials. Siliceous materials can be largely classified into four groups. The magmatic intrusive class embraces granites and diorites and the very stable porphyries. The magmatic extrusive class embraces a large variety, including basalt, andesite, volcanic tuffs and natural glass (e.g. obsidian). The metamorphic class comprises a large variety of quartzites, gneisses and schists. The sedimentary or exogenic cycle derived class includes siliceous or clay-cemented sandstones and breccia but also sinters and opal, a biologically influenced arid weathering product. The ancient Egyptian architects probably found the most stable rock in the red porphyry of Upper Egypt. Columns and stones made of porphyry were used a great deal in many places. All dried, baked or sintered siliceous products such as adobe, terracotta, bricks, glassed bricks and glasses as well as enamel are included in this group. Interestingly, within this group are the so-called stabilized melts such as glass, brick and glazed brick or clinker.

Mixed Mineral Materials (Mainly Carbonate and Silicate). Astonishingly, mixtures of heated carbonates with quartz and other siliceous materials like the heated siliceous mineral compounds of (Portland) cement turned out to be extremely corrosion resistant. Opus cementicium of the Roman engineers is a well-studied example of producing almost miraculous results of stability of materials used in building and engineering. A mixture of sand and ground mollusc shells turned out to be one of the most corrosion-resistant materials of antique technology.

Metallic Materials

Pure metals and many alloys are widely distributed in buildings and objects of art. None of them are really eternally stable. The reinforcing of wood, stone and concrete by metal in buildings, the roofing by lead and copper, metallic sculptures such as the famous Marc Aurel Quadriga, the bronzes of Riace and the mysterious *never* rusting iron column in India are examples of out-door exposure of metal structures. Many metal sculptures designed for indoor exposure have, however, been subject to long periods of burial in soil or water. Patina, films, crusts and other surface changes of metallic products are partially regarded as an integral part of the artistic value of metallic objects. In some cases, artists give a finish to their products that initiates the formation of patina or can be regarded as patina from the beginning. The formation of a hydrogen layer, oxides, sulfates, carbonates on the surface of metallic objects may also contribute to their stability and longevity. All these compounds, on the other hand, contribute to the decay and loss of the original material in many cases. However, also biofilm formation may contribute to preservation although microbial attack on metallic materials is more frequent and protective action less than with mineral surfaces.

Gold, Silver, Copper, Bronze, Brass, Tin. These metals and alloys are mentioned first because they were first coming in use in a growing technological civilization. This is explained by the fact that the temperatures and techniques of processing were first invented or found and did not face humankind with serious problems.

Iron and Steel. In order to recover metallic iron from a melt necessitates higher temperatures. Steel, in contrast to alloys such as bronze and brass needs exact supplements of carbon and other compounds such as chromium, nickel and later vanadium. Stainless steels aside more accidental findings as damascene iron are used only since the 20th Century at a larger scale and sophistication of production. The main aim was to yield highly corrosion-resistant materials. Also these, however, may undergo microbial attack by biopitting processes and other decay mechanisms.

Aluminum, Magnesium, Titanium, Platinum. These last metals have received attention as technical materials only since the onset of the 20th Century. They are very important construction materials of extremely high resistance to corrosion in cases or of importance as ex-

tremely light weight materials in the construction of airplanes, for example. Most organic or plastic replacements pose higher corrosion and decay risks than the metallic compound.

14.4.2 The Mechanisms of Biological Attack on Inorganic Materials

All inorganic materials undergo transformation and destruction, decay, disintegration and solution, even sublimation or evaporation. In many if not all cases, biological and especially microbial interaction cause acceleration of such phenomena. Thus, the natural stability of a chosen material needs to be always regarded with respect to physical, chemical and especially biological processes interfering with the standard stability data. The environment of the final *resting place* of the technical product is of great importance in aesthetical and in a physical–chemical–biological viewpoint.

Krumbein and coworkers [14.110–112] have tried to define and explain the terms frequently in use in this field. Weathering with its meteorological connotation is a somewhat awkward term not directly implying the important biological interactions in the process of rock and material decay. It should be avoided in material sciences when biological processes are involved. Erosion and abrasion involve the physical attack of solids, liquids or gases on solids with the effect of particles detached and transported. Corrosion implies a chemical transfer with surface changes as a consequence. It is used in context with industrial materials and especially with metals and alloys, to a lesser extent with stone and building materials. Degradation is a term for the combination of weathering, wearing down and erosion; it is also frequently used for the biological breakdown of organic or inorganic compounds, which serve as energy, electron or nutrient source for the organism. Also the formation of new mineral lattices and chemical compounds (rust) may be involved. Abrasion has a strong connotation with mechanical forces and material decay in moving parts of machines and other technical equipment. Deterioration and biodeterioration are terms widely used in material sciences. In the following sections we treat mainly biological actions on materials that have a deteriorative effect in terms of cultural heritage conservation efforts. The physical and chemical transfer actions will be described briefly in order to demonstrate the multitude of possible actions occurring in the ageing and decay of objects of art and technology.

14.4.3 Organisms Acting on Inorganic Materials

The durability of inorganic materials is affected by many biological activities and interactions. Biodeterioration has to be regarded as some kind of irreversible loss of information of objects of art made of mineral materials following the attack by living organisms. In this context we have to consider damages caused by man, animals, plants and microorganisms. The destructive activity of man by war, vandalism and neglect is probably the greatest of all biological effects.

Macroorganisms

All macroorganisms acting on materials are eukaryotic. Among macro organisms, roots or the climbing and adhering parts of leaves and stems of plants create a big problem to conservators because they cause partly evident aesthetic damage, partly an alteration of the stone due to (a) a mechanical action of roots, and fixing parts, (b) chemical action through ionic exchange between roots and alkali or earth alkali captions of the stone constituents, (c) vegetation shadowing slows down water evaporation [14.113].

Birds, and in particular pigeons, provoke a remarkable aesthetical and chemical damage by deposition of guano; guano, moreover can be a good growth medium for chemoorganotrophic microorganisms which, in turn, will determine a corrosive action on stone by release of acid metabolites.

There is a multitude of animals that live on and in mineral mixtures (rocks, mortar, mural paintings etc.). They construct their dwellings, seek hide and food within that environment and hereby contribute to the material change and decay as well. The most important among them are spiders, flies, mosquitoes, stone wasps, ants, mites and beetles in common terms. Insects and arthropods are the groups most frequently involved with rock dwelling and rock decay.

Mosses, lichens and algae are macroscopically evident because they cover the material surfaces with visible films of growth. Consequently, first of all an aesthetic alteration is noticed. In addition, they have a corrosive effect on the substrate by release of acid metabolites, some of which are chelating agents that determine a solubilizing and disintegrative action on the constituents. Surficial microbial mats and films and lichen colonies by their exudates (mainly sugars) act as traps of dust and particles, which in turn supply aggressive compounds and nutrients for all kinds of organisms. Lichens provoke physical as well as chemical

damage: acid metabolites solubilize and disintegrate the substrate. One of the most prominent effects of lichen is the formation of pits or crater-shaped holes (Figs. 14.15, 14.16), which are produced in some cases (epilithic lichen) by the algal symbiont, in other cases (mainly endolithic lichen) by the fruiting bodies of the fungal symbiont [14.111, 112]. It is of utmost importance to note that some lichens can act protective, while others on the same rock can act destructive. Therefore cleaning action has to be considered carefully. Many algae form inaeesthetic growth films, slime, which upon their degradation yields biocorrosive actions and can actively perforate the rock.

Microorganisms

It is well known that microorganisms are involved in rock and mineral decay in the geophysiological cycle of elements [14.114, 115].

A correlation between stone decay and the presence of microorganisms presents some difficulties because a great number and variety of species of microorganisms is involved. In fact, many autotrophic and heterotrophic bacteria, algae and fungi are found but a biodeteriorating role has been demonstrated only for some of them. In many cases microorganisms are directly associated to a deteriorating activity on stone materials, in others it is possible that products excreted from the cells under stress or upon lysis serve as nutrients for other heterotrophic decaying microorganisms or act directly on the material without a direct correlation to the organisms. According to terminology, among the rock- and material-damaging microorganisms we can notice that microorganisms are defined as organisms barely or not visible with the naked eye. Microorganisms can belong to the animals, the plants, the fungi, the algae and protozoa (protocists) and to the prokaryotes (bacteria *sensu lato*).

Phototrophic Microorganisms

Lichens and cyanobacteria as the predominant rock dwellers are usually present in association with green and red algae and diatoms. The dominance of one or other of these groups varies both locally and regionally. Cyanobacteria (blue-green algae) and green or red algae growing on surfaces within such buildings as churches or grottoes are well adapted to survive at very low light levels. Communities' color varies with the color and growth form of the dominant forms. Cyanobacteria are predominant in the tropics and arid areas and there is no doubt that this is due in part to high temper-

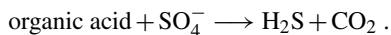
atures and/or extremely high or low high air humidity as well as high or low irradiation. Cyanobacteria can endure strong illumination because their accessory pigments protect them and prevent chlorophyll oxidation in intense light [14.116].

Cyanobacteria and algae can form biofilms and crusts on rock and concrete surfaces that are deep or bright green in humid conditions and deep black, when dry. The black coatings of many rock surfaces can be explained this way. Upon extraction in polar solvents often a typical adsorption between 300 nm and 320 nm is observed besides the classical adsorption peaks in the 400 nm and 600 nm ranges. Apart from the evident aesthetic damage on stone monuments there are many evidences of significant physical and chemical deterioration of the surface by excretion of chelating organic acids and sugar-derived carbonic acids, which initiate the perforating activities of cyanobacteria, some of which are called endolithic, when they exhibit strong perforating activity. The algae have already been mentioned under the section of macroorganisms. Many of these eukaryotic phototrophs are, however, microorganisms and can also act perforating especially in connection with fungi or as symbionts of lichens. Some observations have also been made of the occurrence of anoxygenic phototrophic bacteria in decaying rocks and rock crusts.

Chemolithotrophic Bacteria

Sulfur Compound Oxidizers. Among the chemolithotrophic group, firstly the role of sulfur, sulfide and thio-sulfate oxidizing bacteria has been clarified [14.117–120].

High numbers of strictly autotrophic *Thiobacillus* sp. have been found not only under surfaces of highly deteriorate stones which presented a pulverizing aspect, but also on deeper layers (10 cm) where there was no stone decay yet [14.121]. Some anaerobic species, like *Desulfovibrio desulfuricans*, are not strictly autotrophic and can sometimes utilize organic compounds as electron donors. They can find sulfate from air pollutants or from soil and produce hydrogen sulfide by the reaction



This product is a highly corrosive acid and its salts provoke on open air stone surface the formation of black and/or grey films and crusts often described as patina. Sulfate-reducing bacteria increase the decay activity of sulfur and sulfide or thiosulfate-oxidizing bacteria caus-

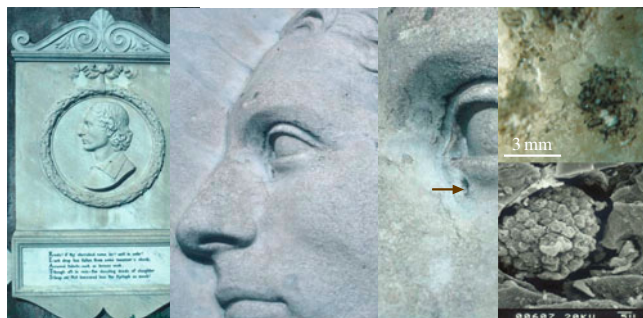


Fig. 14.15 A tear under the eye of the marble portrait of the poet Keats at the Cemetery near the Cestius Pyramid, Rome is visibly incised by black fungi and related microorganisms

ing a deeper biodeteriorating action. In fact, on soil *Desulfovibrio desulfuricans* reduces sulfates to sulfites, thiosulfates and sulfur. By capillarity these compounds can reach the superficial layers of stones where sulfur-oxidizing bacteria will oxidize them to sulfuric acid. This strong acid reacts with Calcium carbonate to form calcium sulfate (gypsum), which is more soluble in water than calcium carbonate (calcite, aragonite, dolomite).

Nitrifying Bacteria. The nitrifying bacteria are commonly found on deteriorated surfaces of rock materials [14.115, 117, 120–125].

Dissolved and particulate ammonia is deposited on rock surfaces with rain and wind from various sources among which agricultural sources (fertilizer, manure) are the most dramatically influential. But also bird excrements and other ammonia and nitrite sources are

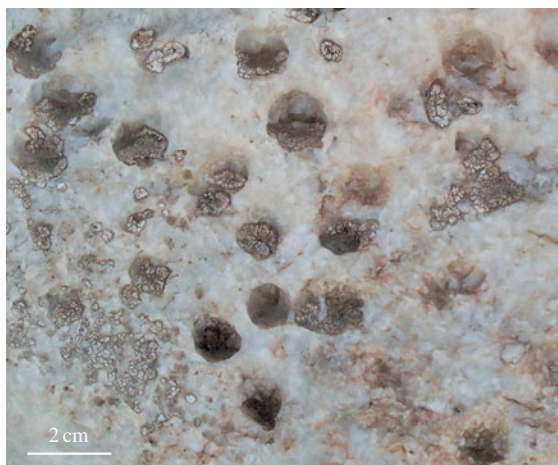


Fig. 14.16 Macropitting by lichens in the Namib desert

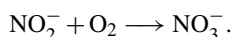
oxidized microbially by chemolithotrophic and, in part also by heterotrophic ammonia oxidizers and nitrite oxidizers to nitrous and nitric acid.

This transformation is divided into two steps.

1. Oxidation of Ammonium by *Nitrosomonas*, *Nitrosococcus*, *Nitrosovibrio*, *Nitrosospira*



2. Oxidation of Nitrite by *Nitrobacter*, *Nitrococcus*, *Nitrospira*



Both of the resulting acids attack calcium carbonate and other minerals. The CO_2 produced is utilized to form organic compounds while calcium cations form nitrates and nitrites, the latter being more soluble than the original mineral phases. Capillary zones can accumulate these products and hydrated and nonhydrated forms of such salts can create considerable damage by volume changes of the mineral phases. The characteristic symptom of the activity of nitrifying bacteria is a change of stone properties. The rock becomes porous, exfoliation occurs and fine powder may fall off, which sometimes is yellow from freshly formed iron oxides. Some evidence of organotrophic bacteria exerting nitrification has also been collected (E. Bock, private communication).

Iron- and Manganese-Oxidizing Microorganisms

The most common iron-oxidizing microorganisms which are not living exclusively in lakes and flowing water like *Gallionella* or *Siderococci* belong to the groups of fungi, chemoorganotrophic bacteria (*Arthrobacter*) or to the autotrophic group like *Thiobacillus ferrooxidans*, *Ferrobacillus ferrooxidans*, *F. sulfoxidans*. The type *Metallogenium symbioticum* has often been reported also in connection to weathering. *Krumbein* and *Jens* [14.116] have isolated numerous Fe- and Mn-precipitating microorganisms from rock varnishes and some of the isolates were closely resembling to *Metallogenium symbioticum*. *Krumbein* and *Schellnhuber* (personal communication) suggest that the organism does not really exist. The structures are fractal physical biogenic phenomena associated with fungal metabolism and iron and manganese oxide deposition outside the cell walls of the fungi. Iron-oxidizing bacteria attack directly iron rocks as well as any structure made of iron associated with stone monuments. Iron oxidation is usually rapid and is sensitive

to pH and oxygen concentration. Ferrous iron is oxidized to ferric iron, which reacts with oxygen to form iron oxide (rust). This latter determines characteristic chromatic alterations on stones. These, however, are often over-emphasized as compared to organic pigments causing the same chromatic alterations [14.126].

Chemoorganotrophic Microorganisms

In recent years a constantly growing number of contributions was made about the impact of chemoorganotrophic microbiota also on the deterioration and bio-transfer of materials of inorganic composition with no direct source of organic substrate. *Paine et al.* [14.127] were about the first authors to attract attention to the effects of chemoorganotrophic bacteria in rock deterioration. *Krumbein* [14.128] showed convincingly that the organic pollution within large cities might increase the abundance of chemoorganotrophic bacteria and especially fungi in rocks transferred from rural environments by a factor of 10^4 within one year. This group of microorganisms requires organic compounds as energy and carbon sources. Stone (as an inorganic material) can support chemoorganotrophic processes for several reasons. Four different types of sources of organic materials are usually present in variable concentrations on rock and mineral surfaces (mural paintings especially). These are

1. consolidating and improving products applied to the surface like wax, casein, natural resins, albumin, consolidants, hydrophobic agents,
2. dust and other atmospheric particles (aerosols) and organic vapors. The latter consist mainly of hydrocarbons from aircraft and car fuels or power plants but also of agricultural applications like manure and harvesting dusts or just pollen and other compounds excreted into the air by plants and animals. In industrial areas and cities manifold organic sources stem from industry and craft such as food factories, bakeries etc. Recently it has been calculated, e.g., that the total amount of fossil fuels in terms of organic carbon could derive from the annual production of pollen and etheric oils and volatile etheric substances (smell of flowers) that are carried into the sea.
3. Not less important is the coexistence of photo- and chemolithotrophic microorganisms with chemoorganotrophic ones in biofilms, biological patina and microbial mats encrusting the upper parts of rocks or the whole paint and mortar layer of frescoes. In this context the chemoorganotrophic bacteria and fungi can survive and reproduce themselves eas-

ily because they have all nutrients from autotrophic organisms.

- Sedimentary rocks usually contain between 0.2% and up to 2% organic matter retained in the rock. These compounds serve as source of energy and carbon for many microorganisms.

Chemoorganotrophic Bacteria. Extremely high numbers of these bacteria have been reported on stones [14.117, 119, 128–132]. Eckhardt [14.115] has estimated that the rate of deposition of chemoorganotrophic bacteria from the air onto stone surface is about 10^6 cells/(cm²·d). Krumbein (personal communication [14.133]), and Warscheid [14.134], however, have reported that airborne bacteria are usually of different genera and species than those settling and dwelling permanently on rocks. Bacteria migrate into porous materials with the flow of groundwater and rain water washings and can reach depths of 160 m in porous rocks. Present-day information confirms, that microorganisms will invariably be detected and active at depths within the Earth's crust, which exhibit temperatures below 110 °C!

Paine et al. [14.127] found *Bacillus* and *Pseudomonas* strains on decaying stones that are also distributed in soil. Detailed investigations of Warscheid [14.134], however, demonstrated that the rock flora considerably differs from the soil flora composition. Vuorinen et al. [14.135] demonstrate a slow decay of Finnish granite due to cultures of *Pseudomonas aeruginosa*. Lewis et al. [14.136] isolated from decaying sandstone *Flavobacterium*, *Bacillus* and *Pseudomonas* strains that showed a severe decay activity in test cultures. Warscheid [14.134] isolated high numbers of gram-positive chemoorganotrophic bacteria from both, carbonaceous and quartzitic sandstones. Most of them were able to grow under oligotrophic conditions. They demonstrated that coryneform bacteria are among the main decomposers of rocks [14.134].

The chemoorganotrophic bacteria (and the fungi) will be especially detrimental and persistent on rock surfaces and within the rock pores when they produce adhesion-promoting extracellular polymeric substances such as slimes, fibrils and other means of attachment such as hydrophobic compounds. Fungi especially may form penetration pegs and hyphae, while at the surface black-stained small and resistant microcolonies occur. The true dimension of the attack is usually made visible only by staining (Fig. 14.17) or complicated thin section techniques (Fig. 14.18). Water availability and water activity in addition largely modifies the aggressiveness of chemoorganotrophic mi-

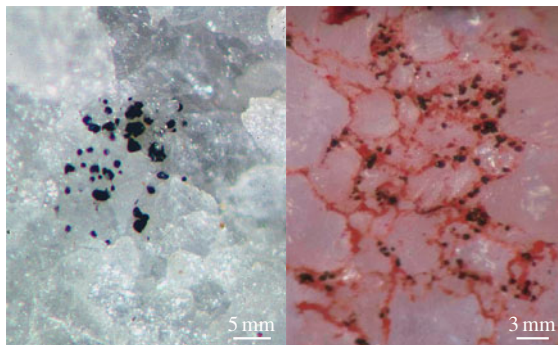


Fig. 14.17 At the surface of marble tiny black colonies and satellite colonies of black yeast are visible to the naked eye. The connecting and nourishing mycelium can only be made visible by PAS-staining for polysaccharides

croorganisms versus mineral substrates. Mineral-bound water, surface films of nanometer-range on minerals and between the layers of hydrated clays as well as bacterially stored water have to be more considered in environments which are under permanent stress of desiccation.

Chemoorganotrophic bacteria further determine their deteriorating action by metabolic products (acidic, alkaline and gaseous) [14.128, 132]. Another mechanism is the production of highly stable pigments. These in turn react with mineral elements causing an aesthetic deterioration and biogenic decay [14.126, 137].

Actinomycetes. These bacteria are thus called, because they similar to fungi form hyphae-like vegetative growth forms and produce spores similar to fungal spores. For this and other reasons their decay mechanism could

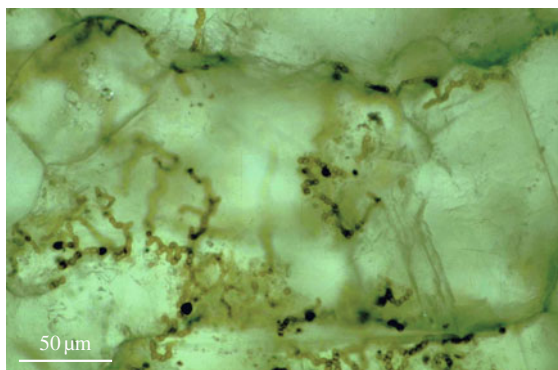


Fig. 14.18 Thin sections of marble can show as well the extent of drilling through grains and fungal penetration along grain boundaries

be the same as of fungi (hyphae penetration and acids release). Among these microorganisms, the genus *Streptomyces* is most frequently occurring in biodeteriorated stone. Penetration of the substrate by their hyphae is increased by their ability to excrete a wide range of enzymes [14.138]. They can form a whitish veil or a granulose patina on mural paintings [14.126]. They also produce water-soluble and insoluble dark pigments. Recently it was documented, however, that they rarely if ever produce noteworthy amounts of organic acids and chelates in a rock-decay environment. They may have less detrimental activities. Their presence in high numbers, however, indicates a very intense population of fungi and other microorganisms. They can perfectly well resist dryness and therefore can be regarded as excellent indicators of a progressed infection of rocks and mural paintings by other microorganisms. Early stages of rock infections usually do not exhibit high numbers of this group of actinomycetes [14.139]. On the other hand the new edition of Bergey's Manual of Systematic Bacteriology suggests placing the Actinobacteria, among which some coryneform bacteria, as already formerly the nocardioform bacteria into the group of actinomycetes or Actinomycetales. The coryneform and nocardioform bacteria, however, have been identified as frequently occurring on rock materials and producing acids from organic pollutants on building stones thus contributing considerably to biocorrosion and biodeterioration [14.134].

Fungi. Fungi are very commonly found on stone surfaces [14.118, 140]. Their deteriorating effect is due to mechanical and chemical action. The first one is related to hyphae penetration of materials that has deep-reaching deteriorating effects such as swelling and deflation as physical effects, channelling water into and keeping it in considerable depths and constant microvibrations through micromotility; the second one is due to production of acid metabolites (oxalic, acetic, citric and other carbonic acids). The latter have a chelating and solubilizing effect on many minerals [14.115, 118, 128, 141].

14.4.4 Biogenic Impact on Rocks

The phenomenological study from geological, chemical and biological groups together with many microbiological analyses of deteriorating rocks in a great number of monuments revealed various forms of deterioration such as pulverization, alveolarization, desquamation, exfoliation, efflorescences, black biofilms, films

(patina), crusts and pitting [14.142–144]. Of these, pulverization and black crusts dominate sandstone and quartzitic sandstone while corrosion by biopitting and biofilms was observed more frequently on limestone and marbles. The mutual relationships and effects of biology and rock destruction phenomena as well as different corrosion levels depending on both the coating of lichens and biofilms or microbial mats and crusts were studied in many places. Environmental conditions including pollution and the mutual influence on rock biota have as well been studied. Therefore, now a selection of some characteristic examples can be described and brought in a biological context.

Pulverization

Both sandstone and quartzitic sandstone are mostly characterized by profound pulverization of the rock. This deterioration is evidenced by a reduction in cohesion and adhesion between structural components, with an increase in porosity and a reduction of the original mechanical strength leading to a spontaneous or weather or shock induced detachment of the rock material in powder form. Pulverization as a sandy surface phenomenon is also observed on limestones and marbles. In these rocks it is, however, usually by far less conspicuous than biopitting. Sometimes, this sanding changes into the formation of alveolar erosion, a deterioration of highly porous rock materials resulting in the formation of big and deep cavities. In its advanced state, it may lead to the tafonis characteristic for many desert environments [14.120, 145, 146].

In all these cases less algae, lichens and other conspicuous microorganisms are visible and involved in the biotransfer process. Chemoorganotrophic bacteria, ammonia- and nitrite-oxidizing bacteria (especially in tafonis) and masses of cocci (or coryneform bacteria) and rod-shaped bacteria forming slimes are often observed in such places and can be correlated with this type of (bio-)corrosion.

Exfoliation, Chipping and Desquamation

Exfoliation and desquamation occur in most sandstone types and granites and gneisses analyzed, but may also be observed on limestones and marbles. These corrosions are marked by a lifting, followed by the detachment, of one or more large thinner (exfoliation), small thinner (chipping), or large thicker (desquamation) rock layers.

Throughout the lichenological study of monuments, the level of this type of (bio-)corrosion is positively correlated to the lichen covering, based on observa-

tions that these structures appear more intensive, the lower the degree of lichen covering, of which particularly the lichen *Lecanora conizaeoides* as well as, e.g., *Acarospora fuscata*, *Candelariella vitellina*, *Lecanora polytropa*, *Lecidea fuscoatra*, and *Physcia orbicularis* were observed on siliceous rocks exhibiting chipping and exfoliation. Often, a significant algal layer occurs besides the lichens mentioned.

Desquamation after crust formation is often observed when an endolithic algal mat is forming under high light conditions or surficial extreme desiccation. Also when dense endolithic layers of iron-mobilizing fungi do transform parts of the cement into new and fresh reddish iron incrustations, large desquamations may occur as it was especially frequently observed in the case of Schlaitdorfer sandstone at the *Kölner Dom* (Cologne cathedral). The same phenomena have also been observed in desert environments.

Patinas and Varnishes; Crusts and Incrustations

More or less dark-colored films, rock varnishes or patinas (often called scialbatura in the Italian and art history literature) as well as thinner or thicker yellow, reddish, brown and black epilithic and endolithic crusts are very typical for many biologically attacked and degrading rocks and tombstones. We are treating these phenomena preliminary in one section because the many different phenotypes have not yet been associated with appropriate chemical, physical and biogenic chemical and physical transfers of the original rock and mineral material.

In pollution-stressed environments sandstones can be covered by a black crust, a product of the transformation of the surface of the material including dust and soot. Its chemical and mineralogical nature and physical characteristics are partly or completely different from those of the substrate material from which it may become separated sometimes by exfoliation in other cases even by pulverization underneath the black film or crust. The crust is composed of different hydrocarbons and alcohols as a result of air pollution agents and biogenic residues, especially EPS (extracellular polymeric compounds). The latter serve like flypaper as a trap and agglutinant for foundry or other ashes and dust particles when wet [14.128]. In the dry state they appear to have extremely high viscosity and serve as a migration and diffusion barrier to chemical compounds before completely rewetted. Even in the wet and swollen stage the EPS drastically reduce the diffusivity of gases and solutes into and out of the rock [14.120, 128, 134]. Gypsum as a biocorrosion product is frequently observed in these black crusts particularly in carbonate cemented sand-

stones, limestone and marble, but even in pure siliceous sandstones and granites. Natural basaltic rocks have also been analyzed and underneath crustose lichens biotransformation products of earth alkali containing feldspars have lead to white gypsum layers between the black basalts and the lichen crusts. The normal approach is, that acid rain especially near industrial centers and in big cities promotes transformation of limestone into gypsum crusts. This, however, is not true. Like in the case of the highly discussed damage to forests by acid rain, acid rain does not really damage building stones. In both cases other reasons are predominant: In the case of mineral transformations this is witnessed and evidenced by gypsum formation in remote desert regions, where no acid rain is documented. The view of microbiologists today is that microbial transformations of sulfur are the most active agent of transformation of calcium carbonate into calcium sulfate.

It is almost premature to analyze the biological impact on the various types of films, crusts, and patinas. Therefore, a few focal points shall be given to initiate discussion and further studies.

1. *Patinas and Varnishes (Scialbatura)*. Yellow, red, brown, and black varnishes and surface films on many rock types are usually the product of repeated colonization by thin epilithic crustose lichens and/or fungal films on and beneath the surface of relatively dense rock materials such as the extremely low porosity marbles and quartzitic sandstone or silicified rock. A typical product of the biotransfer of mineral matter within these films (patina, scialbatura, rock varnish) is (1) the indicative high enrichment of manganese(IV) versus iron(III) with respect to rock derived and dust derived manganese/iron ratios (2) the often observed ring-type distribution of such films, (3) the presence of calcium oxalates (weddelite and whewellite as well as iron and manganese oxalates such as humboldtine). A recent survey on biogenic pigmentations was given by *Krumbein* [14.126].
2. *Crusts and Incrustations*. Crusts and incrustations are often brought about by the same biotransferring microbiota namely biofilms and microbial mats of algae, cyanobacteria, fungi, lichenized fungi, and often also endolithic lichens with characteristic fruiting bodies. Epilithic biofilms and microbial mats on hard substrates will form *crusts* and crustose outwards-directed growth zones. Epi-endolithic biofilms and microbial mats will form more or less deep incrustations underneath the original and trans-

ferred rock surface. In these cases the degree of light penetration, humidity regimes and other biotic factors as well as the porosity of the usually more porous rocks will regulate the thickness of the incrustation and also the question whether the physical decay phenomena will lead to exfoliation, desquamation or other effects. *Krumbein* [14.145] has given a schematic presentation of the biofilm-derived entrapping and outgrowing crusts, which will lead to an addition above the original rock surface under desquamation or exfoliation of the outwards growing crusts together with some of the rock material underneath in cases.

Incrustations and the fate of the rock material in the case of incrustation by biofilms, slimes and microbial mats forming an endolithic dense network have been first described by *Krumbein* [14.145] and schematically elaborated in a morphological and geophysiological sense by *Krumbein* [14.147]. They occur especially in Mediterranean and arid zones. In some cases also endolithic lichens have been observed to form incrustations. The physical rock development after a hardening and solidifying period is often very thick desquamation of surface parallel layers of the whole building stone or natural rock surface to a depth of up to 1 cm. After desquamation a new crust may develop in turn.

Concretioning and other types of hardening of the original rock substrate may often occur during the bio-transfer process especially in crusts and incrustations. Usually ultimately the rock in question will, however, suffer more serious damage than in the case of less hardened rocks.

Colorations

A phenomenon of rock alteration (physical, chemical and biogenic physical and chemical change) as well as deterioration (worsening of the original rock material also in an aesthetical sense), closely related in most cases, however not in all, with patina, rock varnish, crust and incrustation is a general color change or coloration occurring with building stones and monuments. This is especially unwanted in the case of marble statues and sculptures in general. The surficial films and crusts may have yellow to black colors in special but also all other colors of the rainbow due to the following mostly biological or biologically catalyzed effects and products.

1. *Pigmented salts of iron and manganese.* Iron and manganese are the two most frequently occurring metals in rocks. Many of their hydroxides,

oxides, sulfates, phosphates and oxalates are initiated by chemical reactions with the atmospheric environment and polluting agents but also very considerably by oxido-reduction reactions catalyzed by microbiota. The solution, complexation and precipitation of, e.g., calcium, iron and manganese leads to multicolored light-yellow to black staining on rock surfaces and within rock incrustations which may largely contribute to pigmentation and pigmentation changes in rocks [14.116].

2. *Organogenic pigmentations.* Many organogenic pigments do occur in nature and thus also in microbially influenced rocks. Naturally the mineral content of rocks and the different substratum does influence the coloring considerably. The dark-green to pitch shining black pigmentation of rocks is usually due to chlorophylls of cyanobacteria and algae growing on rock surfaces. When dry, all chlorophylls appear deep and shining black or lead-grey depending on substrate, concentration of chlorophyll per surface area and degree of wetness. Only in very rare completely wet conditions (growth period, not to be confused with the annual seasonality of, e.g., plankton blooms) the crusts will appear olive, bright, or dark green. Often one observes also brownish, grey and even black pigmentations of the biogenic crusts and biofilms when actinomycetes and some melanin-producing fungi are predominant. Protective pigments of the carotene type and other pigments may be produced and embedded into the EPS of algae and cyanobacteria as a shield against UV-light and further modify the pigmentation and coloration of rock films and crusts. Yellow to deep-brown and black stains may occur in very rare cases in which microbial nitric acid production leads to yellow to brown xanthoprotein reactions; perhaps even the caramelization effect of sugars and other organic compounds may be produced by especially (biogenic?) sulfuric acid attack. This *caramelization* or *coalification* through concentrated acids has, however, never been proved on rocks. The Maillard reaction, however, which is so well known in the cooking environment (brown sauces) may play an important role also in the natural rock decay environment [14.126]. Lastly, the possibility exists that – upon the death of any microorganism – enzymes are excreted from the protected cell interior, which may react and form melanin in the environment of decaying cell masses. These processes, however, need enormous amounts of cells and proteins. It is thus probably rarely

observed in comparison to other above-mentioned active staining processes, among which the tremendous potential of the black yeast-like fungi needs to be mentioned. *Gorbushina* et al. [14.148] gave an excellent insight into this exceptionally modern topic. The topic is modern in as much as it explains color changes in a new and logical way. The essence of this line of research is, that organic pigments attached or adsorbed to rock and soil particles may explain the color of soils and rocks in a much simpler way than any inorganic chemical pathway involving iron and manganese transformations.

Some of the aesthetically most detrimental and yet not fully understood colorations of marble, alabaster and other white rock sculptures and ornamental elements of buildings are pink, orange, cadmium and even carmine to violet red stains in many marble sculptures and mosaics. These stains have also been observed in some marbles of the Acropolis, Athens.

3. *Colored dust trapping and binding.* Certainly dust particles entrapped and agglutinated mainly by the EPS of biofilms and rock-covering microbial mats in their active growth stages or after rewetting will be other major factors of coloration and pigmentation (flypaper effect). In the northern hemisphere it is usually the black of coal soot and flight ashes. In special cases flight ashes will also produce red colors, when originating from iron foundries and cokeries of lignite (brown or low-vitrinized coal). In other regions red stains are derived from hematite desert dust, which is carried through the stratosphere to far away regions. This was observed many times by Ehrenberg in the 19th Century.
4. *Special heavy metal stains.* Special colorations (e.g., of surface films and crusts on metal containing monuments) may be derived from the (bio-)solubilization oxido-reduction and redeposition of the salts and minerals of copper, manganese, cobalt, silver, sulfur, and other elements. The most typical colors occurring on cemeteries are black and grey through lead letters, green and blue through copper alloys, red through iron and other specific stains usually biologically mediated [14.116].

Efflorescences and Salt Nests and Carpets

Incrustations usually are produced by a large amount of different microorganisms and their metabolic products as well as by the water supply and modification of the pore space by biological and chemical activi-

ties. In the process of this some salts are produced and remain stable for considerable time that are quite soluble alkali and earth alkali salts and double salts with often astonishing capacities of volume changes with temperature and humidity regimes. Up to 300% volume changes have been reported for such salts [14.128]. These salts frequently are the product of the rock-inhabiting microflora [14.128]. Often, the black surface crust is thus accompanied by efflorescences of salts. These crystalline formations of soluble salts on the surface of the object are whitish in color and incoherent. They may, however, be colored by the admixture of traces of reduced and oxidized iron as already suggested in [14.120, 128, 149]. Besides the typical crystals of gypsum, chlorides and nitrates and double sulfates have been analyzed by x-ray diffraction and EDX-studies. Oxalates (whewellite, weddellite and some rarer minerals such as the iron oxalate humboldtine, the magnesium oxalate glushinskite and the yet unnamed oxalates of manganese and copper or oxammite, ammonium oxalate) have been identified as microbial mineral transformation products in crusts and efflorescences [14.147, 150]. Depending on both, the rock material and the environmental conditions, the specific composition of these salts cannot be generalized. The efflorescences may be induced below the crust, which becomes then more and more separated from the substrate material. Many of the soluble salts may come and go with the waterfronts passing through the rock. It has been suggested that the mineralization is independent from the biological activities. This is, however not true. In and underneath lichenic crusts and in and underneath biofilms halophilic and highly halotolerant bacteria were found. In their vicinity new minerals have been shown to occur, such as the phosphates apatite, struvite, dahllite, lazulite, wavellite, and even turquoise or novaculite. Sometimes, the biogenic mineral formations only ephemerally play a destructive role and are later only identified by empty places of a specific mineral form near bacterial aggregates. The cleavaging and fissuring effect and the strongest efflorescences are usually limited to the lower part of the tombstones, as a result of interactions with rising water from the subsoil that also contributes nutrients and rare energy sources such as hydrogen sulfide, methane and other compounds. Special salts like jarosite have been shown in many other places to be biogenic efflorescences and recently we have found much more salt efflorescence in highly saline mural paintings. In order to complete or almost complete the list of biologically influenced efflorescence minerals the sulfates, nitrates

and even chlorides shall be mentioned that are a consequence of mainly chemolithoautotrophic bacteria but also of some chemoorganotrophs as is the case with oxalates and phosphates. Highly detrimental and often observed together with bacteria are the mixed (double-) salts of sodium, potassium, calcium and magnesium as glauberite, astrakanite, mirabilite, but also nitronatrite and nitrokalite. In special cases aluminum and silica salts and even new clay mineral formations have been reported but not yet solidly evidenced [14.115].

Biopitting

The term pitting as a synonym for smaller or larger crater-shaped cavities forming in many decaying rocks is derived from *coal and iron pit mining* of the primitive technological societies. The definition according to geological nomenclature is: *small indentation or depression left on a rock surface as a result of some corrosive or eroding process such as etching or differential solution*. We have identified and defined biopitting as the sole source of these crater-shaped cavities in many places, publications leading back to the book of Moses (Leviticus). *Krumbein* [14.145]; *Krumbein and Jens* [14.116], *Gehrmann et al.* [14.111, 112] and other scientists have now fully elaborated the micro-, meso- and macropitting as being caused mainly by endolithic and epilithic lichens. *Danin et al.* have substantially developed some of the work on biopitting [14.151]. On limestone and marbles biopitting, chipping, cracking and fissuring are frequently seen of which the biocorrosion by biopitting dominates. In all cases of studied biopitting the latter was correlated positively with epilithic or endolithic lichen species. This phenomenon of biocorrosive crater erosion was first introduced into literature by *Krumbein* [14.145]. *Gehrmann et al.* [14.111, 112] have classified these characteristic holes and cavities into three size groups namely (1) micro-, (2) meso- and (3) macro-pitting of the rock surface. Of these, both, micropits and mesopits were identified, upon maceration, as produced by the activities of the calcicole lichen *Caloplaca flavescens*. The specific pitting pattern indicated by the penetration of bundles of hyphae (mesopits) as well as by individual hyphae (micropits) is clearly to be seen on the rock surface. When the pits fuse they may cause kinds of alveolarization but of a significantly different morphology [14.145]. In view of the general importance of this biogenic process the present classification is given here

1. *Micropitting*. In this case etching figures are observed which correspond very much to the pencil

etching described by mineralogists. They are caused by individual cells and trichomes or mycelia of fungi and are only visible by scanning electron microscopy. The diameter of these micropits is between 0.5 and 20 μm . The depths can reach several micrometers and even hundreds of micrometers in special cases.

2. *Mesopitting*. In this case we are dealing with the etching figures of the fruiting bodies of endolithic lichens, in some cases also with the *nap-shaped* grooves of cyanobacteria and/or algae underneath a crustose lichen film. They form little pockets which, upon further biocorrosion or chemical weathering have the shapes of half-ellipsoids or lens type cavities. Also fungal hyphae can be associated with this pitting type. The diameter of the craters is usually between 20–800 μm .
3. *Macropitting*. These are the typical pits and scars clearly visible on many statues and marble monuments all around the Mediterranean but also on a smaller scale in Potsdam and northern areas. A schematic model of pit formation has already been published [14.147]. In this case we are dealing with the not yet sufficiently analyzed *fusion* of several pits in which fractal physical patterns may also play an important role. Some of the macropits are also derived from deeply incising epilithic lichens of ill-defined taxonomy. The macropits usually range in diameter from 1 mm to maximally 2 cm and depths between 1 and 5 mm.

The processes of mesopitting and macropitting produce characteristic depressions, which are ovoid or circular at the rock surface, the diameter of which is usually at least double the size of the depth. The process of biopitting is well separated from the well-known, but very badly understood process of alveolization of many limestones and sandstones. Water potential and availability as well as microchemical gradients play an important role in these interesting formations observed also in many Greek temples (Akrokorinth). Alveoli usually reach sizes of 1 to several cm in diameter and are almost always deeper than their diameter.

Pitting or better biopitting thus is an exclusively biological process related to endolithic and epilithic lichens in almost all cases with a few exceptions of lichenized fungi without a defined lichen thallus and fructification.

Swelling

Another deterioration phenomenon, formerly assumed as abiogenic was called *swelling*. Swelling leads to

a gradual physical relaxation of the mineral context within the complex aggregate called a rock or a building stone. It has to be kept in mind that physically, chemically and mineralogically a rock is not something in which particles or minerals are glued together by a sort of glue or cement. On the contrary: rocks are aggregates of smaller or larger individual mineral or rock particles of which some, because they are younger or smaller are conventionally called *cementing minerals* that by physical and chemical history are intimately mixed and entangled into a more or less solid, more or less hard, more or less age and decay resistant, more or less porous aggregate. The contacts between the smaller or larger particles follow all the same physical rules of electrostatic, van der Waal or other adhesion and *stickiness* promoting forces including very thin-layered water molecule, organic molecule and gas molecule films. The best example of such a noncemented aggregate perhaps is marble with its relatively uniform calcium carbonate crystals, its micro- and macroporosity and its sudden structural disintegration. It has to be kept in mind, however, that all other rock types, albeit more complex are nothing else but densely packed particles. The weakening of the adhesive forces can be brought about by mechanical causes (less load after quarrying, earthquakes, vibrations, even storm shock waves), chemical causes (gases, liquids, redox-processes) and especially by biogenic forces and products as described before. Swelling (namely of *EPS*) is a very typical biogenic physical rock transfer action that contributes largely to pulverization, chipping, exfoliation and even to pitting.

A lichen crust that is often bending out before it breaks away from the surface always has some rock particles adhering. Such patterns of biogenic initial stages of desquamation is connected with epilithic crustose lichens, especially *Acarospora fuscata*, *Candelariella vitellina*, *Lecanora grumosa*, *Lecanora polytropa*, *Lecanora rupicola*, *Lecanora sulfurea* and *Lecidea fuscoatra*. Removing the lichen crust, an advanced state of incoherence of the rock surface layers is recognizable, characterized by an increase in porosity and an apparent decline in the original mechanical strength. Moreover, longitudinal sections of such lichen-encrusted sandstones reveals an extensive compact network of hyphae penetration up to 3 mm inside the rock. Often and even in the absence of lichen hyphae a very dense, slimy layer of *EPS* is observed in contact with the mineral grains and the uppermost layers of an epilithic or epilithic rock film or microbial mat. These slimes or *EPS*, among which a high percentage of polysac-

charides and their acids have a phenomenal capacity of swelling with water. Many bacterial *EPS* (often also designated as alginates) and lower and higher eukaryote water retention systems as, e.g., *Laminaria* spp. and *Sphagnum* spp. may swell with sufficient water supply to 1600% of the dry weight and can reach more than tenfold volumina easily. These swelling and contraction stresses are some of the most dramatic biogenic physical transfers in the disintegration of aggregates such as rock, plaster, mural paintings and other materials. *EPS*, cellular and hyphae swelling and water retention and transport capacities are usually more damaging even as the volume changes in the alkali and earth alkali salts mentioned in the section on internal and external efflorescences.

14.4.5 Biogenic Impact on Metals, Glass, Pigments

Interaction of Microorganisms with Metals

Microbial degradation of metals is associated with a wide range of biochemical processes, including acid metabolite production and galvanic coupling. Chemolitho- and chemoorganotrophic microorganisms exert an active corrosive action on metals by production of inorganic and organic acids. *Cladosporium resinae* causes corrosion of aluminum alloys by the secretion of citric, isocitric, *cis*-aconitic, and α -oxoglutaric acids, resulting in pitting and selective removal of zinc, magnesium and aluminum, leaving copper and iron aggregates behind. This suggests that microbial acid corrosion plays an important role in pitting corrosion [14.152].

In recent years some bronze monuments have been exhibiting serious corrosion damage in the form of *patina*. It starts as a reddish-brown oxide skin to a black coating, which intermingles with green patina underneath. In this phenomenon also bacteria are involved. In fact, organic matter reacts with mineral particles (from metals in the bronze and/or deposited by the environment) and the consequence is corrosion processes. The loss of material beneath a patina surface is *just* some microns each 100 years or so, but it is these microns that represent a large part of a bronze's artistic qualities.

Bacterial extracellular polymeric substances (*EPS*) are a crucial factor to microbial corrosion. They strongly bind the metals, with a wide range of variations that influence its adhesion to metal surfaces and result in preferential oxidation of particular metal species [14.153]. The primary mechanism of bacterial corrosion of metal surfaces involves the creation,

within an adherent biofilm, of local physicochemical *corrosion cells*. The practical consequence of this perception is that bacteria must be in sustained contact with a metal surface, in well-organized microbial communities before the corrosion process is initiated. Bacterial corrosion seems to occur only within the biofilm! [14.154]. It often shows the same biopitting characteristics as on marble and glass, i.e., small crater-shaped holes and pits going several hundred micrometers deep through patina and material.

Interaction of Microorganisms with Glass

Biocorrosion of glass was observed on optical glass corroded in tropical climates and on church windows and other some objects [14.147, 155, 156]. Even if some authors [14.157] suggest that biodeterioration is a minor and negligible process, others had demonstrated the important role played by lichens [14.158, 159] by fungi and other microorganisms [14.160, 161]. Krumbein et al. stated that microbial growth can occur on clean glass in the presence of sufficient humidity. In addition of the supply of hydrating forces, bacteria and fungi act as physical and chemical agents. They can also metabolize, leach, accumulate and redeposit elements like K, Ca, Mg, Fe, Mn, Ag, P. On dirty glass, water supply and pollutants deposited on it act as growth-supporting substrate. As a result of the establishment of microbial communities often pits are formed and/or other etching figures that can be clearly related to microbial activities.

Interaction of Microorganisms with Pigments

Mineral, plant and animal pigments can be more or less susceptible to light (especially plant pigments), but the most important factor of their susceptibility to degradation is the addition of organic substances like albumen, casein, wax, arabic gum, etc., which are an optimal growth substrate for microorganisms. Some of them provoke chromatic alterations by release of acid or alkaline products (e.g., turning to blue of malachite green). Many fungi and bacteria can cause pigment alterations and addition of detrimental and disturbing fluorescent pigments that are added to the pigments in wall paintings and thus altering the total appearance of the mural painting.

14.4.6 Control and Prevention of Biodeterioration

The main effort in the study of biodeterioration of works of art and the interaction of macro- and microorganisms with the materials of which the objects exist is to under-

stand the deteriorating activity and as a consequence to develop specific and specialized methods for controlling the growth of organisms responsible for and hereby preventing the biodeterioration of these valuable materials for as long as possible.

The choice of methods is related to (1) the nature of the material (stone, wood, paintings, paper, glass, etc.), (2) its location (archeological area, museum, church, library, etc.), (3) the extension and form of treated surfaces (little objects, statues, buildings, walls), (4) the processes physical/chemical and organisms involved (macro- or microorganisms). In fact, no method exists that is an overall remedy for all materials, objects and organisms. Impregnations with consolidants and water-repellent substances have been frequently proposed and used and the interactions of these compounds with microbiota were discussed [14.128, 162, 163]. The substances that have been tested and used range from silanes and siloxanes over acrylic resins and polyurethanes to epoxy materials, vinyl polymers, inorganic materials to natural oils, waxes and other substances. Very dangerous and perilous substances seem to be fluorosilicon compounds and several hydroxides that have been frequently used as well as water glass in the past centuries and in the early decades of this century.

In the context of this mainly microbiological review, however, biological methods of treatment and the microbial interaction with chemical consolidants is far more of interest. In the control of biodeteriogenic organisms growing on and in buildings or monuments, as well as other objects of art, the first step should be to eliminate the most determining factors favoring or accelerating biodeterioration: light, temperature, relative humidity (RH), nutritive factors, dust, dirt, etc. This is easier in indoor environments while it is not always possible in outdoor environments, where however, the use of particular devices like environmental recovery and protective measures can keep these parameters in a range of acceptability. Prevention of biodeterioration of indoor objects is largely determined by the conditions of the environment where the object is kept (exhibition or storage). Low RH, conditioning systems and periodic cleaning can control growth of microorganisms. *Valentin* et al. [14.164] found that the combination of low RH and low oxygen levels significantly decreases microbial activity on solid support. Previously *Curri* (pers. comm.) suggested keeping valuable sculptures made of marble under an inert atmosphere of nitrogen. Nitrogen, however, may not prevent totally microbial growth in humid conditions. Thus the preven-

tion of humidity must be added. These latter methods, however, are noninvasive, safe and relatively inexpensive and could be an important alternative in the field of conservation of art materials in museums.

As stated by the relevant Italian Committee (Normal B doc. 33/88) presently mechanical, physical, biological and chemical treatment methods are in use. These techniques have been published by *Pochon* and *Tardieux* [14.165] and are mostly still in use. Molecular techniques are amply described in *Saiz-Jimenez* [14.163]. Detail microscopy can be applied following classical direct and replica techniques. Recently we have applied also atomic force microscopy (AFM) which enables quantitative approaches to the volume of material loss by, e.g., biopitting.

The choice of methods should be taken with care because such methods affect frequently not only the organism causing deterioration but also the work of art itself or the stabilizing and consolidant additives.

- *Mechanical methods* consist in the manual removal of biological structures. This is actually what Hooke did with his valuable book infected by the imperfect fungus revealed for the first time to the eye of a microscopist. These methods, however, have not a great efficiency because they do not totally eliminate the organisms present. They have a useful function, however, in the first step of cleaning operations when it is useful to reduce the biomass and then to continue with other treatments.
- *Physical methods* have a narrow range of applications and have been used to control the growth of algae and cyanobacteria in indoor plaster and walls (MUVU) [14.166] and as deterrent for pigeons (low electricity impulses). Gamma irradiation is used to sterilize library materials and was tested at Sans Soucis in the last Century.
- *Biological methods* utilize either specific nutritive requirements of organisms or biological antagonisms of different species to eliminate undesirable growth [14.167]. Lal Gauri and coworkers have proposed a biotechnological treatment of sulfated marble (black crust) using a broth containing a mixed culture of an oxidizing bacterial biofilm producer and an anaerobic bacterium *Desulfovibrio desulfuricans* that transforms gypsum into calcite. These methods are subject to criticism of their control and incomplete removal after treatment.
- *Chemical methods* are the most frequently employed. They consist in the application or fumigation in the environment by chemical compounds

with biocidal activity. The choice of biocides to be used during conservation and restoration of works of art is not easy. It involves factors like

- specific efficiency towards the biodeteriorative agents
- toxicity towards the person applying the technique
- damage potential towards the work of art
- relative ease of application and availability.

Before applying this kind of products, e.g., on stone in objects of art they must firstly fulfil some prerequisites

- a) efficacy – it is influenced by: (1) dose expressed as amount of product/surface unit; (2) action spectrum (range of sensibility of microorganisms involved); (3) persistence of the active principle.
- b) toxicological characteristics and pollution potential – it should be considered from the view of operators care and environmental risks,
- c) noxious interference with the substrate,
- d) outdoor environments (archeological area, buildings, statues of different material).

Mineral Materials

The microbial attack and thus the necessity of treatment of rock and mineral material is usually restricted to outdoor objects, since indoor objects rarely exhibit serious microbial decay phenomena. We have, however, several times been asked to analyze serious fungal infections of statues which are stored in humid conditions in magazines and store rooms and have persistent fungal infections. Detailed recommendations on use and application of biocides on stones are described in the Document Normal 33/88 (CNR-ICR, 1988). It is stressed, as a partly general criterion, that biocides in order to avoid the interference with substrate must have no coloration, no chemical or physical reactivity capable to modify the characteristics of stone. Biocides, also, must be washed (pulled off) after their time of action. In this way risks of interference between residues of the applied products and stones are reduced to a minimum. Also the danger of damage to the personnel and visitors is reduced this way. Some indication on modern approaches to polyphasic biocidal treatments can be viewed on the Website of BIOGEMA under EU projects (<http://www.biogema.de>).

Tests with biocides on different kinds of stones and other mineral materials (*Groß* and *Krumbein*, personal communication) have put in evidence, that the efficiency of a biocide of a given concentration in direct

contact with the material to be treated can largely vary with lithotypes (e.g., effectless when applied to lime-

stone, while considerable effect is stated when applied to the same flora on sandstone).

14.5 Coatings and Coating Materials

14.5.1 Susceptibility of Coated Surfaces to Fungal and Algal Growth

It is widely recognized that surface coatings can be susceptible to contamination and spoilage by microbial growth during service [14.168]. Examples of growth of fungi and algae on exterior facades are common (Fig. 14.19) and strategies to limit their growth are widely accepted in the industry. In general, these strategies rely on the inclusion of an antimicrobial agent [14.169] into the formulation and its presence inhibits the growth of microorganisms when the coating is used in areas where microbial growth is known to occur. In exterior conditions, growth is often an aesthetic problem although as it progresses, physical damage to the coating can occur. However, in interior situations, growth of certain fungi on surfaces has been implicated in human respiratory disorders [14.170]. In these circumstances limiting fungal growth on coatings has an impact on human health. Coatings for submerged surfaces such as the hulls of ships also suffer from problems associated with the growth of microorganisms (principally algae) along with colonization by species of molluscs and crustaceans.

While behavior under normal conditions of use will always be regarded as the definitive test for performance, a number of laboratory tests have been developed to provide a more reproducible and rapid



Fig. 14.19 Growth of algae on a painted facade

means of gathering data. These tests can be combined with weathering studies ranging from simple leaching in water, through the use of weathering cabinets, to the prior exposure of coated surfaces under field conditions as is employed in studies on the efficacy of treatments on timber against blue-stain in service (Sect. 14.2).

Aside from field exposure, there are two major approaches that are employed to examine the susceptibility of surface coatings to fungal and algal growth. In the first, an artificial substrate (such as a glass fiber or paper filter) is coated and then placed onto a semi-solid microbiological growth medium in a petri dish. The coating and, in some cases, the medium is then inoculated with either single strains of test species or a combination of such strains (Fig. 14.20). This provides a highly accelerated mechanism of testing although it can be argued that the presence of a growth medium, which may diffuse into the coating, can result in the growth of species that are not true biodeteriogens of the coatings system under test. This is especially true when testing for activity against fungi and in some instances a nonnutrient medium (or at least one lacking a source of carbon) is employed such that it simply provides a source of mois-

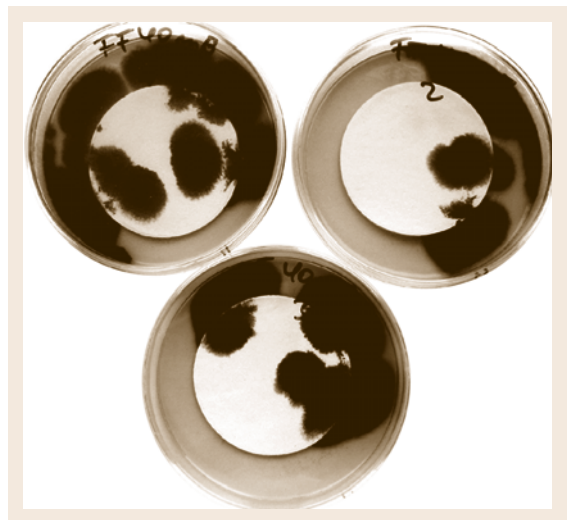


Fig. 14.20 Growth of fungi on a coated filter paper (EN15457)

ture and, occasionally, certain essential trace elements. Of course when testing algae a source of light is essential and this is usually defined in the method and in some cases reproduces a normal diurnal cycle. The major test protocols employed for surface coatings are given in Table 14.12 below, although in some instances, where particular specifications are being defined (such as powder-coated materials for military applications) methods such as ISO 846 and BS2011 Part 2J are employed. Until relatively recently many workers have based their tests on the conditions described in ASTM D5590-00. However, especially within the EU, the guidelines provided by VdL have formed the basis of so-called *filter paper tests* for many laboratories and companies. These guidelines have also formed the basis for two EN norms (EN15457 and EN15458) intended for use in providing data on the suitability of biocidal products to protect paint films in support of requirements of the Biocidal Products Directive [14.171]. While these *filter paper tests* can provide data on compatibility of biocidal products with coating formulations and may even be correlated with performance under field conditions in some circumstances, many coating companies and test institutes regard them as useful screening tests and prefer cabinet-based simulation tests. Probably the most widely employed cabinet-based tests are BS3900 Part G6 (in Europe), ASTM D3273-00 (in the USA) for fungi and the IBRG algal test (Table 14.12).

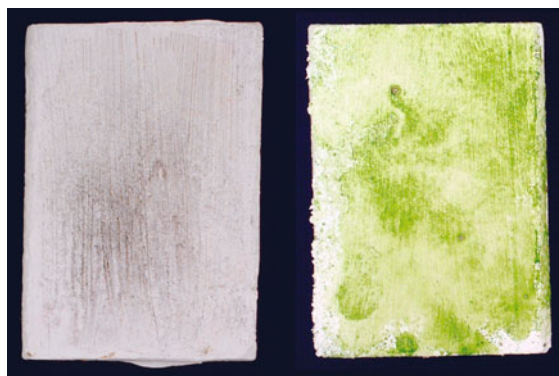


Fig. 14.21 Fungal and algal growth on panels from a cabinet test (BS3900 Part G 6 and IBRG Algal Test)

In all cases the same basic principle is applied where a combination of either fungal spores or algal cells are applied to the surface of replicate test panels. These panels are then incubated under conditions that are suitable for the growth of the species under test. After the specified interval, the panels are inspected for growth and rated and, probably most importantly, their appearance is recorded photographically (Fig. 14.21). As discussed earlier, coatings can be subjected to a number of ageing processes prior to inoculation/incubation to simulate a service cycle (e.g., paint might be aged in the can prior to application, be subjected to exposure

Table 14.12 Methods used to examine the resistance of surface coatings to fungal and algal growth

Reference	Title	Description	Major principle
BS3900 Part G6	Assessment of resistance to fungal growth	Replicate test panels coated with the test coating are inoculated with a suspension of spores of fungi known to grow on the surface of paints and related materials. The samples are then incubated under conditions suitable to support fungal growth ($23 \pm 2^\circ\text{C}$ and high humidity/surface condensation). In the published standard, condensation on the test panels is achieved by increasing the temperature in a water bath below the samples for short periods of time. Revisions are in progress which may obviate this step. The method is validated by the need for fungal growth/germination of spores to be observed on a standard coatings known to be susceptible to fungal growth after incubation for 2 weeks. After incubation growth is rated in accordance with a scale related to the percent cover with fungal growth (following visual and microscopic examination). A natural and artificial soiling agent are described in the method which can be employed when appropriate	Growth cabinet based test
ASTM D3273-00	Standard test method for resistance to growth of mold on the surface of interior coatings in an environmental chamber	Replicate test panels coated with the test coating are inoculated with a suspension of spores of fungi known to grow on the surface of paints and related materials. The samples are then incubated under conditions suitable to support fungal growth	Growth cabinet based test
ASTM WK4201	Standard test method for resistance to mold growth on building products in an environmental chamber	Replicate test panels coated with the test coating are inoculated with a suspension of spores of fungi known to grow on the surface of paints and related materials. The samples are then incubated under conditions suitable to support fungal growth	Growth cabinet based test

Table 14.12 (continued)

Reference	Title	Description	Major principle
ASTM D5590-2000 (2005)	Standard test method for determining the resistance of paint films and related coatings to fungal defacement by accelerated four-week agar plate assay		Agar plate test
SS345 Appendix B	Formal title missing at present	The bottom of glass petri dishes are coated with paint. After drying a culture of algae in a suitable growth liquid medium is placed into the dish and incubated under conditions suitable for algal growth	Liquid immersion test
EN15457	Paints and varnishes – Laboratory method for testing the efficacy of film preservatives in a coating against fungi	Coatings are applied to glass fiber discs and then placed in intimate contact with the surface of nutrient agar plates. The coatings and surrounding media are then inoculated with a mixed suspension of spores of 4 fungal species selected from a list of 10. The plates are then incubated at 24 °C for X d and then assessed for growth using a rating scale. The test is intended to support claims that a biocide can have an effect in a surface coating in support of its listing in the relevant use category within the EU BPD. It is not intended to assess the performance of surface coatings	Zone diffusion assay/agar plate test
AS 1157.10 – 1999	Australian standard – Methods of testing materials for resistance to fungal growth Part 10: Resistance of dried or cured adhesives to fungal growth	Test materials coated onto glass microscope slides are inoculated with a suspension of spores of a range of fungal species and then incubated on the surface of a mineral salts based agar for 14 d and then assessed for growth	Agar plate test
EN 15458	Paints and varnishes – Laboratory method for testing the efficacy of film preservatives in a coating against algae	Coatings are applied to glass fiber discs and then placed in intimate contact with the surface of nutrient agar plates. The coatings and surrounding media are then inoculated with a mixed suspension of 3 algal species selected from a list of 5. The plates are then incubated at 23 °C under illumination (16 h day length, 1000lx) for X d and then assessed for growth using a rating scale. The test is intended to support claims that a biocide can have an effect in a surface coating in support of its listing in the relevant use category within the EU BPD. It is not intended to assess the performance of surface coatings	Zone diffusion assay/agar plate test
VdL RL06	Guideline to evaluate the resistance of coating materials against mould growth	Coatings are applied to paper discs and then placed in intimate contact with the surface of nutrient agar plates. The coatings and surrounding media are then inoculated with a mixed suspension of spores of <i>A niger</i> and <i>Penicillium funiculosum</i> . The plates are then incubated at 28 °C for 3 weeks and assessed for growth using a rating scale after 1, 2 and 3 weeks. Coatings for exterior use and <i>wet</i> applications are leached in water prior to testing	Zone diffusion assay/agar plate test
VdL RL07	Guideline to evaluate the resistance of coating materials against mould growth	Coatings are applied to paper discs and then placed in intimate contact with the surface of nutrient agar plates. The coatings and surrounding media are then inoculated with a mixed suspension of <i>Scenedesmus vacuolaris</i> and <i>Stichococcus bacillaris</i> . The plates are then incubated at 23 °C for 3 weeks under illumination (16 h day length, 1000lx) and assessed for growth using a rating scale after 1, 2 and 3 weeks. Coatings for exterior use and <i>wet</i> applications are leached in water prior to testing	Zone diffusion assay/agar plate test
IBRG Algal Test	Method to determine the resistance of surface coatings to algal growth	Replicate test panels coated with the test coating are inoculated with a suspension of cells of algae known to grow on the surface of paints and related materials. The samples are then incubated under conditions suitable to support algal growth (18 ± 2 °C and high humidity/surface condensation/illumination – 1 Klx, 16 h photoperiod) for up to 12 weeks. After incubation, growth is rated in accordance with a scale related to the percent cover with fungal growth (following visual and microscopical examination)	Growth cabinet based test

with water spray and UV-light in an exposure cabinet, be soiled or abraded). Multiple inoculation events can also be employed and soiling agents applied. Such approaches have been applied to a wide range of coating applications from traditional exterior and interior coatings to powder-coated panels used in air-conditioning systems. One of the great strengths of cabinet-based tests is the ability to use a substrate appropriate to the coating under test (wood, plaster, concrete, steel etc.) and study interactions between the substrate and the coating. Modifications can even be used to explore the impact of environmental factors such as temperature and relative humidity on colonization and growth.

As discussed earlier, outdoor exposure trials are often considered to be the definitive means of testing coated surfaces (and indeed almost the only method employed for marine and freshwater anti-fouling products) however, care needs to be taken to ensure useful data is obtained. The amount of growth that is obtained on test panels differs greatly from location to location. Panel orientation (vertical, horizontal, north facing, south facing etc.), height above ground level and even the time of year in which the trial is initiated can have a highly significant impact on the outcome. This has been examined extensively in [14.172] and many companies employ multiple sites and long-term exposure periods to ensure they gain a thorough understanding of the potential performance of their systems (often in support of products developed using laboratory-based methods and already on the market).

Susceptibility of Coating Systems to Microbiological Growth in Their Wet-State

Many coatings systems are either entirely or at least substantially water-based and, without some form of protection, are susceptible to spoilage through microbial contamination of the product in its wet state [14.173]. Continued regulatory pressure is also resulting in the reduction/elimination of cosolvents that contribute to the overall concentration of volatile organic carbon (VOC). This is leading to an increase in the degree of susceptibility of many products including those which have formerly been protected by the antimicrobial properties of cosolvents present in the formulation (e.g., 2-butoxy ethanol in waterborne paints for automotive applications [14.174]). In-can preservation systems are now used in many coating formulations to prevent spoilage due to microbiological growth such as the development of foul odors, discoloration, loss of structure and the generation of gasses that might distort/damage the final packaging. The protection pro-

vided includes the interval during manufacture as well as storage both within the plant and prior to sale. The protection should be sufficient to provide a shelf-life suitable for the product and may be extended to allow storage of part-used containers by the end user.

By far the most common approach to assessing both the susceptibility of a coating formulation to microbiological spoilage and the potential efficacy of a preservation system is a microbiological challenge test. A relatively limited number of standard test protocols have been developed over the last few decades (e.g. ASTM D 2574-06) and some operators have tried to employ methods based on those described in the various pharmacopoeias for cosmetics and pharmaceutical products although these have been found to be far from satisfactory. The International Biodeterioration Research Group (IBRG) has been developing a test protocol for testing the in-can preservation of paints and varnishes. Although still under development it is the most common method employed by workers in the field although in many cases some modification is made to the method described [14.175]. The method uses a combination of microorganisms which have been demonstrated to grow in water-based paints to challenge a paint formulation on a number of occasions. Preincubation of samples at elevated temperatures prior to inoculation can be used to explore the interaction of biocidal products with the formulation as well as the loss of highly volatile materials and the decay of other reactive components. It has been argued that only two repeat inoculations are required to simulate the interaction of the microorganisms with a paint formulation [14.176], however, most workers in the field recommend that a minimum of three repeat inoculations (usually at weekly intervals) be applied [14.175]. However, care must be taken not to continue re-inoculation until growth is achieved in the formulation. While this could be used to bioassay the concentration of preservative within a system, it provides less information about the interaction of a preservative system and the paint formulation than a carefully structured trial including phases of ageing and relatively short campaigns of microbiological challenge. As with the number of inoculations, both the cell density and the volume of inoculum should be kept within a sensible range both to prevent the test from becoming a disinfection test and the formulation being diluted unnecessarily. Typical total bioburden applied is often in the region of 10^7 colony forming units/g with an inoculum volume of between 100–500 μ l per challenge.

After inoculation, the paint is examined for the presence of viable microorganisms. The paint is examined

at least just prior to the next inoculation although in some cases analysis at intervals between the two inoculations (e.g. 1 and 3 days) can provide useful information. Many works utilize some form of semi quantitative technique to estimate the size of any population surviving after challenge using the argument that any significant growth/survival represents a failure of the in-can preservation system. The use of a fully quantitative technique (with appropriate neutralization of preservative) can be useful in some circumstances. Techniques such as impediometry and the measurement of metabolic markers like adenosine triphosphate (ATP) have been employed with success, however, care must be taken to ensure no adverse interaction between the formulation and the system results in misleading data.

While it is important that challenge studies on coating formulations use a relatively wide range of microorganisms (principally bacteria, but certain yeast and filamentous fungi can be relevant to certain formulations), a significant fraction of these should have been derived from spoiled formulations at some time in the past. They should obviously be maintained in such a manner that they do not lose the ability to grow in paint matrices and some form of passaging may be required to ensure this (Sect. 14.6). Ideally, at least part of the challenge microorganisms should be shown to actually be capable of growing in the unprotected formulation under examination. Although they can be relevant to the spoilage of paint, care should be taken when considering the use of endospore-forming bacteria (and the spores of some species of fungi) as the survival of spores within the system can prove difficult to interpret. In many cases, studies with these species should be performed at least alongside the main challenge studies. In many variants of the basic challenge method, the cell suspensions used to create the challenge consortia are prepared from organisms grown on solid nutrient media. However, it can be argued that organisms grown in carefully standardized liquid culture (e.g., in shake flasks) are more suitable as they better mimic the manner in which contamination is introduced in practice (i. e., through the contact of paint with contaminated wash water in a production environment and via water contained in brushes and rollers used to apply the product). The use of contaminated paint has been used as a mechanism to inoculate test products but this can be difficult to standardize, may be highly selective toward certain components of a consortium and may stimulate the formation of capsules and exopolysaccharide in the challenge species and lead to the prediction of the need for excessive concentrations of preservative.

The principle of the challenge test can be a useful tool in the prediction of both the susceptibility of a coating formulation to microbiological contamination and spoilage and the efficacy of systems designed to preserve it. Careful use of appropriate ageing, incubation conditions (temperature etc.) and challenge consortia can be used to match a method to a wide range of system types from emulsion paints to industrial electrocoat systems. In-can protection of water-based tinters have been studied with success using the principles described above, however, the simulation of growth of fungi on the surface of such systems has yet to be successfully simulated in the laboratory and is the subject of concerted international research at the time of publication [14.177].

Hygienic Coatings

Although antimicrobial activity has been a component of certain coating systems for many decades, in the last few years this activity has been extended to provide a wider spectrum of activity and coatings are now being produced which are intended to provide hygienic benefits to the surfaces coated with them [14.178, 179]. In part, these developments have been fuelled by a raised public interest in hygiene resulting from high profile food poisoning outbreaks and the current high rate of hospital acquired infections.

The control of microbial activity associated with the spoilage of coated surfaces as described above, usually depends on the use of antimicrobial agents to prevent growth in association with the material to be protected [14.169]. In traditional applications, the addition of the antimicrobial agent is intended to protect the coating either during manufacture, in storage or in service. For example, a coating system intended for use on the outside walls of a building might be formulated with the addition of a fungicide and algicide to defend it from attack by microfungi and algae and so protect the film from aesthetic defacement and surface deterioration in service. In this instance the use of antimicrobial agents in the coating is intended to prevent microbiological deterioration of the surface. However, in recent years a new form of interaction between surface coatings and microbial populations has emerged along with a plethora of other materials modified to elicit similar effects [14.180]. In part, these new materials can be viewed as demonstrating either an extension of the degree of protection provided to them by the inclusion of an antimicrobial agent or as the transfer of the properties of external treatments into the material itself. The inclusion of the antimicrobial agent is now not simply intended to

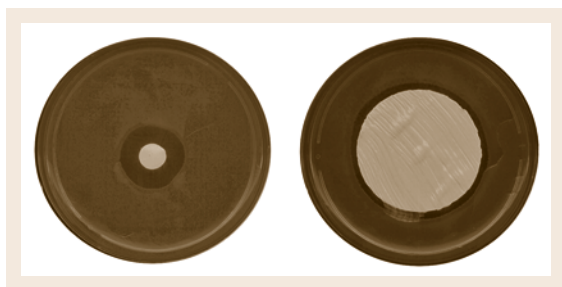


Fig. 14.22 Zone diffusion assay using liquid paint (*left*) and a coated filter paper (*right*). In both cases only an in-can preservative is present

protect the material from deterioration but to exert a biological effect either to the immediate surrounding of that material or to items that come into contact with it. These effects may range from the prevention of growth of undesirable microbial populations on a material to which they pose no physical, chemical or biological threat, (e.g., the proliferation for bacterial species such as *Listeria monocytogenes* on surfaces in a cook/chill production unit) to the immediate destruction of individual microbial cells as they come into close association with its surface (possibly without even coming into direct physical contact). In all cases the effect is external to the material and is not merely present to protect either the material or the article/surface itself. In this context, we are now dealing with treated articles [14.181]. Coatings which impart such properties on the surfaces to which they are applied can be considered to be transforming technologies. They transform objects/surfaces into treated articles. For example, a door handle coated with a powder coating which claims to have antimicrobial properties has transformed that door handle into a treated article and the testing technology needs to be able to provide data that is consistent with the claim made.

As mentioned above, there are several methods in use around the world which are employed to examine the effect of microorganisms on coated surfaces and measure the performance of additives used to protect them from microbial spoilage (mainly fungi and algae). A number of examples are given in Table 14.12. However, there are no formal tests which are intended to measure the *hygienic* effects of antimicrobial coatings although in some cases (e.g., inhibition of fungal growth), certain tests described in Table 14.12 could be employed for that purpose. A number of test methods do exist for other treated articles (e.g., nonporous polymeric materials see Table 14.13) and some of these may again prove appropriate for coated surfaces. These

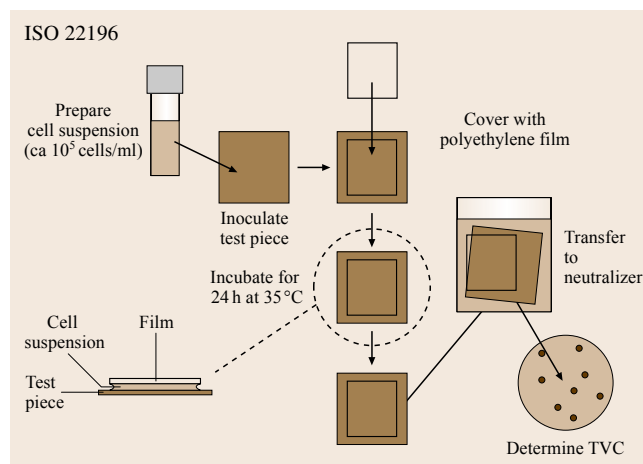


Fig. 14.23 Schematic representation of ISO 22196

methods predominantly examine the effects of such articles against bacteria but, again, these could be modified to suit other types of microorganism (e.g., yeasts and fungal spores). Although no standard methods yet exist for the determination of virucidal activity on surfaces, a test based on JIS Z 2801: 2000 has been described.

Many bacterial test assays rely on the production of growth on nutrient media to visualize their effect. Zone diffusion assays are commonly employed to investigate antibacterial agents such as antibiotics [14.182]. Their use for examining antibacterial coatings could be confusing, however, as in some systems it would be difficult to separate the residual effect of the in-can preservative from true antibacterial activity (Fig. 14.22, [14.170]). These methods also do not generate the truly quantitative data which will be required for the support of claims for treated articles.

Antibacterial activity of hygienic surfaces tends to fall into two distinct categories.

1. Surfaces which are bactericidal (i.e., a material which results in a significant reduction in bacterial numbers following a specific contact time).
2. Surfaces which are bacteriostatic (i.e., a material on which a small bacterial population did not exhibit significant growth during exposure).

A number of test protocols have been described (e.g. [14.178]) which are based on the Japanese Industrial Standard JIS Z 2801: 2000 [14.183] (Fig. 14.23). In these methods, a bacterial cell suspension is held in intimate contact with a coated surface using a sterile

Table 14.13 Methods used to examine the antimicrobial activity of nonporous surfaces

Reference	Title	Description
JIS Z 2801: 2000	Antimicrobial products – Test for antibacterial activity and efficacy	The surface of replicate sample (3 for each treatment and 6 for the blank reference material – usually 50 mm × 50 mm) are inoculated with a suspension of either <i>E. coli</i> or <i>Staph aureus</i> in a highly diluted nutrient broth. The cell suspension is then held in intimate contact with the surface by the use of a sterile polyethylene film (usually 40 mm × 40 mm) for 24 h at 35 °C under humid conditions. The size of the population on the treated surface is then compared with the size on the control surface both prior to and after incubation. A neutralizer for certain biocide types is employed. Antibacterial activity is certified if the difference between the log ₁₀ of the population on the treated sample and that on the control surface is > 2
ISO 22196	Plastics – Measurement of antibacterial activity on plastics surfaces	This is the current New Work Proposal at ISO created from JIS Z 2801 by the SIAA of Japan. Modification and validation is in progress in collaboration with the IBRG. Some changes are expected
XP G 39-010	Propriétés des étoffes – Étoffes et surfaces polymériques à propriétés antibactériennes	Four replicate samples of test material are placed in contact with an agar plate that has been inoculated with a specified volume of a known cell suspension of either <i>Staph aureus</i> and <i>K pneumoniae</i> using a 200 g weight for 1 min. The samples are then removed. Duplicate samples are analysed for the number of viable bacteria both before and after incubation under humid conditions at 37 °C for 24 h. A neutralizer is employed during cell recovery
ASTM E2180-07	Standard test method for determining the activity of incorporated antimicrobial agent(s) in polymeric or hydrophobic materials.	Replicate (3) samples of material are inoculated with cells of either <i>Staph aureus</i> or <i>K pneumoniae</i> suspended in molten semi-solid isotonic saline/agar. This attempts for form an <i>artificial biofilm</i> which holds the suspension in intimate contact with the test surface of inherently hydrophobic materials. Samples are then incubated at a temperature similar to that intended for the final use for a specified period (usually 24 h) under humid conditions. The size of the viable bacterial populations on the control and treated surfaces is then determined using total viable count. Any effect is recorded using percent reduction calculated from the geometric means of the data. A neutralizer may be employed and sonication is used to separate the <i>biofilm</i> from the test surfaces and suspend the agar gel. Subsequent imprinting of the test surface onto solid nutrient media can be performed to look for the presence of adherent viable cells.
ASTM E2149-10	Standard test method for determining the antimicrobial activity of immobilized antimicrobial agents under dynamic contact conditions.	Dynamic shake flask test. Test material is suspended in a buffer solution containing a known number of cells of <i>Klebsiella pneumoniae</i> and agitated. Efficacy is determined by comparing the size of the population before and after a specified contact time.

cover (e.g., either a membrane filter, flexible polypropylene film or a glass microscope cover slip) under humid conditions. After a set contact time, the size of the residual bacterial population is compared with an appropriate control coating using standard microbiological enumeration techniques. ASTM 2180-07 has also been modified to examine such coated surfaces. These test protocols can examine both bactericidal and bacteriostatic performance.

When considering the generation of efficacy test data, it is important to note that the protocols described above rely on the presence of free water to function. It is critical therefore, to interpret the data generated with care as just because an effect is seen during testing it does not necessarily follow that activity would be seen in practice. For example, if the activity of a coating was only exhibited when moisture was present (e.g., due to the presence of a water soluble active ingredient such

as silver ions or triclosan), activity would be detected in the test. If however, the coating was used in dry conditions, it is unlikely that an effect of the same scale would be exhibited and some microbial cells might remain viable on the surface (although this would probably be for a limited period only for many species [14.184]). Clearly under some circumstances (e.g., medical applications) cross-infection could still occur [14.185] despite the presence of an antimicrobial agent intended to prevent it. In this context the relationship between the environment in which the coating will be employed and the conditions under which supporting data were generated become critical factors in providing evidence of efficacy in use.

Similarly, the rate of kill would be important in many circumstances. In the control of cross-infection in clinical situations, surfaces which come into frequent contact with medical staff and patients (e.g., door furniture, bed

frames etc.) may need to be able to deactivate microbial cells very rapidly to provide a useful function. In this context, the contact time becomes a critical factor and tests in which a 24 h contact interval is employed may provide data which provides no useful information relating to efficacy in use. A slower rate of kill might be appropriate, however, to complement hygienic control on walls, flooring and difficult-to-access areas.

Although in many circumstances free water is not present, relatively few methods have been described which can simulate such conditions. Work has been published which examines the interaction of bacteria with polymeric coatings over time by spraying them onto surfaces both with and without the presence of soiling

agents and holding them under differing environmental conditions. Direct vital staining and epifluorescent microscopy was employed to measure the effects [14.186]. Modifications to ISO 22196 (JIS Z 2801) have been described [14.187] which expose the inoculum to a relatively low relative humidity (65%) and measure survival at a number of intervals thereby simulating the effect on bacteria contained in an aqueous deposit coming into contact with the coating and then drying out. A number of methods are also under development in which the inoculum is presented with minimal moisture, but more work is still required before the range of effects claimed for hygienic surfaces can be investigated in a scientifically sound manner.

14.6 Reference Organisms

Methods for the determination of materials performance often require the application of test organisms. For instance, DIN EN 113 describes a test method for determining the protective effectiveness against wood-destroying basidiomycetes using a set of basidiomycetes as test strains. ISO 16869 is a method for the assessment of the effectiveness of fungistatic compounds in plastic formulations where fungal test strains are applied as spore suspensions. ISO 14852 comprises the determination of the ultimate aerobic biodegradability of plastic materials in an aqueous medium. Sludge from a sewage plant is used to inoculate the test, so all organisms inhabiting the sludge can be referred to as test strains.

For comparability of test results, the use of identical test strains is an inevitable prerequisite. These strains should therefore be specified as reference organisms.

Attempts to verify the identity of prokaryotic or eukaryotic test strains in pure culture or in an environmental sample have traditionally been performed by plating dilutions onto certain standard growth media and by assessing certain physiological, morphological and/or chemotaxonomic traits after culturing.

Only recently, through the application of molecular methods such as the polymerase chain reaction (PCR) and sequence analysis, researchers are now in a position to determine genotypic differences of phenotypic similar organisms.

As molecular methods are especially valuable for fast and reliable discrimination and identification of (micro-)organisms, this chapter gives emphasis to

methods for genomic characterization of strains, species and microbial communities.

14.6.1 Chemical and Physiological Characterization

The chemical composition or the physiological potential of organisms is often used for characterizing strains and species and even for microbial communities. Methods such as gas chromatography, thin layer chromatography, high performance liquid chromatography, and various forms of spectroscopy are employed.

This paragraph will describe two techniques which are widely used for the characterization of strains and microbial communities.

Fatty Acid Analysis

Bacteria and fungi possess a cytoplasmic membrane as a component of their cell envelope, the composition of which is approximately 50% lipid. The membrane lipids are a diverse group of molecules which are frequently used as markers for the identification and classification of microorganisms. In particular, the amphipathic lipids (possessing hydrophilic and hydrophobic regions) have great relevance to microbial systematics.

Usually, in this approach fatty acids are released from the cells, methylated to increase volatility and subjected to gas chromatography. The fatty acid profile of an unknown sample can be compared to computer databases for identification.

Although phospholipids are the most widely known polar lipids, the cytoplasmic membrane may also con-

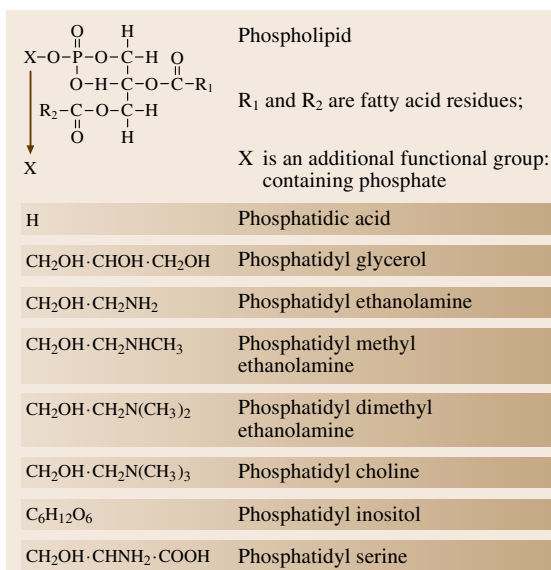


Fig. 14.24 Generalized structure of frequently encountered diacyl phospholipids (after [14.173])

tain glycolipids, polar isoprenoids, and aminolipids. The most commonly encountered lipids consist of a glycerol backbone to which either acyl groups (ester linkage) or alkyl groups (ether linkage) are attached. Polyunsaturated fatty acids generally do not occur in prokaryotes, though they do have significance in fungal characterization [14.173] Fig. 14.24.

Phospholipid fatty acid analysis has also been used as a culture-independent method to characterize microbial communities, but an important limitation of this method has to be considered [14.187]: In general, in bacteria and fungi, the types of fatty acids vary with growth conditions and environmental stresses. Consequently, if cells are cultured prior to fatty acid analysis, this has to be done under standard conditions. If microbial communities are characterized without prior cultivation, phospholipid profiles can be correlated with the presence of some groups of organisms, but they may not necessarily be unique to only those groups under all conditions, thus giving rise to false community profiles.

Carbon Utilization Profiles – BIOLOG, BIOLOG MicroLog

One of the more widely used culture-dependent methods of analyzing and characterizing microorganisms (bacteria and fungi) is the commercially available BIOLOG identification system. This system is also used extensively for the analysis of microbial

communities in natural environments [14.188]. The organism/microbial community of interest is inoculated into a specialized microtiter tray with 95 different carbon sources. Utilization of each substrate is detected by the reduction of a tetrazolium dye, which forms an irreversible, highly colored formazan when reduced. The microtiter trays are read with a conventional plate reader, and the results are compared with a computer database, allowing identification.

As pointed out by Hill et al. [14.171], there are a number of considerations in the use of this method for community analysis. Beside the crucial step of the requirement of a standardized inoculum of *vital* cells, it has to be kept in mind that the color formation in each well is not solely a function of the number of organisms present in the sample (as is often assumed). Some strains may use a certain substrate more efficiently than others, thereby appearing to dominate the sample. In addition, the substrates found in commercially available BIOLOG microtiter trays are not necessarily ecologically relevant. Therefore, the method still suffers from similar bias problems as encountered with culture plating methods and future work with ecologically meaningful substrates should render it more suitable for the characterization of microbial communities.

14.6.2 Genomic Characterization

A major area of research in microbial characterization has been the development of molecular methods for genotyping organisms. Genotypic methods can be highly specific and sensitive and are largely independent of the physiological or growth-state of the organism. Especially the development of the PCR and PCR-based techniques provides sensitive and specific tools to detect and characterize microorganisms in the absence of growth.

Polymerase Chain Reaction

The polymerase chain reaction (PCR) is a molecular method for amplifying DNA fragments. Using PCR and PCR-based techniques, rapid detection and identification of micro- and higher organisms in laboratory cultures as well as in environmental samples is possible.

The DNA fragment to be amplified is determined by the selection of appropriate primers. Primers are short, artificial DNA strands of approximately 20–30 nucleotides, that exactly match the beginning and end of the DNA fragment to be amplified. This means that the exact DNA sequence must already be known. Primers

can be constructed in the lab or purchased from commercial suppliers.

There are three basic steps in PCR (Fig. 14.25). First, the target genetic material must be denatured – that is, the strands of its helix must be unwound and separated – by heating to 90–96°C. The second step is hybridization or annealing, in which the primers bind to their complementary bases on the now single-stranded DNA. The third is DNA synthesis by a polymerase. Starting from the primer, the polymerase can read a template strand and match it with complementary nucleotides very quickly. The result is two new helices in place of the first, each composed of one of the original strands plus its newly assembled complementary strand. A cyclic repetition of denaturation, primer annealing and DNA synthesis results in the exponential amplification of the desired DNA fragment.

The development of group-specific or species-specific primers enables sensitive detection and rapid identification of selected organisms in culture and environmental samples.

ARDRA – Amplified Ribosomal DNA Restriction Analysis

In the ARDRA technology PCR-amplified ribosomal RNA (rRNA) genes are digested with restriction enzymes (enzymes that cut double stranded DNA at enzyme-specific recognition sites, Fig. 14.26) and the resulting fragments are separated electrophoretically. Comparison of patterns to those obtained from a database allows assignment of isolates to species, whereby the resolving power is depending on the restriction enzymes chosen.

This method, which can be used to screen large numbers of isolates rapidly, has gained widespread application in the detection and identification of fungi in laboratory cultures and natural substrates.

Ribosomal DNA is the molecule under investigation, because it is particularly well suited to the development of taxon-specific primers due to interspersed regions of relatively conserved (18S rDNA-, 5.8S rDNA-, 28S rDNA-gene) and nonconserved (ITS I, ITS II) sequences and a large copy number per genome [14.172, 174, 175]. Universal primers, e.g., ITS1 and ITS 4 [14.189], or primer pairs specific for higher fungi (ITS1-F/ITS4-B) or basidiomycetes (ITS1/ITS4-B) [14.190], are used for the amplification of rRNA genes and inserted ITS sequences. The PCR fragments are subjected to restriction digestion, and depending on the position of restriction sites, bands of different number and sizes appear af-

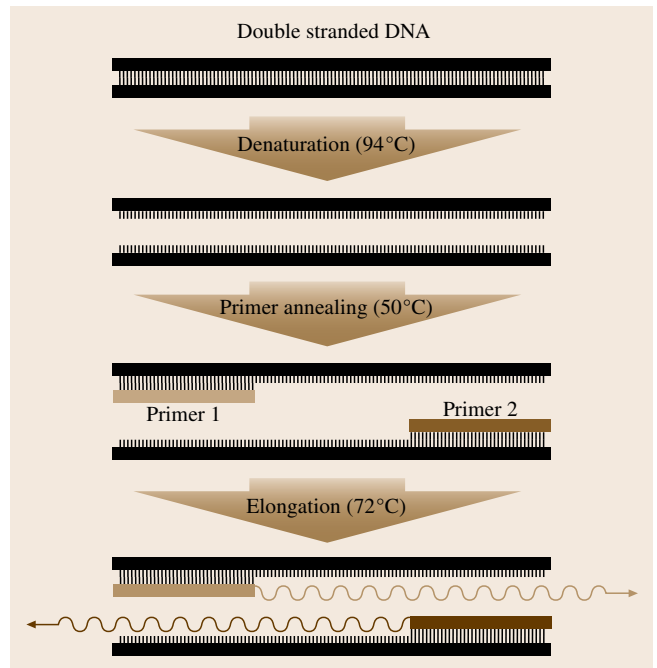


Fig. 14.25 The three basic steps in PCR

ter gel electrophoresis (Fig. 14.27). The majority of ARDRA profiles generated by any given enzyme are unique at the species level, but restriction digestion with *AluI*, *HpaII*, *HaeIII* and *TaqI* proved to be especially useful for the discrimination of decay fungi [14.175].

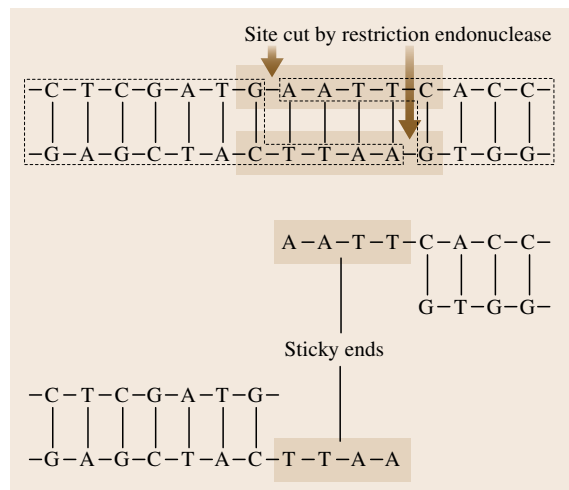


Fig. 14.26 Scheme for restriction enzyme activity. Restriction enzymes recognize a specific sequence of nucleotides and produce a double stranded DNA cut

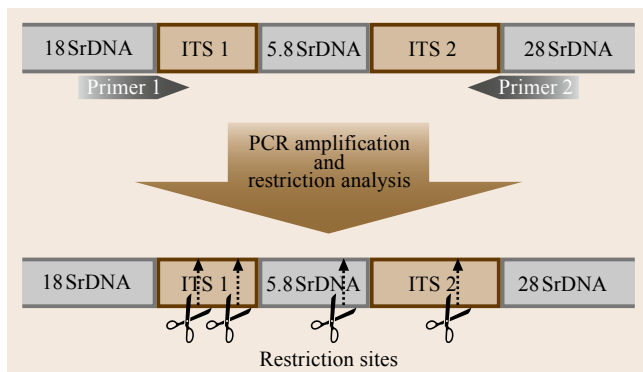


Fig. 14.27 Scheme for amplified ribosomal DNA restriction analysis (ARDRA)

RAPD – Random Amplified Polymorphic DNA (Arbitrarily-Primed PCR)

Random amplified polymorphic DNA (RAPD) or arbitrarily primed PCR (AP-PCR) is a method that creates genomic arrays of DNA fragments (fingerprints) from species of which too little sequence information is available in order to design specific primers. It is used to identify strain-specific variations in (chromosomal) DNA [14.191] (Fig. 14.28).

Arbitrarily chosen primers are used to prime DNA synthesis from genomic sites which they fortuitously match or almost match, which results in the amplification of intervening DNA. Typically, PCR is performed under conditions of low stringency. The number and position of the primer binding sites will vary amongst different strains and consequently will lead to different strain-specific fingerprints. As a prerequisite, the primers must be within reasonable distance of each other, as the DNA polymerase must synthesize a product long enough so that it contains the site for annealing to the other primer. How soon the polymerase falls off the template depends on the purity and the constituents (GC-content) of the template itself.

BRENDA – Bacterial Restriction Endonuclease Nucleic Acid Digest Analysis and RFLP – Restriction Fragment Length Polymorphism

The BRENDA approach is mainly used for the characterization of prokaryotic, i. e., bacterial strains. Chromosomal DNA is digested with diverse restriction endonucleases and the DNA fragments are separated electrophoretically. Depending on the genome size and the enzymes used, the frequencies of restriction sites differ between strains, resulting in different fragment

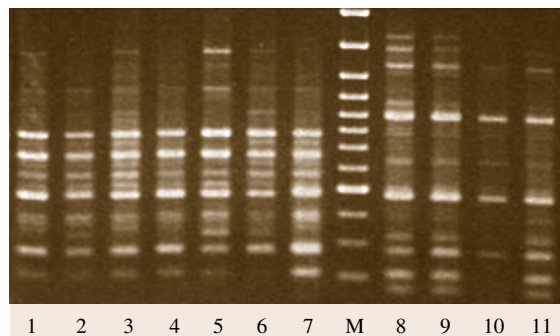


Fig. 14.28 RAPD patterns of eleven different strains of the wood degrading basidiomycete *Coniophora puteana* obtained with the same random primer. All strains were originally considered to be identical and used in the European Standard EN113. M: molecular size marker (2.0, 1.5, 1.2, 1.0, 0.9, 0.8, 0.7, 0.6, 0.5, 0.4, 0.3, 0.2, 0.1 kb) (after [14.191])

profiles. Usually, the profiles are highly complex and therefore difficult to analyze.

The number of detectable bands is reduced in the RFLP approach. Chromosomal DNA is submitted to a restriction digest and gel electrophoresis. Then, the DNA fragments are transferred and immobilized on a solid support such as a cellulose or nylon membrane. A target nucleotide sequence can be detected by a hybridization process, whereby a labelled DNA fragment (DNA probe) binds to the complementary target gene on the membrane. The presence or absence of the restriction endonuclease sites in two strains under investigation will cause differences in the length of the fragments that contain the targeted gene (Fig. 14.29). This technique, like the BRENDA approach, enables discrimination between strains [14.173].

Various systems for labelling and detection of nucleic acid probes are available nowadays. Radio-labelled probes are visualized using autoradiography, nonradioactive systems are based on the enzymatic, photochemical, or chemical incorporation of a reporter group (e.g., fluorescent dyes, marker enzymes coupled to chemiluminescence detection or to silver enhancement) which can be detected with high sensitivity by optical, luminescence, fluorescence, or metal-precipitating detection systems. For details about synthesis, labelling and detection of DNA probes (Hames and Higgings [14.192]).

As rRNA genes have some highly conserved regions (across species) which permits to use rRNA from one organism, e.g., *E. coli*, as a universal probe, these genes

are regularly used as target genes. This so-called *ribotyping* which can be regarded as a special kind of RFLP, examines differences in the restriction pattern of rRNA genes between strains. Usually, the pattern is more complex than observed after RFLP targeting other genes, because rRNA genes are present in multiple copies per genome. The resolving power of ribotyping is dependent on the species studied and the restriction enzyme chosen.

Ribotyping has been facilitated by the availability of commercial, fully automated systems such as the Ribo-Printer Microbial Characterization system (Qualicon Inc., Wilmington, DE). This molecular workstation performs the restriction digest (using *EcoRI* or other restriction enzymes) of the chromosomal DNA, separates the restriction fragments by gel electrophoresis, and simultaneously blots the DNA fragments to a membrane. DNA fragments are hybridized to a bacterial probe that is based on the conserved regions of the genes for the ribosomal DNA operon. Each fingerprint is stored in a database, so it can be accessed for future comparisons and identifications. The Ribo-Printer system is frequently used for quality control and authentication.

Gene probes addressing genes responsible for particular physiological activities (e.g., nitrification, nitrogen fixation, virulence associated genes etc.) are useful to characterize a subset of microorganisms or a microbial community, where the taxonomy or species composition of the community are of minor interest.

FISH – Fluorescence in situ Hybridization

Fluorescence in situ hybridization has been used primarily with prokaryotic communities. It allows the direct identification and quantification of specific or general taxonomic groups of microorganisms within their natural microhabitat. As whole cells are hybridized, artefacts arising from bias in DNA extraction, PCR amplification and cloning are avoided. FISH is a powerful tool that can be used not only for studying individuals within a population, but also has the potential to study population dynamics and tracking microorganisms released into the environment.

The composition of complex microbial communities is most often analyzed by rRNA-targeted nucleic acid probes: Whole cells are fixed, their 16S or 23S rRNA is hybridized under stringent conditions with fluorescently labelled taxon specific oligonucleotide probes. The labelled cells are viewed by fluorescence microscopy. Scanning confocal laser microscopy (SCLM) surpasses epifluorescence microscopy in sen-

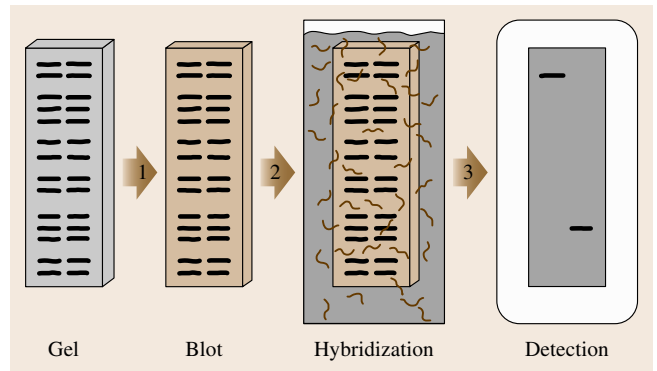


Fig. 14.29 Scheme for the RFLP approach. (1) Digested DNA of two strains under investigation is separated by gel electrophoresis, denatured and transferred (blotted) onto a nylon or cellulose membrane. (2) The blotted DNA is incubated with a labelled DNA probe which binds to the complementary target gene on the membrane. (3) After removal of unspecifically bound DNA probe, the targeted gene can be detected, e.g. by autoradiography (courtesy of S. Schwibbert)

sitivity and allows to assess the distribution of several taxonomic groups simultaneously.

The large amount of rRNA in most cells and the availability of huge rRNA databases for comparative sequence analysis are the major advantages of rRNA targeted nucleic acid probes. With the ARB software package, rRNA oligonucleotide probes can be designed in a straightforward fashion [14.193]. Specific organisms or groups can be selected and parameters such as probe length, G+C content, and target region can be defined and the ARB probe design tool will then search for potential target sites against the background of the full sequence data set. As the ARB database is frequently updated, old probes should not be used without re-checking the database.

Microbial groups without a common diagnostic target site should be detected with more than one probe. For increased sensitivity, as for the detection and tracking of functional genes, the application of horseradish peroxidase-labelled oligonucleotide probes is advisable. Oligonucleotide probes labelled with a variety of fluorochromes can be purchased commercially.

DGGE –

Denaturing Gradient Gel Electrophoresis

Denaturing gradient gel electrophoresis is widely used in recent years for profiling microbial consortia. This method is particularly useful when temporal and spatial dynamics of the population structure are analyzed. It al-

lows the separation of DNA fragments of the same size but different nucleotide sequences by their denaturing profiles. For the characterization of microbial communities, ribosomal RNA genes are obtained directly from a bulk DNA sample by PCR and subjected to DGGE. The resulting banding pattern serves as a fingerprint of the microbial community.

During electrophoresis in an increasing gradient of denaturant (e.g. urea) or in an increasing temperature gradient (TGGE – temperature gradient gel electrophoresis), DNA molecules remain double-stranded until they reach the denaturant concentration or temperature that melts the molecules. Melting DNA branches and thus displays reduced mobility in the gel. As the melting behavior is mainly determined by the nucleotide sequence, theoretically any rDNA gene found

in the mixed template DNA could be specifically amplified and resolved on a DGGE gel. Following DGGE electrophoresis, rDNA fragments can be sequenced and analyzed for similarity to other known sequences in public-domain databases. It has to be kept in mind that one band often does not represent only one species, so this approach is better suited for less complex communities.

This technique also might be limited by Dann extraction efficiency, which differs among microorganisms and type of environment (soil, mud, water). Amplification bias has also been shown to occur for templates that differ substantially in abundance, with preferential amplification of more abundant sequences [14.194]. For a detailed review of possible sources of amplification bias, see [14.195].

References

- 14.1 H.W. Rossmore (Ed.): *Handbook of Biocide and Preservative Use* (Blackie, London 1995)
- 14.2 A.D. Russell, W.B. Hugo, G.A.J. Ayliffe (Eds.): *Principles and Practice of Disinfection, Preservation and Sterilization* (Blackwell Science, Oxford 1999) pp.124–144
- 14.3 W. Paulus: *Directory of Microbicides for the Protection of Materials: A Handbook* (Kluwer, Dordrecht 2005)
- 14.4 J.S. Webb, M. Nixon, I.M. Eastwood, M. Greenhalgh, G.D. Robson, P.S. Handley: Fungal colonization and biodeterioration of plasticised PVC, *Appl. Environ. Microbiol.* **66**, 3194–3200 (2000)
- 14.5 D.J. Knight, M. Coole (Eds.): *The Biocide Business: Regulation, Safety and Applications* (Wiley-VCH, Weinheim 2002)
- 14.6 European Community: January 2006 Version of the Manual of Decisions For Implementation of Directive 98/8/EC Concerning the Placing on the Market of Biocidal Products (2006)
- 14.7 S.D. Worley, Y. Chen: Biocidal polystyrene hydan-toin particles, US Patent 6548054 (2001)
- 14.8 D. Grosser: *Pflanzliche und tierische Bau- und Werkholz-Schädlinge* (DRW, Leinfelden 1985), (in German)
- 14.9 J.G. Wilkinson: The deterioration of wood. In: *Industrial Timber Preservation*, The Rentokil Library, ed. by J.G. Wilkinson (Associated Business, London 1979) pp. 87–125, Chap. 5
- 14.10 S. Anagnost: Light microscopic diagnosis of wood decay, *IAWA Journal* **19**(2), 141–167 (1998)
- 14.11 J.E. Winandy, J.J. Morrell: Relationship between incipient decay, strength and chemical composition of Douglas Fir heartwood, *Wood Fibre Sci.* **25**(3), 278–288 (1993)
- 14.12 J. Bodig: The process of NDE research for wood and wood composites, e-J. Nondestr. Test. **6**(3) (2001), www.ndt.net (last accessed March 2001)
- 14.13 R. Ross, R.F. Pellerin: *Nondestructive Testing for Assessing Wood Members in Structures: A Review*, Gen. Tech. Rep., FPL-GTR-70 (rev.) (US Department of Agriculture, Forest Service, Forest Products Laboratory, Madison 1994) p. 40
- 14.14 M. Grinda: *A Field Study on the Suitability of the European Lap-Joint Test*, IRGWP 01-20239 (IRG, Stockholm 2001)
- 14.15 T. Nilsson, M.L. Edlund: *Laboratory Versus Field Tests for Evaluating Wood Preservatives: A Scientific View*, IRGWP 00-20205 (IRG, Stockholm 2000)
- 14.16 CEN/TR 14723: *Durability of Wood and Wood-based Products – Field and Accelerated Conditioning Tests (FACT) for Wood Preservative out of Ground Contact* (CEN European Committee for Standardization, Brussels 2003)
- 14.17 L. Machek, H. Miltitz, R. Sierra-Alvarez: The use of an acoustic technique to detect wood decay in laboratory soil-bed tests, *Wood Sci. Technol.* **34**, 467–472 (2001)
- 14.18 S.C. Jones, H.N. Howell: Wood-destroying insects. In: *Handbook of Household and Structural Insect Pests*, ed. by R.E. Gold, S.C. Jones (Entomological Soc. America, Lanham 2000) pp. 99–127
- 14.19 R. Schmidt, S. Göller, H. Hertel: Computerized detection feeding sounds from wood boring beetle larvae, *Material und Organismen* **29**, 295–304 (1995)
- 14.20 R.A. Haack, T.M. Poland, T.R. Petrice, C. Smith, D. Treece, G. Allgood: Acoustic detection of *Anoplophora glabripennis* and native woodbor-

- ers (Coleoptera: *Cerambycidae*), Gen. Tech. Rep. NE **285**, 74–75 (2001)
- 14.21 S.E. Brooks, F.M. Oi, P.G. Koehler: Ability of canine termite detectors to locate live termites and discriminate them from non-termite material, *J. Econ. Entomol.* **96**, 1259–1266 (2003)
- 14.22 J.-D. Gu: Microbiological deterioration and degradation of synthetic polymeric materials: Recent research advances, *Int. Biodeterior. Biodegrad.* **52**, 69–91 (2003)
- 14.23 W.H. Stahl, H. Pessen: Funginertness of internally plasticized polymers, *Mod. Plast.* **54**, 111–112 (1954)
- 14.24 S. Berk, H. Ebert, L. Teitell: Utilization of plasticizers and related organic components by fungi, *Ind. Eng. Chem.* **49**(7), 1115–1123 (1957)
- 14.25 M. Pantke: Test methods for evaluation of susceptibility of plasticised PVC and its components to microbial attacking. In: *Biodeterioration Investigation Techniques*, ed. by H. Waters (Applied Science, London 1977) pp. 51–76
- 14.26 V.T. Breslin: Degradation of starch–plastic composites in a municipal solid waste landfill, *J. Environ. Polym.* **1**(2), 127–141 (1993)
- 14.27 N.S. Allen, M. Edge, T.S. Jewitt, C.V. Horie: Initiation of the degradation of cellulose triacetate base motion picture film, *J. Photogr. Sci.* **38**(2), 54–59 (1990)
- 14.28 W.G. Glasser, B.K. McCartney, G. Samaranyake: Cellulose derivatives with low degree of substitution: 3. The biodegradability of cellulose esters using a simple enzyme assay, *Biotechnol. Prog.* **10**, 214–219 (1994)
- 14.29 Y. Tokiwa, T. Suzuki: Hydrolysis of polyesters by lipase, *Nature* **270**, 76–78 (1977)
- 14.30 E. Marten, R.-J. Müller, W.-D. Deckwer: Studies on the enzymatic hydrolysis of polyesters: I. Low molecular mass model esters and aliphatic polyesters, *Polym. Degrad. Stab.* **80**(3), 485–501 (2003)
- 14.31 E. Marten, R.-J. Müller, W.-D. Deckwer: Studies on the enzymatic hydrolysis of polyesters: II. Aliphatic–aromatic copolyesters, *Polym. Degrad. Stab.* **88**(3), 371–381 (2005)
- 14.32 A. Linos, M.M. Berekaa, R. Reichelt, U. Keller, J. Schmitt, H.-C. Flemming, R.M. Kroppenstedt, A. Steinbüchel: Biodegradation of *cis*-1,4-polyisoprene rubbers by distinct actinomycetes: Microbial strategies and detailed surface analysis, *Appl. Environ. Microbiol.* **66**(4), 1639–1645 (2000)
- 14.33 U. Pagga: Testing biodegradability with standardized methods, *Chemosphere* **35**(12), 2953–2972 (1997)
- 14.34 K.J. Seal, H.O.W. Eggins: The biodeterioration of materials. In: *Essays in Applied Microbiology*, ed. by J.R. Norris, M.H. Richmond (Wiley, New York 1981)
- 14.35 M. Pantke: Test methods for evaluation of susceptibility of plasticised PVC and its components to microbial attack. In: *Biodeterioration Investigation Techniques*, ed. by H. Waters (Applied Science, London 1977) pp. 51–76
- 14.36 M. Itävaara, M. Vikman: An overview of methods for biodegradability testing of biopolymers and packaging materials, *J. Environ. Polym. Degrad.* **4**(1), 29–36 (1996)
- 14.37 M. Pantke, K.J. Seal: An interlaboratory investigation into the biodeterioration testing of plastics, with special reference to polyurethanes; Part 2: Soil burial experiments, *Mater. Org.* **25**(2), 88–98 (1990)
- 14.38 U. Pagga, D.B. Beimborn, J. Boelens, B. DeWilde: Determination of the biodegradability of polymeric material in a laboratory controlled composting test, *Chemosphere* **31**(11/12), 4475–4487 (1995)
- 14.39 M. Tosin, F. Degli Innocenti, C. Bastioli: Effect of the composting substrate on biodegradation of solid materials under controlled composting, *J. Cond. Environ. Polym. Degrad.* **4**(1), 55–63 (1996)
- 14.40 A. Ohtaki, N. Sato, K. Nakasaki: Biodegradation of poly(ϵ -caprolactone) under controlled composting conditions, *Polym. Degrad. Stab.* **61**(3), 499–505 (1998)
- 14.41 J. Tuominen, J. Kylmä, A. Kapanen, O. Venelampi, M. Itävaara, J. Seppälä: Biodegradation of lactic acid based polymers under controlled composting conditions and evaluation of the ecotoxicological impact, *Biomacromolecules* **3**(3), 445–455 (2002)
- 14.42 F. Degli Innocenti, M. Tosin, C. Bastioli: Evaluation of the biodegradation of starch and cellulose under controlled composting conditions, *J. Environ. Polym. Degrad.* **6**(4), 197–202 (1998)
- 14.43 S.M. McCartin, B. Press, D. Eberiel, S.P. McCarthy: Simulated landfill study on the accelerated biodegradability of plastics materials, *Am. Chem. Soc. Polym. Prepr.* **31**(1), 439–440 (1990)
- 14.44 G.P. Smith, B. Press, D. Eberiel, S.P. McCarthy, R.A. Gross, D.L. Kaplan: An accelerated in laboratory test to evaluate the degradation of plastics in landfill environments, *Polym. Mater. Sci. Eng.* **63**, 862–866 (1990)
- 14.45 S.P. McCarthy, M. Gada, G.P. Smith, V. Tolland, B. Press, D. Eberiel, C. Bruell, R.A. Gross: The accelerated biodegradability of plastic materials in simulated compost and landfill environments, *Annu. Tech. Conf. Soc. Plast. Eng.* **50**(1), 816–818 (1992)
- 14.46 P. Püchner, W.R. Müller, D. Bartke: Assessing the biodegradation potential of polymers in screening- and long-term test systems, *J. Environ. Polym. Degrad.* **3**(3), 133–143 (1995)
- 14.47 T. Walter, J. Augusta, R.-J. Müller, H. Widdecke, J. Klein: Enzymatic degradation of a model polyester by lipase, *Enzym. Microbiol. Technol.* **17**, 218–224 (1995)
- 14.48 M. Vikman, M. Itävaara, K. Poutanen: Measurement of the biodegradation of starch based materials by enzymatic methods and composting, *J. Environ. Polym. Degrad.* **3**(1), 23–29 (1995)

- 14.49 Z. Gan, J.F. Fung, X. Jing, C. Wu, W.M. Kulicke: A novel laser light scattering study of enzymatic biodegradation of poly(caprolactone) nanoparticles, *Polymer* **40**(8), 1961–1967 (1999)
- 14.50 K. Welzel, R.-J. Müller, W.-D. Deckwer: Enzymatischer Abbau von Polyester-Nanopartikeln, *Chem. Ing. Tech.* **74**(10), 1496–1500 (2002), (in German)
- 14.51 E. Ikada: Electron microscope observation of biodegradation of polymers, *J. Environ. Polym. Degrad.* **7**(4), 197–201 (1999)
- 14.52 D. Abou-Zeid: Anaerobic biodegradation of natural and synthetic polyesters. Ph.D. Thesis (Technical University Braunschweig, Braunschweig 2001)
- 14.53 Y. Kikkawa, H. Abe, T. Iwata, Y. Inoue, Y. Doi: Crystal morphologies and enzymatic degradation of melt crystallized thin films of random copolyesters of (R) 3-hydroxybutyric acid with (R) 3-hydroxyalkanoic acids, *Polym. Degrad. Stabil.* **76**(3), 467–478 (2002)
- 14.54 B. Erlandsson, S. Karlsson, A.-C. Albertsson: The mode of action of corn starch and a prooxidant system in LDPE: influence of thermooxidation and UV irradiation on the molecular weight changes, *Polym. Degrad. Stabil.* **55**, 237–245 (1997)
- 14.55 V.T. Breslin: Degradation of starch plastic composites in a municipal solid waste landfill, *J. Environ. Polym. Degrad.* **1**(2), 127–141 (1993)
- 14.56 H. Tsuji, K. Suzuyoshi: Environmental degradation of biodegradable polyesters 1. Poly(ϵ -caprolactone), poly[(R)-3-hydroxybutyrate], and poly(L-lactide) films in controlled static seawater, *Polym. Degrad. Stabil.* **75**(2), 347–355 (2002)
- 14.57 U. Witt, T. Einig, M. Yamamoto, I. Kleeberg, W.-D. Deckwer, R.-J. Müller: Biodegradation of aliphatic-aromatic copolyesters: Evaluation of the final biodegradability and ecotoxicological impact of degradation intermediates, *Chemosphere* **44**(2), 289–299 (2001)
- 14.58 J. Hoffmann, I. Reznicekova, S. Vanöková, J. Kupec: Manometric determination of biological degradability of substances poorly soluble in aqueous environments, *Int. Biodeterior. Biodegrad.* **39**(4), 327–332 (1997)
- 14.59 U. Pagga, A. Schäfer, R.-J. Müller, M. Pantke: Determination of the aerobic biodegradability of polymeric material in aquatic batch tests, *Chemosphere* **42**(3), 319–331 (2001)
- 14.60 A. Calmon, L. Dusserre Bresson, V. Bellon Maurel, P. Feuilloley, F. Silvestre: An automated test for measuring polymer biodegradation, *Chemosphere* **41**(5), 645–651 (2000)
- 14.61 W.R. Müller: Sauerstoff und Kohlendioxid gleichzeitig messen, *LaborPraxis Sept.*, 94–98 (1999), (in German)
- 14.62 R. Solaro, A. Corti, E. Chiellini: A new respirometric test simulating soil burial conditions for the evaluation of polymer biodegradation, *J. Environ. Polym. Degrad.* **5**(4), 203–208 (1998)
- 14.63 M. Itävaara, M. Vikman: A simple screening test for studying the biodegradability of insoluble polymers, *Chemosphere* **31**(11/12), 4359–4373 (1995)
- 14.64 K. Richterich, H. Berger, J. Steber: The 'two phase closed bottle test' a suitable method for the determination of 'ready biodegradability' of poorly soluble compounds, *Chemosphere* **37**(2), 319–326 (1998)
- 14.65 G. Bellina, M. Tosin, G. Floridi, F. Degli Innocenti: Activated vermiculite, a solid bed for testing biodegradability under composting conditions, *Polym. Degrad. Stabil.* **66**(1), 65–79 (1999)
- 14.66 G. Bellina, M. Tosin, F. Degli Innocenti: The test method of composting in vermiculite is unaffected by the priming effect, *Polym. Degrad. Stabil.* **69**, 113–120 (2000)
- 14.67 A.M. Buswell, H.F. Müller: Mechanism of methane fermentation, *Ind. Eng. Chem.* **44**(3), 550–552 (1952)
- 14.68 D.-M. Abou-Zeid, R.-J. Müller, W.-D. Deckwer: Degradation of natural and synthetic polyesters under anaerobic conditions, *J. Biotechnol.* **86**(2), 113–126 (2001)
- 14.69 D.-M. Abou-Zeid, R.-J. Müller, W.-D. Deckwer: Biodegradation of aliphatic homopolyesters and aliphatic-aromatic copolyesters by anaerobic microorganisms, *Biomacromolecules* **5**(5), 1687–1697 (2004)
- 14.70 S. Gartsier, M. Wallrabenstein, G. Stiene: Assessment of several test methods for the determination of the anaerobic biodegradability of polymers, *J. Environ. Polym. Degrad.* **6**(3), 159–173 (1998)
- 14.71 A. Reischwitz, E. Stoppok, K. Buchholz: Anaerobic degradation of poly(3-hydroxybutyrate) and poly(3-hydroxybutyrate-co-3-hydroxyvalerate), *Biodegradation* **8**, 313–319 (1998)
- 14.72 K. Budwill, P.M. Fedorak, W.J. Page: Anaerobic microbial degradation of poly(3-hydroxyalkanoates) with various terminal electron acceptors, *J. Environ. Polym. Degrad.* **4**(2), 91–102 (1996)
- 14.73 A.-C. Albertsson: Biodegradation of synthetic polymers II. A limited microbial conversion of ^{14}C in polyethylene to $^{14}\text{CO}_2$ by some soil fungi, *J. Appl. Polym. Sci.* **22**, 3419–3433 (1978)
- 14.74 M. Tuomela, A. Hatakka, S. Raikola, M. Vikman, M. Itävaara: Biodegradation of radiolabelled synthetic lignin (^{14}C DHP) and mechanical pulp in a compost environment, *Appl. Microbiol. Biotechnol.* **55**(4), 492–499 (2001)
- 14.75 H. Nishida, Y. Tokiwa: Distribution of poly(β -hydroxybutyrate) and poly(ϵ -caprolactone) aerobic degrading microorganisms in different environments, *J. Environ. Polym. Degrad.* **1**(3), 227–233 (1993)
- 14.76 J. Augusta, R.-J. Müller, H. Widdecke: A rapid evaluation plate test for the biodegradability of plastics, *Appl. Microbiol. Biotechnol.* **39**, 673–678 (1993)

- 14.77 Y. Tokiwa, T. Ando, T. Suzuki, T. Takeda: Biodegradation of synthetic polymers containing ester bonds, *Polym. Mater. Sci. Eng.* **62**, 988–992 (1990)
- 14.78 K.E. Jäger, A. Steinbüchel, D. Jendrossek: Substrate specificities of bacterial polyhydroxyalkanoate depolymerase and lipases: Bacterial lipases hydrolyze poly(T-hydroxyalkanoates), *Appl. Environ. Microbiol.* **61**(8), 3113–3118 (1995)
- 14.79 A. Calmon Decriaud, V. Bellon Maurel, F. Silvestre: Standard methods for testing the aerobic biodegradation of polymeric materials. Review and perspectives, *Adv. Polym. Sci.* **135**, 207–226 (1998)
- 14.80 H. Sawada: ISO standard activities in standardization of biodegradability of plastics development of test methods and definitions, *Polym. Degrad. Stabil.* **59**(1–3), 365–370 (1998)
- 14.81 M. Avella, E. Bonadies, E. Martuscelli, R. Rimedio: European current standardization for plastic packaging recoverable through composting and biodegradation, *Polym. Test.* **20**(5), 517–521 (2001)
- 14.82 F. Degli Innocenti, C. Bastioli: Definition of compostability criteria for packaging: Initiatives in Italy, *J. Environ. Polym. Degrad.* **5**(4), 183–189 (1997)
- 14.83 J.D. Gu, S. Coulter, D. Eberiel, S.P. McCarthy, R.A. Gross: A respirometric method to measure mineralization of polymeric materials in a matured compost environment, *J. Environ. Polym. Degrad.* **1**(4), 293–299 (1993)
- 14.84 A. Starnecker, M. Menner: Assessment of biodegradability of plastics under simulated composting conditions in a laboratory test system, *Int. Biodeterior. Biodegrad.* **37**, 85–92 (1996)
- 14.85 M. Van der Zee, J.H. Stoutjesdijk, H. Feil, J. Feijen: Relevance of aquatic biodegradation tests for predicting degradation of polymeric materials during biological solid waste treatment, *Chemosphere* **36**(3), 461–473 (1998)
- 14.86 U. Pagga: Compostable packaging materials test methods and limit values for biodegradation, *Appl. Microbiol. Biotechnol.* **51**(2), 125–133 (1999)
- 14.87 M. Itävaara, M. Vikman, O. Venelampi: Windrow composting of biodegradable packaging materials, *Compost Sci. Util.* **5**(2), 84–92 (1997)
- 14.88 M.H. Dang, F. Birchler, E. Wintermantel: Toxicity screening of biodegradable polymers II. Evaluation of cell culture test with medium extract, *J. Environ. Polym. Degrad.* **5**(1), 49–56 (1997)
- 14.89 F. Degli Innocenti, G. Bellia, M. Tosina, A. Kapanen, M. Itävaara: Detection of toxicity released by biodegradable plastics after composting in activated vermiculite, *Polym. Degrad. Stabil.* **73**(1), 101–106 (2001)
- 14.90 M. Day, K. Shaw, D. Cooney: Biodegradability: an assessment of commercial polymers according to the Canadian method for anaerobic conditions, *J. Environ. Polym. Degrad.* **2**, 121–127 (1994)
- 14.91 N.E. Sharabi, R. von Bartha: Testing of some assumptions about biodegradability in soil as measured by carbon dioxide evolution, *Appl. Environ. Microbiol.* **59**(4), 1201–1205 (1993)
- 14.92 Y. Yakabe, N. Kazuo, T. Hara, Y. Fujin: Factors affecting the biodegradability of biodegradable polyesters in soil, *Chemosphere* **25**(12), 1879–1888 (1992)
- 14.93 A. Calmon, S. Guillaume, V. Bellon Maurel, P. Feuilloley, F. Silvestre: Evaluation of material biodegradability in real conditions. Development of a burial test and an analysis methodology based on numerical vision, *J. Environ. Polym. Degrad.* **7**(3), 157–166 (1999)
- 14.94 K.L.G. Ho, L. Pometto: Temperature effects on soil mineralization of polylactic acid plastic in laboratory respirometers, *J. Environ. Polym. Degrad.* **7**(2), 101–108 (1999)
- 14.95 H. Nishide, K. Toyota, M. Kimura: Effects of soil temperature and anaerobiosis on degradation of biodegradable plastics in soil and their degrading microorganisms, *Soil Sci. Nutr.* **45**(4), 963–972 (1999)
- 14.96 S. Grima, V. Bellon Maurel, P. Feuilloley, F. Silvestre: Aerobic biodegradation of polymers in solid state conditions: A review of environmental and physicochemical parameter settings in laboratory, *J. Environ. Polym. Degrad.* **8**(4), 183–195 (2000)
- 14.97 E. Abrams: *Microbiological Deterioration of Organic Material: Its Prevention and Methods of Test*, NBS Publ., Vol. 188 (NBS, Washington 1948)
- 14.98 J. La Brijn, H.R. Kauffman: Fungal testing of textiles: A summary of the cooperative experiments carried out by the working group on textiles of the International Biodeterioration Research Group (IBRG). In: *Biodeterioration of Materials*, Vol. 2, ed. by A.H. Walters, E.H. Heuck Van de Plas (Applied Science, London 1972)
- 14.99 J.S. Webb, M. Nixon, I.M. Eastwood, M. Greenhalgh, G.D. Robson, P.S. Handley: Fungal colonization and biodeterioration of plasticised PVC, *Appl. Environ. Microbiol.* **66**, 3194–3200 (2000)
- 14.100 M. Stranger-Johannessen: The role of microorganisms in the formation of pitch deposits in pulp and paper mills, *Biotechnol. Adv.* **2**(2), 319–327 (1984)
- 14.101 H.R. Arai: Microbiological studies on the conservation of paper and related cultural properties (Part 1): Isolation of fungi from the foxing on paper, *Sci. Conserv.* **23**, 33–39 (1984)
- 14.102 W. K. Wilson: Environmental guidelines for the storage of paper records, NISO-TR01-1995 (1995)
- 14.103 W. Paulus: *Directory of Microbicides for the Protection of Materials: A Handbook* (Kluwer, Dordrecht 2005)
- 14.104 European Community: Doc-Biocides-2002/04-Rev3 Guidance document agreed between the Commission services and the competent authorities of the

- Member States for the Biocidal Products Directive 98/8/EC – Guidance Notes on Treated Articles (2004)
- 14.105 W. Hewitt, S. Vincent: *Theory and Practice of Microbiological Assay* (Academic, New York 1989)
- 14.106 P. Raschle: Personal communication (2004)
- 14.107 Svensk Standard SS 876 00 19 Sjukvårdstextil – Bakteriepenetrations – Våt (Bacterial Penetration Test) (1994)
- 14.108 EDANA Test Method 190.1-02 Dry Bacterial Penetration (2002)
- 14.109 EDANA Test Method 200.1-02 Wet Bacterial Penetration (2002)
- 14.110 W.E. Krumbein, B.D. Dyer: This planet is alive. Weathering and biology, a multi-faceted problem. In: *The Chemistry of Weathering*, ed. by J.M. Drever (Reidel, Dordrecht 1985) pp. 143–160
- 14.111 C. Gehrman, W.E. Krumbein, K. Petersen: Lichen weathering activities on mineral and rock surfaces, *Stud. Geobot.* **8**, 33–45 (1988)
- 14.112 C. Gehrman, K. Petersen, W.E. Krumbein: Silicole and calcicole lichens on jewish tombstones – interaction with the environment and biocorrosion, VI. Int. Congr. Deterior. Conserv. Stone (Nicholas Kopernikus Univ., Torun 1988) pp. 33–38
- 14.113 A. Villa: Desherbement des surfaces recouvertes de mosaïques a ciel ouvert, Atti I Congresso sulla Conservazione dei Mosaici (ICROM, Roma 1977) pp. 45–49, (in French)
- 14.114 H.L. Ehrlich: *Geomicrobiology* (Dekker, New York 1990)
- 14.115 F.E.W. Eckhardt: Solubilization, transport and deposition of mineral cations by microorganisms. Efficient rock weathering agents. In: *Chemistry of Weathering*, ed. by J.I. Drever (Reidel, New York 1985) pp. 161–173
- 14.116 W.E. Krumbein, K. Jens: Biogenic rock varnishes of the Negev Desert (Israel) an ecological study of iron and manganese transformation by cyanobacteria and fungi, *Oecologia* **50**, 25–38 (1981)
- 14.117 C. Jaton, G. Oriol: Processus microbiologiques des altérations des briques, Atti Convegno “Il mattone di” (Fondazione Cini, Venezia 1979) pp. 163–170, (in French)
- 14.118 A. Koestler, E. Charola, M. Wypyski: Microbiologically induced deterioration of dolomitic and calcitic stone as viewed by scanning electron microscopy, Proc. Vth Int. Congr. Deterior. Conserv. Stone (Presses Polytechniques Romandes, Lausanne 1985) pp. 617–626
- 14.119 W.E. Krumbein: Role des microrganismes dans la genèse, la diagenèse et la dégradation des roches en place, *Rev. Ecol. Biol. Sol* **9**, 283–319 (1972), (in French)
- 14.120 W.E. Krumbein, J. Pochon: Ecologie bactérienne des pierres alterées des monuments, *Ann. Inst. Pasteur* **107**, 724–732 (1964), (in French)
- 14.121 M. Thiebaud, J. Lajudie: Associations bactériennes et altérations biologiques des monuments en pierre calcaire, *Ann. Inst. Pasteur* **105**, 353–358 (1963), (in French)
- 14.122 H. Kaltwasser: Destruction of concrete by nitrification, *J. Appl. Microbiol.* **3**, 185–192 (1976)
- 14.123 J. Kauffmann: Rôles des bactéries nitrifiantes dans l’altération des pierres calcaires des monuments, *C. R. Acad. Sci.* **34**, 2995 (1952), (in French)
- 14.124 J. Kauffmann: Corrosion et protection des pierres calcaires des monuments, *Corros. Anticorros.* **8**, 87–95 (1960), (in French)
- 14.125 E. Bock, W. Sand, M. Meincke, B. Wolters, B. Ahlers, C. Meyer, F. Sameluck: Biologically induced corrosion of natural stones. Strong contamination of monuments with nitrifying organisms. In: *Biodeterioration*, ed. by D.R. Hughton, R.N. Smith, H.O.W. Eggings (Elsevier, London 1987) pp. 436–440
- 14.126 W.E. Krumbein: Patina and cultural heritage – a geomicrobiologist’s perspective. In: *Cultural Heritage Research: A Pan European Challenge. European Communities*, ed. by R. Kozłowski (Academy of Science, Krakow 2003) p. 415
- 14.127 S.G. Paine, F.V. Lingood, F. Schimmer, T.C. Thrupp: The relationship of micro-organisms to the decay of stone, *Philos. Trans. R. Soc. B* **222**, 97–127 (1933)
- 14.128 W.E. Krumbein: Zur Frage der Gesteinsverwitterung. Über geochemische und mikrobiologische Bereiche der exogenen Dynamik. Ph.D. Thesis (Univ. Würzburg, Würzburg 1966) p. 149, (in German)
- 14.129 F.E.W. Eckhardt: Microbial degradation of silicates – Release of cations from aluminosilicate minerals by yeasts and filamentous fungi. In: *Biodeterioration*, ed. by T.A. Oxley, G. Becker, D. Allsopp (Pitman, The Biodeterioration Society, London 1978) pp. 107–116
- 14.130 W.E. Krumbein: Zur Frage der biologischen Verwitterung: Einfluß der Mikroflora auf die Bausteinverwitterung und ihre Abhängigkeit von edaphischen Faktoren, *Z. Allg. Mikrobiol.* **8**, 107–117 (1968), (in German)
- 14.131 W.E. Krumbein: Über den Einfluß von Mikroorganismen auf die Bausteinverwitterung – eine ökologische Studie, *Dtsch. Kunst Denkmalpfl.* **31**, 54–71 (1973), (in German)
- 14.132 D.M. Webley, M.E.K. Henderson, I.F. Taylor: The microbiology of rocks and weathered stones, *J. Soil Sci.* **14**, 102–112 (1963)
- 14.133 W. E. Krumbein: Private communication (2004)
- 14.134 T. Warscheid: Untersuchungen zur Biodeterioration von Sandsteinen unter besonderer Berücksichtigung der chemoorganotrophen Bakterien. Ph.D. Thesis (Univ. Oldenburg, Oldenburg 1990) p. 147, (in German)
- 14.135 A. Vuorinen, S. Mantere-Almonen, R. Uusinoka, P. Alhonen: Bacterial weathering of Rapabiu granite, *Geomicrobiol. J.* **2**, 317–325 (1981)
- 14.136 F. Lewis, E. May, B. Daley, A.F. Bravery: The role of heterotrophic bacteria in the decay of

- sandstone from ancient monuments, *Biodeterior. Constr. Mater. Proc. Summer Meet. Biodeterior. Soc. (Biodeterioration Society, Delft 1987)* pp. 45–53
- 14.137 A.A. Gorbushina, W.E. Krumbein, M. Volkmann: Rock surfaces as life indicators: New ways to demonstrate lives and traces of former life, *Astrobiology* **2**, 203–213 (2002)
- 14.138 S.T. Williams: Streptomycetes in biodeterioration. Their relevance, detection and identification, *Int. Biodeterior.* **21**, 201–209 (1985)
- 14.139 B. Chamier: Über den Einfluß von Actinomyceten auf die Materialzerstörung. M.Sc. Thesis (Univ. Oldenburg, Oldenburg 1991) p. 113, (in German)
- 14.140 J.M.B. Coppock, E.D. Cookson: The effect of humidity on mould growth constructional materials, *J. Sci. Food Agric.* **2**, 534–537 (1952)
- 14.141 M.E.K. Henderson, R.B. Duff: The release of metallic and silicate ions from minerals, rocks and soils by fungal activity, *J. Soil Sci.* **14**, 236–246 (1963)
- 14.142 H.-C. Flemming: Biofilme und ihre Bedeutung für die mikrobielle Materialzerstörung. In: *Mikrobielle Materialzerstörung*, ed. by H. Brill (Fischer, Stuttgart 1995) pp. 24–47, (in German)
- 14.143 H.-C. Flemming: Auswirkungen mikrobieller Materialzerstörung. In: *Mikrobielle Materialzerstörung*, ed. by H. Brill (Fischer, Stuttgart 1995) pp. 15–23
- 14.144 H.-C. Flemming: Mikrobielle Korrosion von Beton. In: *Zementgebundene Beschichtungen in Trinkwasserbehältern*, ed. by H. Wittmann, A. Gerdes (Aedificatio, Freiburg 1996) pp. 53–65, (in German)
- 14.145 W.E. Krumbein: Über den Einfluß der Mikroflora auf die exogene Dynamik (Verwitterung und Krustenbildung), *Geol. Rundsch.* **58**, 333–363 (1969), (in German)
- 14.146 G. Grote: Mikrobieller Mangan- und Eisentransfer an Rock Varnish und Petroglyphen arider Gebiete. Ph.D. Thesis (Univ. Oldenburg, Oldenburg 1991) p. 335, (in German)
- 14.147 W.E. Krumbein: Mikrobiologische Prozesse und Baumaterialveränderung, 2. Int. Kolloqu. Werkstoffwiss. Bausanier., ed. by F.H. Wittmann (Technische Akademie, Esslingen 1986) pp. 45–62, (in German)
- 14.148 A. Gorbushina, W.E. Krumbein, L. Panina, S. Soukharjevsk, U. Wollenzien: On the role of black fungi in color change and biodeterioration of antique marbles, *Geomicrobiol. J.* **11**, 205–221 (1993)
- 14.149 W.E. Krumbein, J. Pochon, M.A. Chalvignac: Recherches biologiques sur le Mondmilch, *C. R. Acad. Sci.* **258**, 5113–5114 (1964), (in French)
- 14.150 D. Jones, M.J. Wilson: Chemical activities of lichens on mineral surfaces – A review, *Int. Biodeterior. Bull.* **21**, 99–104 (1985)
- 14.151 A. Danin, R. Gerson, J. Garty: Weathering patterns on hard limestone and dolomite by endolithic lichens and cyanobacteria: supporting evidence for eolian contribution to Terra Rossa Soil, *Soil Sci.* **136**, 213–217 (1983)
- 14.152 D. Allsopp, K.S. Seal: *Introduction to Biodeterioration* (Arnold, London 1986)
- 14.153 T.E. Ford, J.S. Maki, R. Mitchell: Involvement of bacterial exopolymers in biodeterioration of metals. In: *Biodeterioration*, Vol. 7, ed. by D.R. Hughton, R.N. Smith, H.O.W. Eggings (Elsevier, London 1987) pp. 378–384
- 14.154 J.W. Costerton, G.G. Geesey, P.A. Jones: Bacterial biofilms in relation to internal corrosion monitoring and biocide strategies, *Mater. Perform.* **12**, 49–53 (1988)
- 14.155 W. Kerner-Gang: Zur Frage der Entstehung von Schimmelpilzspuren auf optischen Gläsern, *Mater. Org.* **3**, 1–17 (1968), (in German)
- 14.156 W. Kerner-Gang: Evaluation techniques for resistance of optical lenses to fungal attack. In: *Biodeterioration Investigation Techniques*, ed. by A.H. Walters (Appl. Sci., London 1977) pp. 105–114
- 14.157 R. Newton, S. Davison: *Conservation of Glass* (Butterworth, London 1989)
- 14.158 E. Mellor: Les lichens vitricole et la deterioration des vitraux d'église. Ph.D. Thesis (Paris 1922), (in French)
- 14.159 E. Mellor: Lichens and their action on the glass and leadings of church windows, *Nature (London)* **112**, 299–300 (1923)
- 14.160 N.H. Tennent: Fungal growth on medieval glass, *J. Br. Soc. Master Glass Paint.* **17**, 64–68 (1981)
- 14.161 G. Callot, M. Maurette, L. Pottier, A. Dubois: Biogenic etching of microfractures in amorphous and crystalline silicates, *Nature (London)* **328**, 147–149 (1987)
- 14.162 R.J. Koestler, D.R. Houghton, B. Flannigan, H.W. Rossmore: *International Biodeterioration Special Issue: Biodeterioration of Cultural Property* (Elsevier, Barking 1991), 340 pp. including a bibliography by R. J. Koestler and J. Vedral
- 14.163 C. Saiz-Jimenez (Ed.): *Molecular Biology and Cultural Heritage* (Swets Zeitlinger, Lisse 2003), 278 pp.
- 14.164 N. Valentin, M. Lidstrom, F. Preusser: Microbial control by low oxygen and low relative humidity environment, *Stud. Conserv.* **35**, 222–230 (1990)
- 14.165 J. Pochon, P. Tardieux: *Techniques d'analyse de microbiologie du Sol* (Ed. La Tourelle, St. Mandé 1962) p. 104, (in French)
- 14.166 J.M. Van Der Molen, J. Garty, B.W. Aardema, W.E. Krumbein: Growth control of algae and Cyanobacteria on historical monuments by a mobile UV unit (MUVU), *Stud. Conserv.* **25**, 71–77 (1980)
- 14.167 G. Caneva, O. Salvadori: Biodeterioration of stone. In: *The Deterioration and Conservation of Stone*, ed. by L. Lazzarini, R. Pieper (Unesco, Paris 1989) pp. 182–243

- 14.168 A. Downey: The use of biocides in paint preservation. In: *Handbook of Biocide and Preservative Use*, ed. by W. Paulus (Blackie, London 1995)
- 14.169 W. Paulus: *Directory of Microbicides for the Protection of Materials. A Handbook* (Kluwer, Dordrecht 2005)
- 14.170 B. Flannigan, E.M. McCabe, F. McGarry: Allergenic and toxigenic micro-organisms in houses. In: *Pathogens in the Environment*, ed. by B. Austin (Blackwell, Oxford 1991)
- 14.171 G.T. Hill, N.A. Mitkowski, L. Aldrich-Wolfe, L.R. Emele, D.D. Jurkonie, A. Ficke, S. Maldonado-Ramirez, S.T. Lynch, E.B. Nelson: Methods for assessing the composition and diversity of soil microbial communities, *Appl. Soil Ecol.* **15**, 25–36 (2000)
- 14.172 M. Viaud, A. Pasquier, Y. Brygoo: Diversity of soil fungi studied by PCR-RFLP of ITS, *Mycol. Res.* **104**, 1027–1032 (2000)
- 14.173 J.W. Lengeler, G. Drews, H.G. Schlegel (Eds.): *Biology of the Prokaryotes* (Thieme, Stuttgart 1999) pp. 695–700
- 14.174 O. Schmidt, U. Moreth: Identification of the dry rot fungus, *Serpula lacrymans*, and the wild Merulius, *S. himantoides*, by amplified ribosomal DNA restriction analysis (ARDRA), *Holzforschung* **53**, 123–128 (1999)
- 14.175 J. Jellison, C. Jasalavich: A review of selected methods for the detection of degradative fungi, *Int. Biodeterior. Biodegrad.* **46**, 241–244 (2000)
- 14.176 K. Winkowski: Efficacy of in can preservatives, *Eur. Coat. J.* **1–2**, 87–90 (2001)
- 14.177 B. Schmidt, J. Lunnenberg, P.D. Askew: Documents of the Project Sub-Group on Preservation of Tinter Pastes (International Biodeterioration Research Group 2005)
- 14.178 P.D. Askew: Antibacterial coatings: Fact or fiction?, *Proc. Coat. Compliance Community Care, PRA Int. Symp.* **18**, Brussels (2001)
- 14.179 P.D. Askew: Relating Performance to Claims for Antimicrobial Coatings, Additives in Coatings – Innovation in Formulation, Frankfurt, Germany / Surface Coatings International (2008)
- 14.180 P.D. Askew: Hygienic coatings – Defining the terms and supporting the claims, *Proc. Third Glob. Conf. Hyg. Coat. Surf.*, Paris (2005)
- 14.181 European Community: Doc-Biocides-2002/04-Rev3 Guidance document agreed between the Commission services and the competent authorities of the Member States for the Biocidal Products Directive 98/8/EC – Guidance Notes on Treated Articles (2004)
- 14.182 W. Hewitt, S. Vincent: *Theory and Practice of Microbiological Assay* (Academic, New York 1989)
- 14.183 JIS: Antimicrobial products – Test for antimicrobial activity and efficacy, *Jpn. Ind. Standard JIS Z 2801: 2000 (E)* (2000)
- 14.184 S. McElDowney, M. Fletcher: The effect of temperature and relative humidity on the survival of bacteria attached to dry solid surfaces, *Lett. Appl. Microbiol.* **7**, 83–86 (1988)
- 14.185 A. Jawad, H. Seifert, A.M. Snelling, J. Heritage, P.M. Hawkey: Survival of *Acinetobacter baumannii* on dry surfaces: Comparison of outbreak and sporadic isolates, *J. Clin. Microbiol.* **36**, 1938–1941 (1998)
- 14.186 L. Boulangé-Petermann, E. Robine, S. Ritoux, B. Cromières: Hygienic assessment of polymeric coatings by physico-chemical and microbiological approaches, *J. Adhes. Sci. Tech.* **18(2)**, 213–225 (2004)
- 14.187 S.K. Haack, H. Garchow, D.A. Odelson, L.J. Forney, M.J. Klug: Accuracy, reproducibility, and interpretation of fatty acid methyl ester profiles of model bacterial communities, *Appl. Environ. Microbiol.* **60**, 2483–2493 (1994)
- 14.188 A. Konopka, L. Oliver, R.F. Turco Jr.: The use of carbon substrate utilization patterns in environmental and ecological microbiology, *Microbiol. Ecol.* **3(5)**, 103–115 (1998)
- 14.189 T.J. White, T. Bruns, S. Lee, J. Taylor: Amplification and direct sequencing of fungal ribosomal RNA genes for phylogenetics. In: *PCR Protocols*, ed. by M.A. Innis, D.H. Gelfand, J.J. Sninsky, T.J. White (Academic, San Diego 1990) pp. 315–322
- 14.190 M. Gardes, T.D. Bruns: ITS primers with enhanced specificity for basidiomycetes – Application to the identification of mycorrhizae and rusts, *Mol. Ecol.* **2**, 113–118 (1993)
- 14.191 K. Göller, D. Rudolph: The need for unequivocally defined reference fungi – Genomic variation in two strains named as *Coniophora puteana* BAM Ebw. 15, *Holzforschung* **57**, 456–458 (2003)
- 14.192 B.D. Hames, S.J. Higgings (Eds.): *Gene Probes 1. A Practical Approach* (Oxford Univ. Press, Oxford 1995)
- 14.193 R. Amann, W. Ludwig: Ribosomal RNA-targeted nucleic acid probes for studies in microbial ecology, *FEMS Microbiol. Rev.* **24**, 555–565 (2000)
- 14.194 M.T. Suzuki, S.J. Giovanni: Bias caused by template annealing in the amplification mixtures of 16S rRNA genes by PCR, *Appl. Environ. Microbiol.* **62**, 625–630 (1996)
- 14.195 F. van Winzingerode, U.B. Gobel, E. Stackebrandt: Determination of microbial diversity in environmental samples: Pitfalls of PCR-based rRNA analysis, *FEMS Microbiol. Rev.* **21**, 213–229 (1997)

15. Material–Environment Interactions

There is no usage of materials without interaction with the environment. Material–environment interactions are relevant for all types of materials, be they of inorganic or organic in origin. Interactions with the environment can cause damage to materials but also might lead to an improvement of materials properties (e.g. oxidative passivation of aluminium or patina formation on copper surfaces). Interactions with the environment might also occur prior to the usage of materials, i. e. in the production phase. For example, before steel can be used for manufacturing of metal products, iron ore has to be extracted and processed.

The impact of the environment on the processes of the *materials cycle* (Fig. 1.15) will be discussed in Sect. 15.1.1 of this chapter. An important material–environment interaction, especially for inorganic materials, is corrosion, which has already been addressed in Chap. 12. Also the biological impact on organic and inorganic materials can be manifold and are presented in Chap. 14. Environmental mechanisms that impair the functioning of organic polymeric materials – such as weathering, ultraviolet (UV) radiation, moisture, temperature and high-pH environments – are the topics of Sect. 15.1.2. The influence of materials on the indoor climate and measurement methods to characterize emissions from materials are treated

15.1 Materials and the Environment	845
15.1.1 Environmental Impact of Materials	845
15.1.2 Environmental Impact on Polymeric Materials.....	848
15.2 Emissions from Materials	860
15.2.1 General.....	860
15.2.2 Types of Emissions.....	860
15.2.3 Influences on the Emission Behavior	861
15.2.4 Emission Test Chambers	862
15.2.5 Air Sampling from Emission Test Chambers.....	863
15.2.6 Identification and Quantification of Emissions	864
15.2.7 Time Behavior and Ageing.....	866
15.2.8 Secondary Emissions.....	869
15.3 Fire Physics and Chemistry	869
15.3.1 Ignition	869
15.3.2 Combustion	873
15.3.3 Fire Temperatures	875
15.3.4 Materials Subject to Fire.....	877
15.3.5 Fire Testing and Fire Regulations....	878
References	883

in Sect. 15.2. Fire exhibits a drastic impact on materials; methods to characterize the flammability and fire behavior of materials are discussed in Sect. 15.3.

15.1 Materials and the Environment

15.1.1 Environmental Impact of Materials

The flow of materials has a significant global impact on the environment. Whereas at the beginning of the 20th century approximately 40% of the materials flow was attributed to renewable resources such as wood, fibres or agricultural products, this fraction dropped to only 8% by the end of the century [15.1]. The enormous increase in materials consumption within the United States is displayed in Fig. 15.1. The materials with the highest consumption rate are construction materials

(sand, gravel, stones, cement) and fossil fuels (oil, gas, coal). Other categories selected for Fig. 15.1 are minerals (clay, bauxite, phosphate rock, salt), iron and steel, wood and agricultural products (with 5 Mt in 2000 not visible in the diagram). Wood and products from agriculture and fishery are the only renewable resources from this point of view. All data are derived from the US Geological Survey [15.2]. The pattern of consumption is steadily increasing with some major historical events visible in the chart (World Wars I and II, the depression in the 1930s, the oil crisis in the mid 1970s

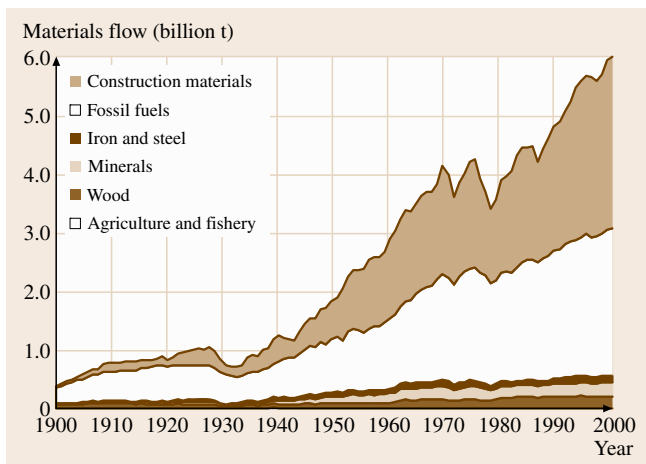


Fig. 15.1 Consumption of selected materials in the United States from 1900 to 2005 (after [15.2]). See text for material categories

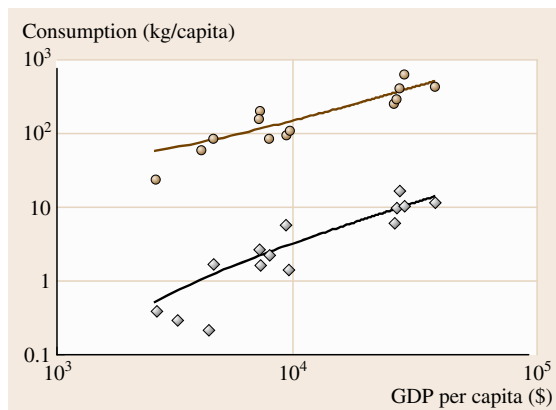


Fig. 15.2 The consumption of steel (*circles*) and copper (*diamonds*) per c.p.t. as a function of the gross domestic product per c.p.t. (after [15.3])

and later recessions). The figures suggest that the materials consumption per c.p.t. has increased by a factor of 6 from 2 t to 20 t per c.p.t. [15.1].

The environmental impact of materials usage is not easy to quantify. However, there are expressions which display the driving forces of this impact. *Graedel* and *Allenby* [15.4] describe the environmental impact as the product of population, gross domestic product (GDP) per person and environmental impact per unit of per c.p.t. GDP

$$\text{Environmental impact} = \text{population} \times \frac{\text{GDP}}{\text{person}} \times \frac{\text{environmental impact}}{\text{unit of per c.p.t. GDP}} \quad (15.1)$$

Population, the first term in (15.1), is still increasing globally. However, the population in most industrialized countries is more or less stable. GDP per person is a criterion for prosperity and varies from country to country. The general trend is positive. The last term in the equation is strongly technology-related. From (15.1) it is obvious that the production of materials using more efficient technologies and less waste production might lead to a reduced environmental impact if the effect of the first two terms can be compensated for. The fact that materials consumption is a function of the GDP per c.p.t. is shown exemplarily for steel and copper in Fig. 15.2.

The technology-related term, environmental impact per unit of per c.p.t. GDP, is the reciprocal value of the efficiency. One possibility to quantify the efficiency of materials production is to estimate the specific

energy consumption (SEC), i.e. the consumption of energy per mass of material produced. The world's SEC for steel has dropped significantly by almost 75% from 46 to 12 GJ/t since 1950 [15.5, 6]. However, the world production of steel is more than 400% of that in 1950 (1950: 190 Mt/a, 2000: 848 Mt/a [15.2]) and increased even more to 1351 Mt/a in 2007 [15.7]. Thus, the global energy consumption for steel production, i.e. the product of global production and SEC, increased from 8750 to 16 000 PJ/a. The environmental impact is directly related to energy consumption (e.g. consumption of fossil fuels, emissions etc.). As a result the environmental impact of steel production has increased, although the figure representing the technology term reduced to $\approx 25\%$ of the initial value.

Specific energy consumption for the production of a certain material is only one part of the total impact of materials production on the environment. The concept of total material requirement (TMR) is an attempt to quantify the environmental impact of materials. TMR is the sum of domestic and imported primary natural resources and their hidden flows [15.8]. Hidden flows are often not considered in environmental analyses because they are attributed with no cost. However, overburden from mining, earth-moving for construction and soil erosion are major sources of ecological damage. The concept of TMR is exemplarily shown in Fig. 15.3 for the production of steel. From mined minerals to the final products a series of process steps takes place (exploration, mine-site development, extraction, milling, washing, concentration, smelting, refining, fabrication),

Table 15.1 The TMR of some metals, minerals and fuels

Material	TMR (t/t material)	Global production (t)	TMR (Mt/a)	References
Sand and gravel	1.18	8 000 000 000	9440	[15.10]
Hard coal	2	3 740 000 000	8826	[15.10]
Phosphate	34	130 000 000	4420	[15.10]
Gold	1 800 000	2445	4401	[15.9]
Crude oil	1.22	3 485 000 000	4252	[15.10]
Copper	300	12 900 000	3870	[15.9]
Iron	5.1	571 000 000	2912	[15.9]
Silver	7500	160 000	1200	[15.9]
Uranium	11 000	45 807	504	[15.9]
Lead	95	2 980 000	283	[15.9]
Platinum	1 400 000	178	249	[15.9]
Aluminum	10	23 900 000	239	[15.9]

each step is connected to other input flows such as energy or other resources. The run-of-mine coal and the mined iron ore are the hidden flows within this example. The hidden flows for metals related to metal-ore mining have been investigated by Halada et al. [15.9]. Table 15.1 lists the data for some metals, together with the data for some minerals and fuels.

The TMR in the United States in the 1990s was 80–100 t per c.p.t., in the European Union (EU-15) it was approximately 50 t per c.p.t. [15.11]. Although the TMR concept is widely accepted, there are no economic incentives to reduce TMR. However, attempts have been made to lower the environmental impact without reduction of economic wealth. Many companies evaluate the eco-efficiency of their products. Eco-efficiency is defined as the ratio of economic benefit per environmental and resource impact [15.12]

$$\text{Eco-efficiency} = \frac{\text{Benefits}}{\text{Costs}} = \frac{\text{Economic benefit of good or service}}{\text{Environmental and resource impacts}} \quad (15.2)$$

The objective is to maximize environmental and economic benefits and reduce both environmental and economic costs. That this approach is advantageous for the economy is supported by numerous examples from industry [15.13]. The concept of ecomaterials (ecomaterials = environmentally conscious materials) was developed in Japan and follows a similar direction [15.14]. Ecomaterials are defined as materials with green environmental profile, hazardous substance-free materials, recyclable materials and materials with high material efficiency. All four types of ecomaterials lead to a reduction in TMR and thus higher eco-efficiency.

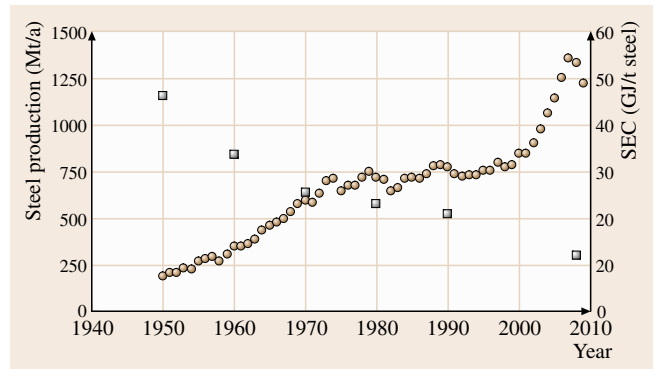


Fig. 15.3 Global steel production and specific energy consumption (global average) for the production of steel since 1950 (circles – steel production (Mt/a), squares – SEC (GJ/t steel))

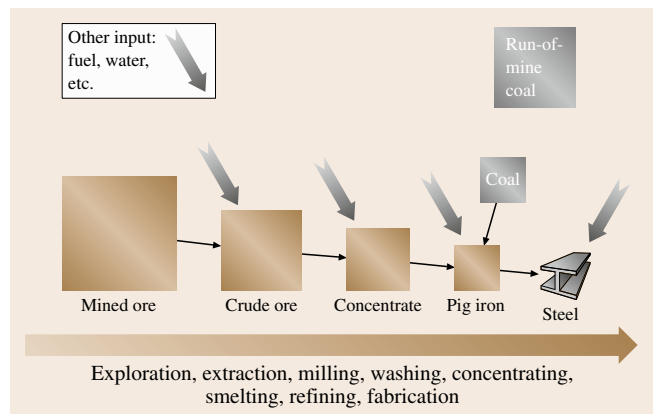


Fig. 15.4 The concept of TMR. The brown boxes are regarded as the hidden flows and account for the estimates of TMR. The sizes of the boxes are not to scale

15.1.2 Environmental Impact on Polymeric Materials

Relevant Environmental Factors

In chemistry, a differentiation is usually made between inorganic and organic matter. This discrimination is not an arbitrary one but rather reflects the completely different nature of the two. While the corrosion of metals as the economically most important environmental impact on inorganic matter has already been dealt with in Chap. 12, this subsection will look exclusively at polymeric materials. The latter not only present the most important sector of organic material but also exhibit an abundant variety of reactions and in general complex reaction behavior.

For (technical) polymeric materials, some special environmental factors are of basic relevance. Bond energies of a few eV (the solar UV comprises the range 3.1–4.1 eV) make them sensitive to UV radiation, which makes weathering resistance a basic topic for polymers. Other relevant environmental factors will be only shortly discussed here.

Ageing – all the irreversible physical and chemical processes that happen in a material during its service life – often limits the serviceable lifetime to only a few years or even months. Thermodynamically, ageing is an inevitable process, however its rate ranges widely as a result of the different kinetics of the single reaction steps involved. Ageing becomes noticeable through changes of different properties, varying from slight loss in appearance properties to total mechanical–technical failure. Ageing is mostly associated with a worsening of material properties, but sometimes it can also result in an improvement of properties, e.g. UV hardening.

Relevant environmental factors for the ageing of polymers are

1. solar radiation (see *weathering exposure* in the following),
2. heat,
3. chemical environment,
4. mechanical stress,
5. ionizing radiation,
6. biological attack.

Heat. Because of their low bond energies technical polymers can only be used in a limited temperature range [15.15]. Polyvinylchloride (PVC) for instance is only suited for permanent use up to 70 °C, polycarbonate (PC) up to 115 °C.

Thermal properties in general are dealt with in Chap. 8.

Chemical Environment. Exposed to water some polymers, like polyamides (PA), polyester, polyurethane, can be hydrolyzed, the mechanism for which may depend on acidity. Other polymers show a high sensitivity to atmospheric pollution, e.g. polyamides and polyurethanes even at room temperature are attacked by SO₂ and NO₂.

Akahori [15.16] used exposure to neutral oxygen radicals, produced by a plasma generator, for accelerated ageing tests.

Mechanical Stress. In the case of mechanical exposure, free radicals can be formed by rupturing chemical bonds, which is used as the initiation step in stress chemiluminescence [15.17].

Ultrasonic degradation can be used to produce polymers with a definite molecular size [15.18] or to degrade polymeric waste products. Frequent freezing/thawing cycles may also lead to degradation of dissolved polymers.

Ionizing Radiation. The impact of high-energy radiation (γ -, x-ray) leads to degradation and/or crosslinking [15.19]. In the presence of oxygen, degradation predominates.

Biological Attack. Not counting the mainly mechanical attacks of rodents or termites, microorganisms – such as mildew, algae and bacteria, that colonize their surfaces – can damage polymeric materials. Damage mechanisms vary for different polymers [15.20]. The microorganisms may attack in a direct way by breaking chemical bonds, or can act indirectly, e.g. increasing the migration of stabilizers. Producing their own pigments they can also disturb the appearance of the surfaces by color change.

In contrast with protecting polymeric materials from biological attacks (biocides) the opposite strategy is followed in sensitizing polymers to biodegradation for recycling.

Chapter 14 deals with the biogenic impact on materials in general.

Often the combined action of these environmental factors, which occur as synergistic or antagonistic effects, has to be considered.

Weathering Exposure

Ageing of polymeric materials by the impact of weathering is mainly initiated by the action of so-

lar radiation. However, other climatic quantities such as heat, moisture, wetting and ingredients of the atmosphere, influence the photochemical ageing and are answerable for the final ageing results. To date there are no satisfactory general answers to the questions of the accurate mechanisms of the photooxidation and photodegradation of pure polymers, not to mention technical polymeric materials.

General Principles of Photoinitiated Ageing. From a theoretical point of view, pure aliphatic polymers show no absorption in the spectrum of solar radiation. For example, the UV absorption bands of pure polyethylene, which contains only C–C and C–H bonds, are located at wavelengths below 200 nm. Only polymers with aromatic groups or conjugated double bonds absorb natural solar UV radiation. For this reason, many polymers should be capable of withstanding the action of solar radiation during outdoor exposure.

The spectral response of a property change of a polymer in the solid phase does not coincide with its absorption spectrum in the spectral range of solar radiation. Even in many aromatic-type polymers, the absorption of radiation, which is responsible for the initiation of ageing, takes place through chemical irregularities or impurities. These originate either during the polymerization process and the processing of the polymers or are residues of catalysts. These chromophores, which are capable of absorbing the UV portion of terrestrial solar radiation, are unavoidable in technical polymers. *Menzel and Schlüter* [15.21] for example describe an increase of absorption at wavelengths above 300 nm and a decrease of weathering resistance after multiple processing of PVC.

Photoinitiated ageing of polymeric materials can be caused

1. directly via an excitation of a molecule in a non-binding state that leads to photolytic chain scission (dissociation);
2. indirectly via an excitation of a molecule in a bound singlet state S_x that can be deactivated by several reaction paths, e.g. an oxidative reaction of the excited polymer molecule with O_2 .

The multistage processes of photoageing can be illustrated by the rough scheme in Fig. 15.5, which shows the levels of the excited states of an organic molecule A. The levels S_1 and S_2 (singlet states) and T_1 and T_2 (triplet states) are the most important energy levels in photochemistry. The thin lines above these levels indicate the vibrational and rotational levels. The nearly ver-

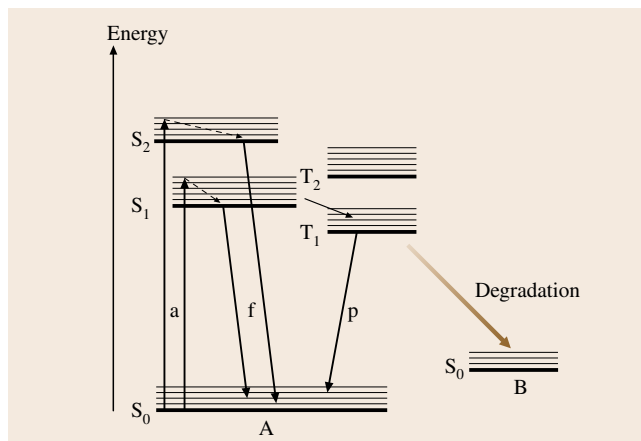


Fig. 15.5 Scheme of the energy levels and transfers in an organic molecule, a – absorption, f – fluorescence, p – phosphorescence and photochemical degradation

tical solid arrows indicate the absorption and emission of radiation, the dashed arrows show radiationless energy transfers. The main processes are described below.

1. Absorption of radiation is the initiating photophysical reaction. At room temperature the polymer molecule A is in the ground state S_0 . By the absorption of a photon, it is transferred from the ground state S_0 to the excited state S_1 (including vibrational and rotational levels) and, at a higher photon energy, also to the excited state S_2 . Under conditions of natural and artificial weathering, the absorption of radiation can be considered as largely independent of any external influences.
2. This is followed by deactivation of excited states. The electronically excited states are no longer in a thermal equilibrium and try to transfer the absorbed energy within a very short time. This deactivation takes place by several competing processes:
 - a) Intramolecular deactivation. This energy transfer takes place from the excited state S_1 by fluorescence, or after internal conversion, intersystem crossing and relaxation from higher vibrational energy levels from the excited state T_1 by phosphorescence. This type of deactivation does not change the polymer molecule. Therefore, the absorption of radiation is not a sufficient condition for an ageing process. Even if the absorbed energy is high enough to rupture a bond, the energy has to be accumulated in this bond.

- b) Intermolecular deactivation. This also takes place from the excited states S_1 and T_1 by radiative and radiationless transitions to an acceptor. This energy transfer plays an important role in photostabilization and even the photosensitization of polymers.
- c) Deactivation by chemical reactions. In a non-binding electronically excited state, the weakest of the bonds involved dissociates into two radicals. These reactive intermediate pieces can recombine or react with many other molecules to form stable final products.

For a comprehensive survey of the photochemistry of polymers see, e.g., *Calvert and Pitts* [15.22] or *Ranby and Rabek* [15.23].

This short and superficial representation of the complex reaction processes during photochemical ageing gives an idea of the numerous factors that can influence photoinitiated ageing at many stages. These influences on the ageing behavior of polymers can only be roughly predicted by means of theoretical considerations. Quantitative results on the influence of the different climatic quantities have to be determined by experiments.

To interpret the results from artificial weathering tests, it is necessary to have an idea of the influences of the different climatic quantities on photochemical ageing. This paper summarizes some results of investigations on the spectral response of polymers and on the influence of heat, moisture, the style of wetting, acid precipitation and biofilms on ageing results.

Spectral Response of Polymers. The spectral response of polymers is usually expressed in terms of their spectral sensitivity or activation spectrum, which unfortunately are not used consistently in literature. Data on the spectral response of polymers can be obtained in principle by two methods

1. A direct method, where the effect of a wavelength of radiation is determined by irradiation with a small spectral band or line of radiation with known irradiance. This technique determines the spectral sensitivity (or wavelength sensitivity), see *Trubiroha* [15.24, 25].
2. An indirect method, which ascribes the incremental property change measured behind a pair of filters to the incremental (UV) radiation of a radiation source transmitted by the shorter-wavelength filter of the pair. This technique, the so-called filter technique, is used to determine the activation spectrum of a polymer, described in full, e.g., by *Searle* [15.26].

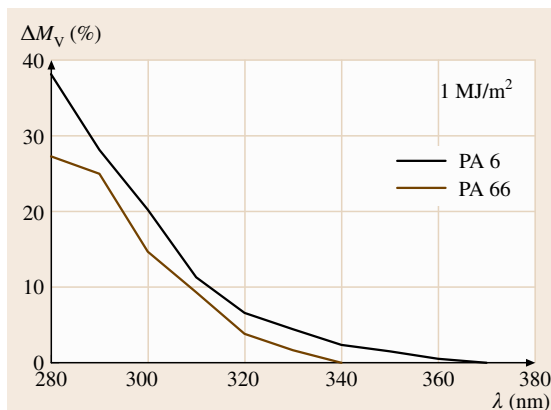


Fig. 15.6 Spectral sensitivity of polyamides, change in molar mass M_v as a function of wavelength of irradiation

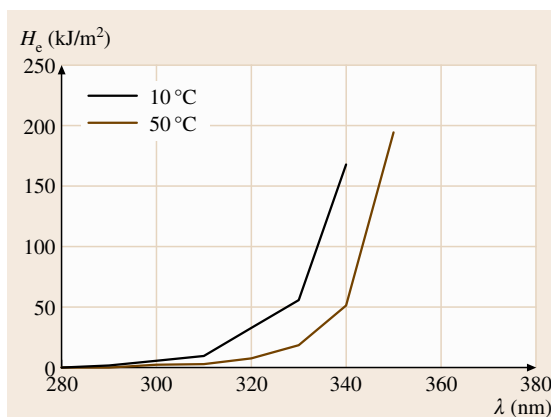


Fig. 15.7 Spectral sensitivity of polycarbonate at 10 and 50 °C. The graph shows the radiant exposure H_e , necessary to produce a 10% loss in internal transmittance as a function of the wavelength of irradiation

Spectral Sensitivity (or Wavelength Sensitivity). Spectral sensitivity data can be obtained by

1. observing the changes of a polymer property as a function of an equal radiant exposure with nearly monochromatic radiation at different wavelengths,
2. observing the radiant exposure with nearly monochromatic radiation, necessary to produce a defined change of the polymer property, if the change of the property is not linearly dependent on the radiant exposure.

The spectral sensitivity of the decrease of molar mass of additive-free polyamide films with a thickness of about 40 μm is illustrated in Fig. 15.6. The

changes were normalized for an equal radiant exposure of 1 MJ/m^2 at each wavelength in the spectral range 280–380 nm. The figure shows the decrease of the molar mass M_v of the two polyamides PA 6 and PA 66 with wavelength of irradiation. The change of M_v was linearly dependent on the radiant exposure in the investigated range.

PA 6 was more sensitive than this PA 66. The sensitivity of molecular degradation increases strongly with decreasing wavelength. Molecular degradation of the PA 6 film was only sensitive to wavelengths shorter than 370 nm. The PA 66 film only degraded at wavelengths below 340 nm.

The spectral sensitivity of the yellowing of a PC film with a thickness of 0.7 mm specimen temperatures of 10 and 50 °C is shown in Fig. 15.7. Because the yellowing of PC is not linearly dependent on the radiant exposure the figure shows the radiant exposure H_e which is necessary to reduce the internal transmittance of the PC film at 360 nm by 10%. With increasing wavelength higher radiant exposures are required to produce this defined change of internal transmittance. With increasing temperature the curve shifts to longer wavelengths by about 10 nm, when the temperature rises from 10 to 50 °C, which means that the spectral sensitivity increases with increasing temperature.

Activation Spectrum. The activation spectrum is the polymer spectral response data measured using the filter technique and is specific to a defined type of radiation source and a fixed exposure time.

An example of the calculated activation spectrum (AS) of the PA 6 film with a thickness of $40 \mu\text{m}$ mentioned above to solar global radiation E_{glob} and the spectral sensitivity (SS) are given in Fig. 15.8. A simplified qualitative definition of an activation spectrum is the superimposition of the spectral sensitivity (SS) of a property change of a test specimen onto the spectral irradiance $E_{e\lambda}$ of a given radiation source. At short wavelengths the activation spectrum must be zero where the spectral irradiance of the radiation source is zero; at long wavelengths the activation spectrum must be zero where the spectral sensitivity is zero. Therefore, information on an activation spectrum needs to be accompanied by information on the spectral irradiance of the radiation source.

Many other unstabilized and stabilized polymers show no remarkable response to radiation of wavelengths above 400 nm [15.24, 26]. However, investigations of very light-sensitive papers by the National Institute for Standards and Technology (NIST) [15.27]

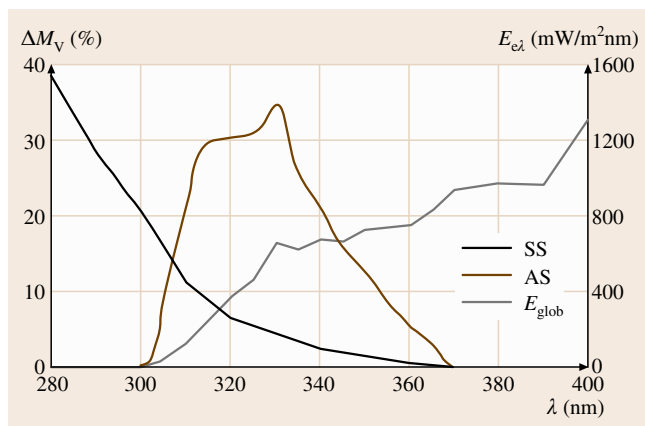


Fig. 15.8 Polyamide 6 film: spectral sensitivity (SS) and activation spectrum (AS) at solar global radiation E_{glob}

and of TiO_2 -pigmented polymers and paints by *Kämpf* and *Papenroth* [15.28] ascertained a slight response to wavelengths up to about 450 nm. Only very light-sensitive color pigments fade strongly on exposure to visible radiation.

These experimental determinations of the spectral response of polymers have to be considered as typical results that can be influenced for example by the temperature, the degree of crystallinity and the thickness of the specimen or the duration of exposure, not to mention additives and pigments, which can be photostabilizers or photosensitizers, see *Trubiroha* et al. [15.29].

Irradiance Level. Besides the wavelength, the irradiance level during exposure may also have an influence on the degradation behavior of transparent test specimens.

Figure 15.9a shows the decrease of radiant flux in a clear transparent film for three different values of the product μd (absorption coefficient \times thickness of a film/sheet) in relative units. If the photochemical ageing only depended on the absorbed energy, the ageing results (Fig. 15.9b) would run parallel to the curves of radiant flux in the film, calculated according to $E = E_0 10^{-\mu d}$.

Figure 15.9b illustrates schematically the changes of carbonyl concentration in a low-density polyethylene (PE-LD) sheet with a thickness of 3 mm as a function of depth at different partial pressures of oxygen, measured by *Furneaux* et al. [15.30]. In a pure oxygen atmosphere, the change of the carbonyl index (infrared (IR) absorption region of the oxidation products) runs parallel to the decrease of radiant flux. However, the radiation exposure in air shows a strong formation of carbonyl groups at the

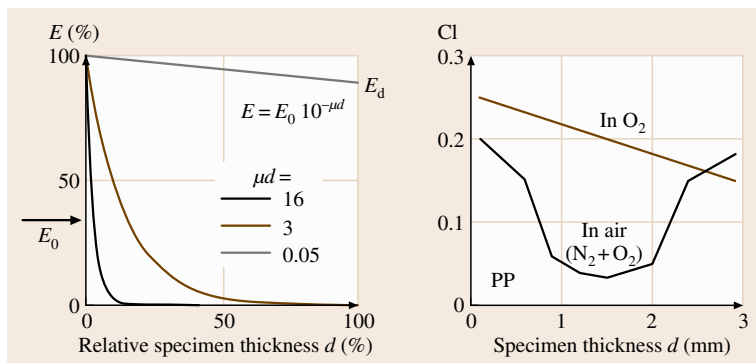


Fig. 15.9 (a) Radiant flux in a transparent sheet, (b) change of carbonyl index (CI) in a low-density polyethylene sheet with depth and partial pressure of oxygen

two surfaces of the sheet. In the specimen's core thickness of 1 mm only very low carbonyl concentrations could be found. The rate of photooxidation definitely depends on oxygen diffusion, and thereby on the irradiance level, which implies an indirect dependence on the specimen temperature.

Photodegradation: Influence of Heat. Increased temperatures do not only increase diffusion rates but generally most chemical reactions. Figure 15.10 shows the loss of gloss of a white TiO₂-rutile-pigmented paint with a binder system consisting of linseed oil/alkyd as a function of the temperature of the specimen surface. It shows the decrease of the reflectometer value at 20, 35, and 50 °C, with time of weathering exposure. With increasing temperature, there is an increasing loss of gloss.

The strong dependence of many photodegradation reactions on the specimen temperature explains why it was not successful to establish a weathering station high

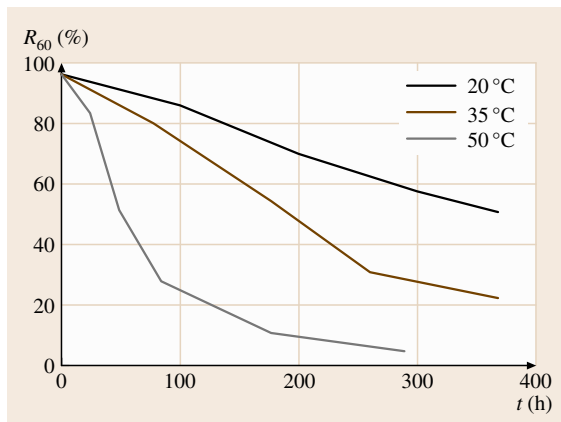


Fig. 15.10 Loss of 60° gloss of a paint with exposure duration t and specimen temperature

in the Alps, although there is a higher level of UV radiation. The mean temperature was about 20 °C lower than in weathering stations at sea level. Even *Boysen's* attempts to combine the natural weathering under daylight with artificial UV exposure during the night did not show the estimated acceleration due to the influence of temperature [15.31]. The low temperature of the specimen surfaces in the night with artificial irradiation changed the ageing processes.

It has to be mentioned here that the increase of surface temperature by irradiation can be different under natural and artificial irradiation, depending on the source of radiation and the color of the specimen. This temperature difference influences the acceleration factors for specimens with different colors.

Photodegradation: Influence of Moisture and Wetness. For unpigmented translucent PVC no dependence of the discoloration in the range of relative humidities between 10 and 90% RH could be found. However, the yellowing of white TiO₂-rutile-pigmented PVC used for window frames, which occurred as a weathering effect, showed a strong dependence on the relative humidity during irradiation [15.32].

Figure 15.11 shows the discoloration of eight specimens of PVC frames with different stabilizers and modifiers expressed in color differences ΔE corresponding to the grades of the greyscale after UV radiant exposure of about 190 MJ/m² at 50 °C. The discoloration in the moist climate was much lower than in the dry climate. This effect can be explained by the photoactivity of TiO₂ at high relative humidity, which destroys the polyene sequences in PVC.

The influence of relative humidities of 10 and 90% RH in the temperature range from 0–50 °C on the photodegradation of PA 6 is shown in Fig. 15.12. The figure shows the changes of molar mass M_v after UV

radiant exposure of about 3.5 MJ/m^2 . With increasing relative humidity and temperature, increasing degradation can be seen. In the temperature range $20\text{--}40^\circ\text{C}$ a stronger increase of the dependence, which probably correlates with the change of the glass-transition temperature, can be observed.

In contrast to *Matsuda and Kurihara* [15.33], who observed a strong influence of moisture content on changes of mechanical properties of PE-LD during weathering, *Löschau and Trubiroha* [15.34] could not confirm this result in the 1970s with three different PE-LD samples. Investigations with different high-density polyethylene (PE-HD) films however, showed a distinct influence of moisture on the changes of mechanical properties, decrease of molecular mass and the formation of carbonyl groups. After UV radiant exposure of 13 MJ/m^2 in a Global UV-Test device at 40°C and relative humidities of 20, 55 and 95%, the carbonyl index increased from 0.6 at 20% RH to 2.5 at 95% RH; the decrease of molar mass increased from 14% at 25% RH to 23% at 95% RH.

From these results, one cannot conclude that the photooxidation of PE-HD is dependent on moisture in contrast to PE-LD. The PE-LD was a pure polymer whilst PE-HD contained additives.

Other important parameters may be the type of wetting, e.g. dew or rain, and the duration of the wetness of the wet–dry cycles, which can cause mechanical stresses during the absorption or desorption of water.

Photodegradation: Influence of Atmospheric Acid Precipitation. Investigations on atmospheric precipitation show that rain with a pH of 2.4–5.5, fog with a pH of 2.2–4.0 and dew with a pH ≥ 2.0 are not rare phenomena, and not only observed in industrial regions. Acid atmospheric precipitation is formed when specific pollutants combine with water or dust particles in the atmosphere. By far the largest contribution to this problem arises from sulphur dioxide SO_2 , a by-product of fossil-fuel combustion. In the atmosphere, SO_2 concentrations of up to 1 ppm are no rarity during the morning rush hours with the increased use of heating systems. When oxidized to sulphuric acid, H_2SO_4 , it accounts for 62–79% of the acidity of rain. Most of the remaining acid is from nitrogen oxides NO_x , found mainly in automobile exhaust fumes, which are oxidized to nitric acid HNO_3 (15–32%). In addition to these two main species, hydrochloric acid HCl (2–16%), also produced by burning coal, is found in the atmosphere [15.35].

However, rain, dew, fog and dust with pH ≥ 2.0 are not the final forms of the acid precipitation which can

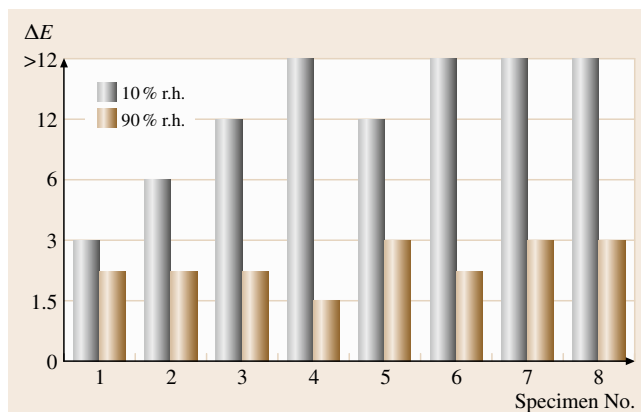


Fig. 15.11 Weathering-induced discoloration ΔE of white polyvinylchloride at low and high relative humidity

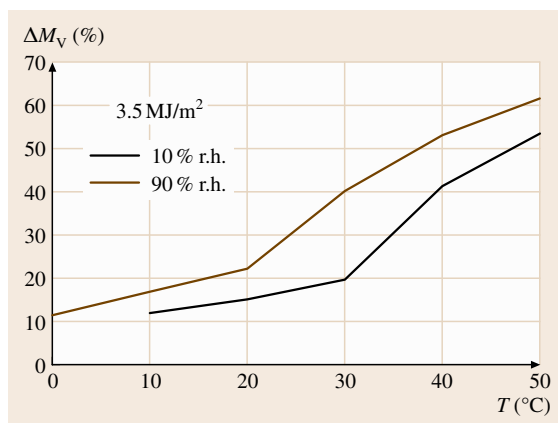


Fig. 15.12 Photodegradation of polyamide 6 with temperature and relative humidity after UV radiant exposure of about 3.5 MJ/m^2 , where M_v is the molar mass

act on surfaces of polymeric materials. Following the vapor–pressure curves it can be stated that the acid precipitation will concentrate up to about 70% sulphuric acid on hot and inert surfaces by the evaporation of H_2O , HNO_3 and HCl . A summary of the influence of acid precipitation on different polymers has been published [15.36, 37]. Hindered amine light stabilizers can be another weak point of technical polymeric materials [15.38].

Results generally show a synergetic effect of acid precipitations with UV radiation which accelerates the effect of artificial weathering tests, but there are also hints that the ageing processes of some polymers, e.g. unstabilized PE and PC, can also be slowed down by acid precipitations.

Photodegradation: Influence of Biofilms. Any surface of a material has a biofilm. This biomaterial or products of their metabolism may also have a synergistic effect on the weathering behavior of polymeric materials, e.g. the mildew growth that causes pinholes in automotive coatings, especially in warm and humid climates like in South Florida. An attempt to produce the formation of these pinholes by means of standardized laboratory mildew tests that did not incorporate radiation failed [15.39].

Dragonflies that confuse a glossy clear coat with a water surface lay their eggs on this surface. Because of heating by solar radiation and the photochemical action of UV radiation, these eggs will be destroyed. *Stevani* et al. have demonstrated that the degradation products can hydrolyze acrylic/melamine resins that are in common use for clear coats [15.40].

Photodegradation: Influence of the Prior History of Test Specimens. *Menzel* and *Schlüter* [15.21], see above, described a decrease of weathering resistance after repeated processing of PVC. Similar results were obtained by *Chakraborty* and *Scott* for PE-LD [15.41].

This means that results from weathering, as well as being influenced by climatic quantities, may also be affected by the prior history of the exposed specimen (surface), for example by the quality of the specimen surface. Figure 15.13 demonstrates the influence of surface roughness on the discoloration of a white specimen of an extruded PVC window frame. By artificial irradiation in a dry climate, dark brown stripes develop over some areas, where the unexposed specimen showed a reduced gloss from processing.

Drying conditions of a coating may influence its ageing behaviour different loss of stabilizer. An increase of the degree of crystallinity of polyamide by annealing can increase its stability. Therefore, different prior his-

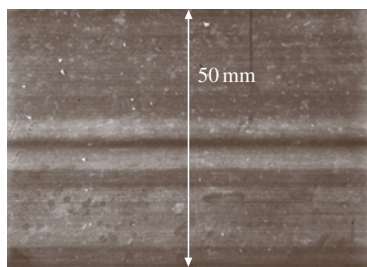


Fig. 15.13 Effect of surface roughness on the discoloration of a white polyvinylchloride specimen. Surface areas that were originally glossy show a light color change, surface areas that were dull show a strong dark brown color

tory of test specimens are often the cause of varying weathering results.

Natural Weathering. In practice, many polymeric materials are exposed to the whole variety of climatic conditions in the world. High levels of UV irradiance, annual UV radiant exposure, temperature, and humidity are extreme conditions for most polymeric materials. However, depending on the anticipated market of the polymer product, other exposure conditions may be important, e.g. maritime exposure to salt spray.

Corresponding to the variety of climates that are a result of latitude, altitude, and special geographical conditions, there are numerous natural-weathering sites across the world.

Benchmark climates for natural-weathering tests are the warm and humid, subtropical climate in Florida and the hot and dry, desert climate in Arizona, see *Wypych* [15.42].

At a given exposure site the real action of weather conditions can be varied by different exposure angles from the horizontal to vertical, by exposure under glass, by sun-tracking exposure or by Fresnel solar concentrators.

The following considerations have to be taken into account

1. It is very difficult to really reproduce results from an outdoor exposure in weathering devices, because the outdoor exposure results vary for different locations, e.g. outdoor exposures at geographical locations such as Florida or Arizona, which accelerate the ageing of polymers compared to Europe, do not duplicate the ageing results of outdoor exposures in Europe. Even at one geographical location, the weather conditions of a season or a year, and therefore the ageing results, are not repeatable within a manageable time.
2. Any accelerated test, either artificial or outdoor, is only an approximation to the exposure stress in the field.

Artificial Weathering. To estimate the service life of products made from polymers or for the development of more stable polymers, the conditions of outdoor exposure are simulated in accelerated artificial-weathering devices. These machines were introduced in 1918, but a long period of time was required for the development from the first purely artificial radiation sources equipped with a carbon arc to artificial weathering devices. In the course of time, these devices have become

good simulators of the actinic portion of the solar radiation. This means that there may be a good simulation of the first photophysical reaction of photochemical ageing in these machines. The other climatic quantities of the weather can never be simulated perfectly due to time compression or acceleration; for this reason, deviations can influence the ageing result and affect the correlation with results from outdoor exposures.

There are a number of different concepts for these weathering devices

1. Devices equipped with xenon arc lamp(s). These machines show good simulation of the maximum of spectral irradiance in the UV and visible (Vis) range of terrestrial solar radiation at vertical incidence of direct solar radiation.

The main advantage of these devices is that even very light-sensitive materials, i.e. sensitive to Vis radiation, can be investigated. The main disadvantage is the high thermal charge to the specimen surfaces by Vis and IR radiation, which makes conditioning of the surfaces at low temperatures and high relative humidity during irradiation impossible.

2. Devices equipped with fluorescent UV lamps. These machines show good simulation of the actinic portion of terrestrial solar radiation with fluorescent type 1 (340) UV lamps and a combination of different types of fluorescent UV lamps.

The big advantage of these devices is their low energy consumption and a very low thermal charge to the specimen surfaces by Vis and IR radiation. Therefore, irradiated surfaces of specimens can be easily conditioned over wide temperature and relative humidity ranges. However, there are some limitations concerning lightfastness tests of specimens that are very sensitive to visible radiation.

3. Devices with carbon arc(s). These machines show a spectral distribution of irradiance that differs strongly from that of terrestrial solar radiation. Additionally there is the same disadvantage as for xenon-arc machines: a high thermal charge to the specimen surfaces by Vis and IR radiation

These machines are mainly used in the Asian market.

Weathering Standards. There are hundreds of national and international standards and company specifications that prescribe exposure conditions for artificial and outdoor weathering exposure tests considering usual and specific conditions, e.g. in the automotive industry or for roofing materials.

Most of these tests procedures are based on the following International Organization for Standardization (ISO) standards

- for the natural exposure of plastics: ISO 877 Plastics – methods of exposure to solar radiation (Part 1: General guidance, Part 2: Direct weathering and weathering using glass-filtered solar radiation, Part 3: Intensified weathering using Fresnel mirrors);
- for paints and varnishes: ISO 2810 Paints and varnishes – natural weathering of coatings – exposure assessment.
- artificial exposure procedures are described for plastics in: ISO 4892 Plastics – methods of exposure to laboratory light sources, parts:
 - a) general guidance,
 - b) xenon-arc sources,
 - c) fluorescent UV lamps,
 - d) open-flame carbon-arc lamps,
- and for paints and varnishes in: ISO 11341 Paints and varnishes – artificial weathering of coatings and exposure of coatings to artificial radiation alone – exposure to filtered xenon-arc radiation (09.94); and ISO 11507 Paints and varnishes – exposure of coatings to artificial weathering – exposure to fluorescent UV and water.

Some failures of polymeric materials from outdoor exposure may not be able to be reproduced in artificial-weathering devices using standard weathering conditions. In these cases, it may be necessary to deviate from the standard conditions.

Determination of Property Changes. Before a property change due to environmental impact can be detected, it is of the utmost importance to characterize the material to be exposed as thoroughly as possible in the unexposed state. It has to be taken into account that the production process of the material might already have resulted in a heterogeneous material in regard to its properties on the surface compared to the bulk.

In most cases, an environmental impact on a material first affects its surface before it accumulates and spreads over the bulk of the material. This brings up two consequences for the determination of property changes: especially in the early stages of an environmental impact a heterogeneous distribution of property changes between the surface and bulk will result [15.43] and secondly, the first effects of weathering will be able to be detected by surface-emphasizing detection techniques.

Generally, weathering-induced degradation will start on a molecular level. For instance impurities in the material or external contamination with highly reactive secondary molecules can cause an increased reactivity in this region and act as the starting point of the degradation process, which can then spread like an infection until ultimately the whole bulk of the material is affected by the degradation process [15.43]. This means that detection techniques for weathering effects that are able to detect changes on a molecular level have the potential to detect the earliest stages of a degradation process.

Guidance for the determination of property changes of general interest is given for plastics by ISO 4582 (Plastics – determination of changes in color and varia-

tions in properties after exposure to daylight under glass, natural weathering or laboratory light sources) and for paints and varnishes by ISO 4628 (Paints and varnishes – evaluation of degradation of coatings; designation of quantity and size of defects, and of intensity of uniform changes in appearance), Parts 1–10.

A number of detailed techniques for the investigation of individual property changes are described in separate standards. Common testing procedures of effects of environmental impacts and – as far as they exist – their respective standards can be found in Table 15.2.

A review of the analytical techniques to look for the reasons for the observed changes can be found in *Kämpf* [15.44] and other references [15.45–49]. A number of these techniques are listed in the following.

Table 15.2 Common test procedures for property changes due to environmental impact on plastics, paints and varnishes

Property category	Individual property assessed	Standard
General	Mass Dimension	
Appearance	Gloss retention	ISO 2813
	Light transmission	ISO 13468-1
	Haze	ISO 14782
	Blistering	ISO 4628-2
	Cracking	ISO 4628-4
	Flaking	ISO 4628-5
	Chalking	ISO 4628-6 (tape method) ISO 4628-7 (velvet method)
	Corrosion around a scribe	ISO 4628-8
	Filiform corrosion	ISO 4628-10
	Cracking or crazing	
	Delamination	
	Warping	
	Colorimetry, for instance yellowing	ISO 7724-1
	Biofilm formation	
Migration of components from inside to surface		
Mechanics	Tension (particular elongation at break)	ISO 527, all parts
	Flexibility	ISO 178
	Impact strength	
	Charpy impact strength	ISO 179-1, ISO 179-2
	Izod impact strength	ISO 180
	Puncture test	ISO 6603-1, ISO 6603-2
	Tensile impact strength	ISO 8256
	Vicat softening temperature	ISO 306
	Temperature at deflection under load	ISO 75, parts 1–3
Dynamic mechanical thermal analysis	ISO 6721, parts 1, 3, and 5	
Chemistry	Effect of immersion of sample in chemicals	ISO 175
	Chemical changes (such as the detection of oxidation products by infrared spectroscopy)	

Table 15.3 Analytical techniques that can be used for spot and surface analysis (see also Sect. 6.1, surface chemical analysis)

Acronym	Meaning	Principle/assessed property	Resolution	References
EMA	Electron beam micro-analysis	Excitation by electrons, emission of x-ray photons for elements boron to uranium. Applications: detection of inorganic inhomogeneities in polymeric materials	Lateral: 0.1–3 μm (minimum 13 nm)	[15.50]
SEM + EDX	Scanning electron microscopy coupled to energy dispersive analysis	As above, but energy dispersive analysis instead of focusing wavelength dispersive analysis. For light elements slightly inferior spectral resolution and lower sensitivity than EMA	Lateral: 1 μm , Depth: \approx 1 μm	[15.51, 52]
TEM	Transmission electron microscopy	Scattered and unscattered electrons are detected after excitation with electrons. In crystalline regions electron diffraction occurs	Lateral: 0.2–10 μm	[15.53]
LAMMA	Laser microprobe mass analysis	Excitation by photons. Laser light is focussed through a light microscope onto the sample, which is caused to evaporate. Emitted ions are detected in time-of-flight mass spectrometer. Detection limit better than 10^{-18} – 10^{-20} g or concentrations in ppb range	Lateral: better than 1 μm Depth: > 0.1 μm	[15.54, 55]
ESCA (XPS)	Electron spectroscopy for chemical analysis (x-ray photoelectron spectroscopy)	Photoionization of electrons on inner atomic shells by characteristic x-ray irradiation. Quantitative identification of atoms, determination of bonding state, oxidation states, depth profiling, identification of polymers. Detection of inorganic or polymeric impurities on polymer matrix. Crude depth profiling possible by angle-resolved XPS (control of analyzer collection angle)	Lateral: 1–1000 μm . Imaging: e.g. 0.1–10 mm Depth: 1–10 nm	[15.56, 57]
AES	Auger electron spectroscopy	Emission of secondary electrons after excitation with x-ray. In combination with ablation by sputtering allows depth profiling	Lateral: 0.1–3 μm Depth: 0.4–2.5 nm	[15.58]
(TOF-) SIMS	(Time-of-flight) secondary ion mass spectrometry	Surface is sputtered with positively charged ions. Emitted particles are neutral as well as secondary ions; the latter are detected by means of mass spectrometry Trace detection of polymers, composition of copolymers and polymer blends, detection of additives or contamination on polymer surfaces, determination of molecular mass	Lateral: < 50 μm , (imaging SIMS: 200 nm), Depth: 1 nm	[15.59, 60]
XFA	X-ray fluorescence analysis	Excitation by photons, emission of photons. Applicable for trace detection of impurities at 10^{10} – 10^{13} atoms/cm ²	Lateral: 1 μm	[15.61]
ATR-IR	Attenuated reflection infrared spectroscopy	Absorption spectroscopy with infrared radiation source. Sample is characterized using multiply attenuated reflection of IR between sample surface and totally reflecting crystal on top. Vibrational spectra allow qualitative and quantitative analysis of functional groups and render information on the constitution. Carbonyl bands can give measure for oxidative ageing	Lateral: \approx 3 mm	[15.62]
Micro-IR	Micro-infrared spectrometry	Coupling of infrared spectrometer to microscope	Lateral: 1 μm	[15.63]
AFM	Atomic force microscopy	The force between the tip and the surface of the sample is monitored while scanning over it	Depth: 0.5 nm	[15.64]
LM	Light microscopy	Photons of visible light transmitted through, or reflected from, the sample material are depicted	Lateral: \approx 1 μm	[15.65]

Table 15.4 Analytical techniques allowing the investigation of bulk changes

Acronym	Meaning	Principle/assessed property	References
	Optical transmission spectroscopy (IR, Vis, UV)	Species are identified by the frequencies and structures of absorption, emission, or scattering features, and quantified by the intensities of these features. Enable trace analysis of organic additives such as heat and UV stabilizers, flame retardants, slip and deforming agents, solvent or monomeric or oligomeric residues, softeners	[15.66]
	Thermo-analytical techniques	Investigate a physical property of the sample as a function of a controlled temperature program. Increased analytical value by coupling to infrared or mass spectrometers, for instance TG-FTIR or TG-MS	[15.67]
AAS	Atomic absorption spectrometry	Atomized either by flame or electrothermally; AAS is characterized by selective resonance absorption of neutral atoms of the light of monochromatic light, proportional to its concentration	[15.68]
XFA	X-ray fluorescence analysis	Emission and detection of characteristic x-ray radiation of atoms after excitation by means of high-energy γ -ray Bremsstrahlung. Allows multi-element analysis. Semiquantitative analysis of inorganic components in polymers	[15.61]
ICP-MS	Inductively coupled plasma mass spectrometry	Ionization of a sample and separation of the ions in a mass spectrometer. Allows multi-element analysis. Remarkably lower detection limits (ppt range) than AAS. Only low concentration solutions usable	[15.69]
GPC	Gel permeation chromatography	The molar mass of polymers dissolvable in GPC solvents (most commonly tetrahydrofuran or chloroform) can be determined as retention time in chromatographic columns that work according to the size exclusion principle. Requires calibration of molar mass as function of retention time. Gives the complete molecular-weight distribution curve	[15.70]
CL	Chemiluminescence	Weak photon emission in first approach linear to reaction rate of oxidation reaction detected by for instance photomultipliers. Very sensitive means to follow oxidative ageing kinetics of polymers. Depending on transmission properties of the sample surface biased. No direct information on emitting species	[15.71–73]

Spot Analysis of Polymer Surfaces. The aforementioned spatial heterogeneous reaction of most interactions between polymeric materials and the environment implies the necessity for imaging microscopic techniques. These allow a distinctive analysis of spots within the bulk as well as the surface to be done.

Polymer Bulk Detection Techniques. *Changes in the Composition (Polymer-Copolymer-Additives-Fillers).* The techniques listed under this topic also look at bulk properties but particularly allow conclusions to be drawn about the composition of a multicomponent system.

Limits of Lifetime Predictions. For lifetime predictions many industrial areas have already made the transition from strong dependence on long-term practical tests to strong reliance on short-term laboratory test results. In these cases the lifetime of the material mostly depends on the impact of only one or two, often relatively constant, exposure parameters, e.g. the temperature, that dominate the limitation of lifetime.

For polymeric materials exposed to natural weathering conditions lifetime predictions based on laboratory tests are much more complex. The results of property changes of polymeric materials as a consequence of

Table 15.5 Techniques particularly suited to determine changes in composition

Acronym	Meaning	Principle/assessed property	References
NMR	Nuclear magnetic resonance	Resonance interaction between the nuclear spins of, for instance, ^1H or ^{13}C atoms of the sample, which is placed in a homogenous external magnetic field, with high-frequency radio waves. Allows analysis of composition and structural changes, such as chain branching and stereochemical configuration. NMR is not sensitive enough for minor components	[15.74, 75]
IR	IR/Raman spectroscopy	Vibrational spectra allow qualitative and quantitative analysis of functional groups (kind and concentration) and render information on the constitution. Carbonyl bands can give measure for oxidative ageing	[15.76]
UV/Vis	UV/Vis micro-spectrophotometry	For depth profiling, typically microtome cross-section slices of the sample are investigated in transmission mode. Allows the detection of the formation or disappearance of chromophoric groups, such as degradation products of the polymer as well as additives	[15.77]
ESCA	Electron spectroscopy for chemical analysis	For the principles see Table 15.3. Applicable for depth profiling in combination with sputtering	Sect. 6.1.2
SIMS	Secondary-ion mass spectrometry	For principles see Table 15.3. Applicable for depth profiling in combination with sputtering	Sect. 6.1.3
Pyrolysis-MS	Pyrolysis mass spectrometry	A sample is pyrolyzed using heat, and the fractions are analyzed by a mass spectrometer to which the pyrolysis cell is coupled	[15.78]

accelerated artificial and long-term outdoor exposures may depend on

1. the specific material under test (e.g. polymer type, formulation, dimensions, processing conditions, the age and the initial moisture content of the test specimen at the start of exposure),
2. the exposure conditions (e.g. mean and maxima of the UV irradiance, temperature, relative humidity and time of wetness, acidic or biological attack, the season when outdoor exposure is started and when it is terminated), and
3. the type of analytical determination and evaluation of the property changes (e.g. physical or chemical properties, surface- or bulk-influenced properties).

This means that lifetime prediction for polymeric materials needs a lot of information on the ageing behavior of the material under consideration, on the artificial and outdoor exposure conditions and on the determination of relevant material properties. These requirements mean that lifetime prediction remains an art rather than a science.

For several decades, scientists had a fundamental knowledge of the weathering performance of the different types of polymeric material in use. Developments of

new formulations or techniques mostly did not dramatically decrease or increase their performance. Because of a lack of confidence in results from artificial accelerated tests the different lifetimes of these new polymeric materials were, estimated by comparative artificial or/and short-time outdoor exposure tests.

During this period, the normally applied procedure of lifetime prediction consisted in simply comparing the radiant exposures from artificial tests with the expected radiant exposures in the field of application. There was no consideration of the influence e.g. of different spectral distributions of irradiance, temperatures, relative humidities and cycles of wet and dry periods. And, even now, we have no confirmation that the reciprocity law is generally valid for the different irradiance levels applied in natural and laboratory exposure tests [15.79, 80]. Only over the last two decades, the lack of confidence in results from artificial accelerated tests is decreasing and knowledge on the influence of different climatic quantities and other weather factors is continually growing.

Today, the rapid progress of developing new polymeric materials with clearly changed formulations and additives that meet the demands of new processing technologies and environmental restrictions, e.g. the

reduction of volatile organic compounds and waste disposal, does not allow sufficient durability testing by outdoor exposure. For the lifetime of their products, the producing and processing industries have to rely on data determined by accelerated exposure tests and on lifetime predictions on the basis of these data.

Therefore, there is an increasing activity of research on different methods of lifetime prediction based on reliable laboratory tests [15.25].

15.2 Emissions from Materials

15.2.1 General

Emissions from materials influence the surrounding environment. Gaseous emissions – mainly volatile organic compounds (VOCs) – into indoor air are of special interest due to the fact that they affect indoor air quality (IAQ). VOCs are of importance because they are strongly related to the so-called sick-building syndrome (SBS). Materials are not the only source of indoor air pollution. Other important sources are every type of combustion (e.g. fire places, gas cooking), especially smoking (environmental tobacco smoke (ETS)) and the use of household chemicals (sprays, solvents e.g.). Whereas these kinds of sources can be influenced by the user (to use or not to use it) materials emissions cannot be influenced by the user to the same extent. Often the user is simply not aware that materials might have emissions.

To reduce emissions from materials, first of all knowledge is needed about

1. what is contained in the material,
2. what is emitted (quality),
3. how much is emitted (quantity),
4. duration of the emissions (time behavior, ageing).

In addition to these material parameters environmental parameters such as temperature, relative

humidity, and air exchange rate influence the emissions or the resulting concentration in air.

1. understanding actual in-service conditions and its variability,
2. understanding the influence of the variety of actions caused by outdoor exposure, and
3. confidence in results from laboratory tests at controlled exposure conditions.

To measure materials emissions, emission test chambers are used, which simulate environmental conditions such as those mentioned above. Air sampling and analysis is an essential part of emission testing.

15.2.2 Types of Emissions

Emissions from materials can be divided into classes of volatility and product classes depending on their field of application.

Classes of Volatility

According to [15.81,82] volatile organic compounds are divided into very volatile organic compounds (VVOCs), VOCs, semi-volatile organic compounds (SVOCs) and particulate organic matter/organic compounds associated with particulate organic matter (POM) (Table 15.6) depending on their volatility.

An important sum parameter for VOCs is the so-called total volatile organic compounds (TVOCs) value. According to ISO 16000-6, the TVOC is defined as sum of volatile organic compounds sampled on Tenax TA and eluting between and including *n*-hexane and *n*-hexadecane in a nonpolar gas-chromatography (GC) column.

Table 15.6 Classification of organic indoor pollutants according to their volatility

Description	Abbreviation	Boiling point range* (°C)
Very volatile (gaseous) organic compounds	VVOC	< 0 to 50–100
Volatile organic compounds	VOC	50–100 to 240–260
Semivolatile organic compounds	SVOC	240–260 to 380–400
Organic compounds associated with particulate matter or particulate organic matter	POM	> 380

* Polar compounds are at the higher end of the range

Product Classes

Depending on the material and its intended field of use many chemicals are contained that might be released during the use of the material. Some examples of materials relevant to indoor use are listed here

1. lacquer, paints, coatings,
2. wood, wood-based materials,
3. furniture,
4. construction products,
5. insulating materials,
6. sealants,
7. adhesives,
8. flooring materials,
9. wall papers,
10. electronic devices,
11. printed circuit boards.

Even in the simple case of e.g. a single polymer it can still contain remaining monomers or solvents and additives from the production that can generally be emitted. Additionally special types of polymers like e.g. polycondensated resins (e.g. urea-formaldehyde resins) can be hydrolyzed and release monomers. Furthermore materials can contain a wide spectrum of additives like, e.g.

1. plasticisers,
2. biocides (e.g. from production, pot preservatives, film preservatives),
3. flame retardants,
4. photoinitiators,
5. stabilizers.

15.2.3 Influences on the Emission Behavior

The emission behavior of materials is influenced by material and environmental parameters.

Material Parameters

The following material parameters are of importance for emission behavior

1. type of material,
2. ingredients,
3. structure,
4. composition,
5. surface,
6. age.

According to [15.83] the rate of emission of organic vapors from indoor materials is controlled by three fun-

damental processes: evaporative mass transfer from the surface of the material to the overlaying air, desorption of adsorbed compounds, and diffusion within the material.

Environmental Parameters

The following environmental parameters influence emission behavior

1. temperature (T),
2. relative humidity (RH),
3. air exchange rate (n),
4. area specific ventilation rate (q),
5. air velocity.

According to [15.83] temperature affects the vapor pressure, desorption rate, and the diffusion coefficients of the organic compounds. Thus, temperature affects both the mass transfer from the surface (whether by evaporation or desorption) and the diffusion mass transfer within the material. Increases in temperature cause increases in the emissions – as can be seen in Fig. 15.14 as an example – due to all three mass-transfer processes mentioned above.

The air exchange rate is another important parameter that affects the concentration of organic compounds in indoor air. The air exchange rate is defined as the flow of outdoor air entering the indoor environment divided by the volume of the indoor space, usually expressed in units of h^{-1} . The higher the air exchange rate the greater the dilution, assuming that the outdoor air is cleaner, and the lower the concentration (see Fig. 15.15 for example).

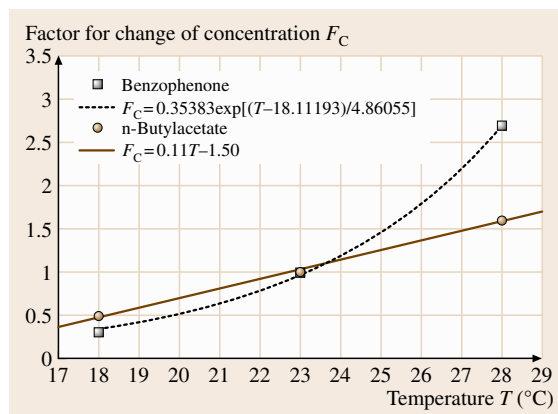


Fig. 15.14 Influence of temperature on the concentration (here the factor for the change of concentration) for a VOC and a SVOC emitted from a UV-curing acrylic lacquer applied to wood

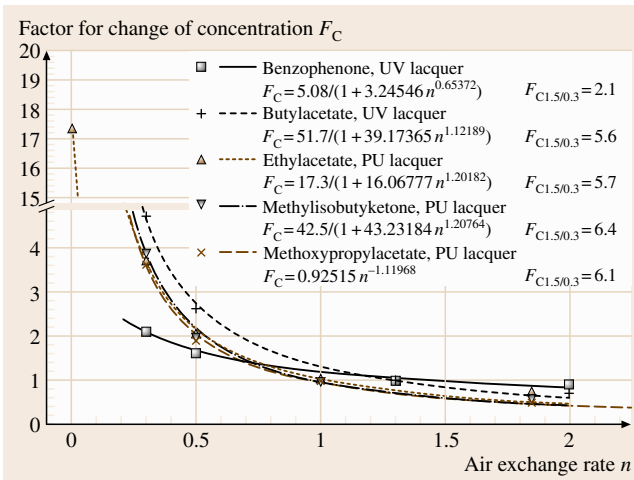


Fig. 15.15 Influence of the air exchange rate on the concentration (here the factor for the change of concentration) for some VOCs emitted from different lacquers (polyurethane (PU) lacquer, UV-curing acrylic lacquer) both applied to wood

Variation of the air exchange rate by a factor of 5 (Fig. 15.15: $F_{C1.5/0.3}$ ($n = 1.5 \text{ h}^{-1}/0.3 \text{ h}^{-1}$)) results in a change of concentration (F_C) of 5.6 to 6.4 with the exception of benzophenone. For benzophenone the concentration changes only by a factor 2.1, which is assumed to be due to adsorption effects of this SVOC.

15.2.4 Emission Test Chambers

Emission test chambers are necessary to provide defined environmental conditions for the evaluation of mater-

ials emissions. In addition to those mentioned above the following criteria have to be met

1. clean air supply,
2. emission-free or low-emission chamber materials (stainless steel or glass, low-emission sealings),
3. sufficient mixing of the chamber air,
4. tightness of the chamber,
5. low adsorption on chamber walls,
6. easy cleaning of the chamber after tests.

In Europe and meanwhile international a distinction is made between emission test chambers (EN ISO 16000-9 [15.84]) and emission test cells (EN ISO 16000-10 [15.85]). Furthermore EN ISO 16000-11 [15.86] exists, describing sampling and storing of material samples and the preparation of test specimen. It should be mentioned that these standards are made for the testing of building products, but the emission test chambers and, in the case of planar products, also the emission test cells are applicable for other kinds of materials. The chamber/cell parameters are listed in Table 15.7.

In Fig. 15.16 a general description of an emission test chamber according to EN ISO 16000-9 is shown. In Fig. 15.17 an example of an emission test cell according to EN ISO 16000-10 can be seen.

In the USA small emission test chambers are described in [15.83]. According to this standard small chambers have volumes between a few liters and 5 m^3 . Chambers with volumes of more than 5 m^3 are regarded as large chambers.

Table 15.7 Specifications for emission test chambers/cells

Volume (V)	Not specified
Temperature (T)	$23 \pm 2 \text{ }^\circ\text{C}$
Relative humidity (RH)	$50 \pm 5\% \text{RH}$
Air exchange rate (n)	See q
Product loading factor (L)	See q
Area specific air flow rate ($q = n/L$)	
Flooring materials	$1.3 \text{ m}^3 \text{ m}^{-2} \text{ h}^{-1}$
Wall materials	$0.4 \text{ m}^3 \text{ m}^{-2} \text{ h}^{-1}$
Sealing materials	$44 \text{ m}^3 \text{ m}^{-2} \text{ h}^{-1}$
Air velocity at the sample surface	$0.1 - 0.3 \text{ m s}^{-1} *$
Background concentration	
Single VOC	$2 \text{ } \mu\text{g}/\text{m}^3$
TVOC	$20 \text{ } \mu\text{g}/\text{m}^3$
Minimum standard air sampling times (duplicate sampling)	$72 \pm 2 \text{ h}$ $28 \pm 2 \text{ d}$

* only for EN ISO 16000-9, not mandatory for EN ISO 16000-10

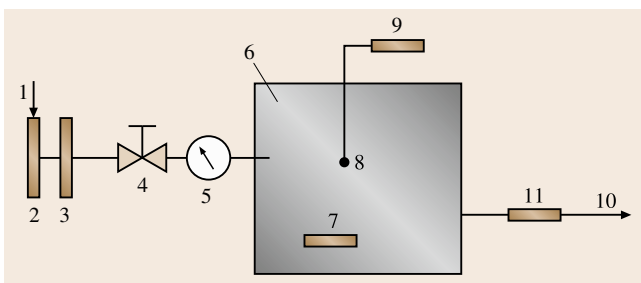


Fig. 15.16 General description of an emission test chamber (1: air inlet, 2: air filter, 3: air-conditioning unit, 4: air flow regulator, 5: air flow meter, 6: test chamber, 7: device to circulate air and control air velocity, 8: temperature, humidity, and air velocity sensors, 9: monitoring system for temperature and humidity, 10: exhaust outlet, 11: manifold for air sampling)

For Japan small emission test chambers are described in [15.87]. Small chambers in this standard are defined to have volumes between 20 l and 1 m³. The test temperature is 28 ± 1 °C, differing from EN ISO 16000-9 and 16000-10 where it is fixed to 23 ± 2 °C.

In Europe as well as in the USA additional standards for the testing of formaldehyde emissions and emissions from wood-based materials exist. These are EN 717-1 [15.88], ASTM D 6007-02 [15.89], ASTM D 6330-98 [15.90] and ASTM E 1333-10 [15.91].

In Fig. 15.18 a 1 m³ chamber is shown loaded with an adhesive applied to glass plates for emission testing. The test specimen is brought into the center of the chamber where the air velocity is adjusted to 0.1–0.3 m/s. Before loading of the chamber the background concentration has been proven to be below the limits described in Table 15.7. The chamber shown [15.92] allows cleaning by thermal desorption at temperatures of up to 240–260 °C in combination with a purging with clean dry air of up to four air exchanges per hour.

In Fig. 15.19 a 20 l chamber is shown also loaded with an adhesive applied onto glass plates. The conditions of temperature, relative humidity, area specific ventilation rate, air velocity, and clean air supply are the same as for the 1 m³ chamber shown in Fig. 15.18.

In Fig. 15.20 a photograph of a FLEC is shown. The test conditions are the same as described above. Therefore even the FLEC with a volume of only 35 ml allows emission rates comparable to the emission test chambers as long as planar homogenous materials are investigated with a smooth surface where emission from small edges plays no major role.

Larger chambers with volumes of more than 1 m³ [15.87], 5 m³ [15.83], or 12 m³ [15.88] might be useful if complex products like e.g. machines (e.g. printers, copiers) have to be tested for emissions. Emissions from hard-copy devices (TVOC, styrene, benzene, ozone and dust) can also be measured [15.93]. This test method has been published for measurements according to the German Blue Angel mark [15.94] and is based on the international standards for emission test chambers EN ISO 16000-9 and ISO 16000-6 for air sampling and analysis, see Sects. 15.2.5 and 15.2.6.

15.2.5 Air Sampling from Emission Test Chambers

The appropriate air sampling method depends on what has to be measured. The most common method

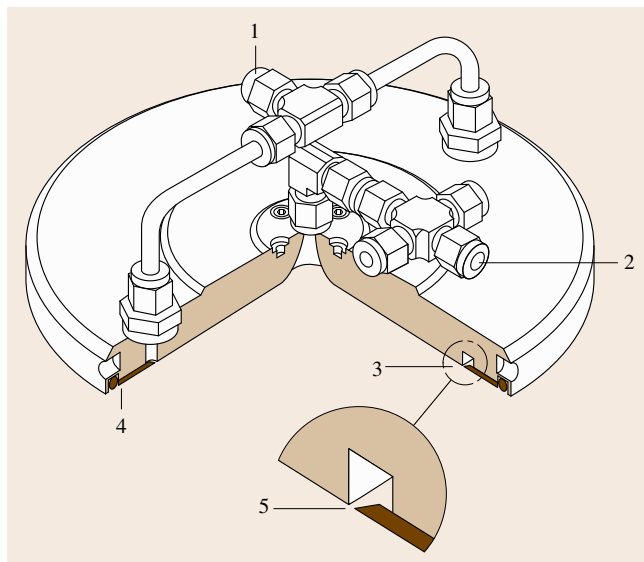


Fig. 15.17 Description of an example of an emission test cell: general description in three dimensions of the field and laboratory emission cell (1: air inlet, 2: air outlet, 3: channel, 4: sealing material, 5: slit)



Fig. 15.18 1 m³ emission test chamber loaded for a test with a flooring adhesive on glass plates (courtesy of BAM)

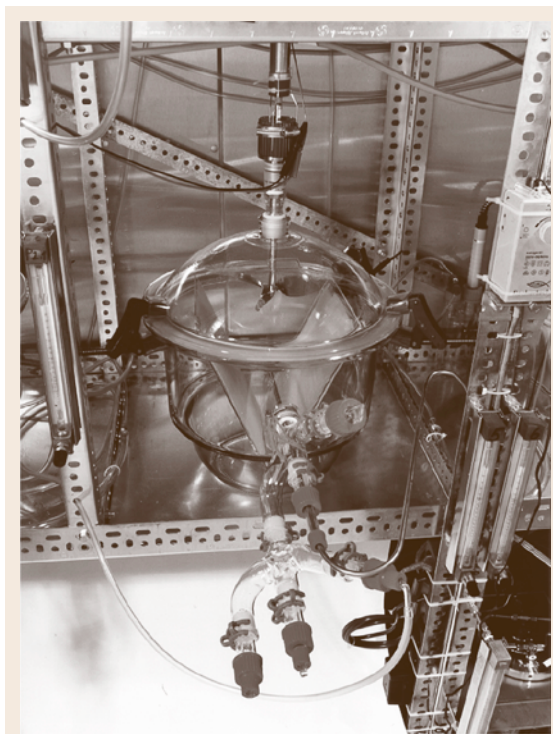


Fig. 15.19 201m³ emission test chamber – loaded with a flooring adhesive on glass plates (courtesy of BAM)

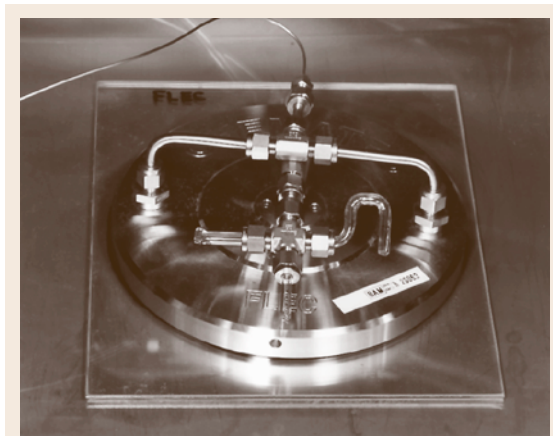


Fig. 15.20 Field and laboratory emission cell (FLEC) according to EN ISO 16000-10) (courtesy of BAM)

for VOC is sampling on Tenax (polyphenylenoxide, based on 2,6-diphenylphenol) as absorbance for enrichment according to ISO 16000-6 [15.95] and

ISO 16017 [15.96] followed by thermal desorption and analysis with gas-chromatography mass spectrometry (GC/MS, see Sect. 15.2.6). Another method being of increasing importance is sampling on 2,4-dinitrophenylhydrazine (DNPH) cartridges according to ISO 16000-3 [15.97] followed by solvent desorption (acetonitrile) and analysis by high-performance liquid chromatography (HPLC) using a diode-array detector (DAD) or UV detection (Sect. 15.2.6).

For sampling of VVOCs from air a wide spectrum of method exists that strongly depend on what has to be measured.

SVOCs can either be sampled by Tenax up to boiling points of about 360 °C (*n*-C₂₂-alkane) [15.98] or, for higher boiling SVOCs, by special polyurethane foam (PUF) [15.99, 100] with subsequent solvent extraction. The sampling of SVOCs on PUF has been practiced successful for biocides [15.101] and flame retardants [15.102].

Table 15.8 gives an overview on sorbents for sampling of volatile organic compounds belonging to different ranges of volatility.

Figure 15.21 shows examples of sorbent tubes used for sampling of volatile organic compounds from (chamber) air.

15.2.6 Identification and Quantification of Emissions

The most common method for the identification and quantification of volatile organic compounds from air is gas chromatography with subsequent mass spectrometry (GC/MS). Using GC (Sect. 1.2) the substance mixtures are separated into the single compounds and, by MS (Sect. 2.1), the mass spectra are generated. Mass spectra can often be used successful for library searches to obtain initial information on the identity of substances. For the confirmation of identity, calibration, and quantification, authentic standards has to be used. High-performance liquid chromatography with either diode-array detectors (HPLC/DAD) or UV detectors (HPLC/UV) (Sects. 1.2 and 2.2) is used for substances for which GC is not suitable, e.g. for substances that are thermally unstable.

Figure 15.22 shows a chromatogram resulting from a chamber test of PVC flooring, air sampled with Tenax TA followed by thermal desorption and GC/MS analysis.

In Table 15.9 the substances are listed with their concentration on different days over the testing time of

Table 15.8 Guidelines for sorbent selection (after [15.103, 104])

Sample tube sorbent	Approx. analyte volatility range	Maximum, Temperature (°C)	Specific surface area (m ² /g)	Example analytes
CarbotrapC CarbopackC Anasorb GCB2	(<i>n</i> -C ₈ to <i>n</i> -C ₂₀)	> 400	12	Alkyl benzenes and aliphatics ranging in volatility from <i>n</i> -C ₈ to <i>n</i> -C ₁₆
Tenax TA	bp 100–400 °C (<i>n</i> -C ₇ to <i>n</i> -C ₂₆)	350	35	Aromatics except benzene, apolar components (bp > 100 °C) and less-volatile polar components (bp > 150 °C)
TenaxGR	bp 100–450 °C (<i>n</i> -C ₇ to <i>n</i> -C ₂₆)	350	35	Alkyl benzenes, vapor-phase PAHs and PCBs and as above for Tenax TA
Carbotrap CarbopackB Anasorb GCB1 (<i>n</i> -C ₄) Chromosorb 102	(<i>n</i> -C ₄ /C ₅ to <i>n</i> -C ₁₄)	> 400	100	Wide range of VOCs incl., ketones, alcohols, and aldehydes (bp > 75 °C) and all apolar compounds within the volatility range specified. Plus perfluorocarbon tracer gases
Chromosorb 106	bp 50–200 °C	250	350	Suits a wide range of VOCs incl. oxygenated compounds and haloforms less volatile than methylene chloride
Chromosorb 106	bp 50–200 °C	250	750	Suits a wide range of VOCs incl. hydrocarbons from <i>n</i> -C ₅ to <i>n</i> -C ₁₂ . Also good for volatile oxygenated compounds
Porapak Q	bp 50–200 °C (<i>n</i> -C ₅ to <i>n</i> -C ₁₂)	250	550	Suits a wide range of VOCs including oxygenated compounds
Porapak N	bp 50–150 °C (<i>n</i> -C ₅ to <i>n</i> -C ₈)	180	300	Specifically selected for volatile nitriles; acrylonitrile, acetonitrile and propionitrile. Also good for pyridine, volatile alcohols from EtOH, MEK, etc.
Spherocarb*	–30–150 °C (C ₃ to <i>n</i> -C ₈)	> 400	1200	Good for very volatile compounds such as VCM, ethylene oxide. CS ₂ and CH ₂ Cl ₂ . Also good for volatile polars e.g. MeOH, EtOH and acetone
Carbosieve SIII* Carboxen 1000* Anasorb CMS*	–60–80 °C	400	800	Good for ultra-volatile compounds such as C ₃ and C ₄ hydrocarbons, volatile haloforms and freons
Zeolite Molecular Sieve 13X**	–60–80 °C	350		Used specifically for 1,3-butadiene and nitrous oxide
Coconut Charcoal* (rarely used)	–80–50 °C	> 400	> 1000	Rarely used for thermal desorption because metal content may catalyze analyte degradation. Petroleum charcoal and Anasorb 747 are used with thermal desorption in the EPA's volatile organic sampling train (VOST), methods 0030 and 0031

* These sorbents exhibit some water retention. Safe sampling volumes should be reduced by a factor of 10 if sampling a high relative humidity (> 90%)

** Significantly hydrophilic. Do not use in high-humidity atmospheres unless silicone membrane caps can be fitted for diffusive monitoring purposes. CarbotrapC, CarbopackC, CarbopackB, Carboxen and Carbosieve SIII are all trademarks of Supelco, Inc., USA; Tenax is a trademark of the Enka Resean Institute; Chromosorb is a trademark of Manville Corp.; Anasorb is a trademark of SKC, Inc.; Porapak is a trademark of Waters Corporation

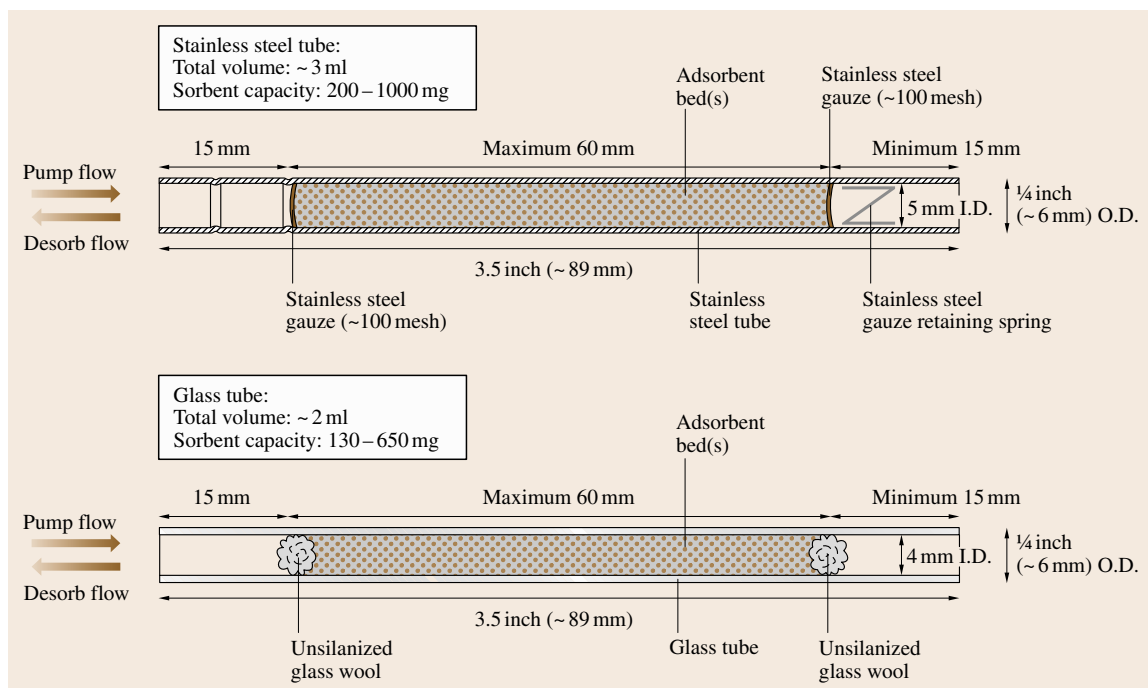


Fig. 15.21 Example of the construction of commercially available adsorbent tubes for thermal desorption

28 d. All named substances are quantified by calibration using authentic standards. The unidentified **VOCs** are quantified by toluene equivalents (according to ISO 16000-6 [15.95]).

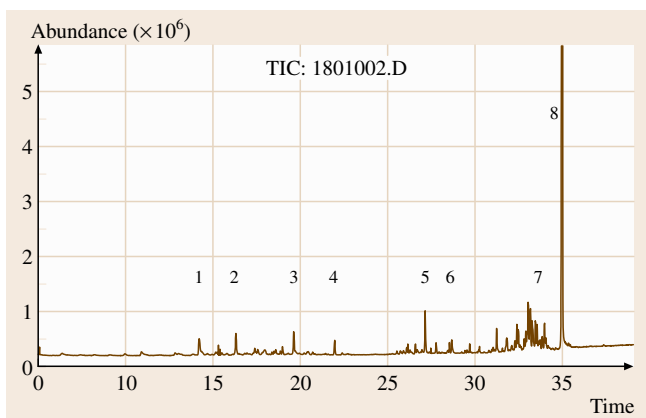


Fig. 15.22 Chromatogram from the measurement of a **PVC** flooring on the 28th day. 1: Methylisobutylketone (**MIBK**); 2: Decane; 3: Undecane; 4: Cyclodecane (internal standard); 5: Butyldiglykol; 6: *n*-methylpyrrolidone; 7: different **VOCs**; 8: 2,2,4-trimethyl-1,3-pentanediol diisobutyrate (**TXIB**)

Calculation of Emission Rates

From the concentration of **VOCs** in the chamber air, emission rates (**ER**) or specific emission rates (**SER**) can be calculated. The most common for the expression of specific emission rates for materials is the area specific emission rate (**SER_a**) [15.84, 85], which is calculated from the concentration *C* at a certain time (e.g. 3 d (72 h) or 28 d) according to

$$\text{SER}_a = Cq = CnL^{-1}, \quad (15.3)$$

where **SER_a** is the are specific emission rate at a certain time [$\mu\text{g m}^{-2} \text{h}^{-1}$], *C* is the concentration at a certain time [$\mu\text{g m}^{-3}$], *q* is the area specific ventilation rate [$\text{m}^3 \text{m}^{-2} \text{h}^{-1}$], *n* is the air exchange rate [h^{-1}], *L* is the product loading rate [$\text{m}^2 \text{m}^{-3}$].

Specific emission rates can also be expressed as length, volume or unit specific emission rates. Often specific emission rates are named emission factors (**EF**) [15.83, 87].

15.2.7 Time Behavior and Ageing

Time behavior of material emissions can also be evaluated by means of emission test chambers. After introducing the test specimen into the chamber, 100% of

Table 15.9 List of emitted substances and their concentrations for PVC flooring for different times of testing

PVC	Concentration ($\mu\text{g}/\text{m}^3$)						
	24 h	3rd day	7th day	10th day	14th day	21st day	28th day
MIBK (methylisobutylketone)	111	65	53	45	39	32	30
Decane	55	35	28	25	23	20	16
Undecane	44	28	22	20	18	16	13
Butyldiglycol	123	75	40	48	44	35	31
N-Methylpyrrolidon	45	30	17	20	15	13	15
VOCs ($n \approx 23$)	438	308	273	253	221	175	159
TXIB (2,2,4-trimethyl-1,3-pentandiol diisobutyrat)	1251	863	760	698	641	614	539
TVOC	2067	1404	1193	1109	1001	905	803

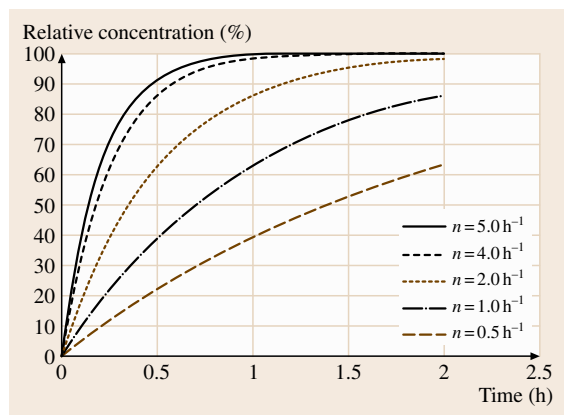
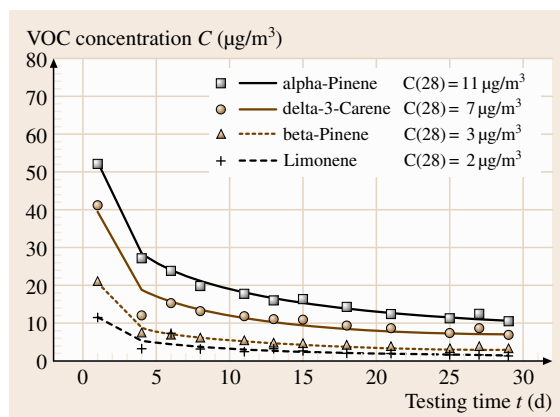
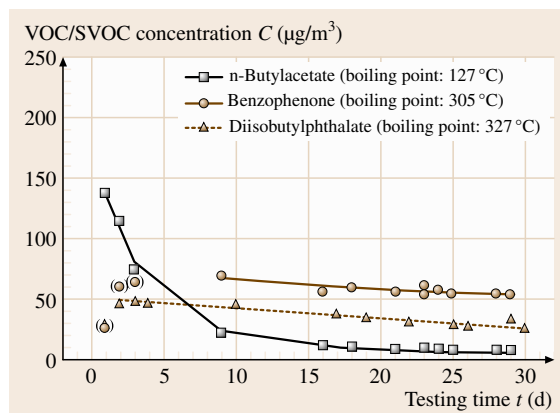
the equilibrium concentration is usually reached within a few hours for VOCs, depending on the air exchange rate (Fig. 15.23); the concentration is given by

$$C = \text{SER}_a(1 - e^{-nt})LV^{-1}n^{-1}, \quad (15.4)$$

where V is the chamber volume [m^3].

This increase of concentration at the beginning of the emission test is mainly of interest if short-time emissions are to be investigated, for example to study the emissions from fast printing hard-copy devices (where printing time is often less than half an hour) in order to consider this for the calculation of emission rates.

If the testing time is long enough at least a trend for the variation of concentration or specific emission rates over time can be evaluated. Typically measurements in test chambers run over 28 d. VOCs during this time usually show decreasing concentrations, as can be


Fig. 15.23 Theoretical percent concentration profiles for various air exchange rates

Fig. 15.24 Terpene emissions from a particleboard over the testing time of 29 days ($T = 23^\circ\text{C}$, $\text{RH} = 45\%$, $n = 1 \text{ h}^{-1}$, $L = 1 \text{ m}^2 \text{ m}^{-3}$, $q = 1 \text{ m}^3 \text{ m}^{-2} \text{ h}^{-1}$)

Fig. 15.25 Variation of concentration of a VOC and two SVOCs over time. Notice the increase of concentration for the SVOCs over the first few days

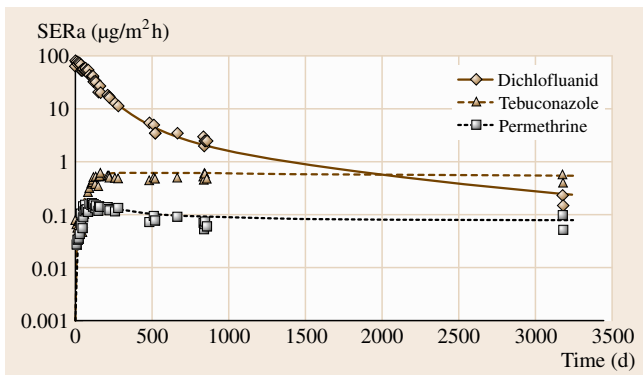


Fig. 15.26 Area specific emission rate (SER_a) for the three biocides dichlofluanid, tebuconazole and permethrine. For the increase at the beginning the SER_a has to be regarded as apparent specific emission rate due to adsorption (sink effects) on the chamber surfaces that result in reduced concentrations in air. The experiment was started in 1994 and is still running

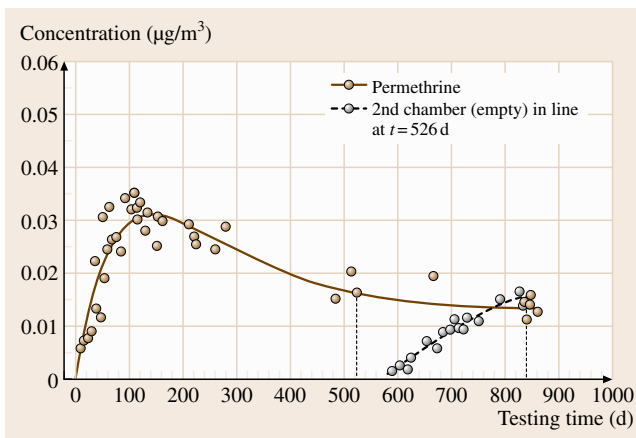
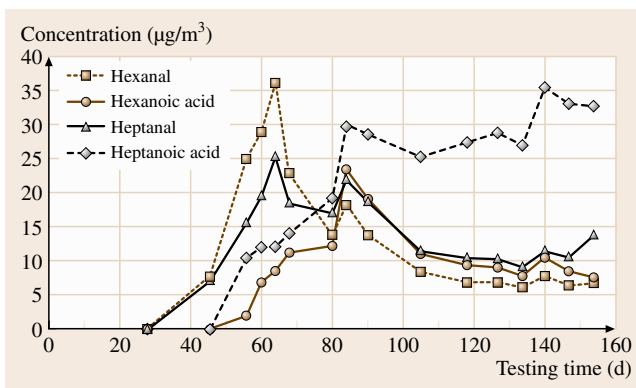


Fig. 15.27 Empty chamber connected to the test chamber: permethrine (after [15.105])



seen for example in Fig. 15.24 for terpene emissions from a particleboard. The terpene emissions result from the pine wood used for the production of the particleboard.

For SVOC emissions the decrease over time is normally not as strong as they have lower vapor pressures and therefore depletion of the boundary layer of the material takes longer. Furthermore they can show a longer increase at the beginning of the test due to adsorption effects (Fig. 15.25).

For extremely-low-volatility SVOC – often called POMs (Table 15.6) – a distinct emission behavior can generally be observed. For these substances increasing concentrations over weeks and months can be observed as shown in Fig. 15.26 for some biocides [15.101].

The time to reach the maximum concentration was about 125 d for tebuconazole and permethrine. After reaching its maximum, the concentration remained almost constant over time for nearly ten years (tebuconazole) or showed only a slight decrease (permethrine).

Generally it should be stated, that organic substances with extremely low vapor pressure show a tendency to adsorb strongly on surfaces. One result of this is that SVOC/POM are retained by the material itself and thus possibly only show slow migration to the surface of the material, slow desorption from materials surface and therefore delayed emissions. Another reason for slowly increasing concentrations is the adsorption of emitted low-volatility organic substances on inner surfaces of the emission test chamber (chamber walls): so called sink effects. Figure 15.27 illustrates this behavior for the example of a biocide (permethrin) where a second chamber was switched in line to a first chamber that was already in equilibrium [15.105]. As can be seen it took about 250 d until the second chamber was also in equilibrium. Relevant amounts of biocide were adsorbed on chamber walls that acted as sinks. This could be shown by elution of the chamber walls after the end of the test. Knowing the amount of substance transported out of the chamber by air flow together with the amount of substance adsorbed on chamber walls generally allows, even for this very-low-volatility substance, one to calculate emission rates after a shorter testing time.

Fig. 15.28 Secondary emissions from a flooring adhesive (solid line with boxes: hexanal, dashed line with boxes: hexanoic acid, solid line with circles: heptanal, dashed line with circles: heptanoic acid) ◀

15.2.8 Secondary Emissions

Secondary emissions are a special case of emissions. Measurements have shown that these emissions do not occur from the beginning of the test. They are sometimes formed during testing, as was shown for emissions from a flooring adhesive [15.103]. At the be-

ginning of the test only typical VOC emissions (mainly solvents) were detected. After more than 28 d, when a test is normally broken off, increasing concentrations of aldehydes and organic acids were already observed (Fig. 15.28). It is supposed that these are secondary products of autoxidation processes of unsaturated oils in the material or on the material's surface.

15.3 Fire Physics and Chemistry

Fire may be defined as an uncontrolled process of combustion generating heat, smoke and toxic. It is essentially of fuel available for gas phase combustion that controls the fire intensity. In fires it is the heat transfer from flames that heats liquid or solid fuels and thereby generating gaseous fumes which reacts with the oxygen in the air. This feedback process make fires an in general instable process which may either grow or go out.



Fig. 15.29 Ignition of the left side cardboard boxes occurs when the combustible volatiles are leaving the surface at a sufficient rate (courtesy of SP)

Fires cause a lot of damage to the society in form of deaths and injuries as well as economical losses. In Europe, North America, Australia and Japan the national losses of lives in fires is between 0.7 and 2.0 persons per 100 000 each year and lot more get injured. The direct economical losses are in the order of 0.1–0.3% of the GDP per year [15.106]. The cost of fire protection of buildings amounts to as much as 2.5–5% of the total cost of building and construction.

Designers and product developers strive at minimizing weight and material consumption by using materials with low densities and making products for the same purpose smaller and smaller. As will be explained below both low density and small thicknesses make materials prone to ignite and burn faster, it is important that the issue of fire properties is considered already in an early stage when developing new materials and products.

It is obvious that fire is an important aspect of the materials–environment interactions treated in this chapter, which may detrimentally influence the performance of materials, products and technical systems.

In the following – based on a brief review of the fundamentals of fire physics and chemistry – methods and techniques to characterize the fire behaviour of materials are compiled.

In addition to the methods for fire testing presented in this chapter, methods to characterize the general thermal properties of materials are compiled in Chap. 8 on thermal properties.

15.3.1 Ignition

A mixture of air and a gaseous fuel may *ignite* and burn if the concentration ratio of the fuel and the air is within the upper and lower combustion limits. For instance, the lower flammable limit of methane in air at normal temperature and pressure is 5% by volume, and the upper limit is 15% by volume. As a matter of fact, for most simple hydrocarbons, the lower and upper flammable limits in air correspond to an equivalence ra-

Table 15.10 Critical temperatures of some liquids (after *Quintiere* [15.107])

Liquid	Formula	Flash point (K)	Boiling point (K)	Autoignition point (K)
Propane	C ₃ H ₈	169	231	723
Gasoline	Mixture	≈ 228	≈ 306	≈ 644
Methanol	CH ₃ OH	285	337	658
Ethanol	C ₂ H ₅ OH	286	351	636
Kerosene	≈ C ₁₄ H ₃₀	≈ 322	≈ 505	≈ 533

tio of approximately 0.5 and 3, respectively. For further information about ignition reference [15.106].

Gas mixtures can be ignited either by *piloted ignition* or by *autoignition*. Piloted ignition occurs when a local source of heat or energy is introduced, while autoignition may occur momentarily for the entire volume, normally at much higher temperatures than piloted ignition.

A liquid or solid may start to burn when combustible volatiles are leaving the surface at a sufficient rate to form a combustible concentration. Piloted ignition occurs when the concentration of combustible fumes near a pilot (e.g. a small flame or a spark igniter) reaches the lower flammable limit.

The rate of evaporation for a liquid is controlled by the liquid temperature. Therefore liquids will at certain conditions reach the lower limit concentration at a given temperature called the *flash point* depending on the ease of evaporation. Table 15.10 gives the flash point temperatures, boiling temperatures and autoignition temperatures for some liquid fuels.

Time to Ignition

Most common combustible solids ignite by piloted ignition when the surface reaches a temperature of 250–450 °C. The autoignition temperature exceeds normally 500 °C, see Table 15.10 for some liquids and Table 15.11 for some plastics.

The time it takes the surface of a material (solid or liquid) to reach a critical temperature like the ignition temperature when heated depends on the dimensions and the thermal properties of the material. Two typical

Table 15.11 Ignition temperatures of some plastics, grouped by category (after *Babrauskas* [15.106])

Category of solid	Ignition temperature (°C)	
	Piloted	Auto
Thermoplastics	369 ± 73	457 ± 63
Thermosetting plastics	441 ± 100	514 ± 92
Elastomers	318 ± 42	353 ± 56
Halogenated plastics	382 ± 79	469 ± 79

cases can be identified, *thin solids* and *thermally thick solids* approximated as *semi-infinite solids*.

For *thin solids*, less than about 2 mm, the temperature is assumed uniform and the thickness is decisive for the ignition time. Then when assuming a constant total heat flux \dot{q}''_{tot} (by radiation and convection) to a body surface and constant material properties, the temperature rise is proportional to the time and the heat flux over the parameter group ρcd

$$T_s - T_i = \frac{\dot{q}''_{\text{tot}} t}{\rho cd}, \quad (15.5)$$

where T_s is the exposed body surface temperature, T_i the initial temperature, t time, ρ density, c specific heat capacity and d thickness. That means that time to ignition is directly proportional to the density and the thickness of a thermally thin material, i. e. the surface weight.

When a thin solid is surrounded by air at ambient temperature and heat by radiation \dot{q}''_{tot} in (15.5) may be replaced by incident radiation \dot{q}''_r . This yield in practice just slight underestimations of time to ignition due to the disregard of cooling by convection and emitted radiation at elevate surface temperatures.

A similar expression as given by (15.5) can be derived for *thermally thick solids*, i. e. the thickness is larger than $2\sqrt{at}$, where t is time and a is thermal diffusivity, and where in turn $a = k/(c\rho)$, where k is the thermal conductivity. Then for a constant net heat flux \dot{q}''_{tot} and constant thermal properties, the surface temperature rise can ideally be calculated as

$$T_s - T_i = \frac{2\dot{q}''_{\text{tot}}\sqrt{t}}{\sqrt{\pi}\sqrt{k\rho c}}. \quad (15.6)$$

The above expression indicates that the rate of surface temperature rise and thereby the time to ignition is proportional to the product of the heat conductivity k , the specific heat capacity c and the density ρ . The grouped property $\sqrt{k\rho c}$ is designated the *thermal inertia* of the material.

In this case the influence by convection and emitted radiation from the exposed surface when the tempera-

Table 15.12 Example of material thermal properties at room temperature (after *Quintiere* [15.107])

Material	Density (kg/m ³)	Conductivity (W/(m K))	Specific heat capacity (J/(kg K))	Thermal inertia (W s ^{1/2} /(m ² K))
Polyurethane foam	20	0.03	1400	29
Fiber insulating board	100	0.04	2000	89
Wood, pine	500	0.14	2800	440
Wood, oak	700	0.17	2800	580
Gypsum plaster	1400	0.5	840	770
Concrete	2300	1.7	900	1900
Steel (mild)	7850	46	460	12900
Copper	8930	390	390	36900

ture rises must be considered. Thus

$$\dot{q}_{\text{tot}}'' = \varepsilon(\dot{q}_r'' - \sigma T_s^4) + h(T_g - T_s), \quad (15.7)$$

where ε is the surface emissivity and absorptivity coefficient, σ the Stefan–Boltzmann constant, h the convection heat transfer coefficient, and T_g the ambient gas temperature. Now the net heat flux \dot{q}_{tot}'' is not constant anymore as it depends of the surface temperature T_s . A numerical integration is therefore needed to calculate the development of T_s and thereby the time to reach the ignition temperature.

Given the incident radiation is \dot{q}_r'' and the ambient gas temperature equal to the initial temperature are constant, a constant \dot{q}_{tot}'' can, however, be obtained for calculating the time to reach ignition temperature explicitly from (15.6). Then heat transfer at the surface is approximated as

$$\dot{q}_{\text{tot}}'' = \varepsilon \dot{q}_r'' - \dot{q}_{\text{cr}}'', \quad (15.8)$$

where \dot{q}_{cr}'' is the critical flux at ignition i. e. the equilibrium heat flux when the surface has reached the ignition temperature T_{ig} . It may be identified from (15.6) as

$$\dot{q}_{\text{cr}}'' = \varepsilon \sigma T_{\text{ig}}^4 + h(T_{\text{ig}} - T_g). \quad (15.9)$$

This approximation is a constant upper limit of the magnitude of the cooling term \dot{q}_{cr}'' before ignition and leads to overestimates of the times to ignition. For further information on alternative approximative solutions see [15.106].

As an example the time to ignition of a surface of thick wood suddenly exposed to an incident radiation of 25 kW/m² is estimated. The wood is initially at room temperature and surrounded by air at the same temperature, 20 °C. The wood surface emissivity ε is assumed equal unity, convection heat transfer coefficient $h = 12 \text{ W/m}^2 \text{ K}$, the other thermal properties accord-

ing to Table 15.12 for pine and the ignition temperature 350 °C. Calculated surface temperature development is shown in Fig. 15.30. The full line shows the temperature when applying the heat flux according to (15.7), while the dashed line is obtained when assuming the heat flux constant with time according to (15.8) and (15.9). From Fig. 15.30 it can be noted that the ignition time is 65 s according to the full line while the approximative theory yields 100 s. The latter value can also be calculated by inserting (15.8) and (15.9) into (15.6) and solve for the time t when the surface temperature equals the ignition temperature. (A general observation by the author is that much better agreements are generally obtained by the simplified approach if the critical heat flux in (15.8) is reduced by 30%.)

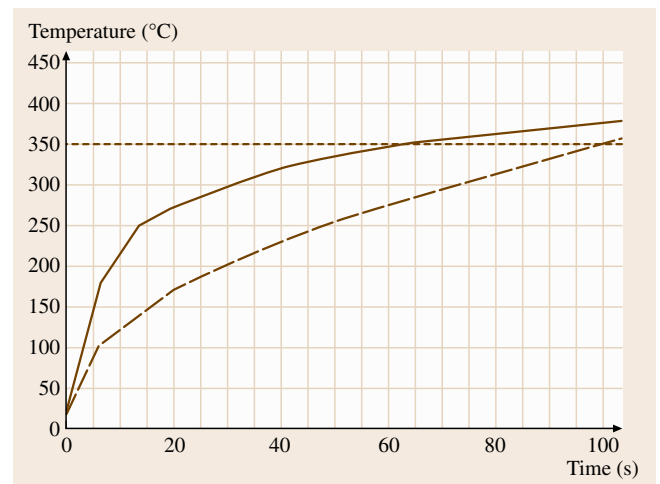


Fig. 15.30 Calculated temperature development of a wood surface exposed an incident radiation of 25 kW/m². The *full line* indicates the temperature development when applying (15.7) and the *dashed line* when approximating the heat according to (15.8,15.9)

Anyhow, the estimated of times to ignition as given above are very crude and based on the assumption of homogeneous materials with constant material properties, not varying with temperature or time. The formulas are, however, very useful for the intuitively understanding of which material properties govern the ease of ignition.

The thermal inertia varies over a very large range for common materials. It depends on the product of density and conductivity, and as conductivity in turn increases with increasing density. Insulating materials have low conductivities k (by definition) and low densities ρ . Therefore the influence of a change in density has a considerable influence on products fire behaviour. The specific heat capacity on the other hand depends on the chemical composition of the material and does not vary much between common materials except for wood which has a relatively high specific heat capacity. Table 15.12 shows how the thermal inertia increases considerably with density for various combustible and noncombustible materials. Note for instance that the thermal inertia of an efficient insulating material like polyurethane foam is less than a hundredth of the corresponding value of wood.

As an example a low density wood fiber board may have a density of 100 kg/m^3 and a conductivity of 0.04 W/(mK) , while a high density wood/fiber board have a density of 700 kg/m^3 and a conductivity of 0.15 W/(mK) . As such boards can be assumed to have about the same specific heat capacity, it can be calculated that the thermal inertia of the high density fiber board is more than 25 times higher of that of the low density board. The low density fiber board can therefore ideally be estimated to ignite 25 times faster than the high density fiber board when exposed to the same constant heating conditions.

Thickness and thermal inertia have also a decisive influence on *flame spread properties* of a material or product. Flame spread can be seen as a continuous ignition process and is therefore governed by the same thermal material properties as ignition. Thus the fire hazard of a material or a product can as a rule of thumb be estimated based on its density as this property governs how easily the temperature of its surface can be raised to the ignition temperature. Table 15.12 gives the thermal properties of some solid materials. These values are approximative and indicative and may vary depending on material quality as well as on measuring techniques.

Spontaneous Ignition

Self-heating leading to spontaneous ignition (commonly used interchangeable with spontaneous combustion) can take place in porous materials or in bulks of granulate solids [15.106]. It involves exothermal (heat generating) processes which raises the temperature of the material. Whether the self-heating process leads to thermal runaway and spontaneous ignition of the material or not, is a competition between heat generation and heat dissipation.

The most common heat generating process is the oxidation of organic materials in the solid phase and oxygen in the gas phase. Therefore porous materials are more susceptible to self-heating than solid materials as oxygen can diffuse through the material and reach surfaces with combustible substances in the interior of the material. A classical example of spontaneous ignition is a rag with absorbed vegetarian oil. Unsaturated fatty acids in the oil are readily oxidised, and with the large surface area and poor heat dissipation of the rag, the temperature rise is fast and leads commonly to ignition.

The problem of self-heating frequently arises in storages of e.g. agricultural products, coal, wood fuels and municipal waste. Another example is self-heating of fiberboards in storages after production [15.108]. Storages of wood chips or pellets are examples of fuels that commonly self-heat and ignite.

In storage of fuels like wood pellets, biological reactions dominate at temperatures below 100°C , when the temperature has reached that level, the rate of chemical oxidation increases and the chemical reactions could further increase the temperature. The content of moisture is of importance for the self-heating process as it is necessary for the growth of biological organisms. Generally, wood fuel containing less than 20% moisture does not self-heat [15.109]. Further, vaporization and condensation of water in the bulk transport heat within the material. The moisture content of the material additionally influences the heat conduction properties. The Winds could further augment heat generating reactions by increasing the availability of oxygen.

Glowing and Smouldering Ignition

When a surface of a combustible solid is exposed to intense heat, it is changed either by melting or charring and it liberates gaseous products. The surface of a charring material may obtain very high temperatures and undergo rapid oxidation, which may be described as *glowing* ignition. When glowing in ambient air the temperature is typically in excess of 1000°C . Flaming may

also occur either before or after the glowing ignition of the surface. Wood and fabrics are examples of products which may ignite first by glowing at the surface and then burn by flaming [15.106].

Smouldering can be defined as a propagating, self sustained exothermic reaction wave deriving its heat from oxidation of a solid fuel. It is a relatively slow combustion process controlled by the rate of air entering the combustion zone. The smouldering can only sustain if the material is insulating so that the combustion zone does not lose too much heat and high temperatures can be maintained. Smouldering is only common with porous or granular materials that can char. Materials which are known to smoulder under certain circumstances include [15.106]

1. wood and cellulosic products in finely divided form,
2. paper,
3. leather,
4. cotton,
5. forest duff, peat and organic soil,
6. latex foam,
7. some types of polyurethane, polyisocyanurate and phenol formaldehyde foams.

Smouldering may also occur in insulation products of mineral wool containing high levels of binders as well as in cellulose loose-fill insulations.

A smouldering fire may break out into flaming, when the combustion zone reaches for example a wood surface or when for some reason more oxygen becomes available. As smouldering fires are very slow they may last very long and may reach flaming conditions not until very long times, could in some cases be several months.

15.3.2 Combustion

A burning candle may serve as a general illustrator of burning processes. Due to heating from the flame, fuel evaporates from the wick and is transported by diffusion towards the surrounding air/oxygen. The combustion takes place at the flame, which emit light. Hot combustion products are transported upwards as they are lighter than the cool ambient air. Inside the flame envelope there are fuel vapours and no oxygen and outside it is vice versa, there is no fuel and ambient concentrations of oxygen. A candle flame is an example of a laminar diffusion flame governed by molecular diffusion.

Flames may be categorized as diffusion flames or premixed flames. In *diffusion flames* fuel gas and oxygen are transported into a reaction zone and mixed due

to concentration differences. In *laminar flames* the diffusion is by molecular diffusion. In flames larger than about 30 cm the laminar flow breaks up into eddies and we get a *turbulent diffusion flame*. Although laminar flames may be important in the ignition phase of a fire, the *turbulent* diffusion flames are the most significant in real fires.

Burning Rate

Burning rate is defined as the mass loss of solid or liquid fuel consumed by combustion per unit time. A general formula the mass burning rate may be written as

$$\dot{m}'' = \frac{\dot{q}}{L},$$

where \dot{q} is the net heat flux to the fuel surface and L the heat of gasification. The latter is a material property. Typical values of L are given in Table 15.13.

When burning the fuel surface is heated by radiation and convection by nearby flames and hot gases. Heating by *radiation* may also come from other sources like remote flames, layers of combustion gases or hot surfaces. The temperature of the surface of thermoplastics and liquids will in principle be at the boiling point. For charring materials like wood and thermosetting plastics an insulating char layer will form, which will hamper the heat flux to the surface and thereby reduce the burning rate.

The *heat release rate (HRR)* or energy release is the most important quantity for characterizing a fire. It rep-

Table 15.13 Values of heat of gasification and effective heat of combustion (after *Quintiere* [15.107])

Fuel	L (MJ/kg)	ΔH_c (MJ/kg)
Liquids		
Gasoline	0.33	43.7
Heptane	0.50	43.2
Kerosene	0.67	43.2
Ethanol	1.00	26.8
Methanol	1.23	19.8
Thermoplastics		
Polyethylene	1.8–3.6	43.3
Polypropylene	2.0–3.1	43.3
Polymethyl methacrylate (PMMA)	1.6–2.8	24.9
Nylon 6/6	2.4–3.8	29.6
Polystyrene foam	1.3–1.9	39.8
Char formers		
Polyvinylchloride (PVC)	1.7–2.5	16.4
Woods	4.0–6.5	13.0–15.0

Table 15.14 Yields of carbon monoxide Y_{CO} and mass optical density D_m depending on ventilation (after *Quintiere* [15.107])

Fuel	Overventilated or fuel lean conditions	D_m (m ² /kg)	Underventilated or fuel rich conditions
	Y_{CO} (kg/kg)		Y_{CO} (kg/kg)
Propane	0.005	160	0.23
Heptane	0.01	190	NA
Wood	0.004	37	0.14
Polymethyl methacrylate (PMMA)	0.01	109	0.19
Polystyrene	0.06	340	NA
Polyurethane flexible foam	0.03	330	NA
Polyvinylchloride (PVC)	0.06	400	0.36

represents the size of the fire and relates directly to flame height and production rates of combustion products like smoke and toxic gas species.

The heat release rate \dot{q} is the product of the burning rate \dot{m}'' and ΔH_c

$$\dot{q} = \dot{m}'' A \Delta H_c$$

where A is the fuel area involved. The effective heat of combustion is a material property (Table 15.13).

Combustion Products

The nature of the combustion products developed in a fire depends on the fuel as well as on the entire fire process. The chemical reactions occurring in the decomposition of the fuel and in the reaction with oxygen depend on temperature, gas flow conditions, ratio between fuel and air available for the combustion process etc. If more air is available than needed for a complete burning process the condition is assumed to be over ventilated or process fuel lean. For less air, the process is termed underventilated or fuel rich. If the fuel to air ratio perfectly match the burning process is *stoichiometric*. A parameter that quantitatively represents over- and underventilation in fires is the equivalence ratio ϕ defined as

$$\phi = \frac{(\text{mass of fuel}/\text{mass of air})}{(\text{mass of fuel}/\text{mass of air})_{\text{stoich}}}$$

Thus for $\phi < 1$ the fire is fuel lean and for $\phi > 1$ fuel rich.

In a similar way as the heat of combustion gives the energy release, *yields* give the mass production rate of combustion product species per unit mass of fuel. As an example the rate of CO mass produced \dot{m}_{CO} can be calculated as

$$\dot{m}_{CO} = \dot{m} Y_{CO}$$

where \dot{m} is the rate of burning and Y_{CO} the yield of CO. The yields of various species are reasonably constant as the fire conditions are well ventilated $\phi < 1$. Under fuel rich conditions $\phi > 1$, however, the yields changes and the production rates increases for many toxic species. Yields of carbon monoxide are given in Table 15.14.

Light is attenuated by *smoke* mainly due to soot particles. Smoke has in many cases a decisive influence on the ability to escape a fire. Therefore the propensity of a material to release smoke is an essential fire property of a material. The reduced intensity of light I can be measured with a lamp and photocell at a distance l away and be expressed as

$$I = I_0 e^{-\kappa l},$$

where I_0 is the original intensity. The parameter κ is the extinction coefficient with the dimension one over unit length (m⁻¹). For a given mass of fuel burnt material m in a closed volume V the extinction coefficient κ may be obtained as

$$\kappa = \frac{m D_m}{V},$$

where D_m is the mass optical density with the dimensions mass over area (kg/m²), which is a material property for overventilated conditions. Values for some common products are given in Table 15.14.

Toxic Products

Organic fuels like wood and polymers contain mainly carbon and hydrogen. Thus when burning with enough oxygen available (fuel lean conditions) the combustion process may be completed and mainly carbon dioxide and water are generated. However, under fuel rich conditions or when the combustion process is interrupted due to cooling (quenching), the combustion process is incomplete and several chemical species are generated

which may be toxic. The most important is *carbon monoxide* which is the cause of most fire casualties. Products containing *nitrogen* like polyurethane may generate toxic substances like hydrocyanic acid HCN and *isocyanates* which have a very high toxic potency.

Soot particles may also constitute a toxicological threat as they can transport toxic species from fires adhered to their surfaces deep into the lungs.

Corrosive Products

Some products like polyvinylchloride PVC generate acid gases like HCl when burning, which is irritating for the eyes and air passages although not necessarily fatal during inhalation. This may hamper the evacuation of a building on fire. In addition HCl dissolves in water droplets and forms hydrochloric acid, which is highly corrosive and may deposit on metal surfaces and cause damages. Such corrosive damages may show up long after a fire and cause a great threat to electronic equipment which in many cases must be discarded after a fire although not being directly exposed flames or hot gases and seemingly being undamaged.

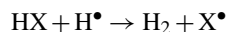
Flame Retardants

There are numerous chemical compounds used to inhibit the combustion process in materials, mainly plastics. Flame retardants can function by intervening in the combustion process chemically or physically, or through a combination of both. Common for all flame retardants is that they interfere early in the combustion process during the heating phase or the ignition phase.

Physically a flame retardant additive can act as a barrier by forming a layer of char when exposed to heat. This layer then protects the underlying material from heat and thereby from degradation and the ensuing generation of combustible fumes. Further, these flame retardants remove the direct connection between the oxygen in air and the fuel [15.110]. Flame retardants can also act by cooling. In such cases the additive degrades endothermally, thereby cooling and possibly diluting the gas mixture of the combustion process, for example through the production of water vapour. In certain instances additives can be used that act only by diluting the material with inert substances such as fillers. This will typically reduce the heat release from a certain weight of a material but have little effect on the ignitibility of the material per se.

Chemically flame retardants can act by accelerating the initial breakdown of the material, causing the material to withdraw from or to flow away from the ignition source or by promoting the generation of a char

layer. Other flame retardants may act in the gas phase through removal of free radicals that are the motor in the exothermic combustion process. The process is shown by the formula below



where X represents a halogen.

The main families of flame retardants are *halogenated* (i.e., containing chlorine or bromine), *phosphorous* based, *nitrogen* based, inorganics and others (including antimony trioxide and nanocomposites). Many of these systems work either in isolation or together with some systems exhibiting synergistic effects when used in combination.

Brominated flame retardants have the highest market share in terms of turnover while *aluminum hydroxide* has the highest market share by weight. A global growth of approximately 3% has been projected by the flame retardants industry in the near future with inorganic flame retardants (e.g. aluminum hydroxide) having the highest projected growth rate.

Flame retardants have received broad application in correlation with the ubiquitous use of plastics in our society. While certain plastics have unacceptable ignition and flame spread properties, they also exhibit highly desirable mechanical properties, i.e., their ability to be formed into a myriad of shapes and applications. Thus, the safe application of plastics has at least partially been dependent on the use of flame retardant additives to modify undesirable ignition and flame spread properties.

In recent years *environmental concerns* about many of these additives has prompted questions about the suitability of their broad use. Legislation is under way in Europe and elsewhere to control the use of these chemicals. Research into quantifiable tools to determine the true environmental impact of the use of flame retardants to obtain a high level of fire safety have, however, clearly identified the need to consider such issues holistically [15.111].

15.3.3 Fire Temperatures

Temperatures in natural fires depend on actual combustion conditions such as fuel/air ratio and heat losses to the environment mainly by radiation. Thus the maximum temperature of turbulent diffusion flames of free-burning fires is in the order of 800–1200 °C. Fires in enclosures with limited openings may at the most reach temperatures in the order of 1200 °C.

Mechanically ventilated fires may under certain very favourable conditions for combustion develop extremely high temperatures. Thus fires in tunnels may reach temperatures of nearly 1400 °C with ordinary fuels of cellulosic materials. Temperatures of that order of magnitude were measured in several tests carried out in a tunnel in Norway 2003 where fires in trailers loaded with wood pallets and furniture were simulated. Such temperature levels expose the surrounding tunnel walls to devastating thermal loads causing concrete linings to spall and fall off in pieces. Therefore tunnels linings must be designed to resist much higher temperatures than other building structures.

Room Fires

The various stages of a fire in a room or compartment with limited openings are shown in Fig. 15.31. Initially the fire is not affected by the surrounding structures. In this *growth stage*, which may last from a few minutes to several hours, the fire intensity is *fuel controlled*. As the fire intensity increases the temperature rises and more and more combustible fumes are released. At a certain stage the fire may start to grow rapidly and *flashover*. After that in the *post-flashover* stage the fire consumes all available oxygen inside the compartment. It is then a *ventilation controlled* or *fully developed* fire. The combustion rate at this stage depends on the amount of oxygen or air that can enter the fire compartment, i. e. it depends on the size and shape of the compartment openings. At this stage the fire generates a lot of heat, smoke and toxic gases, and the temperature of the combustion gases is at least 600 °C and rises as the surrounding structures, i. e. walls, floors and ceilings heats up. Excess combustible fumes will at this stage emerge

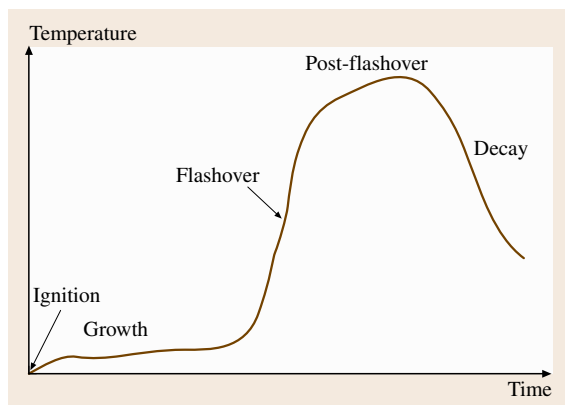


Fig. 15.31 General description of the various stages of a room fire (courtesy of SP)

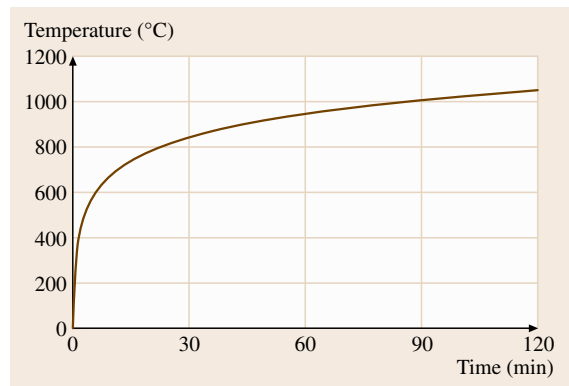


Fig. 15.32 The standard time–temperature curve according to EN 1363 or ISO 834

outside the compartment openings and burn as flames shooting out from the openings. *Flashover* represents a crucial event in the development of a fire as it goes from being a local fire in one room or compartment to a much more severe fire having the potential of rapidly spreading heat and smoke throughout a building.

Significant building components must be designed to resist a fully developed fire. Such a fire is then usually simulated by the so called standard fire curve as shown in Fig. 15.32. This time–temperature curve is meant to simulate a typical fire at the post-flashover stage.

Compartments fire developments can be numerically modelled in three ways [15.112]. The simplest are the *one-zone models* where the entire compartment gas volume is assumed to be at uniform temperature. Mass flow in and out of the compartment is driven by buoyancy. Hot fire gases are lighter than the ambient air and flow out at the top of the openings and are replaced by cool fresh air further down. The fire temperature development will depend on the thermal inertia of the surrounding structure and on the size and height of the openings. Lower thermal inertia (in principle low density) and large openings implies faster fire growth higher temperatures. One-zone models are suited only for fully developed fires. In *two-zone models* the fire compartment is divided into an upper hot zone with fire gases and a lower zone with air at ambient temperature (Fig. 15.33) models are suited for fires before reaching flashover. More advanced are the so called **CFD** (computational fluid dynamics) models where the compartment is divided to a large number of volume elements. Then arbitrary fire conditions can be analysed in terms of temperature as well as concentrations of smoke and (toxic) gas species. **CFD** models are very

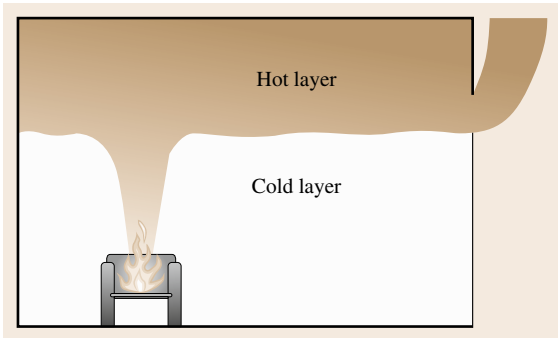


Fig. 15.33 Two-zone model of a room fire with an upper hot layer and a lower layer at ambient temperature (courtesy of SP)

powerful but require substantial computer capacities and detailed material property data.

15.3.4 Materials Subject to Fire

Structural Materials

The temperature in structures exposed to fully developed fires with gas temperatures reaching 800–1200 °C will gradually increase and eventually the structures may lose their load-bearing capacity as well as their ability to confine the fire to a limited space. In building codes fire resistance requirements are usually expressed in terms of time of a structure to resist a nominal or standard fire defined for example in the international standard ISO 834 or the corresponding European standard EN 1363-1 (Fig. 15.32). In USA the corresponding standard for determining fire resistance of building components is ASTM E-119.

Steel starts to lose both strength and stiffness at about 400 and above 600 °C more than half the strength is lost [15.113]. Therefore structural steel elements must in most cases be fire insulated by sprayed on compounds, boards, mineral wool or intumescent paint to keep sufficient load-bearing capacity when exposed to fire. An example of a steel structure failure due to fire was the collapse of two World Trade Center towers on September 11, 2001 after each of them had been hit by a big passenger airplane. A tremendous impact on the buildings but they did not collapse until after about half an hour. The jet fuel had started intense fires and when the strength and stiffness of the steel structures had been eroded due high temperatures the structures failed.

Concrete also loses strength and stiffness at high temperature [15.114]. This is, however, generally not

a problem as concrete has a high density and specific heat capacity as well as a low thermal conductivity. Therefore temperature rises slowly in concrete structures and even the steel reinforcement bars are in general well protected. More problematic is the tendency of concrete to spall when exposed to high temperatures. In particularly high strength concrete qualities are prone to spall. Spalling is not least a problem when designing road and railway tunnels where fire temperatures may be extremely high and where a collapse of a tunnel lining may have devastating consequences.

Wood loses both strength and stiffness as well at elevated temperature. It burns and chars gradually at a rate of about 0.5 mm/min when exposed to fire conditions. The char layer protects the wood behind from being directly exposed to fire conditions and thereby quickly heated and losing its load-bearing capacity. Timber structures therefore resist fire rather very well and can in many cases be used unprotected, see e.g. Eurocode 5 [15.115]. In many cases structural timber members like wall studs are protected from direct exposure by fire boards of for example gypsum and can therefore resist fire for very long periods of time.



Fig. 15.34 The jet fuel started intense fires that caused the World Trade Center towers to collapse on September 11, 2001

Polymers and Composite Materials

Thermoplastics and thermosetting materials decompose differently when exposed to heat. Thermoplastics can soften without irreversible changes of the material, while thermosetting materials are infusible and can not undergo any simple phase changes. They do not have a fluid state.

Many thermoplastics and thermosetting materials form chars when decomposed by heat. This char is as for wood in general a good insulator and can protect the underlying virgin material from heat and slow down the decomposition process.

The polymers possess different hazards in fires depending on their physical constitution and chemical composition. Foamed plastics and thin plastics ignite more easily and burn more vigorously than solid plastics. Below some characteristics are given for a few commercially important polymers. The thermal stability of *polyolefins* like polyethylene and polypropylene depends on branching of the molecule chains, with linear polymers most stable and polymers with branching less stable. *Polyvinylchloride (PVC)* has in general good fire properties as the chloride works as a flame retardant agent. However, the hydrogen chloride HCl, which is generated while burning, is corrosive and irritating and toxic and can impede the evacuation from a fire. *Polyurethanes (PU)* contain nitrogen and forms very toxic products like hydrogen cyanide and isocyanates. *PVC* and *PU* do also generate very dens smoke.

Composite materials consisting of a polymer and suitable reinforcing fibers (typically, glass, carbon or aramide material), also called fiber reinforced plastics (*FRP*), have become increasingly used in many areas of construction, such as airplanes, helicopters and high-speed crafts, due to the high strength/weight ratio. These materials are also chemically very resistant and do not corrode or rust. They are, however, combustible and as they are often meant to replace noncombustible materials, (steel, concrete) they could introduce new fire hazards. Another concern is that inhalable fibers might be generated from *FPR*-materials when burning. These fibers may also penetrate the skin causing irritation and inflammation, and carry toxic substances into the body. This could be a particular hazard when composite materials are mechanically destructed, e.g. in an air plane crash, when large amounts of fibers are released and become airborne.

15.3.5 Fire Testing and Fire Regulations

A lot of products to be put on the market need some kind of documentation, approval or certification, on their fire properties. These documents are usually based on fire tests performed according to various standards. Several organizations issue such standards which describes in detail how the tests shall be carried out. Nationally the most well known standards organizations issuing fire test standards are *BSI* in UK, *DIN* in Germany, and *ASTM* and *NFPA* in USA. Internationally both the European Committee for Standardization *CEN* and the International Organization for Standards *ISO* are very active in the field of fire safety.

There are mainly three categories of fire tests, reaction-to-fire, fire resistance and fire suppression tests. The *reaction-to-fire tests* evaluate materials and products properties in the early stage of a fire. They measure for example ignitibility and flame spread properties. Tests for measuring generations of smoke and toxic gases are often also associated with this cate-



Fig. 15.35 Fire-resistance testing of a glazed partition (courtesy of SP)

gory of tests. *Fire resistance tests* measure how long structural and separating building components can resist a fully developed fire from spreading from one compartment to another. A fire is then simulated in a fire resistance test furnaces (Fig. 15.35), where the temperature develops according to a standardized time-temperature curve as specified in e.g. EN 1363-1, ISO 834 or ASTM E-119. The specimen is then exposed to the simulated fire conditions. The temperature is measured on the other unexposed side and must during the test not rise so much that ignition can occur there. Neither must any flames come out on the unexposed side. Load-bearing elements must be able to carry their design load during the entire test period. *Fire suppression tests* are carried out on extinguishing media, e.g. dry powders and fire extinguishing foams, and on extinguishing equipment like sprinklers, portable extinguishers etc. The latter are tested in full scale and classified according the type of fires, cellulosic fuels, gasoline or electric equipment, and size of fires they can extinguish.

Buildings

A new testing and classification system for building materials and products has been developed within the European Committee for Standardization CEN and is gradually being introduced in the national regulations of the EU member states. Many building materials and products need to be tested as a basis for classification

and CE-marking. This is a harmonized way of declaring certain product properties regulated by EU member states.

For *reaction-to-fire* the so called Euroclasses A–F with several subclasses have been defined for construction products [15.116]. F means that no fire criterion has been declared. The classes A1 and A2 mean the products are denoted as more or less noncombustible. Example of class A1 products are totally inert materials like steel or concrete. A2 products contain limited amounts of combustibles like mineral wool insulations where the binder is combustible and may burn. Methods for carrying out the appropriate test are defined in the standards EN ISO 1182 Noncombustibility and EN ISO 1716 Calorific potential. For class A2 tests in the SBI (single burning item) apparatus according to EN 13823 (Fig. 15.36), are required as well.

To reach class B–D tests have to be done in the SBI apparatus and in the small flame test rig according to EN ISO 11925-2. Typical materials in class B are gypsum boards covered with carton. In class D you find for example solid wood panels.

The level of fire safety requirements in various types of buildings and occupancies are specified in national building codes. The level of safety depends on the character of the building in terms of height, occupants and use etc. The most rigorous requirements are in large and tall buildings and in public buildings where people stay overnight, e.g. hotels and hospitals. Surface linings

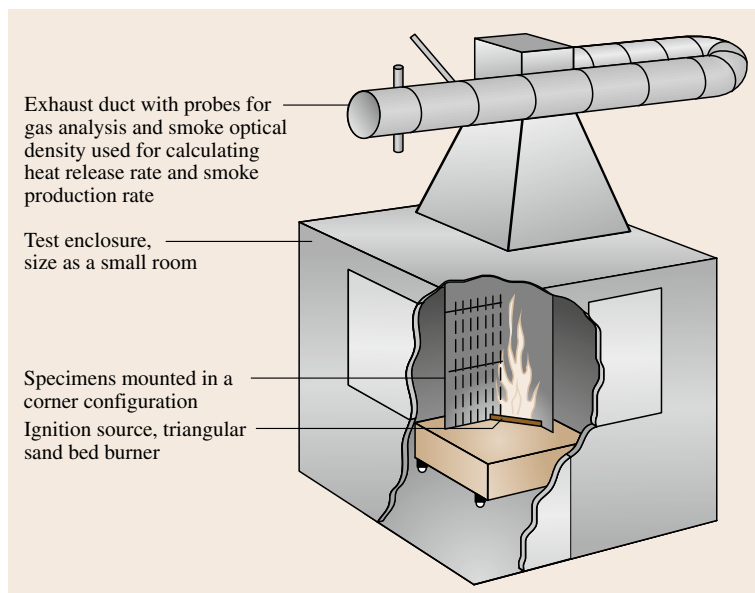


Fig. 15.36 In the SBI method (EN 13823) the 1500 mm high test specimens are placed in a corner (courtesy of SP)

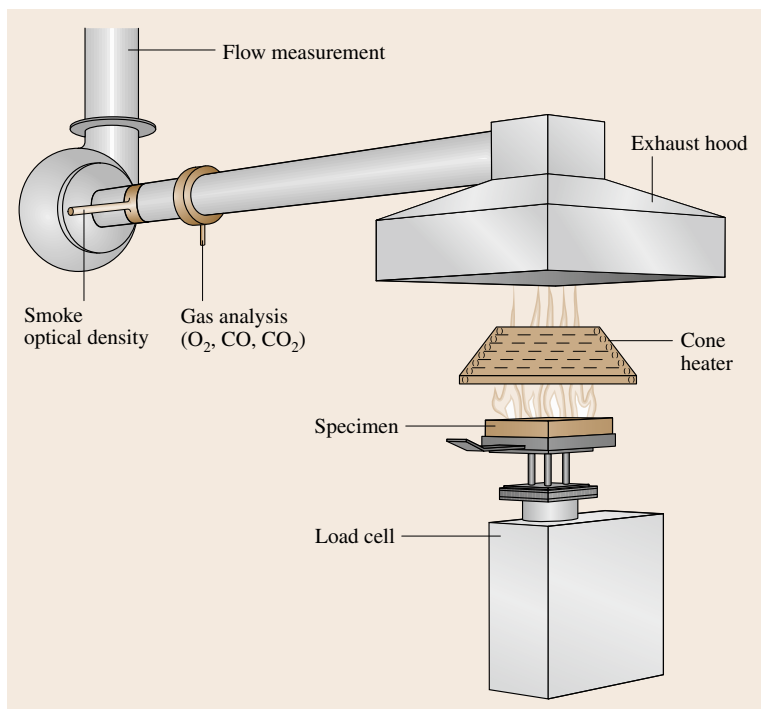


Fig. 15.37 The cone calorimeter measures heat release per unit area when a specimen is exposed to a given heat irradiance (courtesy of SP)

in for example escape routes must generally have very good fire properties, of class B or better.

Building elements may fail a fire resistance test as described above either by integrity, insulation or loss of load-bearing capacity. An integrity failure means that flames penetrate through an element meant to separate two rooms or fire cells in a building. Correspondingly an insulation failure means in short that the temperature rise on the unexposed side of a separating element exceeds 140 °C. Building elements are classified in terms of their fire resistance time, i. e. the time elapsed before failure in a fire resistance test. National building codes then specifies required fire resistance times of building elements and components depending on the level of risk of a failure, mostly in the range of 30–120 min. The former may refer to apartment doors in domestic dwellings and the latter to structural elements in high rise buildings.

In USA the so called Steiner tunnel test [ASTM E 84](#) is the major test method used for determining surface burning characteristics of wall lining materials.

Internationally [ISO](#) has published similar standards as [CEN](#) for testing fire properties of building products. Of special interest for material developers is the Cone Calorimeter [ISO 5660-1](#), as shown in [Fig. 15.37](#), for measuring heat release rates per unit area as a func-

tion of time of products when exposed to specified levels of heat irradiance. The results of these tests can among other things be used in fire safety engineering to calculate the heat release rates in full scale scenarios [[15.117](#)].

Transportation

Combustible plastics are increasingly used in transportation vehicles. They have in comparison with metallic materials several advantages. However, they all burn more or less. Therefore several test methods have been developed in the various sectors of transportation to evaluate their burning behaviour. The transportation industry is by nature very international, as vehicles are often marketed worldwide and used in several countries. Rules and regulation as well as test methods are therefore increasingly international. In some cases test methods are published by international standards bodies. In other areas the rules of US authorities have become so dominating worldwide that they in practice can be considered as international. Below some fire test methods used internationally in various sectors are presented briefly.

For *motor vehicles* the US Federal Motor Vehicle Safety Standards ([FMVSS](#)) has great influence on the industry worldwide. The most significant standard is the

small scale flame spread test **FMVSS 302** [15.118] for motor vehicle interior components (Fig. 15.38).

The **UIC** (Union Internationale des Chemins de Fer) has established a code covering regulations and recommendations for *rail vehicles* or *trains*. The fire tests in this code are mainly simple ignition tests. The code has, however, only partly been adopted in some European countries. Thus there has been work going on within **CEN** and **CENELEC** since 1991 to form a harmonised standard named **EN 45545** Railway Applications – Fire protection of railway vehicles. The new standard will use modern fire test methods like the cone calorimeter (**ISO 5660**) and the smoke density chamber (**ISO 5659**). It will also require smoke toxicity assessment of interior materials in trains.

There are numerous national test standards for trains. In Germany **DIN 5510** the vertical Brandschacht test (**DIN 54 837**) is the main method regulating ignition, fire spread, smoke and flaming droplets. France uses **NFF 16-101** which also includes toxicity assessment of materials. In Great Britain the national standard is **BS 6853** which divides train vehicles into operation categories with varying fire requirements, the main test being a radiant panel test for flame spread. The British standard also considers design and demands on fire detection, suppression and alarm systems.

For *aircrafts* most countries have adopted wholly or in relevant parts the Federal Aviation Regulations (**FAR**) [15.120] of the US Federal Aviation Administration (**FAA**). The methods used to fire test the materials and components of the holds of transport airplanes are for example described in **FAR** part 25. The requirements for military aircrafts are partly similar.

For most parts used in the interior of aircrafts **FAR** part 25 requires that material and components shall pass so called Bunsen burner-type tests where the specimen is mounted in different angles depending of end use. Figure 15.39 shows the test where the specimen is mounted horizontally used for demonstrating that materials are *self-extinguishing*. Other fire tests are specified for components like seat cushions, cargo compartment liners, etc. Some tests not used elsewhere are specified for measuring certain fire properties. Thus for example the so called **OSU** apparatus is specified for measuring heat release, and a special *fireproof* and *fire-resistance* test is described in **FAR** part 23 for materials and parts used to confine fires in designated fire zones.

Safety of international *trading ships* is regulated by the International Convention for the Safety of Life at Sea (**SOLAS**) since 1974. **SOLAS** includes a set of fire safety regulations in its chapter II-2. This chap-

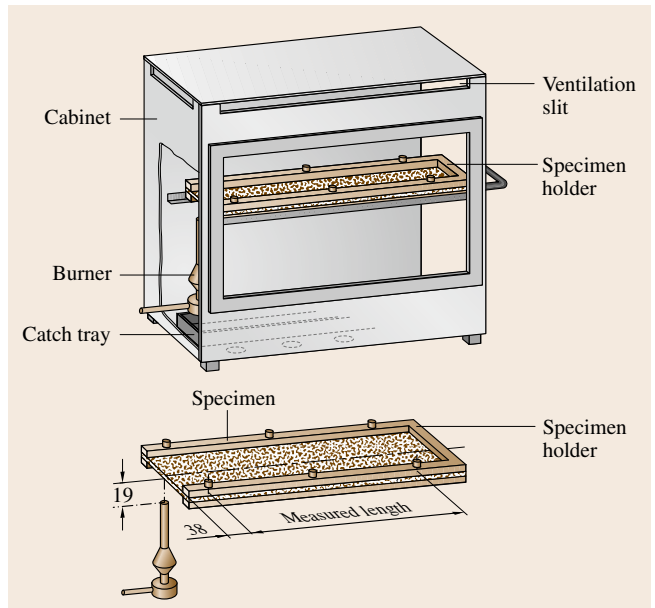


Fig. 15.38 US Federal Motor Vehicle Safety Standard **FMVSS 302** rate of flame spread test for motor vehicle interior components (after [15.119])

ter is reviewed by the Fire Protection Sub-Committee (**FP**) of the International Maritime Organization (**IMO**). In 1996, **IMO FP** developed the Fire Test procedures Code (**FTP Code**) which contains the test procedures for fire safe constructions and materials used on board ships.

Electrical Engineering

Combustible plastics are used extensively in electrical engineering because of their durability, corrosion resistance, strength and not least electrical insulation properties. However, plastics can burn and as any energized circuit inherently is a fire hazard special precautions must be taken with these products. The International Electrotechnical Commission (**IEC**) and the European Electrotechnical Standardization Commission **CENELEC** prepare and publish fire test standards for electro technical products and cables. Thus a comprehensive series of fire tests have been published in the standard **IEC 60695** for characterizing various fire properties like ignitability, flammability, smoke obscuration, toxic potency, and resistance to abnormal heat. In Europe **CEN** is underway to make available a similar classification system for cables as for building materials. It will be based on the preliminary test standard prEN 50399-2.

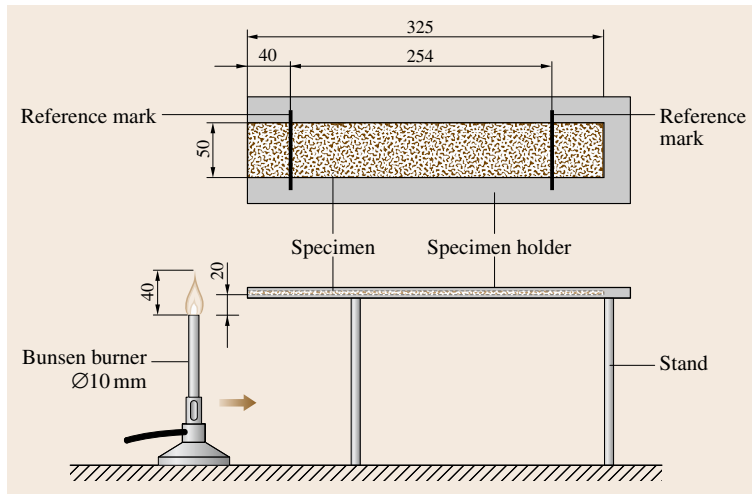


Fig. 15.39 FAR part 25 testing in horizontal position (after Troitzsch [15.119])

Furniture

Furniture, in particular upholstered furniture of polymer foams like foam rubber, can burn intensively and is therefore a potential fire hazard unless properly designed. Most countries have strict building regulations but the fire safety requirements on the building contents like furniture is in general very modest although a survey in Europe [15.119, 121] shows that fires in furniture cause nearly 50% of all fatal fires in private dwellings.

There are several test methods published by various standardization bodies. The European Standard Organization CEN has published four ignition test standards for upholstered furniture and for mattresses. EN 1021-1 and EN 1021-2 are cigarette and small-flame tests for upholstered seatings, and EN 597-1 and EN 597-2 are cigarette and small-flame tests for mattresses [15.119].

Furniture is a complicated product comprising many different materials and assemblies. Fire may develop in cavities and beneath the covering layer etc. or as pool fires underneath a piece of furniture. Therefore any small scale test of individual materials is not always suitable for assessing the fire hazard of composites of cover and filling. To estimate the fire behaviour of these in more realistic fire situation, full scale test data from e.g. the furniture calorimeter as described in NT FIRE 032 is needed (Fig. 15.40). An internationally wide spread method is the full-scale room test according to Technical Bulletin 133 of the State of California [15.122]. This method is in part intended for furniture in high-risk and public occupancies like prisons, health care facilities, public auditoriums and hotels.

The Cone Calorimeter ISO 5660 has been used for testing the burning rates of furniture components and combinations of upholstery and coverings in small scale. The results have been used to predict burning rates of furniture in the full scale the furniture calorimeter as defined in NT Fire 032 [15.123].

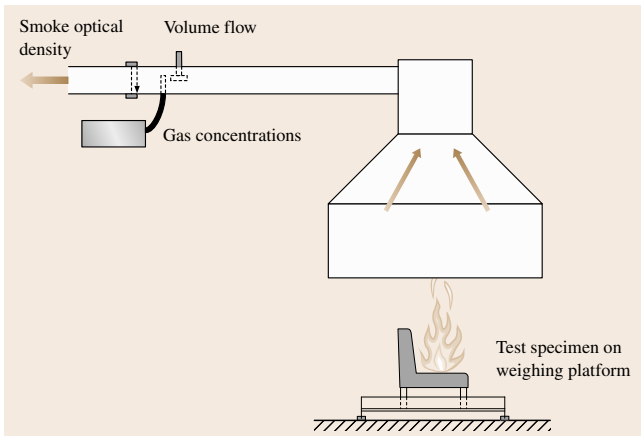


Fig. 15.40 Furniture calorimeter for measuring heat release at full scale of pieces of furniture (courtesy of SP)

References

- 15.1 G. Matos, L. Wagner: Consumption of materials in the United States 1900–1995, *Annu. Rev. Energy Environ.* **23**, 107–122 (1998)
- 15.2 T. Kelly, D. Buckingham, C. DiFrancesco, K. Porter, T. Goonan, J. Sznopce, C. Berry, M. Crane: *Historical Statistics for Mineral and Material Commodities in the United States*, US Geological Survey, Open-File Report 01–006 (Reston 2004)
- 15.3 W.D. Menzie, J.H. DeYoung, W.G. Steblez: *Some Implications of changing patterns of minerals consumption*, US Geological Survey, Open-File Report 03–382 (Reston 2000)
- 15.4 T.E. Graedel, B.R. Allenby: *Design for the Environment* (Prentice Hall, Upper Saddle River 1998)
- 15.5 A.K. Bhaktavatsalam, R. Choudhury: Specific energy consumption in the steel industry, *Energy Fuels* **20**(12), 1247–1250 (1995)
- 15.6 World Steel Association: *2008 Sustainability Report of World Steel Industry* (World Steel Association, Brussels 2008), www.worldsteel.org
- 15.7 World Steel Association: *World Steel in Figures* (World Steel Association, Brussels 2009), www.worldsteel.org
- 15.8 A. Adriaanse, S. Bringezu, A. Hammond, Y. Moriguchi, E. Rodenburg, D. Rogisch, H. Schütz: *Resource flows: The material basis of industrial economies* (World Resource Institute (WRI), Washington 1997)
- 15.9 K. Halada, K. Ijima, N. Katagiri, T. Okura: An approximate estimation of total materials requirement of metals, *J. Jpn. Inst. Met.* **65**(7), 564–570 (2001)
- 15.10 F. Schmidt-Bleek: *Das MIPS-Konzept* (Droemer Knauer, München 1998)
- 15.11 S. Bringezu: *Towards Sustainable Resource Management in the European Union* (Wuppertal-Institute for Climate, Environment, Energy, Wuppertal 2002), paper 121
- 15.12 Five Winds International: *Eco-efficiency and Materials* (Int. Council. Met. Environ., Ottawa 2001)
- 15.13 E.U. von Weizsäcker, J.D. Seiler-Hausmann (Eds.): *Ökoeffizienz, Management der Zukunft* (Birkhäuser, Berlin 1999)
- 15.14 K. Halada, R. Yamamoto: The current status of research and development on ecomaterials around the world, *MRS Bull.* **26**(11), 871–879 (2001)
- 15.15 W. Schnabel: *Polymer Degradation: Principles and Practical Applications* (Hanser, Munich 1981)
- 15.16 M. Akahori, T. Kajino: A new test method for weatherability prediction by using a remote plasma reactor, *Proc. XXVII FATIPEC Congr.*, Vol. 1 (2004) pp. 1–14
- 15.17 L. Zlatkevich (Ed.): *Luminescence Techniques in Solid State Polymer Research* (Dekker, New York 1989)
- 15.18 A.M. Striegel: Influence of chain architecture on the mechanochemical degradation of macromolecules, *J. Biochem. Biophys. Methods* **56**, 117–139 (2003)
- 15.19 M.R. Cleland, L.A. Parks, S. Cheng: Applications for radiation processes of materials, *Nucl. Instrum. Methods Phys. Res. B* **208**, 66–73 (2003)
- 15.20 J.-D. Gu: Microbiological deterioration and degradation of synthetic polymeric materials: Recent research advances, *Int. Biodeterior. Biodegrad.* **52**, 69–91 (2003)
- 15.21 G. Menzel, H.-G. Schlüter: Probleme der dynamisch-thermischen Stabilität von Polyvinylchlorid hart, *Kunststoffe* **65**, 295–297 (1975)
- 15.22 J.G. Calvert, J.N. Pitts: *Photochemistry* (Wiley, New York 1967)
- 15.23 B. Ranby, F.J. Rabek: *Photodegradation, Photo-oxidation and Photostabilization of Polymers* (Wiley, London 1975)
- 15.24 P. Trubiroha: The spectral sensitivity of polymers in the spectral range of solar radiation. In: *Advances in the Stabilization and Controlled Degradation of Polymers*, Vol. I, ed. by A.V. Patsis (Technomic, Lancaster 1989) pp. 236–241
- 15.25 A. Geburtig, V. Wachtendorf: Determination of the spectral sensitivity and temperature dependence of polypropylene crack formation caused by UV-irradiation, *Polym. Degrad. Stab.* **95**, 2118–2123 (2010)
- 15.26 N.D. Searle: Wavelength sensitivity of polymers. In: *Advances in the Stabilization and Controlled Degradation of Polymers*, Vol. I, ed. by A.V. Patsis (Technomic, Lancaster 1989) pp. 62–74
- 15.27 NIST: *Preservation of the Declaration of Independence and the Constitution of the United States* (NIST, Washington 1951), NBS-Circular No. 505
- 15.28 G. Kämpf, W. Papenroth: Einflußparameter bei der Kurzbewitterung pigmentierter Kunststoffe und Lacke, *Kunststoffe* **72**, 424–429 (1982)
- 15.29 P. Trubiroha, A. Geburtig, V. Wachtendorf: Determination of the spectral response of polymers, 3rd Int. Symp. Service Life Prediction, Sedona, ed. by J.W. Martin, R.A. Ryntz, R.A. Dickie (Federation of Societies for Coating Technology, Blue Bell 2005) pp. 241–252
- 15.30 G.C. Furneaux, K.J. Ledbury, A. Davis: Photo-oxidation of thick polymer samples – Part I: The variation of photo-oxidation with depth in naturally and artificially weathered low density polyethylene, *Polym. Degrad. Stab.* **3**, 431–435 (1981)
- 15.31 M. Boysen: Untersuchung der Kombination von natürlicher und künstlicher Bewitterung, *Kunstst. Fortschr.* **5**, 209–218 (1980)

- 15.32 P. Trubiroha: Der Einfluß der Luftfeuchte bei der Verfärbung von PVC während der Bewitterung und bei der anschließenden Dunkellagerung, *Angew. Makromol. Chem.* **158/159**, 141–150 (1988)
- 15.33 T. Matsuda, F. Kurihara: The effect of humidity on UV-oxidation of plastic films, *Chem. High Polym.* **22**, 429–434 (1965)
- 15.34 G. Löschau, P. Trubiroha: Influence of UV radiation to the strength of plastics films, Proc. 6th iapri-World Conf., Hamburg (AFTPVA, Paris 2004) pp. 541–551
- 15.35 W.R. Rodgers, G.D. Garner, G.D. Cheever: Study of the attack of acidic solutions on melamine-acrylic basecoat/clearcoat paint systems, *J. Coat. Techn.* **70**, 83–95 (1998)
- 15.36 P. Trubiroha, U. Schulz: The influence of acid precipitations on weathering results, *Polym. Polym. Compos.* **5**, 359–367 (1997)
- 15.37 U. Schulz: *Accelerated Testing Nature and Artificial Weathering in the Coatings Industry* (Vincentz Network, Hannover 2009)
- 15.38 U. Schulz, K. Jansen, A. Braig: Stabilizers in automotive coatings under acid attack, *Macromol. Symp.* **187**, 835–844 (2002)
- 15.39 U. Schulz, V. Wachtendorf, A. Geburtig: Mildew growth and pinholes on automotive coatings after outdoor weathering in South Florida – A new challenge for developing an appropriate test method, Proc. XXVII FATIPEC Congr. 2004, Vol. 3 (AFTPVA, Paris 2004) pp. 805–815
- 15.40 C.V. Stevani, D.L.A. de Faria, J.S. Porto, D.J. Trindade, E.J.H. Bechara: Mechanism of automotive clearcoat damage by dragonfly eggs investigated by surface enhanced Raman scattering, *Polym. Degrad. Stab.* **68**, 61–66 (2000)
- 15.41 K.B. Chakraborty, G. Scott: The effect of thermal processing on the thermal oxidative and photo-oxidative stability of low density polyethylene, *Eur. Polym. J.* **13**, 731–737 (1977)
- 15.42 G. Wypych: *Handbook of Material Weathering*, 3rd edn. (ChemTec, New York 2003) p. 3
- 15.43 N.C. Billingham: Localization of oxidation in polypropylene, *Makromol. Chem. Macromol. Symp.* **28**, 145–163 (1989)
- 15.44 G. Kämpf (Ed.): *Characterization of Plastics by Physical Methods: Experimental Techniques and Practical Application* (Hanser Macmillan, Munich 1986), German edn.: *Industrielle Methoden der Kunststoff-Charakterisierung: Eigenschaften polymerer Werkstoffe, physikalische Analysenverfahren* (Hanser, München 1996)
- 15.45 J.I. Kroschwitz, M. Howe-Grant, R.E. Kirk, D.F. Othmer: *Kirk-Othmer Encyclopedia of Chemical Technology, Supplement (Aerogels-Xylene Polymers): Surface and Interface Analysis*, 4th edn. (Wiley, New York 1991)
- 15.46 B.W. Rossiter, R.C. Baetzold (Eds.): *Investigations of Surfaces and Interfaces, Part A. Physical Methods of Chemistry*, Vol. 9A, 2nd edn. (Wiley, New York 1993)
- 15.47 D.J. Connor, B.A. Sexton, R.S.C. Smart (Eds.): *Surface Analysis Methods in Materials Science*, Ser. Surf. Sci., Vol. 23 (Springer, Berlin, Heidelberg 1992)
- 15.48 J.C. Riviere (Ed.): Monographs on the physics and chemistry of materials. In: *Surface Analytical Techniques* (Oxford Univ. Press, New York 1990)
- 15.49 R. Holm, S. Storp: Surface and interface analysis in polymer technology: A review, *Surf. Interface Anal.* **2**, 96 (1980)
- 15.50 J.I. Goldstein, D.E. Newbury, P. Echlin, D.C. Joy, C. Fiori, E. Lifshin: *Scanning Electron Microscopy and X-Ray Microanalysis* (Plenum, New York 1981)
- 15.51 L.E. Murr (Ed.): *Electron and Ion Microscopy and Microanalysis: Principles and Applications*, Opt. Eng., Vol. 29, 2nd edn. (Dekker, New York 1991)
- 15.52 L. Reimer (Ed.): *Scanning Electron Microscopy*, Springer Ser. Opt. Sci., Vol. 45 (Springer, Berlin, Heidelberg 1985)
- 15.53 L. Reimer (Ed.): *Transmission Electron Microscopy*, Springer Ser. Opt. Sci., Vol. 36, 3rd edn. (Springer, Berlin, Heidelberg 1993)
- 15.54 R. Kaufmann, F. Hillenkamp: LAMMA and its applications, *Ind. Res. Dev.* **21**(4), 145ff (1979)
- 15.55 R. Kaufmann, F. Hillenkamp, R. Wechsung: Laser microprobe mass analysis, *ESN Eur. Spectrosc. News* **20**, 41 (1978)
- 15.56 K. Siegbahn, C. Nordling, A. Fahlman, H. Hamrin, J. Hedman, G. Johansson, T. Bergmark, S.E. Karlsson, J. Lindgren, B. Lindberg: *Electron Spectroscopy for Chemical Analysis – Atomic, Molecular and Solid State Structure Studies by Means of Electron Spectroscopy* (Almqvist Wiksell, Stockholm 1967)
- 15.57 G.E. Muilenburg (Ed.): *Handbook of X-Ray Photoelectron Spectroscopy. Physical Electronics Div*, 2nd edn. (Perkin-Elmer, Norwalk 1993)
- 15.58 D. Briggs, M.P. Seah (Eds.): *Practical Surface Analysis – Auger and X-Ray Photoelectron Spectroscopy*, 2nd edn. (Wiley Interscience, New York 1990)
- 15.59 D. Briggs, M.P. Seah (Eds.): *Practical Surface Analysis: Ion and Neutral Spectrometry*, Vol. 2 (Wiley, Chichester 1992)
- 15.60 N.M. Reed, J.C. Vickerman: The Application of Static Secondary Mass Spectrometry (SIMS) to the Surface Analysis of Polymer Materials. In: *Surface Characterization of Advanced Polymers*, ed. by L. Sabbatini, P.G. Zamboni (Verlag Chemie, Weinheim 1993)
- 15.61 E.P. Bertin: *Principles and Practice of X-Ray Spectrometric Analysis* (Plenum, New York 1975)
- 15.62 J.G. Grasselli, M.K. Snavely, B.J. Bulkin: *Chemical Applications of Raman Spectrometry* (Wiley, New York 1981)
- 15.63 R.G. Messerschmidt: *Infrared Microspectrometry. Theory and Application* (Dekker, New York 1988)

- 15.64 H. Fuchs: Atomic force and scanning tunneling microscopies of organic surfaces, *J. Mol. Struct.* **292**, 29 (1993)
- 15.65 D.A. Hemsley: *Applied Polymer Light Microscopy* (Elsevier Applied Science, New York 1989)
- 15.66 J.I. Steinfeld: *Molecules and Radiation: An Introduction to Modern Molecular Spectroscopy*, 2nd edn. (MIT, Cambridge 1978)
- 15.67 B. Wunderlich: *Thermal Analysis* (Academic, Boston 1990)
- 15.68 W.J. Price: *Spectrochemical Analysis by Atomic Absorption* (Heyden, London 1979)
- 15.69 K.E. Jarvis, A.L. Gray, R.S. Hook: *Handbook of Inductively Coupled Plasma Mass Spectrometry* (Blakie, London 1992)
- 15.70 T. Provder (Ed.): *Chromatography of Polymers: Characterization by SEC and FFF*, ACS Symp. Ser., Vol. 521 (American Chemical Society, Washington 1993)
- 15.71 I. Blakey, B. Goss, G. George: Chemiluminescence as a probe of polymer oxidation, *Aust. J. Chem.* **59**, 485–498 (2006)
- 15.72 V. Wachtendorf, A. Geburtig: Chemiluminescence for the early detection of weathering effects of coatings Part I: Fundamentals, *JCT CoatingsTech* **7**(April), 66–71 (2010)
- 15.73 V. Wachtendorf, A. Geburtig: Chemiluminescence for the early detection of weathering effects of coatings Part II: Experimental setup and examination, *JCT CoatingsTech* **7**(May), 38–44 (2010)
- 15.74 E. Klesper, G. Sielaff: High resolution nuclear magnetic resonance. In: *Polymer Spectroscopy*, ed. by D.O. Hummel (Verlag Chemie, Weinheim 1974)
- 15.75 D.A.W. Wendisch: Nuclear magnetic resonance in industry, *Appl. Spectrosc. Rev.* **28**, 165 (1993)
- 15.76 H.W. Siesler, K. Holland–Moritz: *Infrared and Raman Spectroscopy of Polymers* (Dekker, New York 1980)
- 15.77 S.J. Valentry: *Polym. Mater. Sci. Eng.* **53**, 288 (1985)
- 15.78 S. Lai, J. Shen: *SPE ANTEC* **34**, 1258 (1988)
- 15.79 J.W. Martin, J.W. Chin, T. Nguyen: Reciprocity law experiments in polymeric photodegradation: A critical review, *Progr. Org. Coat.* **47**, 292–311 (2003)
- 15.80 P. Trubiroha, A. Geburtig, V. Wachtendorf: The principle of reciprocity and its limits, *Proc. 3rd Eur. Weather. Symp. Nat. Artif. Ageing Polym.*, Krakow (2007) pp. 243–258
- 15.81 European Commission: European Collaborative Action (ECA), Report No. 14, Sampling strategies for volatile organic compounds (VOCs) in indoor air, Report EUR 16051 EN (1994)
- 15.82 World Health Organisation (WHO): *Indoor Air Quality – Organic Pollutants*, EURO Rep. Studies, Vol. 111 (WHO, Copenhagen 1989)
- 15.83 American Society for Testing and Materials (ASTM): Standard Guide for Small–Scale Environmental Chamber Determination of Organic Emissions from Indoor Materials/Products. ASTM D 5116–10 (ASTM, West Conshohocken 2010)
- 15.84 EN ISO 16000–9: Indoor air – Part 9: Determination of the emission of volatile organic compounds from building products and furnishing – Emission test chamber method (2006)
- 15.85 EN ISO 16000–10: Indoor air – Part 10: Determination of the emission of volatile organic compounds from building products and furnishing – Emission test cell method (2006)
- 15.86 EN ISO 16000–11: Indoor air – Part 11: Determination of the emission of volatile organic compounds from building products and furnishing – Sampling, storage of samples and preparation of test specimens (2006)
- 15.87 Japanese Industrial Standard (JIS): Determination of the emission of volatile organic compounds and aldehydes for building products – Small chamber method. JIS A 1901 (2009)
- 15.88 EN 717–1: Wood–based panels – Determination of formaldehyde release – Part 1: Formaldehyde emission by the chamber method (2004)
- 15.89 American Society for Testing and Materials (ASTM): Standard Test Method for Determining Formaldehyde Concentration in Air from Wood Products Using a Small Scale Chamber, ASTM D 6007–02 (ASTM, West Conshohocken 2008)
- 15.90 American Society for Testing and Materials (ASTM): Standard Practice for Determination of Volatile Organic Compounds (Excluding Formaldehyde) Emissions from Wood–Based Panels Using Small Environmental Chambers Under Defined Test Conditions, ASTM D 6330–98 (ASTM, West Conshohocken 2008)
- 15.91 American Society for Testing and Materials (ASTM): Standard Test Method for Determining Formaldehyde Concentrations in Air and Emission Rates from Wood Products Using a Large Chamber, ASTM E 1333–10 (ASTM, West Conshohocken 2010)
- 15.92 U. Meyer, K. Möhle, P. Eyerer, L. Maresch: *Development, construction and start-up of a 1 m³ climate test chamber for the determination of emissions from indoor components*, Vol. 54 (Springer, Berlin, Heidelberg 1994) pp. 137–142, *Staub – Reinhaltung der Luft* (in German)
- 15.93 BAM: Test method for the determination of emissions from hardcopy devices – With respect to awarding the environmental label for office devices RAL–UZ 62, RAL–UZ 85 and RAL–UZ 114. In: *Development of a Test Method for and Investigations into Limiting the Emissions from Printers and Copiers within the Framework of Assigning the Environmental Label*, ed. by O. Jann, J. Rockstroh, O. Wilke, R. Noske, D. Broedner, U. Schneider, W. Horn (Federal Environmental Agency, Dessau 2003), Res. Report 201 95 311/02, UBA–Texte 88/03
- 15.94 RAL–UZ 114: *Office Equipment with Printing Function (Printers, Copiers, Multifunction Devices)*

- (RAL, Sankt Augustin 2009), http://www.blauerengel.de/en/products_brands/vergabegruendlage.php?id=147
- 15.95 ISO 16000-6, Indoor air – Part 6: Determination of volatile organic compounds in indoor and test chamber air by active sampling on Tenax TA sorbent, thermal desorption and gas chromatography using MS/FID, March (2010)
- 15.96 ISO 16017-1: Indoor, ambient and workplace air – Sampling and analysis of volatile organic compounds by sorbent tube/thermal desorption/capillary gas chromatography – Part 1: Pumped sampling (ISO, Geneva 2000)
- 15.97 ISO 16000-3: Indoor air – Part 3: Determination of formaldehyde and other carbonyl compounds; Active sampling method (ISO, Geneva 2001)
- 15.98 O. Jann, O. Wilke: Capability and limitations on the determination of SVOC emissions from materials and products, VDI Reports **1656**, 357–367 (2002), (in German)
- 15.99 American Society for Testing and Materials (ASTM): Standard Practice for Sampling and Selection of Analytical Techniques for Pesticides and Polychlorinated Biphenyls in AirASTM designation. ASTM D 4861 (ASTM, West Conshohocken 2005)
- 15.100 Verein Deutscher Ingenieure (VDI): *VDI-Richtlinie 4301, Blatt 2. Measurement of indoor air pollution. Measurement of pentachlorophenol (PCP) and gamma-hexachlorocyclohexene (Lindane) – GC/MS method. VDI-Handbuch Reinhaltung der Luft*, Vol. 5 (Beuth, Berlin 2000)
- 15.101 W. Horn, O. Jann, O. Wilke: Suitability of small environmental chambers to test the emission of biocides from treated materials into the air, *Atmos. Environ.* **37**, 5477–5483 (2003)
- 15.102 S. Kemmlein, O. Hahn, O. Jann: Emissions of organophosphate and brominated flame retardants from selected consumer products and building materials, *Atmos. Environ.* **37**, 5484–5493 (2003)
- 15.103 O. Wilke, O. Jann, D. Brödner: VOC- and SVOC-emissions from adhesives, floor coverings and complete floor structures, Indoor Air 2002, Proc. 9th Int. Conf. Indoor Air Quality and Climate, Monterey, ed. by H. Levin (Indoor Air, Santa Cruz 2002) pp. 962–967
- 15.104 World Fire Statistics: Information Bulletin of the World Fire Statistics, #20, October 2004
- 15.105 O. Jann, O. Wilke: Sampling and analysis of wood preservatives in test chambers. In: *Organic Indoor Air Pollutants. Occurrence, Measurement-Evaluation*, ed. by T. Salthammer (Wiley, New York 1999) pp. 31–43
- 15.106 V. Babrauskas: *Ignition Handbook* (Fire Science, Issaquak 2003)
- 15.107 J.G. Quintiere: *Principals of Fire Behavior* (Delmar, Florence 1998)
- 15.108 J.R. Mehaffey, L.R. Richardson, M. Batista, S. Guer-guiev: Self-heating and spontaneous ignition of fibreboard insulating panels, *Fire Technol.* **36**(4), 226–235 (2000)
- 15.109 H. Kubler: Heat generating processes as cause of spontaneous ignition in forest products, *For. Prod. Abstr.* **10**(11), 299–327 (1987)
- 15.110 A.R. Horrocks, D. Price (Eds.): *Fire Retardant Materials* (CRC Woodhead, Cambridge 2001)
- 15.111 M. De Portere, C. Schonbach, M. Simonson: The fire safety of TV set enclosure materials. A survey of European statistics, *Fire Mater.* **24**, 53–60 (2000)
- 15.112 B. Karlsson, J.G. Quintiere: *Enclosure Fire Dynamics* (CRC, Boca Raton 2000)
- 15.113 EN 1993-1-2, Eurocode 3: Design of steel structures – General rules – Structural fire design (CEN, 2005)
- 15.114 EN 1992-1-2, Eurocode 2: Design of concrete structures – General rules – Structural fire design (CEN, 2004)
- 15.115 EN 1995-1-2, Eurocode 5: Design of timber structures – General rules – Structural fire design (CEN, 2004)
- 15.116 Commission Decision 2000/147/EC of 8 February 2000 implementing Council Directive 89/106/EEC as regards the classification of the reaction to fire performance of construction products, Official Journal of the European Commission, 23.2.2000
- 15.117 U. Wickström, U. Göransson: Full-scale/bench-scale correlations of wall and ceiling linings. In: *Heat Release in Fires*, ed. by V. Babrauskas, S.J. Grayson (Elsevier, Amsterdam 1992)
- 15.118 Title 49: Transportation §571 302. Standard 302: Flammability of interior materials (valid Sep. 1972), US-Federal Register **36**, 232 (1972)
- 15.119 J. Troitzsch (Ed.): *Plastic Flammability Handbook* (Hanser, Berlin 2004)
- 15.120 Federal Aviation Regulation (FAR): *Airworthiness Standards* (Department of Transportation, Federal Aviation Administration)
- 15.121 J.A. de Boer: Fire and furnishing in buildings and transport – Statistical data on the existing situation in Europe, Conf. Proc. Fire Furnish. Build. Transp., Luxembourg (CFPA Europe, Stockholm 1990)
- 15.122 State of California: Flammability test procedure for seating furniture for use in public occupancies, *Tech. Bull.*, Vol. 133 (1991)
- 15.123 B. Sundström (Ed.): *CBUF Fire Safety of Upholstered Furniture – the Final Report of the CBUF Research Programme* (Interscience, London 1995)

Performance

16. Performance Control: Nondestructive Testing and Reliability Evaluation

The performance of materials – as constituents of the components of engineering systems – is essential for the functionality of engineering systems in all branches of technology and industry. Instrumental for characterizing the performance of materials are

1. methods to study and assess the basic damage mechanisms that detrimentally influence the proper functioning of materials, such as materials fatigue and fracture (Chap. 7), corrosion (Chap. 12), friction and wear (Chap. 13), biogenic impact (Chap. 14), materials–environment interactions (Chap. 15)
2. methods to study and assess the performance of materials in engineering applications and to support condition monitoring of materials' functional behavior.

In this chapter the following experimental and theoretical methods for performance control and condition monitoring are compiled.

- Nondestructive evaluation (NDE) methods
- Methods of industrial radiology
- Methods of computed tomography (CT)
- Embedded sensors techniques to monitor structural health and to assess materials performance in situ under application conditions
- Methods to characterize the reliability of materials with statistical tools and test strategies for structural components and complex engineering systems.

16.1	Nondestructive Evaluation	888
16.1.1	Visual Inspection.....	888
16.1.2	Ultrasonic Examination: Physical Background.....	889
16.1.3	Application Areas of Ultrasonic Examination.....	894
16.1.4	Magnetic Particle Inspection.....	897
16.1.5	Liquid Penetrant Inspection.....	898
16.1.6	Eddy-Current Testing.....	899
16.2	Industrial Radiology	900
16.2.1	Fundamentals of Radiology.....	901
16.2.2	Particle-Based Radiological Methods.....	906
16.2.3	Film Radiography.....	907
16.2.4	Digital Radiological Methods.....	908
16.2.5	Applications of Radiology for Public Safety and Security.....	914
16.3	Computerized Tomography – Application to Organic Materials	915
16.3.1	Principles of X-ray Tomography.....	915
16.3.2	Detection of Macroscopic Defects in Materials.....	917
16.3.3	Detection of the Damage of Composites on the Mesoscale: Application Examples.....	918
16.3.4	Observation of Elastomers at the Nanoscale.....	919
16.3.5	Application Assessment of CT with a Medical Scanner.....	920
16.4	Computerized Tomography – Application to Inorganic Materials	921
16.4.1	High-Energy CT.....	921
16.4.2	High-Resolution CT.....	921
16.4.3	Synchrotron CT.....	922
16.4.4	Dimensional Control of Engine Components.....	923
16.5	Computed Tomography – Application to Composites and Microstructures	927
16.5.1	Refraction Effect.....	927
16.5.2	Refraction Techniques Applying X-ray Tubes.....	928
16.5.3	3-D Synchrotron Refraction Computed Tomography.....	929
16.5.4	Conclusion.....	932
16.6	Structural Health Monitoring – Embedded Sensors	932
16.6.1	Basics of Structural Health Monitoring.....	932
16.6.2	Fiber-Optic Sensing Techniques.....	935
16.6.3	Piezoelectric Sensing Techniques.....	945

16.7	Characterization of Reliability	949	16.7.5	System Reliability.....	962
16.7.1	Statistical Treatment of Reliability ..	951	16.7.6	System Reliability Estimation	
16.7.2	Weibull Analysis.....	952		in Practice.....	964
16.7.3	Reliability Test Strategies.....	956	16.A	Appendix	967
16.7.4	Accelerated Lifetime Testing	959	References		968

16.1 Nondestructive Evaluation

Nondestructive evaluation is an important method for performance control and condition monitoring. In engineering systems, flaws and especially cracks in the

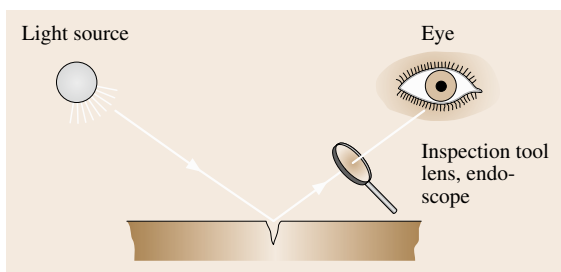


Fig. 16.1 Direct visual inspection

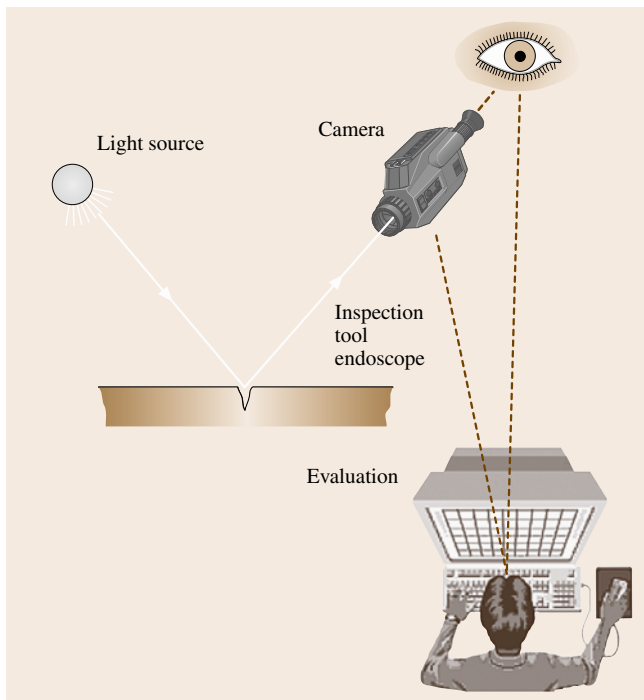


Fig. 16.2 Indirect or remote visual inspection

materials of structural systems' components can be crucially detrimental to functional performance. For this reason the detection of defects is an essential part of quality control of engineering systems and their safe successful use. Control techniques are often listed under a variety of headings such as nondestructive testing (NDT), nondestructive evaluation (NDE) or sometimes nondestructive inspection. Applications of NDT techniques, however, are much deeper and broader in scope than just the detection of defects. The determination of various material properties, such as elastic constants of solids or the microstructure and texture of solids are also covered under the NDT title.

According to the wide scope of this field, a plethora of physical methods are employed. Established methods include *radiography, ultrasound, eddy current, magnetic particle, liquid penetration, thermography* and *visual inspection techniques*. Applications of NDE in industry are as wide ranging as the techniques themselves and include *mechanical engineering, aerospace, civil engineering, oil industry, electric power industry* etc. A large number of components are also in the focus of interest because engineered structures are an integral part of the technological base necessary for our lives and the public infrastructure. The operation of NDT techniques in several industries is standard practice, for example to support condition monitoring for the proper functioning of the daily use of electricity, gas or liquids in which pressure vessels or pipes are employed and where the correct operation of components under applied stress plays a large role for safety and reliability.

16.1.1 Visual Inspection

Visual examination means, in principle, inspection with eyesight [16.1,2]. (For the fundamentals of optical sensing see Sect. 11.7.) In the case of NDT, visual inspection has a much broader meaning. There are differences in the aim of the visual inspection if: (i) *only* surface characteristics, such as scratches, wear or corrosion

phenomena are of interest, or (ii) detection of cracks or deformation is included.

The first point (i) can be described as integral visual inspection and the second point (ii) as specific or selective visual inspection. If between the eye of the inspector and the surface of the test object the optical path is not broken then a direct visual inspection is performed (Fig. 16.1). Such inspection is either integral or selective. Direct visual inspection means examination using eyesight and sometimes simple tools such as artificial illumination. Selective visual inspection uses additional equipment including hand lenses, mirrors, optical microscopes and telescopes and, for the documentation of the inspection results, storage media such as photography or cameras in combination with a monitor. If inspection is carried out by the evaluation of photographs, video films or by robotics an indirect or remote visual inspection is performed (Fig. 16.2). Visual inspection can be carried out in almost all areas where preventive maintenance is required. Visual inspection is the oldest and most common form of corrosion inspection, applied to surface corrosion, intergranular stress corrosion, and some kinds of pitting. Several corrosion phenomena are detectable using direct visual inspection techniques. An example showing a corroded surface is presented in Fig. 16.3. Clearly visible is the scarred surface in the elbow region of the pipe. This example illustrates that the visual technique is quick and in most cases economical. Various types of failure are detectable but the reliability of the inspection is highly dependent on the skill and training of the examiner.



Fig. 16.3 Corroded pipe

16.1.2 Ultrasonic Examination: Physical Background

Sound travels in solids, liquids and gases with a velocity depending on the mechanical properties of the material. Imperfections such as cracks, pores or inclusions cause sound-wave interactions which result in reflection, scattering and general dampening of the sound wave [16.3–6]. This dampening of the sound waves is responsible for the distance traveled by the sound. In liquids sound can travel large distances; on the other hand, in coarse-grained solids the traveling distance may be only a few centimeters due to scattering. Sound directions and the estimation of the distance to the source are not easily obtainable by simple methods. More precise techniques are necessary to overcome these problems. This requires the use of narrow sound beams.

In nondestructive evaluation (NDE) narrow sound beams using short wavelengths can be formed when the ultrasonic source size is much larger than the wavelength. Nondestructive testing is carried out using ultrasonic waves at high frequencies above the audible range, higher than approximately 20 kHz and up to the range of some hundred MHz.

Historically, the development of methods for ultrasonic materials testing in the industry started at the end of the Second World War. Although the orientation of bats using sound waves was an established phenomena, the discovery of the piezoelectric effect by Jacques and Pierre Currie 1880 and 1881 [16.3] was of critical importance for the application of ultrasound. The theory of sound propagation in solids was developed by Lord Rayleigh between 1885 and 1910, as well as the development of early electronic devices.

Sound-field generation and reception is performed using special devices, so called ultrasonic transducer or ultrasonic probes. The active sound-field generation tool is in the most cases a special ceramic with piezoelectric properties. A piezoelectric material has the characteristic that, if it is deformed by an external mechanical pressure, electric charges are produced on its surface (Fig. 16.4). This effect was discovered in 1880 by the brothers Curie. The reverse phenomenon, according to which such a material, if placed between two electrodes, changes its form when an electric potential is applied, was discovered soon afterwards in 1881 (Fig. 16.5). The first effect is referred to as the direct piezoelectric effect, and the second as the inverse piezoelectric effect. The direct effect is used for measuring and the inverse effect for producing mechanical pressures, deformations and oscillations.

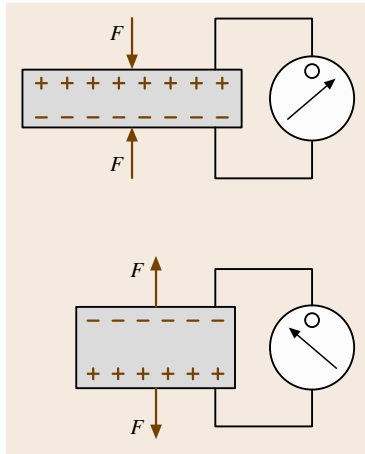


Fig. 16.4 Direct piezoelectric effect

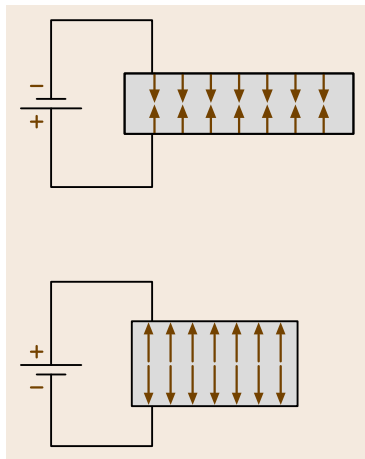


Fig. 16.5 Inverse piezoelectric effect

Generation of Ultrasound

Most transducers used in ultrasonic nondestructive inspection are based on the piezoelectric effect. Generation of ultrasound is achieved using the inverse piezoelectric effect, and the receiving procedure is carried out with the direct piezoelectric effect. The principle of the generation and reception of ultrasound was explained and demonstrated with the help of the quartz crystal. However for the time being other materials with piezoelectric properties can be used to advantage. Today, piezoelectric ceramic is most commonly used, typical examples include barium titanate (BaTiO_3),

lead zirconate titanate ($\text{PbZrO}_3\text{-PbTiO}_3$ solid solution **PZT**), lead meta-niobate (PbNb_2O_6), barium sodium niobate ($\text{Ba}_2\text{NaNb}_5\text{O}_{15}$) and the polymer polyvinylidene fluoride (**PVDF**). The manufacturing process and material properties can be varied within certain limits, achieving a large range of acoustical properties, which are normally customized to a specific application. These materials have a much higher so-called electromechanical coupling factor than quartz. The frequency of the ultrasonic signal comes from the thickness of the piezoelectric ceramic plate. The correlation between thickness and frequency f_0 is given by (16.1).

$$f_0 = \frac{c}{2t}, \quad (16.1)$$

where c is the velocity of sound, and t is the thickness of the piezoelectric ceramic plate.

With knowledge of the sound velocity c of the piezoelectric ceramic, the frequency f_0 is adjustable by varying the thickness t of the ceramic. In Table 16.1 the average sound velocities of common ceramic materials are listed.

Such ceramic material, in the form of *monolithic* discs, were, and are used for ultrasound generation. In the meanwhile, also other crystal configurations are the basis for ultrasound generation. The use of 1–3 composite materials has the advantage due to a higher coupling coefficient and a better effectiveness for ultrasound generation in comparison with monolithic ceramics and polymers. At the Pennsylvania State University's Materials Research Laboratory developed a large variety of piezoelectric composite materials that consist of a ceramic and a polymeric phase with different connectivities [16.7, 8]. The connectivity in one, two, or three dimensions in a composite is designated as "1, 2, or 3". Therefore, a piezocomposite consisting of piezoelectric ceramic rods aligned in parallel and embedded in a polymeric resin matrix is called a "1–3" composite. The ceramic rods are connected in only one direction, namely the poled direction of the material, having a connectivity of "1". On the other hand, the polymer phase connects in all three dimensions, having a connectivity of "3". Figure 16.6 shows schematically the 1–3 piezocomposite arrangement [16.9–11]. From the picture in Fig. 16.6, it seems to be easily to produce such ceramic ma-

Table 16.1 Sound velocities of piezoelectric ceramic materials used for ultrasonic transducers

Material	BaTiO_3	PZT (P5)	PbNb_2O_6	PVDF
Sound velocity (m/s)	5200	4200	3300	1500–2600

materials with the knowledge of wafer technology, but there are some difficulties looking to the manufacturing processes. These difficulties have limited, to a degree, their applicability and have increased the cost of manufacturing piezocomposite probes. Research and development activities in the past try to improve these processes and to introduce piezocomposite transducers for NDT.

Piezoelectric ceramic materials are mainly used for the preparation of ultrasonic transducers, nevertheless other physical properties can be utilized for generating and receiving ultrasound. Although many of these methods produce weaker signals than are obtainable by the piezoelectric effect, they offer a number of advantages that in special cases makes their application in the testing of materials useful. For many of these alternative techniques the energy is transmitted by electrical or magnetic fields, which in principle make mechanical contact with the metallic test piece unnecessary. The conversion into, or from, acoustic energy takes place in the surface of the workpiece concerned. Compared with the piezoelectric oscillator, which requires direct coupling, normally with a suitable medium, e.g. water, to the workpiece, the surface of the workpiece forms in this a part of the acoustic transducer.

Other possibilities for the generation of ultrasound are the use of mechanical shock or friction effects, the application of thermal effects by heating the surface of a body suddenly (*heat shock*) the exploit of electrodynamic effects based on the Lorentz force and the magnetostrictive effect. Apart from the generation of ultrasound using the electrodynamic effect the others methods play at present a small role into the NDE field.

Reflection and Transmission of Ultrasonic Waves at Boundaries

Normal Beam Incidence. The behavior of an ultrasonic wave in an unlimited material is only possible on a theoretical level because in reality every material has boundaries. At such boundaries the traveling wave is disturbed. If the boundary is in a direct contact with a vacuum, transmission of the ultrasonic wave through the boundary is impossible; total reflection occurs. Consider an incident longitudinal plane wave traveling perpendicular to a boundary or interface between two materials, as demonstrated in the schematic diagram in Fig. 16.7 [16.3, 4]. For symmetrical reasons only the reflected P_r and transmitted P_t waves are possible. The part of the reflected wave is characterized by the reflection coefficient R and the part of the trans-

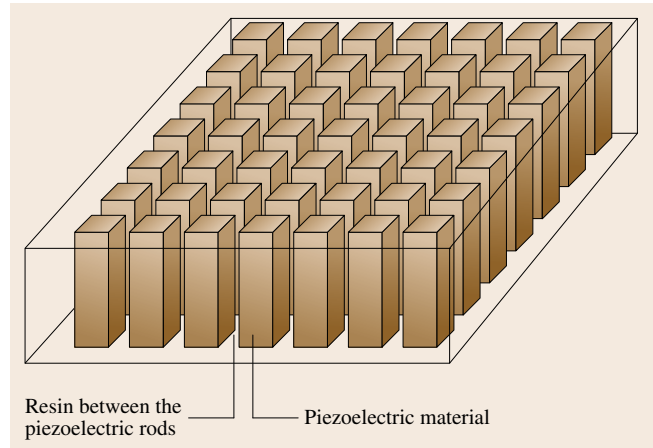


Fig. 16.6 Piezocomposite arrangement

mitted wave by the transmission coefficient T . In this special case the reflection and transmission coefficients only depend on the acoustic impedance $W = \rho c_L$ where ρ is the density of the material and c_L the sound velocity of the longitudinal wave. The equation for the calculation of the two coefficients are as follows

$$R = \frac{W_2 - W_1}{W_1 + W_2} \quad \text{and} \quad T = \frac{2W_2}{W_1 + W_2} \quad (16.2)$$

The indexes 1 or 2 are used to define the two media (Fig. 16.7). It is clearly visible from these equations that 100% of the sound is transmitted through the interface if W_1 is equal W_2 . In reality what happens for a steel–water interface is a combination of impedances often given in ultrasonic examination ($W_1 = 45 \times 10^6 \text{ Ns/m}^3$ for steel and $W_2 = 1.55 \times 10^6 \text{ Ns/m}^3$ for water) for a steel–water interface. With these values a reflection

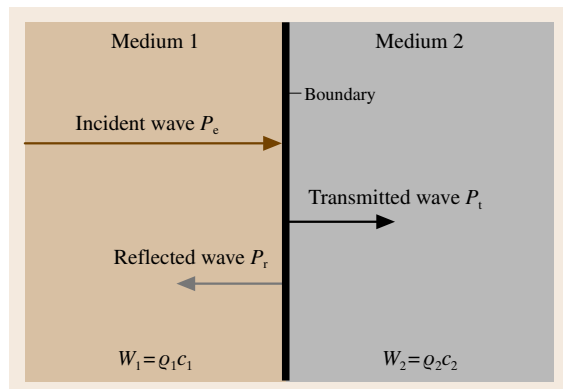


Fig. 16.7 Normal incidence of a sound wave on a boundary

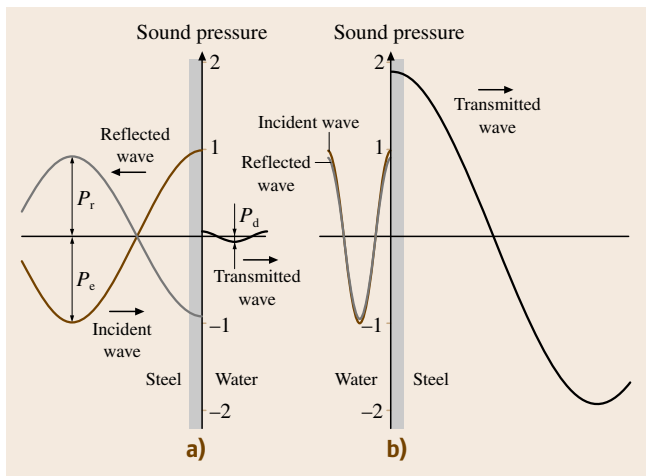


Fig. 16.8 Sound pressure values by reflection at a steel/water interface

coefficient of -0.935 and a transmission coefficient of 0.0065 is calculated. That means that 93.5% of the sound field is reflected at the steel–water interface (Fig. 16.8). The negative value of the reflection coefficient means that the phase of the reflected ultrasonic wave has changed by 180° compared with the incident wave. If we assume an interface steel–air then R is -0.99998 , i. e. nearly 100% . Such a material combination is given for instance if a crack is located in a steel component. Therefore, when the sound wave strikes the crack surface at a normal angle it can be detected with a high probability.

Equations (16.2) are valid if the sound wave is traveling perpendicular to the interface. The behavior is

more complex if the sound strikes the surface with an angle $> 0^\circ$ (Fig. 16.9). A mode conversion as illustrated in the figure must be assumed, i. e. an incidence longitudinal wave is reflected at the boundary as well as a shear wave. A longitudinal and a shear wave are transmitted into the second medium. This circumstances must be taken into consideration by the calculation of the reflection and transmission coefficient. The situation is similar if an incidence shear wave is assumed. For each case presented in Fig. 16.9 two reflection and two transmission factors are obtained.

Inclined Beam Incidence. If an ultrasonic longitudinal plane wave strikes a liquid–solid interface at an angle α as demonstrated in Fig. 16.10 one reflected wave and two transmitted waves are generated. The reflected angle α is equal to the incidence angle whereas the transmitted angles are different. These two angles are dependent on the sound velocity for the different wave types corresponding to the two materials. The calculation of these angles can be carried out using Snell's law

$$\frac{\sin \alpha_1}{\sin \alpha_2} = \frac{c_1}{c_2} \quad (16.3)$$

Using (16.3), all angles can be calculated if the sound velocities and one angle are known. In the following some consequences derived from the Snell's law are considered. The Plexiglas–steel interface is important for ultrasonic angle beam probe construction and therefore we will regard this material combination in the following. The sound velocity for the longitudinal wave is on average 2740 m/s for Plexiglas (perspex) and 5920 m/s for steel as well as 3255 m/s for the shear wave in steel. Consideration of Snell's law indicates that two critical angles exist with respect to the refraction process on the interface. The first critical angle is given when $\alpha_2 = 90^\circ$, i. e. the total reflection of the longitudinal wave. In this case only shear waves exist in material 2. The second critical angle occurs when the shear refracted angle is 90° . If only shear waves will be used in the practical application the Plexiglas wedge angle β should be between 27.6 and 57.3° . These values are calculated using the above printed sound velocities. Angle beam probes generating shear waves used for the examination therefore have angles of incidence between 35 and 80° .

Ultrasonic Transducers

In the following, the description of generating and receiving ultrasound with transducers (probes) will focus on piezoelectric ceramic material [16.3, 5, 6] due to the

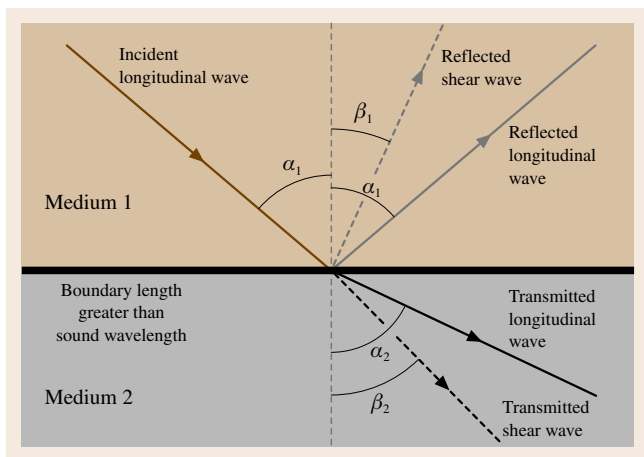


Fig. 16.9 Wave mode conversion at a boundary

importance in practical applications. Such ultrasonic transducers are optimized for different areas of application [16.12–14] but the basic construction principle nearly always remains the same. Figure 16.11 shows schematically typical commercial ultrasonic transducers as a part of the basic equipment for ultrasonic examinations.

A longitudinal wave is generated using a straight beam probe, presented in a schematic sketch in Fig. 16.11a. The piezoelectric ceramic plate is behind a protective coating (wear shoe/plate) and the backing material (damping element) is largely responsible for the pulse form. Together with an electrical adaptation the ultrasonic pulse can be formed and optimized to a particular application. As explained the thickness of the ceramic delivers the middle frequency of the pulse. This kind of probe has such a construction that the waves have a perpendicular (straight) radiation in relation to the test object's surface. The size of the piezoelectric ceramic together with the middle frequency will determine important ultrasound probe parameters, including the near-field length, divergence angle and beam diameter, which are required to perform reliable inspection. All these parameters of an ultrasonic probe can be measured or calculated using simple equations. Figure 16.11b shows the principle drawing of an angle beam probe for shear-wave generation. The shear waves are generated due to refraction of the incident longitudinal wave on the coupling surface. A common ultrasonic angle beam probe can be employed to generate shear waves only. This is achieved if the wedge has an angle between the first and the second critical angle. So far, for the material combination perspex/carbon steel, conventional probes are available generating shear

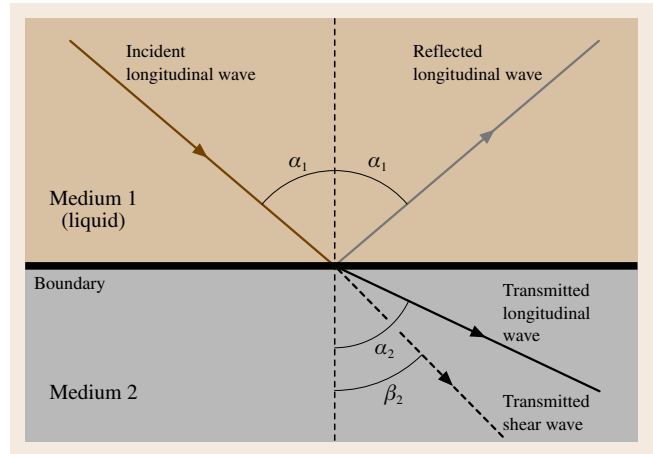


Fig. 16.10 Inclined incidence at a liquid/solid boundary

waves with incidence angles of 45, 60 and 70°. In recent years with the development of electronic beam forming so-called phased array probes [16.3] with variable incidence angles have become available. The principle of the phased array probe can be explained with the help of Fig. 16.12. The crystal is divided into several elements. In the given example, eight elements are illustrated. Each element is connected with the transmitter/receiver part of special ultrasonic controlling equipment (phased array equipment). The time for transmitting the main bang (transmitter pulse) is controlled by the equipment in such a way that different transmitter times can be achieved between the individual elements. When the delay time Δt between the elements is constant decreasing or increasing a variation of the incidence angle will occur. If Δt follows

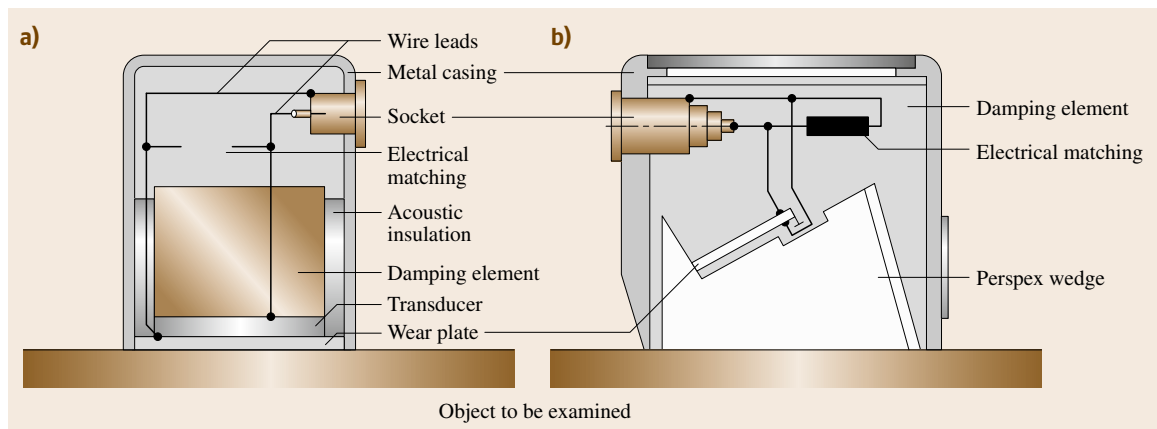


Fig. 16.11a,b Normal or straight beam probe (a) and angle beam probe (b)

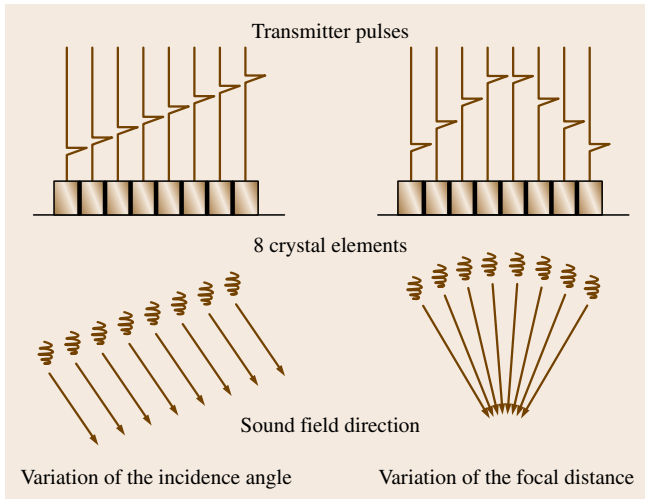


Fig. 16.12 Principle of a phased array probe

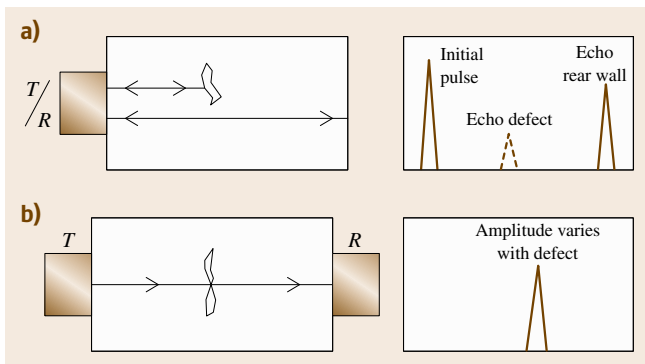


Fig. 16.13a,b Pulse-echo technique (a) and through-transmission technique (b)

a predetermined curvature (like a lens) the sound field can be focused at a certain distance. Further a combination of both is also possible. With such a phased array probe all incidence angle can be realized for longitudinal as well as for shear waves. For the second case, if Δt is specified by the curvature of a lens, a variation of the focal distance is given by changing the curvature. With advanced phased array equipment both changing the angle and focal distance can be carried out in one stage.

In the following some of sound-field distributions of different kinds of probes are presented.

Sound Propagation in Solids

Sound propagation in materials is always connected with an interaction of the ultrasonic pulse and the struc-

ture of the material. Especially for solid materials such as steel the interaction with the grain size (scattering and reflection) is sometimes not negligible mainly if the wavelength and the grain size are within the same dimensional range. Due to this interaction the sound loses energy i. e. an attenuation of the sound will happen along the propagation direction. Another effect is the frictional motion of the particles of the solid which also has an attenuation effect but is based on the absorption of the ultrasonic intensity. Therefore the total attenuation of the ultrasonic intensity is given as the sum of the scattering and absorption coefficient (16.4)

$$\mu = \mu_s + \mu_a \quad (16.4)$$

This attenuation must be taken into consideration during the examination.

Principle of the Pulse-Echo and Through Transmission Methods

Defects in materials caused scattering and reflection of the ultrasonic wave and the detection of the reflected or transmitted waves allows the location of the defect. A general illustration of the *pulse-echo* and *through transmission* methods is shown in Fig. 16.13. The through transmission normally requires access to both sides of a component and is applied if the back-reflection method cannot provide sufficient information about a defect. For example, when small defects are detectable which do not give adequate reflection signals.

The pulse-echo technique requires access to only one side of the component. This is one advantage of this method compared with the through-transmission technique. Another advantage of the pulse-echo method is given due to the time-of-flight measurement because the defect location (distance from the coupling surface) can be estimated from the time required for the pulse to travel from the probe to the discontinuity and back and can be displayed on an oscilloscope. If the horizontal sweep of the oscilloscope is calibrated with the sound velocity into the material to be inspected, the required travel time from the probe to the reflector and back corresponds to the distance of the reflector from the coupling surface. This method is used extensively in practice.

16.1.3 Application Areas of Ultrasonic Examination

The application range of ultrasonic examination is very broad. It covers, for example, wall thickness measurement of structural components and the detection of wall

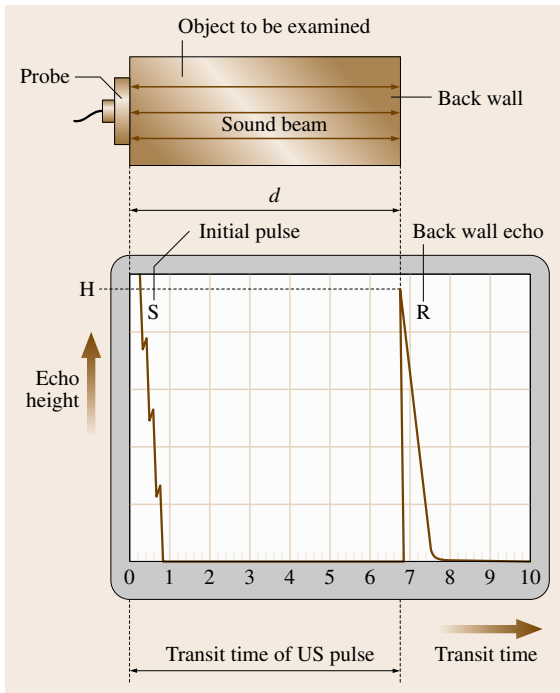


Fig. 16.14 Principle of wall thickness measurements

thickness losses due to corrosion, erosion, wear etc. Other application areas include the measurement of material properties such as sound velocity, elastic constants and the detection of flaws, e.g. cracks, slag inclusions, lack of fusions, pores. The following examples illustrate the application of ultrasonic examination for performance control of components and engineering systems in various areas of technology and industrial sectors.

Wall Thickness Measurement of Components

During the lifetime of a component their surface are subjected to environmental stresses. Depending on the environment corrosion phenomena must be taken into consideration. A reduction of wall thickness can occur and as a consequence the safety factor that was the basis for the construction may no longer be valid. The principle of thickness measurement is illustrated in Fig. 16.14 [16.15]. A straight-beam longitudinal probe is coupled on the surface and the pulse echo from the parallel flat opposite surface (back wall) is received and displayed on the screen. The transit time of the pulse corresponds with the wall thickness if the equipment was calibrated with the correct sound velocity. This method is sometimes known as a simple length measurement.

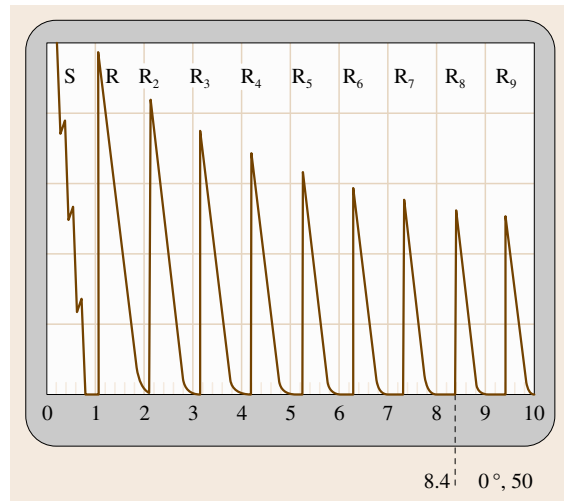


Fig. 16.15 Wall thickness measurement using multiple echoes

Another method is to analyze multiple echoes which are observed, i.e. multiple reflections of an acoustic pulse propagating between the coupling surface and the back wall (Fig. 16.15). Since the constant distances between the echoes corresponds to the specimen thickness d , then the whole transit time of the multiple echo indications on the screen is also a multiple of the wall thickness. An example of a corroded aluminum plate from the aircraft industry is plotted in Fig. 16.16.

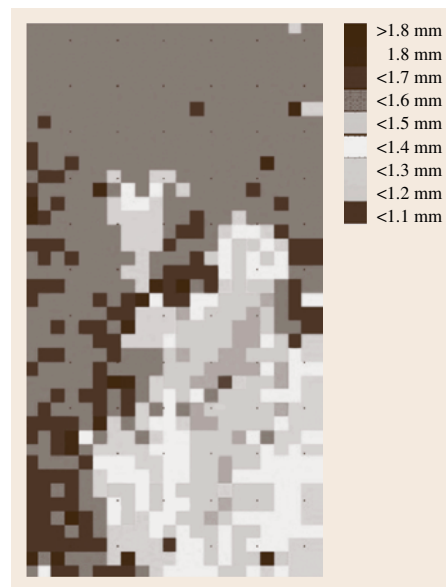


Fig. 16.16 Wall thickness measurement

For wall thickness estimation the measurement was carried out using a mechanized ultrasonic immersion technique. The different gray scales correspond with different wall thicknesses.

All thickness measurement using ultrasound have in common that the coupling conditions of the transducer must be performed in the same manner, however also care must be taken to use the correct sound velocity in the material.

Weld Inspection

Ultrasonic weld inspection is done extensively around the world, and the pertinent literature is published in a multitude of journals, proceedings and technical reports [16.14]. Usually, a shear-wave angle beam transducer is used to examine the weld and the adjacent region in a halfskip and skip distance (Fig. 16.17). In the figure the method of examining the root, the interior and the top layer of the weld is presented. The skip distance can be calculated (16.5) where d is the thickness of the specimen and α the beam angle

$$S_k = 2d \tan \alpha . \quad (16.5)$$

The examination of welds requires that the skip distance, the beam angle, the beam spread and the probe index point are well known. Further information, such as the surface conditions, coupling media to be used, system of marking welds, system of indicating defects found, access conditions for examination of welds and use of other, possible NDT methods should be known before examination. The number of beam angles depends strongly on the wall thickness of the component to be examined. After the checking sensitivity and setting up of the whole ultrasonic system (transducer and equipment) the inspection procedure can be carried out for the detection of longitudinal defects. The shear-wave probe should be placed on the coupling surface and kept during the movement perpendicular to the weld centerline while swiveling the probe head lightly. The ultrasonic probes used for weld inspection must take

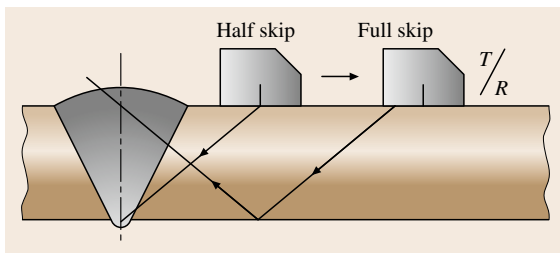


Fig. 16.17 Weld inspection

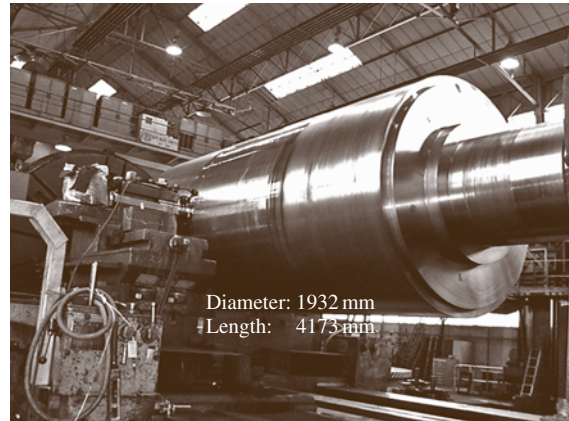


Fig. 16.18 Turbine shaft

into consideration the geometry of the component and the weld. Different weld joints include square groove, bevel groove, v -groove, u -groove and weld types including butt, lap, T , edge, and corner; although this list is not complete, different ultrasonic probes with special sound-field characteristics must be used to overcome this examination problem. Examination procedure and problems are described in several standards, codes and guidelines. For example the detection of defects direct or in the neighborhood of the coupling surface require so-called transmitter receiver probes. The main measuring principle that justifies the use of such probes is the separation of the transmitter and receiver function which is accomplished by using two crystals in the probe. However the choice of the optimal inspection techniques for reliable examination results requires, in addition to the knowledge of the standards, a skilled examiner.

Examination of Forged and Rolled Machinery Parts

With regard to high machining cost, the examination of large forgings should start in the earliest stages of production. In recent times the inspection of components such as turbine shafts, railway wheels etc. are carried out using mechanized testing. Figure 16.18 shows an example of the examination of a turbine shaft with a diameter of about 2 m. The examination was performed using phased array probes [16.16]. During the shaft rotation the incidence angles for longitudinal waves were changed in a range between -30° and 30° with steps of 3° . For every full circle an echotomogram was reconstructed. After the whole examination of the shaft the defect situation in the shaft, in the ra-

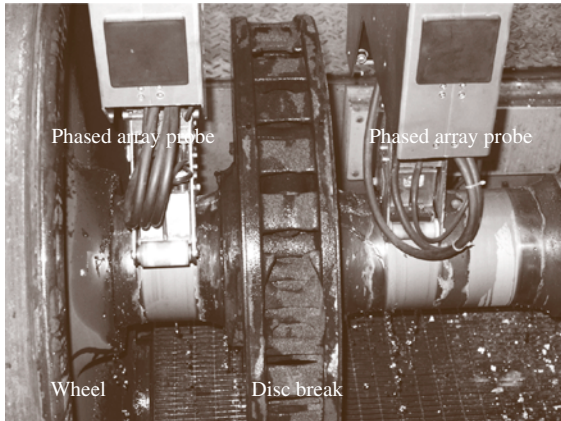


Fig. 16.19 Railway axel inspection with phased array probes

dial and axial directions, was visualized with the help of a computer program called *glassy shaft*.

Another example where mechanized testing is used is the inspection of railroad axels with phased array probes (Fig. 16.19). Two coupled phased array probes on the axel surface are presented in the figure (two probes for each side). Thus for this special application case four phased array probes are necessary for the examination of the area beneath the wheels and the disc brakes. Phased array probes with the possibility of steering the incidence angle have advantages because of the limited accessibility between the wheel and the disc brake.

Inspection of Semi-finished Industrial Products

A wide field for NDT is the inspection of semi-finished products such as rods, pipes plates, casting products etc. Defects in this group of products can either be on or near the surface and internal (embedded) defects. In the case of steel rods, manual ultrasonic inspection using the pulse-echo technique is implemented in practice as well as mechanized inspection. Straight and angle beam probes are for the detection of the different defects such as shrinking cracks, inclusions, cavities, pores etc. There are several different techniques for identifying defects, which can be achieved by mechanized inspection. One main difference is the handling of the rod during the inspection, e.g. whether only longitudinal movement or rotation of product is performed. The probe arrangement will depend on the type of mechanical rod movement that takes place. A more or less simple movement of the rod can be carried out if phased array probes or real-time scanners are used. The reason

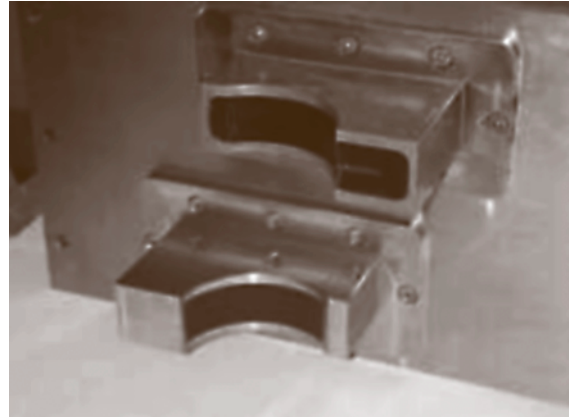


Fig. 16.20 Array transducers for the examination of longitudinal welds in pipes (GE Inspection Technologies)

is, that a complicated mechanical movement is substituted by the sound movement. One example of such a transducer arrangement is presented in Fig. 16.20. The geometry of the array transducer is adapted to the geometry of the pipe to be inspected. In this case the longitudinal weld of pipes will be examined. In addition with the help of some of ultrasonic transducers a simple mechanized movement of a rod is also possible. Three probe holders in a circumferential position of 120° in each and the combination of angle and straight-beam transducers sufficiently guarantee the detection of embedded and near-surface longitudinal defects.

16.1.4 Magnetic Particle Inspection

The physical principles of magnetic particle inspection have been well known for a long time. At the beginning of the 20th century it was discovered that, when steel parts are machined while held in a magnetic chuck, the iron grindings formed patterns around cracks on the surface. The disturbance of magnetic fields by surface defects in magnetized ferromagnetic specimens is the

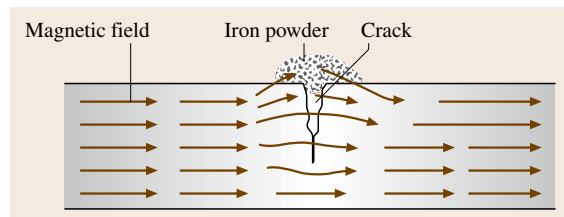


Fig. 16.21 Principle of magnetic particle inspection

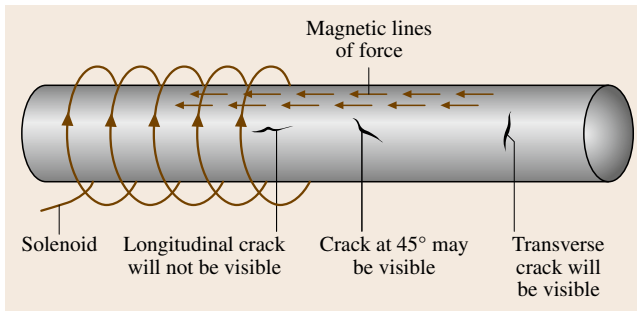


Fig. 16.22 Crack orientation in relation to the magnetic field

principle of the magnetic particle inspection method. The defect will cause some of the lines of magnetic force to depart from the surface and thus to create a magnetic leakage field. Fine iron (powder) particles, applied to the surface of the specimen, are attracted to the area of flux leakage, creating a visible indication of the flaw. The magnetic leakage field will hold the particles in a ridge on top of the crack (Fig. 16.21). By taking advantage of this effect an accumulation of magnetic particle forms, which is much wider than the

crack itself, thus making an otherwise invisible crack visible.

If, for example, a crack is oriented perpendicular to the flux lines the effect of disturbance of the magnetic field is at a maximum compared with other orientations. However, in this situation the leakage field is strongest and provides the clearest indication of a defect. Figure 16.22 demonstrates the orientation of a crack in relation to the direction of the magnetic field. The cylindrical object was magnetized with a solenoid coil that provides longitudinal magnetization of the workpiece, suitable for the examination of transverse cracks. Longitudinal cracks are not visible using this magnetization procedure. From the previous example it is clear that a good magnetic particle inspection should always be carried out with the magnetic field in two different directions, preferable in two orthogonal directions.

16.1.5 Liquid Penetrant Inspection

Liquid penetrant inspection is an old but effective *NDT* method of examining surface areas for cracks, or discontinuities. In railway and casting fabrication this technique is widely practiced to examine the surfaces by the *oil and whitening* method. This involves dunking parts, such as locomotive parts or big bells (made from bronze), in large tanks filled with heavy oil diluted with kerosene. After removal and cleaning, the surface of the specimen is then coated with a fine suspension of chalk in alcohol so that a white surface layer was formed. The residual oil in the surface-opening cracks seeps out and colors the white coating grey. At the time, more-effective penetrating oils containing highly visible dyes (usually red) were developed to enhance flaw detection capability. This method known as *color-contrast dye penetrant* is still used quite extensively. Due to the reason that this method is relatively simple (although care must be taken because there are several requirements which have to be regarded during examination) to handle. It should be clear that this method is restricted to defects open to the surface. The principle procedure of liquid penetrant inspection is illustrated in Fig. 16.23. The penetrant is drawn down into the open crack by capillary action (a). Excess surface penetrant is then removed (b). Developer powder on the surface draws out penetrant liquid, which seeps into and discolors the powder. The crack becomes visible on the surface. One of the advantages of liquid penetrant inspection is that all materials can be inspected if it is guaranteed that the material is resistant to the liquid used.

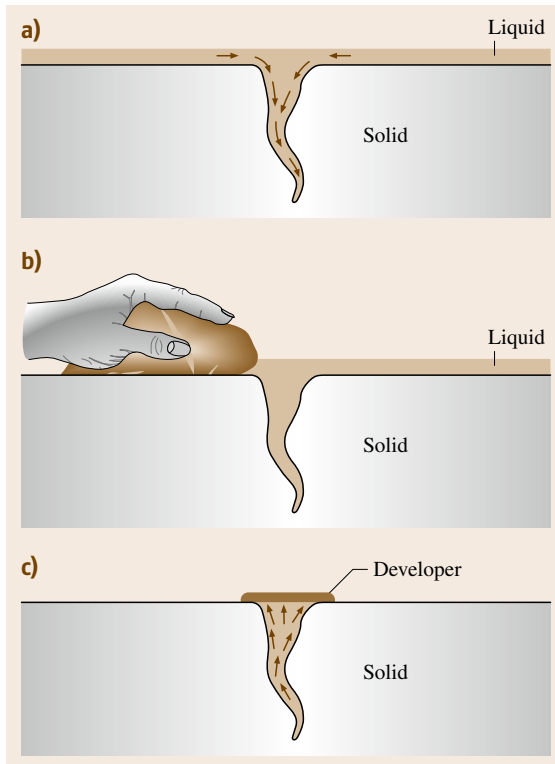


Fig. 16.23a–c Principle of liquid penetrant inspection

16.1.6 Eddy-Current Testing

A varying electric current flowing in a coil (eddy-current probe) generates a varying magnetic field [16.17, 18]. In a specimen with electric conductivity in the proximity of this coil, eddy currents flowing in a closed loop in the surface layer of the specimen are produced (Fig. 16.24). Defects at materials surfaces in the opposite of the eddy-current probe can be detected by the change of the electric coil impedance, which will be, e.g., displayed for evaluation by the test instrument connected to eddy-current probe. Cracks and other surface in homogeneities or discontinuities modify the eddy currents generated in the specimen. The coil impedance is changed in relation to a surface without defects. Practical application using eddy-current techniques is only possible if sensitive electronic devices are available that are able to measure the very small changes of the magnetic field caused by a defect. An important phenomena of eddy-current testing is the so called skin effect. There is no homogenous current distribution within the specimen; it is mainly concentrated at the contact surface of the eddy-current probe. This physical phenomenon is the reason why eddy-current testing is basically limited to thin test objects or only in a surface layer of thicker objects. The penetration depth δ of eddy current can be calculated using (16.6) and depends on the

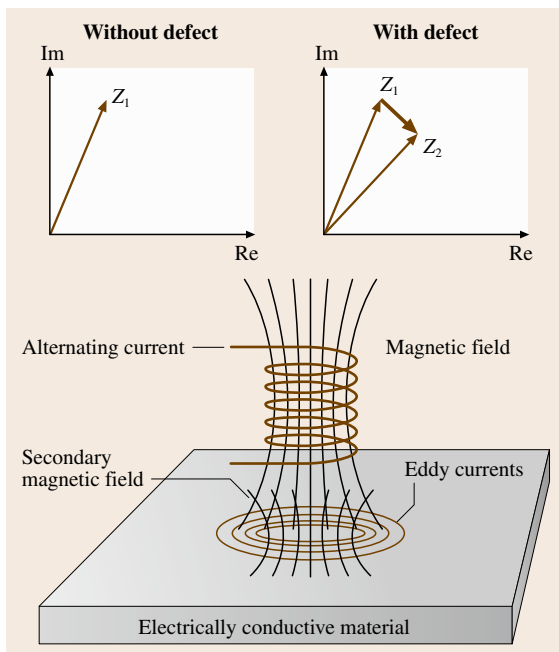


Fig. 16.24 Principle of eddy-current testing

frequency ν , the conductivity σ , the permeability of the free space μ_0 and the relative magnetic permeability μ_r . For nonferromagnetic materials μ_r is equal to 1

$$\delta = \frac{1}{\sqrt{\pi\nu\mu_0\mu_r\sigma}} \quad (16.6)$$

The frequency used in eddy-current testing ranges from a few kHz to more than 5 MHz. At lower frequencies the penetration depth δ is relatively high, as derived from (16.6), but the sensitivity to the detection of discontinuities is poor, while the opposite is true at higher frequencies. Values of δ versus the frequency are plotted in Fig. 16.25. However, it should be considered that these estimations have been made under simplified assumptions. In practical applications the penetration depth δ also depends on the characteristic of the eddy-current probe. For crack detection in and near the surface area, the penetration depth δ must be optimized in relation to the sensitivity of detection. For wall thickness measurement (detection of corrosion phenomena) δ must be at least that of the component thickness.

Figure 16.25 demonstrates that ferritic materials have very high permeability values and therefore only low penetration depth can be achieved (fractions of millimeter). This is the reason why eddy-current techniques cannot be applied to defect detection in certain depths or wall thickness measurements. A magnetizing facility up

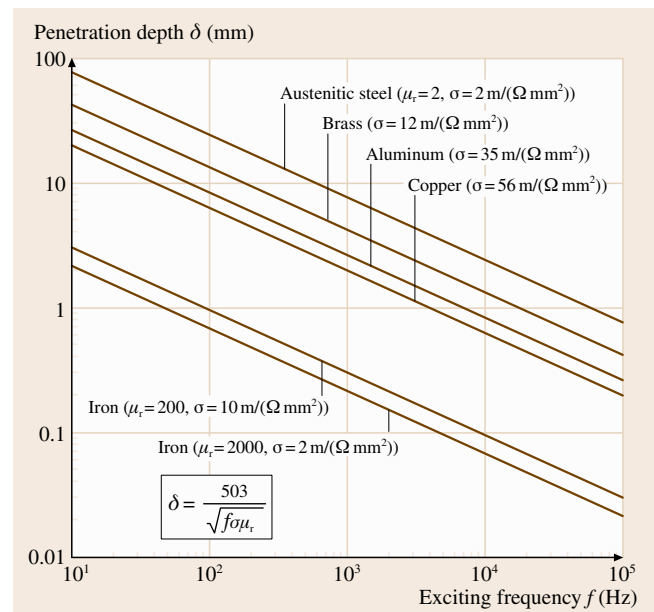


Fig. 16.25 Penetration depth versus eddy-current frequency

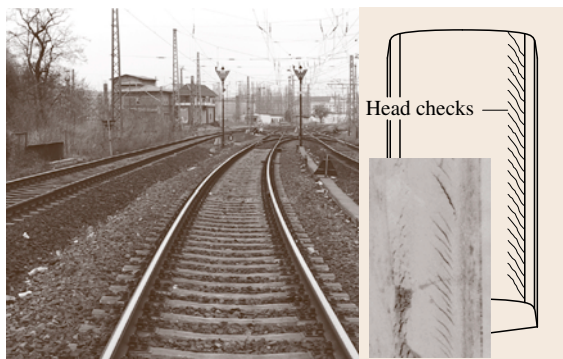


Fig. 16.26 Head checks at the gauge corner

to the saturation field can be helpful due to the reduction of the relative permeability.

On the other hand austenitic steel or nonferrous materials are suitable for the application of eddy-current methods, and a broad application of this method is in the aircraft industry.

The application of eddy-current techniques embraces a wide industrial field from the aircraft industry, the railway industry to the power-generation industry etc. Out of these wide fields of use, an example from the railway industry will be presented [16.19]. The inspection of railway wheels, known and referred to as the inspection of the railway gauge corner using eddy current, has increased in recent years. In Fig. 16.26 a special defect type is shown: so-called head checks. Head checks are cracks in the gauge corner and can be identified by their high number, having a separation of 2–7 mm. Head checks initially grow into the interior of the rail at an inclination angle of 15 to 30°. Rail gauge corner inspection is necessary to avoid rail damage such



Fig. 16.27 Broken rail caused by head checks

as that illustrated in Fig. 16.27 and is necessary to avoid accidents and save human lives.

However, an increase in surface or near-surface defects, such as head checks (Fig. 16.26) requires inspection techniques with a high detection and sizing potential to facilitate the identification of such defects. Another condition has to be considered, which is the speed of the inspection train. Inspection can be performed at up to 100 km/h.

To summarize, the eddy-current techniques proved to be most suitable for such application, because eddy-current probes have a high resolution when the head check distance is within the range of a few millimeters and modern technology means measurements can take place at higher speeds, which is an important economic factor.

16.2 Industrial Radiology

Industrial radiology is typically applied for the volumetric inspection of industrial products and installations [16.20,21]. The basic set up consists of a radiation source in front of the object to inspect and an area detector behind the object. The classical detector is an x-ray film. New electronic area detectors are gradually substituting film. The radiation source can be an x-ray generator, a gamma source or a particle radiator. Objects of all possible materials and thicknesses can be inspected, provided the right radiation source and energy is selected. There exist practical limitations to the upper

material thickness, e.g. 50 cm penetration length in steel or 2 m in concrete (at a radiation energy of 12 MeV).

Radiology dates back to the discovery of x-rays by W.C. Roentgen in 1895 and the discovery of gamma radiation by H. Becquerel in 1896. After the development of high-vacuum x-ray tubes with energies up to 100 keV in 1913, radiological techniques have been introduced into industrial practice. The description of the first computerized tomography (CT) system by G. Hounsfield and A. Cormack in 1973 was a further milestone in the development of radiation techniques

in medical and industrial applications. In acknowledgement all four scientists received Nobel prizes (for the methods of computerized tomography see Sects. 16.3 and 16.5). Over the last decades tremendous progress in hardware has occurred, such as the development of radiosopic systems with x-ray image intensifiers, microfocussing x-ray tubes, digital detector systems. This progress was accompanied by an enormous increase in computing capabilities which made the introduction of digital techniques possible, such as digital image processing and enhancement, automated defect recognition, data reconstruction, and three-dimensional CT applications. Nowadays, the increased capabilities of digital detection systems, such as phosphor imaging plates (computed radiography) and flat-panel detectors (digital detector arrays), indicate a new era in radiology.

16.2.1 Fundamentals of Radiology

Generation of Radiation

Radiation is used in industry, due to its capability to penetrate opaque material to visualize the inner structure of components. The radiation photon has a dual character, acting sometimes like a particle and at other times like a wave. Consequently, the radiation photon is characterized by its energy E or its wavelength λ or frequency ν . Planck postulated that the energy of a photon is proportional to its frequency

$$E = h\nu \quad (16.7)$$

with Planck's constant h . All photons have equal velocity,

$$c = \nu\lambda, \quad (16.8)$$

no electric charge, and no magnetic moment. x-ray or gamma radiation is fully characterized by its energy. They are distinguishable only due to their origin but not due to their properties.

X-rays are usually produced by the deceleration of high-energy electron impinging by a metallic target. Gamma rays are of nuclear origin. Whereas x-rays originate in the electron structure of the atom, gamma rays are emitted by the de-excitation of atomic nuclei in a nuclear reaction. The emission of gamma rays is usually associated with the emission of alpha and beta particles.

X-rays are generated in x-ray tubes, which consist of a cathode and an anode made from heavy high melting metal (Fig. 16.28). Electrons are emitted from the cathode and accelerated to the anode in a high-voltage electrical field. When the electrons with kinetic energy

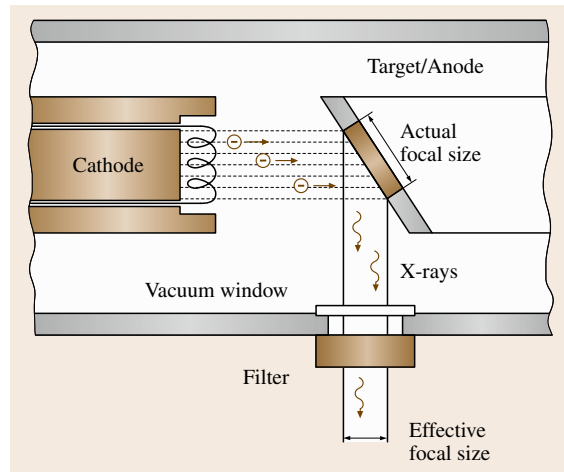


Fig. 16.28 Principle of the x-ray tube

$m_e v^2/2$ hit the target of the x-ray tube the energy is transformed in several ways yielding the production of: (i) bremsstrahlung with a continuous spectrum, and (ii) characteristic radiation (Fig. 16.29).

Bremsstrahlung is produced when the electron interacts directly with the nucleus of the target atom. The electron is stopped by the nucleus (near field) and all its kinetic energy is transformed into a quantum of radiation. Because most of the impinging electrons also interact with the electrons of the target atoms they lose a part of their energy to remove an electron from an atom. The remaining kinetic energy of the electron can be transformed into an x-ray photon. In general, x-rays photons of many energies are emitted forming the continuous bremsstrahlung spectrum. The voltage of the

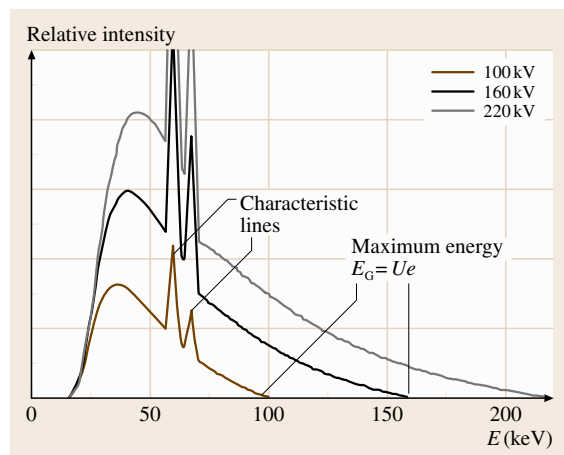


Fig. 16.29 Typical x-ray spectrum

accelerating electrical field gives the maximum energy of the emitted x-ray photons.

When an electron is removed from the target atom by the impinging electron, the atom is left in an excited state. Recombination processes within the electron shell yield the emission of one or more photons with energy characteristic for the atom. As a result, the continuous bremsstrahlung spectrum is overlaid by characteristic spectral lines (compare Fig. 16.29).

The target of a x-ray tube can stop all impinging electrons (thick or absorption target) as used in most of the industrial x-ray tubes, or stop only a part of the electrons (thin or transmission target) as used in micro-focus tubes. Because most of the electron's energy is converted into heat (about 95%), overheating of the target has to be avoided. Therefore, the anode to which the target is attached typically consists of a material with high thermal conductivity, such as copper. Often it is necessary to cool the anode by directly injecting coolant. Another way of solving the problem of localized overheating of the target is by using a rotating anode.

Gamma rays are emitted during the spontaneous decay of unstable isotopes. The decay is accompanied by the emission of alpha or beta particles. Each emission transforms the parent isotope into a daughter isotope having a different mass and nuclear charge. This process continues until the daughter isotope is stable. This is described by the half-life T required for one half of the original number of atoms to decay or change to the daughter atoms. The number of atoms disintegrating per unit time can be expressed by

$$N = N_0 e^{-\lambda t} \quad (16.9)$$

with the total number of parent atoms N_0 , and the decay constant λ . The half-life is given by

$$T = \ln 2 / \lambda = 0.693 / \lambda \quad (16.10)$$

Artificially produced isotopes such as Ir-192 or Co-60 are widely used as sources of radiation for technical radiography. The emitted gamma-ray spectrum consists of separated lines with energies characteristic for the particular isotope. Both isotopes are obtained by neutron bombardment of the naturally existing stable isotopes Co-59 and Ir-191

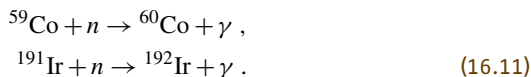


Figure 16.30 shows the disintegration scheme for Co-60. As a result two gamma lines with 1.173 and 1.332 MeV are observed.

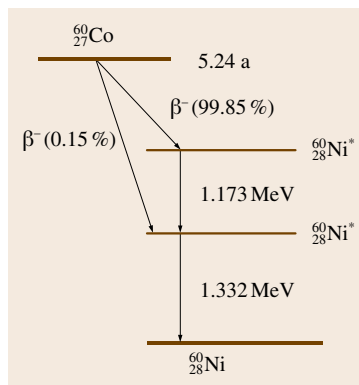


Fig. 16.30 Disintegration series of Co-60

Interaction with Matter

Attenuation Law. Photons interact with a nucleus or an orbital electron of the attenuating material. The interaction of photons with matter can be classified into three predominant types: (i) the photoelectric effect, (ii) scattering, and (iii) pair production. Photodisintegration is neglected due to its minor contribution. The attenuation law is described assuming a narrow beam geometry and monochromatic radiation (Fig. 16.31). Considering an incremental attenuating layer of thickness dx at depth x , the change in the beam intensity dI in dx is proportional to the intensity I at that depth x and the thickness of the layer dx

$$dI = -\mu I dx \quad (16.12)$$

with the proportionality constant μ , which is the linear attenuation coefficient given in one per unit length. Integration of (16.12) yields

$$I_P = I_0 e^{-\mu d} \quad (16.13)$$

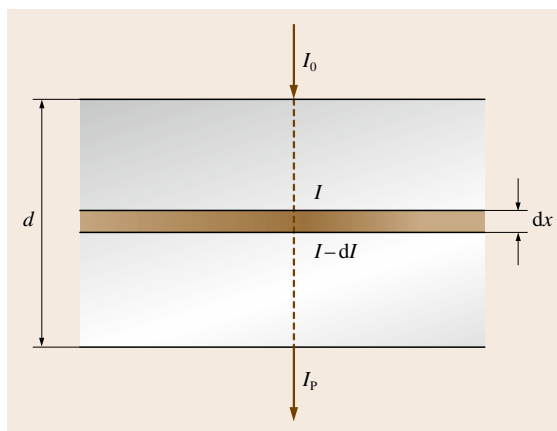


Fig. 16.31 Attenuation law

where I_0 is the intensity of the incident beam and I_p is the primary intensity after penetrating material of thickness d . Equation (16.13) is referred to as the attenuation law. The linear attenuation coefficient is given by the sum of the interaction coefficients for each of the various processes mentioned above

$$\mu = \tau + \sigma_S + \pi . \quad (16.14)$$

Here τ is the attenuation coefficient due to the photoelectric effect, σ_S that due to scattering, and π that due to pair production.

Photoelectric Effect. If a photon of energy E transfers its total energy to an electron in some shell of an atom, the process is called the photoelectric effect (Fig. 16.32). The energy of the photon can be sufficient to lift an electron from an inner to an outer shell or to remove the electron completely and to ionize the atom. In the second case, the photoelectron obtains a kinetic energy given by the difference between the photon's energy and the binding energy of that particular electron. As the energy of the photon increases absorption becomes possible by inner shell electrons. When the energy of the photon reaches the binding energy of a particular shell of electrons the absorption coefficient increases abruptly because more electrons are available for interaction. The energy at which this sharp increase occurs is called an absorption edge, which is characteristic for every atom. Otherwise the absorption coefficient decreases with increasing photon energy. The energy dependence of the linear absorption coefficient for lead is shown in Fig. 16.33. As secondary effects, recombination processes within the electron shell yield either x-ray fluorescence (Fig. 16.32) or the emission of Auger electrons.

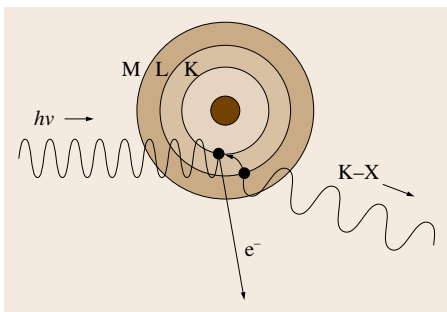


Fig. 16.32 Photoelectric interaction of an incident photon with an orbital electron may yield x-ray fluorescence due to recombination of electrons from a higher to a lower orbital

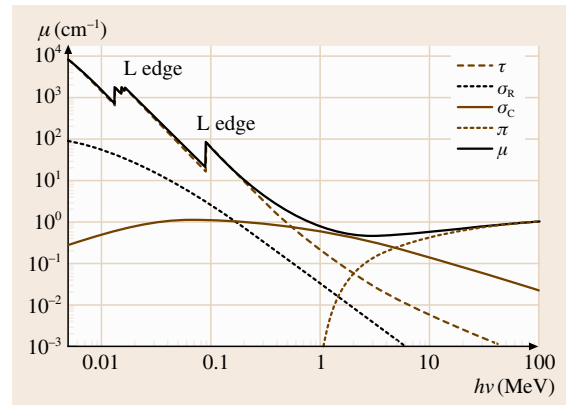


Fig. 16.33 Linear attenuation coefficient μ for lead as a function of energy $h\nu$: τ photoelectric effect, σ_R Rayleigh scattering, σ_C Compton scattering, and π pair production

Scattering of Photons. Scattering can be incoherent, which is known as Compton scattering, or coherent, which is called Rayleigh scattering (Fig. 16.34). Whereas a photon transfers its total energy to an orbital electron while undergoing an absorption event, it loses no or only a part of its energy and is redirected if a scattering event occurs.

The analysis of the Compton process shows that the energy of the scattered photon E' is always less than that of the primary photon $E > E'$. The remaining energy is transferred to the struck electron as kinetic energy. The energy shift predicted depends only on the scattering angle θ and not on the nature of the scattering medium. The larger the scattering angle the larger the energy shift observed. The relationship between the scattering angle and the energy shift can be found from the conservation of energy and momentum during the collision when assuming particle properties of the photon. The scattering of a photon by a free electron is described by the Klein–Nishina formula, providing an accurate prediction of the differential cross section with respect to the solid scattering angle. If considering electron binding effects the Klein–Nishina formula has to be corrected by the incoherent scattering function, which decreases the free-electron cross section in the forward direction, for low energies E , and for high atomic numbers Z . The linear Compton coefficient for lead can be found in Fig. 16.33. In general it decreases with the photon energy, starting at an energy characteristic of the material.

The coherent or Rayleigh scattering involves no energy loss of the photon upon being scattered by an

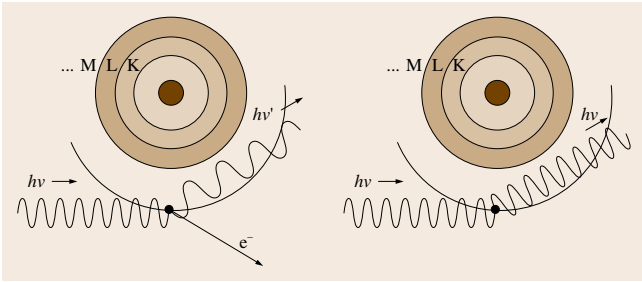


Fig. 16.34 Scattering effects: Compton scattering in which an incident photon ejects an electron and a lower-energy photon (*left*); Rayleigh scattering of a photon without energy loss

atom. It is only a photon process that does not produce electrons. The angle distribution for coherent scattering of a photon by a free electron does not depend on the photon's energy and is given by the Thomson formula, which is equivalent to the Klein–Nishina formula at zero energy. To take account of electron binding effects, the Thomson formula has to be corrected by the coherent atomic form factor. It yields a strong forward directionality of Rayleigh scattering, which increases with the photon energy. Rayleigh scattering occurs only for soft radiation for which the binding energy of the electrons in their atomic shell is important. It is most important for elements of low atomic number Z and high photon energies E . The Rayleigh cross section decreases with energy (compare Fig. 16.33). The contribution of this type of scattering to the total attenuation coefficient is never greater than about 20%.

Pair Production. If the photon energy exceeds double the electron mass of rest, i. e. if $E = hv > 1.022 \text{ MeV}$, the photon is converted in the electrical field of the nucleus into an electron and a positron. This process is called pair production (Fig. 16.35). Photons with lower energy are not able to produce an electron–positron pair. The photon energy that exceeds the

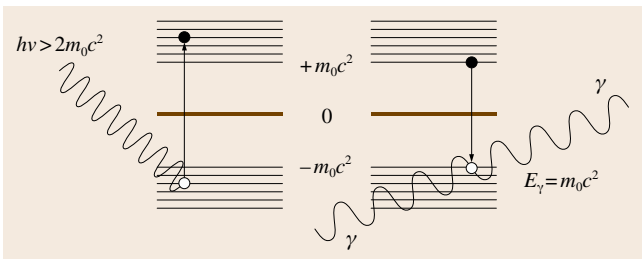


Fig. 16.35 Pair production (*left*) and positron–electron annihilation (*right*)

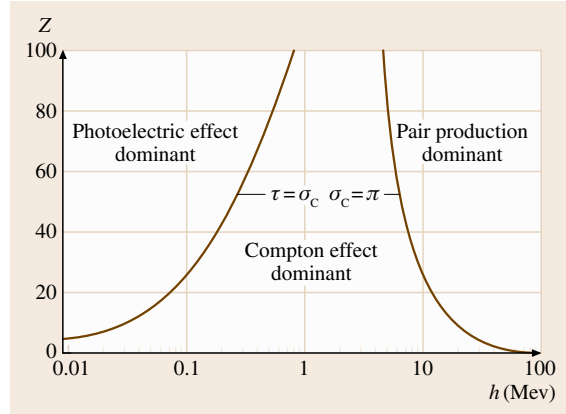


Fig. 16.36 Relative importance of photon interactions

needed minimal energy for producing an electron–positron pair appears as the kinetic energy of the pair. The probability of occurrence of this process increases approximately logarithmically with the energy above the threshold value and then levels off for extremely high photon energies (compare Fig. 16.33). The produced pair loses its kinetic energy within a very short time of about 10^{-12} s . The remaining resting electron–positron pair has a lifetime of about 10^{-9} s before annihilation. As a result two gamma photons are emitted in opposite direction with energy of exactly 511 keV.

As seen in Fig. 16.33, different attenuation mechanisms are dominant at different energies. The photoelectric absorption is the dominant effect for lower energies, whereas Compton scattering becomes important for medium photon energies. For higher energies pair production is the most probable interaction mechanism. Figure 16.36 shows the relative importance of the different photon interactions with matter. The lines show the values of the atomic number Z and the energy for which the two neighboring effects are of equal importance.

Image Quality

The image quality is the characteristic of a radiographic image that determines the degree of detail it shows. It is influenced by a large variety of influencing factors originating in the inspected object (material, thickness), the radiation source (radiation quality), the imaging system (detector properties), and geometry (focal spot size, source-to-object distance, object-to-detector distance). Image quality can be measured by image quality indicators (IQI).

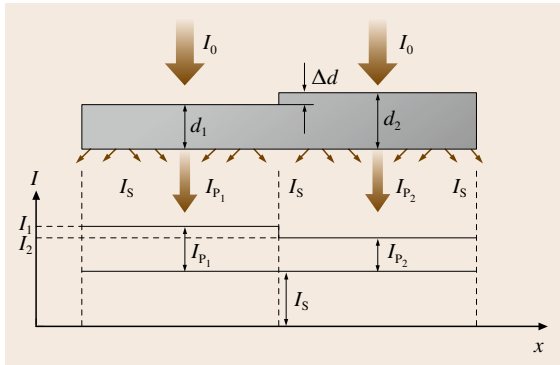


Fig. 16.37 Image formation

Contrast. The formation of a radiographic image can be easily explained in terms of a simple step object (Fig. 16.37). The intensity or density difference seen between two thicknesses at a given detection intensity I or density in an object on a radiograph represents the radiographic contrast in the image (approach for small thickness differences)

$$C_1 = I_1 - I_2 \quad (16.15)$$

with the intensities I_1 and I_2 after penetrating a material of thickness d_1 and d_2 , respectively. Introducing $I_P = I_{P_1}$ as a reference primary intensity, a linear relation follows between the absolute contrast ΔI and the thickness difference from the attenuation law (16.13)

$$\Delta I = I_P \mu \Delta d. \quad (16.16)$$

For the interpretation of radiographs the relative contrast with which an indication is imaged is important

$$C_r = \frac{\Delta I}{I} \quad (16.17)$$

where $I = I_S + I_P$ gives the total intensity. For small thickness differences, it follows from using (16.16) that

$$C_r = \frac{I_P \mu \Delta d}{I_S + I_P} = \frac{\mu}{1+k} \Delta d = C_{sp} \Delta d \quad (16.18)$$

with the scattering ratio $k = I_S/I_P$ and the specific contrast $C_{sp} = \mu/(1+k)$. Hence, the relative and the specific contrast increase with the attenuation coefficient, but decrease with increasing scattering ratio and increasing material thickness. As result, high-energy radiation yields higher contrast for large thicknesses (steel > 50 mm; aluminum > 100 mm) than lower energy radiation because the increase of contrast due to decreasing scatter ratio is larger than the decrease of contrast due to decreasing attenuation coefficient. This

effect can be achieved either by using higher-energy sources (increase of kilovoltage for x-ray tubes, application of gamma radiation) or by using filters to increase the quality of radiation.

Noise and Granularity. The perception of any indication depends on the contrast-to-noise ratio (CNR). The image noise is measured quantitatively as the standard deviation of the mean value of the intensity or density in a projected area of constant object thickness. Density fluctuations are described as the granularity of film systems. The visual impression is the graininess. The term *noise* is used dominantly in digital radiology. The CNR increases with the square root of the required exposure time of a film system or digital detector. This is the reason why slow film systems provide higher contrast sensitivity than fast ones. The human perception depends on the shape of the object. Linear edges, cracks and wires are already recognizable at $CNR > 0.7$. For the perception of small volumetric objects or flaws (e.g. balls, pores) the required CNR is > 2.5 .

Unsharpness. The sharpness of the outline of an image is directly affected by the geometrical unsharpness generated by the source size, the source-to-object and the object-to-detector distances (SOD, ODD), and the inherent unsharpness u_i of the detector.

The blurring of an edge image due to a final focal spot size S is defined by the geometrical unsharpness u_g (Fig. 16.38, left)

$$u_g = \frac{b}{a} S = (M - 1) S \quad (16.19)$$

with the magnification factor M according to Fig. 16.38 (right).

$$M = \frac{a+b}{a}. \quad (16.20)$$

Additionally the detector system contributes to the system unsharpness. Due to the properties of the detector an additional edge blurring is observed. In the case of film radiography there can be drawbacks, e.g. to the use of intensifying screens and to the scattering of photons or electrons in the film emulsion. This contribution is called inherent unsharpness u_i .

The total unsharpness u_t observed in a radiograph when neglecting the effect of motion during exposure can be approximated by

$$u_t = \sqrt{u_i^2 + u_g^2}. \quad (16.21)$$

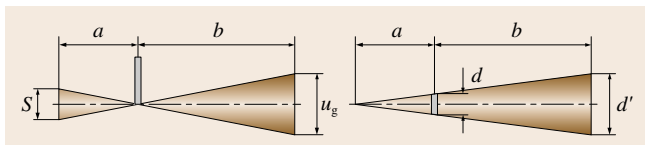


Fig. 16.38 Geometrical unsharpness (*left*) and magnification (*right*)

The optimal geometry for taking radiographs with minimum effective unsharpness (u_t divided by magnification) can be determined if the inherent and geometrical unsharpness are chosen equivalent. From this condition the optimal ratio of the SOD and SDD follows

$$\left(\frac{a}{b}\right)_{\text{opt}} = \frac{S}{u_i} \quad (16.22)$$

As long as the projection $d' = Md$ of an object of size d is larger than the total unsharpness the contrast of the indication is not decreased and follows (16.16). If the unsharpness exceeds d' a decrease of the indication contrast is observed (compare Fig. 16.39).

Image-Quality Indicators (IQI). Image-quality indicators are standardized devices consisting of a series of elements of graded dimensions, which enable a measure of the image quality to be obtained. IQIs are usually included in every radiograph to check on the adequacy of the radiographic technique. The elements of IQIs are commonly wires and steps or plates with holes. IQIs together with their usage are described in detail in the

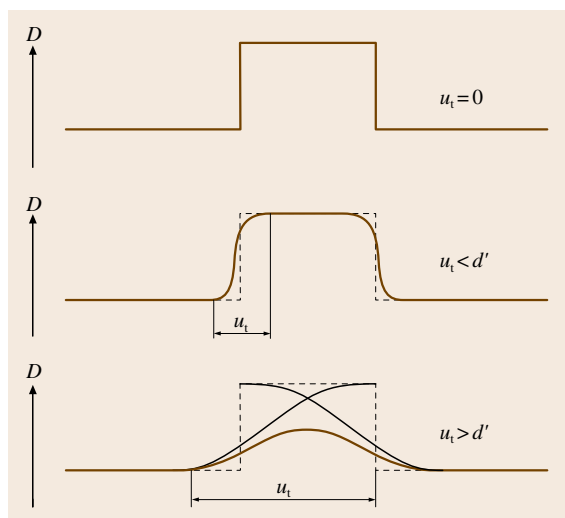


Fig. 16.39 Influence of unsharpness to image contrast

European standards EN 462 part 1–5 and, in the USA, standards ASTM E 747, E 1025, and E 2002.

Wire-type IQIs consist of wires that are arranged by diameter, all with the same length (Fig. 16.40a). The wire material is chosen to match the material of the investigated object. It measures the thickness resolution of the radiographic technique.

The European step hole IQI system is based on a series of steps of different thickness d and holes of diameter equal to the step thickness (Fig. 16.40b). The material is chosen to match the material of the investigated object. The image-quality value is given by the number of the smallest hole that is visible on the radiograph.

The American plate hole IQI (ASTM E 1025) consists of a small rectangular or circular piece of metal usually containing several holes, the diameters of which are related to the thickness of the plate. The ASTM penetrometer contains three holes of diameters T , $2T$, and $4T$, where T is the thickness of the plate. The material is again chosen to match the material of the investigated object. The IQI gives the equivalent penetrometer sensitivity (EPS) in terms of contrast resolution, which is a measure for the minimal resolvable thickness difference together with the minimal resolvable detail influenced by the total unsharpness (compare Fig. 16.39).

Duplex wire indicators (Fig. 16.40c) are used when it is necessary to evaluate and measure the total image unsharpness (spatial resolution) separately from contrast sensitivity measurements. Every element consists of two circular wires of certain diameter, which equals the spacing between the wires. Highly attenuating material, such as tungsten and platinum, is chosen for the wires. The largest element without identifying space between the images of the two wires is taken as the limit of discernibility.

16.2.2 Particle-Based Radiological Methods

X- and γ -ray radiography are the most important and well-accepted methods in industry. Nevertheless there also exist other methods that are based on the attenuation of neutrons, positrons and electrons. Neutron radiography is dominant in the aircraft and military industries and in research. The attenuation of neutrons in materials follows other laws than x-ray and γ -radiography. Figure 16.41 shows the different attenuation coefficients for thermal neutron- and x-radiography as function of the ele-

ment number in the periodic system. Materials which contain the elements H, B, Li, Cd, Gd, Sm and Eu attenuate neutrons much more than construction metals as Al, Fe, Co and Ni. This enables the radiography of organic components in metallic encapsulation such as rocket motors and ammunition with high contrast of structures and flaws of the organic materials (e.g. explosives). Moisture in aircraft components can also be detected at high contrast. More details about n-radiography as well as positron and electron radiography can be found in the ASNT handbook [16.21].

16.2.3 Film Radiography

Radiography in medicine and industry is carried out under different considerations. Medical applications have to be performed with minimum exposure dose for the patient. Therefore, the typical film system consists of fluorescence screens and film. The optical film density is typically between 1 and 2. Industrial applications for nondestructive testing (NDT) generally use exposure dose values which are 10–100 times higher. The resulting NDT image quality is characterized by higher sharpness and contrast sensitivity. Industrial radiographic films contain usually a higher silver content, which allows higher optical density (blackening) to be obtained. NDT films are applied for density values of 2–4.5. Special high-brightness viewing stations are required. Medical viewing equipment is not sufficient. NDT film systems consist of double-layered films with thin lead screens at the front and back side. The x-rays penetrate the film and expose the front and back sides. The lead screens convert x-rays to fast electrons, which expose the film more efficiently than the x-rays. These screens are used for intensifying the exposure, in particular for high-energy x-rays. Since the lead screens convert the photons to electrons instead of light, the exposed radiographs are not blurred by scattered light. Radiographs taken with fluorescence screens have an unsharpness of 0.2–0.4 mm, depending on the screen thickness and x-ray energy. Film lead screen systems have an unsharpness of 30 μm to a few hundred microns, depending on the screen thickness and energy.

NDT film systems are classified corresponding to the standards ISO 11699, EN 584, JIS K 7627 and ASTM E 1815. The classification requires the user to select the film type and the developer as well as the certified developer temperature and immersion time to prove conformity with the standards.

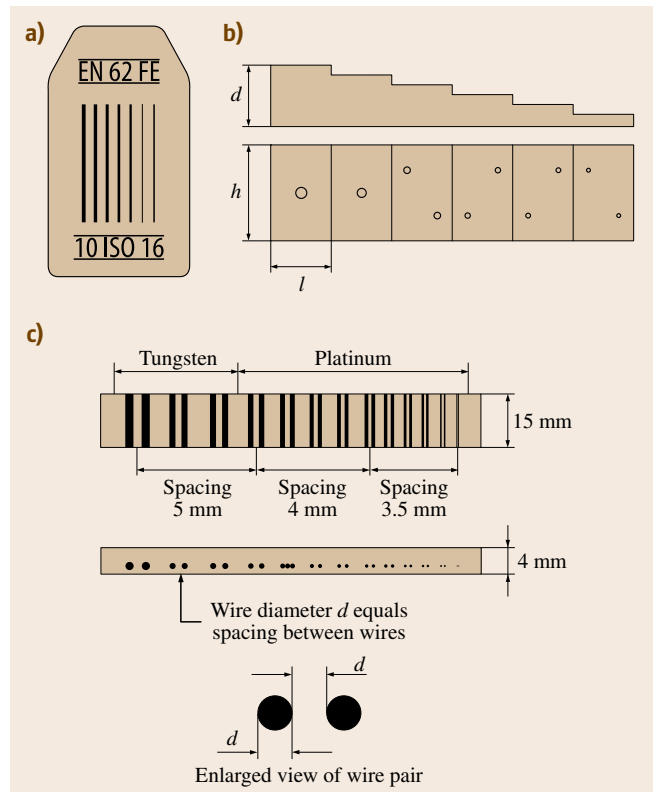


Fig. 16.40a–c Selection of image-quality indicators (IQI), described in European standards: (a) wire IQI; (b) step hole IQI; (c) duplex wire IQI

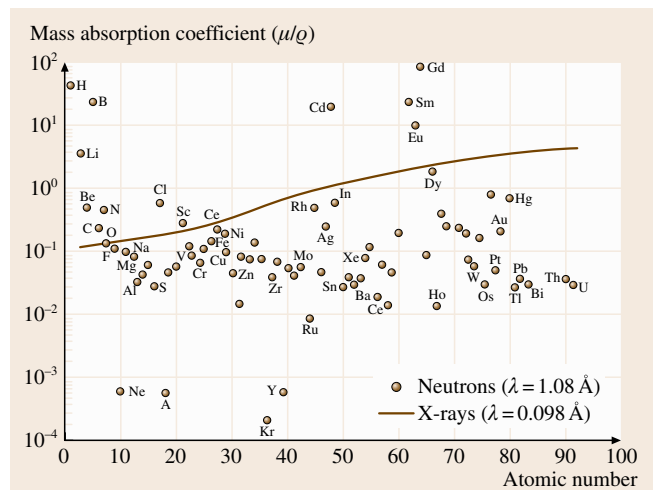


Fig. 16.41 Comparison of mass absorption coefficients for the elements for both x-ray and thermal neutrons. (after: *Thewlis*, Argonne National Laboratory)

16.2.4 Digital Radiological Methods

Users of industrial radiology, who are interested to move from classical film radiography to digital industrial radiology (DIR), should know which particular field they want to enter. Basically there exist unregulated and regulated areas (standards, guidelines and others). Table 16.2 describes the four basic application areas.

Before new methods and detectors will be described, the advantages of traditional film radiography should be summarized. One of the major advantages of x-ray film radiography is its practicability. Important x-ray film properties are

- they are dust- and waterproof packed;
- they consist of flexible and break-proof material;
- the storage period after development is > 50 years (expected shelf life > 500 years);
- the readability is independent of technological development (e.g. independent of data format).

Film Digitization

Film digitization systems can be classified by the sampling technology (Table 16.3).

For example, digitization with a laser scanner proceeds as shown in Fig. 16.42. The film passes a collection tube. A laser beam (wavelength about 680 nm, red) with a fixed diameter (e.g. 50 μm) scans the film. The diffuse transmitted light through the film is integrated by the collection tube and registered by a photomultiplier (PMT) on top of the collection tube (not shown in Fig. 16.42). During the scan the folding mirror deflects the laser beam and moves the spot along a horizontal line on the film. The film is advanced with a constant speed. The resulting voltage at the photo multiplier is proportional to the light intensity behind the film. After logarithmic amplification a digitization with

Table 16.3 Classification of digitization systems by technology

Principle	Scanner type
Point-by-point digitization	Laser scanner
Line-by-line digitization	CCD line scanner
Array digitization	CCD camera

12 bits yields grey values that are proportional to the optical density of the film.

The essential difference to other digitization principles is the reversed optical alignment. The laser scanner illuminates with focused light and measures the diffuse light intensity behind the film. All other methods illuminate the whole area of the film with diffuse light (the film is illuminated with a diffuser) and measure the light intensity that passes the film in one direction at each spot (camera objective or human eye in classical film inspection).

Complementary metal-oxide-semiconductor (CMOS) cameras, which generate a logarithmic output signal relative to the input light intensity, are also available. In this case the digitized grey values will be proportional to the film density, and do not follow the exponential characteristics as digitized with charge-coupled device (CCD) chips. This is an advantage over CCD chips for the digitization of radiographic films, but the signal-to-noise ratio for CMOS detectors is usually considerable lower than for CCD chips.

The standard ISO/EN 14096-1/2 defines the qualification procedure and the minimum requirements for film digitizers in NDT. This is particularly important for microradiography. NDT applications employ x-ray energies of 50–12 000 keV. The standards require a spatial pixel size of 15–250 μm depending on the energy. This corresponds to a required spatial resolution of 16.7 lp/mm (line pairs per millimeter) for energies < 100 keV and e.g. 1 lp/mm for 1300 keV.

Table 16.2 Application areas of digital industrial radiology (DIR)

Digital industrial radiology			
Film replacement		New industrial areas	
Standards, regulations	Nonstandard applications	Serial part inspection	Computed tomography
Welding	Wall thickness, corrosion, erosion	Automated defect recognition (ADR)	3-D-casting inspection
Casting	Buildings, bridges	Completeness test	Ceramic composites, plastics
Electronics	Plastics, composites	Dimensional check	Special applications
	Food, tires, wood ...		

On the basis of the image quality of film radiography the standard requires three quality classes: **DA**, **DB** and **DS**. The user may select the testing class based on the needs of the problem.

- **DS**: the enhanced technique, which performs the digitization with an insignificant reduction of signal-to-noise-ratio and spatial resolution; application field: digital archiving of films (digital storage);
- **DB**: the enhanced technique, which permits some reduction of image quality; application field: digital analysis of films; films have to be archived;
- **DA**: the basic technique, which permits some reduction of image quality and further reduced spatial resolution; application field: digital analysis of films; films have to be archived.

Image Processing

A digital image is physically not more than a data file in a computer system linked to a program capable of displaying its contents on a screen or printout dot by dot. That means it consists of an array of individual image points. These are called picture elements (pixel). The pixels are in practice small rectangles (squares) showing a certain color and brightness.

The image resolution depends on the number of pixels within a given area; the more the better (Fig. 16.43). Radiography commonly deals only with grey-level images.

The numerical values of any pixels within an image can be subjected to various kinds of calculations. Each pixel is characterized by a grey (intensity) value, which is proportional to its brightness. The most trivial step is to adjust brightness and contrast. This allows one to overcome the lower brightness of monitors compared to commercial film viewers. While the human eye can only distinguish between some 60–120 grey values (at a given adaptation, equivalent to 6–7 bits of information) a digital image may contain up to 65 536 grey levels (i. e. 16 bits). The contrast and brightness operations are essential to select the range of interest. The *gamma* transformation alters the linearity of the transfer from the original digital values listed in the image file to its brightness displayed on the screen, taking into account the brightness sensitive perception of human eyes.

Multiple-point calculations take advantage from relationships between adjacent pixels of the image (matrix operations). They are based on a variety of so-called filter algorithms that are supposed to extract the desired features from the total image information. They

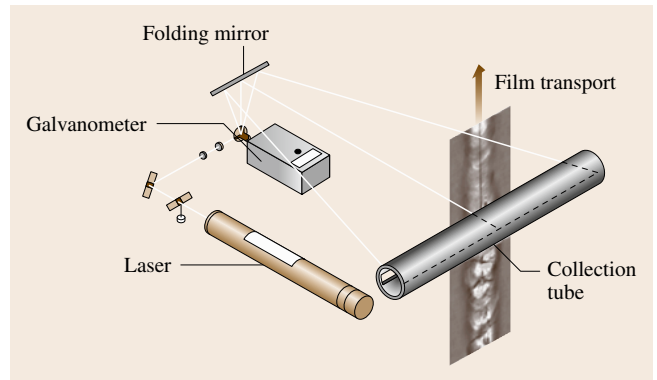


Fig. 16.42 Principle of a laser scanner (“LS 85”, Kodak, USA)

may eliminate unwanted large, patchy intensity fluctuations or noise masking other image details. Typical filters are described in Table 16.4. Processing of radiographic images shows astonishing results that can be found, together with *filter recipes*, in different textbooks [16.22, 23].

Computed Radiography and its Industrial Application

Phosphor imaging plates (**IP**) are image media for filmless radiography. The technique is also called computed radiography (**CR**). **IPs** are routinely used in medicine and biomedical autoradiography. Different systems are

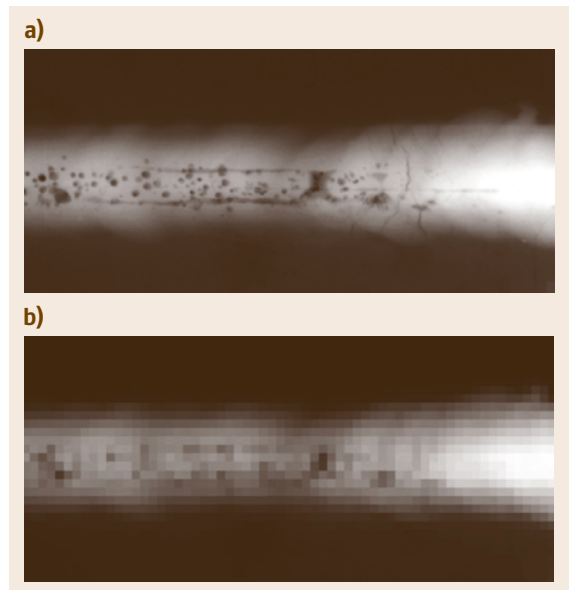


Fig. 16.43a,b Radiographic image of a test weld BAM5, (a) 1024 × 512 pixels; (b) 64 × 32 pixels

Table 16.4 Typical image-processing filters

Filter	Advantage	Disadvantage
Low-pass filter (smoothing)	Increases the signal-to-noise ratio	Reduces the spatial resolution
High-pass filter	Increases the contrast of fine details in relation to intensity changes in a wide range	Reduces the signal-to-noise ratio
Median filter	Increases the signal-to-noise ratio, removes single peaks and outliers (single white or black pixels such as <i>salt and pepper</i> distortions), does not smooth edges	Reduces the spatial resolution
Edge filter	Enhances edges or extracts edges to lines	Increases the noise

available for NDT applications. Novel applications in addition to film radiography emerge taking advantage of the higher sensitivity (shorter exposure time) and the digital processing as well as the capability to analyze digital radiographs with affordable computer systems. A set of standards was published 2005 in Europe and USA, which defines the classification and practice of CR systems [16.24].

IPs are handled nearly in the same way as radiographic films. After exposure, they are read by a laser scanner producing a digital image instead of being developed like a film (Fig. 16.44). Any remaining latent image can be erased with a bright light source so that the same IP can be recycled up to more than 1000×. An IP consists of a flexible polymer support which is

coated with the sensitive layer which is sealed with a thin transparent protective layer. The sensitive layer of the most common systems consists of a mixture of BaFBr doped with Eu^{2+} . X-ray or gamma-ray quanta result in an avalanche of charge carriers i. e. electrons and holes in the crystal lattice [16.25].

These charge carriers may be trapped at impurity sites i. e. electrons at a halogen vacancy (F-center) or holes at an interstitial Br_2^+ molecule (H-center). Red laser light (600–700 nm) excites electrons trapped in a Br^- vacancy (F_{Br} -center) to a higher state from which they may tunnel and recombine with a nearby trapped hole. Transfer of the recombination energy excites a nearby located Eu^{2+} ion. Upon return to its ground state this Eu^{2+} ion emits a blue photon (390 nm). This process is described as photostimulated luminescence (PSL).

The advantages of IP technology are

- linearity with radiation dose
- high dynamic range, up to 10^5
- sensitivity higher than with film
- reusable for 1000 cycles
- no chemical darkroom processing
- capability for direct image processing.

The disadvantages are

- limited spatial resolution, except in new high-definition systems
- high sensitivity in the low-energy range
- sensitive to scattered radiation.

The available systems of phosphor imaging plates and corresponding laser scanners cover radiation dose differences of up to 10^5 . This feature reduces the number of exposures for objects with a high wall-thickness difference. It also compensates partly for incorrectly calculated exposure conditions. The number of so-called test exposures is reduced. The IP reader is typically separated from the inspection site. CR is based

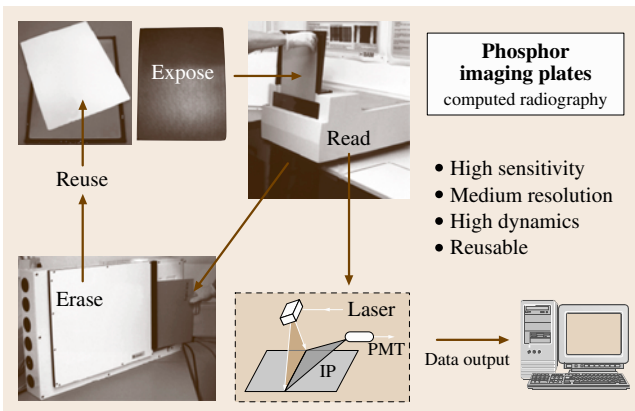


Fig. 16.44 Principle of application of phosphor imaging plates (IP) for computed radiography (CR). The plate is exposed in a lightproof cassette. The scanner reads the IP with a red laser beam. All exposed areas emit stimulated blue light. The photomultiplier collects the blue light through a blue filter and converts it into an electrical signal. The signal intensity values are converted to digital grey values and stored in a digital image file. Remnants of the image on the IPs are erased by intensive light. They can be used usually 100–1000× if they are handled carefully

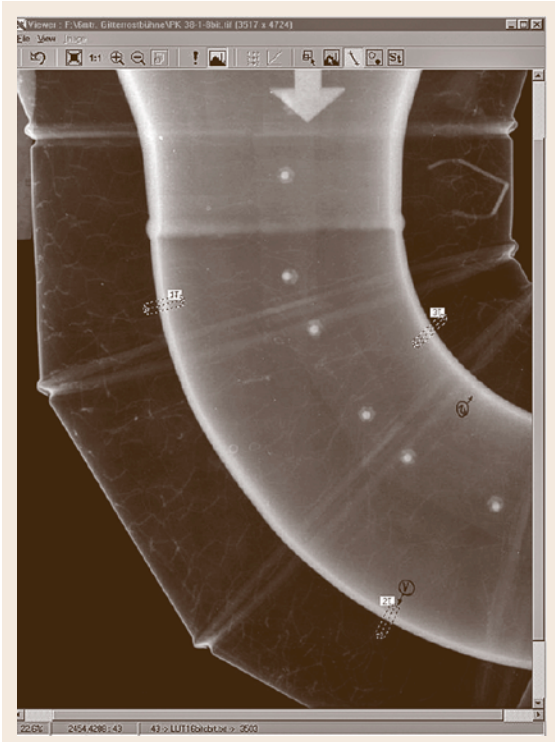


Fig. 16.45 Computer-based inspection of an insulated pipe by projection radiography. The wall thickness is measured by image processing in the *marked areas*

on flexible IPs [16.26]. High-definition CR systems can provide a spatial resolution of better than $25\ \mu\text{m}$. This is sufficient for weld and casting inspection of small components at lower x-ray voltages as well as large components.

Measurement of Pipe Wall Thickness for the Evaluation of Corrosion, Erosion and Deposit

A typical application of the CR technology is radiographic corrosion inspection in the chemical industry. Figure 16.45 presents a typical example with a thermally insulated pipeline. The insulation is covered with an aluminum envelop. The radiographic inspection can be performed without removing the insulation. This is a considerable advantage relative to the other known methods. Radiographic pipe inspection for corrosion and wall thickness measurement is a major NDT technique for predictive maintenance. CR is also more and more applied for inspection of valves and armatures for functionality check and deposit search.

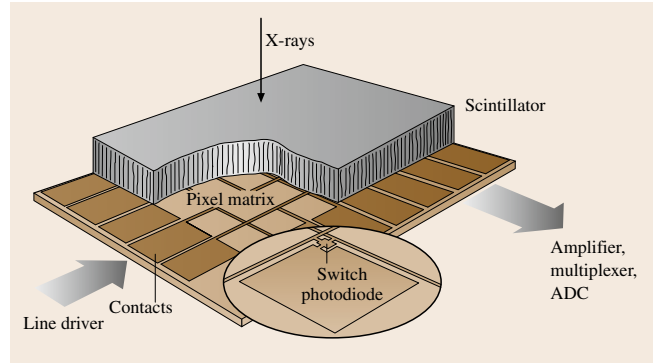


Fig. 16.46 Scheme of a flat-panel detector: The scintillator converts x- or γ -rays into light, which is detected by the photodiodes. They are read out by thin-film transistors (TFT) on the basis of amorphous silicon, which is resistant to radiation

Radiography with Digital Detector Arrays (DDA)

Flat-Panel Detectors. Two types of DDAs, also called flat-panel detectors, are available on the market. The first design (Fig. 16.46) is based on a photodiode matrix connected to thin-film transistors (TFT) [16.27]. These components are manufactured of amorphous silicon and they are resistant against ionizing radiation. Alternatively to the amorphous silicon panels CMOS arrays can be applied. The photodiodes are charged by light which is generated by a scintillator converting the incoming x- or gamma rays. This scintillator can be a polycrystalline layer that causes some additional unsharpness by light scattering or a directed crystalline system which acts like a face plate with lower unsharpness due to inhibited light scattering (Fig. 16.47). The next generation (second type of DDAs) of flat panels is based on a photoconductors like amorphous selenium [8] or CdTe on a multi-microelectrode plate, which is also read out by TFTs (Fig. 16.48b). Direct converting photodiode systems (Fig. 16.48a) are not used in NDT yet, due to their low quantum efficiency.

DDAs are suitable for in-house and in-field applications. In-field applications are characterized by harsh environmental conditions in some areas, which implies the risk of hardware damage and restricts the mobile application of DDAs. Alternatively, digital data may be obtained by film digitization or directly by the application of CR.

Line Detectors. The classical concept of NDT with line detectors is based on a fixed radiation source, moving objects and a fixed line camera. This is

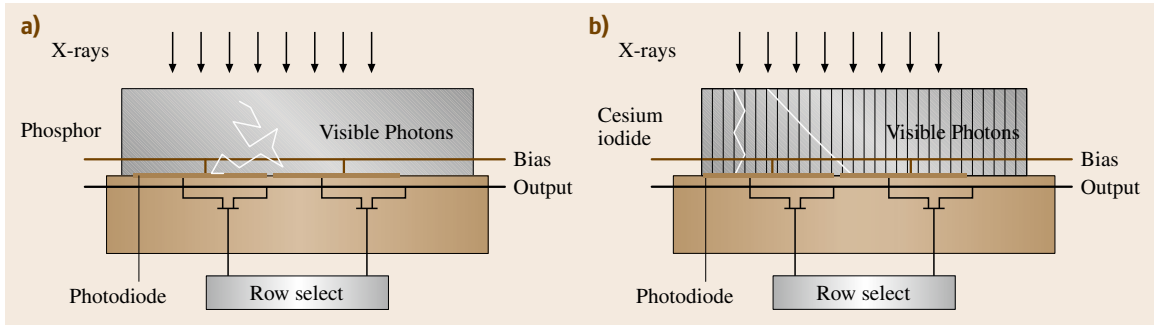


Fig. 16.47a,b Principle of amorphous-silicon flat panels with fluorescence screens. **(a)** Additional unsharpness is generated in the phosphor layer due to light scattering. **(b)** Needle crystals of CsI on the surface of the photodiodes improve the spatial resolution because the crystals conduct the light to the photodiodes like fiber light conductors

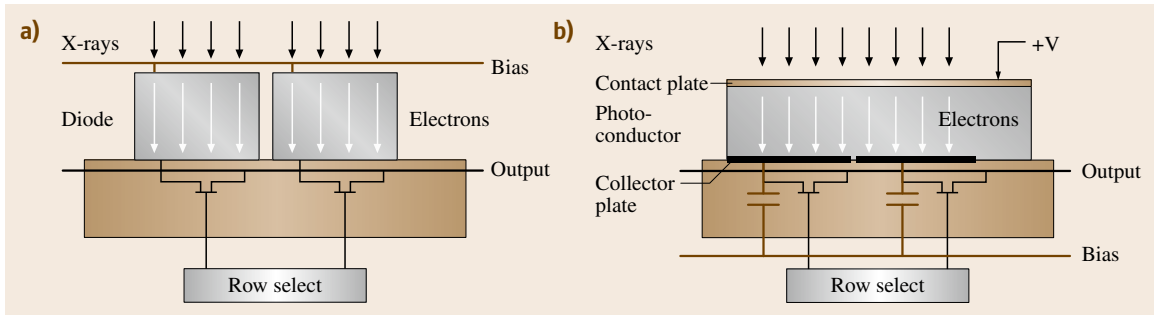


Fig. 16.48a,b Principle of direct converting flat panels with amorphous silicon thin-film transistor arrays for read out. There is no light scattering process involved. The spatial resolution is determined by the pixel size of the detector array. **(a)** Photodiodes convert directly the x-ray photons to electrons. This technique is suitable for low-energy applications. **(b)** A semiconductor (e.g. amorphous selenium or CdTe) is located on microelectrodes in a strong electrical field. Radiation generates charges, which can be stored in microcapacitors

the typical concept for baggage, car and truck inspection. Line detectors are available with a resolution of 0.25–50 mm. The most common principle is the combination of scintillator and photodiodes. The scintillator is selected in accordance to the energy range.

Mechanized X-ray Inspection of Welds. High-resolution lines have been introduced for weld inspection [16.28]. Figure 16.49 shows a mechanized x-ray inspection system, which is based on an x-ray tube, a manipulation system and a line camera. The camera consists of an integrated circuit with about 1200 photodiodes. A GdOS scintillator screen is coupled to the diodes. New applications take advantage of TDI (time-delayed integration) technology to speed up the scan [16.29]. Several hundred lines are used in parallel. The signal is transferred from line to line synchronously

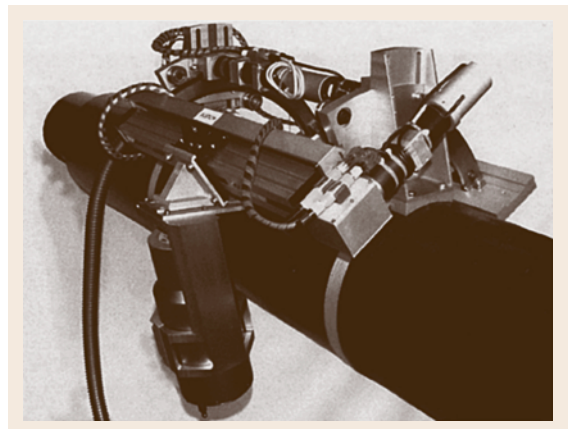


Fig. 16.49 View of the line scanner. The x-ray tube and camera are mounted on a manipulator for mechanized inspection of pipes

with the movement of the object or the scanning system. The information is integrated on the chip and the speed enhancement corresponds to the number of lines used.

Specialized tomographic routines were developed to reconstruct a three-dimensional (3-D) image of the weld [16.28]. This method is very sensitive to cracks and lack of fusion. The depths and shape of these defects can be reconstructed and measured. Figure 16.50 shows the image of a reconstructed crack in an austenitic girth weld in comparison to a cross-sectional metallography.

Automated Evaluation of Digital X-ray Images: Serial Inspection in Automotive Industry

Fast digital x-ray inspection systems are used in the serial examination of industrial products since this technique is capable of detecting flaws rather different in their nature such as cracks, inclusions or shrinkage. They enable a flexible adjustment of the beam direction and of the inspection perspective as well as online viewing of the radioscopic image to cover a broad range of different flaws. This economic and reliable technique has become of essential significance for different applications. The configuration of such systems is schematically represented in Fig. 16.51.

The object, irradiated from one side by x-rays, causes a radioscopic transmission image in the detector plane via central projection. The relation between the focus–detector distance (FDD) and the focus–object distance (FOD) determines the geometrical magnification of the image. An image converter such as an x-ray image intensifier, a fluorescence screen or a digital detector array (DDA), also called a flat-panel

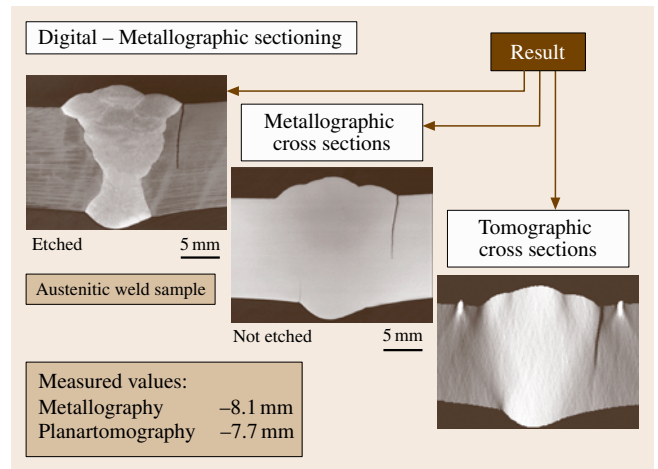


Fig. 16.50 Reconstructed crack in an austenitic weldment compared to the metallographic cross sections

detector, converts the x-ray image to a digital image.

Light alloy castings are widely used, especially in automotive manufacturing. Due to imperfections of the casting process, these components are prone to material defects (e.g. shrinkage cavities, inclusions). These parts are frequently used in safety-relevant applications, such as steering gears, wheels and increasingly wheel suspension components. These parts have to undergo a 100% x-ray inspection for safety.

A fully automated x-ray inspection system for unattended inspection can guarantee objective and reproducible defect detection (see example in Fig. 16.52). The decision whether to accept or to reject a specimen is carried out according to the user's acceptance

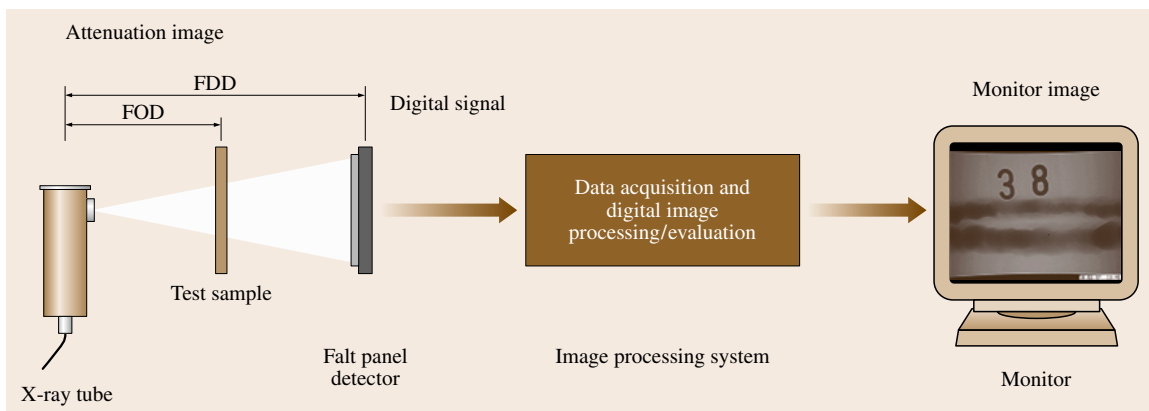


Fig. 16.51 Schematic set up of a digital industrial radiology system

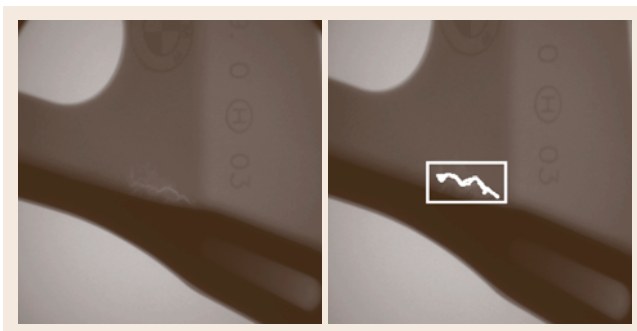


Fig. 16.52 Defect detection with an automated system. *Left*: original image; *right*: detected flaw

specification. These systems are known as automated defect-recognition (ADR) units.

Automated x-ray inspection is also used for a novel field of application: the check of completeness and function. For example, when the presence and deformation of parts have to be checked. Fur-

thermore distances and spatial dimensions can be examined.

16.2.5 Applications of Radiology for Public Safety and Security

Public safety and security is yet another application field of digital industrial radiology. Since explosives entail a considerable threat it is a central issue of all security measures to detect them in time. There exist a variety of different methods for explosive detection [16.30].

Inspection of Unexploded Ordnance (UXO)

Grenades containing warfare substances are identified by the presence of a liquid surface visible in the respective radiograph (Fig. 16.53). They have to be inspected to assign them to the appropriate way of safe disposal. To detect a putative liquid filling, the suspected ammunition is radiographically inspected in a tilted position. If this shows the surface of the liquid, then the grenade is filled with a warfare substance (such as e.g. mustard gas or phosgene). Image processing reveals further details. Figure 16.54 shows how the digital radiograph of a shrapnel grenade was enhanced by image processing.

Dual-Energy Radiography for Baggage Control

The dual-energy technique is widespread in modern baggage-inspection equipment. It provides additional information about the chemical composition of the inspected material. The technique takes advantage of the fact that radiation of different energy is absorbed differently by the various elements. The absorption is a function of the atomic number of the absorbing elements. As a consequence, radiographs taken at a lower and a higher x-ray energy level are not identical. The ratio between the logarithmic grey values of such a pair of images represents the chemical composition of the absorbing material and is independent of its layer thickness. Figure 16.55 shows a dual x-ray tube set and a typical dual-energy radiograph of a bag. This technique provides the operator with color-coded images, where the color indicates the chemical composition of the inspected specimen. This can provide hints of the presence of explosives or contraband. Advanced versions of inspection units include an additional spectrometer to measure the spectrum of the scattered radiation. This method is rather sensitive and allows the detection and specification of various chemical compounds within the object.



Fig. 16.53 Inspection of a grenade of World War I, filled with chemical warfare. The chemical agent can be detected, by visualization of the liquid-level line inside the grenade

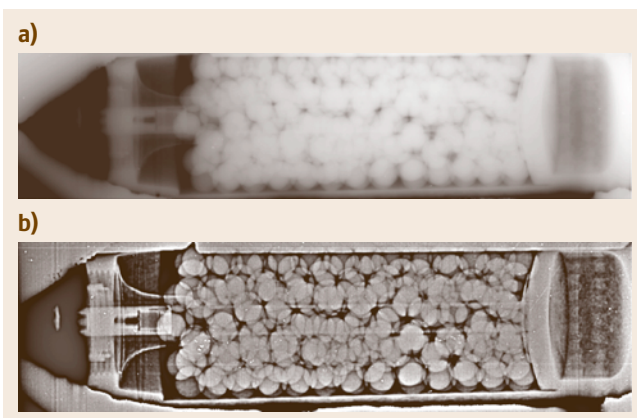


Fig. 16.54a,b Radiograph of a shrapnel grenade: (a) original image, and (b) high-pass-filtered image

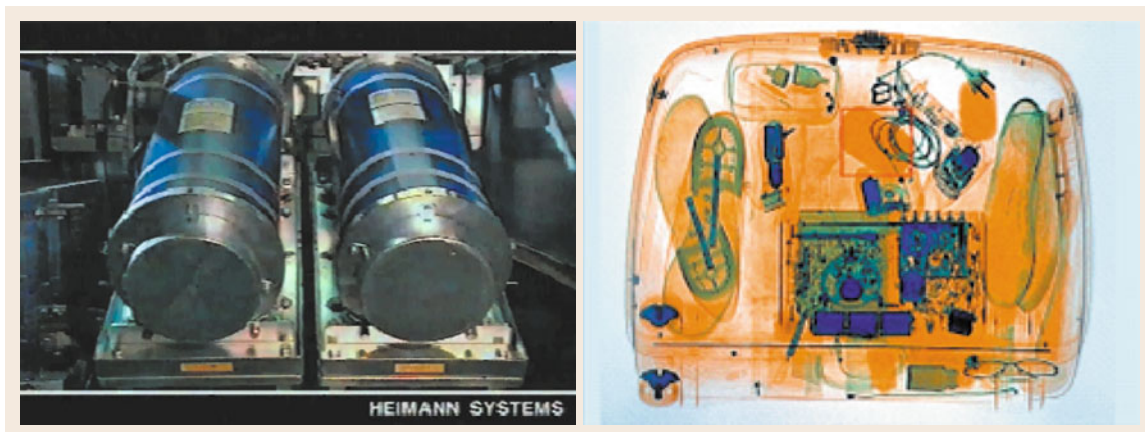


Fig. 16.55 Dual x-ray tube assembly for dual-energy inspection of baggage and typical image of a bag. The atomic number of the components in the object are usually represented by the color: *blue* – high atomic numbers (e.g. metals); *green* – medium atomic numbers (e.g. glass, polyvinyl chloride); *yellow to brown* – low atomic numbers (e.g. carbon hydrates)

16.3 Computerized Tomography – Application to Organic Materials

For tasks of materials performance control, tomography with x-rays supported by computers, in short computerized tomography (CT), is gradually spreading in industry. Tomography, born in the medical field, makes it possible to show 0.1% differences in the density of materials. Moreover, the tomographic section of an object under study, which is reconstructed in three-dimensional space, is not affected by the rest of the volume exposed to irradiation, and the geometry is well defined. The section-by-section reconstruction makes it possible to achieve a complete exploration of the object. For materials classes like polymers, such as natural rubber (NR) or styrene butyl rubber (SBR), and composite materials, such as polymer matrix composites, this method is efficient, gives high resolution and reliable results. However, industrial application of a medical scanner, as presented here, is applicable only for low-density materials ($4 < \text{g/cm}^3$). The application of CT to materials of higher density is discussed in Sect. 16.4.

We can discern four application fields for computer tomography

1. nondestructive testing of big components;
2. nondestructive of small pieces;
3. materials study;
4. microtomography.

In this section, we will present the method and the terminology within the scope in which the medical scanner

is commonly used. Then, we will deal with examples chosen to share the performances of this technique for industrial applications.

16.3.1 Principles of X-ray Tomography

When x-ray tomography is used, a collimated beam goes through the tested object before being received by a row of detectors opposite the x-ray source. The object is then rotated through an angle of 180° . During the rotation, the attenuation of the intensity of the x-ray beam is measured in a finite number of angular increments. Data acquisition is achieved by a computer that carries out the reconstruction of the object with the help of a suitable algorithm.

A x-ray CT is essentially based on the measurement of the different absorption coefficient of the materials crossed by a penetrating beam such as x- or γ -rays [16.31–39]. The CT image gives linear attenuation coefficients in the slice for each point, which depend on the physical density of the material, its effective atomic number and x-ray beam energy. The attenuation in the intensity of a single x-ray beam is then defined by the equation of Lambert–Beer as the following;

$$I = I_0 \exp(-\mu L), \quad (16.23)$$

where I_0 is the incident intensity, I is the transmitted intensity, μ is the linear attenuation coefficient and L is the thickness of the absorber.

Thus, a tomographic system measures the attenuation of intensity from different angles to determine cross-sectional configuration with the aid of a computerized reconstruction. The general view of the medical scanner (x-ray CT) equipped with a mechanical test device – electrical jack plus carbon-fiber tube and also the scanning system – is shown schematically in Fig. 16.56. It consists of an x-ray source, a collimator, a detector array and a computer system with data-storage media.

When going through a material, a beam of x-ray undergoes an absorption that depends on the three following parameters.

1. The nature of the materials, or more exactly the respective densities of the elements that make up the material that is put in the path of the radiation (the linear absorption coefficient);
2. The thickness of each of these elements;
3. The incident intensity of the radiation.

The attenuation of the radiation through an object complies with the Lambert–Beer law, which governs every absorption phenomenon

$$I = I_0 e^{-\mu L} \quad (16.24)$$

The medical scanner is able to measure the x-ray attenuation in Hounsfield units or tomography density even if it does not give local mass density. To obtain this, it is necessary to make a calibration versus a reference which is water. The tomography density (DT) is a relative measure of the attenuation coefficient with regard to the water. For this reason, we need to know the value given to water in the tomography scale in Hounsfield units (H). Basically with a constant X photon energy,

the DT depends of the attenuation coefficient by a theoretical relation where K is a constant equal to 1000

$$D = \frac{\mu - \mu_w}{\mu_w} \quad (16.25)$$

This relation of conversion between the attenuation coefficient and the tomographic density is based on water attenuation coefficient value, which is 1.8 cm^{-1} at 73 keV, corresponding to density zero in the Hounsfield tomography scale.

This conversion is done in two steps.

- An intermediate scale is chosen. In this new scale, for the water, there is a relation between K and C of

$$K = C\mu_w \quad (16.26)$$

and the attenuation coefficient for a given material is given by

$$\mu_{\text{int}} = \frac{K}{\mu_w} \mu \quad (16.27)$$

The tomographic density is linear with regard to the intermediate attenuation μ_{int} and the water density must be equal to zero.

- Make a translation in order to fulfil the condition

$$DT = \mu_{\text{int}} - K \quad (16.28)$$

so that

$$DT = \frac{K}{\mu_w} \mu - K = \frac{\mu - \mu_w}{\mu_w} K \quad (16.29)$$

Calibration has been done with several materials in order to have an empirical relation average DT of materials and respective attenuation coefficient. Table 16.5 presents some results.

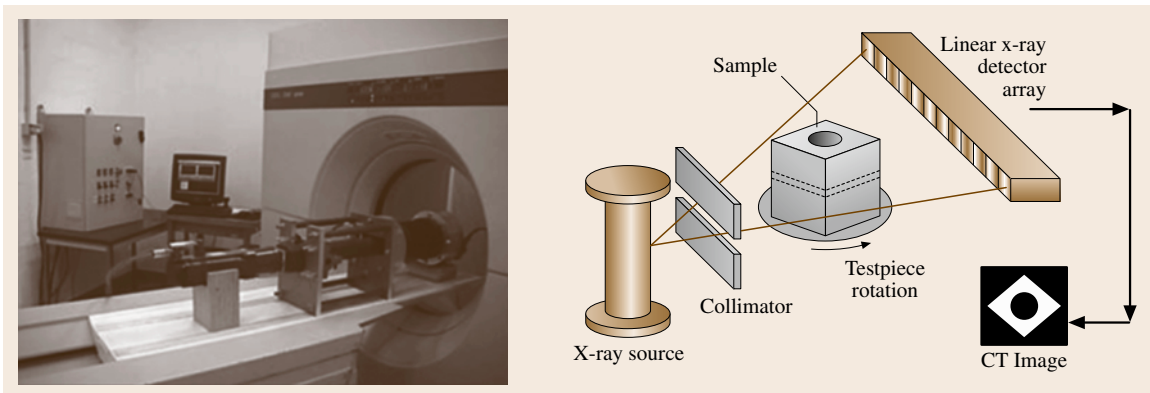


Fig. 16.56 Medical scanner equipped with a mechanical test device (electrical jack plus carbon fiber tube) and schematic of computed tomography system

Table 16.5 Attenuation coefficients and tomographic densities of some materials obtained with a medical scanner

Material	$\mu(\text{cm}^{-1})$	DT (H)
Polyethylene	0.172	-72
Water	0.191	-0.4
Nylon	0.210	90
Polyester	0.217	139
Araldite	0.219	147
Rubber 18160/52	0.224	165
Delrin	0.262	349
Ebonite	0.288	434
Rubber 19199/48	0.340	729
Teflon	0.340	729

Conventional radiography makes it possible to show defects bound up with variations of density compared with the material as a whole. Thus, under most circumstances, inclusions, cracks, porosities, etc. can be shown.

Nevertheless, radiography takes into account everything the beam meets while going through the material and gives a plane projection of them. That is why cracks perpendicular to the beam are liable to escape detection.

Tomography breaks free from the drawbacks of x-radiography by exploring the object with a 180° rotation, thanks to three-dimensional reconstruction, so it is possible to know the absorption density of any point within a given volume.

The units of absorption density are those used in medicine. The following references are given:

1000 H (Hounsfield) units	Density of dried bone
0	Density of water
-1000 H units	Density of air

This scale is suitable for composite materials whose H density is about a few hundred units because of their nature. The standardization carried out to associate the medical unit with the density of the bulk $\Delta\rho$ gives for one H unit: $\Delta\rho = 1 \times 10^{-3}$ with a 120-kV x-ray source.

This implies that the medical scanner makes it possible to show variations of volumetric density of about a thousandth.

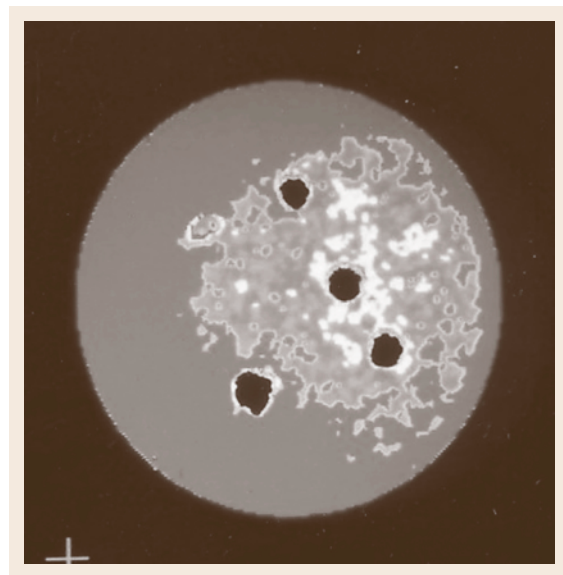
The highest Z material that can be evaluated with a medical scanner is aluminum.

The objectives of this paragraph are to present the performances of x-ray tomography in order

- to detect internal geometric defects,
- to perceive the evolution of mechanical, physical, chemical damage,
- to display homogeneous variation related to processing,
- to observe differences in texture, chemical concentration at the meso- and nanoscale.

16.3.2 Detection of Macroscopic Defects in Materials

Using a medical scanner, metal matrix composites processed by squeeze casting have studied. The first step was to test the alumina preforms, which are disks with 85 mm diameter and 15 mm thickness. In some disks, spherical defects were introduced during the processing. Figure 16.57 presents the results of the tomographic examination. The average Hounsfield density of the ceramic preform is about -215. However, there is a large difference of x-ray attenuation between the center of the specimen and the edge, where the density is a maximum of 118. In fact, the density is lower in the center of the specimen because the volume fraction of alumina is smaller than near the edge. Thus, it is possible to check the processing of the preform with tomographic observation as well as the repartition of alumina platelets which is very difficult using regular experimental methods. Of course, it is very easy to detect defects in ceramic preforms, as is shown in Fig. 16.57.

**Fig. 16.57** Defects in ceramic preform

16.3.3 Detection of the Damage of Composites on the Mesoscale: Application Examples

Putting aside the mechanical interpretation of composite damage in polymers, is it possible to characterize the damage of these materials based on a single method that combines the physical and chemical interpretations? The answer must evidently be no. The problems calls for nondestructive testing methods, which include ultrasonics, x-rays, thermography, and others methods. At

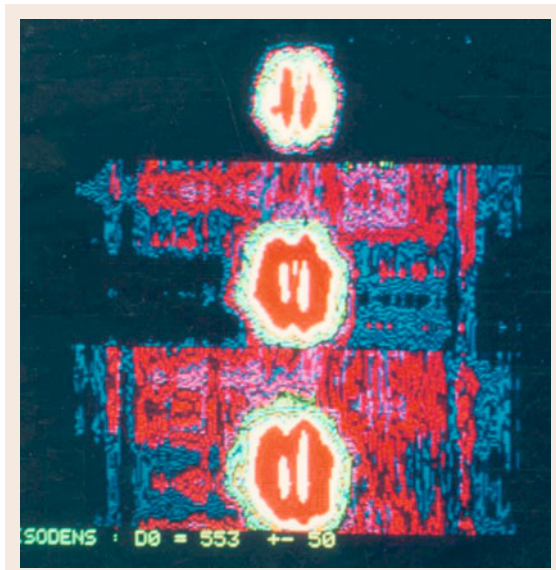


Fig. 16.58 Three cross sections of the specimen after impact

the microscopic level, an electron or acoustic microscope is the required nondestructive evaluation tool.

Between the macroscopic and microscopic levels, there exists a very important middle domain, typical of composite materials, which is treated at the mesoscopic level: that of transverse cracking, distribution of reinforcements and of porosity, that is, the domain of sequential cells. It is very difficult today to characterize defects at these different levels other than by radiography.

The various applications of x-ray tomography allow for the study of composite materials at any level, macroscopic, mesoscopic or microscopic. This instrument is well adapted to reveal defects on a centimeter scale, such as a delamination, but it is also capable of revealing the distribution of the reinforcements on a millimeter scale, and of detecting fiber cracking as well as cracking along fiber matrix interfaces on a micrometer scale. In addition, the attenuation of x-rays, which depends on the physical and chemical nature of the composites constituents, can be measured by x-rays scanners.

Changes in the polymeric matrix due to aging, or even the transformation of amorphous polymers into crystallites, can be studied by x-ray tomography. This astonishing tool, long used by the medical field, is also well adapted to the study of composite materials and polymers due to its ability to detect defects on a wide range of scales, as well as its ability of physical and chemical analysis by measuring x-ray attenuation.

X-ray scanning can thus provide information on the physical and chemical aspects of the material and on the geometry of flaws and damage on any scale. This

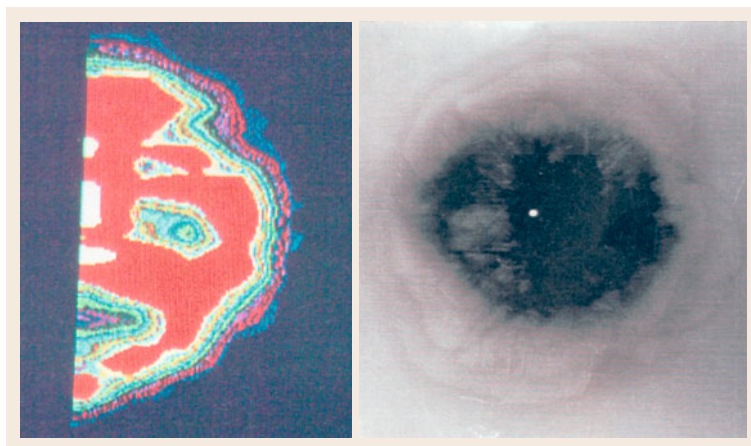


Fig. 16.59 Comparison of radiography (*right*) and tomography (*left*) of delamination

tool provides solutions to many problems faced by the materials scientist, as demonstrated in the following results.

Damage in a Carbon Epoxy Composite Plate Specimen After an Impact

The specimen studied is a rectangular coupon whose dimensions are $255 \times 172 \times 8.5$ mm. It is made up of 64 plies of carbon-epoxy fiber. The stacking sequence is (45/90/–45/0) 8 s.

The specimen was subjected to the impact of an aluminum ball 12.7 mm in diameter moving at a speed of 120 m/s. Then it was cycled in compression under 110 MPa to intensify the damage.

In this case, the scanner examination has been complemented by radiography, zinc-iodide-enhanced x-ray, and by optical micrography. This was done in collaboration with the NASA Langley Research Center in Hampton, Virginia.

Global Examination of the Plain Specimen

A study on the axial slices and on the frontal slices has been carried out. On the frontal views, we note a strongly damaged area whose density is higher than 550 H, slightly elliptical shaped, and whose largest dimension is orientated in the compression direction (Fig. 16.58).

Modeling of the Damage

The damage of this composite specimen is complex because of the great number of plies. The envelope of the damaged area has the shape of a barrel, delaminations being more numerous in the center of the plain specimen than near the surface.

Synthesis of the Observations Made on the Impacted Specimen

To facilitate the interpretation of observations made with medical scanners, damage to the impact specimen is examined by radiography at a microscopic scale and by scanning electronic microscopy at a microscopic scale.

A comparison between radiography and tomography is made (Fig. 16.59). We would like to note that the scanner provided much better resolution of the outline of the damaged area. Nevertheless, enhanced x-ray radiography was required to reveal the very complicated network of microcracks.

To conclude, we emphasize that the resolution of the images of the microcracks with the medical scanner is not satisfactory at the moment.

Damage in Rubber Submitted to High Hydrostatic Pressure

It is well known that triaxiality of stresses including a high hydrostatic pressure has a large effect on the mechanical behavior of rubbers and particularly on fatigue mechanisms.

In a pancake specimen loaded in tension the hydrostatic pressure is about $2.5 \times$ the shear modulus of rubber for an elongation of 20% in NR. From observations by x-ray tomography, it seems that the first cavities are formed in the center of the specimen at 20% of elongation for a fracture at 380% (Fig. 16.60).

It must be pointed out that no other NDT method is available to observe cavitation in rubber.

16.3.4 Observation of Elastomers at the Nanoscale

The damage caused by fatigue and cracking in rubber or in composites with elastomer matrices seems to be considerably influenced by the transformation from an

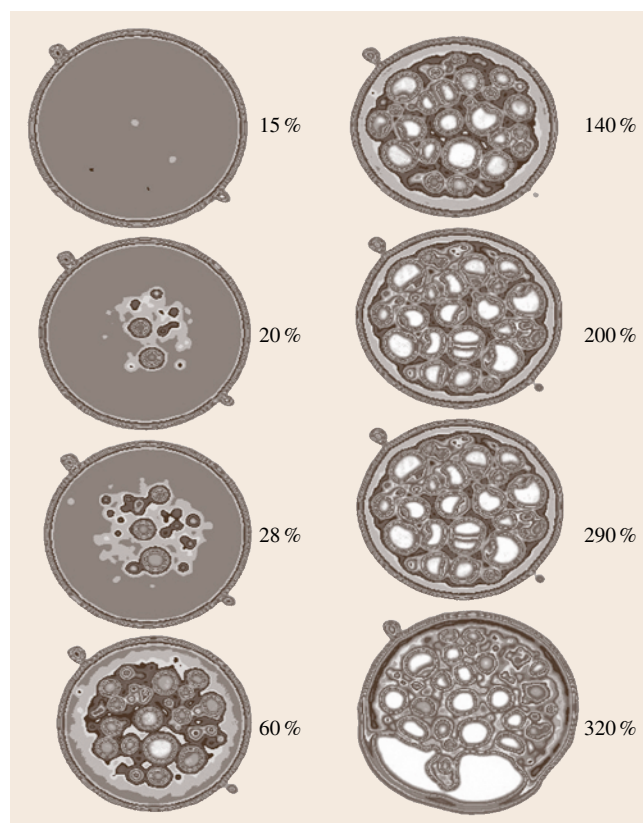


Fig. 16.60 Cavitation growth due to high hydrostatic pressure (NR)

amorphous to a crystalline phase, when this latter phase exists. This hard-to-detect transformation is generally studied by x-ray diffraction, a method by which we cannot detect the gradients of transformation within the rubber nor make local observations.

In contrast, x-ray tomography allows for the observation of the crystalline transformation of rubber and its localization owing to the images generated by scanner. The attenuation of the intensity of the x-ray beam, similar to x-ray diffraction, reveals the existence of crystallites.

In order to validate this hypothesis, test samples of natural, crystallisable rubber (NR) and of synthetic, noncrystallizable rubber (SBR) were studied at different temperatures, knowing that low temperatures induce a partial crystallization of NR.

The crystallization of rubber (NR) may be observed on the samples, which were cooled down to -200°C . This microscopic phenomenon can clearly be evaluated by means of x-rays CT on the mesoscopic scale, which is another benefit of medical scanning. To show this effect, some of the tests were carried out on the axisymmetric hourglass-shaped specimens of NR and compared with SBR, which does not show this phenomenon as it is always amorphous. Hourglass-shaped specimens are very suitable for this test due to their large outer surface [16.32, 33]. So, the variation of mean values of the TD becomes complex; the TD value is maximal at the level of 227 K (-46°C) (Fig. 16.61), it exceeds 1180, whereas at lower temperatures (83 K, -190°C) the value is 1135.

This variation in TD displayed a crystallite state between 300 K (27°C) and 227 K (-46°C) above which the amorphous state again becomes predominant between 227 K (-46°C) and the transition temperature (T_g) of rubber. When there is no crystallization, variation in density certainly modifies the attenuation (TD).

In the case of SBR, which is always amorphous, only the density varies with temperature, related to the dilatation. An increasing in the temperature causes naturally the increasing of the volume and the decreasing of the density and finally the decreasing of the TD (pixel). Figure 16.61b shows the evolution of the TD curve as a function of the temperature for the SBR specimens. It decreases from 1185 to 1120 in the temperature range from 175 (-98°C) to 300 K (27°C). However, it shows a transition zone at the level of 200 K (-73°C), corresponding to the transition temperature, T_g , between the glassy and rubbery phase. This zone is found between 1155 and 1160, corresponding to this glassy transformation.

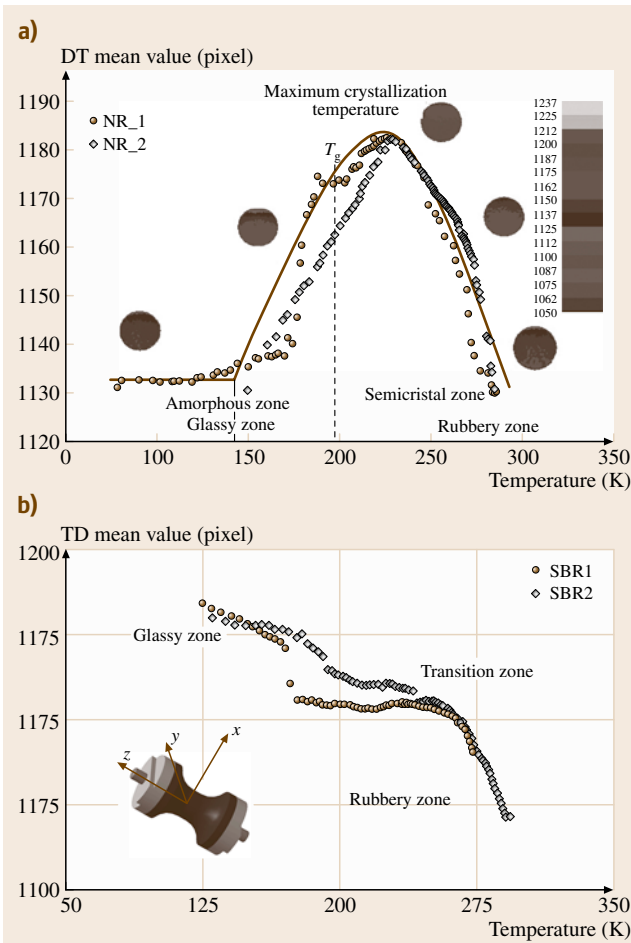


Fig. 16.61a,b Evolution of the TD depending on the temperature in NR (a) and SBR (b)

16.3.5 Application Assessment of CT with a Medical Scanner

The application examples show quite obviously that the medical scanner is adapted to nondestructive evaluation of composite materials from a technical point of view and if we do not take into account the price of the device. The advantages of the method have been presented with its excellent results. They confer on the medical scanner a double role, which may form the subject of two developments.

1. A nondestructive testing instrument with an industrial purpose,

- An instrument comparable to the electronic microscope with a more scientific purpose and able to give information at a microscopic scale (several hundreds of microns).

In the first case, the resolution power of the medical scanner is good enough for a device of classical **NDT**. We have found only one major inconvenience, namely the lack of reliability of the scanner to make precise measurements of the dimensions of the defects within more than 25%.

In the second case, the resolution of the scanner is not good enough to study the transverse cracks in the matrix. We can estimate the spatial resolution of the scanner at some hundreds of micrometers,

whereas we would need 10 μm . We are dealing here with an important need which needs more investigation.

Nevertheless, we should point out that the resolution in density of the scanner is of the order of 10^{-3} , which makes it possible to resolve all the defects contained by composites whether they are cracks, delaminations, fiber bundles, or porosities. The variation of the Hounsfield density must be related at the volumetric density but also to the modification of the chemical microstructure of the materials. From this point of view, the scanner enables studies of the crystallization of polymeric matrix of rubbers, for example. This means that x-ray tomography is a multiscale **NDT** method.

16.4 Computerized Tomography – Application to Inorganic Materials

The study of volume properties as well as of dimensional features with computed tomography requires an optimized selection of source–detector combination depending on the material composition (energy-dependent linear attenuation coefficient μ), the size of the samples and the maximum thickness of material that has to be irradiated, d . Additionally the manipulator system and the mounting need to suffice the required accuracy. The maximum **SNR** of a **CT** measurement of a homogenous sample is given for $\mu d \cong 2$, corresponding to a transmission of about 11% [16.40]. This value is valid only for line detectors with a sufficient detector collimator and shielding between single detector elements. Due to some limitations, especially for flat detectors, the conditions for optimum image quality differ from this theoretical value.

For organic materials with low atomic numbers and low density, medical scanners can be applied in many cases. As an example fiber-reinforced helicopter blades have been investigated for many years by computed tomography, using commercial medical scanners [16.41]. Inorganic materials require radiation sources with higher energy and appropriate detector systems. The different kinds of computed tomography equipment developed at Federal Institute for Materials Research and Testing (**BAM**) represents the state of the art on this field and are described in the following knowing well that commercial solutions are in general more efficient with regard to saving of time and user guidance.

16.4.1 High-Energy CT

This field covers roughly the energy range given by 420 kV x-ray tubes over some radionuclide sources up to electron linear accelerators with a maximum energy of 12 MeV. Most of the high-energy scanners used have line detectors which can be shielded against the scattered radiation. Starting with a translation/rotation scanning principle and multidetector systems, today line detectors are common with several hundred detector elements and scanning times in the range of some minutes and lower. At **BAM** a scanner for a 380-kV x-ray tube and a ^{60}Co radionuclide source was described as early as 1985 [16.42]. This universal scanner was extended for measurements with a 12-MeV electron linear accelerator (**LINAC**, Raytech 4000) in combination with a multi-detector system with step-motor-controlled collimator slits [16.43]. The actual research covers the study of some effects of high-energy cone beam **CT** with a **LINAC** and ^{60}Co using an *a*-Si flat-panel detector (Perkin Elmer, 16-bit **ADC**, 256×256 pixel, pixel size is 0.8 mm^2). Due to the focal spot size of high-energy radiation sources, which is on the order of about 1.5 mm, the spatial resolution is limited to a few tenths of a mm.

16.4.2 High-Resolution CT

Using magnification techniques a much higher spatial resolution can be reached. The condition hereby is that the focal spot size can be lowered to the mi-

rometer range, which is possible with microfocus x-ray tubes. The usable energy range of commercial x-ray tubes extends up to 225 kV. For many objects it would be desirable to extend the energy range of microfocus x-ray tubes. As an example most cellular metals are made from aluminum and thus have a high penetration depth for x-rays. However, they are often used to produce objects of irregular shapes (with an outer cover of a different material or the foam skin itself). This produces artefacts due to the high-attenuation parts. In some applications foams of high-attenuation materials (up to iron) are used. In these cases the choice of an x-ray energy as high as possible reduces the artefacts from beam hardening and exponential edge-gradient effects.

Figure 16.62a gives a graph that shows the gain in attenuation possible with an extended range of kV. For CT measurements the maximum absorption to free beam ratio is about 20. From the graph it is seen that this means an extension of measurable *material in object thickness* from 20 to 30 mm of steel. At the end of 2002 a 320-kV microfocus x-ray tube (MX-5 tube, build by YXLON, Halfdangsgade 8, 2300 S Copenhagen) was integrated into a CT system (Fig. 16.62a). The bipolar tube is build up from a standard -200 kV tube. The original probe head is changed to the bipolar part which has a build in anode with an additional high voltage supply of up to $+120$ kV. The distance between x-ray spot to tube outside is enlarged to 25 mm because the target position is no longer at ground voltage level. This means that the tube in this modification has a lower maximal magnification, but this corresponds to the bigger object

size. For example with 320 kV and 0.1 mA the optimum spatial resolution is about $35 \mu\text{m}$.

In practical operation the second part is fixed to $+120$ kV while the variation in energy is done with the first. A range of 130 kV to 320 kV results. To the first part a standard microfocus target can be attached and the tube can thus be used as normal 200 kV microfocus tube with high magnification. As detector an *a*-Si flat-panel detector (Perkin Elmer, 16-bit ADC, 1024×1024 pixel, pixel size is 0.4 mm^2) is used [16.44].

16.4.3 Synchrotron CT

With transmission target x-ray tubes the focal spot size can be lowered to $1\text{--}5 \mu\text{m}$, corresponding to a spatial resolution of less than $10 \mu\text{m}$. Due to the limited intensity given by electron scattering and the heat generated, which can melt the target, measuring times are increasing to some hours and more. Synchrotron radiation sources offer photon flux densities, which are several orders of magnitude higher compared to laboratory x-ray tubes. The additional advantage is the fact that the high photon flux density can be reached with monochromatic radiation giving some advantages over tomography, such as the absence of beam-hardening artefacts.

To extend the usable energy range at the Berlin Electron Storage Ring Company for Synchrotron Radiation (BESSY) a 7-T wavelength shifter with a critical energy of 13.5 keV has been installed in the storage ring to operate the first hard x-ray beam line at BESSY, called BAMline. The main optical components of the beam line are a double crystal monochromator (DCM)

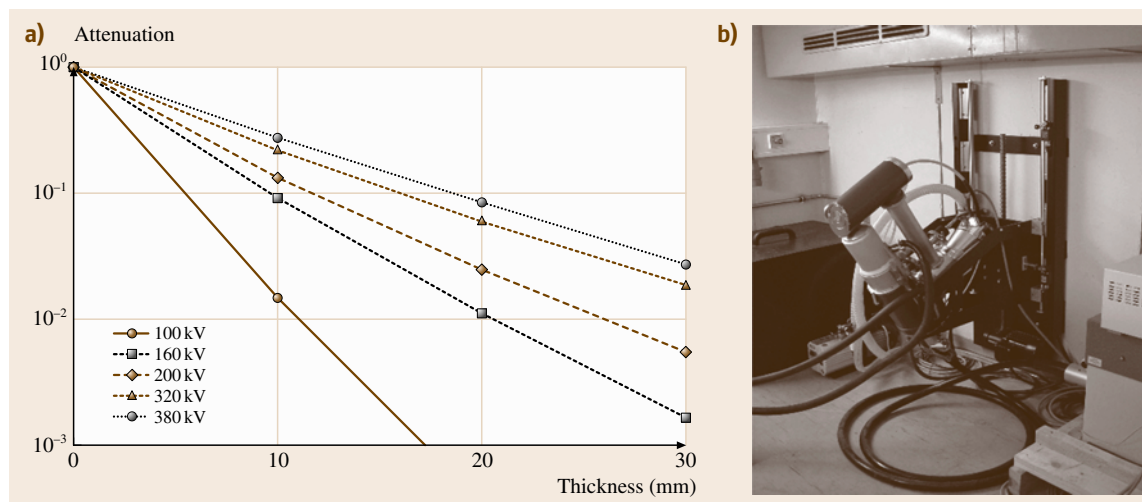


Fig. 16.62 (a) Attenuation curve for iron as function of x-ray energy (b) 320-kV micro-focus tube

and, for the first time for imaging, a double multilayer monochromator (DMM, 320 double layers of W and Si, with thicknesses of 1.2 and 1.6 nm, respectively). The latter is preferred for use in tomographic facilities, giving a factor of 100 higher photon flux due to the increased bandwidth of 2% compared with 0.01% of the DCM [16.45–47]. The detector system consists of a 2048 × 2048 photometric camera system together with a scintillator screen of GdOS. Depending on the lens combination used nominal voxel sizes of 1.5–7.2 μm can be used.

16.4.4 Dimensional Control of Engine Components

A current research topic is the improvement of dimensional control with CT. As an example Fig. 16.63 shows a cross section of an aluminum test sample investigated with the 320-kV equipment. This sample was measured additionally with the LINAC CT. Standard operation for a comparison is the conversion of the voxel data in a point cloud and the analysis of files in the stereolithographic data format (STL).

The comparison performed using the STL data shows principal deviations between the computer-aided design (CAD) model and real sample, which are due to the limited energy of the 320-kV equipment and especially the smoothed edges in the LINAC measurement due to the limited detector pixel size.

Fault Detection in Telecommunication Equipment

The transmission characteristics of glass-fiber cables can be changed after installation or during lifetime.

To localize such flaws optical time-delay reflection (OTDR) methods are frequently used. The location of flaws can be determined with an accuracy of a few mm. An analysis of the type and size of flaws together with geometry control of the complex-shaped cable can be performed with CT. Figure 16.64 shows a vertical slice of a section (length 48 mm) of the cable together with two horizontal slices. The bunches of four glass fibers are embedded in a protective covering. One of the seven coverings contains no fibers. The diameter of each glass fiber is 125 μm. The outer diameter of the cable is 16 mm. Some protective coverings show flaws (Fig. 16.64 bottom right) and an incomplete embedding of fiber bunches. To avoid the influence of sample preparation the investigated sample volume was part of a 15-m-long cable segment.

Flaw Extraction in Cu Samples

As a first example results are shown for flaw extraction in electron-beam-welded Cu samples (size about 40 × 100 × 300 mm) using high-energy 3-D CT (Fig. 16.65). For studies of probability of detection (POD) a 100% inspection of volumetric flaws are performed. Due to the limited size of the flat-panel detector the sample was measured in three positions and the overlapping data sets are joined after the image reconstruction. The reconstructed images show some artefacts given by scattered radiation, beam hardening and inherent detector effects. Therefore a filter was used to reduce these artefacts. Figure 16.65 shows as result a cross section through the sample.

The flaws are evaluated twofold; by a local threshold operation using some image-processing modules (e.g.



Fig. 16.63 Test sample of aluminum (\varnothing about 100 mm). The image (*left*) shows a cross section of the measurement with the 320-kV equipment (320-kV x-ray: 220 kV, 100 μA; prefilter: 1.5 mm Sn; projections: 900/360°; exposure time: 2.28 s per projection; voxel: (0.12 mm³); matrix: 1023 × 1023 × 605). The image (*middle*) shows the deviation against the CAD data and the image (*right*) the deviation against the measurement with LINAC (10.5 MeV, 20 Gy; prefilter: 90 mm Fe; projections: 720/360°; exposure time: 0.8 s per projection; voxel: (0.65 mm³); matrix 255 × 255 × 201)

an STL converter module) developed for the image-processing system AVS and the Volume Graphics (VG Studio Max) image-processing tool. The geometry of the envelope and the voids are lead together and converted to STL format for comparison with ultrasonic results and for theoretical simulation of the irradiation process. The volume of all flaws of the sample is 1100 voxels, determined with the AVS system, which is in good agreement with the result from the VG system, which gives a volume of a 1072 voxel. The total volume is 4 304 500 voxels.

Calibration of NDT Methods

The CT imaging method combined with the geometrical correctness of the dimensions of the investigated

samples are the main advantages to the use of CT for the calibration of other NDT methods, such as ultrasonic technique (UT) or eddy-current techniques. As an example Fig. 16.66 shows the investigation of flaws of coated turbine blades. With optical methods only the flaws in the coating layer can be visualized but not in the matrix material. With high-resolution CT the crack configuration was analyzed. The result was used for calibration of other NDT techniques (the eddy-current method).

Pore Detection and Pore-Size Calculation in Al Foam

Depending on the type of foam there are two ways to measure the size of the pores inside.

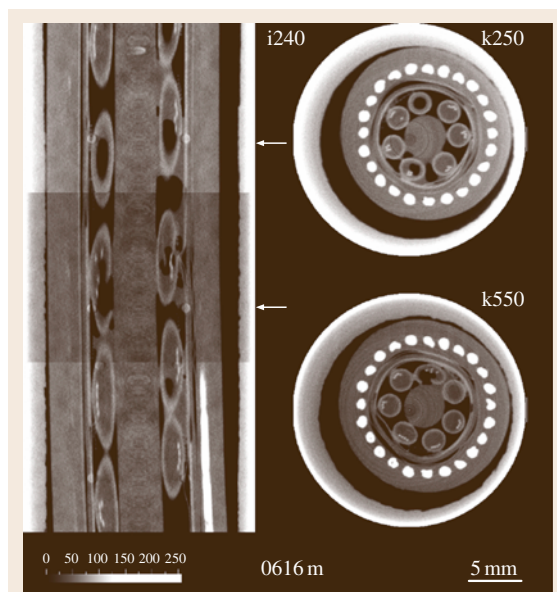


Fig. 16.64 Vertical and two horizontal cross sections of a glass-fiber cable

- If the pores are closed, a threshold operation is first used to obtain the binary area of all pores. Starting on one edge, an algorithm then searches in 3-D for the first marked voxel and colors all adjacent as belonging to the same pore until no more connected voxels are found. The searching algorithm then goes on to the next pore. Figure 16.67 (left image) shows the result; the image is a slice through the searched foam, the different colors of each pore are used to detect pores, which were not separated. The size distribution is given in Fig. 16.67 (right image). While the volume is searched for pores, the volume and the center of gravity are also stored, and further parameters can be calculated. From these parameters a simplified model of the foam can be generated and calculation of real foams with finite-element method (FEM) programs becomes possible. The center image of Fig. 16.67 shows the same foam, representing the pores as spheres with the same diameter.
- If the pores are open, the inverted nonmetal part has to be 3-D-eroded until single areas result for all the



Fig. 16.65 Electron beam welding of a section (size $40 \times 100 \times 300$ mm) of a Cu canister. The image (left) shows a cross section containing the flaws, flaws after segmentation (middle) projected into a plane and the flaws after conversion to the STL data format (right). Source: LINAC 10.5 MeV, 15 Gy; prefilter: 90 mm Fe; projections: $720/360^\circ$; exposure time: 0.2 s per projection; voxel: (0.653 mm^3) ; matrix: $255 \times 255 \times 532$

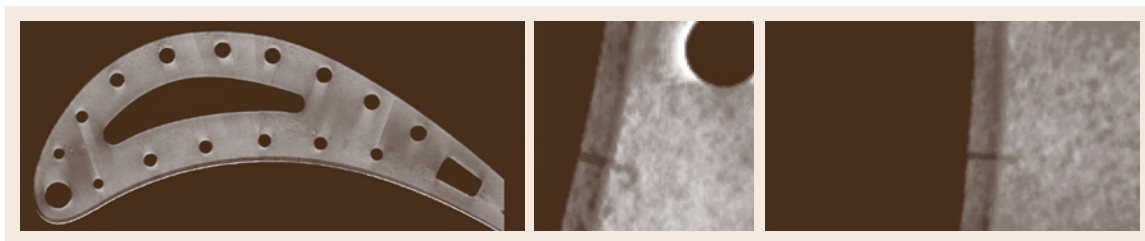


Fig. 16.66 Turbine blade with protective layer (layer thickness of about 400 μm). The CT cross sections show a crack only in the protective layer (*right image*) and a crack in the matrix material

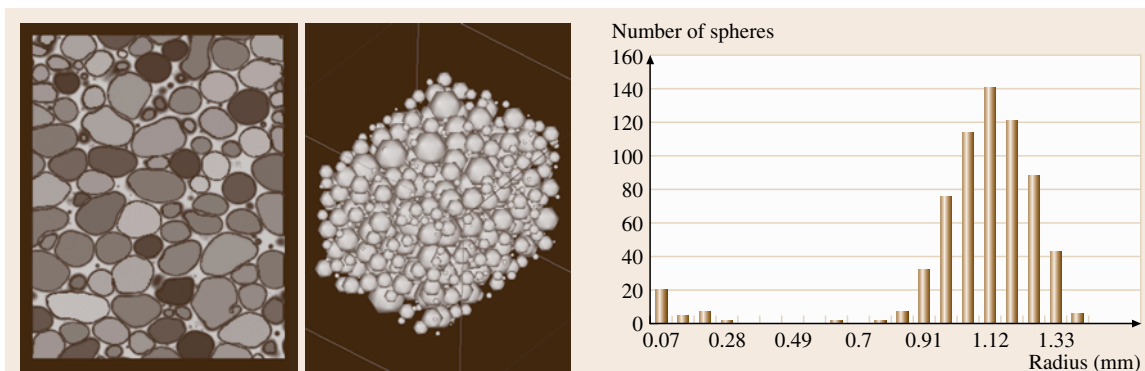


Fig. 16.67 Pore detection (*left*). Spheres with a diameter as calculated from the volume of found pores (*right*) at position of pore centers. The pore size distribution is shown in the diagram on the *right*

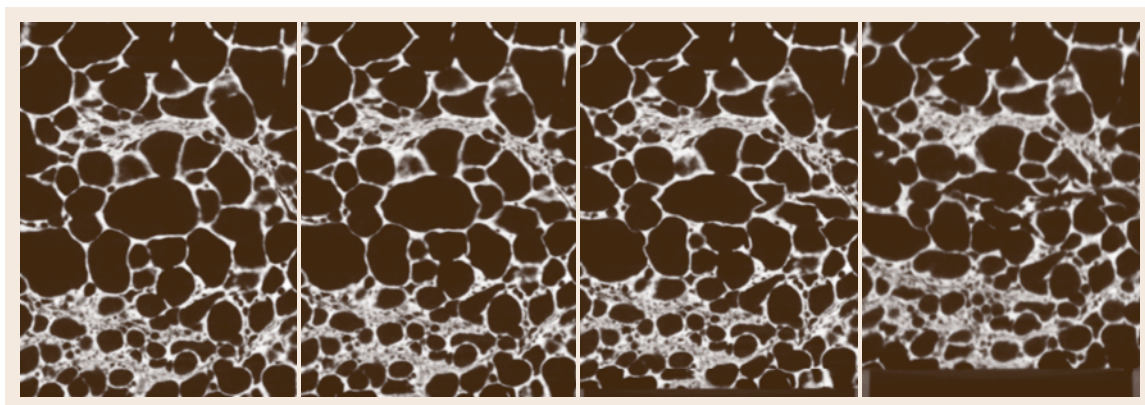


Fig. 16.68 A vertical slice through the foam before and after three compression states (from *left* to *right*). From the different 3-D image data sets the same slice was extracted showing the internal deformation of the foam

pores. The pore radius can then be calculated from the number of voxels counted per pore. Knowing the number of erode steps, the pore radius has to be enlarged by this value.

Internal Deformation

The failure mechanisms of strength-tested foams were studied on samples before compression and after compression. 3-D CT images of the samples were used

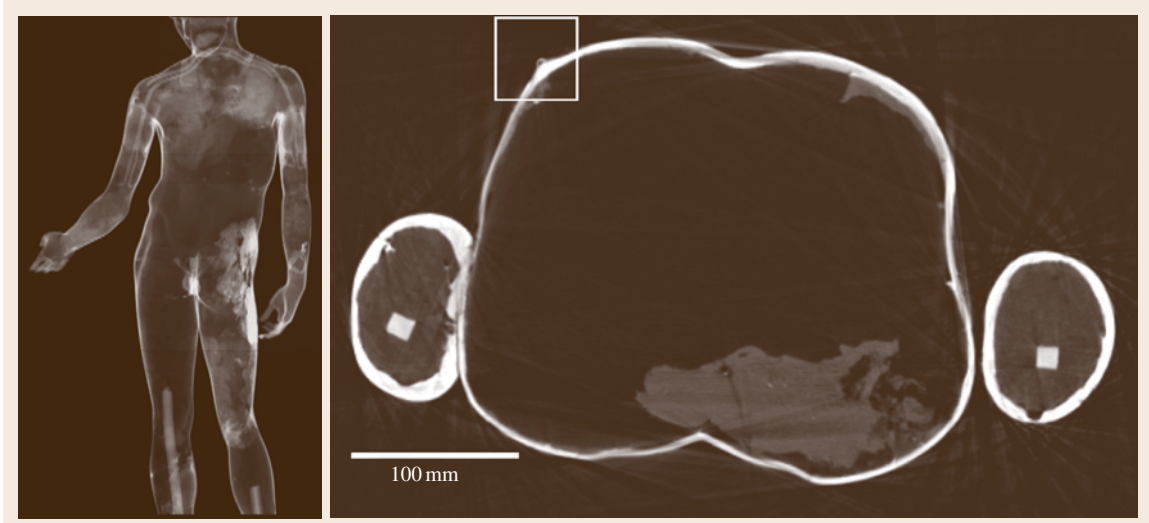


Fig. 16.69 Digital radiography of the antique bronze statue *Idolino* (left image). A cross section is shown on the right, representing the inner structure as well as the technique to fit together the separate cast parts of the statue

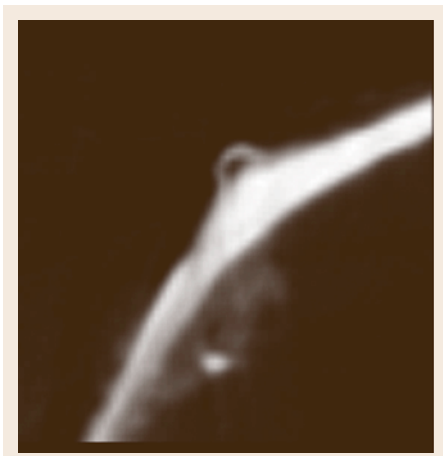


Fig. 16.70 Enlarged detail (fivefold magnification), marked in Fig. 16.69 by the white square

to find out where foam deformation has started, for which a program for image comparison in 3-D was developed. First the size of the region to be compared with the region of the sample after the compression test has to be defined. This region has to be bigger than the mean pore size. The region is moved in different directions in 3-D until it fits best with the initial sample, and the shift of the parts of the strength-

tested sample is written to an array. In this way, for all small regions of the probe we obtain shifts with respect to the initial sample in three directions: Δx , Δy and Δz .

The displacement after the compression test is shown (unit mm) using different grey levels, which are painted over the original foam structure, in order to show the displacement of compressed foam compared to original foam (Fig. 16.68).

Art Objects

Nondestructive methods such as x-ray techniques have been focused on art objects since the discovery of x-rays by W.C. Roentgen. In a long-standing collaboration with the Antikensammlung Berlin several large Greek and Roman bronzes were examined, to evaluate work traces and the interior of these archaeological samples. In 2000 the interior of the hellenistic *Getty Bronze* and the early Augustan *Idolino* in Florence were investigated at BAM [16.48, 49]. From the still being results Fig. 16.69 shows a digital radiography (left image) which is used to localize the precise location of cross sections. The tomogram (right image of Fig. 16.69) gives a view of the interior of the statue, with parts of the structure fitting the different cast parts. A detail of the tomogram shown in Fig. 16.69 is presented in Fig. 16.70 with a fivefold enlargement.

16.5 Computed Tomography – Application to Composites and Microstructures

In computed tomography (CT) the interface contrast of heterogeneous materials can be strongly enforced by x-ray refraction effects. This is especially desirable for materials with low absorption or mixed phases of similar absorption that result in low contrast. X-ray refraction [16.50, 51] is an ultras-small-angle scattering (USAXS) phenomenon. Refraction contrast has also been applied for planar refraction topography, a scanning technique for improved nondestructive characterization of high-performance composites, ceramics and other low-density materials and components [16.52].

X-ray refraction occurs when x-rays interact with interfaces (cracks, pores, particles, phase boundaries), preferably at low angles of incidence, similarly to the behavior of visible light in transparent materials, e.g. lenses or prismatic shapes. X-ray optical effects can be observed at small scattering angles of between several seconds and a few minutes of an arc, as the refractive index n of x-rays is nearly unity ($n \cong 1 - 10^{-5}$). In other terms, due to the short x-ray wavelength below 0.1 nm, x-ray light scattering is sensitive to inner surfaces and interfaces of nanometer dimensions.

16.5.1 Refraction Effect

In analogy to visible optics the interaction of x-rays with small transparent structures with dimensions above several nanometers results in coherent scattering governed by wavelength, structural dimensions and shape, local phase shift and absorptive attenuation. However, differently from optical conditions, the refractive index of x-rays near 1 causes beam deflections into the same small-angle region of several minutes of arc as diffraction. Thus the resulting interference is due to phase modulation due to the refractive index and the absorptive and Rayleigh diffraction, both of which depend on the path length through matter.

However if the dimensions of the scattering objects are much larger than several tens of nanometers, as is common in classical small-angle scattering, the interference fringes are no longer observable by classical small-angle cameras as they are too narrow. The resulting smeared angular intensity distribution is then simply described by a continuous decay according to the rules for refraction by transparent media, e.g. applying Snell's law [16.51]. This purely geometrical refraction approach is appropriate for

small-angle x-ray (and neutron) scattering effects by micrometer-sized structures and is applied in the following.

If ε is the real part of the complex index of refraction n , ρ is the electron density and λ is the x-ray wavelength, then n is

$$n = 1 - \varepsilon, \quad \text{with } \varepsilon \approx \rho\lambda^2 \quad \text{and } \varepsilon \cong 10^{-5} \quad (16.30)$$

for glass under 8 keV radiation. In contrast to optics convex lenses cause divergence of x-rays as $n < 1$. Figure 16.71 demonstrates the effect of small-angle scattering by refraction of cylindrical lenses: a bundle of 15- μm glass fibers (for composites) deflects a pin-hole x-ray beam within several minutes of an arc. In fibers and spherical particles the deflection of x-rays occurs twice, when entering and when leaving the object (insert Fig. 16.71). The oriented intensity distribution is collected by an x-ray film or a CCD camera while the straight (primary) beam is removed by a beam stop. The shape of the intensity distribution of such cylindrical objects is a universal function independent of materials,

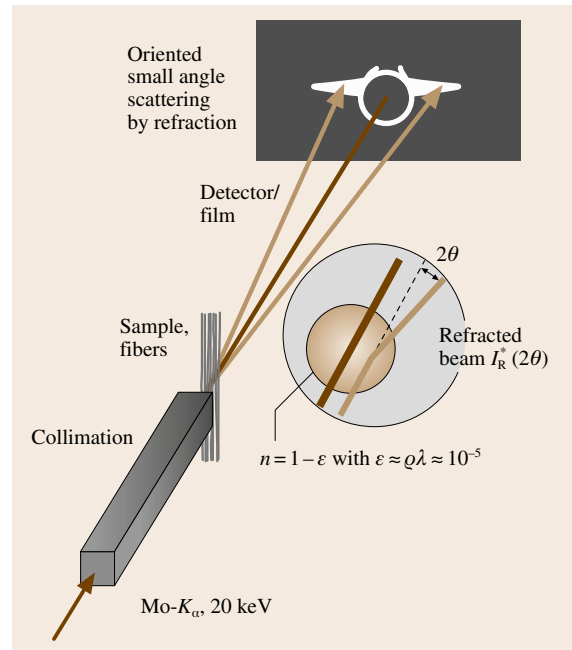


Fig. 16.71 Effect of oriented small-angle scattering by refraction of glass fibers; n index of refraction, ε real part of n , λ wavelength

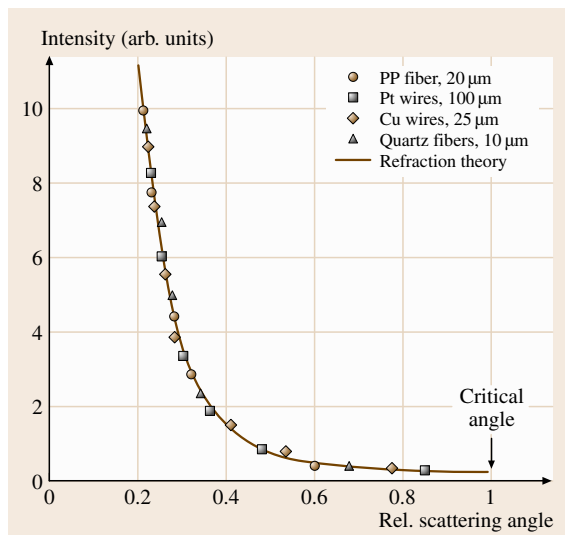


Fig. 16.72 The normalized shape of the angular intensity distribution of cylindrical objects; PP – polypropylene

if normalized to the *critical angle* θ_C of total reflection (Fig. 16.72) defined by the refractive index $\theta_C^2 = 2\varepsilon$. The intensity of the deflected x-rays becomes nearly zero at the critical angle (Fig. 16.72), with a small contribution from total reflection.

Applying a Kratky-type high-resolution small-angle scattering camera with slit collimation a cross section of 10^{-3} of the fiber diameter contributes to the detectable intensity typically above 2 min of arc. Total reflection of x-rays occurs as well but only 10^{-6} of the cylinder diameter is involved and this is therefore negligible, although planar surfaces may scatter all the primary intensity if well aligned. Based on Snell's Law the angular intensity distribution of cylinders has been modeled and

fitted to measurements on most different fibers, as illustrated by Fig. 16.72. The refracted intensity I_R^* of a cylinder (without absorption effects) can be expressed by [16.51]

$$I_R^*(2\theta') = \frac{J_0 2R}{\varepsilon} \sin^3 \left(\arctan \frac{\varepsilon}{\theta'} \right) \cong \frac{J_0 2R \varepsilon^2}{\theta^3} \quad (16.31)$$

J_0 is the irradiation density of the incident x-rays, R is the cylinder radius and $2\theta' = \theta$ is the scattering angle. In the case of spherical particles or pores I_R^* becomes

$$I_R^*(2\theta') \cong \frac{J_0 2R \varepsilon^2}{\theta^4} \quad (16.32)$$

The conventional understanding of *continuous* small-angle x-ray scattering (SAXS) is governed by the interpretation of diffraction effects. Both the well-known Guinier's theory [16.53] for separated particles and Porod's theory [16.54] of densely packed colloids are based on diffraction of Rayleigh scattering. Nevertheless Porod approximates the same angular intensity decay as in (16.32). However both diffraction approaches are about scattering objects two orders of magnitude smaller.

16.5.2 Refraction Techniques Applying X-ray Tubes

The SAXS instrumentation with an x-ray fine-structure tube and a Kratky camera is relatively straightforward. The camera needs an additional scattering foil for the primary-beam attenuation measurement and a micro-manipulation device for the sample (Fig. 16.73). For practical measurements the refraction detector remains at a fixed scattering angle $2\theta'$, so that the relative surface density C of the specimen can be measured according to [16.52]

$$C = \frac{1}{d} \left(\frac{I_R I_{A_0}}{I_{R_0} I_A} - 1 \right), \quad (16.33)$$

where I_R and I_{R_0} are measured by the refraction detector with and without sample, respectively, I_A and I_{A_0} are measured by the absorption detector, and where d the wall thickness of a sample. Apart from the choice of materials the relative surface density C depends solely on the scattering angle and the radiation wavelength. The absolute *inner surface density* (specific surface, surface per unit volume) is determined by comparison with

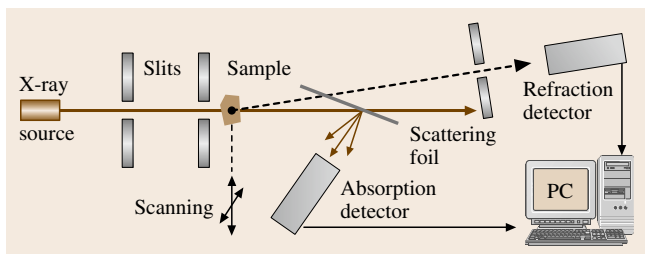


Fig. 16.73 Schematic of a SAXS instrumentation with a collimated x-ray beam, sample manipulator, refraction detector for refracted intensity, I_R with sample or I_{R_0} without sample, and an absorption detector for the attenuation intensity, I_A or I_{A_0} of the primary beam

a known calibration standard at retained boundary conditions (wavelength and scattering angle).

As well as the inner surface of pores and particles, interfaces and cracks such as fiber debonding in composites can also be determined. A model composite has been made to demonstrate the refraction behavior of a bonded and a debonded 140 μm sapphire fiber in a polymer matrix (Fig. 16.74, left). Figure 16.74 (middle) shows the resulting intensity distribution of a two-dimensional refraction scan of the model composite. The upper ray crosses the bonded fiber–matrix interface, causing a small amount of deflected intensity. At the debonded fiber and at the matrix surfaces (lower ray) many more x-rays are deflected, due to the larger difference of the refractive index against air. The polymer channel is clearly separated from the fiber surface. For comparison a mapping of I_A yields the transmission topograph containing only the absorption information of the projected densities, like in conventional radiography (Fig. 16.74, right). In the case of a real composite material the much thinner fibers are not spatially resolved, but the higher refraction signal of debonded fibers reveals quantitatively the percentage of debonded fibers.

Beyond the capabilities for two-dimensional topographs the set up of Fig. 16.73 can be employed for conducting computed tomography of a transversal section. This requires vertical linear scans and rotation of the sample to gain multiple projections for the parallel-beam reconstruction procedure. A section of a C/C ceramic matrix composite (CMC) for high-temperature applications is investigated to image the different crack patterns developing during manufacture by pyrolysis. The three samples (Fig. 16.75, left) are based on different phenolic resin carbon-fiber-reinforced polymer (CFRP) green bodies of good, intermediate and bad fiber/matrix bonding.

The absorption signals are reconstructed according to the rules for *parallel-beam filtered back-projection* as shown by Fig. 16.75, center. The resulting transversal sections reveal major cracks and homogeneous domains.

The refraction and the absorption intensities permit the reconstruction of the relative inner surface density according to (16.33) (Fig. 16.75, right) which shows a significantly higher number and finer cracks. Additionally the average intensity levels reveal the quantitative crack density without resolving individual cracks. These findings have proved for the first time that the degree of fiber debonding is retained during processing from the green state to high-temperature treatment [16.55].

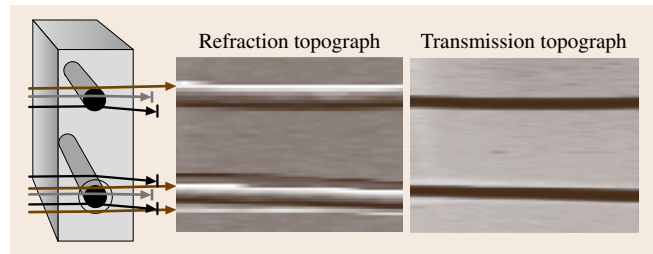


Fig. 16.74 x-ray scanning topography; *left*: model composite of polymer matrix and embedded bonded (*top*) and debonded (*bottom*) 140- μm sapphire fiber; *middle*: x-ray refraction topograph of C -values resolving debonding spatially: an interface image, free from absorption effects; *right*: absorption projection

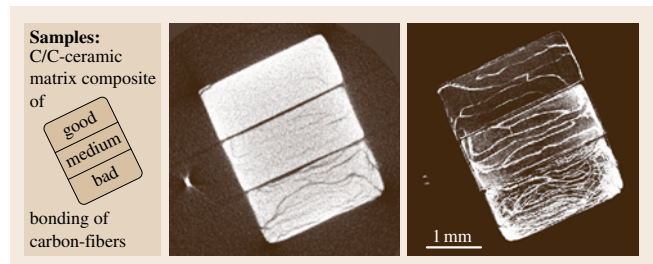


Fig. 16.75 x-ray computed tomography (CT) of carbon/carbon-ceramic matrix composite (C/C-CMC); *left*: sample arrangement, *middle*: crack pattern by conventional (x-ray absorption) CT, *right*: highly contrasted cracks by refraction computed tomography

16.5.3 3-D Synchrotron Refraction Computed Tomography

2-D refraction CT by conventional x-ray tubes has disadvantages. It is limited to low x-ray energies from characteristic Cu and Mo radiation and thus restricted to low-density materials. The thickness of the investigated layer is as large as 1 mm and the measurements require over 10 h. To overcome these limitations 3-D synchrotron refraction CT is employed. At the BAMline at BESSY, Berlin the available monochromatic energy ranges from 5 keV up to 60 keV. Further advantages are the high photon flux, the selectable energy and the highly parallel photon flux.

The experimental set up is sketched in Fig. 16.76 [16.56]. A parallel monochromatic beam (up to 60 keV) at about 2% bandwidth is delivered by a double multilayer monochromator (DMM). At the experimental stage a beam of several 10 mm² is reflected sequentially by two Si(111) single crystals at their Bragg condition for the chosen energy. An x-ray-sensitive CCD camera of about 5 \times 5 μm^2 resolution is placed behind the

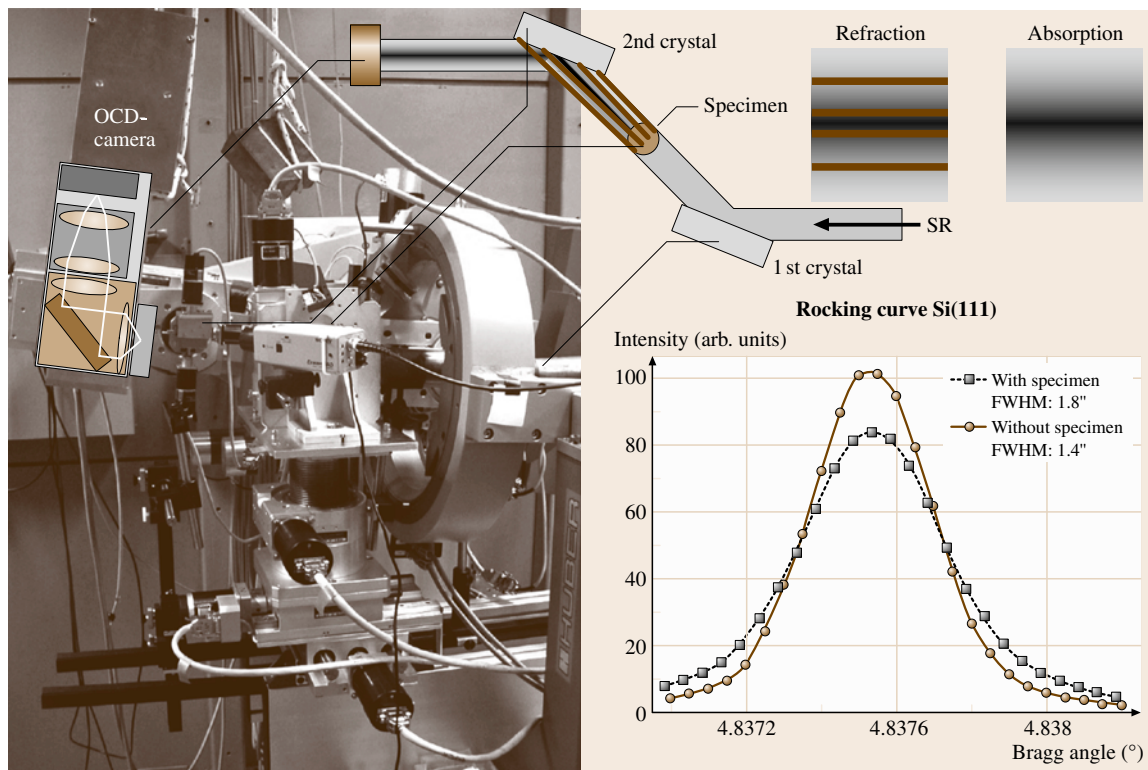


Fig. 16.76 Experimental setup for 3-D refraction CT at the synchrotron BAMline; left and top: goniometer and beam components, right: rocking curve of the second Si(111) crystal (symmetric) with specimen (squares) and without specimen (circles)

second crystal. A small inclination of the second crystal varies the reflected intensity. The resulting *rocking curve* width is 4×10^{-4} full width at half-maximum (FWHM) (Fig. 16.76, circles). In contrast to the set up for phase-contrast CT, the sample is positioned between the two crystals. Thus the most-parallel beam traverses the specimen and is attenuated according to the mass distribution. Additionally, the beam is deflected due to the refraction effect at all interfaces (Fig. 16.76, top right). This leads to a broadening of the rocking curve (Fig. 16.76, squares).

The presented investigation is performed on cylindrical tensile test samples of metal matrix composites (MMCs, MTU Aero Engines, München). The most advanced new material for aero engine compressor components with high tensile strength at low specific weight is based on a Ti matrix embedding SiC fibers. Their mechanical properties depend on the fiber/matrix bonding and their high crack resistance under high loads. Both characteristics require non-destructive characterization.

First a conventional 3-D CT investigation is carried out employing a fine-focus x-ray tube. Figure 16.77 shows the density reconstruction of one out of 300 planes at 100-kV tube voltage and $5 \times 5 \times 5 \mu\text{m}^3$ voxel resolution (720 projections, rotation about cylinder axes, Fourier-filtered back-projection). It shows a transversal section of a low cycle fatigue (LCF) sample. Higher density appears brighter. The reinforcing SiC fibers appear as dark discs with a slightly darker (carbon) core. Solely in the selected plane of Fig. 16.77, bottom, a dark shaded crack area appears due to reduced absorption.

Synchrotron refraction computed tomography of the same sample is performed at the BAMline with the described set up at 50-keV radiation and $5 \times 5 \times 5 \mu\text{m}^3$ detector voxel resolution (360 projections, Fourier-filtered parallel-beam back-projection). The reconstruction of Fig. 16.78 images the same cross section of the MMC LCF sample, but now the crack area appears bright (color enhanced) and is much more detailed. Also some debonded fibers can be identified by

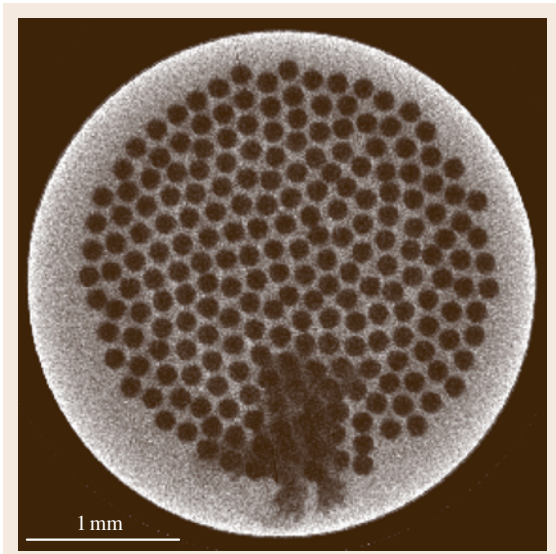


Fig. 16.77 Conventional CT reconstruction of the absorption measurement on Ti-SiC MMC sample after fatigue; fine-focus tube, 100-kV single-slice 3-D measurement

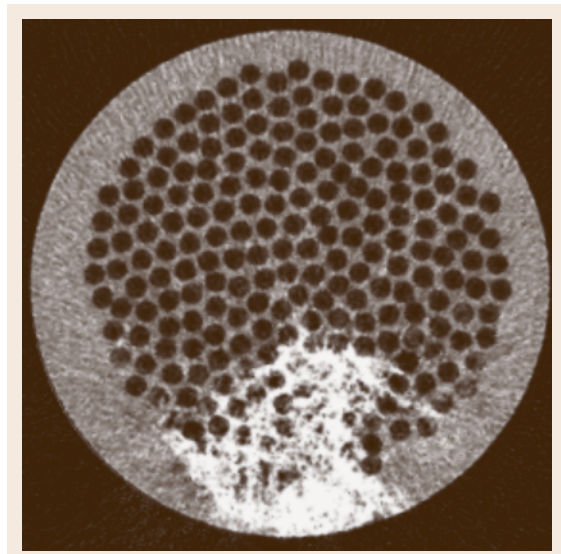


Fig. 16.78 Synchrotron refraction CT of same slice (Fig. 16.76); monochromatic 50-keV radiation, sample between two crystals at maximum reflection (after [16.56])

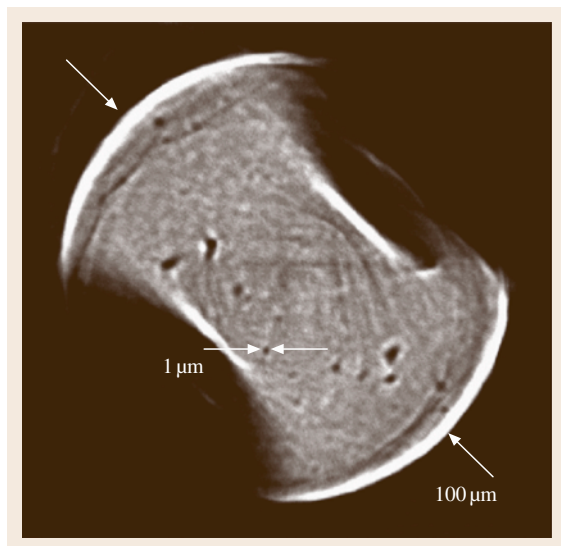
bright surrounding rings. In contrast to conventional absorptive CT measurements the refraction contrast provides crack indications in about 20% of the 300 reconstructed slices of the sample [16.56].

The high inverse contrast (compared to Fig. 16.77) originates from the rejection of deflected x-rays by the second Si crystal in front of the CCD detector due to refraction and total reflection interaction at the crack boundaries. The refraction contrast is nearly independent of the width of the cracks as it is a surface effect. However, the contrast depends strongly on the angle of the incident beam, which is only effective at $(0 \pm 1)^\circ$ (plane crack). In the given set up, with both Si crystals set to the top of their rocking curves, the image information from absorption and refraction effects are both present. If desired they can be separated by different operation of the Si crystals.

Much higher spatial resolution can be achieved, when the second crystal (Fig. 16.76) is replaced by an asymmetric-cut crystal (Fankuchen cut). In this the crystal surface is inclined against the re-

flecting lattice plane, resulting in a broadened exit beam of up to 100 \times magnification. An example of such nanometer-resolution refraction CT is given by Fig. 16.79, which presents the reconstruction of a horizontal section of a standing steel micro-drill (100 μm diameter) using 19-keV radiation. Dark tubular pores below 1 μm diameter, and refraction

Fig. 16.79 3-D nano-refraction CT; reconstructed plane of steel micro-drill from 19-keV projections; dark tubular pores below 1 μm diameter; refraction contrast at outer edges and around pores; magnification by Fankuchen-cut single-crystal Si (at the center of the rocking curve) ►



contrast at the outer edges and around pores are visible.

16.5.4 Conclusion

The presented findings demonstrate the high performance of refraction CT for inner surfaces and inter-

faces, including microcracks. Even beyond the spatial resolution of the reconstruction average crack densities are determined. The techniques are expected to close an essential gap in the spectrum of nondestructive techniques for a better understanding of microstructures of materials down to the nanometer scale and their behavior under thermal and mechanical loads.

16.6 Structural Health Monitoring – Embedded Sensors

The final decade of the 20th century brought many technological achievements, not only in regard to the development of innovative and high-performance materials but also in regard to advanced sensing techniques. The embedment of sensors into materials or structures opens up new possibilities to detect, e.g., the presence of cracks or the onset of failure, to estimate the extent of degradation, and to locate damaged zones. This is the basic idea of structural health monitoring, which has gained more importance within the last years. This is an emerging technology that deals with the development of techniques and systems for the continuous monitoring, inspection and damage detection of structures. Today structural health monitoring can be found in a wide area of industrial applications: starting from A for aircraft and ending at Z for Zeppelin. Innovative bridge design, higher safety requirements, extended operation time, reduction of maintenance and inspection costs (e.g. less or no visual and NDT inspection) are the driving forces for the usage of structural health monitoring systems. The ultimate goal is to eliminate current schedule-based inspection and replace it with condition-based maintenance or repair.

This chapter introduces the concept of structural health monitoring, gives an overview of state-of-the-art sensing techniques used for performance control and condition monitoring, and reviews topical applications from different industrial areas. Further detailed descriptions of a wide range of practical applications can be found e.g. in [16.58–63].

16.6.1 Basics of Structural Health Monitoring

The basic idea of structural health monitoring (SHM) can simply be described as the integration of a type of sensing system that provides information on demand about any significant change or damage occurring in an aerospace, civil and mechanical engineering infrastructure [16.64]. The structural health monitoring process involves the observation of a structure over time using periodically sampled dynamic response measurements from an array of sensors. The extraction of damage-sensitive features from these measurements and the statistical analysis of these features is then used to determine the current state of structural health. For long-term structural health monitoring, the output of this process is periodically updated information regarding the ability of the structure to perform its intended function in light of the inevitable aging and degradation resulting from operational environments. After extreme events, such as earthquakes or blast loading, structural health monitoring is used for rapid condition screening and aims to provide, in near real time, reliable information regarding the integrity of the structure [16.65]. During operational use structural health monitoring attempts to measure the inputs to and responses of a structure before damage so that regression analysis can be used to predict the onset of damage and deterioration in structural condition.

By combining the information of structural health monitoring, current environmental and operational con-

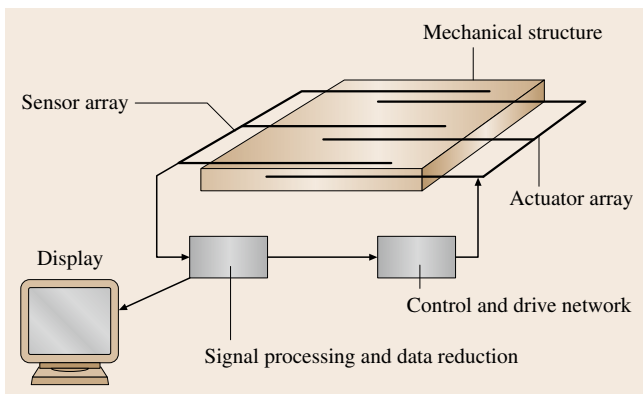


Fig. 16.80 Conceptual diagram of a smart structure (after [16.57])

ditions, previous component testing, nondestructive testing, and numerical modeling, a prognosis is possible to estimate the remaining useful life of the structure. By adding an actuator network and a related control and drive system, the structure can be improved to a so-called *smart material* or *smart structure*. It is able to monitor itself and/or its environment to respond to changes in its conditions (Fig. 16.80) [16.57].

As mentioned before the detection and prediction of onset of damage is the main target of structural health monitoring. Damage in engineering structures is defined as intentional or unintentional changes to the material and/or functional or geometric properties of these structures, including changes to the boundary conditions and system connectivity, which adversely affect the current or future performance of that structure. All damage begins at the material level and, under appropriate loading scenarios, progresses to component- and structure-level failure at various rates. Materials degradation and failure can occur in different ways.

- Gradually (e.g. fatigue, creep, corrosion, wear, biodegradation, chemical degradation);
- Suddenly and unpredictably (e.g. fracture, fiber breakage, matrix cracking, fiber splitting, delamination, debonding).

All material degradation and failure precedes a change of mechanical and/or chemico-physical characteristics of the material. In this context mechanical characteristics (e.g. elasticity, strength) and chemico-physical characteristics (e.g. thermal expansion, temperature dis-

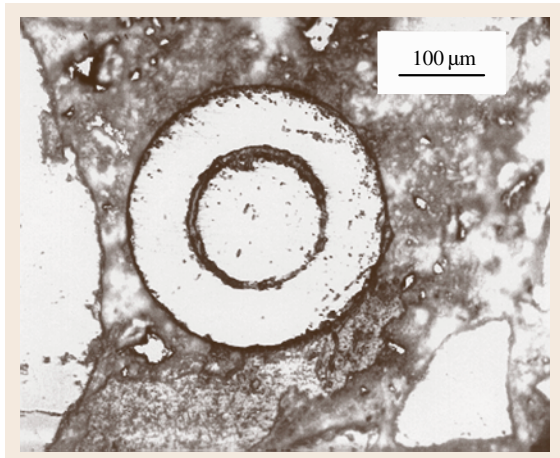


Fig. 16.81 Cross section of a fiber-optic sensor embedded into concrete (after [16.66])

tribution, humidity, oxidation or corrosion status) have special meaning. These characteristics and/or associated auxiliary variables (such as, e.g., strain) must be detected by means of physical sensor effects or measurable quantities and converted into a useful output signal. In all cases the sensing system must be able to resolve the parameter of interest as a function of both position and time throughout the structure. The spatial and temporal bandwidths that are required to address these detection needs must be adapted to the special requirements of the structure being monitored.

Sensing capabilities can be given to materials or structures by externally attaching sensors or incorporating them within the material or structure during manufacturing. In the first place the incorporation of the sensing system must be in compatibility with the material structure. This means that the functional characteristics and performance of the material may not be impaired by the sensor integration. The embedding of piezoelectric sensors into fiber-reinforced composites or of fiber-optic sensors into concrete are typical examples for such a way of integration (Fig. 16.81). On the other hand the sensor must be robust enough to survive the manufacturing process (e.g. high temperatures during curing process), withstand chemical attacks from

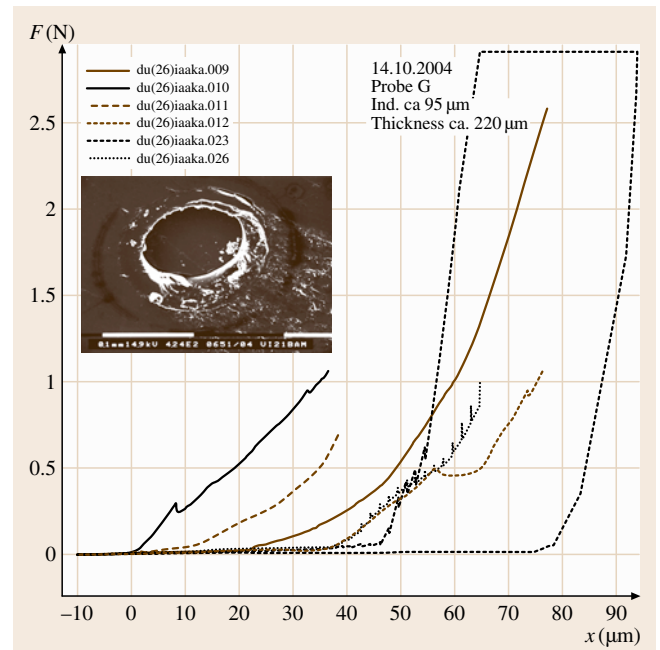


Fig. 16.82 Strain transfer of a two-layer coated fiber measured by indentation testing (after [16.67])

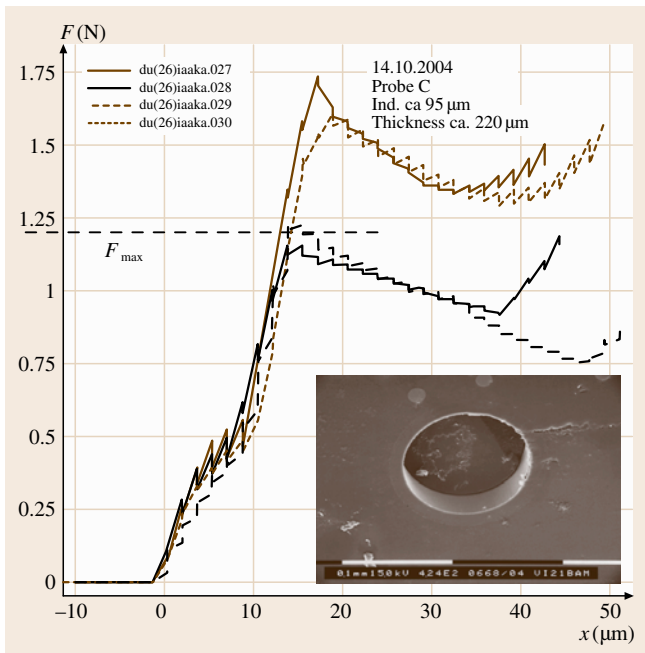


Fig. 16.83 Strain transfer of a polyimide-coated fiber measured by indentation testing (after [16.67])

the material (e.g. very high pH environment in concrete), and withstand extreme mechanical loads (e.g. highly elastic behavior of plastics) (Figs. 16.82 and 16.83).

A wide range of physical sensor effects can be used to detect changes of mechanical and/or chemico-physical characteristics of a material. Preferably electrical (e.g. piezoelectric materials) or optical sensing effects (e.g. optical fibers) are used. Table 16.6 gives an overview about common sensor effects, which are used today for smart materials or structures.

To monitor a complete structure or a part of material, different architectures of sensor arrangement can be used. Basically the following variations are of practical interest [16.57].

- A *point sensor* is one that monitors a particular parameter at a closely confined point defined by the effective cross-sectional area of the sensor element. In principle, the point sensor only sees a sample of the measurand at one particular point.
- An *integrating sensor* is one that takes an average value of a particular measurand over an area or length that is comparable to the area or length of the structure being monitored. Integrating sensors

are sometimes spatially weighted (e.g. by variation of sensitivity) to ensure that they are sensitized to particular spatial distributions and not others.

- A *distributed sensor* is capable of evaluating the parameter of interest as a function of position throughout the geometry of the sensor element. The ability to perform distributed measurements is particularly important in structural health monitoring since it enables the derivation of the measurand at a large number of points throughout the structure using a single interrogation port and thereby eliminates the need for complex wiring harnesses.
- A *multiplexed sensor system* is one that combines a number of point, integrating, or distributed sensors into a complex system. It could go through an electronic interface and use techniques derived from the field. It can also be implemented at the sensor technology level. Here the multiplexing may be effected on the measurand subcarrier.
- A *quasi-distributed sensor system* combines a number of integrating sensors into a single system that is multiplexed in the measurand carrier domain.

Finally the role of *signal processing* in structural health monitoring should not be understated. Signal-processing procedures can be divided into basic and advanced methods [16.65]. A typical basic procedure is *data normalization*. Data normalization is a procedure to normalize data sets so that signal changes caused by operational and environmental variations of the structure can be separated from structural changes of interest, such as structural or material deterioration or degradation.

The purpose of *data fusion* is to integrate data from a multitude of sensors with the objective of making a more robust and confident decision than is possible with any one sensor alone. In many cases, data fusion is performed in an unsophisticated manner, as when one examines relative information between various sensors. At other times, such as those provided by artificial neural networks, complex analyses of information from sensor arrays are used in the data-fusion process.

Data cleansing is the process of selectively choosing data to accept for, or reject from, the feature selection process. The data-cleansing process is usually based on knowledge gained by individuals directly involved with the data acquisition.

Feature extraction is the process of identifying damage-sensitive properties, derived from the measured vibration response, which allows one to distinguish between the undamaged and damaged structure. The

Table 16.6 Typical sensor effects to detect material degradation and failure

Material characteristics/ measurand	Sensor effects	
	Electrical signals	Optical signals
Mechanical: <ul style="list-style-type: none"> • Strain • Displacement • Vibration • Acceleration • Force • Pressure 	<ul style="list-style-type: none"> • Piezoelectric effect • Piezoresistive effect • Change of resistance 	<ul style="list-style-type: none"> • Change of <ul style="list-style-type: none"> - Transmission - Wavelength - Phase - Time of flight - Brillouin scattering
Chemico-physical: <ul style="list-style-type: none"> • Temperature • Humidity • pH value • O₂ concentration • Heat flow 	<ul style="list-style-type: none"> • Thermo resistance • Thermoelectric effect • Chemical resistance • Conductivity 	<ul style="list-style-type: none"> • Fluorescence • Change of <ul style="list-style-type: none"> – Transmission – Wavelength – Phase – Raman scattering – Brillouin scattering

best features for damage detection are typically application specific. Numerous features are often identified for a structure and assembled into a feature vector. In general, a low-dimensional feature vector is desirable. It is also desirable to obtain many samples of the feature vectors. There are no restrictions on the types or combinations of data contained in the feature vector. A variety of methods is employed to identify features for damage detection. Past experience with measured data from a structure, particularly if damaging events have been previously observed for that structure, is often the basis for feature selection. Numerical simulation of the damaged structure's response to postulated inputs is another means of identifying features. The application of artificial flaws, similar to those expected in actual operating conditions, to laboratory specimens can identify parameters that are sensitive to the expected damage. Damage-accumulation testing, during which structural components of the system under study are subjected to a realistic loading, can also be used to identify appropriate features. Fitting linear or non-linear, physical-based, or non-physical-based models of the structural response to measured data can also help identify damage-sensitive features.

Statistical model development is concerned with the implementation of the algorithms that operate on the extracted features to quantify the damage state of the structure. The algorithms used in statistical-model development usually fall into three categories. When data are available from both the undamaged and damaged structure, the statistical pattern-recognition algorithms fall into the general classification referred to as supervised learning. Group classification and regression analysis are supervised learning algorithms. Unsuper-

vised learning refers to the class of algorithms that are applied to data not containing examples from the damaged structure.

The damage state of a structure can be described as a five-step process [16.68]. The damage state is described by answering the following questions.

1. Is there damage in the structure (existence)?
2. Where is the damage in the structure (location)?
3. What kind of damage is present (type)?
4. How severe is the damage (extent)?
5. How much useful life remains (prognosis)?

Answers to these questions in the order presented represent increasing knowledge of the damage state. The statistical models are used to answer these questions in an unambiguous and quantifiable manner.

16.6.2 Fiber-Optic Sensing Techniques

Basics

Basic element of a fiber-optic sensor is a thin optical fiber made of a highly transparent glass or plastic (polymeric) material. The optical fiber consists of a core having a refractive index n_{core} and a surrounding cladding having a refractive index n_{cladd} . In such a fiber the propagation of light can be explained by different models. The models are based on some fundamental postulations and have certain limits of application. Ray optics explains the kinematics of propagation. Wave optics explains diffraction and interference phenomena. Electromagnetic optics makes possible an exact analysis of the phenomena of classic optics, including the effect of energy at the interfaces. Finally quantum optics

Table 16.7 Overview of most common types of silica optical fibers used for sensors

Fiber type	Multimode step index	Multimode graded index	Single-mode step index
Refractive-index profile			
Light propagation (schematic)			
Geometry			
Typical diameter	Core: 50 μm Cladding: 125 μm Coating: 140 μm to 250 μm	Core: 50 μm Cladding: 125 μm Coating: 140 μm to 250 μm	Core: 6 μm (870 nm) 9 μm (1300 nm) Cladding: 125 μm Coating: 140–250 μm

explains all the known optical phenomena, including interaction of light with matter. In this section the explanations are limited to ray and wave optics, because they allow a simple and practical understanding of fiber optic sensing techniques. A comprehensive and detailed introduction to all models (including Maxwell's equations) can be found in [16.69, 70].

Based on ray optics, light propagation in an optical fiber can be understood as follows. When light is launched into one end of the fiber and $n_{\text{core}} > n_{\text{cladd}}$

is true, it propagates along the fiber to the other end corresponding to the physical effect of total internal reflection. Only light that is launched for $0 < \theta < \theta_{\text{max}}$ can be guided along the fiber (assuming that θ_{max} is the maximum value of the range of the accepted angles θ) (Fig. 16.84). It is continuously reflected at the interface between the core and the cladding; the critical angle α_{max} must not be exceeded. Light that strike the end face of the fiber at an angle greater than θ_{max} is no longer completely reflected at the core/cladding

boundary; instead it is partly refracted into the cladding so that it is no longer completely available for further propagation.

The properties of light guidance through a fiber are governed largely by the profile of the refractive index of the core and cladding. In a step-index-profile fiber the refractive index is constant across the entire cross section of the core and cladding (Table 16.7) while the light rays propagate along straight lines in the core and are completely reflected at the core/cladding boundary. The individual light rays cover different distances, so that there are considerable differences in their respective transit times. This is called a multimode fiber. Very small core diameters ($< 10\ \mu\text{m}$) allow only one mode to travel through the fiber (called single-mode fibers). Fibers with a graded-index profile are made up of a core having a radius-dependent refractive index and a cladding with a constant refractive index. Those rays converging in the center travel a shorter distance, but because of the higher refractive index there, they travel at a lower speed. On the other hand, the smaller refractive index near the cladding causes the rays traveling there to have a higher velocity, but they have a longer distance to travel. By choosing a suitable profile exponent it is possible to compensate for these differences in transit time.

An optoelectronic unit, which contains a light source and a detector, and a processing unit for data acquisition, data processing and instrument control complete the fiber-optic sensing system (Fig. 16.85). Depending on the sensor type, semiconductor laser diodes (LD), vertical-cavity surface-emitting lasers (VCSEL), or light emitting diodes (LED) are used preferably. As detectors photo diode with p-i-n semiconductor structure (PIN diode), avalanche photodiodes (APD), or miniaturized spectrometers are mostly integrated into the optoelectronic unit. A comprehensive and detailed explanation of common light sources and detectors for fiber-optic sensing techniques can be found in [16.69,70]. For special or high-resolution measurements more complex measuring equipment like an optical time-domain reflectometer (OTDR) or a high-resolution optical spectrum analyzer are used.

Fiber Fabry–Pérot Interferometer

A *fiber Fabry–Pérot interferometer* sensor consists of a cavity defined by two mirrors that are parallel to each other and perpendicular to the axis of the optical fiber. There are two arrangements of Fabry–Pérot interferometer (FPI) sensors: first, the (intrinsic) in-fiber FPI sensor, where the cavity is formed by two mirrors at lo-

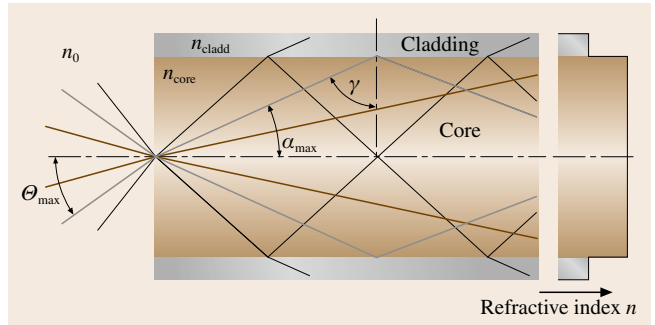


Fig. 16.84 Light propagation in a multimode fiber

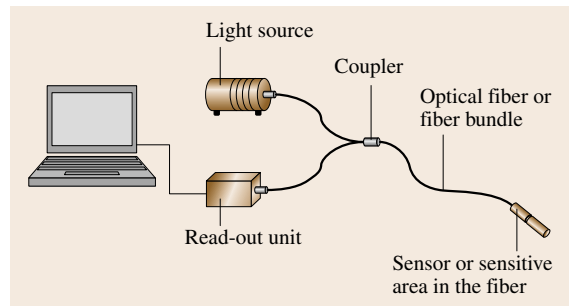


Fig. 16.85 Principle setup of a complete fiber optic sensor system

cations in the length of the fiber. The maximum distance of the mirrors (cavity length) can reach some mm and defines the gauge length. The second type is the extrinsic FPI sensor (EFPI). The optical cavity is formed by the air gap (usually about $10\text{--}100\ \mu\text{m}$) between to uncoated fiber faces (Fig. 16.86). The most widely used design is to fix into position the two fiber ends in a hollow tube. The fiber end-faces act as mirrors and produce the interference fringes.

The functional principle of an FPI sensor is as follows. The incoming light reflects twice: at the interface glass/air at the front of the air gap (the reference (Fresnel) reflection) and at the air/glass interface at the far end of the air gap (sensing reflection). Both reflections interfere in the input/output fiber. The sensor effect is induced by force-induced or temperature-induced axial deformation of the hollow tube. This leads to a shift of the fiber end-faces inside the tube (because they are only fixed at the ends of the tube), which results in changes on the air gap length (gap width s). From this follows a phase change between the reference reflection and the sensing reflection that is detected as an intensity change in the output interference signal.

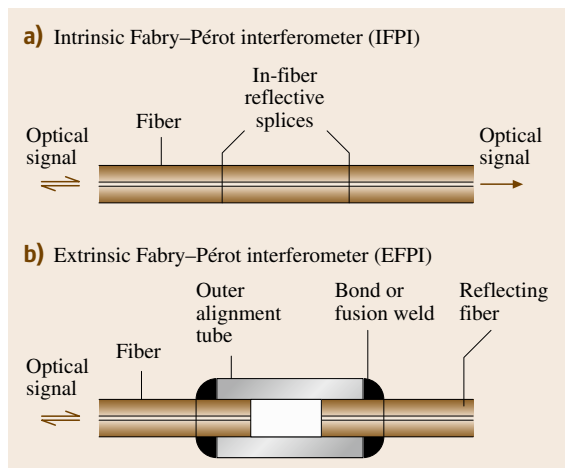


Fig. 16.86a,b Common types of fiber Fabry-Pérot interferometer (after [16.71])

FPI sensor systems are commercially available for strain, temperature and pressure measurements. They allow local measurements of strain in a range between $-5000 \mu\text{m}/\text{m}$ (shortening) and $+5000 \mu\text{m}/\text{m}$ (elongation) with a resolution of up to $0.1 \mu\text{m}/\text{m}$. Available gauge lengths are in the range 1–20 mm. Because of their excellent response time behavior of up to 2 MHz, they can also be used for detection of mechanical vibrations and acoustic waves. However, the interrogation unit used defines the dynamic behavior. With regard to measuring performance and applicability, the fiber Fabry-Pérot interferometer (FPI) sensor is the most often applied interferometric *point sensor* type for structural health monitoring.

Fiber Bragg Grating Sensor

The discovery of the photosensitivity in germanium-doped fibers by Hill and coworkers in 1978 was the basis for fabrication of *in-fiber reflective Bragg grating* filters with a narrow-band, back-reflected spectrum. They discovered that the refractive index n of a fiber increases when ultraviolet (UV) light is incident upon such a fiber. Today fiber grating manufacturing is well established at special wavelengths with a given periodically changing refractive index and spacing between the individual grating planes (grating period or pitch Λ). *Fiber Bragg gratings (FBG)* are usually 1–25 mm long and act as *typical point sensors*.

The distance Λ between the grating planes can vary; the common FBG satisfies the condition $\Lambda < \lambda$ where Λ is less than $1 \mu\text{m}$ (in contrast to so-called long-period gratings with $\Lambda \gg \lambda$, where Λ is 100–500 μm). Fiber

Bragg gratings for sensor applications are primarily referred to as uniform gratings: the grating along the fiber has a constant pitch and the planes are positioned normally to the fiber axis (Fig. 16.87). The principle of function is as follows: when a broadband light signal passes through the fiber Bragg grating, only a narrow wavelength range λ_B which satisfies the Bragg condition

$$\lambda_B = 2n_{\text{eff}}\Lambda \quad (16.34)$$

is reflected back due to interference between the grating planes (n_{eff} is the effective refractive index of the fiber core and Λ is the grating period). The quantity of the Bragg resonance wavelength λ_B is determined by the grating pitch Λ manufactured and corresponds to twice the period of the refractive index modulation of the grating. The grating periodicity is relatively small, typically less than $1 \mu\text{m}$. From (16.34) it can be derived that the Bragg resonance wavelength λ_B will change when n_{eff} changes (for example by temperature variation) or Λ changes (due to pitch changes by fiber-grating deformation). That means that changes in strain or temperature (or both together) will shift the reflected center wavelength. In general, λ_B increases when the fiber is strained ($\Delta\varepsilon > 0$) and decreases when the fiber is compressed ($\Delta\varepsilon < 0$). By means of a spectrum analyzer this wavelength shift can be measured. In this way, one can determine strain variations (for constant temperature) or temperature variations (without any deformation of the grating).

Assuming uniform axial strain changes in the grating area and the absence of lateral deformation of the grating, the strain seen by a grating can be computed by a simple linear equation

$$\varepsilon = K \frac{\Delta\lambda_B(\varepsilon_z)}{\lambda_B} + \xi \Delta T, \quad (16.35)$$

where K has to be estimated by a calibration procedure [16.72]. The strain sensitivity depends on the wavelength used (Table 16.8). With regard to ther-

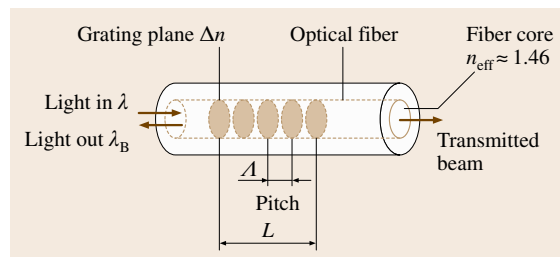


Fig. 16.87 Fiber Bragg grating sensor

Table 16.8 Typical strain and temperature sensitivities of FBGs

Wavelength	Strain sensitivity (pm/ $\mu\epsilon$)	Temperature sensitivity (pm/K)
800 nm	0.63–0.64	5.3–5.5
1300 nm	1.0	8.67–10.0
1550 nm	1.15–1.22	10.0–13.7

mal sensitivity the Bragg resonance wavelength shift is dominated by the temperature-induced change of the refractive index. Only a very small thermal-induced wavelength change comes from the thermal expansion of the glass material (coefficient of expansion of optical fiber glass is 0.55 K^{-1}).

Bragg grating sensors possess a number of advantages that make them attractive compared with other sensor arrangements.

- *Linear response.* The Bragg wavelength shift is a simple linear response to the sensor deformation as shown in (16.34). In contrast to FPI sensors the sensor signal has no ambiguity for strain/compression changes.
- *Absolute measurement.* The strain or temperature information obtained from a measurement system is inherently encoded in the wavelength (strain and/or temperature, index changes due to cladding affection); an interruption in the power supply does not lead to a loss of measurement information.
- *Line neutrality.* The measured data can be isolated from noisy sources, e.g. bending loss in the leading fiber or intensity fluctuations of the light source.
- *Separation of the interrogation unit from sensor.* Removal of the reading unit or exchange of leading

cable using special connectors with polished angled end-faces do not influence the signal response.

- *Potential for quasi-distributed measurement with multiplexed sensing elements.* Because a number of gratings (sensor array) can be written along the fiber and be multiplexed, a quasi-distributed sensing of strain and temperature is possible by serial interrogation of a limited number of gratings. The distance between the gratings can be designed according to the requirements.

There are different techniques to read the grating response under the influence of a measurand. The basic operation principles of fiber-grating-based Bragg grating sensors are monitoring either the shift in the wavelength or change in intensity of the return signal due to measurand-induced changes. To get high-precision monitoring of wavelength shift, laboratory-grade instrumentation based on highly resolving monochromators or optical spectrum analyzers (OSA) have to be used. For applications that do not have high requirements on strain resolution in the submicron or micron range low-cost portable reading units are commercially available (Table 16.9). These interrogation units fit laboratory as well as on-site requirements. When choosing a reading unit for on-site applications, a set of requirements has to be considered, e.g. scan frequency, number of gratings to be read simultaneously, long-term reproducibility of wavelength shift, immunity to optical power fluctuations, low sensitivity to temperature and vibrations, easy handling and a reasonable price.

To exploit the multiplexing capability of FBG sensor, two different methods can principally be used. Because of the wavelength-encoded nature of grating, each sensor in the fiber can be designed to have its own

Table 16.9 Commercially available interrogation units for FBG sensors

Parameter	si 720 Micron Optics	I-MON 400E Ibsen	Spectraleye SE600 FOS&S
Wavelength range	1510–1590 nm	1520–1585 nm	1527–1565 nm
Resolution	0.25 pm wavelength at 0.5 Hz	0.5 pm	1 pm
Uncertainty in wavelength scanning	1 pm	5 pm	± 10 pm
Maximum scan frequency	5 Hz	970 Hz	1 Hz
Number of channels	2 (8 optional)	> 50 FBGs	1
Weight	15.5 kg	0.6 kg	1.3 kg
Specialty	Fabry–Pérot sensors, long-period gratings	Vibration analysis, distributed strain measurements	90 min battery operation
Preferred use; operating temperature	Laboratory, 0°C to $+50^\circ\text{C}$	Small system with USB interface for field applications, 0°C to $+50^\circ\text{C}$	Handheld system for field applications, 0°C to $+40^\circ\text{C}$

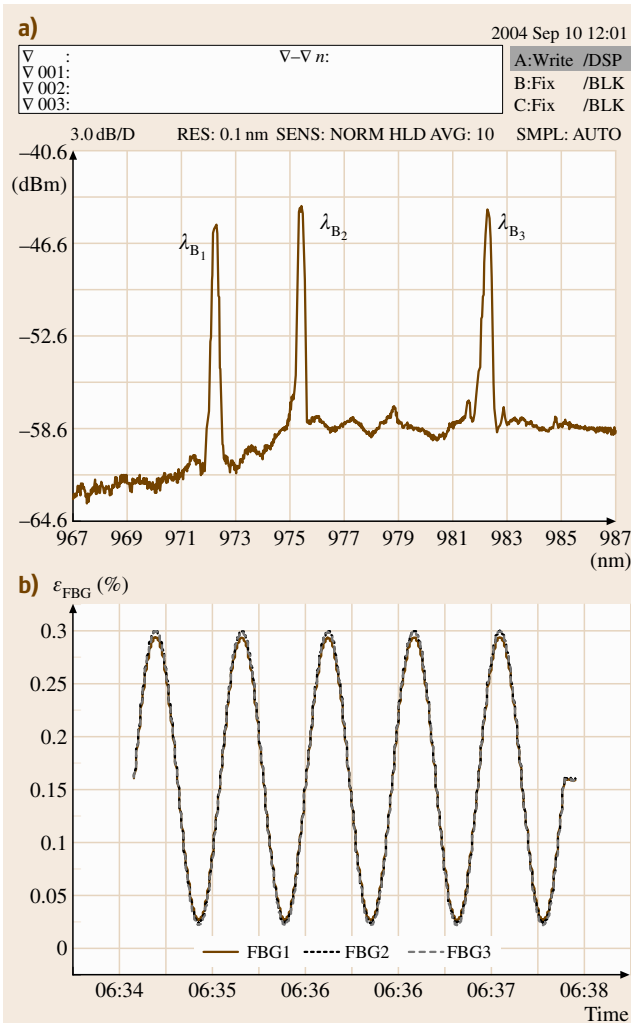


Fig. 16.88 (a) Distributed strain measurement in a composite structure of a rotor blade for a windmill by three FBG; (b) FBG signals after 10 Mio. cycles of dynamic loading during reliability testing

wavelength within the available source spectrum. Then, using wavelength multiplexing, a *quasi-distributed sensing* of strain, temperature or other measurands associated with spatial location of the measurand is possible. The number of sensors depends on the bandwidth of the source (typically about 70 nm), on the Bragg reflection bandwidth (typically 0.4 nm) and on the wavelength range needed for pulse shifting due to measurand changes (sometimes up to ± 3.5 nm). Using this method, up to 20 sensors can be interrogated in series (Fig. 16.88).

Low-Coherence Interferometry

An *integrating* or long-gauge-length *sensor* can be realized by the concept of *low-coherence interferometry*. It is based on a double Michelson interferometer and a low-coherence source (e.g. a LED or a thermal light source) (Fig. 16.89). A sensing interferometer uses two fiber arms – a measurement fiber that is in mechanical contact with the structure, and a reference arm, which compensates for the temperature dependence of the measuring fiber. The reference fiber must not be strained and needs to be installed loose near the first fiber. When the measurement fiber is contracted or elongated, deformation of the structure results in a change of the length difference between the two fibers. By the second interferometer, which is placed in the portable reading unit, the path-length difference of the measurement interferometer can be evaluated. This procedure can be repeated at arbitrary times and, because the displacement information is encoded in the coherence properties of the light (coherence length of a typical LED: 10–100 μm) and does not affect its intensity. Due to its physical principal and easy set up, not only the precision but also the repeatability of measurements is high for this sensor type. The measurement system can be switched off between two measurement events or components such as connectors or cable can be exchanged without zero-point data loss.

Typical parameters of commercially available long-gauge-length sensor are

- measuring length: 50 cm to several 10 m
- measuring range: 0.5% in shortening, 1.0% in elongation
- precision in measurement: 2 μm (error of measurement: $\Delta\epsilon = \pm 1.25 \times 10^{-5}$)
- proportionality factor between the measured delay and the applied deformation: $(128 \pm 1) \mu\text{m}/\text{ps}$.

Such sensors can be provided as tube sensors or as flat tape sensors. Tape sensors allow its integration into composites or into interface zone of multilayer materials. Several sensors can be interrogated by multiplexing.

Optical Time-Domain Reflectometry

A *quasi-distributed sensor system* within a material or construction can be realized by fiber-optic techniques in the following way. By measurement of the time of flight of an ultrashort light pulse transmitted into the fiber and backscattered on markers (splices, photoinduced reflectors, or squeezing points) at the end of these sections,

the measurand can be determined at definite locations along the fiber (Fig. 16.90). An elongation (compression or contraction) of a measuring section, determined by two reflector sites on the fiber, changes the time of flight of the pulse: $\Delta\varepsilon \sim \Delta t_p[(c/2L_0)n]$, where c is the speed of light and n the index of refraction. Based on this relationship, the changes in the average strain of a chain of marked sections along the fiber can be interrogated by an OTDR device.

This method allows the evaluation of strain profiles in large components without using sensor fibers containing discrete sensor points along the fiber. The OTDR device used determines the strain resolution achievable. A high-resolution picosecond OTDR device enables the resolution of elongation to 0.2 mm, assuming the minimum distance between two reflectors in the measuring section is not less than 100 mm [16.74]. Using this method, a reflector shift of 0.35 mm can be resolved, however only long-term reproducibility of reflector shifts of 0.85 mm can be achieved. This value is sufficient to recognized dangerous changes in the material or loss of bonding integrity. Automatic scanning run takes between one and some ten seconds depending on the wanted precision. The sensor sections are interrogated one after another. Offline measurements are preferred because the rather expensive OTDR devices should alternatively be used for other measurement tasks, too.

The length of the fibers evaluated by conventional OTDR technique is limited by the permissible power loss along the fiber (quality of the markers), and can reach up to several hundreds meters, or tens of sensing sections. This method has a serious advantage: determination of the position of all reflectors can be referred to one stable position (reference reflector). Therefore, there is no propagation of error due to propagating from one reflector to the next one.

The examples considered above were focused on strain or deformation measurement in direction of the fiber axis. However in composites, transversely applied pressure, arising forces or beginning delamination might be of interest. For such purposes, single-mode birefringent fibers can be embedded. Internal birefringence can be induced by using a noncircular core geometry of the fiber or by the introduction of stress anisotropy around the core such as done in panda or bow-tie fibers. The refractive-index difference of the two orthogonal polarization modes produces a differential propagation velocity. Any damage or parameter change in the composite or material structure will perturb the birefringence parameters in the sensor fiber. Using the time-delay measurement technique, the in-

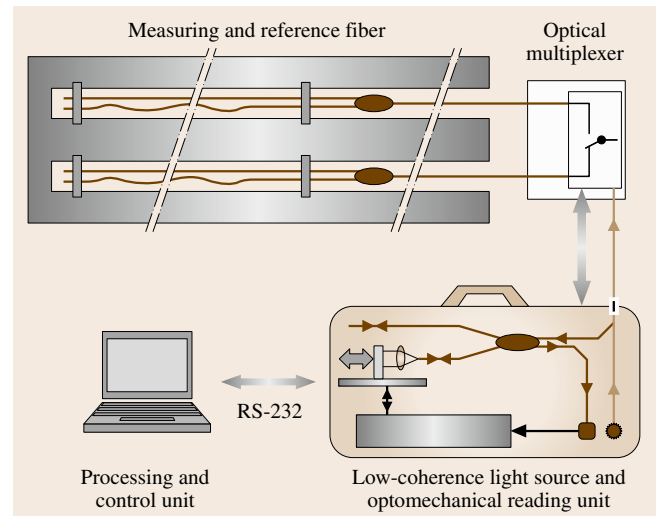


Fig. 16.89 Fiber-optic low-coherence interferometry sensor system (after [16.73])

tensity and position of the perturbation can be located with an uncertainty of about 10 cm [16.75]. However, a reproducible correlation between affecting external events and optical effects in the fiber is quite difficult because the interface zone of the sensing fiber strongly influences the response of the sensor. Nowadays, fiber Bragg gratings will be written into birefringence fibers to make multiple parameter sensing with the capability to discriminate between them [16.76].

Brillouin Scattering

In optical fibers *Brillouin scattering* arises due to the interaction of light with phonons. Phonons are quantized acoustic waves. In essence, the light is scattered from variations in the index of refraction associated with acoustic waves. Light which is scattered off these phonons is frequency shifted by an amount of determined by the acoustic velocity of the phonons. The

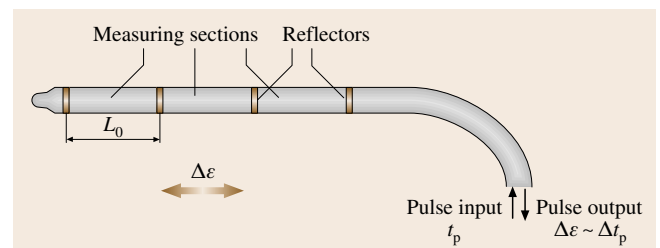


Fig. 16.90 Quasi-distributed fiber-optic sensor based on backscattering signal evaluation

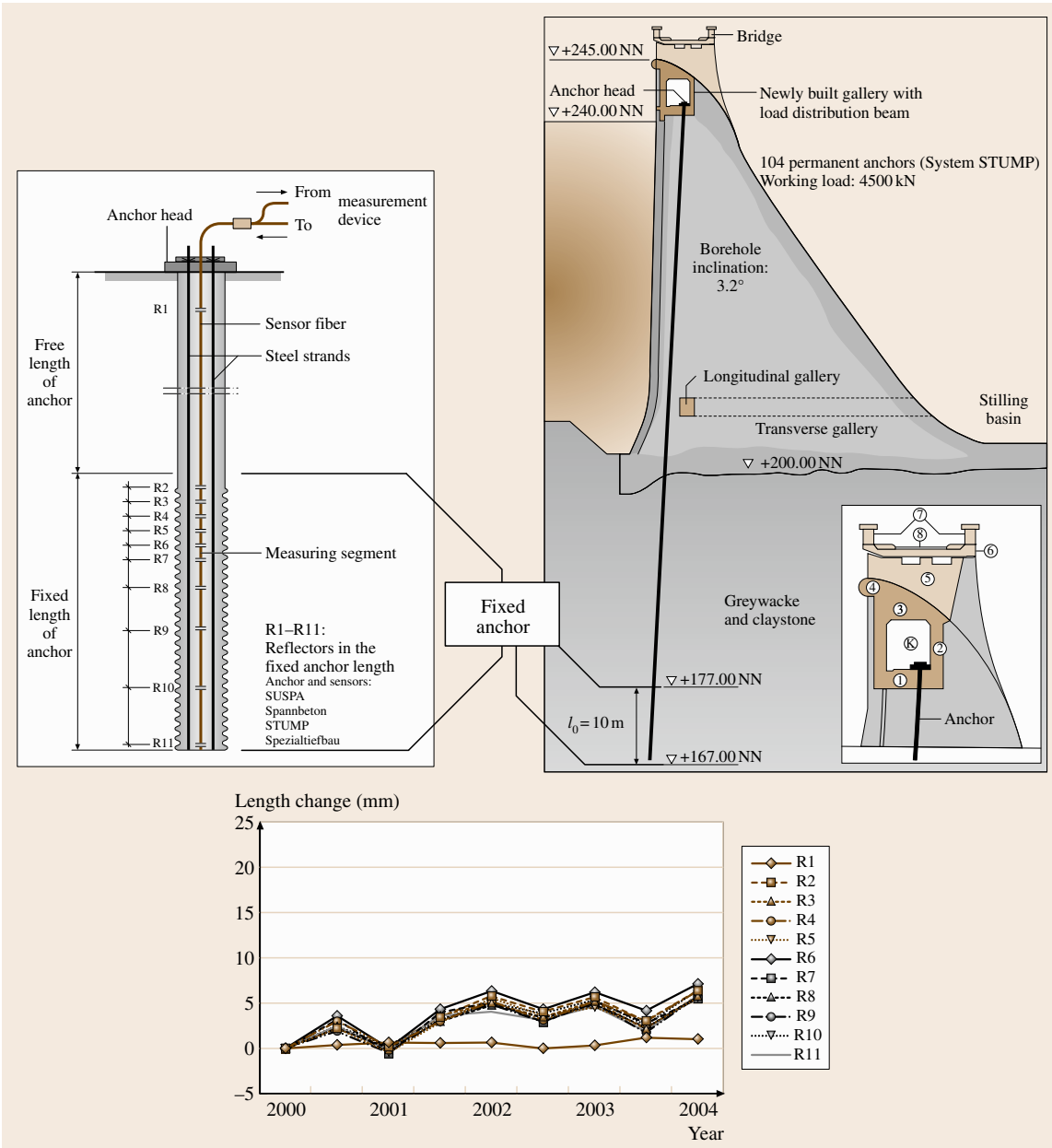


Fig. 16.91 Monitoring of the bonding behavior along the fixed anchor length by quasi-distributed fiber-optic sensors (Eder Gravity Dam Germany) (after [16.77])

acoustic velocity is in turn dependent on the density of glass and thus the material temperature. The Brillouin frequency shift is given by

$$v_B = 2n \frac{V_a}{\lambda}, \quad (16.36)$$

where V_a is the velocity of sound in glass and is a function of (T, ϵ) , n is the effective index of refraction, and λ is the free-space wavelength of operation. The frequency shift is linearly dependent on both the temperature and strain in the fiber [16.78, 79].

The sensitivity of the frequency shift is of the order $4.6 \times 10^{-6} \mu\epsilon^{-1}$ for strain and $9.4 \times 10^{-5} / ^\circ\text{C}$ for temperature.

Since this technique was first published, several developments and technical innovations have led to dramatic advances in the capabilities of the Brillouin approach. Today, several devices based on Brillouin optical-fiber time-domain analysis (BOTDA) are commercially available. One typical example is an arrangement where the sensing fiber follows a double path in the structure to be monitored. One path is attached to the structure or embedded in the material and is thus subjected to both temperature and strain. The return path is loosely installed, measuring only the temperature profile. By such an arrangement a temperature resolution of

1°C and a strain sensitivity of $25 \mu\epsilon$ with a spatial resolution of approximately 1 m have been achieved [16.81].

Figure 16.92 shows zones of shifted Brillouin frequencies with an 11-km-long optical fiber [16.80]. A closer look on these zones demonstrates the temperature and strain resolution of such a set up. The peak difference of both indications is in the order of 3 MHz, which represents a temperature resolution of 2.6°C or a strain resolution of 0.006%.

An alternative approach is named Brillouin optical-fiber frequency-domain analysis (BOFDA) [16.82]. The BOFDA operates with sinusoidally amplitude-modulated light and is based on the measurement of a baseband transfer function in frequency domain by a network analyzer. A signal processor calculates the inverse fast Fourier transform (IFFT) of the baseband transfer function. In a linear system this IFFT is a good approximation of the pulse response of the sensor and resembles the strain and temperature distribution along the fiber (Fig. 16.93a). The frequency-domain method offers some advantages compared to the BOTDA concept. One important aspect is the possibility of a narrow-bandwidth operation in the case of BOFDA. In a BOTDA system broadband measurements are necessary to record very short pulses, but in a BOFDA system the baseband transfer function is determined point-wise for each modulation frequency, so only one frequency component has to be measured by a network analyser with a narrow resolution bandwidth. The use of a narrow bandwidth operation (detectors) improves the signal-to-noise ratio and the dynamic range compared to those of a BOTDA sensor without increasing the measurement time. Another important advantage of a BOFDA sensor is that no fast sampling and data acquisition techniques are used. This reduces costs. Particularly, the low-cost-potential of BOFDA sensors is very attractive for industrial applications.

For stabilization and reinforcement of geotechnical structures like dikes, dams, railway track ballasts, embankments, landfills and slopes geotextiles are commonly used. The incorporation of optical fibers in geotextiles leads to additional functionalities of the textiles, e.g. monitoring of mechanical deformation, strain, temperature, humidity, pore pressure, detection of chemicals, measurement of the structural integrity and the condition of the geotechnical structure (structural health monitoring). Especially solutions for distributed measurement of mechanical deformations over extended areas of some hundred meters up to some kilometers are urgently needed. Textile-integrated distributed fiber optic sensors can provide

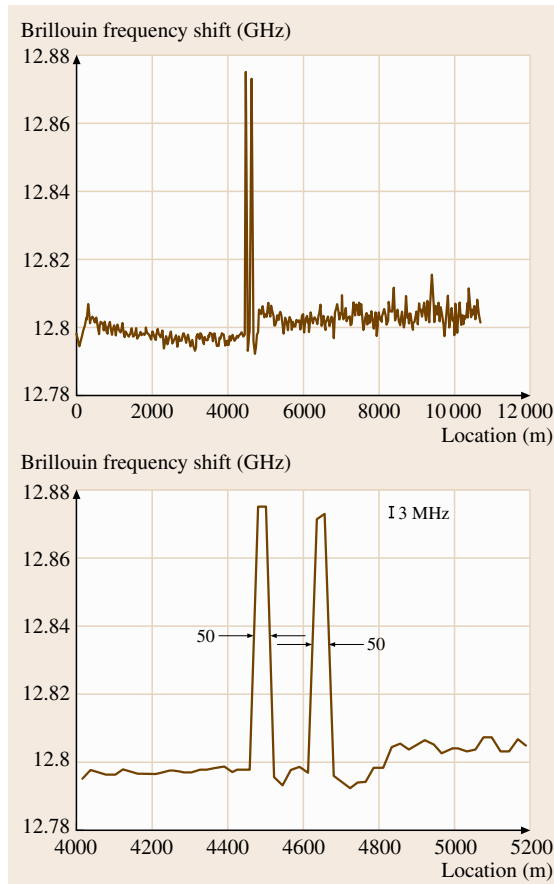


Fig. 16.92 Zones of shifted Brillouin frequencies within an 11-km-long optical fiber (upper). A closer look at these zones demonstrates that the resolution of 3 MHz represents a temperature resolution of 2.6°C or a strain resolution of 0.006% (after [16.80])

for any position of extended geotechnical structures information about critical soil displacement or slope slides via distributed strain measurement along the fiber with a high spatial resolution of less than 1 m [16.83]. So an early detection of failures and damages in geotechnical structures of high risk potential can be ensured.

Figure 16.93c shows the result of a validation test at a test dike at the University of Hannover. A sensor-based geotextile was installed on top of the dike and was covered with a thin soil layer. To simulate a mechanical deformation/soil displacement, a lifting bag was embedded into the soil and was inflated by air pressure. This induced a break of the inner slope of the dike and a soil displacement. The soil displacement was clearly

detected and localized by the BOFDA system. The distribution of the mechanical deformation (strain) in the dike measured by the BOFDA system at two different air pressure values is shown in Fig. 16.93c.

However, the excellent measurement technique based on Brillouin scattering in silica fibers reaches its limits when strong mechanical deformations, i.e. strain of more than 1% occurs. In such a case sensors based on silica fibers cannot be reliably used. Furthermore, silica fibers are very fragile when installing on construction sites and, therefore, special robust and expensive glass fiber cables have to be used. For that reason, the integration of polymer optical fibers (POF) as a sensor into geotextiles has become very attractive because of the high elasticity, high breakdown strain

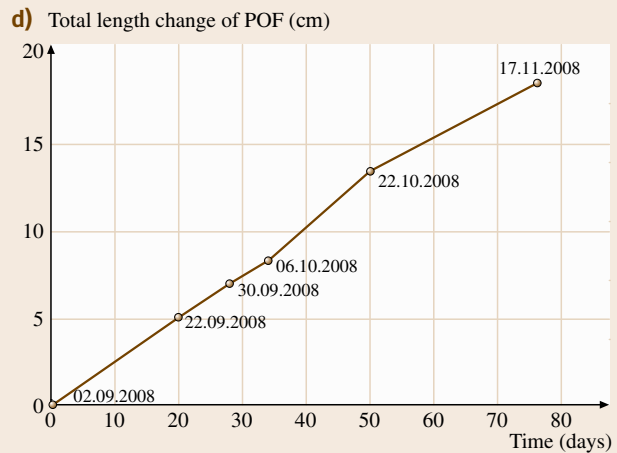
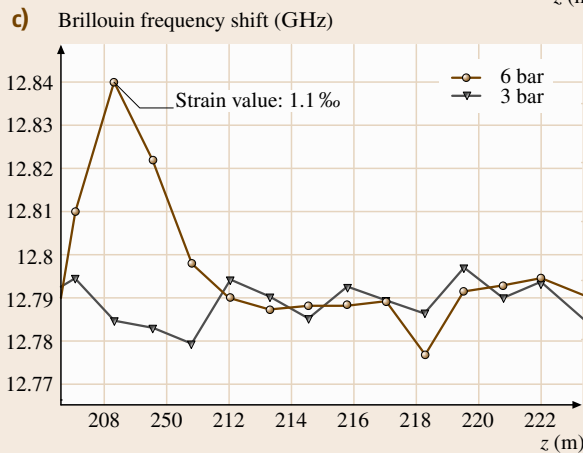
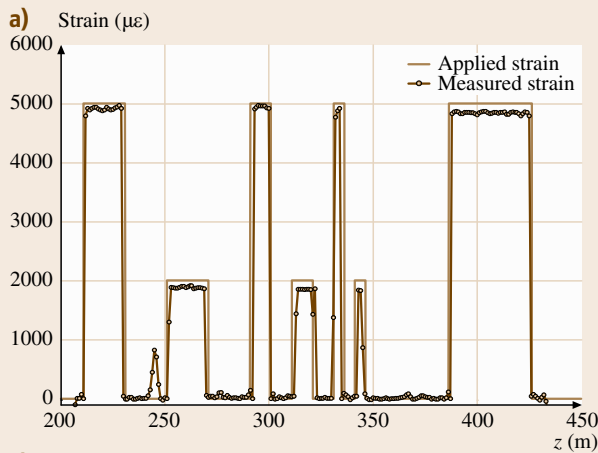


Fig. 16.93 (a) Distributed strain profile measured on a single-mode silica fiber using BOFDA (after [16.83]); (b) Geotextile with embedded glass fiber cables manufactured by STFI, Germany; (c) Detection of soil displacement (induced strain) in a test dike using a BOFDA system (after [16.83]); (d) Creep behaviour of a slope at a coal pit measured with a POF sensor-equipped geogrid (after [16.84])

and the capability of POF of measuring strain of more than 40%. Especially the monitoring of relative small areas with an expected high mechanical deformation such as endangered slopes takes advantage of the outstanding mechanical properties of POF. The monitoring of slopes is a very important task in the geotechnical engineering for prevention of landslide disasters. To overcome the limit of glass-fiber-based geotextiles novel distributed fiber optic sensors based on low-priced standard POF and using OTDR (optical time-domain reflectometry) were developed and embedded into geotextiles [16.85].

Figure 16.93d shows the result of a field application of a POF sensor-equipped geogrid at a coal pit. The 10 m long geogrid was installed directly on top of a creeping slope. It was covered with a 10 cm thick sand layer. The textile is installed with the POF sensor bridging the cleft perpendicular to the opening. Measurements were conducted before and after installation. Figure 16.93d shows a relative linear increase of the POF length with time. The measurements indicate that the creep velocity of the slope was constant during the time of observation with an average rate of about 2 mm per day [16.84].

16.6.3 Piezoelectric Sensing Techniques

Basics

The origin of the *piezoelectric effect* is related to an asymmetry in the unit cell of the crystal and the resultant generation of electric dipoles due to mechanical distortion. However, it was not until 1946 that scientists discovered that barium titanate (BaTiO_3) ceramics could be made piezoelectric by application of an electric field. The polycrystalline ceramic materials have several advantages over single crystals, such as higher sensitivity and ease of fabrication into a variety of shapes and sizes. In contrast, single crystals must be cut along certain crystallographic directions, limiting the possible number of geometrical shapes. After the BaTiO_3 ceramics, scientists discovered a number of *piezoceramics* and in particular the lead zirconate titanate (PZT) class in 1956. With its increased sensitivity and higher operating temperature, PZTs soon replaced BaTiO_3 and are still the most widely used piezoceramics. In the sixties, new varieties of piezoelectrics were developed based on both ceramics and polymers. Piezoelectrics are available in different forms, such as film, powder, paint, multilayered or single fiber. They are available in several types, such as polyvinylidene fluoride (PVDF) lanthanide-modified piezoceramic (PLZT) or the popu-

lar class of lead zirconate titanate piezoceramics. This list is not complete, because the composition of the piezoelectric materials allows a large variety of piezoelectrics, and new piezoelectric classes are expected to be developed in the near future [16.86]. The properties of piezoceramics have attracted a large group of industries such as the aerospace and automotive industries.

The piezoceramics offer a large selection of materials with different electromechanical properties [16.87]. The common electromechanical properties are the coupling factor, piezoelectric charge constant, piezoelectric voltage constant, mechanical quality factor, dielectric loss and relative dielectric constant. The *coupling factor* is defined as the ratio of the mechanical energy stored to the electrical energy applied, at a given frequency or frequency range. It could also be defined as the ratio of the electrical energy stored to the mechanical energy applied. The coupling factor characterizes the coupling between the electrical and mechanical properties of the piezoceramic. The *piezoelectric constant* d also called the charge constant, is the ratio of the electric charge generated per unit area to an applied force. It can also be defined as the ratio of the strain developed by the applied electric field. Another piezoelectric constant exists, called the voltage constant, which is derived from the charge constant. The piezoelectric voltage constant g is the ratio of the strain developed to the charge applied or the electric field developed to the mechanical stress applied. The *mechanical quality factor* is the ratio of the reactance to the resistance in the series equivalent circuit (RS, CS) identifying a piezoelectric resonator. The relative dielectric constant, also called the relative permittivity, is defined as the ratio of the material dielectric constant ϵ to the free-space dielectric constant ϵ_0 . The dielectric loss, also known as loss tangent in the literature, is defined as the ratio of the imaginary component of the complex dielectric to its real component.

However, the most important electromechanical properties are the coupling factor and the piezoelectric constants. A high coupling factor gives a greater sensitivity to the piezoceramic in converting the Lamb waves into an electrical signal. A high piezoelectric charge constant is desirable for materials intended to generate ultrasonic waves such as Lamb waves, because for an applied electric field, or excitation signal, a large developed strain is necessary to propagate over a long distance.

Other nonelectromechanical parameters also exist and play a large role in the selection of the PZT; the most important are the mechanical elastic constants, the

Curie temperature and thermal coefficients of expansion. The value of the elastic constants needs to be as low as possible to reduce the local stress inside the PZT as well as in its vicinity. The Curie temperature is the temperature at which the piezoceramic loses its piezoelectric properties. The Curie temperature has to be as high as possible to allow a large working-temperature range and must be higher than the curing temperature of the composite laminate to prevent the loss of piezoelectric properties. Typically, the working temperature has to be 100 °C lower than the Curie temperature. The thermal coefficients of expansion have to be similar to those of the composite to reduce the stresses in the transducer and the composite.

Four main piezoceramic materials are commercially available; lead zirconate titanate, modified lead titanate, lead metaniobate and bismuth titanate. For transducers used in damage detection as well as sensitive detectors and actuators, the class of PZT is considered to be a suitable material because of its high coupling factor, high charge constant, high Curie temperature, low mechanical quality factor and thermal coefficients similar to those of composites. The dimension of the embedded piezoceramic element has a direct influence on the way the PZT works, that is, the functioning characteristics of the PZT. Some PZT coefficients, such as the coupling factor, the relative dielectric constant or the mechanical quality factor, are dependent on the PZT dimensions. Moreover, the piezoceramic dimensions are chosen by analytical methods based on the properties of wave propagation in the composite.

Embedment Techniques

Two principle configurations with embedded piezoceramic transducers are described in the literature. The technique concerns how to embed the PZT transducer in the composite. Some researchers have chosen to cut the composite plies surrounding the embedded piezoceramic transducer, as done by *Elspass et al.*, *Hagood et al.* [16.88, 89], *Moulin et al.* or *Luis and Crawley* [16.90–92]. Other researchers directly embedded the PZT transducers to avoid cutting the fibers, as done by *Bourasseau et al.*, *Neary et al.* or *Shen et al.* [16.93–95].

Elspass et al. manufactured a piezoceramic transducer to be embedded in carbon-fiber-reinforced thermoplastic composites [16.90]. The material in the interconnectors was the same as the composite. The two interconnectors were placed on each side of the piezoceramic element. The electrical insulation from the upper and lower interconnectors was achieved by two glass-fiber-reinforced thermoplastics, as shown in Fig. 16.94.

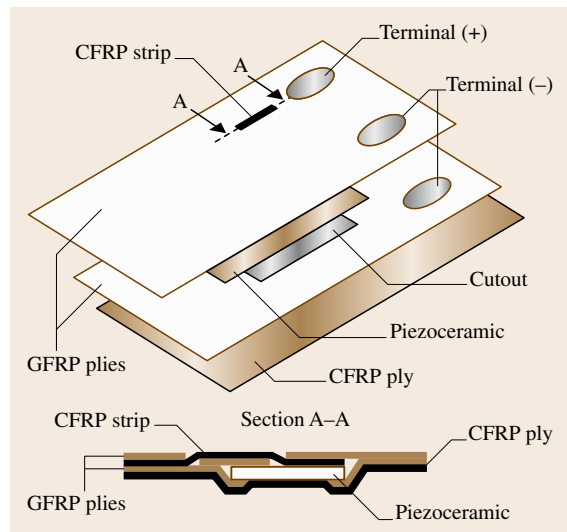


Fig. 16.94 Piezoceramic element embedded in a carbon-fiber-reinforced thermoplastic composite

Cutouts in the glass- and carbon-fiber-reinforced thermoplastic were performed to allow electrical contact between the terminals and the embedded piezoceramic element. The manufacture of such a lay out was complex.

Hagood et al., similar to *Elspass et al.*, used a cut-out technique to embed piezoceramic transducers in glass-fiber-reinforced polymer (GFRP) laminates. A cut-out window had about the same dimension as the PZT element. Slits were also cut in the plies directly above and below the piezoceramic element to allow the connectors to be drawn out to the edges, as shown in Fig. 16.95. The connectors were wires that were soldered to the faces of the piezoceramic element. *Hagood* also embedded the piezoceramic element in conducting material, such as carbon-fiber-reinforced polymer (CFRP). To electrically insulate the piezoceramic transducer from the surrounding material, a polyamide layer was often used to encapsulate both the piezoceramic element and the connectors, as shown in Fig. 16.96.

A research group of Stanford University developed a commercial transducer called the Stanford multi-actuator receiver transduction layer (SMART Layer). The SMART Layer was similar to the transducers used by *Mall and Hsu* [16.96]. The transducer SMART Layer could be customized in a variety of sizes, shapes and complexity, allowing its embedment in many composite structures, such as pressure vessels, pipes or wings, as shown in Fig. 16.97. The PZT elements were PKI-

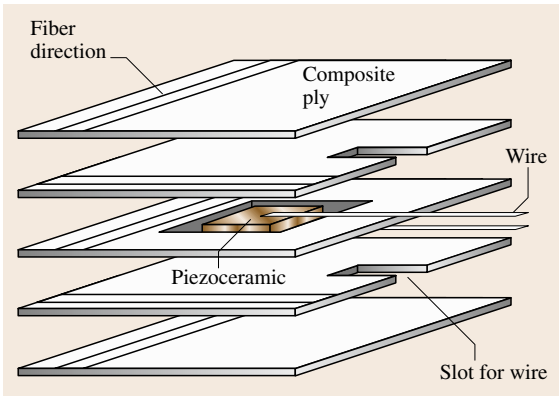


Fig. 16.95 Piezoceramic element embedded in a glass/epoxy laminate

400, with a thickness of 254 μm . The connector was made of a copper layer bonded on a polyamide film. The connector was shaped to provide a perfect fit to be embedded in the composite. The conductive adhesive linking the PZT element to the connector was probably a silver/epoxy compound. The transducer could withstand over 200 $^{\circ}\text{C}$, required for embedment in aerospace composite structures.

Damage Detection Using Lamb Wave Response

Lamb waves are sensitive to damage in the composite, resulting in changes in the Lamb wave response. The interaction between damage and Lamb waves is complex and difficult to predict. Two different approaches to research on Lamb waves for damage detection have been seen in the literature. There are research groups that try to simplify Lamb wave generation, and others that directly postprocess the Lamb wave response without simplification in the Lamb wave generation. To generate simple Lamb waves, researchers use wedged PZT to create an incidence angle between the PZT and the composite plate, which allows the generation of specific Lamb wave modes. In the case of this thesis, the piezoceramic transducers were embedded in the composites, which excluded the use of wedges with the transducers. Nevertheless, it is still possible to improve the generation of Lamb waves by means of PZT size optimization or simplify them by using arrays of embedded transducer. The latter has so far only been done on surface-bonded PZT transducers. This section deals then with postprocessing techniques that are used to track damage information in the Lamb wave response.

In 1885, the English scientist *Lord Rayleigh* demonstrated theoretically that waves can be propagated along

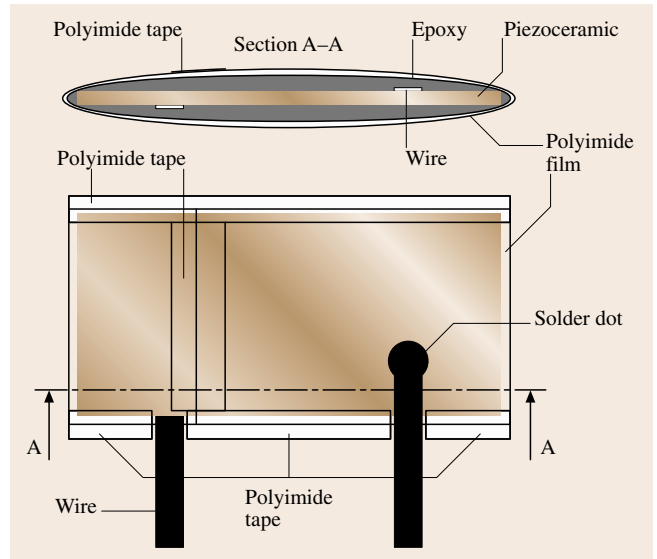


Fig. 16.96 Insulation of a piezoceramic transducer

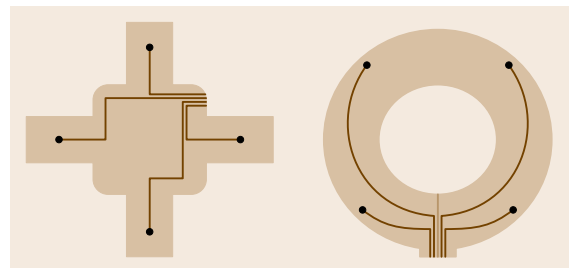


Fig. 16.97 Piezoceramic transducer network for embedment in composite plates (*left*) and pressure vessels (*right*)

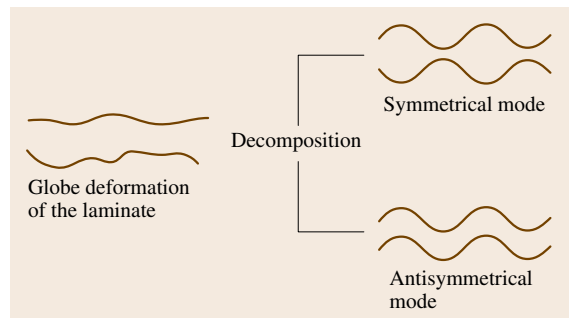


Fig. 16.98 Decomposition in symmetric and antisymmetric modes

the boundary of an elastic half-space and vacuum or sufficient rarefied medium (for example air). It was only in 1914 that *Stoneley* generalized the propagation of waves in two different solids. In 1917, *Lamb* in-

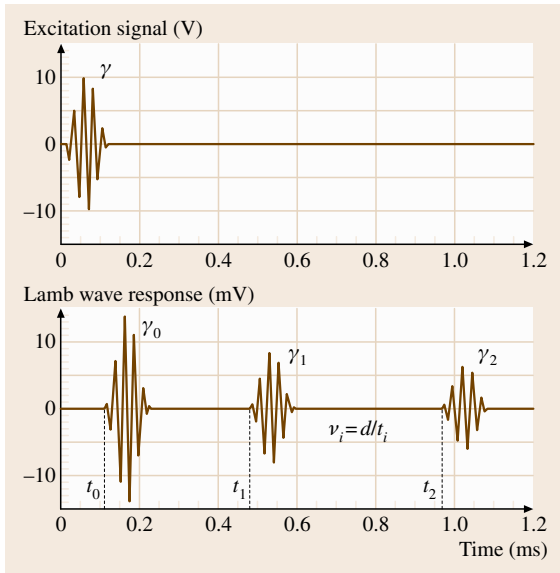


Fig. 16.99 Example of an excitation signal (*upper*) and a multimode response

roduced a third solid defined as a thin layer of finite thickness. This allowed the study of wave propagation in multilayered materials, such as in composites. The waves propagating in this multilayered material were then called Lamb waves. The term Lamb waves refer to elastic waves propagating in a solid plate with free boundaries. The displacements of the Lamb waves occur both in the direction of the wave propagation and perpendicularly to the plane of the plate. A comprehensive description of physical the-

ory and application of Lamb waves can be found in [16.97].

Lamb waves consist of several waves γ_i of the same waveform γ that propagate with different propagation velocities v_i called the group velocities. The waveform is often called a mode. Each Lamb wave mode can propagate symmetrically or antisymmetrically within the laminate, as shown in Fig. 16.98.

The amplitude of γ_i depends on the composite used. Up to now no theory exists that can exactly predict the amplitude of the Lamb waves. Figure 16.99 shows an example of multimode signal containing three modes [16.97]. The time t_i is the time of flight of the Lamb wave mode γ_i . In the present case, the Lamb wave generator and receiver are separated by a distance d . The response given in Fig. 16.98 does not correspond in detail to Lamb waves, because a real Lamb wave response would be too complex for the educational purpose of this section.

Indeed, a Lamb wave response would include not only the Lamb wave modes but also their reflections, which do not exist in the multimode response of Fig. 16.99. Besides, it is possible that at the excitation frequency, some Lamb wave modes might be dispersive, meaning that their corresponding waveform may not be similar to the waveform of the excitation signal. The group velocity v_i of the mode γ_i is given by

$$v_i = \frac{d}{t_i} \tag{16.37}$$

However, the number of waveforms, or modes, propagating in a laminate as well as their time of flight can be predicted by the dispersion curves. Two types of dispersion curves are mostly used for the Lamb wave technique: the phase velocity c and group velocity v , as shown in Figs. 16.100 and 16.101, respectively. The phase velocity corresponds to the ratio of the spatial component, i.e. the wavenumber ξ , to the temporal component, i.e. that is the angular frequency $\omega = 2\pi f$, of a harmonic wave. The group velocity may be described as the energy velocity of the Lamb wave modes in relation to the laminate. The phase-velocity curves are mainly used to determine whether or not the Lamb wave modes will be dispersive, and also to obtain the wavelength λ of each Lamb wave mode generated in the laminate, using the following relationship

$$\lambda = c/f, \tag{16.38}$$

where f is the frequency spectrum of all Lamb wave modes generated in the laminate. To find out if a Lamb

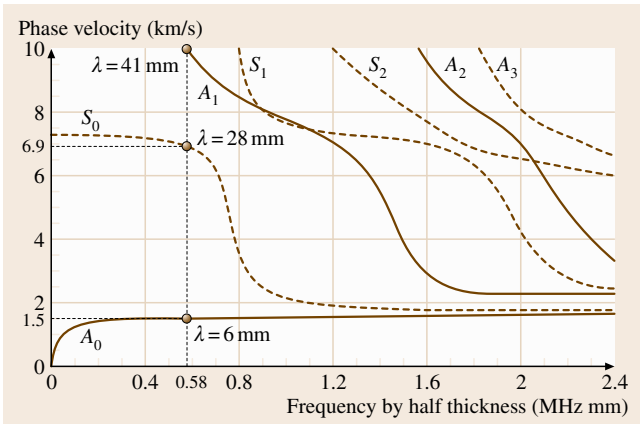


Fig. 16.100 Phase velocity for the cross-ply laminate $[0_4/90_4/0_4/90_4/0_2]_s$

wave mode is dispersive or not, the derivative of the phase velocity is used. If, at a given excitation frequency, the derivative of the phase velocity is zero, then the Lamb wave modes should be nondispersive. Most of the time, nondispersive Lamb waves are chosen, because their corresponding waveforms generally remain the same throughout the propagation. Moreover, the phase and group velocities of a nondispersive wave are theoretically identical. Indeed, both velocities are governed by the following equation

$$\frac{1}{v} = \frac{1}{c} \left(1 - f \frac{dc}{df} \right). \quad (16.39)$$

For a nondispersive wave $\frac{dc}{df} = 0$ and therefore (16.39) leads to $v = c$.

The wavelength of each Lamb wave mode is directly related to the sensitivity of the Lamb waves to the detection of damage. In principle a Lamb wave of wavelength λ is able to interact with damage on the order of or greater than λ . The dispersion curves depend on the composite material and lay out used. Often the dispersion curves are given as a function of the product fh (frequency by half laminate thickness). Two examples of dispersion curves are given in Figs. 16.100 and 16.101, for a stacking sequence of $[0_4/90_4/0_4/90_4/0_2]_s$ and the composite material HTA/6376C. In the figures, S and A stand for symmetric and antisymmetric modes, respectively, and the subscript corresponds to the mode number.

The dispersion curves are important for characterizing the active system that detects damage in the composite [16.98]. The frequency spectrum of all Lamb wave modes is, in principle, equal to the frequency spectrum f of the excitation signal of the Lamb wave generator. In the example shown in Fig. 16.101, the frequency of the excitation signal is 240 kHz for a composite thickness of 4.83 mm. Figure 16.101 therefore shows that the only Lamb wave modes that can exist in

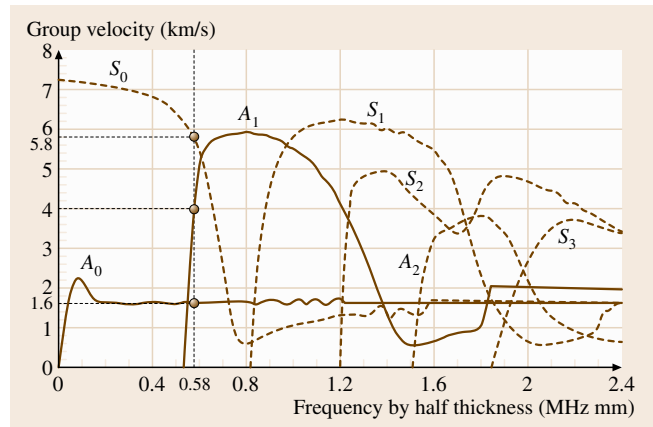


Fig. 16.101 Group velocity of Lamb waves propagating in the laminate $[0_4/90_4/0_4/90_4/0_2]_s$

this composite would be the modes A_0 , S_0 and A_1 with group velocities of 1.6 km/s, 5.8 km/s and 4 km/s, respectively. Figure 16.100 further allows determination of the wavelengths of those modes A_0 , S_0 and A_1 , which are about 6, 28 and 41 mm, respectively. In such an example, the mode A_0 would be able to detect damage of at least 6 mm or larger, with the condition that its amplitude is large enough for the mode to be measured. Note that for higher frequencies, the wavelength of the mode A_0 , for example, is smaller than 6 mm. This would therefore allow the detection of damage smaller than 6 mm. Unfortunately, the propagation distance of the Lamb wave modes tends to decrease with increasing frequency.

Several developments have occurred in this area since the technique was first reported, which have led to new possibilities and advances in the capabilities of structural health monitoring [16.99, 100]. Special focus has been given to the monitoring of composites for aircraft applications [16.101].

16.7 Characterization of Reliability

Reliability is a statement of whether or not a device fulfills its function after a certain time of operation. The scientific definition of reliability reads as follows [16.102]: *Reliability is the probability that an item will perform a required function without failure under stated conditions for a stated period of time.*

As the lifetime of a device *scatters*, reliability is a quantity that can only be described by means of

statistic tools, which will be introduced briefly in the first Sect. 16.7.1. Additionally, we will show that the scatter in lifetime originates from the scatter of both the strength of the device and the scatter of the stresses to which it is exposed. Both can be described by distribution functions, and the region of interference of both distributions will be shown to be a measure for the failure probability.

In Sect. 16.7.2, the Weibull analysis will be introduced, as it has become the major tool in science and industry to analyze failure data. Due to the importance of this issue, this section is the longest in this chapter.

Section 16.7.3 will show different test strategies. Those address the basic problem of how to characterize reliability with a small number of sample devices with the smallest possible time effort.

A similar question is addressed in Sect. 16.7.4, introducing the important acceleration techniques. The basic idea is to apply higher stresses to the device than under real-life conditions to provoke failures. By means of physical models describing the degradation process, the lifetime under real conditions can be estimated.

In the last Sect. 16.7.5, quantitative reliability estimation for complex systems will briefly be discussed. The failure behavior of a complex system consisting of single components can be calculated from the component reliabilities. Here, we restrict discussion to the simple case where the system solely consists of components with serial and parallel functionality.

In this chapter, special emphasis will be placed on the following

- enabling the reader to become familiar quickly with the basic concepts of reliability
- restricting discussion to the main tools presently used in science and industry.

For further reading, key literature is given. To completely understand this material it is inevitable that more-sophisticated literature, which deals with special topics in more depth than is possible here, will have to be consulted.

There are some standard textbooks available that introduce the basic concepts. Some of them have handbook character and are designed for daily use in practice [16.102–106]. Others emphasize the mathematical background and statistical tools [16.107].

Also there are several websites available dealing with reliability. Some of these websites, e.g. [16.108, 109], offer excellent tutorials and introductions to reliability. Further websites are found in the survey paper [16.110].

The Bathtub Curve

In order to describe the time dependence of a device's failure behavior, a reliability parameter called the failure rate $\lambda(t)$ rate is used. Simply speaking, this describes the (average) number of failures per time unit. An exact definition will be given in the next section.

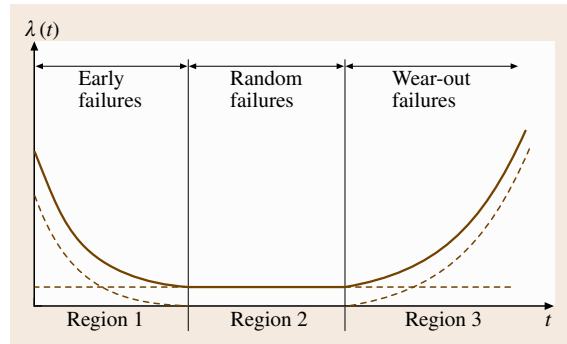


Fig. 16.102 The typical bathtub curve (*thick line*), as a superimposition of the three failure rates belonging to independent failure mechanisms dominating in the regions 1–3 (*dashed lines*)

In most cases, if $\lambda(t)$ is plotted against time, a typical bathtub shaped curve is observed (Fig. 16.102) [16.102, 111].

The bathtub curve is categorized into three regions.

- Region 1 exhibits a falling failure rate and covers the so-called *early failures* (*infant mortality*). The origin of those failures in most cases is not related to material properties, but rather to the quality of the manufacturing process of the whole device.
- Region 2 is characterized by a constant failure rate and covers *random failures* that are not governed by a single failure mechanism. In this region, the device fails due to miscellaneous interactions with its environment, e.g. peak-like overloads, misuse, high temperatures and others.
- Region 3 is the region where material-related failures start to dominate. Therefore, the somewhat imprecise phrase *wear-out failures* is commonly used for this phase. The failure modes in this region are often initiated by detrimental changes of the devices' material components, caused by the service loads applied to the device. The mechanisms leading to failures are called *degradation mechanisms*. Those mechanisms lead to a strong increase of the failure rate with time. Typical degradation mechanisms are mechanical fatigue (Chap. 7), corrosion (Chap. 12), wear (Chap. 13), biogenic impact (Chap. 14), and material–environment interactions (Chap. 15).

A very important statement is that the Weibull analysis (Sect. 16.7.2) enables us to judge to which category the investigated product belongs using the failure data analysis.

16.7.1 Statistical Treatment of Reliability

Since reliability is defined as a statistical quantity, statistical tools are needed to describe it. In the following section, the origin of the statistical scatter will be described by means of static and dynamic stress–strength interference models. In the following section, reliability functions and reliability parameters describing the time-dependent failure behavior are introduced.

Reliability Functions

For a given time value t , $F(t)$ describes the probability for the event that the device will fail within the time interval between 0 and t .

To describe this quantitatively, we introduce the *lifetime* L of the device. L may be given in unit of time, cycle number, or any other quantity related to the life of the device. Then the failure probability $F(t)$ is defined as the probability P that L is smaller than or equal the observation time:

$$F(t) = P(L \leq t). \quad (16.40)$$

$F(t)$ may also be written as integral over its *failure density* $f(t)$

$$F(t) = \int_0^t f(t') dt'. \quad (16.41)$$

The failure density function has practical meaning, since distribution functions are commonly given in this expression. As an example, the well known bell-shaped curve is the *density function* of the Gaussian normal distribution, but not the distribution function itself.

Given the failure probability, the probability of survival is expressed as its complement $R(t)$. $R(t)$ is called the *reliability function*, or simply the *reliability*

$$R(t) = 1 - F(t) = 1 - P(L \leq t) = P(L > t). \quad (16.42)$$

The failure rate, which was introduced earlier in a qualitative manner, can now be defined precisely as

$$\lambda(t) = \frac{f(t)}{R(t)} \quad (16.43)$$

and describes the probability that the device survives until $t + dt$ under the condition that it already survived until t .

Figure 16.103 presents all these functions within one schematic diagram.

Stress–Strength Interference

The time dependence of the failure probability originates from both the interaction of the statistical scatter of the applied *stress* and the statistical scatter of material properties determining the macroscopic *strength* (Sect. 7.3) of the component under load [16.112]. In this context, *stress* means any physical process acting on the device, for example mechanical stress, voltage, temperature or humidity. *Strength*, on the other hand, means the ability of the device to withstand the stress. Both quantities have the same physical dimension and are here – in accordance to mechanical stress and strength – generally described by σ .

- The *strength* σ_S ($S = strength$) scatters due to scatters of manufacturing quality and due to scatters of the material properties.
- The *stress* σ_L ($L = load$) scatters due to different users and due to varying use conditions.

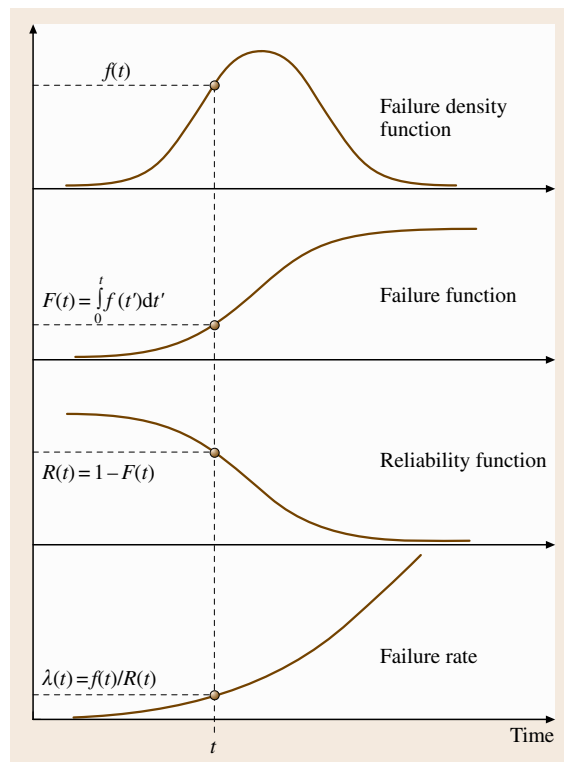


Fig. 16.103 Schematic drawing of all four relevant functions discussed in Sect. 16.7.1. In particular, the relation between the failure density function and the other functions is shown

Failure takes place as soon as the stress exceeds the strength. The failure probability is therefore dependent on the probability that a randomly chosen stress condition exceeds the strength of a randomly chosen device. This probability is dependent on the overlap of the distribution functions, as illustrated in Fig. 16.104a showing the so-called *static stress–strength interference*.

The area under both curves is calculated as [16.112]

$$F = P(\sigma_L > \sigma_S) = \int_{-\infty}^{\infty} f_L(\sigma) \left[\int_{-\infty}^{\sigma} f_S(\sigma) d\sigma \right] d\sigma \tag{16.44}$$

where f_L and f_S are the density functions of the distributions of the stress and the strength, respectively.

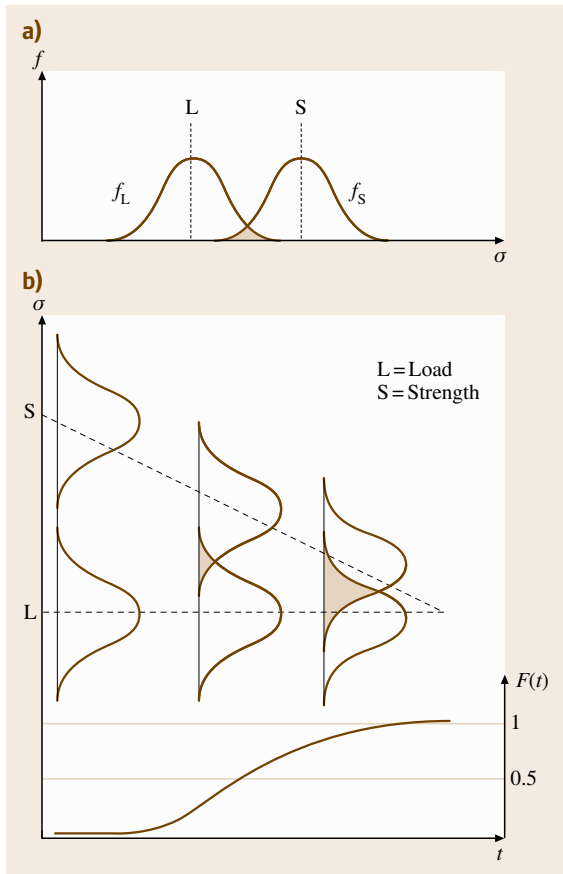


Fig. 16.104 (a) Static, and (b) dynamic interference model. The failure probability of a device depends on the area under the distribution densities for stress and strength (after [16.102, 113])

The same argumentation holds for the *dynamic interference model* (Fig. 16.104b). Here, the failure probability is zero at $t = 0$ since the overlap of both distribution functions is negligible. Then, during the time of operation, microstructural changes within the material reduce the mean value of the strength and so F increases significantly with increasing operation time.

The interference model has the great advantage that it describes the probabilistic origin of time-dependent failure probabilities in a plausible manner. However, it is not suitable for determining the reliability of a device quantitatively, because the application of (16.44) requires the exact knowledge of the distribution functions of stress and strength near their tails. This demand is usually improperly fulfilled in practice.

16.7.2 Weibull Analysis

One of the main topics in reliability engineering is to analyze a given set of failure data. These data may originate from a reliability test performed in the lab or from a warranty analysis of field data. The Weibull analysis makes use of the famous and widely used Weibull distribution, and has become the major tool in modern industry. Many publications document the importance of this tool [16.104]. It should be mentioned that there exist other distributions which are also important. Especially in the case of degradation and fatigue strength phenomena, the lognormal distribution is important [16.114, 115]. In [16.116], the author compared the pros and cons of both distributions for the analysis of wear-out (region 3 of the bathtub curve) failure data.

The Weibull Distribution Function

The Weibull distribution is a multipurpose distribution, which by varying the independent parameters, can be adjusted to almost every failure behavior. The failure function $F(t)$ and the failure density function $f(t)$ of the Weibull distribution read as follows [16.104, 117]

$$F(t) = 1 - e^{-\left(\frac{t}{\eta}\right)^\beta}, \tag{16.45}$$

$$f(t) = \frac{\beta}{\eta} \left(\frac{t}{\eta}\right)^{\beta-1} e^{-\left(\frac{t}{\eta}\right)^\beta}. \tag{16.46}$$

The reliability function $R(t) = 1 - F(t)$ is given by

$$R(t) = e^{-\left(\frac{t}{\eta}\right)^\beta}. \tag{16.47}$$

The Weibull distribution has the following parameters.

- The shape parameter β (also called the Weibull parameter or slope),
- The characteristic life η .

(An additional parameter, the failure free time, will be introduced later in this section.)

The most important parameter is the shape parameter β , since the distribution can be adapted to the given failure phenomenon by varying β . In Fig. 16.105, the density function and the failure function are plotted for constant η and different β , showing that the characteristics are different for different β .

A very important result is that the value of the shape parameter corresponds to the three regions of the bathtub curves as follows (Fig. 16.102).

1. $\beta < 1$ – corresponds to region 1 of the bathtub curve, since $\beta < 1$ results in a decreasing function in the failure rate plot.
2. $\beta = 1$ – corresponds to region 2 of the bathtub curve, since $\beta = 1$ results in a horizontal line in the failure rate plot. For $\beta = 1$, the Weibull distribution becomes an *exponential distribution function*, which is an important special case. The fact that the failure probability is independent of time is represented in the term *memory loss*. As an example, electronic devices often show such a time-independent failure behavior.
3. $\beta > 1$ – corresponds to region 3 of the bathtub curve, since $\beta > 1$ results in an increasing failure rate function. For $\beta > 1$, the density function exhibits a maximum value, and for $\beta \approx 3$ it is similar to the Gaussian bell-shaped curve (compare Fig. 16.105).

Weibull Analysis Procedure

In the previous section, we outlined the importance of determining the Weibull parameters in order to categorize the failure phenomena. In this section, it will be described how the parameters η and β are determined from a given set of failure data.

Two common methods for Weibull analysis are known. The first one is the so-called median rank regression (MRR), the other one is maximum-likelihood estimation (MLE).

The latter is a numerical method that needs intensive computation, while the first one is more instructive and often used. Therefore, we will restrict the discussion to the MRR here.

The median rank Weibull analysis MRR contains the following steps.

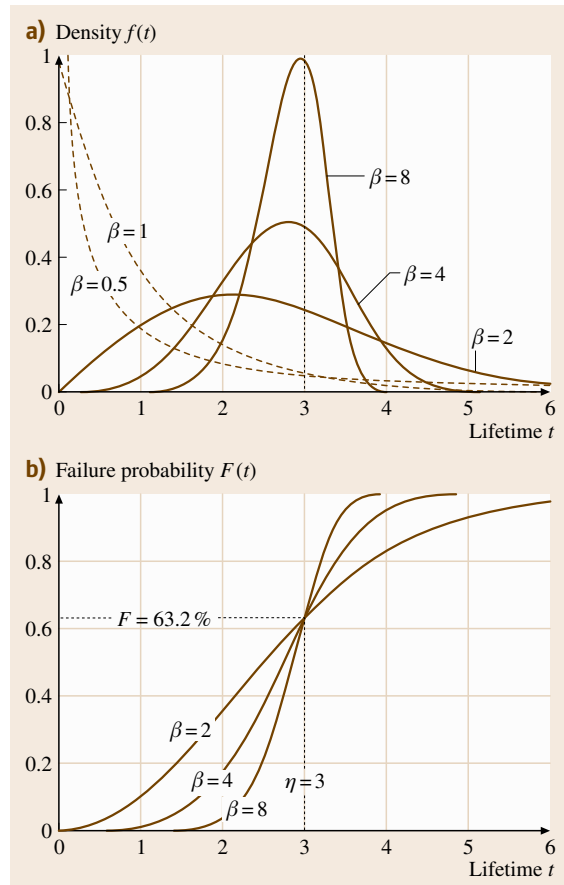


Fig. 16.105 Weibull density function (a) and failure probability (b) for different β and $\eta = 3$. From the density function plot, we see that a *bell-shaped curve* is only reached for $\beta > 1$. In the case $\beta < 1$, no local extrema are present. From the probability plot, we see the peculiarity that the characteristic life is independent of β

Step 1: Collecting Lifetime Data. n samples are tested, yielding n lifetimes L_1, L_2, \dots, L_n . The lifetimes L_i of the specimen are arranged in ascending order in a table (Table 16.10).

Step 2: Median Rank Calculation. This is the procedure that is characteristic of this method. The basic idea is that each sample is assigned a failure probability $F(L_i)$. This is necessary, since from the experiment we only know the lifetime data L_i but not the corresponding failure probabilities. This probability cannot be determined experimentally, but must be found from theoretical considerations. The understanding of its derivation is not

essential for proceeding; however, the interested reader may find it in [16.103]. At this point, one hint is helpful: The failure probability $F(L_i)$ itself follows a statistical distribution known as the binomial distribution. Since the binomial distribution cannot be rearranged such that $F(L_i)$ can be calculated directly, some approximation must be introduced.

In the literature, a vast amount of different methods for approximating the failure probability is known, but the formula for median ranks introduced by Bernard [16.102, 103] has turned out to be the most often used. This formula reads

$$F_{50\%}(L_i) \approx \frac{i - 0.3}{n + 0.4} \tag{16.48}$$

The index 50% indicates that the median of the failure probability distribution is meant.

Instead of calculating the values using (16.48), they can also be looked up in tables for median ranks [16.102].

An excerpt of such a table is given in the appendix to this chapter for different sample sizes up to $n = 12$.

Step 3: Probability Plotting. The probabilities of failure are plotted against the lifetime or number of survived cycles on so-called Weibull paper, what can be seen in Fig. 16.106 for the example $n = 8$. Weibull paper is commercially available, or can be constructed by the method described in [16.116]. If the data points obey the Weibull distribution, then they yield a straight line with little scatter of the data points. The straight line is also plotted on the Weibull paper, and will serve to determine the parameters β and η .

Step 4: Linear Regression. Equation (16.45) is rearranged as follows by taking the double logarithm of both sides of the equation:

$$\begin{aligned} F(L_i) = 1 - \exp(L_i/\eta)^\beta &\Rightarrow 1 - F(L_i) = \exp(L_i/\eta)^\beta \\ &\Rightarrow \ln\{-\ln[1 - F(L_i)]\} = \beta \ln(L_i) - \beta \ln \eta \end{aligned} \tag{16.49}$$

With the general linear equation $y = Ax + B$ we can now identify

$$y_i = \ln\{-\ln[1 - F(L_i)]\}; \quad x_i = \ln L_i \tag{16.50}$$

and

$$A = \beta; \quad B = -\beta \ln \eta \tag{16.51}$$

These equations allow the determination of the goodness of fit and the Weibull parameters β and η , which is described in the following.

Step 5: Estimation of the Goodness of Fit: the Correlation Coefficient (CC). In the case of a Weibull-distributed basic population, a straight line is produced in the Weibull plot. If the data do not obey a linear behavior, the basic population may not be Weibull distributed. As a measure for the linearity of the data, the correlation coefficient (CC), which is well known from standard statistic tools [16.118, 119], is commonly used. The CC is defined as

$$CC = \frac{\sigma_{xy}}{\sigma_x \sigma_y} \tag{16.52}$$

where σ_{xy} is the covariance and σ_x and σ_y are the standard deviations of the x_i and y_i , respectively.

By calculating x_i and y_i from the values $F(L_i)$ and L_i in Table 16.10 by means of (16.50), we can apply the CC to the obtained data pairs. CC takes a value between 0 and 1, and the higher CC, the better is the fit.

Two problems arise when applying CC.

- It is left to the judgement of the user to decide what correlation coefficient means a good or a poor fit.

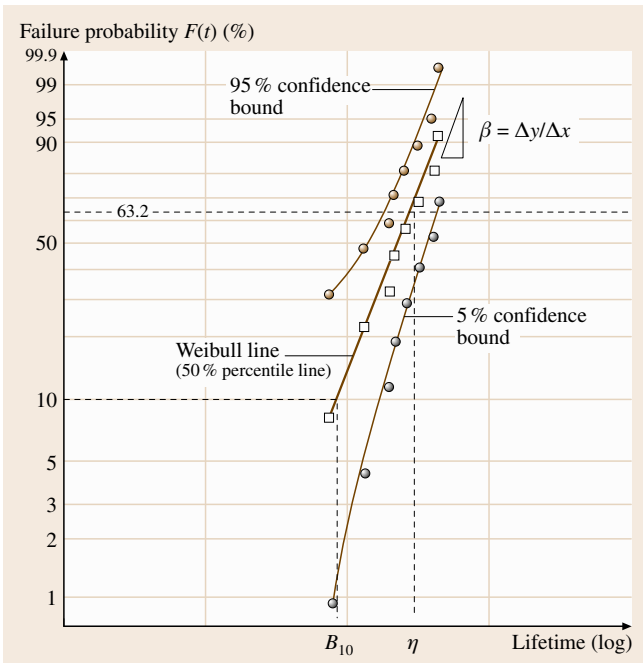


Fig. 16.106 Schematic drawing of a Weibull plot. The square data points show the measured lifetimes and the corresponding median ranks $F(L_i)$. The darker circles represent the 5% and 95% confidence bounds. The Weibull parameter β is estimated from the slope of the weibull line, the characteristic life is estimated from the intersection of the regression Weibull line with the 63.2% line. Additionally, we find the so-called B_{10} life as the lifetime where $F = 10\%$ is reached

Table 16.10 Measured lifetime data L_i and median failure probabilities $F_{50\%}(L_i)$, as well as the $F_{5\%}$ and $F_{95\%}$ -percentiles needed for the confidence bound, which is introduced in Step 7

Sample # i	Lifetime L_i	$F_{50\%}(L_i)$ = ((16.48) or Appendix)	$F_{95\%}$ (Appendix)	$F_{5\%}$ (Appendix)
1	L_1	8.3	31.2	0.6
2	L_2	20.1	47.1	4.6
3	L_3	32.1	59.9	11.1
4	L_4	44	71.7	19.3
5	L_5	55.9	80.7	28.9
6	L_6	67.9	88.9	40
7	L_7	79.8	95.4	52.9
8	L_8	91.7	99.4	68.8

A possible approach to overcome this problem is shown in [16.120].

- The regression of the y -values versus the x -values is somewhat unsatisfactory and overestimates the goodness of the fit because the y -values are predetermined by the rank calculation. In contrast, the measured lifetime values are in fact the values that show scatter. Therefore, *Abernethy* [16.104] recommends doing the regression of x versus y .

In standard mathematical calculation software, linear regression is a standard tool and the calculation of the correlation coefficient CC – sometimes also denoted by the symbol R – is also standard.

It should be mentioned that there are some other, more sophisticated and more accurate tests available such as the Chi-squared test and the tests by Kolmogorov–Smirnov and Mann–Scheuer–Fertig (see references in [16.116]), however, for daily practical application, CC appears to be the easiest and quickest method.

Step 6: Determination of η and β . From the linear regression performed in Step 4, η and β can easily be calculated by applying (16.51)

$$\beta = A; \quad \eta = \exp(-B/\beta). \quad (16.53)$$

The characteristic life can also be directly determined from the Weibull plot in Fig. 16.106. If we introduce $t = \eta$ in (16.45), we obtain $F(\eta) = 63.2\%$.

Therefore, the Weibull line crosses the $F = 63.2\%$ line at $t = \eta$. This is indicated in Fig. 16.106 by an arrow.

The slope β can be determined graphically only if a special, commercially available Weibull paper is used for the graphical analysis [16.108]. In addition to the paper used in Fig. 16.106, this paper has a second y -axis

where β can be found by a method described in [16.103] and [16.108].

Step 7: Introducing the Confidence Interval α . The confidence interval α is a very important parameter. The confidence bound is a demand given from the user of the Weibull analysis, representing his demands on the trustworthiness of the analysis.

In many practical cases, the confidence interval of $\alpha = 90\%$ is demanded. If $\alpha = 90\%$ holds, then the upper and lower confidence bounds are the 95% and 5% percentiles. Similar to the 50% percentiles, these values can be found in the tables given in Step 3. These values are added to the two columns $F_{5\%}$ and $F_{95\%}$ in the table. These values can then also be plotted in the Weibull graph (Fig. 16.106).

The meaning of the confidence bounds is as follows. To require a confidence level of, e.g., $\alpha = 90\%$, means that the probability that the true Weibull regression line lies within the confidence bounds is 90%. In Fig. 16.106 this demand can be found by noting that any Weibull line that is compatible with the confidence bounds is a possible solution to our problem.

To avoid frequent misunderstanding, it should be mentioned that the width of the confidence bound does *not* depend on the *scatter* of the measured lifetime data. The width of the confidence bound solely depends on the number of specimen tested. The larger n , the smaller the confidence bound becomes. This is logical, since the significance of the statistical argumentation becomes higher with increasing sample size.

Step 8: Estimation of the Confidence Bounds of β and η . Since the confidence bounds determined in Step 7 lead to more than one possible Weibull line, we also find a range of values for β and η which we need to determine. To do so, one possibility is to de-

termine the Weibull line with maximum and minimum slope still compatible with the confidence bounds (compare Fig. 16.106) and then determine β_{\max} , β_{\min} , η_{\max} , η_{\min} directly. Another possible method is to directly calculate these parameters as described in [16.103, 119].

Three-Parameter Weibull Analysis

There is an additional form of the Weibull distribution containing a third parameter, the so-called failure-free time t_0 . In the three-parameter form, the Weibull failure function and density function read

$$F(t) = 1 - e^{-\left(\frac{t-t_0}{\eta-t_0}\right)^\beta}, \quad (16.54)$$

$$f(t) = \frac{\beta}{\eta-t_0} \left(\frac{t-t_0}{\eta-t_0}\right)^{\beta-1} e^{-\left(\frac{t-t_0}{\eta-t_0}\right)^\beta}. \quad (16.55)$$

The failure-free time t_0 is a parameter that, in the case $\beta > 1$, serves to properly describe an *incubation period*, often observed in degradation experiments. Before t_0 no failure is observed. This behavior cannot be described with the same accuracy using the two-parameter Weibull distribution. This becomes necessary if the reliability of complex systems must be calculated from the reliability functions of the single components the system is made of. In [16.121] four criteria are given when the introduction of t_0 is indicated.

- There must be 20 or more failures,
- The physics of failure shall support the existence failure-free time,
- The two-parameter weibull plot shows curvature,
- The distribution analysis must favor the three-parameter form meaning that the correlation coefficient becomes larger when trying several $t_0 \neq 0$.

The failure-free time can be estimated by means of graphical methods from the Weibull plot. A simple and commonly used method is introduced by *Dubey* which described in detail in [16.103, 122]. So far, the theoretical justification and the method to determine the failure-free time was discussed. In Sect. 16.7.5, where system reliability issues are discussed, the relevance of the failure-free time t_0 to practical problems will be illustrated in more detail.

16.7.3 Reliability Test Strategies

So far, we have assumed that the failure data are already available and that all tested items have failed within the observation period. In this section, we will introduce several methodologies for how the data are created

either in practical reliability tests in the lab or from warranty data.

In practice we always have the constraint that the sample size as well as the testing time is limited, or that the data set obtained from a warranty analysis is incomplete.

Censored Tests

A censored test is a test where either not all items fail or where not all failures are taken into account for analysis. Censoring becomes necessary for the following reasons [16.108].

- Some failure modes that occur are different from those anticipated and such units are withdrawn from the test;
- We need to make an analysis of the available results before test completion (time constraints);
- A warranty analysis is to be made of all units in the field (nonfailed and failed units). The nonfailed units are considered to be suspended items.

Different types of censoring may occur in practice. Here we will restrict the discussion to the most important. Other types of data are presented in [16.123].

Figure 16.107 shows the following cases.

- a) Some items fail within the observation time (◆), some survive (→).
- b) Some items fail (◆), and some are removed from the test (●). We call these suspended items. A possible reason for suspension is that these items failed due to another failure mechanism than the one of interest.
- c) No item fails. This special case will be dealt with below.

In the following, we discuss how the data are analyzed in the given cases.

Case (a): Some Items Fail Within the Observation Time, Some Survive. In this case, the Weibull analysis is performed as described for complete tests in Sect. 16.7.2. Care must be taken that the n used here is the number of all items, that means, the failures and the survivors (in our example in Fig. 16.107, this means $n = 6$ and not $n = 3$).

This test has special practical meaning since field data are often of this type: a batch of devices has been delivered to customers. After a certain time, some failures are documented, and the rest of the items

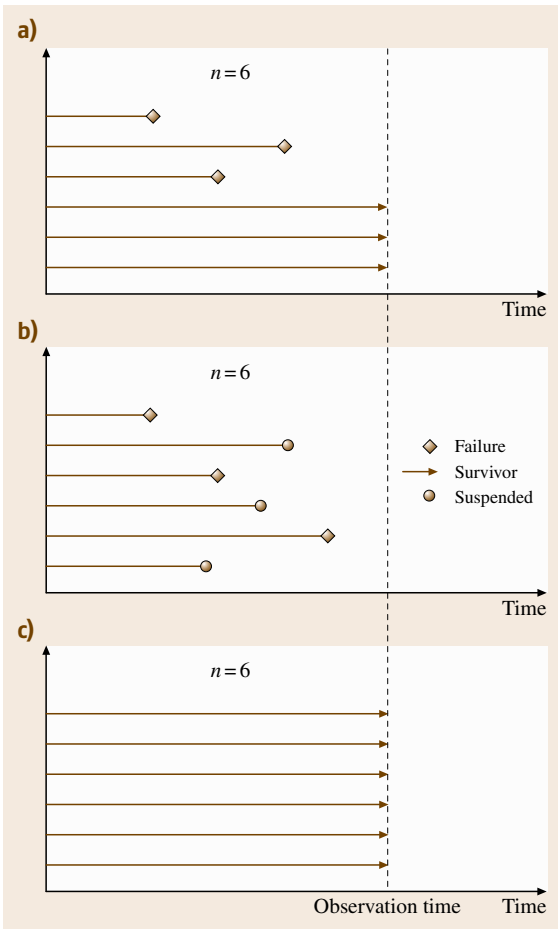


Fig. 16.107a–c Different events during a reliability tests during the testing period: (a) Some items fail (◆), some survive (→). (b) Some items fail (◆), others are suspended from the test (●). (c) All items pass the test (Sect. 16.7.3)

positions i must be adjusted because assigning the usual positions $i = 1 - n$ to each item, regardless of whether it is neglected in the analysis or not, is not appropriate. Instead, the procedure is the following [16.103]:

- Step 1: Collect data as usual, and assign it a capital F (= failed) or S (= suspended), and list the data in a table in ascending order (Table 16.11).
- Step 2: Calculate the rank positions for the failed items, and add them to the table. Suspended data are neglected. The new rank positions for the failed items are calculated using the following rule [16.124, 125]. This is necessary, because a suspended item causes an uncertainty at which rank position the suspended and the following item are located. We therefore need to calculate a mean rank position, which is no longer necessarily a natural number.

The rank of the j -th item i_j is calculated as the sum of the previous rank i_{j-1} and an increment y

$$i_j = i_{j-1} + y_j \tag{16.56}$$

with the increment y_j being

$$y_j = \frac{n + 1 - i_{j-1}}{1 + n_{>j}} \tag{16.57}$$

with n being the overall (not only the failed) sample size, and $n_{>j}$ being the remaining number of items with index being greater than the actual j .

- Step 3: Calculate the median ranks according to (16.57) and add them to the table.
- Step 4: Perform a Weibull analysis as described in Sect. 16.7.2.

is still in function. Those data can be analyzed as described.

Case (b): Some Items Fail, and Some Are Removed from the Test. The Weibull analysis of those data requires a technique that differs slightly from that presented above. In particular, the rank

Item # j	Lifetime L_j	Event F/S	Increment (4.14) y_i	Rank position (4.13) i	Median rank (4.1) F_i
1	L_1	F	1	1	0.109
2	L_2	F	1	2	0.263
3	L_3	S	1.25	-	-
4	L_4	F	1.25	3.25	0.461
5	L_5	S	1.875	-	-
$n = 6$	L_6	F	1.875	5.125	0.754

Table 16.11 Calculation of the adjusted rank positions if censored items are present (for this example, $n = 6$). By the arrows it is shown how the rank positions of failures following a suspension are calculated

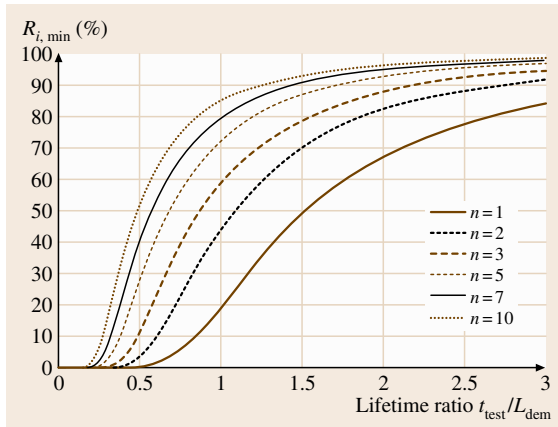


Fig. 16.108 Guaranteed least reliability $R_{i,\min}$ of a device tested in a success run as a function of the lifetime ratio and of the number of samples n . The figure indicates that with smaller sample number the testing time must increase in order to maintain the same reliability level. It is helpful in practice to know the rule of thumb that a reliability of 90% can be guaranteed when three test specimen survive 2–2.5× the demanded lifetime

Case (c) All Items Still in Function – Success Run. The success run has become one of the major tools in reliability engineering. This is because it combines the number of test specimen and the testing time. Additionally, the meaning of the confidence interval α for reliability estimation becomes most obvious in this kind of test.

The typical task is the following. We have to guarantee a minimum reliability $R_{i,\min}$ for a device at a given demanded lifetime L_{dem} . To do so, we have a limited number of specimens (e.g. $n = 3$) which we test for a time t_{test} .

If we assume the basic population to be Weibull distributed, then the formula for this test reads as follows:

$$R_{i,\min}(L_{\text{dem}}) = (1 - \alpha) \left[n \left(\frac{t_{\text{test}}}{L_{\text{dem}}} \right)^\beta \right]^{-1} \quad (16.58)$$

For the derivation of this expression see [16.105]. Its meaning is that, if n components survive a reliability test of duration $t_{\text{test}} > L_{\text{dem}}$, then we can guarantee a minimum reliability $R_{i,\min}$ of the device at the demanded lifetime L_{dem} at a confidence level of α .

In practice, it is often the case that a confidence level as well as the least guaranteed reliability at the demanded lifetime are given. From (16.56), we

can calculate the necessary number of specimen and the corresponding testing time which is necessary to confirm that the given reliability can be guaranteed. This important result is seen in Fig. 16.108 where the least guaranteed reliability is plotted as a function of the so-called lifetime ratio $t_{\text{test}}/L_{\text{dem}}$ and the sample number.

The main drawback of the test is that the Weibull parameter β must be known in advance. It cannot be determined using this method. It must be known from experience, similar studies or from tests under simplified conditions.

Degradation Tests

Degradation testing is a rather new method that has recently attracted many researchers [16.126, 127]. This kind of testing is possible if there is a parameter that can be measured during the operating time of the device and which indicates the degradation process. The plotting of the parameter versus the lifetime describes the so-called degradation path. As an example, the abrasion of a car tyre can be measured during a test and plotted versus the driven kilometers. From the data points we can extrapolate to longer lifetimes and estimate the time when the abrasion reaches a critical value. The extrapolation data from n devices tested result in n lifetimes that can be analyzed with Weibull as described before. The benefit is that the test can be truncated at a time much smaller than the expected lifetime. Some research is ongoing on how long a device must be tested until the extrapolation becomes good enough [16.128].

Example. A ferroelectric memory chip can distinguish between logic 1 and 0 if the polarization states $P(N)$ after N polarization reversals (cycles) do not fall beyond 80% of the initial value P_0 . $P(N)/P_0 = 80\%$ is therefore the failure criterion of the device. Let us assume a cycling test with four samples was carried out, where $P(N)$ is measured after a discrete number of cycles. In order to save time, the measurements are truncated after 10^8 cycles, although the failure criterion is not reached. From the literature, it is known that $P(N)$ is related to N by $P(N)/P_0 = \exp(-N/N^*) + C$, where N^* and C are constants [16.129]. This model can be fitted to the data points and extrapolated to higher cycle numbers than 10^8 in order to find the lifetimes L_i where the failure criterion is fulfilled (Fig. 16.109). With L_i given, a Weibull analysis may be performed as already described in Sect. 16.7.2.

Fig. 16.109 Degradation test. Four devices were tested and the data were extrapolated to the critical failure value of 80% remaining polarization. The lifetime data can now be analyzed by means of the Weibull analysis ▶

16.7.4 Accelerated Lifetime Testing

Accelerated lifetime testing (ALT) is a frequently used method for reducing test time. Many publications deal with the special problems arising from this procedure [16.130].

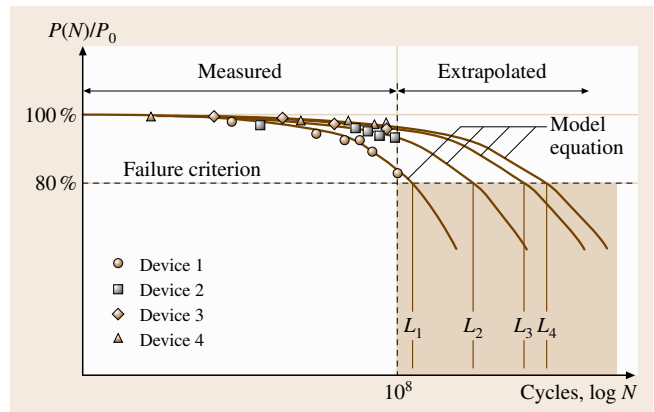
The basic idea of an accelerated lifetime test is to apply higher stresses to the device than it experiences under real service conditions in order to provoke a reasonable number of failures within a reasonable time. Here, stress means any physical process that influences the lifetime of the device; it may be mechanical stress, electrical voltage, current, temperature, humidity and so on. New questions arise from this procedure.

- By what factor do the higher stresses accelerate the degradation process? How are higher stresses and shortened lifetime physically related?
- In how far do higher stresses influence the failure mode? Will higher stresses produce failure modes that would not have occurred under normal conditions?

In ALT it must be assured that the observed failures at higher loading originate from the same failure mechanism that would be expected under use conditions in practise. A proof for this is the following rule.

- Failures that origin from the same failure mechanism show the same shape parameter in the Weibull net, and therefore are shifted parallel to each other. They only differ in their lifetime, which is shorter for higher stresses (Fig. 16.110).
- Only the *lifetime* L of the device, which may be expressed by any parameter related to the distribution (MTTF, η , B_{10} , ...) is affected by the acceleration.

Fig. 16.110 The Weibull line obtained from measurements at higher stress is transferred to the Weibull line that would have been achieved from experiments at use stresses by multiplying the lifetime (here the characteristic life) by an acceleration factor κ . The Weibull parameter β is assumed to remain constant if the failure mode is the same at both stress levels ▶

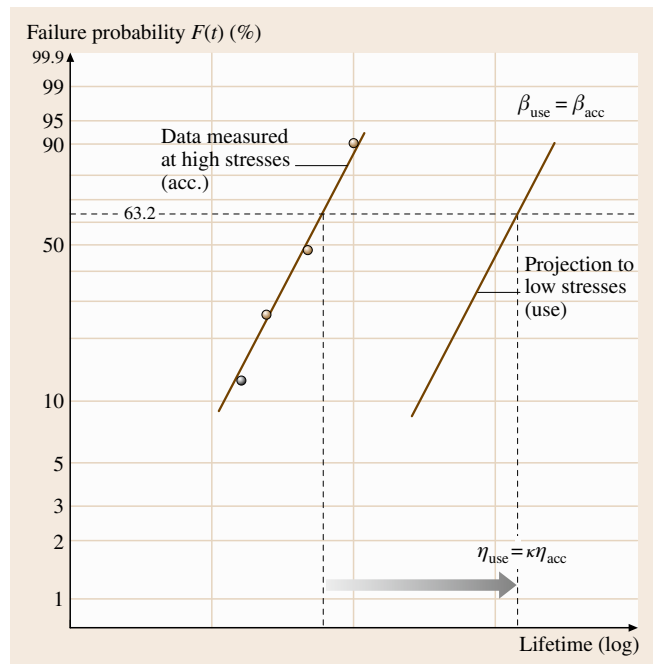


Analysis Procedure

The acceleration is measured by the ratio by which the lifetime is shortened by applying a higher stress. This number is called the acceleration factor.

Let us assume that we can calculate the time to failure L from a model equation $L(S)$, where S is the stress level applied to the item. $L(S)$ is the functional description of the dependency of the lifetime on the given physical quantity.

Now let us assume that we test the device at two different stress levels with $S_{acc} > S_{use}$. (where "acc" stands for acceleration, and "use" means the normal use con-



dition of the device) Then we define the acceleration factor κ as follows

$$\kappa = \frac{L(S_{use})}{L(S_{acc})} \tag{16.59}$$

The basic rule for how an accelerated reliability test is to be performed can be summarized as follows (Fig. 16.110).

- Step 1: Collect failure data at higher stresses S_{acc} .
- Step 2: Perform a Weibull analysis as described in Sect. 16.7.2.
- Step 3: Calculate the lifetime at normal use conditions by applying a suitable physical model describing the acceleration. Those acceleration models are described below.

Acceleration Models

Using acceleration models, the mechanistic origin of the acceleration is described. For any accelerated lifetime testing, this is a crucial point at which the validity of the whole test is decided. Two basic problems arise at this point

- In most cases, the physical model must be known from preknowledge on the physical origin of the ob-

served failure. It is not sufficient to adjust model equations to the given failure data.

- Physical models contain parameters (such as the activation energy, for instance; see below) that have to be estimated or known from the literature. In a few cases only these parameters can be calculated from the failure data directly.

In the following Table 16.12, some of the common acceleration test models are discussed in order to show the principle. Here, we restrict the discussion to the Arrhenius, the inverse power law (IPL) and the Coffin–Manson model.

Advanced Acceleration Techniques

In recent years, some acceleration methods have arisen that differ markedly from the scheme above sketched. In particular, the highly accelerated lifetime testing (HALT) and highly accelerated stress screening (HASS) methods have gained increasing attraction in the near past.

The goal of these methods is to find weaknesses of a product at an early stage of development, e.g. for a prototype, rather than predicting the lifetime of the device.

Table 16.12 Commonly used acceleration models, with their applications, model equations and acceleration factors. These and further models can be found in [16.109]

Model	Application	Model equation	Acceleration factor
Arrhenius	Failure mechanisms that depend on chemical reactions, diffusion processes or migration processes. It covers many of the nonmechanical (or nonmaterial fatigue) failure modes that cause electronic equipment failure	$L(T) = A \exp\left(\frac{\Delta H}{k_B T}\right)$ <p>T: temperature (K) A: constant k_B: Boltzmann constant ΔH: activation energy of the process (must be known in advance)</p>	$\kappa_T = \frac{L(T_{use})}{L(T_{acc})} = \exp\left[\frac{\Delta H}{k} \left(\frac{1}{T_{use}} - \frac{1}{T_{acc}}\right)\right]$
Inverse power law (IPL)	Stresses which are non-thermal in nature; in most cases the stress is given to be electrical voltage, e.g., capacitors often follow the IPL relationship	$L(U) = AU^{-b}$ <p>U: driving voltage of the device A: constant b: characteristic exponent</p>	$\kappa_U = \frac{U_{use}}{U_{acc}} = \left(\frac{U_{acc}}{U_{use}}\right)^b$
Coffin–Manson	Mechanical failure, material fatigue or material deformation, crack growth in solder and other metals due to repeated temperature cycling as equipment is turned on and off	$\Delta \varepsilon_p N_f^c = A$ <p>$\Delta \varepsilon_p$: plastic strain amplitude (peak–peak) N_f: number of cycles to fail c: cycling exponent (must be known in advance) A: material constant</p>	$\kappa_{\Delta \varepsilon} = \frac{N_f(\Delta \varepsilon_{use})}{N_f(\Delta \varepsilon_{acc})} = \left(\frac{\Delta \varepsilon_{acc}}{\Delta \varepsilon_{use}}\right)^{\frac{1}{c}}$

We will mention these methods in brief here, and recommend the papers referred to in [16.131] for further information on this topic.

Step Stress Profile Testing. In this test, test specimens are first subjected to a given level of stress for a certain period of time, and are then subjected to a higher level of stress. The process continues at increasing levels of stress, until either all the specimens fail, or the time period at the maximum stress level ends. The advantage of this method is, that failure modes are provoked, however, with this technique it is very difficult to model the acceleration properly [16.131].

It is mainly used for defining the operating envelope of a product and as a possibility to compare variants in a short period of time. An example for a step stress of a semiconductor transistor (in this case a high-electron mobility transistor) is shown in Fig. 16.111 [16.132]. In this case the drain voltage (black line) of the transistor is increased stepwise nearly every 100 min until 80 V. At ≈ 60 V the gate current (brown line) excess $100 \mu\text{A}$ rapidly leading to a catastrophic degradation of the device.

HALT (Highly Accelerated Lifetime Testing). HALT is an development test with the intention to detect weak spots in a system within a short time using a small number of samples.

The main motivation of HALT is not the survival of the product under specified conditions but to provoke the product/system to fail and detect dormant defects and provide the opportunity to improve reliability of the product. This method should be performed at the beginning of a product development as soon as a prototype is available so that redesign efforts are still affordable. A generalised illustration of the goal behind using HALT is shown in Fig. 16.112 [16.133]. The upper part shows the limits of a prototype before performing HALT. The abscissa represents the stress (vibration, temperature, voltage, etc.) the specimen is subjected to. The black continuous lines indicate the operational area defined by the product specifications. The inner dotted lines represent its operational limits, at which the device remains in a state of operation and at which any further increase in stress will cause a recoverable failure. The outer dotted lines represent the destruction limits, meaning that a stress exceeding these limits will destroy the device. By subjecting the specimen to increasing stress levels of temperature and vibration (independently and in combination) and other stresses specifically related to the product beyond operating conditions, it is possible

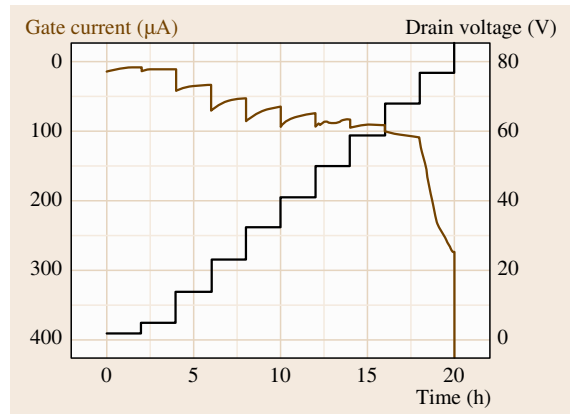


Fig. 16.111 On-Wafer Step-Stress-Tests until catastrophic degradation of a semiconductor transistor. The drain voltage (black line) of the transistor is increased stepwise nearly every 100 min until 80 V. At ≈ 60 V the insulating fails and the gate current (brown line) excess $100 \mu\text{A}$ rapidly leading to a catastrophic degradation of the device (after [16.132])

to determine the above-mentioned functional operating and destructions limits, multiple failure modes and root causes. Based on the obtained results improvements of

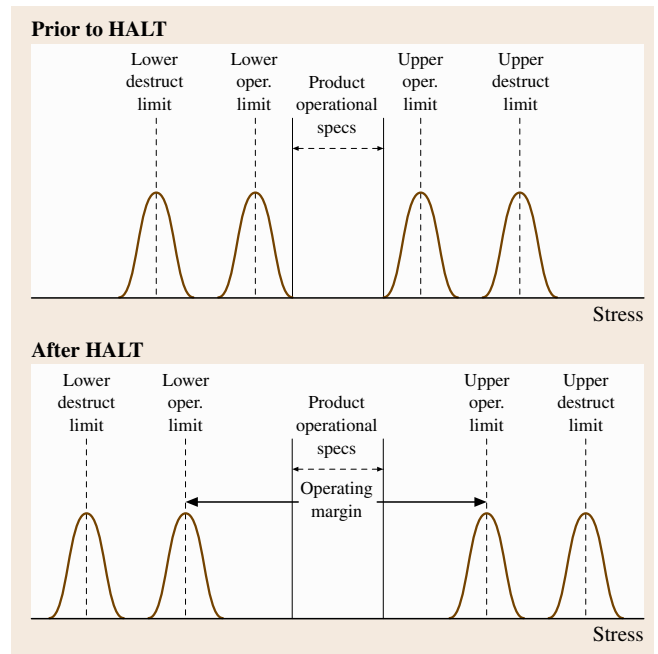


Fig. 16.112 An illustration of the enhanced operating limits due to HALT (after [16.133])

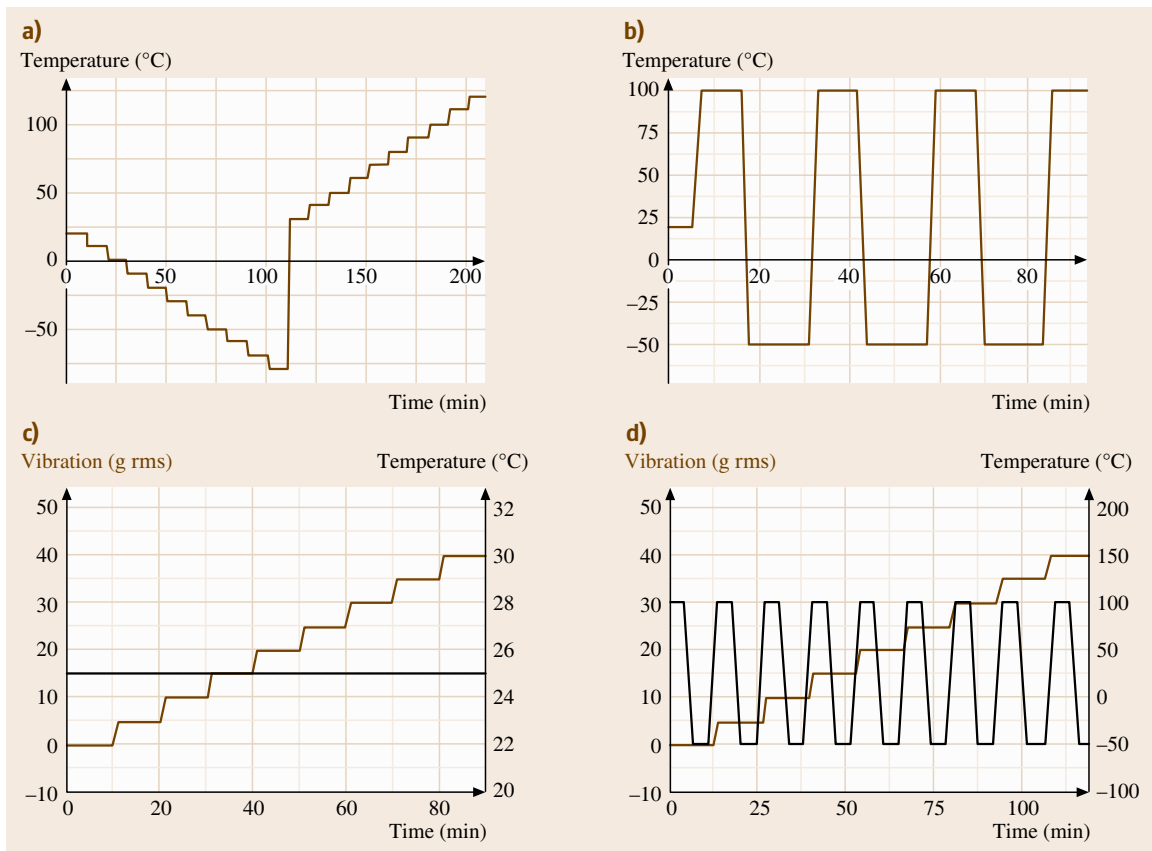


Fig. 16.113a–d An exemplary overview of possible tests including temperature and vibration loads

the prototype are carried out, leading to a higher robustness of the prototype shown in the lower part of Fig. 16.112. The prototype shows an increased operational area and the operation and destruction limits are shifted to higher levels.

Figure 16.113 shows an exemplary overview of different tests, which can be used for HALT. Graph a shows a temperature test, in which the temperature is decreased and later increased stepwise over the time. Graph b shows rapid thermal transitions causing rapid expansion and contraction of the prototype. Graph c illustrates a test, in which the acceleration levels of the random vibration are increased at a constant temperature. In the last graph d two loads are combined, in this case increasing vibration levels and rapid thermal transitions.

The obtained results can also be used later for HASS (see below). Complaints with HALT are the inability of reproducing failure modes because of the random nature of HALT tests and the inability to predict the reliability based on statistical data.

HASS (Highly Accelerated Stress Screening). HASS is a form of accelerated environmental stress screening and it is used for screening in the production process detecting weak products and changes in the manufacturing process. Samples of product assemblies are exposed to all stresses simultaneously for a very limited time period. The level of stresses can exceed beyond operating limits and near destruct limits obtained by HALT beforehand. These levels were predefined in a process called Proof-of-screen (POS) with the goal that HASS detects relevant defects without removing too much life from the test items. By passing HASS successfully, it is possible to ensure that a product has passed its infancy (see bathtub curve region 1) before being delivered to a customer. These and further information can be found in [16.134].

16.7.5 System Reliability

In many practical cases, a system is manufactured from several single components. The reliability R_S of the

whole system depends on the reliability of the single components R_i .

Serial Systems

In practice, it is often the case that the system's functionality depends on the component functionality such that a failure of any component means a failure of the whole device. For example, the system reliability of a car depends on the reliability of the tyre as well as on the engine. From this example, we see that the components do not necessarily need to interact with each other directly.

The underlying system structure can be interpreted as a serial system structure, which is shown in Fig. 16.114a.

For a serial system, the reliability of the system at a given time t is calculated to be the product of the reliabilities of the components, what follows from basic rules for probability calculations:

$$R_{S,\text{serial}}(t) = R_1 R_2 \dots R_n = \prod_i R_i(t) \quad (16.60)$$

or, by using $F_S = 1 - R_S$ and $F_i = 1 - R_i$

$$F_{S,\text{serial}}(t) = 1 - \prod_i [1 - F_i(t)]. \quad (16.61)$$

From these relations, we can draw some important conclusions

- the more components with given reliabilities, the smaller the system reliability becomes;
- in order to maintain a high reliability of the system, the reliability of the components must be improved;
- the system cannot be better than the worst component.

The reliabilities of the components as well as the system reliability can be visualized in a Weibull plot. In Fig. 16.115 we see this for the case of a three-component system. The thick line represents the Weibull distribution of the whole system as a result of the multiplication rule introduced above.

From this plot, we find further interesting facts.

- The system Weibull line is always located towards lower lifetimes. (This is identical to the above statement that the system has a lower reliability than the components.)
- Due to the sensitivity of the system reliability to the component reliability, it makes a significant difference if we use the two- or three-parameter

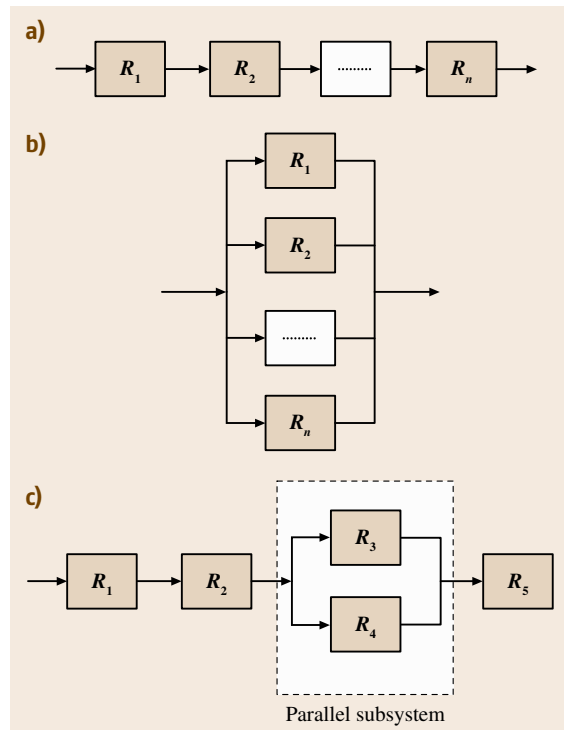


Fig. 16.114 (a) Serial system; (b) parallel system; (c) combined system

Weibull distribution for the components. If the two-parameter distribution is used although a three-parameter distribution is *justified*, then the failure probability is overestimated. This leads to an over-dimensioning of the device. Especially in mechanical engineering, where the strength of a device is dependent on the material amount, this plays an important role from an economical and ecological point of view [16.135].

Parallel Systems, Redundancy

If the system contains components that are able to fulfil the same functionality as other components, then the system contains redundancy. In the system structure, those components are represented as parallel structures, as shown in Fig. 16.114b.

In contrast to a serial system, additional redundant components increase the reliability. This is also indicated in the system equations for parallel systems where the failure probabilities $F(t)$, rather than the reliabilities, are multiplied

$$F_{S,\text{parallel}}(t) = F_1 F_2 \dots F_n = \prod_i F_i(t) \quad (16.62)$$

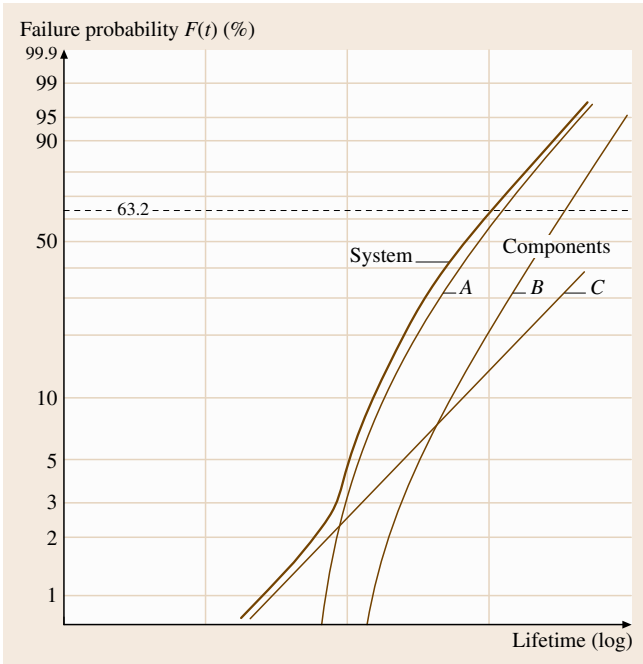


Fig. 16.115 The reliability of a system as a result of the reliabilities of its components, here for the example $n = 3$ and for a serial system. We see that the system reliability is always lower than the reliability of the weakest part. In this example, the system reliability is dominated either by component C or A , depending on the region of the failure probability. Component B , on the other hand, has minor influence since it is more reliable than the others in the whole region

or, expressed in terms of the reliability functions $R_i(t) = 1 - F_i(t)$

$$R_{S,parallel}(t) = 1 - [(1 - R_1)(1 - R_2) \dots (1 - R_n)]$$

$$= 1 - \prod_i [1 - R_i(t)] \quad (16.63)$$

Combined Systems

In practice, it is often the case that within a system some components are in series and others are parallel. In this case, the system reliability can be calculated from the rules of Boolean algebra. A simple example will elucidate the principle.

In Fig. 16.114c we see the functional structure of a system. The system reliability calculates as follows

$$R_S = R_1 R_2 \underbrace{[1 - (1 - R_3)(1 - R_4)]}_{= \text{parallel subsystem}} R_5 \quad (16.64)$$

16.7.6 System Reliability Estimation in Practice

Despite the fact that the theoretical background of reliability engineering, as illustrated in brief in the preceding sections, is well defined, the application of these tools in practice is far from straightforward. There are several practical problems of which the following are the most prominent [16.136]: (a) systems are tending to become more complex. (b) Mechanical, electronic and software components are simultaneously included in the functionality of systems, for example *X-by-wire* techniques. Such *mechatronic systems* will be one of the future challenges in reliability engineering, which has also been documented by the increasing number of publications in this field over the last years [16.137].

In the following example, we will elucidate all these problems by following the procedure in reliability estimation as sketched above. We will show that all above-mentioned problems will be addressed in this example, giving a better understanding of the underlying methodology. The example chosen here was subject of a detailed reliability investigation performed by the authors. We will refer to a previous publication [16.138] where this work is already described in detail. The system to be investigated in our example is an active interface (AI), which was designed for actively damping unwanted vibrations as well as noise in an automobile, Fig. 16.116 [16.139].

According to the above sketched procedure, the reliability analysis was conducted following this sequence of steps: i) System analysis, ii) Determination of component reliabilities, iii) Determination of the system reliability.

i) System Analysis

As already described above, the aim is to find the underlying abstraction of the system structure according to Fig. 16.114, which will be the basis for the later system reliability calculation. To do so, the system was subdivided into the following main subsystems.

- Mechanics,
- Electronics,
- Actuators,
- Control.

From a function analysis performed by the experts in the field of the different technical domains, it became clear that a failure of one of these subsystems will result in a system failure. Furthermore, the analysis revealed

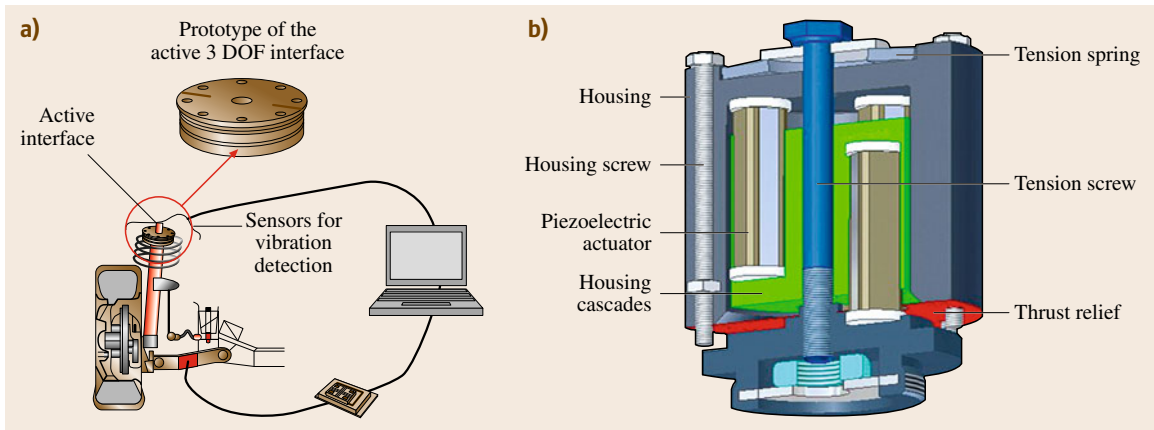


Fig. 16.116 (a) The active interface is located within the spring dome of a car. Sensors detect the unwanted vibrations, the signals are transferred to a controller and a power unit, which drives the piezoelectric actuators acting against the vibrations. (b) Inner construction of the active interface

that the failure behaviour in each subsystem is in large parts independent of the failure behaviour of the others. It must be stated that the determination of this independence is by far not trivial, since in many practical cases not all possible failure modes are known in advance. In our case, a thorough failure mode and effects analysis (FMEA) was performed prior to the reliability investigation, and so a broad knowledge on possible failure modes was present [16.140]. The system structure of the active interface is therefore given as a serial structure shown in Fig. 16.117.

The subsystems themselves were further analysed in order to determine their reliability structure. For instance, for parts of the mechanical construction a combined structure (serial and parallel elements, compare Fig. 16.114c) was found as sketched in Fig. 16.118.

ii) Determination of Component Reliabilities

In this section, the determination of the reliabilities of the aforementioned subsystems mechanics, electronics, actuators and control will be described. It will be shown that the underlying method is different in each domain. Further more, state of the art within the domains also widely differs. The main problem in daily practice is that we need failure data of the components for the calculation of system reliabilities following the schemes sketched above. Those failure data – as we have outlined in the previous sections – are not sufficiently represented by giving a lifetime of the device. Instead, the failure behavior in the form of the Weibull parameters, containing information about the average life *and* the scatter, is needed. As already mentioned, these values

are not documented in public data bases. Exceptions are failure rates for electronic devices and structural durability data for metallic components [16.114].

Mechanics. The reliability of the construction of the active interface is characterized by standard methods of structural durability. For information and further references see [16.114] as well as Chap. 7 in this handbook.

Electronics. The determination of the reliability of electronic components is fixed in international standards. One of the first standards in this field was the MIL-Std 217 [16.141], another newer standard is the IEC TR 62380 [16.142]. In both cases, a constant failure

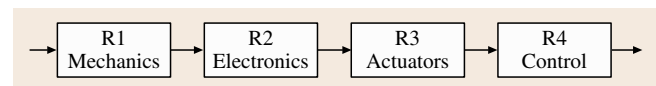


Fig. 16.117 Serial reliability structure of the active interface

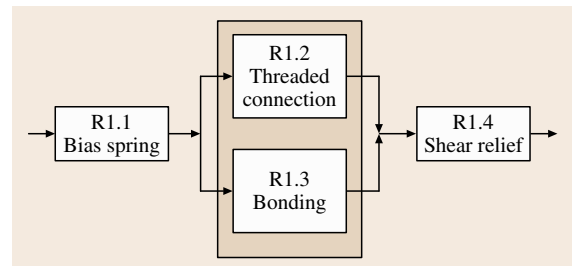


Fig. 16.118 Combined reliability structure of a part of the subsystem mechanics

rate for the electronic components is assumed, which depends on the load conditions (temperature, moisture, mechanical vibrations, . . .). The reliability of the whole electronic subsystem is determined by addition of all failure rates.

Actuators. Additional challenges arise from the fact that mechatronic systems often include new materials that serve as actuators or sensors. This class of materials is called *smart materials*. These active materials, which include ferro- and piezoelectric ceramics [16.143, 144] and shape-memory alloys [16.145], exhibit failures under long-term operation that are not well understood despite intensive work over the last decades. In particular, it is not understood which failures occur under which service conditions (electrical, mechanical stress, temperature, etc.), and the failure probability functions under those service conditions are not yet known.

The actuators used in the AI consist of piezoelectric materials. Piezoelectric materials have been used in the context of adaptronic systems for several years, however, reliability data available from manufacturers refer to service conditions from other applications like fuel injection systems or micro positioning. It is therefore a challenging task to transfer the given reliability data to the actual service conditions of the AI. This can only be done by combination of expert judgement and experimental tests where necessary.

Control. The controllers at one hand consist of electronic hardware, which was already described in the previous section. On the other hand, it consists of software components, which differ markedly from hardware components with respect to their failure behavior. Up to now, there is no general reliability model for software available [16.146]. Present methods of software reliability estimation, as e.g. described in [16.147, 148], are able to quantify implementation failures mainly. Implementation failures origin from human programming errors [16.149]. State of the art is the assumption of a correlation between the amount of generated codes and the amount of failures, which is, on the other hand, not generally accepted [16.150]. A quantification of specification errors is not possible at current state of the art [16.149].

iii) System Reliability

Based on the information gained from the above described procedure, it was possible to estimate the Weibull parameters characteristic lifetime, Weibull

module and failure free time for the subcomponents (compare Sect. 16.1.2).

Under the given preassumption, that the failure behaviors of the subcomponents are independent, the system reliability function of the AI reads, following Sect. 16.1.5, as follows

$$R_{\text{Active interface}} = R_{\text{mechanics}} \times R_{\text{electronics}} \times R_{\text{actuator}} \times R_{\text{control}} \quad (16.65)$$

The system reliability function R_{AI} is obtained from multiplication of the component reliability functions according to (16.65). In case of time-dependent failure behavior, the analytical solution of the multiplication in these equations can only be solved by computation. This was done by means of the software package SYSLEB, which was developed at the IMA (Institute of Machine Components, University of Stuttgart) for the purpose of conducting several analyses. SYSLEB is a powerful software package to analyse life cycle data using different distributions (e.g. Weibull, normal, lognormal, exponential). Computation of Weibull distribution parameters including confidence limits as well as extensive mathematic and graphic illustrations are more SYSLEB-features used for this work. Maximum-Likelihood estimation for combinations of several distribution functions and Monte-Carlo-simulation are further possibilities to use SYSLEB for analyzing system reliability.

In order to visualize the Weibull lines for the system reliability function $R_{\text{AI}}(t)$ as well as for the subcomponents, the Weibull lines are plotted into a Weibull diagram, what is also a feature of the SYSLEB software tool, Fig. 16.119. As can be seen, The Weibull lines for the components actuator (red), bias spring (blue), controller (magenta), amplifier (yellow) as well as the resulting system reliability line (green) are shown in one graph according to the schematic drawing in Fig. 16.115.

For the electronic components like controller and amplifier, a constant failure rate was assumed, what is typical of electronic components. In the Weibull plot, this is expressed by a straight line. The other components were assumed to have a wear-out failure behavior with a given failure-free time. As can be seen from the plot, the system reliability curve at lower lifetimes depends on the failure behavior of the electronic components. However, after reaching the failure free time of the actuators, the actuators start to dominate. Only after very long lifetimes, the bias spring gives a significant contribution to the system reliability function. As can be seen from the Weibull

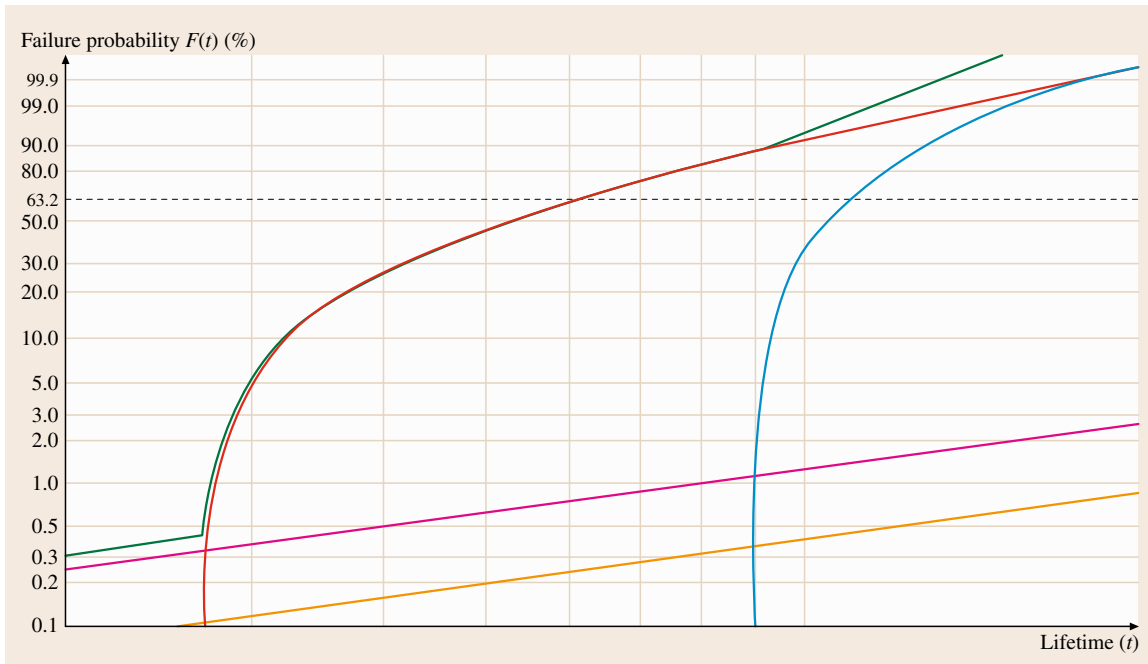


Fig. 16.119 Weibull plot of the components actuator (*red*), bias spring (*blue*), controller (*magenta*), amplifier (*yellow*) as well as the resulting system reliability line (*green*) (after [16.138])

plot, an improvement in the reliability of the actuators will have the greatest impact on the system reliability.

The example shows, how a quantitative reliability estimation of a complex system can be performed by application of the Weibull distribution and Boolean system theory.

It also shows that there are several preconditions to be met. On system level the interactions of the components must be understood at a depth allowing for a judgement of the independence of the components,

which is a necessary precondition for the applicability of the above sketched procedure.

Furthermore, knowledge about the failure behaviour of the components must be available for the analysis. At this point, the quality of the available data is most crucial. The general experience is that the data available do not allow a straightforward introduction to the system reliability analysis without prior interpretation of the available data and without prior expert judgement.

The availability of lifetime data of high quality will be a main challenge in reliability engineering in the future.

16.A Appendix

In the following table, the median rank regression for the 5, 59 and 95% percentiles of the failure probability F (in %) are listed for sample sizes from $n = 3$ up

to $n = 12$. The values are of interest for the Weibull analysis introduced in Sect. 16.7.2.

i	n														
	3			4			5			6			7		
	5	50	95	5	50	95	5	50	95	5	50	95	5	50	95
1	1.7	20.6	63.2	1.3	15.9	52.7	1	12.9	45.1	0.8	10.9	39.3	0.7	9.4	34.8
2	13.5	50	86.5	9.8	38.6	75.1	7.6	31.4	65.7	6.3	26.4	58.2	5.3	22.8	52.1
3	36.8	79.4	98.3	24.9	61.4	90.2	18.9	50	81.1	15.3	42.1	72.9	12.9	36.4	65.9
4				47.3	84.1	98.7	34.3	68.6	92.4	27.1	57.9	84.7	22.5	50	77.5
5							54.9	87.1	99	41.8	73.6	93.7	34.1	63.6	87.1
6										60.7	89.1	99.2	47.9	77.2	94.7
7													65.2	90.6	99.3

i	n														
	8			9			10			11			12		
	5	50	95	5	50	95	5	50	95	5	50	95	5	50	95
1	0.64	8.3	31.2	0.6	7.4	28.3	0.5	6.7	25.9	0.5	6.1	23.8	0.4	5.6	22.1
2	4.6	20.1	47.1	4.1	18	42.9	3.7	16.2	39.4	3.3	14.8	36.4	3	13.6	33.9
3	11.1	32.1	59.9	9.8	28.6	55	8.7	25.9	50.7	7.9	23.6	47	7.2	21.7	43.8
4	19.3	44	71.1	16.9	39.3	65.5	15	35.5	60.7	13.5	32.4	56.4	12.3	29.8	52.7
5	28.9	55.9	80.7	25.1	50	74.9	22.2	45.2	69.6	20	41.2	65	18.1	37.9	60.9
6	40	67.9	88.9	34.5	60.7	83.1	30.4	54.8	77.8	27.1	50	72.9	24.5	46	68.5
7	52.9	79.8	95.4	45	71.4	90.2	39.3	64.5	85	35	58.8	80	31.5	54	75.5
8	68.8	91.7	99.4	57.1	82	95.9	49.3	74.1	91.3	43.6	67.6	86.5	39.1	62.1	81.9
9				71.7	92.6	99.4	60.6	83.8	96.3	53	76.4	92.1	47.3	70.2	87.7
10							74.1	93.3	99.5	63.6	85.2	96.7	56.2	78.3	92.8
11										76.2	93.9	99.5	66.1	86.4	97
12													77.9	94.4	99.6

References

- 16.1 K.G. Bøving: *NDE Handbook, Non-destructive Examination Methods* (Butterworth, London 1989)
- 16.2 C.J. Hellier: *Handbook of Nondestructive Evaluation* (McGraw-Hill, New York 2001)
- 16.3 J. Krautkrämer, H. Krautkrämer: *Ultrasonic Testing of Materials*, 4th edn. (Springer, Berlin Heidelberg New York 1990)
- 16.4 J.L. Rose: *Ultrasonic Waves in Solid Media* (Cambridge Univ. Press, Cambridge 1999)
- 16.5 V. Deutsch, M. Platte, M. Vogt: *Ultraschallprüfung – Grundlagen und industrielle Anwendung* (Springer, Berlin Heidelberg New York 1997), (in German)
- 16.6 L. Cartz: *Nondestructive Testing* (ASM International, Metals Park 1995)
- 16.7 R.E. Newnham, L.J. Bowen, K.A. Klicker, L.E. Cross: Composite piezoelectric transducers, *Mater. Eng.* **2**(93), 93–106 (1980)
- 16.8 R.E. Newnham, J.F. Fernandez, K.A. Markowski, J.T. Fielding, A. Dogan, J. Wallis: Composite piezoelectric sensors and actuators, *Mat. Res. Soc. Symp. Proc.*, Vol. 360 (1995)
- 16.9 D.Y. Wang, K. Li, H.L.W. Chan: Lead-free BNBt-6 piezoelectric ceramic fibre/epoxy 1–3 composites for ultrasonic transducer applications, *Appl. Phys. A* **80**, 1531–1534 (2005), DOI: 10.1007/s00339-003-2390-3
- 16.10 G. Splitt: Piezocomposite Transducers – a milestone for ultrasonic testing, *NDTnet* **1**(7) (1996)
- 16.11 R. Ramesh, R.M.R. Vishnubhatla: Estimation of material parameters of lossy 1–3 piezocomposite plates by non-linear regression analysis, *J. Sound Vib.* **226**(3), 573–584 (1999)
- 16.12 H. Wüstenberg: Characteristic sound field data of angle beam probes, Possibilities for their theoretical and experimental determination, 7th Int. Conf. Non-Destruct. Test., Warszawa (1973)
- 16.13 A. Erhard, H. Wüstenberg, G. Schenk, W. Möhrle: Calculation and construction of phased array-UT probes, *Nucl. Eng. Design* **94**, 375–385 (1986)

- 16.14 E. Mundry, H. Wüstenberg: Theory and experiments of ultrasonic defect size determination with the double probe and the single-probe technique, 5th Int. Conf. Non-Destruct. Test., Montreal (1967) p. 58/62
- 16.15 K. Matthies: *Thickness Measurement with Ultrasound* (DVS, Berlin 1998) pp. 941–945
- 16.16 H. Wüstenberg, B. Rotter, H.-P. Klanke, D. Harbecke: Ultrasonic phased arrays for nondestructive inspection of forgings, *Mater. Eval.* **51**, 669–672 (1993)
- 16.17 H.L. Libby: *Introduction to Electromagnetic Non-destructive Test Methods* (Wiley Interscience, New York 1971)
- 16.18 D.J. Hagemaijer: *Fundamentals of Eddy Current Testing* (Am. Soc. Nondestruct. Test., Columbus 1990)
- 16.19 R. Pohl, A. Erhard, H.-J. Montag, H.-M. Thomas, H. Wüstenberg: NDT techniques for railroad wheel and gauge corner inspection, *Nondestruct. Test. Eval.* **37**, 89–94 (2004)
- 16.20 R. Halmshaw: *Industrial Radiology, Theory and Practice* (Chapman & Hall, London 1995)
- 16.21 L.E. Bryant, P. McIntire (Eds.): Radiography and Radiation Testing. In: *Nanodestructive Testing Handbook*, Vol. 3, 2nd edn. (ASNT, Columbus 1985)
- 16.22 C.A. Lindley: *Practical Image Processing in C, Acquisition, Manipulation, Storage* (Wiley, New York 1991)
- 16.23 R.C. Gonzalez, R.E. Woods: *Digital Image Processing*, 2nd edn. (Prentice Hall, New Jersey 2002)
- 16.24 CR-Standards, CEN EN 14874; ASTM E 2007, E 2033, E 2445, E 2446
- 16.25 U. Ewert, J. Stade, U. Zscherpel, M. Kaling: Lumineszenz-Speicherfolien für die Radiographie, *Materialprüfung* **37**, 474–478 (1995), (in German)
- 16.26 U. Ewert, U. Zscherpel: New Detectors and Perspectives in Industrial Radiography, *NAARR, Bulletin XII(1)*, 59–71 (2005)
- 16.27 J.M. Casagrande, A. Koch, B. Munier, P. de Groot: *High Resolution Digital Flat-Panel X-Ray Detector – Performance and NDT Application*, 15th edn. (WCNDT, Rome 2000), available at <http://www.wcndt.net/article/wcndt00/papers/idn615/idn615.htm>
- 16.28 B. Redmer, J. Robbel, U. Ewert, V. Vengrinovich: Mechanised weld inspection by tomographic computer-aided radiometry (TomoCAR), *Insight* **44(9)**, 564–567 (2002)
- 16.29 O. Dupius, V. Kaftandjian, S. Drake, A. Hansen, J.-M. Casagrande: *FFreshex: A Combined System for Ultrasonic and X-Ray Inspection of Welds*, 15th edn. (WCNDT, Rome 2000), available at <http://www.ndt.net/article/wcndt00/papers/idn286/286.htm>
- 16.30 H. Schubert, A. Kuznelsov (Eds.): *Detection of Bulk Explosives* (Kluwer, Dordrecht 2004)
- 16.31 S.D. Antolovich, A.M. Gokhale, C. Bathias: Application of quantitative fractography and computed tomography to fracture process in materials, *ASTM-STP* **1085**, 325 (1990)
- 16.32 M.J. Dennis: Industrial computed tomography. In: *Metals Handbook*, Vol. 17 (ASM Int., Materials Park 1989) p. 358
- 16.33 K. Legorju-Jago, C. Bathias: Fatigue initiation and propagation in natural and synthetic rubbers, *Int. J. Fatigue* **24**, 85–92 (2002)
- 16.34 S. Saily: Ph.D. Thesis (CNAM, Paris 2001)
- 16.35 M. Gonzalez: Ph.D. Thesis (Ecole Centrale, Paris 2001), p. 27
- 16.36 Q. Shi: Ph.D. Thesis (CNAM, Paris 2003), p. 74
- 16.37 M. Gonzalez, C. Domínguez, C. Bathias: Some results from X-ray computed tomography applied to metal matrix composites, *J. Compos. Technol. Res.* **24**, 45 (2000)
- 16.38 R. Piras: Ph.D. Thesis (Supmeca/LISMA, Paris 2003), p. 15
- 16.39 R.H. Bossi, G.E. Georgeson: The application of X-ray computed tomography to materials development, *J. Mater.* **43(9)**, 8–15 (1991)
- 16.40 L. Grodzins: Optimum energies for X-ray transmission tomography of small samples, *Nucl. Instrum. Methods* **206**, 541–545 (1983)
- 16.41 R. Oster: Computed Tomography (CT) as a non-destructive test method used for composite helicopter components, *Int. Symp. on Computerized Tomography for Industrial Applications*, Berlin 8–10 June 1994 (DGZfP-Berichtsband, Berlin 1994) pp. 234–241
- 16.42 H. Heidt, J. Goebbels, P. Reimers, A. Ketschau: Development and Application of an universal CAT-Scanner, 11th World Conf. NDT, Las Vegas Nov. 3–8, 664–671 (1985)
- 16.43 M.R. Sené, M. Bailey, B. Illerhaus, J. Goebbels, O. Haase, A. Kulish, N. Godon, J.J. Choucan: Characterisation of Accessible Surface Area of HLW Glass Monoliths by High Energy Accelerator Tomography and Comparison with Conventional Techniques, *Proj. Rep. Nucl. Sci. Technol. EUR 19119 EN*, 62 (1999)
- 16.44 Y. Onel, B. Illerhaus, J. Goebbels: Experiences in using a 320 kV micro focus X-ray tube and a large sized amorphous silicon detector for 3D-CT, *Int. Symp. on Computed Tomography and Image Processing for Industrial Radiology*, June 23–25, 2003 Berlin DGZfP. Proc. DGZfP (BB84-CD) pp. 53–60
- 16.45 H. Riesemeier, K. Ecker, W. Görner, B.R. Müller, M. Radtke, M. Krumrey: Layout and first XRF Applications of the BAMline at BESSY II, *X-Ray Spectrom.* **34**, 160–163 (2004)
- 16.46 H. Riesemeier, J. Goebbels, B. Illerhaus, Y. Onel, P. Reimers: 3-D Mikrocomputertomograph für die Werkstoffentwicklung und Bauteilprüfung, *DGZfP Berichtsband* **37**, 280–287 (1993), (in German)
- 16.47 H. Riesemeier, J. Goebbels, B. Illerhaus, E. Becker: Computertomographie zur Qualifizierung von Testkörpern für die Wirbelstromprüfung, *Jahresta-*

- gung der DGZfP, 5–7 Mai 1997 Dresden, DGZfP BB 59.2, pp. 801–807
- 16.48 H. Czichos: *Was ist falsch am falschen Rembrandt? und wie hart ist Damaszener Stahl* (Nicolai, Berlin 2002), (in German)
- 16.49 W.-D. Heilmeyer: Ancient workshops and ancient 'art', *Oxford J. Archaeol.* **23**(4), 403–415 (2004)
- 16.50 A.H. Compton, S.K. Allison: *X-Ray in Theory and Experiment* (Macmillan, London 1935)
- 16.51 M.P. Hentschel, R. Hosemann, A. Lange, B. Uther, R. Brückner: Röntgenkleinwinkelbrechnung an Metalldrähten, Glasfäden und hartelastischem Polypropylen, *Acta Cryst. A* **43**, 506 (1987), (in German)
- 16.52 K.-W. Harbich, M.P. Hentschel, J. Schors: X-ray refraction characterization of nonmetallic materials, *NDT&E International* **34**, 297 (2001)
- 16.53 A. Guinier, G. Fournet: *Small-Angle Scattering of X-Rays* (Wiley, Chichester 1955)
- 16.54 G. Porod: Die Röntgenkleinwinkelstreuung von dichtgepackten kolloidalen Systemen, 1. Teil *Kolloid.-Z.* **124**, 83–144 (1951), (in German)
- 16.55 M.P. Hentschel, A. Lange, R.B. Müller, J. Schors, K.-W. Harbich: Röntgenrefraktions-Computertomographie, *Materialprüfung/Mater. Test.* **42**, 217 (2000), (in German)
- 16.56 B.R. Müller, A. Lange, M. Harwardt, M.P. Hentschel, B. Illerhaus, J. Goebels, J. Bamberg, F. Heutling: Refraction computed tomography, *Materialprüfung/Mater. Test.* **46**, 314 (2004)
- 16.57 H. Sohn, C.R. Farrar, F.M. Hemez, D.D. Shunk, D.W. Stinemat, B.R. Nadler: *A Review of Structural Health Monitoring Literature: 1996–2001* (Los Alamos National Laboratory Report, 2003), LA-13976-MS
- 16.58 C. Boller, W.J. Staszewski (Eds.): *Structural Health Monitoring*, 2nd Eur. Workshop Struct. Health Monit., Munich July 7–9, 2004 (DEStech Publ., Lancaster 2004) pp. 7–9
- 16.59 F. Ansari (Ed.): *Condition Monitoring of Materials and Structures* (American Society of Civil Engineers Press, Reston 2000)
- 16.60 L. Faravelli, B.F. Spencer Jr. (Eds.): *Proceedings of the US-Europe Workshop on Sensors and Smart Structures Technology* (Wiley, Chichester 2003)
- 16.61 F. Casciati (Ed.): *Proceedings of the Third World Conference on Structural Control* (Wiley, Chichester 2003)
- 16.62 J.P. Ou, H. Li, Z.D. Duan (Eds.): *Structural Health Monitoring and Intelligent Infrastructure* (Taylor & Francis, Leiden 2006)
- 16.63 C. Boller, F.-K. Chang, Y. Fujino (Eds.): *Encyclopedia of Structural Health Monitoring* (Wiley Blackwell, Chichester 2009)
- 16.64 International Society for Structural Health Monitoring of Intelligent Infrastructure (SHM): Glossary of Terms, <http://www.ishmii.org>
- 16.65 B. Culshaw: *Smart Structures and Materials* (Artech House, Norwood 1996)
- 16.66 W. Habel, D. Hofmann, B. Hillemeier: Deformation measurements of mortars at early ages and of large concrete components on site by means of embedded fiber-optic microstrain sensors, *J. Cem. Concr. Compos.* **19**, 81–101 (1997)
- 16.67 K. Krebber, W. Habel, T. Gutmann, C. Schram: Fiber Bragg grating sensors for monitoring of wind turbine blades, 17th Int. Conf. Opt. Fibre Sens., May, 2005 (2005) pp. 1036–1039
- 16.68 A. Rytter: *Vibration Based Inspection of Civil Engineering Structures*. Ph.D. Thesis (Aalborg University/Denmark, Dept. of Building Technology and Structural Eng., Aalborg 1993)
- 16.69 J.M. Lopez-Higuera: *Handbook of Optical Fibre Sensing Technology* (Wiley, Chichester 2002)
- 16.70 R.M. Measures: *Structural Monitoring with Fiber Optic Technology* (Academic, New York 2001)
- 16.71 K.T.V. Grattan, T. Sun: Fiber optic sensor technology: An overview, *Sens. Actuators* **82**, 40–61 (2000)
- 16.72 VDI/VDE 2660 Blatt 1: *Experimental stress analysis – Optical strain sensor based on fibre Bragg grating – Fundamentals, characteristics and sensor testing* (Beuth, Berlin 2010)
- 16.73 D. Inaudi, A. Elamari, L. Pflug, N. Gisin, J. Breguet, S. Vurpillot: Low-coherence deformation sensors for the monitoring of civil-engineering structures, *Sens. Actuators A* **44**, 125–130 (1994)
- 16.74 W.R. Habel: Long-term monitoring of 4,500 kN rock anchors in the Eder gravity dam using fibre-optic sensors, *Int. Symp. Geotech. Meas. Model.* (Balkema, Rotterdam 2003) pp. 347–354
- 16.75 W.J. Staszewski, C. Boller, G.R. Tomlinson: *Health Monitoring of Aerospace, Structures – Smear Sensor Technologies and Signal Processing* (Wiley, Chichester 2004)
- 16.76 O. Frazao, D.A. Pereira, J.L. Santos, F.M. Aranjó, L.A. Ferreira: Strain and Temperature Discrimination using a Hi-Bi Grating, Partially Exposed to Chemical Etching, 17th Int. Conf. Opt. Fibre Sens., Vol. 5855, ed. by M. Voet, R. Willsch, W. Ecke, J. Jones, B. Culshaw (SPIE, 2005) pp. 755–758
- 16.77 W. Habel, T. Gutmann: Embedded Quasi-distributed Fibre Optic Sensors for, Long-term Monitoring of 4,500 kN Rock Anchors in the Eder Gravity Dam in Germany, *Int. Conf. Struct. Health Monit. Intell. Infrastruct.*, Shenzhen, SHMII–November 16–18 (2005) pp. 216–218
- 16.78 X. Bao, D.J. Webb, D.A. Jackson: Characteristics of Brillouin Gain based, distributed temperature sensors, *Electr. Lett.* **29**, 1543–1544 (1993)
- 16.79 T. Horiguchi, T. Kurashima, M. Tateda, K. Ishirara, Y. Wakui: Measurement of temperature and strain distribution by Brillouin frequency shift in silica optical fibers, *SPIE-Int. Soc. Opt. Eng.*, Vol. 1797, ed. by J.P. Dakin, A.D. Kersey (1993) pp. 2–13

- 16.80 K. Krebber: Ortsauflösende Lichtleitfaser-Sensorik für Temperatur und Dehnung unter Nutzung der stimulierten Brillouin-Streuung basierend auf der Frequenzbereichsanalyse. Ph.D. Thesis (Ruhr-Universität Bochum, Bochum 2001)
- 16.81 X. Bao, D.J. Webb, D.A. Jackson: Combined distributed temperature and strain sensor based on Brillouin loss in an optical fiber, *Opt. Lett.* **141**, 16 (1994)
- 16.82 D. Garus, K. Krebber, F. Schliep, T. Gogolla: Distributed sensing technique based on Brillouin optical-fiber frequency-domain analysis, *Opt. Lett.* **21**, 17 (1996)
- 16.83 N. Noether, A. Wosniok, K. Krebber, E. Thiele: A distributed fiber-optic sensor system for monitoring of large geotechnical structures, 4th Int. Conf. Struct. Health Monit. Intel. Infrastruct. (SHMII-4, 2009)
- 16.84 S. Liehr, P. Lenke, M. Wendt, K. Krebber, R. Gloetzel, J. Schneider-Gloetzel, L. Gabino, L. Krywult: Distributed Polymer Optical Fiber Sensors in Geotextiles for Monitoring of Earthwork Structures, 4th Int. Conf. Struct. Health Monit. Intel. Infrastruct. (SHMII-4, 2009)
- 16.85 S. Liehr, P. Lenke, M. Wendt, K. Krebber, M. Seeger, E. Thiele, H. Metschies, B. Gebreselassie, J.C. Muenich: Polymer Optical Fibre Sensor for Distributed Strain Measurement and Application in Structural Health Monitoring, *IEEE Sens. J.* **9**, 11 (2009)
- 16.86 T. Ikeda: *Fundamentals of Piezoelectricity* (Oxford Univ. Press, Oxford 1990)
- 16.87 B. Jaffe, W.R. Cook Jr., H. Jaffe: *Piezoelectric Ceramics* (Academic, London New York 1971)
- 16.88 W.J. Elspass, J. Kunzmann, M. Flemming, D. Baumann: Design, manufacturing and verification of piezoceramics embedded in fiber-reinforced thermoplastics, *Proc. SPIE* **2443**, 327–333 (1995)
- 16.89 N.W. Hagood, E.F. Crawley, J. de Luis, E.H. Anderson: Development of integrated components for control of intelligent structures, *Smart Mater. Struct. Math. Issues, US Army Res. Off. Workshop, Blacksburg* (1988) pp. 80–104
- 16.90 W.J. Elspass, J. Kunzmann, M. Flemming, D. Baumann: Design, manufacturing and verification of piezoceramics embedded in fiber-reinforced thermoplastics, *SPIE, Vol. 2443*, ed. by I. Chopra (San Diego, 1995), 327–333
- 16.91 E.F. Crawley, J. de Luis: Use of piezoelectric actuators as elements of intelligent structures, *J. Am. Inst. Aeronaut. Astronaut.* **25**(10), 1373–1385 (1987)
- 16.92 E. Moulin, J. Assad, C. Delebarre, H. Kaczmarek, D. Balageas: Piezoelectric transducer embedded in a composite plate: Application to Lamb wave generation, *J. Appl. Phys.* **82**(5), 2049–2055 (1997)
- 16.93 S. Bourasseau, P. Blanquet, D. Coutellier, M. Dupont, M. Pernice, C. Delebarre, A. Thiriot, T. Demol: Integration of optical fibers and piezoelectric ceramics in composite materials, *Proc. SPIE* **2779**, 180–185 (1996)
- 16.94 T.E. Neary, D.R. Huston, J. Wu, W.B. Spillman: In-situ damage monitoring of composite structures, *Proc. SPIE* **2718**, 202–217 (1996)
- 16.95 B.S. Shen, M. Tracy, Y.-S. Roh, F.-K. Chang: Built-in piezoelectrics for processing and health monitoring of composite structures, *J. Am. Inst. Aeronaut. Astronaut.* **1310**, 390–397 (1996)
- 16.96 S. Mall, T.L. Hsu: Electromechanical fatigue behaviour of graphite/epoxy laminate embedded with piezoelectric actuator, *Smart Mater. Struct.* **9**, 78–84 (2000)
- 16.97 I.A. Viktorov: *Rayleigh and Lamb Waves – Physical Theory and Applications* (Plenum, New York 1967)
- 16.98 N. Guo, P. Cawley: The interaction of Lamb waves with delaminations in composite laminates, *J. Acoust. Soc. Am.* **94**(4), 2240–2246 (1993)
- 16.99 S.H.D. Valdés, C. Soutis: Real-time nondestructive evaluation of fibre composite laminates using low-frequency lamb waves, *J. Acoust. Soc. Am.* **111**(4), 2026–2033 (2002)
- 16.100 S.S. Kessler, S.M. Spearing, C. Soutis: Damage detection in composite materials using Lamb wave methods, *Smart Mater. Struct.* **11**(2), 269–278 (2002)
- 16.101 M. Kehlenbach: Integrierte Sensorik zur Schädigungserkennung in Faserverbundstrukturen für die Luftfahrt. Ph.D. Thesis (TU Darmstadt, Darmstadt 2003), (in German)
- 16.102 P.D.T. O'Connor: *Practical Reliability Engineering*, 4th edn. (Wiley, New York 2001)
- 16.103 B. Bertsche: *Reliability in Automotive and Mechanical Engineering*, 1st edn. (Springer, Berlin 2008)
- 16.104 R. Abernethy: *The New Weibull Handbook*, 4th edn. (Abernethy, North Palm Beach 1994)
- 16.105 A. Meyna, B. Pauli: *Handbook on Reliability and Safety Engineering* (Hansa, München 2003), (in German)
- 16.106 H. Pham (Ed.): *Springer Handbook of Engineering Statistics* (Springer, Berlin Heidelberg New York 2006)
- 16.107 A. Birolini: *Reliability Engineering, Theory and Practice*, 4th edn. (Springer, Berlin Heidelberg New York 2003)
- 16.108 ReliaSoft Corp.: www.weibull.com (last accessed May 20, 2011)
- 16.109 NIST/SEMATECH: *e-Handbook of Statistical Methods*, <http://www.itl.nist.gov/div898/handbook/>
- 16.110 Y. Lu: Web site survey, *Qual. Reliab. Eng. Int.* **19**(6), v–vi (2003)
- 16.111 B. Dodson, D. Nolan: *Reliability Engineering Handbook* (Marcel Dekker, New York 2002)
- 16.112 C. Lipson, N.J. Sheth: Stress–strength interference give parts of failure *Journal, SAE* **77**(4), 38–45 (1969)
- 16.113 E. Haibach: *Structural Durability*, 2nd edn. (Springer, Berlin Heidelberg 2002), (in German)
- 16.114 C.M. Sonsino: *Principles of Variables Amplitude Fatigue Design and Testing*, *ASTM STP* **1439**, ed. by

- P.C. McKeighan, N. Ranganathan (ASTM Int., West Conshohocken 2003)
- 16.115 C. Berger, K.-G. Eulitz, P. Heuler, K.-L. Kotte, H. Naundorf, W. Schuetz, C.M. Sonsino, A. Wimmer, H. Zenner: Betriebsfestigkeit in Germany – An Overview, *Int. J. Fatigue* **24**, 603–625 (2002)
- 16.116 C.-C. Liu: A Comparison between the Weibull and Lognormal Models used to Analyse Reliability Data, Ph.D. Thesis (University of Nottingham, 1997)
- 16.117 W. Weibull: A statistical distribution function of wide applicability, *J. Appl. Mech.* **18**, 293–297 (1951)
- 16.118 I.A. Bronstein, K.A. Semendjajev: *Handbook of Mathematics* (Springer, Berlin Heidelberg New York 2004)
- 16.119 C. Reichelt: Numerical Determination of Weibull Parameters, *Fortschrittsber. VDI-Z* **1**(56) (1978), (in German)
- 16.120 C.D. Tarum: *Determination of the Critical Correlation Coefficient to Establish a Good Fit for Weibull and Log-Normal Failure Distributions* (SAE Technical Paper Series 1999-01-0057, 1999)
- 16.121 www.weibullNEWS.com/Fulhomem.htm (last accessed May 20, 2011)
- 16.122 S.D. Dubey: On some permissible estimators of the location parameter of the weibull and certain other distributions, *Technometrics* **9**(2), 293–307 (1967)
- 16.123 J.L. Romeu: Censored Data, *START* **11**(3), 1–8 (2004)
- 16.124 L.G. Johnson: *The Statistical Treatment of Fatigue Experiments* (Elsevier, New York 1964)
- 16.125 L.G. Johnson: *Theory and Technique of Variation Research* (Elsevier, New York 1964)
- 16.126 W. Zhao, E.A. Elsayed: An accelerated life testing model involving performance degradation, reprinted from *Proc. Annu. Reliab. Maintainab. Symp.*, Los Angeles, California, USA (2004) pp. 324–329
- 16.127 V. Oliviera, E.A. Colosimo: Comparison of methods to estimate the time-to-failure distribution in degradation tests, *Qual. Reliab. Eng. Int.* **20**, 363–373 (2004)
- 16.128 H.-F. Yu, S.-T. Tseng: On-line procedure for terminating an accelerated degradation test, *Stat. Sin.* **8**, 207–220 (1998)
- 16.129 V.Y. Shur, E.V. Nikolaeva, E.I. Shishkin, I.S. Baturin, D. Bolten, O. Lohse, R. Waser: Fatigue in PZT Thin Films, *MRS Symp. Proc.* **655**, C10.8.1–C10.8.6 (2001)
- 16.130 W. Nelson: *Accelerated Testing* (Wiley, New York 1990)
- 16.131 N.H. Criscimagna: Accelerated testing, *START* **6**(4), 1–5 (2003)
- 16.132 <http://www.fbh-berlin.com/business-areas/gan-electronics/reliability>, Ferdinand-Braun-Institut, Leibniz-Institut fuer Hoechstfrequenztechnik (03.12.2010)
- 16.133 H.B. Schwartz, P. Conde: HALT (highly accelerated life test) for Lead Free Soldering, *IPC/JEDEC 4th Int. Conf. on Lead Free Electronic Components and Assemblies*, Frankfurt, Germany, October 21–22 (2003)
- 16.134 B. Dodson, H. Schwab: *Accelerated Testing – A Practitioner's Guide to Accelerated and Reliability Testing* (SAE, Warrendale 2006)
- 16.135 A. Seifried, H. Schröpel, B. Bertsche: Statistical size effect and failure free time in dimensioning of machine components, *Konstruktion* **6**, 69–74 (2002), (in German)
- 16.136 B. Bertsche, P. Göhner, U. Jensen, W. Schinköthe, H. Wunderlich: *Zuverlässigkeit mechatronischer Systeme: Grundlagen und Bewertung in frühen Entwicklungsphasen* (Springer, Berlin Heidelberg 2009), (in German)
- 16.137 W. Yang: *Mechatronic Reliability* (Springer, Berlin Heidelberg 2002)
- 16.138 D. Flaschenträger, J. Nuffer, D. Hofmann, J. Gäng, B. Bertsche: Reliability assessment of an adaptronic system, *Konstruktion* **1/2** (2011), (in German)
- 16.139 M. Matthias, T. Melz, M. Thomaier: Entwicklung, Bau und Test eines multiaxialen, modularen Interfaces zur aktiven Schwingungsreduktion für Automotive Anwendungen (in German), presented at Adaptronic Congress, Göttingen (2005)
- 16.140 R. Platz, D. Mayer, J. Nuffer, M. Thomaier, K. Wolf: FMEA zur qualitativen Bemessung der Zuverlässigkeit eines aktiven Interfaces zur Schwingungsreduktion in PKW, *VDI Tagung Technische Zuverlässigkeit TTZ* (2007), (in German)
- 16.141 MIL-HDBK-217F: *Reliability Prediction of Electronic Equipment* (Department of Defense, Washington DC 1990)
- 16.142 International Electronic Council: *Reliability Data Handbook* (IEC, Geneva 2004)
- 16.143 D.C. Lupascu: *Fatigue in ferroelectric ceramics and related issues*, Springer Ser. Mater. Sci., Vol. 61, ed. by R. Hull, R.M.J. Osgood, J. Parisi, H. Warlimont (Springer, Berlin Heidelberg 2004)
- 16.144 C.S. Lynch, W. Yang, L. Collier, Z. Suo, R.M. McMeeking: Electric field induced cracking in ferroelectric ceramics, *Ferroelectrics* **166**, 11–30 (1995)
- 16.145 M. Mertmann: Fatigue in nitinol actuators, *Actuator 2006*, 10th Int. Conf. Actuators (2006) pp. 461–466
- 16.146 P. Jäger: *Zuverlässigkeitsbewertung mechatronischer Systeme in frühen Entwicklungsphasen*, Dissertationsschrift, Institut für Maschinenelemente IMA, Universität Stuttgart (2007), (in German)
- 16.147 J.D. Musa, A. Iannino, K. Okumoto: *Software Reliability: Measurement, Prediction, Application*, Software Eng. Ser. (McGraw Hill, New York 1987)
- 16.148 Reliability Engineer's Toolkit, The Rome Laboratory (1993)
- 16.149 Health Safety Executive (GB): *Out of Control* (HSE Books, Bootle 1995)
- 16.150 N.E. Fenton, M. Neil: A Critique of Software Defect Prediction Models, *Software Eng.* **25**(5), 675–689 (1999)

Modelling **Part E**

Part E Modeling and Simulation Methods

17 Molecular Dynamics

Masato Shimono, Tsukuba, Japan

18 Continuum Constitutive Modeling

Shoji Imatani, Kyoto, Japan

19 Finite Element and Finite Difference Methods

Akira Tezuka, Tsukuba, Japan

20 The CALPHAD Method

Hiroshi Ohtani, Kitakyushu, Japan

21 Phase Field Approach

Toshiyuki Koyama, Nagoya, Japan

22 Monte Carlo Simulation

Xiao Hu, Tsukuba, Japan

Yoshihiko Nonomura, Ibaraki, Japan

Masanori Kohno, Tsukuba, Japan

Molecular Dynamics

17. Molecular Dynamics

This chapter gives an overview of the molecular dynamics (MD) simulation method. In the first section, the basics techniques of MD will be introduced so that the reader is able to start actual calculations. In the following three sections, several applications of MD simulation, some adapted for actual materials and others concerned with idealized model systems, will be presented. In the second section, a simulation study of diffusionless transformations such as the martensitic transformation and solid-state amorphization is presented. Analysis of amorphous and crystalline structures is described in Chap. 5 in this handbook. MD calculations of the processes involved in the preparation of amorphous alloys by rapid solidification as well as annealing processes in these alloys are discussed in the third section. In the last section, the investigation of atomic diffusion processes in liquid and solid (crystalline and amorphous) phases by MD simulation is explored. Readers may also refer to Chap. 7 concerning atomic diffusion processes in materials.

17.1	Basic Idea of Molecular Dynamics	975
17.1.1	Time Evolution of the Equations of Motion	975
17.1.2	Constraints on the Simulation Systems	978
17.1.3	Control of Temperature and Pressure	980
17.1.4	Interaction Potentials	985
17.1.5	Physical Observables	987
17.2	Diffusionless Transformation	988
17.2.1	Martensitic Transformation	988
17.2.2	Transformations in Nanoclusters	991
17.2.3	Solid-State Amorphization	993
17.3	Rapid Solidification	995
17.3.1	Glass-Formation by Liquid Quenching	995
17.3.2	Annealing of Amorphous Alloys	999
17.3.3	Glass-Forming Ability of Alloy Systems	1004
17.4	Diffusion	1006
17.4.1	Diffusion in Crystalline Phases	1006
17.4.2	Diffusion in Liquid and Glassy Phases	1008
17.5	Summary	1010
	References	1010

17.1 Basic Idea of Molecular Dynamics

In this section, the basic formalism of MD simulation will be introduced, and some useful methods invented for MD calculations will then be presented.

17.1.1 Time Evolution of the Equations of Motion

The essential task in MD simulation is to solve the Newtonian equation of motion numerically. Hence, techniques for numerical solution of differential equations will be explained in this section. The main topics are numerical recipes used for this purpose such as the Verlet and the Gear methods.

The basic idea of molecular dynamics is simple: to follow the motion of all atoms in the system by solving

the Newtonian equations of motion

$$d^2\mathbf{r}_i(t)/dt^2 = \mathbf{F}_i(t)/m_i, \quad i = 1, 2, 3, \dots, N, \quad (17.1)$$

or

$$d^2r_{i\alpha}(t)/dt^2 = -\frac{1}{m_i} \partial\phi/\partial r_{i\alpha}(t), \quad \alpha = 1, 2, 3 \quad (17.2)$$

if the Lagrangian of the system has the following form

$$L_0 = \frac{1}{2} \sum_i m_i \mathbf{v}_i^2 - \phi(\mathbf{r}_1, \mathbf{r}_2, \dots). \quad (17.3)$$

In the numerical integration of the differential equation (17.1), we should calculate the coordinates of

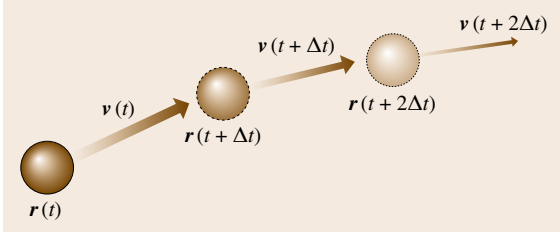


Fig. 17.1 An illustrative view of the integration steps of a particle trajectory in MD simulation

all particles in the system step by step in time, as depicted in Fig. 17.1. For simplicity, let us use a one-dimensional expression $x(t)$ for the particle coordinates. The basic equation for the purpose of predicting the coordinates $x(t + \Delta t)$ at a future time $t + \Delta t$ is the Taylor expansion

$$x(t + \Delta t) = x(t) + x'(t)\Delta t + x''(t)(\Delta t)^2/2 + x'''(t)(\Delta t)^3/3! + \dots, \quad (17.4)$$

where the prime denotes the functional derivative. For a practical calculation, we should truncate the Taylor expansion at a finite order of Δt , and also include the information of the Newtonian equation of motion. To achieve the latter, we use the following relation, which holds for the second time derivative of the particle coordinates at any time

$$x''(t) = F(t)/m. \quad (17.5)$$

Based on this idea, a large number of algorithms have been suggested. We shall explore some of the popular algorithms together with their merits and drawbacks.

Verlet Method

The first example of the popular algorithms is the Verlet method [17.1], which can be derived as follows. Let us write the Taylor series of a forward time step and a backward time step up to third order

$$x(t + \Delta t) = x(t) + x'(t)\Delta t + x''(t)(\Delta t)^2/2 + x'''(t)(\Delta t)^3/3! + O[(\Delta t)^4], \quad (17.6)$$

$$x(t - \Delta t) = x(t) - x'(t)\Delta t + x''(t)(\Delta t)^2/2 - x'''(t)(\Delta t)^3/3! + O[(\Delta t)^4]. \quad (17.7)$$

By adding the above expansions, the third-order terms cancel and, using the equation of motion (17.5), we

get

$$x(t + \Delta t) = 2x(t) - x(t - \Delta t) + F(t)(\Delta t)^2/m, \quad (17.8)$$

which holds up to third order in the time step Δt . This relation is called the Verlet leap-frog algorithm.

An advantage of this method is its simple form, which allows us to code a program very easily. For example, the coding processes can be

- Step 1 Specify the initial position $x(t_0)$ and the position at the first step $x(t_0 + \Delta t)$
- Step 2 Calculate the force $F(t_0 + \Delta t)$ at the first step
- Step 3 Compute $x(t_0 + 2\Delta t)$ according to (17.8)
- Step 4 Repeat steps 2 and 3 with $t_0 \rightarrow t_0 + \Delta t$.

Throughout the whole calculation processes, we only need to record the two latest positions of the particles in the Verlet method, which saves computer memory space.

The form of (17.8) includes only particle coordinates and no velocity terms. The velocity $v(t)$ can be evaluated by rewriting (17.8) as follows

$$x(t + \Delta t) = x(t) + v(t)\Delta t + F(t)(\Delta t)^2/2m, \quad (17.9)$$

$$v(t) = [x(t + \Delta t)] - x[t - \Delta t)]/2\Delta t. \quad (17.10)$$

Although the Verlet method has merit due to its simple form, we encounter a difficulty when the force $F(t)$ depends on the velocity $v(t)$, because the velocity (17.10) can be computed only after calculating the forward-step coordinate $x(t + \Delta t)$, which is itself calculated using the velocity $v(t)$. This is something of a vicious circle. Since the force term rarely includes the velocity for usual atomic interactions, this deficiency is not always a limitation. However, as we shall discuss later, when we try to control the temperature or the pressure of the simulation system by introducing a fictitious variable, we inevitably encounter this problem caused by a velocity-dependent force term.

To avoid this situation, a slightly more complicated prescription, called the predictor–corrector scheme is commonly used, where the coordinates $\tilde{x}(t + \Delta t)$ at a forward step is temporarily calculated, and then subsequently corrected using the force term $F(t + \Delta t)$ calculated at the next time step.

Gear Method

Among the methods using the predictor–corrector scheme, the most popular method is one called the Gear predictor–corrector method [17.2]. The calculation procedure consists of two parts. The first step is called

the predictor step, which is just a Taylor expansion expressed in vector representation for a set of coordinates $x(t)$ and their time derivatives $x'(t)$, $x''(t)$, $x'''(t)$, ...

$$\tilde{\mathbf{q}}(t + \Delta t) = G\mathbf{q}(t), \text{ where}$$

$$G = \begin{pmatrix} 1 & 1 & 1 & 1 & \cdots \\ 0 & 1 & 2 & 3 & \cdots \\ 0 & 0 & 1 & 3 & \cdots \\ 0 & 0 & 0 & 1 & \cdots \\ \vdots & \vdots & \vdots & \vdots & \ddots \end{pmatrix}, \quad \mathbf{q}(t) = \begin{pmatrix} x(t) \\ x'(t)\Delta t \\ x''(t)(\Delta t)^2/2! \\ x'''(t)(\Delta t)^3/3! \\ \vdots \end{pmatrix}. \quad (17.11)$$

One advantage of the Gear method is that we can choose the order of time step Δt in the Taylor expansion to take into account. If we choose to calculate up to order $(\Delta t)^{p-1}$, or equivalently we choose the coordinate vector $\mathbf{q}(t)$ as a p -component vector, then we call it the p -th order Gear method.

Using the predicted coordinates $\tilde{\mathbf{q}}(t + \Delta t)$, we then calculate the force $F(t + \Delta t)$ in the second, corrector step as follows

$$\mathbf{q}(t + \Delta t) = \tilde{\mathbf{q}}(t + \Delta t) + \mathbf{A}(\Delta t)^2 \times [F(t + \Delta t) - \tilde{x}''(t + \Delta t)] / 2, \quad (17.12)$$

where \mathbf{A} is a constant vector called the correction vector.

The forms of the matrix G and vector \mathbf{A} depend on the order of the method. Whereas G is uniquely determined by the order p , there is no unique choice for the correction vector \mathbf{A} that make the third component A_3 unity and thereby satisfy the equation of motion at $t + \Delta t$. Gear determined [17.2] the vector \mathbf{A} so that the numerical errors do not accumulate monotonically. For the fourth-, fifth- and sixth-order algorithms, the prescribed values are listed below

$$G = \begin{pmatrix} 1 & 1 & 1 & 1 \\ 0 & 1 & 2 & 3 \\ 0 & 0 & 1 & 3 \\ 0 & 0 & 0 & 1 \end{pmatrix}, \quad \mathbf{A} = \begin{pmatrix} 1/6 \\ 5/6 \\ 1 \\ 1/3 \end{pmatrix}, \quad (17.13)$$

for $p = 4$,

$$G = \begin{pmatrix} 1 & 1 & 1 & 1 & 1 \\ 0 & 1 & 2 & 3 & 4 \\ 0 & 0 & 1 & 3 & 6 \\ 0 & 0 & 0 & 1 & 4 \\ 0 & 0 & 0 & 0 & 1 \end{pmatrix}, \quad \mathbf{A} = \begin{pmatrix} 19/120 \\ 3/4 \\ 1 \\ 1/2 \\ 1/12 \end{pmatrix}, \quad (17.14)$$

for $p = 5$,

$$G = \begin{pmatrix} 1 & 1 & 1 & 1 & 1 & 1 \\ 0 & 1 & 2 & 3 & 4 & 5 \\ 0 & 0 & 1 & 3 & 6 & 10 \\ 0 & 0 & 0 & 1 & 4 & 10 \\ 0 & 0 & 0 & 0 & 1 & 5 \\ 0 & 0 & 0 & 0 & 0 & 1 \end{pmatrix}, \quad \mathbf{A} = \begin{pmatrix} 3/20 \\ 251/360 \\ 1 \\ 11/18 \\ 1/6 \\ 1/60 \end{pmatrix}, \quad (17.15)$$

for $p = 6$.

Consequently, the coding process is as follows

- Step 1 For the p -th order method, specify the initial position $x(t_0)$ and its derivatives $x'(t_0)$, $x''(t_0)$, ..., and $x^{(p-1)}(t_0)$.
- Step 2 Calculate the predicted coordinates $\tilde{\mathbf{q}}(t_0 + \Delta t)$ at the first step according to (17.11).
- Step 3 Calculate the force $F(t_0 + \Delta t)$ at the first step using $\tilde{\mathbf{q}}(t_0 + \Delta t)$.
- Step 4 Compute the corrected $\mathbf{q}(t_0 + \Delta t)$ according to (17.12).
- Step 5 Repeat steps 2 to 4 with $t_0 \rightarrow t_0 + \Delta t$.

In the course of numerical integration, it is inevitable that numerical errors will accumulate. The size of these errors depends on the numerical integration method used, as well as the time step Δt . To estimate the order of the numerical errors, we calculate the trajectory $x(t)$ of a simple harmonic oscillator of unit mass

$$x''(t) = -x(t), \quad (17.16)$$

and evaluate the deviation from the analytical solution for different integration methods and different time steps.

Figure 17.2 shows the results for the deviation of the numerically integrated trajectory from the exact solution after 100 oscillation periods (200π). As one can see from the slope of a linear approximation to the plots depicted in the figure, the numerical error of the p -th Gear method scales as $(\Delta t)^p$. This behavior is just what one would expect from (17.11), but it is not straightforward, because the number of calculation steps grows as $(\Delta t)^{-p}$ for a constant interval T , although the error for each step is assured to be as low as $(\Delta t)^p$ in the p -th Gear method. In this context, it is interesting that the numerical error of the Verlet method behaves as $(\Delta t)^2$, even though the error at each step is kept as low as $(\Delta t)^4$. In this sense, the Verlet method is considered to be a second-order formalism.

The tendency in Fig. 17.2 tells us that we can keep the numerical errors low if we use the Gear method with a sufficiently small time step compared to a typical time scale for characteristic motion of

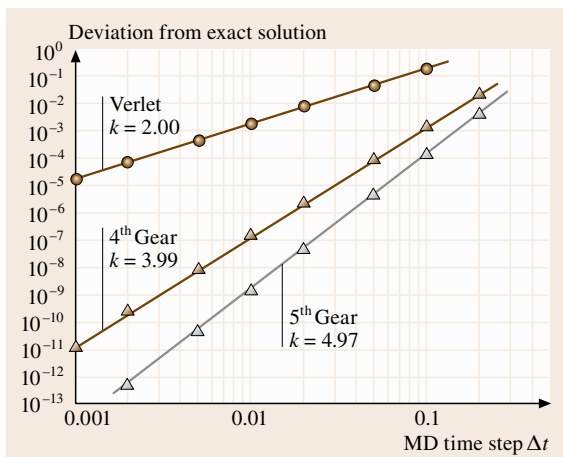


Fig. 17.2 The relation between the deviation in particle trajectory from the exact solution of the harmonic oscillator after 100 cycles and the calculation time step Δt . The slope k of the linear approximation of each set of plots is also depicted

the system considered. However, in the case of the simulation of complex systems of many atoms, numerical errors might also originate from other factors such as an artificial cutoff of the interactions or computer roundoff errors in the numerical treatment. So, we cannot definitely conclude that the higher-order Gear methods are superior to the Verlet method. In some practical simulations of a small protein [17.3], the Verlet method does show more accurate energy conservation than the higher-order (fourth to eighth) Gear methods for a considerably large time step, although the calculation time is shorter and the consumed memory space is lower for the Verlet methods. In a practical sense, we should choose these numerical methods depending on available computational resources such as calculation speed and memory storage.

Program Languages and Computational Platforms

To end this section, we consider the program languages in which the calculation code is written and the platforms on which the MD calculations are performed. The program that executes MD calculations on computers are usually written in particular languages. The FORTRAN language is one of the most popular due to its historical use for supercomputers. Of course, other program languages such as the C or JAVA are also good for the coding MD programs.

In terms of the platform for the simulation, any type of computer, for example supercomputers, workstations, personal computers (PCs), or others, can be used for MD simulations. Any type of operating system, such as UNIX, Windows, Macintosh, or Linux, will work, as long as it supports the language used. In particular, since the main part of the MD calculations consists of the computation of forces acting on each particle, which can be calculated independently, the use of computers with vector or parallel processors makes the calculation highly efficient. In addition, the computing power of modern personal computers is sufficient to perform MD simulations at a satisfactory speed. Examples of typical calculation time of MD simulations on a PC will appear in the following section.

17.1.2 Constraints on the Simulation Systems

MD simulation is inevitably restricted by computational power. Therefore, in this section, we shall introduce two remedies for this deficiency: periodic boundary conditions and the bookkeeping method.

Since the typical time scale for atomic motions is of the order of a picosecond (10^{-12}) or less, we should use values of the order of a femtosecond (10^{-15}) for the time step Δt to keep the numerical errors small. Therefore, it takes many more than a million iterations to follow the motion of a single atom for just a microsecond. Moreover, the number of calculations required grows rapidly as the number of atoms N in the system increases. Under these circumstances, we should satisfy ourselves with the calculation of a small system with fewer than a million atoms and a short physical process over less than a few microseconds. Thus there is always a large discrepancy in both length and time scale between the real macroscopic system and the simulation system we can handle. For example, the typical size of a million-atom system is as small as a few tens of nanometers, which means that the simulation system is far from macroscopic.

Periodic Boundary Condition

A popular remedy for the length scale problem is the use of periodic boundary conditions. As shown schematically in Fig. 17.3, we first confine all the atoms to a box, and then copy the box, together with the atoms in the box, identically in three directions. By repeating this procedure, we can fill the whole space with the original

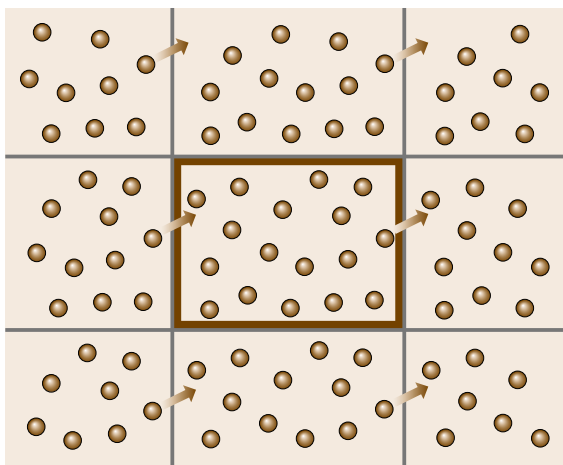


Fig. 17.3 An illustrative view of periodic boundary conditions

configuration and its replicas. Consequently, an atom leaving the box to the right through one boundary can be identified with an atom entering from the left at the opposite boundary. A system constructed in this way can be taken as having infinite size and an infinite number of atoms.

Of course the periodic system cannot be identical to an infinitely large bulk system. Some drawbacks caused by periodic boundary conditions will be discussed in later sections.

Bookkeeping Method

The main part of the calculational cost in solving the equations of motion is due to the calculation of the interactive forces between atoms, because, roughly speaking, the number of combinations of interacting atomic pairs grows as N^2 or faster with the total number of atoms N . If the atomic force has a long-range interaction range, such as the Coulomb interaction, this problem is very serious, and the complicated Ewald method [17.4] is needed to perform calculations effectively. On the other hand, if the interaction is short-range, which is the case for most metallic systems, a simple prescription called the bookkeeping method effectively saves us a lot of calculation time.

The bookkeeping concept is simple: we keep a book, in which a table of the neighboring atoms is written down for all atoms in the system, and is regularly updated with a proper period $\Delta t N_{\text{book}}$. More concretely, we first calculate the members within a distance $r_{\text{book}} = r_c + r_{\text{margin}}$ of each atom, where r_c is the interaction range, and write them down in the book,

as illustrated schematically in Fig. 17.4. Then we need only consider interactions between the atom and its neighbors, as written in the book, in the following N_{book} numerical integration steps. After every N_{book} integration steps, we update the list of neighbors in the book by calculating the distances between all atomic pairs. The period N_{book} for updating the book should be determined according to $N_{\text{book}} v \Delta t = r_{\text{margin}}$, where v is the average velocity of the atoms.

As previously mentioned, the calculation time required for the force calculation grows like N^2 in a pairwise-interacting system, if we calculate the interaction for all pairs of atoms. On the other hand, when we use the bookkeeping method, the time required only grows linearly with N , because the average number of atoms neighboring each particle is almost constant and does not depend on N .

Figure 17.5 shows the relation between the calculation time needed for 100 integration steps and the total number of atoms N in a simulation cell. In this calculation, we choose a system consisting of pairwise-interacting atoms and use $r_{\text{book}} = 1.32r_c$ and $N_{\text{book}} = 50$. The calculation program was coded in the FORTRAN language and executed on a PC with a single processor. In Fig. 17.5, we have shown the slope k of the linear approximation to each data set in log-log plots. Note that the calculation time for the simulation *with* bookkeeping scales almost linearly, while that of the simulation *without* bookkeeping scales almost quadratically, which leads to a difference of nearly a thousand times in the calculation time for $N = 20\,000$ atoms.

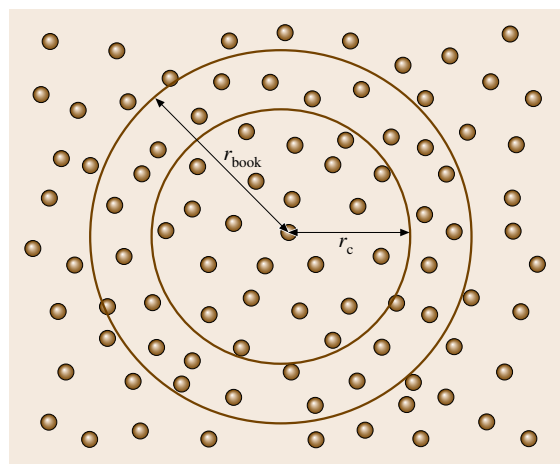


Fig. 17.4 An illustrative view of the regions related with the bookkeeping method

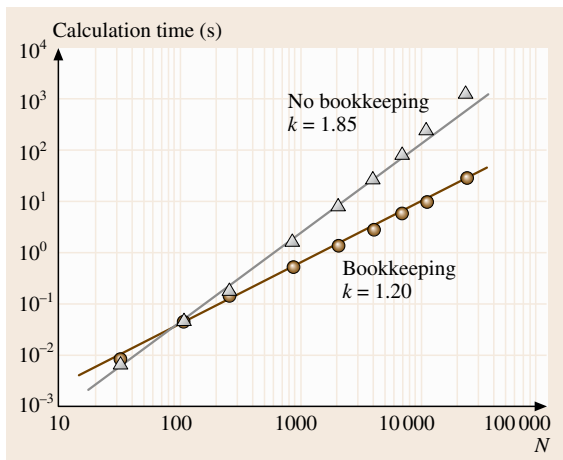


Fig. 17.5 The relation between the calculation time for 100 MD steps and the total number N of atoms in the simulation system with and without bookkeeping

17.1.3 Control of Temperature and Pressure

To compare the simulation results with experimental results, we must control the thermodynamical conditions such as the temperature and the pressure of the simulation system. The techniques for controlling the temperature and the pressure of the simulation system will be introduced in this section: the momentum-scaling method and the Nose–Hoover thermostat for temperature control, and the Andersen and Parrinello–Rahman methods for pressure control.

Before introducing the control methods, we note that the use of the control methods discussed below includes a subtle point; the standard way of temperature or pressure control for the simulation system lies outside the description of the Newtonian equations of motion. Consequently, the deterministic nature of the MD simulation will be lost and there is a risk that the simulation results might depend on the control method we use. Therefore, care should be taken when using such control methods in MD simulations.

Momentum-Scaling Method

To control the temperature of the simulation system, several methods have been presented. One of the simplest methods is the momentum-scaling method [17.5, 6]. The temperature T of the system is defined by the average kinetic energy of all the atoms as

$$\frac{3}{2}k_{\text{B}}T = \frac{1}{2} \sum_i m_i v_i^2, \quad (17.17)$$

where k_{B} is the Boltzmann constant. Accordingly, when we want the system temperature to be T_0 , we rescale the kinetic momenta of all atoms by a factor of $\sqrt{T_0/T}$.

By executing this rescaling procedure repeatedly, the system temperature will approach the desired temperature. Even though this method appears too naive and basic, it has been verified [17.7] that the thermodynamical quantities will approach their equilibrium values after iterated equilibration processes using momentum rescaling if the number of atoms N is sufficiently large.

One of advantages of this method is that the coding procedure is simple. For example, supposed that the rescaling of the momenta is to be carried out every N_{rescale} steps, we would calculate the temperature T of the system according to (17.17), and insert the momentum-scaling transformation for all atoms as

$$p_i \rightarrow \sqrt{T_0/T} p_i, \quad (17.18)$$

after every N_{rescale} integration steps.

In Fig. 17.6, we have depicted two examples of the time evolution of the system temperature T in a simulation in which the temperature is controlled by the momentum-scaling method. Starting from an equilibrated state at $T = 200$ K, we have changed the temperature to 400 K at $t = 1000$ steps, and then to

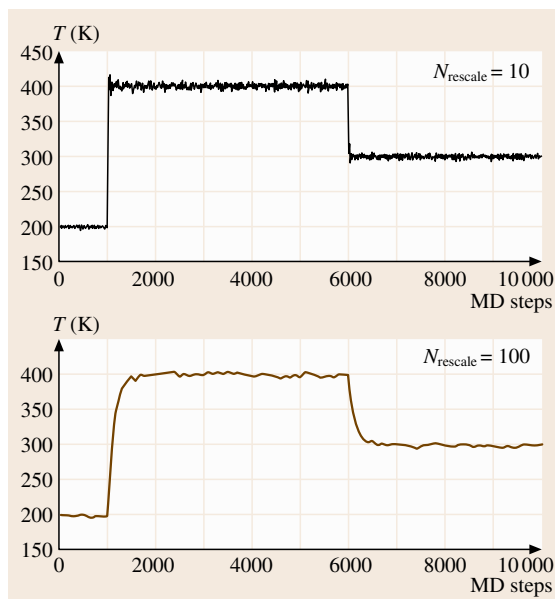


Fig. 17.6 Time evolution of the effective temperature T of the simulation system calculated from the total kinetic energy of the atoms

300 K at $t = 6000$ steps. The upper graph shows the case with $N_{\text{rescale}} = 10$, while the lower graph shows the case with $N_{\text{rescale}} = 100$, where the convergence to the desired temperature is slower. In both cases, the temperature of the system is well controlled to the desired value except for accompanying small fluctuations.

Stochastic Method

There is another temperature-control method called the stochastic method [17.8]. In this method, we pick an atom at random and exchange its velocity with a value taken at random from a Maxwell–Boltzmann distribution with the desired temperature T_0 . By executing this prescription repeatedly every N_{exch} steps, the system should approach thermal equilibrium. However, it is difficult to determine a proper value for the interval N_{exch} . An interval that is too short will generate a jiggling behavior of atoms within a small configuration space, while an interval that is too long will result in a very long calculation time to obtain the thermal equilibration at the desired temperature. In addition, there is another shortcoming to the stochastic method, which might bring about an unwanted steady state in the simulation system. Therefore, one should consult [17.9] if using this method.

Nose–Hoover Thermostat

In contrast to the stochastic nature of the previous method, there is a sophisticated temperature-control method with a deterministic nature, called the Nose–Hoover thermostat method [17.10, 11]. In this method, a fictitious variable S , which plays the role of a temperature controller, is introduced into the mechanics of the simulation system. The variable S serves as a sort of friction of atoms, and its value depends on the difference between the system temperature T and the desired temperature T_0 . The equations of motion of the extended system are the following

$$\frac{d^2 \mathbf{r}_i}{dt^2} = -\frac{1}{m_i} \frac{\partial \phi}{\partial \mathbf{r}_i} - \frac{\dot{S}}{S} \mathbf{v}_i, \quad (17.19)$$

$$\frac{d^2 S}{dt^2} = \frac{S}{Q} \left(\sum_i m_i \mathbf{v}_i^2 - 3Nk_B T_0 \right) + \frac{\dot{S}^2}{S}, \quad (17.20)$$

where Q is the fictitious mass of the variable S . The dotted symbols denote their time derivatives.

The role of the variable S can be seen more clearly if we introduce a variable $\zeta = \dot{S}/S$ and rewrite (17.19) and (17.20) as

$$\frac{d^2 \mathbf{r}_i}{dt^2} = -\frac{1}{m_i} \frac{\partial \phi}{\partial \mathbf{r}_i} - \zeta \mathbf{v}_i, \quad (17.21)$$

$$\frac{d\zeta}{dt} = \frac{2}{Q} \left(\frac{1}{2} \sum_i m_i \mathbf{v}_i^2 - \frac{3}{2} Nk_B T_0 \right). \quad (17.22)$$

We can see that the second term on the right-hand side of (17.21), which is proportional to atom velocities, serves as a sort of friction term, whose value depends on the difference between the system temperature T and the desired temperature T_0 . It has also been verified [17.7] that this extended system gives the same partition function as that of the original system in the thermal equilibrium limit.

If we consider the fictitious variable S as the coordinate of an additional atom, which has a peculiar equation of motion (17.20), then a coding procedure can be executed similarly. However, since (17.19–17.22) contain velocity dependent terms, a simple leap-frog method does not work straightforwardly. In this case, use of a predictor–corrector method is appropriate. For example, using the Gear method, the coding procedure is the following: (Here we shall use one dimensional expression $x_i(t)$ for the atom coordinates for simplicity.)

- Step 1 For the p -th order method, specify the initial position $x_i(t_0)$ and its derivatives $x_i'(t_0)$, $x_i''(t_0)$, \dots , and $x_i^{(p-1)}(t_0)$ and assign them to $\mathbf{q}_i(t_0)$ for $i = 1$ to N .
- Step 2 Consider $S(t)$ as coordinates of the $(N+1)$ -th atom, specify the initial value for $S(t_0)$ and its derivatives $S'(t_0)$, $S''(t_0)$, \dots , and $S^{(p-1)}(t_0)$, and assign them to $\mathbf{q}_{N+1}(t_0)$.
- Step 3 Calculate the predicted coordinates $\tilde{\mathbf{q}}_i(t_0 + \Delta t)$ for $i = 1$ to $N+1$ at the first step according to (17.11).
- Step 4 Calculate the force $F_i(t_0 + \Delta t)$ at the first step for $i = 1$ to N according to (17.19) by using $\tilde{\mathbf{q}}_i(t_0 + \Delta t)$.
- Step 5 Calculate the force $F_{N+1}(t_0 + \Delta t)$ at the first step according to (17.20) by using $\tilde{\mathbf{q}}_i(t_0 + \Delta t)$.
- Step 6 Compute the corrected $\mathbf{q}(t_0 + \Delta t)$ according to (17.12) for $i = 1$ to $N+1$.
- Step 7 Repeat steps 3 to 6 with $t_0 \rightarrow t_0 + \Delta t$.

Here one point should be noted about the methods in which fictitious variables are introduced, such as the Nose–Hoover thermostat. Once the *motion* of the fictitious variables has settled down, the fictitious variable does not harm the simulation system. On the other hand, for example, if we try to increase the system temperature by a large amount, the value of the fictitious variable starts to change very rapidly, so the temperature of the system will rise to the target value. However,

when the system temperature reaches the desired value, the motion of the fictitious variables goes on due to their inertia, which results in the temperature continuing to rise until the motion of the variable stops. This type of overshooting behavior is an inevitable result of methods with fictitious variables. We shall see an example of such undesirable behavior in the case of pressure control in the following.

Boundary Box Scaling

If the simulation system has a fixed boundary, we cannot control the pressure of the system. Therefore, pressure control methods are always accompanied by changes of the boundary conditions. Suppose that the simulation system is contained in a boundary box of volume V , the internal pressure of the system can be calculated using the virial formula

$$P_{\alpha\beta}^{\text{int}} = \frac{1}{3V} \sum_i (m_i v_{i\alpha} v_{i\beta} - q_{i\alpha} \partial\phi / \partial q_{i\beta}), \quad (17.23)$$

where the Greek symbols take the Cartesian values 1, 2, or 3. So a simple method is to enlarge the size of the simulation cell if we want to decrease the pressure, and vice versa. In more concrete words, if the boundary box has a pallerelpiped shape spanned by the three vectors $(\mathbf{a} \ \mathbf{b} \ \mathbf{c}) = \mathbf{h}$, where $h_{\alpha\beta}$ is a 3×3 tensor, we can control the pressure P^{int} of the system by varying the cell shape according to

$$h_{\alpha\beta} \rightarrow h_{\alpha\beta} \left[1 - \varepsilon (P_{0\alpha\beta} - P_{\alpha\beta}^{\text{int}}) \right], \quad (17.24)$$

where P_0 is the desired pressure and ε is an appropriate small parameter. This method is similar to the momentum-scaling method in some sense.

Andersen Method

As in the case of temperature control, there are some more sophisticated methods for the pressure control in which a fictitious variable is introduced in order to control the system pressure. In this case, the simulation cell itself is taken as a fictitious dynamical variable just like the Nose–Hoover thermostat S . The total Lagrangian L is defined as

$$L = L_0 + L_{\text{cell}}, \quad (17.25)$$

$$L_0 = \frac{1}{2} \sum_i m_i \mathbf{v}_i^2 - \phi(\mathbf{r}_1, \mathbf{r}_2, \dots), \quad (17.26)$$

$$L_{\text{cell}} = K_{\text{cell}} - P^{\text{ext}} V, \quad (17.27)$$

where K_{cell} is the *kinetic* term of the simulation cell, which depends on the method, P^{ext} is the external stress, and $V = \det h$ is the cell volume.

Several forms of K_{cell} have been proposed. In Andersen's scheme [17.8], the shape of the cell is restricted to be cubic, that is, $h_{\alpha\beta} = V^{1/3} \delta_{\alpha\beta}$. The dynamics are described by

$$K_{\text{cell}}^{\text{A}} = \frac{1}{2} M \dot{V}^2, \quad (17.28)$$

where the dotted variables denote their time derivatives and M is the effective *mass* of the cubic cell. In this case, the equations of motion are the followings

$$d\mathbf{r}_i / dt = \mathbf{p}_i / m_i + \frac{1}{3} V^{-1} \dot{V} \mathbf{r}_i, \quad (17.29)$$

$$d\mathbf{p}_i / dt = -\partial\phi / \partial \mathbf{r}_i - \frac{1}{3} V^{-1} \dot{V} \mathbf{p}_i, \quad (17.30)$$

$$d^2 V / dt^2 = \frac{1}{M} \left[\frac{1}{3V} \sum_i (m_i \mathbf{p}_i^2 - \mathbf{r}_i \cdot \partial\phi / \partial \mathbf{r}_i) - P^{\text{ext}} \right], \quad (17.31)$$

where the third equation means that the cell motion is triggered by the deviation of the internal stress from the external stress.

By introducing scaled coordinates s_i parameterized as $\mathbf{r}_i = L \mathbf{s}_i$ by the edge length $L = V^{1/3}$ of the cubic cell, (17.29–17.31) can be rewritten as

$$d^2 s_i / dt^2 = -\frac{L^{-1}}{m_i} \partial\phi / \partial \mathbf{r}_i - 2L^{-1} \dot{L} \dot{s}_i, \quad (17.32)$$

$$d^2 L / dt^2 = \frac{L^{-2}}{3M} \left[\frac{1}{3V} \sum_i (m_i (L \dot{s}_i)^2 - \mathbf{r}_i \cdot \partial\phi / \partial \mathbf{r}_i) - P^{\text{ext}} \right] - 2L^{-1} \dot{L}^2. \quad (17.33)$$

These expressions are more easy to handle for coding in many cases.

Parrinello–Rahman Method

In the Parrinello–Rahman method [17.12], which is a generalization of Andersen's method, the shape of the simulation cell is allowed to deform more flexibly. The periodic box has a pallerelpiped shape spanned by the three vectors $(\mathbf{a} \ \mathbf{b} \ \mathbf{c}) = \mathbf{h}$, as shown in Fig. 17.7. The kinetic part is written as

$$K_{\text{cell}}^{\text{PR}} = \frac{1}{2} M \text{tr}({}^t \dot{h} \dot{h}), \quad (17.34)$$

where ${}^t h$ denotes the transpose of h and the dotted variables denote their time derivatives again. The equations

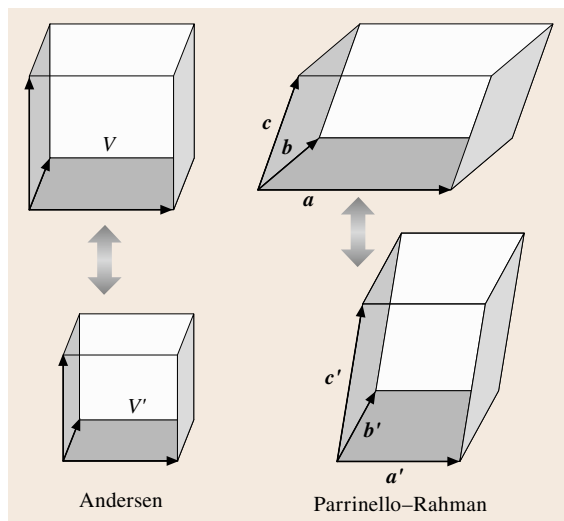


Fig. 17.7 Illustrative images of a deformation of the periodic boundary cell in the Andersen and the Parrinello–Rahman scheme

of motion can then be written down by using scaled coordinates s_i parameterized as $\mathbf{r}_i = h\mathbf{s}_i$ in the following forms

$$ds_i/dt = h^{-1}\mathbf{p}_i/m_i, \quad (17.35)$$

$$d\mathbf{p}_i/dt = -\partial\phi/\partial\mathbf{r}_i - {}^t h^{-1}{}^t \dot{h}\mathbf{p}_i, \quad (17.36)$$

$$d^2h/dt^2 = \frac{V}{M}(\Pi - P^{\text{ext}}) {}^t h^{-1}, \quad (17.37)$$

where

$$(\Pi - P^{\text{ext}})_{\alpha\beta} = \frac{1}{V} \sum_i [m_i(h\dot{s}_i)_\alpha(h\dot{s}_i)_\beta - r_{i\alpha}\partial\phi/\partial r_{i\beta}] - P_{\alpha\beta}^{\text{ext}} \quad (17.38)$$

is the deviation of the internal from the external stress tensor.

As schematically illustrated in Fig. 17.7, the dynamical variable fictitiously introduced into the simulation system is the volume V in the Andersen method, while its counterpart is the shape tensor h in the Parrinello–Rahman method; in both of these methods the periodic simulation cell can change its shape according to the dynamical variable V or h . In both Andersen’s method and the Parrinello–Rahman method, the coding procedure is carried out by taking the fictitious parameters V or h as additional *atoms* just like in the Nose–Hoover thermostat method. In addition, since (17.29–17.33) and (17.35–17.38) contain velocity-dependent terms, use of a predictor–corrector

method is appropriate. For example, to code the Andersen’s constant-pressure method by using the Gear algorithm, the outline is the following: (Here we shall also use one-dimensional expression $x_i(t)$ for the atom coordinates and $s_i(t) = L(t)^{-1}x_i(t)$ for the scaled coordinates for simplicity.)

- Step 1 For the p -th order method, specify the initial (scaled) position $s_i(t_0)$ and its derivatives $s_i'(t_0), s_i''(t_0), \dots$, and $s_i^{(p-1)}(t_0)$ and assign them to $\mathbf{q}_i(t_0)$ for $i = 1$ to N .
- Step 2 Consider $L(t)$ (or $V(t)$) as coordinates of the $(N+1)$ -th atom, specify the initial value for $L(t_0)$ (or $V(t_0)$) and its derivatives, and assign to $\mathbf{q}_{N+1}(t_0)$.
- Step 3 Calculate the predicted coordinates $\tilde{\mathbf{q}}_i(t_0 + \Delta t)$ for $i = 1$ to $N+1$ at the first step according to (17.11).
- Step 4 Calculate the force $F_i(t_0 + \Delta t)$ at the first step for $i = 1$ to N according to (17.32) by using $\tilde{\mathbf{q}}_i(t_0 + \Delta t)$.
- Step 5 Calculate the force $F_{N+1}(t_0 + \Delta t)$ at the first step according to (17.33) by using $\tilde{\mathbf{q}}_i(t_0 + \Delta t)$.
- Step 6 Compute the corrected $\mathbf{q}_i(t_0 + \Delta t)$ according to (17.12) for $i = 1$ to $N+1$.
- Step 7 Repeat step 3 to 6 with $t_0 \rightarrow t_0 + \Delta t$.

As noted above, there is a risk that the fictitious variables introduced to control temperature or pressure might harm the real dynamics of the atoms. In this regard, we shall see how the fictitious variables control the system pressure in the constant-pressure formalism. In Fig. 17.8, an example of the time evolution of the internal pressure $P = (P_{11}^{\text{int}} + P_{22}^{\text{int}} + P_{33}^{\text{int}})/3$ of a simulation system is shown. The system consists of 4000 atoms with face-centered cubic (fcc) structure interacting via a Lennard-Jones potential, which will be explained in the following section. By using the Parrinello–Rahman method, the external pressure is changed from 0 to 1 GPa at MD time step = 2000. Overshooting behavior is found just after the moment at which the pressure is changed until the pressure settles down around the desired value. This overshooting deviation reaches nearly 1 GPa. A similar behavior could be also found in the time evolution of the temperature for the Nose–Hoover thermostat method.

Even after the internal pressure has come to its equilibrium value there remains a small fluctuation of the pressure due to the thermal motion of the simulation cell, as found in Fig. 17.8. This type of breathing behavior inevitably exists in formulations using fictitious variables, and its properties strongly

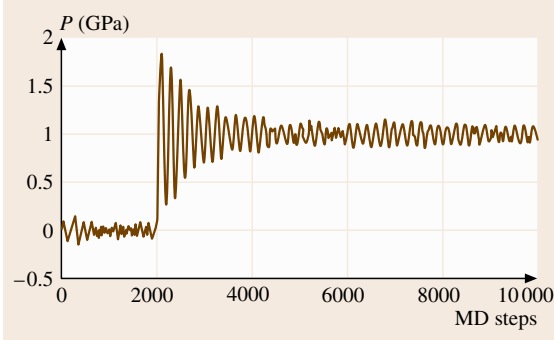


Fig. 17.8 Time evolution of the internal pressure P of the simulation system

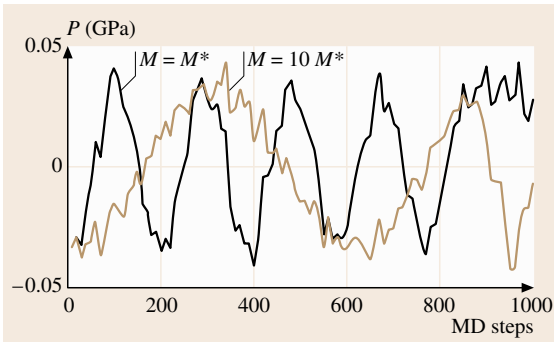


Fig. 17.9 Breathing behavior of the internal pressure P of the simulation system

depend on the *mass* of the fictitious variable. For the same simulation system as shown in Fig. 17.8, we can calculate the breathing behavior of the internal pressure P due to the thermal fluctuation in the cases of different two masses M^* and $10M^*$ of the Parrinello–Rahman cell. (The mass M^* will be defined soon.) The results are shown in Fig. 17.9, where we can see the frequency of the breathing strongly depends on the mass M of the simulation cell.

In general, a large mass gives a small overshoot but a slow convergence, while a small mass gives a large overshoot but a rapid convergence. In any case, the dynamics of the atoms in the simulation is inevitably affected by the motion of the fictitious variables [17.13]. In this context, Parrinello suggested [17.14] that the mass of the simulation cell should be determined such that the periods of the MD cell oscillation and that of sound waves are of the same order. The suggested value is $M^* = 3 \sum m_i / 4\pi^2$, where m_i are the atom masses.

NPT Ensemble

By combining the temperature-control and pressure-control methods, we can perform the simulation of an *NPT* ensemble, which is most appropriate for comparison with experimental results under ordinary conditions. For example, if we take the Nose–Hoover thermostat method for temperature control and the Andersen method for pressure control, the equation of motions of the total system are the following

$$d^2 s_i / dt^2 = - \frac{L^{-1}}{m_i} \partial \phi / \partial r_i - (S^{-1} \dot{S} + 2L^{-1} \dot{L}) \dot{s}_i, \quad (17.39)$$

$$d^2 S / dt^2 = - \frac{S}{Q} \left[\sum_i m_i (L \dot{s}_i)^2 - 3Nk_B T_0 \right] + S^{-1} \dot{S}^2, \quad (17.40)$$

$$d^2 L / dt^2 = \frac{L^{-2}}{3M} \left[\frac{1}{3V} \sum_i [m_i (L \dot{s}_i)^2 - r_i \cdot \partial \phi / \partial r_i] - p^{\text{ext}} \right] + S^{-1} \dot{L} - 2L^{-1} \dot{L}^2, \quad (17.41)$$

where S is the Nose–Hoover thermostat variable with a mass Q , L is the edge length of the cubic simulation cell with a mass M in Andersen’s method, and s_i are rescaled coordinates defined through $r_i = L s_i$. A coding procedure using the p -th order Gear method would be along the following lines

- Step 1 Specify the initial position $s_i(t_0)$ and its derivatives $s'_i(t_0)$ to $s_i^{(p-1)}(t_0)$ and assign them to $q_i(t_0)$ for $i = 1$ to N .
- Step 2 Consider $S(t)$ and $L(t)$ as coordinates of the $(N+1)$ -th and the $(N+2)$ -th atom, specify the initial values for $S(t_0)$ and $L(t_0)$ and their derivatives, and assign each to $q_{N+1}(t_0)$ and $q_{N+2}(t_0)$, respectively.
- Step 3 Calculate the predicted coordinates $\tilde{q}_i(t_0 + \Delta t)$ for $i = 1$ to $N+2$ at the first step according to (17.11).
- Step 4 Calculate the force $F_i(t_0 + \Delta t)$ at the first step for $i = 1$ to N according to (17.39) by using $\tilde{q}_i(t_0 + \Delta t)$.
- Step 5 Calculate the force $F_{N+1}(t_0 + \Delta t)$ and $F_{N+2}(t_0 + \Delta t)$ at the first step according to (17.40) and (17.41) by using $\tilde{q}_i(t_0 + \Delta t)$.
- Step 6 Compute the corrected $q_i(t_0 + \Delta t)$ according to (17.12) for $i = 1$ to $N+2$.
- Step 7 Repeat steps 3 to 6 with $t_0 \rightarrow t_0 + \Delta t$.

We can also perform a simulation of the *NPT* ensemble by combining the momentum-scaling method for temperature control and the Parrinello–Rahman method for pressure control. A coding procedure using the p -th order Gear method is similar to the preceding case

- Step 1 Specify the initial position $s_i(t_0)$ and its derivatives $s_i'(t_0)$ to $s_i^{(p-1)}(t_0)$ and assign them to $\mathbf{q}_i(t_0)$ for $i = 1$ to N .
- Step 2 Specify the initial values for $h_{\alpha\beta}(t_0)$, that is, the shape of the simulation cell, and their derivatives, consider $h_{\alpha\beta}(t)$ as coordinates of the $(N+1)$ -th to the $(N+9)$ -th atom, and assign each to $\mathbf{q}_{N+1}(t_0)$ to $\mathbf{q}_{N+9}(t_0)$.
- Step 3 Calculate the predicted coordinates $\tilde{\mathbf{q}}_i(t_0 + \Delta t)$ for $i = 1$ to $N+9$ at the first step according to (17.11).
- Step 4 Calculate the force $F_i(t_0 + \Delta t)$ at the first step for $i = 1$ to N according to (17.35) and (17.36) by using $\tilde{\mathbf{q}}_i(t_0 + \Delta t)$.
- Step 5 Calculate the force $F_{N+i}(t_0 + \Delta t)$ at the first step for $i = 1$ to 9 according to (17.37) by using $\tilde{\mathbf{q}}_i(t_0 + \Delta t)$.
- Step 6 Compute the corrected $\mathbf{q}_i(t_0 + \Delta t)$ according to (17.12) for $i = 1$ to $N+9$.
- Step 7 Repeat steps 3 to 6 with $t_0 \rightarrow t_0 + \Delta t$.
- Step 8 Rescale the atomic momenta $p_i(t)$ for $i = 1$ to N according to (17.18) after every N_{rescale} steps.

17.1.4 Interaction Potentials

The time evolution of the simulation system completely depends on the forces interacting between atoms, which are usually derived from interaction potentials. Possible forms of the interaction potentials popularly used in simulations will be presented in this section. Among them, the Lennard-Jones two-body potential and the embedded-atom method (EAM) many-body potential, both of which are used repeatedly throughout this chapter, will be given special attention.

The functional form $\phi(\mathbf{r}_1, \mathbf{r}_2, \dots)$ of the potential function plays a crucial role in MD simulation, not only in the physical aspects but also in the technical aspects for coding. In this respect, the potential forms can be classified into two following categories: two-body potentials and many-body potentials. The former can be expressed as a sum of functions of atomic distances as

$$\phi(\mathbf{r}_1, \mathbf{r}_2, \dots) = \sum_{(i,j)} \phi_{ij}(|\mathbf{r}_i - \mathbf{r}_j|). \quad (17.42)$$

Lennard-Jones Potential

One of the simplest and commonly used two-body potentials is the $m-n$ Lennard-Jones (LJ) potential, in which the pairwise interaction between elements A and B separated by distance r is written as

$$\phi^{\text{AB}}(r) = e_0^{\text{AB}} \left[\left(\frac{r_0^{\text{AB}}}{r} \right)^m - \frac{m}{n} \left(\frac{r_0^{\text{AB}}}{r} \right)^n \right]. \quad (17.43)$$

Here the parameters m and n can be adjusted according to the elements in the system and are taken to be integers in many cases. For example, $(m, n) = (12, 6)$ is used for rare gasses, while $(m, n) = (8, 4)$ has been proved [17.15] to be adequate to describe metallic systems. The potential has its minimum, $-e_0^{\text{AB}}$, at the distance r_0^{AB} . Therefore, we can consider these two parameters as the chemical bond strength and the atomic size, respectively.

EAM Potential

It is well known that two-body potentials cannot reproduce the Cauchy discrepancy between the elastic constants and the correct vacancy formation energy. A straightforward remedy for the problem is to use many-body potentials. Among them, one of the most popular many-body potentials used for metallic systems is called the embedded-atom method (EAM) [17.16], which is based on the effective medium theory. In this framework, the potential energy is written as

$$\phi = \sum_i F^{\text{A}}(\rho_i) + \sum_{(i,j)} \varphi_{ij}^{\text{AB}}(r_{ij}). \quad (17.44)$$

Here the first term $F^{\text{A}}(\rho_i)$ corresponds to the energy required to embed atom i into the electron density ρ_i , while the second term φ_{ij}^{AB} corresponds to the core-to-core repulsion energy between atom i and atom j separated by the distance r_{ij} expressed in a pairwise functional. The suffices A and B denote the species of the atoms. The former term incorporates the many-body effect through the electron density assumed to be a linear superposition

$$\rho_i = \sum_{(i,j)} f_i^{\text{A}}(r_{ij}), \quad (17.45)$$

where $f_i^{\text{A}}(r_{ij})$ is the contribution to the electron density ρ_i at atom i due to atom j at the distance r_{ij} .

The functional forms of $f(r)$ and $\varphi(r)$ are determined so as to reproduce the static properties such as the cohesive energy, lattice constants, elastic constants,

and the vacancy formation energy. For example, simple exponential forms such as

$$f^A(r) = f_0^A \exp(-\beta_A r/r_0^{AA}), \quad (17.46)$$

$$\varphi^{AB}(r) = \varphi_0^{AB} \exp(-\gamma_A r/r_0^{AB}), \quad (17.47)$$

are often used, where f_0^A , φ_0^{AB} , β_A and γ_A are parameters, and r_0^{AB} is the equilibrium nearest-neighbor distance.

On the other hand, the standard way to determine the embedding function $F^A(\rho_i)$ is rather more complicated. In the original scheme suggested by Foiles [17.17], the Rose equation of state is used to determine the form of $F^A(\rho_i)$. The Rose equation of state is given from the empirical experimental data and shows the dependence of the cohesive energy of a cubic crystal on the nearest-neighbor distance r as

$$E^A(r) = -E_c^A [1 + \alpha_A (r/r_0^{AA} - 1)] e^{-\alpha_A (r/r_0^{AA} - 1)}, \quad (17.48)$$

where E_c^A is the cohesive energy with the equilibrium lattice parameter and the parameter α_A is defined as

$$\alpha_A = 3\sqrt{\Omega_0^A B_0^A / E_c^A}, \quad (17.49)$$

using the equilibrium atomic volume Ω_0^A and the bulk modulus B_0^A of the equilibrium state. By using the expression (17.44), the embedding function is calculated as

$$F^A(\rho) = E^A(r) - \frac{1}{2} \sum_j \varphi_{ij}^{AA}(r_{ij}), \quad (17.50)$$

where the calculation is performed for a cubic lattice with the nearest-neighbor distance r , and r would be varied around its equilibrium value r_0^{AA} to obtain the value of $F^A(\rho)$ around the equilibrium electron density ρ_0 .

From a practical point of view, the value of the electron density ρ does not significantly deviate from its equilibrium value ρ_0 . Therefore, a polynomial approximation around ρ_0 is sufficient for calculations except for cases with highly defective structure, such as a surface structure

$$F^A(\rho) = \sum_i F_i^A (\rho - \rho_0)^i, \quad i = 0, 1, 2, \dots, \quad (17.51)$$

where the coefficients F_i^A are determined so as to reproduce the experimental properties.

According to the tight-binding theory, another functional form $F(\rho)$ has also been suggested. Up to the second-moment approximation, the functional form of the embedding function is evaluated as

$$F(\rho) = F_0^{\text{FS}} \sqrt{\rho/\rho_0}. \quad (17.52)$$

This type of potential is called the Finnis–Sinclair potential [17.18] and has been widely used in simulations of metallic systems.

Cutoff Procedure

Since the functional forms found in (17.43–17.47) have an infinite interaction range, we usually make a cutoff termination to the potential functions to decrease the calculational cost in MD simulations. For each function to be modified, we set both the starting distance r_s where the termination starts and the cutoff distance r_c where the modified function vanishes.

The two typical terminating processes are as follows. One is to exchange the potential function with a cutoff function $g_c(r)$ for $r > r_s$, which is continuous at r_s to the potential function up to the second derivative, and vanishes for $r > r_c$. For the choice of $g_c(r)$, a polynomial form is often taken

$$g_c(r) = \sum_i c_i (r - r_c)^i, \quad \text{for } r_s < r < r_c, \quad (17.53)$$

where the parameters c_i are determined to satisfy continuity at r_s to the potential function up to the second derivative, and $i = 2, 3, 4, 5, \dots$. For example, a modified LJ potential with terminating at the third-order polynomial starting at its inflection point is called the LJ-spline potential. For the case $(m, n) = (8, 4)$, which we shall use in the following sections, the parameters in (17.53) are uniquely determined as $c_2 = -(10\,240/3159)(5/9)^{(1/2)}r_0^{-2}$, $c_3 = -(655\,360/369\,603)(5/9)^{(3/4)}r_0^{-3}$, and the terminating position $r_c = (103/64)r_s \sim 1.864r_0$ by requiring continuity to the potential function up to the second derivative at the inflection point $r_s = (9/5)^{(1/4)}r_0 \approx 1.158r_0$. For a smoother cutoff at r_c , the fourth-order function ($i = 3, 4$) would be used.

The other approach is to multiply by a switching function $g_s(r)$ that satisfies the properties $g_s(r_s) = 1$, $g'_s(r_s) = g''_s(r_s) = 0$, and $g_s(r_c) = g'_s(r_c) = g''_s(r_c) = 0$ to the potential function on the interval $[r_s, r_c]$. For example, if we take a polynomial function

$$g_s(r) = \sum_i d_i (r - r_c)^i, \quad \text{for } r_s < r < r_c \quad (17.54)$$

of fifth order, that is, $i = 3, 4, 5$, then the coefficients in (17.54) are determined as $d_3 = 10(r_s - r_c)^{-3}$,

$d_4 = -15(r_s - r_c)^{-4}$, and $d_5 = 6(r_s - r_c)^{-5}$. An exponential form such as

$$g_s(r) = \exp \left[\frac{(r - r_s)^3}{(r - r_s)^2 - (r_s - r_c)^2} \right], \quad (17.55)$$

can be also used for the switching function.

17.1.5 Physical Observables

The method of extracting physical observables will be explained in this subsection. Various observables can be calculated by the MD simulations, including volume, energy, pressure, elastic moduli, diffusivity, viscosity, radial distribution function, etc. Here only formulas for evaluating the observables are shown in this section, while the examples applied to the actual MD simulations will appear in later sections.

Thermodynamical Properties

In the course of the MD simulation, thermodynamical properties such as the total volume V and the internal energy E are always calculated, so they are easy to monitor. The internal pressure P of the simulation system can also be monitored by using (17.23). In ordinary MD simulations, we consider a long-time average of the thermodynamical properties as an ensemble average

$$\langle O \rangle_{\text{ensemble}} = \langle O \rangle_{\text{time}}. \quad (17.56)$$

In the actual estimation of these observables, we usually take an average over 100–10 000 time steps, among which the longer time averages reduce the effect of thermal fluctuations and statistical errors. Other thermodynamical properties, such as the specific heat or the thermal expansion rate, can be estimated from the change of E and V with T or P .

Structural Properties

The radial distribution function provides a lot of information about atomistic structure. It can be directly calculated from the atomic coordinates $\mathbf{r}_i(t)$. In many cases, by taking a time average of the pair distribution

$$\sum_{\langle i,j \rangle} \left[\mathbf{r}_i(t) - \mathbf{r}_j(t) \right]^2, \quad (17.57)$$

we can greatly reduce the effect of thermal vibrations.

Microscopic structural properties such as the number of atomic pairs or local symmetry properties around each atom also yield important information [17.19]. One of the popular methods used to investigate the microscopic structure is Voronoi polyhedra analysis. Some examples will be given in Sect. 17.3.2.

Dynamical Properties

Among the dynamical and transport properties, the diffusivity is easy to estimate because we know the position of all atoms. That is, we can estimate the self-diffusion coefficient D from the linear part in the time evolution of the mean square displacement of the atoms as

$$\frac{1}{N} \sum_i \left\langle \left[\mathbf{r}_i(t_0) - \mathbf{r}_i(t_0 + t) \right]^2 \right\rangle = \frac{1}{6} D t + \text{const.}, \quad (17.58)$$

where the time average $\langle \dots \rangle$ starts from the initial time t_0 . The diffusivity D can be also calculated from the zero mode of the velocity autocorrelation function

$$\frac{1}{N} \sum_i \langle \mathbf{v}_i(t_0) \cdot \mathbf{v}_i(t_0 + t) \rangle \quad (17.59)$$

as

$$D = \frac{1}{3} \int_0^\infty dt \frac{1}{N} \sum_i \langle \mathbf{v}_i(t_0) \cdot \mathbf{v}_i(t_0 + t) \rangle / \langle \mathbf{v}_i(t_0)^2 \rangle. \quad (17.60)$$

In the same manner, the viscosity $\eta_{\alpha\beta}$ can be estimated from the stress autocorrelation function as

$$\eta_{\alpha\beta} = \frac{1}{k_B T} \int_0^\infty dt \frac{\langle P_{\alpha\beta}(t_0) P_{\alpha\beta}(t_0 + t) \rangle}{\langle P_{\alpha\beta}(t_0)^2 \rangle}, \quad (17.61)$$

where the stress tensor $P_{\alpha\beta}$ is found from (17.23), and the Greek symbols take the Cartesian values 1, 2, or 3.

Elastic moduli can be calculated [17.20] from a thermodynamical fluctuation formula. From a long-time average of the fluctuation of the stress tensor $P_{\alpha\beta}$, the adiabatic elastic coefficients $C_{\alpha\beta;\gamma\delta}$ can be calculated as

$$\begin{aligned} C_{\alpha\beta;\gamma\delta} = & - \frac{\langle V \rangle}{k_B T} \left(\langle P_{\alpha\beta} P_{\gamma\delta} \rangle - \langle P_{\alpha\beta} \rangle \langle P_{\gamma\delta} \rangle \right) \\ & + \frac{N k_B T}{\langle V \rangle} \left(\delta_{\alpha\delta} \delta_{\beta\gamma} + \delta_{\alpha\gamma} \delta_{\beta\delta} \right) \\ & + \frac{1}{\langle V \rangle} \left\langle \sum_{\langle i,j \rangle} r_{ij}^{-2} \left(\partial^2 \phi / \partial r_{ij}^2 - r_{ij}^{-1} \partial \phi / \partial r_{ij} \right) \right. \\ & \left. \times r_{ij\alpha} r_{ij\beta} r_{ij\gamma} r_{ij\delta} \right\rangle, \quad (17.62) \end{aligned}$$

where $\delta_{\alpha\beta}$ is the Kronecker delta, and k_B is the Boltzmann constant.

The vibration modes of atomic motion can also be calculated from the velocity autocorrelation (17.59); examples will appear in Sect. 17.3.2.

17.2 Diffusionless Transformation

In MD simulations, we can only handle short-time phenomena of the order of nanoseconds. Therefore, it is difficult to simulate processes or transformations that rely upon long-range diffusion of atoms. In this section, as examples of diffusionless transformations, we shall pick the martensitic transformation and solid-state amorphization, and investigate the microscopic mechanism underlying these transformations by using the MD simulation.

17.2.1 Martensitic Transformation

The martensitic transformation, which is a typical diffusionless transformations, will be studied from an atomistic point of view using MD simulation in this section. The martensitic transformation of ordered alloys as well as that from fcc iron into a body-centered cubic (bcc) structure will be investigated. The difference between the martensitic transformation in nanoclusters and the bulk will be also discussed.

For a typical system in which a martensitic transformation takes place, we consider here a 1 : 1 alloy system where the higher-temperature phase is the B2 phase, like the Au-Cd or Ti-Ni system. In most alloy systems where the B2 phase is found as a stable phase, the atomic size difference would play an important role in making the B2 structure stable. Therefore, for a simple model for binary alloys, the interaction between atoms is assumed to be described by the 8–4 Lennard-Jones potential ϕ^{AB}

$$\phi^{\text{AB}}(r) = e_0^{\text{AB}} \left[\left(\frac{r_0^{\text{AB}}}{r} \right)^8 - 2 \left(\frac{r_0^{\text{AB}}}{r} \right)^4 \right]. \quad (17.63)$$

Here the set of parameters e_0^{AB} and r_0^{AB} are determined [17.21] to reproduce the experimental data on molar volumes, cohesive energy and heat of formation of Ti, Ni and B2 phase of the Ti-Ni alloy.

The fitted values of the parameters used in the present simulation are listed in Table 17.1, where atom 1

Table 17.1 Parameters for the LJ potential in (17.63)

r_0^{11}	1.0000
r_0^{22}	0.8494
r_0^{12}	0.8947
e_0^{11}	1.13375
e_0^{22}	1.03387
e_0^{12}	1.24900

corresponds to the Ti atom and atom 2 to Ni; the length scale is expressed in units of the diameter of atom 1, while the energy scale is expressed in 0.5 eV. As a cut-off, a terminating process using third-order polynomial functions, which starts at the inflection point of the 8–4 LJ potential function (17.63), is taken, as discussed in Sect. 17.1.4. For simplicity, we suppose that atoms 1 and 2 have the same atomic mass m . Throughout this section, all units are normalized by the atomic mass m , the diameter r_0^{11} of atom 1, and the energy unit 0.5 eV in Table 17.1.

For an MD simulation in the NPT ensemble of this binary system, we adopt the momentum-scaling method for temperature control and the Parrinello–Rahman method for pressure control. The period N_{rescale} of the momentum scaling is taken to be 10. The bookkeeping radius r_{book} is set at $r_c + 0.6$ and the period N_{book} for updating the *book* ranges from 25 to 100 according to the temperature. The time integration is performed by the fifth Gear algorithm with a time step of $\Delta t = 0.005$ in the normalized units.

As an initial configuration, a $16 \times 16 \times 16$ B2 lattice with an equilibrium lattice parameter $a = 0.9365$ is prepared; snapshots are illustrated in Fig. 17.10. The same number $N/2 = 4096$ atoms of elements 1 and 2 are arranged on the lattice points alternatively, and small velocities randomly taken from the Boltzmann distribution at a temperature $T = 0.001$ (≈ 5.5 K) are assigned to all atoms. After annealing at $T = 0.001$ for 10^5 time integration steps, the system remains in the B2 structure. This means that the B2 structure is at least a metastable phase at low temperature.

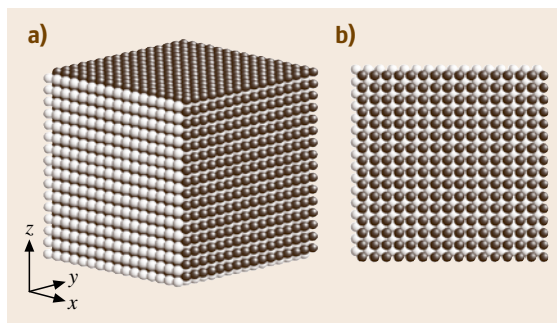


Fig. 17.10a,b Snapshots of a B2 structure: (a) a perspective view and (b) a top view from the z -direction. The light gray spheres and the dark gray spheres denote the elements 1 and 2, respectively

After the annealing process at $T = 0.001$, a heating procedure is performed in a stepwise way, as shown in Fig. 17.11. The size of each heating step is $0.01 (= 2.005 \text{ eV/atom} \approx 55 \text{ K})$ and every step is followed by a 10 000 integration step equilibration period. The physical values, such as the atomic volume and energy, are determined by averages over the last 1000 steps of the equilibration period. To minimize the artificial effect induced by the momentum-scaling process, we execute the scaling procedure only if the effective temperature (17.17) of the system deviates from the desired value by more than 2%. Consequently, the scaling procedures are concentrated in the first 1000 steps of the equilibration period.

Here one point should be noted about the rate of temperature change in an MD simulation. In the stepwise heating shown in Fig. 17.11, the average heating rate is 2.0×10^{-4} in the normalized units. This corresponds to an extraordinarily high rate, around 10^{12} K/s ,

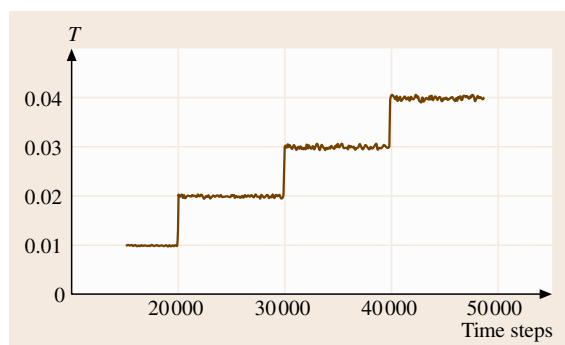


Fig. 17.11 A snapshot of the time evolution of the system temperature T calculated from the total kinetic energy of atoms in a stepwise heating procedure

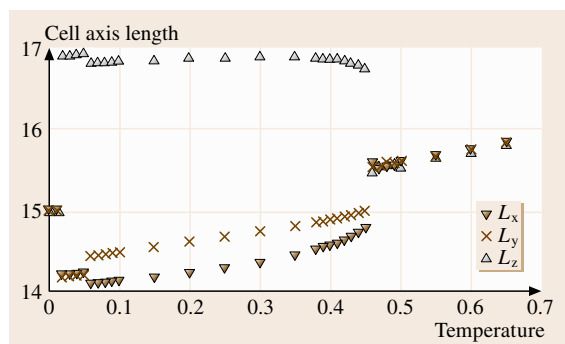


Fig. 17.12 The temperature dependence of the axis length of the simulation cell in the heating process starting from a B2 structure

although this rate is so low that it takes a considerable calculation time of the order of hours. We shall encounter this type of discrepancy between the time scale in the simulation and the actual calculation time in every stage of MD simulations.

To take the statistical and thermal nature into account, several heating runs are carried out from different initial perturbations. Before the crystal starts to melt, the crystal structure experiences some structural transformations. By monitoring the shape of the periodic simulation cell, we can see how the transformation evolves.

The time evolution of the shape of the simulation cell in the heating procedure starting from a B2 phase is shown in Fig. 17.12, where the cell axis lengths are shown as functions on the temperature. The B2 phase immediately transforms into a tetragonal phase with a symmetry $L_x = L_y \neq L_z$ at $T = 0.02$, and then transforms into an orthorhombic phase with $L_x \neq L_y \neq L_z$ at $T = 0.06$. We call the former phase $L1'_0$ and the latter phase $L1''_0$, because both phases are understood as slight modifications of an fcc-based close-packed structure $L1_0$ with a long-period modulation. Snapshots of the $L1'_0$ phase and the $L1''_0$ phase are shown in Figs. 17.13

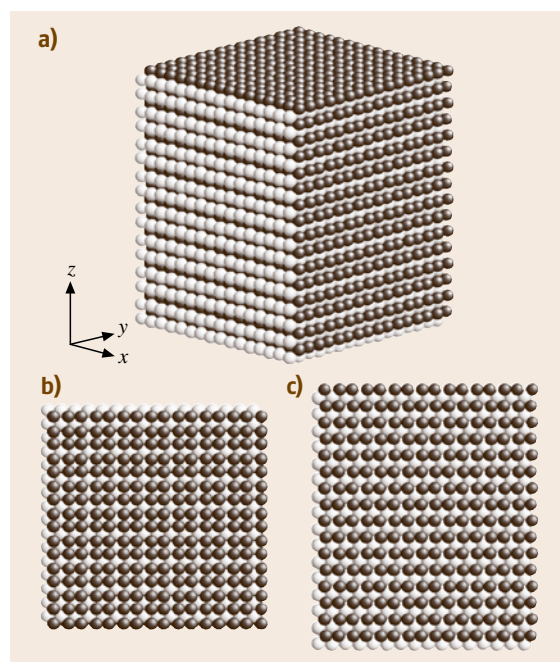


Fig. 17.13a-c Snapshots of an $L1'_0$ structure: (a) perspective view, (b) a top view from the z -direction, and (c) a side view from the x -direction. The atoms are shown using the same colors as in Fig. 17.10

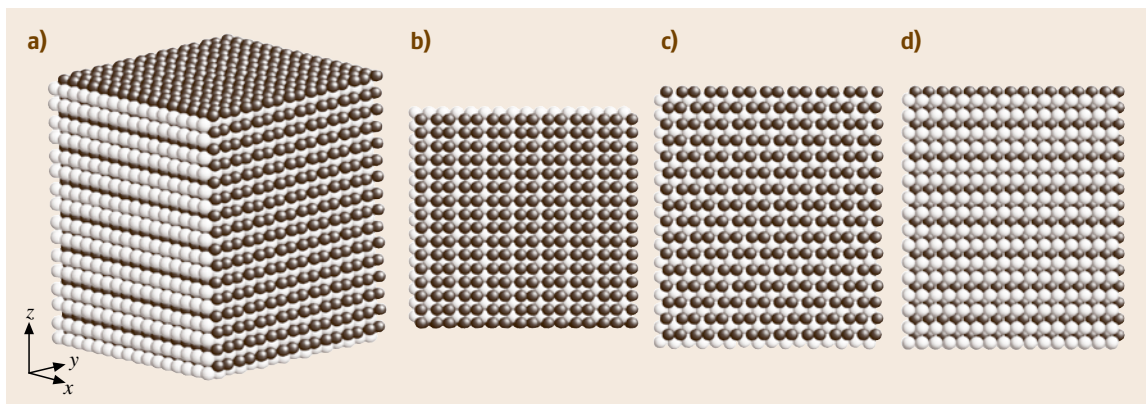


Fig. 17.14a–d Snapshots of an $L1''_0$ structure: (a) a perspective view, (b) a top view from the z -direction, (c) a side view from the x -direction, and (d) a side view from the y -direction. The atoms are shown using the same colors as in Fig. 17.10

and 17.14, respectively. Upon further heating, the system transforms back into the B2 phase at $T = 0.46$, and finally, the B2 crystal melts into the liquid phase at $T = 0.66$.

To understand the phase evolution in the heating process shown above, we shall estimate the enthalpy of each phase found in the simulation. Once we know the atomic configuration of the phase, we can calculate the enthalpy at 0 K of each structure using an energy-minimization process, which is equivalent to an MD calculation at 0 K, if the corresponding structure has a marginal stability at 0 K. The calculated energy levels at 0 K for the B2, the $L1'_0$, and the $L1''_0$ phase are shown in Fig. 17.15. This suggests that the $L1''_0$ phase is the ground state and the B2 phase is a fragile metastable state at 0 K. Therefore, the B2-to- $L1'_0$ transition at $T = 0.02$ is considered to be a simple transition from an unstable state to the ground state, while the $L1'_0$ -to- $L1''_0$ transition at $T = 0.06$ and the $L1''_0$ -to-B2 transition at $T = 0.46$ are understood as the phase transitions to the

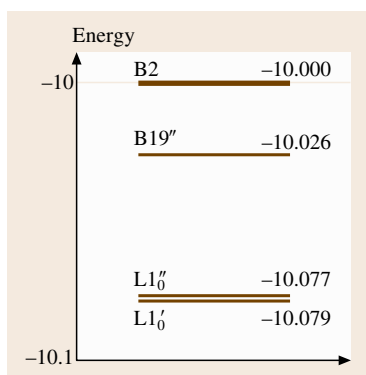


Fig. 17.15 Energy levels of (meta-)stable structures found at 0 K

higher enthalpy states driven by the entropy contribution to the free energies.

The character of the transition between the B2 and the $L1''_0$ phase can be seen from the temperature dependence of the potential energy. If we stop the heating process at a temperature between $T = 0.46$ and 0.65 before melting and cool down the system, we can observe the transition from the B2 phase to the $L1''_0$ phase. Figure 17.16 shows the change of the potential energy per atom in a heating process (triangles) and a cooling process (circles) at a rate of 2.0×10^{-4} . We can see a hysteresis behavior, which means that there is some extent of superheating (supercooling) in the heating (cooling) process with such a high heating (cooling) rate.

For traditional reasons, the transition temperature M_s of a martensitic transformation is defined by the transition from the high-temperature phase into the low-temperature phase, and the transition temperature from the low-temperature phase into the high-temperature phase is called the reverse transformation temperature A_s . Following this convention, Fig. 17.16 tells us that the martensitic temperature M_s of the B2-to- $L1''_0$ transformation is 0.39 and the reverse martensitic temperature A_s of the $L1''_0$ -to-B2 transformation temperature is 0.46 at this cooling/heating rate. It also suggests that the equilibrium temperature T_0 between the $L1''_0$ phase and the B2 phase should be around 0.43. It should also be noted that the potential energy jumps up at the $L1''_0$ -to-B2 transition, which means that this is certainly an entropy-driven transformation.

In general, it is likely that the higher-temperature phase has a structure with higher symmetry. In this

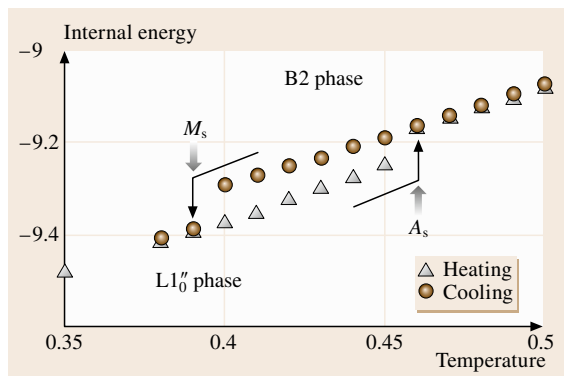


Fig. 17.16 Change of the potential energy per atom with temperature in a heating and a cooling process

context, it is natural that the highest-temperature phase B2 has a cubic symmetry, $L_x = L_y = L_z$. However, it is somewhat strange that the lowest-temperature phase $L1'_0$ has a tetragonal symmetry $L_x = L_y \neq L_z$, while the middle-temperature phase $L1''_0$ only has orthogonal symmetry $L_x \neq L_y \neq L_z$. This can be understood if we look into the translational symmetry. As shown in Figs. 17.13 and 17.14, the lower-temperature phases $L1'_0$ and $L1''_0$ show a breakdown of translational symmetry due to the presence of a periodic modulation of the position of atoms, which makes the translational period of the corresponding direction twice as long as that of the B2 phase. For the $L1'_0$ phase, this type of breakdown of translational symmetry is found in the x - and z -directions, while it is found in all three directions for the $L1''_0$ phase. Therefore, in this sense, the translational symmetry reduces step by step from the B2 phase to the $L1'_0$ phase.

Although the LJ potential parameters used here are determined by the static properties of the Ti-Ni system, the structure of low-temperature phases ($L1'_0$ and $L1''_0$) found in the simulation is different from that experimentally observed in the system, which is a hexagonal phase called B19'. We have also calculated the energy of hexagonal based structure starting from the B19 structure, and found a metastable structure that is a sort of modulation of B19, tentatively called B19''. However, the energy of the B19'' phase is higher than those of $L1'_0$ and $L1''_0$, although it is lower than that of B2, as shown schematically in Fig. 17.15.

In spite of these drawbacks of this LJ potential, this model system has interesting features found in many martensitic transformations, that is, the existence of the martensites with long-period modulation, a series of martensites at low temperatures, and the hysteresis be-

havior in the upward/downward transformation. It is quite amazing that such a simple two-body potential can reproduce a variety of aspects common to martensitic transformations. Therefore, in the next section, we shall use this model to investigate how the transformation properties would change in nanoclusters.

17.2.2 Transformations in Nanoclusters

Some physical properties become different from those in the bulk in nanosized clusters. In this section, we shall investigate how the phase-transformation behavior changes in such nanoclusters by performing the MD simulation for the model for B2 alloy clusters and iron clusters with a special focus on the martensitic transformation.

In general, physical properties change in small clusters. For example, the melting temperature goes down in nanosized clusters of pure metals [17.22]. Even the stable phases change dramatically in nanoclusters of alloys [17.23]. On the other hand, due to the finiteness of the total number of atoms in the system, nanoclusters are appropriate targets for MD simulation. Therefore, we shall investigate how the transformation properties would change for nanoclusters by using the simple model of martensitic transformation discussed in the previous section as well as a pure-iron system described by a simple EAM potential.

Transformation in B2 Alloy Clusters

A spherical nanocluster specimen with a B2 structure is prepared at a temperature around A_s for the bulk system, as depicted in Fig. 17.17a. The temperature-control method and the bookkeeping method are the same as in the bulk case discussed in the preceding section, while there is no need for boundary conditions for a free sin-

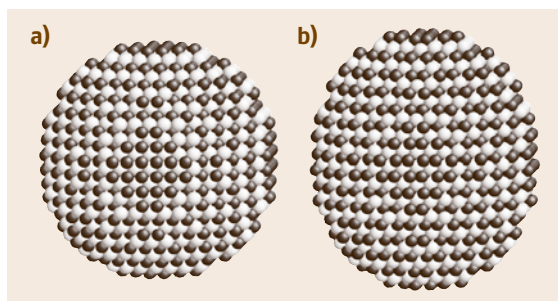


Fig. 17.17a,b Snapshots of nanoclusters with $N = 4279$ atoms: (a) a B2 cluster and (b) an $L1''_0$ cluster. The atoms are shown using the same colors as in Fig. 17.10

gle cluster, or equivalently, a fixed boundary condition is imposed. By lowering the temperature, we can observe a martensitic transformation into the $L1'_0$ structure as we found in the bulk case with periodic boundary conditions. A snapshot of the $L1'_0$ cluster of the low-temperature phase is also depicted in Fig. 17.17b). When we observe a martensite at low temperatures, we raise the temperature to observe a reverse transformation as well as melting of the cluster. By performing such simulation processes for the various sizes of nanoclusters, we can detect [17.24] the dependencies of the martensitic transformation temperature M_s , the reverse transformation temperature A_s , and the melting temperature T_m on the cluster size.

The calculated cluster-size dependencies of the transformation temperatures M_s (closed triangles), A_s (open triangles), and the melting temperature T_m (closed circles) are shown in Fig. 17.18, where the temperature is expressed in the same units as in Fig. 17.16. Throughout the simulations the cooling and the heating rate is 2.0×10^{-4} . All transformation temperatures decrease on decreasing the cluster size. In particular, the dependence of both A_s and M_s on the cluster size shows good agreement with the experimental data on Au-Cd alloy nanoclusters [17.25]. These results indicate that the decrease of the martensitic temperature is caused not by the increase of the activation barrier of the

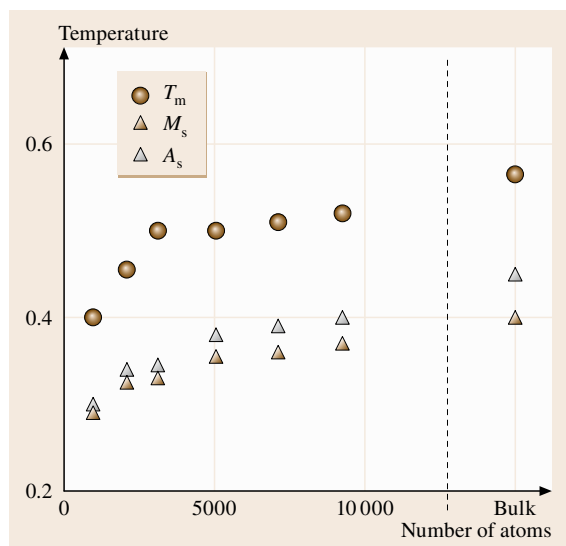


Fig. 17.18 The size dependence of the melting temperature T_m and the martensitic temperatures M_s and A_s of the B2 nanoclusters, together with those for the bulk B2 phase on the right edge of the graph

transformation, but by the decrease of the equilibrium temperature T_0 between the B2 phase and the martensite in this model. Moreover, since both the martensitic transformation and the melting are entropy-driven transformations, these results also suggest that the origin of the peculiar transformation behavior of nanoclusters should be mainly due to the fact that the thermal vibrational state of atoms changes in nanoclusters due to the drastic increase of the population of atoms belonging to the free surface.

Transformations in Iron Clusters

As pointed out above, the transformation properties of nanoclusters are closely related to the existence of a large portion of surface atoms in nanoclusters. In this context, we shall investigate the effect of the surface by using another model for iron clusters.

For an iron potential, we use a simple EAM potential developed by Johnson and Oh [17.26]. In their model, the electron-density function $f(r)$ and the two-body potential $\varphi(r)$ have the following forms

$$f_i^A(r) = f_0^A (r_0^A/r)^{-\beta}, \quad (17.64)$$

$$\varphi^A(r) = \sum_{i=0}^3 \varphi_i^A (r/r_0^A - 1)^i, \quad (17.65)$$

together with terminating procedures using third-order polynomials starting at $r_s = 1.20253r_0^{\text{Fe}}$ and vanishing at $r_c = 1.39385r_0^{\text{Fe}}$ for both functions $f(r)$ and $\varphi(r)$. To include the strong core-core repulsion in the two-body term, Johnson and Oh introduced the stiffening modification

$$\varphi_a^A(r) = \varphi^A(r) + k_a [\varphi^A(r) - \varphi^A(r_0^A)] (r/r_0^A - 1)^2, \quad (17.66)$$

which is valid for $r < r_0^{\text{Fe}}$.

The embedding function $F(\rho)$ has the analytic form

$$F(\rho) = F_0 [1 - \ln(\rho/\rho_0)] (\rho/\rho_0)^n, \quad (17.67)$$

where ρ_0 is the equilibrium electron density of the bcc phase with equilibrium lattice parameter $2/\sqrt{3}r_0^{\text{Fe}}$, and F_0 and n are fitting parameters.

Table 17.2 Parameters for the EAM potential (17.64–17.67)

r_0^{Fe} (Å)	2.4824	ϕ_0 (eV)	−0.2651
f_0 (Å ^{−3})	1.0000	ϕ_1 (eV)	−0.8791
β	6.0000	ϕ_2 (eV)	9.2102
F_0 (eV)	−2.5400	ϕ_3 (eV)	−13.3088
n	0.3681	k_a	12.0630

The potential parameters found in (17.64–17.67) are listed in Table 17.2, and are determined [17.26] by the available experimental data of the atomic volume, the cohesive energy, the bulk modulus, the Voigt average shear modulus, the anisotropy ratio, and the unrelaxed vacancy-formation energy for bcc iron.

Due to the lack of explicit magnetic contribution to the potential energy in this simple scheme, this potential cannot reproduce the phase stability between fcc iron and bcc iron at a given temperature. Instead, this potential stabilizes the bcc structure at any temperature for the bulk as well as clusters [17.27]. Therefore, if we start the simulation from a metastable fcc phase, we can observe the fcc-to-bcc martensitic transformation if there is enough thermal excitation to overcome the activation barrier from the fcc-to-bcc structure, but the opposite transformation cannot be observed. However, we can investigate an atomistic mechanism at the beginning stage of the fcc-to-bcc martensitic transformation by using this model.

In this case, we first prepare fcc clusters with various sizes ranging from $N = 400$ to 10 000 atoms at very low temperatures (≈ 10 K). The system temperature is controlled by the momentum-scaling method. After a annealing and relaxing period of 10 000 time steps with $\Delta t = 0.005$ ps, all clusters retain their initial fcc structure, independent of their size. This means that there is some potential barrier in the transformation path between the fcc phase and the bcc phase for nanoclusters. Then the clusters are heated up to melt at a heating rate of around 5 K/ps.

In the heating process, an fcc-to-bcc transition is observed [17.27] for the clusters with $N < 8000$ and the transformation temperature increases as the cluster size increases, while no explicit phase transformation is observed before melting in the larger clusters. In contrast

to the previous case for the B2 alloy clusters, these results suggests that the cluster-size dependence of the fcc-to-bcc martensitic transformation temperature originates from the change in the height of the activation barrier.

In this sense, the activation barrier is expected to have a close relation to the surface structures of the nanoclusters. Hence the initial stage of the fcc-to-bcc transformation is analyzed with special attention to the motion of surface atoms. As shown in Fig. 17.19, the transformation starts from the surface of the nanocluster and proceeds into the interior of the cluster. By analyzing the atomic correspondence between the initial configuration of an fcc cluster and the final configuration of a bcc cluster, a uniaxial transformation called the Bain transformation takes place in this case. Moreover, further simulation study reveals [17.27] that a vortex-like collective motion is activated on the surface of the clusters according to the temperature, and the collision between two collective modes induces atomic collective motion similar to the Bain transformation, and stimulates the creation of an embryonic martensitic transformation on the surface.

17.2.3 Solid-State Amorphization

Under extreme conditions, such as severe plastic deformations or irradiation damage, some alloy systems show a crystal-to-amorphous transition. This solid-state amorphization is considered as a sort of diffusionless transformation. The physics behind the mechanism of the solid-state amorphization will be investigated by MD simulation for a model system in this section.

It is well known that the atomic size ratio between the constituent elements plays an important role in the amorphous formation of alloys [17.28]. Therefore, to

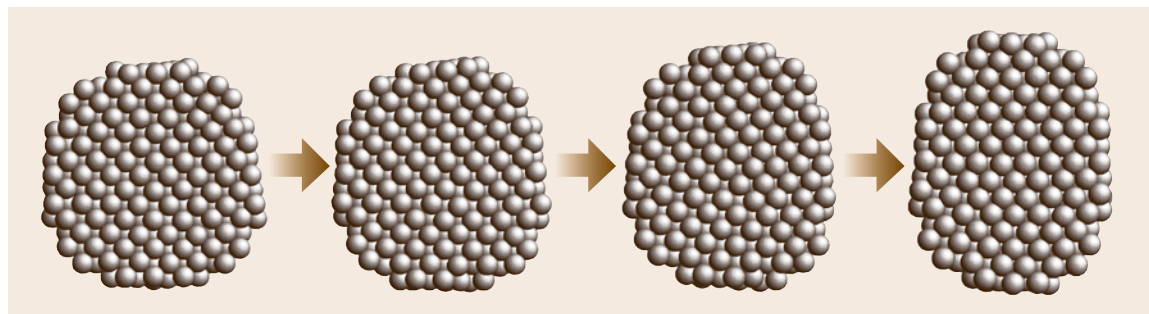


Fig. 17.19 Snapshots of a transformation procedure of a Fe nano-cluster from fcc to bcc. The Bain transformation starts from the *upper-right surface* and proceeds into the *lower-left*, in which the (100) plane of fcc changes into the (110) plane of bcc

investigate the mechanism of solid-state amorphization, we shall examine a binary system where the interaction is described by the 8–4 LJ potential (17.63) as a model for binary alloys, since we can easily vary the atomic size ratio by changing the parameter r_0^{AB} .

Here we deal with the binary system composed of elements 1 and 2, and, without loss of generality, assume $r_0^{11} = 1$ and $r_0^{22} \leq 1$. The atomic distance between different elements is defined as $r_0^{12} = (r_0^{11} + r_0^{22})/2$. To focus on the atomic size effect, we make a further simplification that all chemical bonding parameters are identical, that is, $e_0^{11} = e_0^{22} = e_0^{12} = 1$. The atomic masses of both elements are also supposed to be the same unit mass. Consequently, the binary system is characterized by only two variable parameters: the atomic size ratio r_0^{22} of element 2 to element 1, and the concentration x_2 of element 2. All physical quantities are expressed in the above units in this section.

The crystal-to-amorphous transformation processes are simulated in the following procedures. We first prepare an fcc solid solution at nearly zero temperature by randomly assigning the solute atoms to the fcc lattice sites. After an annealing and relaxation period, we then slowly heat up the system at a rate of 2.0×10^{-4} . In a system that has high glass-forming ability for alloys, the stability of the solid-solution phase against the amorphous phase would be lost, and solid-state amorphization, that is, the transition from the solid solution to an amorphous phase, should be observed if the system acquires enough thermal excitation to overcome an activation barrier.

MD calculations for a 4000-atom system with periodic boundary conditions have been performed [17.29]. The pressure of the system is kept to zero by using the

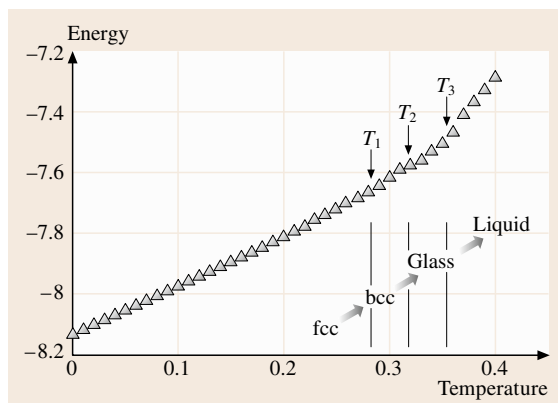


Fig. 17.20 Potential energy dependence on the temperature in a heating process from the fcc solid solution of the $(r_2, x_2) = (0.82, 0.50)$ system

Parrinello–Rahman method. The temperature of the system is set to the desired value by the momentum-scaling method. Figure 17.20 shows the potential energy evolution in a heating process from an fcc solid solution of the system where the atomic size ratio r_0^{22} is 0.82 and the composition x_2 of the smaller elements 2 is 0.50. The fcc solid solution (or strictly speaking, face-centered tetragonal or fct phase) first evolves into bcc solid solution (body-centered tetragonal or bct phase) at $T_1 = 0.28$, and then into an amorphous phase at $T_2 = 0.32$, and finally into the liquid phase at $T_3 = 0.35$. The snapshots of each phase found in this heating process are shown in Fig. 17.21, where the light gray spheres and the dark gray spheres denote the elements 1 and 2, respectively. Note that there is only a small jump in the potential energy at the phase transition at T_1 and

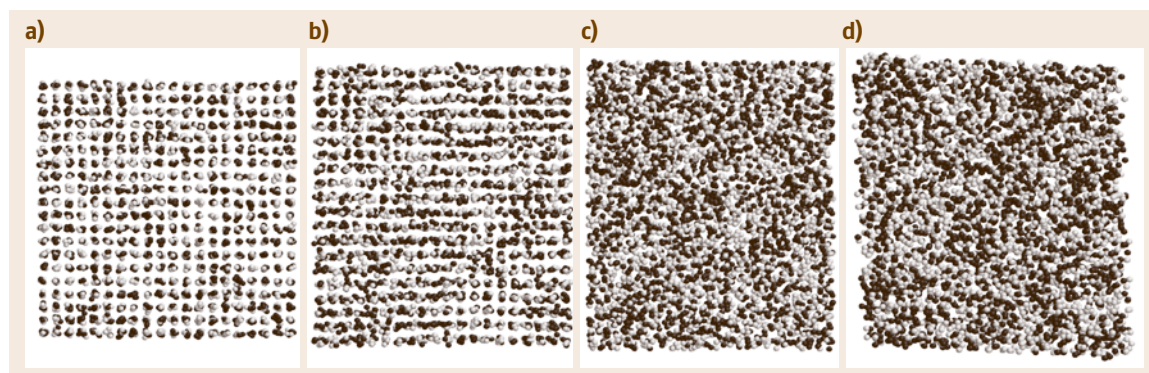


Fig. 17.21a–d Snapshots of the phases appearing in the heating process shown in Fig. 17.20: (a) an fcc solid solution (fct) phase ($T = 0.25$), (b) a bcc solid solution phase (bct) phase ($T = 0.29$), (c) a glassy phase ($T = 0.33$), (d) a liquid phase ($T = 0.39$). The light gray spheres and the dark gray spheres denote the elements 1 and 2, respectively

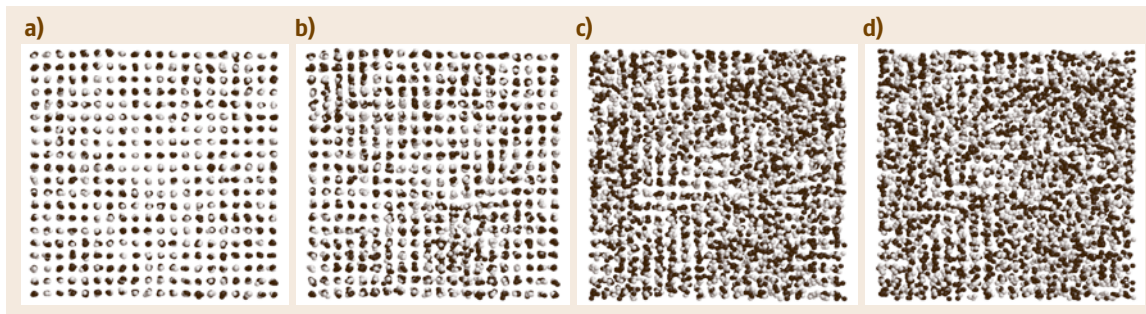


Fig. 17.22a–d Snapshots of atomic configuration of the prepared samples arranged on the *fcc* lattice sites and annealed at $T = 0.001$ in several systems with different atomic size ratio r_0^{22} : (a) the $(r_0^{22}, x_2) = (0.82, 0.50)$ system, (b) the $(r_0^{22}, x_2) = (0.81, 0.50)$ system, (c) the $(r_0^{22}, x_2) = (0.80, 0.50)$ system, and (d) the $(r_0^{22}, x_2) = (0.79, 0.50)$ system. The colors of the atoms are the same as in Fig. 17.21

T_2 , while drastic structural changes are found between the different phases, as shown in Fig. 17.21.

Similar calculations were performed while varying the atomic size ratio r_0^{22} at $x_2 = 0.25$, and 0.75. At each concentration, we observe the transition from solid solutions to amorphous phases if r_0^{22} is less than some corresponding critical ratio r_c^{SS} , while no amorphization but melting accompanying with a potential energy jump is observed if r_0^{22} is larger than r_c^{SS} . Especially, if r_0^{22} is considerably below r_c^{SS} , we find a solid-state amorphization in the preparation stage of the initial *fcc* configuration at nearly zero temperature, as shown in Fig. 17.22 for the $x_2 = 0.50$ case.

Thus, for a given atomic size ratio, we can roughly estimate the composition range where the solid-state amorphization would be observed in the heating and annealing processes in the simulation. The results are shown by the shaded region in Fig. 17.23. This suggests that a large atomic size ratio produces a high glass-forming ability into the binary alloy systems. The same tendency in the glass-forming ability for a binary system was reported in a similar MD study using

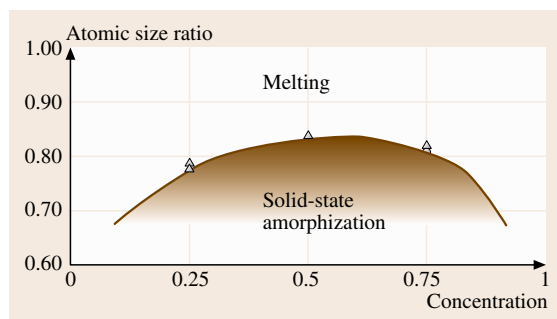


Fig. 17.23 The atomic size dependence of the composition range in which solid-state amorphization is observed

the 12–6 LJ potential [17.30]. We also note that the effect of the atomic size ratio on the glass-forming ability has a slightly asymmetric nature, that is, the glass-forming tendency is higher at $x_2 = 0.75$ than at $x_2 = 0.25$ ($x_1 = 0.75$). This feature can be found in the atomic size effect on the glass-forming ability under rapid solidification, which is one of the topics to be discussed in the next section.

17.3 Rapid Solidification

The rapid solidification procedure is also a short-time process that can be handled by MD simulation. In this area, there are a lot of interesting topics, such as the physics of glass transition, the local structure and vibrational state of glassy materials, the preparation of amorphous alloys, and nanocrystallization found in the annealing process of amorphous phases. In this section, we shall tackle these problems in the MD framework.

17.3.1 Glass-Formation by Liquid Quenching

In this section, rapid solidification processes from the melt are simulated for Ti–Al binary alloy systems. The glass-forming condition is discussed in relation to the experimental observations.

One of the most popular preparation methods of amorphous alloys is the rapid solidification process from the melt. In ordinary rapid solidification processes,

the cooling rate is in the range $1-10^5$ K/s, which is hard to handle by MD simulation. However, the Ti-Al binary system has such poor glass-forming ability that the amorphous phase can be obtained only by sputtering deposition [17.31]. The effective cooling rate in vapor deposition experiments might reach the order of 10^{10} K/s or more, which is tractable even in MD simulations. In this sense, the Ti-Al system is adequate for MD studies on amorphous formation and its crystallization.

In addition, Ti-Al alloys have both technical and theoretical interest, because their excellent mechanical properties strongly depend on their composition and the microstructure. The microstructure can be controlled by heat treatment through a metastable state such as the amorphous phase. Hence it is important to understand the microscopic mechanism involved in the formation and crystallization of the amorphous phases.

We use an EAM potential for Ti and Al developed by Oh and Johnson [17.32]. In their scheme, the electron-density function $f(r)$ and the two-body potential $\varphi(r)$ for the pure metal A are supposed to have the exponential forms

$$f^A(r) = f_0^A \exp[-\beta_A(r/r_0^{AA} - 1)], \quad (17.68)$$

$$\varphi^{AA}(r) = \varphi_0^A \exp[-\gamma_A(r/r_0^{AA} - 1)], \quad (17.69)$$

where f_0^A , φ_0^A , β_A and γ_A are parameters, and r_0^{AA} is the equilibrium nearest-neighbor distance. The embedding function $F^A(\rho)$ is determined by the Rose function $E^A(r)$ according to the procedure discussed in Sect. 17.1.4 by using the modified form of the Rose function

$$E^A(r) = -E_c^A [1 + \alpha_A(r/r_0^{AA} - 1) \{ (r/r_0^{AA})^{-m_A} - m_A(r/r_0^{AA})^{-1} + m_A \}] e^{-\alpha_A(r/r_0^{AA} - 1)}, \quad (17.70)$$

Table 17.3 Parameters of the EAM potential for the Ti-Al system

r_0^{TiTi} (Å)	2.9511	r_0^{AlAl} (Å)	2.8635
f_0^{Ti} (Å ⁻³)	0.4	f_0^{Al} (Å ⁻³)	1.0
β_{Ti}	6.0000	β_{Al}	5.000
ϕ_0^{Ti} (eV)	0.51132	ϕ_0^{Al} (eV)	0.09539
χ_{Ti}	8.9971	χ_{Al}	11.5
E_c^{Ti} (eV)	4.85	E_c^{Al} (eV)	3.58
α_{Ti}	4.743	α_{Al}	4.594
m_{Ti}	2.4	m_{Al}	2.37

and (17.49) and (17.50). The potential parameters found in (17.68–17.70) are listed in Table 17.3; these are determined [17.32] by the available experimental data of the atomic volume, the cohesive energy, the bulk modulus, the Voigt average shear modulus, the anisotropy ratio, and the unrelaxed vacancy formation energy for fcc Al and hexagonal close-packed (hcp) Ti.

The Ti-Al cross potential is created by using Johnson's method [17.33], in which the cross potential between the elements A and B can be written by using the functions from the pure A–A and the pure B–B potential as

$$\varphi^{AB}(r) = \frac{1}{2} \left[\frac{f^B(r)}{f^A(r)} \varphi^{AA}(r) + \frac{f^A(r)}{f^B(r)} \varphi^{BB}(r) \right]. \quad (17.71)$$

The only fitting parameter in (17.71) is the ratio f_0^A/f_0^B . We have determined the ratio $f_0^{\text{Ti}}/f_0^{\text{Al}}$ to reproduce the experimental value of the heat of solution [17.34]. The fitted value is also listed in Table 17.3.

Here one point should be noted about the EAM potential above. The potential is prescribed so as to reproduce the static properties of hcp Ti and fcc Al such as the cohesive energy, the lattice constant and the elastic constants. But it cannot reproduce correctly the formation energy of the intermetallics in the Ti-Al system such as Ti₃Al, TiAl, and TiAl₃.

Since we have a particular interest in the effect of the difference of the potential used in the simulation on the simulation results, the 8–4 LJ potential is also used in another series of simulations. The parameters used in the simulations are listed in Table 17.4, which are fitted [17.35] so as to reproduce a Ti-rich portion of the phase boundaries in the Ti-Al system in the cluster variation method (CVM) framework.

To perform the MD simulation of NPT ensembles, we use the momentum-scaling method every 10 steps and the Parrinello–Rahman method to keep the internal pressure zero. The flexible mobility of the simulation

Table 17.4 Parameters of the LJ potential for the Ti-Al system

r_0^{TiTi} (Å)	2.922
r_0^{AlAl} (Å)	2.864
r_0^{TiAl} (Å)	3.029
e_0^{TiTi} (eV)	0.812
e_0^{AlAl} (eV)	0.559
e_0^{TiAl} (eV)	0.812

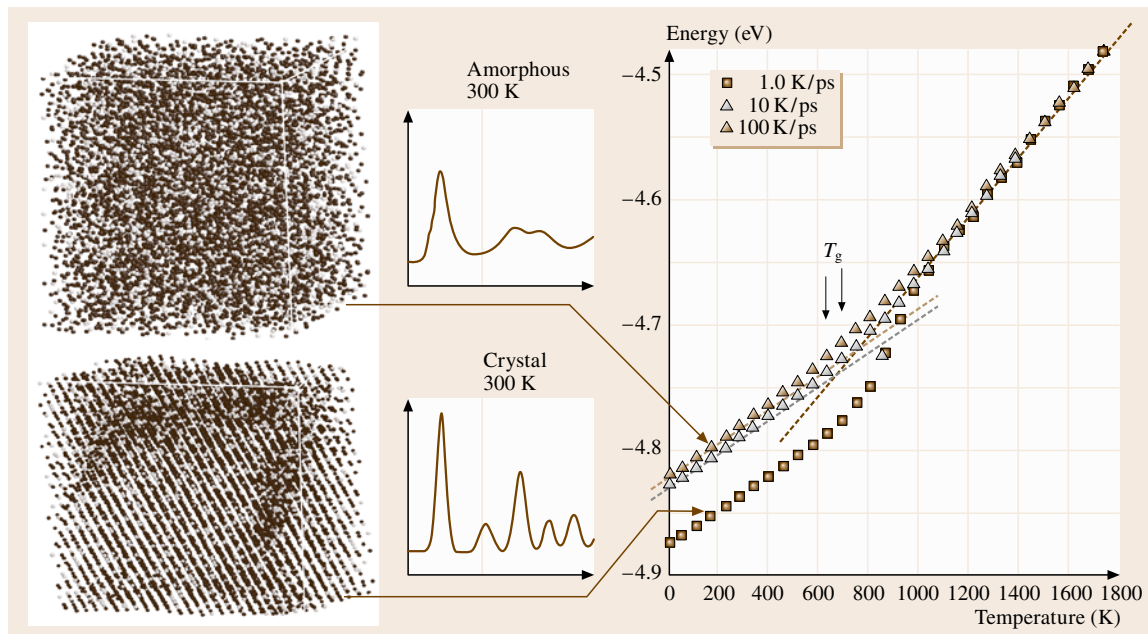


Fig. 17.24 The temperature dependence of the internal energy of the Ti-25 at. % Al system in the cooling processes: the squares, the open triangles, and the closed triangles correspond to the case with the cooling rate of 1.0, 10, and 100 K/ps, respectively. The left graphs are snapshots of atomic configuration and the pair distribution functions of an amorphous phase (upper) and a crystalline phase (lower) at 300 K

cell in the Parrinello–Rahman scheme has the advantage of minimizing the restriction due to the periodic boundary conditions, which is especially important in crystallization processes. The equation of motion is numerically integrated using the fifth Gear algorithm with a time integration step of 0.004 ps.

The MD simulation of the rapid solidification process in the Ti-Al systems of various compositions is carried out in the following way. In the first stage, to make a liquid phase of Ti-Al alloys, we prepare an fcc solid-solution as an initial configuration in a similar manner discussed in Sect. 17.2.3. By annealing it at a high temperature (≈ 2000 K) above the melting point, the initial structure immediately melts. Since the atomic diffusion rate is high in the liquid phases, an isothermal annealing period of 2×10^5 steps (≈ 0.8 ns) is considered to be enough to acquire a sample of the equilibrium liquid state at a given composition.

In the next stage, we choose a liquid phase obtained by the aforementioned prescription as a starting configuration. Then we cool the system down to 10 K in a stepwise manner with various rates ranging from 10^{11} to 10^{15} K/s. Whether we obtain a crystalline phase or an amorphous phase at the end of the cooling process

depends on both the cooling rate and the composition. If we have an amorphous phase, we then raise the temperature of the system up to melting, or, if necessary, keep it at some temperature for isothermal annealing. In the course of the heating or annealing procedure, a structural relaxation process in the amorphous phase and, in some cases, a crystallization process from the amorphous state could be observed.

Some typical evolutions of the internal energy during cooling processes for the Ti-25 at. % Al system of 4096 atoms are shown in Fig. 17.24, where the squares, the open triangles, and the closed triangles correspond to the cooling rate with 1.0, 10, and 100 K/ps. The sudden drop of the internal energy at around $T = 900$ K in the slowest cooling case corresponds to a liquid-to-crystal transition. On the other hand, the discontinuity in the slope in the two faster cooling cases corresponds to a glass transition, using which we can define the glass transition temperature T_g , as denoted in Fig. 17.24. The left graphs in Fig. 17.24 are snapshots of atomic configurations of an amorphous phase (upper) and a crystalline phase (lower) at 300 K together with the pair distribution functions of the corresponding phase, which reflects a typical feature in each phase, that is,

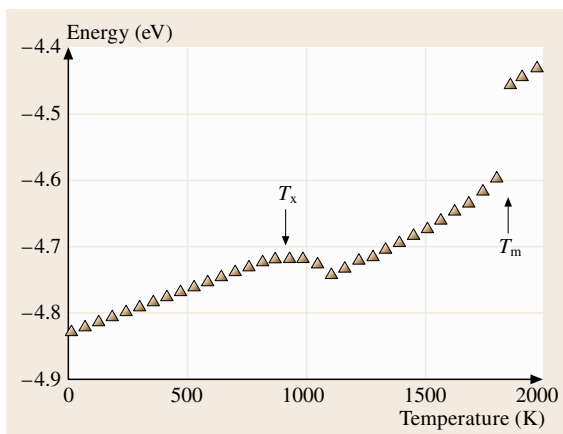


Fig. 17.25 The temperature dependence of the internal energy of the Ti-25 at.% Al system with 4096 atoms in a heating process from an amorphous phase. The heating rate is 1.0 K/ps

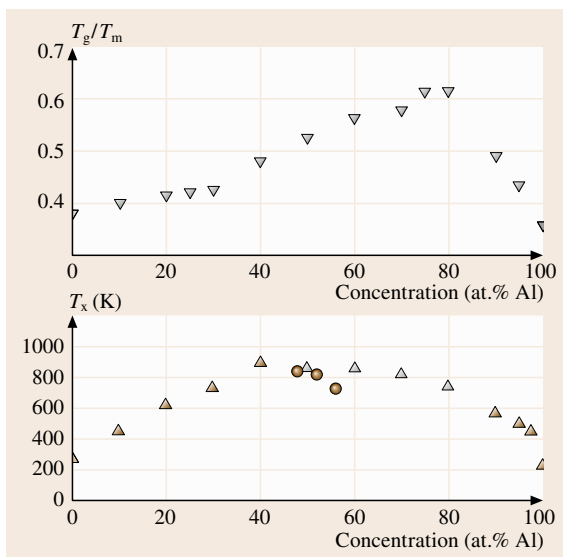


Fig. 17.26 The composition dependence of the glass-transition temperature (*upper column*) and the crystallization temperature (*lower column*) observed in the Ti-Al system. The glass-transition temperature is rescaled by the melting point at each composition. The crystallization temperatures taken from the heating procedure with the rate of 1.0 K/ps are denoted by the closed triangles, those from a long time annealing are denoted by the *open triangles*, and those from the experimental observation (after [17.36]) are denoted by the *closed circles*

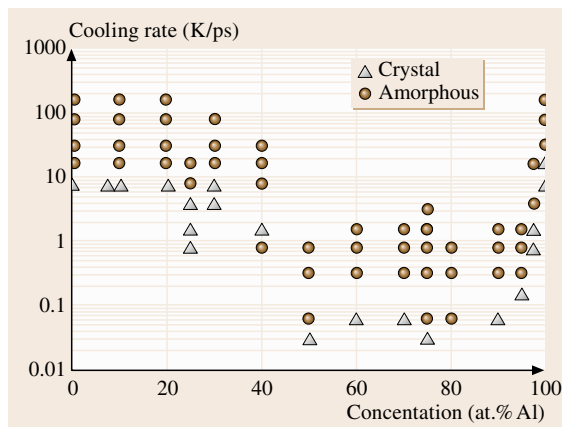


Fig. 17.27 The solidified phases after the cooling process mapped onto the cooling rate versus composition plane. The *squares* and the *circles* correspond to the crystalline and amorphous phases, respectively

a split-shaped second peak in the amorphous phase and a shell structure in the crystalline phase.

In glass transitions it is a general feature [17.37] that a lower cooling rate gives a lower T_g . This tendency is also observed in the simulation. By comparing the results between the case with the cooling rate 10 K/ps and that with the rate 100 K/ps in Fig. 17.24, we find that the lower cooling rate gives the lower energy amorphous state and, consequently, gives the lower T_g . The dependence of T_g on the cooling rate is approximately estimated as that cooling rate that is 10 times higher gives a 50 K increase in T_g .

Figure 17.25 shows an example of the time evolution of the internal energy in a heating procedure from an amorphous phase for the Ti-25 at.% Al case. The drop at around 800 K corresponds to amorphous-to-crystal transition, while the subsequent jump at 1900 K corresponds to melting. Thus we can define the crystallization temperature T_x and the melting point T_m of this composition.

By performing this procedure for different compositions, we can obtain [17.38] the composition dependence of the glass-transition temperature T_g and the crystallization temperature T_x in the Ti-Al system. The results are shown in Fig. 17.26. Since T_g as well as T_x depends on the cooling/heating rate, the plotted data are rescaled values corresponding to a constant rate of 1.0 K/ps. In the upper graph, the compositional dependence of the glass-transition temperature T_g are plotted, where the value of T_g is normalized by the observed

melting point T_m at each composition. In the lower graph, the composition dependence of the crystallization temperature T_x taken from the heating procedure with constant rate are denoted by the closed triangle, while those from long-time annealing are denoted by the open triangle, and those from experimental observations [17.36] are denoted by the closed circles. We find an agreement between the simulation results and the experimental observations.

We can also map the obtained phase after quenching onto the cooling rate–composition plane in Fig. 17.27, where the open triangles denote crystalline phases, while the closed circles denote amorphous phases. By using these plots, we can estimate the amorphous-forming composition range at a given cooling rate.

The results are shown in Fig. 17.28, where the upper two results are from the sputtering deposit experiments [17.31], the middle two are from the MD simulations with the EAM potentials, and the lower two are from the MD simulations with the LJ potentials. Considering that the effective cooling rate in the sputtering deposition experiments is the order of 10^8 – 10^{12} K/s, the MD simulations with EAM potentials show better agreement with the experiments than those with the LJ potentials.

As mentioned before, there is a risk that the periodic boundary condition might harm the dynamics of the simulation system. Hence we investigate the effect of the system size on the critical cooling rate by varying N from 218 to 8000 atoms for the pure Al system. In Fig. 17.29, we have mapped the final phases on the cooling rate–system size plane using the same symbols as used in Fig. 17.27. This shows that the effect is significant in small systems with less than 1000 atoms. The similar effect of size on the thermodynamical observables such as the melting point, the crystallization temperature, and the glass-transition temperature, are also calculated and plotted in Fig. 17.30, where the effect appears smaller than on the critical cooling rate, but with a similar nature. So, we conclude that we need at least a few thousand atoms in simulations using periodic boundary conditions to reduce the effect of the boundary conditions.

17.3.2 Annealing of Amorphous Alloys

The annealing procedure of the Ti–Al amorphous alloys is simulated in this subsection. The atomistic mechanism of the structural relaxation in amorphous alloys as well as that of crystallization is investigated by MD simulation with special attention to the local atomic

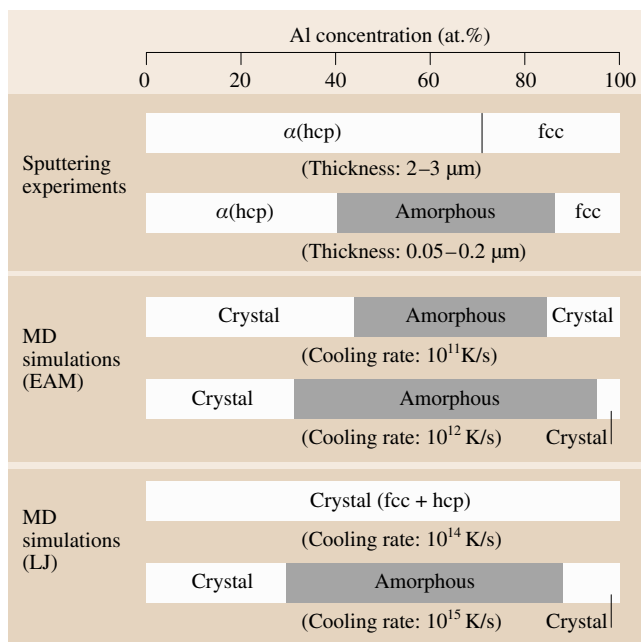


Fig. 17.28 Glass-forming ranges of the Ti–Al system given by experiments and simulations. The *upper two* are given from the sputtering deposition experiments (after [17.31]), the *middle two* are given from the MD simulations with the EAM potentials, and the *lower two* are given from MD simulations with the LJ potentials, respectively. The crystal structure found in the simulations is fcc, hcp, or their mixture in any case

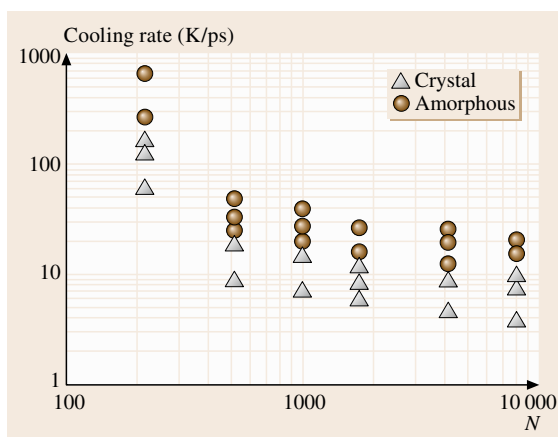


Fig. 17.29 The system-size dependence of the critical cooling rate when varying the total number N of atoms in the simulation for the pure Al system. The quenched phases are denoted by the same symbols as used in Fig. 17.27

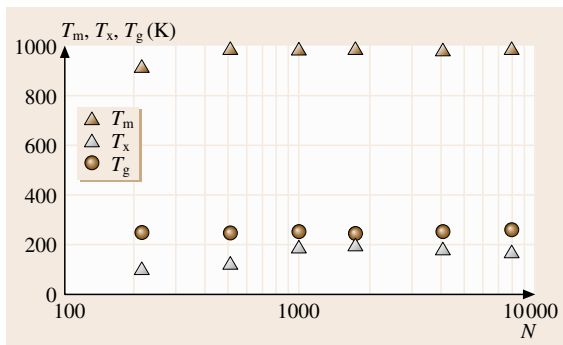


Fig. 17.30 The system-size dependence of the melting point T_m , the crystallization temperature T_x , and the glass-transition temperature T_g when varying the total number N of atoms in the simulation for the pure Al system

structure of the amorphous phases and the vibrational modes characteristic of the amorphous states.

In amorphous alloys, neither the local atomistic structure nor the mechanism of the structural relaxation is clearly understood. To clarify these problems, the structural change at the atomistic level will be investigated in the relaxation and crystallization process of amorphous phases in the Ti-Al binary system by using the MD simulation discussed in the previous subsection. To analyze the local structure in the amorphous phases obtained in the simulations, we shall introduce some local order parameters, which will shed light on the basic feature of the atomistic structure of the amorphous phases from different angles.

Icosahedral Symmetry

From experimental observations [17.39] and MD simulations [17.19], it has been established that icosahedral

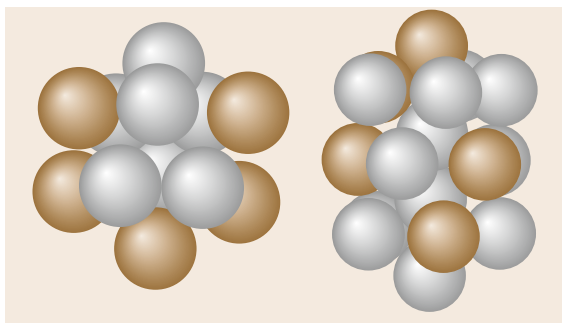


Fig. 17.31 Icosahedral clusters found in Ti-Al amorphous alloys obtained in the simulations. The *brown spheres* and the *white spheres* denote the Ti atoms and the Al atoms, respectively

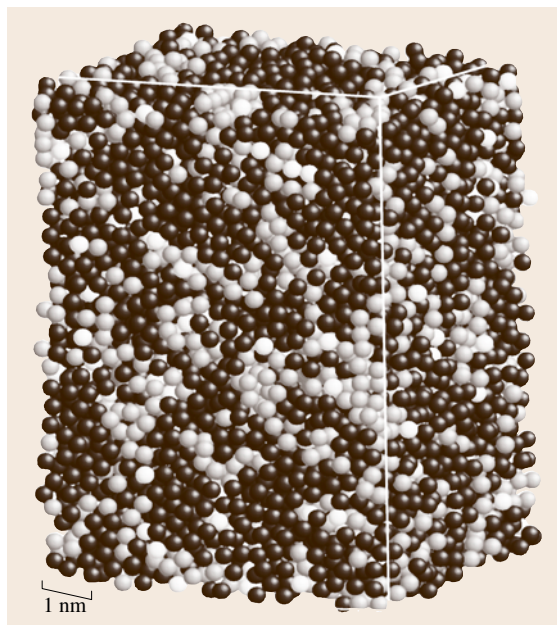


Fig. 17.32 The medium-range structure in a Ti-50 at. % Al amorphous alloy with 8000 atoms after the classification of the atoms according to the symmetry of the surrounding atoms. The *dark gray*, *light gray*, and *white spheres* denote the atoms with icosahedral symmetry, the atoms with crystalline symmetry, and the other atoms with somewhat distorted surroundings, respectively

structures are the basic building blocks of the amorphous state in monatomic systems. Since the atomic size difference between Ti and Al is small (a few %), Ti-Al amorphous alloys might include such icosahedral structures. Indeed, we can find [17.34] many types of icosahedral clusters in the Ti-Al amorphous phases obtained by the simulations, as depicted in Fig. 17.31. Therefore, we shall investigate the local atomic structure while paying particular attention to this icosahedral symmetry to analyze the microstructure of the phases emerging in the heating and annealing processes.

For this purpose, the Voronoi tessellation technique [17.19] is useful to analyze the local symmetry of atomic configuration around each atom. Dividing the whole configuration space by the bisecting planes for all atomic pairs, we can assign the Voronoi polyhedron or the Wigner–Seitz cell to each atom. The shape of the Voronoi polyhedron reflects the local structure around the corresponding atom. Thus we can assign [17.19] the environmental character to the atoms from the distribution of the faces of the corresponding Voronoi polyhedron.

By evaluating the shape of the Voronoi polyhedra, we can classify the atoms into three groups according to their surrounding structure [17.38]: atoms with an environment of icosahedral symmetry, atoms with an environment of crystalline symmetry, and other atoms with somewhat distorted surroundings. Figure 17.32 shows the above classification applied to a Ti-50 at. % Al amorphous alloy with 8000 atoms, where the icosahedral-like atoms, the crystal-like atoms, and the other atoms are depicted by the dark gray, light gray, and white spheres, respectively. The remarkable feature is that there is a region with crystalline symmetry even in the amorphous phase and it forms a medium-range ordered structure on the nanometer scale together with a region with icosahedral symmetry. The geometrical origin of the medium scale is understood as follows.

The essence of glass-formation is the competition between the locally stable state (icosahedral cluster) and the globally stable state (crystalline ordering) and the domination of the former. However, the icosahedral clusters have fivefold symmetry so they cannot fill up all space by themselves and there is some limit of order at the nanometer scale for such icosahedral packing. That is why the inhomogeneity on a medium scale exists in the amorphous states.

Thus we can take the fraction X_{ico} of the atoms with icosahedral symmetry and the fraction X_{cry} of the atoms with crystalline symmetry as order parameters which reflect the local symmetry.

In a similar sense, we use the fraction X_{penta} of the pentagons in the total Voronoi faces as an order parameter, since all the faces of the Voronoi polyhedron with icosahedral packing consist of pentagons, while those with *bcc*, *fcc*, or *hcp* crystal consist of squares and hexagons.

DRP Structure

Historically, the first model of atomistic structure for amorphous alloys is the dense random packing (DRP) model [17.40]. In the DRP model, the basic structure is the closest packing of hard spheres and the basic unit is the tetrahedron made of four mutually contacting spheres. Since such closest packing is almost ideally realized in the icosahedral clusters, the abundance of the icosahedral clusters in the amorphous phase reflects the existence of the DRP structure and hence the tetrahedral packing in its basis. Therefore, by counting the number of tetrahedra made of four mutually neighboring atoms in the amorphous alloys, we can use the number N_{tetra} of tetrahedral clusters per atom as an order parameter to characterize the order of the DRP structure.

Free Volume

Next we introduce the notion of free volume following the idea of *Cohen* and *Grest* [17.41]. The atoms surrounded by enough free volume can move by the length of the order of atomic distance, while those having little space around them can only make oscillatory moves around their equilibrium positions. Those atoms having enough free volume are called liquid-like atoms. In the free volume theory, the glass-to-liquid transition can be understood as a percolation of free volume or the liquid-like atoms. In this context, we take a simple definition for the free volume as follows.

Firstly we define the nearest neighbors of an atom by the atoms within a distance of 1.4 times of its atomic size, which corresponds to the first minimum in the radial distribution. Then we define an atom as having enough free volume if it has fewer than 12 neighbors. Under this definition, atoms surrounded by a crystal packing such as *fcc*, *hcp*, or *bcc* are not atoms with free volume, and neither do atoms surrounded by the icosahedral structure. On the other hand, even in a crystal, the atoms neighboring a defect structure such as a vacancy are atoms with free volume. Thus we have another parameter X_{free} which is the fraction of atoms with enough free volume.

Figure 17.33 shows the time evolution of the above order parameters in the annealing process of amorphous alloys. The left column corresponds to a Ti-25 at. % Al amorphous alloy annealed at 520 K and the right column corresponds to a Ti-50 at. % Al amorphous alloy annealed at 810 K. The common feature is the decrease in the atomic volume and the energy, as well as that in the free volume. On the other hand, the striking difference is in the evolution of X_{penta} and X_{cry} , that is, an increase in X_{penta} and X_{ico} together with a decrease in X_{cry} are observed in the right column, while a decrease in X_{penta} and X_{ico} together with an increase in X_{cry} are observed in the left column. This indicates that a more stable amorphous phase with less free volume would form in the annealing procedure for the system with the composition 50 at. % Al, while embryos of crystalline phases would form in the annealing period for the system with the composition 25 at. % Al. Consequently, in the relaxation period, the microscopic process proceeds differently depending on the Al concentration of the system. At the midway composition, where the glass-forming ability is high, less free volume and hence more stable amorphous phase forms, while the early stages of crystallization take place at low Ti or low Al

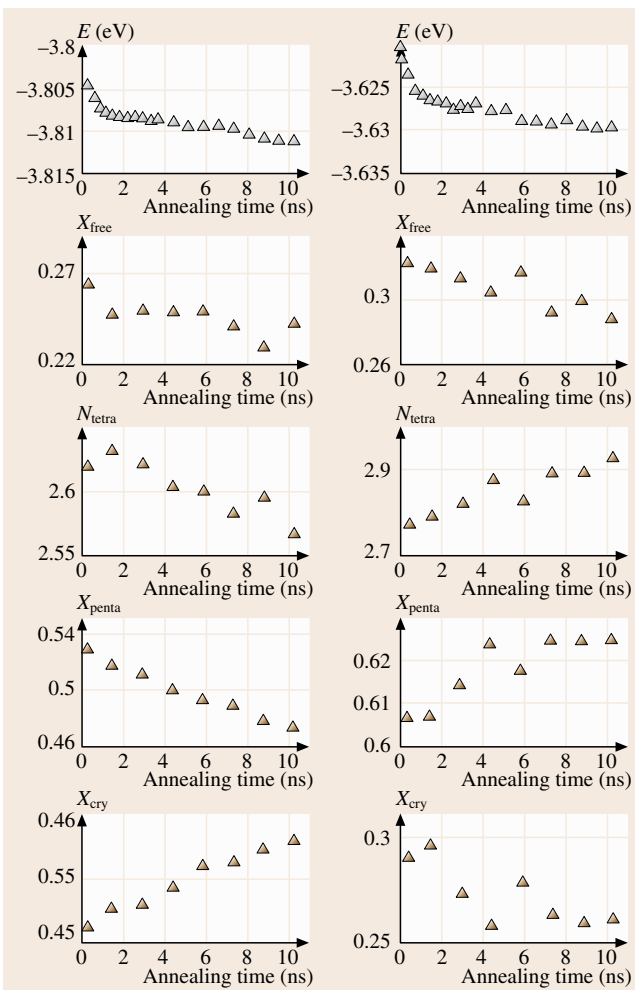


Fig. 17.33 The time evolution of the internal energy E and the structure parameters, X_{free} , N_{tetra} , X_{penta} , and X_{cry} . The left column corresponds to the Ti-25 at. % Al system with 8000 atoms annealed at 520 K, while the right column corresponds to the Ti-50 at. % Al system of the same size annealed at 810 K

concentration where the glass-forming ability is rather low.

Next we investigate how the above parameters that show local structures change in crystallization processes. Figure 17.34 shows the time evolution of the internal energy E , the fraction X_{penta} of the pentagons, the fraction X_{cry} of atoms with crystalline symmetry, the fraction X_{free} of free volume atoms, and the number N_{tetra} of tetragonal clusters in the annealing process at 580 K of a Ti-25 at. % Al amorphous alloy with 8000 atoms. The drastic change in

the parameters at $t = 11$ ns apparently corresponds to the amorphous-to-crystal transition. This can also be seen from the snapshots of atomic configuration of a) the as-quenched state (annealing time $t = 0$ ns), b) a relaxed amorphous state ($t = 10.3$ ns), c) a partially crystallized state ($t = 11.4$ ns), and d) a fully crystallized state ($t = 15$ ns), which are depicted in the right of Fig. 17.34. By using this type of analysis, we can depict a time-temperature-transformation (TTT) curve of the simulation system, as shown in Fig. 17.35, where the tentative TTT-curve of the Ti-25 at. % Al amorphous alloy is shown by the bold line.

Finally we proceed to investigate the vibration modes in the amorphous state. The vibrational state of thermal atomic motion is closely related to the local atomic structure. In this sense, an excess of vibration states experimentally observed [17.42] in many types of amorphous phases is thought to play an important role. This is called the boson peak and seems to be a universal feature of amorphous states. However, its structural origin is not clearly understood yet. Indeed, some pioneering MD studies have shown that these modes are closely related to the local atomistic structure [17.43] and a cooperative motion on the nanometer scale [17.44]. Hence we here try to uncover the microscopic origin of the boson peak by investigating the atomic vibrational state in the Ti-Al amorphous phases during the annealing procedure. The investigation of the microscopic origin of the boson peak helps us to understand the physics of the glass transition and the amorphous state itself.

As mentioned in Sect. 17.1.5, we can calculate the power spectrum $f(\omega)$ of the atomic vibration energy from the velocity autocorrelation function of the atoms as

$$f(\omega) = \frac{2}{\pi} \int_0^{\infty} dt \cos \omega t \langle \mathbf{v}(0)\mathbf{v}(t) \rangle / \langle \mathbf{v}^2 \rangle, \quad (17.72)$$

where the brackets means the average over all atoms. In Fig. 17.36, the calculated vibration energy spectrum of three different phases of Ti-25 at. % Al alloys in the annealing process at 580 K shown in Fig. 17.34, are depicted, where the full line, dashed line, and dotted line correspond to the as-quenched amorphous state (annealing time $t = 0$ ns), a relaxed amorphous state ($t = 10.3$ ns), and a crystallized state ($t = 15$ ns), respectively. We can easily see the excess of states in both the low- and high-frequency

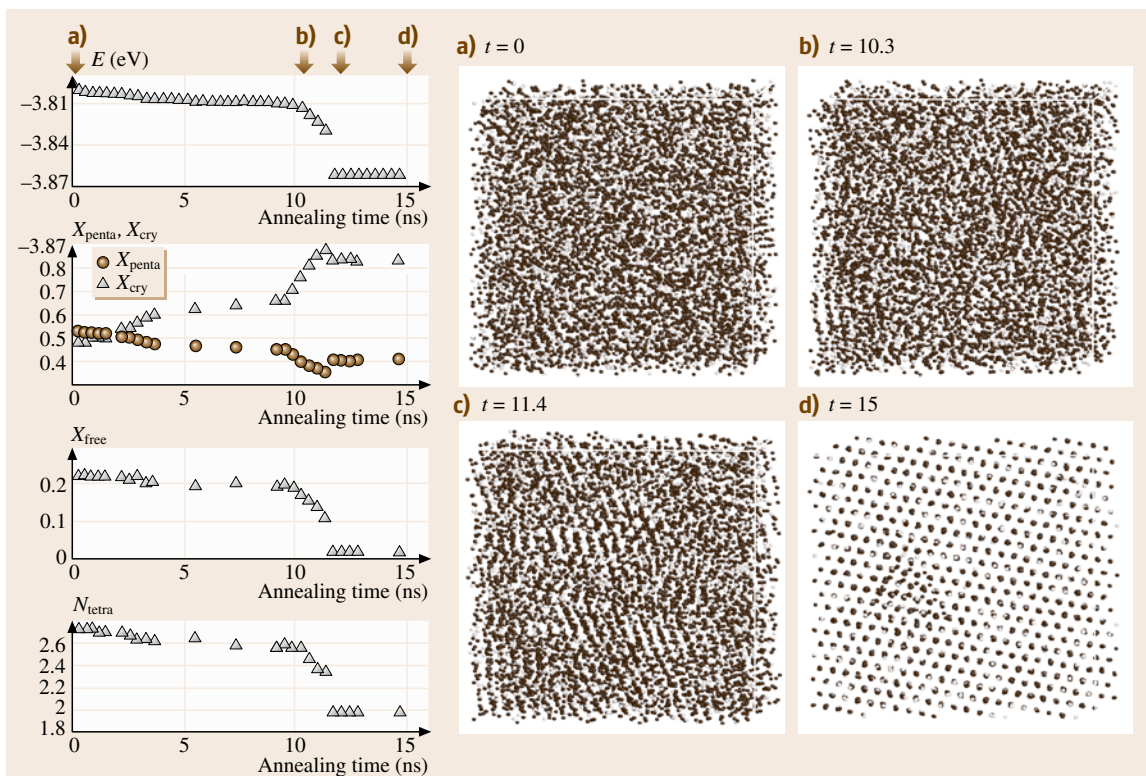
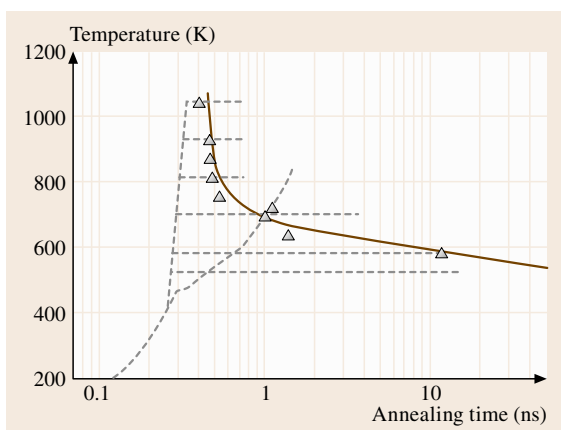


Fig. 17.34a–d The time evolution of the internal energy E , the fraction X_{penta} of the pentagons, the fraction X_{cry} of atoms with crystalline symmetry, the fraction X_{free} of free volume atoms, and the number N_{tetra} of tetragonal clusters in the annealing process at 580 K of the Ti-25 at. % Al amorphous alloy with 8000 atoms. The right graphs are snapshots of atomic configuration at the annealing times (a) $t = 0$ ns, (b) $t = 10.3$ ns, (c) $t = 11.4$ ns, and (d) $t = 15$ ns

tail in the amorphous states and that the amount of the excess decreases with time of annealing. Especially, the excess in the low-frequency tail that



corresponds to the boson peak is shown in the inset of Fig. 17.36.

To clarify the microscopic origin of the boson peak, we next investigate the differences between the contributions made to the excess of vibration modes by different local structures. For this purpose, the classification into three regions based on the atomic local symmetry illustrated in Fig. 17.32 is used, and the contribution to the vibrational spectrum from each region is calculated. The results calculated at 10 K for a Ti-50 at. % Al amorphous alloy with 8000 atoms are shown in Fig. 17.37, where the solid line, dashed line, and dotted line correspond to the icosahedral-like atoms,

Fig. 17.35 The calculated TTT curve of an annealed Ti-25 at. % Al amorphous alloy (bold line). The dotted lines denote the histories of the heat treatments performed in the simulations and the triangles denote the points where crystallization is observed ◀

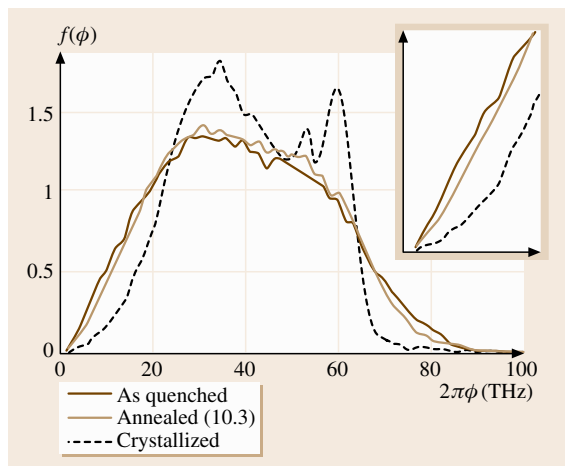


Fig. 17.36 The time evolution of the vibration spectrum in the annealing process at 580 K of the Ti-25 at. % Al amorphous alloy with 8000 atoms. The *solid line*, the *dashed line*, and the *dotted line* correspond to the as-quenched amorphous phase, the relaxed amorphous phase after 10 ns annealing, and the crystallized phase after 15 ns annealing, respectively. The *inset* denotes the low frequency tails

the crystalline-like atoms, and the other atoms, respectively, and the inset shows the lower frequency tails. This means that the contribution to the boson peak from atoms with more free volume and fewer neighbors is the largest, while that from the icosahedral atoms is next, and that from crystalline atoms is the smallest. This is consistent with the fact that the decrease in the boson peak during the annealing process is accompanied by a decrease in free volume. But the quantitative difference is so small that we could only discern it in the inset of Fig. 17.37.

17.3.3 Glass-Forming Ability of Alloy Systems

In order to acquire the high glass-forming ability of alloy systems, there are well-known empirical rules [17.28]: large atomic size difference and negative heat of mixing between the alloying elements. In this section, the microscopic origin of these rules is explored by using MD calculations for a model system in which the atomic size ratio and the heat of mixing between the constitute elements can be varied independently.

Here we again choose a binary system where the interaction is described by the 8–4 LJ poten-

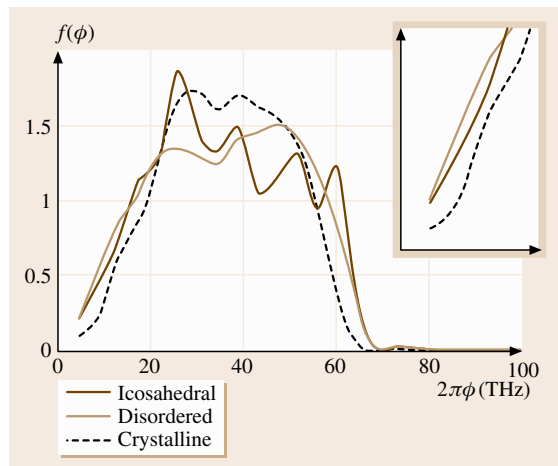


Fig. 17.37 The contribution to the vibration spectrum from the atoms with different local structures calculated at 10 K for a Ti-50 at. % Al amorphous alloy with 8000 atoms. The *solid line*, the *dashed line*, and the *dotted line* correspond to atoms with icosahedral symmetry, atoms with crystalline symmetry, and other atoms with distorted surrounding, respectively. The *inset* denotes the low-frequency tails

tial as a model for binary alloys, which is discussed in Sect. 17.2.3. There are two reasons for using this model. The first is that we can independently vary the atomic size ratio and the heat of mixing by changing the parameter r_0^{AB} and e_0^{AB} , respectively. The second reason can be found in Fig. 17.28, which shows the calculated amorphous-forming range in the Ti-Al system both for the EAM potential and the LJ potential. Quantitatively, the results from the LJ potential are poorer than those from the EAM potential compared to the experimental observations, but qualitatively, the predicted composition range that has maximum glass-forming ability is almost the same for both potentials. In addition, the predicted critical cooling rate for the LJ potential is a thousand times higher than that for the EAM potential, which means the necessary calculation time is much lower for the LJ potential. In this sense, the MD simulation using the LJ potential is a counterpart of the acceleration experiment, if we are only interested in the glass-forming range.

The model system used in the simulation is almost the same as that used in Sect. 17.2.3, except that we assume that $e_0^{11} = e_0^{22} = 1$ and that the heat of mixing is controlled by varying the interaction parameter e_0^{12} . That is, $e_0^{12} < 1$ means a positive heat of mixing, while

$e_0^{12} > 1$ means a negative heat of mixing. All physical quantities are expressed in the above units in this section. Note that the unit of cooling rate is around 5×10^{15} K/s for typical alloy systems.

To simulate rapid solidification processes, we first prepare a liquid phase in the same manner as mentioned in Sect. 17.3.1, and then rapidly quench the system to solidify. Depending on the cooling rate as well as the atomic size ratio and the heat of mixing of the system, we have a crystalline phase or an amorphous phase. By varying the cooling rate, we can estimate the critical cooling rate needed for amorphization by melt quenching. Alternatively, by varying the atomic size ratio r_0^{22} , the chemical interaction e_0^{12} , and the concentration x_2 of the solute element, we can calculate the glass-forming range by melt quenching under a constant cooling rate.

First we show the pure geometrical effect on the glass-forming ability. In Fig. 17.38a, the shaded regions denote the glass-forming ranges in the rapid solidification on the (x_2, r_0^{22}) plane at fixed chemical interaction of $e_0^{12} = 1$. The darker shading corresponds to the lower cooling rate. For the midway compositions, the glass-forming ability is extremely high if the atomic size ratio is less than 0.9.

We note that the glass-forming ranges are not symmetric in composition and are slightly shifted to higher solute concentration. This suggests that the glass-forming ability should be higher when the adding element has a larger atomic size than the main constituent than when the adding element has a smaller size, assuming that the solute element is added in the same amount.

To investigate the chemical effect on the glass-forming ability for melt quenching, we next fix the atomic size ratio at $r_0^{22} = 1$ and vary the chemical bond strengths between $0.5 < e_0^{12} < 1.5$. In this case, however, we cannot observe any obvious change in the critical cooling rate compared to the system with $e_0^{12} = 1$.

Then we turn to the system with a fixed atomic size ratio of 0.95 and vary e_0^{12} . Figure 17.38b shows the glass-forming range in this case, where the heat of mixing ΔH is defined as $\Delta H = (e_0^{11} + e_0^{22})/2 - e_0^{12}$. The larger negative ΔH gives a greater glass-forming ability, although no amorphization is observed in the cases at low cooling rates less than 1×10^{-4} .

The above results show the following two features: 1) The effect of the chemical factor on the glass-forming ability is rather smaller than that of the geometrical fac-

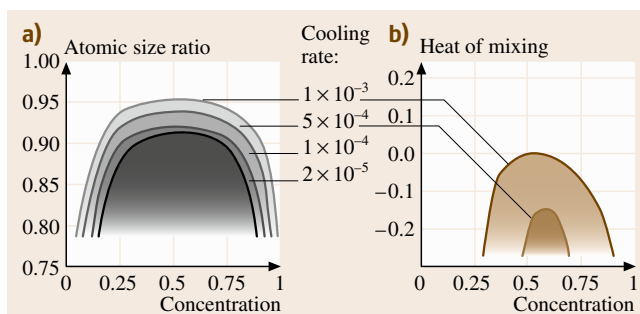


Fig. 17.38a,b Composition ranges in which amorphous phases are formed by melt quenching in the model binary systems. (a) Glass-forming ranges under the variation of r_0^{22} with $e_0^{12} = 1$; (b) glass-forming ranges under the variation of e_0^{12} with $r_0^{22} = 0.95$. The darker shading corresponds to the lower cooling rate

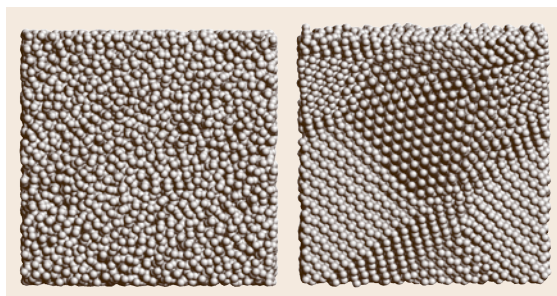


Fig. 17.39 An amorphous phase (left) and a nanocrystalline phase (right) prepared by rapid solidification

tor and it becomes significant if it is combined with the geometrical effect. 2) Both the geometrical and the chemical factor act asymmetrically, in other words, the glass-forming ability is different whether we add the larger atomic size element to the main constituent element or add the smaller one.

Finally, we show an interesting possibility for control of the nanostructure of rapidly solidified phases. Figure 17.39 shows snapshots of an amorphous phase (left) and a nanocrystalline phase (right) obtained by rapid solidification processes with different conditions. That is, they are obtained in different binary systems with different atomic size ratios under different cooling rates. These snapshots indicates that, to choose the parameters such as the atomic size ratio properly, we could control the grain size of nanocrystalline phases by rapid solidification, as well as we could control the formation of the glassy phases.

17.4 Diffusion

In this section, we shall focus on atomic diffusion. The atomistic mechanism for diffusion is investigated by the MD simulation in a number of cases: the diffusion via vacancies or interstitials in crystalline phases including ordered phases, and the diffusion in the liquid and the glassy phases.

17.4.1 Diffusion in Crystalline Phases

In this section, the atomic diffusion process in crystalline phases is investigated by MD simulation. The atomic-level processes are clarified in the cases of diffusion via vacancies and that via interstitials. The difference between the diffusion properties in pure metallic systems and those in ordered alloy systems is discussed.

To investigate diffusion properties in crystalline phases, here we choose the alloy model discussed in Sect. 17.2.1 where the atomic interactions are described by the 8–4 LJ potential. Therefore, all units used in this section are the same as those found in Sect. 17.2.1. The advantage of using this model is that we can find three ordered phases in this system, that is, the $L1'_0$ and the $L1''_0$ (fcc-based) phases at low temperatures, and the B2 (bcc-based) phase at high temperatures. So we can compare the diffusion properties of the ordered alloys with those of pure metals.

The atomic diffusion in crystalline phases is mainly due to vacancies and interstitials. In MD simulations, the atomic diffusivity can easily be calculated from the atomic mean square displacement as in (17.58), while diffusion experiments are always accompanied with many difficulties. We introduce a single vacancy

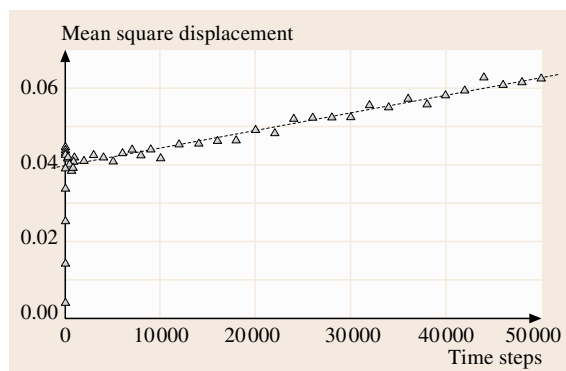


Fig. 17.40 Time evolution of average mean square displacement of atoms in an fcc phase introduced one vacancy into $N = 4000$ atoms at $T = 0.6$

into an fcc crystalline phase consisting of $N = 4000$ atoms of element 1 at $T = 0.60$. Figure 17.40 shows a time evolution of the atomic mean square displacement in the fcc phase introduced a single vacancy. The slope of the time dependence denoted by the dotted line in Fig. 17.40 corresponds to the atomic diffusivity D , while the intersection point of the dotted line with the vertical axis corresponds to the average value of thermal vibration. Note that the temperature $T = 0.6$ amounts to 90% of the melting temperature of the fcc structure of elements 1, and the drawback of the MD calculation of the diffusivity is that we can barely estimate the diffusivity at low temperatures far away from the melting point within the available calculation time.

According to the prescription discussed above, we can estimate the diffusivity via vacancies in the fcc phase of element 1 as well as the alloy phases of the element 1 and the element 2, that is, the B2 phase and the $L1''_0$ phase by introducing a pair of vacancies of the element 1 and 2 into a perfect crystalline phase. The results are shown in Fig. 17.41. The temperature dependence of the atomic diffusivity in each phase are denoted by closed circles (fcc), open triangles (B2), and closed triangles ($L1''_0$). In the calculation, a pair of vacancies is introduced into an $N = 4000$ system for the fcc phase, and into an $N = 3456$ system for the ordered phases. The values T^{-1} on the horizontal axis are normalized by the melting temperature of each phase,

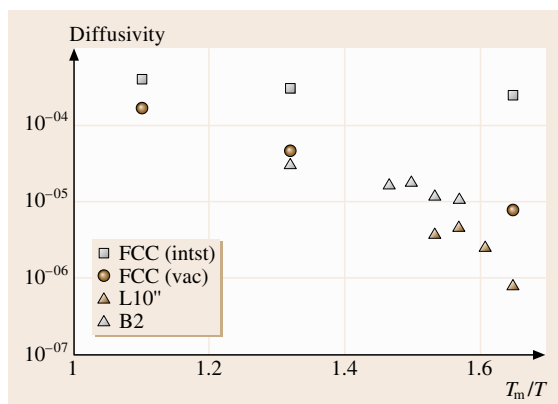


Fig. 17.41 The temperature dependencies of the diffusivity in a B2 phase (open triangles), an $L1''_0$ phase (closed triangles), and an fcc phase (closed circles) with the vacancy concentration ≈ 0.0005 and that of diffusivity in an fcc phase with the same interstitial concentration (open squares)

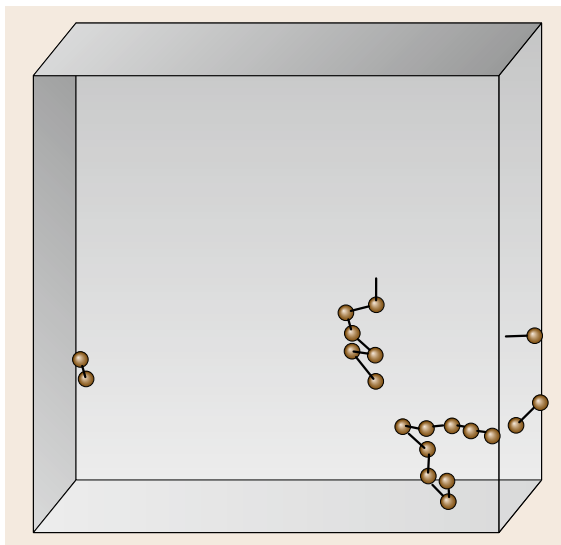


Fig. 17.42 Trajectories of largely moved atoms in an **fcc** phase with two vacancies at $T = 0.30$. The *balls* denote the final positions of atoms and the *sticks* connect them to the initial positions

except the $L1'_0$ phase, which is normalized by the melting temperature of the B2 phase.

Although the calculated values include a considerable amount of statistical errors, especially at low temperatures, we can recognize the following properties. Comparing the diffusivity in the B2 phase with that in the $L1'_0$ phase, the atomic diffusion is suppressed in the latter phase, mainly because the $L1'_0$ phase has a structure based on a close-packed structure. Comparing the diffusivity in the **fcc** phase with that in the $L1'_0$ phase, both of which are based on close-packed structure, the atomic diffusion is also suppressed in the latter phase, which suggests that the atomic diffusion would be suppressed in ordered alloys. We have also calculated the diffusivity in the **fcc** phase by introducing a pair of interstitials into an $N = 4000$ system; the results are plotted in Fig. 17.41. The results indicate that diffusion via interstitials has a much higher rate and lower activation energy than that via vacancies.

In the MD simulations, we can easily pick up the atoms that contribute the diffusion. In Fig. 17.42, we have depicted the trajectories of atoms which have moved a distance larger than half of the nearest neighbor distance within 10^5 time steps in an **fcc** phase of element 1 having introduced a pair of vacancies at $T = 0.30$, where the balls denote the final positions of

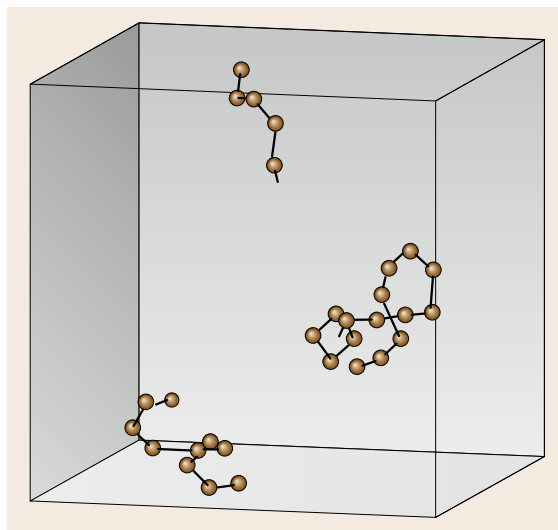


Fig. 17.43 Trajectories of largely moved atoms in an **fcc** phase with two interstitials at $T = 0.25$. The *balls* denote the final positions of atoms and the *sticks* connect them to the initial positions

such atoms and the sticks connect them to their initial positions. Two strings of atom trajectories can be identified, one of which looks broken into three parts due to the periodic boundary conditions. These two strings correspond to two vacancies introduced into a perfect **fcc** crystal.

In Fig. 17.43, similar trajectories of atoms that have moved significant distances after 10^5 time steps are depicted for an **fcc** phase, having introduced a pair of interstitials at $T = 0.25$. The two figures look similar, but there are two differences between them. One is the history of the string of the sequence of the moving atoms has been made. Each string looks like a row of tadpoles and has two ends: one end is the *head* of the leading tadpole, and the other end is the *tail* of the tadpole at the opposite end of row. So we call the former the head of the string and the latter the tail of the string. For the case of diffusion via vacancies, the atomic *jump* starts from the head of the string and ends with the tail of the string, while the direction of the time sequence is opposite for the case of diffusion via interstitials. The second difference is in the distance of each atomic jump. For the case of diffusion via vacancies, the distance of each atomic jump is nearly always the nearest-neighbor distance, while that for the case of the diffusion via interstitials is less than the nearest-neighbor distance. These characteristics of atomic diffusion will be revisited in the next

section, where the diffusion in liquid and glassy phases are discussed.

17.4.2 Diffusion in Liquid and Glassy Phases

The diffusion mechanism in the liquid phase or the glassy phase is not clearly understood. So, in this section, we try to clarify the mechanism in those phases by MD simulation for a model system. The qualitative change in diffusion property during the liquid quench process found in the simulations is discussed in relation to conventional theories of glass transitions.

The physics behind the glass transition is a long-standing problem in materials science. The discovery [17.45, 46] of bulk metallic glasses has given us a good opportunity to investigate the glass transition in a nearly ideal situation because of the broad stable supercooled liquid region in the system. Indeed, experimental observations [17.28, 47–49] of atomic transport phenomena such as diffusivity and viscosity in metallic glasses have gradually revealed the dynamical nature of the glass transition. Especially, recent nuclear magnetic resonance (NMR) measurements [17.50] have shed light on the microscopic transport mechanism in both supercooled liquid and glassy phases. Moreover, many tasks using MD simulations also give [17.51–54] us useful information about the intrinsic nature of the glass transition from an atomic point of view. In this context, we shall describe a series of MD simulations while focusing on transport phenomena such as atomic diffusion in both liquid and glassy states by using the same model of binary alloys as discussed in Sect. 17.3.3.

MD calculations for an idealized alloy system interacting via the 8–4 LJ potential are performed under periodic boundary conditions. The pressure of the system is kept at zero by using the Parinello–Rahman method and the temperature of the system is controlled by the momentum-scaling method. In order to investigate transport properties in supercooled liquid and glassy phases, we need to prevent nucleation of the crystalline phase during the observation. In other words, we should select the potential parameters such that the system should have a high glass-forming ability, or equivalently, a stable supercooled liquid region. The glass-forming ability of the system under rapid solidification has been investigated in Sect. 17.3.3 by another series of MD simulations and it was shown that a large atomic size difference plays a decisive role. Hence we take the atomic size ratio as $r_0^{22} = 0.8$ and vary the concentra-

tion x_2 of the element 2. For simplicity, we assume an equi-chemical interaction, $e_{11} = e_{22} = e_{12} = 1$. We also assume the interaction distance between different elements is $r_{12} = (r_{11} + r_{22})/2$. All physical quantities are expressed in this units in this section as in Sect. 17.3.3.

The melting temperature T_m of the pure system is around 0.67 in these reduced units. We prepare the binary mixture with $x_2 = 0.2, 0.5$, and 0.7 at $T = 0.8$ and slowly cool the system down. The cooling rate 1×10^{-4} corresponds to about 10^{-11} K/s for a typical metallic system. The liquid-to-glass transition is observed in every case and the nucleation of crystalline phases has not been observed in any case. The glass-transition temperature T_g is determined by the discontinuity of the specific heat, as discussed in Sect. 17.3.1. The atomic self-diffusion coefficients D are calculated by the mean square displacement, as shown in the preceding section.

Figure 17.44 shows the time evolution of the total diffusion coefficient D in the equimolar ($x_2 = 0.5$) system in a cooling procedure. The temperature dependence goes down remarkably beyond some critical temperature T_c and then changes to another behavior below the glass-transition temperature T_g , as indicated in the figure. According to the temperature dependence of the diffusivities, we can classify the phases during the liquid-to-glass transition into three stages. That is, ordinary liquid or weakly supercooled liquid phases (region I), strongly supercooled liquid phases (region II), and

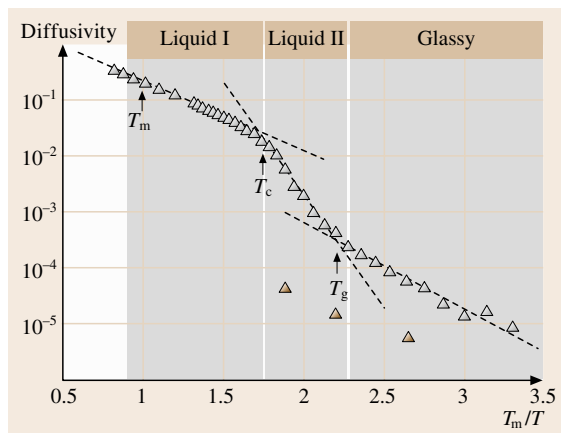


Fig. 17.44 Three stages of the temperature dependence of atomic diffusivity during rapid solidification of a binary system with an atomic size ratio of 1 : 0.8 and a concentration of 50%

glassy phases (region III), as shown schematically in Fig. 17.44.

The transition from region I to II looks a transition from viscous flow to restricted diffusion caused by structural arrest or infinitely slow relaxation processes, while the transition from II to III is understood as the so-called glass transition because it coincides with the T_g determined calorimetrically. In other words, T_c corresponds to the beginning of the structural arrest or structural slowing down and T_g corresponds to the completion of the structural arrest or structural freezing. Note that the latter change of the diffusion rate at T_g has been detected in experimental observations [17.48–50] for metallic glasses.

On the other hand, the former change has not been experimentally observed yet. The Arrhenius behavior of the temperature dependence in region II suggests that the atomic diffusion needs some activation processes such as cooperative motion. The activation energies estimated from the Arrhenius plots are 6.0 in region II and 1.6 in region III in the LJ units. These correspond to 3.0 and 0.8 eV for a typical metallic system, respectively, both of which are consistent with the experimental results [17.28, 49].

We have also plotted the temperature dependence of the diffusivity in a crystalline phase in Fig. 17.44 by the closed triangles, which are obtained during a solidifica-

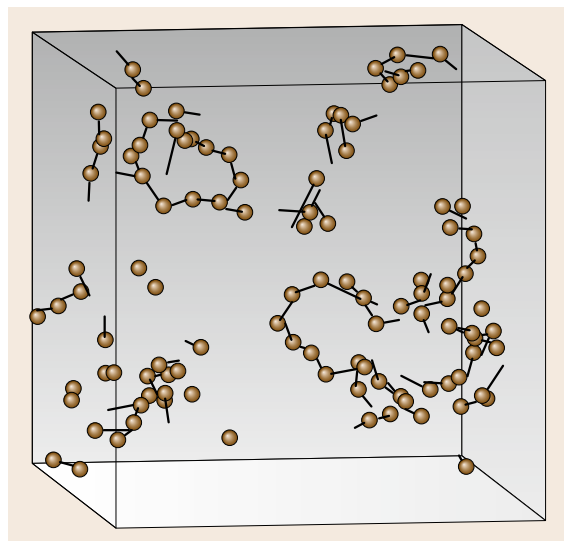


Fig. 17.45 Trajectories of chain-like collective motions in a glassy phase at $T = 0.15$. The *balls* denote the final positions of atoms and the *sticks* connect them to the initial positions

tion process of the pure system with $x_2 = 0$. Compared to the diffusivity in glassy phases, this indicates that the atomic mobility would be much higher in glassy phases than in crystalline phases.

For the systems with other compositions ($x_2 = 0.2$ and 0.7), we can also recognize three regions I–III in both cases, although T_c as well as T_g depends on the solute composition. Therefore, the three-stage feature of diffusivity found in the simulations seems to be a universal character in glass transitions.

To investigate the microscopic nature of atomic diffusion processes in the supercooled liquid and glassy phases, we calculate the atom trajectories, as discussed in the previous section. We first pick the atoms that have moved more than half of the nearest neighbor distance in a time period and then draw lines from the initial to the final position of such atoms. Figure 17.45 shows the trajectories of such atoms in a glassy phase at $T = 0.15$ of the equimolar system in the interval of 10^5 time steps. Many chain-like trajectories are observed. Although these chain-like trajectories look very similar to those found in crystalline phases depicted in Figs. 17.42 and 17.43, the time analysis reveals the following different features in these motions.

Firstly, the motion of atoms in the same chain occurs almost simultaneously (within a few picoseconds), while the sequence of motions found in crystalline phases takes place in a *one after another* way and ranges over a longer period. This indicates that collective motion should exist in the glassy phases. Another feature is that this collective motion is not exactly simultaneous, but seems to start from the tail and end with the head of the chain, as in diffusion via interstitials.

Similar analyses have been done for the liquid phases (regions I and II). We also found the chain-like cooperative motion in the supercooled liquid phases. However, the atomic motion in the liquid phases is complicated and other types of collective motion seem to exist, so more extended analysis is needed; this is one direction for future work.

We have found that three independent regimes exist during the liquid-to-glass transition, which show the different diffusion characteristics: ordinary (or weakly undercooled) liquid phases (region I), strongly supercooled liquid phase (region II), and glassy phase (region III). We believe that this will be a universal feature in glass-transition phenomena. For bulk metallic glasses, the transition from II to III has been observed [17.28], while that from I to II has not yet. However, for ionic glasses, a sign of transition from I to II has been observed in the relaxation property by

neutron scattering experiments [17.55]. The landscape theory [17.56] as well as the free-volume theory [17.57] and the mode-coupling theory [17.58] might provide a key to understanding the nature of this three-stage behavior. From this viewpoint, this peculiar behavior in atomic transport might have its microscopic origin

in atomic cooperative motions or the redistribution of atomic free-volumes. Since MD simulation is a convenient method to clarify the microscopic nature of atomic transport phenomena, it is well worth trying to continue MD study for the glass transition along this line.

17.5 Summary

Due to the increasing power of modern computers, computer simulations will become the third class of investigation method along side the experimental and theoretical method. Among these simulation methods, MD simulation is a powerful tool to investigate the microscopic mechanism in various types of phenomena, since all information about the atoms in the simulation system can be available. A main drawback of this method is the limit in both length scale and time scale due to a lack of sufficient computational power. Even under such limitations, we can apply this method to the investigations of various types of phenomena in materials, as discussed in this chapter

- martensitic transformation in bulk and nano-clusters,
- solid-state amorphization,
- glass-formation by rapid solidification,
- structural relaxation and crystallization of amorphous alloys,
- atomic diffusion in crystalline phases, glassy phases, and liquid phases.

Of course, there will be an infinite number of other applications for MD simulation in materials science. Therefore, it is very promising to cultivate this method in this field.

References

- 17.1 L. Verlet: Computer "experiments" on classical fluids. I. Thermodynamical properties of Lennard-Jones molecules, *Phys. Rev.* **159**, 98–103 (1967)
- 17.2 C.W. Gear: *Numerical Initial Value Problems in Ordinary Differential Equations* (Prentice Hall, New Jersey 1971)
- 17.3 H.J.C. Berendsen, W.F. van Gunsteren: Practical algorithms for dynamic simulations. In: *Molecular-Dynamics Simulation of Statistical-Mechanical Systems*, ed. by G. Ciccotti, W.G. Hoover (Elsevier, Amsterdam 1986)
- 17.4 J.C. Slater: *Insulators, Semiconductors and Metals* (McGraw-Hill, New York 1967)
- 17.5 L.V. Woodcock: Isothermal molecular dynamics calculations for liquid salts, *Chem. Phys. Lett.* **10**, 257–261 (1971)
- 17.6 J.M. Haile, S. Gupta: Extensions of the molecular dynamics simulation method. II. Isothermal systems, *J. Chem. Phys.* **79**, 3067–3076 (1983)
- 17.7 S. Nose: A unified formulation of the constant temperature molecular dynamics methods, *J. Chem. Phys.* **81**, 511–519 (1984)
- 17.8 H.C. Andersen: Molecular dynamics simulations at constant pressure and/or temperature, *J. Chem. Phys.* **72**, 2384–2393 (1980)
- 17.9 B.L. Holian: Simulations of vibrational relaxation in dense molecular fluids. In: *Molecular-Dynamics Simulation of Statistical-Mechanical Systems*, ed. by G. Ciccotti, W.G. Hoover (Elsevier, Amsterdam 1986)
- 17.10 S. Nose: A molecular dynamics method for simulations in the canonical ensemble, *Mol. Phys.* **52**, 255–268 (1984)
- 17.11 W.G. Hoover: Canonical dynamics: Equilibrium phase-space distributions, *Phys. Rev. A* **31**, 1695–1697 (1985)
- 17.12 M. Parrinello, A. Rahman: Crystal structure and pair potentials: A molecular-dynamics study, *Phys. Rev. Lett.* **45**, 1196–1199 (1980)
- 17.13 M. Shimono, H. Onodera, T. Suzuki: fcc–bcc phase transformation in iron under a periodic boundary condition, *Mater. Trans. JIM* **40**, 1306–1313 (1999)
- 17.14 M. Parrinello: Molecular-dynamics study of crystal structure transformations. In: *Molecular-Dynamics Simulation of Statistical-Mechanical Systems*, ed. by G. Ciccotti, W.G. Hoover (Elsevier, Amsterdam 1986)
- 17.15 J.M. Sanchez, J.R. Barefoot, R.N. Jarrett, J.K. Tien: Modeling of γ/γ' phase equilibrium in the nickel-aluminum system, *Acta Metall.* **32**, 1519–1525 (1984)

- 17.16 M.S. Daw, M.I. Baskes: Semiempirical, quantum mechanical calculation of hydrogen embrittlement in metals, *Phys. Rev. Lett.* **50**, 1285–1288 (1983)
- 17.17 S.M. Foiles: Calculation of the surface segregation of Ni–Cu alloys with the use of the embedded–atom method, *Phys. Rev. B* **32**, 7685–7693 (1985)
- 17.18 M.W. Finnis, J.E. Sinclair: A simple empirical N -body potential for transition metals, *Philos. Mag.* **50**, 45–55 (1984)
- 17.19 F. Yonezawa: Glass transition and relaxation of disordered structures. In: *Solid State Phys*, Vol. 45, ed. by H. Ehrenreich, D. Turnbull (Academic, San Diego 1991)
- 17.20 J.R. Ray, M.C. Moody: Molecular dynamics calculation of elastic constants for a crystalline system in equilibrium, *Phys. Rev. B* **32**, 733–735 (1985)
- 17.21 T. Suzuki, M. Shimono: A simple model for martensitic transformation, *J. Phys. IV (France)* **112**, 129–132 (2003)
- 17.22 M. Takagi: Electron-diffraction study of liquid–solid transition of thin metal films, *J. Phys. Soc. Jpn.* **9**, 359–363 (1954)
- 17.23 H. Mori, H. Yasuda: Effect of cluster size on phase stability in nm-sized Au–Sb alloy clusters, *Mater. Sci. Eng. A* **217/218**, 244–248 (1996)
- 17.24 T. Suzuki, M. Shimono, M. Wuttig: Martensitic transformation in micrometer crystals compared with that in nanocrystals, *Scr. Mater.* **44**, 1979–1982 (2001)
- 17.25 K. Asaka, T. Tadaki, Y. Hirotsu: Transmission electron microscopy and electron diffraction studies on martensitic transformations in nanometre-sized particles of Au–Cd alloys of near-equiatomic compositions, *Philos. Mag. A* **82**, 463–478 (2002)
- 17.26 R.A. Johnson, D.J. Oh: Analytic embedded atom method model for bcc metals, *J. Mater. Res.* **4**, 1195–1201 (1989)
- 17.27 T. Suzuki, M. Shimono, S. Takeno: Vortex on the surface of a very small crystal during martensitic transformation, *Phys. Rev. Lett.* **82**, 1474–1477 (1999)
- 17.28 A. Inoue: *Bulk Amorphous Alloys: Preparation and Fundamental Characteristics* (Trans Tech, Zurich 1998)
- 17.29 M. Shimono, H. Onodera: Geometrical and chemical factors in the glass-forming ability, *Scr. Mater.* **44**, 1595–1598 (2001)
- 17.30 M. Li, W.L. Johnson: Instability of metastable solid solutions and crystal to glass transition, *Phys. Rev. Lett.* **70**, 1120–1123 (1993)
- 17.31 H. Onodera, T. Abe, T. Tsujimoto: Formations of metastable phases in vapor quenched Ti–Al–Nb alloys, *Curr. Adv. Mater. Process.* **6**, 627 (1993)
- 17.32 D.J. Oh, R.A. Johnson: Simple embedded atom method model for fcc and hcp metals, *J. Mater. Res.* **3**, 471–478 (1988)
- 17.33 R.A. Johnson: Alloy models with the embedded–atom method, *Phys. Rev. B* **39**, 12554–12559 (1989)
- 17.34 M. Shimono, H. Onodera: Molecular dynamics study on liquid-to-amorphous transition in Ti–Al alloys, *Mater. Trans. JIM* **39**, 147–153 (1998)
- 17.35 H. Onodera, T. Abe, T. Tsujimoto: Modeling of α/α_2 phase equilibrium in the Ti–Al system by the cluster variation method, *Acta Metall.* **42**, 887–892 (1993)
- 17.36 T. Abe, S. Akiyama, H. Onodera: Crystallization of sputter deposited amorphous Ti–52 at.% Al alloy, *Iron Steel Inst. Jpn. Int.* **34**, 429–434 (1994)
- 17.37 A.J. Kovacs, J.M. Hutchinson, J.J. Aklonis: *The Structure of Noncrystalline Materials* (Taylor Francis, London 1977)
- 17.38 M. Shimono, H. Onodera: Molecular dynamics study on formation and crystallization of Ti–Al amorphous alloys, *Mater. Sci. Eng. A* **304–306**, 515–519 (2001)
- 17.39 J. Farges, M.F. de Feraudy, B. Raoult, G. Torchet: Noncrystalline structure of argon clusters. I. Polyicosahedral structure of Ar_N clusters, $20 < N < 50$, *J. Chem. Phys.* **78**, 5067–5080 (1983)
- 17.40 J.D. Bernal: A geometrical approach to the structure of liquids, *Nature* **183**, 141–147 (1959)
- 17.41 M.H. Cohen, G.S. Grest: Liquid–glass transition, a free-volume approach, *Phys. Rev. B* **20**, 1077–1098 (1979)
- 17.42 K. Suzuki, K. Shibata, H. Mizuseki: The medium- and short-range collective atomic motion in Pd–Si(Ge) amorphous alloys, *J. Non-Cryst. Solids* **156–158**, 58–62 (1993)
- 17.43 V.A. Luchnikov, N.N. Medvedev, I.Y. Naberukhin, V.N. Novikov: Inhomogeneity of spatial distribution of vibrational modes in a computer model of amorphous argon, *Phys. Rev. B* **51**, 15569–15572 (1995)
- 17.44 H.R. Schober, B.B. Laird: Localized low-frequency vibrational modes in glasses, *Phys. Rev. B* **44**, 6746–6754 (1991)
- 17.45 A. Inoue, T. Zhang, T. Masumoto: Zr–Al–Ni amorphous alloys with high glass transition temperature and significant supercooled liquid region, *Mater. Trans. JIM* **31**, 177–183 (1990)
- 17.46 A. Parker, W.L. Johnson: A highly processable metallic glass: $Zr_{41.2}Ti_{13.8}Cu_{12.5}Ni_{10}Be_{22.5}$, *Appl. Phys. Lett.* **63**, 2342–2344 (1993)
- 17.47 H.S. Chen: A method for evaluating viscosities of metallic glasses from the rates of thermal transformations, *J. Non-Cryst. Solids* **27**, 257–263 (1978)
- 17.48 H.S. Chen, L.C. Kimerling, J.M. Poate, W.L. Brown: Diffusion in a Pd–Cu–Si metallic glass, *Appl. Phys. Lett.* **32**, 461–463 (1978)
- 17.49 U. Geyer, S. Schneider, W.L. Johnson, Y. Qiu, T.A. Tombrello, M.–P. Macht: Atomic diffusion in the supercooled liquid and glass states of the $Zr_{41.2}Ti_{13.8}Cu_{12.5}Ni_{10}Be_{22.5}$ alloy, *Phys. Rev. Lett.* **75**, 2364–2367 (1995)
- 17.50 X.–P. Tang, U. Geyer, R. Busch, W.L. Johnson, Y. Wu: Diffusion mechanisms in metallic supercooled liquids and glasses, *Nature* **402**, 160–162 (1999)

- 17.51 B. Bernu, J.P. Hansen, Y. Hiwatari, G. Pastore: Soft-sphere model for the glass transition in binary alloys: Pair structure and self-diffusion, *Phys. Rev. A* **36**, 4891–4903 (1987)
- 17.52 S.-P. Chen, T. Egami, V. Vitek: Local fluctuations and ordering in liquid and amorphous metals, *Phys. Rev. B* **37**, 2440–2449 (1988)
- 17.53 G. Wahnström: Molecular-dynamics study of a supercooled two-component Lennard-Jones system, *Phys. Rev. A* **44**, 3752–3764 (1991)
- 17.54 M. Shimono, H. Onodera: Criteria for glass-forming ability accessible by molecular dynamics simulations, *Mater. Trans. JIM* **45**, 1163–1171 (2004)
- 17.55 F. Mezei, W. Knaak, B. Farago: Neutron spin echo study of dynamic correlations near the liquid-glass transition, *Phys. Rev. Lett.* **58**, 571–574 (1987)
- 17.56 F.H. Stillinger: A topographic view of supercooled liquids and glass-formation, *Science* **267**, 1935–1939 (1995)
- 17.57 D. Turnbull, M.H. Cohen: Free-volume model of the amorphous phase: Glass transition, *J. Chem. Phys.* **34**, 120–125 (1961)
- 17.58 W. Götze, L. Sjögren: Relaxation processes in supercooled liquids, *Rep. Prog. Phys.* **55**, 241–376 (1992)

18. Continuum Constitutive Modeling

Constitutive models play an important role when characterizing structural materials in order to evaluate their thermomechanical behavior. The experimental characterization of materials (using techniques discussed in Part C of this Handbook) involves measuring and controlling macroscopic variables such as force, displacement and temperature. Concise models are also of great use when characterizing the continuous media used to create structural materials, because phenomenological modeling can be carried out regardless of the internal material structure. This continuum modeling usually successfully describes the behavior of various classes of material under complex boundary conditions.

This chapter presents phenomenological constitutive models from both macroscopic and microscopic viewpoints:

- Starting from viscoplasticity models, model performance is reviewed in order to predict the mechanical response under creep–plasticity interaction conditions, taking into account internal state variables.
- Material anisotropy is discussed; mathematical modeling of initial anisotropy and induced anisotropy based on the representation theorem for higher order isotropic tensors is presented.
- Thermomechanical coupling phenomena involving phase transformations predominate

18.1 Phenomenological Viscoplasticity	1013
18.1.1 General Models of Viscoplasticity....	1013
18.1.2 Inelasticity Models	1015
18.1.3 Model Performance	1016
18.2 Material Anisotropy	1018
18.2.1 Description of Material Anisotropy..	1018
18.2.2 Initial Anisotropy	1019
18.2.3 Induced Anisotropy	1021
18.3 Metallothermomechanical Coupling	1023
18.3.1 Phase Changes.....	1023
18.3.2 Numerical Methodology	1025
18.3.3 Applications to Heat Treatment and Metal Forming.....	1025
18.4 Crystal Plasticity	1026
18.4.1 Single-Crystal Model.....	1026
18.4.2 Grain Boundary Sliding	1029
18.4.3 Inhomogeneous Deformation	1029
References	1030

in engineering applications of heat treatment and material processing. A continuum model is presented that takes into account the way structural rearrangement evolves in materials.

- Finally, microscopic analysis based on crystal plasticity, which relates the resolved shear stress to crystal slip, is applied to describe the inhomogeneous deformation process in polycrystalline materials.

In the context of Part E of this Handbook, which deals with various methods of modeling and simulation, the subject of this chapter – *continuum modeling* – sits be-

tween the *molecular modeling* methods explored in the previous chapter and the *finite element modeling* methods discussed in the next chapter.

18.1 Phenomenological Viscoplasticity

18.1.1 General Models of Viscoplasticity

Materials exhibit a wide variety of phenomena in their thermal and mechanical behavior. If we consider struc-

tural materials specifically, they are usually composed of large numbers of crystals and they show clear yield points that occur when the stress exceeds a certain limit. The mechanical behavior after yield is termed as the

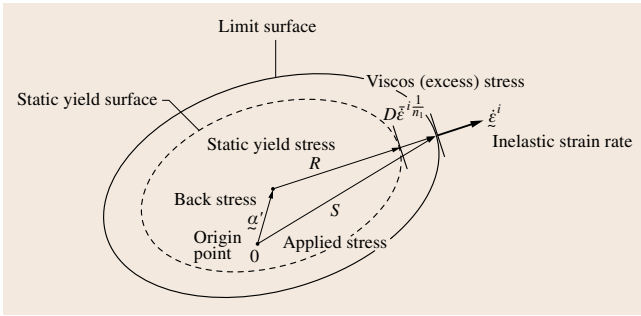


Fig. 18.1 Schematic illustration of unified inelasticity model based on excess stress hypothesis

plasticity regime and is believed to be independent of time. However, the materials even exhibit permanent deformation below the yield point, particularly at elevated temperature. This deformation is called *creep* and it is believed that different mechanisms apply to this low-stress creep compared to those that occur during metal plasticity. On the other hand, when the stress is high, materials exhibit complicated behavior arising from a mixture of the two components (plasticity and creep).

The equations used to investigate the thermomechanical behavior of materials are derived from (a) conservation laws for mass, linear momentum, angular momentum and energy, (b) kinematic relationships relating displacement to strain, and (c) constitutive equations. Among these, the constitutive equations reflect the specific response of a material from mechanical and thermal viewpoints, while the other equations are independent of the material under consideration and so they all are common to any kind of boundary value problems. The linear elasticity model is a typical example of a constitutive equation, where the Young's modulus and Poisson's ratio (or in another form, Lamé's constants) specify the mechanical response of the material. The Fourier law of heat conduction is another one, where the heat flux is proportional to the gradient of temperature. The coefficient in the Fourier law simply corresponds to the elasticity constant. For convenience we limit our discussion to isothermal processes in this section; nonisothermal problems are discussed in Sect. 18.3 (including heat treatment processes).

Viscoplasticity models have been proposed in order to deal with rate-dependent behavior. Among these, the so-called *superposition model* is the model that simply combines the conventional plastic strain ε_{ij}^p with the creep strain ε_{ij}^c as

$$\varepsilon_{ij} = \varepsilon_{ij}^e + \varepsilon_{ij}^p + \varepsilon_{ij}^c. \quad (18.1)$$

Here we tacitly assume the independence of the elastic strain ε_{ij}^e . In contrast, the *unified constitutive model* gives the rate-dependent viscoplastic (or inelastic) strain ε_{ij}^{vp} ($= \varepsilon_{ij}^p + \varepsilon_{ij}^c$) regardless of the plasticity and creep. The latter formulation is sometimes advantageous because it can be hard to distinguish between plasticity and creep deformation. We employ the Cartesian coordinate system throughout this section and denote the strain tensor $\boldsymbol{\varepsilon}$ by ε_{ij} ; the index notation merely indicates the components of the tensors within a particular Cartesian coordinate system. We also write equations in direct notation where it does not cause confusion.

The phenomenological modeling and the thermodynamic considerations of unified constitutive models were first discussed by *Malvern* [18.1] and *Perzyna* [18.2] in the early 1960s, and more sophisticated models have since been proposed that include internal state variables, which allow us to predict the creep-plasticity interaction and cyclic hardening/softening behavior. A modern treatment of unified constitutive models can be found in monographs by *Miller* [18.3] and *Krausz* [18.4], and these models are applied to finite element codes in order to analyze the structural responses of real machine components.

When modeling a unified inelastic constitutive equation, the following assumptions are widely employed: the stress–strain curve is static independent of the time scale used, the stress is explicitly dependent on the evolution of the viscoplastic strain rate, and the normality rule applies to the flow potential F . A schematic illustration is shown in Fig. 18.1, where kinematic back stress is introduced at the center of the yield surface. The viscoplastic strain rate is expressed as

$$\dot{\varepsilon}_{ij}^{vp} = \Phi(\boldsymbol{\sigma}, \boldsymbol{\alpha}) \frac{\partial F}{\partial \sigma_{ij}}, \quad (18.2)$$

where the function Φ describes the magnitude of the strain rate, while the second term describes the direction of the strain rate. The function Φ is chosen such that the steady creep rate can be expressed in terms of the stress $\boldsymbol{\sigma}$ and the internal state variables $\boldsymbol{\alpha}$ (scalar or tensor). The internal state variables (or simply the *internal variables*) are introduced from a phenomenological point of view in such a way that the model reflects hardening and/or softening behavior depending on the prior deformation history of the material. They may correspond to a physical property such as back stress or drag stress in some cases, while the dislocation density can also be chosen as an internal variable in other cases.

Based on the previous discussion and the illustration in Fig. 18.1, a typical evolution law for viscoplastic

strain can be derived as follows [18.5]. Many materials obey a power law for creep and kinematic hardening can be idealized using the back stress α . Introducing the static yield stress r as the threshold for the onset of yield, we can write the viscoplastic strain rate as

$$\dot{\varepsilon}_{ij}^{\text{vp}} = \left\langle \frac{F(\boldsymbol{\sigma} - \boldsymbol{\alpha}) - r}{D} \right\rangle^n \frac{\partial F}{\partial \sigma_{ij}}, \quad (18.3)$$

where F stands for the effective stress given by

$$F = \left[\frac{3}{2} (\sigma'_{ij} - \alpha'_{ij}) (\sigma'_{ij} - \alpha'_{ij}) \right]^{1/2}. \quad (18.4)$$

Here the prime (') denotes the deviatoric part. If we neglect the back stress and yield stress, (18.3) is identical to the well-known creep equation obtained by following the Norton rule. In contrast, the solution of (18.3) for uniaxial stress leads to

$$\sigma = r + D (\dot{\varepsilon}^{\text{vp}})^{1/n} + \alpha. \quad (18.5)$$

When a large value is employed for the power factor n , the second term of the right-hand side becomes negligible and so we obtain an almost rate-independent stress-strain curve. Consequently, this constitutive model is expected to cover a wide range of stress-strain responses, from steady creep to rate-independent plastic behavior.

Internal state variables play a key role when modeling the unified inelasticity model, through which complicated loading histories can be predicted. The internal state variables reflect macroscopic and/or microscopic changes in internal structures [18.6]. The back stress, for example, can be measured in such a way that the Bauschinger effect is produced by the variation, while the back stress cannot be controlled during the deformation process. Therefore, the evolution laws may involve the external variables χ , their rates, and the internal state variables $\boldsymbol{\alpha}$ themselves

$$\dot{\boldsymbol{\alpha}} = \mathbf{A}(\boldsymbol{\chi}, \boldsymbol{\alpha}) : \dot{\boldsymbol{\chi}} + \mathbf{B}(\boldsymbol{\chi}, \boldsymbol{\alpha}). \quad (18.6)$$

Any evolution equation in a constitutive model follows the above principle. Identifying specific parameters is, however, another issue. Material parameters are usually specified using stress-strain diagrams, by trial and error.

18.1.2 Inelasticity Models

Some of typical inelastic constitutive models are summarized here. We assume that the total strain rate is decomposed into an elastic part and an inelastic part.

The elastic part is expressed by Hooke's law, and the temperature and other effects are neglected for simplicity.

(a) The Conventional Superposition Model

This type of constitutive model has been widely used and is still often used in real structural analysis due to its simplicity. The model employs the same basic assumed decomposition of strain as (18.1), and the plasticity and creep models are introduced independently. For example, an isotropic plasticity model can be written in terms of the von Mises yield criterion as

$$F = \frac{1}{2} (\sigma'_{ij} - \alpha'_{ij}) (\sigma'_{ij} - \alpha'_{ij}) - \frac{1}{3} \bar{\sigma}_y^2 = 0, \quad (18.7)$$

where the evolution of the back stress $\boldsymbol{\alpha}$ follows Prager's law,

$$\dot{\alpha}'_{ij} = C \frac{2}{3} \dot{\varepsilon}_{ij}^{\text{p}}. \quad (18.8)$$

Here a , b and c are material parameters. For the creep model, Norton's law is introduced with the form

$$\dot{\varepsilon}_{ij}^{\text{c}} = \frac{3}{2} M A \sigma^{N-1} t^{M-1} \sigma'_{ij}, \quad (18.9)$$

where A , N , and M are material parameters and t is the time. Other types of plasticity and creep laws are also available using this model.

(b) The Chaboche Model [18.5]

Chaboche proposed a unified constitutive model with the type of power law used in (18.3) through (18.5). The key point of the model is the decomposition of back stress. In the original model, three kinds of back stress (namely $\boldsymbol{\alpha}^{(1)}$, $\boldsymbol{\alpha}^{(2)}$ and $\boldsymbol{\alpha}^{(3)}$) are introduced via

$$\boldsymbol{\alpha} = \sum_{k=1}^3 \boldsymbol{\alpha}^{(k)}. \quad (18.10)$$

It is also assumed that the static yield stress r is decomposed into a constant part r_0 and a development R . Taking the nonlinear hardening laws into account, the evolutions are given by

$$\dot{\alpha}^{(1)} = c_1 \left[a_1 \frac{2}{3} \dot{\varepsilon}^{\text{vp}} - \bar{\varepsilon}^{\text{vp}} \alpha'^{(1)} \right] - h \bar{\alpha}^{m-1} \alpha^{(1)}, \quad (18.11a)$$

$$\dot{\alpha}^{(2)} = c_2 \left[a_2 \frac{2}{3} \dot{\varepsilon}^{\text{vp}} - \bar{\varepsilon}^{\text{vp}} \alpha'^{(2)} \right], \quad (18.11b)$$

$$\dot{\alpha}^{(3)} = c_3 \frac{2}{3} \dot{\varepsilon}^{\text{vp}}, \quad (18.11c)$$

$$\dot{R} = b(Q - R) \bar{\varepsilon}^{\text{vp}} - \gamma R^q. \quad (18.12)$$

Here $\bar{\varepsilon}^{vp}$ is the equivalent viscoplastic strain rate and $\bar{\alpha}$ the effective back stress. There are many material parameters here and they need to be identified from conventional test data.

(c) The Miller Model [18.7]

Miller applied Garofalo's macroscopic creep equation to a unified constitutive model. The function Φ in (18.2) is expressed as

$$\Phi = B\theta \left\{ \sinh \left[\left(\frac{F(\sigma - \alpha)}{\sqrt{D_0 + D}} \right)^{1.5} \right] \right\}^n. \quad (18.13)$$

Here B , θ , n and D_s are constants. The temperature dependence is expected to depend on the parameter θ the most. Since the function $\sinh(\cdot)$ shows a steep change with variations in F , the model describes quasi-rate-independent yielding without a static yield stress component. The evolution equations for back stress α and drag stress D should suitably be defined.

(d) The Krempl Model [18.8]

This model can be regarded as an extension of viscoelasticity based on a generalized form of the Maxwell and Voigt models. Using nonlinear functions for the coefficients of viscoelasticity, a simple form can be written as

$$m[\sigma - g[\varepsilon]] \dot{\varepsilon} + g[\varepsilon] = \sigma + k[\sigma - g[\varepsilon]] \dot{\sigma}. \quad (18.14)$$

The function $g[\varepsilon]$ describes a static stress-strain diagram. Since the following relationship holds

$$E = \frac{m[\sigma - g[\varepsilon]]}{k[\sigma - g[\varepsilon]]} \quad (18.15)$$

around the stress origin (E stands for the elasticity constant), the total strain rate is expressed as

$$\dot{\varepsilon} = \frac{\dot{\sigma}}{E} + \frac{\sigma - g[\varepsilon]}{E k[\sigma - g[\varepsilon]]}. \quad (18.16)$$

If we regard the second term as the viscoplastic strain rate, choosing $g[\varepsilon]$ and $k[\sigma - g[\varepsilon]]$ appropriately enables us to describe real nonlinear stress-strain responses. The substantial part contributing to the viscoplastic strain rate $\sigma - g[\varepsilon]$ is called the *over-stress*.

(e) The Bodner Model [18.9]

This model was developed in order to cover a wide range of deformations at high strain rate. The flow rule of the viscoplastic strain rate is subject to the isotropic Levy-Mises condition. The second invariant of the viscoplastic

strain rate D_2 , which is the evolution, is defined by

$$D_2^2 = D_0^2 \exp \left[- \left(\frac{Z^2}{3} \right)^n \left(\frac{n+1}{n} \right) / J_2^n \right]. \quad (18.17)$$

Here D_0 and n are material constants and J_2 is the second invariant of the deviatoric part of the stress; Z is the internal state variable related to the visoplastic work W_p via

$$Z = Z_1 + (Z_0 - Z_1) \exp(-mW_p) \quad (18.18a)$$

$$m = m_0 + m_1 \exp(-\alpha W_p) \quad (18.18b)$$

Z_0 , Z_1 , m_0 , m_1 and α are material parameters. Estrin [18.10] refined this model, taking into account metallurgical considerations, and applied it to various deformation histories involving plasticity and creep.

(f) The Endochronic Model [18.11]

Valanis assumes the existence of an intrinsic time measure ζ particular to each material using

$$d\zeta^2 = \alpha^2 d\xi^2 + \beta^2 dt^2. \quad (18.19)$$

Here ξ is a parameter related to the strain accumulation, while t means the real time scale. This means that ξ reflects a combined history of deformation and time. He further assumes an intrinsic time scale $z(\zeta)$, which increases monotonically with ζ . Let z be, for example, expressed as

$$z = \frac{1}{\beta} \log_e (1 + \beta\zeta). \quad (18.20)$$

Using proper functions for $\mu(\zeta)$ and $K(\zeta)$, the stress deviator and the mean stress are integrated over the intrinsic time as

$$s = 2 \int_{z_0}^z \mu(z - z') \frac{\partial \boldsymbol{\varepsilon}}{\partial z'} dz', \quad (18.21a)$$

$$\sigma_m = \int_{z_0}^z K(z - z') \frac{\partial \varepsilon}{\partial z'} dz'. \quad (18.21b)$$

It should be noted that these material functions imply tangent moduli not under the real time scale, but under the intrinsic time scale.

18.1.3 Model Performance

As described in the previous section, a large number of inelasticity models have been proposed [18.12–15]. One is based on a macroscopic creep law, another one

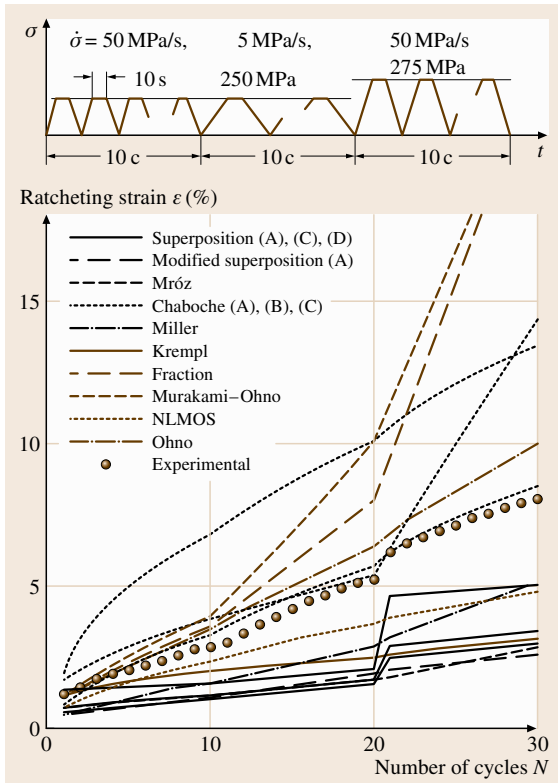


Fig. 18.2 Accumulation of ratcheting strain under various stress levels

reflects the physical deformation mechanism. In order to clarify the performance of each model, benchmark tests [18.16–18] have been carried out by the Subcommittee on Inelastic Analysis and Life Prediction under the support of the Committee on High Temperature Strength of Materials, The Society of Materials Science, Japan. A few examples are demonstrated here. The test material employed was 2.1/4Cr–1Mo ferrite steel, and the experiments were performed at an elevated temperature of 600 °C.

Metallic materials reveal a dependence of the mechanical behavior on rate at elevated temperatures, due to creep deformation, and the test material showed remarkable rate dependence at this temperature. Each model was used to predict the strain accumulated when the tensile stress is loaded at different rates and various holding times are used. Figure 18.2 shows the accumulation of strain for various stress rates and stress levels [18.17]. Since the strain always increases and accumulates with the number of cycles, this accumulation is called ratcheting. As shown in the figure, at least ten models are compared. It should be noted that different results are predicted, even by the same model, when the set of material parameters used is changed. This means that the specification of material parameters is not unique for a model and that even small differences in basic test data for monotonic tension, cyclic loading and monotonic creep seriously influence the ratcheting behavior. It has been reported that the responses under

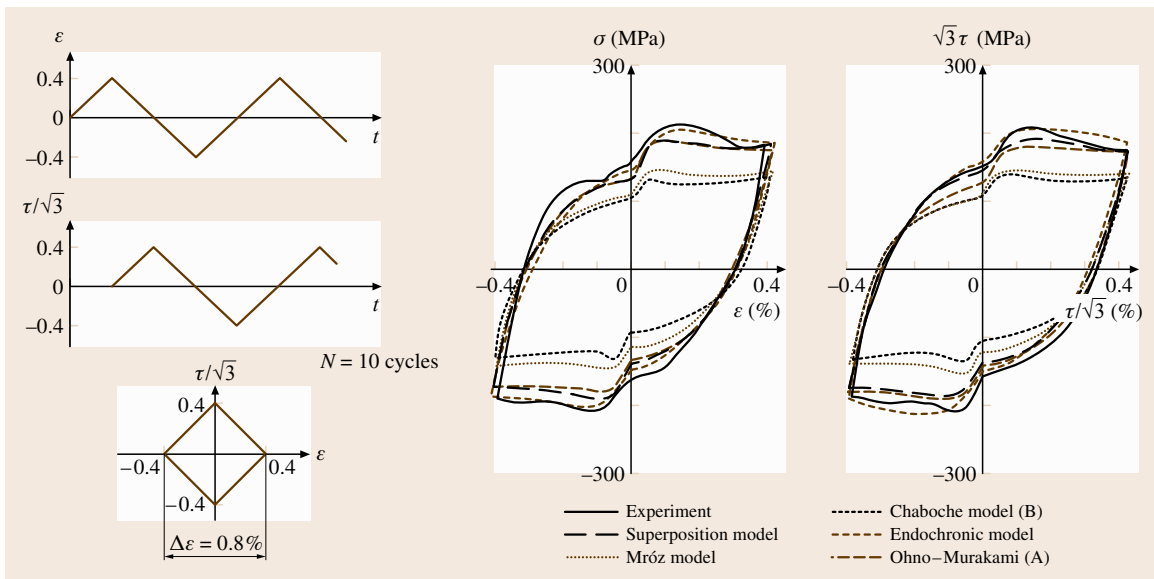


Fig. 18.3 Stress–strain responses under an out-of-phase strain path with square form

controlled stress tests generally exhibit large amounts of scatter.

The next example is stress response under combined states of tension and torsion, where a thin-walled tubular specimen is employed to realize the multiaxial stress. An out-of-phase strain path with a square pattern is imposed on the specimen, as shown on the left-hand side of Fig. 18.3 [18.18]. The stress components show a complicated trajectory due to the out-of-phase strain path. Where the strain trajectory has a corner, the stress trajectory suddenly changes in order to follow the normality

rule, and the magnitude of the stress is generally larger than the normal stress under uniaxial loading. Most of the constitutive models follow the exact trajectory, and the performance of the model is due to the modeling of additional hardening under nonproportional loading. Since all of the parameters used in constitutive models are taken from conventional test data obtained under conditions of uniaxial stress, this particular hardening behavior cannot be predicted in principle. Multiaxiality should preferably be introduced in the model while the parameters are to be simply determined.

18.2 Material Anisotropy

18.2.1 Description of Material Anisotropy

Solids are usually defined in such a way that the material has a reference configuration and that a resistance to deformation occurs. If the resistance of the material depends on the direction, the material is said to be anisotropic, while it is said to be isotropic if the same response is observed for any direction. The anisotropy is characterized by the existence of so-called *anisotropic axes* or *preferred orientations* in material. There are various classes of anisotropy, such as *orthotropy*, *planar anisotropy*, and so on. Here we summarize a rational method of obtaining a concrete form of an anisotropic constitutive equation based on the representation theorem for isotropic tensors [18.19]. Here it should be noted that the term *isotropic tensor* means an objective tensor that is independent of a change of frame; in other words *isotropic* means something very different here to when we use it in relation to isotropic and/or anisotropic material properties. Figure 18.4 describes the fundamental concept of material anisotropy. Let $\mathbf{m}^{(1)}, \mathbf{m}^{(2)}, \dots$ be vectors lying along the anisotropic axes, whose components are given by $m_i^{(k)}$ ($k = 1, 2, \dots$) under a particular orthonormal basis \mathbf{e}_i . For example, three kinds of anisotropic axes exist in orthotropic materials, which are mutually orthogonal. Without any loss of generality we can assume that each

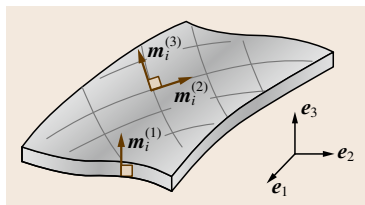


Fig. 18.4 Basic concept of material anisotropy

vector is a unit vector and therefore the following relationship holds

$$m_i^{(1)} m_j^{(1)} + m_i^{(2)} m_j^{(2)} + m_i^{(3)} m_j^{(3)} = \delta_{ij}. \quad (18.22)$$

Here δ_{ij} stands for the Kronecker delta.

Any tensor function used in continuum mechanics must fulfill the principle of objectivity. This requires the components to be invariant under the orthogonal transformation Q_{ij} . Suppose that a tensor $T_{ij\dots k}$ is expressible as a function with p sets of vectors $u_i^{(p)}$ and q sets of second-order tensors $U_{ij}^{(q)}$. Then it is expressed as

$$\begin{aligned} & Q_{il} Q_{jm} \cdots Q_{kn} T_{lm\dots n} \left[u_s^{(p)}, U_{st}^{(q)} \right] \\ &= T_{ij\dots k} \left[Q_{ls} u_s^{(p)}, Q_{ts} Q_{mt} U_{st}^{(q)} \right]. \end{aligned} \quad (18.23)$$

The orthogonal transformation of a vector and a second-order tensor takes the form

$$Q_{il} Q_{jm} U_{lm}^{(p)} = U'_{ij}{}^{(p)}, \quad (18.24)$$

$$Q_{il} u_i^{(q)} = u_i{}^{(q)}. \quad (18.25)$$

Using the representation theorem for isotropic tensors discussed by *Spencer* [18.19], a second-order symmetric isotropic tensor function can be reduced by taking the derivative of a scalar such that

$$T_{ij} = \frac{\partial I}{\partial K_{ij}}. \quad (18.26)$$

Here the scalar function indicates an invariant scalar with arguments that is linear on a symmetric tensor K_{ij} . The scalar I is expressed as

$$I = \phi_1 J_1 + \cdots + \phi_r J_r, \quad (18.27)$$

where J_r stands for invariants that are linear on K_{ij} together with arguments $U_{ij}^{(p)}$ and $u_i^{(q)}$; ϕ_r are coefficients expressed as polynomial functions of the invariants of $U_{ij}^{(p)}$, $u_i^{(q)}$ and possible combinations of them. In this case (18.26) can be rewritten in the form

$$T_{ij} = \sum_{s=1}^r \phi_s \frac{\partial J_s}{\partial K_{ij}}. \quad (18.28)$$

The full list of invariants with vectors, symmetric tensors, and skew-symmetric tensors can be found in the literature [18.19, 20]. Isotropic tensors are expressible as multilinear forms of the arguments using this technique.

When we take a symmetric tensor A_{ij} as an argument, the scalar I with K_{ij} is expressed by

$$I = \phi_1 K_{ii} + \phi_2 K_{ij} A_{ji} + \phi_3 K_{ij} A_{jk} A_{ki}. \quad (18.29)$$

A second-order symmetric isotropic tensor with one kind of argument is then given via (18.28) by

$$T_{ij} = \phi_1 \delta_{ij} + \phi_2 A_{ij} + \phi_3 A_{ik} A_{kj}, \quad (18.30)$$

where ϕ_r ($r = 1, 2, 3$) denote scalar coefficients which are also polynomial functions with the invariants of A_{ij} . When we adopt the second Piola–Kirchhoff stress tensor in T_{ij} and the Green strain tensor in A_{ij} , (18.30) leads to the most general representation for a hyperelastic material. When we pick a special representation which is linear on A_{ij} , (18.30) is reduced to

$$T_{ij} = \phi_1 A_{kk} \delta_{ij} + \phi_2 A_{ij}, \quad (18.31)$$

where ϕ_r ($r = 1, 2$) are now constant. When we regard the Cauchy stress as T_{ij} and the infinitesimal strain as A_{ij} , this coincides with the linear elasticity constitutive equation

$$\sigma_{ij} = E_{ijkl} \varepsilon_{kl} = (\lambda \delta_{ij} \delta_{kl} + 2\mu \delta_{ik} \delta_{jl}) \varepsilon_{kl}, \quad (18.32)$$

where ϕ_r have been replaced by Lamé's constants λ and μ .

For the anisotropic elasticity model, the scalar I involves a second-order symmetric tensor A_{ij} and skew-symmetric tensors X_{ij} . Since any skew-symmetric tensor can be characterized by an axial vector m_i using the relationship

$$X_{ij} = \varepsilon_{ijk} m_k \quad (18.33)$$

we can add vectors in deducing the full representation of general anisotropic materials. In the case of planar anisotropy, where one kind of vector lies

perpendicular to the plane, we have five material parameters among the elasticity constants [18.20]. In the most general anisotropic materials within the linear formulation, we have 21 constants because of the following condition imposed on the elasticity constants

$$E_{ijkl} = E_{jikl} = E_{ijlk} = E_{klij}. \quad (18.34)$$

No other condition is imposed on the material parameters.

18.2.2 Initial Anisotropy

Next we discuss the mathematical formulation of plasticity models accounting for initially anisotropic materials that (mainly for simplicity) initially exhibit orthotropy. When materials – particularly ductile metallic materials – deform under certain conditions, the anisotropic axes may change direction. They may not then be mutually orthogonal, even though they were orthogonal in the initial state. The evolution of the anisotropic axes, if the anisotropic vectors are embedded in the material, takes the form

$$\hat{m}_i = \dot{m}_i - W_{ij} m_j = D_{ij} m_j, \quad (18.35)$$

where \hat{m} means the Jaumann rate of the vector m . D and W are the stretching tensor and spin tensor respectively. It should be noted that this form is just one of the possible forms, and we do not exclude other formulations. If the orthotropy is maintained throughout the deformation, another type of evolution may be preferable.

A typical yield function for isotropic materials reads

$$F = \frac{1}{2} \sigma'_{ij} \sigma'_{ij} - \frac{1}{3} \bar{\sigma}_y^2 = 0. \quad (18.36)$$

Here σ'_{ij} denotes the deviatoric part of the stress and $\bar{\sigma}_y$ refers to the yield stress. One generalized form with a quadratic yield function was proposed by Hill [18.21], where a fourth-order tensor reflecting material anisotropy plays a central role

$$F = \frac{1}{2} N_{ijkl} \sigma_{ij} \sigma_{kl} - \frac{1}{3} \bar{\sigma}_y^2 = 0. \quad (18.37)$$

When N_{ijkl} takes the form

$$N_{ijkl} = \frac{1}{2} (\delta_{ik} \delta_{jl} + \delta_{il} \delta_{jk}) - \frac{1}{3} \delta_{ij} \delta_{kl}, \quad (18.38)$$

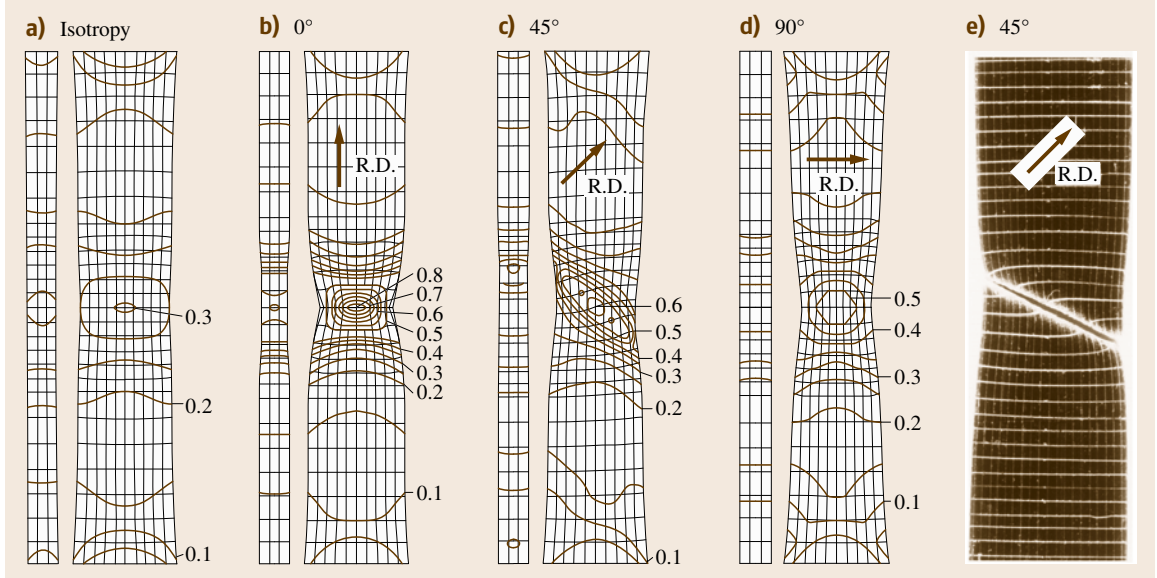


Fig. 18.5a–e Strain localization behavior of a rolled sheet for various stretch directions

(18.37) is reduced to (18.36). When N_{ijkl} involves $\mathbf{m}^{(1)}$ and $\mathbf{m}^{(2)}$, the fourth-order tensor takes the form

$$\begin{aligned}
 N_{ijkl} = & \lambda_1(\delta_{ik}\delta_{jl} + \delta_{il}\delta_{jk}) + \lambda_2\delta_{ij}\delta_{kl} \\
 & + \frac{1}{2}a_1(\delta_{ij}G_{kl} + G_{ij}\delta_{kl}) \\
 & - \frac{3}{8}a_1(\delta_{ik}G_{jl} + G_{ik}\delta_{jl} + \delta_{il}G_{jk} + G_{il}\delta_{jk}) \\
 & + a_2G_{ij}G_{kl} + \frac{1}{2}a_3(\delta_{ij}H_{kl} + H_{ij}\delta_{kl}) \\
 & - \frac{3}{8}a_3(\delta_{ik}H_{jl} + H_{ik}\delta_{jl} + \delta_{il}H_{jk} + H_{il}\delta_{jk}) \\
 & + a_4H_{ij}H_{kl} + \frac{1}{2}a_5(G_{ij}H_{kl} + H_{ij}G_{kl}),
 \end{aligned} \tag{18.39}$$

where a_1 , a_2 , and a_5 are material parameters with the following symbols

$$G_{ij} = m_i^{(1)}m_j^{(1)} - \frac{1}{3}m_k^{(1)}m_k^{(1)}\delta_{ij}, \tag{18.40a}$$

$$H_{ij} = m_i^{(2)}m_j^{(2)} - \frac{1}{3}m_k^{(2)}m_k^{(2)}\delta_{ij}. \tag{18.40b}$$

When the norm of the anisotropic vector is kept unitary, the above formulations become slightly simpler because $m_k^{(p)}m_k^{(p)} = 1$ ($p = 1, 2$). Suppose that the anisotropic axes coincide with the base vector, so that they are (1,0,0) and (0,1,0) for example; in this case we can prove that (18.37) is completely identical to Hill's

original model. Since the anisotropic axes change direction during deformation, it is preferable to generalize the representation so that it is applicable to general anisotropy, and this can be done by introducing a more general fourth-order tensor.

In order to examine the effect of initial anisotropy, finite element analysis is implemented based on the updated Lagrangian (U-L) formulation [18.22]. In the U-L formulation, the stress in the constitutive law is regarded as the Jaumann rate of the Kirchhoff stress and the strain rate as the stretching. The balance equation is based on the equilibrium under the Lagrangian system at the current state and the rate-type formulation is employed for this elastic-plastic boundary value problem. This implies that the rate of Lagrange stress is equilibrated and related to the Jaumann rate of the Kirchhoff stress. Converting these terms into discrete levels, we have

$$\begin{aligned}
 & \sum_e \int_{V_e} [\mathbf{B}^T(\mathbf{D}^{\tan} - \mathbf{F})\mathbf{B} + \mathbf{E}^T\mathbf{Q}\mathbf{E}] dV \dot{\mathbf{u}}^n \\
 & = \sum_e \int_{S_e} \mathbf{N}^T \bar{\mathbf{i}} dS
 \end{aligned} \tag{18.41}$$

for the finite element stiffness in the rate-type formulation. Here \mathbf{N} , \mathbf{B} and \mathbf{E} are the shape function, the strain-displacement matrix and the velocity gradient matrix; \mathbf{F} and \mathbf{Q} are compensation terms due to U-L formulation, and the body force is neglected for simplicity. The sim-

ulation proceeds step-by-step by solving the stiffness equation to unknown nodal displacement rate $\dot{\mathbf{u}}^n$.

Figure 18.5 demonstrates the necking behavior of an initially orthotropic sheet [18.23]. A three-dimensional simulation was carried out since the anisotropic vectors could change direction during the course of deformation. The material parameters are obtained from data on carbon steel sheets. The flow stress in a steel sheet is the lowest in the rolling direction (RD) and the highest in the perpendicular direction, while aluminium sheets show an opposite tendency. Figure 18.5a shows simulated results for isotropic material, and the last photograph corresponds to the results of a uniaxial rupture test performed at 45° to the rolling direction. The higher the strain concentration, the lower the tensile stress. This implies that the strain concentration in b and c are reasonable, and that the onset of strain localization is affected by the flow stress in the tensile direction. Figure 18.5b shows a characteristic aspect of strain localization where the localization appears in a band inclined to both the rolling direction and the tensile direction. The same tendency is also observed in the experiment.

18.2.3 Induced Anisotropy

The Bauschinger effect is a phenomenon where materials later show anisotropy even when they exhibit isotropy in the initial state. The kinematic hardening law is useful for dealing with this type of anisotropy. In this case, the yield surface is translated in stress space while the shape is not changed. Another type of anisotropy as well as this one is usually found in experiments, called the *cross effect* or the *corner effect* according to pioneering work by *Phillips* [18.24] and *Ikegami* [18.25]. Several models have been proposed so far to describe the subsequent anisotropy, which can be roughly classified into two categories

- (A) Where the yield function includes higher order tensors representing the anisotropy, as discussed in the previous section. *Baltov* and *Sawczuk* [18.26] proposed a model based on Hill's quadratic yield function [18.21], and other researchers [18.27, 28] have also employed this concept. The models are simply expressed by

$$F = \frac{1}{2} N_{ijkl} \sigma_{ij} \sigma_{kl} - \frac{1}{3} \bar{\sigma}_y^2 = 0. \quad (18.42)$$

- (B) The other type of formulation assumes that the yield function is composed of the combination of the second and third invariants of the stress J_2 and J_3 .

This procedure was proposed by *Drucker* and *Prager* [18.29]. A typical representation [18.30] takes the form

$$F = J_2 - \sum_I \xi_I J_2^{n_I} J_3^{m_I} - \bar{\sigma}_y^2 = 0. \quad (18.43)$$

Here ξ_I, \dots express the inelastic deformation history.

The former is superior to the latter from the viewpoint of parameter identification because (18.43) provides lots of possibilities for the concrete representation of power factors. Taking into account the back stress concept, (18.42) can be modified to

$$F = \frac{1}{2} N_{ijkl} (\sigma_{ij} - \alpha_{ij}) (\sigma_{kl} - \alpha_{kl}) - \frac{1}{3} \bar{\sigma}_y^2 = 0 \quad (18.44)$$

and the kinematic back stress α (or equivalently the plastic strain when employing the Prager hardening rule) and additional variables are introduced into the fourth-order tensor N_{ijkl} . When the fourth-order tensor involves one kind of second-order tensor ξ_{1ij} , the fourth-order tensor N_{ijkl} is simply expressed by

$$N_{ijkl} = \frac{1}{2} (\delta_{ik} \delta_{jl} + \delta_{il} \delta_{jk}) - \frac{1}{3} \delta_{ij} \delta_{kl} + P_1 \xi_{1ij} \xi_{1kl}. \quad (18.45)$$

In order to justify the physical dimension we add the nondimensional back stress: $\xi_{1ij} = \sqrt{3/2} \alpha'_{ij} / \bar{\sigma}_y$. The final form of the yield function is

$$F = \frac{1}{2} (\sigma'_{ij} - \alpha'_{ij}) (\sigma'_{ij} - \alpha'_{ij}) + \frac{3}{4 \bar{\sigma}_y^2} [(\sigma'_{ij} - \alpha'_{ij}) \alpha'_{ij}]^2 - \frac{1}{3} \bar{\sigma}_y^2 = 0 \quad (18.46)$$

although the fourth-order tensor is not a full representation. This yield function is identical to the Baltov–Sawczuk yield function [18.26] and it describes elliptical shapes with the yield as locus with the development of ξ_{1ij} (the kinematic back stress α_{ij} or plastic strain ϵ_{ij}^p). In order to describe higher order distortions [18.31] such as the cross effect, we introduce another kind of second-order tensor ξ_{2ij} into the representation of N_{ijkl} , and then we have

$$N_{ijkl} = \frac{1}{2} (\delta_{ik} \delta_{jl} + \delta_{il} \delta_{jk}) - \frac{1}{3} \delta_{ij} \delta_{kl} + P_1 \xi_{1ij} \xi_{1kl} + P_2 \xi_{2ij} \xi_{2kl} + \frac{Q}{2} (\xi_{1ij} \xi_{2kl} + \xi_{2ij} \xi_{1kl}). \quad (18.47)$$

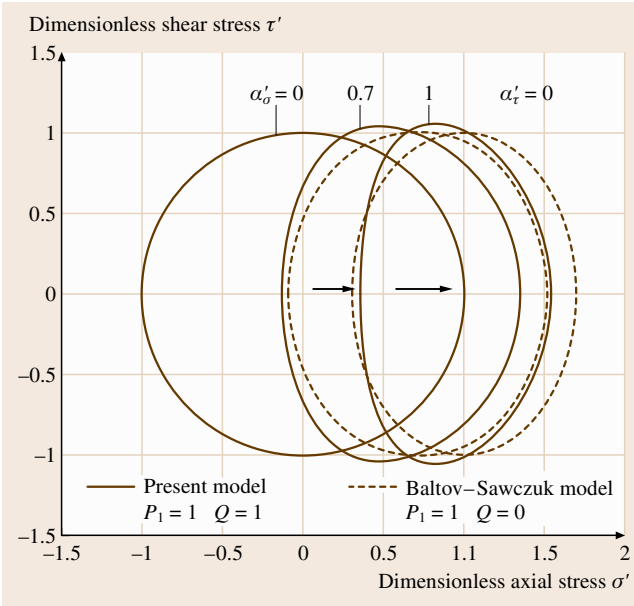


Fig. 18.6 Descriptions of higher order anisotropy for the cross effect and the corner effect

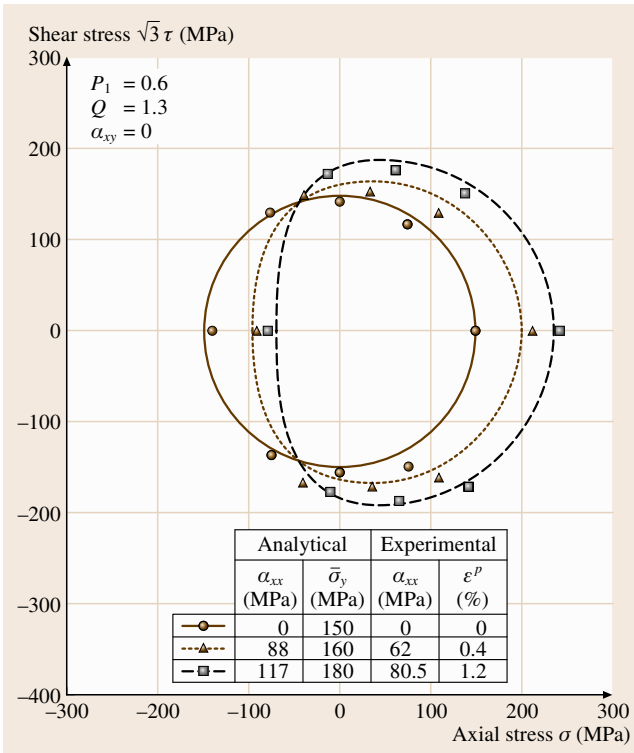


Fig. 18.7 Yield loci under monotonic tension

Here we adopt a nondimensional stress deviator in ξ_{2ij} . Finally the following yield function is obtained

$$F = (S_{ij} - A_{ij})(S_{ij} - A_{ij}) + P_1[(S_{ij} - A_{ij})A_{ij}]^2 + P_2[(S_{ij} - A_{ij})S_{ij}]^2 + Q[(S_{ij} - A_{ij})A_{ij}][(S_{kl} - A_{kl})S_{kl}] - 1 = 0, \tag{18.48}$$

where we have

$$\xi_{1ij} = \sqrt{\frac{3}{2}} \frac{\alpha'_{ij}}{\bar{\sigma}_y} \equiv A_{ij}, \tag{18.49a}$$

$$\xi_{2ij} = \sqrt{\frac{3}{2}} \frac{\sigma'_{ij}}{\bar{\sigma}_y} \equiv S_{ij}, \tag{18.49b}$$

for simplicity. In terms of choosing parameters, P_1 is dominant for the Bauschinger effect, $P_2 = 0$ ensures initial isotropy, and Q is related to the description of the cross effect. Since the second-order tensors adopted in the model reflect the current state of back stress and stress deviator, particular anisotropy with the path/history dependence can not be described by the model.

Figure 18.6 shows the basic performances of the yield functions [18.31] and the variation in yield locus is shown for a combined tension–torsion stress state, in which the axial and shear stresses are displayed in nondimensional ways such that the values are normalized by the yield stress. Dashed lines exhibit elliptical shapes given by the Baltov–Sawczuk theory, while the solid lines show the results from the higher order theory used to describe the cross effect, which exhibits characteristic hardening backward and perpendicular to the tensile direction. As the deformation increases, the kinematic back stress increases and then the elliptical shape shrinks towards the tensile direction. Since the deformation shown in the figure corresponds to a uniaxial stretch, the yield loci can be determined experimentally.

Experimental verification was performed on stainless steel at an elevated temperature, as shown in Fig. 18.7 [18.31]. Small cyclic loadings under combined tension and torsion were performed as uniaxial tension was applied, and the subsequent yield stresses for these small cycles were measured. The 304 stainless steel shows both kinematic hardening and isotropic hardening, and the parameters are chosen to obtain best fit curves for the yield loci. The development of deformation enhances the anisotropy while expanding the yield locus. The yield locus in particular expands backward and perpendicular to the loading direction. The

model successfully describes the development of this kind of higher order induced anisotropy. However, when one wishes to include the history effect of asymmetric shape and the corner effect at the loading point,

this model is of no use because it involves current values of stress and back stress. This problem can be overcome introducing a multisurface model in stress space [18.32].

18.3 Metallothermomechanical Coupling

18.3.1 Phase Changes

Engineering processes involving temperature changes, such as casting, welding, heat treatment and so on, are widely used to produce materials and improve their strength and/or functions. In such cases variations in temperature and internal structure dominate the dimensional accuracy of and residual stresses in the final product. Any metallic material has a specific structure, known as a *phase*, under certain conditions of stress, temperature and so on, which is virtually stable for small disturbances. Carbon steels have perlite and bainite structures at room temperature when they are produced via moderate heat treatment processes. On the other hand, when they undergo rapid cooling from high temperatures, the phase changes from austenite to martensite, and the martensitic structure is quasi-stable at room temperature. Quite a large volumetric change is involved during the quenching process, inducing residual stresses. This implies that temperature, internal structure and stress/strain are all coupled together. Metallothermomechanical coupling theories have been proposed to deal with such processes [18.33–35]. Figure 18.8 illustrates the interactions between temperature, structure and stress [18.36]. When the temperature changes during a process, thermal stresses (1) are induced, while the metallic phase may also change (2) depending on the conditions. Stress and strain are also influence the temperature (3) due to plastic mechanical work, while they also influence the onset of phase change (6). Mechanical properties are obviously affected by the internal structure, and the volumetric change due to a phase change is a typical example of how to affect the stress/strain field (5). Latent heat (4) is generated during the phase change, which affects the temperature field.

Based on the mixture theory concept [18.37], a simplified model has been proposed for dealing with such complicated processes. Here we regard a particle at point \mathbf{x} as being occupied by a number of components, namely 1, 2, ... and N . The material

properties and/or physical quantities ϕ of the particle are assumed to be average values based on the lever rule

$$\phi = \sum_{I=1}^N \xi_I \phi_I . \quad (18.50)$$

Here ϕ_I is the property of the I -th constituent and ξ_I indicates the volume fraction of the I -th component. Generally the following relationship holds for the volume fractions

$$\sum_{I=1}^N \xi_I = 1 . \quad (18.51)$$

This means that one of the N volume fractions is not derived independently but is automatically given by the above equation. Using this simple idea, a conventional thermoelastoplasticity theory can be extended into a theory that accounts for metallothermomechanical coupling.

The thermoelastic theory is formulated as follows [18.38, 39]. The elastic strain is expressed in terms of stress, temperature and the volumetric change in structure, and these contribute linearly to the strain. For macroscopically isotropic materials, this is expressible as

$$\varepsilon_{ij} = \left(\frac{1+\nu}{E} \delta_{ik} \delta_{jl} - \frac{1}{E} \delta_{ij} \delta_{kl} \right) \sigma_{kl} + \alpha (T - T_0) \delta_{ij} + \sum_I \beta \xi_I \delta_{ij} . \quad (18.52)$$

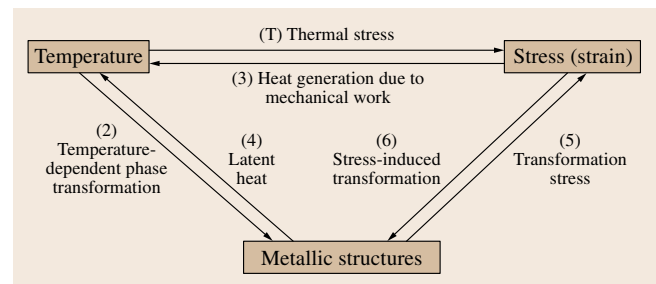


Fig. 18.8 Interaction diagram for thermometalomechanical coupling

Here E and ν are the Young's modulus and Poisson ratio of the material. α is the thermal expansion coefficient, and β_I is the dilatation parameter due to the change in the I -th constituent. The variation in the temperature T plays an important role here. The elasticity parameters and thermal expansion are averaged, and the average values are calculated through (18.50). Taking into account the mechanical work done due to inelastic (plastic) work and the latent heat generation, the heat conduction equation is given by

$$\rho c \frac{\partial T}{\partial t} = \frac{\partial}{\partial x_i} \left(k \frac{\partial T}{\partial x_i} \right) + \sigma_{ik} \dot{\epsilon}_{ki}^p + \sum_I l_I \dot{\xi}_I, \quad (18.53)$$

where ρ , c and k are the mass density, the specific heat and the thermal conductivity of the mixture, which are also averaged in the sense of (18.50). Clearly the mechanical work from the second term is only generated during the process of inelastic deformation, and the latent heat of the third term is only dominant when a phase change occurs. The last two factors can be regarded as macroscopic heat generation terms. The conventional plasticity theory is also modified to a generalized form. When we employ the von Mises yield criterion with isotropic hardening, the yield function takes the form

$$F = \frac{1}{2} \sigma'_{ij} \sigma'_{ij} - \frac{1}{3} \bar{\sigma}_y(\kappa, T, \xi_I)^2 = 0, \quad (18.54)$$

in which the yield stress under uniaxial stress involves not only a hardening parameter κ , such as the equivalent plastic strain, but also the temperature T and even the volume fraction ξ_I of each constituent. In order to obtain the current stress, temperature and structures, these equations are implemented in incremental calculations, so the rate-type formulation is employed and adopted in the numerical scheme.

The kinetics of phase transformation is another issue to be discussed. Typical phase transformations in metallic structures include austenite–perlite, ferrite, martensite and bainite transformations [18.40–42]. These solid–solid phase transformations are classified into two or three categories: the diffusion-driven phase transformation, the nondiffusion-driven type transformation, and a mixture of them. The perlite and ferrite phase transformations are characterized by the first category, while the martensite transformation falls into the second category. Here we summarize typical evolution laws for volume changes due to phase transformations. The dependence of phase transformations on stress involves another topic called *transformation plasticity*, in which permanent deformation is induced by low stress levels. However, we will not discuss this topic here; instead we limit our discussions to the kinetics associated with phase changes.

Johnson and Mehl [18.43] proposed the following volume fraction for the phase transformation from austenite to perlite

$$\xi_P = 1 - \exp(-V_e). \quad (18.55)$$

Here ξ_P refers to the perlite nucleated from the austenite. ξ_A is the volume fraction of austenite, while V_e stands for the residual volume of austenite, which is expressed by

$$V_e = \int_0^t \frac{4}{3} \pi \dot{S} R^3 (t - \tau) d\tau. \quad (18.56)$$

Here \dot{S} and R are the rates of nucleation and growth respectively. It is assumed in this theory that nuclei are spherical. The integrand is affected by both temperature and stress, and so we have

$$V_e = \int_0^t f(T, \sigma_m) \cdot (t - \tau) d\tau. \quad (18.57)$$

The material function $f(T, \sigma_m)$ can be specified from a so-called T–T diagram (or S-curve) under various stress states (pressures). The phase transformation therefore depends on both stress and temperature, and the volume change affects the stress field due to the changes in parameters, while the latent heat influences the heat conduction.

There are also several models for the process of martensite transformation, and a phenomenological treatment proposed by Magee [18.44] is introduced here. The martensite transformation starts at a point M_s

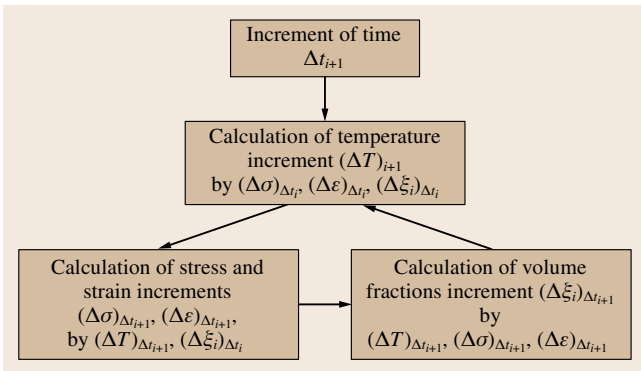


Fig. 18.9 Numerical algorithm for solving the coupled system of equations

where two phases have different free energy levels. This is due to the characteristics of nondiffusion-type phase transformation. Combining the stress-induced terms, the volume of martensite ξ_M is given by

$$\xi_M = 1 - \exp[\phi_1(M_s - T) + \phi_2\sigma_m + \phi_3J_2^{1/2}]. \quad (18.58)$$

Here ϕ_1 , ϕ_2 and ϕ_3 are material parameters. The temperature is dominated by the first term while the mean stress and the deviatoric stress also affect the martensite transformation. If a perlite phase ξ_P exists at the onset of martensite transformation, the above equation is modified to

$$\xi_M = (1 - \xi_P) \times \left\{ 1 - \exp[\phi_1(M_s - T) + \phi_2\sigma_m + \phi_3J_2^{1/2}] \right\}. \quad (18.59)$$

This means that only the austenite contributes to the nucleation of martensite. These are typical kinetics equations of solid–solid phase transformations. As well as these equations, one has to consider solid–liquid transformation when dealing with welding and casting. In this case, however, one must return to the original idea that any material parameter is given in an averaged manner, because the constitutive equation of liquids is completely different to that of solids, and the shear viscosity is generally much smaller in liquid.

18.3.2 Numerical Methodology

It is important to find an efficient procedure that can be used to solve the process of thermometalomechanical coupling in a system. The mechanical equations comprise a set of elliptic-type differential equations, while thermal conduction is governed by a typical diffusion (parabolic) equation. The kinetics of phase transformation are also given explicitly. This implies that the temperature and stress/strain are solved using a finite element/finite volume method, while the variation in internal structure can be taken into account using internal state variables. In order to obtain the numerical solution step-by-step, a suitable algorithm needs to be constructed. Using simple estimation of the sensitivity to each term, it becomes clear that thermal conduction is generally dominant, and that the time step should be controlled with reference to the thermal conduction if the mechanical equation is based on quasi-static motion. The next greatest influence is the effect of a phase change on the stress/strain response. Using this, the following numerical scheme can be established.

A schematic of the algorithm is shown in Fig. 18.9 [18.36]. Let Δt be the time increment prescribed on an object. The temperature is first updated using the solution for ΔT where ΔT is obtained using only the values at the current time step t_i . The time increment Δt is small enough to obtain a stable solution for the temperature. Using this temperature increment ΔT , the kinetics are then updated and the volume fractions $\Delta\xi_j$ are modified during the time increment Δt . Since the change in the volume fraction affects the stress/strain field, the stress and strain are calculated, with the temperature variation, last of all. When the mechanical equation is solved for dynamic motion, substeps with smaller time increments are superimposed on the time step Δt [18.39]. Although this iterative process should proceed until the solution converges from one time step t_i to the next t_{i+1} , reasonable solutions can be found even when the calculation only passes through each step once.

18.3.3 Applications to Heat Treatment and Metal Forming

Thermometalomechanical coupling simulations have been applied in the fields of heat treatment, welding, casting and so on, which have the greatest need for dimensional accuracy and to know residual stresses. For example, when a steel is rapidly cooled from a high-temperature austenitic state, the structure changes to martensite below the M_s transformation state. The volume increases during this process due to dilatation, which generally induces compressive stresses. We now demonstrate a few examples of this from the field of metal forming.

The austenitic stainless steel type SUS304 has a characteristic feature where the austenite at room temperature is said to be quasi-stable and transformed into martensite under large inelastic deformation. This implies that the stainless steel shows phase transformation during the course of forming. Figure 18.10 shows the volume fraction of the martensite during a stamping process [18.39]. A rigid die pushes down from the top of the object, which generates friction between the die and the material. The upper figure shows experimental data for the volume of martensite in % [18.45], while the lower figure corresponds to simulated results. The distribution of the martensite structure observed is caused by both the deformation and the rate of deformation, while the thermal conditions also influence the structural distribution to some degree. Due to the constraints from the friction between the die and material, the center of the top of the material is almost fixed and so less deformation is

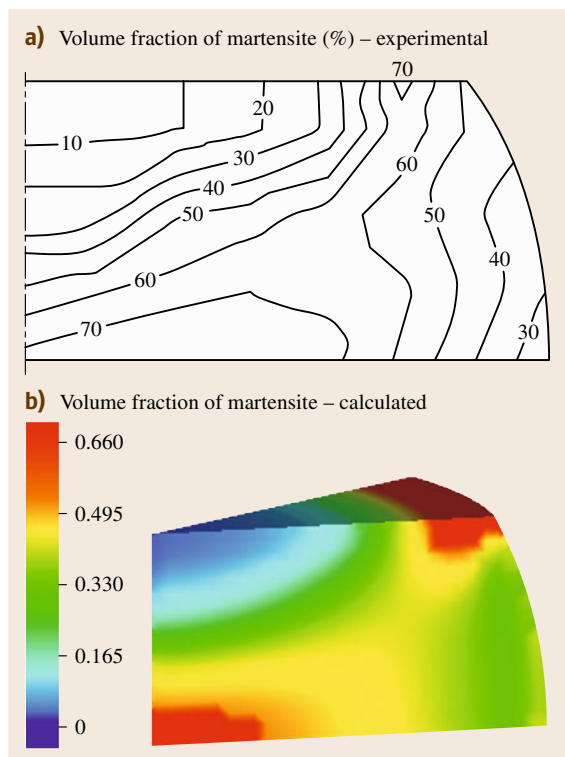


Fig. 18.10a,b Experimental and calculated martensite volume fractions caused by stamping

induced here during the process. The martensite distribution in the experiment is obtained by a coupled usage of magnetic measurement and x-ray diffraction. The simulation successfully grasps the martensite transformation

18.4 Crystal Plasticity

18.4.1 Single-Crystal Model

The phenomenological plasticity models discussed so far have been successful used to describe various classes of material behavior, not only for complex loading histories but also for nonisothermal conditions with varying temperature. However, we have not yet discussed the real physical mechanism of crystal deformation, and so this has not been reflected in the models. Real plastic deformation is mainly caused by slip in grains, as was pointed out from a continuum mechanics viewpoint by *Taylor* [18.47] and *Hill* [18.21], and materials are hardened due to the pile up of dislocations [18.48, 49]. Grain boundary sliding also plays

and shows a good agreement in tendency with the experimental ones.

The advantage of using this type of simulation is that the temperature, stress/strain and metallic structure can be obtained at any time. The next example, shown in Fig. 18.11, demonstrates the effect of friction on the internal structure and the rate of forming on the stress level [18.46]. The upper figures indicate the residual martensite structure after the forging. The left side (Fig. 18.11a) shows the martensite structure when a small friction coefficient (0.1) between the die and material is used, and the right-hand side (Fig. 18.11b) corresponds to a larger friction coefficient of 0.2. Since larger shear stress is induced when overcoming the resistance from the die with larger friction, we expect more strain to be generated, particularly at the teeth of the die. This implies that more martensite appears around the bottom of the teeth. The simulated equivalent stress distributions for the first stroke with a friction coefficient of 0.1 during high strain rate and low strain rate forging are depicted in the lower parts of Fig. 18.11c, d. The martensite distributions in both of these cases at this stage are similar and small values are obtained. The stresses for a high strain rate are higher than the stresses for a low strain rate from the beginning of the stroke until the end of the loading stage shown in Fig. 18.11c, d. During this period, the hardening behavior of the material is determined mainly by austenite, since the martensite content is low. However, with the generation of martensite, the flow stress becomes strongly dependent on the martensite fraction in the material. The low strain rate produces much higher stresses at the end of the simulation due to larger amounts of martensite.

an important role in mechanical behavior at elevated temperatures [18.50]. *Asaro* and coworkers [18.51] proposed a concise model for single crystals which relates the crystal slip to the macroscopic strain. In this section we discuss plastic material behavior from a microscopic view based on the *Asaro* model, and relate the microscopic deformation to continuum deformation at the macroscopic level. Infinitesimal deformation theory is employed throughout here, and this enables us to reduce the simulation load drastically. Detailed discussions on finitely deforming crystals can be found in the original and related articles.

Metallic materials have a certain regularity of atomic configuration, such as body-centered cubic

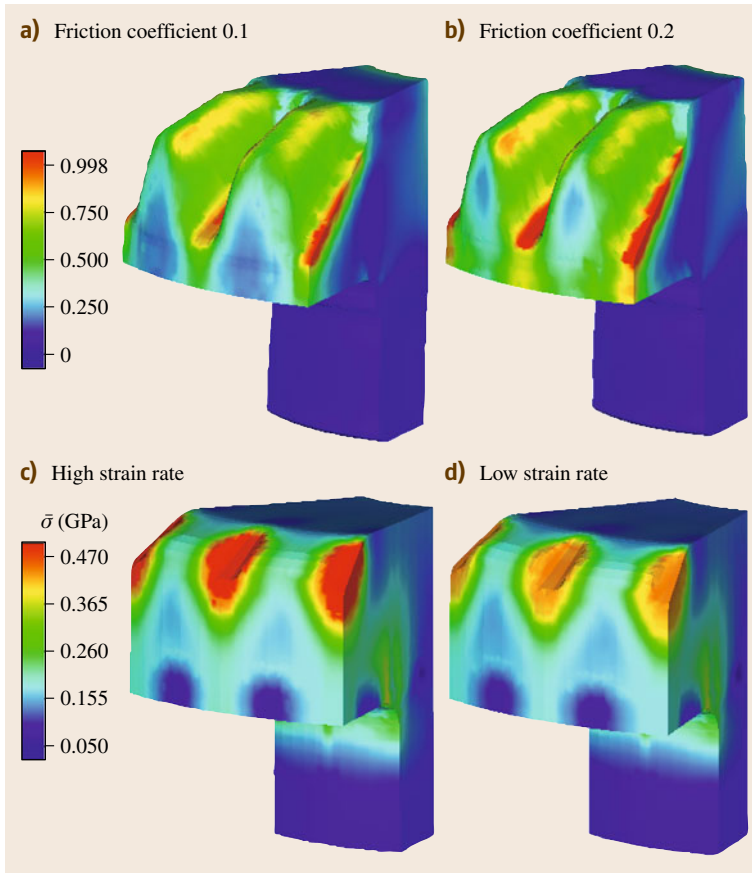


Fig. 18.11a–d The effects of friction and speed on the forging process. The *top* figures demonstrate the effect of friction on martensite transformation under low deformation rate, while the *bottom* figure shows the equivalent stress levels under different punch speeds

(bcc), face-centered cubic (fcc), hexagonal close packed (hcp), and so on. Each crystal structure has a particular plane and direction of permanent deformation. For example, an fcc crystal has 12 primary slip systems. Once we obtain a suitable model for describing the local slip due to the local stress acting on a crystal, we can then expect to be able to predict macroscopic deformation as the sum of all local deformations. When slip occurs in a crystal, the change of configuration can be expressed by the geometrical information of the system that has undergone slip and the amount of slip γ . Figure 18.12 illustrates the basic idea of crystal slip. Let $\mathbf{m}^{(\alpha)}$ be the plane and $\mathbf{s}^{(\alpha)}$ be the direction associated with the slip system (α). Taking into account the distortion of the crystal lattice due to elasticity, the total deformation gradient \mathbf{F} (F_{ij}) can be expressed as

$$F_{ij} = F_{ik}^* F_{kj}^p. \quad (18.60)$$

Here \mathbf{F}^* indicates the distortion and translation that are mainly due to elastic deformation, while \mathbf{F}^p is the permanent deformation due to crystal slip. The velocity

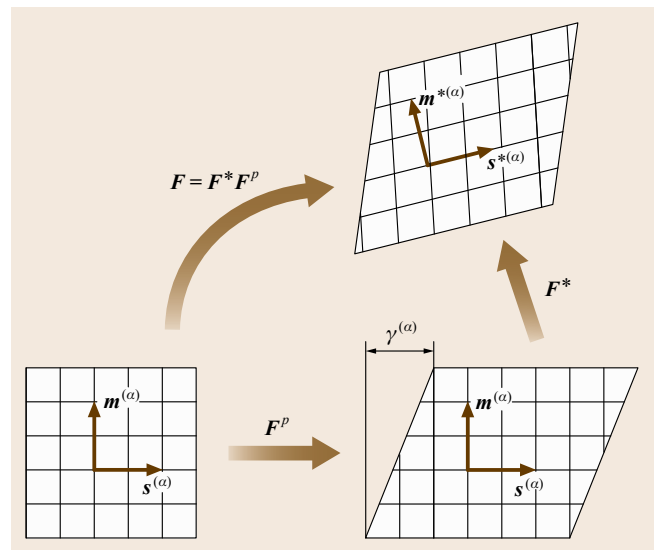


Fig. 18.12 Schematic view of a slip system and the decomposition of deformation

gradient then takes the form

$$L = \dot{F}^* F^{*-1} + F^* \dot{F}^P F^{P-1} F^{*-1} . \quad (18.61)$$

The slip system can be addressed using infinitesimal deformation theory. Assuming that plastic deformation is only caused by the sum of primary slips, the evolution of the plastic part is composed of

$$\dot{F}^P F^{P-1} = \sum_{\alpha} \dot{\gamma}^{(\alpha)} s^{(\alpha)} m^{(\alpha)} , \quad (18.62)$$

where γ^P stands for the amount of shear strain of the slip system (α). The plastic strain rate is then given by the symmetric part of the above equation. Elastic strain covers the rest of the strain rate, and the elastic rate is related to the stress rate via elasticity moduli. The resolved shear stress acting on the system (α) can be expressed using the stress theorem as

$$\tau^{(\alpha)} = s^{(\alpha)} \left(\sigma^T m^{(\alpha)} \right) . \quad (18.63)$$

It is then necessary to connect the shear strain rate and the resolved shear stress. A power law formula involving the resolved shear stress and strain rate was proposed by Hutchinson [18.52], Pan and Rice [18.53] as

$$\dot{\gamma}^{(\alpha)} = a_0 \left| \frac{\tau^{(\alpha)}}{g^{(\alpha)}} \right|^{1/m-1} \left[\frac{\tau^{(\alpha)}}{g^{(\alpha)}} \right] . \quad (18.64)$$

Here the function $g(\gamma^P)$ is the resistance, a kind of drag stress, under constant shear strain rate. The evolution of $g(\gamma^P)$ is governed not only by the shear slips themselves but also by the interactions of different slip systems. This implies that the rate of $g(\gamma^P)$ is expressed by

$$\dot{g}^{(\alpha)} = \sum_{\beta} h_{\alpha\beta} \left| \dot{\gamma}^{(\beta)} \right| . \quad (18.65)$$

The coefficient $h_{\alpha\beta}$ addresses the effect of slip (β) on another slip (α). This coefficient $h_{\alpha\beta}$ is suitably defined using a function involving total shear strain, critical shear stress, interaction parameters and so on. From these considerations, the total strain rate at the macroscopic level is related to the microscopic deformation as follows: (1) The stress is decomposed into the resolved shear stress of a particular slip system, (2) the local stress then acts on the shear slip, and finally (3) each slip is summed, giving the macroscopic strain. Solving the above equation for the stress rate, we obtain

$$\dot{\sigma}_{ij} = E_{ijkl} \dot{\epsilon}_{kl} - \sum_{\alpha} \dot{\gamma}^{(\alpha)} E_{ijkl} P_{kl}^{(\alpha)} \quad (18.66)$$

using the infinitesimal deformation theory. In the above equation $\dot{\gamma}^{(\alpha)} P^{(\alpha)}$ stands for the symmetric part of (18.62) and therefore the plastic strain rate under infinitesimal deformation. The effect of the crystal grain size has also been considered, taking the strain gradient into account [18.54].

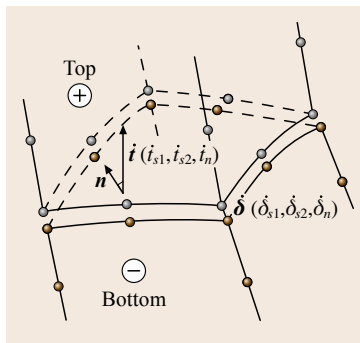


Fig. 18.13 Grain boundary sliding using a contact/slide element

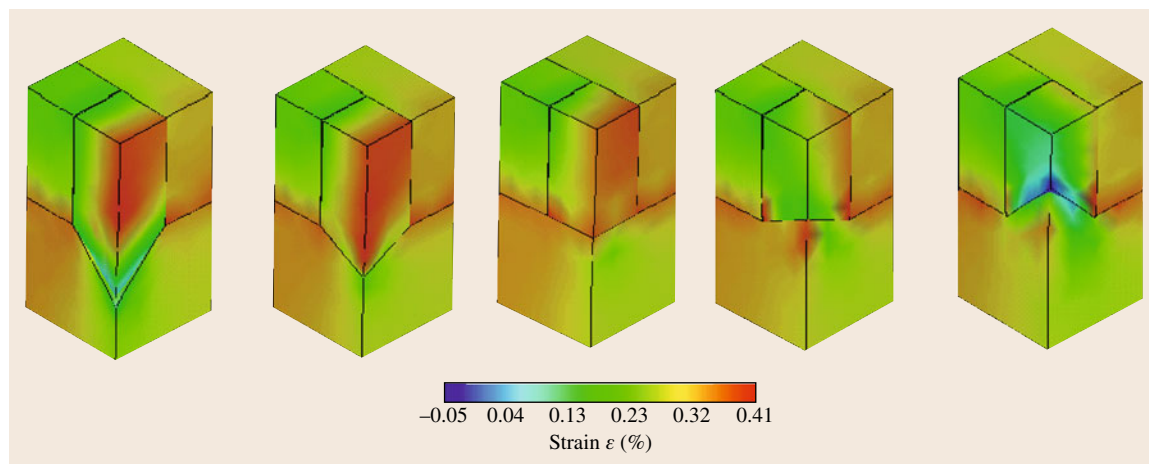


Fig. 18.14 Strain concentration behavior with different grain boundary geometries

18.4.2 Grain Boundary Sliding

Most metallic materials are composed of large numbers of crystal grains, each of which is located in a particular neighborhood defined via grain boundaries. The orientation of each crystal is believed to be random; the macroscopic deformation behavior of polycrystalline materials is reflected in this randomness. The material isotropy of polycrystalline materials is caused by the competing/misfitting effects of crystal slip on neighborhoods. Since the grain boundary can be regarded as a discontinuous plane under strain, it is particularly important to ensure that the mechanical analysis and the boundary sliding model successfully describes not only polycrystal deformation but also damage evolution at elevated temperatures [18.55].

One simple way to idealize grain boundary sliding is to use a special contact/slip model for the grain boundary. A stiffness is introduced as shown in Fig. 18.13, where the contact model is readily applied to the contact/slide element in the finite element technique [18.56]. The local coordinate system can be defined at the grain boundary such that the connecting force is decomposed into the normal force (t_n) and shear force (t_{s1} , t_{s2}). In the case of linear stiffness, we have

$$\begin{pmatrix} t_{s1} \\ t_{s2} \\ t_n \end{pmatrix} \begin{bmatrix} k_s & 0 & 0 \\ 0 & k_s & 0 \\ 0 & 0 & k_n \end{bmatrix} \begin{pmatrix} \delta_{s1} \\ \delta_{s2} \\ \delta_n \end{pmatrix}. \quad (18.67)$$

The normal component is devoted to the opening and closing (δ_n) of the grain boundary, while the shear component is related to relative sliding (δ_{s1} , δ_{s2}). The normal stiffness k_n is set to a large enough value that it causes neither detaching nor overlapping with the neighboring crystal. Permanent shear sliding is also allowed and modeling is also performed on the basis of the Mohr–Coulomb yield condition. The constitutive model for the contact/sliding is then similar to the model for the bulk crystal. It should be pointed out, however, that stiffness parameters are rarely specified in conventional test data, and it is even believed that large variations in stiffness occur which affect the real evolution of damage. *Tvergaard* and coworkers [18.55] employed viscous sliding at the grain boundary which they applied to investigate tertiary creep and damage evolution.

18.4.3 Inhomogeneous Deformation

In this section two examples of simulation are described: one considers the role of the geometry of the grain boundary while the other investigates the devel-

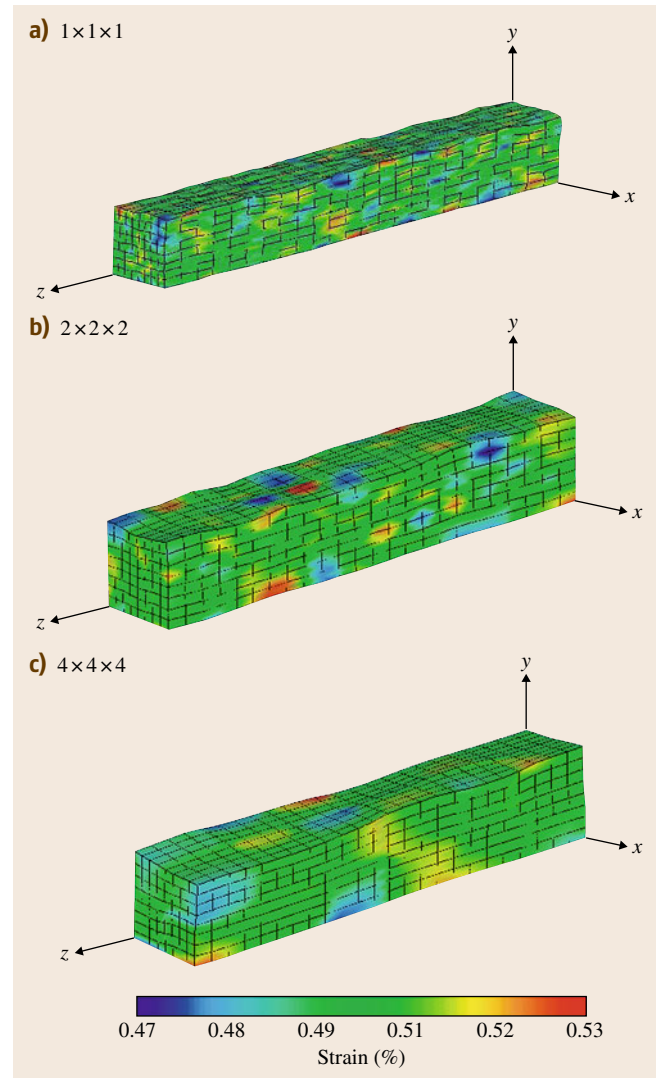


Fig. 18.15a–c Inhomogeneous deformation and surface roughness. The formation of a wavy pattern is observed in a large-scale simulation

opment of surface roughness. In order to evaluate the effects of the grain boundary, we look at (a) combinations of slip systems, (b) the contact geometry, and (c) the contact stiffness. It was found that the contact stiffness (c) and the interactions of slip systems (a) have relatively small effects on the variation in strain concentration. When the stiffness is large, nodal discrepancy is restrained and so the strain concentration is enhanced to some extent, but this is not a significant factor compared to the effect of geometry (b). Figure 18.14

shows how the strain distribution relates to the inclined geometry of the grain boundary [18.57]. The strain distribution varies greatly in models of highly inclined crystals. Since the effect of a slip system is examined in the central figure, where the grain boundary forms a horizontally flat surface, the differences observed in the other figures reflect the effect of grain boundary geometry. It follows from these figures that the strain distribution around the grain boundary is strongly affected by its geometry. Although the influence of the boundary geometry is usually far less than the factors related to mechanical behavior, the randomness of the geometry dominates the variation in the strain, and the variation in the strain may be related to damage evolution in polycrystalline materials.

The size of the crystal grain affects statistical properties related to mechanical behavior. Here we examine the effect of size on the surface roughness. It is worth noting that the real size is not taken into account because the crystal model does not reflect the real size. Introduction of higher order variables such as strain gradient or nonlocal variables covering a certain range of physical distance is a promising way to capture the real size effect in crystal grains. Figure 18.15 depicts the deformed shape of a finite element mesh

under monotonic tension along the z -direction [18.57]. Grain boundary sliding is not introduced in the model. $8 \times 8 \times 24 = 1536$ cubic elements are located in the objective domain, and each element has random crystal slip system in Fig. 18.15a. $2 \times 2 \times 2 (= 8)$ elements compose a block corresponding to a crystal grain, associated with the same slip system used in Fig. 18.15b, and $4 \times 4 \times 4 (= 64)$ elements form a block with the same slip system used in Fig. 18.15c. The displacement on the surface is magnified to emphasize the surface state. The variation in strain occurs due to competing/misfitting effects with a neighboring grain (block); in other words the strain concentration increases when the slip system has a large misfit with the neighborhood. It should be pointed out that a wavy pattern is predicted by every simulation model, and that the wavelength seems to be proportional to the block (grain) size. In fact, experimental results suggest that surface roughness is enhanced during plastic deformation, and that the wavelength of this is equal to the several times the average crystal grain size. The simulated results qualitatively agree with this tendency, although other kinds of uncertainties, in for example mechanical parameters, grain boundary stiffness and variation in grain sizes, apply to real materials.

References

- 18.1 L.E. Malvern: *Introduction to the Mechanics of a Continuous Medium* (Prentice-Hall, Englewood 1969)
- 18.2 P. Perzyna: Thermodynamic theory of viscoplasticity, *Adv. Appl. Mech.* **11**, 313–354 (1971)
- 18.3 A.K. Miller: *Unified Constitutive Equations for Creep and Plasticity* (Elsevier, London 1987)
- 18.4 A.S. Krausz, K. Krausz: *Unified Constitutive Laws of Plastic Deformation* (Academic, San Diego 1996)
- 18.5 J. Lemaitre, J.L. Chaboche: *Mechanics of Solid Materials* (Cambridge Univ. Press, Cambridge 1994)
- 18.6 G.A. Maugin: *Thermomechanics of Plasticity and Fracture* (Cambridge Univ. Press, Cambridge 1995)
- 18.7 A.K. Miller: An inelastic constitutive model for monotonic, cyclic, and creep deformation, *Trans. ASME J. Eng. Mater. Technol.* **98**, 97–105 (1976)
- 18.8 M.C.M. Liu, E. Krempl: A uniaxial viscoplastic model based on total strain and overstress, *J. Mech. Phys. Solids* **27**, 377–391 (1979)
- 18.9 S.R. Bodner, A. Merzer: Viscoplastic constitutive equations for copper with strain rate history and temperature effects, *Trans. ASME J. Appl. Mech.* **100**, 388–394 (1978)
- 18.10 Y. Estrin, H. Mecking: An extension of the Bodner-Partom model of plastic deformation, *Int. J. Plasticity* **1**, 73–85 (1985)
- 18.11 K.C. Valanis: A theory of viscoplasticity without a yield surface, *Arch. Mech.* **23**, 517–551 (1971)
- 18.12 D. Kujawski, Z. Mroz: A viscoplastic material model and its application to cyclic loading, *Acta Mech.* **36**, 213–230 (1980)
- 18.13 Y.F. Dafalias, E.P. Popov: A model for nonlinear hardening materials for complex loading, *Acta Mech.* **21**, 173–192 (1975)
- 18.14 N. Ohno: A constitutive model for cyclic plasticity with a nonlinear strain region, *Trans. ASME J. Appl. Mech.* **49**, 721–727 (1982)
- 18.15 O. Watanabe, S.N. Atluri: Constitutive modeling of cyclic plasticity and creep using internal time concept, *Int. J. Plasticity* **2**, 107–134 (1986)
- 18.16 T. Inoue, N. Ohno, A. Suzuki, T. Igari: Evaluation of inelastic constitutive models under plasticity-creep interaction for 2.1/4Cr-1Mo steel, *Nucl. Eng. Des.* **114**, 295–309 (1989)

- 18.17 T. Inoue, F. Yoshida, N. Ohno, M. Kawai, Y. Niitsu, S. Imatani: Evaluation of inelastic constitutive models under plasticity-creep interaction in multiaxial stress state, *Nucl. Eng. Des.* **126**, 1–11 (1991)
- 18.18 T. Inoue, S. Imatani, Y. Fukuda, K. Fujiyama, K. Aoto, K. Tamura: Inelastic stress-strain response for notched specimen of 2.1/4Cr-1Mo steel at 600°C, *Nucl. Eng. Des.* **150**, 129–139 (1994)
- 18.19 A.J.M. Spencer: Theory of invariants. In: *Continuum Physics*, Vol. 1, ed. by C.A. Eringen (Academic, New York 1971) pp. 239–353
- 18.20 A.J.M. Spencer: Isotropic invariants of tensor functions. In: *Application of Tensor Functions in Solid Mechanics*, CISM Courses and Lectures, Vol. 292, ed. by J.P. Boehler (Springer, Berlin, Heidelberg 1987) pp. 141–169
- 18.21 R. Hill: *The Mathematical Theory of Plasticity* (Oxford Univ. Press, Oxford 1950)
- 18.22 Y. Tomita, A. Shindo: Onset and growth of wrinkles in thin square plates subjected to diagonal tension, *Int. J. Mech. Sci.* **30**, 921–931 (1988)
- 18.23 S. Imatani, T. Saitoh, K. Yamaguchi: Finite element analysis of out-of-plane deformation in laminated sheet metals based on an anisotropic plasticity model, *Mater. Sci. Res. Int.* **1**, 89–94 (1995)
- 18.24 A. Phillips, R. Kasper: On the foundation of thermoplasticity: An experimental investigation, *Trans. ASME J. Appl. Mech.* **40**, 891–896 (1973)
- 18.25 E. Shiratori, K. Ikegami: Studies of the anisotropic yield condition, *J. Mech. Phys. Solids* **17**, 473–491 (1969)
- 18.26 A. Baltov, A. Sawczuk: A rule of anisotropic hardening, *Acta Mech.* **1**, 81–92 (1965)
- 18.27 J.F. Williams, N.L. Svensson: A rationally based yield criterion for workhardening materials, *Mechanica* **6**, 104–114 (1971)
- 18.28 D.W.A. Rees: The theory of scalar plastic deformation function, *Z. Angew. Math. Mech.* **63**, 217–228 (1983)
- 18.29 D.C. Drucker: Relation of experiments to mathematical theories of plasticity, *Trans. ASME J. Appl. Mech.* **16**, 349–357 (1949)
- 18.30 P. Mazilu, A. Meyers: Yield surface description of isotropic materials after cold prestrain, *Ing. Archiv.* **55**, 213–220 (1985)
- 18.31 S. Imatani, M. Teraura, T. Inoue: An inelastic constitutive model accounting for deformation-induced anisotropy, *Trans. JSME A* **55**, 2042–2048 (1989)
- 18.32 N. Ohno, J.D. Wang: Kinematic hardening rules with critical state of dynamic recovery, *Int. J. Plasticity* **9**, 375–390 (1993)
- 18.33 F.D. Fischer, M. Berveiller, K. Tanaka, E.R. Oberainger: Continuum mechanical aspects of phase transformations in solids, *Arch. Appl. Mech.* **64**, 54–85 (1994)
- 18.34 F.D. Fischer, G. Reisner, E. Werner, K. Tanaka, G. Cailletaud, T. Antretter: A new view on transformation induced plasticity (TRIP), *Int. J. Plasticity* **16**, 723–748 (2000)
- 18.35 Q.P. Sun, K.C. Hwang: Micromechanics modelling for the constitutive behavior of polycrystalline shape memory alloys, *J. Mech. Phys. Solids* **41**, 1–17 (1993)
- 18.36 T. Inoue, Z.G. Wang: Coupling between stresses, temperature and metallic structures during processes involving phase transformation, *Mater. Sci. Tech.* **1**, 845–850 (1985)
- 18.37 R.M. Bowen: Theory of mixture. In: *Continuum Physics*, Vol. 3, ed. by C.A. Eringen (Academic, New York 1976) pp. 1–127
- 18.38 T. Inoue, T. Yamaguchi, Z.G. Wang: Stresses and phase transformations occurring in quenching of carburized steel gear wheel, *Mater. Sci. Tech.* **1**, 872–876 (1985)
- 18.39 P. Ding, T. Inoue, S. Imatani, D.Y. Ju, E. de Vries: Simulation of the forging process incorporating strain-induced phase transformation using the finite volume method (Part I: Basic theory and numerical methodology), *Mater. Sci. Res. Int.* **7**, 19–26 (2001)
- 18.40 S. Bhattacharyya, G. Kehl: Isothermal transformation of austenite under externally applied tensile stress, *Trans. ASM* **47**, 351–379 (1955)
- 18.41 M. Fujita, M. Suzuki: The effect of high pressure on the isothermal transformation in high purity Fe-C alloys and commercial steels, *Trans. ISIJ* **14**, 44–53 (1974)
- 18.42 S.V. Radcliffe, M. Schatz: The effect of high pressure on the martensitic reaction in iron-carbon alloys, *Acta Metall. Mater.* **10**, 201–207 (1962)
- 18.43 W.A. Johnson, F.R. Mehl: Reaction kinetics in processes of nucleation and growth, *Trans. AIME* **135**, 416–458 (1939)
- 18.44 C.L. Magee: The nucleation of martensite. In: *Phase Transformation*, ed. by H.I. Aaronson (ASM Int., Metals Park 1968)
- 18.45 K. Shinagawa, H. Nishikawa, T. Ishikawa, Y. Hosoi: Deformation-induced martensitic transformation in type 304 stainless steel during cold upsetting, *Iron Steel* **3**, 156–162 (1990)
- 18.46 P. Ding, D.Y. Ju, T. Inoue, S. Imatani, E. de Vries: Simulation of the forging process incorporating strain-induced phase transformation using the finite volume method (Part II: Effects of strain rate on structural change and mechanical behavior), *Mater. Sci. Res. Int.* **7**, 27–33 (2001)
- 18.47 G.I. Taylor: Plastic strain in metals, *J. Inst. Metals* **62**, 307–324 (1938)
- 18.48 C. Teodosiu: Dislocation modelling of crystalline plasticity. In: *Large Plastic Deformation of Crystalline Aggregates*, CISM Courses and Lectures,

- Vol. 376, ed. by C. Teodosiu (Springer, Wien, New York 1997) pp. 21–80
- 18.49 E.C. Aifantis: The physics of plastic deformation, *Int. J. Plasticity* **3**, 211–247 (1987)
- 18.50 V. Tvergaard: Influence of grain boundary sliding on material failure in the tertiary creep range, *Int. J. Solids Structures* **21**, 279–293 (1985)
- 18.51 R.J. Asaro: Micromechanics of crystals and polycrystals, *Adv. Appl. Mech.* **23**, 1–115 (1983)
- 18.52 J.W. Hutchinson: Bounds and self-consistent estimates for creep of polycrystalline materials, *Proc. R. Soc. London A* **348**, 101–127 (1976)
- 18.53 J.R. Rice: Inelastic constitutive relations for solids, *J. Mech. Phys. Solids* **19**, 433–455 (1971)
- 18.54 T. Inoue, S. Torizuka, K. Nagai, K. Tsuzaki, T. Ohashi: Effect of plastic strain on grain size of ferrite transformed from deformed austenite in Si–Mn steel, *Mater. Sci. Tech.* **17**, 1580–1588 (2001)
- 18.55 E. van der Giessen, V. Tvergaard: A creep rupture model accounting for cavitation at sliding grain boundaries, *Int. J. Fracture* **48**, 153–178 (1991)
- 18.56 G. Beer: An isoparametric joint/interface element for finite element analysis, *Int. J. Num. Meth. Eng.* **21**, 585–600 (1985)
- 18.57 R. Kawakami, S. Imatani, R. Maeda: Effects of crystal grain and grain boundary sliding on the deformation of polycrystal, *J. Soc. Mater. Sci. Jpn.* **52**, 112–118 (2003)

19. Finite Element and Finite Difference Methods

Finite element methods (FEM) and finite difference methods (FDM) are numerical procedures for obtaining approximated solutions to boundary-value or initial-value problems. They can be applied to various areas of materials measurement and testing, especially for the characterization of mechanically or thermally loaded specimens or components. (Experimental methods for these fields have been treated in Chaps. 7 and 8.)

The principle is to replace an entire continuous domain of a body of interest by a number of subdomains in which the unknown function is represented by simple interpolation functions with unknown coefficients. Thus, the original boundary-value problem with an infinite number of degrees of freedom is converted into a problem with a finite number of degrees of freedom approximately.

19.1	Discretized Numerical Schemes for FEM and FDM	1035
19.2	Basic Derivations in FEM and FDM	1037
19.2.1	Finite Difference Method (FDM)	1037
19.2.2	Finite Element Method (FEM)	1038
19.3	The Equivalence of FEM and FDM Methods	1041
19.4	From Mechanics to Mathematics: Equilibrium Equations and Partial Differential Equations	1042
19.4.1	Heat Conduction Problem in the Two-Dimensional Case	1043
19.4.2	Elastic Solid Problem in the Three-Dimensional Case	1043
19.5	From Mathematics to Mechanics: Characteristic of Partial Differential Equations	1047
19.5.1	Elliptic Type	1048
19.5.2	Parabolic Type	1048
19.5.3	Hyperbolic Type	1048
19.6	Time Integration for Unsteady Problems	1049
19.6.1	FDM	1049
19.6.2	FEM	1050
19.7	Multidimensional Case	1051
19.7.1	Finite Difference Method	1051
19.7.2	Finite Element Method	1052
19.8	Treatment of the Nonlinear Case	1055
19.9	Advanced Topics in FEM and FDM	1055
19.9.1	Preprocessing	1055
19.9.2	Postprocessing	1056
19.9.3	Numerical Error	1056
19.9.4	Relatives of FEM and FDM	1057
19.9.5	Matrix Calculation and Parallel Computations	1057
19.9.6	Multiscale Method	1059
19.10	Free Codes	1059
	References	1059

A finite element analysis includes the following basic steps.

- Discretization or subdivision of the domain of the body of interest.
- Selection of the interpolation functions to provide an approximation of the unknown solution within an element.
- Formulation of the system of equations (using, for example, the typical Ritz variational and Galerkin methods).

- Solution of the system of equations. If the system of equations is solved, the desired physical variables at the nodes can then be computed and the results displayed in form of curves, plots, or color pictures, which are more meaningful and interpretable.

Finite element methods (FEM) use a complex system of points called *nodes*, which make up a grid called a *mesh*. This mesh is programmed to contain the *material and structural properties* that define how the structure will

react to certain loading conditions. Nodes are assigned at a certain density throughout the material depending on the anticipated stress levels of a particular area. Regions that receive large amounts of stress usually have a higher node density than those that experience little or no stress. Points of interest may concern, for example, fracture points of previously tested materials (Sect. 7.4) or high-stress areas. The mesh acts like a spider web in that from each node, there extends a mesh element for each of the adjacent nodes. This web of vectors is what carries the *material properties* to the object, creating many elements.

As a typical example, consider a material or a body in which the distribution of an unknown variable – such as temperature or displacement – is required. The first step of any finite element analysis is to divide the actual geometry of the structure using a collection of discrete portions called *finite elements*. The elements are joined together by shared nodes. The collection of nodes and finite elements is known as the *mesh* (Fig. 19.1).

The variable to be determined in the analysis is assumed to act over each element in a predefined manner. The number and type of elements is chosen to ensure that the variable distribution over the whole body is adequately approximated by the combined elemental representations. After the problem has been divided into discrete units, the governing equations for each element are formulated and then assembled to give a system of equations that describe the behavior of the body as a whole.

Finite difference methods (FDM) are also based on the similar idea. In this method, the elements and mesh are called grids and grid, respectively (Fig. 19.2). The major differences of FDM from FEM are (1) Governing partial differential equations are approximated directly by finite difference approximation, not by interpolation functions nor via the Galerkin method, (2) The discretized whole domain is not covered by a finite number of interpolation functions, but is represented by a finite number of sampling nodes. A finite difference analysis can be summarized as follows.

- Discretization or subdivision of the domain of the body of interest
- Selection of the finite difference functions to provide an approximation of the derivatives of unknown solution at a node

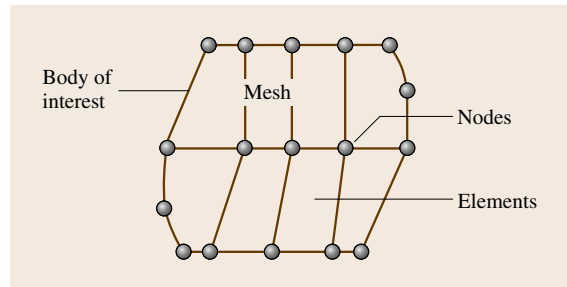


Fig. 19.1 Collection of nodes and finite elements (mesh) in FEM

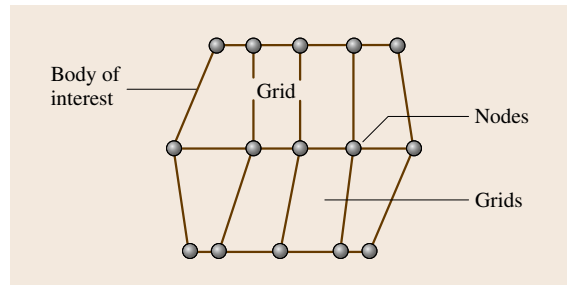


Fig. 19.2 Collection of nodes and grids in FDM

- Formulation of the system of equations at all the nodes
- Solution of the system of equations. If the system of equations is solved, the desired physical variables at the nodes can then be computed and the results displayed in form of curves, plots, or color pictures, which are more meaningful and interpretable, just as FEM does.

In this chapter, both FEM and FDM are explained. The contents include the basics necessary to understand the formulation, more advanced topics, practical information, and information on the use of commercial software. This chapter is for nonspecialists in macroscopic mechanics and computational mechanics, so only the key concepts are focused on in the discussion. Since the reader might not be accustomed to tensor representation, all derivations are shown without tensor notations. The explanation will focus on a steady or unsteady heat conduction problem in the one-dimensional case, however, multidimensional and nonlinear cases are also handled within the limited pages.

19.1 Discretized Numerical Schemes for FEM and FDM

FEM and FDM are classified into so-called discretized numerical schemes. Discretized numerical schemes are approximated ways to solve boundary problems, described by partial differential equations, with complex shaped domain with complicated boundary conditions, which can usually not be solved analytically by hand calculation. It should be noted that FEM and FDM are not applicable to phenomena that cannot be represented by partial differential equations.

In this section, we will focus on the process of discretized numerical schemes by using a simple example of a two-coupled spring model.

The relationship between a displacement u and a force F can be connected with a spring constant k as in the following equation, based on the knowledge of high school's physics

$$ku = F. \quad (19.1)$$

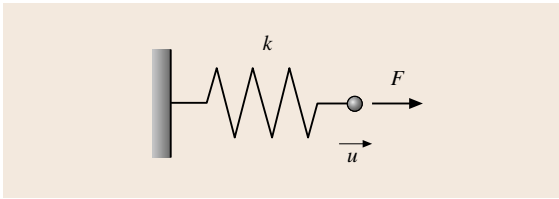


Fig. 19.3 Simple spring model

For the preparation to consider a more complicated case, we'd like to extend (19.1) for a more general case by introducing a spring model element, as shown in Fig. 19.4.

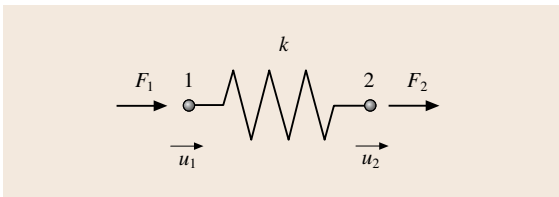


Fig. 19.4 Spring model element

By introducing u_1 , F_1 , u_2 , and F_2 at nodes 1 and 2, the spring model element can be represented with matrix notation

$$\begin{pmatrix} k & -k \\ -k & k \end{pmatrix} \begin{pmatrix} u_1 \\ u_2 \end{pmatrix} = \begin{pmatrix} F_1 \\ F_2 \end{pmatrix}. \quad (19.2)$$

By setting $u_1 = 0$ as a boundary condition, this matrix system is reduced to (19.1) in the following fashion

$$\begin{pmatrix} k & -k \\ -k & k \end{pmatrix} \begin{pmatrix} 0 \\ u_2 \end{pmatrix} = \begin{pmatrix} F_1 \\ F_2 \end{pmatrix}, \quad (19.3)$$

$$\begin{pmatrix} -k \\ k \end{pmatrix} (u_2) = \begin{pmatrix} F_1 \\ F_2 \end{pmatrix}. \quad (19.4)$$

Since the first row cannot be used for calculation due to the unknown value of F_1 , we can get the same equation as (19.1) by omitting the first row in (19.4)

$$ku_2 = F_2. \quad (19.5)$$

This is just a warm-up explanation of the two-coupled spring model below.

Now let's think about the following two-spring coupling model.

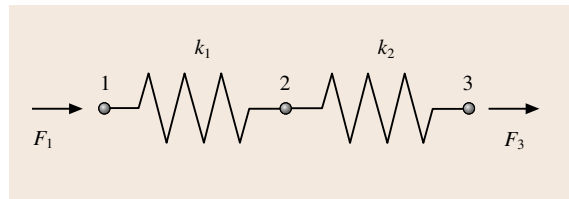


Fig. 19.5 Two-coupled spring model

The two-coupled spring model can be divided into two spring-model elements as shown in Fig. 19.6.

By combining two matrices in Fig. 19.6, we get the following system of equations

$$\begin{pmatrix} k_1 & -k_1 & 0 \\ -k_1 & k_1 & 0 \\ 0 & 0 & 0 \end{pmatrix} \begin{pmatrix} u_1 \\ u_2 \\ u_3 \end{pmatrix} = \begin{pmatrix} F_1 \\ F_{21} \\ 0 \end{pmatrix}$$

$$\begin{pmatrix} 0 & 0 & 0 \\ 0 & k_2 & -k_2 \\ 0 & -k_2 & k_2 \end{pmatrix} \begin{pmatrix} u_1 \\ u_2 \\ u_3 \end{pmatrix} = \begin{pmatrix} 0 \\ F_{22} \\ F_3 \end{pmatrix}$$

$$\rightarrow \begin{pmatrix} k_1 & -k_1 & 0 \\ -k_1 & k_1 + k_2 & -k_2 \\ 0 & -k_2 & k_2 \end{pmatrix} \begin{pmatrix} u_1 \\ u_2 \\ u_3 \end{pmatrix} = \begin{pmatrix} F_1 \\ F_{21} + F_{22} \\ F_3 \end{pmatrix}. \quad (19.6)$$

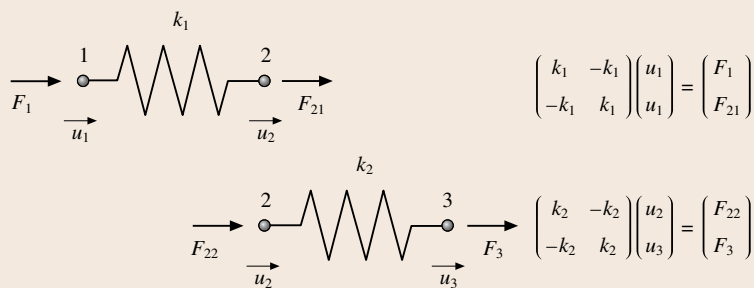


Fig. 19.6 Two elements of the two-spring model

Since the inner force is always balanced, $F_{12} + F_{22} = 0$. Then,

$$\begin{pmatrix} k_1 & -k_1 & 0 \\ -k_1 & k_1 + k_2 & -k_2 \\ 0 & -k_2 & k_2 \end{pmatrix} \begin{pmatrix} u_1 \\ u_2 \\ u_3 \end{pmatrix} = \begin{pmatrix} F_1 \\ 0 \\ F_3 \end{pmatrix}. \quad (19.7)$$

However, the combined matrix above cannot be inverted due to the singularity of the matrix, which is physically interpreted such that the position of the balancing springs in air is not determined explicitly. We need a fixed point to solve this matrix, which is called a (first) boundary condition. Suppose that node 1 is fixed as $u_1 = 0$. In this case, the matrix becomes solvable in the following way.

1. Substitute $u_1 = 0$ into the matrix system

$$\begin{pmatrix} k_1 & -k_1 & 0 \\ -k_1 & k_1 + k_2 & -k_2 \\ 0 & -k_2 & k_2 \end{pmatrix} \begin{pmatrix} 0 \\ u_2 \\ u_3 \end{pmatrix} = \begin{pmatrix} F_1 \\ 0 \\ F_3 \end{pmatrix}; \quad (19.8)$$

2. Omit the first column in the matrix

$$\begin{pmatrix} -k_1 & 0 \\ k_1 + k_2 & -k_2 \\ -k_2 & k_2 \end{pmatrix} \begin{pmatrix} u_2 \\ u_3 \end{pmatrix} = \begin{pmatrix} F_1 \\ 0 \\ F_3 \end{pmatrix}; \quad (19.9)$$

3. Since F_1 is an unknown value, the first row is omitted. Then we get a 2×2 matrix system that is now

solvable

$$\begin{pmatrix} k_1 + k_2 & -k_2 \\ -k_2 & k_2 \end{pmatrix} \begin{pmatrix} u_2 \\ u_3 \end{pmatrix} = \begin{pmatrix} 0 \\ F_3 \end{pmatrix}. \quad (19.10)$$

By solving the matrix system of (19.10), we get the following solutions, which is equivalent to the formula of the two-coupled spring model $1/k = 1/k_1 + 1/k_2$

$$\begin{aligned} u_2 &= \frac{F_3}{k_1}, \\ u_3 &= \frac{F_3}{k_1} + \frac{F_3}{k_2}. \end{aligned} \quad (19.11)$$

The procedure above can be summarized as follows.

1. Discretize the targeted domain into basic element models.
2. Construct a balancing (equilibrium) equation (local matrix) at each basic element model.
3. Combine all local matrices, add boundary conditions, and then solve global the matrix.

The process explained above is common among so-called discretized numerical schemes such as **FEM** and **FDM**. Usually the spring constant above becomes a *spring* coefficient matrix in these methods. The only difference between **FEM** and **FDM** can be summarized in the way to derive the *spring matrix* part. We'll treat basic derivations in **FEM** and **FDM** in the following section.

19.2 Basic Derivations in FEM and FDM

The governing equation of steady heat conduction problems in the one-dimensional case is given by the following equation, where u is a temperature, k is a heat conduction coefficient, and f is a heat source

$$k \frac{\partial^2 u}{\partial x^2} = -f. \quad (19.12)$$

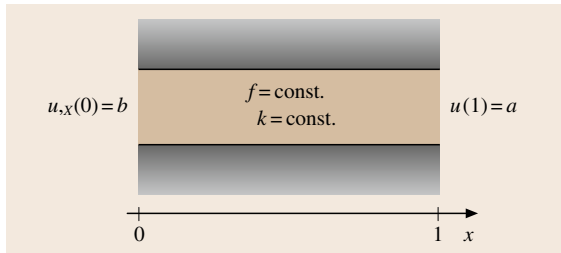


Fig. 19.7 One-dimensional steady heat conduction problem

Suppose that the boundary conditions (please recall Sect. 19.1) are provided as follows

$$\begin{aligned} u(1) &= a \quad (u = a \text{ at } x = 1), \\ u_x(0) &= b \quad \left(\frac{\partial u}{\partial x} = b \text{ at } x = 0 \right). \end{aligned} \quad (19.13)$$

Here, $u(x_0) = a$ is called either the first boundary condition or the Dirichlet boundary condition, while the boundary condition of $u_x(x_0) = b$ is named the second boundary condition or Neumann boundary condition. The problem represented by (19.12) and (19.13) is defined as a boundary value problem. (For unsteady problems, please refer to Sect. 19.6.)

Of course, the analytical solution of this problem can be given in the following form in this case, but we would like to consider the approximated numerical simulation by FDM and FEM in the following parts

$$u(x) = a + (x-1)b + \int_x^1 \left[\int_0^y f(z) dz \right] dy. \quad (19.14)$$

The exact solution function with respect to (wrt) the x -coordinate, under the parameters of $a = 1$, $b = 0.2$, $f = 1$, $h = 0.5$, and $k = 1$, is

$$\begin{aligned} u(x) &= -0.5x^2 + 0.2x + 1.3, \\ [u(0) &= 1.300, u(0.5) = 1.275, u(1) = 1.000]. \end{aligned} \quad (19.15)$$

19.2.1 Finite Difference Method (FDM)

In FDM, the derivatives of the governing equation are replaced by so-called finite difference approximations.

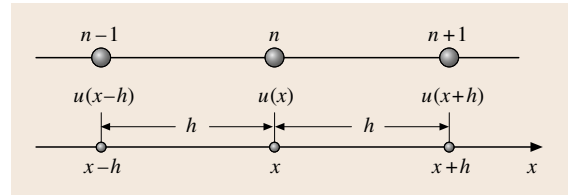


Fig. 19.8 Finite difference approximation of the first derivative of u wrt x

To approximate first derivative $\partial u / \partial x$ at node n in Fig. 19.8, there exist three schemes in FDM. The central difference scheme in (19.16) guarantees second-order accuracy with respect to x , and first-order accuracy in the other two *one-sided* methods in (19.17) and (19.18) [19.1].

Central difference scheme

$$\begin{aligned} \frac{\partial u}{\partial x} &= \lim_{h \rightarrow 0} \frac{u(x+h) - u(x-h)}{2h} \\ &\approx \frac{u(x+h) - u(x-h)}{2h}; \end{aligned} \quad (19.16)$$

Backward difference scheme

$$\frac{\partial u}{\partial x} = \lim_{h \rightarrow 0} \frac{u(x) - u(x-h)}{h} \approx \frac{u(x) - u(x-h)}{h}; \quad (19.17)$$

Forward difference scheme

$$\frac{\partial u}{\partial x} = \lim_{h \rightarrow 0} \frac{u(x+h) - u(x)}{h} \approx \frac{u(x+h) - u(x)}{h}. \quad (19.18)$$

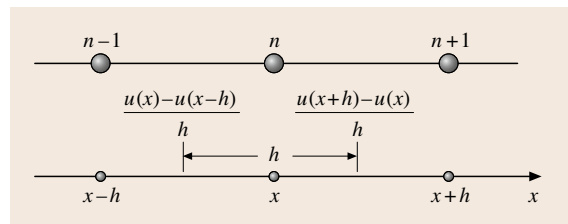


Fig. 19.9 Finite difference approximation of the second derivative of u wrt x

We can derive the following finite difference approximation on the second derivative of u , $\partial^2 u / \partial x^2$, by applying the backward difference scheme at $x = x - h/2$ and the forward difference scheme at $x = x + h/2$ on the first derivative of u , $\partial u / \partial x$

$$\begin{aligned} \frac{\partial^2 u}{\partial x^2} &\approx \frac{\frac{\partial u}{\partial x} \Big|_{x=x+\frac{h}{2}} - \frac{\partial u}{\partial x} \Big|_{x=x-\frac{h}{2}}}{h} \\ &\approx \frac{\frac{u(x+h) - u(x)}{h} - \frac{u(x) - u(x-h)}{h}}{h} \\ &= \frac{u(x+h) - 2u(x) + u(x-h)}{h^2}. \end{aligned} \tag{19.19}$$

Now we can apply the above finite difference approximations to the given problem in Fig. 19.7

$$k \frac{\partial^2 u}{\partial x^2} = -f, \tag{19.20}$$

$$u(1) = a(u = a \text{ at } x = 1),$$

$$u_x(0) = b \left(\frac{\partial u}{\partial x} = b \text{ at } x = 0 \right). \tag{19.21}$$

Equation (19.22) leads to the following solvable system of two equations with two variables u_1 and u_2 , after deleting u_0 and u_3 by using the relationship in (19.23).

$$\begin{cases} \frac{u_2 - 2u_1 + (u_2 - 2hb)}{h^2} = -f \\ \frac{a - 2u_2 + u_1}{h^2} = -f \end{cases}. \tag{19.24}$$

If $a = 1$, $b = 0.2$, $f = 1$, $h = 0.5$, and $k = 1$, then we get the following FD-approximated solutions at nodes 1 and 2, which are numerically equivalent to the exact solutions described at the end of Sect. 19.1, by chance

$$\begin{cases} u_1 = 1.300 \\ u_2 = 1.275 \end{cases}$$

where $a = 1$, $b = 0.2$, $f = 1$, $h = 0.5$, and $k = 1$.

Once the values u at all the nodes are obtained, the derivative values $\partial u / \partial x$ can be calculated by applying finite difference approximations in (19.16–19.18).

19.2.2 Finite Element Method (FEM)

With the same problem setting as in (19.20) and (19.21), the formulation of FEM is visualized in the following part.

First of all, we introduce a weight function w , which is an arbitrary function with zero value at the nodes of first boundary conditions. Multiplying the governing equation by the weight function w , and taking the integral over the domain results in the following equation

$$\int_0^1 \left(k \frac{\partial^2 u(x)}{\partial x^2} + f \right) w(x) dx = 0. \tag{19.25}$$

Integrating by parts gives

$$\begin{aligned} \int_0^1 f w(x) dx + k \frac{\partial u(x)}{\partial x} u(x) w(x) \Big|_0^1 \\ - \int_0^1 \frac{\partial w(x)}{\partial x} k \frac{\partial u(x)}{\partial x} dx = 0. \end{aligned} \tag{19.26}$$

Considering both the first and second boundary conditions in (19.21) and the nature of weight function w described above we obtain the following

$$\int_0^1 k \frac{\partial w(x)}{\partial x} \frac{\partial u(x)}{\partial x} dx = \int_0^1 f w(x) dx - k w(0) b. \tag{19.27}$$

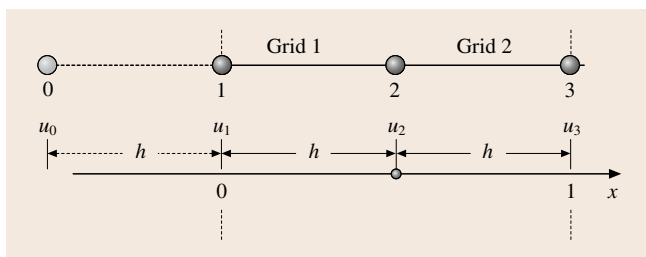


Fig. 19.10 Finite difference grids with a mirror node introduced

Suppose that the domain is discretized into two grids. Applying the difference scheme for second derivatives to the governing equation in (19.20) at the non-first-boundary condition-imposed nodes 1 and 2, we get the system of equations in (19.22). From the first and second boundary conditions in (19.21), the simultaneous equations are obtained as shown in (19.23). Here node 0 is a mirror node, which is artificially introduced as shown in Fig. 19.8, for the treatment of second boundary condition.

$$\begin{cases} \frac{u_2 - 2u_1 + u_0}{h^2} = -f \\ \frac{u_3 - 2u_2 + u_1}{h^2} = -f \end{cases}, \tag{19.22}$$

$$\begin{cases} u_3 = a \\ \frac{u_2 - u_0}{2h} = b \end{cases}. \tag{19.23}$$

This equation is usually called the *weak form*. It should be noted that the second boundary condition is *naturally* embedded in the weak form during the derivation. Due to this characteristic, the first and second boundary conditions are called essential and natural boundary conditions in FEM, respectively.

Up to (19.27), we just used a conceptual derivation in the continuous exact model without introducing any approximated discretization. To calculate (19.27) we introduce some approximated discretized functions in u and w .

Now we consider the following finite element model with two linear finite elements.

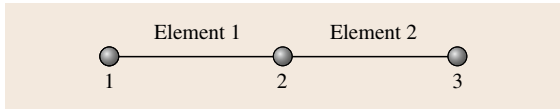


Fig. 19.11 Finite element model

The finite difference method is a scheme with respect to nodes, while the finite element method is an element-oriented scheme with element-integral weak form. Thus (19.27) can be represented as the summation of an element-wise weak form in FEM as

$$\int_{\text{element}\#1} k \frac{dw(x)}{dx} \frac{du(x)}{dx} dx + \int_{\text{element}\#2} k \frac{dw(x)}{dx} \frac{du(x)}{dx} dx = \int_{\text{element}\#1} fw(x) dx + \int_{\text{element}\#2} fw(x) dx - kw(0)b. \quad (19.28)$$

The linear finite-element-approximated function selected here is represented in Fig. 19.10 and (19.29). The finite element function can be interpreted as an interpolation function of the physical values at nodes 1 and 2 in an element by looking at (19.29) carefully. The upper suffix h in (19.29) represents the element-wise discretized approximated function.

Since the weight function can be arbitrary with zero values at the nodes of first boundary conditions, the same function as the finite element function is applied in this case.

This setting is usually used in FEM, and is called the Galerkin (or Bubnov–Galerkin) method. If a different weight function is selected other than the finite element-approximated function, we call it the Petrov–Galerkin method, which is the stabilized upwind case FEM for

fluid dynamics [19.2])

$$\begin{aligned} u^h(x) &= u_1 N_1(x) + u_2 N_2(x), \\ w^h(x) &= w_1 N_1(x) + w_2 N_2(x), \\ \text{where } N_1(x) &= \frac{x_2 - x}{h}, \quad N_2(x) = \frac{x - x_1}{h}. \end{aligned} \quad (19.29)$$

Matrix manipulation in both elements 1 and 2 are presented below.

Element 1

$$\begin{aligned} \int_{\text{element}\#1} k \frac{dw(x)}{dx} \frac{du(x)}{dx} dx &= \int_{\text{element}\#1} fw(x) dx - kw(0)h, \\ \int_{\text{element}\#1} k \begin{pmatrix} w_1 & w_2 \end{pmatrix} \begin{pmatrix} \frac{dN_1(x)}{dx} \\ \frac{dN_2(x)}{dx} \end{pmatrix} & \times \begin{pmatrix} \frac{dN_1(x)}{dx} & \frac{dN_2(x)}{dx} \end{pmatrix} \begin{pmatrix} u_1 \\ u_2 \end{pmatrix} dx \\ &= \begin{pmatrix} w_1 & w_2 \end{pmatrix} \int_{\text{element}\#1} f \begin{pmatrix} N_1(x) \\ N_2(x) \end{pmatrix} dx \\ & \quad - k \begin{pmatrix} w_1 & w_2 \end{pmatrix} \begin{pmatrix} N_1(0) \\ N_2(0) \end{pmatrix} b, \\ \begin{pmatrix} w_1 & w_2 \end{pmatrix} \frac{k}{h} \begin{pmatrix} 1 & -1 \\ -1 & 1 \end{pmatrix} \begin{pmatrix} u_1 \\ u_2 \end{pmatrix} & \\ &= \begin{pmatrix} w_1 & w_2 \end{pmatrix} \begin{pmatrix} \frac{fh}{2} \\ \frac{fh}{2} \end{pmatrix} - k \begin{pmatrix} w_1 & w_2 \end{pmatrix} \begin{pmatrix} 1 \\ 0 \end{pmatrix} b; \end{aligned} \quad (19.30)$$

Element 2

$$\begin{aligned} \int_{\text{element}\#2} k \frac{dw(x)}{dx} \frac{du(x)}{dx} dx &= \int_{\text{element}\#2} fw(x) dx, \\ \int_{\text{element}\#2} k \begin{pmatrix} w_1 & w_2 \end{pmatrix} \begin{pmatrix} \frac{dN_1(x)}{dx} \\ \frac{dN_2(x)}{dx} \end{pmatrix} \begin{pmatrix} \frac{dN_1(x)}{dx} & \frac{dN_2(x)}{dx} \end{pmatrix} & \times \begin{pmatrix} u_1 \\ u_2 \end{pmatrix} dx = \begin{pmatrix} w_1 & w_2 \end{pmatrix} \int_{\text{element}\#2} f \begin{pmatrix} N_1(x) \\ N_2(x) \end{pmatrix} dx, \\ \begin{pmatrix} w_1 & w_2 \end{pmatrix} \frac{k}{h} \begin{pmatrix} 1 & -1 \\ -1 & 1 \end{pmatrix} \begin{pmatrix} u_1 \\ u_2 \end{pmatrix} &= \begin{pmatrix} w_1 & w_2 \end{pmatrix} \begin{pmatrix} \frac{fh}{2} \\ \frac{fh}{2} \end{pmatrix}, \\ \text{where } N_1(x) &= \left(\frac{x_2 - x}{h} \right), \quad N_2(x) = \left(\frac{x - x_1}{h} \right). \end{aligned} \quad (19.31)$$

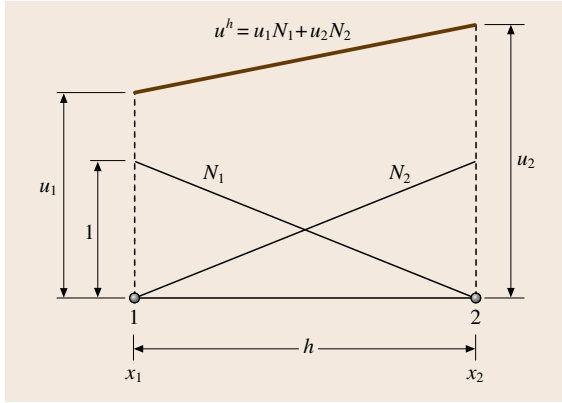


Fig. 19.12 Two-node linear-finite-element approximated function

By combining (19.30) and (19.31) we get the following total system of equations

$$\begin{aligned} (w_1 \ w_2 \ w_3) \frac{k}{h} \begin{pmatrix} 1 & -1 & 0 \\ -1 & 1+1 & -1 \\ 0 & -1 & 1 \end{pmatrix} \begin{pmatrix} u_1 \\ u_2 \\ u_3 \end{pmatrix} \\ = (w_1 \ w_2 \ w_3) \left[\begin{pmatrix} \frac{fh}{2} \\ fh \\ \frac{fh}{2} \end{pmatrix} - \begin{pmatrix} kb \\ 0 \\ 0 \end{pmatrix} \right]. \end{aligned} \quad (19.32)$$

Since w_3 is zero due to the nature of the weight function,

$$\begin{aligned} (w_1 \ w_2) \frac{k}{h} \begin{pmatrix} 1 & -1 & 0 \\ -1 & 2 & -1 \end{pmatrix} \begin{pmatrix} u_1 \\ u_2 \\ u_3 \end{pmatrix} \\ = (w_1 \ w_2) \left[\begin{pmatrix} \frac{fh}{2} \\ fh \end{pmatrix} - \begin{pmatrix} kb \\ 0 \end{pmatrix} \right]. \end{aligned} \quad (19.33)$$

Considering the first boundary condition of $u_3 = a$,

$$\begin{aligned} (w_1 \ w_2) \frac{k}{h} \begin{pmatrix} 1 & -1 \\ -1 & 2 \end{pmatrix} \begin{pmatrix} u_1 \\ u_2 \end{pmatrix} \\ = (w_1 \ w_2) \left[\begin{pmatrix} \frac{fh}{2} - kb \\ fh \end{pmatrix} - \frac{k}{h} \begin{pmatrix} 0 \\ -a \end{pmatrix} \right]. \end{aligned} \quad (19.34)$$

Since w_1 and w_2 are arbitrary we can get the following solvable system of two equations with two variables $\mathbf{Ku} = \mathbf{f}$ in (19.35). It should be noted that the treatment of the second boundary condition is not needed in the

matrix manipulation part in FEM, which is a different point from FDM's case

$$\frac{k}{h} \begin{pmatrix} 1 & -1 \\ -1 & 2 \end{pmatrix} \begin{pmatrix} u_1 \\ u_2 \end{pmatrix} = \begin{pmatrix} \frac{fh}{2} - kb \\ fh \end{pmatrix} - \frac{k}{h} \begin{pmatrix} 0 \\ -a \end{pmatrix}. \quad (19.35)$$

If $a = 1$, $b = 0.2$, $f = 1$, $h = 0.5$, and $k = 1$, then we get the following FE-approximated solutions at nodes 1 and 2, which are numerically the same as the exact solutions described at the end of Sect. 19.1, by chance

$$\begin{cases} u_1 = 1.300 \\ u_2 = 1.275 \end{cases},$$

where $a = 1$, $b = 0.2$, $f = 1$, $h = 0.5$, and $k = 1$.

In FEM, the derivative values $\partial u^h / \partial x$ are obtained from the derivative of interpolated function such as in (19.36)

$$\begin{aligned} \frac{\partial u^h(x)}{\partial x} &= u_1 \frac{\partial N_1(x)}{\partial x} + u_2 \frac{\partial N_2(x)}{\partial x}, \\ \frac{\partial w^h(x)}{\partial x} &= w_1 \frac{\partial N_1(x)}{\partial x} + w_2 \frac{\partial N_2(x)}{\partial x}, \end{aligned}$$

where $N_1(x) = \frac{x_2 - x}{h}$, $N_2(x) = \frac{x - x_1}{h}$,

$$\frac{\partial N_1(x)}{\partial x} = -\frac{1}{h}, \quad \frac{\partial N_2(x)}{\partial x} = \frac{1}{h}. \quad (19.36)$$

This is all for the basic derivations in FDM and FEM, but a few important remarks in both FDM and FEM should be added.

1. The final shape of FDM and FEM calculation is $\mathbf{Ku} = \mathbf{f}$, where \mathbf{K} is a sparse matrix, \mathbf{u} is a solution vector and \mathbf{f} is a given force vector. \mathbf{K} can be symmetric or nonsymmetric depending of the physical problems. \mathbf{K} could be nonlinear if \mathbf{K} is a function of \mathbf{u} , although \mathbf{K} is linear in the problem above. The treatment of the nonlinear case is discussed in Sect. 19.8.
2. In this problem setting, both FDM and FEM reached numerically acceptable solutions compared with analytical exact solutions. Unfortunately this is just by chance. Usually both FDM and FEM provide only approximated solutions and in most cases you may need careful verification of the obtained numerical solutions, especially in multidimensional cases. (In the world of FDM and FEM, there exists a big difference among the one-dimensional case, two-dimensional case, and three-dimensional case.) This topic will be treated in Sect. 19.9.

3. The good news is that both FDM and FEM must be converged to more accurate solutions if the grid size or mesh size h is close to zero. To utilize this nature, the convergence test to evaluate the accuracy is possible in discretized methods, although the matrix size becomes bigger with a tiny grid or mesh size. It should be noted that the grid (mesh) size doesn't have to be uniform. If the accuracy is to be improved locally, for example, around a singular point, it is a good idea to use a smaller mesh size around the targeted local domain. However, a rapid change of mesh size distribution usually leads to bad results. An adaptive mesh in FEM and a boundary-fitted grid in FDM provide some solution to it. This important matter will be discussed in Sect. 19.9.
4. The obtained finite element function $u^h(x)$ [for example, in (19.35)] are continuous even between elements, however, the finite element derivative function $\partial u^h(x)/\partial x$ is not continuous, which means the derivative value at a node with two elements (in the 1-D case) is not unique. To obtain the derivative value, such as heat flux in heat conduction problems and stress in solid mechanics (see Sect. 19.4), post-processing is inevitable and is treated in Sect. 19.9.
5. Since a function is not defined within a grid in the finite difference method, there are no problems in the derivations of the derivative value at a node. However you may have another problem regarding how to select a proper definition among (19.16–19.18). Usually, the central difference scheme has a good reputation due to second-order accuracy, but you need some tricks in the multidimensional case [19.1].
6. Mathematically, FEM is governed by function analysis [19.3] since the concept of *norm* can be introduced due to the shape of weak form. Using function analysis, a new established finite element formula can be evaluated in advance of real calculations in a normal sense in functional analysis.
7. As was discussed, a finite element domain is packed with element-wise finite element functions. Since the field is represented by the summation of FE functions, FEM is very strong at local resolution, for example, in stress distributions in solid mechanics, if the mesh is fine enough for the analysis. On the contrary, if the mesh is poor (too coarse for the problem), it is possible to obtain unexpected oscillations, for example, in fluid dynamics. The stabilized FEM, such as the streamline-upwind Petrov–Galerkin method (SUPG) and the Galerkin/least squares scheme (GLS), is one solution for it. A finite difference domain is not filled for any functions that are strong for unexpected oscillations, but not suitable for local resolution in solid mechanics.
8. As a general summary, FEM is good for arbitrary-shaped domains, treatment of second boundary conditions, solid mechanics, and parallel computations, while FDM is only valid for regular shaped domains, but suitable for fluid mechanics. The rough summary table, considering other related numerical schemes, is given in Table 19.1 in Sect. 19.9.

19.3 The Equivalence of FEM and FDM Methods

A reader might be wondering whether the treatment of FDM and FEM are equivalent to each other. In this section, we'll consider the equivalence of these two forms by explaining the variational method.

According to linear algebra [19.4], the following three forms are equivalent, where \mathbf{K} , \mathbf{f} and \mathbf{u} are a positive, definite symmetric matrix, a given force vector and an unknown vector, respectively

$$\text{(Form 1) } \mathbf{Ku} - \mathbf{f} = 0, \tag{19.37}$$

$$\text{(Form 2) } \mathbf{w} \cdot (\mathbf{Ku} - \mathbf{f}) = 0, \quad \forall \mathbf{w} \in \mathbb{R}^n, \tag{19.38}$$

$$\text{(Form 3) } \mathbf{F}(\mathbf{v}) - \mathbf{F}(\mathbf{u}) \geq 0, \quad \forall \mathbf{v} \in \mathbb{R}^n, \tag{19.39}$$

where $\mathbf{K} = \mathbf{K}^t$,
 $\mathbf{F}(\mathbf{v}) = \frac{1}{2} \mathbf{v} \cdot \mathbf{Kv} - \mathbf{v} \cdot \mathbf{f}.$

We now extend the discussion to the boundary-value problem below [19.5]. Again consider the same problem as treated in Sect. 19.2 by (19.20) and (19.21), which is Form 1 shown below. Form 2 is the weak form already explained in (19.27). Form 3 is called the variational form, which means the solution u is the minimizer of the function $\mathbf{F}(v)$.

$$\text{(Form 1) } k \frac{\partial^2 u}{\partial x^2} = -f \quad \text{in } (0, 1), \quad u(1) = a, \quad \frac{\partial u}{\partial x}(0) = b; \tag{19.40}$$

$$\text{(Form 2) } \int_0^1 \left(k \frac{\partial u}{\partial x} \frac{\partial w}{\partial x} - fw \right) dz - kw(0)b = 0, \quad \forall w \text{ with } w(1) = 0; \tag{19.41}$$

$$\text{(Form 3)} \quad u(1) = a, \quad F(v) \geq F(u), \quad \forall v \text{ with } v(1) = a, \quad (19.42)$$

$$\text{where} \quad F(v) = \frac{1}{2} \int_0^1 k \left(\frac{dv}{dx} \right)^2 dx - \int_0^1 f v dx - kv(0)b, \quad \forall v \text{ with } v(1) = a.$$

First we derive Form 1 from Form 3 in the following proof.

Proof [(Form 3) → (Form 1)]

Suppose that u is the minimizer of the function F , which is satisfied with the given first boundary condition in the interval $(0, 1)$

$$u(1) = a, \quad F(v) - F(u) \geq 0, \quad \forall v \text{ with } v(1) = a. \quad (19.43)$$

Substituting $v = u \pm \varepsilon w$, by introducing w , where ε is a positive real number,

$$u(1) = a, \quad F(u \pm \varepsilon w) - F(u) \geq 0, \quad \forall w \text{ with } w(1) = 0. \quad (19.44)$$

It should be added that w is an arbitrary function such that $w(1) = 0$, since $v(1) = a$, $u(1) = a$.

By rewriting (19.44),

$$\pm \varepsilon \left[\int_0^1 \left(k \frac{\partial u}{\partial x} \frac{\partial w}{\partial x} - fw \right) dx - kw(0)b \right] + \frac{1}{2} \varepsilon^2 \int_0^1 k \left(\frac{\partial w}{\partial x} \right)^2 dx \geq 0. \quad (19.45)$$

If $\varepsilon \rightarrow 0$ after dividing the equation by $\varepsilon (> 0)$,

$$\text{(Form 2)} \quad \int_0^1 \left(k \frac{\partial u}{\partial x} \frac{\partial w}{\partial x} - fw \right) dx - kw(0)b = 0. \quad (19.46)$$

By integration by part with $w(1) = 0$,

$$\int_0^1 \left[-\frac{\partial}{\partial x} \left(k \frac{\partial u}{\partial x} \right) - f \right] w dx + k \frac{\partial u}{\partial x}(0)w(0) - kw(0)b = 0. \quad (19.47)$$

Since w and $w(1)$ are arbitrary, the equation above ascribes to the following shape, which is nothing else but Form 1.

Now we derive Form 3 from Form 1.

Proof [(Form 1) → (Form 3)]

Subtracting $F(u)$ from $F(v)$,

$$F(v) - F(u) = \int_0^1 \left[k \frac{\partial u}{\partial x} \frac{\partial}{\partial x} (v - u) - f(v - u) \right] dx - k(v - u)(0)b + \frac{1}{2} \int_0^1 k \left[\frac{\partial}{\partial x} (v - u) \right]^2 dx. \quad (19.48)$$

Since the function u and v must satisfy the first boundary condition, $(v - u)(0) = 0$ gives the following equation

$$u(1) = a, \quad \int_0^1 \left[k \frac{\partial u}{\partial x} \frac{\partial}{\partial x} (v - u) - f(v - u) \right] dx - h(v - u)(0)b = 0, \quad \forall v \text{ with } v(1) = a. \quad (19.49)$$

According to the derivations above, we finally obtain Form 3

$$F(v) - F(u) = \frac{1}{2} \int_0^1 k \left(\frac{d}{dx} (v - u) \right)^2 dx \geq 0. \quad (19.50)$$

It is recommended that one refer to the explanation in Sect. 19.2.2 again, after reading this section.

19.4 From Mechanics to Mathematics: Equilibrium Equations and Partial Differential Equations

Although (19.20) was given without any logical derivation, the governing partial differential equations are always derived from both equilibrium equations in a mechanical sense and material constitutive equations

in a material property sense. In this section, we derive mathematics from mechanics.

The governing equations describe the relationship between the force-related variables as input and the

motion-related variables as output. The equilibrium equations represent the mechanical balancing relationship, while material constitutive equations characterize the empirical material properties of the target. In short, the former is related to mechanics and the latter is concerned with materials

Governing equations

= Equilibrium equations (from mechanical balancing)
 + Material constitutive equations (from experiments).

It should be noted from Sect. 19.1 that the material constitutive equation directly represents the governing equation in (19.1), which is a special case.

19.4.1 Heat Conduction Problem in the Two-Dimensional Case

Let us take a look at the balance of heat flux in an infinitesimal element as shown in Fig. 19.13, where q_x and q_y show heat fluxes, the functions of x and y , in the x and y directions, respectively.

Considering in and out heat flux,

$$Q \nabla t = \left\{ \left[q_x \left(x - \frac{1}{2} \nabla x, y \right) - q_x \left(x + \frac{1}{2} \nabla x, y \right) \right] \nabla y - \left[q_y \left(x, y - \frac{1}{2} \nabla y \right) - q_y \left(x, y + \frac{1}{2} \nabla y \right) \right] \nabla x + f \nabla x \nabla y \right\} \nabla t. \quad (19.51)$$

By dividing the equation above by $\Delta x \Delta y \Delta t$ and taking the limit as Δx and $\Delta y \rightarrow 0$, we get

$$\lim_{\nabla x \nabla y \rightarrow 0} \frac{Q}{\nabla x \nabla y} = -\frac{\partial q_x}{\partial x} - \frac{\partial q_y}{\partial y} + f. \quad (19.52)$$

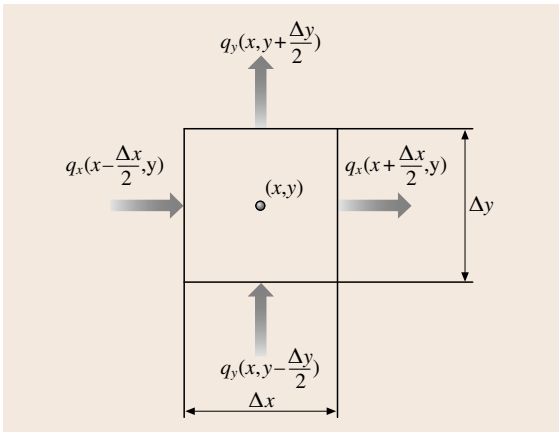


Fig. 19.13 Balance of heat flux in an infinitesimal element

On the other hand, Q can be defined by introducing the heat capacity c_p and the density ρ

$$Q = \rho c_p \dot{u} \Delta x \Delta y. \quad (19.53)$$

Then we obtain the following equilibrium equation

$$\rho c_p \dot{u} = -\frac{\partial q_x}{\partial x} - \frac{\partial q_y}{\partial y} + f. \quad (19.54)$$

As for the material property of heat conduction, Fourier's law, which was modeled by experiments, is known as

$$\begin{cases} q_x = -k_{xx} \frac{\partial u}{\partial x} - k_{xy} \frac{\partial u}{\partial y}, \\ q_y = -k_{yx} \frac{\partial u}{\partial x} - k_{yy} \frac{\partial u}{\partial y}. \end{cases} \quad (19.55)$$

Combining the equilibrium heat equation and the material constitutive equation, we finally obtain the unsteady heat conduction equation in the two-dimensional case. Equation (19.20) is a one-dimensional steady-state version

$$\rho c_p \dot{u} = \frac{\partial}{\partial x} \left(k_{xx} \frac{\partial u}{\partial x} + k_{xy} \frac{\partial u}{\partial y} \right) + \frac{\partial}{\partial x} \left(k_{yx} \frac{\partial u}{\partial x} + k_{yy} \frac{\partial u}{\partial y} \right) + f. \quad (19.56)$$

19.4.2 Elastic Solid Problem in the Three-Dimensional Case

Solid mechanics problems are rather complicated to explain, since there exist three components such as stress, strain, and displacement.

What is needed now are the following.

1. Equilibrium relationship on stress;
2. Displacement-strain relationship;
3. Stress-strain relationship including material constitutive equations.

The three recipes above are explained in the following parts, to derive the governing equation of elastic solid deformation problems. Some additional discussion on stress is necessary to avoid a misunderstanding of the physical meanings. The three-dimensional case is treated here, since the two-dimensional case is a degenerated case with some additional assumptions.

Equilibrium Relationship on Stress

Now let us think about the balance of forces in the x -direction in a three-dimensional infinitesimal element

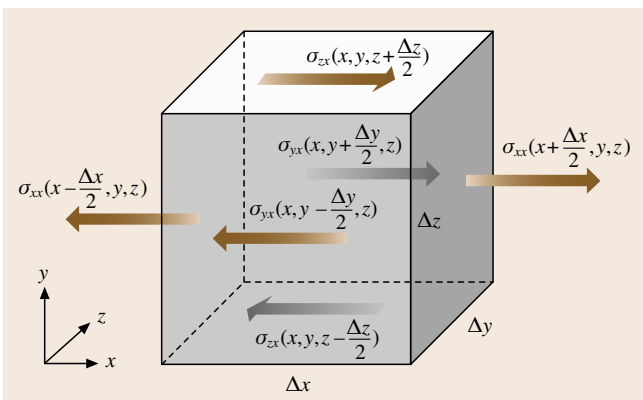


Fig. 19.14 Balance of forces in the x -direction in an infinitesimal element

in Fig. 19.14, where $\sigma_{\alpha\beta}$ is a stress (local pressure) value on the α -plane (the plane perpendicular to α -coordinate) in the β -direction, which is a function of x , y , and z . For example, σ_{zx} represents the component of stress in the x -direction on the z -plane.

The equilibrium in the x -direction is

$$\begin{aligned} & \left[-\sigma_{xx} \left(x - \frac{1}{2} \nabla x, y, z \right) \right. \\ & \quad \left. + \sigma_{xx} \left(x + \frac{1}{2} \nabla x, y, z \right) \right] \nabla y \nabla z \\ & + \left[-\sigma_{yx} \left(x, y - \frac{1}{2} \nabla y, z \right) \right. \\ & \quad \left. + \sigma_{yx} \left(x, y + \frac{1}{2} \nabla y, z \right) \right] \nabla z \nabla x \\ & + \left[-\sigma_{zx} \left(x, y, z - \frac{1}{2} \nabla z \right) \right. \\ & \quad \left. + \sigma_{zx} \left(x, y, z + \frac{1}{2} \nabla z \right) \right] \nabla x \nabla y \\ & + \varrho f_x \nabla x \nabla y \nabla z = 0. \end{aligned} \quad (19.57)$$

After dividing by $\Delta x \Delta y$ and applying $\Delta x \Delta y \rightarrow 0$, we get

$$\frac{\partial \sigma_{xx}}{\partial x} + \frac{\partial \sigma_{yx}}{\partial y} + \frac{\partial \sigma_{zx}}{\partial z} + \varrho f_x = 0. \quad (19.58)$$

Applying the same steps in the y - and z -directions leads to the following equations

$$\begin{aligned} \frac{\partial \sigma_{xy}}{\partial x} + \frac{\partial \sigma_{yy}}{\partial y} + \frac{\partial \sigma_{yz}}{\partial z} + \varrho f_y &= 0, \\ \frac{\partial \sigma_{xz}}{\partial x} + \frac{\partial \sigma_{yz}}{\partial y} + \frac{\partial \sigma_{zz}}{\partial z} + \varrho f_z &= 0. \end{aligned} \quad (19.59)$$

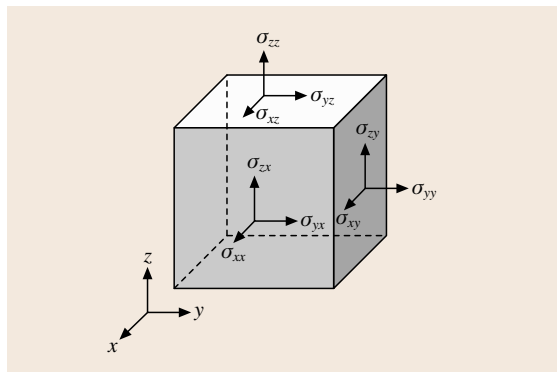


Fig. 19.15 Stress components

The stress components in (19.58) and (19.59) are sometimes represented in matrix form (19.60), which is physically visualized in Fig. 19.15

$$\boldsymbol{\sigma} = \begin{pmatrix} \sigma_{xx} & \sigma_{yx} & \sigma_{zx} \\ \sigma_{xy} & \sigma_{yy} & \sigma_{yz} \\ \sigma_{xz} & \sigma_{zy} & \sigma_{zz} \end{pmatrix}. \quad (19.60)$$

Considering the momentum equilibrium in Fig. 19.15, the symmetry of the stress is obtained. The shearing stress σ_{xy} is sometimes described as τ_{xy} , but the meaning is the same

$$\sigma_{xy} = \sigma_{yx}, \quad \sigma_{yz} = \sigma_{zy}, \quad \sigma_{zx} = \sigma_{xz}. \quad (19.61)$$

Displacement–Strain Relationship

Let us consider the case that a point P is moved to a point P' after some deformation of the body, as shown in Fig. 19.16.

Suppose vectors \mathbf{a} and \mathbf{x} are position vectors of points P and P' , individually. For the convenience of notation, subscripts 1, 2, and 3 represent x , y , and z ,

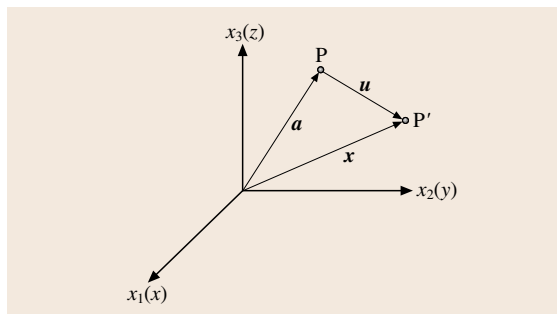


Fig. 19.16 Deformation

respectively in the following parts

$$\mathbf{u} = \mathbf{x} - \mathbf{a} \quad (\text{or } u_k = x_k - a_k)$$

where $x_1 = x$, $x_2 = y$, and $x_3 = z$. (19.62)

If you consider a differential line near points P and P', then

$$|d\mathbf{x}|^2 + |d\mathbf{a}|^2 = \sum_{i=1}^3 dx_i dx_i - \sum_{k=1}^3 da_k da_k,$$

where $x_1 = x$, $x_2 = y$, and $x_3 = z$. (19.63)

According to the differential rule

$$da_k = \sum_{i=1}^3 \frac{\partial a_k}{\partial x_i} dx_i \quad (19.64)$$

(19.64) changes to

$$\begin{aligned} & \sum_{i=1}^3 dx_i dx_i - \sum_{k=1}^3 da_k da_k \\ &= \sum_{i=1}^3 dx_i dx_i - \sum_{k=1}^3 \left(\sum_{i=1}^3 \frac{\partial a_k}{\partial x_i} dx_i \right) \left(\sum_{i=1}^3 \frac{\partial a_k}{\partial x_i} dx_i \right) \\ &= \sum_{i=1}^3 \sum_{j=1}^3 \left(\delta_{ij} - \sum_{k=1}^3 \frac{\partial a_k}{\partial x_i} \frac{\partial a_k}{\partial x_j} \right) dx_i dx_j. \end{aligned} \quad (19.65)$$

If the following definition of strain tensor ε_{ij} is introduced

$$\varepsilon_{ij} = \frac{1}{2} \left(\delta_{ij} - \sum_{k=1}^3 \frac{\partial a_k}{\partial x_i} \frac{\partial a_k}{\partial x_j} \right) \quad (19.66)$$

and taking the derivative of ∂x_i in (19.63)

$$\frac{\partial u_k}{\partial x_i} = \delta_{ki} - \frac{\partial a_k}{\partial x_i} \quad (19.67)$$

then we obtain

$$\varepsilon_{ij} = \frac{1}{2} \left(\frac{\partial u_i}{\partial x_j} + \frac{\partial u_j}{\partial x_i} - \frac{\partial u_k}{\partial x_i} \frac{\partial u_k}{\partial x_j} \right). \quad (19.68)$$

If the higher term is neglected in (19.68), we obtain the following displacement–strain relationship, which is called a Cauchy infinitesimal strain tensor. It should be noted that there exists a lot of stress tensors in nonlin-

ear solid mechanics that allow finite deformation and rotation [19.6]

$$\varepsilon_{ij} = \frac{1}{2} \left(\frac{\partial u_i}{\partial x_j} + \frac{\partial u_j}{\partial x_i} \right). \quad (19.69)$$

As a summary, the displacement and strain are connected to each other in the following relationship, where u , v , and w are displacement in the x , y , and z directions, respectively.

$$\begin{cases} \varepsilon_{xx} = \frac{\partial u}{\partial x} \\ \varepsilon_{yy} = \frac{\partial v}{\partial y} \\ \varepsilon_{zz} = \frac{\partial w}{\partial z} \\ \varepsilon_{xy} = \varepsilon_{yx} = \frac{1}{2} \left(\frac{\partial u}{\partial y} + \frac{\partial v}{\partial x} \right) \\ \varepsilon_{yz} = \varepsilon_{zy} = \frac{1}{2} \left(\frac{\partial v}{\partial z} + \frac{\partial w}{\partial y} \right) \\ \varepsilon_{zx} = \varepsilon_{xz} = \frac{1}{2} \left(\frac{\partial w}{\partial x} + \frac{\partial u}{\partial z} \right) \end{cases} \quad (19.70)$$

Stress–Strain Relationship Including Material Constitutive Equations

The constitutive equation for three-dimensional isotropic elastic material, which describes the stress–strain relationship, is modeled by experiments, as an extension of Hooke's law, where E , ν , and G are Young's modulus (modulus of elasticity), Poisson's ratio, and the modulus of elasticity in shear, respectively. For the definition of Young's modulus and Poisson's ratio, please refer to Sect. 19.7.1. It should be emphasized that (19.71) and (19.72) are only valid for three-dimensional *isotropic elastic* material

$$\begin{cases} \varepsilon_{xx} = \frac{1}{E} [\sigma_{xx} - \nu (\sigma_{yy} + \sigma_{zz})] \\ \varepsilon_{yy} = \frac{1}{E} [\sigma_{yy} - \nu (\sigma_{zz} + \sigma_{xx})] \\ \varepsilon_{zz} = \frac{1}{E} [\sigma_{zz} - \nu (\sigma_{xx} + \sigma_{yy})] \\ \varepsilon_{xy} = \frac{1}{G} \sigma_{xy} \\ \varepsilon_{yz} = \frac{1}{G} \sigma_{yz} \\ \varepsilon_{zx} = \frac{1}{G} \sigma_{zx} \end{cases} \quad (19.71)$$

or

$$\boldsymbol{\sigma} = D\boldsymbol{\varepsilon}$$

where

$$\boldsymbol{\sigma} = \begin{pmatrix} \sigma_1 \\ \sigma_2 \\ \sigma_3 \\ \sigma_4 \\ \sigma_5 \\ \sigma_6 \end{pmatrix} = \begin{pmatrix} \sigma_{xx} \\ \sigma_{yy} \\ \sigma_{zz} \\ \sigma_{yz} \\ \sigma_{zx} \\ \sigma_{xy} \end{pmatrix}, \quad \boldsymbol{\varepsilon} = \begin{pmatrix} \varepsilon_1 \\ \varepsilon_2 \\ \varepsilon_3 \\ \varepsilon_4 \\ \varepsilon_5 \\ \varepsilon_6 \end{pmatrix} = \begin{pmatrix} \varepsilon_{xx} \\ \varepsilon_{yy} \\ \varepsilon_{zz} \\ 2\varepsilon_{yz} \\ 2\varepsilon_{zx} \\ 2\varepsilon_{xy} \end{pmatrix},$$

$$D = \begin{pmatrix} \lambda + 2G & \lambda & \lambda & 0 & 0 & 0 \\ \lambda & \lambda + 2G & \lambda & 0 & 0 & 0 \\ \lambda & \lambda & \lambda + 2G & 0 & 0 & 0 \\ 0 & 0 & 0 & G & 0 & 0 \\ 0 & 0 & 0 & 0 & G & 0 \\ 0 & 0 & 0 & 0 & 0 & G \end{pmatrix},$$

$$\lambda = \frac{E\nu}{(1-2\nu)(1+\nu)}, \quad G = \frac{E}{2(1+\nu)}. \quad (19.72)$$

As in the two-dimensional case, there are two degenerated cases: the plane stress case is for plates with in-plane forces imposed, while the plane strain case is for a beam-like structure along the z direction with equally distributed forces acting on the long side. The former and latter are described by the conditions of $\sigma_{zz} = \sigma_{zx} = \sigma_{zy} = 0$ and $\varepsilon_{zz} = \varepsilon_{zx} = \varepsilon_{zy} = 0$, respectively [19.7]

$$\begin{pmatrix} \sigma_{xx} \\ \sigma_{yy} \\ \sigma_{xy} \end{pmatrix} = \begin{pmatrix} \frac{E}{1-\nu^2} & \frac{E\nu}{1-\nu^2} & 0 \\ \frac{E\nu}{1-\nu^2} & \frac{E}{1-\nu^2} & 0 \\ 0 & 0 & G \end{pmatrix} \begin{pmatrix} \varepsilon_{xx} \\ \varepsilon_{yy} \\ \varepsilon_{xy} \end{pmatrix}$$

(plane stress case),

$$\lambda = \frac{E\nu}{(1-2\nu)(1+\nu)}, \quad G = \frac{E}{2(1+\nu)}, \quad (19.73)$$

$$\begin{pmatrix} \sigma_{xx} \\ \sigma_{yy} \\ \sigma_{xy} \end{pmatrix} = \begin{pmatrix} \lambda(1-\nu) & \lambda\nu & 0 \\ \lambda\nu & \lambda(1-\nu) & 0 \\ 0 & 0 & G \end{pmatrix} \begin{pmatrix} \varepsilon_{xx} \\ \varepsilon_{yy} \\ \varepsilon_{xy} \end{pmatrix}$$

(plane strain case),

$$\lambda = \frac{E\nu}{(1-2\nu)(1+\nu)}, \quad G = \frac{E}{2(1+\nu)}. \quad (19.74)$$

So far, the derivation of the governing equation on the three-dimensional isotropic elastic solid problem

has been explained. In solid mechanics, stress values are very important and are directly linked to breakage, crash, and fatigue. A further explanation of stress is provided below to avoid a misunderstanding of physical meanings.

Further Explanation of Stress

Now let's study stress more deeply. The stress (pressure) value at a point cannot be determined uniquely if the acting plane information is not given. To represent the stress condition, the information on both an evaluation point and an evaluation plane is needed.

Figure 19.17 shows a tetrahedral element, where \mathbf{t} is a traction vector, the shaded face is a targeted plane, and \mathbf{n} is a normal unit vector of the targeted plane. It should be added that the traction vector \mathbf{t} is not an applying force from outside to the tetrahedral, but a reaction force from the tetrahedral element to outside.

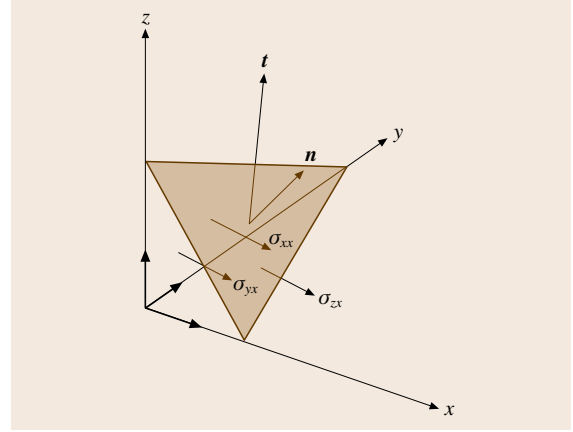


Fig. 19.17 Stress components at a tetrahedral element

We represent the traction vector \mathbf{t} with stress components in xyz -coordinates. Considering the x direction in Fig. 19.17, we get the following equation, where ΔA , ΔA_α , ΔV , ρ , and f_x are the area of the shaded plane, the area of α -plane (tetrahedral face normal to α -coordinate), the volume of the tetrahedral, the density, and the x component of the volume force

$$\sigma_{xx} \Delta A_x + \sigma_{yx} \Delta A_y + \sigma_{zx} \Delta A_z - \rho f_x \Delta V = t_x \Delta A. \quad (19.75)$$

Since $\Delta A_x = n_x \Delta A$, ... (n_x is x component of the normal unit vector \mathbf{n}), we get

$$(\sigma_{xx} n_x + \sigma_{yx} n_y + \sigma_{zx} n_z) \Delta A - \rho f_x \Delta V = t_x \Delta A. \quad (19.76)$$

Considering $\Delta A \rightarrow 0$ (at the same time, $\Delta V \rightarrow 0$),

$$\begin{aligned} t_x &= \sigma_{xx}n_x + \sigma_{yx}n_y + \sigma_{zx}n_z, \\ t_y &= \sigma_{xy}n_x + \sigma_{yy}n_y + \sigma_{zy}n_z, \\ t_z &= \sigma_{xz}n_x + \sigma_{yz}n_y + \sigma_{zz}n_z, \end{aligned} \tag{19.77}$$

or

$$\begin{pmatrix} t_x \\ t_y \\ t_z \end{pmatrix} = \begin{pmatrix} \sigma_{xx} & \sigma_{yx} & \sigma_{zx} \\ \sigma_{xy} & \sigma_{yy} & \sigma_{zy} \\ \sigma_{xz} & \sigma_{yz} & \sigma_{zz} \end{pmatrix} \begin{pmatrix} n_x \\ n_y \\ n_z \end{pmatrix}. \tag{19.78}$$

Now the traction force vector t on the shaded plane is represented with a stress component matrix σ in (19.78) and a normal vector. It should be noted that the stress matrix σ is a second-rank tensor since it contains the directional information of acting force and imposed plane.

Mathematically the 3×3 matrix has the following important properties.

1. It has three eigenvalues, including multiple roots, which are real numbers.
2. The eigenvectors are orthogonal to each other.

With these properties the stress matrix can be transformed as follows after some coordinate changes. The physical meaning is illustrated in Fig. 19.18, where σ_x , σ_y , and σ_z are called the principal stress. It should be added that the left and right sides of Fig. 19.18 are physically identical since the transformation is just a change of coordinate setting.

The 3×3 stress matrix has three invariants against coordinate settings. The von Mises stress value in (19.79), which is a good estimator of the strength, is

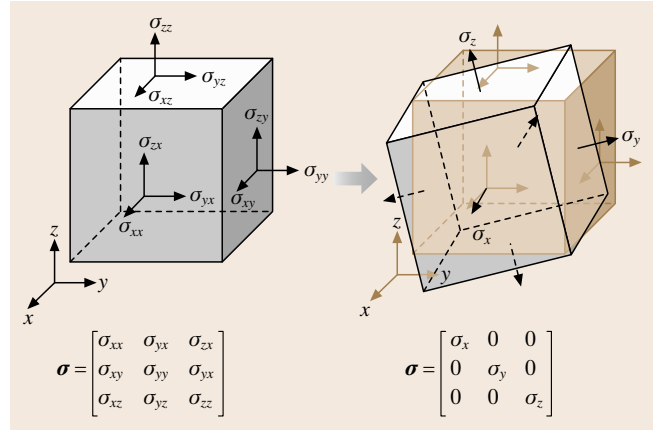


Fig. 19.18 Principal stresses

one of them

$$\begin{aligned} \sigma_{\text{von Mises}} &= \sqrt{\frac{1}{2} \left[(\sigma_x - \sigma_y)^2 + (\sigma_y - \sigma_z)^2 + (\sigma_z - \sigma_x)^2 \right]} \\ &= \sqrt{\frac{1}{2} \left[(\sigma_{xx} - \sigma_{yy})^2 + (\sigma_{yy} - \sigma_{zz})^2 + (\sigma_{zz} - \sigma_{xx})^2 \right] + 3 \left(\sigma_{xy}^2 + \sigma_{yz}^2 + \sigma_{zx}^2 \right)}. \end{aligned} \tag{19.79}$$

It must be added in this section that these governing equations are only valid for continuum mechanics since the material constitutive equations are derived from experimental data obtained in a continuum modeling sense.

19.5 From Mathematics to Mechanics: Characteristic of Partial Differential Equations

In the previous section, we studied the derivation of mathematical governing equations for heat conduction problems and solid deformation problems from mechanical points of view. In this section, we take a look at the characteristics of physical (mechanical) representations of partial differential equations, categorized in a mathematical sense.

Equation (19.80) represents the general form of second-order partial differential equations

$$\begin{aligned} A \frac{\partial^2 \phi}{\partial x^2} + B \frac{\partial^2 \phi}{\partial x \partial t} \\ + C \frac{\partial^2 \phi}{\partial t^2} + D \frac{\partial \phi}{\partial x} + E \frac{\partial \phi}{\partial t} + F \phi + G = 0. \end{aligned} \tag{19.80}$$

Depending on the value of $B^2 - 4AC$ in (19.80), it can be categorized into elliptic, parabolic, and hyperbolic types as in (19.81), which are linked with steady heat conduction problems, potential flow problems, steady perfect elastic deformation problems, and so on

$$\begin{aligned} \text{elliptic type} & \quad B^2 - 4AC < 0, \\ \text{parabolic type} & \quad B^2 - 4AC = 0, \\ \text{hyperbolic type} & \quad B^2 - 4AC > 0. \end{aligned} \quad (19.81)$$

In the following part, we study the characteristic of three types.

19.5.1 Elliptic Type

If an independent variable t is replaced by y under the conditions of $A = C = 1$, $B = D = E = F = 0$ and $G = f(x, y)$ in (19.80), we get a so-called Poisson equation

$$\frac{\partial^2 \phi}{\partial x^2} + \frac{\partial^2 \phi}{\partial y^2} = f(x, y). \quad (19.82)$$

The Laplace equation is in the case of $f(x, y) = 0$

$$\frac{\partial^2 \phi}{\partial x^2} + \frac{\partial^2 \phi}{\partial y^2} = 0. \quad (19.83)$$

This type represents the problem of finding the steady distribution of the target value inside the domain with some boundary conditions such as steady heat conduction problems (see Sect. 19.4.1), potential flow problems (under the assumption of zero rotation = no viscosity) and steady perfect elastic deformation problems (see Sect. 19.4.2).

From images of these phenomena, the characteristics of elliptic-type phenomena can be summarized as

1. The equation type is usually for steady problems.
2. The solution at some point tends to be the averaged values of the surrounding points.

19.5.2 Parabolic Type

Typical parabolic-type phenomena are unsteady heat conduction or unsteady diffusion problems. For example, by setting $A = -1$, $E = 1$, and $B = C = D = F = 0$, we obtain the following equation, where t , x , and $\phi(x, t)$ are time, the x -coordinate in one-dimension, and the physical variable dependent on x and t , such as density or temperature

$$\frac{\partial \phi}{\partial t} = \frac{\partial^2 \phi}{\partial x^2}. \quad (19.84)$$

Both unsteady heat conduction problems and unsteady diffusion problems belong to this type.

Equation (19.85) represents both unsteady heat conduction problems and unsteady diffusion problems in one-dimensional case, where k is the heat conduction coefficient and a diffusive coefficient, respectively

$$\frac{\partial u(x, t)}{\partial t} - k \frac{\partial^2 u(x, t)}{\partial x^2} = -f. \quad (19.85)$$

With the information above, the characteristics of parabolic-type phenomena can be summarized as

1. Nondirectional distribution of the solution in space
2. Rapid diffusion of the solution in time over the domain.

19.5.3 Hyperbolic Type

A typical hyperbolic type is the wave equation below, which is the case with $A = -c^2$, $C = 1$, and $B = D = E = F = 0$ in (19.80). This equation represents the wave propagation along the x direction with the velocity c , which is called the wave equation

$$\frac{\partial^2 \phi}{\partial t^2} = c^2 \frac{\partial^2 \phi}{\partial x^2}. \quad (19.86)$$

The second part of factorized equation below is called an advection equation, which has almost equivalent characteristics as a wave equation

$$\frac{\partial^2 \phi}{\partial t^2} - c^2 \frac{\partial^2 \phi}{\partial x^2} = \left(\frac{\partial}{\partial t} - c \frac{\partial}{\partial x} \right) \left(\frac{\partial}{\partial t} + c \frac{\partial}{\partial x} \right) \phi. \quad (19.87)$$

The characteristics of hyperbolic-type phenomena can be summarized as

1. Directional distribution of the solution in space
2. Diffusion of the solution with given velocity in time in some part of domain.

The advection–diffusion equation is given in (19.88), where ϕ , u , k , and f are density, advective velocity, diffusive coefficient, and source term, respectively

$$\frac{\partial \phi}{\partial t} + u \frac{\partial \phi}{\partial x} - k \frac{\partial^2 \phi}{\partial x^2} = f. \quad (19.88)$$

As one can see from the previous explanation, hyperbolic and parabolic types show the opposite characteristics. Since the advection–diffusion equation is the combination of these two types, there exist some difficulties for numerical calculations. The flow problem, described by Navier–Stokes equation, is a nonlinear version of the advection–diffusion equation in a mathematical sense.

19.6 Time Integration for Unsteady Problems

The governing equation of the unsteady heat conduction problem in the one-dimensional case is represented as follows, where u , k , and f are the temperature, the heat conduction coefficient, and the heat source, respectively

$$\frac{\partial u(x, t)}{\partial t} - k \frac{\partial^2 u(x, t)}{\partial x^2} = -f. \quad (19.89)$$

Suppose that we know the values of u and $\partial u/\partial x$ at time n , which is represented by u^n and \dot{u}^n . Now we want to obtain u^{n+1} from u^n and \dot{u}^n .

Figure 19.19 visualizes the problem. The shaded part is $u^{n+1} - u^n$, which is what we want to obtain. The finite difference idea is applied to this problem.

Let us simplify the problem by introducing the generalized trapezoidal method description [19.2], which is nothing but a generalized finite difference description using the parameter α

$$\begin{aligned} u^{n+1} &= u^n + \Delta t \dot{u}^{n+\alpha}, \\ \dot{u}^{n+\alpha} &= (1-\alpha)\dot{u}^n + \alpha\dot{u}^{n+1}. \end{aligned} \quad (19.90)$$

If $\alpha = 0$, then $u^{n+\alpha} = \dot{u}^n \rightarrow u^{n+1} = u^n + \Delta t \dot{u}^n$, which means $u^{n+1} - u^n$ is calculated by the known value \dot{u}^n at the n th time step as shown by the lower dotted line in Fig. 19.19. This is a forward difference scheme *wrt* time, which is called the forward Euler or the explicit method.

If $\alpha = 1$, then $\dot{u}^{n+\alpha} = \dot{u}^{n+1} \rightarrow u^{n+1} = u^n + \Delta t \dot{u}^{n+1}$, which means $u^{n+1} - u^n$ is calculated by the unknown value \dot{u}^{n+1} at $(n+1)$ th time step. In Fig. 19.19, the upper dotted line illustrates this case. This is the backward

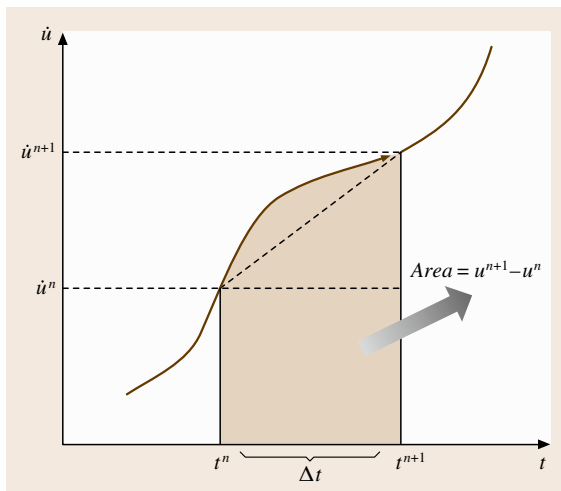


Fig. 19.19 Time integration between t^n and t^{n+1}

difference method in time, named the backward Euler or the implicit method.

If $\alpha = 0.5$, then $\dot{u}^{n+\alpha} = (\dot{u}^n + \dot{u}^{n+1}/2) \rightarrow u^{n+1} = u^n + \Delta t(\dot{u}^n + \dot{u}^{n+1}/2)$, which means $u^{n+1} - u^n$ is calculated by both known and unknown values \dot{u}^n , \dot{u}^{n+1} at the n th time step. In Fig. 19.19, this is the diagonal dotted line. This is called the trapezoidal rule, the midpoint rule, or the Crank–Nicolson method.

According to Fig. 19.19, the Crank–Nicolson method ($\alpha = 0.5$ case) seems to be the best solution, however \dot{u}^{n+1} is not known at the n th time step. Since \dot{u}^{n+1} is also calculated with the Crank–Nicolson algorithm, it is not a simple discussion. Based on experience, the Crank–Nicolson method with $\alpha = 0.51 \approx 0.55$ is recommended in most cases.

Usually the unknown value \dot{u}^{n+1} is obtained by a matrix inversion process in the implicit method or Crank–Nicolson method in discretized numerical schemes. In nonlinear cases, equilibrium iterations, for example, the Newton–Raphson method (see Sect. 19.8) within a time step is usually omitted in explicit time integration.

In the following, the derivations of FDM and FEM for the unsteady heat conduction problem in the one-dimensional case is explained by the time integration scheme explained above.

19.6.1 FDM

By applying the generalized finite difference description in time to a finite difference formulation at node $u^n(x)$, we get

$$\begin{aligned} & \frac{u^{n+1}(x) - u^n(x)}{\Delta t} \\ & - k \left[(1-\alpha) \frac{u^n(x+h) - 2u^n(x) + u^n(x-h)}{h^2} \right. \\ & \left. + \alpha \frac{u^{n+1}(x+h) - 2u^{n+1}(x) + u^{n+1}(x-h)}{h^2} \right] \\ & = -f. \end{aligned} \quad (19.91)$$

After modifying the equation, it becomes

$$\left(\alpha \frac{k}{h^2} \frac{1}{\Delta t} - 2\alpha \frac{k}{h^2} \quad \alpha \frac{k}{h^2} \right) \begin{pmatrix} u^{n+1}(x-h) \\ u^{n+1}(x) \\ u^{n+1}(x+h) \end{pmatrix}$$

$$\begin{aligned}
& + \left((1-\alpha) \frac{k}{h^2} - \frac{1}{\Delta t} - 2(1-\alpha) \frac{k}{h^2} \quad (1-\alpha) \frac{k}{h^2} \right) \\
& \times \begin{pmatrix} u^n(x-h) \\ u^n(x) \\ u^n(x+h) \end{pmatrix} = -f. \quad (19.92)
\end{aligned}$$

If $\alpha = 0$, the local FD equation becomes the following one in matrix representation

$$\begin{aligned}
& \begin{pmatrix} 0 & \frac{1}{\Delta t} & 0 \end{pmatrix} \begin{pmatrix} u^{n+1}(x-h) \\ u^{n+1}(x) \\ u^{n+1}(x+h) \end{pmatrix} \\
& + \begin{pmatrix} \frac{k}{h^2} & -\frac{1}{\Delta t} - 2\frac{k}{h^2} & \frac{k}{h^2} \end{pmatrix} \begin{pmatrix} u^n(x-h) \\ u^n(x) \\ u^n(x+h) \end{pmatrix} = -f. \quad (19.93)
\end{aligned}$$

After summing this equation for all nodes, we get the following matrix system

$$\frac{1}{\Delta t} \mathbf{I} \mathbf{u}^{n+1} + \mathbf{K}_2 \mathbf{u}^n = \mathbf{F}. \quad (19.94)$$

Equation (19.94) means that a solution vector at $(n+1)$ th time step \mathbf{u}^{n+1} can be obtained merely by $\mathbf{u}^{n+1} = \Delta t(\mathbf{F} - \mathbf{K}_2 \mathbf{u}^n)$ without any matrix inversion. This is an explicit case.

If $\alpha = 1$, we get the following local matrix system

$$\begin{aligned}
& \begin{pmatrix} \frac{k}{h^2} & \frac{1}{\Delta t} - 2\frac{k}{h^2} & \frac{k}{h^2} \end{pmatrix} \begin{pmatrix} u^{n+1}(x-h) \\ u^{n+1}(x) \\ u^{n+1}(x+h) \end{pmatrix} \\
& + \begin{pmatrix} 0 & -\frac{1}{\Delta t} \frac{k}{h^2} & 0 \end{pmatrix} \begin{pmatrix} u^n(x-h) \\ u^n(x) \\ u^n(x+h) \end{pmatrix} = -f. \quad (19.95)
\end{aligned}$$

After summing all equations,

$$\mathbf{K}_1 \mathbf{u}^{n+1} - \frac{1}{\Delta t} \frac{k}{h^2} \mathbf{I} \mathbf{u}^n = \mathbf{F}. \quad (19.96)$$

This matrix system denotes that a solution vector at the $(n+1)$ th time step \mathbf{u}^{n+1} is calculated by $\mathbf{u}^{n+1} = \mathbf{K}_1^{-1}(\mathbf{F} + 1/\Delta t \ k/h^2 \ \mathbf{I} \mathbf{u}^n)$ which involves the matrix inversion \mathbf{K}_1^{-1} . This is an implicit case. The Crank–Nicolson case with $\alpha = 0.51$ – 0.55 belongs to an implicit case, since it needs matrix inversion calculation.

19.6.2 FEM

In FEM, the space domain is spanned by the finite element interpolation function, but the finite difference idea in time is applied in the time domain.

Again, starting from the weak form, we get

$$\int_0^1 \left(\frac{\partial u(x, t)}{\partial t} + k \frac{\partial^2 u(x, t)}{\partial x^2} + f \right) w(x, t) dx = 0, \quad (19.97)$$

$$\begin{aligned}
& \int_0^1 w \frac{\partial u(x, t)}{\partial t} dx + \int_0^1 k \frac{\partial w(x, t)}{\partial x} \frac{\partial u(x, t)}{\partial x} dx \\
& = \int_0^1 f w(x, t) dx - k w(0) b. \quad (19.98)
\end{aligned}$$

By introducing the finite element functions as in Sect. 19.1,

$$\begin{aligned}
& \int_{\text{element } j} \begin{pmatrix} w_1(t) & w_2(t) \end{pmatrix} \begin{pmatrix} \frac{dN_1(x)}{dx} \\ \frac{dN_2(x)}{dx} \end{pmatrix} \\
& \times \begin{pmatrix} \frac{dN_1(x)}{dx} & \frac{dN_2(x)}{dx} \end{pmatrix} \begin{pmatrix} \dot{u}_1(t) \\ \dot{u}_2(t) \end{pmatrix} dx \\
& + \int_{\text{element } j} \begin{pmatrix} w_1(t) & w_2(t) \end{pmatrix} \begin{pmatrix} \frac{dN_1(x)}{dx} \\ \frac{dN_2(x)}{dx} \end{pmatrix} \\
& \times \begin{pmatrix} \frac{dN_1(x)}{dx} & \frac{dN_2(x)}{dx} \end{pmatrix} \begin{pmatrix} u_1(t) \\ u_2(t) \end{pmatrix} dx \\
& = \begin{pmatrix} w_1(t) & w_2(t) \end{pmatrix} \int_{\text{element } j} f \begin{pmatrix} N_1(x) \\ N_2(x) \end{pmatrix} dx \\
& - k \begin{pmatrix} w_1(t) & w_2(t) \end{pmatrix} \begin{pmatrix} N_1(0) \\ N_2(0) \end{pmatrix} b. \quad (19.99)
\end{aligned}$$

Omitting weight function vector,

$$\begin{aligned}
& \sum_{\text{element } j} \int \begin{pmatrix} \frac{dN_1(x)}{dx} \\ \frac{dN_2(x)}{dx} \end{pmatrix} \\
& \times \begin{pmatrix} \frac{dN_1(x)}{dx} & \frac{dN_2(x)}{dx} \end{pmatrix} dx \begin{pmatrix} \dot{u}_1(t) \\ \dot{u}_2(t) \end{pmatrix} \\
& + \sum_{\text{element } j} \int k \begin{pmatrix} \frac{dN_1(x)}{dx} \\ \frac{dN_2(x)}{dx} \end{pmatrix} \\
& \times \begin{pmatrix} \frac{dN_1(x)}{dx} & \frac{dN_2(x)}{dx} \end{pmatrix} dx \begin{pmatrix} u_1(t) \\ u_2(t) \end{pmatrix} \\
& - \sum_{\text{element } j} \int f \begin{pmatrix} N_1(x) \\ N_2(x) \end{pmatrix} dx - k \begin{pmatrix} N_1(0) \\ N_2(0) \end{pmatrix} b = 0. \quad (19.100)
\end{aligned}$$

Now we get the following matrix representation, where \mathbf{M} and \mathbf{K} are called the mass matrix and stiffness matrix, respectively

$$\mathbf{M}\dot{\mathbf{u}}(t) + \mathbf{K}\mathbf{u}(t) = \mathbf{F}(t)$$

$$\begin{aligned} \text{where } M &= \sum_{\text{element } j} \int \left(\frac{dN_1(x)}{dx} \frac{dN_2(x)}{dx} \right) \\ &\quad \times \left(\frac{dN_1(x)}{dx} \frac{dN_2(x)}{dx} \right) dx, \\ K &= \sum_{\text{element } j} \int k \left(\frac{dN_1(x)}{dx} \right) \\ &\quad \times \left(\frac{dN_1(x)}{dx} \frac{dN_2(x)}{dx} \right) dx, \\ F &= \sum_{\text{element } j} \int f \begin{pmatrix} N_1(x) \\ N_2(x) \end{pmatrix} dx \\ &\quad - k \begin{pmatrix} N_1(0) \\ N_2(0) \end{pmatrix} b. \end{aligned} \quad (19.101)$$

Combining the definition of the generalized trapezoidal method as follows

$$\begin{aligned} \mathbf{M}\dot{\mathbf{u}}^{n+1} + \mathbf{K}\mathbf{u}^{n+1} &= \mathbf{F}^{n+1}, \\ \mathbf{u}^{n+1} &= \mathbf{u}^n + \Delta t \dot{\mathbf{u}}^{n+\alpha}, \\ \dot{\mathbf{u}}^{n+\alpha} &= (1-\alpha)\dot{\mathbf{u}}^{n+\alpha} + \dot{\mathbf{u}}^{n+1}, \end{aligned} \quad (19.102)$$

we finally get the following algorithm

$$\begin{aligned} &\frac{1}{\alpha\Delta t} (\mathbf{M} + \alpha\Delta t\mathbf{K}) \mathbf{u}^{n+1} \\ &= \mathbf{F}^{n+1} + \frac{1}{\alpha\Delta t} \mathbf{M} [\mathbf{u}^n + (1-\alpha)\Delta t\dot{\mathbf{u}}^n]. \end{aligned} \quad (19.103)$$

It should be noted that both \mathbf{u}^n and $\dot{\mathbf{u}}^n$ should be stored in the code for the Crank–Nicolson method.

In the case of $\alpha = 0$, that is, the forward Euler case, if the left-hand side mass matrix \mathbf{M} is lumped (summing the diagonal terms), \mathbf{u}^{n+1} can be obtained without serious matrix inversion. This is an explicit method, where LS-DYNA and PAM-CRASH for crash FE analysis are the most common pieces of software used for this type.

In the explicit time integration scheme (both in FDM and FEM), the Courant–Friedrichs–Lewy (CFL) condition is a key issue to determine a proper time step. The CFL condition says that a time step must be less than the time for some significant action to occur. In other words, the Courant number defined in (19.104) must be less than 1, where c , h , and Δt are dissipation speed, mesh size, and time step. This means if one uses a very fine mesh, one should also use a proper tiny time step. The mesh size and the time step are linked together in the explicit method by

$$v = \frac{c}{\left(\frac{h}{\Delta t}\right)} = c \frac{\Delta t}{h}. \quad (19.104)$$

19.7 Multidimensional Case

The multidimensional case is basically the extension of one-dimensional case, but it is usually difficult to have an image of derivations in matrix forms. Here we study it without tensor description.

Let us consider the two-dimensional heat conduction problem, described by (19.105). In this case, we consider isotropic heat conduction without any directional references (see (19.56) for a general description)

$$\frac{\partial q_x}{\partial x} + \frac{\partial q_y}{\partial y} = f,$$

$$\text{with } u = a \text{ on } \Gamma_a, \quad -\mathbf{qn} = b \text{ on } \Gamma_b,$$

$$\text{where } \mathbf{q} = \begin{pmatrix} q_x \\ q_y \end{pmatrix} = - \begin{pmatrix} k & 0 \\ 0 & k \end{pmatrix} \begin{pmatrix} \frac{\partial u(x, y)}{\partial x} \\ \frac{\partial u(x, y)}{\partial y} \end{pmatrix}$$

$$\text{(Fourier's law in the isotropic case)}. \quad (19.105)$$

By substituting Fourier's law to the partial differential equation (19.105), we get

$$k \left(\frac{\partial^2 u(x, y)}{\partial x^2} + \frac{\partial^2 u(x, y)}{\partial y^2} \right) = -f. \quad (19.106)$$

In the following part, we only consider (19.106) without boundary conditions for simplicity.

19.7.1 Finite Difference Method

By extension of the one-dimensional definition in finite difference operators, we can easily obtain the following operators in the two-dimensional case

$$\begin{aligned} \frac{\partial \phi(x, y)}{\partial x} &\approx \frac{\phi(x+h, y) - \phi(x-h, y)}{2h_x}, \\ \frac{\partial \phi(x, y)}{\partial y} &\approx \frac{\phi(x, y+h) - \phi(x, y-h)}{2h_y}, \end{aligned}$$

$$\frac{\partial^2 u(x, y)}{\partial x^2} \approx \frac{u(x+h, y) - 2u(x, y) + u(x-h, y)}{h_x^2},$$

$$\frac{\partial^2 u(x, y)}{\partial y^2} \approx \frac{u(x, y+h) - 2u(x, y) + u(x, y-h)}{h_y^2}.$$

(19.107)

Now let us consider two-dimensional finite difference grids in Fig. 19.20.

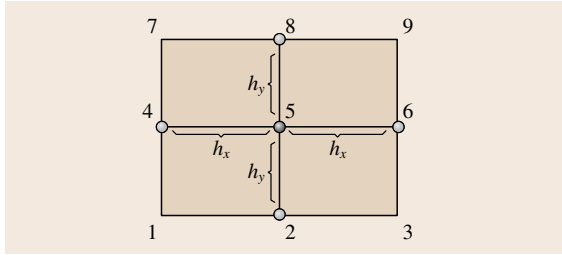


Fig. 19.20 Finite difference grids in the two-dimensional case

Applying (19.107) to (19.106) at node 5 in Fig. 19.19 gives

$$k \left(\frac{\partial^2 u(x, y)}{\partial x^2} + \frac{\partial^2 u(x, y)}{\partial y^2} \right) \approx k \left(\frac{u_4 - 2u_5 + u_6}{h_x^2} + \frac{u_2 - 2u_5 + u_8}{h_y^2} \right), \quad (19.108)$$

which is visualized by the local and global matrix representations in Fig. 19.21. The whole global matrix for (19.106) is piled up without any overlap between rows.

19.7.2 Finite Element Method

As in Sect. 19.2, the weak form can be generated by multiplying the weight function w with the governing equation in (19.106). It should be noted that all functions are assumed to be functions *wrt* x and y .

$$\int_{\Omega} \left(\frac{\partial q_x(x, y)}{\partial x} + \frac{\partial q_y(x, y)}{\partial y} - f \right) w(x, y) d\Omega = 0 \quad (19.109)$$

By applying integration by parts, or the Green-Gauss theorem, we obtain

$$-\int_{\Omega} f w(x, y) d\Omega + \int_{\Gamma_b} w(x, y) \left(\frac{\partial q_x}{\partial x} n_x + \frac{\partial q_y}{\partial y} n_y \right) d\Gamma$$

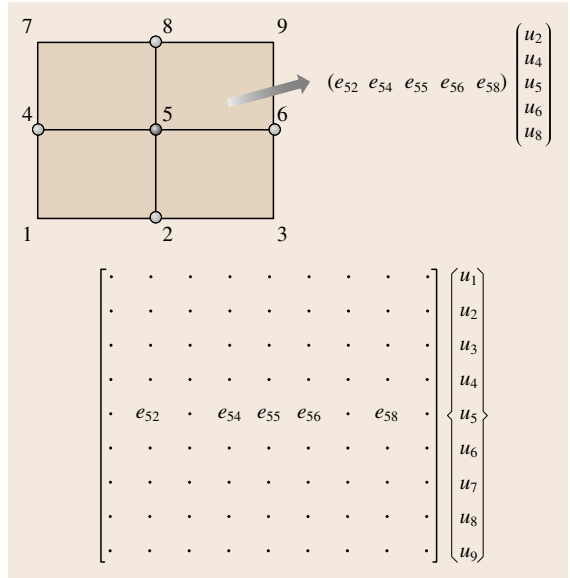


Fig. 19.21 Local (upper) and global matrix in two-dimensional FDM

$$-\int_{\Omega} \left(\frac{\partial w(x, y)}{\partial x} q_x + \frac{\partial w(x, y)}{\partial y} q_y \right) d\Omega = 0. \quad (19.110)$$

After substituting Fourier's law into (19.110), we get the matrix form

$$\int_{\Omega} \left(\frac{\partial w(x, y)}{\partial x} \frac{\partial w(x, y)}{\partial y} \right) \begin{pmatrix} k & 0 \\ 0 & k \end{pmatrix} \begin{pmatrix} \frac{\partial u(x, y)}{\partial x} \\ \frac{\partial u(x, y)}{\partial y} \end{pmatrix} d\Omega = \int_{\Omega} f w(x, y) d\Omega + \int_{\Gamma_b} w(x, y) b d\Gamma. \quad (19.111)$$

Now we consider the left-hand term only, which is

$$\int_{\Omega_j} \left(\frac{\partial w(x, y)}{\partial x} \frac{\partial w(x, y)}{\partial y} \right) \begin{pmatrix} k & 0 \\ 0 & k \end{pmatrix} \begin{pmatrix} \frac{\partial u(x, y)}{\partial x} \\ \frac{\partial u(x, y)}{\partial y} \end{pmatrix} d\Omega. \quad (19.112)$$

As in Sect. 19.1, the variable (and its derivatives) are represented by finite element shape functions, where we consider the four-node bilinear quadrilateral finite

element

$$\begin{aligned}
 & \begin{pmatrix} \frac{\partial u(x, y)}{\partial x} \\ \frac{\partial u(x, y)}{\partial y} \end{pmatrix} \\
 &= \begin{pmatrix} \frac{\partial N_1(x, y)}{\partial x} & \frac{\partial N_2(x, y)}{\partial x} & \frac{\partial N_3(x, y)}{\partial x} & \frac{\partial N_4(x, y)}{\partial x} \\ \frac{\partial N_1(x, y)}{\partial y} & \frac{\partial N_2(x, y)}{\partial y} & \frac{\partial N_3(x, y)}{\partial y} & \frac{\partial N_4(x, y)}{\partial y} \end{pmatrix} \\
 & \times \begin{pmatrix} u_1 \\ u_2 \\ u_3 \\ u_4 \end{pmatrix}. \tag{19.113}
 \end{aligned}$$

Substituting (19.113) into (19.112) gives

$$\begin{aligned}
 & \int_{\Omega_j} (w_1 \ w_2 \ w_3 \ w_4) \begin{pmatrix} \frac{\partial N_1}{\partial x} & \frac{\partial N_1}{\partial y} \\ \frac{\partial N_2}{\partial x} & \frac{\partial N_2}{\partial y} \\ \frac{\partial N_3}{\partial x} & \frac{\partial N_3}{\partial y} \\ \frac{\partial N_4}{\partial x} & \frac{\partial N_4}{\partial y} \end{pmatrix} \begin{pmatrix} k \ 0 \\ 0 \ k \end{pmatrix} \\
 & \times \begin{pmatrix} \frac{\partial N_1}{\partial x} & \frac{\partial N_2}{\partial x} & \frac{\partial N_3}{\partial x} & \frac{\partial N_4}{\partial x} \\ \frac{\partial N_1}{\partial y} & \frac{\partial N_2}{\partial y} & \frac{\partial N_3}{\partial y} & \frac{\partial N_4}{\partial y} \end{pmatrix} \begin{pmatrix} u_1 \\ u_2 \\ u_3 \\ u_4 \end{pmatrix} d\Omega. \tag{19.114}
 \end{aligned}$$

Omitting vectors \mathbf{w} and \mathbf{u} ,

$$\begin{aligned}
 & K_j = \int_{\Omega_j} \begin{pmatrix} \frac{\partial N_1}{\partial x} & \frac{\partial N_1}{\partial y} \\ \frac{\partial N_2}{\partial x} & \frac{\partial N_2}{\partial y} \\ \frac{\partial N_3}{\partial x} & \frac{\partial N_3}{\partial y} \\ \frac{\partial N_4}{\partial x} & \frac{\partial N_4}{\partial y} \end{pmatrix} \\
 & \times \begin{pmatrix} k \ 0 \\ 0 \ k \end{pmatrix} \begin{pmatrix} \frac{\partial N_1}{\partial x} & \frac{\partial N_2}{\partial x} & \frac{\partial N_3}{\partial x} & \frac{\partial N_4}{\partial x} \\ \frac{\partial N_1}{\partial y} & \frac{\partial N_2}{\partial y} & \frac{\partial N_3}{\partial y} & \frac{\partial N_4}{\partial y} \end{pmatrix} d\Omega. \tag{19.115}
 \end{aligned}$$

Since FEM handles an arbitrary shaped domain, an element's shape is usually arbitrary. For this reason, finite element functions in natural coordinates are used in the

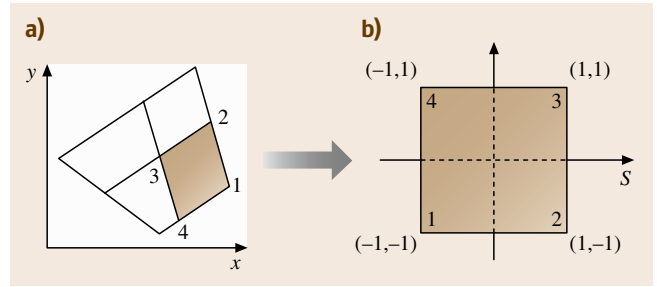


Fig. 19.22a,b Bilinear quadrilateral element: (a) Physical coordinates, (b) natural coordinates

multidimensional case

$$\begin{aligned}
 u(x, y) &= \sum_{k=1}^4 u_k N_k(s, t), \\
 x(s, t) &= \sum_{k=1}^4 x_k N_k(s, t), \\
 y(s, t) &= \sum_{k=1}^4 y_k N_k(s, t), \\
 \frac{\partial [x(s, t), y(s, t)]}{\partial (s, t)} &= \begin{pmatrix} \frac{\partial x(s, t)}{\partial s} & \frac{\partial x(s, t)}{\partial t} \\ \frac{\partial y(s, t)}{\partial s} & \frac{\partial y(s, t)}{\partial t} \end{pmatrix}, \\
 \begin{cases} N_1(s, t) = \frac{1}{4}(1-s)(1-t), \\ N_2(s, t) = \frac{1}{4}(1+s)(1-t), \\ N_3(s, t) = \frac{1}{4}(1+s)(1+t), \\ N_4(s, t) = \frac{1}{4}(1-s)(1+t). \end{cases} \tag{19.116}
 \end{aligned}$$

It should be noted that all finite element functions always have, in general, the following property

$$\begin{cases} N_\alpha(s_\beta, t_\beta) = \delta_{\alpha\beta}, \\ \sum_{\alpha=1}^n N_\alpha(s, t) = 1. \end{cases} \tag{19.117}$$

Considering the Jacobian matrix between (x, y) and (s, t) ,

$$K_j = \int_{\Omega_j} \begin{pmatrix} \frac{\partial N_1}{\partial s} & \frac{\partial N_1}{\partial t} \\ \frac{\partial N_2}{\partial s} & \frac{\partial N_2}{\partial t} \\ \frac{\partial N_3}{\partial s} & \frac{\partial N_3}{\partial t} \\ \frac{\partial N_4}{\partial s} & \frac{\partial N_4}{\partial t} \end{pmatrix} \begin{pmatrix} k \ 0 \\ 0 \ k \end{pmatrix}$$

$$\times \begin{pmatrix} \frac{\partial N_1}{\partial s} & \frac{\partial N_2}{\partial s} & \frac{\partial N_3}{\partial s} & \frac{\partial N_4}{\partial s} \\ \frac{\partial N_1}{\partial t} & \frac{\partial N_2}{\partial t} & \frac{\partial N_3}{\partial t} & \frac{\partial N_4}{\partial t} \end{pmatrix} \left| \frac{\partial(x, y)}{\partial(s, t)} \right| d\Omega . \tag{19.118}$$

Local and global matrix representations around node 5 are visualized in Fig. 19.23.

Let us now show that the local stiffness matrix \mathbf{K}_j in the linear elastic solid case, which is treated in Sect. 19.4, has the following form for the reader's future reference.

The relationship in (19.70) and (19.72) can be summarized as shown in (19.119)

$$\begin{pmatrix} \varepsilon_{xx} \\ \varepsilon_{yy} \\ \varepsilon_{zz} \\ 2\varepsilon_{yz} \\ 2\varepsilon_{zx} \\ 2\varepsilon_{xy} \end{pmatrix} = \begin{pmatrix} \frac{\partial}{\partial x} & 0 & 0 \\ 0 & \frac{\partial}{\partial y} & 0 \\ 0 & 0 & \frac{\partial}{\partial z} \\ 0 & \frac{\partial}{\partial z} & \frac{\partial}{\partial y} \\ \frac{\partial}{\partial z} & 0 & \frac{\partial}{\partial x} \\ \frac{\partial}{\partial y} & \frac{\partial}{\partial x} & 0 \end{pmatrix} \begin{pmatrix} \frac{\partial u}{\partial x} \\ \frac{\partial u}{\partial y} \\ \frac{\partial u}{\partial z} \end{pmatrix} . \tag{19.119}$$

Considering (19.119), the local stiffness matrix $\mathbf{K}^{\text{element } j}$ for an eight-node brick element can be defined as below, where the \mathbf{D} matrix is the same as in (19.72) for the isotropic elastic cases. This is schematic view of the $\mathbf{K}^{\text{element } j}$ matrix and the treatment in Fig. 19.22 is not visualized here. For further details, please refer to [19.2].

$$\mathbf{K}^{\text{element } j} \mathbf{u}^{\text{element } j} = \left(\int_{\Omega_j} \mathbf{B}^T \mathbf{D} \mathbf{B} d\Omega \right) \mathbf{u}^{\text{element } j}$$

where $\mathbf{B} = \begin{bmatrix} \frac{\partial N_1}{\partial x} & 0 & 0 & \dots & \frac{\partial N_8}{\partial x} & 0 & 0 \\ 0 & \frac{\partial N_1}{\partial y} & 0 & \dots & 0 & \frac{\partial N_8}{\partial y} & 0 \\ 0 & 0 & \frac{\partial N_1}{\partial z} & \dots & 0 & 0 & \frac{\partial N_8}{\partial z} \\ 0 & \frac{\partial N_1}{\partial z} & \frac{\partial N_1}{\partial x} & \dots & 0 & \frac{\partial N_8}{\partial z} & \frac{\partial N_8}{\partial x} \\ \frac{\partial N_1}{\partial z} & 0 & \frac{\partial N_1}{\partial x} & \dots & \frac{\partial N_8}{\partial z} & 0 & \frac{\partial N_8}{\partial x} \\ \frac{\partial N_1}{\partial y} & \frac{\partial N_1}{\partial x} & 0 & \dots & \frac{\partial N_8}{\partial y} & \frac{\partial N_8}{\partial x} & 0 \end{bmatrix}$

$$\mathbf{u}^{\text{element } j} = \begin{pmatrix} u_1^{\text{element } j} \\ v_1^{\text{element } j} \\ w_1^{\text{element } j} \\ \vdots \\ u_8^{\text{element } j} \\ v_8^{\text{element } j} \\ w_8^{\text{element } j} \end{pmatrix} . \tag{19.120}$$

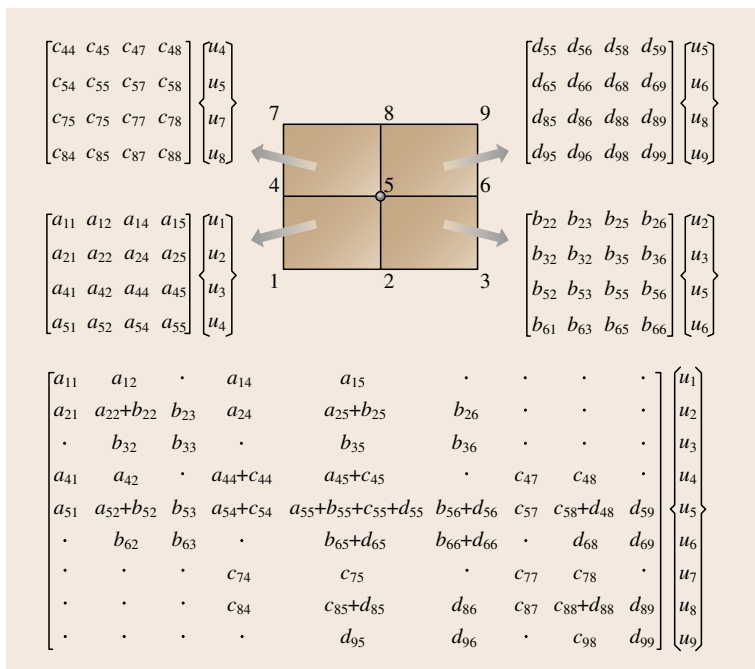


Fig. 19.23 Local and global matrix in two-dimensional FEM

19.8 Treatment of the Nonlinear Case

Nonlinear problems can be classified into several patterns, such as material nonlinearity, geometrical nonlinearity (including large strain/stress and buckling), and boundary nonlinearity (including moving boundary and contact/friction). Since nonlinearity among these classes is so different on a numerical sense, the reader should be careful, when using nonlinear commercial software. Even the defined strain is different in some settings (for further information, refer to [19.6]).

As for the numerical treatment of the nonlinear problem, we want to pick up one typical method here. The Newton–Raphson method [19.4] is the method used to solve a nonlinear equation $g(x) = 0$ by iterative calculation of the derivative of $g(x)$ (or Jacobian in the multidimensional case) as shown in (19.121)

$$g(x) = 0. \quad (19.121)$$

By applying a Taylor's expansion to the nonlinear iterative equation $g(x^{k+1}) = 0$ around x^k and omitting higher-order terms, we get

$$g(x^{k+1}) \approx g(x^k) + g'(x^k)(x^{k+1} - x^k) = 0. \quad (19.122)$$

Rewriting (19.122) results in the following representation, which drives the $k+1$ th step approximated solution x^{k+1} from the value x^k at the previous k th step

$$x^{k+1} = x^k - [g'(x^k)]^{-1} g(x^k), \quad g'(x^k) \neq 0. \quad (19.123)$$

It should be noted that Newton–Raphson method is valid for multidimensional nonlinear problems as

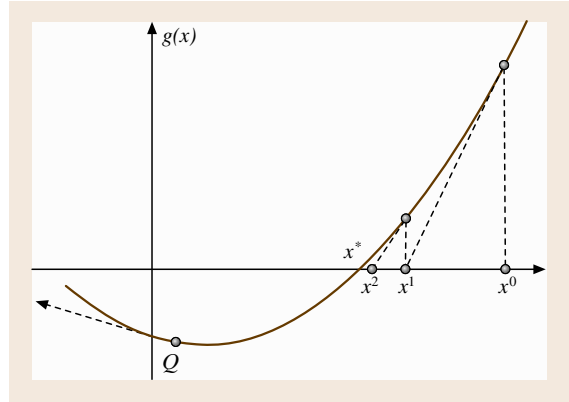


Fig. 19.24 Newton–Raphson method

shown in (19.124)

$$\begin{aligned} g_1(x_1, \dots, x_n) &= 0, \\ &\dots \\ g_n(x_1, \dots, x_n) &= 0. \end{aligned} \quad (19.124)$$

If the nonlinearity of the equation is not severe and the initial guess x^0 is not far from the solution, this algorithm offers a numerically acceptable converged solution x^* by applying (19.123) iteratively from an initial guess x^0 , as shown in Fig. 19.24. However if an initial guess x^0 is too far from a converged solution x^* (for example, the point Q is selected as an initial guess x^0 in Fig. 19.24) or if the function $g(x) = 0$ is highly nonlinear, the method might still diverge, even after many iterations. In this case, more stable methods such as the Riks method [19.6] should be applied.

19.9 Advanced Topics in FEM and FDM

Some advanced topics are treated in this section. You may encounter some of the problems when you use FEM or FEM software packages. The explanation below is just a sample for the reader, with references provided for more information.

19.9.1 Preprocessing

Until now we have been talking about theoretical aspects with an algorithm explanation. However, the most time-consuming part in the numerical analysis (espe-

cially in three-dimensional case) is modeling, which is the process of making FE mesh or FD grids in advance of simulation.

Some so-called *automatic* mesh/grid generator software is available, however, the reader should recognize that there are two categories of automatic model generation schemes: the interactive mapped mesh half-automatic generation approach and the noninteractive nonmapped mesh full-automatic generation approach. The former requires an interactive, time-consuming task to help the automatic mesh generation software.

The basic idea of mapped mesh approach [19.8] is based on the conforming mapped function as shown in Fig. 19.22a,b.

Since FDM handles regular shaped domains in most cases because of its limitation, mesh generation is done using the interactive mapped mesh approach basically [19.9]. However, FEM can treat the domain of an arbitrary shape, thus the noninteractive nonmapped mesh approach might be a better tool for modeling [19.10].

It should be noted that the modeling method greatly affects the quality of solution in discretized methods. The reader should always recognize that what the discretized numerical method can do is provide an approximated solution.

19.9.2 Postprocessing

As mentioned in remark (4) in Sect. 19.2.2, the first derivative of an FE function is discontinuous between elements. This implies that a node has m derivative values if the node is surrounded by m elements. To obtain a representative value at a node, Winslow's weighted averaging scheme (19.125) in [19.11] or super convergent patch scheme [19.12] is usually applied, which is nothing but a process to convert element-wise values to nodal values

$$x_n = \frac{\sum_{n,j=1}^{m_j} x_{g_{nj}} w_{nj}}{\sum_{n,j=1}^{m_j} w_j}, \quad (19.125)$$

where x_n is the target variable at node n , x_{nj} is the centroid coordinates at finite elements $j(j = 1, m_j)$ connected with the node n , and w_{nj} is a weight (1 in this case) at element j . Visualization software sometimes does this kind of postprocessing automatically, which can conceal unacceptable unsmoothed solutions with nice visualizations in some cases.

19.9.3 Numerical Error

If we get some unacceptable numerical results as compared with experimental data, there might be several causes for the errors. Basically, a numerical simulation involves three stages, as shown in Fig. 19.25. The major error source might lie between the *real problem* and *physical model*, which is related to the simplification process of the real target problem with selecting a proper physical property. For example, if the head conduction coefficient is improper (inaccu-

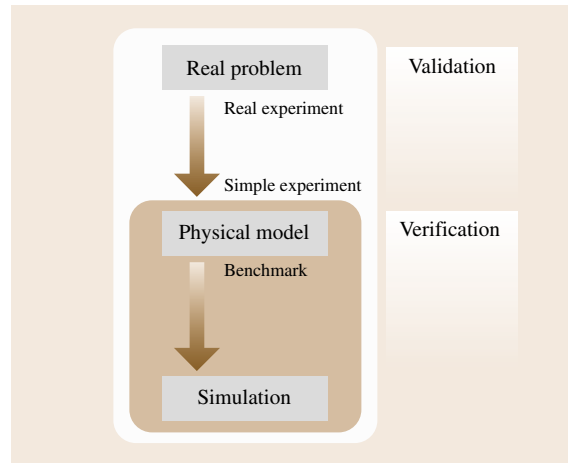


Fig. 19.25 Three stages of simulation

rately approximated) to model the considered problem, we cannot get an acceptable numerical solution even with very accurate numerical schemes applied. The responsibility of numerical schemes only covers physical models and simulation, although it gives rise to serious error due to an inefficient number of grids or meshes. To distinguish the discussion between the former and the latter, the terminology *verification and validation* is sometimes used [19.13]. Validation is *confirmation by examination and provisions of objective evidence that the particular requirements for a specific intended use are fulfilled*, while verification is *confirmation by examination and provisions of objective evidence that specified requirements have been fulfilled*, according to IEEE definition [19.13]. Thus, in discussion above, the former is related to validation, while the latter is linked with verification.

As described above, infinitely fine mesh/grid leads to the exact solution, which requires an infinite scale matrix calculation. It is an important idea for engineers to establish acceptable numerical analysis within the limitation of real computational power available. Since the quality of FD/FE analysis greatly depends on the quality of mesh/grid, the reader must be careful in real simulations. Automatic mesh/grid control schemes, such as the adaptive finite element method [19.12] or boundary-fitted finite difference method [19.9], can be useful for this purpose. Most commercial software provides this function for better results. It should be emphasized that this is only related to the verification stage.

As for the worse cases, solutions themselves can sometimes not be obtained due to the improper set-

tings in numerical analyses. For example, the treatment of incompressibility in fluids and solids is one of the typical matters to be noted. In incompressible flows, the equations for velocity and pressure are usually solved separately in a weakly coupled fashion. In this case, the feasible combination of velocity-element and pressure-element is limited by the Ladyzhenskaya–Babuska–Brezzi (LBB or BB) condition in the usual FE formulation [19.14], while staggered-type grids are needed in popular FD formulation [19.14]. It should be added that there are no uniform general numerical formulation proposed that are valid for both incompressible and compressible flows. In the same manner for fluid, the treatment of incompressible materials in solid FEA should be carefully treated, which can be a cause of so-called locking in the simulation. The treatment of magnetic problems usually needs some techniques. The problems above might be described in the manuals in most commercial FE/FD software, but the reader should keep them in mind.

Usually FEM and FDM are conducted with the information of material properties, domain's shape, and boundary conditions, to obtain the distribution of temperature in thermodynamics, displacement/strain/stress in solid mechanics, velocity/pressure in fluid dynamics, and so on. If and only if the quality of the simulation is highly reliable, material properties can be *measured* by applying FEM and FDM iteratively with the technique of minimum search. This inverse problem setting is sometimes useful, especially when the direct measurement is impossible for some reason, although the uniqueness of the inverse solutions is not always guaranteed. For information on the state-of-the-art of this subject, please refer to [19.15].

19.9.4 Relatives of FEM and FDM

There exist other methods categorized in discretized numerical schemes. We briefly introduce some of them.

Finite Volume Method (FVM)

FVM is an effective scheme for fluid dynamics, where flux-balancing is considered in a finite volume (control volume) [19.16]. The domain is discretized into infinite number of finite volumes, and its shape can be arbitrary. Unknown variables are defined at the center of the control volume, while the flux on its boundary is linked with the unknown variables in some way.

Boundary Element Method (BEM)

The derivation of BEM is based on Green's theorem with the use of fundamental solutions in various phenomena [19.17]. BEM mainly supports linear analysis. According the Green's theorem, an n -dimensional problem can be treated as an $(n - 1)$ -dimensional problem setting but only homogenous material can be handled in BEM. The main advantage of this method is that it can treat infinite domain such as in magnetic or acoustic problems without any theoretical difficulties. The matrix is a dense matrix, while it is a sparse matrix in other discretized methods.

Constrained Interpolated Profile (CIP) Method

The CIP method is very powerful for moving boundary problem and multiphysics problems [19.18,19]. It is one of multimeasure methods with a spline-interpolation function in FDM's category, which utilizes both variables and its derivatives for calculation.

Particle Method

The biggest weak point of discretized methods is that it cannot easily handle complicated moving boundary unsteady problems, including explosions, since the topology of grid/mesh must be fixed during time-step calculations. Particle methods, such as the discrete element method (DEM), smooth particle hydrodynamics method (SPH), and related various methods, are good for these unflavored problems. Because of limited space in this chapter, please refer to [19.20] for details.

Including the additional methods treated above, a rough summary of the properties of each method is shown in Table 19.1. The information listed might be not a complete set, but serves as a reference for a reader.

19.9.5 Matrix Calculation and Parallel Computations

As shown above, the coefficient matrix in FEM and FDM is a diagonal-dominated (banded) sparse matrix. The matrix can be symmetrical in heat and elastic solid problem or nonsymmetrical in fluid and nonlinear solid problems.

There are two categories in matrix calculation: direct method and iterative method. The direct matrix solvers are based on Gauss-elimination and its modifications, such as the skyline method for symmetric matrices, frontal (wave front) method for a nonsymmetric matrix. Since the banded size around the diagonal varies according to the numbering of the nodes, which

Table 19.1 Summary of discretized numerical schemes

	Strong points	Weak points	Major targets	Software
FEM	2nd BC treatment Local resolution Arbitrary shape	Calculation time Complex derivation Sensitive solution	Nonlinear solid/thermal/fluid/ vibration	ANSYS (multiphysics) LS-DYNA (crash/solid) FIDAP (fluid), etc.
FDM	Calculation time Stable solution Simple derivation	Stable solution Regular shape Heuristic aspects	Simple derivation	Flow-3D (fluid), etc.
FVM	Calculation time Stable solution Moving boundary	Local resolution Heuristic aspects	Thermal/fluid	FLUENT (fluid), etc.
BEM	Simple modeling	Limited to linear/ homogeneous case Dense matrix	Linear elastic/linear flow/ acoustic/magnetic	BEASY (solid), etc.
CIP	Complex problem Stable solution Multiphysics	New method No sales software	Thermal/fluid/solid	[19.17]
PM	No mesh/grid Explosion Highly nonlinear	Calculation time New method No sales software	Nonlinear solid/explosion	[19.18]

greatly affects the calculation time and required memory size, some renumbering algorithms to reduce the bandwidth are proposed.

The iterative methods can be classified into two groups: (1) The stationary iterative methods, such as the Jacobi method, Gauss–Seidel method, and successive overrelaxation (SOR) method, and (2) the nonstationary method, such as the conjugate gradient (CG) method, the biconjugate gradient stabilized (Bi-CGSTAB) method, quasiminimal residual (QMR) method, and generalized minimal residual (GMRES) method [19.21]. The rough algorithm in the stationary iterative methods can be represented by (19.126)

$$\begin{aligned} \mathbf{Ax} &= \mathbf{b} \rightarrow \mathbf{Mx} = (\mathbf{M} - \mathbf{A})\mathbf{x} + \mathbf{b}, \\ \mathbf{Mx}^{k+1} &= (\mathbf{M} - \mathbf{A})\mathbf{x}^k + \mathbf{b}, \end{aligned} \quad (19.126)$$

where (1) \mathbf{M} = diagonal part of \mathbf{A} , (2) \mathbf{M} = triangular part of \mathbf{A} , and (3) \mathbf{M} = combination of (1) and (2) part of \mathbf{A} .

The basic algorithm on nonstationary method is represented in (19.127), where \mathbf{r} , \mathbf{p} , and \mathbf{x} are the residual vector, direction vector, and the solution vector, respectively.

$$\begin{aligned} \mathbf{r}^0 &= \mathbf{b} - \mathbf{Ax}^0 \\ \text{for } k &= 0, 1, 2, \dots \end{aligned}$$

$$\begin{aligned} \mathbf{p}^{k+1} &= \mathbf{p}^k + \alpha \mathbf{r}^k \\ \mathbf{x}^{k+1} &= \mathbf{x}^k + \beta \mathbf{p}^{k+1} \\ \mathbf{r}^{k+1} &= \mathbf{b} - \mathbf{Ax}^{k+1} \\ \text{convergence check} \\ \text{end.} \end{aligned} \quad (19.127)$$

To accelerate convergence of the iterations, the algorithm with some preconditioners is proposed as in [19.21]

$$\begin{aligned} \mathbf{r}^0 &= \mathbf{b} - \mathbf{Ax}^0 \\ \text{for } k &= 0, 1, 2, \dots \\ \mathbf{z}^k &= \mathbf{M}^{-1} \mathbf{r}^k \\ \mathbf{p}^{k+1} &= \mathbf{p}^k + \alpha \mathbf{z}^k \\ \mathbf{x}^{k+1} &= \mathbf{x}^k + \beta \mathbf{p}^{k+1} \\ \mathbf{r}^{k+1} &= \mathbf{b} - \mathbf{Ax}^{k+1} \\ \text{convergence check} \\ \text{end.} \end{aligned}$$

Some of the related subroutines above are available from [19.22].

For the parallel calculation method such as the domain decomposition method, please refer to [19.23] and [19.24]. Table 19.2 shows the summary of matrix calculation methods.

Table 19.2 Summary of matrix calculation methods

		For ill-conditioned matrix	For parallel calculation	Method	
Direct matrix solver		o	×	Skyline Frontal	Symmetric Nonsymmetric
Iterative matrix solver	Stationary	×	o	Jacobi Gauss–Seidel SOR	M = diagonal part of A M = triangular part of A M = diagonal and triangular parts of A
	Non-stationary	×	o	CG Bi-CGSTAB QMR GMRES	Symmetric/FEM/solid Nonsymmetric/FEM/solid Nonsymmetric/FEM/fluid Nonsymmetric/FEM/fluid

19.9.6 Multiscale Method

To bridge the macroscopic scale and mesoscopic scale, the multiscale approach was recently considered to be important. The homogenization method is one of the so-

lutions that carries numerical material testing between macroscale (usual FE mesh) and microscale (FE mesh at material level) to get real-time stress–strain constitutive behavior for FEA in macroscale. The key points of this method are introduced in reference [19.25].

19.10 Free Codes

Some internet URLs for FEM and FDM are provided for the reader’s convenience. This is not a recommended selection; the reader must use the information at their own risk.

1. Information on modeling, FEM, and FDM
http://homepage.usask.ca/~ijm451/finite/fe_resources/fe_resources.html (Internet Finite Element Resources; general information on FEM including free codes)
<http://morden.csee.usf.edu/dragon/kpalbrec/mesh.html> (Meshing Research Corner; survey of mesh generation schemes and codes)
2. Parallel computations in FEM, FDM, and FVM
[http://www.ibase.aist.go.jp/infobase/pcp/platform-](http://www.ibase.aist.go.jp/infobase/pcp/platform-en/index.html)

[en/index.html](http://www.netlib.org/) (Parallel Computing Platform/PCP developed by AIST and FUJIRIC; perfect solution for parallelization of FEM/FDM/FVM codes, free from headaches from matrix handling, MPI commands and memory allocations, sample programs of FEM/FDM/FVM are also provided)

3. Related libraries
<http://www.netlib.org/> (collection of mathematical software, papers, and databases)
4. Modeling-related free software
<http://www.netlib.org/voronoi/index.html> (Voronoi; 2-dimensional Voronoi diagram, Delaunay triangulation)
<http://www.geuz.org/gmsh/> (Gmsh mesh generation code with TRI/QUAD/TETRA/HEXA element)

References

- 19.1 J.W. Thomas: *Numerical Partial Differential Equations: Finite Difference Methods* (Springer, Berlin, Heidelberg 1995)
- 19.2 T.J.R. Hughes: *The Finite Element Method: Linear Static and Dynamic Finite Element Analysis* (Dover, New York 2000)
- 19.3 A.N. Kolmogorov, S.V. Fomin: *Elements of the Theory of Functions and Functional Analysis* (Dover, New York 1999)
- 19.4 G. Strang: *Introduction to Applied Mathematics* (Wellesley–Cambridge, Cambridge 1986)
- 19.5 N. Kikuchi: *Finite Element Methods in Mechanics* (Cambridge Univ. Press, New York 1986)
- 19.6 T. Belytschko, W.K. Liu, B. Moran: *Nonlinear Finite Elements for Continua and Structures* (Wiley, New York 2000)
- 19.7 S.P. Timoshenko, J.N. Goodier: *Theory of Elasticity* (McGraw–Hill, New York 1970)

- 19.8 O.C. Zienkiewicz, D.V. Phillips: An automatic mesh generation scheme for plane and curved surfaces by isoparametric coordinate, *Int. J. Numer. Methods Eng.* **3**, 519–528 (1971)
- 19.9 J.F. Thompson, Z.U.A. Warsi, C.W. Mastin: *Numerical Grid Generation* (North-Holland, Amsterdam 1985)
- 19.10 A. Tezuka: 2D mesh generation scheme for adaptive remeshing process, *Jpn. Soc. Mech. Eng.* **38**, 204–215 (1996)
- 19.11 A.M. Winslow: Numerical solution of the quasi-linear poisson equation in a nonuniform triangle mesh, *J. Comput. Phys.* **2**, 149–172 (1967)
- 19.12 M. Ainsworth, J.T. Oden: *A Posterior Error Estimation in Finite Element Analysis* (Wiley, New York 2000)
- 19.13 P.J. Roache: *Verification and Validation in Computational Science and Engineering* (Hermosa, Socorro 1998)
- 19.14 R. Peyret: *Handbook of Computational Fluid Mechanics* (Academic, New York 1996)
- 19.15 K.A. Woodbury: *Inverse Engineering Handbook* (CRC, Boca Raton 2002)
- 19.16 J.H. Ferziger, M. Peric: *Computational Methods for Fluid Dynamics* (Springer, Berlin, Heidelberg 2001)
- 19.17 C.A. Brebbica: *The Boundary Element Method for Engineers* (Pentech, London 1978)
- 19.18 T. Nakamura, R. Tanaka, T. Yabe, K. Takizawa: Exactly conservative semi-Lagrangian scheme for multidimensional hyperbolic equations with directional splitting technique, *J. Comput. Phys.* **174**, 171–207 (2001)
- 19.19 CIPUS (CIP User's Society): www.mech.titech.ac.jp/~ryuutai/cipuse.html (2011) by T. Yabe
- 19.20 W.K. Liu, S. Li: Meshfree and particle methods and their applications, *Appl. Mech. Rev.* **55**, 1–34 (2002)
- 19.21 G.H. Golub, C.F. Van Loan: *Matrix Computations* (Johns Hopkins Univ. Press, Baltimore 1996)
- 19.22 W.H. Press, S.A. Teukolsky, W.T. Vetterling, B.P. Flannery: *Numerical Recipes in Fortran 90: The Art of Parallel Scientific Computing*, 2nd edn. (Cambridge Univ. Press, Cambridge 1996)
- 19.23 B.F. Smith, P.E. Bjrstad, W.D. Gropp: *Domain Decomposition: Parallel Multilevel Methods for Elliptic Partial Differential Equations* (Cambridge Univ. Press, Cambridge 1996)
- 19.24 Parallel Computing Platform/PCP: www.ibase.aist.go.jp/infobase/pcp/platform-en/index.html (2011)
- 19.25 J.M. Guedes, N. Kikuchi: Preprocessing and post-processing for materials based on the homogenization method with adaptive finite element methods, *Comput. Methods Appl. Mech. Eng.* **83**, 143–198 (1990)

The CALPHAD

20. The CALPHAD Method

Phase diagrams offer various areas of materials science and technology indispensable information for the comprehension of the properties of materials. The microstructure of solid materials is generally classified according to the size of the constituents – for example, at the electron, atomic, or granular level (Sect. 1.3). Accordingly, fundamental principles like quantum mechanics, statistical mechanics, or thermodynamics are applied individually to describe the physical properties. Phases are important features of material because they characterize homogeneous aggregations of matter with respect to chemical composition and uniform crystal structure. The various functions of a material are closely related to the phases and structures of the material's composition. Therefore, to develop a material with a maximum level of desired functions, it is essential to undertake design of the structure in advance.

Phase diagrams are composed by means of experimental measurements, as well as statistical thermodynamic analysis. The construction of phase diagram calculations based on experiments and thermodynamic analysis are generally referred to as the calculation of phase diagrams (CALPHAD) approach [20.1]. This method provides a very accurate understanding of the properties originating in the macroscopic character of the material under study.

This chapter is organized in three parts:

- In the first part, a brief outline of the CALPHAD method is summarized.
- In the second part, the method for deriving the Gibbs free energies incorporating the ab initio calculations is presented in order to clarify the uncertainty of thermodynamic properties for metastable solution phases, taking the Fe–Be-based bcc phase as an example. Some results

20.1	Outline of the CALPHAD Method	1062
20.1.1	Description of Gibbs Energy	1062
20.1.2	Equilibrium Conditions	1064
20.1.3	Evaluation of Thermodynamic Parameters.....	1065
20.2	Incorporation of the First-principles Calculations into the CALPHAD Approach .	1066
20.2.1	Outline of the First-principles Calculations .	1066
20.2.2	Gibbs Energies of Solution Phases Derived by the First-principles Calculations.....	1067
20.2.3	Thermodynamic Analysis of the Gibbs Energies Based on the First-principles Calculations	1071
20.2.4	Construction of Stable and Metastable Phase Diagrams.....	1071
20.2.5	Application to More Complex Cases.....	1073
20.3	Prediction of Thermodynamic Properties of Compound Phases with First-principles Calculations	1079
20.3.1	Thermodynamic Analysis of the Fe–Al–C System	1079
20.3.2	Thermodynamic Analysis of the Co–Al–C and Ni–Al–C Systems	1083
	References	1090

for metastable phase equilibria in the Fe–Be, and Co–Al binary systems are shown.

- In the third part the application to predict thermodynamic properties of compound phases is discussed. The thermodynamic modeling for the Perovskite carbide with an E₂₁-type structure in the Fe–Al–C, Co–Al–C and Ni–Al–C ternary systems is illustrated, and constructions of phase diagrams are performed.

20.1 Outline of the CALPHAD Method

Phase diagrams provide basic and important information especially for the design of new materials. However, by using experimental techniques only, a lot of time and labor is required in construction of even a partial region of a phase diagram, because the practical materials are composed of multicomponent alloys, more than ternary systems. In order to break this difficult situation, the method of calculation of phase diagrams was advocated and is referred to as the CALPHAD method. CALPHAD was originally a name for this researcher's group, however it has recently become the name for the technique by which a phase diagram is calculated on the basis of thermodynamics. In this method a variety of experimental values concerning the phase boundaries and the thermodynamic properties is analyzed according to an appropriate thermodynamic model and the interaction energies between atoms are evaluated. By using this technique, phase diagrams outside the experimental range can be calculated based on thermodynamic proof. Difficulty in extension of the calculated results to higher-order systems is much less than that in the case of experimental work, since the essence of the calculation does not change so much between a binary system and a higher-order system. This method provides a very accurate understanding of the properties originating in the macroscopic character of the material under study. However, a shortcoming of this approach is that it is hard to obtain information on metastable equilibria, or on undiscovered phases, since the thermodynamic parameters from this method can only be evaluated from experimental data.

The empirical model of *de Boer* et al. [20.2] has often been used to deduce the thermodynamic quantities of systems where the experimental values do not exist. In this model, generally called Miedema's model, the crystal lattice is divided into Wigner-Seitz cells. The simple expression for the formation energy in alloys is derived by considering the change in the electron density states at the interface between the cells, as shown in (20.1)

$$\Delta E \propto -P (\Delta\Phi)^2 + Q \left(\Delta n_{\text{WS}}^{1/3} \right)^2. \quad (20.1)$$

Here, Δn_{WS} is the difference in electron density based on the volume of the Wigner-Seitz cell between different species of atoms. This term always leads to local perturbations that give rise to a positive energy contribution in (20.1). On the other hand, $\Delta\Phi$ presents a difference between the chemical potentials of the different species of atoms at the cell surfaces, and leads to

an attractive term in (20.1). The constants P and Q are proportionality constants, derived empirically. Equation (20.1) does not contain any parameters that refer to the crystal structure, and therefore, the heats of solution of face-centered-cubic (fcc), body-centered-cubic (bcc), and hexagonal-close-packed (hcp) structures, as well as liquids, are predicted. However, it is known that the absolute values are not always predicted accurately, although this model predicts the correct sign for the formation enthalpy in various alloy systems. For example, thermodynamic analysis of the Fe-Pd system predicts the enthalpy of formation for the $L1_0$ and the $L1_2$ ordered phases to be -14 kJ/mol and -22 kJ/mol, respectively, while the predicted values from Miedema's model are -6 kJ/mol for the $L1_0$ phase and -4 kJ/mol for the $L1_2$ phase [20.3]. The large difference between these values means that incorporating Miedema's model with a thermodynamic analysis is rather difficult.

Such serious problems, which are intrinsic to the CALPHAD approach, should be solved with the assistance of the first-principles energetic calculation method. Thus, in the present chapter, a new approach to introduce some thermodynamic quantities obtained by the ab initio band energy calculations in the conventional CALPHAD-type analysis of some alloy systems is presented.

20.1.1 Description of Gibbs Energy

Gibbs Free Energy

Using the Regular Solution Approximation

The selection of a thermodynamic model by which Gibbs free energy of an alloy system is described is the most important factor when using the CALPHAD method. In a system in which interaction between alloying elements is not so strong, the regular solution model is well known to describe the thermodynamic properties of the alloys comparatively well. For instance, the free energy of the A-B binary alloy is expressed as (20.2)

$$G_m = x_A {}^0G_A + x_B {}^0G_B + x_A x_B L_{AB} + RT(x_A \ln x_A + x_B \ln x_B), \quad (20.2)$$

where 0G_i is the Gibbs energy of the pure component i in the standard, and x_i is the mole fraction of i . L_{AB} shows the interaction energy for A atoms and B atoms, and is given by

$$L_{AB} = NZ \left[\varepsilon_{AB} - \frac{1}{2} (\varepsilon_{AA} + \varepsilon_{BB}) \right], \quad (20.3)$$

where N denotes the so called Avogadro's number, Z is the coordination number, and ε_{AB} , ε_{AA} and ε_{BB} show the cohesion energies between A–B, A–A, B–B atomic pair, respectively. The ordering between unlike atoms occurs for $L_{AB} < 0$ because the A–B atom pair is more stable than the average of the A–A and B–B atom pairs. On the other hand, the clustering of the like atom is caused in case of $L_{AB} > 0$. For $L_{AB} = 0$, no atomic interaction exists, and then the solution shows the random mixing of atoms. This interaction parameter should not be constant but a function of the temperature and the chemical compositions of alloys. From a qualitative point of view, the first term of (20.2) represents the energies of mechanical mixing, the second term stands for excess energy which shows deviation from the ideal solution, and the third is ideal mixing entropy.

Gibbs Free Energy Using the Sublattice Model

For the simplest case of the sublattice model [20.4], let us consider a phase represented by the formula $(A, B)_a(C, D)_b$, containing two elements A and B in one sublattice "1" and two elements C and D in the other sublattice "2". The coefficients a and b show the number of sites in each sublattice and the size of the sublattices may be generally chosen as $a + b = 1$ for convenience. There are four elements in the system, however the degrees of freedom in varying in composition are two, because the total numbers of atoms in each sublattice are fixed. Thus these two composition parameters are conveniently plotted on a square where the corners

represented the four basic end members A_aC_b , A_aD_b , B_aC_b , and B_aD_b , as shown in Fig. 20.1a. The symbols y_B^1 and y_D^2 denote the mole fractions, respectively, for the sublattices 1 and 2, and they are represented as follows:

$$y_B^1 = \frac{n_B^1}{n_A^1 + n_B^1}, \quad y_D^2 = \frac{n_D^2}{n_C^2 + n_D^2}. \quad (20.4)$$

In this equation n_i^j denotes the number of i atoms in the j sublattice. The nonplanar surface composed of four reference states, i. e., one each for the compounds A_aC_b , A_aD_b , B_aC_b , and B_aD_b , is called the surface of reference as shown in Fig. 20.1b, and represented by

$$G_m^{\text{ref}} = y_A^1 y_C^2 G_{A_aC_b} + y_A^1 y_D^2 G_{A_aD_b} + y_B^1 y_C^2 G_{B_aC_b} + y_B^1 y_D^2 G_{B_aD_b}. \quad (20.5)$$

For the entropy term, the following Gibbs energy of mixing can be obtained, assuming the atoms mix randomly within each sublattice

$$G_{\text{mix}}^{\text{ideal}} = RT \left[a \left(y_A^1 \ln y_A^1 + y_B^1 \ln y_B^1 \right) + b \left(y_C^2 \ln y_C^2 + y_D^2 \ln y_D^2 \right) \right]. \quad (20.6)$$

It seems difficult to accept that the interaction between A and B atoms should be quite independent of whether the other sublattice is occupied by C and D atoms. Thus the regular solution model should be defined as the power series representation of excess Gibbs free energy

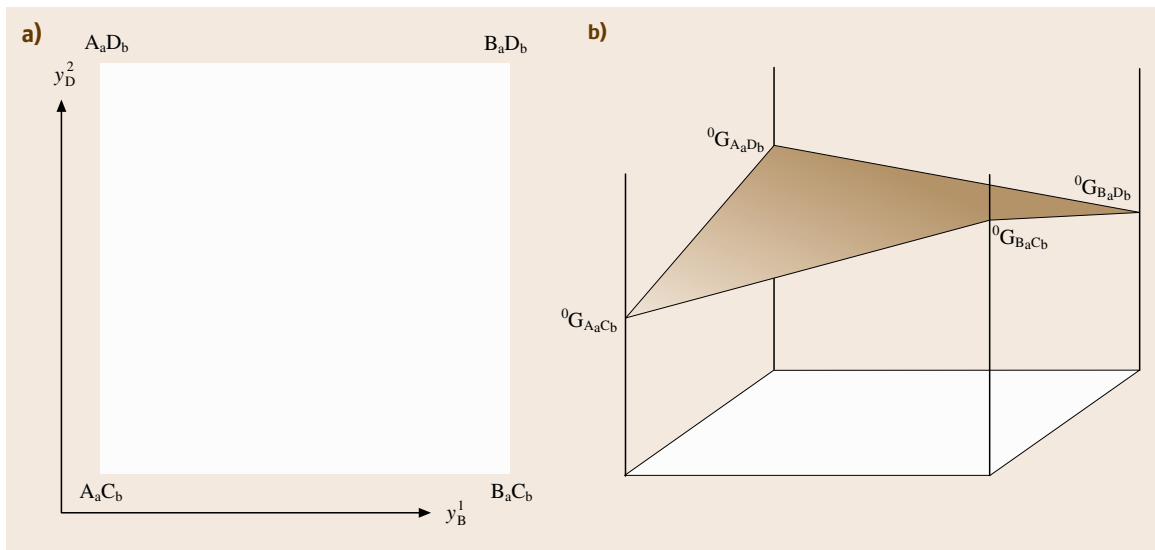


Fig. 20.1 (a) Composition square in a quaternary system $(A, B)_a(C, D)_b$ and (b) surface of reference for the free energy

by the following equation

$$G_{\text{mix}}^{\text{xs}} = y_{\text{A}}^1 y_{\text{B}}^1 y_{\text{C}}^2 L_{\text{A,B:C}} + y_{\text{A}}^1 y_{\text{B}}^1 y_{\text{D}}^2 L_{\text{A,B:D}} + y_{\text{C}}^2 y_{\text{D}}^2 y_{\text{A}}^1 L_{\text{A:C,D}} + y_{\text{C}}^2 y_{\text{D}}^2 y_{\text{B}}^1 L_{\text{B:C,D}}, \quad (20.7)$$

where $L_{i,j;k}$ (or $L_{i;j,k}$) is the interaction parameter between unlike atoms on the same sublattice. Consequently the Gibbs energy for one mole of the phase, denoted as $(\text{A}, \text{B})_{\text{a}}(\text{C}, \text{D})_{\text{b}}$, can be represented by the two-sublattice model as shown in (20.8):

$$G_m = G_m^{\text{ref}} + G_{\text{mix}}^{\text{ideal}} + G_{\text{mix}}^{\text{xs}}. \quad (20.8)$$

Gibbs Energy for Interstitial Solutions Represented by Sublattice Model

The Gibbs energy for interstitial phases is very important in steels and ferrous alloys, where the elements such as C, N, S, or B occupy the interstitial sites of solid solutions. The structure of such a phase is considered as consisting of two sublattices, one occupied by substitutional elements and the other occupied by the interstitial elements as well as vacancies. Let us consider the austenite phase for the Fe–Cr–C system, for instance. The occupation of the sublattices is shown as $(\text{Cr}, \text{Fe})_1(\text{C}, \text{Va})_1$, since the number of sites in each sublattice is 1 : 1 in the case of an fcc structure. The Gibbs energy is given by the following equation:

$$\begin{aligned} G_m = & y_{\text{Cr}}^1 y_{\text{Va}}^2 {}^0G_{\text{Cr:Va}} + y_{\text{Fe}}^1 y_{\text{Va}}^2 {}^0G_{\text{Fe:Va}} \\ & + y_{\text{Cr}}^1 y_{\text{C}}^2 {}^0G_{\text{Cr:C}} + y_{\text{Fe}}^1 y_{\text{C}}^2 {}^0G_{\text{Fe:C}} \\ & + RT \left[\left(y_{\text{Cr}}^1 \ln y_{\text{Cr}}^1 + y_{\text{Fe}}^1 \ln y_{\text{Fe}}^1 \right) \right. \\ & \left. + \left(y_{\text{C}}^2 \ln y_{\text{C}}^2 + y_{\text{Va}}^2 \ln y_{\text{Va}}^2 \right) \right] \\ & + y_{\text{Cr}}^1 y_{\text{Fe}}^1 y_{\text{Va}}^2 \sum_v {}^vL_{\text{Cr,Fe:Va}} \left(y_{\text{Cr}}^1 - y_{\text{Fe}}^1 \right)^v \\ & + y_{\text{Cr}}^1 y_{\text{Fe}}^1 y_{\text{C}}^2 \sum_v {}^vL_{\text{Cr,Fe:C}} \left(y_{\text{Cr}}^1 - y_{\text{Fe}}^1 \right)^v \\ & + y_{\text{Cr}}^1 y_{\text{C}}^2 y_{\text{Va}}^2 \sum_v {}^vL_{\text{Cr:C,Va}} \left(y_{\text{C}}^2 - y_{\text{Va}}^2 \right)^v \\ & + y_{\text{Fe}}^1 y_{\text{C}}^2 y_{\text{Va}}^2 \sum_v {}^vL_{\text{Fe:C,Va}} \left(y_{\text{C}}^2 - y_{\text{Va}}^2 \right)^v. \end{aligned} \quad (20.9)$$

The first two terms represent the Gibbs energy of fcc Cr and Fe, because the second sublattice consists of vacancies. The next two terms represent the Gibbs energy of

the CrC and FeC compounds, where the interstitial sites are completely filled with C. The second line shows the ideal entropy term, while the residual lines represent the excess terms of the Gibbs energy. When $y_{\text{C}}^2 = 0$ in the equation, the Gibbs energy equation coincides with the equation for the simple substitutional mixing of Cr and Fe.

Magnetic Contribution to Gibbs Energy

In magnetic materials containing Fe, Ni and Co, there is polarization of electron spins, and it is necessary to consider the magnetic contribution to the Gibbs energy, by adding the extra term to the paramagnetic Gibbs energy G_m as follows:

$$G = G_m + G_{\text{mag}}. \quad (20.10)$$

The magnetic contribution to the Gibbs free energy, G_{mag} , is given by the expression

$$G_{\text{mag}} = RT f(\tau) \ln(\beta + 1), \quad (20.11)$$

where

$$\begin{aligned} f(\tau) = & 1 - \frac{1}{A} \left[\frac{79\tau^{-1}}{140p} + \frac{474}{497} \left(\frac{1}{p} - 1 \right) \right. \\ & \left. \times \left(\frac{\tau^3}{6} + \frac{\tau^9}{135} + \frac{\tau^{15}}{600} \right) \right], \quad \text{for } \tau < 1 \end{aligned} \quad (20.12)$$

and

$$f(\tau) = -\frac{1}{A} \left(\frac{\tau^{-5}}{10} + \frac{\tau^{-15}}{315} + \frac{\tau^{-25}}{1500} \right), \quad \text{for } \tau \geq 1, \quad (20.13)$$

and

$$A = \frac{518}{1125} + \frac{11692}{15975} \left(\frac{1}{p} - 1 \right). \quad (20.14)$$

The variable τ is defined as T/T_C , where T_C is the Curie temperature and β is the mean atomic moment expressed in Bohr magnetons μ_B . The value of p depends on the structure, and $p = 0.28$ for the fcc phase.

20.1.2 Equilibrium Conditions

Figure 20.2 shows the so-called Gibbs energy-composition diagram for the A–B binary system. This figure schematically shows the relationship between a eutectic type of binary phase diagram and the Gibbs energy curves of each phase. Let us consider the case in which the microstructure of the alloy is composed of the

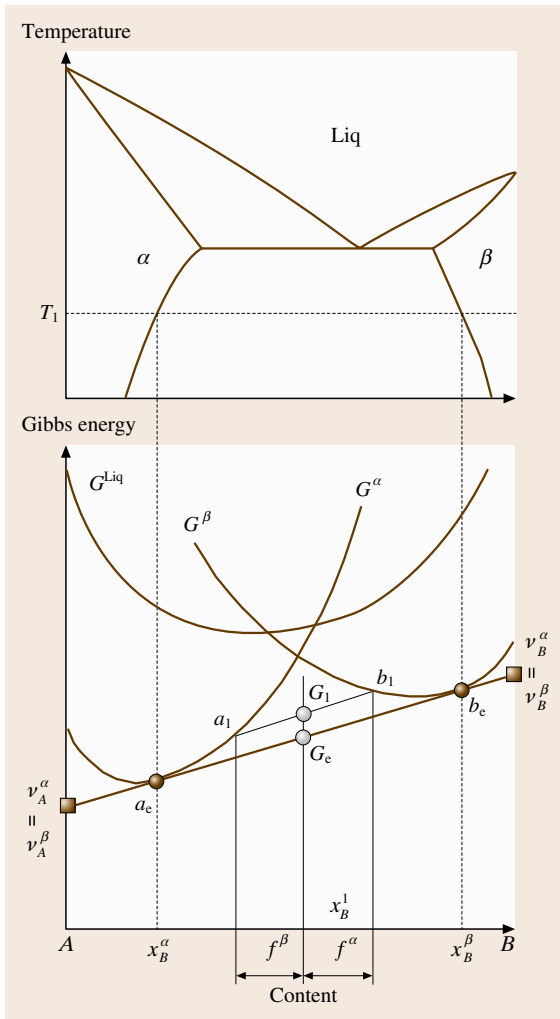


Fig. 20.2 Eutectic type of phase diagram and corresponding Gibbs energy-composition diagram for hypothetical A–B binary system

α and β phases. When the Gibbs energies of the α and β phases are given by the points a_1 (G_1^α) and b_1 (G_1^β), respectively, the total energy of the solution is represented by the line $a_1 b_1$ in the figure. At the alloy composition x_B^1 , the Gibbs energy is G_1 and each phase has the volume fraction of f^α and f^β . Then the following relation holds:

$$G_1 = G_1^\alpha f^\alpha + G_1^\beta f^\beta. \tag{20.15}$$

The thermodynamic equilibrium is achieved under the condition of the lowest energy of the alloy. According to this criterion, the point G_1 is not the lowest energy state,

but decreases further to G_e by changing f^α and f^β . The line $a_e b_e$ is a common tangent of Gibbs energy G^α and G^β , and the equilibrium composition of each phase is given as x_B^α and x_B^β . In the calculation of the phase equilibrium, it is convenient to use these chemical potentials as the basic equations. For instance, to obtain the equilibrium between phase α and phase β , (20.16) should be calculated by using the numerical analytic method

$$\begin{aligned} \mu_A^\alpha &= \mu_A^\beta, \\ \mu_B^\alpha &= \mu_B^\beta. \end{aligned} \tag{20.16}$$

The chemical potential μ of each element is obtained by using

$$\mu_i = G_m - \sum_{j=1}^2 x_j \frac{\partial G_m}{\partial x_j} + \frac{\partial G_m}{\partial x_i} \tag{20.17}$$

and hence the chemical potentials of A and B species in the ϕ phase are expressed as:

$$\begin{aligned} \mu_A^\phi &= {}^0G_A^\phi + RT \ln x_A^\phi + (x_B^\phi)^2 L_{AB}^\phi, \\ \mu_B^\phi &= {}^0G_B^\phi + RT \ln x_B^\phi + (x_A^\phi)^2 L_{AB}^\phi. \end{aligned} \tag{20.18}$$

20.1.3 Evaluation of Thermodynamic Parameters

The interaction parameters included in the free energy expression can be directly evaluated from the experimental values on activity. For example the activity of Pb over the Pb–Sb binary liquid have been determined as shown in Table 20.1 [20.5]. The liquid state of the elements is adopted as its standard. If the composition dependency of the interaction parameter is expressed as (20.19), the chemical potential of Pb in the binary system can be derived as (20.20)

$$L_{\text{PbSb}} = {}^0L_{\text{PbSb}} + (x_{\text{Pb}} - x_{\text{Sb}})^1 L_{\text{PbSb}}, \tag{20.19}$$

$$\begin{aligned} \mu_{\text{Pb}} &= {}^0G_{\text{Pb}} + RT \ln x_{\text{Pb}} + (1 - x_{\text{Pb}})^2 \\ &\times \left[{}^0L_{\text{PbSb}} + (4x_{\text{Pb}} - 1)^1 L_{\text{PbSb}} \right]. \end{aligned} \tag{20.20}$$

Table 20.1 Experimental data on activity of Pb in the Pb–Sb binary liquid

x_{Pb}	0.05	0.1	0.2	0.3	0.4	0.5
a_{Pb}	0.04	0.08	0.162	0.247	0.338	0.433
x_{Pb}	0.6	0.7	0.8	0.9	0.95	
a_{Pb}	0.555	0.674	0.785	0.897	0.946	

This is straightforwardly arranged as

$$\frac{RT \ln \left(\frac{a_{\text{Pb}}/x_{\text{Pb}}}{(1-x_{\text{Pb}})^2} \right)}{+ 4x_{\text{Pb}} {}^1L_{\text{PbSb}}} = \left({}^0L_{\text{PbSb}} - {}^1L_{\text{PbSb}} \right) \quad (20.21)$$

since the relation $\mu_{\text{Pb}} = {}^0G_{\text{Pb}} + RT \ln a_{\text{Pb}}$ holds. Therefore, if the left-hand side of (20.21) is calculated from the activity data shown in Table 20.1 and the each value is plotted against x_{Pb} , the interaction parameters ${}^0L_{\text{PbSb}}$, ${}^1L_{\text{PbSb}}$ can be obtained, respectively, from the intercept of the ordinate and the slope of the straight line as:

$${}^0L_{\text{PbSb}} = -2900 \text{ J/mol}, \quad {}^1L_{\text{PbSb}} = -200 \text{ J/mol}. \quad (20.22)$$

The calculated activity of Pb in the liquid phase was compared with the experimental values in Fig. 20.3. Considering the other observed data set at a different temperature yields the dependence on the temperature for the interaction parameters ${}^0L_{\text{PbSb}}$, ${}^1L_{\text{PbSb}}$.

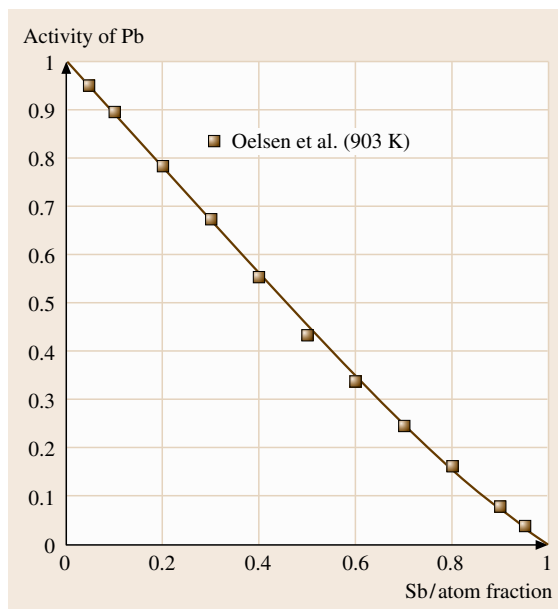


Fig. 20.3 Calculated activity of Pb in the Pb–Sb binary liquid compared with experimental values [20.5]

20.2 Incorporation of the First-principles Calculations into the CALPHAD Approach

In this section, in order to clarify the uncertainty of thermodynamic properties for metastable solution phases, the method for deriving the Gibbs free energies incorporating the first-principles calculations is presented, taking the Fe–Be-based *bcc* phase as the example. First, a set of some superstructures is selected to be representative of a series of *bcc*-based ordered phases, and the total energies are calculated using the first-principles calculations. Next, the effective cluster interaction energies can be extracted from these formation energies using the cluster expansion method (CEM). This leads to a set of composition-independent parameters, from which the energy of the set of superstructures can be reproduced in terms of a set of correlation functions. Once we know the cluster interaction energies for the alloy system, the enthalpy term is expressed by the combination of effective cluster interaction and the correlation functions for the clusters. The entropy term in the Gibbs energy expression is calculated using the cluster variation method (CVM) with the tetrahedron approximation to

calculate the configurational entropy. Minimizing the grand potential with respect to all the correlation functions allows for the Gibbs energy of mixing to be obtained as a function of composition at a constant temperature.

20.2.1 Outline of the First-principles Calculations

First-principles calculations using density functional theory (DFT) have proved to be quite reliable in condensed matter physics. There still remains a barrier to overcome in application to materials science, for instance, stoichiometric deviations, surfaces, impurities, and grain boundaries, however, for certain materials, the direct application of this technique has been attempted in studying the various properties using 100 or more atoms in a unit cell. According to the theorem based on DFT, the total energy E_{tot} of a nonspin-polarized system of interacting electrons in an external potential is given as a function of the ground state electronic

density ρ as in the following equation:

$$E_{\text{tot}}(\rho) = \int V(r)\rho(r)d^3r + T[\rho] + \frac{e^2}{2} \int \frac{\rho(r)\rho(r')}{|r-r'|} d^3r d^3r' + E_{\text{XC}}[\rho]. \tag{20.23}$$

Here the first term $\int V(r)\rho(r)d^3r$ denotes the Coulomb interaction energy between the electrons and nuclei, $T[\rho]$ is the single-particle kinetic energy, $\frac{e^2}{2} \int \frac{\rho(r)\rho(r')}{|r-r'|} d^3r d^3r'$ is the Hartree component of the electron–electron energy, and $E_{\text{XC}}[\rho]$ is the exchange–correlation functional.

Kohn and Sham [20.6] showed that the correct density in the equation is given by the self-consistent solution of a set of single particles following Schrödinger-like equations as

$$\varepsilon_i \Psi_i(r) = \left[-\frac{\hbar}{2m} \nabla^2 + V(r) + e^2 \int \frac{\rho(r')}{|r-r'|} d^3r' + V_{\text{XC}}(r) \right] \Psi_i(r). \tag{20.24}$$

In (20.24), V_{XC} represents the exchange correlation potential and $V_{\text{XC}}(r) = \partial E_{\text{XC}}[\rho] / \partial \rho(r)$. Thus we can obtain an appropriate electronic density in much easier way as compared with solving a many-body Schrödinger equation. In calculations, the single particle Kohn–Sham equation in (20.24) is solved separately on a grid of sampling points in the irreducible part of the Brillouin zone, and the obtained orbitals are used to construct the charge density.

The first-principles calculations based on DFT may be, at this time, divided into two methods; one employing pseudopotentials and relatively simple basis sets,

and the other using much more complex basis sets such as the full potential linearized augmented plane wave (FLAPW), which gives accurate results on formation energies for metals. The FLAPW method, as embodied in the WIEN2k software package [20.7], is one of the most accurate schemes for electronic calculations, and allows for very precise calculations of the total energies in a solid, and will be employed in the present energetic calculations. The FLAPW method uses a scheme for solving many-electron problems based on the local spin density approximation (LSDA) technique. In this framework, a unit cell is divided into two regions: nonoverlapping atomic spheres and an interstitial region. Inside the atomic spheres, the wave functions of the valence states are expanded using a linear combination of radial functions and spherical harmonics, while a plane wave expansion is used in the interstitial region. The LSDA technique includes an approximation for both the exchange and correlation energies, and it has been recently enhanced by the addition of electron density gradient terms to the exchange–correlation energy. This has led to a generalized gradient approximation (GGA), as suggested by Perdew et al. [20.8], and we used this improved method rather than the LSDA approach.

20.2.2 Gibbs Energies of Solution Phases Derived by the First-principles Calculations

The formation enthalpies of some binary ordered structures derived by the first-principles calculations are compared with experimental data in Table 20.2 [20.9]. In this comparison, alloy systems where the thermodynamic analysis had already been completed, are

Table 20.2 Comparison of the estimated formation enthalpies for some ordered structures with the appropriate evaluated data

Alloy systems	Structures	Temperature (K)	Experimental values (kJ/mol)	Calculated values (kJ/mol)
Al–Ni	B2	298	– 71.7	– 69.5
	L1 ₂	298	– 41.0	– 40.5
Al–Ti	L1 ₀	298	– 39.8	– 39.6
	D0 ₁₉ (Ti ₃ Al)	298	– 27.5	– 27.3
Be–Cu	B2	298	– 21.4	– 19.0
Fe–Pd	B2	298	– 15.6	– 13.2
Fe–Ti	B2	298	– 51.6	– 46.5
Ni–Ti	B2	999	– 34.2	– 34.1
	D0 ₂₄ (Ni ₃ Ti)	827	– 54.0	– 51.4
Al–Li	B32	298	– 22.8	– 23.1

selected. The *bcc*- and *fcc*-based ordered phases are included in the calculations. As can be seen in this table, the calculated values and evaluated data are reasonably consistent, and this close agreement encourages us to proceed to the next step to evaluate the Gibbs free energies of solution phases.

First-principles Calculations of the Gibbs Free Energy

The *bcc* phase in the Fe–Be binary system is illustrated as an example to derive the Gibbs energy on the basis of ab initio method, since the phase is metastable and located in the central part of the phase diagram, the thermodynamic properties in this region are unknown.

An outline for deriving the Gibbs free energies of the *bcc*-based structures incorporating the ab initio calculations is as follows. First, a set of superstructures {A–A2, A₃B–D0₃, AB–B2, AB–B32, AB₃–D0₃, B–A2} are selected to be representative of a series of *bcc*-based ordered phases, the total energies were calculated using the FLAPW method. With the known total energies, the formation energy of the *bcc*-based superstructures, $\Delta E_{\text{form}}^{\phi}$, is defined by averaging the total energy of the elements with chemical composition to the segregation limit, as shown in the following equation

$$\Delta E_{\text{form}}^{\phi}(V) = E_{\text{tot}}^{\phi}(V) - (1 - x_{\text{Be}}^{\phi}) E_{\text{tot}}^{\text{bccFe}}(V_{\text{Fe}}) - x_{\text{Be}}^{\phi} E_{\text{tot}}^{\text{bccBe}}(V_{\text{Be}}), \quad (20.25)$$

where ϕ denotes the type of superstructure and V is the volume.

Then, the effective cluster interaction energies, $\{v_i(V)\}$, can be extracted from these formation energies using the cluster expansion method (CEM) developed by Connolly and Williams [20.10]. This leads to a set of composition-independent parameters, from which the energy of the set of superstructures can be reproduced in terms of a set of correlation functions $\{\xi_i^{\phi}\}$,

$$\Delta E_{\text{form}}^{\phi}(V) = \sum_{i=0}^{\gamma} v_i(V) \times \xi_i^{\phi}, \quad (20.26)$$

where $v_i(V)$ is the effective interaction energy of the i -point cluster, and ξ_i^{ϕ} is the correlation function for cluster i in the phase ϕ ; ξ_i^{ϕ} is defined as the ensemble average of the spin operator $\sigma(p)$, which takes values of ± 1 , depending on the atom occupancy of the lattice site p . The values of ξ_i^{ϕ} for the superstructures considered in this study are summarized in Table 20.3. The formation energies to the segregation limit for the Fe–Be binary system in the D0₃, B2, B32, and A2 structures in the ground state are summarized in Table 20.4 [20.11].

The upper limit of the summation in (20.26) γ specifies the largest cluster that participated in the expansion. In the case of the Fe–Be system, a tetrahedron cluster is considered, as schematically illustrated in Fig. 20.4, as being the largest cluster, since in the *bcc* structure, the tetrahedron forms an irregular shape containing both the

Table 20.3 The values of ξ_i^{ϕ} for the *bcc* superstructures {A–A2, A₃B–D0₃, AB–B2, AB–B32, AB₃–D0₃, B–A2}

Ordered structures	ξ_0	ξ_1 point	ξ_2 n.n.pair	ξ_3 n.n.n.pair	ξ_4 triangle	ξ_5 tetrahedron
A- <i>bcc</i>	1	1	1	1	1	1
A ₃ B–D0 ₃	1	1/2	0	–1	–1	–1
AB–B2	1	0	–1	1	–1	1
AB–B32	1	0	0	–1	0	1
AB ₃ –D0 ₃	1	–1/2	0	–1	1	–1
B- <i>bcc</i>	1	–1	1	1	–1	1

Table 20.4 The formation energies to the segregation limit for the Fe–Be binary system in the D0₃, B2, B32, and A2 structures in the ground state

Basic lattice	Composition of Be		Structure	Formation enthalpy (kJ/mol)
<i>bcc</i>	0	Fe	A2	0.0
<i>bcc</i>	0.25	Fe ₃ Be	D0 ₃	–12.3
<i>bcc</i>	0.5	FeBe	B2	–31.4
<i>bcc</i>	0.5	FeBe	B32	–9.3
<i>bcc</i>	0.75	FeBe ₃	D0 ₃	–18.6
<i>bcc</i>	1	Be	A2	0.0

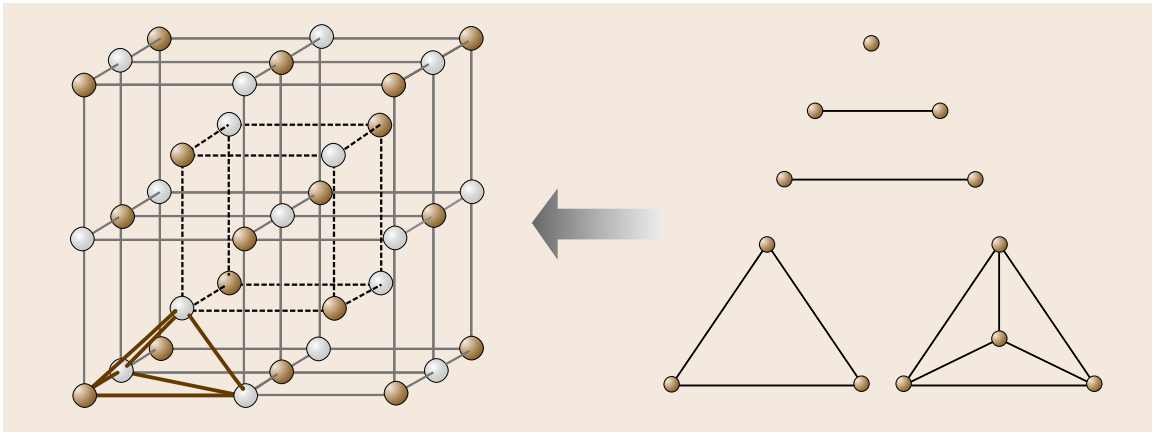


Fig. 20.4 Various clusters consisting of ordered structures

first- and second-nearest neighbor distances. The second pair interaction was also taken into account, which leads to the consequence that mathematically, five γ should represent six types of cluster. From Table 20.3, we can see that $\{\xi_i^\phi\}$ is a 6×6 matrix and that it is a regular matrix. The matrix inversion of (20.26) yields the effective interaction energies as

$$v_i(V) = \sum_{i=0}^5 \left(\xi_i^\phi\right)^{-1} \Delta E_{\text{form}}^\phi(V). \quad (20.27)$$

Thus the interatomic interactions can be estimated by expanding the total energies of the ordered structures obtained from the band-energy calculations.

Using the Murnaghan equation of states [20.12], as shown in (20.28), the total energies of the A2, B2, B32, and the D0₃ structures were expressed as a function of the volume

$$E(V) = \frac{BV}{B'(B' - 1)} \left[B' \left(1 - \frac{V_0}{V} \right) + \left(\frac{V_0}{V} \right)^{B'} - 1 \right] + E(V_0), \quad (20.28)$$

where B , B' , and V_0 are the bulk modulus, its pressure derivative, and the equilibrium volume, respectively, at normal pressures. Table 20.5 shows the coefficients in (20.28) for each ordered structure. In this table, $E(V)$ is the total energy of each ordered structure in the equilibrium volume of the B2 structure; i.e., $V_0 = 124.0438 \text{ a.u.}^3$. The formation energy of each structure is represented as $\Delta E_{\text{form}}^\phi$, by defining the average concentration of the total energy of the bcc Fe and the bcc Be phases at the segregation limit. By applying (20.28) to these formation energies, the

Table 20.6 The effective interaction $\{v_i(V)\}$ corresponding to the clusters

Effective cluster interactions (kJ/mol)	
Tetrahedron CVM	
v_1	-4.0
v_2	28.8
v_3	-4.8
v_4	4.0
v_5	6.2

Table 20.5 The coefficient of the Murnaghan equation of states for the bcc superstructures

Structures	B (GPa)	B' (Ry/a.u. ³)	$E(V_0)$ (Ry)	V_0 (a.u. ³)
Fe (bcc)	334.2450	5.5525	-5091.1796	155.5298
Fe ₃ Be (D0 ₃)	75.3890	0.7851	-3833.1698	144.3524
FeBe (B2)	180.8774	3.6243	-2575.1689	124.0438
FeBe (B32)	87.6360	5.9438	-2575.1367	122.6823
FeBe ₃ (D0 ₃)	81.5496	3.6914	-1317.1225	112.6662
Be (bcc)	244.0350	3.0866	-59.0657	105.6658

effective interaction, $\{v_i(V)\}$, corresponding to each cluster is calculated, as shown in Table 20.6, where the positive numbers define the attractive force working between unlike atoms. The value of v_2 represents the interaction energy between the nearest neighbor atoms, while v_3 denotes the next-nearest neighbor interaction.

The Gibbs free energies of the metastable bcc-based phase in the Fe–Be binary system are evaluated using the effective cluster interaction energies up to the tetrahedron cluster, including a second pair interaction as

$$\Delta E = \sum_{i=0}^5 v_i \xi_i . \quad (20.29)$$

At a finite temperature T the free energy of a phase of interest ΔG can be obtained by adding a configurational entropy term ΔS to the internal energy as follows [20.13, 14]:

$$\Delta G = \Delta E - T\Delta S . \quad (20.30)$$

The cluster variation method (CVM) with the tetrahedron approximation are used to calculate the configurational entropy. For the bcc structure, the entropy

formula is

$$\Delta S = k_B \times \ln \frac{\left\{ \prod_{i,j,k} (Nz_{ijk})! \right\}^{12} \left\{ \prod_i (Nx_i)! \right\}}{\left\{ \prod_{i,j,k,l} (Nw_{ijkl})! \right\}^6 \left\{ \prod_{i,j} (Ny_{ij})! \right\}^4 \left\{ \prod_{i,j} (Ny_{ij})! \right\}^3} , \quad (20.31)$$

where x_i , y_{ij} , y_{ij} , z_{ijk} , and w_{ijkl} are the cluster probabilities of finding the atomic configurations specified by the subscript(s) at a point, the nearest neighbour pair, the second-nearest neighbour pair, the triangle, and the tetrahedron clusters, respectively, and N is the number of lattice points. Minimizing the grand potential with respect to all the correlation functions allows for the Gibbs energy of mixing to be obtained as a function of composition at a constant temperature, T .

The compositional variation of the formation enthalpy derived by the cluster expansion and the cluster variation methods is shown in Fig. 20.5 [20.11]. The solid lines show the results of thermodynamic analyses described in the following section. The open squares denote the corresponding Gibbs free energy derived by the method shown in this section.

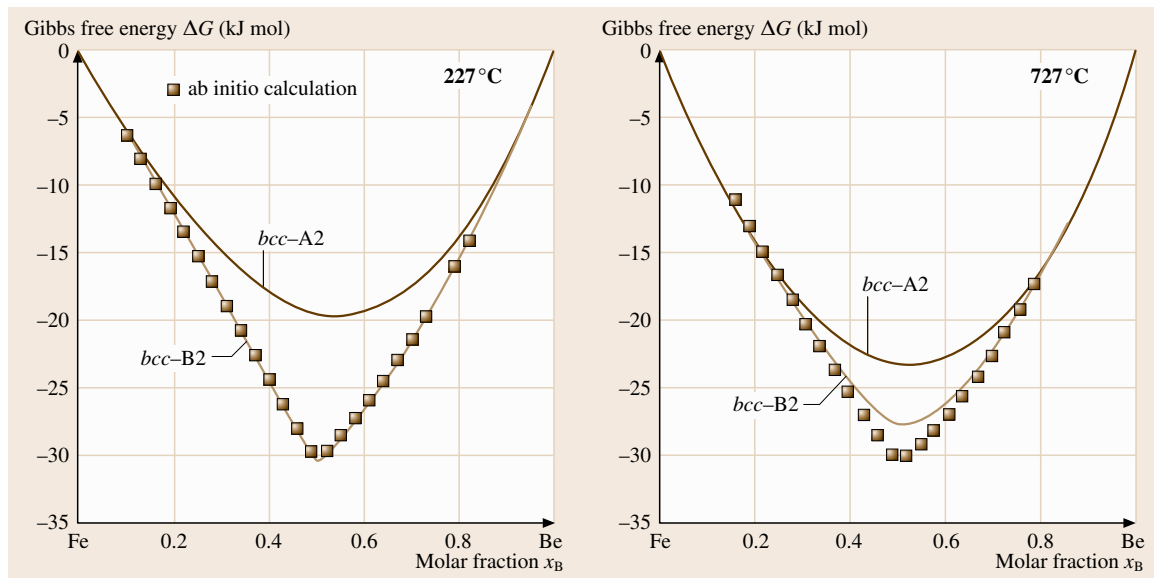


Fig. 20.5 The Gibbs energies of mixing in the α bcc solid solution at 227°C and 727°C based on ab initio energetic calculations

20.2.3 Thermodynamic Analysis of the Gibbs Energies Based on the First-principles Calculations

The Gibbs free energy of the *bcc* phase derived using the first-principles calculations is analyzed according to the two-sublattice model. According to Table 20.4, the most stable ordered structure in the Fe–Be *bcc* phase is recognized as a B2 structure, and hence the Gibbs free energy for this simple structure is described in this section. The Gibbs energy for one mole of ϕ phase, denoted as $(\text{Fe}, \text{Be})_m(\text{Fe}, \text{Be})_n$, is represented by the two-sublattice model as described in Sect. 20.1.1 as the following equation:

$$\begin{aligned} G^\phi &= y_{\text{Fe}}^1 y_{\text{Fe}}^2 {}^0G_{\text{Fe:Fe}}^\phi + y_{\text{Fe}}^1 y_{\text{Be}}^2 {}^0G_{\text{Fe:Be}}^\phi \\ &+ y_{\text{Be}}^1 y_{\text{Fe}}^2 {}^0G_{\text{Be:Fe}}^\phi + y_{\text{Be}}^1 y_{\text{Be}}^2 {}^0G_{\text{Be:Be}}^\phi \\ &+ RT \left[\frac{m}{m+n} \left(y_{\text{Fe}}^1 \ln y_{\text{Fe}}^1 + y_{\text{Be}}^1 \ln y_{\text{Be}}^1 \right) \right. \\ &+ \left. \frac{n}{m+n} \left(y_{\text{Fe}}^2 \ln y_{\text{Fe}}^2 + y_{\text{Be}}^2 \ln y_{\text{Be}}^2 \right) \right] \\ &+ {}^{\text{ex}}G^\phi + G_{\text{mag}}. \end{aligned} \quad (20.32)$$

The term y_i^s denotes the site fraction of element i in the sublattice s . The terms m and n are variables denoting the size of the sublattice s , and straightforwardly, the relationships of $m = 0.5$ and $n = 0.5$ hold for the B2 structure. ${}^0G_{i;j}$ denotes the Gibbs energy of a hypothetical compound $i_{0.5}j_{0.5}$, and terms relative to the same stoichiometry are identical, whatever the occupation of the sublattice. The excess Gibbs energy term, ${}^{\text{ex}}G^\phi$, contains the interaction energy between unlike atoms, and is expressed using the following polynomial

$$\begin{aligned} {}^{\text{ex}}G^\phi &= y_{\text{Fe}}^1 y_{\text{Be}}^1 y_{\text{Fe}}^2 L_{\text{Fe,Be:Fe}} + y_{\text{Fe}}^1 y_{\text{Be}}^1 y_{\text{Be}}^2 L_{\text{Fe,Be:Be}} \\ &+ y_{\text{Fe}}^2 y_{\text{Be}}^2 y_{\text{Fe}}^1 L_{\text{Fe:Fe,Be}} + y_{\text{Fe}}^2 y_{\text{Be}}^2 y_{\text{Be}}^1 L_{\text{Be:Fe,Be}}, \end{aligned} \quad (20.33)$$

where $L_{i,j;k}$ (or $L_{i;j,k}$) is the interaction parameter between unlike atoms on the same sublattice. The magnetic contribution to the Gibbs free energy G_{mag} was given by (20.11).

The thermodynamic parameters obtained by fitting the ab initio values to (20.32) are shown as follows:

$$\begin{aligned} G_{\text{Be:Fe}}^\beta &- 0.5 {}^0G_{\text{Be}}^{\text{bcc}} - 0.5 {}^0G_{\text{Fe}}^{\text{bcc}} \\ &= -37\,100 + 9T \text{ (J/mol)}, \end{aligned}$$

$$\begin{aligned} G_{\text{Fe:Be}}^\beta &- 0.5 {}^0G_{\text{Be}}^{\text{bcc}} - 0.5 {}^0G_{\text{Fe}}^{\text{bcc}} \\ &= -37\,100 + 9T \text{ (J/mol)}, \end{aligned}$$

$${}^0L_{\text{Be,Fe:Be}}^\beta = {}^0L_{\text{Be:Be,Fe}}^\beta = -4T \text{ (J/mol)},$$

$${}^0L_{\text{Fe:Be,Fe}}^\beta = {}^0L_{\text{Be,Fe:Fe}}^\beta = -380 - 4T \text{ (J/mol)}.$$

The calculated Gibbs energies of mixing in the α *bcc* solid solution at 227 and 727 °C are drawn in Fig. 20.5 using the solid lines for the ordered state (*bcc*–B2) and the disordered state (*bcc*–A2), respectively. The convex curvature of the free energy in the vicinity of the equiatomic composition corresponds to the formation of the B2 structure.

20.2.4 Construction of Stable and Metastable Phase Diagrams

The information on the experimental data on the phase boundaries and other thermodynamic quantities are thermodynamically analyzed together with the estimated metastable quantities of the *bcc* phase described in the foregoing section.

The calculated results of the Fe–Be phase diagram are compared with the experimental data in Fig. 20.6. The shaded area shown in this figure is the metastable (*bcc*+B2) two-phase region, which is accompanied by the ordering of the *bcc* structure on formation. The dotted line shows the order–disorder transition line, along which the two-phase field expands into the higher temperature range. The age hardening of this alloy has been investigated experimentally and the results are summarized in [20.15], and a brief outline of the ageing process of this alloy is as follows. The disordered *bcc* structure forms in the initial stage, and consequently, the B2-type ordered structure separates in the *bcc* phase. A (100) modulated structure with changes in concentration was observed in some samples using electron microscopy. This ordering behavior of the *bcc* structure is possibly explained by the metastable equilibria in Fig. 20.6.

It is well known that the solubility of Be in *bcc* Fe (α) deviates significantly from the Arrhenius equation; i. e., a proportional relationship exists between the logarithm of the solubility and the reciprocal of the temperature. The solubility of Be in the α phase is shown in Fig. 20.7. The solubility would be denoted by the broken line if there were neither an order–disorder transition nor a magnetic transition in the *bcc* Fe phase. This is approximated by the straight line following the Arrhenius law for dilute solutions. Thus, the deviation of the solubility from the ideal Arrhenius law is repre-

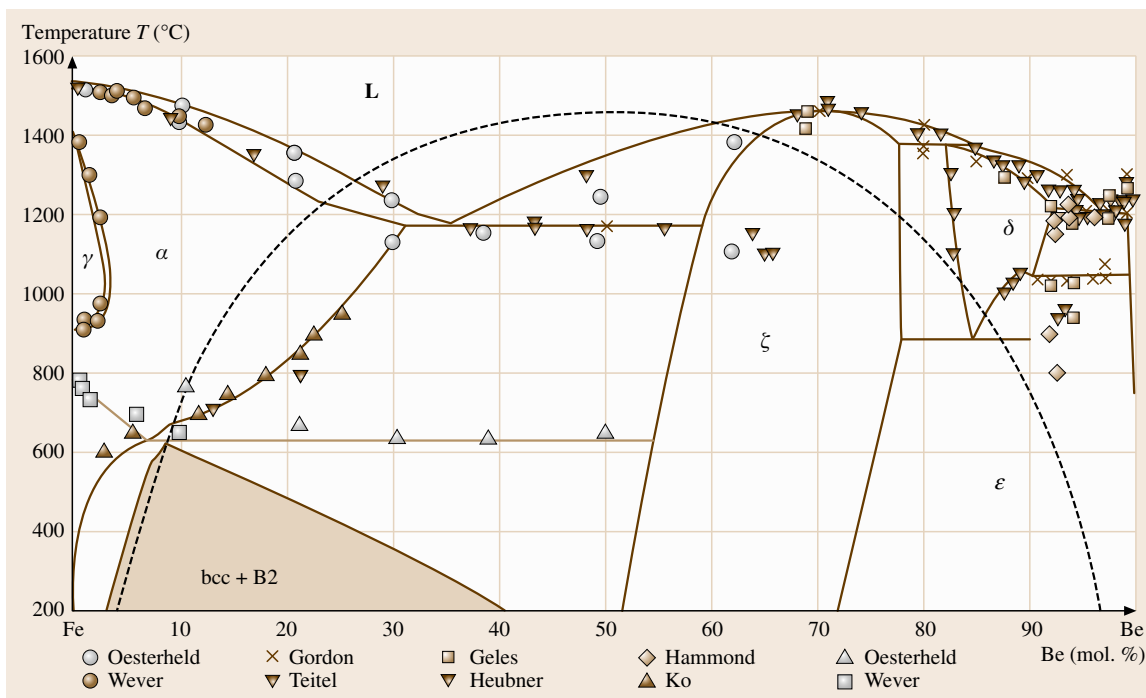


Fig. 20.6 Calculated Fe–Be phase compared with experimental data

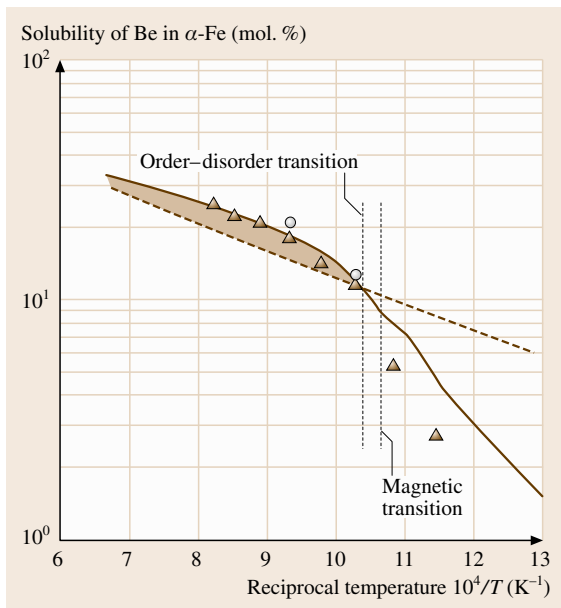


Fig. 20.7 Solubility of Be in the α phase

sented by the shaded areas. The dashed lines show the order–disorder transition temperature and the magnetic transition temperature of the bcc Fe phase. The solubility of Be decreases in the lower temperature region below 650°C , while it increases in the higher temperature region. The decrease in solubility in the lower temperature region can be explained from the viewpoint of the change in magnetism [20.16]. On the other hand, the solubility increases owing to the order–disorder transition of the bcc phase in the higher temperature range. Figure 20.8 shows the change in the order parameter along a solubility line for the α phase. The order parameter was defined by

$$\eta = y_{\text{Be}}^1 - y_{\text{Be}}^2 \quad (20.34)$$

The solubility line in Fig. 20.8a intersects the order–disorder transition line indicated by the dotted line at about 650°C . As can be seen in Fig. 20.8b, the order parameter along the solubility line increases at a higher temperature than 650°C , yielding the progress of the B2 ordering in the bcc disordered phase.

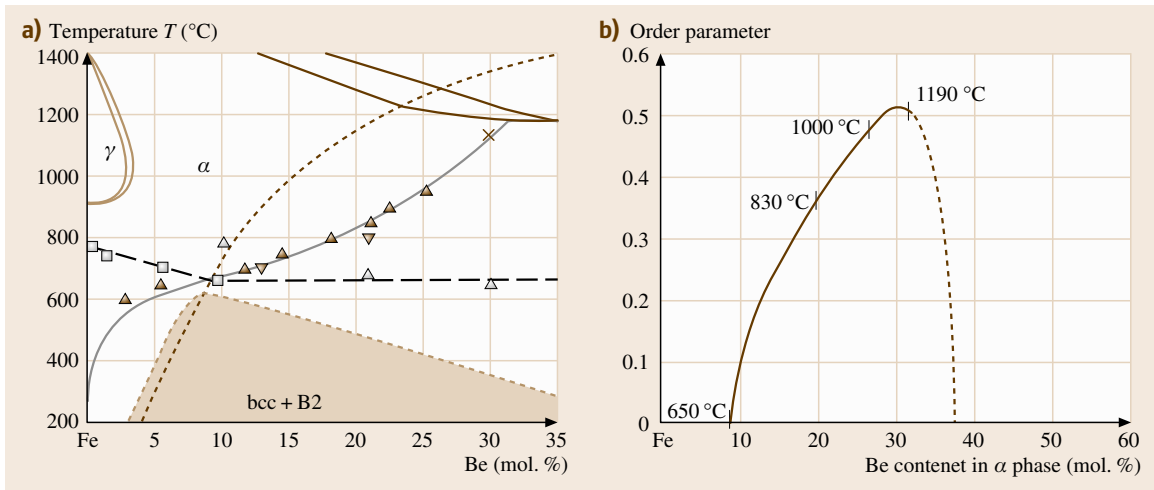


Fig. 20.8 (a) Enlarged Fe-rich portion of the calculated Fe–Be binary phase diagram. The *dotted* line shows the order–disorder transition line. (b) Change in the order parameter along the solubility line for the α phase

20.2.5 Application to More Complex Cases

In the foregoing Sect. 20.2.3, two-sublattice formalism was applied to describe the Gibbs energies derived from the first-principles calculations. However, it is generally true that a more complex thermodynamic formalism such as a four-sublattice model is appropriate so as to reflect directly the results of the *ab initio* values in phase diagram computations, since several stoichiometric compositions are selected for superstructures, i. e., $\text{A}_3\text{B–D0}_3$, AB–B2 , AB–B32 , $\text{AB}_3\text{–D0}_3$ etc. in the bcc phase. Then in this section, an analysis of metastable phase separation of bcc phase in the Co–Al and Ni–Al binary systems is presented [20.17] using the four-sublattice model. The more complex thermodynamic modeling brings a detailed knowledge about the metastable phase equilibria in these binary systems.

The Co–Al phase diagram consists of liquid, two fcc solid solutions γ (Co) and γ (Al), hcp Co(ϵ), β with CsCl structure, and the intermetallic phases Co_2Al_5 , CoAl_3 , $\text{Co}_4\text{Al}_{13}$, and Co_2Al_9 , as shown in Fig. 20.9. There exists one eutectic reaction concerning the liquid phase and six invariant reactions between the solid phases. The B2 (β) phase has a large homogeneity range at higher temperatures, but the range decreases remarkably in the lower temperature region. It has been confirmed experimentally that the two-phase region for the $\text{Al}(\gamma)/\text{B2}(\beta)$ phases extends over a wide composition range with decreasing temperature. Owing to a sudden drop in the homogeneous region, these experimental values were debatable.

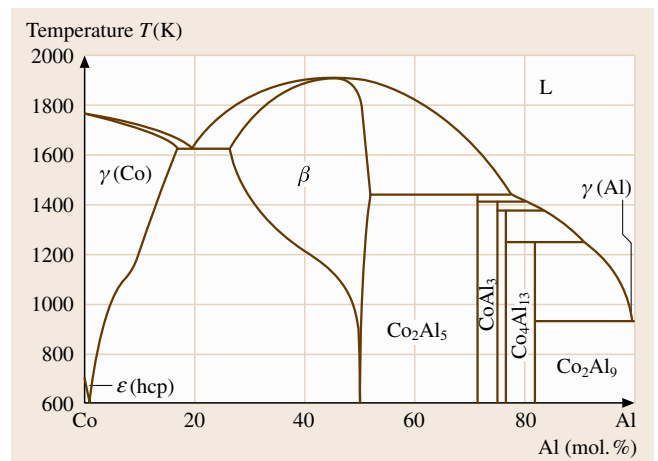


Fig. 20.9 Outline of the Co–Al binary phase diagram

Formation Energies of Superstructures for the Co–Al System

The formation energies to the segregation limit for the Co–Al system in the D0_3 , B2, B32 structures in the ground state are summarized in Table 20.7, where the corresponding values for the Ni–Al system are included. The Gibbs free energies of the metastable bcc -based phase are evaluated using the effective cluster interaction energies up to the tetrahedron cluster, including the second pair interactions. Using the same procedure as in Sect. 20.2.2, the Gibbs energy of mixing can be obtained as a function of composition at a constant temperature T .

Table 20.7 Formation energies to the segregation limit for Co–Al and Ni–Al in the D0₃, B2, B32, and A2 structures in the ground state

Alloy system	Molar fraction of Al	Structure	Formation energy (kJ/mol)
Co–Al	0.25	D0 ₃	–12.7
	0.5	B2	–62.3
	0.5	B32	–23.7
	0.75	D0 ₃	–18.3
Ni–Al	0.25	D0 ₃	–40.7
	0.5	B2	–69.5
	0.5	B32	–34.0
	0.75	D0 ₃	–18.2

Expression of Gibbs Energy of the B2 Phase Using the Four-Sublattice Model

The β phase was described using a four-sublattice model, so as to reflect the results of the ab initio calculations on the phase diagram computation as

$$\left(\text{Al}_{y_{\text{Al}}^1}^1 \text{M}_{y_{\text{M}}^1}^1 \right)_{0.25} \left(\text{Al}_{y_{\text{Al}}^2}^2 \text{M}_{y_{\text{M}}^2}^2 \right)_{0.25} \left(\text{Al}_{y_{\text{Al}}^3}^3 \text{M}_{y_{\text{M}}^3}^3 \right)_{0.25} \left(\text{Al}_{y_{\text{Al}}^4}^4 \text{M}_{y_{\text{M}}^4}^4 \right)_{0.25} \quad (20.35)$$

The number of each sublattice site is 0.25, and the four sites are therefore equivalent. The disordered state is described when the site fractions of the different species are the same in the four sublattices. For the ordered structures, if two sublattices have the same site fractions, as do the two others, but are different, then the

model describes the B2 and B32 phases. If three sublattices have the same site fractions, and are different from the fourth, then D0₃ ordering is described.

The Gibbs energy of the β phase is expressed by

$$G_m = \sum_i \sum_j \sum_k \sum_l y_i^1 y_j^2 y_k^3 y_l^4 {}^0G_{i:j:k:l} + \frac{RT}{4} \sum_{s=1}^4 \sum_i y_i^s \ln(y_i^s) + \sum_{s=1}^4 \sum_i \sum_{j>i} \sum_k \sum_l \sum_m y_i^s y_j^s y_k^r y_l^r y_m^u L_{i,j:k:l:m} \quad (20.36)$$

where ${}^0G_{i:j:k:l}$ denotes the Gibbs energy of a compound $i_{0.25}j_{0.25}k_{0.25}l_{0.25}$, and terms relative to the same stoichiometry are identical, whatever the occupation of the sublattice. $L_{i,j:k:l:m}$ is the interaction parameter between unlike atoms on the same sublattice.

Calculated Phase Equilibria in the Co–Al Binary System

The calculated Gibbs free energy of the bcc phases at 727 °C was compared with the results from the ab initio energetic calculations in Fig. 20.10. The calculated Co–Al binary phase diagram is compared with the experimental data in Fig. 20.11. The characteristic features of the binary phase diagram are well reproduced by the calculations. The dotted line shows the metastable two-phase separated region between the A2 (bcc-Co) and the B2 (β) phases. The two-phase separation, based on the bcc structure, closely relates the anomaly in the phase boundaries in the Co–Al binary system. This situation is schematically illustrated in Fig. 20.12, where the Gibbs free energies of the B2 (β) and the A1 (γ (Co)) phases are drawn. The two-phase separation of the β phase does not occur at higher temperatures T_1 mainly owing to the effect of the en-

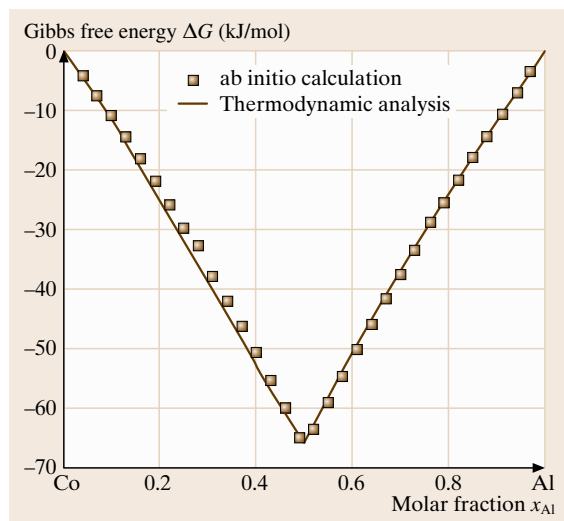


Fig. 20.10 The calculated Gibbs free energy of the bcc phase in the Co–Al binary system at 727 °C compared with the results from the ab initio energetic calculations

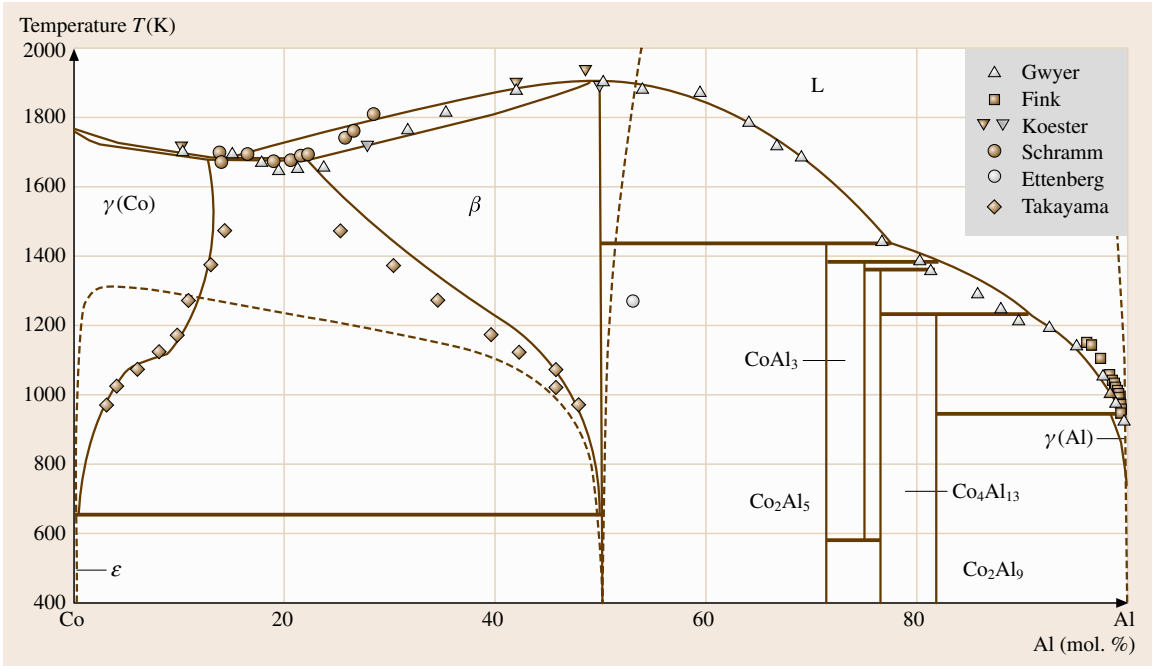


Fig. 20.11 A comparison of the calculated Co–Al binary phase diagram with previous work

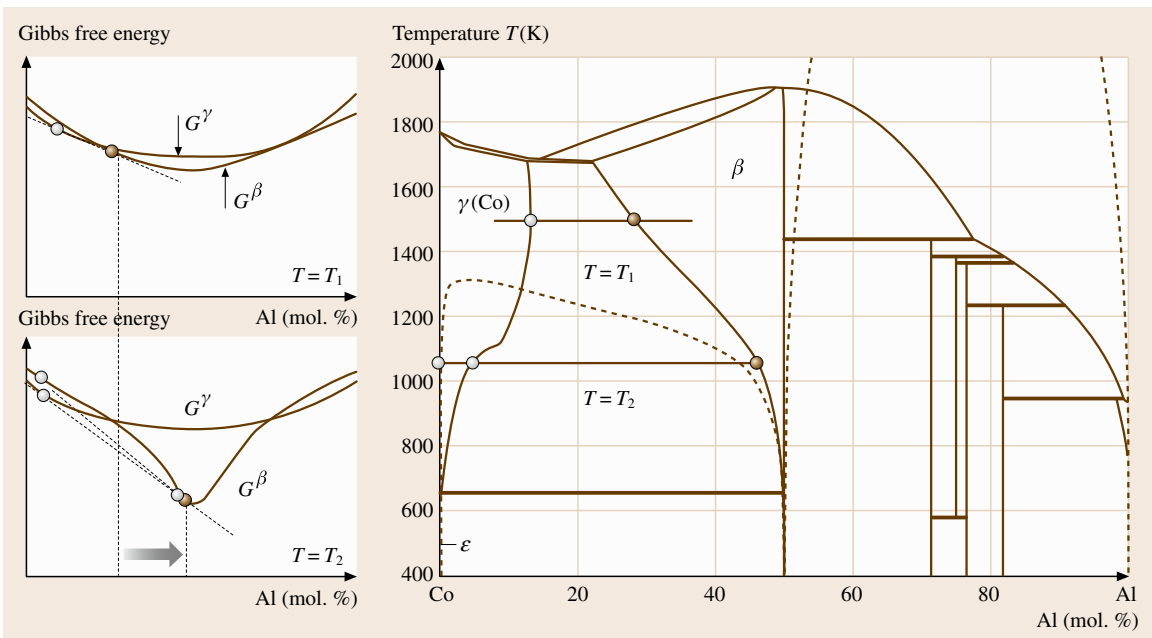


Fig. 20.12 The schematic Gibbs free energies of the B2 (β) and A2 ($\gamma(\text{Co})$) phases in the Co–Al system

ropy of random mixing on the atomic arrangement. On the other hand, the tendency towards ordering becomes stronger at lower temperatures T_2 . In the B2 structure, the interaction between unlike atoms strength-

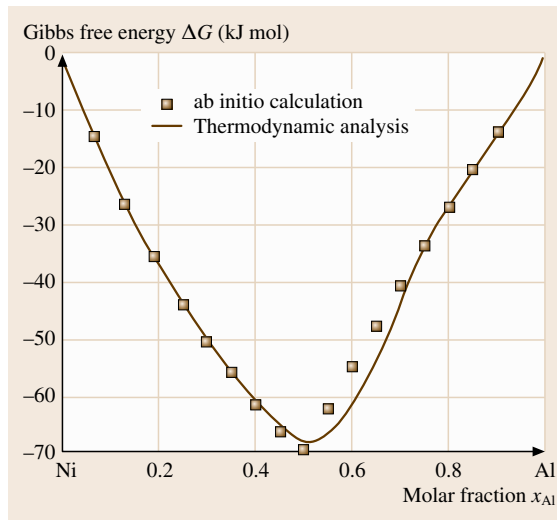


Fig. 20.13 Calculated Gibbs free energy of the bcc phase in the Ni–Al binary system at 727 °C compared with the results from the ab initio energetic calculations

ens around the 50% Al composition, since the degree of order reaches a maximum at the equiatomic composition. The decrease in the enthalpy term due to the attractive interaction results in the acute point in the free energy curve in the vicinity of the 50% Al composition, and consequently, a two-phase separation in the β phase forms. This situation yields a significant shift of the phase boundary for the $(\gamma(\text{Co}) + \beta)/\beta$ composition to the equiatomic composition.

The procedure used for the Co–Al binary system is applied to the Ni–Al binary system. The calculated Gibbs free energy of the bcc phase is compared with the results of the ab initio energetic calculations in Fig. 20.13. The calculated Ni–Al binary phase diagram is compared with the experimental data in Fig. 20.14. The phase separation of the A2 and B2 structures can not be observed in this binary system.

Origin of Phase Separation in the Co–Al and Ni–Al Systems

The formation energies to the segregation limit for Co–Al and Ni–Al in the D0₃, B2, B32, and A2 structures in the ground state, as listed in Table 20.7, are plotted versus Al concentration in Fig. 20.15. In comparing the two systems, it can be seen that in the Co–Al system, the energy of the D0₃ structure at the 25% Al

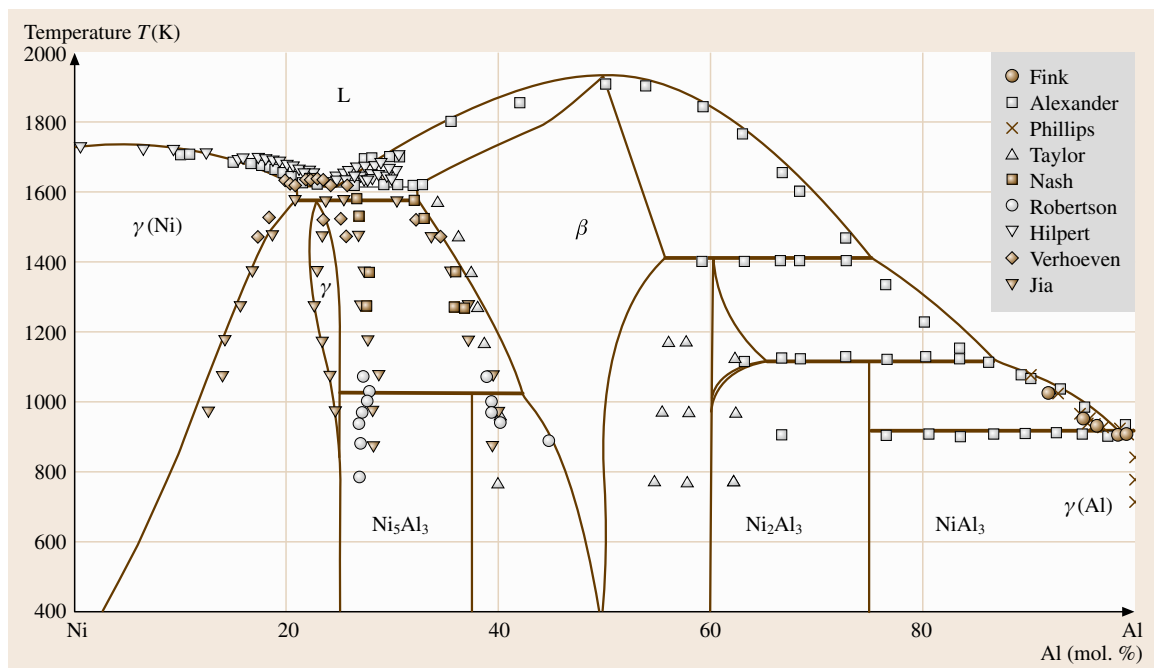


Fig. 20.14 A comparison of the calculated Ni–Al binary phase diagram with previous work

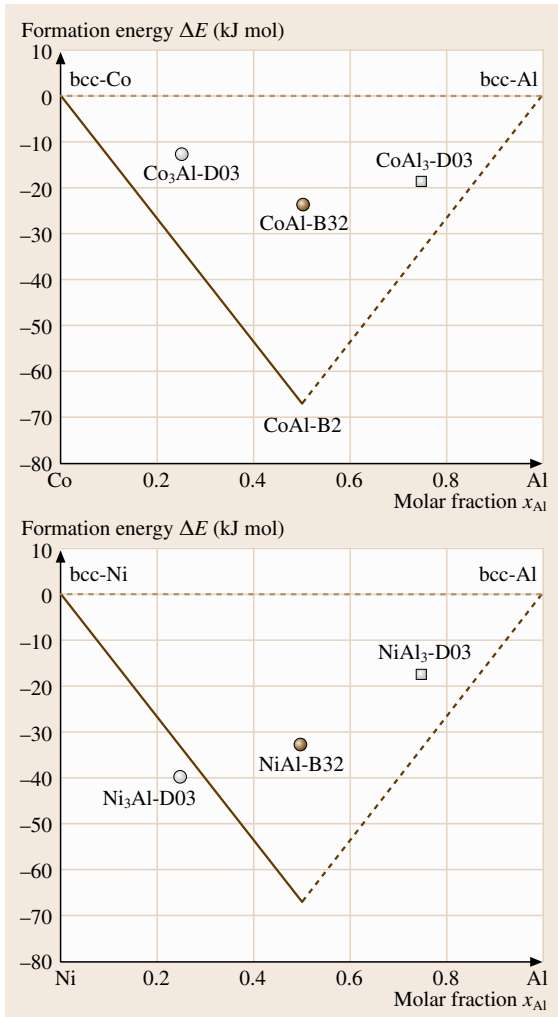


Fig. 20.15 Variation of the formation energies to the segregation limit for Co–Al and Ni–Al with concentration of Al

composition is located slightly above the straight line connecting the energy values at the 0% Al and 50% Al compositions, which results in a two-phase separation of the A2 (bcc-Co) and B2 (β) structures in Co–Al that is more stable than the formation of the Co₃Al–D0₃ structure in the ground state. On the other hand, the energy plot of the Ni–Al system shows the stabilization of the Ni₃Al–D0₃ structure compared with the two-phase separation of the A2 (bcc-Ni) and B2 (β) structures, since the formation energy of the D0₃ phase is lower than the straight line connecting the energy values at the 0% Al and 50% Al compositions. This energetic analy-

sis suggests that a two-phase separation of the bcc-Co and B2 (β) phases occurs on the Co rich side in Co–Al system, while such a separation is not realized in the Ni–Al system.

Figure 20.16 shows the density of states (DOS) of the B2 (β) structure in the Co–Al and Ni–Al alloy systems. In this figure, E_F denotes the Fermi energy, where no electrons occupy the electronic states above this energy level. It can be seen that the distribution of the DOS of the B2 phase in the two systems is similar, with both showing a low DOS at the Fermi level. However, when observing the DOS of the D0₃ phase for these two systems, as shown in Fig. 20.17, we observe a marked difference between these two systems, in that the Fermi level is located near the peak of the DOS for the Co₃Al–D0₃ phase but decreases in a region with a very low DOS in the Ni₃Al–D0₃ phase. This fact indicates that from an energetic point of view, the stable D0₃ structure of the Ni₃Al phase is highly preferred, while in the Co₃Al–D0₃ phase is unstable with respect to separation of the A2 and B2 phases in the Co–Al system.

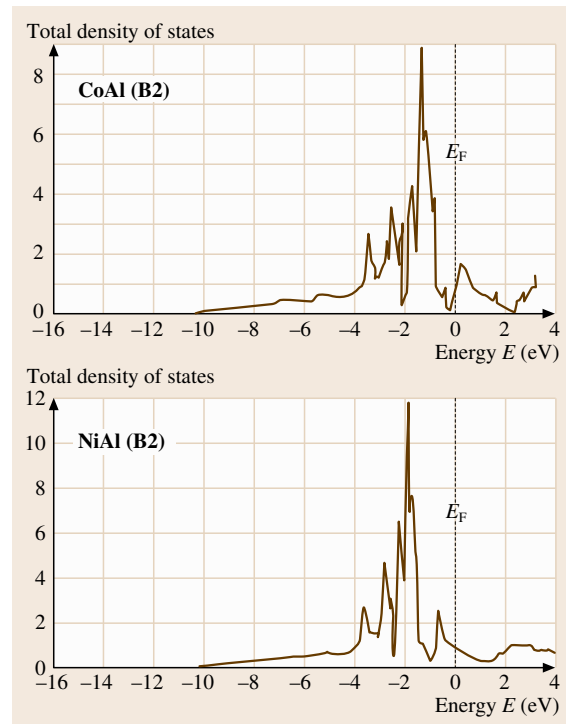


Fig. 20.16 The density of states of the B2 (β) structure in the Co–Al and Ni–Al alloy systems

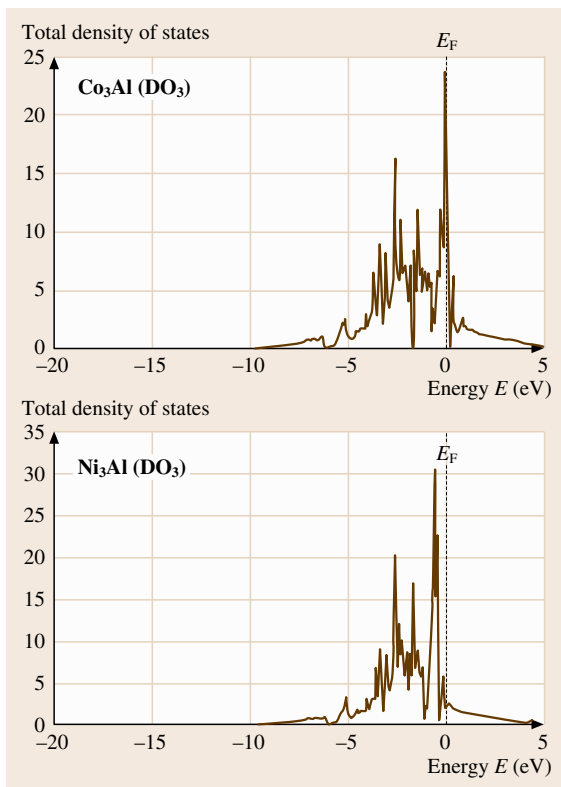
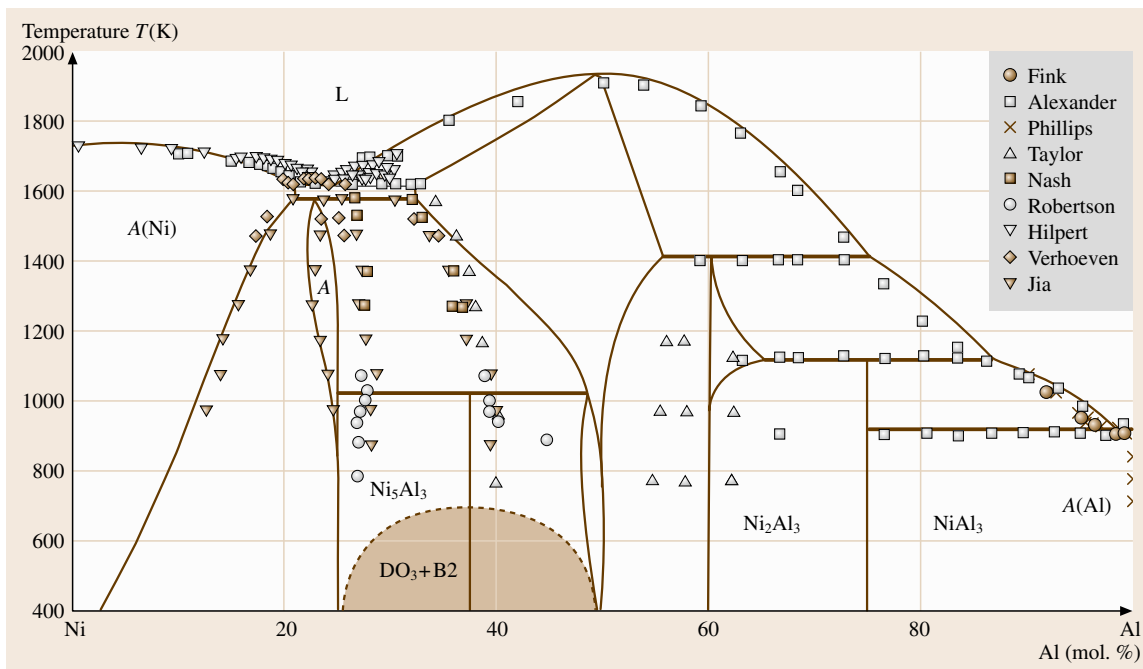


Fig. 20.17 The density of states of the $D0_3$ structure in the Co–Al and Ni–Al alloy systems

This difference in the density of states at the Fermi level might be considered to be the result of the extra d-electron in Ni versus Co. From the point of view of the rigid band approximation, this difference in the number of electrons for two neighboring elements shifts the Fermi level towards the higher energy side in the Ni–Al system versus the Co–Al system. This raises the different relative positions of the Fermi level in the DOS curve, which consequently leads to the different structural stabilities.

The ground state analysis of the Ni–Al system suggests that the phase separation concerning the $D0_3$ structure forms at absolute zero. When assuming that such a two-phase separation forms at a finite temperature, however, the agreement between the calculated phase boundaries and experimental data is insufficient. For example, Fig. 20.18 shows the phase diagram in the case that a two-phase separation between the metastable $D0_3$ and B2 structures occurs around 500°C . The homogeneity range of the B2 single phase is compar-

Fig. 20.18 The calculated Ni–Al phase diagram assuming that the critical temperature of the two-phase separation between the metastable $D0_3$ and B2 structures was around 500°C



actively reduced owing to the influence of the metastable miscibility gap with decreasing temperature, and accordingly, the calculated phase boundaries deviate from

the experimental data. Therefore, the phase separation of the DO_3 structure is not likely in the experimentally observable temperature range.

20.3 Prediction of Thermodynamic Properties of Compound Phases with First-principles Calculations

In an analysis of phase equilibria containing compound phases, physical properties of metastable structures are often required. The necessity appears clearly for instance in the following case. Figure 20.19 shows the isothermal phase diagram for the Fe–Cr–C ternary system. In this ternary system, several types of carbides form in which some amount of alloying element is soluble. If we consider the cementite, Cr substitutes more than 10% of Fe, and it forms the ternary line compound. In such a case, the Gibbs energy of the cementite phase is usually described by using sublattice model as the $(\text{Fe}, \text{Cr})_3\text{C}$ formula. Then if we want to evaluate the thermodynamic function for this phase, we need the formation energy of Cr_3C , which is metastable in the Cr–C binary system. In the procedure of CALPHAD approach, this parameter is usually determined on the basis of the experimental data in the Fe-rich side. However, it could be easily understood that this technique follows large amount of errors in estimation. Applying the first-principles calculation may possibly solve this difficulty. Thus in the present section, some examples for application to predicting thermodynamic properties of compound phases and phase diagram calculations will be illustrated.

Carbides and nitrides play a key role in the microstructure control of steels, due to a fine dispersion of these precipitates. The effectiveness of the first-principles calculations to the analysis of thermodynamic properties of these compounds might be an interesting issue. A comparison of the calculated formation energies with the experimental values is attempted for some typical carbides observed in steels to clarify the validity of the FLAPW method. Table 20.8 [20.18] shows the formation energy, $\Delta E_{\text{form}}^\phi$, defined by averaging the total energy of the constituent elements with chemical composition up to the segregation limit, as follows

$$\Delta E_{\text{form}}^\phi = E_{\text{tot}}^\phi - x_M^\phi E_{\text{tot}}^M - (1 - x_M^\phi) E_{\text{tot}}^C, \quad (20.37)$$

where ϕ denotes the type of carbide, and M and C represent a metallic element and graphite, respectively. For example, the formation energy of Fe_3C in the paramag-

netic state is calculated to be 17.9 kJ/mol, while the formation energy of Fe_3C , by considering the spin polarization, is 8.1 kJ/mol. This result shows the effect of the ferromagnetism of the Fe_3C phase in the lower temperature region. Furthermore, because the formation energy from bcc-Fe and graphite is positive, the Fe_3C structure is less stable than graphite at absolute zero. The calculated formation energies for the Cr_7C_3 and Cr_{23}C_6 phases show a reasonable agreement with the thermodynamic data reported in the literature [20.19]. From consideration of the data shown in Table 20.8, the thermodynamic properties for metallic carbides evaluated by the first-principles calculations can be applied to the general procedures used in the CALPHAD method.

20.3.1 Thermodynamic Analysis of the Fe–Al–C System

The Perovskite carbide in this ternary system, Fe_3AlC (κ), is an fcc-based ordered phase with an E2_1 -type

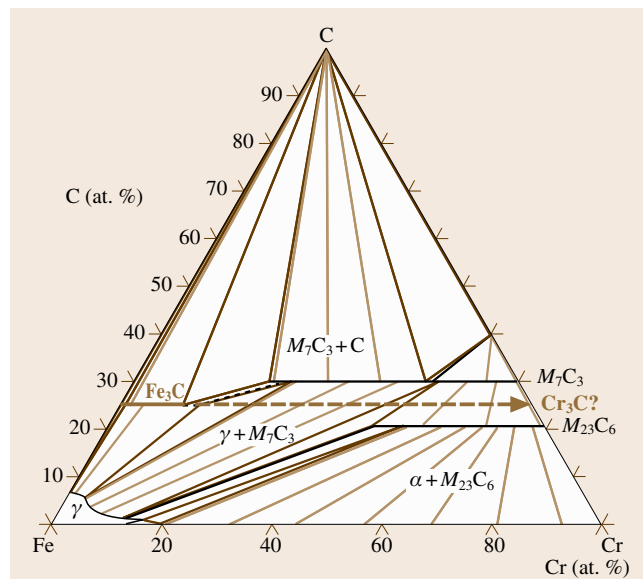


Fig. 20.19 The isothermal phase diagram for the Fe–Cr–C ternary system

Table 20.8 Comparison of the calculated formation energies with the experimental values for some typical steel carbides

Carbides	Space group	Calculated lattice parameter (nm)	Observed lattice parameter (nm)	Calculated formation enthalpy in the ground state (kJ/mol)	Observed formation enthalpy at 25 °C (kJ/mol)
Fe ₃ C (paramagnetic)	Pnma	<i>a</i> = 0.4871 <i>b</i> = 0.6455 <i>c</i> = 0.4330	— — —	+ 17.9	— — —
Fe ₃ C (ferromagnetic)	Pnma	<i>a</i> = 0.5018 <i>b</i> = 0.6650 <i>c</i> = 0.4460	<i>a</i> = 0.5078 <i>b</i> = 0.67297 <i>c</i> = 0.45144	+ 8.1	+ 6.3
Cr ₇ C ₃	Pnma	<i>a</i> = 0.4373 <i>b</i> = 0.6772 <i>c</i> = 1.1730	<i>a</i> = 0.4526 <i>b</i> = 0.7010 <i>c</i> = 1.2142	− 19.8	− 22.8
Cr ₂₃ C ₆	Fm-3m	<i>a</i> = 1.0475	<i>a</i> = 1.06595	− 21.8	− 19.7

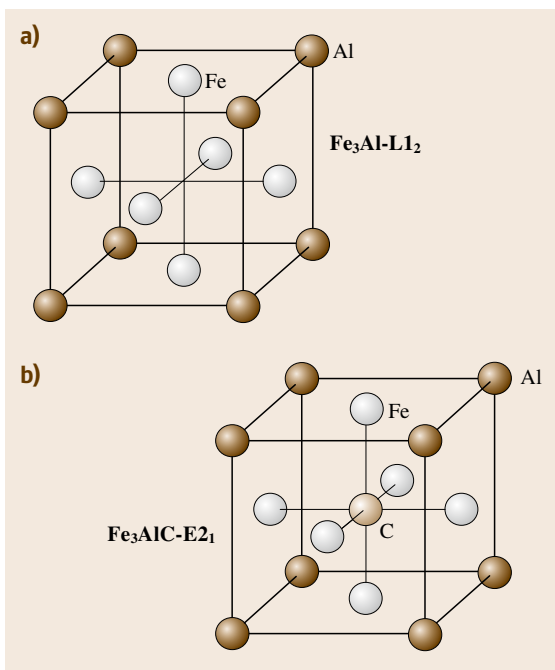
structure. The application of this material as a heat resistant alloy from the formation of a coherent fine microstructure consisting of an fcc solid solution and the κ phase is attracting great attention [20.20]. Regardless of such a promising potential for this new material, little information on the thermodynamic properties of this carbide phase is known. Thus, an attempt to calculate the full phase equilibria of the Fe–Al–C ternary system is made, introducing the first-principles values for Fe₃AlC into a CALPHAD-type thermodynamic analysis.

In the Fe₃AlC structure, the Fe and Al atoms are arranged in an L1₂-type superlattice, in which the C atoms occupy interstitial sites, resulting in an E2₁ superstructure. Figures 20.20a, 20.20b show schematic diagrams of the Fe₃Al–L1₂ and Fe₃AlC–E2₁ structures, respectively. If the C atom occupies only the body-centered sites, then it is surrounded by six Fe atoms, and this is preferable from an energetic point of view. Occupation of the other fcc interstitial sites enhances the tetragonality of the L1₂ crystal structure, yielding a larger strain energy. The only difference between these two structures is the existence of C atoms in the octahedral interstitial sites. Therefore, the Gibbs free energies of these two ordered structures should be described by the same thermodynamic model. The two-sublattice model denoted by the formula,

$$\left(\text{Fe}_{y_{\text{Fe}}^{(1)}}\text{Al}_{y_{\text{Al}}^{(1)}}\right)_3 \left(\text{Fe}_{y_{\text{Fe}}^{(2)}}\text{Al}_{y_{\text{Al}}^{(2)}}\right)_1,$$

was generally applied to the L1₂ structure, and the three-sublattice model,

$$\left(\text{Fe}_{y_{\text{Fe}}^{(1)}}\text{Al}_{y_{\text{Al}}^{(1)}}\right)_3 \left(\text{Fe}_{y_{\text{Fe}}^{(2)}}\text{Al}_{y_{\text{Al}}^{(2)}}\right)_1 \left(\text{C}_{y_{\text{C}}^{(3)}}\text{Va}_{y_{\text{Va}}^{(3)}}\right)_1,$$

**Fig. 20.20a,b** Crystal structures for (a) Fe₃Al–L1₂ and (b) Fe₃AlC–E2₁

is applied to the κ phase. The Gibbs free energy for the κ phase is calculated using (20.38):

$$G^\kappa = y_{\text{Al}}^{(1)}y_{\text{Al}}^{(2)}y_{\text{C}}^{(3)0}G_{\text{Al:Al:C}}^\kappa + y_{\text{Al}}^{(1)}y_{\text{Al}}^{(2)}y_{\text{Va}}^{(3)0}G_{\text{Al:Al:Va}}^\kappa \\ + y_{\text{Al}}^{(1)}y_{\text{Fe}}^{(2)}y_{\text{C}}^{(3)0}G_{\text{Al:Fe:C}}^\kappa + y_{\text{Al}}^{(1)}y_{\text{Fe}}^{(2)}y_{\text{Va}}^{(3)0}G_{\text{Al:Fe:Va}}^\kappa \\ + y_{\text{Fe}}^{(1)}y_{\text{Al}}^{(2)}y_{\text{C}}^{(3)0}G_{\text{Fe:Al:C}}^\kappa + y_{\text{Fe}}^{(1)}y_{\text{Al}}^{(2)}y_{\text{Va}}^{(3)0}G_{\text{Fe:Al:Va}}^\kappa$$

$$\begin{aligned}
 &+ y_{\text{Fe}}^{(1)} y_{\text{Fe}}^{(2)} y_{\text{C}}^{(3)} G_{\text{Fe:Fe:C}}^{\kappa} + y_{\text{Fe}}^{(1)} y_{\text{Fe}}^{(2)} y_{\text{Va}}^{(3)} G_{\text{Fe:Fe:Va}}^{\kappa} \\
 &+ 3RT \left(y_{\text{Al}}^{(1)} \ln y_{\text{Al}}^{(1)} + y_{\text{Fe}}^{(1)} \ln y_{\text{Fe}}^{(1)} \right) \\
 &+ RT \left(y_{\text{Al}}^{(2)} \ln y_{\text{Al}}^{(2)} + y_{\text{Fe}}^{(2)} \ln y_{\text{Fe}}^{(2)} \right) \\
 &+ RT \left(y_{\text{C}}^{(3)} \ln y_{\text{C}}^{(3)} + y_{\text{Va}}^{(3)} \ln y_{\text{Va}}^{(3)} \right) \\
 &+ y_{\text{Al}}^{(1)} y_{\text{Fe}}^{(1)} y_{\text{Al}}^{(2)} y_{\text{C}}^{(3)} L_{\text{Al,Fe:Al:C}}^{\kappa} \\
 &+ y_{\text{Al}}^{(1)} y_{\text{Fe}}^{(1)} y_{\text{Al}}^{(2)} y_{\text{Va}}^{(3)} L_{\text{Al,Fe:Fe:Va}}^{\kappa} \\
 &+ y_{\text{Al}}^{(1)} y_{\text{Fe}}^{(1)} y_{\text{Fe}}^{(2)} y_{\text{C}}^{(3)} L_{\text{Al,Fe:Fe:C}}^{\kappa} \\
 &+ y_{\text{Al}}^{(1)} y_{\text{Fe}}^{(1)} y_{\text{Fe}}^{(2)} y_{\text{Va}}^{(3)} L_{\text{Al,Fe:Fe:Va}}^{\kappa} \\
 &+ y_{\text{Al}}^{(1)} y_{\text{Al}}^{(2)} y_{\text{Fe}}^{(2)} y_{\text{C}}^{(3)} L_{\text{Al:Al,Fe:C}}^{\kappa} \\
 &+ y_{\text{Al}}^{(1)} y_{\text{Al}}^{(2)} y_{\text{Fe}}^{(2)} y_{\text{Va}}^{(3)} L_{\text{Al:Al,Fe:Va}}^{\kappa} \\
 &+ y_{\text{Fe}}^{(1)} y_{\text{Al}}^{(2)} y_{\text{Fe}}^{(2)} y_{\text{C}}^{(3)} L_{\text{Fe:Al,Fe:C}}^{\kappa} \\
 &+ y_{\text{Fe}}^{(1)} y_{\text{Al}}^{(2)} y_{\text{Fe}}^{(2)} y_{\text{Va}}^{(3)} L_{\text{Fe:Al,Fe:Va}}^{\kappa} \\
 &+ y_{\text{Al}}^{(1)} y_{\text{Al}}^{(2)} y_{\text{C}}^{(3)} y_{\text{Va}}^{(3)} L_{\text{Al:Al:C,Va}}^{\kappa} \\
 &+ y_{\text{Al}}^{(1)} y_{\text{Fe}}^{(2)} y_{\text{C}}^{(3)} y_{\text{Va}}^{(3)} L_{\text{Al:Fe:C,Va}}^{\kappa} \\
 &+ y_{\text{Fe}}^{(1)} y_{\text{Al}}^{(2)} y_{\text{C}}^{(3)} y_{\text{Va}}^{(3)} L_{\text{Fe:Al:C,Va}}^{\kappa} \\
 &+ y_{\text{Fe}}^{(1)} y_{\text{Fe}}^{(2)} y_{\text{C}}^{(3)} y_{\text{Va}}^{(3)} L_{\text{Fe:Fe:C,Va}}^{\kappa} \quad (20.38)
 \end{aligned}$$

Calculation of the Thermodynamic Properties of the κ Phase

The thermodynamic parameters required by the model in the $(\text{Fe}, \text{Al})_3(\text{Fe}, \text{Al})_1(\text{C}, \text{Va})_1$ form are evaluated using first-principles calculations and the results are listed in Table 20.9. The calculated values denote the formation enthalpies based on the stable structure of the pure element in the ground state. The ferromagnetic state of the κ phase is calculated to be almost 10 kJ/mol more stable than its paramagnetic state, and the magnetic moment of the phase was calculated to be 3.05 μB . Besides these cohesive energies for the stoichiometric components, the interactions between atoms on the same sublattice are defined in the same way as for the thermodynamic parameters, and these interaction parameters, as well as the entropy term of the formation energy, are estimated using the experimental phase boundaries.

Electronic Structure and Phase Stability of the κ Phase

As shown in Fig. 20.20, a crystallographic similarity exists between the Perovskite carbide κ and the $\text{Fe}_3\text{Al-L1}_2$ structure, i. e., a C atom is placed in the center of an octahedron composed of six Fe atoms occupying the face-centered positions in the L1_2 structure. The actual calculated equilibrium lattice constant of the $\text{Fe}_3\text{Al-L1}_2$ structure is 0.3502 nm, while that of the κ phase is 0.3677 nm, which correspond well with the experimental results of Palm and Inden [20.21]. This fact implies that occupation by the C atoms in the octahedral interstitial sites causes an expansion of the L1_2 lattice. Since the calculated enthalpy of formation of the κ phase (-27.9 kJ/mol of atoms) is much lower than that of the $\text{Fe}_3\text{Al-L1}_2$ structure (-8.8 kJ/mol of atoms), it is concluded that the interstitial C atoms enhance the stability of the L1_2 structure. Thus, the role of the C atoms will be discussed in the context of their electronic structure.

Table 20.9 Calculated thermodynamic parameters required by the $(\text{Fe}, \text{Al})_3(\text{Fe}, \text{Al})_1(\text{C}, \text{Va})_1$ -type three-sublattice model

Structure	Structure symbol	Magnetism	Calculated lattice parameter (nm)	Observed lattice parameter (nm)	Calculated formation enthalpy in the ground state (kJ/mol of compound)
Fe_3AlC	E2_1	Paramagnetic Ferromagnetic	0.3677 0.3677	– 0.3781	–128.5 –139.5
Al_3FeC	E2_1	Paramagnetic	0.3890	–	+190.5
Fe_3Al	L1_2	Paramagnetic	0.3502	–	–35.2
FeAl_3	L1_2	Paramagnetic	0.3734	–	–67.6
Fe_4C	–	Paramagnetic	0.3645	–	+88.4
Al_4C	–	Paramagnetic	0.4057	–	+160.5

Figures 20.21 and 20.22 show the total density of states (total DOS) and the angular-momentum-resolved density of state for each element (p-DOS) for the $\text{Fe}_3\text{AlC-E}2_1$ (κ) and $\text{Fe}_3\text{Al-L}1_2$ structures, respectively. The term E_F denotes the Fermi energy, and no electrons occupy electronic states above this energy level. In both structures, the DOS mainly consist of the contribution from the Fe d-electrons. However, while

observing these diagrams, we noticed a marked difference between these two structures, in that the Fermi level is located near the peak of the total DOS for the $\text{Fe}_3\text{Al-L}1_2$ structure, but decreases in a region with a very low DOS in the $\text{Fe}_3\text{AlC-E}2_1$ structure. This fact indicates that from an energetic point of view, the stable $E2_1$ structure of the κ phase is highly preferred, compared with the $\text{Fe}_3\text{Al-L}1_2$ structure.

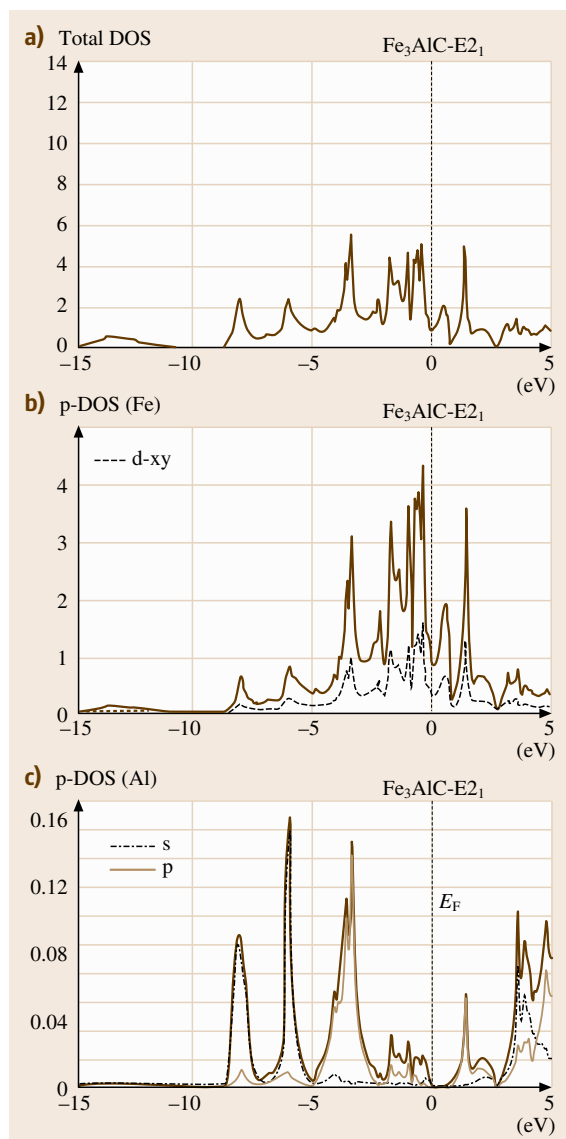


Fig. 20.21 (a) Total density of states, and angular-momentum-resolved density of states for: (b) Fe and (c) Al for the $\text{Fe}_3\text{AlC-E}2_1$ (κ) structure

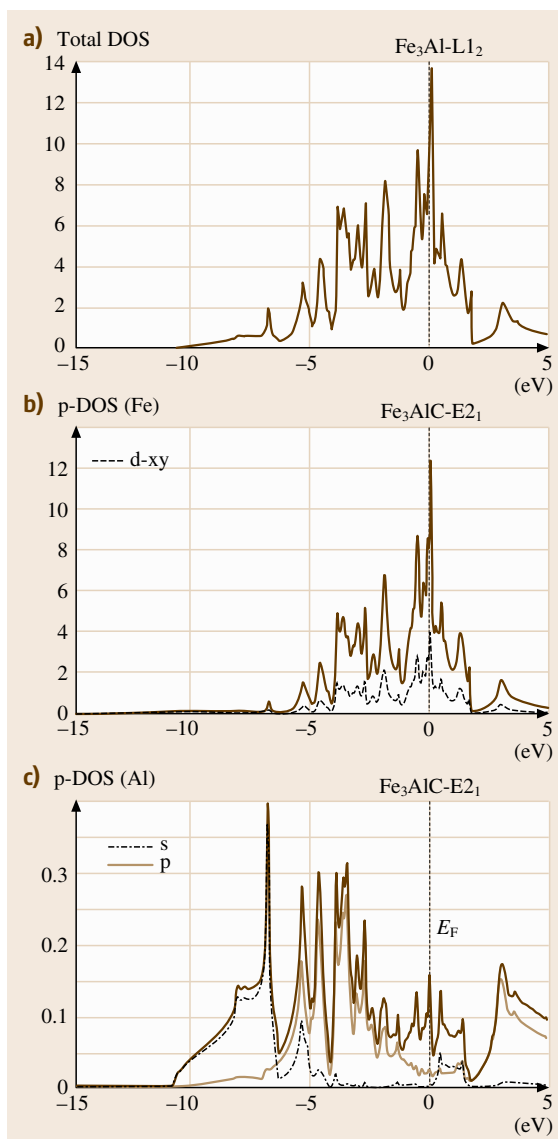


Fig. 20.22 (a) Total density of states, and angular-momentum-resolved density of states for: (b) Fe and (c) Al for the $\text{Fe}_3\text{Al-L}1_2$ structure

Figures 20.23a and 20.23b show the calculated electron charge density plots of the $\text{Fe}_3\text{AlC-E}2_1$ (κ) and $\text{Fe}_3\text{Al-L}1_2$ structures in the $(00\frac{1}{2})$ plane, where the contour lines correspond to an electron density of 100 e/nm^3 . The Fe atoms can be seen in the middle of the horizontal and vertical axes, while the C atoms are located in the center of the Fig. 20.23a. From these con-

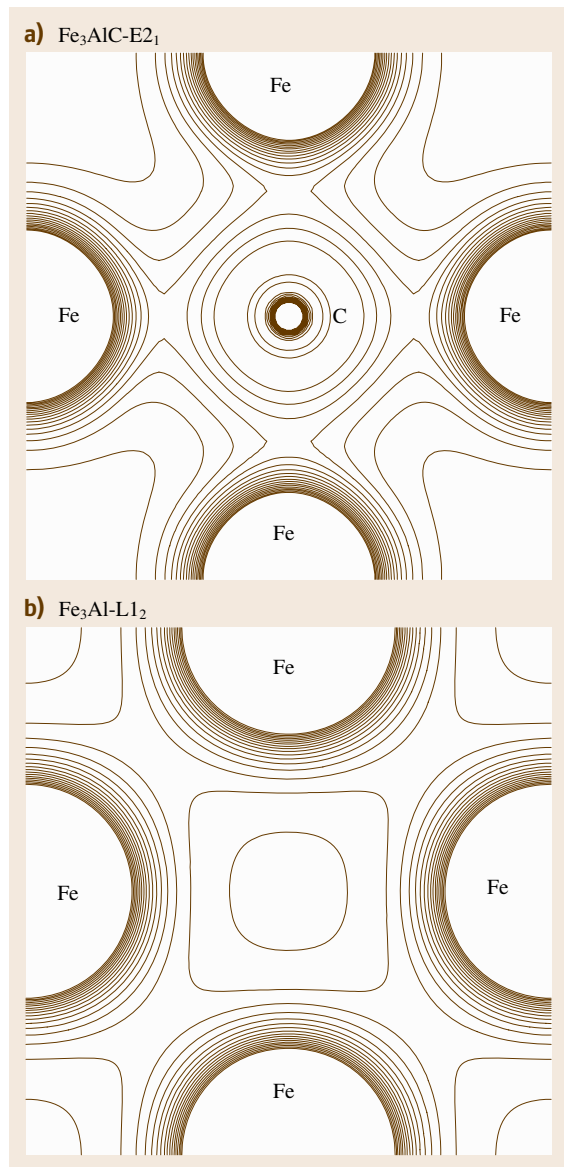


Fig. 20.23a,b Calculated electron charge density plots of: (a) the $\text{Fe}_3\text{AlC-E}2_1$ (κ) and (b) the $\text{Fe}_3\text{Al-L}1_2$ structures in the $(001/2)$ plane

tour plots, it can be seen that bonding between the Fe and C atoms occurs in the $\text{Fe}_3\text{AlC-E}2_1$ structure, since a finite charge density between these atoms can be observed. This interaction between the atoms enhances the energetic stability of the $\text{Fe}_3\text{AlC-E}2_1$ structure.

Comparison of the Calculated Phase Equilibria with the Experimental Data

The calculated Fe–Al–C ternary phase diagrams are shown in Fig. 20.24 for temperatures, $T = 800, 1000,$ and $1200\text{ }^\circ\text{C}$. The enlarged portion of the isothermal section diagrams is compared with the experimental phase boundaries determined using X-ray diffraction and metallographic observation [20.21]. From EPMA measurements, they reported that the chemical composition of the κ phase shifted remarkably from its stoichiometric composition. The homogeneity range of the κ phase extends from $\text{Fe}_{2.9}\text{Al}_{1.1}\text{C}_{0.7}$ to $\text{Fe}_{2.8}\text{Al}_{1.2}\text{C}_{0.7}$ according to the calculations.

20.3.2 Thermodynamic Analysis of the Co–Al–C and Ni–Al–C Systems

The microstructures of Ni-based superalloys contain the $\text{Ni}_3\text{Al-L}1_2$ phase, which shows an anomalous flow-stress dependence on temperature [20.22]. In addition, because they exhibit very high melting temperatures and have good resistance to oxidation, alloys with complex phase structures containing the $\text{NiAl-B}2,$ $\text{fcc-Ni},$ and $\text{Ni}_3\text{Al-L}1_2$ phases have been investigated for technological applications. On the other hand, it is difficult to produce Co–Al-based superalloys with a microstructure consisting of fcc-Ni and $\text{Ni}_3\text{Al-L}1_2$, because of the absence of a stable strengthening $\text{L}1_2$ phase in the Co–Al binary system. However, the addition of carbon to this alloy stabilizes the formation of the Perovskite type carbide ($\text{E}2_1$) with the composition, M_3AlC (κ phase), as seen in Fig. 20.18, and this carbide is anticipated to form a fine coherent microstructure in a Co-based solid solution. Then the entire phase equilibria of the Co–Al–C ternary system is attempted to be clarified by coupling the CALPHAD and ab initio calculations. The same procedure is applied to the Ni–Al–C system, and the results are compared to the Co–Al–C system.

Calculation of the Co–Al–C Phase Diagram

The same thermodynamic model as $(\text{Fe}, \text{Al})_3(\text{Fe}, \text{Al})_1(\text{C}, \text{Va})_1$ is applied to the Co–Al–C and Ni–Al–C based κ phase, and the parameters necessary for this model are evaluated using first-principles calculations,

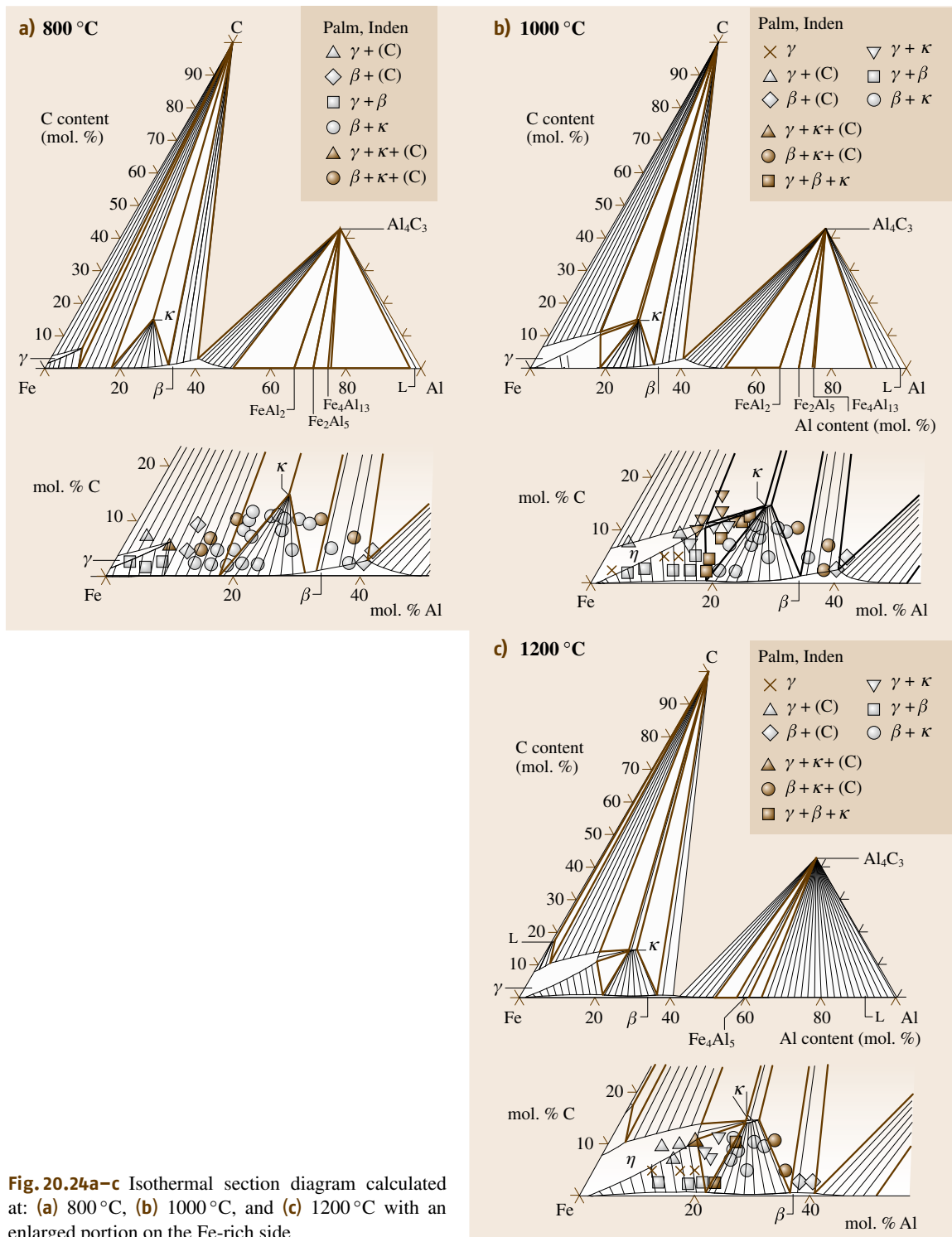


Table 20.10 The calculated thermodynamic parameters required by the $(M, \text{Al})_3(M, \text{Al})_1(\text{C}, \text{Va})_1$ -type three sublattice model

Structure	Structure symbol	Calculated lattice parameter (nm)	Observed lattice parameter (nm)	Calculated formation enthalpy in the ground state (kJ/mol of compound)
Co ₃ AlC	E2 ₁	0.3675	0.3700	-179.0
Al ₃ CoC	E2 ₁	0.3909	—	+113.5
Co ₃ Al	L1 ₂	0.3515	—	-79.6
CoAl ₃	L1 ₂	0.3726	—	-90.4
Co ₄ C	—	0.3621	—	+98.0
Al ₄ C	—	0.4057	—	+160.5
Ni ₃ AlC	E2 ₁	0.3713	—	-141.0
Al ₃ NiC	E2 ₁	0.3905	—	+64.5
Ni ₃ Al	L1 ₂	0.3504	0.3572	-169.5
NiAl ₃	L1 ₂	0.3774	—	-91.6
Ni ₄ C	—	0.3645	—	+61.0

as listed in Table 20.10. The calculated Co–Al–C ternary phase diagrams are shown in Fig. 20.25 for temperatures of 900 °C, 1100 °C, and 1300 °C. The enlarged portion of the isothermal section diagrams at 1100 °C was compared with the experimental data [20.21].

The κ phase only appears at the stoichiometric composition in our results, while a small homogeneity range is exhibited by this phase in the experimental phase diagrams. This aspect is closely related to the large, positive formation energies in the metastable ordered structures, such as Al₃CoC and Al₄C. As the formation energy of Co₃AlC shows an extremely large negative value when compared to these structures, the κ phase only forms at the stoichiometric position. The homogeneity can be expressed by introducing interaction parameters between unlike atoms in the same sublattice. However, this treatment is not applied in the present analysis, because the experimental phase boundaries of the κ phase are still uncertain.

The calculated vertical section diagrams at constant 10 mol % C and 30 mol % Al are shown in Fig. 20.26b. The calculated values agree well with the experimental results, and hence, the new type of approach based on the incorporation of the CALPHAD method into ab initio calculations has proven to be applicable to phase diagram calculations for higher-order systems.

Calculation of the Ni–Al–C Phase Diagram

In the Ni–Al–C system, on the other hand, it has been experimentally verified that the κ phase does not appear in the vicinity of the stoichiometric composition. Figures 20.27a–c show the calculated isothermal section diagrams at 900, 1000, and 1300 °C, respectively.

Phase Separation of the κ Phase in the Co–Ni–Al–C Quaternary System

According to the first-principles calculations, there was a large difference in the phase stability between the Co₃Al–L1₂ and Ni₃Al–L1₂ phases, compared to the difference between the Ni₃AlC–E2₁ and Co₃AlC–E2₁ phases. In such an energetic situation, a two-phase separation should occur, depending on the difference in the formation energies of the compounds, given by the following expression

$$\Delta G = {}^0G_{\text{Ni}_3\text{Al}} + {}^0G_{\text{Co}_3\text{AlC}} - {}^0G_{\text{Co}_3\text{Al}} - {}^0G_{\text{Ni}_3\text{AlC}} \quad (20.39)$$

This miscibility gap originates in the energy difference between the terminal compounds, and as the absolute value of ΔG increases, then the critical temperature of the miscibility gap increases. Such a phase separation is often observed in some complex carbonitrides or alloy semiconductor systems. Figure 20.28 shows the calculation of a miscibility gap in the Co₃AlC–Ni₃AlC–Co₃Al–Ni₃Al pseudoquaternary system at $T = 1000$ °C. In this model calculation, only the formation enthalpies of the stoichiometric compounds are used, designated by the four vertices of the composition square. One can see that a two-phase separation forms in the direction of the Co₃AlC and Ni₃Al diagonal. Therefore, a two-phase separation between these terminal compounds will be involved in the phase equilibria of the quaternary system.

Using the thermodynamic description of the four ternary systems that comprise the Co–Ni–Al–C quaternary system, a vertical section diagram is calculated

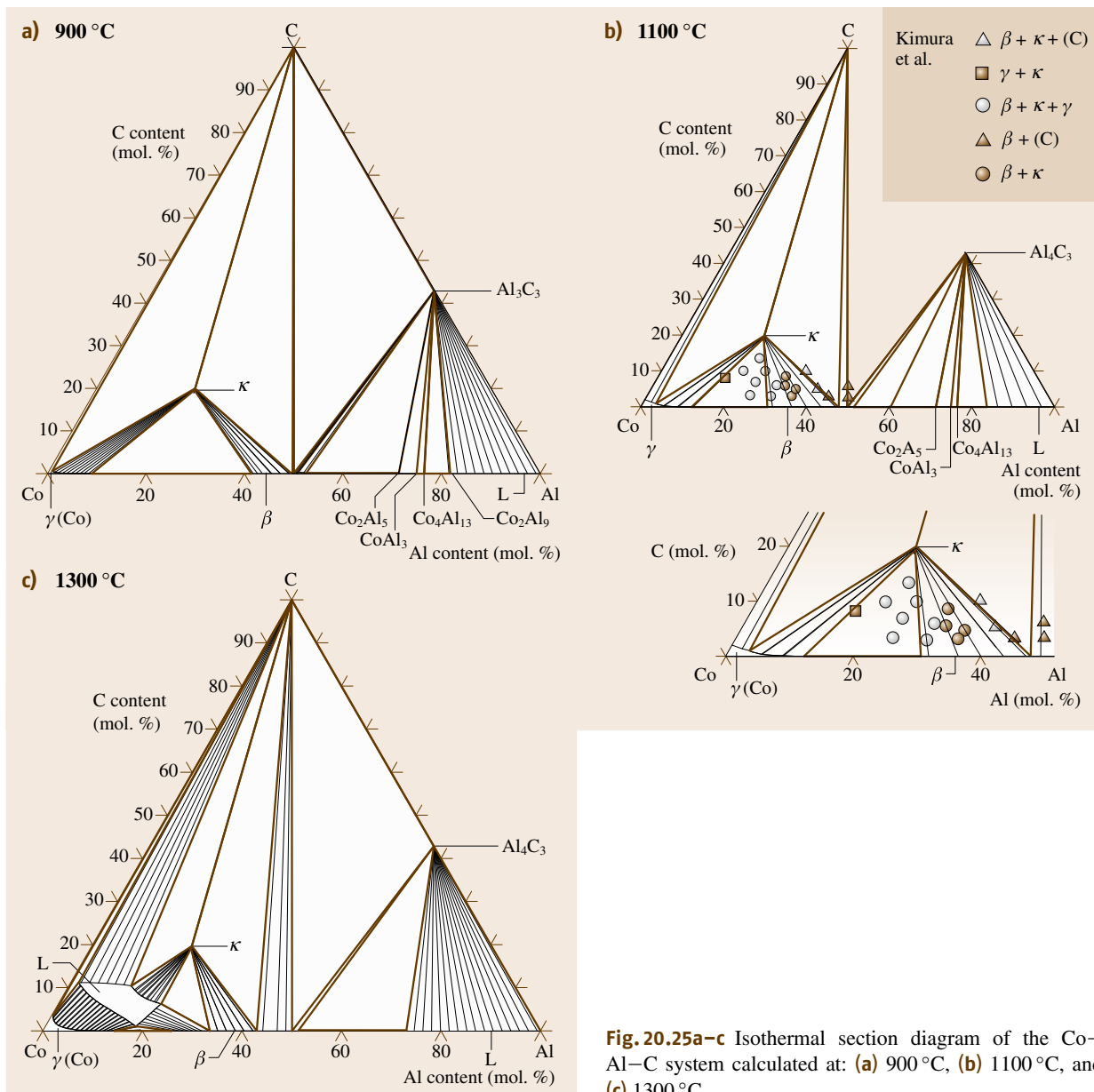


Fig. 20.25a–c Isothermal section diagram of the Co–Al–C system calculated at: (a) 900 °C, (b) 1100 °C, and (c) 1300 °C

at a constant C content of 4 mol %, and an Al content of 23 mol %, as shown in Fig. 20.29. In this figure, the term κ_1 denotes the Ni-based $L1_2$ structure, while the Co-based Perovskite structure is represented by κ_2 . At higher temperatures, the $E2_1$ structure forms a homogeneous solution, and this phase is designated as κ .

The κ phase gradually changes its character from the Co_3AlC -based carbide to the Ni_3Al -based intermetallic compound with increasing Ni content in the alloy. The precipitates decompose into almost stoichiometric Co_3AlC and Ni_3Al phases in the lower temperature range.

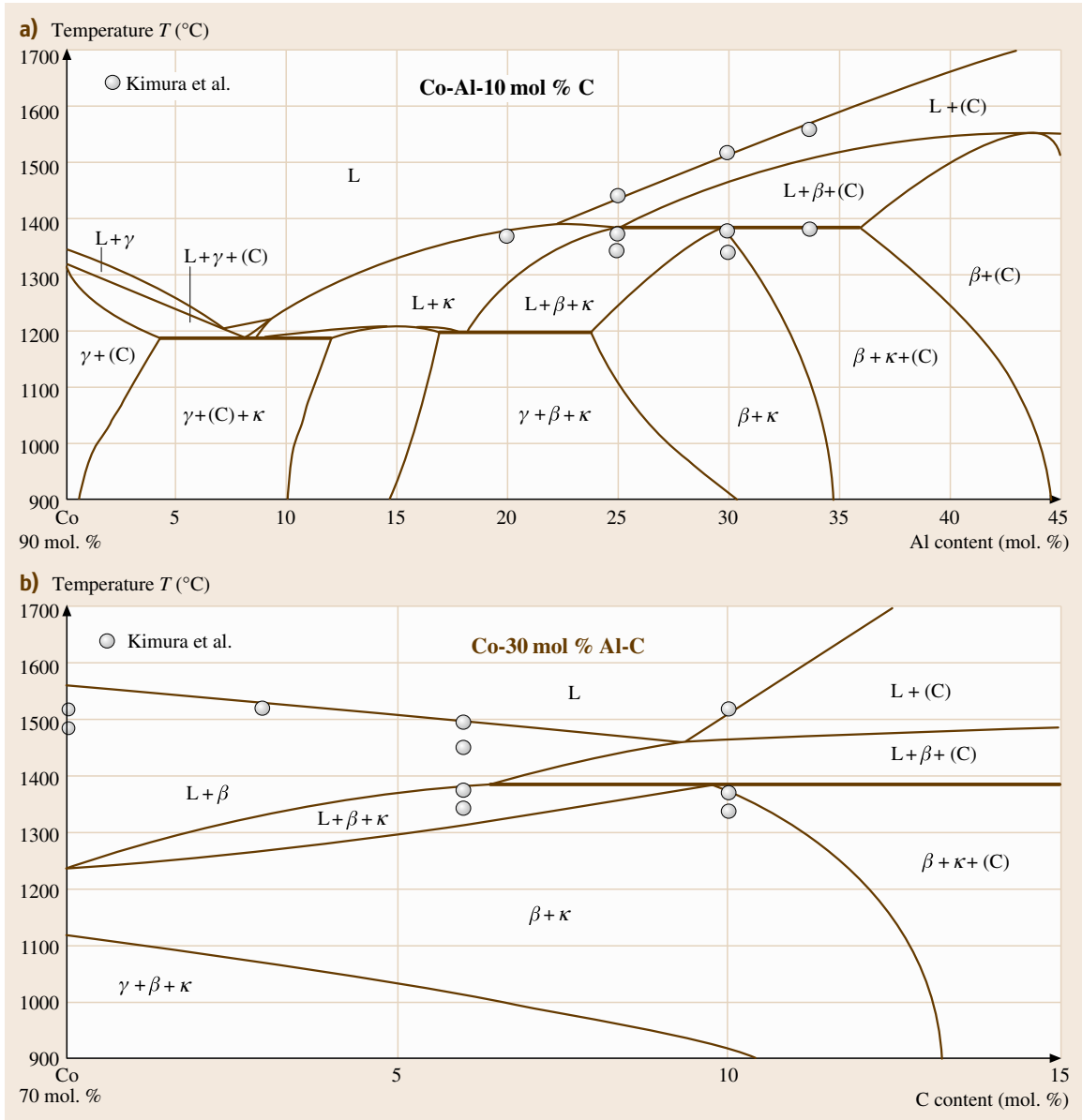
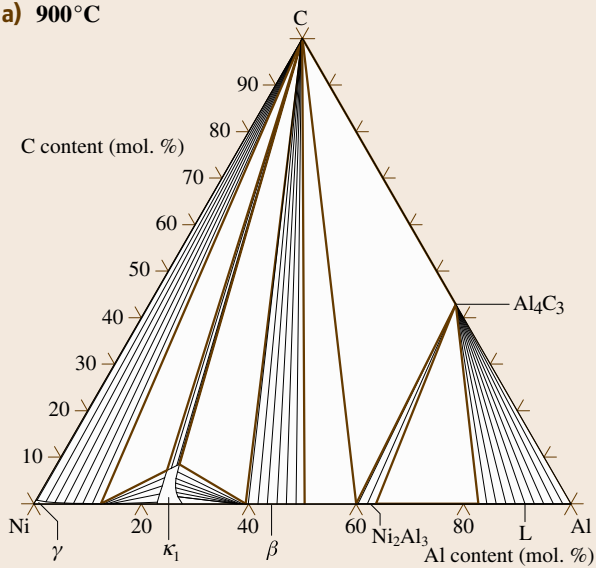
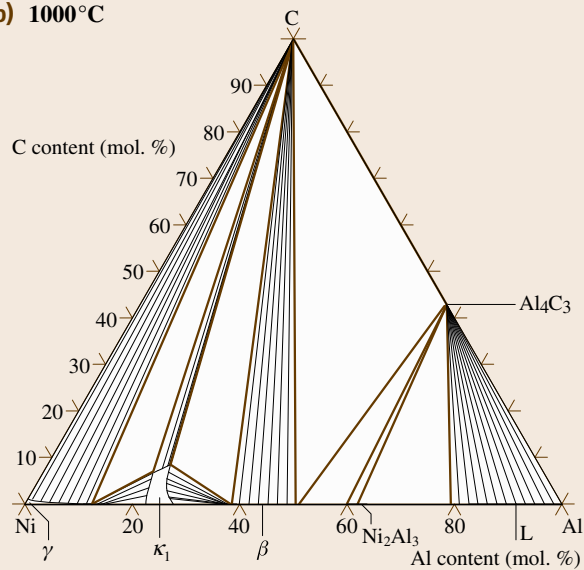


Fig. 20.26a,b Calculated vertical section diagrams at constant (a) 10 mol % C and (b) 30 mol % Al

a) 900°C



b) 1000°C



c) 1300°C

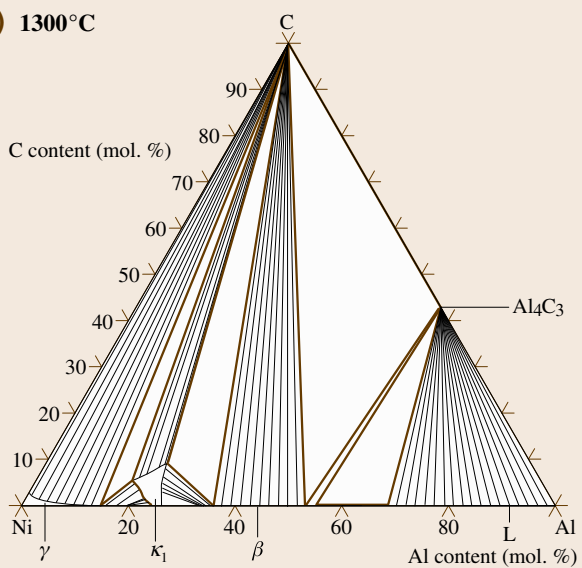


Fig. 20.27a–c Isothermal section diagram of the Ni–Al–C system calculated at (a) 900°C, (b) 1000°C, and (c) 1300°C

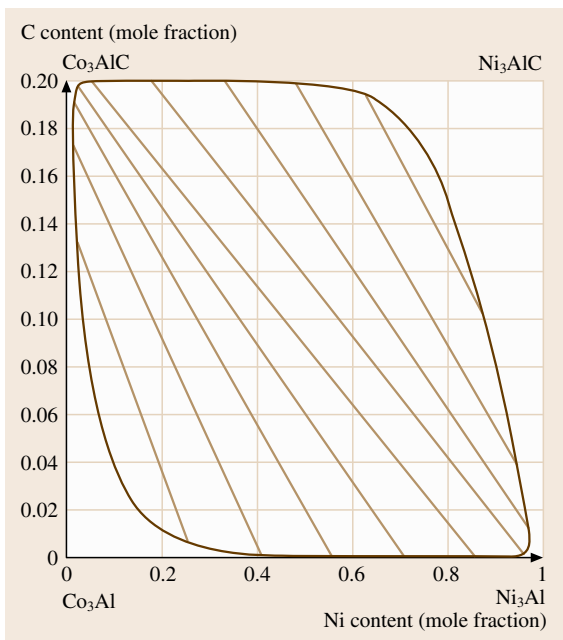


Fig. 20.28 Calculated miscibility gap in the Co_3Al C– Ni_3Al C– Co_3Al – Ni_3Al pseudoquaternary system at 1000°C

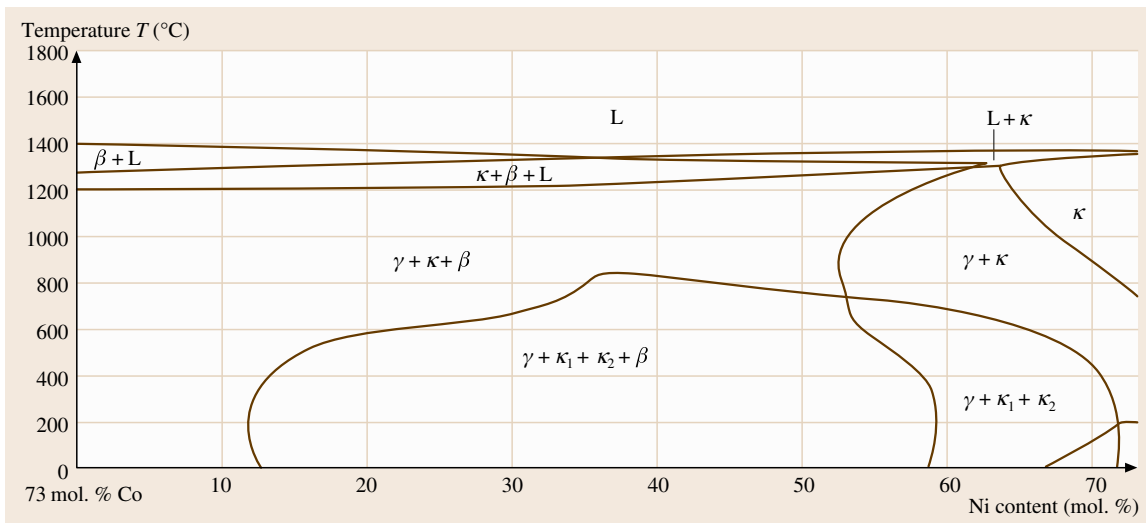


Fig. 20.29 Vertical section diagram calculated at a constant C content of 4 mol % and an Al content of 23 mol %

References

- 20.1 N. Saunders, A.P. Miodownik: *CALPHAD (Calculation of Phase Diagrams): A Comprehensive Guide* (Elsevier, Oxford 1998)
- 20.2 F.R. de Boer, R. Boom, W.C.M. Mattens, A.R. Miedema, A.K. Niessen: *Cohesion in Metals, Transition Metals Alloys* (North-Holland, Amsterdam 1988)
- 20.3 G. Ghosh, C. Kantner, G.B. Olson: Thermodynamic modeling of the Pd-X (X = Ag, Co, Fe, Ni) systems, *J. Phase Equil.* **20**, 295–308 (1999)
- 20.4 M. Hillert, L.-I. Staffansson: The regular solution model for stoichiometric phases and ionic melts, *Acta Chem. Scand.* **24**, 3618–3626 (1970)
- 20.5 W. Oelsen, F. Johannsen, A. Podgornik: *Erzmetall* **9**, 459–469 (1956)
- 20.6 W. Kohn, L.J. Sham: Self-consistent equations including exchange and correlation effects, *Phys. Rev.* **140**, A1133–1138 (1965)
- 20.7 P. Blaha, K. Schwarz, G.K.H. Madsen, D. Kvasnicka, J. Luiz: *WIEN2k, An Augmented Plane Wave and Orbitals Program for Calculating Crystal Properties* (Karlheinz Schwarz, Tech. Universit t Wien, Vienna 2001)
- 20.8 J.P. Perdew, K. Burke, Y. Wang: Generalized gradient approximation for the exchange–correlation hole of a many–electron system, *Phys. Rev. B* **54**, 16533–16539 (1996)
- 20.9 H. Ohtani, M. Hasebe: Thermodynamic analysis of phase diagrams by incorporating ab initio energetic calculations into CALPHAD approach, *Bull. Iron Steel Inst. Japan* **9**, 223–229 (2004)
- 20.10 J.W.D. Connolly, A.R. Williams: Density-functional theory applied to phase transformations in transition–metal alloys, *Phys. Rev. B* **27**, 5169–5172 (1983)
- 20.11 H. Ohtani, Y. Takeshita, M. Hasebe: Effect of the order–disorder transition of the bcc structure on the solubility of Be in the Fe–Be binary system, *Mater. Trans.* **45**, 1499–1506 (2004)
- 20.12 F.D. Murnaghan: The compressibility of media under extreme pressures, *Proc. Nat. Acad. Sci. USA* **30**, 244–247 (1944)
- 20.13 M.H.F. Sluiter, Y. Watanabe, D. de Fontaine, Y. Kawazoe: First-principles calculation of the pressure dependence of phase equilibria in the Al–Li system, *Phys. Rev. B* **53**, 6137–6151 (1996)
- 20.14 T. Mohri, Y. Chen: First-principles investigation of L1₀-disorder phase equilibrium in the Fe–Pt system, *Mater. Trans.* **43**, 2104–2109 (2002)
- 20.15 H. Ino: A pairwise interaction model for decomposition and ordering processes in b.c.c binary alloys and its application to the Fe–Be system, *Acta Metall.* **26**, 827–834 (1978)
- 20.16 T. Takayama, M.Y. Wey, T. Nishizawa: Effect of magnetic transition on the solubility of alloying elements in bcc iron and fcc cobalt, *Trans. Japan Inst. Met.* **22**, 315–325 (1981)
- 20.17 H. Ohtani, Y. Chen, M. Hasebe: Phase separation of the B2 structure accompanied by an ordering in Co–Al and Ni–Al binary systems, *Mater. Trans.* **45**, 1489–1498 (2004)
- 20.18 H. Ohtani, M. Yamano, M. Hasebe: Thermodynamic analysis of the Fe–Al–C ternary system by incorporating ab initio energetic calculations into the CALPHAD approach, *ISIJ Intern.* **44**, 1738–1747 (2004)
- 20.19 R. Hultgren, P.D. Desai, D.T. Hawkins, M. Gleiser, K.K. Kelley: *Selected Values of the Thermodynamic Properties of Binary Alloys* (ASM, Metals Park 1973)
- 20.20 Y. Kimura, M. Takahashi, S. Miura, T. Suzuki, Y. Mishima: Phase stability and relations of multiphase alloys based on B2 CoAl and E21 Co₃AlC, *Intermet.* **3**, 413–425 (1995)
- 20.21 M. Palm, G. Inden: Experimental determination of phase equilibria in the Fe–Al–C system, *Intermet.* **3**, 443–454 (1995)
- 20.22 H. Ohtani, M. Yamano, M. Hasebe: Thermodynamic analysis of the Co–Al–C and Ni–Al–C systems by incorporating ab initio energetic calculations into the CALPHAD approach, *Comp. Coupling Phase Diag. Thermochem.* **28**, 177–190 (2004)

Phase Field Approach

The term *phase field* has recently become known across many fields of materials science. The meaning of phase field is the spatial and temporal order parameter field defined in a continuum–diffused interface model. By using the phase field order parameters, many types of complex microstructure changes observed in materials science are described effectively. This methodology has been referred to as the phase field method, phase field simulation, phase field modeling, phase field approach, etc. In this chapter, the basic concept and theoretical background for the phase field approach is explained in Sects. 21.1 and 21.2. The overview of recent applications of the phase field method is demonstrated in Sects. 21.3 to 21.6.

Phase field models have been successfully applied to various materials processes including solidification, solid–state phase transformations and microstructure changes. Using phase field methodology, one can deal with the evolution of arbitrary morphologies and complex microstructures without explicitly tracking the positions of interfaces. This approach can describe different processes such as diffusion–controlled phase separation and diffusionless phase transition within the same formulation. It is rather straightforward to incorporate the effect of coherency and applied stresses, as well as electrical and magnetic fields.

Since phase field methodology can model complex microstructure changes quantitatively, it will be possible to search for the most desirable microstructure using this method as a design simulation, i. e., through computer trial–and–error testing. Therefore, the most effective strategy for developing advanced materials is as follows. First, we elucidate the mechanism of microstructure changes experimentally, then we model the microstructure evolutions using the phase–field method based on the experimental results, and

21.1	Basic Concept of the Phase-Field Method	1092
21.2	Total Free Energy of Microstructure	1093
	21.2.1 Chemical Free Energy	1093
	21.2.2 Gradient Energy	1095
	21.2.3 Elastic Strain Energy	1097
	21.2.4 Free Energy for Ferromagnetic and Ferroelectric Phase Transition ..	1101
21.3	Solidification	1102
	21.3.1 Pure Metal	1102
	21.3.2 Alloy	1104
21.4	Diffusion-Controlled Phase Transformation	1105
	21.4.1 Cahn–Hilliard Diffusion Equation ...	1105
	21.4.2 Spinodal Decomposition and Ostwald Ripening	1107
21.5	Structural Phase Transformation	1108
	21.5.1 Martensitic Transformation	1108
	21.5.2 Tweed–Like Structure and Twin Domain Formations	1108
	21.5.3 Twin Domain Growth Under External Stress and Magnetic Field ..	1109
21.6	Microstructure Evolution	1110
	21.6.1 Grain Growth and Recrystallization	1110
	21.6.2 Ferroelectric Domain Formation with a Dipole–Dipole Interaction ...	1111
	21.6.3 Modeling Complex Nanogranular Structure Formation	1112
	21.6.4 Dislocation Dynamics	1112
	21.6.5 Crack Propagation	1113
	References	1114

finally we search for the most desirable microstructure while simultaneously considering both the simulation and experimental data.

21.1 Basic Concept of the Phase-Field Method

Over the last two decades, the phase-field approach [21.1–7] has been developed for many fields in materials science as a powerful tool to simulate and predict complex microstructure developments (for example, solidification [21.3, 8–12], spinodal decomposition [21.13, 14], Ostwald ripening [21.15], crystal growth and recrystallization [21.16–19], domain microstructure evolutions in ferroelectric materials [21.20, 21], martensitic transformation [21.22], dislocation dynamics [21.23–25], crack propagation [21.26], etc.).

An essence of the phase-field method is based on a diffuse-interface approach [21.6] proposed more than a century ago by van der Waals [21.27] and independently almost a half-century ago by *Cahn* and *Hilliard* [21.28, 29]. Because the phase-field methodology has an efficient ability to model various types of complex microstructure changes quantitatively, there is large possibility to search for the most desirable microstructure using this method as a design simulation, i. e., trial-and-error testing on a computer.

Since the phase-field method has developed over a wide range within the field of materials science, the definition of the method has divided into two main categories. One is the interface-tracking approach commonly used in solidification simulation of dendrite growth, and the other is the continuum diffuse-interface model, which describes the temporal and spatial developments of the dynamics of inhomogeneous order parameter fields during phase transformations.

In phase-field modeling, the determination of order parameters that are well defined and called phase-field variables is the most important step. The order parameters are, in general, classified into two types: the conserved order parameters and the nonconserved ones. Typical examples of the former and the latter are the composition of a solute atom and the long-range order parameter describing an order–disorder phase transition, respectively. There is no systematic criterion for selecting the order parameters, but it is usually enough for the order parameters to describe the targeted microstructure morphology and its total free energy, quantitatively.

In order to simulate the temporal and spatial microstructure developments the total free energy of the inhomogeneous microstructure should first be evaluated. The total free energy of microstructure G_{sys} is defined by a sum of a chemical free energy density g_c , a gradient energy density f_{grad} , an elastic strain energy density e_{str} , a magnetic energy density f_{mag} , and an

electric energy density f_{ele} , so that the functional G_{sys} is written as

$$G_{\text{sys}} = \int_{\mathbf{r}} \left[\begin{array}{l} g_c(c_i, s_j) \\ + f_{\text{grad}}(c_i, s_j) + e_{\text{str}}(c_i, s_j) \\ + f_{\text{mag}}(c_i, s_j) + f_{\text{ele}}(c_i, s_j) \end{array} \right] d\mathbf{r}, \quad (21.1)$$

where $c_i(\mathbf{r}, t)$ and $s_j(\mathbf{r}, t)$ are the order parameters of the conserved and nonconserved fields, respectively, and these are the function of spatial position \mathbf{r} and time t . The subscripts i and j of each order parameter are the numbers by which it is determined if the order parameter belongs to the same category. The order parameters, such as $c_i(\mathbf{r}, t)$ and $s_j(\mathbf{r}, t)$, are commonly called the phase-field variables in the phase-field method. Since g_c , f_{grad} , e_{str} , f_{mag} , and f_{ele} are expressed as a function of order parameters $c_i(\mathbf{r}, t)$ and $s_j(\mathbf{r}, t)$, these parameters interact with each other through the total free energy during microstructure changes.

The temporal evolution of field variables in a phase-field model can be obtained by solving (21.2) and (21.3) including the dynamic coupling term of the time variation of the order parameters (see the second term of the right-hand side of both equations)

$$\frac{\partial c_i(\mathbf{r}, t)}{\partial t} = \nabla \cdot \left[M_{ij} \left(\nabla \frac{\delta G_{\text{sys}}}{\delta c_j} + \xi_{c_j} \right) \right] + K_{ij}^c \frac{\partial s_j(\mathbf{r}, t)}{\partial t}, \quad (21.2)$$

$$\frac{\partial s_i(\mathbf{r}, t)}{\partial t} = -L_{ij} \left(\frac{\delta G_{\text{sys}}}{\delta s_j} + \xi_{s_j} \right) + K_{ij}^s \frac{\partial c_j(\mathbf{r}, t)}{\partial t}, \quad (21.3)$$

where the symbols M_{ij} and L_{ij} is the mobility concerning the changes of the corresponding order parameters. These are precisely described as a function of the order parameters, but in many actual calculations the mobility is often set constant or regarded as a function of temperature. ξ_p is a Gaussian thermal noise term for the order parameter p ($= c_i$ or s_i). The second terms in the right-hand side of (21.2) and (21.3) represent the dynamic coupling of each phase-field variable, where K_{ij}^c and K_{ij}^s are the coupling coefficients. These are often assumed to be constant, or set to 0 when the dynamic interaction between order parameters is ignored. The microstructure change, which this coupling term should introduce, is actually limited to the case when a highly complex morphology of microstructure is formed almost as far from equilibrium, e.g., the dendrite growth, the fractal pattern formation, and so on.

21.2 Total Free Energy of Microstructure

In order to simulate microstructure changes quantitatively, the precise evaluation of the total free energy of the microstructure is required. In this section, the detail of the equations used for estimating the total free energy of microstructure is explained.

21.2.1 Chemical Free Energy

Several types of description for chemical free energy for a homogeneous state (i. e., mean field) have been proposed for phase-field simulations. They are mainly classified into two categories. One is the expression based on the polynomial expansion with respect to the order parameters known as a Landau expansion method [21.30], the other is the case where the well-defined chemical free energy curves for specific crystal structures are connected to each other continuously using phase-field variables. Some typical examples are provided below.

Grain Growth

The chemical free energy density g_c utilized for a crystal grain growth in polycrystalline single-phase materials is given by

$$g_c(s_1, s_2, s_3, \dots, s_p) = \sum_{i=1}^p \left(-\frac{A}{2} s_i^2 + \frac{B}{4} s_i^4 \right) + C \sum_{i=1}^p \sum_{j>i}^p s_i^2 s_j^2, \quad (21.4)$$

where $s_i = s_i(\mathbf{r}, t)$, ($i = 1, 2, \dots, p$) are the order parameters describing the probability to find the crystal with its orientation designated by i at position \mathbf{r} and time t [21.16]. Each integer number $i (= 1 \sim p)$ corresponds to the specific orientation of the crystal structure, respectively. The probability of finding the grain with orientation i at position \mathbf{r} and time t is defined by $|s_i(\mathbf{r}, t)|$. The symbols A , B , and C are the numerical constants determined phenomenologically. If we only employ $i = 1$, (21.4) reduces to

$$g_c(s_1) = -\frac{A}{2} s_1^2 + \frac{B}{4} s_1^4 \quad (21.5)$$

$$= -\frac{A}{2} s_1^2 \left(1 + s_1 \sqrt{\frac{B}{2A}} \right) \left(1 - s_1 \sqrt{\frac{B}{2A}} \right).$$

Hence $g_c(s_1) = 0$ is satisfied at $s_1 = 0, \pm\sqrt{2A/B}$, and the function $g_c(s_1)$ has a maximum at $s_1 = 0$, a minimum at $s_1 = \pm\sqrt{A/B}$, which is determined from the condition $\partial g_c / \partial s_1 = 0$.

The last term in the right-hand side of (21.4) is the penalty term, which forbids the coexistence of crystals with different orientation at the same position (because the coefficient C is defined as $C > 0$).

As an extended application of (21.4) to the two-phase mixture [21.31], the chemical free energy for a polycrystal containing grains of different phase is written as

$$g_c \left(c; s_1^\alpha, s_2^\alpha, \dots, s_p^\alpha; s_1^\beta, s_2^\beta, \dots, s_q^\beta \right) = -\frac{A}{2} (c - c_m)^2 + \frac{B}{4} (c - c_m)^4 + \frac{C_\alpha}{4} (c - c_\alpha)^4 + \frac{C_\beta}{4} (c - c_\beta)^4 + \sum_{i=1}^p \left[-\frac{U_\alpha}{2} (c - c_\beta)^2 (s_i^\alpha)^2 + \frac{V_\alpha}{4} (s_i^\alpha)^4 \right] + \sum_{i=1}^q \left[-\frac{U_\beta}{2} (c - c_\alpha)^2 (s_i^\beta)^2 + \frac{V_\beta}{4} (s_i^\beta)^4 \right] + \frac{W}{2} \sum_{\alpha} \sum_{\beta} \sum_{i=1}^p \sum_{j=1}^q (s_i^\alpha)^2 (s_j^\beta)^2, \quad (21.6)$$

where the composition field $c = c(\mathbf{r}, t)$ is also considered, and c_α and c_β are the composition of α and β phase, respectively; c_m is defined by $c_m = (c_\alpha + c_\beta)/2$. Symbols A , B , C_α , C_β , U_α , U_β , V_α , V_β and W are the phenomenologically determined numerical constants. The phase-field order parameters for different crystal structures, α and β , are denoted by $s_i^\alpha = s_i^\alpha(\mathbf{r}, t)$ and $s_i^\beta = s_i^\beta(\mathbf{r}, t)$, respectively.

Phase Separation Between Different Crystal Structure Phases (Landau Expansion)

A typical example is the case that both a phase separation and a structural phase transition from cubic to tetragonal occur simultaneously [21.32]. The chemical free energy function is expressed based on the Landau expansion as

$$g_c(c, s_1, s_2, s_3) = \frac{1}{2} A (c - c_1)^2 + \frac{1}{2} B (c - c_2) \left(s_1^2 + s_2^2 + s_3^2 \right) - \frac{1}{4} C \left(s_1^4 + s_2^4 + s_3^4 \right) + \frac{1}{6} D \left(s_1^6 + s_2^6 + s_3^6 \right) + U \left(s_1^2 s_2^2 + s_2^2 s_3^2 + s_3^2 s_1^2 \right) + V \left[s_1^4 \left(s_2^2 + s_3^2 \right) + s_2^4 \left(s_1^2 + s_3^2 \right) + s_3^4 \left(s_1^2 + s_2^2 \right) \right] + W s_1^2 s_2^2 s_3^2, \quad (21.7)$$

where $s_i = s_i(\mathbf{r}, t)$ are the order parameters indicating the probability of finding the tetragonal phase designated by i at position \mathbf{r} and time t . Index i ($= 1, 2, \text{ and } 3$) corresponds to the direction of the c -axis of the tetragonal phase. (In the structural phase transition from cubic to tetragonal, there are three orientation relations between cubic and tetragonal phases, i. e., three variants.) The specific state $s_1 = s_2 = s_3 = 0$ corresponds to cubic phase. The order parameter $c = c(\mathbf{r}, t)$ is a solute composition at position \mathbf{r} and time t . The symbols $c_1, c_2, A, B, C, D, U, V,$ and W are constants.

Phase Separation Between Different Crystal Structure Phases (Use of Thermodynamic Database of Phase Diagrams)

The construction method of chemical free energy using a thermodynamic database of phase diagrams is proposed in the phase-field method for alloy solidification [21.1, 2, 9]. In this formulation, since the chemical free energy is directly related to the real phase diagrams and we can simulate phase transformations in accord with the phase diagrams, this methodology is quite important and useful for practical engineering purposes, and the details are as follows.

First we suppose, for instance, that the α and β phase have different crystal structure in the A–B binary alloy system, and that the chemical free energy curves for these two phases are denoted as $g_c^\alpha(c, T)$ and $g_c^\beta(c, T)$, respectively, where c is the solute composition of component B. The chemical free energy function for each phase is easily obtained from the thermodynamic database of phase diagrams such as ThermoCalc, Pandat, etc. [21.33].

Next, we define the phase-field variable $s = s(\mathbf{r}, t)$, that is, the probability of finding the β phase at position \mathbf{r} and time t . Therefore, the cases $s = 0$ and $s = 1$ correspond to the α single phase and the β one, respectively. Utilizing the phase-field variable s , we are able to formulate the chemical free energy surface as a function of c and s , which is expressed as

$$g_c(c, s, T) = g_c^\alpha(c, T) [1 - h(s)] + g_c^\beta(c, T) h(s) + W_c^{\alpha \leftrightarrow \beta}(T) g^2(s), \quad (21.8)$$

where $W_c^{\alpha \leftrightarrow \beta}(T)$ is an energy barrier originating in the latent heat during $\alpha \leftrightarrow \beta$ structural phase transition. In the phase-field method the function $g(s)$ is usually defined by

$$g(s) \equiv s(1 - s). \quad (21.9)$$

As for the function $h(s)$, two different definitions have mainly been employed in the phase-field method, that is

$$h(s) = \frac{\int_0^s g(s') ds'}{\int_0^1 g(s') ds'} = s^2(3 - 2s) \quad (21.10)$$

and

$$h(s) = \frac{\int_0^s g^2(s') ds'}{\int_0^1 g^2(s') ds'} = s^3(10 - 15s + 6s^2). \quad (21.11)$$

It seems that there is no significant effect on the simulation result as to whether (21.10) or (21.11) is employed. Clearly recognized from (21.10) and (21.11), the function $h(s)$ shows an S-shaped curve, the value of which ranges from 0 to 1. The function $g^2(s)$ is 0 when $s = 0$ and $s = 1$, and a maximum value at $s = 0.5$. Equation (21.8) constructs the energy surface connecting the chemical free energy curves of the α and β phase smoothly using function $h(s)$. The physical meaning of the third term in the right-hand side of (21.8) is the latent heat induced with a structural phase transition. (The detail for the formulation of a chemical free energy for each single phase is explained in Chap. 20.)

It should be noted that the free energy surface defined by (21.8) is a conveniently determined surface with no strict physical meaning. For instance, the atomic structure corresponding to the state of $s = 0.5$ is not defined in the phase-field method. (The same definition of atomic arrangement may be possible for $s = 0.5$, but the explicit image for the atomic arrangement is not needed because the phase-field method is a continuum model for microstructure calculation where only an energy is evaluated depending on the local order parameter values.)

The chemical free energy of the multicomponent and multiphase system is expressed as an extended form

$$g_c(c_1, c_2, \dots, c_{N_c}, s_1, s_2, \dots, s_{N_s}, T) = \sum_{i=1}^{N_s} g_c^{\phi_i}(c_1, c_2, \dots, c_{N_c}, T) h(s_i) + \frac{1}{2} \sum_{i=1}^{N_s} \sum_{j=1}^{N_s} W_c^{\phi_i \leftrightarrow \phi_j}(T) g(s_i, s_j), \quad (21.12)$$

where N_c and N_s are the number of components and phases considered. The function $g_c^{\phi_i}(c_1, c_2, \dots, c_{N_c}, T)$ is a chemical free energy of ϕ_i phase denoted by i . In this case, since $s_i = s_i(\mathbf{r}, t)$ is a phase-field variable indicating the probability to find the ϕ_i phase at position \mathbf{r} and time t , the condition $\sum_{i=1}^{N_s} s_i(\mathbf{r}, t) = 1$

must be satisfied. The function $g(s_i, s_j)$ is defined by $g(s_i, s_j) \equiv (1 - \delta_{ij})s_i^2 s_j^2$ and $g(s_i, s_j) \equiv (1 - \delta_{ij})s_i s_j$ for a binary system and the other multicomponent system, respectively, where δ_{ij} is Kronecker's delta, i. e., $\delta_{ij} = 1$ for $i = j$ and $\delta_{ij} = 0$ for $i \neq j$. This distinction is to avoid the appearance of a concave region on the free energy curve constructed by order parameters s_i .

21.2.2 Gradient Energy

A gradient energy F_{grad} [21.29–34] is given by a gradient squire approximation for the order parameter profile in the phase-field method, which is expressed as

$$F_{\text{grad}} = \int_{\mathbf{r}} \left[\frac{1}{2} \sum_{i=1}^{N_c} \kappa_c (\nabla c_i)^2 + \frac{1}{2} \sum_{i=1}^{N_s} \kappa_s |\nabla s_i|^2 \right] d\mathbf{r}, \quad (21.13)$$

where symbols κ_c and κ_s are the gradient energy coefficients.

It is sometimes treated that a gradient energy is same as an interfacial energy. Strictly speaking, this is not correct. The interfacial energy where the interface is defined by the diffused order parameter profile not only includes the gradient energy but also the chemical free energy. Since the physical meaning of an interfacial energy is the total free energy at the interface, a gradient energy is different from an interfacial energy.

Equation (21.13) is derived by means of the Taylor expansion of a chemical free energy with respect to the gradient and curvature of the order parameter profile and with the higher order terms removed. The key idea is that the gradient and the curvature of the order parameter profile are treated as invariant variables except for the order parameter itself. The physical meaning of this equation is explained as follows.

In order to make the argument simple, we only consider the composition field $c(\mathbf{r})$ for the A–B binary alloy system, and focus on $c(\mathbf{r}_1) = 0.5$ at arbitrary position \mathbf{r}_1 . When we only consider the chemical free energy for the total free energy at \mathbf{r}_1 , the total free energy value is not changed even if the gradient and curvature of the composition profile at \mathbf{r}_1 is altered. But when the composition profile is extremely sharp, such that it is observed in the modulated structure during spinodal decomposition, the number of A–A, B–B, and A–B atom pair at \mathbf{r}_1 will depend on the shape of the composition profile across the position \mathbf{r}_1 . This deviation is evaluated by considering the composition field information $c(\mathbf{r}_1 \pm \Delta\mathbf{r})$ around \mathbf{r}_1 , i. e.,

the deviation is described using the gradient and the curvature of the composition profile as an invariant variable. Therefore, the composition gradient energy is the excess energy induced from the spatial fluctuation of composition field, and in this case, the chemical free energy is the mean field energy without composition fluctuation.

The Orientation Dependence of Gradient Energy

The interface between phases with different crystal structure and orientation is often considered in the phase-field method, and commonly, the orientation dependence is introduced into the gradient energy coefficient [21.1, 2] in (21.13). Therefore, the variation calculation for the gradient energy is significantly influenced in this case. For simplicity, we consider the composition field of the A–B binary alloy system, and a two-dimensional calculation is supposed. Under this condition, the composition gradient energy coefficient is defined by $\kappa_c \equiv \varepsilon^2(\theta)$, where ε is a function of the orientation θ . Then the composition gradient energy is given as

$$F_{\text{grad}} = \frac{1}{2} \int \varepsilon^2(\theta) (\nabla c)^2 d\mathbf{r}. \quad (21.14)$$

We consider the phase separated microstructure, and let \mathbf{n} be a unit normal at the interface between precipitate and matrix. The relations among \mathbf{n} , θ , and $c(\mathbf{r}, t)$ are given by

$$\begin{aligned} \mathbf{n} &= (n_1, n_2) = (\cos \theta, \sin \theta) \\ &= -\frac{\nabla c}{|\nabla c|} = -\frac{1}{\sqrt{C, x^2 + C, y^2}} (C, x, C, y), \\ \therefore \tan \theta &= \frac{n_2}{n_1} = \frac{C, y}{C, x} \rightarrow \theta = \tan^{-1} \frac{C, y}{C, x}, \end{aligned} \quad (21.15)$$

where C, x and C, y are defined by $C, x \equiv \partial c / \partial x$ and $C, y \equiv \partial c / \partial y$, respectively. It is worth noting that (21.15) insists θ and $c(\mathbf{r}, t)$ are not independent. Since the orientation of θ at the interface is a function of a composition gradient, the composition gradient energy coefficient κ_c is also a function of a composition gradient. Therefore, the variation calculation should be performed in (21.14) not only for the gradient squared part but also for the composition gradient energy coefficient itself. The explicit form of the variation

calculation is written in the form

$$\begin{aligned}
\frac{\delta F_{\text{grad}}}{\delta c} &= -\frac{d}{dx} \left(\frac{\partial f_{\text{grad}}}{\partial C, x} \right) - \frac{d}{dy} \left(\frac{\partial f_{\text{grad}}}{\partial C, y} \right) \\
&= \frac{d}{dx} \left(\varepsilon \varepsilon' C, y - \varepsilon^2 C, x \right) \\
&\quad - \frac{d}{dy} \left(\varepsilon \varepsilon' C, x + \varepsilon^2 C, y \right) \\
&= -\varepsilon^2 (C, xx + C, yy) - \left(\varepsilon'^2 + \varepsilon \varepsilon'' \right) \\
&\quad \times (\theta, yC, x - \theta, xC, y) \\
&\quad - 2\varepsilon \varepsilon' (\theta, xC, x + \theta, yC, y) , \quad (21.16)
\end{aligned}$$

where $f_{\text{grad}} \equiv (1/2)\varepsilon^2(\theta)(\nabla c)^2$, $\varepsilon' \equiv \partial\varepsilon/\partial\theta$, $\varepsilon'' \equiv \partial^2\varepsilon/\partial\theta^2$, $C, xx \equiv \partial^2c/\partial x^2$, $C, yy \equiv \partial^2c/\partial y^2$, $C, xy \equiv \partial^2c/\partial x\partial y$, $\theta, x \equiv \partial\theta/\partial x$, and $\theta, y \equiv \partial\theta/\partial y$.

The diffusion potential concerning the composition gradient energy has to be calculated by (21.16), when the composition gradient energy coefficient has an orientation dependence. In the case when a facet interface is observed, further modification is required in (21.16), the detail of this modification is discussed by *Eggleston et al.* [21.35].

Gradient Energy Expression for Multicomponent and Multiphase Systems

We first consider the composition field for the $N_c + 1$ component system ($i = 0 \sim N_c$). The composition gradient energy in this case is obtained by

$$\begin{aligned}
F_{\text{grad}} &= \frac{1}{2} \kappa_c \int_r \sum_{i=0}^{N_c} (\nabla c_i)^2 dr \\
&= \frac{1}{2} \kappa_c \int_r \sum_{i=1}^{N_c} \sum_{j=1}^{N_c} (\delta_{ij} + 1) (\nabla c_i) (\nabla c_j) dr , \quad (21.17)
\end{aligned}$$

where the condition $\sum_{i=0}^{N_c} c_i = 1$ is used and we assume κ_c to be a constant. δ_{ij} is Kronecker's delta. As for the ternary alloy system, (21.17) is reduced to

$$F_{\text{grad}} = \kappa_c \int_r \left[(\nabla c_1)^2 + (\nabla c_2)^2 + (\nabla c_1)(\nabla c_2) \right] dr . \quad (21.18)$$

Note that the cross-term $(\nabla c_1)(\nabla c_2)$ appears.

On the other hand, in the case for the multiphase system where the number of phases is $i = 1 \sim N_\phi$, the phase-field order parameter ϕ_i , ($0 \leq \phi_i \leq 1$) is intro-

duced, and the gradient energy is given by

$$\begin{aligned}
F_{\text{grad}} &= \frac{1}{2} \int_r \sum_{i=1}^{N_\phi} \sum_{j=1}^{N_\phi} \kappa_\phi |\phi_j \nabla \phi_i - \phi_i \nabla \phi_j|^2 dr , \\
\sum_{i=1}^{N_\phi} \phi_i &= 1 . \quad (21.19)
\end{aligned}$$

This is an irreducible expression for the gradient energy [21.36].

How to Derivate the Equation of Composition Gradient Energy

As a typical example for the derivation of a gradient energy equation, the formulation of the composition gradient energy that was proposed in the spinodal theory is explained [21.28, 29]. We concretely derive the composition gradient energy equation for the A–B binary alloy system and the solute composition of B component is referred to $c(\mathbf{r}, t)$ that is a function of local position \mathbf{r} and time t . In this formulation, since we employ the composition gradient ∇c and the curvature $\nabla^2 c$ as invariant variables, the chemical free energy is expanded in Taylor series form as follows

$$\begin{aligned}
g_c(c, \nabla c, \nabla^2 c) &= g_c(c, 0, 0) + K_0(c)(\nabla c) \\
&\quad + K_1(c)(\nabla^2 c) + K_2(c)(\nabla c)^2 \\
&\quad + K_3(c)(\nabla^2 c)^2 + K_4(c)(\nabla c)(\nabla^2 c) + \dots \\
&\cong g_c(c, 0, 0) + K_0(c)(\nabla c) \\
&\quad + K_1(c)(\nabla^2 c) + K_2(c)(\nabla c)^2 , \quad (21.20)
\end{aligned}$$

where we ignored the higher order terms in the Taylor series. $K_i(c)$ is an expansion coefficient and a function of composition. A function $g_c(c, 0, 0)$ corresponds to the chemical free energy with no composition fluctuation (i. e., homogeneous single phase state). Expression (21.20) is the chemical free energy of the inhomogeneous system including the information of the composition profile shape.

Here, we focus on the free energy at position x_0 of the one dimensional composition profile with arbitrary shape. The chemical free energy at x_0 should be written as $g_c\{c(x_0), \nabla c(x_0), \nabla^2 c(x_0)\}$. When the coordinate conversion of a flip horizontal is performed to the function g_c around x_0 , i. e., it corresponds to the case that the point x_0 is looked at from back, the chemical free energy at x_0 is given as $g_c\{c(x_0), -\nabla c(x_0), \nabla^2 c(x_0)\}$. Since energy must be invariant with the coordinate conversion

because energy is a scalar quantity, it is necessary to satisfy the following relation

$$\begin{aligned} & g_c \{c(x_0), \nabla c(x_0), \nabla^2 c(x_0)\} \\ &= g_c \{c(x_0), -\nabla c(x_0), \nabla^2 c(x_0)\}. \end{aligned} \quad (21.21)$$

Substituting (21.20) into (21.21), we obtain

$$\begin{aligned} & g_c \{c(x_0), 0, 0\} + K_0 \{c(x_0)\} \{\nabla c(x_0)\} \\ &+ K_1 \{c(x_0)\} \{\nabla^2 c(x_0)\} + K_2 \{c(x_0)\} \{\nabla c(x_0)\}^2 \\ &= g_c \{c(x_0), 0, 0\} - K_0 \{c(x_0)\} \{\nabla c(x_0)\} \\ &+ K_1 \{c(x_0)\} \{\nabla^2 c(x_0)\} + K_2 \{c(x_0)\} \{-\nabla c(x_0)\}^2, \\ &\therefore K_0 \{c(x_0)\} \{\nabla c(x_0)\} = 0 \rightarrow K_0 \{c(x_0)\} = 0. \end{aligned}$$

Hence $K_0(c)$ must be 0 identically because (21.21) should be satisfied at any position x_0 . Therefore, the chemical free energy for an inhomogeneous system has to be written as

$$\begin{aligned} & g_c(c, \nabla c, \nabla^2 c) \\ &= g_c(c, 0, 0) + K_1(c)(\nabla^2 c) + K_2(c)(\nabla c)^2. \end{aligned} \quad (21.22)$$

Therefore, the excess term originating in the composition fluctuation is expressed as

$$\begin{aligned} F_{\text{grad}} &= \int_V \left[K_1(c)(\nabla^2 c) + K_2(c)(\nabla c)^2 \right] dV \\ &= \int_V K_1(c)(\nabla^2 c) dV + \int_V K_2(c)(\nabla c)^2 dV. \end{aligned} \quad (21.23)$$

F_{grad} is a composition gradient energy. Furthermore, the first term of the right-hand side of (21.23) is transformed as

$$\begin{aligned} & \int_V K_1(c)(\nabla^2 c) dV \\ &= \int_S K_1(c) \{(\nabla c) \cdot \mathbf{n}\} dS - \int_V (\nabla K_1) \cdot (\nabla c) dV \\ &= \int_S K_1(c) \{(\nabla c) \cdot \mathbf{n}\} dS - \int_V \frac{\partial K_1}{\partial c} (\nabla c)^2 dV \\ &= - \int_V \frac{\partial K_1}{\partial c} (\nabla c)^2 dV, \end{aligned} \quad (21.24)$$

where the divergence theorem of Gauss, $\int_V f \nabla \cdot \mathbf{g} dV = \int_S f \mathbf{g} \cdot \mathbf{n} dS - \int_V \nabla f \cdot \mathbf{g} dV$, is utilized and \mathbf{n} is a unit normal at the surface of the object. The reason the term for the surface integral in (21.24) has been eliminated is that the integrated value over the whole surface of

the object becomes 0 statistically. Therefore, (21.23) is rewritten as

$$\begin{aligned} F_{\text{grad}} &= \int_V K_1(c)(\nabla^2 c) dV + \int_V K_2(c)(\nabla c)^2 dV \\ &= \int_V \left[K_2(c) - \frac{\partial K_1}{\partial c} \right] (\nabla c)^2 dV. \end{aligned} \quad (21.25)$$

Defining $\kappa(c)$ by

$$\kappa(c) = K_2(c) - \frac{\partial K_1}{\partial c}, \quad (21.26)$$

finally, we obtain

$$F_{\text{grad}} = \int_V \kappa(c)(\nabla c)^2 dV, \quad (21.27)$$

where $\kappa(c)$ is the so-called composition gradient energy coefficient. From (21.26), strictly speaking, $\kappa(c)$ is a function of a composition, but $\kappa(c)$ is often assumed to be constant and given by $\kappa = k\Omega d^2$, where Ω is an atomic interchange energy, d is the interatomic distance, and k is a phenomenological constant.

21.2.3 Elastic Strain Energy

In this section, the evaluation for the elastic strain energy of the coherent two-phase microstructure in A–B binary alloy system is explained as a simple example [21.37,38]. The steps for evaluating the elastic strain energy is as follows

Step 1 The eigenstrain [21.38] $\varepsilon_{ij}^0(\mathbf{r})$ is expressed as a function of the local composition $c(\mathbf{r})$, where \mathbf{r} is a position vector. The subscripts i and j take the integer values 1, 2, and 3.

Step 2 The total strain $\varepsilon_{ij}^c(\mathbf{r})$ is divided into two parts: $\varepsilon_{ij}^c(\mathbf{r}) = \bar{\varepsilon}_{ij}^c + \delta\varepsilon_{ij}^c(\mathbf{r})$, where $\bar{\varepsilon}_{ij}^c$ is the spatial average of $\varepsilon_{ij}^c(\mathbf{r})$, and $\delta\varepsilon_{ij}^c(\mathbf{r})$ is the deviation from $\bar{\varepsilon}_{ij}^c$. Therefore, the following relations should be satisfied

$$\bar{\varepsilon}_{ij}^c = \int_{\mathbf{r}} \varepsilon_{ij}^c(\mathbf{r}) d\mathbf{r}, \quad \int_{\mathbf{r}} \delta\varepsilon_{ij}^c(\mathbf{r}) d\mathbf{r} = 0.$$

Step 3 The equation to calculate the displacement, that is initially an unknown quantity, is deduced from the mechanical equilibrium equation using the $\varepsilon_{ij}^0(\mathbf{r})$ as a boundary condition, then $\delta\varepsilon_{ij}^c(\mathbf{r})$ is calculated from $u_i(\mathbf{r})$ directly.

Step 4 The elastic strain energy is written as a function of $\varepsilon_{ij}^c(\mathbf{r})$ and $\varepsilon_{ij}^0(\mathbf{r})$.

Step 5 $\bar{\varepsilon}_{ij}^c$ is determined from a constraint condition for the whole body.

Utilizing steps 1 to 5, we are able to evaluate the elastic strain energy of the coherent two-phase microstructure. When we try to calculate the elastic strain energy, it is important to distinguish the known variables and the unknown ones. In this case, the given variable is $\varepsilon_{ij}^0(\mathbf{r})$ that is calculated directly from the composition field $c(\mathbf{r})$, and the unknown variable is $\varepsilon_{ij}^c(\mathbf{r})$. The following formulation of elastic strain energy may look complicated, but the basic idea is simple. We evaluate the unknown variable using the known one through the mechanical equilibrium equation and the boundary conditions. Detail of the evaluation method is explained along the lines of step 1 to 5 as follows.

Step 1

When the lattice parameter a is a linear function of the composition, i.e., the Vegard's law is satisfied, a is given by

$$a(\mathbf{r}) = a_0 + \frac{da}{dc}c(\mathbf{r}), \quad (21.28)$$

where $c(\mathbf{r})$ is a local solute composition of component B at position \mathbf{r} , and a_0 is the lattice parameter for pure A component. In this case, the eigenstrain is defined by

$$\begin{aligned} \varepsilon_{ij}^0(\mathbf{r}) &\equiv \frac{a(\mathbf{r}) - a_0}{a_0} = \eta c(\mathbf{r}) \delta_{ij}, \\ \eta &\equiv \frac{1}{a_0} \frac{da}{dc}, \end{aligned} \quad (21.29)$$

where η is a lattice mismatch that is calculated from the lattice parameters of pure A and B metals. Since the lattice parameters of pure component and the composition field $c(\mathbf{r})$ are given in advance, the spatial distribution of the eigenstrain $\varepsilon_{ij}^0(\mathbf{r})$ in the microstructure is easily calculated from (21.29).

Step 2

Next, the total strain $\varepsilon_{ij}^c(\mathbf{r})$ is defined by

$$\varepsilon_{ij}^c(\mathbf{r}) \equiv \bar{\varepsilon}_{ij}^c + \delta\varepsilon_{ij}^c(\mathbf{r}), \quad (21.30)$$

$$\int_{\mathbf{r}} \delta\varepsilon_{ij}^c(\mathbf{r}) d\mathbf{r} = 0, \quad (21.31)$$

where $\bar{\varepsilon}_{ij}^c$ is a volume average of $\varepsilon_{ij}^c(\mathbf{r})$, $\delta\varepsilon_{ij}^c(\mathbf{r})$ is the deviation from $\bar{\varepsilon}_{ij}^c$, and is defined using the displacement vector $u_i(\mathbf{r})$ as

$$\delta\varepsilon_{kl}^c(\mathbf{r}) \equiv \frac{1}{2} \left[\frac{\partial u_k(\mathbf{r})}{\partial r_l} + \frac{\partial u_l(\mathbf{r})}{\partial r_k} \right]. \quad (21.32)$$

The elastic strain $\varepsilon_{ij}^{\text{el}}(\mathbf{r})$ is defined by

$$\varepsilon_{ij}^{\text{el}}(\mathbf{r}) \equiv \varepsilon_{ij}^c(\mathbf{r}) - \varepsilon_{ij}^0(\mathbf{r}). \quad (21.33)$$

On the basis of the linear elasticity theory, the stress is evaluated based on Hook's law

$$\sigma_{ij}^{\text{el}}(\mathbf{r}) = C_{ijkl} \varepsilon_{kl}^{\text{el}}(\mathbf{r}) = C_{ijkl} \left[\varepsilon_{kl}^c(\mathbf{r}) - \varepsilon_{kl}^0(\mathbf{r}) \right], \quad (21.34)$$

where C_{ijkl} is an elastic constant.

Step 3

The mechanical equilibrium equation is expressed as

$$\sigma_{ij}^{\text{el}}, j(\mathbf{r}) = \frac{\partial \sigma_{ij}^{\text{el}}(\mathbf{r})}{\partial r_j} = 0, \quad (21.35)$$

where the no body force condition is assumed. Substituting (21.29), (21.32), and (21.34) into (21.35) yields

$$C_{ijkl} \frac{\partial^2 u_k}{\partial r_j \partial r_l} = C_{ijkl} \eta \delta_{kl} \frac{\partial c}{\partial r_j}. \quad (21.36)$$

The functions $c(\mathbf{r})$, u_i and $\delta\varepsilon_{ij}^c(\mathbf{r})$ are expressed in the form of a Fourier integral as follows

$$c(\mathbf{r}) = \int_{\mathbf{k}} \hat{c}(\mathbf{k}) \exp(i\mathbf{k} \cdot \mathbf{r}) \frac{d\mathbf{k}}{(2\pi)^3} \quad (21.37)$$

$$u_i(\mathbf{r}) = \int_{\mathbf{k}} \hat{u}_i(\mathbf{k}) \exp(i\mathbf{k} \cdot \mathbf{r}) \frac{d\mathbf{k}}{(2\pi)^3} \quad (21.38)$$

$$\delta\varepsilon_{ij}^c(\mathbf{r}) = \int_{\mathbf{k}} \delta\hat{\varepsilon}_{ij}^c(\mathbf{k}) \exp(i\mathbf{k} \cdot \mathbf{r}) \frac{d\mathbf{k}}{(2\pi)^3}, \quad (21.39)$$

where $\mathbf{k} = (k_1, k_2, k_3)$ is a reciprocal wave vector in Fourier space. Substituting (21.37–21.39) into (21.36) and focusing on the amplitude part of the Fourier expression, we obtain

$$C_{ijkl} k_j k_l \hat{u}_k(\mathbf{k}) = -i C_{ijkl} \eta \delta_{kl} k_j \hat{c}(\mathbf{k}). \quad (21.40)$$

This is a Fourier expression of the mechanical equilibrium equation. (Note that the upright i is the imaginary number, not an index for vector or tensor.) Here, we define the following equations

$$G_{ik}^{-1}(\mathbf{k}) \equiv C_{ijkl} k_j k_l, \quad (21.41)$$

$$\sigma_{ij} \equiv C_{ijkl} \eta \delta_{kl}. \quad (21.42)$$

Using (21.41) and (21.42) in (21.40), the $\hat{u}_k(\mathbf{k})$, that is a Fourier transform of $u_k(\mathbf{r})$, is given by

$$\begin{aligned} \hat{u}_k(\mathbf{k}) &= -i G_{ik}(\mathbf{k}) C_{ijkl} \eta \delta_{kl} k_j \hat{c}(\mathbf{k}) \\ &= -i G_{ik}(\mathbf{k}) \sigma_{ij} k_j \hat{c}(\mathbf{k}). \end{aligned} \quad (21.43)$$

Since the Fourier transform of (21.32) is

$$\delta\hat{\varepsilon}_{kl}^c(\mathbf{k}) = i\frac{1}{2} [\hat{u}_k(\mathbf{k})k_l + \hat{u}_l(\mathbf{k})k_k], \quad (21.44)$$

substituting (21.43) into (21.44) yields

$$\begin{aligned} \delta\hat{\varepsilon}_{kl}^c(\mathbf{k}) &= i\frac{1}{2} [\hat{u}_k(\mathbf{k})k_l + \hat{u}_l(\mathbf{k})k_k] \\ &= i\hat{u}_k(\mathbf{k})k_l \\ &= -iiG_{ik}(\mathbf{k})k_jk_l\sigma_{ij}\hat{c}(\mathbf{k}) \\ &= G_{ik}(\mathbf{k})k_lk_jC_{ijmn}\eta\delta_{mn}\hat{c}(\mathbf{k}). \end{aligned} \quad (21.45)$$

The values of the elastic constant C_{ijkl} and the lattice mismatch η are given from the materials parameters in advance. Since the composition field $c(\mathbf{r})$ is given beforehand, $\hat{c}(\mathbf{k})$ is calculated by the first Fourier transform of $c(\mathbf{r})$ numerically. Therefore, $\delta\hat{\varepsilon}_{kl}^c(\mathbf{k})$ is directly calculated based on (21.45) and obtained as a function of \mathbf{k} , then $\delta\varepsilon_{kl}^c(\mathbf{r})$ is calculated through the inverse first Fourier transform of $\delta\hat{\varepsilon}_{kl}^c(\mathbf{k})$ numerically.

Step 4

The elastic strain energy is given as

$$\begin{aligned} E_{\text{str}} &= \frac{1}{2} \int_{\mathbf{r}} C_{ijkl} \varepsilon_{ij}^{\text{el}}(\mathbf{r}) \varepsilon_{kl}^{\text{el}}(\mathbf{r}) \mathbf{d}\mathbf{r} \\ &= \frac{1}{2} \int_{\mathbf{r}} \left\{ C_{ijkl} \left[\bar{\varepsilon}_{ij}^c + \delta\varepsilon_{ij}^c(\mathbf{r}) - \varepsilon_{ij}^0(\mathbf{r}) \right] \right. \\ &\quad \left. \times \left[\bar{\varepsilon}_{kl}^c + \delta\varepsilon_{kl}^c(\mathbf{r}) - \varepsilon_{kl}^0(\mathbf{r}) \right] \right\} \mathbf{d}\mathbf{r}, \end{aligned} \quad (21.46)$$

where the elastic strain is defined by

$$\begin{aligned} \varepsilon_{ij}^{\text{el}}(\mathbf{r}) &\equiv \varepsilon_{ij}^c(\mathbf{r}) - \varepsilon_{ij}^0(\mathbf{r}) \\ &= \bar{\varepsilon}_{ij}^c + \delta\varepsilon_{ij}^c(\mathbf{r}) - \varepsilon_{ij}^0(\mathbf{r}) \end{aligned} \quad (21.47)$$

and we are able to rewrite (21.46) using (21.47) as

$$E_{\text{str}} = \frac{1}{2} \int_{\mathbf{r}} \left\{ C_{ijkl} \left[\bar{\varepsilon}_{ij}^c + \delta\varepsilon_{ij}^c(\mathbf{r}) - \varepsilon_{ij}^0(\mathbf{r}) \right] \right. \\ \left. \times \left[\bar{\varepsilon}_{kl}^c + \delta\varepsilon_{kl}^c(\mathbf{r}) - \varepsilon_{kl}^0(\mathbf{r}) \right] \right\} \mathbf{d}\mathbf{r}$$

$$\begin{aligned} &= \frac{1}{2} \int_{\mathbf{r}} C_{ijkl} \bar{\varepsilon}_{ij}^c \bar{\varepsilon}_{kl}^c \mathbf{d}\mathbf{r} + \frac{1}{2} C_{ijkl} \bar{\varepsilon}_{ij}^c \int_{\mathbf{r}} \delta\varepsilon_{kl}^c(\mathbf{r}) \mathbf{d}\mathbf{r} \\ &\quad - \frac{1}{2} C_{ijkl} \bar{\varepsilon}_{ij}^c \int_{\mathbf{r}} \varepsilon_{kl}^0(\mathbf{r}) \mathbf{d}\mathbf{r} \\ &\quad + \frac{1}{2} C_{ijkl} \bar{\varepsilon}_{kl}^c \int_{\mathbf{r}} \delta\varepsilon_{ij}^c(\mathbf{r}) \mathbf{d}\mathbf{r} \\ &\quad + \frac{1}{2} \int_{\mathbf{r}} C_{ijkl} \delta\varepsilon_{ij}^c(\mathbf{r}) \delta\varepsilon_{kl}^c(\mathbf{r}) \mathbf{d}\mathbf{r} \\ &\quad - \frac{1}{2} C_{ijkl} \int_{\mathbf{r}} \delta\varepsilon_{ij}^c(\mathbf{r}) \varepsilon_{kl}^0(\mathbf{r}) \mathbf{d}\mathbf{r} \\ &\quad - \frac{1}{2} C_{ijkl} \bar{\varepsilon}_{kl}^c \int_{\mathbf{r}} \varepsilon_{ij}^0(\mathbf{r}) \mathbf{d}\mathbf{r} \\ &\quad - \frac{1}{2} \int_{\mathbf{r}} C_{ijkl} \varepsilon_{ij}^0(\mathbf{r}) \delta\varepsilon_{kl}^c(\mathbf{r}) \mathbf{d}\mathbf{r} \\ &\quad + \frac{1}{2} \int_{\mathbf{r}} C_{ijkl} \varepsilon_{ij}^0(\mathbf{r}) \varepsilon_{kl}^0(\mathbf{r}) \mathbf{d}\mathbf{r} \\ &= \frac{1}{2} C_{ijkl} \bar{\varepsilon}_{ij}^c \bar{\varepsilon}_{kl}^c \int_{\mathbf{r}} \mathbf{d}\mathbf{r} - C_{ijkl} \bar{\varepsilon}_{ij}^c \int_{\mathbf{r}} \varepsilon_{kl}^0(\mathbf{r}) \mathbf{d}\mathbf{r} \\ &\quad + \frac{1}{2} C_{ijkl} \int_{\mathbf{r}} \varepsilon_{ij}^0(\mathbf{r}) \varepsilon_{kl}^0(\mathbf{r}) \mathbf{d}\mathbf{r} \\ &\quad - C_{ijkl} \int_{\mathbf{r}} \delta\varepsilon_{ij}^c(\mathbf{r}) \varepsilon_{kl}^0(\mathbf{r}) \mathbf{d}\mathbf{r} \\ &\quad + \frac{1}{2} \int_{\mathbf{r}} C_{ijkl} \delta\varepsilon_{ij}^c(\mathbf{r}) \delta\varepsilon_{kl}^c(\mathbf{r}) \mathbf{d}\mathbf{r} \\ &= \frac{1}{2} C_{ijkl} \bar{\varepsilon}_{ij}^c \bar{\varepsilon}_{kl}^c - C_{ijkl} \bar{\varepsilon}_{ij}^c \delta_{kl} \eta \int_{\mathbf{r}} c(\mathbf{r}) \mathbf{d}\mathbf{r} \\ &\quad + \frac{1}{2} C_{ijkl} \delta_{ij} \delta_{kl} \eta^2 \int_{\mathbf{r}} \{c(\mathbf{r})\}^2 \mathbf{d}\mathbf{r} \\ &\quad - \frac{1}{2} C_{ijkl} \int_{\mathbf{r}} \delta\varepsilon_{ij}^c(\mathbf{r}) \varepsilon_{kl}^0(\mathbf{r}) \mathbf{d}\mathbf{r} \\ &= \frac{1}{2} C_{ijkl} \bar{\varepsilon}_{ij}^c \bar{\varepsilon}_{kl}^c - C_{ijkl} \bar{\varepsilon}_{ij}^c \delta_{kl} \eta c_0 \\ &\quad + \frac{1}{2} C_{ijkl} \delta_{ij} \delta_{kl} \eta^2 \overline{\{c(\mathbf{r})\}^2} \\ &\quad - \frac{1}{2} \int_{\mathbf{k}} n_i \sigma_{ij} \Omega_{jk}(\mathbf{n}) \sigma_{kl} n_l |\delta\hat{c}(\mathbf{k})|^2 \frac{\mathbf{d}\mathbf{k}}{(2\pi)^3}, \end{aligned} \quad (21.48)$$

where \mathbf{n} is a unit vector in the \mathbf{k} direction, $\mathbf{n} \equiv \mathbf{k}/|\mathbf{k}|$, and $\Omega_{ik}^{-1}(\mathbf{n}) \equiv C_{ijkl}n_j n_l$. The following equations

$$\begin{aligned} \int_{\mathbf{r}} \delta \varepsilon_{ij}^c(\mathbf{r}) \, d\mathbf{r} &= 0, \\ \int_{\mathbf{r}} \varepsilon_{ij}^0(\mathbf{r}) \, d\mathbf{r} &= \delta_{ij} \eta \int_{\mathbf{r}} c(\mathbf{r}) \, d\mathbf{r} = \delta_{ij} \eta c_0, \\ \int_{\mathbf{r}} C_{ijkl} \delta \varepsilon_{ij}^c(\mathbf{r}) \varepsilon_{kl}^0(\mathbf{r}) \, d\mathbf{r} &= \int_{\mathbf{r}} C_{ijkl} \delta \varepsilon_{ij}^c(\mathbf{r}) \delta \varepsilon_{kl}^c(\mathbf{r}) \, d\mathbf{r}, \end{aligned}$$

are used for formulation of (21.48). The last relation of the above equations is obtained as follows

$$\begin{aligned} \int_S \delta \sigma_{ij}^c(\mathbf{r}) u_i(\mathbf{r}) n_j \, dS - \int_{\mathbf{r}} \delta \sigma_{ij,j}^c(\mathbf{r}) u_i(\mathbf{r}) \, d\mathbf{r} &= 0, \\ \left[\because \delta \sigma_{ij}^c(\mathbf{r}) n_j = 0, \quad \delta \sigma_{ij,j}^c(\mathbf{r}) = 0 \right], \\ \int_{\mathbf{r}} \delta \sigma_{ij}^c(\mathbf{r}) \delta \varepsilon_{ij}^c(\mathbf{r}) \, d\mathbf{r} &= 0, \\ \int_{\mathbf{r}} C_{ijkl} \delta \varepsilon_{ij}^c(\mathbf{r}) \{ \delta \varepsilon_{kl}^c(\mathbf{r}) - \varepsilon_{kl}^0(\mathbf{r}) \} \, d\mathbf{r} &= 0, \\ \therefore \int_{\mathbf{r}} C_{ijkl} \delta \varepsilon_{ij}^c(\mathbf{r}) \varepsilon_{kl}^0(\mathbf{r}) \, d\mathbf{r} &= \int_{\mathbf{r}} C_{ijkl} \delta \varepsilon_{ij}^c(\mathbf{r}) \delta \varepsilon_{kl}^c(\mathbf{r}) \, d\mathbf{r}, \end{aligned}$$

where $\delta \sigma_{ij}^c(\mathbf{r}) = C_{ijkl} \{ \delta \varepsilon_{kl}^c(\mathbf{r}) - \varepsilon_{kl}^0(\mathbf{r}) \}$ and the Gauss integral is used. Furthermore, the mechanical equilibrium equation and the force balance at the body surface, i. e., the pressure on the surface is assumed to be 0, are considered.

Step 5

In the final stage of evaluating the elastic strain energy, the average value of the total strain $\bar{\varepsilon}_{ij}^c$ is determined. $\bar{\varepsilon}_{ij}^c$ is commonly evaluated by one of the following four types of boundary conditions.

1. The surface of the body is rigidly constrained and there is no external stress field. Since the surface is fixed, the average of the total strain should be 0, i. e.,

$$\bar{\varepsilon}_{ij}^c = 0. \quad (21.49)$$

2. The body is constrained under homogeneous external strain $\bar{\varepsilon}_{ij}^a$. In this case, the average total strain is the same as $\bar{\varepsilon}_{ij}^a$, i. e.,

$$\bar{\varepsilon}_{ij}^c = \bar{\varepsilon}_{ij}^a, \quad (21.50)$$

where the $\bar{\varepsilon}_{ij}^a$ is a known variable given by the boundary condition.

3. The surface of the body is unfixed and there is no external stress.

In this case, since the object can be expanded or contracted freely, the average total strain under a stable state should satisfy the condition

$$\frac{\partial E_{\text{str}}}{\partial \bar{\varepsilon}_{ij}^c} = 0. \quad (21.51)$$

Substituting (21.48) into (21.51), we obtain the following relation

$$\begin{aligned} \frac{\partial E_{\text{str}}}{\partial \bar{\varepsilon}_{ij}^c} = C_{ijkl} \bar{\varepsilon}_{kl}^c - C_{ijkl} \delta_{kl} \eta c_0 &= 0, \\ \therefore \bar{\varepsilon}_{kl}^c &= \delta_{kl} \eta c_0. \end{aligned} \quad (21.52)$$

4. The surface of the body is unfixed and the external stress σ_{ij}^a is applied.

In this case, the Gibbs energy is given as

$$G = E_{\text{str}} - \sigma_{ij}^a \bar{\varepsilon}_{ij}^c. \quad (21.53)$$

Since the average of total strain under the stable state should satisfy the condition

$$\frac{\partial G}{\partial \bar{\varepsilon}_{ij}^c} = 0, \quad (21.54)$$

substituting (21.53) and (21.48) into (21.54) yields

$$\begin{aligned} \frac{\partial G}{\partial \bar{\varepsilon}_{ij}^c} = C_{ijkl} \bar{\varepsilon}_{kl}^c - C_{ijkl} \delta_{kl} \eta c_0 - \sigma_{ij}^a &= 0, \\ \therefore \bar{\varepsilon}_{kl}^c = C_{ijkl}^{-1} \sigma_{ij}^a + \delta_{kl} \eta c_0, \end{aligned} \quad (21.55)$$

where C_{ijkl}^{-1} is an elastic compliance, i. e., an inverse matrix of C_{ijkl} .

It is worth noting that the elastic strain is expressed using (21.52) as

$$\begin{aligned} \varepsilon_{ij}^{\text{el}}(\mathbf{r}) &= \varepsilon_{ij}^c(\mathbf{r}) - \varepsilon_{ij}^0(\mathbf{r}) \\ &= \bar{\varepsilon}_{ij}^c + \delta \varepsilon_{ij}^c(\mathbf{r}) - \eta \delta_{ij} c(\mathbf{r}) \\ &= \delta_{ij} \eta c_0 + \delta \varepsilon_{ij}^c(\mathbf{r}) - \eta \delta_{ij} c(\mathbf{r}) \\ &= \delta \varepsilon_{ij}^c(\mathbf{r}) - \eta \delta_{ij} [c(\mathbf{r}) - c_0]. \end{aligned} \quad (21.56)$$

This equation means that the phrases *the mechanical equilibrium condition of the uniform strain is considered* and the *eigenstrain is redefined as $\varepsilon_{ij}^0(\mathbf{r}) \equiv \eta \delta_{ij} [c(\mathbf{r}) - c_0]$* are equivalent.

As for the multicomponent and multiphase system, the eigenstrain is expressed as a linear function of the order parameters ϕ_p as

$$\varepsilon_{ij}^0(\mathbf{r}, t) = \sum_p \varepsilon_{ij}^{00}(p) \phi_p(\mathbf{r}, t), \quad (21.57)$$

where ϕ_p corresponds to the composition field c and the squire of crystal structure field s^2 . $\varepsilon_{ij}^{00}(p)$ is a lattice mismatch concerning the order parameter ϕ_p . The derivation of elastic strain energy in this case is straightforward.

The evaluation of E_{str} mentioned above is for the homogeneous case, i. e., the elastic constant does not depend on the local order parameter. The elastic strain energy calculation in inhomogeneous case has been proposed and discussed in [21.39, 40].

21.2.4 Free Energy for Ferromagnetic and Ferroelectric Phase Transition

The order parameter used to describe ferromagnetic phase transition is a magnetization moment M , and the polarization moment P is employed as an order parameter for representing the ferroelectric phase transition in dielectric materials. In order to describe the ferromagnetic or ferroelectric domain microstructure formation in the phase-field method, the order parameters, M and P , are defined as a function of position \mathbf{r} and time t .

Since a description of the energy for the ferromagnetic and ferroelectric phase transition has a quite similar formulation, we explain the total free energy description for a ferroelectric phase transition during the structural phase transformation from cubic to tetragonal along the line of Wang's analysis [21.20].

In this field, the Landau-type bulk free energy density is commonly expressed by a six-order polynomial of the spontaneous polarization

$$\begin{aligned} g_c = & \alpha_1(P_1^2 + P_2^2 + P_3^2) + \alpha_2(P_1^4 + P_2^4 + P_3^4) \\ & + \alpha_3(P_1^2 P_2^2 + P_2^2 P_3^2 + P_3^2 P_1^2) \\ & + \alpha_4(P_1^6 + P_2^6 + P_3^6) \\ & + \alpha_5 \left[P_1^4(P_2^2 + P_3^2) + P_2^4(P_3^2 + P_1^2) \right. \\ & \left. + P_3^4(P_1^2 + P_2^2) \right] \\ & + \alpha_6 P_1^2 P_2^2 P_3^2, \end{aligned} \quad (21.58)$$

where three variants are considered, and α_i are constant coefficients. The subscripts $i = 1, 2$, and 3 ; indicate a variant number. In the Ginzburg–Landau theory, the free energy function also depends on the gradient of the order parameter (that is, corresponding to the gradient energy). For ferroelectric materials, the polarization gradient energy represents the ferroelectric domain wall energy. For simplicity, the lowest order of the gradient

energy density takes the form

$$\begin{aligned} f_{\text{grad}} = & \frac{1}{2} \kappa_1 (P_{1,1}^2 + P_{2,2}^2 + P_{3,3}^2) \\ & + \kappa_2 (P_{1,1} P_{2,2} + P_{2,2} P_{3,3} + P_{3,3} P_{1,1}) \\ & + \frac{1}{2} \kappa_3 \left[(P_{1,2} + P_{2,1})^2 + (P_{2,3} + P_{3,2})^2 \right. \\ & \left. + (P_{1,3} + P_{3,1})^2 \right] \\ & + \frac{1}{2} \kappa_4 \left[(P_{1,2} - P_{2,1})^2 + (P_{2,3} - P_{3,2})^2 \right. \\ & \left. + (P_{1,3} - P_{3,1})^2 \right], \end{aligned} \quad (21.59)$$

where κ_i are gradient energy coefficients and $P_{i,j}$ denotes the derivative of the i th component of the polarization vector P_i with respect to the j th coordinate.

In the phase-field simulations, each element is represented by an electric dipole with its strength of the dipole being given by a local polarization vector P_i . The multiple dipole–dipole electric interactions play a crucial role in calculating the morphology of a domain structure and in the process of domain switching as well. The multiple dipole–dipole electric interaction energy density is calculated by

$$f_d(\mathbf{r}) = -\frac{1}{2} f_{\text{dip}}(\mathbf{r}) \cdot \mathbf{P}(\mathbf{r}), \quad (21.60)$$

where

$$\begin{aligned} f_{\text{dip}}(\mathbf{r}) = & -\frac{1}{4\pi\varepsilon} \int_{r'} \left\{ \frac{\mathbf{P}(r')}{|\mathbf{r} - \mathbf{r}'|^3} \right. \\ & \left. - \frac{3(\mathbf{r} - \mathbf{r}')\mathbf{P}(r') \cdot (\mathbf{r} - \mathbf{r}')}{|\mathbf{r} - \mathbf{r}'|^5} \right\} d\mathbf{r}' \end{aligned} \quad (21.61)$$

is the electric field at point \mathbf{r} induced by all dipoles. When there is an externally applied electric field E_a , an additional electrical energy

$$f_a = -E_i^e P_i \quad (21.62)$$

should be taken into account in the simulations. The spontaneous strains are associated with spontaneous polarizations. The eigenstrains are linked to the polarization components in the following form

$$\begin{aligned} \varepsilon_{11}^0 &= Q_{11} P_1^2 + Q_{12} (P_2^2 + P_3^2), \\ \varepsilon_{22}^0 &= Q_{11} P_2^2 + Q_{12} (P_1^2 + P_3^2), \\ \varepsilon_{33}^0 &= Q_{11} P_3^2 + Q_{12} (P_1^2 + P_2^2), \\ \varepsilon_{12}^0 &= \varepsilon_{21}^0 = Q_{44} P_1 P_2, \\ \varepsilon_{23}^0 &= \varepsilon_{32}^0 = Q_{44} P_2 P_3, \\ \varepsilon_{31}^0 &= \varepsilon_{13}^0 = Q_{44} P_1 P_3, \end{aligned} \quad (21.63)$$

where Q_{ij} are the electrostrictive coefficients. When a dipole is among other dipoles with different orientations, there exist multiple dipole–dipole elastic interactions. The multiple dipole–dipole elastic interactions play an essential role in the determination of a domain structure. A twin-like domain structure is formed when the multiple dipole–dipole elastic interactions predominate.

Due to the constraint of the surroundings, the polarization-related strains include two parts: the elastic strain and the eigenstrain. The elastic strain related to polarization and/or polarization switching is given by

$$\varepsilon_{ij}^{\text{el}} = \varepsilon_{ij}^{\text{c}} - \varepsilon_{ij}^{\text{o}}. \quad (21.64)$$

When there exists an externally applied homogeneous stress σ_{kl}^{a} , using the superposition principle, we have the total elastic strains of the system

$$\varepsilon_{ij}^{\text{el}} = \varepsilon_{ij}^{\text{c}} - \varepsilon_{ij}^{\text{o}} + S_{ijkl}\sigma_{kl}^{\text{a}}, \quad (21.65)$$

where S_{ijkl} is the elastic compliance matrix. Finally, the elastic strain energy density under the cubic approximation is given by

$$e_{\text{str}} = \frac{1}{2}C_{11} \left[\left(\varepsilon_{11}^{\text{el}} \right)^2 + \left(\varepsilon_{22}^{\text{el}} \right)^2 + \left(\varepsilon_{33}^{\text{el}} \right)^2 \right] + C_{12} \left(\varepsilon_{11}^{\text{el}}\varepsilon_{22}^{\text{el}} + \varepsilon_{22}^{\text{el}}\varepsilon_{33}^{\text{el}} + \varepsilon_{33}^{\text{el}}\varepsilon_{11}^{\text{el}} \right)$$

21.3 Solidification

21.3.1 Pure Metal

The interface between a liquid phase and a solid one is expressed by the continuum scalar function ϕ , which is called a phase-field variable and takes values from 0 (liquid phase) to 1 (solid phase) as illustrated in Fig. 21.1. The variable ϕ is a function of spatial position $\mathbf{r} = (x, y, z)$ and time t , and then the solidification process is represented by a temporal development of the ϕ field. Indicating the interface using ϕ , we are able to treat the complex changes of interface shapes such as a dendrite. The conditions of the interface curvature and temperature distribution around the interface are automatically satisfied by employing the parameters obtained from the physical properties at the interface.

The total free energy of the pure metal during solidification is given by

$$F = \int_V \left[f(\phi, T) + \frac{1}{2}\varepsilon^2 |\nabla\phi|^2 \right] dV, \quad (21.68)$$

$$+ 2C_{44} \left[\left(\varepsilon_{12}^{\text{el}} \right)^2 + \left(\varepsilon_{23}^{\text{el}} \right)^2 + \left(\varepsilon_{31}^{\text{el}} \right)^2 \right]. \quad (21.66)$$

As described above, the elastic strain energy is a function of polarization and applied stresses. An applied electric field can change the polarization and consequently vary the elastic strain energy density. On the other hand, an applied stress field can also change the polarization and thus change the electric energy density.

Integrating the free energy density over the entire volume of a simulated ferroelectric material yields the total free energy, F_{ele} , under externally applied electrical and mechanical loads, E_i^{c} and σ_{kl}^{a} . Mathematically, we have

$$F_{\text{ele}} = \int_{\mathbf{r}} \left[g_{\text{c}}(P_i) + f_{\text{grad}}(P_{i,j}) + e_{\text{str}}(P_i, \sigma_{kl}^{\text{a}}) \right] d\mathbf{r} + \int_{\mathbf{r}} \left[f_{\text{d}}(P_i) + f_{\text{a}}(P_i, E_i^{\text{c}}) \right] d\mathbf{r}. \quad (21.67)$$

As for the energy description for a ferromagnetic phase transition, the order parameter is changed from P to M . The bulk Landau free energy density, in this case, corresponds the magnetocrystalline anisotropy energy. The formulation of another parts is almost the same and straightforward.

where $f(\phi, T)$ is a chemical free energy defined by

$$f(\phi, T) \equiv h(\phi)f^{\text{s}}(T) + [1 - h(\phi)]f^{\text{l}}(T) + Wg(\phi). \quad (21.69)$$

Functions $f^{\text{s}}(T)$ and $f^{\text{l}}(T)$ are the chemical free energy for the solid and the liquid phase, respectively, given as a function of temperature T . The function $h(\phi)$ is a monotonic increasing function satisfying the constraint $h(0) = 0$ and $h(1) = 1$. The product $Wg(\phi)$ in the right-hand side of (21.69) is the energy barrier term, which takes a maximum value W within $0 < \phi < 1$ and $g(0) = g(1) = 0$, and is introduced in order to not mix the solid and liquid phases. The second term inside the integral of the right-hand side in (21.68) is a gradient energy that corresponds to the interfacial energy, and ε^2 is the gradient energy coefficient. When orientation dependence on the interfacial energy is considered, ε is assumed as a function of orientation.

In the phase-field method, the temporal and spatial development of the ϕ field is assumed to be proportional

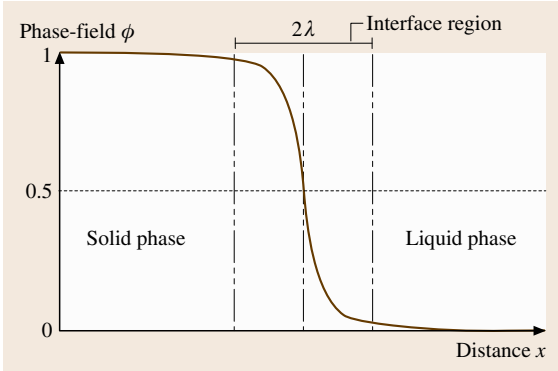


Fig. 21.1 Schematic illustration of the one-dimensional profile of phase-field order parameter ϕ across the interface. The variable ϕ is commonly defined as a function of spatial position \mathbf{r} and time t , and the field dynamics, such as a solidification process, is represented by a temporal development of the field $\phi(\mathbf{r}, t)$

to the variation of the total free energy F with respect to ϕ , therefore the following differential evolution equation

$$\frac{\partial \phi}{\partial t} = -M_{\phi} \frac{\delta F}{\delta \phi}, \quad (21.70)$$

is employed, where M_{ϕ} is a mobility of the interface motion. As for the temporal and spatial changes of a temperature field, the thermal diffusion equation

$$\frac{\partial T}{\partial t} = D \nabla^2 T - p(\phi) \frac{L}{C_p} \frac{\partial \phi}{\partial t} \quad (21.71)$$

is applied. The second term of the right-hand side of (21.71) means the diverging term of heat produced from latent heat during solidification. Symbols D , L , and C_p are thermal diffusivity, latent heat, and specific heat, respectively. A function $p(\phi)$ satisfies the conditions $\int_0^1 p(\phi) d\phi = 1$ and $p(0) = p(1) = 0$, which is often defined by $p(\phi) \equiv \partial h / \partial \phi$ using the function $h(\phi)$. The phase-field method for the solidification simulation in a pure metal is calculated based on (21.70) and (21.71). The parameters M_{ϕ} , W , and ε are determined from the interface thickness 2λ (Fig. 21.1) and the interfacial energy density σ . The relations between them are summarized as

$$M_{\phi} = \frac{T_m \mu \sigma}{\varepsilon^2 L}, \quad \sigma = \frac{\varepsilon \sqrt{W}}{3\sqrt{2}}, \quad 2\lambda = 2.2\sqrt{2} \frac{\varepsilon}{\sqrt{W}}. \quad (21.72)$$

T_m is the melting temperature, and μ is the kinetic coefficient determined by $v_n / \mu = f^L - f^S - 2\sigma / R$ that

is an equation of the sharp interface motion, where v_n and R are an interface velocity and a curvature at the interface. The numerical technique to solve the nonlinear differential equations is commonly a finite difference simulation. Since the calculation method is mathematically equivalent to that solving the differential equation describing temporal field dynamics, we can utilize many techniques developed in the field of the computational fluid dynamics.

The result of a two-dimensional simulation of dendrite growth in pure metal is shown in Fig. 21.2. The black and white parts are the solid and liquid phase, respectively. Note that the complex morphological change of the realistic dendrite growth is quite reasonably calculated.

Since the width of the solid–liquid interface in the solidification process commonly has the length of an atomic scale, the temperature field causes numerical errors in the gradual interface as shown in Fig. 21.1, if the numerical difference calculation is performed using coarse difference dividing cells. Since the parameter M is derived assuming the temperature is constant within the interface, a small calculation mesh size is required to neglect the temperature change though the interface region in the numerical simulation. Hence, the interface width should be negligibly small as compared to the capillary length and theoretically at the sharp interface limit. However, the value of the interface width is sometimes selected as large beyond the restriction for the computational efficiency.

This made the limit of the phase-field method at an early stage when this simulation method was proposed, but the new technique (called the thin interface limit model) of amending the point mentioned above has already been proposed. For example, *Karma* and *Rappel* [21.10] derived the phase-field mobility in the thin interface limit to relax the restriction of the interface

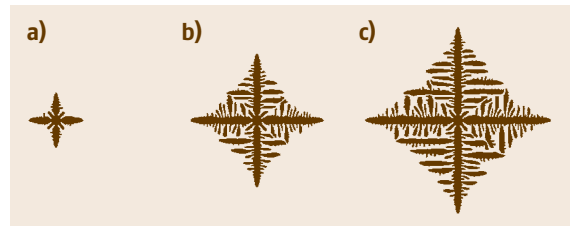


Fig. 21.2a–c Two-dimensional phase-field simulation of a dendrite growth process in pure metal is represented from (a)–(c). The black and white parts represent a solid and liquid phase, respectively

width and expressed it as follows

$$M^{-1} = \frac{\varepsilon^2 L}{T_m \sigma} \left(\frac{1}{\mu} + \frac{\delta L}{4 D C_p} K \right)^{-1},$$

$$K = \int_0^1 \frac{h(\phi) [1 - h(\phi)]}{\phi(1 - \phi)} d\phi. \quad (21.73)$$

This thin interface limit model not only improves computer efficiency but also removes the limitation for the kinetic coefficient. They showed that the numerical calculation of the dendrite shape using the phase-field model agreed well with the solvability theory in both 2-D and 3-D. Therefore, we should emphasize that the idea that the phase-field method always physically requires a smooth interface is a mistake, and the phase-field method can be applied to the sharp interface with one atomic layer.

21.3.2 Alloy

In the phase-field model for alloy solidification, the local solute composition c is also employed as one of the phase-field order parameters and the gradient energy term for the solute composition field is introduced into the total free energy functional. But when the interface region is small relative to the entire microstructure simulated, a similar problem explained for the temperature field in the above section arises for the composition field. The thin interface model considering the composition field was proposed by *Kim et al.* [21.11]. They defined the interface as a fraction weighted mixture of the solid and liquid with different compositions and free energy, where the compositions of solid and liquid at the interface are determined to have the same chemical potential μ , i.e., the local equilibrium is assumed to be

$$\begin{aligned} f^s &= c_S f_B^s(T) + (1 - c_S) f_a^s(T), \\ f^L &= c_L f_B^L(T) + (1 - c_L) f_a^L(T), \\ c &= h(\phi) c_S + [1 - h(\phi)] c_L, \\ \mu^s(c_S) &= \mu^L(c_L). \end{aligned} \quad (21.74)$$

The local solute composition of the solid phase and the liquid one is denoted by c_S and c_L , respectively. This model is called the **KKS** model (Kim–Kim–Suzuki model) [21.11], where a solute diffusion equation is solved simultaneously as

$$\frac{\partial c}{\partial t} = \nabla \cdot \left(\frac{D_c(\phi)}{f_{cc}} \nabla f_c \right), \quad (21.75)$$

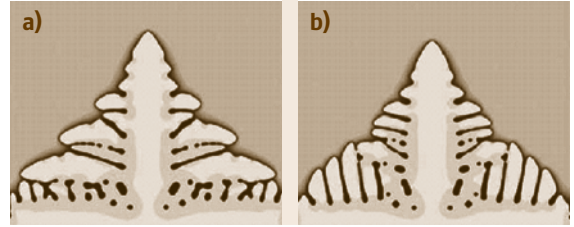


Fig. 21.3a,b The change in dendrite shape of steel due to a ternary alloying element is demonstrated for (a) Fe-0.5 mol % C; and (b) Fe-0.5 mol % C-0.001 mol % P (after [21.12]). The simulation results show that a small addition of phosphorus changes the secondary arm spacing significantly even when it does not significantly change the interface velocity

where D_c is the solute diffusivity and f_c and f_{cc} are the first and the second derivatives of the chemical free energy density. The parameters, ε and W , are the same as the ones in the pure material solidification case defined by (21.72). The mobility M in the thin interface limit was also derived by *Kim et al.* as

$$M^{-1} = \frac{\varepsilon^2}{\sigma} \left[\frac{RT}{V_m} \frac{1 - k^e}{m^e} \frac{1}{\mu} + \frac{\varepsilon}{D_L \sqrt{2W}} \zeta(c_S^e, c_L^e) \right],$$

$$\zeta(c_S^e, c_L^e) = f_{cc}^s(c_S^e) f_{cc}^L(c_L^e) (c_L^e - c_S^e)^2$$

$$\times \int_0^1 \frac{h(\phi) [1 - h(\phi)]}{[1 - h(\phi)] f_{cc}^s(c_S^e) + h(\phi) f_{cc}^L(c_L^e)} \frac{1}{\phi(1 - \phi)} d\phi, \quad (21.76)$$

where D_L is a diffusion coefficient of liquid phase, k^e and m^e are a partition coefficient and a gradient of liquidus line on the corresponding phase diagram, respectively. V_m is a molar volume and the superscript e indicates that the parameter is in a local equilibrium state.

The phase-field simulation of the dendrite shape changes performed by *Suzuki et al.* for Fe-0.5 mol % C binary alloy and Fe-0.5 mol % C-0.001 mol % P ternary alloy at 1780 K is shown in Fig. 21.3 [21.12]. The secondary arms develop well and the arm spacing becomes narrow with a small addition of phosphorus because the phosphorus is likely to enrich the interface and reduce the interface stability. The simulation results show that a small addition of phosphorus changes the secondary arm spacing significantly even when it does not significantly change the interface velocity.

21.4 Diffusion-Controlled Phase Transformation

21.4.1 Cahn–Hilliard Diffusion Equation

Since the relation between the kinetics and the thermodynamics of phase transformations is plainly formulated in the diffusion theory treating an interdiffusion, the diffusion controlled phase decomposition in solid-solid phase transformations is a very good example for explaining the relation between energetics and dynamics in microstructure evolution. In this section, the basis of the diffusion equation concerning phase decomposition is explained [21.41].

From a physical viewpoint, atom diffusion in solids is formulated based on the equation of the friction. Because the diffusion of the atom inside the solid corresponds to the movement of the object in the medium with a very strong viscosity, the inertia term in the equation of motion (the so-called Ranjuban equation) attenuates exponentially and only the friction term will remain. We consider the case where atom A moves with speed \mathbf{v}_1 and a thermodynamic driving force to move this atom is assumed to be \mathbf{F}_1 . The \mathbf{F}_1 is defined by

$$\mathbf{f}_1 = -\nabla\mu_1, \quad (21.77)$$

where μ_1 is the chemical potential of component A. Thus, the velocity of atom A, \mathbf{v}_1 , is given by the equation of the friction

$$\mathbf{v}_1 = M_1 \mathbf{f}_1 = -M_1 \nabla\mu_1, \quad (21.78)$$

where M_1 is the mobility for atom A diffusion, which is a parameter indicating the easiness of atom movement and is physically equivalent to the reciprocal of the friction coefficient. M_1 is, exactly, a function of the local composition around the atom A in diffusing, but it is often assumed to be constant for simplicity. Using (21.78), we obtain the diffusion flow of component A, \mathbf{J}_1 , which is induced by a driving force \mathbf{F}_1 , as

$$\mathbf{J}_1 = c_1 \mathbf{v}_1 = -M_1 c_1 \nabla\mu_1, \quad (21.79)$$

where c_1 is a local composition of component A.

Next, we derive the equation of interdiffusion for the diffusion couple of A–B binary system. Henceforth, the element names A and B are referred to as 1 and 2, respectively, at the symbol subscript. The equation describing the interdiffusion is derived by eliminating \mathbf{v}_0 in the right-hand side of the following equations, which are the governing equations for a macroscopic flux flow of the solute element

$$\begin{aligned} \mathbf{J}_1 &= -c_1 M_1 \nabla\mu_1 + \mathbf{v}_0 c_1, \\ \mathbf{J}_2 &= -c_2 M_2 \nabla\mu_2 + \mathbf{v}_0 c_2, \end{aligned} \quad (21.80)$$

where \mathbf{v}_0 is a macroscopic flux flow of the solute element, for instance, in the diffusion couple, it corresponds to the macroscopic velocity of coupling interface. According to the conservation law, the diffusion equation is defined as

$$\begin{aligned} \frac{\partial c_1}{\partial t} &= -\nabla \cdot \mathbf{J}_1 = \nabla \cdot (c_1 M_1 \nabla\mu_1 - \mathbf{v}_0 c_1), \\ \frac{\partial c_2}{\partial t} &= -\nabla \cdot \mathbf{J}_2 = \nabla \cdot (c_2 M_2 \nabla\mu_2 - \mathbf{v}_0 c_2). \end{aligned} \quad (21.81)$$

Therefore, the relation

$$\begin{aligned} \frac{\partial(c_1 + c_2)}{\partial t} &= \nabla \cdot (c_1 M_1 \nabla\mu_1 + c_2 M_2 \nabla\mu_2 - \mathbf{v}_0) = 0 \\ \therefore c_1 M_1 \nabla\mu_1 + c_2 M_2 \nabla\mu_2 - \mathbf{v}_0 &= C : \text{const} \end{aligned}$$

is obtained by considering $c_1 + c_2 = 1$. Furthermore, if we assume $\nabla\mu_1 = 0$, $\nabla\mu_2 = 0$ and $\mathbf{v}_0 = 0$ at the position far from the coupling interface, the value of C should be 0. Because C is a constant and independent of position. Therefore, the velocity of the coupling interface is given by

$$\mathbf{v}_0 = c_1 M_1 \nabla\mu_1 + c_2 M_2 \nabla\mu_2. \quad (21.82)$$

Substituting (21.82) into (21.81), we obtain the interdiffusion equation as a form of

$$\begin{aligned} \mathbf{J}_1 &= -(c_2 M_1 + c_1 M_2) c_1 \nabla\mu_1 \\ &= -(c_2 M_1 + c_1 M_2) c_1 c_2 \nabla(\mu_1 - \mu_2) \\ &= -(c_2 M_1 + c_1 M_2) c_1 c_2 \nabla \left(\frac{\partial g_c}{\partial c_1} \right) \\ &= -(c_2 M_1 + c_1 M_2) c_1 c_2 \left(\frac{\partial^2 g_c}{\partial c_1^2} \right) \nabla c_1, \\ \mathbf{J}_2 &= -(c_2 M_1 + c_1 M_2) c_2 \nabla\mu_2 \\ &= -(c_2 M_1 + c_1 M_2) c_1 c_2 \nabla(\mu_2 - \mu_1) \\ &= -(c_2 M_1 + c_1 M_2) c_1 c_2 \nabla \left(\frac{\partial g_c}{\partial c_2} \right) \\ &= -(c_2 M_1 + c_1 M_2) c_1 c_2 \left(\frac{\partial^2 g_c}{\partial c_2^2} \right) \nabla c_2. \end{aligned} \quad (21.83)$$

In the formulation of (21.83), the Gibbs–Duhem relations

$$\begin{aligned} c_1 d\mu_1 + c_2 d\mu_2 &= 0, \\ \rightarrow c_1 d\mu_1 + c_2 d\mu_1 &= c_2 d\mu_1 - c_2 d\mu_2, \\ \therefore d\mu_1 &= c_2 d(\mu_1 - \mu_2) \end{aligned}$$

and

$$\begin{aligned}\frac{\partial g_c}{\partial c_1} &= \mu_1 - \mu_2 + c_1 \frac{\partial \mu_1}{\partial c_1} + c_2 \frac{\partial \mu_2}{\partial c_1} \\ &= \mu_1 - \mu_2, \\ \frac{\partial g_c}{\partial c_2} &= \mu_2 - \mu_1,\end{aligned}$$

are used, where g_c is a chemical free energy density. According to (21.83), the interdiffusion coefficient is expressed as follows

$$\begin{aligned}\tilde{D}_1 &= (c_2 M_1 + c_1 M_2) c_1 c_2 \left(\frac{\partial^2 g_c}{\partial c_1^2} \right), \\ \tilde{D}_2 &= (c_2 M_1 + c_1 M_2) c_1 c_2 \left(\frac{\partial^2 g_c}{\partial c_2^2} \right).\end{aligned}\quad (21.84)$$

In particular, when g_c is a chemical free energy for an ideal solid solution, we find the relation $\partial^2 g_c / \partial c_1^2 = \partial^2 g_c / \partial c_2^2 = RT / (c_1 c_2)$ and entering this into (21.84), we have

$$\tilde{D}_1 = \tilde{D}_2 = c_2 M_1 RT + c_1 M_2 RT = c_2 D_1^* + c_1 D_2^*, \quad (21.85)$$

where $D_1^* = M_1 RT$ and $D_2^* = M_2 RT$ are the Einstein's relations, R is the gas constant and T is the absolute temperature, and D_i^* is a self-diffusion coefficient.

On the other hand, the phenomenological equation for the generalized Fick's first law is defined as

$$\begin{aligned}\mathbf{J}_1 &= -L_{11} \nabla \mu_1 - L_{12} \nabla \mu_2, \\ \mathbf{J}_2 &= -L_{21} \nabla \mu_1 - L_{22} \nabla \mu_2,\end{aligned}\quad (21.86)$$

where L_{ij} is the Onsager coefficient, which should satisfy the relation

$$L_{11} + L_{21} = 0, \quad L_{12} + L_{22} = 0, \quad L_{12} = L_{21}. \quad (21.87)$$

The above relation is derived from the restriction of solute conservation law and the condition of the detailed balance of local equilibrium. Considering (21.87) in (21.86), we get

$$\begin{aligned}\mathbf{J}_1 &= -L_{11} \nabla (\mu_1 - \mu_2), \\ \mathbf{J}_2 &= -L_{22} \nabla (\mu_2 - \mu_1).\end{aligned}\quad (21.88)$$

Since (21.83) and (21.88) should be the same equation, the Onsager coefficient is given by

$$\begin{aligned}L_{11} &= L_{22} = (c_2 M_1 + c_1 M_2) c_1 c_2, \\ L_{12} &= L_{21} = 0.\end{aligned}\quad (21.89)$$

An important point is that the interdiffusion and Onsager coefficients are obtained using (21.84) and (21.85), if a self-diffusion coefficient and a chemical free energy function g_c are experimentally determined.

Although we considered the chemical free energy g_c in the formulation mentioned above, the more general evolution equation that is able to describe the microstructure changes in the diffusion controlled phase transformation can be deduced using the total free energy of the microstructure G_{sys} instead of the chemical free energy g_c . For instance, the diffusion flux \mathbf{J}_2 is expressed as

$$\mathbf{J}_2 = -(c_2 M_1 + c_1 M_2) c_1 c_2 \nabla \frac{\delta G_{\text{sys}}}{\delta c_2}. \quad (21.90)$$

By comparing (21.83) and (21.90), the mobility M_c should be written as

$$M_c(c_2) = (c_2 M_1 + c_1 M_2) c_1 c_2. \quad (21.91)$$

Therefore, the nonlinear diffusion equation describing diffusion-controlled phase transformations is given as

$$\frac{\partial c_2}{\partial t} = \nabla \cdot \left[M_c(c_2) \nabla \frac{\delta G_{\text{sys}}}{\delta c_2} \right], \quad (21.92)$$

where the composition fluctuation term (i. e., the random noise term) is ignored.

This equation is a general form for the diffusion equation, and the Cahn–Hilliard equation [21.29] is also constructed from this equation. In the spinodal theory, the total free energy G_{sys} of the phase decomposed inhomogeneous microstructure is expressed as

$$\begin{aligned}G_{\text{sys}} &= \frac{1}{L} \int_x \left[g_c(c) + \eta^2 Y_{(hkl)} (c - c_0)^2 + \kappa \left(\frac{\partial c}{\partial x} \right)^2 \right] dx, \\ &\quad (21.93)\end{aligned}$$

where the one-dimensional system (the one-dimensional spatial direction is denoted by x with a total length L) is considered for simplicity, and c is a local solute composition of element B in an A–B binary alloy system. The quantities η , $Y_{(hkl)}$, and κ are the lattice mismatch, the function of the elastic constants, and the composition gradient energy coefficient, respectively. The first, second, and third terms in the integral at the right-hand side of (21.93) correspond to a chemical free energy, an elastic strain energy, and a composition gradient energy, respectively. If F is defined by the sum of these three terms and the variation principle is applied to F

with respect to the invariant variables c , x , and $(\partial c/\partial x)$, the variation $\delta G_{\text{sys}}/\delta c$ is given as

$$\begin{aligned} \frac{\delta G_{\text{sys}}}{\delta c} &= \frac{\partial F}{\partial c} - \frac{d}{dx} \left(\frac{\partial F}{\partial (\partial c/\partial x)} \right) \\ &= \frac{\partial g_c(c)}{\partial c} + 2\eta^2 Y_{(hkl)}(c - c_0) - 2\kappa \left(\frac{\partial^2 c}{\partial x^2} \right), \end{aligned} \quad (21.94)$$

where the Euler equation is considered. $\delta G_{\text{sys}}/\delta c$ is commonly called as a diffusion potential. Substituting (21.94) into (21.92), we obtain the nonlinear diffusion equation

$$\frac{\partial c}{\partial t} = \frac{\partial}{\partial x} \left[\tilde{D} \left(\frac{\partial c}{\partial x} \right) \right] - 2 \frac{\partial}{\partial x} \left[\tilde{K} \left(\frac{\partial^3 c}{\partial x^3} \right) \right], \quad (21.95)$$

where

$$\begin{aligned} \tilde{D} &\equiv M_c(c) \left[\frac{\partial^2 g_c(c)}{\partial c^2} + 2\eta^2 Y_{(hkl)} \right], \\ \tilde{K} &\equiv M_c(c)\kappa. \end{aligned} \quad (21.96)$$

In many textbooks of spinodal decomposition, M_c is assumed to be a constant and \tilde{K} has been moved out beside the differentiation in the second term at the right-hand side in (21.95). The value \tilde{D} , defined by (21.96), is then the interdiffusion coefficient for the coherent phase decomposition.

In the practical viewpoint for the actual numerical simulation, it is effective to directly solve the equation

$$\frac{\partial c}{\partial t} = \frac{\partial}{\partial x} \left[M_c \left(\frac{\partial \mu_{\text{sys}}}{\partial x} \right) \right] \quad (21.97)$$

instead of (21.95). In order to solve (21.97), the diffusion potential $\mu_{\text{sys}} \equiv \delta G_{\text{sys}}/\delta c$ is first calculated as a function of local position x and time t , and then (21.97) is solved using a numerical simulation technique such as a finite difference method.

21.4.2 Spinodal Decomposition and Ostwald Ripening

Two-dimensional simulation of the spinodal decomposition in the Fe-40 at. % Mo alloy within *bcc* crystal structure during isothermal aging at 773 K is represented in Fig. 21.4 [21.14], where the Mo composition is indicated using grayscale, i. e., the black part corresponds to the Mo-rich region. The phase decomposition is clearly recognized to progress with aging. The lattice mismatch of the Fe-Mo alloy system is so large

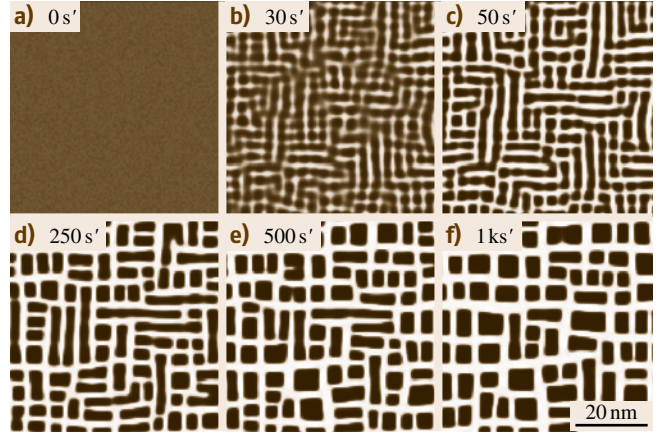


Fig. 21.4a-f Two-dimensional simulation of the spinodal decomposition in the Fe-40 at. % Mo binary alloy with *bcc* crystal structure during isothermal aging at 773 K, where the Mo composition is indicated by *gray scale*, i. e., the *black* part corresponds the Mo rich region. The lattice mismatch of the Fe-Mo alloy system is so large that a modulated structure, i. e., the microstructure with fine Mo-rich zones along the $\langle 100 \rangle$ directions, is produced by the mechanism of spinodal decomposition. Numerical values in the figure are the dimensionless aging time

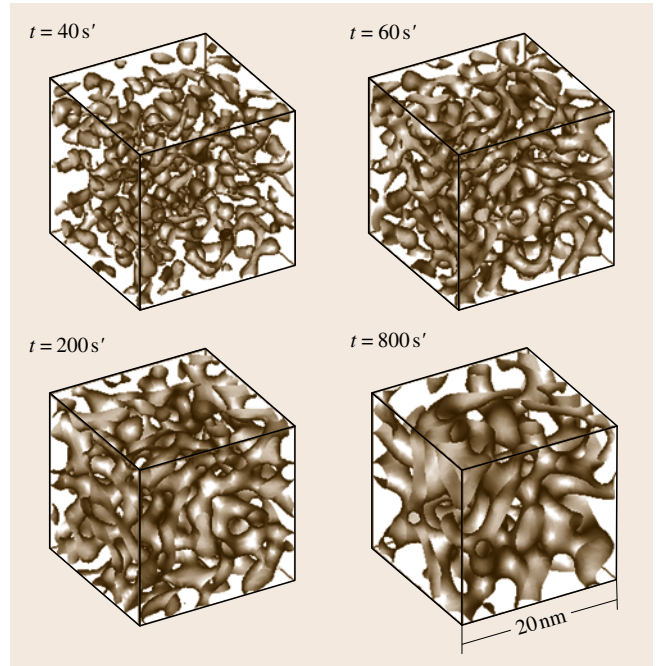


Fig. 21.5 Three-dimensional phase field simulation for the spinodal decomposition of Fe-40 at. % Cr binary alloy at 773 K. The symbol t is a dimensionless normalized aging time. The precipitate phase is represented by an isocomposition surface of 40 at. % Cr

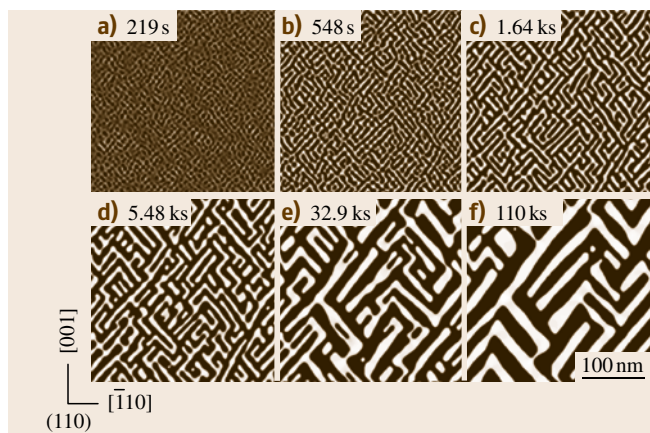


Fig. 21.6a–f Two-dimensional simulation of the spinodal decomposition of the ZrO_2 -8 mol % $\text{YO}_{1.5}$ partially stabilized zirconia at 1773 K. The calculation is performed on the two-dimensional plane of (110). The completely black and white regions indicate the composition of 16 and 0 mol % Y, respectively. Numerical values in the figure are the aging time

that a modulated structure, i. e., the microstructure with fine Mo-rich zones along $\langle 100 \rangle$ directions, is produced by the mechanism of spinodal decomposition. Since the volume fraction of precipitates becomes higher, the encounter of precipitates happens so that the rod-shaped particles are temporarily produced in many places, as seen in Fig. 21.4d. However, with further aging particle-

splitting can be observed in Fig. 21.4f. This suggests that uniformity of particle size caused by elastic interactions becomes more energetically dominant than the usual particle coarsening controlled by the interfacial energy. Figure 21.4d–f clearly shows that the microstructure is self-regulated by the elastic interaction energy so as to produce a periodic microstructure with uniform particle size. The identical microstructures have experimentally been recognized in many real alloy systems such as Ni-base superalloys.

Figure 21.5 shows three-dimensional simulation of spinodal decomposition of Fe-40 at. % Cr alloy aged at 773 K. The precipitate is represented by an isocomposition surface of 40 at. % Cr. With aging, the fine microstructure coarsens according to the Ostwald ripening mechanism that is driven by the reduction of the interfacial energy.

Figure 21.6 demonstrates the two-dimensional simulation of the spinodal decomposition of the ZrO_2 -8 mol % $\text{YO}_{1.5}$ partially stabilized zirconia at 1773 K [21.42]. The calculation is performed on the two-dimensional plane of (110). The completely black and white regions indicate the composition of 16 and 0 mol % Y, respectively. The orientation of the modulated microstructure is mainly controlled by elastic strain energy. Since the phase-field simulation is a continuum model, this simulation method is directly applicable for the phase transformation in ceramics and polymer materials.

21.5 Structural Phase Transformation

21.5.1 Martensitic Transformation

Figure 21.7 shows the simulation results of the cubic \rightarrow trigonal martensitic transformation in AuCd alloys calculated by Wang et al. [21.22]. For the cubic \rightarrow trigonal transformation, four lattice-correspondence variants are considered, i. e., four types of martensite orientation variants, with trigonal axes along the $[111]$, $[\bar{1}\bar{1}1]$, $[\bar{1}\bar{1}\bar{1}]$, and $[1\bar{1}\bar{1}]$ directions of the parent phase, are numbered 1, 2, 3, and 4, and are distinguished by shades of gray. The phase-field order parameter used in the simulation is the possibility of finding the trigonal martensite phase with variant i ($i = 1, 2, 3, 4$) at position \mathbf{r} and time t . The symbols τ and ζ indicate the reduced time and the ratio of the typical transformation strain energy to the chemical driving force, respectively.

The microstructures for $\zeta = 1$ and $\zeta = 5$ at $\tau = 30$ are presented in Fig. 21.7a and b, respectively. The effect of the contribution of elastic strain energy to the total free energy is demonstrated. Since the system with a higher value of ζ coarsens faster, Fig. 21.7a,b actually corresponds to the coarsening process of the domain structures. The microstructure is a herringbone type structure with coarsened domains. The schematic illustration of the arrangement of the domains in Fig. 21.7d is represented in Fig. 21.7c, which coincides with that observed in experiment of this alloy system [21.43].

21.5.2 Tweed-Like Structure and Twin Domain Formations

Figure 21.8 shows the calculated microstructure changes of the cubic (c) \rightarrow tetragonal (t) structural

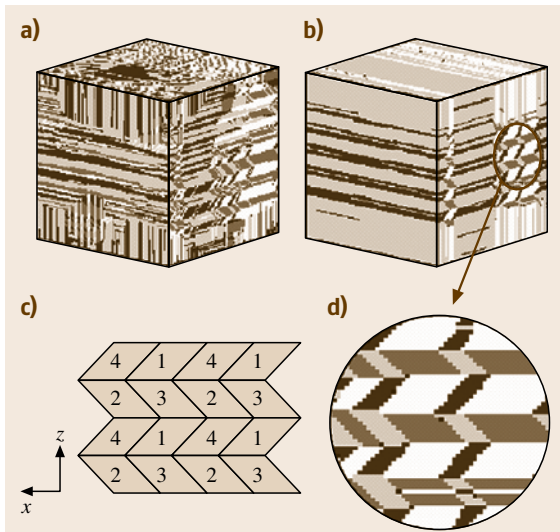


Fig. 21.7a–d Simulated three-dimensional microstructures in a single crystal computational volume faceted by the $\{100\}$ planes: (a) $\zeta = 1$ at $\tau = 30$; (b) $\zeta = 5$ at $\tau = 30$. (c) The schematic illustration of the herringbone structure shown in (d), where the numbers 1, 2, 3, and 4 represent the four types of variant domains (after [21.22])

phase transformation in Ni_2MnGa during isothermal aging, where the final equilibrium state is a single t phase and the chemical driving force for $c \rightarrow t$ phase transition is assumed to be $\Delta G^{c \rightarrow t} = -40 \text{ J/mol}$ [21.44]. This driving force seems to be relatively small compared to that for the normal martensitic transformation, because we supposed the calculation condition of aging temperature to be just below the $c \rightarrow t$ phase transition temperature. This calculation is performed on the two-dimensional plane (001). The initial condition of the microstructure is a single c phase and the grayscale of the figure means the value of $s_1^2(\mathbf{r}, t)$, so the white part is t_1 phase (e.g., t phase with variant p is written as t_p phase), and the black part corresponds to the t_2 phase. But only for Fig. 21.8a, cubic phase is also included in the black part. Numerical values in the figure are the dimensionless aging time (the time unit is described as s' not s).

At the initial stage of phase transformation, the tweed-like structure with $\langle 110 \rangle$ striation appears as shown in Fig. 21.8a,b. From Fig. 21.8c–e, t -phase domains grow gradually during aging, then a lamellar-shaped twin microstructure emerges (Fig. 21.8e) and the straight twin domain with narrow width begins to shrink

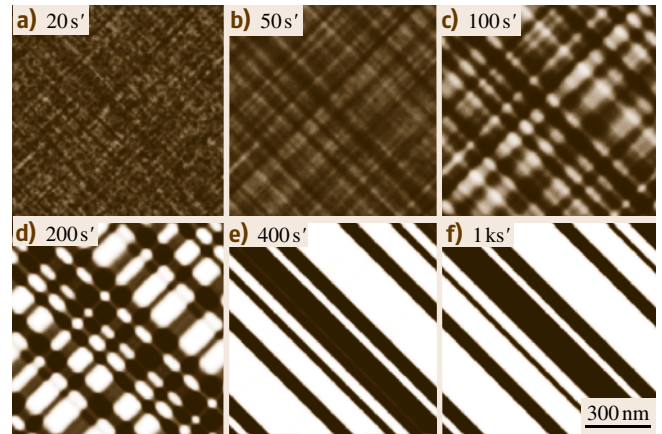


Fig. 21.8a–f Two-dimensional simulation result of the cubic \rightarrow tetragonal structural phase transformation in Ni_2MnGa during isothermal aging calculated on the two-dimensional plane of (001). The white part is the t_1 phase, e.g., the t phase with variant p is written as t_p phase, and black part corresponds to the t_2 phase ($\Delta G^{c \rightarrow t} = -40 \text{ J/mol}$). Numerical values in the figure are the dimensionless aging time

by twin boundary motion (Fig. 21.8f). The morphological changes of the microstructure are in very good agreement with the martensitic transformation induced by the weak first order structural phase transition that is observed, for instance, in the Fe-Pd system experimentally.

21.5.3 Twin Domain Growth Under External Stress and Magnetic Field

Figure 21.9 shows the twin microstructure developments under external stress and magnetic fields [21.44]. The microstructure in Fig. 21.8f is employed as the initial condition for the simulation of Fig. 21.9, and the white and black parts in the figure correspond to the t_1 phase and t_2 phase, respectively. The microstructure changes from Fig. 21.9a–c demonstrate the twin domain growth with twin boundary motion under the condition of 1 MPa compressive applied stress along the vertical direction. It is recognized that the t_2 phase (black part) preferentially grows upwards. Because the c -axis of the unit cell for t_2 phase coincides with the direction along the y -axis (vertical direction) and the tetragonality of the t phase is less than unity, the compressive force makes the t_2 phase more stable. On the other hand, the microstructure changes under the external magnetic field along the x -axis (horizontal di-

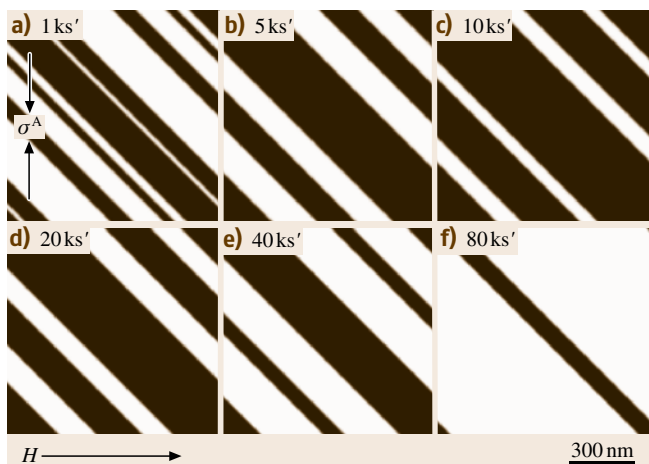


Fig. 21.9a–f The twin microstructure developments under external stress and magnetic fields. The microstructure of Fig. 21.8f is employed as the initial condition for the simulation of Fig. 21.9, and the *white* and *black parts* in the figure correspond to t_1 phase and t_2 phase, respectively. ($\Delta G^{c \rightarrow t} = -40 \text{ J/mol}$). Numerical values in the figure are the dimensionless aging time

reaction) without applied stress are demonstrated from Fig. 21.9c–f. In this case, the t_1 phase (white part) grows conversely. This is because t_1 phase has the c -axis, that is, the easy axis for magnetization, along the x -axis (horizontal direction), therefore, the magnetic energy of the t_1 phase is lower than that of t_2 phase.

21.6 Microstructure Evolution

21.6.1 Grain Growth and Recrystallization

In crystal grain growth dynamics, several phase-field models have been proposed with the first being proposed by *Chen and Yang* [21.16], in which the grains of different crystallographic orientations are represented by a set of nonconserved order parameter fields (multiorder parameter model). The temporal development of

the order parameter field is calculated by the Allen–Cahn equation [21.34].

On the other hand, an interesting phase-field model was recently proposed for studying the crystalline grain growth [21.17, 18]. It uses two order parameters to describe a polycrystal structure; one represents the crystalline order and the other indicates the value of the local orientation of the crystal. Whereas this model can also simulate grain rotation, which is absent from the multiorder parameter models, this order parameter is undefined in a disordered liquid state.

A typical example of the three-dimensional grain growth simulation by *Krill and Chen* [21.16] is shown in Fig. 21.10. It was obtained using a multiorder parameter free energy model with 25 order parameters. With increasing simulation time, the grains are eliminated by a mechanism of the grain boundary migration, and owing to the conservation of total volume, the average grain size increases steadily. The square of average grain size increases proportional to time, that is, expected for curvature-driven grain boundary migration.

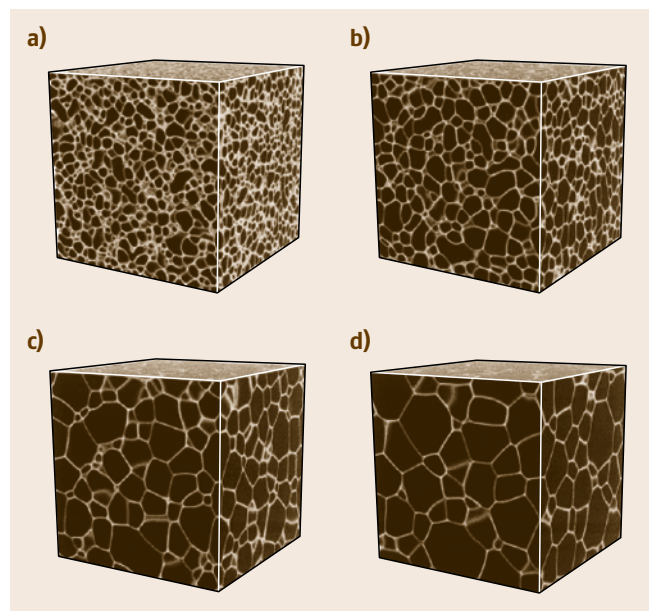


Fig. 21.10a–d A typical grain evolution process obtained from a three-dimensional phase-field simulation of grain growth assuming isotropic grain boundary energy and isotropic boundary mobility (after [21.16]). The *white lines* show the grain boundary. With increasing simulation time from (a)–(d), the grains are eliminated by the mechanism of grain boundary migration and, owing to the conservation of total volume, the average grain size increases steadily

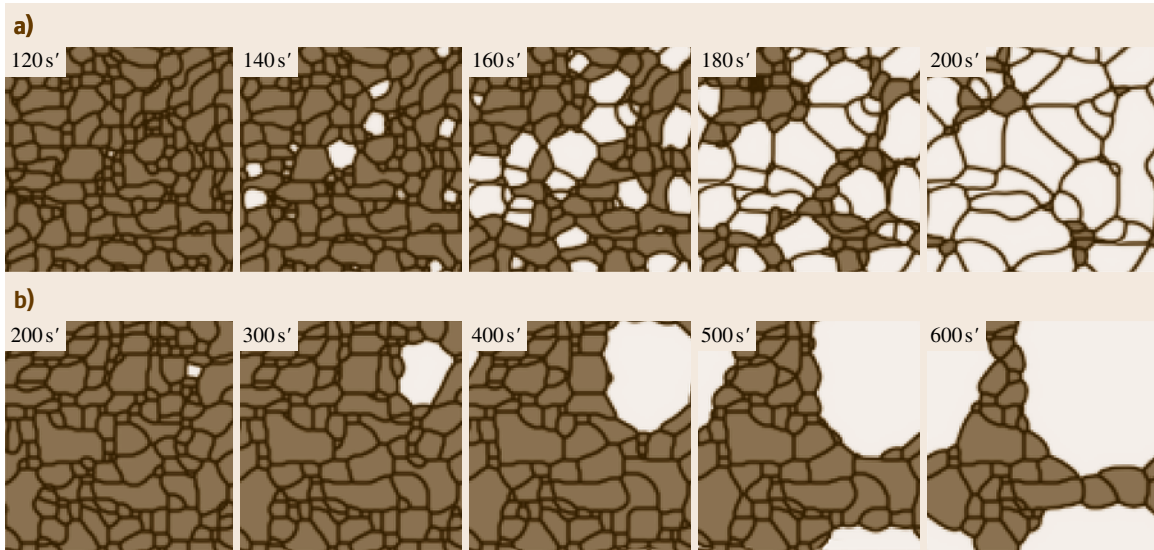


Fig. 21.11a,b Two-dimensional simulation of the recrystallization process. The microstructure changes of the *upper* and *lower layer* correspond to the case that the initial strain in the polycrystal is large and small, respectively. The *gray parts* are primary grain, and the *white grains* correspond to recrystallized ones. Numerical values in the figure are the dimensionless aging time

Figure 21.11 shows a two-dimensional simulation of the recrystallization process. The microstructure changes of upper and lower layer correspond to the case that the initial strain in the polycrystal is large and small, respectively. When the initial polycrystal is highly deformed, recrystallization frequently occurs in the place of grain growth, on the other hand, with less deformation, grain growth takes place sparsely.

21.6.2 Ferroelectric Domain Formation with a Dipole–Dipole Interaction

Figure 21.12 shows the temporal evolution of a dielectric domain structure without an external electric field. At the beginning of the evolution, a Gaussian random fluctuation was introduced to initiate the polarization evolution process. The shade regions imply the polarization domain and the orientation of polarization moment is indicated by the arrows in Fig. 21.12f. After $t = 4 s'$ (the symbol s' means the dimensionless time unit), the polarization is still in the nucleation state. Figure 21.12b illustrates the polarization distribution after $t = 12 s'$, where the 90° and 180° domain walls appear. Figure 21.12b–f demonstrate the temporal domain structure evolution, where the morphology of domain structure is changed by domain wall motion and the coarsening of domains is progressed.

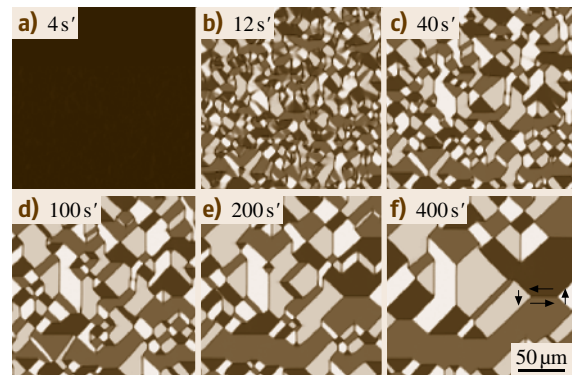


Fig. 21.12a–f Temporal evolution of the domain structure development in dielectric materials without an external electric field. The *shaded regions* imply the polarization domain and the orientation of the polarization moment is indicated by *arrows* in (f). Numerical values in the figure are the dimensionless aging time

Figure 21.13a–f shows the temporal evolution of polarization switching when an external electric field is applied along the x -direction (rightward direction). Comparing Figs. 21.12 and 21.13 indicates that the applied electric field drives the domain walls to align their polarization moment along the applied field.

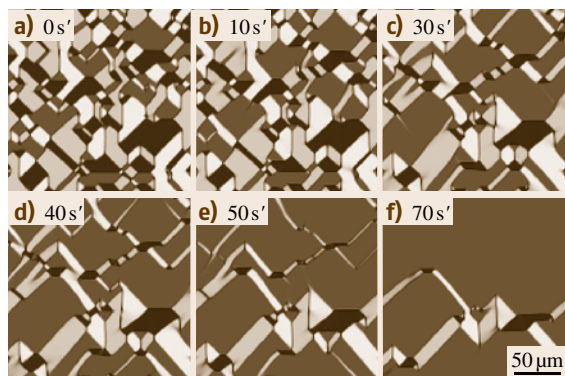


Fig. 21.13a–f Temporal evolution of the domain structure development in dielectric materials under external electric field in the x -direction. Note that the applied electric field drives the domain walls to align their polarization moment along to the applied field. Numerical values in the figure are the dimensionless aging time

21.6.3 Modeling Complex Nanogranular Structure Formation

As a typical example of modeling complex microstructure evolution using the phase-field method, the FePt nanogranular microstructure formation during sputtering and the order–disorder phase transition of FePt nanoparticle in nanogranular thin films during subsequent annealing are demonstrated [21.45]. FePt nanogranular structure is well known as the candidate for the next generation of high-density recording media because of its large magnetocrystalline anisotropy. The simulation is performed on the nanostructure formation in FePt nanogranular thin film during sputtering and a subsequent phase transformation of FePt nanoparticles from A1 to L1₀ structure with isothermal aging.

Figure 21.14 shows the two-dimensional simulation result for the FePt nanogranular structure formation and

the ordering of FePt nanoparticles at 923 K [21.45]. The composition of the FePt phase is set at Fe-45 at. % Pt. The black and white regions with droplet shape are FePt nanoparticles, and the degree of white means the degree of L1₀ order. Therefore, a black particle is an FePt(A1) disordered phase, and a white particle is an FePt(L1₀) ordered phase. The matrix (gray part) is an amorphous alumina phase. Numerical values in the figure are normalized aging time.

At the initial stage (as-spattered stage), as shown in Fig. 21.14a and b, the FePt phase takes a disordered state. With the aging progress, it is understood from Fig. 21.14c–e that ordering from A1 to L1₀ proceeds during coarsening of the FePt phase. It is noteworthy that the speed of ordering for a particle with small size seems to delay (see the left arrow in Fig. 21.14e). The antiphase boundary is also recognized in the FePt particle (see the right arrow in Fig. 21.14e). It is quite interesting that the degree of order decreases as the particle size becomes small (see the arrowed particle in Fig. 21.14g). This size dependence on ordering of FePt phase has already been observed experimentally by Takahashi et al. [21.46]. These microstructure changes agree well with features of FePt nanogranular structure formation experimentally observed.

We would like to emphasize that once the morphological shape of a microstructure is quantitatively obtained using phase-field modeling, it is possible to calculate magnetic properties such as a magnetic hysteresis based on the micromagnetics simulation [21.47, 48] using the calculated microstructure data as boundary conditions.

21.6.4 Dislocation Dynamics

A quite advanced phase-field modeling of the dislocation dynamics has been proposed by Wang et al. [21.26]. In order to describe a multidislocation system using a set of order parameters, they employed discontinuous relative displacements between the two lattice

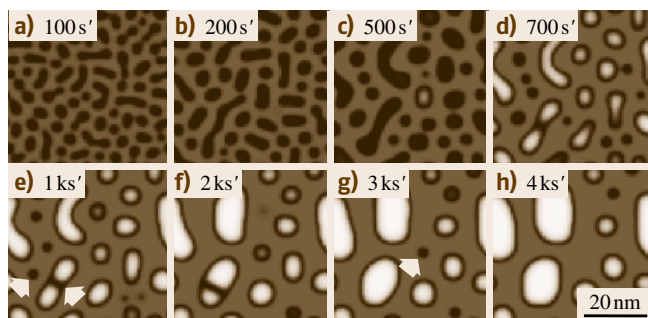


Fig. 21.14a–h Two-dimensional simulation for the FePt nanogranular structure formation and the ordering of FePt (Fe-45 at. % Pt) nanoparticles at 923 K. The *black* and *white* regions with droplet shape are FePt nanoparticles, and the degree of white means the degree of L1₀ order. Therefore, a *black particle* is FePt(A1) disordered phase, and a *white particle* is FePt(L1₀) ordered phase, respectively. The matrix (*gray part*) is the amorphous-alumina phase. Numerical values in the figure are the dimensionless aging time

planes below and above the slip plane, measured in units of Burgers' vectors, as a phase-field order parameters. The temporal evolution of the order parameter fields is obtained by solving the governing equation for nonconserved order parameters. This model not only takes into account the stress-induced long-range interactions among individual dislocations but also automatically incorporates the effects of short-range interactions, such as multiplication and annihilation between dislocations.

Figure 21.15 shows a three-dimensional simulation of Frank–Read source calculated by Wang et al. The periodic boundary condition is used and the rectangular shaped loop is introduced as the pinned source segments initially. In terms of inclusion formalism, a succession of dislocation generation through the Frank–Read mechanism should be interpreted as *sympathetic* nucleation of new thin lamellar inclusions.

Figure 21.16 shows an example from a phase-field simulation of plastic deformation of a model alloy under a uniaxial tensile stress imposed along vertical direction. The temporal dislocation generation during deformation was provided by randomly placed Frank–Read sources in the system. Figure 21.16a,b shows the dislocation microstructure at points a and b on the stress–strain curve. This model can be extended to the polycrystal and to systems where phase transformations and dislocation dynamics are simultaneously evolved.

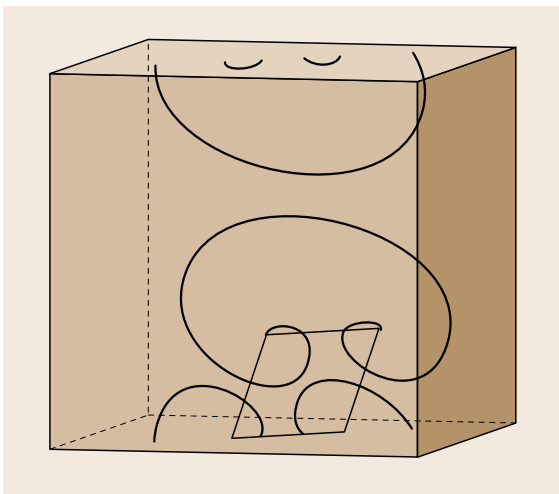


Fig. 21.15 Three-dimensional phase-field simulation of a Frank–Read source under a periodic boundary condition, where the *rectangular loop* (thin plate inclusion) serves as the pinned source segments (after [21.23])

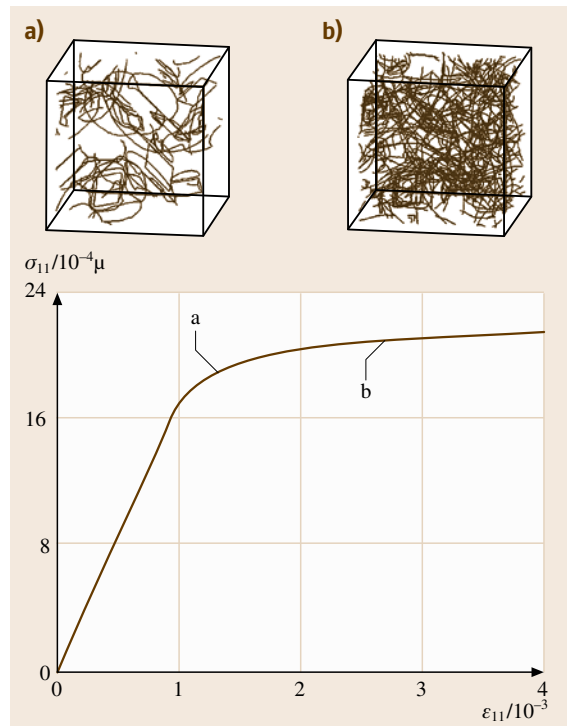


Fig. 21.16a,b The stress–strain curve obtained from a three-dimensional phase-field simulation of an *fcc* crystal under uniaxial loading (after [21.23]). The figures (a) and (b) show the dislocation microstructure at points a and b on the stress–strain curve

21.6.5 Crack Propagation

The phase-field simulation is also applicable to multicrock systems in polycrystalline materials if elastic isotropy is assumed [21.26]. In this case, the grain rotation does not change the components of the elastic modulus, and thus the polycrystal can be treated as an elastically homogeneous medium. However, the grain rotation in the polycrystal changes the crack propagation paths because it rotates the direction of permitted cleavage planes. Since the cleavage planes have different orientations in different grains, the crack picks up new energetically favored cleavage planes when it crosses the grain boundaries. The phase-field model explicitly takes into account this effect as well as the elastic coupling between cracks in different grains.

Figure 21.17 shows the phase-field simulation of crack propagation in a two-dimensional polycrystal calculated by Wang et al. [21.26]. The initial polycrystal

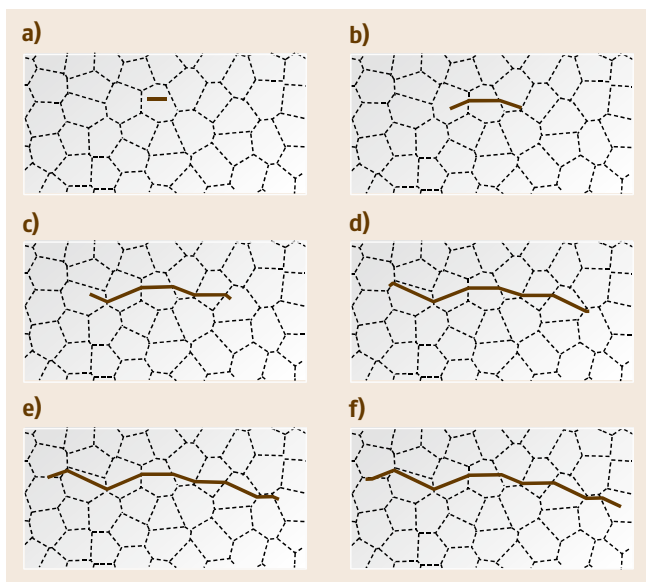


Fig. 21.17a–f Phase-field simulation of crack propagation in two-dimensional polycrystal. Under uniaxial stress in the y -direction (vertical direction of the figure), the pre-existing crack (a) starts to grow. When it crosses the grain boundary, the crack changes its original propagation path and picks up the energetically favored cleavage planes in the neighboring grains (b)–(f). The resultant meandering path is shown in (f) (after [21.26])

is generated by the Voronoi tessellations under a periodic boundary constraint. The simulation sequence is described briefly as follows: (1) 40 grain seeds are randomly positioned in the 512×256 computational cell;

(2) each point in the space belongs to the grain whose seed is the nearest to this point; and (3) a rotation angle is randomly assigned to each grain. The generated polycrystalline structure composed of 40 randomly oriented grains is shown as the dotted lines in Fig. 21.17. Two cleavage planes, (100) and (010), are assumed for each grain.

Uniaxial stress is applied to the polycrystal in the y -direction (vertical direction), and as shown in Fig. 21.17a, a preexisting crack is introduced in one grain. The simulation results are shown in Fig. 21.17a–f. When the crack crosses through the grain boundary and enters the neighboring grain, the energetically favored cleavage plane is automatically picked up. This results in the meandering cleavage path, as shown in Fig. 21.17f.

References

- 21.1 R. Kobayashi: Modeling and numerical simulations of dendritic crystal growth, *Physica D* **63**, 410–423 (1993)
- 21.2 A.A. Wheeler, W.J. Boettinger, G.B. McFadden: Phase-field model for isothermal phase transitions in binary alloys, *Phys. Rev. A* **45**, 7424–7439 (1992)
- 21.3 W.J. Boettinger, J.A. Warren, C. Beckermann, A. Karma: Phase-field simulation of solidification, *Annu. Rev. Mater. Res.* **32**, 163–194 (2002)
- 21.4 L.-Q. Chen: Phase-field models for microstructure evolution, *Annu. Rev. Mater. Res.* **32**, 113–140 (2002)
- 21.5 M. Ode, S.G. Kim, T. Suzuki: Recent Advances in the phase-field model for solidification, *Iron Steel Inst. Jpn. Int.* **41**, 1076–1082 (2001)
- 21.6 H. Emmerich: *The Diffuse Interface Approach in Materials Science* (Springer, Berlin, Heidelberg 2003)
- 21.7 D. Raabe: *Computational Materials Science* (Wiley-VCH, Weinheim 1998)
- 21.8 J.J. Robinson (Ed.): Solidification and microstructure, *J. Min. Met. Mater. Soc.* **56**(4), 16–68 (2004)
- 21.9 J.A. Warren, W.J. Boettinger: Prediction of dendritic growth and microsegregation patterns in a binary alloy using the phase-field method, *Acta Metall. Mater.* **43**, 689–703 (1995)
- 21.10 A. Karma, W.-J. Rappel: Quantitative phase-field modeling of dendritic growth in two and three dimensions, *Phys. Rev. E* **57**, 4323–4349 (1998)
- 21.11 S.G. Kim, W.T. Kim, T. Suzuki: Phase-field model for binary alloys, *Phys. Rev. E* **60**, 7186–7197 (1999)
- 21.12 T. Suzuki, M. Ode, S.G. Kim: Phase-field model of dendritic growth, *J. Cryst. Growth* **237–239**, 125–131 (2002)
- 21.13 T. Miyazaki, T. Koyama: Computer simulations of the phase transformation in real alloy systems based on the phase field method, *Mater. Sci. Eng. A* **312**, 38–49 (2001)
- 21.14 T. Koyama: Computer simulation of phase decomposition in two dimensions based on a discrete type non-linear diffusion equation, **39**, 169–178 (1998)
- 21.15 J.Z. Zhu, T. Wang, A.J. Ardell, S.H. Zhou, Z.K. Liu, L.Q. Chen: Three-dimensional phase-field simulations of coarsening kinetics of γ' particles in binary Ni–Al alloys, *Acta Mater.* **52**, 2837–2845 (2004)
- 21.16 C.E. Krill III, L.-Q. Chen: Computer simulation of 3-D grain growth using a phase-field model, *Acta Mater.* **50**, 3059–3075 (2002)
- 21.17 A.E. Lobkovsky, J.A. Warren: Phase-field model of crystal grains, *J. Cryst. Growth* **225**, 282–288 (2001)

- 21.18 J.A. Warren, R. Kobayashi, W.C. Carter: Modeling grain boundaries using a phase-field technique, *J. Cryst. Growth* **211**, 18–20 (2000)
- 21.19 T. Miyazaki: Recent developments and the future of computational science on microstructure formation, *Mater. Trans.* **43**, 1266–1272 (2002)
- 21.20 J. Wang, S.-Q. Shi, L.-Q. Chen, Y. Li, T.-Y. Zhang: Phase-field simulations of ferroelectric/ferroelastic polarization switching, *Acta Mater.* **52**, 749–764 (2004)
- 21.21 Y.L. Li, S.Y. Hu, Z.K. Liu, L.-Q. Chen: Effect of substrate constraint on the stability and evolution of ferroelectric domain structures in thin films, *Acta Mater.* **50**, 395–411 (2002)
- 21.22 Y.M. Jin, A. Artemev, A.G. Khachaturyan: Three-dimensional phase field model of low-symmetry martensitic transformation in polycrystal: Simulation of ζ_2' martensite in AuCd alloys, *Acta Mater.* **49**, 2309–2320 (2001)
- 21.23 Y.U. Wang, Y.M. Jin, A.M. Cuitino, A.G. Khachaturyan: Nanoscale phase field microelasticity theory of dislocations: Model and 3D simulations, *Acta Mater.* **49**, 1847–1857 (2001)
- 21.24 D. Rodney, Y. Le Bouar, A. Finel: Phase field methods and dislocations, *Acta Mater.* **51**, 17–30 (2003)
- 21.25 S.Y. Hu, L.-Q. Chen: A phase-field model for evolving microstructures with strong elastic inhomogeneity, *Acta Mater.* **49**, 1879–1890 (2001)
- 21.26 Y.U. Wang, Y.M. Jin, A.G. Khachaturyan: Phase field microelasticity theory and simulation of multiple voids and cracks in single crystals and polycrystals under applied stress, *J. Appl. Phys.* **91**, 6435–6451 (2002)
- 21.27 J.S. Rowlinson: Translation of J.D. van der Waals' "The thermodynamic theory of capillarity under the hypothesis of a continuous variation of density", *J. Stat. Phys.* **20**, 197–244 (1979)
- 21.28 W.C. Carter, W.C. Johnson (Eds.): *The Selected Works of J.W. Cahn* (Min. Met. Mater. Soc., Warrendale 1998)
- 21.29 H.I. Aaronson (Ed.): *Phase Transformation* (ASM, Metals Park 1970) p. 497
- 21.30 C. Kittel, H. Kroemer: *Thermal Physics* (Freeman, New York 1980)
- 21.31 D. Fan, L.-Q. Chen: Topological evolution during coupled grain growth and Ostwald ripening in volume-conserved 2-D two-phase polycrystals, *Acta Mater.* **45**, 4145–4154 (1997)
- 21.32 D. Fan, L.-Q. Chen: Possibility of spinodal decomposition in yttria-partially stabilized zirconia (ZrO_2 - Y_2O_3) system – A theoretical investigation, *J. Am. Ceram. Soc.* **78**, 1680–1686 (1995)
- 21.33 N. Saunders, A.P. Miodownik: *CALPHAD (Calculation of Phase Diagrams): A Comprehensive Guide* (Pergamon, New York 1998)
- 21.34 S.M. Allen, J.W. Cahn: A microscopic theory for antiphase boundary motion and its application to antiphase domain coarsening, *Acta Metall. Mater.* **27**, 1085–1095 (1979)
- 21.35 J.J. Eggleston, G.B. McFadden, P.W. Voorhees: A phase-field model for highly anisotropic interfacial energy, *Physica D* **150**, 91–103 (2001)
- 21.36 I. Steinbach, F. Pezzolla, B. Nestler, M. Seeselberg, R. Prieler, G.J. Schmitz, J.L.L. Rezende: A phase field concept for multiphase systems, *Physica D* **94**, 135–147 (1996)
- 21.37 A. Khachaturyan: *Theory of Structural Transformations in Solids* (Wiley, New York 1983)
- 21.38 T. Mura: *Micromechanics of Defects in Solids*, 2nd edn. (Kluwer, Dordrecht 1991)
- 21.39 L.-Q. Chen, J. Shen: Applications of semi-implicit Fourier-spectral method to phase field equations, *Comput. Phys. Commun.* **108**, 147–158 (1998)
- 21.40 P.H. Leo, J.S. Lowenngub, H.J. Jou: A diffuse interface model for microstructural evolution in elastically stressed solids, *Acta Mater.* **46**, 2113–2130 (1998)
- 21.41 M.E. Glicksman: *Diffusion in Solids* (Wiley, New York 2000)
- 21.42 M. Doi, T. Koyama, T. Kozakai: Experimental and theoretical investigation of the phase decomposition in ZrO_2 - $Y_{0.5}$ system, Proc. Fourth Pac. Rim Int. Conf. Adv. Mater. Process (PRICM 4), Honolulu 2001, ed. by S. Hanada, Z. Zhong, S.W. Nam, R.N. Wright (The Japan Institute of Metals, Sendai 2001) 741–744
- 21.43 K. Otsuka, C.M. Wayman (Eds.): *Shape Memory Materials* (Cambridge Univ. Press, Cambridge 1998)
- 21.44 T. Koyama, H. Onodera: Phase-field simulation of microstructure changes in Ni_2MnGa ferromagnetic alloy under external stress and magnetic fields, *Mater. Trans. JIM* **44**, 2503–2508 (2003)
- 21.45 T. Koyama, H. Onodera: Modeling of microstructure changes in FePt nano-granular thin films using the phase-field method, *Mater. Trans. JIM* **44**, 1523–1528 (2003)
- 21.46 Y.K. Takahashi, T. Koyama, M. Ohnuma, T. Ohkubo, K. Hono: Size dependence of ordering in FePt nanoparticles, *J. Appl. Phys.* **95**, 2690–2696 (2004)
- 21.47 A. Hubert, R. Schafer: *Magnetic Domains* (Springer, Berlin, Heidelberg 1998)
- 21.48 H. Kronmüller, M. Fähnle: *Micromagnetism and the Microstructure of Ferromagnetic Solids* (Cambridge Univ. Press, Cambridge 2003)

Monte Carlo

22. Monte Carlo Simulation

In the general overview on materials and their characteristics, outlined in Sect. 1.3, it has been stated that *materials and their characteristics result from the processing of matter*. Thus, *condensed matter physics* is one of the fundamentals for the understanding of materials. The Monte Carlo Method, which is a powerful method in this respect, is presented in this final chapter of the Handbook's Part E on Modelling and Simulation Methods as follows:

First, the principles of this simulation technique are introduced

- Monte Carlo Method: the fundamentals
- Improved Monte Carlo algorithms
- Quantum Monte Carlo Method.

Second, the application of the Monte Carlo Method is explained in considering selected areas of materials science.

- Electronic correlations: antiferromagnetism
- Perfect conductance of electricity: superconductivity
- Vortex states in condensed matter physics
- Quantum critical phenomena.

22.1	Fundamentals of the Monte Carlo Method	1117
22.1.1	Boltzmann Weight	1118
22.1.2	Monte Carlo Technique	1118
22.1.3	Random Numbers	1119
22.1.4	Finite-Size Effects	1120
22.1.5	Nonequilibrium Relaxation Method	1121
22.2	Improved Algorithms	1121
22.2.1	Reweighting Algorithms	1121
22.2.2	Cluster Algorithm and Extensions	1122
22.2.3	Hybrid Monte Carlo Method	1123
22.2.4	Simulated Annealing and Extensions	1124
22.2.5	Replica Monte Carlo	1125
22.3	Quantum Monte Carlo Method	1126
22.3.1	Suzuki-Trotter Formalism	1126
22.3.2	World-Line Approach	1126
22.3.3	Cluster Algorithm	1127
22.3.4	Continuous-Time Algorithm	1128
22.3.5	Worm Algorithm	1129
22.3.6	Auxiliary Field Approach	1130
22.3.7	Projector Monte Carlo Method	1130
22.3.8	Negative-Sign Problem	1132
22.3.9	Other Exact Methods	1133
22.4	Bicritical Phenomena in O(5) Model	1133
22.4.1	Hamiltonian	1134
22.4.2	Phase Diagram	1134
22.4.3	Scaling Theory	1135
22.5	Superconductivity Vortex State	1137
22.5.1	Model Hamiltonian	1138
22.5.2	First Order Melting	1138
22.5.3	Continuous Melting: B ab Plane	1141
22.6	Effects of Randomness in Vortex States	1143
22.6.1	Point-Like Defects	1143
22.6.2	Columnar Defects	1144
22.7	Quantum Critical Phenomena	1146
22.7.1	Quantum Spin Chain	1146
22.7.2	Mott Transition	1147
22.7.3	Phase Separation	1148
	References	1149

22.1 Fundamentals of the Monte Carlo Method

In material science, we are always facing systems composed of a huge number of atoms or molecules, typically of order 10^{23} . Knowing the interactions among the particles, one can, in principle, predict the individual trajectories from a given initial configuration, specified by the positions and the velocities of the particles (for

quantum systems the initial wave functions), and thus know the destination of the system. However, even with the most advanced supercomputer, the system one can treat in this way is very much limited. On the other hand, in most cases, we are interested in the total, averaged behaviors of the system, such as density of gas

and magnetic polarization of a magnet, upon various external conditions such as temperature, pressure and magnetic field, instead of the detailed trajectories of individual particles. The statistical mechanics is such a disciplinary, which reveals simple rules governing systems of huge numbers of components. In many interesting cases, unfortunately, statistical mechanics cannot provide a final compact expression for the desired physical quantities because of the many-body effect of the interactions among components, although the bare interaction is two-body. Many approximate theories have been developed which make the field called condensed matter physics very rich. With the huge leaping of power of computers, the Monte Carlo approach based on the principle of statistical mechanics has been developed in the recent decades. This chapter is devoted to introducing the basic notions for the Monte Carlo method [22.1], with several examples of application.

22.1.1 Boltzmann Weight

According to the principle of statistical mechanics, the probability for a particular *microscopic* state appearing in an equilibrium system attached to a heat reservoir with temperature T is given by the Boltzmann weight

$$p_i = e^{-\beta E_i} / \sum_i e^{-\beta E_i} \equiv e^{-\beta E_i} / Z, \quad (22.1)$$

where $\beta = 1/k_B T$, E_i the energy of the system at the particular state, and Z the partition function. The expectation value of any physical quantity, such as the magnetic polarization of a magnet, can be evaluated by

$$\langle O \rangle = \frac{1}{Z} \sum_i O_i e^{-\beta E_i}. \quad (22.2)$$

The difficulty one meets in applications is: there are too many possible states such that it is practically unable to compute the partition function and the expectation values for desired physical quantities.

22.1.2 Monte Carlo Technique

The Monte Carlo techniques overcome this difficulty by choosing a subset of possible states, and approximate the expectation value of a physical quantity by the average within the subset of states of limited number. The way for picking up the subset of states can be specified by ourselves, and is very crucial to the accuracy of the estimation thus made. A successful Monte Carlo simulation thus relies heavily on the way of sampling.

Importance Sampling

One can regard the statistical expectation value as a time average over the states a system passes through the course of a measurement. This suggests that we can take a sample of the states of the system such that the possibility of any particular state being chosen is proportional to its Boltzmann weight. This importance sampling method is the simplest and most widely-used in Monte Carlo approaches. It is easy to see that the estimation for the desired expectation value is given simply by

$$\langle O \rangle_M = \sum_{i=1}^M O_i / M, \quad (22.3)$$

since the Boltzmann weight has been already involved into the process of sampling. This estimation is much more accurate than a simple sampling process, especially at low temperatures where the system spends the large portion of time in several states with low energies.

The implementation of the above importance sampling is achieved by Markov processes. A Markov process for Monte Carlo simulation generates a Markov chain of states: starting from the state a , it indicates a new one b , and upon inputting b it points the third one c , and so on. A certain number of the states at the head of these Markov chains are dropped, since they depend on initial state a . However, after running a sufficiently long time, the picked states should obey the Boltzmann distribution. This goal is guaranteed by the ergodicity property and the condition of detailed balance.

Ergodicity

This property requires that any state of the system can be reached via the Markov process from any other state supposing we run it sufficiently long. The importance of this condition is very clear since otherwise the missing states will have zero weight in our simulation which is not the case in reality. It is noticed that one still has room to set the *direct* transition probability from one state to many others to zero, as usually done in many algorithms.

Detailed Balance

This condition is slightly subtle and requires some consideration. For the desired distribution vector \mathbf{p} , with the components of the vector being the Boltzmann weight for each state, suppose we find an appropriate Markov process characterized by a set of transition probabilities among possible states such that

$$\sum_j p_i P(i \rightarrow j) = \sum_j p_j P(j \rightarrow i), \quad (22.4)$$

where p_i is the probability of the state i and $P(i \rightarrow j)$ the transition probability from i -state to j -state. The above condition is necessary since the desired distribution, namely the Boltzmann distribution, is the one for equilibrium state. However, the Markov process satisfying the above condition does not necessarily generate the desired distribution, even when the Markov chain is run long enough. Actually, it is possible that a dynamic limit cycle is realized as

$$\mathbf{p}'(t+n) = P^n \mathbf{p}'(t) \quad (22.5)$$

with $n > 1$, so that the desired distribution \mathbf{p} can never be reached. In order to avoid this situation, we set the detailed balance condition

$$p_i P(i \rightarrow j) = p_j P(j \rightarrow i). \quad (22.6)$$

It is easy to see that this condition eliminates the possibility of limit cycles. Then from the Perron–Frobenius theorem, it can be shown that the desired distribution \mathbf{p} is the only one that can be generated by the transition matrix P .

To be short, a Markov process satisfying the conditions (i) the ergodicity condition, (ii) $\sum_i P(i \rightarrow j) = 1$, and (iii)

$$P(i \rightarrow j)/P(j \rightarrow i) = p_j/p_i = e^{-\beta(E_j - E_i)}, \quad (22.7)$$

will generate the Boltzmann distribution at equilibrium.

Acceptance Ratio

There is still freedom when composing the transition probabilities. One can take a selection probability g and the acceptance ratio A such that

$$P(i \rightarrow j) = g(i \rightarrow j)A(i \rightarrow j). \quad (22.8)$$

For simplicity, one usually takes the constant selection probability for all possible states during the one-step transition. As for the acceptance ratio, we can take them as large as possible provided they satisfy the condition (22.7), which makes the Markov chain move more efficiently around the sampling space. It is easy to see that the acceptance ratio is given by

$$A(i \rightarrow j) = \begin{cases} e^{-\beta(E_j - E_i)}, & \text{for } E_j - E_i > 0; \\ 1, & \text{otherwise.} \end{cases} \quad (22.9)$$

This is the Metropolis algorithm [22.2].

With the selection probability and the acceptance ratio determined, a Monte Carlo simulation goes like

the following: from a given initial state we pick up a candidate for the next state out of the possible ones according to the selection probability; then we check if the candidate state is to be accepted according to the probability specified by the acceptance ratio. This routine is repeated for sufficiently long time before we insert a measurement step where we calculate physical quantities for the realized state.

It is then clear that the Markov chain of states thus generated is stochastic, which is the most important feature of the Monte Carlo techniques in comparison with other deterministic methods such as molecular dynamics. The rules which specify a particular simulation algorithm govern the distribution of the realized states when a large number of states are piled up.

22.1.3 Random Numbers

The stochastic property of Monte Carlo simulations comes in because one chooses a new state from the old one in a *random* fashion. This process is realized by random numbers. Therefore, generation of a sequence of random numbers is of crucial importance for accurate Monte Carlo simulations. Of course, as long as such a sequence is generated by a deterministic procedure written in a computer code, it cannot be really random. It is usually called *quasi* random provided it satisfies the following two conditions characteristic to *true* random numbers.

Condition I: The period of the quasi random numbers should be longer than the total length of simulations.

Condition II: The quasi random numbers should be k -dimensional equidistributed with large enough k . In other words, all possible sets consisting of k sequential numbers appear with the same frequency in a period, except the one of k zeros.

Classical Random Number Generators

The linear congruential sequence is given by

$$\mathbf{x}_{i+1} = a\mathbf{x}_i + b \pmod{2^w}, \quad i = 0, 1, \dots, \quad (22.10)$$

where w stands for the number of bits of random numbers \mathbf{x}_i , and a and b are suitable sets of numbers which maximizes the period of the quasi random numbers to 2^w . The merit of this sequence is its simplicity. However, it has several shortcomings. First, the period is not sufficiently long even with $w = 31$. Second, a random number is determined only by the previous one, and there exists strong correlation among sequential numbers. Third, the multiple operation is time consuming.

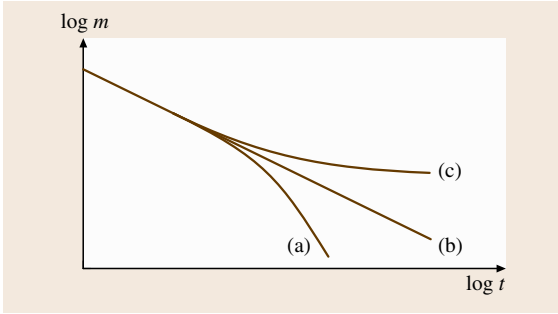


Fig. 22.1 Schematic figure of nonequilibrium relaxation of order parameter from a fully polarized configuration for (a) $T > T_c$, (b) $T = T_c$ and (c) $T < T_c$

way

$$\langle m_i m_j \rangle - \langle m_i \rangle^2 \sim \frac{e^{-|i-j|/\xi}}{|i-j|^{d-2+\eta}}, \quad (22.18)$$

$$\xi \sim |T - T_c|^{-\nu}, \quad (22.19)$$

where m_i stands for the order parameter at position i , and ν and η are the critical exponents for the correlation length and critical correlation function. While the critical temperature T_c depends on details of systems such as lattice structures, the critical exponents are not changed by such details, a property known as the universality of critical phenomena.

In a finite system, phase transition is supposed to take place at the temperature where a correlated cluster becomes as large as the system size, namely $\xi \sim L$. Finite-size scaling theory claims that physical quantities around the critical temperature can be expressed as a function of L/ξ in the following fashion

$$Q(L, T) \sim L^{\varphi/\nu} f_{\text{sc}}[L^{1/\nu}(T - T_c)], \quad (22.20)$$

where $f_{\text{sc}}(x)$ is a scaling function.

Several statements can be derived from the finite-size scaling form (22.20): (1) At $T = T_c$, this form

is reduced to $Q(L, T_c) \sim L^{\varphi/\nu}$, which stands for the power-law size dependence at the critical temperature. (2) When $L^{-\varphi/\nu} Q(L, T)$ is plotted versus $L^{1/\nu}(T - T_c)$, the curves for different L should collapse to each other in the vicinity of T_c provided T_c , ν and φ are known. Alternatively, one can use this so-called finite-size scaling plot to evaluate the critical point and critical exponents.

22.1.5 Nonequilibrium Relaxation Method

As discussed above, measurement of physical quantities should be made after equilibration of the system. However, the relaxation process also contains valuable information of equilibrium state, such as the transition point and critical exponents. As an example, we consider the magnetic polarization of a ferromagnet, which presuming nonvanishing value only below the transition temperature as $m(T) \sim (T_c - T)^\beta$. If one starts from a fully polarized configuration, the order parameter m decays exponentially to zero as MC update proceeds for $T > T_c$; it converges to a finite value for $T < T_c$, as shown in Fig. 22.1. The dynamical scaling form [22.8,9] in the thermodynamic limit is given by

$$m(T; t) \sim t^{-\beta/(z\nu)} F_{\text{sc}}[t^{1/(z\nu)}(T - T_c)], \quad (22.21)$$

where z is the dynamical critical exponent. At $T = T_c$, (22.21) reduces to

$$m(T_c; t) \sim t^{-\beta/(z\nu)}. \quad (22.22)$$

Therefore, it is possible to evaluate the critical temperature T_c and a combination of critical exponents $\beta/(z\nu)$ [22.10–13]. Another combination of critical exponents $1/(z\nu)$ is evaluated from the “finite-time” scaling of (22.21). Extensions to quantum systems [22.14–16] and Kosterlitz–Thouless [22.17] and first-order [22.18] phase transitions are possible.

22.2 Improved Algorithms

The conventional Monte Carlo algorithm explained above suffers from the problem of slow relaxation in cases such as nucleation process in first-order phase transitions, critical slowing down in the vicinity of second-order phase transitions, and complex free-energy landscape of random and/or frustrated systems. Several improved algorithms are proposed and shown

to be very efficient. Readers can refer to [22.19] for a well-written review.

22.2.1 Reweighting Algorithms

Suppose the number of states between E and $E + dE$ is given by $D(E)dE$ with the density of states (DOS)

$D(E)$, the probability for the system presuming energy E is $P(E, T) \sim D(E)e^{-\beta E}$, known as the canonical distribution. If the canonical distribution at a temperature β_0 is given, that at β is obtained by the reweighting formula [22.20]

$$P(E; T) = \frac{e^{-(\beta-\beta_0)E} P(E; T_0)}{\int e^{-(\beta-\beta_0)\varepsilon} P(\varepsilon; T_0) d\varepsilon}. \quad (22.23)$$

Since the histogram $P(E; T_0)$ has a sharp peak around the averaged energy of the system at T_0 , $P(E; T)$ can be evaluated from $P(E; T_0)$ with small enough statistical errors only if T is close enough to T_0 . This limitation can be overcome by taking data for several temperatures around the target one [22.21, 22].

The essential point of the histogram method is to notice that the probability distribution used in simulations can be different from that used for evaluating thermal averages of physical quantities, namely the Boltzmann distribution. In the multicanonical method [22.23, 24], the simulated probability distribution is taken as $P(E; T) \approx 1/E_0(T)$, where $E_0(T)$ stands for the range of the energy covered in simulations at temperature T . The reason that the multicanonical simulation works efficiently can be seen taking the example of a first-order phase transition. Since the canonical distribution has a sharp peak around the equilibrium energy, nucleation processes governed by the two free-energy minima with finite separation results in slow relaxation. This difficulty is overcome by the broad energy range covered by the multicanonical weight.

Since the DOS $D(E)$ is not known *a priori*, it should be evaluated in preliminary runs, and the approximate DOS $D_0(E; T)$ is utilized in simulations. The probability distribution

$$P_{MC}(E; T) = D_0^{-1}(E; T)D(E)/E_0(T) \quad (22.24)$$

does not have to be completely flat, and the reweighting formula is given by

$$P(E; T) = \frac{e^{-\beta E} D_0(E; T) P_{MC}(E; T)}{\int e^{-\beta\varepsilon} D_0(\varepsilon; T) P_{MC}(\varepsilon; T) d\varepsilon}. \quad (22.25)$$

From a practical point of view, construction of the flat histogram (or precise estimation of the DOS) is the crucial point of the multicanonical method, and various algorithms have been proposed [22.25–30] after the original one. In all these algorithms, the DOS is evaluated by accumulating the entry number of a random walk in the energy space. As the system size increases, the deviation of the DOS grows exponentially, and the

estimation within limited preliminary runs by simple accumulation becomes difficult.

In order to overcome this difficulty, a new algorithm [22.31, 32] was proposed based on a “biased” random walk in the energy space

0. Set $i = 0$, $D(E) \equiv 1$ and $n = 1$.
1. Select a site at random and measure the initial energy E_b .
2. Choose a Monte Carlo move to the state with energy E_a by the transition probability $p(E_b \rightarrow E_a) = \min[D(E_b)/D(E_a), 1]$.
3. Update the DOS at the energy of the chosen state as $D(E) \rightarrow D(E)f_i$, with a modification factor $f_i > 1$.
4. If $n < N$, set $n \rightarrow n + 1$ and go to step 1.
5. If $n = N$, set $f_i \rightarrow f_{i+1} (< f_i)$, $i \rightarrow i + 1$, $n = 1$, rescale the DOS and go to step 1.
6. Continue this process until $f_i \rightarrow 1$.

The essential point of this algorithm is the introduction of the modification factor f_i . When f_0 and N are taken so that f_0^N is comparable to the total number of states, the deviation of the DOS is reproduced in the early stage of the iteration. Of course, $f_i > 1$ means that the detailed balance condition is not satisfied (in this sense this algorithm does not belong to Monte Carlo ones), and the DOS during the iteration has a systematic discrepancy from the equilibrium one. The true DOS is obtained at the final stage of the iteration, where $f_i = 1$ eventually holds.

The reweighting algorithm discussed above has a bonus that some physical quantities not available in conventional Monte Carlo algorithm can be treated by this method. For example, the energy dependence of the free-energy landscape can be evaluated [22.33, 34], which is suitable for the analysis of the first-order phase transition.

22.2.2 Cluster Algorithm and Extensions

In the vicinity of the critical temperature T_c of a second-order phase transition, the correlation time τ of a physical quantity Q defined in

$$\langle Q(t_0)Q(t_0+t) \rangle \sim e^{-t/\tau}, \quad (22.26)$$

diverges as $\tau \sim (T - T_c)^{-z\nu}$, where z is a dynamical critical exponent. The critical slowing down makes computer simulations around the critical point very time consuming. In order to overcome this difficulty, the cluster algorithm (Swendsen–Wang (SW) algorithm) was proposed [22.35].

Here we explain this algorithm using the Ising model

$$-\beta\mathcal{H} = K \sum_{(i,j)} \sigma_i \sigma_j, \quad \sigma_i = \pm 1. \quad (22.27)$$

First, we consider the Hamiltonian $\mathcal{H}_{l,m}$ in which the interaction between sites l and m are removed. Then, we define the conditional partition functions $Z_{l,m}^P$ and $Z_{l,m}^{AP}$ for $\sigma_l \sigma_m = +1$ and -1 by

$$Z_{l,m}^P = \text{Tr}_\sigma e^{-\beta\mathcal{H}_{l,m}} \delta_{\sigma_l \sigma_m, 1}, \quad (22.28)$$

$$Z_{l,m}^{AP} = \text{Tr}_\sigma e^{-\beta\mathcal{H}_{l,m}} \delta_{\sigma_l \sigma_m, -1}. \quad (22.29)$$

The partition function is expressed as

$$Z = \text{Tr}_\sigma e^{-\beta\mathcal{H}} = e^K Z_{l,m}^P + e^{-K} Z_{l,m}^{AP}. \quad (22.30)$$

Using

$$Z_{l,m} = \text{Tr}_\sigma e^{-\beta\mathcal{H}_{l,m}} = Z_{l,m}^P + Z_{l,m}^{AP}, \quad (22.31)$$

we can rewrite (22.29) as

$$Z = e^K \left[(1 - e^{-2K}) Z_{l,m}^P + e^{-2K} Z_{l,m} \right]. \quad (22.32)$$

This expression can be interpreted as: “If the spins at sites l and m are parallel, create a bond with the probability $p = 1 - e^{-2K}$.” When this procedure is repeated for all nearest-neighbor pairs of spins, each spin is assigned to one of the clusters. The system is now mapped on a percolation problem with N_c clusters [22.36, 37]

$$Z = \text{Tr} p^b (1 - p)^n 2^{N_c}, \quad (22.33)$$

where b is the number of bonds and n is the number of interactions which do not form bonds, and the trace is taken for all possible configurations of clusters. In each Monte Carlo step, we assign a new Ising variable for each cluster independently. This nonlocal update using percolation clusters reduces significantly the relaxation time.

It was then proposed [22.38] that one can flip a single cluster in one step which is grown from a randomly chosen site. This process improves the efficiency of the SW cluster algorithm [22.39].

The algorithm discussed above can be applied to the Heisenberg model [22.38]

$$-\beta\mathcal{H} = K \sum_{(ij)} \mathbf{S}_i \cdot \mathbf{S}_j, \quad \mathbf{S}_i^2 = 1, \quad (22.34)$$

using an operator $R(\mathbf{r})$ with respect to a randomly chosen unit vector \mathbf{r} in the spin space

$$R(\mathbf{r})\mathbf{S} = \mathbf{S} - 2(\mathbf{S} \cdot \mathbf{r})\mathbf{r}, \quad (22.35)$$

and a spin cluster is formed in the procedure: “If the spins at sites l and m satisfies $M \equiv (\mathbf{S}_l \cdot \mathbf{r})(\mathbf{S}_m \cdot \mathbf{r}) > 0$, create a bond with the probability $p = 1 - e^{-2KM}$.” This rule is a natural extension of the SW algorithm in the Ising model (22.27), and \mathbf{r} is updated in each Monte Carlo step. A similar extension has been made to the six-vertex model [22.40]. Since this model is a classical counterpart of the quantum Heisenberg model, this extension enabled the cluster-update version of quantum Monte Carlo simulations, as will be discussed later.

Further developments of the cluster algorithm took place in connection with percolation theories. The invaded cluster algorithm [22.41, 42] which automatically tunes physical parameters to the critical point is a typical example. It turns out that a simple algorithm to tune the probability p directly until critical percolation is observed [22.43] works better.

Another important progress is the worm algorithm [22.44], which enables accelerated dynamics as fast as the cluster update within the local update. Although this algorithm is based on the closed-path configurations appearing in high-temperature expansions, it shares the fundamental concept with the cluster algorithm, namely Monte Carlo simulations in alternative representations of original systems. Since this algorithm exhibits its merits more clearly in quantum Monte Carlo simulations, it will be explained later in this chapter.

22.2.3 Hybrid Monte Carlo Method

As far as the ergodicity and detailed balance condition are satisfied, any kind of update process can be adopted in a certain Monte Carlo algorithm. Then, it is interesting to hybridize Monte Carlo and molecular dynamics (MD) simulations. Since MD process corresponds to a forced particle move on an equal-energy surface, it is expected to be effective in frustrated systems at low temperatures. An implementation in this direction is formulated for the Heisenberg spin glass model [22.45, 46]

$$\mathcal{H} = \sum_{(ij)} J_{ij} \mathbf{S}_i \cdot \mathbf{S}_j, \quad \mathbf{S}_i^2 = 1, \quad (22.36)$$

with the equation of motion

$$\hbar \frac{d\mathbf{S}_i}{dt} = \mathbf{S}_i \times \mathbf{H}_i, \quad \mathbf{H}_i = \frac{\partial \mathcal{H}}{\partial \mathbf{S}_i} = \sum_j J_{ij} \mathbf{S}_j. \quad (22.37)$$

The MD treatment for all spins is inserted in each Monte Carlo step for certain time intervals.

22.2.4 Simulated Annealing and Extensions

In complex free-energy landscapes of random and/or frustrated systems as shown in Fig. 22.2, conventional Monte Carlo algorithms result in trapping to a metastable state. Applications of the multicanonical and cluster algorithms brought some progress but the results were not so satisfactory, since for example frustrations suppress the formation of large clusters. One therefore needs special treatments for this class of problems.

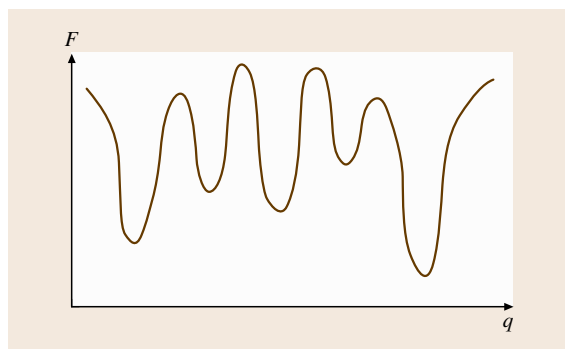


Fig. 22.2 Schematic figure of a complex free-energy landscape

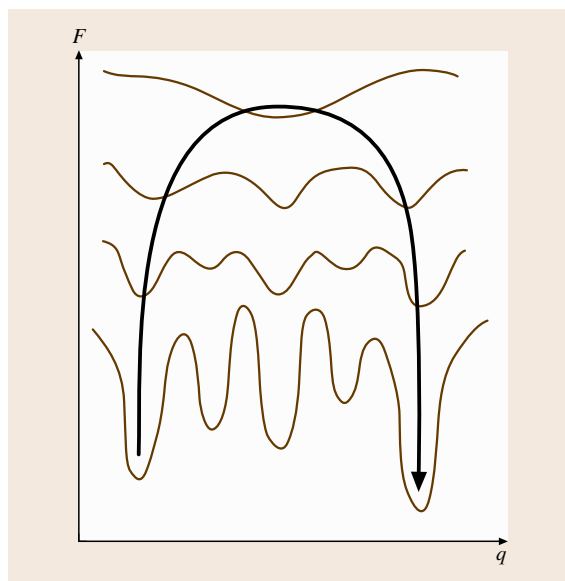


Fig. 22.3 Deep valleys of the free-energy landscape at low temperatures (at the *bottom*) can be bypassed with high-temperature configurations (*upper ones* correspond to higher temperatures)

The simulated annealing [22.47] was originally proposed for optimization problems, namely searching the state which minimizes a cost function. The cost function can be taken as the energy of a physical system. One can then introduce an auxiliary *temperature*, and define a *free energy* at finite temperatures. The benefit is that one can then search the global energy minimum via some passes activated naturally by finite temperatures. The simulation is started from a high temperature, and the system is cooled down gradually.

Simulated Tempering

In the simulated tempering [22.48, 49] the inverse temperature β is treated as a dynamical variable, such that both the cooling and heating processes are implemented in the algorithm. The reason this algorithm works well is explained in Fig. 22.3. The probability distribution of the original system

$$P(\mathbf{x}) = \frac{e^{-\beta\mathcal{H}(\mathbf{x})}}{Z(\beta)}, \quad Z(\beta) = \sum_{\mathbf{x}} e^{-\beta\mathcal{H}(\mathbf{x})}, \quad (22.38)$$

is extended to a larger parameter space of \mathbf{x} and $\{\beta_m\}$ ($m = 1, 2, \dots, M$) as

$$P(\mathbf{x}, \beta_m) = \frac{e^{-\beta_m\mathcal{H}(\mathbf{x})}}{Z(\beta_m)} \tilde{\pi}_m, \quad (22.39)$$

$$\tilde{\pi}_m \propto \exp[g_m + \log Z(\beta_m)], \quad \sum_m \tilde{\pi}_m = 1. \quad (22.40)$$

One choice of the function g_m is $g_m = -\log Z(\beta_m)$, which results in $\tilde{\pi}_m = 1/M$. That is, all β_m are visited equally.

Choosing several discrete inverse temperatures can make the simulation efficient, and the optimal number and distribution of $\{\beta_m\}$ are estimated as follows [22.49, 50]. First, the acceptance ratio of the flip between different temperatures is given by

$$\begin{aligned} & \exp[-(\beta_m\mathcal{H}(\mathbf{x}_m) - \beta_{m+1}\mathcal{H}(\mathbf{x}_{m+1}))] \\ & \approx \exp[-(\Delta\beta)^2 d\mathcal{H}/d\beta] \\ & = \exp[-(\Delta\beta)^2 NC/\beta_m^2], \end{aligned}$$

where N and C are the number of particles and the specific heat, respectively. In order to keep the acceptance ratio independent of the system size, $\Delta\beta \sim N^{-1/2}$ or $M \sim N^{1/2}$ should be satisfied. If C diverges at the critical temperature, one should take $M \sim N^{[1+\alpha/(d\nu)]/2}$, with the critical exponent α of C and the space dimension d .

Next, each β_m is determined iteratively in preliminary runs. A new set $\{\beta'_m\}$ is constructed from the old

set $\{\beta_m\}$ as

$$\beta'_1 = \beta_1, \quad (22.41)$$

$$\beta'_m = \beta'_{m-1} + (\beta_m - \beta_{m-1}) \frac{p_m}{c} \quad (m = 2, \dots, M), \quad (22.42)$$

$$c = \frac{1}{M-1} \sum_{m=2}^M p_m, \quad (22.43)$$

with $\beta_1 < \beta_2 < \dots < \beta_M$. The acceptance ratio p_m at β_m is also evaluated during preliminary runs. The above procedure arrives at equilibrium when all values of $\{p_m\}$ become equal, which is consistent with the initial choice of g_m .

Monte Carlo simulations are performed using the above sets of $\{\beta_m\}$ and $\{g_m\}$. Since g_m only depends on β_m , update without changing β_m is the same as the standard one, and the weight for update of β_m is proportional to $e^{-\beta_m \mathcal{H} + g_m}$. Measurements on physical quantities are made similarly to the conventional Monte Carlo algorithm at each β_m .

Exchange Monte Carlo

Instead of treating one system as in the simulated tempering, the exchange Monte Carlo method [22.50] takes M replicated systems at β_m ($m = 1, 2, \dots, M$), and exchanges the configurations between replicas of close temperatures. The optimal distribution of β_m is evaluated similarly to that in the simulated tempering as given in (22.41)–(22.43). Update in a replica is the same as the conventional one, and exchange of replicas at β_m and β_{m+1} is introduced by comparison of the weights $\exp[-\beta_m \mathcal{H}(\mathbf{x}_m) - \beta_{m+1} \mathcal{H}(\mathbf{x}_{m+1})]$ and $\exp[-\beta_m \mathcal{H}(\mathbf{x}_{m+1}) - \beta_{m+1} \mathcal{H}(\mathbf{x}_m)]$. This algorithm can be regarded as a parallelized version of the simulated tempering, and is often called parallel tempering.

This algorithm has several advantages compared with the simulated tempering. First, it is unnecessary to introduce the nontrivial function g_m . Since determination of g_m (or equivalently $Z(\beta_m)$) is complicated and time consuming, this property simplifies the coding and accelerates simulations. Second, existence of fixed sets of β_m throughout simulations is suitable for observing the replica overlap, which is important in the study of spin glasses. Third, this algorithm fits very well with parallel coding. Most calculations can be done independently in each replica (i. e., in each CPU), and only information on exchange rates and temperatures have to be sent to other CPUs.

22.2.5 Replica Monte Carlo

The replica Monte Carlo [22.51] implemented for spin glass models can be regarded as a mixture of the exchange Monte Carlo and the cluster algorithm. Consider the Ising spin glass model

$$\mathcal{H} = - \sum_{\langle ij \rangle} \beta J_{ij} \sigma_i \sigma_j, \quad (22.44)$$

and take M replicas. The pair Hamiltonian of two close temperatures is defined as (for simplicity, $m = 1$)

$$\mathcal{H}_{\text{pair}}(\sigma^1, \sigma^2) = - \sum_{\langle ij \rangle} \left(\beta^1 J_{ij} \sigma_i^1 \sigma_j^1 + \beta^2 J_{ij} \sigma_i^2 \sigma_j^2 \right). \quad (22.45)$$

Using a new Ising variable $\tau_i^{(m)} = \sigma_i^{(m)} \sigma_i^{(m+1)}$, (22.45) is written as

$$\mathcal{H}_{\text{pair}}(\sigma^1; \tau^1) = - \sum_{\langle ij \rangle} \left(\beta^1 + \beta^2 \tau_i^1 \tau_j^1 \right) J_{ij} \sigma_i^1 \sigma_j^1. \quad (22.46)$$

The pair Hamiltonian is divided into clusters within which $\tau_i^1 \tau_j^1 = +1$ is satisfied. When each cluster is represented by an effective Ising variable $\eta_a^{(m)}$ with the index a of clusters, the pair Hamiltonian is expressed as

$$\mathcal{H}_{\text{cl}}(\eta^1) = - \sum_{\langle a,b \rangle} k_{a,b} \eta_a^1 \eta_b^1, \quad (22.47)$$

$$k_{a,b} = (\beta^1 - \beta^2) \sum_{\langle i \in a, j \in b \rangle} J_{ij} \sigma_i^1 \sigma_j^1. \quad (22.48)$$

The cluster update is introduced as Monte Carlo flips of the variable η_a^1 starting from configurations with all-up η_a^1 spins.

After the cluster flip, original Ising variables are changed as $\sigma_i^{1,2} \leftarrow \eta_a^1 \sigma_i^{1,2}$ for $i \in a$, and conventional Monte Carlo flips are performed in each replica to assure the ergodicity.

In the representation (22.46), the exchange Monte Carlo corresponds to a simultaneous flip of all $\tau^1 = -1$ clusters. Although the present algorithm was proposed as early as the cluster algorithm itself and much earlier than the exchange Monte Carlo, it has not been used so popularly to date due to complex coding and limited applicability in comparison with the exchange Monte Carlo. However, a recent study [22.52] showed that in two dimensions this algorithm is much faster than the exchange Monte Carlo.

22.3 Quantum Monte Carlo Method

The quantum Monte Carlo method is a powerful method to investigate both finite- and zero-temperature properties of quantum systems. The results are exact within error bars. This method can be applied to large-size systems in any dimensions. However, it has a problem when applied to the systems with large frustrations or strong correlations. In such systems, almost half of samples have negative weights, and Monte Carlo simulations do not work well. Hence, readers had better take care in using the quantum Monte Carlo method for such systems. The negative-sign problem is explained in Sect. 22.3.8.

There are several types of quantum Monte Carlo algorithms. Depending on the model, the most suitable algorithm should be chosen: For spin systems without magnetic fields, the cluster algorithm is effective (Sect. 22.3.3). Under magnetic fields, the worm algorithm or the directed-loop algorithm is better (Sect. 22.3.5). The continuous-time algorithm makes simulations efficient (Sect. 22.3.4). For electron systems, the auxiliary-field algorithm is appropriate, especially for the Hubbard model (Sect. 22.3.6). To investigate the ground-state properties, projection methods are suitable (Sect. 22.3.7).

There are other Monte Carlo methods to investigate quantum systems. Here, we only consider the quantum Monte Carlo algorithms by which results converge to the exact value in principle. Hence, approximate methods like variational Monte Carlo methods or fixed-node approximations are beyond our scope.

22.3.1 Suzuki–Trotter Formalism

Quantum Monte Carlo simulations in d -dimensional systems are generally performed through mapping to

the corresponding $(d + 1)$ -dimensional classical systems. The Suzuki–Trotter transformation is the most typical procedure of this mapping using the Trotter formula. In order to explain the basics of quantum Monte Carlo methods, we review first the Suzuki–Trotter formalism [22.53].

The partition function of quantum systems is generally defined as

$$Z = \text{Tr} e^{-\beta \mathcal{H}}, \quad (22.49)$$

where β and \mathcal{H} are the inverse temperature and the Hamiltonian, respectively. Using the generalized Trotter formula, the exponential of quantum Hamiltonians can be decomposed into the product of exponentials in infinitesimal time-slices as

$$e^{\beta \mathcal{H}} = \lim_{n \rightarrow \infty} \left(\prod_i e^{-\Delta \tau \mathcal{H}_i} \right)^n, \quad (22.50)$$

where $\Delta \tau = \beta/n$, and \mathcal{H}_i is a local Hamiltonian that satisfies $\mathcal{H} = \sum_i \mathcal{H}_i$. Inserting complete sets between time slices, the partition function can be expressed in terms of local weights as

$$Z = \sum_A W(A), \quad W(A) = \prod_i w(a_i). \quad (22.51)$$

Here, A denotes a configuration such as shown in Fig. 22.4a, and a is a local configuration on a plaquette. Their weights are represented by $W(A)$ and $w(a)$, respectively. Plaquette weights are defined on shaded plaquettes in Fig. 22.4a.

In this way, the system is mapped onto a $(d + 1)$ -dimensional classical system. This transformation is called the Suzuki–Trotter transformation [22.54, 55]. Quantum Monte Carlo simulations are performed through updates of configurations in the $(d + 1)$ -dimensional space-time. For recent progress see [22.56, 57].

22.3.2 World-Line Approach

In order to explain how quantum Monte Carlo simulations are performed in the $(d + 1)$ -dimensional space-time, we here review the world-line algorithm. As an example, we consider the spin-1/2 Heisenberg model, which is defined by the following Hamiltonian

$$\mathcal{H} = J \sum_{\langle i, j \rangle} \mathbf{S}_i \cdot \mathbf{S}_j, \quad (22.52)$$

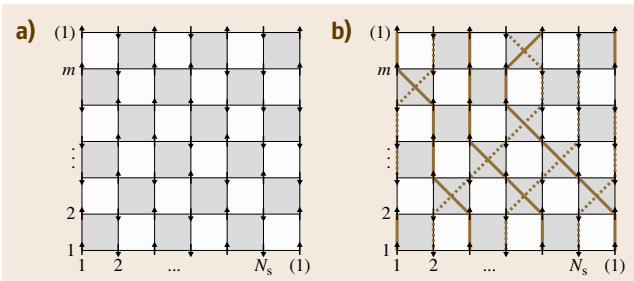


Fig. 22.4 (a) $(d + 1)$ -dimensional space-time for N_s site quantum system. (b) World-line configuration. The vertical axis represents the Trotter axis, and m is the Trotter number

where the summation is taken over nearest-neighbor sites, and S_i denotes the spin operator at site i . All the possible local configurations and weights of plaquettes in a time-slice are listed in Table 22.1.

Up spins (or down spins) may be joined by lines as illustrated in Fig. 22.4b. These lines are called world-lines [22.58]. In the world-line algorithm, world-line configurations are updated. One way to update them is the following: As illustrated in Fig. 22.5, we try to flip four spins (a, b, c, d), taking care so that the flip satisfies the conservation law of the model. The new world-line configuration is accepted with the probability

$$P = \frac{\rho'_1 \rho'_2 \rho'_3 \rho'_4}{\rho_1 \rho_2 \rho_3 \rho_4 + \rho'_1 \rho'_2 \rho'_3 \rho'_4}, \quad (22.53)$$

based on the heat-bath algorithm (or the Metropolis algorithm). In this way, world-lines are locally moved. This process is called a local flip. Since the ergodicity is not satisfied by this type of updates only [22.59], we need other types of flips. If up spins (or down spins) align in the imaginary time direction or in the diagonal directions, they can flip simultaneously. If up and down spins align alternately in the space direction, they can also flip simultaneously. These types of flips are called global flips [22.60]. Combining these two types of flips, world-line configurations are updated. Physical quantities such as magnetization, susceptibilities, energy and specific heat can be measured using spin configurations, local weights and their derivatives in the $(d + 1)$ -dimensional space-time [22.61–63].

In the world-line algorithm, the width of the time slice is finite. Hence, the extrapolation $\Delta\tau \rightarrow 0$ is necessary after simulations. The error due to the finite $\Delta\tau$ is systematic: It is proportional to $\Delta\tau^2$ or $\Delta\tau^4$, etc., depending on the way of decomposition in (22.50) [22.64, 65]. In the continuous-time algorithm, the discreteness of the Trotter slice is removed by taking $\Delta\tau \rightarrow 0$ in the definition of local probabilities as will be discussed later.

22.3.3 Cluster Algorithm

Spin configurations in the $(d + 1)$ -dimensional space-time can be updated more efficiently by using the cluster algorithm. For the cluster algorithm in quantum systems [22.35, 40], readers may refer to excellent overviews in [22.66, 67]. In the cluster algorithm, spin configurations as in Fig. 22.4a are mapped onto graphs [22.68, 69]. The weights $V(G)$ of graph G are

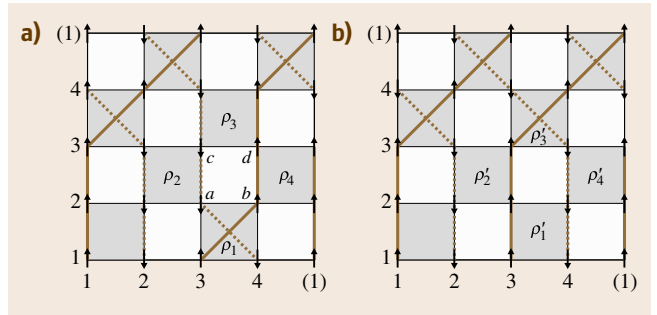


Fig. 22.5a,b Local flip in the world-line algorithm in a four-spin system with the Trotter number $m = 4$

defined in order to satisfy the following relation

$$W(A) = \sum_G V(G) \Delta(A, G), \quad (22.54)$$

where $\Delta(A, G)$ is one if spin configuration A is compatible with graph G , and otherwise zero. Similarly, it is possible to define the local version of (22.54) as

$$w(a) = \sum_g v(g) \delta(a, g). \quad (22.55)$$

For the Heisenberg model defined in (22.52), $\delta(a, g)$ is chosen as shown in Table 22.2.

The probability $P(g|a)$ of assigning graph g to configuration a is given by

$$P(g|a) = \frac{\delta(a, g)v(g)}{w(a)}. \quad (22.56)$$

Table 22.1 Local configurations and their weights

a	$w(a)$
$\begin{pmatrix} \uparrow & \uparrow \\ \uparrow & \uparrow \end{pmatrix}, \begin{pmatrix} \downarrow & \downarrow \\ \downarrow & \downarrow \end{pmatrix}$	$e^{-\frac{\Delta\tau J}{4}}$
$\begin{pmatrix} \uparrow & \downarrow \\ \uparrow & \downarrow \end{pmatrix}, \begin{pmatrix} \downarrow & \uparrow \\ \downarrow & \uparrow \end{pmatrix}$	$e^{\frac{\Delta\tau J}{4}} \cosh\left(\frac{\Delta\tau J}{2}\right)$
$\begin{pmatrix} \uparrow & \downarrow \\ \downarrow & \uparrow \end{pmatrix}, \begin{pmatrix} \downarrow & \uparrow \\ \uparrow & \downarrow \end{pmatrix}$	$-e^{\frac{\Delta\tau J}{4}} \sinh\left(\frac{\Delta\tau J}{2}\right)$

Table 22.2 Function $\delta(a, g)$ for mapping of local configurations to graphs

$a \backslash g$	\parallel	$=$
$\begin{pmatrix} \uparrow & \uparrow \\ \uparrow & \uparrow \end{pmatrix}, \begin{pmatrix} \downarrow & \downarrow \\ \downarrow & \downarrow \end{pmatrix}$	1	0
$\begin{pmatrix} \uparrow & \downarrow \\ \uparrow & \downarrow \end{pmatrix}, \begin{pmatrix} \downarrow & \uparrow \\ \downarrow & \uparrow \end{pmatrix}$	1	1
$\begin{pmatrix} \uparrow & \downarrow \\ \downarrow & \uparrow \end{pmatrix}, \begin{pmatrix} \downarrow & \uparrow \\ \uparrow & \downarrow \end{pmatrix}$	0	1

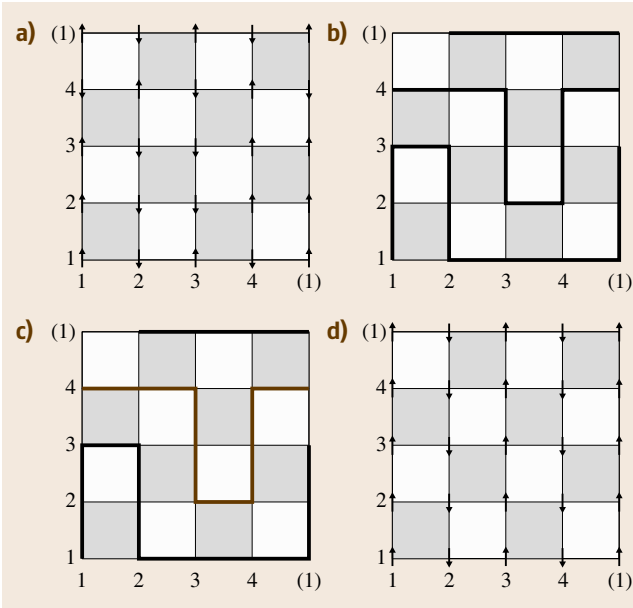


Fig. 22.6a–d Update of spin configurations through graph representation. See text for details

The updating procedure in the cluster algorithm is illustrated in Fig. 22.6: For a spin configuration Fig. 22.6a, graphs are assigned as in Fig. 22.6b with probability given in (22.56), which results in clusters (or loops). The clusters are flipped with probability $1/2$. If the graph shown in a red line in Fig. 22.6c is flipped, the spin configuration becomes as in Fig. 22.6d. In the cluster algorithm, a large number of spins flip simultaneously. Hence, the auto-correlation time is greatly reduced compared with the world-line algorithm [22.40, 70, 71]. Also, it is easy to take the limit of $\Delta\tau \rightarrow 0$ [22.72]. For isotropic Heisenberg models and XXZ models with XY -anisotropy, clusters form loops. Hence, the cluster algorithm for these models are called the loop algorithm [22.40].

Table 22.3 Local configurations and their weights in the limit of $\Delta\tau \rightarrow 0$

a	$w(a)$
$(\uparrow\uparrow), (\downarrow\downarrow)$	$1 - \frac{\Delta\tau J}{4}$
$(\uparrow\downarrow), (\downarrow\uparrow)$	$1 + \frac{\Delta\tau J}{4}$
$(\uparrow\downarrow), (\downarrow\uparrow)$	$-\frac{\Delta\tau J}{2}$

The cluster algorithm is also applied to the models with general spin S [22.73]. Since spin- S operators can be represented by $2S$ spin- $1/2$ operators, simulations in the N_s -site system with spin S can be performed by mapping the system onto the $2SN_s$ -site system with spin- $1/2$ operators under the special boundary condition in the imaginary-time direction [22.74]. The boundary condition is set in order to project out the unphysical states with $S_t^2 < S(S+1)$.

Simulations under the magnetic field (H) can be performed by the cluster algorithm, replacing the flipping probability with

$$P_{\text{flip}} = \frac{e^{\beta H M_{\text{new}}}}{e^{\beta H M_{\text{new}}} + e^{\beta H M_{\text{old}}}}, \quad (22.57)$$

where M_{new} and M_{old} are the magnetizations of the cluster in the new and old configurations, respectively. We should be careful about the use of it in the low-temperature regime under high magnetic fields, because in such situations the flipping probability defined in (22.57) becomes exponentially small [22.75]. Hence, in this case, other algorithms such as the worm algorithm [22.76, 77] or the directed-loop algorithm [22.78] are suitable.

22.3.4 Continuous-Time Algorithm

Based on the cluster algorithm, the limit of $\Delta\tau \rightarrow 0$ is taken [22.72]. The local weights in Table 22.1 become as in Table 22.3 in the limits of $\Delta\tau \rightarrow 0$. The probability of assigning graphs $P(g|a)$ is given in Table 22.4, using (22.56). The positions of new vertices are statistically determined in the continuous time. According to Table 22.4, the probability that a new vertex is created during the interval τ_L between antiparallel spins is $1 - e^{-\frac{\tau_L J}{2}}$. The procedure of the continuous-time loop algorithm is illustrated in Fig. 22.7: For a spin configuration Fig. 22.7a, graphs are assigned as in Fig. 22.7b with probabilities given in Table 22.4. The loops are

Table 22.4 Probability $P(g|a)$ of assigning graphs to configurations in the limit of $\Delta\tau \rightarrow 0$.

$a \backslash g$	$ $	$=$
$(\uparrow\uparrow), (\downarrow\downarrow)$	1	0
$(\uparrow\downarrow), (\downarrow\uparrow)$	$1 - \frac{\Delta\tau J}{2}$	$\frac{\Delta\tau J}{2}$
$(\uparrow\downarrow), (\downarrow\uparrow)$	0	1

flipped with probability 1/2. If the graphs shown in red lines in Fig. 22.7c are flipped, the spin configuration becomes as in Fig. 22.7d.

Physical quantities are calculated in the same way as in the discrete-time loop algorithm. Since in the continuous-time algorithm, the limit of $\Delta\tau \rightarrow 0$ is already taken, it is unnecessary to extrapolate data to $\Delta\tau \rightarrow 0$. Another merit is that the memory cost is generally smaller than the discrete-time loop algorithm.

The stochastic series expansion (SSE) algorithm [22.79–81] is an alternative quantum Monte Carlo algorithm which does not depend on the Trotter formula and can produce exact results within error bars without extrapolations at finite temperatures. In the SSE algorithm, the partition function defined in (22.49) is expressed as

$$Z = \sum_{n=0}^{\infty} \frac{(-\beta)^n}{n!} \text{Tr} \mathcal{H}^n. \quad (22.58)$$

This expansion converges exponentially for $n \sim N_s\beta$. Here, a truncation at $n = L$ of this order is imposed. The number L is adjusted during equilibration so that the highest value of n appearing in the simulation does not exceed L . In this case, truncation errors become completely negligible. Using this L , the partition function is rewritten as

$$Z = \sum_{S_L} \frac{\beta^m (L-m)!}{L!} \text{Tr} \prod_{i=1}^L \mathcal{H}_{a_i, b_i}, \quad (22.59)$$

where S_L denotes a sequence of operator indices: $S_L = [a_1, b_1], [a_2, b_2], \dots, [a_L, b_L]$, with $a_i \in \{1, 2\}$ and $b_i \in \{1, \dots, M\}$ (M : the number of bonds), or $[a_i, b_i] = [0, 0]$. Here, $\mathcal{H}_{1,j}$ and $\mathcal{H}_{2,j}$ denote diagonal and off-diagonal parts of the local Hamiltonian on bond j , respectively. (A positive constant is added to $\mathcal{H}_{1,j}$ in order to make all matrix elements positive, if necessary.) The operator $\mathcal{H}_{0,0}$ is defined as the unit operator: $\mathcal{H}_{0,0} = 1$. The number of non-[0,0] elements in S_L is denoted by m . Simulations are performed in the $N_s L$ site system in the $(d+1)$ -dimensional space-time. Spin configurations are updated through updates of indices at vertices $[1, b] \leftrightarrow [0, 0]$ or $[1, b_i][1, b_j] \leftrightarrow [2, b_i][2, b_j]$. The latter process is improved by the operator-loop update [22.82], which is naturally extended to the directed-loop algorithm [22.78].

22.3.5 Worm Algorithm

In the cluster algorithm, it is difficult to investigate properties in the low-temperature regime under high

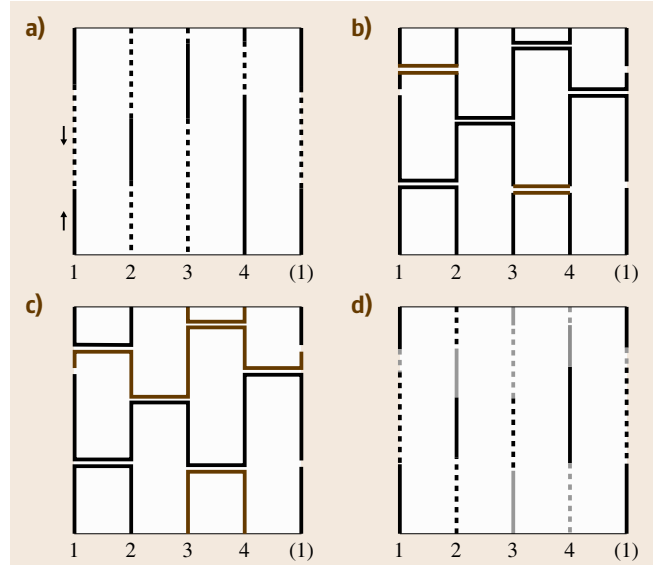


Fig. 22.7a–d Update of spin configurations through graph representation in the limit of $\Delta\tau \rightarrow 0$. In (a) and (d), up and down spins are represented by *solid* and *dotted* lines, respectively. In (b), new vertices are joined by *red* lines. See text for details

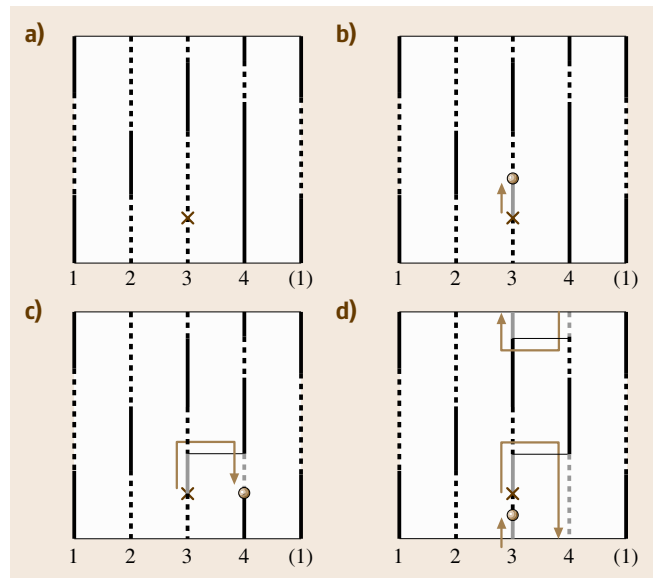


Fig. 22.8a–d Update of spin configurations by the directed-loop algorithm

magnetic fields, because the flipping probability of clusters becomes exponentially small. This difficulty can be removed by taking the effects of magnetic fields

into account in the process of loop formations, as in the worm algorithm [22.76, 77] and the directed-loop algorithm [22.78]. The updating procedure of the directed-loop algorithm is illustrated in Fig. 22.8: A starting point is randomly chosen in the $(d+1)$ -dimensional space-time as in Fig. 22.8a. From this starting point, the worm moves in one of the two directions as in Fig. 22.8b. The worm can hop to another site stochastically as in Fig. 22.8c. Reaching a vertex, the worm jumps to the other site as in Fig. 22.8d with the probability one. These motions are continued until the worm goes back to the starting point. (The worm may turn back at vertices, if probabilities are defined to allow such processes.) The trajectory of the worm forms a loop as in the loop algorithm. In the worm algorithm, two worms (or the head and tail of a worm) are created randomly at nearby times in the $(d+1)$ -dimensional space-time. Then, the worms move randomly until they meet again. The off-diagonal correlations like $\langle S^+ S^- \rangle$ can also be calculated by using the worms [22.76, 77].

22.3.6 Auxiliary Field Approach

The basic strategy of the auxiliary field quantum Monte Carlo algorithm is the following: Auxiliary fields are introduced in the path integral representation. Quantum (fermionic) degrees of freedom are integrated exactly, and the remaining degrees of freedom for (classical) auxiliary fields are integrated by Monte Carlo techniques. There is a powerful auxiliary field algorithm for the Hubbard model [22.83–86]. We consider the Hubbard model defined by the following Hamiltonian

$$\mathcal{H} \equiv \mathcal{H}_t + \mathcal{H}_U, \quad (22.60)$$

$$\mathcal{H}_t \equiv -t \sum_{(i,j),\sigma} (c_{i\sigma}^\dagger c_{j\sigma} + c_{j\sigma}^\dagger c_{i\sigma}), \quad (22.61)$$

$$\mathcal{H}_U \equiv U \sum_i n_{i\uparrow} n_{i\downarrow}, \quad (22.62)$$

where $c_{i\sigma}$ and $n_{i\sigma}$ denote the annihilation operator and the number operator with spin σ at site i , respectively. The partition function defined in (22.49) can be decomposed as

$$\text{Tr} e^{-\beta\mathcal{H}} = \lim_{n \rightarrow \infty} \text{Tr} (e^{-\Delta\tau\mathcal{H}_t} e^{-\Delta\tau\mathcal{H}_U})^n, \quad (22.63)$$

where $\Delta\tau = \beta/n$. The exponential of the U -term can be expressed in terms of auxiliary fields s_i as [22.87]

$$e^{-\Delta\tau U n_{i\uparrow} n_{i\downarrow}} = \frac{1}{2} \sum_{s_i = \pm 1} e^{(2as_i - \frac{\Delta\tau U}{2})n_{i\uparrow}} \times e^{(-2as_i - \frac{\Delta\tau U}{2})n_{i\downarrow}}, \quad (22.64)$$

where $\cosh 2a = e^{\frac{\Delta\tau U}{2}}$. Since the U -term is decomposed into up- and down-spin parts as

$$e^{-\Delta\tau\mathcal{H}_U} = \frac{1}{2^{N_s}} \sum_{s_1, \dots, s_{N_s}} e^{-\Delta\tau\mathcal{H}_U^\uparrow(s_1, \dots, s_{N_s})} \times e^{-\Delta\tau\mathcal{H}_U^\downarrow(s_1, \dots, s_{N_s})}, \quad (22.65)$$

the partition function becomes

$$Z = \lim_{n \rightarrow \infty} \frac{1}{2^{N_s n}} \sum_{\{s\}} \text{Tr} \prod_{\sigma} \prod_{l=1}^n \left(e^{-\Delta\tau\mathcal{H}_t^\sigma} e^{-\Delta\tau\mathcal{H}_U^\sigma(\{s_l\})} \right) = \lim_{n \rightarrow \infty} \frac{1}{2^{N_s n}} \sum_{\{s\}} W^\uparrow(\{s\}) W^\downarrow(\{s\}), \quad (22.66)$$

where $\{s\} = s_{i,l}$ ($i = 1, \dots, N_s$, $l = 1, \dots, n$), $\{s_l\} = s_{i,l}$ ($i = 1, \dots, N_s$), and N_s denotes the number of sites. It should be noted that in this expression the interactions between up and down spins are removed in each auxiliary-field configuration. This reduces the problem to noninteracting fermions under local magnetic fields produced by auxiliary fields. It is easy to solve the noninteracting fermion problem. The effects of interactions are taken into account through Monte Carlo samplings for the auxiliary fields. By taking the trace over the fermionic degrees of freedom, the weight W^σ is obtained as

$$W^\sigma(\{s\}) = \det \left[I + \prod_{l=1}^n \left(e^{-\Delta\tau\mathcal{H}_t^\sigma} e^{-\Delta\tau\mathcal{H}_U^\sigma(\{s_l\})} \right) \right]. \quad (22.67)$$

Simulations are performed by updating auxiliary-field configurations in the $(d+1)$ -dimensional space-time.

The auxiliary-field Monte Carlo algorithm is also used to investigate ground-state properties, replacing the trace of the partition function in (22.49) by the expectation value of a trial state. This corresponds to a kind of projection method.

22.3.7 Projector Monte Carlo Method

The basic principle of the projection method is to extract the ground-state component by repeatedly applying the Hamiltonian many times to a trial state. In the process of multiplication of the Hamiltonian, configurations are generated by Monte Carlo techniques [22.88, 89]. Here, as an example, we take the Monte Carlo power method which is the simplest projection method.

Let us suppose that a trial state ($|\psi\rangle$) has finite overlap with the ground state ($|\phi_0\rangle$), i. e. $\langle\phi_0|\psi\rangle \neq 0$. Then, physical quantities in the ground state are evaluated as

$$\bar{O} = \lim_{p \rightarrow \infty} \bar{O}_p, \quad \bar{O}_p \equiv \frac{\langle\psi|\hat{\mathcal{H}}^p O \hat{\mathcal{H}}^p|\psi\rangle}{\langle\psi|\hat{\mathcal{H}}^{2p}|\psi\rangle}, \quad (22.68)$$

where $\hat{\mathcal{H}} \equiv \mathcal{H} - C$, and C is chosen such that $|E_0 - C| > |E_i - C|$. Here, E_0 is the ground-state energy, and E_i ($i = 1, 2, 3, \dots$) the energy of i th excited state. In Monte Carlo simulations, the trial state is expanded in terms of the states which are used in Monte Carlo updates such as site representation as $|\psi\rangle = \sum_i a_i |i\rangle$. The denominator of \bar{O}_p is expressed as

$$\begin{aligned} \langle\psi|\hat{\mathcal{H}}^{2p}|\psi\rangle &= \sum_{i_0, i_1, \dots, i_{2p}} a_{i_{2p}}^* a_{i_0} \prod_{j=1}^{2p} \langle i_j | \hat{\mathcal{H}} | i_{j-1} \rangle \\ &= \sum_{i_0} |a_{i_0}|^2 \sum_{\text{path}} (WP)_{\text{path}}, \\ W &= \frac{a_{i_0}}{a_{i_{2p}}} \prod_{j=1}^{2p} \langle i_{j-1} | \hat{\mathcal{H}} | i_j \rangle, \\ P &= \prod_{j=1}^{2p} \frac{|a_{i_j}|^2}{|a_{i_{j-1}}|^2}. \end{aligned} \quad (22.69)$$

Similarly, the numerator of \bar{O}_p can also be expressed in terms of $|i\rangle$. Using Monte Carlo techniques, states are generated according to the distribution determined by $|a_{i_0}|^2$. From a configuration ($|i_0\rangle$), we choose one of the configurations which are reached by multiplying the Hamiltonian with probability $|a_{i_1}|^2/|a_{i_0}|^2$. This procedure is repeated $2p$ times to obtain the weight (W) of a path. \bar{O}_p is calculated as the ratio of $\langle\psi|\hat{\mathcal{H}}^p O \hat{\mathcal{H}}^p|\psi\rangle$ to $\langle\psi|\hat{\mathcal{H}}^{2p}|\psi\rangle$, which are approximately obtained as the average of weights over all paths produced by Monte Carlo samplings.

Monte Carlo updates for $|i_0\rangle$ are performed by the algorithm of the variational Monte Carlo method. In this sense, the Monte Carlo power method corresponds to the extension of the variational Monte Carlo method to make it possible to extract the ground-state component from the variational trial state. As is well known, the variational Monte Carlo method does not suffer from the negative-sign problem. However, the Monte Carlo power method does in general, because the weights W can be negative. If we use the trial state that has the same node structure with the ground state, the negative sign problem does not appear. If negative weights can be removed due to some special symmetry, the negative-sign problem can also be avoided. Improved algorithms

of the Monte Carlo power method have been proposed such as the power Lanczos method [22.90] which makes the convergence faster by adopting the principle of the Lanczos algorithm.

Here, we briefly review the ground-state version of the auxiliary-field quantum Monte Carlo algorithm. As a trial state, the state in the following form is used

$$\begin{aligned} |\Phi\rangle &= |\Phi^\uparrow\rangle \otimes |\Phi^\downarrow\rangle, \\ |\Phi^\sigma\rangle &= \prod_{j=1}^M \left(\sum_{i=1}^{N_s} \Phi_{i,j}^\sigma c_{i,\sigma}^\dagger \right) |0\rangle, \end{aligned} \quad (22.70)$$

where M and N_s are the numbers of up- (or down-) spins and lattices, respectively. Using auxiliary fields, the expectation value of the exponentials of the Hamiltonian by the trial state is expressed as

$$\begin{aligned} \rho_n &= \langle\Phi|(e^{\Delta\tau\mathcal{H}})^n|\Phi\rangle \\ &= \sum_{\{s_1, \dots, s_n\}} W_\uparrow(\{s\}) W_\downarrow(\{s\}), \\ W_\sigma(\{s\}) &= \det \left[{}^t\Phi^\sigma \prod_{l=1}^n (U_\sigma^l(\{s_l\}) K^l) \Phi^\sigma \right], \end{aligned}$$

where U_σ^l is a diagonal matrix whose diagonal elements are $1/\sqrt{2} \exp(2as_{i,l}\sigma - (\Delta\tau U/2))/\sqrt{2}$, and $K^l = \exp(-\bar{K})$. Here, \bar{K} has non-zero matrix elements $-\Delta\tau t$ for (i, j) components, where i and j are the nearest neighbors. Updates for the auxiliary fields are performed in the same way as in the finite-temperature algorithm.

The stochastic reconfiguration method [22.91–93] is a projection method which is based on an extension [22.94,95] of the fixed-node approximation [22.96,97]. In this method, configurations of walkers are rearranged so as not to increase negative weights under the condition that expectation values of some operators remain unchanged.

In principle, the ground state is obtained by projection methods through a large number of projection steps, if trial states have finite overlap with the ground state. However, special attention should be paid for the choice of trial states in practice. If the symmetry of the ground state is known, the trial state should be chosen to have the same symmetry as the ground state. Then, the simulations can be performed within the subspace of this symmetry, and the convergence becomes faster. Even though a trial state $|\phi_0\rangle$ has a lower energy than a state $|\phi_s\rangle$ which has the same symmetry as the ground state, the energy starting from $|\phi_s\rangle$ can become lower than that from $|\phi_0\rangle$ at finite projection steps. The sym-

metries of the ground state that need to be taken into account commonly are, for example, the total spin $S = 0$ and total momentum $K = 0$. Such a trial state may be better than ordered states as an initial state of projection methods.

22.3.8 Negative-Sign Problem

In quantum Monte Carlo simulations, partial Boltzmann weights may be negative. Since the Markov process cannot be defined for negative weights, simulations are based on the absolute values of weights. The statistical average of a physical quantity is obtained by dividing the average of physical quantity with signs of weights by the average of signs. Generally, at low temperatures or in large systems, the average of signs becomes exponentially small, and its statistical error becomes exponentially large. This difficulty is called the negative-sign problem.

Here, we show a simple example that exhibits the negative-sign problem. We consider the Heisenberg model defined by (22.52) in a three-site cluster with the Trotter number three. There are three types of world-line configurations as shown in Fig. 22.9. Other world-line configurations can be obtained by inversion of spin directions or translations.

The weights of these configurations are

$$\text{a) } w \begin{pmatrix} \uparrow & \uparrow & \uparrow \\ \uparrow & \uparrow & \uparrow \end{pmatrix}^3,$$

$$\text{b) } w \begin{pmatrix} \downarrow & \uparrow \\ \downarrow & \uparrow \end{pmatrix} w \begin{pmatrix} \uparrow & \uparrow \\ \uparrow & \uparrow \end{pmatrix}^2 \text{ and}$$

$$\text{c) } w \begin{pmatrix} \uparrow & \downarrow \\ \downarrow & \uparrow \end{pmatrix}^3,$$

where local weights are defined in Table 22.1. Since $w \begin{pmatrix} \uparrow & \downarrow \\ \downarrow & \uparrow \end{pmatrix}$ is negative, the weight of (c) is negative. If we define the probability as in (22.53), the probability of (c) from (b) (or (b) from (c)) becomes negative. Thus, we decouple the weight W into the positive weight W' and the sign S as $W = W' \times S$. The probability is then redefined as $P = W'_{\text{new}} / (W'_{\text{new}} + W'_{\text{old}})$. The average of physical quantity Q is obtained as

$$\begin{aligned} \langle Q \rangle &= \frac{\sum_A W(A) Q(A)}{\sum_A W(A)} \\ &= \frac{\sum_A W'(A) S(A) Q(A)}{\sum_A W'(A) S(A)} \\ &= \frac{[\sum_A W'(A) S(A) Q(A)] / [\sum_A W'(A)]}{[\sum_A W'(A) S(A)] / [\sum_A W'(A)]} \\ &= \frac{\langle SQ \rangle'}{\langle S \rangle'}, \end{aligned} \quad (22.71)$$

where $\langle \cdot \rangle'$ denotes the average with respect to W' . When the number of negative weights is as large as that of positive weights, $\langle S \rangle'$ becomes almost zero. Then, the statistical error becomes large. The negative sign problem is generally severe in the low-temperature regime.

Spin models without frustration do not suffer from the negative-sign problem, because all the weights can be chosen as positive by a gauge transformation. The Hubbard models on bipartite lattices with attractive interactions ($U < 0$) or those with repulsive interactions ($U > 0$) at half-filling do not have negative weights. One-dimensional electron systems with nearest-neighbor hopping also do not suffer from the negative-sign problem in general.

Even with frustrations or strong correlations, some models can be simulated without negative-sign problems by using special algorithms. For some frustrated Heisenberg chains, quantum Monte Carlo simulations can be performed free of negative-sign problems by the algorithm shown in [22.98]. In this algorithm, the representation basis is changed from the conventional S^z -basis to the dimer basis. Using this dimer basis, the system is described as a single chain where dimer units are connected with a single effective coupling. The

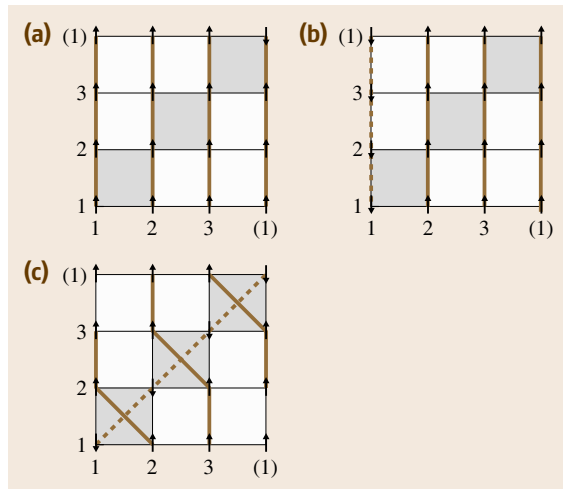


Fig. 22.9a–c World-line configurations for a three-site system

suppression of negative weights can be proved by a non-local unitary transformation with appropriate coupling constants.

Another algorithm which does not suffer from the negative-sign problem for strongly-correlated electron systems is shown in [22.99, 100]. This algorithm is based on a cluster algorithm and called the meron-cluster algorithm. The model considered here is the fermionic version of the spin-1/2 Heisenberg model without chemical potentials. For fermionic systems, there are two types of clusters, one changing their signs by a flip, and the other not. The former is called meron-clusters. Only the configurations without meron-clusters contribute to the average of the sign (Sign), since in the cluster algorithm without magnetic fields (which correspond to chemical potentials for fermionic systems), clusters flip independently with probability 1/2: Configurations with meron-clusters cancel signs by a flip ($(+1 - 1)/2 = 0$). For the calculation of susceptibilities $\chi = \langle O^2 \text{Sign} \rangle / \langle \text{Sign} \rangle$, only the configurations with zero or two meron-clusters contribute. Thus, updating configurations with the restriction that there are at most two meron-clusters, susceptibilities can be calculated with sufficient statistics.

22.3.9 Other Exact Methods

There are some methods which give exact results for large quantum systems in principle other than quan-

tum Monte Carlo methods. One is the high-temperature expansion method [22.101, 102]. In this method, the partition function is expanded in powers of the inverse temperature. Thus, this method gives exact results in the high-temperature limit and is applicable to any models in the thermodynamic limit. Properties in the low-temperature regime are investigated by extrapolating data using the Padé approximation.

The density-matrix renormalization group (DMRG) method also gives accurate results in large-size systems [22.103, 104]. In this method, the ground state is approximated by eigen states of the density matrix with large weights. The states are updated by adding or readjusting local sites. Hence, this method is effective for one-dimensional systems with open boundary conditions. This method has been extended to investigate finite-temperature properties [22.105–109].

In order to investigate electron systems without suffering from the negative-sign problem, the path-integral renormalization group (PIRG) method has been developed [22.110–112]. In this method, the ground state is approximated by a linear combination of nonorthogonal single-particle states in the form of (22.70). The states are selected so as to minimize the energy. Single-particle trial states are generated in the same way as in the auxiliary-field quantum Monte Carlo method. This method is applicable to the Hubbard models in any dimensions even with frustrations [22.113–115].

22.4 Bicritical Phenomena in O(5) Model

Several applications of the Monte Carlo techniques are reviewed in the remaining part of this chapter. The first one is for a classical O(5) model. The competition between antiferromagnetism (AF) and superconductivity (SC) is observed in high- T_c superconductors and several others including organic ones, where the effects of strong correlations among electrons are important. This feature has led to the SO(5) theory, where the U(1) symmetry of SC and SU(2) symmetry of AF is unified to a group of SO(5) [22.116, 117]. The SO(5) symmetry is achieved through the competition between the two orders at a bicritical point [22.118, 119] in the phase diagram. In general, however, the symmetry of a fixed point, or even its existence, depends on the dimensionality, the number of degrees of freedom, as well as biquadratic perturbations [22.120, 121]. In literature [22.122], the following picture for the stability of the multicritical point for 5 spin-components in

three dimensions is provided by the ε expansions of the renormalization group (RG) theory: for positively large, biquadratic AF-SC couplings, the normal(N)-AF and N-SC transitions switch from second to first order before the two critical lines touch because of thermal fluctuations, resulting in two tricritical points and a triple point in the phase diagram; the stable fixed point should be a decoupled, tetracritical point characterized by a negative biquadratic AF-SC coupling.

Our Monte Carlo (MC) simulations on the O(5) Hamiltonian in three dimensions [22.123, 124] indicate however that the bicritical point is stable as far as the biquadratic coupling is nonnegative, and that for negative biquadratic couplings the biconical, tetracritical point takes the place, in contrast to the RG results. We have formulated a scaling theory on the order parameters, which provides a powerful tool for estimation of the bicritical point and the bicritical and crossover exponents.

22.4.1 Hamiltonian

The Hamiltonian is given by [22.123]

$$\mathcal{H} = - \sum_{\langle i,j \rangle} J_{ij}^{\text{AF}} \mathbf{s}_i \cdot \mathbf{s}_j - \sum_{\langle i,j \rangle} J_{ij}^{\text{SC}} \mathbf{t}_i \cdot \mathbf{t}_j + g \sum_i s_i^2 + w \sum_i s_i^2 t_i^2, \quad (22.72)$$

on the simple cubic lattice. The couplings are limited to nearest neighbors. The vector $\mathbf{s}(\mathbf{t})$ of three(two) components is for the local AF(SC) order parameter, and $s_i^2 + t_i^2 = 1$. The Hamiltonian (22.72) is O(3) and O(2) symmetric with respect to the rotations in the two subspaces for \mathbf{s} and \mathbf{t} , respectively. The symmetries are broken spontaneously when temperature is below the corresponding critical points. The system enjoys a higher O(5) symmetry for $J_{ij}^{\text{AF}} = J_{ij}^{\text{SC}}$ and $g = w = 0$, while anisotropy in coupling constants breaks the O(5) symmetry. There are two other fields which break the symmetry: g field associated with the chemical potential of electrons and w field with the quantum effects of Gutzwiller projection of double occupancy of electrons [22.125, 126]. Higher-order terms are known to be irrelevant to critical phenomena and thus are omitted in our study.

In a typical MC simulation process, we generate a random configuration of superspins at a sufficiently high temperature, and then cool down the system gradually. The conventional Metropolis algorithm is adopted, with 50 000 MC steps for equilibration and 100 000 MC steps for statistics on each superspin at a given temperature. The system size for data shown here is $L^3 = 40^3$ with periodic boundary conditions. We have simulated up to $L^3 = 80^3$ and confirmed that finite-size effects do not change our results.

22.4.2 Phase Diagram

For the long-range order parameters of SC, we adopt the helicity modulus defined by

$$\Upsilon \equiv \lim_{\theta \rightarrow 0} \frac{F(\theta) - F(0)}{(\theta/L)^2 S}, \quad (22.73)$$

where the free energy $F(\theta)$ is for the system under a twist, for example, along x direction, $\varphi \rightarrow \varphi + \theta \times (1 - 2x/L)$ with $S = L^2$ for the cross section. For the long-range order parameter of AF, the staggered magnetization is used

$$m = \frac{1}{N} \sqrt{\left\langle \left(\sum_i s_i \right)^2 \right\rangle}. \quad (22.74)$$

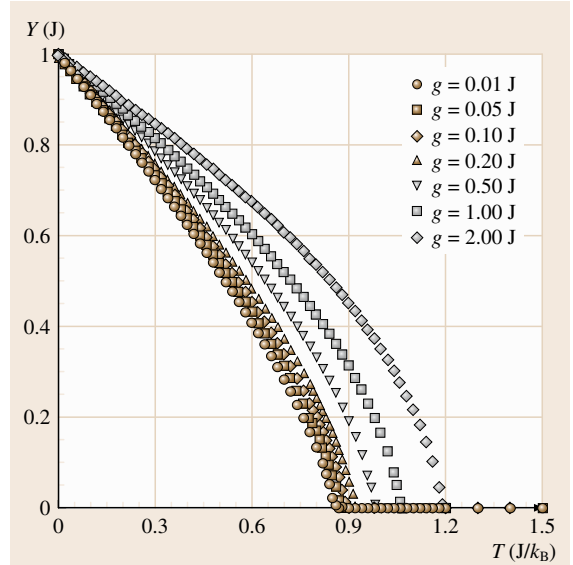


Fig. 22.10 Temperature and g dependence of the helicity modulus for isotropic couplings and $w = 0$ (after [22.123, 124])

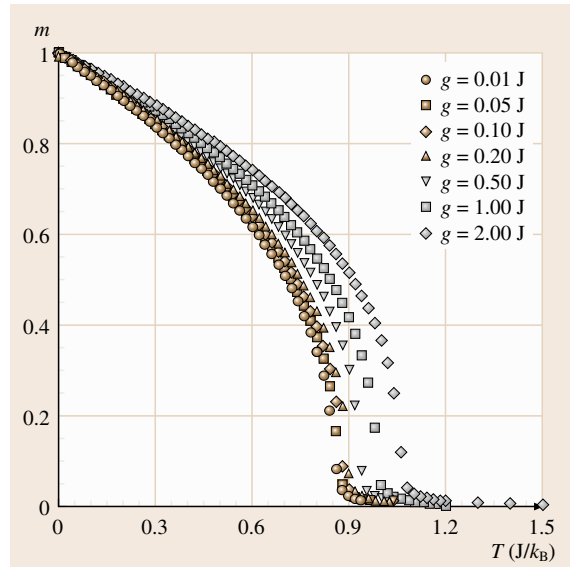


Fig. 22.11 Temperature and g dependence of the staggered magnetization for isotropic couplings and $w = 0$ (after [22.123, 124])

First we show the simulation results for the simplest case of $J_{ij}^{\text{AF}} = J_{ij}^{\text{SC}} (= J)$ and $w = 0$ in Figs. 22.10 and

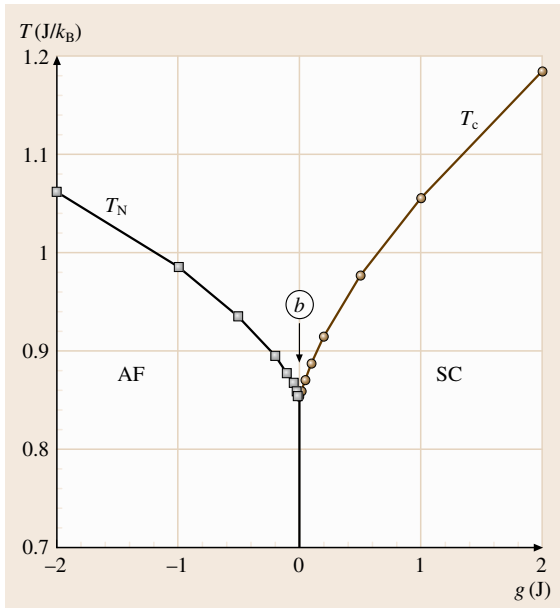


Fig. 22.12 g - T phase diagram with a bicritical point for isotropic couplings and $w = 0$ (after [22.123, 124])

22.11. The helicity modulus (staggered magnetization) is zero for $g < 0$ ($g > 0$).

The phase diagram thus obtained is depicted in Fig. 22.12. The bicritical point is located at $[g_b, T_b] = [0, 0.845J/k_B]$, at which the two critical lines merge tangentially. We shall address the crossover phenomenon in Fig. 22.12 as $g \rightarrow 0$ later.

We have also turned on the anisotropy in the coupling constants: $J_c^{\text{SC}} = J/10$, namely the SC coupling along the c crystalline axis is 1/10 of other coupling constants, while keeping $w = 0$. The bicritical point is achieved at $[g_b, T_b] = [1.18J, 0.67J/k_B]$ [22.127]. It is interesting to observe that the O(5) symmetry broken by the coupling anisotropy is recovered by tuning the g field to the common tangent of the two critical lines starting from the bicritical point.

Next, we check the stability of the bicritical point upon introducing a positive w field. It is revealed that the Gutzwiller projection out of the double occupancy of electrons in high- T_c cuprates should result in a positive biquadratic AF-SC coupling [22.125, 126]. Without losing generality, let us set $w = 0.1J$ in Hamiltonian (22.72). For $g \geq 0.012J$ and $g \leq 0.010J$ we observe long-range SC and AF orders, respectively. At $g = 0.011J$ either AF or SC is realized depending on the initial random configuration and cooling process, same as at $g = g_b = 0$ for $w = 0$. No homogeneous co-

existence between AF and SC can be observed, and all the phase transitions upon temperature reduction are second order, and thus there is no fluctuation-induced first-order transition suggested by the RG ε expansions. The phase diagram for $w = 0.1J$ is the same as that in Fig. 22.12 for $w = 0$ except that the bicritical point shifts to $g_b = 0.011J$ [22.123].

We have increased the w field to $w = 0.5J$ supposing that it should result in stronger first-order N-AF and N-SC phase transitions in wider regimes, if any. Systems have also been enlarged up to $L^3 = 80^3$ in order to check possible finite-size effects. All we have observed are second-order N-AF and N-SC transition and a stable bicritical point.

For the negative biquadratic coupling $w = -0.1J$, we observe a biconical, tetracritical point at $g_t = -0.011J$ (of the same absolute value of g_b for $w = 0.1J$) as shown in Fig. 22.13. There is a region in the phase diagram where AF and SC coexist homogeneously.

22.4.3 Scaling Theory

For positively large enough g field, there is a sufficiently large temperature region above the SC critical line where AF fluctuations are irrelevant to the critical phenomenon. This critical region characterizing the

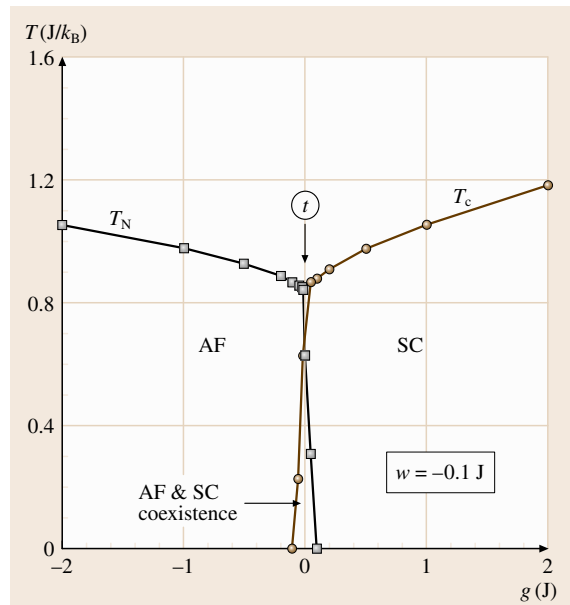


Fig. 22.13 g - T phase diagram with a bicritical point for isotropic couplings and $w = -0.1J$ (after [22.123, 124])

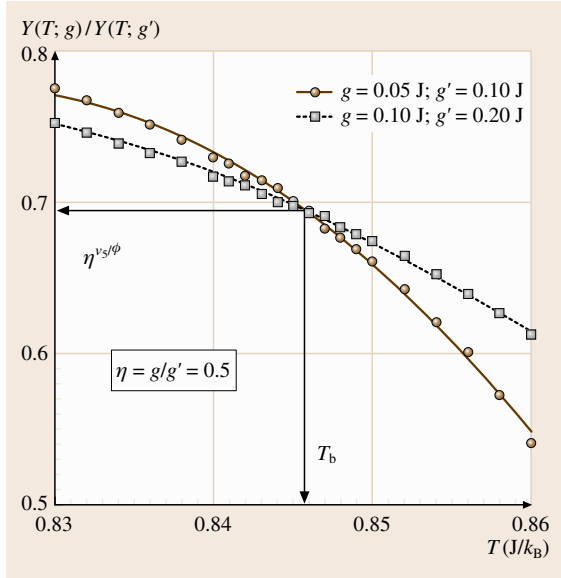


Fig. 22.14 Scaling plot for estimation on the bicritical point and the ratio ν_5/ϕ according to (22.79) (after [22.123, 124])

O(2) symmetry breaking is, however, shrinking as g is reduced. This can be read from the temperature dependence of the helicity modulus in Fig. 22.10, and can be understood easily, at least qualitatively, since in Hamiltonian (22.72) thermal fluctuations associated with the O(5) symmetry become more important as g decreases. Similar behaviors are observed for the Néel order parameter for $g < 0$.

In order to analyze the crossover phenomenon quantitatively, we develop the scaling theory for order parameters below the critical lines (see [22.128] for the scaling theory for the response functions above the critical lines)

$$\Upsilon(T; g) \simeq A g^{\nu_5/\phi} \times f\left((T/T_b - 1)/g^{1/\phi}\right), \quad (22.75)$$

with ν_5 for the bicritical singularity of $n = 5$ and ϕ the crossover exponent. For simplicity, we consider here the case of $g_b = 0$, noticing that extension to cases $g_b \neq 0$ is straightforward. The scaling function $f(x)$ should have the following properties

$$f(x) \simeq \begin{cases} (-x)^{\nu_5}, & \text{as } x \rightarrow -\infty; \\ (B_2 - x)^{\nu_2}, & \text{as } x \rightarrow B_2, \end{cases} \quad (22.76)$$

with B_2 defined by

$$B_2 g^{1/\phi} = T_c(g)/T_b - 1, \quad (22.77)$$

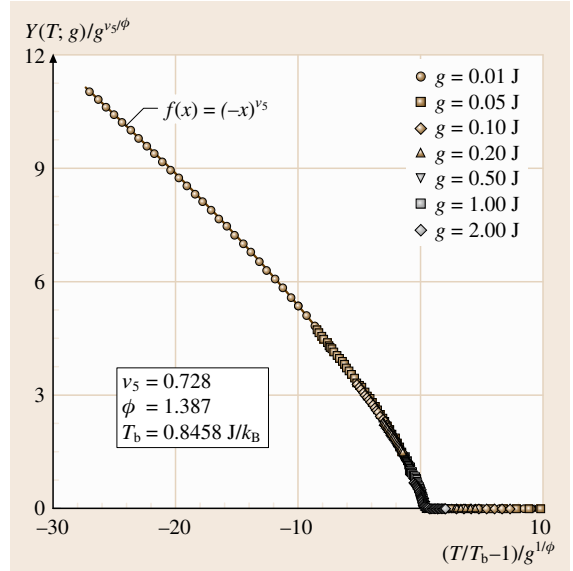


Fig. 22.15 Scaling plot for the data on helicity modulus in Fig. 22.10 according to (22.75) (after [22.123, 124])

which describes the SC critical line. With the properties (22.76), we can arrive at

$$\Upsilon(T; g) \simeq \begin{cases} A \times (1 - T/T_b)^{\nu_5}, & \text{for } g = 0; \\ A \times (1 - T/T_c(g))^{\nu_2}, & \text{for } g > 0. \end{cases} \quad (22.78)$$

This formulation of the bicritical scaling theory permits us to evaluate the bicritical and crossover exponents as well as the bicritical point in high precisions from the MC simulation results.

From the scaling ansatz (22.75), one should have

$$\Upsilon(T_b; \eta g)/\Upsilon(T_b; g) = \eta^{\nu_5/\phi}. \quad (22.79)$$

In order to fully utilize this relation, we plot in Fig. 22.14 the g and temperature dependence of $\Upsilon(T_b; \eta g)/\Upsilon(T_b; g)$ for $\eta = 1/2$. The two curves should cross at the point $[T_b, \eta^{\nu_5/\phi}]$ according to (22.79). Therefore, we estimate $T_b \simeq 0.8458 \pm 0.0005 J/k_B$ and $\nu_5/\phi \simeq 0.525 \pm 0.002$. Each point in Fig. 22.14 is obtained by 3 million MC steps on each superspin.

The crossover exponent ϕ can be evaluated from the slope $\kappa[\eta; g]$ of $\Upsilon(T; \eta g)/\Upsilon(T; g)$ with respect to temperature at the bicritical point T_b in Fig. 22.14

$$\phi = \ln(g_2/g_1)/\ln(\kappa[\eta; g_1]/\kappa[\eta; g_2]). \quad (22.80)$$

In this way, we have $\phi = 1.387 \pm 0.030$ with the error bar estimated from those of the slopes. Finally, we arrive at $\nu_5 = 0.728 \pm 0.018$.

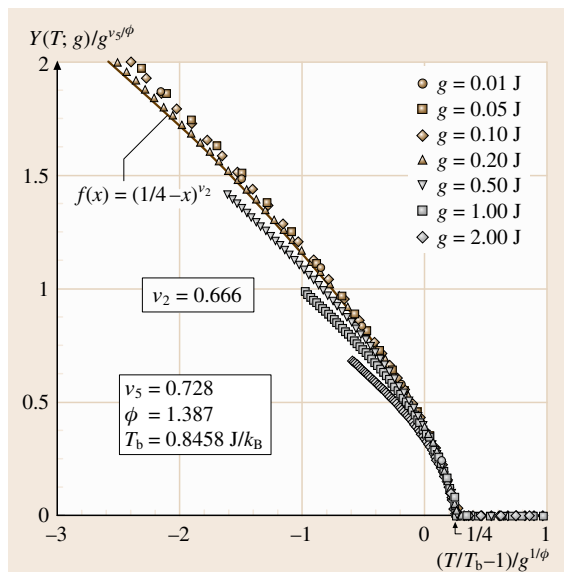


Fig. 22.16 Zoom in of Fig. 22.15 around the origin (after [22.123, 124])

With the estimates on the bicritical point and the bicritical, crossover exponents, we can plot the data in Fig. 22.10 in the scaled way described in (22.75). The result is depicted in Figs. 22.15 and 22.16, where we have $A \simeq 1.0$ and $B_2 \simeq 1/4$. The singularity at $x = B_2$ can be fitted very well by the critical exponent for

22.5 Superconductivity Vortex State

Superconductivity is one of the most fascinating physical phenomena, because of its perfect conduction of electricity. Its prominent character is however the peculiar magnetic property, namely the diamagnetism known as the Meissner effect. A deeply related phenomenon is the quantization of magnetic flux by superconductivity. There are two kinds of superconductors, type I and II. The superconductivity in type I samples is broken discontinuously by increasing magnetic field to a critical value. For type II superconductors, according to the mean-field theory by Abrikosov [22.130, 131], who shared the Nobel Prize of Physics in 2003 with Ginzburg and Leggett, there exist two critical magnetic fields: at the lower critical field H_{c1} quantized fluxes start to penetrate into the sample and form a triangular lattice of flux lines; at the upper critical field H_{c2} superconductivity is suppressed because of the overlapping of flux cores. Both

the pure XY model of O(2) symmetry $\nu_2 \simeq 0.67$ as in (22.78). To the best of our knowledge, the scaling theory for bicritical phenomena is verified in such a precise way for the first time.

The scaling analysis for the AF order parameters for $g < 0$ can be performed in the same way. Beside the critical exponents we have obtained the coefficient $B_3 \simeq 1/6$ which describes the critical line of AF order

$$B_3(-g)^{1/\phi} = T_N(g)/T_b - 1. \quad (22.81)$$

The ratio $B_2/B_3 = 3/2$ is given by the inverse ratio of the two degrees of freedom and should be a universal constant for the competition between two orders of two and three components such as in the high- T_c superconductivity.

Since the helicity modulus is related to the London penetration depth $\Upsilon \sim 1/\lambda^2$, the scaling theory is expected to be useful for analyzing experimental results. Another interesting issue for the AF-SC competition is the magnetic-field effect. When we apply an external magnetic field, the long-range SC order is achieved in the form of the Abrikosov flux-line lattice. The N-SC transition becomes first order accompanied by the melting of flux-line lattice. Because the strong thermal fluctuations in the SC sector, the N-AF transition becomes first order nearby the AF-SC phase boundary. There is a tricritical point on the N-AF phase boundary where the N-AF transition is switched back to second order [22.129].

the translation and rotation symmetry associated with the spatial distribution of flux lines and the local U(1) gauge symmetry are broken at the upper critical field H_{c2} . In the mean-field theory, this phase transition is *second order*.

Although the theory by Abrikosov is ground breaking, thermal fluctuations are not treated sufficiently. The discovery of high- T_c superconductivity in cuprates makes the thermal-fluctuation regime accessible. A first-order melting of the flux-line lattice was proposed based on transport measurements, in which resistance drops discontinuously. Later on, experiments on thermodynamic quantities, such as magnetization and the specific heat, revealed clearly the first-order nature of the phase transition. For review articles, see [22.132–134].

A theoretical understanding toward the phase transition in vortex states beyond mean-field theory is not

easy. It is shown by the ε expansions of renormalization group (RG) that the superconductivity to normal phase transition should be *first order*, up to the lowest order of ε [22.135]. This result is natural since the melting of the flux-line lattice is understood to be similar to most other melting phenomena in reality ($d = 3$). However, the upper critical dimension for the superconductivity vortex state is $d_u = 6$, above which mean-field theory is correct, since thermal fluctuations in the two dimensions perpendicular to the magnetic field are cut off by the vortex spacing and thus cannot contribute to the long-range order, noticing $d_u = 4$ for superconductivity without magnetic field. The treatment on RG flows is therefore quite hard using quantities only to the lowest order of $\varepsilon = d_u - d = 3$. As a matter of fact, the conclusion on the first-order melting transition of vortex lattice from RG was challenged by others.

22.5.1 Model Hamiltonian

This situation motivated many computer simulation works. As the melting temperature is much lower than $T_{c2}(B)$, where the Meissner effect sets on, it is a reasonable approximation to neglect fluctuations in the amplitude of the complex order parameter when the melting transition is concerned. In addition, the high- T_c superconductors are extremely type-II, in which the penetration length of magnetic field is much larger than the correlation length. This permits one to take the magnetic induction uniform and equal to the applied magnetic field.

With these two approximations we can derive the following three-dimensional frustrated XY model [22.136, 137] from the Ginzburg–Landau (GL) Lawrence–Doniach (LD) free-energy functional for layered superconductors [22.138, 139]

$$H = - \sum_{(i,j)} J_{ij} \cos \left(\varphi_i - \varphi_j - \frac{2\pi}{\phi_0} \int_i^j \mathbf{A} \cdot d\mathbf{r} \right). \quad (22.82)$$

Namely, the main effects of thermal fluctuations come from the phase degrees of freedom of superconductivity order parameter, which are defined on the simple cubic lattice in simulation. The couplings are limited to nearest neighbors and $J_{ij} = J$ with $J = \phi_0^2 d / 16\pi^3 \lambda_{ab}^2$ for links $\langle ij \rangle$ parallel to the superconducting layer while $J_{ij} = J/\Gamma^2$ for the perpendicular. The lattice constant along the c direction is the separation between neighboring CuO_2 layers d , while the lattice constant in

the ab planes l_{ab} can be taken in a range satisfying $\xi_{ab} \ll l_{ab} \ll \lambda_{ab}$. Then the anisotropy parameter should be given by the relation $\Gamma l_{ab} = \gamma d$ if one wants to simulate a superconductor with anisotropy parameter $\gamma = \lambda_c / \lambda_{ab}$.

For magnetic fields parallel to the c axis, one can set $A_z = 0$. The strength of the magnetic field is given in a dimensionless way $f \equiv B l_{ab}^2 / \phi_0$. Vortices are figured out, including vorticity n , by counting the gauge invariant phase differences around any plaquette

$$\sum_{(i,j)} [\varphi_i - \varphi_j - A_{ij}] = 2\pi(n - f). \quad (22.83)$$

In the ground state, the areal density of vortices should be equal to f .

In the above model, we assume a finite amplitude of *local* superconductivity order parameter on each site, which gives the coupling strength. At high temperatures, the phases fluctuate significantly and thus a coarse grain to any length scales larger than that given initially in the model will result in a vanishing amplitude of superconductivity order parameter. As for the long-range order of superconductivity, one needs to investigate the coherence of the phase degrees of freedom in the present system. The helicity modulus proportional to the rigidity of the system under an imposed phase twist as in (22.75) should be taken as the true *long-range* superconductivity order parameter.

22.5.2 First Order Melting

Here we present some of our results published in [22.140–142], with simulation techniques developed partially in early studies [22.143]. Similar results are reported by other groups [22.144–146]. For the convenience of simulation, we take $\Gamma = \sqrt{10}$ when modeling the moderately anisotropic high- T_c superconductor $\text{YBa}_2\text{Cu}_3\text{O}_{7-\delta}$ of $\gamma = 8$. The magnetic field is $f = 1/25$. The system size is $L_{ab} \times L_{ab} \times L_c = 50 \times 50 \times 40$, where $N_v = 100$ vortices induced by the external magnetic field are contained in each ab plane. Periodic boundary conditions (PBCs) are set in all the directions. The conventional Metropolis algorithm is adopted. The number of MC sweeps at each temperature is 50 000 for equilibration and 100 000 for sampling. Around the transition temperature, we have simulated up to several million MC sweeps.

The Specific Heat

In Fig. 22.17 we display the temperature dependence of the specific heat per vortex line per length d evaluated

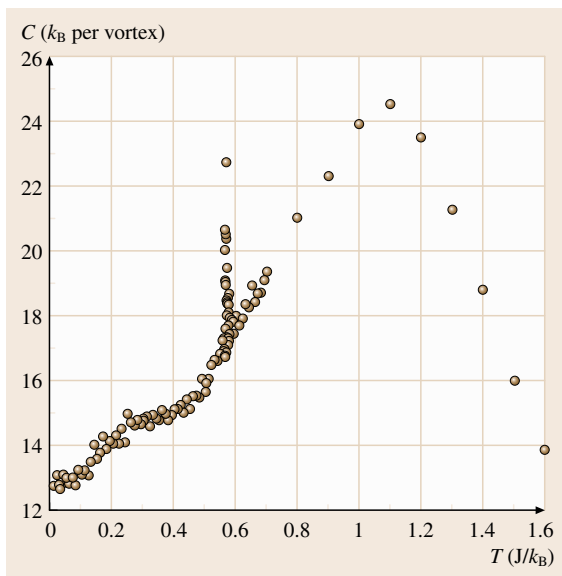


Fig. 22.17 Temperature dependence of the specific heat per vortex line per length d

via the fluctuation-dissipation theorem

$$C = (\langle H^2 \rangle - \langle H \rangle^2) / k_B T^2. \quad (22.84)$$

A sharp spike is observed in the specific heat around the temperature $T_m \simeq 0.567 J/k_B$. Quantitatively, the specific heat is $C_+ \simeq 18.5 k_B$ just above T_m , $C_{\max} \simeq 23 k_B$ right on T_m , and $C_- \simeq 17.5 k_B$ just below T_m in a narrow regime of temperature.

Figure 22.18 displays the variation of the internal energy around the transition temperature T_m . A kink-like anomaly takes place, and from the two straight lines in Fig. 22.18 the latent heat is estimated as $Q \simeq 0.07 k_B T_m$ per flux per layer. The data on the specific heat and the latent heat indicate very clearly that a first-order phase transition occurs at T_m .

According to the finite-size scaling theory for a first-order phase transition [22.1], one has

$$C^{\max} = \frac{Q^2}{4k_B T_m^2} L_{ab}^2 L_c f + \frac{C_+ + C_-}{2}, \quad (22.85)$$

$$\Delta T = \frac{2k_B T_m^2}{Q L_{ab}^2 L_c f}, \quad (22.86)$$

providing that the system is already large enough such that the estimate of the latent heat in the way described in Fig. 22.18 is accurate enough. It has been checked that our data satisfy these two relations very

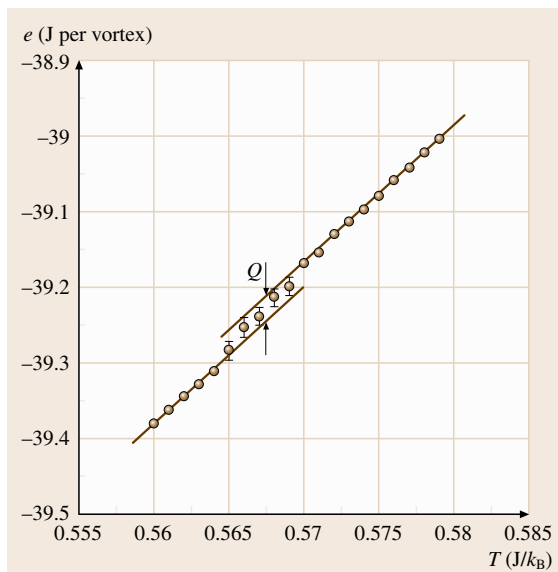


Fig. 22.18 Temperature dependence of the internal energy per vortex line per length d

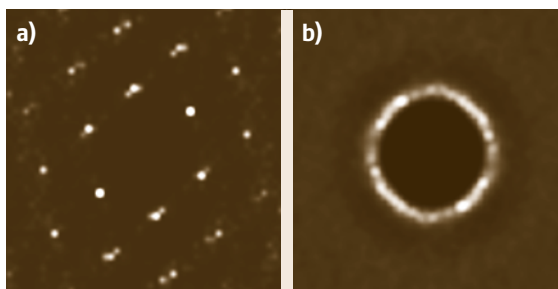


Fig. 22.19a,b Structure factors for vortex lattice at low temperature (a) and vortex liquid at high temperatures (b)

well. Therefore, we can say that the present simulation results are statistically and thermodynamically correct.

Structure Factor

The correlation functions of vortices can be described by a structure factor defined by

$$S(\mathbf{q}_{ab}, z) = \frac{1}{N_v} \int_{-\infty}^{\infty} \frac{dq_c}{2\pi} e^{iq_c z} \langle n(\mathbf{q}) n(-\mathbf{q}) \rangle, \quad (22.87)$$

where $n(\mathbf{q}) = \sum_{\mathbf{r}} n(\mathbf{r}) \exp(-i\mathbf{q} \cdot \mathbf{r})$ and $n(\mathbf{r})$ is the vorticity in the c direction (i. e., along the magnetic field) at position \mathbf{r} . Two typical structure factors $S(\mathbf{q}_{ab}, z=0)$ for the in-plane correlation functions of vortices are depicted in Fig. 22.19. It becomes clear that the first-order

phase transition is a melting transition of the vortex lattice of hexagonal symmetry into the isotropic vortex liquid.

Helicity Modulus

The temperature dependence of the helicity modulus along the c axis

$$\begin{aligned} \Upsilon_c = & \frac{1}{L_{ab}^2 L_c} \left\langle \sum_{(i,j)} J_{ij} \cos(\varphi_i - \varphi_j) (\hat{e}_{ij} \cdot \hat{c})^2 \right\rangle \\ & - \frac{1}{k_B T L_{ab}^2 L_c} \left\langle \left[\sum_{(i,j)} J_{ij} \sin(\varphi_i - \varphi_j) (\hat{e}_{ij} \cdot \hat{c}) \right]^2 \right\rangle \\ & + \frac{1}{k_B T L_{ab}^2 L_c} \left\langle \sum_{(i,j)} J_{ij} \sin(\varphi_i - \varphi_j) (\hat{e}_{ij} \cdot \hat{c}) \right\rangle^2, \end{aligned} \quad (22.88)$$

is presented in Fig. 22.20. It increases from zero to a finite value $\Upsilon_c(T_m) \simeq 0.6 \text{ J}/\Gamma^2$ in a narrow temperature region around T_m as the system is cooled down. Therefore, the phase transition at T_m is the normal to superconducting phase transition. The sharp onset of Υ_c is another indication of first-order transition. The helicity modulus in the ab plane remains zero even below the transition temperature T_m . Therefore, the system is superconducting only along the c axis even below T_m .

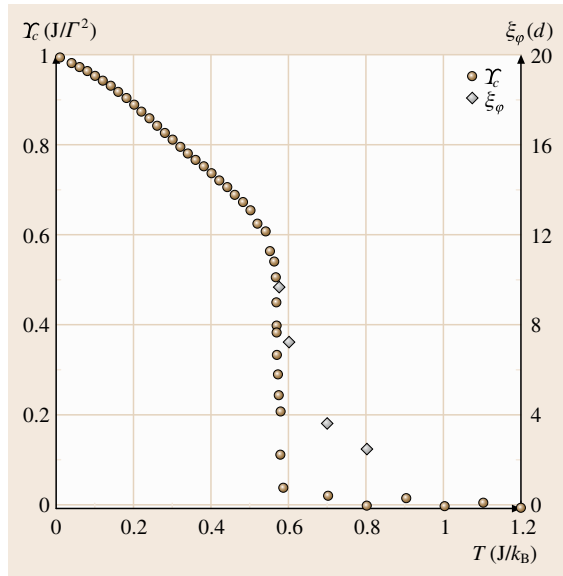


Fig. 22.20 Temperature dependence of the helicity modulus and the correlation length

The correlation length of phase variables along the c direction increases with cooling and reaches to $\xi_{\varphi,c} \simeq 10d$ at the melting temperature. We notice that our system size is $L_c = 40$ in units of d , and is therefore sufficient for simulating the true phase transition of the vortex system of the given parameters. If a smaller system of $L_c \leq 20$ was taken, the system would behave as if a long-range SC order had established at a temperature above the melting point, where the structure factor evolves from that of the liquid into the lattice. Then one would be led to two phase transitions, instead of the true single one.

Phase Diagram

By tuning the magnetic field, or equivalently the anisotropy parameter, we have mapped out the B - T phase diagram of the pancake vortices as shown in Fig. 22.21. The decreasing melting temperature with increasing magnetic field is consistent with the Clausius–Clapeyron relation

$$\Delta B = -4\pi \Delta s / (dB_m/dT), \quad (22.89)$$

where Δs is the entropy jump of unit volume. Taking into account the temperature dependence of the penetration depth, and thus that of the coupling strength in our model, we can [22.142] compare our numerical results with experiments. The agreement is quite satisfactory as in Table 22.5.

The hump in the specific heat at $T_v \simeq 1.1 \text{ J}/k_B$ is produced by a huge number of thermal excitations of vortices in the form of closed loops. Even local superconductivity order parameters cannot sur-

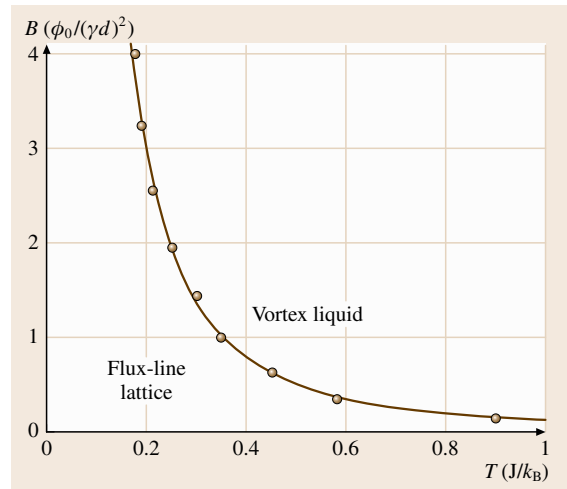


Fig. 22.21 B - T phase diagram (after [22.142])

Table 22.5 Comparison between our simulation results and experimental observations for $\text{YBa}_2\text{Cu}_3\text{O}_{7-\delta}$. ΔS denotes the entropy jump per flux line per length d

$B = 8$ Tesla	$T_m[\text{K}]$	$\Delta S[\text{k}_B]$	$\Delta B[\text{G}]$
Simulation	81	0.55	0.19
Experiment	79	0.4	0.25

vive at any scale larger than the grid, which indicates $T_v = T_{c2}$. Therefore, treating thermal fluctuations successfully makes the mean-field phase transition at H_{c2} a crossover.

22.5.3 Continuous Melting: $B||ab$ Plane

When the external magnetic field is applied parallel to the CuO_2 layers of a high- T_c superconductor, magnetic induction tends to penetrate the sample through the positions where superconductivity concentration is lower, namely the so-called block layers. Because of the Josephson couplings, magnetic induction is still quantized, the so-called interlayer Josephson vortices. A Josephson vortex is of a large size along the ab plane and squeezed in the c direction. The inter-vortex repulsion in this geometry is highly anisotropic, and meanwhile vortex lines feel strong layer pinning for motions along the c axis. In spite of much effort, which

certainly makes the vortex physics very rich [22.148–158], a unified picture for possible phases, phase transitions and phase diagrams is still not yet available. We have performed extensive Monte Carlo simulations of the frustrated XY model (22.82). The main prediction from computer simulation [22.147, 159] (see also [22.160, 161]) is that there is a multicritical point in the B - T phase. For magnetic fields above the critical value, there is an intermediate phase characterized by intraplane (2-D) quasi-long-range crystalline order of vortex lines in between the liquid and the 3-D lattice.

The model Hamiltonian is given in (22.82) with a gauge $A_{xy} = 0$. We take Γ as the anisotropy constant $\gamma = 8$ of the material $\text{YBa}_2\text{Cu}_3\text{O}_{7-\delta}$. The unit length of our grid is then d for all the three directions. For the convenience of simulation, we choose $f = 1/32$ and put the system size as $L_x = 384$, $L_y = 200$ and $L_z = 20$ with $N_v = 240$ flux lines in the system.

The Specific Heat

The specific heat is displayed in Fig. 22.22. There are sharp spikes in the specific heat for $\gamma = 8$ and 9 at $T_m \simeq 0.96 \text{ J/k}_B$, which indicates a first-order melting. As the total latent heats are very small, we plot in Fig. 22.23 the expectation values for the cosine function of the gauge invariant phase difference between neighboring layers, which is proportional to the Josephson energy. There

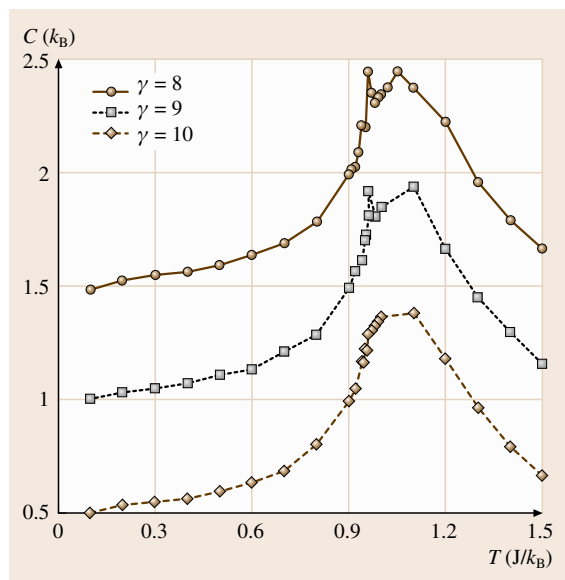


Fig. 22.22 Temperature dependence of the specific heat for several anisotropy parameters (after [22.147]). Data for $\gamma = 8$ and 9 are shifted by constants

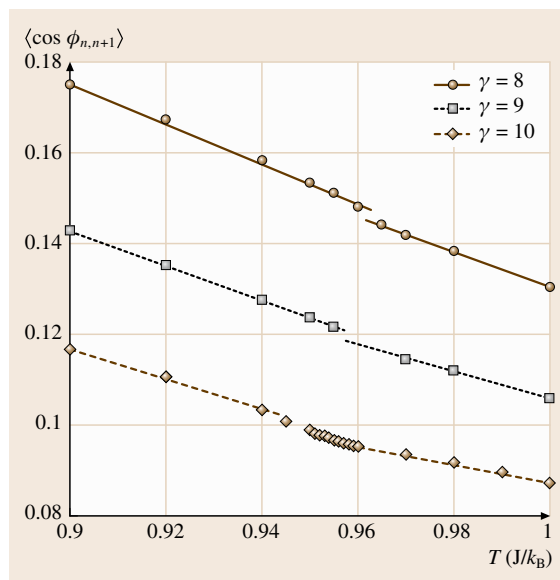


Fig. 22.23 Temperature dependence of the Josephson energy for several anisotropy parameters (after [22.147]). Data for $\gamma = 8$ and 9 are shifted by constants

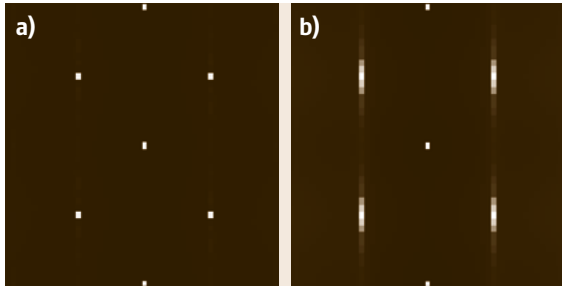


Fig. 22.24a,b Structure factors for Josephson vortices $S(k_x, k_c, y=0)$ at $T = 0.65\text{J}/k_B$ (a) and $T = 0.70\text{J}/k_B$ (b). The panels are for wave numbers within $k_x \in [-25\pi/192d, 25\pi/192d]$ (horizontal) and $k_c \in [-2\pi/d, 2\pi/d]$ (vertical) (after [22.159])

are discontinuous jumps in this quantity for $\gamma = 8$ and 9, corresponding to the spikes in the specific heat.

However, the first-order melting transition is suppressed when the anisotropy parameter is increased to $\gamma = 10$, for which the spike in the specific heat and the discontinuous jump in the Josephson energy disappear as in Figs. 22.22 and 22.23. It is discussed in [22.147] that there is a critical value of $f\gamma$ above which the intralayer repulsion force becomes significantly stronger than the interlayer one, such that the intralayer order establishes first upon cooling. For a more careful discussion please refer to our original paper [22.159]. It is easy to see that this critical magnetic field should be above

the following value when the anisotropy parameter γ is given [22.153]

$$B = \frac{1}{2\sqrt{3}\gamma d^2}. \quad (22.90)$$

To determine the value of the critical magnetic field demands a lot of simulation time, and has actually not yet been done. Nevertheless, the above relation seems to give a reasonable estimate for moderately anisotropic superconductors such as $\text{YBa}_2\text{Cu}_3\text{O}_{7-\delta}$.

Structure Factor

The above scenario has been verified by checking the vortex correlation function. In Fig. 22.24, we present the structure factors for $f = 1/32$ and $\gamma = 20$. For $T = 0.65\text{J}/k_B$ there is a 3-D long-range crystalline order characterized by the δ -function Bragg peaks; for $T = 0.7\text{J}/k_B$ the Bragg spots smear out significantly in the k_c direction, corresponding to short-range correlation in the c direction.

The k_x profile for the Bragg spot at $(k_x, k_c) = (\pm 2f\pi/d, \pm\pi/d)$ is plotted in Fig. 22.25 for several temperatures, from which we found that the real-space correlation functions show power-law decay with exponents $1 \leq \eta \leq 2$. The cusp singularity in the k_x profiles is suppressed at $T \simeq 0.96\text{J}/k_B$ where $\eta \simeq 1.97$. The suppression of the quasi long-range order upon

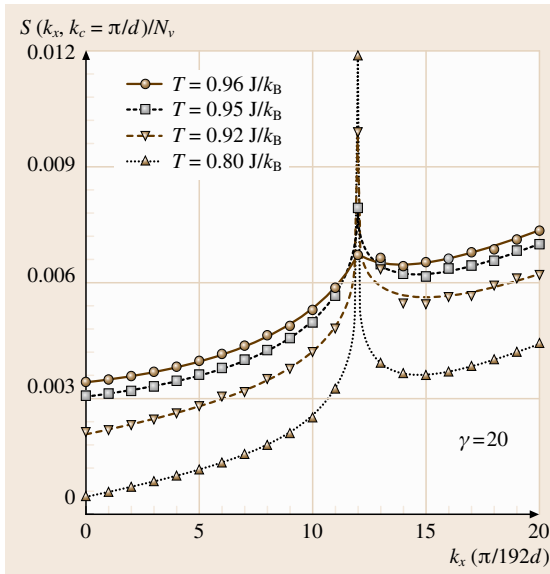


Fig. 22.25 k_x profiles for the Bragg spots (after [22.159])

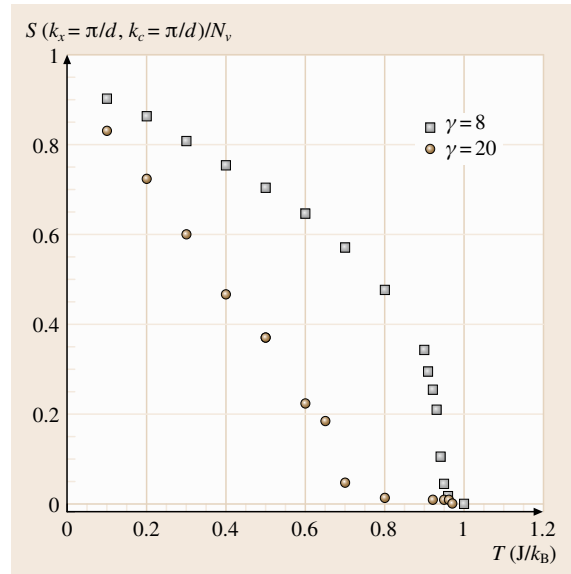


Fig. 22.26 Temperature dependence of intensity of Bragg peaks (after [22.159])

heating should be a Kosterlitz–Thouless (KT) transition [22.159].

The temperature dependence of the intensity of Bragg peaks is displayed in Fig. 22.26 is such a fashion that for quasi long-range orders the intensity should be zero at the thermodynamics limit. As our system is finite, small values of normalized intensity can be seen for $\gamma = 20$ which increases very slowly with decreasing temperature in the region $0.7J/k_B \leq T \leq 0.95J/k_B$. Across $T_x \simeq 0.65J/k_B$ where the Bragg spots become δ -function like, the intensity increases noticeably. The onset of 3-D long-range order is revealed as a second-order phase transition in the 3-D XY universality class. In a sharp contrast, the intensity of Bragg peaks for $\gamma = 8$ increases very sharply with decreasing temperature as soon as they become observable at the melting point $T_m \simeq 0.96J/k_B$ as shown in Fig. 22.26.

22.6 Effects of Randomness in Vortex States

It is highly nontrivial whether the vortex lattice can survive when defects are introduced into the system. The answer depends on the dimensions of the space and the type of defects. In the elastic theory, the Hamiltonian of vortex states including point-like randomness is given by

$$\mathcal{H} = \frac{c}{2} \int [\nabla u(x)]^2 d^d x - \int V(x)\rho(x)d^d x, \quad (22.91)$$

where the first term stands for the simplified elastic energy associated with deviations of flux lines $u(x)$ from their equilibrium positions, and $V(x)$ and $\rho(x)$ denote the random potential and the density of flux lines, respectively. Larkin [22.163, 164] proposed an approximation to replace the second term by

$$\int V(x)\rho(x)d^d x \approx \int f(x)u(x)d^d x, \quad (22.92)$$

where $f(x)$ is the Gaussian random force.

Then, the situation becomes similar to Imry–Ma’s argument [22.165] for the random-field model. Let us compare the energy between a polycrystal containing domains of the linear size $\sim L$ with the perfect vortex lattice. The elastic energy loss and the pinning energy gain are proportional to L^{d-2} and $L^{d/2}$, respectively. Since the second term is larger than the first one for large enough L in $d < 4$, the vortex lattice is unstable for infinitesimal randomness in $d < 4$. This simple consideration turns out to be insufficient and the picture

Right now experimental verifications of the multicritical point and the KT phase are carried on by several groups. For an estimate, we foresee the critical field at $H \approx 50$ Tesla for $\text{YBa}_2\text{Cu}_3\text{O}_{7-\delta}$ of $\gamma = 8$ and $H \approx 2$ Tesla for $\text{Bi}_2\text{Sr}_2\text{CaCu}_2\text{O}_{8+y}$ of $\gamma = 150$.

Since it is still not easy to simulate the vortex states of low vortex density, namely small magnetic field, the total phase diagram is not available merely by the computer simulation. Recently, using the density functional theory, we [22.162] find in certain magnetic field regimes below that given by (22.90) a smectic phase [22.154, 155], characterized by long-range correlation along the c axis and short-range correlations in the ab plane, that may exist in between the lattice and liquid phases. The melting is then two-step: first-order lattice-smectic and second-order smectic-liquid transitions.

of a Bragg glass is now established where the vortex correlations become quasi long ranged [22.166–170].

22.6.1 Point-Like Defects

Here our Monte Carlo simulations based on the frustrated XY model are reviewed. Modeling of point-like randomness is not unique in the frustrated XY model. One possible way is to introduce a Gaussian random variable ε_{ij} with $\langle \varepsilon_{ij} \rangle = 0$ and $\langle \varepsilon_{ij}^2 \rangle = 1$ as $J_{ij} = J + p\varepsilon_{ij}$ [22.171]. In this definition, randomness is included in every bond, and the strength of randomness p can be treated as a continuous thermodynamic variable like temperature. On the other hand, the pinning force of these randomly-modulated interactions to vortices may be very weak.

We introduced [22.172] point defects as the plaquettes which consist of four weaker couplings and are randomly distributed in the xy plane with probability p . Couplings are given by $J_{ij} = (1 - \varepsilon)J$ ($0 < \varepsilon < 1$) on the point defects, and $J_{ij} = J$ elsewhere. This formulation of point defects is schematically drawn in Fig. 22.27. As will be seen later, most phases observed experimentally in vortex states are reproduced by this modeling.

Bragg Glass

Monte Carlo simulations are performed for $f = 1/25$, $\Gamma = 20$, $p = 0.003$, and various pinning strengths ε with the system size $L_x = L_y = 50$ and $L_c = 40$. The same algorithm for the clean system discussed previ-

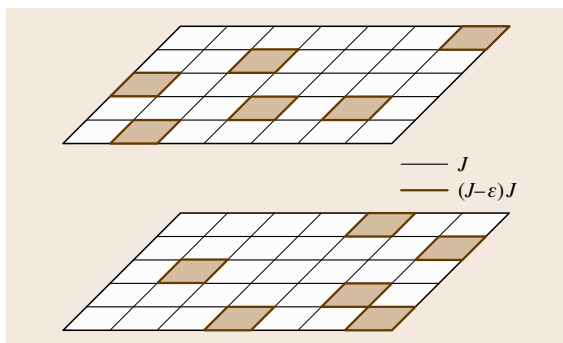


Fig. 22.27 Modeling for point-like defects (after [22.172])

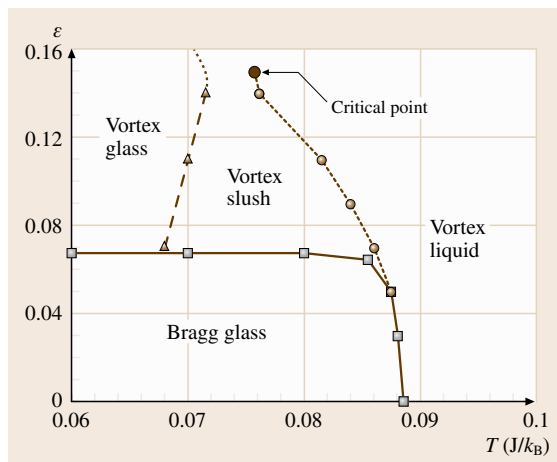


Fig. 22.28 ϵ - T phase diagram of vortex states with the point defects (after [22.172, 173])

ously is adopted. The ϵ - T phase diagram is displayed in Fig. 22.28.

The first-order melting transition between the Bragg glass (BrG) and vortex liquid (VL) phases is similar to

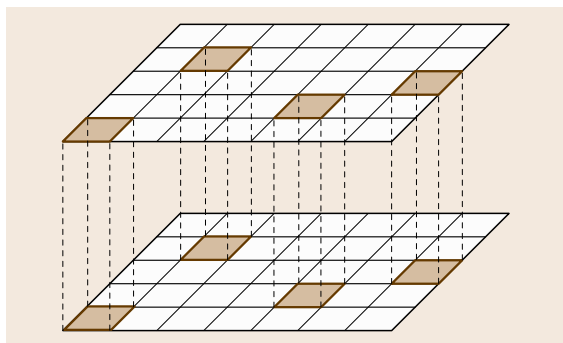


Fig. 22.29 Modeling for columnar defects (after [22.174])

that of the vortex lattice and VL phases in pure systems as shown previously. As the strength of point-like defects ϵ increases, the melting temperature T_m decreases, which shows a sharp contrast to the case with columnar defects as will be discussed later.

The Bragg glass is destroyed when the pinning force becomes large enough even though temperature is low, and thus thermal fluctuations are not significant. This *randomness-induced* melting was first observed numerically in the random-field XY model [22.175] and the Lawrence–Doniach model [22.176]. The first-order nature of this phase transition is clarified in more detail by precise numerical studies on the phase boundary. We showed [22.172] that the latent heat on the boundary is one order smaller than that on the *thermal* melting line. It was also reported [22.171] that the latent heat is vanishing within error bars while discontinuity in other physical quantities remains observable on the phase boundary.

Possible Vortex Glass

As a possible thermodynamic phase above the BrG, the vortex glass (VG) phase [22.177, 178], where flux lines are tightly pinned by point-like defects, has been considered. In the early stage of numerical simulations, the VG-VL boundary was detected by the jump of the correlation time [22.179] or the deviation of flux lines [22.180]. In the frustrated XY model, the VG phase is characterized by finite helicity modulus along the c axis and vanishing Bragg peak [22.172]. Although the absence of the VG was once argued [22.171], stability of the VG phase without the screening has now been established [22.181–183]. It is noticed that the stability of VG phase including the screening is still unsettled [22.184, 185].

Vortex Slush

There is a vortex slush phase [22.186–188] in the phase diagram (Fig. 22.28). The vortex slush shares the same symmetry of the liquid. The two phases are separated by a first-order transition line characterized by the jump of the density of dislocations in the xy plane [22.189, 190]. As in the gas–liquid case, this transition line is terminated by a critical point as shown in Fig. 22.28. It is interesting to notice that even above the critical point, a step-like anomaly of the specific heat was reported [22.173, 191].

22.6.2 Columnar Defects

Columnar defects created by heavy-ion irradiation along the c axis work as strong correlated pinning

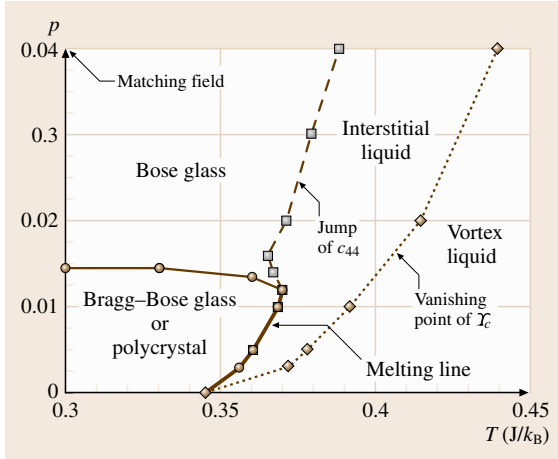


Fig. 22.30 p - T phase diagram for vortex states with the columnar defects (after [22.174])

centers to the vortex lines and produce new vortex states such as the Bose glass (BG) [22.192–194]. We introduced [22.174] columnar defects as the correlated plaquettes surrounded by four weak couplings $J_{ij} = (1 - \varepsilon)J$ with probability p in the xy plane and $J_{ij} = J$ elsewhere, as shown in Fig. 22.29. Since the density of defects p plays an essential role in vortex states with columnar defects, we tune the parameter p while fixing ε . Parameters for simulation are $\Gamma = 5$, $f = 1/25$, $\varepsilon = 0.1$, and $L_x = L_y = 50$ and $L_c = 80$.

Bose Glass

The p - T phase diagram obtained by Monte Carlo simulations is displayed in Fig. 22.30. When the number of columnar defects exceeds that of flux lines, the BG is stable at low temperatures. Here, we concentrate on small densities of columnar defects, ranging from the pure system with $p = 0$ to the matching case $p = f = 1/25$.

In order to evaluate the BG phase boundary, the tilt modulus c_{44} is evaluated. The Hamiltonian under the transverse field H^\perp is given by $\mathcal{H}' = \mathcal{H} - H^\perp m^\perp$ with the transverse magnetization m^\perp , and c_{44} is given [22.195] by

$$c_{44} \sim \left[\frac{\partial \langle m^\perp \rangle}{\partial H^\perp} \Big|_{H^\perp=0} \right]^{-1} \sim N_{\text{flux}} k_B T / \left\langle \left(m^\perp \right)^2 \right\rangle \Big|_{H^\perp=0}, \quad (22.93)$$

aside from a coefficient. The BG phase boundary is signaled by a large jump of c_{44} , which is expected to be infinite in the thermodynamic limit.

Interstitial Liquid

When the number of columnar defects is smaller than that of flux lines and the temperature is slightly higher than the BG transition temperature, columnar defects still trap some flux lines, while other interstitial flux lines can move around. This state is known as the interstitial liquid (IL) [22.196]. The helicity modulus along the c axis Υ_c takes a finite value as long as some of the flux lines are trapped by columnar defects. Therefore, the vanishing of the helicity modulus Υ_c corresponds to the boundary of the IL region.

Possibility of Bragg–Bose Glass

Similar to the BrG phase of vortex state with point-like defects, a Bragg–Bose glass (BBG) was proposed in the presence of columnar defects [22.197], which is characterized by quasi-long-range crystalline order and diverging tilt modulus. However, stability of this phase is not so trivial. At the ground state, flux lines are perfectly parallel to the magnetic field and the columnar defects. The system is then equivalent to the two-dimensional vortex states with point defects, where the absence of the BrG phase at $T = 0$ was shown numerically [22.198]. Therefore, the BBG (if exists) may be a kind of order caused by thermal fluctuations.

For small enough p and low enough temperatures, the structure factor shows sharp Bragg peaks, which is consistent with the BBG. As the temperature increases, the maximum value of the structure factor S_q^{max} drops just on the BG boundary with a narrow coexistence region, and the δ -function peak of the specific heat is observed. These facts indicate that the first-order melting transition of the BBG phase occurs just on the BG

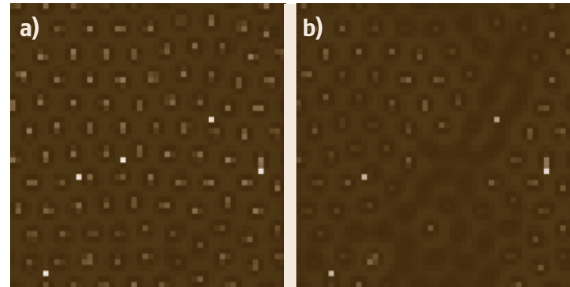


Fig. 22.31a,b Density of vortices in the xy plane averaged along the c axis in the (a) BBG and (b) IL phases with the same configuration of columnar defects (after [22.174]). The defects are painted in yellow (no flux lines) to red (filled with flux lines), and other regions are painted in violet (no flux lines) to light blue (largest probability of flux lines)

boundary at low density of columnar defects. The **BBG** at low temperature can be destroyed by introducing more columnar defects, indicated by a sharp change of S_q^{\max} . It is found that the **BBG-BG** phase boundary is almost independent of temperature, as shown in Fig. 22.30.

As can be seen in Fig. 22.31a for **BBG** phase, all flux lines are localized and form a triangular lattice. There exist some unoccupied columnar defects (yellow dots). The defects far from stable positions of vortex lattice remain unoccupied in the **BBG** phase. On the other hand, in Fig. 22.31b for the **IL** phase, most defects are occupied unless other occupied ones are very close by chance. Owing to such *selected pinning* of flux lines in

the **BBG**, introduction of more columnar defects to certain density enhances energy gain by trapping more flux lines using defects close to stable positions of vortex lattice, without destroying the lattice structure. This results in increase of the melting temperature. When p becomes large enough, the vortex lattice will be destroyed by the overwhelming pinning energy and the **BG** phase becomes stable.

The above description is consistent with the simulations based on the boson model [22.199], while the simulations based on the density-functional theory results in a different picture characterized by the two-step melting transition with the “**BrG** phase” surrounded by the **BG** phase [22.200, 201].

22.7 Quantum Critical Phenomena

Here we show several examples investigated by quantum Monte Carlo simulations, which is helpful for understanding the methodology.

22.7.1 Quantum Spin Chain

It was naively expected that low-energy excitations of spin systems are described by spin waves. In the spin-wave approximation, low-energy excitations are always gapless, regardless of the length of spins. However, Haldane predicted that in one dimension

low-energy excitations have a finite gap for integer spin systems [22.203, 204]. This prediction was later confirmed by numerical simulations [22.205–207] and experiments [22.208–211]. Further, Affleck extended Haldane’s argument to bond-alternating systems and predicted that integer spin chains can have a gapless excitation with special values of the alternating strength [22.212–214].

Some compounds that can be regarded as spin $S = 1$ bond-alternating Heisenberg chains have been found experimentally [22.215–219]. Among them, the susceptibility of $[\text{Ni}(\text{333-tet})(\mu\text{-N}_3)](\text{ClO}_4)_n$ (333-tet denotes tetraamine N,N' -bis(3-aminopropyl)-1,3-propanediamine) shows a gapless behavior [22.220]. In order to confirm whether this compound can really be described by an $S = 1$ bond-alternating Heisenberg chain, numerical simulations have been performed [22.202]. Since the model is a nonfrustrated Heisenberg model, quantum Monte Carlo simulations can be performed without negative-sign problems as explained in Sect. 22.3.8. Hence, the loop algorithm (Sect. 22.3.3) is applied to this system. The comparison between the result of the quantum Monte Carlo simulation and the experimental result is shown in Fig. 22.32. In the wide temperature range, numerical and experimental data agree well. This indicates that the magnetic properties of this compound are well described by the $S = 1$ bond-alternating Heisenberg chain at the gapless point. Only in the very low temperature regime, data show a little difference which may be due to single-ion anisotropy of this compound.

It was also predicted that at the gapless point low-energy properties are described by the level $k = 1$

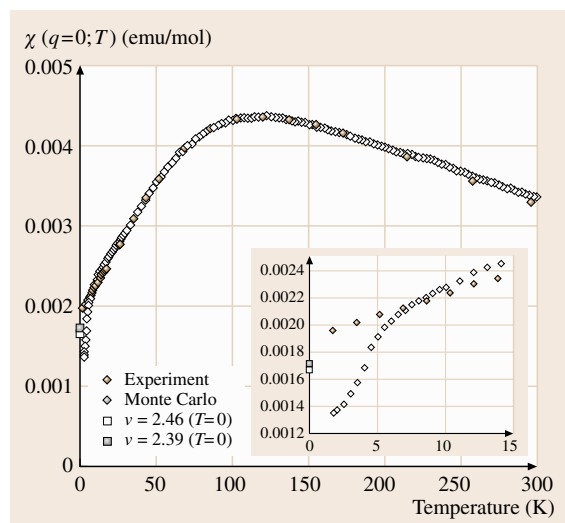


Fig. 22.32 Uniform susceptibility $\chi(q = 0; T)$ obtained by the quantum Monte Carlo simulation and experiments (after [22.202])

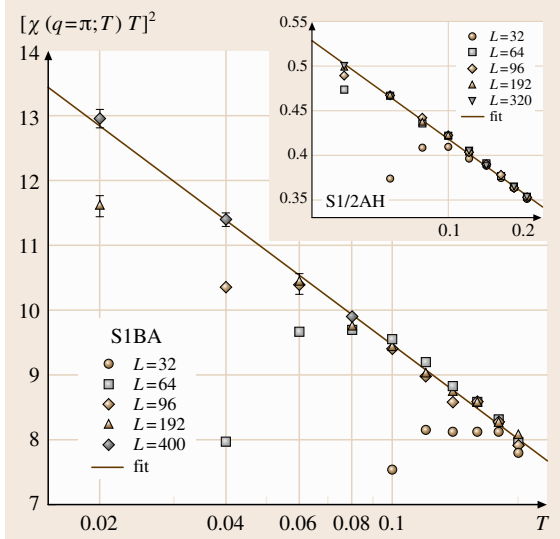


Fig. 22.33 Staggered susceptibility $\chi(q = \pi; T)$ obtained by the quantum Monte Carlo simulation (after [22.202]). S1BA and S1/2AH denote the $S = 1$ bond-alternating Heisenberg chain at the gapless point and the $S = 1/2$ Heisenberg chain, respectively

SU(2) Wess–Zumino–Witten (WZW) model [22.212–214], which is the same universality class as the $S = 1/2$ Heisenberg chain. The critical properties at the gapless point are also investigated by the quantum Monte Carlo simulation [22.202]. It is known that in the WZW universality class staggered susceptibility $\chi(q = \pi; T)$ and staggered structure factor $S(q = \pi; T)$ diverge toward the critical point [22.221, 222] as

$$\chi(q = \pi; T) \propto T^{-1} [\ln(T_\chi/T)]^{1/2}, \quad (22.94)$$

$$S(q = \pi; T) \propto [\ln(T_S/T)]^{3/2}. \quad (22.95)$$

Figures 22.33 and 22.34 show the numerical results for $\chi(q = \pi; T)$ and $S(q = \pi; T)$. The scaling properties of (22.94) and (22.95) are clearly observed.

In this way, quantum Monte Carlo simulations are powerful to investigate properties of spin systems. There are many other examples to show the power of quantum Monte Carlo simulations [22.66].

22.7.2 Mott Transition

It is widely believed that for the high- T_c superconductivity strong correlations near the Mott transition play an important role. In the insulating phase, there is a magnetic order and the spin and charge excitations are

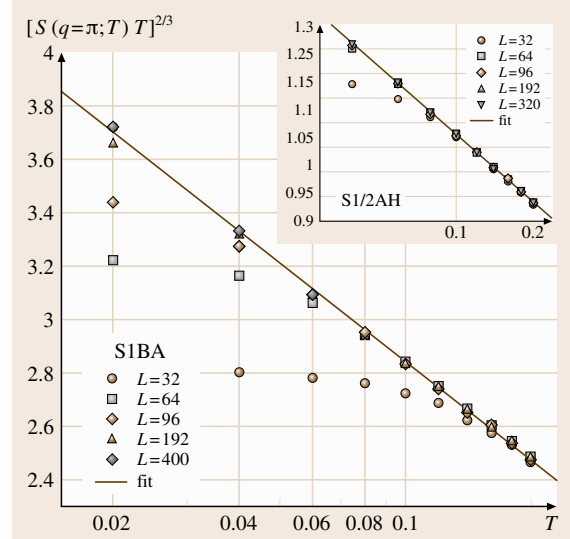


Fig. 22.34 Staggered structure factor $S(q = \pi; T)$ obtained by the quantum Monte Carlo simulation (after [22.202])

separated. On the other hand, in the metallic phase, it is expected that spin and charge degrees of freedom are strongly coupled, and the excitations may be described by fermionic quasi particles at least in the low electron-density regime. The difficulty of approaching the Mott transition comes from the complexity of the transit of these two-types of states. Since the Hubbard and t - J models are known to be insulators at half filling and become metallic by doping, characteristic features of Mott transitions would be described by these models.

Properties near the metal-insulator transition have been numerically investigated by quantum Monte Carlo simulations. For the two-dimensional Hubbard model, Furukawa and Imada applied the auxiliary-field quantum Monte Carlo method (Sect. 22.3.6) and found nontrivial power-law behaviors toward the Mott transition point [22.223]: The compressibility κ and the spin structure factor $S(Q)$ diverge as

$$\kappa \propto \delta^{-1}, \quad (22.96)$$

$$S(Q) \propto \delta^{-1}, \quad (22.97)$$

where δ denotes the doping concentration. Equation (22.97) suggests that the antiferromagnetic correlation length ξ_m diverges as

$$\xi_m \propto \delta^{-1/2}, \quad (22.98)$$

assuming that the spin–spin correlations behave as $\langle S_0 S_r \rangle \propto e^{iQr} \cdot e^{-r/\xi_m}$. These features are observed by

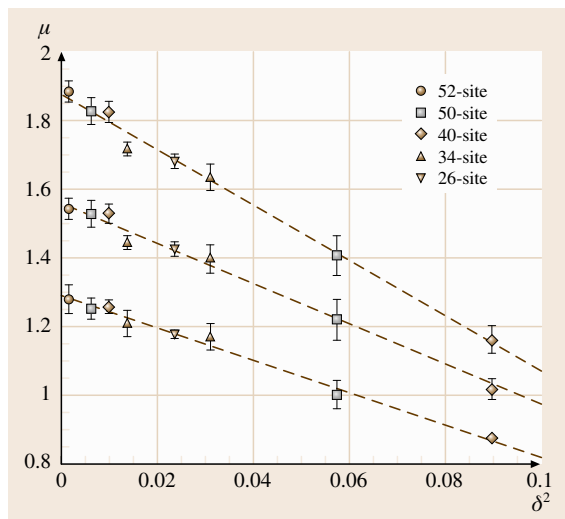


Fig. 22.35 Scaling behavior of chemical potential μ as a function of doping δ for the two-dimensional t - J model (after [22.227])

experiments [22.224–226]. For the two-dimensional t - J model, a similar analysis has been made based on the numerical results obtained by a Monte Carlo power method (Sect. 22.3.7) [22.227] as shown in Figs. 22.35 and 22.36. The results are qualitatively the same as the Hubbard model. Here, compressibility κ behaves as $\kappa \propto \partial\delta/\partial\mu$.

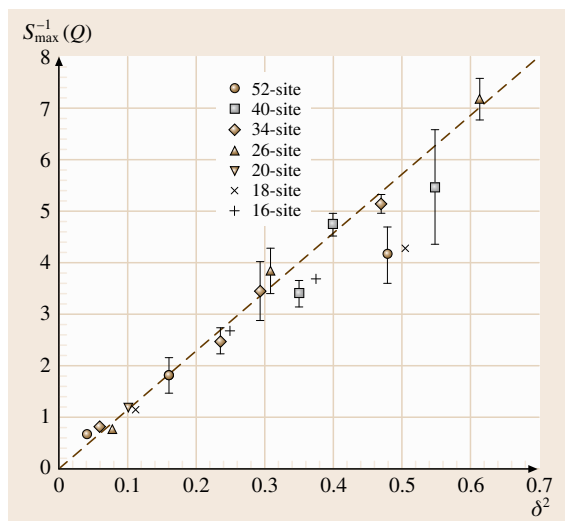


Fig. 22.36 Scaling behavior of spin structure factor $S_{\max}^{-1}(Q)$ as a function of doping δ for the two-dimensional t - J model (after [22.227])

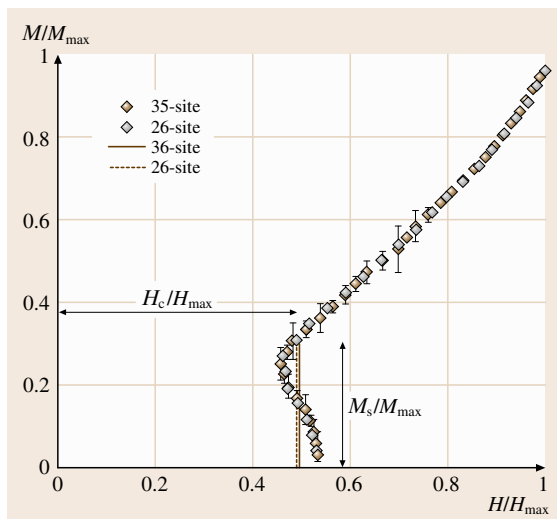


Fig. 22.37 Magnetization process of the $S = 1/2$ XXZ model with Ising-like anisotropy on a square lattice (after [22.228]). Solid and dotted lines denote the magnetization jump determined by the Maxwell construction

These numerical simulations suggest that spin and charge fluctuations diverge toward the Mott transition point. There is a possibility that such large fluctuations may lead to the high- T_c superconductivity.

In this way, properties of strongly correlated electron systems can be investigated by quantum Monte Carlo simulations.

22.7.3 Phase Separation

Quantum Monte Carlo simulations can also be applied to investigate first-order phase transitions. For example, in the two-dimensional t - J model, the phase-separation boundary has been investigated by a Monte Carlo power method [22.227] (Sect. 22.3.7). In finite systems, the energy obtained in canonical ensembles as a function of the electron density becomes concave downward in the region of phase separation. In order to satisfy the thermodynamic requirement, a tangent has to be drawn based on the Maxwell construction. Thus, the phase-separation boundary can be estimated using quantum Monte Carlo data in finite clusters. Since very accurate simulations are necessary in order to determine the precise position of the phase-separation boundary in the very small doping regime for the two-dimensional t - J model, it is a subtle problem and still controversial [22.227, 229–239].

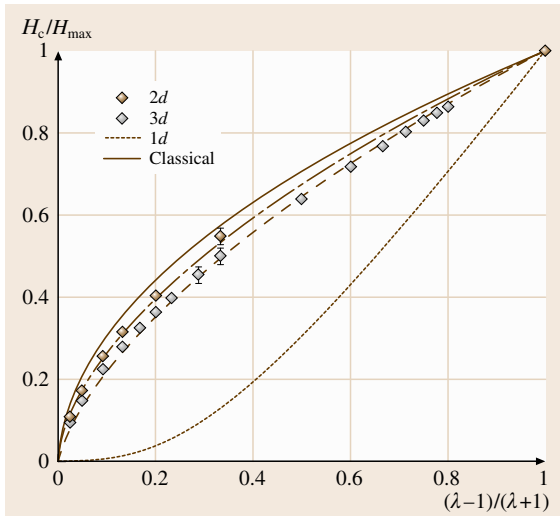


Fig. 22.38 Critical field H_c for the $S = 1/2$ XXZ model with Ising-like anisotropy (after [22.228]). Here, λ denotes the anisotropy parameter. At the isotropic point, $\lambda = 1$

A similar analysis has been made for the magnetization process of the $S = 1/2$ XXZ models with Ising-like anisotropy in two and three dimensions by using the cluster algorithm [22.228] (Sect. 22.3.3). Magnetization curves (M - H curves) are obtained by the quantum Monte Carlo simulation in canonical ensembles in finite systems as shown in Fig. 22.37. This figure shows the nonmonotonic behavior of magnetization M as a function of magnetic field H , indicating the phase separation (i.e., the magnetization jump). The phase-separation boundary determined by the Maxwell construction has little size effect as shown in Fig. 22.37.

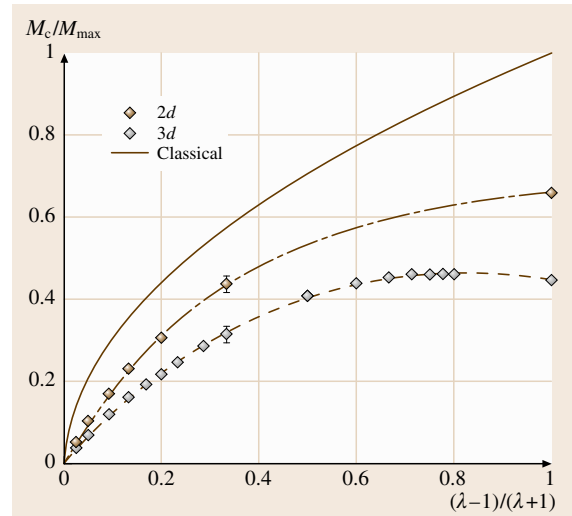


Fig. 22.39 Magnetization jump M_s for the $S = 1/2$ XXZ model with Ising-like anisotropy (after [22.228])

The critical field H_c and the magnetization jump M_s are shown in Figs. 22.38 and 22.39. The results in two and three dimensions are quite different from the one-dimensional result. In one dimension, there is no region of the phase separation, and the critical field near $\lambda = 1$ behaves as $H_c \propto \exp[-\pi^2/2\sqrt{2(\lambda-1)}]$ [22.240], where λ denotes the anisotropy parameter. (At the isotropic point, $\lambda = 1$.)

It should be noted that the $S = 1/2$ XXZ model can be mapped onto the Bose–Hubbard model with nearest-neighbor repulsions in the hard-core limit. Thus, numerical results for the $S = 1/2$ XXZ model imply that the corresponding Bose–Hubbard model also shows the first-order transition.

References

- 22.1 K. Binder, Q.W. Heermann: *Monte Carlo Simulation in Statistical Physics*, Springer Series in Solid-State Sciences (Springer, Berlin Heidelberg 1988) p. 80
- 22.2 N. Metropolis, A.W. Rosenbluth, M.N. Rosenbluth, A.H. Teller, E. Teller: Equation of state calculations by fast computing machines, *J. Chem. Phys.* **21**, 1087–1092 (1953)
- 22.3 A.M. Ferrenberg, D.P. Landau, Y.J. Wong: Monte Carlo simulations: Hidden errors from “good” random number generators, *Phys. Rev. Lett.* **69**, 3382–3384 (1992)
- 22.4 M. Matsumoto, Y. Kurita: Twisted GFSR generators, *ACM Trans. Model. Comput. Siml.* **2**, 179–194 (1992)
- 22.5 M. Matsumoto, Y. Kurita: Twisted GFSR generators II, *ACM Trans. Model. Comput. Siml.* **4**, 254–266 (1994)
- 22.6 M. Matsumoto, T. Nishimura: Mersenne Twister: A 623-dimensionally equidistributed uniform pseudorandom number generator, *ACM Trans. Model. Comput. Siml.* **8**, 3–30 (1998)
- 22.7 The source codes in various languages and original articles can be downloaded from the web-

- site <http://www.math.sci.hiroshima-u.ac.jp/~m-mat/MT/emt.html>
- 22.8 M. Suzuki: Linear and nonlinear dynamic scaling relations in the renormalization group theory, *Phys. Lett. A* **58**, 435–436 (1976)
- 22.9 M. Suzuki: Static and dynamic finite-size scaling theory based on the renormalization group approach, *Prog. Theor. Phys.* **83**, 1142–1150 (1977)
- 22.10 N. Ito: Non-equilibrium critical relaxation of the three-dimensional Ising model, *Physica A* **192**, 604–616 (1993)
- 22.11 N. Ito, T. Matsuhisa, H. Kitatani: Ferromagnetic transition of $\pm J$ Ising spin glass model on square lattice, *J. Phys. Soc. Jpn.* **67**, 1188–1196 (1998)
- 22.12 N. Ito, K. Hukushima, K. Ogawa, Y. Ozeki: Nonequilibrium relaxation of fluctuations of physical quantities, *J. Phys. Soc. Jpn.* **69**, 1931–1934 (2000)
- 22.13 Z.B. Li, L. Schülke, B. Zheng: Dynamic Monte Carlo measurement of critical exponents, *Phys. Rev. Lett.* **74**, 3396–3398 (1995)
- 22.14 Y. Nonomura: New quantum Monte Carlo approach to ground-state phase transitions in quantum spin systems, *J. Phys. Soc. Jpn.* **67**, 5–7 (1998)
- 22.15 Y. Nonomura: New quantum Monte Carlo study of quantum critical phenomena with Trotter-number-dependent finite-size scaling and non-equilibrium relaxation, *J. Phys. A* **31**, 7939–7954 (1998)
- 22.16 T. Nakamura, Y. Ito: A quantum Monte Carlo algorithm realizing an intrinsic relaxation, *J. Phys. Soc. Jpn.* **72**, 2405–2408 (2003)
- 22.17 Y. Ozeki, K. Ogawa, N. Ito: Nonequilibrium relaxation analysis of Kosterlitz–Thouless phase transition, *Phys. Rev. E* **67**, 026007(1–5) (2003)
- 22.18 Y. Ozeki, K. Kasono, N. Ito, S. Miyashita: Nonequilibrium relaxation analysis for first-order phase transitions, *Physica A* **321**, 271–279 (2003)
- 22.19 Y. Iba: Extended ensemble Monte Carlo, *Int. J. Mod. Phys. C* **12**, 623–656 (2001)
- 22.20 A.M. Ferrenberg, R.H. Swendsen: New Monte Carlo technique for studying phase transitions, *Phys. Rev. Lett.* **61**, 2635–2638 (1988)
- 22.21 A.M. Ferrenberg, R.H. Swendsen: Optimized Monte Carlo data analysis, *Phys. Rev. Lett.* **63**, 1195–1198 (1989)
- 22.22 A.M. Ferrenberg, D.P. Landau: Critical behavior of the three-dimensional Ising model: A high-resolution Monte Carlo study, *Phys. Rev. B* **44**, 5081–5091 (1991)
- 22.23 B.A. Berg, T. Neuhaus: Multicanonical algorithms for first order phase transitions, *Phys. Lett. B* **267**, 249–253 (1991)
- 22.24 B.A. Berg, T. Neuhaus: Multicanonical ensemble: A new approach to simulate first-order phase transitions, *Phys. Rev. Lett.* **68**, 9–12 (1992)
- 22.25 J. Lee: New Monte Carlo algorithm: Entropic sampling, *Phys. Rev. Lett.* **71**, 211–214 (1993)
- 22.26 P.M.C. de Oliveira, T.J.P. Penna, H.J. Herrmann: Broad histogram method, *Braz. J. Phys.* **26**, 677–683 (1996)
- 22.27 P.M.C. de Oliveira, T.J.P. Penna, H.J. Herrmann: Broad histogram Monte Carlo, *Eur. Phys. J. B* **1**, 205–208 (1998)
- 22.28 R.H. Swendsen, B. Diggs, J.-S. Wang, S.-T. Li, C. Genovese, J.B. Kadane: Transition matrix Monte Carlo, *Int. J. Mod. Phys. C* **10**, 1563–1569 (1999)
- 22.29 J.-S. Wang, T.K. Tay, R.H. Swendsen: Transition matrix Monte Carlo reweighting and dynamics, *Phys. Rev. Lett.* **82**, 476–479 (1999)
- 22.30 J.-S. Wang: Flat histogram Monte Carlo method, *Physica A* **281**, 147–150 (2000)
- 22.31 F. Wang, D.P. Landau: Efficient, multiple-range random walk algorithm to calculate the density of states, *Phys. Rev. Lett.* **86**, 2050–2053 (2001)
- 22.32 F. Wang, D.P. Landau: Determining the density of states for classical statistical models: A random walk algorithm to produce a flat histogram, *Phys. Rev. E* **64**, 1–16 (2001)
- 22.33 J. Lee, J.M. Kosterlitz: New numerical method to study phase transitions, *Phys. Rev. Lett.* **65**, 137–140 (1990)
- 22.34 J. Lee, J.M. Kosterlitz: Finite-size scaling and Monte Carlo simulations of first-order phase transitions, *Phys. Rev. B* **43**, 3265–3277 (1991)
- 22.35 R.H. Swendsen, J.-S. Wang: Nonuniversal critical dynamics in Monte Carlo simulations, *Phys. Rev. Lett.* **58**, 86–88 (1987)
- 22.36 P.W. Kasteleyn, C.M. Fortuin: Phase transitions in lattice systems with random local properties, *J. Phys. Soc. Jpn. Suppl.* **26**, 11–14 (1969)
- 22.37 C.M. Fortuin, P.W. Kasteleyn: On the random cluster model. I: Introduction and relation to other models, *Physica* **57**, 536–564 (1972)
- 22.38 U. Wolff: Collective Monte Carlo updating for spin systems, *Phys. Rev. Lett.* **62**, 361–364 (1989)
- 22.39 P. Tamayo, R.C. Brower, W. Klein: Single-cluster Monte-Carlo dynamics for the Ising-model, *J. Stat. Phys.* **58**, 1083–1094 (1990)
- 22.40 H.G. Evertz, G. Lana, M. Marcu: Cluster algorithm for vertex models, *Phys. Rev. Lett.* **70**, 875–879 (1993)
- 22.41 J. Machta, Y.S. Choi, A. Lucke, T. Schweizer, L.V. Chayes: Invaded cluster algorithm for equilibrium critical points, *Phys. Rev. Lett.* **75**, 2792–2795 (1995)
- 22.42 J. Machta, Y.S. Choi, A. Lucke, T. Schweizer, L.V. Chayes: Invaded cluster algorithm for Potts models, *Phys. Rev. E* **54**, 1332–1345 (1996)
- 22.43 Y. Tomita, Y. Okabe: Probability-changing cluster algorithm for Potts models, *Phys. Rev. Lett.* **86**, 572–575 (2001)
- 22.44 N. Prokof'ev, B. Svistunov: Worm algorithms for classical statistical models, *Phys. Rev. Lett.* **87**, 160601(1–4) (2001)

- 22.45 F. Matsubara, T. Iyota, S. Inawashiro: Dynamical simulation of the Heisenberg spin glass in three dimensions, *J. Phys. Soc. Jpn.* **60**, 41–44 (1991)
- 22.46 F. Matsubara, T. Iyota: Hybrid Monte-Carlo spin-dynamics simulation of short-range $\pm J$ Heisenberg models with and without anisotropy, *Prog. Theor. Phys.* **90**, 471–498 (1993)
- 22.47 S. Kirkpatrick, C.D. Gelatt, M.P. Vecchi: Optimization by simulated annealing, *Science* **220**, 671–680 (1983)
- 22.48 E. Marinari, G. Parisi: Simulated tempering: A new Monte Carlo scheme, *Europhys. Lett.* **19**, 451–458 (1992)
- 22.49 W. Kerler, P. Rehberg: Simulated-tempering procedure for spin-glass simulations, *Phys. Rev. E* **50**, 4220–4225 (1994)
- 22.50 K. Hukushima, K. Nemoto: Exchange Monte Carlo method and application to spin glass simulations, *J. Phys. Soc. Jpn.* **65**, 1604–1608 (1996)
- 22.51 R.H. Swendsen, J.-S. Wang: Replica Monte Carlo simulation of spin-glasses, *Phys. Rev. Lett.* **57**, 2607–2609 (1986)
- 22.52 J.-S. Wang, R.H. Swendsen: Replica Monte Carlo simulation (revisited), *Prog. Theor. Phys. Suppl.* **157**, 317–323 (2005)
- 22.53 M. Suzuki: *Quantum Monte Carlo methods in Condensed Matter Physics*, ed. by M. Suzuki (World Scientific, Singapore 1993)
- 22.54 M. Suzuki: Relationship between d -dimensional quantum spin systems and $(d+1)$ -dimensional Ising systems – equivalence, critical exponents and systematic approximants of the partition function and spin correlations, *Prog. Theor. Phys.* **56**, 1454–1469 (1976)
- 22.55 M. Suzuki: Generalized Trotters formula and systematic approximants of exponential operators and inner derivations with applications to many-body problems, *Commun. Math. Phys.* **51**, 183–190 (1976)
- 22.56 M. Suzuki: General theory of higher-order decomposition of exponential operators and symplectic integrators, *Phys. Lett. A* **165**, 387–395 (1992)
- 22.57 M. Suzuki: General nonsymmetric higher-order decomposition of exponential operators and symplectic integrators, *J. Phys. Soc. Jpn.* **61**, 3015–3019 (1992)
- 22.58 J.E. Hirsch, R.L. Sugar, D.J. Scalapino, R. Blankenbecler: Monte Carlo simulations of one-dimensional fermion systems, *Phys. Rev. B* **26**, 5033–5055 (1982)
- 22.59 H. De Raedt, A. Lagendijk: Monte-Carlo simulation of quantum statistical lattice models, *Phys. Rep.* **127**, 233–307 (1985)
- 22.60 M. Suzuki: *Quantum Monte Carlo Methods in Equilibrium and Nonequilibrium Systems*, ed. by M. Suzuki (Springer, Berlin Heidelberg 1987)
- 22.61 M. Suzuki, S. Miyashita, A. Kuroda: Monte Carlo simulation of quantum spin systems I, *Prog. Theor. Phys.* **58**, 1377–1387 (1977)
- 22.62 T. Sakaguchi, K. Kubo, S. Takada: Monte Carlo simulation for the in-plane susceptibility of 1-D spin 1/2 and 1 XY model, *J. Phys. Soc. Jpn.* **54**, 861–864 (1985)
- 22.63 S. Miyashita: Thermodynamic properties of spin 1/2 antiferromagnetic Heisenberg model on the square lattice, *J. Phys. Soc. Jpn.* **57**, 1934–1946 (1988)
- 22.64 M. Suzuki: Fractal decomposition of exponential operators with applications to many-body theories and Monte Carlo simulations, *Phys. Lett. A* **146**, 319–323 (1990)
- 22.65 M. Suzuki: General theory of fractal path integrals with applications to many-body theories and statistical physics, *J. Math. Phys.* **32**, 400–407 (1991)
- 22.66 H.G. Evertz: The loop algorithm, *Adv. Phys.* **52**, 1–66 (2003)
- 22.67 N. Kawashima, K. Harada: Recent developments of world-line Monte Carlo methods, *J. Phys. Soc. Jpn.* **73**, 1379–1414 (2004)
- 22.68 N. Kawashima, J.E. Gubernatis: Dual Monte Carlo and cluster algorithms, *Phys. Rev. E* **51**, 1547–1559 (1995)
- 22.69 N. Kawashima, J.E. Gubernatis: Generalization of the Fortuin-Kasteleyn transformation and its application to quantum spin simulations, *J. Stat. Phys.* **80**, 169–221 (1995)
- 22.70 N. Kawashima: Cluster algorithms for anisotropic quantum spin models, *J. Stat. Phys.* **82**, 131–153 (1996)
- 22.71 N. Kawashima, J.E. Gubernatis, H.G. Evertz: Loop algorithms for quantum simulations of fermion models on lattices, *Phys. Rev. B* **50**, 136–149 (1994)
- 22.72 B.B. Beard, U.-J. Wiese: Simulations of discrete quantum systems in continuous Euclidean time, *Phys. Rev. Lett.* **77**, 5130–5133 (1996)
- 22.73 N. Kawashima, J.E. Gubernatis: Loop algorithms for Monte Carlo simulations of quantum spin systems, *Phys. Rev. Lett.* **73**, 1295–1298 (1994)
- 22.74 S. Todo, K. Kato: Cluster algorithms for general-S quantum spin systems, *Phys. Rev. Lett.* **87**, 047203(1–4) (2001)
- 22.75 V.A. Kashurnikov, N.V. Prokofev, B.V. Svistunov, M. Troyer: Quantum spin chains in a magnetic field, *Phys. Rev. B* **59**, 1162–1167 (1999)
- 22.76 N.V. Prokof'ev, B.V. Svistunov, I.S. Tupitsyn: Exact, complete, and universal continuous-time world-line Monte Carlo approach to the statistics of discrete quantum systems, *Sov. Phys. JETP* **87**, 310–321 (1998)
- 22.77 N.V. Prokof'ev, B.V. Svistunov, I.S. Tupitsyn: “Worm” algorithm in quantum Monte Carlo simulations, *Phys. Lett. A* **238**, 253–257 (1998)

- 22.78 O.F. Syljuåsen, A.W. Sandvik: Quantum Monte Carlo with directed loops, *Phys. Rev. E* **66**, 046701(1–28) (2002)
- 22.79 A.W. Sandvik, J. Kurkijärvi: Quantum Monte Carlo simulation method for spin systems, *Phys. Rev. B* **43**, 5950–5961 (1991)
- 22.80 A.W. Sandvik: Generalization of Handscomb's quantum Monte-Carlo scheme – Application to the 1-D Hubbard-model, *J. Phys. A* **25**, 3667–3682 (1992)
- 22.81 A.W. Sandvik: Finite-size scaling of the ground-state parameters of the two-dimensional Heisenberg model, *Phys. Rev. B* **56**, 11678–11690 (1997)
- 22.82 A.W. Sandvik: Stochastic series expansion method with operator-loop update, *Phys. Rev. B* **59**, R14157–R14160 (1999)
- 22.83 J.E. Hirsch: Monte Carlo study of the two-dimensional Hubbard model, *Phys. Rev. Lett.* **51**, 1900–1903 (1983)
- 22.84 J.E. Hirsch: Two-dimensional Hubbard model: numerical simulation study, *Phys. Rev. B* **31**, 4403–4419 (1985)
- 22.85 S.R. White, D.J. Scalapino, R.L. Sugar, E.Y. Loh, J.E. Gubernatis, R.T. Scalettar: Numerical study of the two-dimensional Hubbard model, *Phys. Rev. B* **40**, 506–516 (1989)
- 22.86 M. Imada, Y. Hatsugai: Numerical studies on the Hubbard model and the t - J model in one- and two-dimensions, *J. Phys. Soc. Jpn.* **58**, 3752–3780 (1989)
- 22.87 J.E. Hirsch: Discrete Hubbard–Stratonovich transformation for fermion lattice models, *Phys. Rev. B* **28**, 4059–4061 (1983)
- 22.88 J. Kuti: Stochastic method for the numerical study of lattice fermions, *Phys. Rev. Lett.* **49**, 183–186 (1982)
- 22.89 R. Blankenbecler, R.L. Sugar: Projector Monte Carlo method, *Phys. Rev. D* **27**, 1304–1311 (1983)
- 22.90 Y.C. Chen, T.K. Lee: t - J model studied by the power Lanczos method, *Phys. Rev. B* **51**, 6723–6726 (1995)
- 22.91 S. Sorella: Green function Monte Carlo with stochastic reconfiguration, *Phys. Rev. Lett.* **80**, 4558–4561 (1998)
- 22.92 S. Sorella, L. Capriotti: *Phys. Rev. B* **61**, 2599–2612 (2000)
- 22.93 S. Sorella: Generalized Lanczos algorithm for variational quantum Monte Carlo, *Phys. Rev. B* **64**, 024512(1–16) (2001)
- 22.94 H.J.M. van Bemmelen, D.F.B. ten Haaf, W. van Saarloos, J.M.J. van Leeuwen, G. An: Fixed-node quantum Monte Carlo method for lattice fermions, *Phys. Rev. Lett.* **72**, 2442–2445 (1994)
- 22.95 D.F.B. ten Haaf, H.J.M. van Bemmelen, J.M.J. van Leeuwen, W. van Saarloos, D.M. Ceperley: Proof for an upper bound in fixed-node Monte Carlo for lattice fermions, *Phys. Rev. B* **51**, 13039–13045 (1995)
- 22.96 D.M. Ceperley, B.J. Alder: Ground state of the electron gas by a stochastic method, *Phys. Rev. Lett.* **45**, 566–569 (1980)
- 22.97 D.M. Ceperley, B.J. Alder: Quantum Monte-Carlo, *Science* **231**, 555–560 (1986)
- 22.98 T. Nakamura: Vanishing of the negative-sign problem of quantum Monte Carlo simulations in one-dimensional frustrated spin systems, *Phys. Rev. B* **57**, R3197–R3200 (1998)
- 22.99 S. Chandrasekharan, U.-J. Wiese: Meron-cluster solution of fermion sign problems, *Phys. Rev. Lett.* **83**, 3116–3119 (1999)
- 22.100 S. Chandrasekharan, J. Cox, J.C. Osborn, U.-J. Wiese: Meron-cluster approach to systems of strongly correlated electrons, *Nucl. Phys. B* **673**, 405–436 (2003)
- 22.101 C. Domb, M.S. Green: *Phase Transitions and Critical Phenomena*, Vol. 3, ed. by C. Domb, M.S. Green (Academic, London 1974)
- 22.102 G.A. Baker Jr. (Ed.): *Quantitative Theory of Critical Phenomena* (Academic, San Diego 1990)
- 22.103 S.R. White: Density matrix formulation for quantum renormalization groups, *Phys. Rev. Lett.* **69**, 2863–2866 (1992)
- 22.104 S.R. White: Density-matrix algorithms for quantum renormalization groups, *Phys. Rev. B* **48**, 10345–10356 (1993)
- 22.105 T. Nishino: Density matrix renormalization group method for 2-D classical models, *J. Phys. Soc. Jpn.* **64**, 3598–3601 (1995)
- 22.106 R.J. Bursill, T. Xiang, G.A. Gehring: The density matrix renormalization group for a quantum spin chain at non-zero temperature, *J. Phys.: Condens. Matter* **8**, L583–L590 (1996)
- 22.107 N. Shibata: Thermodynamics of the anisotropic Heisenberg chain calculated by the density matrix renormalization group method, *J. Phys. Soc. Jpn.* **66**, 2221–2223 (1997)
- 22.108 X. Wang, T. Xiang: Transfer-matrix density-matrix renormalization-group theory for thermodynamics of one-dimensional quantum systems, *Phys. Rev. B* **56**, 5061–5064 (1997)
- 22.109 K. Maisinger, U. Schollwöck: Thermodynamics of frustrated quantum spin chains, *Phys. Rev. Lett.* **81**, 445–448 (1998)
- 22.110 M. Imada, T. Kashima: Path-integral renormalization group method for numerical study of strongly correlated electron systems, *J. Phys. Soc. Jpn.* **69**, 2723–2726 (2000)
- 22.111 T. Kashima, M. Imada: Path-integral renormalization group method for numerical study on ground states of strongly correlated electronic systems, *J. Phys. Soc. Jpn.* **70**, 2287–2299 (2001)
- 22.112 M. Imada, T. Mizusaki: Quantum-number projection in the path-integral renormalization group method, *Phys. Rev. B* **69**, 125110–1–125110–10 (2004)

- 22.113 T. Kashima, M. Imada: Magnetic and metal-insulator transitions through bandwidth control in two-dimensional Hubbard models with nearest and next-nearest neighbor transfers, *J. Phys. Soc. Jpn.* **70**, 3052–3067 (2001)
- 22.114 H. Morita, S. Watanabe, M. Imada: Nonmagnetic insulating states near the Mott transitions on lattices with geometrical frustration and implications for κ -(ET)₂Cu₂(CN)₃, *J. Phys. Soc. Jpn.* **71**, 2109–2112 (2002)
- 22.115 S. Watanabe, M. Imada: Precise determination of phase diagram for two-dimensional Hubbard model with filling- and bandwidth-control Mott transitions: grand-canonical path-integral renormalization group approach, *J. Phys. Soc. Jpn.* **73**, 1251–1266 (2004)
- 22.116 S.-C. Zhang: A unified theory based on SO(5) symmetry of superconductivity and antiferromagnetism, *Science* **275**, 1089–1096 (1997)
- 22.117 E. Demler, W. Hanke, S.-C. Zhang: SO(5) theory of antiferromagnetism and superconductivity, *Rev. Mod. Phys.* **76**, 909–974 (2004)
- 22.118 K.-S. Liu, M.E. Fisher, D.R. Nelson: Quantum lattice gas and the existence of a supersolid, *J. Low. Temp. Phys.* **10**, 655–683 (1973)
- 22.119 M.E. Fisher, D.R. Nelson: Spin flop, supersolids, and bicritical and tetracritical points, *Phys. Rev. Lett.* **32**, 1350–1353 (1974)
- 22.120 D.R. Nelson, J.M. Kosterlitz, M.E. Fisher: Renormalization-group analysis of bicritical and tetracritical points, *Phys. Rev. Lett.* **33**, 813–817 (1974)
- 22.121 D.R. Nelson, M.E. Fisher, J.M. Kosterlitz: Bicritical and tetracritical points in anisotropic antiferromagnetic systems, *Phys. Rev. B* **13**, 412–432 (1976)
- 22.122 A. Aharony: Comment on “Bicritical and tetracritical phenomena and scaling properties of the SO(5) theory”, *Phys. Rev. Lett.* **88**, 059703(1) (2002), and references therein
- 22.123 X. Hu: Bicritical and tetracritical phenomena and scaling properties of the SO(5) theory, *Phys. Rev. Lett.* **87** (2001)
- 22.124 X. Hu: Bicritical phenomena and scaling properties of O(5) model, *Physica A* **321**, 71–80 (2003)
- 22.125 E. Arrigoni, W. Hanke: Renormalized SO(5) symmetry in ladders with next-nearest-neighbor hopping, *Phys. Rev. Lett.* **82**, 2115–2118 (1999)
- 22.126 E. Arrigoni, W. Hanke: Critical properties of projected SO(5) models at finite temperatures, *Phys. Rev. B* **62**, 11770–11777 (2000)
- 22.127 X. Hu: Reply to “Comment on ‘Bicritical and tetracritical phenomena and scaling properties of the SO(5) theory’”, *Phys. Rev. Lett.* **88**, 059704(1–4) (2002)
- 22.128 P. Pfeuty, D. Jasnow, M.E. Fisher: Crossover scaling functions for exchange anisotropy, *Phys. Rev. B* **10**, 2088–2112 (1974)
- 22.129 X. Hu, T. Koyama, M. Tachiki: Phase diagram of a superconducting and antiferromagnetic system with SO(5) symmetry, *Phys. Rev. Lett.* **82**, 2568–2571 (1999)
- 22.130 A.A. Abrikosov: On the magnetic properties of superconductors of the second group, *Zh. Eksp. Teor. Fiz.* **32**, 1442 (1957)
- 22.131 A.A. Abrikosov: On the magnetic properties of superconductors of the second group, *Sov. Phys. JETP* **5**, 1174–1182 (1957)
- 22.132 G. Blatter, M.V. Feigelman, V.B. Geshkenbein, A.I. Larkin, V.M. Vinokur: Vortices in high-temperature superconductors, *Rev. Mod. Phys.* **66**, 1125–1388 (1994)
- 22.133 G.W. Crabtree, D.R. Nelson: Vortex physics in high-temperature superconductors, *Phys. Today* **50**, 38–45 (1997)
- 22.134 T. Nattermann, S. Scheidl: Vortex-glass phases in type-II superconductors, *Adv. Phys.* **49**, 607–704 (2000)
- 22.135 E. Brezin, D.R. Nelson, A. Thiaville: Fluctuation effects near H_{c2} in type-II superconductors, *Phys. Rev. B* **31**, 7124–7132 (1985)
- 22.136 Y.-H. Li, S. Teitel: Vortex-line-lattice melting, vortex-line cutting, and entanglement in model high- T_c superconductors, *Phys. Rev. Lett.* **66**, 3301–3304 (1991)
- 22.137 R.E. Hetzel, A. Sudb, D.A. Huse: First-order melting transition of an Abrikosov vortex lattice, *Phys. Rev. Lett.* **69**, 518–521 (1992)
- 22.138 P.G. de Gennes: *Superconductivity of Metals and Alloys* (Addison-Wesley, Redwood City, CA 1966), translated by P.A. Pincus
- 22.139 W.E. Lawrence, S. Doniach: *Proceedings of LT12, Tokyo, 1970*, ed. by E. Kanda (Keigaku, Tokyo 1971)
- 22.140 X. Hu, S. Miyashita, M. Tachiki: Simulation for the first-order vortex-lattice melting transition in high- T_c superconductors, *Physica (Amsterdam)* **282-287C**, 2057–2058 (1997)
- 22.141 X. Hu, S. Miyashita, M. Tachiki: δ -function peak in the specific heat of high- T_c superconductors: Monte Carlo simulation, *Phys. Rev. Lett.* **79**, 3498–3501 (1997)
- 22.142 X. Hu, S. Miyashita, M. Tachiki: Monte Carlo simulation on the first-order melting transition of high- T_c superconductors in \hat{c} , *Phys. Rev. B* **58**, 3438–3445 (1998)
- 22.143 S. Miyashita, H. Nishimori, A. Kuroda, M. Suzuki: Monte Carlo simulation and static and dynamic critical behavior of the plane rotator model, *Prog. Theo. Phys.* **60**, 1669–1685 (1978)
- 22.144 A.E. Koshelev: Point-like and line-like melting of the vortex lattice in the universal phase diagram of layered superconductors, *Phys. Rev. B* **56**, 11201–11212 (1997)
- 22.145 A.K. Nguyen, A. Sudbø: Phase coherence and the boson analogy of vortex liquids, *Phys. Rev. B* **58**, 2802–2815 (1998)

- 22.146 P. Olsson, S. Teitel: Correlation lengths in the vortex line liquid of a high- T_c superconductor, *Phys. Rev. Lett.* **82**, 2183–2186 (1999)
- 22.147 X. Hu, M. Tachiki: Possible tricritical point in phase diagrams of interlayer Josephson-vortex systems in high- T_c superconductors, *Phys. Rev. Lett.* **85**, 2577–2580 (2000)
- 22.148 K.B. Efetov: Fluctuations in layered superconductors in a parallel magnetic field, *Sov. Phys. JETP* **49**, 905–910 (1979)
- 22.149 B.I. Ivlev, N.B. Kopnin, M.M. Slomaa: Vortex-lattice/vortex-liquid states in anisotropic high- T_c superconductor, *Phys. Rev. B* **43**, 2896–2902 (1991)
- 22.150 B.I. Ivlev, N.B. Kopnin, V.L. Pokrovsky: Shear instability of a vortex lattice in layered superconductors, *J. Low. Temp. Phys.* **80**, 187 (1990)
- 22.151 L.V. Mikheev, E.B. Kolomeisky: Melting of a flux-line fluid confined by CuO_2 planes: Lindemann-criterion failure, *Phys. Rev. B* **43**, 10431–10435 (1991)
- 22.152 S.E. Korshunov, A.I. Larkin: Problem of Josephson-vortex-lattice melting in layered superconductors, *Phys. Rev. B* **46**, 6395–6399 (1992)
- 22.153 G. Blatte, B.I. Ivlev, J. Rhyner: Kosterlitz-Thouless transition in the smectic vortex state of a layered superconductor, *Phys. Rev. Lett.* **66**, 2392–2395 (1991)
- 22.154 L. Balents, D.R. Nelson: Fluctuations and intrinsic pinning in layered superconductors, *Phys. Rev. Lett.* **73**, 2618–2621 (1994)
- 22.155 L. Balents, D.R. Nelson: Quantum smectic and supersolid order in helium films and vortex arrays, *Phys. Rev. B* **52**, 12951–12968 (1995)
- 22.156 Y. Iye, S. Nakamura, T. Tamegai: Absence of current direction dependence of the resistive state of high temperature superconductors in magnetic fields, *Physica* **159C**, 433–438 (1989)
- 22.157 W.K. Kwok, U. Welp, G.W. Crabtree, K.G. Vandervoort, R. Hulscher, J.Z. Liu: Direct observation of dissipative flux motion and pinning by twin boundaries in $\text{YBa}_2\text{Cu}_3\text{O}_{7-\delta}$ single crystals, *Phys. Rev. Lett.* **64**, 966–969 (1990)
- 22.158 W.K. Kwok, J. Fendrich, U. Welp, S. Fleshler, J. Downey, G.W. Crabtree: Suppression of the first order vortex melting transition by intrinsic pinning in $\text{YBa}_2\text{Cu}_3\text{O}_{7-\delta}$, *Phys. Rev. Lett.* **72**, 1088–1091 (1994)
- 22.159 X. Hu, M. Tachiki: Decoupled two-dimensional superconductivity and continuous melting transitions in layered superconductors immersed in a parallel magnetic field, *Phys. Rev. B* **70**, 064506(1–13) (2004)
- 22.160 X. Hu, M. Tachiki: Structure and phase transition of Josephson vortices in anisotropic high- T_c superconductors, *Phys. Rev. Lett.* **80**, 4044–4047 (1998)
- 22.161 X. Hu: Pinning effects in vortex states of high- T_c superconductors: Monte Carlo simulations, *J. Low. Temp. Phys.* **131**, 979–986 (2003)
- 22.162 X. Hu, M.-B. Luo, Y.-Q. Ma: Density functional theory for freezing transition of vortex-line liquid with periodic layer pinning, *Phys. Rev. B* **72**, 174503(1–6) (2005)
- 22.163 A.I. Larkin: Effect of inhomogeneities on the structure of the mixed state of superconductors, *Sov. Phys. JETP* **31**, 784–786 (1970)
- 22.164 A.I. Larkin, Y.N. Ovchinnikov: Pinning in type II superconductors, *J. Low. Temp. Phys.* **34**, 409–428 (1979)
- 22.165 Y. Imry, S.-K. Ma: Random-field instability of the ordered state of continuous symmetry, *Phys. Rev. Lett.* **35**, 1399–1401 (1975)
- 22.166 T. Nattermann: Scaling approach to pinning: Charge density waves and giant flux creep in superconductors, *Phys. Rev. Lett.* **64**, 2454–2457 (1990)
- 22.167 S.E. Korshunov: Replica symmetry breaking in vortex glasses, *Phys. Rev. B* **48**, 3969–3975 (1993)
- 22.168 T. Giamarchi, P. Le Doussal: Elastic theory of pinned flux lattices, *Phys. Rev. Lett.* **72**, 1530–1533 (1994)
- 22.169 T. Giamarchi, P. Le Doussal: Elastic theory of flux lattices in the presence of weak disorder, *Phys. Rev. B* **52**, 1242–1270 (1995)
- 22.170 T. Giamarchi, P. Le Doussal: Phase diagrams of flux lattices with disorder, *Phys. Rev. B* **55**, 6577–6583 (1997)
- 22.171 P. Olsson, S. Teitel: Disorder driven melting of the vortex line lattice, *Phys. Rev. Lett.* **87**, 137001(1–4) (2001)
- 22.172 Y. Nonomura, X. Hu: Effects of point defects on the phase diagram of vortex states in high- T_c superconductors in the $B \parallel c$ axis, *Phys. Rev. Lett.* **86**, 5140–5143 (2001)
- 22.173 Y. Nonomura, X. Hu: Crossover behaviors in liquid region of vortex states above a critical point caused by point defects, *cond-mat/0302597*
- 22.174 Y. Nonomura, X. Hu: Possible Bragg-Bose glass phase in vortex states of high- T_c superconductors with sparse and weak columnar defects, *Europhys. Lett.* **65**, 533–539 (2004)
- 22.175 M.J.P. Gingras, D.A. Huse: Topological defects in the random-field XY model and the pinned vortex lattice to vortex glass transition in type-II superconductors, *Phys. Rev. B* **53**, 15193–15200 (1996)
- 22.176 S. Ryu, A. Kapitulnik, S. Doniach: Field-driven topological glass transition in a model flux line lattice, *Phys. Rev. Lett.* **77**, 2300–2303 (1996)
- 22.177 M.P.A. Fisher: Vortex-glass superconductivity: A possible new phase in bulk high- T_c oxides, *Phys. Rev. Lett.* **62**, 1415–1418 (1989)
- 22.178 M.P.A. Fisher, D.S. Fisher, D.A. Huse: Thermal fluctuations, quenched disorder, phase transitions, and transport in type-II superconductors, *Phys. Rev. B* **43**, 130–159 (1991)
- 22.179 A. van Otterlo, R.T. Scalettar: Phase diagram of disordered vortices from London Langevin simulations, *Phys. Rev. Lett.* **81**, 1497–1500 (1998)

- 22.180 R. Sugano, T. Onogi, K. Hirata, M. Tachiki: The effect of pointlike pinning on vortex phase diagram of $\text{Bi}_2\text{Sr}_2\text{CaCu}_2\text{O}_{8+\delta}$, *Physica C* **357–360**, 428–431 (2001), and references therein
- 22.181 A. Vestergren, J. Lidmar, M. Wallin: Vortex glass transition in a random pinning model, *Phys. Rev. Lett.* **88**, 117004(1–4) (2002)
- 22.182 P. Olsson: Vortex glass transition in a frustrated 3-D XY model with disorder, *Phys. Rev. Lett.* **91**, 077002(1–4) (2003)
- 22.183 J. Lidmar: Amorphous vortex glass phase in strongly disordered superconductors, *Phys. Rev. Lett.* **91**, 097001(1–4) (2003)
- 22.184 F.O. Pfeiffer, H. Rieger: Numerical study of the strongly screened vortex-glass model in an external field, *Phys. Rev. B* **60**, 6304–6307 (1999)
- 22.185 H. Kawamura: Simulation studies on the stability of the vortex-glass order, *J. Phys. Soc. Jpn.* **69**, 29–32 (2000)
- 22.186 T.K. Worthington, M.P.A. Fisher, D.A. Huse, J. Toner, A.D. Marwick, T. Zabel, C.A. Feild, F. Holtzberg: *Phys. Rev. B* **46**, 11854–11861 (1992)
- 22.187 T. Nishizaki, K. Shibata, T. Sasaki, N. Kobayashi: New equilibrium phase diagram of $\text{YBa}_2\text{Cu}_3\text{O}_y$ under high magnetic fields, *Physica C* **341–348**, 957–960 (2000)
- 22.188 K. Shibata, T. Nishizaki, T. Sasaki, N. Kobayashi: Phase transition in the vortex liquid and the critical endpoint in $\text{YBa}_2\text{Cu}_3\text{O}_y$, *Phys. Rev. B* **66**, 214518(1–7) (2002)
- 22.189 J. Kierfeld, V. Vinokur: Dislocations and the critical endpoint of the melting line of vortex line lattices, *Phys. Rev. B* **61**, R14928–14931 (2000)
- 22.190 G.P. Mikitik, E.H. Brandt: Effect of pinning on the vortex-lattice melting line in type-II superconductors, *Phys. Rev. B* **68**, 054509(1–15) (2003)
- 22.191 F. Bouquet, C. Marcenat, E. Steep, R. Calemczuk, W.K. Kwok, U. Welp, G.W. Crabtree, R.A. Fisher, N.E. Phillips, A. Schilling: An unusual phase transition to a second liquid vortex phase in the superconductor $\text{YBa}_2\text{Cu}_3\text{O}_7$, *Nature* **411**, 448–451 (2001)
- 22.192 M.P.A. Fisher, P.B. Weichman, G. Grinstein, D.S. Fisher: Boson localization and the superfluid-insulator transition, *Phys. Rev. B* **40**, 546–570 (1989)
- 22.193 D.R. Nelson, V.M. Vinokur: Boson localization and pinning by correlated disorder in high-temperature superconductors, *Phys. Rev. Lett.* **68**, 2398–2401 (1992)
- 22.194 D.R. Nelson, V.M. Vinokur: Boson localization and correlated pinning of superconducting vortex arrays, *Phys. Rev. B* **48**, 13060–13097 (1993)
- 22.195 J. Lidmar, M. Wallin: Critical properties of Bose-glass superconductors, *Europhys. Lett.* **47**, 494–500 (1999)
- 22.196 L. Radzihovsky: Resurrection of the melting line in the Bose glass superconductor, *Phys. Rev. Lett.* **74**, 4923–4926 (1995)
- 22.197 T. Giamarchi, P. Le Doussal: Variational theory of elastic manifolds with correlated disorder and localization of interacting quantum particles, *Phys. Rev. B* **53**, 15206–15225 (1996)
- 22.198 C. Zeng, P.L. Leath, D.S. Fisher: Absence of two-dimensional Bragg glasses, *Phys. Rev. Lett.* **82**, 1935–1938 (1999)
- 22.199 S. Tyagi, Y.Y. Goldschmidt: Effects of columnar disorder on flux-lattice melting in high-temperature superconductors, *Phys. Rev. B* **67**, 214501(1–15) (2003)
- 22.200 C. Dasgupta, O.T. Valls: Two-step melting of the vortex solid in layered superconductors with random columnar pins, *Phys. Rev. Lett.* **91**, 127002(1–4) (2003)
- 22.201 C. Dasgupta, O.T. Valls: Melting and structure of the vortex solid in strongly anisotropic layered superconductors with random columnar pins, *Phys. Rev. B* **69**, 214520(1–16) (2004)
- 22.202 M. Kohno, M. Takahashi, M. Hagiwara: Low-temperature properties of the spin-1 antiferromagnetic Heisenberg chain with bond alternation, *Phys. Rev. B* **57**, 1046–1051 (1998)
- 22.203 F.D.M. Haldane: Nonlinear field theory of large-spin Heisenberg antiferromagnets: semiclassically quantized solitons of the one-dimensional easy-axis Néel state, *Phys. Rev. Lett.* **50**, 1153–1156 (1983)
- 22.204 F.D.M. Haldane: Continuum dynamics of the 1-D Heisenberg antiferromagnet: identification with the $O(3)$ nonlinear sigma model, *Phys. Lett. A* **93**, 464–468 (1983)
- 22.205 M.P. Nightingale, H.W. Blöte: Gap of the linear spin-1 Heisenberg antiferromagnet: a Monte Carlo calculation, *Phys. Rev. B* **33**, 659–661 (1986)
- 22.206 M. Takahashi: Spin-correlation function of the $S=1$ antiferromagnetic Heisenberg chain at $T=0$, *Phys. Rev. B* **38**, 5188–5191 (1988)
- 22.207 Y. Kato, A. Tanaka: Numerical study of the $S=1$ antiferromagnetic spin chain with bond alternation, *J. Phys. Soc. Jpn.* **63**, 1277–1280 (1994)
- 22.208 W.J.L. Buyers, R.M. Morra, R.L. Armstrong, M.J. Hogan, P. Gerlach, K. Hirakawa: Experimental evidence for the Haldane gap in a spin-1 nearly isotropic, antiferromagnetic chain, *Phys. Rev. Lett.* **56**, 371–374 (1986)
- 22.209 M. Steiner, K. Kakurai, J.K. Kjems, D. Petitgrand, R. Pynn: Inelastic neutron scattering studies on 1-D near-Heisenberg antiferromagnets: A test of the Haldane conjecture, *J. Appl. Phys.* **61**, 3953–3955 (1987)
- 22.210 I.A. Zaliznyak, L.P. Regnault, D. Petitgrand: Neutron-scattering study of the dynamic spin correlations in CsNiCl_3 above Néel ordering, *Phys. Rev. B* **50**, 15824–15833 (1994)

- 22.211 J.P. Renard, M. Verdagner, L.P. Regnault, W.A.C. Erkelens, J. Rossat-Mignod, W.G. Stirling: Presumption for a quantum energy-gap in the quasi one-dimensional $S=1$ Heisenberg-antiferromagnet $\text{Ni}(\text{C}_2\text{H}_8\text{N}_2)_2\text{NO}_2(\text{ClO}_4)$, *Europhys. Lett.* **3**, 945–951 (1987)
- 22.212 I. Affleck: The quantum Hall-effects, σ -models at $\theta = \pi$ and quantum spin chains, *Nucl. Phys. B* **257**, 397–406 (1985)
- 22.213 I. Affleck: Exact critical exponents for quantum spin chains, nonlinear σ -models at $\theta = \pi$ and the quantum Hall-effect, *Nucl. Phys. B* **265**, 409–447 (1986)
- 22.214 I. Affleck, F.D.M. Haldane: Critical theory of quantum spin chains, *Phys. Rev. B* **36**, 5291–5300 (1987)
- 22.215 E. Coronado, M. Drillon, A. Fuyentes, D. Beltran, A. Mosset, J. Galy: Structural and magnetic study of $\text{Ni}_2(\text{EDTA})(\text{H}_2\text{O})_4 \cdot 2\text{H}_2\text{O}$ – alternating Landé factors in a two-sublattice 1-D system, *J. Am. Chem. Soc.* **108**, 900–905 (1986)
- 22.216 R. Vicente, A. Escuer, J. Ribas, X. Solans: The first nickel(II) alternating chain with two different end-to-end azido bridges, *Inorg. Chem.* **31**, 1726–1728 (1992)
- 22.217 A. Escuer, R. Vicente, J. Ribas, M.S.E. Fallah, X. Solans, M. Font-Badría: Crystal structure and magnetic properties of *trans*- $[\text{Ni}(333\text{-tet})(\mu\text{-N}_3)]_n(\text{ClO}_4)_n$ and *cis*- $[\text{Ni}(333\text{-tet})(\mu\text{-N}_3)]_n(\text{PF}_6)_n$: two novel kinds of structural nickel(II) chains with a single azido bridge. Magnetic behavior of an alternating $S=1$ chain with $\alpha = 0.46$, *Inorg. Chem.* **33**, 1842–1847 (1994)
- 22.218 J.J. Borrás-Almenar, E. Coronado, J. Curely, R. Georges: Exchange alternation and single-ion anisotropy in the antiferromagnetic Heisenberg chain $S=1$. Magnetic and thermal properties of the compound $\text{Ni}_2(\text{EDTA}) \cdot 6\text{H}_2\text{O}$, *Inorg. Chem.* **34**, 2699–2704 (1995)
- 22.219 A. Escuer, R. Vicente, X. Solans, M. Font-Badría: Crystal structure and magnetic properties of $[\text{Ni}_2(\text{dpt})_2(\mu\text{-ox})(\mu\text{-N}_3)]_n(\text{PF}_6)_n$: a new strategy to obtain $S=1$ alternating chains, *Inorg. Chem.* **33**, 6007–6011 (1994)
- 22.220 M. Hagiwara, Y. Narumi, K. Kindo, M. Kohno, H. Nakano, R. Sata, M. Takahashi: Experimental verification of the gapless point in the $S=1$ antiferromagnetic bond alternating chain, *Phys. Rev. Lett.* **80**, 1312–1315 (1998)
- 22.221 O.A. Starykh, R.R.P. Singh, A.W. Sandvik: Quantum critical scaling and temperature-dependent logarithmic corrections in the spin-half Heisenberg chain, *Phys. Rev. Lett.* **78**, 539–542 (1997)
- 22.222 O.A. Starykh, A.W. Sandvik, R.R.P. Singh: Dynamics of the spin-1/2 Heisenberg chain at intermediate temperatures, *Phys. Rev. B* **55**, 14953–14967 (1997)
- 22.223 N. Furukawa, M. Imada: Two-dimensional Hubbard model – metal insulator transition studied by Monte Carlo calculation, *J. Phys. Soc. Jpn.* **61**, 3331–3354 (1992)
- 22.224 A. Ino, T. Mizokawa, A. Fujimori, K. Tamasaku, H. Eisaki, S. Uchida, T. Kimura, T. Sasagawa, K. Kishio: Chemical potential shift in overdoped and underdoped $\text{La}_{2-x}\text{Sr}_x\text{CuO}_4$, *Phys. Rev. Lett.* **79**, 2101–2104 (1997)
- 22.225 N. Harima, A. Fujimori, T. Sugaya, I. Terasaki: Chemical potential shift in lightly doped to overdoped $\text{Bi}_2\text{Sr}_2\text{Ca}_{1-x}\text{R}_x\text{Cu}_2\text{O}_{8+y}$ ($\text{R}=\text{Pr}, \text{Er}$), *Phys. Rev. B* **67**, 172501(1–4) (2003)
- 22.226 R.J. Birgeneau, D.R. Gabbe, H.P. Janssen, M.A. Kastner, P.J. Picone, T.R. Thurston, G. Shirane, Y. Endoh, M. Sato, K. Yamada, Y. Hidaka, M. Oda, Y. Enomoto, M. Suzuki, T. Murakami: Antiferromagnetic spin correlations in insulating, metallic, and superconducting $\text{La}_{2-x}\text{Sr}_x\text{CuO}_4$, *Phys. Rev. B* **38**, 6614–6623 (1988)
- 22.227 M. Kohno: Ground-state properties of the two-dimensional t - J model, *Phys. Rev. B* **55**, 1435–1441 (1997)
- 22.228 M. Kohno, M. Takahashi: Magnetization process of the spin-1/2 XXZ models on square and cubic lattices, *Phys. Rev. B* **56**, 3212–3217 (1997)
- 22.229 V.J. Emery, S.A. Kivelson, H.Q. Lin: Phase separation in the t - J model, *Phys. Rev. Lett.* **64**, 475–478 (1990)
- 22.230 W.O. Putikka, M.U. Luchini, T.M. Rice: Aspects of the phase diagram of the two-dimensional t - J model, *Phys. Rev. Lett.* **68**, 538–541 (1992)
- 22.231 W.O. Putikka, M.U. Luchini: Limits on phase separation for two-dimensional strongly correlated electrons, *Phys. Rev. B* **62**, 1684–1687 (2000)
- 22.232 P. Prelovšek, X. Zotos: Hole pairing and clustering in the two-dimensional t - J model, *Phys. Rev. B* **47**, 5984–5991 (1993)
- 22.233 E. Dagotto, J. Riera, Y.C. Chen, A. Moreo, A. Nazarenko, F. Alcaraz, F. Ortolani: Superconductivity near phase separation in models of correlated electrons, *Phys. Rev. B* **49**, 3548–3565 (1994)
- 22.234 J. Jaklič, P. Prelovšek: Thermodynamic properties of the planar t - J model, *Phys. Rev. Lett.* **77**, 892–895 (1996)
- 22.235 C.S. Hellberg, E. Manousakis: Phase separation at all interaction strengths in the t - J model, *Phys. Rev. Lett.* **78**, 4609–4612 (1997)
- 22.236 C.S. Hellberg, E. Manousakis: Green's-function Monte Carlo for lattice fermions: application to the t - J model, *Phys. Rev. B* **61**, 11787–11806 (2000)
- 22.237 S.R. White, D.J. Scalapino: Density matrix renormalization group study of the striped phase in the 2-D t - J model, *Phys. Rev. Lett.* **81**, 1272–1275 (1998)

- 22.238 S.R. White, D.J. Scalapino: Energetics of domain walls in the 2-D t - J model, *Phys. Rev. Lett.* **81**, 3227–3230 (1998)
- 22.239 C.T. Shih, Y.C. Chen, T.K. Lee: Revisit phase separation of the two-dimensional t - J model by the power-Lanczos method, *J. Phys. Chem. Sol.* **62**, 1797–1811 (2001)
- 22.240 J.D. Cloizeaux, M. Gaudin: Anisotropic linear magnetic chain, *J. Math. Phys. (N.Y.)* **7**, 1384–1400 (1966)

Acknowledgements

B.5 Nanoscopic Architecture and Microstructure

by Koji Maeda, Hiroshi Mizubayashi

The authors would like to thank Drs. M. Hasegawa, A. Hida, K. Hono, M. Ichihara, H. Jinnai, R. Matsuo, A. Momose, S. Morita, T. Nish, K. Oshima, Y. Satow, T. Sekiguchi, I. Shimada and I. Yonenaga for useful discussions or kindly supplying us with unpublished materials and data.

B.6 Surface and Interface Characterization

by Martin Seah, Leonardo De Chiffre

The authors would like to thank Ian Gilmore and Steve Spencer, National Physical Laboratory, for critical reading of the text and preparing some of the Figs, Pietro Lonardo, University of Genova, for valuable contributions during preparation of the section on surface topography, and Jørgen Garnæs, Danish Fundamental Metrology, for valuable contributions during preparation of the text on scanning probe microscopy. Part of this work is supported by the National Measurement System of the UK Department of Trade and Industry through the Valid Analytical Measurements Programme.

C.7 Mechanical Properties

by Sheldon M. Wiederhorn, Richard J. Fields, Samuel Low, Gun-Woong Bahng, Alois Wehrstedt, Junhee Hahn, Yo Tomota, Takashi Miyata, Haiqing Lin, Benny D. Freeman, Shuji Aihara, Yukito Hagihara, Tetsuya Tagawa

Sect. 7.1. The authors are grateful to ASTM International and to ASM International for giving us permission

to republish copyrighted figures from their publications. Figures 7.4 to 7.12 are reprinted with permission of ASTM International, 100 Barr Harbor Drive, West Conshohocken, PA 19428. The ASTM standard designation number and title for each figure are given in the figure caption and in the reference to the figure. Figures 7.13 to 7.15 were reprinted with the permission of ASM International, Materials Park, OH (2000).

Sect. 7.6. We gratefully acknowledge partial support of this work by the Chemical Sciences, Geosciences and Biosciences Division, Office of Basic Energy Sciences, Office of Science, US Department of Energy (grant no. DE-FG03-02ER15362). This research work was also partially supported by the US Department of Energy's National Energy Technology Laboratory under a subcontract from Research Triangle Institute through their prime contract no.: DE-AC26-99FT40675.

E.21 Phase Field Approach

by Toshiyuki Koyama

The author would like to thank Prof. T. Miyazaki, Prof. M. Doi, and Prof. H. Onodera for useful discussions on many occasions. He also thanks Dr. M. Ode for useful comment concerning the thin interface model of the phase-field method. This work was partly supported by the Special Coordination Funds for Promoting Science and Technology on Nanohetero Metallic Materials, the NAREGI Nanoscience Project, Ministry of Education, Culture, Sports, Science and Technology, Japan, and the CREST of the Japan Science and Technology Agency.

About the Authors



Shuji Aihara

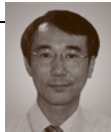
Nippon Steel Corporation
Steel Research Laboratories
Chiba, Japan
s-aihara@re.nsc.co.jp

Chapter C.7, Sect. 7.5

Dr. Shuji Aihara is an expert in the field of welding metallurgy and fracture mechanics. He received awards from the Society of Naval Architects, Japan and the Institute of Steel and Iron, Japan for his achievements in the research of fracture mechanics and metallurgy of high-strength low-alloy welded structural steels.

Tsutomu Araki

Osaka University
Graduate School of Engineering Science
Osaka, Japan
araki@me.es.osaka-u.ac.jp



Chapter C.11, Sect. 11.7

Professor Tsutomu Araki received his Ph.D. degree in applied physics from Osaka University, Japan, in 1977. After being a post doctoral Fellow with the University of Wisconsin, Madison, he joined the faculty of the University of Tokushima, Japan and received the Ph.D. degree in medical sciences from the University of Tokushima in 1986. He is currently a Professor in the Department of Mechanical Sciences and Bioengineering of Osaka University. His research interests include development of a new biomedical and biophysical measurement systems using a fast pulse laser. He is a member of the Society for Applied Spectroscopy, the Optical Society of America, the Japan Society of Mechanical Engineering, and the Japan Society of Applied Physics.

Masaaki Ashida

Osaka University
Graduate School of Engineering Science
Osaka, Japan
ashida@mp.es.osaka-u.ac.jp



Chapter C.11, Sects. 11.1, 11.4

Professor Masaaki Ashida received the PhD degree in physics from Kyoto University, Japan, in 1994. He has worked on laser spectroscopy on solids. In 2003 he joined the department of Materials Engineering Science at Osaka University. His current interests are in ultrafast optical nonlinearity of strongly correlated electron systems and nanoscale materials. He recently developed an ultra broadband THz time-domain spectroscopy. He is a member of the Physical Society of Japan, the Japan Society of Applied Physics and the Optical Society of America.



Peter D. Askew

IMSL, Industrial Microbiological Services
Limited
Hartley Wintney, Hants, UK
peter.askew@imsl-uk.com

Chapter D.14, Sects. 14.1, 14.3, 14.5

Pete has been working since 1977 as an industrial microbiologist and is the Managing Director of IMSL, a specialised microbiological testing and consultancy service. As well as qualifications in microbiology, he is an Associate of the Oil and Colour Chemists Association and is a consultant to the OECD on treated articles and Secretary General of the International Biodeterioration Research Group.



Heinz-Gunter Bach

Heinrich-Hertz-Institut
Components/Integration Technology,
Heinrich-Hertz-Institute
Berlin, Germany
Heinz-Gunter.Bach@hhi.fraunhofer.de

Chapter C.9, Sect. 9.4

Heinz-Gunter Bach received the M.S. degree in electrical engineering from TU Berlin, Germany. From 1978 to 1981 he was with the Hahn-Meitner-Institute Berlin working on the electrical characterization of BCCDs. He received the Ph.D. degree in 1982. In 1981 he joined the Heinrich-Hertz-Institut für Nachrichtentechnik Berlin GmbH heading the electrical characterization group within the photonics division. He was involved in III-V materials characterization, heterostructure analysis, and device optimization. Further he was engaged in project management of topics such as HEMT optimization, optoelectronic packaging and within the last 13 years on ultra-high-speed photodetector development and photoreceiver integration. He gives annual lectures at the Technical University on "optoelectronic semiconductor devices" and "measurement techniques for semiconductor devices". He is member of VDE, Elektrotechnischer Verein (ETV) e.V. / ITG and serves as a technical committee member of the international conference on Optical Fiber Communications.

Gun-Woong Bahng

Korea Research Institute of Standards and Science
Division of Chemical and Materials Metrology
Daejeon, South Korea
gwbahng@kriss.re.kr



Chapter C.7, Sect. 7.3

Gun-Woong Bahng received his B.S. in 1976 from Seoul National University and his Ph.D. in 1982 from Northwestern University, Evanston. He is Chairman of the APEC network for Materials Properties Evaluation (2002–2006). His scientific work concentrates on mechanical behaviour of materials at low temperature, hardness standards, certified reference materials, the traceability and metrology of materials properties, and standard reference data. In 2004 he received the Science and Technology Medal from the Korean Government.

Claude Bathias

Conservatoire National des Arts et Métiers, Laboratoire ITMA
Institute of Technology and Advanced Materials
Paris, France
bathias@cnam.fr



Chapter D.16, Sect. 16.3

Claude Bathias is Professor “Classe Exceptionnelle” at the Conservatoire National des Arts et Métiers, School of Science and Technology for Engineering in Paris, France. He is Director of ITMA and Head of the MS Education (Materials Engineering). Professor Claude Bathias has dedicated his research career to the fracture of materials by fatigue in both of fundamental and technological aspects. Three periods can be distinguished in his activity: In the 1970ies he has worked about the modelling of fatigue crack growth and has displayed the mechanism of cyclic plastic deformation at the fatigue crack tip. In the 1980ies he applied fracture mechanics to the delamination of laminate composite materials and to the fatigue crack propagation in elastomers. Finally, in the 1990ies Professor Bathias and co-workers gave the experimental confirmation, for the first time, that all of the metals can fail in fatigue beyond the quadrillion of cycles range which is evidence of that the concept of infinite fatigue life does not exist.

Günther Bayreuther

University of Regensburg
Physics Department
Regensburg, Germany
guenther.bayreuther@physik.uni-regensburg.de



Chapter C.10, Sect. 10.4

Günther Bayreuther is Professor of Physics at the University of Regensburg and at the Max Planck Institute of Microstructure Physics in Halle/Germany. He has a long experience in magnetic films and surfaces. Current areas of research are ferromagnetic order and phase transitions in epitaxial nanostructures, spin-dependent transport phenomena in epitaxial metal-semiconductor layered structures, spin injection into semiconductors and ultrafast magnetization dynamics.

Bernd Bertsche

University of Stuttgart
Institute of Machine Components
Stuttgart, Germany
bernd.bertsche@ima.uni-stuttgart.de



Chapter D.16, Sect. 16.7

Bernd Bertsche studied Mechanical Engineering at the University of Stuttgart, Germany and received his academic degree Dipl.-Ing. in 1984. From 1984–1989, he was a Research Assistant in Reliability Engineering at the Institute of Machine Components and was conferred the academic degree Dr.-Ing. from the University of Stuttgart in 1989. From 1989–1992, he was a development engineer at Daimler-Benz AG in Stuttgart. His main projects were: development of automotive transmissions and four-wheel drive cars. From 1993–1996 he was a Professor in Mechanical Engineering at the University of Applied Science in Albstadt, Germany. Since 1996, he is a Professor of Mechanical Engineering at the Institute of Machine Components, University of Stuttgart, and Head of the Reliability Engineering Department. Since 2000, he also is Chief Executive Officer of the Technology Transfer Initiative GmbH of the University of Stuttgart. Since 2001, he is Head of the Institute of Machine Components.

Brian Brookman

LGC Standards Proficiency Testing
Bury, Lancashire, UK
brian.brookman@lgstandards.com



Chapter A.3, Sect. 3.6

Brian Brookman has over thirty years experience in analytical science, the past twenty years in the field of analytical quality, particularly concerned with reference materials and proficiency testing. Brian has been involved in various training and consultative projects concerned with developing proficiency testing in other countries and the accreditation of PT providers. He has been invited to lecture on proficiency testing at various events around the world. He is very active at the national, European and international level with respect to the development and harmonisation of good practice in proficiency testing. He is currently the Chair of the EURACHEM Proficiency Testing Working Group, Chair of the EA-EUROLAB-EURACHEM Joint Working Group on Proficiency Testing in Accreditation, Chair of the UK Working Group on Proficiency Testing and a member of the ILAC (International Laboratory Accreditation Cooperation) Proficiency Testing Consultative Group. He was a member of the ISO/CASCO Working Group which is developed the new ISO/IEC 17043 standard "Conformity assessment – General requirements for proficiency testing"

Wolfgang Buck

Physikalisch-Technische Bundesanstalt
Berlin, Germany
wolfgang.buck@ptb.de



Chapter C.8

Wolfgang Buck has 30 years of experience in metrological work gained at the Physikalisch Technische Bundesanstalt (PTB). Most of these years he worked in field of low-temperature physics and thermometry and in the development of the Provisional Low-Temperature Scale 2000. He made contributions to the planning and construction of highly magnetically shielded rooms and an low-energy electron storage ring for synchrotron radiation. In 2002 he became the Head of the Division "Temperature und and Synchrotron Radiation" and head of the Berlin Institute of PTB. After retirement he is now the Chairman of the Physical Society of Berlin.

Richard R. Cavanagh

National Institute of Standards and
Technology (NIST)
Surface and Microanalysis Science
Division, Chemical Science and
Technology Laboratory (CSTL)
Gaithersburg, MD, USA
richard.cavanagh@nist.gov

Chapter B.4

Richard R. Cavanagh earned his Ph.D. from Harvard University. He came to NIST in 1979 to pursue postdoctoral studies in the area of Surface Science. Since that time, he has published over 100 papers in the area of molecular processes at surfaces, incorporating measurement methods ranging from inelastic neutron scattering, picosecond and femtosecond lasers spectroscopy, and near-field optics. Dr. Cavanagh is the Chief of the Surface and Microanalysis Science Division, overseeing programs in microanalysis research, surface and interface research, and analytical microscopy. His Division provides the measurement science that underpins micro- and nanoscale chemical characterization of natural and man-made structures. Expertise in the Division spans electron microscopy, x-ray diffraction and fluorescence, SIMS, Raman, IR, NLO, scanned probes, optical microscopy, and AES.

Leonardo De Chiffre

Technical University of Denmark
Department of Mechanical Engineering
Kgs. Lyngby, Denmark
ldch@mek.dtu.dk

Chapter B.6

Leonardo De Chiffre is an internationally recognized expert in manufacturing and metrology. He has created and directed since its formation the Centre for Geometrical Metrology at the Technical University of Denmark which is part of the Danish Primary Laboratory for Length. Professor De Chiffre is active member of CIRP, panel member of the Foundation Committee of Euspen, and Associate Editor of Precision Engineering.

Steven J. Choquette

National Institute of Standards and Technology
Biochemical Science Division
Gaithersburg, MD, USA
steven.choquette@nist.gov



Chapter B.4, Sect. 4.1

Steven Choquette is a Research Chemist at the National Institute of Standards and Technology, Gaithersburg, Maryland. He has been employed in the Analytical Chemistry Division since 1987. His current research interests are in the development of performance validation standards for Near Infrared and Raman spectroscopy. He is a member of several ASTM committees and currently serves as the vice-chair of ASTM E 13.08 committee on Raman Spectroscopy. He obtained a Ph.D. in analytical chemistry in 1987 at the Virginia Polytechnical Institute and State University, Blacksburg, VA. His B.S. degree in Chemistry and Electrical Engineering was obtained from Santa Clara University, in Santa Clara, CA in 1980.

Horst Czichos

University of Applied Sciences Berlin
Berlin, Germany
horst.czichos@t-online.de



Chapters A.1, A.3, Sects. 3.4, 3.10

Horst Czichos has been President of BAM, the German Federal Institute for Materials Research and Testing (1992–2002) and President of EUROLAB, the European Federation of National Associations of Measurement, Testing and Analytical Laboratories (1999–2003). He holds degrees in precision engineering, physics and materials science from the Free University and the Technical University of Berlin, and obtained a Dr. h.c. from KU Leuven University for his research work in tribology. He is currently Professor of Mechatronics at the University of Applied Sciences, BHT Berlin, and received 2007 the Beuth Award for achievement in engineering education.

Werner Daum

Federal Institute for Materials Research and Testing (BAM)
Division VIII.1 Measurement and Testing
Technology; Sensors
Berlin, Germany
werner.daum@bam.de

Chapter D.16, Sect. 16.6

Dr. Werner Daum studied electrical engineering with a major in measuring techniques at the Technical University of Berlin. Upon graduation in 1984 he entered Federal Institute for Materials Research and Testing (BAM). Until 1989 his main activity was R&D in the field of non-destructive testing with special focus on digital image processing and radiography. In 1989 he became head of the laboratory for optical measuring methods and experimental stress analysis and commenced with the development of optical NDT methods. In 1994 he received his PhD. from the Technical University of Berlin. In 1996 he became a Director and Professor at BAM and head of the division Measurement and Testing Technology; Sensors. The emphasis of his work is the development of sensor technology to be embedded into materials and structures, of fiber-optic sensors, and of sensor technology for smart structures and materials. Since 1999 he is chairman of the German Society of Experimental Structure Analysis (GESA).

Paul DeRose

National Institute of Standards and Technology
Biochemical Science Division
Gaithersburg, MD, USA
paul.derose@nist.gov

Chapter B.4, Sect. 4.1

Paul DeRose is a physical/analytical chemist who came to NIST as a National Research Council Postdoctoral Fellow in 1996. Before coming to NIST, he earned his Ph.D. in chemistry from the University of Pennsylvania where he studied laser spectroscopy and excited-state dynamics. His current research interests concern the development of fluorescence standards and methods for validation of chemical and clinical assays.

Stephen L.R. Ellison

LGC Ltd.
Bioinformatics and Statistics
Middlesex, UK
s.ellison@lgc.co.uk



Chapter A.3, Sect. 3.3

Dr. Ellison is head of the Bioinformatics and Statistics section at LGC. Originally qualified as a chemist, his research and application interests include statistics, chemometrics and computing applied to chemical and biological measurement. He is a recognised international expert in measurement uncertainty and traceability for analytical methods, and has contributed to a range of national and international committees and guidance documents in that field.

Anton Erhard

Federal Institute for Materials Research and Testing (BAM)
Department Containment Systems for Dangerous Goods
Berlin, Germany
anton.erhard@bam.de



Chapter D.16, Sect. 16.1

Prof. Dr.-Ing. Anton Erhard studied metal physics at the Technical University Berlin. Since 1976 he is employed at the Bundesanstalt für Materialforschung und -prüfung (BAM) Berlin. His scientific work was honored with two awards; 1984 from the German Society of Non-Destructive Testing (DGZfP) and 1985 from the American Society for Nondestructive Testing (ASNT). His scientific results are presented in more than 200 publications.

Uwe Ewert

Federal Institute for Materials Research and Testing (BAM)
Division VIII.3 Radiology
Berlin, Germany
uwe.ewert@bam.de

Chapter D.16, Sect. 16.2

Dr. Uwe Ewert is Director and Professor of the division Radiology in the Department Non-destructive Testing of BAM, the Federal Institute for Materials Research and Testing. He received his Ph.D. from the Humboldt-University in Berlin on calculations of electron spin resonance (ESR) spectra of metal complex compounds. He developed tomography systems at the centre of scientific instruments in Berlin-Adlershof up to 1990 and developed pulsed ESR tomography methods at the Cornell University in New York State. Since 1992 he is engaged at BAM in material characterisation, new intelligent testing methods of industrial components and their standardization. He is chairman of the radiology committee of the German Society of NDT since 1997.

Richard J. Fields

National Institute of Standards and Technology
Materials Science and Engineering Laboratory
Gaithersburg, MD, USA
richard.fields@nist.gov

Chapter C.7, Sect. 7.2

Richard J. Fields is a Ph.D. metallurgist and has worked at the National Institute of Standards and Technology and the National Bureau of Standards for the past 27 years, supervising groups of scientists doing research in metal forming, nanolaminates, and powder metallurgy. His group also certifies the U.S. national standards for Rockwell B and C hardness scales.

David Flaschenträger

Fraunhofer Institute for Structural Durability and System Reliability (LBF)
Darmstadt, Germany
David.flaschentraeger@lbf.fraunhofer.de



Chapter D.16, Sect. 16.7

David Flaschenträger studied Mechanical Engineering in Darmstadt, Germany and obtained his Master of Science degree in 2008. Since then David Flaschenträger is with the Fraunhofer Institute for Structural Durability and System Reliability (LBF) performing research on the reliability assessment of complex adaptive and mechatronic systems.

Benny D. Freeman

The University of Texas at Austin, Center for Energy and Environmental Resources
Department of Chemical Engineering
Austin, TX, USA
freeman@che.utexas.edu



Chapter C.7, Sect. 7.6

Dr. Freeman's research is mass transport of small molecules in polymers. He directs 15 PhD students and 3 postdoctoral fellows performing fundamental research in gas and liquid separations using polymer membranes and barrier packaging. Current topics include vapor separation materials, new materials for hydrogen separation, natural gas purification, and water desalination as well as reactive barrier packaging, and new materials for improving fouling resistance in liquid separations.

**Holger Frenz**

University of Applied Sciences
Gelsenkirchen
Business Engineering
Recklinghausen, Germany
frenz@fh-gelsenkirchen.de

Chapter A.3, Sect. 3.7

After his graduation in Materials Science and Engineering at the Technical University in Braunschweig, he received his Ph.D. degree in Material Science from the Technical University Berlin. Between 1987 and 1997 he was head of a laboratory for mechanical testing at the Federal Institut for Materials Research and Testing (BAM). His main focus is on quality management systems in testing laboratories, the production of metallic reference materials, and the organization of proficiency tests. He is managing director of the Institut for Proficiency Testing, Marl, Member of the Board of EUROLAB-Germany, and currently Chair of the Technical Committee for Materials Testing of the German Accreditation Body DAkkS. Since 1997 Holger Frenz is Professor for Materials Testing at University of Applied Sciences, FH Gelsenkirchen.

**Jochen Gäng**

JHP – consulting association for product
reliability
Stuttgart, Germany
gaeng@jhp-beratung.de

Chapter D.16, Sect. 16.7

Jochen Gäng studied Mechanical Engineering in Stuttgart, Germany and obtained his Diploma degree in 2006. Afterwards Mr. Gäng was a scientific researcher in the field of reliability of mechatronics in early phases of development at the Institute of Machine Components, University of Stuttgart. Since 2010 Mr. Gäng works at JHP, a consulting association for product reliability.

Anja Geburtig

BAM Federal Institute for Materials
Research and Testing
Division III.1, Dangerous Goods Packaging
Berlin, Germany
anja.geburtig@bam.de



Chapter D.15, Sect. 15.1.2

Dr. Anja Geburtig studied physics at the Humboldt University in Berlin and received her PhD in 2002 at the Technical University of Berlin investigating plastic deformation of alloys with means of optical surface techniques. Since 2002 she has been working on weathering of polymers at the Federal Institute for Materials Research and Testing.

Mark Gee

National Physical Laboratory
Division of Engineering and Processing
Control
Teddington, TW11 0LW, UK
mark.gee@npl.co.uk



Chapter D.13

Mark Gee is an NPL Fellow in the Materials Division at the National Physical Laboratory. He manages projects which are concerned with the development of an improved infrastructure for friction and wear testing in the UK. Particular research interests are the mechanisms of abrasive wear for ceramics and other hard materials. He has published over 200 papers and reports. He has recently been Chairman of the Institute of Physics Tribology Group, and is now Secretary of the Surface Engineering Division Board and the Coatings and Surface Treatments Committees of the Institute of Materials, Mining and Minerals. He is also a member of the International Advisory Editorial Board of Tribology International. He is a member of ASTM Committee G2 on Wear, and represents the UK on standards committees CEN 352 Nanotechnologies, ISO TC 206 Fine Ceramics, and ISO TC 229 Nanotechnologies.

**Jürgen Goebbels**

Federal Institute for Materials Research
and Testing (BAM)
Radiology (VIII.3)
Berlin, Germany
juergen.goebbels@bam.de

Chapter D.16, Sect. 16.4

Dr. Jürgen Goebbels received his Ph.D. from the Technical University Karlsruhe in 1976 on Surface resistance of amorphous superconducting films. He has worked for six years in the field of low-temperature solid-state physics and nuclear magnetic resonance (NMR) at the Karlsruhe Nuclear Research Centre and at the Free University Berlin. Since 1982 he is at the Federal Institute for Materials Research and Testing (BAM) and is at present head of the working group 'Computed tomography'. Since the foundation 1987 he is chairman of the subcommittee 'Computed Tomography' of the German Society of Non-destructive Testing (DGZfP).


Manfred Golze

Chapter A.3, Sect. 3.4

BAM Federal Institute for Materials Research and Testing
S.1 Quality in Testing
Berlin, Germany
manfred.golze@bam.de

Manfred Golze has a diploma and a PhD in chemistry from the Free University Berlin. He did research at the Fritz-Haber-Institute of the Max-Planck-Society and the FU Berlin in the field of surface analysis. Since 1987 he is with the BAM Federal Institute for Materials Research and Testing, since 1992 head of the section Quality in Testing. Current interest is focussed on conformity assessment and technical issues of quality assurance in testing.

Anna A. Gorbushina

Chapter D.14, Sect. 14.4

Federal Institute for Materials Research and Testing (BAM)
Department Materials and Environment
Berlin, Germany
anna.gorbushina@bam.de



Anna Gorbushina studied Biology, Material Sciences and Physics at St. Petersburg University. She received her Ph.D. from Komarov Institute, Russian Academy of Sciences. Professor Gorbushina is teaching materials science and microbiology at the Applied University Cologne and mycology and landscape ecology (architectural ecology) at Oldenburg University. She is working on biodeterioration by and molecular ecology of micromycetes (lower fungi). She is a member of International Board of Environmental Biogeochemistry. Since April 2009 she is professor at the Free University of Berlin and Head of Department 4 Materials and Environment of BAM Federal Institute for Materials Research and Testing.

Robert R. Greenberg

Chapter B.4, Sect. 4.1

National Institute of Standards and Technology
Analytical Chemistry Division
Gaithersburg, MD, USA
robert.greenberg@nist.gov



Dr. Greenberg has been a Research Chemist at NBS/NIST since 1976, and the Group/Team Leader of the Nuclear Methods Group/Team since 1989. His research has focused on the development and application of high-accuracy nuclear and radioanalytical chemistry methods for elemental analysis, the development of complete uncertainty budgets for the nuclear analytical chemistry methods, and the establishment of quality assurance procedures.

Manfred Grinda

Chapter D.14, Sect. 14.2



Berlin, Germany
manfred.grinda@t-online.de

Diplom Holzwirt Manfred Grinda studied wood science and technology at the University of Hamburg. He was the head of the project group "Reliability and Resistance of Materials to Biodeterioration at the Federal Institute for Materials Research and Testing (BAM)". Until his retirement he was a member of several working groups of CEN/TC 38 "Durability of Wood and Derived Materials". His main interests are the methodology of meaningful materials testing against wood destroying fungi.


Roland Grössinger

Chapter C.10, Sect. 10.3

Technical University Vienna
Institut für Festkörperphysik
Vienna, Austria
rgross@ifp.tuwien.ac.at

Roland Grössinger studied Technical Physics at the Technical University in Vienna where he received the title Diplom Ingenieur. During his employment at the Institute of Experimental Physics at the Technical University Vienna he received the Doctor for Technical Sciences in 1975. In 1983 he graduated as "Dozent" for Experimental Metal Physics, and was awarded the Planseepreis for the industrial development of a magnet key in 1985. In 1993 he was awarded the title Universitäts Professor. He has more than 400 publications in international journals and gave more than 500 talks and presentations at international conferences. His research interests are physical properties of magnetic materials and physics and technology of high magnetic fields and their measurement methods.

Yukito Hagihara

Sophia University
Faculty of Science and Technology,
Department of Engineering and Applied
Science
Tokyo, Japan
hagihara@me.sophia.ac.jp



Chapter C.7, Sect. 7.5

Professor Yukito Hagihara's main area of research is the fracture of steel and the integrity of welded structures based on fracture mechanics. He received his Dr. Eng. from the University of Tokyo in 1973. He worked at the Nippon Steel Corporation for 28 years (1973–2001) and at the National Institute for Materials Science for 3 years (2001–2004), where he was engaged in the ultra-steel project.

Junhee Hahn

Korea Research Institute of Standards
and Science (KRIS)
Division of Industrial Metrology
Daejeon, South Korea
juny@kriss.re.kr



Chapter C.7, Sect. 7.3

Junhee Hahn's research fields are the synthesis of nanostructured thin films, the assessment of mechanical reliability of nanostructured materials and standardizing test methods. His current research activities comprise the development of atomic force acoustic microscopy (AFAM) technique to determine local elastic properties of multiple materials integrated on the sub micrometer scale. He participates in standardizing the instrumental indentation test method and prepared the first draft of nanoindentation standard.

Holger Hanselka

Fraunhofer-Institute for Structural
Durability and System Reliability (LBF)
Darmstadt, Germany
holger.hanselka@lbf.fraunhofer.de

Chapter D.16, Sect. 16.7

Holger Hanselka studied general machine engineering at the Technical University of Clausthal and worked as Scientific Assistant at the German Centre 01' Aviation and Spare Travel in Braunschweig. In 1992 he graduated with a PhD from TU Clausthal. In 1997, he was called to lecture at the Otto-von-Guericke University of Magdeburg; Hanselka held the Chair of Adaptronics and was head of the work group Experimental Mechanics. Since 2001 he is Head of the Fraunhofer-Institute of Structural Durability and System Reliability (LBF) in Darmstadt and holds the Chair for System reliability and Machine Acoustics at the University of Technology in Darmstadt, of which he is Vice-President. He is Head of the Fraunhofer-Alliance "Materials" and member of the board of the Fraunhofer-Gesellschaft. Professor Hanselka coordinates several large-scale projects such as the Collaborative Research Center SFB 805, the LOEWE-Center AdRIA as well as System Research on Electromobility.

Werner Hässelbarth

Berlin, Germany
werner.haesselbarth@t-online.de

Chapter A.3, Sect. 3.8

Werner Hässelbarth is a chemist with strong influences from theoretical physics and mathematics. His university research career (15 years) was focussed on theoretical and physical chemistry. Later he worked at Federal Institute for Materials Research and Testing (BAM) in different areas including chemical safety, gas analysis and quality management. Having retired in 2007, he is still active in dedicated scientific fields, especially in measurement uncertainty.

Martina Hedrich

BAM Federal Institute for Materials
Research and Testing
S.1 Quality in Testing
Berlin, Germany
martina.hedrich@bam.de

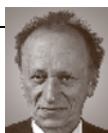


Chapter A.3, Sect. 3.7

Martina Hedrich has majored in chemistry and received her PhD degree from Berlin Free University (FUB). Her areas of competence include analytical chemistry, quality management, metrology in chemistry and reference materials (RM). Joining BAM in 1989 she has been the head of working groups characterizing RM with nuclear techniques, gas analysis and metrology. Currently, she is BAM Quality Manager, lecturer at FUB, involved in education and training programmes (TrainMiC, EURACHEM) and convener of BAM's Certification Committee for RM.

Manfred P. Hentschel

Federal Institute for Materials Research and Testing (BAM)
VIII.3, Nondestructive Testing
Berlin, Germany
manfred.hentschel@bam.de



Chapter D.16, Sect. 16.5

Dr. Manfred P. Hentschel is manager of working group “X-Ray Scattering Topography” at Federal Institute for Materials Research and Testing (BAM) and Professor at the Technical University Berlin. He received his Ph.D. in physics from the Free University of Berlin. For developing new imaging and computed tomography techniques of x-ray scattering he was awarded the Roentgen Plaque in 2000. He is co-editor of RNDE and “Materialprüfung/Materials Testing”.

Horst Hertel

Federal Institute for Materials Research and Testing (BAM)
Division IV.1
Berlin, Germany
horst.hertel@bam.de

Chapter D.14, Sect. 14.2

Horst Hertel is biologist with a Ph.D. in Natural Sciences. He is lecturer at the Institute of Neurobiology, Free University of Berlin and , Head of Division Biology in Materials Protection and Environmental Issues” at the Federal Institute for Materials Research and Testing (BAM). His main interests are in materials protection against wood destroying insects on a biological basis.

Daniel Hofmann

University of Stuttgart
Institute of Machine Components
Stuttgart, Germany
daniel.hofmann@ima.uni-stuttgart.de

Chapter D.16, Sect. 16.7

Daniel Hofmann studied Mechanical Engineering at the University of Stuttgart in Germany and obtained his academic degree Dipl.-Ing. in 2007. Since 2007, he is a Research Assistant in Reliability Engineering at the Institute of Machine Components. From October 2010 until February 2011 he was a Visiting Researcher at the University of Ottawa, Canada.

Xiao Hu

National Institute for Materials Science
World Premier International Center for
Materials Nanoarchitectonics
Tsukuba, Japan
hu.xiao@nims.go.jp



Chapter E.22

Xiao Hu got his PhD degree from the University of Tokyo (1990). He was a Research Associate and Associate Professor at the Institute for Material Research, Tohoku University (1991–1995); Senior Scientist, Group Director at the National Institute for Materials Science (NIMS) (1995–2007). Now he is a PI at the WPI Center for Materials Nanoarchitectonics (MANA-NIMS), and since 2007 a Professor at the University of Tsukuba. His major interest is in theory of condensed matter and computer simulation in materials science. His current research interests cover the vortex states in type-II superconductors, terahertz electromagnetic radiation based on Josephson effects, and theoretical design of novel spintronics materials.

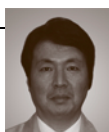
Ian Hutchings

University of Cambridge, Institute for
Manufacturing
Department of Engineering
Cambridge, UK
imh2@cam.ac.uk



Chapter D.13

Currently Professor of Manufacturing Engineering at the University of Cambridge, Ian Hutchings is also Editor-in-Chief of the journal *Wear*, and has research interests in the tribological behavior of materials, surface engineering, and manufacturing processes for all classes of materials. He is a Fellow of the Royal Academy of Engineering and holds the Tribology Trust Silver Medal (1994), the NPL Award for Materials Metrology (2000) and the Staudinger-Durrer Prize from ETH Zürich (2007).

Shoji Imatani

Kyoto University
Department of Energy Conversion Science
Kyoto, Japan
imatani@energy.kyoto-u.ac.jp

Chapter E.18

Shoji Imatani started his research on inelastic constitutive modeling and finite element simulation in the middle of 1980's. His current interest is in the field of nonlinear continuum mechanics, particularly in material inhomogeneity and macro-/micro-combined analysis of inelastic materials.


Hanspeter Ischi

The Swiss Accreditation Service (SAS)
Berne, Switzerland
hanspeter.ischi@sas.ch

Chapter A.3, Sects. 3.2, 3.9, 3.11

After his graduation as an analytical chemist Hanspeter Ischi worked in the chemical industry in the field of quality control. In this function he gained first experience in establishing industrial quality management systems and quality assurance in analytical chemistry already in 1980. Afterwards he continuously improved his knowledge in modern management systems including development of staff in the area of communication, leadership, organization and conflict management, as well as in quality assurance in testing. He is the head of the Swiss Accreditation Service since 1991 and presently a member of the Executive Committee of the European Cooperation for Accreditation (EA). For several years he was also member of the Executive committee of the International Laboratory Accreditation Cooperation (ILAC) and he is one of the past chairmen of the laboratory committee of EA.

Bernd Isecke

Federal Institute for Materials Research
and Testing (BAM)
Department Materials Protection and
Surface Technologies
Berlin, Germany
bernd.isecke@bam.de



Chapter D.12

Bernd Isecke has a Diploma in Materials Science (1974) and a PhD (1977) from the Technical University in Berlin. Since 1978 he is with the Federal Institute for Materials Research and Testing (BAM), where he became head of the Division "Corrosion and Corrosion Protection" in 1989 and in 2009 head of the department "Materials Protection and Surface technologies". His main areas of research include corrosion in steel reinforced concrete, corrosion monitoring and testing, stainless steels and hydrogen embrittlement of high strength materials. Dr. Isecke is Chairman of the Gesellschaft für Korrosionsschutz GfKorr, Past President of the European Federation of Corrosion EFC, German Delegate to the International Corrosion Council ICC, Chairman and member of various Standardisation committees in ISO, CEN and DIN and editor of the journal Materials and Corrosion.

Tadashi Itoh

Osaka University
Institute for NanoScience Design
Osaka, Japan
itoh@insd.osaka-u.ac.jp



Chapter C.11, Sects. 11.2, 11.3

Tadashi Itoh is the vice-director, Institute for NanoScience Design, Osaka University since 2010. He was graduated from the Graduate School of Engineering Science, Osaka University with PhD in 1974. He continued to work at Tohoku University until 1998 and, afterward, at Osaka University until 2010. His research fields include photophysics of bulk and nanostructured materials, nonlinear and time-resolved laser spectroscopy, optical microspectroscopy, and the fabrication of nanostructured opto-materials. He is members of the Physical Society of Japan, the Japan Society of Applied Physics, the Society of Nanoscience and Nanotechnology, the Materials Research Society, and the Institute of Physics.


Tetsuo Iwata

The University of Tokushima
Department of Mechanical Engineering
Tokushima, Japan
iwata@me.tokushima-u.ac.jp

Chapter C.11, Sect. 11.1

Tetsuo Iwata received his Ph.D. degree in applied physics from Osaka University, Osaka, Japan, in 1984. He is currently a Professor with the Department of Mechanical Engineering, the University of Tokushima and with the Division of Energy System, Institute of Technology and Science, Graduate school of Tokushima University. His research interests are the development of optical and spectroscopic instruments based on new ideas.


Gerd-Rüdiger Jaenisch

Chapter D.16, Sect. 16.2

Federal Institute for Materials Research and Testing (BAM)
Non-destructive Testing
Berlin, Germany
gerd-ruediger.jaenisch@bam.de

Dr. habil. Jaenisch, a physicist by education, received his Ph.D. in 1992 in theoretical nuclear physics and his habilitation in 2001 in materials science from Dresden University of Technology, Germany. Since 1992 he has been working in the field of non-destructive testing at the Federal Institute for Materials Research and Testing (BAM) in Berlin, Germany. His area of expertise extends to modelling and reconstruction in quantitative non-destructive evaluation with special focus on radiation techniques. Many activities were performed in cooperation with industrial partners. Since 2002 he has been appointed as university lecturer at Dresden University of Technology.

Oliver Jann


Chapter D.15, Sect. 15.2

Federal Institute for Materials Research and Testing (BAM)
Environmental Material and Product Properties
Berlin, Germany
oliver.jann@bam.de

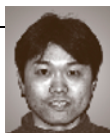
Dr. Oliver Jann studied environmental engineering at the Technical University Berlin (1981-1987). Since 1987 he was scientist at the Federal Institute for Materials Research and Testing (BAM). During this time he received his Dr.-Ing. in 1993 and was project leader since 1996, and became Head of the BAM-laboratory Emissions from Materials in 1997. Since 2009 he is Head of the BAM-devison IV.2 Environmental Material and Product Properties. His scientific activities include research on emissions coming from materials and products and development of related test methods.

Enrico Janssen


Chapter D.16, Sect. 16.7

Fraunhofer Institute for Structural Durability and System Reliability (LBF)
Darmstadt, Germany
enrico.janssen@lbf.fraunhofer.de

Enrico Janssen studied Mechanical Engineering in Darmstadt, Germany and obtained his Diploma degree in 2005. Since 2006 Enrico Janssen is with the Fraunhofer Institute for Structural Durability and System Reliability (LBF) performing research on the reliability assessment of complex adaptronic and mechatronic systems.


Masanori Kohno

Chapter E.22

National Institute for Materials Science
Computational Materials Science Center
Tsukuba, Japan
kohno.masanori@nims.go.jp

Dr. Masanori Kohno received his Ph.D. degree in Physics from the university of Tokyo in 1998. Prior to joining National Institute for Materials Science, he worked at Mitsubishi Research Institute as a staff researcher. He mainly studied effects of strong correlations in condensed matter by using numerical techniques such as quantum Monte Carlo methods and the density-matrix renormalization method.


Toshiyuki Koyama

Chapter E.21

Nagoya Institute of Technology
Department of Materials Science and Engineering
Nagoya, Japan
koyama.toshiyuki@nitech.ac.jp

T. Koyama received the DE degree in materials science and engineering from Nagoya Institute of Technology (NIT) in 1996 during Research Associate at the NIT (1990–2001). After the Senior Researcher, Group Leader at the National Institute for Materials Science (NIMS) (2002–2009), he is Associate Professor at the NIT since 2010. His current research focuses on the total free energy based analysis for the complex microstructure formation and the computer simulation of phase transformations based on the phase-field method.

Gary W. Kramer


Chapter B.4, Sect. 4.1

National Institute of Standards and Technology
Biospectroscopy Group, Biochemical Science Division
Gaithersburg, MD, USA
gary.kramer@nist.gov

Gary W. Kramer is the leader of the Biospectroscopy Group (BSG) at NIST. The BSG Group is responsible for developing, producing, and certifying instrument performance standards for molecular spectroscopy. Dr. Kramer, probably best known for his laboratory automation activities, received a Pioneer in Laboratory Robotics Award in 1985, the Association for Laboratory Automation (ALA) Achievement Award in 1998, and the ALA Charter Member Award in 2004.

Wolfgang E. Krumbein

Biogema
Material Ecology
Berlin-Lichterfelde, Germany
wek@biogema.de



Chapter D.14, Sect. 14.4

Wolfgang E. Krumbein, Professor of Geomicrobiology at Oldenburg, Germany, acted 10 years as Obmann in VDI Commissions, founded EUREKA-EUROCARE, served twice as President of the Committee of Leading Marine Scientists and was founding director of the Institute for Chemistry and Biology of the Marine Environment, ICBM. Krumbein received the Credner-Price, the Lise Meitner-Alexander von Humboldt Price, and the Pasteur Medal, and several honorary Dr. degrees. He presently works as Chairman of Biogema, a consulting company on materials science and biodegradation in the fields of restoration of objects of art and intelligent building materials.

**George Lamaze**

National Institute of Standards and Technology
Analytical Chemistry Division
Gaithersburg, MD, USA
george.lamaze@nist.gov

Chapter B.4, Sect. 4.1

Dr. George Lamaze received his Ph.D. in nuclear physics in 1972 from Duke University. At NIST (formerly NBS) he measured standard neutron cross sections in the Center for Radiation Research using both LINAC and reactor sources. In the Analytical Chemistry Division his main activity was the measurement of depth profiles with cold neutrons. Dr. Lamaze retired in 2004.

**Haiqing Lin**

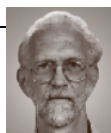
Membrane Technology and Research, Inc.
Menlo Park, CA, USA
Haiqing.lin@mtrinc.com

Chapter C.7, Sect. 7.6

Dr. Lin graduated from the University of Texas at Austin in 2005 and is currently a senior research engineer at Membrane Technology and Research, Inc, Menlo Park, CA. He is working on new membrane materials and processes for gas separations in refinery and natural gas applications.

Richard Lindstrom

National Institute of Standards and Technology
Analytical Chemistry Division
Gaithersburg, MD, USA
richard.lindstrom@nist.gov



Chapter B.4, Sect. 4.1

Richard Lindstrom obtained his BS from the University of Wisconsin in 1963 and his PhD from the University of California, San Diego in 1970. He did postdoctoral work with D. Lal at the Tata Institute of Fundamental Research in Mumbai, India and Raymond Davis, Jr. at Brookhaven National Laboratory. He is at NIST since 1972. His research areas are high-sensitivity and high-accuracy radionuclide measurement, conventional and prompt gamma neutron activation analysis, gamma-ray spectrometry, analytical chemistry, radiochemistry, and computer applications and nuclear data.

Samuel Low

National Institute of Standards and Technology
Metallurgy Division, Materials Science
and Engineering Laboratory
Gaithersburg, MD, USA
samuel.low@nist.gov



Chapter C.7, Sect. 7.3

Samuel Low is Materials Research Engineer at NIST for 27 years in the fields of properties and testing of materials. He began managing the NIST hardness standardization program in 1995. Currently, he is Chairman of the ASTM-International Committee on Indentation Hardness Testing, Head of the USA delegation to ISO TC164/SC3 on hardness testing, and Secretary of the CIPM Working Group on hardness.

**Koji Maeda**

The University of Tokyo
Department of Applied Physics
Tokyo, Japan
maeda@exp.t.u-tokyo.ac.jp

Chapter B.5

Professor Koji Maeda research focuses on defects in solids, especially extended ones and point defects in semiconductors. His recent activities are directed to atomic and molecular manipulation by electronic excitations and the development of various schemes of nanospectroscopical measurements using STM. His hobby is mountaineering.

**Ralf Matschat**

Berlin, Germany
ralf.matschat43@web.de

Chapter B.4, Sects. 4.3, 4.5

Ralf Matschat studied physics at the Humboldt University Berlin, Germany, and received the PhD degree in 1971. He headed different laboratories of analytical atomic spectrometry and was in his last position Head of Division of Inorganic Chemical Analysis, CRMs at BAM, the Federal Institute for Materials Research and Testing, Berlin. He was convener of metrological IAWG of METCHEM and one of the initiators of the European ERM program. He published more than 70 scientific papers and presented more than 200 oral or poster conference contributions.

Willie E. May

National Institute of Standards and Technology (NIST)
 Chemical Science and Technology Laboratory (CSTL)
 Gaithersburg, MD, USA
willie.may@nist.gov



Chapter B.4

Willie E. May obtained his B.S. from Knoxville College in 1968 and his Ph.D. from the University of Maryland in 1977. Dr. May is currently Director of the Chemical Science and Technology Laboratory (CSTL). CSTL is one of the seven technical Operational Units within the National Institute of Standards and Technology and has ≈ 325 technical staff members. CSTL is entrusted with the responsibility of developing, maintaining, advancing, and enabling the chemical measurement system for the United States of America. CSTL is organized into five Divisions along disciplinary lines: Biotechnology, Process Measurements, Surface and Microanalysis Science, Physical and Chemical Properties and Analytical Chemistry. He has a long list of awards among which are the Arthur Flemming Award for Outstanding Federal Service, 1986; NOBCCHE Percy Julian Award for Outstanding Research in Organic Analytical Chemistry and Presidential Rank Award of Meritorious Federal Executive, 1992; the Department of Commerce Gold Medal, 1992; the American Chemical Society Distinguished Service in the Advancement of Analytical Chemistry Award, 2001; the NOBCCHE Henry Hill Award for exemplary work and leadership in the field of chemistry, and the Science Spectrum Magazine Emerald Award, 2005.

Takashi Miyata

Nagoya University
 Department of Materials Science and Engineering
 Nagoya, Japan
miyata@numse.nagoya-u.ac.jp



Chapter C.7, Sect. 7.5

In 1972 Takashi Miyata earned his Dr.Eng. from Tokyo University. From 1972-1974 he was Lecturer in the Department of Materials Sciences and Engineering and from 1974-1990 Associate Professor at Nagoya University. He spent 1974-1976 as Guest Researcher at the Materialprüfungsanstalt (MPA), University of Stuttgart, Germany. From 1990 to present he is Professor in Department of Materials Science and Engineering, Nagoya University, Japan.

Hiroshi Mizubayashi

University of Tsukuba
 Institute of Materials Science
 Tsukuba, Japan
mizuh@ims.tsukuba.ac.jp



Chapter B.5

Hiroshi Mizubayashi is a scientist in metal physics and Professor Emeritus at University of Tsukuba, Japan. He has found new phenomena in amorphous alloys associated with a collective motion of many atoms and characteristic mechanical properties of nanostructured metals.

Bernd R. Müller

BAM Federal Institute for Materials Research and Testing
 Berlin, Germany
bernd.mueller@bam.de



Chapter D.16, Sect. 16.5

Bernd R. Müller studied physics at the Technical University of Berlin, Germany, where he earned his doctorate in physics of atomic spectroscopy in 1990. He continued basic research concerning x-ray optics at different European Synchrotron Radiation Laboratories. In 1995 he joined the Federal Institute for Materials and Testing (BAM), Department of Nondestructive Testing, where he is responsible for x-ray topography and computed tomography. Since 2000 he has been developing and realizing the BAM hard x-ray laboratory BAMline at the Berlin Synchrotron Storage Ring BESSY. Since 2009 he is head of the working group X-Ray Topography.

Rolf-Joachim Müller

Gesellschaft für Biotechnologische
Forschung mbH
TU-BCE
Braunschweig, Germany
rju@gbf.de



Chapter D.14, Sect. 14.3

Dr. Rolf-Joachim Müller studied chemistry at the Technical University Braunschweig, Germany and made his dissertation on molecular characterization of high molecular synthetic polymers at the Institute of Technical Chemistry in Braunschweig. Since 1986, he is at the GBF, working on the characterization of biopolymers and the development and testing of biodegradable synthetic polymers.

Kiyofumi Muro

Chiba University
Faculty of Science, Department of
Physics
Chiba, Japan
muro@physics.s.chiba-u.ac.jp



Chapter C.11, Sect. 11.5

Professor Kiyofumi Muro's current research activities are spectroscopies based on fibre photonics, high sensitivity and high resolution spectroscopy based on microcavity, and terahertz spectroscopy of condensed matter with a femtosecond fibre laser. He has 15 years of industrial experience and more than 10 US patents in the development of diode-pumped solid-state lasers and high-power pump lasers.

Yoshihiko Nonomura

National Institute for Materials Science
Computational Materials Science Center
Ibaraki, Japan
nonomura.yoshihiko@nims.go.jp



Chapter E.22

Yoshihiko Nonomura received his Ph.D. at the Graduate School of Physics, University of Tokyo in 1994. Then he worked on classical and quantum random spin systems numerically at the Tokyo Institute of Technology and RIKEN. Currently he is studying superconducting vortex systems (especially effects of impurities and layered structures) using Monte Carlo and other numerical methods at the National Institute for Materials Science (NIMS) since 1998.

Jürgen Nuffer

Fraunhofer Institute for Structural
Durability and System Reliability (LBF)
Darmstadt, Germany
juergen.nuffer@lbf.fraunhofer.de



Chapter D.16, Sect. 16.7

Jürgen Nuffer studied Physics in Frankfurt/Main, Germany and obtained his Diploma degree in Physics in 1997. In 2000 he received his PhD in Materials Science from the University of Technology Darmstadt. Since 2003 Dr. Nuffer is with the Fraunhofer Institute for Structural Durability and System Reliability (LBF) performing and coordinating research on the reliability assessment of complex adaptronic and mechatronic systems. Since 2006 he is leader of the System Reliability Group in the Mechatronics/Adaptronics Department.

Jan Obrzut

National Institute of Standards and
Technology
Polymers Division
Gaithersburg, MD, USA
jan.obrzut@nist.gov



Chapter C.9, Sect. 9.5

Jan Obrzut received a PhD degree from Cracow University of Technology, Poland, in 1981. After a postdoctoral appointment at the Polymer Science Department, University of Massachusetts, he joined IBM in 1988 as an advisory engineer where he conducted exploratory work on applications of dielectric and electrooptic materials for microelectronics. He has been with the National Institute of Standards and Technology since 1997, where he pursues research in metrology of dielectrics and nanostructured hybrid materials.

Hiroshi Ohtani

Kyushu Institute of Technology
Department of Materials Science and
Engineering
Kitakyushu, Japan
ohtani@matsc.kyutech.ac.jp



Chapter E.20

Professor, Hiroshi Ohtani received doctor degree from Tohoku University (Japan) in 1985. His research activities have been concentrating on the thermodynamic analysis of alloys, ceramics and other materials using the CALPHAD method and first-principles calculations.


Kurt Osterloh

Chapter D.16, Sect. 16.2

Federal Institute for Materials Research and Testing (BAM)
Division VIII.3
Berlin, Germany
kurt.osterloh@bam.de

After studies in chemistry and biology from 1969–1975 Dr. Osterloh received his Ph.D. in 1979. He did post-doctoral research in Munich (Germany) from 1980–1984, in Harrow/London (UK) from 1984–1986, in Mobile AL (USA) from 1986–1987, in New York NY (USA) 1987–1989, again in Munich (Germany) from 1989–1990, he spent the years from 1990–1994 in pharmaceutical industry in Berlin (Germany). After 5 years research at the Free University of Berlin (1995–2000) and development of ESR spectrometry at Magnetech in Berlin (1995–2000) he joined the Federal Institute for Materials Research and Testing (BAM) in 2000 working on radiology in safety and security applications.


Michael Pantke

Chapter D.14, Sect. 14.1

Federal Institute for Materials Research and Testing (BAM)
Division IV.1, Materials and Environment
Berlin, Germany
michael.pantke@bam.de

Michael Pantke has a Diploma in Microbiology from the Free University of Berlin. He has experience in recognizing causes of damage by microbial attack on organic materials. He does prenormative research for developing test methods for determining the behaviour of plastics to microbial attack. He works in cooperation with national (DIN) and international (CEN, IEC, ISO) standardization bodies. He is coordinator of international standardization activities in the field of biologically degradable plastics.

Karen W. Phinney

Chapter B.4, Sect. 4.1

National Institute of Standards and Technology
Analytical Chemistry Division
Gaithersburg, MD, USA
karen.phinney@nist.gov



Karen Phinney received her Ph.D. in analytical chemistry from the University of Hawaii-Manoa. She is currently a Research Chemist in the Analytical Chemistry Division at NIST. Her research interests include chiral separations, dietary supplements, forensic analysis, and various separation techniques, including capillary electrophoresis and supercritical fluid chromatography.

Rüdiger (Rudy) Plarre

Chapter D.14, Sect. 14.2

Federal Institute for Materials Research and Testing (BAM)
Environmental Compatibility of Materials
Berlin, Germany
ruediger.plarre@bam.de



Rudy Plarre is Head of the working group Materials Protection against Fungi and Insects. This group conducts research in the field of applied pest control in urban environments including efficacy testing of integrated pest control strategies. Rudy is an entomologist by training and received his degree at the Free University of Berlin.


Kenneth W. Pratt

Chapter B.4, Sect. 4.1

National Institute of Standards and Technology
Analytical Chemistry Division
Gaithersburg, MD, USA
kenneth.pratt@nist.gov

Kenneth Pratt holds a Ph.D. from Iowa State University, Ames, USA. At NIST he is responsible for research and SRM certification in electrochemical analysis (coulometry, pH, conductimetry). He is active in international metrological organizations including CCQM and IUPAC working groups. Particular research interests are constant-current coulometry, classical analysis, absolute measurement of electrolytic conductivity and primary pH metrology.


Michael H. Ramsey

Chapter A.3, Sect. 3.1

University of Sussex
School of Life Sciences
Brighton, UK
m.h.ramsey@sussex.ac.uk

Professor Michael H. Ramsey has published over 140 scientific papers, mainly on aspects of uncertainty in sampling and in measurement, as well as the effects of this uncertainty on decision making. Recent research projects include investigation of uncertainty from sampling of contaminated land (TSB funded) and contaminated food (FSA funded). He is currently Chair of the Eurachem/Eurolab/Citac/Nordtest/AMC Working Group on Uncertainty from Sampling, and co-author of the Eurachem Guide on this subject.

Peter Reich

Berlin, Germany
peterreichberlin@email.de



Chapter B.4, Sect. 4.4

Dr. Peter Reich studied chemistry at the Technical University of Dresden from 1955 to 1963 where he also finished his Dr. rer. nat. in 1975. He obtained his Dr. sc. nat. in 1998 and became Professor (non-scheduled) for Analytical Chemistry at the Technical University of Berlin. From 1992 to 2002 he was leader of the Division I.3, Structure Analysis at the Federal Institute for Materials Research and Testing (BAM) in Berlin. His fields of work are applications of spectroscopic methods for materials analysis. He has published 80 papers, 1 monograph, and owns 2 patents.

Gunnar Ross

Magnet-Physik Dr. Steingroever GmbH
 Köln, Germany
ross@magnet-physik.de



Chapter C.10, Sect. 10.2

Dr.-Ing. Gunnar Ross is Development and Production Manager for measuring equipment for magnetic quantities and magnetic material properties. He is Head of a Calibration Laboratory for magnetic quantities that is accredited in the Deutscher Kalibrierdienst (DKD).

Steffen Rudtsch

Physikalisch-Technische Bundesanstalt
 (PTB)
 Berlin, Germany
steffen.rudtsch@ptb.de

Chapter C.8

Dr. Steffen Rudtsch is the head of the working group Applied Thermometry at the Physikalisch-Technische Bundesanstalt (PTB), Germany. He has 12 years of experience in thermophysical properties measurements at the Brandenburg Technical University at Cottbus. Between 1999 and 2002 he was working at PTB and at the National Institute of Standards and Technology (NIST) in the US on adiabatic and differential scanning calorimetry. His current field of work is the development of a new generation of metallic, fixed points of the International Temperature Scale of 1990 (ITS-90).

Lane Sander

National Institute of Standards and
 Technology
 Chemical Science and Technology
 Laboratory, Analytical Chemistry Division
 Gaithersburg, MD, USA
lane.sander@nist.gov

Chapter B.4, Sect. 4.1

Lane Sander attended the University of Washington and received a Ph.D. in analytical chemistry in 1982. He is currently Leader of the Organic Chemical Metrology Group, in the Analytical Chemistry Division. Research interests include synthesis and characterization of novel stationary phases for liquid chromatography; elucidation of solute retention mechanisms; molecular modeling; and chromatographic metrology in environmental, clinical and food science disciplines.

Erich Santner

Bonn, Germany
esantner@arcor.de



Chapter D.13

Erich Santner studied Physics in Berlin (Freie Universität) where he received his DSc for investigations in solid state physics. In the following years he concentrated on radiation protection and nuclear fuel analysis at the Federal Institute for Materials Research and Testing (BAM), intermittently working for one year as a technical officer in the Ministry of Economy in Bonn, Germany. He was then Head of the Division of Tribology and Wear Protection at BAM. His research and development activities were focused on the tribology of thin hard coatings, failure analysis, and on micro- and nanotribology.

Michele Schantz

National Institute of Standards and
 Technology
 Analytical Chemistry Division
 Gaithersburg, MD, USA
michele.schantz@nist.gov



Chapter B.4, Sect. 4.1

Dr. Michele Schantz is a research chemist in the Analytical Chemistry Division at the National Institute of Standards and Technology (NIST). She is currently the team leader for the gas chromatography team and has been involved in the certification of numerous environmental Standard Reference Materials and coordinating and participating in interlaboratory studies for organics in marine tissue and sediment, marine mammal blubber, and PM_{2.5} air particulate.



Anita Schmidt

Chapter A.3, Sect. 3.4

Federal Institute for Materials Research and Testing (BAM)
Berlin, Germany
anita.schmidt@bam.de

Anita Schmidt has a diploma and PhD in chemistry from the Justus Liebig University Giessen. Since 2000 she is with the BAM Federal Institute for Materials Research and Testing. Since 2008 she is Head of the section Information Management and since 2010 of the merged sections Quality assurance and Information Management in the department Dangerous Goods Packaging. Current interests are in chemical compatibility.



Guenter Schmitt

Chapter D.14

Iserlohn University of Applied Sciences
Laboratory for Corrosion Protection
Iserlohn, Germany
schmitt.g@fh-swf.de

Professor Guenter Schmitt received his Ph.D. in Chemistry in 1971 from RWTH Aachen, Germany. He had professorships at Universities of Aachen, Bochum and Iserlohn, Germany. He is a member of major national and international scientific societies, the past president of GfKORR, the German Society for Corrosion Protection and Chairman of the EFC working Group Corrosion and Scale Inhibition. He is a NACE Fellow and was awarded the Rahmel-Schwenk-Medal of GfKORR.

Bernd Schumacher

Chapter C.9, Sects. 9.1, 9.2

Physikalisch-Technische Bundesanstalt
Department 2.1 DC and Low Frequency
Braunschweig, Germany
bernd.schumacher@ptb.de



Dr. Bernd Schumacher received the PhD degree in Electrical Engineering in 1991 from the University of Technology, Aachen, Germany. He joined the Physikalisch-Technische Bundesanstalt (PTB) Braunschweig, Germany, in 1991. He is Head of the working group DC-Measuring Techniques. His main research topic is the improvement of measuring techniques for resistance standards and other DC quantities. This includes resistance measurement bridges based on the cryogenic current comparator and voltage calibration based on the Josephson effect.

Michael Schütze

Chapter D.12

Karl-Winnacker-Institut
DECHEMA e.V.
Frankfurt am Main, Germany
schuetze@dechema.de



Professor Michael Schütze earned his Dipl.Ing. in Materials Science from the University of Erlangen-Nürnberg, Germany in 1978 and his Dr.Ing. from RWTH Aachen in 1983, followed by his State Doctorate in 1991. Since 1996 he is Director of DECHEMA's Karl-Winnacker-Institut in Frankfurt/Main, Germany and has a full professorship at RWTH Aachen since 1998. He was awarded the Friedrich-Wilhelm-Award (RWTH Aachen, 1991), the Rahmel-Schwenk-Medal (1999). Dr. Schütze was the past chairman of the Gordon Research Conference on Corrosion, is Chairman of EFC Working party and Convenor of ISO work group on high temperature corrosion. He has more than 200 publications, owns 18 patents and has written 6 books.



Karin Schwibbert

Chapter D.14, Sect. 14.6

Federal Institute for Materials Research and Testing (BAM)
Division IV.1 Materials and Environment
Berlin, Germany
karin.schwibbert@bam.de

Dr. Karin Schwibbert is currently a research associate for microbiology at the Federal Institute for Materials Research and Testing (BAM). She obtained her PhD from the University of Bonn in 1999 and continued her research at the University of Münster in the Department of Biochemistry. Her scientific interests are in the areas of: soil microbiology, biodeterioration and biodegradation, and the development of methodologies for identification and classification of microorganisms.

**John H. J. Scott**

Chapter B.4, Sect. 4.2

National Institute of Standards and Technology
Surface and Microanalysis Science
Division
Gaithersburg, MD, USA
johnhenry.scott@nist.gov

John Henry currently works as a physicist at NIST in Gaithersburg, MD. His research involves chemical characterization techniques in electron beam instruments, primarily analytical transmission electron microscopy (ATEM), as well as Monte Carlo simulation, correction procedures for quantitative microanalysis, and multivariate statistical methods.

Martin Seah

Chapter B.6

National Physical Laboratory
Analytical Science Division
Teddington, UK
martin.seah@npl.co.uk



Dr. Martin Seah founded the research group at NPL leading work in standards for measurements and quantification in the surface analysis techniques of Auger electron spectroscopy, x-ray photoelectron spectroscopy, static secondary ion mass spectrometry and atomic force microscopy. He is Chair of a subcommittee for ISO TC 201 on Surface Chemical Analysis and set up relevant activities in the Consultative Committee for Amount of Substance and in VAMAS. He is a Fellow of the Institute of Physics, the Institute of Materials, Minerals and Mining and the American Vacuum Society. He has won awards from the American Society for Metals, American Vacuum Society, Institute of Physics and International Union for Vacuum Science, Technique and Applications.

Steffen Seitz

Chapter C.9, Sect. 9.3

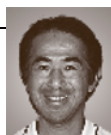
Physikalisch-Technische Bundesanstalt (PTB)
Dept. 3.13 Metrology in Chemistry
Braunschweig, Germany
steffen.seitz@ptb.de



Dr. Steffen Seitz received his diploma as physicist from the Ludwig Maximilians University in Munich and earned his PhD in Engineering from the Technical University of Braunschweig in 2007. He joined PTB (National Metrology Institute providing scientific and technical services) in 2004, where he optimized the electrooptic sampling of ultrashort electrical pulses. Since 2007 he is working in the electrochemical working group on the development and application of primary conductivity measurement procedures.

Masato Shimono

Chapter E.17



National Institute for Materials Science
Computational Materials Science Center
Tsukuba, Japan
shimono.masato@nims.go.jp

Dr. Masato Shimono is research scientist at the National Institute for Materials Science (NIMS), Particle Simulation and Thermodynamics Group. He is currently working on projects in materials science and computational physics.

John R. Sieber

Chapter B.4, Sect. 4.1



National Institute of Standards and Technology
Chemical Science and Technology
Laboratory
Gaithersburg, MD, USA
john.sieber@nist.gov

Dr. John R. Sieber is a research chemist in the Inorganic Chemical Metrology Group of the Analytical Chemistry Division, National Institute of Standards and Technology. He specializes in x-ray fluorescence spectrometry. Dr. Sieber spent nine years in the petroleum industry and is a member of ASTM International.

Franz-Georg Simon

Chapter D.15, Sect. 15.1

Federal Institute for Materials Research and Testing (BAM)
Waste Treatment and Remedial
Engineering
Berlin, Germany
franz-georg.simon@bam.de



Dr. Simon studied chemistry in Frankfurt/Main (Diploma 1985) and Mainz (PhD 1989), Germany and gained a master's degree in business engineering (AKAD Zurich, Switzerland 1997). He joined the Federal Institute for Materials Research and Testing (BAM) as Head of Division in 1998 after working for eight years in an industrial research centre in Switzerland. His scientific activities encompass research on thermal waste treatment, groundwater remediation and ecomaterials.

John Small

National Institute of Standards and Technology
Surface and Microanalysis Science
Division
Gaithersburg, MD, USA
john.small@nist.gov



Chapter B.4, Sect. 4.2

John A. Small is the Group Leader of the Microanalysis Research Group and a Senior Research Chemist in the Surface and Microanalysis Science Division at the National Institute for Standards and Technology (NIST). His research has focused on the quantitative chemical analysis of individual particles using x-ray microanalytical techniques. Recent research interests include x-ray microanalysis of nanoscale particles. He currently is a member of (NEHI) under the NNI, and works with the ESH working group under the NNI-Chi CBAN.

Melody V. Smith

National Institute of Standards and Technology
Biospectroscopy Group
Gaithersburg, MD, USA
melody.smith@nist.gov

Chapter B.4, Sect. 4.1

Melody Smith is a physical science technician who has been with the Analytical Chemistry Division of the National Institute of Standards and Technology since 1981. Before that, she was with the NBS Office of Standard Reference Materials. Her duties in the Biospectroscopy Group include the production and certification of spectrophotometric standard reference materials.

Petra Spitzer

Physikalisch-Technische Bundesanstalt (PTB)
Dept. 3.13 Metrology in Chemistry
Braunschweig, Germany
petra.spitzer@ptb.de

Chapter C.9, Sect. 9.3

The emphasis of Ms. Spitzer's work is the development and application of primary electrochemical methods. She is head of the working group "Metrology in Electrochemistry" at the Physikalisch-Technische Bundesanstalt (PTB), Braunschweig, Germany. By education Ms. Spitzer is a physical chemist and received her diploma as chemist from the Humboldt University in Berlin, Germany. Before 1991 she worked on electrochemistry and adsorption at the Central Institute of Physical Chemistry, former Academy of Science.

Thomas Steiger

Federal Institute for Materials Research and Testing (BAM)
Department of Analytical Chemistry;
Reference Materials
Berlin, Germany
thomas.steiger@bam.de



Chapter A.3, Sect. 3.8

Thomas Steiger studied Chemistry at the University of Leipzig focusing on theoretical and quantum chemistry. He received a PhD degree from the Academy of Sciences of GDR, Berlin in 1977 on the application of quantum chemical methods for interpretation of NMR and vibrational spectra. Since 1992 he has been working at BAM Federal Institute for Materials Research and Testing in the field of analytical chemistry and related reference materials. Currently, his special interests are quality assurance and metrology in analytical chemistry.

Ina Stephan

Federal Institute for Materials Research and Testing (BAM)
Division IV.1 Biology in Materials
Protection and Environmental Issues
Berlin, Germany
ina.stephan@bam.de



Chapter D.14, Sect. 14.2

Dr. Ina Stephan has a Ph.D. in Wood Science and Technology from the University of Hamburg, Germany and is head of the working group on the resistance of materials to microorganisms at the Federal Institute for Materials Research and Testing (BAM). Her main interests are in the testing of materials against fungi, algae and bacteria in a meaningful manner and the international harmonization of test standards for biodeterioration.

**Stephan J. Stranick**

Chapter B.4, Sect. 4.2

National Institute of Standards and Technology
Department of Commerce, Surface and Microanalysis Science Division
Gaithersburg, MD, USA
stranick@nist.gov

Stephan Stranick received a PhD in Chemistry from the Pennsylvania State University in 1995. Stephan is currently a Research Chemist in the Chemical Science and Technology Laboratory of the National Institute of Standards and Technology, where his present research focuses on the development of novel super-resolution probes of surface physicochemical properties. He has published over sixty papers on the subject and has been awarded fourteen patents associated with scanning probe microscopies for chemical and electrical characterization. Stephan's awards include the American Chemical Society's Nobel Laureate Signature Award and Arthur F. Findeis Award.

**Hans-Henning Strehblow**

Chapter D.12

Heinrich-Heine-Universität
Institute of Physical Chemistry
Düsseldorf, Germany
henning@uni-duesseldorf.de

Dr. Hans-Henning Strehblow is Professor of Physical Chemistry at the Heinrich-Heine-Universität, Düsseldorf, Germany since July 1982. He studied Chemistry at Freie Universität, Berlin (1959–1964) where he also earned his Ph.D. in Physical Chemistry (1971) as well as his State Doctorate in Physical Chemistry (1977). He is Fellow of the Electrochemical Society since 2005. His professional interests are electrochemistry, corrosion, surface analysis and physical chemistry of surfaces.

Tetsuya Tagawa

Chapter C.7, Sect. 7.5

Nagoya University
Department of Materials Science and Engineering
Nagoya, Japan
tagawa@numse.nagoya-u.ac.jp



Tetsuya Tagawa is Associate Professor at Nagoya University since 2000, where he also received his Ph.D. in 1994.

Akira Tezuka

Chapter E.19

National Institute of Advanced Industrial Science and Technology
Tsukuba, Japan
tezuka.akira@aist.go.jp



Akira Tezuka obtained his BS (Mechanical Engineering) from the University of Tokyo in 1983, his MS (Mechanical Engineering and Applied Mechanics) from the University of Michigan in 1989, and his PhD from the University of Tokyo in 1994. He started his career as a researcher at Hitachi Ltd. in 1984. After the experience in Industrial Products Research Institute, Mechanical Engineering Laboratory, and as a visiting scholar at Stanford University, his current interests are multi-scale/multi-physics computational mechanics on extended-FEM with the emphasis on adaptivity and parallel computing for the real application for manufacturing fields. He is a member of the Executive Council of the Japan Society for Computational Engineering and Science and a former member of the General Council of the International Association of Computational Mechanics.

**Yo Tomota**

Chapter C.7, Sect. 7.4

Ibaraki University
Department of Materials Science, Faculty of Engineering
Hitachi, Japan
tomota@mx.ibaraki.ac.jp

Professor Yo Tomota's current research topics include neutron diffraction studies of phase transformation, microstructural evolution and mechanical behavior of ecomaterials. The development of environmentally conscious materials, so called ecomaterials are his concern for realizing a sustainable human society. Therefore, Professor Tomota is studying material flow and recycling, ecomaterials, mainly steels design etc. Nanostructure analysis using neutron diffraction is a powerful tool to develop nanocrystalline ecomaterials and to study the deformation and fracture of materials.

**John Travis**

Chapter B.4, Sect. 4.1

National Institute of Standards and Technology
Analytical Chemistry Division (Retired)
Gaithersburg, MD, USA
john.travis@nist.gov

John Travis joined NBS/NIST after earning his Ph.D. in physics from the University of Texas in 1967. His research generated over 85 papers in Mössbauer spectroscopy, applications of tunable lasers to chemical analysis, Fourier transform spectroscopy, atomic emission and molecular absorption spectrometry. He retired in October of 2004, becoming an Emeritus Scientist pursuing intrinsic standards for molecular absorption spectrometry.

Peter Trubiroha

Chapter D.15, Sect. 15.1.2

Berlin, Germany
peter.trubiroha@t-online.de



Peter Trubiroha studied Physics at the Freie Universität Berlin. From 1970 until 2003 he was with the Federal Institute of Material Research and Testing (BAM), Berlin, Germany. His area of work was the climatic resistance of polymeric materials especially studies on the influence of different climatic quantities on photo degradation and to develop new test procedures.

Gregory C. Turk

Chapter B.4, Sect. 4.1

National Institute of Standards and Technology
Analytical Chemistry Division
Gaithersburg, MD, USA
turk@nist.gov



Dr. Gregory C. Turk is leader of the Inorganic Chemical Metrology Group at the National Institute of Standards and Technology, where he has worked in the area of spectrochemistry since 1976. His research background includes the use of laser spectroscopy for trace metal analysis, including the development of Laser Enhanced Ionization Spectrometry. Present research includes the development of improved strategies for instrument calibration in spectrochemical analysis. He received his Ph.D. degree from the University of Maryland.

**Thomas Vetter**

Chapter B.4, Sect. 4.1

National Institute of Standards and Technology (NIST)
Analytical Chemistry Division
Gaithersburg, MD, USA
thomas.vetter@nist.gov

Thomas Vetter is an inorganic analytical chemist at NIST. Over the past 25 years at NIST he has assayed major constituents in numerous Standard Reference Materials by gravimetry coupled with instrumental techniques and by gravimetric titrimetry. In addition, over the past 15 years, he has promoted a step-wise quantification of measurement uncertainty to improve measurement quality.

**Volker Wachtendorf**

Chapter D.15, Sect. 15.1.2

BAM Federal Institute for Materials Research and Testing (BAM)
Division VI.3, Durability of Polymers
Berlin, Germany
volker.wachtendorf@bam.de

Volker Wachtendorf obtained his diploma in chemistry from the Technical University of Clausthal, Germany, where he also achieved his doctor's degree with a thesis on the monitoring of the ageing of polymers using chemiluminescence. The practical part of his thesis already was done at the Federal Institute for Materials Research and Testing (BAM) in Berlin, Germany, where he currently heads the working group Weathering Stability of Polymers. His interests are in the fields of weathering exposure, ageing of polymers and its analytics in early stages of exposure.

Andrew Wallard

Chapter A.2

Pavillon de Breteuil
Bureau International des Poids et Mesures
Sèvres, France
fjoly@bipm.org



Professor Wallard has been Director of the International Bureau of Weights and Measures (BIPM) since January 2004. The BIPM's task is to ensure uniformity of measurements world-wide and has interests in physics, engineering, chemistry, laboratory medicine and other areas in which traceable measurement is important. Professor Andrew Wallard has left the BIPM as of 31 December 2010, and is now Director Emeritus of the BIPM.

Joachim Wecker

Siemens AG
Corporate Technology, CT T DE
Erlangen, Germany
joachim.wecker@siemens.com



Chapter C.10, Sect. 10.1

Dr. Joachim Wecker is leading the Global Technology Field Organic Electronics at Siemens Corporate Technology, Erlangen, Germany. He earned his PhD in Physics from the University of Göttingen, Germany. Previous and current field of work are hard and soft magnetic materials, superconductors, thin film magnetoelectronic and organic electronic devices. Dr. Wecker is member of the Advisory Board of the German Materials Society (DGM) and the magnetism section of the German Physical Society.

Wolfhard Wegscheider

Montanuniversität Leoben
General and Analytical Chemistry
Leoben, Austria
wegschei@unileoben.ac.at



Chapter A.3, Sect. 3.5

Wolfhard Wegscheider is Professor of General and Analytical Chemistry at the University of Leoben, Austria. He received his education from the Graz University of Technology majoring in Technical Chemistry with a specialisation in Biochemistry and Food Chemistry. As Fulbright Scholar he worked in Denver, CO, mainly on energy-dispersive x-ray fluorescence spectrometry. Much of his research centers on the development of chemometric procedures for analytical chemical problems. Professor Wegscheider is member of several learned societies, past chairman of CITAC and EURACHEM, has cooperation on International Traceability in Analytical Chemistry, Austrian Delegate to EURACHEM where he is member of the Executive Committee, of the Working Group on Education and Training, of the Working Group on Measurement Uncertainty and Traceability, and of the Working Group Analytical Quality Assurance at Universities. Currently he serves as Vice-President of the Austrian Society of Analytical Chemistry – ASAC. He is a consultant to the Austrian Federal Ministry for Agriculture, Forestry, Environment and Water Management and a lead auditor in the Austrian Accreditation of Laboratories.

Alois Wehrstedt

DIN Deutsches Institut für Normung
Normenausschuss Materialprüfung (NMP)
Berlin, Germany
alois.wehrstedt@din.de



Chapter C.7, Sect. 7.3

Alois Wehrstedt studied materials science at the Technical University Dresden, Germany. He is manager of the department for materials testing at the Central Institute for Solid State Physics and Material Science in Dresden. Since 1989 he worked in the Standardization Committee for Materials Testing (NMP) of the German Institute for Standardization in Berlin for which he is the manager since 2005. Since 1994 he is the secretary of the international standardization committee ISO/TC 164/SC 3 Hardness Testing of Metallic Materials.

Michael Welch

National Institute of Standards and
Technology
Gaithersburg, MD, USA
michael.welch@nist.gov



Chapter B.4, Sect. 4.1

Dr. Welch received a Ph.D. in analytical chemistry from Arizona State University in 1976 and has been at the National Institute of Standards and Technology since 1978. His research interests focus on development of mass spectrometry based reference methods and standard reference materials for organic analytes in blood, drugs of abuse in urine, hair, and other matrices, and nutrients in foods.

Ulf Wickström

SP Swedish National Testing and
Research Institute
Department of Fire Technology
Borås, Sweden
ulf.wickstrom@sp.se



Chapter D.15, Sect. 15.3

Professor Ulf Wickström is Heading the Department of Fire Technology at the Swedish National Testing and Research Institute (SP). The department has a staff of about 50 involved in fire testing and research and is one of the leading laboratories of its kind in the world. Professor Wickström has a PhD from the Lund University of Technology (1979) in Fire Technology, a Master of Science from University of California (1977), Berkeley. Professor Wickström's special scientific interest is heat transfer analysis of structures exposed to fire where he has published several scientific papers. Among other things he has developed the computer code TASEF for calculating temperature in fire exposed concrete and steel structures.

Sheldon M. Wiederhorn

National Institute of Standards and
Technology
Materials Science and Engineering
Laboratory
Gaithersburg, MD, USA
sheldon.wiederhorn@nist.gov

Chapter C.7, Sect. 7.1

Sheldon M. Wiederhorn received his B.S. degree in 1956 from Columbia University and his Ph.D. degree in 1960 from the University of Illinois. He joined the National Institute of Standards and Technology in 1963, where he developed methods for quantifying subcritical crack growth in glasses and ceramics. He was elected a member of the National Academy of Engineering in 1991.

Scott Wight

National Institute of Standards and
Technology
Surface and Microanalysis Science
Division
Gaithersburg, MD, USA
scott.wight@nist.gov

Chapter B.4, Sect. 4.2

Scott Wight is a Research Chemist in the Surface and Microanalysis Science Division at NIST. Scott received his B.S. in Chemistry from State University of New York, Plattsburgh in 1986 and a MS in analytical-nuclear-environmental chemistry from the University of Maryland in 1989. His current research is in Auger electron spectroscopy and he is active in ASTM E42 and ISO TC 201 committees for surface analysis.

Michael Winchester

National Institute of Standards and
Technology
Analytical Chemistry Division
Gaithersburg, MD, USA
mrw@nist.gov



Chapter B.4, Sect. 4.1

Dr. Michael Winchester has been a Research Chemist at NIST for over twenty years (first two years as a National Research Council Postdoctoral Fellow). His research focuses mainly on plasma source atomic spectroscopy. He is also involved in the production and certification of Standard Reference Materials. Dr. Winchester earned the PhD in Analytical Chemistry from Clemson University in 1990.

Noboru Yamada

Matsushita Electric Industrial Co., Ltd.
Optical Media Group, Storage Media
Systems Development Center
Moriguchi, Japan
yamada.noboru@jp.panasonic.com



Chapter C.11, Sect. 11.6

Dr. Noboru Yamada graduated from Kyoto University and entered the Central Research Laboratory of Matsushita Electric in 1974. He first found an epoch-making phase-change in GeTe-Sb₂Te₃ in 1987 and developed DVD-RAM media in 1998. He obtained his Ph.D. in engineering from Kyoto University in 2001 and received the Matsushita science prize in 2001 and 24th JJAP Paper Award from the Japan Applied Physics Society in 2002.

**Rolf Zeisler**

National Institute of Standards and Technology
Analytical Chemistry Division
Gaithersburg, MD, USA
rolf.zeisler@nist.gov

Chapter B.4, Sect. 4.1

Dr. Rolf Zeisler joined NIST in 1978 with his degree from the Technical University, Munich, Germany (1974) on instrumental neutron activation analyses of tissues and their application to investigations of metallosis. Activation analysis formed the core of his research, expanding the technique's applications in the life sciences and in chemical metrology. Post doctoral studies at Texas A&M University, assignment to the IAEA Laboratories, Austria, and many collaborations allowed him to explore the various forms of nuclear based analysis.

**Uwe Zscherpel**

Federal Institute for Materials Research and Testing (BAM)
Division "NDT – Radiological Methods"
Berlin, Germany
uwez@bam.de

Chapter D.16, Sect. 16.2

Dr. Uwe Zscherpel received his Ph.D. from the University of Leipzig, Germany, on Fourier transform infrared spectroscopy of zeolites. In 1992 he changed to non-destructive testing and since 1996 he is head of the working group "Digital Radiology and Image Analysis" at the Federal Institute for Materials Research and Testing (BAM), Berlin, Germany. His area of expertise is digital image processing in industrial radiology, including NDT film digitization, digital image analysis, pattern recognition and digital reference catalogues for weldings and castings. Additional working fields are new radiographic image detectors such as imaging plates and digital detector arrays for industrial applications, standardization and reliability.

Adolf Zschunke

Leipzig, Germany
zschunke35@aol.com



Chapter A.3, Sect. 3.7

Adolf Zschunke was head of the department Analytical Chemistry; Reference Materials at the Federal Institute for Materials Research and Testing (BAM) and Professor of Analytical Chemistry at the Humboldt-University in Berlin, Germany. He was chairman of the international working group on Reference Materials of EURACHEM, EUROLAB, EUROMET and EA. He retired in 2002. He is still member of Executive Committee of EURACHEM.

Detailed Contents

List of Abbreviations	XXV
------------------------------------	-----

Part A Fundamentals of Metrology and Testing

1 Introduction to Metrology and Testing

<i>Horst Czichos</i>	3
1.1 Methodologies of Measurement and Testing	3
1.1.1 Measurement	3
1.1.2 Testing	5
1.1.3 Conformity Assessment and Accreditation	7
1.2 Overview of Metrology	9
1.2.1 The Meter Convention	9
1.2.2 Categories of Metrology	9
1.2.3 Metrological Units	11
1.2.4 Measurement Standards	12
1.3 Fundamentals of Materials Characterization	13
1.3.1 Nature of Materials	13
1.3.2 Types of Materials	15
1.3.3 Scale of Materials	16
1.3.4 Properties of Materials	17
1.3.5 Performance of Materials	19
1.3.6 Metrology of Materials	20
References	22

2 Metrology Principles and Organization

<i>Andrew Wallard</i>	23
2.1 The Roots and Evolution of Metrology	23
2.2 BIPM: The Birth of the Metre Convention	25
2.3 BIPM: The First 75 Years	26
2.4 Quantum Standards: A Metrological Revolution	28
2.5 Regional Metrology Organizations	29
2.6 Metrological Traceability	29
2.7 Mutual Recognition of NMI Standards: The CIPM MRA	30
2.7.1 The Essential Points of the MRA	30
2.7.2 The Key Comparison Database (KCDB)	31
2.7.3 Take Up of the CIPM MRA	31
2.8 Metrology in the 21st Century	32
2.8.1 Industrial Challenges	32
2.8.2 Chemistry, Pharmacy, and Medicine	33
2.8.3 Environment, Public Services, and Infrastructures	34
2.9 The SI System and New Science	34
References	37

3	Quality in Measurement and Testing	
	<i>Michael H. Ramsey, Stephen L.R. Ellison, Horst Czichos, Werner Hässelbarth, Hanspeter Ischi, Wolfhard Wegscheider, Brian Brookman, Adolf Zschunke, Holger Frenz, Manfred Golze, Martina Hedrich, Anita Schmidt, Thomas Steiger</i>	39
3.1	Sampling	40
3.1.1	Quality of Sampling	40
3.1.2	Judging Whether Strategies of Measurement and Sampling Are Appropriate	42
3.1.3	Options for the Design of Sampling	43
3.2	Traceability of Measurements	45
3.2.1	Introduction	45
3.2.2	Terminology	46
3.2.3	Traceability of Measurement Results to SI Units	46
3.2.4	Calibration of Measuring and Testing Devices	48
3.2.5	The Increasing Importance of Metrological Traceability	49
3.3	Statistical Evaluation of Results	50
3.3.1	Fundamental Concepts	50
3.3.2	Calculations and Software	53
3.3.3	Statistical Methods	54
3.3.4	Statistics for Quality Control	66
3.4	Uncertainty and Accuracy of Measurement and Testing	68
3.4.1	General Principles	68
3.4.2	Practical Example: Accuracy Classes of Measuring Instruments	69
3.4.3	Multiple Measurement Uncertainty Components	71
3.4.4	Typical Measurement Uncertainty Sources	72
3.4.5	Random and Systematic Effects	73
3.4.6	Parameters Relating to Measurement Uncertainty: Accuracy, Trueness, and Precision	73
3.4.7	Uncertainty Evaluation: Interlaboratory and Intralaboratory Approaches	75
3.5	Validation	78
3.5.1	Definition and Purpose of Validation	78
3.5.2	Validation, Uncertainty of Measurement, Traceability, and Comparability	79
3.5.3	Practice of Validation	81
3.6	Interlaboratory Comparisons and Proficiency Testing	87
3.6.1	The Benefit of Participation in PTs	88
3.6.2	Selection of Providers and Sources of Information	88
3.6.3	Evaluation of the Results	92
3.6.4	Influence of Test Methods Used	93
3.6.5	Setting Criteria	94
3.6.6	Trends	94
3.6.7	What Can Cause Unsatisfactory Performance in a PT or ILC?	95

3.6.8	Investigation of Unsatisfactory Performance	95
3.6.9	Corrective Actions	96
3.6.10	Conclusions	97
3.7	Reference Materials	97
3.7.1	Introduction and Definitions	97
3.7.2	Classification	98
3.7.3	Sources of Information	99
3.7.4	Production and Distribution	100
3.7.5	Selection and Use	101
3.7.6	Activities of International Organizations	104
3.7.7	The Development of RM Activities and Application Examples	105
3.7.8	Reference Materials for Mechanical Testing, General Aspects	107
3.7.9	Reference Materials for Hardness Testing	109
3.7.10	Reference Materials for Impact Testing	110
3.7.11	Reference Materials for Tensile Testing	114
3.8	Reference Procedures	116
3.8.1	Framework: Traceability and Reference Values	116
3.8.2	Terminology: Concepts and Definitions	118
3.8.3	Requirements: Measurement Uncertainty, Traceability, and Acceptance	119
3.8.4	Applications for Reference and Routine Laboratories	121
3.8.5	Presentation: Template for Reference Procedures	123
3.8.6	International Networks: CIPM and VAMAS	123
3.8.7	Related Terms and Definitions	126
3.9	Laboratory Accreditation and Peer Assessment	126
3.9.1	Accreditation of Conformity Assessment Bodies	126
3.9.2	Measurement Competence: Assessment and Confirmation	127
3.9.3	Peer Assessment Schemes	130
3.9.4	Certification or Registration of Laboratories	130
3.10	International Standards and Global Trade	130
3.10.1	International Standards and International Trade: The Example of Europe	131
3.10.2	Conformity Assessment	132
3.11	Human Aspects in a Laboratory	134
3.11.1	Processes to Enhance Competence – Understanding Processes	134
3.11.2	The Principle of Controlled Input and Output	135
3.11.3	The Five Major Elements for Consideration in a Laboratory	136
3.11.4	Internal Audits	136
3.11.5	Conflicts	137
3.11.6	Conclusions	137
3.12	Further Reading: Books and Guides	138
	References	138

Part B Chemical and Microstructural Analysis

4 Analytical Chemistry

<i>Willie E. May, Richard R. Cavanagh, Gregory C. Turk, Michael Winchester, John Travis, Melody V. Smith, Paul DeRose, Steven J. Choquette, Gary W. Kramer, John R. Sieber, Robert R. Greenberg, Richard Lindstrom, George Lamaze, Rolf Zeisler, Michele Schantz, Lane Sander, Karen W. Phinney, Michael Welch, Thomas Vetter, Kenneth W. Pratt, John H. J. Scott, John Small, Scott Wight, Stephan J. Stranick, Ralf Matschat, Peter Reich</i>	145
4.1 Bulk Chemical Characterization	145
4.1.1 Mass Spectrometry	145
4.1.2 Molecular Spectrometry	147
4.1.3 Atomic Spectrometry	156
4.1.4 Nuclear Analytical Methods	161
4.1.5 Chromatographic Methods	168
4.1.6 Classical Chemical Methods	173
4.2 Microanalytical Chemical Characterization	179
4.2.1 Analytical Electron Microscopy (AEM)	179
4.2.2 Electron Probe X-ray Microanalysis	180
4.2.3 Scanning Auger Electron Microscopy	183
4.2.4 Environmental Scanning Electron Microscope	185
4.2.5 Infrared and Raman Microanalysis	186
4.3 Inorganic Analytical Chemistry: Short Surveys of Analytical Bulk Methods	189
4.3.1 Inorganic Mass Spectrometry	190
4.3.2 Optical Atomic Spectrometry	192
4.3.3 X-ray Fluorescence Spectrometry (XRF)	192
4.3.4 Neutron Activation Analysis (NAA) and Photon Activation Analysis (PAA)	194
4.4 Compound and Molecular Specific Analysis: Short Surveys of Analytical Methods	195
4.5 National Primary Standards – An Example to Establish Metrological Traceability in Elemental Analysis	198
References	199

5 Nanoscopic Architecture and Microstructure

<i>Koji Maeda, Hiroshi Mizubayashi</i>	205
5.1 Fundamentals	211
5.1.1 Diffraction and Scattering Methods	211
5.1.2 Microscopy and Topography	215
5.1.3 Spectroscopy	226
5.2 Crystalline and Amorphous Structure Analysis	232
5.2.1 Long-Range Order Analysis	232
5.2.2 Medium-Range Order Analysis	235
5.2.3 Short-Range Order Analysis	237

5.3	Lattice Defects and Impurities Analysis	239
5.3.1	Point Defects and Impurities	240
5.3.2	Extended Defects	252
5.4	Molecular Architecture Analysis	258
5.4.1	Structural Determination by X-Ray Diffraction	258
5.4.2	Nuclear Magnetic Resonance (NMR) Analysis	259
5.4.3	Chemophysical Analysis	267
5.5	Texture, Phase Distributions, and Finite Structures Analysis	269
5.5.1	Texture Analysis	269
5.5.2	Microanalysis of Elements and Phases	271
5.5.3	Diffraction Analysis of Fine Structures	273
5.5.4	Quantitative Stereology	274
	References	277
6	Surface and Interface Characterization	
	<i>Martin Seah, Leonardo De Chiffre</i>	281
6.1	Surface Chemical Analysis	282
6.1.1	Auger Electron Spectroscopy (AES)	285
6.1.2	X-ray Photoelectron Spectroscopy (XPS)	294
6.1.3	Secondary Ion Mass Spectrometry (SIMS)	298
6.1.4	Conclusions	307
6.2	Surface Topography Analysis	308
6.2.1	Stylus Profilometry	312
6.2.2	Optical Techniques	316
6.2.3	Scanning Probe Microscopy	318
6.2.4	Scanning Electron Microscopy	320
6.2.5	Parametric Methods	321
6.2.6	Applications and Limitations of Surface Measurement	322
6.2.7	Traceability	322
6.2.8	Summary	325
	References	326

Part C Materials Properties Measurement

7 Mechanical Properties

	<i>Sheldon M. Wiederhorn, Richard J. Fields, Samuel Low, Gun-Woong Bahng, Alois Wehrstedt, Junhee Hahn, Yo Tomota, Takashi Miyata, Haiqing Lin, Benny D. Freeman, Shuji Aihara, Yukito Hagihara, Tetsuya Tagawa</i>	339
7.1	Elasticity	340
7.1.1	Development of Elasticity Theory	340
7.1.2	Definition of Stress and Strain, and Relationships Between Them	341
7.1.3	Measurement of Elastic Constants in Static Experiments ...	344

7.1.4	Dynamic Methods of Determining Elastic Constants	349
7.1.5	Instrumented Indentation as a Method of Determining Elastic Constants	352
7.2	Plasticity	355
7.2.1	Fundamentals of Plasticity	355
7.2.2	Mechanical Loading Modes Causing Plastic Deformation ...	357
7.2.3	Standard Methods of Measuring Plastic Properties	358
7.2.4	Novel Test Developments for Plasticity	365
7.3	Hardness	366
7.3.1	Conventional Hardness Test Methods (Brinell, Rockwell, Vickers and Knoop)	368
7.3.2	Selecting a Conventional Hardness Test Method and Hardness Scale	374
7.3.3	Measurement Uncertainty in Hardness Testing (HR, HBW, HV, HK)	376
7.3.4	Instrumented Indentation Test (IIT)	378
7.4	Strength	388
7.4.1	Quasistatic Loading	389
7.4.2	Dynamic Loading	398
7.4.3	Temperature and Strain-Rate Effects	401
7.4.4	Strengthening Mechanisms for Crystalline Materials	402
7.4.5	Environmental Effects	404
7.4.6	Interface Strength: Adhesion Measurement Methods	405
7.5	Fracture Mechanics	408
7.5.1	Fundamentals of Fracture Mechanics	408
7.5.2	Fracture Toughness	410
7.5.3	Fatigue Crack Propagation Rate	419
7.5.4	Fractography	424
7.6	Permeation and Diffusion	426
7.6.1	Gas Transport: Steady-State Permeation	427
7.6.2	Kinetic Measurement	429
7.6.3	Experimental Measurement of Permeability	431
7.6.4	Gas Flux Measurement	433
7.6.5	Experimental Measurement of Gas and Vapor Sorption ...	436
7.6.6	Method Evaluations	440
7.6.7	Future Projections	442
	References	442

8 Thermal Properties

	<i>Wolfgang Buck, Steffen Rudtsch</i>	453
8.1	Thermal Conductivity and Specific Heat Capacity	454
8.1.1	Steady-State Methods	456
8.1.2	Transient Methods	458
8.1.3	Calorimetric Methods	461
8.2	Enthalpy of Phase Transition, Adsorption and Mixing	462
8.2.1	Adiabatic Calorimetry	464
8.2.2	Differential Scanning Calorimetry	465

8.2.3	Drop Calorimetry	466
8.2.4	Solution Calorimetry	467
8.2.5	Combustion Calorimetry	468
8.3	Thermal Expansion and Thermomechanical Analysis	469
8.3.1	Optical Methods	469
8.3.2	Push Rod Dilatometry	470
8.3.3	Thermomechanical Analysis	470
8.4	Thermogravimetry	471
8.5	Temperature Sensors	471
8.5.1	Temperature and Temperature Scale	471
8.5.2	Use of Thermometers	474
8.5.3	Resistance Thermometers	475
8.5.4	Liquid-in-Glass Thermometers	477
8.5.5	Thermocouples	478
8.5.6	Radiation Thermometers	479
8.5.7	Cryogenic Temperature Sensors	480
References	482

9 Electrical Properties

	<i>Bernd Schumacher, Heinz-Gunter Bach, Petra Spitzer, Jan Obrzut, Steffen Seitz</i>	485
9.1	Electrical Materials	486
9.1.1	Conductivity and Resistivity of Metals	486
9.1.2	Superconductivity	487
9.1.3	Semiconductors	488
9.1.4	Conduction in Polymers	490
9.1.5	Ionic Conductors	490
9.1.6	Dielectricity	491
9.1.7	Ferroelectricity and Piezoelectricity	492
9.2	Electrical Conductivity of Metallic Materials	493
9.2.1	Scale of Electrical Conductivity; Reference Materials	493
9.2.2	Principal Methods	494
9.2.3	DC Conductivity, Calibration of Reference Materials	496
9.2.4	AC Conductivity, Calibration of Reference Materials	496
9.2.5	Superconductivity	497
9.3	Electrolytic Conductivity	498
9.3.1	Scale of Conductivity	498
9.3.2	Basic Principles	499
9.3.3	The Measurement of the Electrolytic Conductivity	501
9.4	Semiconductors	507
9.4.1	Conductivity Measurements	507
9.4.2	Mobility Measurements	510
9.4.3	Dopant and Carrier Concentration Measurements	513
9.4.4	I - V Breakdown Mechanisms	518
9.4.5	Deep Level Characterization and Minority Carrier Lifetime	519
9.4.6	Contact Resistances of Metal-Semiconductor Contacts	523

9.5	Measurement of Dielectric Materials Properties	526
9.5.1	Dielectric Permittivity	527
9.5.2	Measurement of Permittivity	529
9.5.3	Measurement of Permittivity Using Microwave Network Analysis	532
9.5.4	Uncertainty Considerations	536
9.5.5	Conclusion	537
	References	537

10 Magnetic Properties

	<i>Joachim Wecker, Günther Bayreuther, Gunnar Ross, Roland Grössinger</i>	541
10.1	Magnetic Materials	542
10.1.1	Diamagnetism, Paramagnetism, and Ferromagnetism	542
10.1.2	Antiferromagnetism, Ferrimagnetism and Noncollinear Magnetism	543
10.1.3	Intrinsic and Extrinsic Properties	544
10.1.4	Bulk Soft and Hard Materials	544
10.1.5	Magnetic Thin Films	544
10.1.6	Time-Dependent Changes in Magnetic Properties	545
10.1.7	Definition of Magnetic Properties and Respective Measurement Methods	545
10.2	Soft and Hard Magnetic Materials: (Standard) Measurement Techniques for Properties Related to the $B(H)$ Loop	546
10.2.1	Introduction	546
10.2.2	Properties of Hard Magnetic Materials	549
10.2.3	Properties of Soft Magnetic Materials	555
10.3	Magnetic Characterization in a Pulsed Field Magnetometer (PFM) ...	567
10.3.1	Industrial Pulsed Field Magnetometer	568
10.3.2	Errors in a PFM	569
10.3.3	Calibration [3.1]	573
10.3.4	Hysteresis Measurements on Hard Magnetic Materials	575
10.3.5	Anisotropy Measurement	576
10.3.6	Summary: Advantages and Disadvantages of PFM	579
10.4	Properties of Magnetic Thin Films	579
10.4.1	Saturation Magnetization, Spontaneous Magnetization ...	579
10.4.2	Magneto-Resistive Effects	583
	References	585

11 Optical Properties

	<i>Tadashi Itoh, Tsutomu Araki, Masaaki Ashida, Tetsuo Iwata, Kiyofumi Muro, Noboru Yamada</i>	587
11.1	Fundamentals of Optical Spectroscopy	588
11.1.1	Light Source	588
11.1.2	Photosensors	590
11.1.3	Wavelength Selection	592

11.1.4	Reflection and Absorption	594
11.1.5	Luminescence and Lasers	598
11.1.6	Scattering	602
11.2	Microspectroscopy	605
11.2.1	Optical Microscopy	605
11.2.2	Near-field Optical Microscopy	606
11.2.3	Cathodoluminescence (SEM-CL)	607
11.3	Magneto-optical Measurement	609
11.3.1	Faraday and Kerr Effects	609
11.3.2	Application to Magnetic Flux Imaging	610
11.4	Nonlinear Optics and Ultrashort Pulsed Laser Application	614
11.4.1	Nonlinear Susceptibility	614
11.4.2	Ultrafast Pulsed Laser	618
11.4.3	Time-Resolved Spectroscopy	620
11.4.4	Nonlinear Spectroscopy	623
11.4.5	Terahertz Time-Domain Spectroscopy	624
11.5	Fiber Optics	626
11.5.1	Fiber Dispersion and Attenuation	627
11.5.2	Nonlinear Optical Properties	630
11.5.3	Fiber Bragg Grating	632
11.5.4	Fiber Amplifiers and Lasers	635
11.5.5	Miscellaneous Fibers	638
11.6	Evaluation Technologies for Optical Disk Memory Materials	641
11.6.1	Evaluation Technologies for Phase-Change Materials	641
11.6.2	Evaluation Technologies for MO Materials	647
11.7	Optical Sensing	649
11.7.1	Distance Measurement	649
11.7.2	Displacement Measurement	651
11.7.3	3-D Shape Measurement	651
11.7.4	Flow Measurement	652
11.7.5	Temperature Measurement	653
11.7.6	Optical Sensing for the Human Body	655
	References	656

Part D Materials Performance Testing

12 Corrosion

	<i>Bernd Isecke, Michael Schütze, Hans-Henning Strehblow</i>	667
12.1	Background	668
12.1.1	Classification of Corrosion	669
12.1.2	Corrosion Testing	670
12.2	Conventional Electrochemical Test Methods	671
12.2.1	Principles of Electrochemical Measurements and Definitions	671
12.2.2	Some Definitions	673

12.2.3	Electrochemical Thermodynamics	674
12.2.4	Complex Formation	676
12.2.5	Electrochemical Kinetics	676
12.2.6	The Charge-Transfer Overvoltage	676
12.2.7	Elementary Reaction Steps in Sequence, the Hydrogen Evolution Reaction	679
12.2.8	Two Different Reactions at One Electrode Surface	681
12.2.9	Local Elements	683
12.2.10	Diffusion Control of Electrode Processes	684
12.2.11	Rotating Disc Electrode (RDE) and Rotating Ring-Disc Electrode (RRDE)	686
12.2.12	Ohmic Drops	689
12.2.13	Measurement of Ohmic Drops and Potential Profiles Within Electrolytes	690
12.2.14	Nonstationary Methods, Pulse Measurements	692
12.2.15	Concluding Remarks	695
12.3	Novel Electrochemical Test Methods	695
12.3.1	Electrochemical Noise Analysis	695
12.4	Exposure and On-Site Testing	699
12.5	Corrosion Without Mechanical Loading	699
12.5.1	Uniform Corrosion	700
12.5.2	Nonuniform and Localized Corrosion	701
12.6	Corrosion with Mechanical Loading	705
12.6.1	Stress Corrosion	706
12.6.2	Corrosion Fatigue	709
12.7	Hydrogen-Induced Stress Corrosion Cracking	714
12.7.1	Electrochemical Processes	715
12.7.2	Theories of H-Induced Stress Corrosion Cracking	716
12.7.3	Environment and Material Parameters	717
12.7.4	Fractographic and Mechanical Effects of HISCC	717
12.7.5	Test Methods	718
12.8	High-Temperature Corrosion	718
12.8.1	Main Parameters in High-Temperature Corrosion	718
12.8.2	Test Standards or Guidelines	719
12.8.3	Mass Change Measurements	721
12.8.4	Special High-Temperature Corrosion Tests	729
12.8.5	Post-Test Evaluation of Test Pieces	731
12.8.6	Concluding Remarks	732
12.9	Inhibitor Testing and Monitoring of Efficiency	732
12.9.1	Investigation and Testing of Inhibitors	733
12.9.2	Monitoring of Inhibitor Efficiency	734
12.9.3	Monitoring Inhibition from Corrosion Rates	736
	References	738

13 Friction and Wear

<i>Ian Hutchings, Mark Gee, Erich Santner</i>	743
13.1 Definitions and Units	743
13.1.1 Definitions	744
13.1.2 Types of Wear	744
13.1.3 Units for Wear	745
13.2 Selection of Friction and Wear Tests	747
13.2.1 Approach to Tribological Testing	747
13.2.2 Test Parameters	748
13.2.3 Interaction with Other Degradation Mechanisms	750
13.2.4 Experimental Planning and Presentation of Results	750
13.3 Tribological Test Methods	751
13.3.1 Sliding Motion	751
13.3.2 Rolling Motion	751
13.3.3 Abrasion	752
13.3.4 Erosion by Solid Particles	753
13.3.5 Scratch Testing	753
13.4 Friction Measurement	754
13.4.1 Friction Force Measurement	754
13.4.2 Strain Gauge Load Cells and Instrumentation	754
13.4.3 Piezoelectric Load Sensors	755
13.4.4 Other Force Transducers	755
13.4.5 Sampling and Digitization Errors	756
13.4.6 Calibration	756
13.4.7 Presentation of Results	758
13.5 Quantitative Assessment of Wear	759
13.5.1 Direct and Indirect Quantities	759
13.5.2 Mass Loss	759
13.5.3 Dimensional Change	759
13.5.4 Volume Loss	760
13.5.5 Other Methods	762
13.5.6 Errors and Reproducibility in Wear Testing	762
13.6 Characterization of Surfaces and Debris	764
13.6.1 Sample Preparation	764
13.6.2 Microscopy, Profilometry and Microanalysis	765
13.6.3 Wear Debris Analysis	767
References	767

14 Biogenic Impact on Materials

<i>Ina Stephan, Peter D. Askew, Anna A. Gorbushina, Manfred Grinda, Horst Hertel, Wolfgang E. Krumbein, Rolf-Joachim Müller, Michael Pantke, Rüdiger (Rudy) Plarre, Guenter Schmitt, Karin Schwibbert</i>	769
14.1 Modes of Materials – Organisms Interactions	770
14.1.1 Biodeterioration/Biocorrosion	770
14.1.2 Biodegradation	771

14.1.3	Summary	771
14.1.4	Role of Biocides	771
14.2	Biological Testing of Wood	774
14.2.1	Attack by Microorganisms	776
14.2.2	Attack by Insects	781
14.3	Testing of Organic Materials	789
14.3.1	Biodeterioration	789
14.3.2	Biodegradation	791
14.3.3	Paper and Textiles	803
14.4	Biological Testing of Inorganic Materials	811
14.4.1	Inorganic Materials Subject to Biological Attack	811
14.4.2	The Mechanisms of Biological Attack on Inorganic Materials	813
14.4.3	Organisms Acting on Inorganic Materials	814
14.4.4	Biogenic Impact on Rocks	818
14.4.5	Biogenic Impact on Metals, Glass, Pigments	823
14.4.6	Control and Prevention of Biodeterioration	824
14.5	Coatings and Coating Materials	826
14.5.1	Susceptibility of Coated Surfaces to Fungal and Algal Growth	826
14.6	Reference Organisms	833
14.6.1	Chemical and Physiological Characterization	833
14.6.2	Genomic Characterization	834
	References	838

15 Material–Environment Interactions

	<i>Franz–Georg Simon, Oliver Jann, Ulf Wickström, Anja Geburtig, Peter Trubiroha, Volker Wachtendorf</i>	845
15.1	Materials and the Environment	845
15.1.1	Environmental Impact of Materials	845
15.1.2	Environmental Impact on Polymeric Materials	848
15.2	Emissions from Materials	860
15.2.1	General	860
15.2.2	Types of Emissions	860
15.2.3	Influences on the Emission Behavior	861
15.2.4	Emission Test Chambers	862
15.2.5	Air Sampling from Emission Test Chambers	863
15.2.6	Identification and Quantification of Emissions	864
15.2.7	Time Behavior and Ageing	866
15.2.8	Secondary Emissions	869
15.3	Fire Physics and Chemistry	869
15.3.1	Ignition	869
15.3.2	Combustion	873
15.3.3	Fire Temperatures	875
15.3.4	Materials Subject to Fire	877
15.3.5	Fire Testing and Fire Regulations	878
	References	883

16 Performance Control: Nondestructive Testing and Reliability Evaluation

Uwe Ewert, Gerd-Rüdiger Jaenisch, Kurt Osterloh, Uwe Zscherpel, Claude Bathias, Manfred P. Hentschel, Anton Erhard, Jürgen Goebbels, Holger Hanselka, Bernd R. Müller, Jürgen Nuffer, Werner Daum, David Flaschenträger, Enrico Janssen, Bernd Bertsche, Daniel Hofmann, Jochen Gäng

	887
16.1 Nondestructive Evaluation	888
16.1.1 Visual Inspection	888
16.1.2 Ultrasonic Examination: Physical Background	889
16.1.3 Application Areas of Ultrasonic Examination	894
16.1.4 Magnetic Particle Inspection	897
16.1.5 Liquid Penetrant Inspection	898
16.1.6 Eddy-Current Testing	899
16.2 Industrial Radiology	900
16.2.1 Fundamentals of Radiology	901
16.2.2 Particle-Based Radiological Methods	906
16.2.3 Film Radiography	907
16.2.4 Digital Radiological Methods	908
16.2.5 Applications of Radiology for Public Safety and Security ...	914
16.3 Computerized Tomography – Application to Organic Materials	915
16.3.1 Principles of X-ray Tomography	915
16.3.2 Detection of Macroscopic Defects in Materials	917
16.3.3 Detection of the Damage of Composites on the Mesoscale: Application Examples	918
16.3.4 Observation of Elastomers at the Nanoscale	919
16.3.5 Application Assessment of CT with a Medical Scanner	920
16.4 Computerized Tomography – Application to Inorganic Materials	921
16.4.1 High-Energy CT	921
16.4.2 High-Resolution CT	921
16.4.3 Synchrotron CT	922
16.4.4 Dimensional Control of Engine Components	923
16.5 Computed Tomography – Application to Composites and Microstructures	927
16.5.1 Refraction Effect	927
16.5.2 Refraction Techniques Applying X-ray Tubes	928
16.5.3 3-D Synchrotron Refraction Computed Tomography	929
16.5.4 Conclusion	932
16.6 Structural Health Monitoring – Embedded Sensors	932
16.6.1 Basics of Structural Health Monitoring	932
16.6.2 Fiber-Optic Sensing Techniques	935
16.6.3 Piezoelectric Sensing Techniques	945
16.7 Characterization of Reliability	949
16.7.1 Statistical Treatment of Reliability	951
16.7.2 Weibull Analysis	952
16.7.3 Reliability Test Strategies	956
16.7.4 Accelerated Lifetime Testing	959

16.7.5	System Reliability	962
16.7.6	System Reliability Estimation in Practice	964
16.A	Appendix	967
References	968

Part E Modeling and Simulation Methods

17 Molecular Dynamics

<i>Masato Shimono</i>	975
17.1	Basic Idea of Molecular Dynamics	975
17.1.1	Time Evolution of the Equations of Motion	975
17.1.2	Constraints on the Simulation Systems	978
17.1.3	Control of Temperature and Pressure	980
17.1.4	Interaction Potentials	985
17.1.5	Physical Observables	987
17.2	Diffusionless Transformation	988
17.2.1	Martensitic Transformation	988
17.2.2	Transformations in Nanoclusters	991
17.2.3	Solid-State Amorphization	993
17.3	Rapid Solidification	995
17.3.1	Glass-Formation by Liquid Quenching	995
17.3.2	Annealing of Amorphous Alloys	999
17.3.3	Glass-Forming Ability of Alloy Systems	1004
17.4	Diffusion	1006
17.4.1	Diffusion in Crystalline Phases	1006
17.4.2	Diffusion in Liquid and Glassy Phases	1008
17.5	Summary	1010
References	1010

18 Continuum Constitutive Modeling

<i>Shoji Imatani</i>	1013
18.1	Phenomenological Viscoplasticity	1013
18.1.1	General Models of Viscoplasticity	1013
18.1.2	Inelasticity Models	1015
18.1.3	Model Performance	1016
18.2	Material Anisotropy	1018
18.2.1	Description of Material Anisotropy	1018
18.2.2	Initial Anisotropy	1019
18.2.3	Induced Anisotropy	1021
18.3	Metallothermomechanical Coupling	1023
18.3.1	Phase Changes	1023
18.3.2	Numerical Methodology	1025
18.3.3	Applications to Heat Treatment and Metal Forming	1025

18.4	Crystal Plasticity	1026
18.4.1	Single-Crystal Model	1026
18.4.2	Grain Boundary Sliding	1029
18.4.3	Inhomogeneous Deformation	1029
	References	1030

19 Finite Element and Finite Difference Methods

	<i>Akira Tezuka</i>	1033
19.1	Discretized Numerical Schemes for FEM and FDM	1035
19.2	Basic Derivations in FEM and FDM	1037
19.2.1	Finite Difference Method (FDM)	1037
19.2.2	Finite Element Method (FEM)	1038
19.3	The Equivalence of FEM and FDM Methods	1041
19.4	From Mechanics to Mathematics: Equilibrium Equations and Partial Differential Equations	1042
19.4.1	Heat Conduction Problem in the Two-Dimensional Case ..	1043
19.4.2	Elastic Solid Problem in the Three-Dimensional Case	1043
19.5	From Mathematics to Mechanics: Characteristic of Partial Differential Equations	1047
19.5.1	Elliptic Type	1048
19.5.2	Parabolic Type	1048
19.5.3	Hyperbolic Type	1048
19.6	Time Integration for Unsteady Problems	1049
19.6.1	FDM	1049
19.6.2	FEM	1050
19.7	Multidimensional Case	1051
19.7.1	Finite Difference Method	1051
19.7.2	Finite Element Method	1052
19.8	Treatment of the Nonlinear Case	1055
19.9	Advanced Topics in FEM and FDM	1055
19.9.1	Preprocessing	1055
19.9.2	Postprocessing	1056
19.9.3	Numerical Error	1056
19.9.4	Relatives of FEM and FDM	1057
19.9.5	Matrix Calculation and Parallel Computations	1057
19.9.6	Multiscale Method	1059
19.10	Free Codes	1059
	References	1059

20 The CALPHAD Method

	<i>Hiroshi Ohtani</i>	1061
20.1	Outline of the CALPHAD Method	1062
20.1.1	Description of Gibbs Energy	1062
20.1.2	Equilibrium Conditions	1064
20.1.3	Evaluation of Thermodynamic Parameters	1065

20.2	Incorporation of the First-principles Calculations into the CALPHAD Approach	1066
20.2.1	Outline of the First-principles Calculations	1066
20.2.2	Gibbs Energies of Solution Phases Derived by the First-principles Calculations	1067
20.2.3	Thermodynamic Analysis of the Gibbs Energies Based on the First-principles Calculations	1071
20.2.4	Construction of Stable and Metastable Phase Diagrams	1071
20.2.5	Application to More Complex Cases	1073
20.3	Prediction of Thermodynamic Properties of Compound Phases with First-principles Calculations	1079
20.3.1	Thermodynamic Analysis of the Fe–Al–C System	1079
20.3.2	Thermodynamic Analysis of the Co–Al–C and Ni–Al–C Systems	1083
	References	1090

21 Phase Field Approach

	<i>Toshiyuki Koyama</i>	1091
21.1	Basic Concept of the Phase-Field Method	1092
21.2	Total Free Energy of Microstructure	1093
21.2.1	Chemical Free Energy	1093
21.2.2	Gradient Energy	1095
21.2.3	Elastic Strain Energy	1097
21.2.4	Free Energy for Ferromagnetic and Ferroelectric Phase Transition	1101
21.3	Solidification	1102
21.3.1	Pure Metal	1102
21.3.2	Alloy	1104
21.4	Diffusion-Controlled Phase Transformation	1105
21.4.1	Cahn–Hilliard Diffusion Equation	1105
21.4.2	Spinodal Decomposition and Ostwald Ripening	1107
21.5	Structural Phase Transformation	1108
21.5.1	Martensitic Transformation	1108
21.5.2	Tweed-Like Structure and Twin Domain Formations	1108
21.5.3	Twin Domain Growth Under External Stress and Magnetic Field	1109
21.6	Microstructure Evolution	1110
21.6.1	Grain Growth and Recrystallization	1110
21.6.2	Ferroelectric Domain Formation with a Dipole–Dipole Interaction	1111
21.6.3	Modeling Complex Nanogranular Structure Formation	1112
21.6.4	Dislocation Dynamics	1112
21.6.5	Crack Propagation	1113
	References	1114

22 Monte Carlo Simulation

<i>Xiao Hu, Yoshihiko Nonomura, Masanori Kohno</i>	1117
22.1 Fundamentals of the Monte Carlo Method	1117
22.1.1 Boltzmann Weight	1118
22.1.2 Monte Carlo Technique	1118
22.1.3 Random Numbers	1119
22.1.4 Finite-Size Effects	1120
22.1.5 Nonequilibrium Relaxation Method	1121
22.2 Improved Algorithms	1121
22.2.1 Reweighting Algorithms	1121
22.2.2 Cluster Algorithm and Extensions	1122
22.2.3 Hybrid Monte Carlo Method	1123
22.2.4 Simulated Annealing and Extensions	1124
22.2.5 Replica Monte Carlo	1125
22.3 Quantum Monte Carlo Method	1126
22.3.1 Suzuki-Trotter Formalism	1126
22.3.2 World-Line Approach	1126
22.3.3 Cluster Algorithm	1127
22.3.4 Continuous-Time Algorithm	1128
22.3.5 Worm Algorithm	1129
22.3.6 Auxiliary Field Approach	1130
22.3.7 Projector Monte Carlo Method	1130
22.3.8 Negative-Sign Problem	1132
22.3.9 Other Exact Methods	1133
22.4 Bicritical Phenomena in $O(5)$ Model	1133
22.4.1 Hamiltonian	1134
22.4.2 Phase Diagram	1134
22.4.3 Scaling Theory	1135
22.5 Superconductivity Vortex State	1137
22.5.1 Model Hamiltonian	1138
22.5.2 First Order Melting	1138
22.5.3 Continuous Melting: $B ab$ Plane	1141
22.6 Effects of Randomness in Vortex States	1143
22.6.1 Point-Like Defects	1143
22.6.2 Columnar Defects	1144
22.7 Quantum Critical Phenomena	1146
22.7.1 Quantum Spin Chain	1146
22.7.2 Mott Transition	1147
22.7.3 Phase Separation	1148
References	1149
Acknowledgements	1159
About the Authors	1161
Detailed Contents	1185
Subject Index	1203

Subject Index

- γ - γ angular correlation 250
 γ -ray 247–250
 ω - 2θ (θ - 2θ) scan 233
 xyz actuator 318
 λ_c (cut-off) filter 313
 λ_s (sampling) filter 313
 0.2% proof stress 392
 ^{14}C -labeling 798
 2-D parameter 314
 2-D-ACAR (2-D-angular correlation of annihilation radiation) 250
 2-D-angular correlation of annihilation radiation (2-D-ACAR) 250
 3-D areal measurement 310
 3-D parameter 315
 3-D-TEM (three-dimensional TEM) 276
-
- A**
- ab initio calculations 1061
 abrasion 745, 813
 abrasion testing 752
 abrasive
 – wear 752
 abrasive wear 745
 absorbance spectrum 148
 absorbed energy 399
 absorption 211, 594
 – change 623
 – coefficient 256, 595
 – edge 597
 AC conductivity
 – calibration 496
 AC method 496
 Acarospora fuscata 819
 accelerated lifetime testing (ALT) 959
 accreditation 8
 accuracy class of instrument 69
 acoustic detection 786
 acoustic gas
 – thermometer 472
 acrylic resin 824
 actinobacteria 818
 actinomycetes 817
 activation
 – analysis 160
 – energy 643, 646
 – thermal 401
- active mode-locking 620
 activity 1065
 adaptive finite element method 1056
 additive
 – biocides 861
 – flame retardants 861
 – photoinitiators 861
 – plasticisers 861
 – stabilizers 861
 adenosine triphosphate 830
 adhesive strength 406
 adiabatic calorimetry 461
 adiabatic potential 244
 ADR (automated defect recognition) 914
 aerobic 798
 AFNOR 799
 ageing 848, 866
 – accelerated 775
 – artificial 775
 – evaporative 775
 AgInSbTe 642
 AGM (alternating gradient field magnetometer) 545, 553
 AGM/AFGM (alternating (field) gradient magnetometer) 582
 algae 812, 814, 827
 algal 827
 alloy 15
 alloy semiconductor system 1085
 ALT (accelerated lifetime testing) 959
 alternating (field) gradient magnetometer (AGM/AFGM) 582
 alternating gradient field magnetometer (AGM) 545, 553
 American Society for Testing and Materials (ASTM) 104, 751, 798
 amino acids (peptide) 258
 Amontons law 744
 amorphous 276
 – solid 642
 – state 641
 amplified ribosomal DNA restriction analysis (ARDRA) 835
 amplified spontaneous emission (ASE) 600, 636
 AMR (anisotropic magneto-resistance) 583
- AMRSF (average matrix relative sensitivity factor) 292, 297
 anaerobic 798
 anaglyph image 275
 analysis of variance (ANOVA) 41
 analytical chemistry 145
 analytical reagent 177
 anchor monitoring 942
 Andersen method 982
 andesite 812
 anelastic relaxation 242
 anelastic strain 231
 anelasticity 231
 angle-resolved photoemission spectroscopy (ARPES) 517
 angle-resolved XPS 282
 angular momentum 229
 angular-momentum-resolved density of state 1082
 anharmonic potential 615
 anisotropic axes 1018
 anisotropic magneto-resistance (AMR) 583
 anisotropy 554, 555
 anobiid 785
 Anobium punctatum 787
 anobium punctatum 785, 786
 anomalous dispersion 213, 238
 – method 232
 ANOVA (analysis of variance) 41
 antibacterial 809, 831
 antiferromagnetism 543
 antimicrobial 809
 antiphase boundary 254
 anti-Stokes scattering 603
 ants 782
 APCI (atmospheric pressure chemical ionization) 172
 APD (avalanche photodiode) 937
 apertureless SNOM 225
 APMP (Asian-Pacific Metrology Program) 29
 applications and limitations of surface measurement 322
 arc lamp 588
 Archard wear equation 746
 ARDRA (amplified ribosomal DNA restriction analysis) 835
 area specific emission rate 866, 868
 areal 315
 arithmetic average 314

- arithmetic mean height 315
 ARPES (angle-resolved photoemission spectroscopy) 517
 Arrhenius
 – equation 491, 1071
 – law 1072
 – plot 522, 647
 ascomycete 776
 ASE 601
 ASE (amplified spontaneous emission) 600, 636
 Asian–Pacific Metrology Program (APMP) 29
 ASTM (American Society for Testing and Materials) 104, 751, 798
 ASTM C 1341-00 348
 ASTM C 1419-99a 349
 ASTM C 674-88 348
 ASTM D 3379-75 347
 ASTM D 638 347
 ASTM D 882 347
 ASTM E 111 347, 352
 ASTM E 132 347
 ASTM E 143 348
 ASTM E 1875 351
 ASTM E 1876 351
 ASTM E 1876-01 350
 astrakanite 822
 athermal stress 402
 atmospheric pressure chemical ionization (APCI) 172
 atomic
 – absorption spectrometry (AAS) 156, 193
 – emission detector (AED) 168
 – emission spectrometry (AES) 146
 – force microscopy (AFM) 224, 282, 292, 303, 309, 310, 318, 383, 606, 757, 796, 825
 – image 607
 – operation mode 319
 – scanner 319
 – force tip 606
 – layer 282, 298
 – mixing 300, 301
 – probe 226
 – scattering factor 213, 232
 – spectrometry 156
 ATR (attenuated total reflection) 188
 attenuated total reflection (ATR) 188
 attenuation length 297
 Auger electron 222, 231, 272
 – spectroscopy (AES) 184, 231, 272, 281, 282, 285, 645, 695
 – differential mode 286
 – direct mode 286
 autocorrelation function 618
 autofocus 310, 316
 automated defect recognition (ADR) 914
 avalanche breakdown 519
 avalanche photodiode (APD) 937
 average matrix relative sensitivity factor (AMRSF) 292, 297
- B**
-
- BAAS (British Association for the Advancement of Science) 25
 Bacillus 817
 back stress 1015
 background noise 323
 backscattered electron 222
 backscattering
 – electron 271
 – factor 291
 backward difference scheme 1037
 bacteria 776, 814
 Bailey–Hirsch 403
 balanced design 41
 BAM reference procedures 123
 bandgap 597
 barium titanate (BaTiO₃) 492
 bark beetle 787
 basalt 812
 basidiomycete 776
 BaTiO₃ (barium titanate) 492
 Bauschinger effect (BE) 393
 Bavendam-test 777
 BCCD (buried charge-coupled device) 516
 BCS gap 598
 BE (Bauschinger effect) 393
 bearing curve parameter 315
 Beer's law 595
 beetle 781, 783, 785
 – wood boring 785
 bending 395
 BER (bit error rate) 645, 646
 Berg–Barrett method 221
 Bi-CGSTAB (biconjugate gradient stabilized method) 1058
 biconjugate gradient stabilized method (Bi-CGSTAB) 1058
 binding energy
 – reference 295
 biological testing
 – wood 774
 biocidal activity 773
 – algistatic 773
 – bacteriostatic 773
 – fungistatic 773
 biocide 772, 811
 – permethrine 868
 biocorrosion 770, 771, 789, 818
 biodegradation 770, 771, 792
 biodeterioration 770, 789, 791, 810, 811, 813
 biofilm 770, 791, 811
 biofouling 770
 biogenic impact 770
 biological attack 848
 biological patina 816
 biomaterial 16, 625
 biomolecule 218, 258, 605
 biopitting 813
 biostatic activity 773
 biostatic repellency 773
 BIPM (Bureau International des Poids et Mesures) 9, 26
 BIPM data bases 124
 birefringence 236, 617
 bismuth- and gallium-doped yttrium-iron garnets 611
 bispectral luminescence radiance factor (BLRF) 151
 bit error rate (BER) 645, 646
 Bitter decoration technique 609
 black coating 815
 black patina 815
 blackbody 480, 653
 – radiation 653
 blend 790
 Bloch waves 220
 BLRF (bispectral luminescence radiance factor) 151
 blue LED 589
 blue stain 776
 blu-ray disc 641
 body contours 655
 body-centered cubic 1027
 Boltzmann
 – approximation 512
 – constant 474
 – distribution 599
 bomb calorimeter 468
 bookkeeping method 979
 Born approximation 213
 Borrmann effect 220, 257
 boson peak 1002
 BOTDA (Brillouin optical-fiber time-domain analysis) 943
 bottom-up approach 41
 boundary
 – element method (BEM) 1057
 – lubrication 746, 750

- boundary condition
 – periodic 978
 boundary-fitted finite difference method 1056
 boundary-value problem 1033
 boxcar integrator 621
 Bragg
 – condition 212, 252, 257
 – resonance wavelength 938
 – wavelength 634
 brain tomography 655
 brass 813
 bright field image 219, 252
 Brillouin optical-fiber time-domain analysis (BOTDA) 943
 Brillouin scattering 603, 941
 British Association for the Advancement of Science (BAAS) 25
 brittle fracture 390, 425
 broadband frequency 318
 broadband optical continuum 640
 bronze 813
 brown rot 776
 Bubnov–Galerkin method 1039
 bulging 393
 bulk
 – conduction 523
 – method 189
 – modulus 1069
 Bureau International des Poids et Mesures (BIPM) 9, 26
 Burgers vector 252
 buried charge-coupled device (BCCD) 516
 burner rig tests 729
 burning rate 873
 business domains (Europe) 132
- C**
- C/N (carrier-to-noise ratio) 645, 646
 cabinet based simulation 827
 cabinet based test 804
 Cahn–Hilliard diffusion equation 1105
 calcium carbonate 812
 calibration
 – and measurement capability (CMC) 10, 47, 120
 – diagram 70
 – interval 49
 – liquid chromatography 169
 – of instruments 323
 – of load cell 345, 346
 – of measurement instruments 70
 – of measuring and testing devices 48
 – of optical instruments 324
 – of SPM 324
 – using reference procedures 122
 Callendar–van Dusen equation 475
 Caloplaca flavescens 822
 calorific value 468
 CALPHAD 1061
 Camponotus 785
 Candelariella vitellina 819
 cantilever 224, 318
 capability of test systems 114
 capacitance 251, 492
 – measurement 514
 – spectroscopy 520
 – transient 522
 capillary
 – electrophoresis (CE) 171, 268
 – gel electrophoresis (CGE) 171
 – isoelectric focusing (CIEF) 171
 – isotachopheresis (CITP) 171
 – zone electrophoresis (CZE) 171
 carbon 259
 – balance 801
 – ceramic resistor 481
 – fiber-reinforced polymer (CFRP) 946
 – glass resistor 481
 – resistor 481
 – utilization profile 834
 carbonitride
 – complex 1085
 carotene 820
 carpenter ant 783, 785, 786
 Carrara marble 812
 carrier concentration 510
 – intrinsic 520
 – measurement 511, 513
 – profile 514
 – temperature dependence 512
 carrier-to-noise ratio (C/N) 645, 646
 CARS (coherent anti-Stokes Raman spectroscopy) 654
 CASCO (Committee on Conformity Assessment) 8
 cathode discharge lamp 156
 cathodic reaction of corrosion 677
 cathodoluminescence (CL) 222, 607
 – image 608
 – spectroscopy 605, 607
 – spectrum 608
 Cauchy 341
 cavitation erosion 745
 cavity perturbation method 536
 CBED (convergent beam electron diffraction) 235, 272
 CC (correlation coefficient) 954
 CCD (charge-coupled device) 150, 594, 599
 CCT (center-cracked tension) 714
 cct (critical crevice corrosion temperature) 703
 Cd_{1-x}Mn_xTe quantum well 611
 CE (counter electrode) 672
 cell constant 503
 cellulose 776
 cement 812
 cementite 1079
 CEN (European Standards Organization) 132
 CENELEC (European Electrotechnical Standardization Commission) 132
 censored test 956
 center line average (CLA) 314
 center-cracked tension (CCT) 714
 central difference scheme 1037
 ceramics 15
 – shear modulus 349
 – Young's modulus 347
 CERT (constant-extension-rate test) 715
 certified reference material (CRM) 6, 120, 149, 174
 CFD (constant fraction discriminator) 621
 CG (conjugate gradient method) 1058
 CGPM (General Conference on Weights and Measures) 26
 chalcogenide
 – alloy 641
 – fiber 639
 – film 641
 – glass 642
 challenge test 829
 channeling effect 241, 271
 characteristics 19
 characterization 308
 charge transfer devices 159
 charge-coupled device (CCD) 150, 594, 599
 – camera 622
 charged particle activation analysis (CPAA) 165
 Charpy impact test 110, 398
 chemical
 – environment 260, 848

- etching 252
- free energy 1093
- potential 1065
- shift 259
- standard 198
- substitution 232
- chemolithotrophic bacteria 815
- chemoorganotrophic microorganism 814
- chemophysical analysis 267
- chipping 818
- chirality 268
- chirped grating 634
- chromatic dispersion 628
- chromatogram 267, 866
- CIPM (Comité Internationale des Poids et Mesures) 26, 27, 45
- CIPM Consultative Committee 30
- circular
 - dichroism (CD) 268
 - polarization 247
 - polarized light 268
 - polarized photoluminescence 247
- cis-aconitic acid 823
- citric acid 818, 823
- CL (cathodoluminescence) 222, 607
- CLA (center line average) 314
- cladding pumping 637
- Cladosporium resinae 823
- classification
 - of corrosion 669
 - of material 13
- Clausius–Mosotti equation 472
- cleavage fracture 425
- clock 646
- cluster 239
 - expansion method (CEM) 1066
 - interaction 1066
 - ion 305
 - variation method (CVM) 1066
- clustering 1063
- CMA (cylindrical mirror analyzer) 185
- CMC (calibration and measurement capability) 10, 47, 120
- CMC data base 124
- CMR (colossal magneto-resistance) 584
- CNR (contrast-to-noise ratio) 905
- Co–Al 1073
- Co–Al–C 1083
- coarse-grained (CG) HAZ 418
- coating 826
- coating material 826
- coaxial line configuration 531
- coaxial probe
 - open ended 531
 - short-terminated 531
- coaxial test fixture 531
- Code d'Indexation des Materiaux de Reference (COMAR)
 - reference material (RM) database 99
- coefficient of friction 744
- coefficients of thermal expansion (CTE) 722
- coercimeter 547, 558
- coercivity 547, 558
- coherent anti-Stokes Raman spectroscopy (CARS) 654
- collaborative trial in sampling (CTS) 42
- colloid 274
- color center 244
- color plot 313
- coloration 820
- colossal magneto-resistance (CMR) 584
- combined measurement uncertainty 72
- combustion 873
 - calorimetry 468
 - product 874
- Comité Internationale des Poids et Mesures (CIPM) 26, 27, 45
 - Consultative Committee 27, 28
 - Mutual Recognition Arrangement (MRA) 30
- Committee on Conformity Assessment (CASCO) 8
- compact tension (CT) 714
- compact test specimen 411
- comparative method 457
- comparison of static and dynamic methods 352
- complex
 - carbonitride 1085
 - dielectric constant 595
 - optical indices 529
 - permeability 563
 - permittivity measurement 529
 - refractive index 626
- composite 16
 - monitoring of 949
 - strengthening 407
- composition depth profiling 287
- composition gradient energy 1096
- compostability
 - in soil 799
- compound analysis 195
- compression test 393
- computed radiography (CR) 909
- computed tomography 275, 779
- concrete 877
- concreting 820
- condition monitoring 932
- conductivity
 - electrical 485
 - electrolyte solution 503
 - electrolytic 498
 - fishbone 503
 - high-purity water 505
 - ionic 491
 - measurement 494
 - metallic material 493
 - metals 494
 - molar 500
 - polymer 490
 - polymeric materials 490
 - rectangular shaped sample 509
 - scale 499
 - semiconductor 508
 - temperature correction 503
 - thermal 454
 - thin layer 509
 - voltage–current measurement 495
- conductivity cell
 - differential 504
 - four-electrode 505
 - inductive 505
 - the principle 507
 - three-electrode 505
 - two-electrode 504
- conductor resistance 486
- cone angle 312
- confidence
 - bound 955
 - interval 955
 - ring 7
- configuration coordinate 244
- configurational entropy 1066
- confocal 218
 - microscope 309
 - microscopy 316
- conformation 262, 268, 276
- conformity assessment 7, 133
 - body (CAB) 8, 133
- Co–Ni–Al–C 1085
- conjugate gradient method (CG) 1058
- consolidant 816
- constant fraction discriminator (CFD) 621
- constant strain testing 708

- constant-extension-rate test (CERT) 715
- constrained interpolated profile (CIP) method 1057
- contact
- geometry 749
 - metal–semiconductor 523
 - mode 319
 - resistance 524
- contacting 308
- contamination of samples 45
- continuous excitation 351
- continuous wave (CW) 154
- contour plot 313, 1083
- contrast-to-noise ratio (CNR) 905
- control of damage 303
- controlled potential coulometry 176, 177
- conventional microscopy 605
- conventional MOL 611
- convergent beam electron diffraction (CBED) 235, 272
- pattern 235
- convolution analysis 622
- COOMET (Euro–Asian Cooperation of National Metrology Institutes) 29
- Cooper pair 598
- coordination number 239
- copolymer 790
- copper 493, 813
- coptoterm 785
- Coptotermes formosanus 787
- core electron 231
- excitation 231
- core excitation 239
- edge 232
- corner effect 1021
- correct sampling protocol 40
- correction algorithm 516
- correlated spectroscopy (COSY) 265
- correlation coefficient (CC) 954
- correlation functions 1066
- corrosion 667, 812, 813
- anodic reaction of 677
 - fatigue 710
 - process 669
 - product 875
 - products 701
 - rate 700
 - testing 718
 - thermodynamics of 674
 - uniform 700
- COSY (correlated spectroscopy) 265
- Cotton effect 268
- coulometry 176
- counter electrode (CE) 672
- coupling 1023
- spin–orbit 230, 245
 - spin–spin 260
- Courant number 1051
- Courant–Friedrichs–Lewy (CFL) condition 1051
- CPAA (charged particle activation analysis) 165
- cpt (critical pitting temperature) 703
- CR (computed radiography) 909
- crack 1113
- determination 925
 - initiation 400
 - propagation 400
 - propagation testing 713
 - tip opening displacement (CTOD) 408, 410
- Crank–Nicolson method 1049
- crashworthiness 366
- creep 319, 1014
- crevice corrosion 702
- critical crevice corrosion temperature (cct) 703
- critical magnetic induction 498
- critical pitting temperature (cpt) 703
- critical temperature 497
- CRM (certified reference material) 6, 120, 149, 174
- cross effect 1021
- cross peak 265
- cross-conductivity standard 495
- cross-sectional HRTEM 256
- crust 812, 819
- crystal
- diffraction 212
 - plasticity 1026
 - rotation 254
 - slip 1026
 - state 641
- crystallinity 793
- crystallite size 273
- crystallization 642
- speed 643, 644
 - temperature 643
- CT (compact tension) 714
- CTE (coefficients of thermal expansion) 722
- CTS (collaborative trial in sampling) 42
- Curie
- point 648
 - temperature 493, 543, 553, 562, 579, 580
- current conduction mechanism 524
- current injection 600
- cut-back method 627
- cut-off 312
- effect 232
 - filter 312
 - digital Gaussian 312
- C–V method 514
- CW (continuous wave) 154
- CW laser 601, 618
- cyanobacteria 814
- cylinder method 456
- cylindrical mirror analyzer (CMA) 185
-
- ## D
-
- damage 935
- cross section 303
 - detection 935, 947
- dark current 519
- dark glass 642
- dark-field (DF) 271
- image 219
- data determination
- reference 121
- data fusion 934
- DBTT (ductile-to-brittle transition temperature) 399
- DC (direct current) 147, 159
- DC conductivity 496
- DDA (digital detector array) 911, 913
- de Broglie waves 212
- dead time 289
- Debye
- relaxation model 527
 - rings 233
- Debye length 515
- correction 516
 - problem 516
- Debye–Scherrer camera 233
- decohesion theory 716
- deep cavity 322
- deep level 251
- transient spectroscopy (DLTS) 251, 508, 519
 - signal 522
 - spectrum 521
 - technique 521
- deep level transient spectroscopy (DLTS) 519
- defect 239
- complex 239

- definition 793
- definitive method 119
- deflection method 778
- deformation map 401
- degradation 789, 813
 - enzymatic 796
 - mechanisms 950
 - photo 792
 - test 958
 - thermal 792
- degree of order 1076
- delta layer 301
- demagnetizing field 579
- denaturing gradient gel electrophoresis (DGGE) 837
- dense random packing (DRP) model 1001
- density functional theory (DFT) 1066
- density of states (DOS) 1077
- depletion
 - approximation 514
 - capacitance 521
- deposit corrosion 704
- depth
 - of field 320
 - profile 241, 250
 - profiling 147, 159
 - resolution 292, 299
- derivatization
 - with dinitrophenylhydrazine (DNPH) 864
- design 308
- desquamation 818
- Desulfovibrio desulfuricans 815
- detection 264
- detector
 - thermal 591
- deterioration 811, 813
- Deutsche Industrie Norm (DIN) 794
- DF (dark-field) 271
- DFG (difference-frequency generation) 616
- DFT (density functional theory) 1066
- DGGE (denaturing gradient gel electrophoresis) 837
- diamagnetic current 259
- diamond tip 312
- dielectric
 - constant 491
 - constant gas thermometer 472
 - displacement 492
 - effect 526
 - function 625
 - loss 492, 526
 - loss tangent 527
 - material 491, 526
 - metrology 529
 - permittivity 527, 529, 535
 - permittivity spectrum 528
 - polarization 526
 - property 526
 - relaxation 242, 526, 527
 - resonance 529
- dielectric constant
 - complex 595
- difference-frequency generation (DFG) 616
- differential 623
 - amplifier (DA) 673
 - cell 504
 - scanning calorimetry 461
 - thermal analysis 643
- diffraction 211, 212
 - blazed grating 593
 - limit 605, 607
 - mode 219
- diffractometer 233
- diffuse scattering 273
- diffuse-interface model 1092
- diffusion 426, 1006
 - coefficient 242
 - control of electrode process 684
 - controlled phase transformation 1105
 - equation 1105
- diffusion rate
 - thermal 642, 643
- diffusivity
 - thermal 454
- digital
 - storage oscilloscope 621
- digital detector array (DDA) 911, 913
- digital Gaussian
 - cut-off filter 312
- dilatometry 469
- dimensional control 923
- dimetric 313
- dimple 425
- DIN (Deutsche Industrie Norm) 794
- diorite 812
- dipole moment 492
- dipole-coupled 264
- dipole–dipole interaction 230, 261, 266, 1101
- direct current (DC) 147, 159
- direct heating method 457
- direct method 232, 259
- Dirichlet boundary condition 1037
- disappearance cross section 305
- discrete Fourier transform 318
- discretized numerical scheme 1035
- discrimination
 - fungal species 835
 - fungal strains 835
- disintegration 795
- dislocation 239, 249, 252, 355, 1112
 - edge 356
 - motion 258
 - screw 356
 - theory 716
- dispersion
 - compensation 635
 - parameter 629
 - shifted fiber 629
- displacement–strain relationship 1044
- display 490
- dissolved organic carbon (DOC) 799
- distributed sensor 934, 945
- distributed strain measurement 940
- distributed strain profile 944
- DLTS (deep level transient spectroscopy) 519
- DOC (dissolved organic carbon) 799
- documentary standard 309
- domain-wall displacement detection (DWDD) 649
- dominant texture direction 322
- donor 489
- dopant
 - atom 300
 - concentration 302
 - distribution 282
- doped semiconductor 625
- doping profiling 514
- Doppler effect 251
- DOS (density of states) 1077
- double quantum process 262
- double-cantilever displacement gage 411
- double-clad fiber 638
- Dresden agreement 133
- drift mobility 513
- drop calorimetry 461
- Drude model 597
- drug detection 626
- drywood termite 785
- ductile fracture 390, 425
- ductile-to-brittle transition temperature (DBTT) 399

- duplicate method
 – for uncertainty estimation 41
 durability of wood 774
 DVD-RAM 641, 644
 DVD-RW 641
 DWDD (domain-wall displacement detection) 649
 dynamic
 – effect 235
 – heterogeneity 528
 – loading 398
 – mechanical analysis 469
 – methods of determining elastic constants 349
 – motion 259
 – range 318
 – shear modulus 351
 – SIMS 283, 299
 – strain aging 402
 – theory 212, 219, 256
 – Young's modulus 350
- E**
- EAL (European Cooperation for Accreditation of Laboratories) 377
 easy magnetization direction (EMD) 578
 EBIC (electron-beam-induced current) 222
 eco-efficiency 847
 EDFA (Er-doped fiber amplifier) 635, 636
 EDFA configuration 636
 EDMR (electrically detected magnetic resonance) 247
 effective area of fiber 632
 effective cluster interaction energies 1066
 effective density of states 512
 effective interaction energy 1068
 effective mass 512, 517
 effective thickness 414
 effectiveness 780
 efficiency 305
 effluorescence 818
 EFPI (extrinsic FPI sensor) 937
 Egypt 23
 EHL (elastohydrodynamic lubrication) 750
 eigenstrain 1097
 Einstein coefficient 599
 Einstein relation 491
 elastic
 – aftereffect 231
 – backscattering spectrometry (EBS) 297
 – compliance method 414
 – constant 340, 341
 – limit 355, 391
 – modules 273
 – modulus 353
 – modulus, measurement uncertainty 72
 – scattering 602
 – solid problem 1043
 – strain energy 1097
 elastic constants
 – resonance techniques 350
 – ultrasonic pulse technique 349
 elasticity 6, 340
 elastic-plastic fracture mechanics (EPFM) 408
 elastohydrodynamic lubrication (EHL) 750
 electric conductivity 597
 electric field gradient 251
 electric potential-difference technique 422
 electric susceptibility 595
 electrical
 – energy dissipation 526
 – modeling 475
 – property 485, 778
 – sheet 559
 – storage 485
 electrical conductivity 485
 – eddy current method 494
 – measurement method 494
 – metallic materials 485
 – voltage-current method 494
 electrically detected magnetic resonance (EDMR) 247
 electrochemical
 – impedance spectroscopy (EIS) 695
 – kinetics 676
 – noise analysis (ENA) 695
 – testing 671
 electrode kinetics 671
 electrodeposition 174
 electrolytic conductivity 485, 498
 – measurement 501
 electron 211
 – attenuation length 286
 – beam induced current (EBIC) 508
 – capture detector (ECD) 168
 – charge density plot 1082
 – cloud 246
 – detector 289
 – diffraction (ED) 645
 – energy-loss spectroscopy (EELS) 179, 230
 – nuclear double resonance (ENDOR) 246
 – paramagnetic resonance (EPR) 230
 – paramagnetic resonance (EPR) spectroscopy 197
 – probe microanalysis (EPMA) 285
 – probe microanalyzer (EPMA) 272
 – probe microscopy 282
 – probe x-ray microanalyzer (EPMA) 180
 – spin resonance (ESR) 230
 electron channeling 220
 – pattern (ECP) 270
 electron lattice coupling 244
 electron paramagnetic resonance (EPR) 245
 electron-beam-induced current (EBIC) 222
 electronic
 – density 232
 – dipolar transitions 244
 – materials 485
 – polarization 492
 – Raman scattering 604
 – spins 229
 electron-probe microanalyzer (EPMA) 644
 electrooptic sampling 626
 element 239, 275, 1034
 – analysis 226
 ellipsometry 298, 595, 626, 644
 elliptically polarized light 268
 elongation
 – uniform 392
 embedded atom method (EAM)
 – potential 985
 embedded sensor 933
 embedded-atom method 985
 embedment techniques 946
 EMD (easy magnetization direction) 578
 emission 159
 – factor (EF) 866
 – rate (ER) 866
 emission test chamber
 – air exchange rate 862
 – area specific air flow rate 862
 – relative humidity 862
 – temperature 862
 endlessly single-mode PCF 640
 endolithic fungi 819
 endolithic lichen 814

- endoscope 785
 endothermic peak 643
 energy
 – conservation 603
 – dispersion 159
 – dispersive spectrometer (EDS) 181
 – dispersive x-ray (EDX) 272
 – level diagram 285
 – loss 526
 – product 547
 – quantum 211
 – release rate 410
 enhancement technique 313
 environment 789
 environmental
 – compartment 775
 – contaminant 295
 – factors 848
 – scanning electron microscope (ESEM) 185
 – test 646, 649
 – tobacco smoke (ETS) 860
 enzyme 790, 792
 EPFM (elastic–plastic fracture mechanics) 408
 epilithic fungi 814
 epilithic lichen 814
 EPMA (electron-probe microanalyzer) 644
 EPR (electron paramagnetic resonance) 245
 EPS (equivalent penetrometer sensitivity) 906
 EPS (extracellular polymeric compounds) 819
 EPS (extracellular polymeric substances) 823
 Epstein frame 547, 559, 560
 EPTIS (European proficiency testing information system) 89
 equation of elastic equilibrium 342
 equilibrium
 – thermal 474
 equilibrium volume 1069
 equivalent penetrometer sensitivity (EPS) 906
 erasability 645
 Er-doped fiber amplifier (EDFA) 635, 636
 erosion 790, 813
 – by solid particles 745
 – testing 753
 error source 322
 ESIS (European Structural Integrity Society) 366
 estimate of the maximum concentration 43
 estimate of the mean concentration 43
 estimated life 647
 etch pit 252, 356
 ETSI 132
 EU directives 131
 Eu-based MOL 610
 eucentric tilting 321
 EURAMET (European Association of National Metrology Institutes) 29
 Euro–Asian Cooperation of National Metrology Institutes (COOMET) 29
 EUROLAB (European Federation of National Associations of Measurement, Testing, and Analytical Laboratories) 105
 European Association of National Metrology Institutes (EURAMET) 29
 European Cooperation for Accreditation of Laboratories (EAL) 377
 European Electrotechnical Standardization Commission (CENELEC) 132
 European Federation of National Associations of Measurement, Testing, and Analytical Laboratories (EUROLAB) 105
 European proficiency testing information system (EPTIS) 89
 European standardization 131
 European Standards Organization (CEN) 132
 European Structural Integrity Society (ESIS) 366
 EuS MOL 612
 evaluation length 313
 evanescent wave 218, 225, 606
 evolution 264
 Ewald
 – method 979
 – sphere 212, 233
 EXAFS (extended x-ray absorption fine structure) 238
 exchange bias 584
 exchange correlation functional 1067
 exchange interaction 230, 260, 542
 excitation 159
 excited state 244
 exciton 596
 exfoliation 816
 exothermic peak 643
 experiment 623
 exposure furnace 724
 exposure testing at high temperatures 724
 extended defect 239, 252
 extended x-ray absorption fine structure (EXAFS) 238
 extensometer 346
 exterior facade 826
 external magnetic field 260, 1109
 external quantum-effect detector
 – photomultiplier tube 590
 – phototube 590
 external shape 214
 external standard approach 170
 external stress 1109
 extinction coefficient 595, 644
 extinction distance 219, 235
 extracellular polymeric compounds (EPS) 819
 extracellular polymeric substance 817
 extracellular polymeric substances (EPS) 823
 extrinsic FPI sensor (EFPI) 937
 extrinsic stacking fault 255
-
- F**
-
- Fabry–Pérot interferometer (FPI) 937, 938
 Fabry–Pérot resonator 601
 facade paint 827
 face-centered cubic (fcc) 1027
 failure density function 951
 failure mode and effects analysis (FMEA) 965
 failure rate 950
 Faraday
 – cup 290
 – effect 609
 – imaging technique 609
 – method 562
 – microscopy 609, 613
 – rotation 609, 611, 612
 fast neutron activation analysis (FNAA) 160, 167
 fast neutrons 212
 fatigue 399
 – crack propagation 419
 – life 400
 – precrack 411
 – strength 400
 fatigue-limit diagram 400

- fatty acid analysis 833
 FBG fabrication 633
 fcc (face-centered cubic) 1027
 FDM (finite difference method) 1033
 FEA (finite element analysis) 366, 387, 1020
 feature extraction 934
 Fe–Cr 1107
 FEM (finite element method) 1033
 Fe–Mo 1107
 FePt 1112
 Fermi energy 487, 1077
 Fermi level (FL) 288, 294, 512
 ferrimagnetic 647
 ferrimagnetism 543
 ferroelectric
 – domain 1111
 – material 492
 – phase transition 1101
 ferroelectricity 492
 ferromagnetic
 – phase 251
 – phase transition 1101
 – state 1081
 ferromagnetism 1079
 FET (field-effect transistor) 513
 FFP (fitness for purpose) 41
 FIB (focused ion beam) 180, 765
 fiber
 – amplifier 635
 – Bragg grating (FBG) 632, 634, 938
 – dispersion 627
 – fabrication 627
 – laser 637
 – loss 627
 – optic sensor system 937
 – refraction
 x-ray 928
 – reinforced plastics (FRP) 878
 fiber-reinforced material 406
 fiber-saturation point 776
 Fick's first law 1106
 FID (flame ionization detector) 168
 FID (free induction decay) 154, 263
 field
 – and laboratory emission cell (FLEC) 864
 – emission gun 223
 – evaporation 275
 – exposure 804
 – fluctuation 262
 – ion microscope (FIM) 225, 275
 – test 779, 780
 field-effect transistor (FET) 513
 filter 312
 finite difference method (FDM) 1033
 finite element analysis (FEA) 366, 387, 1020
 finite element method (FEM) 1033
 finite volume method (FVM) 1057
 Finnis–Sinclair potential 986
 fire
 – resistive steel 366
 – testing 878
 buildings 879
 electrical engineering 881
 transportation 880
 first boundary condition 1037
 first-order Laue zone (FOLZ) 235
 first-principles calculations 1066
 FISH (fluorescence in situ hybridization) 837
 fishbone 503
 fitness for purpose (FFP) 41
 fixed points of ITS-90 473
 Fizeau interference microscope 317
 FL (Fermi level) 288, 294, 512
 flame ionization detector (FID) 168
 flame photometric detector (FPD) 168
 flame retardant 875
 flame-brushing 633
 FLAPW (full potential linearized augmented plane wave) 1067
 flashover 876
 Flavobacterium 817
 flaw size extraction 923
 flight hole 782
 flow
 – calorimeter 468
 – curve 393
 – through cell 507
 – visualization 653
 fluctuation 242
 fluorescence 149–151
 – line narrowing 600
 – resonant energy transfer (FRET) 269
 fluorescence in situ hybridization (FISH) 837
 fluorochromes 218
 fluorosilicone 824
 fluxmeter 547, 555
 FMEA (failure mode and effects analysis) 965
 FNAA (fast neutron activation analysis) 160, 167
 focused ion beam (FIB) 180, 765
 folic acid 307
 FOLZ (first-order Laue zones) 235
 force standards 757
 force transducer 755
 form fit 312, 313
 formaldehyde 863
 formation enthalpy 1070
 forward difference scheme 1037
 forward projection 300
 forward-focusing effect 298
 Fourier transform (FT) 152, 239, 262, 263
 – inverse 214, 228, 232
 – spectroscopy 227
 Fourier transformation 214, 232, 618, 626
 Fourier-transform filtering 613
 Fourier-transform infrared (FTIR) 440
 Fourier-transform limited 618
 four-point probe 508
 four-sublattice model 1073
 four-wave mixing (FWM) 618, 624, 631
 FPD (flame photometric detector) 168
 FPI (Fabry–Pérot interferometer) 937, 938
 fractal dimension 315
 fractography 424
 fracture
 – mechanics 408
 – toughness 410
 fragmentation 307
 Frank partial dislocation 255
 Frank–Read source 1113
 frass 783–785
 free carrier concentration 515
 free energy 1093
 free induction decay (FID) 154, 263
 free volume theory 1001
 frequency
 – analysis 321
 – chirp 617
 – conversion 615, 616
 – domain analysis 318
 – factor 646
 fresh water environment 781
 fretting 744
 friction 743
 – internal 231
 – measurement 747, 754
 FT (Fourier transform) 152, 239, 262, 263

FTIR (Fourier-transform infrared) 440
 full potential linearized augmented plane wave (FLAPW) 1067
 fumigation 825
 function 308
 functional analysis 313
 functional behavior 322
 – of a surface 308
 fungal decay
 – nondestructive testing 778
 fungi 814, 826
 FVM (finite volume method) 1057
 FWM (four-wave mixing) 618, 624, 631

G

gain
 – coefficient 600
 – flattening 636
 – saturation 636
 GaInAs photodiode 519
 Galileo 340
 Gallionella 816
 galvanostat 673
 gamma radiation 778
 gas chromatography (GC) 168, 267, 435
 – infrared (GC-IR) 153
 – with subsequent mass spectrometry (GC/MS) 864
 gas laser 601
 gas thermometer 472, 474
 GaSe 625
 gaseous secondary electron detector (GSED) 186
 Gaussian 624
 Gauss–Seidel method 1058
 GC (gas chromatography) 168, 267, 435
 GD-MS (glow discharge mass spectrometry) 191
 GD-OES (glow discharge optical emission spectrometry) 192
 GD-OES (glow discharge optical emission spectroscopy) 158
 GDP (gross domestic product) 846
 GE (gel electrophoresis) 268
 Ge(Sb₇₅Te₂₅)–Sb 642
 gear method 976
 gel electrophoresis (GE) 268
 General Conference on Weights and Measures (CGPM) 26
 generalized gradient approximation (GGA) 1067

generalized minimal residual method (GMRES) 1058
 generation 308
 generation–recombination noise 243
 geometrical product specification 309
 geometry of the stylus 322
 geotechnical structure 943, 944
 geotextile 804, 943, 944
 germanate fiber 638
 GeTe–Sb₂Te₃ 644
g-factor 229
 GFRP (glass-fiber-reinforced polymer) 946
 GGA (generalized gradient approximation) 1067
 giant magnetoimpedance effect (GMI) 566
 giant magneto-resistance (GMR) 545, 584
 Gibbs energy-composition diagram 1064
 Gibbs free energy 1062
 Giorgi 26
 GIXRR (grazing-incidence x-ray reflectance) 298
 glass 812
 – transition 997
 – transition temperature 641, 643
 glass-fiber-reinforced polymer (GFRP) 946
 glass-forming ability 1004
 glauberite 822
 global trade 130
 glow discharge 146, 147, 158, 159
 glow discharge mass spectrometry (GD-MS) 191
 glow discharge optical emission spectrometry (GD-OES) 192
 glow discharge optical emission spectroscopy (GD-OES) 158
 glowing ignition 872
 glucose monitoring 656
 GMI (giant magnetoimpedance effect) 566
 GMR (giant magneto-resistance) 545, 584
 GMRES (generalized minimal residual method) 1058
 gnawing sound 786
 gold 813
 goniometer 233
 Gorsky relaxation 242
 Gouy method 563
 governing equations 1043

gradient energy 1095
 grain
 – boundary 239, 252, 258, 286, 1029
 – growth 1110
 – refinement 403
 – size 270
 grain boundary
 – small-angle 256
 grand potential 1070
 granite 811
 gravimetric titrimetry 176
 gravimetry 173
 grayscale mapping 313
 grazing-incidence x-ray reflectance (GIXRR) 298
 green wood beetle 787
 grid 1034
 groove 252
 gross domestic product (GDP) 846
 ground state 244
 – analysis 1078
 – degeneracy 512
 group delay dispersion 618
 group velocity dispersion (GVD) 618, 628
 group velocity of Lamb waves 949
 group-IV material
 – semiconducting property 489
 GSED (gaseous secondary electron detector) 186
 G-SIMS 306
 G-SIMS-FPM 307
 guarded hot plate method 456
 guide to the expression of uncertainty in measurement (GUM) 5, 199, 377
 – method 5
 guided wavelength 529
 Guinier plot 273
 Guinier–Preston (GP) zone 273
 GUM (guide to the expression of uncertainty in measurement) 5, 199, 377
 GVD (group velocity dispersion) 618, 628
 gypsum 815

H

HAADF-STEM (high-angle annular dark-field STEM) 241
 Hall
 – constant 510
 – effect probe 609
 – factor 513

- mobility 513
 - Hall–Petch relation 404
 - halo diffraction ring 237
 - halogen cycle 589
 - hard magnetic materials 541
 - hard material
 - magnetically 544
 - hard pulse 263
 - hardness testing 109
 - Havriliak–Negami relaxation function 528
 - HAZ (heat-affected zone) 418
 - hazard class 775
 - hcp (hexagonal close packed) 1027
 - heat 848
 - affected zone (HAZ) 418
 - conduction problem 1043
 - flow meter apparatus 457
 - flux sensor 457
 - release rate 873
 - heating rate 643
 - heavy atom method 232
 - heavy atoms substitution method 259
 - heavy-metal fluoride glass fiber (HMFG) 638
 - helicity 268
 - helium 192
 - Helmholtz coil 554, 562
 - hemicellulose 776
 - hemispherical analyzer (HSA) 185
 - heterogenous mixed electrode 681
 - hexagonal close packed (hcp) 1027
 - Heydweiller bridge 497
 - hidden detail 322
 - high performance liquid chromatography (HPLC) 735
 - high rate plastic testing 366
 - high-angle annular dark-field STEM (HAADF-STEM) 241
 - high-angle scattering 274
 - high-density polyethylene (PE-HD) 853
 - higher-order Laue zones (HOLZ) 235
 - higher-order structure 258
 - high-performance liquid chromatography (HPLC)
 - with subsequent ultraviolet (UV) or diode array detection (DAD) 864
 - high-resolution NMR 259, 262
 - high-resolution transmission electron microscopy (HRTEM) 220, 254
 - high-speed deformation 388
 - high-temperature
 - corrosion 718
 - superconductor (HTS) 497
 - hillock 252
 - HL (hydrodynamic lubrication) 750
 - HMFG (heavy-metal fluoride glass fiber) 638
 - hollow glass waveguide 639
 - hollow-core PCF 640
 - hollow-core photonic bandgap fiber 640
 - holographic technique 633
 - HOLZ (higher-order Laue zones) 235
 - homogeneous
 - broadening 605
 - width 600
 - Hooke 340
 - Hopkinson split-bar method 398
 - horizontal lap-joint method 779
 - horntail 783
 - hot strip method 459
 - HPLC (high performance liquid chromatography) 735
 - HRR stress field 410
 - HRTEM (high-resolution transmission electron microscopy) 220, 254
 - HSA (hemispherical analyzer) 185
 - Huang scattering 240
 - human aspects in a laboratory 134
 - HV (Vickers hardness) 394
 - hybridization 836
 - hydrocarbon 816
 - hydrodynamic lubrication (HL) 750
 - hydrogen 242, 243
 - attack 404
 - embrittlement 404
 - evolution 679
 - induced stress corrosion testing 714
 - loading 633
 - hydrolysis 792
 - hygienic coating 830
 - hygienic surface 831
 - Hylotrupes bajulus 787
 - hylotrupes bajulus 785
 - hyperfine structure 246
 - hysteresis 319, 492, 547, 557
 - AC 559
 - DC, ring method 555
 - DC, yoke method 557
 - for hard magnetic materials 547
-
- I**
- IACS (International Annealed Copper Standard) 493
 - IAQ (indoor air quality) 860
 - IBRG (International Biodeterioration Research Group) 805
 - IBRG algal test 827
 - IC (ion chromatography) 735
 - ICP (inductively coupled plasma) 145, 644
 - ICP OES (ICP optical emission spectrometry) 157, 192
 - ICP optical emission spectrometry (ICP OES) 157, 192
 - ICP-AES (inductively coupled plasma atomic emission spectrometry) 157
 - ICP-MS (inductively coupled plasma mass spectrometry) 157, 190
 - ICPS (inductively coupled plasma spectrometry) 735
 - ideal entropy 1064
 - IEC (International Electrochemical Commission) 27
 - IERF (intensity–energy response function) 290, 296
 - ignition 869
 - autoignition 870
 - piloted ignition 870
 - time to ignition 870
 - ILAC (International Laboratory Accreditation Cooperation) 8, 27, 29, 45
 - ILC (interlaboratory comparison) 87
 - illumination mode 606, 607
 - image-quality indicators (IQI) 904
 - imaging
 - mode 219
 - plates (IP) 909
 - IMFP (inelastic mean free path) 291
 - impact ionization 518, 519
 - impact wear 745
 - impedance 530
 - analyzer 530
 - bridge 547, 563
 - complex 529
 - measurement 530
 - implantation profile 514, 516, 517
 - impulse excitation 350
 - impurity 178, 239
 - INAA (instrumental NAA) 161

- in-can preservation 829
- incrustation 820
- indentation technique 352
- in-depth profiling 515
- index-guiding PCF 640
- indoor air quality (IAQ) 860
- inductance 563
- induction current 263
- inductively coupled plasma (ICP) 145, 644
- inductively coupled plasma atomic emission spectrometry (ICP-AES) 157
- inductively coupled plasma mass spectrometry (ICP-MS) 157, 190
- inductively coupled plasma spectrometry (ICPS) 735
- inelastic mean free path (IMFP) 291
- inelastic scattering 228, 602
- inert gas ion sputtering 287
- infrared (IR) 779, 785
 - active 603
 - fiber 638, 639
 - spectroscopy 152, 197, 228
- infrared absorption spectroscopy (IRAS) 226, 243
- inhibitor
 - action 733
 - testing 732
 - testing technique 736
- inhomogeneous broadening 605
- inhomogeneous spectral broadening 605
- initial-value problem 1033
- inorganic 189
- inorganic mass spectrometry 190
- insect 781, 785
- inspection
 - visual 782
- instrument bias 113
- instrumental NAA (INAA) 161
- instrumented indentation test 352, 353
- insulator 486, 596
- integral
 - breadth 273
 - method 321
- integrated circuit inspection 626
- integrating sensor 934, 940
- intensity scale 290, 295
 - calibration 290, 295
- intensity–energy response function (IERF) 290, 296
- interaction energy 1062
- intercrystalline corrosion 705
- interdiffusion coefficient 1106
- interface
 - broadening 301
 - strength 405
- interference 159
 - function 214, 273
 - measurement method 630
 - microscopy 215, 309, 317
 - optical microscopes 236
- interferogram 228
- interferometric method 317
- interferometry 227, 316, 317
- intergranular corrosion 704
- intergranular fracture 425
- interlaboratory comparison (ILC) 87
- interlaboratory validation approach 75
- intermetallic phase 1073
- intermittent contact mode 319
- internal
 - friction 231
 - magnetic field 251
 - quality 112
 - standard approach 170
 - state variables 1014
- internal quantum-effect detector
 - photoconductive detector 591
 - photovoltaic detector 591
- International Annealed Copper Standard (IACS) 493
- International Biodeterioration Research Group (IBRG) 805
- International Electrochemical Commission (IEC) 27
- International Federation of Clinical Chemists 27
- International Laboratory Accreditation Cooperation (ILAC) 8, 27, 29, 45
- International Organization for Standardization (ISO) 149
- International Organization of Legal Metrology (OIML) 11
- international standards 130
- International System of Units (SI) 11
- International Temperature Scale of 1990 473
- interplanar spacings 233
- interrogation unit 939
- interstitial atom 239, 241
- interstitial site 1080
- interstitial solution 1064
- intralaboratory validation approach 75
- intrinsic
 - carrier concentration 520
 - stacking fault 255
- inverse
 - Fourier transform 214, 228, 232
- inverse power law (IPL) 960
- inversion 313
 - domain boundary 254
 - symmetry 603, 614, 623
- invisibility criterion 253, 255
- ion
 - cyclotron resonance (ICR) 147
 - exchange 174
 - milling 218
 - mobility 500
 - sputtering 282
 - trap 147
- ion chromatography (IC) 735
- ionic
 - conductivity 491
- ionic crystal
 - electrical conduction 491
- ionization
 - cross section 291, 296
 - energy 513
 - rate 518
- ionized donor 512
- ionized impurity scattering 513
- ionizing radiation 848
- IPL (inverse power law) 960
- IQI (image-quality indicators) 904
- IR (infrared) 779, 785
- IRAS (infrared absorption spectroscopy) 226, 243
- Irganox 1010 305
- iron 813
 - oxidizer 816
- irradiation 792
- ISO (International Organization for Standardization) 149
- ISO 12085 314, 315
- ISO 1302 314
- ISO 13565 314
- ISO 13565-1 315
- ISO 13565-2 315
- ISO 13565-3 315
- ISO 14577-1:2002 Ed. 1 354
- ISO 14577-2:2002 Ed. 1 354
- ISO 14577-3:2002 Ed. 1 354
- ISO 14577-4 Ed. 1 354
- ISO 14577-5 Ed. 1 354
- ISO 4287 314
- ISO 4288 314
- ISO standard 283–285, 793
- ISO standards for surface texture 309

ISO TC 201 285
 isobaric interference 147
 isocitric acid 823
 isometric 313
 isotope 259, 283
 – dilution 170, 190
 isotropic hardening 394
 isotype layer 510
 ITS-90 473, 475, 476, 479, 480

J

J integral 410
 Jacobi method 1058
 Jahn–Teller distortion 245
 Japanese Standardization Organization (JIS) 798
 JCGM (Joint Committee for Guides in Metrology) 5
J-coupling 260, 264
 JCTLM (Joint Committee for Traceability in Laboratory Medicine) 34
 JIS (Japanese Standardization Organization) 798
 jitter 645, 646
 Joint Committee for Guides in Metrology (JCGM) 5
 Joint Committee for Traceability in Laboratory Medicine (JCTLM) 34
 Jones cell 503
J–*R* curve 414

K

KC (key comparison) 31, 120
 KC data base 124
 Kelvin contact configuration 525
 Kelvin probe 691
 Kennedy correction 517
 Kerr
 – effect 609
 Kerr effect 609, 648
 Kerr lens mode-locking 617, 620
 key comparison (KC) 31, 120
 key comparison database (KCDB) 31
 Kikuchi lines 235, 270
 Kikuchi patterns 220
 killing effect
 – algicidal 773
 – bactericidal 773
 – fungicidal 773
 – protisticidal 773
 – sporicidal 773

– virucidal 773
 kilogram 27, 28, 35
 kilogram of the archives 11
 kinematic hardening 394
 kinematical theory 212, 219, 256
 Kissinger plot 643
 Kissinger's equation 643
 KKS model (Kim–Kim–Suzuki model) 1104
 Kleinman's relation 614
 Kohlrausch cell 504
 Kohlrausch's law 500
 Kohn–Sham equation 1067
 Kramers–Kronig relation 596, 598, 617
 Kramers–Kronig transformation 626
 kurtosis 315

L

laboratory accreditation 126
 laboratory validation approach 76
 Ladyzhenskaya–Babuska–Brezzi (LBB or BB) condition 1057
 Lamé constant 343
 Lamb wave 948, 949
 – generation 947
 – mode 947, 949
 – response 947, 948
 Landau expansion 1093
 Lang camera 221
 large crystals 214
 large scale yielding condition 409
 large-range AFM 320
 Larmor 259
 – angular frequency 230
 – frequency 245, 247, 248, 263
 laser 601
 – beam detector 316
 – cavity 601
 – diode (LD) 937
 – Doppler velocimeter (LDV) 652
 – flash method 459
 – modulation 645
 – scanning confocal microscopy (LSCM) 217, 269, 275
 – single-mode 618
 laser diode (LD) 601
 laser Doppler velocimeter (LDV) 652, 655
 laser-induced fluorescence (LIF) 654
 Lasius 785
 latent heat 1023
 lateral resolution 309, 316, 606, 607

latex 274
 lattice
 – defect 239
 – misfit 254
 – parameter 233
 Laue zone
 – second-order (SOLZ) 235
 LBZ (local brittle zones) 418
 LC (liquid chromatography) 169
 LC/MS (liquid chromatography/mass spectrometry) 172
 LC/MS/MS (liquid chromatography/tandem mass spectrometry) 172
 LD (laser diode) 601
 LDOS (local density of states) 224
 LDV (laser Doppler velocimeter) 652, 655
 leaching 775
 lead zirconate titanate (PZT) 945
 leading edge decay length 300
 Lecanora grumosa 823
 Lecanora polytropa 819, 823
 Lecanora rupicola 823
 Lecanora sulfurea 823
 LEFM (linear-elastic fracture mechanics) 408
 legal traceability
 – of samples/measurements 45
 Lennard-Jones potential 985
 level population 262
 lichen 814
 LIF (laser-induced fluorescence) 654
 life sciences 307
 lifetime 598, 951
 light 211
 – element 276
 – emitting diode (LED) 150, 937
 – propagation 936, 937
 lignin 776
 – degrading 777
 limestone 812
 limits of detection 193
 line shape parameters 250
 linear system theory (LST) 695
 linear variable differential transformer (LVDT) 346, 754
 linear-elastic fracture mechanics (LEFM) 408
 linearly polarized light 268
 line-broadening 273
 liquid chromatography (LC) 169, 267
 liquid chromatography/mass spectrometry (LC/MS) 172

- liquid chromatography/tandem mass spectrometry (LC/MS/MS) 172
 liquid crystals 237
 liquid impact erosion 745
 liquid metal ion gun 305
 liquid-in-glass thermometer 477
 L-joint method 779
 load 312
 – cell 754
 load-line displacement 413
 local brittle zones (LBZ) 418
 local density of states (LDOS) 224
 local element 683
 – current distribution 688
 local spin density approximation (LSDA) 1067
 local vibrational modes (LVM) 243
 localized corrosion 701
 long-range order 232
 Lorentz force 510
 Lorentz oscillator model 596
 Lorentzian 624
 loss
 – angle 563
 – hysteresis 547
 – total 547, 561
 low-coherence interferometry 940, 941
 low-Cr zone 405
 low-temperature superconductor (LTS) 497
 LSDA (local spin density approximation) 1067
 LS-DYNA 1051
 LST (linear system theory) 695
 LTS (low-temperature superconductor) 497
 lubricant reservoir 322
 lubrication
 – boundary 746, 750
 – elastohydrodynamic (EHL) 746, 750
 – hydrodynamic 746, 750
 luggage inspection 626
 luminescence 604, 623
 – cathodoluminescence 598
 – chemiluminescence 598
 – electroluminescence 598
 – line narrowing 600
 – photoluminescence 598
 lumped element circuit frequency limit 531
 LVDT (linear variable differential transformer) 346, 754
 LVM (local vibrational modes) 243
 lyctid beetle 785
 Lyctus brunneus 787
- ## M
-
- Mach–Zehnder interferometer 653, 654
 macromolecule 235, 258
 macroorganism 814
 macropitting 822
 MAD (median absolute deviation) 66
 magic angle 296
 Magna Carta 23
 magnetic
 – aftereffect 242, 545
 – amplifying magneto-optical system (MAMMOS) 649
 – anisotropy 543, 579
 – balance 562
 – circular dichroic absorption (MCDA) 247
 – circular dichroism (MCD) 268
 – circular polarized emission (MCPE) 230, 247
 – contribution 1064
 – dipole moment 553, 555, 563
 – field
 internal 251
 – flux imaging 610
 – flux pattern 612
 – moment 229, 230, 563, 1081
 – patterns of superconducting films 609
 – polarization 555
 – property 541
 – random access memory (MRAM) 541
 – resonance imaging (MRI) 276
 – scale 547, 562
 – sector 147
 – solid-state memory (MRAM) 541
 – super-resolution technologies 649
 – thermometer 481
 – thin film 580
 – thin films 544
 – transition 1072
 – ultrathin film 580
 – x-ray circular dichroism (MXCD) 546
 magnetically
 – hard material 544
 – soft material 544
 magnetism 541
 – diamagnetism 542
 – ferromagnetism 542
 – paramagnetism 542
 magnetogyric ratio 229, 259
 magneto-optic effect 582
 magneto-optic Faraday effect 583
 magneto-optic Kerr effect (MOKE) 546, 583
 magneto-optical 647
 – disk (MO) 641
 – effect 609, 648
 – imaging 610
 – layer (MOL) 609
 – measurement 609
 magneto-resistance 541, 583
 magnetoresistive 609
 magnetostriction 242, 564
 majority carrier 513
 – emission 521
 manganese oxidizer 816
 marble 812
 Marie Curie 27
 marine environment 781
 Mariotte 340
 mark length 645
 mark-edge 646
 martensite 1025
 martensitic transformation 988, 1108
 mass accuracy 304
 mass change
 – evaluation 728
 – measurement 721
 mass loss 780
 mass spectrometry (MS) 146, 147, 168, 735
 mass spectroscopy 196
 material
 – anisotropy 1018
 – atomic bonding 13
 – conductivity scale 487
 – cycle 19
 – damage 933
 – degradation 933, 935
 – dielectric 526
 – failure 935
 – grain 14
 – lattice defect 14
 – performance 19
 – phase 14
 – principal characteristics 486
 – reference (RM) 6, 34, 48, 109, 110, 493
 – response 316
 – scale 16
 – smart 933

- spatial atomic structure 14
- structural 877
- superconducting 488
- type 15
- wood-based 863
- material property
 - dielectric 526
 - electrical 485
 - magnetic 541
 - mechanical 339
 - optical 587
 - thermal 453
- materialized reference 5
- materials characterization
 - fundamental 13
- materials metrology 20
- matrix effects 147, 159
- matrix elements 291
- maximum detectable slope 316
- maximum entropy method (MEM) 233
- maximum-likelihood estimation (MLE) 953
- Maxwell's equation 527
- MCA (multichannel analyzer) 621
- MCP (microchannel plate) 622
- MD (minidisc) 641
- MDM (minimum detectable mass) 180
- mean line 313
- measurement 3, 308, 624
 - and filtering 312
 - conductivity 493
 - instrument accuracy 69
 - method
 - resonant 535
 - of elastic constants 344
 - specific resistance 511
 - standard 5, 12
 - uncertainty 69
- measurement service
 - reference 121
- measurement standard 126
 - reference 126
- measuring instruments directive (MID) 11
- measuring system 3
- MECC (micellar electrokinetic capillary chromatography) 171
- mechanical
 - characteristic 7
 - equilibrium equation 1098
 - property 339
 - spectroscopy 231
 - strength 273
- stress 848
- mechatronic system 964
- median absolute deviation (MAD) 66
- median rank determination 954
- median rank regression (MRR) 953
- medium to sample 44
- medium-energy ion scattering (MEIS) 297
- medium-range order 235
- MEIS (medium-energy ion scattering) 297
- melanin 820
- melting temperature 642, 643
- MEM 234
- MEM (maximum entropy method) 233
- MEMS (microelectromechanical systems) 352, 747
- mesa diode 523
- mesh 1034
- mesomacropitting 822
- metal 486, 597
 - bivalent 487
 - forming 1025
 - matrix composites (MMC) 930
 - resistance 494
- metal–insulator–semiconductor FET (MISFET) 513
- metal–insulator–semiconductor (MIS) 514
- metallic carbide 1079
- metallic material 15, 486
- Metallogenium symbioticum 816
- metal–oxide–semiconductor (MOS) 516
- metal–semiconductor contact 523
- metastable equilibria 1062, 1071
- metastable phase separation 1073
- meter convention 9
- meter of the archives 11
- meter, kilogram, second, ampere (MKSA) 11
- method
 - primary 119
 - reference 118
- method versus procedure 118
- methodology of measurement 3
- metric system 11
- metrological traceability 198
- metrological unit 11
- metrology 9
 - AFM 320
 - category 9
 - industrial 10
- legal 10
- of materials 20
- scientific 9
- MFD (mode field diameter) 632
- MIC (microbially induced corrosion) 771
- micellar electrokinetic capillary chromatography (MECC) 171
- Michelson 26
 - interferometer 651
- microanalysis 271
- microbial community
 - characterization 838
- microbial mat 814
- microbially induced corrosion (MIC) 771
- microchannel plate (MCP) 622
- microclimate 781
- microelectromechanical systems (MEMS) 352, 747
- microgeometry 308
- microluminescence excitation spectroscopy 605
- microorganism 774, 789, 791, 792, 811
- microphotoluminescence spectroscopy 605
- micropitting 822
- microprobe tip 606
- microscopy 215
- microspectroscopy 605
- microstructure evolution 1091, 1110
- microthermal analysis 282
- microvoid 249
 - coalescence type of fracture 425
- microwave
 - network 532
 - analyzer 532
 - signal flow graph 532
- MID (measuring instruments directive) 11
- middle tension specimen M(T) 420
- Mie scattering 602
- Miedema's model 1062
- Miller's rule 616
- minidisc (MD) 641
- minimize financial loss 43
- minimum detectable mass (MDM) 180
- minimum mass fraction (MMF) 180
- minority carrier
 - lifetime 519
 - trap 522

- mirabilite 822
 MIS
 (metal–insulator–semiconductor) 514
 miscibility gap 1085
 MISFET (metal–insulator–semiconductor FET) 513
 MITI (Ministry of International Trade and Industry of Japan) 799
 mixing 266
 MKS units 26
 MKSA (meter, kilogram, second, ampere) 11
 MLE (maximum-likelihood estimation) 953
 MLLSQ (multiple linear least squares) 182
 MMF (minimum mass fraction) 180
 MnBi 647
 mobile carrier
 – effective mass 517
 – profile 517
 mobility 491
 mode field diameter (MFD) 632
 mode locking 601, 619
 mode of sampling 44
 model structures 232
 modeling approach to measurement uncertainty 75
 mode-locked fiber laser 637
 mode-locked laser 619, 621
 modulus of elasticity (MOE) 341, 778
 MOE (modulus of elasticity) 341, 778
 moiré pattern 256
 moiré topography 652, 655
 moisture resistance 647
 MOKE (magneto-optic Kerr effect) 546, 583
 MOL 614
 MOL based on semimagnetic semiconductor 611
 molar purity 155
 molecular
 – analysis 195
 – architecture 258
 – displacement 528
 – dynamics (MD) 975
 – technique 825
 moment-measuring coil 547, 554
 momentum conservation 603
 momentum-scaling method 980
 monitoring of
 – composites 949
 monitoring of efficiency of inhibitor 732
 monochromator 227, 594
 monolayer 292
 MOS (metal–oxide–semiconductor) 516
 Mößbauer spectroscopy 197, 250
 motif parameter 315
 motional narrowing 267
 mouth opening displacement 412
 MRA (mutual recognition arrangement) 99
 MRR (median rank regression) 953
 MS (mass spectrometry) 146, 147, 168, 735
 multiaxiality 1018
 multichannel advantage 594
 multichannel analyzer (MCA) 621
 multimode operation 601
 multiple linear least squares (MLLSQ) 182
 multiple-phonon scattering 604
 multiplex advantage 594
 multiplexed sensor 934
 multiscale method 1059
 multiscaled heterogeneous deformation 395
 muon spin resonance 230
 muon spin rotation 247
 Murnaghan equation 1069
 muscle spindle 649
 mutual exclusion 604
 mutual inductor 560
 mutual recognition arrangement (MRA) 99
 Mètre des Archives 24
-
- N**
- NAB (national accreditation body) 88
 nanogranular 1112
 nanoparticle 796
 nanoscale field distribution 607
 nanoscopic architecture 205
 nanostructured semiconductor material 605
 narrow-band filtering 634, 635
 national accreditation body (NAB) 88
 National Bureau of Standards 25
 National Institute of Standards and Technology (NIST) 149, 503
 national measurement institute (NMI) 88
 National Metrology Institute (NMI) 149, 377
 National Physics Laboratory (NPL) 25, 496
 national standard 198
 natural
 – constant 5
 – glass (obsidian) 812
 – material 16
 Navier 341
 Nd:YAG laser 616, 619
 NDE (nondestructive evaluation) 21, 888
 NDT (nondestructive testing) 778, 888, 907
 near infrared (NIR) 149
 near-edge x-ray absorption fine structure (NEXAFS) 239
 near-field luminescence image 607
 near-field optical microscopy (NOM) 605, 606
 near-field transmission image 607
 necking 391
 negative temperature 600
 neighbor distances 239
 nematic phase 237
 Nernst equation 672, 674
 net plane 212, 237
 network analyzer 532
 Neumann boundary condition 1037
 neutral axis 340, 341
 neutron 211, 238
 – activation analysis (NAA) 161, 194
 – depth profiling (NDP) 163
 – diffraction 269
 – generator 160
 – reflectance (NR) 298
 new approach (European economy) 131
 Newton–Raphson method 1055
 NEXAFS (near-edge x-ray absorption fine structure) 239
 Ni₂MnGa 1109
 Ni–Al 1073
 Ni–Al–C 1083
 NIR (near infrared) 149
 NIST (National Institute of Standards and Technology) 503
 nitrifying bacteria 815
 nitrogen 259, 824
 nitrokalite 822
 nitronatrite 822

- NMI (national measurement institute) 88
 NMI (National Metrology Institute) 149, 377
 NMR (nuclear magnetic resonance) 230, 545, 546
 NMR spectroscopy 196
 node 1034
 NOE (nuclear Overhauser effect) 261, 266
 NOESY (nuclear Overhauser effect spectroscopy) 266
 noise
 – figure 636
 – spectroscopy 242
 – thermometer 472
 NOM (near-field optical microscopy) 605, 606
 Nomarski microscope 217
 nominal
 – strain 389
 – stress 389
 noncontact AFM 224
 noncontact mode 319
 nondestructive evaluation (NDE) 21, 888
 nondestructive testing (NDT) 778, 888, 907
 nonlinear 319
 – crystal 617
 – dielectric response 528
 – fluorescent microscopy 275
 – optics 614
 – refractive index 617, 630, 632
 – spectroscopy 623
 – susceptibility 614, 616
 nonlinearity 289
 – second-order 615, 616
 nonmetallic material 15
 nonproportional loading 1018
 nonradiative decay 599
 nonradiative process 623
 nonwoven 806
 Nose–Hoover thermostat 981
 NPL (National Physics Laboratory) 496
 NPL primary conductivity standard 497
 NRA (nuclear reaction analysis) 298
 NTC thermistor 477
 nuclear magnetic moment 259
 nuclear magnetic resonance (NMR) 230, 545, 546
 – analysis 259
 – spectroscopy 154
 nuclear orientation thermometry 481
 nuclear Overhauser effect (NOE) 261, 266
 nuclear Overhauser effect spectroscopy (NOESY) 266
 nuclear quadrupole interaction 230
 nuclear reaction analysis (NRA) 298
 nuclear spin 229, 259
 nucleic acid probe 837
 number of samples 44
 numerical aperture 626
 numerical error 1056
n-value 392
 Nyquist formula 472
 Néel temperature 543
-
- O**
-
- OA (operational amplifier) 672
 object-to-detector distance (ODD) 905
 OCT (optical coherent tomography) 655
 ODD (object-to-detector distance) 905
 ODF (orientation distribution function) 270
 ODMR (optically detected magnetic resonance) 230, 247
 odor control 811
 OECD 797
 off-resonance 263
 Ohm's law 475, 476
 ohmic contact 524
 oil 816
 OIML (International Organization of Legal Metrology) 11
 one-dimensional (1-D) NMR 263
 on-site corrosion testing 699
 opal 812
 opening mode 408
 operating parameter 7
 operation
 – single-mode 601
 operational amplifier (OA) 672
 operationally defined properties 119
 optical
 – absorption 268
 – atomic spectrometry 192
 – coherent tomography (OCT) 655
 – conductivity 598
 – constant 595, 644
 – emission spectrometry (OES) 158, 159, 193
 – fiber 626, 627
 – fiber type 936
 – flat 323
 – force detection 318
 – gain 600
 – indices
 – complex 529
 – Kerr effect 617
 – Kerr shutter 622, 623
 – laser distancemeter 650
 – microscopy (OM) 215
 – parametric amplifier (OPA) 620
 – parametric generation (OPG) 616
 – property 587
 – pulse method 629
 – pumping 600
 – pyrometry 654
 – rectification 616
 – rectification (OR) 625
 – rotary dispersion (ORD) 268
 – scanning techniques 308
 – sectioning 652
 – spectroscopy 196
 – spectrum analyzer (OSA) 939
 – stylus profilometry 316
 – technique 316
 – time domain reflectometry (OTDR) 941
 – time-domain reflectometer (OTDR) 627, 937, 940
 – time-domain reflectometry (OTDR) 628
 – tip 606
 optical disk 642, 645
 – memory 641
 – rewritable optical disk 641
 optically detected magnetic resonance (ODMR) 230, 247
 opus cementicium 812
 OR (optical rectification) 625
 orbital angular momenta 229
 order–disorder transition 1071
 ordering 1063
 organic
 – layer 298
 – material 15
 – pollution 816
 – vapor 816
 organogenic pigmentation 820
 orientation distribution function (ODF) 270
 Orowan loop 403

oscillator model 614
 Ostwald ripening 1107
 OTDR (optical time-domain reflectometry) 628
 outdoor exposure trial 829
 output coupler 601
 overlapping signal 262
 overwrite 646
 oxalate film 812
 oxidation 792
 – behavior 721
 – kinetics 721
 – rate 723
 oxoglutaric acid 823
 oxygen 243
 – sputtering 301

P

PA (polyamides) 848
 PAA (photon activation analysis) 165, 194
 PAC (perturbed angular correlation) 230, 248, 546
 PAHs (polycyclic aromatic hydrocarbons) 150
 PAM-CRASH 1051
 paper 803
 paracrystal 235
 parallel electron loss spectroscopy 282
 parallel-plate resonator 536
 paramagnetic current 259
 paramagnetic state 1081
 parametric method 321
 Paris' equation 401
 Paris' law 420
 Parrinello–Rahman method 982
 partial differential equation 1035
 – second-order 1047
 partial dislocation 254, 255
 partial distribution function 238, 239
 particle
 – induced x-ray emission (PIXE) 166
 – method 1057
 – shape 274
 – size 44
 particulate organic matter (POM) 860
 PAS (positron annihilation spectroscopy) 249
 passive mode-locking 620
 path-independent contour integral 410

patina 813
 Patterson function 232
 PC (polycarbonate) 303
 PC antenna 626
 PCF (photonic crystal fiber) 639
 PCR (polymerase chain reaction) 833, 834
 PDMS (poly(dimethyl siloxane)) 428
 PDMS (poly(dimethyl siloxane)) 295, 304
 peak 322
 – broadening 257
 – separation 233
 – shift 258
 peer assessment 136
 PE-HD (high-density polyethylene) 853
 Pendellösung 220, 255
 penetrating radar 778
 penetration depth of electrons 608
 Penning ionization 146
 peptide 268
 performance 19
 – control 887
 periodic
 – boundary condition 978
 permalloy 544, 584
 permeability 547, 557, 561, 563
 – complex 563
 permeameter 557
 permeation 426
 permittivity, complex 527
 permutation symmetry 614
 Perovskite 1079
 perpendicular magnetic anisotropy 648
 perpendicular magnetization 641, 647
 PERSF (pure element relative sensitivity factor) 286, 291, 297
 perturbation expansion 615
 perturbed angular correlation (PAC) 230, 248, 546
 Petrov–Galerkin method 1039
 PGAA (prompt gamma activation analysis) 162
 phase
 – boundary 254
 – compression 630
 – contrast computed tomography 929
 – diagrams 1061
 – mask technique 633
 – problem 232
 – separation 1076
 – shift method 629
 – stress 404
 – transformation 356, 1023, 1091
 phase matching 623
 – condition 617
 phase-change optical disk 641
 phase-field method 1092
 phase-shift interferometry (PSI) 317
 PHB (poly(β -hydroxy butyrate)) 796
 pheromone 786
 phonon 211, 228, 596
 phosphorescence 149–151
 photoabsorption 244
 photoacoustic method 460
 photoacoustic spectroscopy 599
 photocalorimetric
 – spectroscopy 599
 photochemical ageing 849
 photodiode 519
 photoelectron emission 231
 photogrammetry 321
 photoinitiated ageing 849
 photoionization detector (PID) 168
 photoluminescence (PL) 244
 photomultiplier tube (PMT) 159, 600, 908
 photon activation analysis (PAA) 165, 194
 photonic crystal fiber (PCF) 639
 photosensitivity 633
 photosensor
 – APD 620
 – PD 620
 – PMT 620
 photostimulated luminescence (PSL) 910
 photothermal method 460
 Physikalisch-Technische Bundesanstalt (PTB) 504
 pick-up 312
 PID (photoionization detector) 168
 piezoactuator 223
 piezoceramics 945
 piezoelectric
 – effect 945
 – load cell 755
 – material 319
 piezoelectricity 493
 pigeon 814
 pipe method 458
 pitting 701, 818
 PL (photoluminescence) 244
 PL excitation spectroscopy 600
 PL spectroscopy 599

- planar defect 254
 Planck distribution 599
 Planck's law 472, 479, 480
 plane-strain fracture toughness 411
 plasma frequency 597
 plasmon 218, 231
 plastic
 – anisotropic coefficient 359, 362
 – constraint 410
 – optical fiber 639
 – strain hardening 359, 360
 – strain ratio 359, 362
 – strain-rate sensitivity 360
 – work hardening 359, 360
 plastic loading modes
 – ball punch 364, 365
 – bending 364
 – biaxial tension, indentation 358
 – compression tests 362
 – compression, tension 358
 – drift expansion 365
 – earing 365
 – flanging 365
 – flattening 365
 – hardness, multiaxial compression 358
 – ring expansion 365
 – shear 364
 – shear testing 363
 – shear, bending, torsion 358
 – torsion 364
 – torsion testing 364
 – torsion testing, hot tensile, multiaxial 366
 – tube ring hydraulic pressure 365
 – uniaxial tension test 360
 – uniaxial tension, compression 358
 plastic yielding
 – Tresca criterion 355
 – von Mises criterion 355
 plasticity 355, 1014
 – clay 356
 – creep 361
 – dependency, creep 361
 – isotropic hardening 366
 – kinematic hardening 366
 – superplasticity 362
 – temperature effects, time 361
 plastics 789
 – biodegradable 789
 – compostability 799
 plate capacitor model 514
 plidulation 649
 PMMA (poly(methyl methacrylate)) 440
 PMMA (poly(methyl methacrylate)) 304
 PMT (photomultiplier tube) 159, 600, 908
 point group 235
 point sensor 934
 point-by-point
 – scan 308
 – technique 633
 Poisson's ratio 340, 343, 391, 1045
 – determination by static methods 347
 – on ceramics 348
 polar Kerr effect 641
 polar Kerr magnetometer 648
 polariton 596
 polarizability 228
 polarization 595, 596
 – dielectric 485
 – electronic 492
 – of electron spin 1064
 – orientation 492
 – saturation 528
 – selection rule 604
 pole
 – coil 551
 – figure 269
 poly(1-trimethylsilyl-1-propyne) (PTMSP) 433, 442
 poly(dimethyl siloxane) (PDMS) 295, 304, 428
 poly(methyl methacrylate) (PMMA) 304, 440
 poly(β -hydroxy butyrate) (PHB) 796
 polyacetylene 490
 polyamides (PA) 848
 polyaniline 490
 polyatomic ion 305
 polycarbonate (PC) 303
 polycrystalline AgBrCl fiber 639
 polycyclic aromatic hydrocarbons (PAHs) 150
 poly-L-lysine 306
 polymer 15, 235, 258, 791, 848
 – amorphous 796
 – blend 303
 – conducting 490
 – elastic constants 347
 – optical fiber (POF) 944, 945
 polymerase chain reaction (PCR) 833, 834
 polymers and composite materials 878
 polypyrrole 490
 polytetrafluoroethylene (PTFE, Teflon) 153, 304
 polyurethane 824
 polyvinylchloride (PVC) 303, 772, 790
 polyvinylidene fluoride (PVDF) 890, 945
 POM (particulate organic matter) 860
 pop-in 414
 population inversion 600
 pore 322
 pore size evaluation 925
 porphyr 812
 positron annihilation spectroscopy (PAS) 249
 positron lifetime 249
 postsputtering oxidation 301
 post-test evaluation 731
 potential profiles measurement 690
 potential-pH diagram 675
 potentiometric method 476
 potentiostatic corrosion testing 672
 Pourbaix diagram 675
 powder diffraction 233, 269
 P-profile
 – primary 312
 Pr-doped fiber amplifier 637
 precipitation hardening 403
 precision 115
 preconditioning, natural 776
 preferential sputtering 292
 preparation 264
 preservation of samples 45
 primary
 – cell, flow-through 507
 – method 119
 – P-profile 312
 – reference measurement procedure 119
 – reference solution 503
 – standard 198
 – structure 258
 principal stress 1047
 prism 593
 probe 318
 – tip 223
 procedure 323
 – reference 6, 118
 – versus method 118
 process
 – single-quantum 262
 process control 313
 – parameter 322
 proficiency test (PT) 48, 76, 88

profile parameter 314
 profilometry 761
 projection 313
 prokaryote 814
 prompt gamma activation analysis (PGAA) 162
 property of materials 17
 property, mechanical 790
 proportion of total variance 43
 proportional limit 359, 391
 protein 258, 268, 303
 protocist 814
 proton 259
 proton-hopping mechanism 501
 protozoa 814
 provisional low temperature scale of 2000 473
 pseudo-eucentric tilting 321
Pseudomonas 817
Pseudomonas aeruginosa 817
 pseudopotentials 1067
 PSI (phase-shift interferometry) 317
 PSL (photostimulated luminescence) 910
 PT (proficiency test) 48, 88
 PT reference values 121
 PTB (Physikalisch-Technische Bundesanstalt) 504
 PTC thermistor 477
 PTFE, Teflon
 (polytetrafluoroethylene) 153, 304
 PTMSP
 (poly(1-trimethylsilyl-1-propyne)) 433, 442
 pulse
 – calorimetry 462
 – field magnetometer (PFM) 546
 – measurement 693
 – oximetry 655
 – sequence diagram 263
 pulsed laser 601, 618
 pulse-field magnetometer 541
 pulse-width modulation (PWM) 559
 pulverization 818
 pump–probe experiment 621, 623, 624
 pure element relative sensitivity factor (PERSF) 286, 291, 297
 purity 178
 purity of water conductivity 506
 push rod dilatometry 470
 PVC (polyvinylchloride) 303, 772, 790

PVDF (polyvinylidene fluoride) 890, 945
 PWM (pulse-width modulation) 559
 PZT (lead zirconate titanate) 945

Q

QMR (quasiminimal residual method) 1058
 QNMR (quantitative proton nuclear magnetic resonance) 155
 Q-switch 618
 quadrupole 147
 – splitting 251
 qualification 111
 quality
 – assurance (QA) 98
 – control (QC) 98
 – control chart 116
 – internal 112
 quantification 301, 308
 – of inhomogeneous samples 292
 – of thin homogeneous overlayers 297
 quantitative analysis 286
 quantitative proton nuclear magnetic resonance (QNMR) 155
 quantum
 – efficiency 599
 – spectroscopy 529
 quantum-based standards 28, 29
 quantum-well magneto optic layer 613
 quasicrystal 237
 quasi-distributed sensor 934, 940–942
 quasiminimal residual method (QMR) 1058
 quasistatic test procedure for elastic constant determination 346
 quasistatic-loading 388
 quaternal structure 258
 Q-value 618

R

radiation
 – solar 848
 radiation source
 – thermal 588
 radiation thermometer 472, 479
 radiative decay 599
 radioactive tracer technique 762
 radiochemical NAA (RNAA) 161
 radiofrequency (RF) 147, 159

radionuclide wear measurement 762
 radius of gyration 273
 Raman
 – active 603
 – gain 631
 – scattering 228, 239, 272, 603
 – spectroscopy 151, 197, 243, 603
 – tensor 604
 random amplified polymorphic DNA (RAPD) 836
 range of scalability 320
 RAPD (random amplified polymorphic DNA) 836
 rapid solidification 995
 rare-earth transition-metal (RE-TM) 647
 raster scanning 318
 rate equation 598
 rate window 522
 Rayleigh scattering 602, 627
 RBS (Rutherford backscattering spectrometry) 240, 297, 645
 RDE (rotating disc electrode) 685, 686
 reabsorption 600
 reaction rate constant 646
 reciprocal lattice 212
 reciprocal space 215
 reconstruction from stereo pairs 321
 recording density 646
 recrystallization 1110
 reduction in area 392
 redundancy 963
 reentrance 322
 reference
 – binding energy 295
 – data determination 121
 – electrode (RE) 672
 – laboratory 126
 – material (RM) 6, 34, 48, 109, 110, 493
 – measurement procedure 118
 primary 119
 – measurement service 121
 – measurement standard 126
 – method 118
 – organism 833
 – procedure 6, 118
 – product 774
 – solution
 primary 503
 – spectrophotometer 148
 – value 117
 reflection 594

– signal 316
 reflectivity 594
 refractive index 217, 236, 595, 644
 – complex 626
 regenerative amplifier 620
 regional metrology organization (RMO) 10, 29, 31
 regular solution model 1062
 relative complex permittivity 529
 relative sensitivity factor (RSF) 147, 296, 301
 relaxation
 – peak 231
 – spectroscopy 242
 – time 231, 242
 reliability function 951
 remanence 547
 repetition rate 621
 representation theorem 1018
 requirements for reference procedures 119
 resistance 486
 – bridge 476
 – measurement 494
 – thermometer 475
 resolution 310
 resolved shear stress 1028
 resonance transition 529
 resonant Raman scattering 229, 243, 604
 resonant transition 528
 resonant vibrating cantilever mode 319
 restriction endonucleases 836
 restriction fragment length polymorphism (RFLP) 836
 retention time 267
 reticuliterme 785
 Reticulitermes santonensis 787
 retina examination 655
 RE-TM (rare-earth transition-metal) 647
 reversed-phase liquid chromatography (RPLC) 169
 reversible phase transition 641
 RF (radiofrequency) 147, 159
 RFLP (restriction fragment length polymorphism) 836
 rhodium–iron thermometer 477
 ribosomal RNA (rRNA) 835
 ribotyping 837
 Rietveld method 234
 rigid band approximation 1078
 ring specimen 556
 river pattern 425

RMO (regional metrology organization) 10, 29, 31
 RNAA (radiochemical NAA) 161
 rock varnish 816
 rolling direction 1021
 rolling motion 751
 room fire 876
 root mean square 314
 – deviation 315
 rotating disc electrode (RDE) 685, 686
 rotating ring disc electrode (RRDE) 686
 roughness 312
 – measurement 312
 – R-profile 312
 RPLC (reversed-phase liquid chromatography) 169
 RRDE (rotating ring disc electrode) 686
 rRNA (ribosomal RNA) 835
 RSF (relative sensitivity factor) 147, 296, 301
 ruthenium-oxide sensor 481
 Rutherford backscattering spectrometry (RBS) 240, 297, 645
r-value 392

S

S/N (signal-to-noise ratio) 154
 SAD (selected area diffraction) 234
 SADC MET (Southern African Development Community Cooperation in Measurement Traceability) 29
 sample rotation 293
 sampling 40, 312
 – and analytical quality control scheme (SAQCS) 45
 – length 313
 – proficiency test (SPT) 42
 – target 44
 – uncertainty 41
 sandstone 812
 sap stain 777
 sapphire crystalline fiber 639
 satellite spots 234
 saturation
 – coil 547, 562
 – magnetization 543
 – magnetometer 562
 – polarization 562
 Savitzky and Golay smoothing 290
 SBS (sick-building syndrome) 860
 scale of materials 16
 scanner tube 319
 scanning confocal laser microscopy (SCLM) 837
 scanning electrochemical microscopy (SECM) 690
 scanning electron microscopy (SEM) 180, 222, 292, 308, 309, 320, 424, 607, 645
 – cathodoluminescence mode (SEM-CL) 257
 scanning force microscopy (SFM) 689
 scanning nanoindenter 273
 scanning near-field optical microscopy (SNOM) 225, 272, 282
 scanning probe microscopy (SPM) 223, 281, 308, 318
 scanning reference electrode technique (SRET) 691
 scanning transmission electron microscopy (STEM) 179, 221
 scanning tunneling microscopy (STM) 223, 241, 282, 309, 318, 672, 689
 scanning tunneling spectroscopy (STS) 224
 scanning vibrating electrode technique (SVET) 691
 scanning white-light interferometry (SWLI) 317
 scattering 211, 602
 – parameter 532
 – wave vector 213
 Scherzer defocus 221, 254
 schlieren 653, 654
 Schottky
 – contact 514
 – defect 491
 Schrödinger equation 1067
 scialbatura 812
 SCLM (scanning confocal laser microscopy) 837
 scratch test 407, 753
 screening of electric field 609
 SD (strength difference) 393
 SDO (standards development organization) 361
 sealed x-ray tube 233
 SEC (specific energy consumption) 846
 SECM (scanning electrochemical microscopy) 690

- second boundary condition 1037
 secondary electron SEM (SEM-SE) 222
 secondary emission 868, 869
 secondary ion mass spectrometry (SIMS) 159, 281, 282, 298, 645
 secondary ion mass spectroscopy (SIMS) 517
 secondary structure 258
 second-harmonic generation (SHG) 616, 624, 655
 – microscopy 275
 second-order
 – Laue zone (SOLZ) 235
 – nonlinearity 615, 616
 – partial differential equation 1047
 seconds pendulum 24
 Seebeck effect 478
 segregated phosphorus 287
 selected area diffraction (SAD) 234
 selection rule 228, 247, 603, 623
 selective corrosion 704
 selective polarization inversion (SPI) 264
 self-diffusion coefficient 1106
 self-focusing 617
 self-phase modulation (SPM) 617, 630
 Sellmeier equation 628
 SEM (scanning electron microscopy) 180, 222, 292, 308, 309, 320, 424, 607, 645
 semiconductor 15, 486
 – band bending 514
 – characterization method 508
 – compound 489
 – conductivity measurement 507
 – deep level 519
 – device 523
 – doping profile 515
 – electrical property 488
 – implanted 516
 – laser 601
 – property 508
 – purity 513
 semi-volatile organic compound (SVOC) 860, 867
 SEM-SE (secondary electron SEM) 222
 SENB (single-edge notch bend) 714
 sensing technique 932
 sensitivity factor 302
 sensor 932, 934
 – effect 935
 – integration 933
 SER (specific emission rate) 866
 SFG (sum-frequency generation) 616
 SFM (scanning force microscopy) 689
 shadowgraph 653, 654
 shape of contact asperities 322
 SHE (standard hydrogen electrode) 673
 shear
 – lag model 407
 – modulus 340, 343
 – strain 396
 – stress 396
 sheet carrier concentration 510
 sheet resistance 525
 SHG (second-harmonic generation) 616, 624, 655
 shiny 316
 Shirley background 295
 Shockley partial dislocation 255
 short-range order 237
 short-terminated probe 531
 SI (International System of Units) 11
 SI unit 25, 26, 35, 198
 sick-building syndrome (SBS) 860
 side groove 414
 Siderococcus 816
 signal amplitude 646
 signal processing 934
 signal-to-noise ratio (S/N) 154
 silane 824
 silica optical fiber 936
 silicon
 – doping level 524
 – drift detector (SDD) 181
 – lattice 489
 siloxane 824
 silver 813
 SIM (Sistema Interamericano de Metrología) 29
 SIMS (secondary ion mass spectrometry) 159, 282, 298, 645
 SIMS (secondary ion mass spectroscopy) 517
 single crystal 258
 single quantum dot spectroscopy 605
 single-edge notch bend (SENB) 714
 single-edge notched (SEN) bend specimen 411
 single-mode
 – laser 618
 – operation 601
 single-molecule
 – spectroscopy 605
 single-quantum
 – process 262
 single-sheet
 – tester (SST) 547, 560
 singularity zone 409
 sinter 812
 Sistema Interamericano de Metrología (SIM) 29
 size 214, 273
 – effect 258
 skewness 315
 skin
 – spectroscopy 655
 sliding motion 751
 slimicide 805
 slow neutrons 212
 slow strain rate testing 708
 small crystals 214
 small-angle
 – grain boundary 256
 small-scale yielding condition 409
 smart
 – material 932, 933
 – structure 932, 933
 SMART layer (Stanford multi-actuator receiver transduction layer) 946
 smectic phase 237
 smouldering ignition 872
 S–N curve 399
 Snoek relaxation 242
 SNOM (scanning near-field optical microscopy) 225, 272, 282
 SOD (source-to-object distance) 905
 soft
 – magnetic materials 541
 – material magnetically 544
 – pulse 263
 – rot 776
 – surface 316
 software gage 323
 soil burial trial 804
 solar
 – radiation 848
 solidification 1102
 solid-solution hardening 403
 solid-state
 – amorphization 993
 – laser 601
 – NMR 248
 soliton 630
 solubility 1071

- solute retention 169
 solution calorimetry 467
 sonic stress wave 778
 SOR (successive overrelaxation method) 1058
 sorbent for air analysis 865
 sounds tapping 786
 source of measurement uncertainty 72
 source-to-object distance (SOD) 905
 Southern African Development Community Cooperation in Measurement Traceability (SADCMET) 29
 space charge region 514
 S-parameter set 315
 spark 159
 Spark OES (spark optical emission spectrometry) 158
 spark optical emission spectrometry (Spark OES) 158
 spatial resolution 215, 272, 282, 285, 607, 613
 – beyond the diffraction limit 606
 specific contact resistance 525
 specific emission rate (SER) 866
 specific energy consumption (SEC) 846
 specific heat capacity 454
 specific resistance
 – measurement 511
 specific wear rate 747
 specimens to measure elastic constants 344
 spectral band radiation thermometers 479
 spectral response 850
 spectral sensitivity 850
 spectrometer 600, 644
 – energy scale 288, 295
 – transmission function 290
 spectrophotometer
 – reference 148
 spectroscopy 623
 – photocalorimetric 599
 – single-molecule 605
 – skin 655
 spectrum meter 646
 specular reflection 233
 SPF (superplastic forming) 362, 365
 SPI (selective polarization inversion) 264
 spin
 – decoupling 264
 – echo 264
 – finish 803
 – glass 544
 – Hamiltonian 230, 245
 – operator 1068
 – wave 580
 spin–lattice relaxation 261
 – time 248
 spinodal decomposition 1107
 spin–orbit
 – coupling 230, 245
 spin–spin
 – coupling 260
 – relaxation 261
 split cavity resonator 536
 split-post dielectric resonator 536
 SPM (scanning probe microscopy) 223, 281, 308, 318
 SPM (self-phase modulation) 617, 630
 spontaneous emission 599
 spontaneous ignition 872
 spontaneous magnetization 543, 579
 spring back 365
 sputter depth profiling 282, 292, 298
 sputtering 147, 159
 – yield 293
 SQUID (superconducting quantum interference device) 497
 SQUID magnetometer 545, 580, 581
 SRE (stray radiant energy) 148
 SRET (scanning reference electrode technique) 691
 SRS (stimulated Raman scattering) 631
 stable crack extension 413
 stacking fault 239, 252, 254, 258
 – intrinsic 255
 stain 776
 standard addition approach 170
 standard hydrogen electrode (SHE) 673
 standard platinum resistance thermometer 473
 standard time–temperature curve 876
 standard uncertainty 503
 standards development organization (SDO) 361
 Stanford multi-actuator receiver transduction layer (SMART layer) 946
 static bending technique 778
 static SIMS 283, 303
 static tester 644
 statistical surface description 321
 steel 813, 877
 Stefan–Boltzmann
 – constant 654
 – law 472, 475, 480
 STEM (scanning transmission electron microscopy) 179, 221
 STEM-EELS 272
 step-meter 644
 stereogram 274
 stereographic projection 269
 steric local configuration 261
 stimulated Brillouin scattering 631
 stimulated Raman scattering (SRS) 631
 – stitching 320
 STM (scanning tunneling microscopy) 223, 241, 282, 309, 318, 672, 689
 stochastic method 981
 Stokes
 – process 603
 – scattering 603
 – shift 228, 244, 631
 Stokes–Wilson scattering 240
 storage oscilloscope
 – digital 621
 strain 341, 342
 – distribution 273
 – gauge 754
 – localization 1021
 – measurement 346
 – nominal 389
 – sensitivity 938, 939
 – true 390
 stray radiant energy (SRE) 148
 streak camera 621, 622
 strength difference (SD) 393
 strength of materials 388
 Streptomyces 818
 stress 273, 341
 – athermal 402
 – corrosion 706
 – corrosion cracking (HISCC) 706
 – corrosion cracking (SCC) 405
 – corrosion test 707
 – intensity factor 408
 – intensity factor range ΔK 419

- nominal 389
- strength interference 952
- thermal 402, 1023
- true 390
- yield 359
- stress–strain
- curve 389, 1113
- relations 343
- relationship 1045
- stretched zone (SZ) 425
- width (SZW) 417
- striations 426
- structural
- analysis 258
- health monitoring (SHM) 932
- material 877
- phase transformation 1108
- structure
- primary 258
- structure factor 214, 232
- structure–property relation 7
- STS (scanning tunneling spectroscopy) 224
- stylus 310, 312
- instrument 312
- profilometry 308, 312
- subaerial biofilm 811
- subaquatic biofilm 811
- sublattice model 1063
- success run 958
- successive overrelaxation method (SOR) 1058
- sum-frequency generation (SFG) 616
- superconducting material 488
- superconducting quantum interference device (SQUID) 497
- superconductor 497, 598, 625
- ceramic 488
- high- T_c 488
- supercooled liquid 642
- super-hyperfine structures 246
- superlattice 234
- superplastic forming (SPF) 362, 365
- superstructure 1068, 1069
- surface
- analysis 283
- charge density 492
- chemical analysis 282
- contamination 287
- enhanced Raman scattering 229
- erosion 792
- inversion point 516
- mapping 320
- of reference 1063

- plasmon resonance 274
- potential microscope (SPOM) 645
- recombination 523
- replication 765
- roughness 222, 1029
- soft 316
- state parameter 523
- tester 312
- texture calibration standard 323
- topography analysis 308, 325
- worn 764
- surrounding coil 549
- susceptibility 547, 563
- SVET (scanning vibrating electrode technique) 691
- SVOC (semi-volatile organic compound) 860, 867
- swarming insect 786
- swelling 818
- swelling of the crater floor 301
- SWLI (scanning white-light interferometry) 317
- symmetry property 614
- synchrotron radiation 221, 232, 274, 277
- synchrotron refraction computed tomography 929
- system reliability 962
- systematic errors
- from sampling 42, 50
- SZ (stretched zone) 425

T

- TAC (time-to-amplitude converter) 621
- Tafel plot 679, 682
- tapping sound 786
- TBCCO (tellurium-barium-calcium-copper-oxide) 497
- TC213 309
- TDI technology (time-delayed integration) 912
- TDS (time-domain spectroscopy) 625
- TDS (total dissolved solid) 499
- Te₈₁Ge₁₅Sb₂S₂ 642
- Te-based eutectic alloy 642
- technical object 6
- tellurium-barium-calcium-copper-oxide (TBCCO) 497
- TEM (transmission electron microscope) 270
- temper brittle 286
- temperature
- dependent-color material 654
- melting 793
- sensitivity 939
- sensor 471
- unit kelvin 473
- template for reference procedures 123
- tensile
- strength (TS) 392
- test specimen 115
- tension test 389
- tensor 614
- terahertz (THz) 625, 656
- imaging 626
- termite 781, 783, 785, 786, 788
- dog 786
- galleries 783
- tubes 783
- terpene 867
- tertiary structure 258
- test
- field 795
- high cycle fatigue (HCF) 730
- laboratory 796
- low cycle fatigue (LCF) 730
- respirometric 797
- simulation 795
- specimens to measure elastic constants 344, 345
- wood 779
- tester
- single-sheet (SST) 547, 560
- testing 3
- tetrahedron cluster 1068
- tetramethylsilane (TMS) 155
- textile 803
- texture 269
- TFT (thin-film transistors) 911
- theoretical strength 402
- thermal
- activation 401
- conductivity 454
- conductivity detector (TCD) 168
- cycling oxidation testing 725
- desorption mass spectrometry (TDS) 645
- detector 591
- diffusion rate 642, 643
- diffusivity 454
- effusivity 454
- equilibrium 474
- gravimetric analysis-infrared (TGA-IR) 153
- inertia 870, 872

- ionization mass spectrometry (TIMS) 191
 - magnetic recording 647
 - neutrons 212
 - property 453
 - radiation source 588
 - stress 402, 1023
 - thermalization 249
 - thermocouple 478
 - thermodynamic equilibrium 1065
 - thermodynamic temperature 472
 - thermodynamics
 - of corrosion 674
 - thermograph 655
 - thermogravimetry 471
 - thermomechanical analysis 469
 - thermometer
 - acoustic gas 472
 - standard 473
 - total radiation 480
 - vapor pressure 473
 - THG (third-harmonic generation) 616, 617
 - THG spectroscopy 617
 - thickness 218, 231, 256
 - fringe 220
 - thin-film transistors (TFT) 911
 - Thiobacillus 815
 - thiosulfate 815
 - third-harmonic generation (THG) 616, 617
 - third-order nonlinear effect 617
 - third-order nonlinearity 615
 - third-order polarization 615
 - three-dimensional atom probe (3-DAP) microanalysis 275
 - three-dimensional TEM (3-D-TEM) 276
 - three-parameter Weibull analysis 956
 - THz (terahertz) 625, 656
 - THz wave 656
 - Ti:sapphire laser 620, 625
 - time integration 1049
 - time of flight (TOF) 147, 275, 649
 - time to ignition 871
 - time-correlated single-photon counting 621
 - time-domain spectroscopy (TDS) 625
 - time-resolved imaging 612
 - time-resolved spectroscopy 600, 620, 622
 - time-to-amplitude converter (TAC) 621
 - tin 813
 - tip 318
 - radius 312
 - TIRFM (total internal reflection fluorescence microscopy) 217, 269
 - titrimetry 174
 - Tl-Se 642
 - Tl-Te 642
 - Tm-doped fiber amplifier 637
 - TMR (total material requirement) 846
 - TMR (tunnel magneto-resistance) 545, 584
 - TMS (tetramethylsilane) 155
 - TOF (time of flight) 147, 275, 649
 - tolerance verification 313
 - top-down approach 42
 - topography 215, 224, 308
 - torque magnetometer 547, 554, 582
 - torsion 395
 - total dissolved solid (TDS) 499
 - total internal reflection 218
 - total internal reflection fluorescence microscopy (TIRFM) 217, 269
 - total material requirement (TMR) 846
 - total radiation
 - thermometer 480
 - total reflection x-ray fluorescence spectrometry (TXRF) 194
 - total volatile organic compound (TVOC) 860
 - toxic product 874
 - toxic value 780
 - toxicity 802
 - traceability 322
 - chain 4, 110, 502
 - of measurements 45
 - to reference values 117
 - trace-particle 652
 - tracing 312
 - speed 312
 - trailing edge decay length 300
 - transfer spectrophotometer 148
 - transfer standard 324
 - transformation plasticity 1024
 - transient absorption 623, 624
 - transient hot wire method 458
 - translation vector 254
 - translational symmetry 239
 - transmission 594
 - change 623
 - characteristic 312
 - electron microscope (TEM) 645
 - electron microscopy (TEM) 179, 218, 252, 282, 293, 298
 - line method 525
 - transmission electron microscope (TEM) 270
 - transmittance 594
 - transmitter 262
 - transparent 316
 - trans-polyacetylene conductivity 490
 - transverse time constant 261
 - trap 786
 - filling phase 521
 - Tresca criterion 396
 - triangulation 649, 650
 - tribological testing 747
 - tribology 743
 - triple point of water 473
 - true
 - 3-D characterization 322
 - strain 390
 - stress 390
 - trueness 115
 - truncation 313
 - TS (tensile strength) 392
 - T–T–T diagram 1024
 - tunable laser 594
 - tungsten lamp 589
 - tungsten strip lamp 480
 - tunnel magneto-resistance (TMR) 545, 584
 - tunneling 518
 - current 223
 - TVOC (total volatile organic compound) 860
 - tweed-like structure 1108
 - twin boundary 254, 258
 - twin domain 1108
 - twinning 402
 - two-beam condition 252
 - two-dimensional (2-D) NMR 264
 - two-electrode cell 503
 - two-phase separation 1074, 1085
 - two-photon absorption 623, 624
 - coefficient 617
 - two-photon microscopy 275
 - two-photon process 229
 - two-sublattice model 1071
 - TXRF (total reflection x-ray fluorescence spectrometry) 194
 - types of corrosion 670
-
- ## U
-
- UHV (ultrahigh vacuum) 184
 - ultimate tensile strength (UTS) 359, 360, 392
 - ultrahigh spatial resolution 605

ultrahigh vacuum (UHV) 184
 ultrashort pulse 618
 ultrasmall-angle scattering (USAXS) 927
 ultrasonic attenuation 231
 ultrathin gate oxide 298
 uncertainty 4, 111
 – budget 7
 – budgeting 324
 – evaluation 75
 – of measurement 69
 – of reference values 117
 – relation 618
 – source 503
 UNI 799
 unified constitutive model 1014
 uniform
 – corrosion 700
 – elongation 392
 United States Pharmacopeia (USP) 503
 unpaired electron 246
 up-conversion 623
 updated Lagrangian formulation 1020
 Urbach tail 597
 usable working distance 320
 USAXS (ultrasmall-angle scattering) 927
 use class 775
 USP (United States Pharmacopeia) 503
 UTS (ultimate tensile strength) 359, 360, 392
 UV LED 589
 UV resistance 848
 UV-light 829

V

V parameter 626
 vacancy 239, 247, 249, 355, 356
 vacuum level 288
 validation 78, 1056
 validation using reference procedures 122
 valley 322
 valley connectivity 322
 VAMAS (Versailles Project on Advanced Materials and Standards) 20, 125
 van der Pauw
 – method 495
 – structure 510
 – test sample geometry 512
 van der Waals force 319

vapor pressure
 – thermometer 473
 varnish 816
 VCSEL (vertical-cavity surface-emitting laser) 937
 vector model 230, 262
 velocimetry 652
 Verdet constant 610
 verification 323, 1056
 Verlet method 976
 Versailles Project on Advanced Materials and Standards (VAMAS) 20, 125
 – network 125
 vertical
 – range 312
 – resolution 309
 – time constant 261
 vertical-cavity surface-emitting laser (VCSEL) 937
 very volatile organic compound (VVOC) 860
 vibrating sample magnetometer (VSM) 545, 547, 552, 580, 648
 vibrating tip 319
 vibration 211
 Vickers hardness (HV) 394
 Vienna agreement 133
 vinyl polymer 824
 virtual electronic state 228
 virucidal 831
 visual estimation 779
 visualization 308, 313
 VOC (volatile organic carbon) 829
 VOC (volatile organic compound) 860, 867
 volatile organic carbon (VOC) 829
 volatile organic compound (VOC) 860, 867
 voltage–current method 493
 voltmeter–ammeter method 547, 561
 von Grotthuss type 501
 von Mises criterion 396
 von Mises stress 1047
 Voronoi polyhedron 1000
 VSM (vibrating sample magnetometer) 545, 547, 552, 580, 648
 VVOC (very volatile organic compound) 860

W

water for injection (WFI) 503
 water repellent 824

wattmeter method 547, 560
 wave propagation 526
 waveform 625
 waveguide dispersion 629
 wavelength 211, 644
 – dispersive 159
 – dispersive spectrometer (WDS) 181
 – locking 635
 – of full-amplitude modulation 316
 wavenumber 211
 wavevector 212
 waviness 312
 wax 816
 weak form 1039
 weak-beam dark-field method 254
 wear 743
 – abrasive 752
 – coefficient 746
 – debris 764
 – debris analysis 767
 – down 813
 – factor 747
 – mapping 751
 – measurement 747
 – mild 746
 – severe 746
 – testing errors 762
 weathering 813, 848
 weaving ancillary 803
 weddellite 819
 Weibull analysis 952
 Weibull distribution function 952
 wet-state 829
 WFI (water for injection) 503
 Wharf beetle 785
 Wheatstone bridge 476
 whewellite 819
 white
 – light 318, 594
 – rot 776
 white-light continuum 623
 – generation 617
 white-light interferometry 310
 Whitworth 24
 Wien's law 654
 Wiener–Khinchine theorem 243
 Williamson–Hall plot 274
 Winchester yard 24
 Winslow's weighted averaging scheme 1056
 wire bonding 406
 WLI 310
 wood 877
 – ant 784, 785
 – based product 774

- biological testing 774
- boring beetle 785
- insect attack 781
- mass loss 776
- natural durability 774
- preservative 779
- strength loss 776
- test 779
- wasp 787
- wood-based
 - material 863
- work function 524
- workhardening 390, 403
- World Trade Organization (WTO) 9
- worn
 - surface 764
- WTO (World Trade Organization) 9

X

- xanthoprotein 820
- Xe lamp 589
- x-ray 211, 779, 785
 - absorption near-edge structure (XANES) 239
 - absorption spectroscopy (XAS) 695

- computed tomography (XCT) 276
- diffraction (XRD) 213, 258, 269, 645, 695
- diffuse scattering 240
- fluorescence 159, 222, 231
- fluorescence spectrometry (XRF) 192
- interface contrast 929
- magnetic circular dichroism (XMCD) 583
- method 779
- micro analyzer (XMA) 644
- phase contrast imaging (PCI) 276
- photoelectron spectroscopy (XPS) 281, 282, 294, 645, 695
- photoemission spectroscopy (XPS) 231, 239
- refraction 927
- spectroscopy 607
- topography (XRT) 221, 256

Y

- Yb-doped fiber amplifier 637
- yield
 - locus 1022

- strength (YS) 355, 392
- stress 359
- yielding surface 394
- Young 341
- Young's modulus 340, 343, 391, 1045
- on ceramics 348

Z

- ZBLAN 638
- Z-contrast 222
- Zeeman splitting 245
- Zener relaxation 242
- zero-dispersion wavelength 629
- zero-phonon line 244
- zero-quantum process 262
- zero-resistance ammeter (ZRA) 696
- zeroth-order Laue zone (ZOLZ) 234
- Ziegler–Klausmann–Kar profile correction 516
- ZOLZ (zeroth-order Laue zone) 234
- ZRA (zero-resistance ammeter) 696
- Z-scan 624
 - measurement 617